AD-A237 955

RED6461-EE-02.

ION IMPLANTATION TECHNOLOGY

(1)

Proceedings of the Eighth International Conference on
Ion Implantation Technology
University of Surrey, Guildford, UK, 30 July–3 August 1990

DTIC
ELECTE
JUL 09 1991
S
C
D

Editors
K.G. STEPHENS
P.L.F. HEMMENT
K.J. REESON
B.J. SEALY
J.S. COLLIGON

NORTH-HOLLAND

ION IMPLANTATION TECHNOLOGY

Proceedings of the Eighth International Conference on
Ion Implantation Technology
University of Surrey, Guiidford, UK, 30 July–3 August 1990

Editors

K.G. STEPHENS

P.L.F. HEMMENT (Conference Chairman)

K.J. REESON

B.J. SEALY

University of Surrey, Guildford, UK

J.S. COLLIGON

University of Salford, Salford, UK

With assistance from

D.W. PALMER (Conference Co-chairman)

University of Sussex, Brighton, UK

M.F. JACKSON (Conference Secretary)

University of Surrey, Guildford, UK

Accession For
NTIS GRA&I ☑
DTIC Tab ☐
Unannounced ☐
Justification
By
Distribution/
Availability Codes
Dist | Avail and/or Special
A-1

QUALITY INSPECTED 4

91 7 05 088

1991

NORTH-HOLLAND

91-04045

· Elsevier Science Publishers B V , 1991
All rights reserved No part of this publication may be reproduced, stored in a retrieval system or transmitted, in any form or by any means, electronic, mechanical photocopying, recording or otherwise without the written permission of the Publisher, Elsevier Science Publishers B V , P O Box 103, 1000 AC Amsterdam, The Netherlands

Special regulations for readers in the USA - This publication has been registered with the Copyright Clearance Center Inc (CCC) Salem, Massachusetts Information can be obtained from the CCC about conditions under which photocopies of parts of this publication may be made in the USA All other copyright questions including photocopying outside of the USA, should be referred to the Publisher

No responsibility is assumed by the Publisher for any injury and/or damage to persons or property as a matter of products liability, negligence or otherwise, or from any use or operation of any methods, products, instructions or ideas contained in the materials herein Although all advertising material is expected to conform to ethical standards, inclusion in this publication does not constitute a guarantee or endorsement of the quality or value of such product or of the claims made of it by its manufacturer

This publication is printed on acid-free paper

Reprinted from
NUCLEAR INSTRUMENTS AND METHODS IN PHYSICS RESEARCH
Section B Beam Interactions with Materials and Atoms Volume B55, Nos 1-4

The Manuscript of the Proceedings was received by the Publisher August, December 1990

PRINTED IN THE NETHERLANDS

Editorial

The Conference on Ion Implantation Technology held in the University of Surrey, Guildford from July 30th to August 3rd, 1990 was the eighth in a series of conferences. It was co-sponsored by the Institute of Physics (UK) and the University of Surrey, together with a large number of other, mainly industrial, sponsors from many countries. It is worth noting that the first conference in this series has been attributed to Salford in 1977 which in fact was also sponsored and organised by the Institute of Physics and the Universities of Salford and Surrey with the proceedings published as Low Energy Ion Beams in the Institute of Physics Conference Series (no. 38) in 1978. Subsequently conferences were held in Trento (1978), Kingston (1980), Berchtesgaden (1982), Burlington (1984), Berkeley (1986) and Kyoto (1988).

The scope of the conference, as always, was broad with no parallel sessions, and was divided into eight oral and three poster sessions. The conference began with overviews of the applications of ion implantation, both looking back and to the future. The subsequent sessions then dealt with problems of real-time processing, throughput and yield, and developments of ion sources, beam transport systems and advanced machines. New applications of ion implantation into semiconductors and future trends completed the technical coverage of the conference.

About 350 people attended, some 250 of whom came from 32 countries other than the UK. There were 54 oral papers presented. 14 of them invited, plus 200 poster papers, ensuring that the technical content of the conference was well covered. A special feature was the guest lecture by J.H. Freeman, of ion source fame, who spoke on Ion Beams in Retrospect, which was a fascinating look back on the development of the subject of this conference. Several other activities, characteristic of these conferences, were included at Guildford. A three-day School on Ion Implantation Science and Technology was held immediately before the conference, 26th–28th July, which attracted over 100 participants. During the conference there was a most impressive exhibition in the Great Hall of the University with 37 exhibitors demonstrating their recent products to a very interested audience.

The success of the conference was due to the enthusiasm, not only of the organising and programming committees headed by the Chairman and Co-Chairman, the Conference Secretary and his secretary, but also to the enthusiastic cooperation of the participants and the members of the International Committee who ensured that there was generous financial and other support from 22 companies, and other organisations, including Elsevier Science Publishers, whilst CEI-Europe/Elsevier provided prizes for the best poster in each session.

There were of course many others who contributed to ensure that IIT'90 ran smoothly, both technically and socially; these included many colleagues both in the Department of Electronic and Electrical Engineering and elsewhere in the University, their relatives and friends.

In producing these proceedings the guest editors need to acknowledge the freely given help of the many referees and the response of the authors to requests for revisions as well as the support of the staff of the publishers, North-Holland Physics. However, this help would have been of no avail but for the support provided by Brenda Kirk and Jan Whitcombe who coped admirably with the demands of five guest editors.

The next, 9th Conference in the series will be held in 1992 at the University of Gainesville, Florida, at a time to be decided, under the joint chairmenship of Kevin Jones and Geoff Ryding.

K.G. STEPHENS
for the Guest Editors

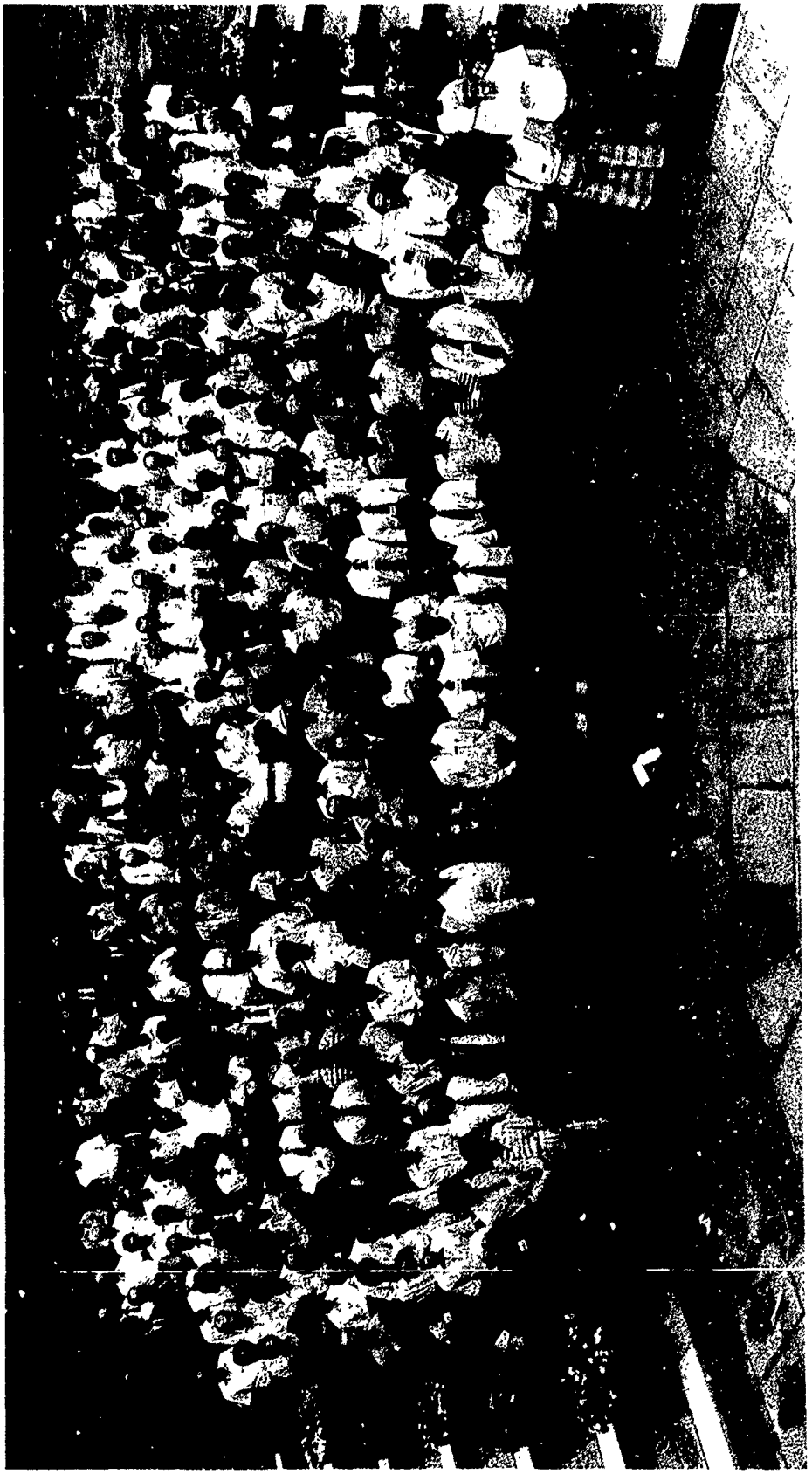

Special invited talk: Ion beams in retrospect

The implantation of semiconductor devices as a manufacturing routine is a relatively recent development. But there is a much longer-standing tradition of scientific interest in the production of focussed beams of heavy ions and in the various ways in which they interact with surfaces. This has its origins in Goldstein's 1886 description of "Kanalstrahlen" in an electric discharge. However, the real significance of this – almost inadvertent – observation of collimated beams of energetic ions only became apparent in 1911 when J.J. Thomson described the detailed behaviour of such "positive rays" in his parabola-ray apparatus. He gave a convincing explanation of the phenomenon of ionisation and he provided a pioneering account of ion implantation when he noted that: "some of the atoms constituting the positive rays seem to enter a metal against which they strike and either combine with the metal or get absorbed by it". The intensity of these ion beams was evidenced by his description of the extent of the "spluttering" in his apparatus, as well as by his report of the effects of ion bombardment in the presence of reactive gases. Despite these striking observations, the overwhelming interest in beams of heavy ions in the following years was directed to the development of mass spectrometers for studies of isotope abundance and atomic weight. Although a number of groups did in fact achieve the mass separation of small, but measurable, amounts of various isotopes during the 1930s, the first major advance in heavy-ion accelerators resulted from the requirements in the United States in the early 1940s for substantial quantities of highly enriched ^{235}U. Under the inspired direction of E.O. Lawrence this led to a programme of machine development on a quite unprecedented scale. It resulted in the construction of over 1000 massive electromagnetic isotope separators ("calutrons") each with an ion beam capability of tens or even hundreds of milliamperes. Although this enterprise ended in 1945 when diffusion was chosen as the preferred route for uranium enrichment, a small number of the calutrons remained in use to meet the nuclear physics' needs for modest quantities of an extensive range of isotopically enriched nuclides. This same requirement also led to the construction of a variety of low-current, heavy-ion accelerators elsewhere, notably in Europe. To a large extent it is these ion-source and accelerator developments which provided the foundation for the now commonplace use of intense beams of heavy ions in industrial-scale implantation.

J.H. FREEMAN
British Embassy, 35 Rue du Faubourg St. Honoré, 75383 Paris Cedex 08, France

Conference Chairman

Peter Hemment

Co-chairman

Derek Palmer

Conference Secretary

Mike Jackson

Secretary

Brenda Kirk

International Committee

D. Aitken (UK)
L.J. Chen (Taiwan)
N.W. Cheung (USA)
M.I. Current (USA)
G. Dearnaley (UK)
A.D. Giles (UK)
H.K. Glawischnig (Germany)
J. Gyulai (Hungary)
P.L.F. Hemment (UK)
R.E. Kaim (USA)
R. Koudijs (The Netherlands)
C.M. McKenna (USA)
S. Mader (USA)
K. Matsuda (Japan)
J W. Mayer (USA)
O. Meyer (Germany)
J A. Pals (UK)
S. Peterson (Sweden)
K.H. Purser (USA)
R.D. Rathmel (USA)
P.H. Rose (USA)
G. Ryding (USA)
H. Ryssel (Germany)
P.J. Scanlon (Canada)
M. Setvak (Czechoslovakia)
K.G. Stephens (UK)
T. Takagi (Japan)
M. Tamura (Japan)
S.C. Tsou (PR China)
A.F. Vyatkin (USSR)
W. Weisenberger (USA)
J.S. Williams (Australia)
A.B. Wittkower (USA)
G.K. Wolf (Germany)
I. Yamada (Japan)
J.F. Ziegler (USA)

Organising Committee

G. Bennett (Motorola)
S.D. Brotherton (Philips)
M. Bruel (LETI)
J.S. Colligon (Univ. of Salford)
T. Conlon (AEA)
P. Connock (Applied Materials, Horsham)
A. Donleavy (STC Components Ltd.)
H.K. Glawischnig (Siemens, Germany)
L.I. Haworth (Univ. of Edinburgh)
A. Hawryliw (Hughes Microelectronics)
P.L.F. Hemment (Univ. of Surrey) (*Chairman*)
I. Jackson (LSI)
M.F. Jackson (Univ. of Surrey) (*Secretary*)
R. Oakley (Plessey)
D.W. Palmer (Univ. of Sussex) (*Co-chairman*)
G. Proudfoot (AEA)
B.J. Sealy (Univ. of Surrey)
K.G. Stephens (Univ. of Surrey)
J.M. Walls (VG-W Technology)
R.P. Webb (Univ. of Surrey)
B.L. Weiss (Univ. of Surrey)
I.H. Wilson (Univ. of Surrey)
J.F. Ziegler (IBM)

Programme Committee

J.S. Colligon
P.L.F. Hemment (*Chairman*)
C. Hill
D.W. Palmer (*Co-chairman*)
F. Plumb
G. Proudfoot
H. Ryssel
B.J. Sealy
K.G. Stephens
B.L. Weiss
I.H. Wilson
J.F. Ziegler

Sponsors

Institute of Physics
University of Surrey
Applied Materials
Genus Inc.
Royal Society
Eaton Corporation
AEA Technology
LETI, CEA
CEI-Europe/Elsevier
Leybold Ltd.
STC Technology Ltd.
European Research Office of the US Army
Electrostatic International Inc.
Ibis Technology Corporation
Varian/Extrion Division
Nissin Electric Co. Ltd.
High Voltage Engineering Europa B.V.
Elsevier Science Publishers B.V.
ULVAC Corporation
University of Surrey Research Park
European Office of Aerospace Research & Development of the US Air Force
Prometrix

Exhibitors

Applied Materials
Foundry Lane, Horsham, W Sussex RH13 5PY, UK

Biorad Microscience Ltd.
Marylands Ave., Hemel Hempstead, Herts HP2 7TD, UK

Caburn UHV/MDC Vacuum Products
1 Castle Ditch Lane Lewes, E Sussex, UK

Cascade Scientific Ltd.
ETC Building, Brunel Univ., Uxbridge, Middlesex UB8 3PH, UK

CEI Europe/Elsevier
P.O. Box 910, S-61201 Finspong, Sweden

Chell Instruments Ltd.
Tudor House, Grammar School Road, North Walsham, Norfolk NR28 9JH, UK

CTI Cryogenics Ltd.
Unit 4, Avenue 2, Station Lane Industrial Estate, Witney, Oxon OX8 6YD, UK

CVC Scientific Products Ltd.
Hogwood Industrial Estate, Finchampstead, Wokingham, Berks RG11 4QW, UK

Darchem Automation Ltd.
Salters Lane, Sedgefield, Co Durham, UK

Eaton Corporation
108 Cherry Hill Drive, Beverly, MA 01915, USA

Edwards High Vacuum Int.
Manor Royal, Crawley, W Sussex RH10 2LW, UK

Euro III-Vs Review
Elsevier Advanced Technology, Mayfield House, 256 Banbury Road, Oxford OX2 7DH, UK

Ferrofluidics Ltd.
Floor 2, Seacourt Tower, Botley, Oxford, Oxon OX2 0JJ, UK

Glassman Europe Ltd.
Studio 4, Intec 2, Wade Road, Basingstoke, Hants RG24 0NE, UK

Grant Test & Measurement Ltd.
Maxet House, Liverpool Road, Luton, Beds LU1 1RS, UK

Hiden Analytical Ltd.
231 Europa Blvd., Gemini Business Park, Warrington WA5 5TN, UK

High Voltage Engineering Europa B.V.
P.O. Box 99, 3800 AB Amersfoort, The Netherlands

Ibis Technology Corporation
32A Cherry Hill Drive, Danvers, MA 01923, USA

Intertrade Scientific Ltd
Linford Wood Business Centre, Sunrise Parkway, Linford Wood, Milton Keynes, Bucks MK14 6LP, UK

Jandel Engineering Ltd.
1 Redwood Close, Wing, Leighton Buzzard, Beds LU7 0TP, UK

Le Carbone (GB) Ltd.
South Street, Portslade, Sussex BN41 2LX, UK

Leybold Ltd.
Waterside Way, Plough Lane, London, SW17 7AB, UK

Macrotron (UK) Ltd.
The Forum, Marlborough Rd., Old Town, Swindon, Wilts SN3 1QT, UK

Megatech Ltd.
8 Kinscroft Court, Ridgway, Havant, Hants PO9 1LS, UK

Megavolt Ltd.
Cornhill, Ilminster, Somerset, UK

Nissin Electric Co. Ltd.
47 Umezu-Takase-cho, Ukyo-ku, Kyoto 615, Japan

Oxford Engineering
Industrial Estate, Radley Road, Abingdon, Oxon OX14 3RY, UK

Potentials Inc.
P.O. Box 9560, Austin, TX 78766, USA

Prometrix
3255 Scott Blvd., Building 6, Santa Clara, CA 95054, USA

SERC Central Facility for Microelectronics
Dept. of Electronic and Electrical Engineering, Univ. of Surrey, Guildford, Surrey GU2 5XH, UK

Spectra-Metrics
Leda House, Tunstall Road, Knypersley, Stoke-on-Trent, Staffordshire ST8 7TY, UK

Surrey Research Park
Univ. of Surrey, Guildford, Surrey GU2 5XH, UK

Tylan General (UK) Ltd.
Unit 19, Westmead Industrial Estate, Westlea, Swindon, Wilts SN5 7YT, UK

UKAEA
Harwell Laboratories, Oxon, UK

Varian Associates Ltd.
Manor Road, Walton-on-Thames Surrey KT12 2QF, UK

Vat Vacuum Products Ltd.
235 Regents Park Road, Finchley, London N3 3LG, UK

Wallis Hivolt Ltd
Dominion Way, Worthing, W. Sussex BN14 8NW, UK

Contents

Editorial ... vii
Conference photograph ... viii
Ion beams in retrospect (*Special invited talk*)
Freeman, J H. ... ix
Committees ... x
Sponsors and exhibitors ... xi

Section I. Overviews

Ion implantation in bipolar technology (*Invited paper*)
Hill, C and P. Hunt ... 1
Application of ion implantation in submicron CMOS processes (*Invited paper*)
Küsters, K.H., H.M. Mühlhoff and H Ceiva ... 9
Implantation in the 1990s (*Invited paper*)
Seidel, T E ... 17

Section II. Real time processing problems

A detailed study of elemental contamination in a Varian 180XP high-current implanter
Taylor, M.C., S. Mehta and R.J. Eddy ... 20
Energy contamination in ion implantation
Van Herk, J., A.N van der Steege, M L C van Meyl and P C Zalm ... 25
Energetic neutral contamination in modern high-current implanters
Cherekdjian, S. and W. Weisenberger ... 30
Real time, in situ particle monitoring of the Applied Materials PI9200 ion implanter
Leung, S. B Adibi, S. Moffatt, B Fishkin and P. Kinney ... 35
Channeling control for large tilt angle implantation in Si ⟨100⟩
Simonton, R.B., D.E. Kamenitsa, A.M. Ray, C Park, K.M. Klein and A.F. Tasch ... 39
Energy contamination of P^{2+} ion beams on the Varian, EXTRION 220 medium current implanter
Van der Meulen, P F.H.M., S Mehta and R.E. Kaim ... 45
Control of BF_2 dissociation in high-current ion implantation
Downey, D.F and R.B. Liebert ... 49
A RGA study of the cross-contamination of dopant species and low level impurities and the use of the RGA as a process monitor in a Varian 180XP
Cummings, J.J. and D.T. Enloe ... 55
An analysis of vacuum effects on ion implanter performance
Renau, A., M.E. Mack, J.P. O'Connor and N. Tokoro ... 61
Particle contamination control in the EXTRION 220
Milgate, R. and J. Pollock ... 66
Control of metal contamination in the Varian Extrion 1000 ion implantation system
Liebert, R.B., S. Satoh, B.O. Pedersen, D.F. Downey, T. Sakase and E. Evans ... 71
Control of wafer charging on the Varian EXTRION 1000 ion implanter
Satoh, S, B.O. Pedersen, D.F. Downey, T. Sakase, R B. Liebert and S.B Felch ... 77
Device charge-to-breakdown studies on a high-current implanter
Felch, S.B., S. Mehta, S. Kikuchi and S. Kitahara ... 82

Control of ion beam density and profile for high current ion implantation systems
Tanjyo, M., S. Fujiwara, H. Sakamoto and M. Naito 86
A high-resolution beam profile measuring system for high-current ion implanters
Fujishita, N., K. Noguchi, S. Sasaki and H. Yamamoto 90
An electron-beam charge neutralization system for ion implanters
Leung, K.N., K.C. Gordon, W.B. Kunkel, C.M. McKenna, S.R Walther and M.D. Williams ... 94
New approaches to charging control
Strain, J.A., Y. Tanaka, N.R. White and R.J. Woodward 97
Implantation-equipment data management for cost reduction, equipment optimization and process enhancement
Yarling, C., R. Eddy and J. Turner 104
The use of tertiarybutylarsine (TBA) and tertiarybutylphosphine (TBP) as liquid reagents for ion implantation
Larson, L.A., M. Sakshaug and W. Weiner 109

Section III. Processing, throughput and yield

Gate oxides in high curent implanters: how do they survive? (*Invited paper*)
Sinclair, F. 115
Process-induced defects in VLSI (*Invited paper*)
Kolbesen, B.O., W. Bergholz, H. Cerva, B. Fiegl, F. Gelsdorf and G Zoth 124
A survey of implant particulate process control and yield effects (*Invited paper*)
Larson, L.A. 132
Wafer charging study on a Varian 160 XP ion implanter with charge-sensitive devices
Nee, R., S. Mehta, S B Fetch and S. Kikuchi 137
Charging studies with "CHARM"
Lukaszek, W., R.K. Nahar, A. McCarthy, W Weisenberger, S. Cherekdjian and D. Lindsey ... 143
Gauge-capability study of ion-implant monitors
Johnson, W.H , W.A. Keenan and T. Wetteroth 148
Maximization of DRAM yield by control of surface charge and particle addition during high dose implantation
Horvath, J. and S. Moffatt 154
Effects of molybdenum contamination resulting from BF_2 implantation
Cubina, A. and M. Frost 160
A micro-uniformity test structure
Keenan, W.A., W.H. Johnson, L. Mantalas, L. Nguyen and L.A. Larson 166
Monitoring the micro-uniformity performance of a spinning disk implanter
Current, M.I., T Guitner, N. Ohno, K. Hurley, W.A. Keenan, W. Johnson, R.J. Hillard and C. Jeynes 173
Daily 2×10^{12} monitoring of an ion implanter
Cherekdjian, S. and W. Weisenberger 178
Spectroscopic ellipsometry for depth profiling of ion implanted materials
Vanhellemont, J., Ph. Roussel and H.E. Maes 183
Process control issues for ion implantation using large tilt angles
Simonton, R.B., D.E. Kamenitsa and A.M. Ray 188
Annealing behaviors of residual defects in high-dose BF_2^+-implanted (001)Si under different implantation conditions
Chu, C.H., E.L. Tsai, W.Y. Chao and L.J. Chen 193
Knock-on of contaminants causing instabilities of transistor characteristics
Kröner, F. 198
Implant uniformity evaluation using a Varian/Extrion scan compensator module on an electrostatic scanning ion implanter
Howard, K. 202

The use of negative ions to enhance beam currents at low energies in an MeV ion implanter
O'Connor, J.P., M.E. Mack, A. Renau and N. Tokoro 207
Charging measurement and control in high-current implanters
Angel, G., N. Meyyappan, F. Sinclair and W. Tu 211
Effects of P^+-implanted poly-Si electrodes on the gate dielectric characteristics of thin oxides
Chang, H.-C. and W.-S. Chen 216
Investigation of backscattering and re-implantation during ion implantation into deep trenches
Posselt, M., E. Sobeslavsky and G. Otto 220
Proximity gettering by MeV-implantation of carbon: microstructure and carrier lifetime measurements
Skorupa, W., R. Kögler, K. Schmalz and H. Bartsch 224
Comparison of modern uniformity-mapping techniques
Keenan, W.A., W.H. Johnson and C.B. Yarling 230
The history of uniformity mapping in ion implantation
Yarling, C.B., W.A. Keenan and L.A. Larson 235
Techniques for dose matching between ion implanters
Lundquist, P., S. Mehta, T. Black and D. Jackson 243
Monitoring of dose in low dose ion implantation
Hara, T., H. Hagiwara, R. Ichikawa, W.L. Smith, C. Welles, S.K. Hahn and L. Larson 250
Implant dose uniformity simulation program
Nagai, N 253
Nondestructive determination of damage depth profiles in ion-implanted semiconductors by multiple-angle-of-incidence single-wavelength ellipsometry
Fried, M., T. Lohner, F. Jároli, C. Hajdu and J. Gyulai 257
Limitations of the spreading resistance technique for ion implant profile measurements
Montserrat, J., J. Bausells and E. Lora-Tamayo 261
Thermal wave characterization of silicon implanted with MeV phosphorus ions
Anjum, M., G.S. Sandhu, S. Cherekdjian and W. Weisenberger 266
RTP temperature uniformity mapping
Keenan, W.A., W.H. Johnson, D. Hodul and D. Mordo 269
Ion implant standard
Larson, L.A., W.A. Keenan and W.H. Johnson 275
Development of a process to achieve residue-free photoresist removal after high-dose ion implantation
McOmber, J.I. and R.S. Nair 281

Section IV. Innovations in ion source and beam transport

Ion beam systen design for ULSI device requirements (*Invited paper*)
White, N.R 287
Improvement of an ECR multicharged ion source
Ishii, S. 296
An increased implant current by combining a long-slit microwave ion source with a converging lens
Sakudo, N., H. Koike, T. Seki and K. Tokiguchi 300
Plasma cathode oxygen ion source
Shibuya, T., S. Hashimoto, E. Yabe and K. Takayama 305
A dual source low-energy ion implantation system for use in silicon molecular beam epitaxy
Gottdang, A., K. Eich, A. Hassenburger, W.H. Schulte, B. Cleff, D.J.W. Mous, R. Koudijs, G.F.A. van de Walle and J. Politiek 310
A silicon MBE-compatible low-energy ion implanter
Gordon, J.S., A. Bousetta, J.A. van den Berg, D.G. Armour, R. Kubiak and E.H.C. Parker 314
Direct extraction of a Na^- beam from a sodium plasma
Sasao, M., H. Yamaoka, M. Wada and J. Fujita 318

Negative-ion sources for ion implantation
Holmes, A.J.T. and G. Proudfoot 323
A low-energy fast-atom beam source
Gorbatov, Yu.B., A.F. Vyatkin and V.I. Zinenko 328
Double hollow cathode ion source for metal ion-beam production
Tonegawa, A., H. Taguchi and K. Takayama 331
A cold-hollow-cathode lateral-extraction Penning ion source
Ma, M., J.E. Mynard, B.J. Sealy and K.G. Stephens 335
Ion beam injection system for a variable energy RFQ accelerator
Amemiya, K., K. Tokiguchi, Y. Hakamata and N. Sakudo 339
Milliampere metal ion beam formation using multipoint emission by an impregnated-electrode-type liquid-metal ion source
Ishikawa, J., H. Tsuji and Y. Gotoh 343
Possible mechanisms for particle transport in ion implanters
Brown, D.A., P. Sferlazzo and J.F. O'Hanlon 348
A high-current low-energy multi-ion beam deposition system
Tsukakoshi, O., S. Shimizu, S. Ogata, N. Sasaki and H. Yamakawa 355
Development of a four-electrode extraction system for a large area ion source with a wide range of operational conditions
Maeno, S., M. Tanjyo, K. Tanaka and J. Fujita 359
Production of oxygen plasmas using radio-frequency magnetron-discharge
Shibuya, T., S. Hashimoto, E. Yabe and K Takayama 364
Development of a high current and high energy metal ion beam system
Inami, H., Y. Inouchi, H. Tanaka, T Yamashita, K. Matsunaga and K. Matsuda 370
Beam optics research for a 600 keV heavy ion implanter
Zhao Qihua, Jiang Xinyuan, Lin Chenglu and P Tanguy 374

Section V. Advanced machine technologies

Ion implantation challenges in the drive towards 65 Mb and 256 Mb memory cell type devices (*Invited paper*)
Giles, A.D. and A. van de Steege 379
Development of ion implantation equipment in the USSR (*Invited paper*)
Vyatkin, A.F., V.V. Simonov and A I Kholopkin 386
The Nissin NH-20SP medium-current ion implanter
Nagai, N., T. Kawai, M. Nogami, T Shin'yama, T. Yuasa, Y Kibi, H. Kawakami, K Nishikawa and M. Isobe 393
A high-current ion implanter system
Nasser-Ghodsi, M., M Farley, J. Grant, D Bernhardt, M. Foley, S Holden, T. Bowe, C. Singer, K Dixit and G. Angel 398
Mechanically scanned ion implanters with two-axis disk tilt capability
Tami, T., M. Diamond, B. Doherty and P. Splinter 408
Charge neutralisation in the PI9000 series implanters
Wauk, M.T., N. White, B. Adibi, M. Current and J. Strain 413
Parallel beam ion implanter: IPX-7000
Mihara, Y., K. Niikura, O. Tsukakoshi and Y Sakurada 417
A system and performance overview of the EXTRION 220 medium-current ion implanter
Pippins, M.W. 423
Advances in the Extrion 1000 and XP Series high-current ion implantation systems
Harris, M. 428
The beam performance of the Genus G-1500 ion implanter
Tokoro, N., J.P. O'Connor, A. Renau and M.E. Mack 434

Vacuum system design for ion implanters
Hucknall, D.J. and M. Kuhn 439
The Nissin PR-80A high current ion implantation system
Kawai, T., M. Chotokudani, M. Naito, T. Hiramatsu, M. Sasaki, T. Sunouchi, Y. Nishigami, T. Matsumoto, M. Nakaya and M. Nakazawa 443
System and process enhancements of the Applied Materials Precision Implant 9200
Jaffe, P.R. and K.P. Fairbairn 448
The EXTRION 220 parallel scan magnet
Kaim, R.E. and P.F.H.M. van der Meulen 453
Improved wafer charge neutralization system in Varian high current implanters
Mehta, S., R.F. Outcault, C.M. McKenna and A. Heinonen 457
Operating procedure for improving ion source lifetime for the 80-180XP ion implanter
Walther, S.R. and R.F. Outcault 465
Particulate performance for robotics-based wafer handing ion implant system
Nasser-Ghodsi, M., D. McCarron, M. Foley, S. Holden, D. Veinbachs, S Mooney and S. Ward . 469
Initial performance results from the NV1002 high energy ion implanter
McIntyre, E., D. Balek, P. Boisseau, A. Dart, A.S. Denholm, H. Glavish, C. Hayden, L. Kaminski, B. Libby, N. Meyyappan, J. O'Brien, F. Sinclair and K. Whaley 473
A versatile ion implanter for planar and 3D device construction
Dykstra, J.P., A.M. Ray and R.B. Simonton 478
Simulation of the geometrical characteristics of a mechanically scanned high current implanter
Sinclair, F. 482
Beam incidence variations in spinning disk ion implanters
Ray, A.M. and J.P. Dykstra 488
The MeV ion implantation system "RFQ-1000" and its applications
Hirakimoto, A., H. Nakanishi and M Asari 493
A 500 keV ion accelerator with two types of ion source
Agawa, Y., M. Takai, S. Namba, T Uchiyama, R Fukui and H. Yamakawa 502
A broad-beam, high-current metal-ion implantation facility
Brown, I.G. M.R. Dickinson, J.E. Galvin, X Godechot and R.A MacGill 506
A versatile WiBS 200 kV ion implanter for materials modification
Bond, P., D. Duckworth, R.G. Elliman, R. Henshaw, S.T. Johnson, M C. Ridgway, R.P. Thornton, J.S Williams, P. Byers and D.J. Chivers 511
The phased linear scanner
Aitken, D. 517
A universal sample manipulator with 50 kV negative bias
Kenny, M.J., L S. Wielunski, M.D. Scott, R.A. Clissold, D. Stevenson and G. Baxter 522
Computer modelling for ion-beam system design
Ito, H and N.R White 527

Section VI. Materials science

Amorphous Si – the role of MeV implantation in elucidating defect and thermodynamic properties (*Invited paper*)
Poate, J.M., S. Coffa, D.C Jacobson, A. Polman, J.A Roth, G.L. Olson, S. Roorda, W. Sinke, J.S. Custer, M.O. Thompson, F. Spaepen and E. Donovan 533
Recent progress in depositing epitaxial metal films by an ionized cluster beam (*Invited paper*)
Yamada, I. 544
BF_2^+ implantation in predamaged Si with Ge^+ or Si^+ at doses lower than amorphization
Kase, M., M. Kimura, Y. Kikuchi, H. Mori and T. Ogawa 550
Formation of thin silicon films using low energy oxygen ion implantation
Robinson, A.K., C.D. Marsh, U. Bussmann, J.A. Kilner, Y. Li, J. Vanhellemont, K.J. Reeson, P.L.F. Hemment and G.R. Booker 555

Measurements and applications of high energy boron implants in silicon
La Ferla, A., E. Rimini, A. Carnera, A. Gasparotto, G. Ciavola and G. Ferla 561
Ultra low energy (100–200 eV) boron implantation into crystalline and silicon-preamorphized silicon
Bousetta, A., J.A. Van den Berg, R. Valizadeh, D.G. Armour and P.C. Zalm 565
Shallow junction formation by dual Ge/B, Sn/B and Pb/B implants
Hašlar, V., P. Seidl, P. Hazdra, R. Gwilliam and B. Sealy 569
Sublimation and diffusion of arsenic implanted into silicon at rapid electron beam annealing
Grötzschel, R., V.A. Kagadey, N.I. Lebedeva and D.I. Proskurosvky 573
Thermal-annealing effects on the structural and electrical properties of heavy-ion-implanted silicon layers
Said, J., G. Ghibaudo, I. Stoemenos and P. Zaumseil 576
Expitaxial regrowth and lattice location of indium implanted in arsenic-preamorphized silicon
Alves, E., M.F. Da Silva, J.C. Soares, A.A. Melo, J. May, V. Hašlar, P. Seidl, U. Feiser and R. Vianden 580
Effect of SiN_x coating in lateral solid phase epitaxy of implanted amorphous Si films
Ishiwara, H. and K. Fukao 585
Near-surface damage created in silicon by BF_2^+ implantation
Li Xiaoqin, Lin Chenglu, Yang Genqin, Zhou Zuyao and Zhou Shichang 589
Custom profiles by automated multi-step implantation
Crook, J P., M.I. Current, B. Adibi, S. Leung and L.A. Larson 593
The annealing behaviour of ion-implanted Si studied using time-resolved reflectivity
Thornton, R.P., Y.H. Li, R.G. Elliman and J.S. Williams 598
MeV ion-beam annealing of semiconductor structures
Williams, J.S., M.C. Ridgway, R.G. Elliman, J.A. Davies, S.T. Johnston and G.R. Palmer . . 602
Distribution of paramagnetic defects formed in silicon by MeV ion implantations
Yajima, Y , N. Natsuaki, K. Yokogawa and S. Nishimatsu 607
Evolution of low-fluence heavy-ion damage in Si under high energy ion irradiation
Battaglia, A., F Priolo, C. Spinella and E. Rimini 611
Channeling implantation of B and P in silicon
Schreutelkamp, R.J , V. Rainen, F.W. Saris, R.E. Kaim, J.F. Westendorp, P.F.H.M. van der Meulen and K.T.F. Janssen 615
Annealing behavior of dislocation loops near the projected ion range in high-dose As^+- and P^+-implanted (001) Si
Hsu, S.N. and L.J. Chen 620
Acivation of shallow implants in Si by pulse laser irradiation
Wesch, W., T. Bachmann, G. Götz, F. Hagemann and A Heft 625
Centers of spin-dependent recombination in structures formed by N^+ ion implantation into Si
Karanovich, A.A., A.V Dvurechenskii, I E. Tyschenko and G.A. Kachurin 630
Anomalous redistributions of As and Sb atoms in As-implanted Sb-doped and Sb-implanted As-doped Si during annealing
Yokota, K., H. Furuta, S. Ishihara and I. Kimura 633
The influence of implantation temperature and subsequent annealing on residual implantation defects in silicon
Hazdra, P., V. Hašlar and M. Bartoš 637
Some properties of amorphous silicon produced by helium ion implantation
Buravlyov, A.V., A.F. Vyatkin, V.K. Egorov, V.V. Kireiko and A.P Zuev 642
Electrical activation process of erbium implanted in silicon and SIMOX
Tang, Y.S. and B.J. Sealy 647
Isotope effects for ion-implantation profiles in silicon
Svensson, B.G. and B. Mohadjeri 650

The enhanced diffusion of boron in silicon after high-dose implantation and during rapid thermal annealing
Marou, F., A. Claverie, Ph. Salles and A. Martinez 655
Channeling implants of boron in silicon
Rainieri, V., G. Galvagno, E. Rimini, A. La Ferla, S. Capizzi, A. Carnera and G. Ferla 661
Calculation of channeling effects in ion implantation
Bausells, J., G. Badenes and E. Lora-Tamayo 666
Molecular complexes on implanted surfaces: unenhanced surface Raman study
Mathur, M.S., J.S.C. McKee and C.B. Kwok 671
A new method to calculate range and damage distributions by direct numerical solution of Boltzmann transport equations
Posselt, M. 676
Transport-theoretical studies of static and dyanmic recoil mixing
Jimenez-Rodriguez, J.J., I. Abril, J.A. Peinador and A. Gras-Marti 681
High-dose oxygen implantation into silica
Chater, R.J., J.A. Kilner, K.J. Reeson, A.K. Robinson and P.L.F. Hemment 686
The study of $Si_{0.5}Ge_{0.5}$ alloy implanted by high dose oxygen
Zhang, J.P., P.L.F. Hemment, U. Bussmann, A.K. Robinson, J.E. Castle, H.D. Liu, J.F. Watts, S.M. Newstead, A.R. Powell, T.E. Whall and E.H.C. Parker 691
An investigation of $Si_{0.5}Ge_{0.5}$ alloy oxidation by hgh dose oxygen implantation
Castle, J.E., H.D. Liu J.F. Watts, J.P. Zhang, P.L.F. Hemment, U. Bussmann, A K Robinson, S.M. Newstead, A.R. Powell, T.E. Whall and E.H C. Parker 697
Amorphisation and solid phase epitaxial regrowth of the silicon overlayer in SIMOX structures
Starkov, V V., P.L.F. Hemment and A.F. Vyatkin 701
The IR properties in SOI wafers formed by oxygen implantation into silicon
Lu Diantong, Zheng Lirong, Wang Zhonglie and P.L.F. Hemment 705
Raman measurement of local SOI structure by SIMOX
Kato, K., M. Takai, S. Namba, R. Schork and H Ryssel 710
Raman scattering and photoluminescence analysis of SOI/SIMOX structures obtained by sequential implantation and annealing correlated with cross sectional TEM
Pérez, A., J. Portillo, A. Cornet, J Jimenez, J.R. Morante, P.L.F. Hemment and K.P Homewood 714
Microscope-spectrophotometric analysis to determine the origins of the colour variations on SIMOX wafers
Reeson, K.J., A.J Criddle, P Pearson, R.J Chater, K. Christensen, J. Alderman, G.R Booker and J A. Kilner 718
Thermal-wave measurements of high-dose ion implantation
Taylor, M., K. Hurley, K. Lee, M. LeMere, J. Opsal and T O'Brien 725
Optical characteristics of multi-layer structures formed by ion beam synthesis and their computer simulation
Yu, Y., C. Lin, X. Liu, S. Zou and P.L.F Hemment 730
Buried insulator formation by nitrogen implantation at elevated temperatures
Hatzopoulos, N., U. Bussmann, A.K. Robinson and P.L.F. Hemment 734
Studies on $Si^+ + B^+$ dual implantations into the top silicon layer of SIMNI material
Zhang, S., C. Lin, Z. Zhou and S. Zou 738
SOI structure formed by 95 keV N_2^+ and N^+ implantation and epitaxial growth
Lin Chenglu, Li Jinghua, Zhang Shunkai, Yu Yuehui and Zou Shichang . . . 742
The effects of epitaxy and oxidation on the properties of SIMNI and SIMOX materials
Li Jinghua, Lin Chenglu, Lin Zhixing, Jin Yuqing and Zou Shichang 746
The peculiarities of the new phase formation by O^+ ion implantation into silicon under thermo-ionization excitation
Belgorokhov, A.I., A.B. Danilin, Yu.N. Erokhin, A.A. Kalinin, V.N. Mordkovich, V.V. Saraikin and I.I. Khodos 750

SOI structures produced by oxygen ion implantation and their annealing behaviour
Zheng Lirong, Lu Diantong, Wang Zhonglie, Zhang Bei and P.L.F Hemment 754

Radiation damage in As^+ implanted $TiSi_2$ films
Hsu, C.T., C.J. Ma and L.J. Chen 758

Comparison of models for the calculation of ion implantation moments of implanted boron, phosphorus and arsenic dopants in thin film silicides
Cole, P.D., G.M. Crean, J. Lorenz and L. Dupas 763

Ion beam synthesis of cobalt silicide: effect of implantation temperature
Dekempeneer, E.H.A., J.J.M. Ottenheim, D.E.W. Vandenhoudt, C.W.T. Bulle-Lieuwma and E.G C. Lathouwers 769

Cobalt silicide formation caused by arsenic ion beam mixing and rapid thermal annealing
Ye, M., E. Burte, P-H. Tsien and H. Ryssel 773

The application of a 600 keV heavy ion implanter
Jiang Xinyuan, Zhao Qihua, Guan Anmin, Shao Tianhao and Lin Chenglu 778

Preparation of W–Th films by ion beam sputtering
Griepentrog, M., R.-A. Noack, M. Rosengarten and W. Schneider 782

X-ray diffraction studies of radiation damage in gallium arsenide
Van Berlo, W.H. and T. Pihl 785

Defect production in ion implanted GaAs, GaP and InP
Wendler, E., W. Wesch and G. Götz 789

Characterization of Si-implanted gallium antimonide
Su, Y.K., K.J. Gan, F.S. Juang and J S. Hwang 794

Rapid thermal annealing of Mg^+ and P^+ implanted InP
Shen, H., G Yang, Z. Zhou and S. Zou 798

Section VII. Future trends and applications

The technology of finely focused ion beams (*Invited paper*)
Harriott, L.R. 802

Plasma immersion ion implantation for ULSI processing (*Invited paper*)
Cheung, N.W. 811

Sub-100 nm p + /n junction formation using plasma immersion ion implantation
Qian, X Y., N.W. Cheung, M.A Lieberman, M I Current, P.K Chu, W.L. Harrington, C.W Magee and E.M Botnick 821

SIMOX-material quality in a semi-industrial production
Lamure, J M., J Margail, B Baisse, J F. Michaud, A. Soubie, C. Pudda, F. Gusella and C. Jaussaud 826

Annealing behaviour of BF_2^+ implanted (001) and (111)Si inside miniature size oxide openings
Nieh, C.W. and L.J. Chen 831

Dose dependence of crystallinity and resistivity in ion beam sythesised $CoSi_2$ layers
Spraggs, R S., K J Reeson, R.M. Gwilliam, B.J. Sealy, A. De Veirman and J. van Landuyt . . 836

Contouring of SIMOX profiles by oxygen ion energy change
Wittkower, A., M. Guerra, B. Cordts, R. Dolan and P. Sandow 842

SIMOX wafers with low dislocation density produced by a 100 mA-class high-current oxygen implanter
Nakashima, S. and K. Izumi 847

Energy and dose dependence of silicon top layer and buried oxide layer thickness in SIMOX substrates
Bussmann, U., A.K. Robinson and P.L.F. Hemment 852

Oxygen implantation through patterned masks: a method for forming insulated silicon device islands while maintaining a planar wafer surface
Bussmann, U., P.L.F. Hemment, A.K. Robinson and V.V. Starkov 856

Nitrogen implantation for local oxidation (NILO) of silicon
Molle, P., C. Jaussaud and M. Bruel 860
Channeling contrast analysis of local damage distributions induced by maskless implantation
Kinomura, A., M. Takai, K. Hirai and S. Namba 866
Effect of deposition temperature of arsenic implanted poly-Si-on-insulator on grain size and residual stress
Takai, M., K. Kato, S. Namba, U. Pfannenmüller and H. Ryssel 870
Epitaxial growth of carbon-doped p-type GaAs films by ionized cluster beam
Takaoka, G.H., Y. Haga, H. Tsuji and J. Ishikawa 873
Preparation of atomically flat gold films by ionized cluster beam
Yamada, I., G.H. Takaoka, H. Usui, F. Satoh, Y. Itoh, K. Yamashita, S. Kitamoto, Y. Namba, Y Hashimoto, Y. Maeyama and K. Machida 876
A system for complex processing of semiconductor structures in vacuum
Yankelevich, E.B. and V.S. Budishevsky 880
A plasma immersion ion implantation reactor for ULSI fabrication
Qian, X.Y., D Carl, J. Benasso, N.W. Cheung, M A. Lieberman, I.G. Brown, J.E. Galvin, R.A. MacGill and M.I. Current 884
Plasma immersion Pd ion implantation seeding pattern formation for selective electroless Cu plating
Qian, X Y., M.H. Kiang, J Huang, D. Carl, N.W Cheung, M.A. Lieberman, I G. Brown, K.M. Yu and M.I. Current 888
Metal vapor vacuum arc ion implantation for seeding of electroless Cu plating
Qian, X.Y., M.H Kiang, N W. Cheung, I.G. Borwn, X. Godechot, J E. Galvin, R A MacGill and K.M. Yu 893
Conformal implantation for trench doping with plasma immersion ion implantation
Qian, X.Y., N W Cheung, M.A. Lieberman, R Brennan, M.I. Current and N. Jha 898
Ion projection lithography process on dry resist
Kholopkin, A I., M.N. Lyakhov, D.A. Pankratenko, V V. Simonov and A F Vyatkin 902

Author Index 905

Nuclear Instruments and Methods in Physics Research B55 (1991) 1–8
North-Holland

Section I. Overviews

Ion implantation in bipolar technology *

Chris Hill and Peter Hunt
Plessey Research Caswell Ltd., Caswell, Towcester, Northants NN12 8EQ, UK

Over the past 15 years, ion implantation has increased its role in advanced bipolar integrated circuit technology from zero to 80–90% of the doping steps The history of this change is briefly described, and the technical reasons for fabrication of each component using ion implantation are discussed. During the next decade, considerable further improvements in speed and packing density of bipolar integrated circuits will be achieved by the adoption of novel structures and materials. Some likely applications of ion implantation in this context are described

1. Introduction

Ion implantation was a doping technique with many years experience behind it when it first started to be used in integrated circuit fabrication in the early 1970s The basic science and engineering required to build machines of high doping uniformity and purity, and the materials science of fabrication of MOS and bipolar devices were all well-established prior to 1970, and successful devices had been demonstrated. All this necessary science and engineering infrastructure was funded not by the semiconductor industry, but mainly by Government funded programmes in the UK and USA as a spin-off from the mass-separator and ion-defect programmes associated with the development of nuclear power. The capital cost and novelty of ion implantation, and the adequacy of chemical deposition techniques for the low complexity circuits then fabricated, delayed incorporation of ion implantation into IC technology until the mid-70s. Once incorporated in process lines, the technique rapidly found many applications To understand how this happened in bipolar technology, this paper briefly describes some characteristic features of the bipolar transistor (section 2), the increasing importance of ion implantation in the evolution of bipolar technology to date (section 3), the advantages and disadvantages of ion implantation in fabricating each region of the bipolar circuit (section 4) and lastly some exciting new possibilities for ion implantation in future bipolar technologies (section 5).

2. Characteristics of the bipolar transistor

The bipolar transistor is a three-terminal current valve in which the current flow between the semiconductor emitter and collector regions is controlled by modulating the potential barriers associated with an intervening narrow base region of opposite semiconductor type. Schematic diagrams of a basic n–p–n transistor and its associated load resistor are shown in fig. 1a. A voltage applied between emitter and collector contact results in no significant current flow until the potential barrier of the emitter–base n–p junction is lowered by applying an appropriate voltage between base contact and emitter Electrons are then emitted into the p-type base region, across which they diffuse as minority carriers into the depletion layer associated with the base–collector p–n junction, where the junction field accelerates then into the collector. Ideally, no current flows in the control loop (base–emitter), but in real devices some holes always recombine with electrons, either in the base itself, in the oxide–semiconductor interface, in the emitter–base depletion region, or in the emitter This gives rise to a small hole current i (fig. 1b). An important parameter of a bipolar transistor is the current gain, the ratio of the output current I to the control current i. Typical steady state values of gain are 50–200. High values of gain, especially for low values of I, are necessary for efficient low power bipolar circuits, and this requires optimised vertical dopant distribution profiles in emitter, base and collector, a low density of recombination at surfaces and in the bulk, and high quality p–n junctions.

Switching speed is of paramount importance in bipolar transistors since this is their main advantage over MOS transistors. The switching speed is determined by the total time taken to transfer charge backwards and forwards across the device, and this is made up of a number of weighted time constants ($t = wRC$) associated with the resistance R and capacitance C of various components of the structure (fig. 1c), plus the transit time t_t for electrons to cross the base region. The whole history of improvement in switching speed in bipolar

* Invited paper.

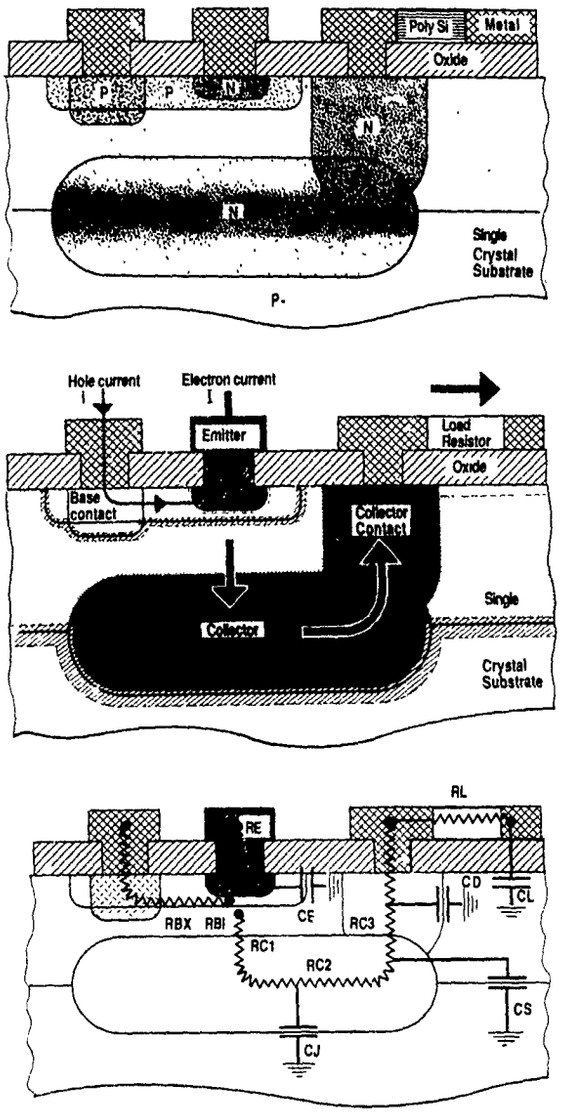

Fig. 1 Schematic sections through a simple VLSI bipolar transistor and load resistor, showing (a) the distribution of the doped regions, (b) the current flows and depletion layers (hatched) under forward bias conditions, and (c) the resistances and capacitances arising from the doped silicon regions and the depletion layers, respectively, which contribute RC time delays to the speed with which the transistor can be switched on and off

circuits has been associated with reducing these three parameters R, C and t_f.

The fabrication techniques universally used for bipolar transistors (fig. 1a) give intrinsically low transit times t_f, because of the narrow base widths attainable by controlling the vertical spacing of emitter, base and collector through controlling the vertical dopant profiles which constitute these regions. Thus, base widths in bipolar devices have never been tied to photolithographic resolution, as the equivalent dimension, channel length, has always been in MOS devices, typically base widths have remained a factor of ten smaller than MOS channel lengths. At very high switching speeds, the gain of bipolar devices falls, and a convenient figure of merit is the unity gain frequency f_T at which $I/i = 1$. Very roughly, an optimised circuit can be usefully run at clock speeds of about $f_T/10$.

An important consequence of the narrow base regions of bipolar devices is their sensitivity to vertical line defects [2]. By acting either as rapid diffusion routes for emitter dopant or as precipitation sites for metals, one such defect can electrically short emitter to collector, destroying transistor action. The short transit times, also mean, however, that bipolar devices can be very tolerant of recombination centres within the base region.

3. Implantation in bipolar technology 1970–1990

Although Shockley patented the concept of forming the bipolar base by ion implantation as early as 1954 [3], the first decade of planar bipolar integrated circuits development (1965–1975) proceeded almost entirely without the use of implantation. A transistor structure characteristic of the end of this era is shown in fig. 2a. All the selectively doped areas were fabricated by a chemical deposition of dopant (usually in compound form) followed by a higher temperature "driven-in" stage in which the dopant penetrated laterally and vertically into the single crystal silicon. This approach is adequate and cost effective (and still used) where geometries are undemandingly large ($\geqslant 3$ μm) and base widths are sufficiently wide ($\geqslant 0.5$ μm) that doping variations do not significantly change the base width. The need for implantation arose when attempts to further increase f_T from 0.7 GHz by narrowing the boron base under a phosphorus emitter resulted in irreproducible high resistance bases [4], resulting from base compensation by a fast-diffusing phosphorus "tail" in the emitter profile [5]. It was already known that this effect could be avoided by the use of high concentration arsenic emitters using either a solid arsenic doped germanosilicate glass [6] or a metallic arsenic vapour [7] as doping source. These techniques were not satisfactory for production; however, ion implanted arsenic emitters were satisfactory, if followed by a high temperature heat treatment to anneal the damage, to move the emitter–base junction away from the implanted region by solid state diffusion, and to create the steep-fronted arsenic depth profile characteristic of high concentration arsenic diffusion [8]. The availability of commercial ion implanters, developed initially in Government laboratories as a spin-off from the large UK and USA

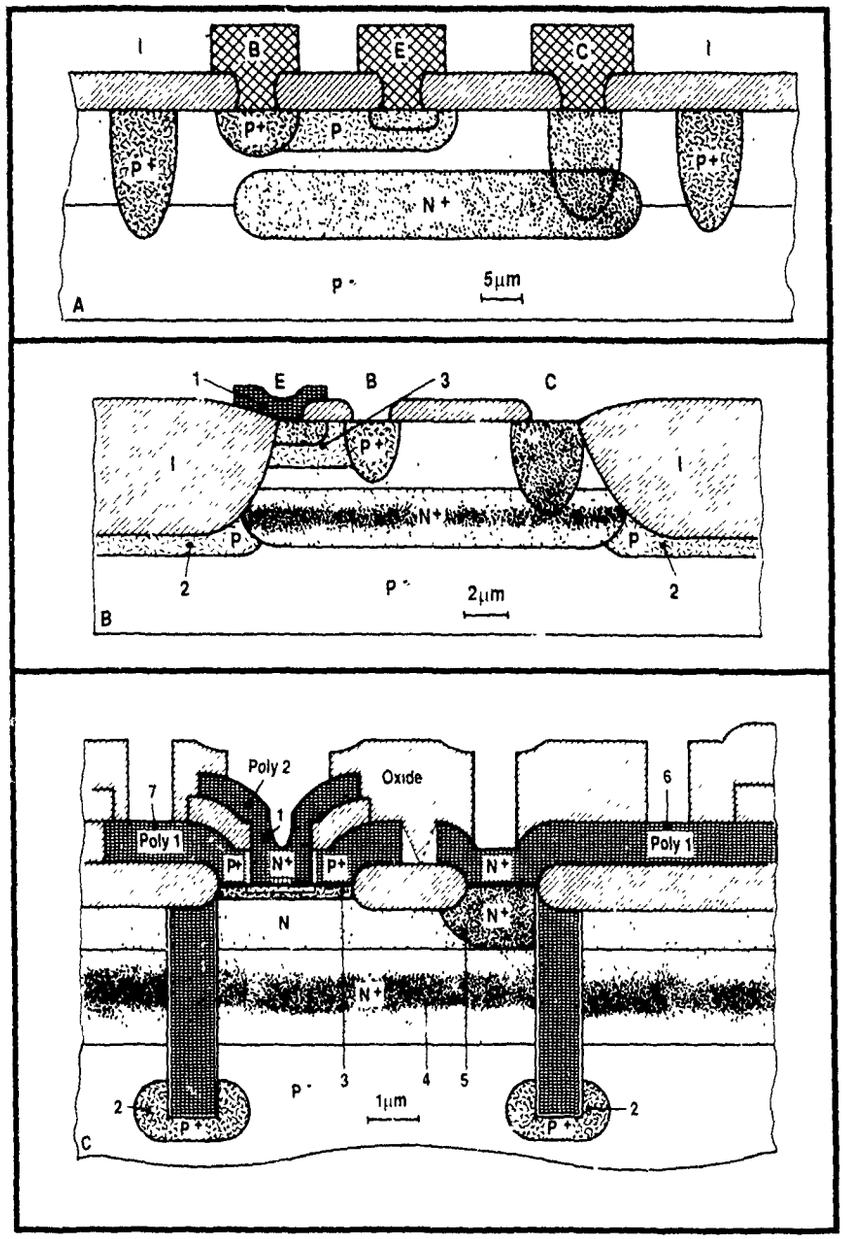

1975

1982

Emitter

Base

Channel stop

1989

Emitter

Base

Channel stop

Buried N+

Base contact

Collector contact

Resistor

Fig 2. Schematic sections through silicon integrated circuit bipolar transistor structures, showing the evolution of the structures over the first 15 years and the gradual incorporation of ion implantation for fabricating the doped regions (A) Structure typical of the mid-1970s, (B) structure typical of the early 1980s and (C) a 1989 one-micron feature size structure Numbered regions are those doped by ion implantation (1) polysilicon emitter (As), (2) channel stop (B), (3) base (B); (4) buried n + collector (As); (5) collector contact (P); (6) polysilicon resistor (P or As); (7) base contact (B)

Table 1
Summary of the incorporation of ion-implanted doped regions into silicon bipolar integrated circuit technology The table shows each region of the transistor, the dopant used, the approximate implant energy range and dose range, the typical date of incorporation and the frequency of usage of implantation in modern process technology.

BIPOLAR DEVICE REGION	Dopant	Energy			Dose		Timescale		Usage	
		<30	30-50	>70	$<10^{14}$	$>10^{15}$	◄75	85►	Few	Most
Buried N^+Collector	As,Sb		▨			▨		▨	▨	
Channel Stop	B		▨		▨	▨		▨	▨	
Collector contact	P		▨	▨		▨		▨	▨	
Isolation	B		▨		▨	▨	▨	▨	▨	▨
Base	B	▨			▨	▨	▨			▨
Base contact										
Single XSTL	B	▨					▨			
Polysilicon	B	▨	▨			▨	▨	▨		▨
Emitter										
Single XSTL	As		▨			▨	▨			
Polysilicon	As		▨			▨	▨	▨		▨
Resistor										
Single XSTL	B	▨			▨		▨			
Polysilicon	B,P	▨			▨	▨		▨		▨

Table 2
Characteristics and advantages of implantation as a doping source for each region of the bipolar integrated circuit, as compared with the alternative chemical sources shown The size of the plus and minus signs indicates the relative advantage or disadvantage of implantation; zero indicates no advantage or disadvantage.

Region of Bipolar Circuit Structure to be Fabricated	Advantages of Ion Implantation Source						Alternative Source		
	Doping Element	Depth Control	Dose Control	Auto-Registn.	Colli-mation	Defect density	Solid/ Liquid	Gas	Surface Glass
Buried N^+Collector	As, Sb	0	+	+	0	+			(AsSiO)
Collector Contact	P	0	0	+	0	0	$POCL_3$ →	$POCL_3$ →	(PSiO)
Isolation Doping									
1. p-n Junction only	B	0	0	+	0	0	BN →	(BOH) →	(BSiO)
2. Oxide + Channel stop	B	0	+	+	0	—	BN →	(BOH) →	(BSiO)
3. Trench + Channel stop	B	0	+	+	+	—	BN →	(BOH →	(BSiO)
Base	B	+	+	+	−	−	BN →	(BOH) →	(BSiO)
Base contact									
Single XSTL	B	+	+	+	0	0	BN →	(BOH) →	(BSiO)
Polysilicon	B	+	+	+	0	0	Deposited		Doped
Emitter									
Single XSTL	As	0	+	0	0	−	As →	As →	
Polysilicon	As	+	+	0	0	0	Deposited		Doped
Resistor									
Single XSTL	B	0	+	+	0	0	Bn →	(EOH) →	(BSiO)
Polysilicon	B,P	0	+	+	0	0	Deposited		Doped

mass-separator programmes of the 40s and 50s [9], enabled production processes incorporating arsenic emitters to appear in the late seventies. A crucial development for this application was the development of the stable high current Freeman ion source [10], which made the high implantation doses required by emitters (5×10^{15}–2×10^{16} ions/cm^2) a commercial possibility.

Once implantations were installed in process lines, and damage annealing techniques were established, the advantages of ion implantation for doping other regions was discovered. In parallel with this, other aspects of bipolar technology had been changed to achieve higher speeds and packing densities so that a typical transistor of the early 80s was as shown in fig. 2b. The emitter is still arsenic-implanted, but the implant is into a polysilicon overlayer from which out-diffusion into the single crystal occurs during anneal, thus enabling very shallow emitter regions of low edge capacitance to be fabricated independently of impact energy and damage. An implanted base allows even narrower base widths to be achieved reproducibly. Recessed oxide isolation, replacing traditional p–n junction isolation, reduces capacitance C_d, and increases packing density. Ion implantation made this important change possible, by facilitating the fabrication of a precisely doped channel stop region under the oxide, which prevented the occurrence of n-type surface channels in the silicon substrate material adjacent to the oxide Segregation of boron during thermal oxidation and the polarity of oxide charge favour the formation of such channels in p-type substrates doped below 10^{16}/cm^3.

Considerable further development during the 80s has resulted in modern structures similar to that shown schematically in fig. 2c. Use of self-alignment techniques in emitter, base and isolation, and the addition of an implanted boron polysilicon base contact, produces a very compact, low capacitance emitter–base structure. Ion implantation is used for all the other selective doping steps, i e. in deep trench isolation channel stop, in buried n^+ collector, in collector contact, and in polysilicon resistor fabrication The reductions in device area, capacitance and resistance thus achieved enabled circuits with $f_T = 12$ GHz, clock frequency 2 GHz and arrays of 100000 resistors to be fabricated successfully [11]. A summary of the introduction of ion implantation into bipolar component fabrication, with typical doses and energies used, is given in table 1.

4. Characteristics and advantages of ion implantation for each region of the modern bipolar circuit

4 1. Characteristics and advantages

A summary of these is given in table 2. The main characteristics of a doping technique are depth, control, dose control, autoregistration capability, collimation, and defect density produced overall. It can be seen that, as compared with alternative doping sources, ion implantation has considerable advantages in most characteristics for the fabrication of most bipolar components. In particular, dose control and autoregistration capability are the two characteristics which have ensured the replacement of most other doping methods by ion implantation. The precise dose control not only guarantees a reproducible, transferable process for the number of ions in each bipolar component, but also, through the dopant-concentration dependence of solid state diffusion, guarantees the precise location of the p–n junctions. Autoregistration, in which the same photoengraved feature is used successively to define several selectively doped regions, allows much denser packing of components than the alignment tolerances between successive photolithographic steps would normally allow. Ion implantation, being a ballistic rather than a thermal doping technique, allows the use of organic photoresist layers as sacrificial doping barriers, thus enormously simplifying self-alignment strategies. In addition to these general advantages, there are aspects of ion implantation particular to each component fabrication, examples of which will now be briefly described.

4.2 Trench isolation

The deep oxide-filled trenches shown in fig. 2c need a channel stop region at the bottom as shown The collimation characteristic of ion implantation is ideal in this application, since before filling, the deep narrow trench can be precisely doped at its base by a boron implant at 90° to the wafer surface The defects created by this implant have to be very carefully controlled, however, since they are well placed to act as dislocation sources if mechanical stresses act on the trench region Such stresses arise inevitably from the trench-filling processes and associated heat treatments. With careful engineering of dose, energy and anneal, an adequate dislocation-free channel stop can be fabricated [12].

4.3. Base region

In this case, the collimation characteristic of ion implantation is unwanted, and can give rise to different lateral penetration distances on either side of the base implant window [13] This occurs because, in order to avoid channelling down major crystal directions, the implant beam is usually misaligned with the wafer surface normally by a few degrees. Line-of-sight shadowing by one mask edge but not by the other can then produce lateral spreads in ratios up to 1.8 (fig. 3). The depth control of ion implantation, coupled with its easy self-alignment can, however, be used to great effect in achieving very narrow reproducible base regions, as

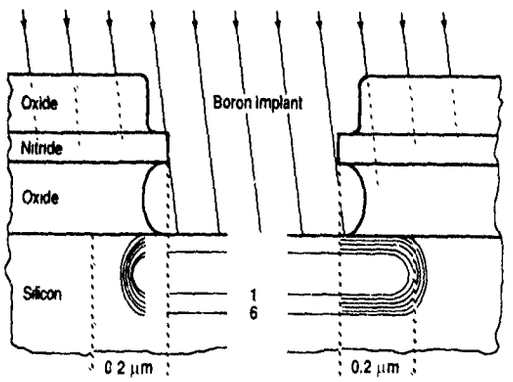

Fig 3 Experimentally measured two-dimensional depth distributions of boron after implantation at 7° to the surface normal through a window in the masking layers shown The boron concentration contours cover the range 1×10^{19} atom/cm^3 (1) to 1×10^{18} atom/cm^3 (6) The difference in lateral penetration of dopant beyond the right and left hand mask edges is 0 1 μm

shown in fig. 4 The natural shape of the boron implant profile, which in a single crystal matrix always has some channelled tail, prevents unlimited reduction of base width by simply reducing implant energy. However, by implanting a precisely placed dose of phosphorus through the emitter window, the critical region of the boron tail profile can be electrically compensated, thus effectively narrowing the base region with little loss of total integrated base electrical dose This technique has been used to increase f_t from 12 GHz to 20 GHz with little deleterious effect on other circuit properties [14].

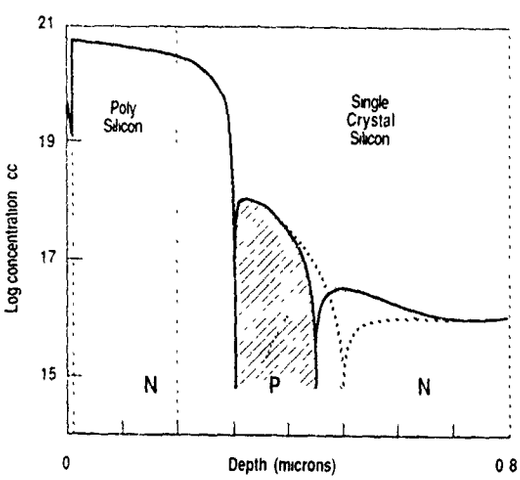

Fig 4. Concentration–depth profiles through the emitter-base–collector region of a high performance bipolar transistor showing the use of a buried phosphorus implant to electrically compensate the channelled tail of the boron base implant and so obtain a narrower base region The carrier concentration profiles in the arsenic-implanted polysilicon plus single crystal n-type emitter region, the boron implanted p-type base region, and the epitaxial n collector are shown by bold lines, the compensating phosphorus implant is shown by a light dotted line. For comparison, the bold dotted line shows the carrier profiles in the base–collector region in an unimproved device (after Wilson [14]).

4 4 *Emitter region*

As can be seen from table 2, the main advantage of ion implantation is the precise control of a high dose of arsenic. In modern devices, this implant is into polysilicon, and the final depth of the n–p junction is determined by the solid state diffusion occurring in emitter (arsenic) and base (boron) regions during the emitter anneal. This approach to shallow junction for-

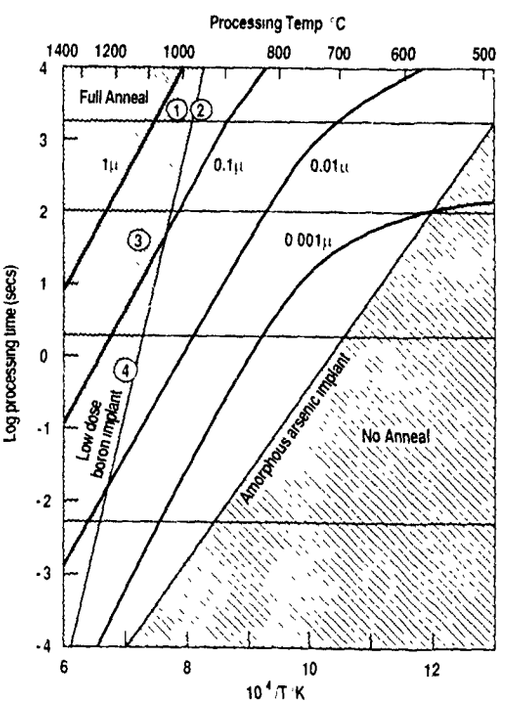

Heat Treatment	Base Width Microns	Year
①	0.2	1975
②	0.1	1985
③	0.06	1990
④	0.03	1995

Fig 5 Time–temperature map showing the region for full anneal of a 40 keV low dose boron implant superimposed on curves giving the loci of time- temperature schedules which redistribute a 10^{16} 40 keV arsenic implant by the diffusion distances ($3\sqrt{Dt}$) shown The numbered locations 1–3 show typical heat treatments used in emitter–base anneal as bipolar technology has evolved; location 4 shows the subsecond heat treatment necessary to anneal future narrower bases, if direct implantation of boron is still used (after Hill [15])

mation is increasingly favoured, and base contact (boron in polysilicon or silicide) and even the base itself (co-diffusion of arsenic and boron from polysilicon) are being seriously investigated. The reason for this is the increasingly difficulty of removing implant anneal damage while restricting broadening of the narrow emitter and base regions by solid state diffusion. The different activation energies of anneal and diffusion have enabled rapid thermal annealing to solve this problem for present technology (location 3, fig. 5), but shorter anneal times are probably impractical. Using the implant to achieve a precise dose, and trapping the implant defects within a polycrystalline overlayer, is a very attractive alternative.

5. Ion implantation in future bipolar development

Analysis of the contributions to delay in switching of modern bipolar integrated circuits [11,16] shows that the major time delays are in the extrinsic components, particularly in the resistance–capacitance products associated with the load resistance R_L and the extrinsic collector capacitance C_{CJ} and load capacitance C_L. Evolutionary improvements in these time delays will arise mainly from decreasing component areas as packing densities increase, and a proposed future technology based on half-micron feature sizes and oxide-isolated collector contact with a total device area of 4 μm^2 is expected to have a unity gain frequency f_t of 30–35 GHz [11]. The role of implantation will still be essentially that shown for the one-micron device of fig. 2c.

Future improvements are possible, both in simplification of the bipolar technology and in even faster switching circuits, using novel technologies. One simplification is the replacement of the implanted collector plus epitaxial silicon overgrowth, by a directly implanted collector into the silicon substrate. In the past, the combination of high dose (5×10^{15} ions/cm^2) and high energy (5 MeV phosphorus) required ruled out this approach. The lateral shrinkage of device geometries below one micron has reduced both dose and energy requirements to a level that can be achieved using recently developed MeV implanters, as shown in table 3. The reduction in implant energy follows from the vertical shrinkage of the device implemented to achieve higher switching speeds. The large reduction in dose shown in table 3 arises from the lessening influence of collector resistance R_C on device speed as compared with the load resistance R_L, which must increase as operating currents decrease to maintain the same output signal. Very low current circuit designs, as CML (cur-

Table 3
Factors determining the implant dose and energy required to fabricate a phosphorus buried n$^+$ collector by direct implantation in three different bipolar circuits. As operating currents decrease, the value of load resistance to generate a required signal voltage increases, thus enabling the resistance of the buried n$^+$ collector in series to also increase with no significant performance penalty.

Parameter	Circuit type	High speed Emitter-coupled logic		Low power Current-mode logic
	Geometry	one micron	half micron	half micron
Emitter–collector current I_C [mA]		1	0.3	0.03
Signal voltage V_S [V]		0.6	0.6	0.2
Load resistor R_L [Ω]		600	2000	6667
Total allowable collector series resistance $R_C = 0.3R_L$ [Ω]		180	600	2000
Epitaxial collector resistance R_1 [Ω]		50	300	300
Collector contact resistance R_3 [Ω]		2	2	2
Maximum allowable buried collector resistance R_2 ($= R_C - R_1 - R_3$) [Ω]		128	298	1698
Maximum allowable buried n$^+$ sheet resistance S [Ω/□]		128	298	1698
Implant conditions to fabricate a buried n$^+$ layer with the above S value underlying a surface region 0.4 μm deep with dopant concentration $< 5 \times 10^{16}$/cm^3.				
Phosphorus dose [ions/cm^2]		1×10^{15}	3×10^{14}	7×10^{13}
Energy [keV]		800	700	600

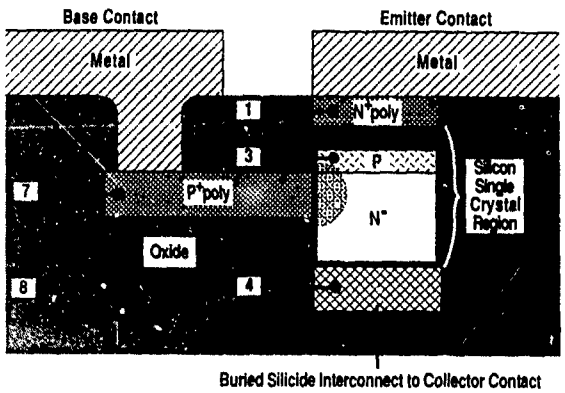

Fig. 6 A possible future minimum resistance and capacitance bipolar transistor structure capable of switching speeds up to 50 GHz Regions likely to be implanted are (1) polysilicon emitter, (3) base region, (4) buried silicide collector, (7) base contact and (8) oxide isolation (SIMOX). After Hunt [11].

rent mode logic) will favour the direct implant buried n^+ approach.

Faster switching speeds will require further minimisation of capacitances, and a radically different technological approach A possible implementation is shown in fig. 6 [11], in which all the silicon doping steps and two compound synthesis steps can be carried out by ion implantation and suitable anneals. The p–n junction areas are reduced to the minimum required for bipolar switching, and oxide isolation is used throughout. The device area is reduced by a buried base contact and buried silicide collector contact. Fabrication could involve oxygen implantation to create the back oxide isolation, cobalt implantation to produce buried silicide, and selective epitaxy in an oxide well to create lateral oxide isolation. Emitter–base fabrication could well be a single step operation by vertical solid state diffusion from an arsenic and boron implanted polysilicon layer, while lateral diffusion from a boron implanted polysilicon layer into the epitaxial material creates the base contact. Such a device should achieve f_T values of 50 GHz [11].

6. Conclusions

Ion implantation has found an increasingly comprehensive and diverse role in selective doping in integrated circuit bipolar technology, and will continue to do so for the forseeable future. Bipolar technologies of the next decade may well incorporate MeV implantation and implanted compound synthesis of SiO_2 and $CoSi_2$. In shallow junction fabrication, implantation into overlayers to combine the precise dose of implantation with the defect-free steep p–n junctions characteristic of high concentration diffusion from a polycrystalline source will probably be favoured.

Acknowledgements

This work was supported by the EEC and GEC-Plessey Semiconductors Ltd., through the collaborative project STORM and TIP-BASE, and thanks are due to both bodies for permission to publish.

References

[1] Physics of Semiconductor Devices (Wiley, New York, 1981).
[2] C Hill, Proc. 5th Int. Conf on Ion Beam Modification of Materials, Nucl. Instr. and Meth B19/20 (1987) 348
[3] W Shockley, US Patent 2787564 (1954)
[4] T Tokayama, T. Ikeda and T. Tsuchimoto, Proc 4th Microelectronics Congress (Oldenburg, Munich, 1970) p 36.
[5] J.C C Tsai, Proc. IEEE 57 (1969) 1499
[6] K Fujinima, T. Sakamoto T. Abe, K. Sato and Y Ohmura, Proc 1st Conf on Solid State Devices, J Jpn Soc. Appl. Phys. 39 (1969) 71
[7] T L. Chiu and H.N Ghosh, IBM J Res. Dev 15 (1971) 464.
[8] V.G.K. Reddi and A.Y C. Yu, Solid State Technol 15 (1972) 35
[9] G Dearnaley, J H Freeman, R S Nelson and J Stephen, Ion Implantation (North-Holland, Amsterdam, 1972).
[10] J H Freeman, Nucl Instr and Meth 22 (1963) 306
[11] P C Hunt, IEDM Tech Digest 1989 (IEEE, Piscataway, NJ, 1989) p. 791.
[12] M C Wilson and D J. Bazley, Plessey Research Caswell Technical Report A11/566/88 (1988)
[13] P J Pearson and C Hill, J Phys (Paris) 49 (1988) C4-515
[14] M.C Wilson, Proc ESSDERC 90, eds. W Eccleston and P Rosser, (Adam Hilger, Bristol, 1990) p. 349.
[15] C Hill, in Laser Solid Interactions and Transient Thermal Processing of Materials, eds. J Narayan, W.L. Brown and R A Lemons (North-Holland, New York, 1983) p 381.
[16] P. Ashburn, IEEE J Solid State Circuits 24 (1989) 512

Nuclear Instruments and Methods in Physics Research B55 (1991) 9–16
North-Holland

Application of ion implantation in submicron CMOS processes *

K.H. Küsters, H.M. Mühlhoff and H. Cerva
Siemens AG, Otto-Hahn-Ring 6, 8000 München 83, Germany

Ion implantation is an essential technology for the development of submicron CMOS processes The most important applications of ion implantation in a CMOS process are, (1) well formation, (2) threshold voltage control of MOS active and parasitic transistors, (3) drain engineering of transistor, (4) formation of n^+, p^+ areas, (5) breakup of native oxides by ion mixing and (6) doping of 3-dimensional structures like DRAM cells. Recent developments in these topics, which are reviewed in this paper, include optimization work based on conventional implantation technology as well as new implantation techniques like MeV implantation, parallel-scan implantation and large-tilt-angle implantation

1. Introduction

Ion implantation is used for most doping steps in VLSI The scaling of CMOS devices into the deep submicron range sets new challenges for the optimization of implantation technology. The design rules of 16 Mbit DRAMs, which are now in pilot production, have moved down to 0.5–0.6 μm. All impurity doping steps (see fig. 1) have to be optimized to improve device performance, particularly isolation and transistor performance. The development of 3-dimensional DRAM cells requires the implantation doping of 3-dimensional structures.

This paper reviews the most important applications of ion implantation in modern CMOS processes and the present work on process optimization concerning impurity doping and new implantation techniques in CMOS processes Furthermore, defect problems in CMOS processes due to implantation damage are discussed.

2. Well formation

In CMOS processes adjustment of bulk doping is usually performed by the formation of n- and p-wells. When designing the well process, several device issues have to be taken into account. Surface concentration has to be high enough that sufficient isolation for active and passive devices can be maintained. Since this is not always the case, additional shallow implantations such as channel implants for active devices and field implants for isolation areas may be necessary. Bulk concentration needs to be at a level to inhibit non-surface-controlled leakage (punchthrough) both in active and isolation devices. Also vertical punchthrough between devices in a well with opposite doping than the substrate and the substrate has to be avoided. In DRAMs with depletion-type trench capacitors, especially high p-well doping levels are necessary to suppress punchthrough between adjacent trenches [1] and to reduce the soft error rate due to alpha particles [2] The latch-up problem inherent in CMOS technology has to

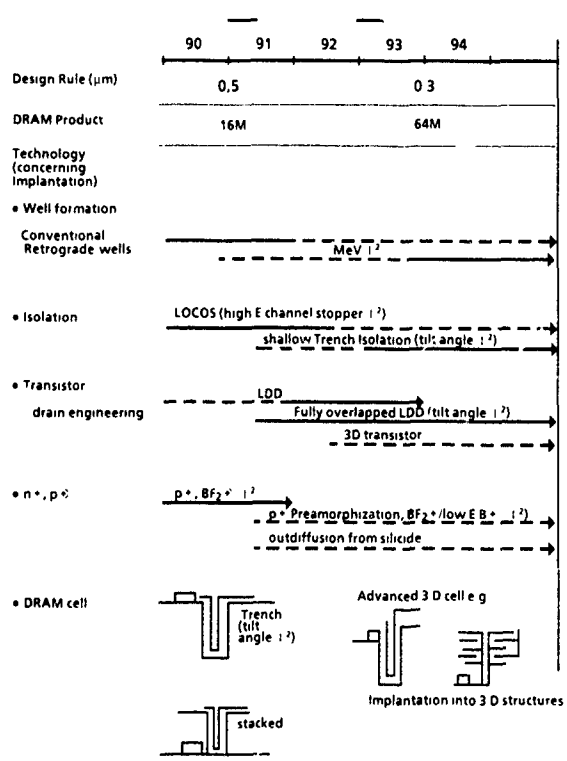

Fig 1. Technology trends in ion implantation.

* Invited paper.

0168-583X/91/$03.50 © 1991 – Elsevier Science Publishers B V (North-Holland)

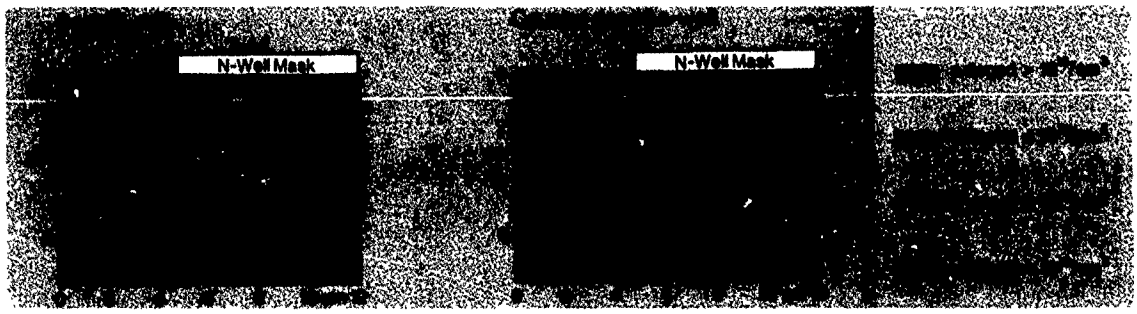

Fig 2. Simulated 2D doping profile of deep n-well, and counter-doped n-well.

be minimized by designing wells with low sheet resistances and minimum β for the parasitic bipolar transistors.

P- and n-wells can be fabricated in a fairly straightforward fashion using two masking steps and low implantation energies To achieve the required well depths, drive-in steps are performed at high temperature (1150–1190 °C). Several hours are needed for DRAMs with trench capacitors because the doping concentration at the trench bottom in 4 μm depth has to be more than 10^{16} cm^{-3}. In order to reduce the mask count, self-adjusting technologies have been suggested [3] employing a local oxidation process. An even simpler approach is an unmasked p-well implantation followed by the implantation of the n-well in masked areas, in which the n-doping counterdopes the p-well, creating a net donor concentration between 5×10^{16} and 10^{17} cm^{-3} [4]. 2D simulation of the doping profile reveals the advantages of this well concept (fig 2) Because the n-well is superimposed on a highly doped p-well background, well pn junctions are fairly abrupt both in the lateral and in the vertical direction The dimension of regions with low net doping (less than 10^{16} cm^{-3} net concentration) is considerably smaller than in conventionally doped wells (0.6 μm vs 2 μm). This permits tighter design rules for n^+–p^+ spacing because no isolation area is wasted with lowly doped well boundaries The dependence of isolation properties of the n-well on separation between well-edge and p^+ junction are shown in fig. 3 The counterdoped n-well even beats a very shallow n-well which was driven in with minimum thermal budget. Well parameters are listed in table 1. High-temperature drive-in steps can be avoided, if higher implantation energies are used. MeV implantation has left the development phase and is now entering production [5–8]. Besides low-temperature processing, an additional advantage consists of being able to make a retrograde doping profile, in which bulk concentration is much higher than surface concentration. Using this technology, highly doped layers can be made underneath field oxide for improved isolation and be made underneath active devices for reduced susceptibility to latch-up [8]. But also conventional or counterdoped well technologies can produce good results with respect to latch-up [4].

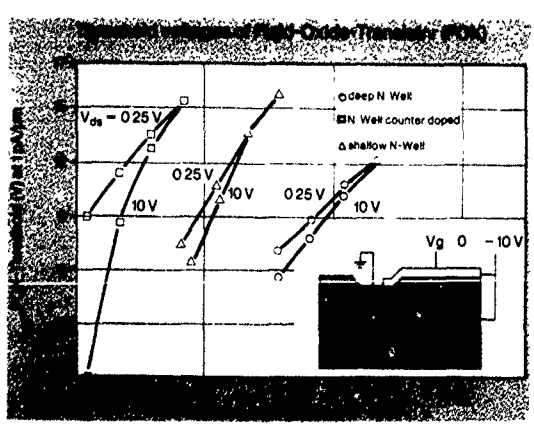

Fig 3. Lateral isolation of n-well. Threshold voltages of FOX-transistor for V_{ds} = 0.25 V and V_{ds} = 10 V at 1 pA/μm.

Fig 4 shows latch-up data for substrate-triggering of p-doped wafers (refer to refs. [9–11] for description of characterization method). This trigger mechanism is dominated by the shunt resistance of the p-substrate and the p-well. Using thin epi can improve latch-up trigger currents by several orders of magnitude 16 Mbit DRAMs with deep p-well have a performance equivalent to 8 to 14 μm epi-substrate.

Trigger currents for well triggering are shown in fig. 5. This trigger mechanism is dominated by the shunt

Table 1
Well parameters

	Deep n-well	Shallow n-well	Counterdoped n-well
Well depth [μm]	4.0	1.5	3
Outdiffusion from masks edge [μm]	3.5	2.0	0.5
Vert d_j $<1\times10^{16}$ [μm]	2.0	0.9	0.6
Lat d_j $<1\times10^{16}$ [μm]	1.4	0.8	0.5

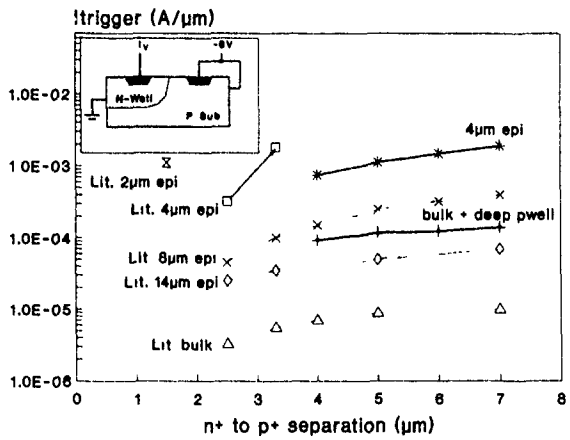

Fig 4 Latch-up substrate triggering Comparison between own data and ref [8].

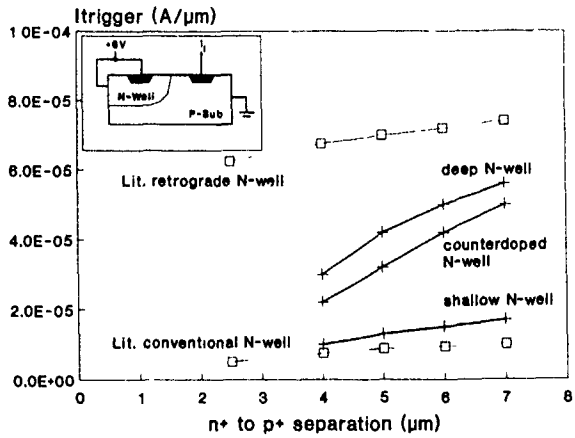

Fig. 5 Latch-up well triggering Comparison between own data and ref [8].

resistance of the n-well. Well trigger currents for conventional deep n-wells are are not much below those of MeV-implanted retrograde n-wells down to 4 µm n^+–p^+ spacing. Figs 4 and 5 compare own data with results taken from the literature [8]. Is is evident that carefully tuned conventional well technologies can be stretched to realize n^+–p^+ spacings of less than 4 µm, which is sufficient for 0.5 µm CMOS processes. For spacings less than 2 µm, however, thin (2 µm) epi-substrate and retrograde wells will be required.

3. Threshold voltage control, MOS active and parasitic transistors

Conventional poly-buffered LOCOS isolation can still be used up to the 16 Mbit DRAM integration level [12,13] Maintaining oxide thicknesses of more than 200 nm becomes difficult with processes where isolation widths of less than 0 7 µm are required. Satisfactory electrical results are shown in fig 6 demonstrating that neither turn-on of the parasitic field-effect transistor nor punchthrough between adjacent source/drain areas occurs down to 0.7 µm separations Due to the different segregation behavior of boron and phosphorus during oxidation, boron concentration underneath the field oxide is very low whereas phosphorus piles up on the silicon side of the interface For this reason channel-stop implantation is usually not required for PMOS isolation areas.

To achieve satisfactory isolation in NMOS areas, additional channel-stop implants are required. If this implantation is carried out before LOCOS growth, lateral outdiffusion will increase the doping concentration in narrow active areas causing higher threshold voltages. This narrow width effect can be eliminated by performing the channel-stop implantation after the LOCOS growth at higher energies (180 keV). Boron atoms at this energy penetrate 400 to 600 nm field oxide. Isolation properties of both doping techniques are compared in fig 6. The narrow-width effect (fig. 7)

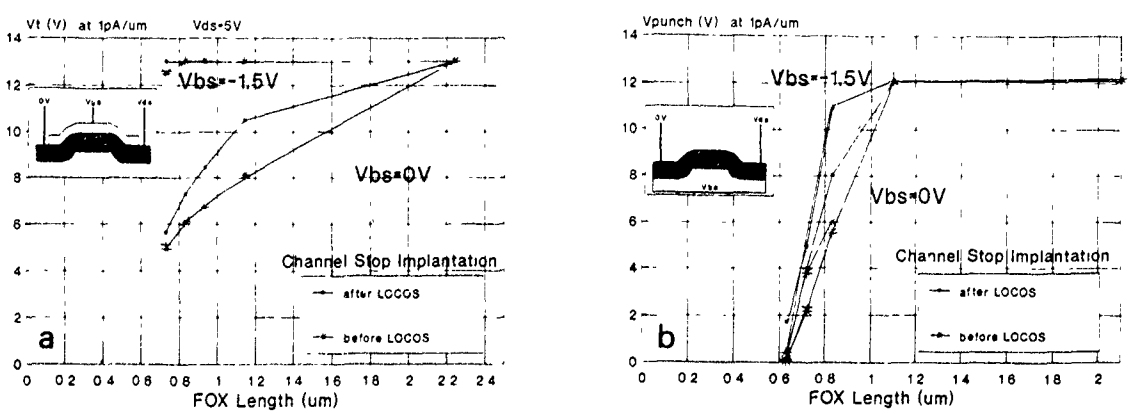

Fig 6 Threshold voltage (a) and punchthrough (b) of parasitic FOX-transistor. Isolation can be maintained down to 0 7 µm

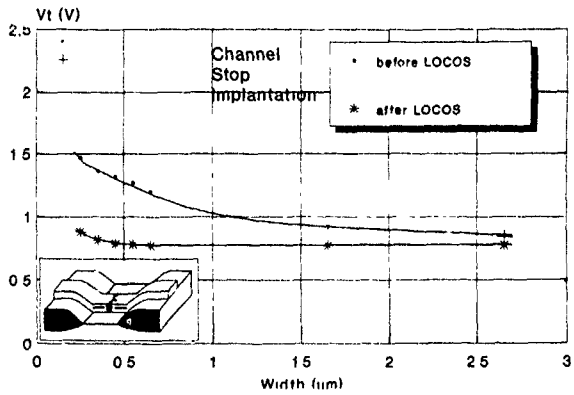

Fig. 7 Comparision of NMOSFET narrow-width effect for two channel-stop implantation techniques: ■ implantation before LOCOS growth, * implantation after LOCOS growth $L_{gate} = 0.8\ \mu m$, $V_{ds} = 3.5$ V and $V_{bs} = -1.5$ V

disappears almost completely and transistors with active area width of 0.25 μm can be realized [14]. Even smaller LOCOS isolation can be made when the pad oxide is scaled down further. A value of 0.5 μm can be acheived when a 5 nm pad oxide under a 50 nm poly-Si film is used [13]. For increased integration densities like 64 Mbit DRAM, shallow trench isolation can be introduced. Isolation properties have to be adjusted by tilt-angle implant of trench sidewalls [15,16].

4. Drain engineering of transistors

The performance of submicron transistors depends on the impurity profile in the vicinity of the drain regions. LDD transistors reduce the peak electric field in the channel and thus reduce hot electron degradation of NMOS transistors. Gate control over n^--LDD regions is crucial for reliability improvement. Therefore the shadowing of the LDD implantation at the gate edge, which gives rise to asymmetric transistors with nonoverlap between gate and source/drain, has to be avoided by rotating the wafers at the LDD implantation [17]. Optimization of deep submicron ($L_g = 0.25\ \mu g$) transistor reliability has led to fully overlapped LDD structures (FOLD) (fig. 8) [18,19]: The LDD implant is performed at tilt angles up to 60°. In addition to reliability gains, current drive capability is increased due to the higher conductivity of the fully overlapped n^- region. This structure is also suitable to suppress gate-induced drain leakage [20] which sets constraints on deep submicron transistors with ultrathin (< 10 nm) gate oxides.

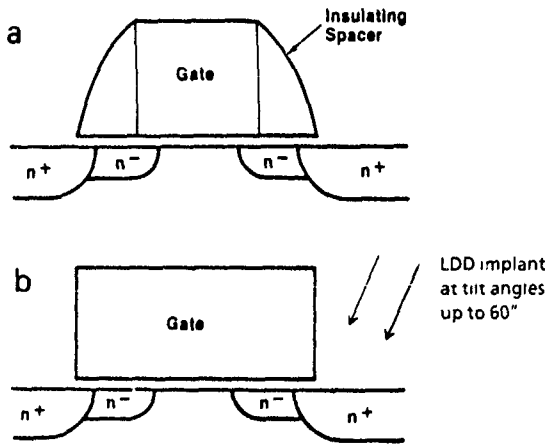

Fig. 8 Schematic drawing of (a) LDD and (b) FOLD transistor.

Fully overlapped LDD structures can also be achieved with conventional implanters (inverse T-gate process) without large-tilt-angle end stations; however, this is achieved at the cost of enhanced process complexity [21,22].

5. n^+-, p-areas junction formation

A scaled CMOS technology requires shallow source/drain junctions. Junction depth for 0.5 μm CMOS technology is approaching 100 nm or less to prevent punchthrough and short-channel effects. Shallow implanted profiles can easily be achieved for As-doped n^+ layers. However, shallow B-doped p^+ profiles can only be realized if the channeling of B^+ ions is prevented. Complete elimination of channeling is possible by preamorphization using a Ge or Si implant prior to B^+ or BF_2^+ implantation [23,24]. Also preamorphization by implantation of F [25] or Sb [26] has been reported. The integration of shallow implanted layers in a CMOS process requires careful work on the control of implantation damage [27]. Defects near the shallow source/drain junctions are detrimental to device performance. The thermal budget for defect anneal has to be kept minimal because of dopant redistribution.

Therefore, control of implantation damage is an important concern of process flow and optimization of implantation parameters. Process options for shallow p^+ layers without defects include the following.

- Use of rather thin preamorphized layers. The annealing time to remove damage is decreasing as the proximity to the surface increases: the shallower the damage, the lower the annealing temperature can be. The use of an amorphized layer as thin as 40 nm is combined with low-energy BF_2^+ (fig. 9) [24] or very-low-energy B implantation [28].
- Outdiffusion from TiSi and CoSi using RTA annealing, which has been intensively investigated [29–33]. Different approaches using ion implantation before or after silicide formation are reported. Process prob-

lems arise from low dopant concentration at the silicide/Si interface, which have been observed, e.g., for B and the $TiSi_2$/Si interface [30]. B tends to precipitate at the $TiSi_2/SiO_2$ interfaces and to form meta'/dopant compounds with Ti. Outdiffusion of B into Si is rather poor (fig. 10). The lack of pileup of boron at the $TiSi_2$/Si interface makes ohmic contact formation difficult. Process optimization for higher surface dopant concentration at the $TiSi_2$/Si interface therefore requires high implant doses, an implantation range as close as possible to the interface, and short-time drive in RTA. Results for the outdiffusion of dopants from $CoSi_2$ indicate that $CoSi_2$ is favourable compared to TiSi. Shallow junctions with high B concentration at the $CoSi_2$/Si interface were reported [32].

Formation of detrimental defects is not only critical for p^+ layers, but also for n^+ layers. Here, defects at mask edges are found after the crystallization of an amorphous layer [34,35]. These defects occur during a typical CMOS process. The high-dose source/drain implantation is performed self-aligned to the gate. The gate/LDD spacer acts as an implantation mask. At the mask edge the amorphous/crystalline interface is curved; solid-phase epitaxial regrowth (fig. 11) proceeds now into both vertical and lateral directions, simultaneously.

Partial crystallization of the amorphous layer reveals a notch on the amorphous/crystalline (a/c) interface, which is shown to be due to the different epitaxial regrowth rates on the various lattice planes. On further annealing, defects are generated when the crystallization fronts on both sides of the notch join. These defects are inevitable if an amorphous zone has sharply curved a/c interfaces. During further processing these defects are in a stress field Fig. 12 shows a dislocation nucleated at the mask edge defect below a stress-inducing thick

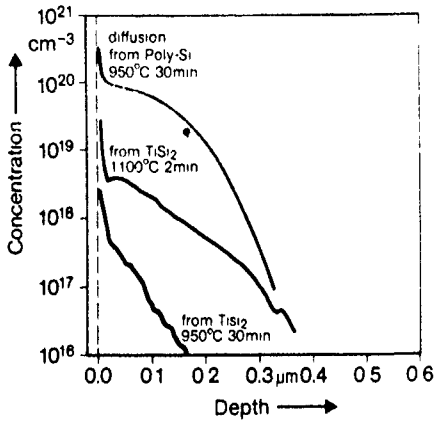

Fig 10 B doping profiles after outdiffusion from $TiSi_2$, data taken from ref. [30] (B in mono-Si)

nitride layer; here a strong leakage current can be observed. Process options to avoid these defects at mask edges, which occur only in As-implanted source/drain regions of N channel transistors, are:

- use of less steep implantation sidewalls to achieve a smoothly rounded a/c interface; however, this may conflict with the trend of increasing integration density;
- use of only n^- doping in stress-sensitive regions;
- diffusion of dopants from doped silicide on Si into Si substrate, to avoid any implantation damage in the substrate.

6. Ion mixing

Ion mixing techniques are used for silicide formation and for poly-Si/Si contacts. The effect of an interface native oxide can largely be suppressed by implanting

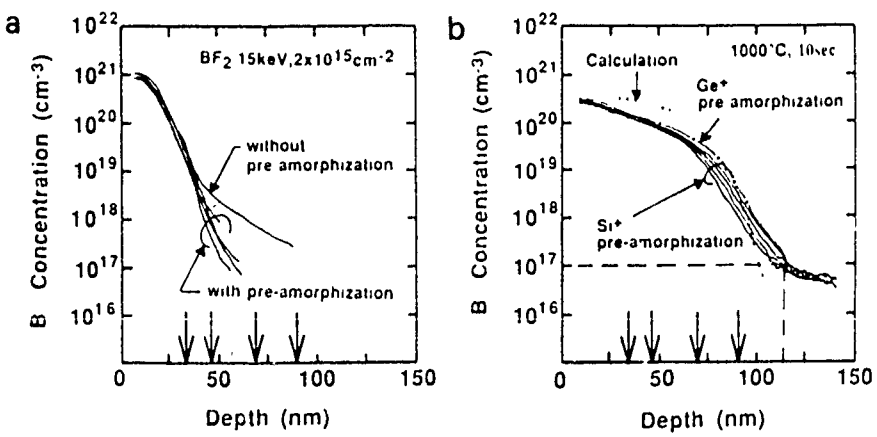

Fig. 9. Doping profiles of BF_2^+-implanted layers with different thicknesses of the preamorphized layer Data taken from ref [24] (a) As-implanted B profiles for preamorphized and crystal samples The arrows indicate the a/c interface positions. (b) Annealed B profiles for preamorphized samples formed by Si^+ and Ge^+ implantations.

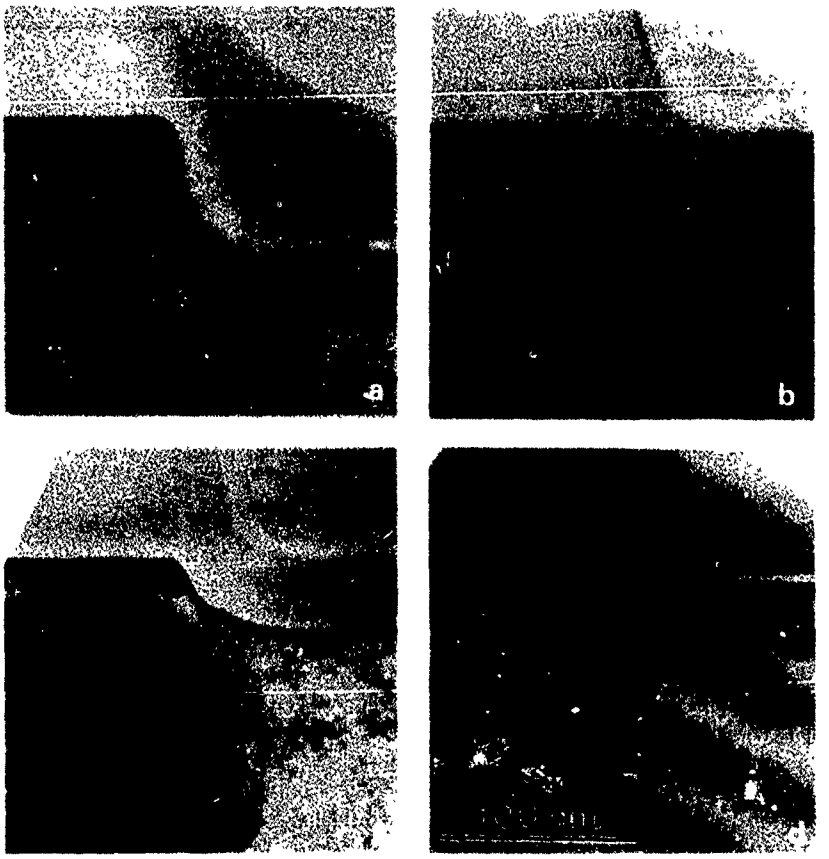

Fig 11 Defect formation during crystallization of an amorphous As-implantation layer near a mask edge (a) As-implanted, (b)-(d) regrowth after: (b) 500 °C, 30 min, (c) 500 °C, 190 min, (d) 900 °C, 60 min.

ions through the deposited-metal/poly-Si layer into the interface [37]. The ion beam mixing breaks up the oxide at the interface.

For silicide processes it has been observed that interface mixing (e.g., by Si^+ implantation or implantation of dopants) enhances the Ti–Si or Co–Si nucleation rate and results in a smooth silicide surface [38]. Furthermore, resistivity uniformity is enhanced. However, junction problems have been reported, e.g., because of mixing of Co into the substrate and loss of dopants during silicide formation.

Ion mixing also serves to reduce the contact resistance of poly-Si/Si contacts [39]. Low specific contact resistivities in the 20 $\Omega\mu m^2$ range are found if the energy is high enough that As^+ ions reach the contact interface. The native oxide is broken up and poly-Si regrowth on Si substrate is epitaxial during subsequent annealing. Also Si^+ ions can be used to break the native oxide and achieve low values of contact resistance after low-energy As^+ ion implantation. Using Si implantation, the degradation of the contact doping profile can be avoided. However, ion mixing of contact areas leads to an amorphous zone in the Si substrate, which may have sharply curved a/c interfaces below the mask edges. During regrowth of the amorphous zones the defect formation at contact borders again becomes an important concern for process optimization (see section 5).

7. Trench capacitor sidewall doping

As the level of integration increases, devices have to be formed below the Si surface or above it. DRAM cells of beyond 1 Mbit integration density (see ref [40]) are based on 3-dimensional cell structures such as stacked capacitors and trench capacitors. Fig. 13 shows a cross section of a 16-Mbit-DRAM trench cell. The doping of a trench capacitor requires implantation of ions into vertical sidewalls of trenches, whose aspect ratio may be as high as 10.

The angle of incidence of the ion on the trenches has to be strictly controlled, therefore implanters with parallel beam scan have to be used [41–43]. To avoid shadowing effects, rotational implantation is necessary. A major concern about trench sidewall doping is con-

trollability and uniformity. The ion dose delivered to trench sidewall/trench bottom depends, e.g., on the implantation angle and energy, which determine the reflection on ions from the sidewalls, and on the trench geometry. The experimental determination of implantation profiles is cumbersome and time-consuming. Computer simulation is used to obtain suitable implantation conditions [44–47]. In simulation studies, the 3-dimensional Monte Carlo technique is used to simulate the trajectories of particles and the final doping profile. To achieve uniform trench doping, optimization of the ion incidence angle is necessary. The optimized ion incidence angle is given by the condition that the ion beam, coming from the mask edge (upper trench edge) is injected into the opposite bottom corner of the trench [44].

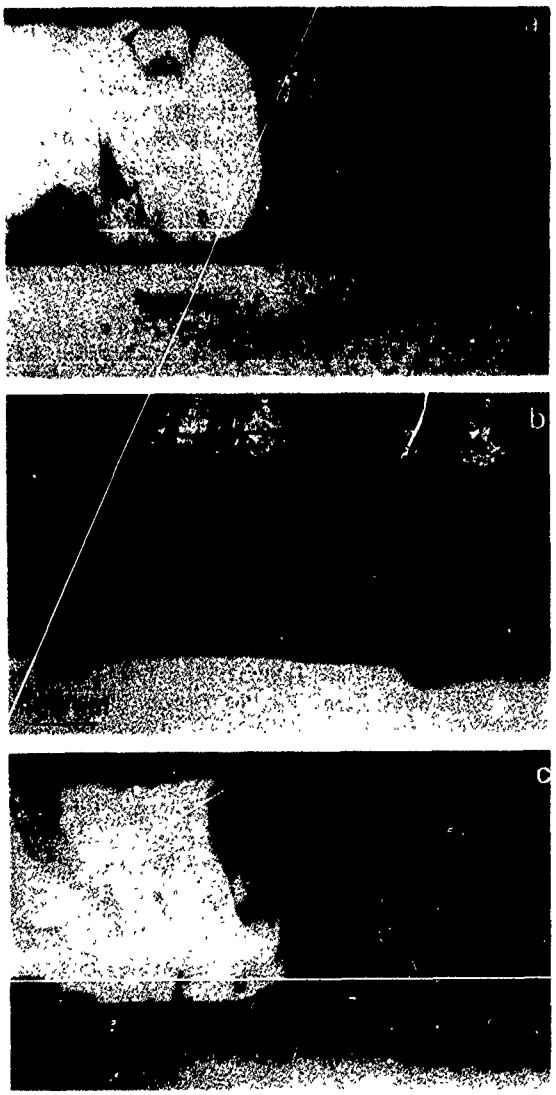

Fig 12 (a) Nucleation of a Hu loop at a residual implantation defect induced by the stress of a thick nitride film (b) Thin nitride film; (c) no nitride film

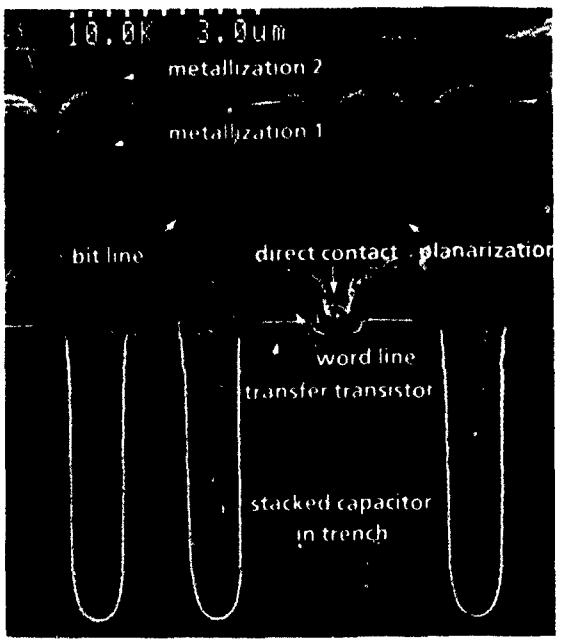

Fig 13 Cross section of 16 Mbit DRAM trench cell.

8. Summary

The application of ion implantation in advanced CMOS processes has been discussed. Recent developments include optimization work based on conventional implantation techniques as well as the application of advanced techniques like

- MeV implants (retrograde well),
- tilt-angle implantation with parallel beam scan (3-dimensional structures, FOLD transistor).

For all implantation applications in VLSI, defect-related problems will need more attention to enable the production of chips with increased packing density at high yield:

- implantation damage has to be characterized, process flow has to be optimized to avoid implantation damage or remove damage with low thermal budget;
- contamination levels have to be reduced, ultraclean techniques [47] will be introduced in VLSI;
- charging of wafers through implantation, which may cause gate damage, has to be avoided

Acknowledgement

The authors are grateful to W Müller for continuous support and encouragement, and to R. Kakoschke and A. Strohbach for helpful discussions.

References

[1] M. Elahy, H. Shichijo, P.K. Chatterjee, A H. Shah, S.K. Banerjee and R.H. Womack, IEDM Tech. Dig. (1984) p. 248.

[2] J.C. Chern, P. Yang, P Pattnik and J.A. Seitchik, IEEE Trans. Electron Devices ED-33 (1986) 822.

[3] L.C. Parillo et al., IEDM Tech. Dig (1980) p. 706.

[4] H.-M. Mühlhoff, F. Lau, P. Küpper and S. Röhl, ESSDERC89 Tech. Dig. 553 (1989)

[5] R.D. Rung, C.J Dell Oca and L.G. Walker, IEEE Trans. Electron Devices ED-28 (1981) 1115.

[6] Y. Taur et al., IEEE Trans. Electron Devices (1985) 203.

[7] R.A. Martin, A.G. Lewis, T.Y. Huang and J.Y. Chen, IEDM Tech. Dig. (1985) p 403.

[8] A G Lewis, R.A. Martin, T.Y Huang, J.Y. Chen and M. Koyanagi, IEEE Trans. Electron Devices ED-34 (1987) 2156.

[9] R.R. Troutman, Latch-up in CMOS Technology (Kluwer Academic Publ., 1986) p 135

[10] C Mazure, W Reczek, D Takacs and W Winnerl, IEEE Trans Electron Devices (1988) 1609.

[11] D Takacs, J. Harter, E P. Jacobs, C Werner, U. Schwabe, J Winnerl and E Lange, IEDM Tech. Dig (1983) p. 159

[12] N Hoshi, S Kayama, T Nishihara, J Aoyama, T Komatsu and T Shimada, IEDM Tech Dig (1986) p 300.

[13] T Nishihara, K. Tokunaga, K. Kobayashi, IEDM Tech Dig 100 (1988).

[14] H-M Mühlhoff, J Dietl, P. Küpper and R Lemme, ESSDERC90 Tech Dig (1990)

[15] G Fuse, H. Ogawa, K Tateiwa, I Nakao, S. Odanaka, M. Fukumoto, H Iwasaki and T Ohzone, IEDM Tech Dig. (1987) p 732.

[16] K Ohe, S Odanaka, K Moriyama, T Hori and G. Fuse, IEEE Trans. Electron Devices ED-36 (1989) 1110.

[17] H-M. Mühlhoff, ULSI Science and Technology, ECS Proc 87-11 (1987) 498.

[18] T Hori, IEDM Tech Dig (1989) p. 772

[19] M. Inuishi, K Mitsiu, S Kusunoki, M Shimizu and K Tsukamoto, IEDM Tech Dig (1989) p 773

[20] T Y Chan, J Chen, P K Ko and C Hu, IEDM Tech Dig (1987) p 718

[21] D.S Wen, C.C-H Hsu, Y Taur, D S Zichermann, T H Ning and M.R Wordemann, IEDM Tech. Dig (1989) p. 765

[22] J E Moon, T. Garfinkel, J. Chung, M Wong, P K Ko and C. Hu, IEEE Electron Device Lett. 11 (1990) 221.

[23] M C. Ozturk, J J Wortman, C.M Osburn, A Ajmera, E. Frey, G A Rozgonyi, W. Chu and C. Lee, IEEE Trans. Electron Devices ED-35 (1988) 659

[24] A Tanaka, T Yamaji, A Uchiyama, T. Hayashi, T. Iwabuchi and S. Nishikawa, IEDM Tech. Dig (1989) p. 785

[25] S. Ando, H. Horie, M. Imai, K. Oikawa, H. Kato, H. Ishiwari and S Hijiya, VLSI Symp Tech. Dig (1990) p 65

[26] B. Davari, E. Ganin, D. Harame and G.A. Sai-Halasz, VLSI Symp. Tech Dig (1990) p 27.

[27] R.B Fair and G.A. Ruggles, Solid State Technol. (1990) 107

[28] S.N. Hong, G.A. Ruggles, J J. Paulos, J.J. Wortman and M.C. Ozturk, Appl Phys. Lett. 53 (1988) 174.

[29] R. Lin, F. Bajocchi, L. Heimbrook, J. Kovatchick D. Malm, D. Williams and W. Lynch, ULSI Science and Technology, ECS Proc 87-11 (1987) 446

[30] A. Mitwalsky, V Probst, R. Burmeister, H R Huff, K.G. Barraclough and J Chikawa, Semicond. Silicon, EC 90-7 (1990) 876

[31] Y.H. Ku, S K Lee and D L Kwong, ULSI Science and Technology, ECS Proc 89 (1989) 144

[32] V. Probst, P Lippens, L. Van den Hove, K. Maex, H. Schaber and R De Keersmaecker, Proc. ESSDERC (1987) p. 437

[33] L. Rubin, D. Hoffman, D. Ma and N Herbots, IEEE Trans. Electron Devices ED-37 (1990) 183.

[34] H Cerva and K.H Kusters, J Appl. Phys. 66 (1989) 4723

[35] M Horiuchi, M Tamura and S. Aoki, J. Appl. Phys. (1989) 2238

[36] M. Tamura and M Horiuchi, J Cryst. Growth 99 (1990) 245.

[37] G.L Patton, J C Brauman and J.D Plummer, IEEE Trans. Electron Devices ED-33 (1986) 1754.

[38] B Davari, Y Taur, D. Moy, F M. d'Heurle and C.Y Ting, ULSI Science and Technology, ECS Proc 87-11 (1987) 368.

[39] K H. Küsters, W. Sesselmann, H. Melzner and B Friesel, J. Phys (Paris) 49 Colloque CY (1988) 503.

[40] P. Chatterjee, IEDM Tech. Dig. (1986) p 128

[41] R. Kakoschke, R E. Kaim, P.F H M Van der Meulen and J.F M Westendorf, IEEE Trans. Electron Devices ED-37 (1990) 1052.

[42] G Fuse, H Ogawa, Y. Naito, K Tamura, K fateiwa and H. Iwasaki, VLSI Symp., San Diego (1988) p. 75.

[43] G. Fuse, H. Umimoto, S. Odanaka, and M. Fukumoto, Application of ion beams in materials science, Proc 12th Int Symp. Hosei Univ Tokyo (1987) p. 191

[44] K Kato, IEEE Trans Electron Devices ED-35 (1988) 1827

[45] S Saler, R. Kassing and R. Kakoschke, Nucl. Instr. and Meth. B44 (1990) 453.

[46] G Hobler and S Selberherr, IEEE Trans Computer-Aided Design 8 (1989) 450.

[47] T Shibata, A Okita, Y. Kato, T. Ohmi and T. Nitta, VLSI Symp., Honolulu (1990) 63.

Nuclear Instruments and Methods in Physics Research B55 (1991) 17–19
North-Holland

Implantation in the 1990s *

Thomas E. Seidel
SEMATECH, 2706 Montopolis Drive, Austin, TX 78741, USA

Requirements for implantation in the 1990s are being driven by both core and specialized processes. A review of these requirements includes difficult topography for deep-submicron MOS transistor structures (shadowing effects) and trench side-wall doping. The usual requirements on gate oxide integrity, contamination and high throughputs are to be maintained or improved. Equipment reliability and operational characteristics (source life) are being driven to more advanced performance levels.

1. Introduction

Implantation in the 1990s will continue with widespread use in manufacturing, development and research that includes doping, damage and synthesis applications [1]. The manufacturing and technology application issues within the silicon arena are discussed in this paper. "Core CMOS" technology is used as a point of discussion for application as it is the technology of choice throughout the 1990s. General operational and technical needs are reviewed. The *cost of ownership* of the implant equipment and the integrated process sequence surrounding the implant steps are keys to competitiveness. Cost of ownership considerations will drive the support of both development pathways and equipment buying decisions.

2. Major trends of silicon technology

In addition to the continued growth of core CMOS as a dominant commercial vehicle in the early 1990s, there is a continued trend to larger wafer sizes. In 1989, 900M square inches of silicon were processed worldwide mainly with 100 mm and 125 mm wafer sizes. In 1992, 1500M square inches are expected to be processed with the dominant wafer size at 150 mm, but about 25% of the total area in 200 mm diameter wafers. Continued growth (~ 17% per year) to about 3B square inches per year is expected by the year 2000. In the mid-90s there will be a wide distribution of design rules ranging from 1.2 to 0.25 μm with "wafer scale integration" carried out at about 0.5 μm. The character of the factories will change so that smaller lots can be produced rapidly with equipment that has serial consolidation features, i.e., integrated sectors of equipment. These sectors will be under development for several years before reliability reaches a level of acceptance.

3. Application shifts in CMOS

Phosphorus n-tub implants have increased to 90% of total CMOS since 1986. N-well designs are emerging as more popular since the performance of the superior n-channel transistor in lightly doped substrates improves. There is also an increase in twin-tub usage.

Retrograde tubs are just coming into manufacture for some n-wells. Field isolation surface implants are mostly with boron. Trench sidewall implants require incident angles that scan onto the sidewall surfaces.

Threshold adjust implants will continue to be used for all CMOS that has n-doped poly because of the "metal-semiconductor" offset potential. Nowadays implantation-doped poly is used with increasing frequency in order to make both MOS transistors become surface-conducting. In this case, and with the body doping increasing to avoid punch-through at deep submicron dimensions, the use of Vt-adj implants will become even more important for both types of transistors.

Lightly doped drains are important for n-MOS since the avalanche rate for electrons is much higher than for holes. Thus, about half the devices in production today use phosphorus Ldd implants. In deep submicron designs, 0.35 μm, the need for limiting avalanche effects in p-MOS becomes important and this activity is in experimental stages (< 5% of use).

Standard source and drain implants for n-MOS are carried out exclusively with arsenic. The need for shallow junctions has driven the use of BF_2 implants for p-MOS junctions. A slow shift away from this practice is seen as practitioners realize the difficulty in controlling the dissociation of BF_2 into B in the implanter's

* Invited paper

0168-583X/91/$03.50 © 1991 – Elsevier Science Publishers B.V. (North-Holland)

column, giving rise to punched-through devices. Use of boron is accompanied by channel tail variations unless additional processing is done The capability to limit BF_2 dissociation remains important.

Advanced source and drain technology includes the use of "elevated drains", where one may implant As, P and B into poly or silicides [2] and then form the shallow junctions by outdiffusion. Alternately, the implantation of Si or Ge to preamorphize [3] the junction region, followed by dopant implant and limited diffusion is another method for producing controlled, non-channeling profiles

4. Approaches to shallow-junction control

Whether one is implanting source and drains into crystalline silicon, preamorphized silicon or elevated drain structures, there are technical concerns and no single approach has emerged as the "technology of preference" for deep submicron technology

Gate shadowing, channelling, "end of range" damage, the formation of quality preamorphized layers, and control of the quality of films (compound precipitation) and interfaces in the elevated drain structures are issues that are still being studied.

There has been an explosion in the variety of approaches that address device architecture for deep submicron application [4,5]. Issues such as effective channel length control (X_j and channelling), controlled breakdown and reliability (drain profile engineering), conductance for the on-state of the MOS transistor and threshold voltage shifts with scaling are driving these multiple developments Process consolidation, i.e., fewer steps, is also key to competitiveness Until a standard approach emerges, the supplier community will be unable to freeze process designs. A "shake-out" in technology approaches will coincide with the ~ 0.35 μm technology timetable around 1991–92. It is clear, however, that with the advent of large-angle tilt (medium-current) and high-energy commercial implanters most needs are met Less mainstream and more difficult applications appear to be the combination capability of high angle plus high current and implanters with very-low-temperature target configurations.

5. Technical and operational issues

Ion sources have a "designed-in" short mean time to repair for 20 years. Practice is, on average, still to change source charges or filaments in less than 100 hours. Safety issues have generally been addressed.

Uniformity has been addressed by new scanning designs. Uniformity, as influenced by wafer charging, is still a concern in some cases but has been heavily studied.

The complex problem of wafer (gate oxide) charging continues to be explored. Charge monitoring devices at the target and approaches which use secondary electrons during overscan are opportunities for solving this problem. The overscan source of secondaries provides electrons in time and space in proportion to their need to neutralize positive-charge buildup.

Particulates control using generic vacuum practices have greatly advanced. The importance of soft roughening and dry neutral gas ambients is recognized. Resist, handling and beam-generated particulates are known as contamination sources.

Resist stripping, using equipment which is "dedicated" to the high-throughput implanter, is an opportunity for equipment integration and serial consolidation About half of the implants done in a manufacturing process are followed by a resist-strip process These general technical and operational issues have an impact on the competitiveness

6. Business community and future competition

The supplier community for implant equipment is international. Major suppliers are TEL, Varian, Eaton, Nissin, AMAT and Genus Although the US and Japan have ownership, European contributions played a role in the emergence of the advanced high-current tool now marketed by AMAT (9200) and the high-angle–medium-current tool now marketed by Varian (E220) Genus is the smallest revenue producer among the companies listed, but they are considered a sole source for high-energy commercial implanters.

Implant technology may compete against new equipment ideas such as CV-doped diffusion (rediscovered), gas-immersion laser doping (GILD) and ECR-like or plasma implantation. These technologies may be capable of providing very low cost for high-dose application, but probably not before ~ 1993

7. Total cost of ownership

In summary, manufacturing equipment and processes are being judged by the overall "cost of ownership." The elements are throughput, total cost, tool utilization on product, and yield. The earliest implant machines had selling prices ~ $50k, while 20 years later the more advanced high-current, high-throughput implanters are sold above $2M, a factor of 25 000 increase in price. Throughput has increased greatly, and cost has increased even faster. Tool utilization capability, i.e., the total percentage time *used on product* (1 – total downtime, both scheduled and unscheduled) and yield objec-

tives are ≥ 90% in the industry today. Improvements are needed. A careful analysis of the cost of ownership will enhance our competitiveness.

Acknowledgements

I thank Frank Robertson and Elaine Custodio-Williams of SEMATECH for their very helpful input and discussions.

References

[1] R B Simonton, Emerging Ion Implantation Processes for the 1990s, No 8500208 (Eaton Corporation, Austin, Texas, 1990)
[2] Y. Ku et al., IEEE Electron Device Lett 9 (1988) 243
[3] M Ozturk et al., IEEE Trans. Electron Devices 35 (1988) 659.
[4] M. Chen et al., IEEE Electron Device Lett. 35 (1988) 2210
[5] T Hori et al., 1988 Symp on VLSI Technology, Digest of Technical Papers, p 15

Nuclear Instruments and Methods in Physics Research B55 (1991) 20–24
North-Holland

Section II. Real time processing problems

A detailed study of elemental contamination in a Varian 180XP high-current implanter *

M.C. Taylor
Intel Corporation, 5200 Elam Young Parkway, Hillsboro, OR 97123, USA

S. Mehta and R.J. Eddy
Varian Ion Implant Systems, Blackburn Industrial Park, Gloucester, MA 01930, USA

Contamination is a major focus for device manufacturers, especially as the industry moves towards 16–64 Mbit memory level integration. This places considerable constraints on the existing ion implantation technology and the choice of materials used in the manufacture and maintenance of ion implanters. Contamination in the ion implantation process can come from a variety of mechanisms: ion-beam sputtering of hardware, cross-contamination from previous implants, in cases of nondedicated systems, end stations (discs, platens etc.), and mass interference effects during species analysis. In this paper, results of contamination analysis of wafers implanted at a customer site on a 180XP Varian implanter will be represented. A wide range of elements, including Al, Fe, Ni, alkali and alkaline earth metals, and previously implanted species were studied. Characterization was done by several techniques including secondary-ion mass spectrometry (SIMS), inductively coupled plasma mass spectroscopy (ICPMS), total-reflection X-ray fluorescence (TXRF) and neutron-activation analysis (NAA). In addition, the effects of beam current on the amounts of sputtered contaminants will be discussed. Preventative measures and maintenance procedures, which can also be potential sources of contamination, will be highlighted.

1. Introduction

The aspect of elemental contamination in semiconductor processing has been a subject of critical attention [1–4]. The stringent requirements for process characterization and control demanded by the advanced VLSI/ULSI devices have both the semiconductor equipment and device manufacturers concerned about the levels of contaminants that would be tolerated by the modern devices. In this paper we will limit our discussions to contamination in ion implantation. Ion implanters whose semiconductor wafers are surrounded by metallic hardware (especially Al or stainless steel) are a potential cause of concern from contamination standpoint. The system hardware and beam optics, if not properly designed, may also result in the interaction of beam with the beam line. Sputtered surface atoms can then be transported to the wafer. This paper presents an investigation of impurities introduced into silicon wafers implanted on a Varian XP high-current production ion implanter. Characterization of the implanted wafers was done by using a wide range of bulk and surface analytical techniques including secondary-ion mass spectrometry (SIMS), inductively coupled plasma mass spectrometry (ICPMS), neutron-activation analysis (NAA) and total-reflection X-ray fluorescence (TXRF). The congruency of results obtained by each technique will be examined and their individual strengths and weaknesses will also be discussed.

2. Experimental description

All wafers for this study were implanted on the Varian 180XP high-current ion implanter. Contamination analysis was conducted for both arsenic and phosphorous species implanted at 30 keV into 150 mm p-type (100) wafers to a dose of 9×10^{15} cm^{-2}. For ICPMS analysis, the implants were performed on wafers through a 900 Å screen oxide to completely stop the implant. Low-energy implants were selected in order to amplify any possibility of the ion beam interaction with the system hardware. High-energy (80 keV) implants at increased beam currents were used to examine the effects of increased beam current and energy on contamination.

3. Results and discussion

A wide range of elements were analyzed by the several techniques employed for this study. This discussion will focus on key elements of interest: the transition and heavy metals, and aluminum.

0168-583X/91/$03.50 © 1991 – Elsevier Science Publishers B.V. (North-Holland)

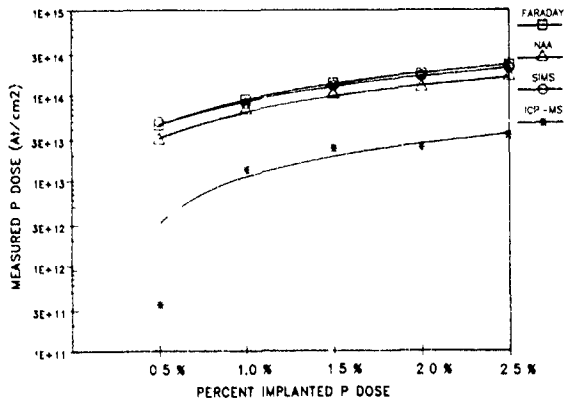

Fig 1. Calibration plot comparing phosphorous levels measured by three bulk techniques used in this study

To examine the relative congruency and accuracy of the characterization tools for reliability purposes, several wafers implanted with 30 keV arsenic to a dose of 9×10^{15} cm^{-2} were reimplanted with phosphorous at doses equal to 0.5%, 1.0%, 1.5%, 2.0% and 2.5% of the arsenic dose. Elemental compositions of these wafers were determined by NAA, SIMS and ICPMS. The various doses of P as determined by these techniques were plotted against the implanted doses, as shown in fig. 1. It is found that the NAA and SIMS results agree very closely with the implanted doses. However, the phosphorous levels as measured by ICPMS are much lower than the actual implanted values. This is due to volatile-compound formation when the implanted oxide reacts with HF/HNO_3 (etchant) which vaporizes during the sample preparation. It also appears that the sensitivity of ICPMS drops at lower dose levels. This was also found to be true for arsenic values.

3.1. Transition elements

Transition metals are known to generate energy levels in the silicon band gap which result in reduced carrier lifetimes in minority carrier devices [5,6]. A plot of the measured levels of several key elements of interest as determined by NAA, SIMS and ICPMS for several implants is depicted in fig. 2. It can be noticed that the contamination levels for the arsenic implants in general are slightly higher among all the wafers analyzed. It is also worth noting that the levels detected for transition metal impurities, especially Fe and Cr, are, for all samples, very low in relation to the implanted dose. This is indicated by results of SIMS analysis in fig. 3. The higher levels of transition (and alkali) metals observed by NAA and ICPMS were traced as cross-contaminants due to sample handling and etching solutions, respectively.

The SIMS results were further substantiated by results of TXRF analysis from wafers implanted with arsenic and phosphorous. Analysis was done at three locations across the wafer for spatial information of the impurities. No transition or heavy metals were detected at any of the three locations on the wafer. These results are summarized in table 1. In some cases, a minor peak of Fe was detected, but the level was too low to be quantified.

3.2. Heavy metals

The presence of heavy metals has detrimental effects on the performance of devices [7].

TXRF analysis of the wafers did not reveal the presence of any heavy metals with the exception of arsenic. However, NAA revealed the presence of small amounts of molybdenum (Mo) in all the wafers analyzed. This element cannot be detected by the TXRF technique. Historically, molybdenum has been found to exist in the ion implantation process but few accounts of its detection in ion-implanted wafers have been published [8]. In this study, this element was detected in very small amounts. Interestingly, its level in the phosphorous-implanted wafers was somewhat higher than in those implanted with arsenic. The origin of this cross-contaminant was traced to the ion source which contained some Mo parts. During the routine implantation

Table 1
TXRF analysis of transition and alkali metals on several wafers (dose and energy for all arsenic implants are 9×10^{15} cm^{-2} and 30 keV, respectively)

Sample ID	Implant description	$\times 10^{12}$ atoms/cm^2						
		Na	K	Ca	Cr	Fe	Ni	Cu
03	Arsenic, 3 mA	nd [a]	nd	nd	nd	pk [b]	nd	nd
06	Arsenic + 0.5% P$^+$	nd	nd	4.0	nd	pk	nd	nd
17	Arsenic + 2.5% P$^+$	nd	nd	5.0	nd	nd	nd	nd
24	Phosphorous, 3 mA	nd	nd	2.0	nd	0.3	nd	nd
27	Phosphorous, 5 mA	nd	nd	3.0	nd	0.5	nd	nd

[a] nd implies not detected.
[b] pk implies that a small peak was seen but was too low to quantify

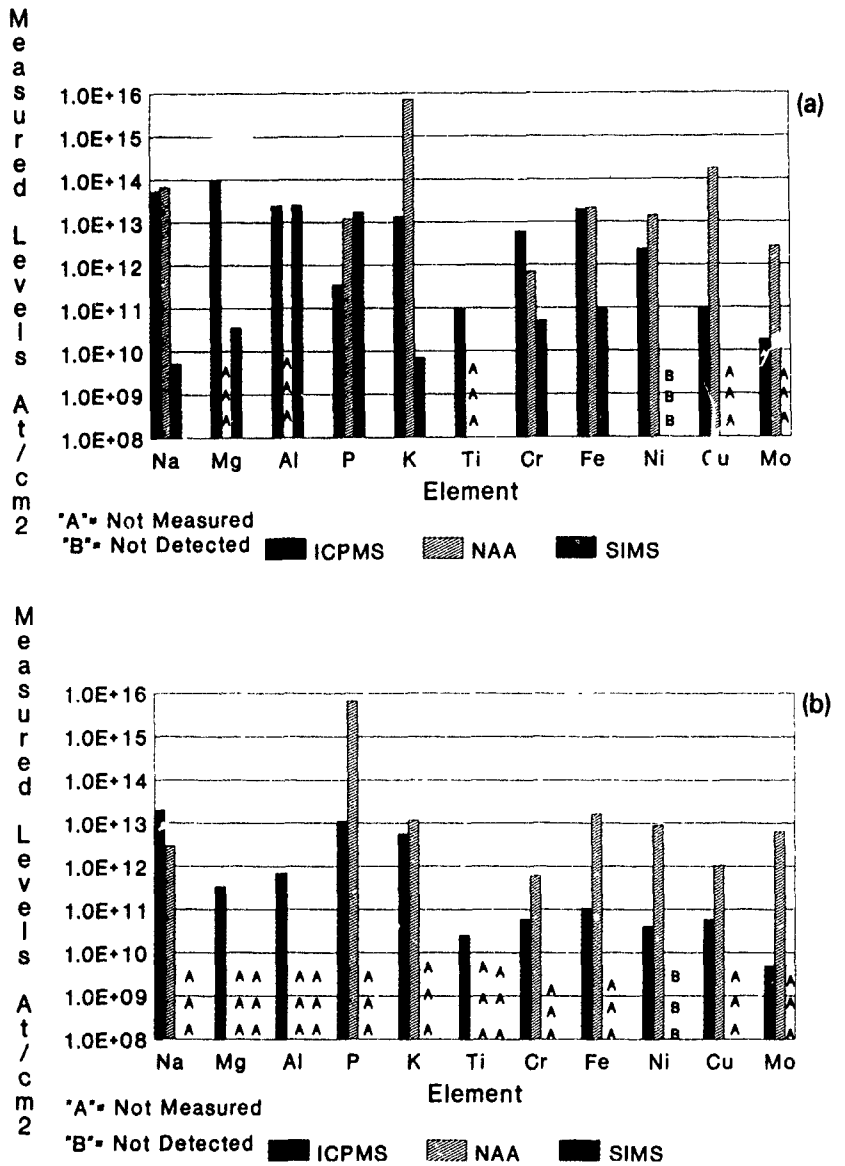

Fig 2 Levels of various contaminants as measured by ICPMS, NAA and SIMS in silicon wafers implanted under different conditions. (a) arsenic, 9.0×10^{15} cm^{-2}, 30 keV, 6 mA; (b) phosphorus, 9.0×10^{15} cm^{-2}, 30 keV, 6 mA

of BF_2, Mo from the source can show up as Mo^{2+} (49) and reach the wafer. The slightly higher Mo levels seen on the phosphorous-implanted wafers can be explained by the significantly higher volume of BF_2 implants run on this end station (ES-1). The Mo-containing parts of the ion source have been replaced with alternative materials

3.3. Aluminum

Aluminum is the major hardware component surrounding the wafer. Of all the elements analyzed it was found to be the most predominant. Since NAA and TXRF cannot detect this element, the analysis was done by SIMS. Concentration depth profiles of the implanted species (As) and aluminum were generated at three locations on the wafer along a diameter. The dose [atoms/cm^2] at each location was computed by integrating the depth profiles.

No differences between the three analyzed locations were observed. The SIMS profiles measured in the center of the three samples and an unimplanted wafer are shown in fig. 3. It is observed that the level of aluminum drops very rapidly from the surface into the bulk of the sample, indicating this may be a near-surface contaminant. The total integrated average dose of Al

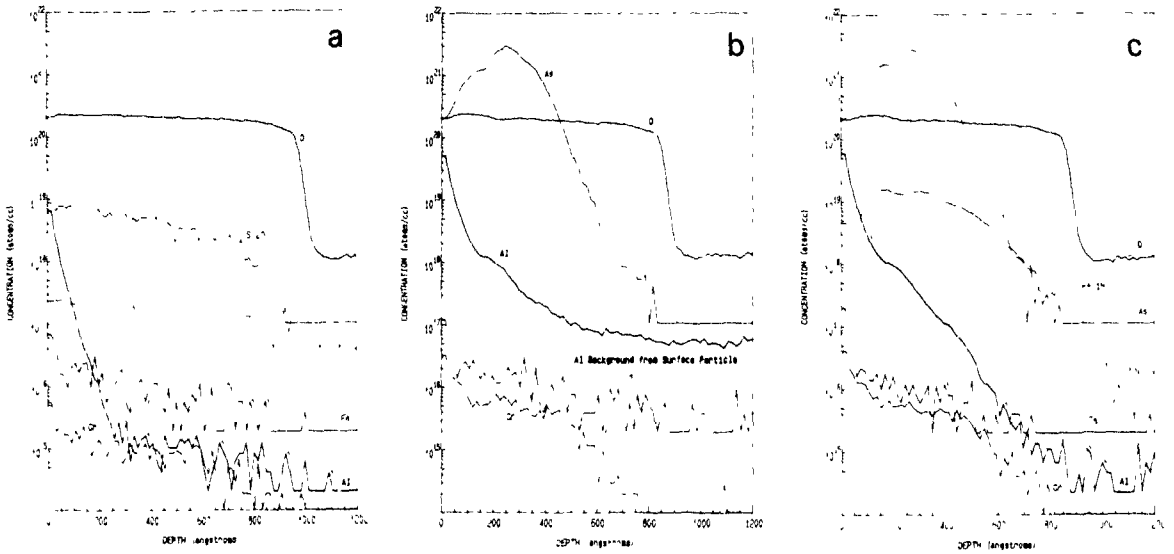

Fig 3 SIMS analysis of (a) an unimplanted 1000 Å oxide film on silicon, (b) a 900 Å oxide film implanted with As^+ (9×10^{15} cm^{-2}), 30 keV, $I_b = 6$ mA, and (c) a 900 Å oxide film implanted with As^+ (9×10^{15} cm^{-2}), 30 keV and P^+ (1.8×10^{14} cm^{-2}), 30 keV.

for the three locations is 2.3×10^{13} cm^{-2} which corresponds to 0.25% of the implanted arsenic dose. ICPMS results also substantiate this finding. In a separate study, it was observed that the aluminum depth below the surface was larger in arsenic wafers than in phosphorous-implanted wafers. This may indicate that aluminum is sputter-deposited onto the wafer during the implantation process and subsequently recoil-implanted into the substrate the incoming ions. The arsenic, by virtue of its larger energy transfer, drives the aluminum deeper into the wafer than phosphorous. In another set of experiments, it was found that increasing the beam current or the energy of the implant did not result in any significant increase in the amount of aluminum.

3.4 Alkali metals

These elements generally indicate poor wafer handling and maintenance procedures. These elements were analyzed by all the above techniques. TXRF results are summarized in table 1. NAA and ICPMS analysis for these elements are not reliable for reasons explained earlier. Furthermore, the analysis of the reagent blanks used for etching the implanted oxide for ICPMS analysis displayed large and variable amounts of alkali metals. SIMS was therefore selected as the technique for these elements. Table 2 compares the level of these elements for a bare (unimplanted) wafer and two implanted samples. The SIMS results show that the amounts of alkali metals in the implanted wafers are not significantly higher than the unimplanted wafer. In a well-controlled and clean environment one can expect to see even lower levels of these elements. In addition, the higher levels of alkali metals detected in the arsenic wafers can be attributed to the larger volume of photoresist wafers that are routinely implanted on the arsenic-dedicated end station (no. 2).

Table 2
Alkali contaminant levels as determined by SIMS (dose and energy for all arsenic implants are 9×10^{15} cm^{-2} and 30 keV, respectively)

Sample ID	Implant description	Atoms/cm^2			
		Na	Mg	K	Ca
T0337-20	No implant	3.6×10^{9}	6.0×10^{8}	8.0×10^{9}	3.7×10^{10}
04	Arsenic, 6 mA	5.2×10^{9}	3.5×10^{10}	6.9×10^{9}	1.2×10^{10}
08	Arsenic + 2% P^+	1.1×10^{10}	4.5×10^{10}	8.7×10^{9}	1.7×10^{10}

4. Conclusions

A detailed analysis of the elements found in a production high-current implanter has been conducted by several advanced techniques. The contaminant levels were found to be low. A further reduction in the levels of transition metals, aluminum and heavy metals can be achieved through the selection of higher-grade materials and improved design configurations of the ion implantation equipment.

Although agreement between the techniques was found to be reasonably good for some elements, their congruency over a complete range of elements is limited by their individual sensitivities towards each element. The contaminants from sample preparation and handling are an additional factor. Therefore, no single analysis method is sufficient for a thorough analysis of a wide range of elements and a combination of several complementary techniques needs to be used.

Although a wide variety of techniques are available for characterization, the levels of certain key elements demanded by the device manufacturers are at or below the detection levels of these instruments. The development of advanced, rapid and reliable techniques is essential to the continued improvement in the design of future semiconductor equipment In addition, the levels of various key elements must be determined empirically by the device manufacturers A partnership of the device process engineers and equipment manufacturers is essential if the needs of the future devices are to be addressed successfully.

Acknowledgements

The authors wish to thank Evans East Inc. for the SIMS and TXRF work. Thanks are also due to Michael Frost of Intel Inc for additional help on SIMS analysis. Thanks are due to Oregon State University and the Radiation Facility of the University of Missouri for NAA work and to Robert Brown of Elemental Research Inc. for ICPMS analysis of the samples. The authors are grateful to Marcus Monell of Varian Implant Systems for helping to keep track of the many wafers analyzed and Jerry Zietz of Intel Inc. for running the implants for this study Many thanks to Pam Mansfield for artwork and preparation of the final manuscript.

References

[1] A. Shimazaki, H Hiratauka, Y. Matsushita and S. Yoshii, Chemical Analysis of Ultrace Impurities in SiO_2 Films, Extended Abstracts of the 16th Int. Conf on Solid State Devices and Materials, Kobe, 1984, p 361
[2] T Shiraiwa, N Fujino, S. Sumita and Y Tanizoe, Semiconductor Fabrication· Technology and Metrology, Ed. D.C. Gupta, ASTM STP 990 (1989)
[3] P.L F Hemment, Vacuum 29 (1979) 439.
[4] R.J Eddy, S. Mehta, R F Outcault and S K Suh, Yield Issues in Ion Implantation, Proc of Technical Sessions, SEMICON Korea (December 1989)
[5] Properties of Silicon, emis Data Reviews Series 4 (INSPEC Publication, 1988)
[6] N.C Einspruch and G B. Larrabee (eds.), VLSI Electronics, Vol 6, (Academic Press, 1983).
[7] S P. Tobin, A C Greenwald, R G Wolfson and P J Drevinsky, Mater Res Soc Symp. Proc 36 (1986) 43.
[8] M I Current and L A Larson, MRS proc 147, Eds. N Cheung, A D Marwick and J Roberto (1989) p. 365

Nuclear Instruments and Methods in Physics Research B55 (1991) 25–29
North-Holland

Energy contamination in ion implantation

J. van Herk
Philips IC ADMC, P O Box 80000, 5600 JA Eindhoven, The Netherlands

A.N. van der Steege and M.L.C. van Meyl
Philips Components, Gerstweg 2, 6534 AE Nijmegen, The Netherlands

P.C. Zalm
Philips Research Laboratories, P O Box 80000, 5600 JA Eindhoven, The Netherlands

Extending the effective energy range of an implanter is possible by implanting multiple-charged species A problem when using these species is energy contamination The energy contamination using P^{3+}, B^{2+} and B^{+} has been investigated on commercially available high-current implanters The major cause of energy contamination is charge exchange reactions due to (the residual) gas inside an implanter. Careful control and design of the vacuum system are therefore important. Energy contamination can also be caused by sputtering/reflection from slits and lining of the implanter Ionisation of residual gas is probably the origin of fluorine contamination when using BF_3 as source feed material The fluorine contamination again stresses the need to control the amount and composition of the residual gas in an implanter

1. Introduction

The energy range of an implanter can be extended using multiple-charged species. In doing so, one must be careful about energy contamination An investigation was started to study the energy contamination using P^{3+} and B^{2+} on an APPLIED PI9000 and a NOVA 20-200 high-current implanter. These machines were selected in order to have sufficient beam intensity for the aforementioned multiple-charged species. Energy contamination was also investigated using singly charged boron on high-current implanters. Energy contamination occurs when the selected dopant is implanted with a different energy than the desired one. The result can be a seriously disturbed concentration profile of the dopant [1] Energy contamination can be caused by (1) charge exchange, (2) molecular breakup, (3) sputtering and reflections from slits and lining of the beam line and (4) ionisation of residual gas in the implanter.

Neutralisation of the ion beam results in energy contamination when charge exchange occurs before the final acceleration/deceleration stage. Since pressure is a dominant factor regarding charge exchange, it is important to control the pressure inside an implanter. Molecular breakup can be another cause of energy contamination. Well documented in the literature is the breakup of the phosphor dimer (P_2^+) prior to entering the mass analyser [1–4]. Sputtering and reflections can cause energy contamination, but to what extent exactly is presently unknown Energy contamination from ionisation of residual gas in the implanter can be controlled by pumping and a careful design of the implanter.

2. Experimental

2.1 Implantations

Boron and phosphorus ions were implanted in 6 inch 1–50 Ω cm p- and n-type (100) silicon wafers with energies ranging from 180 to 500 keV The tilt angle was 7°, the twist angle 30° for all implants Except for a native oxide, the wafers were otherwise bare. SIMS was chosen as the analysis technique to investigate energy contamination because R_{sheet} measurements cannot distinguish between energy contamination and beam neutralisation after final acceleration/deceleration Spreading resistance profiling and C–V measurements were insufficiently accurate to determine the various levels of energy contamination Concentration profiles determined with SIMS were of as-implanted dopant.

Solid phosphorus was used as source feed material, to reduce the pressure between extraction and mass analyser and thus reduce energy contamination of P^+ from breakup of the trimer P_3^+ [2] When implanting boron, BF_3 was used as source feed material. In order to simulate production circumstances, wafers were im-

0168-583X/91/$03 50 © 1991 – Elsevier Science Publishers B V (North-Holland)

planted with and without additional photoresist-coated wafers loaded on the wafer-implant wheel of the high-current implanters. Silicon wafers for R_{sheet} measurement were wafers covered with 30 nm oxide. After implantation the wafers received an RTA anneal at 1000°C for 10 s to activate the implant electrically. After annealing oxide was removed and R_{sheet} measured.

2.2. Secondary-ion mass spectrometry

All SIMS measurements were carried out on a CAMECA ims 4f instrument. Samples of 1×1 cm^2 were cut from the wafer mid-section. For the boron implantations routinely well-focused O_2^+ primary ion beams of 3 to 10 keV were used, with beam currents in the range of 0.2–0.5 μA and rastered over 350×350 μm^2. The highest energies were used to obtain an overall profile of the implants. The lower energies served two purposes: (1) to obtain an improved depth-resolution result of the first 0.5 μm and (2) to reduce the uncertainty for the concentration distribution in the near-surface region caused by the evolution towards steady-state erosion conditions and the extent of possible surface contamination mixed in the topmost layers under the action of the primary beam. Only $^{10}B^+$ or $^{11}B^+$ and $^{28}Si^{2+}$ secondary ions stemming from the central 60 μm diameter region of the sputtered crater were analysed with a low-mass resolution ($M/\Delta M = 300$). The $^{28}Si^{2+}$ signal intensity was used to check the stability of experimental conditions. For phosphorus, a 0.15 μA, 14.5 keV Cs^+ primary ion beam was used with the same raster size/analysed area dimensions. The $^{31}P^-$ secondary-ion signal intensity was exclusively monitored in the high-mass resolving mode ($M/\Delta M = 4000$) in order to avoid interference with the $^{30}SiH^-$ cluster ion. In this mode the instrument's stability is unfortunately less perfect due, among other things, to analyzer magnet drift. Reproducibility was confirmed by repeating measurements on every sample at least twice, in addition to careful primary-current monitoring, and will be discussed in more detail below.

The depth scale was obtained by determining the total crater depth with a micromechanical stylus transducer. Absolute accuracies in this way are no better than 5%, but relative errors for one measurement series (i.e. a single-day run) of 2% are achievable when focussing, current stability of the primary beam and, if applicable, matrix secondary-ion signal stability are good. Occasionally slight differences ($\leq 2\%$) were observed in the peak positions of supposedly identical dopant distributions prepared on different implanters. These may be either due to the aforementioned depth calibration error or to implanter particulars (e.g. standard 7° off the normal angle of incidence of the high-energy implanter used). It was decided to apply a small correction to the depth scale to merge all maxima. Since it is known that this affects the higher moments of the distribution only in second order, it will not influence the intercomparison in any way.

As for the concentration scales, different approaches were adopted for B and P. In the case of boron, all implants were calibrated, somewhat arbitrarily, against the high-energy implanter. That is, it was assumed that the dose claimed for that particular machine was exactly correct. Next, a sensitivity factor was derived by dividing the "known" fluence of an implant by the time-integrated boron signal intensity obtained for that sample. This sensitivity factor was then used to calibrate all others. Repetition of the measurement from the high-energy implanter sample several times during one run ensured reproducibility. For phosphorus this approach proved unfeasible, owing to the inferior mass-spectrometer stability. Here the dose claimed was simply assumed to be true and fed into the conversion.

In this way it was found that boron distributions of a single sample could be measured with a run-to-run reproducibility in the range of 5–10% (even with up to one year delay in between[1]), i.e. variations in the local depth concentration are generally less than these numbers. For phosphorus this was only 15–20%. In the remainder of this paper differences in the dopant distribution of various samples well outside these limits will be considered to be of sufficient significance to merit discussion.

3. Results and discussion

3.1 Energy contamination using P^{3+}

An investigation on energy contamination was started to assess the possible use of P^{3+} on an Applied PI9000 and a Nova 20-200 high-current implanter for energetic, hence deep, dotation. Beam currents in the range of 100 μA were obtained. During repeated start-up of a P^{3+} ion beam it was noticed that a stable P^{3+} ion beam could be more easily started after a few hours of source operation. Automated tuning will further enhance the reproducibility of P^{3+} implants. Sometimes it was possible to obtain quite large beam currents of P^{4+}, in the order of 40–80 μA, but it was not clear to what extent the energy contamination of the charge-exchange reaction of P^+ to P^{2+} between source and analyser [2] contributed to the beam current.

A first indication whether implants with single- and multiple-charged phosphorus ions result in the same concentration profile can be found when one compares the values of the R_{sheet} of these implants. Table 1 gives an overview of the influence of single- and multiple-charged phosphorus implants on the value of R_{sheet}. The P^{2+} implantation has a lower R_{sheet}-value than the

Table 1
Overview of the influence of implant species on the R_{sheet}-values of silicon (1–50 Ω cm) wafers covered with 30 nm oxide, the wafers were implanted with P^+, P^{2+}, P^{3+} and P^{3+} with photoresist-coated wafers added to the implant wheel (P^{3+} + PR), after RTA anneal (10 s, 1000°C) the oxide was removed and the wafers were measured on R_{sheet}

Ion	Dose [ions/cm^2]	Energy [keV]	R_{sheet} (Ω/□)
P^+	5×10^{13}	180	483
P^{2+}	5×10^{13}	180	452
P^{3+}	5×10^{13}	180	459
P^{3+} + PR	5×10^{13}	180	458

P^{3+} implant, which can be explained by molecular breakup The phosphorus trimer P_3^+ exists in smaller amounts in the source plasma than P_2^+, therefore causing less energy contamination The lower R_{sheet}-value of the P^{3+} implant as compared to the P^+ can be caused by energy contamination and beam neutralisation after post-acceleration. In both cases the result is a lower R_{sheet}-value than that obtained for the P^+ implant. Photoresist outgassing can have a large influence on charge-exchange reactions in the ion beam, causing additional beam neutralisation and energy contamination As can be seen from table 1, photoresist outgassing seems to have little influence on the value of R_{sheet}, indicating a minor change in the amount of beam neutralisation/energy contamination.

In order to establish the extent of the energy contamination at high energies, wafers for SIMS were implanted with P^{3+} with a dose of 5×10^{14} ions/cm^2 at 500 keV on the Applied PI9000 and Nova 20-200 with photoresist wafers added to the wheel. The Applied PI9000 was tested using both the standard source and a low-flow source. The low-flow source reduces the pressure between the source and analyser-magnet region The SIMS concentration profiles were compared with a concentration profile of an implant from a high-energy implanter where, due to the design of this implanter, energy contamination was reduced to a minimum [5]. Within the experimental error no distinction could be made between the concentration profiles obtained from the Applied implanter with the low-flow source, the Nova 20-200 and the high-energy implanter. In fig. 1 the concentration profiles obtained from the Applied PI9000 for both the standard and low-flow source are shown

At the surface there seems to be a very shallow phosphorus contamination which is very difficult to quantify since the sputter rate of SIMS is not yet stable in that region. However, the very-low-energy contaminant inevitably shows up exclusively on samples of the high-current implanters and is consequently not a SIMS artefact. The energy contamination of P^{3+} at 500 keV is

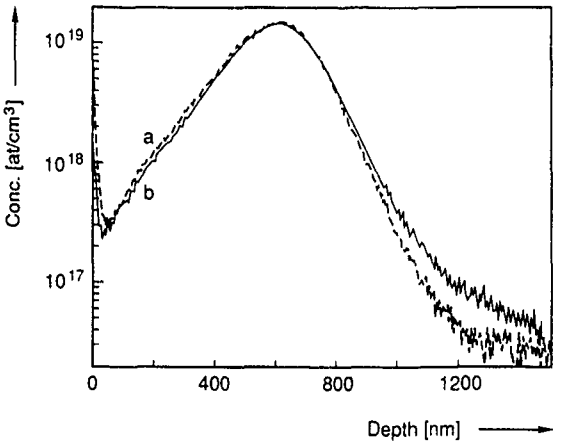

Fig 1 SIMS P concentration profiles of P^{3+} (5×10^{14} ions/cm^2) 500 keV implantations performed on the Applied PI9000 high-current implanter with the standard source (a) and the low-flow source (b)

typically below 2% for the Applied and Nova implanters (excluding the shallow contamination, which is sizable but difficult to quantify reliably) For some IC applications this amount of energy contamination is not detrimental to device operation. At the moment the reproducibility of the P^{3+} implant is monitored using R_{sheet} and transistor measurements.

3.2. Energy contamination using $^{11}B^{2+}$

Energy contamination of a $^{11}B^{2+}$ implant at 400 keV with a dose of 5×10^{14} ions/cm^2 was subsequently investigated on the Nova 20-200 using SIMS. The concentration profiles of the implantations with and without added photoresist-coated wafers are the same within the experimental error Fig 2 shows the ^{11}B (curve labeled a) and ^{10}B concentration profiles of the $^{11}B^{2+}$ implant with no photoresist wafers added to the wheel. For comparison the profile obtained for a 5×10^{14} ions/cm^2 implantation made on a high-energy implanter (a Varian 500XP) is included in fig 2 (curve b). Both profiles are identical at sufficiently large depth (beyond the implantation peak) The $^{11}B^{2+}$ clearly exhibits energy contamination. The estimated contribution is 5×10^{13} ions/cm^2 (difference of the Nova and Varian profiles), i.e. around 10%. This energy contamination shows one unexpected region, corresponding to an implant energy of about 20–30 keV. This is extraordinary since the extraction voltage is at 80 kV and the post-acceleration at 120 kV.

A most surprising contaminant is ^{10}B. Since the ^{10}B concentration profile shows some distinct peaks as compared to the more diffuse ^{11}B profile, the ^{10}B peaks may give some clues as to what the possible causes of the (energy) contamination might be. By comparing the ^{10}B

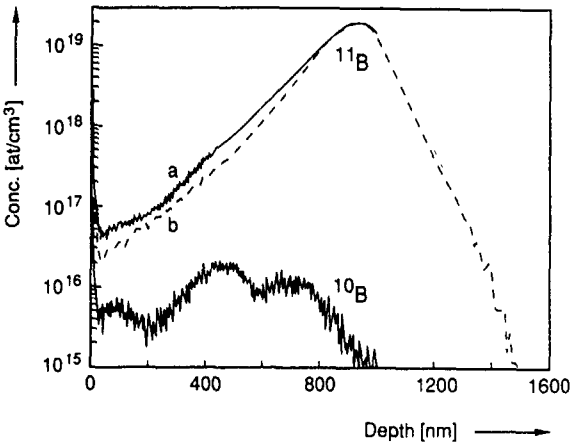

Fig 2 SIMS concentration profiles of a $^{11}B^{2+}$ (5×10^{14} ions/cm^2) 400 keV implantation performed on a Nova 20-200 high-current implanter (a) together with its ^{10}B contamination profile Also shown is a $^{11}B^{+}$ (5×10^{14} ions/cm^2) 400 keV implantation performed on a Varian 500XP implanter (b)

and ^{11}B concentration profiles it is clear that the ^{10}B contamination is not caused by an insufficient mass separation. If the implanter had a poor mass separation, the ^{11}B and ^{10}B peaks should always have a fixed ratio This is clearly not the case. The deepest peak in the ^{10}B concentration profile is near an implant depth corresponding to an implant energy twice the extraction plus once the post-acceleration voltage ($2\times80+120=280$ keV). The second ^{10}B peak is implanted with about twice the extraction energy (160 keV). The energy contamination near an implant depth corresponding to a boron implant of 20–30 keV can be explained by

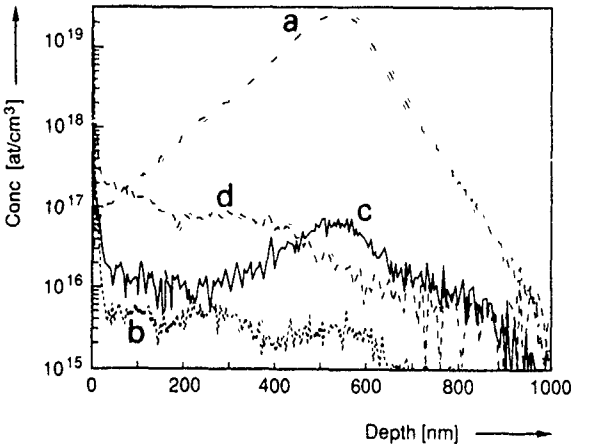

Fig. 3. SIMS concentration profiles of (a) ^{10}B 5×10^{14} ions/cm^2, 200 keV implant, (b) ^{10}B contaminant in a deliberate ^{11}B 5×10^{14} ions/cm^2 200 keV implant, (c) ^{11}B contaminant in a deliberate ^{10}B 5×10^{14} ions/cm^2 200 keV implant (a), and (d) ^{19}F contaminant in a ^{11}B 5×10^{14} ions/cm^2 200 keV implant.

sputtering/reflection and or ionisation of residual gas in the implanter. A detailed cause of the ^{10}B contamination is not yet apparent and necessitates further investigation.

3.3. (Energy) contamination using B^+ on high-current implanters

When implanting $^{11}B^{2+}$, a contamination of ^{10}B occcurred. The cause(s) of the ^{10}B contaminant might be linked with the causes of energy contamination. To study the contaminant origin, the ^{10}B contamination of a deliberate ^{11}B implant and likewise that of the ^{11}B contaminant of a ^{10}B implant was measured. The ^{11}B and ^{10}B implants were done at an energy of 200 keV and a dose of 5×10^{14} ions/cm^2 In fig. 3 the deliberate ^{10}B implant profile is shown together with the contamination profiles of the ^{11}B and ^{10}B implants and the ^{19}F contamination of the ^{11}B implant. The depth of the peak in the ^{19}F concentration profile corresponds to an implant energy of 105–125 keV. The extraction potential during the implant was 80 kV and the post-acceleration voltage was 120 kV. An explanation for the ^{19}F contamination implanted with 105–125 keV is ionisation of neutral feed-gas molecules (or fragments thereof) The fluorine contamination on the two types of high-current implanters investigated was typically $\leq 2\%$.

The ^{10}B contamination profile of the ^{11}B implant shows three distinct peaks near a depth corresponding to an implant energy of 200, 80 and 20–30 keV. Surprisingly "the 80 keV" peak in the ^{11}B contamination of the ^{10}B implant is missing. This discrepancy can only be explained by a possible ^{10}BH contamination during the ^{11}B implant which is absent in the ^{10}B implant Possible causes for the boron contaminant peaks at 200 and 20–30 keV are ionisation of residual gas, molecular breakup, reflections from slits and lining of the beam line. It is unclear how much these various processes contribute to the (total) contamination. The total amount of the ^{10}B contaminant of a deliberate ^{11}B implant, on the two types of implanter investigated, is not very significant, typically $\leq 0.5\%$. The energy contamination of ^{11}B, of a ^{11}B implant, can be between 1% and 6% depending on the vacuum conditions in the implanter (excluding the shallow contaminant). The shallow contaminant is here a SIMS artifact, other than with a similar contribution in the ^{31}P profiles obtained on high-current implanters discussed earlier.

4. Conclusions

Energy contamination was investigated to assess the usefulness of P^{3+} for high-energy implants on two types of high-current implanter. The energy contamination/beam neutralisation can be influenced by controlling

the pressure in various parts of the implanter, especially in the region between source and analyser, and in the beam line and end station. Reducing and controlling the magnitude of the amount of energy contamination and beam neutralisation on high-current implanters opens the way to P^{3+} usage for high-energy implants.

When boron is implanted, a broad spectrum of (energy) contaminants occurs owing to a variety of causes During a boron implant the wafer was also contaminated with ^{19}F due to ionisation of residual gas in the implanter. The partial pressure of residual gas in the implanter has a large influence on these contaminants This again indicates the need for precise control of the vacuum in the implanter. Not only a good vacuum is important, but also the design of the implanter itself influences contamination. Boron implants performed on a medium-current implanter where the beam is made parallel by a dipole lens magnet prior to acceleration show energy contamination with an energy equal to the extraction energy [6] This contamination probably arises due to beam neutralisation between the magnet and the acceleration stage since that region is not actively pumped.

Phosphorus implantations made on high-current machines showed a very shallow contamination at the surface of a few keV. Probable causes may be sputtering and reflections from slits and lining of the beam line. Careful design of the implanter and choice of materials can reduce/control this contaminant.

Acknowledgements

The authors gratefully acknowledge J. Politiek, Applied and Eaton for helpful discussions, as well as H. Bosch, J. van Buul, S Oosterhoff and the process technicians of FAB1 for general assistance and performing part of the implants.

References

[1] P Spinelli, J. Escaron, A Soubie and M Bruel, Nucl Instr and Meth. B6 (1985) 283
[2] J H. Freeman, D.J Chivers and G A Gard, Nucl Instr and Meth 143 (1977) 99
[3] C R. Kalbfus and R Milgate, Nucl Instr and Meth B21 (1977) 400
[4] K. Brack, W Euen and D Hagman, Nucl Instr and Meth B21 (1977) 405
[5] H J. Ligthart and J Politiek, Philips Tech Rev 43 no 7 (1986) 185
[6] R.J Schreutelkamp, F W Saris, J F.M Westendorp, R.E. Kaim, G B Odlum and K T F. Janssen, Mater Sci Eng B2 (1989) 139

Nuclear Instruments and Methods in Physics Research B55 (1991) 30–34
North-Holland

Energetic neutral contamination in modern high-current implanters

S. Cherekdjian and W. Weisenberger
Ion Implant Services, 1050 Kifer Road, Sunnyvale, CA, USA

The presence of energetic neutrals in a high-current, high-energy implant can result in nonuniformities on a silicon wafer. A larger concern is when the energetic neutrals are not of the desired energy. This is a major consideration when designing ion implanters with pre- and post-acceleration stages. This paper investigates the levels of pre-accelerated boron neutrals present in a 180 kV boron implant. The machines investigated were a Nova 20A and an Applied Materials PI9000. A comparison of their vacuum systems and their ability to cope with photoresist batches and argon backfill are presented. Silicon wafers were mapped by four-point probe resistivity measurements and the levels of pre-accelerated neutrals were quantified by spreading resistance profiles (SRPs). It is clearly demonstrated that good uniformity on a bare silicon wafer is not an indicator of a clean ion beam. Even though it is well understood that this problem is vacuum-related, modern high-current implanters are still being built and marketed with improper vacuum isolation and insufficient pumping capability.

1. Introduction

Ion implanters with pre- and post-acceleration stages have become the favored modern implanter style. In this configuration the ions are extracted with pre-acceleration voltages in the region of 20 to 100 kV. The ions are then analyzed and finally post-accelerated to their required energy. These machines have been favored owing to their inherent smaller magnet design, their ion current being insensitive to energy and their easy final ion-energy adjustment.

Unfortunately these machines are susceptible to vacuum-related process problems. Improper vacuum isolation between the exit of the analyzer and the implant chamber or the source region disturbs the energy purity of the ion beam. In the case of doubly charged implants the contaminant is a lower energy peak associated with a loss in charge state; conversely, molecular implants have a higher energy peak related to the dissociation of the molecule prior to post-acceleration. The former event, charge reduction, is still of importance with singular-charged species such as B^+, P^+ and As^+. If beam neutralization occurs after the analyzer, undesirable energetic neutrals will be created. With no neutral trap, a mechanically scanned system ensures that these pre-accelerated neutrals will reach the wafers. In a high-energy implant they will contribute to energy and dosing nonuniformities.

The pressure burst during a high-energy, high-current implant into photoresist batches is often encountered in production and assumed to produce no adverse effects. The ability of these implanters to maintain their energy purity and doping uniformity under these conditions is of concern. This work utilizes various implant conditions and wafer loads to elucidate some of the typical vacuum failings of older implanters that still plague modern high-current implanters.

2. Experimental

The implants were performed on two high-current machines, a Nova 20A and an Applied Materials PI9000. Each machine was operated in standard production mode for maximum throughput. The implant used to investigate the machines was $^{11}B^+$, 1×10^{15} ions/cm^2, 180 kV, 8–9 mA. The PI9000 was configured for 5 in. (batch size of 25) and the Nova was configured for 6 in. (batch size of 15). This ion dose provided the maximum detectable neutral level from the photoresist batches [1]. The high implant energy allowed the maximum separation of the pre- from the post-accelerated neutrals.

The implants consisted of silicon wafer loads with and without photoresist and a variety of different process chamber pressures. Argon leaking or backfill are utilized in the electron flood gun systems of the Nova 20A and the Applied Materials PI9000. All the test wafers were 5 or 6 inch bare silicon n-type ⟨100⟩, 5–10 Ω cm. The sheet photoresist (AZ1350) batches were baked at 100°C for 30 minutes. The test wafers were rapidly thermally annealed at 1100°C for 10 seconds and mapped on a Prometrix 111B four-point prober. Dopant distributions were obtained from spreading resistance profiling (SRP).

0168-583X/91/$03.50 © 1991 – Elsevier Science Publishers B.V. (North-Holland)

3. Discussion

Each machine section discusses the vacuum system from the end station to the analyzer, the measurement resolution and the results obtained.

Table 1 summarizes all the four-point probe, and SRP data. The pre-accelerated boron concentrations were estimated by equating the high-energy boron peaks with the implanted dose of 1×10^{15} ions/cm^2. The level of pre-accelerated neutralization can then be determined by dividing the calculated pre-accelerated boron dose signal with the implanted boron dose of 1×10^{15} ions/cm^2. Theoretical range and straggling data were obtained from PRAL range tables [2].

3.1 The Nova 20A

On the Nova 20A the end-station pumping is provided by a 10 inch cryopump on the side of the process chamber. The beam line is serviced by two turbopumps (fig. 1), one located on the bend of the analyzer and the other placed between the post-acceleration stage and the electron flood gun. This turbopumping isolation before and after the post-acceleration stage protects this region from the detrimental pressure effects from the source, the flood gun and the end station. To increase the pumping isolation between the end station and the beam line, the Nova 20A end station has a high-vacuum interlock. When the end-station pressure has recovered, the ion beam is gated on and the mechanical scan continues.

Table 1
PROMETRIX and SRP data for the Nova 20A and the PI9000

Machine	Run	Conditions	Sheet ρ [Ω/□]	σ [%]	SRP [%]
NOVA 20A	(1)	Si [a]	85 41	0 91	–
	(2)	PR [b]	75 70	4 12	4–5
	(3)	Si, AR [c] (5×10^{-5} Torr)	83 51	0.86	–
	(4)	PR, AR (5×10^{-5} Torr)	74.80	4.32	4–5
PI9000	(1)	Si	85 28	0.81	1.02
	(2)	PR	85 02	1 35	7 80
	(3)	Si, AR (2E-5mbar)	82 40	0 69	4 70
	(4)	PR, AR (2E-5mbar)	84.31	0 71	17 16
	(5)	Si, AR (4E-5mbar)	80.30	0 70	10 40

PI9000, 20 kV neutral component – ratio of (1) to (2)

Percentage (1)		Percentage (2)	
1 02		–	–
1 02	+	6.78	6.65
4 70		–	
4 70	+	12 46	2 65
10 40	+	–	–

[a] Si: Bare silicon wafers
[b] PR. Sheet photoresist wafers + 1 bare silicon wafer
[c] AR Denotes the use of the flood gun (pressure used)

The SRP data for this machine are shown in fig. 1. For 80 keV boron ions, the boron background level at a depth of 270 nm is about 6×10^{18} atoms/cm^3. A minimum detectable signal from pre-accelerated neu-

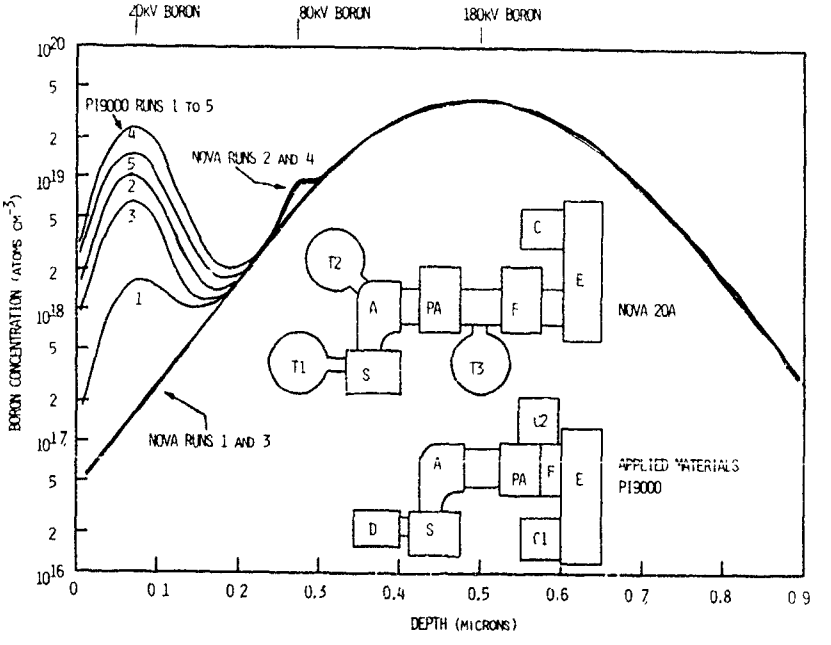

Fig 1. SRP profiles and vacuum schematics (A) analyzer (C) cryopump, (D) diffusion pump, (E) end station, (F) electron flood gun and argon leak, (S) source, and (T) turbopump.

trals at 80 keV needs to be about 1.5×10^{18} atoms/cm^3 (about 3.4×10^{13} ions/cm^2). This is a neutralization of approximately 3.4%, a lower level will be smeared out by the background.

A small signal was detected in both photoresist runs on the Nova 20A. The depth of the signals corresponds to 80 keV boron from the ion source. The level of boron was estimated to be 4–5%. No 80 keV boron signal was detected for the run with only electron flood and 5×10^{-5} Torr argon leak; with photoresist wafers the 80 keV neutrals appear again.

The high pre-acceleration voltage of 80 kV helps to disguise this signal below levels of 3.4% Higher implant doses would further reduce the relative levels and a thermal drive-in anneal would wash it out completely. The pumping isolation of the source and the analyzer could not be determined owing to this high-threshold detection level.

We can deduce that performing molecular or multi-charged implants may be a problem with photoresist batches. A solution would be to place an additional turbopump in line with T3 (see fig. 1). This now resembles a Nova 10-160 end-station vacuum system which has an improved end-station-to-analyzer vacuum isolation [3].

The Nova wafer maps tabulated in table 1 indicate overdosing with the use of the flood gun, the argon leak or with the addition of photoresist wafers. The wafer uniformities ranged from 0.9% to 4.32% (table 1) and no resistivity striation of the wafers was observed in the slow-scan direction. Even though the Nova 20A is the latest generic design, it still suffers, disappointingly, from the interaction of the end-station pressure burst with the wafer doping uniformity. The overdosed central area for these wafers (fig. 2) corresponds to the maximum area of photoresist bursting from the implanted wafers. SRP data from the edge and center of the wafer confirmed that the nonuniformity is mainly from post-accelerated neutrals These resistivity and uniformity issues from photoresist batches can be eliminated by using the Nova pressure compensation (K-factor) software [4]. The K-factor solution is an implant option and

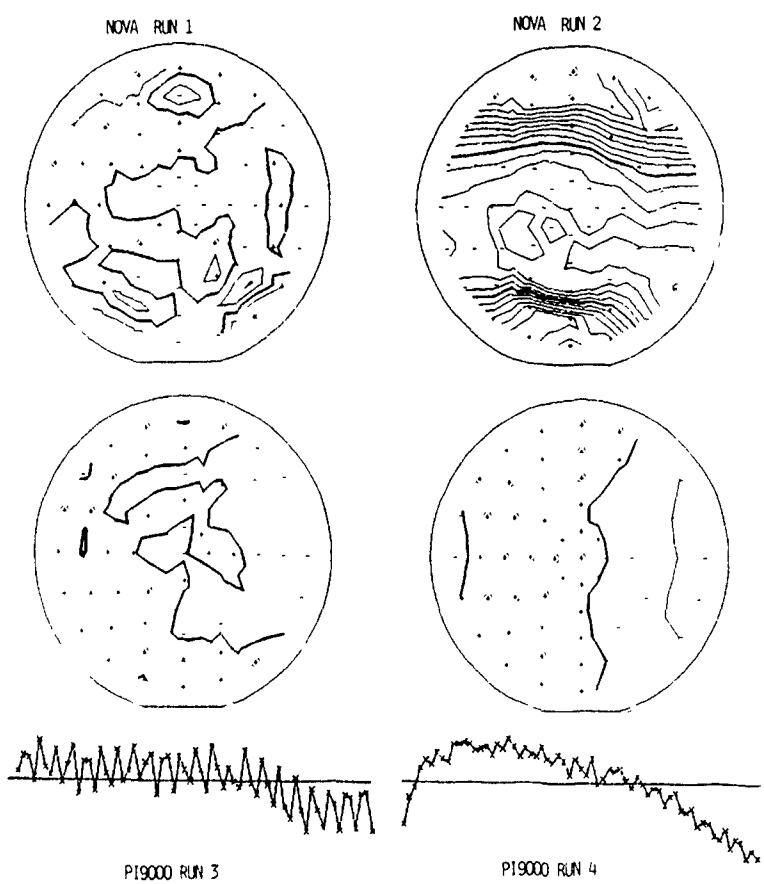

Fig. 2. Resistivity contours and diameter maps

can only be implemented if the exact K-values have been determined for the implant conditions. The energy contamination issue, however, is not corrected.

3.2. The Applied Materials PI9000

The PI9000 beam-line vacuum design has two 10 in. cryopumps, one located at the side of the end station and the other located in a region described as the "differential pumping box", which contains the post-acceleration stage. This pump isolates the end-station pressure effects from the post-acceleration stage. Also, the pump has the floodgun gas leak placed in front of its pumping orifice. There is a vacuum interlock on the end-station pressure, but it is only acknowledged after the implant wheel has completed the scan. This should be improved for batches containing photoresist.

The sensitivity level for pre-accelerated neutrals in this ion implanter is greatly enhanced owing to their shallow 20 keV signal. In this case the background boron signal is now at least an order of magnitude lower around 2×10^{17} atoms/cm^3. Therefore, a detectable signal should be about 1.5×10^{17} cm^3 (corresponding to a 20 keV boron dose of 1.5×10^{12} ions/cm^2). This is a very sensitive neutral resolution level of 0.15%.

Fig. 1 displays the SRP data which is summarized in table 1. The low-energy boron signals in fig 1 at 70 nm agrees well with the PRAL value of 79 nm, confirming their origin is from the source. With no pressure loading (no photoresist or argon leak) a constant 1% level of neutrals is present. This indicates insufficient vacuum isolation between the source and the analyzer. This level could increase as the pumping efficiency of the ion implanter deteriorates with time. The isolation could be improved by running the source leaner and installing conductance-limiting apertures. Better still, the installation of a turbopump between these two regions would be a good solution.

The effect of increasing the process chamber pressure from the base pressure of 2×10^{-6} mbar with no photoresist wafers present to 2×10^{-5} mbar (the recommended argon leak for the use of the electron flood system) and 4×10^{-5} mbar (argon leak) increases the 20 keV neutral level by 3.68% and 9.38%, respectively. The addition of 24 photoresist wafers increases the 20 keV neutrals by 6.78% with no argon leak and 12.46% with an argon leak of 2×10^{-5} mbar, respectively.

The presence of photoresist wafers results in the largest detection of energetic neutrals. If this machine is configured for 6 or 8 rather than 5 inches, the increase in the photoresist bursting would be a theoretical maximum of 44% and 74%, respectively. The single cryopump (C2 in fig. 1) over the post-acceleration stage appears inadequate.

These levels of neutralization can be understood by shutting the ion beam down and vacuum-testing the

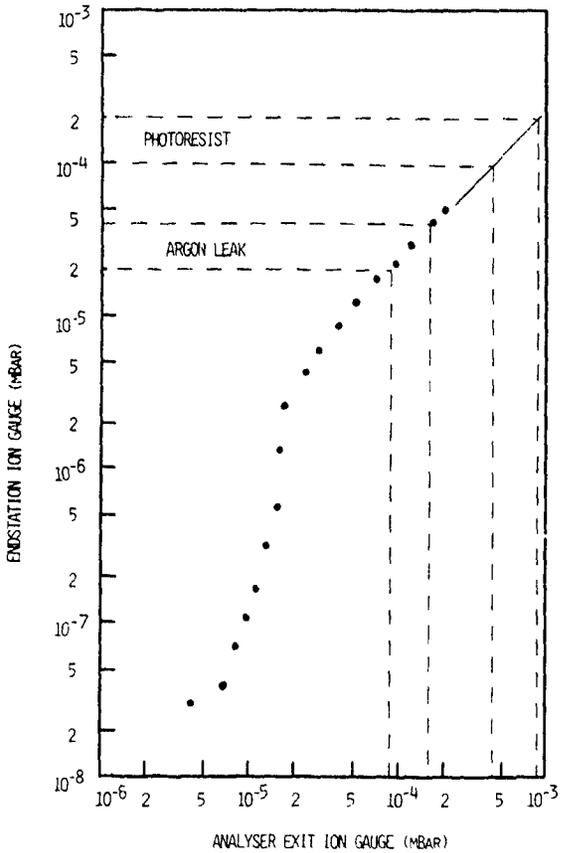

Fig 3 PI9000 end-station ion gauge versus analyzer ion gauge

isolation between the end station and the exit of the analyzer. An ion gauge was placed at the exit of the analyzer and its reading is plotted as a function of the end-station argon leak in fig. 3. It can be seen that the end-station argon leak of $(2-4) \times 10^{-5}$ mbar increases the analyzer pressure from 9×10^{-5} to 1.6×10^{-4} mbar, respectively. Photoresist effects typically range from 1×10^{-4} to 2×10^{-4} mbar; at the end station this would then raise the analyzer from 4.4×10^{-4} to 9×10^{-4} mbar. Although, for photoresist, a more accurate representation would warrant the gas leaked to be hydrogen, it nevertheless reflects the poor pumping capability of the system. The data here was also extrapolated from the last data point at 5×10^{-5} mbar. This assumes the pumping gradient does not change. It should be noted that specifying the electron flood raises the end station to 2×10^{-5} mbar and consequently increases the pressure at the exit of the analyzer to 9×10^{-5} mbar. Even with no photoresist this will cause process problems when molecular and multicharged species are run.

A possible redesign of the vacuum system should move the wafers away from the post-acceleration stage. Two in-line cryopumps could be added and the post-

acceleration stage should be placed between these two additional pumps and the original cryopump (C2 in fig. 1). The original now pumps the analyzer while the other two isolate the end station. The flood gun and its gas leak may be located in the cryopump closest to the end station. Two additional cryopumps are a direct consequence of the large pumping load the end station presents as its very large volume is argon-backfilled during electron-flood-gun runs, usually containing photoresist wafers. In this configuration the post-acceleration suppression electrode should be moved close to the wafers to eliminate beam blowup effects [5].

To interpret the uniformity of the wafer maps listed in table 1, the effect of two main contributions of beam neutralization must be considered: (1) the increase in pressure at the exit of the analyzer as the argon flood gun leak is increased and (2) the pressure burst from the photoresist wafers. The former results in a relatively constant flux of 20 kV boron neutrals while the latter is a time-varying component modulating with the photoresist bursting. Assuming these effects can be linearly superimposed, their individual contributions are shown in table 1. The worst uniformity is observed in run 2, where the ratio of (2) to (1) is the greatest. This nonuniformity disappears in run 4 where the higher argon pressure has increased the level of constant 20 keV neutrals from (1).

The most interesting effect is the left-to-right (slow-scan direction) dosing striation observed in runs 3 and 4 (see fig. 2). The common factor in both runs is the 2×10^{-5} mbar argon leak. The additional neutralization from the photoresist wafers from run 4 help to reduce the degree of striation. Conversely no striping of the wafer has been observed in run 5 where the argon pressure is now 4×10^{-5} mbar. No difference in ion beam dimensions were observed from the PI9000 beam profiler prior to these runs. We can only speculate that a neutral hot spot present in run 3 has increased in run 5 beyond the critical x-axis (slow scan) dimension required for wafer striping.

4. Conclusion

It has been demonstrated that the indication of a good wafer-contour map is no measure of the macroscopic uniformity or the purity of an ion-implant process.

Ideally, high-current ion implanters should be impervious to end-station pressure effects. The achievement of this goal would lead to a more reliable and reproducible implant. Unfortunately this paper has shown that modern high-current machines, currently available to the process engineer, have limitations in this area.

Acknowledgements

Thanks are due to J. Schuur and V. Dinh of Integrated Device Technology, D.W. Lindsay of Ion Implant Services, M. Anjum of Micron Technology and C.B. Yarling of Varian.

References

[1] S. Cherekdjian and I.H. Wilson, Radiat. Eff. 98 (1986) 179.
[2] J. Biersack and J. Ziegler, Nucl. Instr. and Meth. 194 (1982) 93.
[3] S. Cherekdjian, IIS internal report.
[4] Nova Engineering Bulletin, ECO no. 4877M.
[5] M.E. Mack, G. Ryding, D.H. Douglas-Hamilton, K. Steeples, M. Farley, V. Gillis, N. White, A. Wittkower and R. Lambracht, Nucl. Instr. and Meth. B6 (1985) 405.

Nuclear Instruments and Methods in Physics Research B55 (1991) 35–38
North-Holland

Real time, in situ particle monitoring of the Applied Materials PI9200 ion implanter

Samuel Leung [a], Babak Adibi [a], Steve Moffatt [b], Boris Fishkin [b] and Pat Kinney [b]

[a] *Applied Materials, Implant Division, Foundry Lane, Horsham, West Sussex RH13 5PY, England*
[b] *Applied Materials, Implant Division, 3050 Bowers Ave, Santa Clara, CA 95954, USA*

Real time monitoring of particles in the process chamber and the roughing line of high current implanters has recently been of invaluable assistance to equipment manufacturers and fabrication line process engineers. Earlier in situ particle monitors were limited in their performance by the size (> 0.5 μm), velocity (< 750 cm/s) and concentration of the particles (< 100 particles/s) to be detected. The results from a recently developed particle monitor capable of measuring particle sizes down to > 0.22 μm, installed in a PI9200 ion implanter are discussed here. It is demonstrated that an equipment engineer can study, test, and improve autoclean cycles with the effect of any hardware change. The development of SPC charts and possible processing interlocks are discussed.

1. Introduction

Particulate contamination is one of the prime contributors to yield loss in advanced IC fabrication [1]. There are semiconductor products on the market today that are sensitive to particles as small as 0.1 μm. This is beyond the leading edge of the detection capability of today's monitoring equipment. However, the requirement for the number of particles added on the wafer surface to be < 0.03 particles/cm^2 (measured at 0.3 μm) will soon be here, and equipment clean enough to manufacture and monitor these devices is yet to be developed.

In the interest of minimizing particulate contamination sources, the Applied Materials PI9000 series uses a loadlock to transfer wafers under vacuum into the implant chamber of the system and a low abrasion wafer handling design. Having a uniform, repeatable wafer-handling regime means that numerous variables can be eliminated, making it much simpler to track down sources of contamination. Fig. 1 illustrates the relative particle performance differences between processes. It also represents an analysis of factors contributing to wafer handling.

Particulate contributions from very fine particles that are transported with the ion beam account for 60 to 90% of the defect density [2]. Given this fact, a much more desirable approach to particle control in vacuum systems would have an in situ, vacuum compatible particle monitor placed underneath the beam line for direct, real-time particle detection. This would allow optimization of particle reduction with fewer ambiguities of the actual particle sources.

The purpose of this paper is to report the development of an in situ particle monitor installed in the target chamber of the Applied Materials PI9200 high current ion implanter. Initial tests were carried out to determine important information regarding particle generation mechanisms and particle conditions during the implanter's autoclean cycle.

2. In situ particle monitor (ISPM) development

Most observations of particles in processing equipment, particularly in vacuum systems, have been made by running silicon wafers through the equipment and measuring the number of particles added to each wafer. This type of measurement consumes both process equipment time and personnel time. It is also the final judgement of the particles added to wafers. Yet this technique provides only after-the-fact information and

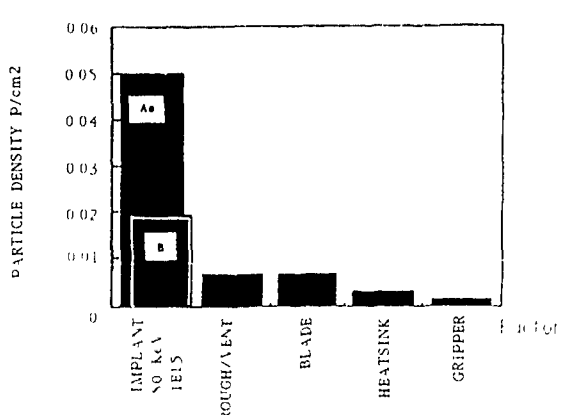

Fig. 1 Pareto analysis of factors contributing to wafer particulate addition from process equipment.

0168-583X/91/$03.50 © 1991 – Elsevier Science Publishers B.V. (North-Holland)

specific particle sources in the equipment are usually difficult to isolate using this method.

Pioneering PFM (particle flux monitor) tools have been thoroughly characterized [3]. It was found that particle monitors were limited in their performance by the size, velocity and concentration of the particles to be detected, and therefore had low count rates The development program described below was initiated to address these limitations, resulting in the creation of a more advanced tool. The anticipated benefits of this new capability are: detection of particulate-generating events at the earlier stages of particle development, quantification of process step contributions to wafer surface contamination, and feedback in developing statistical process control (SPC).

3. Experimental setup

The largest contributor to particle contamination during the whole implant cycle is the exposure to the ion beam. The exact magnitude of the contribution varies in a complicated way with species, energy, dose, current, ion optics, beam size and position. The particle monitor sensor has been installed in the Applied Materials PI920C ion implanter. Fig. 2 shows the location of the sensor in the target chamber. It is mounted directly underneath the last electrode of the beam line. Since the wafers undergo the greatest stress, and are thus most likely to shed particles, when they pass the beam. The effective area of particle detection is in alignment with the wheel so that the sensor will see most of the particles after the wafers pass the beam A schematic diagram of the optical system for the sensor

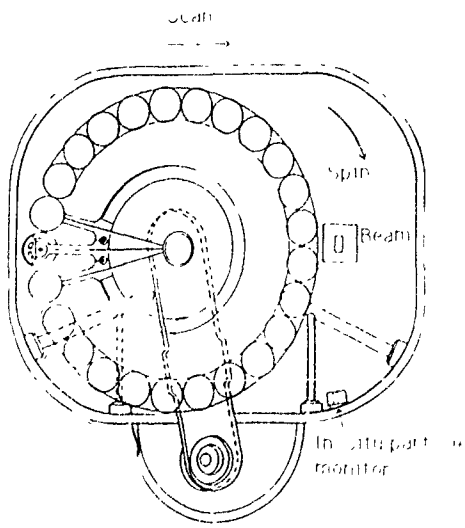

Fig 2 Location of in situ particle monitor in the PI9200 target chamber

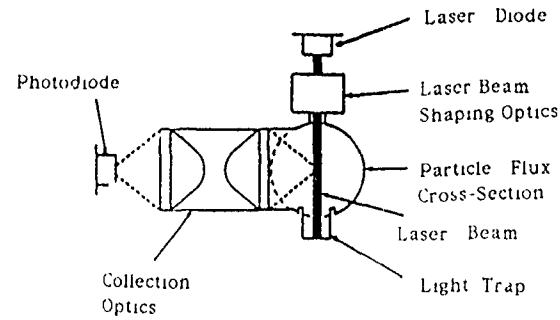

Fig 3 A schematic diagram of the optical system for the sensor

is shown in fig. 3 The sensor consists of a laser diode, beam stop, a set of optical lenses for collecting scattered light and a photodetector. As particles fall through the laser light, they scatter light toward the photodetector The particle-induced scattered light is collected perpendicular to the laser axis to reject the continuous background emission from the laser diode

Particle monitor evaluations were performed both on the bench and in the implanter. Benchtop evaluations with monosized latex spheres were conducted using a 0.1 μm 28.3 l/min (1 cfm) aerosol particle counter as a reference for sizing/counting efficiency. This testing determined that our smallest detectable particle size is 0.22 μm with an estimated detection area for this size of 5 mm^2 Calculated detection area for 0.3 μm particles was 15 mm^2, for 0.509 μm was 40 mm^2, and for 1.09 μm was 75 mm^2

4. Results

Results of particle measurements made on the in situ particle monitor with various beam currents are shown in fig. 4a and b Initial monitoring showed that the particle count was roughly dependent on the current of the beam. Each peak corresponds to the number of particles spinning off the wafers after passing through the beam.

An interesting effect seen in fig. 4a is the reducing of the particle levels with time, which may be due to the depletion of some particle reservoirs. In practice there will be a large number of particle reservoirs (e.g., electrodes, front plate, beamstop, etc.). Any one of these which is disturbed or under stress can produce a total contribution onto the wafer of 10 to 200 particles. Once the disturbance is stabilized, the individual contributors may decrease or stay constant with time.

Although we do not have enough statistical results to show the direct correlation between the particle counts obtained from the particle monitor and the wafer surface, it has been observed in fig. 4a that the ratio of

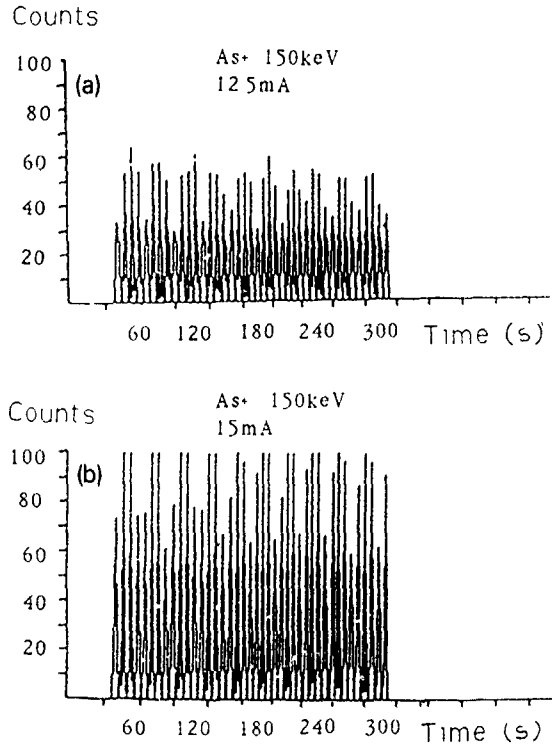

Fig 4 The particle measurements made on the in situ particle monitor with beam current at (a) 12 5 mA and (b) 15 mA

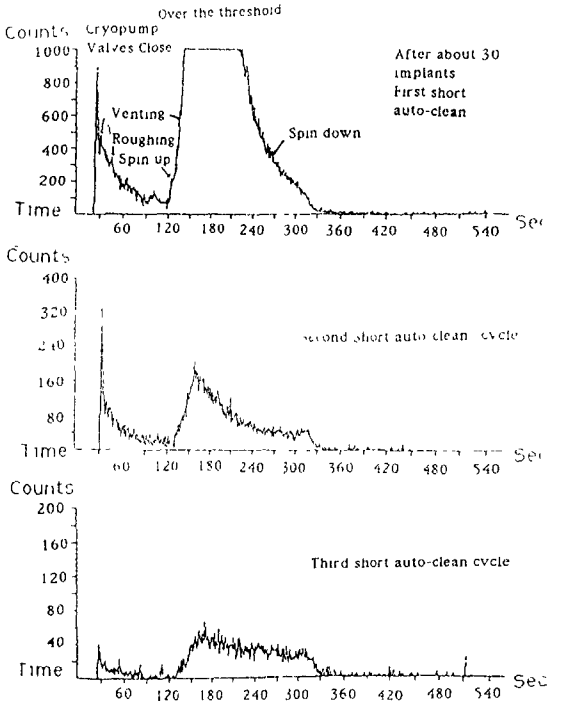

Fig 5 Particle counts in the target chamber during three successive short autoclean cycles

the monitor counts to the wafer counts is much higher than we expect The average particle count for this implant is below 40 ppw at 0 3 μm on a 150 mm wafer. This data strongly suggested that the majority of the particles from the beam line do not stay on the surface of the wafers.

The sensor has also been used to optimize autocleaning cycles The autoclean procedure is an effective way to clear particles from the target chamber It consists of a series of alternating roughs and vents, usually with the wheel spinning This procedure is designed to stir up free particles and pump them out the roughing lines Fig 5 shows the particle counts as a function of time for three successive autocleans All the events during the autoclean cycle are annotated in the figure. Each short autoclean cycle requires 10 minutes. The benefit can be seen with the aid of fig 5 It shows the rapid drop in counts by the third cycle The benefit of an in situ particle monitor is that time can be saved when the target chamber is relatively clean and the number of short autoclean cycles can be reduced This is consistent with earlier results on different implanters [4,5]

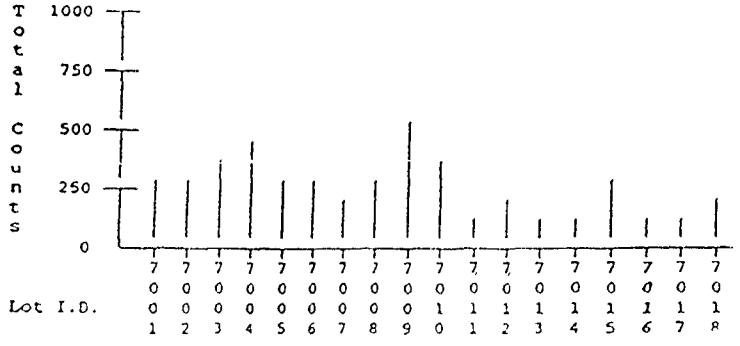

Fig 6 An example of SPC chart used in particle analysis

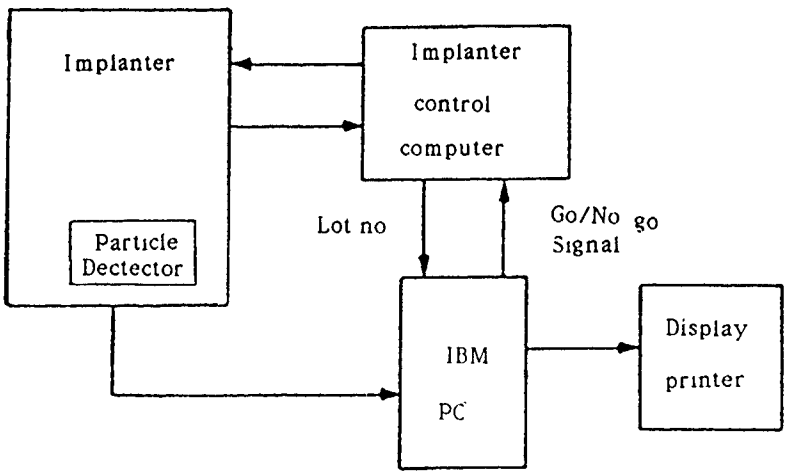

Fig. 7. Flow diagram of closed loop particle control

5. Closed loop particle control

The Applied Materials in situ particle monitor and stand alone PC will provide diagnostic routines which prevent the start of an implant if the monitoring system indicates that a preset particle level is being exceeded The closed loop particle control will then interrupt the process The combination of real time process control and product protection is designed to sustain high product yield levels while maximizing system throughput and availability.

Each time the PI9200 ion implanter processes a batch of wafers, the particle counts collected throughout the whole process will be integrated and stored on the PC hard disk so that it can be displayed on a statistical process control (SPC) chart. Thresholds will be established for the entire run When these thresholds are exceeded, either a warning message will be sent to the equipment operator, or the equipment will be commanded to pause the subsequent runs An example of an SPC chart is shown in fig. 6 Each chart will show the total particles per run for a specific recipe or lot number. Individual recipe names will have control limits and full SPC analysis will be available from the PC

This new version will be able to enter a more automatic mode where the implanter will tell the particle monitor when a process is started or stopped. This will allow the particle monitor to request run information from the implanter, and start and stop particle counting without direct operator intervention This information will be sent to the particle monitor from the implanter in the form of events transmitted over a SECS link (see fig. 7).

6. Conclusion

The new in situ particle monitor, with the minimum detectable particle size of 0 22 μm, shows sensitivity to particle conditions during the ion implanter's autoclean cycle and real time particle detection during arsenic implants with various beam currents The application of SPC will provide an efficient means of recording particle data It will also provide the operator with real time process control information so that immediate action can be taken to stop processing when particle counts exceed a set level.

Acknowledgements

The authors would like to thank Dave McMahon and John Spencer-May for their assistance in setting up hardware for the applications described here

References

[1] J Horvath and S Moffatt, these Proceedings (8th Int Conf. on Ion Implantation Technology, Guildford, UK, 1990) Nucl Instr and Meth B55 (1991) 154
[2] T Hattori and S Koyata, Proc Microcontamination Conf and Exposition, Santa Clara, CA (1988) p 1
[3] J Gregg and P Border 2nd Symp on Particles in Gases and Liquids, 20th Annual Meeting of the Fine Particle Soc., 1989, vol 2, ed K L Mittal (Plenum, New York, 1990)
[4] W Weisenberger, S Chereckdjian, P Borden and W Knodle, Proc 7th Int Conf on Ion Implantation Technology, Kyoto, Japan, 1988, Nucl Instr and Meth B37/38 (1989) 644
[5] W Weisenberger, Semicond Int 6 (1988) 188

Nuclear Instruments and Methods in Physics Research B55 (1991) 39–44
North-Holland

Channeling control for large tilt angle implantation in Si ⟨100⟩

Robert B. Simonton, Dennis E. Kamenitsa and Andrew M. Ray
Eaton Corp Semiconductor Equipment Division, 2433 Rutland Drive, Austin, TX 78758, USA

Changhae Park, Kevin M. Klein and Al F. Tasch
Microelectronics Research Center, University of Texas at Austin, Austin, TX 78712, USA

This investigation will present measurements of silicon ⟨100⟩ wafers, implanted with tilt angles in the range 7–60°, which identify combinations of tilt and azimuthal (twist) angles that avoid major channeling zones The orientations identified in this study minimize channeling effects even for very low dose implantation A stereographic projection demonstrates that all major variations in observed channeling behavior are explained by channeling in the six major (low Miller index) crystallographic axes and planes The implanted wafers were characterized using modulated reflectance and SIMS measurements We investigated the relative severity of ion channeling in major poles and planes and the effect of energy and species variations on channeling behavior The physical basis for the observed variations is explained by employing the concepts of critical channeling angles and average distance traveled within a channel

1. Introduction

Ion implantation processes employing large tilt angles (7–60°) have stimulated great interest in the recent past due to the advanced device fabrication capability this implantation technique offers, particularly when used in conjunction with in situ wafer rotational repositioning [1].

Previous investigations of optimum silicon wafer orientation for channeling (dopant profile) control have typically described the range of tilt angles from 0 to about 10° [2], although the range 0–20° has been characterized by Ziegler and Lever with backscattering techniques [3]. In order to obtained dopant profile control when using larger tilt angles, optimum wafer orientations must be identified which will avoid major channeling zones.

2. Experimental methods

150 mm, prime silicon ⟨100⟩ wafers without a screen oxide were implanted using a systematic matrix of tilt and azimuthal (twist) angle combinations Tilt is defined as the angle between the incident ion beam vector and a vector perpendicular to the wafer's surface at the wafer's center Twist is defined as the rotational angle between a projection of the beam vector onto the wafer's surface and the {110} planes perpendicular to the wafer's major flat.

All implants were performed on an Eaton NV-6200AV, a modern, electrostatically scanned medium current ion implanter which allows any combination of tilt angles 0–60° with twist angles 0–360° [4]. Direct measurements on this implanter system revealed that both the accuracy and precision of the tilt and twist orientation were $< \pm 0.25°$ and $< \pm 2.0°$, respectively The tilt accuracy includes the ⟨100⟩ alignment error of the silicon substrates The advanced digital scan system of this implanter effectively eliminates the cross-wafer nonuniformity resulting from geometric effects at any tilt angle 0 to 60°, allowing a typical implant uniformity of $< 0.5\%$, one sigma [5] throughout the available tilt range.

The majority of the wafers were implanted with a boron, 100 keV, 5×10^{11} cm^{-2} implant Smaller groups of wafers were implanted using boron at energies of 10–400 keV and phosphorus at 50–600 keV

After implantation, all wafers were characterized by modulated reflectance measurements in a Therma-Wave Inc TP-300 [6], using two modes, high spatial density conformal mapping and diameter scans. The cross-wafer uniformity (%, one sigma) and the average value from modulated reflectance measurements on each wafer were plotted as a function of the tilt and twist angle setting for that wafer The measurements are in therma-wave units (TW), an arbitrary unit of modulated reflectance, which is proportional to the damage produced by the implanted ions [7] Therefore, increased channeling would cause a reduction in TW signal, because channeled ions produce less damage in the substrate.

0168-583X/91/$03.50 © 1991 – Elsevier Science Publishers B.V. (North-Holland)

The therma-wave modulated reflectance measurement is quite sensitive to the distortions of the as-implanted profile which result from ion channeling during implantation; this is demonstrated in fig. 1. This figure contains an overlay of seven implant profiles, measured using secondary ion mass spectroscopy (SIMS) [8], from different locations on a radius of the same silicon ⟨100⟩ wafer, the wafer had also been mapped in TW units. This wafer had been implanted (with no screen oxide) using 180 keV, 5×10^{11} cm^{-2} boron in a variable scan angle implanter at a tilt angle of 0° (ion beam aligned with the ⟨100⟩ pole at the wafer center). This resulted in a range of known ion beam orientation angles to the ⟨100⟩ pole at different locations on the wafer's radius SIMS profiles from the seven locations were correlated with the known ion beam orientation angle to the ⟨100⟩ and the measured TW value for each location, resulting in fig 1 As indicated there, a variation of a few percent in TW units means a fairly dramatic shift in the as-implanted profile has occurred.

3. Results

The plots of average TW value and cross-wafer TW uniformity (%, one sigma) for the boron, 100 keV, 5×10^{11} cm^{-2} implant condition are presented in fig. 2 Fig 2a presents this data for a constant twist angle (23°) at various tilts from 0 to 60°. Figs 2b–f provide this data as a function of twist angle for various (fixed) tilt angles

The ion beam is aligned with major channeling features at those orientations in fig 2 which exhibit significantly decreased average TW value and degraded TW uniformity Conversely, orientations which display the best TW uniformities and local maxima in average TW values are orientations where the ion beam is not aligned

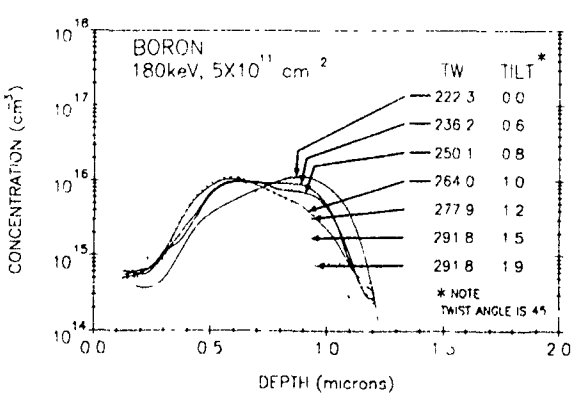

Fig. 1 Therma-wave (TW) modulated reflectance signal sensitivity to as-implanted profile changes from ⟨100⟩ axial channeling variations, determined by SIMS measurements for a boron, 180 keV, 5×10^{11} cm^{-2} implant without a screen oxide

with major channeling features, profile control should be optimum there. Table 1 summarizes the optimum combinations of tilt and twist angles, obtained from the data in fig. 2, for the boron, 100 keV, 5×10^{11} cm^{-2} implant condition.

4. Discussion

All major variations of average TW value and TW uniformity observed in fig 2 can be explained by considering channeling in six major (low Miller index) poles and planes. This is demonstrated by considering fig. 3, a stereographic projection [9] for the silicon lattice as viewed along a ⟨100⟩ pole. This projection represents the entire twist range 0–360° because of the mirror symmetry about the {110} planes and the 90° rotational symmetry about the ⟨100⟩ poles. Note that the 0° twist references in figs. 2 and 3 are the {110} planes because these planes correspond to the major wafer flat, which is the twist orientation reference in most implanter equipment.

The major, low Miller index poles and planes are represented in fig 3 by the largest filled circles and heaviest lines, respectively Higher Miller index poles are represented by smaller filled circles; for simplicity, many of these poles are not indicated here The regions of angle space in the stereographic projection which were investigated by the implants whose TW measurements are plotted in fig 2 are identified by light dashed lines. The electrostatic scan system of the NV-6200AV ion implanter used in this study produces small variations in ion beam orientation as the beam is scanned across the wafer The tilt and twist angle space "sampled" by the scanned ion beam depends on the tilt angle (and wafer size) employed for the implant, the space sampled at higher tilt angles is greatly reduced from that at lower tilt angles The angle space sampled by the area of one 150 mm wafer is visualized by the small ellipses in fig. 3.

By considering each part of fig. 2 in the light of fig 3, all major variations are explained. Wherever the dotted lines (representing the tilt/twist implant matrix) in fig 3 encounter a major plane or pole, a relatively major decrease in TW value and increase in TW nonuniformity appears in the corresponding plot in fig 2 which contains the tilt/twist angles of the encounter

For example, in fig. 2a, the large TW and uniformity variations which occur at 0° tilt, at about 37° tilt, and about 47° tilt are caused by ion beam alignment with the ⟨100⟩ pole, {111} planes, and {110} planes, respectively. (The relatively minor TW variations at about 25° tilt are caused by higher Miller index poles, previously reported by Ziegler and Lever [3], which are not indicated in fig. 3 but which were obvious in the TW conformal maps of these wafers. The effect of these

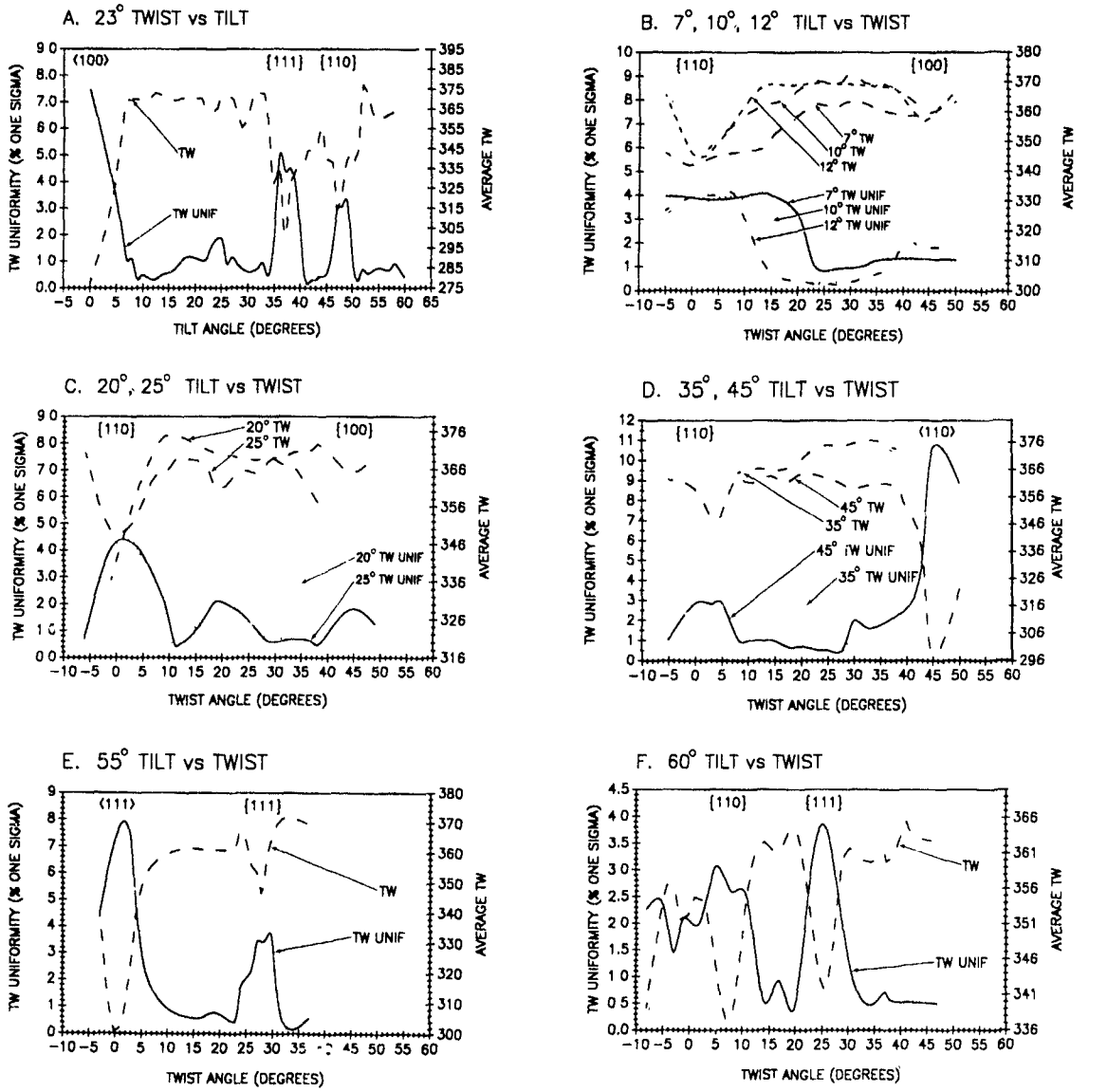

Fig 2 TW average value and cross-wafer uniformity (%, one sigma) for various tilt and twist angle combinations, as noted above (All implants are boron, 100 keV, 5×10^{11} cm^{-2}, without screen oxides.)

poles is also evident at about 20° twist for 25° tilt, and less so for 20° tilt, in fig. 2c.) In this manner, direct comparison of the channeling behavior in fig 2 and the location of poles and planes in fig 3 explains all major channeling variations

The relative magnitude of TW variations in fig. 2 from channeling into the different major features is explained by the data presented in fig. 4. The information in this figure also reveals the effect of energy variations on channeling behavior. This data was obtained by appropriately oriented TW diameter scans of wafers which had been deliberately oriented during implantation so that the ion beam was aligned with a selected channeling zone over a portion of the target surface during scanning. Correlation of the measured TW value with position on the measurement diameter and accurate knowledge of the ion beam scan angles on the target plane allowed plotting of the measured TW values as a function of ion beam alignment with the channeling zone, in degrees. The measured TW values for each wafer have been normalized to the minimum (channeled) value, and are presented as a percent variation in the plots in fig. 4.

By examining the plots in fig. 4, the relative magnitude for channeling of boron ions in several major zones is revealed. Channeling from poles clearly overshadows

Table 1
Optimum wafer orientations for channeling control for boron, 100 keV, 5×10^{11} cm^{-2} implants without screen oxide

Tilt angles [a]	Optimum twist angles [a]
7°	25–33°
10°	23–35°
12°	15–37°
20°	12° or 26–32°
25°	12° or 28–38°
35°	28–38°
45°	18–26°
55°	14–23° or 32–38°
60°	18–20° or 40–45°

[a] Experimental orientation accuracy for tilt and twist angles is $< \pm 0.25°$ and $< \pm 2.0°$, respectively

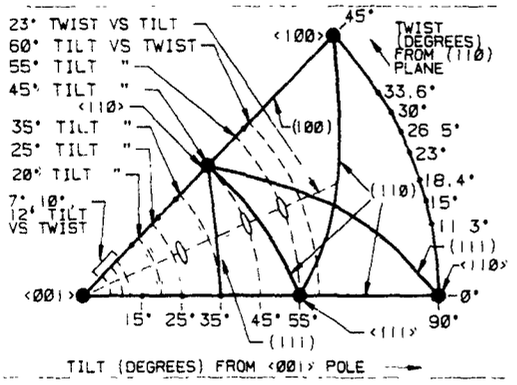

Fig. 3 Stereographic projection of the silicon lattice for the tilt range 0–90° from the ⟨100⟩ pole and the twist range 0–45° from the {110} planes toward the {100} planes.

that from planes, this observation has been reported in previous investigations [3]. Also, {110} planes manifest significantly more severe channeling than {100} planes. This hierarchy explains the relative magnitude for most of the major TW variations in fig. 2, particularly near 0° tilt in fig. 2a and for 0° twist relative to 45° twist at the various tilts in figs. 2b and c.

Table 2
Boron critical angle and average channeled distance

Channel	Critical angle [a] [deg]	Average distance [b] [Å]
⟨110⟩ pole	2.2	3400
⟨111⟩ pole	1.92	1750
⟨100⟩ pole	1.74	1180
{111} plane	1.04	720
{110} plane	0.94	800
{100} plane	0.79	780

[a] Critical angles for 100 keV boron calculated using a ZBL *specific* boron–silicon interatomic potential [11].

[b] Average distance traveled in the channel for boron ions entering at 1° off perfect alignment, calculated using MARLOWE code (at 100 keV for planes and 80 keV for poles).

The severity of channeling in a pole or plane (ignoring dose effects) depends strongly on its critical acceptance angle. This angle is dependent on the atomic number (Z) and energy (E) of the implant species; it is proportional to $(Z/E)^{1/2}$ [10]. A summary of critical angles (for boron at 100 keV) for all major features affecting the measurements in fig. 2 is presented in table 2. These angles were calculated using a ZBL interatomic potential specific to boron and silicon [11], which yields critical angles smaller than previous calculations. Also contained in table 2 are the average distances traveled by a channeled ion in these same major poles and planes, calculated using MARLOWE. As is clear from this table, major poles will have significantly greater channeling effects than major planes, and {110} planes will have worse channeling effects than {100} planes, as is experimentally verified in fig. 4. Consideration of the critical channeling angles and average channeled distance indicates the degree of channeling will be greatest for ⟨110⟩ poles, then ⟨111⟩ poles, followed closely by ⟨100⟩ poles; this is consistent with the behavior observed for these poles in figs. 2a, d, and e. Furthermore, the table predicts that {111} planes manifest channeling

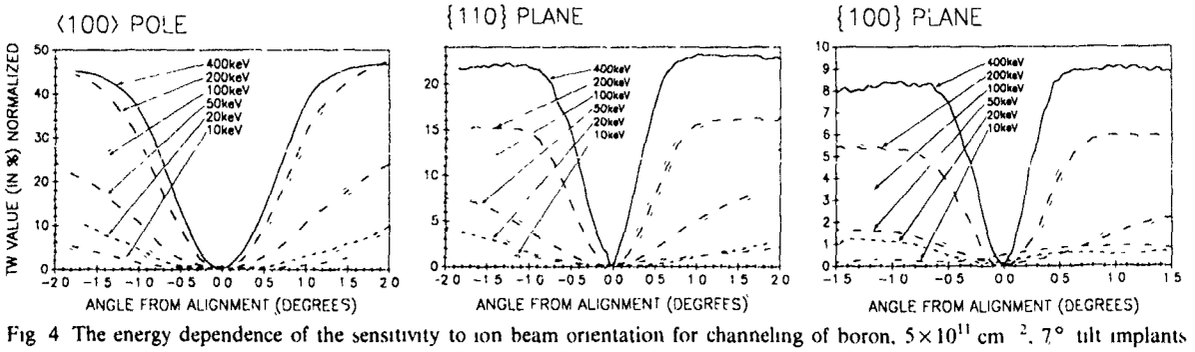

Fig. 4 The energy dependence of the sensitivity to ion beam orientation for channeling of boron, 5×10^{11} cm^{-2}, 7° tilt implants (without a screen oxide) into ⟨100⟩ poles, {110} planes, and {100} planes

slightly worse than {110} planes, which will clearly be worse than {100} planes; this is consistent with the relative variations observed for these planes in figs. 2a and f ({111} vs {110}), fig. 2b, and fig. 4 ({110} vs {100}).

Fig. 4 also demonstrates the variation in channeling behavior as the energy of a 5×10^{11} cm^{-2} boron implant is varied from 400 down to 10 keV. The highest energy implants have the smallest critical angles, but channeling variations are greater at high energy because the sensitivity to small changes in ion beam orientation near alignment is greater. This sensitivity is reduced by reducing the energy, because the critical channeling angle depends on $(Z/E)^{1/2}$, so that lower energy will produce larger channeling acceptance angles. Although this means that acceptance into all major channels is easier, it also means reduced sensitivity to small variations near alignment with any particular channel For example, in fig. 4, when the boron implant energy is below about 20 keV, the manifestation of channeling variation caused by {100} planes is eliminated, even at 5×10^{11} cm^{-2} dose

When increasing the physical tilt angle (θ) while keeping the beam aligned with a planar channel, the average distance traveled by a channeled ion (perpendicular to the wafer's surface) is reduced by a factor cos θ [12], consequently, there is a reduction of channeling variations when θ is large This explains the absence of {100} planar channeling effects for 60° tilt at the 45° twist position and the diminished effect of {110} planar channeling at 0° twist in fig. 2f

In the same manner that boron channeling behavior is characterized in fig. 4, we also characterized channeling in phosphorus 5×10^{11} cm^{-2} implantation. The same general channeling tendencies were observed with phosphorus as with boron, except that the sensitivity of channeling to orientation was reduced by the selection of the heavier species, and reductions in implant energy more quickly reduced this sensitivity for phosphorus than for boron. These effects are expected when the critical acceptance angle is increased by selection of phosphorus ($Z = 15$) instead of boron ($Z = 5$). The changes in channeling behavior from energy and species variations we observed were consistent with previous reports [3]

When comparing our data for phosphorus and boron, we observed the channeling behavior for specific implant conditions with the same $(Z/E)^{1/2}$ ratios is essentially identical This occurs because the 5×10^{11} cm^{-2} dose used here is too low to allow significant channeling differences from accumulated crystal damage to appear in a comparison of these two species. Since channeling is not effectively reduced by increasing the implant dose until an amorphous layer is formed, consideration of critical channeling angles and characterization of orientation sensitivity (as presented in fig. 4) should allow reasonably accurate general predictions of channeling behavior for a wide range of species and energy, at doses up to the formation of amorphous layers.

5. Conclusion

Optimum wafer orientations (tilt/twist combinations) for the tilt range 7–60° have been identified for a boron, 100 keV, 5×10^{11} cm^{-2} implant (table 1). These orientations should provide adequate channeling (profile) control, even for implantations employing very low doses.

A stereographic projection reveals that all major variations in the experimentally observed channeling behavior from 7–60° can be explained by considering channeling in the six major, low Miller index crystallographic poles (⟨100⟩, ⟨110⟩ and ⟨111⟩) and planes ({110}, {111} and {100})

The relative severity of ion channeling in these major poles and planes, and the effect of energy, species and tilt angle variations on the manifestation of channeling can be explained using the concepts of critical channeling angle and average distance traveled for channeled ions

The orientations identified here will apply to a broad range of implant conditions However, implantations employing conditions with a significantly larger $(Z/E)^{1/2}$ ratio (lower energy/higher mass) and/or much higher doses ($\gg 5 \times 10^{14}$ cm^{-2}) will have a larger set of acceptable orientations Conversely, implants with a significantly smaller $(Z/E)^{1/2}$ ratio (higher energy/lower mass) using low doses ($\ll 1 \times 10^{14}$ cm^{-2}) will have a more constrained set of allowable orientations, due to increased sensitivity to ion beam orientation of channeling effects for all crystallographic features in the silicon lattice, particularly higher Miller index poles [3]

Acknowledgements

This work was supported in part by the Semiconductor Research Corporation and Sematech

References

[1] Y Akasaka, Nucl Instr and Meth B37/38 (1989) 9
[2] K. Klein, C Park, A Tasch, R Simonton and S Novak, Ext Abstr Electrochem Soc Conf 90-1 (Pennington, NJ) 359
[3] J. Ziegler and R. Lever, Appl Phys Lett 46 (1985) 358
[4] J Dykstra, A. Ray and R Simonton, these Proceedings (8th Int. Conf. on Ion Implantation Technology, Guildford, UK, 1990) Nucl Instr and Meth B55 (1991) 478

[5] R Simonton, D. Kamenitsa and A. Ray, these Proceedings, (8th Int. Conf. on Ion Implantation Technology, Guildford, UK, 1990) Nucl. Instr. and Meth. B55 (1991) 39
[6] Therma-Wave, Inc., 47734 Westinghouse Drive, Fremont, CA 94534, USA.
[7] W Smith, A Rosencwaig, D Willenborg, J Opsal and M Taylor, Solid State Technol 29 (1986) 85
[8] Charles Evans & Assoc., 301 Chesapeake Dr., Redwood City, CA 94063, USA
[9] L. Azaroff, Elements of X-Ray Crystallography (McGraw-Hill, 1968) p. 23
[10] D Van Vliet, in Channeling: Theory, Observation, and Experiment, ed. D. Morgan (Wiley, New York, 1973).
[11] C Park, K. Klein, A. Tasch and J. Ziegler, Electrochem Soc Conf. 90-1 (Pennington, NJ) 357
[12] G. Fuse, H Umimoto, S Odanaka, M. Wakabayashi, M Fukumoto and T Ohzone, Electrochem. Soc 133 (1986) 996.

Nuclear Instruments and Methods in Physics Research B55 (1991) 45–48
North-Holland

Energy contamination of P^{2+} ion beams on the Varian, EXTRION 220 medium current implanter

P.F.H.M. van der Meulen, S. Mehta and R.E. Kaim
Varian Ion Implant Systems, Gloucester, MA 01930, USA

Singly charged contaminant beams have been analyzed during P^{2+} implants on an EXTRION 220 medium-current ion implanter. A method has been developed for measuring the amount of contamination prior to the actual implant. The measured amount of singly charged energy contamination in the doubly charged ion beam has been related to a shift in sheet resistance of the implanted layer. This shift is proportional to the amount of energy contamination. This measurement proves to be more sensitive than SIMS analysis for the implant that was monitored.

1. Introduction

The use of doubly charged ions for ion implantation is an accepted method to extend the energy range of ion implanters. Doubly charged ion beams have several disadvantages compared to singly charged beams. First, the yield of doubly charged ions in most conventional ion sources is much lower. This limits the available beam current and hence reduces wafer throughput. Second, doubly charged beams can contain ions with an energy different from the main beam. This is called energy contamination. It is caused by the interaction of ions extracted from the ion source with residual gas molecules. Energy contamination can result in a degradation of implant uniformity, junction depth variations and dosimetry problems [1]. In this paper we will discuss how these effects can be measured and controlled on the EXTRION 220 medium-current ion implanter [2,3].

2. Energy contamination

As on most ion implanters, one can distinguish two types of energy contamination on the E-220. The first type of contamination occurs when molecular ions (such as P_2^+) that are extracted from the ion source dissociate before they reach the mass analyzer magnet. The dissociation process leaves an ion with a quarter of the energy of the doubly charged ions. This ion has the same magnetic stiffness as the doubly charged ions and therefore is transmitted through the analyzing magnet.

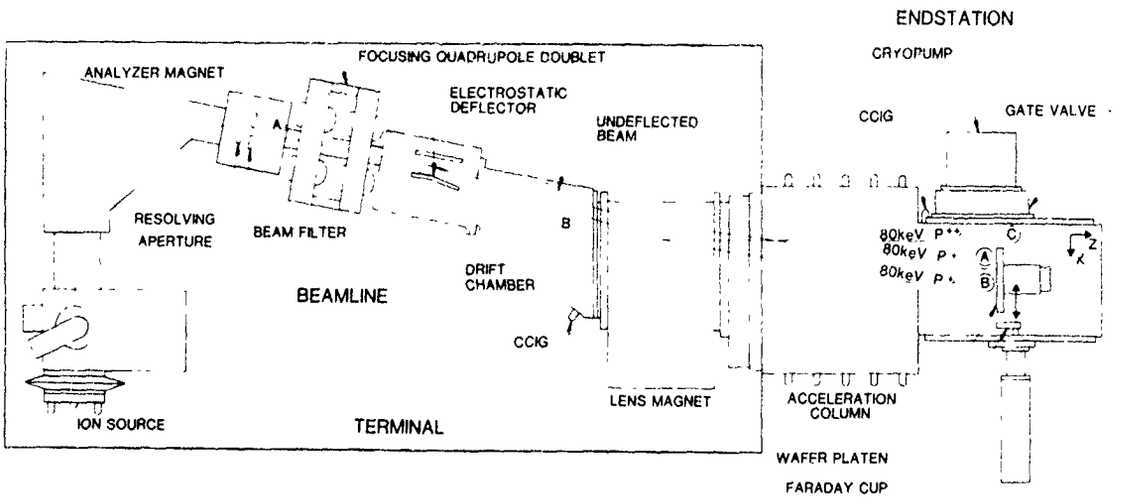

Fig. 1. Ion trajectories in the E-220 beamline for 40 kV extraction and no acceleration voltage. The main contaminant beams are labeled A and B. Beam C is hidden in the main beam.

0168-583X/91/$03.50 © 1991 – Elsevier Science Publishers B.V. (North-Holland)

However, it can be effectively removed from the main beam by an electrostatic beam filter [4,5] The second type of energy contamination occurs after the beam passes through the electrostatic beam filter. Doubly charged ions (I^{2+}) exchange charge with a residual gas molecule/atom (Å).

$$I^{2+} + A^0 \rightarrow I^+ + A^+. \quad (1)$$

The energy loss of the ion I^{2+} in this reaction is negligible compared to its total energy The amount of doubly charged ions in the main beam that lose part of their charge this way is proportional to the pressure in the system and to the length of the path that the ions travel before they reach the wafer surface. The design of the vacuum system and beamline influences the amount of energy contamination and thereby the quality of the implanted layer There are three sections (labeled A, B and C in fig. 1) in the E-220 beamline where this charge exchange occurs

The first section (A) is between the beam filter and the deflector Ions that have lost part of their charge in (A) will be deflected over half the deflection angle of the doubly charged ions

The second section (B) is between the deflector and the angle correction magnet (also referred to as lens magnet) [6] Both singly charged beams produced in section A and B have a higher magnetic stiffness than the main beam This means that they will be underbent (smaller deflection) in the angle correction magnet. The main beam, on the other hand, will be bent in such a way as to become perpendicular to the endstation. Calculations show that contaminant beam A crosses over the main beam somewhere in the acceleration column. Both beams A and B, therefore, end up on the same side of the main beam.

The third section (C) is between the angle correction magnet and the wafer. Ions which undergo charge exchange in this area are not separated from the main beam The contribution of section C to energy contamination is less significant since the pressure in this area is lower than in the rest of the beamline ($\approx 5 \times 10^{-7}$ compared to $1-2 \times 10^{-6}$ Torr). Also the higher energy of the doubly charged ions after acceleration reduces the cross section for charge exchange If the main beam is scanned across the wafer, all three contaminant beams will also scan across, thereby contributing to possible dose offsets and non uniformities

3. Measurement of energy contamination

The electrostatic scanner on the E-220 can be set in spot mode, that is, with a fixed potential on the scan plate The spot mode allows us to measure the integrated ion beam current as a function of position This is done by moving a slotted Faraday cup with a

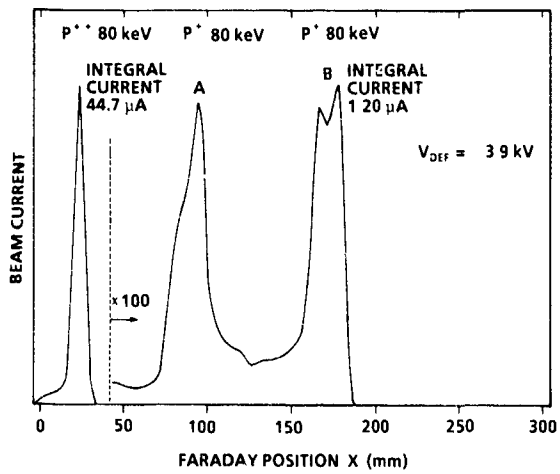

Fig. 2 Beam current measurements as a function of Faraday cup position The doubly charged main beam and singly charged contaminant beams A and B are shown

0.635 cm horizontal and 6.35 cm vertical opening across the end station in the X-axis (fig 1). Since the beam is smaller than the cup in the vertical direction but larger in the horizontal direction, this offers the ability to measure beam current as a function of X-position. In fig. 2 we have plotted the beam current of a doubly charged beam as a function of X-position. The E-220 software calculates the integral beam current over the scanned length The calculated integrated current contains contributions from the contaminant singly charged beams. However, by selecting a lower voltage on the scanner and by using a 100 times larger amplification, we can determine the integral current peaks A and B without getting a contribution from the main beam. Before each implant we perform therefore two integral current measurements. One with the beam in the center of the endstation to measure the total integral current of the main beam and peaks A and B The second measurement is with a lower scanner voltage and a 100 times higher amplification to measure only peaks A and B The relative amount of energy contamination (EC) is then given by (as a percentage of particles)

$$EC = \frac{I^+}{\frac{1}{2}(I^{2+} - I^+)} \times (100\%). \quad (2)$$

In this formula, I^{2+} is the integral current of the main beam plus the contaminants A and B and I^+ is the integral current of only peaks A and B. The factor 2 arises from the fact that each doubly charged ion is counted twice by the dose amplifier The number from eq. (2) can now be related to other measures of energy contamination such as sheet resistance changes or SIMS concentration profiles.

4. Experimental

All measurements were performed on an EXTRION 220 equipped with an electrostatic beam filter set at 28 kV in order to eliminate energy contamination from molecular breakup. Feed material for the Freeman ion source was either solid phosphorus evaporated in a vaporizer or hydrogen buffered 15% PH_3 gas

All implanted wafers were 150 mm (100) p-type (boron) (10–20 Ω cm) SEMI standard wafers with no oxide. Phosphorus implants were done at 180 keV and a 2×10^{14} ions/cm^2 dose with a 7° tilt and a 22° twist to avoid channeling. Wafers used for sheet resistance mapping were RTP annealed at 1100 °C for 10 s. The native oxide was subsequently stripped in buffered HF and the wafers were probed on a Prometrix Omnimap RS30 system. SIMS measurements were performed at Evans East, Inc. on a Perkin Elmer 6300 SIMS system using a 400 nA Cs^+ primary ion beam with an energy of 8 keV. The depth axis was established using a calibrated profilometer Overall accuracy of the profiles is considered to be within 10%.

Implants were performed under three different conditions:

- With a solid phosphorus vaporizer source, to get the lowest amount of contamination.
- With a gaseous phosphine source, resulting in a higher system pressure and hence higher energy contamination caused by the presence of hydrogen
- As before, but with all cryo pumps closed off, resulting in a worst case system pressure

As a comparison to the doubly charged implants, an identical singly charged phosphorus implant was done with the same dose and energy. These implants were used to get an idea of what the result should be in case there was no energy contamination

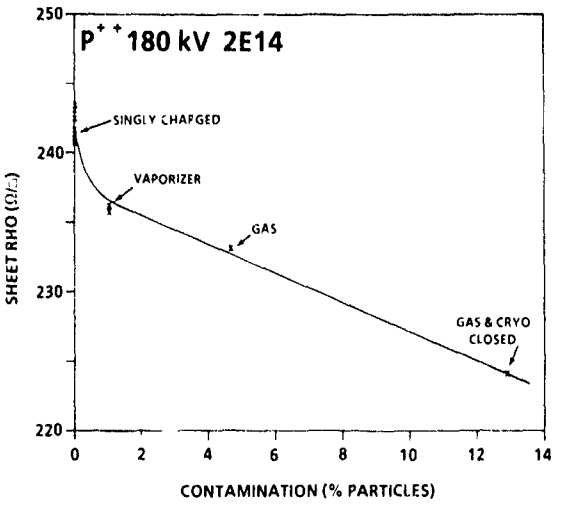

Fig. 4 Sheet resistance as a function of energy contamination for a 180 keV, 2×10^{14} phosphorus implant

5. Results and discussion

In fig. 3 we show three sheet resistance maps of singly and doubly charged implants. As can be seen, the uniformity is maintained well below the 0.5% level, even at the highest amount of energy contamination In fig 4 the mean sheet resistance of all implants is plotted versus the amount of energy contamination measured before the implant For doubly-charged implants, there is a linear relationship between the sheet resistance and the measured amount of energy contamination However, there is a nonlinear change in sheet resistance between 0% energy contamination (singly charged implant) and the first doubly charged implant with the vaporizer

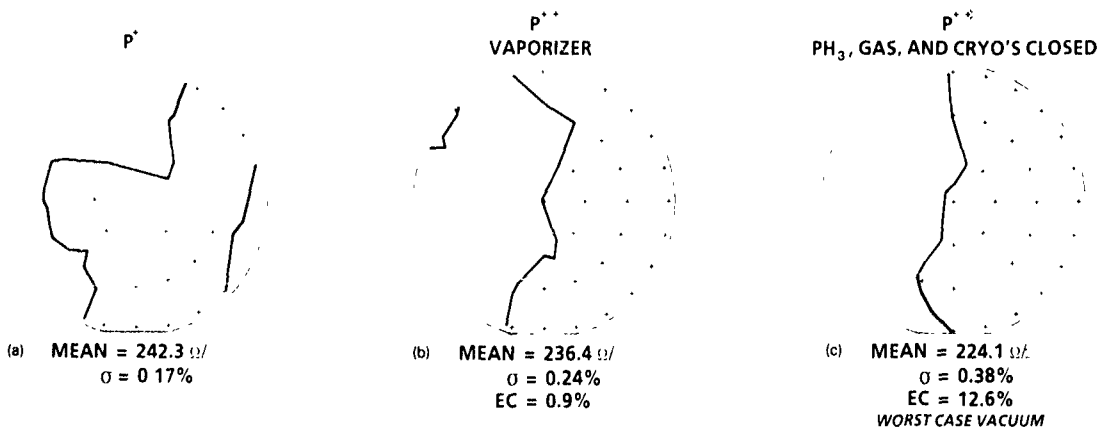

Fig 3 Uniformity maps for 2×10^{14}, 180 keV phosphorus implants Shown are (a) singly charged phosphorus, (b) doubly charged phosphorus with the least amount of contamination, and (c) doubly charged with the largest amount of contamination

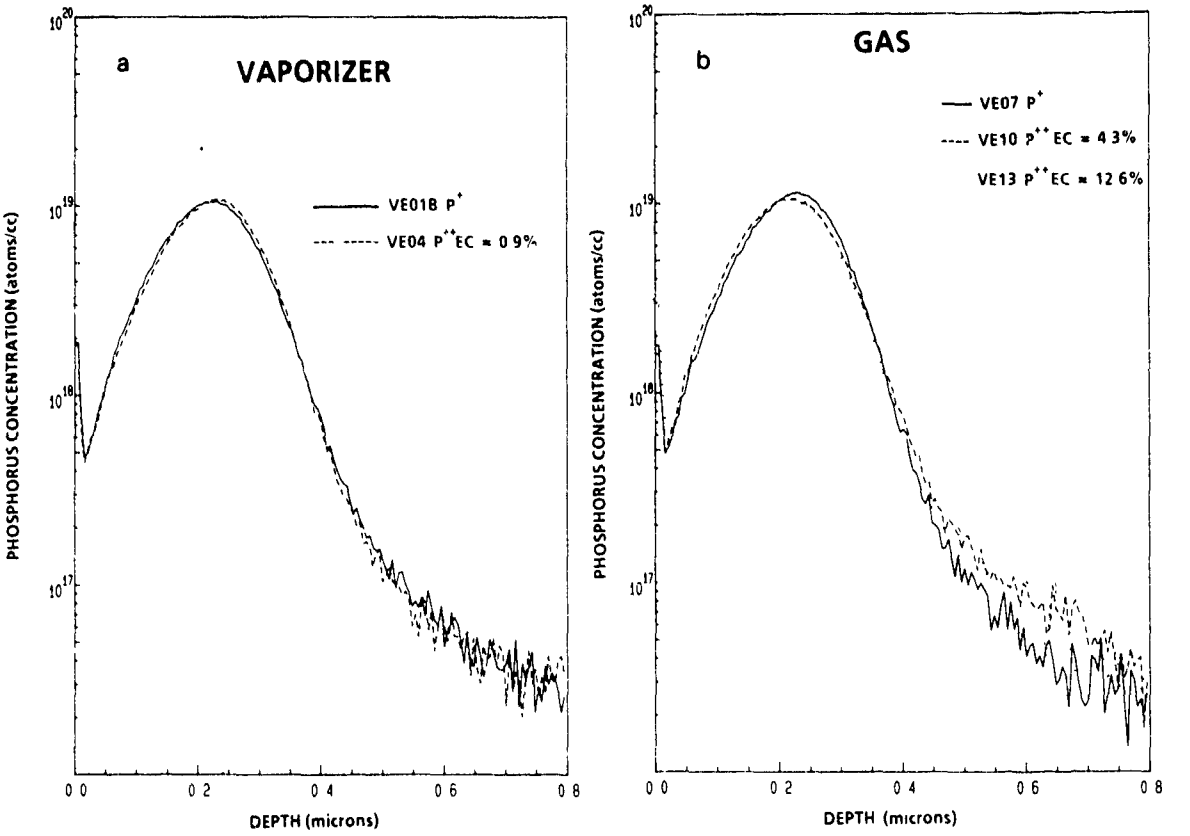

Fig 5 SIMS measurements of as-implanted profiles for a 180 keV, 2×10^{14} ions/cm^2 phosphorus implant Profiles for (a) vaporizer feed and (b) gas feed material.

Fig 5 shows the results of SIMS depth profiles In fig. 5a the profile for a singly charged implant and a doubly charged implant using a vaporizer are plotted. The difference between the two profiles is minimal indicating that the amount of energy contamination is very low indeed. The implanted dose calculated from the profile is the same as in the singly charged implant, within the accuracy of the SIMS measurement. In fig. 5b the results for the implants using PH_3 gas are shown. Again, the singly and doubly charged implants differ very little. Only the implant under worst case vacuum shows a definite change in dose and depth. However, this shift was still not large enough to relate to an amount of contamination.

6. Conclusions

It is possible to measure and monitor the amount of energy contamination on the E-220 implanter. This measurement gives an accurate result that can be related to a shift in sheet resistance for the investigated implantation. The changes are too small to resolve in SIMS measurements for this implant. The described method is much faster and easier to do than a SIMS measurement One can get a value for the EC just before starting the implant instead of afterwards

References

[1] K Brack, W. Euen and D Hagmann, Nucl Instr. and Meth B21 (1987) 405
[2] D.W Berrian, R E Kaim, J W Vanderpot and J F M Westendorp, Nucl Instr and Meth B37/38 (1989) 500
[3] D W Berrian, R E Kaim and J.W. Vanderpot, Nucl Instr and Meth B37/38 (1989) 518.
[4] R.E. Kaim and J F M Westendorp, Solid State Technol (1989) 65
[5] R. Simonton, M King and D.E Kamenitia, Nucl Instr and Meth B37/38 (1989) 616
[6] R E Kaim and P.F H.M. van der Meulen, these Proceedings (8th Int Conf. on Ion Implantation Technology, Guildford, UK, 1990) Nucl. Instr and Meth B55 (1991) 453.

Nuclear Instruments and Methods in Physics Research B55 (1991) 49–54
North-Holland

Control of BF_2 dissociation in high-current ion implantation

Daniel F. Downey and Reuel B. Liebert

Varian Ion Implant Systems, 35 Dory Road, Blackburn Industrial Park, Gloucester, MA 01930, USA

High-current BF_2^+ implants have been studied under various implant conditions, extraction and acceleration voltages and vacuum conditions to determine the critical controls required to eliminate (or minimize) dissociation of BF_2^+ during ion implantation. Dissociated BF_2^+ ions can produce a higher-energy contaminant which extends the junction depth beyond the desired value and destroys devices. In this study, preamorphized Si wafers were used to minimize the channeling tail and optimize the measurement sensitivity. SIMS analysis was performed to determine the size and position of the unwanted energy-contaminant peak (if any). Results are presented and discussed which show that implants between 20 and 60 keV, where the total energy is provided in one stage, have no BF_2 dissociation peak, and for implants between 60 and 80 keV, where the extraction voltage is 60 kV, there is no measurable high-energy contaminant. However, if the extraction voltage is lowered to 20 kV for the equivalent implant, there is a discernible energy contaminant. The size of this peak can vary significantly, depending on the implanter design and pumping capability. In a system with extraction energy limited to low values and/or limited post-analysis pumping, this value can be greater than 5%. In this paper it is shown how this value can be minimized. 130 keV BF_2 implants are also reviewed and comparisons made between 50 keV BF_2^+ and 11.2 keV B^+ implants. In addition a second energy-contamination peak associated with the stripping of the dissociated B^+ ion into B^{++} has been observed at higher beam-line pressure and is discussed in detail in this paper.

1. Introduction

Over the last several years, BF_2^+ ions have been commonly used in the formation of shallow p-type ion-implanted layers. Their use is well documented in the literature [1–13]. The earliest applications of BF_2^+ were driven by the higher beam currents available for BF_2^+ versus those achievable for the equivalent-energy B^+ implant (which is 11/49th of that required for BF_2^+). As time progressed, commercially available ion implanters started to provide increasingly higher beam currents of low-energy boron, but the demand for BF_2^+ implants remained high and it now appears that BF_2^+ will continue to be the species of choice in the fabrication of shallow P^+ junctions for the next generation of devices.

The literature cites several possible reasons for the continued popularity of BF_2^+ implants. One reason is that the additional fluorine decreases the dose required to amorphize the Si substrate [14] and hence reduces the adverse effects resulting from channeling, while improving the annealing characteristics versus those for intentionally preamorphized layers, where a narrow band of extended defects at the original amorphous-to-crystalline interface and other postannealing defects have been observed [15–17]. These problems with preamorphization have been reported to increase leakage currents by three orders of magnitude and hence Wu [17] recommended the use of BF_2^+ implants without preamorphization and RTP anneals to help with stress relaxation [17] and to minimize dopant redistribution [13,11,18]. Recently Wright and Saraswat [19] have reported that the fluorine can have beneficial effects on gate oxides with few, if any, negative effects. In general, fluorine was reported to have produced an improvement in Si/SiO_2 interfacial properties, improving the hot-electron immunity of the devices and at medium doses potentially improving resistance to irradiation. In addition, no dramatic decreases in breakdown voltages (V_{bd}) with a tighter V_{bd} distribution were observed. The charge to breakdown (Q_{bd}) in 130 Å oxides was seen to decrease at fluorine fluences $> 1 \times 10^{15}$, but this effect was not seen on the 410 Å oxides. The fluorine was found not to be a mobile ion in the oxide, but at higher doses fluorine increased the oxide thickness.

In the literature [9,10] there have also been cited disadvantages to the use of BF_2^+. Primarily these have been associated with structure in the boron profile as seen by SIMS, which extends the depth of the implant far beyond the desired value, compromising the integrity of a shallow junction. Sigmon et al. [9] have clearly demonstrated that there exists an energy-contaminant peak which results from the dissociation of BF_2^+, into B^+ and F_2 after mass analysis and prior to final acceleration. The boron energy of this peak is given by

$$E_{\text{boron}} = e\left(\tfrac{11}{49}V_x + V_{\text{acc}}\right). \quad (1)$$

For a 150 keV implant with $V_x = 30$ kV, a contamination peak at $R_p = 0.37$ μm was observed with a boron dose of 0.4% of the total. Queirolo et al. [10] studied this phenomenon further, carefully monitoring various implanter conditions including beam-line pres-

0168-583X/91/$03.50 © 1991 – Elsevier Science Publishers B.V. (North-Holland)

sure and postacceleration voltages on the SIMS boron-ion depth profile. Their results confirmed those of Sigmon et al.; however, curve-fitting analysis could not explain the tail beyond the B^+ contamination peak (which on a two-stage acceleration machine was reported to be 2–5% of the total dose). They concluded that this tail was the result of channeling. Conclusions about the mechanisms responsible for the dissociation of the BF_2^+, whether it was related to gas-phase collisions or collisions with the resolving aperture, were clouded by the inability to accurately measure the pressure in the beam line.

In this paper, BF_2^+ implants into preamorphized Si (to eliminate questions regarding channeling) are conducted at various energies, extraction voltages and pressures, in order to clarify some of the remaining questions about the structure in the boron-ion profile and to help identify the mechanisms involved in the dissociation of BF_2^+. In addition "equivalent"-energy BF_2^+ (50 keV) and B^+ (11.2 keV) implants as a function of RTP and furnace-annealing techniques are compared. Based on this study, the authors hope to provide methods to control the dissociation of BF_2^+ and provide recipes for boron doping equivalent implants using BF_2^+.

2. Experimental

All of the implants were performed in a Varian EXTRION 1000 ion implanter, which was specially configured to allow for separately controlled N_2 gas introduction in the end-station chamber and into the beam-line area between the analyzer magnet and the mass slits. In the Varian EXTRION 1000 the beam-line pressure is measured by a nude Bayard Alpert ionization gauge which is mounted directly on the side of the mass slit chamber; in addition the Extrion 1000 has a turbomolecular pump which specifically pumps this area, and keeps the beam-line pressure typically between 1×10^{-6} and 4×10^{-6} Torr during standard operation, with base pressures down to 2×10^{-7} Torr.

All wafers used were 150 mm ⟨100⟩ n-type wafers, with resistivities between 1 and 20 Ω cm. The preamorphized wafers were implanted twice with ^{28}Si, once at 50 keV (2×10^{15} ions/cm^2) and again at 150 keV (2×10^{15} ions/cm^2) [12].

All SIMS measurements were done by Evans East Inc., employing a Perkin Elmer 6300 secondary-ion mass spectrometer. The primary bombarding species was 5 keV O_2^+ ions at 60° incidence. Quantification of the profiles was provided by a calibrated ion-implanted standard of B in Si. The depth of the sputtered crater was measured by a calibrated profilometer to establish the depth axes. The overall accuracy of the profiles is 10–15%.

The RTP anneals were performed in a Varian RTP-8000, employing a two-step temperature recipe of 800 °C, 5 s (cool-down) + 1100 °C, 10 s. The furnace anneals were done in a Thermtec Model 1320 double-stack furnace at 930 °C for 30 min in a N_2 flow of 20 l/min.

3. Results and discussion

Fig. 1a is an overlay of two SIMS profiles of "as-implanted" 80 keV ($V_x = 60$ kV), 1×10^{15} ions/cm^2 BF_2^+

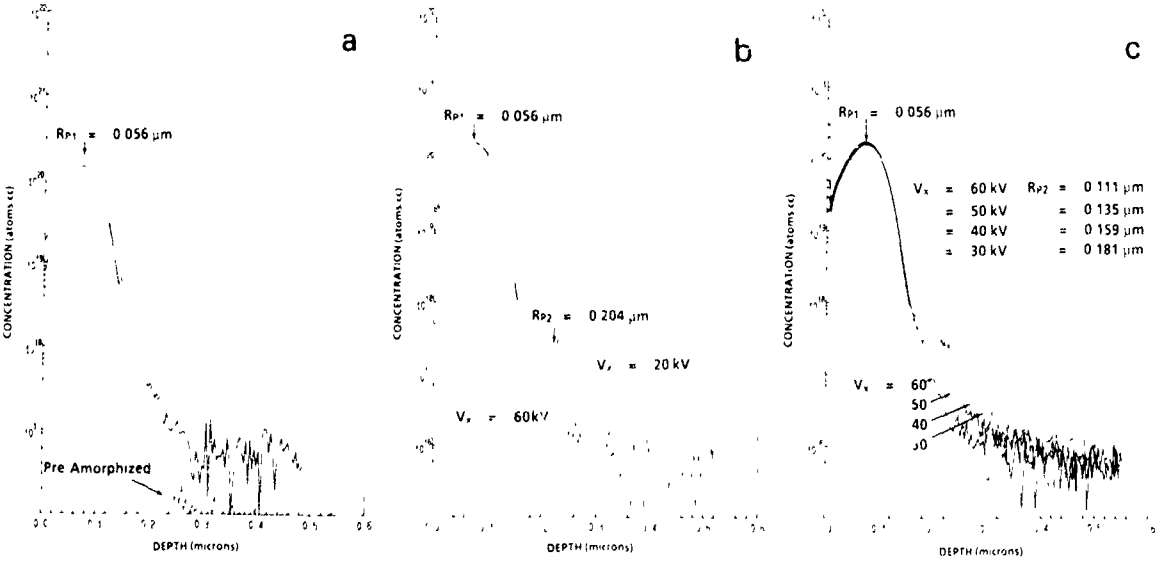

Fig. 1. SIMS profiles of BF_2^+, 80 keV, 1×10^{15} ions/cm^2 implants (a) into single-crystal and preamorphized Si, (b) with extraction voltages of 20 and 60 kV, and (c) with extraction voltages of 30, 40, 50 and 60 kV.

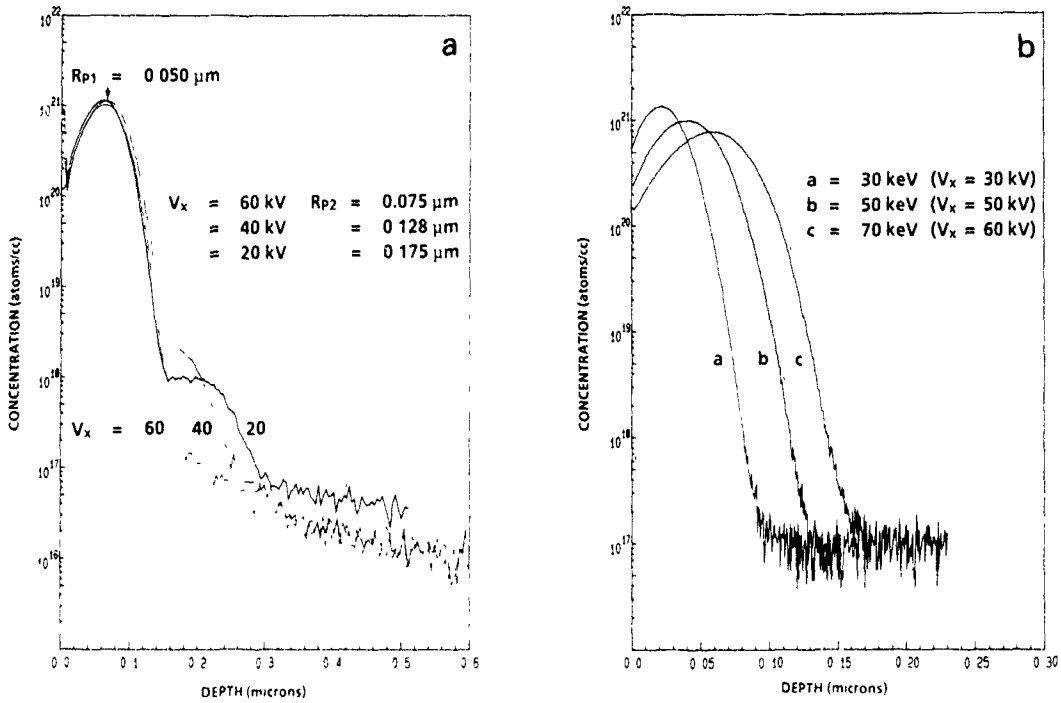

Fig 2 SIMS profiles of BF_2^+, 70 keV, 5×10^{15} ions/cm^2 implants (a) with extraction voltages of 20, 40 and 60 kV, and (b) for 30 keV (V_x = 30 kV), 50 keV (V_x = 50 kV) and 70 keV (V_x = 60 kV)

Table 1
BF_2^+, 1×10^{15} ions/cm^2, 80 keV, $P_{bl} = 2.0\times10^{-6}$ Torr

V_x [kV]	R_{P1} [μm]	R_{P2} [μm]	Dose peak 1 [a] [ions/cm^2]	Dose peak 2 [a] [ions/cm^2]	Dose P2 / Total dose [%]
60	0.056	0.111	1.25×10^{15}	0	0
50	0.056	0.135	1.16×10^{15}	2.4×10^{12}	0.21
40	0.056	0.159	1.13×10^{15}	2.79×10^{12}	0.25
30	0.056	0.181	1.13×10^{15}	2.4×10^{12}	0.21
20	0.056	0.204	1.14×10^{15}	2.47×10^{12}	0.21

[a] Dose integrated from SIMS

Table 2
BF_2^+, 5×10^{15} ions/cm^2, $P_{bl} = (1.2)\times10^{-6}$ Torr

E [keV]	V_x [kV]	R_{P1} [μm]	R_{P2} [μm]	Dose peak 1 [a] [ions/cm^2]	Dose peak 2 [a] [ions/cm^2]	Dose P2 / Total dose [%]
70	60	0.050	0.075	6.5×10^{15}	0	0
70	40	0.050	0.128	7.12×10^{15}	1.11×10^{13}	0.156
70	20	0.050	0.175	6.93×10^{15}	8.83×10^{12}	0.128
30	30	0.023	0.023	4.9×10^{15}	0	0
50	50	0.037	0.037	5.3×10^{15}	0	0
70	60	0.050	0.075	5.1×10^{15}	0	0

[a] Dose integrated from SIMS.

Table 3
BF_2^+, 5×10^{15} ions/cm^2

P_{bl} [Torr]	P_{ex} [Torr]	Energy [keV]	Dose peak 1 [a] [ions/cm^2]	Dose peak 2 [a] [ions/cm^2]	Dose peak 3 [a] [ions/cm^2]	Dose P2 / Total dose [%]
2.0×10^{-6}	1.2×10^{-6}	70 (V_x = 20)	6.5×10^{15}	8.83×10^{12}	–	0.128%
4.4×10^{-6}	1.2×10^{-6}	80 (V_x = 20)	4.6×10^{15}	1.8×10^{13}	–	0.39%
4.8×10^{-6}	5.0×10^{-6}	80 (V_x = 20)	4.9×10^{15}	2.4×10^{13}	–	0.48%
9.0×10^{-6}	1.9×10^{-5}	80 (V_x = 20)	4.8×10^{15}	4.0×10^{13}	–	0.83%
2.2×10^{-5}	8.0×10^{-7}	80 (V_x = 20)	4.7×10^{15}	8.5×10^{13}	–	1.78%
5.0×10^{-5}	1.0×10^{-6}	80 (V_x = 20)	4.6×10^{15}	1.9×10^{14}	1.3×10^{12}	3.97%
4.0×10^{-6}	7.0×10^{-7}	130 (V_x = 60)	4.7×10^{15}	3.1×10^{13}	–	0.66%
5.0×10^{-6}	4.7×10^{-6}	130 (V_x = 60)	4.8×10^{15}	4.3×10^{13}	1.7×10^{12}	0.89%
9.0×10^{-6}	2.0×10^{-5}	130 (V_x = 60)	4.8×10^{15}	8.1×10^{13}	2.3×10^{12}	1.68%
2.2×10^{-5}	8.0×10^{-7}	130 (V_x = 60)	4.4×10^{15}	1.5×10^{14}	3.4×10^{12}	3.30%
5.0×10^{-5}	1.0×10^{-6}	130 (V_x = 60)	4.1×10^{15}	3.3×10^{14}	8.3×10^{12}	7.45%

[a] Dose integrated from SIMS

implants. One implant is into preamorphized Si, while the other is into single-crystal Si. This experiment demonstrates the effectiveness of the preamorphized Si wafer in reducing/eliminating the channeling tail and in enhancing the SIMS sensitivity in distinguishing structure related to higher-energy contaminant peaks. Based on this, all further implants where boron profiles were to be obtained are into preamorphized substrates.

Figs. 1b and 1c dramatically illustrate the effect of the extraction voltage on the boron profile. At V_x = 60 kV, only one peak is observed at 0.0564 μm (the SIMS data is fitted to LSS $^{11}B^+$ distribution) which corresponds to a boron energy of 18.0 keV (which is 11/49th of the BF_2 implant energy). As the extraction is decreased, an energy contaminant of 0.2–0.25% of the total dose (as integrated from the SIMS profile) is

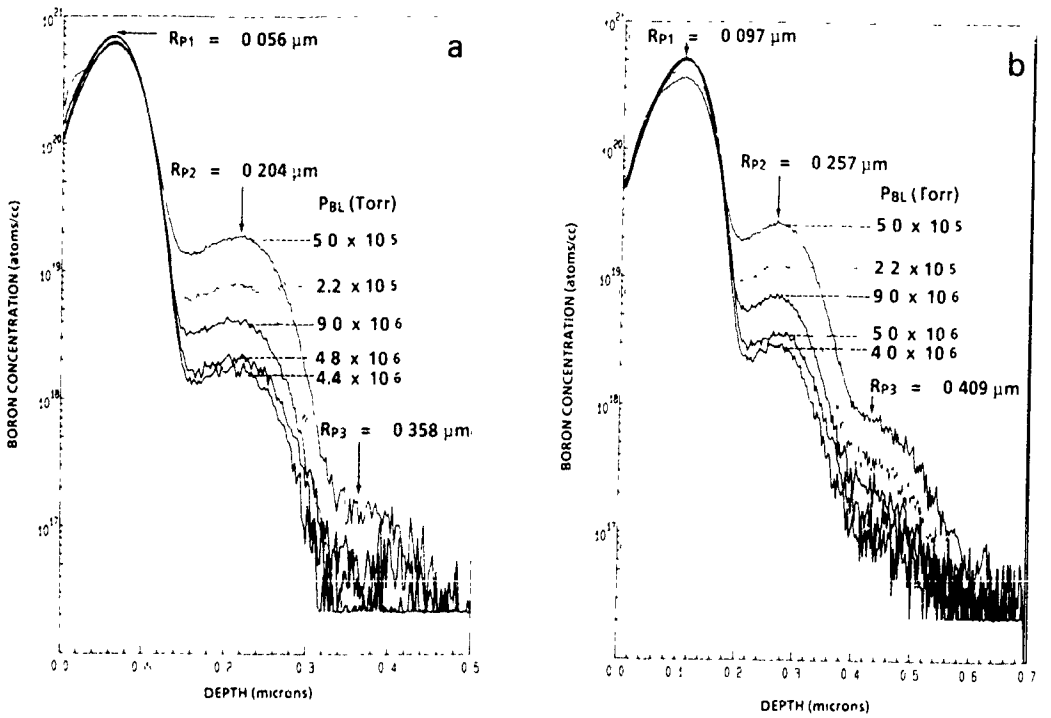

Fig. 3. (a) SIMS profile of a BF_2^+, 80 keV (V_x = 20 kV), 5×10^{15} ions/cm^2 implant as a function of P_{bl}. (b) SIMS profiles of 130 keV (V_x = 60 kV) implants as a function of P_{bl}.

observed at increasingly deeper depths (refer to table 1). The boron energy of this contamination peak is given by eq. (1).

Similar results are depicted in fig 2a for 5×10^{15} ions/cm^2, 70 keV BF_2^+ implants. Here the sizes of the peaks are 0.13–0.16% of the total dose (refer to table 2). Fig 2b is an overlay of a 30, 50 and 70 keV implants, with $V_x = 30$, 50 and 60 kV, respectively. In these cases there are no discernible energy-contaminant peaks.

The effects of varying both the beam line (just before the acceleration tube) and the end-station pressure on 80 ($V_x = 20$ kV) and 130 keV ($V_x = 60$ kV) implants was studied These results are listed in table 3. The SIMS profiles of the 80 keV ($V_x = 20$ kV) are shown in fig. 3a. It should be noted that $V_x = 20$ kV was chosen to emphasize the contamination peak as a function of pressure. The SIMS plots are overlays of the various beam-line pressures (P_{bl}). The following observations can be made from this data:

(1) the size of the contamination peak at 0.204 μm ($E_{boron} = 64.5$ keV) is a linear function of the beam-line pressure and is affected only slightly by the end-station pressure,

(2) there is a third peak which appears at $P_{bl} = 5 \times 10^{-5}$ Torr at close to 0.358 μm, which corresponds to the energy of B^{++} ions, stripped after mass analysis and prior to final acceleration, whose boron energy is given by

$$E_{boron} = \tfrac{11}{49} eV_x + 2eV_{acc}, \qquad (2)$$

which in this case is 124.5 keV The SIMS profiles of the 130 keV ($V_x = 60$ kV) implants (refer to fig 3b) lends further evidence to the existence of the third peak. This peak is now appearing at a P_{bl} value of 5×10^{-6} Torr. A B^{++} ion, stripped after mass analysis, according to eq (2) has an energy of ~ 153.5 keV and, from the LSS distribution an R_p-value of 0.409 μm. This is in excellent agreement with the data. In addition it should be noted that these energy peaks are monotonically increasing functions of P_{bl}, certainly eliminating channeling effects as their cause and highly suggesting that they are produced by gas-phase collisions (with the background gas).

Figs. 4a, b and c are SIMS profiles of a 50 keV ($V_x = 50$ kV), 3×10^{14} ions/cm^2 BF_2^+ comparison with a 11.2 keV boron implant of the same dose. Fig. 4a is the "as-implanted" profile illustrating the effectiveness of the BF_2^+ implant in controlling channeling. Fig. 4b is a two-step RTP anneal (800 °C, 5 s + 1100 °C, 10 s) showing minimal diffusion of the dopants. Fig. 4c is a 930 °C, 30 min furnace anneal depicting large amounts of diffusion. The boron in the BF_2 is now diffusing much more quickly than in the B^+ implant This supports earlier observations that fluorine and the associated higher damage causes enhanced diffusion [11,15]. Four-point probe measurements of these implants show that for the RTP anneals the BF_2^+ has a sheet resistance of 345.6 Ω/□, while the $^{11}B^+$ has a sheet resistance of 345.4 Ω/□. The furnace anneal for BF_2 has a sheet resistance of 483.7 Ω/□, while the $^{11}B^+$ has a sheet resistance of 460.4 Ω/□.

The BF_2^+ experiments investigating the dissociation of BF_2^+ and the related structure in the SIMS boron profile clearly confirm the observations of Sigmon et al [9] They further answer questions raised by Queirolo et

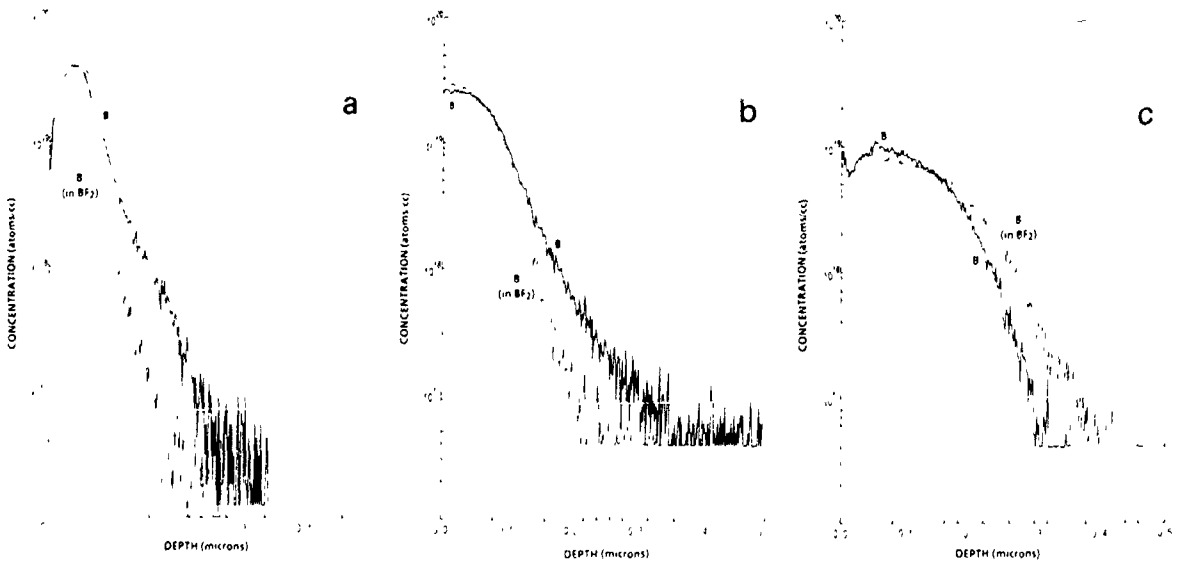

Fig 4 SIMS profiles of BF_2^+, 50 keV, 3×10^{14} ions/cm^2 implants versus equivalent-dose B^+ 11.2 keV implants (a) as-implanted, (b) after RTP anneal and (c) after furnace anneal

al. [10], that is, that the high-energy tail in the SIMS profile beyond the B^+ contaminant peak is not related to channeling but is a distinct third peak which appears to be associated with the stripping of the B^+ ion to B^{++} after mass analysis and prior to final acceleration. The energy of this peak observes eq. (2). Both contamination peaks are monotonically increasing functions of P_{bl} and very slow functions of P_{es}. This fact highly suggests that the mechanism of dissociation is a gas-phase mechanism, involving BF_2^+ ion dissociation with the background gas between mass analysis and final acceleration. To produce SIMS profiles without these contamination peaks, the implants should be performed with $V_x = V_{total}$ (i.e., drift mode or single-stage acceleration) or with V_x as large as possible, in this case $V_x = 60$ kV. At higher energies, e.g. 130 keV, contamination peaks $< 0.5\%$ can be achieved with $p_{bl} \leq 2.0 \times 10^{-6}$ Torr. It should be noted that Queirolo et al. [10] observed levels of 2–5% at reported pressures of 1×10^{-7} Torr. The authors of this paper believe that these pressures were measured too far away from the beam-line area to be truly indicative of that pressure and a P_{bl} value $> 5 \times 10^{-5}$ Torr is probably more indicative of that pressure value. In any case, the beam-line pressure must be measured as close to the region of dissociation as possible if meaningful pressure data is to be obtained. Further reductions in the size of the contaminant peaks require additional pumping (or methods to reduce P_{bl}) or shortening of the beam line.

The annealing studies demonstrate that to achieve BF_2^+ equivalent sheet resistance results RTP annealing has distinct advantages as long as the dose is below the solid-solubility limit. Additional work is in progress by the authors of this paper to investigate higher-dose annealing ($\geq 1 \times 10^{15}$ ion/cm^2) of BF_2^+ implants.

4. Conclusion

BF_2^+ implants into preamorphized Si increase the sensitivity of SIMS in distinguishing energy-contaminant peaks related to BF_2^+ dissociation. This sensitivity allowed for the observation of two contaminant peaks. The first peak, which was first observed by Sigmon et al. [9], and a second peak which is associated with B^{++}, dissociated after mass analysis and prior to final acceleration with an energy given by eq. (2).

These peaks can be eliminated (up to 80 keV) by the appropriate choice of the extraction voltage. That is, $V_x = V_{total}$ or $V_x = 60$ kV for implants from 60 to 80 keV. At higher energies these peaks can be minimized by adequately pumping the beamline region and maintaining a beamline pressure $\leq 2 \times 10^{-6}$ Torr during implantation.

Acknowledgements

The authors would like to thank Dr. Charles Magee of Evans East, Inc. for many helpful discussions, and from Varian Ion Implant Systems, Bjorn Pedersen and Ronald Eddy for helpful discussions, Keith Pierce and Marcus Monell for assistance with the experiments, and Pamela Mansfield and Heather Deacon for preparing the figures and manuscript.

References

[1] T E Seidel, IEEE Electron Device Lett. EDL-4 (1983) 353
[2] R G Wilson, J Appl Phys 54 (1983) 6979
[3] T.M Liu and W G Oldham, IEEE Electron Device Lett. EDL-4 (1983) 59
[4] M E Lunnon, J T Chen and J E Baker, Appl Phys. Lett. 45 (1984) 1056
[5] M E. Lunnon, J T Chen and J E Baker, J Electrochem Soc 132 (1985) 2473
[6] S S Cohen, J F. Norton, E.F Kock and G J Weisel, J Appl Phys 57 (1985) 1200
[7] W Vandervorst, D C Houghton, F.R. Shepherd, M.L Swanson, H H Plattner and G J C Carpenter, Can J Phys. 63 (1985) 863
[8] M Simard-Normandin and S Slaby, J Electrochem Soc 132 (1985) 2218
[9] T W Sigmon, V R Deline, C A Evans and W M Katz, J Electrochem. Soc 127 (1980) 981
[10] G Queirolo, C. Bresolin, L Meda, M Anderle and R Canteri, J. Electrochem. Soc 135 (1988) 777
[11] R A Powell, J. Appl Phys 56 (1984) 2837
[12] R B Simonton, Nucl Instr and Meth B21 490 (1987)
[13] V K Basra and D.F Downey, Nucl Instr and Meth B21 (1987) 505
[14] H Muller, H Ryssel and I Ruge, in Ion Implantation in Semiconductors (Springer, Berlin and New York, 1971) p 85
[15] J Gyulai, in Ion Implantation Science and Technology, 2nd edition, ed J F Ziegler (Academic Press) p. 112.
[16] S.D. Brotherton, J P Gowers, N D Young, J B Clegg and J.R. Ayers, J. Appl Phys 60 (1986) 3567
[17] I W Wu, R.T. Fulks and J C Mikkelson, Jr, J Appl. Phys 60 (1986) 2422.
[18] D F Downey, C.J Russo and J.T White, Solid State Technology (September 1982).
[19] P J Wright and K C Saraswat, IEEE Trans Electron Devices ED-36 (1989) 879

Nuclear Instruments and Methods in Physics Research B55 (1991) 55–60
North-Holland

A RGA study of the cross-contamination of dopant species and low level impurities and the use of the RGA as a process monitor in a Varian 180XP

James J. Cummings and Daniel T. Enloe
Intel Corporation (Mailstop SC1-11), 3065 Bowers Avenue, Santa Clara, CA 95054, USA

Residual gas analysis (RGA) has been used to characterize the process of a Varian 180XP The cross-contamination from dopant species has been investigated along with low level impurities from other sources, specifically resist, pump backstreaming, and implanter parts. This effect is clearly observed using RGA to measure total and partial pressures This study concentrates on selected ranges of energy, dose, and beam current The study also investigates the correlation of particle events in the implanter with a RGA and an in situ particle counter A recommendation on the use of one or both tools as process monitors is made

1. Introduction

High current, batch process ion implanters are a common denominator in the manufacture of nearly all semiconductor products being designed today With the demand for faster and smaller devices, the cleanliness of the process chamber is becoming increasingly important.

High current implanters can cause resist outgassing and possible particle generation due to the high beam powers employed. Effects include: decreased throughput due to the requirement to maintain low pressures, beam neutralization caused non-uniformities, the cross-contamination of species due to sputtering, the generation of particles by photoresist blistering; beam impacts on beamline components causing sputtering. Non-beam-induced effects include contamination by low level impurities, such as mechanical pump and diffusion pump oils All of these effects can influence yields

Other papers have noted the effects of resist outgassing on low and high current machines [1–5]. Smith, Okuyama and Larson have shown that resist outgassing results from the breaking of C–H bonds, forming a mechanically and physically hard film on implanter surfaces [1,2]. Individual gas peaks (H_2, N_2, H_2O) have been monitored by Raicu [4] et al as function of beam current, energy, and species. Raicu [4] indicates that the outgassing is a beam current heating effect and can be controlled by hardbaking and UV curing. Smith, Larson, and Okuyama disagree with this, indicating it is a beam interaction mechanism [1–3].

Our research confirms the existence of the outgassing as well as the formation of the film on surfaces in the vacuum chamber. It confirms that H_2 gas evolution by photoresist is independent of baking. Residual gas analysis (RGA) also confirms the existence of undesired dopant species during implant at surprisingly large relative levels. Pump oils were below detectable levels during normal implants. Finally, an analysis of the RGA and the in situ particle counter for their capability as in situ production monitors is made

2. Experimental

This study involved the monitoring of partial pressures using the UTI 2211 RGA and particle generation using a High Yield Technology (HYT) model 15A in situ particle counter, as a function of resist/no resist, species, and energy The RGA and particle counter (HYT) were mounted in endstation one. The mounting was made on the only existing vacuum port directly above the Faraday, behind the endstation chamber. The total distance of the RGA head to the endstation chamber is nine inches A forty-five degree stub was used to achieve adequate clearance A gate valve was used to isolate the open source RGA from atmosphere during wafer exchange. The gate valve was operated in parallel with the endstation isolation valve. A line connecting the open source to the scan cyro pump was used to pump on the open source when isolated (fig. 1) Both tools used the standard vendor supplied software. 150 mm 13-site disks were used in the endstation with full loads of patterned resist, full loads of wafers with 6000 Å of oxide, as well as mixes of the two The resist used was an advanced submicron Japanese type, with a post bake of 90 °C for one minute. The RGA and HYT were used simultaneously to check for correlation between the two instruments. Particles 0.5 μm and larger were monitored by the HYT, and various selected gasses

0168-583X/91/$03.50 © 1991 – Elsevier Science Publishers B.V (North-Holland)

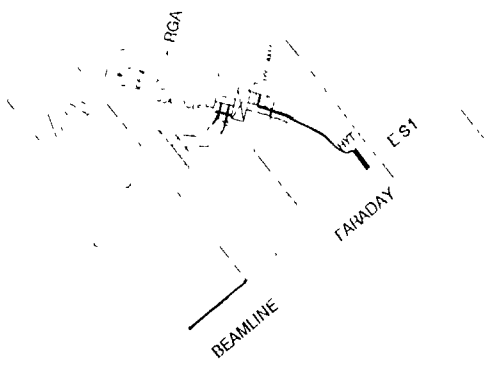

Fig 1 RGA schematic

were monitored using the RGA (^{75}As, ^{11}B, N_2, ^{31}P, BF_2, oils, ^{19}F, etc)

3. Results

Fig. 2 illustrates a typical spectrum from endstation one with the machine in an idle state (with no ion beam, at high vacuum). Note that possible backstreaming CF_3 from the mechanical pumps and C_6H_6 from the diffusion pump are both not detectable Point A represents the beginning of the vent cycle for endstation one, indicating a leak on the RGA isolation valve, confirmed by increases in nitrogen partial pressures. A leaky endstation two isolation valve was also detected this way Point B represents initiation of the rough pumping cycle. Point C represents time of cyro isolation valve opening. All pressures trend down from this point as expected. Monitoring of endstation two was also possible from this location, but at lower partial pressures.

Fig. 3 represents a 150 keV, 10 mA arsenic implant on the 180XP with simulated production on the disk (i.e., resist and oxide mixture on the disk). Point A is the time of endstation one isolation valve opening. The step pressure increase is due to the valve opening when the endstation pressure is 2×10^{-5} Torr Point B marks the beginning of beam tuning. Point C marks the start of the implant. Note the plateau of the arsenic pressure and the magnitude of phosphorous. The other selected peaks decrease during implant The presence of ^{11}B and its decrease indicate a possible sputtering source (likely the disk). Point D marks the beginning of the wafer exchange cycle Point E marks the opening of the end-

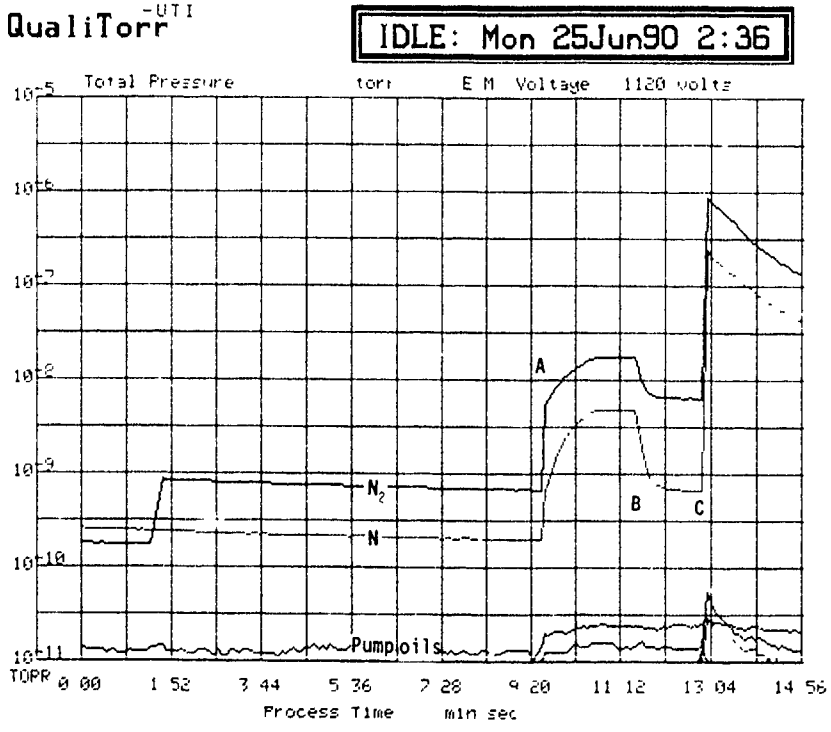

Fig 2 Idle state RGA spectrum

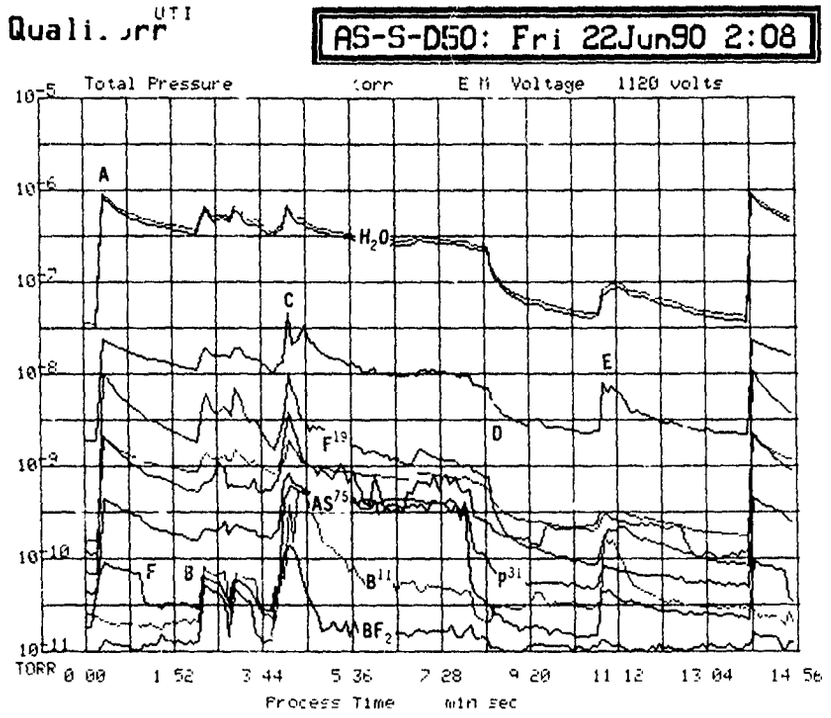

Fig. 3 Typical implant RGA spectrum

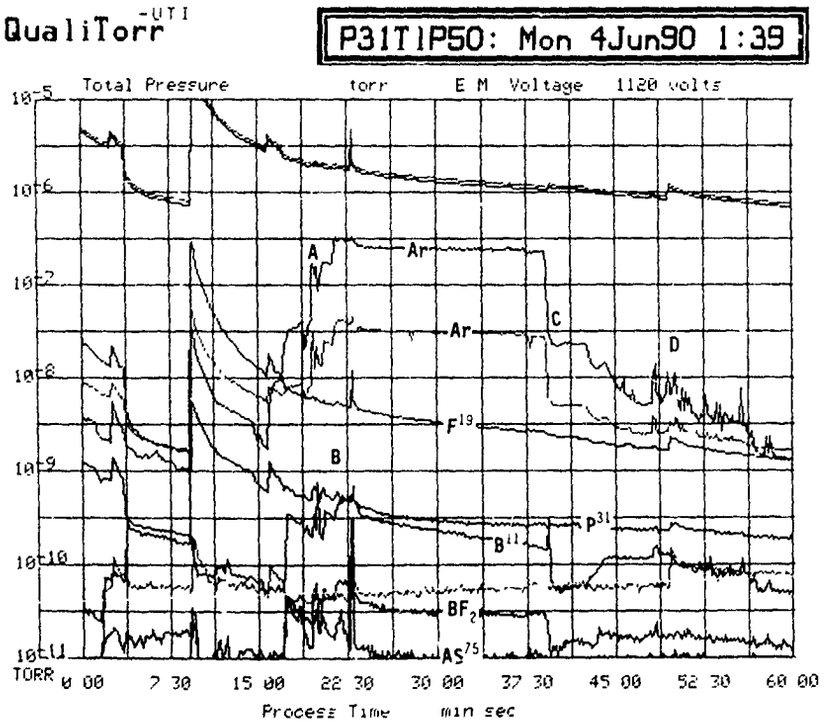

Fig. 4 Argon clean RGA spectrum

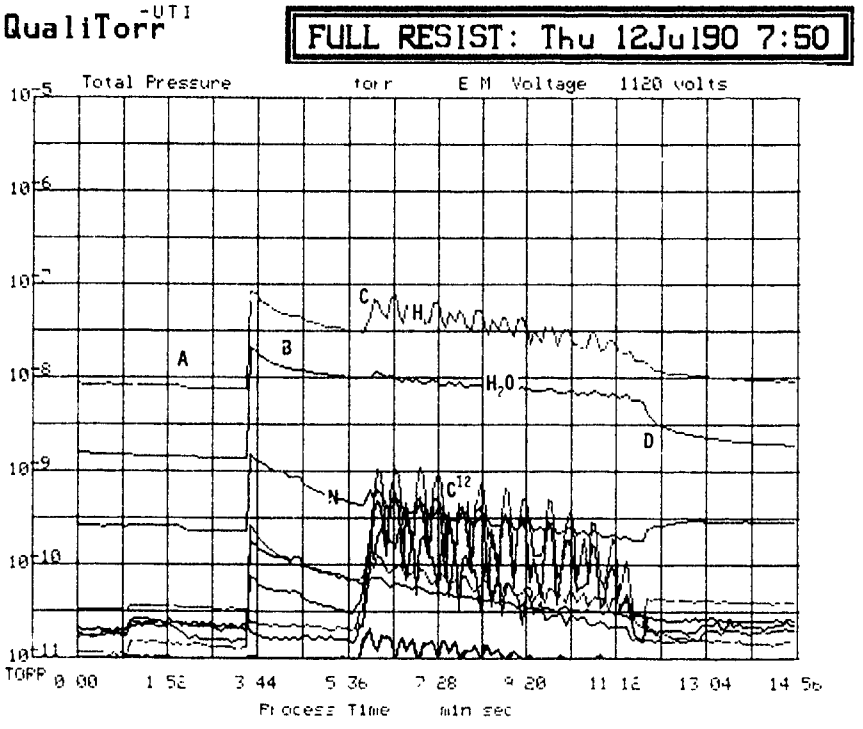

Fig 5 Resist RGA spectrum

station two beam gate. Point F marks the completion of implant on endstation two.

Fig 4 represents a typical argon cleaning cycle on the 180XP. The 150 keV, 10 mA argon beam is kept in the neutral cup for approximately thirty minutes and is used for conditioning the source for the next dopant. Point A marks the start of the cleaning beam operation. Note the decay of partial pressures of selected dopant ions starting at Point B, when full beam power is achieved Point C marks the beginning of a species change on the implanter. Point D marks the opening of the endstation two isolation valve after a purge cycle

Fig. 5 is a typical selected peak monitor obtained during a full disk load of resist Point A represents the baseline for the selected peaks with the beam in the neutral dump The H_2O and N_1 peaks fall off relatively smoothly after the endstation one isolation valve opens (point B) and return to the baseline level before the implant The verification of this point was seen by running bare oxide wafers on the disk and making a comparison between the two spectrums. The H_2O peak is at the same levels as with the resist. The N_1 has some variation in amplitude, but generally the trend is the same. Therefore, the amount of these substances is intrinsic to the vacuum system due to the vent and pumpdown cycles as suggest by Larson et al [1]. The trend of the H_1 and ^{12}C peaks mimic each other with the hydrogen having similar amplitude starting with the beam gate opening at point C. Point D represents the end of implant and the downward trend of all species continues except for N_1 which is a result of the endstation vent cycle

Fig 6 is a typical scan for 0 5 μm and larger particles using the HYT particle counter The figure shows a series of implant and wafer exchange cycles as viewed on the computer's monitor. The only observable effects were the resonance condition between the fluorescent light frequency and the frequency of the laser beam when the door is open The HYT was useful in diagnosing the cause of gross particle excursions. It was used to monitor both endstations for comparison and to generate baseline data

4. Discussion

4 1. Residual gas analyzer

The RGA was obtained for the 180XP for evaluation as a process monitor. It had adequate sensitivity to measure the effectiveness of the argon clean, the sequence of events on the opposite endstation, and to

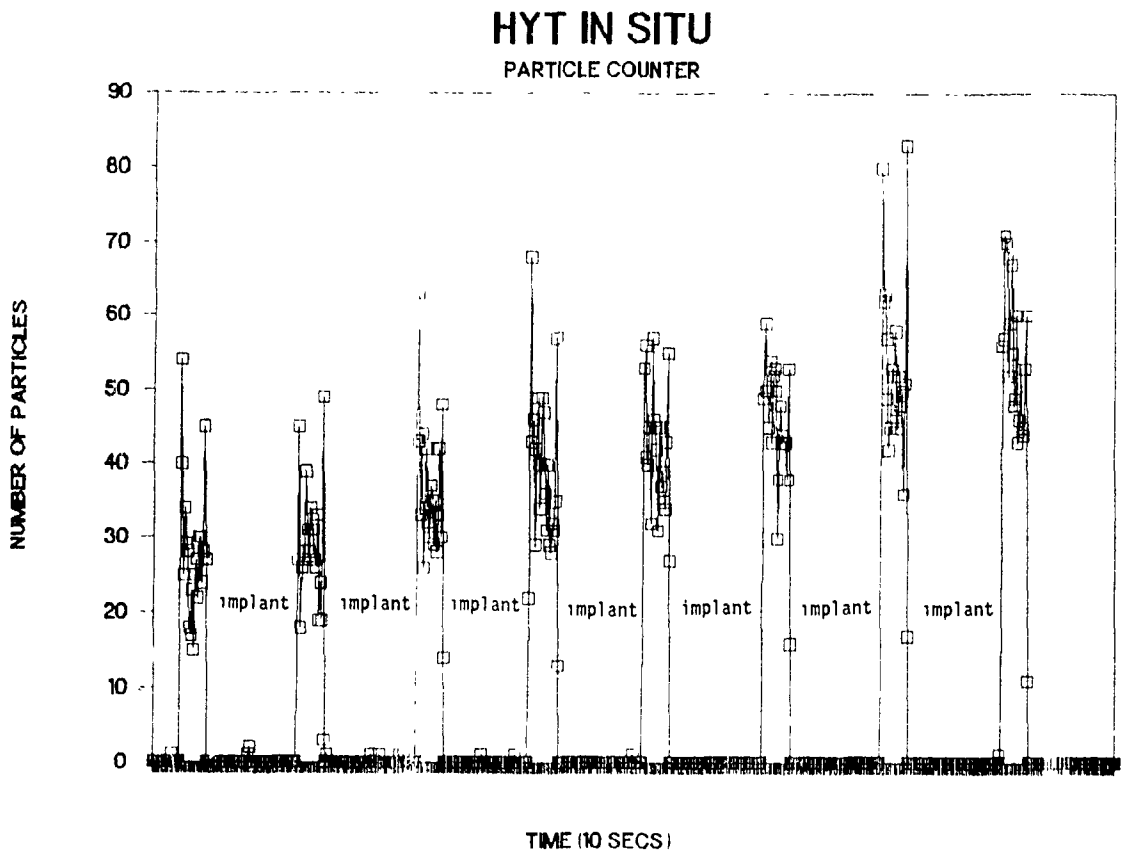

Fig 6 HYT in situ particle counter scan.

monitor for oil backstreaming The system is not complex, except for the custom vacuum piping. It has the ability to be used as a short term diagnostic tool, and in situ monitor, once "fingerprints" of each process step are obtained It is not capable of unattended operation due to its limitation of scanning for only two hours

The RGA illustrated the effectiveness of the protection from pump backstreaming on this machine The scan in fig 2 shows the levels of hydrocarbons and mechanical pump oils to be at barely detectable levels. A full scan of the AMU spectrum shows that all hydrocarbon levels are insignificant In the same figure, the diagnosis of a leaky valve is completely evident with the rise in nitrogen levels and the subsequent pumpdown cycle

The "fingerprint" of a typical implant can be seen in fig 3 This graph illustrates the sensitivity of the system with the detection of events on endstation one. The peaks associated with ^{11}B, BF_2, ^{19}F, ^{31}P and their downward trend as the implant continues suggests the beam sputtering of these dopant species from the disk. The peaks may correspond to the scan of the beam hitting the disk and causing sputtering of the dopants

Fig. 4 demonstrates the effectiveness of argon clean between species. The sharp rise in the argon peaks in the initiation of this procedure. The trend of all dopant species appears to be exponential in nature. The confirmation of this effect is seen in the effect of pumping on the water The water reaches baseline very quickly, while the dopant species continue downward An exponential curve fit may be possible.

Fig. 5 supports the findings of Larson et al [1–3] The H_1 and ^{12}C follow a very similar pattern. The N_1 peak exhibits a similar oscillatory nature, but this fact was noted by Larson [1] et al. as being thermal decomposition of sensitizer component of the resist. However, this fact does contradict his point that $> 50\,^{\circ}C$ softbake was enough to liberate nitrogen from the resist. The resist that was used for this experiment was softbaked at $90\,^{\circ}C$ for 60 s and Larson used a 45 min $90\,^{\circ}C$ softbake [1]. Therefore, this explains the difference in that the resist used in our experiment had more sensi-

tizer remaining This effect was seen only slightly in the first few scans due to lower temperature curing. This observation supports the fact that the resist outgassing is hydrogen evolution and is a beam interaction effect as duly noted by Smith, Okuyama, Larson, et al. [1–5].

4.2 In situ particle counter

The in situ particle counter in its present configuration had limited use on this machine. The majority of particles on the 180XP are less than 0.3 μm. The sensor has a lower limit of 0.5 μm with a 10% capture rate. The particle counter was helpful during one particle excursion event The event involved the burning of resist in the endstations due to low cooling water flow The particle counter was used to monitor vent/purge cycles to obtain a general trend The result was a downward trend from about 500–600 counts ≥ 0.5 μm

One failure encountered during the experiments resulted in the coating of the mirrors by sputtered resist. The coating was removed by cleaning with TCA while the head was out of the machine. This was disturbing in that the head failed after two weeks and low resist loading. This problem may be corrected by relocating the head, or possible heating of the mirrors

The instrument itself was user friendly. The software, supplied by the vendor, is necessary if the instrument is to be used for process monitoring, as it allows for continuous monitoring and storing of data.

5. Conclusions

We have concluded from this comparison that neither the RGA nor the particle counter are reliable and self-sustaining process monitors. The RGA protects against abnormal conditions of resist outgassing, argon clean, leaks and predictive regenerations of cryopumps The inability of the RGA computer to continuously monitor the process is the only disadvantage noted

The particle counter had a good interface with the user in that the software had the ability to continuously store and monitor the data without operator intervention. The rapid coating of the mirrors and the poor sensitivity of the head on this machine are the major flaws with the instrument.

Further areas of research include a comparison of different implanters using the RGA to obtain baseline fingerprints of the machines. A highly desirable investigation will be the effectiveness of inert gas cleaning using time and high voltage arcing as the independent and dependent variables Lastly, a correlation of the chemical analysis of particles to the RGA peaks would be useful for measurement of contamination sources

References

[1] B N. Mehrotra and L A Larson, Advanced Processing and Characterization of Semiconductors III, Proc SPIE, Vol 623, eds D K Sadana and M I Current (1986) p 78
[2] Y Okuyama, T Hashimoto and T Koguchi, J Electrochem Soc 125 (1978) 1293
[3] T C Smith, in, Ion Implantation Equipment and Techniques (Springer, Berlin, 1983) p. 2
[4] B. Raicu, in Ion Implantation Equipment and Techniques (Springer, Berlin, 1983) p 450
[5] D Roche, J F Merchand and M Bruel Ion Beam Processing in Advanced Electronic Materials and Device Technology, MRS Symp Proc , Vol 45, eds B R Appleton, F H Eisen and T W Sigmon (1985) p 203

Nuclear Instruments and Methods in Physics Research B55 (1991) 61-65
North-Holland

An analysis of vacuum effects on ion implanter performance

A. Renau, M.E. Mack, J.P. O'Connor and N. Tokoro

Genus Incorporated, Ion Technology Division, 4 Mulliken Way, Newburyport, MA 01950, USA

The generation of an ion beam and its impact into photoresist-masked wafers will have an adverse effect on the vacuum of an ion implanter. This is particularly significant when doping with boron using BF_3 or BCl_3 as the source feed material. As well as affecting high voltage performance, poor vacuum will allow charge exchange and partial neutralization of the ion beam which could cause energy contamination as well as dosimetry errors. The nature of these effects depends not only on the system design but also on the implanted species and its charge state and energy. This paper discusses these effects on ion implanter performance and shows how a matrix-based general vacuum model may be used to investigate vacuum integrity. A time-dependent vacuum model that simulates the effect of pressure on dosimetry is also described.

1. Introduction

For many years the semiconductor equipment industry has been aware of the adverse effects that poor vacuum can have on the ion implantation process. However, the very nature of ion beam generation from a gas or vapor source, its inefficient transport (mostly due to mass analysis) and the copious quantities of gas that can be produced on impact into the wafer have made this a recurring problem.

In this paper the most common of these adverse effects will be discussed and some simple techniques for improving vacuum system design will be described and illustrated. However, before doing this it is useful to identify and quantify the principal gas loads in a typical ion implanter.

2. Gas loads in an ion implanter

There are various types of gas load that can occur during implantation depending on the species being implanted and the feed material that is used. Each of these will now be described and illustrated, where possible, by using the example of a boron implant from a BF_3 gas feed.

2.1. Arc chamber

If the ion source of an implanter were 100% efficient then every standard cubic centimeter per minute (sccm) of flow into the arc chamber would produce 71.7 mA of singly ionized molecular beam current. However, because this is not usually true, gas or vapor which is not ionized will flow into the beamline.

$$Q_{\text{source}} = I_{\text{beam}} \frac{(\eta^{-1} - 1)}{71.7 f}, \quad (1)$$

where η is the ionization efficiency and f is the ratio of the analyzed beam current, I_{beam} (mA), to the total source drain current. Q_{source} is measured in sccm.

Both η and f depend on the type of source that is used and on the way that it is tuned. The modified hot cathode PIG source used on the Genus G1500 ion implanter [1], for example, has an ionization efficiency of around 0.4 to 0.45. For large-aperture Freeman sources this could be as low as 0.25, whilst efficiencies as high as 0.5 could be attained from sources that use more intense plasma densities. The value of f for BF_3 in the G1500 ion source is around 0.2 to 0.25 (fig. 1). For a well tuned Freeman source this could be as high as 0.4.

It should be noted that, particularly in the case of small extraction aperture sources, the usual conductance formulae for treating this gas load may not be appropriate because of streaming effects. This is discussed further in the section on the matrix method.

2.2. Analyzing magnet flight tube

When boron is being implanted using a BF_3 or BCl_3 feed gas a significant gas load is generated in the analyzing magnet flight tube. This occurs because unresolved halide ions are deposited on the flight tube walls. Since they are volatile they are likely to re-evolve as atomic F or F_2. If it is assumed that only a negligible amount of the extracted beam is intercepted by apertures before the flight tube then this gas load (sccm)

0168-583X/91/$03.50 © 1991 – Elsevier Science Publishers B.V. (North-Holland)

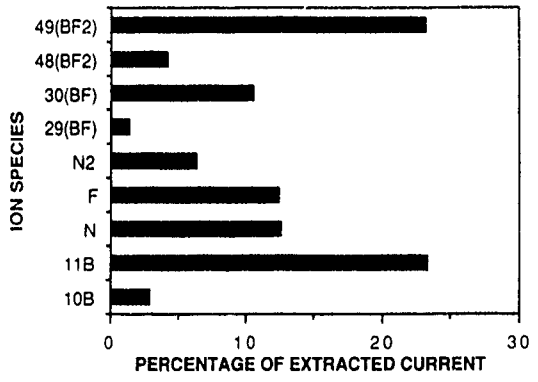

Fig. 1. Typical composition of the extracted beam from the G1500 PIG ion source

may be quantified in terms of the ratio, R, of the total ionized fluorine (atomic mA) in the source beam current to the ^{11}B current

$$Q_{F_2} = \frac{0.5R}{71.7} I_{beam} \quad (2)$$

As can be seen from fig 1, if the contributions from BF_2^+, BF^+ and F^+ are summed, the Genus PIG source has an R value of about 3 This gives the somewhat surprising result that the gas load at the flight tube is as high as 20% of that which leaves the ion source This is just a guideline, however, since R depends not only on the type of source used but also its tuning.

2 3 End station

There is a considerable outgassing load when implanting into photoresist. This is predominantly H_2 and the quantity produced is beam current and energy dependent. Looking at HPR204 positive photoresist, Smith [2] has shown that the outgassing rate (sccm) is highest at the beginning of an implant and remains fairly constant until a critical dose (of about 2×10^{14} cm^{-2}) has been reached:

$$Q_{H_2 max} = 0\ 014\ U\ M_g I_{beam}, \quad (3)$$

where the utilization, U, is the fraction of the beam that is incident on the wafer. For arsenic at 40, 80 and 160 keV Smith gives values for M_g of about 900, 1400 and 2600, respectively.

Using this data and that of O'Connor and Riley [3] and Roche et al. [4], a semi-empirical expression has been derived to describe the outgassing in more general terms:

$$Q_{H_2}(t) = \frac{0.81\ U(t) I_{beam} E^{0\ 765}}{\left(1 + D(t)/D_c\right)^2}, \quad (4)$$

where E is the beam energy in keV. It must be noted that the critical dose, D_c, that is used here is slightly different to that used by Smith because of the simple quadratic fall-off in outgassing rate that is assumed in this expression.

2.4. Other gas loads

Chamber outgassing loads are generally small compared with the other loads that have been discussed. However, this may not be true for graphite apertures or linings upon which the beam is incident. The composition and the rate of gas evolution is very dependent on the type of graphite used, its history and its operating temperature. This is discussed in more detail in a review article by Beitel [5].

In certain instances, additional gas loads are introduced intentionally into the implanter. In the Extrion 160-10 implanter [6], for example, a nitrogen bleed is used to control the effect of space charge on beam focussing. A number of machines also use an inert gas bleed as part of the system for generating low energy flood electrons (see, e g., Renau et al [7]). The quantity of gas which is used in these cases will generally vary from one implant to the next but is typically in the range 1 to 5 sccm

3. Problems caused by poor vacuum

Pressure related degradation of the beam can be represented generically by

$$\epsilon = 1 - \exp(-\mathcal{L}\sigma Pl), \quad (5)$$

where ϵ represents the fraction of the beam which is affected by a reaction for which the cross section is σ (cm^2) after the beam has traversed a path with a pressure-length product of Pl (Torr cm). $\mathcal{L}$ is the Loschmidt number (the number of molecules in a gas at $0\,^\circ C = 3.538 \times 10^{16}$ Torr^{-1} cm^{-3})

There are a number of reactions of this type which can affect the beam at different regions of the implanter Some of the most common will now be discussed

3 1. Dose and uniformity errors

When the ion beam propagates through an elevated pressure region the ions will be partially neutralized. The current arriving at the wafer (or Faraday cup) is no longer an accurate measure of the dose rate The dose will be affected if this reaction occurs anywhere after mass analysis (which filters out the neutrals) and before charge integration Photoresist outgassing is a major influence on the pressure of these regions The neutralization cross section, σ, varies with species, energy and gas type but, typically, it is in the range 10^{-16} to 10^{-15} cm^2.

3.2. Energy contamination

Neutralization or charge exchange (e.g., $A^+ + B^0 \rightarrow A^0 + B^+$) which occurs after analysis but prior to the beam being accelerated to its final energy will result in energy contamination as well as a dose error. The contaminant ions or neutrals will have a different projected range from the rest of the beam thus giving subsidiary peaks on the depth profile. The quantity of contaminant can be calculated from eq. (5). The pressure length product is now the path between the analyzing magnet and the beginning of the acceleration region. This is significant since it may be a poorly pumped region.

3.3. Molecular dissociation

Two common implants suffer because of molecular dissociation. The first is BF_2, which may dissociate in a number of ways after it has been analyzed but before it is accelerated to final energy. For example

$$BF_2^+ \rightarrow B^+ + F_2. \tag{6}$$

In this example, if V_{pre} and V_{post} are the pre- and post-analysis acceleration voltages then the desired implant energy for the boron is $(V_{pre} + V_{post}) \times 11/49$. However, boron from the ions which dissociate as in eq. (6), will have an implant energy which is $V_{post} \times 38/49$ greater than this. The significance of this reaction depends on how large the ratio V_{post}/V_{pre} is, since if it is small the contaminant depth profile may not be noticeable.

The second type of dissociative reaction can occur whenever multiply charged ions are used for implant. Generally only a small fraction of the ion source's output is multiply charged and so dissociation of any of the molecular output prior to analysis can produce a significant contaminant. This can be illustrated by considering a P^{2+} implant. The reaction of interest is:

$$P_2^+ \rightarrow P^+ + P^0 \tag{7}$$

The amount of P^+ produced above can be significant since P_2^+ is generated in much larger quantities by the ion source than P^{2+} [8]. The P^+ produced in this way has almost exactly a quarter of the energy of the P^{2+} and, hence, the same magnetic rigidity. The contaminant ion will therefore be transmitted. However, its implant energy will be $V_{post} + 1.5V_{pre}$ lower than required.

In the context of multiply charged implants it must also be noted that the charge exchange cross sections for these ions are large [8] and so post-analysis energy contamination, as described in section 3.2, can be a major problem.

3.4. General problems

Of the more general problems caused by poor vacuum perhaps the most significant is increased X-ray levels. This occurs because electrons produced by ionization of neutrals can be accelerated in the opposite direction to the ion beam and produce X-rays on impact into high-Z (typically metallic) targets. As well as the obvious safety hazards, these may degrade the high voltage operation of the machine since an X-ray which strikes an insulator can cause photo-ionization which can, in turn, lead to electrical breakdown.

4. Analytical and modelling aids to vacuum design

All of the problems that have been discussed can be reduced greatly by a better approach to vacuum system design. A number of simple theoretical tools have been developed to assist with this process, two of which will be outlined here. A more detailed account will be given in a future publication.

4.1. Matrix method for calculating pressure distributions

If the implanter is considered to be composed of a number of distinct regions in which the pressure is uniform then, with a knowledge of the conductances between each region, it is possible to apply the equation of continuity and calculate the pressure throughout the system:

$$Q_i = P_i S_i + \sum_{k=1}^{n} (P_i - P_k) c_{ik}, \tag{8}$$

where Q_i is the mass flow produced in the ith region and P_i and S_i are the pressure and applied pumping speed. c_{ik} is the conductance between ith and kth elements. Since most regions are not adjacent to each other, most of the c_{ik} values will be zero.

This series of equations lend themselves readily to matrix solution:

$$\begin{pmatrix} S_1 + C_1 & -c_{12} & -c_{13} & & -c_{1n} \\ -c_{21} & S_2 + C_2 & -c_{23} & & -c_{2n} \\ -c_{31} & -c_{32} & S_3 + C_3 & \cdots & -c_{3n} \\ \vdots & \vdots & \vdots & & \vdots \\ -c_{n1} & -c_{n2} & -c_{n3} & & S_n + C_n \end{pmatrix} \begin{pmatrix} P_1 \\ P_2 \\ P_3 \\ \vdots \\ P_n \end{pmatrix} = \begin{pmatrix} Q_1 \\ Q_2 \\ Q_3 \\ \vdots \\ Q_n \end{pmatrix}, \tag{9}$$

where:

$$C_i = \sum_{k=1}^{n} c_{ik}.$$

In the above summation c_{ii} is ignored. The rest of the conductance matrix is readily calculable by using, for example, the various formulae that are given by Roth [9]. For gas loads which have some directionality (streaming) such as the ion source and, in some cases, wafer outgassing, the load matrix may be adjusted to account for this. Assuming molecular flow, it is relatively easy to integrate the velocity distribution (which is probably cosine [9]) over the emitting surface and, thereby, calculate what fraction of the load will flow directly, without collision, into another region. In this way the load from, say, the ion source may be distributed, according to the geometry, between the extraction region, the post-extraction region and the flight tube.

After matrix inversion and multiplication, a piecewise solution to the pressure distribution can be obtained More elements can be used to model regions of particular interest or regions which have a significant pressure gradient. Since the pumping speeds, conductances and loads are gas type dependent, the matrix equation must be solved for each of the partial pressures These may then be summed and, with the relevant cross sections, the impact on the implantation process assessed

To demonstrate the use of this technique, two similarly priced approaches to beamline pumping are compared in fig. 2 In the first, the conductance between the end station and the beamline is minimized. Pumping is done at the terminal end which, for practical reasons, limits the pump size In contrast, the second approach uses a larger (cryogenic) pump at ground potential and maximizes the conductance from the beamline.

When, as in this example, photoresist outgassing is of concern, a useful figure of merit is the normalized effective path-length, L_{eff}. This is the total pressure–length product for beam neutralization, normalized to the end station pressure and is readily calculable from the model. It can be seen from the example illustrated that the open conductance approach to beamline pumping offers considerable advantages.

4.2. Time dependent pressure variations

For problems like photoresist outgassing, the pressure and gas loads are not constant. In such cases it is necessary to refine the technique for analyzing the vacuum. Starting once again from the equation of continuity:

$$V\frac{dP(t)}{dt} = Q_{\text{in}}(t) - SP(t), \tag{10}$$

where V is the region's volume and $Q_{\text{in}}(t)$ is the load, it can be shown, by integration, that

$$P(t+\Delta t) = \frac{Q_{\text{in}}(t)}{S} + \left[P(t) - \frac{Q_{\text{in}}(t)}{S}\right]\exp\left(\frac{-S\,\Delta t}{V}\right) \tag{11}$$

Using this expression, the evolution of the system's pressure can be traced in short time steps (Δt).

In this case of photoresist outgassing, the load is given by eq (4) along with an ambient load which represents chamber outgassing.

$$Q_{\text{in}} = Q_{H_2} + SP_{\text{ultimate}}. \tag{12}$$

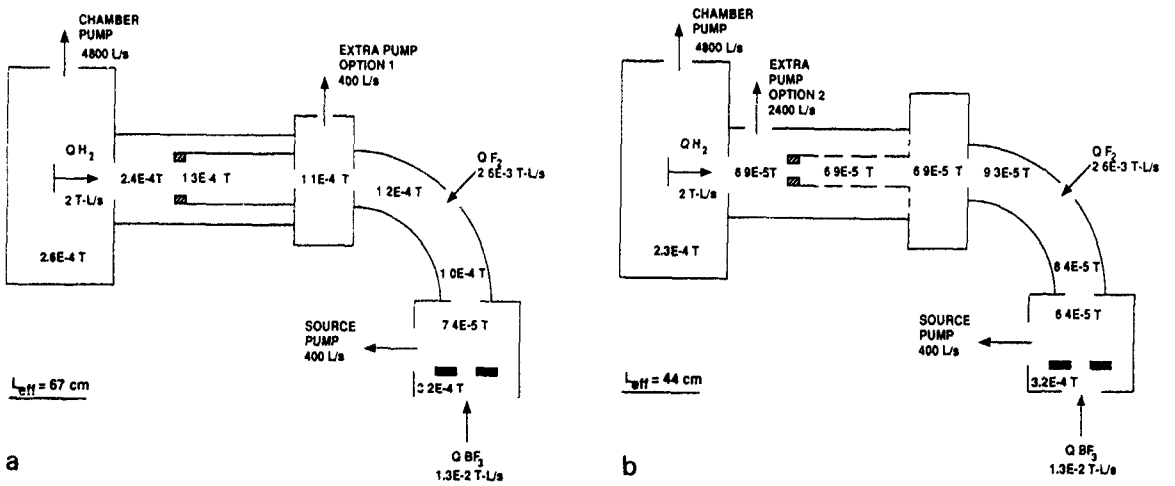

Fig 2 Calculated total pressure distributions in a "generic" implanter. Assuming typical loads and geometries, the effectiveness of (a) directly pumping the beamline from the terminal can be compared to (b) an open conductance design with additional pumping from the ground level. Although both approaches have similar cost, the effective path length (see text) in (a) is 67 cm whilst in (b) it is reduced to 44 cm The pumping speeds given are for nitrogen

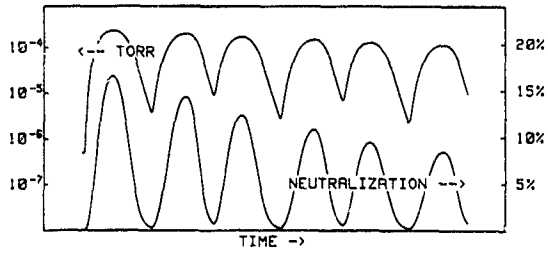

Fig 3 End station pressure and beam current modulation in a batch machine The photoresist outgassing load is calculated from eq (4) with the utilization factor varying as the wafers scan in and out of the beam.

An example of the pressure fluctuations in a batch end station is shown in fig. 3, along with the effect that this has on the beam current assuming an effective normalized path length of 44 cm (see fig. 2) and a neutralization cross section of 5×10^{-16} cm^2. It can be seen that, if the dosimetry system is not designed to cope with this, the effect on dose uniformity is severe.

5. Conclusion

The principal gas loads in an implanter have been quantified and the various detrimental process effects of poor vacuum have been discusssed. A simple tool that can be used for vacuum system design has been described and its use illustrated. The extension of the model to analysis of the effects of time-dependent photoresist outgassing has also been described and demonstrated.

References

[1] N Tokoro, J.P. O'Connor, A Renau and M E Mack, these Proceedings (8th Int Conf on Ion Implantation Technology, Guildford, UK, 1990) Nucl Instr and Meth. B55 (1991) 434
[2] T.C. Smith, in Ion Implantation Science and Technology (2nd ed), ed. J F Ziegler (Academic Press, 1988)
[3] J P O'Connor and J.T Riley, Mater Sci. Eng B2 (1989) 177
[4] D Roche, J.F. Michaud and M Bruel, Mater Res Soc. Symp Proc., 623 (1985) 203
[5] G E Beitel, J. Vac Sci Technol. 8 (1971) 647
[6] R. Liebert, B Pedersen, C. Ehrlich and W Callahan, Nucl Instr. and Meth B6 (1985) 16
[7] A Renau, S Moffatt and F Plumb, U S. Patent Number 4825087 (1989)
[8] J.H Freeman, D.J Chivers and G A. Gard, Nucl Instr. and Meth 143 (1977) 99
[9] A Roth, Vacuum Technology, 2nd ed (North-Holland, 1982)

Nuclear Instruments and Methods in Physics Research B55 (1991) 66–70
North-Holland

Particle contamination control in the EXTRION 220

R. Milgate and J. Pollock

Varian Ion Implant Systems, Blackburn Industrial Park, Gloucester, MA 01930, USA

The design philosophy of the EXTRION 220, a serial implanter, with regard to particle contamination is discussed. The implanter is a hybrid electrostatic/mechanical scan system offering unique performance characteristics Particle control has been studied under stringent test conditions. The evolution of the particle control hardware is explained Data documenting particle contamination levels is presented

1. Introduction

Particle contamination continues to be one of the most important factors affecting yields today in integrated circuit manufacturing. With device geometries shrinking and chip areas growing, equipment requirements governing the allowable size and quantity of particles added to wafers during processing are being tightened accordingly. Ion implantation process cleanliness has become increasingly important because many of the more advanced circuits now being manufactured require multiple implant steps, some as many as 15 [1].

The EXTRION 220 is a new generation medium current ion implanter which has most recently demonstrated outstanding particle performance in the field This paper discusses the initial design philosophies and strategies, describes the wafer handling system, outlines the design evolution of hardware, and presents factory test and field performance data.

2. Design philosophy / system description

The endstation of the EXTRION 220 performs both wafer handling and mechanical scanning functions. The design has concentrated on maximizing reliability and

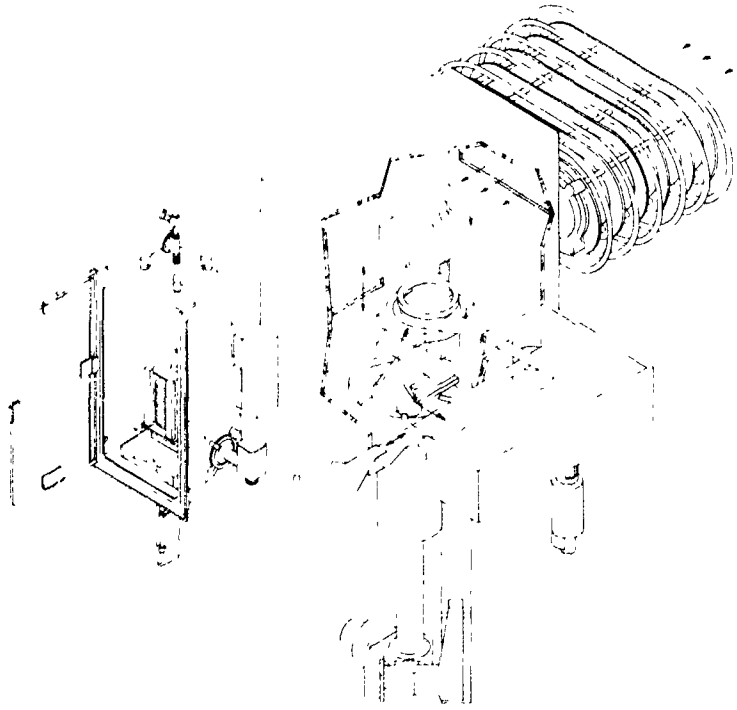

Fig 1. Schematic isometric view of the EXTRION 220 endstation A pair of two-axis wafer handlers pick and place wafers in vacuum

0168-583X/91/$03.50 © 1991 – Elsevier Science Publishers B V (North-Holland)

wafer safety while minimizing wafer contamination. Design philosophies were based primarily on experiences with earlier generation ion implanter particle optimization efforts. Much progress towards reducing contamination levels had already been made on these earlier systems, like the EXTRION 350D and 300XP, with respectable field performance being readily attained after installing retrofit hardware [2]. Despite the encouraging results, it had become clear that the fundamental concept of handling wafers in air and sequentially loadlocking them into the main process chamber was a severely limiting factor in achieving particle performance levels good enough to meet future requirements. Also, edge handling of wafers had been identified as a contributing source of particles in the endstation [3]. These two important observations helped in shaping the EXTRION 220 endstation design concept which became a system using batch vacuum loadlocking of wafers in cassettes, with backside handling of wafers in high vacuum using gentle pick and place methods.

The EXTRION 220 wafer handling system is an in-vacuum horizontal design which handles wafers of up to 200 mm directly from SEMI standard wafer cassettes. Fig 1 shows a schematic isometric view of this system. One centrally located implant site is "served" by a pair of two-axis wafer handlers, one located on each side of the process chamber. Each handler can alternately load and/or unload wafers to and from the horizontally oriented platen by rotating from its neutral "home" position. A wafer lifter built into the implant platen provides the vertical lifting of the wafer to make exchanges with the handlers Two vacuum elevator loadlocks are also served by the same two handlers, with one handler/elevator pair dedicated to each side of the machine (see fig. 2) With the rotary axis of the handler locked, the handler can be translated in and out of the elevator to make wafer exchanges with the cassette Vertical motion of the elevator provides the gentle pick and place exchange with the handlers When the wafer handler is parked at its "home" position, the wafer orienter, below, can make an upward move to contact and lift the wafer from the pick The orienter spins the wafer while an optical detector maps its edge profile. The orienter aligns the wafer flat and centrally replaces the wafer on the pick

All wafer handling motions are motor driven and motion profiled to control acceleration forces acting on the wafers Wafer slippage is prevented and wafer throughput is maximized because mechanisms are run slowly when carrying wafers and fast when not All of the handler mechanisms operate in vacuum, below the wafer handling plane, so that any particulate matter generated by them will fall to the floor of the chamber. Wafers (up to two cassettes full at a time), are brought into the process chamber through the vacuum elevator loadlocks. Because the load-locks were the only chambers to be vacuum cycled during normal machine use, extra careful attention was paid to the design, selection and positioning of components whithin them Motion feedthroughs were located at the bottom of the load lock chamber, adjacent to the rough pumping port, while the vent port was located in the roof of the load lock. A description of the design evolution of the loadlock vent system follows.

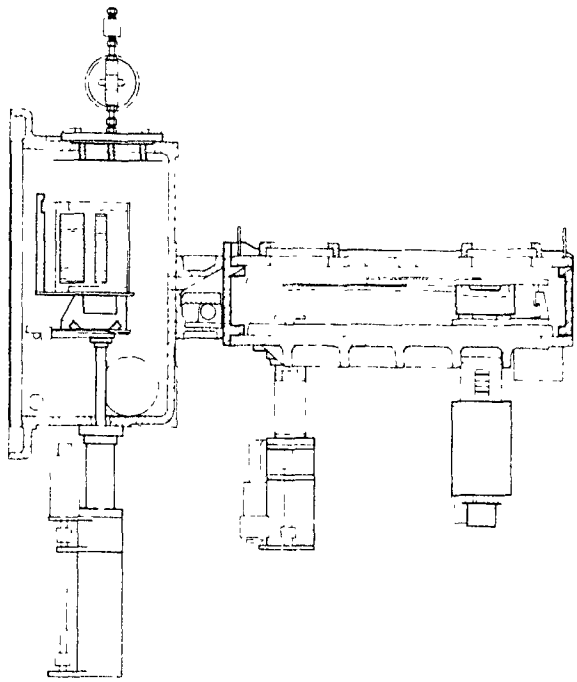

Fig 2. Elevation view of the wafer handler, orienter, and cassette elevator

3. Design evolution

The loadlocks of the EXTRION 220 have remained essentially unchanged throughout the machine's production history, however the venting systems have been revised a number of times (see fig 3). These design improvements have been driven by our observations and theories regarding the effects of gas flow in the loadlocks on wafer surface particle contamination

Recognizing that it would be economically unfeasible, if not impossible, to eliminate every potential particle source in the machine, a more realistic approach was taken, which was to minimize those sources and concentrate on controlling the mechanisms of particle transport. By handling in vacuum, the unpredictable effects of aerodynamic forces on particle transport have been eliminated This in-vacuum handling concept, combined with a handler layout which constrains all the particle generating hardware to be below the wafer

plane, has resulted in a very clean overall design. Early experiments on a prototype EXTRION 220 revealed that the majority of particles were added during gas exchange in the loadlocks, thus validating in-vacuum handling. It also made clear the need to focus on the loadlocks to improve particle performance. Even after improving machine performance to as low as 0.009 particles per cm^2 at 0.3 μm and larger, recent experiments still show that loadlocks are the *only* significant contributor in the EXTRION 220.

The contamination levels in the loadlocks have been reduced by modifying the gas flow into them during venting. To understand the importance of the gas exchange, particularly during venting, it is necessary to consider the mechanics of particle liberation and transport

Near atmospheric pressure, the movement of airborne particles of submicron size is strongly a function of aerodynamic forces The aerodynamic forces acting on these particles are orders of magnitude greater than the force of gravity [4]. However, if these particles come in contact with a surface, they become bound quite tightly there by van der Waals forces. With submicron separations these strong adhesive forces are also much greater than gravitational ones [4] The size of these attached particles makes them all but impervious to further aerodynamic effects as they are small enough to effectively "hide" under the boundary layer that forms between the surface and the surrounding gas flow. There is, however, a gas flow condition which *is* capable of liberating these tightly bound particles, namely sonically choked flow

The condition of sonically choked flow is well known in gas dynamics Briefly stated, whenever the pressure ratio across an orifice becomes less than the critical pressure ratio, flow becomes independent of downstream pressure Regarding particle contamination the significance of this phenomenon lies in what occurs on the downstream side of the orifice during a period of sonically choked flow A plume of locally supersonic, relatively high density gas (compared to the surrounding gas) is formed. This plume of gas is quite well defined, being roughly conical in shape, with its length and diameter determined by the size of the orifice,the pressure on the downstream side of the orifice and the pressure ratio [5]. As the critical pressure ratio for N_2 at standard temperature and pressure is about 0 53, it can be seen that, unless special precautions are taken to avoid it, the condition of sonically choked flow exists whenever a vacuum vessel is vented. During the first few seconds of venting, when the pressure ratio is large, this gas jet has enormous ability to liberate particles from surfaces it comes in contact with This is because the density outside the jet is low, so little or no boundary layer can form at the gas/surface interface. With no protective boundary layer to hide under, the attached particles encounter the full aerodynamic drag forces applied by the gas flow, and are easily stripped away, making them available for redistribution within the load lock

This jet also forms during rough vacuum pumping. In this case, however, it forms within the roughing manifold (not in the loadlock) Provided the roughing manifold is properly designed, particles liberated in the manifold during roughing will not contaminate the loadlock It should be noted that the particle contribution associated with rough pumping a chamber is very dependent on chamber and manifold geometry If flow restrictions are present within the chamber which allow pressure differences greater than the critical pressure ratio to develop during rough pumping, then techniques such as soft start pumping or staged rough pumping may have a significant effect on particle contamination levels Experiments with these devices, however, have shown that they do not significantly improve particle performance when used on the EXTRION 220

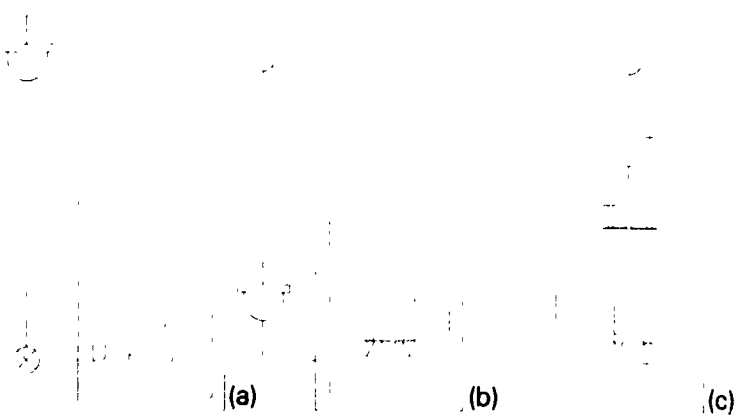

Fig 3. Schematic diagram showing the design evolution of the loadlock venting configuration

The initial configuration of the loadlock provided unidirectional gas flow which had been shown to be important for good particle performance [6], but did not control the shock wave. During prototype evaluation this configuration produced disappointing results (> 1.0 particles/cm^2 at 0.5 μm and larger) which in retrospect, should have been expected.

Fig. 3 shows schematically a history of venting configurations. The first production configuration (fig. 3a) used a number of small orifices to control the rate of flow of vent gas into the chamber The intent was to minimize the size of the jets and place the orifices within the loadlock such that any particles liberated during venting would be confined to an area below the wafer cassette Typical performance measured was 0 077 particles/cm^2 at 0.5 μm and larger for this configuration

A variation of this first production configuration changed the relative locations of the vent shut-off valves and the vent filters, and replaced the multiple orifice vent tube with a single orifice (see fig 3b). Downstream filtration was used to protect the loadlock from particles generated by the valve. This system demonstrated particle performance of 0 066 particles/cm^2 at 0 5 μm and larger This was an insignificant improvement

Although the particle performance was respectable, it fell far short of our goals Additionally, the long vent times being used had significantly decreased wafer throughput At this point in time Mears and others [7] were reportedly demonstrating excellent loadlock particle performance with rapid venting After reviewing the contamination results and the vent design, it appeared that they key to that system was the placement of the point of use filter, truly at the point of entry into the chamber, with no downstream flow restrictions It was postulated that the shock wave was forming on the upstream side of the filter, downstream of the shutoff valve The poor conductance across the filter combined with a lack of restrictions beyond it, prevented the formation of any subsequent shock waves

Based on these observations, a similar vent configuration for the EXTRION 220 was built and tested, which put the vent assembly back on the roof of the loadlock Results were mixed vent times were rapid, particle levels were low, but the top wafer in the cassette was consistently an order of magnitude dirtier than the others Since the problem was confined to the top slice, and the particle size distribution was not biased to large particle sizes, it was felt that this effect was associated with some event in the early portion of the vent cycle Consider, had these particles *not* attached to the top wafer by the time pressures were high enough to sustain airborne particle motion then *all* the wafers in the cassette would have been fairly uniformly contaminated This was not the case

To eliminate the top wafer effect it was decided to permanently install a baffle in the loadlock, directly below the vent port This arrangement (fig. 3c) is the venting system which is in use today. This configuration eliminated the top wafer effect, reduced actual vent times to well under one minute, and demonstrated particle performance levels as low as 0.009 particles/cm^2 at 0 3 μm and larger.

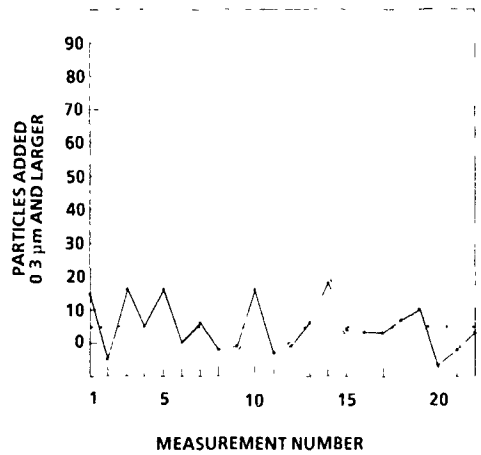

Fig 4 History of particles added to wafers run on a system in around-the-clock production, after having its loadlocks upgraded to the current vent configuration

Fig. 4 shows particle performance history of a 200 mm implanter running product wafers, 168 hours per week using this venting configuration The particle measurements made over a 4-day period showed an average number added of 4.6 particles (0 016 particles per cm^2) at 0 3 μm and larger, with a standard deviation of 7 7

4. Summary

Early experiments regarding particle contamination in the EXTRION 220 verified that the wafer handling concepts were sound, but in order to achieve good contamination control, improvements would be required in the loadlock area The key to making these improvements was controlling the shock wave associated with the venting process. Using flow restrictions to control this shock wave improved particle performance but decreased wafer throughput A final configuration embodying a baffle plate and point of use filtration to achieve shock wave control gave satisfactory results. Field machines fitted with this configuration have reported contamination levels averaging between 0 01 and 0.05 particles per cm^2 at 0 3 μm and larger sizes

Despite the improvements, loadlocks are still the major contributor to particle contamination The fact that a baffle is required to avoid top wafer effects indicates that there is room for further improvement. Loadlock performance as good as 0 003 particles/per

cm^2 at 0.3 μm and larger has been demonstrated with wafers oriented face down. This suggests that there are still liberation problems to address, and that at lower levels of contamination gravitational transport is a consideration. Presumably, this distribution occurs during the time when the lock pressure is too low to sustain airborne particle suspension, a condition which obviously occurs during roughing as well as venting. Additionally, experiments reported by Bader and Strasser [8] indicate that staged or profiled venting could improve loadlock performance to levels better than 0.001 per cm^2.

It is only by understanding the nature of particle liberation and transport that handling systems and loadlocks can be designed to minimize wafer surface contamination. By considering these points, it is possible to manufacture reliable equipment which meets users requirements for both cleanliness and wafer throughput without resorting to the use of exotic materials or expensive components

References

[1] T.C Smith, Nucl Instr and Meth B37/38 (1989) 487
[2] R Milgate and R Simonton, Nucl. Instr and Meth B21 (1987) 383
[3] W H. Weisenberger and M. McCullough, Nucl. Instr and Meth. B6 (1985) 190
[4] W.C. Hinds, in: Aerosol Technology, Properties, Behavior and Measurement of Airborne Particles (Wiley, New York, 1982) p. 130.
[5] B W Schumacher, Ontario Research Foundation, Physics Research Report no. 5806 (1962) p 19
[6] J Pollock et al., Nucl Instr and Meth. B6 (1985) 202
[7] E Mears et al., Wafer Particle Contamination Isolation and Control in the Varian/EXTRION 1000 Ion Implanter (to be published)
[8] G Strasser and M Bader, Microcontamination 8 (1990) 45

Nuclear Instruments and Methods in Physics Research B55 (1991) 71–76
North-Holland

Control of metal contamination in the Varian Extrion 1000 ion implantation system

Reuel B. Liebert, Shu Satoh, Bjorn O. Pedersen, Daniel F. Downey, Takao Sakase and Edward Evans

Varian / Ion Implant Systems, 35 Dory Road, Blackburn Industrial Park, Gloucester, MA 01930-2297, USA

The rapid development of higher-density device structures in recent years has focussed increased attention on all defect-producing by-products of the ion implantation process. In the past, the well-known effects of alkali and transition metals have constrained the materials technology used in ion-source and beam-transport systems of ion implanters. The next generation of high-current ion implanters is being challenged with requirements for minimization of defects caused by other contamination sources. This paper presents data on the levels of metal contamination produced in typical high-dose implants on the Varian Extrion 1000 implanter. It is shown that the aluminum contamination level has been reduced by greater than a factor of 13 using masking techniques.

1. Introduction

The Varian Extrion 1000 ion implantation system, described in a previous paper [1], is a high-current batch implanter covering the 5–200 keV range in energy and using beam currents between 1 μA and 27 mA. In any ion implanter, the ion-beam transport system contains defining apertures, beam dumps to accept unwanted beams, accelerating electrodes and other surfaces which can contact the beam in either steady-state implantation, during the tuning process, or under a fault condition such as a high-voltage spark or sudden pressure burst. The transport system of the Extrion 1000, shown in fig. 1, is designed to allow this contact only on graphite surfaces with the following exceptions:

(a) wafer disc – constructed of aluminum and using wafer retention pads of aluminum,
(b) overscan collector (commonly called the "spillover cup" – constructed of aluminum,
(c) acceleration tube electrodes – constructed of aluminum but guarded from beam interception by upstream beam apertures made of graphite;
(d) small annular region on the outside of the beam gate – constructed of aluminum and retracted from the beam path during implantation;
(e) ion source materials – include molybdenum and tungsten as well as graphite exposed to plasma regions.

Each of these areas is presently being studied experimentally or is in redesign to reduce potential metal contributions. The alternate material of choice is silicon because of expectations that carbon will eventually become a leading contaminant after the others are reduced to tolerable levels. The present study characterizes the performance of the "standard" model Extrion 1000 and evaluates the reduction of aluminum contamination with a system upgrade which masks the disc and overscan area with silicon.

2. Experimental

Several methods were employed to analyze the metal contents of implants done on the Extrion 1000. Total metal doses were measured for some metals using ICPMS (inductively coupled plasma mass spectroscopy). This technique analyzes implanted oxide layers after stripping them chemically. It suffers from interferences and nonrepeatability for some elements (e.g. aluminum) and is susceptible to errors associated with impurities absorbed during the oxidation process.

SIMS analysis offers depth information and was found to be effective in producing integrated dose information for some metals such as aluminum and chromium. Its sensitivity is limited for some elements and it is also sensitive to surface particle contamination which can mimic implanted impurities at the levels found in implanters.

TXRF (total-reflection X-ray fluorescence) was used to search for tungsten on wafer surfaces deposited during electron-flood operation.

SIMS and TXRF analysis was performed by Charles Evans & Associates (Evans East), while the ICPMS analysis was performed by Balasz Laboratories.

The Extrion 1000 was evaluated in three phases using 150 mm wafers.

(a) The performance of the existing system was evaluated using SIMS data for several BF_2 and As implants which were considered typical medium- to high-dose implants.

0168-583X/91/$03.50 © 1991 – Elsevier Science Publishers B.V. (North-Holland)

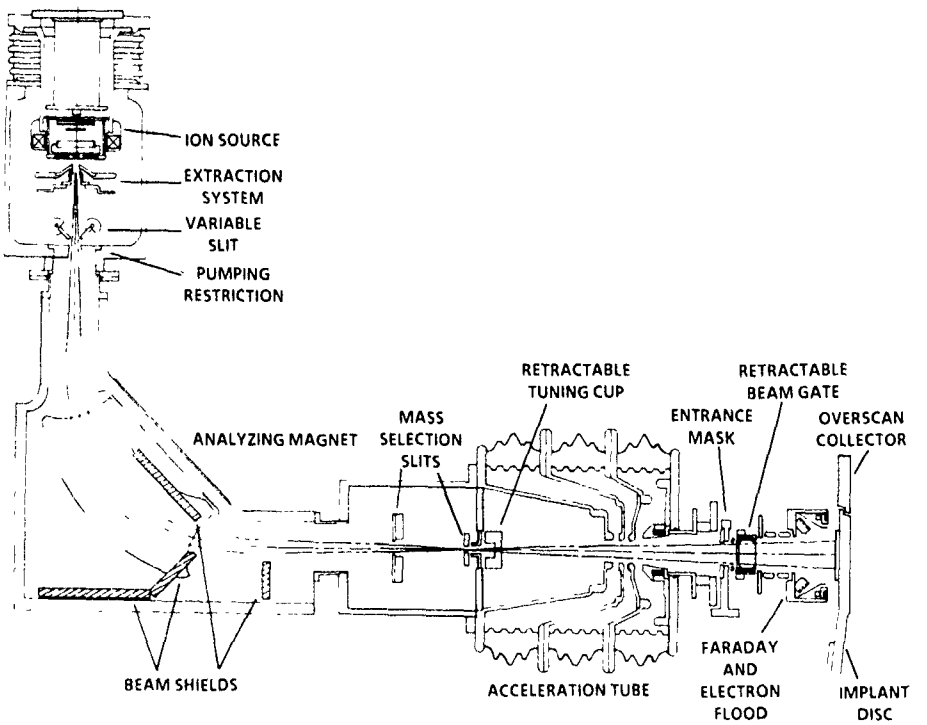

Fig 1 The ion-beam transport system of the Extrion 1000 is shown in schematic form. All areas designed for beam definition are made of carbon.

(b) The "worst-case" high-dose As implant was chosen for a case study.
(c) The overscan collector (spillover cup) was covered with a silicon wafer and the overscan reduced to remove a 1 25 cm annulus of safety margin around the wafer.
(d) The disc was flame-sprayed with 0.075 mm of silicon The coating was inspected after all the implant tests and numerous other implants and found to be undamaged.

The analysis results are discussed in the following section

3. Results

Table 1 shows contamination results from integrating SIMS profiles for aluminum and chromium in arsenic and boron implants and for molybdenum in a BF_2 implant for a variety of energies, beam currents and doses. The worst-case situation occurs for the acceleration mode which is used for high-current arsenic beams at intermediate energies. Lower energies use a drift mode in which no voltage is impressed on the tube Only boron beams are typically used in the deceleration mode which puts large and opposite gradients in sec-

Table 1
Contamination for selected elements before upgrade

Species	Dose [atoms/cm^2]	Energy [keV]	Transport mode	Ion current [mA]	Fraction of implanted dose [ppm]		
					Al	Cr	Mo
As	9×10^{15}	30	drift	6	366	19	
				10 6	548	19	
	5×10^{15}	50	drift	15	95	8	
	1×10^{16}	80	low accel	19 5	1071	32	
	5×10^{15}	160	high accel	12	276	7	
B	2×10^{15}	5	decel	2 8	[a]	[a]	
BF_2	1×10^{15}	80	low accel	7.6	[a]	[a]	130

[a] Below reference wafer correction levels.

tions of the tube, but the low energy of the light boron beam prevents any significant levels of aluminum or chromium from being found Fig. 2 shows the SIMS spectrum for one of the BF_2 wafers and fig. 3 shows the worst-case arsenic implant. It was found that the reference wafers showed a substantial metal content: approximately 2.3×10^{12} and 4.8×10^{10} atoms/cm^2, respectively, for Al and Cr on p-type wafers, while the n-type wafers had corresponding values of 7.6×10^{11} and 2.0×10^{11} atoms/cm^2. Fig. 4 shows a spectrum of an unimplanted reference wafer in which it can be seen that the aluminum peak is much shallower than that seen in the implanted wafers. In all cases, average values of the reference (unimplanted) wafers were subtracted from the raw data to produce the results quoted in the tables and figures

The results are estimated to have a precision of approximately 100–150 ppm (expressed as a fraction of the dopant dose) for aluminum in 1×10^{16} cm^{-2} implants and 20–40 ppm for chromium. No molybdenum subtractions were done because no reference wafers were available for the molybdenum data. The fluctuations between wafers at the same experimental conditions imply that the precision is of the order of 30–50 ppm on a 5×10^{15} cm^{-2} implant

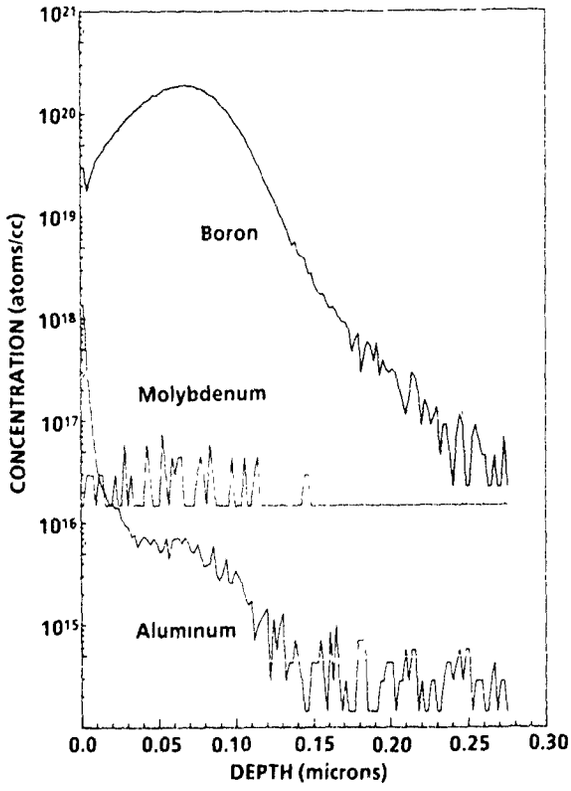

Fig 2 SIMS profile for a BF_2-implanted dose of 1×10^{15} atoms/cm^2 at 80 keV. $^{98}Mo^{++}$ will pass through with the BF_2-analyzed beam

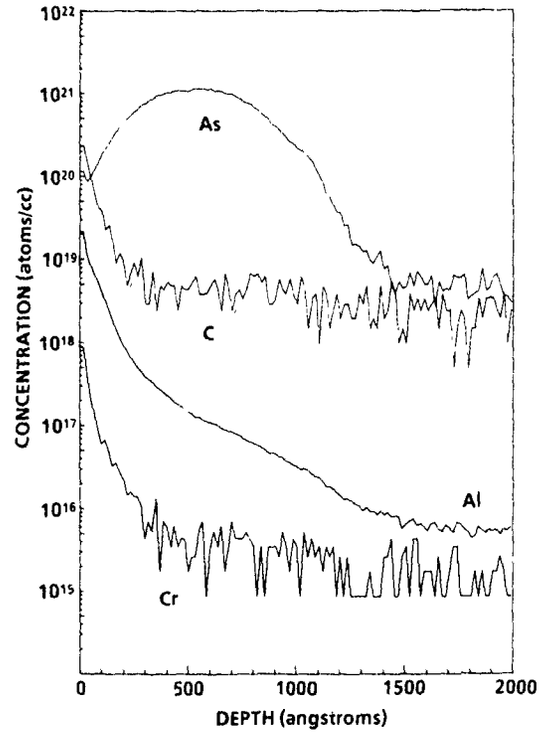

Fig 3 Arsenic implant before upgrades showing the highest fraction of aluminum content in the current tests The implant dose was 1×10^{16} atoms/cm^2 with a beam energy of 80 keV and a current of 19 5 mA

Table 2 shows the integrated SIMS data which resulted from successive runs using a masked spillover cup (graphite), a reduced overscan and masked spillover cup (silicon), and a combination of a silicon-masked spillover cup, a silicon-coated disc and reduced overscan The net effect of the upgrades is to reduce the aluminum fraction from 1071 to 80 ppm (shown graphically in fig. 5). Figs. 6a and 6b show the SIMS profiles which result from adding the graphite spillover cup and the silicon-covered disc configurations, respectively The latter also included a silicon-covered spillover cup and a reduced overscan The results for other trace elements were looked at using ICPMS in the case of the graphite-covered spillover cup and are given in table 3 No reference wafer data was subtracted, and, therefore, the results are considered conservative upper-limit values. The molybdenum contribution for this implant is expected to be lower than in BF_2 implants because of the coincidence of Mo^{++} with BF_2 for the 24% fraction of the molybdenum isotope with mass 98 The largest contributor is the iron peak, and it is seen to reduce by a factor of 3 8 from the original values.

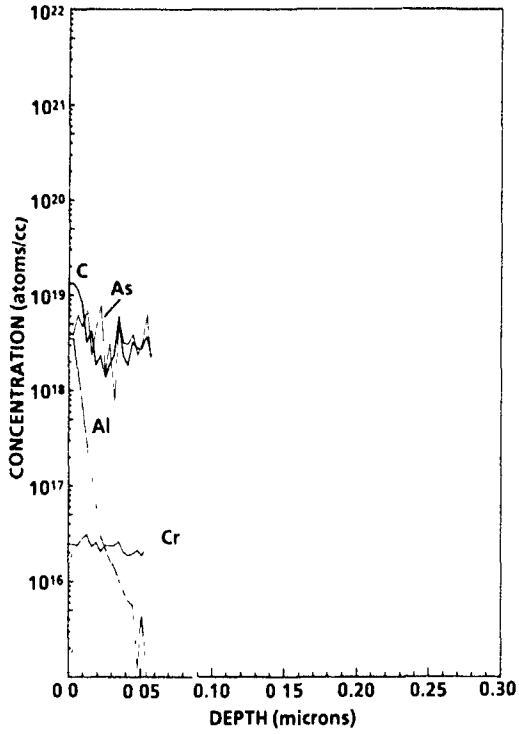

Fig 4 SIMS profile of unimplanted wafer used for reference in background subtractions The aluminum profile drops to low levels in the first 30 nm and to the detection limit in 70 nm

An experiment was also performed on the standard configuration system to determine if any tungsten was detectable from the electron-flood system during implantation Fig. 7 shows the TXRF spectrum for an arsenic implant of 5×10^{15} atoms/cm^2 at 50 keV. No tungsten was found at the detection limit of the technique (approximately 8×10^{10} atoms/cm^2 or 16 ppm of the implant). A peak of iron was found at the 50 ppm level but was unaffected by turning the flood gun on or off. No detectable levels of copper or zinc were found (at approximately 20 ppm detection limit).

Table 3
The effect of spillover-cup upgrade: ICPMS analysis is presented for a selection of metals; the data was taken for As$^+$ 1×10^{16} atoms/cm^2 implants at 80 keV

	Fraction of implanted dose [ppm]				
	Mo	Cu	Cr	Fe	Zn
Standard configuration before upgrade	2	44	84	504	59
Graphite-covered spillover cup	1	17	7	133	28

4. Analysis

The data on the standard-configuration machine show that a substantial aluminum contamination (0 1% of the incident implant) can be obtained under conditions of large incident ions (As) and large beam current Table 4 shows the result of numerical simulations of the sputtering of aluminum from the overscan regions There are three competing effects: dwell time of the beam on overscan surfaces, solid angle for sputtered atoms landing on wafers, and occlusion of the sputtered atoms by the Faraday assembly The dwell time is larger on the outside overscan than on the inside, but the solid angle for sputtering onto the wafer area is larger on the inside. Occlusion by the Faraday is negligible on the outside and is an approximate 20% effect for the inside overscan (for the beam size of 9.6 cm used for the "worst-case" implant under study). A sputtering yield of 1 was assumed and the angular distribution of sputtered atoms was assumed to be a cosine distribution. The model uses the approximation that the dwell-

Table 2
The effect of disc area upgrades integrated SIMS profiles are presented for a selection of metals

	Species	Dose [atoms/cm^2]	Current [mA]	Fraction of implanted dose [ppm]		
				Al	Cr	Mo
Standard configuration	As	1×10^{16}	19 5	1071	32	
Graphite-covered spillover cup	As	1×10^{16}	19 0	406	2	
Silicon-covered	As	1×10^{16}	20 0	670	27	
spillover cup and	As	1×10^{16}	4.8	490	20	
reduced overscan	BF_2	5×10^{15}	8.2	354		17
Silicon-covered disc and spillover cup with reduced overscan	As	1×10^{16}	19 1	80	36	

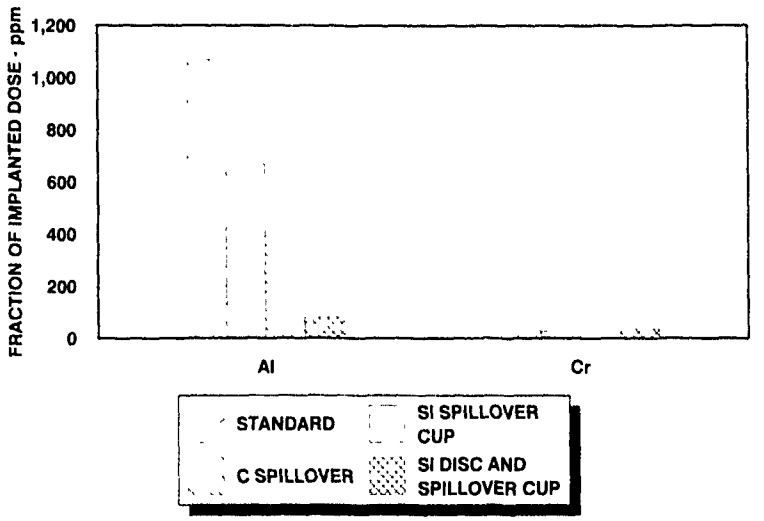

Fig. 5 Comparison of Extrion 1000 integrated SIMS profile data for aluminum and chromium at various stages of the disc area upgrade

time fraction can be simply multiplied by the solid angle of a stationary beam at the full-overscan position. The results can be tested against the spillover-cup experiment The model predicted a reduction of 451 ppm from the original 1071 ppm measured before upgrade, to give a new result of 620. This compares to the graphite spillover-cup result of 406 ppm. Similarly, the value calculated for the reduced-overscan case implies a

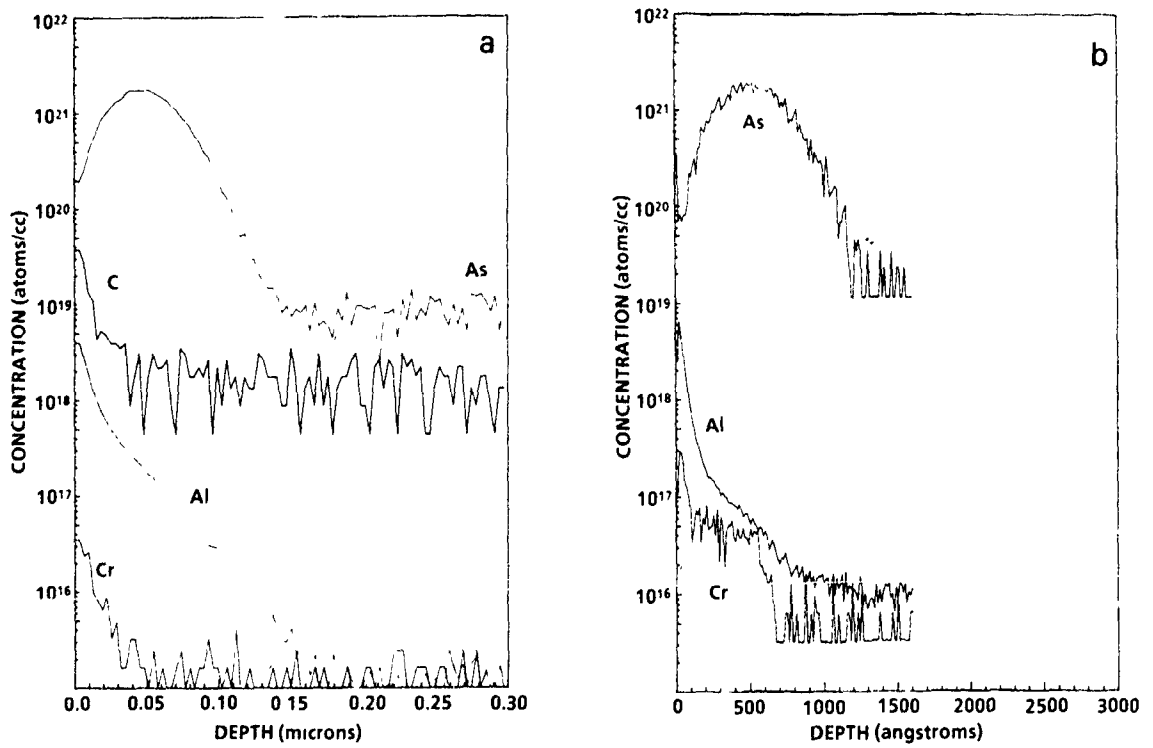

Fig 6. SIMS profiles for disc area upgrades. (a) graphite cover spillover cup and (b) silicon-covered disc and spillover cup with reduced overscan Note that different scales are used in the figures

Table 4
Modelling results for aluminum sputtering from overscan regions

Overscan	Large beam				Small beam			
	Normal		Reduced		Normal		Reduced	
	inner	outer	inner	outer	inner	outer	inner	outer
Occupancy time [%]	18 5	30 2	16 8	26 9	-	-	15 2	22 8
Aluminum sputtering [ppm]	364	451	345	420	-	-	370	404

reduction of 420 ppm and a corresponding result of 651 ppm.

The experimental result is 670 ppm (in good agreement) The effect of beam size is seen to be in the 5-10 ppm range The predicted effect of the silicon-coated disc and spillover cup is to reduce the aluminum to under 256 ppm The fact that the results went down to 80 ppm means that a substantial component was produced in the disc region between the wafers. The remaining areas on the disc which are not coated with silicon are the thin pads surrounding each wafer Future upgrades are planned to coat these parts as well as attack the few areas of the beam line which can potentially contribute

It is clear that work is needed to improve the base level of contamination on unimplanted wafers (and its repeatability) if one intends to reduce the contributions below the present levels. In any case, dose levels of 1×10^{16} atoms/cm^2 or higher are required in order to show the results with acceptable precision

5. Conclusions

The Varian Extrion 1000 ion implantation system was characterized for contamination during high-dose implantation by aluminum and other metals. The contamination was seen to be maximized for high-dose arsenic implants and was reduced by a factor of 13 to the 80 ppm implanted-dose level using silicon coatings for the disc and overscan region Molybdenum contamination was visible between 17 and 130 ppm during BF_2 implants and will only be reduced by reduction of the molybdenum content of the ion source. Other trace elements were seen at levels between 1 and 133 ppm for high-dose arsenic implants after covering the spillover cup with graphite Further gains are expected when the silicon-coated disc is evaluated

Continued upgrades will depend on reduction of unimplanted wafer contamination and improvement of analytical techniques currently available

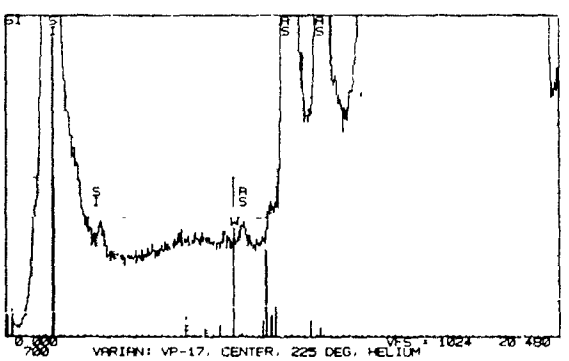

Fig 7 TXRF spectrum taken after BF_2 implant of 1×10^{15} atoms/cm^2 at 50 keV The electron flood was turned on at maximum output during the implant The position expected for tungsten is marked but no peak is present

Acknowledgements

The authors gratefully acknowledge the many useful discussions, cross-calibrations and overtime support given by the staff of Charles Evans & Associates. Also acknowledged is the hard work and support supplied by Pam Mansfield and Heather Deacon in the preparation of figures and tables, and the support offered by the Varian Applications Lab staff in evaluation of analytical techniques and handling of the wafers Keith Pierce is acknowledged for the hours he spent running the system and Eric Mears is thanked for his help in obtaining the materials used for the upgrade test.

Reference

[1] R B Liebert, A. Delforge, R Hertel, H Lulsdorf, E Mears and S Satoh, Nucl Instr and Meth B37/38 (1989) 533

Nuclear Instruments and Methods in Physics Research B55 (1991) 77–81
North-Holland

Control of wafer charging on the Varian EXTRION 1000 ion implanter

Shu Satoh, Bjorn O. Pedersen, Daniel F. Downey, Takao Sakase and Reuel B. Liebert
Varian Assoc., 35 Dory Road, Blackburn Industrial Park, Gloucester, MA 01930, USA

Susan B. Felch
Varian Research Center, Palo Alto, CA 94303-0883, USA

Wafer charging during high current implantation has been one of the major concerns to implanter users not only because of ever-shrinking device structures, but especially because of two to three-fold increases of beam currents available on next-generation high current implanters. In this paper, wafer charging on the Varian EXTRION 1000 was studied under various beam, electron flood gun and vacuum conditions and it was found that it can provide a much better environment in terms of wafer charging control than the previous generation machines. A relatively new technique, J-t test, has been used to measure the charge to breakdown as well as the traditional breakdown voltage measurement. The device yields from the tests were close to 100% for all the tested device wafers. The Q_{bd} results from J-t tests showed good correlation with flood/vacuum conditions and pinpointed the best operating condition. However some results posed difficulty in interpretation, which suggests wafer charging is a very complex phenomenon.

1. Introduction

Since the introduction of a new generation of high current ion implanters [1,2] which deliver almost twice as much beam current as their predecessors, it was commonly believed that wafer charging, which has been at the top of customers' concerns, might be bad enough to negate the advantage of the higher beam current capabilities of the new machines. Despite the concern, our experience after the introduction shows that the problem on the new machine is less severe than for its predecessor. As Current et al. [3] described it, it could be the result of the much lower charge per pass due to the larger disc size, higher rotation speed and larger beam size of the new machines.

One of the problems of designing and evaluating the new machine with regard to wafer charging is the strong dependency on device structure [4] which makes it very difficult to draw any universal conclusion out of a single test on a single device.

In this paper, the wafer charging behavior of the Varian EXTRION 1000 high current ion implanter [1] was studied, using the VRC (Varian Research Center) charging test wafer, which has been used also on a round robin test [5] of the major implanter manufacturers to evaluate and compare their wafer charging results. It is widely recognized throughout the industry as one of the reliable standard test devices.

A lot of effort has been put in using a rather new technique of J–t test as a tool for diagnosing wafer charging recently in our company. It is being accepted as a method for checking oxide integrity [6] and it is hoped that this study will contribute to establish it as a tool for wafer charging.

2. Description of the EXTRION 1000 electron flood system

The Varian EXTRION 1000 delivers up to 27 mA beam current of As and P (10 mA for B and BF_2) to wafers mounted on a mechanically scanned 42 in diam disc rotating at 1200 rpm. For the purpose of dose uniformity control and charging control, the rotating disc has a series of holes for profiling the beam size and locating the centroid [7] in the slow scan direction, which provide valuable information to help reduce the risk of wafer charging.

An electron flood system is located in the Faraday housing which is mounted in front of the rotating disc, of which details are shown in fig. 1 along with its control diagram for emission regulation. There are two primary electron guns, one on each side of the ion beam path, and together they deliver up to 500 mA of primary electrons to secondary electron emitter plates which face the guns obliquely. The geometry was chosen to confine positive ions from residual gas ionization close to the emitters to help neutralize the huge space charge of the slow secondary electrons for efficient electron transport. Also to assist the transport, there is a provision for gas bleeding into the Faraday housing to be used if necessary.

The emission regulation system is quite similar to the one used on the Varian XP series high current machine

0168-583X/91/$03.50 © 1991 – Elsevier Science Publishers B.V. (North-Holland)

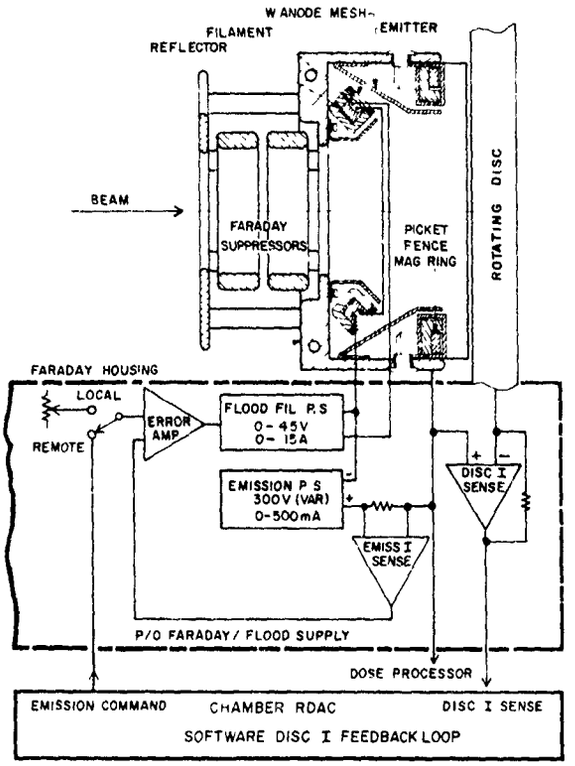

Fig 1. Schematic Diagram of the EXTRION 1000 electron flood system

for several years [8]. In closed loop mode, the current flowing between the disc and Faraday system (referred to as disc current) is measured to keep the current constant by adjusting the flood emission. In open loop mode, the primary emission current is kept constant. In the EXTRION 1000, the feedback is done by one of its branch computers (RDAC) using software with a digital filtering technique

2.1. Description of test devices

The test devices are basically thin-dielectric, polysilicon-gate MOS capacitors isolated by thick field oxide The thermal gate oxide was 170 Å thick, while the LPCVD polysilicon was 4000 Å thick and $POCl_3$-doped to give a sheet resistance of about 20 Ω/sq. The devices were fabricated on 150 mm diam, n-type (100) silicon substrates. The wafers were not exposed to any charging processes during fabrication, all of the photoresist removal and etching were done with wet processing.

Test devices 1C, 1A and 2E each consist of a large, square field capacitor connected to a small, rectangular gate capacitor (15 μm × 10 μm) [4]. Device 1C has no polysilicon edges on gate oxide, while the field capacitor is 150 μm × 150 μm, giving a charge multiplier ratio of 150. Devices 1A and 2E have two polysilicon edges on the gate oxide, while the field capacitor areas are the same as that of 1C for 1A and 64 times larger for 2E This gives a charge multiplier ratio for 2E of 9600 and 150 for 1A.

2.2. Test procedure

The dielectric breakdown voltage of the test devices was measured by recording the voltage produced when a current of 1 μA was forced through the device. The device was always biased in accumulation, which means that a positive voltage was applied to the gate since the substrates were n-type The measurements were performed on a computer-controlled, automatic probing station. A device is considered failed if the measured breakdown voltage is lower than 10 V. Device yield is derived by dividing the number of failed devices by the total number of tested devices.

The charge-to-breakdown (Q_{bd}) of the oxide was measured by an accelerated test called "J–t testing" [9]. In this test, the forced current density (J) is stepped up by a factor of 2.15 in time increments (t) of 5 s so that the average device under test will break down within 2–3 min. This test time is much shorter than that needed to make a Q_{bd} measurement with a fixed current density. During a J–t test, the voltage across the device under test is measured every 20 ms until the present voltage has decreased by at least 15% from the voltage previously measured. This is defined as the breakdown of the oxide. The integrated J–t product is then the Q_{bd} value, or the amount of electric charge conducted by the capacitor before the gate oxide breaks down.

3. Results

Fig. 2 shows the device yields by V_{bd} after implants of 1×10^{16} cm^{-2} of 60 keV As$^+$, 18.5 mA and fig. 3

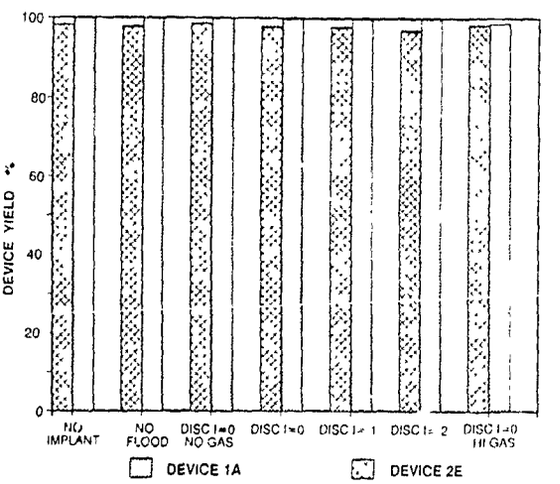

Fig 2 Yields of VRC device 2E and 1A for 60 keV As$^+$, 18.5 mA 1×10^{16} cm^{-2} implants

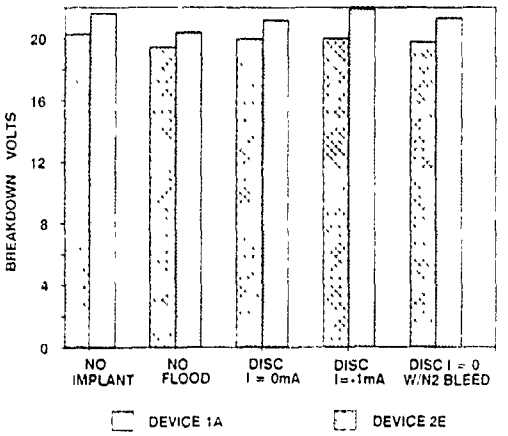

Fig 3. Breakdown voltages of VRC device 2E and 1A for 70 keV BF_2^+, 10 mA 5×10^{15} cm^{-2} implants.

shows the breakdown voltages after implants of 5×10^{15} cm^{-2} of 70 keV BF_2^+, 10 mA for test devices 2E and 1A, under several flood conditions. It is clearly seen that the device yields are very good, even without using the flood system. Most notably, the device 2E, which has been known to be the most sensitive, survived with surprising yields

The benefit of the electron flood system is very pronounced in Q_{bd} measurements shown in figs. 4 and 5, which are the result of J–t tests on device 1C and 2E, respectively. The results of the 2E device in fig. 5 show very dramatic improvement by addition of electron flood Vertical bars in figs. 4 and 5 represent standard deviations of the distributions around mean values. It is understood that the amount of shift from the reference value indicates the level of degradation of oxide quality. Both device results agree that the case with 80 mA of constant emission with a small amount of gas bleed is the best in terms of mean Q_{bd} shift and spread of the distribution, although the difference from the case with closed loop with zero disc current is small. It is a much lighter use of flood gun than the closed loop case, which was known to be close to the best condition on our XP series high-current machine [8]. This difference remains to be solved. It could be caused by the difference in scanning schemes in the two machines, one uses mechanical and the other is hybrid.

Fig. 4 also shows the documented benefit of gas bleeding [10] for charge-up prevention. To be noted, however, is that a very small pressure increase seems to be enough for this purpose in the EXTRION 1000, minimizing the risk of other vacuum-related contamination problems [11].

To see the effect of charge-per-pass, one implant was done with 600 rpm of disc rotation, which is a half of the normal 1200 rpm, keeping other implant parameters the same The result is shown in the far right in fig. 4, and despite our prediction, it showed very little Q_{bd} shift. Other values like breakdown voltage behaved likewise. This is another point to be pursued later, but it shows that wafer charging is a more complex phenomenon than commonly thought.

4. Discussion

The results from this study suggest that wafer charging in the Varian EXTRION 1000 is much more mod-

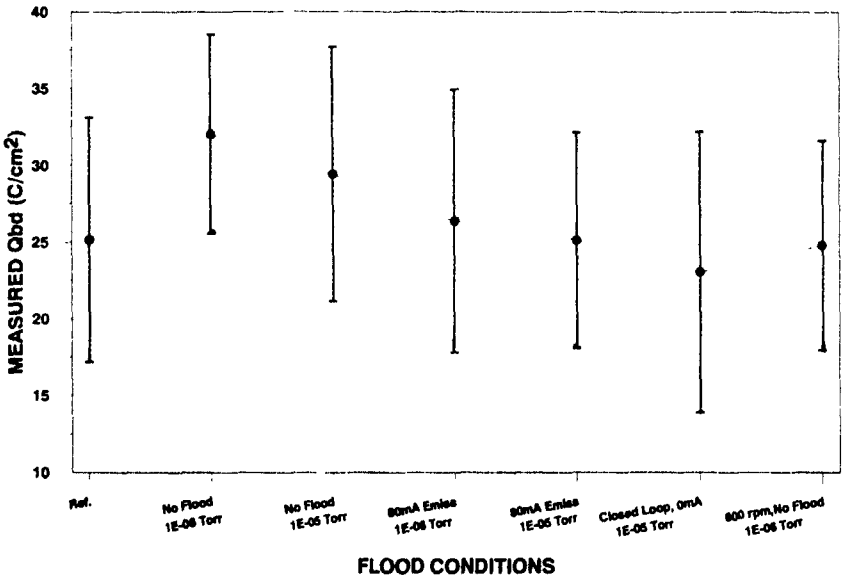

Fig. 4. Q_{bd} changes of VRC device 1C by flood conditions.

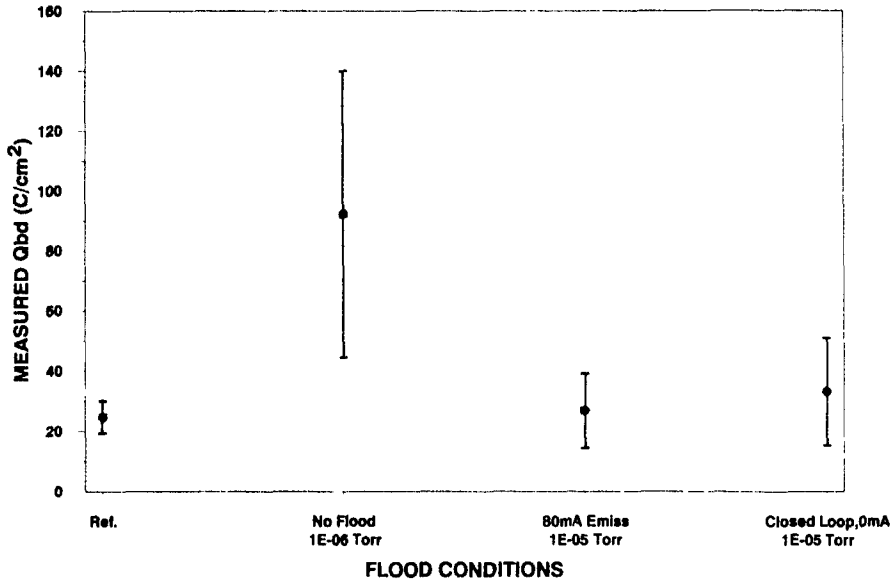

Fig 5. Q_{bd} changes of VRC device 2E by flood conditions

erate than expected from its high beam currents, and the electron flood system functioned efficiently to eliminate the problem. Because of the large disc, fast rotation and larger beam size, the amount of charge per pass is very low, 27 mA of 3-in. high (in slow scan direction) beam gives only 6.4×10^{-7} C/cm^2 pass. A good correlation between charge per pass and device yield was reported [3] before, but one result from this study, the 600 rpm run, did not support the view, and this should therefore be pursued later.

Results from the J–t tests showed great sensitivity, especially on device 2E, to a small change of the environment to which the wafers are exposed during implant. As reported before [4], most of the results showed positive Q_{bd} shifts, which are sometimes interpreted as the result of positive charging during the implant. The results from device 1C seem to support the interpretation except for the 600 rpm case, however the results from 2E give some difficulty to it, which could be due to the exposed gate oxide in 2E.

From the charge per pass and Q_{bd} of the reference device which is about 25 C/cm^2, we can derive the number of passes for the device to fail by Q_{bd}. Considering the charge multiplier ratio, it is about 400 passes for 2E and about 26000 passes for 1C, which translate to 18 s and 22 min, respectively, of continuous exposure to beam without scanning. We can conclude that for 2E it is very possible to fail by Q_{bd}, but for 1C may not be the case as scanning reduces the actual beam exposure.

Since the use of the J–t test as a diagnostic tool for wafer charging during implant is rather new, several interesting but mysterious things were observed. For example, a change of Q_{bd} by implant is interpreted as a result of increased number of traps, that means a change of only 1 C/cm^2 in Q_{bd} corresponds to an increase of the number of traps by 6×10^{18} cm^{-2}, which seems to be an extraordinary large number. In fact, Solomon [12] studied electron trapping in thin oxide after forced Fowler–Nordheim tunneling by a high electric field, but he reported a trap density of only about 10^{12} cm^{-2}, which is six orders less than the above number. This suggests that there might be factors governing the Q_{bd} shift other than pure electrical stress, but so far we have not come up with a good answer.

5. Summary

Wafer charging under several flood conditions was tested on Varian EXTRION 1000 high current implanter using VRC charging test devices. The results suggest that wafer charging under the test conditions was very small and that the electron flood system functioned very efficiently to eliminate the problem. Device yields by V_{bd} were too good to show the effects of flood and vacuum even without using flood on the most sensitive structure used in this test.

J–t tests showed very good sensitivity to small changes of flood and vacuum conditions and the results behaved as predicted, except for one case with no flood, no gas bleed and reduced rpm of the disc, which showed almost no sign of charging.

The results from this study posed several interesting questions, for example, whether the shift of Q_{bd} can tell the polarity of wafer charging, why the shift of Q_{bd} is so large, etc., which will help to deepen understanding

of the basic mechanism behind this complex phenomenon, wafer charging.

References

[1] R B. Liebert, A Delforge, R. Hertel, H. Lulsdorf, E. Mears and S Satoh, Nucl Instr. and Meth B37/38 (1989) 533

[2] M T Wauk and A D. Giles, Nucl. Instr. and Meth. B37/38 (1989) 442.

[3] M.I Current, A. Bhattacharyya and M Khid, Nucl Instr and Meth. B37/38 (1989) 555.

[4] S B Felch, V K. Basra and C.M McKenna, IEEE Trans. Electron Devices ED-35 (1988) 2338

[5] S.B Felch, L.A Larson, M I Current and D.W. Lindsey, Nucl. Instr and Meth B37/38 (1989) 563

[6] D R. Wolters and J J van der Schoot, Philips J Res. 40 (1985) 115

[7] R B. Liebert, S Satoh, A. Delforge and E Evans, Nucl. Inst. and Meth. B37/38 (1989) 464

[8] S Mehta, R.F. Outcault, C.M. McKenna and A Heinonen, these Proceedings (8th Int. Conf. on Ion Implantation Technology, Guildford, UK, 1990) Nucl Instr and Meth B55 (1991) 457

[9] S.B. Felch, S Mehta, S Kikuchi and S. Kitahara, ibid., p 82.

[10] M.E. Mack, Nucl. Instr and Meth B37/38 (1989) 472

[11] D F Downey and R Liebert, these Proceedings (8th Int. Conf. on Ion Implantation Technology, Guildford, UK, 1990) Nucl Instr and Meth. B55 (1991) 49

[12] P. Solomon, J. Appl Phys. 48 (1977) 3843

Nuclear Instruments and Methods in Physics Research B55 (1991) 82–85
North-Holland

Device charge-to-breakdown studies on a high-current implanter

S.B. Felch
Varian Research Center, 611 Hansen Way, Palo Alto, CA 94303, USA

S. Mehta
Varian Ion Implant Systems, Blackburn Industrial Park, Gloucester, MA 01930, USA

S. Kikuchi and S. Kitahara
Tokyo Electron Limited, Kyushu, Japan

Wafer charging studies on a high-current ion implanter were performed using charge-sensitive MOS structures with various charge multiplier ratios. Charge-to-breakdown measurements were made, both before and after implantation, to characterize the charging damage. The shifts observed in these measurements yielded information about the magnitude and polarity of the charge induced in the oxide during the implant. Such shifts have been correlated to the various implant parameters and electron flood conditions chosen for this study. For all the implants, a real-time monitoring of the disk current and the potential developed on each wafer was also made. The relationship between these parameters and the observed shifts in charge-to-breakdown will be discussed.

1. Introduction

Ion implantation is one of the many processes used to fabricate today's semiconductor devices that involve charged particles, since it relies on the transport of positive ions into the target semiconductor wafer. Unfortunately, advanced devices with shrinking gate oxide thicknesses and lateral dimensions are quite susceptible to charging damage and resulting yield loss. In addition, high ion beam currents, which increase wafer throughput for high-dose implants, exacerbate charging problems. In order to prevent surface charge build-up, most high-current implanters are equipped with electron flood systems which supply a steady flow of low-energy electrons to the wafer.

The effectiveness of electron flood systems is usually studied with charge-sensitive MOS test structures. Typically, damage to the test structure is characterized by a change in the breakdown voltage of the thin dielectric in the device. However, the charge-to-breakdown (Q_{BD}) of the thin dielectric has been considered to be a more sensitive parameter [1], which additionally gives information on the polarity of the charging process. In this paper, charge-to-breakdown data will be presented to illustrate the charge neutralization capability of a new experimental electron flood technique under development in a Varian XP high-current implanter.

2. Experiment

All of the charging tests reported here were run on a Varian 160XP high-current ion implanter. A new technique for charge neutralization, which is currently under development, was examined. This study was part of a program to evaluate several new techniques [2] for generating low-energy, charge-neutralizing electrons in the Faraday area, independent of changing conditions in the Faraday. Details of this system will be published at a later date when the system is developed and qualified as a product. During each implant, real-time monitoring of the net disk current and of the charge developed on each wafer was made. Unfortunately, the charge monitor was located 180° away from the test wafer on the disk, so its signal was too small to give sensitivity to any of the implant conditions studied [3].

The test structures used were state-of-the-art, MOS devices fabricated on 150 mm diameter silicon substrates with a 250 Å thick gate oxide (SiO_2). Two devices with different charge multiplier ratios were studied. One had a charge multiplier ratio of 100 000 and a gate oxide area of about 25 μm^2, the other had a charge multiplier ratio of 1000 and a gate oxide area of about 7500 μm^2.

The charge-to-breakdown of the oxide was measured by an accelerated test called "J–t testing" [4]. In this

0168-583X/91/$03.50 © 1991 – Elsevier Science Publishers B.V. (North-Holland)

test, the forced current density (J) is stepped up by a factor of 2.15 in time increments (t) of 5 s so that the average device under test will break down within 2–3 min. This test time is much shorter than that needed to make a Q_{BD} measurement with a fixed current density. During a J–t test, the voltage across the device under test is measured every 20 ms until the present voltage has decreased by at least 15% from the voltage previously measured – this is defined as the breakdown of the oxide. The integrated J–t product is then the charge-to-breakdown, or the amount of electric charge conducted by the capacitor before the gate oxide breaks down

3. Results and discussion

Charge-to-breakdown data is often displayed as a cumulative percent failure distribution [4] Fig. 1 is an example of such plots for the two different devices on a wafer implanted with 80 keV As^+ ions to a dose of 3×10^{15} cm^2 with no electron flooding. The Y-axis of the plot gives the calculated percentage of all tested devices that failed at a value equal to or less than the given value on the X-axis, which is the charge-to-breakdown in C/cm^2. The actual number of failures can easily be calculated by knowing the total number of devices that were tested.

Both test structures shown in fig. 1 had a larger charge-to-breakdown after implant than before This can be seen by the positions of the after-implant curves to the right of the before-implant curves The amount of this shift for the structure with the larger gate oxide area (a) is much greater than that for the structure with the smaller gate oxide area (b). A process that produces a constant defect density would give this result, since the larger area would have a larger number of defects. A so-called "positive" shift in the Q_{BD} curve, like these, is indicative of positive charging caused by the implant. Positive charging will induce positively charged traps in the oxide, which will lead to a higher charge-to-breakdown when the current stress measurement is made [5]. The observation of positive charging is also consistent with the implant condition of no electron flooding.

The relationship between implant condition and the direction of the shift in the Q_{BD} curve is illustrated further in fig. 2. The three wafers whose data are shown were also implanted with As^+ ions under the same implant conditions as above. The results are those for the test structure with the smaller gate oxide area. Plot 2a is identical to fig. 1b and displays the results for the wafer implanted with the electron flood off. A positive shift in the Q_{BD} curve is observed, which agrees with the positive charging expected with no flood and the measured net disk current of about +8.5 mA. Data for the wafer implanted with a medium flood condition is presented in fig 2b This graph shows almost no shift in the Q_{BD} curve, suggesting no charging during the implant The net disk current for this implant was about +2 mA. Fig. 2c gives the results for the wafer implanted with a high flood condition. Here a negative shift in the Q_{BD} curve occurred, which implies that negative charging or overflooding took place. Again, this observation agrees with the flooding condition, even though the net disk current was about +1 mA

Table 1 summarizes the data presented in fig. 2 plus the data from wafers implanted with 30 keV B^+ and 40 keV BF_2^+ under medium flood conditions. All of the

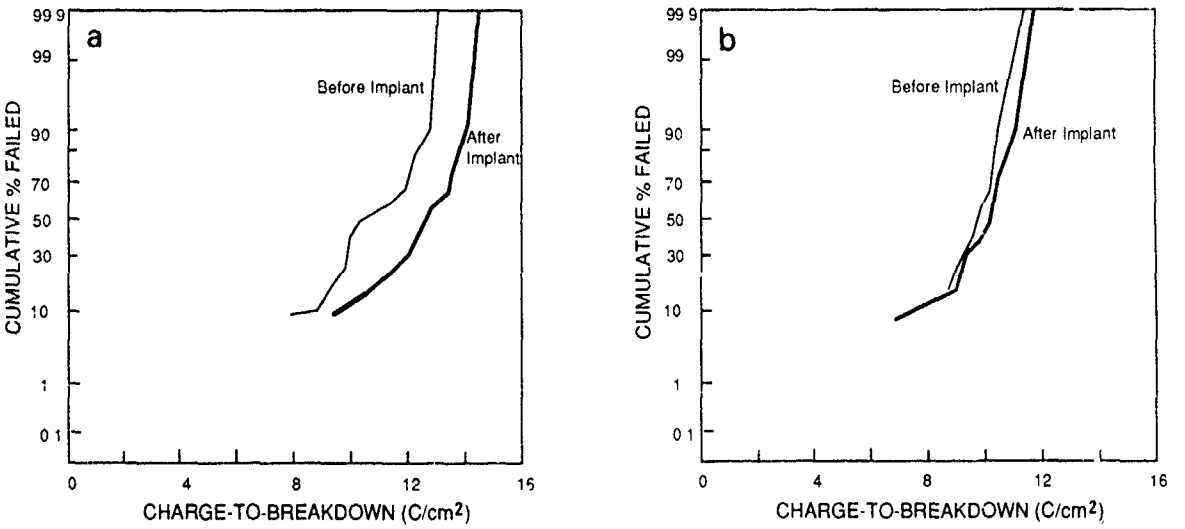

Fig. 1 Cumulative percent failure distributions for devices of larger (a) and smaller (b) gate oxide area on a wafer implanted with As^+ ions with no electron flooding

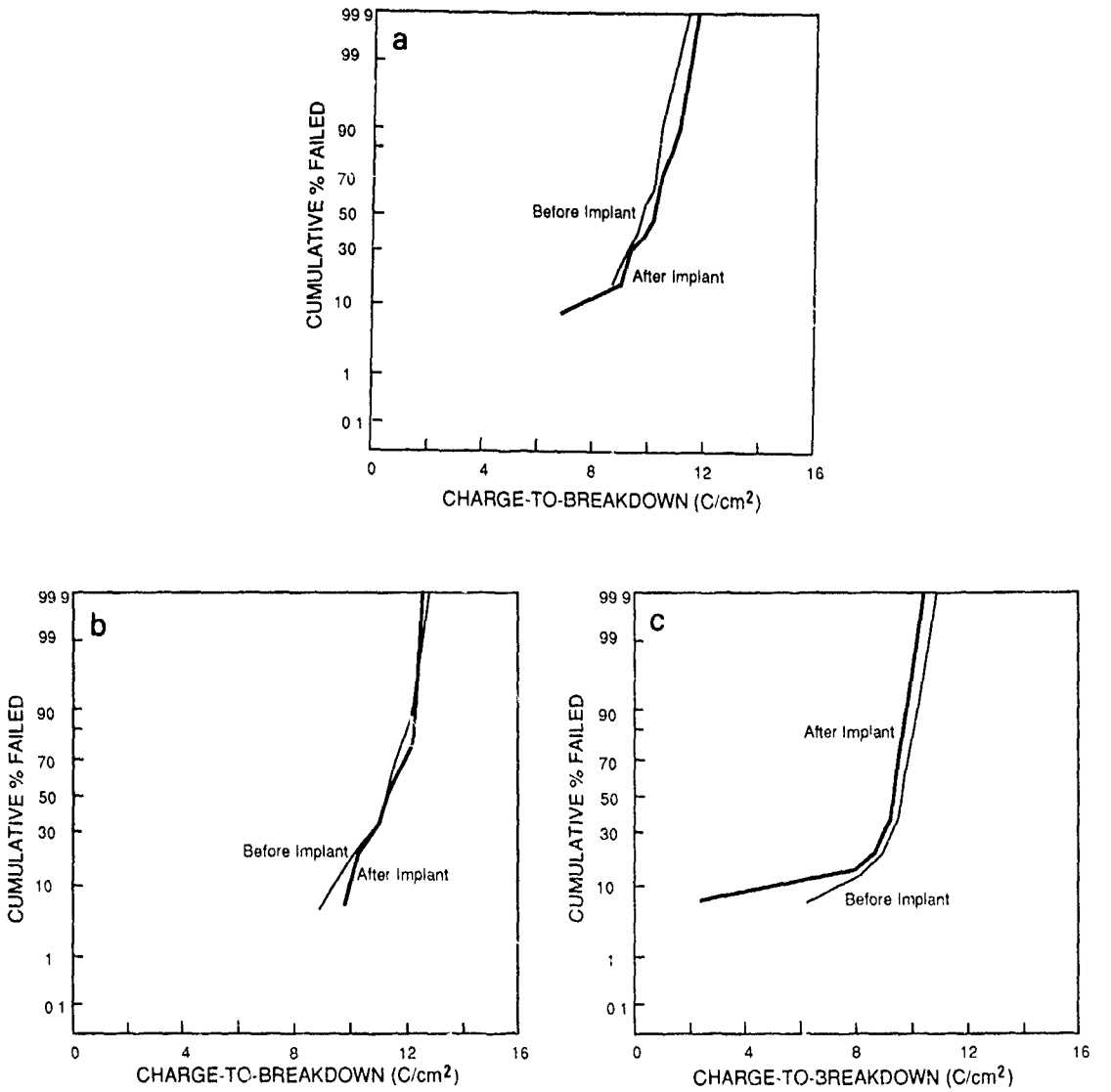

Fig 2 Cumulative percent failure distributions for devices of smaller gate area on wafers implanted with As^+ ions with (a) no electron flooding, (b) a medium flood condition, and (c) a high flood condition The direction of the shift in each plot agrees with the expected polarity of the charging process

Table 1
Difference in median charge-to-breakdown before and after implant

Implant condition	Shift in median Q_{BD} [C/cm^2]
As^+, no flood	+0 33
As^+, medium flood	+0 05
As^+, high flood	−0.38
BF_2^+, medium flood	+0 01
B^+, medium flood	+0 99

doses were 3×10^{15} cm^2, and the results are for the structure with the smaller gate oxide area. The difference between the median charge-to-breakdown (the Q_{BD} value on the X axis corresponding to 50% on the Y-axis) before and after implant is tabulated for each implanted wafer. The As^+ results are the same as those described above. The wafer implanted with no flood showed a positive shift and positive charging; the one implanted with medium flood had almost zero shift and no charging; the wafer implanted with high flood

Table 2
Difference in 10% Q_{BD} points before and after implant

Implant condition	Shift in 10% Q_{BD} points [C/cm^2]
As^+, no flood	−2.06
As^+, medium flood	+0.73
As^+, high flood	−3.69

suffered a negative shift and overflooding. Clearly, the medium flood condition is optimal.

A comparison of the B^+ and BF_2^+ results is also interesting. The B^+-implanted wafer displayed a large positive shift (+0.99), indicating positive charging. The net disk current for this implant was about −1 mA. However, the BF_2^+ wafer had almost zero shift (+0.01), implying no charging and agreeing with the net disk current of about 0 mA. This phenomenon can be explained by the different beam spot sizes for the two ion species. The B^+ ion beam is tightly focused and results in a high charge density on the wafer. On the other hand, the BF_2^+ ion beam is much broader, giving a lower charge density and less device damage [6].

Table 2 presents the difference in the 10% points on the cumulative percent failure distributions between the before-implant data and the after-implant data for the three As^+ wafers. This difference gives an indication of the number of test devices that catastrophically failed, or suffered dielectric breakdown during the implant. The wafer implanted with medium flood displayed a positive difference in the 10% points, meaning that the 10% Q_{BD} value after implant was greater than the before-implant value. This implies that very little charging damage occurred and that a near-optimal electron flood condition was used. In contrast, the two wafers implanted with no flood and high flood showed large, negative differences in the 10% points (the value after implant is smaller). These wafers had serious dielectric damage from the implant and represent undesirable flooding conditions.

4. Conclusions

The ability of a new electron flood technique to provide optimal charge neutralization has been demonstrated on charge-sensitive MOS structures under a variety of implant conditions. More work is currently in progress to qualify this technique as a production-worthy system. In addition, this study has shown the usefulness of dielectric charge-to-breakdown as a measurement parameter for device damage, especially since it also gives information on the polarity of the charging process.

Acknowledgements

The authors wish to express their sincere gratitude to an industry source for providing the MOS test structures and the Q_{BD} measurement capability for this work. The valuable assistance of M. Inoue of TEL Varian Ltd. and M. Hamada of TEL, Kyushu, in running the tests is also greatly appreciated. Finally, we would like to thank Dr. Charles McKenna and Ronald J. Eddy of Varian Ion Implant Systems for many technical discussions.

References

[1] D.R. Wolters and A.T.A. Zegers-van Duynhoven, Proc. Eur. RELCON, eds. J. Moltoft and F. Jensen (North-Holland, Amsterdam, 1986) p. 315.
[2] K.N. Leung, K.C. Gordon, W.B. Kunkel, C.M. McKenna, S.R. Walther and M.D. Williams, these Proceedings (8th Int. Conf. on Ion Implantation Technology, Guildford, UK, 1990) Nucl. Instr. and Meth. B55 (1990) 94.
[3] S. Mehta, R.F. Outcault, C.M. McKenna and A. Heinonen, ibid., p. 457.
[4] S.B. Felch, L.A. Larson, M.I. Current and D.W. Lindsey, Nucl. Instr. and Meth. B37/38 (1989) 563.
[5] I.C. Chen, S. Holland and C. Hu, IEEE Electron Dev. Lett. EDL-7 (1986) 164.
[6] R. Nee, S. Mehta, S.B. Felch, and S. Kikuchi, these Proceedings (8th Int. Conf. on Ion Implantation Technology, Guildford, UK, 1990) Nucl. Instr. and Meth. B55 (1990) 137.

Nuclear Instruments and Methods in Physics Research B55 (1991) 86--89
North-Holland

Control of ion beam current density and profile for high current ion implantation systems

Masayasu Tanjyo, Shuichi Fujiwara, Hiromichi Sakamoto and Masao Naito
Nissin Electric Co., Ltd, 47, Ukyo-ku, Kyoto 615, Japan

One solution for the problems of the local temperature increase and the charge-up of a wafer during high current ion implantation is to decrease the beam current density while maintaining the total beam current necessary on the wafer. To solve these problems, a method, that maintains the beam spatial profile on a wafer by controlling the normalized perveance and the pole face angle of the analyzing magnet for various beam currents, has been developed experimentally. As a result, under the experimental conditions of 1 to 8 mA of 35 keV As^+, the beam uniformity, defined as [average current density]/[maximum current density], became more than 0.2 and the beam profile on the wafer was maintained by using a suitable value of the perveance.

1. Introduction

The local temperature increase and charge-up of a wafer caused by a high current ion beam can degrade the performance of ion implantation systems. Lower beam current density implantation is one solution. Recently a new methodology has been developed to control the spatial profile of the ion beam current density. This has been applied to the Nissin high current ion implantation system (PR-80A [1]). This paper describes the experimental procedure, results from the use of this new method and its application to high current ion implantation.

2. Experimental parameters

2.1 Normalized perveance

In all ion beam systems the perveance is a parameter that indicates the status of the extracted ion beams. The effects of the space charge downstream of the beam extraction electrodes are characterized by the poissance $\Pi = I_{ext}/V^{3/2}$, where I_{ext} is the extraction current and V is the extraction voltage. The perveance, defined by the Child–Langmuir equation for the one-dimensional parallel plate model, is $P_C = (4\epsilon_0/9)(2e/M)^{1/2}(A/d_0^2)$, where d_0 is the gap width of the extraction electrodes, A is the area of the slit of the plasma electrode and the other notations are as defined in ref. [2]. We define the effective gap width $d_e (= d_0 + t)$ as d_0, where t is the thickness of the extraction electrode. The normalized perveance is one of the important beam optics matching parameters to control the spatial profile and is characterized by $P_N = \Pi/P_C$. When an ion species and a beam energy are fixed, the normalized perveance is expressed by $P_N = K(I_{ext}/d_e^2)$, where K is a constant. Therefore, the value of the normalized perveance can be adjusted by varing the extraction current and the gap width.

2.2. Pole face angle

One way of shaping the spatial profile of the beam is to make use of the fringing field of the entrance or the exit pole face of the analyzing magnet [3]. In the PR-80A system, the entrance pole face angle of the analyzing magnet is denoted by α and the exit pole face angle is denoted by β, as shown in fig. 1. In the experiments, the β dependence was investigated thoroughly.

2.3 Beam uniformity

The spatial profile of the beam at the target is equivalent to the transverse current density profile of

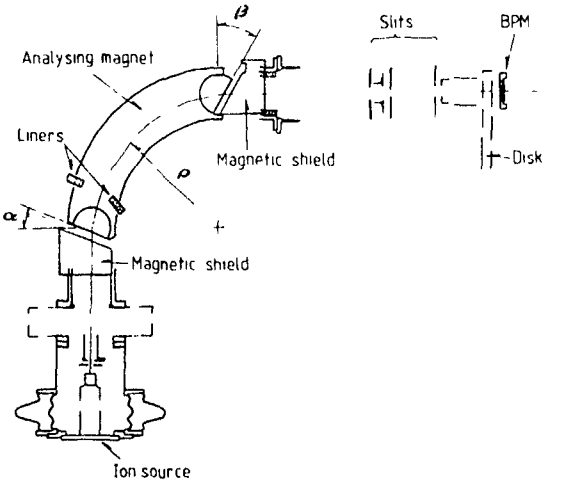

Fig. 1. Schematic of the beam line of the PR-80A system

0168-583X/91/$03.50 © 1991 – Elsevier Science Publishers B V. (North-Holland)

the ion beam at the target. The beam uniformity is defined as $J_N = J_{AVE}/J_{MAX}$, where J_{AVE} and J_{MAX} are the average and the maxmum beam current densities, respectively, within an area of 70 mm (width W) × 190 mm (height H) on the target. The criterion adopted was that $J_N > 0.2$.

3. Apparatus

Some representive elements of the beam optics of PR-80A are shown in fig. 1. The ion beam from a Freeman type ion source is extracted from a slit with dimensions 2 mm (W) and 60 mm (H). Typical beam currents on target are 1 to 8 mA of 35–50 keV As^+ and 1 to 3 mA of 30–50 keV B^+. The analyzing magnet has an optical radius of 500 mm and a 90° bending angle. The entrance pole face angle (α) is normally set to +20° and the exit pole face angle (β) to 0°. In the beam line, there is an analyzing slit of 18 mm (W) × 110 mm (H) and, also, a shaping slit of 24 mm (W) × 110 mm (H). The distance between the ion souce and the entrance of the analyzing magnet and between the exit of the analyzing magnet and the target are 500 mm and 1050 mm, respectively. The beam trajectories have one focal point in the x (horizontal) plane between the analyzing magnet and the target. The beam (spatial) profile monitor, "BPM", is installed behind the disk, as shown in fig. 1.

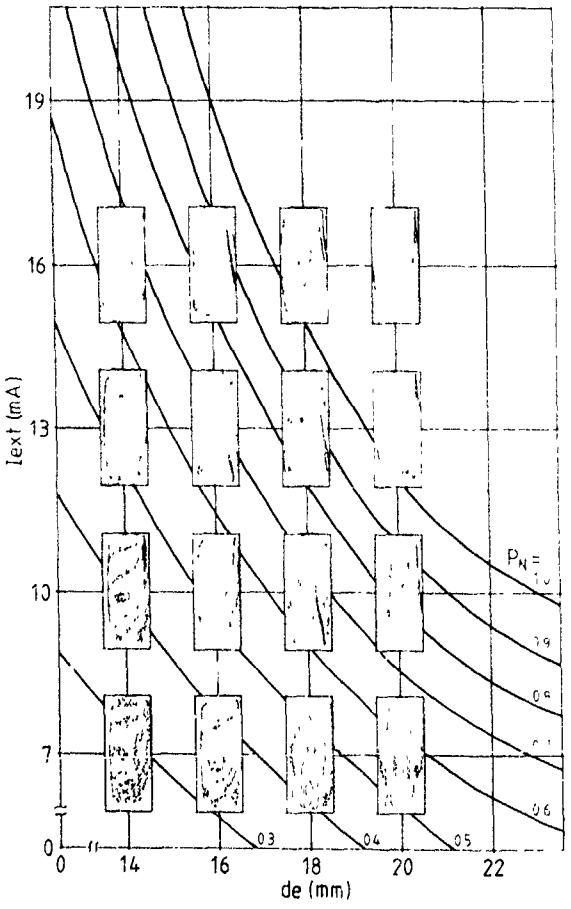

Fig. 2 As^+ beam spatial profiles on target showing the P_N dependence.

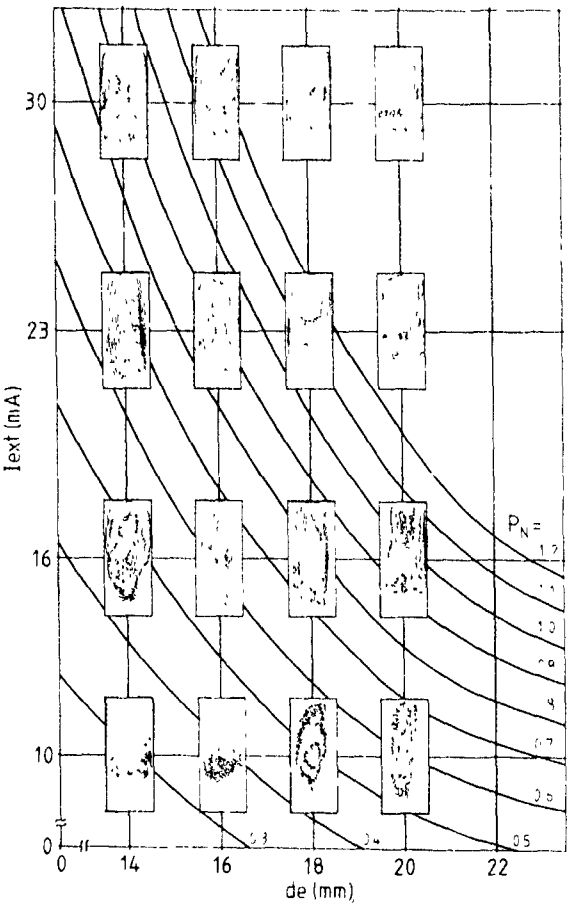

Fig. 3. B^+ beam spatial profiles on target showing the P_N dependence

4. Results

4.1. Control of the spatial profile

Spatial profiles of beams of 35 keV As^+ and 30 keV B^+ in the plane of the target are shown in fig. 2 and fig. 3, respectively. The following conclusions can be drawn:

- Both As^+ and B^+ beams have similar profiles for a given value of P_N.
- When P_N is smaller than 0.6, the spatial profile becomes broad, and it becomes narrower when P_N is changed to larger values.

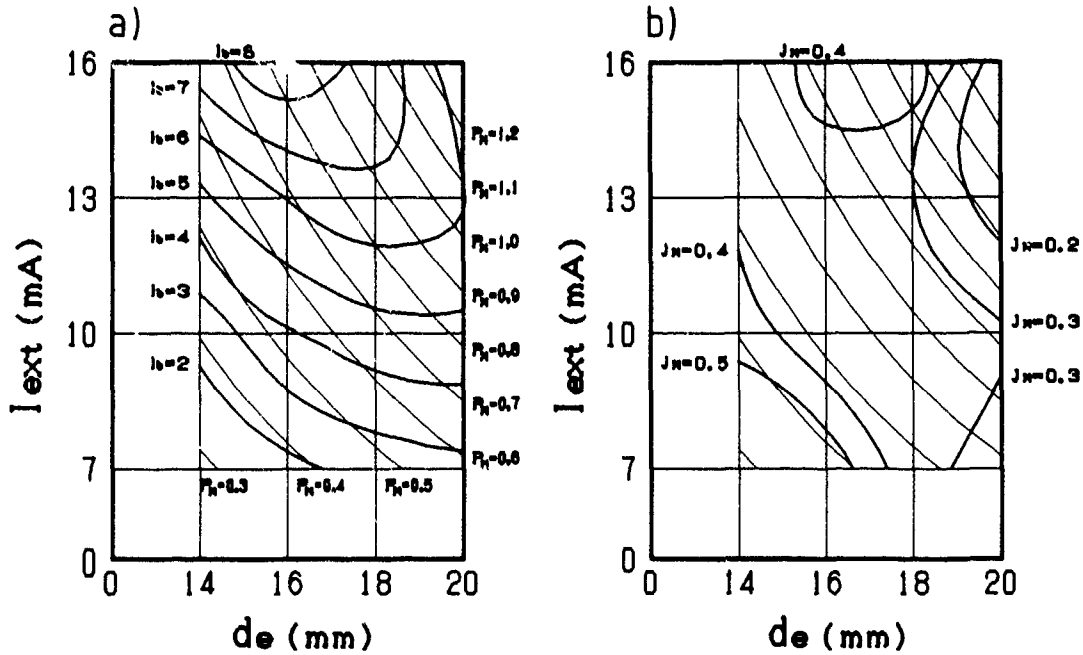

Fig 4 (a) Contours of the beam current on target, and (b) contours of the beam uniformity on target The ion beam is As^+

- When P_N is between 0.6 and 0 8, the spatial profile has a single maximum (peak) and the current density is a maximum. With increasing P_N, the spatial profile becomes a trapezoid.
- For P_N larger than 0.8, the beam diverges and when $P_N = 1\,0$ the profile has two maxima ("two-peak distribution")

The relationship between the beam uniformity, J_N, and and the target beam current, I_b, is shown in fig. 4. From fig. 4, one can choose the parameters to give the optimum beam current and uniformity. For example, for an As^+ beam with $I_b = 8$ mA and $J_N > 0.2$, values of $d_e = 16$ mm and $I_{ext} = 16$ mA should be selected.

4.2 Determination of β

The focussing of the fringing field on the exit side of the analyzing magnet was investigated by studying the dependence of the beam transport efficiency and the spatial profile upon the parameter β. Typical experimental data are shown in fig. 5 from which it can be deduced that the optimum values of β are $-30°$ for 35 keV As^+ and $-20°$ for 30 keV B^+.

5. Conclusions

The spatial profile of the beam on the target is determined and controlled by the normalized perveance (P_N). This is possible because the spatial profile of the

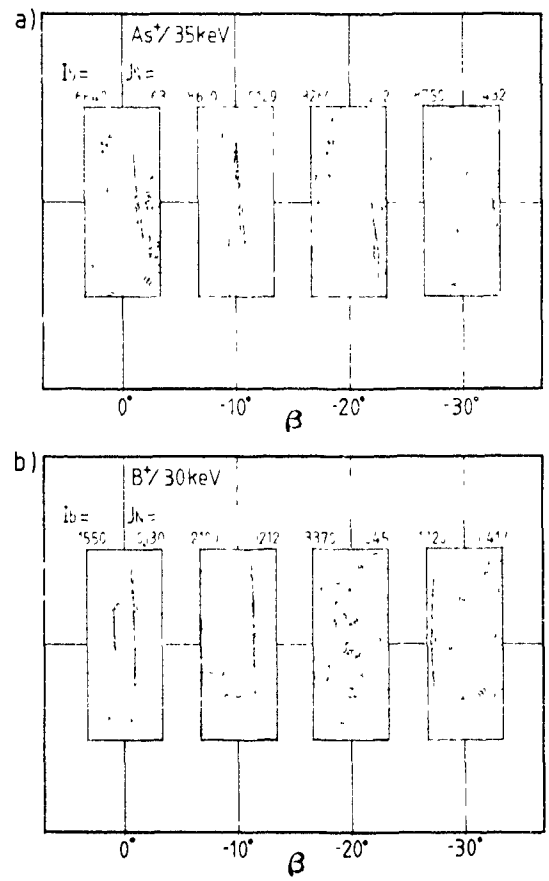

Fig 5. Beam spatial profile on target showing the β dependence: (a) 35 keV As^+, and (b) 30 keV B^+.

extracted beam can be maintained during transport through the analyzing magnet and the slits. Therefore, by setting P_N, which is achieved by setting the extraction current and the gap width, one can reduce the beam current density on the target and yet still transport the required high beam current. This is an effective method of suppressing the local temperature increase and charge-up on a wafer.

References

[1] T. Kawai et al., these Proceedings (8th Int. Conf on Ion Implantation Technology, Guildford, UK, 1990) Nucl Instr. and Meth B55 (1991) 443.

[2] L. Lejeune, in. Advances in Electronics and Electron Physics , Suppl. 13C, ed A Septier (Academic Press, 1983) p. 207.

[3] H.A. Enge, in: Focussing of Charged particles, vol. 2, ed. A. Septer (Academic Press, 1967) chap. 4.2.

Nuclear Instruments and Methods in Physics Research B55 (1991) 90–93
North-Holland

A high-resolution beam profile measuring system for high-current ion implanters

N. Fujishita, K. Noguchi and S. Sasaki

Manufacturing Development Laboratory, Mitsubishi Electric Corporation, Amagasaki, Hyogo, 661 Japan

H. Yamamoto

Kita-Itami Works, Mitsubishi Electric Corporation, Itami, Hyogo, 664 Japan

A high-resolution beam profile measuring system (BPM) has been developed to analyze the correlation between charging damage and the ion beam profile for high-current ion implanters. With the increase of the ion beam current, insulators such as thin oxide layers of VLSI devices are subject to charging damage during ion implantation. To obtain accurate information on the local current density of the ion beam, 125 Faraday cups are placed in the BPM. This system has two measuring modes. One is a topographic mode that can detect the ion beam current density of 12500 sampling points in 30 s. A high-resolution contour map of the current density distribution is displayed on a CRT. The other is a real-time mode in which the current density distribution (125 sampling points) of the ion beam can be monitored every half second on the CRT. In this mode, fine adjustment of the ion beam profile is easily possible by visual control. The charging damage of insulating layers in the TEG (test element group) to the beam profile was investigated using this newly developed BPM. It has been proven that the damage probability increases rapidly above some threshold level of the beam current density. It is confirmed that for high-current implantation a uniform current density distribution of the ion beam is very effective to prevent charging damage. It is concluded that this measuring system is valuable not only for quick analysis of damage phenomena, but also for evaluating machine performance.

1. Introduction

With the increasing integration of VLSI devices, the gate area and the thickness of the oxide layer decrease in size, and dielectric breakdown of the gate oxide by charging due to high-current ion implantation has become a serious problem. Several experimental investigations have been performed, for example on the dependence of the breakdown yield on ion beam conditions, the construction of end stations and device structures [1–3]. There are some reports where dielectric breakdown decreases the yield if the ion beam current is increased or the beam width is reduced. To reduce damage from excessive surface charge buildup in a high-current implanter, the amount of total charge delivered to a wafer during a single pass in the ion beam, Q_{pp}, is a very important parameter [1]. In a rotational disk scan system, Q_{pp} is given by:

$$Q_{pp} = I/Rv,$$

where I is the ion beam current, v is the wafer velocity along the fast-scan direction and R is the ion beam width along the radial direction of the rotational disk.

To analyze the effect of the ion beam profile on charging damage, a high-resolution beam profile measuring system (BPM) has been developed and the charging damage of MOS transistors on TLG wafers was investigated using this BPM.

2. Beam profile measuring system

A schematic diagram of the newly developed measuring system is shown in fig. 1. It is constructed with a sensing head, an X–Y table, current-to-voltage converters, multiplexers, an isolated-amplifier, an analog-to-digital converter and a computer. We developed two types of high-resolution beam profile measuring systems (BPM) for different commercial high-current ion implanters. The BPM A is attached to a side wall of an end station of the implanter, and the ion beam density is detected by 61 Faraday cups (13 × 5 array except for corners). The BPM B, shown in fig. 2 is attached to a head lining of an end station, and has 125 Faraday cups (19 × 7 array except for corners). The sensing head, which is a part of a Faraday cup to detect the total beam current, consists of beam collectors placed on an insulating plate at intervals of 1 cm in a square lattice arrangement, a carbon plate with entrance apertures of 1 mm diameter, and a secondary electron suppression plate (−200 V), and is cooled to avoid the increase of its temperature caused by the irradiation by the ion beam.

0168-583X/91/$03.50 © 1991 – Elsevier Science Publishers B.V. (North-Holland)

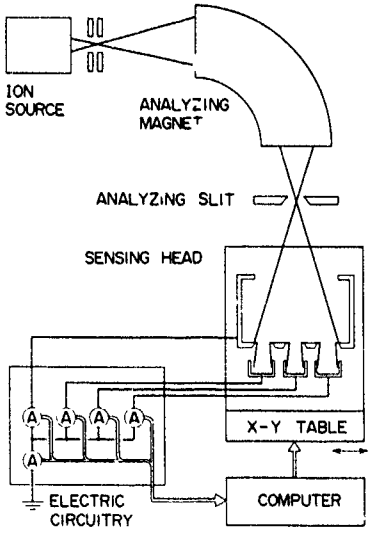

Fig. 1. Schematic diagram of the high-resolution beam profile measuring system.

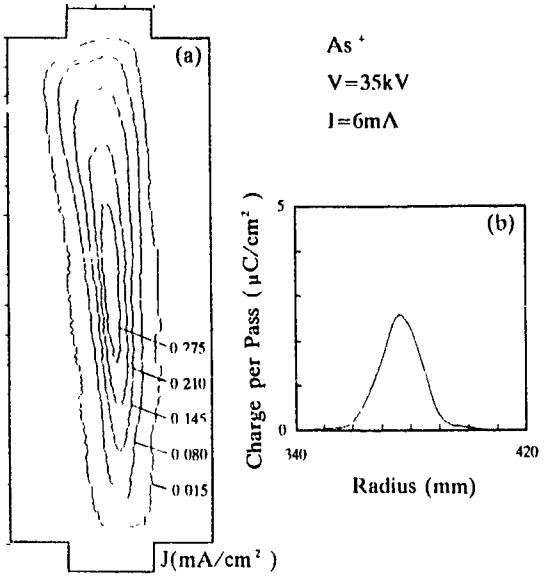

Fig 3. Ion beam current density distribution measured by the BPM B: (a) contour map; (b) distribution of charge per pass. The velocity of rotation was 300 rpm.

The current from each cup is serially detected by multiplexers, and is displayed graphically on a CRT at intervals of half a second (real-time mode). The current of each cup can be detected up to 50 μA (6.4 mA/cm^2 on the BPM) with accuracy of 0.5%. In this mode, the ion beam profile can be adjusted visually.

To obtain accurate and rapid information on the local ion beam current density, the sensing head moves by an X–Y table at intervals of 1 mm over a 10 mm × 10 mm area measuring the current at each interval (topographic mode). The vacuum pressure of the end station is kept at less than 10^{-4} Pa ($\sim 10^{-6}$ Torr) by a bellows sealing.

In the case of the BPM B, the density at 12500 sampling points is detected and is stored in disk memories. A high-resolution contour map of the current density distribution is displayed on the CRT, typically within 10 s (drawing 5 lines) as shown in fig. 3. The lowest level and the interval of the contour map can be arbitrarily selected.

In other modes of data processing a horizontal section, a vertical section, an integrated view along the X or Y axis and a density distribution of charge delivered per pass of the wafer through the ion beam, as shown in fig. 3b, are displayed. The detailed performance of each BPM is listed in table 1.

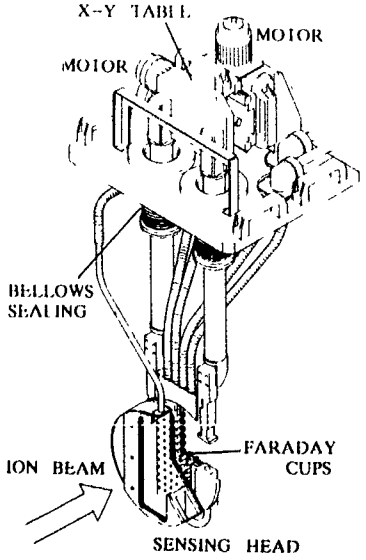

Fig. 2. Schematic diagram of the BPM B

Table 1
Comparison of beam profile measuring systems

Parameter	BPM A	BPM B
Area of measurement [mm × mm]	50 × 130	70 × 190
Diameter of aperture [mm]	1	1
Number of sampling points	61 × 100	125 × 100
Maximum Range [mA/cm^2]	6.4	6.4 (0.64)
Accuracy [%]	0.5	0.5
Area of X–Y table [mm × mm]	10 × 10	10 × 10
Measurement time [s]	45	30
Display time [s/line]	15	2

3. Experimental conditions

To evaluate the effect of the ion current density distribution, TEG (test element group) wafers were implanted with 35 keV As^+ to a dose of 3×10^{15} ions/cm^2 at a beam current ranging from 3 mA to 8 mA with various beam profiles. An electron shower system was not used when clarifying the yield dependence on the ion beam current density distribution. The effective radius of the rotational disk was 375 mm, and the velocity of rotation was from 300 to 1000 rpm. The ion beam current density distribution was measured by the BPM B which was placed 86 mm behind the wafer position on the disk.

The sample device structure was a MOS transistor fabricated on an n-type 150 mm silicon wafer, whose resistivity was in the range of 5.5 ± 2 Ω cm. On the (100) surface of the wafer, a field oxide layer of 450 nm thickness was grown except for active regions, where a gate oxide layer of 20 nm thickness was stacked by a gate polysilicon layer of 250 nm thickness. The gate area was 5 μm long and 100 μm wide. The gate polysilicon layer was extended onto the field oxide. The extended part, of which the area was 4×10^5 μm^2, provided a pad electrode for the gate on electrical measurements. The implanted wafers were tested to breakdown and the yields were sampled at 125 locations on each wafer.

4. MOS transistor yield results

There were two groups of maximum electric field which could be sustained before catastrophic breakdown of tested sample devices. One was less than 2 MV/cm, the other was more than 8 MV/cm and the former group was caused by charging phenomena. The variation in yield loss with some ion beam profile parameters is shown in fig. 4.

The variation in yield loss with the maximum value of local charge per pass, q_{pp}, is shown in fig. 4a. Yield loss at the rotational velocity of 300 rpm was observed for the maximum value of local charge per pass of 2.7 μC/cm^2 and greater. The threshold of significant yield loss decreased with increasing velocity of rotation. Including different velocities of rotation, yield loss rather depended on the maximum of local charge per time, q_{pt}, shown in fig. 4b.

5. Discussion

At the condition of $q_{pp} = 2.7$ μC/cm^2, (if discharge is ignored) the electric field in the gate oxide is greater than 165 MV/cm, which is more than the usual electric field at breakdown (~ 11 MV/cm). Most of the charge delivered to a wafer in the ion beam was immediately lost by surface conduction, conduction through insulators and secondary electrons from the surroundings.

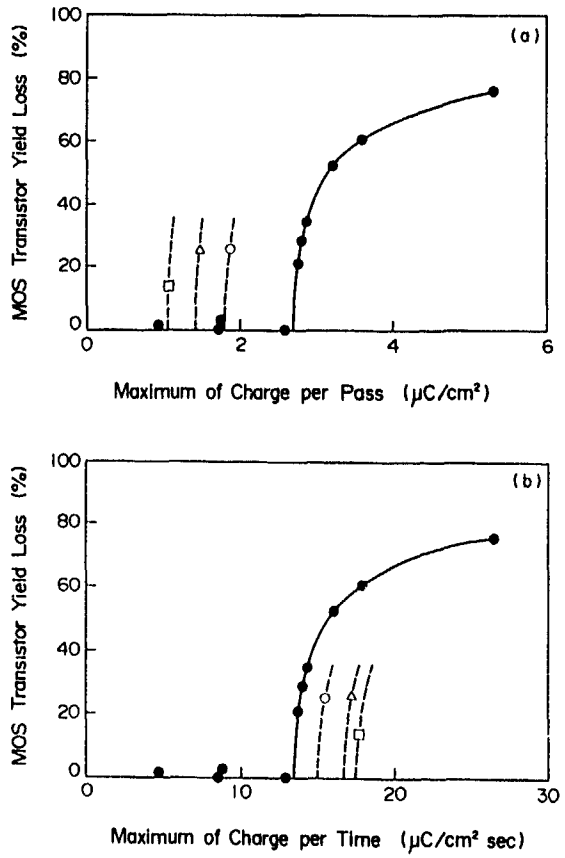

Fig 4. MOS transistor yield loss dependence on some beam profile parameters (a) yield loss vs charge per pass; (b) yield loss vs charge per time. TEG wafers were implanted with 35 keV As^+ to a dose of 3×10^{15} ions/cm^2 at a beam current ranging from 3 to 8 mA with various beam profiles and wafer velocities (●) 300 rpm, (○) 500 rpm, (△) 700 rpm, (□) 1000 rpm

At a constant velocity, the assumption that the charge per pass was an effective parameter for the yield was in agreement with yield results. However, when changing the velocity, the threshold of q_{pp} was inversely proportional to the velocity, and this assumption was not valid. The maximum value of charge per time, q_{pt}, is a rather important parameter. The breakdown did not occur by the charge delivered to a wafer during a single pass of the beam, but it did occur after several beam passes. The mechanism of charge buildup depends on the velocity of rotation or the diameter of the disk.

6. Conclusion

The importance of the ion beam current density distribution in a high-current implanter has been demonstrated by testing the yield of MOS transistors with the high-resolution beam profile measuring system. The maximum value of charge per time, q_{pt}, is an important parameter. The yield loss of MOS transistors on TEG wafers increased as the q_{pt} values increased above 13 $\mu C/cm^2$ s at the velocity of 300 rpm.

References

[1] M.I. Current, A. Bhattacharyya and M. Khid, Nucl. Instr. and Meth. B37/38 (1989) 555.
[2] S.B. Felch, L.A. Larson, M.I. Current and D.W. Lindsey, Nucl. Instr. and Meth. B37/38 (1989) 563.
[3] N. Nagai, T. Kawai, M. Naito, Y. Nishigami, H Fujisawa and K. Nishikawa, Nucl. Instr. and Meth. B37/38 (1989) 572.

Nuclear Instruments and Methods in Physics Research B55 (1991) 94–96
North-Holland

An electron-beam charge neutralization system for ion implanters *

K.N. Leung [a], K.C. Gordon [a], W.B. Kunkel [a], C.M. McKenna [b], S.R. Walther [b] and M.D. Williams [a]

[a] *Lawrence Berkeley Laboratory, University of California, Berkeley, CA 94720, USA*
[b] *Varian/Extrion Division, Gloucester, MA, USA*

A new wafer-charge neutralization system which employs a curved solenoid magnetic guiding field and a large-area LaB_6 cathode is described. This system generates a directed beam of low-energy electrons with total current of about 100 mA. The majority of the electrons that impinge on the wafer surface have energies less than 10 eV. This neutralization system is simple and compact, and could be easily incorporated into the existing high-current ion implanters.

1. Introduction

Semiconductor fabrication often involves the implantation of ions into insulating structures. Excess charge can accumulate on the wafer and may generate breakdown and other electrical problems. Wafer charging can also affect beam propagation resulting in a nonuniform implant. Electron flooding is the most frequently used form of charge compensation in high-current implantation. The energies of the electrons used in this neutralization scheme are low (~ 10 eV). However, production of these low-energy electrons and subsequent irradiation of the wafer is not a simple matter [1]. For this reason, we have designed and tested a new charge neutralization system which employs a curved solenoid magnetic guiding field and a large-area lanthanum hexaboride (LaB_6) cathode to form a directed flow of low-energy electrons. It is demonstrated that low-energy electrons ($E < 30$ eV) with a total current of 100 mA can be transported from a large-area LaB_6 cathode through a right-angle turn onto a target surface. The following sections summarize the development of the system and the results of the experimental investigation.

2. Experimental setup

Fig. 1 is a schematic diagram of the experimental arrangement. An electron beam is first extracted from a circular (5 cm diameter) directly heated LaB_6 cathode. LaB_6 is chosen as the cathode material because it has the appropriate physical properties, such as a high melting point, chemical inertness and resistance to erosion under ion bombardment. When heated to a temperature of 1600 K or higher, LaB_6 is a copious emitter of electrons.

Since the normal operating temperature for a LaB_6 cathode is relatively low, one would expect that the evaporation rate for the LaB_6 material is also small [2]. Accordingly, the lifetime of a LaB_6 cathode should be much longer than that of tungsten or tantalum cathodes. In fact, lifetime tests have shown that a LaB_6 emitter can last several thousands of hours at relatively modest current densities, in the range 10–20 A/cm^2 [3].

Previously, we demonstrated that directly heated LaB_6 *filaments* can be fabricated and that they perform satisfactorily in plasma or ion sources where tungsten or

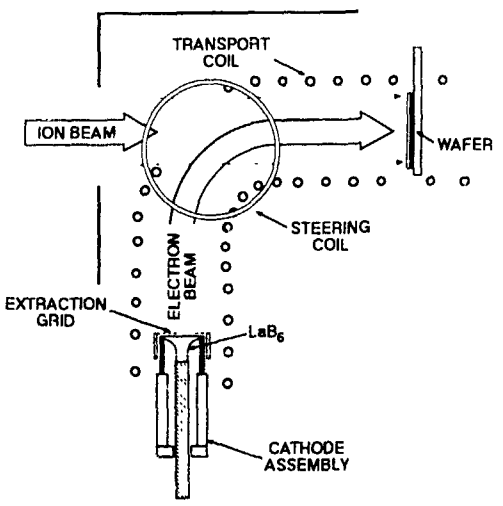

Fig. 1. A schematic diagram of the magnetically guided low-energy electron beam wafer neutralizer.

* This work is supported by Varian/Extrion Division, and the US Dept. of Energy under Contract No. DE-AC03-76SF00098.

0168-583X/91/$03.50 © 1991 – Elsevier Science Publishers B.V. (North-Holland)

tantalum filaments are normally employed [2]. In some experiments, very low electron energies are required. The magnetic field generated around the filament by the high heater current is strong enough to prevent low-energy electrons from leaving the filament. This problem can be solved by using a coaxial cathode structure to cancel the magnetic field produced by the heater current [4].

Recently, we have modified the coaxial arrangement to form a 5 cm diameter, directly heated LaB_6 cathode [5]. The shape of this cathode is properly designed so as to achieve a uniform emission current density. In order to generate an electron current of 100 mA ($J \approx 5$ mA/cm^2), the LaB_6 cathode is operated at a temperature of about 1400 K. This temperature is so low that the lifetime of the cathode will be extremely long and the evaporation of LaB_6 material will become minimal.

For space-charge-limited extraction, one can estimate from the Child–Langmuir equation (with $V \approx 10$ V and $J \approx 5$ mA/cm^2) that the separation between the cathode and anode is approximately 2 mm. A tungsten mesh with 74% transparency was mounted in front of the cathode surface for extraction purposes.

Once the electrons are extracted, they will be guided by a solenoid magnetic field and then impinge normally on the wafer surface. The 90° bend keeps the cathode out of the line of sight with the wafer. An opening in the coil allows the ion beam to merge with the electron beam which can also provide the necessary space charge for beam neutralization. Since the guiding field is weak, the perturbation of the positive ion trajectories will be very small. A plot of the calculated magnetic field together with the coil geometry is shown in fig. 2.

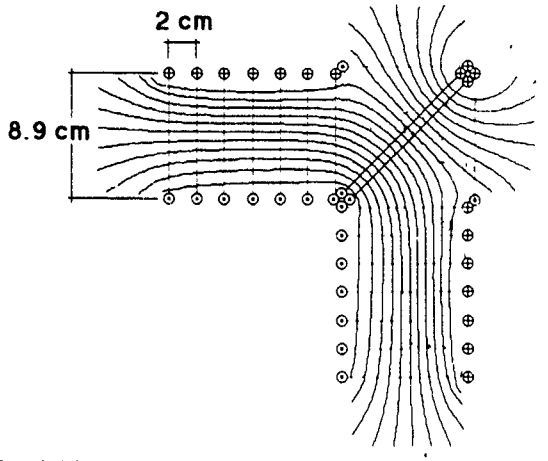

Fig. 2. The calculated magnetic field distribution generated by a right-angle solenoid.

3. Experimental results

3.1 Transport in a straight solenoid geometry

The experiment was initially performed in the first straight section of the solenoid shown in fig. 1. A *segmented* copper collector was installed at the end of the solenoid coil to simulate a wafer. With this arrangement, the radial electron current density distribution could be determined. In this experiment, it was found that a coil current of ~ 60 A ($B \approx 30$ G) was quite adequate to transport a low-energy electron beam.

The experiment was first performed in a background pressure of about 1×10^{-6} Torr. The extraction grid, the solenoid coil and the target collector were all maintained at ground potential while the cathode was biased negatively with respect to ground. With the LaB_6 cathode operated at a temperature of 1400 °C and an extraction voltage of 55 V, only 3 mA of electrons could be transported to the collector. However, the transported electron current increased rapidly as soon as a small quantity of xenon gas was added to the chamber. Electron currents exceeding 100 mA could now be easily obtained with an extraction voltage of 55 V and with a xenon pressure of 1.7×10^{-5} Torr. This result indicates that positive ions are required for space charge neutralization. Positive xenon ions are produced by the beam electrons when the extraction voltage is greater than the ionization potential of xenon.

The cathode was directly heated by passing the heater current through the LaB_6 material. The temperature on the cathode surface was monitored by means of an optical pyrometer. Fig. 3 is a plot of the collected electron current as a function of the cathode temperature with the extraction voltage maintained at ~ 54 V and the xenon pressure at 1.7×10^{-5} Torr. A total electron current of 100 mA or higher could be obtained when the cathode temperature exceeded 1300 °C. Both

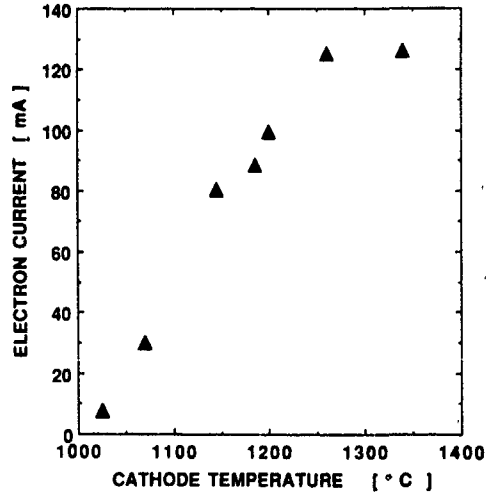

Fig. 3 Transported electron current as a function of cathode temperature.

the beam profile and the beam current were optimized with a solenoid current of 60 A. The electron current density at the collector was uniform within a region of about 5 cm diameter, which was approximately the same area as the LaB_6 cathode.

In order to investigate the energy distribution of the collected electrons, a small plane Langmuir probe was installed just in front of the copper collector. The probe trace showed the space potential of the background plasma was almost the same as the coil or ground potential. Superimposed on the beam electrons was a group of background electrons which could be represented by a Maxwellian distribution with a temperature of 2.25 eV. The distribution of the probe current indicated that the majority of the electrons arriving at the collector had an energy less than 10 eV. In this case, the cathode bias voltage and therefore the primary beam energy was about 20 eV.

3.2. Transport through a right-angle solenoid

With the completion of the straight coil experiment, a right-angle solenoid coil was installed as shown schematically in fig. 1. When the cathode was turned on, it was observed that the electron beam could only propagate in the first straight section of the coil. When the beam arrived at the corner of the coil, it would drift either above or below the plane formed by the coil (depending on the direction of the coil current). A large fraction of the beam was lost to the coils of the second straight section. As a result, the current measured at the collector was very small.

The change in the direction of beam propagation could arise from either the $E \times B$ or the curvature B drift of the electrons. In order to steer the electron beam around the corner, a vertical or perpendicular component of the B-field is needed. This B-field can be generated by a pair of Helmholtz coils at the corner of the solenoid. The position where the beam impinges on the collector can be easily optimized by adjusting the strength of this steering field. A vertical B-field of about 5 G was normally required to center the beam on the collector.

By applying the steering field, a total electron current of 96 mA was obtained on the target collector for an extraction voltage of -30 V. The electron current density at the collector was very uniform within 5 cm diameter, as shown by the profile distribution plot in fig. 4. If the extraction voltage was increased to 34 V, the total collected current became 117 mA. Langmuir probe traces obtained in this new solenoid arrangement were very similar to that of the straight section. Thus, the majority of the electrons impinging on the target collector were again low-energy electrons with $E < 10$ eV.

In conclusion, we have demonstrated that a beam of low-energy electrons can be transported from a large 5 cm diameter LaB_6 cathode through a right-angle solenoid coil to a target collector. In order to achieve a total electron current of 100 mA, a small quantity of xenon gas is needed for low-voltage extraction and to provide the positive ions for space charge neutralization. The electrons that impinge on the collector have a distribution of energy. The majority of these electrons have energies less than 10 eV.

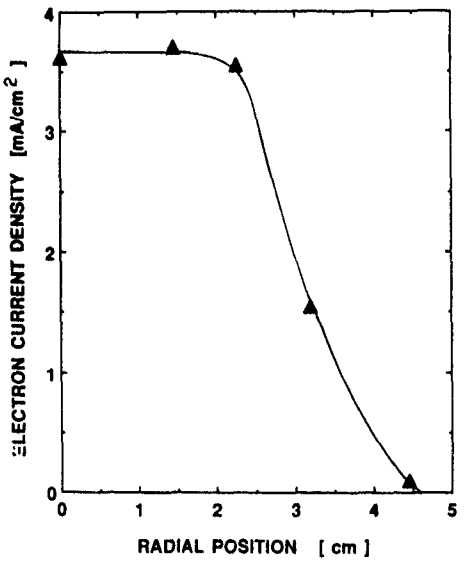

Fig. 4. Electron current density as a function of radial position. The origin represents the center of the wafer target.

Acknowledgement

We would like to thank S. Wilde, G.J. DeVries and members of their group for technical assistance. This work is supported by Varian/Extrion Division, and the US Dept. of Energy under Contract No. DE-AC03-76SF00098.

References

[1] R. Outcault, C. McKenna, T. Robertson and L. Biondo, Nucl. Instr. and Meth. B21 (1987) 354.
[2] K.N. Leung, P.A. Pincosy and K.W. Ehlers, Rev. Sci. Instr. 55 (1984) 1064.
[3] Y. Mori, A. Takagi, K. Ikegami and S. Fukumoto, Proc. Int. Symp. on the Production and Neutralization of Negative Ions and Beams, Upton, NY, USA, 1986 (Am. Inst. Phys., Conf. Proc. 158).
[4] K.N. Leung, D. Moussa and S.B. Wilde, Rev. Sci. Instr. 57 (1986) 1274.
[5] P. Purgalis, K.N. Leung, S.B. Wilde and M.D. Williams, Bull. Am. Phys. Soc. 33 (1988) 2091.

Nuclear Instruments and Methods in Physics Research B55 (1991) 97–103
North-Holland

New approaches to charging control

Julie A. Strain, Yoichiro Tanaka, Nicholas R. White and Richard J. Woodward
Applied Materials Implant Division, Foundry Lane, Horsham, West Sussex, RH13 5PY, England

In space charge neutralised beams a plasma exists. In a 20 mA, 50 keV arsenic beam used for source drain implants the Debye length is around 0.5 mm. Understanding and exploitation of this plasma is necessary in the control of wafer charging levels within each die, as opposed to wafer-scale control, so as to prevent current passing through thin gate oxides. This approach allows electrons of very low energy to be used for charge control. Many existing flood gun systems produce electron energy distributions with high energy tails. Exploiting the properties of the beam plasma allows true low energy (< 20 eV) electron guns to be used.

1. Introduction

An inherent part of the process of ion implantation is the transport of charge to the wafer. In the presence of insulating layers of photo-resist or oxide this leads to a build-up of charge on the surface of the wafer. Excess charge build-up can cause catastrophic breakdown or more subtle dielectric damage through Fowler-Nordheim tunnelling leading to a degradation in oxide strength. For example in CMOS FET gates current flow from the gate through oxide to the substrate gives progressive gate oxide damage. Oxide damage will occur if the voltage developed on the gates exceeds the threshold for Fowler–Nordheim tunnelling and a significant fraction of charge to breakdown (Q_{BD}) is passed by the end of an implant. The problem is worse for devices with a large polysilicon to gate oxide area ratio.

The solution is to supply excess low energy electrons, in other words a greater electron current density than ion beam current density. However negative charge build-up can also cause damage, so overflooding with energetic electrons must also be avoided. This means that electron flood system settings on modern implanters must be optimised for maximum device yield each time a new process is qualified. Negative charge build-up should not be a problem if the energy of the electrons is low enough, as the electrons cannot charge the wafer to a voltage greater than their own potential. Low-energy electrons can be produced but are difficult to transport from their source to the wafer. In hard vacuum the space charge limit for 20 eV electrons is only 400 μA. However, low energy electrons can be transported to positively charged regions on the wafer via the plasma that is associated with the ion beam.

2. The plasma associated with an ion beam

A high-current ion beam comprises a fast ion component propagating through a plasma [1,2]. The plasma consists of beam ions, slow ions (formed by ionisation or charge exchange between beam ions and residual gas) and thermalised electrons [1,2]. As in a plasma without the fast ion component, the centre region of the system has a fairly constant potential, dropping rapidly towards the outside or sheath region [3]. The most important criteria for the existence of a plasma is that the Debye length be small compared with the dimensions of the system. The Debye length defines the distance over which steady state potentials can have a large influence and is given by

$$\lambda_D = \left(\epsilon_0 kT/n_0 e^2\right)^{1/2}, \quad (1)$$

where T is the electron temperature in Kelvin, n_0 the electron density cm^{-3}, e the charge on an electron, k Boltzmanns constant and ϵ_0 the permittivity of free space. Using the Bohm criteria [1] the current density at the plasma sheath transition is given by

$$J_i = n_i e\left(kT/M\right), \quad (2)$$

where M is the ion mass and n_i is the slow ion density at the plasma boundary. It is shown by Forrester [1] that the plasma density at the boundary is approximately a factor of 2 lower than in the constant potential region.

3. Use of the plasma for charge control

Plasma electrons respond strongly to different potentials. If a plasma exists close to the wafer, plasma electrons will flow to wafer locations with a positive

0168-583X/91/$03.50 © 1991 – Elsevier Science Publishers B.V (North-Holland)

charge and be repelled from those with a negative charge.

A plasma tends to remain neutral, and will adjust to the addition of extra electrons, and provide a conductive path for them. Extra electrons can arise from secondary electrons from the wafer, secondary electrons from flood gun primary electrons and ionisation of neutrals. These may be thermalised through elastic collisions with other electrons within the plasma. Via these mechanisms the plasma environment provides a means of transporting low-energy electrons to the wafer. An advantage of the use of the ion beam plasma for electron transport is the fact that if the beam drops out, the plasma disperses and electrons therefore cease to travel so the system can be self regulating.

4. Double Langmuir probes

Electrical probes have been used to measure plasma parameters for many years, the method having been developed by Langmuir in 1924. In this investigation we used a double probe arrangement as described by Hutchinson [4] and Chen [5].

Two probes are positioned at the edge of the plasma, a voltage is applied between the probes and the current flow between the probes is measured. This arrangement causes minimal disturbance to the plasma as no net current is drawn from it. A typical double probe current–voltage characteristic is shown in the inset in fig. 1 for equal area probes. When the voltage difference V_d is zero the current flow to each probe from the plasma is equal, so no current flows between them. At large potential differences (values greater than A or B on the inset diagram) one or the other probe collects saturation ion current I_{is}. For the sharply changing region in between it can be shown [5] that current flow between the probes, I_d, is given by

$$I_d = I_{is} \tanh(eV_d/2kT), \tag{3}$$

The electron temperature can be extracted using

$$\tfrac{1}{4}(V_1 + V_2) = kT/e, \tag{4}$$

where V_1 and V_2 are found from the intersection of the saturation current lines with the tangent to the steepest part of the slope. This means the electron temperature can be calculated. The slow-ion current density can be calculated from the saturation ion current using eq. (2).

5. Experimental details

A schematic diagram of the experimental arrangement is given in fig. 2. It comprises a mock-up of an ion-beam–wafer endstation arrangement with a flood gun mounted on an aluminium tube through which the beam is passed. Two flood guns were used, the standard flood gun used on the Applied Materials PI9000 series [6] and a prototype low-energy gun, both of which can have Ar gas supplied to enhance their efficiency. To

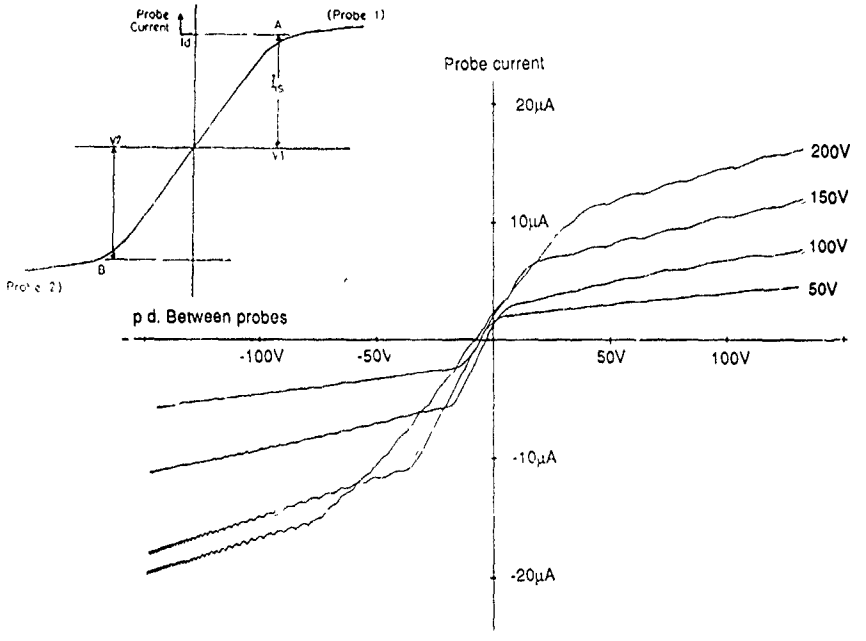

Fig. 1. Raw double-probe data for the standard flood gun at various primary electron accelerating potentials (numbers in brackets) for zero Ar bleed, with a theoretical or ideal double Langmuir probe characteristic shown in the inset.

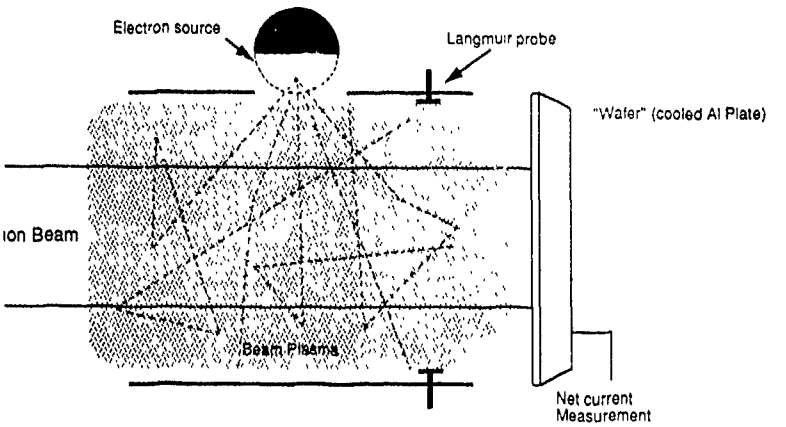

Fig 2. A schematic diagram of the experimental arrangement showing the "wafer", probes and flood gun at the wall of an Al tube with the ion beam passing through the tube

simulate an implanted wafer a cooled aluminium plate was used which could have a bias voltage applied to it. The unsuppressed current flowing to this "wafer" was monitored. The probes were aluminium discs of equal area positioned at the inner surface of the aluminium tube.

All measurements were taken using a 20 keV Ar^+ beam at 5 or 10 mA (the beam current was measured on a suppressed Faraday style beamstop with the "wafer" out of the beam). The beam dimensions were 60 mm by 60–70 mm. The influence of flood gun electron energy and argon bleed on plasma parameters was measured as well as the influence of a positive bias on the "wafer".

6. Results

6.1. Comparison of standard and low-energy flood guns

The first series of tests described involved a comparison of the standard PI9000 series flood gun with a low energy prototype gun using a 5 mA Ar ion beam. The

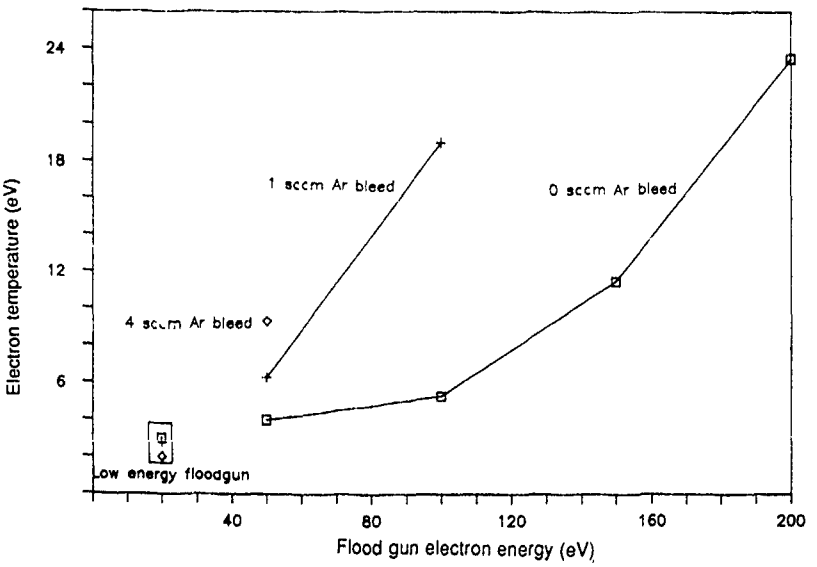

Fig. 3. Electron temperature plotted as a function of flood gun electron energy for different Ar bleed settings, showing data for both standard and low-energy gun using an Ar 20 keV 5 mA ion beam. The low-energy gun data is boxed

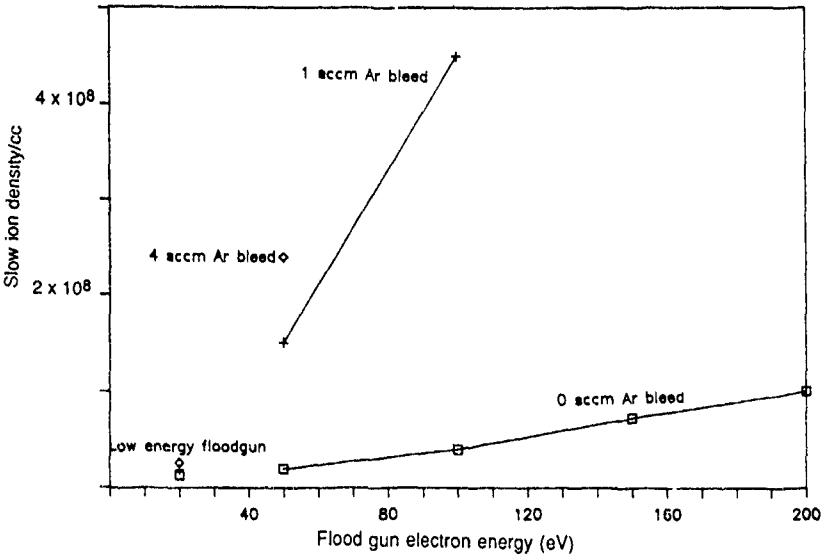

Fig. 4 The corresponding variation of slow-ion density with flood gun electron energy for the electron temperatures of fig 3

flood gun electron energy was 20 eV on the prototype gun and varied between 50 and 200 eV on the standard gun. Double Langmuir probe data for a variety of flood gun conditions was obtained. The double-probe characteristics were of similar shape to that described in the inset in fig. 1 for the low-energy flood gun and for the standard gun, provided the energy and Ar bleed were not too high. An example of raw Langmuir probe data is given in fig. 1 for the standard gun at various energies. The plots for the standard gun at higher Ar bleed and electron energies exhibited large asymmetric peaks suggesting some sort of asymmetric, non-plasma be-

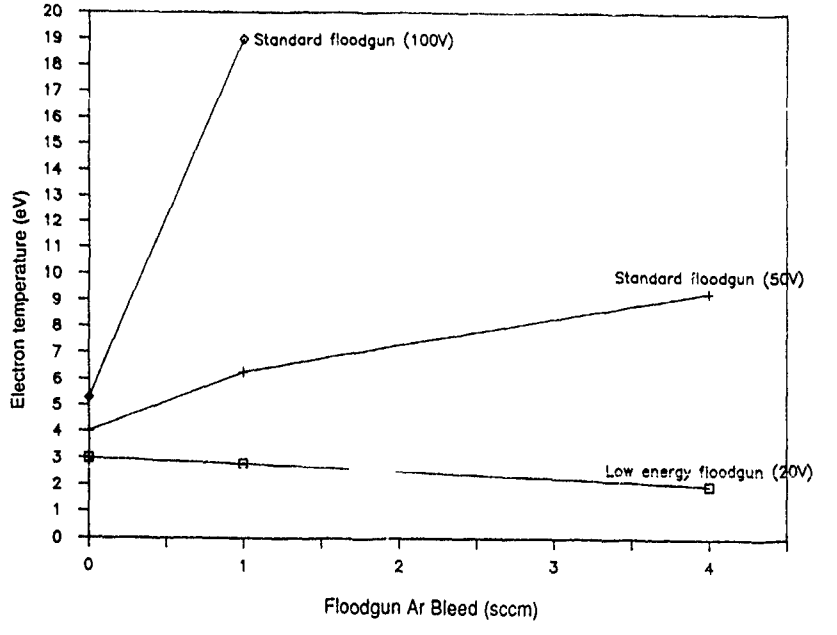

Fig. 5. Electron temperature plotted against argon gas flow. Numbers in brackets are the potential across which primary electrons have been accelerated determining their energy.

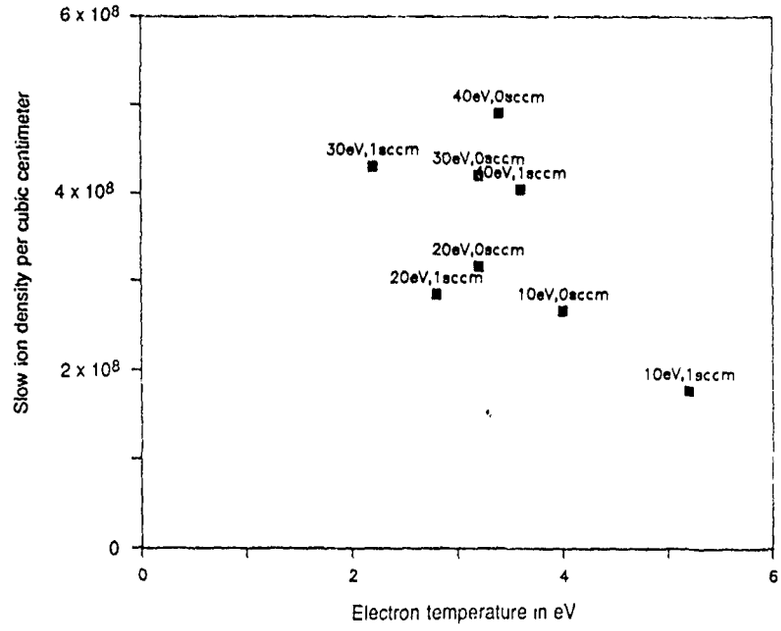

Fig. 6 A plot of slow-ion density plotted against electron temperature for a 10 mA 20 keV Ar beam Numbers beside the plots give primary electron energy and gas bleed flow

haviour. This gun is not normally operated under these conditions.

Electron temperature and slow ion density were obtained as described above for the "well behaved" plots. Figs. 3 and 4 show these plotted as a function of flood gun electron energy. Electron temperatures start at 2 eV for 20 eV flood electrons and rise rapidly as the flood gun electron energy is increased. A steady rise in slow-ion density is also observed with energy. The figs. include curves for 0 and 1 sccm floodgun Ar bleed and

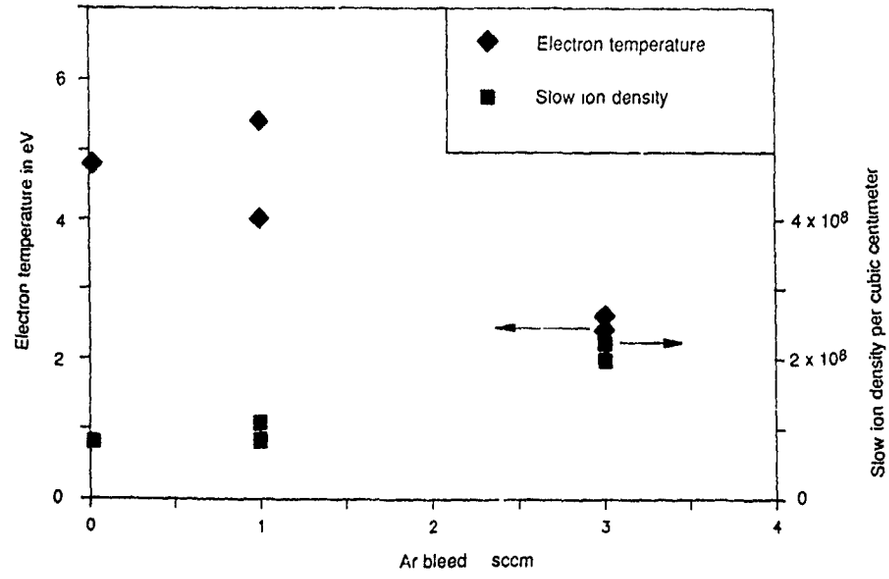

Fig. 7. The influence of Ar bleed on electron temperature and slow-ion density for 20 eV flood gun electrons for a 10 mA 20 keV Ar beam.

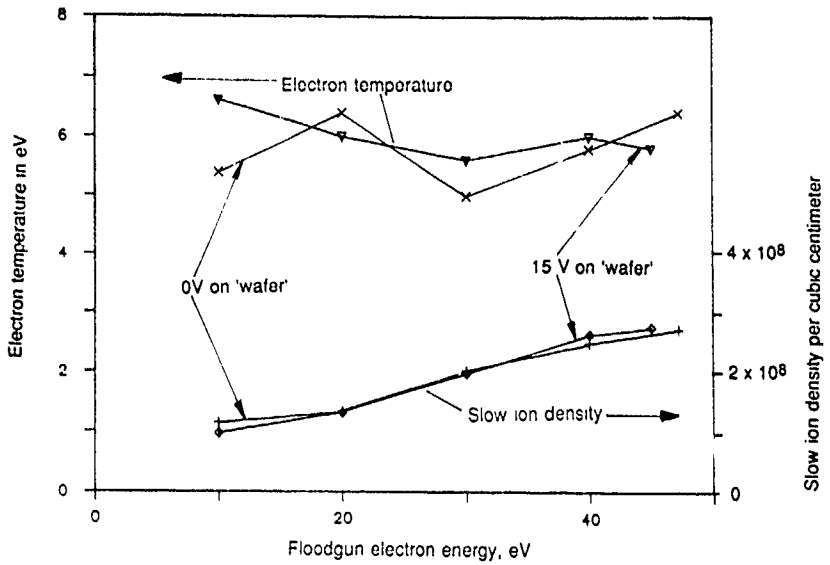

Fig. 8 Slow ion density and electron temperature plotted against flood gun electron energy for 1 sccm Ar bleed flow for a 10 mA 20 keV Ar beam showing the influence of "wafer" bias on the plasma.

some points at 4 sccm (sccm = standard cubic centimetres per minute). As may be expected, the slow-ion density is greater for the higher argon flows. Fig. 5 shows the effect of Ar bleed on the electron temperature. For the low-energy gun at 20 eV the electron temperature is seen to decrease with increasing Ar flow while the standard gun shows an unexpected increase in electron temperature with flow at electron energies of both 50 and 100 eV.

6.2 *The low-energy gun in more detail*

The next series of tests involved a more detailed study of the low-energy flood gun behaviour using a 10 mA Ar beam. The flood gun electron energy was varied between 10 and 47 eV, Ar bleed varied between 0 and 3 sccm and the effect of wafer charge-up on the plasma investigated by biasing the "wafer" positively at 15 V. "Well behaved" double-probe characteristics were obtained for all these conditions.

Fig. 6 shows electron temperature and slow-ion density plotted as a function of flood gun electron energy for 0 and 1 sccm Ar bleed. The slow-ion density shows a steady rise with flood electron energy while there is no discernible trend in electron temperature. The addition of 1 sccm Ar bleed also has little effect on the plasma parameters. Fig. 7 shows similar plasma parameters plotted as a function of Ar bleed. As in the previous data the slow-ion density increases with Ar bleed and the decrease in electron temperature as the Ar bleed is increased from 1 to 3 sccm confirms the low energy flood gun data of fig. 4.

The data of fig. 8 shows the effect of adding a 15 V bias to the "wafer". The plasma parameters are plotted as a function of flood electron energy and again show an increased slow ion density with electron energy and no trend in electron temperature. The positive bias on the "wafer" has no significant effect on density or temperature. The data in fig. 8 was obtained with a "hashy" ion beam and this may explain the consistently higher electron temperature (5 to 7 eV) compared with the other data for the low-energy gun (figs. 6 and 7) which is 2 to 5 eV. To look at the effect of beam width near the charge control/probe system, probe data was obtained with a beam defining aperture placed before the Al tube on which the flood gun is mounted. A reduction in electron temperature was observed from the more typical 3 to 5 eV to 1.4 eV for 20 eV electrons and 1 sccm Ar bleed. Hence beam conditions do influence the data obtained, possibly because of changes in the proximity of the beam to the aluminium tube and probe arrangement.

7. Discussion

The Debye length for the ion beam plasma system described above can be calculated from the slow-ion density and electron temperature using eq. (1). This gives a Debye length ~ 1 mm for all the data described in section 2 for the low-energy flood gun with a 10 mA ion beam. Hence the condition $\lambda_D \ll$ plasma dimensions is satisfied for the beam used which is ~ 60 mm × 70 mm. The probe diameter is 10 mm which

means the condition $\lambda_D \ll$ probe dimensions is satisfied well enough to obtain meaningful plasma data with the arrangement used.

The low-energy flood gun data shows an increase in slow-ion density with electron energy and Ar bleed A decrease in electron temperature is seen between 1 and 3 sccm of Ar bleed in the flood gun and there seems to be no trend in electron temperature over this flood gun electron energy range (10 to 45 eV). The condition of the ion beam also has to be taken into account in some instances.

The standard flood gun, provided it is not operated above 200 V at 0 sccm and 100 V at 1 sccm also gives good double Langmuir probe plots from which plasma parameters can be calculated. In this case the electron temperature increases with Ar bleed. This is not as expected but the data is reproducible.

Perhaps the most promising observation is the insignificant influence of "wafer" bias on the plasma, shown in fig. 8. This suggests that a positively charged wafer passing through the ion-beam-plasma, does not disrupt the plasma and should be neutralised by the plasma electrons. One should also note that the unsuppressed "wafer" current when biased at 15 V was -10 mA compared with $+15$ mA for the unbiased case (20 eV electrons 1 sccm Ar). This is a measure of how effectively electrons reach a positively biased wafer from the plasma. "Wafer" current readings with no beam present were -1 mA for the same flood gun conditions with the "wafer" biased and 0 with no bias on the "wafer" showing that few electrons reach the wafer unless the beam is present.

8. Conclusions

A plasma exists in the wafer/beam/floodgun environment. A double Langmuir probe arrangement can be used to measure the properties of this plasma provided the energy of the flood gun electrons is low enough.

The plasma and consequently the ion beam must be present if low-energy electrons are to be transported to the wafer. For the low-energy electron gun the plasma is enhanced by the Ar bleed.

The slow ion density for the system is $\sim 10^8/\mathrm{cm}^3$ compared with a neutral density of $\sim 10^{12}$. There is a lot of scope for increasing the plasma density, for example by improved confinement.

The potential on the wafer does not significantly perturb the plasma.

References

[1] A.T Forrester, Large Ion Beams (Wiley-Interscience, New York, 1988).

[2] N.R White, these Proceedings (8th Int. Conf. on Ion Implantation Technology, Guildford, UK, 1990) Nucl. Instr. and Meth B55 (1991) 287

[3] H. Ito and N.R. White, these proceedings (8th Int Conf. on Ion Implantation Technology, Guildford, UK, 1990) Nucl. Instr and Meth. B55 (1991) 527

[4] I.H Hutchinson, Principles of Plasma Diagnostics (Cambridge Univ Press, 1987).

[5] F F. Chen, in: Plasma Diagnostic Techniques, eds R H. Huddlestone and S L Leonard (Academic Press, New York, 1965).

[6] A Renau, S Moffatt and F. Plumb, US patent 4825087 (1989).

Nuclear Instruments and Methods in Physics Research B55 (1991) 104–108
North-Holland

Implantation-equipment data management for cost reduction, equipment optimization and process enhancement

C. Yarling [a], R. Eddy [a] and J. Turner [b]

[a] *Varian Ion Implant Systems, Gloucester, MA 01930, USA*
[b] *Particle Measuring Systems, Boulder, CO, USA*

Most problems with existing ion-implantation equipment do not require complex statistical analyses to ascertain a solution or to subsequently provide verification of production-worthy performance. However, knowledge of performance goals, measurement parameters and data-reduction techniques are helpful in methodically and systematically solving recurring problems These facets necessitate the implementation of a data-management program that provides an ongoing useful tool which measures equipment performance The utility of such a program can be measured with benefits of optimized equipment utilization, improvements in equipment throughput, as well as increase in wafer die yield. This paper will identify common methods, measurements and tools which have demonstrated measurable improvements in performance of ion-implantation equipment Data collected from as-required maintenance versus optimized-scheduled maintenance programs will show that preventive maintenance should be the principle focus of any useful ongoing semiconductor fab maintenance effort. Process optimization and the extent to which the equipment manufacturer can support the user in that regard will be discussed. It will be shown that motivation, knowledge and participation of both management and supporting personnel of the IC manufacturer as well as the equipment vendor can be combined to develop a partnership that will accelerate and solidify the optimization process

1. Introduction

In the semiconductor-manufacturing environment, productivity may be defined as consisting of three components: yield, throughput and availability. As such, maximum productivity is a fundamental goal that is sought by managers on all levels. Yet, all to often this goal is addressed by separate departments, addressing each of these components individually. When only two of these components have been optimized with respect to each other, only partial improvement in productivity is achieved; maximum productivity is realized only when all three components have been fully optimized with each other [1,2].

Statistical data, the medium most often used to measure these fundamental components of productivity, frequently originate from a variety of sources within the wafer fab (table 1). Unfortunately, these sources are usually different departments, each of which are guided by their own responsibilities. Although the overall plan addresses maximum productivity, individual departments can be in opposition to each other in their own modus operandi, without knowing of the other's needs or contributions to this effort.

An example of this is shown as follows. From the viewpoint of the maintenance or facilities manager, the two primary goals of data management are minimization of non-machine-related downtime components (such as delays to initiation of maintenance procedures as well as excessive wait-times due to delivery of spare parts) and maximization of equipment uptime and productivity (such as retrofit of equipment improvements and/or upgrades, throughput, reduction of unscheduled downtime, and optimized scheduled maintenance activities). These goals are not usually fundamental to the process- or device-engineering departments and are, therefore, often ignored. However, progress towards these two goals necessarily equates to optimum performance of the other two departments: manufacturing and process engineering.

Another overlooked contributor to maximum productivity is the relationship between the equipment

Table 1
Sources of data for productivity

Component	Department	Source(s)
Yield	Process and/or device engineering	Yield at various steps, machine condition(s) and setup, process control
Throughput	Manufacturing/ production	Number of wafers and lots, number of different implanter specifications, operator wait-times, production holds
Availability	Maintenance/ production	Maintenance cycles (both scheduled and unscheduled) wait-time, and requalification time

0168-583X/91/$03.50 © 1991 – Elsevier Science Publishers B.V. (North-Holland)

producer and the equipment users in the fab. When performed at a high enough level, information exchange between these important counterparts enables optimum performance of production equipment and its related support systems. An active partnership between these two "occasionally divergent parties" will produce benefits that will ensure the long-term success of both.

2. Maintenance activities/contributors

Most implanter-equipment manufacturers provide either general or customized scheduled maintenance routines to their customers. With proper implementation, these types of procedures have been shown to minimize unscheduled downtime. From a practical standpoint, however, occasions will arise in the wafer fab when scheduled maintenance activities must be delayed due to immediate production demands. In these cases, use of a customized maintenance schedule will provide enough flexibility to allow equipment use to be extended for a reasonable period of time. This type of schedule will most likely have been generated through a historical evaluation of the implanter in question.

Typically, scheduled maintenance activities use a timed and/or throughput-based sequence of actions based upon the recommendations of the manufacturer's equipment-design engineers. These recommendations are not often flexible enough for the variety of processes or operational variables to which equipment is exposed in the production environment. Equipment manufacturers are now recognizing that this practice is not necessarily an efficient method to enhance the reliability of their equipment nor to optimize its throughput.

Varian has recently addressed the flexibility requirements of the semiconductor industry with introduction of a tailored-scheduled maintenance program designed around the specific mechanical and process demands of any batch or serial implanter. This flexible maintenance package, referred to as Modularized Action Program or MAP [3] began with an intensive evaluation of machine-performance data from a large database of implanters. The management of this data has resulted in a program that is a pro-active approach to traditional preventive or scheduled maintenance activities.

Whereas the conventional annual PM took four to five consecutive days (and more if difficulties were encountered), the MAP introduces an innovative approach to maintenance by separating the previous annual maintenance parameters into modularized components, each one taking less than twenty-four hours (Table 2). Thus, the time for required scheduled maintenance activities has become modularized and is easily nested into other planned maintenance activities. The usual post-overhaul troubleshooting and requalification is greatly minimized since the areas of potential trouble or error have been greatly reduced from the entire implanter to just the modular area being addressed at any single time. The overall annual availability of the implanter to manufacturing is remarkably increased. The MAP program provides previously unavailable flexibility for the maintenance and manufacturing departments to pro-actively schedule required maintenance for each ion implanter.

Table 2
Modular Action Plan (MAP) components

Medium-current implanter	*High-current implanter*
- High-voltage terminal	- Source region
- Beam line	- Beam line and analyzer
- End station	- End station
- Vacuum and cooling	- Vacuum and cooling
	- Wafer-handling system

3. Implementation of equipment options and upgrades

The implanter manufacturer often has the capability to support the IC manufacturer in the investigation and refinement of the equipment that has been purchased, such as enhancements, options or upgrades. In most cases, the philosophy of the user mandates that these kinds of tests be performed off-line, i.e., outside of the fab, so as to avoid disrupting ongoing production flow and/or possibly risking equipment integrity. However, best results are only obtained through beta-site testing of preproduction assemblies of new equipment options or enhancements on-site at the customer's facility. Indeed, optimum process results must ultimately be tested in the fab for the following reasons:

(1) uniqueness of the process flow in the fab;
(2) potential contamination from an external test;
(3) specific combination of process-related options;
(4) process/dopant memory from previous implants

From the vendor's viewpoint, there must be a careful balance of supplying new techniques or options to the user as soon as they appear ready for the production environment versus expediting the delivery of the new technique or option to him with an undetected flaw. However, before any real comparative tests can be made, both the equipment and the product must have established a stable, existing process. With a stable implant-process-capable system (in our case, material, material preparation, implantation, post-implant processing), the reporting of results from newly installed additions to the implanter can be tracked by a simple computer program. Thus, lot-to-lot comparisons can be made in a cost-effective manner, i.e., a minimum number of lots, runs or wafers, with high confidence factors. Then the resulting trends can be fully evaluated, thus

beneficial to the fab user as well as the equipment vendor.

4. Automation and data management

New-generation ion-implantation equipment used in today's IC fabrication facilities is being designed with an increasing number of features which allow the equipment to be encapsulated within its automated and controlled environment. This scenario allows a host control system to sends process recipes to awaiting equipment, which then performs the following: it processes the recipe, sets up and tunes the equipment, and then cycles the correct wafers through the equipment. Processed wafers are then directed by host control to be transported to the next process step by clean robotic control or clean air tracks.

Realistically, before an implanter can be fully automated, all key facets of its operation must be identified, understood, and tracked. Once all individual pieces of equipment are stable and process-ready, they can be integrated into the fully automated fab environment. Although this type of automated process is functional in today's semiconductor industry, it is still the exception, rather than the rule. For example, only about 5% of the installed equipment are currently using SECS protocols [4].

The success of full automation will ultimately depend upon the availability and format of data reported back from the equipment itself. Most, if not all, ion-implantation equipment currently being manufactured has built-in capability of transmitting various kinds of data taken during the implant process into other forums. This includes lot-tracking information, machine data from specific implant steps, as well as machine performance data such as error messages, machine failure records, and preventive maintenance prediction. However, maximum performance of each machine cannot be obtained unless the information being reported meets three important guidelines: (1) is it useful to the user, (2) can it be massaged into a usable format, and (3) will it bring positive results when factored back into the manufacturing process? The following examples place these guidelines into proper perspective.

One of the available software options on the EXTRION 1000 ion implanter is the Operator Report. This access level controlled function provides the user

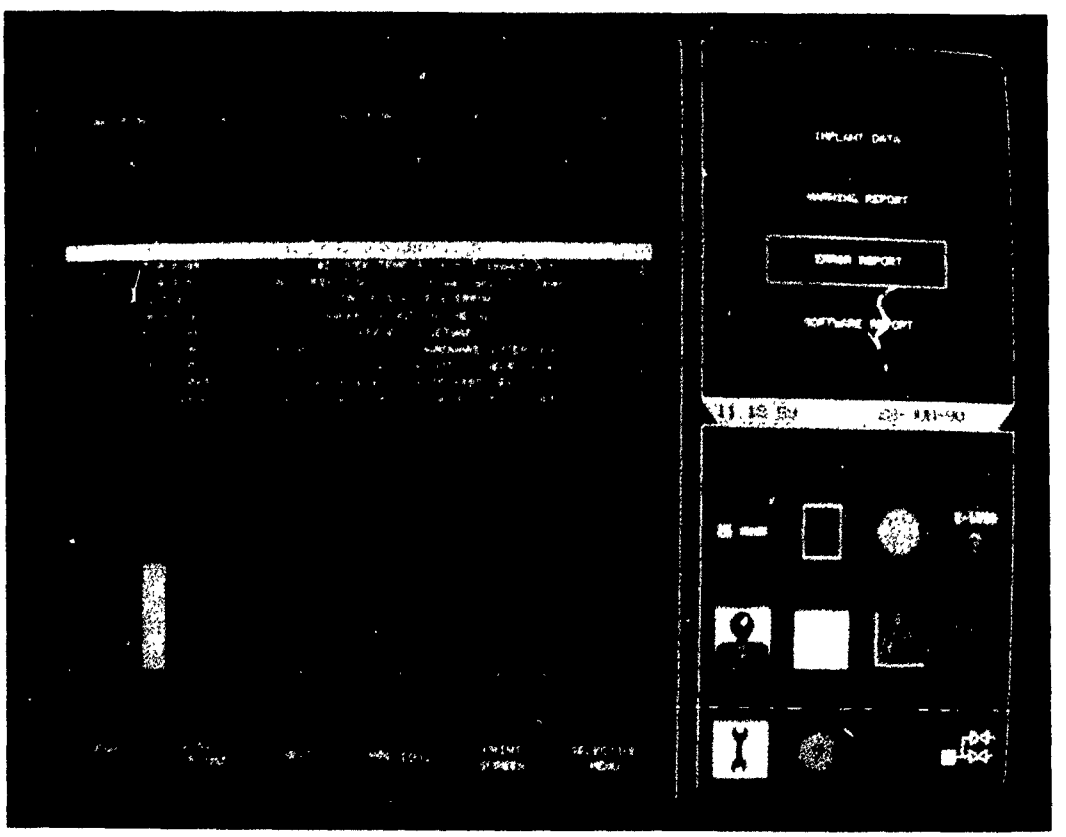

Fig. 1. The frequency-versus-error graph from the EXTRION 1000 is a detailed listing of logged error messages presented in Pareto analysis format such that the most troublesome error is shown first.

with a quick and easily understood summary of available machine data. The report topics available are the Implant Log, Software Report, the Error Report and the Warning Report. Line items in each report are capable of being viewed, printed or purged. The Error and Warning Reports include the capability of being plotted by frequency versus code, day or month. These reports have been designed for maintenance, production and process engineering departments as reflected in table 1.

Fig. 1 is an example of this type of machine-generated performance data from the EXTRION 1000 ion implanter. This figure shows the Frequency Versus Error graph for various logged error messages. The errors shown were logged when the implanter was being first brought into service on the production floor. The Error Codes represent a software description of the the error type; the Error Message is a brief description of the error; the presentation is in Pareto Analysis format such that the most troublesome error is shown first. With this type of data, machine performance can be evaluated, logged errors can be itemized, and problem areas can be quickly prioritized and addressed.

Another example of the utility of automated machine-performance data is in fig. 2. In this example, predicted-scheduled maintenance is shown on the Routine Maintenance screen of the EXTRION 220 Ion Implanter. This screen shows a listing of various items that require periodic routine maintenance, the life time of the serviceable item (in hours or cycles), the present age of that item, how much time is left before next service (as a percentage of scheduled or predicted lifetime) and appropriate information on the previous service (name and date). Any item that is overdue for a maintenance activity is highlighted in red. When the service activity has been completed, the counter is reset for that item. If required, the service engineer may review instructions for the maintenance procedure directly from the screen. Thus, all preventive maintenance activities can be monitored and tracked right at the computer console of the implanter. And when needed, this information can be downloaded to a floppy disk in a spreadsheet format for use by maintenance or process engineers responsible for logging this type of information onto an external maintenance computer system.

The Routine Maintenance screen is an excellent example of software capability that readily addresses the needs of the customer to provide the best service for his equipment. The information generated from this screen is presently being compiled and will be used to refine maintenance service information (i.e., cycle time/periods) for optimization of the MAP program into this

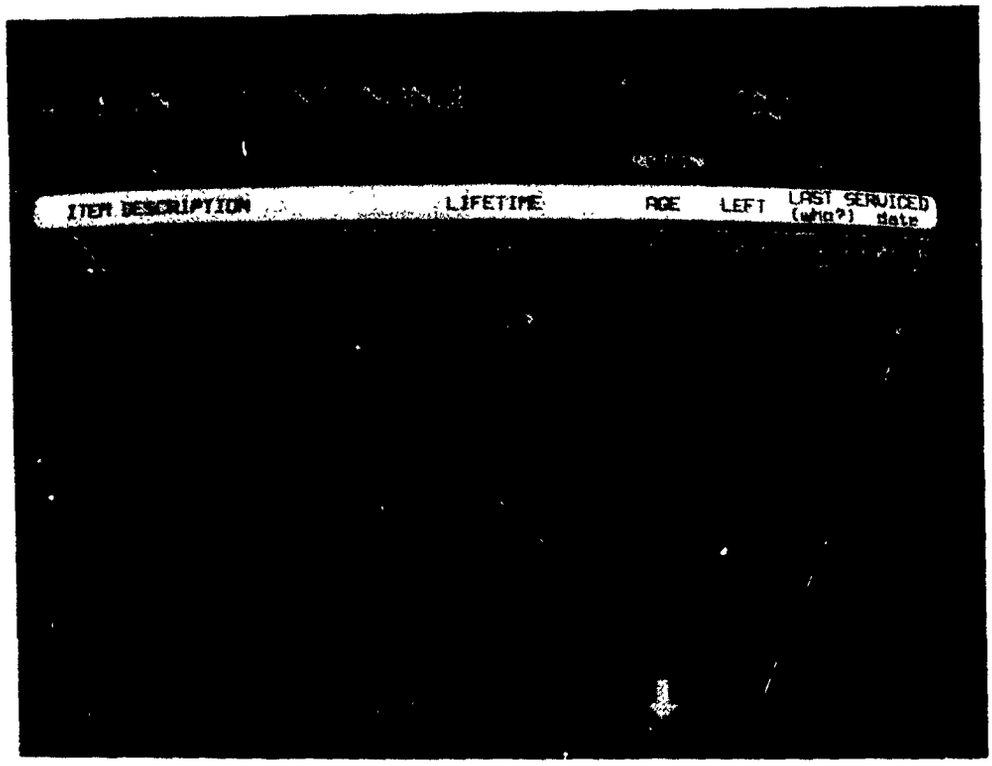

Fig. 2. The Routine Maintenance screen from the EXTRION 220 lists predicted and scheduled maintenance activities in tabular form. Also available from this screen is a listing of the service procedure for each activity.

new product. This same activity is ongoing for another new generation implanter, the EXTRION 1000. These new MAP programs will address a wide range of production and maintenance requirements for various customers of modern ion-implantation equipment.

5. Equipment/user partnership

A solid partnership between the IC manufacturer and the capital equipment vendor can improve not only the user's productivity and yield, but can also improve the lifetime of the equipment as well as the cost of ownership. In addition, a continuous, stable relationship can lead to the development of unique operating conditions, assemblies, and/or options to existing equipment. As unit cells (individual equipment) work towards becoming fully automated , the partnership will pay off with improved productivity.

For example, a major semiconductor manufacturer dedicated one end station of a 120XP dual end station high-current batch implanter to arsenic and boron implants on 150 mm wafers. During a two-month time period, particle levels in this machine averaged 20.21 defects per wafer with a standard deviation of 13.51. During this period, three particle maintenance events occurred which were attributed to unscheduled maintenance, which by definition caused unscheduled delays to production. The customer had become so used to these unscheduled events that he was ready to implement a scheduled preventive maintenance procedure to address the situation. However, upon consultation, Varian recommended use of a hithertofore under-utilized software feature: the user-defined Vent-Purge Cycle [5]. This software feature allows the process engineer to preselect an automatic vent-purge time, whereby the implanter automatically commences a slow particle-purge cycle initiated by the operator. This particular customer implemented the procedure on a once-per-day basis and reduced the particle levels (> 0.3 μm on 150 mm wafers) to an average of 11.55 per wafer with a standard deviation of 5.17 over a period of three months. During this time period, only one maintenance event was required. Thus a partnership agreement between vendor and customer brought about a reduction in unscheduled maintenance with a resultant increase in implanter performance and productivity. In addition, all three sectors outlined in table 1 benefited from the results.

A recent editorial in a semiconductor-equipment trade journal remarked on the importance of designing for manufacturability [6]. It was pointed out that chip designers could easily improve manufacturability as well as increase yield on their product simply by incorporating existing data into their design with only a slight layout change. However, because the designer was unaware that the data existed, and therefore was unable to ask for it, an easily attainable improvement in yield was not accrued. This is another example of where inefficiency in data management techniques have allowed the NIH (not invented here) syndrome to affect productivity at the capital equipment producer's site or in the wafer fab. The bottom line is that a successful vendor–customer partnership does not allow this type of situation to occur since there is already in existence a proven two-way communication program that includes a significant amount of data transfer. This action is the ultimate utility of data management.

6. Conclusion

As semiconductor manufacturers slowly progress towards total factory automation, published technical information such as that provided by Kaminski and Abegglen [7] and others will aid fab architects in reaching this auspicious goal in the near future. In the mean time, equipment vendors must continue their relationship with the customer, i.e., the manufacturer, and provide him with the necessary automation and data-management capabilities that will help him in achieving this worthy accomplishment.

References

[1] C M. McKenna, Nucl. Instr and Meth. B37/38 (1989) 448
[2] C.B. Yarling, Microelectronic Manufacturing and Testing 12(13) (1989).
[3] For information, contact John Appelgren at the Varian Customer Support Department, Varian Associates, 48664 Milmont Drive, Fremont, CA 94538, USA; tel 415-490-8333.
[4] C.F. Hiatt, Technical Proc of Semicon/Europa, 1988 (Semiconductor Equipment and Materials Institute, Mountain View, CA) pp 5–14.
[5] Batch Ion Implantation System Software Manual No M-105145 (Varian Publication, October 1985).
[6] P.H. Singer, Semiconductor International 13(5) (April 1990) 13.
[7] G. Kaminski and R. Abegglen, ibid., 13(6) (May 1990) 165

Nuclear Instruments and Methods in Physics Research B55 (1991) 109–114
North-Holland

The use of tertiarybutylarsine (TBA) and tertiarybutylphosphine (TBP) as liquid reagents for ion implantation

Lawrence A. Larson [1] and Mike Sakshaug
National Semiconductor Corporation, PO Box 58090, Santa Clara, CA 95052-8090, USA

Wayne Weiner
American Cyanamid Company, Wayne, NJ, USA

The safety and environmental concerns regarding the widespread use of phosphine and arsine gas in the semiconductor industry have given rise to the use of alternative, less hazardous replacement substances, such as tertiarybutylphosphine (TBP) and tertiarybutylarsine (TBA). TBP and TBA are less hazardous than the hydride gases under sudden release scenarios because they are (1) liquids, and (2) have a lower acute toxicity than the gases. For applications in ion implantation, the use of TBP and TBA could potentially reduce the costly downtime resulting from the heating and cooling cycles of the solid source vaporizers. In comparison with the gases, the use of liquids can extend the period of implanter operation before chemical sources need replacement. In this paper, data is presented which demonstrates the performance of these materials in a production environment, with the discussion focusing on issues such as source lifetime, implanter maintainability and overall performance.

1. Introduction

Ion implantation is now a ubiquitous process in the fabrication of semiconductor devices. The most common elements implanted into silicon in production facilities are phosphorus, arsenic and boron. The source materials for producing ion beams of these elements are typically phosphine and arsine gas and boron trifluoride (BF_3). Alternatively, metallic arsenic and phosphorus have been used [1].

The use of gases or solids as source materials for ion implantation has particular handling disadvantages. Arsine and phosphine gas, for example, are extraordinarily toxic materials. In addition, they are stored under pressure thus representing an extreme potential hazard to the production facility and to the surrounding community in the event of an uncontrolled release. The increasing awareness of these hazards has caused a ground swell of regulatory activity in the USA, increasing the requirements for the use, transport, and inventory of these gases. In certain cases, expensive capital costs are required in order to continue to use these materials in existing facilities [2].

The uses of arsine and phosphine gas for ion implantation is distinguished from the use of these gases for other electronic applications (such as LPCVD or diffusion doping) by an additional safety consideration. Whereas the other applications can accommodate the gases located in a remote bunker or gas cabinet, for ion implantation, the gases can only be used with the bottles immediately inside the implanter. Gas bottles are then necessarily located directly on the production floor. This makes the changing of gas bottles for the implanter, the operation with the highest probability of incident, a particularly cumbersome procedure; both time consuming and hazardous.

Although solid sources avoid the issues discussed above, they still are difficult to handle, particularly with regard to arsenic dust. Most importantly, the solid source vaporizers are notoriously difficult to operate, and can require 1–2 h for heating up and cooling down. This amounts to an undesirable loss of potential production time, which renders the use of solid source material prohibitive for facilities which must switch implanters from one source to another frequently.

The use of liquids as source materials for ion implantation represents a possible solution to the disadvantages of both gases and solids. Two liquids in particular have been chosen for study: tertiarybutylarsine (TBA) and tertiarybutylphosphine (TBP). These organometallic sources for arsenic and phosphorus are readily available in electronic grade purity and have sufficient vapor pressures at room temperature such that they can be handled in essentially the same way as the source gases. But because TBA and TBP are not stored under pressure their use represents a substantial reduction in hazards in comparison to the compressed gases arsine and phosphine. A further benefit to the liquids is

[1] Present address: Sematech, 2706 Montopolis Dr., Austin, TX 78739, USA.

0168-583X/91/$03.50 © 1991 – Elsevier Science Publishers B.V. (North-Holland)

that they are significantly less toxic than the gases. In fact, TBP is not regarded as a poisonous liquid!

In comparing the use of the liquids to the solid sources, the relative ease of control of the liquids is attractive. Most significantly, the use of solid vaporizers can be eliminated and the wasted productive time used for vaporizer heating and cooling can be regained.

The present work is an extension of a previous study which demonstrated the feasibility of using TBP as a liquid phosphorus source on a medium-current implanter [3] The present work is focused on the use of both TBA and TBP on a daily basis in a production environment. In particular, it will be shown that the use of the liquids can occur in a manner which is transparent to the use of gases with regard to machine operability, maintenance, and source lifetime To our knowledge, this represents the first account of the use of liquid sources of phosphorus and arsenic for production applications, and establishes an important alternative method for production facilities

2. Experimental

TBA and TBP are manufactured in 99 9999% purity by the American Cyanamid Company, Wayne, New Jersey The material is supplied in returnable, stainless-steel ampoules In addition to the current work, TBA and TBP have been used extensively as replacements for arsine and phosphine in the MOCVD growth [4] of InP and GaAs materials, as well as dopant sources for in-situ-doped polysilicon [5] and in the CVD growth of BPSG and PSG films [6].

The physical properties and toxicological properties of these materials are shown in tables 1 and 2, respectively Note that the liquids have a lower acute inhalation toxicity than the gases. In addition, as expected, the liquids have been shown by modelling studies to disperse orders of magnitude less readily than the gases, and can therefore be regarded as significantly less hazardous in the event of a leak [7].

Fig. 1 shows a diagram of the installation of the liquid bubbler in the gas distribution system of a Varian

Table 2
Acute toxicity

Material	LC_{50}
Tertiarybutylarsine (TBA) [a]	70 ppm (4 h)
Tertiarybutylphosphine (TBP) [a]	>1100 ppm (3 h) [b]
Arsine [c]	5–45 ppm (4 h)
Phosphine [a]	11–50 ppm (4 h)

[a] Internal Testing, American Cyanamid Company
[b] Exposure to TBP was halted after three hours of exposure to 1100 ppm. There were no deaths at this concentration. Actual LC_{50} was not determined.
[c] Four-hour LC_{50} data for arsine are still not definitively established. This range is an estimate that generally reflects the industry's perception on arsine's toxicity at this time The National Institute of Environmental Health Sciences has reported an LC_{50} in mice of approximately 25 ppm in recent studies (personal communication)

Table 1
Physical properties of TBA and TBP

	TBA	TBP
Formula	$C_4H_{11}As$	$C_4H_{11}P$
Structure	$CH_3-\underset{\displaystyle CH_3}{\overset{\displaystyle CH_3}{\overset{\vert}{\underset{\vert}{C}}}}-AsH_2$	$CH_3-\underset{\displaystyle CH_3}{\overset{\displaystyle CH_3}{\overset{\vert}{\underset{\vert}{C}}}}-PH_2$
Weight (amu)	134	90
Density (g/ml, @ 20 °C)	1 0	0 71
Boiling Point (°C, @ 760 mm Hg)	65	54
Melting Point (°C)	−1	4
Vapor Pressure (mm Hg, K)	$\ln P = 16.68\ (3475/T)$	$\ln P = 17\ 47-(3544/T)$
Appearance (@ 25 °C)	Clear, mobile liquid	
Solubility	Insoluble in water, soluble in most organic solvents	
Reactivity	Strong reducing agent, ignites upon exposure to air (pyrophoric), non-corrosive toward stainless steel; indefinite shelf life when stored under an inert atmosphere	

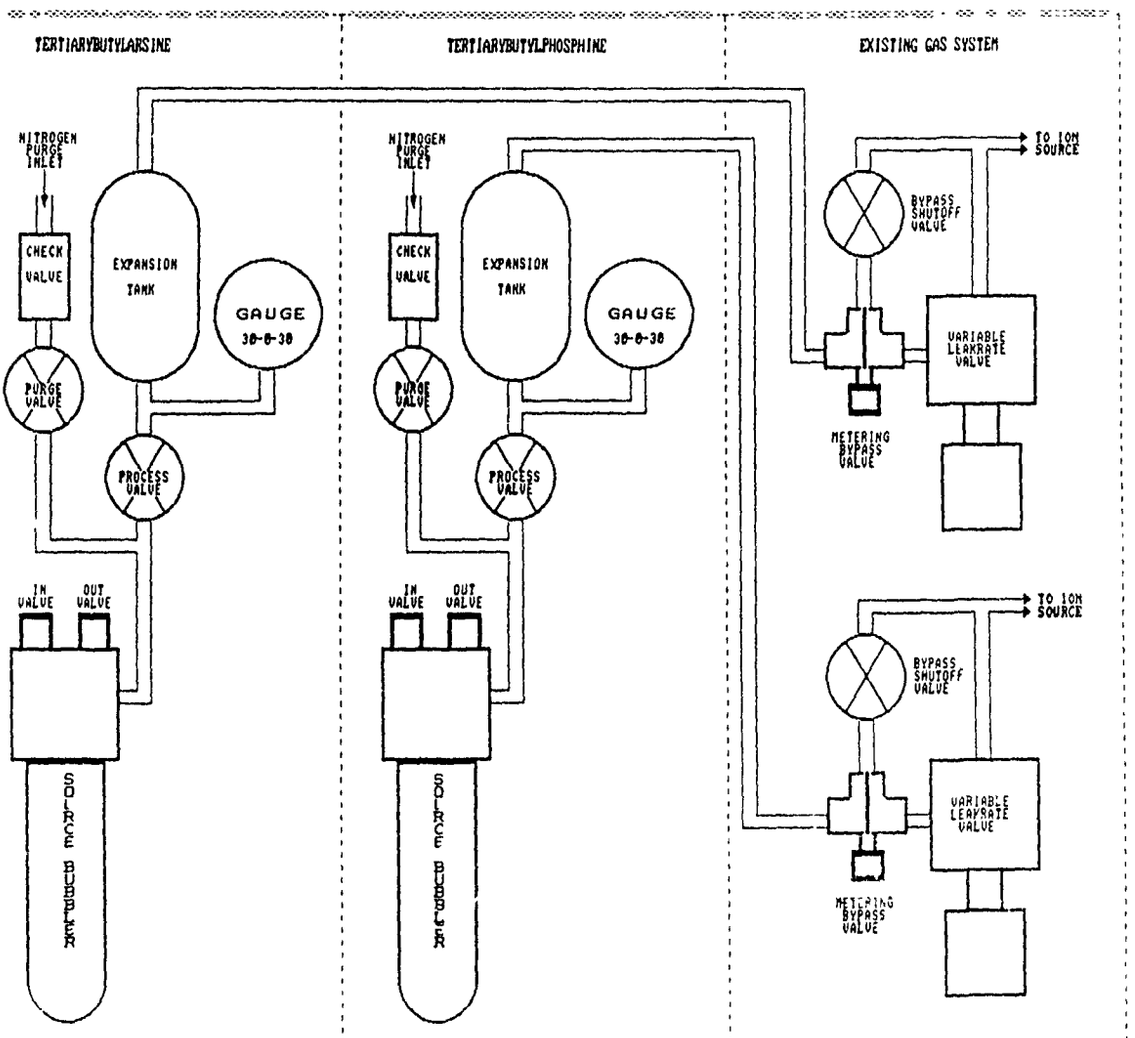

Fig 1 Source gas manifold as configured for liquid materials

DF4 implanter The only deviation from a direct connection is the addition of an expansion chamber between the bubbler and the leak valves This expansion chamber increases the volume of the vapor that is available and reduces the source instabilities due to high rates of mass flow. Without an expansion chamber, running the source at higher mass flow rates will pull vacuum on the liquid and push it towards its triple point. At the triple point the liquid will freeze and boil simultaneously and sufficient vapor pressure to feed the source will not exist for a time. This is observed as an instability in the source current.

Two modifications to the source construction were also carried out over the course of this experiment to overcome the effects of carbon deposition on the source lifetime The first was to add a protective cover to the insulators for the extraction anode. This was to overcome shorting of the extraction potential that occurs readily in an unprotected situation. The second was to add re-entrant insulators to the filament itself At high rates of carbon deposition, these insulators would coat and short through the arc chamber. A re-entrant design provides sufficient insulating surface area that this mechanism is defeated

Following installation of the bubblers and the extraction anode modification, the TBA and TBP sources were qualified for production with all the product lines at the National Semiconductors Santa Clara facility and put into production. As such, the data presented here represents an analysis of production performance rather

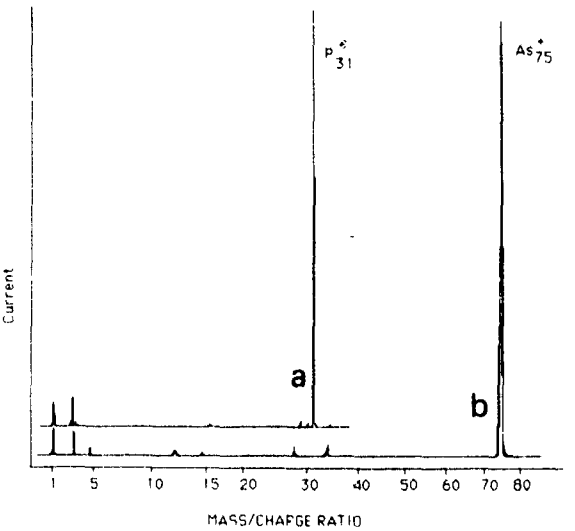

Fig 2. Mass spectra of the two liquids: (a) TBP, (b) TBA

than a carefully controlled experimental study. Presently slightly over six months of production data have been gathered and the source continues to be used.

3. Process results

The mass spectra of TBP and TBA are shown in fig. 2. It is clear that there are few peaks other than the primary peaks. These peaks are clear and distinguished making it the obvious choice for tuning. Other peaks which are observable include P^{2+}, mass 28 (N_2 and/or CO), and N^+ – all of these are not an issue in the machine setup.

Tests verifying the resistivity and uniformity of the implant were performed. As expected, these were indistinguishable from the gas or solid sources in every way. Split lot qualification tests were also done with all product lines in the Santa Clara plant. These include bipolar, CMOS, and NMOS production lines and processes that mix most of these technologies. The results of these split lots were also that the source was indistinguishable and full production was allowed.

4. Maintenance results

Fig. 3 is a plot of the number of hours of ionization source lifetime for the implanter using the liquid re-

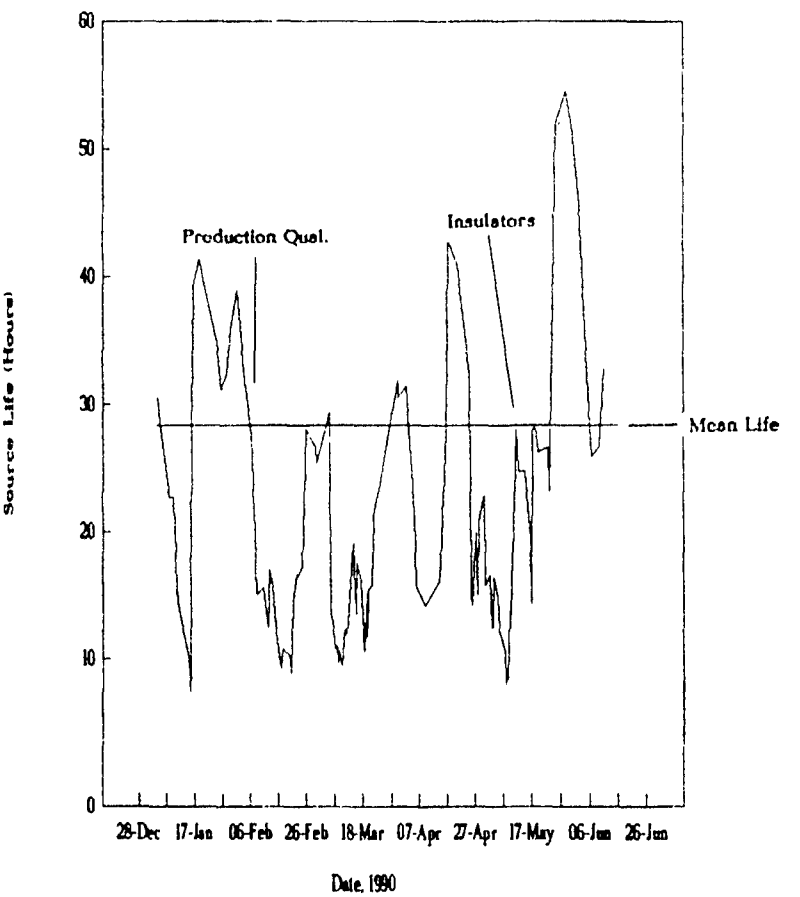

Fig. 3. Source lifetime as experienced in the first six months of 1990

agents as a function of date. This is compared to the average life of the other implanters in the facility which operate using PH_3, AsH_3, and BF_3 gases. The jagged line in fig. 3 is composed of aproximately 120 source changes which occured over a six-month period. For example, the source installed on May 22nd operated for 28 hours before failure; near the average for the facility. Of the 28 hours of operation, 12 hours were devoted to phosphorus (TBP) and arsenic (TBA) implantation. On the average 20% of the operating hours of each ionization source was devoted to phosphorus and arsenic implants; the remainder to boron. In the initial phases of this project this percentage was limited by the source lifetime. Presently this ratio is limited by the production volume. In fact, the present operation will switch from liquid sources to BF_3 and back several times during the source life.

Several points are observable in this chart. Initially the lifetime was relatively high as the liquid sources had not passed product line qualification. When production started the source lifetime fell and was extremely low ($\sim$ 10 h) with regular short lifetime failures. This gradually improved as all of the technicians learned to build and setup the source. The time when the re-entrant filament insulators were introduced is noted. This gives a definite increase in lifetime. This was particularly noticable in that the primary cause of source failure was once again filament burnout rather than shorting. The end result, as evidenced by the last six weeks, is operation which is well within the distribution of "normal" source lifetime.

Two caveats should be mentioned regarding this performance. The first is that implants done on this machine are limited to those below 4×10^{14} ions/cm^2. This is because the fab is operated as an implant center and higher dose implants are staged onto other machines. As such, the beam current is seldom taken above 150 μA – a particularly easy operations mode as compared to either specified current or operation of more modern machines. The second is that the fab underwent a major reorganization during the time period that this test was run. Turnover was relatively high and the distribution of source lifetimes is somewhat lower than that which is expected! This is why the liquid-source lifetime is compared to the distribution as established during the same time period. We do not expect that the sources for the liquid-source machine received particularly different treatment from the others so this is considered a proper comparative evaluation.

5. Discussion

The use of TBP for ion implantation was first demonstrated on a medium-current implanter. One of the issues in using these materials is the effect of carbon deposition on the ionization chamber.

Inspection of the mass spectra of the extracted beam (fig. 3) reveals that there can be very little ionized beam attributed to carbon; the spectrum is essentially identical to those obtained when using the hydride gases. This suggests that most of the carbon of the tertiarybutyl group is deposited as carbon in the ionization chamber, or is pumped out of the system as hydrocarbon fragments. Visual inspection of the ionization chamber reveals substantial amounts of black carbonaceous residue, and suggests that a substantial amount of the carbon plates out in the arc chamber.

While this is advantageous from the standpoint of ionization efficiency, the carbon deposition in the chamber can form on the filament insulators. After a period of time, this can cause shorting and premature failure of the arc and/or the filament. For this reason, it is essential to operate the liquid sources using the minimum vapor flow needed to maintain the desired beam current. The effect of running more vapor than necessary is what we believe is observed in the middle section of the source lifetime results (fig. 3). Here the lifetime was often 20% or less of the value that was obtained as an experience base was gained. The utilization of re-entrant filament insulators greatly reduces the potency of this failure mechanism. In this case the insulators are constructed such that the carbon buildup has less opportunity to coat a shorting path.

The other modification necessary for consistant flow of the vapor is the ballast chamber manifold (fig. 1). This manifold supplies a large volume of the vapor (at its nominal vapor pressure) which provides sufficient material to support the mass flow necessary to hold a steady pressure. Without the use of the manifold the vapor flow tends to become erratic. This is due to a "boiling/freezing" phenomenon that occurs as high vacuum pulls the liquid/vapor interface to the triple point of the material.

6. Conclusions

This work has shown, for the first time, the viability of using liquid phosphorus (TBP) and liquid arsenic (TBA) sources for ion implantation in a production environment. It has been demonstrated that the performance and overall operability of the implanter using the liquid sources is indistinguishable to the use of gas sources when medium current machines are operated at routine beam current levels.

The substitution of the gases by TBA and TBP leads to a significant decrease in risk of operating the ion implanter, particularly in the area of changing gas bottles or other such maintenance intervention in the gas manifold. By nature of the fact that liquids are more

dense than gases, the molar equivalent of phosphorus or arsenic molecules in a given volume is 20–30 times that found in a 15% gas mix. It is expected then, that the frequency of gas bottle changes may be decreased by a factor of 20–30, enabling a significant incremental gain in available production implanter time

Further work will be aimed at expanding this technology. The borderline as to when (if at all) higher current performance is affected in medium current machines has not been explored. Similarly, this technology will be expanded to test the performance in high-current ion implanters

Acknowledgements

The authors would like to thank Paul Daniels of the Extrion Division of Varian for the original work in setting up the expansion chamber and the extraction anode shields. We would also like to thank the maintenance technicians at NSC, as a crew, for putting up with the original learning curve portion of using this source. In particular, Frank Nurkowski and Dai Tran for their work on the insulators

References

[1] H Ryssel and I. Rub , Ion Implantation, (Wiley, 1986).
[2] Ordinance no. 2314-90 City Council of Sunnyvale CA, USA, February 6, 1990
[3] P. Daniel, H D. Sarge and W. Weiner, Electrochem. Soc Meeting, October 1989, Hollywood, Florida, USA, Abstract No 735RNP.
[4] T. Kikkawa, H. Tawaka and J Komeno, J Appl Phys 97 (1990) 7576;
B.I. Miller, M. Young, M. Ovon, U Koren and D. Kisker, Appl. Phys. Lett 56 (1990) 1439.
[5] T E Tang, Technical Digest Int Electron Device Conf (IEEE, New York, 1989).
[6] Applications Note No. 8, American Cyanamid Company, Electronic Chemicals Department, Wayne, New Jersey, USA.
[7] Applications Note No 2, American Cyanamid Company, Electronic Chemicals Department, Wayne, New Jersey, USA,
G Miller, Solid State Tech. 32 (1989) 59.

Nuclear Instruments and Methods in Physics Research B55 (1991) 115–123
North-Holland

Section III. Processing, throughput and yield

Gate oxides in high current implanters: how do they survive? *

Frank Sinclair
Eaton Corporation, Beverly, MA 01915, USA

The use of thinner gate oxides in ULSI, susceptible to catastrophic breakdown at lower voltages, presents an increasingly difficult problem for ion implanter manufacturers. The center of a high current ion beam can be modeled as a voltage source whose potential depends on the current density in the beam, the neutralization of the beam by electrons and the geometry of the process chamber. Many measurements using a variety of methods support the validity of these models The peak voltages are almost always larger than the expected breakdown voltages of thin gate oxides and thus would predict zero yields.

Studies of oxide failure in electrical tests have shown two distinct classes of effects: some devices fail promptly with characteristics consistent with a localized defect that leads to a reduced breakdown voltage, while other devices have reduced reliability that correlates with reduced charge to breakdown. The charge to breakdown test typically gives results in the range from 1×10^{18} to 1×10^{21} electrons/cm^2, much greater than the total dose in an implant, so that a simple charge based model would predict 100% yields

This paper puts forward some physical models based on recent experimental results aimed at approaching the problem from an interdisciplinary perspective. First, we characterize the environment in an implanter using in situ measurements, and conclude that at scales larger than the beam it behaves like a pure current source, while at scales smaller than the beam it behaves like a voltage source with a surprisingly high current limit Second we review some recent trends in electrical tests of gate oxides, and finally we put forward some hypotheses that could be tested in future experiments.

1. Introduction

The integrated circuit industry is on the well-known treadmill of decreasing device lateral dimensions by a factor of two every five years As an essential part of this programmed revolution, gate oxides are inexorably getting thinner, albeit at a slightly less dramatic rate. This scaling means that charging (and particulates) will be with us forever as an area where our customers will require continued improvement in performance. Thinner gate oxides have lower breakdown voltages and therefore require reduced supply voltages. The SRC five-year projection made last year predicts that in 1994 gate oxides will be 5 nm thick and supply voltages will be down to 3.3 V.

Ion implant users often have problems with the yield of their devices, and in several cases the cause of gate oxide failure has been traced to a high current implanter If no mechanism is used to neutralize the charge in the beam, the target will charge up to very high voltages. Thus all high current implanters use electron showers or gas bleeds or both to neutralize the charge on the surface of the wafer and thus to reduce the destruction of the fragile gate oxides [1–3]. The success of this scheme is evident from the output of large number of CMOS devices from our fabrication lines. The details of the physical interaction are not well understood, however, and to continue to keep up with the scaling treadmill we need to apply some real physical understanding to the design of charge neutralization systems.

2. The implanter environment

The environment of a high current implanter is at first sight a very hazardous territory for a fragile integrated circuit. The beam contains ions with kinetic energies of 10–200 keV, the power density can be as high as 1 kW/cm^2, the wafers spin on a disk requiring centripetal accelerations of 1000 g, photoresist dissociates to produce hydrogen, and electrons are deliberately introduced to shower down on the wafer. The success of the process has been demonstrated many times, however, and it is only by an examination of the individual processes in detail that we can assess realistically the important issues involved.

2.1. A single ion

The processes that occur on an atomic level in an ion implant step are mostly well known; there are several time and size scales that are important. During the first 1×10^{-15} s, the ion passes through the first atomic layer of the target, and very likely leads to the emission of secondary electrons as illustrated in fig. 1. It may

* Invited paper.

0168-583X/91/$03 50 © 1991 – Elsevier Science Publishers B.V (North-Holland)

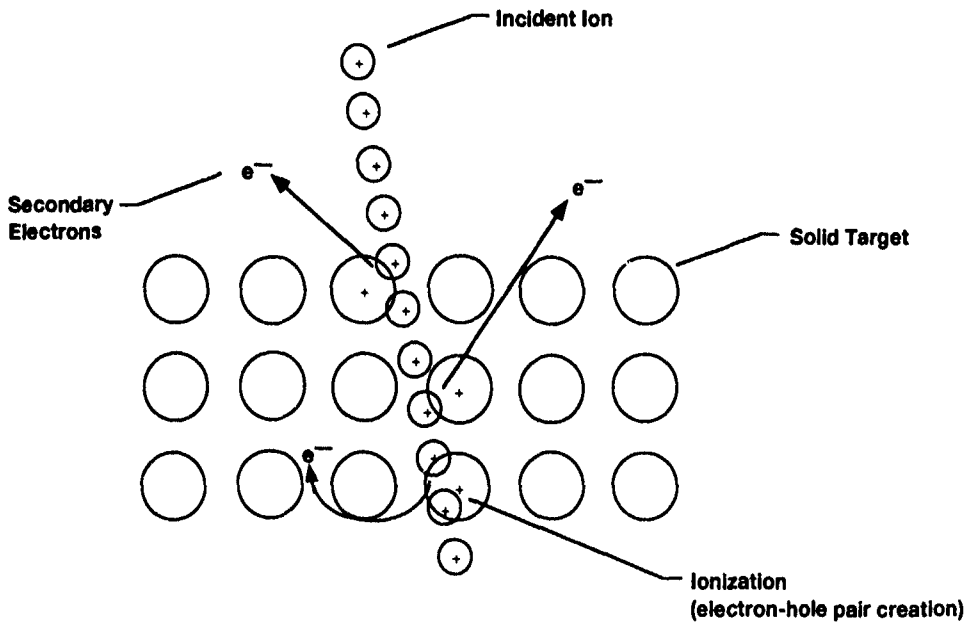

Fig. 1. Sketch showing the effects that occur during the first femtosecond of the interaction

also emit sputtered atoms, most of which one would expect to be neutral. The emission of secondary electrons means that the net charge imparted to the target during this event is more than one positive electron charge.

During the next 10^{-13} to 10^{-12} s, the ion enters the bulk of the target and come to rest as shown in fig. 2. During the time that it is slowing down, the ion may exchange charges with the target material, leading rapidly to an equilibrium charge state for the projectile. The first order approximation for this equilibrium is given by the "Bohr velocity matching" condition. Essentially, if one considers a projectile traveling at a given velocity v through the matrix, and assuming that one of its electrons comes to rest in the matrix, then it will have a velocity v in the frame of the projectile. This

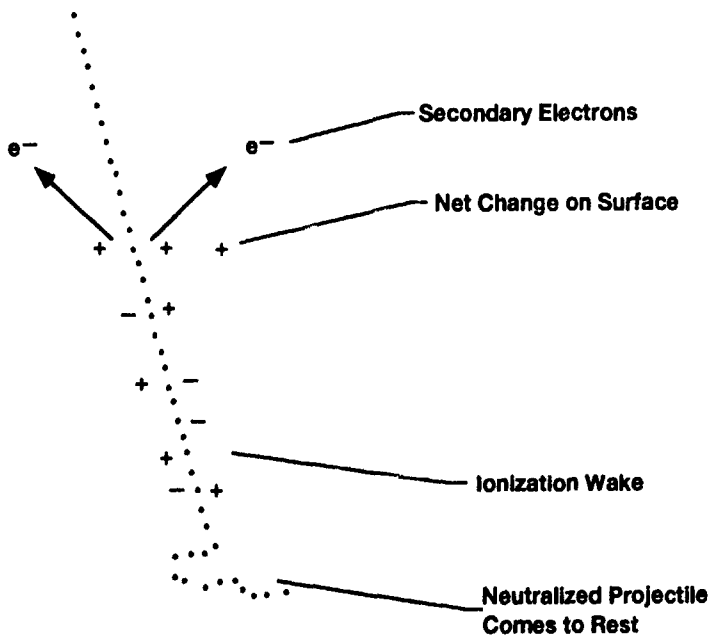

Fig. 2. Sketch illustrating the main effects as a single ion comes to rest.

corresponds to a kinetic energy for the electron, and if this kinetic energy is larger than the ionization potential, the electron will stay behind, and the projectile will become more positively charged. Conversely, if the projectile is initially charged, it may pick up an electron from the matrix, liberating an ionization energy and accelerating the electron to its own velocity. At a low enough velocity this reaction becomes exoenergetic, and therefore the ion tends to neutralize as it slows down. This calculated equilibrium charge state is shown in fig. 3. Notice that, under most typical implant conditions, one would expect the projectiles to be neutral. Experimental data often shows a wide spread, and the rapid interaction rate in solids may favour higher charge states [4].

If the projectile ion does carry some charge deep into the target, it seems that the ionization wake will persist for a time of the order of the minority carrier recombination time, ns to μs depending on conditions, and that the charge will be conducted to the surface during that time.

Thus, after the projectile has come to rest, we can assume that there is a net charge on the surface of the target. This charge is almost certainly positive and will be given by the charge on the incident ion plus the charge due to the escape of secondary electrons.

2.2. An ion beam

The center of a high current ion beam can be modeled as a voltage source whose potential depends on the current density in the beam, the neutralization of the beam by electrons and the geometry of the process chamber [5].

It is useful to distinguish three fluxes of electrons. First, those which are injected from outside the beam either from an electron shower or by emission from the side walls of the beam guide induced by stray ions. These have significant kinetic energy when they reach the center of the beam, and as such are likely to escape to the side walls unless they can be thermalized by the particles already in the beam. Consideration of the energy loss cross sections indicates that other electrons already in the beam would be much more effective at slowing down the injected electrons, but that at the densities expected the mean free path may be several beam diameters. Second, electrons that are the result of ion beam collisions with the residual gas and thus with little kinetic energy at the bottom of the potential energy well formed by the beam. Either of these first two fluxes of electrons will reduce the beam potential and also will reduce the net charge on the wafer [1]. Third, there are secondary electrons produced by the beam striking its target. These electrons will also reduce the beam potential, but if the beam is striking the wafer, they will increase the net electrical current to the surface of the wafer [2].

These are very complicated issues to analyze in detail. Some of the important issues such as the kinetic energy distribution of the electrons at different positions are very poorly understood, and may also vary by

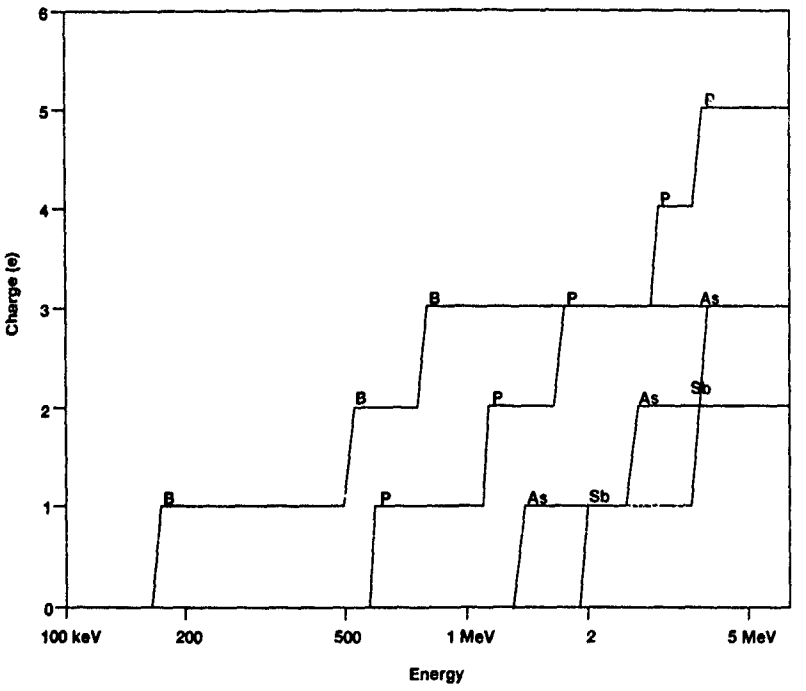

Fig. 3. Equilibrium charge on an ion calculated from the Bohr velocity matching equilibrium condition.

several orders of magnitude depending on beam parameters such as species, energy, current, etc. In the simplest assumption, the potential is zero at the conducting beam tube wall by definition and in equilibrium the field is also zero. The positive ions are presumably more tightly bunched than the negative electrons, but if the field is zero at the wall, the total charge per unit length of beam line comes close to canceling. Given these assumptions, the potential is positive everywhere, even in the positions where the electron density is higher than the ion density, as shown in fig. 4. The peak potential is a strong function of the extent of neutralization, the diameter of the beam tube and relative diameters of the ion and electron distributions.

Many measurements using a variety of methods support the validity of these models. We have made several different in situ measurements at Eaton [1,6,7] that seem to confirm reports from other labs [2,8–10]. Please refer to a parallel submission [7] at this conference to see the details of our most recent in situ measurements. The peak voltages for typical process parameters are higher than the breakdown voltages for very thin gate oxides, and this is why the results of these measurements have been suppressed on at least some occasions.

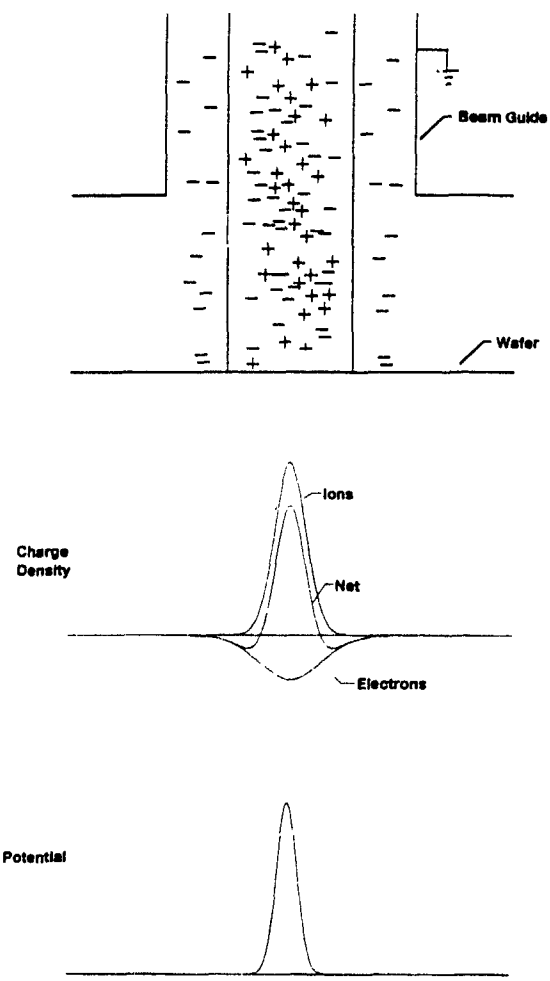

Fig. 4 Sketch showing the relationship between the space charge distribution and the beam potential.

2.3. Currents at the wafer surface

One of the key observations we made is that the potential measured on a small capacitor dot is essentially independent of the input impedance of the measurement circuit over quite a wide range, and that in many instances we saw currents an order of magnitude higher than expected from the ion beam current density. On the wafer scale, however, the voltages developed seem to be reasonably explained by arguments based on current balances. Essentially, the signal observed on a local scale (smaller than the beam dimension) is determined by the beam potential while on a larger scale (larger than the beam dimension) it is determined by the beam current.

In order to maintain potentials on the small scale, to the extent of sinking or sourcing currents larger than the incident ion current on a small area, we must assume that local currents flow quite readily close to or on the surface of the wafer. This is quite a natural conclusion; the volume close to the target surface is a region of intense electrical activity, with many electrons and secondary ions. The surface of the solid itself has an elevated temperature and many of the ionization events produced in the bulk by the ion beam may lead to mobile charges that migrate to the surface where there is a large density of states. Thus we would expect that an in situ measurement of resistance between conducting contacts separated by a dielectric surface would show a very low resistance while in the ion beam. These surface currents thus flow to maintain the potential imposed by the beam. In the specific example of a small test capacitor held at a high potential, a large current can flow in an external circuit only if electrons are flowing away from it, either into the weak plasma near the surface or along the surface.

3. Breakdown mechanism

Studies of oxide failure in electrical tests have shown two distinct classes of effects: some devices fail promptly with characteristics consistent with a localized defect that leads to a reduced breakdown voltage, while other devices have reduced reliability and break down after some period of time in service. Recently among our customers there has been a trend away from measuring the breakdown voltage (V_{bd}) as a way of characterizing the quality of thin gate oxides; rather it has been found that measurements that focus on the charge per unit

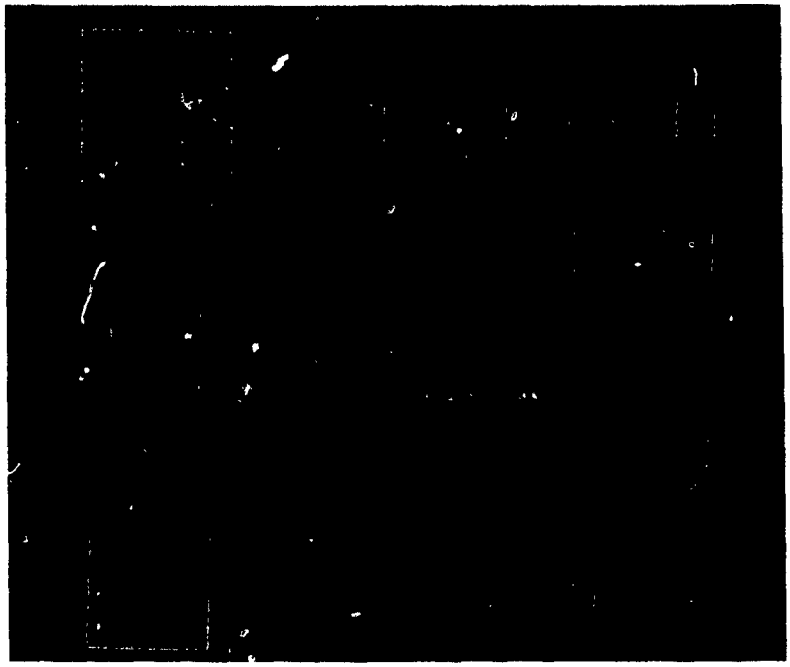

Fig. 5 Micrograph of an array of MOS capacitors on test wafers In each device, the metallization fully overlays the gate oxide area The gate oxide thickness was 46 nm, while a field oxide of 83 nm surrounded the gate in all cases

area that the oxide can conduct before suffering irreversible damage (Q_{bd}) is a parameter that relates more directly to observed reliabilities, is more useful in diagnosing chemical contamination in the process and represents the useful life of the dielectric in a more meaningful way [11]

The theoretical underpinning of the Q_{bd} test lies in current theories of the breakdown mechanism [12–14]. At these current levels, as well as at the current levels expected in an implanter, the oxide conducts charge by Fowler–Nordheim tunneling This is the quantum mechanical process whereby an electron in the conduction band of the silicon can move to a physical location in the oxide where the potential of the conduction band is the same or lower than that in the silicon, without ever occupying the space between and thus avoiding any violation of the conservation of energy [15]. The current density due to this mechanism varies exponentially with the voltage, producing a current density of about 100 $\mu A/cm^2$ with an applied voltage of 22 V through an oxide of 20 nm [11].

This process results in a significant electron current

Table 1
Median V_{bd} for each test site on each of three wafers before (B) and after (A) implant

Device	Breakdown voltage V_{bd} [V]					
	Wafer no. 1		Wafer no 2		Wafer no 3	
	B	A	B	A	B	A
1	69	70	88	86	69	91
2	91	111	73	115	89	95
3	81	82	71	88	81	75
4	80	70	70	71	76	90
5	71	69	63	66	68	67
6	72	58	64	94	70	67
7	73	82	66	62	78	94
8	60	65	61	66	58	65
9	65	70	58	79	63	72
13	61	84	58	79	59	69

through the oxide in the conduction band of the oxide. These electrons generate point defects in the oxide, possibly by charging small cross section trapping sites. Once these point defects have built up to a sufficiently high concentration, a low resistance conduction path opens up and the oxide fails catastrophically.

The key results of charge to breakdown testing is that the value of Q_{bd} can be very high and quite insensitive to the current used or the thickness of the oxide tested. Typical results show the same Q_{bd} for current densities up to 200 mA/cm^2 [16] or 5 A/cm^2 [13], much higher than the expected current densities in a high current implanter beam. The breakdown is observed to occur at charges per unit area in the range from 10^{18} to 10^{21} electrons/cm^2 [11,16], much greater than the total dose in an implanter. If the only charges available to cause damage to the oxides were those in the beam, even with reasonable allowance for secondary electron ejection, one would expect no significant loss of reliability in a high dose implant step.

3.1. Test structure

In order to investigate the mechanisms leading to the failures of gate oxides in high current implanters, we felt that it was essential to develop a test structure that would allow investigation of the effects of various parameters. We have therefore developed a set of capacitors as shown in a micrograph in fig. 5.

The gate oxides were grown at 1100 °C in an atmosphere of dry oxygen with some trichloroethane. The average gate oxide thickness in our first test was 452 Å with a 1.48% (1σ) variation within one wafer and 1.76% between wafers. The breakdown voltage of these devices before and after implant was measured using an Eaton Autoprobe 3007 and Waferspec using a measurement protocol that ramped the voltage at a rate of 20 V/ms, and recorded the voltage at which the current exceeded 10 μA. A total of 153 measurements were made of each type of device on each wafer, spread roughly uniformly over the whole area, but with different individual dies tested before and after implant. Breakdown voltages were measured directly after implant, with no anneal or other heat treatment.

3.2. Yield results

The implants were all performed on an NV-10 to a dose of 9.6×10^{15} As/cm^2 at 40 keV with a beam current of 2 mA. Wafer no. 1 was implantedwith an electron shower primary current of 30 mA, while wafer no. 2 used 100 mA and wafer no. 3 used 200 mA. Table 1 shows the median breakdown voltages measured for

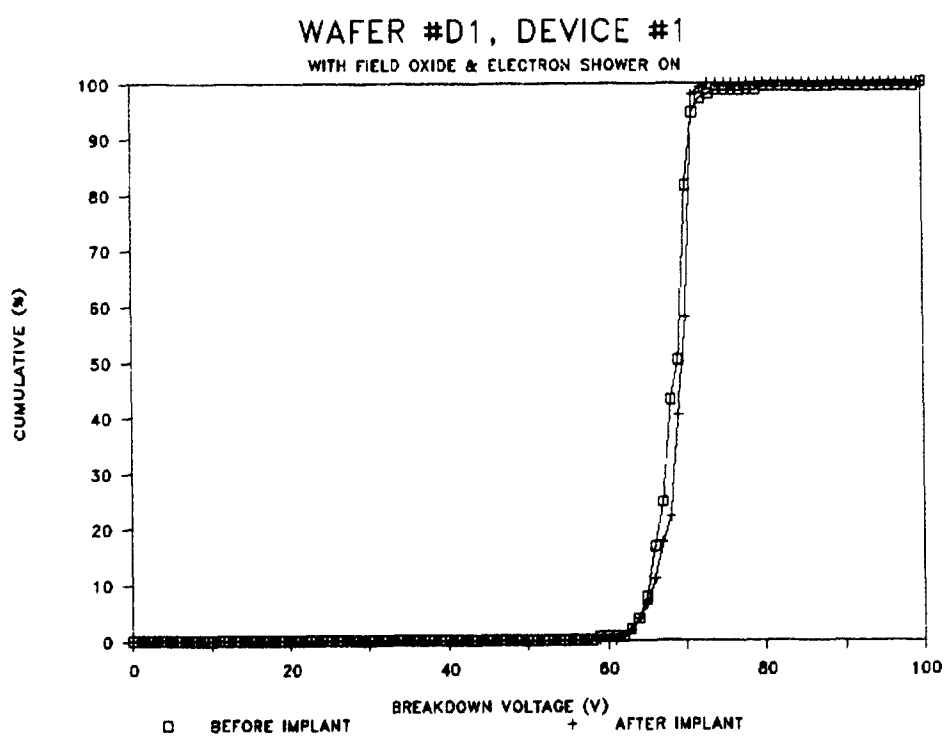

Fig. 6 Cumulative failure as a percentage of 153 tests of device no. 1 as a function of voltage, before and after a 2 mA, 40 keV 9.6×10^{15} As implant. The electron shower primary current was 30 mA.

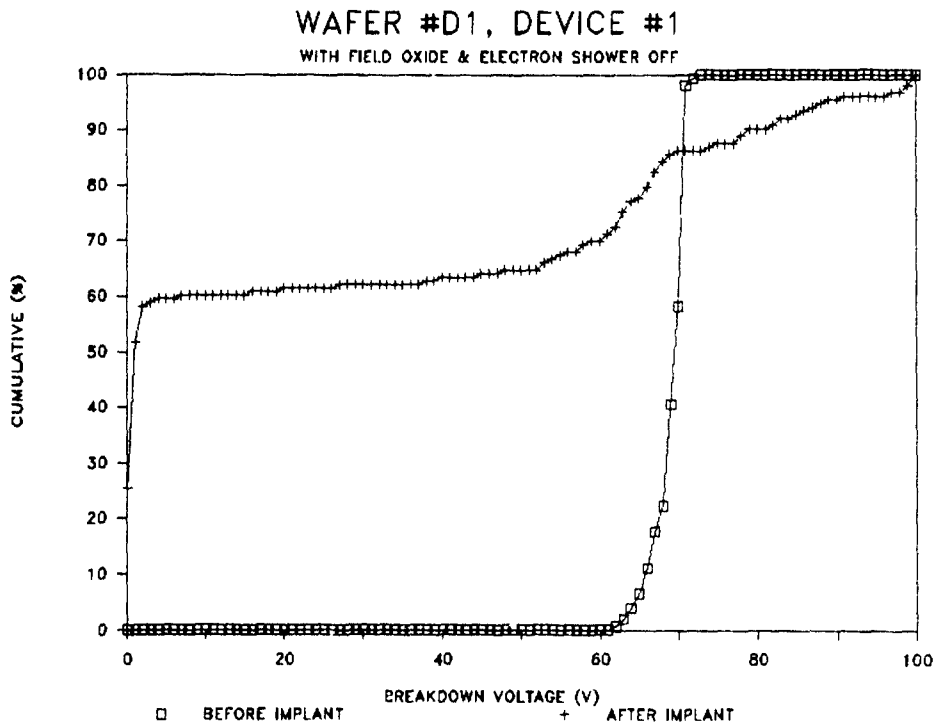

Fig 7 Cumulative failure for the case with no electron shower

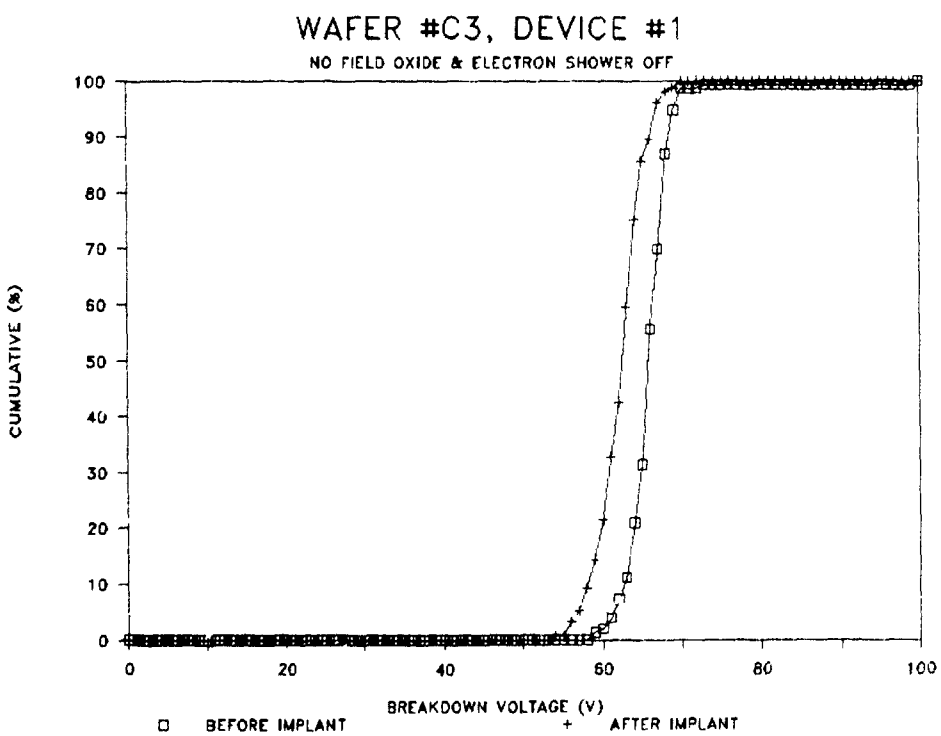

Fig. 8 Cumulative failure as a function of breakdown voltage with no electron shower on a wafer with no field oxide The edge of the metallization corresponded to the edge of the 46 nm gate oxide

III. THROUGHPUT & YIELD

ten device types on these wafers before and after implant. The other device types suffered from poor contacts with the probe card as detected by the measured capacitance, and the data are not shown. The average breakdown field in these experiments was 16.5 MV/cm, in reasonable agreement with high quality oxides produced at other facilities. Notice that in the majority of cases the breakdown voltage has increased following implant. Given the relatively small voltages that are generated by these beams in our in situ measurements, in the range from 8 to 16 V, it is not surprising that we have suffered no loss in oxide quality. The apparent increase in breakdown voltage has been observed at other facilities, and while there is no consensus on the cause of this effect, it may be due to thermal annealing or some electrical analogue.

Fig. 6 shows the cumulative percentage of device breakdown voltages for device no 1 before and after implant with an electron shower primary current of 30 mA. As can be seen, there is very little difference between the measurements, indicating once again negligible effects due to the implantation. Fig. 7 shows the same results for the case with no electron shower present at all. As can be seen, about 60% of the devices are dead shorts, and most of the remainder have significantly reduced breakdown voltages. Under these circumstances, our in situ measurements show very high beam potentials, of the order of a hundred volts. In this case, we used two different types of wafers. One used a field oxide 83 nm, while the other had only a single oxide thickness of 46 nm As can be seen, we find significant degradation in the example with a field oxide, but very little loss of quality in the case with no field oxide This observation does fit the model developed in the earlier section. Given the same beam potential in front of the device, the case with the thinner field oxide will sink more current to the wafer along the surface. Because of the more effective current sink in the case with the thinner field oxide, the potential across the gate oxide (which was the same thickness in both cases) is reduced and the occurrence of a destructive breakdown is much less.

These results are only the initial experiment with this type of structure, and further work must investigate the effects of thinner gate oxides, and the nature of the surfaces that are in the beam at the same time as the test device. Work is also progressing to develop a charge to breakdown test which may be much more informative about subthreshold effects on the oxides.

4. Discussion

The model developed here would suggest that the expected yields on real devices are neither 0 nor 100%, but lie somewhere between these two extremes. Implanter manufacturers should continue to develop improved charge control systems to serve two intersecting goals: first to add electrons to the beam to minimize the net charge delivered by the beam so that large area conducting components do not collect enough charge to produce voltages high enough to produce discharges from the wafer to ground, and second to sufficiently neutralize the space charge of the beam and control its spatial dimensions so that the electrostatic beam potential itself does not rise to levels much above the breakdown strength of the gate oxides. In either case, it is important to realize that large potential voltages are only dangerous if they can deliver significant net charge per unit area through the oxide.

Several experiments could be useful in confirming this model. An in situ resistance measurement across the surface of the wafer as it passes through the beam would be a very direct way of evaluating the current carrying capacity of different surfaces. More yield studies with a range of different field and gate oxide thicknesses, extending down to less than 10 nm, would allow experimentation with device structures that might deliberately drain any excess charge on the gate to the substrate during the implant step. This might lead to an approach to device layout and design with charging damage prevention built in.

In the future, we can look forward to a much greater emphasis on in situ monitoring to monitor conditions in the implanter in real time. These might be used to stabilize the net current transported to the wafer or the beam potential. We can probably also look forward to continued anxiety and heated debate on this topic, while integrated circuit manufacturers continue to produce useful devices.

References

[1] B J Doherty and D J McCarron, Nucl. Instr and Meth B37/38 (1989) 559
[2] M I Current, A. Bhattacharyya and M Khid, Nucl Instr and Meth B37/38 (1989) 555.
[3] C.P. Wu, F Kolondra and R Hesser, RCA Review, 44 (1983) 62.
[4] J Heinemeier and P Hvelplund, Nucl Instr and Meth 148 (1978) 65
[5] A.J T Holmes, Phys Rev A19 (1979) 389, Radiat Eff 44 (1979) 47.
[6] V. Benveniste, H E Friedman, M E. Mack and F Sinclair, Nucl. Instr. and Meth B37/38 (1989) 658
[7] G Angel, N. Meyyappan, F. Sinclair and W Tu, these Proceedings (8th Int Conf on Ion Implantation Technology, Guildford, UK, 1990) Nucl Instr and Meth B55 (1990) 211
[8] S B Felch, L.A Larson, M I Current and D W. Lindsey, Nucl Instr and Meth B37/38 (1989) 563

[9] S.B Felch, V K. Basra and C.M. McKenna, IEEE Trans. Electron Devices 35 (1988) 2338; Microelectronic Manufacturing and Testing 11 (1988) 1.
[10] A. McCarthy and W. Lukaszek, A New Wafer Surface Charge Monitor (CHARM), Semiconductor Research Corporation Report C88445 (November 1988), See also: N. Baran, Byte (April 1990) p. 20.
[11] M Davis and R. Lahri, IEEE Electron Device Lett. 9 (1988) 183; Wafer Level Reliability, National Semiconductor GOI Meeting, Arlington, TX (February 1990).
[12] C M. Osburn and D.W. Ormond, J Electrochem. Soc. 119 (1972) 591 et seq.
[13] E. Harari, J Appl. Phys. 49 (1978) 2478
[14] D.R Wolters and A.T A. Zegers-van Duynhoven, On the Mechansim of Intrinsic Breakdown in Thin Dielectrics, Philips Research Labs, 5600JA Eindhoven, The Netherlands (1987).
[15] S M. Sze, Physics of Semiconductor Devices (Wiley–Interscience, 1969).
[16] N. Novkovski, M Dutoit and J Solo de Zaldivar, Appl Phys Lett. 56 (1990) 2120.

Nuclear Instruments and Methods in Physics Research B55 (1991) 124–131
North-Holland

Process-induced defects in VLSI *

B.O. Kolbesen [a], W. Bergholz [a], H. Cerva [b], B. Fiegl [a], F. Gelsdorf [a] and G. Zoth [a]

[a] *Siemens AG, Semiconductor Group, Technology, Otto-Hahn-Ring 6, D-8000 Munchen 83, Germany*
[b] *Siemens AG, Corporate Research and Development, Otto-Hahn-Ring 6, D-8000 Munchen 83, Germany*

Shrinking device dimensions enhance the susceptibility of the devices to defects in the electrically active regions of the silicon substrate and the gate oxide Typical harmful defects are discussed which may occur in micron and submicron silicon technology if processes are not optimized. Ion implantation is involved in the formation of most of those defects Since economic mass production of devices in VLSI (very-large-scale integration) requires overall defect density levels below 1 cm^{-2}, strategies and remedies for reducing defect densities are a major task Some recently developed techniques for the characterisation and monitoring of defects and metal contamination are described

1. Introduction

The progress in silicon microelectronics technology is still vigorous, even in the very-large-scale integration (VLSI) era. Advancing miniaturization combined with increasing packing density and fabrication on silicon substrates with larger diameters (150 and 200 mm) still provide continuous cost reduction in terms of cost per bit of semiconductor memories In the case of MOS memory technology the progress was also facilitated by a number of important innovations which pushed packing density or helped to overcome problems inherent to micron and submicron devices such as hot electron effects [1]. Important examples of such innovations are the trench capacitor and the stacked capacitor, the multilayer dielectric [*o*xide/*n*itride/*o*xide (ONO)], the fully overlapping direct contact and the *l*ightly *d*oped *d*rain (LDD) transistor. However, those innovations drastically increased the process complexity – the fabrication of the 4M (megabit) DRAM (*d*ynamic *r*andom-*a*ccess *m*emory) needs more than 400 process steps – and required novel processes such as etching of deep trenches (5 μm) into the silicon substrate [2].

On the other hand, the ongoing miniaturization of structures and enlargement of chip sizes (90 mm^2 for the 4M, 140 mm^2 for the 16M DRAM) enhance the susceptibility of the devices to detrimental crystallographic defects in the silicon substrate and defects in the gate dielectric films [3–6]. Moreover, the scenario of defect formation in VLSI becomes more and more complex due to the increasing process complexity. Defect formation has to be considered as a synergetic action of driving forces and potential defect nucleation sites from various sources: e.g., mechanical stresses by temperature gradients or films, supersaturations of intrinsic point defects and impurities (dopants, oxygen, metallic contaminants), residual lattice damage from ion implantation and dry etching.

By contrast, economic mass production of VLSI devices requires overall defect density levels below 1 cm^{-2}. Therefore, strategies and remedies for reducing defect densities are a major and continuous task in the development and production of large volume devices such as memories This task comprises monitoring and analysis of defects, exploration of defect sources and defect generation mechanisms and the development and realization of measures for defect prevention ("defect engineering") It requires also the availability of appropriate diagnostic techniques and tools for the monitoring and characterisation of defects and contamination at a routine level.

In the following we discuss some typical examples of crystallographic defects in the silicon substrate and gate oxide which can occur in VLSI technology if processes and materials are not optimized. Emphasis is given to the discussion of defects in the formation of which ion implantation plays a prominent role. Finally, some recently developed techniques and tools for the monitoring and characterisation of defects and metal contamination will be dealt with

2. Ion-implantation-induced stacking faults

For the sub-μm integrated circuits the problem of punching, e.g., trench–trench punching for DRAM devices, becomes more and more important. The punching can be reduced by an enhancement of the n- and p-type doping levels, which can be put into practice by an increase of the ion implantation doses for the well

* Invited paper

0168-583X/91/$03.50 © 1991 – Elsevier Science Publishers B.V (North-Holland)

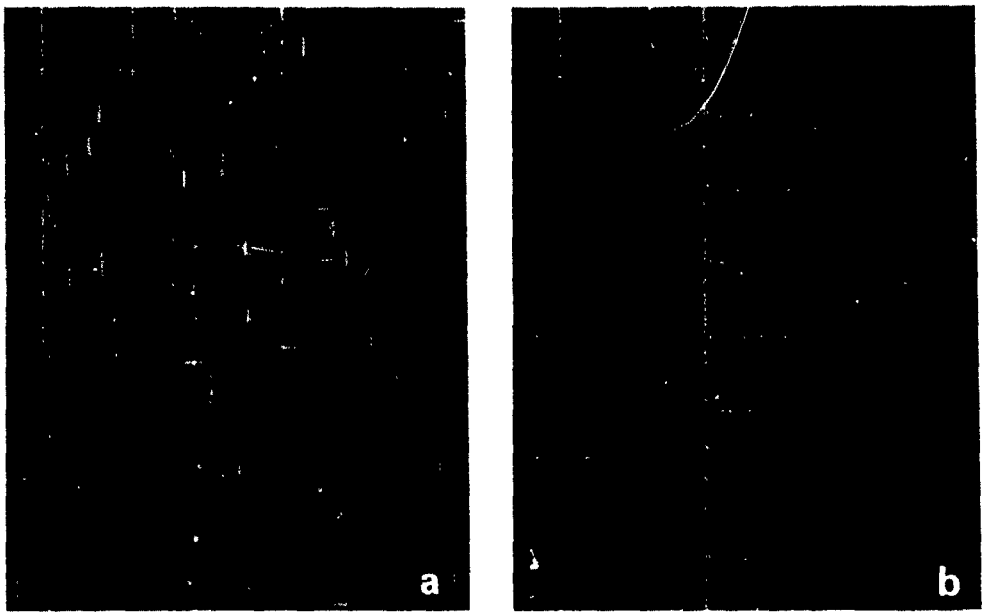

Fig. 1 Ion-Implantation-induced stacking faults on p- and n-well regions revealed by defect etching (200×). (a) Stacking faults of high density are formed during unsuitable annealing; (b) no visible defects ($< 1\ cm^{-2}$) are found for optimized annealing conditions.

regions. An investigation of the well formation process by defect etching points to the boron implantation as the most critical process in this context.

It was found that the ion implantation damage left by boron doses of several $10^{13}\ cm^{-2}$ can induce the formation of stacking faults during the subsequent drive-in, if the anneal conditions are not optimized (fig. 1). Since a whole-wafer boron implantation prior to the n-well phosphorus implantation was used in our experiments, stacking faults are formed during the drive-in also on the n-well regions (fig. 1). The formation of stacking faults and dislocation loops after boron implantation and annealing at high temperatures (1000–1200 °C) was also reported in [9]; the growth of these defects was attributed to the oxidation during the anneal treatment in that case.

For standard drive-in conditions we observe an increase in the stacking fault density with increasing boron dose (fig. 2). For doses below about $2 \times 10^{13}\ cm^{-2}$ the stacking fault density is very small and independent of the drive-in conditions. For boron doses above $\approx 3 \times 10^{13}\ cm^{-2}$, on the other hand, the stacking fault density increases rapidly for unsuitable drive-in conditions, reaching very high values of about $10^5\ cm^{-2}$ for doses of $6 \times 10^{13}\ cm^{-2}$. Nevertheless, even for the highest investigated boron doses the defect density can be reduced to negligible values ($< 1\ cm^{-2}$) by optimizing the annealing conditions during the drive-in (fig. 2).

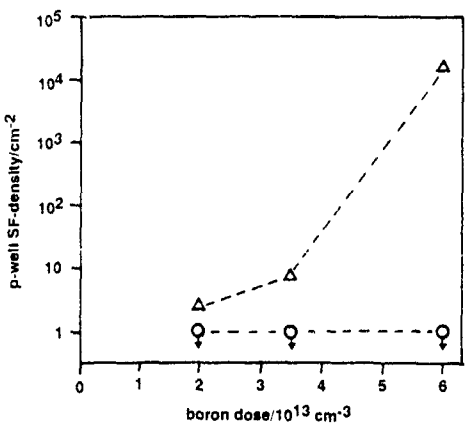

Fig. 2. Stacking fault density on p-well regions as a function of the boron dose: △ standard process; ♀ improved process.

3. Electrical activity of Fe-decorated stacking faults

It is well-known that stacking faults can significantly degrade the electrical parameters of semiconductor devices such as generation lifetime [10] or junction leakage current [11]. It is generally found that the influence of stacking faults on electrical parameters is mainly determined by the amount of decoration with metallic impurities, i.e., the electrical activity of stacking faults increases with increasing impurity decoration.

To examine the influence of stacking fault decoration directly, we performed deep-level transient spectroscopy (DLTS) and current-voltage (I–V) measurements on Schottky diodes containing oxidation induced stacking faults (OSF) and different amounts of iron.

For this purpose a high density of OSFs (several times 10^6 cm^{-2}) was created in a controlled manner by oxidation of mechanically damaged p-type wafers [12]. Various degrees of iron decoration were realized by contaminating samples with iron on the wafer backside prior to oxidation. This results in contamination levels which are about 1–2 orders of magnitude higher than the contamination of as-received state of the art wafers.

For clean, i.e., not intentionally decorated stacking faults DLTS measurements revealed a characteristic level with an activation energy of $E_v + 0.50$ eV which is associated with the boundary dislocation of the stacking faults [13]. For samples with Fe-decorated stacking faults the deep level spectra show neither an increase of the stacking fault line amplitude nor additional OSF- and Fe-related lines.

Results of I–V measurements on Schottky diodes as simple test devices are shown in fig. 3. For samples containing only clean stacking faults (3×10^6 cm^{-2}, [Fe] < 10^{11} cm^{-3}) or dissolved iron (up to several 10^{13} cm^{-3}) no enhancement of the reverse current of the Schottky diodes compared to reference diodes was observed. By contrast, for diodes which contained stacking faults and iron, a strong increase of the reverse current was found (fig. 3). The reverse current enhancement increases with increasing iron concentration (fig. 4), i.e., increasing impurity decoration of the stacking faults.

Measurement of the Schottky barrier heights show a drastic decrease of this quantity from about 0.5 eV for reference diodes to about 0.3 eV for diodes with heavily decorated stacking faults. It appears that this reduction of the Schottky barrier is the main reason for the enhancement of the reverse current, although a contribution of generation currents induced by stacking fault decoration cannot be unambiguously excluded.

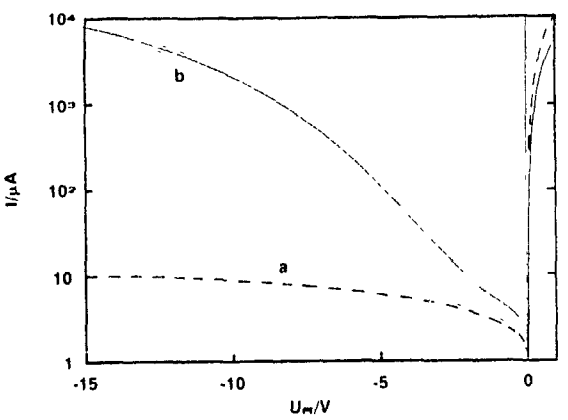

Fig. 3 Current–voltage characteristics of Ti Schottky diodes. (a) Reference diode; similiar curves were measured for diodes containing only clean stacking faults (3×10^6 cm^{-2}) or only dissolved iron (up to several 10^{13} cm^{-3}); (b) diode containing stacking faults (3×10^6 cm^{-2}) and iron (8×10^{13} cm^{-3}).

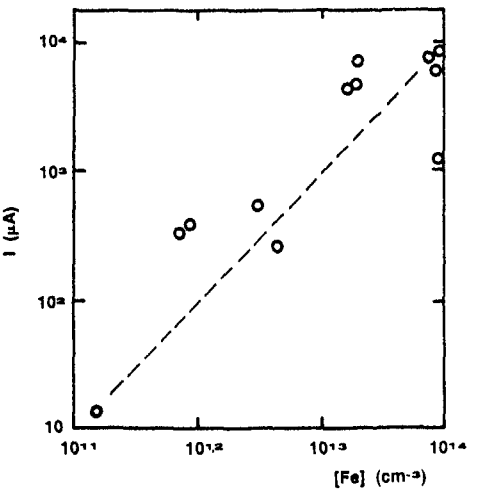

Fig. 4. Reverse current at 15 V for Schottky diodes containing 3×10^6 stacking faults/cm^2 as a function of the iron concentration measured by DLTS.

In summary, these results clearly demonstrate that clean stacking faults have only a negligible influence on electrical parameters of devices and that they become much more detrimental to devices by impurity decoration.

4. Defects induced by ion implantation at mask edges

The scaling down of VLSI devices requires the definition of small doped areas in the silicon substrate. Those are usually fabricated by selfalignment techniques based on ion implantation of the dopant. In the case of MOS transistors the polysilicon gate acts as implantation mask for the implantation of the source/drain regions. In order to reduce hot-electron problems of micron and submicron size MOS transistors, a modification, the so-called lightly doped drain (LDD) transistor, has been introduced. For the LDD transistor two implantations are necessary: First, a phosphorus implantation masked by the polysilicon gate provides the lightly doped drain region, second, an arsenic implantation masked by a so-called (oxide) spacer forms the highly doped source/drain contact region. After the implantations one or several high-temperature annealing steps are applied for electrical activation of the dopant atoms and for removal of the implantation lattice damage.

It is known that As implantations exceeding doses of 5×10^{13} atoms/cm^2 create a buried amorphous layer. At the edge of the oxide spacer, due to the steep side walls the high-dose implanted region terminates abruptly, resulting in a sharply curved amorphous/crystalline interface. During annealing the amorphous

layer vanishes by an epitaxial regrowth process restoring the original lattice. It has been observed [14,15] that extended lattice defects can be created in the silicon beneath the spacer edges in the case of non-optimized processing. In extensive studies by transmission electron microscopy (TEM) [14,15] the formation sequence of those defects has been elucidated. The majority of defects has been identified as vacancy-type dislocation half loops, some more complicated defect configurations turned out to be microtwins. The formation of those defects is described by a model that is based on the different epitaxial regrowth rates for different substrate lattice plane orientations [16].

Such defects created at spacer edges can act as dislocation sources in subsequent process steps and provide sinks for metal precipitation. These defects can degrade device characteristics via enhanced leakage currents and give rise to reliability problems if they extend into active device regions. By optimisation of the implantation and annealing conditions the formation of those defects has been prevented.

5. Ion implantation damage and gate oxide breakdown

It is common practice to enhance the capacitance of MOS-devices by a high-dose arsenic ion implantation ("HiC" implantation). The breakdown voltage can be severely reduced by ion implantation damage, as is demonstrated in the following example, in which the breakdown field for arrays of large-area test capacitors with 20 nm thermally grown oxide was tested in a ramped voltage test [17].

- The test capacitors, which did not receive any ion implantation, break down at an electric field larger than or equal to about 10 MV/cm (intrinsic mode or so-called "*C*-mode") [17] (fig. 5a).
- A large fraction of the test capacitors with As implantation breaks down at an electric field strength much smaller than 10 MV/cm (*B*-mode failure) (fig. 5b). Since such a poor gate oxide quality is quite unacceptable for an advanced highly integrated CMOS device, the process had to be improved.
- The breakdown strength of the ion-implanted test capacitors is practically identical to that of the unimplanted ones (a) after the process improvement (fig. 5c).

It is a general experience that frequently the ion implantations necessary for devices are close to or above a threshhold for defect formation with residual ion implantation damage as nuclei. Process modifications to reduce or eleminate the incidence of ion implantation-correlated defects can be manifold, e.g., improvement of the annealing conditions, modification of the ion implantation energy, improvements in the cleanliness of the process, etc.

6. Trench-induced dislocations

The problem of oxide-edge induced dislocations due to stress concentration at the film edge, has plagued integrated-circuit technology right from the beginning and has been held at bay by a variety of process optimizations, e.g., change of oxide and nitride thicknesses, oxidation temperatures, ramping furnaces from a low stand-by temperature up to the desired annealing temperature, etc.

With the introduction of three-dimensional devices, e.g., trench capacitors in 4M DRAMS [4,11,19] a new problem has arisen, namely the formation of dislocations, e.g., at the substrate corners of the trench capacitors: typically, these dislocations run from the substrate surfaces adjacent to the trenches to a trench sidewall (fig. 6), but it has also been observed with the help of a 3-dimensional preparation technique [20] that dislocations run from a trench sidewall to the sidewall of an adjacent trench or that dislocations originate at the

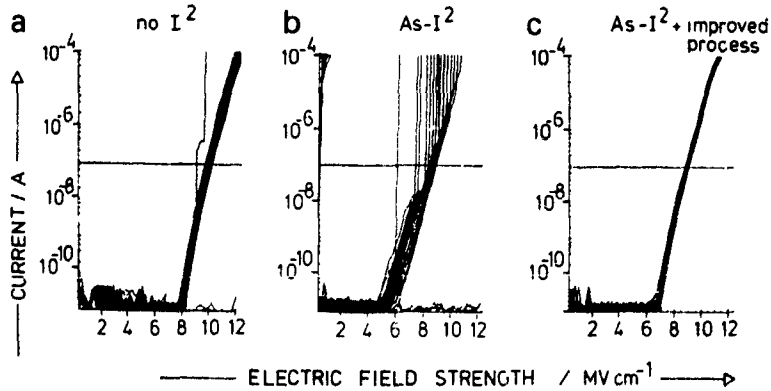

Fig 5. Voltage ramp dielectric breakdown test curves for MOS test structures. The breakdown voltage is defined as the voltage for which the current exceeds 10^{-7} A. (a) No ion implantation, (b) with implantation; (c) with the same implantation as for (b) and an improved process.

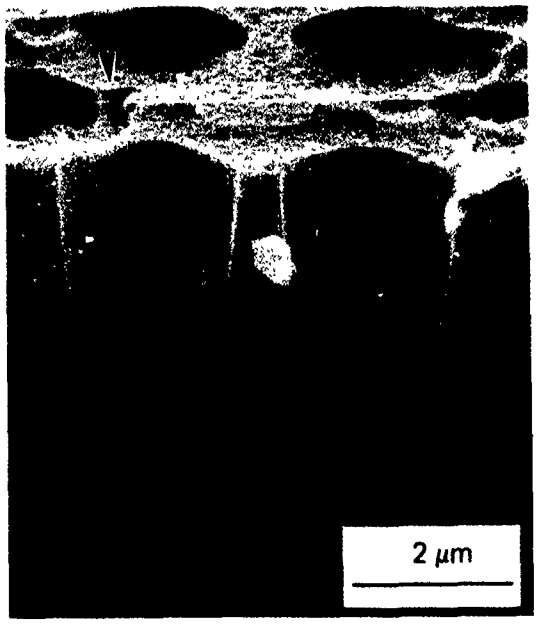

Fig. 6 SEM-micrograph of etch pits due to a trench-induced dislocation. The two dislocation etch pits on the substrate surface and in the trench sidewall are marked by arrowheads.

bottom corner of a trench (fig. 7). Finite-element calculations [21] of the stress at different positions around a trench have indeed shown that maximum stress arises at

Fig. 7. Three-dimensional defect delineation of trench-induced dislocation (SEM-micrograph). The defect marked A originates near the bottom of the trench, defect B connects two trenches.

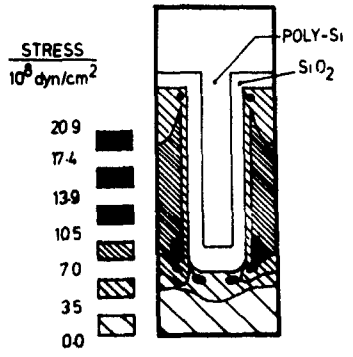

Fig. 8. Example of a calculated shear stress distribution around a trench with an oxide sidewall and which is filled by poly-Si (after ref. [21]). Note the stress maximum occurs near the bottom of the trench.

the upper substrate corners and at the bottom of the trench (fig. 8), and that the magnitude of the stress depends sensitively on the trench shape, e.g., a stress minimum is assumed for a radius of curvature equal to half the trench diameter. Micro-Raman stress measurements have moreover shown that the stress can be reduced by a BPSG (boron phosphorus silicate glass) refill of the trench instead of the more common poly Si refill.

Since trench-induced dislocations cause refresh-failure of the affected memory cells [11] process modifications and optimizations have been carried out to prevent the formation of trench-induced dislocations.

7. Analysis and monitoring techniques for defects and metal contamination

Appropriate analytical techniques and tools are important prerequisites to analyse and solve defect problems and to control low defect levels in VLSI technology. Whereas in the development stage of a technology and in the case of trouble shooting also sophisticated techniques are used to some extent, for monitoring purposes the techniques have to be rather simple, fast, preferably nondestructive and preparation-free and suitable for automated operation in cleanroom environment.

In the following we discuss examples of recently developed analytical techniques which to a large extent meet the requirements imposed on monitoring techniques.

7.1. Crystallographic defect imaging by spatially resolved modulated optical reflection ("thermawave imager")

The most frequently applied analytical technique to detect extended crystal defects is defect etching [22–24],

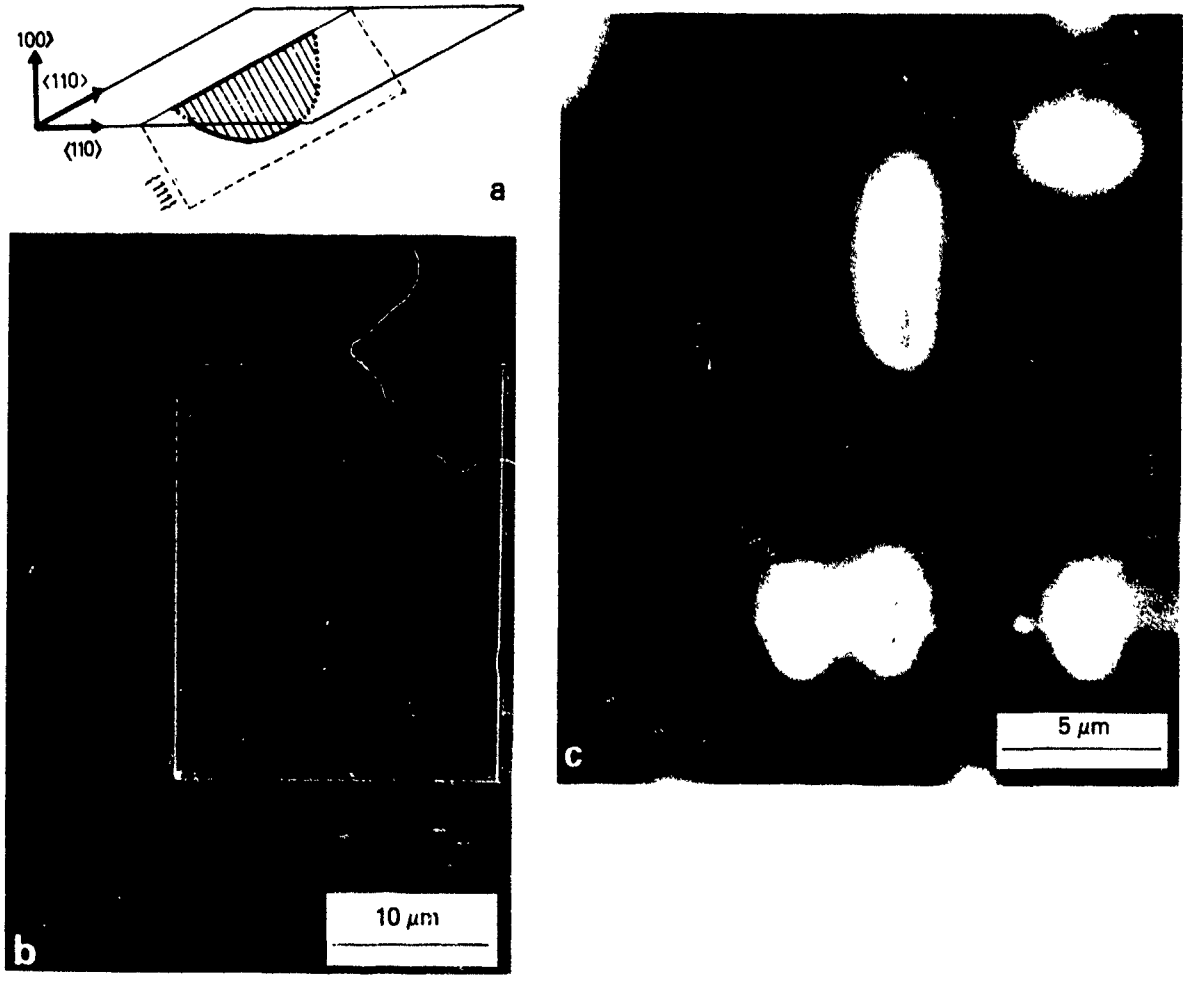

Fig. 9. Imaging of Ni-precipitates in intentionally contaminated CZ-Si. (a) Schematics of the geometry of $NiSi_2$ precipitates, (b) optical micrograph after 30 s defect etching; (c) "Thermawave" image.

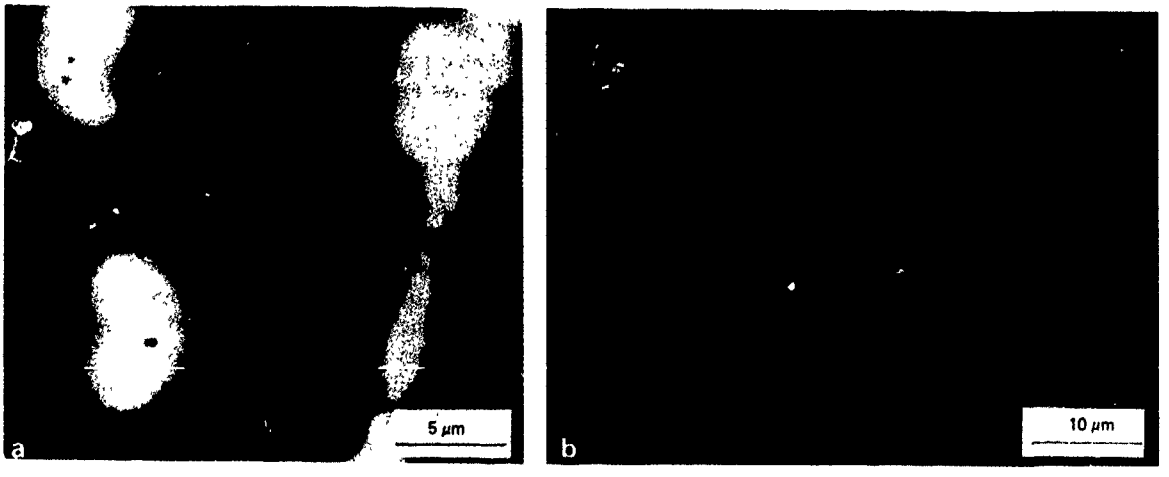

Fig. 10. Imaging of oxidation-induced stacking faults intentionally contaminated by Ni. (a) "Thermawave" image; (b) optical micrograph after 60 s defect etching.

whereas transmission electron microscopy is only used in special cases due to the large amount of preparation necessary. The third more common technique is transmission X-ray topography [25] which is preparation-free but has limited spatial resolution (5–10 μm) and is not sensitive to crystal defects near the surface.

Quite recently, the modulated optical-reflectance technique ("thermawave") [26] has been improved in spatial resolution to such a degree that it is possible to record scanned thermawave images with a spatial resolution of the order of 0.5 μm. First tests have shown that crystal defects are imaged and that the images are to a certain degree similar to the etch figures obtained after crystal defect etching [27], as shown in the following two examples

(1) Ni precipitates are usually in the shape of platelets of $NiSi_2$ on {111}-planes, which intersect the (100) wafer surface in ⟨110⟩ directions (fig 9a). Hence the etch figures are lines along ⟨110⟩ and resemble those of stacking faults (fig. 9b). The thermawave image of the same defects recorded before defect etching is indeed very similar to the etch figure (fig. 9c) and it is even possible to determine to which side of the intersection with the surface the plate-like precipitate is inclined.

(2) Ni-contaminated oxidation-induced stacking faults are imaged in a clearly different manner as the precipitates (fig. 10a): the defect image resembles that of a banana, and it appears that mainly the decorated boundary dislocation gives rise to a much larger signal than the fault plane. Again there is a good correspondence to the defect etch figures (fig. 10b).

The main advantage of the thermawave technique compared to conventional techniques is that it is completely preparation-free and fully in-line compatible. Therefore checking for crystal defects could be an application of the technique in addition to the main routine application to measure ion implantation doses before annealing via the ion implantation damage [28].

7.2. Bulk metal contamination control via diffusion length measurements by surface photovoltage (SPV) and electrolytic metal tracer (Elymat)

Dissolved impurities in the bulk can be monitored easily and fast by minority carrier diffusion length measurements. Among these methods a very powerful tool is a combination of two recently developed techniques, namely the Elymat [29] for recording diffusion length maps and the surface photovoltage (SPV) method for Fe detection in boron-doped silicon [30].

A high-resolution wafer map of the diffusion length is provided by the Elymat. This often allows for a direct identification of the contamination source by revealing its characteristic contamination pattern. An example is given in fig. 11 which shows a diffusion length map of a 4 in. wafer after ion implantation and a rapid anneal

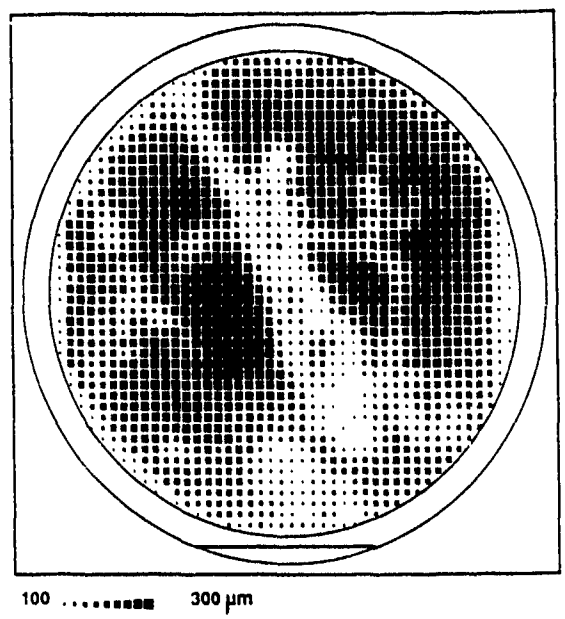

Fig 11. Elymat diffusion length map of a 4 in. wafer contaminated by a manual implanter loading system.

drive-in step. In this case the observed contamination pattern was due to the manual loading system of the implanter.

Fe detection by the SPV method is based on the fact that in boron-doped silicon interstitial iron undergoes a reversible pairing reaction with boron and that interstitial iron is an about ten times more efficient recombination center than FeB. The modulation of the diffusion length induced by iron in the different states is used to determine the Fe concentration. By SPV measurements on the same wafer as shown in fig. 11 it was ascertained that iron was the contaminating species, i.e., the Elymat diffusion length map reflects mainly the distribution of iron. Up to 6×10^{12} cm^{-3} iron was found in regions with small diffusion length, whereas the iron concentration was less than $\approx 3 \times 10^{11}$ cm^{-3} in the other wafer parts.

7.3. Surface metal contamination control by total reflection X-ray fluorescence analysis (TXRF) in combination with vapour phase decomposition (VPD)

In many processes of device fabrication and by handling of the wafers metal impurities are deposited on the surfaces (front side, back side) of the silicon wafers. For a direct control of surface contamination, e.g., for checking the effectiveness of cleaning procedures, VPD in combination with atomic-absorption spectroscopy (AAS) has been in routine use for several years [31]. VPD is a preconcentration technique: the wafer surface is exposed to HF vapour which dissolves

the native or thermal surface oxide. The metal impurities are concentrated in the resulting condensate droplet. Subsequently in the droplet usually only a few key elements are analyzed quantitatively by AAS (sensitivity typically 10^9 to 10^{10} atoms/cm^2). The typical contamination levels of current processes and virgin wafers distinctly exceed these detection limits. TXRF alone which is a preparation-free and multielement method lacks in sensitivity (depending on the equipment detection limits between 10^{10} to 10^{11} atoms/cm^2) [32].

Recently, VPD has been combined with TXRF [33,34] by analyzing the droplet residue by TXRF instead of AAS. Depending on the wafer diameter which determines the preconcentration factor, detection limits can be lowered to 10^8 atoms/cm^2. These are the metal contamination levels specified in Japan for virgin 200 mm wafers used for devices of the 64M generation.

References

[1] See, e.g., IEEE 1989 International Electron Devices Meeting, Technical Digest

[2] W. Beinvogl and E. Hopf, Adv Solid State Phys 28 (1988) 87.

[3] B.O. Kolbesen and H. Strunk, in: VLSI Electronics: Microstructure Science, ed. N.G. Einspruch, vol. 12: Silicon Materials, ed. H.R. Huff (Academic Press, New York, 1985) p. 143.

[4] B.O. Kolbesen, W. Bergholz and H. Wendt, Proc. 15th Int. Conf. Defects in Semiconductors, Mat. Sci. Forum 38–41 (1989) 1.

[5] A. Ohsawa, K. Honda, R. Takizawa, T. Nakanishi, M. Aoki and N. Toyokura, in: Semiconductor Silicon 1990, eds. H.R. Huff, K.G. Barraclough and J. Chikawa (The Electrochem. Soc., Princeton, NJ, 1990) p. 601

[6] L. Jastrzebski, ibid., p. 614.

[7] Y. Akasaka, ibid., p. 759.

[8] K.H. Küsters, H.M. Mühlhoff and H. Cerva, these Proceedings (8th Int. Conf. on Ion Implantation Technology, Guildford, UK, 1990) Nucl. Instr. and Meth. B55 (1991) 9.

[9] L.J. Chen and I.W. Wu, J. Appl. Phys. 52 (1981) 3310.

[10] Y. Ichida, T. Yanada and S. Kawado, in: Lifetime Factors in Silicon, ASTM STP 712 (Philadelphia PA 1979) p. 107

[11] B.O. Kolbesen, W. Bergholz, H. Cerva, F. Gelsdorf, H. Wendt and G. Zoth, Inst. Phys. Conf. Ser. 104 (1989) 421

[12] I. Ishihara, H. Kaneko and S. Matsumoto, Jpn. J. Appl. Phys. 23 (1984) L620.

[13] B. Fiegl and G. Zoth, to be published

[14] H. Cerva and K.H. Küsters, J. Appl. Phys. 66 (1989) 4723.

[15] H. Cerva and H. Oppolzer, Mater. Res. Soc. 183 (1990) in print

[16] L. Csepregi, E.F. Kennedy, T.J. Gallagher, J.W. Mayer and T.W. Sigmon, J. Appl. Phys. 48 (1977) 4234.

[17] W. Bergholz, W. Mohr, W. Drewes and H. Wendt, Mater. Sci. Eng. B4 (1989) 359.

[18] K. Yamabe, K. Taniguchi and Y. Matsushita, in: Defects in Silicon, eds. W.M. Bullis and L.C. Kimerling (The Electrochemical Society, Pennington, NJ, 1984) p. 629.

[19] L. Risch, W. Müller and R. Tielert, Semicond. Int. 11 (1988) 246.

[20] H. Wendt and S. Sauter, J. Electrochem. Soc. 136 (1989) 1568.

[21] S. Nadahara, S. Kambayashi, M. Watanabe and T. Nakakubo, Ext. Abstr. 19th Conf. Solid State Devices and Materials, Tokyo, 1987, p. 327.

[22] F. Secco d'Aragona, J. Electrochem. Soc. 119 (1972) 948.

[23] K.H. Yang, J. Electrochem. Soc. 131 (1984) 1140.

[24] M.W. Wright Jenkins, J. Electrochem. Soc. 124 (1977) 757

[25] A.R. Lang, in: Characterization of Crystal Growth Defects by X-ray Methods, eds. B.K. Tanner and D.K. Bowen (Plenum Press, New York, 1979) p. 161

[26] W.L. Smith, A. Rosencwaigh and D.L. Willenborg, Appl. Phys. Lett. 47 (1985) 584.

[27] W. Bergholz, C. Wells, A. Bivas, G. Götz, B. Fiegl and L. Smith, to be submitted to J. Appl. Phys.

[28] W.L. Smith, A. Rosencwaigh, D. Willenborg, J. Opsal and M. Taylor, Solid State Technol. 29 (1986) 85.

[29] H. Föll, V. Lehmann, G. Zoth, F. Gelsdorf and B. Göttinger, in: Analytical Techniques for Semiconductor Materials and Process Characterization, eds. B.O. Kolbesen, D.V. McCaughan and W. Vandervorst (The Electrochem. Soc., Princeton, NJ, 1990) p. 44

[30] G. Zoth and W. Bergholz, J. Appl. Phys. 67 (1990) 6764.

[31] A. Shimazaki, H. Hiratsuka, Y. Matsushita and S. Yoshii, Ext. Abstrs. 16th Conf. on Solid State Devices and Materials, Kobe, 1984, p. 281

[32] V. Penka and W. Hub, Spectrochim. Acta 44B (1989) 483.

[33] A. Huber, H.J. Rath, P. Eichinger, Th. Bauer, L. Kotz and R. Staudigl, in: Diagnostic Techniques for Semiconductor Materials and Devices, eds. Th.J. Shaffner and D.K. Schroder (The Electrochem. Soc., Princeton, NJ, 1988) p. 109

[34] P. Eichinger, in: Analytical Techniques for Semiconductor Materials and Process Characterization, eds. B.O. Kolbesen, D.V. McCaughan and W. Vandervorst (The Electrochem. Soc., Princeton, NJ, 1990) p. 227

Nuclear Instruments and Methods in Physics Research B55 (1991) 132–136
North-Holland

A survey of implant particulate process control and yield effects *

L.A. Larson [1]

National Semiconductor Corporation, Santa Clara, CA, USA

This paper is a review of current work to improve particulate control in ion implantation equipment The first section includes current published research work which will be outlined and summarized. The second section focusses on work performed at National Semiconductor Corporation on testing and implementing an in situ particle monitoring system. The first equipment test consisted of a single monitor mounted in a medium current implanter. This test indicated that the particle signal correlated to surface scan monitor tests and that operating characteristics of the ion implanters which produce particles were observable. Our followup effort was an implementation of the in situ counters on all the implanters as a single particle counting system for the fab The result of this work was a pareto-like analysis of machine and process issues which result in particle events. A correlation of lot-specific particle counts to yield was also developed The advances in machine particulate control are contrasted with the needs and trends in process development Although the advances in particulate control have been excellent, the predicted future requirements are even more stringent The implications of these needs on both particulate performance and measurement are discussed

1. Introduction

Particulate control is widely recognized as one of the primary concerns in achieving higher yields in the ion implantation steps of semiconductor processing. Early analog and bipolar implant process flows would only have one to three implant steps, the critical area for particle contamination would be small and there would be a large number of die. All of these lead to low impact of particulate contamination. Present day development processes for submicron CMOS include 10–15 implant steps, with a small number of die and large values of the critical area These make particulate contamination during implant an increasing concern.

Several excellent reviews of particulate detection and control have been presented in the literature [1–3]. Several papers discuss specifically the generation and monitoring of particles in semiconductor processing equipment [4–6]. Another topic that is broadly treated is particle control and reduction in semiconductor processing [7–9]. It is the intent of this paper to supplement these reviews more than it is to cover the field totally.

There are multiple effects that occur when a particle comes to rest in an active area of a semiconductor device. These are shown schematically in fig. 1. The primary impact of the particle during implant is that it shields the covered portion of the device from the implant. Implantation depths generally range from a few hundred angstroms to about seven thousand angstroms, at the maximum for standard processing. The linewidths of the circuit may also range as low as seven thousand angstroms. It is not surprizing then, that a particle of three thousand angstroms (the lowest value we can reliably measure) can block the implant and seriously degrade the performance of the circuit through shorting (or opening) the junction Secondary effects that may also occur are that contaminants may be released from the particle by sputtering during the

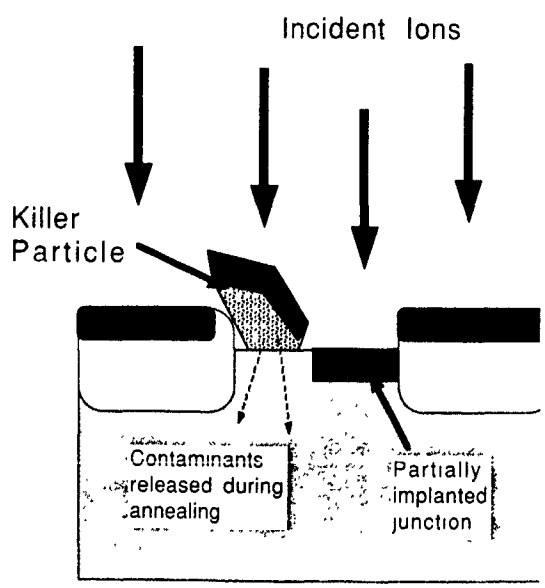

Fig. 1 Effects due to a "killer" particle on an opening in a circuit (after ref [1])

* Invited paper

[1] Presently with Sematech, 2706 Montopolis Drive, Austin, TX 78741 USA.

0168-583X/91/$03.50 © 1991 – Elsevier Science Publishers B V. (North-Holland)

implant or by sintering during the following anneal step.

The effect of particulate contamination on final yield of the wafer is described by a relationship called Murphy's Law. It states that the yield on a water (Y) is dependent on the product of the defect density (D) and on the critical area of the die (A) as by the following relationship:

$$Y = Y_0\left[(1 - \exp\{-AD\})/AD\right]^2.$$

This relationship is shown in fig. 2 for several of the important technologies processed today. At low defect densities the yield loss is nearly linear following the ratio of the number of defects to the number of die. At higher densities this effect mollifies somewhat, because the number of die available that have not already been affected is greatly reduced. As shown in fig. 2, this is a difficult trend to follow as the newer technologies develop. The older bipolar technologies featured a few thousand die on a wafer with linewidths over ten microns. Murphy's law is kind to these processes as the critical area is small and the number of die is large. These are the nearly straight lines denoted as Analog and as TTL/ECL. The trend for advancing CMOS technologies is shown in the lower portion of the same chart. Early estimates of the layout for 64 Mbit DRAMs indicates that a 200 mm wafer will contain about 300 die at linewidths of about 0.5 μm [11]. Murphy's law indicates the extreme yield loss for this case in the lower curve of fig 2

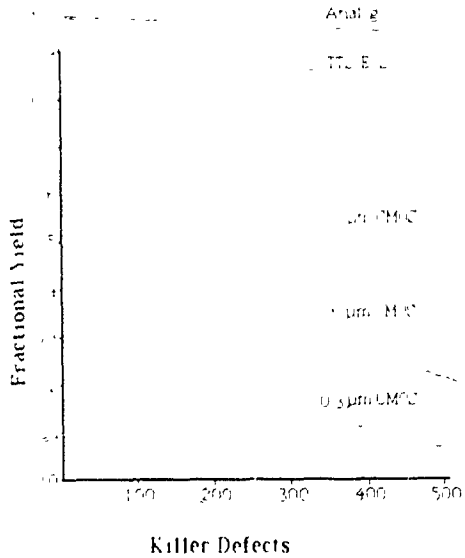

Fig 2 Fractional yield as a function of the number of killer defects as described by Murphy's law for a number of processes in production today.

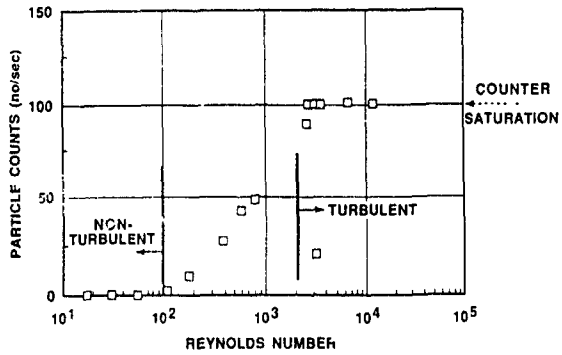

Fig 3 The increase in particle counts as a function of Reynolds number of the gas flow (after ref [13])

2. Vacuum transport

A topic of great interest in the literature is that of the mechanisms which allow the motion of particles in vacuum systems. The driving motives of research on this topic is to develop mechanisms and procedures such that particle motion does not occur, thus allowing the wafer to pass cleanly. It is generally thought that the particle transport occurs through aerodynamic forces [12]. Fig 3 illustrates the results of Chen and co-workers of the University of Santa Barbara [13]. Their work demonstrated clearly that particle count rate is related to the Reynolds flow number of the vacuum system. Given a low Reynolds number (laminar flow) the count rate is very low This increases for Reynolds number that are considered transitional. The particle counter iturates at high (turbulent flow) Reynolds numbers

As a corollary effect, the forces of adhesion for small particles are considered to be Van der Waals in nature [12]. There should then be a limiting value of "air" velocity, below which particles will not move. This concept was explored by a group of authors from the Eaton Corporation [14,15]. Their work is shown in fig

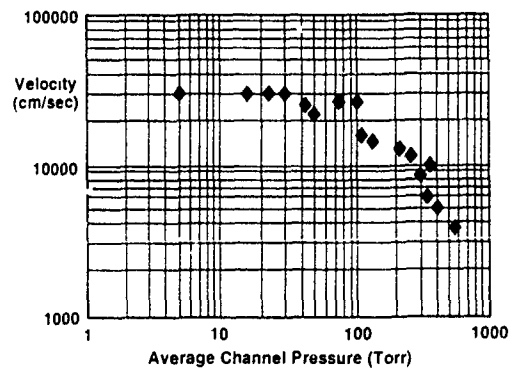

Fig 4 The gas flow velocity necessary to dislodge a 5 μm particle as a function of the average channel pressure (after refs. [14,15]).

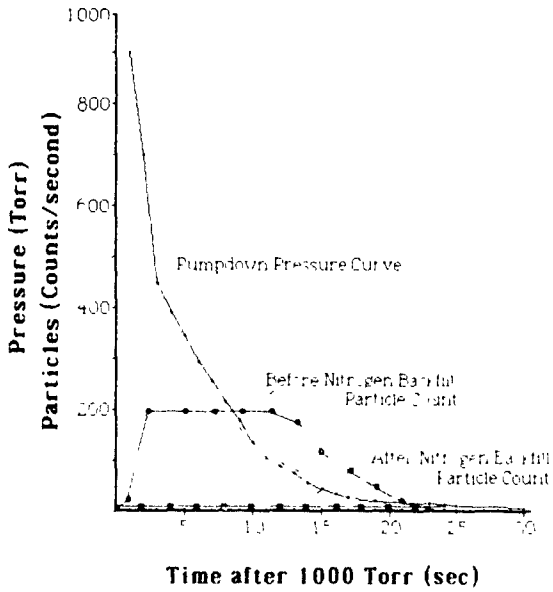

Fig 5 Illustration of condensation by tracking particle counts with and without nitrogen backfill (after ref [17])

4. Here the gas flow velocity necessary to move 5 μm particles of various materials is determined as a function of the pressure. While the particles are generally larger than those of interest in semiconductor device manufacturing, it may be argued that the larger particles will move easier That makes these relationships an appropriate boundary condition to follow in developing pumping and venting pressure-flow curves

Another mechanism that has been of concern is the condensation of water on particles that may occur during the adiabatic cooling of pumpdown. This has been an enabling mechanism for the development of high sensitivity atmospheric particle counters, but in an implanter loadlock it is just as effective as a deposition mechanism. Wu et al. of IBM [16] have published a complete theoretical treatment of this subject with some experimental results. Chen and Hackwood [17] did similar work on a more experimental level. One of their results is shown in fig. 5. There, a large particle signal developed during the pumpdown after regular atmospheric exposure but did not occur when the chamber was carefully backfilled with nitrogen. Any procedure or equipment that removes the residual atmospheric humidity seems to have similar effect Both molecular sieves and other dry gases were tested with the same result.

The consensus is that particle effects in vacuum systems and loadlocks are becoming much better understood and, in particular, are managable. The situation becomes more complex for ion beam systems. Brown et al. [18] have published a theoretical work demonstrating that particles of macroscopic size may be suspended in the fields of an ion beam. Given that the momentum of the beam is directed towards the endstation, it follows that the beam itself may transport contamination to the wafer. This theory has been supported by visual observation of such particles [19] but no direct experimental work has been reported as of yet.

3. In situ monitoring

In situ monitoring has dominated the recent literature on particle detection and monitoring. As a portion of that work is from National Semiconductor, I will demonstrate with our results while commenting on more general principles.

There are three basic techniques for particle detection and monitoring in a production environment. Bare wafer surface scanners have a size resolution of 0.3–0.2 μm and are generally used between one and five times on each production shift for each ion implanter A more advanced technology is the patterned wafer surface scanners. These have poorer size resolution at 1.0–0.5 μm but may be used more frequently as routine production could be sampled (hopefully 10–30 per shift!). As compared to these, an in situ monitor has intermediate resolution, at 0.5–0.3 μm, but monitors every wafer!! This is the primary advantage of the in situ monitoring systems – the process environment is sampled for every wafer rather than sampling being performed at long intervals according to an inspection plan.

The importance of this concept is illustrated in fig 6 [20] Here the in situ particle count rate for a production Varian DF4 implanter is plotted as a function of time over an interesting set of events. Notice that in the first two hours of the data the baseline particle count is slowly decreasing but that there are episodic particle events that are slowly becoming worse. This continues until a wafer sticks in the loadlock just after 18:00 hours. It is expected that this set of episodic signals

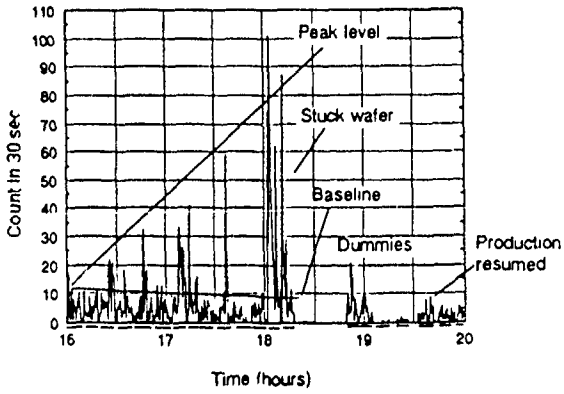

Fig 6 In situ count rate as a function of time for production operation on a DF4 implanter

would probably not be observed with a monitor wafer chosen at random. A second interesting effect is observed in the later portion of the same figure. The established procedure of this fab is that after a maintenance intervention the implanter is "cleaned" with dummy wafers before real production is resumed. The four lots of dummy wafers between 18.45 and 19:30 clearly return the implanter particle signal to much less than the previous baseline. However, as soon as production is resumed at 19.30, the in situ particle signal increases to previous levels

Borden [21] has described these effects through the concept of a particle conservation theory. In this theory, an implanter or any type of vacuum system is considered a closed system for particle generation Particle sources include the production wafers, the process gases used in the loadlock and the intrinsic wear of the system. The particle sinks are the same production wafer leaving the system and the gas flow evacuated from the system. As with any conservation system in equilibrium, this system would seek equilibrium levels of particles based on these sources and sinks. Thus a sporadic event would have forces trying to return the particle levels to the baseline as long as there are no new particle producing events Similarly, when clean dummy wafers are run the system responds by establishing a new, lower baseline level. Unfortunately, as soon as the production is resumed, the system also trends back to the previous baseline levels Clearly, the method to actually reduce the particulate effects for the system as a whole is to reduce the rates of particle introduction from the sources Minor changes may be effected by changing particle populations in a portion of the system, but if the input rates are not affected then it may be predicted that the output rates will return to equilibrium.

Fig 7 illustrates that a much more causal relationship between particles and yield may be established due to the on-line nature of in situ particle counting [22]. This work evaluated the relationship between six months of NMOS production and the in situ particle counts as recorded for four of the implant steps Individual maximum sensitivities for each mask layer were developed using the limiting value of Poissons form of the yield equation. These followed the expected trends as per the criticality of each step and as per the amount of active circuit exposed at that layer The end result of this exercise was that the yield hit was approximately 0.5% per mask layer due to these effects. The average surface scan particle counts during these tests was on the order of 0.5/cm^2 and the in situ particle count was on the order of 10 counts per lot The disturbing part of these results is that the largest number of these three numbers is the number of die killed (number of die killed $\gg$ surface scan particle count > in situ particle count)!! This is again indicative that the surface scan qualification tests do give a particle baseline for the system, but unfortunately it is not the baseline that the production wafers are exposed to!

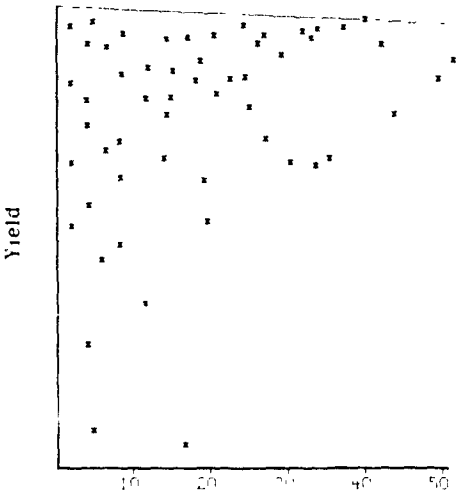

Fig. 7 Process yield as a function of in situ particle count for a single implant as measured on many lots of NMOS product The upper line is the predicted yield limit due to particles at this mask level

4. Future requirements

Present generation implanters are boasting an added particle count on the order of 0.03 to 0.05 particles/cm^2 This is a significant improvement over the machine performances of the late '80s but at best is merely in step with the trends of process shrinks. This performance is expected to be sufficient to meet the needs of 1M DRAM (1.2 μm) and 4M DRAM (0.8 μm) processes but is at best marginal for 16M DRAM (0.5 μm) processes These 0.5 μm processes are in development now and are expected to hit production by 1992 [11]. This is not far in the future! At the same time, development efforts will be on-line for 64M DRAM (0.35 μm) processes The particulate target for these processes is 0.003 particles/cm^2. This is *one* particle per 200 mm wafer per implant step! Clearly more work needs to be done

As a matter of perspective, one can ratio these requirements up to macroscopic sizes. If the 0.3 μm particle is increased to one centimeter, then the die that it would affect increases from 1.44 cm (predicted [11]) to 480 meters on a side. It would obviously be a challenge to even deal with that area ratio, but consider that the 200 mm diameter of the wafer has increased to 6.7 km! This is the size of a city (Dublin for example).

This is a matter of concern in that we all will have to be able to monitor to this scale in order to effectively control these processes and to qualify machines to run them. I have a particular concern with the sampling rate that is implicit with this requirement. Do we declare a machine or process out-of-control when we get a particle count of 1? What sort of sampling frequency is necessary to effectively declare that this is a true reading? The in situ monitors look particularly good when measured against these concerns [23], however even an analysis of their predicted count rates showed a level which is of concern when considering the accuracy of low signal rates. This rate was about one count every four minutes.

5. Conclusions

Several advances in our understanding of particulate generation, transportation and control have been described here. Recent advances in monitoring technology have been described with examples of different analyses that can result from these technologies. In general, advances in equipment particulate control have taken the industry to the point of results on the order of 0.03 to 0.05 particles/cm^2 added. This is adequate for present technologies and for the development of processes for 1-2 years from now. Target technologies for development in the '92-'93 timeframe require added particulate levels of 0.003 particles/cm^2. This is a particularly difficult and agressive goal for both implanters and the equipment that is made to monitor particle levels.

References

[1] T.C. Smith, 20th Meeting of the Fine Particle Society, Boston MA, ed. K.L. Mittal, to be published in Particles in Gases and Liquids II.
[2] T.C. Smith, Nucl. Instr. and Meth. B37/38 (1989) 486.
[3] I. Hattori, Microelectronic Manuf. Test 11(5) (1988) 31.
[4] H.S. Nagaraj, B.L. Owens and R.J. Miller, in: Particles in Gases and Liquids I: Detection, Characterization and Control, ed. K.L. Mittal (Plenum, New York, 1989) p. 283.
[5] P. Borden, Microcontamination 8(2) (1990) 23.
[6] P.B. Keady, K.J. Weyrauch and A.S. Viner, Forum Contaminexpert, Sept. 1989, Versailles, France.
[7] P. Borden, Microcontamination 8(3) (1990) 47.
[8] J.F. O'Hanlon, J. Vac. Sci. Technol. A5 (4) (1987) 2067.
[9] J.F. O'Hanlon, J. Vac. Sci. Technol. A7 (3) (1989) 25.
[10] J. Strain, S. Moffatt and M. Current, Microtamination 7 (5) (1989) 47.
[11] ICE News 21 (2) (May 1990).
[12] K.L. Mittal (ed.), Particles on Surfaces I and Particles on Surfaces II (Plenum, New York, 1989).
[13] D. Chen, T. Seidel, S. Belinski and S. Hackwood, J. Vac. Sci. Technol. A7 (5) (1989) 3105.
[14] M.E. Mack, D.E. Stone, J.A. Jost and P. Sferlazzo, Semicon/East 89 Proc. (SEMI, 1989) p. 107.
[15] P. Sferlazzo, D.K. Stone, J.A. Jost and M.E. Mack, Semicon/Korea 89 Proc. (SEMI, 1989).
[16] J.J. Wu, D.W. Cooper and R.J. Miller, J. Vac. Sci. Technol. A8 (3) (1990) 1961.
[17] D. Chen and S. Hackwood, J. Vac. Sci. Technol. A8 (2) (1990) 933.
[18] D.A. Brown, J.F. O'Hanlon and P. Sferlazzo, IES Proc. (1990) p. 396.
[19] M. Vella, private communication, GSVIUG Meeting, March 1990.
[20] L.A. Larson and P. Borden, ISMSS Proc. (1989) p. 61.
[21] P. Borden, Microcontamination 8(1) (1990) 21.
[22] L.A. Larson and P.A. Haunschild, Fine Particle Society Meeting, August 1990.
[23] P. Borden, GSVIUG Notes, March 1990.

Nuclear Instruments and Methods in Physics Research B55 (1991) 137–142
North-Holland

Wafer charging study on a Varian 160 XP ion implanter with charge-sensitive devices

R. Nee
Motorola Inc., MOS-6, 2200 West Broadway, Mesa, AZ 85202, USA

S. Mehta
Varian Ion Implant Systems, Blackburn Industrial Park, Gloucester, MA 01930, USA

S.B. Felch
Varian Research Center, 611 Hansen Way, Palo Alto, CA 94303, USA

S. Kikuchi
Tokyo Electron Limited, Kyushu, Japan

Device yield is significantly affected by positive surface charge build-up during high current implantation. In order to protect the devices from charging-up, ion implanters are equipped with electron flood systems which supply a steady flow of low energy electrons to the wafer to neutralize the positive charge induced by the ion beam. Excellent device yields have been achieved on the Varian XP series of high current implanters with two different techniques for charge neutralization – auto emission electron flood control system and a new, alternative, charge neutralization method. These two techniques have been evaluated with a state-of-the-art, charge-sensitive MOS structure, involving different gate oxide thicknesses and a high charge multiplier ratio. The effect of several implant parameters, including beam spot size, species, and various electron flood conditions on yield were also examined. Device yield was characterized by breakdown voltage (V_{bd}) measurements.

1. Introduction

Several processes used in the fabrication of modern semiconductor devices involve charged particles. Ion implantation, which relies on the transport of positively charged ions into the target semiconductor wafer, is one of these processes. As the lateral geometries and the gate oxide thicknesses involved in these devices continue to shrink to accommodate the rapid trend towards 4–16 Mb memory level integration, their susceptibility to charging damage during high-current implantation increases proportionally. It is therefore, necessary to somehow neutralize the ion-beam-induced charge to protect the devices from such damage. Most high-current implanters of today are equipped with electron flood systems to neutralize the charge on the wafers. However, the demand for higher beam currents to address the throughput needs of the device manufacturers places considerable constraints upon the ability of modern implanters to provide adequate methods for neutralizing the charging effects of high beam currents. In this paper, the effectiveness of two charge neutralization techniques in a Varian XP high-current implanter, studied with a charge-sensitive MOS structure, will be presented.

2. Experimental

All charging tests conducted for this investigation were run on a Varian 160XP high-current ion implanter. Two different techniques for charge neutralization were examined. These are "electron flood system no. 1" and "electron flood system no. 2". These will be referred to as EFS-1 and EFS-2 respectively, in the remainder of the text. The EFS-1 is available as a product on all XP series of Varian high current implanters, whereas EFS-2 is being tested and is currently under development by the vendor. In the EFS-1, primary electrons from an electrically heated filament mounted on one wall of the Faraday are used to generate charge neutralizing low energy secondaries from the opposite wall of the Faraday cage. A closed loop electronic system varies the primary emission level of the flood system to regulate the net disk current at a user-selected value. More detailed accounts of this electron flood system have

0168-583X/91/$03.50 © 1991 – Elsevier Science Publishers B.V. (North-Holland)

been published elsewhere [1–3]. In the EFS-2, a low energy electron source injects the electrons into the Faraday for charge neutralization. This system differs from EFS-1 in that the energy of the charge-neutralizing electrons is independent of the Faraday conditions. This would result in an increased MTBF from the standpoint of Faraday maintenance. The details of the EFS-2 will be published at a later date when the system will be fully qualified as a product by the vendor.

The effects of several implant parameters such as ion species and beam spot size were also studied. The ion species implanted were; $^{11}B^+$, $^{49}(BF_2^+)$, and $^{75}As^+$. The spot size (or the charge density) of the beam was varied by changing the extraction voltage while maintaining constant beam current and by turning "on" the high voltage suppression bias (−10 kV) in "decel mode" of operation.

Test vehicles used were state-of-the-art MOS test structures with gate oxide thicknesses of 235 and 180 Å, fabricated on 150 mm, p-type (100) silicon wafers. The charge multiplier ratio was about 3.3×10^5, thereby making the test structures extremely charge-sensitive. Electrical characterization of the implanted devices was done by breakdown voltage (V_{bd}) measurements. A controlled voltage ramp was applied across the gate while monitoring the flow of current through the oxide. The criterion for breakdown was the voltage where 1 μA of current was detected through the oxide

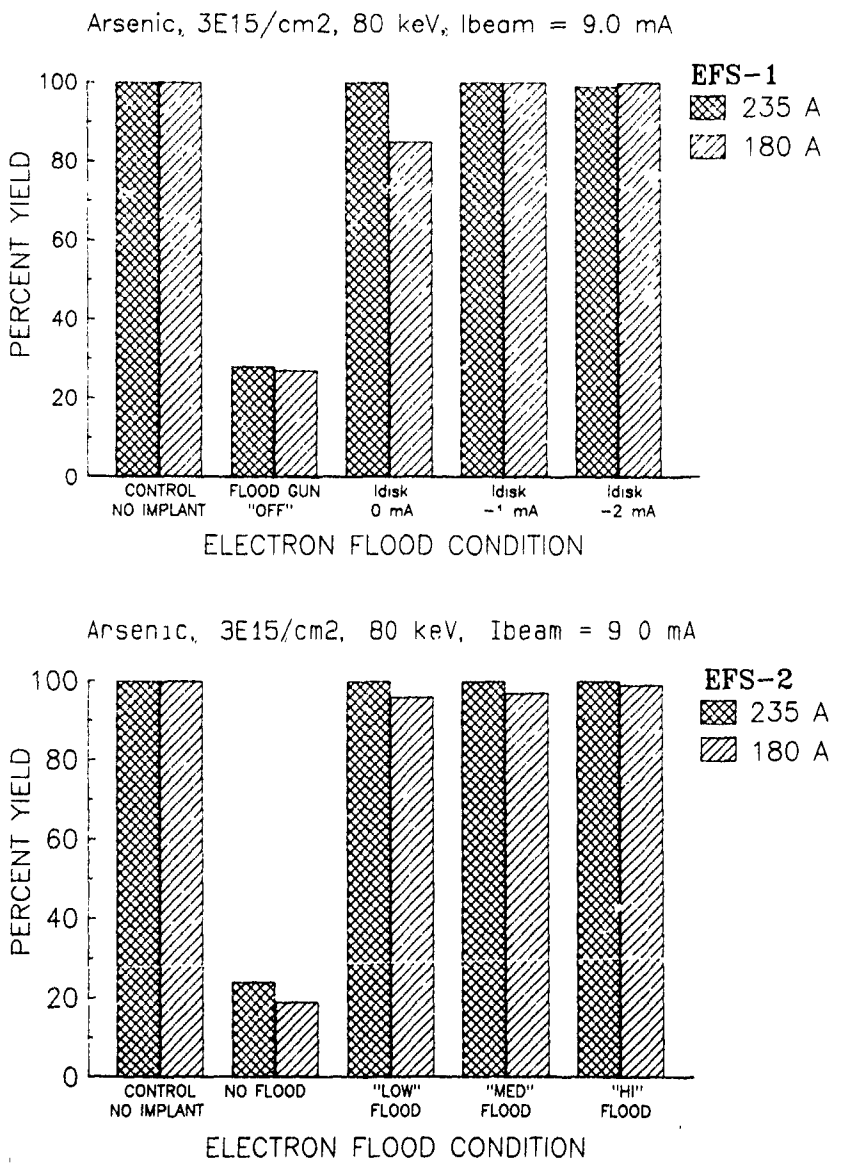

Fig 1. Yield plots for arsenic-implanted charge monitor wafers under various conditions of electron flooding for EFS-1 and EFS-2.

3. Results and discussion

A typical n^+ source/drain implant was used to study the effect of the various flood conditions on both charge neutralization systems. Arsenic ions with 80 keV energy were implanted into the wafers to a dose of 3×10^{15} cm^{-2} at a beam current of 9.0 mA in the "accel mode" of operation. Device yields for wafers implanted with the two flood systems are depicted in fig. 1. The control wafers, which received no implant, had 100% yield for both gate oxide thicknesses, indicating good process control in the fabrication of the devices. On the other hand, wafers implanted without any electron flood showed poor yields on both endstations, clearly demonstrating the need for charge neutralization.

Use of the EFS-1 and EFS-2 markedly improved the device yield for all 3 conditions tested in this experiment. The results of EFS-1 also indicate that optimum charge neutralization is achieved when the disk current is anywhere from 0 to -1 mA (giving 100% yield for both oxide thicknesses at -1 mA). Although this may indicate that slight overflooding is necessary for achieving optimum charge neutralization, the conditions may vary from one device type to another. In addition, for any given flood condition, the yield on a wafer with the thicker gate oxide (235 Å) was always somewhat higher than that on a wafer with a thinner oxide (180 Å). This

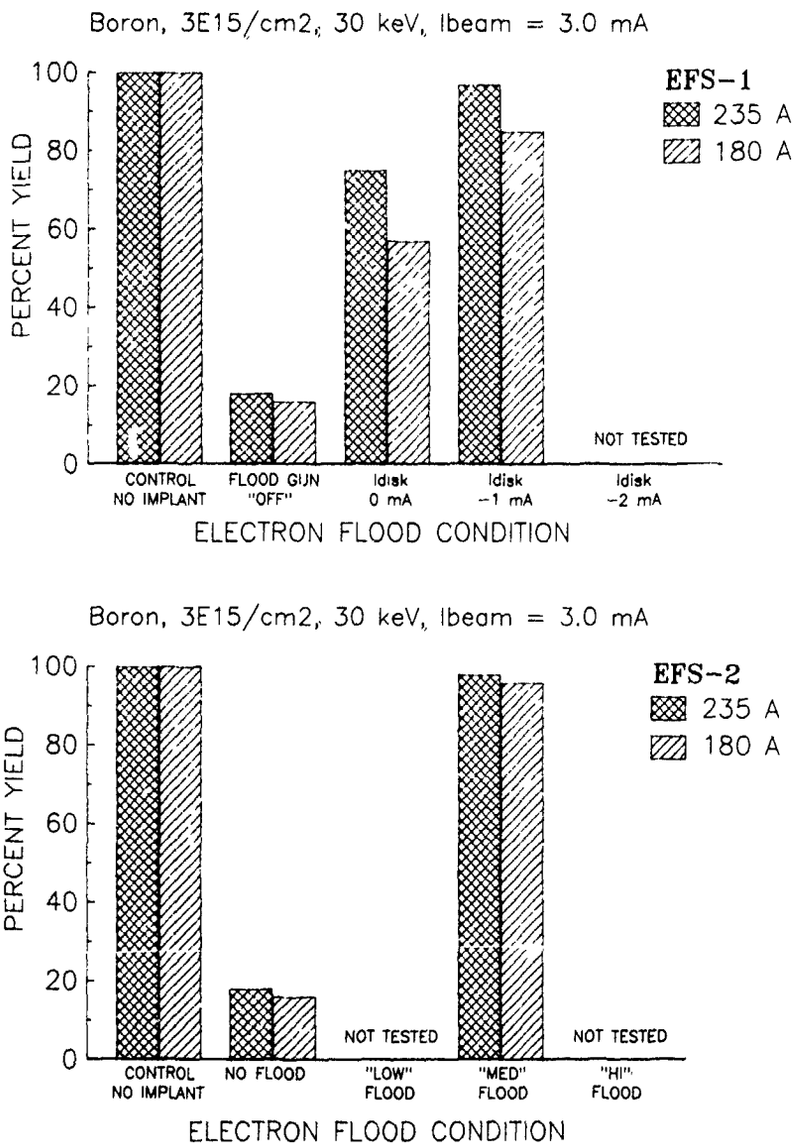

Fig. 2. Yield plots for boron-implanted charge monitor wafers under various conditions of electron flooding for EFS-1 and EFS-2.

is consistent with the fact that the dielectric breakdown voltage decreases with decreasing oxide thickness, thereby making thin oxides more susceptible to charging effects.

In addition to arsenic, the charging effects of several other species such as B^+ and BF_2^+ were studied under implant conditions very similar to those encountered in actual device production. The species were implanted in "decel mode", to a dose of 3×10^{15} cm^{-2}. The beam current for B^+ and BF_2^+ ions was 3.0 and 4.5 mA, respectively. Device yields for the two cases are depicted in figs. 2 and 3. Higher yields were obtained at disk current of ≈ 1 mA, reflecting the consistency with results on the arsenic implants

Among p-type dopants, BF_2^+ implants gave better device yields than were obtained with B^+ implants for both electron flood systems under investigation. This can be explained by the different beam spot sizes and the resulting current densities in the two cases. Due to its larger mass, the space-charge effects will be more pronounced for BF_2^+ than for boron. Consequently, the beam spot size for BF_2^+ ions for the same beam current will be much larger. The reduced charge density is less damaging to the oxide thereby resulting in improved device yield.

The influence of beam spot size (or charge density) on device yield was further studied by a series of tests whereby singly-charged arsenic ions at a beam current

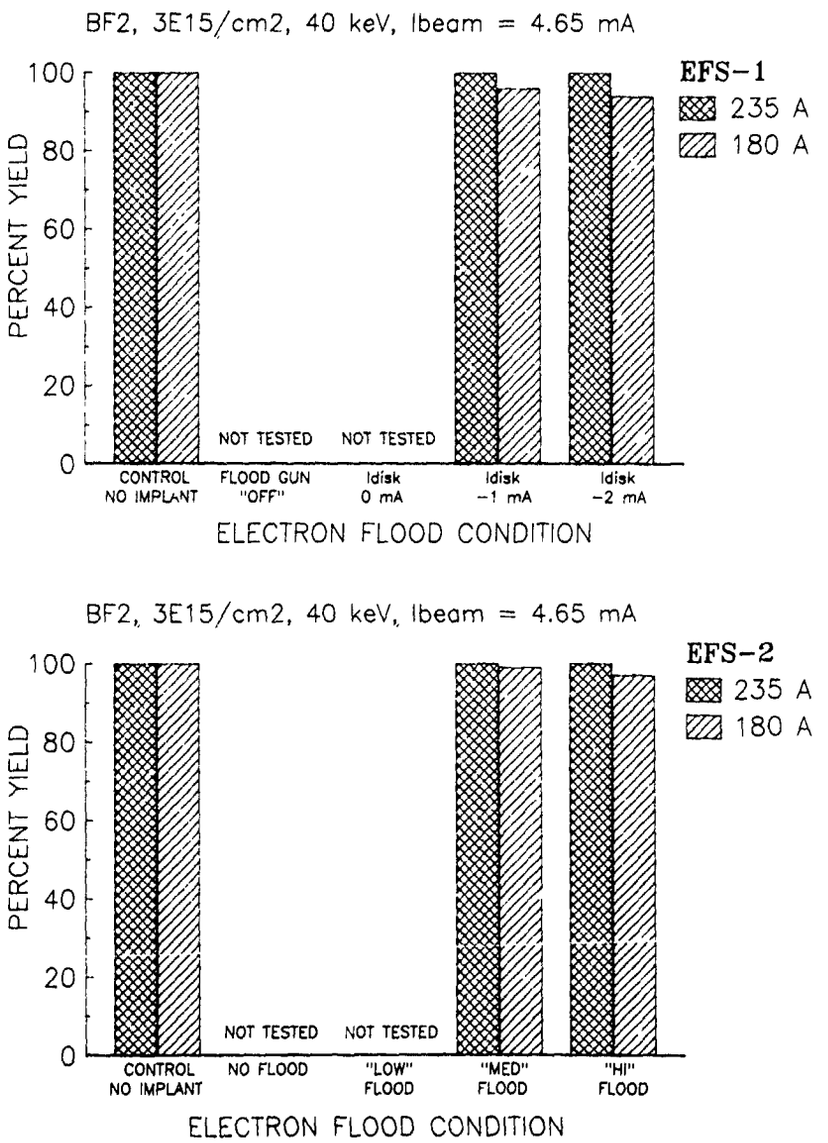

Fig. 3. Yield plots for BF_2-implanted charge monitor wafers under various conditions of electron flooding for EFS-1 and EFS-2

of 4.2 mA were implanted into the test wafers to a dose of 4.5×10^{15} cm^{-2} at 50 keV under a variety of extraction conditions. For all the implants performed for this investigation, the disk current was held constant at 0 mA using the EFS-1. The results for the 235 Å gate oxide device used in these tests are depicted in fig. 4

The results show that as long as the extraction energy of the ions is lower than or equal to the final energy of the species ($V_{ext} = 40$, 45 and 50 keV) or in other words, the implant is performed in "accel mode", high device yields (up to 100%) can be achieved. However, when the extraction energy exceeds the final energy of the species ($V_{ext} = 55$ and 60 keV), thereby rendering the implant to be run in "decel mode", there is a significant drop in yield (64 and 46% at 55 and 60 keV, respectively). The difference in yield can be explained by the different charge densities of the beam in the two modes of operation. In the "accel mode" of operation, both the high voltage suppression (−10 kV) and the pre-Faraday bias (−1 kV) are "on" during the implant. The stripping of the electrons from the beam by these negative potentials causes the beam to blow up, which results in a diluted charge density of the beam Consequently, the devices are not exposed to severe charging conditions, and this results in higher yields.

On the other hand, when the implant is run in the "decel mode", both the −10 and −1 kV suppression biases are automatically turned off Furthermore, the high extraction potentials, cause the ion beam to be sharply focussed as it emerges from the ion source Since the electron suppressing biases are absent in this case, the beam remains space-charge neutralized during its transport to the wafer. Therefore, the charge density of the beam is much higher, which in turn results in charging damage of the devices.

In order to substantiate this finding, the tests were repeated in the "decel mode" with the −10 kV suppression bias turned "on" manually. For both extraction conditions tested, dramatic improvement in yield was observed. These results are shown in fig. 5.

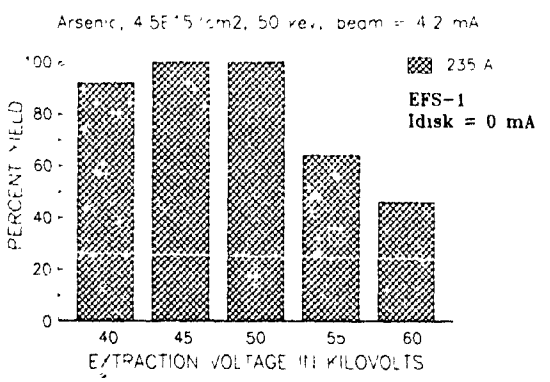

Fig. 4. Plots showing yield as a function of extraction voltage for arsenic-implanted charge monitor wafers while disk current is held constant at 0 mA using EFS-1

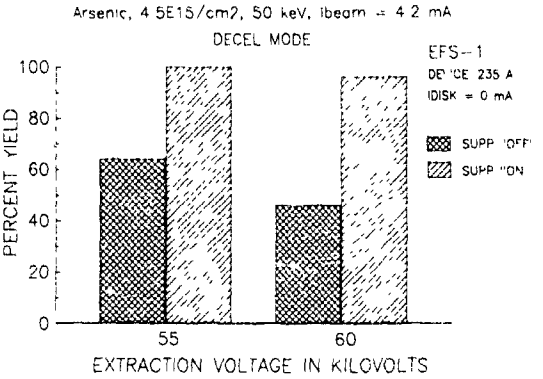

Fig. 5 Effects of (−10 kV) suppression bias on the yield of arsenic-implanted charge monitor wafers with the disk current held constant at 0 mA using EFS-1

4. Conclusions

The effectiveness of two charge neutralization techniques for the Varian XP series of high-current implanters has been studied with charge-sensitive MOS structures. While the EFS-1 is a fully established product for these implanters and continues to perform remarkably well at the production level, the EFS-2 has also demonstrated promising results under the same implant conditions. Further testing needs to be continued to develop the latter into a qualified product. The results of this work also show that the beam spot size plays a very important role in achieving optimum device yields We conclude that, in order to prevent the devices from charging damage during high current implantation, the implant conditions should be chosen so as to keep the charge density as low as possible without sacrificing beam current. In addition, any set of implant conditions optimized for a given device type may not be applicable to another

Acknowledgements

The authors wish to thank Aki Ueda of Motorola for providing valuable assistance in the post-implant testing of the devices. We are also grateful to Dr. Charles McKenna and Ronald J. Eddy of Varian Extrion for many helpful discussions, and Mr Kitahara of Tokyo Electron Limited for providing engineering assistance in running the tests. Thanks are also due to Pam Mansfield for providing graphic arts assistance.

References

[1] S. Mehta, R.F. Outcault, C M McKenna and A. Heinonen, these Proceedings (8th Int Conf on Ion Implantation Technology, Guildford, UK, 1990) Nucl. Instr and Meth B55 (1991) 457.

[2] C M McKenna, B O Pedersen, J.K Lee, R.F Outcault and S. Kikuchi, Proc. 7th Int. Conf. on Ion Implantation Technology, Kyoto, Japan, Nucl. Instr and Meth B37/38 (1990) 492

[3] R.J Eddy, S. Mehta, R F Outcault and S K. Suh, Yield Issues in Ion Implantation, Proc. of Semicon Korea, Technical Sessions, 1989

Nuclear Instruments and Methods in Physics Research B55 (1991) 143–147
North-Holland

Charging studies with "CHARM"

W. Lukaszek, R.K. Nahar and A. McCarthy
Center for Integrated Systems, Stanford University, Stanford, CA 94305, USA

W. Weisenberger, S. Cherekdjian and D. Lindsey
Ion Implant Services, 1050 Kifer Road, Sunnyvale, CA 94086, USA

A novel, EEPROM transistor-based wafer surface-charge monitor has been applied to quantitative assessment of surface charging during 120 kV, 5×10^{15} arsenic ion implants under a variety of beam-current, flood-gun and argon pressure conditions. Least negative charging was observed with argon backfill, in the absence of flood-gun electrons. Comparison of devices with different-sized charge-collection electrodes supports the voltage source model of surface charging.

1. Introduction

The shallow, highly doped n + p junctions required by high-performance ICs are almost universally implemented with high-dose arsenic implants. To improve throughput, ion-implanter manufacturers have been providing the semiconductor industry with high-beam-current ion implanters. Unfortunately, the anticipated throughput improvements have not been completely achieved due to gate-oxide breakdown [1] or other structural damage [2] resulting from charge buildup on the surface of the implanted wafers during high-beam-current implants. To monitor this phenomenon and to establish preventive IC design guidelines, IC manufacturers have used simple, conveniently available, polysilicon capacitors with varying gate oxide–field oxide ratios, area–edge ratios, etc. [1,3]. Relying on determining the number of damaged or destroyed capacitors, this technique has frequently failed to provide definitive answers [3].

Ideally, a monitor is needed which gives a direct measure of the driving force behind the damage: the potential developed on the wafer surface. To this end, implant manufacturers have developed in situ monitors which provide a waveform of the potential developed across a capacitor as the beam sweeps over it [4,5]. This approach, however, employs special fixtures within the implant chamber, is confronted with difficult signal transmission problems, requires considerable knowledge (some of which may be missing) in interpreting the waveforms, and, in the mind of the user, does not sufficiently imitate the conditions occurring on product wafers. To instill this essential confidence, the monitor itself should be a wafer which has the ability to "remember" the peak potential developed on its surface. A step in this direction was taken by Yoshida et al. [6], in monitoring the threshold voltage shift of EEPROM transistors subjected to a variety of process conditions. However, no effort was reported to determine the influence of UV on the final threshold voltage (UV can eject electrons from the floating gate, thus affecting the threshold voltage shift, leading to an erroneous estimate of the surface potential), and the investigation did not encompass the use of different-sized charge-collection electrodes to investigate the presence or absence of the "antenna effect", which is critical to developing circuit layout guidelines and understanding the physical mechanisms underlying wafer surface charging.

In this paper we report experimental results, obtained under a variety of high-current arsenic implants, using a dedicated, EEPROM-based wafer surface-charge monitor which employs devices with different-sized charge-collection electrodes, and "reference" devices which permit separation of the electrostatic and UV influence on the threshold voltage shift of the monitor devices. The experimental conditions examine the effect of beam current, flood-gun current, bias voltage and argon backfill pressure on the surface-charging characteristics of 120 kV, 5×10^{15} As implants performed on an Eaton model NV10-160 ion implanter.

2. Device description

Implemented in clusters populating the entire wafer, the CHARM (charge monitor) device, shown in fig. 1a, employs electrically erasable PROM transistors whose control gates are connected to aluminum charge-collection electrodes located on thick oxide. Electrostatic charge deposited on the collection electrodes gives rise

0168-583X/91/$03.50 © 1991 – Elsevier Science Publishers B.V. (North-Holland)

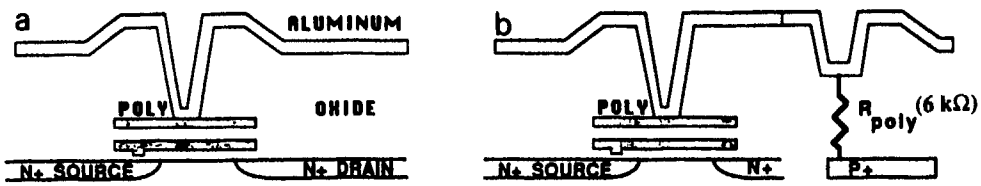

Fig 1. CHARM structure.

to a potential proportional to the amount of deposited charge and the collection electrode-to-substrate oxide thickness. This potential, in turn, programs the EEPROM memory transistors by altering their threshold voltages in proportion to the potential on the charge collection electrodes [7]. The monitor is, therefore, a polarity-sensitive peak voltage detector with memory. Its threshold voltage shift versus control gate potential, shown in curve (a) of fig. 2, is determined during wafer probe by repeated application of external voltages to the charge-collection electrodes.

Two undesirable characteristics may be observed in curve (a): the EEPROM transistor does not respond to applied voltages between −10 V and +10 V, and the threshold voltage shift saturates for applied voltages lower than −25 V or greater than 30 V. The absence of response between −10 and +10 V implies that the applied potential is insufficient to cause electron tunneling through the thin tunnel oxide, while the saturation is due to reverse tunneling across the tunnel oxide when the floating gate potential is sufficiently low (or high) and the external programming voltage is removed. While the saturation places a limit on the maximum surface potential the devices can monitor unambiguously, this limit approaches or exceeds the breakdown voltage of contemporary gate oxides and, consequently, does not impose any practical limitations on the utility of the monitor. Moreover, if the processing medium behaves like a current source, it is possible to extend this limit, as discussed later. The lack of response between −10 and +10 V appears more serious. Fortunately, it can be completely circumvented by preprogramming the monitor EEPROM transistors to their saturated threshold voltage state, where the transistors will respond to the slightest potential of the opposite polarity, as indicated in curves (b) and (c) of fig. 2. Consequently, the entire range of surface potentials between −25 and +30 V can be monitored with this device.

It should also be observed that the EEPROM memory transistor is a rapidly responding device, as evident from fig. 3, which shows its threshold voltage shifts for different duration programming pulses (different batch than given in fig. 2). In view of the 1–5 ms duration of the positive and negative pulses observed with in situ capacitive sensors during high-current implants [5,8], and the less than 3 pF equivalent capacitance of the CHARM monitor, it behaves as a last-toggle device, recording the polarity and peak value of the last pulse it encounters It is important to keep this in mind when interpreting the experimental data.

To determine whether a wafer-processing environment behaves like an area-proportional current source, leading to the "antenna effect", or an area-independent voltage source, monitors employing a broad range of charge-collection electrode areas were implemented. Due

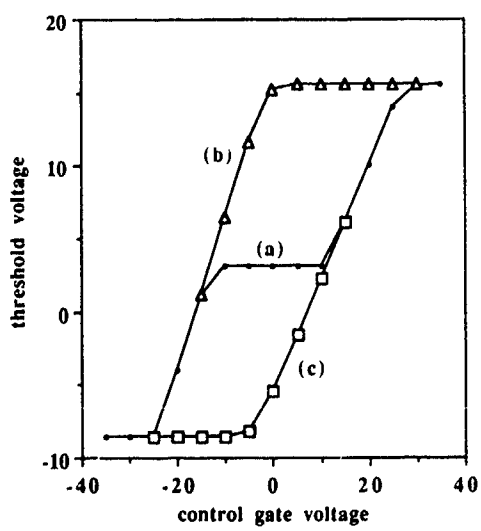

Fig. 2. CHARM response to control gate potential (a) as manufactured, (b) programmed positive to sense negative potential, and (c) programmed negative to sense positive potential.

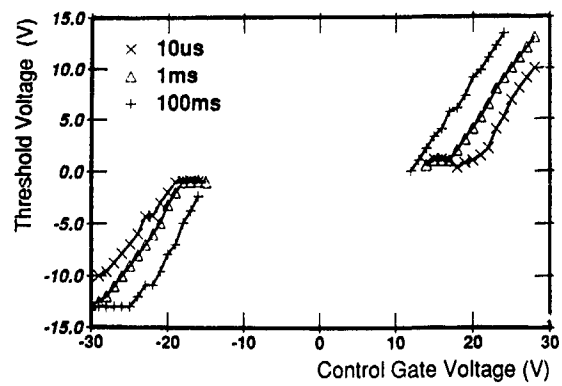

Fig. 3 CHARM pulse response.

to charge sharing between the charge-collection capacitor and the EEPROM memory transistor, the voltage developed on the control gate of the EEPROM transistor depends on the size of the charge-collection electrode. When the charge-collection electrode capacitance is large in comparison to the EEPROM transistor capacitance the voltage developed on the charge-collection electrode approaches the unloaded charge-collection voltage V_H, given by $V_H = Q_S(t_D/\epsilon_{OX})$, where Q_S is the deposited charge per unit area, t_D is the dielectric thickness, and ϵ_{OX} is the associated dielectric constant. When the charge-collection electrode approaches the size of the EEPROM transistor control gate, the voltage developed on the charge-collection electrode approaches V_L, the voltage that would be developed if the charge were deposited on the transistor control gate directly. For the EEPROM transistor layout and dielectric thicknesses employed in the devices used in this study, $V_L = V_H/6$. To span a large range of possible surface potentials, 21 different electrode areas have been employed [9], spanning ratios of 2.25 to 100 in the charge-collection electrode to control gate areas.

Optical removal of charge from the floating gates of the well-shielded monitor memory transistors, which would lead to incorrect measurements of wafer-surface peak charge/voltage, is monitored with reference devices, shown in fig. 1b, which are identical to the monitor devices but have their charge-collection electrodes connected to the substrate through 6 kΩ resistors, with the purpose of providing electrostatic discharge paths. The reference devices are probed and preprogrammed to a high threshold state before the wafers are placed in an ion implanter. Post-implant threshold voltage shifts of the reference transistors can be used to compensate for optical effects in the monitor memory transistors.

3. Experimental conditions and test procedures

The purpose of this experiment was to examine the utility of the CHARM monitor under a variety of high-current arsenic implant conditions. In order to emphasize the influence of flood-gun current, bias, and argon backfill pressure on wafer-charging characteristics, the implant energy and dose were set at 120 kV and 5×10^{15} cm^{-2}, respectively. All implants were performed on the Eaton NV10-160 ion implanter. In order to perform the experiment within a reasonable period of time, we used a total of nine CHARM wafers, assigning two wafers to each split except for splits 5 and 10 which used only one wafer. The experiment was performed in two rounds, involving splits 1–5 in the first round and 6–10 in the second round. The complete experimental matrix is shown in the table accompanying fig. 5.

Wafer preparation prior to implantation consisted of establishing specific threshold voltages on a set of four devices, on 47 sites per wafer. Two devices, a reference device and its corresponding monitor device, were preprogrammed using a 20 V pulse, applied to the charge-collection electrode, which resulted in threshold voltages of approximately 10 V. Two additional monitor devices, each having a different charge-collection electrode area, were electrically erased to a threshold voltage of approximately 3 V. The threshold voltages of these four devices were measured again after the implants.

4. Analysis of results

The analysis of the implant charging results began with a post-implant comparison of the threshold voltage shift of the preprogrammed reference devices. The maximum threshold voltage shift of 0.4 V in the first round of experiments, and 0.0 V threshold voltage shift in the second round, indicated that the several volts post-implant threshold voltage shifts on the monitor devices did not require any compensation for optical erasure of the charge content of the floating gates. (The maximum 0.4 V shift in the first round may be due to initial threshold voltage instabilities typical of floating-gate devices.) Next, a comparison was made of the post-implant threshold voltages of the two monitors with different-sized charge-collection electrodes. A typical result is shown in fig. 4. The identical threshold voltages are a clear indication of the absence of the "antenna effect", confirming the results obtained by Benveniste [5] that the electron cloud around the beam appears to behave like a voltage source. This result also allowed a direct analysis of the post-implant threshold voltages on the preprogrammed monitors, which formed the basis of the summary of charging results shown in fig. 5, derived by first examining the histograms of the final threshold voltages and converting them to surface potential with the help of fig. 2 (or the equation $V_{SURF} = V_{TH} - 16$). It should be observed on the basis of fig. 3 that the

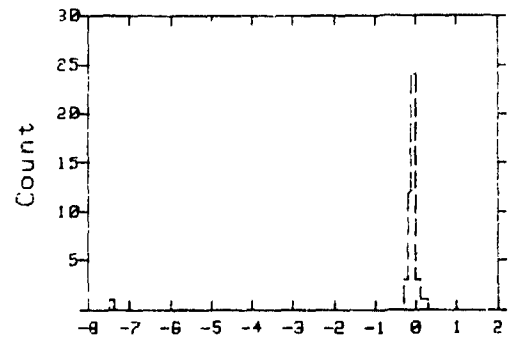

Fig. 4. Difference between post-implant threshold voltages on two monitors having different-sized charge-collection electrodes. No "antenna effect" is evident.

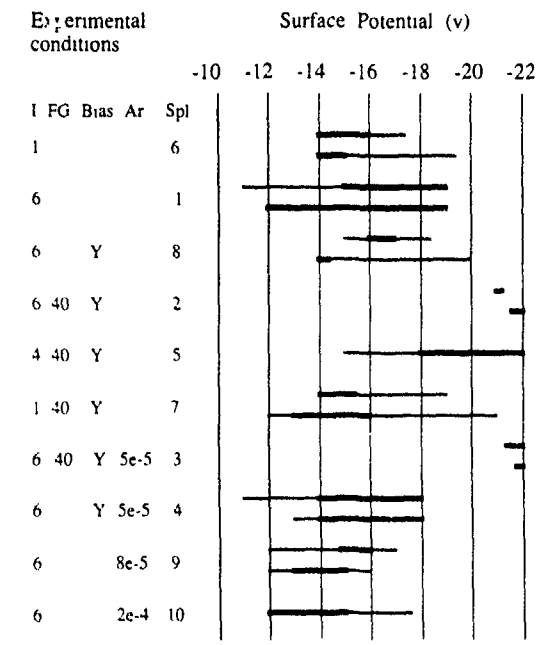

Fig 5 Summary of negative charging results for this experiment

magnitude of the surface voltage obtained in this manner is probably somewhat less than the true value, because the time that the monitor is exposed to the electron cloud is less than the 100 ms programming time used to obtain fig 2. However, in the absence of additional knowledge about the duration of the electron-cloud pulse, except that it probably is longer than 2 ms [5,8], fig. 3 may be used to infer that the absolute error is not greater than 5 V Since it is probably safe to assume that the duration of the electron-cloud pulse is not drastically different for the different implant conditions examined in this experiment, the relative error in fig 5 should be considerably less

Several additional comments are appropriate with regard to the summary of results shown in fig 5. Each of the bar graphs represents the results obtained on a single wafer, and consists of a heavy line which indicates the range containing the main distribution, typically embracing 80–95% of the data, and a thin line which shows the spread of the rest of the data Even though some of the data were far removed from the main distribution, no data was excluded in this presentation. Furthermore, data showing broad distributions was wafer-mapped. Very similar contours were observed in all cases.

5. Discussion of experimental results

Keeping in mind that in its present configuration the CHARM monitor is a fast, last-toggle, peak voltage sensor, many of the results shown in fig. 5 are consistent with expectations. For example, comparison of splits 6 and 1 shows increased charging with increasing beam current, while comparison of splits 6 and 7 indicates that, at 1 mA beam current, the beam does not pick up enough flood-gun electrons to substantially affect negative surface charging. Comparison of split 7 with splits 5 and 2, on the other hand, shows that as the beam current is increased, the number of flood-gun electrons carried to the wafer surface increases, as evidenced by increased negative charging. Given this observation, it might be suspected that eliminating flood-gun electrons should reduce negative charging. This is supported by comparison of split 2 with splits 1 and 8.

From the viewpoint of wafer throughput and survival during high-current arsenic implants, the results obtained with argon backfill are the most interesting. As splits 4, 9 and 10 indicate, increasing the argon pressure decreases the amount of negative charging. Split 3, however, indicates that flood gun electrons can easily override this benefit. Given the results of Doherty and McCarron [4], that the positive charging voltage also decreases with increasing background pressure, these observations suggest the use of argon backfill to control both negative and positive wafer charging without the use of flood guns.

6. Summary

Although the last-toggle characteristic of the present CHARM monitor does not permit independent measurement of both positive and negative charging pulses experienced by devices undergoing ion implantation, its application in this experiment suggests that future configurations, modified to permit this, might prove very useful in the study of wafer-surface charging phenomena. Moreover, the technique permits wafer mapping of surface potential, and the wafers are reusable. Finally, incorporation of reference devices to monitor the magnitude of radiative processes removes any doubt regarding the validity of the threshold shifts measurements on the monitor devices, ensuring correct, quantitative measurements of wafer surface potential

Experimental data obtained in a variety of ion-implant experiments have consistently failed to support the current source model responsible for the "antenna effect". All experimental data collected so far indicate a local equilibration of surface potential, supporting the voltage source model, although process-dependent, across-the-wafer gradients of surface potential have been frequently observed. The surface-potential wafer maps are similar to yield patterns observed on product wafers [10]. The conspicuous absence of the "antenna effect" raises serious questions regarding the use of polysilicon capacitors with different-sized field oxide capacitors for

the purpose of determining design guidelines intended to eliminate yield loss resulting from damage attributed to wafer-surface charging during ion implantation.

Generalizing the quantitative results of this experiment, summarized in fig. 5, it appears that the best arsenic implant results have been obtained without the use of electron flood, but, rather, with the use of argon backfill. The magnitudes of negative charging obtained at a beam current of 6 mA with argon backfill were lower than those obtained at 1 mA without argon backfill.

References

[1] R Tong and P McNally, Nucl. Instr and Meth B6 (1985) 376
[2] C.P. Wu, F Kolondra and R. Hesser, RCA Review 44 (1983) 48
[3] S.B. Felch, L A. Larson, M I Current and D W. Lindsey, Nucl. Instr. and Meth. B37/38 (1989) 563
[4] B J Doherty and D J McCarron, Nucl Instr. and Meth B37/38 (1989) 559
[5] V. Benveniste, H.E Friedman, M.E. Mack and F Sinclair, Nucl. Instr. and Meth. B37/38 (1989) 568.
[6] Y. Yoshida, R. Shirota and K. Azumi, Proc Symp. on Dry Processes, vol 88-7 (Electrochemical Society) p. 110.
[7] A. Kolodny, S T K. Nieh, B Eitan and J. Shapir, IEEE Trans. Electron Devices ED-33 (1986) 835
[8] M E. Mack, Nucl. Instr. and Meth B37/38 (1989) 472
[9] A. McCarthy, Ph.D dissertation, Stanford University (1990)
[10] Ion Implant Services, private information

Nuclear Instruments and Methods in Physics Research B55 (1991) 148–153
North-Holland

Gauge-capability study of ion-implant monitors

W.H. Johnson and W.A. Keenan

Prometrix Corp., 3255 Scott Blvd., Bldg 6, Santa Clara, CA 95054, USA

T. Wetteroth

Motorola Corp BTC, 2200 West Broadway, Mesa, AZ 85202, USA

The ability to control a process is determined by the variability of the process and the variability of the system used to monitor the process. The monitoring system consists of the monitor wafer, the operator, the environment and the test system (gauge) The monitor wafer can be sensitive to short-term and long-term drift, post processing and temperature This decouples the monitoring system from the process and simplifies the control problem. A gauge-capability study helps establish the repeatability (tester variability) and reproducibility (operator variability) of the monitoring system A gauge study was conducted on five sets of production ion implant monitor wafers ranging from 26 to 3000 Ω/□ Ten wafers were available for each implant These were manually measured twice by three operators and twice by an automated wafer handling system. The results were analyzed with respect to operator training and attention, automated wafer handling, probe performance and qualification, temperature variation and the range of sheet resistance of the monitors To adequately control the implant process, the ratio of total repeatability and reproducibility (precision) to the process (tolerance) specification should be less than 0 1 (P/T ratio) This can be achieved with good equipment that is well maintained, dedicated and adequately trained operators, and well controlled fab temperature or temperature compensation

1. Introduction

With increased emphasis on quality improvement and Statistical Process Control (SPC), it is becoming more important to isolate process and measurement variations It is clear that mere process control is no longer sufficient to compete in the world market a process or product must be continually improved to survive This requires knowledge of the process variation and the components that affect this variation All measurement equipment exhibits some variation. Using the best test methods available, the measurement variability often accounts for between 30% and 80% of the total variation [1] Motorola and other companies have set a target of 10% or less as the maximum variability due to the gauge (monitor, operator, environment and measurement tool) [2,3]. This variation becomes part of the overall process evaluation Proper calibration can usually compensate for systematic variation or bias; however, nonsystematic error will show up as noise and can obscure the interpretation of the data. Before any meaningful process-capability study can be attempted, a gauge evaluation must be performed [2,3].

The nonsystematic variations can be broken down into three categories: repeatability, reproducibility and stability. Repeatability is the variation obtained from a single operator using a single gauge to measure the same wafer Reproducibility is the variation of the averages of different operators measuring the same wafer with the same gauge. And stability is the variation of measurements taken at different times by the same gauge on the same part

To estimate the measurement equipment variation, a gauge study was conducted on five sets of production ion-implant monitor wafers ranging from 26 to 3000 Ω/□ The process conditions are listed in table 1 Ten wafers were measured for each implant. These were measured manually twice by three operators and twice by an automated wafer handling system. The results were analyzed with respect to operator training and attention, automated wafer handling, probe performance and qualification, temperature variation and the

Table 1
Process conditions

Set	Species	Dose	Energy [keV]	Spec R_s
A	Boron	1.3×10^{14}	60	520
F	Arsenic	5.0×10^{15}	60	25 9
Q	Phosphorus	5.0×10^{14}	100	145 4
R	Boron	2.2×10^{13}	100	2487
U	Phosphorus	5.0×10^{12}	120	2655

0168-583X/91/$03.50 © 1991 – Elsevier Science Publishers B V. (North-Holland)

range of sheet resistance of the monitors. An attempt was made to systematically eliminate or minimize the sources of error or noise.

2. Procedure

The study was done in three parts. The first part was a traditional gauge capability study [4] using three operators. The second part used an auto-handler [5] to eliminate errors caused by manual wafer placement and orientation. The third part consisted of determining (and eliminating or reducing) sources of error in the measurements on the most difficult wafers and then repeating the gauge study using the automated wafer handler.

The procedure for part 1 required three operators to measure five sets of ion-implant monitors twice. Table 2 shows the results of implant monitor set A. Gauge repeatability and reproducibility were calculated using the formulae listed in the table. It was noticed that operator No. 2 continually produced the highest variation. After observing the operator it became apparent he was paying less attention to positioning the wafer on the tester stage and allowed too much time to elapse between processing successive wafers. Additional training and encouragement reduced his significantly higher variation.

Table 3 summarizes the gauge capability results of all five sets of wafers. Two sets did not pass the desired P/T ratio limit of 0.10, so an effort was made to isolate the source of variation. Because set U gave the largest variation, it became the focus for isolating the variation.

The first step was to check for any drift in the electronics. A 2794 Ω/□ calibrated resistor network (four-point-probe simulator) was used to check the ac-

Table 2
Repeatability and reproducibility analysis results for a 1.3×10^{14} ions/cm^2, 60 keV boron ion implant

GAUGE: OmniMap Model RS50 Target Rs = 520 Ohm/sq Coeff. of
USL = 559 Variation of
PART NAME: MONITOR SET A LSL = 481 SPEC = 2.5 %
CHARACTERISTIC: SHEET RESISTANCE TOTAL TOLERANCE: >> 78 << TT
(6 sigma) or Total Tolerance (=> 1 Sigma = TT/6)

	OPERATOR 1			OPERATOR 2			OPERATOR 3		
ID	FIRST MEAS	SECOND MEAS	Difference (D)	FIRST MEAS	SECOND MEAS	Difference (D)	FIRST MEAS	SECOND MEAS	Difference (D)
1	528.4	528.1	0.3	528.5	528.4	0.1	528.1	528.1	0.0
2	540.8	540.6	0.2	540.7	540.6	0.1	540.5	540.6	0.1
3	527.2	527.3	0.1	527.3	527.2	0.1	527.0	527.0	0.0
4	569.1	569.3	0.2	568.3	568.5	0.2	568.9	569.0	0.1
5	531.5	531.7	0.2	531.5	531.9	0.4	531.1	531.1	0.0
6	554.4	554.6	0.2	554.3	555.3	1.0	553.6	553.6	0.0
7	547.4	547.1	0.3	547.3	547.3	0.0	546.7	546.8	0.1
8	526.2	526.2	0.0	526.1	525.9	0.2	525.7	525.6	0.1
9	549.9	549.8	0.1	550.0	549.9	0.1	549.7	549.2	0.5
10	529.3	529.1	0.2	529.3	528.8	0.5	528.7	528.9	0.2
	X_{11}= 540.4	X_{12}=540.4	R_1=0.2	X_{21}=540.3	X_{22}=540.4	R_2=0.3	X_{31}=540.0	X_{32}=540.0	R_3=0.1
	[1] X_1=540.4			[2] X_2=540.4			[3] X_3=540.0		

[4] $R_l = (R_1+R_2+R_3)/3$=0.2
[5] $R_x = X_h - X_l$ =0.4
[6] $[(Sigma)T]^2$=0.026
[7] $[(Sigma)D]^2 = \{[(1/d2)D * R_x]^2 - [(Sigma)T]^2/n*r\}$=0.045
[8] SQRT [[6] + [7]] =0.27 << (Sigma)e
(1/d2)T =0.862 <- [(one gauge X 10 parts) => A=10] and [(meas. 2X) => B=2]
(1/d2)D =0.524 <- [A=1 and (no. of appraisers) B=2]; n=10, r=2
[9] 6*[8]/TT=0.02 << P/T Ratio
Avg =540.3
[(Sigma)e/Avg] x 100% =0.05%

Table 3
Summary of gauge capability results for various implant conditions

Set	LSL	Target	USL	Coeff. of var. [%]	Total tolerance	P/T ratio [a]			
						1st	2nd	3rd	4th
A	481	520	559	2 5	78	0.02			
F	24	25 9	27 8	2.5	3.8	0 07			
Q	134 5	145.4	156.3	2 5	21.8	0 01			
R	2300	2487	2673	2 5	373	0.16	0.09		
U	2456	2655	2854	2.5	398	0 97	0.50	0 09	0.10

[a] 1st three operators.
2nd: C2C cassette to cassette auto-handler.
3rd: C2C with minimum temperature shift between successive tests.
4th C2C with sheet resistance values corrected for temperature shifts.

curacy for several days. There was no deviation (SD) from the certified value (within the five digits reported). This indicated that the level of noise or variation due to the electronics at this current and voltage range were negligible. To investigate the effect of various currents on the wafer, ten measurements at seven currents around the selected current were made on wafer 8 from set U without moving the wafer or probe The resultant mean sheet resistance and standard deviations are plotted in fig. 1. This plot indicates that a current of 10 μA gave an acceptable standard deviation without changing the sheet resistance. The drop in sheet resistance at 100 μA is attributed to substrate leakage, which increases with increasing current. The increase in sheet resistance at 500 μA is believed to be caused by joule heating.

Much greater noise (SD) was experienced measuring set U than the equivalent resistor network (2794 Ω/□) is most likely due to the contact resistance.

The next step was to check the short term repeatability on different type probes with a probe qualification routine [6]. Fig. 2 plots the mean and standard deviation versus probe tip radius on wafer 8 of set U. As is normally observed for high resistivity layers, the mean increased and the standard deviation decreased as the

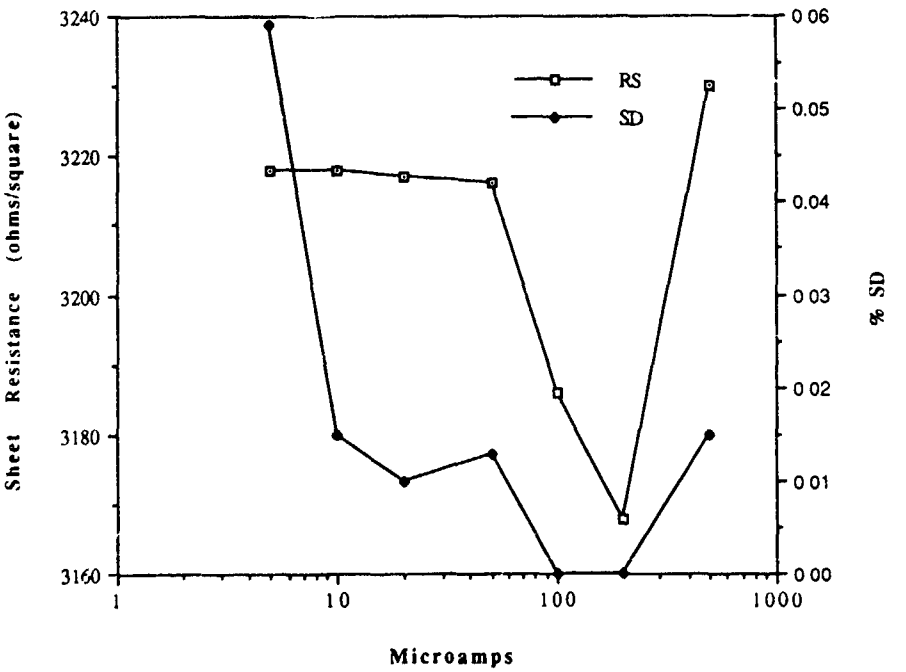

Fig. 1 Sheet resistance and standard deviation for a 5×10^{12} ions/cm^2, 120 keV phosphorus ion implant as a function of measurement current.

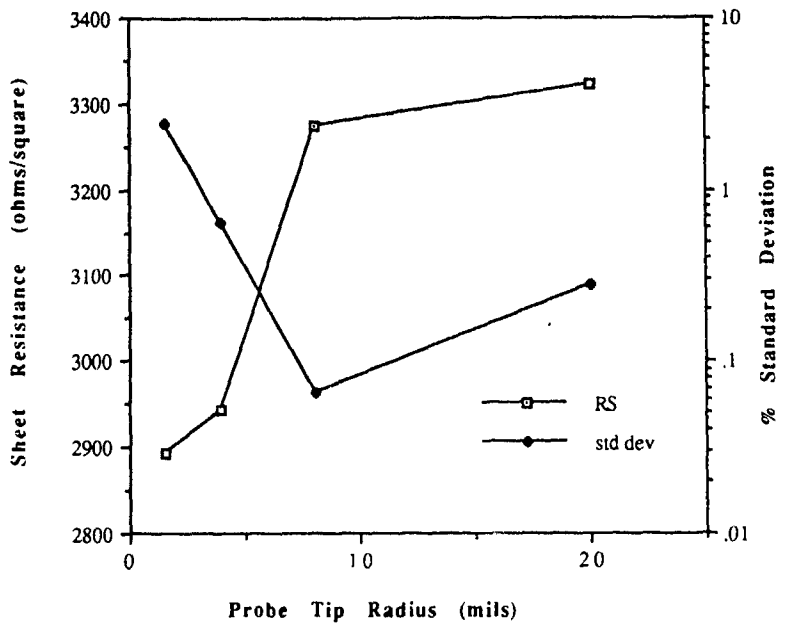

Fig 2 Sheet resistance and standard deviation as a function of probe tip radius for a 5×10^{12} ions/cm^2, 120 keV phosphorus ion implant

probe tip radius increased. The best probe was a Prometrix type C with an 8 mil tip radius of tungsten carbide with 40 mil tip spacing, and 100 g loading The standard deviation of groups of five measurements were all less than the acceptable upper limit of 0.2%. Therefore the noise component due to probe contact repeatability was estimated to be less than 0 2% Fig. 3 shows the maps using the optimum 8 mil probe and the less than optimum 1.6 mil probe. The loss of definition in the map reflects the increased variability caused by the inconsistent probe contact as indicated in the probe qualification tests

In the second part of this study, the wafers were remeasured using an automatic wafer handler to minimize the error caused by misplacement of the wafer on the stage. Based on the contour map (fig. 3) the error would be substantial for low test-site densities. Variations approaching 2% can be seen in areas within 1/2 in of each other With the use of the auto-handler, set U produced a P/T ratio of 0 50. Although this was an

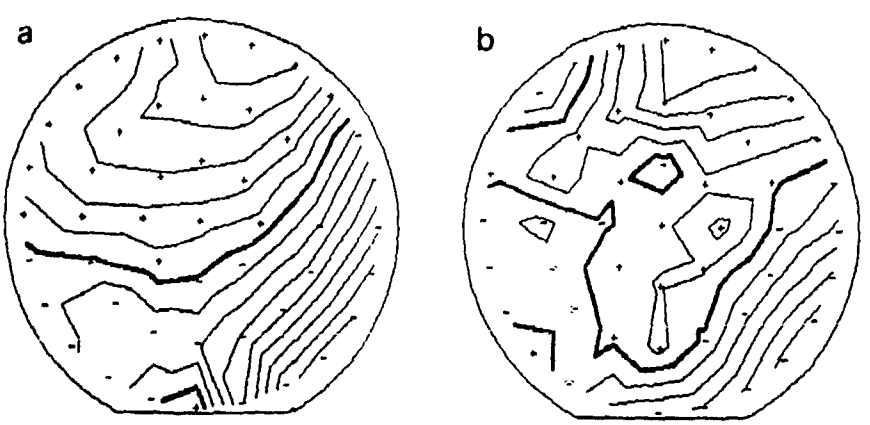

Fig. 3. Sheet-resistance contour maps for a correct and incorrect probe head for a 5×10^{12} ions/cm^2, 120 keV phosphorus ion implant. (a) Mean. 3292.1 Ω/□, standard deviation: 3 357%, contour interval· 1%, probe: 8 mil tip radius; (b) mean: 2856 4 Ω/□, standard deviation· 4.064%, contour interval. 2%, probe. 1 6 mil tip radius.

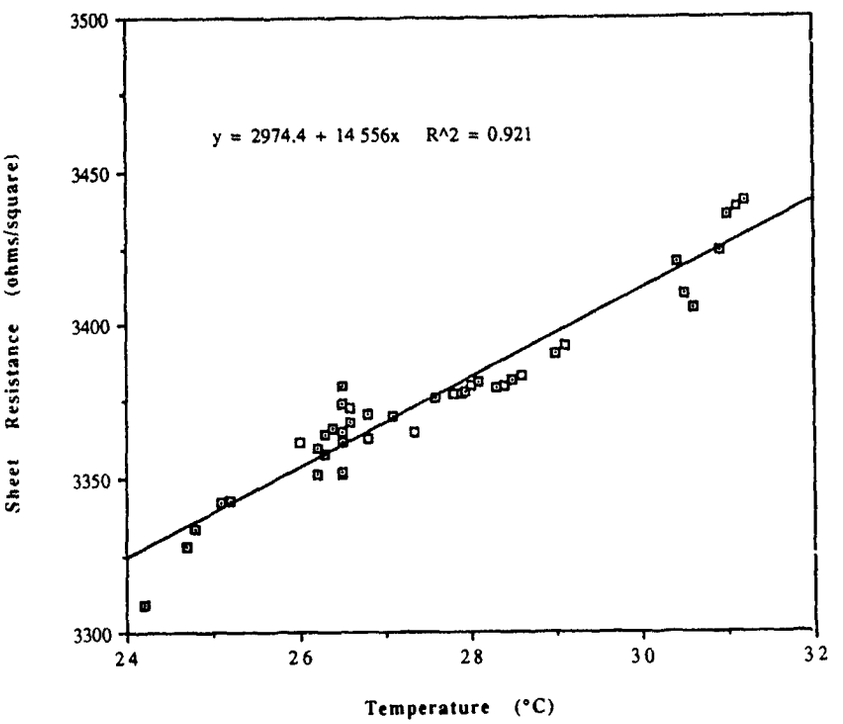

Fig 4 Sheet resistance as a function of temperature for a 5×10^{12} ions/cm^2, 120 keV phosphorus ion implant.

improvement it was a higher than desired or expected P/T ratio based on the probe qualification results.

Because these wafers had been measured at different times of the day (due to tool availability) environmental changes that occurred during the course of a day were investigated as probable causes of the variation. Temperature was found to be the major contributing factor. The test was then repeated in the evening when the temperature variation was minimal. This produced a P/T ratio of 0.09 for set U, which was deemed acceptable. Because in the normal operation it would not be desirable to wait for a specified temperature to measure a wafer, a temperature coefficient was investigated Sheet-resistance and temperature measurements were taken over a period where the temperature changed by 7 °C. The sheet resistance as a function of temperature (shown in fig. 4) indicates a temperature coefficient of 14.5 Ω/□/°C. With a normal temperature swing of 5 °C, this would correspond to a 2.7% sheet resistance shift for set U. Although the temperature variation in our facility is not nearly as well controlled as in a production fab, this could easily account for differences between testers in different locations or on the same instrument between different shifts. Our results would be expected to be worst case for this sample because of the wide temperature swing. Results for higher-resistivity samples would be even worse

3. Conclusion

Gauge capability plays a major role in statistical process control, and there is need to reduce any variation from a gauge to less then 10% of the total acceptable tolerance or specification. It was shown that, for the tested processes, this is possible only with close attention paid to the many variables that affect the measurement. For the most difficult process tested 5×10^{12} phosphorus at 120 keV) the P/T ratio was reduced from 97% of the total tolerance to less than 10% by eliminating placement errors and temperature effects and by optimizing the measurement parameters. It was shown that using an inappropriate probe head or significant deviations in operating parameters can cause considerable shifts in the average sheet resistance (bias) as well as nonsystematic errors (noise).

Although operator training had a slight effect on the gauge capability with regard to wafer placement, temperature changes were found to have the most profound effect on the gauge-capability results. The effect of

temperature was found to be greater with the higher-sheet-resistivity wafers, as would be expected, due to the increased dependence of mobility on temperature at lower concentrations. Although more work needs to be done in this area, this study indicates that for a given implant where the temperature coefficient has been sufficiently charaterized, it is possible to correct the sheet resistance for temperature changes.

One word of caution in any gauge study: "Practice the process you preach". Because of time constraints and wide fluctuations in temperature, we reduced the number of test sites from a full 81 or 121 to 5 or 9. However, this introduced additional sensitivity to wafer placement and orientation. If you monitor 81 sites, then use 81 sites for your gauge study and answer the question "How much of your process window is consumed by your gauge (monitor, operator and tester)?".

Reference

[1] C G. Pfeifer, SPC in the Process Industries, Quality (December 1988) p. 38.
[2] SPC-A Motorola Commitment, A Six Sigma Mandate, BR392/D (Motorola Corporation) p. 14.
[3] GMC-1693 Statistical Process Control Manual (General Motors Corp., Warren, MI, Aug 1986)
[4] J.T. Luftig, Guidelines for a Practical Approach to Gauge Capability Analysis, SQC course given to Ford Motor Co., October 1984.
[5] C2C cassette-to-cassette wafer handler, Prometrix Corp
[6] W.A. Keenan, W. Johnson and A K Smith, Production Monitoring of 200 mm Wafer Processing, Emerging Semiconductor Technology ASTM STD 960, eds D.C Gupta and P H Langer, (American Society for Testing Materials, 1986)

Nuclear Instruments and Methods in Physics Research B55 (1991) 154–159
North-Holland

Maximization of DRAM yield by control of surface charge and particle addition during high dose implantation

J. Horvath
Texas Instruments, 13353 Floyd Road, Dallas, TX 75285, USA

S. Moffatt
Applied Materials, 3050 Bowers Ave, Santa Clara, CA 95054, USA

Ion implantation processing exposes semiconductor devices to an energetic ion beam in order to deposit dopant ions in shallow layers In addition to this primary process, foreign materials are deposited as particles and surface films The deposition of particles is a major cause of IC yield loss and becomes even more significant as device dimensions are decreased Control of particle addition in a high-volume production environment requires procedures to limit beamline and endstation sources, control of particle transport, cleaning procedures and a well grounded preventative maintenance philosophy Control of surface charge by optimization of the ion beam and electron shower conditions and measurement with a real-time charge sensor has been effective in improving the yield of NMOS and CMOS DRAMs Control of surface voltages to a range between 0 and −20 V was correlated with good implant yield with PI9200 implanters for p^+ and n^+ source-drain implants

1. Introduction

Ion implantation is used almost exclusively for the planar doping of silicon in DRAM production We note that IC manufacturing is currently operating in the era of the 1 Mbit and 4 Mbit DRAM. The typical number of implant process steps has risen with generation, increasing from about 8 at 256 Kbit to approximately 15 at 4 Mbit and up to 22 at 16 Mbit Critical dimensions have decreased significantly over these generations and in general gate oxide thicknesses have decreased. All these subjects will be carefully covered by many papers in this conference

We have studied experimentally the actual effects of both surface charging and particle addition during the era of 256 Kbit and the transition to 1 Mbit We have learned some important facts relevant to implant processing as we enter the 16, 64 and 256 Mbit eras. We suggest a methodology to optimize yield based on a simple evaluation of particle addition and surface charge voltage.

In order to construct our model, we need to consider the principle circuit factors which drive yield at implant steps, namely:

(1) Oxide thickness (decreasing).
(2) Charge collector surface, area, geometry, etc. (decreasing).
(3) C_D feature size, mask opening size, etc (decreasing).
(4) Number of steps (increasing).

We expected, therefore, in our experimental investigations to see an increasing sensitivity in the particle addition density and surface voltage with time and this was indeed the case. This paper explains how with correct preventative maintenance of equipment and real-time diagnostics the particle addition and charging voltage was controlled to obtain yield maximization for a 1 Mbit DRAM, based on experience gained with the 256 Kbit DRAM. Initial checks of over 15 observables showed the key control parameters to be:

(1) Measured surface voltage.
(2) Measured surface particle density.
(3) Monitored preventative maintenance activity for implanters.

2. Experimental details

Two PI9200 ion implanters were used; these were fitted with real-time charge sensors (shown in fig. 1) as described in another paper presented at this conference [1]. Particle counts from monitor wafers were obtained at 0.5 μm and 1.0 μm using an Aeronca WIS 150, by a pre-implant measurement, a post-implant measurement and calculating the differences. Particle measurement wafers were included inside each product wafer lot to get a realistic and actual particle count in the presence of photoresist masks, previously deposited particles, etc. Before and after measurements were used with a edge exclusion of 7 mm. One further PI9200 implanter was fitted with a real-time particle monitor [2] to investigate

0168-583X/91/$03.50 © 1991 – Elsevier Science Publishers B.V (North-Holland)

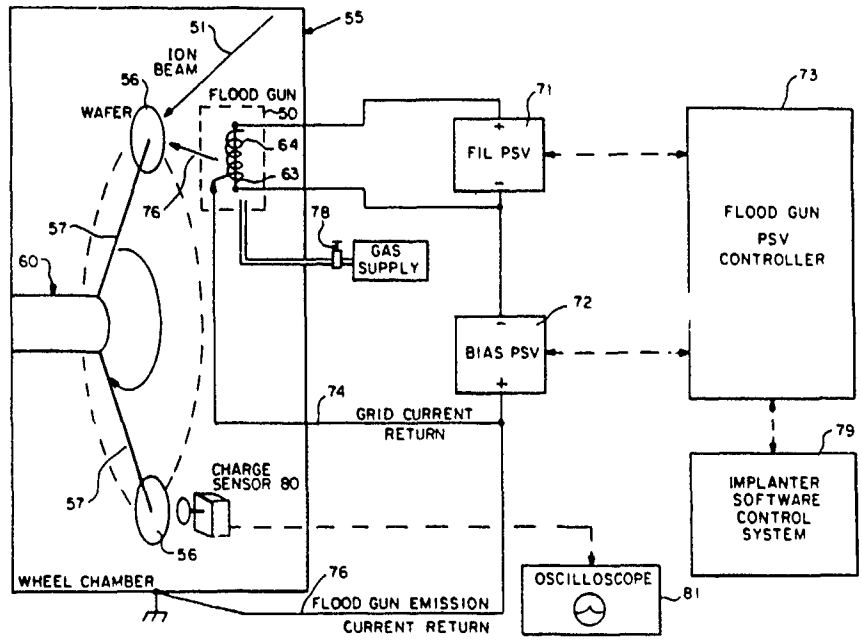

Fig 1 Schematic of charge control system showing capacitive charge sensor and associated electronics

cleaning techniques to control particle addition within defined limits.

We used standard 256 Kbit and 1 Mbit DRAM product wafers and performed designed experiments to establish the optimum charge neutralization. The charge neutralization system, fitted to the implanter, consists of a primary electron space-charge limited diode flood gun of the type invented by Renau et al. [3] In this case, inert gas is introduced into the inter-anode/cathode gap to reduce primary electron energy to between 1 to 15 V

The two PI9200 implanters (A and B) were compared in these experiments with a third implanter (C) from the perspective of an independent control A further implanter (D) (PI9200) was used to perform particulate cleaning tasks

3. Results

Preliminary experiments showed that the n^+ source drain implant performed on the 256 Kbit DRAM had the major implant sensitivity. This is because it is both the highest dose and it inflicts the greatest voltage/time stress on the gate oxide. From this experience the n^+ and p^+ source-drain implants for 1 Mbit were chosen as "test vehicles" for the optimizing process. These are the highest current, highest dose implants in the majority of CMOS designs.

Fig 2 shows the particle counts obtained by the particle measurement loop for the 256K n^+ SD, 1M n^+ SD and 1M p^+ SD The data points are mixed together as the various processes were run sequentially on the two implanters but the combined mean level for implanter A was approximately 4 9 particles added per 150 mm wafer at > 1 μm. Average of > 0.5 μm was 11 particles added. It is important to distinguish these numbers as production values with the implants in the presence of photoresist masks

The simple result was that no sensitivity to particle levels below 30 particles at 0.5 μm was found for either implanter. Above that level some yield losses were measurable at the 60 particle level. A direct increase of bit zero failure is seen above 30 particles Below 30 no improvement was measured.

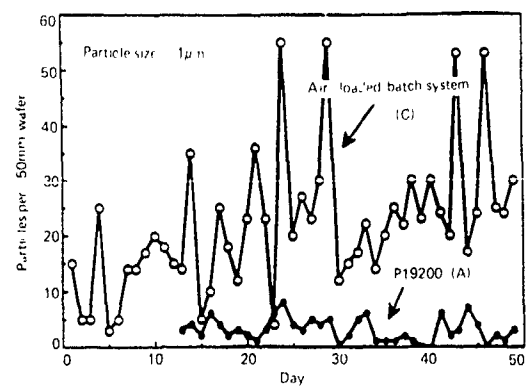

Fig 2 Particle additions on implanters A and C.

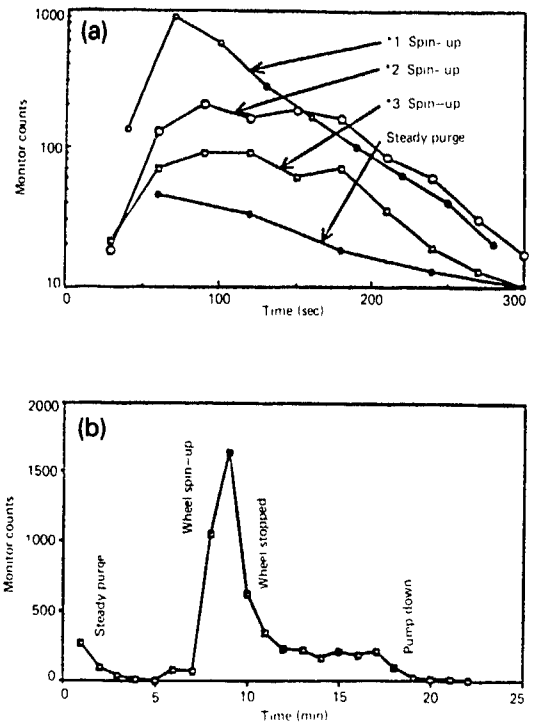

Fig 3 Multiple spin cleans ensure low particle levels of implanter

The high peak values of particle counts (shown in fig. 2) consisted of implants that occurred immediately following the implanter servicing by venting the endstation to air The occurs infrequently because the processing chamber is normally at vacuum (the 9200 implanters, A and B, are loaded by vacuum loadlock). Vacuum loading generally is capable of lower particle additions, note the direct comparison of implanter C an

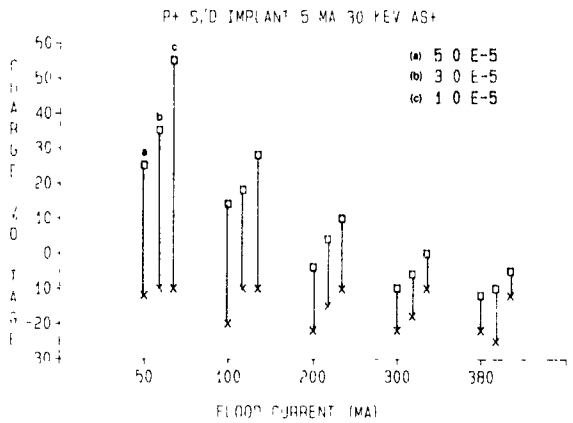

Fig. 4. Charge sensor voltage range as a function of flood emission for P^+ SD

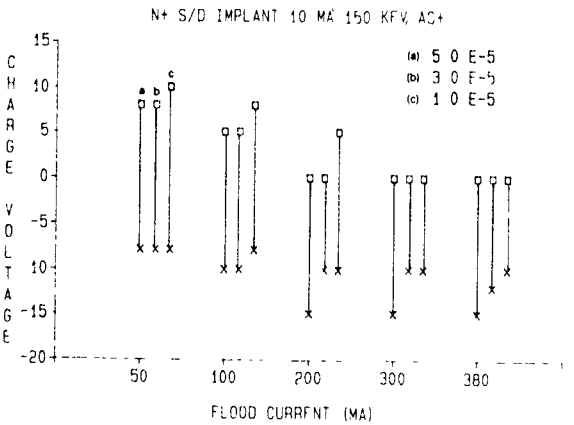

Fig 5 Charge sensor voltage range as a function of flood emission for n^+ SD

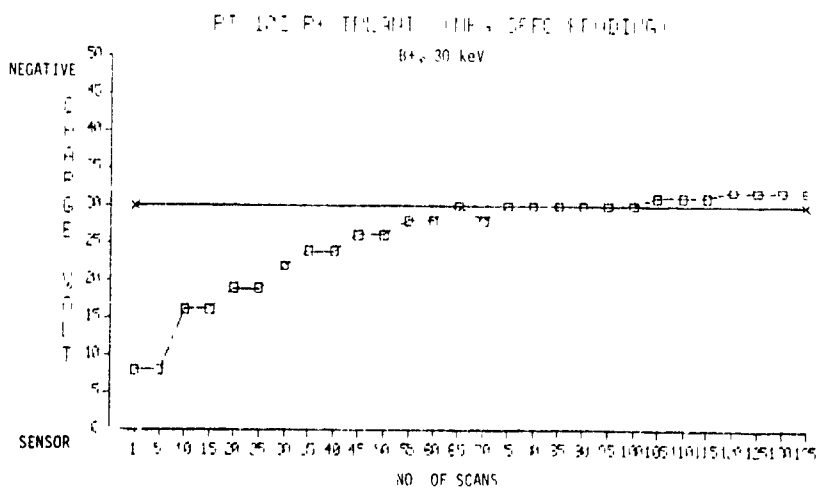

Fig. 6. Charge sensor voltage shown as a function of dose (increasing scans)

air loaded system, which is exposed to venting after each implant.

The high particle levels, after backfilling implanter A endstation, were entirely eliminated by conditioning the post-acceleration to avoid arcing and by spin cleaning the endstation by purging dry N_2 at a pressure of 400 mbar and spinning the wheel at 800 rpm. The effectiveness of this process is shown in fig. 3. We obtained the clean up completion by using a real-time particle detector in the vacuum chamber [2].

The surface potential that was measured on the 1 MBit DRAM wafers for the n^+ and p^+ source-drain implants is shown in figs. 4 and 5. Over the whole emission and gas pressure range it can easily be observed that the range of surface voltage (maximum to minimum) that occurs during mechanical scanning is reduced as the electron flood emission is increased. Also the overall mean value of surface potential shifts more negative with increasing electron flood emission; this is the same characteristic seen with many charge neutralization systems [4], and the quantification of this parameter was found to be very important in this work. As the high dose implant progresses, the endstation pressure, photoresist conductivity and other parameters vary and the measured surface potential changes.

Fig. 6 shows the extreme negative value of charge sensor potential which initially shows approximately -10 V for 50 mA for 3×10^{-5} mbar pressure. As the number of scans increases, the negative potential increases. Eventually, after a dose of about $1 \times 10^{15}\,cm^{-2}$, an equilibrium value is achieved.

We established a manufacturing specification (demonstrated here by the 30 V line). A similar pattern of curves was established for both implants By analyzing the IC yield results the normalized yield for the n^+ process was constructed (fig. 7) as a function of the limit of the negative potential maximum. Negative potentials in excess of -12 V decrease yield for the n^+ implant and a -30 V limit was established similarly for the p^+ process (fig. 6).

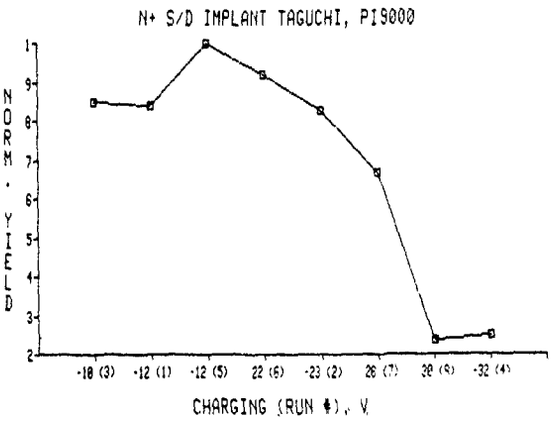

Fig 7 Normalized third yield versus charging for n^+ SD

These negative limits are understood to be the maximum allowed values to avoid significant gate oxide stress. Another technique sometimes used to quantify this limit is the gate oxide integrity test circuit constructed on special test wafers. We used such a test vehicle and could produce visible and measurable results with only very extreme cases. Fig. 8 shows a photograph demonstrating gross capacitor failure which was only obtained with zero flood on implanters A and B.

Over the entire range of electron emission, 50 to 400 mA, no damage to the gate oxide integrity circuit could be found, for either p^+ or n^+ source drain implants.

Fig. 8. Optical microscope photograph of gate oxide integrity test capacitor. The edge failure is clearly marked. It occurred with zero flood.

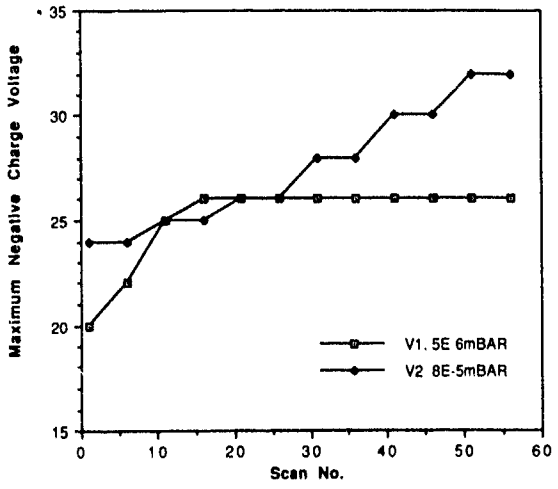

Fig. 9 Charge sensor voltage for high pressure and low pressure cases.

Only the p^+ source drain implant showed these failures without any flood gun emission. Looking at fig. 4 we see that a +50 V or greater potential probably occurs before it is sensed on this gate oxide monitor circuit. The charge sensor has at least one order of magnitude greater sensitivity, and the result is continuously available in real time.

We also found that the capacitive charge sensor was useful in detecting other yield influencing factors that previously were unnoticed. With increased pressure during implant, caused by photoresist outgassing during the first 5×10^{14} cm^{-2} part of the implant [5], the negative surface charge may be increased. Variations will occur in this outgassing, due to effectiveness of air bake, wait time, etc. We have shown that these variations cause significant changes in the negative charging of the wafer surface and this leads to increased I_{DD} device failures. Various other factors can lead to this increased pressure condition including cryo-pump failure, improperly baked photoresist, vacuum leaks, etc.

We noticed about −2 to −5 V increase in negative excursion for resist that had a noticeably greater outgassing characteristic (see fig. 9). In order to produce repeatable results we deliberately altered the pressure in the endstation during the whole implant. This shifted the negative surface voltage enough to cause very major yields loss as demonstrated by fig. 7. A theoretical model will be presented in a later publication by Moffatt and Horvath [6].

4. Conclusion

The use of quantitative techniques that measure: (1) wafer surface voltage on product wafer, and (2) particle addition to wafer added to production lot, can establish control limits in a very simple manner. By picking one or two of the most electrically stressful implants (source drain) and setting controls based on the yield impact curve, a rapid transition to new generation products can be made. We used the 256 Kbit to 1 Mbit DRAM to explain our methodology; it is generally applicable to increasingly complex and sensitive designs.

Table 1
The no-loss yield control values for charge and particle for 1 Mbit DRAM, and the first order yield impact if these limits are exceeded. The results were obtained for Taguchi matrix

Implant	Parameter	No-loss control level	Yield impact
n^+ SD	charge	−12 V	2.1% per volt
	particle	30 particles/ wafer	0.07% per particle per water
p^+ SD	charge	−30 V	5.0% per volt
	particle	30 particle/ wafer	0.07% per particle per wafer

Table 1 shows the control limits set and deviations measured with a five parameter designed (Taguchi) experiment. The control levels are fixed by the family of curves that we obtained in a similar manner to fig. 7. The no-loss control levels are the maximum negative charging voltage as measured by the charge sensor. These values, −30 V for p^+ source drain and −12 V for n^+ source drain, are the critical values. No positive excursion (> 0 V) is allowed. The yield impact caused by exceeding these values is 2.1%/V and 5.0%/V, respectively. Real manufacturing control levels were recommended well inside the safe region. If this parameter is not controlled or if gate oxide monitoring is used a ±50 V variation may easily occur due to wafer causes, machine malfunction or incorrect maintenance for any high current implanter.

In a similar way a particle control limit of 30 particles was established with a 0.07% per particle per wafer sensitivity. For implanters A and B this never happened when we followed the correct spin clean and high voltage conditioning maintenance procedure.

Acknowledgements

The authors would like to thank the staff of DMOS 4, Texas Instruments and Applied Materials, Santa Clara, CA for supporting this work. In particular we would like to thank Scott Edel for device measurements and very useful suggestions, and Babak Adibi for assistance in the charge neutralization work.

References

[1] M.T. Wauk, N.R White, B. Adibi, M.I Current and J.A Strain, these Proceedings (8th Int. Conf. on Ion Implantation Technology, Guildford, UK, 1990) Nucl Instr. and Meth. B55 (1991) 413.
[2] S. Leung, B Adibi, B Fishkin and P. McKinney, ibid., p. 35.
[3] T Renau, S. Moffatt and F Plumb, US Patent 4825087
[4] M. Mack, Nucl. Instr. and Meth B37/38 (1989) 472
[5] T C Smith, Ion Implantation Equipment and Techniques, Berchtesgaden, 1982, pp. 196–213
[6] S. Moffatt and J Horvath, in preparation

Nuclear Instruments and Methods in Physics Research B55 (1991) 160–165
North-Holland

Effects of molybdenum contamination resulting from BF_2 implantation

Alfredo Cubina
Intel Corporation, 250 North Mines Rd., Livermore, CA 94550, USA

Michael Frost
Intel Corporation, 3065 Bowers Ave, Santa Clara, CA 95051, USA

When molybdenum is utilized for the construction of arc chambers for ion implanters, the species $^{98}Mo^{2+}$ is co-implanted during $^{11}B^{19}F_2^+$ implantation, due to its coincident charge-to-mass ratio. The metal ions are generated as the fluorinated species in the source plasma react with the molybdenum arc chamber components The peak molybdenum concentration in the substrate, as measured by secondary ion mass spectrometry, increases with increasing source arc current for a given dose Molybdenum acts as a deep-level impurity, which significantly reduces bipolar transistor gain The diffusion of molybdenum in silicon is studied and its effect on solid state device performance is discussed Tantalum is suggested as an alternative source material

1. Introduction

Molybdenum concentrations as high as 2.3×10^{18} cm^{-3} (45 ppm) were detected in BF_2 implanted silicon wafers by secondary ion mass spectrometry (SIMS). We will show that this contamination occurs while using an implanter having molybdenum source arc chamber components. The doubly ionized species $^{98}Mo^{2+}$ has the same charge-to-mass ratio as the $^{11}B^{19}F_2^+$ molecular ion. As a result, the doubly ionized molybdenum ion is not filtered out by the mass analyzer magnet and the species is co-implanted. Part of this study will identify the ion source parameters that affect the molybdenum concentration in the substrate.

Molybdenum is known to be a strong minority carrier lifetime killer in silicon [1]. Its deep electrical level in the silicon bandgap of 0.31 eV above the valence band makes it a powerful recombination center [2]. Moreover, Mo has been characterized as a fast diffuser, with a diffusivity on the order of 10^{-8} cm^2/s at high temperatures [3]. This makes it a potentially dangerous contaminant, particularly in devices requiring long minority carrier lifetimes such as bipolar transistors and solar cells. We observed that the diffusion of molybdenum in the silicon substrate was strongly influenced by the residual implant damage. This phenomenon has been studied in detail by Tsai et al. [4].

The molybdenum contamination in the substrate can be reduced significantly by cladding the molybdenum components of the implanter source arc chamber with tantalum foil. A split lot experiment was designed around test device wafers implanted using the tantalum cladded source and a standard molybdenum source to understand the impact of the implanted metallic contamination. It was determined that the presence of molybdenum significantly reduced the current gain of both p–n–p and n–p–n parasitic bipolar transistors. This is consistent with the assessment that Mo is a minority carrier lifetime killer.

2. Experimental

The first part of this study consisted of identifying the presence of molybdenum in implanted wafers and understanding the dependence of its concentration on implanter parameters. Using an Eaton Nova NV10-80 high-current implanter, 100 mm phosphorus doped epitaxial silicon wafers with $\rho = 0.45$ Ω cm and $\langle 100 \rangle$ orientation were implanted with BF_2 at 80 keV with 8.0×10^{15} cm^{-2} dose. All implants were performed using a wafer tilt of 7°. A Nova White enhancement source with a molybdenum arc chamber was used. Wafers were implanted at source arc currents ranging from 0.5 to 2.0 A and arc voltage values of 90 and 120 V. All elemental depth profiles were obtained via SIMS analysis performed on a Riber MIQ156 ion microprobe. The instrumental conditions for all SIMS analyses were identical. An oxygen primary beam accelerated to 8 keV was used, with 100 nA of beam current and rastering the beam over a 1.5 mm × 1.5 mm area.

To understand the impact of the molybdenum contaminant on solid state devices, a split lot experiment was performed using an 80 keV, 4.0×10^{15} cm^{-2} BF_2 implant as the p-channel source/drain implant in a single well CMOS process. Three lots of 24 wafers were split between a standard 4.0 mA beam current implant

0168-583X/91/$03.50 © 1991 – Elsevier Science Publishers B.V. (North-Holland)

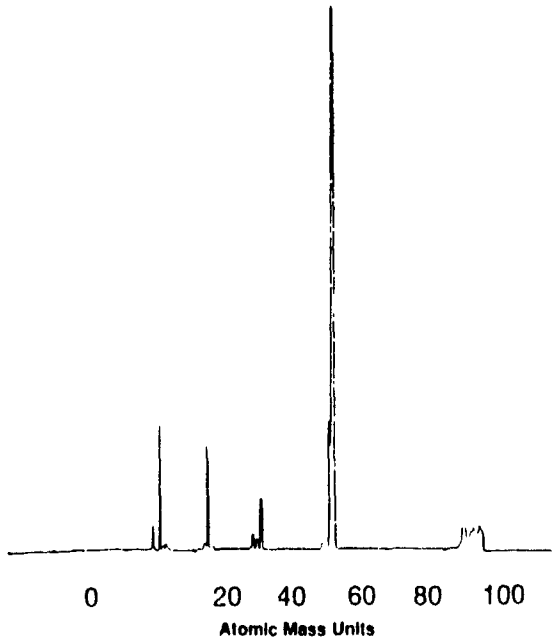

Fig 1. BF_3 feed gas mass spectrum. Arc current = 2 3 A, arc voltage = 90 V, 80 keV

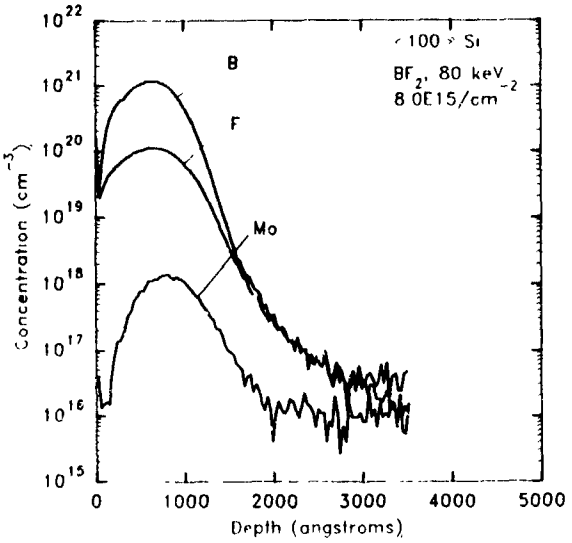

Fig. 2 As-implanted BF_2 SIMS profile

and a 1.0 mA implant with a source lined with tantalum foil to prevent molybdenum ion generation. Parametric electrical MOS and parasitic bipolar test structures were used and the electrical modulation due to the presence of molybdenum is discussed below.

3. Detection of Mo in the substrate

Molybdenum contamination was suspected to be in the BF_2 beam due to the presence of small peaks around 98 amu in the boron trifluoride spectrum. As shown in the beam mass spectrum shown in fig. 1, small peaks in the order of 10 μA are seen in the range where molybdenum occurs (92–100 amu). The most abundant molybdenum isotope is ^{98}Mo, with a natural abundance of 24% [5]. Most components of the Nova White source are constructed of molybdenum, suggesting a likely source of the metal ions. Initially, the presence of a doubly ionized molybdenum species could only be speculated since the intense $^{49}BF_2^+$ peak, which has an equal charge-to-mass ratio, was a direct interference in the spectrum.

To confirm the existence of the molybdenum in the implanted substrates, SIMS analysis was performed on implanted silicon wafers. Fig. 2 shows the as-implanted SIMS profile of the BF_2 implant, clearly indicating the presence of molybdenum.

Silicon wafers were implanted with BF_2^+ at different source arc currents and voltages. Peak molybdenum concentrations for each wafer were obtained by SIMS analysis. Table 1 summarizes the peak as-implanted molybdenum concentrations for each set of source conditions, and shows that an increase in the source arc potential did not cause an appreciable variation in the peak molybdenum concentration. Fig. 3 is a semi-log plot that reveals an exponential relationship between the peak as-implanted molybdenum concentration and the source arc current.

No singly or doubly ionized molybdenum ions were observed in an argon source plasma spectrum, inferring that the molybdenum ions are not generated merely by a plasma sputtering process. The suggested reaction that takes place within the source plasma is:

$$Mo + F_x \rightleftharpoons MoF_x.$$

A surface reaction appears to take place, proceeding via fluoride intermediates as F^- species react with the molybdenum metal from the arc chamber components producing a molybdenum fluoride compound. This compound gets dissociated in the source plasma, gener-

Table 1
Summary of SIMS data vs source parameters (BF_2^+, 80 keV, 8×10^{15} cm^{-2})

Arc current [A]	Arc voltage [V]	Peak molybdenum concentration [cm^{-3}]	Peak boron concentration [cm^{-3}]
0 5	90	$1\,2\times10^{17}$	$1\,0\times10^{21}$
1 0	90	$2\,9\times10^{17}$	$1\,1\times10^{21}$
1 5	90	1.1×10^{18}	$9\,0\times10^{20}$
2 0	90	$2\,3\times10^{18}$	1.2×10^{21}
2.0	120	$1\,2\times10^{18}$	$1\,2\times10^{21}$

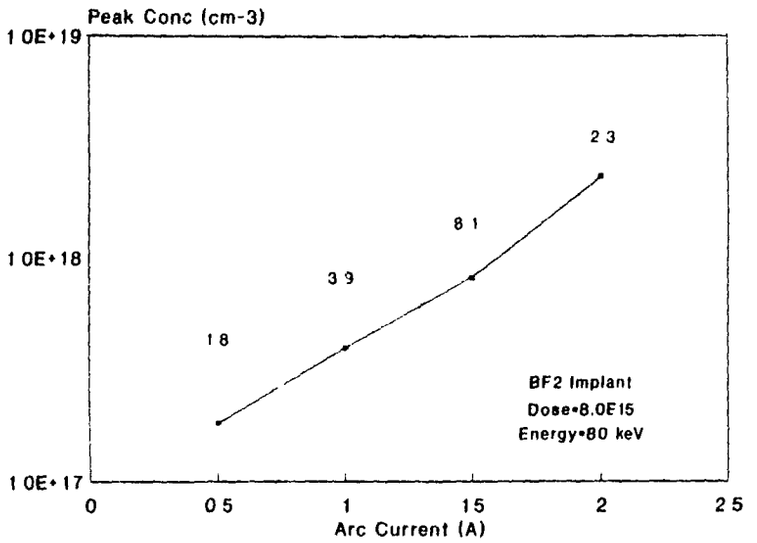

Fig 3 Peak molybdenum concentration vs arc current

ating the molybdenum ions Increasing the source arc current will increase the rate of ionization of the BF_3 feed gas components, producing a higher concentration of fluorine radicals In addition, the arc chamber temperature increases with increasing arc current As a result, the surface reaction rate increases and more molybdenum ions are created. The ratio of molybdenum to BF_2 ions in the beam appears to increase with increasing arc currents, which is confirmed by the reasonably consistent peak boron concentrations listed in table 1

4. Diffusion characteristics of Mo in Si

The phenomenon of Mo contamination is not reported in the literature. However, its distribution after an active anneal can be explained by previously published results. Others have shown how the defects that form during BF_2 implantation act to getter the F in the substrate during annealing [4,6]. Here, we see the gettering effect for both Mo and F.

The BF_2-implanted Si wafer was furnace annealed at 920 °C for 30 min. The resultant depth profile is shown in fig. 4, which compares the annealed elemental distributions with those before annealing. The implant dose (8.0×10^{15} cm^{-2}) creates a shallow amorphous layer After annealing, defect zones appear to be localized to three regions. These zones are believed to be due to the formation of the amorphous layer and damaged crystalline region during implantation [4]. While Mo and F are preferentially gettered to the defect zones, B does not appear to be affected. Note the narrowing of the distribution after annealing, which suggests that the crystal regrowth process and residual defects are not only prohibiting diffusion of Mo deeper into the Si, but also that the low-level Mo which had an implant range beyond the damaged regions is being gettered towards the surface, to the low-energy defect zone.

5. Electrical effects of Mo on devices

An experiment was performed to assess the electrical effects of the molybdenum contaminant on both parasitic bipolar and MOS devices. To get a BF_2 beam free of molybdenum contamination, the implanter source

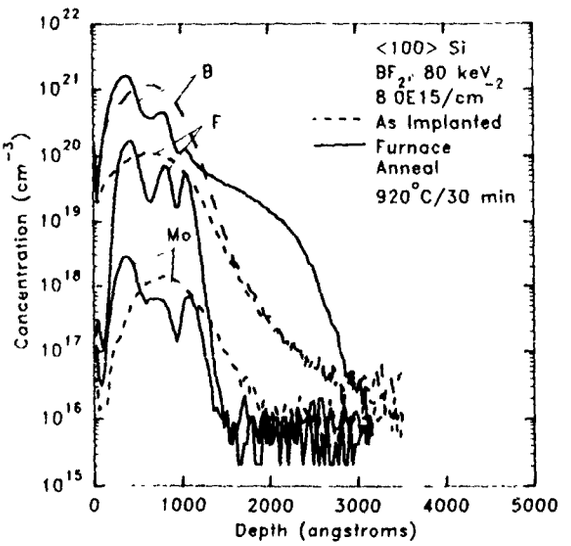

Fig. 4. BF_2-implanted SIMS profiles – furnace anneal.

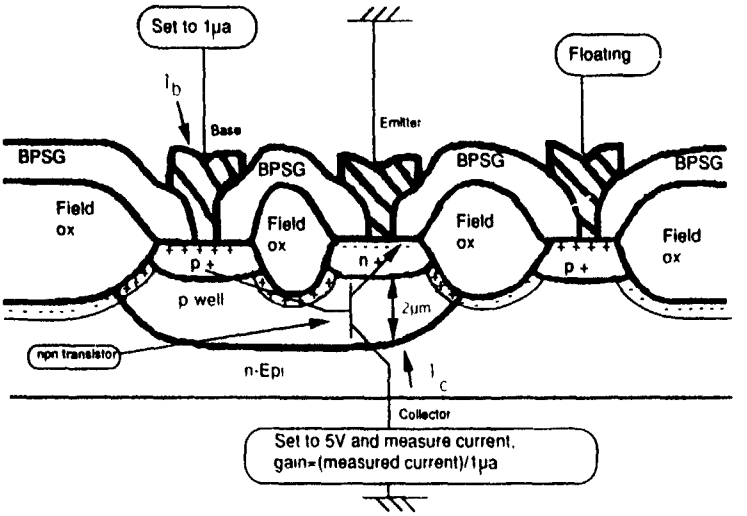

Fig. 5 n–p–n bipolar test structure

arc chamber was clad with tantalum foil. A source plasma arc and a 1.0 mA BF_2 beam were obtained with stable source parameters. An 80 keV, 8.0×10^{15} cm^{-2} beam was used to implant bare silicon wafers. SIMS analysis was performed on the sample and no molybdenum was detected above 1.0×10^{16} cm^{-3}

Three lots of 25 test structure wafers were split in half The first half of the set was implanted using the tantalum arc chamber to ensure a molybdenum-free beam. The BF_2 implant parameters were 4.0×10^{15} cm^{-2} dose, 80 keV energy, at 1.0 mA of beam current with 1.0 A of source arc current. The second half was implanted with the standard molybdenum arc chamber for the same energy and dose as the first half, but at 4.0 mA of BF_2 beam current with 1.5 A of source arc current. Based on SIMS data, the peak as-implanted molybdenum concentration should be in the low 10^{18} cm^{-3} range.

The 100 mm wafers contained diverse electrical test structures of both MOS and bipolar configuration. After processing, the wafers were tested on a Keithley S350 electrical testing system Different locations across each wafer were tested for the same type of device for a total of 495 test results per structure. Statistical analysis was performed for all devices and those that showed significant parametric modulation are discussed below

The parasitic bipolar devices shown in fig. 5 and 6 exhibited the greatest electrical modulation due to the

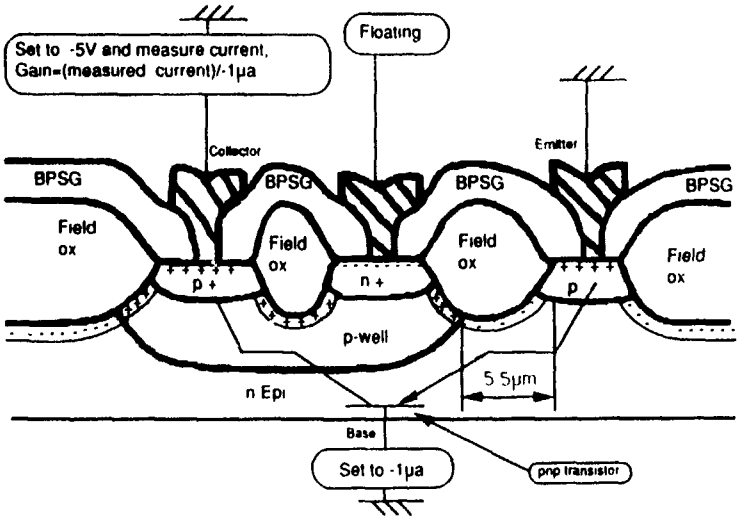

Fig. 6. p–n–p bipolar test structure.

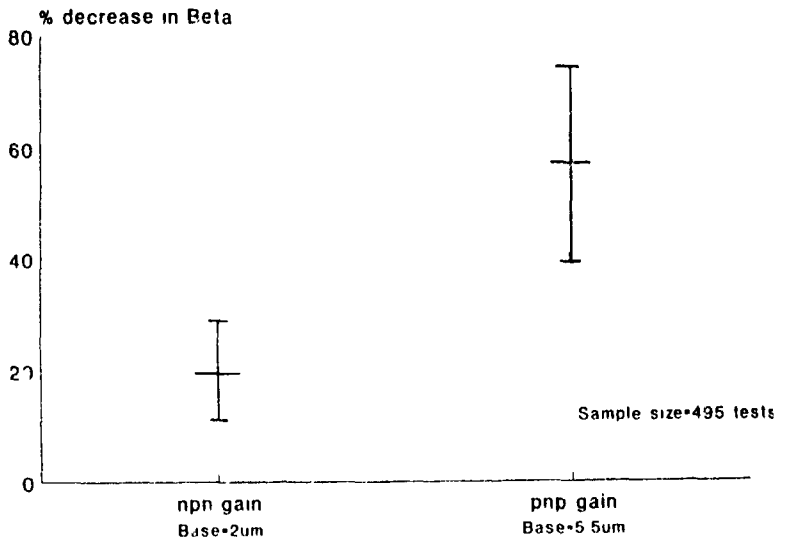

Fig. 7. Parasitic BJT (bipolar junction transistor) gain decrease due to molybdenum arc chamber (95% confidence intervals).

presence of molybdenum in the BF_2-implanted area. In all cases, the p^+ BF_2 implanted region corresponds to the 80 kV, 4.0×10^{15} cm^{-2} implant. A standard current gain (β) test was performed on both structures with electrical biasing as shown in the figures. For both devices, β was calculated as follows.

$$\beta = I_{collector}/I_{base},$$

where $I_{collector}$ is the current in the collector and I_{base} is the current in the base.

The n–p–n transistor shown in fig. 5 utilizes the boron implanted p-well region as the base, while the p^+ BF_2-implanted region serves as the base contact. The effective base length is approximately two microns. The mean β value for the devices implanted with the molybdenum source was 140. As seen in fig. 7, the mean β of the molybdenum contaminated devices was 19% lower than the devices implanted with the tantalum source.

The p–n–p device shown in fig. 6 has a 5.5 μm base residing in the n-epitaxial silicon layer. For this structure, the BF_2-implanted region serves as the p^+ emitter and also as the p^+ collector contact. The mean β value for the devices implanted with the molybdenum source was 0.20. Fig. 7 shows the 57% β reduction due to the presence of molybdenum in the p^+ regions.

For both parasitic bipolar devices the BF_2-implanted region has immediate proximity to the base. The decrease in β on the molybdenum-contaminated wafers is due to a decrease in collector current since the base current is fixed at 1 μA for both tests. A likely mechanism for this decrease in emitter–collector current is an increased concentration of recombination centers in the base. Molybdenum, as stated earlier, has been identified as a powerful minority carrier lifetime killer and is the likely source of these recombination centers. By outdiffusion from the p^+ region to the base region, molybdenum atoms increase the concentration of recombination centers, contributing to decreased minority carrier lifetimes in the base. Further proof of this model is the larger β reduction effect in the longer base device (5.5 μm vs 2 μm). With decreased lifetimes, more minority carriers will recombine in a longer base device before they reach the collector. As a result the magnitude of the current gain decrease is greater on the long base device.

The post-diffusion SIMS profiles (fig. 4) show the molybdenum distribution contained well within the boron profile. It is important to note that the SIMS instrument used in this experiment has a detection limit of approximately 1×10^{16} cm^{-3} for molybdenum in silicon. A significant amount of molybdenum has possibly diffused beyond the implant damage region and the junction depth. The diffusivity of molybdenum, known to be high in the absence of implant damage, suggest the penetration depth can be large, exceeding several microns. The electrical results from the bipolar tests suggest that this mechanism occurs. A recombination trap concentration as low as 10^{10}–10^{11} cm^{-3} in the base is sufficient to degrade transistor gain.

A practical solution to the molybdenum cross contamination problem is the use of different materials to build the source arc chamber. In addition, molybdenum parts should also be avoided around the extraction electrode assembly. The impinging beam is likely to sputter off and ionize molybdenum atoms from the electrode, which can easily incorporate into the beam.

Tantalum appears to be the best alternative due to its high atomic weight, resistant thermal properties, and ease of machining. The tantalum foil used in this experi-

ment was effective in eliminating the molybdenum contamination and sustained little damage after five hours of containing the source plasma.

6. Conclusion

The presence of co-implanted molybdenum in BF_2 implants has been identified, and the mechanism of its incorporation into the ion beam has been proposed. The concentration of molybdenum in the substrate has been shown to increase exponentially with increasing ion source arc current.

Depth profile analysis using SIMS has revealed that much of the molybdenum is gettered during furnace annealing by residual implant damage caused by the implantation process. However, the results of electrical measurements of devices built on substrate contaminated by molybdenum during BF_2 implantation suggests that low levels of the metal species diffuse into the silicon. The most dramatic effect observed was the reduction of parasitic bipolar transistor gain, argued to be caused by the carrier recombination properties of molybdenum in silicon.

The process of molybdenum contamination can effectively be eliminated by constructing the ion source arc chamber of a different material. Preliminary results using tantalum suggest it to be the metal of choice.

Acknowledgements

The authors would like to thank J Jone for the electrical test results, and E. Waterman, T. Spencer, J. Murray and P. Davies for much technical assistance.

References

[1] A. Rohatgi, R.H Hopkins, J R Davis, R.B Campbell and H C' Mollenkopf, Solid-State Electron. 23 (1980) 1185
[2] S.K Ghandhi, VLSI Fabrication Principles, Silicon and Gallium Arsenide (Wiley, 1983) p 25.
[3] S.P Tobin, A C. Greenwald, R C. Wolfson, D L Meier and P J Drevinsky, Mater. Res Soc. Symp Proc 36 (1985) 4
[4] M.Y Tsai, D S Day, B G. Streetman, P Williams and C A Evans Jr, J. Appl Phys 50 (1979) 188
[5] J C. Vickerman, A. Brown and N M Reed, Secondary Ion Mass Spectrometry. Principles and Applications (Clarendon, Oxford, 1989) p 302
[6] M Y. Tsai, B G Streetman, P Williams and C A. Evans Jr, Appl. Phys. Lett 32 (1978) 144

Nuclear Instruments and Methods in Physics Research B55 (1991) 166–172
North-Holland

A micro-uniformity test structure

W.A. Keenan, W.H. Johnson, L. Mantalas and L. Nguyen
Prometrix Corporation, 3255 Scott Blvd., Santa Clara, CA 95054, USA

L.A. Larson [1]
National Semiconductor Corporation, P.O Box 58090, Santa Clara, CA 95052, USA

The uniformity of ion implantation across a chip is becoming more important as the density of devices on a chip increases and the matching tolerance of device parameters across a chip decreases and becomes more critical In order to investigate ion-implant micro-uniformity, a special van der Pauw mask was designed with 400 structures per square centimeter This mask has been used with a polysilicon-on-oxide test structure to investigate chip micro-uniformity Both medium- and high-current implanters have been studied using this dense van der Pauw pattern Contour maps, 3D maps and histograms are used to display the variation of dose across a chip area Results are also presented for micro-nonuniformity patterns deliberately introduced on a wafer Several optical techniques are also presented to map closely spaced stripes across the wafer

1. Introduction

Ion implantation offers many unique advantages in semiconductor manufacturing While making possible low doping levels necessary for new, high-density ULSI devices, ion implantation also provides the important process advantages of repeatability and uniformity. Wafer uniformity of less than 1% is now generally accepted as the industry standard. The question arises as to the dose variation across much smaller dimensions [1]

A great deal of interest has been expressed recently in achieving and measuring micro-uniformity on silicon wafers. Earlier work [2,3] used the measurement of discrete diode capacitors to measure micro-uniformity on 3 inch wafers The density of the capacitors was 10000 cm^{-2}. Perloff [4] recorded uniformity measurements using van der Pauw [5] structures. He also implanted a pattern of rectangular openings in a mask oxide, which had been photolithographically defined. This quilt pattern was tested with the four-point probe, using a precision prober.

This investigation will report on a pattern of van der Pauw structures photolithographically defined and etched into a polysilicon layer This proved to be a particularly interesting study because the difficulty in achieving complete electrical activation in polysilicon [6] had not been anticipated. A very interesting phenomenon of the polysilicon changing optical thickness after ion implantation and annealing was observed Work will also be presented on the measurement of micro-uniformity using an optical technique that involves a microscope-based spectrophotometer (Prometrix FT probe) using CARIS (constant-angle reflectance interference spectroscopy).

2. Structure and experiment

The actual van der Pauw structure used in this work is shown in fig 1 The size of the complete van der Pauw is 300 μm by 400 μm. The test pads are 100 μm square, as is the body of the resistor. The spacing between the structures is 100 μm in the X-direction and 200 μm in the Y-direction, resulting in a density of

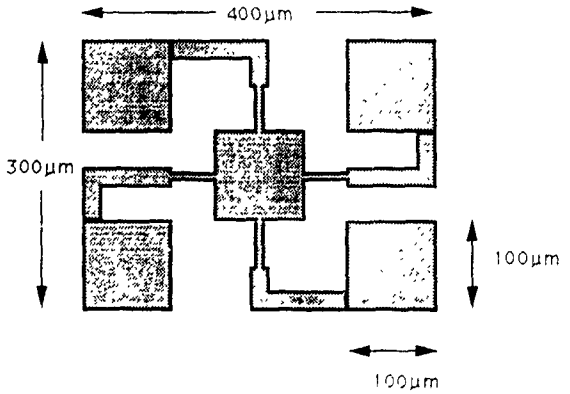

Fig 1 The van der Pauw structure used in this study The size of the structure is 300 μm × 400 μm

[1] Present address Sematech, 2706 Montopolis Dr., Austin, TX 78741, USA.

0168-583X/91/$03.50 © 1991 – Elsevier Science Publishers B V (North-Holland)

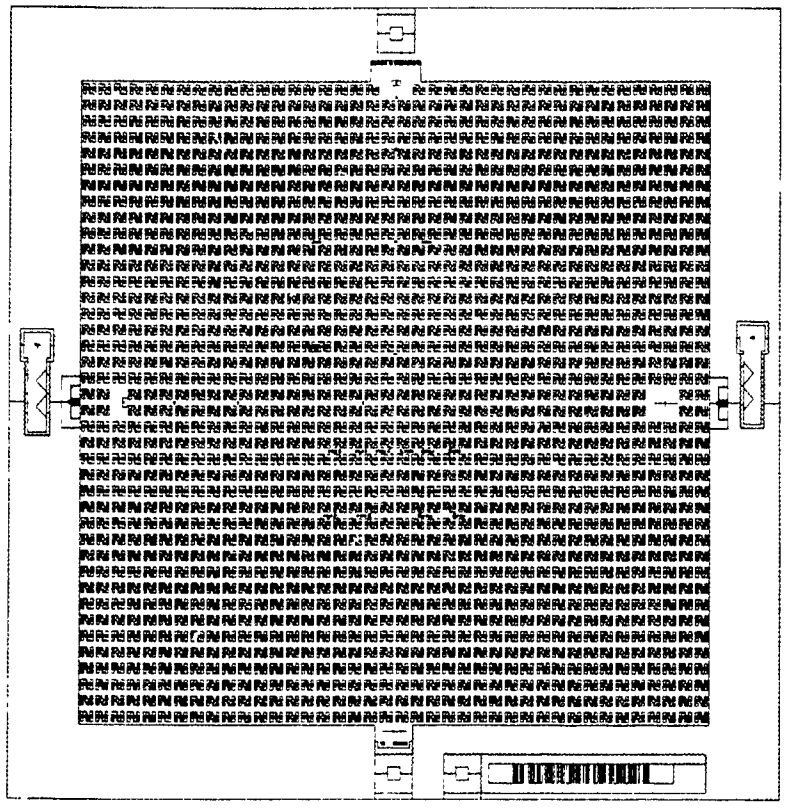

Fig 2 The van der Pauw structure on the 2 cm × 2 cm chip or die The chip has 40 van der Pauw structures in the *X*- and the *Y*-direction, giving a total density of 1600 chips per die

20×20 or 400 cm^{-2}. The masking for this experiment was done on the new Nikon Stepper which provides an image field of 2 cm × 2 cm, for a total of 1600 sites per die. Fig. 2 shows the van der Pauw array Intrinsic polysilicon was deposited on 800 Å of thermal SiO_2, with an average thickness of 3000 Å and a standard deviation of about 10 Å or 0.33% These wafers were exposed courtesy of Andrew Cosio at Nikon Precision

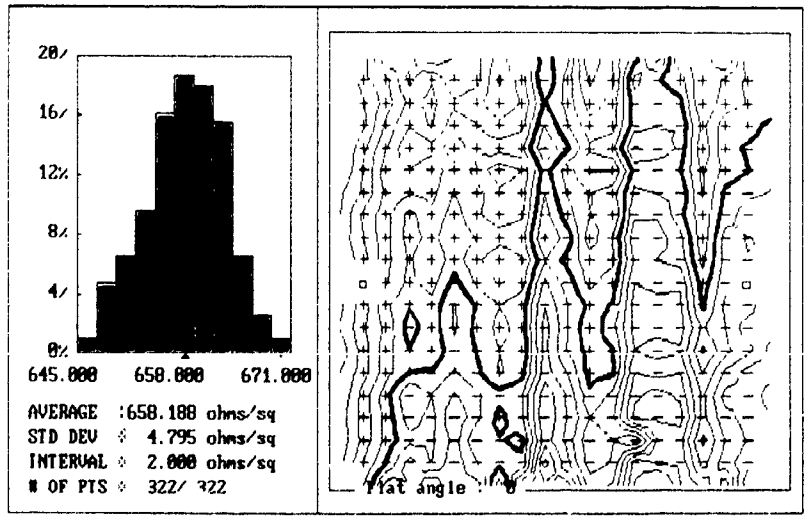

Fig 3 Sheet-resistance map output by the Lithomap for a good chip on one of the wafers in the experiment. Good overall uniformity, but stripes are present

Inc. in Bellmont, CA. The wafers were etched and the photoresist stripped at National Semiconductor. Implants were done at National Semiconductor as well as IICO Corp. of Santa Clara, CA. An advantage of this structure is that the pattern can be etched before the ion implant. After implantation the polysilicon was first investigated optically. The wafers were then annealed for R_s measurements. No contact metallurgy was used.

3. Testing

The test structures were tested using the Prometrix Lithomap, which is an instrument for characterizing photolithographic equipment and processes. A pattern of electrical test structures is etched into a conducting layer, such as a doped polysilicon or metal layer. This conducting layer is isolated from the substrate with an oxide. The Lithomap is capable of measuring line widths down to 0.2 μm with a precision of 0.002 μm. It is also capable of a measuring registration using a unique test structure. The latest enhancement to the Lithomap is the ability to measure defects. Electrical shorts and opens can be measured using an interleaving comb structure and a serpentine structure, respectively. The ability to measure interlayer shorts and opens is also one of its new capabilities. The Lithomap has software to analyze the data to determine the contribution of the various components of the photolithographic equipment.

Fig. 3 shows a Lithomap uniformity map for a chip with good uniformity. The average sheet resistance is 654 Ω/□ with a standard deviation of 0.5%. The histogram shows a tight distribution of sheet-resistance values. In spite of the good uniformity this chip clearly has a striping problem. Fig. 4 shows good uniformity but with a very interesting striping pattern on the chip. The average R_s value is 658 Ω/□ and the standard deviation is 0.7%. The peak-to-valley difference in the stripes is 20 Ω/□ or about 3%.

These results indicate the degree of difficulty in activating heavily dosed polysilicon. These wafers had been implanted at 5×10^{15} and RTP-annealed.

4. Optical tests

Interesting results for unannealed polysilicon were obtained by making thin-film measurements on the implanted wafers. The map of fig. 5 is of the polysilicon thickness on a wafer that received a special implant. The pattern was produced by holding the X-scan fixed and then holding the Y-scan fixed, producing a cross pattern. The diameter scan shown in fig. 6 is a plot of the beam diameter achieved by doing a stripe across the polysilicon wafer. This polysilicon wafer has not been annealed nor patterned. We can see the fine structure of the beam in this thickness measurement. The question is what are we actually measuring? Quadrant implants shown in fig. 7 were done to investigate the effect of dose on this phenomenon. The polysilicon thickness *increases* with dose. This is due to the assumptions made in the measurement. The system assumes that the index of refraction or the dispersion curve of the polysilicon has not changed. The polysilicon surface has changed and become more amorphous due to the implant. What we are looking at is an optical thickness that assumes a constant or unchanging index of refraction. Since $n \times t$ (index × thickness) is measured and n is assumed constant, the system indicates a change in thickness.

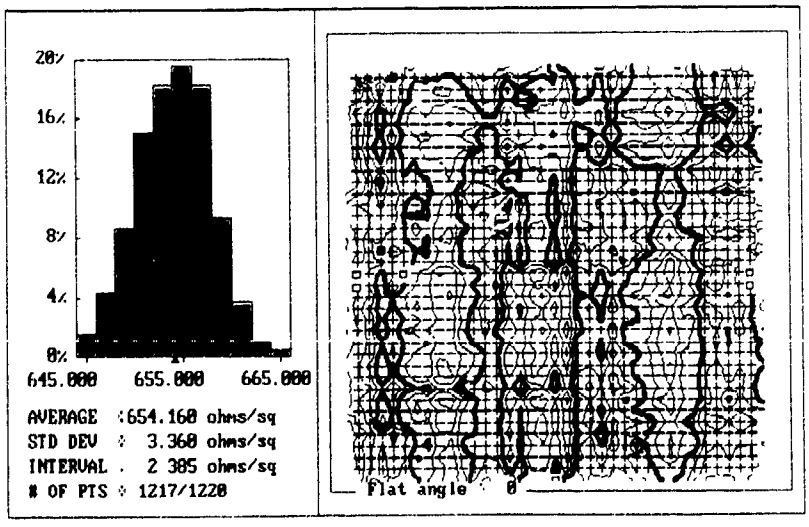

Fig. 4. Sheet-resistance map of a die with good uniformity but showing interesting stripes or microscopic variation across the chip.

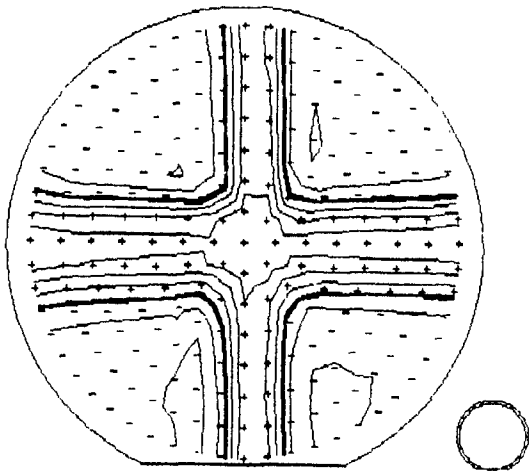

MEAN.....	3158.8		WAFER DIAM.....	125.00 mm / 4.92 in	
STD DEV.....	110.61	3.502 %	TEST DIAM.....	115.00 mm / 4.53 in	
MINIMUM.....	3050.8				
MAXIMUM.....	3393.6		CONTOUR DISPLAY.....	STANDARD	
# SITES/GOOD.....	225/ 225		- INTERVAL.....	50.000	
SUBSTRATE.....	SILICON		LAYER 2 - FILM.....	Polysilicon	
SORTING SIGMA.....	3.0		MEAN-TARGET.....	0.00000	
CORRELATION.....	* NONE		-WARNING.....	0.00000	0.000 %
UNITS	ANGSTROMS		-SPEC.....	0.00000	0.000 %

Fig 5 Cross section of beam in X- and Y-direction

Another set of samples, provided by Michael Current of Applied Materials, were bare silicon wafers implanted on the Applied Materials 9000 with various implant conditions to deliberately create striping. The variables were beam spot size, the rate at which the wheel was spinning and the rate at which the wheel was

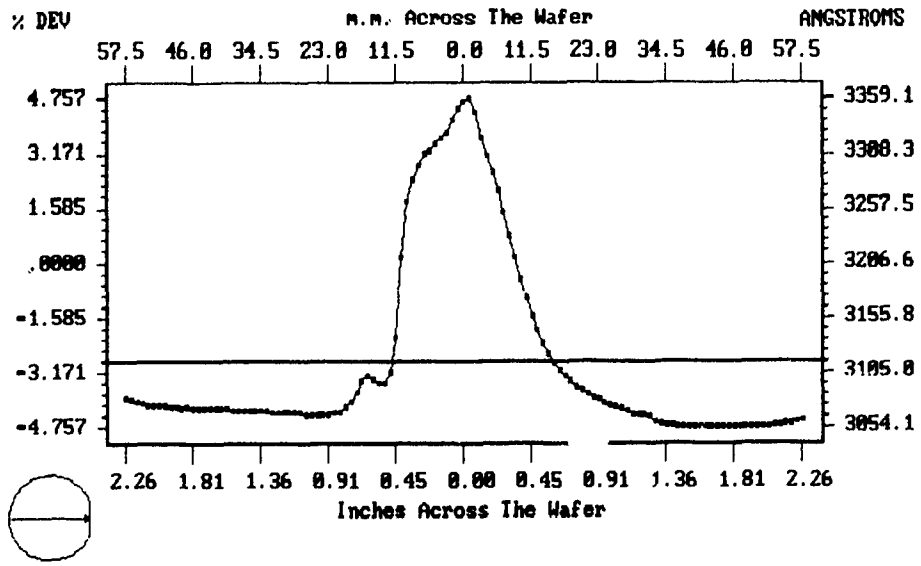

MEAN.....	3115.3		WAFER DIAM.....	125.00 mm / 4.92 in
STD DEV.....	89.657	2.878 %	TEST DIAM.....	115.00 mm / 4.53 in
MINIMUM.....	3054.1		ROTATION.....	0 dg TOP TO BTTM
MAXIMUM.....	3359.1		SCAN DISPLAY.....	FULL SCALE DISPLAY
# SITES/GOOD.....	121/ 121			

Fig 6. Diameter scan across a polysilicon layer that had been implanted using only the X-scan of an electrostatic scan system This shows the Y-cross section of the ion beam

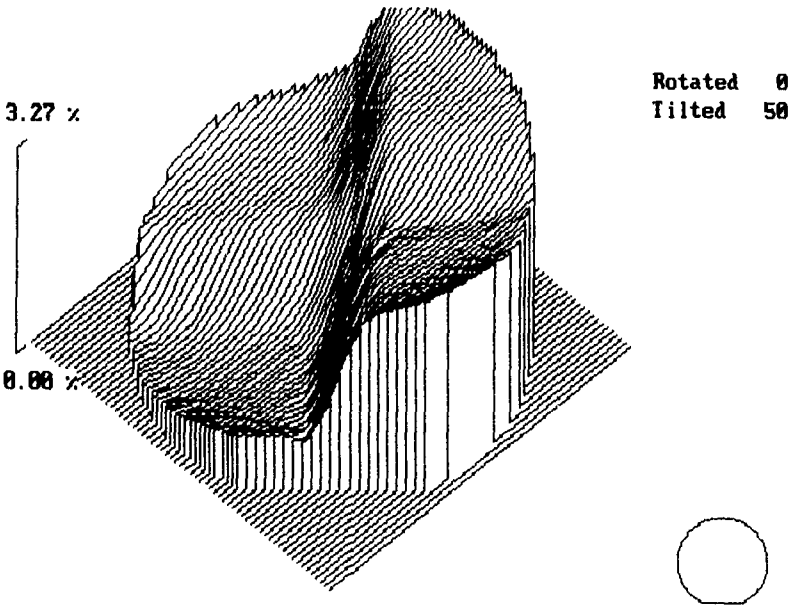

TITLE.....	I/I POLY WAFERS 90 KEV AS IN QUADS				
MEAN.....	3110.3		WAFER DIAM.....	125.00 mm / 4.92 in	
STD DEV.....	31.487	1.012 %	TEST DIAM.....	110.00 mm / 4.33 in	
MINIMUM.....	3061.8				
MAXIMUM.....	3158.5		3D DISPLAY.....	ABSOLUTE DISPLAY	
# SITES/GOOD.....	225/ 225		- ABS MINIMUM.....	3060.0	100.000 %
- ABS MEAN.....	3060.0	ANGSTROMS	- ABS MAXIMUM.....	3160.0	103.268 %

Fig 7 Quadrant implants of polysilicon layer were achieved by doing two half wafer implants at 1×10^{13} and 2×10^{13} ions/cm^2 Resultant quadrant doses are 0, 1, 2 and 3×10^{13} ions/cm^2. Maximum increase in optically measured thickness was about 100 Å

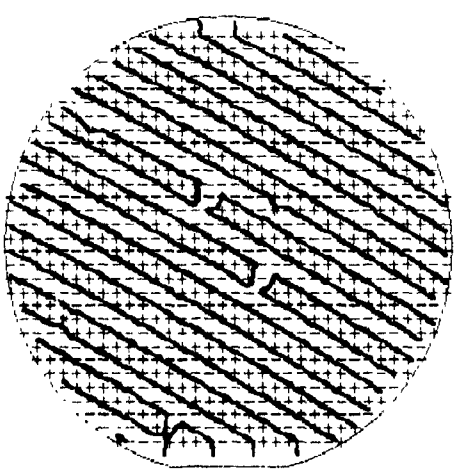

MEAN...	41 668		PATTERN	874 Sites
STD DEV	307 78 m	0.739 %	STEP SIZE	x:1 500 y.1.500
MINIMUM	40.083			
MAXIMUM	42 228		CONTOUR DISPLAY	STANDARD
# SITES/GOOD	874/ 871		- INTERVAL	50.000

Fig. 8 Reflectivity map of a section of a bare silicon wafer that showed microscopic striping Wafer had not been annealed

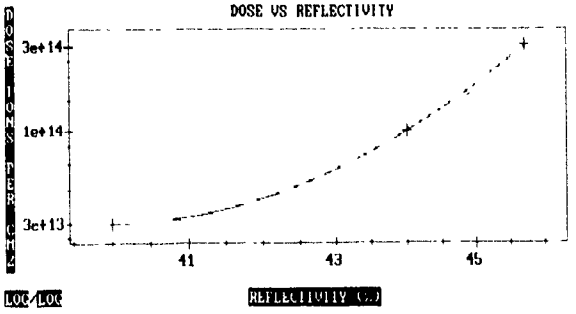

Fig. 9. Calibration curve of dose vs reflectivity for arsenic implants evaluated in this study.

translated across the beam The reflectivity map shown in fig. 8 was taken on a wafer showing macroscopic striping. Monitors were used to generate the calibration curve of fig. 9. The diameter scan of dose in fig. 10 was made with 625 points and a test diameter of 6 24 mm This results in a step size of 10 μm. The spot size of the FT500 was 4 μm (50 × objective). The results for these measurements are very repeatable. These results on the FT500 both for the unannealed polysilicon and for the unannealed silicon are very interesting. Obviously many things can change the reflectivity of a sample, but in this case, where we are looking at variations across the wafer, it is easy to generate a calibration curve of reflectivity versus dose (as in fig 9).

5. Follow-on

The results for implanting the undoped polysilicon were disappointing because of the difficulty of activating polysilicon implants. Several steps will be taken to further this work. One is to start with doped polysilicon and implant it with a dose of 1×10^{12}–1×10^{14} and use the damage as an indication of the implant dose. This would be similar to be double-implant technique [7]. The implant damage will increase the sheet resistance in proportion to the dose. This technique will require a calibration curve.

The second approach is to measure the thickness of the individual unannealed van der Pauw structures with the FT5000, then anneal the wafers and look for very small changes in sheet resistance by probing the van der Pauw structures. Finally the FT500 will be used to measure the reflectivity at one of the interference pattern peaks. This will lend more understanding to the possibilities of using test structures for electrical testing of microuniformity. If feasible, the size of the structure here could certainly be reduced. The size used here was determined simply because it was available as a part of the Lithomap mask library.

The earlier C-V work will be repeated using an MOS structure where the metal dots are replaced by polysilicon dots. The testing technique would be to use the C_{max}/C_{min} ratio to monitor the average channel doping. Also the area under the C–V curve will be integrated to obtain the partial dose [8].

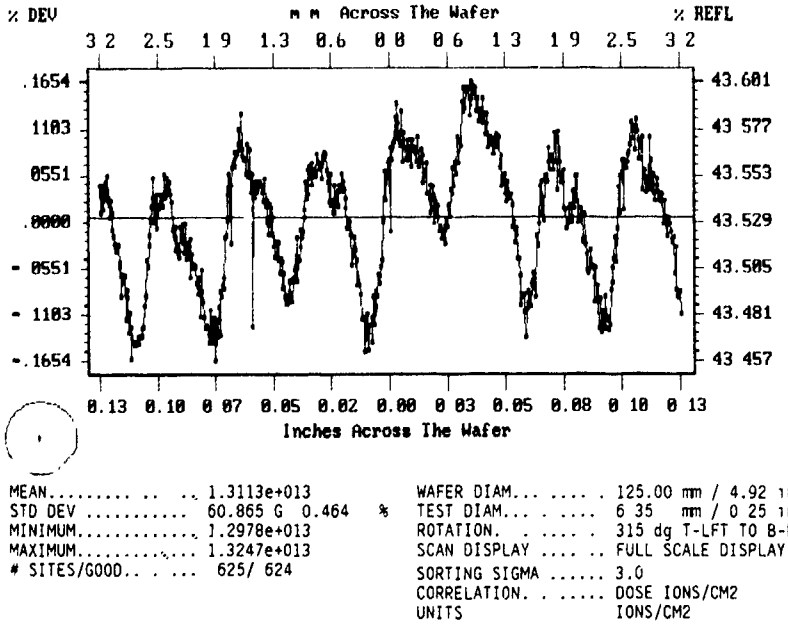

Fig 10 Dose diameter scan that was measured on one of the wafers with the best implant condition The diameter scan was 6 24 mm, with a total of 625 measures giving a step size of 10 μm.

Acknowledgements

The authors want to thank those who contributed to this work, in particular Andy Cosio, who did an excellent job of exposing the van der Pauw chip on the Nikon Stepper, and Jack Jackson of IICO Corp. of Santa Clara, CA.

References

[1] E McGuire, Nucl Instr and Meth. B21 (1987) 431
[2] N. Turner, Nucl. Instr. and Meth 189 (1981) 311
[3] H. Glaveschnig, K Hoerschelmaun, W. Holtschmidt and W Wenzig, Nucl Instr and Meth 189 (1981) 291.
[4] D.S. Perloff, F.E. Wahl and J T. Kerr, Proc 7th Int. Conf on Electron and Ion Beam Science and Technology, Washington, DC (1976) p. 320
[5] L.J van der Pauw, Philips Res Rep 13 (1958) 1
[6] B. Raicu, M I. Current, W A Keenan, D. Mordo and R. Bernnan, High Conduction Polysilicon for Interconnects and Defect Free Shallow Junction Diffusion Sources by High Dose Boron Implantation and Rapid Thermal Annealing, presented at this conference (8th Int. Conf on Ion Implantation Technology, Guildford, UK, 1990)
[7] A.K A. Smith, W H Johnson, W A Keenan, M. Rigik and R Kleppinger, in: Ion Implant Technology, eds M I Current, N.W Cheung, W. Weisenberger and B Kirby (North-Holland, 1987) p. 529
[8] R O Deming and W A. Keenan, Nucl Instr and Meth B6 (1985) 349.

Nuclear Instruments and Methods in Physics Research B55 (1991) 173–177
North-Holland

Monitoring the micro-uniformity performance of a spinning disk implanter

Michael I. Current [a], Tim Guitner [a], Naotsugu Ohno [b,1], Kurt Hurley [c], W.A. Keenan [d], Walt Johnson [d], R.J. Hillard [e] and C. Jeynes [f]

[a] *Applied Materials, Santa Clara, CA 95054, USA*
[b] *Applied Materials Japan, Narita, Japan*
[c] *Therma-Wave Inc., Fremont, CA 47320, USA*
[d] *Prometrix Corp., Santa Clara, CA 95054, USA*
[e] *Solid State Measurements, Pittsburgh, PA 15275, USA*
[f] *Electronic and Electrical Engineering, University of Surrey, Guildford, Surrey GU2 5XH, UK*

Methods for monitoring fluctuations in dose uniformity on spatial scales on the order of 1 cm or less are investigated for the case of a spinning disk ion implanter. Various optical, electrical and physical methods including Therma-Wave signals, optical reflectance, sheet resistance, spreading resistance and Rutherford backscattering are used. Comparison is made to a number of estimates of dose uniformity as a function of beam size and the scanned distance between successive passes through the ion beam.

1. Introduction

Providing uniform distribution of total ion dose over the surface of a wafer is one of the first tasks in the design of an ion implantation system [1]. Measurements of dose uniformity, particularly in the form of contour maps derived from a spatial array of measurements, have become routine techniques for monitoring the performance of ion implantation systems [2,3]. The goal is to ensure that variations in dose level over the wafer are less than the tolerable process limits and within the specified performance of the implantation tool. The number of measurements taken to get a measure of the dose uniformity and to calculate a dose contour map is limited by time allowed for the probing and the spatial resolution of the probe technique. Densities of probe locations of ≈ 1 site/cm^2 are sufficient to reveal large-scale dose variations in a wide variety of situations [3].

As IC chip dimensions grow to 1–4 cm on a side, control of fluctuations in dose on spatial scales which are smaller than the chip dimensions becomes increasingly important. Whereas large-scale, "macro-uniformity" variations can result in wide distributions of IC performance characteristics between various chips, small-scale, "micro-uniformity" variations can result in totally nonfunctional ICs. An example of a potential micro-uniformity effect is the loss of signal synchronization resulting from inter-chip transistor speed variations. The impact of poor micro-uniformity is accentuated if the pattern of dose variations is aligned with the chip layout.

Early studies of dose uniformity on the scale of the beam spot size (≈ 1 cm) were directed at the x-y scanning systems [4–6]. The methods used for evaluation of fine-scale dose variations were measurements from patterned arrays of CV dots or resistors. This work will investigate the effects of beam size and scanning speeds on the dose uniformity for a spinning disk, "R-theta", scanning system [7,8] and will use a variety of optical, electrical and physical measurement tools and mapping techniques.

1.1. Dose equation

In an R-theta scanning system, such as the PI9200 [8], the ion beam dose is distributed over a ring of wafers located at an average distance R_0 from the center of a rapidly spinning wheel. The wheel axis is mounted on a scan arm which allows for translation of the wheel along an approximately radial direction. For a rotation speed of 1250 rpm and R_0 of 61.8 cm, the rotational speed at the edge of a ring of 125 mm wafers is 89.1 m/s. Since the rotational speed is $> 10^3$ faster than the translational speed of the wheel center, V_{scan}, the dose distribution is determined by the translational scanning process.

The fraction of time a small segment of circumferential width, ∂C, of an annulus of width ∂R at distance R is in the ion beam is $\partial C/(2\pi R)$ [7]. The time the beam traverses the width of an annular ring of width ∂R is $\partial R/V_{scan}$. The net time, t, a small segment of the wafer

[1] Now at Kawasaki Steel Corp., Hagagun, Japan

0168-583X/91/$03.50 © 1991 - Elsevier Science Publishers B.V. (North-Holland)

surface at radial distance R and area $\partial C\,\partial R$ is in the ion beam during a single translational scan is $(\partial R/V_{scan})(\partial C/2\pi R)$ The implanted dose, Φ_{pass}, during a single translational scan through a current I comprised of ions of charge state q is:

$$\Phi_{pass} = \frac{I}{q}\frac{t}{\partial C\,\partial R}. \quad (1)$$

Substituting for the time in the beam, t, one gets:

$$\Phi_{pass} = \frac{I}{q}\frac{1}{(2\pi R V_{scan})} \quad (2)$$

By controlling V_{scan} to compensate for the variation in rotational speed with radial position, according to

$$V_{scan} = U_0 R_0/R, \quad (3)$$

where U_0 is the translational speed when the beam is traversing the center of the wafer at a radial position of R_0.

$$\Phi_{pass} = \frac{I}{q}\frac{1}{2\pi R_0 U_0}. \quad (4)$$

Since in the usual nomenclature, a "scan" is two "passes" in front of the ion beam, the total dose for N scans is.

$$\Phi_{total} = \left(\frac{1}{q\pi R_0}\frac{IN}{U_0}\right). \quad (5)$$

In order to maintain a constant dose for these studies, both I and N were varied to compensate as we investigated the effects of the choice of U_0 on micro-uniformity

2. Experimental conditions

Most of the implants which were used in this study were done with 80 keV As^+ at a nominal dose of 10^{14} ions/cm^2 This choice of implant conditions was made to allow for the overlap of the performance range of number of tools. This dose was high enough to provide good electrical characterization and was in the range of strong optical effects from the onset of amorphization Arsenic was chosen as the implant species to allow for ease of RBS analysis. The implantation system used was a Precison Implant 9000 [8] operated with wheel rotation speeds of 640 and 1250 rpm and average lateral scan speeds between 1 7 and 10.2 cm/s. The total number of scans (passes back and forth into the beam) was varied from 2 up to 30 for various beam currents and scan speeds. The beam was focused down to FWHM dimensions as small as 2-6 mm in order to produce clearly resolved uniformity variations The beam size was monitored by a 5-cup profiler which scanned a 10×10 cm area in the plane of the wafer [8]. The wafers were 125 mm diam, p-Si(100) with a nominal resistivity of 10 Ω cm. The wafers were mounted on the wheel with a 7° tilt and a 45° twist orientation to suppress measurement complications resulting from channeling effects [9]. Dose calibration implants were also done at 3×10^{13} and 3×10^{14} ions/cm^2. The electrical measurements were made after an anneal for 10 s at 950 °C in an AG Associates rapid thermal processor.

3. Monitoring methods

In addition to the obvious requirements for spatial resolution, the choice of techniques for micro-uniformity measurements also rests on the need for good stability, precision and sensitivity to slight dose variations [3]. Ideal methods should also require minimal time per site measurement, straightforward data analysis for dose calculations, and ease of interpretation of the data.

3 1 Optical methods

The principal optical technique in this work was dose map measurements with a Therma-Wave laser probe which uses a combination of a modulated Ar laser beam and a CW He–Ne laser probe beam [10]. Typical laser beam spot diameters are 2–4 μm. Therma-Wave probes have demonstrated the ability to resolve device features of less than 1 μm width [11] At doses above the onset of amorphization, the modulated reflected signal of the probe beam, or TW signal, deviates from a monotonic increase with dose and becomes a modulated value with an increasing trend. The reflectivity of the laser beams also varies in a periodic fashion as the thickness of the amorphous layer increases. The thickness of the amorphous layer measured by the reflectivties is fitted to a $(\ln[\text{dose}])^{1/2}$ calibration curve and combined with the TW signal. The dose repeatability of this method is estimated at 2%.

The variation in optical reflectance was measured on several wafers with a Prometrix FT-500 film thickness monitor which had a probe spot of ≈ 2 μm [12] The FT-500 measures the reflectivity of light from a W filament source in the wavelength range of 600–700 nm

3.2 Electrical methods

Sheet resistance measurements have been the mainstay of uniformity mapping since the development of low-noise four-point probe measurements using configuration switching techniques [2,13]. Measurements with four-point probe arrays have demonstrated the ability to resolve dose variations with a width of 1 mm on a linear pattern with a pitch of 5 mm [13]

Annealed wafers were probed with in-line four-point arrays with tip spacings of 1.04, 0 635 and 0.20 mm and a square array with spacing of 0.1 mm Maps with up to 625 probe sites were obtained with circular probe pat-

terns on the Prometrix Omnimap RS50/e and with a 25×25 rectangular array on a Solid State Measurements prober. Line scans along the major stripe patterns were made with four-point and two-point probes.

3.3. Physical measurements

Rutherford backscattering measurements were made on as-implanted wafers with a scan overlap pitch of ≈ 5 cm. The spatial resolution of the 2 MeV He RBS beam was ≈ 1 mm.

4. Maps and line scans

Strong patterns, generated by implants with highly focused ion beams and fast translational scan speeds were easily seen in the Therma-Wave maps (fig. 1). The orientation of the pattern follows the 45° twist of the wafers so that the leading edge of the wafer into the ion beam was the lower left side. Line scans across the dose variation stripes (fig. 2) clearly indicated the lack of sufficient overlap of the beam during these implants. Therma-Wave line scans were able to clearly resolve apparent dose variations of less than 0.4% even though the variation pattern is not seen in the whole-wafer map (figs. 3 and 4).

Certain sheet resistance maps showed strong moiré-like interference patterns (fig. 5). The strong dose variation patterns were resolved by increasing the probe site density to 361 and 625 sites in a circle of 1 cm test radius and reducing the probe tip spacing to 0.2 mm

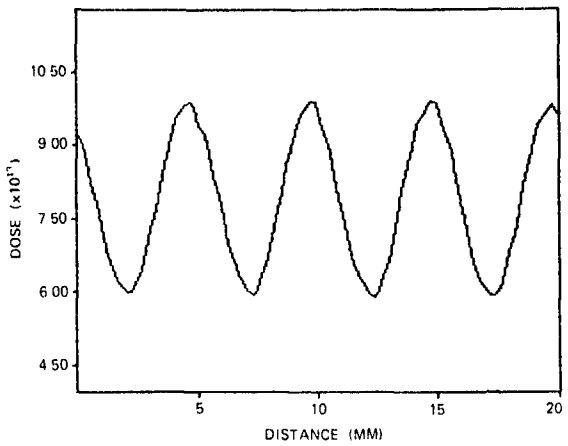

Fig. 2. Therma-Wave line scan along a 2 cm segment across the pattern in fig. 1. Apparent dose variation is 17.4%

(fig. 6). Characteristic stipping patterns were measureable by line scans with four-point probe measurements for scan overlap pitches as small as 1.6 mm.

The apparent values of the dose variations as measured by 2 cm line scans along the dose variation ripples are compared in table 1. For the large-scale ripples, which were easily observed by all of the measurement techniques – including direct visual inspection of the wafers, the apparent dose variation for the same implant pattern ranged from 5.4 to 35%. The optical reflectivity gave a particularly high value of the dose variation. Electrical and Therma-Wave probes gave ob-

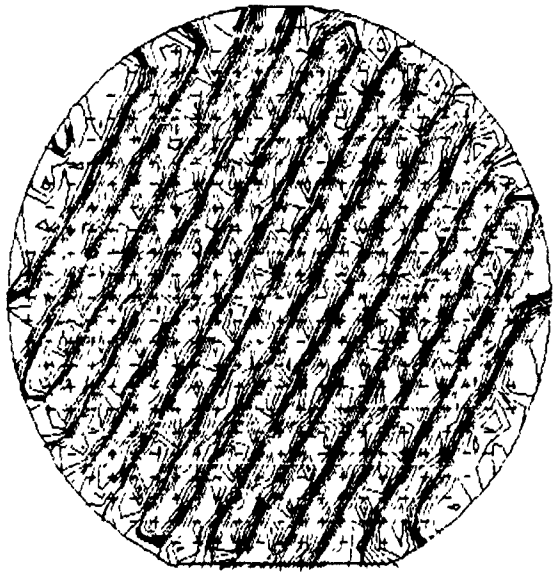

Fig. 1. Therma-Wave full wafer map for an implant with a pitch between passes of 4.9 mm with a beam FWHM of 11 mm. Apparent dose variation is 17.3%.

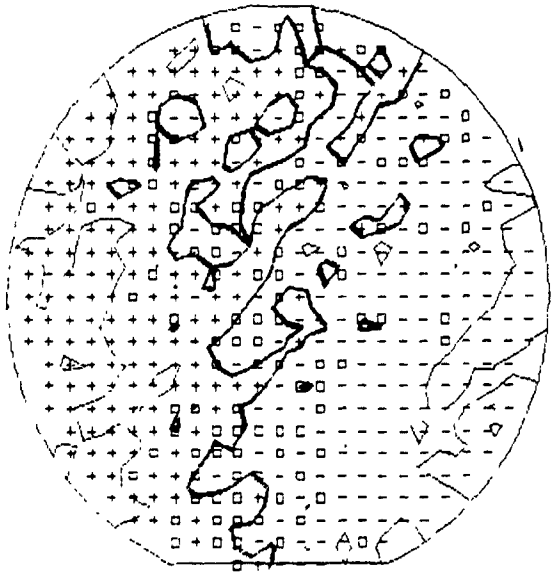

Fig. 3. Therma-Wave full wafer map for an implant with a pitch between passes of 0.8 mm with a beam FWHM of 6 mm. Apparent dose variation is 0.78%.

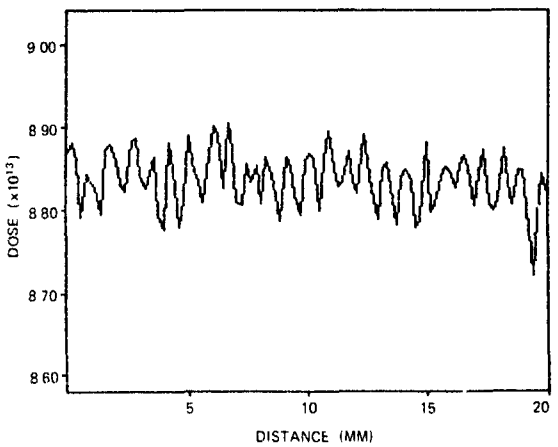

Fig. 4 Therma-Wave line scan along a 2 cm segment across the pattern in fig. 3 Apparent dose variation is 0 38%

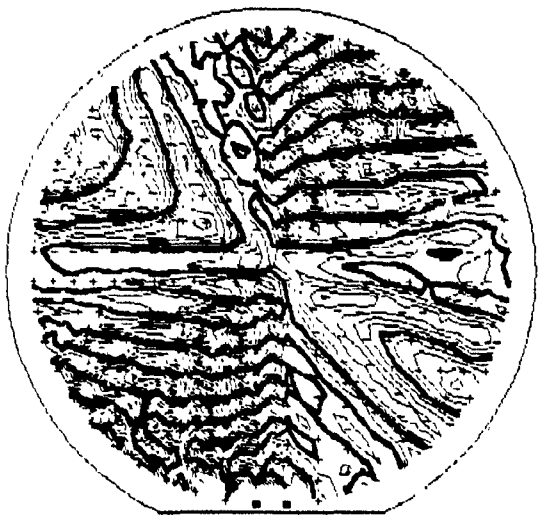

Fig. 5 Full wafer sheet resistance map with 625 sites of an implant with a pitch between passes of 4 9 mm and a beam FWHM of 6 mm Strong moiré interference is seen in the contours between the implant stripes and circular probe pattern The probe tip spacing was 1 mm

served variations between 5 4 and 8.8%. The RBS measurement was 20% for maximum and minimum dose levels (peak to valley).

Table 1
Comparison of apparent dose variations (10^{14} As/cm^2, 0.6 cm FWHM ion beam, 2 cm line scans, RMS values)

Technique	1.7 cm/s scan speed, pitch/FWHM = 0 14, 7 scans	10 2 cm/s scan speed, pitch/FWHM = 0 82, 12 scans
Therma-Wave	$9\,8\times10^{13}$ ions/cm^2 ± 0 89%	$7\,8\times10^{13}$ ions/cm^2 ± 8 76%
Optical reflectance	$1\,0\times10^{14}$ ions/cm^2 ± 4 5%	$1\,07\times10^{14}$ ions/cm^2 ± 35%
Rutherford backscattering		10^{14} As/cm^2 ± 20%
Spreading resistance	668 Ω ± 1 2%,	666 Ω ± 5.9%,
0.1 mm probe spacing	dose variation = 1 8%	dose variation = 8 8%
Sheet resistance		
1 mm probe spacing	603.8 Ω/□ ± 0.09%, dose variation = 0 13%	602 Ω/□ ± 2.66%, dose variation = 3 9%
0 6 mm probe spacing	609 Ω/□ ± 0 13%, dose variation = 0.19%	612 Ω/□ ± 3 6%, dose variation = 5 4%
0.1 mm probe spacing	558 3 Ω/□ ± 0 2%, dose variation = 0 38%	526.4 Ω/□ ± 4.5%, dose variation = 6.75%

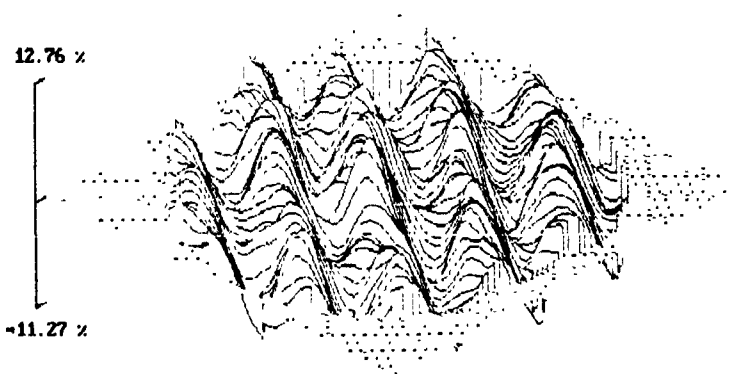

Fig. 6 A three-dimensional map of sheet resistance values in a 22 mm circular segment of the wafer shown in fig. 5. The map was constructed from 625 test sites with a probe tip spacing of 0 2 mm. The apparent dose variation was 6 4%.

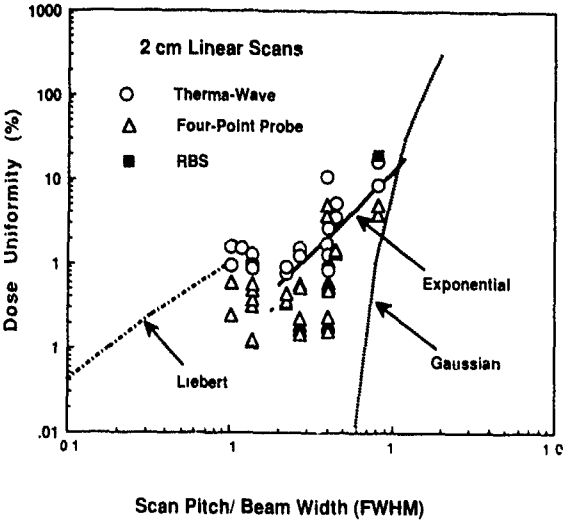

Fig 7 Comparison of apparent dose variations with various dose uniformity models.

For the implants with relatively high degrees of overlap, the apparent dose variation ranged from 0.2 to 4.15%, with the optical reflectivity again giving a substantially higher value than other techniques.

5. Scan overlap models

Early analytical models were based on the assumption of either a Gaussian or "exponential" beam profile [4–6]. A recent approach used a convolution of actual beam profiles and scanning conditions [1]. According to the observations of this work (fig. 7), the assumption of a Gaussian beam shape is a particularly optimistic one for ratios of the pattern pitch to beam size (FWHM) of less than 1. The exponential beam shape is a reasonable fit to the data in the range of pitch to FWHM ratios in this work [5]. The projection of the exponential model and the general trends of our data into the range of "production-worthy" conditions, pitch/FWHM less than 0.1 and dose uniformity variations less than 1%, seems to agee well with the Liebert model.

6. Summary

The delineation of fine-scale dose variations is within the resolution capability of a number of commercially avaliable optical and electrical probes. The interplay between the beam pitch between successive rotations of the wheel and the beam profile size and shape is the dominant effect in determining the micro-uniformity. Increasing the number of scans produced only a very gradual improvement in micro-uniformity values. To obtain micro-uniformity values approaching 0.1%, the scan overlap pitch should be ≈ 10 times smaller than the beam width The large spread in apparent dose variation values for the different measurement techniques clearly shows that additional work is need to establish reliable process control procedures for micro-uniformity.

Acknowledgements

The authors wish to acknowledge the many colleagues who have aided us in this work. In particular, we thank Chris Knowler of Applied Materials Japan for assistance in the ion beam tuning and implants, David Mordo of AG Associates for the annealing processing, Greg Little of Prometrix, Roger Brennan of Solecon Labs, Donald Zier of Solid State Measurements and Mark LeMere and John Opsal of Therma-Wave.

References

[1] R.B Liebert, S. Satoh, A. Delforge and E. Evans, Nucl. Instr. and Meth B37 (1989) 464.
[2] J N. Gan and D.S. Perloff, Nucl Instr. and Meth 189 (1981) 265
[3] M.I. Current, C.B. Yarling and W.A Keenan, in Ion Implantation. Science and Technology, ed J.F. Ziegler 2nd ed (Academic, 1988) p. 377.
[4] H Glawischnig, K. Hoerschelmann, W. Hotschmidt and W Wenzig, Nucl. Instr and Meth 189 (1981) 291.
[5] E.J Rogers, Nucl. Instr. and Meth 189 (1981) 305.
[6] N Turner, Nucl. Instr and Meth. 189 (1981) 311.
[7] G E. Robertson, U S Patent 3778626, 1973.
[8] M.T. Wauk and A.D. Giles, Nuc. Instr. and Meth B37 (1989) 442.
[9] M.I. Current, N. Turner, T.C Smith, D. Crane, Nucl. Instr. and Meth B6 (1985) 336.
[10] J. Opsal, A Rosencwaig and D L. Willenborg, Appl. Opt 22 (1983) 3169,
J Opsel, in: Review of Progress in Quantitative Nondestructive Evaluation, vol 8B, eds. D.O Thompson and D. Chimenti (Plenum, 1989) p. 1241.
[11] W.L Smith, R.A. Powell and J.D. Woodhouse, SPIE Proc 530 (1985) 188.
[12] H.V. Pham, H. Damar, C.L Mallory and D.S. Perloff, Microelectronic Manufacturing and Testing 10 (1987) 8.
[13] W A. Keenan, W.H. Johnson and A K. Smith, in: Emerging Semiconductor Technology, eds. D.C. Gupta and P.H. Langer, Am. Soc Test. Mater. ASTM STD 960 (1986) p. 598.
[14] W.A. Keenan and A.K. Smith, SPIE Proc. 530 (1985) 174.

Nuclear Instruments and Methods in Physics Research B55 (1991) 178–182
North-Holland

Daily 2×10^{12} monitoring of an ion implanter

S. Cherekdjian and W. Weisenberger
Ion Implant Services, 1050 Kifer Rd., Sunnyvale, CA, USA

Low-dose monitoring has always been a problem The monitors drift with time either within minutes of an implant or within days or months Resistivity excursions in excess of 50% are not uncommon. This paper presents data to understand some of the factors affecting the reliability and repeatability of low-dose, 2×10^{12} ions cm^{-2}, sheet resistivity measurements Four-point probe electronic drift, the optimum probe tip size and finish, background silicon substrate doping, surface oxide growth, and silicon surface chemistry are investigated The correct specifications of the wafers, wafer processing and the four-point probe tips enable reproducible measurement of low-dose boron implants.

1. Introduction

A widely used technique for the measurement of ion-implanted layers in the semiconductor industry is the four-point probe method [1,2]. It is commonly used in the dose range of 10^{14}–10^{16} ions cm^{-2} where the measurements can be very accurate [2]. When monitoring a dose of 2×10^{12} ions cm^{-2} the direct probe technique becomes susceptible to the ambient temperature, the background doping variations, changes in the probe geometry, and "surface effects". The measured sheet resistance is, therefore, a convolution of the above with the implant resistance. The term "surface effects" is an evasive variable which has been associated with dangling bonds [3], surface states [3], trapped holes [4], or hydrogen injection [5–7]. In this paper it refers to changes in surface conduction.

The key to reliable and reproducible low-dose direct probe resistivity data is to maintain the measurement variables as constant as possible. This paper demonstrates how this may be achieved. We explore and optimize the three main variables, the probing equipment, the silicon material, and the "surface effects".

2. The probing equipment

The two main factors to consider are the inherent electronic noise of the equipment and the mechanical probe contact variations. The first can be characterized by the daily use of standard resistor packs that replace the four-point probe head. The trend of this data allows the measurement resolution of the system to be determined. In our case, a 7.4 kΩ/□ reading had electronic noise excursions of about 30 Ω/□. The second factor requires the investigation of the performance of various probe tip radii with different lapped surface finishes. Probe tips of 1 6, 4, 8 and 20 mil radius were examined. The head that gave the best probe statistics and most reproducible data was an 8 mil with a 2 μm finish.

Probe tip roughness ranged from 0.25 to 2.0 μm finishes. No difference was observed until the tips were finished with just a chemical etch. Etch-only probe heads initially gave good results but tended to become unstable after probe "conditioning". This "conditioning" increases the roughness of the probe surface, and each protrusion stresses the native oxide to achieve penetration to the conducting layer. It has been shown that "conditioning" with a ceramic plate results in a constant contact probe footprint regardless of the initial topography [8]. In extreme cases, the probe tip changes shape. Under the microscope an old 4 mil head, which performed like an 8 mil head, visually resembled a flat 8 mil head.

There seems to be a trade-off between tip radius and surface roughness in obtaining the optimum electrical contact.

Finally, both of these variables must be monitored on a daily basis. An outline is given below for a procedure for the qualification of a four-point probe system.

(1) Check the system electronics with the use of standard resistor packs.
(2) Perform a probe tip qualification. "Condition" the tip as required.
(3) Probe trend wafers of typical implants of interest. Wafer results must be within expected limits or expected change rate (for low-dose wafers).
(4) Probe bulk NIST (previously NBS) traceable resistivity standards. This can be a monthly check or as required.

When the system passes items 1–4, test wafers may be probed. Under emergencies, a test wafer may be read

0168-583X/91/$03 50 © 1991 – Elsevier Science Publishers B.V. (North-Holland)

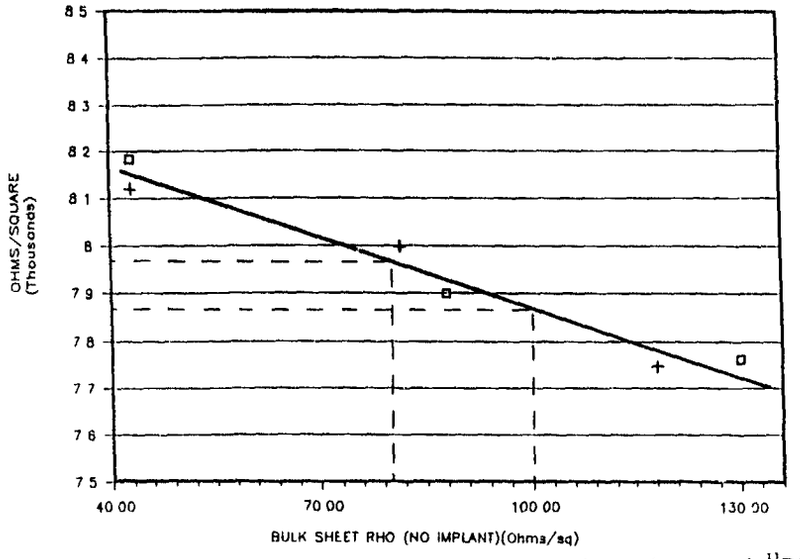

Fig. 1. Bulk sheet resistance (no implant) readings versus measured final resistance after implanting with $^{11}B^+$, 2×10^{12} ions cm^{-2}, 90 kV.

first but test 3 must be carried out immediately to ensure the validity of the pass or fail result from the test wafer.

3. The silicon material

This characterization is shown in fig 1. All the wafers were bare silicon n-type ⟨100⟩ material of various background doping levels from 1–10 Ω cm. The implant was $^{11}B^+$, 2×10^{12} ions cm^{-2} at 90 kV. All the wafers were premeasured on a four-point probe Prometrix 111B, implanted on a Nova 6200 medium current ion implanter, rapid thermally annealed (RTA) in an AG610 heat pulse at 1100°C for 10 s. and then reprobed.

Fig 1 shows the relationship between the measured resistance after implantation and the initial background

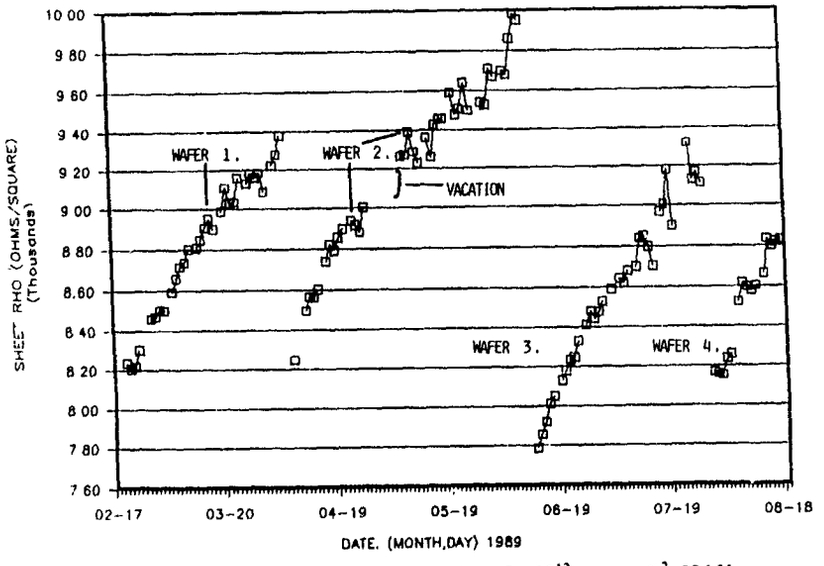

Fig. 2. Boron-implanted daily trends Implant: 2×10^{12} ions cm^{-2}, 90 kV.

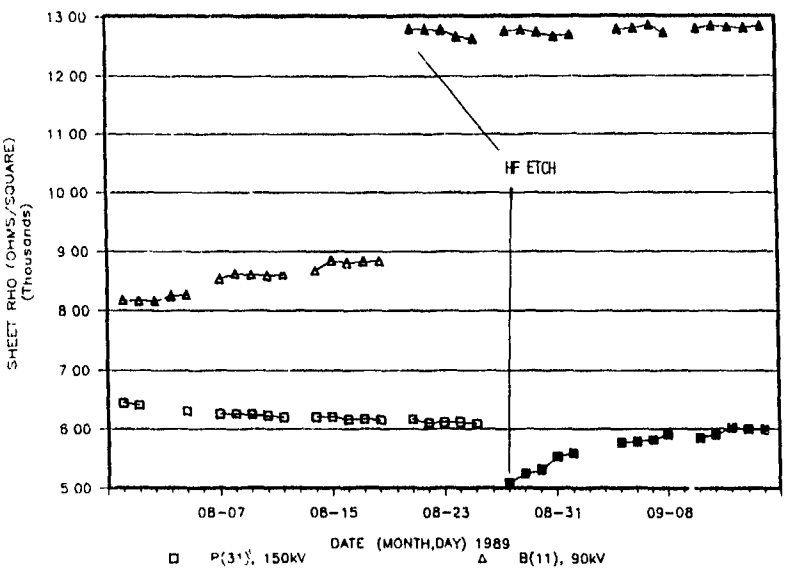

Fig 3 Boron and phosphorus daily trends before and after etching in HF Dose 2×10^{12} ions cm^{-2}

reading. It is observed that a 20% variation in the bulk sheet resistance corresponds to a change in the measured implant reading of around 100 Ω/□. We conclude that the incoming wafer resistivities should be at least 10–12 Ω cm. A higher value of bulk resistivity of around 100 to 120 Ω cm is desirable, but obtaining test or prime n-type wafers of this resistivity is currently very difficult.

4. "Surface effects"

Fig. 2 displays the daily trend data for four individual 2×10^{12} boron-implanted wafers. The sheet resistance increases for all four wafers in a similar manner. The wafer readings rise regardless of probe interval. This dismisses probe-induced damage as a likely cause.

If we consider the movements in the boron trends to be attributed to "surface effects", the measured sheet resistance can be interpreted as a reduction in a surface hole concentration [4]. If these surface holes are present on all silicon surfaces, regardless of the wafer type, a p-type ⟨100⟩ silicon wafer implanted with phosphorus should experience a decrease in sheet resistance. The phosphorus and boron-implanted trends in fig. 3 agree with this model. The surface of silicon has been reported as space charged depleted owing to surface states [4]. We can then assume that the surface states (which can be of the same order of magnitude as these implants [9]) are changing after the rapid thermal anneal.

These trend wafers, in fig. 3, were etched in HF. This drastically modified the sheet resistance in the direction indicated by the slow moving trends, rising 49% for boron and falling 21% for the phosphorus-implanted wafer. X-ray photoelectron spectroscopy (XPS) data of Grundner and Jacobs [10] reported changes in surface chemistry and indicated that a surface oxide would continue to grow for at least 4 weeks after silicon wafers had been etched in HF. The differences in surface

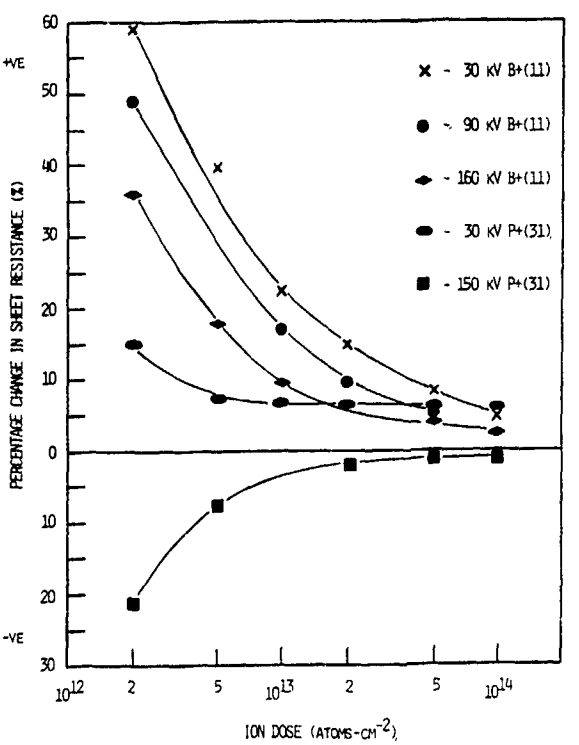

Fig. 4 Variation of the change in sheet resistance with ion dose and energy for boron and phosphorus-implanted silicon wafers.

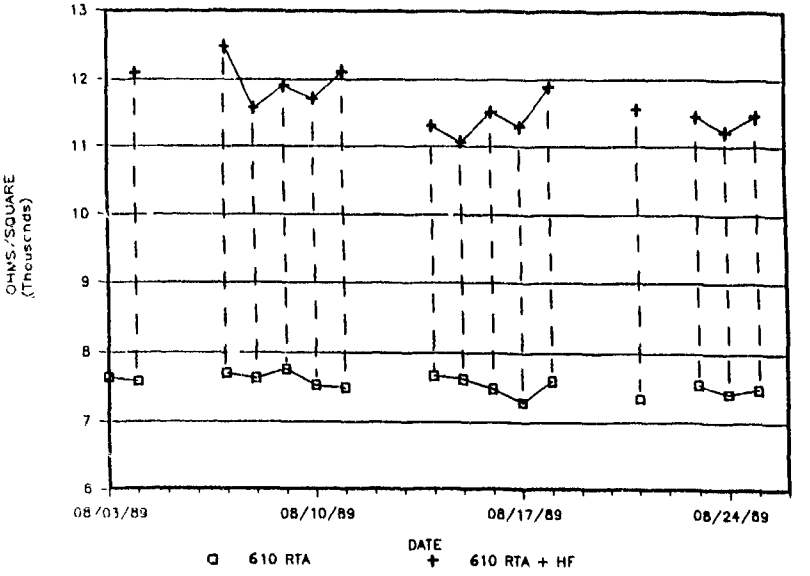

Fig. 5. Nova 6200 trend wafers before and after etching in HF. Implant: $^{11}B^+$, 2×10^{12} ions cm^{-2}, 90 kV

chemistry [10] for hydrophilic and hydrophobic silicon is probably the main contributor to the change in surface conduction, which drastically changes the measured sheet resistance.

The boron trend results seem more stable after etching while the phosphorus slowly creeps up. We can speculate that this may be due to the interaction of the shallower phosphorus implant and the slowly growing surface oxide [10]. This fall and rise effect was observed in p-type wafers with bulk resistivities of less than 10 Ω cm. Sheet resistances increased when p-type wafers greater than 20 Ω cm were etched in HF. The level of the boron dopant concentration (of the bulk) in p-type wafers is, therefore, a determining factor for these changes in resistance.

Fig. 4 displays the percentage sheet resistance change after HF etching of premeasured implanted wafers as a function of the ion dose and the implant energy. Diminishing effects are observed as the dose and the energy are increased. A reduction in energy also im-

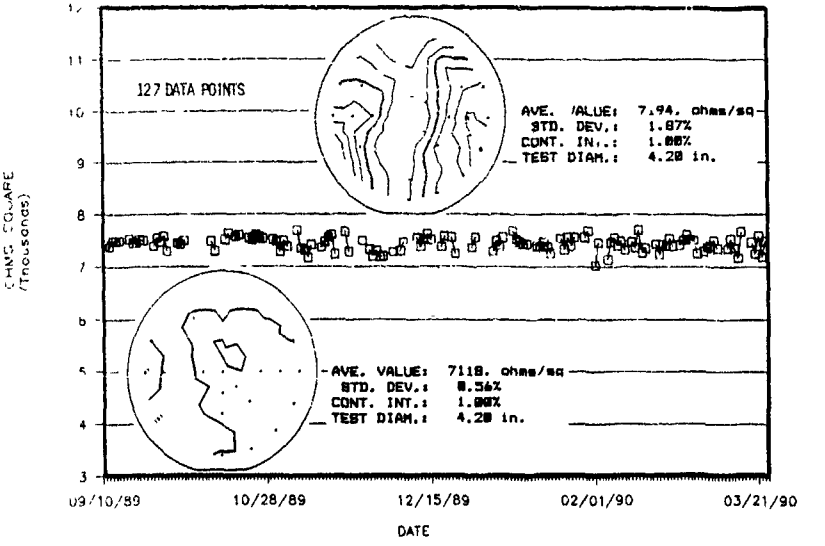

Fig. 6. Nova 6200, $^{11}B^+$, 2×10^{12} ions cm^{-2}, 90 kV daily qualification wafers.

paired the ability of the probe tip to make good surface contact. We conclude that it is important to choose an ion energy that isolates the implanted layer from the interaction of the surface.

Fig. 5 displays the reproducibility of HF-treated bare wafers. The wafers were implanted, annealed, probed, etched in HF and reprobed. The post etch readings indicated larger variations in sheet resistance, even though the HF etch produced a more stable surface (fig. 3). Semiconductor grade HF is one of the chemical reagents commonly used for cleaning and etching silicon, unfortunately it is not very clean. Juleff et al. [11] have identified 32 dissolved trace impurities, 10 of which are transition metals. Also a surface that emerges from an HF etch is very reactive and picks up contaminates and particulates [12,13]. This significantly enhances the rate of impurity absorption, particularly carbon. It can be concluded that the surface is a major contributor to inconsistent measurements.

5. Daily 2×10^{12} monitoring

Based on the previous considerations from section 1, 2, and 3, bare n-type ⟨100⟩ wafers 10–12 Ω cm were used to daily monitor a $^{11}B^{+}$, 2×10^{12}, 90 kV implant on a Nova 6200 The daily monitor results are presented in fig. 6 over a period of 6 months.

Typical maps are displayed in fig. 6, and it can be observed that no large changes in sheet resistance were noticed from channelling effects. Traditionally bare wafer results tend to be plagued by this [14]. In the 2×10^{12} ions cm^{-2} or lower dose regime, the mobility of the carriers starts to saturate [2] and the sheet resistance is, therefore, insensitive to energy.

Bulk and electronic noise levels were estimated in the previous sections as 100 and 30 Ω/□, respectively. The three sigma values of the data seems to line within 400 Ω/□. The channeling variations lie within 270 (400–130) Ω/□. Oxide wafers will produce a tighter distribution only if the HF etch prior to measurement can be eliminated or controlled.

6. Conclusion

Careful maintenance and the use of an 8 mil head on a four-point probe Prometrix 111B has enabled the successful and reproducible probing of 2×10^{12} boron implanted silicon wafers. Bare silicon wafers should be used with as little background resistivity variation as possible.

The measured sheet resistance is described by two components, the surface conduction and the junction depth. At present, leaving the surface alone minimizes any surface effects. If the surface is treated in any way, care must be taken to ensure that the resultant effect on the surface conduction is constant.

Large changes in sheet resistance were observed after HF etching and one may conclude that surface chemistry must play an important part in changing the surface conduction. Unstable etched wafer results are attributed to contaminates before and after the HF etching process.

Acknowledgements

Thanks are due to W. Johnson and A. Keenan of Prometrix, S. Tseng of Sierra, D Conners, and G. Lucchesi of Ion Implant Services

References

[1] S Wolf and R N. Tauber, Silicon Processing for the VLSI Era, vol. 1 (Lattice press, June 1987) pp. 118–123.
[2] P.L F. Hemment, Ion Imp. Sci. and Tech , ed. J F. Ziegler (Academic Press, 1984) pp. 211–260.
[3] S Kramer and A. Ruyven, Solid State Electron. 20 (1977) 1011.
[4] M Woods and R. Williams, J Appl. Phys. 47 (1976) 1082
[5] S.J. Pearton, S S and Integrated Circuit Tech. (Nov. 1989) 56
[6] J.I. Pankove et al , Phys. Rev Lett. 51 (1983) 2224.
[7] D. Chantre et al , J. Electrochem. Soc 135 (1988) 2867
[8] N. Nadeau and S. Perreault, Microelect. Manu and Testing 12 (10) (1989) 35.
[9] S.M. Sze, Physics of Semiconductor Devices (Wiley, New York, 1969) pp. 40, 444–466.
[10] M.L. Grundner and H. Jacob, Appl. Phys A39 (1986) 73.
[11] E.M Juleff, J. McLeod, E.A. Hulse and S Facett, S.S Tech (Sept. 1982) 82.
[12] R C. Henderson, J Electrochem Soc 119 (1972) 772
[13] S.I. Raider, R. Flitsch and M.J. Palmer, J. Electrochem. Soc. 122 (1975) 413
[14] M.I. Current, N.L. Turner, T C. Smith and D. Crane, Nucl. Instr. and Meth. B6 (1985) 336.

Nuclear Instruments and Methods in Physics Research B55 (1991) 183–187
North-Holland

Spectroscopic ellipsometry for depth profiling of ion implanted materials

J. Vanhellemont, Ph. Roussel and H.E. Maes

Interuniversity Micro-Electronics Centre (IMEC), Kapeldreef 75, B-3001 Leuven, Belgium

The application of spectroscopic ellipsometry (SE) to obtain accurate depth profiles of ion-implanted silicon substrates is discussed. Details on the interpretation of SE spectra are given, explaining why such a complex analysis is possible. The power of SE to nondestructively obtain depth profiles of ion implantation damage is illustrated for hydrogen-implanted silicon and on low-dose implanted SIMOX (Separation by IMplanted OXygen) material. The obtained SE results are verified by cross-sectional transmission electron microscopy and by other analytical techniques.

1. Introduction

Spectroscopic ellipsometry has known a real breakthrough during the last few years since a high-quality commercial instrument has become available [1]. Although the theoretical principles of SE were developed more than two decades ago, it is only with the availability of cheaper computer hardware that the technique could be developed to its present mature status. The recorded spectra are based on the measurement of the change of polarization of a circularly polarised incident light beam by interaction with the structure under investigation. The measurement can be performed at a number of different wavelengths largely exceeding the number of unknown parameters, even for complex multilayer structures A detailed regression analysis is then possible, assuming a physically realistic model for the multilayer structure. As the technique is based on the measurement of the change of polarization of the incident light by the interaction with the specimen, it has the advantage of being independent of intensity fluctuations of the light source.

In the present paper a novel powerful application of SE is presented. It is shown that by using an optimised regression algorithm and an optimised structure of reference files for refractive indices, accurate depth profiles of structures with varying refractive index can be obtained.

The multilayer optical spectrometer scanner (MOSS) of SOPRA is used with improved interpretation software [#1]. All SE spectra are recorded at an incident angle of 75°, close to the Brewster angle of the SiO_2/Si system which gives the highest sensitivity. The wavelength window used in this work ranges from 300 to 850 nm and a standard measurement is performed at 111 equidistant wavelengths. The results are compared with those obtained by other techniques such as X-ray diffraction (XRD) to measure the strain distribution, secondary ion mass spectroscopy (SIMS) for the determination of the chemical depth profiles and cross-sectional transmission electron microscopy (TEM) to obtain information on layer thicknesses, different phases and the crystal quality of the implanted layers

[#1] Will be implemented in future SOPRA software

2. Interpretation of SE spectra of multilayer structures

The simulation of SE spectra of multilayer systems is based on the calculation of the optical thicknesses of the different layers as a function of the wavelength. This requires a knowledge of the complex refractive index for each layer at each wavelength. The refractive indices of all components in the multilayer structure must be available as a library in the interpretation software. A sophisticated regression program then allows the best fit to be calculated between the simulated and the recorded SE spectra. During the regression, the incident angle, the thickness and the composition of the various layers can be varied.

2.1. Cubic splines for storage and interpolation of refractive index files

In this work cubic splines are used to store the reference data. In this way an optimum interpolation can be obtained, as the available data are stored as a continuum [2]. The goal is to obtain an optimised approximation $n_a(\lambda)$ for the refractive index n as a function of the wavelength:

$$n(\lambda) \approx n_a(\lambda)$$

0168-583X/91/$03 50 © 1991 – Elsevier Science Publishers B.V. (North-Holland)

When using cubic splines B_i, the problem reduces to:
- the choice of knots, and
- the determination of the coefficients μ_i

$$\sum_{i=1}^{m} [\mu_i n(\lambda)] B_i(\lambda) = n_a(\lambda).$$

$C_i = \mu_i n$ are the spline coefficients, determined by the fit criterion

$$\sum_{j=1}^{d} \left[\sum_{i=1}^{m} (\mu_i n(\lambda_j)) B_i(\lambda_j) - n_a(\lambda_j) \right]^2 = \text{minimum}.$$

The number of knots is increased until this minimum is smaller than S_q, the accuracy which one wants to obtain. In those cases for which the error on the data points is known it should be taken into account in the choice of S_q.

The cubic spline fit program used in this work is a reduced version of the FORTRAN source for cubic splines with constraints taken from ref. [3].

2.2. Calculation of indices of refraction of mixed layers

In the much referenced work of Bruggeman on effective medium approximation (EMA) models for mixed layers, expressions were derived for the dielectric constant of mixed layers for different types of physical mixtures, e.g. lamellae, parallel of perpendicular to the incident beam, spherical inclusions or homogeneous mixtures of spheres, etc. [4].

The EMA which is most commonly used and referred to as the Bruggeman model supposes a homogeneous mixture of spheres of the two components. In the present work three EMAs are used: the Bruggeman model, a model for spherical inclusions, and a model for lammellar inclusions [4]. For these three cases the dielectric function ϵ is respectively determined by

$$\epsilon = 0.25\left[C + (C + 8\epsilon_1\epsilon_2)^{0.5} \right]$$

$$\text{with} \quad C = (3c - 1)(\epsilon_1 - \epsilon_2) + \epsilon_1, \tag{1}$$

$$1 - c = \frac{\epsilon_2 - \epsilon}{\epsilon_2 - \epsilon_1} \sqrt[3]{\frac{\epsilon_1}{\epsilon}}, \tag{2}$$

$$\epsilon = (1 - c)\epsilon_1 + c\epsilon_2, \tag{3}$$

where c is the concentration of component 2 and ϵ_1, ϵ_2 are the dielectric constants of components 1 and 2, respectively. As the dielectric constants ϵ_1, ϵ_2 and thus also ϵ are complex numbers, special care has to be taken to obtain the correct complex refraction index $n = \sqrt{\epsilon}$ from all mathematically possible solutions, especially for expressions (1) and (2) [5].

2.3. Regression analysis

The regression analysis is based on the Levenberg–Marquardt algorithm [6] and is optimised for the highest stability by limiting all parameters to physically meaningful values. Briefly, the Levenberg–Marquardt type of approach can be described as follows: Assume that we have a set of measured values f_i^m. The goal of the regression routine is to minimise the error function G, given by the sum of the squares

$$G = \sum_{i=1}^{n} [f_i^c(\tilde{x}) - f_i^m]^2$$

$$\text{with} \quad \tilde{x} = (x_1, x_2, \ldots, x_p)^T \quad \text{and} \quad p \le n.$$

$f_i^c(\tilde{x})$ are the values of the nonlinear functions $f^c(\tilde{x})$ calculated at the measuring points, based on a model with variable parameters $\tilde{x}$. The superscripts c and m stand for the calculated and for the measured values, respectively.

The iterations of the regression program are then given by

$$\tilde{x}^{\lambda+1} = \tilde{x}^{\lambda} + \tilde{\delta}^{\lambda},$$

with $\tilde{\delta}$ the solution of the set of linear equations

$$(\mathbf{A} + \lambda \mathbf{I})\tilde{\delta} = -\tilde{v}$$

and $\mathbf{A} = \mathbf{J}^T\mathbf{J}$, $\tilde{v} = \mathbf{J}^T\tilde{f}^c$ are calculated at $\tilde{x}^{\lambda}$. The Jacobian $(m \times n)$ matrix $\mathbf{J}$ is defined as

$$[J_{ij}] = \frac{\partial f_i^c}{\partial x_j},$$

and λ is the parameter which is used to control the size of the iteration steps. During the calculation of λ, $\mathbf{A}$ and $\tilde{v}$ are constant so that $\tilde{\delta}$ is a function of λ. $\lambda = 0$ and $\lambda = \infty$ are the two extreme values and correspond to the Gauss–Newton and the steepest descent method, respectively. The steepest descent methods are very stable but have the drawback of being slowly convergent. The Gauss–Newton methods are more daring and converge faster, if at all. They, however, have the drawback of being much less stable. The Levenberg–Marquardt-based methods try to find a better choice of λ, taking into account the evolution of the regression. In most cases a starting value of λ is chosen which is either kept constant, or multiplied with, or divided by a fixed value ν between 1 and 10 for each iteration. A more sophisticated approach allows an optimum value of ν (but still between 1 and 10) to be calculated at each iteration step, thus also optimising λ during the regression [7].

The accuracy of the final fit is expressed by the unbiased estimator σ of the mean square deviation:

$$\sigma = \left(\frac{G}{2n - p} \right)^{1/2}. \tag{4}$$

The error function for the SE spectra can be written as

$$G = \sum_{i=1}^{n} \left[(D_i^c - D_i^m) + (W_i^c - W_i^m)^2 \right], \tag{5}$$

where p is the number of parameters, e.g. film thicknesses, incident angle or film composition, which is

varied during the regression and n is the number of different wavelengths at which a measurement is performed.

To avoid tan ψ having an exaggerated influence in the fitting criterion, so making it insensitive to variations in δ, two fit criteria are used:
- weighting of tan ψ (and cos δ), limiting the variation of both parameters to $[-1, 1]$, i.e.

$$D_i^{c,m} = \frac{2 \cos \delta_i^{c,m} \tan \psi_i^{c,m}}{\tan^2 \psi_i^{c,m} + 1} = \cos \delta_i^{c,m} \sin 2\psi_i^{c,m}$$

and

$$W_i^{c,m} = \frac{\tan^2 \psi_i^{c,m} - 1}{\tan^2 \psi_i^{c,m} + 1} = \cos 2\psi_i^{c,m}; \quad (6)$$

- for small tan ψ an unweighted fit criterion is used with

$$D_i^{c,m} = \cos \delta_i^{c,m} \quad \text{and} \quad W_i^{c,m} = \cos 2\psi_i^{c,m}. \quad (7)$$

The uncorrelated 95% confidence limits and the cross-correlation matrix between the parameters of the regression are also obtained assuming a Gaussian error distribution of the parameters.

3. Depth profile determination

The determination of depth profiles of layers with variable refractive indices is an iterative process. Some preliminary information is required with respect to the location of the layer with variable refractive index. For ion implantation damage a knowledge of the implantation energy and dose and of the implanted species allows us to estimate the depth of the damage peak below the surface. This is illustrated by considering the case of a damage profile in silicon. This procedure is, however, generally applicable for all layers which have varying optical properties with depth.

A simple three-layer model is used, assuming that the structure consists of an undamaged silicon substrate overlain by a damaged layer, which can be modeled as a mixture of single-crystal and amorphous silicon or voids. On top of this damaged layer one assumes, again, an undamaged silicon layer which is in turn covered by a thin native or capping silicon dioxide film. Keeping the incident angle constant during the regression analysis will then yield an approximate thickness of the damaged layer and of the top silicon layer. The next step is to replace this three layer model by a more complex one. Below the undamaged silicon overlayer, the damaged layer is subdivided into a number of thin mixed layers of equal thickness, which have the same total thickness as the damaged layer in three-layer model. In most cases the number of layers cannot be larger than ten, due to the limited number of measured wavelengths and the limited amount of information contained in the spectra. During the regression analysis (still at a constant angle) the thicknesses of the two top layers (silicon dioxide and silicon) are allowed to vary, while for the other, mixed layers, only the concentration of the second component is allowed to float. Some readjustment of the individual layer thicknesses within the damaged layer may be necessary, afterwards, to obtain an optimum profile when the concentration in the outer layers is reduced to zero. When, after a number of iterations the best structural model and therefore also the best fit, is obtained, the incident angle is also allowed to float. Its variation gives an indication of the quality of the proposed physical model. When the model is very good, the angle will remain nearly constant. In other cases, the regression program will try to obtain the best fit by changing the incident angle by more than the (mechanical) accuracy to which it is known (about 0.1°). In some cases a further improvement in the fit and the profile can be obtained by using within the damage layer variable layer thicknesses whereby thinner layers are used in areas where the refractive indices are rapidly changing and thicker ones in areas with small concentration gradients.

4. Two case studies

4.1. Damage profiles in as-implanted implanted silicon

As a first example, results obtained from hydrogen-implanted silicon substrates are presented. (001) silicon wafers are implanted with H_2 fluences of 4×10^{15} and 2×10^{16} cm^{-2} at energies of 15.5 and 75 keV. The damage profiles are obtained with a 12-layer model assuming a native oxide, an undamaged top silicon layer and ten mixed layers of crystalline silicon and voids of fixed thickness but varying composition. The results are shown in fig. 1a. The profiles obtained with SE correspond very well with those obtained independently with XRD (strain profile) and SIMS (chemical profile) represented in fig. 1b. To represent the concentration of voids it is assumed that it is directly proportional to the strain measured by XRD so that the same logarithmic scale can be used. The depth information obtained with SE is very accurate and corresponds well with the results from cross-sectional TEM investigation [9].

SE is thus sensitive for low damage levels It must be pointed out, however, that the obtained quantitative data for the void concentration depend critically on the accuracy of the value of the incident angle of the light beam. Many local minima can occur during the regression especially in the case of the low-dose implants. Knowledge of the approximate location of the maximum damage (from the measurement of the high-dose

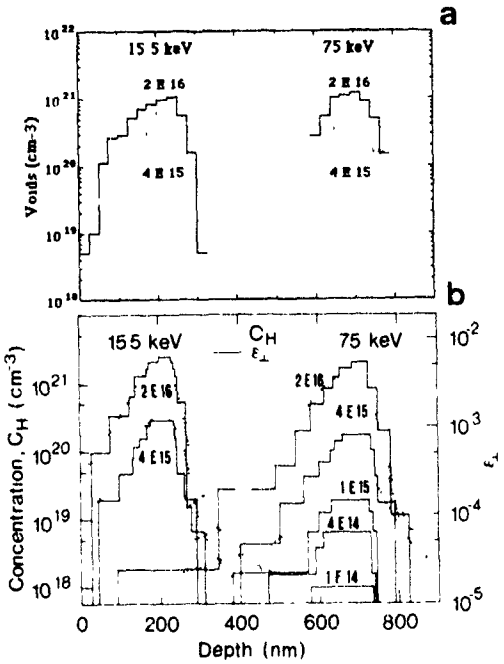

Fig 1 (a) Damage profiles derived from the SE spectra of hydrogen-implanted wafers (b) Strain and the hydrogen profiles obtained with XRD and SIMS (dotted line), respectively [8]

implants) is essential in such cases in order to obtain realistic numbers

4.2. Compositional profiling of SIMOX materials

As a second example, compositional profiling in low-dose implanted SIMOX is illustrated. Buried SiO_2 layers can be formed by high-dose ($> 10^{18}$ cm^{-2}) oxygen ion implantation at energies ranging typically from 150 to 200 keV. Lower doses do not yield a continuous buried oxide layer, is illustrated in the TEM micrograph in fig. 2a. The as-implanted material shows a buried damaged layer in which the optical properties can again be modeled by a mixture of a-Si and Si, or by a mixture of SiO_2 and damaged Si.

After an anneal for 16 h at 1050 °C, a mixed buried layer consisting of SiO_2 precipitates in a silicon matrix is observed, shown in fig. 2a. SE allows us to determine the composition profile of the buried mixed layer for three different EMAs shown in fig. 2b. Calculation of the integrated SiO_2 profile in the annealed wafer also allows us to calculate the implanted oxygen dose. The doses obtained based on eqs. (1)–(3) correspond surprisingly well with the nominal dose of 0.5×10^{18} cm^{-2}. More information on the application of SE to

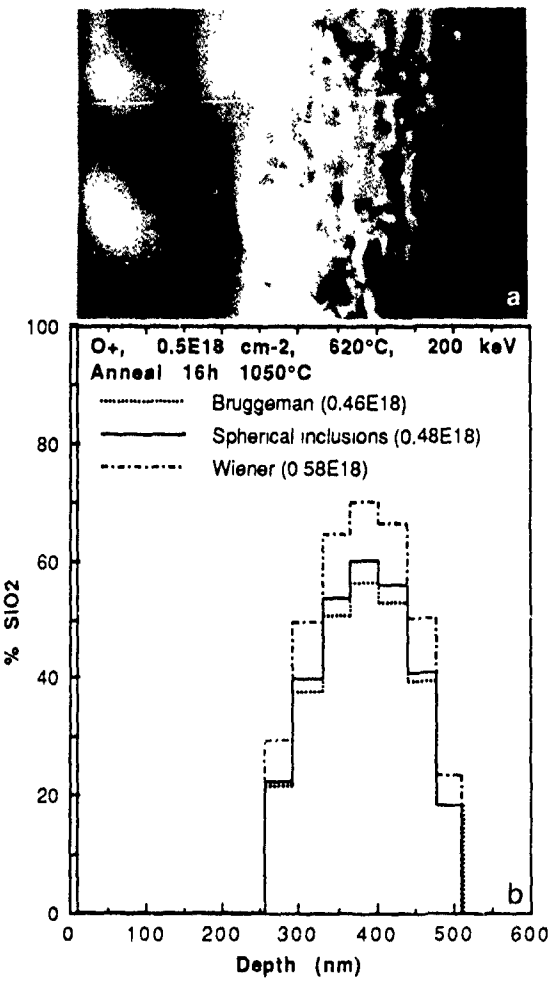

Fig. 2 (a) Cross-sectional TEM micrograph of a low-dose implanted (0.5×10^{18} cm^{-2}, 200 keV) SIMOX structure after a 16 h anneal at 1050 °C [courtesy of A De Veirman]. (b) SiO_2 concentration profiles obtained with SE using three different EMA models. The oxygen implantation doses calculated based on the integrated SiO_2 concentration profile are also indicated

characterise both as-implanted and annealed SIMOX materials can be found in ref [10].

5. Conclusion

The power of spectroscopic ellipsometry, which is a *genuinely nondestructive* technique, to monitor not only damage but also composition profiles in silicon, is demonstrated and verified by comparison with other analytical techniques. It is shown that SE and TEM have a similar thickness accuracy for the observation of these profiles but that SE also allows these profiles to be quantified. The examples illustrate that in many re-

spects SE can be considered as a nondestructive, cheap "poor man's" optical "Rutherford backscattering spectrometer" and even as a one-dimensional optical high-resolution microscope.

References

[1] SOPRA, 68, rue Pierre Joigneaux, 92270 Bois-Colombes, France.

[2] J. Vanhellemont and Ph. Roussel, Proc. Int. Workshop of Spectroscopic Ellipsometry, Paris, April 23–26, 1990 (SOPRA)

[3] P. Dierckx, Computing 24 (1980) 349.

[4] D.A.G Bruggeman, Annalen der Physik 5 (1935) 636.

[5] Ph. Roussel, J. Vanhellemont and H.E. Maes, to be submitted to J. Opt Soc Am.

[6] D. Marquardt, J Soc Indust. Appl. Math. 11 (1963) 431.

[7] R. Fletcher, Atomic Energy Research Establishment, Harwell, UK, Report AERE-R.6799 (1971).

[8] L. Meda, G F Cerofolini, R. Dierckx, G. Mercurio, M. Servidori, F. Cembali, M. Anderle, R. Canteri, G. Ottaviani, C Claeys and J. Vanhellemont, Nucl. Instr and Meth. B39 (1989) 381

[9] J Vanhellemont, C. Claeys and H E. Maes, in: Defect Control in Semiconductors, ed. K Sumino (North-Holland, 1990) p. 501

[10] J. Vanhellemont, A. De Veirman and H.E. Maes, Proc 1st SIMOX Workshop, Surrey, UK, 7–8 November 1988, Vacuum (1990) in press.

Nuclear Instruments and Methods in Physics Research B55 (1991) 188–192
North-Holland

Process control issues for ion implantation using large tilt angles

Robert B. Simonton, Dennis E. Kamenitsa and Andy M. Ray
Eaton Corp., Semiconductor Equipment Division, 2433 Rutland Drive, Austin, TX 78758, USA

Using large tilt angles (7°–60°) and wafer rotational repositioning during ion implantation results in several effects which can compromise process control. These effects include: (1) tilt-related nonuniformity, (2) effective dose reduction from decreased ion flux density, (3) effective ion energy decrease, (4) effective dose reduction from dopant loss by surface scattering, and (5) effective surface film thickness increase. In this paper we characterize these effects and explain their physical basis.

1. Introduction

Ion implantations performed using large tilt angles and wafer rotational (azimuthal) repositioning can provide simplified processing which forms submicron transistors that avoid undesirable device scaling effects [1]. This technique also allows fabrication of three-dimensional structures which avoid the packing density limitations of traditional planar semiconductor processing [2].

However, the use of this new implantation technique requires understanding and control of several effects which impact process results significantly; these effects typically increase in magnitude with increasing tilt angles. This paper investigates these effects for tilt angles up to 60°. Throughout this paper, the tilt angle (θ) will be defined as the angle between a vector perpendicular to the implanted surface and the vector of the incident ion beam at the center of the target wafer.

All the process results in this investigation were obtained by implanting boron and phosphorus into 150 mm, prime, silicon ⟨100⟩ wafers using an Eaton NV-6200AV [3], a modern, electrostatically scanned medium current ion implanter which allows implantation at any combination of tilt angles 0°–60° and twist (azimuthal) angles 0°–360°. This implanter also allows in situ wafer rotational repositioning, using either discrete steps or continuous rotation, in highly flexible user-selectable modes.

The implanted wafers were characterized with sheet resistance measurements using a Prometrix RS-50e; post-implant processing was a furnace anneal (1000°C, 30 min, 100% N_2), followed by BOE/DI water surface preparation. SIMS profiles were also obtained from the center of the wafer for selected samples.

2. Tilt (geometric) nonuniformity

It is well known that tilting the target wafer during implantation when using electrostatic scanning results in cross-wafer dose nonuniformity. This nonuniformity is caused by the changing angle between the center of scan plates and the target surface from one edge of the wafer to the other; it is approximately proportional to $\tan\theta$, where θ is the tilt angle [4]. This effect is easily compensated by modifying the scan voltage waveforms; this compensation has been available on Eaton medium current implanters for some time as "uniformity correction factors" [5]. The NV-6200AV employs the same technique to eliminate this nonuniformity for tilt angles in the entire range 0°–60°, as seen in fig. 1.

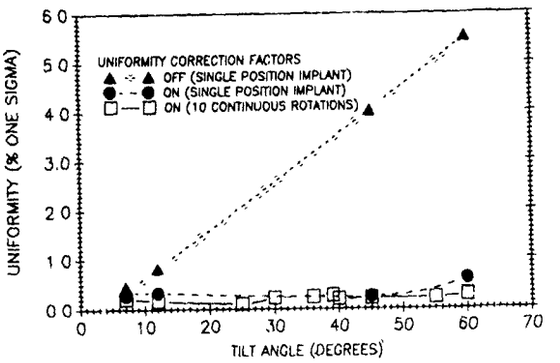

Fig. 1. Cross-wafer sheet resistance uniformity (%, σ) on 150 mm wafers for tilt angles (θ) 7°–60°, with and without NV-6200AV uniformity correction factors. All implants are $^{31}P^+$, 5×10^{14} cm^{-2}, 160 keV, single-position implants used 25° twist and screen oxide (400 Å for $\theta < 45°$, 200 Å for $\theta \geq 45°$).

3. Effective dose reduction

It has been recognized for some time that tilting the wafer relative to the incident ion beam (in any scan system design) will result in reduced dose due to the decreased flux density of the ion beam on the target

0168-583X/91/$03.50 © 1991 – Elsevier Science Publishers B.V. (North-Holland)

surface. This effect is proportional to cos θ; the effective dose $D^1 = D \cos \theta$, where D is the dose on a surface perpendicular to the incident beam [6]. This effect is easily compensated by designing the implanter to make appropriate adjustment to the area factor used to control the dose of the implant. This technique is employed in the NV-6200.AV, eliminating this effect at all tilt angles.

4. Effective energy decrease

This effect has also been recognized for some time; its cause is easily visualized by considering the projection of the incident ion energy (E) vector for a tilted implant onto a vector perpendicular to the wafer's surface. This analysis reveals that the incident ion energy E is reduced by the factor cos θ, resulting in an effective energy $E^1 = E \cos \theta$ [6].

The process variation from this effect is demonstrated in fig. 2; this figure contains average sheet resistance data for two sets of wafers. One set was implanted using constant 100 keV ion energy at increasing tilt angles 7°–60°, and the other set was implanted with constant 7° tilt and decreasing ion energies. These ion energies were selected to be equal to the effective energies of the wafers implanted with constant 100 keV ion energy and increasing tilt angles. As seen in fig. 2, the sheet resistance increases with both decreasing energy (using constant tilt) and with increasing tilt angle (using constant energy).

The reason for this is apparent by examining fig. 3, the SIMS profiles from the center of wafers from both these groups. As the ion energy is decreased or tilt angle is increased, the profiles are shifted to shallower regions and their peak concentration increases. These profile changes result in higher sheet resistance because more of the implanted carriers are placed in regions of lower mobility, and the implant layer thickness is decreased.

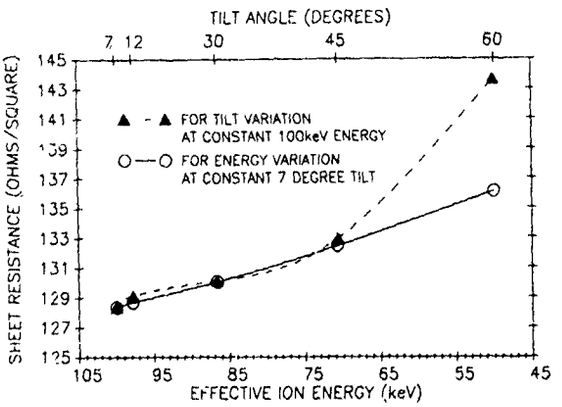

Fig. 2 Average sheet resistance dependence upon increasing tilt angle (at constant 100 keV incident energy) and with decreasing ion energy (at constant 7° tilt angle). All implants are $^{31}P^+$, 5×10^{14} cm^{-2}, with native oxide and continuous rotation.

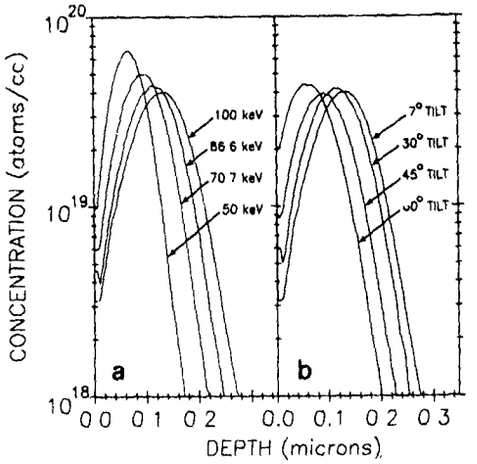

Fig 3. (a) SIMS profiles (as implanted) for $^{31}P^+$, 5×10^{14} cm^{-2} implants with constant 7° tilt angle and decreasing ion energy, as indicated. (b) SIMS profiles (as implanted) for $^{31}P^+$, 5×10^{14} cm^{-2} implants with constant 100 keV ion energy and increasing tilt angles, as indicated

5. Dopant loss

It is apparent in fig. 2 that reducing the incident ion energy (at constant 7° tilt) by a cos θ factor imitates the sheet resistance shift for increased tilt angles (with constant energy) reasonably well up to about 45° tilt. Above that, a significant departure in sheet resistance behavior between the two groups appears.

The reasons for this departure are made apparent by close comparison of fig. 3a and 3b. In fig. 3a, as the energy is reduced (at constant tilt), both the projected range (R_p) and the straggle (ΔR_p) scale with ion energy, causing the peak concentration (N_p) to rapidly increase with reduced energy. However, in fig. 3b, as the tilt angle is increased (with constant ion energy), we see that the profiles at and above 45° tilt are not identical to the corresponding profiles in fig. 3a, which have the same effective energy. This behavior has been previously reported [6].

The difference is more clearly illustrated in fig. 4, which contains the 7° tilt, 50 keV SIMS profile, and the 60°, 100 keV SIMS profile from fig. 3a and 3b, respectively. The experimentally measured parameters (by SIMS) of these two profiles with equal effective energy are also provided in fig. 4. From this figure we can see that, for profiles with increasing tilt angles (at constant ion energy), the range is decreasing faster than for reduced energy (at constant tilt) profiles, and the

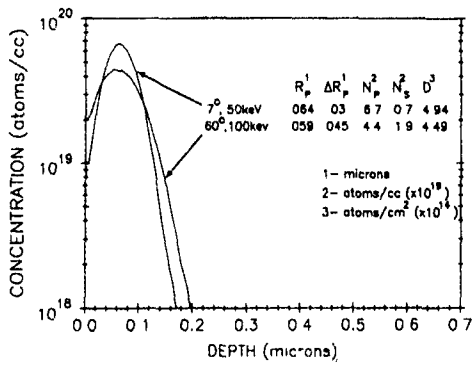

Fig. 4. SIMS profiles (as implanted, $^{31}P^+$ 5×10^{14} cm^{-2}) for two implants at 7° and 60° tilt with the same effective energy (50 keV). The table provides measured values (by SIMS) of implant range (R_p), straggle (ΔR_p), peak concentration (N_p), surface concentration (N_s) and implant dose (D) for these two implants.

straggle is significantly greater in the large tilt angle profile, because it is not scaling with effective energy. Consequently, the 60° tilt angle implant in fig. 4 has a lower peak concentration at a slightly shallower depth, a deeper junction depth, and a significantly higher surface concentration than the corresponding profile at 7° tilt with equivalent effective energy. More important, a significant amount of dopant has been lost from the large tilt angle profile at the implant surface; for the conditions in fig. 4, the 60° profile has lost about 9% of its dose (as measured by SIMS) relative to the 7° profile. [The total phosphorus dose precision for the SIMS measurements in this study was experimentally determined to be ±0.7%, 1σ.] The smaller projected range and dopant loss of the large tilt profile will increase the sheet resistance; however, this is partially offset by the reduced peak concentration and slightly increased junction depth, which will both decrease the sheet resistance by increasing the mobility and thickness of the implanted layer, respectively. As a result, although the 60° implant has ~ 9% lower effective dose, it was only ~.5% higher in sheet resistance than the 7° tilt profile with equivalent energy in fig. 4.

The implications of the behavior illustrated in figs. 3 and 4 is that compensation of sheet resistance increases from effective energy reductions by adjusting the ion implant energy with a cos θ factor will not be generally effective for tilt angles $\geq 45°$. This is demonstrated in fig. 5, which presents sheet resistance variation with tilt angle for phosphorus (fig. 5a) and boron (fig. 5b) implants, in which we have adjusted the incident ion energy to obtain a constant effective (100 keV) energy. As is apparent in this figure, the sheet resistance is well controlled (to about ±0.5%) up to about 45° tilt, above which the sheet resistance increases for both species, as expected. Of more significance is that the increase in sheet resistance is different for phosphorus (+3.1% at 60°, relative to the average sheet resistance between 7°

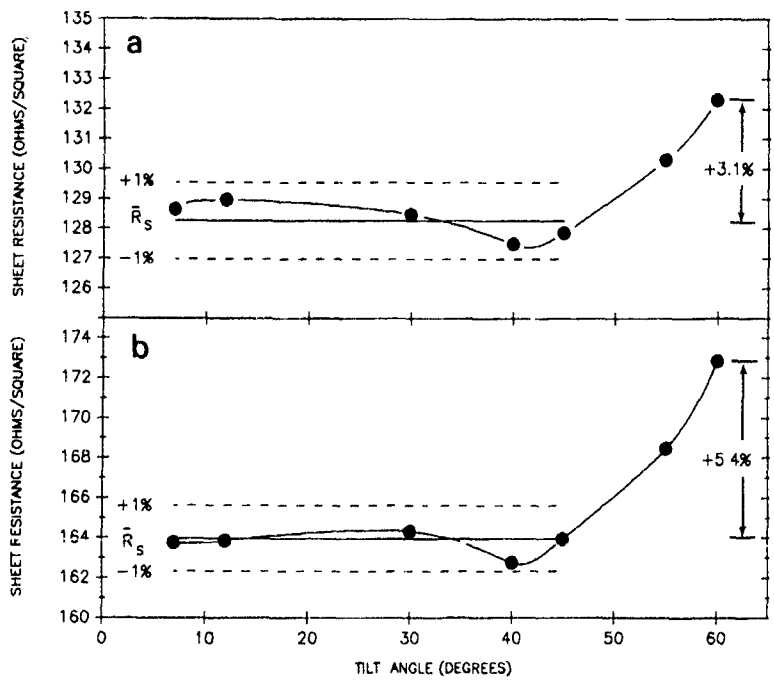

Fig. 5. (a) Average sheet resistance dependence upon tilt angle (θ) using a constant effective energy $E^1 = E\cos\theta = 100$ keV for $^{31}P^+$, 5×10^{14} cm^{-2} implantation using bare wafers and continuous rotation. (b) The same, but for $^{11}B^+$, 5×10^{14} cm^{-2} implantation.

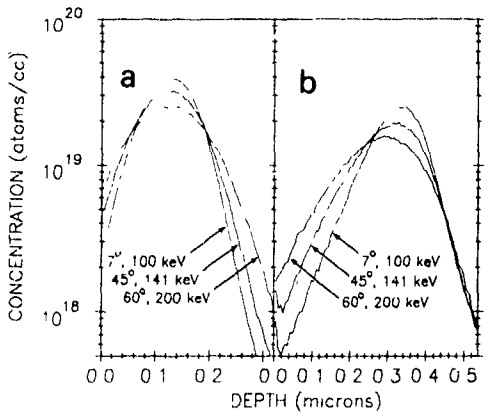

Fig 6 (a) SIMS profiles, (as implanted) for $^{31}P^+$, 5×10^{14} cm^{-2} implants (using native oxide and continuous rotation) with increasing tilt angle (θ) and constant effective energy $E^1 = E\cos\theta = 100$ keV. (b) The same, but for $^{11}B^+$, 5×10^{14} cm^{-2} implantation

and 45°) than for boron (+5.4% at 60°). This demonstrates that attempts to "correct" for the sheet resistance increases above 45° tilt by a factor embodied in the implanter design will not be generally correct, because the profile variations and dopant loss will be a complex function of species, energy, dose and implant surface conditions (amorphous or crystalline, orientation, thickness and type of surface films).

The larger increase in sheet resistance for boron than phosphorus for the implants in fig. 5 is explained by considering the relative profile changes for these two species as the tilt angle is increased. These changes are characterized by SIMS in fig 6 and table 1. [The total boron dose precision for the SIMS measurements in this study was experimentally determined to be ±2.7%, 1σ.] For phosphorus at 60° relative to 7°, the relative range (R_p) reduction is significantly less than for boron, while its relative straggle (ΔR_p) increase is only slightly smaller than for boron, which results in a large relative junction depth increase for phosphorus and a very small increase for boron. There is a similar relative decrease in peak concentration for both species; however, different mobility functions for electrons and holes will impact the resulting sheet resistance shift for phosphorus and boron. Taken together, the impact of these profile variations with species is that the mobility increase and implant layer thickness increase is greater for phosphorus and the dopant loss is comparable for phosphorus (~ 8.7%) and boron (~ 10.8%) at 60° tilt relative to 7° tilt. This results in the smaller sheet resistance increase for phosphorus than boron observed in fig. 5.

The dopant loss at large tilt angles is due to a combination of Rutherford scattering at the sample surface and the range straggle of a Gaussian implant profile placing a portion of the profile outside the sample surface. Sputtering effects can be neglected until doses higher than 1×10^{16} cm^{-2} are employed [7]. The dopant loss at large tilt angles will be increased by increasing the mass or reducing the energy of the incident ions [8]. Calculations using a model based only on Gaussian implant profile straggle will tend to underestimate the degree of dopant lost, whereas a model based on Rutherford scattering at the surface will yield more accurate results [8]. This is particularly true for tilt angles > 60°, which occur for implantation into the vertical sidewall of trenches. In this study, calculations at 60° tilt using only the Gaussian model [8] underestimated the measured dopant loss by a factor of about 50 for boron and less than 2 for phosphorus.

6. Effective film thickness increase

As the tilt angle (θ) is increased, the effective thickness of surface films (e.g., screen oxides) will be increased, proportional to $(\cos\theta)^{-1}$. This is visualized by considering the path length of an incident ion's trajectory through a surface film of thickness t, as the surface is increasingly tilted relative to the incident ion trajectory; the path length increases at $t(\cos\theta)^{-1}$. This effect

Table 1
Measured implant profile parameters: range (R_p), straggle (ΔR_p), peak concentration (N_p) and dose (D), for implants at various tilt angles (θ), whose ion energy (E) was adjusted for a constant effective energy $E^1 = E\cos\theta$ of 100 keV (from SIMS profiles in fig 6)

Implant species	Implant dose [cm^{-2}]	θ [deg]	R_p [μm]	ΔR_p [μm]	N_p [$\times10^{19}cm^{-3}$]	D [$\times10^{14}cm^{-2}$]
$^{31}P^+$	5×10^{14}	7	0.128	0 051	4.0	5.01
$^{31}P^+$	5×10^{14}	45	0.125	0 062	3.25	4 81
$^{31}P^+$	5×10^{14}	60	0.124	0.076	2.55	4.58
$^{11}B^+$	5×10^{14}	7	0 334	0 068	2.66	4 98
$^{11}B^+$	5×10^{14}	45	0.318	0.088	2.04	4 75
$^{11}B^+$	5×10^{14}	60	0 297	0 109	1 65	4 44

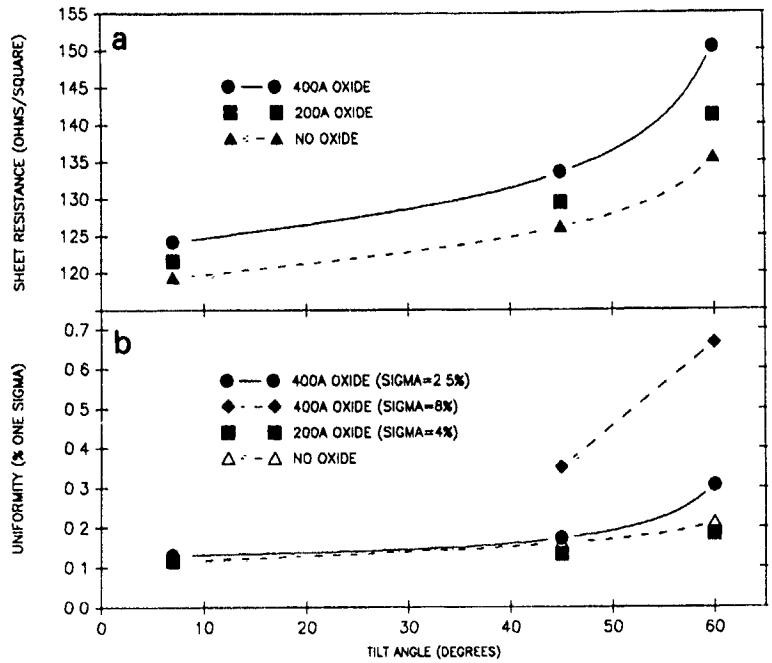

Fig. 7 (a) Average sheet resistance dependence upon large tilt angles from the presence of a 200–400 Å dry thermal oxide. All implants are $^{31}P^{+}$ 5×10^{14} cm^{-2}, 160 keV using ten continuous rotations (b) Cross-wafer sheet resistance nonuniformity with large tilt angles from the presence of 200–400 Å dry thermal oxide; the sensitivity to 400 Å film uniformity is demonstrated. Implants as in (a)

results in increased ion scattering and dose hold-up in surface films with increased tilt angles. Consequently, the average sheet resistance increase and cross-wafer nonuniformity from hold-up in the film will also increase with larger tilt angles. This is demonstrated in fig. 7; as seen in fig. 7a, the sheet resistance of a 160 keV phosphorus implant is measurably increased at tilt angles $>45°$ (relative to bare wafers) by increased implant hold-up in an oxide film as thin as 200–400 Å. In fig. 7b the increased sensitivity to film uniformity at large tilt angles is demonstrated; the cross-wafer sheet resistance uniformity of the 160 keV phosphorus implant at 45–60° is clearly degraded by the nonuniformity of a 400 Å film. These effects increase with heavier species, lower energies and thicker films; they can be avoided by consideration of film hold-up during process design, as discussed in ref. [9].

Acknowledgement

The authors would like to thank Dr. Charles Magee of Evans East, Inc. for the quality of the SIMS analysis which supported this study.

References

[1] T Hori, IEEE Electron Device Lett. (1988) 300.
[2] Y Akasaka, Nucl Instr. and Meth B37/38 (1989) 9
[3] J. Dykstra, A Ray and R. Simonton, these Proceedings (8th Int. Conf. an Ion Implantation Technology, Guildford, UK, 1990) Nucl Instr. and Meth. B55 (1991) 478
[4] J. Keller, Radiat Eff 44 (1979) 71.
[5] D Zrudsky and D Myron, Nucl. Instr. and Meth. B26 (1987) 614
[6] G. Fuse, H. Umimoto, S. Odanaka, M. Wakabayashi, M. Fukumoto and T. Ohzone, J Electrochem. Soc 133 (1986) 996.
[7] K Kato, IEEE Trans Electron Devices 35 (1988) 1820
[8] T. Mizuno, T. Higuchi, H. Ishiuchi, Y Matsumoto, Y. Saitoh, S. Sawada and S. Shinozaki, IEEE Trans Electron Devices 35 (1988) 2323.
[9] D. Zrudsky and R. Simonton, Nucl. Instr and Meth B37/38 (1989) 351

Nuclear Instruments and Methods in Physics Research B55 (1991) 193–197
North-Holland

Annealing behaviors of residual defects in high-dose BF_2^+-implanted (001)Si under different implantation conditions

C.H. Chu [a,1], E.L. Tsai [a], W.Y. Chao [b] and L.J. Chen [a]

[a] *Department of Materials Science and Engineering, National Tsing Hua University, Hsinchu, Taiwan*
[b] *United Microelectronics Corporation, Hsinchu, Taiwan*

The annealing behavior of residual defects in high-dose BF_2^+-implanted (001)Si under different implantation conditions has been studied by cross-sectional transmission electron microscopy and four-point probe sheet resistance measurements. Three kinds of samples were prepared with different implanters. M, MC and H samples were implanted with 80 keV, $4\times10^{15}/cm^2$ BF_2^+ in a medium-current implanter without deliberate end-station cooling, a medium-current implanter with a freon-cooled end station, and a high-current implanter with a water-cooled end station, respectively. The BF_2^+ ion dissociation effects were revealed by the comparison of M or MC and H samples. Rod-like and equi-axial dislocation loops beneath the original a/c interface were observed in the M and MC samples. The dopant activation of the annealed samples was found to correlate well with microstructural changes.

1. Introduction

BF_2^+ implantation has become an important doping technique in the fabrication of p$^+$–n junctions in microelectronic devices. In order to reduce the cost and to increase the throughput of IC fabrication, the medium-current implanter (with a beam current in the range of tens to hundreds of microamperes) has been replaced by the high-current implanter (with a beam current of a few milliamperes for high-dose implantation). Owing to the differences in configuration of different models of implanters, the implantation conditions are varied. Changes in the implantation conditions, such as end-station cooling, molecular ion dissociation and contamination in the vacuum chamber can all influence the results of ion implantation. The channeling of boron during BF_2^+ implantation and the presence of a secondary boron peak as seen from SIMS depth profiling have been attributed to the dissociation of BF_2^+ ions after the mass analysis [1–4]. The dissociation of BF_2^+ ions during implantation results in the deep implantation of B^+ ions and makes the junction depth uncontrollable. Comparing the dissociation efficiency of BF_2^+ ions from a medium-current implanter and a high-current implanter showed that a high efficiency of BF_2^+ ion dissociation occurred in the medium-current implanter [5]. The effect of the dissociation of BF_2^+ ions on the residual defects is therefore of much importance. In this work we study the annealing behaviors of residual defects and dopant activation in samples implanted by medium- and high-current implanters. The residual defects and dopant activation were studied by the cross-sectional transmission electron microscopy and four-point probe sheet resistance measurements.

2. Experimental procedures

Single-crystal, 3–5 Ω cm, phosphorus-doped (001)Si wafers were used in the present study. Samples were implanted with 80 keV BF_2^+ ions at a fluence of $4\times10^{15}/cm^2$. Three kinds of samples were prepared using different implanters. Samples designated M were implanted by a medium-current implanter at room temperature with the beam current maintained at less than 20 μA to minimize heating effects. To determine the effect of substrate cooling during ion implantation, samples labeled MC were prepared by a Varian/Extrion 200-20A2 medium-current implanter with a freon-cooled end station. Finally, in order to determine the effects of high beam current and dissociation of BF_2^+ ions during ion implantation, samples labeled H were prepared in a Varian 120/10 high-current implanter with a water-cooled end station. The beam current was as high as 3 mA. In the Varian/Extrion 200-20A2 implanter, the beam was focused and the scanned area was 60 cm^2. The scanning frequency of the ion beam was 70 Hz along the vertical direction and 1000 Hz along the horizontal direction. In the Varian 120/10 implanter, the beam was elliptic in shape with major and minor axes of about 4 and 2 cm in length, respectively. The scanning frequency and rotation speed of the sample holder were 4.5 cycles/min and 1000 rpm, respectively.

[1] Present address: AT & T Bell Laboratories, 600 Mountain Avenue, Murray Hill, NJ 07974, USA.

0168-583X/91/$03.50 © 1991 – Elsevier Science Publishers B.V. (North-Holland)

The beam was scanned over a strip 3 to 35 cm from the center of the substrate holder. The wafers were oriented 7° off the incident beam direction to alleviate the channeling effect.

Isothermal annealings were performed in a three-zone diffusion furnace at 550–1000 °C for 0.5–1 h in N_2 ambient. High-purity N_2 gas was first passed through a titanium getter tube maintained at 800 °C to reduce the O_2 content for annealings in N_2 ambient. The residual defects were investigated by cross-sectional transmission electron microscopy conducted in a JEOL 200CX STEM. The dopant activation in the annealed samples was determined from the sheet resistances which were measured by the four-point probe technique.

3. Results and discussion

The average thicknesses of the surface amorphous layers of the as-implanted M, MC and H samples were measured to be 120, 138 and 122 nm, respectively. The roughness of the a/c (amorphous/crystalline) interface was found to increase in the order of H, MC and M samples, as shown in fig. 1. A thicker amorphous layer was found in the MC sample than those in the other samples, which is likely to be due to the alleviation of the aggregation of damage clusters by substrate cooling.

Solid state epitaxial growth (SPEG) was not completed in M and MC samples annealed at 500 °C for 1 h. The a/c interfaces were rather rough. The average thickness of the amorphous layers was about 10 nm and 5 nm in the M and MC samples, respectively. The thickness variation of the amorphous layers was about 40 nm and 30 nm in the M and MC samples, respectively. A high density of twins was found in the crystalline surface layers. Twins were found to have grown from a depth of about 40 nm and 60 nm above the original a/c interface in the M and MC samples, respectively. The twins were plates grown on all four {111} planes. The a/c interfaces were found to be delineated by {111} planes. Paired dislocations were evident in the M samples but not in the MC samples. In the H samples, SPEG was found to be completed. The regrowth layer was essentially defect free and the spreading of the defect clusters near the original a/c interface was about 30 nm. Examples are shown in fig. 2.

SPEG was completed in M, MC and H samples annealed at 600 °C. Thick surface twins were formed in the M samples. The width of the region with a high density of twins is about 70 nm. "V"-shaped dislocations, extending from the original a/c interface to the lower boundary of the twin region with a density of $9 \times 10^5/cm^2$, were observed. In the MC samples, only a low density of small twins was observed. The lengths of the microtwin plates were about 10 to 30 nm. In the H samples, the regrowth layer was found to be defect free Defect clusters were observed near the original a/c interface.

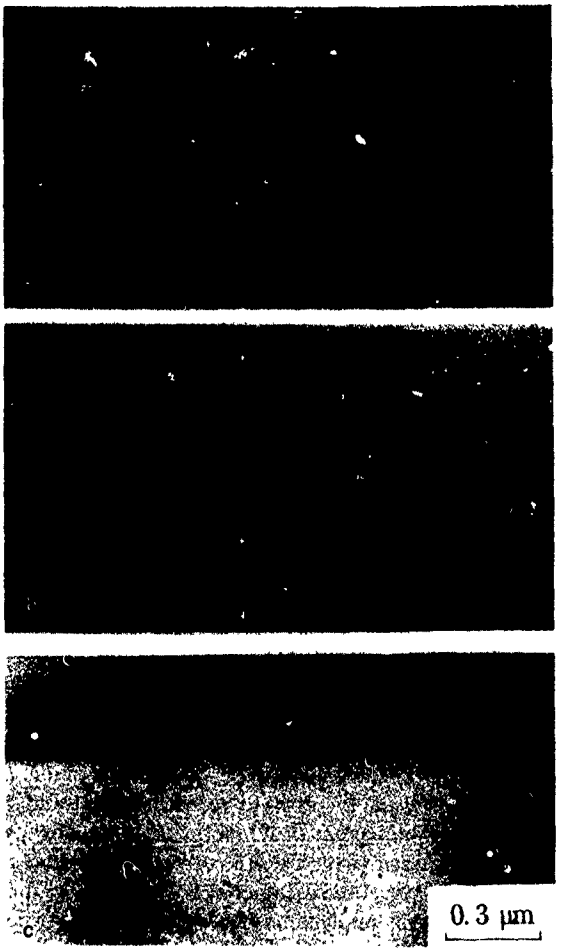

Fig. 1 XTEM micrographs of the as-implanted samples (a) M sample, (b) MC sample and (c) H sample.

In the M samples annealed at 700 °C, ~ 60-nm-long rod-like defects and 20-nm-diameter dislocation loops were observed in a layer extending from the original a/c interface to a depth of ~ 320 nm from the surface. Twins near the surface covered about 28% of the surface area. Paired dislocations were found in the regrowth layers. In MC samples, ~ 10-nm-long rod-like defects and small dislocation loops were observed to be distributed in a 100-nm-thick layer extending from the original a/c interface further into the substrate. In the H samples no dislocation loops were observed beneath the original a/c interface. The defect clusters in the original a/c interface had grown into small dislocation loops in the M, MC and H samples. The depth distribution and general features of defects in 800 °C annealed samples

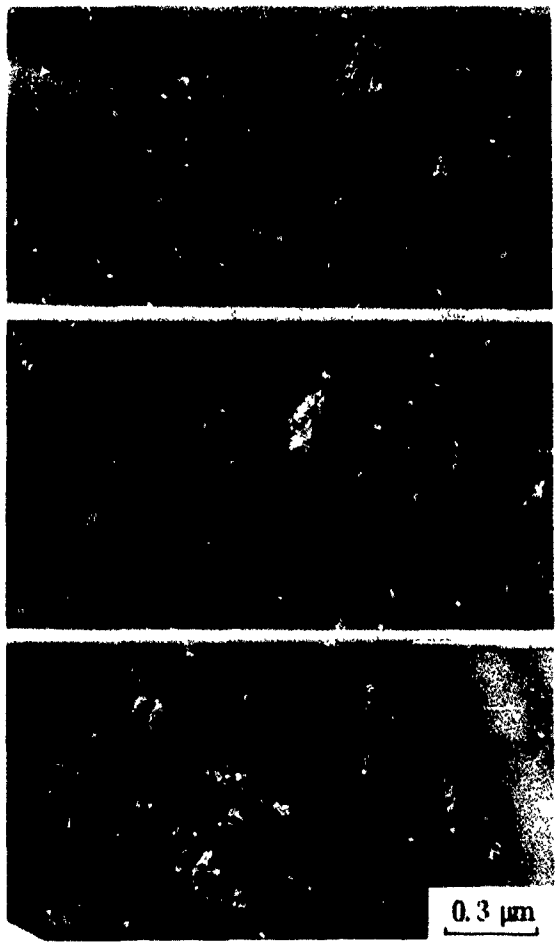

Fig 2. Bright-field (BF) XTEM micrographs of the 550 °C, 1 h annealed samples: (a) M sample, (b) MC sample and (c) H sample.

were found to be similar to those observed in 700 °C annealed samples.

In the M samples annealed at 900 °C, the rod-like defects beneath the original a/c interface were found to grow into loops. "V"-shaped dislocations were found in the near surface regions. A low density of surface twins was observed. In the MC samples, the dislocation loops near the original a/c interface were larger than those in the 800 °C annealed samples. For the H samples, similar results were obtained as those in the 800 °C annealed samples. Examples are shown in fig. 3.

In the M samples annealed at 1000 °C, surface twins and dislocations near the original a/c interface were observed. Discrete and large dislocation loops were observed near the original a/c interface in the MC samples. In the H samples, a lower density of dislocation loops than that found in the MC samples was observed near the original a/c interface.

The most striking difference in the residual defects among the annealed samples is that twins did not form in the H samples, whereas they were annealed out at a lower temperature in the MC samples than in the M samples. Formation of twins in high-dose BF_2^+ implanted (001)Si has been found previously [7]. Although the implantation was nominally performed at room temperature, the temperature can be much higher with poor thermal conduction in the end station. The self-annealing effect is expected to promote the aggregation of the defect clusters induced by ion implantation. The aggregates are rather difficult to remove by thermal annealing [8]. It is thought that the stabilized defect clusters tend to attract the fluorine atoms and hinder the SPEG of the amorphous layer. As the SPEG is slowed down, twins are formed Comparison among M, MC and H samples suggested that the formation of twins in the regrowth layer in BF_2^+-implanted (001)Si is

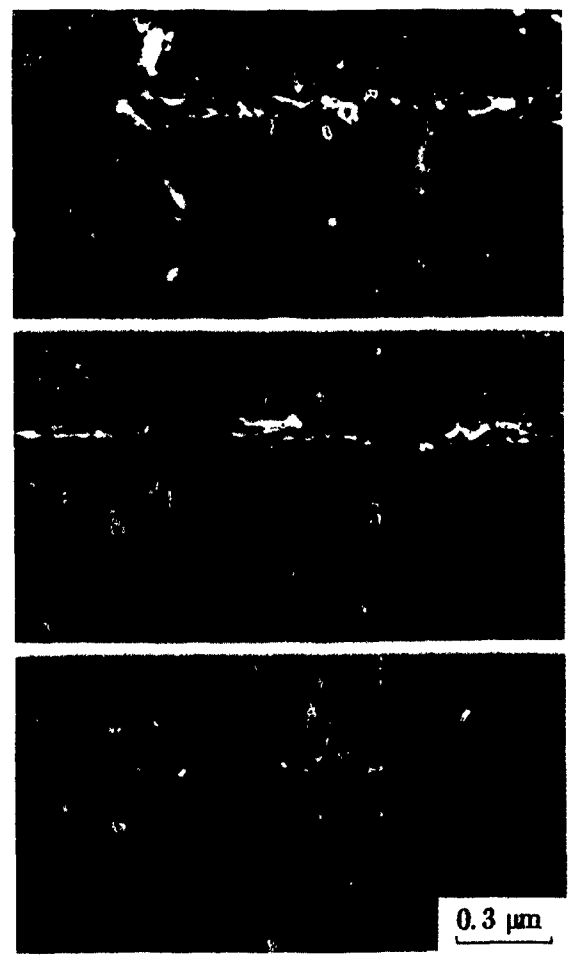

Fig. 3. WBDF micrographs of the 900 °C, 1/2 h annealed samples: (a) M sample, (b) MC sample and (c) H sample.

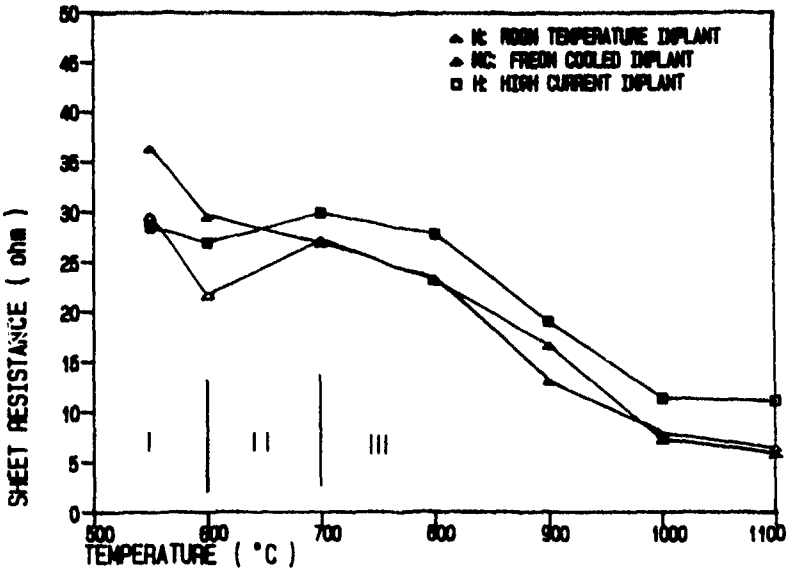

Fig. 4 Sheet resistances of the 550 to 1100 °C annealed M, MC and H samples.

correlated with substrate heating conditions during the implantation.

Rod-like dislocations and equi-axial loops in BF_2^+-implanted samples have been characterized previously [10,11]. In the M samples, the results were similar to those obtained previously. In the MC samples, the temperature range of formation and the size of these dislocations beneath the original a/c interface are narrower and smaller than those of the M samples, respectively. In the H samples, no dislocations beneath the original a/c interface were observed. Using the high-current implanter, BF_2^+ dissociation is less prone to occur. The formation of dislocations beneath the original a/c interface in the M and MC samples suggested that the dissociation of BF_2^+ ions occurred during implantation. The dissociation of BF_2^+ ions during implantation resulted in the implantation of B^+ and F^+ with higher energy into the substrate. Channeling effects may further aggravate tailing of the implant profile [4,5].

The electrical activation of implanted boron ions in the M, MC and H samples was measured by the four-point probe method. The variations of sheet resistance of these samples, as shown in fig. 4, are correlated well with microstructural changes. The sheet resistances of the H samples are higher than those of the corresponding M and MC samples. This difference may be attributed to the difference in dissociation of BF_2^+ ions in the accelerating tubes. In the medium-current implanter, dissociation of BF_2^+ ions occurred during the acceleration stage. The range of the implanted boron profiles in the M and MC samples is longer than that of the high-current implanter implanted samples.

4. Summary and conclusions

The effects of substrate cooling for BF_2^+-implanted (001)Si were revealed by comparing the residual defects in annealed M and MC samples. A high density of surface twins was observed in the M samples. The BF_2^+ ion dissociation effects were demonstrated by comparing M or MC and H samples. Rod-like and equi-axial dislocation loops beneath the a/c interface were observed in the M and MC samples but not in H samples. A monotonic decrease in sheet resistance with annealing temperature was observed for M samples. The variation in sheet resistance with annealing temperature for M, MC and H samples was found to correlate well with the changes in microstructures.

Acknowledgement

This research was supported by the Republic of China National Science Council.

References

[1] T.W. Sigmon, V.R. Deline, C.A. Evans Jr. and W.M Katz, J. Electrochem. Soc. 127 (1980) 981.

[2] R.G Wilson, J. Appl. Phys. 54 (1983) 6879.
[3] S.S. Cohen, J.F Norton, E F. Kock and G.J Weisel, J. Appl. Phys. 57 (1985) 1200
[4] I.W. Wu, R T. Fulks and J.C. Mikkelsen Jr., J. Appl Phys 60 (1986) 2422
[5] G. Queirolo, C. Bresolin, L. Meda, M. Anderle and R. Canteri, J. Electrochem Soc. 135 (1988) 777.
[6] I Suni, U. Shreter, M-A. Nicolet and J.E. Baker, J Appl. Phys. 56 (1984) 273.
[7] C.W. Nieh and L.J. Chen, J. Appl. Phys. 60 (1986) 3114.
[8] G. Queirolo, P Caprara, L Meda, C. Guareschi, M. Anderle, G. Otaaviani and A. Armigliato, J. Electrochem. Soc. 134 (1987) 2950.
[9] T. Sands, J. Washburn, R. Gronsky, W. Maszara, D.K. Sandana and G A Rozgonyi, Appl. Phys Lett. 45 (1984) 982.
[10] L.J. Chen and I.W. Wu, J. Appl Phys. 52 (1981) 3318.
[11] I.W Wu and L J. Chen, J Appl. Phys. 58 (1985) 3032.

Nuclear Instruments and Methods in Physics Research B55 (1991) 198–201
North-Holland

Knock-on of contaminants causing instabilities of transistor characteristics

F. Kröner

Siemens Bauelemente, Siemensstrasse 2, A9500 Villach, Austria

A phenomenon leading to locally distorted breakdown characteristics of MOS power transistors in the range of 0.1 to 1 mA, e.g. very far away from real operating conditions, has been observed. The characteristics might have suggested a reduced second breakdown of the parasitic bipolar transistor, but with the subtle difference that the voltage was normal again at larger currents. The attempt to understand the phenomenon in terms of ordinary transistor theory led to the assumption that small-area n-doping contaminations were present in the silicon substrate. Laborious experiments revealed the fact that the instabilities of the breakdown characteristics were a unique function of the plasma etch equipment used for polysilicon definition. The question of interest was now how is it possible for contaminating atoms to penetrate through a rather thick residual oxide during an isotropic plasma etch step. Therefore, the assumption was made that the contaminants were knocked through the residual oxide during the boron implant immediately after the polysilicon etch. TXRF-analysis and C/V-measurements have shown that sulfur is the most probable candidate for the n-type contamination. The amount of knock-on by boron implants is demonstrated by C/V and doping profile analysis. Finally, the phenomenon was eliminated by changing the seals of the etch chamber as well as the electrode defining ceramic rings to those of more suitable materials in order to avoid the contaminations a priori.

1. Description of the phenomenon

Fig. 1 shows a principal cross section of an MOS power transistor. Short-circuiting gate with source and sweeping the voltage until breakdown of the pn-junction leads to a typical reverse characteristic, as shown in fig. 2.

Due to a newly observed phenomenon the transistor characteristics were affected by what is demonstrated in fig. 3. Taking into account data from all electric parameters and from live tests, the most probable theoretical explanation for the phenomenon was the following. If one regards the source, the p-doped channel region and the n$^-$-doped substrate as an npn-bipolar transistor, the pn$^-$-junction initially has the breakdown behavior of a diode, because the p-region is short circuited with the n$^+$-region by the aluminum contact.

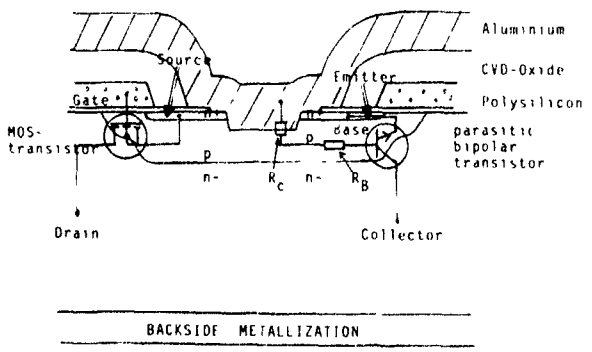

Fig. 1. Cross section of the MOS power transistor and its parasitic bipolar transistor.

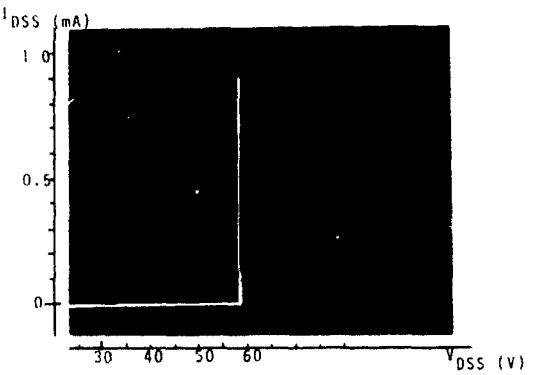

Fig. 2. Normal reverse characteristic.

If for some reason a finite resistance is created between n$^+$-emitter and p-base, also depicted in fig. 1, resulting in a potential drop which is larger than the built-in potential of the n$^+$p-junction, the reverse characteristic has to be regarded in terms of the second breakdown of a bipolar transistor, which in its most simple form may be written as:

$$BV_{CEO} = BV_{CBO}(1-\alpha)^{1/n}, \qquad (1)$$

where BV_{CEO} is the breakdown voltage between emitter and collector with the base opened, and BV_{CBO} that is between the base and collector with the emitter opened,

0168-583X/91/$03.50 © 1991 – Elsevier Science Publishers B.V. (North-Holland)

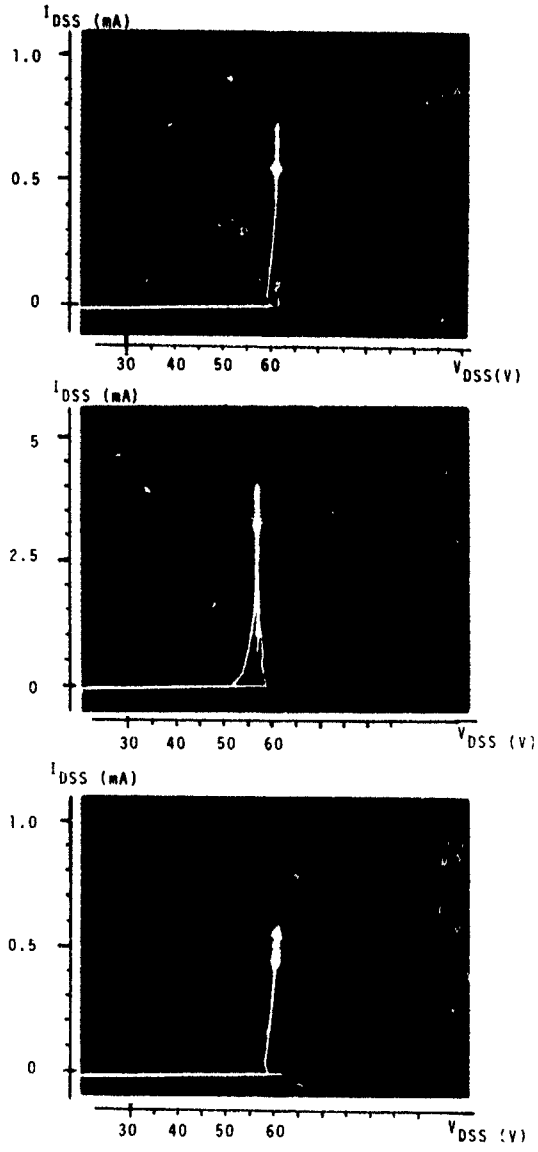

Fig 3 Distorted reverse characteristics

e g. for the pn -diode α is the static common-base current gain, which is related to the static common-emitter current gain β by

$$\beta = \alpha/(1-\alpha) \quad (2)$$

Since β is related to the emitter and base doping, N_E and N_B respectively, and the base width W roughly by

$$\beta \sim N_E/N_B W, \quad (3)$$

either a depletion of N_B or a reduction of W may cause a reduced breakdown according to eq. (1). Also a finite base resistance may change the breakdown behavior from that of a diode to that typical of a bipolar transistor.

An increased base resistance may have its causes either in too little p doping or counterdoping, or an augmented contact resistance. The latter possibility was evidently not the case. Further, it was not possible to shift the unwanted shape and oscillations of the reverse characteristics by a heat treatment of up to 400 °C, or had any weaknesses of the gate oxide been observed.

Finally, it should be stated that at larger reverse currents, e.g. in a current region related to real operating conditions, the voltage was normal again, so we assumed that the defect area was microscopically small.

2. Experimental search

The experimental investigation initially was dominated by the search for a possible diffusion source of an n-doping element, for example unwanted phosphorus diffusion from the LPCVD oxide or the polysilicon doping.

Since this seemingly probable hypothesis failed, and also no geometrical irregularities of the polysilicon edges could be detected, a laborious systematic investigation on the base of comparisons of the individual manufacturing steps in different production lines, revealed that the distorted transistor characteristics were a function of the plasma etch equipment used for polysilicon definition.

A thorough comparison of the hardware details showed that the "bad" machine used seals of a synthetic material rather than a more natural type of rubber, because the synthetic material delivered better results concerning particulates. Also a lighter type of ceramic was used to isolate the etch chamber from ground, because it could be shaped mechanically. It should be remarked that these parts had been in operation several months before they started to cause the phenomenon. After changing the parts, the instabilities of the transistor characteristics disappeared immediately.

In addition to the phenomenological investigation, TXRF analyses of bad transistors were made, which are summarized in table 1. The only real difference between devices which were polysilicon etched with the different

Table 1
Averaged results of TXRF-analysis before and after the change of the seals and the ceramic ring of the etch chamber "–" indicates that values are below the detection limit.

State of machine	Element [10^{12} atoms/cm^2]				
	P	S	Ca	Fe	Cu
"Bad" seal + "bad" ceramic ring	–	33–44	0–7.6	0–0.4	0.3–0.7
"Bad" seal + good ceramic ring	–	24–36	–	–	–
Good seal + good ceramic ring	–	–	–	–	–

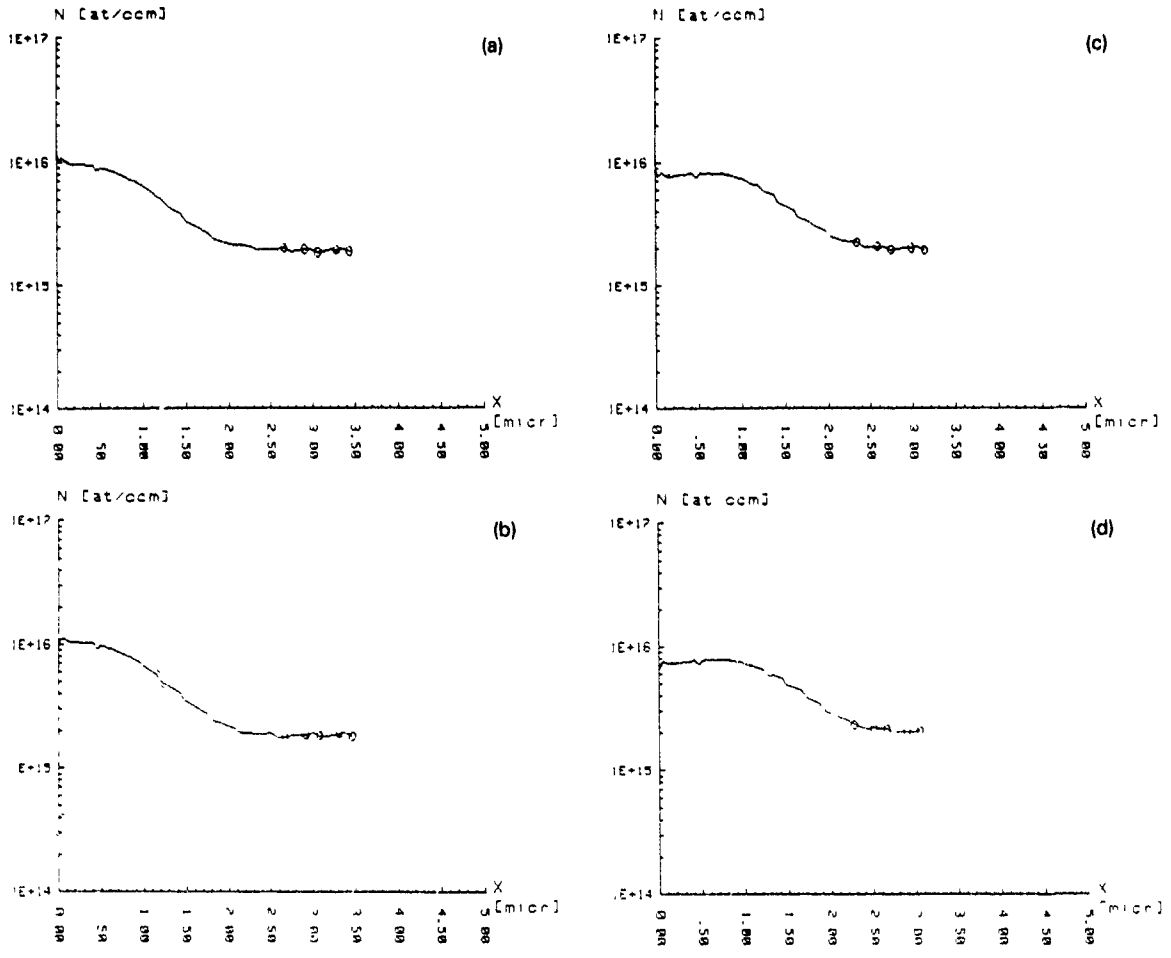

Fig 4. Boron depth profiles in silicon after the processing described in table 2, with: (a) uncontaminated surface, (b) surface contaminated with sulfuric acid, (c) surface contaminated with phosphorus acid, and (d) surface contaminated with SF_6 plasma

machines are the sulfur concentrations. Sulfur behaves as an n-doping element.

3. Knock-on experiments

Since the kinetic energy of any ion in the plasma of an etching apparatus is completely insufficient to knock surface contaminants through the residual oxide, the assumption was made that the unwanted atoms were transported into the substrate during the subsequent boron implant. Therefore, the experiments were made in order to evaluate under what conditions it is possible to knock n-doping elements into the substrate by ion implantation. The process flow of the experiment is shown in table 2.

As fig. 4 demonstrates, a counterdoping of the boron surface concentration of up to 20% is possible if the scattering oxide is treated by either a dip of phosphorus acid or a few seconds of an SF_6 plasma.

SF_6 was used for etching LOCOS nitride in the same

Table 2
Process flow for determination of doping profiles

Starting material, p-doped, 10–20 Ω cm
Cleaning: RCA + H_2SO_4/H_2O_2
Dry oxidation, 400 Å
DELIBERATE SURFACE CONTAMINATION
Boron implant, 180 keV/1×10^{12} cm^{-2}
Oxide etch, buffered HF
Dry oxidation + diffusion
Polysilicon + aluminum electrodes: 1 mm^2 size
C/V measurements: calculation of doping profile

machine, and worked probably in conjunction with the seals of the unsuited materials to produce the problem. It was not possible to counterdope the boron concentration by a treatment with sulfuric acid.

4. Conclusion

An example has been illuminated where contamination introduced during ion implantations did not have its source in the implantation equipment itself, but in a plasma etching apparatus. The necessity of more frequent changes of the seals and the use of higher quality ceramic in the plasma etch system, to assure nonbreakdown of materials that absorb unwanted chemicals, is justified in order to prevent locally counterdoping by knock-on of ions implanted immediately after the etch step.

Nuclear Instruments and Methods in Physics Research B55 (1991) 202–206
North-Holland

Implant uniformity evaluation using a Varian/Extrion scan compensator module on an electrostatic scanning ion implanter

Kenneth Howard

Motorola Semiconductor, 2200 W Broadway Rd, Mesa, AZ 85202, USA

With the ever-increasing demands upon processes used in VLSI technology and trends toward increased wafer size, proportionate demands are being placed on ion implanter manufacturers for improvement in areas such as machine automation, dosimetry, wafer cooling, particle reduction, beam purity, channeling control and wafer charging effects, to name a few This paper will discuss an experimental evaluation of a scan compensator module developed by Varian/Extrion for the purpose of improving implant uniformity This module is utilized on their medium current, electrostatic scanning, serial ion implanters and is offered as a retrofit Gains in uniformity are evident for an earlier machine; however, optimum performance may vary from one situation to another

1. Introduction

Depending on the type and make of ion implanter under discussion, there are various scanning schemes employed to ensure uniform coverage of a desired implant species on a wafer's surface. It is well known that the type of scanning technique designed into an implanter will demonstrate intrinsically different abilities to dose uniformity [1] Other factors critical to the issue of uniformity include wafer channeling effects, which are closely related to the implanter system design, crystallographic orientation of the wafer, and the processing parameters [2]. All of these have a strong influence upon the resultant implanted sheet resistance (R_s) and its uniformity because these parameters depend upon the manner in which the beam of energetic ions are dispersed across the wafer surface and finally come to rest within the silicon crystalline lattice structure.

In an effort to improve implant uniformity on their serial ion implanters, Varian/Extrion has designed and introduced a scan compensator circuit [3]. An analog correction transforms the traditional linear triangular waveform, producing a quadratic waveform signal instead, which is then applied to the electrostatic deflection plates [4]. This methodology intentionally distorts the relationship between voltage and time, resulting in a smooth change in the rate at which the beam sweeps across the wafer. This paper will discuss the experimen-

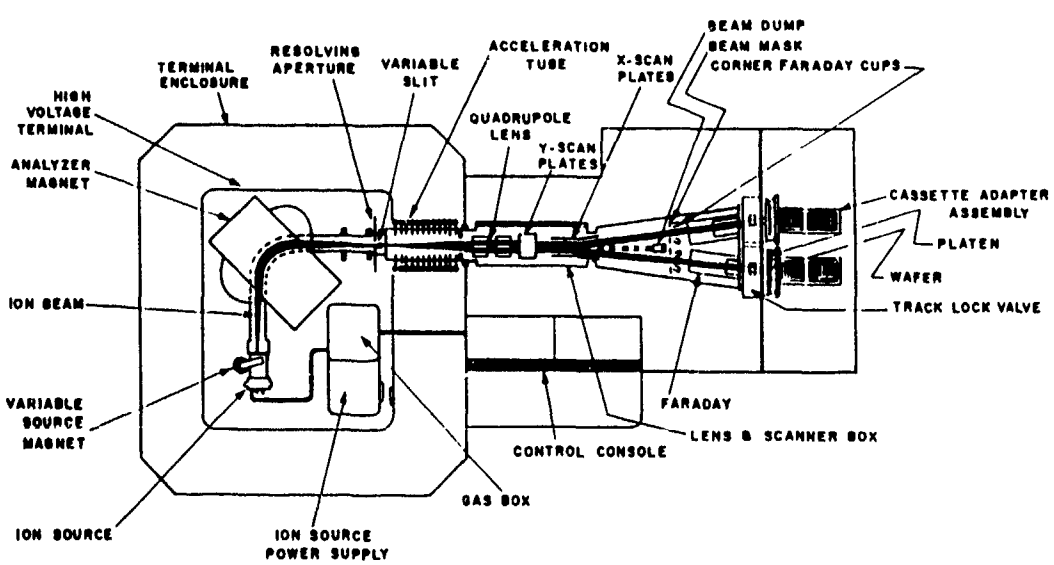

Fig. 1. A simple cutaway diagram displaying the top view of the Varian/Extrion 350D with dual endstation configuration

0168-583X/91/$03.50 © 1991 – Elsevier Science Publishers B.V. (North-Holland)

tal R_s uniformity results obtained in an evaluation of the Varian/Extrion scan compensator module tested in conjunction with an electrostatic (X/Y) scanning ion implanter

2. System under investigation

This evaluation was performed within a research/development pilot line environment of Motorola's Advanced Technology Center (ATC) in Mesa, Arizona. The implanter used was an earlier Varian/Extrion model 350D medium current, electrostatic scanning, serial machine (fig. 1). The design of the dual wafer processing endstation configuration utilizes a fixed implant tilt angle of $+7°$ and $-7°$ relative to the incident beam direction on the horizontal axis. Prior to this investigation, the average percent uniformity difference between the two similarly equipped "HYCOOL" domed endstations ranged from 3.5 to 8%. This two-endstation design presented an opportunity to examine the effect upon implant uniformity between two different endstation platen geometries which forms the basis of this inquiry. Endstation no. 2 was equipped with the "HYCOOL" domed platen assembly, while endstation no. 1 was equipped with the standard, flat platen assembly (without HYCOOL). HYCOOL is a Varian trademark for the system designed for medium to high dose applications where wafer cooling is necessary. Its use prevents the degradation of the photoresist film on wafers by avoiding excessive implanting temperatures. This wafer cooling effect is accomplished by injecting N_2 at a pressure of approximately 20 Torr into the sealed area between the back of the wafer and the platen surface. Another design feature of the HYCOOL platen is its domed geometry This particular configuration flexes the wafer surface approximately 1.8° from the wafer center to its outer edge for 100 mm diameter wafers. (Newer systems flex the wafer less, but require the use of hydrogen or helium for maximum cooling). This system also utilizes a standard X/Y scanning deflection scheme driven by triangular waveforms with frequencies regulated by a crystal-controlled oscillator. The standard scanning frequencies are 117 Hz on the vertical axis and 1019 Hz on the horizontal axis. The amount of deflection in each direction is directly proportional to the voltage applied to the scan plates.

The scan compensator module which Varian/Extrion has developed for the purpose of improving implant uniformity on their electrostatic scanning machines can be easily interchanged with the earlier beam scan controller module. The compensator module has an independent, variable turn potentiometer control for each endstation that is calibrated in percent. This corresponds to the percent change in dose gradient introduced. Here, one turn is equal to one percent. Varian/Extrion cautions that the results may vary by process, so the particular scan settings chosen for this investigation were 0 0 (equivalent to the standard beam scan controller), 2.5, 5.0 and 7.5%.

3. Experimental procedure

For ATC's 350D dual endstation design, this investigation centered on measuring the dependence of sheet resistance (R_s) uniformity as a function of different scan compensator settings for various combinations of ion species, energy, dose and endstation geometries. Thirty-two, n-type ⟨100⟩ substrates (avg. $\rho = 10\ \Omega$ cm; avg. $C_b = 5 \times 10^{14}/\text{cm}^3$) and thirty-two, p-type ⟨100⟩ substrates (avg. $\rho = 18\ \Omega$ cm; avg. $C_b = 8 \times 10^{14}/\text{cm}^3$) were used in this evaluation. The 100 mm diameter test wafers were laser scribed for identification and randomized. The scan compensator module does not compensate for channeling effects. Therefore, in order to reduce channeling effects, approximately 200 Å of screen oxide was thermally grown on all wafers prior to ion implantation. To further minimize the effects of channeling, it is standard practice in our pilot line to rotate the major flats on all wafers 45° with respect to the machine's horizontal plane using the wafer orientor which is an integral part of the platen assembly. As a cross section of our present 48 "standard" medium current pilot line production implants, the implant parameters listed in table 1 were selected.

Wafer-to-wafer repeatability of sheet resistance (R_s) for the same scan compensator setting with a given implant setup was previously demonstrated to be on the order of +0.5% or less with respect to the average R_s. Due to the relatively large undertaking of this investigation within a pilot line operation, it was decided that one wafer per scan setting per implant setup, though statistically "weak", would provide initial R_s data to ascertain the effects of the various compensator settings with different implant and endstation configurations.

Table 1
Implant parameters

Boron
25 keV, $2.2 \times 10^{13}/\text{cm}^2$
40 keV, $1.0 \times 10^{14}/\text{cm}^2$
120 keV, $1.0 \times 10^{14}/\text{cm}^2$
180 keV, $1.5 \times 10^{13}/\text{cm}^2$
Phosphorus
40 keV, $5.0 \times 10^{13}/\text{cm}^2$
180 keV, $1.0 \times 10^{14}/\text{cm}^2$
Arsenic
40 keV, $5.0 \times 10^{13}/\text{cm}^2$
180 keV, $5.0 \times 10^{13}/\text{cm}^2$

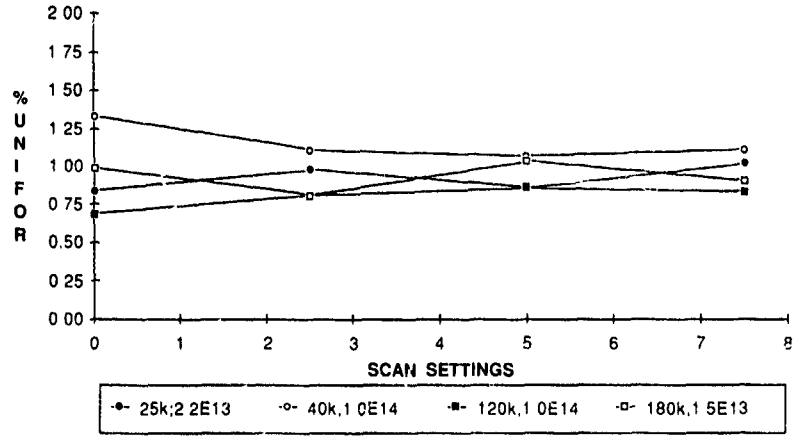

Fig 2 Use of the scan compensator module on endstation no. 1 (non-HYCOOL, flat platen) of the 350D displays mixed boron results A scan setting of "0.0" appears to be optimum for the boron implants chosen at 25 keV, 2.2×10^{13} and 120 keV, 1.0×10^{14}

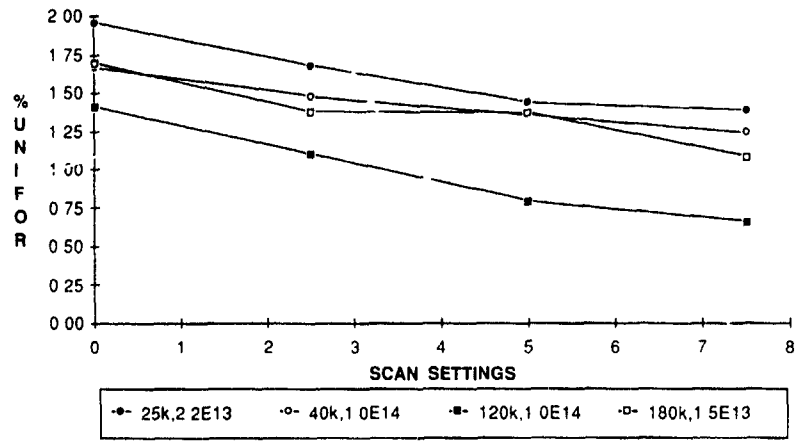

Fig. 3 Use of the scan compensator module on endstation no. 2 (domed platen with HYCOOL) of the 350D displays continued uniformity improvements for all chosen boron implants with increased scan settings A scan setting of "7 5" appears to be optimum.

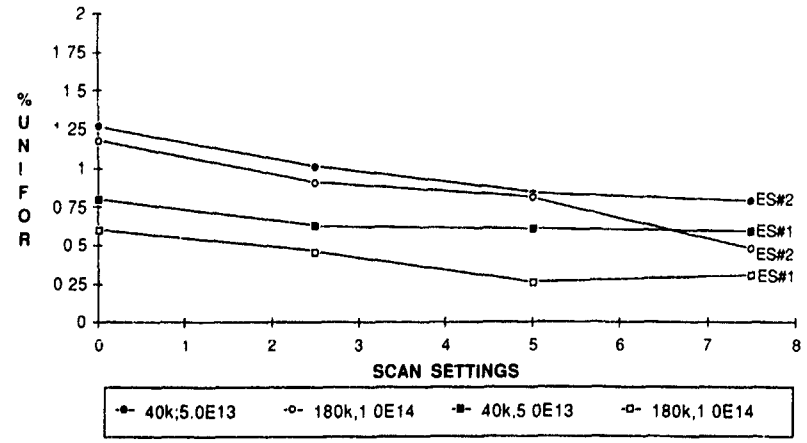

Fig. 4. Use of the scan compensator module on both endstations no. 1 and no. 2 shows steady gains in uniformity from a scan setting of "0.0" to "7 5" for the majority of the phosphorus implants chosen.

The beam currents used were commensurate with implanting times of approximately 10 s. After the implants were completed, the wafers were then sent to the diffusion area for the following separate batch anneals: boron and phosphorus – 900°C, N_2, 30 min, and arsenic – 1040°C, N_2, 25 min. Following the removal of the screen oxide, sheet resistance measurements were obtained using a Prometrix Omni Map system with 45 site contour maps.

4. Experimental results

Figs. 2 through 5 show how the scan compensator affects the implant uniformity at the established scan settings. Bear in mind that a scan setting of "0.0" is equivalent to the "standard" beam scan controller module. Fig. 2 displays mixed results for endstation no. 1. The boron 40 keV, 1.0×10^{14} and 180 keV, 1.5×10^{13} implants show initial improvement on the order of approximately 17% from a setting of "0.0" to "2.5". From there they begin to lose ground. The boron 25 keV, $2.2\text{–}10^{13}$ and 120 keV, 1.0×10^{14} implants suggest a setting of "0.0" as the best. Fig. 3 is very encouraging for all boron implants under study on endstation no. 2. It seems to suggest that a scan setting of "7.5" is definitely to our advantage with 26 to 53% gains in improved uniformity from a setting of "0.0". Fig. 4 shows steady gains in uniformity for phosphorus implants on both endstations. In three out of four cases, a scan setting of "7.5" appears to be the best. Fig. 5 illustrates mixed results for arsenic implants on endstation no. 1. The optimum setting for the 40 keV implant is at "0.0" and worsens from there, while the higher energy, 180 keV, implant shows continued improvement to a setting of "7.5". Both the 40 and 180 keV arsenic implants on endstation no. 2 show approximately a 10% uniformity improvement from a setting of "0.0" to "2.5". The 180 keV implant continues this downward trend to a scan setting of "7.5" where it shows a final improvement of 33%. The 40 keV implant however does not follow this trend and the gains in uniformity for scan settings between "0.0" and "5.0" are lost at "7.5".

5. Discussion

It is apparent that endstation no. 1 with the flat-faced platen assembly has demonstrated better (lower) overall R_s uniformity results when compared to endstation no. 2, regardless of the scan compensator setting. The uniformity results from endstation no. 1 ranged from 19 to 52% better than those from endstation no. 2. This was to be expected, since the flexing of the wafer over the domed platen produces higher nonuniformity at any flat rotation angle [2]. Implant uniformity problems are influenced by channeling effects as a result of the system design (scanning scheme, wafer tilt and rotation, scan angles, compound implant angles due to wafer flexing, etc.) and crystallographic orientation of the wafer. Wafer size is another important factor to consider. The larger the wafer diameter to be implanted on a flexed dome, the more compound angles will be introduced, edge to edge, resulting in greater uniformity variation.

The effects of planar channeling have shown sheet resistance variation as high as 10% indicating that channeling is an overriding factor in obtaining implant uniformity and that this is commonly known to cause junction depth variation of 10 to 50% in implants into bare silicon [4–8]. The scan compensator does not affect channeling, however these effects can be greatly re-

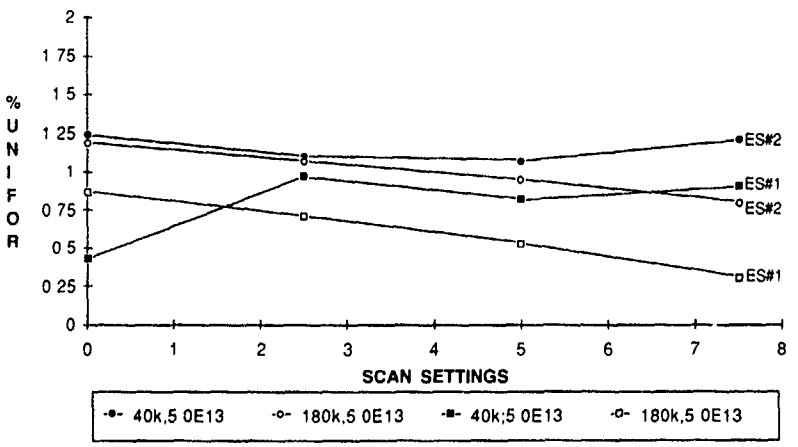

Fig. 5. Use of the scan compensator module with endstations no 1 and no 2 shows continued improvement in uniformity for the arsenic implant at 180 keV, 5.0×10^{13} from a scan setting of "0.0" to "7.5". Mixed uniformity results were obtained for the arsenic implant at 40 keV, $5.0 \times 10^{13}\,cm^{-2}$.

duced by thermally growing a layer of screen oxide on the wafer surface as well as providing some means of implant wafer tilt, usually 7°, and wafer twist. The object of the scan compensator module is to subdue or eliminate geometric nonuniformity effects as the result of implanting wafers at a 7° tilt. The use of a dome-shaped platen as opposed to a flat platen arrangement will have a worsening effect on dose uniformity as well as variation of the dopant depth profile across the wafer.

Due to the many complex interactions involved in this investigation, the various results have not been completely quantified, however the optimum scan setting for endstation no. 1 with its flat-faced platen ranged from "0.0" to "7.5" and appears to be dependent on the type of implant desired, which does not make it very convenient in a normal production mode. Endstation no. 2, with its domed platen face, may have demonstrated higher nonuniformity values than endstation no. 1, but for the majority of the implants in this study, it also showed larger gains in R_s uniformity as the scan setting was increased. The optimum scan setting on endstation no. 2 was typically "7.5".

6. Conclusion

As expected, when comparing percent uniformity between platens only, a flat-faced platen achieved superior values compared to a domed platen face on Varian/Extrion's 350 D medium current ion implanter. This is due to the fact that the wafer is not flexed, reducing the range of compound implant angles across the surface of the wafer One must keep in mind, however, that in this system a flat-faced platen does not have the superior wafer cooling ability as does the domed face platen and the degradation of photoresist due to wafer heating can become a problem with doses much above 1.0×10^{14} ions/cm^2. In this study, when the scan compensator was utilized in conjunction with a flat-faced platen, mixed results were obtained, therefore under these conditions one may wish to abstain from the use of a scan compensator in a production environment and look for other alternatives to improve uniformity. Wafers implanted on a domed platen face, on the other hand, yielded intrinsically higher R_s uniformity values due to channeling effects coupled with the system design. However, if this platen is used in concert with a Varian/Extrion scan compensator module, improvements in uniformity can be significant.

References

[1] A.B. Wittkower, Solid State Technol 25(9) (1982) 77
[2] M.I. Current, N L. Turner, T.C Smith and D Crane, Nucl. Instr. and Meth B6 (1985) 336
[3] P Fisher, Nucl Instr. and Meth. B37/38 (1989) 525.
[4] P A Fisher, Compensated scan wave form generator for ion implantation equipment, U S. Patent No 4851693 (25 July, 1989).
[5] N. Turner, Nucl. Instr and Meth. B6 (1985) 224.
[6] D Voreades and W. Borglum, presentation F-24, 5th Int Conf on Ion Implantation Equipment and Technology, Smuggler's Notch, VT, USA, July 1984.
[7] A. Michel et al., Appl. Phys Lett 44 (1981) 404
[8] M Miuaki et al., J. Electrochem. Soc 130 (1983) 716

Nuclear Instruments and Methods in Physics Research B55 (1991) 207–210
North-Holland

The use of negative ions to enhance beam currents at low energies in an MeV ion implanter

John P. O'Connor, Michael E. Mack, Anthony Renau and Nobuhiro Tokoro
Genus Inc., Ion Technology Division, 4 Mulliken Way, Newburyport, MA 01950, USA

Since the introduction of the G1500 ion implanter, the use of tandem accelerators in production ion implantation systems has become well established. However, the beam currents which are attainable at present at low energies (< 200 keV) are suitable for only low- and medium-dose implants. In this paper, an approach to increase low-energy beam currents in dc tandem accelerators is presented Specifically, the use of negative ions which have been generated in the injector of the implanter are transported to the end station and implanted into the wafers. In this work, beam current measurements which have been performed using the Genus G1500 ion implanter are presented for the typical semiconductor dopants In addition, system changes which are necessary to accomplish implants with negative ions are discussed. A comparison of sheet resistances and uniformities measured with both positive and negative ions at the same energy and from the same G1500 system are presented.

1. Introduction

Over the past few years, the use of high-energy implantation has been primarily confined to the laboratory for the development of next-generation devices. However, in several major fabrication facilities, high-energy implantation has progressed from a purely research and development tool to production This includes production of dynamic random-access memory devices and charge-coupled devices.

For efficient production use of these systems, the capability of the implanter to support low-energy, medium-current implants is important. At present, MeV ion implanters using the dc tandem acceleration technique such as the Genus G1500 attain beam currents at energies below 200 keV which are suitable for only low-dose implants.

To improve the G1500 capabilities, a program has been instituted by Genus to enhance ion beam currents in the MeV system at low energies. The efforts to date have focused on transporting the negative ions produced in the injector of the system through the tandem acceleration structure. These ions are the dopants for the silicon wafers.

In this work, beam current measurements of negative ions for the semiconductor dopants are presented. The transport efficiencies through the tandem accelerator and charge-state-resolving filter magnet are also presented. In addition, G1500 system changes necessary for negative ion implants are discussed. Finally, preliminary experiments have been performed to compare the sheet resistances and uniformities of bare and oxide-coated silicon wafers implanted with positive or negative ions at the same energy and by the same system.

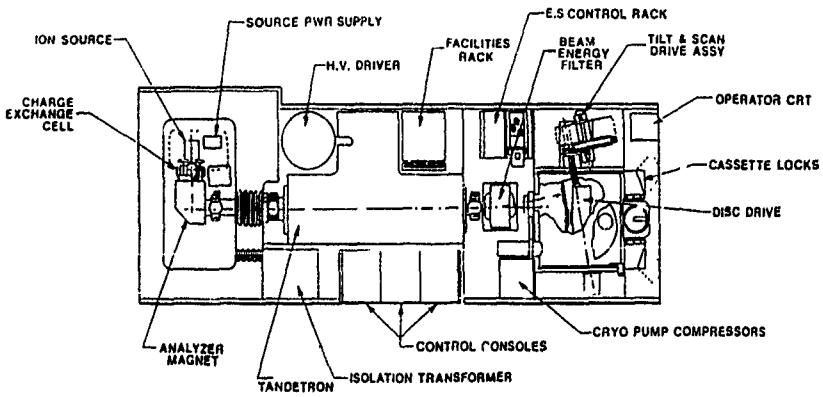

Fig. 1 Overall plan view of the Genus G1500 high-energy ion implanter.

0168-583X/91/$03.50 © 1991 – Elsevier Science Publishers B V (North-Holland)

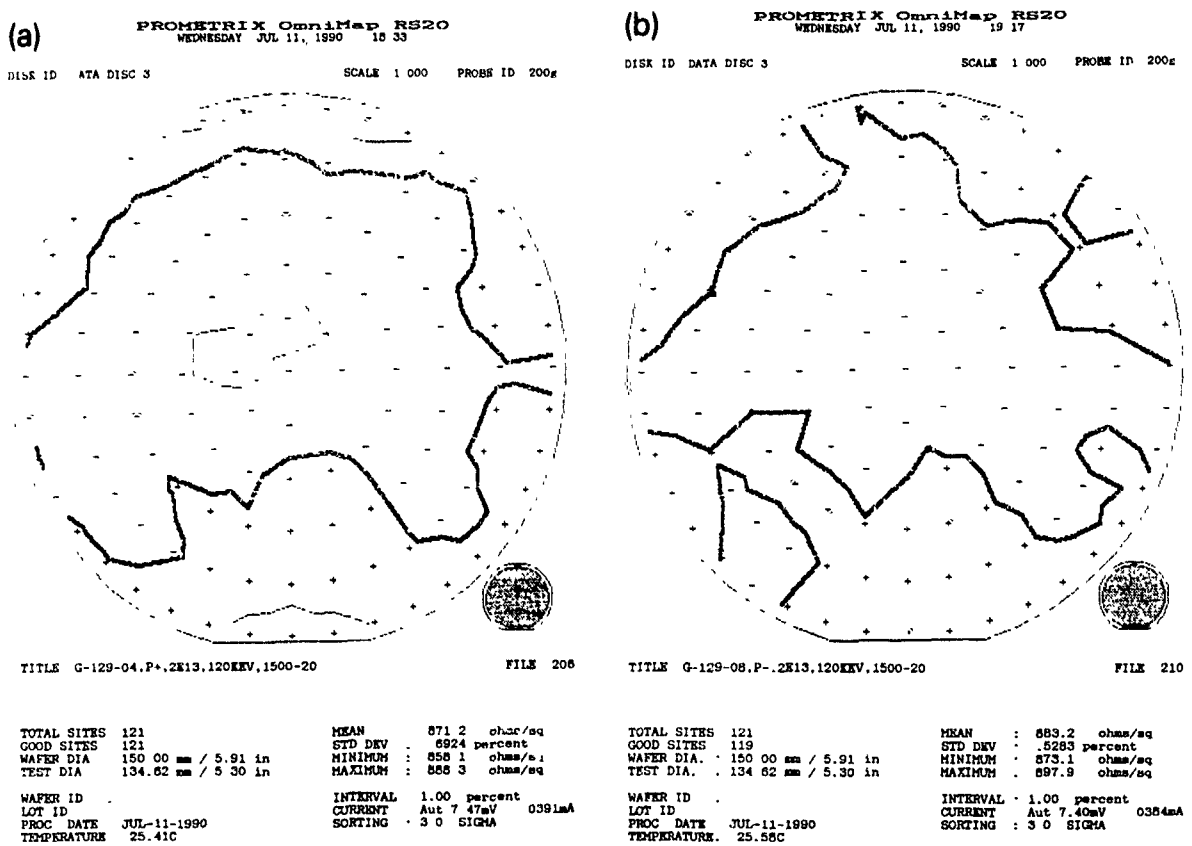

Fig. 2 Sheet resistivity maps of 120 keV (a) P^+ and (b) P^-, 2×10^{13} cm^{-2} implants into bare silicon wafers after a 960 °C, 30 min anneal.

2. Experimental technique

A schematic representation of the G1500 is shown in fig. 1. In typical operation, positive ions are extracted from the ion source at an energy of up to 40 keV and immediately enter a charge exchange cell containing magnesium vapor. In the cell, a fraction of the ions are converted from positive to negative. The desired negative-ion species is selected and focused by the 90° analyzing magnet. The ions are then accelerated back to ground potential through a three-gap region with a resultant energy of up to 130 keV. A Faraday cup may be inserted at this point to monitor and optimize the negative ion current.

After exiting the injector, the negative ions enter the tandem acceleration section of the system. A quadrupole doublet-steerer assembly restores the circular symmetry for optimum transmission through the accelerator. The negative ions are accelerated toward the positive high-voltage terminal at the center of the Tandetron (up to 750 kV) where they pass through a nitrogen gas cell. Electrons are stripped from the ions reversing their polarity from negative to positive. The positive ions are then repelled from the terminal and accelerated back to ground potential. A second quadrupole doublet lens focuses the positive ions which enter the beam energy filter. In this region, the positive ions pass through a uniform 10° magnet which separates the singly, doubly and triply charged ions produced in the nitrogen stripper canal. The desired beam passes into the end station and impinges upon the wafers.

At low energies, the charge exchange efficiency (from -1 to $+1$) at the nitrogen stripper canal is small. Thus, the positive ion currents attained at the end station are not optimum. One method to increase these low-energy beam currents is to close the N_2 leak valve to the stripper canal, set the Tandetron voltage equal to zero, and transport the negative ions through the tandem region. The voltages applied to the quadrupole doublet lens downstream of the Tandetron are reversed to focus the negative ions. In addition, the polarity of the 10° beam filter magnet is reversed from normal operation to deflect negative ions and these ions pass through the final defining aperture and are incident upon the wafers.

For setup and implant control, the only additional change is that the dosimetry system must be modified to use negative current from the setup and disk Faraday cups.

3. Results and discussion

In table 1, typical beam currents which have been obtained in both standard operation of the G1500, and in these measurements are presented. In addition, the beam currents measured at the injector Faraday cup are included as well as the transmission percentages from the injector Faraday cup to the setup Faraday cup. The ratio of the increase of negative ion to positive ion transmission to the water plane is also presented.

As evidenced by the data, there is a significant improvement in low-energy beam performance for each species. The negative-ion transmission results demonstrate the excellent focusing characteristics of the G1500 as the ions are transported a significant distance without acceleration, i.e., from the exit of the pre-acceleration column to the wafer plane. Also, it is interesting to note that the ion source output was not maximized during the measurements. Thus, one would expect substantial increases (approximately a factor of 2) for each species with optimized ion source parameters.

In addition to the beam current measurements, phosphorus implants were performed using both positive and negative ions from the same system and at the same energy. The negative ion implants were the first in a series of measurements which will be performed at Genus. Sample Prometrix maps from 120 keV P^+ and P^- 2×10^{13} cm^{-2} implants into bare silicon wafers are presented in fig. 2. Maps for 120 keV P^+ and P^- 5×10^{13} cm^{-2} implants into silicon wafers coated with 200 Å of silicon dioxide are shown in fig. 3. The data demonstrate that the uniformities are well within specification for both ion polarities. The sheet resistances also agree to within approximately 2%.

4. Summary

It is clear that the G1500 system may be used for both positive and negative implants with good results.

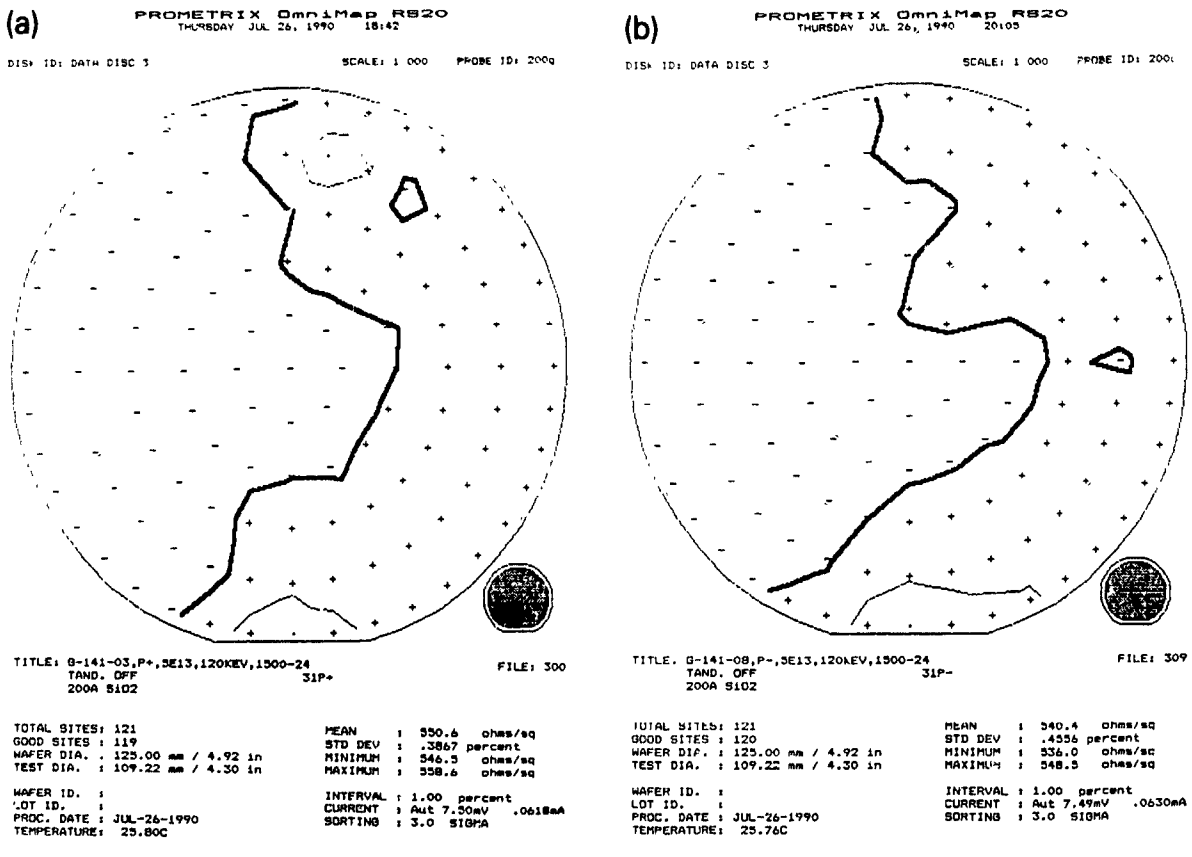

Fig. 3. Sheet resistivity maps of 120 keV (a) P^+ and (b) P^-, 5×10^{13} cm^{-2} implants into silicon wafers coated with 200 Å of silicon dioxide after a 960 °C, 30 min anneal

Table 1
Beam currents measured in standard G1500 operation (+) and by the transmission of negative ions to the end station (−); the injected beam currents at each energy as well as the transmission percentages for each species and the ratio of the negative- to positive-ion transmission percentages are presented

Energy [keV]	Injected current [μA]	Target current [μA]	Transmission [%]	Ratio [−/+]
(1) *Boron results*				
40	80	33 (−)	41	2.6
40	76	12 (+)	16	
100	96	42 (−)	44	1.7
100	86	22 (+)	26	
140	126	76 (−)	60	1.9
140	112	36 (+)	32	
(2) *Phosphorus results*				
40	402	105 (−)	26	1.5
40	395	68 (+)	17	
80	495	173 (−)	35	1.6
80	491	108 (+)	22	
120	511	196 (−)	38	1.8
120	494	104 (+)	21	
(3) *Arsenic results*				
40	73	36 (−)	49	1.8
40	60	16 (+)	27	
80	71	47 (−)	66	1.7
80	65	26 (+)	40	
120	69	53 (−)	77	1.7
120	68	31 (+)	46	

There are only minor system changes necessary to switch from standard positive ion implant mode to the use of negative ions. The increase in beam currents available with negative ions makes their use for implantation attractive. The G1500 is the only production system available with this capability. In future measurements, the small differences in sheet resistivity between the positive and negative phosphorus ion implants will be examined. A study of boron and arsenic negative ion implants will also be performed.

In a separate set of experiments, measurements will be performed to examine the transport of low-energy positive ions directly from the extraction region to the end station. This technique has the potential advantage of injecting substantial beam currents (several mA) into the tandem acceleration region with significant increases in target beam current for ions with energies below 40 keV. These results will be described in a future publication.

Nuclear Instruments and Methods in Physics Research B55 (1991) 211–215
North-Holland

Charging measurement and control in high-current implanters

Gordon Angel, Nara Meyyappan, Frank Sinclair and Weilin Tu
Eaton Corporation, Semiconductor Equipment Division, Beverly, MA 01915, USA

We present data on beam potential measurements in a high-current implanter. The beam potential measurements were made using a test structure on a silicon wafer with a time-resolved in situ data gathering system in the mechanically scanned implanter Data comparing different conditions in the implanter show that the beam potential strongly influences the surface potential of the wafer when it is exposed to the ion beam. This voltage can be effectively controlled by the use of electron injection from an electron shower as currently practiced. Analysis of results in terms of a theoretical model suggests that charge-induced breakdown of very thin gate oxides in ion implantation will not become an insuperable obstacle in the foreseeable future

1. Introduction

The use of thinner (< 10 nm) and thus more sensitive gate oxides in ULSI circuits as device sizes decrease presents an increasingly important constraint on ion implant processes. Ion implanters, particularly high-current (> 1 mA) systems in high-dose ($> 1 \times 10^{15}$ cm^{-2}) applications clearly have a potential for creating a great amount of damage to sensitive structures already on the wafer at that stage in the process [1,2].

Many parameters are important in determining the yield and reliability of such devices: beam current, beam shape, beam residence time [3,4], process chamber pressure, electron injection from showers or floods [5,6], secondary electron yields from the various surfaces, device design [7,8] and wafer grounding schemes. Using

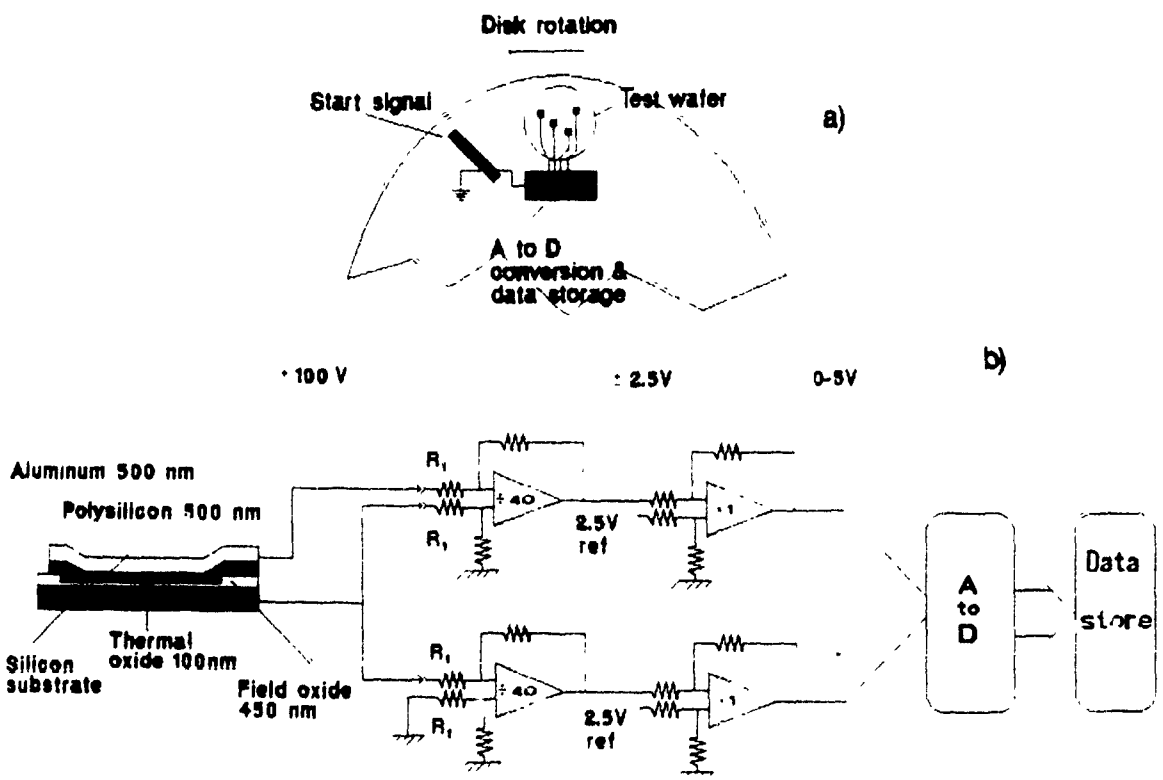

Fig 1. (a) Schematic of the wafer mounted on the implanter disk (b) Cross section of a test site and block diagram of circuit used to measure the voltages on the test structures

0168-583X/91/$03 50 © 1991 – Elsevier Science Publishers B V. (North-Holland)

a specially designed probe [1], we have made measurements of the potential distribution in the beam. The results from these experiments allow the refinement of current physical models of the processes occurring in the beam–wafer interaction.

2. Measurements

We have developed a wafer that contains several test capacitor sites, both 500 μm and 1 mm square, that are linked by metallization traces and wire bonding to an external contact array. Individual sites may be connected to a differential amplifier, analog to digital converter and micro controller for data storage. The wafer and electronics are mounted on the rotating disk of the implanter, shown schematically in fig. 1a. Fig. 1b shows a cross section of a device and a block diagram of the electronics.

The voltage that appeared on the substrate and that of a selected capacitor were monitored simultaneously at a sampling rate of 100 samples per millisecond and an 8 bit resolution between typical limit values of −100 and +100 V using a single card data logger manufactured by Onset Corporation [9], data sampling being initiated by the beam passing over the start bar shown in fig. 1a The final output was obtained by downloading the stored data using a serial RS-232 data link to a PC for subsequent analysis and manipulation.

These experiments were carried out in an Eaton NV-10 high-current implanter with a mark IV electron shower to control the beam space charge and wafer charging. In this device a stream of electrons emitted from a filament is accelerated to 300 V and allowed to impinge upon a secondary target, from which a copious supply of low energy secondary electrons is emitted. These low energy electrons are attracted by the potentials of the beam and the positively charged wafer thus helping to reduce the potential of both. The shower current referred to later in this report is the current of primary electrons leaving the filament.

3. Results

Fig. 2a shows a typical voltage observed between the wafer and ground measured with a 2 mA beam of As^+ ions at 40 keV. Notice the initial positive step as the leading edge of the wafer sweeps into the beam, followed by a similar drop in voltage about 4 ms later as the trailing edge of the 100 mm wafer exits the beam, traveling at a circumferential velocity of 23.5 m/s. After the initial rise to 11 V at 2 ms, there appears to be an *RC* decay to about 4 V with a time constant of 1 or 2 ms. Our interpretation of this process is that, while the voltage of the beam is constant at 11 V, our probe is measuring the voltage of the substrate and this decreases because of the increasing voltage across the capacitor formed by the oxide on the wafer. The surface

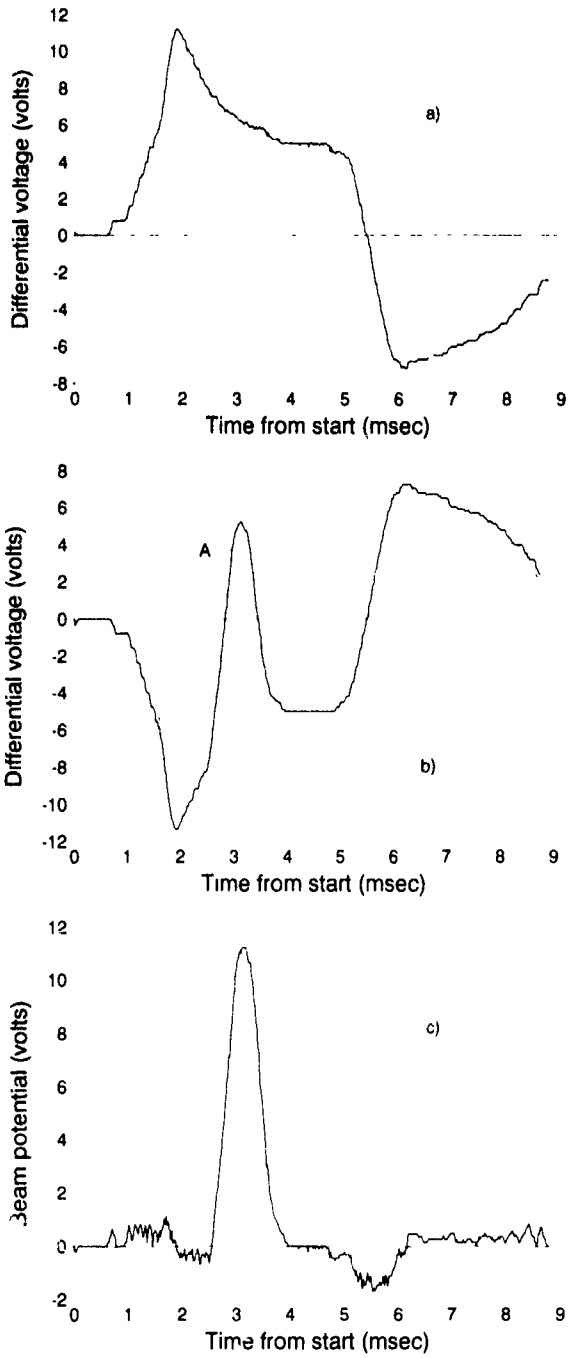

Fig. 2 Results of measurement with a 40 keV, 2 mA As^+ beam (a) Shows the measured substrate to ground voltage, (b) shows the measured test site to substrate voltage, and part (c) shows the sum of these two signals, the test site to ground voltage

of this wafer has a 450 nm field oxide over all the exposed surface, which can be expected to act as a capacitor, with a capacitance of about 0.6 μF. When the outer surface of the oxide is forced to the beam potential of 11 V, the capacitively coupled substrate follows this voltage. The leakage resistances from the substrate to ground and the parallel leakage across the oxide itself, either of which may be enhanced or provided by the weak plasma in the implant chamber, form a differentiator network which allows the substrate potential to decay exponentially from 11 V. An equilibrium is reached, in the case shown at about 4 V, when the networks supplied by the leakage resistances divide proportionately the 11 V beam potential. At this equilibrium, there will be 7 V across the field oxide, corresponding to an electric field of 0.16 MV/cm. This may well be higher at a thin point at the edge of the wafer or some defect.

Once the wafer leaves the beam, the surface of the wafer reverts to 0 V. The substrate potential reflects this 11 V change as would be expected of a differentiator network.

In fig. 2b the measured voltage between the test device and the substrate is shown. Note how the signal consists of a component that is the inverse of the variation of the substrate potential with a superimposed positive peak, shown as A in the figure. The extent to which the initial negative variation of the substrate potential matched the inverse of the substrate potential was investigated and found to be strongly dependent on the value of R_1 (fig. 1b), the input impedance of the differential amplifiers.

As the beam strikes the substrate and drives it positive with respect to ground the test device is driven negative with respect to the substrate, the connection of the measurement circuit supplying the necessary negative charge from ground. In the ideal case, with an infinite input impedance, the test device potential would float with the substrate potential and no negative excursion would be seen. We attempted to increase the values of R_1 to achieve this but even at values as high as 50 MΩ an appreciable negative variation of the site potential was observed. As the value of R_1 was decreased, the negative variation in the site voltage increased until it matched the inverted substrate variation. As the impedance was lowered below 200 kΩ a loss of the peak height in the positive going part was observed. For these experiments a value of 680 kΩ was finally adopted. It was then possible, by measuring the site and the substrate voltages simultaneously, to calculate the potential of the test site to ground by adding the site to substrate voltage and the substrate to ground voltage. If we assume that there is a sufficient exchange of charge between the surface and the beam, this sum, shown in fig. 2c, can be taken to represent the effective beam potential at different positions as the site passes through the beam. Further investigations showed that this potential was independent of the site capacitor size, lending weight to the argument that the beam acts as a voltage rather than a current source, although the decrease in the observed signal as the input impedance is lowered below 200 kΩ suggests that this is a current limited source.

Given the input impedance of 680 kΩ, the total charge flowing through the external circuit can be estimated for a peak of 11 V with a FWHM of 1 ms as 11 V × 1 ms/680 kΩ = 16 nC. This is much larger than that deposited in the test site by the ions in the beam. If we allow one positive charge per ion, assume that the beam has a height in the direction normal to the travel of 20 mm and use a collection area of 0.25 mm^2, then a 2 mA beam will deposit 1.0 nC in a single pass of the wafer through the beam. Thus the actual amount of charge observed on this small test structure is much larger than the beam itself can have supplied, even taking into account reasonable secondary electron yields, (typically about two for the energies of interest here [10]). Thus we see that the signal observed on a local scale (smaller than the beam dimension) is much more readily interpretable in terms of the voltages established than in terms of the expected currents in the beam

Fig. 3a shows the dependence of the maximum beam potential (V_{max}) on the electron shower primary current for a 2 mA B^+ beam at 20, 40 and 60 keV, while Figs. 3b and 3c show the similar data for different As^+ beam conditions. For each beam species and current, the variation of the maximum voltage (V_{max}) as a function of the shower primary current (I_p) can be closely represented by an equation of the form $V_{max} I_p^m = C$ Values of m range between 0.3 and 0.5. The variation of the peak voltage on beam energy is more complex; for boron we see the higher voltages with the higher energy beams, while for arsenic there are several instances when lower energy beams were found to be significantly more tightly focused and to give higher potentials, as shown in fig. 3b.

4. Discussion

We can summarize our model of the physical interactions that occur in a high-current implanter with reference to two different scales of spatial dimension. On a large scale, with dimensions larger than the width of the beam, the net electrical current delivered by the beam is related to the ion beam current and the flow of electrons and this current is responsible for the potential of conductors large enough to trap the whole beam. On a scale smaller than the beam dimension, however, there are potential gradients established by the beam potential and the beam will supply quite large current densities to maintain these potentials on the surface of its target.

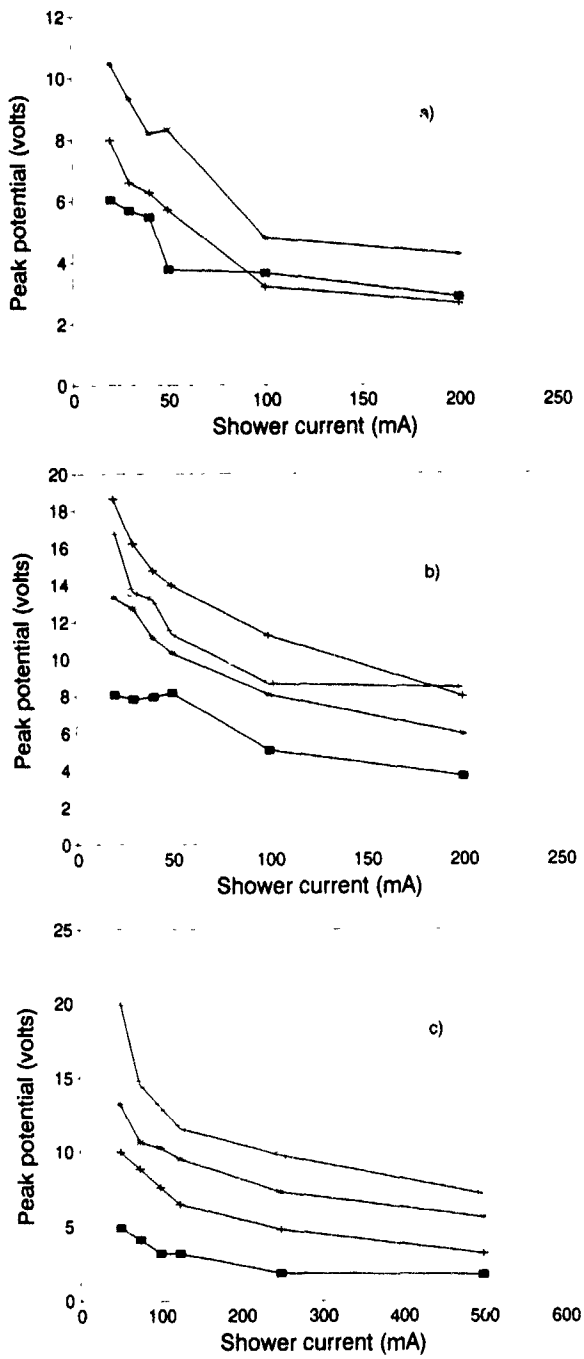

Fig 3 Peak measured voltages as a function of beam kinetic energy and electron shower primary current for the following conditions: (a) 2 mA B^+ beams, (b) 2 mA As^+ beams and (c) 5 mA As^+ beams. In each case beams energies are represented as follows: (■) 20 keV, (+) 40 keV, (*) 60 keV, (□) 80 keV The lines connecting the measured points are intended merely as guides to the eye.

It is useful to distinguish three fluxes of electrons. *First*, those which are injected from outside the beam either from an electron shower or by emission from the sidewalls of the beam guide induced by stray ions. These have significant kinetic energy when they reach the center of the beam, and as such are likely to escape to the sidewalls unless they can be thermalized by the particles already in the beam. Consideration of the energy loss cross sections indicates that other electrons already in the beam would be much more effective at slowing down the injected electrons. This thermalization process, of course, would result in an increase in the net electron temperature in the beam. *Second*, electrons that are the result of ion beam collisions with the residual gas and thus with little kinetic energy at the bottom of the potential energy well formed by the beam. Either of these first two fluxes of electrons will reduce the beam potential and also may reduce the net charge on the wafer [3]. *Third*, there are secondary electrons produced by the beam striking the target. These electrons will also reduce the beam potential, but while the beam is striking the wafer, they will increase the net electrical current to the surface of the wafer [4].

On a scale smaller than the dimensions of the ion beam, it is more useful to consider that the beam has a characteristic potential, determined by the space charge represented by the ions and electrons. Our experiments suggest that the local electrical currents induced in the structures on the wafer respond very quickly to maintain these voltage distributions. The fact that these local current densities are much higher than the net current density transported by the beam must mean that there is a significant component due either to a field extraction of electrons from the surface of the wafer or by surface currents enabled by conduction in the surface of the solid target induced by the impact of the energetic ions.

This analysis argues that charge control systems in high-current implanters should be designed to serve two interrelated goals: first, to add electrons to the beam to minimize the net charge delivered by the beam so that large area conducting components do not collect enough charge to produce excessively high voltages, and second to neutralize sufficiently the space charge of the beam and control its spatial dimensions so that the electrostatic beam potential itself does not rise to a level that will be hazardous to the devices. In either case, it is important to realize that large potential voltages are only dangerous if they can deliver significant net charge per unit area through an oxide.

References

[1] V. Benveniste, H.E. Friedman, M E. Mack and F. Sinclair, Nucl. Instr. and Meth. B37/38 (1989) 658

[2] S B Felch, L A. Larson, M I. Current and D.W Lindsey, Nucl. Instr. and Meth. B37/38 (1989) 563.
[3] B.J. Doherty and D J. McCarron, Nucl. Instr. and Meth. B37/38 (1989) 559.
[4] M.I. Current, A. Bhattacharyya and M Khid, Nucl Instr. and Meth B37/38 (1989) 555.
[5] C P. Wu, F Kolondra and R. Hesser, RCA Rev 44 (1983) 62.
[6] N. Nagai, T. Kawai, M Naito, Y. Nishsigami, H Fujisawa and K. Nishikawa, Nucl Instr. and Meth. B37/38 (1989) 572
[7] S.B Felch, V K. Basra and C.M McKenna, IEEE Trans. Electron Devices ED-35 (1988) 2338.
[8] R. Tong and P. McNally, Nucl. Instr and Meth B6 (1985) 376.
[9] Cnset Computer Corp., PO Box 1030, 199 Main Street, N Falmouth, MA 02556, USA.
[10] B. Svensson and G Holmen, J Appl. Phys 52 (1981) 11.

Nuclear Instruments and Methods in Physics Research B55 (1991) 216–219
North-Holland

Effects of P^+-implanted poly-Si electrodes on the gate dielectric characteristics of thin oxides

Huang-Chung Cheng [a] and Wu-Shiung Chen [b]

[a] *Department of Electronics Engineering and Institute of Electronics, and* [b] *Institute of Applied Chemistry, National Chiao-Tung University, Hsinchu, Taiwan*

Phosphorus implantation into polycrystalline silicon (poly-Si) has been used to dope the gate electrodes in poly-Si and polycide structures. Effects of phosphorus implantation conditions and post-implantation annealing on the time zero dielectric breakdown (TZDB) characteristics of gate oxides of thicknesses 10, 20 and 30 nm were investigated. Higher implantation energy and higher post-implantation annealing temperature result in worse TZDB properties of the gate oxides. Especially, the TZDB characteristics of 10-nm-thick oxides after annealing show a much more significant dependence on the phosphorus implantation energy and post-implantation annealing temperature than those of thicker oxides. Therefore, phosphorus diffusion into the SiO_2/Si interface is the main cause of deterioration of the gate dielectrics. The thicker oxide has a higher endurance to the phosphorus diffusion and consequently achieves a better dielectric property for the higher energy implantation and higher temperature annealing conditions.

1. Introduction

Generally, doped polycrystalline silicon (poly-Si) and polycide (i.e. silicide film on the doped poly-Si layer) structures are used as gate electrodes. Since the speed advantages attained from short-channel design of the smaller components would be offset by the interconnect resistance at the gate level [1,2], heavy doping of poly-Si films is commonly used in both poly-Si and polycide gate structures of metal-oxide-semiconductor (MOS) devices. In this application, ion implantation is widely used to introduce dopants into the poly-Si film. However, a high-temperature furnace annealing to activate the implanted atoms in the poly-Si films results in a considerable redistribution of the dopants and the reliability problems of gate oxides [3,4]. Therefore, studies of dopant redistribution and grain growth of poly-Si electrodes have been reported for the proper design and reliable performance of MOS devices [5–7]. Moreover, post annealings of poly-Si gate also lead to the pileup of doping species at the oxide/poly-Si interface and caused the attendant yield loss and reliability problems in devices due to the defect generation in the gate oxide [8,9].

In this work, we therefore report the effects of phosphorus doping on the dielectric characteristics of gate oxides. We used phosphorus implantation at various energies to simulate the penetration depth of phosphorus impurities in the poly-Si films.

2. Experimental

(100)-oriented p-type silicon wafers of 3 in. diameter and of resistivity 5–15 Ω cm were used to fabricate the investigated MOS capacitors. After standard RCA initial cleaning and HF dip, the wafers were oxidized at 900 °C in dry O_2 ambient to obtain gate oxides of thicknesses 10, 20, and 30 nm and in-situ annealed at the same temperature for 30 min in N_2 ambient. The oxidized silicon wafers were deposited with a layer of low-pressure chemical-vapor-deposited (LPCVD) poly-Si film of the thickness 150, 250, or 400 nm. The poly-Si film was then ion-implanted with phosphorus ions (P^+) at a dose of 5×10^{14}, 2.5×10^{15}, or $5 \times 10^{15}/cm^2$ and an energy of 60, or 110 keV. Then, the specimen was deposited with a SiO_x capping layer using a plasma-enhanced chemical vapor deposition (PECVD) system and subsequently activated in N_2 ambient at 800 °C for 15 min. MOS capacitors of 150 μm diameter were plasma-etched by a DRIE plasma etcher. To lower the sheet resistances of gate electrodes and investigate the electrical reliability of thin oxide after high-temperature processings, these MOS capacitors were all annealed in N_2 ambient at temperatures ranging from 800 to 1000 °C for 30 min. N_2 gas was first purified by titanium getter before entering the annealing furnace. The capping oxide was then removed. Electrical breakdown tests were performed by using a voltage ramp technique [9].

0168-583X/91/$03.50 © 1991 – Elsevier Science Publishers B.V. (North-Holland)

3. Results and discussion

Firstly, the effects of ion-implantation energy on the TZDB field strength of n^+ poly-Si gate structures are investigated to recognize the importance of phosphorus penetration depth. Then, the influences of oxide thickness on the TZDB field of gate dielectrics are proposed to understand the tolerance of phosphorus impurities in the gate dielectrics. The dependence of the TZDB field on the post-annealing temperature is discussed to demonstrate the effects of phosphorus diffusion. The Weibull plots of gate dielectrics are presented to further illustrate the degradation effects of defects induced by phosphorus penetration or diffusion.

3.1. Effects of ion-implantation energy on the TZDB field strength of n^+ poly-Si gate structures

The curves of TZDB field strength versus annealing temperature for the n^+ poly-Si/SiO_2 (10 nm)/Si gate structures implanted with phosphorus ions (P^+) at a dose of $5 \times 10^{15}/cm^2$ and energies of 40, 60, and 110 keV are shown in fig. 1. The value (10 nm) marked after the SiO_2 represents the thickness of gate oxide. The field strength sharply decreases with increasing annealing temperature for the poly-Si gates implanted with P^+ ions at 110 keV. On the other hand, the field maintains a constant level, about 15–16 MV/cm, for the specimens implanted with P^+ ions at 40 or 60 keV and subsequently annealed at 800, 900, or 1000°C. After high-temperature annealing, the phosphorus atoms in the poly-Si films would segregate to the poly-Si/SiO_2 interface and then diffuse into the gate oxide. Hu et al. [10,11] showed that the dielectric breakdown process could be divided into two stages. High density of hole traps or large hole capture cross section at the local spot, or lower effective barrier at zero time due to particulate contamination, crystalline defects or interface asperities in the silicon would cause the "early" breakdown. The implant range and standard deviation of the silicon implanted with P^+ ions at 110 keV are 145 and 49 nm, respectively. For the 250-nm-thick poly-Si film, a direct phosphorus penetration to the bottom of the polysilicon layer to about 1/20 of the peak concentration has been obtained for the 110 keV phosphorus implantation. Thus, a small fraction of the total number of ions penetrates into the oxide. The damage is expected to lead to oxide breakdown. Furthermore, a larger quantity of phosphorus impurities diffuses into the gate oxide during the subsequent annealing and enhances the deterioration of gate dielectric. Hence, it is surmised that the phosphorus impurities penetrating and diffusing into the silicon dioxide and substrate would enhance the probability of electron–hole pair generation via impact ionization and form the localized conduction column. As a consequence, the poly-Si gate implanted with a higher energy of phosphorus ions will gain a larger impact of phosphorus impurities and exhibit a worse TZDB field.

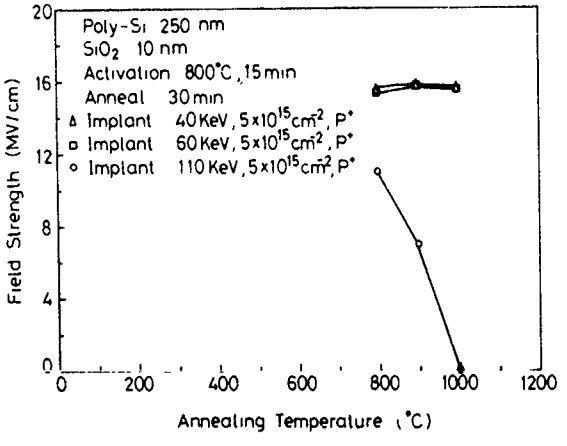

Fig. 1. Curves of TZDB field strength versus annealing temperature for the n^+ poly-Si/SiO_2 (10 nm)/Si samples implanted with P^+ ions at a dose of $5 \times 10^{15}/cm^2$ and energies of 40, 60, and 110 keV, respectively.

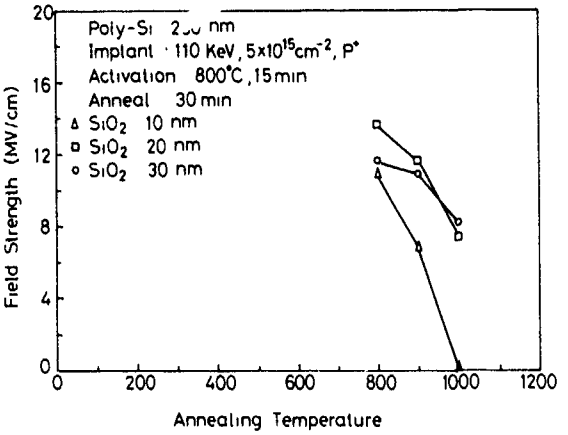

Fig. 2. Curves of TZDB field strength against annealing temperature for the n^+ poly-Si/SiO_2 (10 nm)/Si, n^+ poly-Si/SiO_2 (20 nm)/Si, and n^+ poly-Si/SiO_2 (30 nm)/Si specimens implanted with P^+ ions at $5 \times 10^{15}/cm^2$ and 110 keV, correspondingly.

3.2 Effects of oxide thickness on the TZDB field strength of n^+ poly-Si gate structures

The curves in fig. 2 illustrate the dependence of TZDB field on the annealing temperature for the n^+ poly-Si/SiO_2/Si structures with various thicknesses of the gate oxides. Implantation condition of P^+ ions, $5 \times 10^{15}/cm^2$, and 110 keV were used. The breakdown field significantly decreases with increasing annealing

temperature for the 10-nm-thick oxide. The field strength of the 20-nm-thick oxide exhibits a smaller drop as the annealing temperature increases. Furthermore, the field mildly decreases with increasing annealing temperature for the 30-nm-thick oxide. Obviously, thin oxides have a lower sustainability to the high-temperature annealing. This is predictable because thinner oxides have a lower tolerance of phosphorus diffusion into the interface between SiO_2 and Si substrate.

3.3. Effects of post-annealing temperature on the TZDB field strength of n^+ poly-Si gate structures

As can be seen in figs. 1 and 2, the breakdown field significantly decreases with increasing annealing temperature as the implantation energy is high or the oxide thickness is thin. Previous reports [12,13] showed that phosphorus impurities in the annealed specimens of poly-Si/SiO_2 (10 nm)/Si and WSi_x/poly-Si/SiO_2 (10 nm)/Si structures would diffuse into the SiO_2 films. Since the phosphorus fraction diffused into the substrate could be proportional to $\sqrt{Dt}$, where D is the diffusion coefficient of phosphorus in SiO_2 layer at the annealing temperature and t is the annealing time [9,14,15], high annealing temperatures would enhance the phosphorus diffusion into the SiO_2 dielectric and Si substrate. Hence, a larger fraction of phosphorus impurities will be implanted and diffused into the SiO_2/Si interface to deteriorate the TZDB field of gate dielectric for the higher implantation energy and higher annealing temperature.

3.4. Weibull plots of n^+ poly-Si gate structures

Fig. 3 shows the Weibull plots of n^+ poly-Si/SiO_2 (10 nm)/Si gates annealed at 900 °C for 30 min. Since

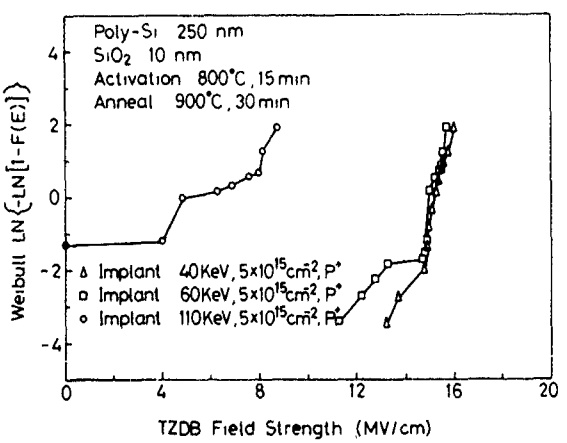

Fig 3 Weibull plots of n^+ poly-Si/SiO_2 (10 nm)/Si gates implanted with P^+ ions at a dose of $5\times10^{15}/cm^2$ and energies of 40, 60, and 110 keV, and subsequently annealed at 900 °C

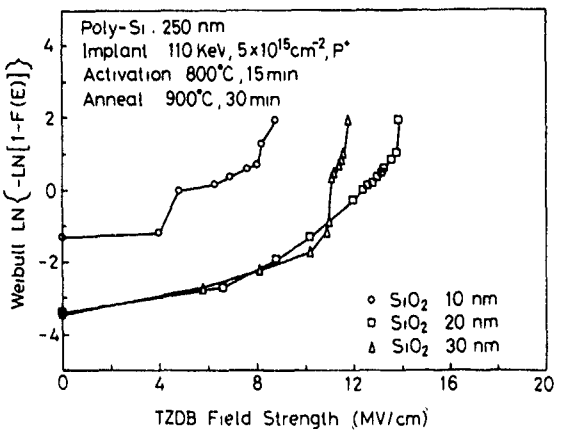

Fig. 4. Weibull plots of n^+ poly-Si gate structures implanted with P^+ ions at $5\times10^{15}/cm^2$ and 110 keV and subsequently annealed at 900 °C for different oxide thicknesses

the cumulative distributions of specimens implanted with P^+ ions at 40 and 60 keV are concentrated at about 15–16 MV/cm, they are conjectured to have an intrinsic breakdown. The distribution for 110 keV implantation is rather scattered. This is because the phosphorus impurities have penetrated into the SiO_2/Si interface of the poly-Si gates implanted with P^+ ions at 110 keV and subsequently annealed at 900 °C for 30 min. As shown in fig. 4, the oxides of thicknesses 20 and 30 nm have steep gradients at the field strengths of 14 and 11 MV/cm, respectively, which just describes the intrinsic breakdowns of the oxides. However, no obvious concentrated field can be observed in fig. 4 for the 10-nm-thick oxide. Since most of the defect-related failures shown in the Weibull plots would disperse over a large range of field strength [9], the 10-nm-thick oxide should induce a larger amount of defects which would cause a more scattered cumulative distribution of field strength than the thicker oxides. This is because thicker oxides lessen the impact of phosphorus diffusion to the SiO_2/Si interface.

4. Conclusions

As the poly-Si gate electrodes are implanted with phosphorus ions (P^+) at an energy of 40 or 60 keV and a dose of $5\times10^{15}/cm^2$, the oxides in the n^+ poly-Si gate structures almost keep a constant level of TZDB field strength even after an anneal at 1000 °C. However, the TZDB field strength of 10-nm-thick oxides in the poly-Si gate electrodes implanted with P^+ ions at 110 keV and $5\times10^{15}/cm^2$ strongly degrades with increasingly annealing temperature. In addition, the degradation tendency of the TZDB fields of gate oxides decreases with the increase of oxide thickness. Hence,

phosphorus diffusion to the SiO_2/Si interface will deteriorate the dielectric characteristics of n^+ poly-Si gate structures. Thicker gate oxides then have a higher endurance to the phosphorus diffuse-in effect

Acknowledgement

The research was supported in part by the Republic of China National Science Council.

References

[1] A K. Sinha, W.S. Lindenberger, D.B Fraser, S.P. Murarka and E.N. Fuls, IEEE Trans. Electron Devices ED-27 (1980) 1425
[2] Y. Shioya, T. Itoh, S.I. Inoue and M. Maeda, J. Appl. Phys 58 (1985) 4194.
[3] A.H Hamid and F.D McDaneil, J. Appl. Phys. 55 (1984) 4162
[4] J Y.W Seto, J Appl. Phys. 46 (1975) 5249
[5] J.R Schwank and D.M Fleetwood, Appl Phys. Lett. 53 (1988) 770.
[6] K. Yamabe and K. Taniguchi, IEEE Trans. Electron Devices ED-32 (1985) 423
[7] T B Hook and T.P. Ma, Appl. Phys Lett 48 (1986) 1208
[8] D. Flowers, J Electrochem. Soc. 134 (1987) 698
[9] H.C Cheng, C Y. Chao, W D. Su, S W. Chang, M.K Lee and C.Y. Wu, Solid-State Electron. 33 (1990) 365
[10] S Holland, I.C. Chen, T.P. Ma and C Hu, IEEE Electron Device Lett. EDL-5 (1984) 302.
[11] I.C Chen, S.E. Holland and C. Hu, IEEE Trans. Electron Devices ED-32 (1985) 413
[12] G S Oehrlein, S.A. Cohen and T.O. Sedgwick, Appl. Phys. Lett. 45 (1984) 417.
[13] N.S. Alvi, S.K. Lee and D.L Kwong, IEEE Electron Device Lett EDL-8 (1987) 197.
[14] M.O Thurston, J.C.C Tsai and K.D Kang, Diffusion of impurities into silicon through an oxide layer, Ohio State University Research Foundation, AD-261201, Contract DA-36-039-SC-83874, Final Report, Columbus, Ohio (March 1961).
[15] L J. van Ijzendoorn, G F. A van De Walle, A A Van Gorkum, A M L. Theunissen, R.A van den Heuvel and J H Barrett, Nucl Instr and Meth B50 (1990) 127

Nuclear Instruments and Methods in Physics Research B55 (1991) 220–223
North-Holland

Investigation of backscattering and re-implantation during ion implantation into deep trenches

M. Posselt, E. Sobeslavsky and G. Otto

Central Institute for Nuclear Research, Rossendorf, PF 19, D(0)-8051 Dresden, Germany

Recently, precise experimental investigations of backscattering and re-implantation have been performed. In these experiments "macroscopic" trench structures were employed. To understand the backscattering and re-implantation processes in more detail, we have developed a two-dimensional simulation model. Backscattering is described by TRIM Monte Carlo simulations whereas analytical approximations are used for re-implantation. The re-implantation profiles calculated by our simulation model are in good agreement with the experimental data from the literature

1. Introduction

Narrow- and deep-trench capacitor technology is often favoured to increase the packing density of VLSI DRAM cells. In several applications doping of the trench sidewalls is required. Ion implantation is an attractive method to dope a trench with a high aspect ratio. Since the ions are implanted with a shallow angle to the sidewall surface, some specific phenomena occur. A considerable number of the incident particles are backscattered and may be re-implanted into the opposite sidewalls of the trench. The enhanced sputtering yield can cause modifications of the trench surfaces if the implantation doses are sufficiently high. Experimental investigations of backscattering and re-implantation in real trench structures are very difficult because of their miniature sizes. Therefore, these processes were studied quantitatively using "macroscopic" structures. The crucial experiments were performed by Fuse et al. [1] and Kakoschke et al. [2,3]. In fig. 1 the experimental setup of Fuse et al [1] is shown schematically. Two silicon slices were arranged so as to face each other; one slice served as a reflector and the other as a collector. The chosen values for θ_0, E_0 and D_0 were characteristic for a real trench implantation. At certain points Y_a, Y_b and Y_c of the collector surface the depth profiles of re-implantation were determined by SIMS. A similar experimental arrangement was used by Kakoschke et al. [2,3]. In contrast to the experiments of Fuse et al. [1] the silicon slices were mounted at an angle of 90°.

To get a better understanding of backscattering and re-implantation processes in the present work, a simulation model is developed (section 2). In particular we consider the special two-dimensional arrangement of Fuse et al. [1]. Our procedure consists of two parts. In a first step the energy and angular distribution of backscattered particles is calculated by TRIM Monte Carlo simulations [4]. Then a fast algorithm to determine the two-dimensional profiles of re-implantation is applied. Here we employ analytical models instead of time-consuming Monte Carlo simulations. Our method of simulation is relatively similar to that of Saler et al [5] which

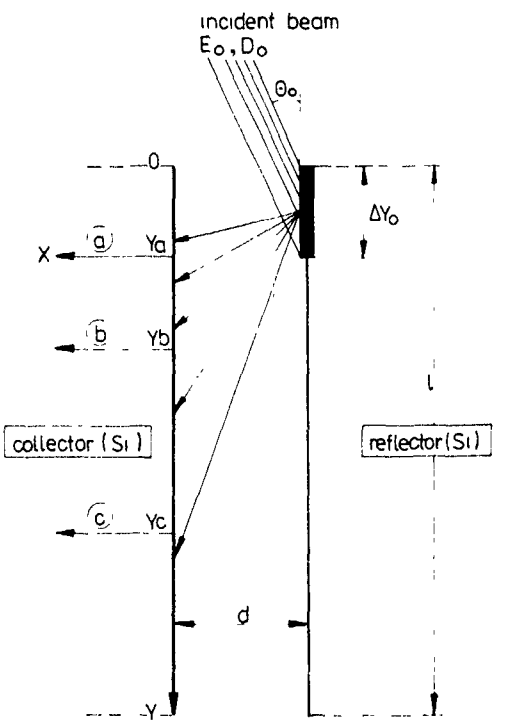

Fig 1 Experimental setup of Fuse et al. [1] Two silicon slices are mounted facing each other One slice serves as a reflector, the other as a collector At the points Y_a, Y_b and Y_c the depth profiles of re-implantation were measured by SIMS

0168-583X/91/$03.50 © 1991 – Elsevier Science Publishers B.V. (North-Holland)

was employed to calculate isoconcentration lines in real trenches. In section 3 of the present work the profiles of re-implantation calculated by our simulation model are compared with the experimental data of Fuse et al. [1].

2. Simulation model

2.1 Description of backscattering

We consider a two-dimensional geometry with a line source of incident ions at the target surface. This is illustrated in fig. 2a. The line source is in the z-direction. For a given incidence angle θ_0 ($0 \le \theta_0 \le \pi/2$) and implantation energy E_0 the energy and directional distribution of the reflected ions depends on two variables: (i) the energy E of the particles and (ii) the direction of motion characterized by the angle ψ ($0 \le \psi \le \pi$). It should be noted that the angle ψ is a polar angle in the x–y plane. In our TRIM Monte Carlo simulations the direction of motion of the particles is characterized by three direction cosines. The projection of this direction on the x–y plane gives the value of the polar angle ψ. During the Monte Carlo simulation we count the number $dY_B(E_0, \theta_0)$ of backscattered ions per incident particle:

$$dY_B(E_0, \theta_0) = y_B(E_0, \theta_0, E, \psi)\, dE\, d\psi, \qquad (1)$$

where $y_B(E_0, \theta_0, E, \psi)$ is the energy and angular distribution of the reflected ions or the differential backscattering yield. The total backscattering yield $Y_B(E_0, \theta_0)$ is obtained from eq. (1) by integration. We studied grazing incidence implantation of As^+ into Si for implantation energies of 80, 115 and 150 keV and incidence angles of 4°, 6°, 8° and 10° to the target surface [6]. About 5000 particle histories were simulated. The values obtained for the backscattering yield are given in table 1. In the case of grazing incidence implantation $Y_B(E_0, \theta_0)$ strongly depends on the incidence angle. For $\theta_0 = 8°$ about 35% of the incoming ions are reflected. The backscattering yields of table 1 are nearly independent of the implantation energy. Fig. 2b shows the energy and angular distribution $y_B(E_0, \theta_0, E, \psi)$ of the reflected particles for 150 keV As^+ implantation and $\theta_0 = 8°$. The figure demonstrates that forward scattering dominates. In the region $3\pi/8 < \psi < \pi$ only a few particles with $E < 0.15E_0$ were found by the TRIM simulations. Therefore, this part of the histogram is not shown in the figure.

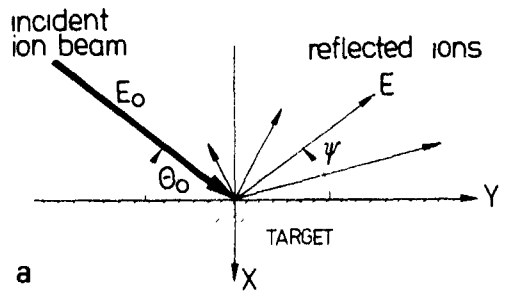

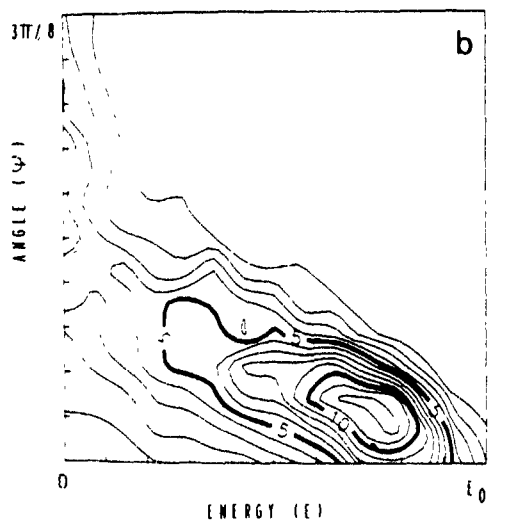

Fig. 2. (a) Two-dimensional geometry used in the calculation of the energy and angular distribution of the backscattered particles. (b) Energy and angular distribution [10^{-3} keV^{-1} rad^{-1}] of backscattered ions (TRIM histogram), $As^+ \rightarrow Si$ ($E_0 = 150$ keV, $\theta_0 = 8°$).

2.2 Simulation of re-implantation

We consider the geometrical arrangement of fig. 1. The whole two-dimensional profile of re-implantation $H(d, \Delta y_0, x, y)$ in the collector is obtained by simple geometrical considerations.

$$H(d, \Delta y_0, x, y) = \frac{1}{\Delta y_0} \int_0^{\Delta y_0} dy_0' \int_0^{E_0} dE \int_0^{\pi/2 + \arctan(y_0'/d)} d\psi \times y_B(E_0, \theta_0, E, \psi) \times G(x, y - y_0' - d \cot\psi, E, \psi). \qquad (2)$$

Table 1
Reflection coefficients

E_0 [keV]	θ_0 [deg]			
	4	6	8	10
80	0.503	0.431	0.363	0.304
115	0.509	0.422	0.349	0.284
150	0.496	0.415	0.362	0.290

The meaning of the variables is illustrated in figs. 1 and 2a. $G(x, y - y_0' - d \cot \psi, E, \psi)$ is the two-dimensional profile of re-implantation of a line source of particles incident on the collector surface at $y = y_0' + d \cot \psi$ with an energy E and an angle ψ to the collector surface. In a relatively rough approximation

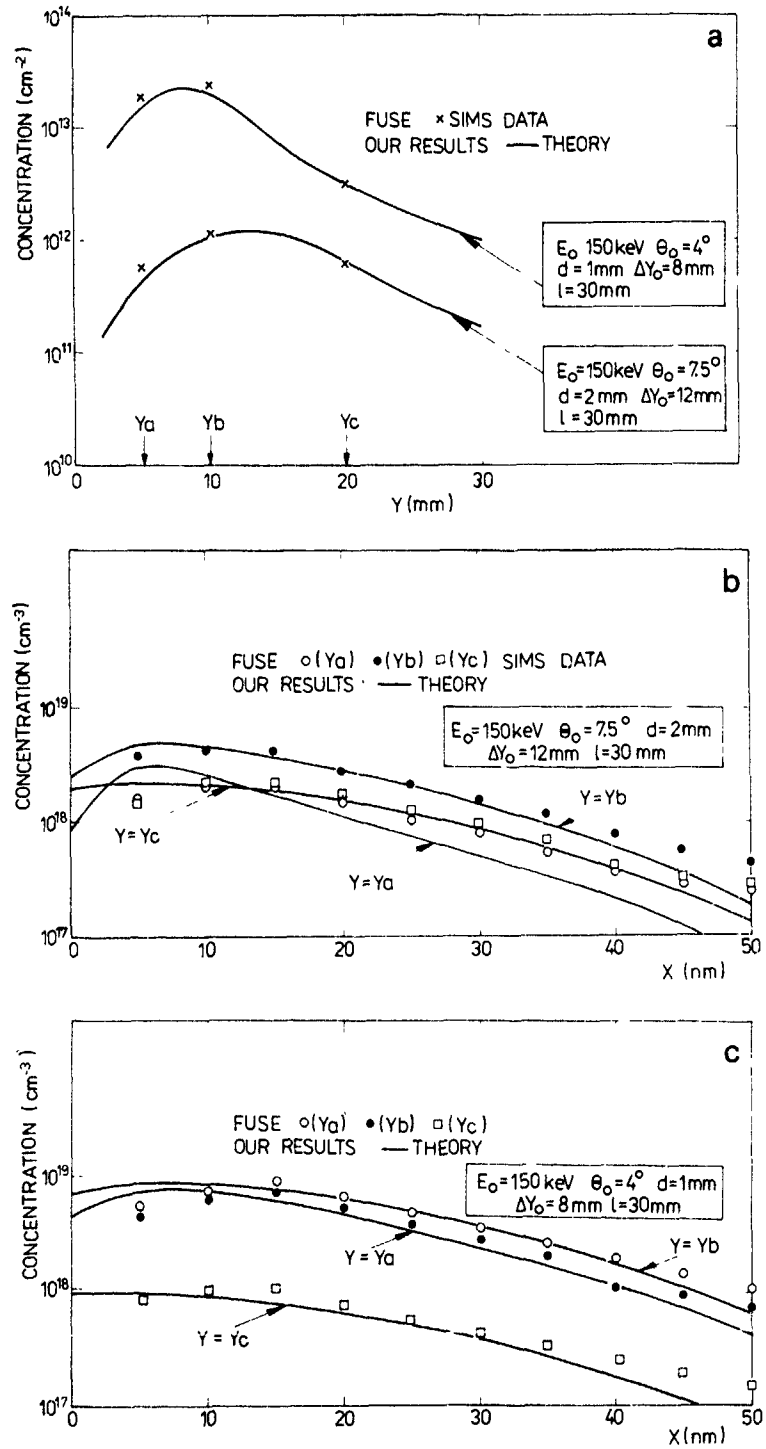

Fig 3. (a) Effective dose of re-implantation (As^+) (shown as a surface concentration) versus the coordinate Y. (b, c) Depth profiles of re-implantation (As^+) at points Y_a, Y_b and Y_c at the collector surface

we assume $G(x, y - y_0' - d \cot \psi, E, \psi)$ to be proportional to the product of a Gaussian depth profile $F(x, E, \psi)$ and a Gaussian lateral distribution $F_L(y - y_0' - d \cot \psi, E, \psi)$:

$$F(x, E, \psi) = \frac{1}{\left[2\pi\left(\Delta R_p^2(E) \sin^2\psi + \Delta R_{pL}^2(E) \cos^2\psi\right)\right]^{1/2}} \times \exp\left(\frac{-\left(x - R_p(E) \sin \psi\right)^2}{2\left[\Delta R_p^2(E) \sin^2\psi + \Delta R_{pL}^2(E) \cos^2\psi\right]}\right), \quad (3)$$

$$F_L(y - y_0' - d \cot \psi, E, \psi) = \frac{1}{\left[2\pi\left(\Delta R_p^2(E) \cos^2\psi + \Delta R_{pL}^2(E) \sin^2\psi\right)\right]^{1/2}} \times \exp\left(\frac{-\left(y - y_0' - d \cot \psi - R_p(E) \cos \psi\right)^2}{2\left[\Delta R_p^2(E) \cos^2\psi + \Delta R_{pL}^2(E) \sin^2\psi\right]}\right), \quad (4)$$

where $R_p(E)$, $\Delta R_p(E)$ and $\Delta R_{pL}(E)$ are the range parameters for normally incident ions with energy E. These parameters are given in the well-known tables of Gibbons, Burenkov [7,8] and other authors. A fraction of the particles incident on the collector surface are backscattered. In the Gaussian approximation discussed above the backscattering yield of particles with energy E and incidence angle ψ is given by [9]

$$Y_B(E, \psi) = \frac{1}{2}\left[1 - \mathrm{erf}\left(\left\{R_p(E) \sin \psi\right\} \times \left\{\left[\Delta R_p^2(E) \sin^2\psi + \Delta R_{pL}^2(E) \cos^2\psi\right]^{1/2}\right\}^{-1}\right)\right]. \quad (5)$$

Then we obtain

$$G(x, y - y_0' - d \cot \psi, E, \psi) = \frac{F(x, E, \psi) F_L(y - y_0' - d \cot \psi, E, \psi)}{(1 - Y_B(E, \psi))}. \quad (6)$$

Re-implantation in the collector as a result of multiple reflection processes between reflector and collector can be neglected. Inserting eq. (6) into eq. (2), the whole profile of re-implantation $H(d, \Delta y_0, x, y)$ is calculated by numerical integration using the energy and angular distributions $y_B(E_0, \theta_0, E, \psi)$ obtained from Monte Carlo simulations.

3. Comparison with experimental data

Fig. 3a shows the effective dose of re-implantation as a function of the coordinate y at the collector surface (cf. fig. 1). The depth profiles of re-implantation at the points Y_a, Y_b and Y_c are shown in figs. 3b and 3c. The values of the parameters E_0, θ_0, d, Δy_0, l, Y_a, Y_b and Y_c are given in the figures. The doses D_0 are chosen such that the incident ion beam intensities per unit surface area of the reflector are always equal to 1.4×10^{14} cm^{-2} [1]. For this low dose the sputtering effect is unimportant. In all examples the agreement between the simulated profiles and SIMS data of Fuse et al. [1] is good. Therefore, we can conclude that the approximation of section 2.2, concerning the two-dimensional profile of re-implantation $G(x, y - y_0' - d \cot \psi, E, \psi)$, was justified.

4. Conclusions

Using a special simulation model we are able to reproduce the results of experimental investigations of backscattering and re-implantation performed by Fuse et al. [1]. The procedure can also be applied to other geometrical arrangements, e.g. to the experimental setup of Kakoschke et al. [2,3]. In our laboratory further experimental and theoretical studies are in progress.

References

[1] G. Fuse, H. Ogawa, K. Tamura, Y. Naito and H. Iwasaki, Appl. Phys. Lett. 54 (1989) 1534

[2] R. Kakoschke, H. Binder, S. Röhl, M. Masseli, I.W. Rangelow, S. Saler and R. Kassing, Nucl. Instr. and Meth. B21 (1987) 142.

[3] M. Masseli, Thesis, Universität Kassel (1987)

[4] J.F. Ziegler, J.P. Biersack and U. Littmark, The Stopping and Range of Ions in Solids (Pergamon, New York, 1985)

[5] S. Saler, R. Kassing and R. Kakoschke, Nucl. Instr. and Meth. B44 (1990) 453.

[6] M. Posselt and G. Otto, to be published in Vacuum (1990)

[7] J.F. Gibbons, W.S. Johnson and S.W. Mylroie, Projected Range Statistics (Healsted, Stroudsburg, 1975)

[8] A.F. Burenkov, F.F. Komarov, M.A. Kumakhov and M.M. Temkin, Tablitsy Parametrov Prostranstvennogo Raspredeleniya Ionnoimplantirovanoi Primesi (Isd. BGU Lenina, Minsk, 1980) in Russian.

[9] G. Fuse, H. Unimoto, S. Odanaka, M. Wakabayashi, M. Fukumoto and T. Ohzone, J. Electrochem. Soc. 133 (1986) 996.

Nuclear Instruments and Methods in Physics Research B55 (1991) 224–229
North-Holland

Proximity gettering by MeV-implantation of carbon: microstructure and carrier lifetime measurements

W. Skorupa and R. Kögler
Central Institute for Nuclear Research, Rossendorf, PF 19, KF, O-8051 Dresden, Germany

K. Schmalz
Institute for Semiconductor Physics, W.-Korsing-Str. 2, PF 409, O-1200 Frankfurt/Oder, Germany

H. Bartsch
Institute for Solid State Physics and Electron Microscopy, O-4020 Halle/Saale, Germany

The gettering efficiency of silicon implanted with carbon at a dose of 1×10^{16} cm^{-2} and energies in the range of 0.33–10 MeV was tested by carrier lifetime measurements. After an intentional contamination of the sample back side with gold as a lifetime killer, on the front side we found values for the generation lifetime of the minority carriers in the range of 27–78 μs and 144–569 μs for the 2.4 MeV and 10 MeV implantation, respectively. These values are higher by 1–2 orders of magnitude as compared to unimplanted silicon. Furthermore, an anomalous doping effect of carbon was found which depends on the annealing method (furnace, RTA). The microstructure of the carbon-implanted layer was investigated by electron microscopy of cross-sectional samples showing dislocation loops which surround the stacking faults. These defects are located within a band of very small precipitates.

1. Introduction

The use of ion implantation to modify the dopant distribution in single crystalline silicon and other semiconductors is widely accepted in the semiconductor industry. The implantation of nondopant elements has also been paid much attention over the last years. Especially, the formation of silicon-on-insulator structures by ion beam synthesis and the introduction of damaged regions to perform gettering are topics of this kind [1–3].

Besides high-dose implantation and the use of nondopant elements, a lot of research effort has been devoted to the use of high implantation energies above 200 keV up to several MeV to produce materials with better and/or new properties. An interesting new technique to produce a region in a silicon wafer, which is able to getter metallic impurities very near to the active device region, was proposed by Wong et al. [4]. High-energy implantation of oxygen or carbon with an energy of up to 4 MeV and a dose in the range of 10^{16} cm^{-2} was used to create a buried damaged region with remarkable gettering efficiency of additionally introduced gold. Wong et al. called this process "proximity gettering". Up to now, this effect was only proved by means of measuring the atomic profile by secondary ion mass spectroscopy (SIMS).

In this paper, we present for the first time a test of the gettering efficiency by measurement of the carrier lifetime. Carbon implantation was used to produce the damage region because this type of MeV-implantation was found to be more effective in gettering [4]. Furthermore, analysis of the implanted samples was performed by SIMS, SRP (spreading resistance profiling), XTEM (transmission electron microscopy at cross-sectional samples) and DLTS (deep level transient spectroscopy) to get more detailed knowledge on the doping behaviour and the microstructure.

2. Experimental

Silicon wafers (⟨100⟩, n-type, 3–5 Ω cm, 2 in. diameter) from a Czochralski-grown crystal were annealed at 1100°C for 4 h in dry nitrogen to create a surface region of 4 μm denuded in oxygen. A silicon dioxide layer was grown at 1000°C in dry oxygen up to a thickness of 100 nm. After thinning the oxide on the lapped back side of the sample to a thickness of 30 nm by chemical etching, gold was implanted into the back side with an energy of 330 keV and a dose of 1×10^{12} cm^{-2}. In this manner gold was used as a lifetime killer to illustrate the gettering effect of the carbon-implanted layer.

0168-583X/91/$03.50 © 1991 – Elsevier Science Publishers B.V (North-Holland)

Then, carbon was implanted at energies of 0.33, 2.4 and 10 MeV and a dose of 1×10^{16} cm^{-2} at room temperature. The implantation at 0.33 MeV was performed by a conventional implanter. For the implantation at the higher energies the Rossendorf tandem accelerator was used. Only the central 2×2 cm^2 (0.33 MeV) or 2×3 cm^2 (2.4 and 10 MeV) part of the wafers was implanted allowing the investigation of gettered and ungettered materials with the same wafer. After implantation, the wafers were diced into four parts to perform different types of post-implantation annealing (FA – furnace annealing; RTA – rapid thermal annealing):

FA: 1000 °C, 1 h, dry nitrogen;
RTA1: 1100 °C, 30 s, dry nitrogen;
RTA2: 1250 °C, 30 s, dry nitrogen;
RTA3: 1350 °C, 30 s, dry nitrogen.

Then, the gate oxide layer on the front side was thinned to about 70 nm by chemical etching to remove organic contaminants and other impurities introduced during vacuum processing. Aluminium contacts were produced on the front side by photolithography (0.5 mm dots) and on the back side (full area). Subsequently, the contacts were annealed at 450 °C for 30 min in dry nitrogen. Capacitance–voltage (C–V) and capacitance-time (C–t) measurements were used to evaluate the doping density and the generation lifetime of the minority carriers, respectively. The lifetime values evaluated from the Zerbst plot are given for a depth region of 1.0–1.5 μm.

After removing the contacts and the gate oxide, several methods were applied to evaluate further properties of the samples by SRP, SIMS, XTEM and DLTS. With the last method Schottky diodes were used.

3. Results and discussion

3.1. Doping behaviour and atomic profile

To our knowledge, only a few papers exist on the investigation of carbon-implanted silicon with doses up to 10^{16} cm^{-2} and they are mostly from the early days of ion implantation [5]. Especially, the influence of carbon on the doping behaviour of silicon was not a matter of interest over the last 20 years of research in ion implantation. So, it was somewhat surprising to see the carrier concentration profiles of our samples as measured by SRP. In fig. 1, such profiles are shown for the case of 2.4 MeV implantation. For furnace annealing (FA), a distinct increase of the donor concentration in the depth region of about 1.5–3.2 μm is observed. The profile has a double peak with maxima at 2.1 and 2.7 μm and a maximum concentration of about 1×10^{16} cm^{-2}, about four times the background donor concentration of the wafer, 2.4×10^{15} cm^{-3}.

The application of rapid thermal annealing (RTA1–RTA3) resulted in a completely different characteristic.

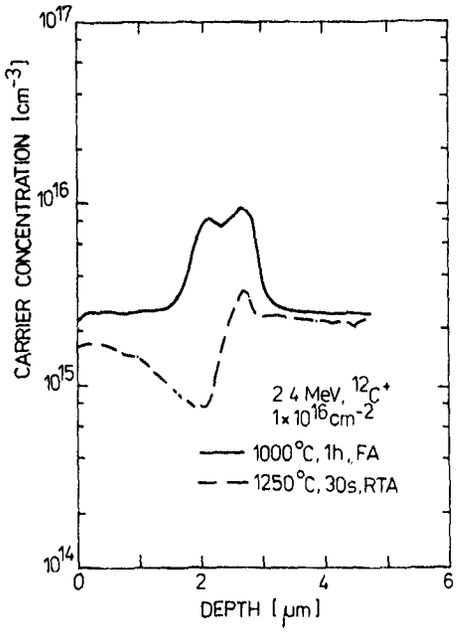

Fig. 1. Carrier concentration profiles from spreading resistance measurements after 2.4 MeV carbon implantation into silicon with a dose of 1×10^{16} cm^{-2} and after different annealing treatments.

It is visible in fig. 1 that, coming from the surface, the profile is characterized by a deep dip pointing to an acceptor-like effect of carbon. This dip is immediately joined to a peak with a maximum carrier concentration only slightly higher than that of the wafer, and not so high as in the case of furnace annealing. The cause for this strange doping behaviour, especially for RTA, could also be related to defect-related doping. For the other implantation energies of 0.33 and 10 MeV, the shape of the profiles is comparable to the case of 2.4 MeV, also showing the difference between FA and RTA.

For the case of 0.33 MeV, the evaluation of the integral dopant density is also possible using the C–V measurements and gave values of about 1×10^{16} cm^{-2} for all annealing variants (table 1). This confirms the results of SRP.

For the implantation energies of 0.33 and 2.4 MeV, we have performed SIMS measurements. In this paper, only the results for the higher energy will be discussed, because the carrier lifetime increase was only found for this energy (see section 3.3). In fig. 2, the profiles for carbon and gold are shown. Phosphorus was also measured but did not show any deviation from the background. The carbon profile shows a typical Gaussian shape (no double peak!) for the two cases of annealing. In both cases the range of the ions is 2.65 μm, comparable to the depth of the deeper lying peak of the carrier concentration profile (2.7 μm) after furnace annealing (fig. 1). No theoretical range data are available for

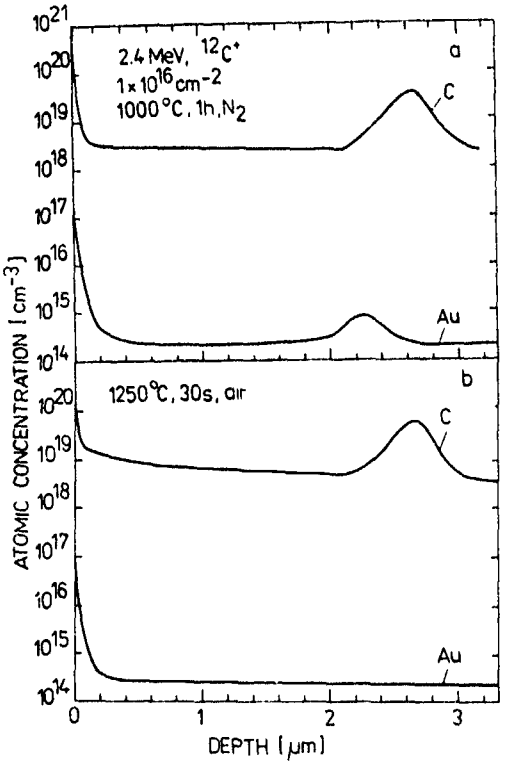

Fig. 2 SIMS profiles after 2.4 MeV carbon implantation into silicon with a dose of 1×10^{16} cm^{-2} and after different annealing treatments

carbon implantation in this energy range. The upper peak of the carrier concentration profile of the furnace-annealed sample lying at 78% of the depth of the deeper peak could be related to the maximum of energy deposition into nuclear processes. The position of $0.8R_p$ is well documented for energies in the keV-range. A more detailed paper concerning the carbon profiles and their modeling will be published in future.

The gold profile shows an accumulation effect in the region of the carbon maximum only for the case of furnace annealing (fig. 2a) corresponding to the results of Wong et al. [4]. For RTA no such accumulation pointing to the gettering of gold is detected (fig. 2b).

3.2. Microstructure

In fig. 3, several XTEM micrographs of the carbon-implanted silicon samples are shown. Generally, a damage band was seen for the three implantation energies, but with different appearances. The depth of the defect band is given in table 1. The best preparation and microscope work was possible for the samples with the lowest energy of 0.33 MeV. For all cases of annealing, a band of loops containing stacking faults is visible lying in all cases within a background of very small precipitates (e.g. fig. 3a). The defect band is located at a depth of about 600–900 nm with the centre at 750 nm. The loop diameter varies between 220 and 400 nm,

Table 1
Experimental data evaluated on silicon implanted with MeV carbon ions at a dose of 1×10^{16} cm^{-2}

E_{impl} (MeV)	Anneal step	R_{DB} [μm]	R_p [μm]	$N_{D\,max}$ [10^{16} cm^{-3}]	$N_{DL,Au}$ [cm^{-3}]		τ_{gen} [μs]	
					unimpl.	impl.	unimpl	impl.
0.33	FA	0.75	0.53	1.13	2.4×10^{12}	$< 10^{11}$	3.0	0.6– 1
	RTA1	0.75	–	0.94	–	–	1.2	0.1
	RTA2	0.75	0.56	1.00	–	–	6.3	4.1
	RTA3	0.75	0.62	1.10	–	–	10.6	7.3– 13.7
2.4	FA	3.00	2.65	0.90	4×10^{12}	$< 10^{11}$	0.3– 3.1	27 – 47
	RTA2	3.00	2.65	0.26	–	–	0.8–13	33 – 78
10.0	FA	11.0	–	1.64	2×10^{12}	$< 10^{11}$	1.1– 2.8	245 –342
	RTA1	11.0	–	0.61	–	–	1.5– 2.3	144 –239
	RTA2	11.0	–	0.59	–	–	4.9–24.1	264 –543
	RTA3	11.0	–	0.47	–	–	16.9–19.5	292 –569

E_{impl} – implantation energy; FA – furnace annealing (1000 °C, 1 h, N_2);
RTA – rapid thermal annealing (1–1100 °C, 30 s; 2–1250 °C, 30 s, 3–1350 °C, 30 s),
R_{DB} – depth of the damage band assessed from XTEM micrographs,
R_p – range data from SIMS measurements;
$N_{D,max}$ – maximum donor concentration (integral value from C–V measurements for 0.33 MeV, maximum carrier concentration from SRP data for 2.4 and 10 MeV);
$N_{DL,Au}$ – concentration of the gold-induced deep levels (DLTS);
τ_{gen} – generation lifetime of the minority carriers.

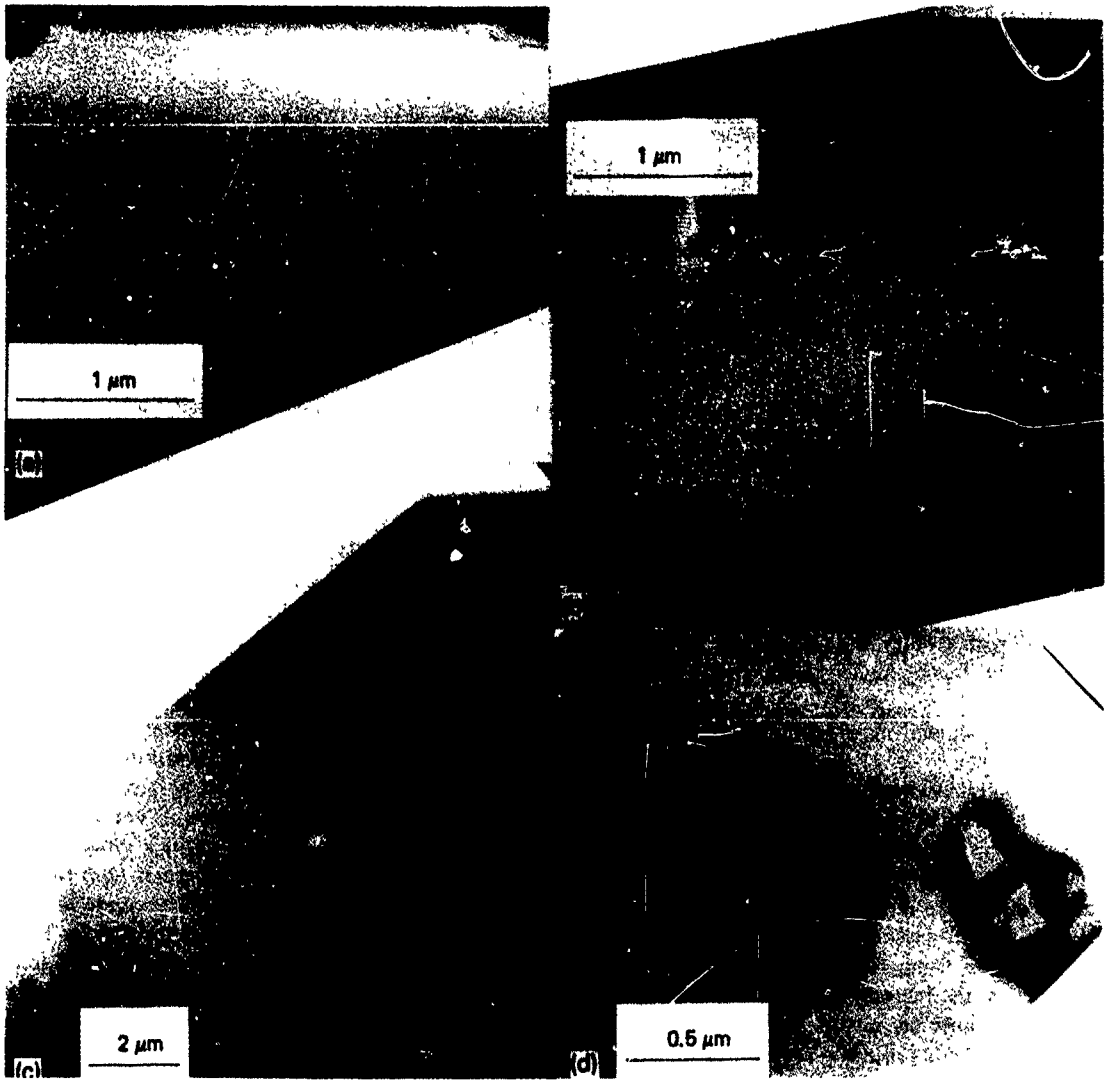

Fig. 3. TEM micrographs of cross-sectional samples after carbon implantation into silicon and annealing: (a) 0.33 MeV, 1350 °C, 30 s, (b) 2.4 MeV, 1000 °C, 1 h; (c) 10 MeV, 1250 °C, 30 s, (d) 0.33 MeV, 1100 °C, 30 s. The implanted dose is generally 1×10^{16} cm^{-2}. The weakly visible defect band in (c) is marked by D

mostly 300 nm. It is worth mentioning that the loops are not of ideal circular shape, but have a rough border line pointing to a decoration with impurities. This is visible in fig. 3d for the case of furnace annealing. Only for the case of RTA3, the highest annealing temperature, the loops were not so rough as in the case of the other annealing variants (fig. 3a). On the contrary, the background band of small precipitates was more clearly visible than in the other cases. This could be caused by a dissolution of the decorated loops into small precipitates.

Dark field imaging showed that the dislocation contrast of the loops is very weak. Assuming that the decoration of the loops (see above) is first of all due to precipitated carbon, the weak contrast could be caused by carbon well matched into the dislocation as well as the planes of the stacking fault. In this manner, carbon reduces the lattice stress around the dislocation due to its low covalent radius.

For the case of 2.4 MeV implantation, the type of formed defects is the same one. The defect region is located at a depth of 3 μm (fig. 3b). This value is higher by 10% than the depth of the deeper lying peak of the SRP data (fig. 1) as well as the carbon maximum measured by SIMS (fig. 2) for the case of furnace annealing. This underlines a correspondence of the defect band with the maximum of the carbon concentration. The loop diameter is about 0.2–0.3 μm, again.

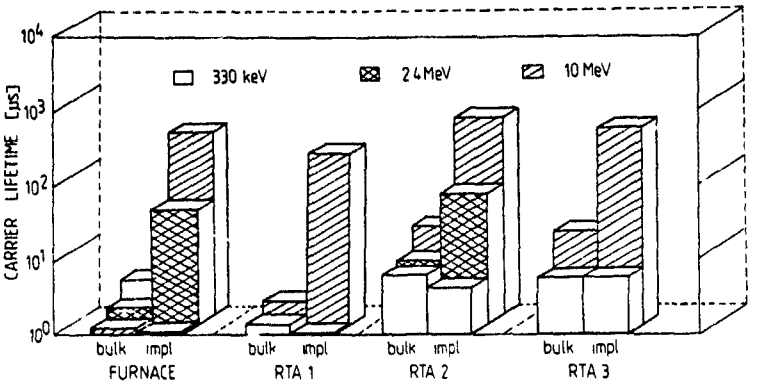

Fig 4 Graphic overview showing the generation lifetime of the minority carriers in silicon after carbon implantation at an energy in the range of 0.33–10 MeV and annealing (for further details, see text) The wafers were only partly implanted to enable a measurement of the carrier lifetime on both the implanted ("impl.") and the unimplanted ("bulk") part of the samples.

After the 10 MeV implantation, only a weakly appearing band with darker contrast lying parallel to the surface is visible (fig. 3c). It is located at a depth of about 11 μm with a width of about 0.3 μm. It could not be better resolved using higher magnification imaging.

3.3. Carrier lifetime and gettering

In fig. 4, a graphic overview of the measured generation lifetime values is represented. The exact data are given in table 1. Generally, a distinct increase in lifetime was found on the implanted parts of the wafers for the implantation energies of 2.4 and 10 MeV. For FA and RTA1, the lifetime values are about two orders of magnitude higher using the 10 MeV implantation. In the other cases, the increase was at least one order of magnitude. The absolute lifetime values are highest for the 10 MeV implantation independently of the annealing method. Whereas these values are generally higher than 150 μs, silicon implanted at an energy of 2.4 MeV shows values in the range of 20–80 μs. In all these cases the unimplanted material is characterized by a carrier lifetime in the 0.3–20 μs region. It is worth noting that carbon implantation does not only increase the carrier lifetime very distinctly but also equalizes the values within one order of magnitude as compared with the scattering of the data from the unimplanted material. They vary within two orders of magnitude. For the 0.33 MeV implantation, no lifetime increase was found on the implanted region. This is due to the fact that the carbon-implanted region is immediately next to the space charge region which was used to inspect the semiconductor. For unimplanted silicon, the inspected volume during the carrier lifetime measurement is defined in a depth region of 1–2 μm. On the implanted part, the space charge region can be driven up to a depth of 0.5–0.6 μm due to the carbon-induced donor concentration of about 1×10^{16} cm^{-3} in this region. The residual defects in the implanted region lead to high generation currents and small lifetime values.

Whereas the carrier lifetime is an indirect measure of the gettering ability of the carbon-implanted layer, the measurement of deep levels typical for gold ($E = 0.54$ eV) at the surface of the wafer directly delivers this property. We found, for the furnace-annealed samples, the level typical for gold on a substitutional position, at the surface of the unimplanted part of the wafer with the concentration given in table 1. On the implanted part, the concentration must be in a range lower than 1×10^{11} cm^{-3}, which is the detection limit of our system. Although the carrier lifetime increase is the same on the samples annealed by furnace and by RTA, no gold levels were found at the unimplanted and implanted parts of the surface of these samples. This result confirms the SIMS data for the case of 2.4 MeV implantation which also did not show any gold accumulation at the implanted carbon for the case of RTA (see fig. 2).

4. Conclusions

(1) Carbon implanted into silicon at MeV-energies and a dose of 1×10^{16} cm^{-2} induces a distinct gettering effect as tested for intentionally introduced gold by measurement of the generation lifetime of the minority carriers as well as deep levels typical for gold. The data show a lifetime increase higher by 1–2 orders of magnitude compared to unimplanted silicon for all types of annealing. Further work is necessary to clarify the contradiction between the observation of the lifetime increase for RTA, but no indication of gold accumulation using SIMS and DLTS. Besides gold, the gettering efficiency of such a carbon implanted layer should also be tested for the transition metals (Fe, Co, Ni, etc.) playing an important role as unwanted impurities both in starting silicon wafers and during their processing.

(2) Silicon implanted with carbon at a dose of 1×10^{16} cm^{-2} shows an anomalous doping behaviour. Whereas furnace annealing at 1000 °C leads to the formation of donors, rapid thermal annealing forms both acceptor-like and donor-like doping effects. These findings need more research work because such doping effects can change the functioning of electronic devices produced above carbon-implanted layers.

(3) It was shown that the type of carbon implantation investigated in this paper induces, after annealing (furnace, RTA), the formation of a buried defect layer consisting of both small precipitates and dislocation loops containing stacking faults.

References

[1] W Skorupa, R. Grötzschel and H. Bartsch, Phys Status Solidi A112 (1989) 661.
[2] W. Skorupa, P Knothe and R Grötzschel, Electron Lett 24 (1988) 464
[3] N W. Cheung, C.L Liang, B.K Liew, R H. Mutikainen and H Wong, Nucl Instr. and Meth B37/38 (1989) 941
[4] H. Wong, N W. Cheung, P.K Chu, J Liu and J.W Mayer, Appl Phys Lett. 52 (1988) 1025
[5] D E. Davies and S Roosild, Solid-State Electron. 14 (1971) 975

Nuclear Instruments and Methods in Physics Research B55 (1991) 230–234
North-Holland

Comparison of modern uniformity-mapping techniques

W.A. Keenan and W.H. Johnson
Prometrix Corporation, Santa Clara, CA 95054, USA

C.B. Yarling
Varian Associates, Inc., Ion Implant Systems, 35 Dory Road, Gloucester, MA 01930, USA

When ion implantation was first introduced for semiconductor processing, implanter specifications of 2% wafer uniformity and 2% wafer-to-wafer repeatability were actually better than the precision of the measurement equipment and techniques available. In the past ten years, the performance of both the ion implanter and its requisite process monitoring equipment has greatly improved. In addition, techniques using modern technology and software have been introduced. Six characterization methods are currently available for monitoring ion implant uniformity: sheet resistance, spreading resistance, pulsed capacitance–voltage ($C-V$), modulated-optical reflectance, optical constant monitoring using ellipsometry, and optical densitometry. Sheet resistance, spreading resistance and pulsed $C-V$ are direct electrical measurements of the active dopant atoms in the implanted wafer. The other three techniques monitor dose by measuring the damage induced by the ion beam: modulated-optical reflectance and optical constant monitoring measure the damage in an implanted wafer, whereas optical densitometry measures the damage in a photoresist coating on a glass substrate. This paper will review each of these methods and discuss their relative merits. It will be clear from this presentation that wise process engineers should use more than one of these methods to characterize ion implant equipment as well as monitor the ion implantation process.

1. Introduction

Ion implantation offers many unique advantages in semiconductor manufacturing. While it makes possible the controlled low doping levels necessary for new high-density ULSI devices, ion implantation also provides the important process advantages of repeatability and uniformity. When the first commercial implanters were introduced, the manufacturers' specifications of 2% for both uniformity and repeatability exceeded the capability of any available measurement technique. It was eventually learned that these specifications were actually based on optimistic vendor calculations. At that time, the four-point probe sheet-resistance measurement had a precision or repeatability of about 5%. Van der Pauw sheet-resistance structures were good to maybe 1%, but required extensive processing. The accuracy of the MOS pulsed capacitance–voltage ($C-V$) technique was approximately 15% and required photodefined dots for uniformity testing. During this time period it was extremely difficult to verify specifications that exceeded the measurement capability of the technique available. Fortunately, the performance of ion implanters as well as of their monitoring techniques has improved significantly in the last ten years. In addition, new monitoring techniques have been introduced [1].

There are essentially six techniques available for ion implantation (I/I) monitoring, particularly for uniformity mapping. These include sheet resistance, spreading resistance, pulsed $C-V$, thermal-wave, optical constant measurement, and optical density measurement. Three of these techniques, sheet resistance, spreading resistance and pulsed $C-V$, are direct electrical measurements of the electrically active dopant atoms. The other three techniques depend on the damage resulting from the implant: thermal-wave and optical constant measurements monitor the damage in the semiconductor of interest, while the optical density technique measures the damage with a specially prepared glass wafer covered with photoresist.

This array of techniques offers the implant engineer several options for measuring and displaying implant uniformity. Each technique has special advantages that make it unique, as well as limitations. Each technique will be reviewed with special attention to convenience, cost, calibration, physical phenomena being used, physical modeling available, sensitivity to changes in dose, pre- and post-processing required, applicable range of energy and dose, resolution or spot size, standards, applicability to device wafers, pre-implant measurement if required, repeatability (wafer-to-wafer and instrument-to-instrument), inherent drift or relaxation, accuracy, dependence on energy and current, necessity for anneal, and applicability to inactive ions. The applicability of the equipment to monitoring other processes and parameters will also be mentioned.

0168-583X/91/$03.50 © 1991 – Elsevier Science Publishers B.V. (North-Holland)

2. Electrical techniques

2.1. Four-point probe

The precision of the four-point probe measurement of sheet resistance was improved to better than 0.2% by the introduction of configuration switching [2]. Configuration switching requires two measurements to be made with each probe impression. Using this data, a geometric correction factor is calculated for each site. This eliminated the errors introduced by current crowding at the edge of the wafer and by probe-spacing variation. At the present time, sheet-resistance mapping [3–6] is the most widely used and accepted means of measuring ion implant uniformity and repeatability. It has become an industry standard, in part because every implant vendor has sheet-resistance mapping equipment. Sheet resistance is physically modeled and has NBS-standard reference material available for equipment calibration. The sensitivity of any implant measurement is defined as the percent change in the measured parameter divided by the percent change in dose The sheet-resistance sensitivity is about 0.7–0.8, which is the best of any technique.

The direct sheet resistance (R_s) technique requires a wafer of the opposite conductivity type from the implanted ion in order to isolate the resistivity change that results from the implant. It is necessary to anneal the wafer to mend the crystal damage done by the incident ions, and to allow them to assume substitutional sites and become electrically active A screen oxide is recommended to minimize contamination, channeling and dopant loss during anneal.

Sheet resistance can be used for the whole range of ion implant dose. The direct or single implant [7] can be used from 2×10^{11} to 1×10^{17} ions/cm^2 and above. Competing background concentration and native oxide charge require the use of high-resistivity substrates and a sulfuric peroxide surface treatment in the 2×10^{11}–5×10^{13} ions/cm^2 range. Below 2×10^{11} ions/cm^2 the double-implant technique [8] uses the change in sheet resistance caused by implant damage to monitor the dose The double implant requires an initial implant and anneal to form a conducting layer, which is followed by a second low-dose implant The sheet resistance of the initial layer is dramatically increased by the damage of the second implant. The advantage of the double-implant sheet-resistance technique is that the sensitivity can be tailored by changing the dose and energy of the initial implant. As with any indirect technique, a calibration curve must be generated to correlate the measured parameter with dose. The technique has been used from 5×10^9 ions/cm^2 (with poor sensitivity) up to 1×10^{14} ions/cm^2. This upper limit is a practical one: the initial implant dose should be 50–100 times the second implant.

2.2. Spreading resistance

The technique of using two probe tips to measure the carrier profile on a beveled sample is called spreading-resistance profiling (SRP). The current density in the silicon is highest at the probe tip, causing the greatest voltage drop with the two contact diameters of the tip. This geometry establishes the spreading-resistance probe as a point technique, whereas the four-point probe is actually a volumetric or bulk technique. The probe must be calibrated to a set of samples spanning the range of measurement. Great care and skill is required to operate the SRP system.

Solid State Measurements has introduced a four-point probe mapping system that uses two spreading-resistance probes as a four-point probe array [9] With this dual-probe arrangement, this system can simultaneously map spreading resistance and sheet resistance with very high resolution. The probe spacing is less than 100 μm and the step size (i.e., distance between measurements sites) is about 50 μm

2.3. Pulsed capacitance–voltage

The pulsed MOS C–V technique is also a direct measurement of the ion implant. It requires a wafer of the same conductivity type as the implant. For best sensitivity, the background concentration should be as low as possible. The same oxide that serves as the screen oxide serves as the MOS oxide. A metal dot acts as one plate of the MOS capacitor. the implanted substrate acts as the second plate. These dots can be quickly deposited by evaporation or sputtering through a metal mask. For best results, the whole back side of the wafer should be stripped of oxide and coated with aluminum. MOS wafers require two anneals, one for the implant and one for the metallization The pulsed C–V technique can be used to calculate the concentration profile of the implanted atoms.

However, there are many problems with this use of the technique, including dot diameter variation, dependence of results on area, and measurement noise amplified by differential calculation. A new technique, introduced to integrate the C–V curve directly, overcomes these problems and yields a fraction of the implanted dose or the partial dose [10].

The partial-dose technique avoids the problems that arise from differentiating the measured data to get the concentration profile by integrating the C–V curve. The measurement is much faster and does not depend on the area of the dots; thus, it is not necessary to use photo-defined dots to measure the partial dose uniformity. This technique is applicable to doses up to about 5×10^{12} ions/cm^2. Above this dose the voltage required to deplete the mobile charge will cause the silicon or the oxide to break down. The extra postprocessing required

for MOS $C-V$ is a consideration, but the technique does provide a direct measurement of low dose. There are no standards available for $C-V$, but the results can be modeled. The spatial resolution is determined by the dot diameter. The advantage of the MOS $C-V$ technique is that it can be used to calculate the concentration profile at any measurement site.

3. Optical techniques

Each optical technique depends on the damage generated by the implanted ions and as such is an indirect measurement of the dose. These techniques do not require an anneal because they are non-electrical; however, because they require a calibration curve for each energy and species, results are difficult to compare from tester to tester. Their sensitivity, which ranges from 0.1 to 0.7, is determined by the implant-damage generation. The phenomenon of room-temperature relaxation of this damage must also be considered when using these techniques. There are no standards and no physical models for calculating the results. These techniques have the advantage that they do not require an anneal and can be used to monitor ions that are not electrically active in silicon. The spatial resolution of the optical techniques is determined by the spot size of the incident light beam.

3.1 Modulated-optical reflectance

One optical measurement tool is the ThermaWave instrument, which uses two lasers to characterize ion implant damage through the measurement of thermal waves [11]. The spot size is on the order of 1 μm so the spatial resolution is excellent, and small features on device wafers can be measured. This is not a differential technique like the other optical measurements. This technique has a sensitivity [12] ranging from about 0.2 at 1×10^{12} ions/cm^2 to about 0.7 at 5×10^{13} ions/cm^2. Above this dose the sensitivity begins to decrease due to the saturation of damage as a continuous amorphous layer is formed. This technique can also be used to measure the dielectric film thickness. The instrument is expensive but very useful in determining whether or not product wafers [13] have been implanted. Software compensates for room-temperature relaxation [14] of I/I damage, but it has been reported that the thermal-wave results depend on the implant current used and show an exaggerated sensitivity to channeling [12]. Another application of this instrument is its ability to measure thin films as well as subsurface defects.

3.2. Ellipsometry

The newest tool available for I/I monitoring is the GRQ ellipsometer [15] which measures the change in the extinction coefficient. The technique of monitoring the change in the optical constants with ion implantation has been reported earlier [16], but this equipment claims to be fast and convenient for mapping. There is little data available, but the sensitivity is less than 0.5 for argon implants into GaAs. The spatial resolution is determined by the spot size of the light on the test wafer. However, this technique is not suitable for device structures since a spot of 0.5 mm and an angle of incidence of 70° result in an effective spot size of 1.5 mm. The instrument can also be used to measure the thickness of dielectric layers. This technique is differential, requiring that the extinction coefficient be measured before and after implant. Any differential technique amplifies the noise of the two individual measurements by taking the difference of their results.

3.3. Optical dosimetry

The Ion Scan [17] measures the change in the optical density of a photoresist-coated glass wafer. It is a differential technique that requires the sample to be measured both before and after implantation. The most attractive feature of the Ion Scan is that no anneal is required and the glass wafer can be measured immediately after implantation [18]. A calibration curve must be generated to correlate the change in optical density with dose. It lacks sensitivity in the very-low-dose region where there is little change in the photoresist density and in the high-dose region where saturation sets in. The spatial resolution is about 3 mm, the diameter of the light spot used to measure the optical density. The technique cannot be used for measuring high-current implants, charging or channeling. There is also a concern with contamination from sodium in the glass and from the iron backing that must be attached to the glass wafer to trigger the photo-sensors on the implanter. The Ion Scan has enjoyed success in the GaAs industry where it is used to monitor ions that are not electrically active in silicon. New photoresist is being investigated that may improve the instrument's sensitivity at low dose [19].

4. Summary

Each of the six techniques presented here have their inherent advantages as well as weaknesses. These are summarized in table 1.

Gone are the days of the Mylar burn. Implant engineers now have an array of characterization tools at their disposal. These tools not only help detect problems but, with mapping and SPC software, provide the information to identify and correct them. The monitoring techniques available have different strengths and weaknesses which tend to complement one another.

Table 1
Mapping techniques compared

Type	Electrical				Optical		
Technique	R_s single I/I	R_s double I/I	Spreading resistance	Pulsed $C-V$	Ion Scan	Therma Wave	GRQ ellipsometry
Measures	Sheet resistance	Damage	Spreading resistance	Depletion capacitance	Photoresist damage	Crystal damage	Crystal damage
Resolution [mm]	0 25	0 25	0 050	0 10	3	0.001	1.5
Species	Active	Both active and inactive	Active	Active	Both	Both	Both
Sensitivity	0 6–0.8	0.5–1.0	0 4–0.9	0 6–0 9	0.3–0.5	0.2–0.6	0 5
Dose range	2×10^{11}–1×10^{17}	1×10^{10}–1×10^{14}	1×10^{10}–1×10^{17}	1×10^{10}–5×10^{12}	1×10^{11}–1×10^{14}	1×10^{11}–1×10^{14}	1×10^{11}–1×10^{14}
Results	Direct	Calibration	Calibration	Direct	Calibration	Calibration	Calibration
NBS Standard	Yes	No	Yes	No	No	No	No
Relaxation	Minor	Serious	Minor	Minor	Serious	Serious	Serious
Substrate	Si opposite σ type	Si	Si either σ type	Si same σ type	Glass with P/R	Any	Any
Require	Anneal	Initial I/I	Anneal	Screen oxide anneal + dots	Measure before and after	Careful control and operation	Measure before and after
Advantage(s)	Monitor whole s/c process Industry Std	Reuse wafer No post-process Tailor sensitivity	Resolution Either Substrate type	Profile available	No post-process	No post-process Contactless Measure on device wafers	No post-process Contactless

Wise process engineers will avail themselves of more than one means to control and understand their implanter.

References

[1] M.I Current, C.B. Yarling and W A Keenan, in Ion Implantation Science and Technology, 2nd edition, ed J F. Ziegler (Academic Press, 1988) p. 377.

[2] D.S. Perloff, J N Gan and F.E Wahl, Solid State Technol 20 (1981) 112.

[3] M I Current and W.A. Keenan, Solid State Technol 28, (1985) 139

[4] L A Larson, J Electrochem. Soc. 136 (1988) 1802

[5] H Glawischnig and G. Lang, Proc. 7th Int. Conf. on Ion Implantation Technology, Kyoto, Japan, 1988, ed. T. Takagi, Nucl. Instr. and Meth. B37/38 (1989) 628

[6] Li Da Han, Jiang Yun Xiang, Yuan Yin and W.A Keenan, Proc 2nd Int Conf on Solid State and Integrated Circuit Technology (ICSSICT), Beijing, PR China, ed Mo Bangxian, Oct 1989 (International Academic Publications, Beijing) p 232

[7] W A Keenan, W H Johnson and A.K A. Smith, Solid State Technol 28 (1985) 143

[8] A K.A. Smith, W H Johnson, W A Keenan, M. Rigik and R. Kleppinger, in: Ion Implantation Technology, eds. M I. Current, N W Cheung, W Weisenberger and B. Kirby (North-Holland, 1987) p. 529.

[9] R.O. Deming and W.A Keenan, Solid State Technol. 28 (1985) 163.

[10] R. Masur, private communication.

[11] A Rosenzwaig, in: VLSI Electronics: Microstructure Science, ed N G Einspruch (Academic Press, 1985) p 227

[12] B J Kirby, L.A Larson and Ru-Yu Liang, in: Ion Implantation Technology, eds M.I. Current, N.W Cheung, W Weisenberger and B Kirby (North-Holland, 1987) p. 550

[13] W.A. Wendman and W L. Smith, ibid., p 559.

[14] J. Schuur, C Waters, J Maneval, N Tripsis, A Rosenzwaig, M Taylor, W.L. Smith, L Golding and J Opsal, ibid , p 554

[15] J.C. Chang, The E-Probe 200 Wafer Probing System (Greater Silicon Valley Implant Users Group, Dec 1985)

[16] N Natsuaki, K. Ohyu and T Tokuyana, Rev. Sci Instr 49 (1978) 1300

[17] J Golin, N Schnell, J Glaze and R Ozarski, Nucl. Instr. and Meth B21 (1987) 542

[18] G A Gruber and N.B. Riley, Semiconductor International (May 1988) 178

[19] J. Driver (Greater Silicon Valley Implant Users' Group, April 1990)

Nuclear Instruments and Methods in Physics Research B55 (1991) 235–242
North-Holland

The history of uniformity mapping in ion implantation

C.B. Yarling [1]
Varian Ion Implant Systems, Blackburn Industrial Park, 35 Dory Road, Gloucester, MA 01930, USA

W.A. Keenan
Prometrix Corp, 3255 Scott Blvd. Bldg 6, Santa Clara, CA 95054, USA

L.A. Larson [2]
National Semiconductor Corp, P.O. Box 58090, Santa Clara, CA 95052-8090, USA

In the early days of semiconductor manufacturing, the four-point probe became established as the tool-of-choice for monitoring diffusion processes. The application of the four-point probe to ion implantation in the early 1960s was basically limited to the single-point measurement of dose, since the equipment did not have the necessary precision or repeatability to provide useful uniformity results. As a result, implanter uniformity was determined by either a visual observation of a heavily doped wafer or by a mylar burn. Unfortunately, these techniques were either subject to interpretation by the user or could not provide a parameter that could be statistically tracked or characterized.

During the last 30 years, the commercial ion implanter as well as the dose and uniformity characterization equipment used to characterize this production tool have progressed significantly. Indeed, several generations of electrical and optical equipment have been developed to measure both the dose and uniformity of the increasingly advanced and complex ion implanter. This paper will review all of the techniques and equipment used to measure the uniformity of ion implantation. In addition, various graphical techniques developed to present early measurement results will be discussed.

1. Overview

Commercial ion implantation was introduced almost 30 years ago as a practical application of the ion beam accelerator to semiconductor manufacturing. Although one of the first uses of implantation in this field was damage enhancement in point-contact diodes in 1952 [1], it was not until 1962 that the first doping implant was performed. In that year, a phosphorus implant into silicon was used in the manufacture of nuclear-radiation detectors [2]. In the following year, phosphorus was implanted during the manufacture of solar cells [3]. And the first use of implantation as a doping technique in MOSFET technology was in 1965 [4].

During this early period, when ion implantation was a new doping technique, the only useful method to measure the dose of a monitor wafer was the four-point probe. The uniformity of an implanted wafer, however, was routinely measured by visual inspection of a heavily doped wafer (fig. 1) or a mylar burn. After inspecting a wafer implanted with high dose, a viewer could estimate the uniformity through the darkened surface due to incident implant damage. A mylar burn was nothing more than "implanting" a piece of mylar attached to a wafer and inspecting the darkened results. The downside of these two techniques was that only qualitative results were available. The advantage was that striping conditions due to electrostatic scan problems (the most common early uniformity problem) were immediately evident – with no time required for post-processing.

The last 30 years have brought about several successive generations of ion implantation equipment as well as dose and uniformity monitoring equipment. In addition, novel techniques have been developed for use by existing measurement equipment. Indeed, uniformity monitoring of the implanter has progressed (table 1) from the mylar burn to full wafer color contour and 3D maps available from modern instrumentation.

2. Ion implant test site – IITS (1973)

Some of the first test-site sheet-resistance maps were reported in 1973 by Seirmarco and Keenan [5] using a pattern of huge resistors (20 × 20 mil) with diffused and

[1] Now at Process Products Corporation, 37 Flagship Drive, No Andover, MA 01845, USA.
[2] Now at Sematech, 2706 Montopolis Drive, Austin, TX 78741, USA.

0168-583X/91/$03.50 © 1991 – Elsevier Science Publishers B.V. (North-Holland)

Table 1
History of uniformity mapping in ion implantation

Visual inspection	pre-1960s
Mylar burn	1960s
Patterned resistors	1973
Van der Pauw resistors	1973
Sheet resistance	1975
Device measurements	1975
C–V dots	1980
Particle measurements	1982
Optical densitometry (ion scan)	1983
Double-implant technique	1983
Partial-dose technique	1984
Modulated-optical reflectance (Therma-Wave)	1984
Bridging-implant technique	1987
Extinction-coefficient meas (GRQ Instruments)	1987
Color contour maps	1987

metallized contacts. This ion implant test structure (IITS) was tested on an automated tester and numerical wafers maps of sheet resistance were output. For many years, all IBM implanters were qualified using the IITS. Uniformity was measured down to 1×10^{12} using 100 Ω cm wafers. This structure was also used to generate sheet-resistance versus dose calibration curves [6], as well as to measure the temperature coefficient of resistance for ion-implanted resistors and generate new mobility curves [7].

3. Test pattern structures (1975)

From the mid-1970s to the early 1980s, before the predominance of four-point probe mapping systems, it was common to ascertain wafer-wide doping uniformity through the electrical probe of van der Pauw resistor structures (fig. 2). These structures were resistors which were processed through standard masking and doping techniques, including ion implant. After probe, software managed the data and displayed the value of the resistors in a wafer-map presentation.

About this same time frame, test structures were becoming more prevalent in wafer manufacturing. Test structures were a collection of various devices representing key parts of a microprocessor which were usually located in the kerf or scribe-line area. Typically, the structures were probed after completion of wafer processing in order to test the success of various stages of wafer processing. Devices within these structures were used to ascertain the yield of the wafer as well as the integrity of the wafer processing procedures. Key electrical measurements included sheet-resistance measurement of van der Pauw resistors, as well as depletion currents (fig. 3) and threshold voltages of MOS transistors located on these test patterns. It was also common for process engineers to use a mask set that replicated these structures over the entire wafer in order to determine overall wafer uniformity of various semiconductor processes.

4. Four-point probe mapping system (1975)

Since the four-point probe was already being used to measure doping processes in the diffusion area, it became the first instrument used to measure implanted dose. The standard practice for many years was to find

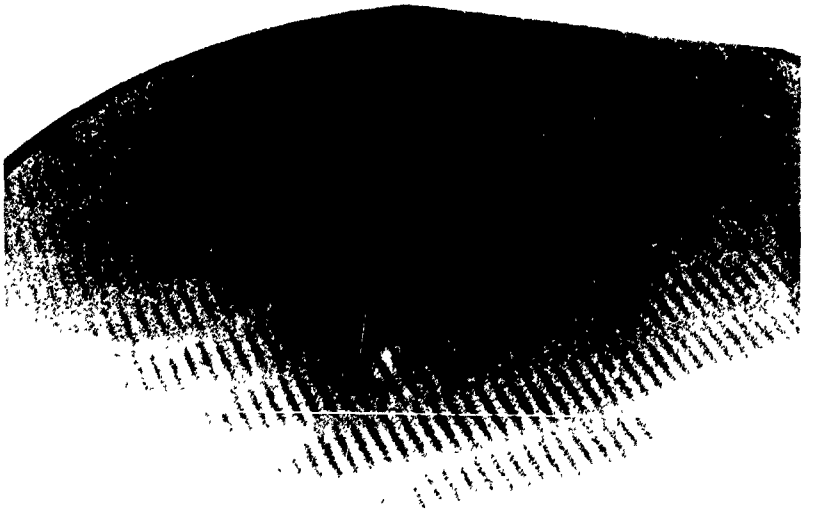

Fig. 1. Pattern on an unannealed wafer reaffirming the present-day utility of visual inspection. This example of "scan lock-up" was the result of a failure in the dither circuit of an electrostatic scan system of a modern implanter. It was observed by an alert process technician, Joan Chandler (Varian Ion Implant Systems), prior to anneal.

the average sheet resistance by manually probing the wafer in four outer spots, plus a fifth one in the center. Uniformity was essentially considered to be the standard deviation of these five measurements.

Early work performed by Perloff while at Signetics in the mid-1970s extended the utility of the four-point probe by automating its measurement capabilities (fig. 4) This action paved the way for the sheet-resistance contour map. One of the first reports of this successful venture was published in 1976 [8].

In the early days of implantation the four-point probe (FPP) was relied upon to measure the uniformity of the ion implanter because its repeatability (2%) was better than the uniformity specification of the equipment (5%). Perloff [9] introduced configuration switching in 1980 which greatly improved the performance of the FPP. By making measurements using two different current–voltage configurations at the same site, a geometric correction factor was calculated. This action eliminated the two main sources of noise in the FPP measurement: variation of probe spacing (probe wobble) and current crowding at the wafer edge. The repeatability of the FPP was improved from 2% to 0.2%. Thus armed with configuration switching and mapping capability, Perloff founded Prometrix in 1983.

5. Transistor threshold measurements (1978)

In the late 1960s, the most widespread semiconductor application for ion implantation was the threshold adjustment of MOS transistors [10], usually in the dose range of 1×10^{10}–5×10^{12} ions/cm^2. Indeed, threshold voltages were found able to be controlled within ±0.3

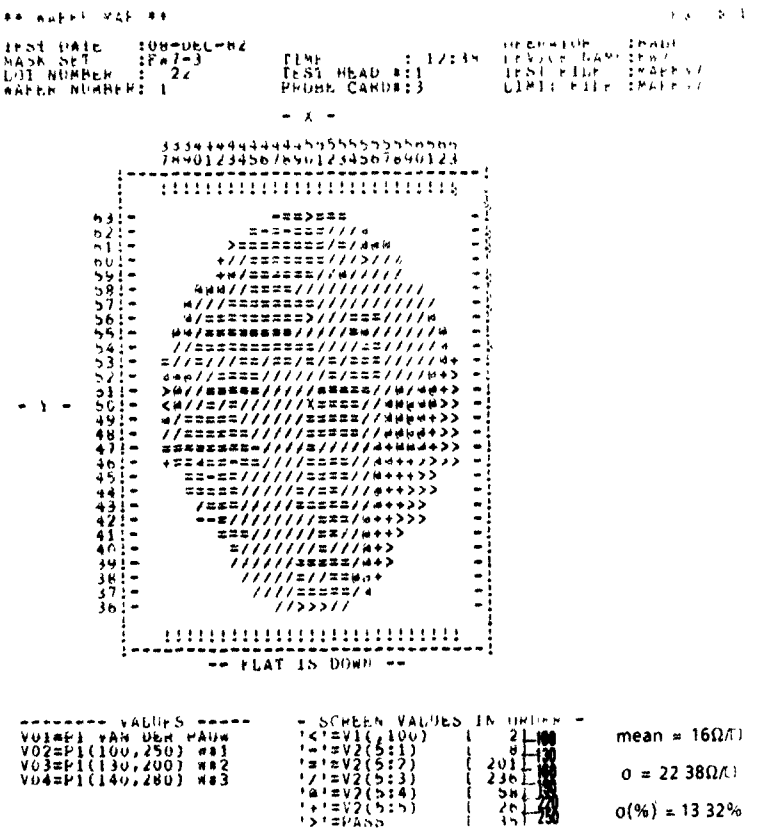

Fig. 2 Van der Pauw resistors were widely used as a resistance mapping tool prior to the introduction of the sheet-resistance mapping system This 1982 contour map shows "scan lock-up" in an early electrostatically scanned implanter.

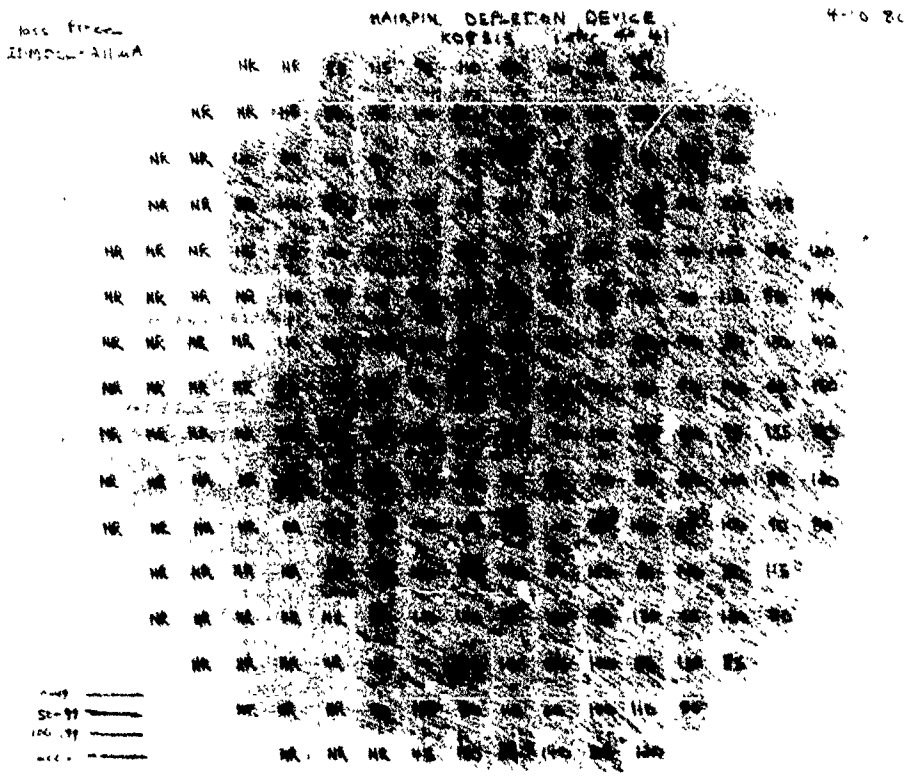

Fig 3 Depletion currents were electrical measurements made on transistors located on test pattern structures beginning in the mid-1970s This figure shows the common practice at that time of hand-plotting resultant data in order to ascertain wafer uniformity relating from a previous implant step

V. Therefore, the doping variations on a wafer were determined by measuring the threshold voltage of a large number of transistors, in conjunction with a threshold-voltage versus dose calibration curve. Depending on the probing equipment and the available number of test sites on a wafer, other information, including depletion current, became useful in measuring implant uniformity. Such measurements were commonly performed on the test structures processed during the last stage in semiconductor manufacturing Since device measurements also depend upon the flat-band voltage and uniformity of oxide thickness, the process engineer must be aware of possible ambiguous results from this technique. Although uniformity maps using this technique were commonly manually mapped by engineers in the late 1970s, published reports of automated measurements did not occur until 1982 [11].

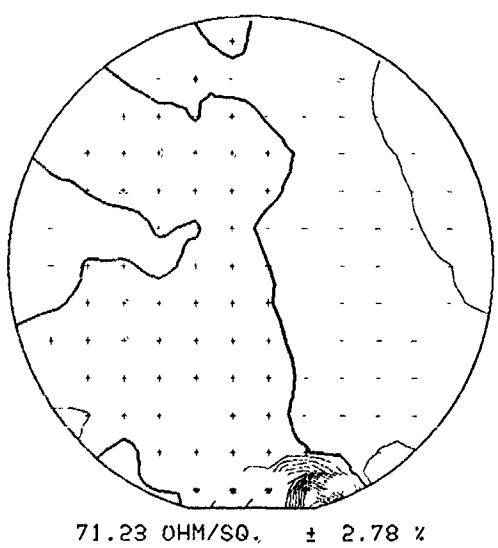

Fig. 4. An early version of the sheet-resistance contour map in 1975 resulting from work by Perloff while at Signetics. Map provided by Dan Downey (Varian Ion Implant Systems)

6. Special sheet-resistance structures

Perloff [12] used two techniques to map the uniformity of implanted wafers in 1976: the van der Pauw structure and a special oxide structure with rectangular openings photo-lithographically defined in it. The four-point probe was used to measure the sheet resistance of the implanted silicon in the rectangular openings. The implanted area was tested with an automated prober

that placed the four-point probe in the same location in every rectangle. This allowed the same geometric correction factor to be used across the whole wafer and avoid errors due to current crowding at the wafer wedge. A variety of types of maps, including numerical and contour, were presented to display the results.

7. Capacitance–voltage dots (1980)

The early application of capacitance–voltage (C–V) measurements in ion implantation was for measurement of low-dose implants such as that required for threshold tailoring of MOS transistors. The dose range required for this implant, usually 1×10^{10} to 5×10^{12} ions/cm^2, placed it outside the range of the four-point probe. With C–V measurements, however, determination of both carrier concentration and doping profiles was possible. Glawischnig et al. provided one of the first C–V uniformity maps in 1981 [13]. This particular map showed strong doping variations due to a scan lock-up condition on an electrostatically scanned implanter with C–V measurements using 4300 test sites on a 3 inch wafer. A more recent application of C–V measurements was reported by Deming et al. using the partial dose technique [14].

8. Optical densitometry (1983)

An instrument introduced in 1983 related changes in dose to changes in optical density of implanted photoresist layers [15]. In this technique, a microdensitometer measures the optical transmission of a photoresist-covered glass substrate prior to implant, using a 390 nm wavelength light source. After implantation, the wafer is re-measured. The ion bombardment by implantation results in a change of the implanted resist layer through graphitization of the long hydrocarbon chains that results from the breakup of H–C bonds [16], yielding a measureable change in its optical density or transmission characteristics. Thus, after the instrument determines the difference in the before and after readings from > 1000 measurement sites (per 150 mm wafer), an average and standard deviation of the data, called mean dose index (MDI), is determined. This data is finally summarized in a contour map. Once a calibration curve has been determined, the MDI is fully representative of the implant conditions (i.e., dose, energy and species). Because the optical densitometry technique essentially measures damage, the technique can measure electrically inactive species such as silicon, argon, etc. Although the manufacturer states that a recent model of the instrument provides a dose resolution from 5×10^{11} to 1×10^{16}, a practical range is more likely to be 5×10^{11} to 1×10^{14} ions/cm^2 [17].

9. Double-implant technique (1983)

The double-implant technique is based on the fact that the damage induced by an implant destroys the crystallinity of the silicon lattice. The displaced dopant atoms in a damaged layer do not contribute to the conductivity of the layer and the displaced silicon atoms greatly reduce the mobility of the free carriers. This technique requires that a wafer be first implanted and annealed with a "dose" roughly 100 times that of the implant to be measured. The low-dose implant modifies the measured sheet resistance from the first implant. Using a previously established calibration curve, the four-point probe mapping system correlates dose of the second implant to the modified sheet resistance [18].

This technique is sensitive from 1×10^{10} ions/cm^2 to a medium dose of about 1×10^{14} ions/cm^2. The lower bound is determined by the lowest dose of first implant that can be accurately read following the second implant. The upper bound is determined from both the first implant approaching solid saturation and the de-activation implant approaching the regions where the produced damage saturates. A major advantage of the double-implant technique is that the sensitivity can be tailored for any particular low dose by adjusting the initial implant. It should be noted, however, that the double-implant technique suffers from temperature- and time-driven effects which have been identified as issues with other damage measurement techniques [19]. Recent work at Motorola [20] indicates that the stability of double-implant results was improved by a 200 °C bake in dry nitrogen for 45 minutes.

10. Partial-dose technique (1984)

MOS monitors are ubiquitous in an FET line, being used to measure insulator integrity, fixed and mobile oxide, average substrate doping and substrate leakage [21]. Pulsed C–V (PCV) measurements on MOS dots [22] were used to measure the concentration profile after low-dose ion implantation ($< 5 \times 10^{12}$) and after subsequent hot processing. The profile was usually very noisy because the calculation involved the difference of two capacitance measurements close in value. The results also depended on the square of the area of the MOS dot or the fourth power of the dot diameter. Thus a small error in the diameter of the dot would lead to a large error in concentration. In order to track the PCV results the peak concentration was reported. The noise in the profile made the peak concentration an unacceptable process monitor parameter. In order to improve the PCV repeatability, the concentration profile was integrated to provide a measure of the implanted dose. This parameter represented part of the implanted dose (the partial dose) under the profile from two Debye

lengths into the silicon to the background concentration. This improved the PCV repeatability from near 10% to about 1%.

The next refinement in this technique was direct integration of the PCV curve [23]. This yielded quicker results than first calculating the profile by differentiating the C–V curve, followed by integration of the profile to get the partial dose. This innovation improved the repeatability to 0.2%, almost another order of magnitude. In addition, an unexpected bonus of this approach was the elimination of the dependence on dot diameter. Thus, it became possible to measure the uniformity of the implant as well as the dose on MOS wafers without photo-defined dots. This technique has been used worldwide by IBM to monitor low-dose uniformity.

11. Modulated-optical reflectance (1984)

In 1984, the Therma-Wave Company developed a dosimetry and uniformity mapping instrument which measured the properties of damaged silicon [25]. The technique of modulated-optical reflectance is based on the change in the reflectance properties of silicon with the implant-induced damage. In this technique, the wafer is first modulated with an argon laser beam. The reflectance changes in phase with the driving modulation, detected using a second laser (He–Ne) which is then processed as the thermal-wave signal. The data is then presented in a contour map (fig. 5) with the average and standard deviation of thermal-wave (TW) units. Due to the large amount of damage that is generally produced per implanted ion, this technique is very sensitive to low- to medium-dose implants. However, some sensitivity loss has been noted with arsenic in the dose range greater than 5×10^{15} ions/cm^2 [26]. Recent work has extended this region of sensitivity significantly into the higher doses [27]; however, long-term application of these new algorithms has yet to be reported. Aside from this recent work in high-dose measurement, the practical measuring range of the Therma-Wave instrument covers the range from approximately 1×10^{11} to 3×10^{14} ions/cm^2 [26]. The sensitivity in the medium- to high-dose regime is limited by the saturation of the lattice damage which starts in the upper 1×10^{13} dose and completes above a dose of 1×10^{15}, depending upon the species and energy of the measured ion. In addition to its low-dose sensitivity, the other unique aspect to this technique is that its spatial resolution is determined by the focussing ability of the lasers. This enables measurements to be done within the die on actual product wafers, which is a true example of real-time statistical process control (SPC). Another application of this spatial resolution is the ability to do micro-uniformity line scans on a dimension relevant to the dimensions of the circuits in a die.

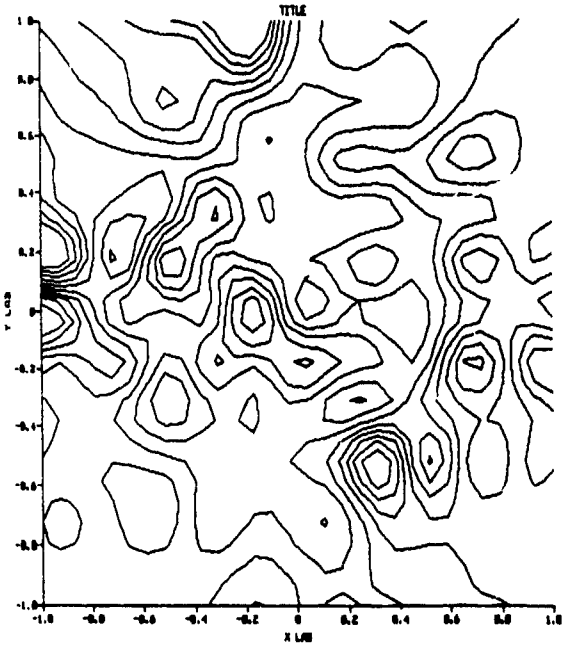

Fig. 5 Modulated-optical reflectance measurements were introduced in 1984 by Therma Wave. This contour map, provided by Lee Smith (Therma Wave), is the first ever made by the system.

12. Bridging-implant technique (1987)

An interesting phenomenon takes place when measuring MeV implants with the four-point probe. The projected range into the silicon is so large that there is essentially no way to measure the deeply implanted layer, since the doped layer does not even contact the wafer surface. The bridging-implant technique forms a resistive link to the deeper layer [24]. In this technique a low-energy implant is first implanted, activated and measured. This implant serves as the bridge. The MeV implant is then implanted and activated, and then the sum of the two implants is measured. The sheet resistance of the deep implant can then be calculated as the difference between the original implant and the combination of the two (treated as two resistors in parallel). Although this technique has not yet been optimized, nor have its sensitivity limits been completely determined, it has been established as an enabling technology for the measurement of deeper implants for which few reliable monitoring techniques are presently available.

13. Extinction-coefficient measurement (1987)

GRQ Instruments introduced a mapping instrument in 1987 that was based upon the fundamental physics of the ellipsometric measurement technique. However, Chang [28] added the measurement of the extinction coefficient to this prior knowledge, thus creating a uniformity mapping tool. This system was introduced with full-color mapping capability – one of the first to do so. The extinction-coefficient technique uses the difference between before-and-after optical properties in the damage layer to determine the depth and extent of the damage, thus extending the sensitivity of the ellipsometry technique. The signal difference is converted back into dose-related units. Since the extinction-coefficient technique is a differential technique, it shares the problems of other damage measurement techniques. However, the ellipsometric technique with added extinction-coefficient measurement is primarily useful where implant damage lies near the saturation region. Therefore, the high-dose regime is the effective region for this technique. With the addition of the extinction coefficient, the practical range of measurement was quoted to be in the range of 1×10^{11} to 1×10^{14} ions/cm^2. Although this tool was originally intended to measure silicon, it has since been primarily dedicated to the measurement of III–V materials.

14. Other

Most of this presentation has been based on uniformity mapping techniques which can be correlated in some manner to measurement of implanted dose. One technique that does not fall into the overall format of this presentation but has been proven to yield useful information about the ion implanter is the wafer particle map. Using the difference between before and after measurements on wafers processed through the implanter, a laser scanning particulate measurement instrument is able to identify the origin of various particle sources within the implanter relating to operations such as wafer clamping and end-station venting [29,30]. One of the first published reports of wafer particle maps in relation to problem solving occurred in 1983 [31].

It is not within the scope of this paper to discuss the relative advantages or disadvantages of the measurement techniques presented herein. While the sensitivity of several measurements discussed herein has been reported previously [17], the reader is referred to the cited references for more in-depth information on specific topics.

References

[1] H. Ryssel and I. Ruge, in: Ion Implantation (Wiley, New York, 1986) English translation, p. 3
[2] T. Alvager and N.J. Hansen, Rev. Sci. Instr. 33 (1962) 367.
[3] W.J. King, J.T. Burrel, S. Harrison, F. Martin and C.M. Kellett, Nucl. Instr. and Meth. 38 (1965) 178.
[4] J.W. Mayer, L. Eriksson and J.A. Davies, in: Ion Implantation in Semiconductors (Academic Press, New York, 1970) p. 233
[5] J.A. Seirmarco and W.A. Keenan, Extended Abstract, no. 152, Electrochemical Society Fall Meeting, Boston, MA (1973).
[6] J.A. Seirmarco, R.C. Joy and W.A. Keenan, Extended Abstract no. 82, Electrochemical Society Spring Meeting, San Francisco, CA (1974)
[7] J.A. Seirmarco, F.A. Montillo and W.A. Keenan, Extended Abstract no. 82, Electrochemical Society Meeting, San Francisco, CA (1985)
[8] A.B. Wittkower, P.H. Rose and G. Ryding, Solid State Technol. 18 (12) (1975) 41
[9] D.S. Perloff, J.N. Gan and F.E. Wahl, Solid State Technol. 24 (2) (1981) 112
[10] R. Dobiner, Electronic News 11 (5) (May 1975) 36.
[11] M.I. Current, D.S. Perloff and L.S. Gutai, in: Ion Implantation Techniques, eds. H. Ryssel and H. Glawischnig, Springer Series in Electrophysics 10 (Springer, New York, 1982) p. 235
[12] D.S. Perloff, F.E. Wahl and J.T. Kerr, Proc. 8th Int. Conf. on Electron and Ion Beam Science and Technology, Seattle, WA, 1978, p. 269.
[13] H. Glawischnig, K. Hoerschelmann, W. Holtschmidt and W. Wenzig, Nucl. Instr. and Meth. 189 (1981) 291
[14] R.O. Deming and W.A. Keenan, Extended Abstract no. 169, Electrochemical Society Spring Meeting, Montreal, Canada (May 1982)
[15] J.C. Chang and G.R. Tripp, Solid State Technol. 26 (11) (1983) 143.
[16] T.C. Smith, in: Ion Implantation Equipment and Techniques, Springer Series in Electrophysics 11, eds. H. Ryssel and H. Glawischnig (Springer, New York, 1983) p. 116
[17] M.I. Current, C.B. Yarling and W.A. Keenan, in: Ion Implantation Technology, ed. J.F. Ziegler (Academic Press, 1988) p. 377
[18] M.J. Markert, D.S. Perloff and E. Lee, Extended Abstract no. 369, Electrochemical Society Spring Meeting, San Francisco, CA, 1983, p. 83
[19] J. Schuur et al., ibid., p. 554
[20] S.L. Sundaram and A.C. Carlson, IEEE Trans. Semiconductor Manufacturing 4 (1989) 146.
[21] E.H. Nicollian and J.R. Brews, MOS Physics and Technology (Wiley, New York, 1982)
[22] C.P. Wu, E.C. Douglas and C.W. Mueller, IEEE Trans. Electron Devices ED-22 (1975) 319.
[23] R.O. Deming and W.A. Keenan, Nucl. Instr. and Meth. B6 (1985) 349.
[24] W.A. Keenan, Nucl. Instr. and Meth. B21 (1987) 563
[25] W.L. Smith, A. Rosenswaig and D.L. Willenborg, Appl. Phys. Lett. 47 (1985) 564.

[26] B.J. Kirby, L / Larson and R.V Liang, Nucl. Instr. and Meth. B21 (1987) 550.
[27] K. Hurley, Greater Silicon Valley Implant Users' Group (April 1990)
[28] J. Chang, Greater Silicon Valley Implant Users' Group (December 1985).
[29] M.I. Current, in: Ion Implantation Science and Technology, eds. J.F. Ziegler and R.L. Brown (1984) p. 501.
[30] J. Pollock, N. Turner, R. Milgate, R. Resnek and R Hertel, Nucl. Instr and Meth. B6 (1985) 202
[31] S. DiNaro, R Hertel and N Turner, in. Ion Implantation Equipment and Techniques, Springer Series in Electrophysics 11, eds. H. Ryssel and H. Glawischnig (Springer, New York, 1983) p. 116.

Nuclear Instruments and Methods in Physics Research B55 (1991) 243–249
North-Holland

Techniques for dose matching between ion implanters

P. Lundquist and S. Mehta
Varian Ion Implant Systems, Gloucester, MA 01930, USA

T. Black and D. Jackson
Intel/Fab 6 5000, W Chandler Blvd., Chandler, AZ 85226, USA

Dose matching between systems installed in a device manufacturer's fab is a critical issue in ion implantation, especially when the process is to be transferred from one system to another. Ion implantation systems, like other types of semiconductor capital equipment, are constantly evolving to keep pace with the ever-increasing demands of device manufacturers Some hardware changes may be retrofitted to existing equipment, while major changes often result in a new system design. As a result older, retrofitted systems as well as the latest generation equipment may be found operating side by side in the wafer fab. While dose uniformity and repeatability for a given implanter have always been specified, dose matching between implanters, allowing the transfer of process from one system to another, is addressed in this paper. Dose matching characteristics for several Varian implanters will be presented and techniques for matching dose between systems will be discussed. In addition, the key hardware and process issues that may cause mismatching in dose will be addressed

1. Introduction

Every implant used in a semiconductor fab is described by a recipe. The recipe specifies: species, dose, energy, beam current, wafer tilt angle, and several other parameters for implant setup. Frequently, when a process is developed in a new fab, the implant recipes are determined by qualification exercises done on the new ion implanters. In contrast, when an existing fab upgrades or purchases new equipment, the goal is for the new or retrofitted equipment to run the established recipes, within the tight control limits of the process, already developed on existing equipment. The goal is driven by the need to bring the equipment on line quickly with the minimum cost, and to avoid getting approvals for recipe changes.

The absolute dose has not been as important as dose matching to the existing process. N.B.S. standards are not available for an implanted dose. Implant round robins done throughout the industry for a given recipe indicate there is approximately a 12% variation of sheet resistance due to the implanters when the wafers are all processed together [1–3] Theoretical models must consider a large number of variables to be able to predict for all recipes, what the sheet resistance should be. Some of the difficult variables are wafer charging, beam neutralization, and onset of wafer amorphization coupled with its change on channeling effects. Hence, one should be cautious about using theoretical models for a target sheet resistance value [3]. A reference value to consider is the baseline implant done during the installation of an implanter. The ion implanter manufacturer can provide these recipes which have been tested on many ion implanters.

Typically, an ion implanter has control capability that allows the user to increase or decrease all of the doses by the same amount for dose matching to the existing process recipes of another ion implanter. On Varian serial ion implanters control of the implant area setting provides this control capability. The implant area setting is a number entered into the dose calculation electronics. The implant area is the effective area (square centimeters) at the wafer plane, which is scanned by the ion beam. For a given wafer size, increasing the area setting will increase all the implanted doses. This paper discusses considerations to be made before adjusting the area setting. The steps for selecting the area setting for matching the dose on two ion implanters are presented along with the data from two production implanters.

2. Variables affecting dose

In dose matching two ion implanters, the average value of the dose (ions/cm^2) implanted into the wafer, the uniformity of the dose across the wafer, and the depth profile must match, for the measurement of wafer dose to match. Dose matching must be checked for each recipe that is used in production. Product device data is the ultimate judge that the dose matching is successful

0168-583X/91/$03.50 © 1991 – Elsevier Science Publishers B.V (North-Holland)

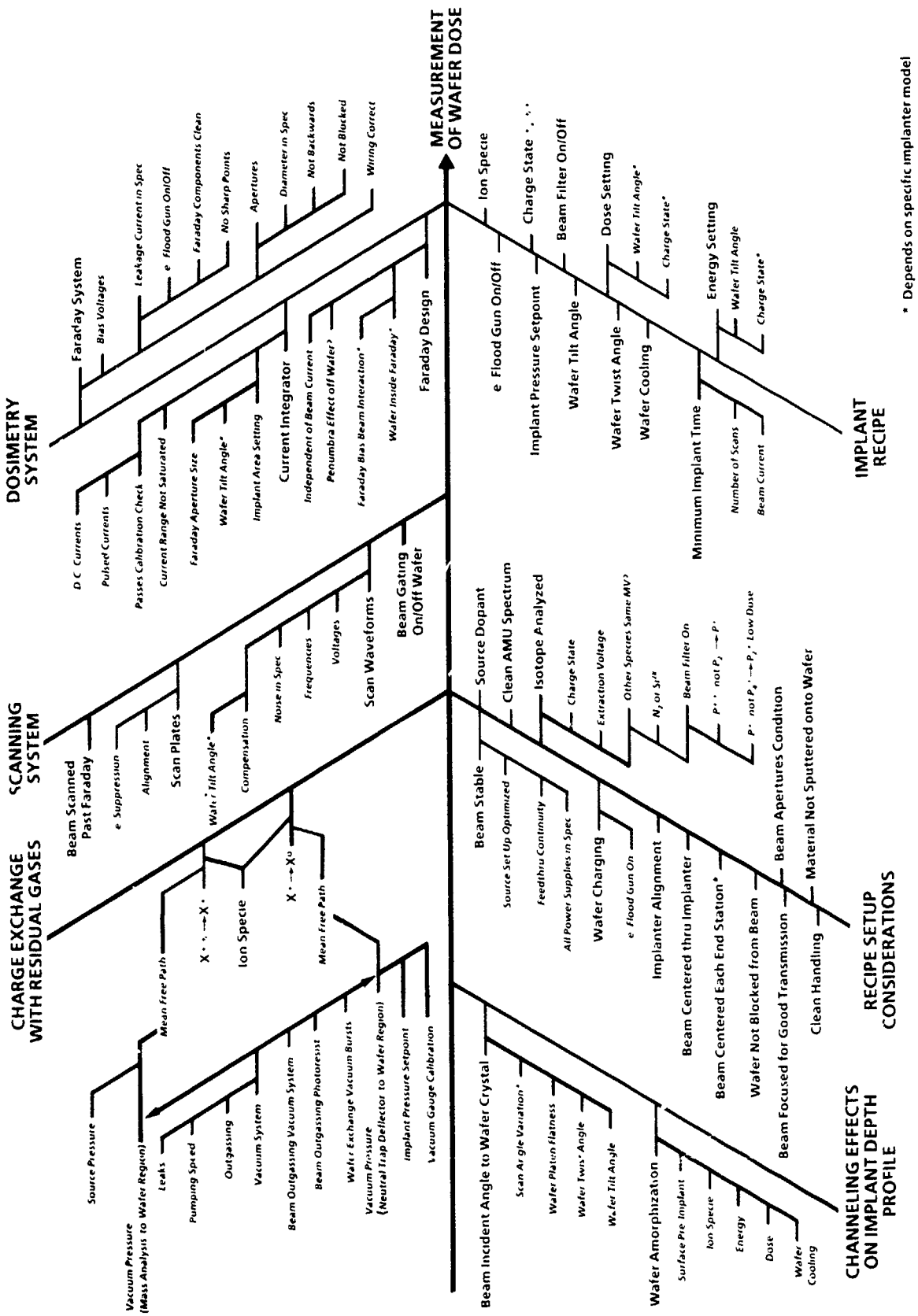

Fig 1(a) Implant variables affecting dose

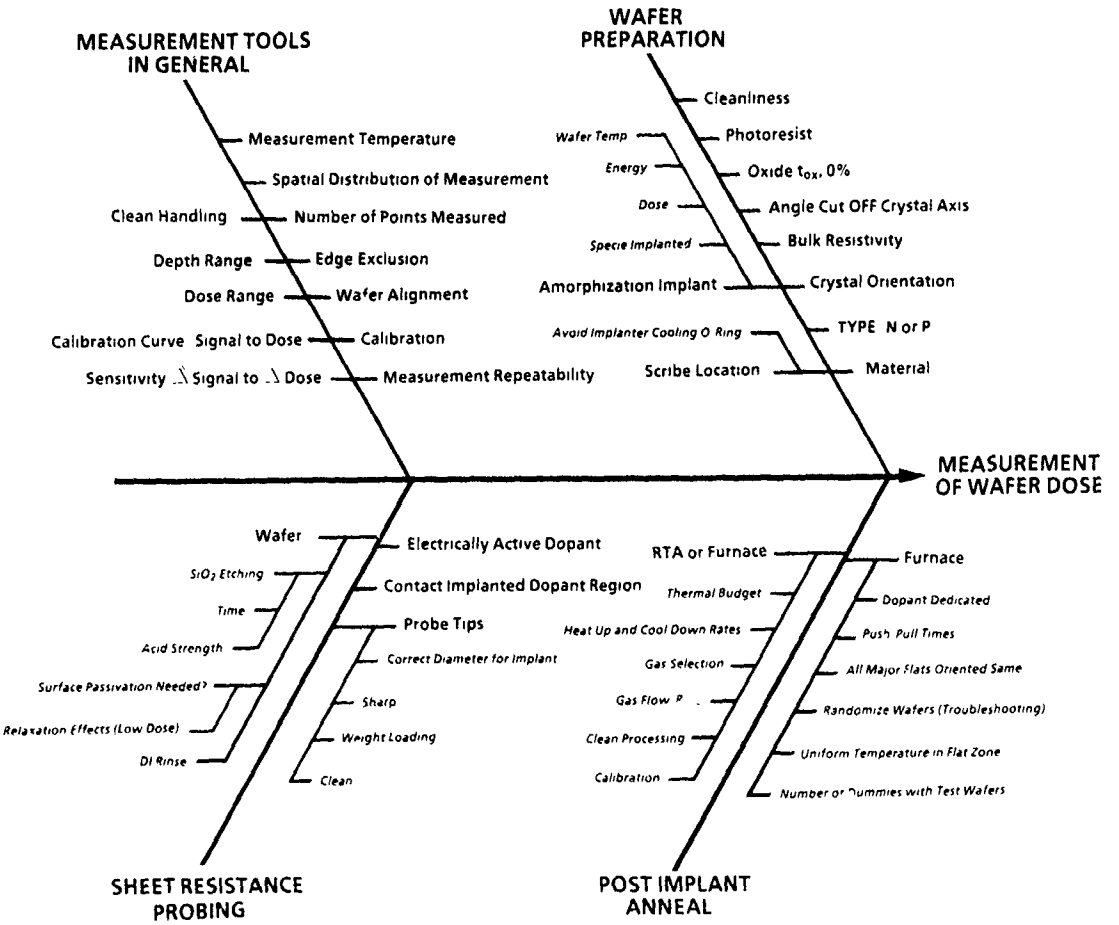

Fig 1(b). Process variables affecting dose

when both implanters' products are within the process control limits.

Fig. 1a is a fishbone (Ishikawa) diagram [4] of serial implanter variables which can cause the "measurement of wafer dose" to change. Six main categories are listed The branches off of the "implant recipe" are the recipe items, any one of which, if changed, could cause a change in the measurement of wafer dose (average value, uniformity, or depth profile). Many of the fishbone items are not called out in a recipe. For example there is a branch off of the "dosimetry system" category called "current integrator". It has branches connecting to it. One branch is "passes calibration check" for "dc currents" and "pulsed currents", which, if out of calibration, will cause the measurement of wafer dose to change. If there is only one current range that is bad, then dose matching between two implanters might be successful except for implants on that current range. Thus, the calibration of modules which could affect dose must be verified to be correct before starting dose matching Newer implanters use software routines to monitor power supplies and check many calibrations, to warn of implanter problems.

A different type of dose matching problem is not due to an implanter failure but to implanter design The "platen flatness" is typically fixed on an implanter. If a fab has two implanters, one with a flat platen, and the other with a domed cooling platen then the "beam incident angle to the wafer crystal" structure will be different between the two implanters. This according to the fishbone diagram could cause "channeling effects on implant depth profiles", which could show up on four-point probe maps as an unusual sheet resistance value with a poorer uniformity map [5]. This would show up less or not at all for high dose, high energy As^+ implants that amorphize the crystal lattice and have minimal channeling. This small difference in implanter configuration could cause the doses on the two implanters to match for some recipes but not for all.

For a particular implanter design, one must look at the fishbone diagram and determine the variables that apply and their corresponding effects. If variables are

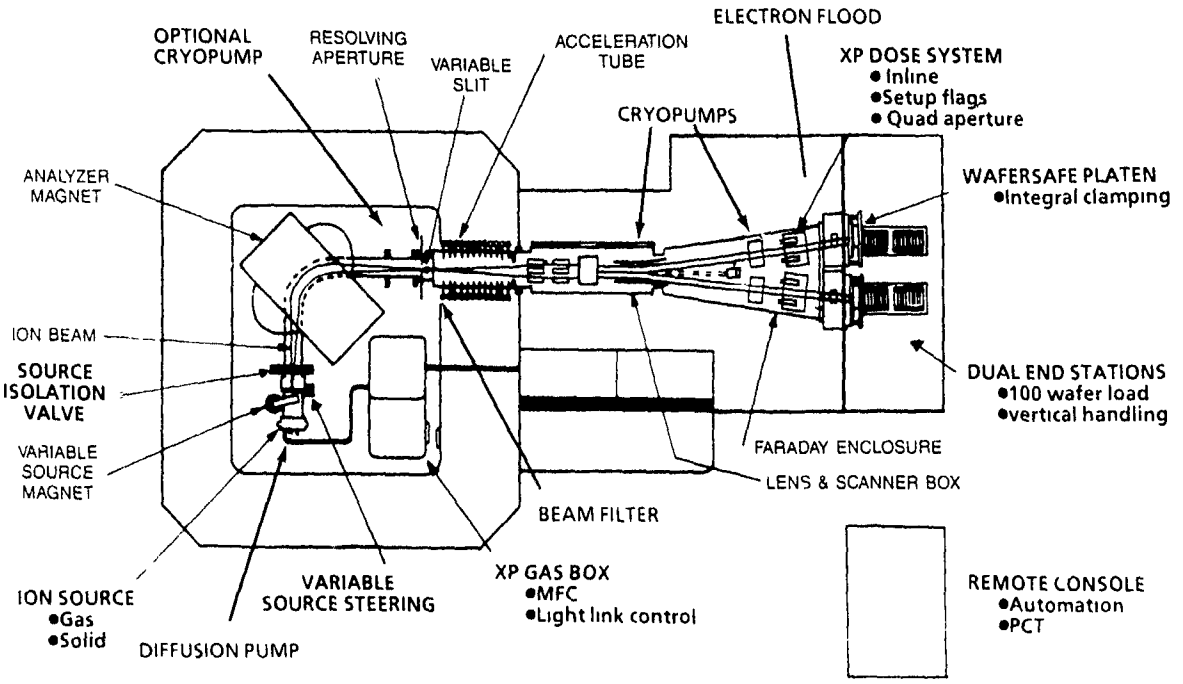

Fig. 2. Varian 300XP layout

added, make sure that they are well defined and measurable. A dose matching checklist can then be made from the customized fishbone diagram. If a variable is not controlled, and dose matching is performed, when that variable changes (which one may not be aware of) the implanter may no longer be dose-matched to the

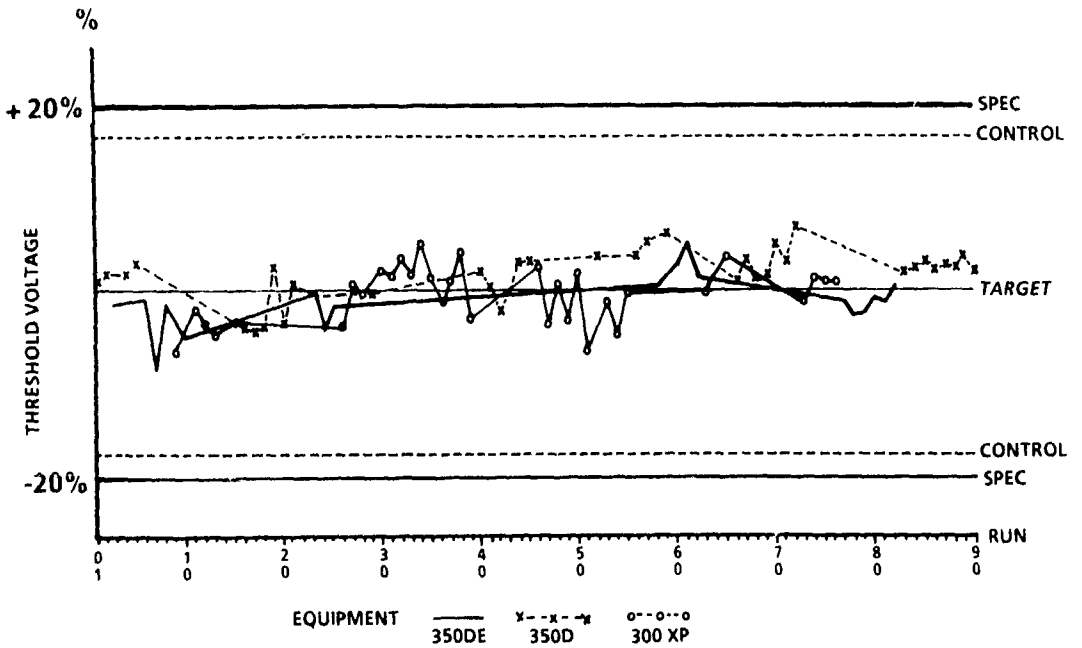

Fig. 3. Dose matching implant must be stable.

other implanter or the process. Fig. 2 is the layout of a 300 XP serial implanter for reference in locating implanter main assemblies mentioned in the fishbone.

Fig. 1b is a fishbone diagram of process variables which can cause the "measurement of wafer dose" to change. Because of all the variables in processing the wafers, it is necessary to split a "lot" of wafers, which meet the wafer requirements through both implanters. Combine the wafers after implant. Randomize the wafers for the anneal, in order to separate the anneal effects from the implanter effects [6]. Measure the wafer dose on the same system. A checklist should also be made for each processing step.

In addition to the recipes that must be matched, it is valuable to develop at least one dose matching monitor. The monitor can be the same as one of the recipes. The monitor should have the following qualities. It should have a quick turn around time of 4 hours or less, compared to a few weeks for device wafers. It must be sensitive to the dose so that it can pinpoint small dose changes. Its measured value must be stable over time, so that the time after implant that the measurement is made does not affect the result [7]. It should have its own control chart like fig. 3. Once the implanters are matched, the monitor can be periodically implanted as a quick partial implanter check. Typical monitoring process is to use an anneal, etch, and 4-point probe, or to use a thermal-wave measurement.

3. Dose matching steps and results

The steps for dose matching implanters will now be presented along with the data from two production implanters.

Step 1. Consider the implanter variables due to calibration, recipe requirements, and implanter configuration. Go through the checklist and fix any problems.

Dose matching was done between a new 300XP serial implanter, and a 350D serial implanter retrofitted with a new Faraday system [8], similar to the one used on the 300XP. The retrofitted 350D is called a 350DE. Before the retrofit was done the 350D and 300XP had been dose-matched. The variables for the 350DE and 300XP implanters were checked. The significant dif-

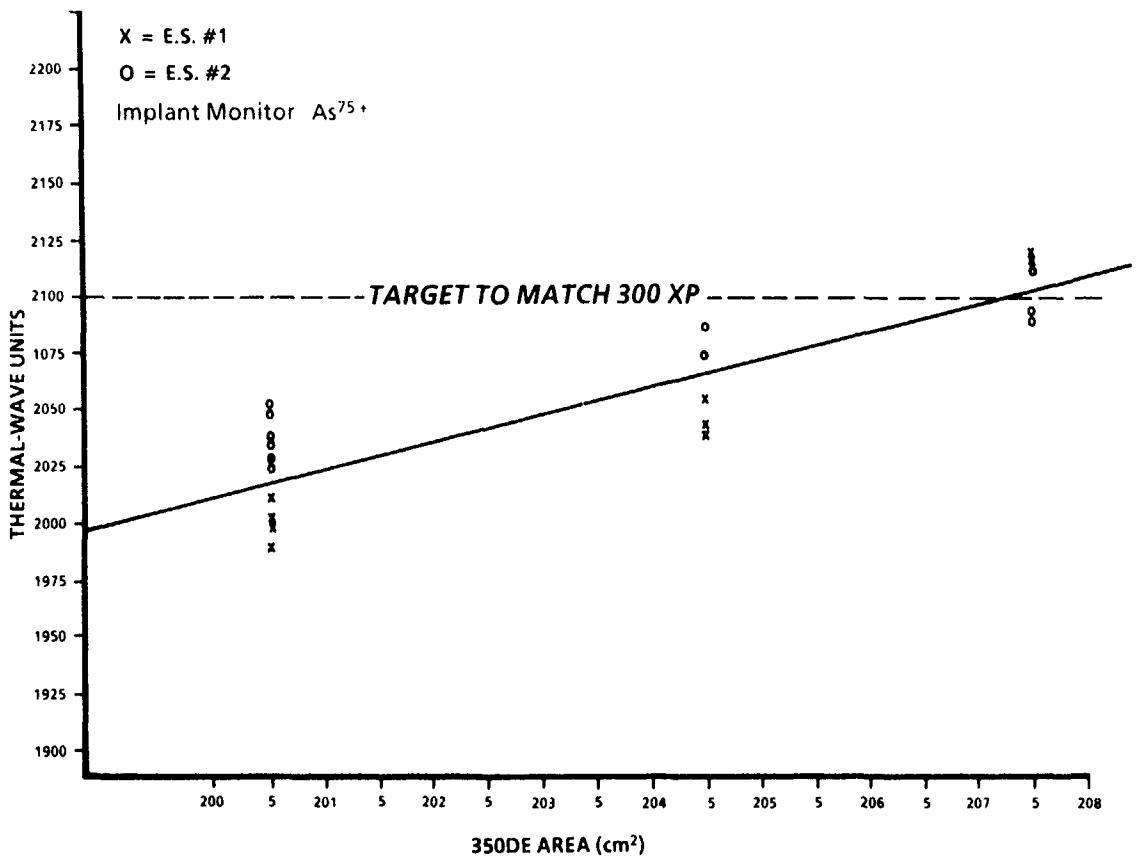

Fig. 4. Selecting an implant area of 207 5 cm^2 on 350DE to match thermal wave signal of 300XP.

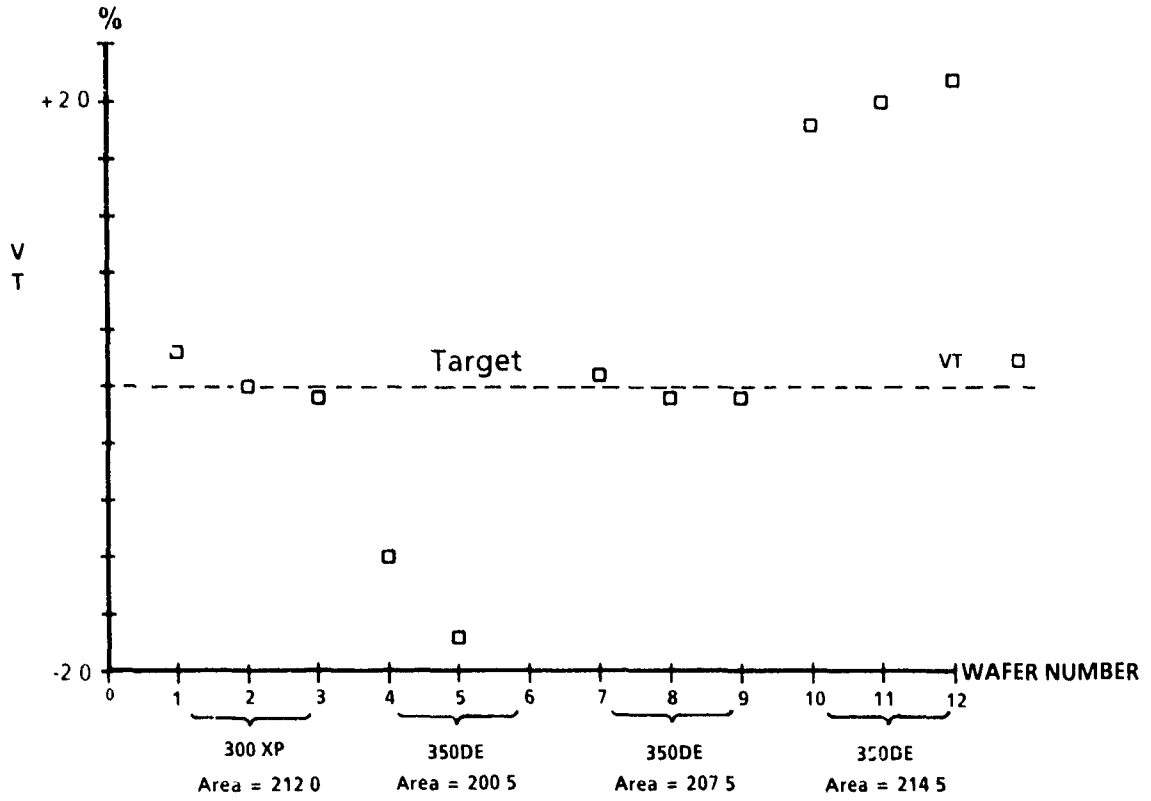

Fig 5. Device threshold voltage measurements demonstrate that an area of 207 5 cm^2 matches 350DE to 300 XP

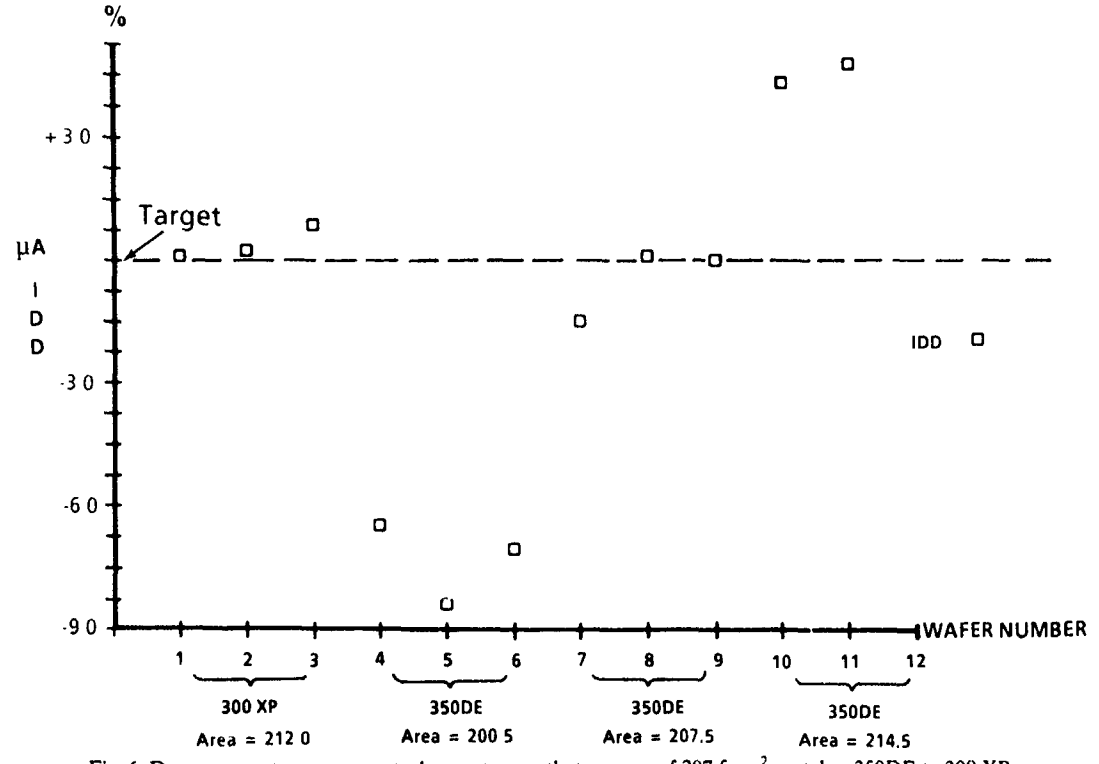

Fig. 6. Device current measurements demonstrating that an area of 207.5 cm^2 matches 350DE to 300 XP

ference between the two implanters was that the 350DE would have a smaller implant area because its construction puts the wafer plane closer to the center of scan.

Step 2. Implant dose matching monitor wafers on both implanters. On the implanter already process qualified, implant the monitors with the production area setting. On the other implanter use three different areas, the calculated area provided by the implanter manufacturer, an area between 2 and 4% greater than, and an area 2 to 4% less than the calculated area. Implant 3 monitor wafers for each area setting. After this test is successfully done, it can be repeated with other monitor implants if desired.

Twelve dose matching monitors were implanted, and measured on a thermal wave system. The 300XP used its production qualified area of 212.0 cm^2. Three areas were implanted with on the 350DE: 200.5, 204.5, and 207.5 cm^2. Fig. 4 is a graph of 350DE area setting vs. thermal wave signal. From it one concludes that an area of 207.5 cm^2 initially matches the 350DE to the 300XP.

Step 3. Implant a split lot of product wafers on both implanters. On the implanter already process qualified, use the production area setting. On the other implanter use three different areas, the dose matching area found in step 2, an area between 2 and 4% greater than, and an area 2 to 4% less than the dose matching area found in step 2. Implant 3 product wafers for each area setting.

This test was performed with microprocessor product wafers. E-test results in fig. 5 show that device threshold voltage measurements demonstrate that the area of 207.5 cm^2 matches the 350DE to the 300XP. E-test results in fig 6 show that a sensitive source to drain depletion current measurement demonstrates that the correct dose matching area is 207.5 cm^2.

Step 4. Repeat step 3 with a larger quantity of wafers to gain more confidence in the measurement [6].

Referring back to fig. 3, it shows the stability of the threshold voltage measurement over time for the 350DE, the 300XP, and another implanter on site, the 350D.

Step 5. Repeat step 3 and step 4 for each recipe. This can be done over the course of a few weeks, so that as time passes more and more recipes are production-qualified on the implanter.

The implant area of 207.5 cm^2 was used on the 350DE to match it to the 300XP for the other device implants. All the implants matched the 350DE with an area of 207.5 cm^2 to the 300XP with an area of 212.0 cm^2.

Since the thermal wave measurement agreed with the product wafer device measurements that the area of 207.5 cm^2 is corr the thermal wave measurement is used as a daily monitor.

4. Conclusions

Dose matching between two implanters must be carefully done taking into account implanter variables, wafer processing, and dose measurement. After the implanter is configured as needed, and passes its checklist, then on serial implanters use a sensitive, stable monitor and we suggest to adjust the implant area to dose-match the implanters. All recipes used must be checked before turning over to full production.

In the event that two different model implanters do not match for all doses, then we would suggest to match them for the one with the tightest control specs. If some of the other recipes fall out of spec, then that recipe dose will have to be changed unless the implanter configuration can be changed to bring that recipe back into spec.

Acknowledgements

The authors acknowledge A. Dranchak for work done on the serial implanters at Intel, and P. Mansfield for work on the figures.

References

[1] H Glawischnig and G Lang, Proc 7th Int. Conf on Ion Implantation Technology, Nucl Instr and Meth B37/38 (1989) 624.
[2] L. Larson, Proc. 7th Int. Conf. on Ion Implantation Technology, Nucl Instr and Meth. B37/38 (1989) 628
[3] L A Larson and G L Kennedy, Proc. 6th Int Conf on Ion Implantation Technology, Nucl Instr and Meth B21 (1987) 421.
[4] K Ishikawa, Guide to Quality Control (Asian Productivity Organization, Japan, 1988) p 18
[5] M I. Current, N.L. Turner, T.C Smith and D Crane, Proc 5th Int Conf. on Ion Implantation Equipment and Techniques, Nucl. Instr. and Meth. B6 (1985) 336
[6] A.R Alvarez, D.J. Welter, and M Johnson, Solid State Technol 26(7) (1983) 127
[7] J.T C Chen, Proc 6th Int Conf on Ion Implantation Technology, Nucl Instr. and Meth B21 (1987) 526.
[8] P Lundquist, C McKenna, R Brick and P Corey, Proc. 6th Int. Conf. on Ion Implantation Technology, Nucl. Instr. and Meth. B21 (1987) 414.

Nuclear Instruments and Methods in Physics Research B55 (1991) 250–252
North-Holland

Monitoring of dose in low dose ion implantation

Tohru Hara [a], Hiroyuki Hagiwara [a], Ryuji Ichikawa [a], W. Lee Smith [b], C. Welles [b], S.K. Hahn [c] and L. Larson [d]

[a] *Electrical Engineering, Hosei University, Koganei, Tokyo 184, Japan*
[b] *Therma Wave Inc., 47320 Mission Falls Ct., Fremont, CA 94539, USA*
[c] *Siltec Corporation, 190 Independent Drive, Menlo Park, CA 94025-1197, USA*
[d] *National Semiconductor Corp., 2900 Semiconductor Drive, Santa Clara, CA 95051, USA*

Monitoring of dose by thermal wave (TW) modulated reflection is investigated for As^+ or B^+ implantation into silicon at low doses (5×10^{10} to 1×10^{13} cm^{-2}) employed in the threshold voltage control of a MOS transistor. This method is shown to be useful to dose levels down to 5×10^{10} and 1×10^{11} cm^{-2} for As^+ and B^+ implantation (100 keV), respectively. The TW intensity has a close correlation with dose and also we can find a correlation of TW intensity with damage density, minority carrier lifetime, sheet conductance and the threshold voltage of a transistor at low doses if we assume that the extrapolation to lower doses is valid. Therefore, this technique is a useful, nondestructive, contactless and highly sensitive method for monitoring the dose.

1. Introduction

Control of the threshold voltage of a metal oxide semiconductor (MOS) transistor is important and has been achieved by varying the dose of ions implanted into the channel region of depletion and enhancement transistors. Therefore, monitoring of the dose for low dose implantations (5×10^{11}–5×10^{12} cm^{-2}) is needed for tight threshold voltage control of an MOS transistor. This improvement leads to the increase of device production yields and of the allowance of device design in very large scale integrated circuits (VLSI).

Dose monitoring has conventionally been done by threshold voltage and drain current measurements of MOS transistors [1]. However, this technique is destructive and very time consuming. The thermal wave (TW) modulated optical reflectance method has offered a nondestructive alternative approach to the characterization of the damage induced during low dose ion implantation. Although the variation of the TW signal intensity with ion dose was studied for high dose implantations employed in source and drain formation [2–4], the correlation of the intensity with damage density for low dose has been studied in few papers [5,6].

2. Experimental procedures

Ion implantation of B and As was performed into n- and p-type (100) Si wafers (resistivity: 8–12 Ω cm) with doses of 5×10^{10} to 1×10^{13} cm^{-2}.

Density of damage formed by the implantation was measured with 1.5 MeV He^+ Rutherford backscattering spectrometry aligned spectra [7]. Measurement was also performed by the thermal wave (TW) modulated reflectance and by minority carrier lifetime.

3. Experimental results

TW intensity measurements were performed for As^+ and B^+ implanted Si, where each implantation was performed through 50 and 200 Å thick oxide layer at 25 and 50 keV, respectively, with low doses (2×10^{11}–5×10^{12} cm^{-2}) employed in threshold voltage control of MOS transistor. The intensity is shown in fig. 1 as a function of dose. The intensity increased monotonically with the increase of dose. A higher intensity was attained in As^+ implantation. This result indicates that the ion implantation dose can be monitored by the TW signal intensity measurement at low doses.

The TW signal intensity for As^+ and B^+ implantations into bare Si at 100 keV was also measured to determine the sensitivity of this technique and the results are shown as a function of dose in figs. 2 and 3. The TW intensities increased linearly with dose in the TW signal intensity (linear scale) versus implant dose plot (logarithmic scale). These measurements indicate that this method is useful to dose levels down to 5×10^{10} and 1×10^{11} cm^{-2} for As^+ and B^+ implantations (100 keV), respectively.

In order to use this technique for dose monitoring, we must obtain the correlation of the TW intensity with ion implanted damage density of ion implanted layers, electrical properties and device parameters.

0168-583X/91/$03.50 © 1991 – Elsevier Science Publishers B.V. (North-Holland)

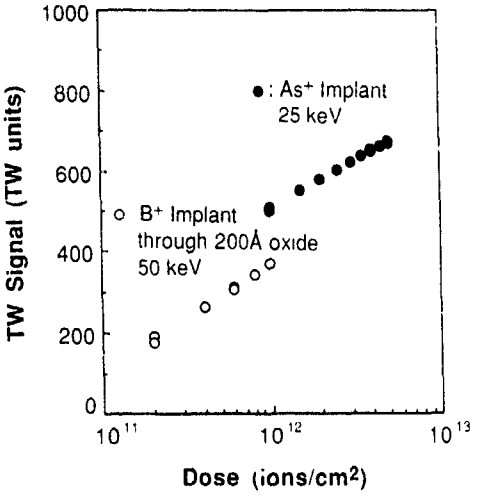

Fig 1 Variation of the thermal wave (TW) signal intensity with dose for As^+ and B^+ implantations in Si, where the implantation of As^+ and B^+ was performed through 50 and 200 Å thick oxide layers at 25 and 50 keV, respectively.

The displaced atom density (DAD) for As^+ implanted Si determined by RBS aligned spectra [7] is also shown in fig 2 The DAD was 2.9×10^{17} cm^{-2} at the dose level of 1×10^{14} cm^{-2}. It decreased monotonically with the decrease of dose and reached 1.5×10^{16} cm^{-2} at a dose of 1×10^{13} cm^{-2} Below 1×10^{13} cm^{-2}, this technique cannot be used because of the sensitivity limit The lowest dose detection limit for B^+ implantation is around 5×10^{14} cm^{-2}. Displaced atom density measurement cannot be used at the low doses employed in threshold voltage control. If the correlation between

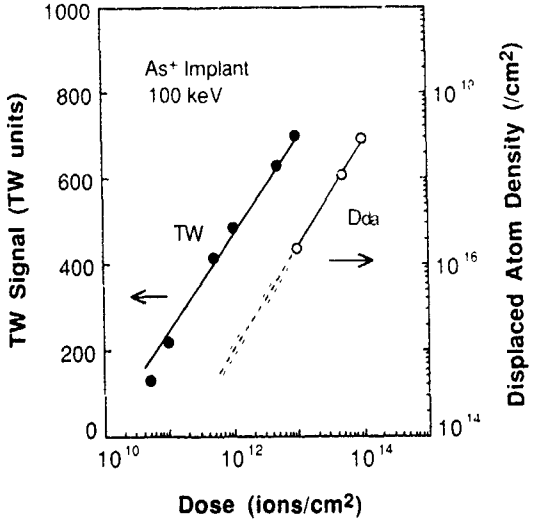

Fig 2 The TW signal intensity and displaced atom density (DAD) in As^+ implantation into Si at 100 keV as a function of ion implantation dose.

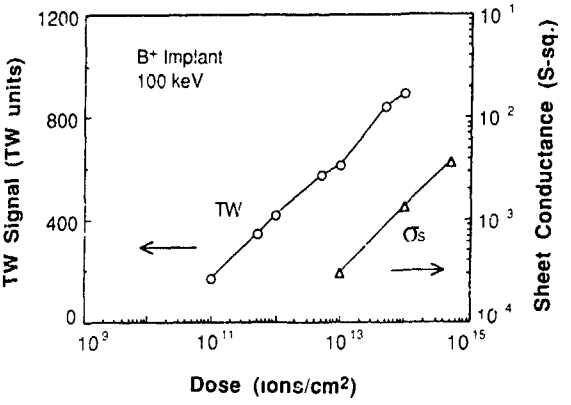

Fig 3. The TW signal intensity (as-implanted) and sheet conductance (annealed) in B^+ implantation into Si at 100 keV as a function of ion implantation dose, where annealing was done at 1000 °C for 20 min in N_2.

TW signal intensity and the DAD is assumed to apply at lower doses, as extrapolated by broken line in this figure, then the displaced atom density formed by this implantation can be monitored by the TW signal intensity measurement

After these layers were annealed at 1000 °C for 20 min, sheet resistance (conductance) was measured. This measurement has been extensively used in ion implantation dose monitoring at high doses. Sheet conductance for B^+ implanted Si at 100 keV is shown in fig. 3 as a function of dose. Sheet conductance decreased monotonically with the decrease of dose. It reached below 3.6×10^{-4} S sq. at doses below 1×10^{13} cm^{-2} This results shows clearly that the TW intensity has a close relation with sheet conductance at implant doses above 1×10^{13} cm^{-2}. Therefore, dose monitoring can be attained below this value if this correlation holds at the lower doses employed in channel doping Furthermore sheet conductance, carrier concentration and threshold voltage can be monitored by the TW signal intensity measurement for the as-implanted layer

A minority carrier lifetime measurement was also performed for As^+ implanted Si, where the implantation was performed at 100 keV through a 430 Å thick oxide layer. The lifetime increased with increasing annealing temperature because of damage recovering. Fig 4 indicates the variation of the minority carrier lifetime with dose after implanted samples were annealed at 800 °C. The lifetime decreased with the increase of dose. These data show that highly sensitive dose monitoring can be achieved by the minority carrier lifetime measurement.

Threshold voltage measurement for a MOS transistor is a useful dose monitoring technique and has been used at low doses. Fig. 5 shows the variation of threshold voltage (V_t) with dose in enhancement tran-

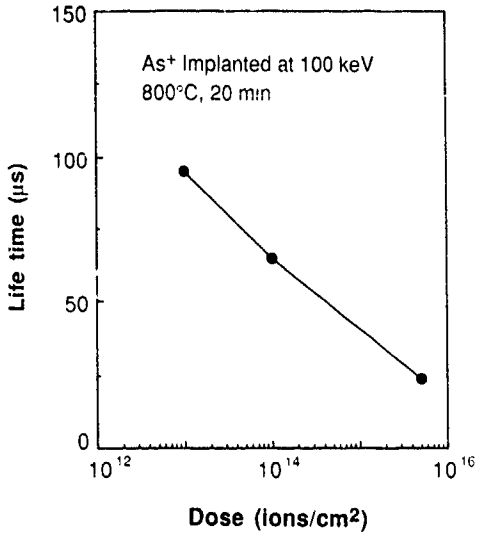

Fig 4 Variation of minority carrier lifetime with dose in As^+ implanted Si, where the implantation was performed at 100 keV and annealed at 800 °C

sistors reported by one of us (W L.S.), where B^+ was implanted into the channel region of a p-channel enhancement MOS transistor at 50 keV through a thin (50 Å thick) oxide. The threshold voltage (V_t) decreased linearly with decreasing dose in the V_t versus log dose plot as seen in this figure Since V_t is a function of carrier concentration in the channel layers, dose and carrier concentration after annealing can be monitored by the threshold voltage measurement. Even though this monitoring technique is highly sensitive, it is destructive and very time consuming for device fabrication The

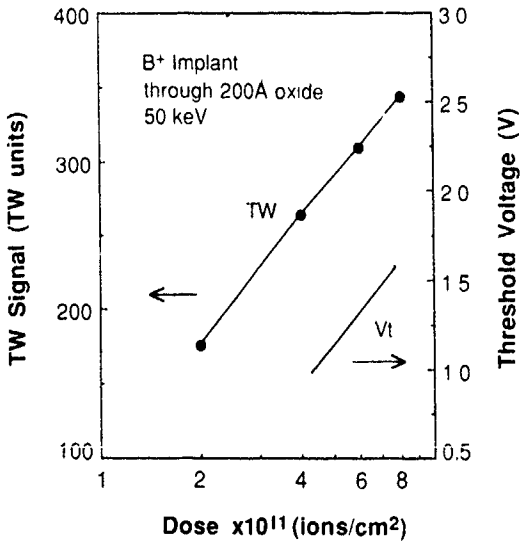

Fig. 5. The thermal wave (TW) signal intensity a id threshold voltage (V_t) observed in a p-channel enhancement transistor [1] as a function of dose. B^+ implantation was performed through a thin (50 Å thick) oxide layer at 50 keV

TW intensity for this implantation in an unpatterned Si wafer is also shown in this figure. The intensity in the B^+ implanted layer has again a close correlation to the threshold voltage of an enhancement transistor. As is evident from these results, the threshold voltage of a MOS transistor can be monitored by the measurement of damage in the as-implanted layer using the TW modulated reflectance method

4. Conclusions

(1) Displaced atom density (DAD) has a close correlation with ion implantation at doses above 1×10^{13} cm^{-2} in As^+ implantation. The lower dose detection limit by the sheet conductance measurement is 5×10^{12} and 1×10^{13} cm^{-2} for As^+ and B^+ implantations, respectively, at 100 keV Therefore, these monitoring techniques can not be used for the monitoring of low dose ion implantation employed for threshold voltage control of MOS transistors.

(2) Thermal wave signal intensity increases monotonically with ion implantation dose. The method is useful to dose levels down to 5×10^{10} and 1×10^{11} cm^{-2} for As^+ and B^+ implantations (100 keV), respectively

(3) Since the TW intensity has a correlation with dose and threshold voltage of enhancement MOS transistors, the threshold voltage can be monitored by the TW intensity measurement for an as-implanted layer The intensity also has correlation with damage density and sheet conductance if we assume the data can be extrapolated to low doses

In conclusion, the TW signal intensity measurement technique is a promising nondestructive and highly sensitive dose and damage monitoring technique.

References

[1] M A Wendman and W L Smith, Nucl Instr and Meth B21 (1987) 559
[2] W L Smith, M W. Taylor and J. Schuur, Soc Photo-Opt Instrum Eng 530 (1985) 201
[3] W L Smith, A. Rosencwaig and D L Willenberg, Appl Phys Lett. 47 (1985) 584
[4] W.L Smith, A Rosencwaig, D.L. Willenborg, J Opsal and M.W. Taylor, Solid State Technol. 29 (1986) 85.
[5] T. Hara, S. Takahashi, H Hagiwara, W.L. Smith, C. Welles, S.K. Hahn, L Larson and C C.D. Wong, Proc. Int. Conf. on Defect Control in Semiconductors, Yokohama, Japan, 1989 (Elsevier, 1990)
[6] T. Hara, S Takahashi, H Hagiwara, W.L. Smith, C. Welles, S K Hahn, L Larson and C C.D. Wong, Appl Phys Lett. 55 (1989) 1315
[7] W K Chu, J.W Mayer and M A Nicolet, Backscattering Spectrometry (Academic Press, New York, 1978) p 21
[8] T. Hara, H. Hagiwara, W L. Smith, C Welles, S K Hahn, L Larson and C.C.D Wong, IEEE Electron Device Lett 11 (1990) 485.

Nuclear Instruments and Methods in Physics Research B55 (1991) 253–256
North-Holland

Implant dose uniformity simulation program

Nobuo Nagai

Nissin Electric Co., Ltd., Ion Equipment Division, 575 Kuze Tonoshiro-cho, Minami-ku, Kyoto, Japan

A two-dimensional implant dose uniformity simulation code consisting of two programs named SCAN and MAP has been developed The code can take account of the effects of beam sweep waveform, beam sweep frequency, beam size, and wafer rotation speed The result of the calculations can be plotted in a two-dimensional contour map similar to a wafer uniformity map.

1. Introduction

It is very useful to simulate implant dose uniformity on a computer because we can simplify the situation and are able to see the dose distribution as implanted without being disturbed by post-process. Sheet resistivity and Therma-wave [1] measurements are the most common techniques to assess the uniformity of the implant dose But those methods do not measure the implanted ions directly, so the results are influenced by some effects other than from the implanter such as anneal conditions and channeling effects. Besides difficulty in the measurement, an ion implanter itself presents many uncertainties that affect the measurements of dose uniformity. For example, fluctuation on ion beam current, noise on beam sweep waveform, channeling effects due to implant angle (wafer tilt and twist angle) can make a complicated pattern in dose uniformity map [2]

To evaluate the essential effects of implanter parameters on implant dose uniformity, a computer simulation program has been developed. The computer code calculates the two-dimensional implant dose distribution over a wafer with given machine parameters such as beam sweep frequencies of x and y directions, a beam sweep waveform, a wafer rotation speed, a wafer tilt angle, and a beam density distribution With this simulation we can predict the optimal conditions for uniform implantation, on an electrostatically scanned serial implanter with or without wafer rotation.

2. Description of simulation code

The computer code simulates ion implantation on a wafer. To simulate the process by a digital computer, area and time have to be quantized. An implant area is divided into a small rectangular mesh pattern as shown in fig. 1. An ion beam sweeping over the wafer leaves a *footprint* for every short constant time interval. The program counts the number of footprints left by an ion beam on each mesh. After implant, the counts of the footprint in one mesh show how many times the mesh (small part of a wafer) is exposed to the ion beam.

The simulation code consists of two programs. The program 1 names SCAN calculates the beam position at every short time interval and makes a data file containing the footprint counts which is later used by the program 2. The program 2 named MAP calculates the uniformity over the wafer and draws a 2-D contour map.

The mesh size must be smaller than the beam size and the uniformity structure which one wants to see on the uniformity map. Using a shorter time interval gives a more precise simulation, but it uses much CPU time A desirable time interval is the time in which a beam scans 1/2 or 1/3 mesh. (The time interval shown in fig 1 is too long.)

In the program SCAN, a beam is assumed to have a

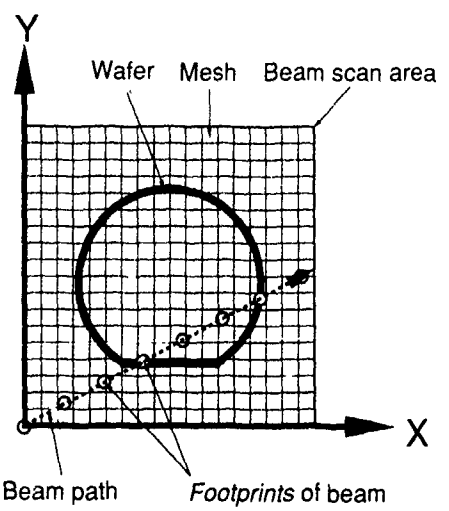

Fig. 1 Coordinate of simulation and mesh

0168-583X/91/$03.50 © 1991 – Elsevier Science Publishers B V (North-Holland)

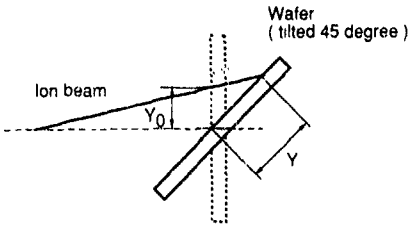

Fig. 2 Treatment of wafer tilt angle

point cross section, but the actual beam has a size and density distribution. To evaluate the effects of beam spot size, in the program MAP, dose data on the wafer for every mesh is calculated by a weighted average of the footprint counts around the mesh. The weight represents the beam density distribution. The resultant dose uniformity data is plotted as a contour map like a sheet resistivity map with the signs switched.

The program SCAN can generate data for MAP if the beam position at any time is known. In the case of an electrostatic-scan implanter (such as a common medium current implanter), the beam position on the wafer is determined by the voltage applied to the scanning electrodes. A tilted wafer is treated as a beam position Y_0 changed to Y as illustrated in fig. 2. When SCAN simulates the wafer rotational implantation [4], the simulation coordinate system is rotated with the wafer.

3. Result of simulation

The result of a simulation for a 45° tilt angle implant is shown in fig. 3a. In the simulated map, a circle indicates the wafer area. The parameters of the simulation used in this case are as follows:

beam scan area:	150 mm (W) × 150 mm (H);
mesh size:	2 mm square;
time interval:	6.53 μs;
beam:	Gaussian distribution (both x and y directions), $\sigma = 3$ mm.

Fig. 3b is an experimentally obtained sheet resistivity map of a 45° tilt angle implant. The comparison of the simulation and the experiment shows a quite good agreement. But it should be noted that the physical quantity shown in each map is different. Fig. 3a represents the dose uniformity and fig. 3b shows the sheet resistivity.

Both maps show the increase of dose from the right bottom to the left top. The pattern is caused by the change in the beam sweep velocity over the wafer [3].

Fig. 4 shows simulation results of a 45° tilt implant with wafer rotation. The simulation parameters are the same as for fig. 3a. It is shown that the rotational implant for a large tilt angle implant is effective to improve uniformity as reported [4,5]. The simulation shows the uniformity improves from 2.66% to 0.16% for an implant with 1.3 rps wafer rotation.

A resonance occurs when the implant time is very short compared with the period of wafer rotation. An example of the resonance pattern is shown in fig. 5a. Fig. 5b is an experimental Therma-wave map. Fig. 5c is derived from fig. 5a using empirical Therma-wave sensitivity. It is shown that the simulation gives fairly good agreement with the experimental result.

A resonance occurs at a certain combination of beam scan frequency and wafer rotation speed. Even a

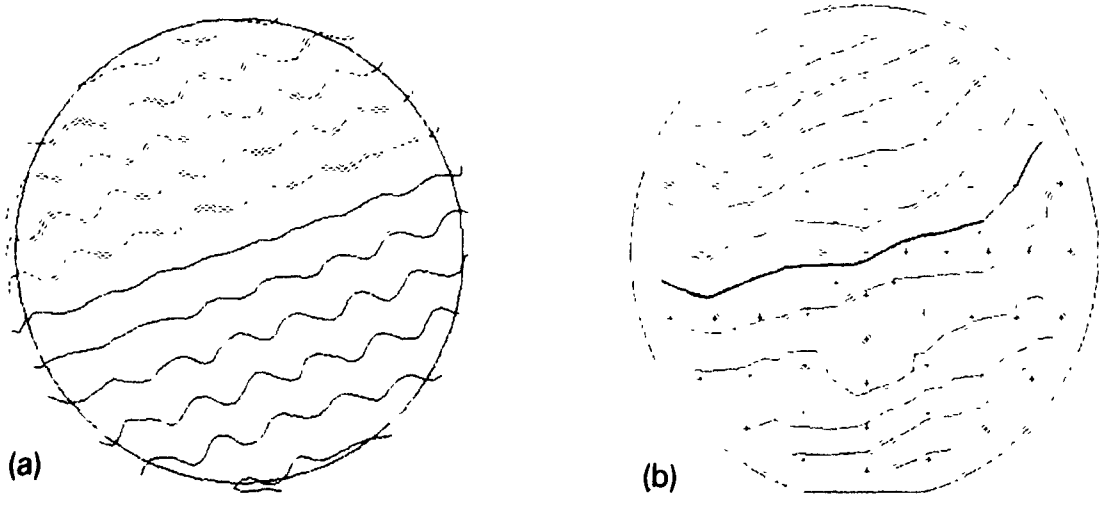

Fig. 3 Uniformity maps of 45° tilt angle implant. (The wafer twist angle is 30°.) (a) A calculated dose uniformity map. The dotted line shows the contour line of a higher dose region and the solid line shows the contour line of a lower dose region. A contour interval is 1% dose. Uniformity is 2.66%. (b) An experimental sheet resistivity map. A higher dose area is indicated by "−" sign. A contour interval is 1% sheet resistivity. Uniformity is 2.67%

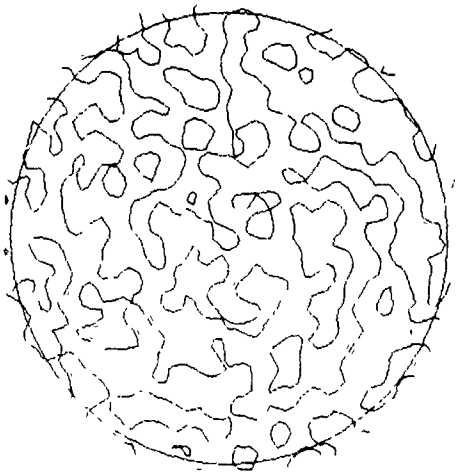

Fig 4 Effect of rotational implant Simulation parameters are the same as for fig 3a Uniformity is 0 16%. Only average lines are shown

small variation of a parameter can result in a very large change in the resonance pattern as shown in figs. 6 and 7

4. Conclusion

A two-dimensional simulation code for implant dose uniformity mapping was developed. This simulation code can be used to examine the effects of beam sweep waveform, beam sweep frequency, beam size, and wafer rotation speed and can help us to predict a "good combination" of the beam scan parameters.

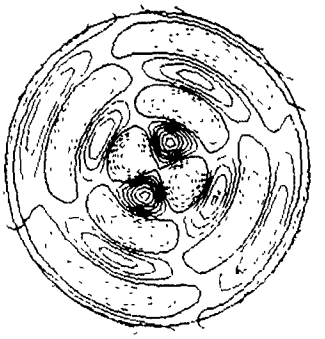

Fig 6. Simulation of beam scan and wafer rotation resonance pattern Vertical beam scan frequency is 504 16 Hz, and other parameters are the same as for fig 5a

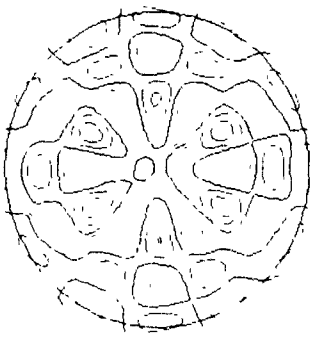

Fig 7 Simulation of beam scan and wafer rotation resonance pattern Vertical beam scan frequency is 501 38 Hz, and other parameters are the same as for fig 5a

References

[1] W L Smith, A Rosencwaig, D L Willenborg, J Opsal and M W Taylor, Nucl Instr and Meth. B21 (1987) 537

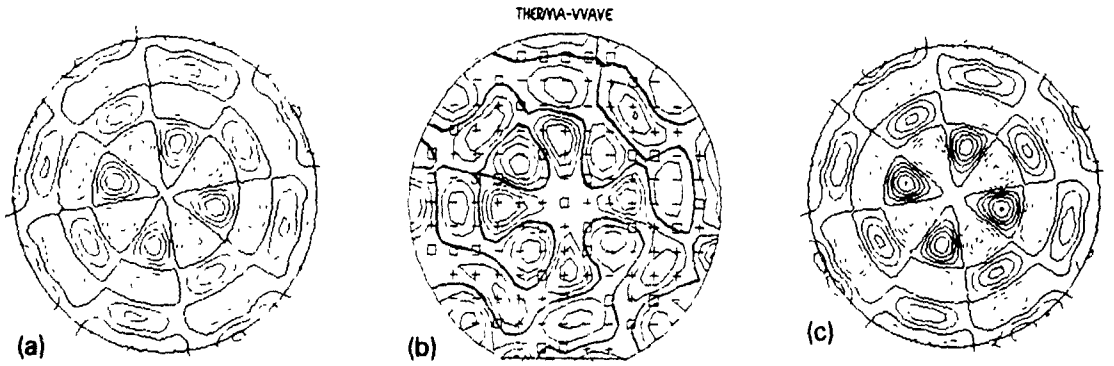

Fig. 5 Simulation of beam scan and wafer rotation resonance pattern Implant time: 5 s, wafer rotation speed. 1 0 rps; beam scan frequency: H: 88 85 Hz, V. 502.13 Hz. (a) Simulation Dose uniformity 6.53%, contour interval: 5% (b) An experimental result Therma-wave (TW) map. TW uniformity 0 80%; contour interval: 0.5%, TW signal: 609.6 TW units (c) Simulation The dose is converted to Therma-wave units. Empirical Therma-wave sensitivity used is as follows $TW = -1580\,61 + 168\,063 \log_{10}(\text{dose})$ TW uniformity. 0 79%; contour interval 0 5%; TW signal. 604 05 TW units

[2] M.I Current, N.L. Turner, T.C. Smith and D. Crane, Nucl. Instr and Meth. B6 (1985) 336.
[3] M. Sasaki, M. Tanaka, H. Kawakami and H. Kumazaki, Nucl. Instr. and Meth. B37/38 (1989) 469.
[4] Y. Tamura, M. Nogami, M. Tanaka, T. Maeda, H Kumasaki and S. Tamura, Nucl. Instr. and Meth. B37/38 (1989) 620.
[5] S. Ohsaki, M. Nagatomo, K. Higashitani, T Takahashi and T. Hirao, Proc. 31st Semiconductor and Integrated Circuit Technology Symp., Tokyo (Dec. 1986) p. 97, in Japanese

Nuclear Instruments and Methods in Physics Research B55 (1991) 257–260
North-Holland

Nondestructive determination of damage depth profiles in ion-implanted semiconductors by multiple-angle-of-incidence single-wavelength ellipsometry

M. Fried, T. Lohner, E. Jároli, C. Hajdu and J. Gyulai
Central Research Institute for Physics, Budapest, 114, H-1525, POB 49, Hungary

Four-parameter fitting of multiple-angle-of-incidence (MAI) ellipsometry data is developed to characterize near-surface layers on semiconductors damaged by implantation. We used coupled half-Gaussians to describe the damage depth profiles. The method was tested on Ge-implanted silicon layers (at a wavelength of 632.8 nm) and was cross-checked with high depth resolution RBS and channeling.

1. Introduction

Preamorphization by implantation of electrically neutral atoms can eliminate channeling tails in implantation, but the control and optimization of this process, especially within the technology, is an important task.

Ion-implantation-induced disorder changes the complex refractive index of the implanted layer, so it can be detected by optical methods such as ellipsometry [1–7]. Ellipsometry is a sensitive, rapid and nondestructive but indirect technique, so a realistic and adequate multilayer optical model must be used to determine the disorder profile from the ellipsometric data alone.

From an ellipsometric measurement at given values of wavelength and angle of incidence, one can determine only two unknown parameters. (In earlier works most optical models have proven to be useful only for monitoring the relative change in the surface layer, or destructive etching was used to get depth information.) A possibility to increase the number of independent experimental data is to use the multiple-angle-of-incidence (MAI) method [8]. However, by introducing more distinct layers in the optical model, the cross-correlations between the unknown parameters increase. (Even with spectroscopic ellipsometry [9–11] the practical limit is ten layers in the model.) The solution of this problem is to use layers of equal thicknesses with damage levels determined by a function of depth. This function is described with a limited number of unknown parameters. The complex refractive index of each layer is calculated from the actual damage level by the Bruggeman effective medium approximation (EMA) [12], using crystalline and totally amorphous semiconductor values as endpoints.

Our method originated from ideas used in earlier investigations [2,4,7,13]. The most similar method is the one used in ref. [13] to determine carrier profiles in silicon by MAI in the infrared wavelength region. During our investigation, we found a recently published paper [14] which uses a similar optical model to determine damage profiles in silicon by reflection measurements.

To demonstrate the method, we measured data on 40 or 60 keV Ge implanted silicon. The MAI results were compared with ion backscattering spectrometry combined with channeling.

2. Ellipsometry

2.1. The optical model

To construct a realistic optical model, we used coupled half-Gaussian functions with four independent parameters (center, height and two standard deviations). Taking into account the fact that the damage level is saturated at the amorphous state, we describe the damage depth profile with the following function:

$$D(x) = 1 - \exp\left\{ -f \exp\left[-(x - rp)^2 / 2\sigma_{1,2}^2 \right] \right\}$$

$$\begin{cases} \sigma_1, & \text{when } x < rp, \\ \sigma_2, & \text{when } x > rp, \end{cases}$$

where rp is the center, f is the height, σ_1 and σ_2 are the standard deviations of the coupled half-Gaussians. (This function originated from the assumption that one single ion track is fully amorphous and a later overlapping ion track does not cause more amorphization.) In addition, we take into account a native oxide layer in the optical model as a fifth unknown parameter (see fig. 1). The number of layers is a result of a compromise between resolution and the required computing time. We used

0168-583X/91/$03.50 © 1991 – Elsevier Science Publishers B.V (North-Holland)

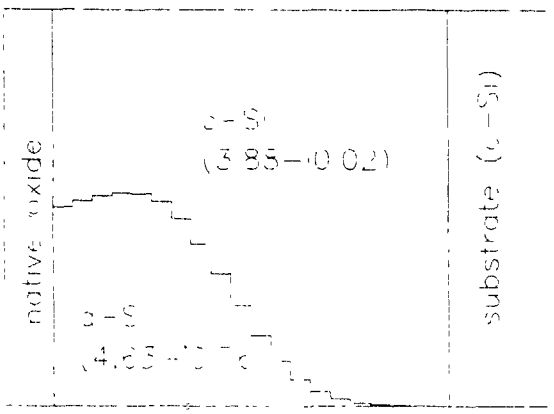

Fig 1 The optical model The complex refractive index of totally amorphous silicon is from refs [6,7].

an IBM compatible (32-bit) PC to evaluate the measurements The computing time was 1–3 h depending on the number of angles of incidence with an optical model of 20 layers.

It is important to note that f is not proportional to the implanted dose. They are related, but exact proportionality would only exist at 0 K. At room temperature, the migration of point defects modifies the situation.

2.2. MAI ellipsometry

In refraction ellipsometry the experimental result is given by

$$\rho = \tan\psi \exp(i\Delta) = R_p/R_s, \tag{1}$$

where ρ is the complex reflectance ratio and R_p and R_s are the complex amplitude reflection coefficients for the parallel and perpendicular polarizations. ρ (and thus ψ and Δ) can be computed knowing all complex refractive indices, layer thicknesses (of the optical model) and device parameters (wavelength and angle of incidence)

Symbolically, the functional dependence of ψ and Δ on the system parameters can be separated into two real equations:

$$\psi = \arctan\left|\rho(n_j^*, d_j, \Phi_0, \lambda)\right|, \tag{2}$$

$$\Delta = \arg\left[\rho(n_j^*, d_j, \Phi_0, \lambda)\right], \tag{3}$$

where $|\rho|$ and $\arg(\rho)$ are the absolute value and argument of the complex equation (1) and are dependent upon many parameters. If we use the $\boldsymbol{D}$ depth profile function to compute n_j^* (d_j are fixed) then we may write

$$\rho = \rho(\boldsymbol{B}, \Phi, \lambda); \qquad \psi = \psi(\boldsymbol{B}, \Phi, \lambda); \tag{4}$$
$$\Delta = \Delta(\boldsymbol{B}, \Phi, \lambda),$$

where $\boldsymbol{B} = (d_{ox}, rp, \sigma_1, \sigma_2, f)$ is the vector containing the unknown parameters. During the computation we used $drp = \sigma_1 + \sigma_2$ and $ddrp = \sigma_1 - \sigma_2$ for programming convenience. This means that even in the case of a high value of f, the profile is also sensitive to the drp and $ddrp$. If we use σ_1 and σ_2 then in the case of a high value of the f, the profile is not sensitive to the σ_1. This fact disturbs the fitting process.

Let us measure at M different angles of incidence. In this case we have $2M$ nonlinear equations from eqs. (4):

$$\psi_j^m = \psi_j^c(\boldsymbol{B}, \Phi_j, \lambda); \quad \Delta_j^m = \Delta_j^c(\boldsymbol{B}, \Phi_j, \lambda), \tag{5}$$

where $j = 1, \cdots, M$. The superscripts m and c distinguish between the measured and computed values of ψ and Δ, respectively. If $M \geq 3$, we have more data than the unknown parameters.

Because of experimental errors and/or model weaknesses (our optical model is an approximation only), eqs. (5) cannot be satisfied exactly, so a least-squares solution must be sought by a computer program The program minimizes the sum of squares of the residuals

$$G(\boldsymbol{B}) = \sum_j \left\{(1/e_1)^2\left|\psi_j^m - \psi_j^c(\boldsymbol{B}, \Phi_j)\right|^2 + (1/e_2)^2\left|\Delta_j^m - \Delta_j^c(\boldsymbol{B}, \Phi_j)\right|^2\right\},$$

where e_1 and e_2 are the experimental errors of the ψ and Δ values (0.1 and 0.3), respectively.

3. Experimental

Wacker-made, p-type Si(111) wafers of 4–8 Ω cm resistivity were implanted with Ge ions at room temperature. The implantation conditions are shown in table 1.

The ellipsometric measurements were performed with a LEM-2 type manual null ellipsometer in PCSA (polarizer, compensator, sample, analyzer) configuration. The wavelength was 632.8 nm (He–Ne laser) The measurements were made at several angles of incidence between 60° and 72°. Three angles are enough to evaluate the measurements, but more angles can yield more precise results At the same time, more angles need more computing time In the case of the samples

Table 1
Implantation conditions

Energy [keV]	Dose [$\times 10^{14}$ Ge^+/cm^2]	Sample no
40	0.25	41
40	0.5	42
40	1	43
40	2	44
60	0.25	61
60	0.5	62
60	1	63
60	2	64

investigated during this work we used five angles. The typical measurement time with our manual ellipsometer is under 10 min (at five angles of incidence). An automatic ellipsometer can measure in seconds.

To check the ellipsometric results we used Rutherford backscattering spectrometry (RBS) combined with channeling. The analyzing beam was a 1.5 MeV $^4He^+$ beam. The detector was positioned to detect ions scattered through 97° (with a glancing exit angle to the surface of 7°). In this geometry, the depth resolution was better than 5 nm. To evaluate the spectra we used the RBX program written by Kótai [15], which can also handle channeled spectra.

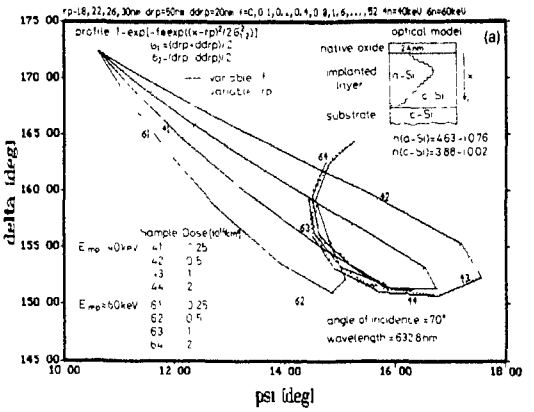

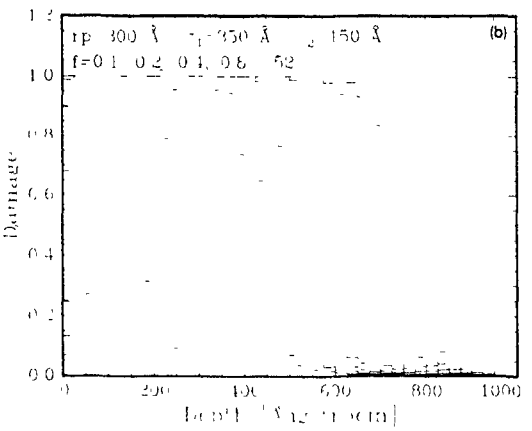

Fig 2 (a) Measured $\psi-\Delta$ values at an angle of incidence of 70° with simulated curves. The varying parameters are *rp* and *f* (b) The profiles related to different *f* values along one fixed *rp* (solid line). *rp* = 30 nm, *f* = 0.1, 0.2, 0.4, ... 52

4. Results and discussion

In MAI ellipsometry, a crucial point is the guessing of the initial values of the unknown parameters. In our case, the ion range data are good for this purpose. (The ion range profile is always deeper and narrower than the damage depth profile for the same ion type and energy.) The height of the profile can be estimated from simulations similar to the one in fig 2a. In fig. 2b we show the profiles related to different *f* values along one fixed *rp* (solid line).

The native oxide is also a problem, especially in the case of small doses (samples 41 and 61). However, we measured its thickness on a virgin part of the same wafer. The thickness was between 20 and 30 Å in all cases This fact can be considered during the computer fitting.

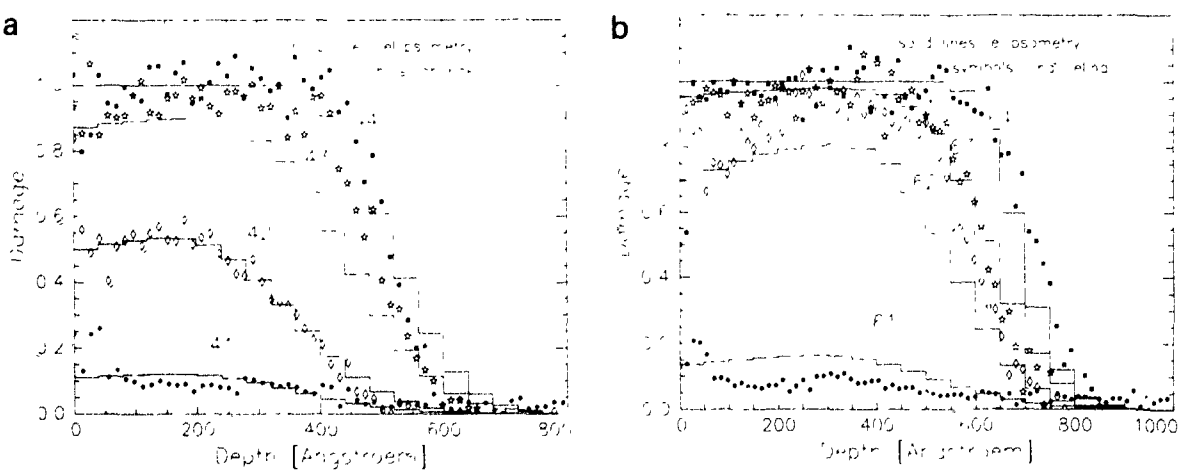

Fig 3 Damage profiles obtained from MAI ellipsometry (histograms) and RBS channeling (symbols) (a) 40 keV implants, (b) 60 keV implants.

Ellipsometry is extremely sensitive to the near-surface region. Our method can detect precisely whether this region is fully amorphized or not. This is important from the point of view of post-implantation annealing.

Above the dose of full amorphization, only the depth and the width of the c/a interface are in question. With this method we can determine these parameters

The depth limit in silicon at this wavelength (λ = 6328 Å) is about 2000 Å. At shorter λ, the sensitivity is better, but the depth limit is less. At longer λ, the situation is the opposite. Naturally, if we measure at different wavelengths (spectroscopic ellipsometry), the method becomes better.

To check the ellipsometric results we made RBS measurements. The evaluated damage profiles can be compared directly with the profiles (histograms) obtained from MAI ellipsometry (see fig. 3). The number of layers in the optical model is a result of a compromise between resolution and the required computing time (The time grows with the square of the number of layers).

The agreement between the results obtained by the two different methods seems to be very good.

5. Summary

We developed an optical model for MAI ellipsometry to determine damage depth profiles in ion-implanted semiconductors To describe a realistic profile, it is enough to use a few fitting parameters. To demonstrate the method, we measured data on Ge-implanted silicon. We checked our results by RBS.

The method can be generalized easily for spectroscopic ellipsometry.

Acknowledgement

The authors are grateful for the helpful assistance of Dr. N.Q. Khanh in RBS measurements.

References

[1] M.M. Ibrahim and N.M. Bashara, Surf. Sci. 30 (1972) 662
[2] J R Adams and N M. Bashara, Surf Sci 49 (1975) 441
[3] A Kucirkova, Radiat. Eff 28 (1976) 129
[4] T. Motooka and K Watanabe, J. Appl. Phys 51 (1980) 4125.
[5] M Delfino and R R Razouk, J Appl Phys 52 (1981) 386
[6] T. Lohner, G Mezey, E Kótai, A Manuaba, F. Pászti, A Dévényi and J Gyulai, Nucl Instr and Meth 199 (1982) 405
[7] M. Fried, T Lohner, E Jároli, Gy Vizkelethy, G Mezey and J. Gyulai, Thin Solid Films 116 (1984) 191
[8] R M A. Azzam and N.M Bashara, Ellipsometry and Polarized Light (North-Holland, New York, 1977)
[9] M. Erman and J.B Theeten, Surf Interf Anal 4 (1982) 98
[10] M Erman and J.B Theeten, Surf. Sci. 135 (1983) 353.
[11] Mo Dang and He Xingfei, Chin Phys Lett. 3 (1986) 229
[12] S.A G Bruggemann, Ann Phys 24 (1935) 636
[13] T. Motooka, T Warabisako, T Tokuyama and T Watanabe, J Electrochem Soc 131 (1984) 174
[14] K. Jezierski and M Kulik, Opt Commun 71 (1989) 285
[15] E. Kótai, The RBX code, to be published

Nuclear Instruments and Methods in Physics Research B55 (1991) 261–265
North-Holland

Limitations of the spreading resistance technique for ion implant profile measurements

J. Montserrat, J. Bausells and E. Lora-Tamayo

Centro Nacional de Microelectrónica – CSIC, Universitat Autónoma de Barcelona, 08193 Bellaterra, Spain

The main problem with the spreading resistance technique is that it yields a net carrier concentration profile measured on a beveled sample and this may be quite different from the corresponding dopant profile due to carrier spilling. We have made theoretical and experimental studies of this phenomenon to evaluate the accuracy of the technique to measure ion-implanted profiles. We see that errors are important when a pn shallow junction is formed with low implant doses.

1. Introduction, the spreading resistance technique

In the research and development of new processes used in the fabrication of semiconductor devices it is fundamental to know the dopant impurity profiles. Today the most used process to introduce dopant impurities in a semiconductor is ion implantation. Characterization of implanted-ion profiles can be performed by physical techniques, such as SIMS or RBS, or by electrical methods. Among the electrical profiling methods for the last few years the spreading resistance (SR) one [1,2] has been the most widely used in silicon.

SR uses two small probes of tungsten–osmium alloy separated by a very short distance, typically 50–100 μm. The probes are moved in steps across the surface of the sample to be studied, measuring the resistance in a small region immediately under the probe tips. The system has a high spatial resolution. We can bevel the sample with a small angle and then by probing on this beveled surface, we obtain a measurement of the resistance versus depth.

Because of the intrinsic complexity of the contact variables between probe and sample, SR cannot be used for absolute measurements. Instead, probes are prepared to standardize the mechanical contact parameters. Measurements are then made by comparison to calibration curves generated for a particular set of probes on bulk silicon samples with uniform and known resistivity, having the same conductivity type, crystallographic orientation and surface finish as the test specimens. Since SR is a comparison technique, the accuracy of the results is strongly dependent on the achievement of a high degree of reproducibility both of the probe contact and of the surface finish on calibration samples and test specimens. Probe tips are conditioned by using the Gorey–Schneider probe grinder [3]. To standardize the sample preparation samples are wax-mounted on beveling fixtures having the desired bevel angle. They are polished with fine diamond abrasive in an oil-based slurry on a frosted glass plate [3]. With this procedure a polished surface with a sharp bevel edge is obtained.

The resistance–depth profile data are converted to a resistivity profile through the calibration curves and a boundary effect correction procedure based on the multilayer approach of Schumann–Gardner [4]. Finally the carrier depth profile is obtained with an improved version of Irvin's curves [5].

The advantages of SR are its speed and that it can measure on a wide range of resistivities and depths. Its disadvantages are the need for calibration and that it is a destructive technique.

2. The carrier spilling problem

The operation of semiconductor devices is determined by the free-carrier distribution but for the process engineer it is more important to exactly know the dopant distribution to fix the technological process.

A fundamental limitation of SR is that it measures the free-carrier density profile, and usually this does not agree with the corresponding dopant concentration profile. This differences are more important when the doping profiles are very steep. This is the case of profiles obtained by ion implantation. In the case of a pn junction there are also differences because of the space-charge region between the two zones.

Because of the doping density gradient, there is a diffusion current. A spatial charge distribution and an electric field appear and an equilibrium situation is reached within the semiconductor, where at different points the doping concentration is different from the free-carrier concentration. This free-carrier redistribution is known as "carrier spilling". All electrical char-

0168-583X/91/$03.50 © 1991 – Elsevier Science Publishers B.V. (North-Holland)

acterization techniques are affected by this phenomenon.

In addition, to measure a depth profile it is necessary to bevel the sample and this introduces an additional redistribution, because the boundary conditions over the surface change. Gauss' law requires the potential lines to bend up perpendicularly to the bevel surface. Physically this is accomplished by a divergence of carrier spilling which becomes two-dimensional in the vicinity of the bevel [6]

If we have a pn junction, there is a metallurgical junction (MJ) where the dopant concentration of the surface layer becomes equal to the opposite-type dopant substrate concentration. There is an electrical junction (EJ) where the free-carrier concentration is minimum. When we measure the electrical junction with SR on bevel we obtain the "on-bevel" electrical junction. This point is where maximum resistance occurs.

In order to know the free-carrier distribution for a known dopant distribution, it is necessary to solve the two-dimensional Poisson equation for this structure [6] If the bevel angle is small the effect of beveling is equivalent to planar material removal and then it is possible to make a set of one-dimensional simulations for the different vertical sections [7]. We have made some theoretical and experimental studies to evaluate the influence of carrier spilling in the SR measurements. We have solved the two-dimensional Poisson equation in beveled samples to find the free-carrier distribution for a given dopant distribution in several cases of interest in order to determine the differences when on bevel, where SR measures. We have prepared some samples by making ion implantations and annealings in different conditions. The samples have been characterized by SR and SIMS. Process modelling has also been done.

3. Results and discussion

Firstly the case of a shallow highly doped p-type layer is studied. A boron ion implantation with a dose of 1.0×10^{15} cm^{-2} was made into an n-type silicon wafer with a nominal resistivity of 4–5 Ω cm ($N_D = 1.0 \times 10^{15}$ cm^{-3}). This wafer was annealed at 950 °C during 30 min in inert ambient in order to activate the dopant impurities and to remove the crystallographic defects created by the ion implantation. A carrier profile was obtained from SR measurements using a SSM-130 made by Solid State Measurements Inc. The calculation of carrier concentration from SR values was made using the software supplied by SSM.

In this case in bulk of the sample the holes originating in the surface layer spill in the underneath region and the EJ in depth is deeper than the MJ. However, in the region where the bevel crosses the MJ this situation changes and the electrons originating in the substrate spill into the superficial layer near the bevel.

The simulation of the process was made with SUPREM-4 [8], a two-dimensional process simulation program, including an etch step to make the beveled region. Then this structure was introduced in PISCES [9], a two-dimensional device simulation program, to calculate the corresponding free-carrier distribution. The result is plotted in fig 1. We can see that the level

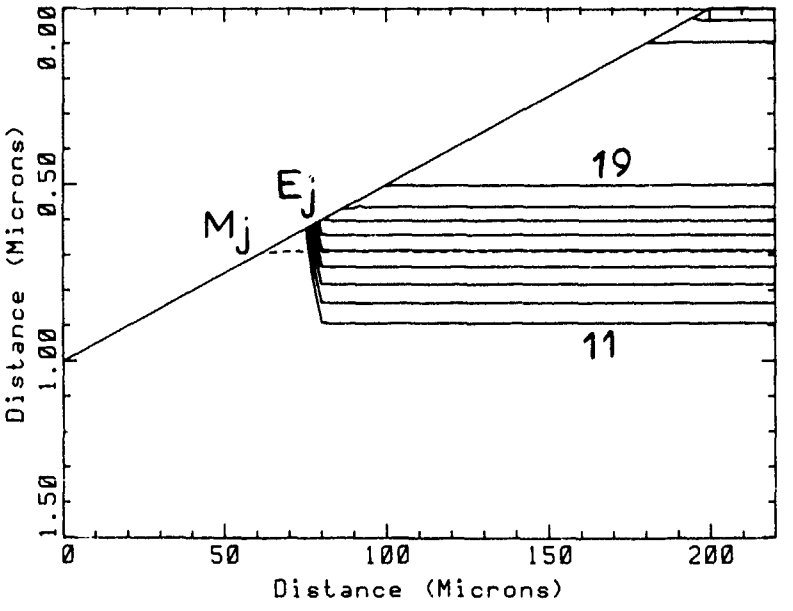

Fig 1 Two-dimensional plot of a beveled sample with a pn junction. Solid lines are the level contours of hole concentration and the dashed line is the metallurgical junction

contours of hole concentration are parallel to the original surface of the sample, but when they approximate to the bevel surface suddenly they bend up. As SR measures on bevel it finds that the EJ is shallower than MJ. In fig. 2 the predicted dopant and free-carrier profiles in depth in the nonbeveled region, and the free-carrier profile along the bevel surface have been plotted, with the distance scaled to the vertical depth. This simulation is compared to the actual SR measurement. Results are presented in the same figure. The predicted on bevel EJ is in good agreement with the measured values, and is shallower than MJ.

Then we made the same process but with a low ion implantation dose ($D = 1.5 \times 10^{11}$ cm^{-2}). In fig. 3 the simulated profiles are plotted. Here we see that the relative difference between on-bevel EJ and MJ is much more important We also see a shift in the depth of the distribution maximum. This can introduce errors if we use the SR technique to determine the mean projected range of the distribution profile of dopant atoms. Moreover, the area under the on-bevel carrier profile is lower than the area under the acceptor impurity profile This can introduce errors in the measure of ion implantation doses Finally we do not obtain the first metallurgical junction

For a number of cases of interest a two-dimensional technological process simulation has been used to obtain the dopant atom distribution and MJ, and a two-dimensional electrical simulation to calculate the free carrier distribution and EJ We studied B ion implantation with doses ranging from 1.0×10^{12} to 3.2×10^{15} cm^{-2} at 100 keV, in an n-type substrate ($N_D = 1.0 \times 10^{15}$ cm^{-3}) and annealings at 1150 °C in a conventional furnace in inert ambient during different times, from 10 to 720 min

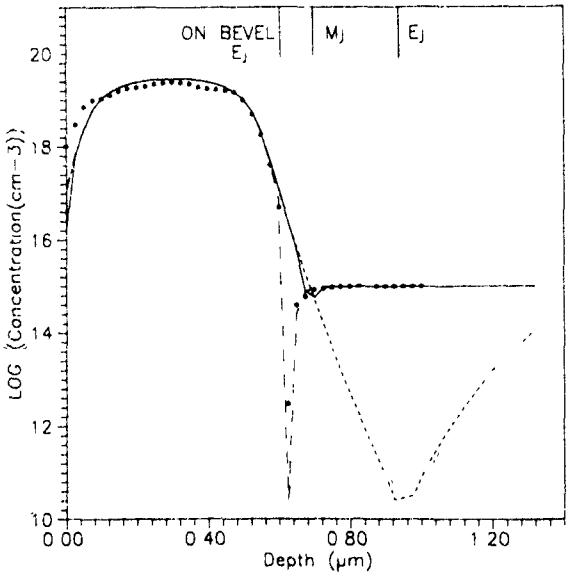

Fig. 2. Simulated and measured concentration profiles for a high ion implantation dose (———) dopant profile in depth, (— — — —) free-carrier profile in depth, (- - - - - -) on-bevel carrier profile, and (* * * *) free-carrier profile obtained by SR measurements

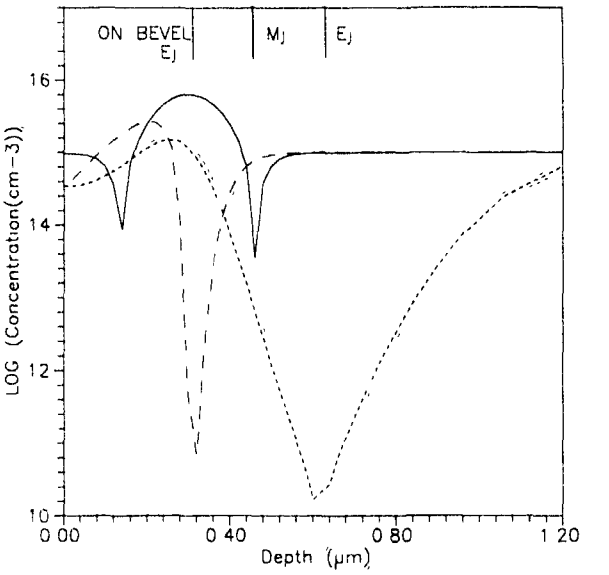

Fig 3 Simulated concentration profiles for a low ion implantation dose (———) dopant profile in depth, (— — —) free-carrier profile in depth; and (- - - - - -) on-bevel carrier profile

In fig 4 the ratio EJ/MJ versus ion implantation dose is plotted for several annealing times In fig 5 the difference between on-bevel EJ and MJ is plotted versus MJ for several ion implantation doses Finally, B im-

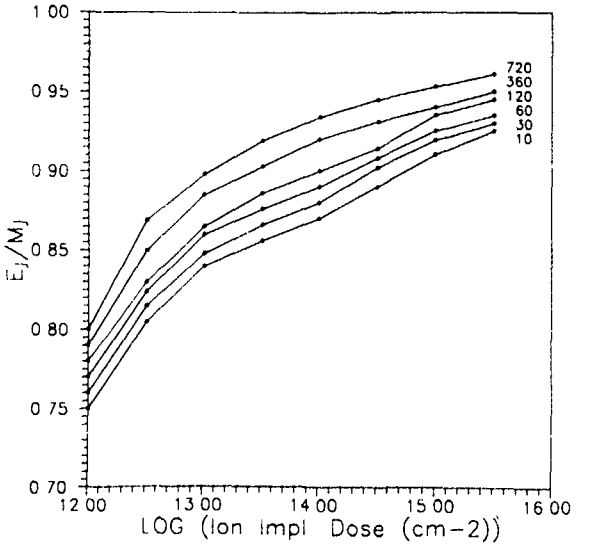

Fig 4 Ratio between on-bevel electrical junction and metallurgical junction (EJ/MJ) versus ion implantation dose for several annealing times [min]

plantations with doses ranging from 10^{11} to 3×10^{15} cm^{-2} at 100 keV have been performed on n-type silicon wafers ($N_D = 1 \times 10^{15}$ cm^{-3}). After 1000 Å PECVD SiO_2 deposition the samples have been annealed by incoherent-light rapid thermal annealing during 10 s at 1150 °C. The resulting profiles have been measured by SR and SIMS.

In the SIMS measurements, made with an Atomika 1000, it is difficult to determine MJ because in the range of 10^{15} the measurements are very noisy. However, if we compare the SIMS and SR tail region of the profiles, the effects of carrier spilling can clearly be seen. In the SR measurements (fig. 6) we obtain an abnormal displacement of the distribution maximum towards the surface when the ion implantation dose decreases. This effect appears already in doses at which it is impossible to explain it as a consequence of carrier spilling. We think that this effect can be related to the algorithm used to make the transformation from the SR depth profile to the resistivity depth profile.

For the larger doses if we compare the experimental results with the results of simulation with SUPREM we observe an enhanced diffusion. The effective diffusion coefficient is approximately 4 times larger than that for a normal process, in agreement with known boron-transient-enhanced diffusion results [10]. For the lower doses the quantity of carriers measured by SR is lower than the dose introduced, considering the reduction introduced by carrier spilling. We think that this is due to an incomplete activation of dopant impurities or to the existence of crystallographic defects that favour carrier recombination, and that have a higher relative importance when the carrier concentration is smaller.

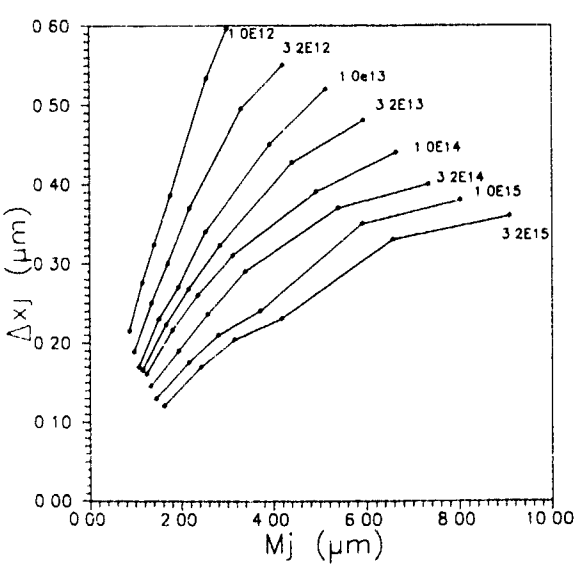

Fig 5 Difference between metallurgical junction (MJ) and on-bevel electrical junction (EJ) versus MJ for several ion implantation doses.

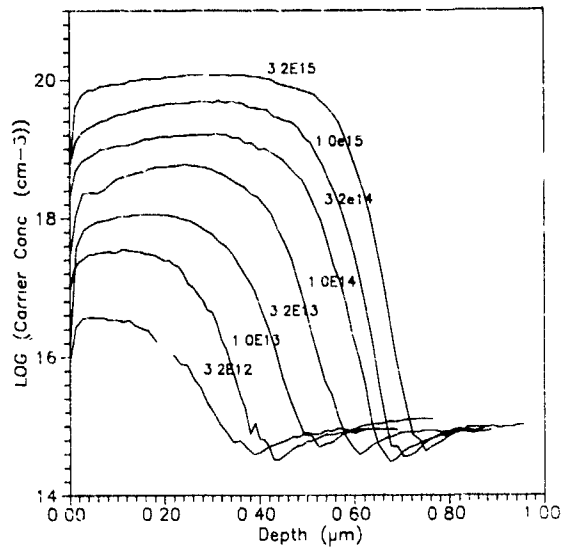

Fig 6 SR measurements of the free-carrier profile for several ion implantation doses at 100 keV after a rapid thermal annealing

4. Conclusion

Presently SR is one of the most commonly used techniques in characterizing ion-implanted profiles. With the improvements in sample preparation, probe conditioning and algorithms for the calculation of correction factors, highly accurate measurements can be obtained. However, several problems have been identified in the last few years, mainly due to the reduction in device geometries. SR measures an electrical on-bevel carrier profile which may be quite different from the corresponding atomic dopant profile. This is due to carrier spilling caused by doping density gradients and special boundary conditions in a beveled surface.

We have studied this phenomenon by process modeling to determine dopant impurity profiles, and then free-carrier profiles have been calculated by solving the two-dimensional Poisson equation. The main discrepancy is that for any profile with a junction the on-bevel electrical-junction location will always be shallower than the metallurgical junction, and also the total quantity of carriers is lower than the implanted dose.

We have fabricated several samples by making ion implantations and annealings in different conditions. The samples have been characterized by SR and SIMS. The predicted results are in good agreement with the measured values.

References

[1] R.G. Mazur and D.H Dickey, J. Electrochem Soc. 113 (1966) 255

[2] Semiconductor Measurement Technology· Spreading Resistance Symposium, Nat. Bur. Stand (US) Spec Publ. 400-10 (1974).

[3] R G. Mazur and G.A Gruber, Solid State Technol. 11 (1981) 64.

[4] P A Schumann and E E Gardner, Solid-State Electron. 12 (1969) 371

[5] J C. Irvin, Bell Syst Tech J. 41 (1962) 387

[6] S.M Hu, J Appl Phys. 53 (1982) 1499.

[7] A. Casel and H. Jorke, Appl. Phys Lett 50 (1987) 989.

[8] TSUPREM-4, Copyright Technology Modeling Associates, Inc.

[9] PISCES-2B, Copyright Technology Modeling Associates, Inc.

[10] R B Fair, Mater. Res Soc. Symp. Proc 35 (1985) 381.

Nuclear Instruments and Methods in Physics Research B55 (1991) 266–268
North-Holland

Thermal wave characterization of silicon implanted with MeV phosphorus ions

M. Anjum and G.S. Sandhu
Micron Technology Inc., 2805 East Columbia Road, Boise, ID 83706, USA

S. Cherekdjian and W. Weisenberger
Ion Implant Services, 1050 Kifer Road, Sunnyvale, CA 94086, USA

We have performed laser-induced photothermal reflectance measurements on p-type (100) silicon wafers implanted with phosphorus in the energy range of 0.5 to 3 MeV. The dose for implants was varied from 1×10^{12} to 1×10^{14} ions/cm^2. The variation of thermal wave signal for different implant angles and species has been studied. The signal was sensitive to the dose, energy and tilt angle of the implantation. We have determined that this technique can be used to monitor high energy implantations into Si substrates.

1. Introduction

Photothermal reflection spectroscopy is a contactless, nondestructive and quick technique for monitoring ion implanter dose accuracy and uniformity. This method uses a modulated laser beam to induce thermal oscillations in the silicon surface and a probe laser to measure resulting fluctuations in the surface reflectivity. The measured signal is dependent on the level and distribution of damage in the surface layers of the sample and thereby on the implanted dose.

Thermal wave measurements on Si substrates implanted with various ion species up to the energy of 400 keV and doses ranging from 1×10^{12} to 1×10^{15} ions/cm^2 have been reported previously [1–4]. It has been stated that this technique can evaluate a depth of approximately 3 μm from the sample surface and measure a minimum dose of 1×10^{10}/cm^2. Little has been reported on the usefulness of this technique for monitoring dose and uniformity in high energy (> 0.5 MeV) ion implanted Si substrates. High energy phosphorus and boron implantation are increasingly coming into use for manufacturing advanced IC chips, for example, in fabrication of retrograde wells and buried grid layers to reduce soft errors in DRAMs. We have performed thermal wave measurements on p-type silicon wafers implanted with high energy phosphorus ions. The sensitivity of the thermal wave method to dose and energy of high energy implantations into silicon is of primary interest in this study.

2. Experimental

P-type (100) Si wafers of 150 mm diameter with 250 Å of thermal SiO_2 were implanted at room temperature with phosphorus ions having energies from 0.5 to 3 MeV using a Genus 1500 X ion implanter at Micron Technology and Ion Implant Services. The implantations were done at a wafer orientation of 25° and tilts of 0 to 7°. Thermal wave measurements were taken immediately after the implantation using a TP-300 made

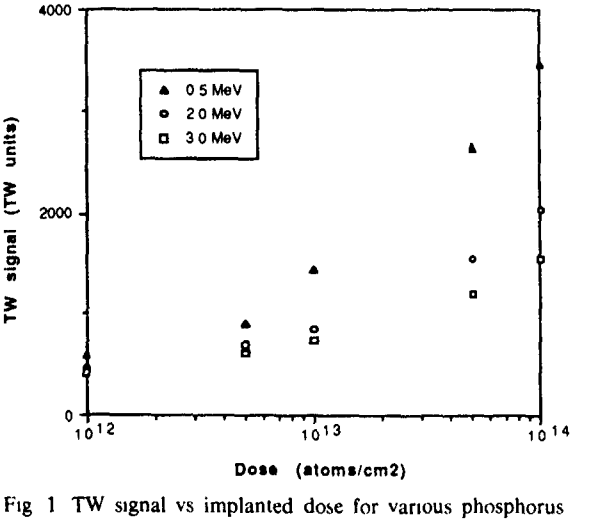

Fig. 1. TW signal vs implanted dose for various phosphorus ion energies in Si.

0168-583X/91/$03.50 © 1991 – Elsevier Science Publishers B.V. (North-Holland)

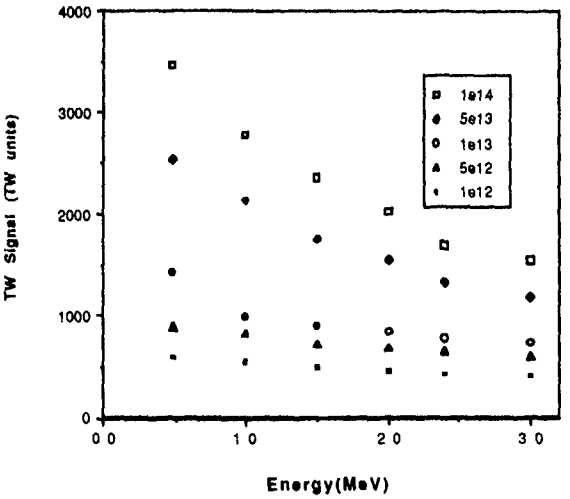

Fig 2 TW signal as a function of phosphorus ion energy at various doses.

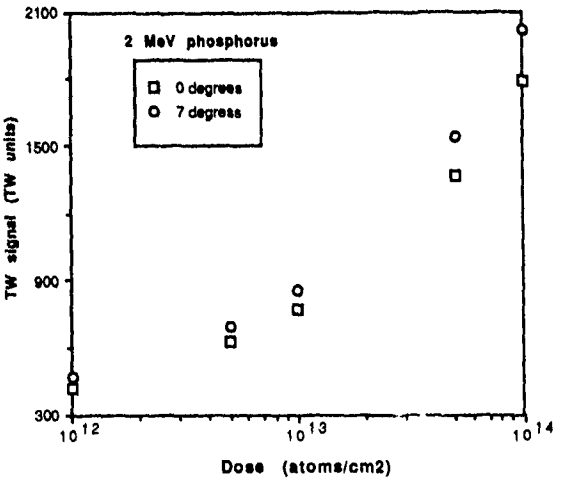

Fig. 3. Sensitivity of TW readings to implant tilt angles for 2 MeV phosphorus implantation into Si

by Therma-Wave Inc. Contour maps of the thermal wave signal and oxide thickness were generated in each case to check for dose uniformity across the wafers. The results are presented in otherwise undefined "thermal wave units" presented by the system. The reader should not expect to reproduce the absolute values in thermal wave units since it depends upon the system used and the measurement and calibration procedure employed. In addition, the thermal wave signal can also depend on the surface states which is a function of sample preparation. However, the various trends observed during this study should be universally repeatable.

3. Results and discussion

Fig. 1 shows the variation in thermal wave (TW) signal with dose for various energies of phosphorus implants into p-type Si. The standard deviation on the contour plot was generally around 0.5% for these sets of data. For the same dose, the TW signal decreases with an increase in energy. At the same time, the difference in TW signals, at different energies, decreases at lower doses. For higher energies, the peak of the damage produced during implantation lies deeper into the substrate. Consequently, thermal waves propagate through larger distances resulting in a smaller TW signal. The TW signal as a function of ion energy for various doses

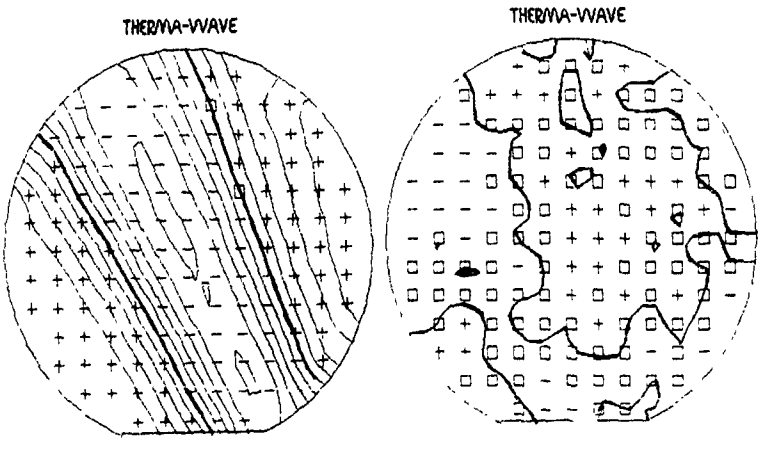

Fig. 4. Contour maps of TW signal showing the effect of channeling for 2 MeV phosphorus ion implantations into Si at (a) 0° and (b) 7° tilt, and 25° rotation

in plotted in fig. 2. The sensitivity of the TW signal to energy is small at the dose of 1×10^{12} ions per cm^2.

Fig. 3 shows that the TW signal is sensitive to the tilt angle during the implantation. The change in damage distribution for channeling directions results in a lower signal. However, the percentage difference in the TW signal between 0 and 7° implants is constant as shown in fig. 3. This indicates that the random and channeled fraction of the incident ions are the same, below the critical dose for amorphization. This gives rise to similar differences in total damage between 0 and 7° implantations at various doses.

Fig. 4 shows contour maps of the TW signal for 2 MeV P implantation into Si at 0 and 7° tilt angles. The 0 and 7° implants resulted in standard deviations of 6.89 and 0.29% respectively. This large difference in standard deviations is due to the effect of channeling. The TW signals for implants with the same energy and dose for P and As ions are shown in fig. 5. The larger signal for As results from a shallower implant range as well as larger damage produced per As ion compared to P ions.

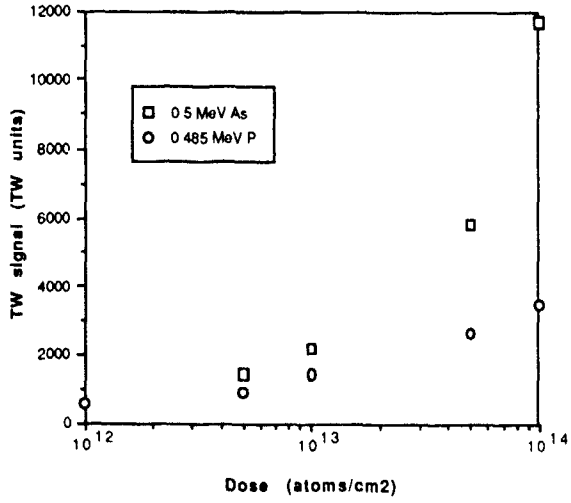

Fig. 5. Variation of TW signal with implanted species. Arsenic ions having the same energy produce larger TW signal compared to phosphorus ions implanted to the same dose.

4. Summary

Thermal wave monitoring of high energy ion implants into silicon has been performed. The sensitivity of the thermal wave signal to energy, dose, implant angle and ion species has been reported. It has been demonstrated that the thermal wave signal is sensitive to energies up to 3 MeV for phosphorus ions implanted into Si. This technique can be used to monitor high energy ion implantations into Si.

Acknowledgement

We thank T. Johnson, R. Burton, C. Locke and other implant engineering staff at Micron Technology Inc. We would also like to thank R. Kuzbyt and A. McFaddan at Ion Implant Services and Neil Bonine from Genus Inc.

References

[1] W.L. Smith, A. Rosencwaig and D.L. Willenborg, Appl. Phys. Lett. 47 (1985).
[2] B.J. Kirby, L.A. Larson and R-Y. Liang, Nucl. Instr. and Meth. B21 (1987) 550.
[3] K. Ishikawa, M. Yoshida and M. Inoue, Nucl. Instr. and Meth. B37/38 (1989) 317.
[4] I.A. Vitkin, C. Christofides and A. Mandelis, Appl. Phys. Lett. 54 (1989).

Nuclear Instruments and Methods in Physics Research B55 (1991) 269–274
North-Holland

RTP temperature uniformity mapping

W.A. Keenan and W.H. Johnson
Prometrix Corporation, 3255 Scott Blvd. Santa Clara, CA 95054, USA

D. Hodul
Varian Research Center, 611 Hansen Way, Palo Alto, CA 94303, USA

D. Mordo
AG Associates, 1325 Borregas Avenue, Sunnyvale, CA 94089, USA

This paper presents innovative software developed to help generate a temperature calibration curve and to mathematically manipulate and combine multi-point wafer maps The software automatically applies the calibration curve to a map of film parameters to provide a quantitative map of temperature uniformity Several process examples are presented to demonstrate the flexibility and convenience of the software

1. Introduction

Temperature uniformity is a critical parameter in RTP equipment because of the very short duration of the heating and cooling cycles Unfortunately, it is extremely difficult to measure temperature accurately and non-invasively at a single point on a wafer during RTP – much less to directly map temperature uniformity over the wafer surface This situation has led to the indirect measurement of temperature uniformity by mapping an appropriate temperature-dependent material property of the processed wafer, such as film thickness or sheet resistance Several techniques are currently used for the indirect measurement of temperature uniformity in RTP equipment, including thermal oxide growth, activation annealing of very-high-dose ion implants, and silicide sintering. In order to use any of these methods, it is necessary to establish a calibration curve of the appropriate materials parameter as a function of temperature In some cases it is also necessary to compare or mathematically manipulate (e g. add, subtract, ratio etc.) the results of several wafer maps, each containing hundreds of data points. Doing this data reduction by hand is time-consuming and does not lend itself to routine process monitoring or quality control

2. Calibration curves

The most obvious application of generating a calibration curve and applying it to a wafer map is mapping ion implant dose uniformity from a sheet resistance map. It is necessary to input the sheet resis-

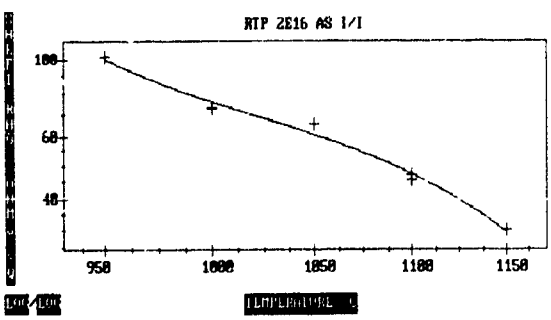

Fig 1 Sheet resistance versus RTP temperature for a wafer implanted with arsenic at 80 keV with a dose of 2×10^{16} ions/cm^2

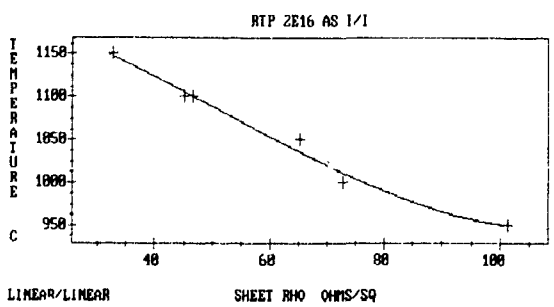

Fig 2 Calibration curve of RTP anneal temperature versus sheet resistance for a 10 s anneal

0168-583X/91/$03 50 © 1991 – Elsevier Science Publishers B V (North-Holland)

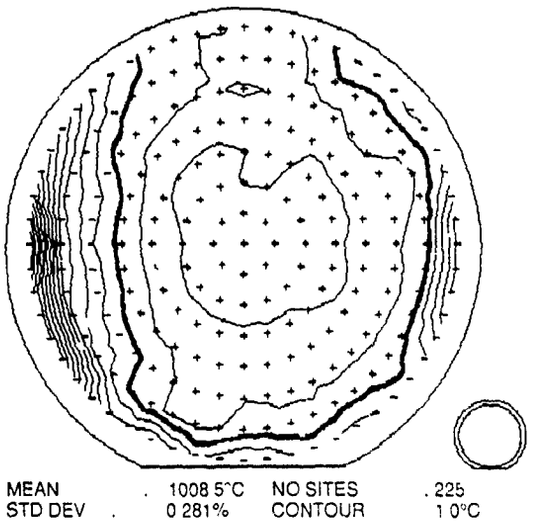

Fig 3 Temperature-uniformity map derived from a sheet-resistance map for a wafer RTP annealed at 1090 °C for 10 s

tance as a function of dose in the calibration curve. This can be done either from experimental results around the dose of interest or from calculations from SUPREM or other process modeling software. The calibration curve software can switch or interchange the *X*- and *Y*-axes which interchanges the independent and dependent variables. In this case the sheet-resistance and dose axes are switched to give a dose versus sheet-resistance curve. The software provides a polynomial fit of the raw data, which is applied to the sheet-resistance map to generate a dose-uniformity map.

3. Activation of ion implant

When rapid thermal processing was first introduced, the primary application was annealing ion-implanted wafers [1–3] It was quickly observed that the sheet-resistance uniformity was a very good indication of the temperature uniformity during the anneal. Several round robins [4] have been conducted by the Greater Silicon

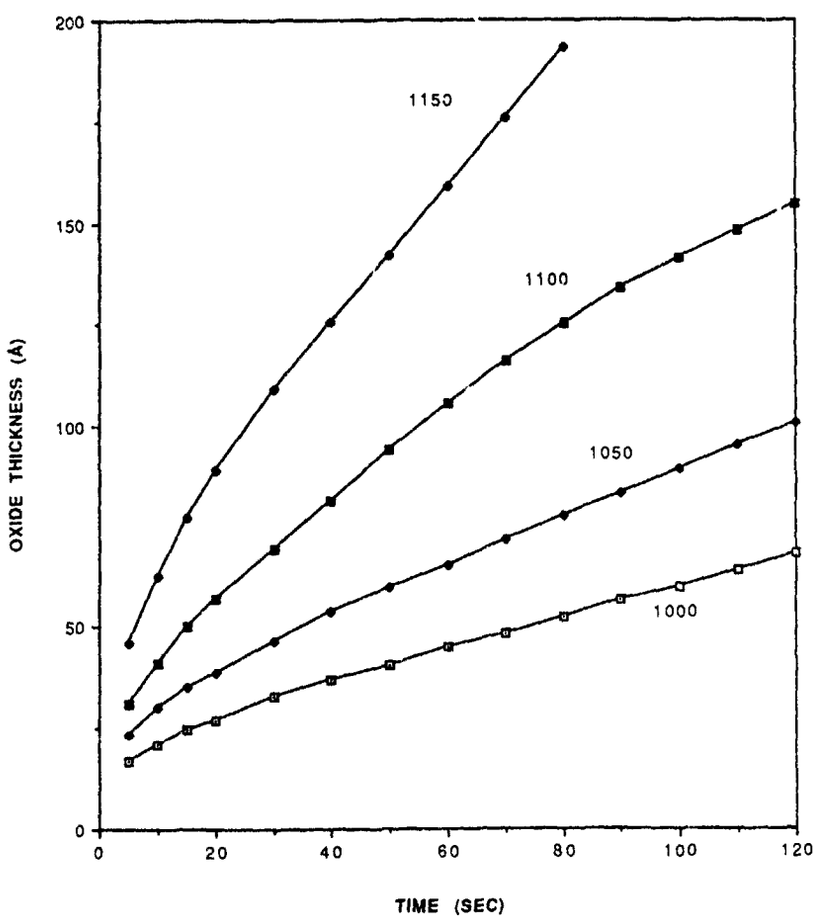

Fig. 4 AG Associates isothermal oxide thickness versus time for several oxidation temperatures between 1000 °C and 1150 °C.

Valley Implant Users Group to verify the uniformity and repeatability available from the various RTP vendors. RTP vendors themselves use ion-implanted wafers as a check of the temperature uniformity.

An experiment was conducted using 150 mm p-type ⟨100⟩ wafers to demonstrate the software. A screen oxide of 200 Å was grown on these wafers at Varian Research using their RTP system. The wafers were then implanted with 50 keV arsenic at a dose of 2×10^{16} ions/cm^2. One wafer was used to verify the emissivity of the backside of the wafer in order to obtain accurate temperature readings with an optical pyrometer. One wafer was furnace-annealed to verify the implant uniformity. The other six wafers were processed at temperatures ranging from 950 °C to 1150 °C in 50 °C steps. Two wafers were processed at 1100 °C to check the repeatability. Since the pyrometer is positioned below the wafer and its field of view includes only a small area in the center of the wafer, the center of each wafer was mapped using 49 sites and a test diameter of 1 cm to develop the sheet-resistance versus temperature calibration curve. The average sheet resistance of each wafer is plotted as a function of the anneal temperature in fig. 1

The software can provide a third-order fit of the data, as well as second- and first-order fits. Using the software to interchange the X- and Y-coordinates, fig. 2 shows the data plotted as temperature versus sheet resistance. This provides the polynomial needed to convert any sheet-resistance value into a temperature value. One wafer had a mean sheet resistance of 73.5 Ω/□, with a standard deviation of 1.28%. Applying the polynomial of fig. 2 to each of the 225 R_s values, the temperature uniformity map of fig. 3 is generated. The mean temperature is 1008 °C and the standard deviation is 2.8 °C or 0.28%. The R_s and T maps are of course similar in appearance with the scale and contour interval changed. The standard contour interval in the temperature map is 1 °C, so the distribution of temperature across the wafer is easily visualized. The flat temperature distribution in the center of the wafer decreases rapidly toward the sides of the wafer. It must be emphasized that to reach the target temperature as rapidly as possible the temperature was ramped up extremely fast, using a ramp rate of 200 °C/second. It was to be expected that this fast ramp rate would seriously degrade the uniformity.

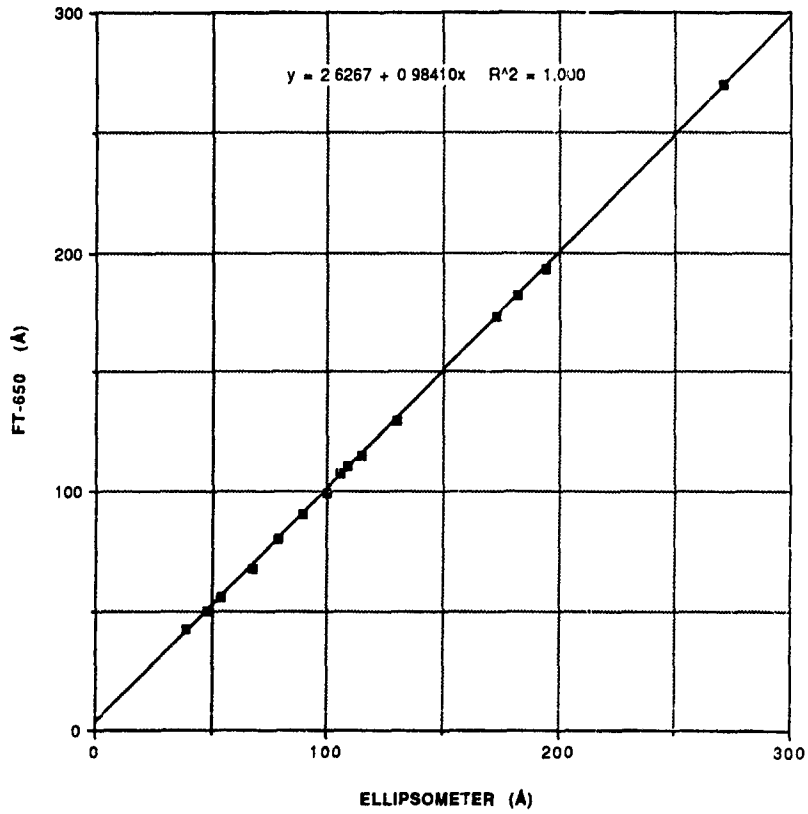

Fig 5 Customer correlation curve of FT versus ellipsometer measurements on wafers with oxides ranging from < 40 to 300 Å in thickness, showing excellent agreement.

4. Very thin oxide layers

One exciting recent application of rapid thermal processing is growing of very thin oxides [4–7]. Fig. 4 shows a set of isothermal growth curves for temperatures ranging from 1000 °C to 1150 °C generated at AG Associates and measured using an ellipsometer. In order to conveniently map oxides below 100 Å, an instrument must be quick and extremely reproducible. It would be convenient if the instrument were also accurate. Unfortunately, there is no standard reference material (SRM) for very thin oxides. It is only recently that the National Institute of Science and Technology (NIST) (formerly known as NBS) introduced a set of three thermal oxide standards with thicknesses of 500, 1000 and 2000 Å.

The reference method always cited in evaluating any thin-film thickness measurement is the ellipsometer. Fig. 5 shows the results of a customer study comparing ellipsometer and Prometrix FT measurements for oxides ranging in thickness from 40 to 300 Å. The FT is a microscope-based film-thickness measurement system using the CARIS technique (constant-angle reflected interference spectroscopy). The resultant correlation coefficient is 1 and with an offset of 2 Å. The FT has a variable spot size ranging from 4 to 40 μm depending on the objective used. The system is capable of repeat-

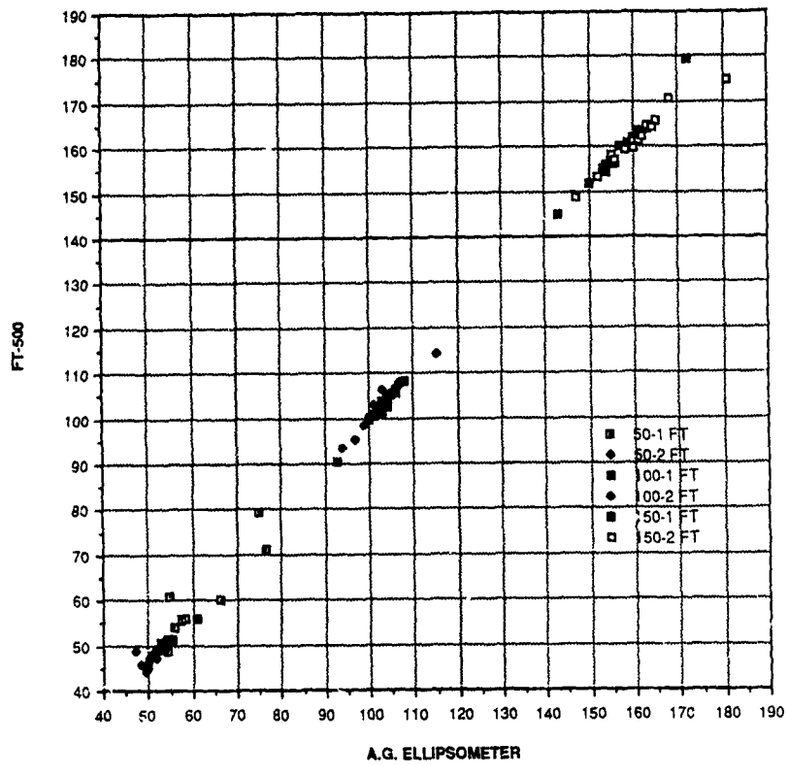

Source	Sum of Squares	Deg of Freedom	Mean Squares	F-Ratio	Prob>F
Model	2 31e+5	1	2 31e+5	7 05e+4	0 00e+0
Error	3 66e+2	112	3 27e+0		
Total	2 31e+5	113			

Coefficient of Determination (R^2)	9 98e-1
Adjusted Coefficient (R^2)	9.98e-1
Coefficient of Correlation (R)	9 99e-1
Standard Error of Estimate	1 81e+0
Durbin-Watson Statistic	1 61e+0

Fig. 6. FT versus ellipsometer readings (19 readings per wafer) for the six AG Associates thin oxide wafers, with nominal thicknesses ranging from 50 to 150 Å

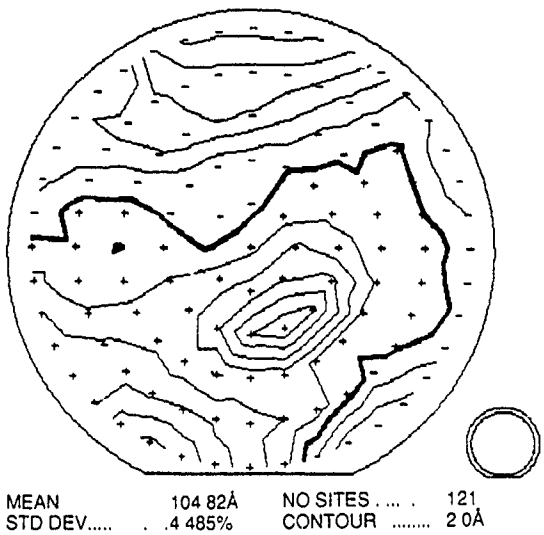

Fig 7 T_{ox} map of a nominal 100 Å wafer for RTP oxidation at 1100 °C for 20 seconds. The mean oxide thickness is 104.8 Å with a standard deviation of 4 7 Å The contour interval is 2 Å.

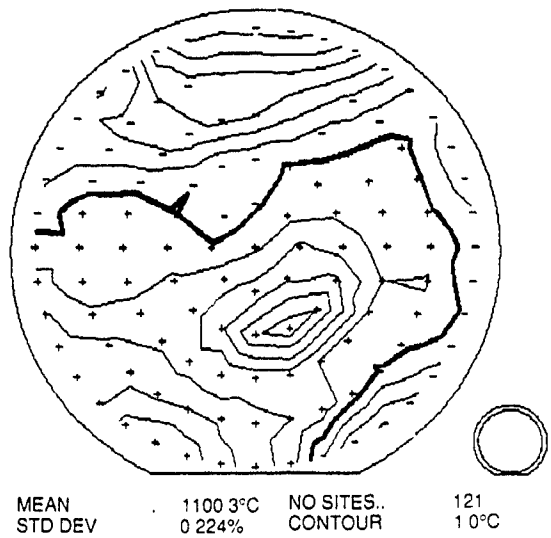

Fig. 9 Temperature map for 1100 ° C, 38 s RTP oxide wafer The mean temperature is 1100.3 ° C and the standard deviation is 2.46 ° C. The contour interval is 1 ° C

ably measuring the oxide thickness down to less than 40 Å. For the wafers used in the thin oxide temperature mapping study, 19 FT measurements per wafer are compared to the ellipsometer results in fig. 6. Six wafers were processed, two at 50 Å, two at 100 Å and two at 150 Å. The coefficient of correlation for this data is 0.999. The flyers or Mavericks are probably due to the positioning accuracy of the ellipsometer and its large spot size (~ 1 mm) compared to the small spot size of the FT (4 μm = 0.004 mm).

The repeatability of the FT results on a 55 Å RTP oxide wafer measured daily for five days was 0.19 A or 0.34%, which is excellent for such a thin oxide. The map in fig. 7 is an oxide thickness map made with 121 sites with a 130 mm test diameter. The contour interval is 2 Å and the standard deviation is 4.7 Å. This oxide was grown at AG Associates using a nominal temperature of 1100 ° C for 38 seconds. Going back to the isothermal T_{ox} versus temperature curves (fig. 4), the data for 38 seconds of T_{ox} was plotted versus temperature and converted into temperature versus oxide thickness in fig. 8. The polynomial was used to convert the oxide thickness map to a temperature-uniformity map as shown in fig. 9. The average temperature is 1100.3 ° C with a standard deviation of 2.46 ° C or 0.22%. The temperature interval is 1 ° C Measurement time is approximately 5 seconds per site, and for 121 sites, this requires about 10 minutes to map the wafer.

The next wafer measured had been targeted for a 50 Å oxide thickness. The average measured thickness is 47 Å with a standard deviation of 3 Å. The wafer was processed at 1050 ° C for 20 seconds The calibration curve of T vs T_{ox} was again derived from fig 4 Fig. 10 shows the temperature versus oxide thickness for an oxidation of 20 seconds. The polynomial for this curve was applied to the T_{ox} map to generate the temperature uniformity map of fig. 11. The mean temperature is 1042.5 ° with a standard deviation of 1.4%. The low temperature at the back of the wafer (opposite the flat) may have been caused by the gas flow into the chamber at this point.

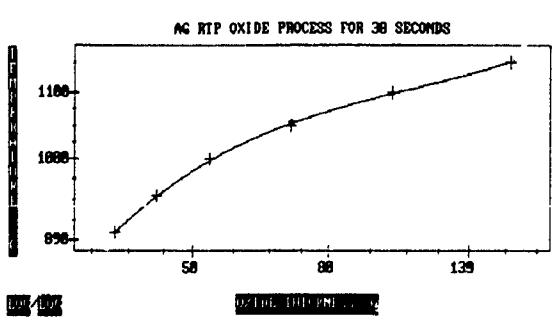

Fig. 8. Temperature versus T_{ox} for a 38 s RTP oxide.

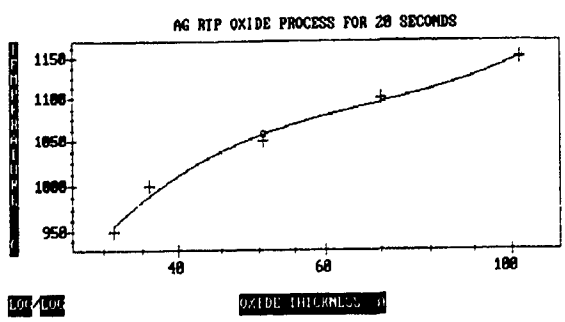

Fig 10. Temperature versus T_{ox} for 20 s RTP oxide.

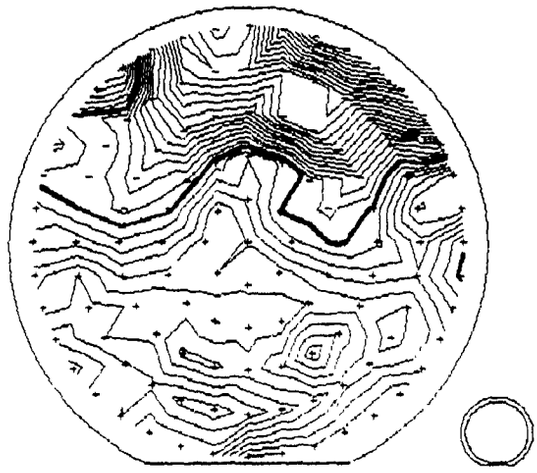

Fig 11 Temperature uniformity map for wafer with 20 s 1050°C RTP oxide The mean temperature is 1042 5°C with a standard deviation is 14 73°C The contour interval is 2°C

The ability to accurately and reproducibly measure oxides of this thickness makes temperature mapping of RTP equipment quick and convenient.

5. Summary and conclusion

The software presented here provides the ability to quickly generate calibration curves and apply them to wafer maps. In order to use this for temperature mapping, a measurable parameter such as T_{ox} or R_s must be plotted as a function of temperature. The software then generates a temperature calibration curve versus the parameter. This calibration curve can automatically be applied to the parameter map to generate a temperature map. The mapping temperature of an RTP system has always used some physical parameter of a wafer processed in the tool. This software makes conversion of a parameter map to a temperature map quick and easy.

References

[1] R Kakoschke and K Ehinger, Nucl. Instr. and Meth. B37/38 (1989) 823.
[2] D Hodul and S Metha, Nucl. Instr. and Meth. B37/38 (1989) 818.
[3] R Kakoschke, Nucl Instr and Meth B37/38 (1989) 753
[4] C.B. Yarling and W.A Keenan, Nucl Instr and Meth. B37/38 (1989) 828
[5] S. Mehta, C Russo and D. Hodul, Proc. SPIE, Los Angeles (Jan 1986) p 123
[6] S. Mehta, D. Hodul and C Russo, Proc 6th Int Conf. on Ion Implantation Technology, Berkeley, CA, J Phys. 4 (1986) 629
[7] M Moslehi, S Shatas and K Saraswat, Appl Phys Lett 47 (1985) 1353
[8] J. Nulman, J Krusius and A. Gat, IEEE Trans. Electron Devices ED-6 (1985) 205

Nuclear Instruments and Methods in Physics Research B55 (1991) 275–280
North-Holland

Ion implant standard

L.A. Larson [1]
National Semiconductor, A2535, PO Box 58090, Santa Clara, CA, USA

W.A. Keenan and W.H. Johnson
Prometrix Corporation, 3255 Scott Blvd, Bldg 6, Santa Clara, CA, USA

The Greater Silicon Valley Implant Users Group (GSVIUG) has been working with the American Society for Testing Materials (ASTM) and the National Institute of Standards and Technology (NIST, previously known as NBS) to develop a standard for ion implantation. This standard would address two critical needs of the industry: (1) standard reference material (SRM) for certifying and calibrating equipment, and (2) a recommended standard procedure for fabricating such a standard.

The SRM would be a wafer that had been implanted with a specified species, energy and dose. Its average sheet resistance and uniformity would be certified to be within certain tolerances. It would be used to verify the performance of the four-point probe and sheet resistance mapping equipment and to calibrate analytical characterization techniques such as secondary ion mass spectroscopy (SIMS), Rutherford backscattering spectroscopy (RBS) and spreading resistance profiling (SRP). An unannealed sample could be used to calibrate Thermawave, ellipsometer and other optical tools and to verify annealing systems. The standard procedure would prescribe the recommended steps to produce the same wafer in the fab. This would help determine if an implanter is operating correctly at the specified conditions.

We have reviewed all the previous implant round robins and studies and solicited input from implant vendors and implant service organizations in recommending a set of implant conditions for a proposed standard. Particular attention was paid to the requirement of stability over time and minimum variation with ambient temperature. Fabrication specifications for species, energy and dose are detailed. Plots are also presented for the sensitivity to various parameters that could influence the results, such as substrate resistivity, screen oxide thickness, anneal time and temperature and measurement conditions.

1. Introduction

In the course of the last five years the Greater Silicon Valley Implant Users Group (GSVIUG) has held two round robin experiments in an attempt to develop a common basis for discussion when differences in dosimetry are noticed [1,2]. The effort to develop these works made it abundantly clear that no standard exists either for the results of an implant or for the methodology to test it. In the literature, three other works exist that approach the same concerns [3–5]. All five efforts worked to characterize different implants. Only two of them detailed the processing conditions well enough for a realistic effort to reproduce the results [2,3]. In the work by Perloff [3], the implant choosen was 5×10^{14} boron/cm^2 at 150 keV and it was annealed at 950 °C in dry nitrogen for 30 min. This recipe was implanted by 85 machines throughout the industry and the wafers processed together. The results indicated that there was a spread in the dosimetry used in various fabs that was as large as 4% in 1-sigma deviation. In the previous Users Group paper by Larson [2] three recipes were tested on about 50 machines throughout the industry. It didn't help, the spread was still at the 4% level. This spread was shown to have components both from differences in the fleets of machines from individual manufacturers and from differences in the normalization of those machines as they are inserted into well-established fabs.

The existence of a standard is important to form a common basis for users of both implanters and implant test equipment. In either case, if a user is entirely self-reliant then there is a need only for consistency. However, the user almost always wants to at least communicate with the manufacturer of his equipment. At that point both must deal with the fact that there is a spectrum of different process and test conditions. The set chosen will be the one which makes the best sense to the engineer setting up the equipment. As a result the semiconductor device manufacturer has results which can only marginally be compared to those from the implanter manufacturer, both of which may be different to those the probing company recommends. Semiconductor manufacturing companies have to take account of this issue in particular. When processes are trans-

[1] Present address: Sematech, 2706 Montopolis, Austin, TX 78741, USA.

0168-583X/91/$03.50 © 1991 – Elsevier Science Publishers B.V. (North-Holland)

ferred between fabs a large amount of the initial effort is spent in simply recreating the implant dose! This is due to the differences in calibration mentioned above, yet this is difficult and time consuming to trace as each fab (if not each implant!) has to be individually cross-calibrated.

The production of an implant standard and/or a standard procedure has been a difficult concept for our normal standard producing institutions, the ASTM and NIST. The issue involved is that the processing procedures necessary to do this are sufficiently involved (and not standardized either) that the result must necessarily be imprecise. This is a problem for institutions that owe both their pride and reputation to the production of materials and procedures to the best available standard of precision. The appropriate people in both organizations have agreed that this is a noble cause and are willing to to be "driven" by the implant community. The purpose of this paper is then to review the work which has been done to date, to examine the variabilities present in standard processing, and to propose a standard implant and process for discussion.

2. Studies reviewed

Previous round robins and studies were reviewed in proposing an ion implant standard. A comparative listing of these are provided in table 1. Almost all of these papers stress the need for standards. The first ion implant round robin was conducted by Gan, Perloff, and Wahl [3] in 1980. This is the best documented round robin to date and also the one with best control over the wafer's variability. The authors provided all of the monitor wafers for the round robin. It was demonstrated that sheet resistance could be used to cross-calibrate implanters. A dose sensitivity (that is the percent change in sheet resistance divided by the percent change in dose) of 0.77 was demonstrated as well as an energy sensitivity of 0.12. This paper was first to call for

Table 1
A comparative listing of dosimetry studies that have been published

Date done	Authors	Ref	Species	Energy [keV]	Dose [cm^{-2}]	Comments
1980	Gan, Perloff and Wahl	NIM (81) SST (81) [3]	B	150	5×10^{14}	Supplied wafers, best documented, call for standard
1982	Ryding	NIM (83) [6]	B	50	5×10^{15}	Call for process and measurement standard
			As	80	1×10^{15}	
			P	80	2×10^{15}	
1982	Gruber	SST (83) [7]	all	several	many	In process testing, 4PP, spreading resistance and CV
1982	Markert and Current	SST (83) [4]	several	several	several	Species and energies not identified
			B	150	5×10^{14}	
1984	Current and Keenan	NIM (85) SST (85) [1]	B	180	1×10^{12}, 5×10^{12}, 1×10^{13}, 1×10^{14}	GSVIUG, snapshot of production implanters, also checked 4PP mappers
			As	80	5×10^{13}, 5×10^{14}, 5×10^{15}, 5×10^{16}	
1982–85	Steeples	NIM (85) [8]	B	150	5×10^{14}	Stressed need for standard, determined sensitivity to process parameters
			As	80, 160	1×10^{15}, 4×10^{15}, 1×10^{16}	
1986	Larson and Kennedy	NIM (87) [9]	B	several	several	All R_s normalized to target, E and doses not identified
			As	several	several	
1986	Larson	ECS (88) [2]	B	80	3×10^{13}, 3×10^{15}	Restressed need for standard, also studied all 4PP mapping system
			As	80	3×10^{15}	
1988	Glawischnig and Lang	NIM (89) [11]	As	80	3×10^{15}	Also studied 4PP system, German Implant Users Group
			P	130	5×10^{15}	
1988	Han et al	ICSICT (89) (China) [5]	B	60	1×10^{14}	Reiterated call for standards

an industry wide ion implant standard. Ryding [6] used sheet resistance maps to compare different Faraday designs and the effects of pressure and beam current and energy on uniformity. Ryding called for both process and measurement standards that would help evaluate the performance of different implanters. Gruber [7] used different electrical testing techniques, including CV, sheet resistance, and spreading resistance to evaluate the performance of several implanters at Siliconix. All the Siliconix implants were listed, but no attempt was made to focus on a standard. Markert and Current [4] reproduced the conditions of the original round robin and also included several other implants, the energies of which were not specified. Their paper also included data for the double implant technique for sheet resistance monitoring of low dose. Results were also included from Ken Steeples of Eaton/Nova and from 23 different implanters within the Philips Corporation located at nine locations in Europe. Unfortunately, the energies and species of these additional implants were not specified Current and Keenan [1], under the auspices of the Greater Silicon Valley Ion Implant Users Group (GSVIUG), did a round robin to check the performance of production implanters being used by the members. This "snap-shot" was completed in two months. The implant conditions were carefully specified, however the participants supplied their own wafers. In the course of this study, five sheet resistance mapping systems, all OmniMaps, were surveyed using boron implants ranging from 1×10^{12} to 1×10^{14} ions/cm^2. This was the first survey of implant monitoring equipment. The need for standards was reiterated. Steeples [8] reported repeatability results for Eaton implanters including a hundred different machines over a three-year period. The species, energy and dose were carefully specified. The Gahn and Perloff energy and dose conditions were included. The sensitivity of the sheet resistance to various process parameters were analyzed. He strongly stressed the need for a standard. Larson and Kennedy [9] reported the results of several dose accuracy experiments at National Semiconductor. Unfortunately the sheet resistance data were normalized by dividing by the target sheet resistance. The actual energies and doses of the implants were not specified and cannot be used to reach a consensus. Larson [2] later reported the results of an industry-wide GSVIUG round robin of dosing accuracy. The implant conditions were specified. The participants provided their own

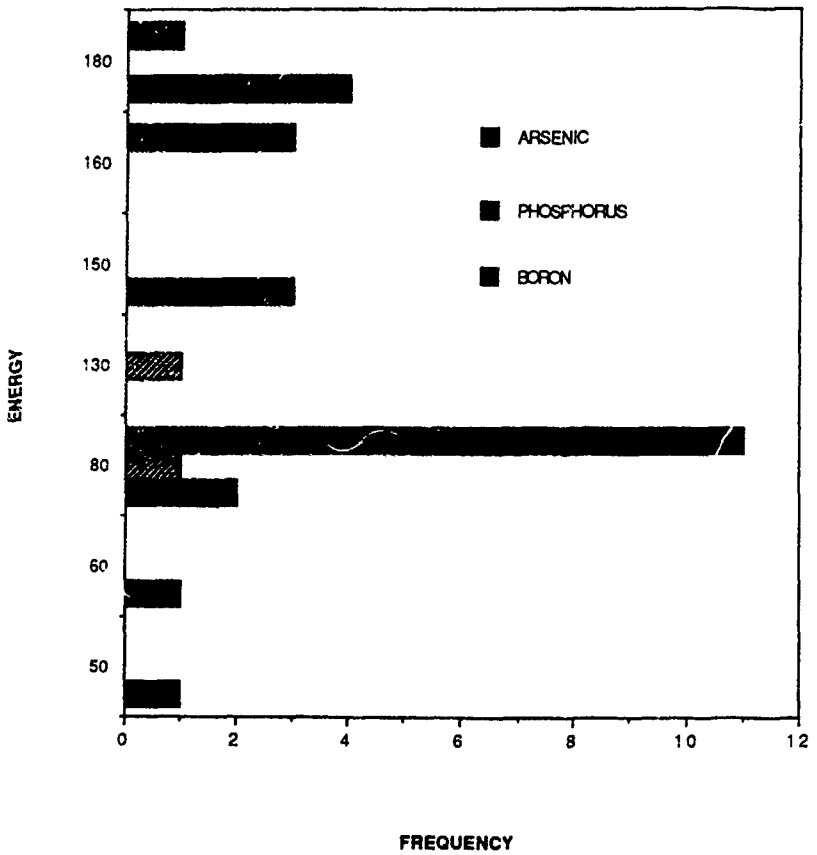

Fig 1. Histogram of the frequency of occurrence of energies and species in implant dosimetry studies (round robins and papers).

wafers, which introduced variability in substrate resistivity and screen oxide. The need for a standard was again stressed. Larson [10], using the wafers from this study, was also able to evaluate the performance of all the sheet resistance mapping equipment available at the time. This is the only evaluation of this type that has been published to date. Glawischnig and Lang [11], under the auspices of the German Implant Users Group, conducted a round robin of ion implanters and four-point probes. The four-point probe evaluation wafers were all produced and measured at Siemens and sent to twenty sheet resistance mapping systems. Twelve of which were made by Prometrix. The implant round robin implants included arsenic and phosphorous. the doses and energies of which were specified. The participants provided their own wafers, which again would contribute to some of the variability of results. Han et al. [5] conducted the first ion implant round robin in China in 1988. The dose, energy, and species were carefully specified and the wafers and post processing were provided by the National Institute of Metrology of China. This paper stressed the importance of establishing standard evaluation procedures and standards wafers for implanters and the implant process.

The histograms of fig. 1 show the various energies and species used in the above studies. Arsenic at 80 keV is the overall winner as 80 keV is a energy that all production implanters can produce. Phosphorus is mentioned in only two studies. Boron is reported in 11 studies, with the maximum occurrence being for the Perloff condition of 150 keV and 5×10^{14} ions/cm^2. Arsenic is the clear winner with 15 studies, with an energy of 80 keV (11 mentions) and a tie between 1 and 3×10^{15} ions/cm^2 dose (3 mentions each).

The ion implant service companies were polled. There was no consensus on the energy or dose except that 80 and 100 keV shows up repeatedly. Three of the implant machine vendors were sampled. They also showed no consensus, 80 keV was used only once even though it has appeared many times in papers by the same vendors

3. Preferred test conditions

The conditions for testing the implant monitor are nearly as important as the conditions of its production. Unfortunately, page limitations for this volume limit the discussion of this topic. In short, our preferred conditions are:

(1) K&S probe, tungsten carbide tips, 4 mil radius of curvature on tips, 40 mil spacing, 100 g load
(2) Dual configuration probing technique.
(3) Repeatability < 0.2%.

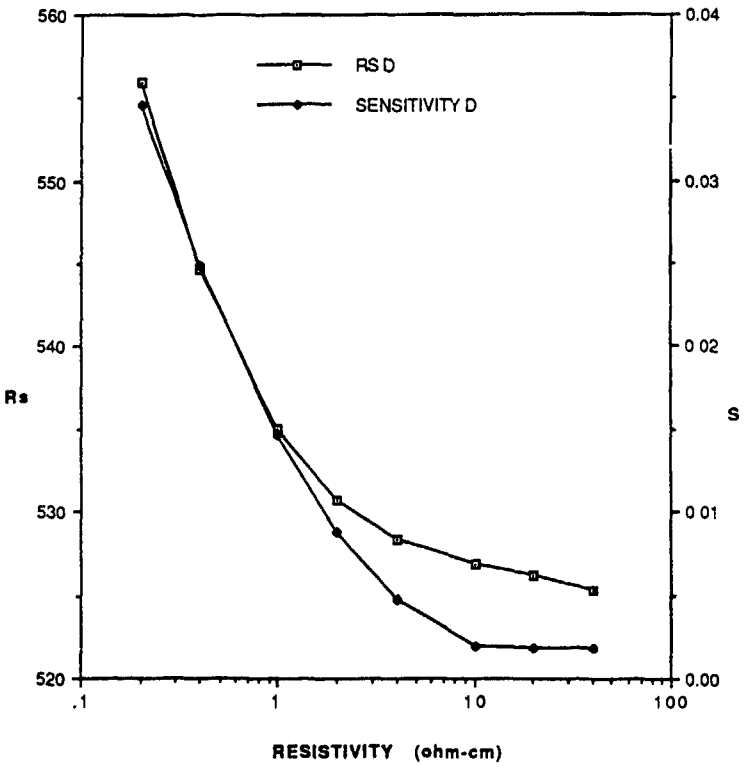

Fig. 2. The relationship of sheet resistance to test wafer resistivity plotted together with the sensitivity to changes in resistivity

(4) Uniform test pattern, < 1 cm^2 per site
(5) Probe current set for a voltage of ~ 7.5 mV.

4. Processing variations

A study of the variations possible in the *processing* of an implant has been carried out using the modelling program SUPREM-III [13]. As one might expect, almost all of the results that can be obtained are cross-coupled to all of the previous choices. This is then an attempt to point out the variations that can occur and to document the variability of the ones considered major.

4.1 Dose / substrate resistivity

The relationship of resistivity/dose to substrate resistivity is shown in fig. 2. In that figure it can be seen that for an implant of 1×10^{14} ions/cm^2 that any base resistivity above 5 Ω cm has a variation of less than 0.5%. Sensitivity, as used in this paper is defined as the percentage change in the sheet resistance as a function of percentage change in the driving parameter. This is shown as the second curve in fig. 2. The relationship between implant dose and substrate resistivity for a given sensitivity will pretty much hold constant as long as the ratio of the two parameters is kept constant. Other regions to avoid are the onset of solid solubility, which is most marked in the region of 5×10^{15} for arsenic, and to avoid having a dose too low to measure reproducibly. The acceptable region for dose is then between 3×10^{13} and 1×10^{15}/cm^2. These can be implanted into wafers in the region of 1–10 Ω, although the higher the substrate resistivity, the more reproducible the result. The basic parameters chosen for the rest of this discussion are an implant of 1×10^{14} ions/cm^2 into a 10 Ω cm wafer of opposite conductivity type.

4.2. Screen oxide

Fig. 3 shows the effect of a screen oxide on an arsenic implant. It also illustrates the sensitivity of the sheet resistance to changes in screen oxide thickness. This was perhaps one of the most startling results of the simulation: all of the dopants showed a significant variation in the resistivity depending simply on whether a screen oxide was there or not. In each case, the difference between 0 Å of oxide and 10 Å (in the simulation) was significant. The general purpose of the screen oxide has been to reduce channeling in implants that are susceptable to this effect, to protect the wafer surface from possible contamination and to raise the surface concentration. This figure illustrates that there is another very important benefit available from using a screen oxide, and that is to make the silicon surface relatively independent of the further treatment it receives. This figure shows that a screen oxide of 100 Å is acceptable in that it does not hold up a sizable percentage of the implant (3% for arsenic), and it is *preferable* to no oxide at all. Channeling implants, such as boron will benefit from an even larger oxide thickness.

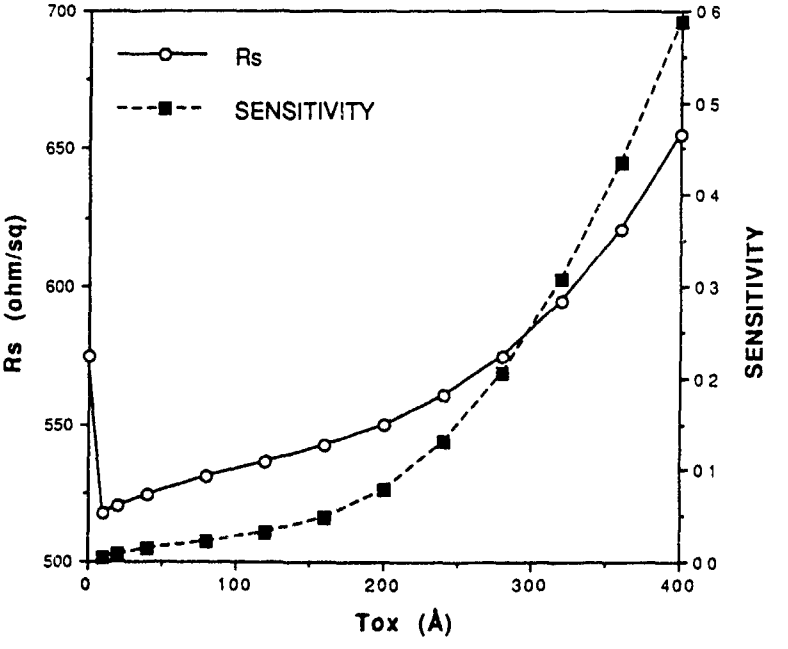

Fig. 3. The effect of screen oxide thickness on subsequent sheet resistance and its sensitivity to that change.

The same figure for boron did not show 3% holdup until a thickness of 1000 Å.

4.3. Anneal

The diffusion characteristics of the dopants are relatively well known and will not be discussed further here. There are two basic points that are appropriate to mention. The first is, in reference to the previous point, the screen oxide. The difference between an oxidizing ambient and a neutral ambient is relatively large. The presence of a screen oxide somewhat mollifies this effect, but as it is harder to maintain a neutral ambient it is preferable to choose a mildly oxidizing one. The other point is that, all enthusiasm for rapid thermal processing aside, it is better to have a long hot anneal to reduce depth effects from the implant, such as channeling. This should also minimize non-uniformities due to temperature distributions, as furnace anneals have been well optimized to remove these effects. The anneal should be chosen such that the final diffusion depth is quite large compared to the implant depth. Note that this makes the choice of energy relatively moot (it should be 80 keV in deference to machines that don't do more than this!). The preferred parameters, based on this reasoning are phosphorus (fast diffusion, low channeling) annealed at 1000 °C for 30 min in an ambient of 5% dry oxygen in nitrogen. In deference to popularity, arsenic is a better choice. This is considerably more popular both as an implanted species and as the subject of tests performed to date. It may be expected that the depth issues resulting from channeling will be relatively small.

5. Conclusions

On the basis of this investigation, the wafer/implant/process that we propose as a standard is:

(1) Starting material: 5–10 Ω cm P⟨100⟩ silicon;
(2) Prepared with a screen oxide of 100 Å;
(3) Implanted with arsenic at 80 keV to a dose of 1×10^{14} ions/cm^2;
(4) Annealed 30 min at 1000 °C in a 5% dry oxygen in nitrogen atmosphere;
(5) Probing should be carried out with a uniform density of test sites, at least 1/cm^2, a probe repeatability of $< 0.2\%$ and a test voltage of ~ 7.5 mV.

The SUPREM analysis indicates that this should "exactly" have a resistivity of 534.09 Ω/□.

References

[1] M.I. Current and W.A. Keenan, Solid State Technol. 28 (1985) 139.
[2] L.A. Larson, J. Electrochem Soc. 135 (1988) 1802.
[3] D.S. Perloff, J.N. Gan and F.E. Wahl, Solid State Technol. 24 (1981) 112.
[4] M. Markert and M.I. Current, Solid State Technol. 26 (1983) 101.
[5] L.D. Han, Y.X. Jiang, Y. Yuan and W.A. Keenan, in: Proc. Int. Conf. on Semiconductor and Integrated Circuit Technology, ed. Mo Baugxian (International Academic Publishers, Beijing, China, 1989)
[6] G. Ryding, Nucl. Instr. and Meth. 189 (1983) 274.
[7] G. Gruber, Solid State Technol. 26 (1983) 156.
[8] K. Steeples, Nucl. Instr. and Meth. B6 (1985) 412.
[9] L.A. Larson and G.L. Kennedy, Nucl. Instr. and Meth. B21 (1987) 421.
[10] L.A. Larson, Nucl. Instr. and Meth. B37/38 (1989) 628
[11] H. Glawischnig and G. Lang, Nucl. Instr. and Meth. B37/38 (1989) 624.
[12] W.A. Keenan, W.H. Johnson and A.K.A. Smith, in: Emerging Semiconductor Technology, eds. D.C. Gupta and P.H. Langer (ASTM, 1986).
[13] SUPREM-III, Rev. 8834, Technical Modeling Associates, Palo Alto, CA, USA.

Nuclear Instruments and Methods in Physics Research B55 (1991) 281–286
North-Holland

Development of a process to achieve residue-free photoresist removal after high-dose ion implantation

Janice I. McOmber

Branson International Plasma Corporation, 31172 Huntwood Avenue, Hayward, CA 94566, USA

Rajesh S. Nair

Motorola Advanced Technology Center, 2200 West Broadway, Mesa, AZ 85202, USA

Photoresist subjected to high-dose ion implantation tends to bubble and explode during the plasma photoresist stripping process in single-wafer ashers. A process has been developed to achieve the goals of complete photoresist removal with no bubbling or residues, minimum particulates, and minimal-CV shifts. These goals are accomplished by suitable photoresist pretreatment and optimization of resist strip parameters. Deep UV bake prior to implantation along with reduced platen temperature topside-lamp-assisted ashing have resulted in a residue-free ash with a low-CV shift.

1. Introduction

Photoresist subjected to high-dose ion implantation (greater than 5×10^{14} ions/cm^2) remains a major challenge to the engineer seeking to use a single-wafer resist ash system. Ion-implanted resist tends to bubble and explode during the stripping process in single wafer downstream ashers. This phenomenon is mainly attributed to the elevated temperatures required to obtain the acceptable ash rates which lead to suitable wafer throughputs for large production facilities [1]. The implantation process causes a carbonized shell to form over the less reacted underlayer [2]. Thermal heating during ashing, which elevates the resist temperature above the preimplant bake temperature, causes solvents from this underlayer to volatilize and burst through the

Fig. 1. High-dose ion-implanted resist after partial ash, demonstrating resist bubbling.

0168-583X/91/$03.50 © 1991 – Elsevier Science Publishers B.V. (North-Holland)

top skin [3] This is shown in fig. 1. These bubbles deposit resist particles over the ash chamber and leave residues which are extremely difficult to remove in the asher or subsequent wet processing [1]. A suitable single-wafer resist process should meet the goals of:

(1) complete organic photoresist removal with no bubbling or residues,
(2) minimal particulates during ashing,
(3) minimal-CV shifts,
(4) understanding the ash properties of the implanted resist (to allow process optimization).

These goals are accomplished by deep UV baking the resist prior to implantation and developing reduced-temperature ash processes which remove the polymerized shell at a temperature lower than the preimplant photoresist bake An asher is used which allows for thermal heating of the wafer by use of a temperature-controlled platen and topside-lamp ash-rate acceleration. Different thermal and lamp treatments before and after implantation, as well as various resist ash processes, will be detailed which lead to our understanding of the optimal ashing of heavily implant-damaged photoresist.

Studies were carried out to understand the chemistry and kinetic properties of the resist shell and bulk, utilizing the ash rate of the resist versus temperature and time to obtain the activation energy of the polymerized shell and bulk and the carbonized shell thickness.

2. Experimental

The resist ash process was developed on a Branson International Plasma Corporation L3300 downstream asher (fig. 2). The L3300 is a remote plasma chamber downstream asher. The plasma is generated in a quartz chamber with external rf electrodes. The plasma chamber is separated from the wafer chamber by two 90° bends in order to prevent ion, electron, and UV light migration into the wafer chamber. Photoresist ashing is accomplished by reactive neutral species only. The wafer

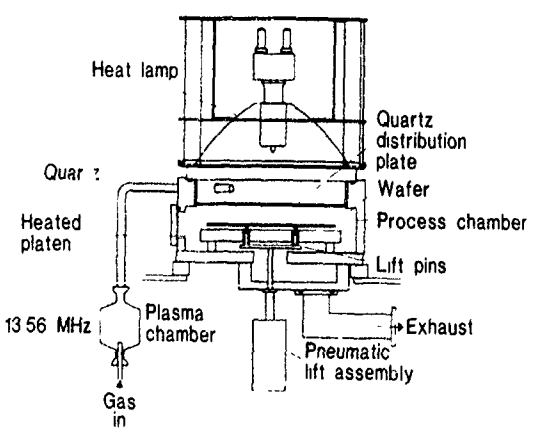

Fig 2 The L3300 downstream asher.

chamber and platen electrically float in order to isolate the wafer from charge damage. The wafer sits on or above the variable-temperature controlled platen. A variable-intensity quartz halogen lamp provides topside lamp heating, providing 100 to 1000 W of visible light. Use of both heat sources increases the tool's versatility for reduced-temperature resist processes [3].

100 mm silicon wafers with 200 Å oxidation were used for particulate experiments. The wafers went through the following steps in sequence: positive photoresist spin, bake, stepper exposure, post-exposure bake (110 °C, 60 s), develop (sodium-free developer), implant (5×10^{15} ions/cm^2 P^+ at 80 keV, 4 mA beam current). A two-way ANOVA study was done to determine a suitable preimplant resist treatment and an optimal ash process with respect to resist residues. Six different resist treatments and five different ash processes were evaluated.

The pretreatment splits are as follows:

(1) No further bake ("standard" process).
(2) 110 °C bake for 150 s.
(3) 110 °C bake for 150 s followed by 1000 mJ (integrated) flood exposure to light of 400 nm wavelength.
(4) Same as step 3, except that the flood exposure was done *after* implant, prior to the ashing.
(5) Ultraviolet (less than 350 nm wavelength) exposure for 20 s.
(6) Ultraviolet exposure with a 230 °C bake for 110 s.

Note that all pretreatments were done prior to implantation except for method 4.

To explain the asher splits, it is advantageous to first describe the ash process in terms of certain elemental steps. The different splits use combinations of these steps with varying platen temperature.

Step I: Quartz pins hold the wafer above the platen during the O_2/N_2O ash using 225 W topside lamp heating. This step is used for slow heat-up during the ash of the "skin".

Step II: The wafer is lowered onto the heated platen during the O_2/N_2O ash using 225 W lamp heating. This step is to complete the ash of the "skin".

Step III: The lamp intensity is increased from 425 to 500 W for the O_2/N_2O ash of the bulk resist

Step IV: The gas mixture is changed to N_2/4% H_2, using 225 to 500 W lamp heating for implant-dopant residue removal [5]

Step V: The gas mixture is changed back to O_2/N_2O with 225 W lamp heating for final residue cleanup.

The five ash processes used are described in table 1. The major variables in these ash processes are platen temperature, intensity of topside lamp heating and the addition of residue cleanup processes. Plasma-chamber variables (pressure, rf power, gas flows) were found in

Table 1
Particle counts as a function of pre-ash and ash treatments

Ash treatment	A	B	C	D	E	Average
Temperature [°C]	150	250	200	200	250	
Steps	1,2,3	1,2	1,2,3,4	1,2,3,4	1,2,4,5	
Pre-ash treatment						
(1) No bake	23	70	47	44	66	50
(2) Bake	31	55	60	49	10	60
(3) Bake, visible light	9	39	39	28	70	37
(4) Bake, visible light, *after* implant	15	56	22	39	57	38
(5) UV flood expose	0	15	10	3	27	11
(6) UV bake, 200–230 °C	1	1	7	6	6	4
Average	13	39	31	28	56	

previous studies [4] to play a much smaller role and were held constant during the experiments. Particulate study and CV wafers were maintained in a clean environment throughout the processing.

The O_2/N_2O process ran at 600 W rf power, 700 mTorr pressure with 500 sccm oxygen and 30 sccm nitrous oxide. The N_2/4% hydrogen process ran at 600 W rf power, 800 mTorr pressure with 900 sccm of nitrogen mixed with 4% hydrogen.

All wafers were processed through a wet clean of 150 °C sulfuric acid with bubbled ozone prior to additional analysis.

Particulate studies were performed using an Inspex EX3500 inspection system, examining residues larger than 0.5 μm in the presence of the implant pattern on the silicon

CV tests were performed after ash on wafers with the following processing: p-type wafers received 400 Å thermal oxidation and were coated and patterned with 1.1 μm of photoresist. Table 3 shows the conditions used for the ash splits. The initial seven wafers had no resist pretreatment prior to ashing Step II alone was used for ash. The final twelve wafers were deep UV-baked prior to ashing. These wafers were processed through steps I, II and III. Use of step IV was a variable. The wafers were then processed through the sulfuric/ozone wet strip. Al/Si was sputtered on, and the metal mask was defined, etched and removed. The wafers received a 450 °C forming gas anneal, and CV measurements were taken. CV charts used −5 to 5 V at room temperature CV traces were taken at room temperature with no prior stress and then at 200 °C with +12 V bias stress prior to cool-down and CV trace.

Resist thickness measurements were taken [5] of boron-implanted wafers (5×10^{15} ions/cm^2 at 80 keV) as they were ashed, using the temperature-controlled platen. Wafers were ashed at temperatures varying from 150 ° to 250 °C in order to determine the temperature-dependent ash-rate activation energy and the carbonized-skin thickness The boundary between the car-

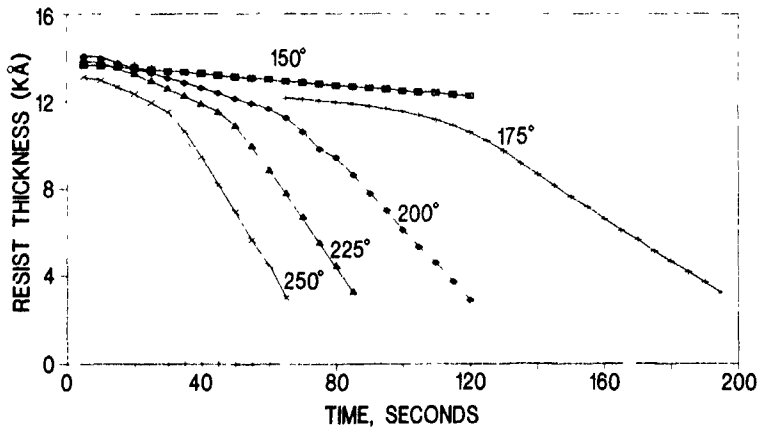

Fig. 3. Resist thickness as a function of ash tie for high-dose implanted resist.

bonized and bulk resist was determined to be the point at which the slope of the curve of resist thickness versus time changed (fig. 3).

3. Results

Fig. 3 shows resist thickness as a function of time for implant-damaged resist at platen temperatures between 150° and 250°C. A similar chart for standard, untreated resist shows a more linear curve, independent of resist thickness [5]. These implant-damaged wafers show a shell thickness of 0.30 μm independent of the ash temperature. The carbonized shell is observed to give an ash rate of 746 Å/min at 150°C, 2395 Å/min at 200°C and 4341 Å/min at 250°C. This is in contrast to ash rates of 4300, 9741 and 15 246 Å/minute, respectively, for the bulk resist. These much reduced ash rates at the lower temperatures are not usable as they are too slow to ensure adequate throughput through the asher. Topside-lamp assistance is used at the reduced temperatures to increase the ash rate closer to the μm/min ash rate required by throughput considerations.

Table 1 contains the particulate data from the ANOVA study. In related work, pretreatment groups 1, 2, 3, 4 and 5 were observed to form vapor bubbles when placed on a 150°C platen (no reactive chemistry) for just 30 s. Group 6 (deep UV baked at 230°C) did not form bubbles when placed on the 150°C platen. Experimentally, we have found that vapor bubbles form on heavily implant-damaged resist when the platen temperature exceeds the temperature of the resist bake. Figs 4 and 5 are bar graphs of particulate counts as a function of pretreat and ash process. The lowest counts were obtained on the wafers which were deep UV baked prior to implantation. Pretreat 5 received a deep UV exposure but with no thermal bake. They bubbled and exploded like the other low-temperature bake wafers during ashing but showed a final particulate count almost as good as pretreat 6 which had the bake. Can the elimination of the photosensitive agents prior to implantation allow for better ash results?

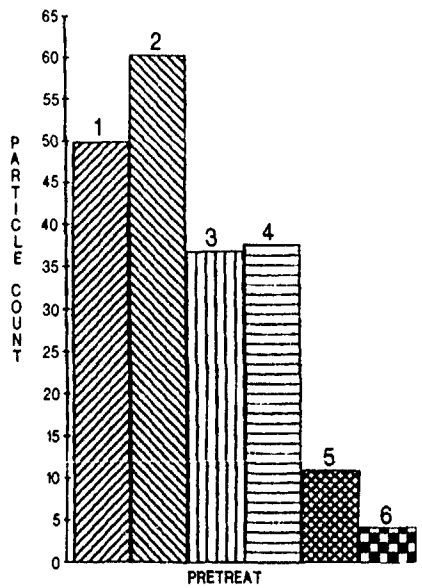

Fig 4. Particle counts as a function of preheat treatment.

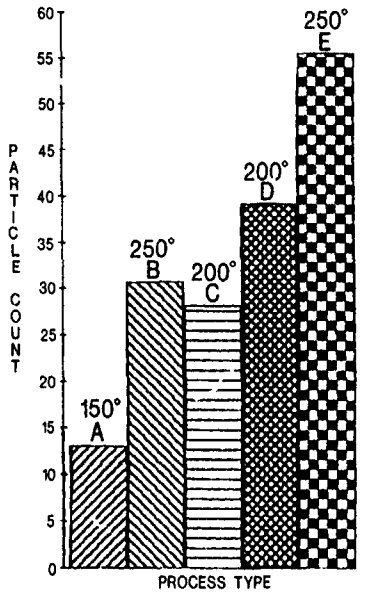

Fig 5 Particle counts as a function of ash process

For those pretreatments that showed resist explosions, the lowest residues occurred for ash processes having the lowest temperature, group A. The amount of residues increased with ash temperature. Table 2 shows that variability is explained significantly by differences in pretreatment and ash process. Tukey's multiple comparison tests indicate that pretreatments 5 and 6 yield lower particle counts than the rest of the pretreatments. The CV results are shown in table 3. The best results are shown for the reduced-temperature resist ash. Lamp assistance to the resist ash is not observed to degrade the CV results at reduced temperature. Degradation of the CV results is demonstrated as the ash temperature is

Table 2
Analysis of variance using an additive model

Source	DF	%var expl	F-ratio	Significance
Pretreat	5	59.0	17.888	0.0000
Process	4	27.8	10.553	0.0001
Residual	20	13.2		
Total	29	100.0		

Table 3
CV results for different ash treatments

Wafer	Lamp control	Platen control [°C]			ΔV_{FB} [V]
1	control	control			−0.088
2	0	150			−0.117
4	0	200			−0 15
6	0	250			−0 136
3	350	150			−0.066
5	350	200			−0 139
7	350	250			−0.270
Wafer	UV bake temp [°C]	Lamp [W]	Platen temp. [°C]	N_2/H_2 step	ΔV_{FB} [V]
9	230	control	control		−0.062
13	200	control	control		−0.06
17	175	control	control		-0 063
21	130	control	control		−0 057
10	230	170/425	150	no	−0 09
14	200	170/425	150	no	−0 082
18	175	170/425	150	yes	−0 083
22	130	170/425	150	yes	- 0 083
11	230	225	250	no	−0 23
15	200	225	250	no	−0 143
19	175	225	250	yes	−0 203
23	130	225	250	yes	−0 194

increased The UV bake process alone shows no CV result degradation.

4. Discussion

Photoresist subjected to high-dose implantation explodes when the carbonized shell is ashed at temperatures above the preimplant bake temperature Subjecting the implant-damaged resist to thermal *or* lamp treatments prior to ash did not reduce the tendency for explosion. Once the carbonized shell is formed, vapor movement through it is limited Prevention of explosions results from:

(1) removing the (reduced temperature boiling point) volatile organics from the resist prior to implantation;
(2) Avoiding raising the resist temperature above this bake temperature during the initial ash.

Deep UV baking prior to implantation and using a reduced-temperature, topside-lamp-assisted ash was the only methodology found in this study to maintain ashed wafers which added less than 0 1 particles/cm^2 (6 particles per 100 mm wafer). We were unable to obtain submicron "clean" wafers using a process which allowed the resist to explode. Redeposited residues from the chamber contributed to higher particulate counts on the wafers. We conclude that the resist ash temperature should not exceed the preimplantation bake temperature. Chemical kinetics limits the capability of resist ashing of standard thermal-baked resist (100 to 130 °C) in single-wafer ashers. It is quite difficult to get reasonable ash rates on single-wafer ashers for standard resist below 150 °C [3]. Lamp assistance cannot bring the ash rate above 5000 Å per minute without adding enough thermal heat to the resist to cause bubbles and explosions. Addition of a secondary gas such as CF_4 or NF_3 [6] to decrease the activation energy low enough to cause ashing would be possible. Some loss of exposed silicon or silicon oxide could be expected. This is generally not acceptable to minimal geometry IC processing. Future work will examine alternative techniques for obtaining faster ash rates between 100 and 130 °C so that deep UV baking is not required for a clean ash

Previous work [3] has shown the standard (nonimplanted) resist ash rate to be first-order with respect to temperature at reduced ash temperatures (100 to 150 °C). A plot of the natural log of etch rate with respect to inverse temperature showed a straight line. We find that as the temperature is raised towards 250 °C for standard resist, the carbonized shell and bulk resist, the Arrhenius plot levels off; the rate of rise is not as great as expected for a first-order reaction. With the increased temperature, an additional factor joins in to affect the ash rate. It is likely either the amount of reactive oxygen reaching the resist surface or interference of the (increased quantity of) volatile reaction by-products with the incoming reactants. This additional effect is minimal from 150 to 175 °C. Using this temperature range, we can calculate an activation energy for the resist ash rate of 8.97 kcal/mole for standard resist, 13 23 kcal/mole for the implant-damaged shell and 8.04 kcal/mole for the bulk of the implant-damaged resist

Similar to Sibbett et al. [7], we see CV degradation with increasing platen temperature, though the magnitude is less The worst case result in this study is a three-fold degradation, compared to the control, to 0 28 V. It is unexpected to observe no CV degradation with lamp assistance at 150 or 200 °C, as a noticeable increase is observed for 250 °C As the asher is designed to eliminate energetic ion bombardment and (plasma generated) UV light, this leaves thermal migration of sodium contamination in the resist (1 ppm nominal) as the most probable cause for the increase in the CV shift. The ash time should then be minimized to reduce the exposure of the thermal oxide to sodium.

Acknowledgements

We would like to acknowledge T.C. Smith, Motorola ATC, for useful discussions; Jim Howden and Amir Jalalpour, Branson/IPC, for assistance in the experi-

mentation; Woody Chung, Ted Liston and John Davies, Branson/IPC, for useful discussion; Richard Savage, Horace Simmons and Tom Metz, SC Technology, for assistance with the activation energy experiments; and Jim McVittie, Stanford University CIS, for useful discussions.

References

[1] W Chung, Proc. Technical Symp. for Advanced Equipment (Semicon, Korea, 1989)

[2] T.C. Smith, in: Ion Implantation Science and Technology, ed. J.F. Ziegler (1988) p. 345.

[3] J.I. McOmber, W.P Marsh and J Ngo, Proc. 8th Int. Symp. on Plasma Processing (1990) p. 423

[4] R.F. Reichelderfer, 1988 Technical Proc. (Semicon, Korea, 1988).

[5] J.T. Davies, T. Metz, R. Savage and H. Simmons, SPIE Conf. Proc. (October 1990)

[6] J.J Hannon and J.M. Cook, J Electrochem. Soc. 131 (1984) 1164.

[7] K.H Sibbett, J I. Ulacia, J.P McVittie and R.F. Reichelderfer, Spring 1987 Plasma Processing Symp., Mater Res Soc. Conf Proc. (1987).

Nuclear Instruments and Methods in Physics Research B55 (1991) 287–295
North-Holland

Section IV. Innovations in ion source and beam transport

Ion beam system design for ULSI device requirements *

Nicholas R. White

Applied Materials Implant Division, Foundry Lane, Horsham, West Sussex, RH13 5PY, England

The requirements of ULSI devices are placing stringent demands on ion source design, ion beam optics and system design. The problems include lower beam energies, the need for precisely controlled profiles both at low and high energies, wafer charging control, and ion beam purity. This paper discusses the physics of the ion beam, specifically the plasma that exists within the ion beam, as it affects these problems.

1 Introduction

This paper discusses the ways in which ion beam system designs may have to respond to the shrinking dimensions and vertical doping profile requirements of submicron devices.

The lowest energy required and the corresponding dose of implants are falling. Device manufacturers require shallow dopant profiles with steep cutoffs and with usable throughputs, and may need full amorphisation for channeling and diffusion control. Techniques for producing sufficiently high currents down to 5 keV are discussed.

A major theme of this paper is the plasma that exists within space-charge-neutralised ion beams. Measurements of beam plasma parameters are presented, as well as theoretical methods of calculating the potentials and fields within the beam, and their use in computer models. Further, since the wafer environment is a plasma, the conditions that will most effectively control wafer charging can be determined using plasma physics techniques.

The dopant profiles obtained using low-energy boron or BF_2 can be compromised by channeling, or in some ion implanter architectures by fast atoms or ions. High-energy dopant profiles are also vulnerable to contamination with slow atoms or ions. The shrinking geometries and the use of vertical transistors are placing stringent requirements on the control of these effects, and both are described.

2. The optics of high-current low-energy ion beams

2.1 Available boron currents

High current ion implanters have for some years delivered from 10 to 27 mA of certain dopant ions at energies of 40 keV and above, but the most crucial interest is in sufficient boron for source/drain implants at energies down to 5 keV and even lower. Fig. 1 shows that the typical behaviour of implanter ion beam systems is for the beam current to fall steeply below a certain threshold energy. Two mechanisms dominate this decrease, both having a characteristic dependence on beam energy. Space-charge forces (the self-repulsion of the beam ions) tend to make the beam diverge; this effect is well known to be inversely proportional to beam energy to the power 3/2. The second mechanism is the matching of the ion beam emittance to the geometrical acceptance of the system [1]. (Beam emittance is the product of minimum beam cross section and the divergence solid angle.) Emittance is inversely proportional to the beam energy, but the geometrical acceptance of the beamline hardware is usually fixed. As the beam energy is reduced, the fraction of the ions transmitted will fall, and neglecting other effects would fall linearly with energy. Thus in all systems it can be predicted that at a low enough energy the combination of these two effects can cause a current dependence on the 5/2 power of beam energy.

From fig. 1 it can be seen that the behaviour of a typical modern high-current implanter exhibits a rapid falloff fitting this description below about 10 keV, and a less steep falloff between 10 and about 20 keV. Fig. 1 also shows the current required to implant 60 150 mm diam wafers per hour, as a function of beam energy. This falls with energy as the required depth of dopant is reduced.

The PI 9200, fitted with the optional "low-flow" ion source, has five times the boron current of today's other high-current implanters at 5 keV. Reasons include the low beam divergence and the very large geometrical acceptance of the short beamline, due in part to the 20 keV extraction energy from the ion source. This reduces the magnet radius, and reduces the range of energies over which the ion beam extraction must be controlled.

* Invited paper.

0168-583X/91/$03.50 © 1991 – Elsevier Science Publishers B.V. (North-Holland)

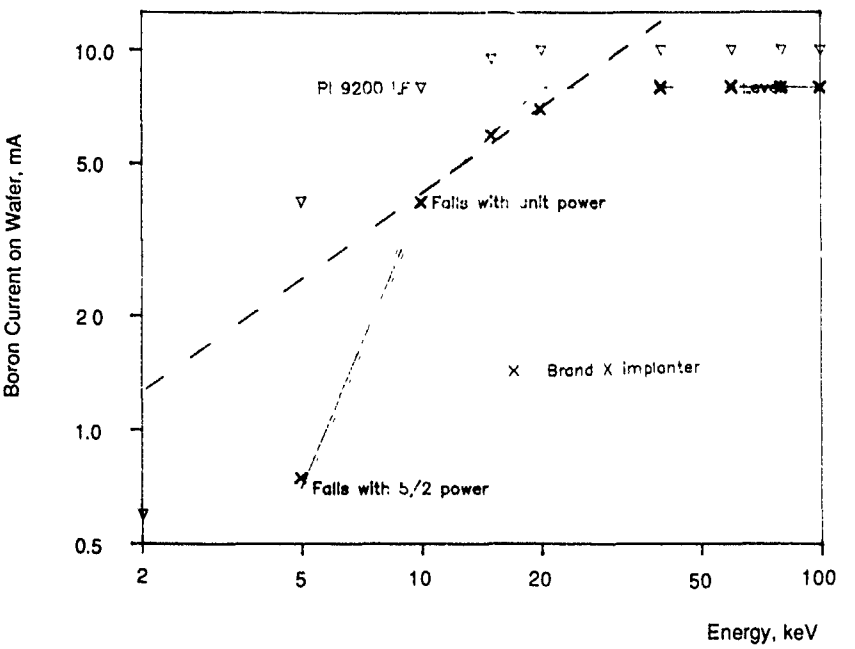

Fig. 1 Boron ion currents available on the PI 9200 high-current implanter and on another typical commercial implanter. Solid line: theory, see text. Dashed lines: the currents required to achieve 60 wafer/hour throughput on 150 mm wafers at the projected doses are also shown.

The "low-flow" ion source is modified to produce a smaller beam with about 1/3 the divergence of the standard source. Fig. 2 shows the computer modeling of a 5 keV boron beam from BF_3: The total current is 37 mA with a divergence of $\pm 2.5°$ (it would be less at higher energies) and an average mass of 23 amu is assumed. The boron is assumed to comprise a fifth of the total current, the remainder being fluoride fractions

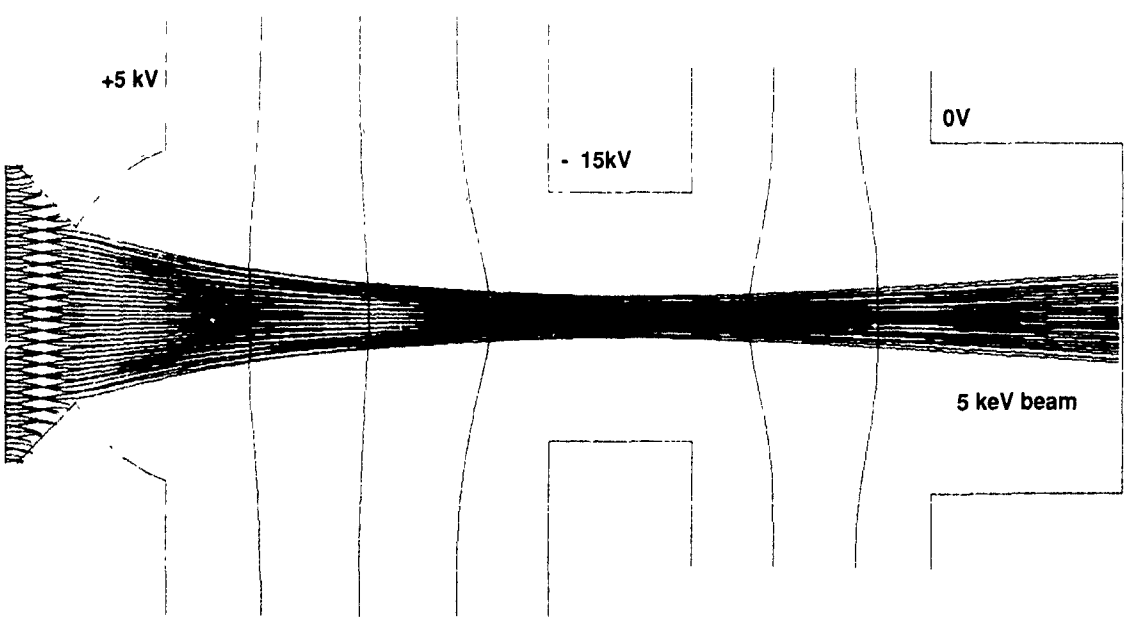

Fig. 2 Ion source extraction system for PI 9200 "low-flow" ion source, modelled by SORCERY [2]. 37 mA total beam current, with a mean mass of 23. Divergence at right is $\pm 2.5°$. With losses, 4.7 mA of B^+ ions at 5 keV should reach wafers.

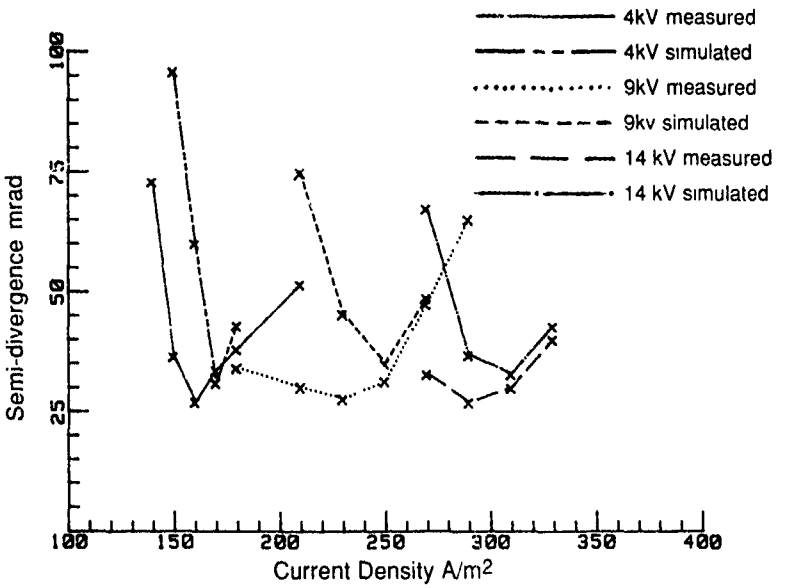

Fig 3 Comparison of SORCERY predictions and measured divergences for 20 keV argon beams for the Applied "low-flow" ion source

from the BF_3 gas. Of this, about 60% is assumed to be transmitted, giving about 4.5 mA boron.

It is assumed in the computer model [2,4] that the ions are extracted from a plasma with a temperature of 3.5 eV. No a priori assumption of plasma boundary shape or beam shape is made; the ions are assumed to have a velocity slightly greater than the Bohm velocity with some transverse "thermal" component, and the

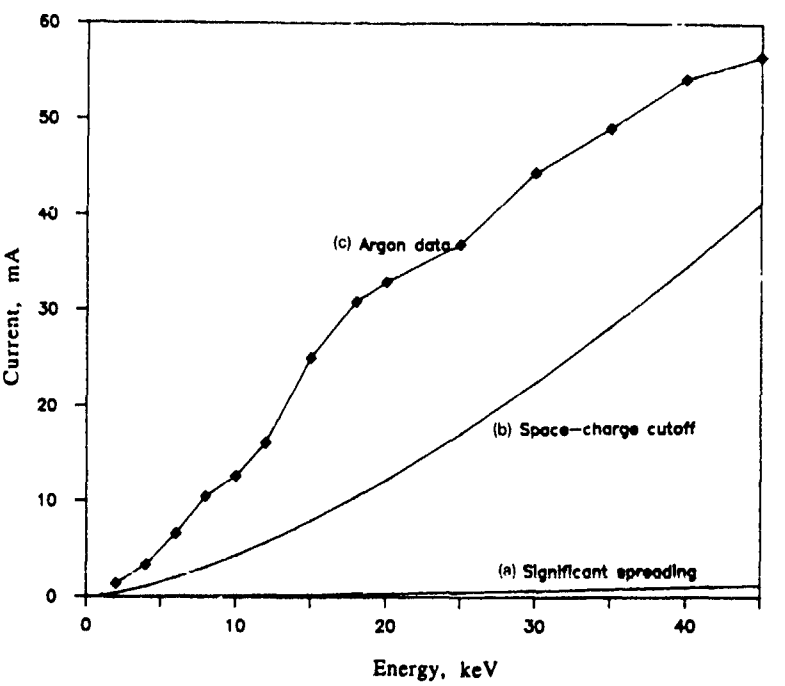

Fig. 4. (a) The practical limit for argon beam current in electrostatically scanned implanters (b) The space-charge cutoff limit (c) Experimental maximum argon currents versus energy, measured through a ±35 mrad defining aperture, with no magnetic analysis

potentials are calculated by iterative solution of Poisson's equation. The physical validity of the model was tested for a number of cases running 20 keV argon beams where the current was varied from 25 to 60 mA. The predicted beam divergence was compared with measurement. Three different focus voltages were used. The comparison of measurement with predicition is shown in fig. 3.

2.2 Space-charge limits

Space-charge effects limit the electrostatically scanned beams of medium-current implanters to about 1 mA at 40 keV, because beam expansion becomes too great and too hard to control. A more fundamental limit arises at approximately 50 times this current: At this point the space-charge causes a potential hill on the axis of the beam so great as to stop any following ions. This is an unattainable current known as the space-charge limit, which is almost independent of the dimensions of the beam. Fig. 4 shows the space-charge limit for argon.

In high-current implanters as in isotope separators, electrostatic fields are eliminated from the beamline allowing electrons to become trapped and neutralise the beam space-charge. Suppression voltages are applied to prevent loss of these electrons at accelerating gaps.

Space-charge neutralised beams of currents many times greater than the space-charge limit can be transported. Overlaid in fig. 4 is the beam from the "low-flow" ion source, measured after travelling for 1 m without magnetic analysis and through an aperture limiting its divergence to $\pm 1.8°$. The maximum attainable current at energies from 2 to 45 keV was plotted. The data is well above the space-charge limit, and its overall dependence on energy is close to linear: it is clearly unrelated to space charge and the limit may be beam emittance, since this would give a linear scaling law.

2.3. The ion beam as a plasma

The main theme of this paper is the fact that a plasma (an approximately neutral mixture of ions and electrons) exists within many ion beams. The large difference in mass means that electrons and ions do not exchange significant energy, whilst electrons rapidly exchange energy with each other and thermalise, long before the ions have moved a significant distance. Without this mechanism space-charge neutralisation could not be so effective, since electrons originating outside the beam would simply oscillate from side to side, contributing little to the space charge at the beam centre, but because of it the electron density n_e is given by a Boltzmann factor,

$$n_e = n_0 \exp(eV/kT), \tag{1}$$

where the potential V is assumed to be zero at the centre of the beam and negative everywhere else accessible to the plasma. T is the temperature of the electrons, and the other symbols have their usual meanings.

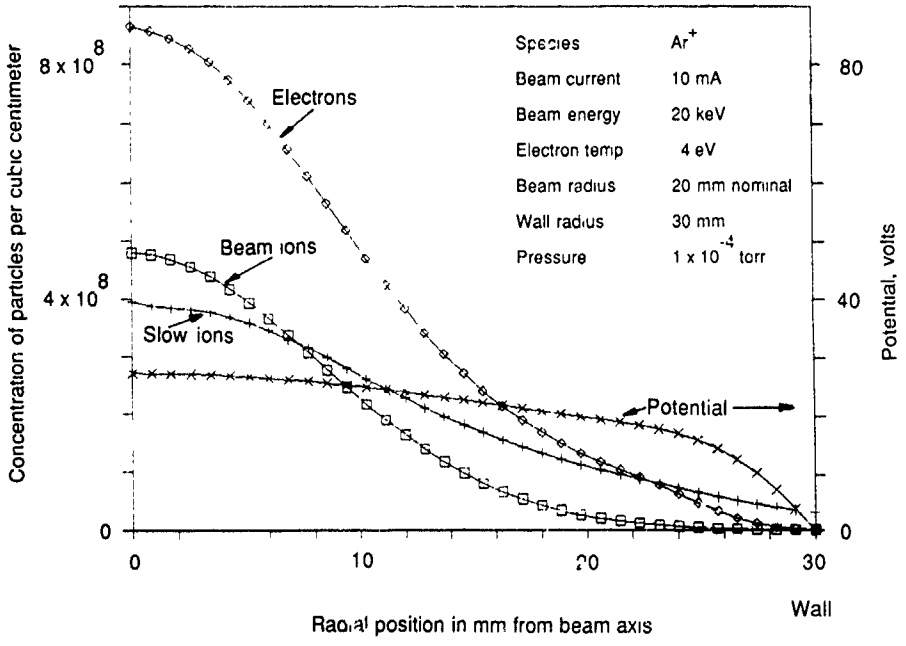

Fig. 5. Graph of calculated beam plasma parameters.

As the beam-generated plasma is atypical it is worth describing our understanding of it in some detail. The beam ionises a small fraction of the residual gas, providing a source of electrons. Another source is secondary electrons emitted when energetic ions or other electrons strike the walls. The beam generates almost stationary ions by charge exchange, with a cross section significantly higher than that for direct ionisation. These slow ions are repelled by the positive space charge of the beam and move radially outward until they strike the walls. Approximately one residual gas atom in 10^4 is ionised under typical conditions. The density of slow ions may equal or even exceed that of the beam ions since they are moving slowly, so the positive space charge is raised by this mechanism. However, this traps electrons electrostatically, and these rapidly come to thermal equilibrium. Holmes [4] describes how the temperature is determined by an energy balance, but data is not available to permit realistic calculation of electron temperatures.

Fig. 5 shows calculated beam and plasma parameters [4]. Some reasonable assumptions have been made to simplify the modeling. The beam is assumed to be travelling through a long cylindrical pipe 60 mm in diameter, and to have a Gaussian current density profile. The beam is 10 mA of argon at 20 keV, and the pressure is 10^{-4} Torr. This pressure is probably realistic for the most distant points from the pumps in many systems, or for the region close to outgassing wafers undergoing implantation. An electron temperature of 4 eV is assumed, based on measurements described later.

The potential at the center of the beam will fall to a value between 5 and 10 times kT/e, where T is the electron temperature. The computer model has been used to solve for the equilibrium condition in which the few electrons that have sufficient energy to reach the walls balance the slow-ion current.

The beam ion density on the axis is approximately equalled by the slow-ion density at this pressure. As the slow-ion cloud continuously expands radially towards the wall and the ions gain speed, the slow-ion density drops a little, but near the wall the beam ions are almost absent. The electron density is very slightly less than the total ion density, except in the region near the wall known as the sheath, where a potential drop of about 4 to 6 times kT/e develops over a very short distance. This is clearly visible in the figure. The thickness of the plasma sheath is a little greater than a Debye length [6].

The radial electric field that causes defocussing of the ion beam has been determined from this model. It increases from zero on the beam axis, slowly rising linearly until it approaches the plasma sheath, then suddenly increases to a high value within the sheath. The importance of this result is that not only does the presence of the beam plasma almost cancel the tendency for the beam to blow up under space-charge forces, but the residual forces are linear, and therefore the emittance of the ion beam is conserved. This is an unexpected result, since space-charge forces under other conditions are usually nonlinear and seriously degrade the effective emittance of ion and electron beams. The potential drop between the centre of the beam and the sheath edge is of the order of kT/e, and that from the centre of the beam to the beam edge (one sigma) is of the order of $kT/2e$. It is possible to approximate the defocussing electric field by the expression

$$E_r = \frac{kTr}{er_{\max}}, \tag{2}$$

and this has been used in the computer program OPTICIAN [4] to model high-current neutralised beams. The quantity $r_{\max}$ is taken as the outer edge of the beam; r

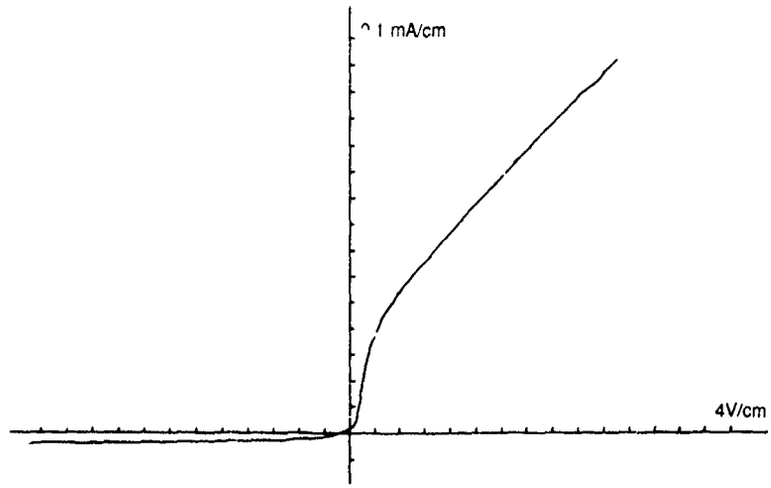

Fig. 6 Langmuir probe plot obtained with 1.5 mm diam probe, 5 mm outside edge of 20 keV argon beam

is the radial coordinate. The electron temperature is typically taken to be from 1 to 5 eV, based on data.

Measurements have been made of the ion beam plasma parameters by using Langmuir probes Fig. 6 is a plot taken with a 1.5 mm diam probe placed 5 mm outside the edge of a 20 keV argon beam. The electron temperature is determined from the region near the origin in which the growth of current is exponential. The almost flat region to the left of the origin shows the saturated ion current, from which the plasma density can be calculated. To the right of the origin the electron current rises more slowly once the plasma potential has been exceeded

Ion densities of 3 to 6×10^8 per cm^3 are usually measured. In this instance the electron temperature was only 0.8 eV, but it is observed that values ranging up to 5 eV are often obtained. One factor influencing the temperature was found to be the field of an analysing magnet situated 200 mm downstream from the probe position. Varying the field from 0 to 0.6 T caused a temperature variation from 0.75 to 1.8 eV with other factors held constant. All these temperatures are so low that the electric fields are too small to materially affect the beam optics Note that this fits with the observed beam behaviour shown in fig. 4 There is also some evidence that the temperature has an inverse relationship with beam current.

If there are rapid fluctuations, "hash", in the beam current, this can upset the beam plasma A 1 μs interruption of the beam would cause a substantial loss of plasma electrons to the walls. Therefore a noisy ion beam will tend to have a higher plasma temperature than a quiet one. The higher the beam current, the greater the sensitivity to noise. Under these conditions the background pressure will affect the recovery time from upsets and hence can affect the plasma conditions.

In the book by Forrester [6], it is assumed that the outer edges of the ion beam peel off into the sheath and get deflected into the walls. In the results of the present modeling the plasma extends significantly beyond the intense region of the beam, and the electric field continues to vary almost linearly well beyond the outer beam ions. This depends on the Debye length, and hence on the pressure, and in practice this effect may be insignificant

3. Wafer charging control and the beam plasma

Immediately in front of a wafer undergoing implantation the pressure is quite high, typically 1×10^{-4} Torr, because of outgassing, sputtering, and the use of argon gas as part of electron flood systems The neutral density is in the region of 3×10^{12} atoms per cm^3, while the ion and electron densities are 3×10^8 per cm^3 Note that the slow ions from this plasma enhance the emission and transport of low-energy electrons from all types of electron flood gun

There will typically be several populations of electrons in this region Direct measurement of all of these

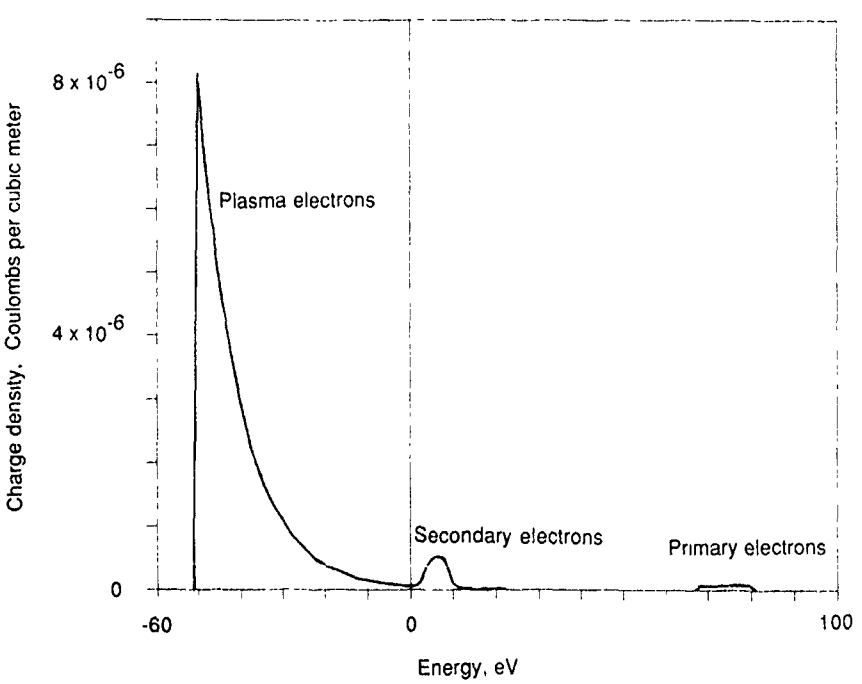

Fig 7 Total elecron spectrum near wafer, deduced from Langmuir probe and other data

by a single technique is impractical, so evidence is assembled from different sources. Primary electrons from the flood gun will be present. Their energy is determined by the negative bias voltage on the filament in the flood gun; this is 60 to 100 eV in the PI 9200 [7], and somewhat higher in most other systems. There are secondary electrons, in some systems from deliberately placed targets, and in others from the walls. Finally there are plasma electrons. These are the only ones that are trapped, and hence their spatial density can far exceed that of the primaries or secondaries. The general picture is shown in fig. 7.

The plasma electrons play a vital role in the control of charging. The current of plasma electrons to a point on the wafer which charges positive will rise exponentially, according to eq. (1), and will rapidly drop if the wafer charges negative. The rate of change is inversely proportional to the plasma temperature. This is discussed in more detail in the paper by Strain et al. [8] in this conference.

4. The control of the implanted dopant profile

4.1 High-energy implants and shallow contaminants

ULSI processes using deep implants often require accurate control of the profile on the shallow side of the peak. Some of these are discussed in other papers in this conference [9]. Kaim [12] pointed out that a very significant drop in surface concentration accompanies strong channeling. This dopant reappears at a greater depth. Mechanisms that cause variations in the profile include some that are fairly universal, and some that apply specifically to the use of multiply charged ions to reach the high energies. Fig. 8 illustrates a number of important mechanisms for the case of doubly charged boron ions. The well known problem with doubly charged phosphorus being contaminated with slow P^+ ions from dissociated P_2^+ [11] does not occur, since boron does not form a dimer from BF_3.

Many of these mechanisms are vacuum related, and none of these can be improved by the use of an electrostatic retarding filter. Vacuum can be strongly affected by wafer outgassing, and in the case of boron beams, fluorine outgasses from the analysing magnet region where the F^+, BF^+ and BF_2^+ ions are dumped.

4.2 Low-energy beams and deep contaminants

Channeling is the most obvious source of serious deep tails on the profiles of low-energy boron implants, critical for source/drain doping. It can be overcome by preamorphisation, which also can help suppress enhanced diffusion during RTA, but the added process step has not been welcomed. Current [13] describes in this conference the use of automated linked implants, in which a low dose of fluorine is used for preamorphisation [14] at production-worthy throughputs.

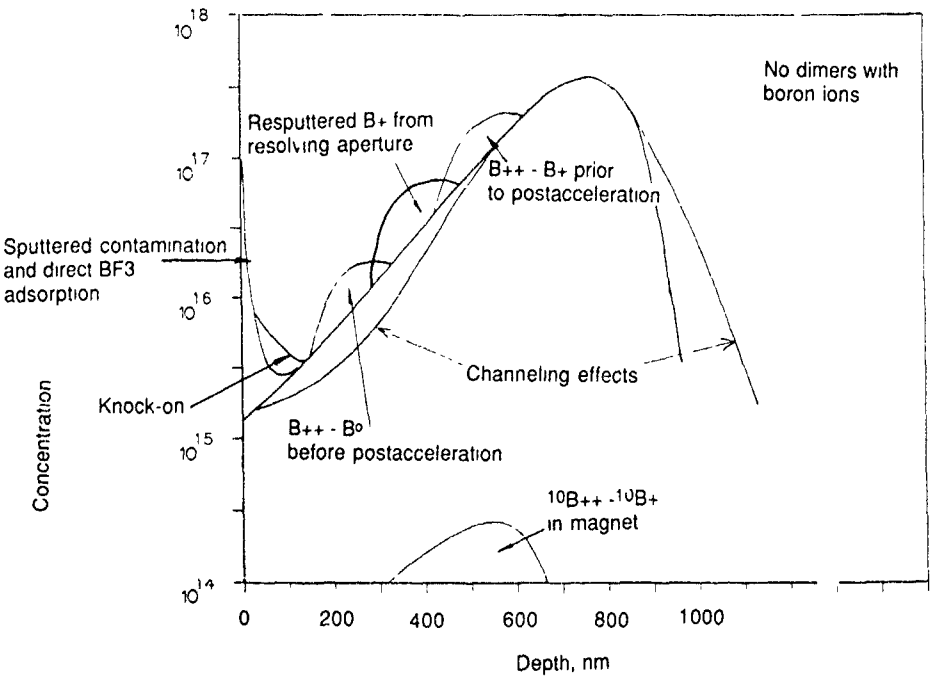

Fig. 8. Diagram of possible energy contaminants to a B^{2+} beam. The base profile was calculated by TRIM.

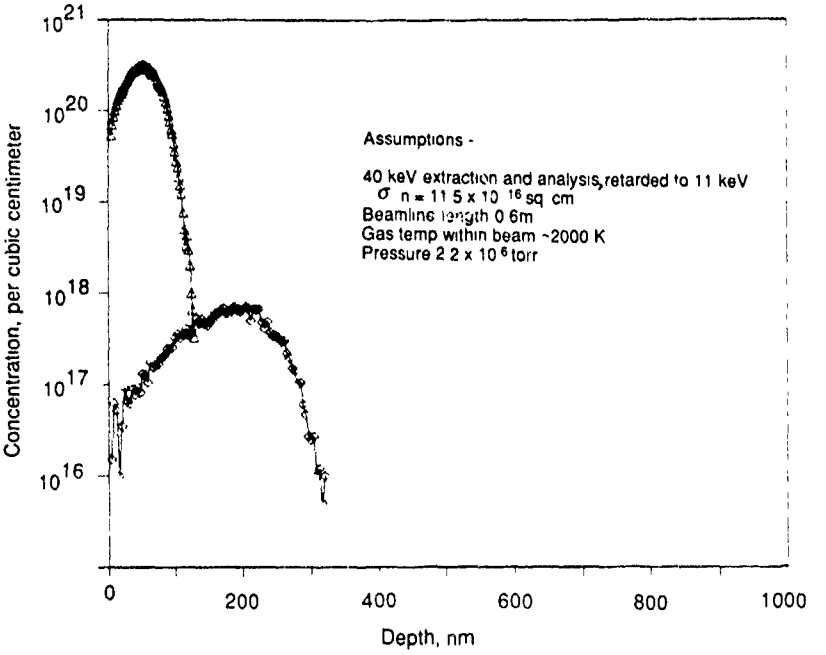

Fig 9 TRIM simulation of the profile of an 11 keV boron implant obtained by retarding a 40 keV boron beam 0 5% of the boron is neutralised and causes a deep tail

BF_2^+ implants on postacceleration implanters are vulnerable to deep tails because a fraction of the molecular ions can be dissociated to atomic boron ions prior to the postacceleration. These atomic ions have excess velocity after acceleration, and penetrate beyond the desired profile

The problems of obtaining high currents of boron at energies of 5 keV and below were discussed earlier in this paper. One apparent solution is the use of retardation: the ion beam extraction and analysis is all performed at high energy, overcoming space-charge and emittance problems, and then the beam is retarded immediately prior to implant to its final energy. This approach has been used very successfully under UHV conditions [15,16], in particular for retardation to energies at which epitaxial deposition can be carried out However, as a practical method of carrying out source/drain implants of boron it will be less successful, since it will produce deep tails similar to those previously discussed Boron has a high cross section for neutralisation (σ_n), and practical beamline pressures, for reasons already discussed, are unlikely to be far below 1×10^{-5} Torr. Under these conditions the fraction of boron neutralised is of the order of 1%. Neutral atoms will not be retarded, and will penetrate deeply into the substrate. Fig. 9 illustrates the mechanism: it is synthesised from two calculations using TRIM [17] with appropriate energies and pressures.

The boron or BF_2 profiles with the steepest cutoff, before and after annealing, are obtained by means of preamorphisation and no acceleration or deceleration after magnetic analysis.

Acknowledgements

The author would like to acknowledge the work of colleagues which has been included in this paper In some cases other papers in this conference cover this work in more detail, but since it is not covered elsewhere the work of Tim Grey Morgan, Andrew Devaney, and David Kennard deserves special mention here.

References

[1] A P Banford, The Transport of Charged Particle beams (Spon, 1966)
[2] N.R White, Nucl Instr and Meth B21 (1987) 339
[3] A. Holmes, Rad Eff 44 (1979) 47
[4] H Ito and N R. White, these Proceedings (8th Int Conf on Ion Implantation Technology, Guildford, UK, 1990) Nucl. Instr. and Meth B55 (1991) 527.
[5] M E Mack, G. Ryding, D.H Douglas-Hamilton, K Steeples, M Farley, V Gillis, N White, A Wittkower and R Lambracht, Nucl. Instr and Meth B6 (1985) 405.
[6] A T. Forrester, Large Ion Beams (Wiley, 1987).
[7] M T. Wauk, N.R. White, B Adibi, M I Current and I A Strain, these Proceedings (8th Int Conf on Ion Implantation Technology, Guildford, UK, 1990) Nucl. Instr and Meth. B55 (1991) 413.

[8] J Strain, Y Tanaka, R. Woodward and N R White, ibid., p. 97
[9] A.N Van der Steege, J van Herk and M L C. van Meyl, presented at the 8th Int. Conf. on Ion Implantation Technology, Guildford, UK, 1990.
[10] S Cherekdjian and W Weisenberger, these Proceedings (8th Int. Conf. on Ion Implantation Technology, Guildford, UK, 1990) Nucl. Instr. and Meth. B55 (1991) 178.
[11] C.R Kalbfus and R Milgate, Nucl Instr and Meth. B21 (1987) 400.
[12] R.E Kaim, in Emerging Trends in Ion Implant Technology, ed M. Vella (American Vacuum Society, 1989)
[13] M I Current, B Adibi, S Leung, P Crook and L.A. Larson, these Proceedings (8th Int. Conf on Ion Implantation Technology, Guildford, UK, 1990) Nucl Instr. and Meth B55 (1991) 173.
[14] B. Biasse, A.M Cartier, P Spinelli and M Bruel, Nucl Instr. and Meth B21 (1987) 493
[15] J.H Freeman, W Temple and G.A. Gard, Vacuum 34 (1984) 305
[16] A. Bousetta, J A. van den Berg, D G Armour and P.C. Zalm, these Proceedings (8th Int. Conf on Ion Implantation Technology, Guildford, UK, 1990) Nucl Instr. and Meth. B55 (1991) 565
[17] TRIM is a Monte Carlo computer program by J F Ziegler and J.P Biersack

Nuclear Instruments and Methods in Physics Research B55 (1991) 296–299
North-Holland

Improvement of an ECR multicharged ion source

Shigeyuki Ishii [1]

Plasma Physics Laboratory, RIKEN, Hirosawa, Wako-shi, Saitama 351-01, Japan

Experimental results are shown for the yield of high charge state ions depending on the field configuration and the type of microwave launcher. The presence of an octupole improves the yield by a factor of 8. A tandem mirror configuration improves the yield by a factor of 7. A multifilar helical antenna on the magnetic axis improves the yield by a factor of 2. Extension of the mirror distance, with the mirror ratio kept unchanged, has little effect on the yield.

1. Introduction

Multicharged ions are desirable in ion implantion since they can be easily accelerated to high energies without high voltage accelerators. Upgrading of the ECR multicharged ion source has so far been carried out exclusively by elevating the microwave frequency and less study has been made on the magnetic field configuration [1]. Increasing the frequency of the microwaves is expensive.

We have been studying an economical source using a low-frequency microwave. In the previous works it was established that the multipole of the minimum B fields should be not so strong as to enhance the cusp loss of plasma, and the mirror ratio should be sufficiently large [2,3].

In the present work we studied how the yield of high charge state ions depended on the field configuration and the type of microwave launcher. The presence of an octupole improved the yield by a factor of 8. A tandem mirror configuration improved the yield by a factor of 7. A multifilar helical antenna on the magnetic axis improved the yield by a factor of 2. Extension of the mirror distance, with the mirror ratio kept unchanged, has little effect on the yield.

2. Experimental arrangement

The experimental setup is depicted in fig. 1. The detailed description has been given elsewhere [3]. Spatial distributions of the field intensities are indicated on top of fig. 1. The mirror field is formed in two ways: by a single mirror (A) and by a tandem mirror (B). The minimum field, in whose region plasmas are trapped, is at an ECR intensity. A mirror ratio, R_m, can be varied with a mirror distance, L_m, kept unchanged. Microwaves of 2.45 GHz frequency are supplied from a magnetron along the magnetic field lines. Two types of antenna are used: rod and multifilar helix [4].

Argon gas is introduced from the left and pumped to a gas pressure as low as 10^{-4}–10^{-3} Pa. Ions flowing out from the right are accelerated by applying a high voltage of 10 kV to the plasma chamber insulated from a beam transport chamber which is grounded. An ion beam is mass separated with a sector magnet and collected with a Faraday cup. Total beam current can be collected with a Faraday cup placed in front of an extractor.

3. Experimental results

3.1. With the mirror field A, and the octupole field

The minimum pressure p which microwave breakdown occurs is equal to about 3×10^{-4} Pa. The beam currents, mass separated, are shown in fig. 2 as functions of p. At each measured point the power is optimized to maximize high charge states. The most abundant species extracted is Ar^{2+}. With increasing p, Ar^{+} increases and saturates, while Ar^{2+} is maximized at $p = 7 \times 10^{-4}$ Pa and then decreases below Ar^{+} at higher pressures. The pressure at which the current is at a maximum decreases as the charge state rises.

3.2. With the mirror field A, but without the octupole field

In this case the minimum gas pressure increases to 1×10^{-3} Pa. The lower the charge state is, the greater is the current over the relevant pressure range. With increasing p, the low charge states saturate, while the high charge states decrease.

[1] Present address: Faculty of Engineering, Toyama Prefectural University, Kosugi, Toyama 939-03, Japan.

0168-583X/91/$03.50 © 1991 – Elsevier Science Publishers B.V. (North-Holland)

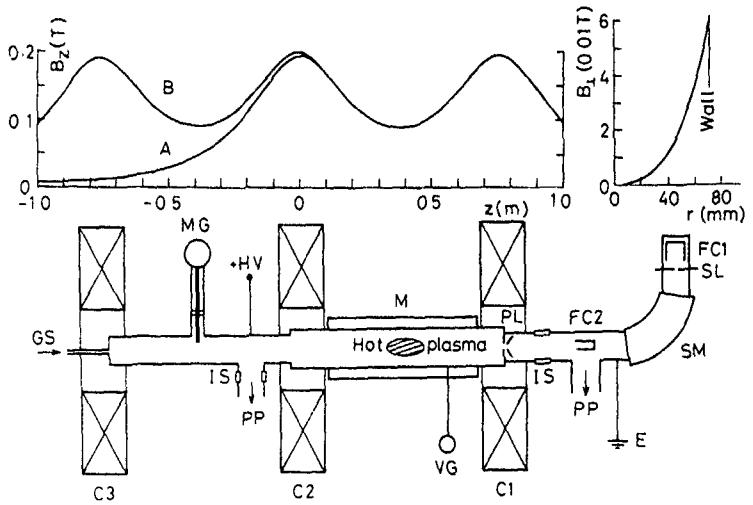

Fig. 1 Experimental setup C1–C3: magnetic coils; M: ferrite magnets, SM: sector magnet; MG: magnetron, GS. gas inlet, PP: pumps, VG vacuum gauge; HV: high voltage; E: ground; IS. insulators, PL: extractor; SL: slit, FC1, FC2. Faraday cups. Top, B_z: axial magnetic field; B: octupole field.

3.3. With the mirror field B (tandem mirror) and with the octupole field

To ensure a reliable comparison, we changed the mirror field promptly from A to B. The charge state distributions in both cases are plotted in fig. 3. The ion currents increase by a factor of about four over all charge states. Ar^{5+} is masked by O^{2+}.

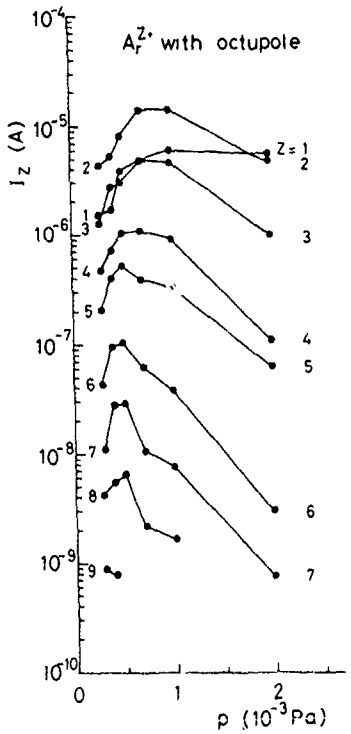

Fig. 2. Variation of beam currents with gas pressure p with the octupole field. Z denotes the charge states of argon ions. $R_m = 2.3$, $L_m = 0.76$ m.

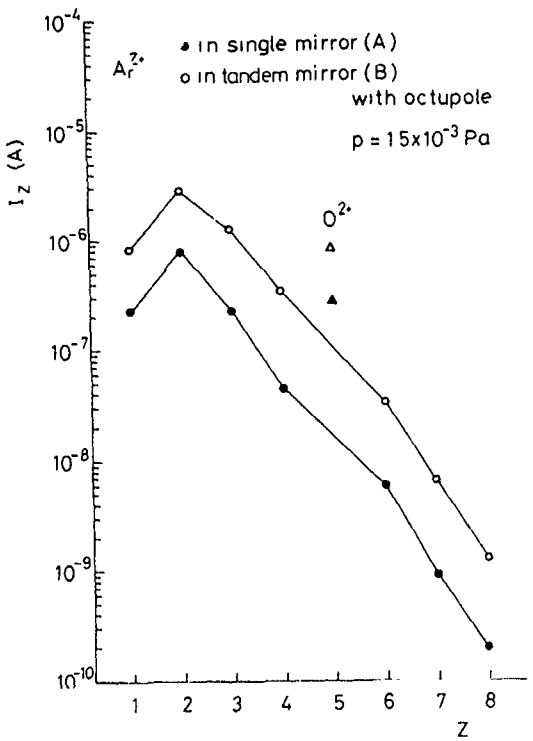

Fig 3. Comparison of the charge state distributions for the single and tandem mirrors with the octupole.

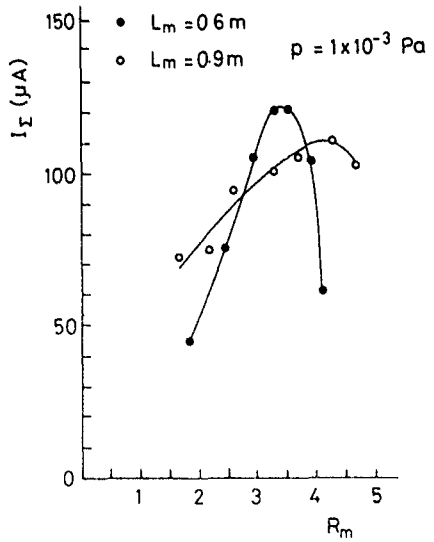

Fig. 4. Variation of the total beam current, I_Σ, with increasing R_m at $L_m = 0.6$ and 0.9 m

3.4. Dependence on the mirror distance

Keeping L_m unchanged we varied R_m. Fig. 4 shows the total beam current, I_Σ, as functions of R_m at two extreme values of L_m. For both cases the curves of I_Σ is peaked and the variation is more gradual at larger L_m. The peak values are nearly equal.

3.5 Multifilar helical antenna on axis

Instead of the rod antenna a multifilar helical antenna [4] was installed on the magnetic axis. The comparison of charge state distributions with the rod antenna case is shown in fig. 5 Although there are differences with fig. 3, the differences in the high charge states are small.

3.6 Overall comparisons of data

We compare the improvements of typical charge states due to change of the experimental conditions, including the results of the past experiments, as shown in table 1. The mirror ratio was varied with L_m kept unchanged [3]. It is seen that R_m is the most effective factor for obtaining high charge states, followed by the octupole field, the tandem mirror field, and the antenna type. The mirror distance is insignificant

4. Discussion

The electron temperature, T_e, ranges from 5–15 eV and monotonically rises with decreasing p [2]. As T_e increases, peaks of the fractional abundance of ions

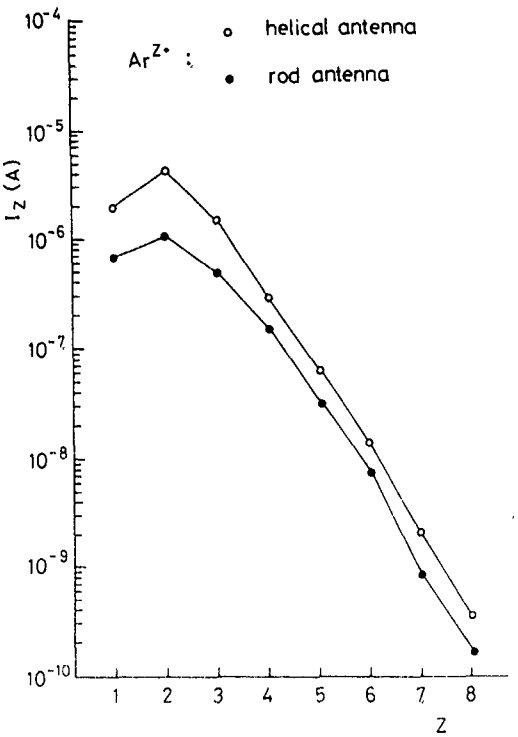

Fig 5 Comparison of the charge state distributions with the rod and helical antenna with the octupole

shift to higher charge states [7]. The shift of the peaks towards lower values of p with increasing Z in fig. 2 can be explained by this temperature dependence.

In the previous work [2] we experimentally elucidated that too intense a multipole field is disadvantageous in obtaining high density plasmas The cusp loss at the wall was considered to be large. The optimum aspect ratio of the multipole to the mirror field can so be determined that the magnetic flux containing the plasma does not touch the sidewall of the plasma chamber between the mirror points The plasma diameter is usually half the chamber diameter. Approximating the

Table 1
Incremental factors due to change of the experimental conditions

Conditions	Ion species		
	Ar^{2+}	Ar^{4+}	Ar^{8+}
R_m: 2.3 → 4.6 [a]	4	6	15
Octupole: off → on	4	5	8
Tandem: off → on	4	7	7
L_m 0.6 → 0.9 m	1	– [b]	– [b]
Antenna rod → helices	4	2	2

[a] Previous work. [3]
[b] Not measured.

profile of the axial field intensity between the mirror points to be quadratic and that of the multipole intensity to be proportional to r^n, where r is the radial distance, we get from an equation of magnetic field line the ratio of the multipole intensity at the wall ($r = R$), B_R, to the minimum axial field intensity at the center ($r = 0$), B_0,

$$\frac{B_R}{B_0} = \frac{(2^n - 2)R(R_m - 1)^{1/2}}{(n-1)L_m \tan^{-1}(R_m - 1)^{1/2}},$$

where the values of n are equal to 2 and 3 for the hexapole and octupole, respectively. This formula gives a reasonable value for the experimental result [2].

Plasma loss due to particle interaction is considered. The particle confinement time in the magnetic mirror, τ_c, is taken to be the sum of the momentum transfer collision time, τ_{ii}, and the flight time, τ_f, along the field line; the ions which fall in loss cone and travel to the mirror points leave the mirror system. From a simple calculation, τ_f is much larger than τ_{ii} for both Ar^{2+} and Ar^{8+} even if we overestimate T_i to be 10 eV. The charge transfer cross section, σ_{cx}, of the multicharged argon can be expressed from ref. [5,6] as $\sigma_{cx} = 4 \times 10^{-19} Z^{3/4}$ m^2. Using this formula it is shown that the charge transfer loss is negligibly small compared with the flight loss. Then from the rate equation for ions: $dn_i/dt = \langle \sigma_i v_e \rangle n_0 n_e - \langle \sigma_{cx} v_i \rangle n_0 n_i - n_i/\tau_c = 0$, where σ_i is the ionization cross section, v_e and v_i are the electron and ion velocities, respectively; n_0, n_e, and n_i are the neutral, electron, and ion densities, respectively, we get $n_i \simeq \langle \sigma_i v_e \rangle n_0 n_e \tau_f = (L_m/\lambda_i)(v_e/v_i) n_e \propto L_m$, where λ_i is the ionization mean free path of Ar. For the tandem mirror, L_m is doubled, while Ar^{2+}, which carries the mean plasma density, is four times larger. Nevertheless, extension of L_m is ineffective (fig. 4). A possible mechanism is as follows: the tandem mirror has two heating zones where electrons are mirror trapped. The electrons in the loss cone in one zone can be trapped in the other because they further gain transverse energy there from the microwaves. Thus the electron density builds up, resulting in the increase of the ion density.

The helical antenna drives the whistler wave whose propagation is not density-limited. With this antenna, however, the increase in the high charge states was small, compared with the low charge states. This is probably because the antenna comes into direct contact with the plasma core and cools the electrons

5. Conclusions

The present work indicates several important aspects in the design of the ECR multicharged ion source:
(1) The multipole field is indispensable. The aspect ratio of this field to the mirror field must be suitably taken.
(2) The large mirror ratio is much more advantageous to the high charge states than to the low ones.
(3) The tandem mirror system is also advantageous to the high charge states. The consequent long system can be shortened without lowering the plasma density.
(4) By meeting these requirements an upgraded ECR multicharged ion source can be expected even with low-frequency microwaves.
(5) The ultimate upgrade should be made by using high-frequency microwaves which are much more costly.

Acknowledgement

The author appreciates the helpful discussions of Dr K. Matsumoto and Dr. Y. Kato of Toyama Prefectural University.

References

[1] R Geller, B Jacquot and P Sortais, Nucl Instr and Meth. A243 (1986) 244
[2] S. Ishii, H Amemiya and M Yanokura, Jpn J Appl. Phys 25 (1986) L712
[3] S Ishii, H. Oyama, and H Odagiri, Nucl Instr and Meth B37/38 (1989) 147
[4] H A Wheeler, Proc IRE 35 (1947) 1484
[5] S C Brown, Basic Data of Plasma Physics, 2nd ed (MIT press, Cambridge, 1966) p 73
[6] P G Carolan and V.A. Piotrowicz, Culham Laboratory Report CLM-P672 (1982)
[7] C Breton, C. de Michel and M Mattioli, J Quant Spectrosc. Radiat. Transfer 19 (1978) 367.

Nuclear Instruments and Methods in Physics Research B55 (1991) 300–304
North-Holland

An increased implant current by combining a long-slit microwave ion source with a converging lens

N. Sakudo [a], H. Koike [b], T. Seki [a] and K. Tokiguchi [a]

[a] *Hitachi Research Laboratory, Hitachi Ltd, 4026 Kuji-cho, Hitachi-shi Ibaraki-ken, 319-12 Japan*
[b] *Naka Works, Hitachi Ltd, Ichige, Katsuta-shi, Ibaraki-ken, 312 Japan*

Pre-deposition implanters, used in semiconductor device manufacturing, need higher currents which can only be realized by increasing the ion emitting areas, i.e., the slits, of the ion sources. A microwave ion source makes it easy to change the form of the ion emitting area. The slit length is enlarged by up to twice the pole gap of the mass separator with the slit width kept at the standard value, 2 mm, in order to maintain the required mass resolution. In the nondispersion plane, the ion beam converges into the pole gap. The beam acceptance of the mass separator in the nondispersion plane can be changed by adjusting the inclination of the pole edge of the separator magnet to the ion beam in the dispersion plane. Mass separated P^+ ions of more than 30 mA and O^+ ions of more than 25 mA have been obtained.

1. Introduction

Pre-deposition implanters need higher currents to increase the wafer throughputs at high dose levels during semiconductor device manufacturing. Most high current ion implanters are composed mainly of a magnetic-sector mass separator and an ion source which has a ribbon beam extracted through a slit. Since the plasma density of such an ion source has reached a maximum, it is impractical to further increase the density for the purpose of getting the desired higher currents. Another solution for higher currents is to enlarge the ion emitting area of the ion source. Many optic modes of an ion implanter have been used. In conventional ion optics which most ion implanters adopt, the sector magnetic field functions as a convex lens to an ion beam in the dispersion plane (x, z). The locations of the ion source slit and the mass resolving aperture correspond to those of the object and the image in the dispersion plane, respectively. Since the slit makes its image at the mass resolving aperture, the beam width at the aperture does not change no matter how large and how variable the beam dispersion angle at the slit is. The slit width s is limited by the required mass resolution, a typical value of which is about 100 for implantation into semiconductors. The mass resolution R_e in a symmetric-sector mass separator of 90° deflection is given as follows:

$$R_e = r/2s, \qquad (1)$$

where r is the beam trajectory radius in the magnetic field and the width of mass resolving aperture is equal to s [1]. In the case of a radius of 400 mm, for example, the slit width s should be less than 2 mm to maintain the needed resolution. On the other hand, the slit length should be shorter than the gap between magnetic poles of the mass separator as long as a parallel beam is extracted in the nondispersion plane (y, z). The typical value of the length for most conventional high current implanters is 40 mm.

In order to overcome these limitations in conventional ion optics, Aitken [2] has proposed an ion optical system in which the ion source is turned through 90° so that the long dimension of the ion source slit is in the dispersion plane. Then the slit length is no longer limited by the size of the pole gaps in the separator magnet. He succeeded in obtaining currents of 30 mA of phosphorus and arsenic with an implanter adopting such optics. However, in the dispersion plane of this optical system, the mass resolving aperture is placed at the focal point of the convex lens of the sector magnetic field, not at the imaging point of the ion exit slit. Therefore, ions should be extracted in parallel to maintain the required mass resolution. The degree of the parallelism determines the beam width at the aperture, hence it also controls the mass resolution. In other words, the mass resolution in this optics is changeable depending on operational conditions and characteristic variations of the ion source.

In this paper, a new method is proposed to increase ion beam currents without reducing the mass resolution. In the dispersion plane (x, z), the ion source slit makes its image at the mass resolving aperture as in conventional separator optics. However, in the nondispersion plane (y, z), ions are extracted through a slit whose length is larger than the pole gap of the separator magnet and they are converged into the pole gap. A microwave ion source which is modified to have a

0168-583X/91/$03.50 © 1991 – Elsevier Science Publishers B.V. (North-Holland)

longer slit than the standard one is adopted to combine with this optics.

2. Improvement of ion beam transmission

Ion beam transmission in a high current implanter is mainly limited by the matching between the beam emittance and the separator acceptance in the nondispersion plane [3]. Fig. 1 shows an example of the relations between the beam emittances and the separator acceptances both in the dispersion plane and in the nondispersion plane. In the nondispersion plane it is possible for the emittance contour to be improved to match the separator acceptance. For improved matching it is better to converge the beam to focus at the middle point of the path in the magnetic field.

Typical ion trajectories in both planes are shown in fig. 2. Since the sector magnetic field acts on charged particles as a convex lens in the dispersion plane, the image of the source slit can be adjusted to be formed at the position of the mass resolving aperture as shown in fig. 2a. In the nondispersion plane there is no lens effect, so long as the ion trajectory in the dispersion plane is perpendicular to the field boundaries of the magnetic field as shown in fig. 2b. When the ion trajectory is not perpendicular to the boundaries, thin-lens effects by the fringing magnetic field appear at the entrance and exit of the magnetic field depending on the inclinations of the ion trajectory in the dispersion plane to the field boundaries at the pole edges, as shown in fig. 3b. The focal lengths of the thin lenses in the nondispersion plane, f_1 at the entrance and f_2 at the exit, are given by the following equations [4]:

$$f_1 = r \cot \epsilon_1, \tag{2}$$

$$f_2 = r \cot \epsilon_2, \tag{3}$$

where ϵ_1 and ϵ_2 are inclination angles at the entrance and exit in the dispersion plane, respectively. Positive

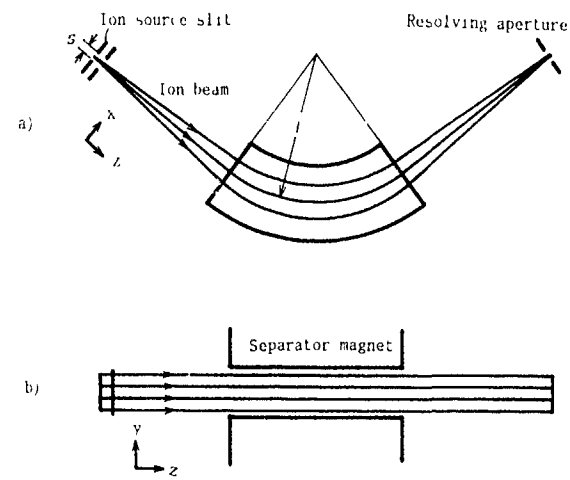

Fig. 2. Ion trajectories of perpendicular boundary optics. (a) In the dispersion plane; (b) in the nondispersion plane

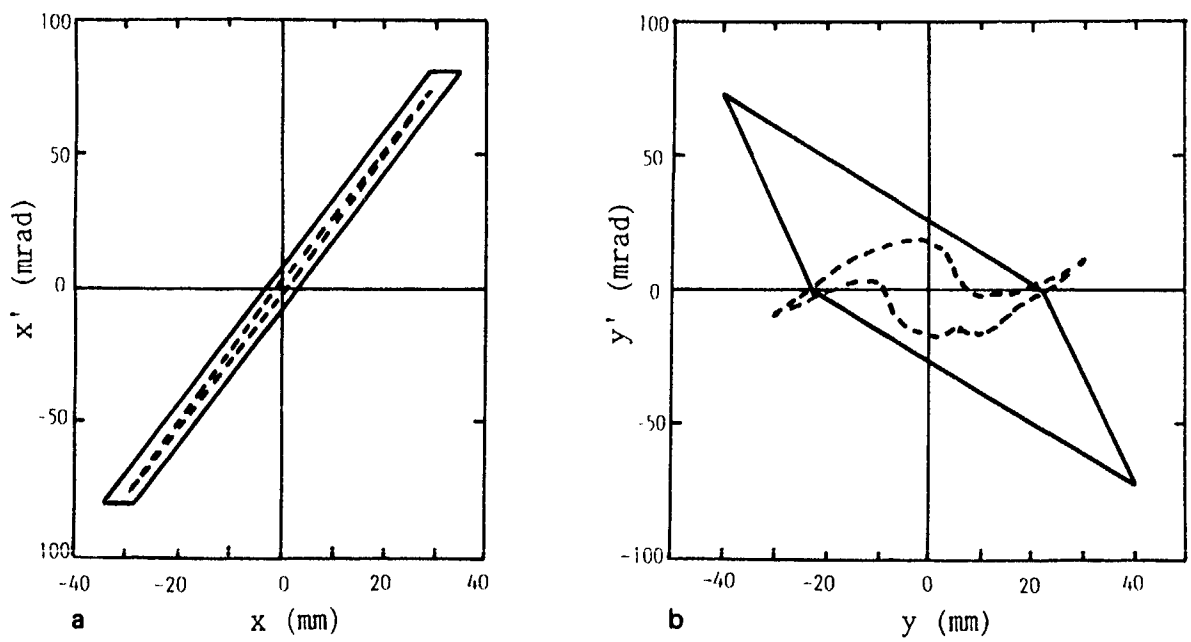

Fig 1 Examples of beam emittances and separator acceptances halfway from the ion source slit to the entrance of the separator magnet. The emittances and the acceptances are shown by dotted and solid lines, respectively. (a) In the dispersion plane; (b) in the nondispersion plane.

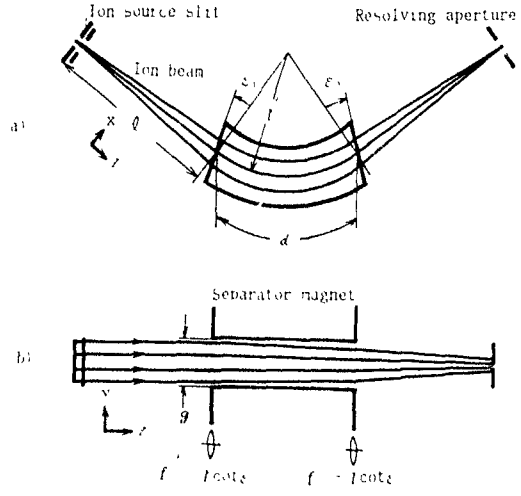

Fig. 3 Ion trajectories of inclined boundary optics. (a) In the dispersion plane; (b) in the nondispersion plane

values of the focal lengths mean convex lenses and negative ones, concave lenses. If the inclination angles ϵ_1 and ϵ_2 are zero, there are no lens effects in the nondispersion plane

The acceptable slit area which emits ions which can pass through the separator magnet can be estimated by simply drawing the ion trajectories in the nondispersion plane The acceptable slit length, l_s, which includes such an area is expressed as follows:

$$l_s = g(1 + 2l_1/d - l_1/f_1), \quad (4)$$

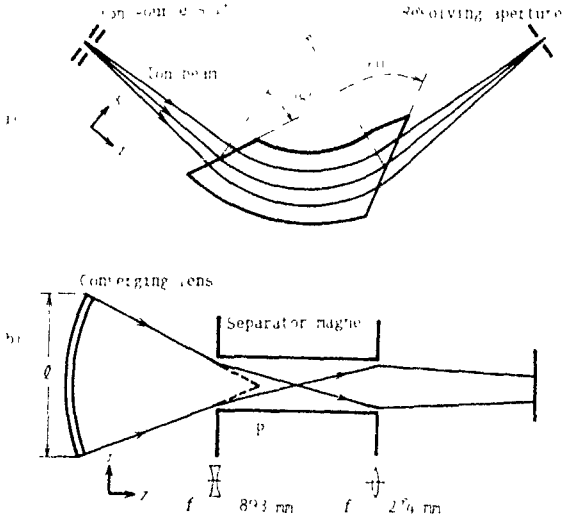

Fig. 4 Improvement of the matching between the beam emittance and the separator acceptance. Ion trajectories (a) in the dispersion plane and (b) in the nondispersion plane In the nondispersion plane there is a thin concave lens at the magnet entrance and a thin convex lens at the magnet exit Point P in the nondispersion plane is the focal point of the new extraction lens of the microwave ion source.

where g is the pole gap width, l_1 is the distance from the source slit to the magnet entrance, and d is the beam path length in the magnetic field. In this case, it is assumed that the only obstructions to the ion path are the magnetic poles and there is a thin-lens effect of a focal length f_1 at the entrance to the magnet.

In order to increase the beam acceptance of this separator magnet in the nondispersion plane, l_s should be increased. For this purpose, f_1 should be a small negative value according to eq. (4). Hence, ϵ_1 should be negative from eq. (2).

In order to match the beam emittance with this acceptance, a converging extraction lens is adopted. A new ion optics with improved separator acceptance in the nondispersion plane is shown in fig. 4 In this case, $r = 475$ mm, $g = 45$ mm, $\epsilon_1 = -28°$, $d = 622$ mm, and $l_1 = 700$ mm.

The acceptable slit length l_s is 182 mm which is several times longer than the slit length of a standard microwave ion source, 40 mm. If all the ions from the slit are extracted so as to converge to the point P which is 230 mm distant from the entrance edge of the magnetic pole, all of them can pass through the pole gap.

With microwave ion sources it is very easy to lengthen the slit, since the volume of the discharge chamber can be designed freely. Extraction electrodes of a microwave ion source are modified to have a 930 mm radius of curvature in order to focus the ions at point F. Hence,

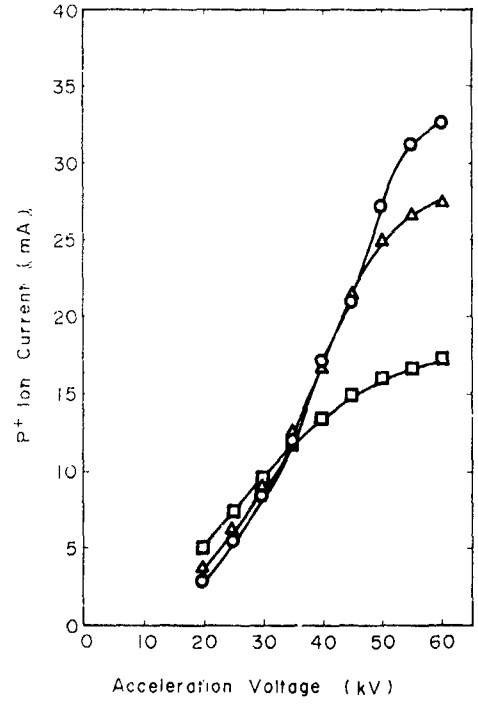

Fig. 5. Mass-separated P^+ ion currents. Pure PH_3 gas was introduced into the ion source.

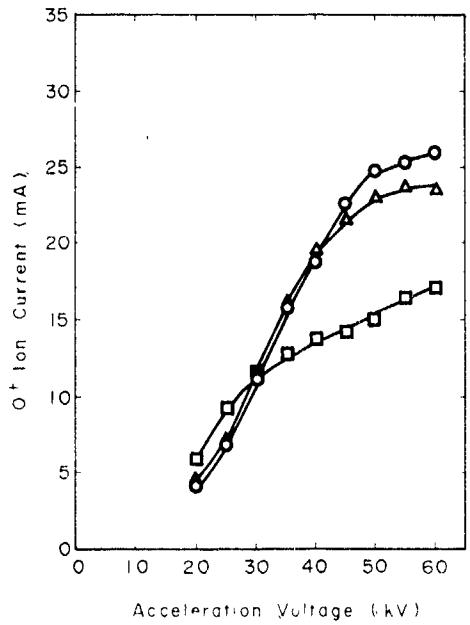

Fig 6 Mass-separated O^+ ion currents O_2 gas was introduced into the ion source.

the crossing point of ions is really moved to the center of the magnet by concave-lens effect at the entrance edge. In order to have the emittance contour included sufficiently inside the acceptance contour, the slit length is determined to be 80 mm considering that there are other obstructions besides the magnetic poles in the actual beam path. This value is twice that of a standard microwave ion source, but far smaller than the acceptable length of 182 mm.

3. Experimental

Fig 5 shows relations between mass-separated P^+ ion currents and extraction voltages. Pure PH_3 gas was introduced into the ion source. Increasing the extraction voltage, ion currents tend to saturate. The saturated currents depended on the PH_3 flow rates and the current values also tended to increase up to the flow rate of 2.0 cm^3 atm/min. The P^+ ion current of 33 mA was obtained at the extraction voltage of 60 kV. The microwave power was 160 W and the PH_3 flow rate was 2.0 cm^3 atm/min The flow rate was rather higher than that of a standard microwave ion source. It was assumed that the higher flow rate was needed to keep the necessary gas pressure in the discharge chamber since the slit area was twice that of a standard ion source The percentage of P^+ ions in all the ion species extracted from the ion source was about 70% as shown in fig. 7a. This value was almost the same as that of a standard microwave ion source.

Fig. 6 shows relations between mass-separated O^+ ion currents and extraction voltages. The characteristics were very similar to those of P^+ ions. Microwave power was 500 W and the O^2 flow rate was 2.2 cm^3 atm/min The O^+ ion current of 26 mA was obtained at the extraction voltage of 60 kV The percentage of O^+ ions in the mass spectrum was 75% as shown in fig. 7b. In both cases of PH_3 and O_2, no degradation of the mass resolution could be observed

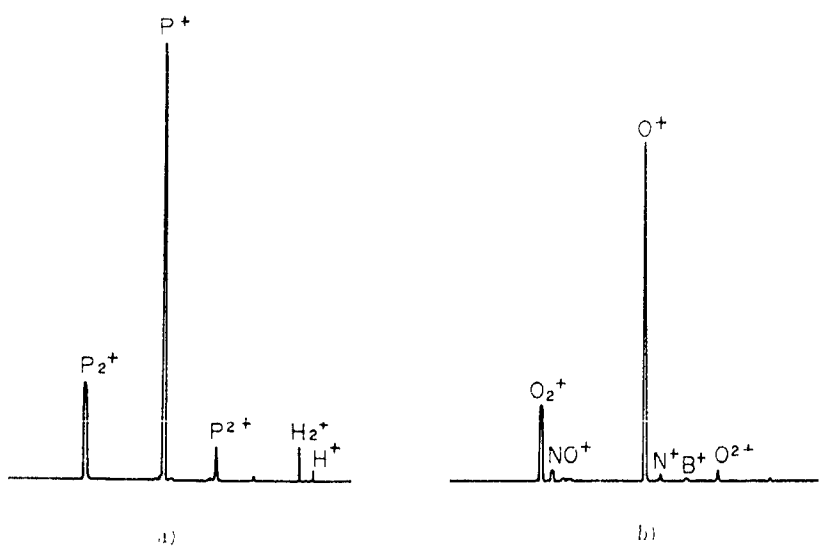

Fig 7 Mass spectra of (a) PH_3 and (b) O_2.

4. Conclusions

A new ion optical system which improves the ion beam current without reducing the mass resolution has been described. A microwave ion source was modified to match the new ion optics and the implant current was increased to about twice that of a conventional implanter. In the experiment the slit of the microwave ion source was lengthened to twice the standard one. However, from a consideration of the separator's acceptance, it is probable that this length can be extended to more than four times that of the standard one. This would further increase the implant current.

References

[1] A. Septier Focusing of Charged Particles II (Academic Press, New York, 1967) p. 218.
[2] D Aitken, Nucl. Instr. and Meth B21 (1987) 274
[3] N. Sakudo, H. Koike, K Tokiguchi, T Seki and K. Sakai, Nucl. Instr. and Meth B37/38 (1989) 184
[4] R. Herzog, Acta Phys. Austriaca 4 (1959) 431.

Nuclear Instruments and Methods in Physics Research B55 (1991) 305–309
North-Holland

Plasma cathode oxygen ion source

Takehisa Shibuya [a], Shizuyo Hashimoto [a], Eiji Yabe [b] and Kazuo Takayama [b]

[a] *Department of Physics, School of Science, and* [b] *Institute of Research and Development, Tokai University, 1117 Kitakaname Hiratsuka Kanagawa 259-12, Japan*

A plasma cathode ion source has been developed to attain a long lifetime for oxygen ion production. In this ion source, an Ar plasma which is non-reactive plasma serves as a cathode for a thermionic hot cathode used in the Kaufman ion source. This ion source consists of two compartments: (1) a plasma generator, and (2) a plasma chamber. The plasma generator is used for generating a plasma cathode, while the plasma chamber is used for producing oxygen ions. Two chambers are connected to each other by an anode hole which has narrow tapered ducts. These two chambers are differentially pumped out, the pressure of the plasma generator has to keep a high pressure, so that the large pressure difference between two chambers prevents oxygen gas from flow into the plasma generator Oxygen gas fed to the plasma chamber does not damage the thermionic hot cathode located in the plasma generator. It has been confirmed that the plasma cathode ion source can produce a stable ion beam and has a long lifetime. Mass spectrometry results show that this ion source has an ability of generating a considerable amount of positive oxygen ions

1. Introduction

Physical properties of thin films produced by ion assisted deposition, commonly referred to as IAD, have been extensively investigated [1–5]. It has been found that ion bombardment significantly increases the mobility of adatoms on a substrate surface. The packing density of resulting thin films on the substrate surface is much higher than that of a thin film formed by the usual techniques without ion bombardment. In the IAD processes, stable operation with a long lifetime is required because chemically reactive ion beams have been extensively utilized in semiconductor fabrication. Furthermore, recently, a need has arisen for an ion source with a large area and uniform irradiation.

A Kaufman-type ion source [6] has been widely used for IAD to produce a large-area ion beam. We have constructed a new version of the compact plasma cathode ion source without a neutralizer. The lifetime of the Kaufman type ion source is limited by that of burning away a metallic hot cathode used in this ion source. Therefore, ion sources without a metallic hot cathode should be of great advantage in order to increase the lifetime of the ion source. This expectation has motivated us to investigate the possibility of replacing the metallic hot cathode used in conventional ion sources by a plasma cathode [7–12]. In the next section, we describe a device construction of the plasma cathode ion source. Measurements of properties for IAD are presented in section 3, and concluding remarks are made in section 4.

2. Structure and operating principle of the ion source

The structure of the newly-designed version of the plasma cathode ion source is schematically shown in fig. 1. Our ion source consists of three components: a plasma generator, a plasma chamber and an anode ring. These two chambers are separated by an anode plate, which is sandwiched by two ceramic insulators with small openings of 1 mm in diameter. The plasma generator is equipped with a metallic hot cathode, ceramic floating electrodes, an anode plate and an inlet for a nonreactive working gas, and the vessel wall is electrically floating. The vessel and the anode plate were cooled with water. The plasma chamber is a cylinder, 35 mm in diameter and 40 mm in length, with a gas-feeding inlet, and an inside wall of cylinder used as an anode in the main discharge. The anode ring mounted on the plasma chamber has a circular slit. A plasma produced in the plasma chamber is extracted through the slit of the anode ring.

The essential points of the design principle of the plasma cathode, are as follows: Nonreactive gas (for example Ar gas) is supplied to the plasma generator with a considerably high pressure increasing the lifetime of the metallic hot cathode. The discharge in the plasma generator is maintained between the inner surface of the small opening of the anode plate and the metallic hot cathode. Then a plasma expands out into the plasma chamber, forming the plasma cathode.

An Ar plasma cathode is produced in the plasma generator at a neutral pressure of 0.1–1 Torr. This

0168-583X/91/$03.50 © 1991 – Elsevier Science Publishers B.V. (North-Holland)

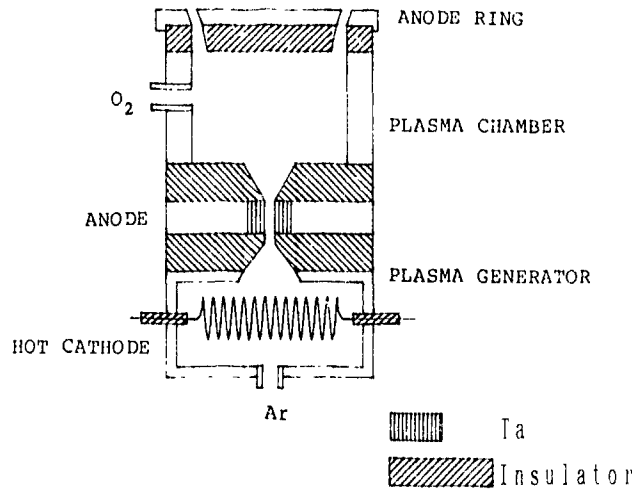

Fig. 1 Schematic diagram of the plasma cathode ion source

plasma flows into the plasma chamber due to the large pressure difference between the plasma generator and the plasma chamber generated by differential pumping. In the plasma chamber, an arc discharge is formed between the plasma cathode and the inside wall of the vessel at an operating pressure of 10^{-3}–10^{-2} Torr. The feed gas supplied to the plasma chamber is ionized both by the arc discharge and by contact with the plasma cathode which has a high temperature and density and is also highly ionized. Neutral atoms and ions in the plasma chamber cannot flow back into the plasma generator, because of the large pressure difference between these chambers, therefore, even a corrosive gas fed to the plasma chamber never causes deterioration of the hot cathode in the plasma generator. This fact and a fairly high gas pressure in the plasma generator permits a long operation of the ion source and, moreover, production of oxygen ions. To obtain ion beams with a uniform large area of irradiation, we adopted the anode ring with a circular slit. A plasma produced in the plasma chamber is extracted through the slit of the anode ring. The plasma generator is normally operated at discharge current I_{pg} ranging from 1 to 3 A. The arc discharge in the plasma chamber can be operated with a current I_{pc} in the range of 1 to 4 A, and in the anode ring I_{ar} up to 2 A.

3. Characteristics of the ion source

For the experimental results reported in this paper, the discharge gas in the plasma generator is Ar and the feed gases in the plasma chamber are Ar and O_2. The discharge voltage of the plasma generator, V_{pg}, was approximately between 30 and 50 V, depending on the its pressure P_{pg} and the discharge current I_{pg}. The arc discharge voltage between the plasma cathode and the plasma chamber, V_{pc}, was below 100 V, and the voltage between the plasma cathode and the the anode ring, V_{ar}, was around 100 V. Ion current density is measured by a Langmuir probe, ion species are analyzed by a quadruple mass spectrometer and the energy distributions of ions are measured by a Faraday cup with three grids, respectively. Uniformity of the density distribution of ion currents extracted from the ion source is measured by a movable single probe. Fig. 2 shows the ion current density distribution for various values of the arc discharge current I_{ar}. The ion current density, I_i, increases as I_{ar} is increased. This enables us to adjust I_i just by

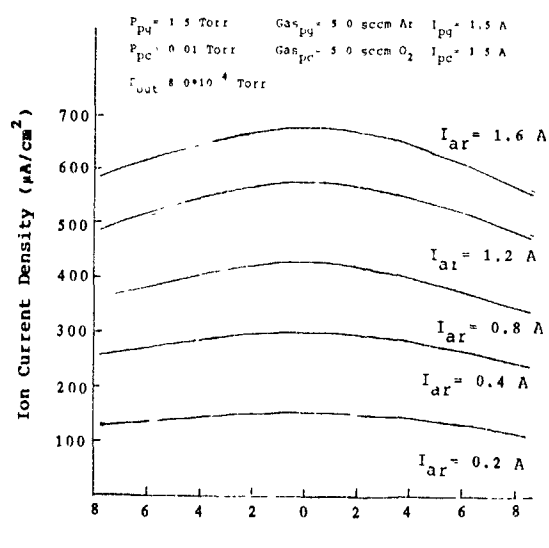

Fig. 2 Uniformity of density profile of the ion currents extracted from the ion source

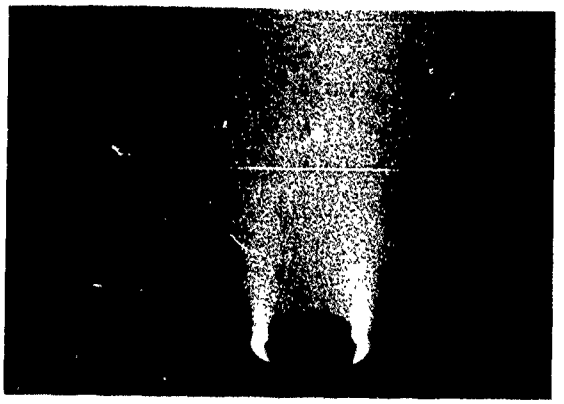

Fig 3 A picture of oxygen plasma from the plasma cathode ion source.

tuning I_{ar} without changing any other parameter. Uniformity of the ion density at a distance of 15 cm from the ion source in a 15 cm diameter area was better than 0 85 (minimum density/maximum density). This result indicate that the anode ring is useful for a large-area of irradiation. The operation of the ion source is pictured in fig. 3. The lifetime of the ion source was found to be more than 100 h with argon gas and the discharge currents of 2 A in the plasma generator. It is limited by the metallic hot cathode lifetime and deterioration of the insulator between the electrodes. The former happens by evaporation of the metallic hot cathode and the sputtering by Ar ions, whereas the latter comes from contamination on the surface of the insulators.

Fig. 4 shows ion mass spectra for four values of the arc discharge current I_{ar} in the anode ring. It is seen from the spectra that Ar^+, O^+ and O_2^+ ions are generated in the ion source. The peak values of the spectra increase with increasing I_{ar}. In these spectra, the O^+ peak value is found to be larger than peak values for any other ions. This fact indicates that the arc discharge in the anode ring can control the ionization of the plasma.

The energy distribution of ions is important for thin-film fabrication. The energy distribution obtained at two values of the anode ring voltage V_{ar} are shown in fig. 5. The energy spread of the peak value of the beam increases and the number of peaks in the distribution appear when the anode ring voltage V_{ar} is equal or lower than the plasma chamber voltage V_{pc} (a) When $V_{ar} > V_{pc}$ (b), the distribution shows only a single peak. Our results suggest that the ion energy distribution can be easily controlled by changing V_{ar}.

The demonstration of ion assisted deposition using this ion source was performed for an optical thin film. The substrates were fused silica, with the surfaces polished flat and parallel to within a few fringes so that accurate estimates of transmittance of the coated surface could be made taking account of the multiple reflections between the coated and uncoated surfaces of the substrate. Neutral oxygen could not be introduced into

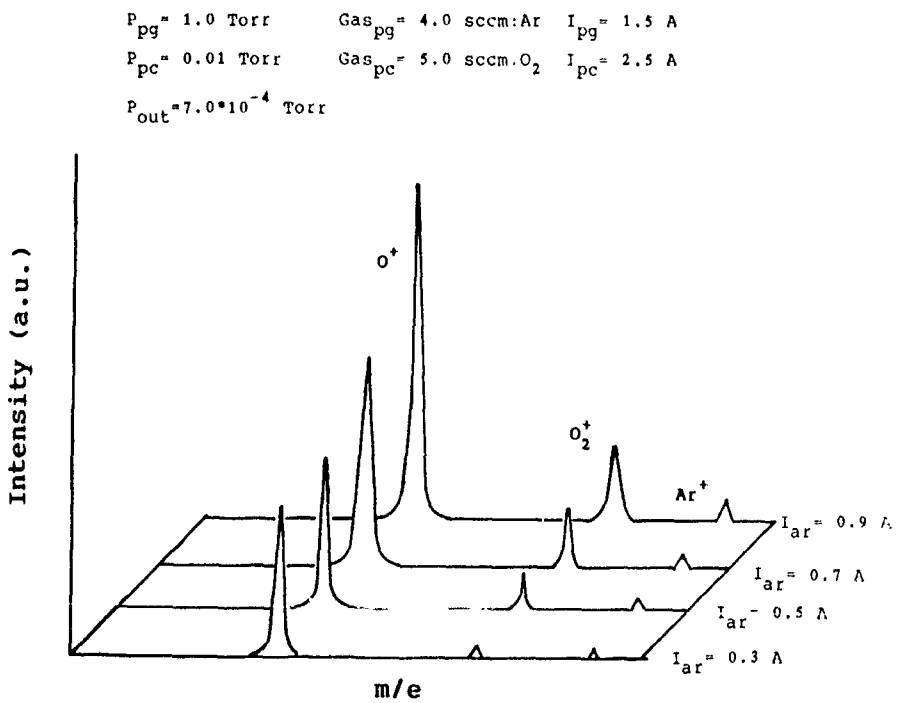

Fig 4 Mass spectra of ion beams for various values of I_{ar}.

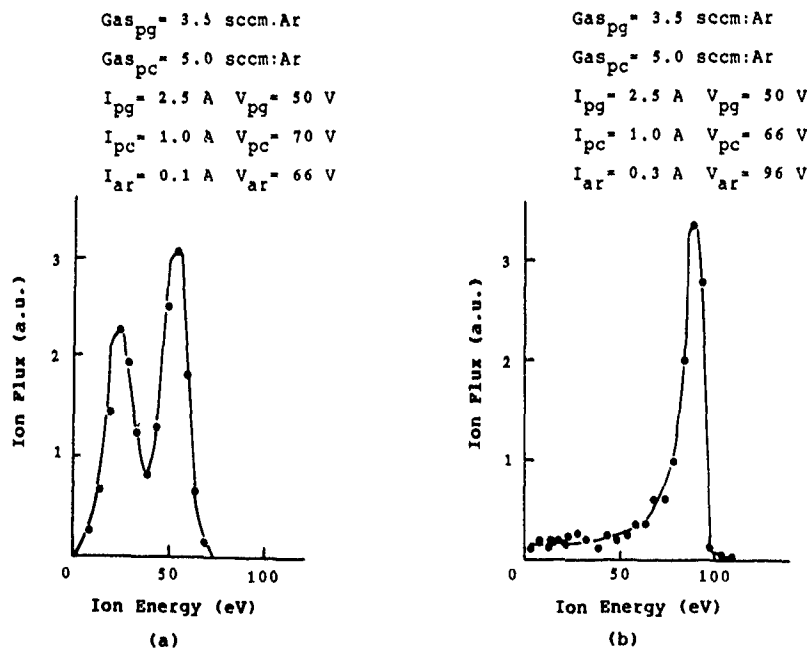

Fig 5 Energy distribution of ion beams produced by plasma cathode ion source· (a) low anode ring voltage, and (b) high anode ring voltage.

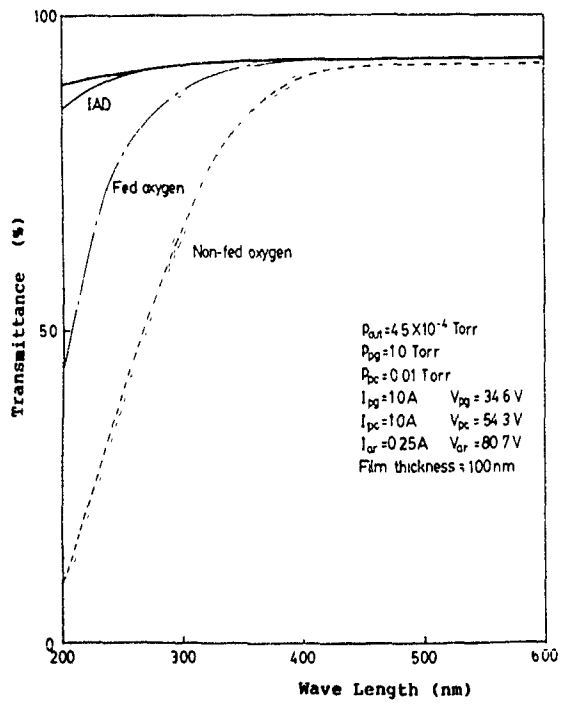

Fig 6. Transmittance of SiO_2 films on fused silica for 100 eV O^+/O_2^+ ion bombardment Film thickness in all cases is around 100 nm

the vacuum system to assist oxidation during reactive evaporation in this work. Fig. 6 shows the transmittance of SiO_2 films of about 100 nm physical thickness. The beam energy of the O^+/O_2^+ ions was around 100 eV. The advantage of ion bombardment is clear and can be seen by comparing the film transmittance for non-bombardment with that for bombardment present during deposition.

4. Conclusion

It was confirmed that a plasma cathode oxygen ion source can produce a stable ion beam and has a long lifetime. An ion source of this type proves to be useful for producing reactive ion beams. Furthermore, it has been recognized that this ion source can be used effectively for ion assisted deposition processes.

Acknowledgement

The authors would like to express their gratitude to Professor S. Kojima of Tokai University for his encouragement throughout this work.

References

[1] P.J. Martin, R.P. Netterfiled, W.G. Sainty, G.J. Clark, W.A. Lanford and S.H. Sie, Appl. Phys. Lett 43 (1983) 711.

[2] P.J. Martin, H.A. Macleod, R.P. Netterfield, G C. Pacey and W G. Sainty, Appl. Opt 22 (1983) 178.

[3] J.R. McNeil, A.C. Barron, S.R. Wilson and W.C Herrmann Jr., Appl. Opt. 23 (1984) 522

[4] W.G. Sainty, R.P Netterfiled and P.J. Martin, Appl. Opt. 23 (1984) 1116.

[5] C M. Kennemore III and V J Gibson, Appl Opt. 23 (1984) 3608.

[6] H.R. Kaufman, NASA Tech. Note, D-585 (1961).

[7] E. Yabe, S. Takeshiro, K. Sunako, K. Takayama, R Fukui, K. Takagi, K. Okamoto and S. Komiya, Nucl. Instr. and Meth. B6 (1985) 119.

[8] E. Yabe, A. Tonegawa, D. Satoh, K. Takayama, R Fukui, K. Takagi, K. Okamoto and S. Komiya, Vacuum 36 (1986) 43.

[9] E. Yabe, N Ishizaka, T Shibuya, A Tonegawa, K Takayama, R. Fukui, K. Takagi, R. Kikuchi, K. Okamoto and S. Komiya, Nucl. Instr. and Meth. B21 (1987) 190.

[10] E. Yabe, Rev. Sci. Instr. 58 (1987) 1.

[11] E. Yabe and R. Fukui, Jpn. J. Appl Phys. 26 (1987) 1179

[12] T. Shiono, T. Shibuya, Y. Harano, E. Yabe and K. Takayama, Nucl. Instr and Meth. B37/38 (1989) 166.

Nuclear Instruments and Methods in Physics Research B55 (1991) 310–313
North-Holland

A dual source low-energy ion implantation system for use in silicon molecular beam epitaxy

A. Gottdang, K. Eich, A. Hassenbürger, W.H. Schulte and B. Cleff
Institute of Nuclear Physics, University of Münster, 4400 Munster, Germany

D.J.W. Mous and R. Koudijs
High Voltage Engineering Europa B V, P.O Box 99, 3800 AB Amersfoort, The Netherlands

G.F.A. van de Walle and J. Politiek
Philips Research Laboratories P O. Box 80000, 5600 JA Eindhoven, The Netherlands

Recently an ion implanter for low-energy ion doping during molecular beam epitaxy has been developed The unit consists of a dual source injection system operating at 30 kV extraction, a beam transport system and a deceleration stage, located in an ultrahigh-vacuum MBE chamber Tests have shown that in the energy range of 150–2000 eV target currents of up to 100 μA can be reached with controllable beam focusing For uniform wafer implantation the decelerated beam can be electrostatically scanned with a lateral displacement from +70 to −70 mm at target position To obtain sharp doping transitions, the system is designed to switch within 1 s between the two independent microwave sources.

1. Introduction

Doping of silicon during molecular beam epitaxy (MBE) by the use of co-evaporation often presents difficulties because of low incorporation probabilities and surface segregation effects. However, these fundamental problems can be largely overcome when low-energy (< 2 keV) ion implantation is used to dope the growing layer [1–4]. Moreover, a better control of the doping profile can be achieved via target current monitoring. In several publications it has been shown that lattice damage and a decrease in electrical quality of the wafer as a result of low-energy ion doping are encouragingly small [5–7]. These are the main reasons for the growing interest on accelerated ion doping during MBE.

In order to create controllable high doping levels and to have the possibility to form sharp p–n transitions we recently developed a dual-source low-energy ion implantation system. The system fits to an already existing ultrahigh-vacuum Si MBE system at the Philips Research Laboratories, which is capable of handling 6 in. wafers [8]. The design aim was a 100 μA beam of boron, phosphorus, germanium and silicon and implantation energies of < 2 keV, with a switching time of < 1 s between the two sources.

2. System description

Fig. 1 shows a schematic layout of the low-energy implantation (LEI) system. The two microwave ion sources are fed with fluorine-containing gases (BF_3, PF_3, GeF_4 or SiF_4). The sources use the electron cyclotron resonance to obtain high ionization efficiency and low energy spread. A T-shaped antenna couples the microwave power into the plasma and hence no filament is needed, which ensures long lifetime of the source. The source operates at 30 kV extraction potential and is described in detail elsewhere [9].

An electrostatic switcher selects one ion beam for transport to the MBE vessel. After the electrostatic switcher a 90° magnet and slit system provide mass separation. The slit system consists of two pair of slits. The first one, with a fixed width is used for mass separation ($M/\Delta M > 80$) whereas the second pair of slits is motor driven and controls and stabilizes beam current via feedback of the target current. Moreover it enables sharp gradients in doping concentration to be obtained in a controllable fashion. After the slit system the beam subsequently passes a quadrupole-triplet, a 90° deflection magnet, an einzel lens and the deceleration stage.

0168-583X/91/$03.50 © 1991 – Elsevier Science Publishers B.V (North-Holland)

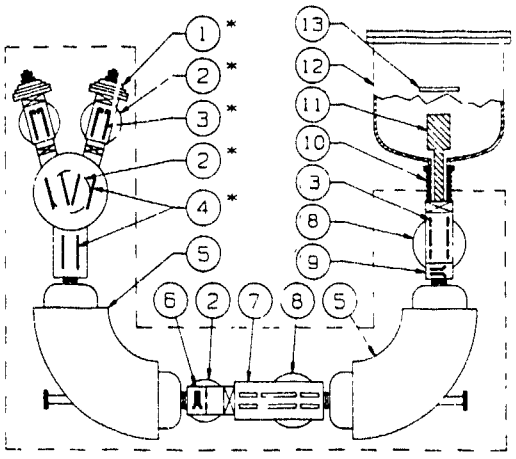

Fig 1 Schematic layout (side view) of the LEI system (1) ion sources, (2) turbomolecular pumps, (3) einzel lenses, (4) electrostatic switcher, (5) 90° magnets, (6) beam-profile monitor and slit system, (7) quadrupole triplet, (8) cryopumps, (9) beam-profile monitor, (10) 30 kV insulator, (11) deceleration stage, (12) MBE vessel, (13) 4-6 in wafer holder. The dashed line indicates the high-voltage area. Items marked with an asterisk are rotated 90° for clarity

The optical design of the system was done by the use of computer simulations based on matrix formalism. Fig 2 shows the beam-transport simulation from the source to the entrance of the deceleration stage. For the input parameters the High Voltage Engineering cold-cathode penning-source emittance data (4π mm mrad $(\mathrm{MeV})^{1/2}$) were used. Although emittance data of the microwave ion source were not yet available, experiments have shown that the beam quality of the microwave source is at least comparable to that of the penning source

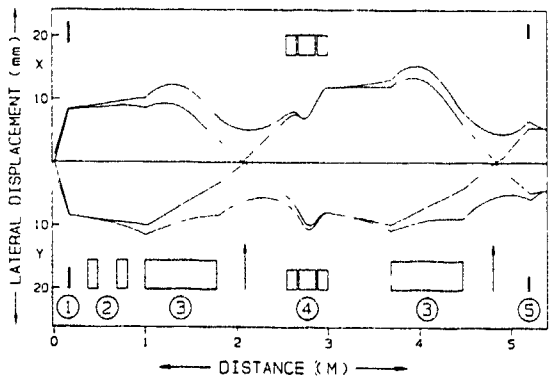

Fig 2 Beam transport simulation of the LEI system. The picture shows the envelope and central trajectory with maximal divergence in X and Y directions from the source to the entrance of the deceleration stage: (1) source and einzel lens, (2) electrostatic switcher, (3) 90° magnets, (4) quadrupole triplet, (5) einzel lens in front of the deceleration stage Arrows indicate the position of the beam-profile monitors

In fig. 2 arrows indicate the position of two beam-profile monitors, which display the X and Y beam profiles on an oscilloscope. During operation the beam transport parameters are adjusted to give a waist at the monitor positions which ensures a transport through the system in accordance with the beam transport calculations

During operation the ion beam is adjusted to the final implantation energy E_0 by setting the total LEI system at a voltage of $E_0/q - 30$ kV.

To ensure minimal gas load for the MBE system during source operation, the apparatus is equipped with a five-stage differential pumping vacuum system. In the beam line three 360 l/s turbomolecular pumps are followed by two 1500 l/s cryopumps, and after the second magnet only metal sealing is used. Most of the controls for vacuum operation and safety interlocks are located at beam-line potential ($E_0/q - 30$ kV). Controls needed for operation during implantation are located on ground potential They are connected to the system at beam-line potential by light guides

The LEI system is designed to switch within 1 s all beam transport parameters, including implantation current and energy, from one preset value (source 1) to the other (source 2) by a one-switch operation. To obtain fast switching of the magnetic fields, the magnet power supplies are especially designed to rapidly absorb or supply electrical energy. Moreover the magnetic fields are measured by Hall probes and are fed back to the supplies to avoid hysteresis.

3. Deceleration stage

Before reaching the target, the 30 keV ions are decelerated in a multiple-electrode system The unit is partly placed inside the MBE vessel (see fig. 1) and consists of an einzel lens to match the beam optics to the actual deceleration section, a multiple-electrode system for deceleration of the ions and an electrostatic focusing and deflection system All components that might be hit by the beam after deceleration are made of silicon to avoid contamination of the substrate due to sputtering Moreover, all elements that face the heated target are made of tantalum, aluminum oxide or silicon to avoid outgassing during operation.

The deceleration stage was designed by the use of the AXCEL-GSI program [10]. It calculates single beam trajectories and takes space-charge effects into account In order to test the designed unit, measurements were performed on a prototype with lithium and potassium ion beams and with different currents. In the test setup the beam profile was measured by scanning wires placed 220 mm behind the exit of the deceleration stage. This

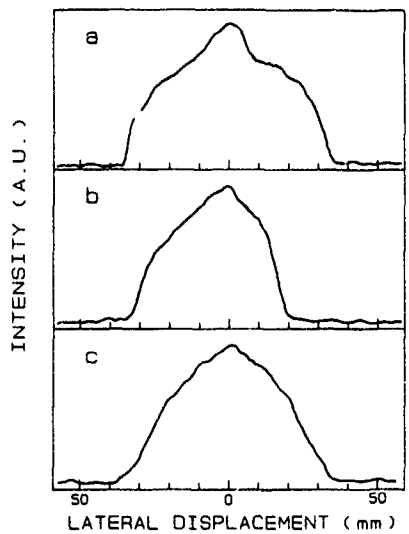

Fig 3. Beam profiles for three different focusing voltages ((a) low, (b) optimized, and (c) high) measured for a 22 μA, 250 eV Li^+ beam. Profiles were measured 220 mm behind deceleration stage.

position is comparable to the target position in the MBE vessel.

Figs. 3 and 4 show the focusing and scanning properties for a 22 μA, 250 eV Li^+ beam and a 27 μA, 500 eV K^+ beam, respectively. Fig. 3 shows the focusing properties for different voltages of the last electrode, which acts as an einzel lens. It was found that for the specified current and energy the beam could be focused to a spot of 60 mm diameter at target position.

To achieve uniform wafer implantation the scanning performances were investigated. Fig. 4 gives the beam position and profile in X and Y directions during a scan in Y direction. The beam was scanned from +70 to −70 mm at target position without a serious influence on the beam profile.

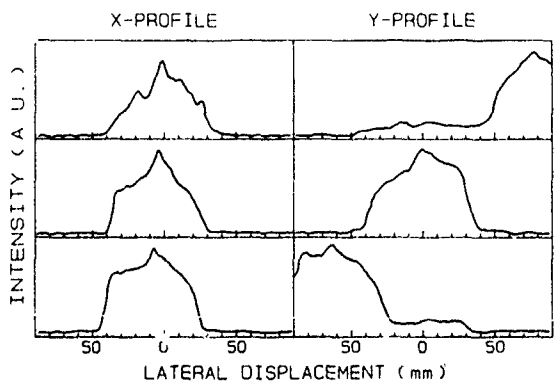

Fig. 4. Measured beam position and profile for different deflection voltages in Y direction and a 27 μA, 500 eV K^+ beam.

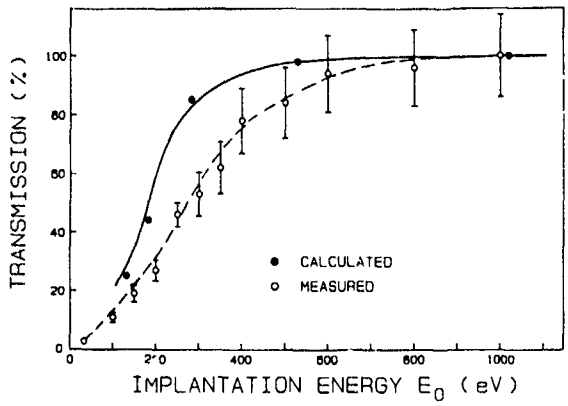

Fig. 5. Transmission of the deceleration stage as a function of the final implantation energy E_0. A 100 μA Li^+ beam was used as input for the deceleration stage Lines are drawn to guide the eye

Finally, the measured and the calculated transmission of the deceleration stage are given in fig. 5 in the case of a 100 μA Li^+ beam entering the deceleration stage. A transmission of > 80% was obtained for energies > 500 eV, whereas for energies < 500 eV the transmission falls off proportionally to the final energy E_0.

4. Summary

A newly developed dual ion source system for low-energy ion implantation is described. The system is designed to switch within 1 s from one source to another with simultaneous adjustment of all beam transport parameters including doping concentration and implantation energy. Tests have shown that in the energy range of 150–2000 eV target currents of up to 100 μA can be achieved with controllable beam focusing For uniform wafer implantation the beam can be electrostatically scanned from +70 to −70 mm at target position.

References

[1] Y. Ota, J. Appl. Phys 51 (1980) 1102.
[2] A Rockett, S.A. Barnett and J.E Greene, J. Vac. Sci Technol. B2 (1984) 306.
[3] R.P. de Carvalho, N. Djebbar, J Gutierrez and A Vapaille, J Vac. Sci. Technol B5 (1987) 515.
[4] M.A. Hasan, J. Knall, S.A. Barnett, J-E Sundgren, L.C. Markert, A. Rockett and J.E. Greene, J. Appl. Phys. 65 (1989) 172.
[5] M.W. Denhoff, D.C. Houghton, T.E. Jackman, M.L. Swanson and N.R. Parikh, J. Appl. Phys 64 (1988) 3938.
[6] J.-P. Noël, J.E Greene, N.L. Rowell, S. Kechang and D.C. Houghton, Appl. Phys. Lett. 55 (1989) 1525.

[7] J.-P. Noël, J.E. Greene, N.L. Rowell and D.C Houghton. Appl. Phys Lett. 56 (1990) 265.
[8] A A. van Gorkum, G.F.A van de Walle, R.A. van den Heuvel, D.J. Gravesteyn and C W. Fredriksz, Thin Solid Films 184 (1990) 207.
[9] W H. Urbanus, J.G. Bannenberg, S. Doorn, S. Douma, J. Ishikawa and F.W. Saris, Nucl Instr. and Meth. A267 (1988) 237.
[10] P Spädtke, Thesis (Gesellschaft für Schwerionenforschung, Darmstadt, FRG, 1987).

Nuclear Instruments and Methods in Physics Research B55 (1991) 314–317
North-Holland

A silicon MBE-compatible low-energy ion implanter

J.S. Gordon
VSW Scientific Instruments, Manchester M16 0JT, England

A. Bousetta, J.A. van den Berg and D.G. Armour
Department of Electronic and Electrical Engineering, University of Salford, Salford M5 4WT, England

R. Kubiak and E.H.C. Parker
Department of Physics, University of Warwick, Coventry CV4 4AL, England

The design of an ion implanter for the doping of shallow layers grown by silicon molecular beam epitaxy to a concentration 10^{20} cm^{-3} or higher is described. This requires a capability to deliver beams into the UHV growth chamber with ion energies in the range 500 eV down to 50 eV and lower, fluxes in the range 1 to 50 $\mu A\ cm^{-2}$ and uniformity over a 100 mm diameter wafer. The instrument has been designed to operate simultaneously with the MBE growth process, without having to compromise the latter. The practical problems which arise from attaching to an existing silicon MBE installation in which the position, electrical potential and environment of the target are predetermined have also influenced the final design.

1. Introduction

The provision of consistent and controllable in-situ doping of molecular beam epitaxy (MBE) grown semiconductor layers remains a major challenge. This is particularly so in silicon MBE, where there are physical and technical problems with the usual dopant species. Doping methods compatible with the proven ability of

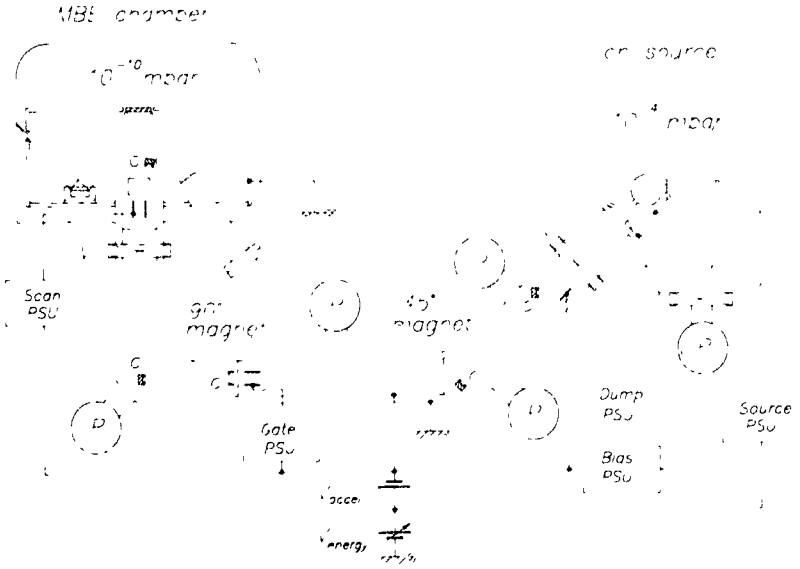

Fig. 1. Schematic diagram of the low-energy ion implanter. P indicates a high-vacuum pump, V a vacuum valve and C an ion current monitor. The dump and gate power-supply units allow zero-contamination mass switching, and the scan power supply rasters the beam over the target.

0168-583X/91/$03.50 © 1991 – Elsevier Science Publishers B.V. (North-Holland)

MBE to grow high-quality layers with thicknesses in the nanometer range and atomically sharp interfaces are required.

The most flexible doping method is to incorporate a mass-analyzed very-low-energy ion implanter with the MBE system [1–4]. This allows essentially any dopant species to be introduced without growth chamber contamination problems, and with accurate dosimetry. In this note we describe a very-low-energy ion implanter now being designed and built to attach to an existing silicon MBE system (VG Semicon V90) as part of the UK SERC Low Dimensional Structures and Devices Programme. The equipment is being used to grow and dope silicon and silicon–germanium low-dimensional structures. A high-temperature effusion cell for boron has been fitted to the MBE system which is giving good p-type co-evaporation doping performance particularly at substrate temperatures below 500°C. Compatible n-type doping is required at the growth temperatures below 600°C which are needed to realise the full potential of Si and SiGe low-dimensional structures. The prime task of the low-energy ion implanter is therefore to enable doping with phosphorus, arsenic or antimony, with a similar level of control to that being achieved with co-evaporation boron doping. In the longer term, it is planned to investigate the use of ion-assisted growth to enable epitaxial-growth temperatures to be reduced towards room temperature.

The features of the low-energy implanter are illustrated schematically in fig. 1. Ions are extracted from a universal source, accelerated to a transport potential of 10 kV, mass analysed and directed into the MBE growth chamber, where they are decelerated to the required energy prior to striking the target. Electrostatic deflectors are provided for beam gating and rastering, and there are current monitors at five locations along the beam line and in the growth chamber. Specifications for the instrument are given in table 1.

2. Physical design constraints

There are a number of constraints on the nature of the beam at the target for it to be compatible with simultaneous silicon MBE. These concern the following:
- choice of species,
- beam purity and accompanying gas load,
- ion energy range and incidence angle,
- flux and areal coverage.

The use of the well-established Freeman ion source [5] ensures compatibility with all the silicon dopant elements, plus a wide range of other species, including silicon itself, that may prove valuable for ion-assisted growth, ion etching, or ion-beam deposition within the MBE processing environment. The low emittance of the source is also important for magnetic mass analysis and for well-controlled ion deceleration.

The need for a very pure source feed material is considerably relaxed by comparison with UHV evaporators or non-mass-analyzed ion-beam attachments. The calculated typical resolving power of 150 (5% valley between adjacent masses) provides sufficient mass resolution to give pure monoisotopic beams of the silicon dopant species.

Sputtering of beam-line components by the ion beam could introduce very undesirable metallic impurities into the growing film. High-density, high-purity graphite components are used where 10 keV ions will strike surfaces, and careful arrangement of baffles along the beam line minimizes the possibility of sputtered material proceeding towards the MBE growth chamber. The final aperture before the growth chamber is constructed

Table 1
Design specifications of the silicon MBE-compatible low-energy implanter

Source	Freeman universal type, 45° angled
Acceleration voltage	10 kV
Mass-resolving magnet	45°, 350 mm radius, 0.65 T maximum field
Neutral-elimination magnet	90°, 300 mm radius, 0.75 T maximum field
Magnet switching, 0 to B_{max}	< 5 s
Gas load into MBE chamber	$< 5 \times 10^{-8}$ mbar l s^{-1}
Ion energy	10 keV down to 50 eV or lower
Neutral content of beam	≪ 0.1%
Beam size on target	25×20 mm^2
Beam-current density	up to 50 μA cm^{-2} before rastering (final target value 100 μA cm^{-2})
Uniform coverage	central 100 mm diameter of 150 mm diameter wafers to better than 10% uniformity (final target value 2%)
Raster frequency x	3000 Hz
y	12 Hz

from a silicon wafer to ensure that any sputtered material in this critical region is benign. The gas load into the growth chamber is arranged to be no greater than that expected from a typical effusion cell. This is achieved using five stages of differential pumping to reduce the pressure from 10^{-4} to 10^{-5} mbar in the implanter source chamber to 10^{-8} mbar prior to the MBE growth chamber.

Whilst the first mass-resolving magnet removes the neutral flux from the source from the ion beam, it is vital to take further steps to eliminate the high energy neutrals formed when ions in the beam charge exchange with residual gas species. These neutrals have the full acceleration energy and are of course unaffected by the deceleration field. The second electromagnet, therefore, as well as performing beam steering, removes unwanted neutrals from the ion beam. The opportunity for further fast neutral creation beyond the magnet is considerably reduced in the ultrahigh-vacuum (UHV) conditions that then prevail (10^{-8} mbar and better). Experience on a UHV low-energy ion-beam implantation and deposition system at the University of Salford has shown that neutral trapping at this stage effectively eliminates damage to silicon substrates from high-energy neutrals [6].

Ion energies in the sub-500 eV range are needed to ensure that the dopant can be confined only to the growing surface region. Choice of ion energy for MBE-compatible implantation involves more than simply selecting on the basis of the projected range, however. It is also necessary to take into consideration radiation damage, sticking coefficients and the efficiency of incorporation of the dopant ions into active sites for a given dopant/substrate combination. The bombardment of silicon at MBE growth temperatures with ions capable of producing significant atom displacements leads to the formation of highly stable complex defects which cannot be annealed out below about 1000 K. High temperature anneals after an implant are usually out of the question, as the resulting diffusion would destroy the nanometer scale doping profiles created during the growth process. Since it has been shown that several silicon atoms are displaced from lattice sites per incident ion during bombardment by an argon beam of only 60 eV [6], it is clearly important to try to reach the lowest possible energies to search for the point where there is still good incorporation efficiency, but stable damage structures are not formed.

The ability to achieve a uniform beam at low energies is dependent upon having a low-emittance beam undergoing a well-controlled deceleration. Experience on the University of Salford low-energy implanter has shown that beam quality can be maintained with less than 10 V difference between source and target potential [7]. In the instrument described here, however, the retardation optics must not alter significantly the MBE growth chamber. The solution adopted has been to use the cold shields of the chamber itself as the final lens element. Initial ion-optic simulations have shown acceptable performance down to 50 eV. It is an aim of the project to explore the low-energy performance limit.

The retardation geometry features normal beam incidence onto the target, as this has been found to give the best control at low energies. Normal incidence is also predicted to give better doping profiles than non-normal incidence [7]. The possible detrimental effects of channeling on doping profiles are currently under investigation [8], but it is not expected that the choice of normal beam incidence will be a significant disadvantage. Practically any incidence angle will reveal a channelling effect at these low energies because of the large critical angles for channelling.

The required beam flux at the target can be derived simply from the required doping level and known MBE growth rates. Taking the volume doping level N_a [cm^{-3}] to be given by

$$N_a = N_v \frac{f_i}{f_n} \frac{(I/ne)(a/A)}{J_n},$$

where N_v is the atom density of the film, J_n the molecular beam flux (atoms cm^{-2} s^{-1}), f_i and f_n the fractions of the incident ion and molecular beam fluxes which are incorporated into the growing film, I the beam current density (A cm^{-2}), n the ionic charge state, e the electronic charge, a the beam area and A the area over which the beam is rastered. Taking the case of silicon growing at one monolayer per second ($J_n = 10^{15}$ cm^{-2} s^{-1}), assuming f_i/f_n is unity and a/A is 1/32, the ion-beam current must be 10 μA cm^{-2} to reach doping levels in the 10^{20} cm^{-3} range. Based on the performance of the system at Salford University, a maximum current density of 50 μA cm^{-2} is expected, relatively independent of the selected energy. Even higher doping levels should be achievable by reducing the MBE growth rate (or halting it temporarily) or by reducing raster area

3. Technical and practical considerations

The physical arrangement of the system is shown in fig. 2. The overall geometry is fixed by the position and orientation of the target in the MBE growth chamber, and the normal beam incidence requirement. The electron beam evaporators used for silicon growth require the target to be horizontal, and facing downward. The normally incident ion beam must therefore enter the chamber vertically from below. This is achieved using a 90° deflecting magnet placed under the growth chamber. This section of the beam line must be disconnected from the remainder of the system and from the growth chamber, and moved clear whenever it is necessary to

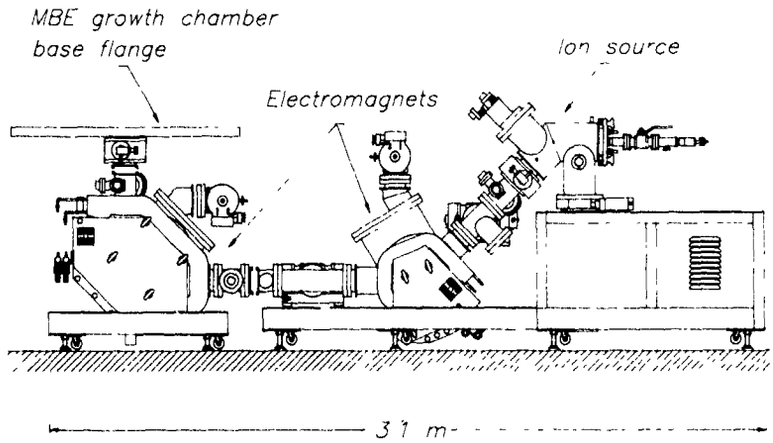

Fig 2 Elevation view of the low-energy ion implanter

lower the growth chamber flange to recharge the MBE evaporators.

The ion source is conventional except in that the arc chamber is attached at 45° so that a beam can be extracted at that angle down towards the first electromagnet. The target wafer and cooling shields of the MBE system cannot be taken to high voltage, therefore it has been necessary to design an isolated high-voltage flight tube to transport the ions from the source extraction lens to the retardation stage in the growth chamber. This runs within the (grounded) vacuum envelope, supported by ceramic insulators. Pumping conductance into the inner tube is provided with high-transmission mesh. A special mechanism withdraws the inner flight tube to allow gate valves at either end of the beam line to close. The choice of a 10 kV transport potential is a compromise which gives acceptable transport efficiency in a system in which totally effective space-charge compensation cannot be relied upon in the ultrahigh-vacuum stages, with good deceleration performance, operational convenience and acceptable levels of sputtering and heating in the beam line.

Using the two electromagnets with Hall probe feedback, and an electrostatic beam dump and fast beam gate, it is possible to switch between two species being extracted from the source with zero possibility of target contamination, and accurate dose control. A two-axis beam raster provides one complete coverage of 100 mm diameter in 40 ms, a time short compared to the time for one monolayer to be deposited. The practical performance of the retardation optics when the beam is deflected well off-axis is the subject of investigation.

4. Conclusions

The design of a low-energy MBE-compatible ion implanter differs considerably from conventional medium- and high-energy implanters. The combination with silicon MBE should allow the growth of low-dimensional structures with p- and n-type doping, and also longer-term investigations into ion-assisted growth processes.

Practical investigations are necessary into the achievable low-energy limit and the behaviour of the beam when it is deflected well off-axis for large wafer coverage.

Acknowledgements

The authors acknowledge the mechanical design skills of Simon Head of VSW. The project has been funded as part of the SERC Low Dimensional Structures and Devices Programme.

References

[1] Y. Ota, J. Appl Phys 51 (1980) 1102
[2] J C. Bean and E.A Sadowski, J. Vac Sci. Technol. 20 (1982) 137
[3] D C. Houghton, M W. Denhoff, T E. Jackman, M.L Swanson and N Parikh, J. Electrochem. Soc. 135 (1988) 3109.
[4] J.-P. Noël, J.E. Greene, N.L. Rowell and D C. Houghton, Appl. Phys. Lett. 56 (1990) 265
[5] J H Freeman, Nucl. Instr. and Meth. 22 (1963) 306
[6] A.H. Al-Bayati, K.G Orrman-Rossiter, R Badheka and D.G Armour, accepted for publication in Surface Science
[7] D G Armour, MRS Symp Proc. 100 (1988) 127
[8] A. Bousetta, J A. van den Berg, D G. Armour and P.C Zalm, these Proceedings (8th Int. Conf. on Ion Implantation Technology, Guildford, UK, 1990) Nucl. Instr. and Meth. B55 (1991) 565.

Nuclear Instruments and Methods in Physics Research B55 (1991) 318–322
North-Holland

Direct extraction of a Na^- beam from a sodium plasma

Mamiko Sasao [a], Hitoshi Yamaoka [b], Motoi Wada [c] and Junji Fujita [a]

[a] *National Institute for Fusion Science, Nagoya, Japan*
[b] *The Institute of Physical and Chemical Research, Saitama, Japan*
[c] *Department of Electronics, Doshisha University, Kyoto, Japan*

Negative sodium ions (Na^-) were extracted from a small multi-cusp ion source. A steady state sodium plasma was produced by primary electrons in a sodium gas evaporating from a metal sample placed in the discharge chamber. The Na^- current density of 1.5 $\mu A/cm^2$ was obtained from a single aperture of 1.5 mm diameter at relatively low discharge power of about 0.4 W and filament power of 50 W. Extraction characteristics were studied by changing the plasma electrode bias. The extracted Na^- current showed a dependence on the bias voltage similar to that of H^- or Li^- volume production.

1. Introduction

Volume production of H^- and Li^- ions is currently attracting considerable interest, not only from a viewpoint of using these ions in high-energy neutral beam heating and diagnostic systems for fusion plasmas [1–3], but also from a viewpoint of studying the production mechanism of negative ions in a plasma volume [4,5]. The H^- and Li^- ions are considered to be produced in the plasma volume by dissociative attachment (DA) of low energy electrons to diatomic molecules. In the case of H^- production, the DA process is strongly enhanced when hydrogen molecules are highly excited to vibrational and/or rotational states, dominantly through collisional excitation with fast electrons. However, the main destruction process of the H^- and Li^- ions in the plasma volume is detachment in collision with high energy electrons. Suppression of high-energy electrons in the extraction region by applying a filter magnetic field or by shaping the main plasma into a sheet is an effective way to increase the output current. It is also known that the negative ion current reaches a maximum when the plasma electrode facing the extraction region plasma is biased a few volts positive with respect to the anode potential [1,3].

In a volume plasma, Na^- ions are presumed to be formed under a more severe condition than H^- or Li^-: the electron affinity of Na is only 0.54 eV, smaller than that of hydrogen (0.76 eV) or lithium (0.62 eV). In the present paper evidence of direct extraction of Na^- ions from a sodium plasma is shown, and the dependence of extracted current on discharge voltage and the plasma electrode bias voltage are described. The effect of the magnetic filter is examined. The results are compared with the extraction characteristics of H^- and Li^- volume production sources.

2. Experimental arrangement

Fig. 1 shows a schematic diagram of the ion source and the geometry of the extraction and measurement of the negative ion current. The ion source consists of a cylindrical stainless-steel chamber (6 cm diameter by 7.5 cm long) surrounded externally by eight columns of samarium–cobalt magnets. Inside the chamber is a stainless-steel heat shield of 4.8 cm inner diameter. A plasma is produced by primary electrons emitted from a tungsten filament of 0.35 mm diameter and 80 mm long. The wall of the heat shield serves as an anode. A piece of sodium metal, placed in the heat shield evaporates dominantly due to the radiation from the filament which is heated with a typical power of 50 W. The heat shield temperature is monitored by a thermocouple at a position away from the filament. Only at the beginning of the operation argon gas is introduced to initiate a discharge. When the heat shield temperature reaches above 230 °C, the gas introduction is terminated and the steady-state sodium plasma is sustained with sodium vapour. A pair of external permanent magnets is fixed in the region adjacent to the plasma electrode. The maximum strength of the magnetic filter field is 207 G and this peak field is located 0.9 cm apart from the plasma electrode hole.

The beam is extracted by a two-electrode extraction system (a plasma electrode and an extraction electrode). The plasma electrode, which forms the end of the source cylinder, can be biased at a voltage, V_b, relative

Elsevier Science Publishers B.V. (North-Holland)

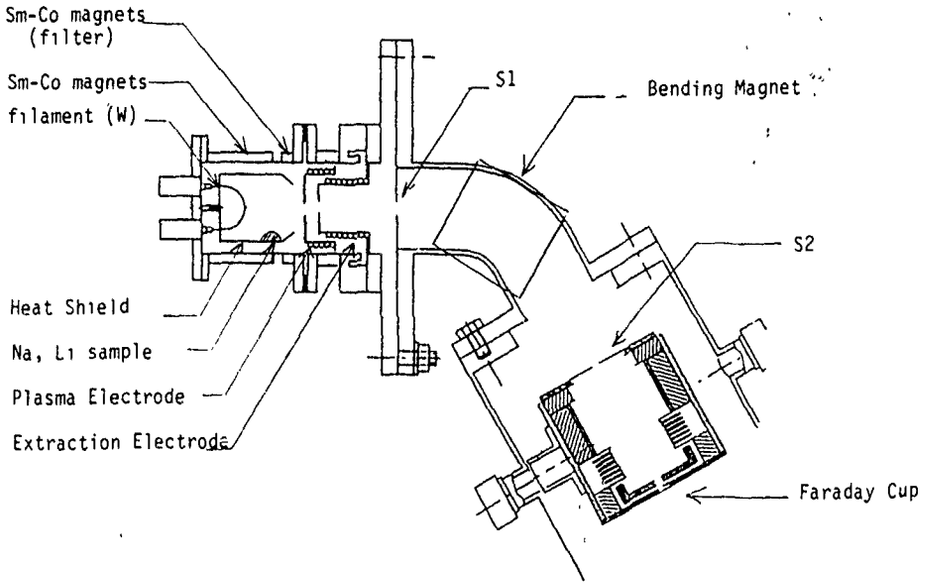

Fig 1 Schematic diagram of the experimental apparatus

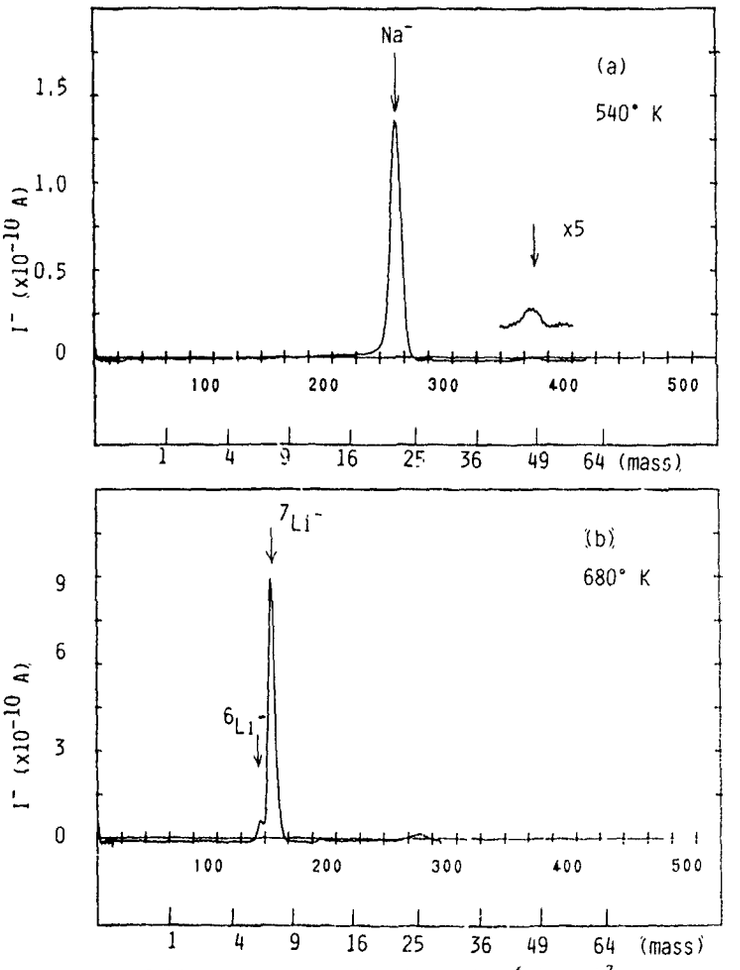

Fig. 2. Momentum spectra of (a) Na^-, and (b) $^6Li^-$ and $^7Li^-$

to the anode. The extractor aperture of each electrode is 1.5 mm in diameter. The extracted beam is detected with a Faraday cup after 60° bending with an electromagnet. In order to keep enough resolution in the momentum spectrum, two defining slits, S1 and S2, of 1.1 mm width each are inserted at the entrance of the bending section and that of the Faraday cup.

3. Experimental results and discussions

3.1. Characteristics of Na^- extraction

The extraction of a Na^- beam is examined on the momentum spectra. In this experiment, lumps of sodium and lithium metal are placed in the heat shield together. When the heat shield temperature reaches above 215°C, a signal of Na^- beam can be seen as shown in fig. 2(a). It disappears when the sodium is all consumed. Meanwhile, a peak of Li^- beam starts to appear as shown in 2b, when the temperature is above 300°C. The momentum of the peak in fig. 2a is defined to be that of Na^- by comparison with those of $^6Li^-$ and $^7Li^-$, and the mass of the ion species is confirmed by changing the acceleration potential from 200 to 500 V. In fig. 2a, a small peak of mass number 46 is seen, indicating a possible existence of Na_2^- in the extracted beam.

In fig. 3 the Na^- beam current as a function of the heat shield temperature is plotted. If thermal equilibrium is assumed in the heat shield, the dependence of the extracted Na^- current on the sodium vapour pressure, P, is roughly expressed as $I^- \propto P^{1/2}$, and it can be

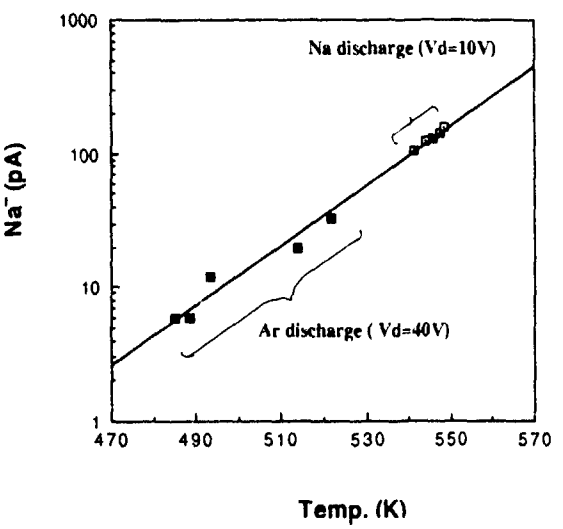

Fig. 3. The dependence of the Na^- beam current upon the heat shield temperature.

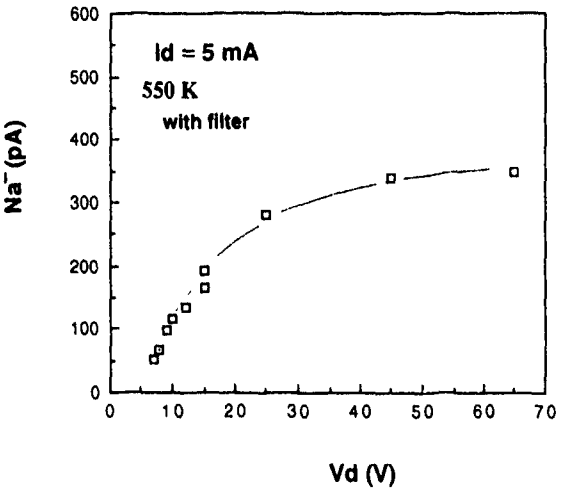

Fig. 4 The dependence of the Na^- beam current on the discharge voltage measured with the magnetic filter

scaled almost independently from the amount of introduced argon gas.

The dependence of the Na^- beam current on the discharge voltage is shown in fig. 4. Here, the discharge current and the heat shield temperature are kept almost constant, to be 5 mA and 550 K, respectively, and the plasma electrode bias is fixed at 0.5 V. The output current increases as the discharge voltage (V_d). There is a tendency for this to saturate at higher values of V_d.

The total beam current has been measured when the two slits S1, S2 are removed, and most of the beam is detected with the Faraday cup of 3.5 cm inner diameter. The Na^- current density of 1.5 $\mu A/cm^2$ was obtained at a relatively low discharge power of about 0.4 W and a filament power of 50 W.

3.2. The effect of the magnetic filter

In order to investigate the similarity with H^- and Li^- volume production, the dependence of the plasma electrode bias voltage (V_b) and the effect of the magnetic filter are examined. In fig. 5 the V_b dependences of the Na^- beam current (I^-) are shown, measured without the filter magnets (a) and with them (b). The drain current to the plasma electrode, I_b, is also shown in the figures. The I^- dependence on V_b is similar to those of H^- and Li^- extraction experiments [1,3]. Except that the current to the plasma electrode in the electron saturation region is suppressed by the filter field in (b) and the plasma potential to the anode is slightly different, the overall features are same in both cases. Rough estimations of the electron temperature and the density of the plasma in the extraction region can be made from the region of the I_b–V_b trace where the effect of the magnetic field is small. The validity of

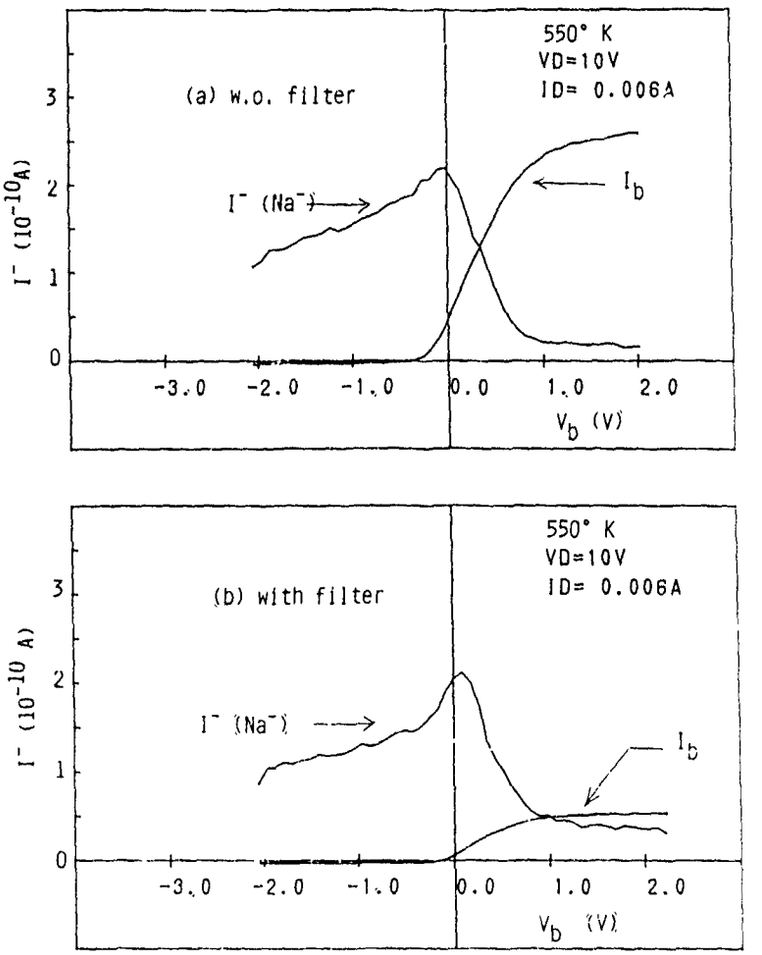

Fig 5 The dependence on the plasma electrode bias voltage (V_b) of the Na^- current and the drain current of to the plasma electrode (I_b), (a) without the magnetic filter, and (b) with it

the analysis is discussed in reference [6]. The electron temperatures are about 0.15 eV for both cases and the ion saturation currents are almost the same. These similarities may explain the fact that the extracted currents are the same at the maximum or when V_b is negative. On the other hand I^- in the electron saturation region without the filter field is less than a half of that with the filter, indicating the possibility of the destruction of Na^- by electrons near the extraction region.

The comparison of the dependence of I^- normalized to the discharge power upon the discharge voltage can be seen in fig. 6. Here the plasma electrode bias voltage was optimized so that the I^- takes a maximum. They are almost the same and the magnetic filter effect cannot be seen at V_d less than 15 V, as can be expected from the fact that the electron temperature is very low. On the other hand, at the higher discharge voltage, the normalized I^- measured with filter gradually decreases as the V_d increases, but it is constant when the filter magnets are removed.

4. Conclusions

Negative sodium ions (Na^-) were directly extracted from a self-sustained sodium plasma confined in a small multi-cusp ion source. The extracted Na^- current shows dependence on the plasma electrode bias voltage similar to that of H^- or Li^- volume production. When the plasma electrode voltage is in ion saturation or in the transition region, the effect of the magnetic filter on the extracted current is not observed, because the plasma in the extraction region is not affected by it within the present operational conditions. The Na^- beam current is almost proportional to the discharge voltage without the magnetic filter. The Na^- current density of 1.5 $\mu A/cm^2$ was obtained from a single aperture of 1.5 mm

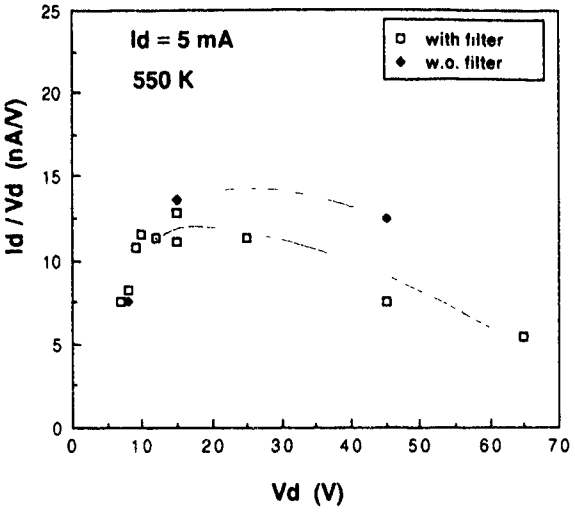

Fig 6 The normalized Na current (I^-) divided by the discharge voltage (V_d) as a function of V_d. Open symbols indicate measurements with the magnetic filter and closed symbols without it

diameter at relatively slow discharge power of about 0.4 W and filament power of 50 W.

References

[1] K.N. Leung, K.W Ehlers and M Bacal, Rev. Sci. Instr. 54 (1983) 56.
[2] S.R. Walther, K.N Leung and W B. Kunkel, Appl Phys Lett. 51 (1987) 566.
[3] M. Wada, H. Tsuda and M. Sasao, Rev Sci Instr 61 (1990) 433
[4] M. Bacal, Phys Scripta 2/2 (1982) 467.
[5] M.W. McGeoch and R.E. Schlier, Phys. Rev. A33 (1986) 1708.
[6] M. Wada, H Tsuda and M Sasao, to be submitted

Nuclear Instruments and Methods in Physics Research B55 (1991) 323–327
North-Holland

Negative-ion sources for ion implantation

A.J.T. Holmes and G. Proudfoot
AEA Technology, Culham Laboratory, Abingdon, Oxon, UK

The development of negative-ion sources has now reached the state where they can be considered for implanter applications. In the following paper a conceptual negative-ion source is described, based on production by dissociative attachment in the plasma. This type of source reduces some of the problems encountered with positive-ion sources such as surface charging and impurity ions and has the additional advantage of variable beam current at fixed beam energy.

1. Introduction

The implantation of ions into semiconductors can be readily achieved by the impact of a high-energy beam of low current density on the semiconductor surface. The beam energy determines the depth of penetration and is typically in the range 5–200 keV. However, the electric charge carried by the beam leads to a buildup of charge on the surface which modifies the beam energy and can lead to electrical breakdown problems.

The use of positive-ion beams always requires high-resolution mass analysis in order to achieve the desired low impurity levels. However, a negative-ion beam has a natural low impurity level. As a result substantially different system concepts can be considered for negative-ion implantation which could influence both process cost and reliability.

1.1 Charging effects

In the case of positive-ion beams, which have been used so far for ion implantation, this charge buildup is enhanced by secondary-electron emission from the surface so that the charging current is $(1 + \gamma_+)I_b$, where γ_+ is the secondary-electron emission coefficient per incident ion. Typically for normal incidence γ_+ lies on the range of 1 to 10 but takes on lower values for clean surfaces.

There exist two solutions to this problem. We could use a neutral-atom beam for the implant formed by passing the positive-ion beam through a gas cell. However, this solution has unattractive aspects; the gas load formed by the cell would cause pumping difficulties, beam control and mass analysis would be almost impossible and the conversion efficiency is low at high implanter beam energies. Alternatively we could use a negative ion beam for implantation. In this case the charging current is $(1 - \gamma_-)I_b$. There are very few experimental measurements of γ_- but Dixit and Ghosh [1] have observed that γ is similar for positive and negative ion beams of similar electronic configurations and ion velocities. Hence the effective charging current for low values of γ (i.e. around 1 to 2) is much reduced for negative ion beams but this relative effect becomes of lower importance if γ is large.

Table 1
List of negative-ion states for elements of interst for implanters

Element	State	Electron affinity [eV]	Comments
H	H^-	0.75	only stable state known
O	O^-	1.46	
	O_2^-	0.5	higher states exist
Li	Li^-	0.61	only state known
P	P^-	0.77	only state known
As	As^-	0.80	only state known
Cl	Cl^-	3.7	
F	F^-	3.6	
Ge	Ge^-	1.2	only state known
C	C^-	1.3	
N	N^-	?	
B	B^-	0.92	only state known

1.2 Beam purity

In a typical positive-ion discharge, the plasma contains many species of ion, impurities being present both as molecular ions and multicharged ions. Elements with stable negative polarity ions are listed in table 1 and include O^-, P^- As^-, Ge^- and B^-, all of which are routinely used dopants in the semiconductor industry. Unlike positive ions, there is virtually no evidence for the existence of stable molecular negative ions apart from oxygen which has O_2^- and O_3^- ionic states [2]. Some unstable molecular negative ions do exist, however, which have lifetimes in the picosecond range. It has been reported (but not in open literature) that some

0168-583X/91/$03.50 © 1991 – Elsevier Science Publishers B.V. (North-Holland)

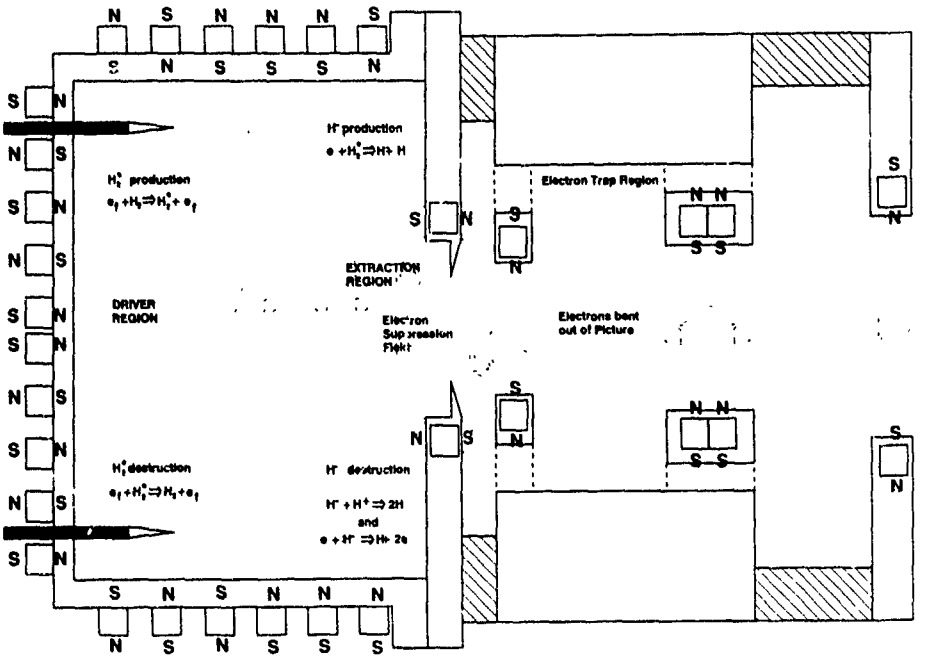

Fig. 1 A schematic of a volume negative-ion source and triode accelerator

experiments have seen evidence for molecular negative ions arising from magnetic momentum analysis. These ions could be impurities associated with oxygen or OH radicals. However, they are likely to be well separated from the ion mass of interest in momentum and hence easily analysed. In practise, therefore, negative-ion extraction and analysis can select the ion of interest with minimal impurity levels, provided the correct source materials are used. One aspect of beam purity special to negative-ion systems concerns the electron beam co-extracted with the negative ions from the discharge. Extensive work has shown that to a large extent this electron current in the beam can be reduced to a small fraction of the ion current, provided steps are taken to suppress and trap electrons within the accelerator.

1 3. Conceptual design

A conceptual design of a heavy-negative-ion source is shown in fig. 1. While similar in many ways to its positive-ion counterpart, there are significant differences in the design of the discharge chamber to enhance negative-ion formation and in the accelerator design to reduce electron extraction. This concept is based on an H^- accelerator which has been developed over the last few years in the Fusion and Strategic Defense Initiative Programmes. However, for heavy ions subtle changes are needed to optimise the performance to that needed for industry.

In the rest of this paper we discuss the design of negative-ion sources suitable for implanter applications and the likely performance that can be achieved.

2. Formation of negative ions

Three major methods of producing negative ions have emerged over the past few years. The first of these is the production of negative ions by double electron capture by a low-energy positive-ion flux passing thorugh a vapour. The second is by single-electron capture by absorbed neutral atoms on a low-work-function surface, such as a monolayer of cesium or bulk barium metal. The third is direct formation within a plasma discharge via dissociative attachment of vibrationally excited molecules in the gas phase of the element to be implanted.

All three techniques have been used to produce intense beams of H^- but there is a fundamental difference between the latter two techniques. The second method forms negative ions with initial energies of typically 200–400 eV, of which 2–5% is transverse to the beam axis [3]. This leads to low-quality beam optics with high transverse temperatures ~ 10 eV compared with 0.5 eV for dissociative attachment with resultant mass-analysis problems downstream when the desired ion species is separated from impurity ions. In addition, there is an effusion of the converter material (i.e. caesium or barium) at a low rate from the source. Neither situation is desirable. The dissociative-attachment tech-

nique has the advantage that the ions are formed at low energy and this yields highly collimated beams [4] with consequent high transmission to the target. Furthermore, there is virtually no effusion of impurities from the source. In the rest of this paper we will focus on sources based on dissociative attachment.

The fundamental process involved in the production of the negative ion occurs in essentially two steps. The first of these is the formation of vibrationally excited molecules via fast electron impact on unexcited molecules,

$$e_{fast} + X_2 \rightarrow X_2(\nu) + e_{fast},$$

where X_2 is the molecule of the desired element in the ground state and the electron energy is typically in excess of 20 eV. The term ν indicates that the molecule is elevated to a vibrational level ν. The second stage is the dissociative-attachment collision itself,

$$e_{slow} + X_2(\nu) \rightarrow X_2^- \rightarrow X^- + X.$$

In this instance the electron energy is usually about 1 eV and only the vibrational levels with internal energies which exceed about 0.6 of the dissociation energy of the X_2 molecule have a significant cross section.

As well as the production processes, there are various destruction processes for negative ions both in the plasma and on the walls of the discharge chamber The low binding energy of the extra electron leads to electron-detachment collisions,

$$e + X^- \rightarrow X + 2e,$$

which have a very large cross section (typically 100-fold the production cross section) for energetic electrons ($T_e > 10$ eV). There is also ion- ion recombination,

$$X^+ X^- \rightarrow X + X^*,$$

where X^* denotes an excited state. This cross section falls rapidly with increasing ion energy

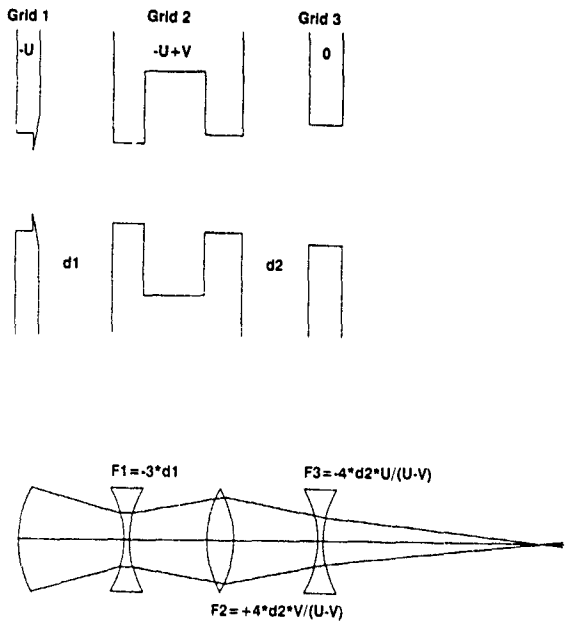

Fig. 2 Thin-lens model of the triode accelerator

3. Negative-ion source design

The above processes indicate the dilemma faced by the designers of negative-ion sources Fast electrons are

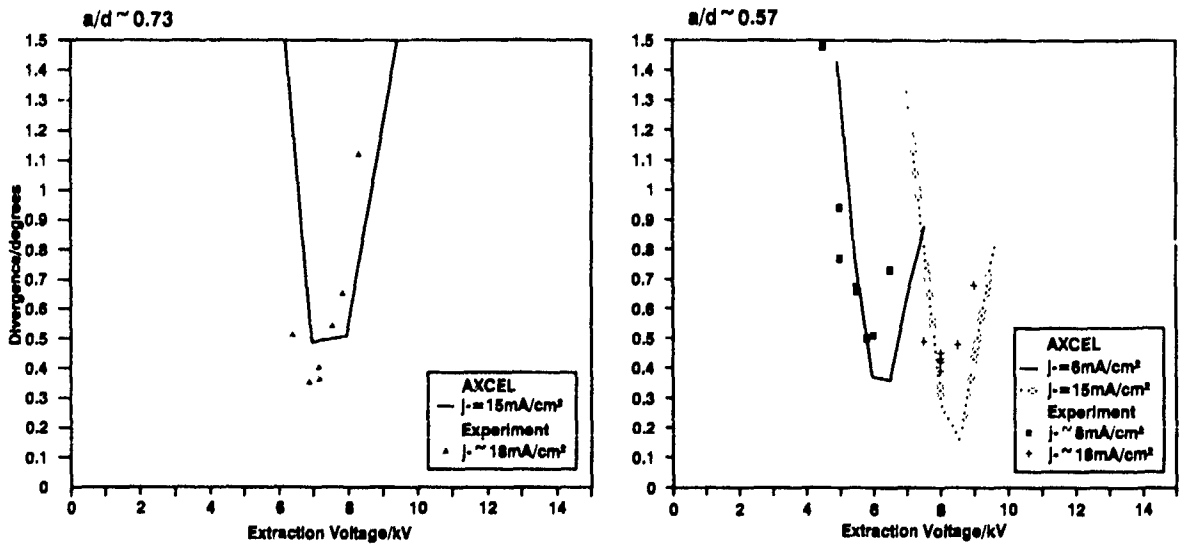

Fig 3 A comparison of AXCEL predictions of beam divergence vs extraction voltage to experimental data for two values of a/d (triode, H^-, $U = 70$ kV).

needed for vibrational molecule production (in particular for large values of v) but at the same time only slow electrons are needed for X^- production and the presence of fast electrons would reduce the density of X^-. These problems have been overcome by use of the so-called "magnetic filter".

The basic concept is shown in fig. 1 for an H^-/D^- source. The discharge chamber is a magnetic multipole confinement volume where fast electrons are emitted from hot wire filaments at the back. Here the plasma is ionised and vibrational molecules are formed. The magnetic filter is a long-range field created by the arrangement of magnets on the sides of the source [5] but can be also created by internal magnets within the discharge [6]. This field preferentially transmits low-energy electrons as only these electrons have the necessary collisionality to escape being trapped on field lines. The effective temperature change ΔT is given by

$$\frac{\Delta T}{T_2} = 0.6 \ln\left(\frac{n_1}{n_2}\right),$$

where n_1 and n_2 are the electron densities on the production and extraction sides of the filter and T_2 is the electron temperature on the extraction side of the filter and should be not more than 1 eV in a good source design. The dc arc discharge is not essential and a comparable approach would be possible with, for example, and rf-excited discharge of reactive ions.

The accelerator is also shown in fig. 1 and contains two accelerating gaps with bar magnets in all three electrodes. The function of the magnets in the plasma electrode facing the discharge is to suppress electrons from being extracted from the plasma. The transverse magnetic flux F created by the magnets, for the plasma electrode at plasma potential, attenuates the electrons by a factor

$$I_e = J_{e0} \exp(-Fv_e/8T_2),$$

where J_{e0} is the random electron flux in the plasma (i.e. $J_{e0} = en_2v_e$) and v_e is the thermal-electron speed and I_e is the electron current which is eventually extracted.

It is not practical to totally suppress the electrons as the stray fields of this structure interfere with the discharge so some electrons do enter the accelerator. These are swept out of the beam path by magnets in the upstream face of the second electrode, as shown in fig. 1, and are collected in the recess in the bulk of this electrode. Thus the maximum electron energy is just the first gap potential. The magnets in the downstream face of the second electrode and the third electrode serve to correct the trajectories of the X^- ions so that they exit the accelerator on the mechanical axis of the system. The magnetic flux is cancelled to the second order so that there is neither beam deflection or displacement.

4. Beam transport

Collimation of a beam produced from the negative ion accelerator described described above is straightforward; it is achieved by merely adjusting the ratio of the voltages across the two gaps. An explanation of this voltage ratio can be seen in fig. 2. There exist three lenses in the system where each lens located at a step change in axial electric field; a strong focusing and defocusing lens on either side of the second electrode and a weak defocusing lens at the third electrode. Only the focusing lens is variable over a significant range by altering the second electrode potential and collimation is achieved for a unique value of this voltage.

Fig. 3 shows experimental and numberical calculations of the beam divergence for different values of this voltage vor various beam currents of H^- ions. The final beam energy is constant, indicating that negative-ion triode accelerators do not have a unique beam perveance for collimation (unlike positive ion systems) which allows the ion dose rate to varied without readjusting the final beam energy. This could be a significant advantage.

5. Ion species

Many, but not all, of the elements of the periodic table can form stable negative ions, the major exceptions being the noble gases (except He). Table 1 lists the elements of interest for implantation and their binding energies.

Because of its low binding energy the more stable ion (if two or more states or species can form) is highly preferentially formed. Thus a small impurity of oxygen in a hydrogen discharge leads to virtually only O^- being created with the H^- ions being a minor fraction. This rules out using gaseous compounds of elements to produce discharges of the desired element if the ion of the combining element is more stable. It is preferable to create discharges by evaporation from an oven containing the required ion element.

At present H^- and D^- are formed from discharges of this type at energies of up to 100 keV and beam currents from a single aperture of more than 100 mA [7,8]. Negative-lithium beams have been formed at low energies and modest currents from a small discharge chamber [10] and O^- beams have been produced. In the latter case filament erosion is a serious problem and an rf discharge technique has been successfully developed [9].

In the case of the other elements no experimental work has been done but the technology of positive-ion sources in this area can be transferred directly to the design of a negative-ion source, as the only major difference is the addition of a magnetic filter within the

discharge chamber. However, the potential of negative-ion-beam-based systems is significant – not only could charging effects be reduced but mass analysis could be considerably simplified and the attendant impurities caused by beam impingement substantially reduced. Such a capability could be particularly important for the low-energy beams required for shallow doping. Alternatively, crude mass analysis could produce very-high-purity beams.

References

[1] S.D. Dixit and S.N. Ghosh, Indian J. Phys B55 (1981) 87
[2] H S W. Massey, Negative Ions (Cambridge University Press, 1976)
[3] C F A. Van Os, A.W Kleyn, L M Lea and A.J T Holmes, Rev. Sci. Instr 60 (1989) 539
[4] A.J T Holmes and M P S Nightingale, Rev Sci Instr 57 (1986) 2402
[5] A.J T. Holmes, T S Green, M Inman, A Walker and N Hampton, Proc 3rd Conf on Heating in Toroidal Plasmas, Grenoble, EUR 7979 EN (Commission of European Communities, 1982)
[6] K.N. Leung, K W Ehlers and M Bacal, Rev. Sci Instr. 54 (1983) 56
[7] R McAdams, A.J T Holmes and M P S Nightgale, Rev Sci Instr 59 (1988) 895.
[8] J.W Kwan, Private communication
[9] G Proudfoot, C M O Mahony and R. Perrin, Nucl. Instr. and Meth B37/38 (1989) 103
[10] S R Walter, K N Leung and W B. Kunkel, Appl Phys Lett 51 (1987) 566

Nuclear Instruments and Methods in Physics Research B55 (1991) 328–330
North-Holland

A low-energy fast-atom beam source

Yu.B. Gorbatov, A.F. Vyatkin and V.I. Zinenko

Institute of Microelectronics Technology and High Purity Materials, USSR Academy of Sciences, 142432 Chernogolovka, Moscow District, USSR

The characteristics of a low-energy (1–1.5 keV) fast-atom beam (FAB) source have been investigated The FAB was produced by resonance charge exchange of argon ions extracted from an rf multiaperture ion source on the gas flowing out of the source. A 20 mm diameter, 1.5 keV argon FAB with an equivalent current density of 0 9 mA/cm^2 has been obtained.

1. Introduction

Great interest has been recently shown in the use of fast-atom beams (FABs) for analytical and technological applications. The use of FABs instead of ion beams is essential for secondary-ion mass spectrometry when solving problems related to charging of dielectric surface [1,2]. A FAB is preferable from the viewpoint of reducing disruption of stoichiometric oxides [3] and the values of the interface charge and the surface state density in SiO_2–Si structures [4,5]

Efficient FAB sources are required to implement the advantages of FAB processing of dielectric and semiconductor materials As in the case of ion beam etching, this calls for a FAB with a beam diameter of several centimeters operating in the range 0.5–2 keV at an equivalent current density of about 1 mA/cm^2 The known low-energy argon FAB sources are based on charge exchange of Ar^+ ions into fast Ar^0 atoms immediately in the gas discharge plasma of the ion source [6,7]. Therefore, the yield and energy of fast atoms are determined by the parameters of gas discharge in the ion source (pressure, discharge voltage). This presents problems for independent control of such FAB parameters as energy and current density [6] The FAB source suggested is to a large extent free from this disadvantage.

2. Generation of fast-atom beams

The only way to produce an inert-gas FAB is the charge-exchange method. The greatest fast-atom yield is achieved in the low-energy region in the case of resonance charge exchange of ions on the parent gas. This is due to the large value of the resonance charge-exchange cross section σ_{10} at low energies. For instance, for the reaction $Ar^+ + Ar \rightarrow Ar^0 + Ar^+$, $\sigma_{10} \simeq 2 \times 10^{-15}$ cm^2 at an energy of 1 keV [1].

The conventional procedure for producing fast-atom beams in experiments on the physics of atomic collisions consists of passing an ion beam through a gas target in a collision chamber The part of the ion beam transformed into low-energy fast atoms can be estimated from.

$$F_0 \simeq 1 - \exp\left(-3.2 \times 10^{16} p \ell \sigma_{10}\right), \qquad (1)$$

where σ_{10} [cm^2] is the charge-exchange cross section, p [Torr] is the gas pressure in the collision chamber and ℓ [cm] is the length of the collision chamber. Estimates indicate that at $\ell = 10$ cm and $p = 5 \times 10^{-3}$ Torr over 90% of the 1 keV Ar^+ ions can be transformed into fast atoms with the same energy. Eq. (1) is only valid if the capture cross section σ_{10} is much larger than the loss cross section σ_{01}. However, this scheme of producing a low-energy FAB with a large diameter is difficult to realize since it also requires large diameters of the inlet and outlet channels of the collision chamber. This leads to considerable gas leak-in and necessitates the use of vacuum pumps with a high pumping speed. Moreover, the use of the collision chamber results in the location of the sample to be farther from the ion source and the decrease of the equivalent fast-atom current density owing to the angular divergence of the low-energy FAB. Therefore, we rejected the collision chamber and made an attempt to realize Ar^+-ion charge exchange in the parent neutral gas flowing from the ion source

3. Description of the fast-atom beam source

The source of positive ions was based on an rf ion source. The latter operates at a relatively high gas pressure in the discharge chamber ($p \simeq 10^{-2}$ Torr) as contrasted to, for instance, the Kaufman source ($p \simeq 10^{-3}$ Torr). This enables charge exchange of positive ions extracted from the source on the parent gas flowing from the source. It is well known that a "thick" extrac-

0168-583X/91/$03 50 © 1991 – Elsevier Science Publishers B.V. (North-Holland)

tor with a channel several millimeters long is used in rf sources to ensure the difference in pressure between the discharge chamber of the source and the high-vacuum chamber. When extracting ions from such sources, a negative effect is observed which is caused by a significant ion loss as a result of charge exchange of ions into fast atoms on the gas in the long extractor channel [8]. This phenomenon was used to produce an argon FAB of a large diameter utilizing a multiaperture "thick" extractor.

The schematic diagram of the multiaperture fast argon atom source is shown in fig. 1. The discharge chamber of the rf source is made of quartz. An argon rf discharge was excited by an inductor connected to an rf generator ($P = 400$ W, $f = 13.56$ MHz). An extracting ion optical system included a screen grid made of 0.5 mm thick molybdenum foil and a "thick" extractor. The screen grid had 40 holes, 2 mm in diameter, arranged over a 20 mm diameter circle. The extractor had 2 mm diameter cylindrical channels. The spacing between the screen grid and the extractor was 1 mm. When passing through the long extractor channels, part of the Ar^+ ions extracted from the source were transformed into fast atoms by way of resonance charge exchange on the parent gas flowing from the source. As a result, a compound beam of ions and fast atoms with equal energy was formed at the source outlet. The ions were removed from the beam by an electrostatic field and a pure beam of fast argon atoms struck the target. The high-vacuum chamber connected to the source was pumped down by a 600 l/s diffusion pump.

The radial distribution of the fast-atom equivalent current density was measured by a moving thermocouple detector which was an 8 mm diameter disk made of 50 μm thick tantalum foil. A thermocouple was welded

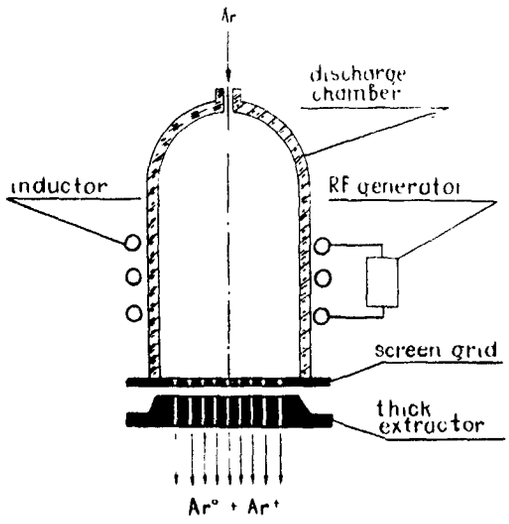

Fig 1 Schematic diagram of the FAB source

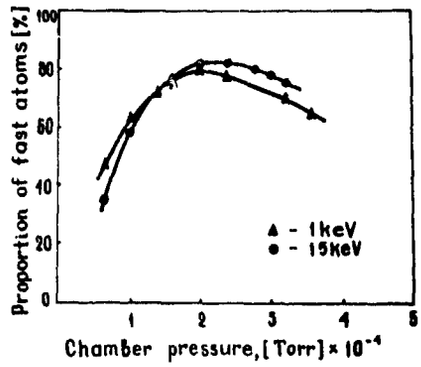

Fig. 2. Proportion of fast atoms in the beam versus chamber pressure.

onto the reverse side of the disk. The inlet aperture of the detector was 2 mm in diameter. The detector was calibrated by an ion beam with known energy. The sensitivity of the detector was 1.6×10^{-2} V/W. At the same time it could operate in the Faraday cup mode to measure the ion component current of the beam.

4. Experimental results and discussion

From eq. (1) it follows that the dependence of the yield of fast argon atoms upon resonance charge exchange at a given energy is defined by the product of the gas pressure in the extractor channel, p, and the channel length ℓ The channel length was varied from 5 to 12 mm. The pressure in the channels could be indirectly estimated by the argon pressure in the high-vacuum chamber.

Fig. 2 shows the percentage of fast argon atoms in the beam at the rf source outlet versus pressure in the high-vacuum chamber for an optimal extractor channel length of 10 mm Measurements were taken on the

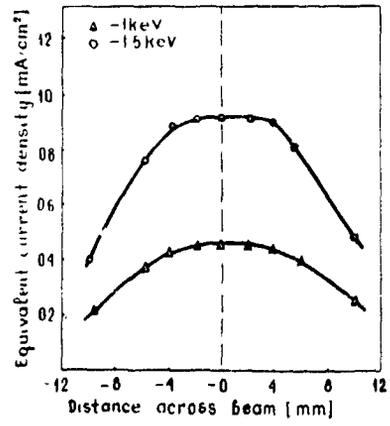

Fig 3 Radial distribution of FAB equivalent current density.

beam axis at a distance of 7 cm from the rf source at energies of 1 and 1.5 keV. It is seen that at an optimal pressure the beam contains up to 80% fast argon atoms.

Fig 3 illustrates the radial distribution of the equivalent current density of the fast argon atoms at 1 and 1.5 keV, respectively, measured in the optimal-operation mode of the rf source (high-vacuum chamber pressure $= 2 \times 10^{-4}$ Torr). At 1.5 keV the fast-atom equivalent current density reaches 0.9 mA/cm^2 which is sufficient for the use of this source in the etching of dielectric materials The equivalent current density may be increased by increasing the geometric transparency of the electrodes of the ion extraction system. In principle there are no restrictions on the increase of beam diameter. No impurities were observed in the mass spectrum of ions extracted from the source

5. Conclusion

It has been shown that an efficient low-energy fast-inert-gas atom source can be created on the basis of the rf ion source using resonance charge exchange of ions on the parent gas emerging from the source. In the optimal-operation mode, up to 80% Ar^+ ions are transformed into fast atoms. The obtained equivalent current densities of the fast Ar^0 atoms appreciably exceed those obtained with the use of other ion sources.

References

[1] N Klays, Vacuum 35 (1985) 131
[2] J.A. Van den Berg, Vacuum 36 (1986) 981
[3] S O Saied, J L. Sullivan, T Choudhury and C.G Pearce, Vacuum 38 (1988) 917.
[4] P V McCaughan, R A Kushner, D.L Simms and C W White, J Appl Phys 51 (1980) 299.
[5] T Mizutani and S Nishimatsu, J Vac Sci Technol A6 (1988) 1417
[6] S O Saied, J L Sullivan and R K Fitch, Vacuum 38 (1988) 111
[7] F Shimokawa and K Nagai, Nucl Instr and Meth B33 (1988) 867.
[8] A.N Serbinov and V I Moroka, Prib Tekh Eksp N5 (1960) 27, in Russian

Nuclear Instruments and Methods in Physics Research B55 (1991) 331–334
North-Holland

Double hollow cathode ion source for metal ion-beam production

Akira Tonegawa, Hirokazu Taguchi and Kazuo Takayama

Department of Physics and Institute of Research and Development, Tokai University, 1117 Kitakaname, Hiratsuka, Kanagawa 259-12, Japan

A double hollow cathode ion source can produce high current and a high amount of metal ions (Mo, Ta, etc.) by using a new sputtering mode of hollow cathode discharge. A high density plasma is formed inside the narrow canal of the second hollow cathode, which is located between the first hollow cathode and an anode along an axial magnetic field (0.6–1.5 kG). A negative sputter voltage is applied to the second hollow cathode with respect to the anode, resulting in sputtering and ionization of the refractory material of this cathode. In the case of a Mo or Ta sputter target with an argon carrier gas, the metal ion ratio reaches 49–51% at a sputter voltage in the range 460–580 V. A total ion beam current of 9.0 mA is obtained at an extraction voltage of 20 kV.

1. Introduction

The use of ion beams as an effective means for changing the surface properties of materials has gained increasing interest in the last few years. There is a great demand for ions of various kinds of refractory materials, such as molybdenum (Mo), titanium (Ti) and tantalum (Ta), for new material production and plasma processing.

Cathode sputtering is the most universal method to feed metal ions into an ion source discharge. However, the amount of metal ions in the total ion beam is 10 to 20% and the metal ion beam current is several hundred μA.

In order to increase the amount of metal ions and metal ion beam current, a double hollow cathode ion source has been developed for the production of ions of various refractory materials by using the sputtering technique of hollow cathode discharge [1,2]. This ion source consists of two hollow cathode tubes with different diameters, connected in series and made of refractory materials. The discharge path becomes narrow in the second hollow cathode, which is located between the first hollow cathode and an anode. An axial magnetic field serves to further compress the narrowed discharge path. The role of these structures of the ion source is as follows. A high density plasma is formed inside the narrow canal of the second hollow cathode. A negative high voltage (~1 kV) is applied to the second hollow cathode with respect to the anode, resulting in sputtering of the refractory material of this cathode. The sputtering efficiency can be increased by increasing the negative voltage without affecting the main discharge conditions. The sputtered refractory materials of the second hollow cathode can be effectively ionized by this high density plasma and a new discharge mode: hollow cathode discharge with inverse magnetron mode.

In this paper, we describe our ion source developed

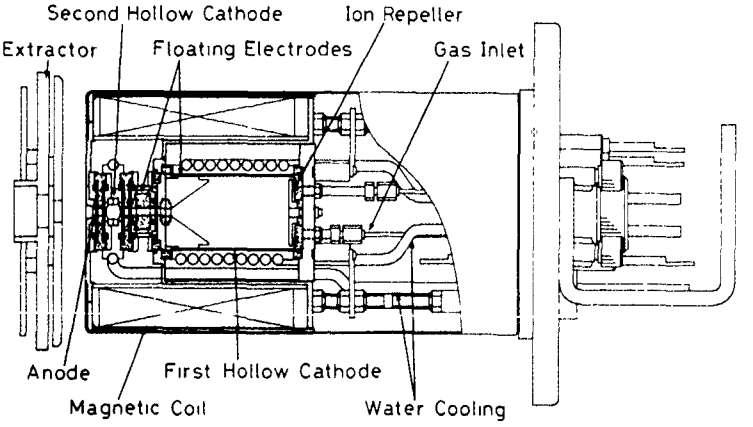

Fig. 1. Schematic diagram of the double hollow cathode metal ion source.

0168-583X/91/$03.50 © 1991 – Elsevier Science Publishers B.V. (North-Holland)

to produce metal ions of Mo or Ta and investigate the characteristics of extracted ion beams.

2. Experimental apparatus

Our ion source (fig. 1) consists of three parts: a cylindrical hollow cathode, a second narrow hollow cathode as a sputter target, and an anode. The dimensions of the first cylindrical hollow cathode are 40 mm diameter and 70 mm length. In front of the first hollow cathode, there is a narrow orifice (4 mm diameter) which is formed by a tapered electrode and a floating electrode (4 mm diameter and 16 mm length) which is made of ceramic insulator. The second narrow hollow cathode, which has a small canal (4–8 mm diameter and 12 mm length), is electrically insulated from the other electrode. Both the first and the second hollow cathode, which are made of a refractory metal (Mo, Ti or Ta), serve as a sputter target. The construction of the second hollow cathode is such that it is easy to replace the target material. The anode is the inner surface of a canal (4 mm diameter and 2 mm length). An axial magnetic field of up to 0.6–1.5 kG is produced by a magnetic coil, and a mild steel yoke surrounds the first hollow cathode region. Argon carrier gas is fed through a small orifice (1 mm diameter) in the back of the ion repeller (30 mm diameter) at the bottom of the cathode. The copper blocks which are in thermal contact with the first and second hollow cathodes are water-cooled in order to sustain a cold hollow cathode discharge mode. Hollow cathode effects [3,4] help to produce a high density plasma and ionize the metal ions in our ion source. Also, the hollow cathode may be one of the solutions to improve the lifetime of the ion source because of a large electron emitting capability [5,6]. In this ion source, the large pressure difference between the hollow cathode tube and an ion beam region can be easily maintained. The pressure in the first hollow cathode tube is typically between 0.2 and 0.7 Torr, while the pressure in the ion beam region is maintained to below 1×10^{-4} Torr by differential pumping

Fig 2 shows the geometrical, magnetic and electrical parameters of our ion source. A discharge is formed between the first hollow cathode and the anode inside the small canal. The plasma is compressed when it flows through the small canal of the second hollow cathode along the axial magnetic field; as a result, the temperature and density of the plasma in this cathode are raised significantly A highly ionized, relatively dense plasma exists near the anode. When a negative sputter voltage (up to 1 kV) with respect to the anode is applied to the second hollow cathode as shown in fig. 2, the target material of the second hollow cathode is sputtered by dense plasma inside the canal. At the same time, the motion of the emitted electrons from the second hollow

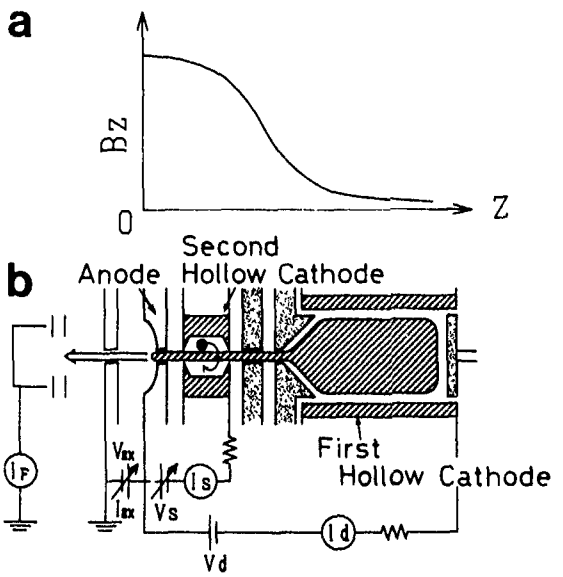

Fig 2 Magnetic and electric parameters of our ion source (a) magnetic field distribution, (b) design and electric circuit.

cathode is an inverse magnetron one along an axis perpendicular to both B and E in this cathode. The resulting motion is effective for the ionization of the metal atoms. In this method, the metal ion beam current and the metal ion ratio can be easily increased by changing the negative sputter voltage applied to the second hollow cathode without changing the other discharge conditions.

Ions are extracted through a small outlet aperture on the anode They are accelerated by the potential difference between the anode and the extractor. The extraction voltage for ion beams is ~ 5–20 kV. The total ion beam current is measured by a movable Faraday cup placed just behind the extractor. The mass spectrum is analyzed by a 90° sector magnet.

3. Experimental results

We have investigated some characteristics of the double hollow cathode metal ion source using a sputter target made of Mo or Ta.

Fig. 3 shows the extracted current I_{EX} (○, △, □) and the total ion beam current I_F (●, ▲, ■) as functions of the extracted voltage V_{EX} at a discharge current of 0.4 A and a gas pressure of 0.3 Torr by using the Mo sputter target. When the potential of the second hollow cathode is floating, I_{EX} is saturated with the increase of the extracted voltage V_{EX}. However, when the sputter voltage is applied up to $V_s = 600$ V, I_F is unsaturated and reaches up to 9.0 mA at the extracted voltage of 20 kV. It is clear that the plasma density is increased in the second hollow cathode by applying the sputter voltage.

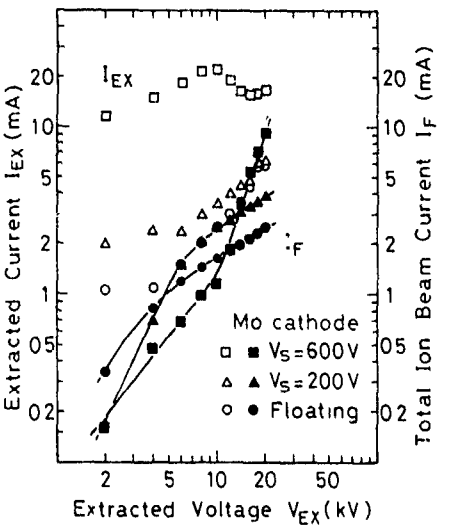

Fig. 3 The extracted current I_{EX} (○, △, □) and the total ion beam current I_F (●, ▲, ■) as functions of the extracted voltage V_{EX} at a discharge current I_d of 0.4 A and a gas pressure of 0.3 Torr

Fig. 4 shows the ion beam current of Ar^+ and Mo^+ plotted against the sputter voltage V_s at an extracted voltage of 5 kV. The diameter d of the second hollow cathode changes as 4 (○, ●), 6 (△, ▲) and 8 mm (□, ■). The argon pressure in the first hollow cathode tube is approximately 0.2 Torr and the discharge current I_d is fixed at 0.8 A. In the case of $d = 8$ mm, Mo^+ rapidly rises with increasing V_s, although Ar^+ decreases.

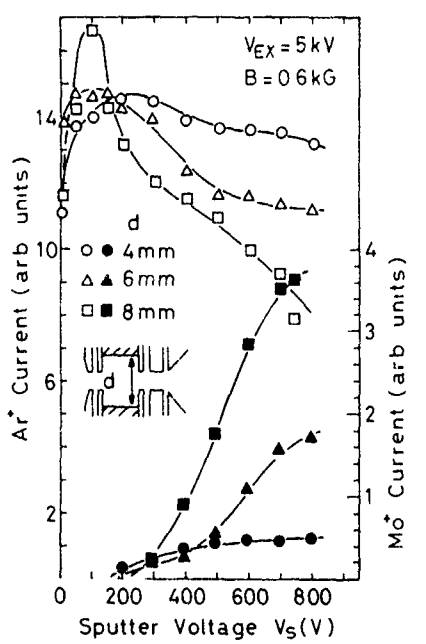

Fig. 4. The ion beam current of Ar^+ and Mo^+ is plotted against the sputter voltage V_s when the diameter d of the second hollow cathode is changed from 4 to 8 mm, at a gas pressure of 0.2 Torr and a discharge current of 0.8 A.

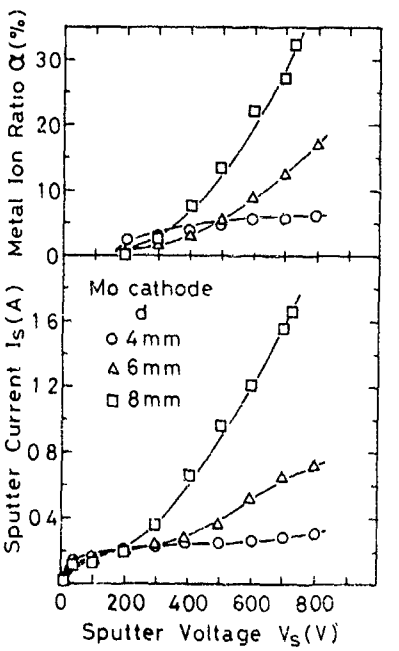

Fig. 5. The metal ion ratio α and the sputter current I_s are plotted against the sputter voltage V_s under the same conditions as in fig. 4.

In fig. 5 the metal ion ratio α ($Mo^+/(Ar^+ + Mo^+)$) and the sputter current I_s are plotted against the sputter voltage V_s at the same conditions as in fig. 4. The I_s initially increases like the ion-saturation characteristic until $V_s = 200$ V. After that, the V_s–I_s curve shows substantial deviation from the ion-saturation curve with the increase of d of the second hollow cathode. It is evident that the discharge mode is shifted from the conventional sputter mode to a new discharge mode with increasing V_s. This new discharge mode caused both sputtering and ionization: the hollow cathode discharge with inverse magnetron motion. In particular, when $d = 8$ mm, I_s rapidly increases with increasing V_s. When V_s is equal to 700 V, α and I_s are ~ 34% and 1.7 A (~ 674 mA/cm^2), respectively.

Table 1
Typical parameters and the metal ion ratio of our ion source for an extracted voltage of 5 kV

Metal	Discharge power $I_d \times V_d$ [W]	Sputter power $I_s \times V_s$ [W]	Metal ion ratio α [%]
Mo	0.8×300	1.74×580	51
Ta	0.8×320	1.72×460	49

Typical parameters of the discharge characteristics and the metal ion ratio α for the Mo and Ta sputter targets are given in table 1 for a 5 kV extracted voltage at a gas pressure of 0.3 Torr. At a sputter voltage in the range 460–580 V, I_s is ~ 1.7 A and α is 49–51%

The lifetime of this ion source is about 6 h and it is limited by the dielectric breakdown between the anode and the sputter target

4. Conclusions

We have developed the double hollow cathode metal ion source in order to increase the metal ion ratio and the ion beam current When the sputter voltage is applied perpendicular to the axial magnetic field in the second hollow cathode, a new discharge mode is obtained: the hollow cathode discharges with inverse magnetron motion Our experimental results with this ion source have shown that refractory materials (Mo (· Ta) of the second hollow cathode can be effectively sputtered and ionized by this new discharge mode by changing its diameter from 4 to 8 mm. At the sputter voltage from 400 to 700 V, the metal ion ratio α is ~ 30–51% The total ion beam current obtained is ~ 9 0 mA for a 20 kV extracted voltage

Acknowledgement

This work is supported by a Grant-in-Aid for Scientific Research from the Ministry of Education, Science and Culture, Japan

References

[1] S Kogure, A Tonegawa, K Takayama, R. Fukui and K Takagi, Nucl. Instr and Meth B37 (1989) 201
[2] A Tonegawa, H Taguchi and K. Takayama, Proc 12th Symp on ISIAT'90, Tokyo, vol 1 (1990) p 71
[3] A. Gunthershlultze, Z Tech Phys, 11 (1930) 49
[4] H Schuler, Phys Z 22 (1921) 264
[5] A Tonegawa, T Shimoyama, E Yabe, K Takayama, K Takagi, R Fukui, R Kikuchi, K Okamoto and S Komiya, Nucl. Instr and Meth B21 (1987) 212
[6] A Tonegawa, E Yabe, K Sunako, K Takayama, K Takagi, R Fukui, K Okamoto and S Komiya, Nucl Instr and Meth B6 (1985) 127

Nuclear Instruments and Methods in Physics Research B55 (1991) 335–338
North-Holland

A cold-hollow-cathode lateral-extraction Penning ion source

M. Ma, J.E. Mynard, B.J. Sealy and K.G. Stephens

Department of Electronic and Electrical Engineering, University of Surrey, Guildford, Surrey GU2 5XH, UK

A cold-cathode lateral-extraction ion source has been developed. This source has two hollow cathodes made of either graphite or titanium, which allows an increase in the arc current and a reduction in both the arc voltage and the discharge pressure. As a consequence the ion current is larger and a good yield of multicharged ions and atomic ions can be realised from a compound source material.

1. Introduction

An ion source which can produce multicharged ion beams is important for high-energy ion implantation research. So far, the most universally used is the Penning source, especially the cold-cathode lateral-extraction Penning source. However, one of the most important limiting features of this source, as outlined in ref. [1], is the rapid wear of the cathodes by sputtering under positive-ion bombardment. When the indentation worn in the cathode becomes about as deep as its radius, the arc becomes unstable and difficult to strike. To overcome this problem, we use two cylindrical hollow cathodes, instead of the original solid cathodes, which were in the form of a column. In this paper we discuss the structure of the new source and present some experimental results of its use and application.

2. The structural characteristics of the ion source

The structure of the ion source is shown in fig. 1. Details of the various components of the source follow.

2.1 The cathode

There are two hollow cathodes. Both are made in the shape of a cup as shown in fig. 1 (number 4). Their internal diameter is 5.5 mm and the depth 6.5 mm. Ideally the cathodes should be made of a material with a high secondary-electron emission coefficient, a low ion-sputtering coefficient and a high melting point. In this work both carbon and titanium have been used for the cathodes. As the hollow cathode should work in an area free of magnetic fields [2], a magnetic shielding ring of stainless steel (fig. 1, number 5) is placed around each of the cathodes.

2.2 The arc chamber

This was designed, from data given by ref. [3], as a graphite cylinder with an internal diameter of 8 mm and length 32 mm. In order to allow the arc chamber to operate at a high temperature (e.g., 450°C), a small gap was maintained between the chamber and the source body to increase the heat resistance, enabling the source to use some solid materials.

2.3 The extraction system

The ion-emitting aperture is a circular hole of 2 mm diameter in the wall of the anode. The cold-cathode Penning ion source needs to have a relatively high magnetic field. For lateral extraction sources, the ions emitted from the anode must cross over the magnetic field lines, which deflect them. This is unfavourable to the transport of ion beams in the implanter system. To minimise this deflection, the extraction electrode is made of a magnetic stainless steel, which acts as a screen to the source magnetic field. In doing this, however, it is necessary to prevent this screen from partially shorting out the magnetic field of the source, which would weaken and distort the magnetic field in the arc chamber. This shorting effect is minimised by making the extractor in the form of a circular cone with a 3 mm extraction hole, as shown in fig. 1 (number 6).

2.4 The feed system for source materials

This is a typical combined system of a gas inlet and a crucible for solid materials. The crucible is made of graphite and can be heated by directly passing an electrical current through its thin wall. Tests show that the temperature can rise to 600°C when the heating current is 40 A.

0168-583X/91/$03.50 © 1991 – Elsevier Science Publishers B.V. (North-Holland)

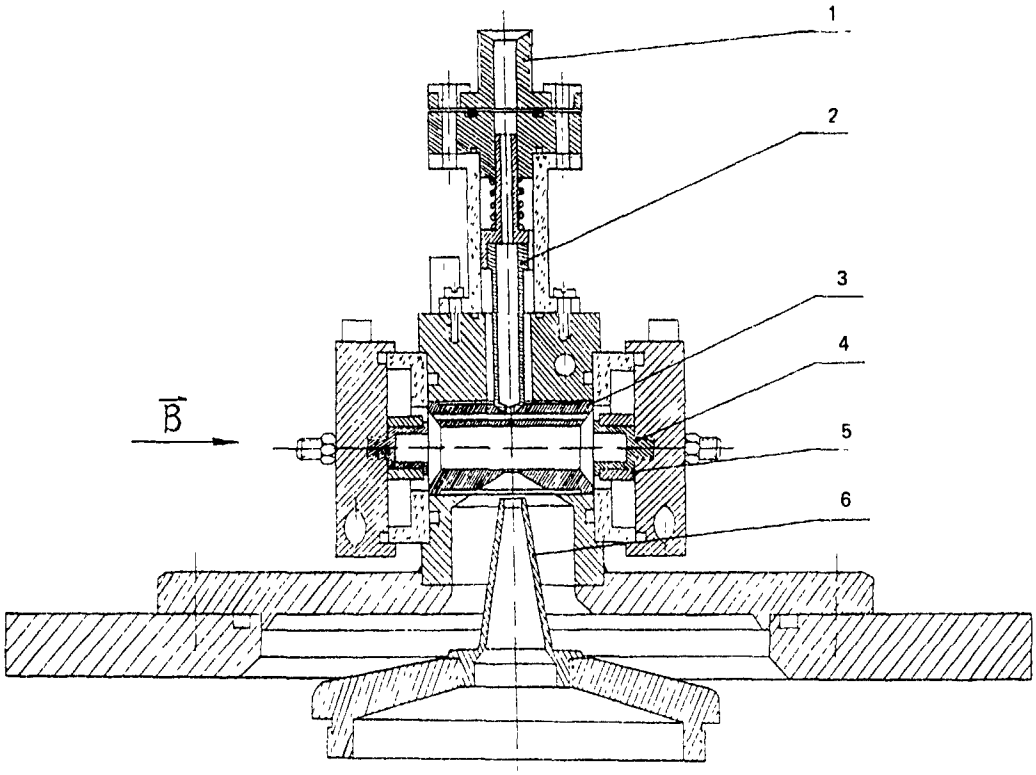

Fig. 1 The structure of the ion source (1) gas inlet, (2) crucible, (3) anode, (4) hollow cathodes, (5) magnetic shield and (6) extraction electrode

2 5. The magnetic field

The axial magnetic field plays a vital part in the Penning discharge, and sometimes its value required for the discharge is very critical Because of this, a small electromagnet was designed. The magnetic field in the middle of the arc chamber is shown in fig. 2 as a function of coil current; it should be noted that the magnetic field near the surface of the magnetic pole is about twice this value.

3. The hollow-cathode Penning discharge

So far we have tested the discharge characteristics using hollow cathodes of carbon, titanium (and stainless

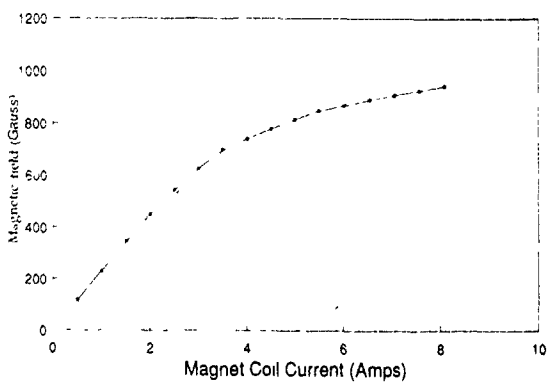

Fig 2. Magnetic field vs coil current of the electromagnet.

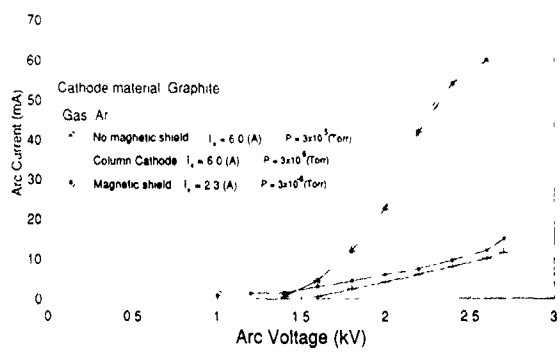

Fig 3 Comparison of the hollow cathode with a magnetic shield, the hollow cathode without the magnetic shield and the column cathode in a discharge

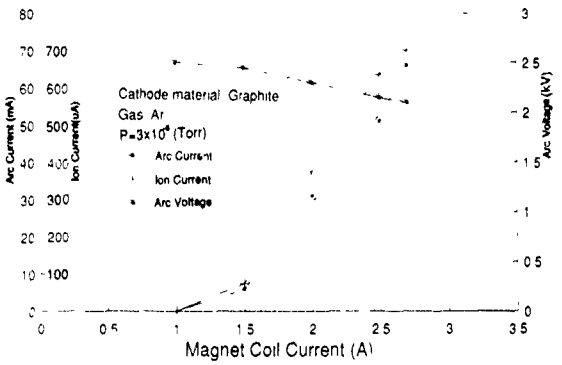

Fig 4. The discharge characteristics with the carbon hollow cathode in a low pressure

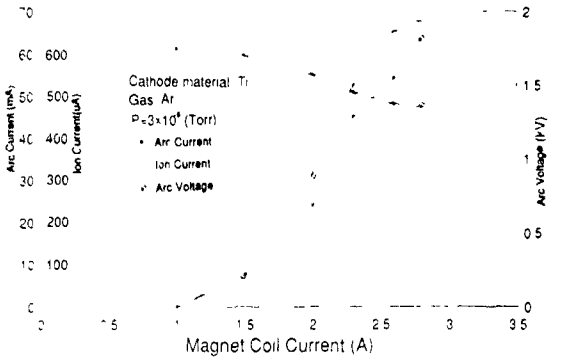

Fig. 6 The discharge characteristics with a titanium hollow cathode in a low pressure

steel for comparison) with gases of Ar, N_2 and SiF_4, respectively These experiments have shown that the effects of the hollow cathode in a discharge are significant.

3 1 The comparison of a hollow cathode with a column cathode in a discharge

Fig. 3 gives three curves. They are obtained, respectively, using the hollow cathode with a magnetic shield, the hollow cathode without a magnetic shield, and for the conventional cathode in column form. From these curves we can conclude that the magnetic shield plays an important role in the discharge and that the hollow cathode does increase the arc current, at a lower discharge pressure, thereby enabling the use of a lower arc voltage and consequently a smaller source magnetic field. Note that the pressure given in this paper was measured in the vacuum system after the ion source, not inside the discharge chamber. The lifetime of the cathodes is no longer limited by the sputtering of ions as mentioned in section 1. The experiments show that the hollow cathode will work well for more than 50 hours until its wall is punctured by the sputtering of ions.

We have searched for reasons why the arc current is higher with a hollow cathode. One explanation is that the slow-moving electrons of the plasma in the hollow cathode join the ionisation discharge in the main chamber, because although the positive ions in the hollow-cathode plasma are quickly extracted to the walls of the hollow cathode, the electrons in this plasma only reach the anode with some difficulty. Thus these slow electrons will accumulate and this will result in a potential difference being established between the two plasmas inside and outside of the hollow cathode. In this way the slow moving electrons in the hollow-cathode plasma may be accelerated by this potential difference and consequently obtain enough energy to join the ionisation discharge.

3 2. The characteristics of the discharge

Figs. 4–7 present the characteristics of the discharge with carbon and titanium cathodes using different discharge parameters. From these figures we can see that:

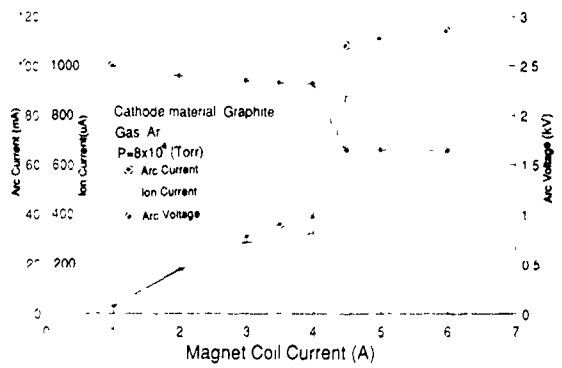

Fig 5 The discharge characteristics with the carbon hollow cathode in a high pressure

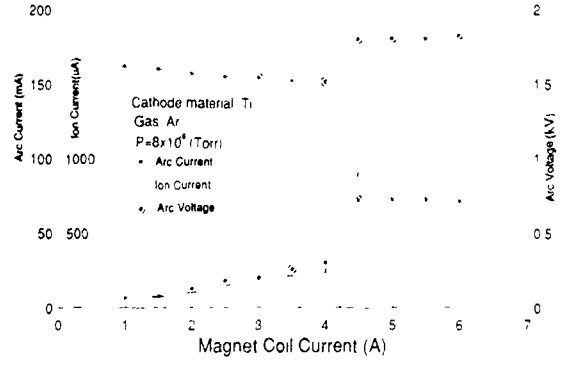

Fig. 7 The discharge characteristics with a titanium hollow cathode in a high pressure.

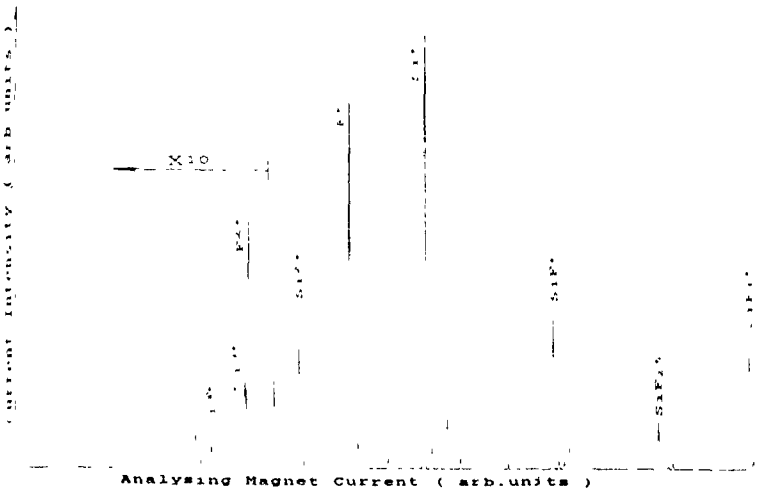

Fig. 8. The spectrum of an ion beam using SiF_4 measured on a 500 keV ion implanter

(i) with a pressure of $< 5 \times 10^{-6}$ Torr, the arc current varies smoothly with magnetic field or arc voltage (see fig. 3), but the discharge becomes unstable (hashy) when the magnetic field is above that for a coil current of 3 A;

(ii) with a pressure $> 5 \times 10^{-6}$ Torr the discharge appears to have two working positions, a high-voltage–low-current one and a low-voltage–high-current one, as the arc voltage and (or) magnetic field varies, the change between these two positions is abrupt;

(iii) that the discharge is different with different materials and sizes of cathode; furthermore the arc voltage is lower with a titanium cathode than with a carbon cathode for the same arc current.

Note also that a stainless-steel cathode was tested for comparison, but although the discharge was good, the sputtering was too severe for any useful application. From the measurement we have deduced that as the internal diameter of the hollow cathode is reduced, so is the arc current, but only down to a diameter of 5 mm. Below this value the discharge becomes unstable and we do not appear to have the high-current–low-voltage discharge position.

4. Ion beam extraction and use of the source on a 500 keV ion implanter

Figs. 4–7 have shown that the total ion beam currents extracted from the ion source can reach 900 μA, in this case the beam current density is about 250 mA/cm^2 for each ampere of arc current, and the extraction efficiency (i.e., the ratio of extraction beam current to the loading current of the extraction supply) is more than 95%, which implies that the design of the extraction system is successful.

This ion source has been tested on the Surrey 500 keV ion implanter. The ion beam mass-analysing spectrum with a source gas of SiF_4 is shown in fig. 8. The currents of different charge states of silicon after passing through the beam line of length 8 m into the target were: Si^+, 57 μA; Si^{2+}, 22 μA; Si^{3+}, 3.2 μA; Si^{4+}, 0.42 μA; Si^{5+}, 0.05 μA. Fig. 8 shows the relative contents of multicharged ions, compound ions and atomic ions, e.g., Si^+ relative to the ions of Si^{2+}, SiF^+, SiF_2^+ and SiF_3^+ in the ion beam. The fraction of Si^+ and Si^{2+} of the total ion beam is larger than that usually achieved in ion implanters.

5. Conclusion

A cold-hollow-cathode lateral-extraction Penning ion source has been developed. Compared with the conventional cold-cathode sources in ion implanters it gives larger ion beam currents, containing a significantly higher fraction of both singly charged and multicharged, atomic ions when using compound source gases. The hollow-cathode design enables large arc currents to be used and prolongs the lifetime of cathodes to more than 50 hours. These preliminary results are encouraging, but we have yet to test the source with solid materials.

References

[1] J.K.J. Bennett, IEEE Trans. Nucl. Sci. NS-19 (1972) 48.
[2] G. Sidenius, Nucl. Instr. and Meth. 38 (1965) 19.
[3] Song Zhizhong, Yu Jinxiang, Li Renxing and Yuan Zhongxi, Vacuum 36 (1986) 897.

Nuclear Instruments and Methods in Physics Research B55 (1991) 339–342
North-Holland

Ion beam injection system for a variable energy RFQ accelerator

K. Amemiya, K. Tokiguchi, Y. Hakamata and N. Sakudo
Hitachi Research Laboratory, Hitachi Ltd., 4026 Kuji-cho, Hitachi-shi, Ibaraki-ken 319-12, Japan

A new injection system designed for a variable energy RFQ (radio frequency quadrupole) accelerator was developed from the viewpoint of introducing a high current ion beam into the RFQ. This injection system consists of a high current multiply charged ion source, a sector-type mass-separator, and a magnetic quadrupole triplet. The ion source is designed for effective production of a milliampere class lower-charge-state multiply charged ion beam. The mass-separator has a double-focusing action in order to mass-separate the high current beam. The quadrupole lens functions to focus the beam at the RFQ inlet position. In the experiments an Ar^+ injection beam current of 2.2 mA and an Ar^{2+} current of 1.7 mA are obtained. The injection beam size is 10 mm ∅. A combination of this injection system with a variable energy RFQ accelerator should provide a milliampere class MeV ion implanter.

1. Introduction

There is an increasing demand for a high energy ion implantation technique to be applied in silicon device fabrications [1,2] and surface modifications [3,4]. For these applications, a milliampere class MeV ion beam is necessary to obtain high throughput. An RFQ accelerator can provide an accelerated beam current of milliampere class. We designed a new variable energy RFQ accelerator system driven by an external LC resonant circuit [5]. This system can provide a beam of wide energy range using multiply charged ions.

To realize the MeV range beam of milliampere class, it is necessary to introduce a several milliampere class beam of small beam diameter into the RFQ. The beam size of 10 mm ∅ is the upper limit of an acceptable beam size which can be introduced into the RFQ since the conventional RFQ has a bore radius of about 5 mm. We have already designed a new type of microwave multiply charged ion source and a sector-type mass-separator [6,7]. The mass-separated Ar^{2+} beam current reached 3.0 mA at 20 kV and the beam had a square size of 22 mm × 22 mm. In order to inject the 10 mm ∅ ion beam into the RFQ, we adopted a magnetic quadrupole triplet. This is because a stigmatic beam image is easily obtained by triplet lens operation and this magnetic lens is suitable for high current beam transportation. The static magnetic field does not generate a beam divergence due to the space charge effect, unlike when using an electric field.

This paper describes the results of high current beam focusing characteristics of the new injection system. The usefulness of this system especially for RFQs is also demonstrated.

2. Experimental apparatus

A schematic diagram of the beam injection system and beam measurement system is shown in fig. 1. The ion source has a single plasma chamber, which is cylindrical with an inner diameter of 90 mm and a length of 211 mm. Two types of magnetic fields, a mirror and an octupole magnetic field, are superimposed on the entire plasma chamber and a 2.45 GHz microwave is introduced into the chamber. The mass-separator is a 90° deflector with a 270 mm radius for the beam trajectory. The gap of the magnetic separator is 40 mm. A double-focusing action is used to obtain a high current mass-separated beam. Typical characteristics of the mass-separated beam are shown in fig. 2.

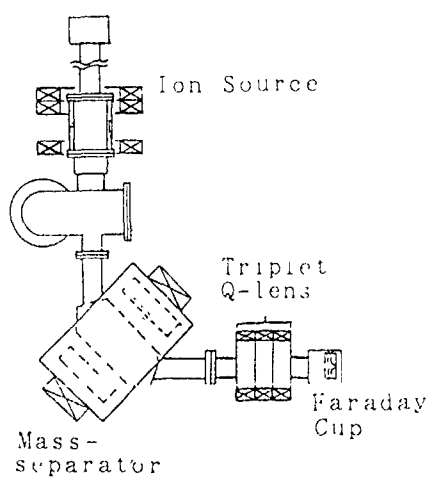

Fig. 1. Schematic diagram of the experimental apparatus.

0168-583X/91/$03.50 © 1991 – Elsevier Science Publishers B.V. (North-Holland)

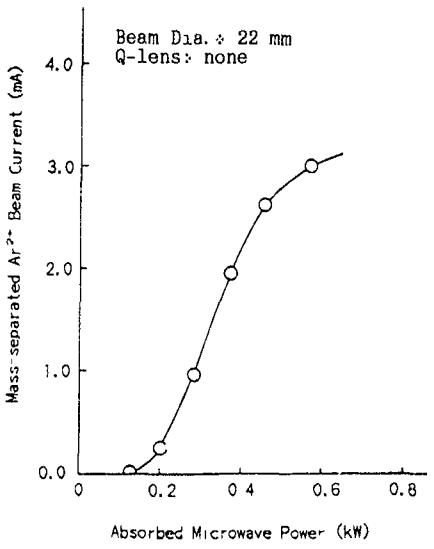

Fig 2 Dependence of mass-separated Ar^{2+} beam current on absorbed microwave power The beam current was measured by a Faraday cup of 22×22 mm^2

The magnetic quadrupole triplet consists of three lenses of the same specifications (Q1, Q2, Q3) Each lens has an aperture diameter of 77 mm, a length of 110 mm and a magnetic pole radius of 44 mm, and is set with a 190 mm separation We considered the maximum ion mass number to be 84 (Kr) and the maximum energy, 20 kV The total length of this triplet lens is 870 mm.

The focused beam is measured by a Faraday cup which is set at the injection point of the RFQ The aperture in front of the cup has a 10 mm diameter. It was observed that most beams are injected into the cup An example of a beam trajectory calculation is shown in fig. 3 for a stigmatic condition. In this figure, the starting point (left) is the ion extraction point of the ion source, and the ending point (right) is the entrance of the Faraday cup. The image magnification is about 0.8

3. Results and discussion

This section describes mainly the focused beam characteristics of Ar^{2+}, because the beam, accelerated by the RFQ, is proportional to the charge number of the ion and the Ar^{2+} beam current is over a milliampere after passing through the mass-separator.

3.1 Dependence on lens field strength

The dependence of focused Ar^{2+} beam current on the Q_1-lens coil current, which is proportional to the magnetic field of the lens, is shown in fig 4 Q_2- and Q_3-lens currents were tuned so as to obtain the maximum beam current as given by a beam trajectory calculation. In this experiment, the measurement conditions were: argon gas pressure in the plasma chamber, 9.9×10^{-2} Pa; absorbed microwave power, 400 W, and extraction voltage, 24 kV A maximum Ar^{2+} current of 1.3 mA is obtained at a under the coil current of 7.0 A, however, the beam current decreases at all other current values. At low currents, the lens strength is insufficient for focusing the beam into 10 mm ∅. On the other hand, at higher currents than 7.0 A, the lens field strength is too high to obtain a high current focused beam. The beam trajectory simulation indicates a high lens-field-strength results in the beam stopping against an inner wall of the vacuum pipe inserted in these quadrupole lenses. This means that an increase in the

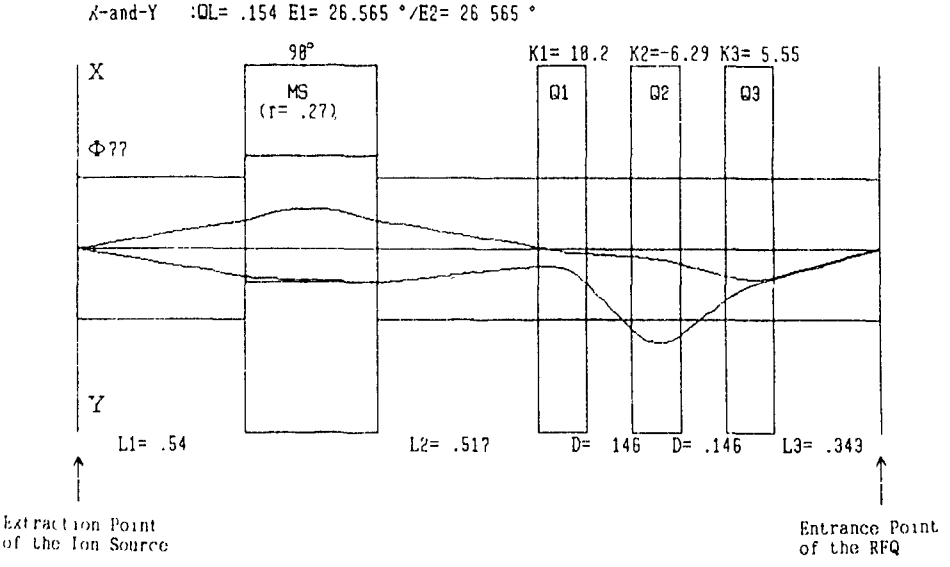

Fig 3. Example of the calculation of beam trajectory

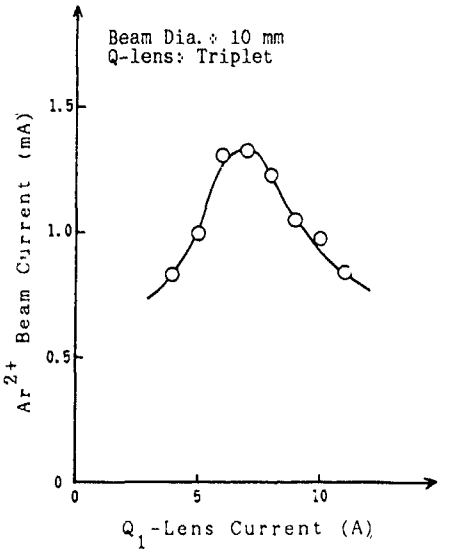

Fig 4 Dependence of Ar^{2+} beam current on lens field strength This beam was measured by a Faraday cup of 10 mm ø aperture

lens aperture size will increase the focused beam current in our system.

3.2 Operating conditions of the ion source

The operating conditions of the ion source were changed and the focused beam current was investigated with the optimum Q-lens condition, which is shown in fig. 4. The dependence of Ar^{2+} beam current on gas pressure is shown in fig 5. The absorbed microwave power was 400 W, and extraction voltage was 24 kV. An Ar^{2+} beam of 1.7 mA is obtained at a pressure in the plasma chamber of 1.1×10^{-1} Pa. The reason for the decrease of Ar^{2+} current at the high pressure region is the low production efficiency of multiply charged ions in this region. It is important to set the pressure suitable for obtaining maximum Ar^{2+} current, because mainly the gas pressure determines the production efficiency of multiply charged ions.

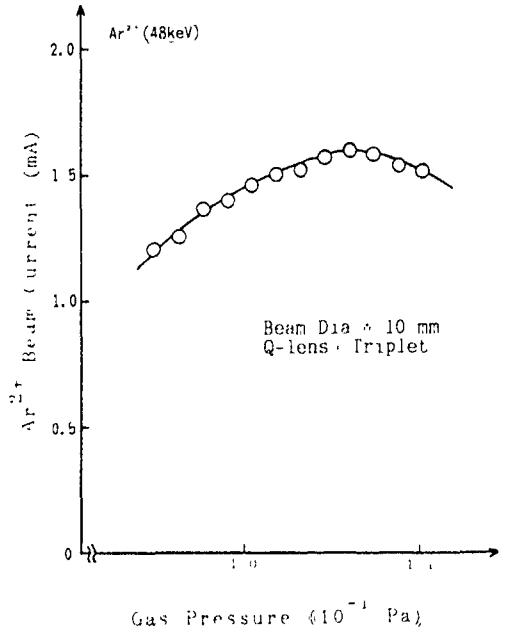

Fig 5. Dependence of Ar^{2+} beam current on gas pressure This beam was measured by a Faraday cup of 10 mm ø aperture.

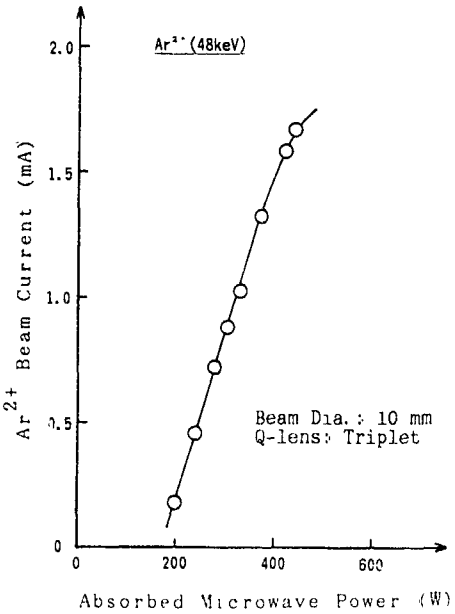

Fig 6 Dependence of Ar^{2+} beam current on absorbed microwave power This beam was measured by a Faraday cup of 10 mm ø aperture.

The dependence of focused Ar^{2+} current on absorbed microwave power is shown in fig. 6. In this experiment, argon gas pressure in the plasma was 1.0×10^{-1} Pa, and extraction voltage was 24 kV. The Ar^{2+}

Table 1
Principal data obtained with the new beam injection system

(a) Ion beam injection system for RFQ			
Ion source:	2.45 GHz microwave discharge (mirror + octupole magnetic field)		
Separator:	90° deflector with 270 mm radius		
Lens:	triplet magnetic quadrupole		
(b) 10 mm ø beam current			
Ion	Current [mA]	Beam energy [keV]	Microwave power [W]
Ar^{+}	2.2	24	370
Ar^{2+}	1.7	48	440

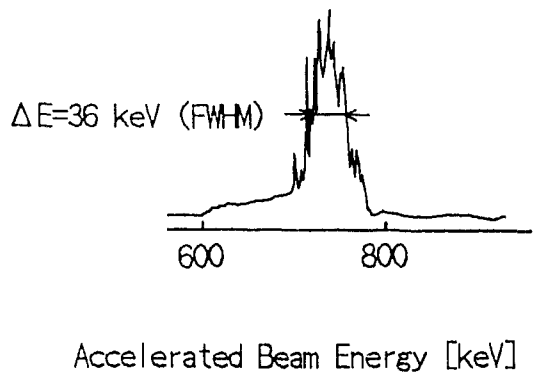

Fig. 7. Energy spectrum of the accelerated 740 keV Ar^{2+} beam RF: 15 MHz (10.5 kW), RFQ. 1 3 m.

current is almost proportional to the absorbed microwave power, and reached 1.7 mA at the microwave power of 440 W. It is apparent that a higher absorbed microwave power in the plasma is very effective to produce the Ar^{2+} beam.

Principal operation conditions and obtained data are summarized in table 1

3 3. Ar^{2+} beam acceleration test

Fig. 7 shows the results of Ar^{2+} beam acceleration. The vane length of the RFQ was 1.3 m and operating frequency was 15 MHz. An RF power of 10.5 kW was introduced into the RFQ system The beam energy was measured by a cylindrical electrostatic analyzer. Results show that an Ar^{2+} beam of 740 keV is accelerated with an FWHM of 36 keV. Accelerated beam current measurements just after the RFQ are scheduled in the near future.

4. Conclusion

A new injection system consisting of a microwave multiply charged ion source, a sector-type mass-separator, and a magnetic quadrupole triplet was shown to be very useful for a variable energy RFQ accelerator system. An Ar^{+} beam of 2.2 mA and an Ar^{2+} beam of 1.7 mA were obtained under a 500 W microwave power in the new injection system. Widening the quadrupole lens aperture was found to be effective for obtaining a larger beam current. As the RFQ has a high transparency (> 50%), a combination of this new beam injection system with a variable energy RFQ system has a good potential for obtaining a milliampere class MeV ion beam. To apply this injection system to a future MeV ion implanter, a beam emittance value which is measured at the entrance of the RFQ must be investigated with the beam current Measurements of the beam current and emittance value, and acceleration tests are scheduled in the near future.

Acknowledgement

This work was performed under the Research and Development Program "Advanced Material Processing and Machining System", conducted under the direction of the New Energy and Industrial Technology Development Organization.

References

[1] D Pramanik and M Current, Solid State Technol 27 (1984) 211
[2] J.F Ziegler, Nucl Instr and Meth B6 (1985) 270.
[3] M A Z Vasconcellos et al , Nucl Instr and Meth. B37/38 (1989) 653
[4] F W Saris, Vacuum 39 (1989) 173
[5] K Tokiguchi et al , Nucl Instr and Meth. B37/38 (1989) 253
[6] K Tokiguchi et al , Vacuum 38 (1988) 487
[7] K Amemiya et al , Nucl. Instr and Meth B37/38 (1989) 87

Nuclear Instruments and Methods in Physics Research B55 (1991) 343–347
North-Holland

Milliampere metal ion beam formation using multipoint emission by an impregnated-electrode-type liquid-metal ion source

Junzo Ishikawa, Hiroshi Tsuji and Yasuhito Gotoh
Department of Electronics, Kyoto University, Kyoto 606, Japan

Intense metal ion beams are required in advanced materials science in which the kinetic energy and the potential energy should be controlled. In the present study, intense metal ion beams were formed using multipoint emission by a high-intensity impregnated-electrode-type liquid-metal ion source. New ion sources with respectively five and eight emission points were developed and their characteristics were examined with germanium and gold as source materials. As a result, it was shown that an ion current proportional to the number of cusps of the emitter tip could be obtained by multipoint emission. A maximum germanium ion current of more than 4 mA was obtained with the eight-point emission source. The multipoint emission of the impregnated-electrode-type liquid-metal ion source proved to be a potential method for developing a high-current metal ion source.

1. Introduction

Intense metal ion beams are required in advanced materials science in which the kinetic energy and the potential energy of the depositing particle should be controlled. Generally, metal ion sources, such as the Freeman type [1], are of the plasma type, in which the material to be ionized is fed as a pure material at a very high temperature or as a compound vapour such as halide [2]. In these cases, severe problems of heat and corrosion arise; the power consumption is very high and the corrosive gas flows out into the vacuum chamber. When a compound gas is used, a mass separator with high mass-resolution power is needed. Thus, a metal ion source with a low power consumption and with a capability of utilizing pure metal materials at low temperatures is desired. One promising candidate for the general metal ion source that has the features described above is a liquid-metal ion source, in which metal ions are produced on a metal surface and are directly extracted. Liquid-metal ion sources have some unique features such as high brightness [3] and the capability of operation at relatively low temperatures as compared with plasma-type metal sources. However, conventional sources, i.e. needle-type and capillary needle-type sources have several drawbacks: (a) they cannot deliver the ion currents desired in the materials science, and (b) metals whose vapour pressures at their melting points are as high as 10^{-3} Torr cannot be used as source materials [4]. The reason for the former is a poor controllability of liquid flow during transportation towards the emission point. The reason for the latter is that, at temperatures corresponding to a vapour pressure of 10^{-3} Torr, most of the metal atoms thermally evaporate during the feeding of the liquid metal to the emission point. These drawbacks are attributed to their structures.

To overcome the drawbacks described above, the authors recently developed an impregnated-electrode-type liquid-metal ion source with a porous tip structure [5–8]. This ion source can deliver high-current ion beams of several hundreds of microamperes even from a single emission point, because the flow rate of the liquid metal can be controlled by the porous region. Ion currents of more than 100 μA were extracted from Li, Cu, Ga, Ge, Ag, In, Sn, Au and Pb sources with single emission points. Besides large ion currents, metals with high vapour pressures of 10^{-1} Torr can be ionized, since the liquid metal is fed through the porous region. Thus, the impregnated-electrode-type liquid-metal ion source is a promising candidate as an intense metal ion source. If the number of the emission points is multiplied to a large value, a milliampere-class ion source will be easily realized. The authors have already reported on an intense metal ion beam formation by the three-point emission of an impregnated-electrode-type liquid-metal ion source [9,10]. The present report describes the result of further intensification of the impregnated-electrode-type liquid-metal ion source by multiplying the number of emission points to numbers up to eight.

2. Structure of ion source

The impregnated-electrode-type liquid-metal ion source has a porous tip made of a refractory metal. The ion source has a cylindrical reservoir for liquid metal which is typically made of tungsten. The reservoir also

0168-583X/91/$03.50 © 1991 – Elsevier Science Publishers B.V (North-Holland)

serves as a heater for melting the metal to be ionized. A heating current is supplied through molybdenum knife-edged electrodes by which the reservoir is rigidly held.

Fig. 1 shows a schematic diagram of five kinds of ion sources: (a) prototype, (b) has most of its porous tip surface covered for high-vapour-pressure metals and (c) has multipoint emission cusps for high-current operation. The cross-sectional shape of the reservoir is a circle with a diameter of 2 mm for sources (a) and (b), and an ellipse with radii of 1 and 2.5 mm, respectively, along the minor and the major axis for source (c). In the present study, new types of sources, (d) and (e), which have five and eight emission cusps, respectively, were developed. The cross-sectional shape of the reservoir for source (d) is the same as that for source (c). For source (e), the radius along the major axis was prolonged to 5 mm.

3. Multipoint emission

As previously confirmed, the impregnated-electrode-type liquid-metal ion source can be operated with three-point emission. In this report, further multiplication of the emission points was performed with the new sources (d) and (e) which are shown in fig. 1.

In multiplying the emission points, careful design of the extractor is needed to realize effective and stable operation. The ion-optics in the extraction region affects the ion beam trajectories in the following space. The authors designed the shape of the extractor with the aid of a three-dimensional computer simulation. The calculation was carried out to form electric fields of the same strength and direction upon the apexes of the cusps. The details of the simulation are described elsewhere [11]. The calculation revealed that a slit-type extractor with an open side was suitable for the present source geometry. If a rectangular aperture were to be used as an extractor, the electric field on the apex of the end of the tip would have a fairly large component towards the outer direction. To correct the electric field, the edge of the extractor aperture, which affects the electric field in the outer direction on the apex of the corner, should be placed far away from the tip. With the slit extractor, such an edge does not exist.

Besides ion-optics, the configuration of the extractor involves another serious problem: bombardment of the tip by secondary electrons produced by the impact of the extracted ion beam. The bombardment by the electrons heats the emitter tip excessively, often resulting in unstable operation. Furthermore, a large secondary electron current is a heavy load for the extraction power supply. The best way to reduce the secondary electron current is to decrease the ion current that hits the extractor. In order to do this, the extractor was modified so as to have a slope, as shown in fig. 2 This extractor showed an excellent result on the present subject [11] The electron current including an indistinguishable ion current to the extractor was reduced down to one-fifth, compared with the flat plate extractor.

3.1. Five-point emission

Ion emission from five points were experimentally confirmed with both a germanium and a gold ion source.

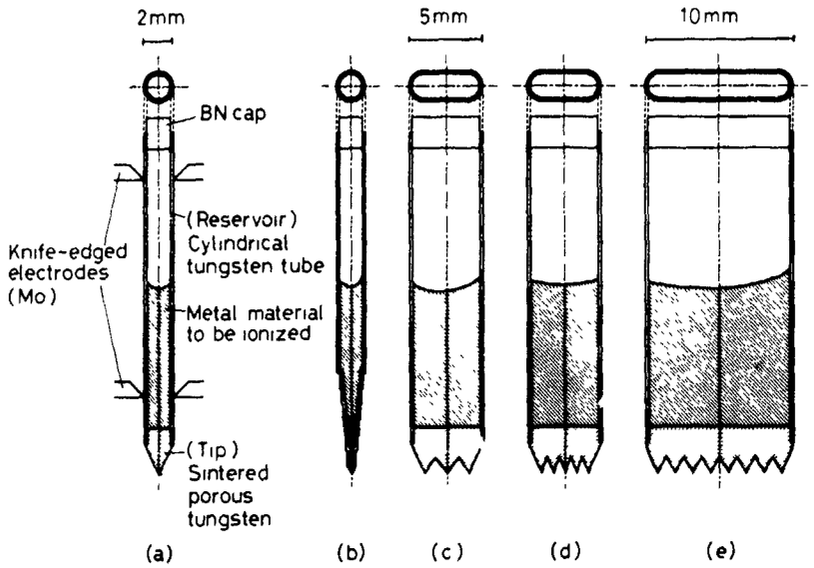

Fig. 1. Schematic diagram of five kinds of impregnated-electrode-type liquid-metal ion sources. (a) prototype, (b) for metals with high vapour pressures, (c) for three-point emission, (d) for five-point emission, and (e) for eight-point emission.

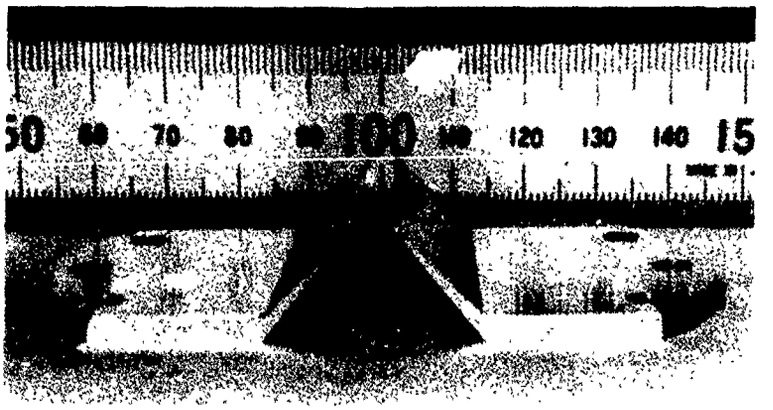

Fig. 2. Photograph of the sloped slit-type extractor.

Ion currents were measured just below the ion source with a Faraday cup to suppress the secondary electrons produced at the collector. Since mass-separation was not performed, the measured ion current included all kinds of positively charged ions such as singly charged atomic ions, multiply charged atomic ions and charged particles that are composed of more than two atoms. Fig. 3a shows the typical current–voltage characteristics of a germanium ion source. The maximum ion current of 1.8 mA was obtained. This maximum current is reasonable, although the value is a little smaller than that expected from the maximum current of a single-point emission source. Fig 3b shows the typical current–voltage characteristics of a gold ion source. The maximum ion current of 1 5 mA was obtained. This maximum ion current is approximately five times as large as that of a single-point emission source. Thus, milliampere metal ion beams were obtained by multi-point emission of impregnated-electrode-type liquid-metal ion sources

3 2. *Eight-point-emission*

Eight-point emission was also confirmed with a germanium ion source A heating current of 120 A was required to heat the tip up to 950 °C. Fig. 4 shows a

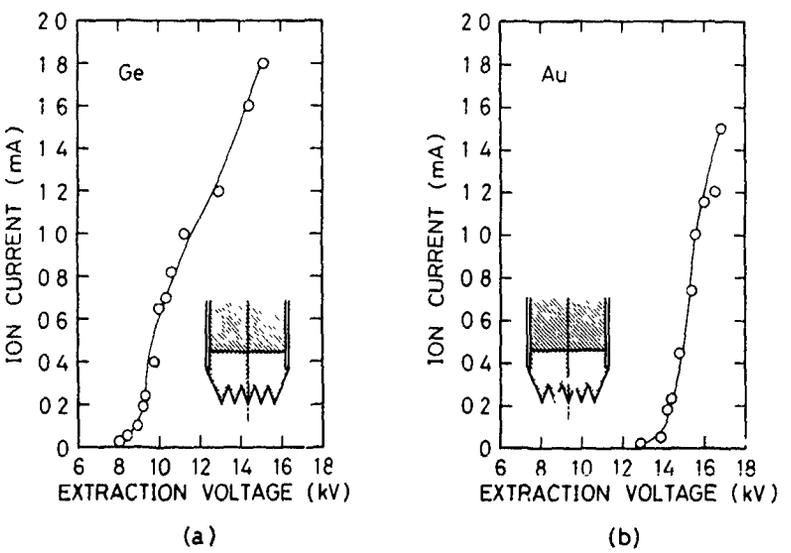

Fig. 3. Typical current–voltage characteristics of the five-point emission sources: (a) for germanium ion source and (b) for gold ion source.

Fig 4. Photograph of the eight-point emission tip in operation

Table 1
Summary of multipoint emission

	Au			Ge			
Number of cusps	1	3	5	1	3	5	8
Maximum current [mA]	0 30	0.85	1 3	0 50	1 3	1 8	4 2
Effective point-number	1	2 8	4 2	1	2 6	3 6	8.4
Average current from 1 point [mA]	0 30	0 28	0 26	0 50	0.43	0 36	0 53

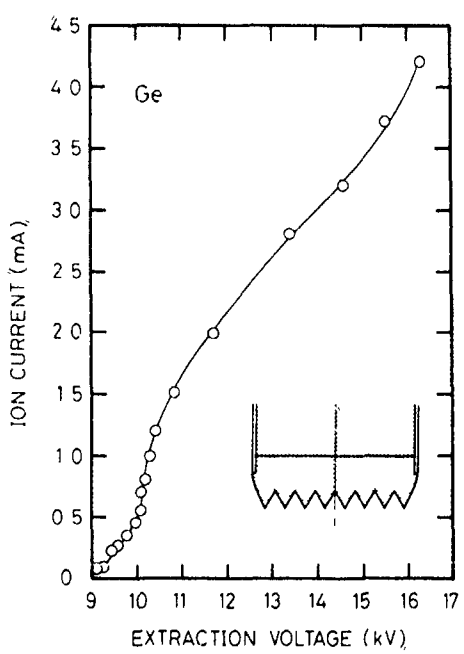

Fig 5 Typical current–voltage characteristics of the eight-point emission source

photograph of the germanium eight-point source in operation Eight plasma balls are clearly seen The ions are emitted in the same direction. Fig. 5 shows the typical current–voltage characteristics of the eight-point source The maximum ion current of 4 2 mA was obtained This value is approximately eight times as large as that of a single emission source Table 1 shows the summary of the multipoint emission. Here the effective point-number is defined as the ratio of the maximum ion current with multipoint emission source to that with a single-point emission source. The effective point-number agrees well with the number of cusps. The results indicate that the ion current of multipoint emission is proportional to the number of cusps From the present results, multipoint emission proved to be a potential method for developing a high-current liquid-metal ion source

4. Further intensification of the source

In order to intensify the ion source, two methods can be considered: (a) further multiplication of the emission

cusps in a tip, and (b) parallel operation of multipoint emission tips. In the former method, there is a problem of heating current increase. On the other hand, in the latter method, attention should be paid to heating several tips equally. In the present study, the possibility of parallel operation was confirmed. Two tips of source (e) set in parallel with independent knife-edged electrodes were heated up to approximately the same temperatures of 940 °C and 990 °C, respectively. Ion emissions from both tips were confirmed. Thus, further increases in the extractable ion current from the impregnated-electrode-type liquid-metal ion source are expected.

5. Conclusion

The intensification of the impregnated-electrode-type liquid-metal ion source was achieved up to 4 mA by using an eight-point emission source. The possibility of parallel operation was confirmed.

References

[1] J H. Freeman, Nucl Instr. and Meth. 22 (1963) 306.
[2] R.G. Wilson and G.R. Brewer, Ion Beams (Wiley, 1973) p 405.
[3] R L. Seliger, J W Ward, V Wang and R.L Kubena, Appl. Phys Lett 34 (1979) 310
[4] A Wagner and T.M. Hall, J Vac. Sci Technol. 16 (1979) 1871.
[5] J. Ishikawa and T. Takagi, J. Appl. Phys. 56 (1984) 3050
[6] J. Ishikawa and T Takagi, Vacuum 36 (1986) 825
[7] J Ishikawa, Y. Gotoh, H. Tsuji and T. Takagi, Nucl Instr. and Meth B21 (1987) 186.
[8] J Ishikawa, H. Tsuji, T Kashiwagi and T. Takagi, Nucl. Instr and Meth B37/38 (1989) 155
[9] J Ishikawa, Nucl. Instr and Meth B40/41 (1989) 1037.
[10] J. Ishikawa, H. Tsuji, Y. Aoyama and T Takagi, Rev Sci Instr. 61 (1990) 592
[11] H Tsuji, Y Aoyama and J Ishikawa, Proc 13th Symp on Ion Sources and Ion-Assisted Technology, ISIAT '90, Tokyo (The Ion Engineering Society of Japan, 1990) p. 53

Nuclear Instruments and Methods in Physics Research B55 (1991) 348–354
North-Holland

Possible mechanisms for particle transport in ion implanters

D.A. Brown
ECE Department, University of Arizona, Tucson, AZ 85721, USA

P. Sferlazzo
Eaton Semiconductor Equipment Division, Beverly, MA 01915, USA

J.F. O'Hanlon
ECE Department, University of Arizona, Tucson, AZ 85721, USA

Possible mechanisms for the charging and entrapment of particulate contamination in a cylindrical ion beam are investigated A model is developed which describes the charging, and steady-state charge acquired by the particle Confinement within the beam is then investigated by comparing the resulting electric force with the opposing force of gravity The model predicts a region about the center of the beam where a net trapping force may exist Calculations of this force for various operating conditions suggest a strong dependence on parameters that affect the beam-ion density

1. Introduction

Current developments in semiconductor technology are pushing the minimum feature size of devices and microelectronic circuits down into the submicron range. With these reduced dimensions, particulate contamination during processing has become of increased concern. Particles with dimensions of the order of tenths of microns are becoming unacceptable.

In ion implantation, a number of areas have been the object of close scrutiny. Improved venting and roughing schemes have reduced the number of particles added during implantation to a point where more subtle effects, such as beam particle transport, must be taken into consideration [1,2]. An effort is presented here to identify and calculate the currents and forces acting on a particle placed in the vicinity of a cylindrical high-current ion beam.

Holmes [3] has developed a model that describes the electric field and charge densities characteristic of an intense cylindrically symmetric ion beam. This model is used as a framework to calculate the currents incident on a conducting particle in the vicinity of the beam. From these currents, the particle charge is determined. Utilizing the electric field calculated by Holmes, the electric force acting on the particle is derived. When this force is greater than gravity, entrapment can occur.

2. Beam model

The relevant features of Holmes' model may be summarized by the following equations:

$$n_b = n_{b0} \exp\left\{-(r/r_0)^2\right\}, \tag{1}$$

$$n_e = n_{e0} \exp\left\{-\tfrac{1}{2}(1+\beta^2)(r/r_0)^2\right\}, \tag{2}$$

$$\Phi(r) = -\Phi_w\left\{1 - \exp\left[-\beta^2(r/r_0)^2\right]\right\}, \tag{3}$$

0168-583X/91/$03 50 © 1991 – Elsevier Science Publishers B V (North-Holland)

in which n_b is the beam-ion density as a function of the radial position r, n_{b0} is the beam-ion density along the axis, n_e is the spatial electron density with an axial value of n_{e0}, r_0 is a characteristic dimension of the cylindrical beam, defined to be the beam radius, $\Phi(r)$ describes the beam potential and Φ_w is the magnitude of the beam potential far from the axis. The factor β represents the ratio of the characteristic potential radius to the radius of the beam.

This model has been tested by Holmes, and independently examined by Klabunde [4]. Its predictions are in good agreement with experimental observations.

3. Beam currents

Collisions of beam ions with apertures and residual gas molecules generate secondary electrons and ionized gas molecules which give rise to a beam comprised of high-energy beam ions produced in the source, low-energy ionized residual gas molecules (slow-ions), trapped-electrons confined by the electric potential of the beam, and fast electrons possessing sufficient kinetic energy to escape the positive space charge of the beam. Each of these components contributes to the flow of charge through any point inside the beam. It can be shown, however, that the current contributions of the slow ions and the fast electrons are small when compared to the other two current components and may be neglected [5].

3 1. Beam-ion current

In the axial direction, the beam energy, and hence its velocity, is assumed to be constant at all points along a linear trajectory, displaying no radial dependence. Under this condition, the current density due to the beam ions at any radial position r is given by

$$\boldsymbol{J}_b = q v_b n_{b0} \exp\left[-(r/r_0)^2\right] \boldsymbol{e}_z, \tag{4}$$

where $\boldsymbol{e}_z$ is a unit vector parallel to the beam axis and oriented in the direction of the beam-velocity, q is the elementary unit of charge ($= 1.6 \times 10^{-19}$ C) and v_b is the beam velocity.

3 2. Trapped-electron and net currents

Following Holmes, the trapped electrons are assumed to display a Maxwellian distribution of velocities in which the high-energy tail is truncated by the loss of fast electrons possessing radial velocity components greater than $\sqrt{2q\Phi_w/m_e}$. All axial velocities are allowed, but the non-axial velocities are constrained by the relation $v_x^2 + v_y^2 \leqslant (2q\Phi_w/m_e)$. Here, the x–y plane is centered on and normal to the beam, with the positive z-axis pointing in the direction of positive ion flow. Cylindrical symmetry is assumed. Calculation of the normalized electron distribution function yields [5]:

$$f_e(v) = \left(\frac{m_e}{2\pi kT}\right)^{3/2}\left[1 - \exp\left(-\frac{q\Phi_w}{kT}\right)\right]^{-1} \exp\left[-\frac{m_e}{2kT}\left(v_x^2 + v_y^2 + v_z^2\right)\right], \tag{5}$$

where m_e is the electron mass, k is Boltzmann's constant and T is the electron temperature.

Of particular interest is the distribution of velocity components outwardly directed and parallel to a given radial line. This can be calculated by integrating eq. (5) over two degrees of freedom. Again all axial velocities are allowed, but v_y is restricted to values $v_y \leqslant \sqrt{(2q\Phi_w/m_e) - v_x^2}$. Performing the integration, the distribution function becomes:

$$f_e(v_x) = \left[1 - \exp\left(-\frac{q\Phi_w}{kT}\right)\right]^{-1}\left(\frac{2m_e}{\pi^2 kT}\right)^{1/2} \exp\left(-\frac{m_e v_x^2}{2kT}\right)\int_0^{\left(\frac{q\Phi_w}{kT} - \frac{m_e v_x^2}{2kT}\right)^{1/2}} \exp(-u^2)\, du. \tag{6}$$

At any radial position r, the trapped-electron current density will be determined by the electron energy.

It will be assumed that the electrons are created with negligible kinetic energy [3,6,7], and that the net angular acceleration due to collisions is negligible. Under these conditions electrons trapped in the space charge of the beam will oscillate about the beam axis, and only those electrons crossing the axis with a velocity $v \geq \sqrt{-2q\Phi(r)/m_e}$ will have sufficient kinetic energy to reach the point r.

Utilizing eq. (6) the trapped-electron current density can now be found. From eq. (2) the density of electrons very near the axis is n_{e0}. Multiplying eq. (6) by $-qn_{e0}v_r\,dv_x$ and integrating from the minimum velocity $v_r = \sqrt{-2q\Phi(r)/m_e}$ to the maximum velocity $v_x = \sqrt{2q\Phi_w/m_e}$ provides the desired result. Combining this outwardly directed vector component with the axial component of eq. (4) the net current density as a function of radial position is obtained:

$$\boldsymbol{J} = qn_{b0}v_b \exp\left[-\left(\frac{r}{r_0}\right)^2\right]\boldsymbol{e}_z - qn_{e0}\frac{\exp\left(-\frac{q\Phi_w}{kT}\right)}{1-\exp\left(-\frac{q\Phi_w}{kT}\right)}\left(\frac{2kT}{\pi^2 m_e}\right)^{1/2}$$

$$\times\left\{\exp\left[\frac{q}{kT}(\Phi(r)+\Phi_w)\right]\int_0^{\left[\frac{q}{kT}(\Phi(r)+\Phi_w)\right]^{1/2}}\exp(-z^2)\,dz - \left[\frac{q}{kT}(\Phi(r)+\Phi_w)\right]^{1/2}\right\}\boldsymbol{e}_r. \qquad (7)$$

4. Particle charging

Consider a conducting sphere of diameter d_0 located at a radial position r within the beam. Such a particle presents a cross-sectional target area $\pi d_0^2/4$ in all directions; thus, the current becomes $I = (\pi d_0^2/4)J$, where J is the algebraic sum of the components in eq. (7). As the particle accumulates charge, it develops an electric field that perturbs the trajectories of surrounding charges. The ion current is dominated by beam ions which are of sufficiently high energy so as to remain undisturbed by the presence of the charged particle, but this is not true for the trapped electrons. As the potential on the particle rises, so does the minimum kinetic energy required for an electron to transit the region between the axis and the particle. This minimum energy is the beam potential at the location of the particle plus the particle's floating potential V. An electron incident on the particle must cross the axis with a velocity $v \geq \sqrt{-(2q/m_e)(\Phi(r)+V)}$. The total current to the particle is, therefore, given by:

$$I(r) = \frac{q\pi d_0^2}{4}\left\{n_{b0}v_b \exp\left[-\left(\frac{r}{r_0}\right)^2\right] - n_{e0}\frac{\exp\left(-\frac{q\Phi_w}{kT}\right)}{1-\exp\left(-\frac{q\Phi_w}{kT}\right)}\left(\frac{2kT}{\pi^2 m_e}\right)^{1/2}\right.$$

$$\times\left[\exp\left[\left(\frac{q}{kT}\right)(\Phi(r)+\Phi_w+V)\right]\int_0^{\left[\frac{q}{kT}(\Phi(r)+\Phi_w+V)\right]^{1/2}}\exp(-z^2)\,dz\right.$$

$$\left.\left.-\left[\frac{q}{kT}(\Phi(r)+\Phi_w+V)\right]^{1/2}\right]\right\}. \qquad (8)$$

4.1. Floating potentials

Under steady-state conditions, the net current to the particle is zero. The two terms in eq. (8) may be equated and solved for $V(r)$.

$$V(r) = \frac{kT}{q}\left\{\ln\left[\left(\frac{1-\exp\left(-\frac{q\Phi_w}{kT}\right)}{\exp\left(-\frac{q\Phi_w}{kT}\right)}\right)\left(\frac{\pi^2 m_e}{2kT}\right)^{1/2}\left(\frac{n_{b0}}{n_{e0}}\right)v_b \exp\left[-\left(\frac{r}{r_0}\right)^2\right] + \left[\frac{q}{kT}(\Phi(r)+\Phi_w+V)\right]^{1/2}\right]\right.$$

$$\left. - \ln\int_0^{\left[\frac{q}{kT}(\Phi(r)+\Phi_w+V)\right]^{1/2}} \exp(-z^2)\,dz - \frac{q}{kT}(\Phi(r)+\Phi_w)\right\}. \quad (9)$$

Eq. (9) represents the magnitude of the floating potential at equilibrium. The minimum potential needed for entrapment is found by equating the gravitational and electric forces. This yields:

$$V_{min}(r) = -\frac{1}{2\epsilon_0}\frac{1}{12\beta^2}\frac{d_0^2 r_0^2}{\Phi_w}\frac{\rho g}{r}\exp\left[\beta^2\left(\frac{r}{r_0}\right)^2\right]. \quad (10)$$

4.2. Charging time

Invoking the relation

$$\frac{\partial V(r,t)}{\partial t} = \frac{1}{2\pi\epsilon_0 d_0}\frac{\partial Q(r,t)}{\partial t} = \frac{1}{2\pi\epsilon_0 d_0} I_e$$

eq. (8) may be inverted and integrated to yield the time required for the beam to alter the particle's potential. Letting $\chi = (q/kT)(\Phi(r)+\Phi_w+V)$, and performing the integration, the time required to charge the particle from an initial potential V_1 to a second potential V_2 is given by.

$$t = \frac{8\epsilon_0 kT}{q^2 d_0 n_{b0} v_b}\int_{\chi_1}^{\chi_2}\{d\chi\}\left\{\exp\left[-\left(\frac{r}{r_0}\right)^2\right] - \frac{n_{e0}}{n_{b0}}\left[\frac{\exp(-q\Phi_w/kT)}{1-\exp(-q\Phi_w/kT)}\right]\left(\frac{2kT}{\pi^2 m_e v_b^2}\right)^{1/2}\right.$$

$$\left.\times\left[\exp(\chi)\int_0^{\chi}\exp(-z^2)\,dz - \sqrt{\chi}\right]\right\}^{-1}. \quad (11)$$

5. Forces

If a particle is to be confined within the beam, the net force acting on the particle must be directed towards the central axis. In the region of the beam under investigation, two principal forces may be identified: the central force of the electric field and gravity. There is also a third force due to momentum transfer from the beam ions to the particle. However, this force is perpendicular to the Coulomb attraction and has no primary effect on trapping, other than affecting the residence time of the particle inside the beam.

5.1. Electric force

From eq. (9), the steady-state charge on the particle may be obtained from $Q = 2\pi\epsilon_0 d_0 V$. The electrostatic force is proportional to the negative gradient of the potential and, utilizing eq. (3), is expressible as: $F_e = -Q\nabla\Phi(r) = Q2\Phi_w\beta^2(r/r_0^2)\exp[-\beta^2(r/r_0)^2]$. Then from eq. (9), at a fixed point r,

the charged particle will experience the following steady-state electric force:

$$F_c = \frac{4\pi\beta^2\Phi_w\epsilon_0 d_0 kT}{qr_0^2} r \exp\left[-\beta^2\left(\frac{r}{r_0}\right)^2\right]\left\{\ln\left[\left(\frac{1-\exp\left(-\frac{q\Phi_w}{kT}\right)}{\exp\left(-\frac{q\Phi_w}{kT}\right)}\right)\left(\frac{\pi^2 m_e}{2kT}\right)^{1/2}\left(\frac{n_{b0}}{n_{e0}}\right)v_b \exp\left[-\left(\frac{r}{r_0}\right)^2\right]\right.\right.$$

$$\left.\left.+\left[\frac{q}{kT}(\Phi(r)+\Phi_w+V)\right]^{1/2}\right] - \ln\int_0^{\left[\frac{q}{kT}(\Phi(r)+\Phi_w+V)\right]^{1/2}} \exp(-z^2)\,dz - \frac{q}{kT}(\Phi(r)+\Phi_w)\right\}. \tag{12}$$

5.2. Normalized force

In general, depending on the angular position of the particle in the beam, the Coulomb and gravitational forces are not directly opposing. To assess the trapping ability of the positive field, the focus will be narrowed to the case of a particle situated at the bottom of the beam where the principle forces are maximally opposing. The net force acting on the particle is then $F_c + F_g$, where $F_g = g(\pi/6)\rho d_0^3$, ρ being the particle's density, g the acceleration due to gravity and d_0 the particle's diameter. Let F_N be the normalized force defined by:

$$F_N = \frac{F_g + F_c}{F_g} = 1 + \frac{F_c}{F_g}. \tag{13}$$

Then, if the value of eq. (13) is negative, the Coulomb force exceeds the gravitational force, and entrapment can occur. In this discussion, the particle is assumed to be created at rest, and the effects of initial conditions are not taken into consideration.

Before presenting the final form of the normalized force, certain simplifications may be introduced. It can be shown that for the beam under consideration, $kT \approx q\Phi_w$ and $\beta^2 \approx \frac{1}{3}$ [3,5]. Moreover, the plasma condition of charge neutrality along the beam axis, $n_{b0} \approx n_{e0}$, may be invoked. The expression for the normalized force thereby becomes:

$$F_N(r) = \frac{8\epsilon_0}{g\rho}\left(\frac{\Phi_w}{r_0 d_0}\right)^2 r \exp\left[-\frac{1}{3}\left(\frac{r}{r_0}\right)^2\right]$$

$$\times\left\{\ln\left[\left(\frac{\pi^2 m_e}{2\lambda q\Phi_w}\right)^{1/2} v_b \exp\left[-\left(\frac{r}{r_0}\right)^2\right] + \left[\exp\left[-\frac{1}{3}\left(\frac{r}{r_0}\right)^2\right] + \frac{V}{\Phi_w}\right]^{1/2}\right]\right.$$

$$\left. - \ln\int_0^{\left[\exp\left(-\frac{1}{3}\left(\frac{r}{r_0}\right)^2\right)+\frac{V}{\Phi_w}\right]^{1/2}} \exp(-z^2)\,dz - \exp\left[-\frac{1}{3}\left(\frac{r}{r_0}\right)^2\right]\right\} + 1, \tag{14}$$

where

$$\lambda = \frac{\exp\left(-\frac{q\Phi_w}{kT}\right)}{1-\exp\left(-\frac{q\Phi_w}{kT}\right)} = \frac{e^{-1}}{1-e^{-1}} = 0.582.$$

6. Calculations and discussion

Eqs. (9) and (11), which are implicit functions of V, were evaluated numerically using an iterative technique, and the value of V so obtained was used to calculate eq. (14).

Fig. 1 illustrates the normalized force exerted on a 1 μm Al particle in a 100 keV, 10 mA, 3 cm diameter As beam. The beam-line residual gas pressure was entered as 5.0×10^{-6} Torr. As is evident from the graph, eq. (14) predicts a region in which a particle may become entrapped, with a maximum trapping force occurring slightly outside the beam radius.

In fig. 2, the dependence of the maximum trapping force on beam-ion mass is displayed. For a beam of fixed current, energy and diameter, more massive molecules produce a greater trapping force. Correspondingly, for a particular beam-ion species, calculations of the trapping force as a function of beam energy at a constant current indicate that the force decreases with energy. Both situations reflect variations in the beam-ion density. With increasing velocity, space charge decreases, resulting in reduced field strength and a weaker Coulomb force.

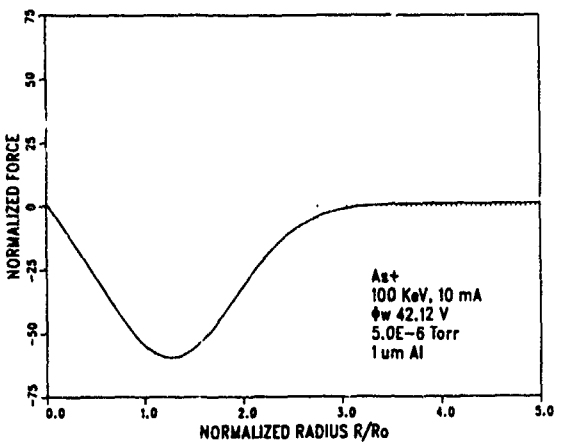

Fig 1 Variation of the normalized force with radial position expressed in terms of the radius ratio r/r_0. At the point 1 0 on the abscissa, the particle is located at the beam radius The point of maximum trapping is seen to lie just beyond the radius of the beam

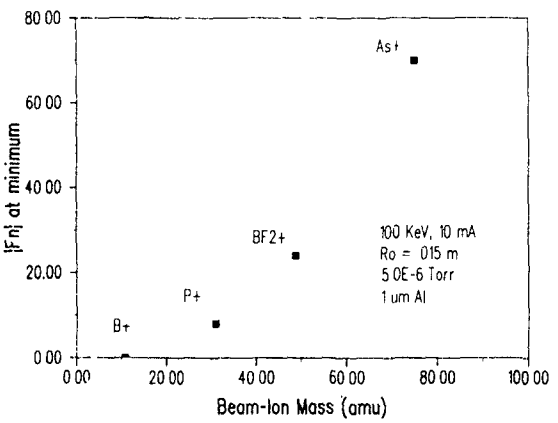

Fig 2 Variation of the maximum magnitude of the trapping force with beam-ion species For a fixed beam energy and current, increased ion mass leads to a lower beam velocity. This increases the charge density and leads to an enhancement of the Coulomb force acting on the particle

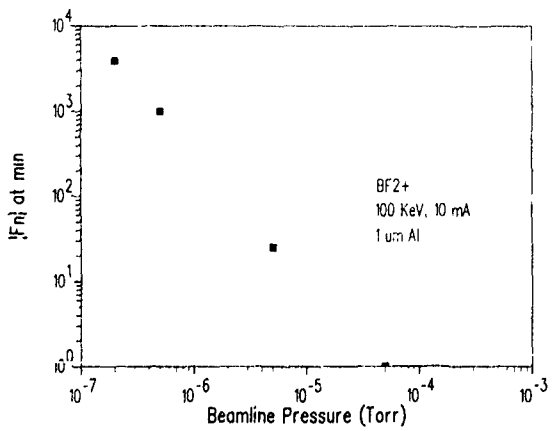

Fig 3. Dependence of the magnitude of the normalized force at maximum trapping with residual gas pressure Density of the background gas affects the space-charge neutralization of the beam and thereby influences the charging and electric field experienced by the particle.

The model developed here is valid for pressures ranging from approximately 10^{-8} to 10^{-4} Torr. Fig. 3 depicts the effect of pressure on a 100 keV, 10 mA BF_2 beam propagating through a chamber maintained at constant temperature (27° C). A decrease of two orders of magnitude in the pressure is seen to induce a force enhanced by three orders of magnitude. A greater gas density results in greater beam-ion neutralization and reduced space charge.

In order for trapping to occur, the charging time must be short with respect to residence times. The time necessary for a 1 μm Al particle to acquire the minimum trapping charge (i.e., the charge determined from eq. (10)) was calculated at the point of maximum trapping. For various beam conditions, it was found to range from ~ 1 ns to ~ 1 μs. Because the time scales for particle motion are typically orders of magnitude larger than these charging times, the charged state of the particle can be considered in equilibrium. In other words, the mobility of ions and electrons far exceeds the mobility of the particle, and a condition of instantaneous charging may be assumed.

7. Conclusions

Within an intense cylindrical ion beam, conditions may exist that can lead to the charging and confinement of particulate contamination. These conditions will be affected by the initial state of the particle. However, for a static, initially uncharged particle, the model developed here predicts that certain beams may support an electric force stronger than the opposing force due to gravity. Moreover, the time required for the particle to attain the necessary charge is sufficiently small so as not to preclude entrapment.

The experimental evidence on particle trapping in an ion beam is sketchy and contradictory. The purpose of this calculation is to provide some guidelines and to predict general trends which may be verified by more systematic experiments or by reviewing past accumulated data from various processes. Clearly, the numbers given here cannot be simply applied to beams of different geometry, but it is reasonable to assume that conclusions may be drawn from this analysis that are applicable under a variety of conditions.

Acknowledgement

The support of the University of Arizona Sematech Center of Excellence in Contamination/Defect Control is gratefully acknowledged.

References

[1] T C Smith, Nucl Instr and Meth B37 (1989) 486
[2] M. Mack, D Stone, J Jost and P Sferlazzo, Prevention of Aerodynamic Particle Transport in Air Handling Water Processing Equipment, Techn Proc Semiconductors East 107 (Boston, MA, 1989)
[3] A.J T Holmes, Phys Rev A19 (1979) 389
[4] J. Klabunde and A Schoenlein, Beam Transport With Space Charge Compensation, Proc. Linear Accelerator Conf. Stanford, SLAC Rep 303 (Palo Alto, CA, 1986) 296
[5] D A Brown, Theoretical Study of Particle Charging and Entrapment in a Cylindrical Ion Beam, M Sc Thesis, (University of Arizona, Tucson, AZ, 1990)
[6] M E Rudd and T Jorgensen, Phys Rev 131 (1963) 666.
[7] M. Gryzinski, Phys Rev 115 (1959) 374.

Nuclear Instruments and Methods in Physics Research B55 (1991) 355–358
North-Holland

A high-current low-energy multi-ion beam deposition system

Osamu Tsukakoshi, Saburo Shimizu, Seiji Ogata, Naruyasu Sasaki and Hiroyuki Yamakawa
ULVAC Japan, Ltd. 2500, Hagisono, Chigasaki, Kanagawa 253, Japan

A high-current, low-energy multi-ion beam deposition system has been developed aiming at the fabrication of new materials This system consists of two ion sources, a dual-sector-type mass analyzer and a decelerating system Several ion species are extracted successively from the two ion sources by switching the mass analyzer selection Artificially structured materials, especially having a layered structure, can be grown by the fine control of the growth process of each layer The developed ion beam deposition system, including the design concept, is described in detail The deceleration characteristics of this system using Ar^+ ion are also shown

1. Introduction

The use of low-energy ion beam in thin film growth is very important and attractive in the fabrication of artificially structured new materials having well-controlled composition and structure almost on an atomic scale. Various methods such as ionized cluster beam deposition, mass-separated low-energy ion beam deposition and dual ion beam sputter deposition have been employed for the preparation of these films Among these, mass-separated low-energy ion beam deposition is quite attractive, because it can control the growth parameters precisely by selecting the ion species and ion energy independently. The authors have used mass-separated, low-energy group-V ion beam for the epitaxial growth of III–V compound semiconductors [1–5]. Recently, ORNL group has been trying to obtain various semiconductor films such as β-SiC/α-SiC [6], GaAs/Si [7] and GaAs/Ge [8] by using low-energy direct ion beam deposition

However, the ion beam deposition systems used in these experiments are not satisfactory from the viewpoint of the deposition of films with characteristic features, because ion beam current is relatively low (several μA–several tens of μA) and the number of ion species utilized for the film growth is only one with some exceptions [4,6,7] Therefore, the further development of the low-energy ion beam deposition system is inevitable to realize new properties of films.

We have developed a high-current, low-energy multi-ion beam deposition system. In this paper, the design of the system and the results of Ar^+ ion beam deceleration in order to characterize the beam characteristics are reported

2. Physical basis of the design

Taking into account the space charge effect, the paraxial ray equation, which describes the beam envelope for a radially uniform beam, is written as follows:

$$d^2r/dz^2 + (dV/dz)(dr/dz)(2(V - V_0 - V_s))^{-1} + (d^2V/dz^2)r(4(V - V_0 - V_s))^{-1} - I(m/2e)^{-1/2}(4\pi\epsilon_0 r)^{-1}(V - V_0 - V_s)^{-3/2} = 0, \quad (1)$$

where r is the radius of the ion beam starting from the ion source at potential V_s with a starting kinetic energy of V_0(eV), V is the potential on the axis at z, e and m are the charge and the mass of the ion respectively. ϵ_0 is the dielectric constant of the vacuum The fourth term which represents the space charge effect shows that the ion beam spreads in inverse proportion to 3/2 power of the kinetic energy. Thus, the spread of the ion beam becomes serious with the diminution of its energy To overcome this difficulty, the ion beam deposition system is designed as follows

(1) The substrate is set at the ground potential; (2) the ion energy at the substrate is controlled by adjusting the potential of the ion sources, (3) the ion beam extracted from the ion sources is transported at negative high voltage (from −20 to −35 kV) and decelerated just in front of the substrate; (4) a voltage of 2 kV lower than that of the transport region is applied to two electrodes (the exit of the ion extraction system and the entrance of the ion deceleration system) to enhance the space charge neutralization by trapping slow electrons

0168-583X/91/$03.50 © 1991 - Elsevier Science Publishers B V (Nor h-Holland)

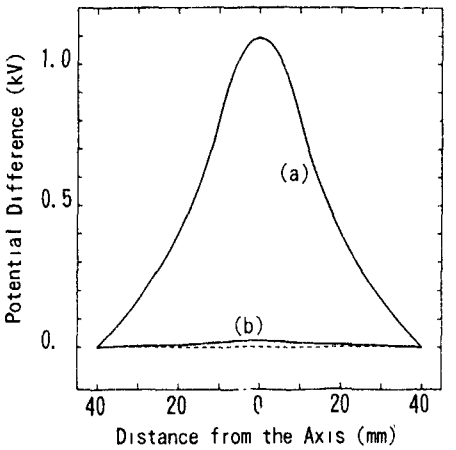

Fig. 1. Cross sections of the potential calculated from eq. (2). The curve (a) shows the potential without the neutralization and the curve (b) shows that with a neutralization of 98%. The dotted line shows the potential of the metal tube.

in the beam channel; (5) the ion beam is controlled not electrostatically but electromagnetically throughout the ion beam transportation.

To estimate the potential due to the space charge, we consider a radially uniform ion beam flowing in a metal cylinder of inner radius R. The potential $V(r)$ at radius r is given as

$$V(r) = (m/2e)^{1/2}(4\pi\epsilon_0)^{-1}(1-h) \times I(V_s + V_0 - V)^{-1/2} \times 2\log(R/r), \qquad r > r_1,$$

$$V(r) = (m/2e)^{1/2}(4\pi\epsilon_0)^{-1}(1-h) \times I(V_s + V_0 - V)^{-1/2} \times \left[1 + 2\log(R/r_1) - (r/r_1)^2\right], \qquad r < r_1, \quad (2)$$

where V is the mean potential in the beam, r_1 is the envelope radius of the beam, I is the total current and h is the degree of the neutralization. For example, cross sections of the potential calculated from eq. (2) for a 23 kV W^+ beam with a current of 5 mA and a radius of 10 mm injected into a metal cylinder of 80 mm inner diameter are shown in fig. 1. Though the potential on the axis without the neutralization amounts to about 1 kV, that of a 98% neutralized beam [9] is reduced to only about 20 V.

3. Design of the system

3.1 Ion beam transport system

A bird's eye view of this system is shown in fig. 2. The system is equipped with two ion sources – a plasma filament type [10] and a double hollow cathode type [11] – to supply various kinds of ion species. The former is for the production of the metal ions having relatively low vapor pressure such as In^+, Ga^+, As^+ and P^+ and the latter for the refractory metal ions such as W^+, Nb^+ and Mo^+. Each ion source can produce more than two ion species simultaneously. The ion beams extracted from the ion sources are mass separated by a dual-sector-type mass analyzer, focused by a triplet magnetic quadrupole lens and then deflected by a magnetic deflector to eliminate high-energy neutral atoms. After the

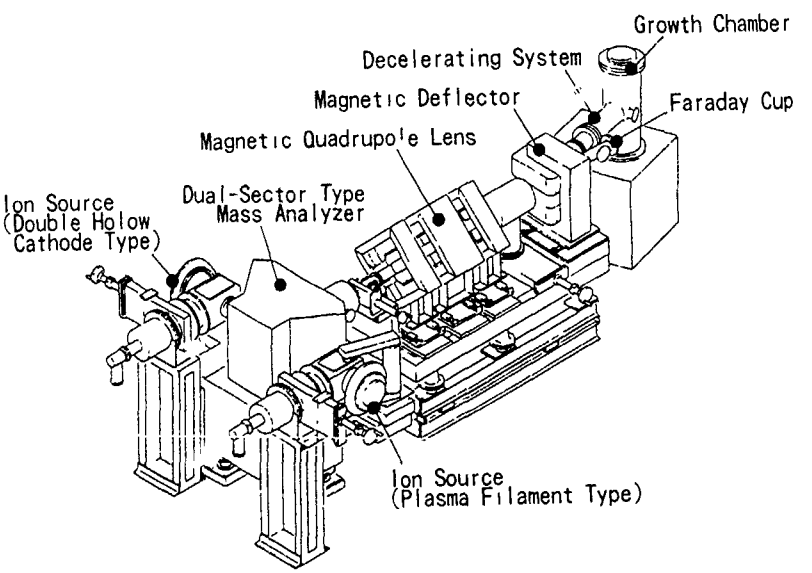

Fig. 2 Bird's eye view of the system.

deflection, the ion beams are introduced into a growth chamber which is kept at the ultrahigh vacuum of 1×10^{-8} Pa and then decelerated just in front of the substrate. The design concept of this decelerating system will be described in section 3.2.

Thin shims designed by computer simulation are attached at the periphery of the pole-pieces of the dual-sector-type magnet and the deflection magnet respectively. The rotatable shims are mounted on the pole-pieces of the dual-sector-type magnet at the entrance sides.

Both a quick switching of the ion species and a stable ion current are needed by the following two reasons: (1) To minimize the contamination on the substrate, it is desired that the useless interval in which the substrate is left without any injection of the ion beam while switching the ion species is as short as possible; (2) to supply the required ion species successively, a magnetic field must be controlled with a high reproducibility.

A high-speed and high-precision control of the electromagnet is realized by a feedback via a magnetic field monitor using a Hall probe. Since the Hall probe is sensitive to the temperature, an IC thermosensor monitors the temperature and these devices are kept at almost constant temperature ($< 0.5°C$) by an isolated cooling system. Two electromagnets, the dual-sector type and the deflector, are equipped with this control system. The fluctuation is reduced to less than 5×10^{-4} by utilizing this control system. When the ion beams are extracted from the different ion source, it is necessary to turn the polarity of the dual-sector-type magnet. The time needed to turn the polarity of the magnet (from +10000 to −10000 G) is less than 30 s. When the turning of the polarity is not required, the time to attain to the maximum magnetic field available (from 0 to 11000 G) is as short as 5 s.

All electromagnets are controlled via optical fiber links by a factory computer (NEC FC-9801V) at the ground potential. Since parallel digital signals are latched at ground level, discharge in the high-voltage region will cause no deviation from the programmed behavior.

3.2 *Ion beam decelerating system*

The ion beam is decelerated down to an energy of several eV–several hundred eV by the decelerating system. Since the ion beam passes through an electric field with a high gradient, a sophisticated design was performed for the decelerating system. Throughout the design of dimensions and applied potentials of the electrodes, a computer simulation of the ray tracing considering the space charge effect was carried out. The finite element method was used to solve the Poisson equation.

The decelerating system is composed of three cylindrical electrodes. The first electrode operates to trap the slow electrons in the transport region as described in section 2. The second and the third electrode, between which a large difference of potential of up to about 50 kV is supplied, produce a strong converging lens field. This converging field is indispensable to cancel the diverging force due to the following two reasons. First, a decelerated ion beam diverges owing to its space charge. Second, a decelerating electric field between a cylindrical electrode and a flat metal plate produces a diverging lens field.

One of the examples of computer-simulated ion beam trajectories in the decelerating system is shown in fig. 3. A W^+ ion beam (100 eV) with a current as high as 5 mA can be obtained using this decelerating system. Potentials applied to the first, second and third electrodes are −25.0, −50.0 and −2.9 kV respectively. The potential of the third electrode is optimized automatically by the computer.

4. Ar^+ ion deceleration

We have carried out decelerating experiments with an Ar^+ ion beam. The maximum current incident on

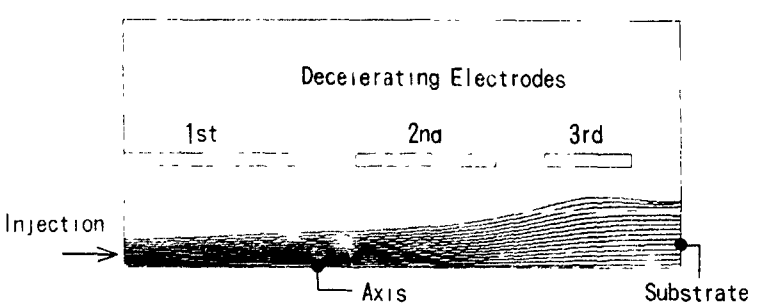

Fig. 3. Computer-simulated ion beam trajectory. The ion species is W^+, the current is 5 mA and the kinetic energy is 100 eV. Potentials applied to the first, second and third electrodes are −25.0, −50.0 and −2.9 kV respectively.

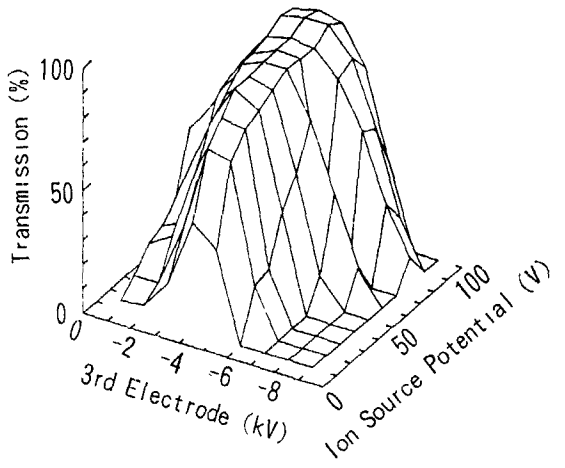

Fig. 4 Experimental results of the transmission as a function of the potentials of the third electrode and the ion source. Potentials applied to the transport region, the first electrode and the second electrode are −30.0, −33.0 and −38.0 kV respectively.

the substrate up to the present was 1.2 mA with the ion source potential of 100 V. The ion beam current injected into the decelerating system is monitored by a Faraday cup, shown in fig. 2, when the magnetic deflector does not operate. The transmission, which is defined as a ratio of the ion current incident on the substrate to the injected current, did not depend on the injected current in the range 0–1.5 mA. Therefore, a larger ion source gives a higher current at the substrate.

The transmission is most sensitive to the potential of the third electrode among the three decelerating electrodes. In fig. 4, an experimental result of the transmission is shown as a function of the ion source potential and the potential of the third electrode. Transmissions over 0.8 were obtained for ion source potentials over 40 V. Even for an ion source potential as low as 10 V, a transmission over 0.4 was obtained. The optimum potential of the electrode observed for each ion source potential agreed satisfactorily with that obtained by the computer simulation.

5. Conclusion

We have developed a high-current low-energy multi-ion beam deposition system aiming at the fabrication of new materials. By monitoring the magnetic fields using Hall probes, a high-speed and high-precision control of the ion beam was realized. Up to the present, an ion beam of 1.2 mA incident on the substrate with an energy of 100 eV was obtained.

Acknowledgements

The authors wish to express their sincere gratitude to Dr. C. Hayashi who supported us throughout the present project. They are also indebted to Dr. T. Katagawa, Messrs. T. Fujita and T. Nomura for their cooperation to design and construct the present system.

This work was performed under the Research and Development Program on "Advanced Material Processing and Machining System", conducted under a program set by the New Energy and Industrial Technology Development Organization

References

[1] S. Shimizu, O. Tsukakoshi, S. Komiya and Y. Makita, Jap. J. Appl. Phys. 24 (1985) 1130
[2] S. Shimizu, O. Tsukakoshi, S. Komiya and Y. Makita, J. Vac. Sci. Technol. B3 (1985) 554
[3] S. Shimizu, O. Tsukakoshi, S. Komiya and Y. Makita, Jap. J. Appl. Phys. 24 (1985) L115
[4] S. Shimizu and Y. Makita, Proc. 10th Symp. on ISIAT'86, Tokyo (Ion Engineering Society of Japan, Tokyo, 1986) p. 313
[5] S. Shimizu and S. Komiya, J. Cryst. Growth 81 (1987) 243
[6] S.P. Withrow, K.L. More, R.A. Zuhr and T.E. Haynes, Vacuum 39 (1989) 1065.
[7] T.E. Haynes, R.A. Zuhr, S.J. Pennycook and B.R. Appleton, Appl. Phys. Lett. 54 (1989) 1439
[8] T.E. Haynes, R.A. Zuhr, S.J. Pennycook and B.C. Larson, Proc. 12th Symp. on ISIAT'89, Tokyo (Ion Engineering Society of Japan, Tokyo, 1989) p. 363
[9] O. Tsukakoshi, T. Terasawa, K. Komatsu, N. Niikura, K. Yui, E. Kouno, T. Katagawa, K. Takagi, H. Yamakawa and S. Komiya, Proc. 11th Symp. on ISIAT'87, Tokyo (Ion Engineering Society of Japan, Tokyo, 1987) p. 225
[10] R. Fukui, K. Takagi, T. Tsugueda, H. Tsuboi, R. Kikuchi, E. Yabe and K. Takayama, Nucl. Instr. and Meth. B37/38 (1989) 140
[11] H. Taguchi, A. Tonegawa and K. Takayama, Proc. 13th Symp. on ISIAT'90, Tokyo (Ion Engineering Society of Japan, Tokyo, 1990) p. 71

Nuclear Instruments and Methods in Physics Research B55 (1991) 359–363
North-Holland

Development of a four-electrode extraction system for a large area ion source with a wide range of operational conditions

Shuichi Maeno, Masayasu Tanjyo, Kazuhiko Tanaka and Jyota Fujita
Nissin Electric Co., Ltd, 47, Ukyo-ku, Kyoto 615, Japan

We have developed a four-electrode extraction system for a large area ion source with a wide range of operational conditions, that is, a beam energy of 1–100 keV, a beam current density of 7 nA/cm^2–7 μA/cm^2, and ion source gases of BF_3 or PH_3. Uniformity of the beam profile was less than ±10% in the 15×15 cm^2 area. Control of the beam optics was done by varying the electric field in the extraction region. The optimum field intensity was investigated experimentally and the result agreed quite well with that of the computer simulation. By designing the gap ratio (the distance of the extraction region / the distance of the acceleration region) with a small value, we could control the beam with energies of 1–100 keV by varying the extraction voltage from 0 to 2 kV.

1. Introduction

Recently, it has been popular to apply ion beam systems to industrial uses other than semiconductor implantations, such as the implantation of impurities for solar cells and thin film transistors of liquid crystal drivers, beam etching for magneto-heads and non-spherical lenses, and surface modification of metals and ceramics. Requirements for some of these latter uses are high beam currents, high performance, large area uniformity, wide area treatment, good controllability and easy maintenance. An ion shower system which uses a multi-hole electrode extraction ion source, typically a bucket type ion source, is suitable for many of the above requirements. Generally speaking, this system has two disadvantages compared with the ion implanter. One is that using the usual three-electrode extraction ion source, the lower the beam energy the lower the

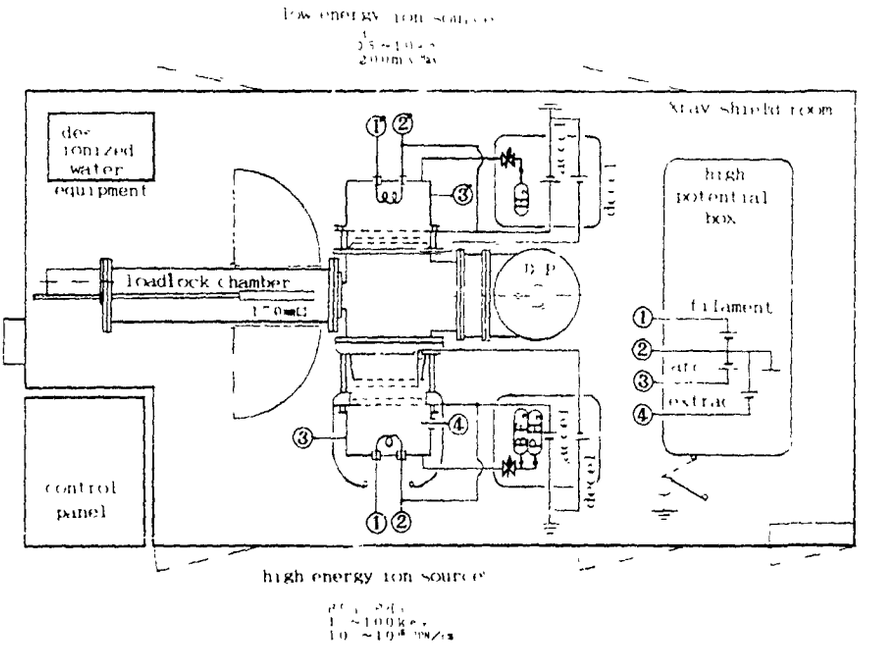

Fig. 1. Schematic drawing of the ion shower system with a four-electrode ion source for 100 keV B and P ion beams and the three-electrode ion source for a 10 keV H ion beam.

0168-583X/91/$03.50 © 1991 – Elsevier Science Publishers B.V. (North-Holland)

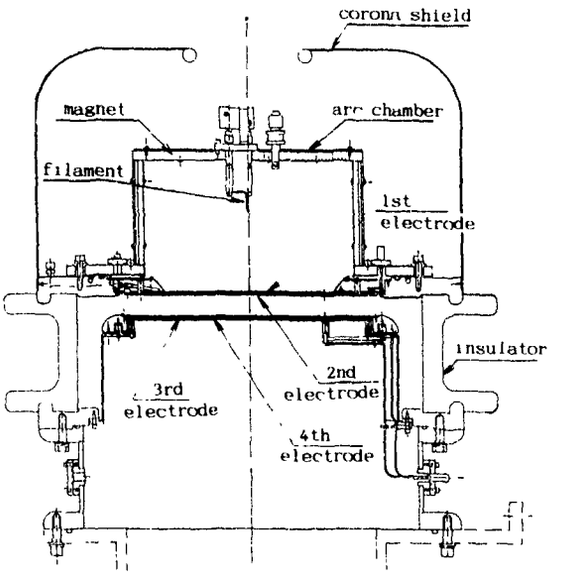

Fig 2. Schematic of the four-electrode ion source

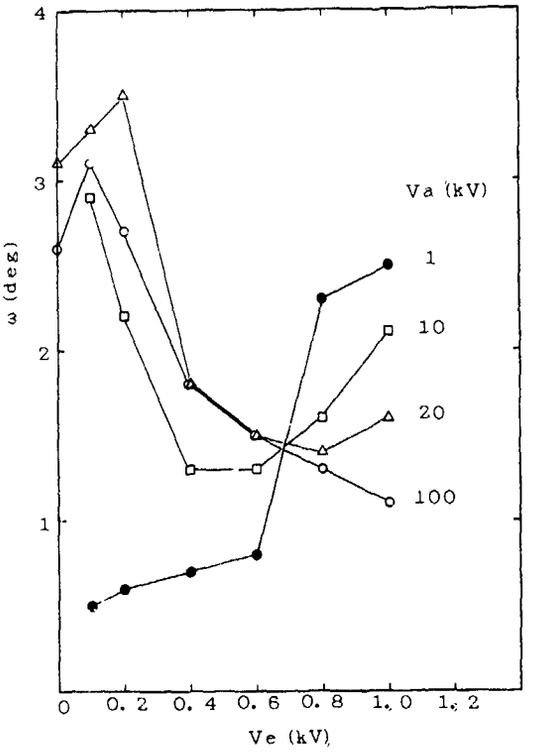

Fig. 4 Calculated beam divergence ω with varying parameters V_a and V_e (PH_3). V_a = 1, 10, 20, 100 kV, V_e = 0.1–1 kV

beam current to obtain a good beam uniformity, because beam current is proportional to beam energy $Va^{3/2}$ under similar beam optics. Another is that mass separation is difficult.

We investigated whether a four-electrode extraction large area ion source could operate with a wide range of operational conditions required for an ion shower system which is applied to implantation for solar cells and thin film transistors of liquid crystal drivers The required specifications are that the beam energy should vary from 1 to 100 keV with the same current density (10 μA/cm^2) and that the beam current is variable from 10 nA/cm^2 to 10 μA/cm^2 for the same beam energy (around 100 keV) with good beam uniformity ($< \pm 10\%$) on the 15 cm × 15 cm target.

A four-electrode extraction ion source has been investigated in detail by the JAELI groupe [1] for the neutral beam injection system. Their purpose is to get a minimum beam divergence at high beam current. On the other hand, in this work the purposes were to achieve a uniform beam profile with widely varying operational conditions, and good controllability

2. Apparatus, the four-electrode ion source

In fig 1 the ion shower system is shown, which is equipped with a four-electrode ion source and with the usual three-electrode ion source. The former is used as a boron (B) and phosphorus (P) ion beam source with high energy (100 keV) and low current (4 mA) The latter is used as a hydrogen (H) ion beam source with low energy (10 keV) and high current (200 mA). Plasma production is done by dc discharge, the power of which

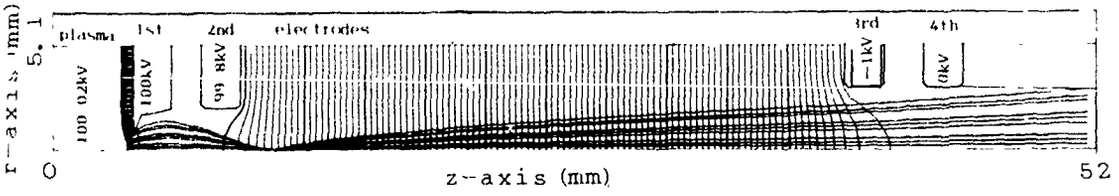

Fig 3. Typical beam trajectory calculated by computer simulation with a beam acceleration voltage V_a = 100 kV and an extraction voltage V_e = 0.2 kV (PH_3) J_i = 300 μA/cm^2, I_b = 5.5 μA, ω = 2.7°, a = 1 mm, d(1–2) = 1.5 mm, d(2–3) = 30 mm, t(1–4) = 2 mm

is supplied by a filament power supply and an arc power supply in the high potential box. These power supplies are alternatively used for both ion sources. The process chamber is evacuated by an oil diffusion pump with a pumping speed of 5000 l/s. In the loadlock chamber, a 150 cm × 150 cm size specimen can be installed. To measure the beam profile, there is a Faraday cup array which consists of nine cups, where the cup hole size is 4 mm in diameter and a has pitch of 25 mm, attached to the specimen holder. It is scanned horizontally.

A schematic of the four-electrode source is shown in fig. 2 The plasma chamber is enclosed with a multi-cusp magnetic field and a filament installed in it. The ion source gas is fed in at the top of the chamber. The ion beam is transported by the four-electrode system. The first electrode is the plasma electrode, the second one is for extraction, the third one is for acceleration and the fourth one is the earth electrode. The multi-holes of 529 pieces are made in the 22 cm × 22 cm square area for each electrode coaxially.

3. Computer simulation of beam trajectory

For designing the beam optics of the four-electrode system, the main factors are the Perveance ratio (P/P_e) which is concerned with the beam divergence at the extraction region, the electric field ratio $f = E_1/E_2$ which controls the lens effect between the extraction ($E_1 = V_e/d_1$) and the acceleration ($E_2 = (V_a - V_e)/d_2$) regions, and the potential ratio $p = V_e/(V_a - V_e)$ which describes the beam collimation intensity at the acceleration region. Here V_e is the extraction voltage between the first and second electrodes, V_a is the acceleration voltage between the first and fourth electrodes, d_1 is the distance between the first and second electrodes, and d_2 is that between the second and third electrodes. As the distance between the electrodes and the target is 30 cm, the beam divergence (ω) must be designed to have a suitable minimum value of $\omega = 30$ mrad (2°), otherwise a too small divergence results in a multi-spot beam profile

A typical example of a PH_3 ion beam trajectory at the single hole calculated with a computer simulation is shown in fig 3. The main parameters are shown in the figure, namely the ion saturation current $J_i = 300$ $\mu A/cm^2$, $V_a = 100$ kV, $V_e = 0.2$ kV, the radius of the hole of the first electrode $a = 1$ mm, the gap between the first and second electrodes $d(1-2) = 1.5$ mm, the gap between the second and and third electrodes $d(2-3) = 30$ mm, and the thickness of each electrode $t = 2$ mm In the results, the beam current $I_b = 5.5$ μA and the beam divergence angle $\omega = 2.7°$. As the calculated Perveance ratio of the extraction region is 1.4, the plasma meniscus has a convex shape. Then with an electric field

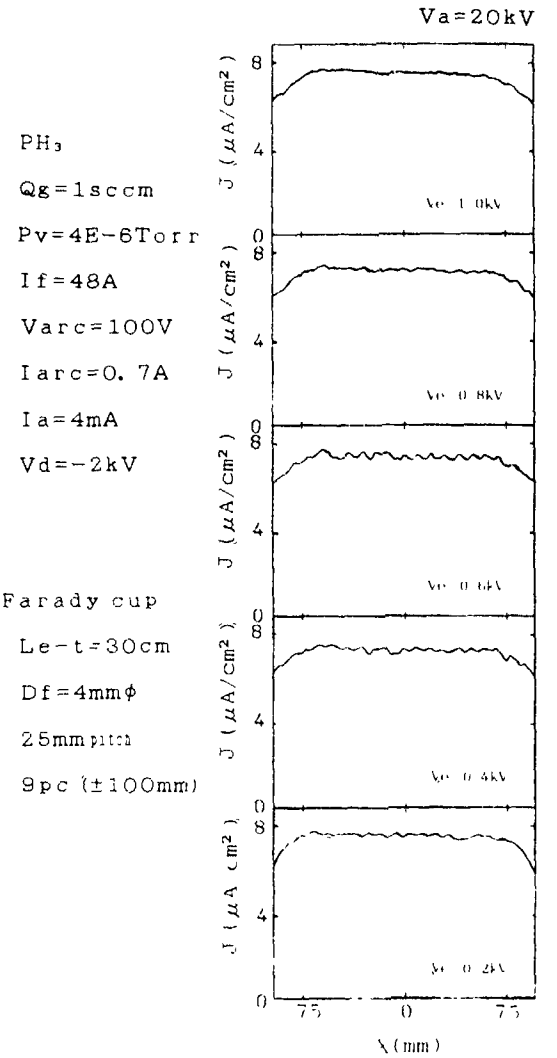

Fig. 5 Beam profiles at the midplane with $V_a = 20$ kV and $V_e = 0.2$–1.0 kV (PH_3).

ratio $f = 0.02$, beam focusing occurs because of the strong convex lens effect. As the potential ratio is $p = 0.002$, the beam is collimated at the acceleration region

The calculated values for ω are shown in fig. 4 for V_e in the range $V_e = 0.1$–1 kV, and values for V_a of V_a = 100, 10 and 1 kV. As V_a decreases, V_{em}, the value of V_e which gives the minimum ω, decreases.

4. Experimental results

The ion beam profile was measured by means of a scanning Faraday cup array. In fig. 5, beam profiles at the midplane are shown with $V_a = 20$ kV, $V_e = 0.2$–1.0 kV, other conditions as shown. At $V_e = 0.6$ kV, a multi-

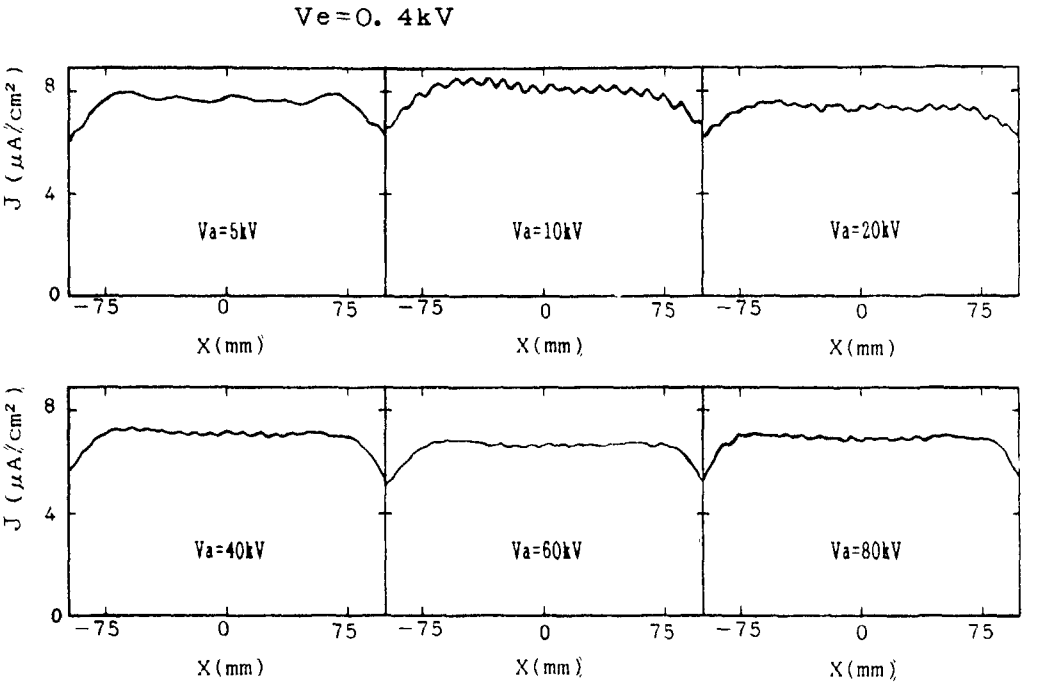

Fig 6 Beam profiles at the midplane with V_a = 5–80 kV and V_e = 0.4 kV (PH_3)

spot beam profile appeared. which suggests the beam divergence to be at a minimum. So it is recognized that the optimum V_e is 0.2 kV

In fig. 6, beam profiles at the midplane with V_e = 0.4 kV and V_a = 5–80 kV are shown At V_a = 10 kV, a multi-spot beam profile appears.

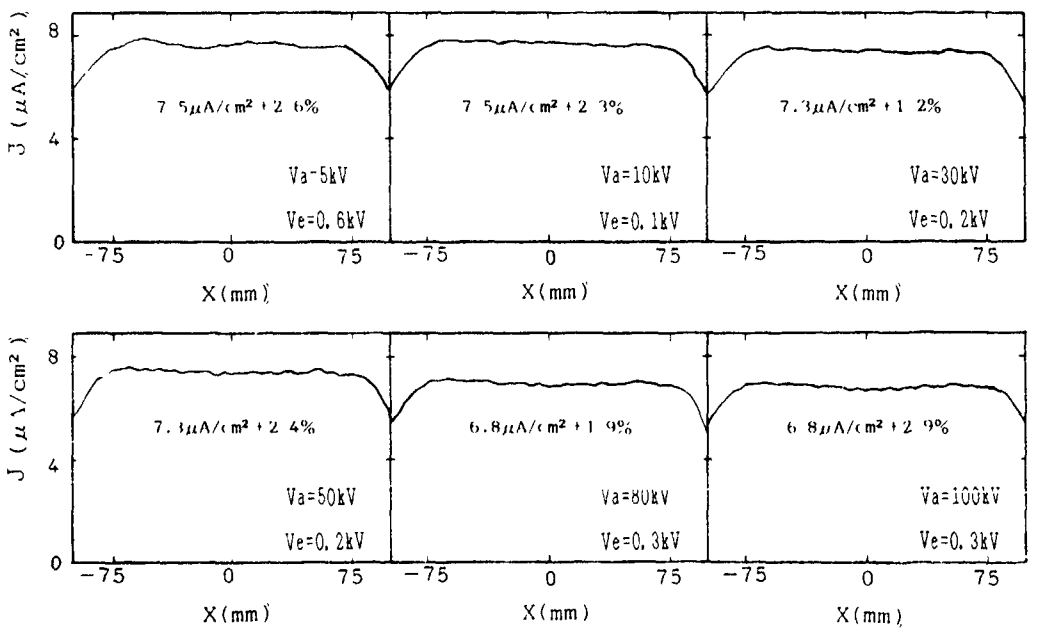

Fig. 7 Beam profiles at the midplane with V_a = 5–100 kV and optimized V_e for good beam profile (PH_3)

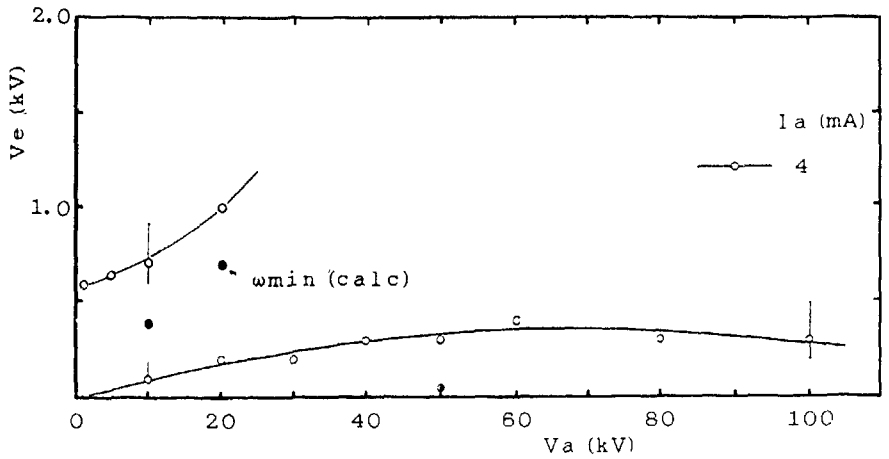

Fig 8. Optimum V_e vs V_a for a good beam profile and minimum divergence conditions deduced from the computer simulation (PH_3).

Considering the experimental and computational results stated above, the measured beam profiles at optimum V_e for $V_a = 5$–100 kV are shown in fig. 7. It is shown that the average beam current density is almost the same at 7 $\mu A/cm^2$ and the uniformity of the profile is less than $\pm 3\%$ in the ± 75 cm^2 area. The beam uniformity in a 150 mm × 150 mm square area is less than $\pm 10\%$. In fig. 8, the optimum V_e versus V_a to obtain a good beam profile are plotted and the minimum divergence conditions as deduced from computer simulation are also plotted.

5. Conclusions

(1) It is concluded that using a four-electrode ion source, a constant beam current and a good beam profile can be achieved for the 5–100 keV energy range. Computer simulation results agreed fairly well with the experiment, which suggests that using this extraction system, the beam optics does not follow the $I \propto V^{3/2}$ law but can be controlled by the suitably selected extraction voltages V_e.

(2) For this four-electrode extraction ion source, the suitable extraction voltage V_e is somewhat lower or higher than the extraction voltage V_{em} which gives a minimum divergence angle. The lower value is $V_e =$ 100–300 V for the beam energy $V_a = 10$–100 keV. The higher value increases rapidly as V_a increases, so the available conditions are $V_a < 20$ kV and $V_e = 0.5$–1 kV. It is expected that a high beam current density requires a high extraction voltage.

Acknowledgements

The author would like to acknowledge Messrs. K. Nakata and Y. Miyai for their advice and support with the high voltage power supply circuits He also thanks Messrs. H. Nakazato, I. Ito, Y. Kawakita, T. Amemiya, M. Tanii, and Y Goino for their help and encouragement.

Reference

[1] Y Ohara, J. Appl Phys 49 (1978) 4711

Nuclear Instruments and Methods in Physics Research B55 (1991) 364–369
North-Holland

Production of oxygen plasmas using radio-frequency magnetron-discharge

Takehisa Shibuya [a], Shizuyo Hashimoto [a], Eiji Yabe [b] and Kazuo Takayama [b]

[a] *Department of Physics, School of Science, and* [b] *Institute of Research and Development, Tokai University, 1117 Kitakaname Hiratsuka Kanagawa 259-12, Japan*

A new type of oxygen ion source has been developed in order to substantially prolong the lifetime of a conventional oxygen ion source for various plasma processes In this ion source, an oxygen plasma is produced by coupling a 13 56 MHz radio-frequency (rf) field to a pair of rf electrodes placed in the region of a line cusp field. Two electrodes are positioned in such a way that accelerated electrons undergo magnetron type motion around them, efficiently producing a plasma around the electrodes (rf magnetron discharge) This plasma diffuses along the magnetic field line into the center region of the cusp field where the field strength is almost nil. The above process makes it possible to produce a large volume of uniform plasma As a result, extraction of a large area oxygen-ion-beam from the new ion source is relatively easy. The lifetime of this ion source is virtually limitless, because it does not have any corrosive parts, such as a hot filament The new ion source can be used with any kind of reactive gases as well as oxygen

1. Introduction

The ion sources have been used in ion assisted technologies such as ion beam etching, ion beam deposition and ion implantation for high speed ion beam processing [1–6]. In the plasma processes, stable operation with a long lifetime is required because chemically reactive ion beams have been extensively utilized in semiconductor fabrication. Furthermore, recently, the need has arisen for an ion source to extend the ability for uniform irradiation over a large area. For the above-mentioned reason, the development of a radio-frequency magnetron type ion source was started. A new type of rf magnetron-discharge oxygen plasma source has been developed to substantially prolong the lifetime of the conventional oxygen plasma source for various plasma processes. In comparison with a dc plasma source, the rf plasma source has several advantages: (1) it is a simple structure, (2) it produces a uniform plasma density, (3) it produces easily a large-area ion beam, (4) it can be used with any reactive gas, and (5) finally, as it has no filament it has a long

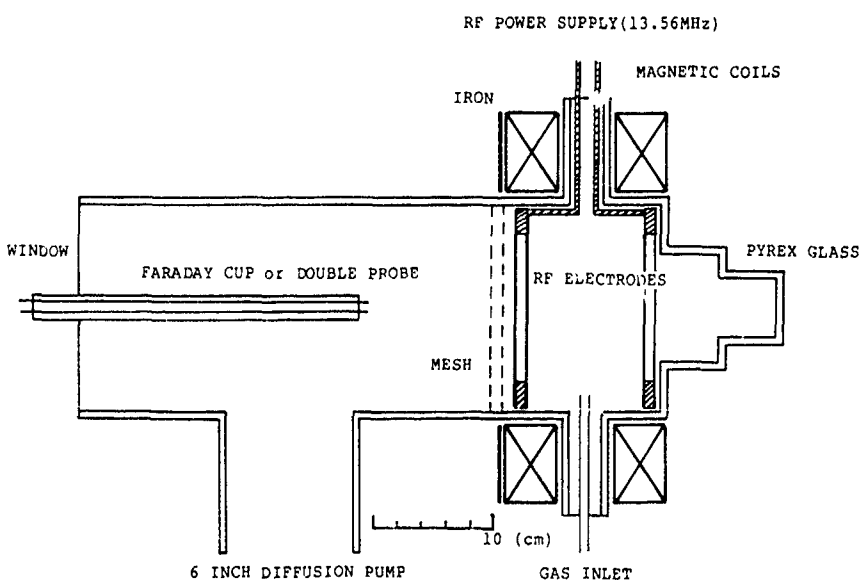

Fig. 1 Schematic diagram of the rf magnetron type ion source.

0168-583X/91/$03 50 © 1991 – Elsevier Science Publishers B V. (North-Holland)

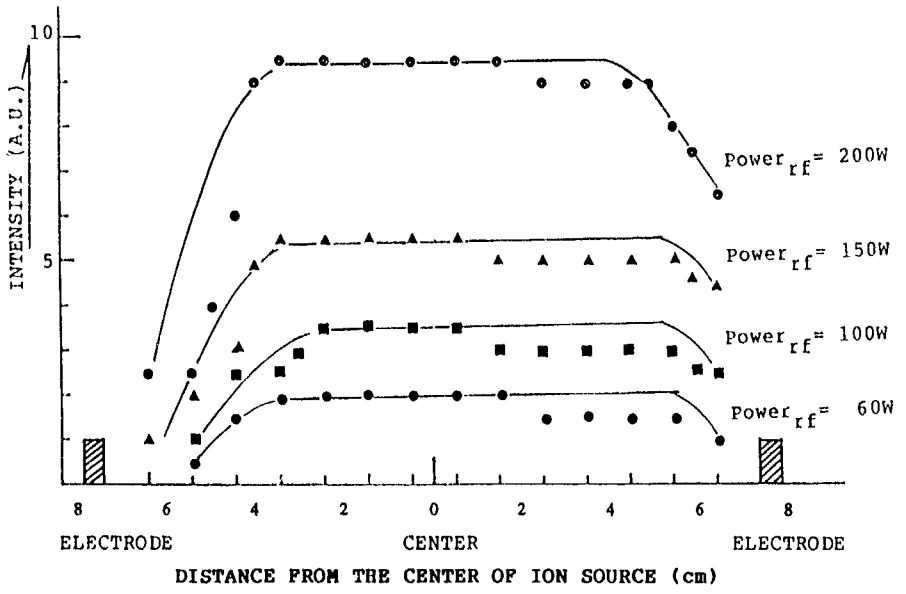

Fig 2 Intensity distribution as a function of the rf power in the cusp field O_2 gas, $P = 3.0 \times 10^{-4}$ Torr, cusp magnetic field (90 G), O_2 spectral line

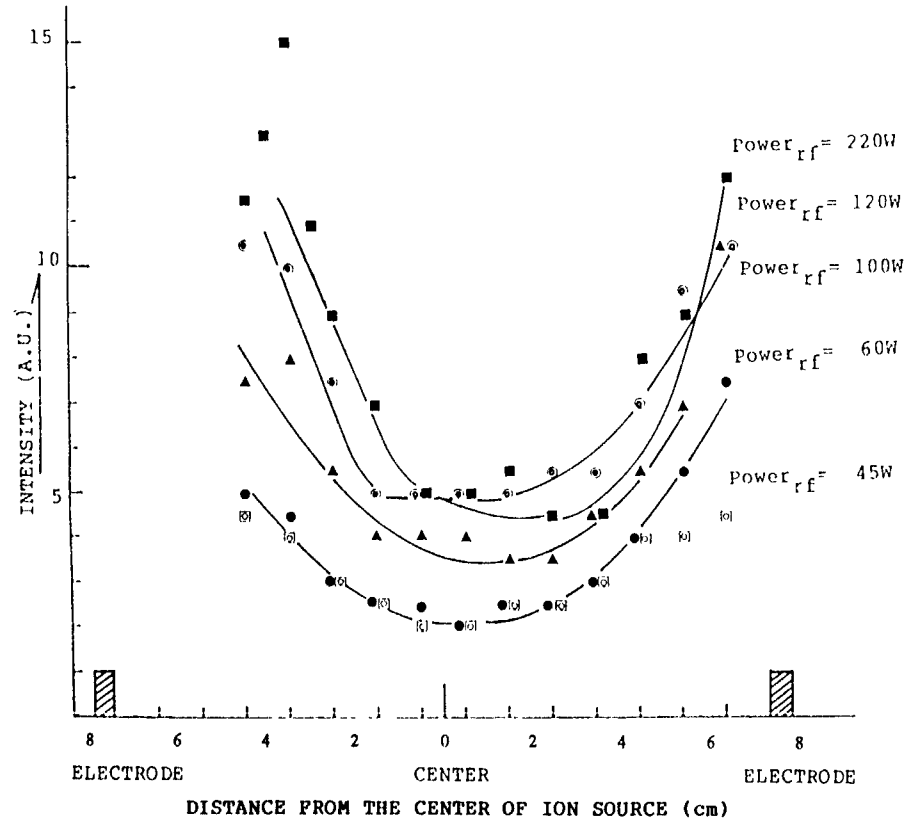

Fig. 3 Intensity distribution as a function of the rf power in the mirror field O_2 gas, $P = 3 \times 10^{-4}$ Torr, mirror magnetic field (140 G), O_2 spectral line

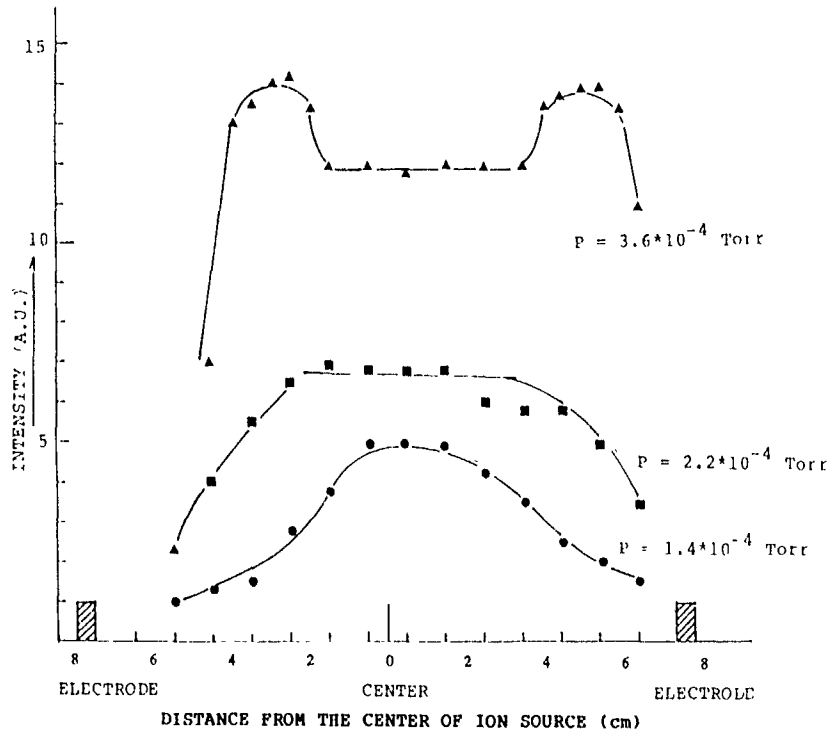

Fig 4 Intensity distribution as a function of the pressure of the ionization chamber in the cusp field O_2 gas, rf power = 200 W, cusp magnetic fields (90 G), O_2 spectral line

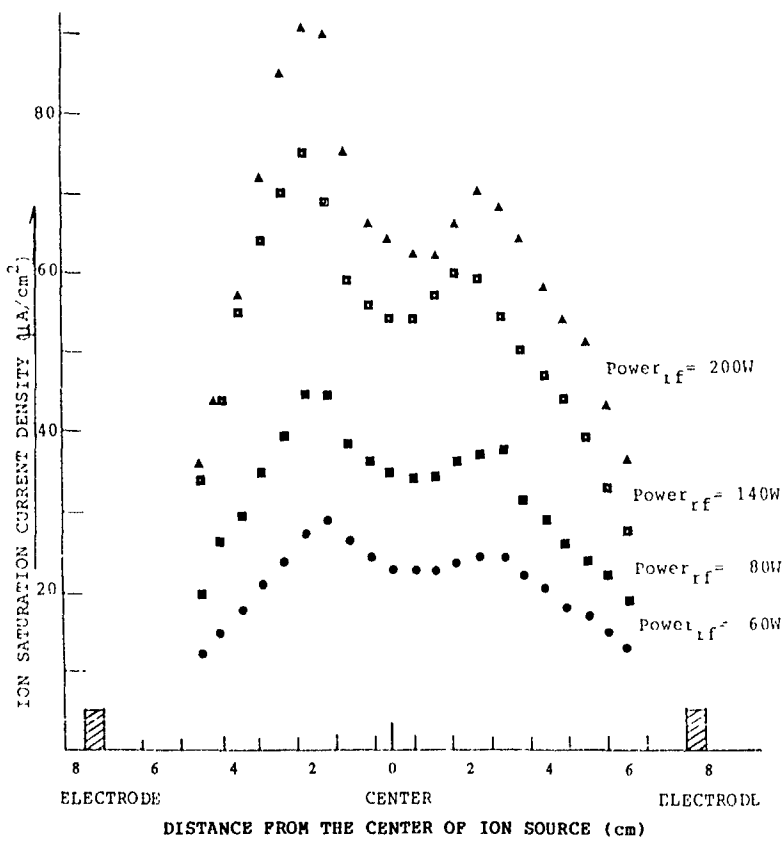

Fig 5 Ion current density distribution as a function of the rf power in the cusp field. O_2 gas, $P = 4.4 \times 10^{-4}$ Torr, cusp magnetic field (90 G).

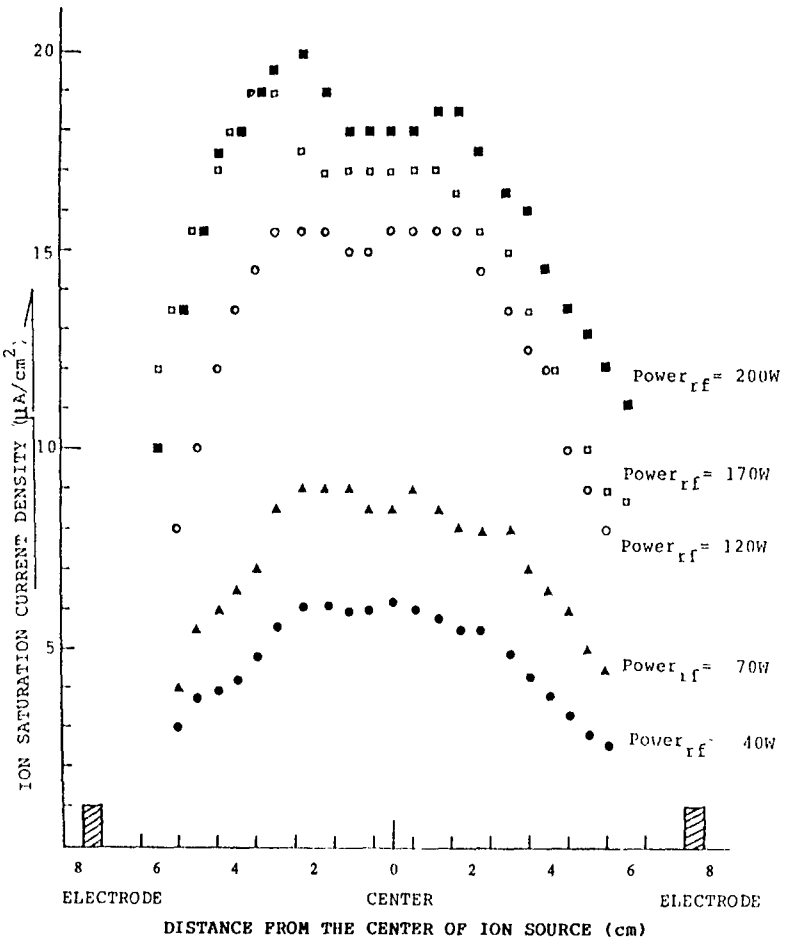

Fig 6 Ion current density distribution as a function of the rf power in the mirror field O_2 gas, $P = 3.0 \times 10^{-4}$ Torr, mirror magnetic field (140 G)

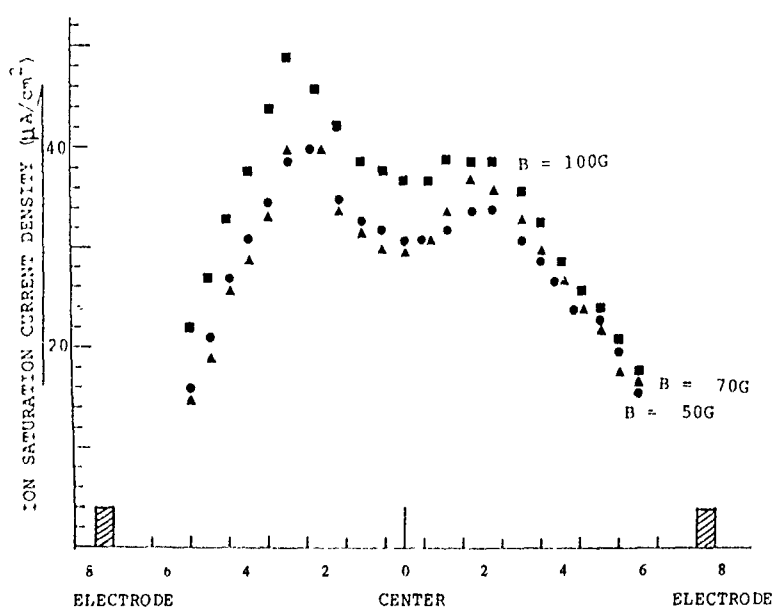

Fig. 7 Ion current density distribution as a function of B in the cusp field, O_2 gas, $P = 2.5 \times 10^{-4}$ Torr, rf power = 100 W, cusp magnetic field

lifetime. We have constructed a new version of a compact rf magnetron ion source.

In this paper, the operational principles and preliminary test results are reported.

2. Structure and operating principle of the ion source

The structure of the newly designed version of the rf magnetron-type ion source is schematically shown in fig. 1. This ion source consists of a cylindrical ionization chamber, the magnetic coils and the rf electrodes. The geometrical and electrical characteristics of the ion source are the following: Interior diameter of the ionization chamber in pyrex glass, 150 mm, length of the vessels 150 mm. The ionization chamber is surrounded with a pair of magnetic coils which produce a magnetic field in the chamber. The pair of magnetic coils were placed at an interval of 100 mm. The magnetic flux density is about 100 G near the wall. This magnetic field produces a line cusp field. A pair of rf electrodes in a ring is placed in the region of the line cusp field at an interval of 100 mm. The rf discharge is sustained by an rf generator of maximum rf power output of 1 kW and the oscillation frequency is from 0.001 to 20 MHz. The discharge gas O_2 is fed into the ionization chamber through a mass flow controller. Ultimate pressure obtained is 10^{-7} Torr using an oil diffusion pump of 6 in. diameter. The rf power of around 200 W and oscillation frequency of 13.56 MHz is applied to the rf electrodes, via a SWR meter and an impedance matching network which is a homemade design. Two electrodes are positioned in such a way that the accelerated electrons undergo a magnetron-type motion around them, efficiently producing a plasma ring around the electrodes. This initially produced a diffuse plasma along the magnetic field line into the center region of the cusp field when the field strength is almost nil.

3. Characteristics of the ion source

In all measurements reported here, oxygen was used as the discharge gas in the ionization chamber. Ion current densities were measured by the Faraday cup without a grid. Uniformity of the plasma density distribution in the ionization chamber was checked by the spectral analysis. The intensity of the spectral line (O_2 5585 Å) with the spectroscope is shown in fig. 2 for various values of the rf power in the cusp field The intensity of the spectral line increases as the rf power increase and in the center part it is almost flat Fig. 3 shows the intensity as a function of the rf power in the

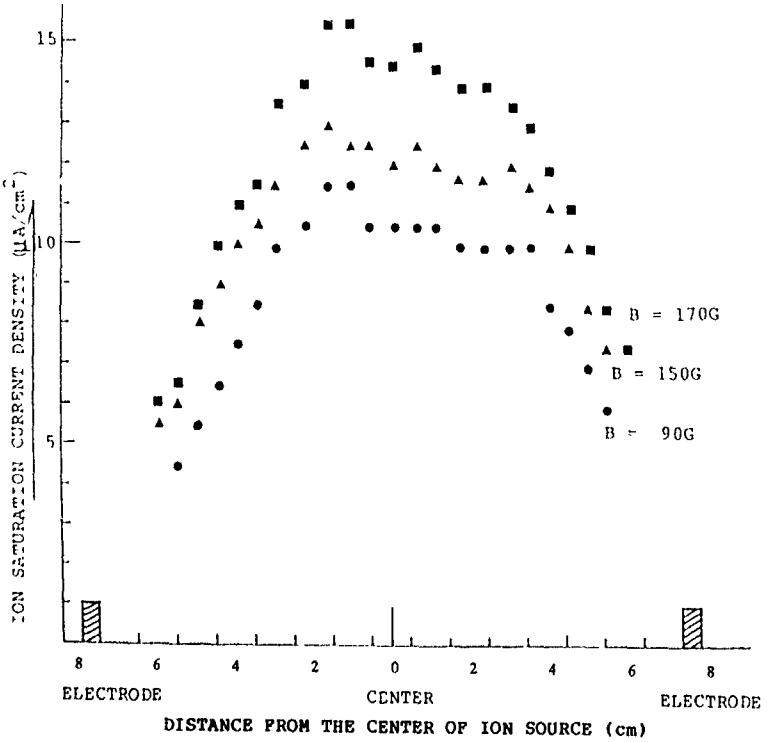

Fig 8. Ion current density distribution as a function of B in the mirror field. O_2 gas, $P = 2.5 \times 10^{-4}$ Torr, rf power = 150 W, mirror magnetic field.

mirror field. In this case, the intensity of the center part is lower than that of the end parts. In order to obtain a uniform distribution of the plasma, the cusp field must be stronger than the mirror field.

Fig. 4 shows the intensity distribution for three values of the pressure in the ionization chamber. It is seen that the intensity increases as the pressure increases. At lower pressures the intensity of the center parts is higher than that of the end parts. However, at a high pressure, the intensity of the end part is higher than that of the center parts.

In figs. 5–8 results are given when the ion current densities are examined by the Faraday cup Fig. 5 shows the ion current density distribution as a function of the rf power in the cusp field. The ion current density increases with increasing rf power, but the ion current density distribution is not uniform. Fig. 6 shows plots of the ion current density distribution against the rf power in the mirror field. In this case, the ion current density also increases with increasing rf power. This data tells us the ion current density of the cusp field is higher than that of the mirror field.

The effect of the magnetic field B for the ion production was examined. The ion current density distribution is shown in fig. 7 for various values of B in the cusp field. The results indicate that an increase in the ion current density up to 100 G results in no significant increase. Fig. 8 shows plots of the ion current density distribution against B in the mirror field. The ion current density increases with increasing B. The results indicate that the cusp field is better than the mirror field for ion production and a large-area irradiation.

4. Conclusion

It was confirmed that the rf magnetron type ion source can produce a large-area ion beam and have a long lifetime. Furthermore, this ion source can be used effectively for producing an oxygen ion beam. It is suggested that a cusp field is better than a mirror field for ion production.

Acknowledgement

The authors would like to express their gratitude to Professor S. Kojoma of Tokai university for his encouragement throughout this work.

References

[1] P.J. Martin, R.P. Netterfield, W.G. Sainty, G.J. Clark, W.A. Lanford and S.H. Sie, Appl. Phys. Lett. 43 (1983) 711
[2] P.J. Martin, H.A. Macleod, R.P. Netterfield, G.C. Pacey and W.G. Sainty, Appl. Opt. 22 (1983) 178.
[3] J.R. McNeil, A.C. Barron, S.R. Wilson and W.C. Herrmann Jr., Appl. Opt. 23 (1984) 522
[4] W.G. Sainty, R.P. Netterfield and P.J. Martin, Appl. Opt. 23 (1984) 1116
[5] C.M. Kennemore III and V.J. Gibson, Appl. Opt. 23 (1984) 3608
[6] H.R. Kaufman, NASA Techn. Note D-585 (1961)

Nuclear Instruments and Methods in Physics Research B55 (1991) 370–373
North-Holland

Development of a high current and high energy metal ion beam system

H. Inami, Y. Inouchi, H. Tanaka, T. Yamashita, K. Matsunaga and K. Matsuda
Nissin Electric Co., Ltd., 47, Umezu-Takase-cho, Ukyo-ku, Kyoto 615, Japan

A high current metal ion accelerating system, which consists of a metal vapor plasma ion source with a multicusp magnetic field and a single gap acceleration column, has been developed. The following results were obtained experimentally: (1) a 110 mA aluminum ion beam and a 95 mA chromium ion beam were extracted from the ion source, (2) the impurities contained in the beams were less than 1%, and (3) the aluminum ion beam was accelerated up to 90 keV at 50 mA on the target.

1. Introduction

Surface modification of several kinds of materials (metals, ceramics, etc.) by metal ion implantation has been investigated and improvements of wearness and/or hardness of these materials have been reported [1–4]. Some kinds of ion beams of metal elements (for example aluminum, chromium, silicon, titanium, etc.) at an energy above 100 keV have been used. It should be emphasized that a high dose of above 10^{17} ions/cm^2, which is two or three orders of magnitude higher than the dose used for ordinary ion implantation for semiconductor devices, is required to achieve an effective improvement.

Therefore, in order to complete implant processing to an area of about 100 cm^2 in a few minutes, a high current and high energy metal ion beam system is necessary. Besides making a system simple and compact, a non-mass-analyzed system is desirable. Therefore the purity of the ion beam extracted must be as high as possible.

So far, several types of high current metal ion sources have been developed [5–7]. The authors also developed a metal vapor plasma ion source [8,9]. Using this type of ion source, a 60 mA aluminum beam could be extracted stably for three hours. And it was found that the purity of the beam was high compared with the purities of beams extracted from ion sources in which chloride or fluoride gases of metals for feed materials are used.

Then the authors tried to enhance further the beam current and purity. In order to increase the beam energy, a post-acceleration column of a single gap was used.

2. Experimental setup

The metal ion beam is extracted from the multicusp ion source, and the beam is accelerated by the single gap acceleration column. The characteristics of the beam are measured by a profile monitor, a calorimeter and a mass analyzer. The schematic diagram of the experimental setup is shown in fig. 1.

The metal ion source has double radiation shields in the discharge chamber. The shields are heated to high temperature to prevent the condensation of metal vapor in the ion source. The metal vapor plasma is produced, without any pre-ionized gases by an arc discharge,

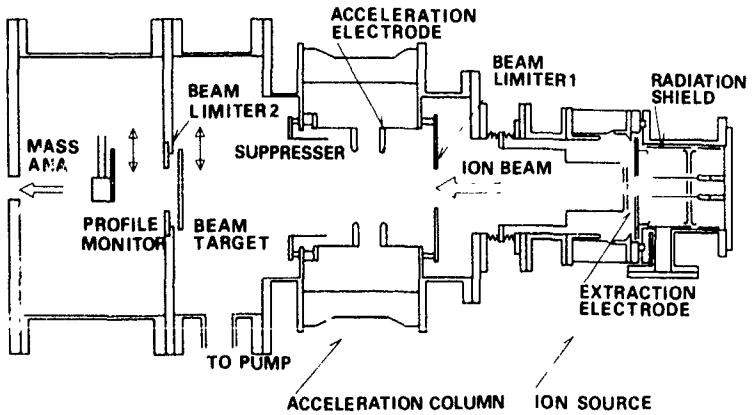

Fig. 1. Schematic diagram of the experimental setup

0168-583X/91/$03.50 © 1991 – Elsevier Science Publishers B.V. (North-Holland)

where the metal to be ionized is fed as vapor from the crucible set in the radiation shields. The ion beam is extracted from multi-slit electrodes (each slit is 0.3 cm wide and 7 cm long; the extraction area is 7.5 cm^2). The details of the ion source have been described elsewhere [8,9].

In order to accelerate a high current ion beam up to 100 keV, we designed the single gap, acceleration column with an inner diameter of 12 cm and a gap distance d of 4 or 6.5 cm. At the entrance of the acceleration column, beam limiter 1, with a 7 cm diameter aperture is set to reduce the beam bombardment on the acceleration electrodes. Behind the acceleration electrodes a suppressor biased negatively is placed to suppress the streaming back of secondary electrons produced by the beam bombardment on a beam target. The distance between the extraction electrode and beam limiter 1 is 38 cm.

The beam current on the beam target is measured calorimetrically. The two-dimensional spatial profile of the beam is measured by an array of Faraday cups (a profile monitor). The purities of the extracted beam are studied by using a magnetic mass analyzer

The residual gas pressure (P) in the chamber during the experiments was below 2×10^{-4} Pa.

3. Experimental results

3.1. Characteristics of the extracted ion beam

Measurements of the extraction characteristics of the beams were carried out. Fig. 2 shows the extraction characteristics of aluminum and chromium. From the figure it is seen that a maximum of 110 mA of aluminum ions and 95 mA of chromium ions were extracted.

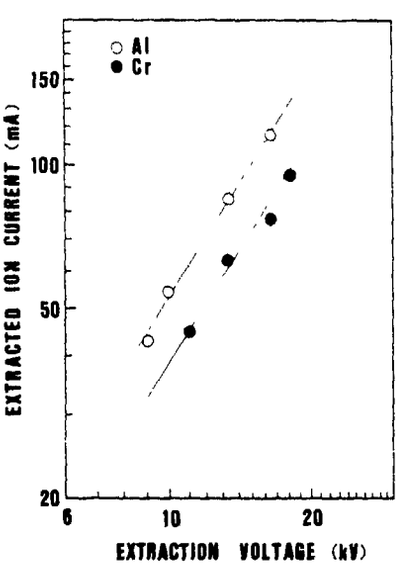

Fig. 2. Characteristics of ion beam extraction.

Table 1
Results of mass analysis of the extracted beam

Element	Single charge [%]	Double charge [%]	Impurities [%]
Al	96	3	1
Cr	79	20	1

The impurities contained in the ion beam were measured by the magnetic mass analyzer. The results are listed in table 1. The impurities were less than 1%. The components of these impurities were mainly Ta and/or W, which are the materials of the radiation shields and the filaments in the ion source. For aluminum ion beams, a ratio of singly-charged aluminum ions to total ions of 96% was achieved by reducing the arc voltage

3.2 Beam transport efficiency and characteristics of the ion beam acceleration

The beam transport efficiency is one of the most important parameters to get a high current and high energy ion beam. So, we investigated the ion beam transport from the ion source to the beam target in the experimental configuration (shown in fig. 1) with the post acceleration column. The acceleration current (I_{acc}) and the target current (I_{tar}) were obtained as a function of the acceleration voltage (V_{acc}) under the conditions of an extraction voltage (V_{ext}) of 20 kV and an extrac-

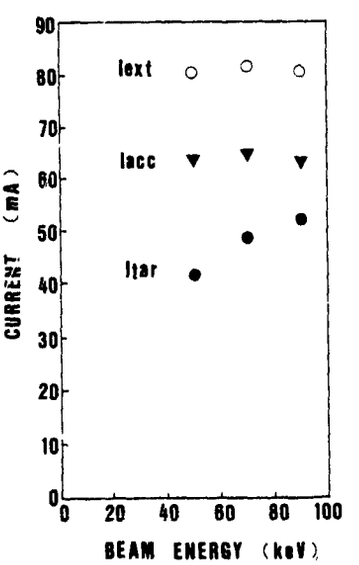

Fig. 3. Aluminum ion beam currents vs beam energy I_{ext}: extraction current, I_{acc}: acceleration current; I_{tar} beam current on the target (extraction voltage = 20 kV)

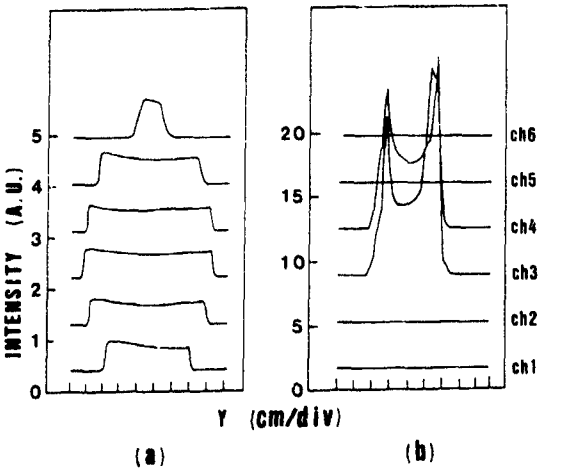

Fig. 4 Spatial profile of the accelerated aluminum ion beam Symbols "ch$n$" denote the nth Faraday cup of the profile monitor (a) $V_{acc} = 30$ kV; (b) $V_{acc} = 70$ kV ($I_{acc} = 15$ mA, $d = 65$ mm, $P = 1.9 \times 10^{-4}$ Pa).

tion current (I_{ext}) of about 80 mA. The experimental results for Al ions are shown in fig. 3. Here the gap of the acceleration electrodes was 4 cm, and the suppressor was biased at -3.8 kV, which was sufficient to suppress the secondary electrons produced on the beam target From the figure it is found that the transport efficiency from the ion source to the acceleration column, $\eta_1 (= I_{acc}/I_{ext})$ is about 75%. On the other hand the transport efficiency from the acceleration column to the beam target, $\eta_2 (= I_{tar}/I_{acc})$ increases with the beam energy and reaches 83% at a beam energy of 90 keV ($I_{tar} = 50$ mA) This increment of the transport efficiency may be caused by far the following reasons The spread of the beam at low energies is larger than the size of the beam target, so the beam target was not enough to catch the whole beam. As the beam energy increases, the beam spread gradually becomes smaller.

To confirm this idea, measurement of the beam profile was carried out. The profile monitor was set behind beam limiter 2 with a 70 mm diameter aperture, through which the beam irradiated the profile monitor. Figs. 4 and 5 show the dependence of the beam profile, which is in the perpendicular direction (Y) to the long side of the extraction slits, on the acceleration voltage at low current ($I_{acc} = 15$ mA) and high current ($I_{acc} = 50$ mA), respectively. Here the signal from each channel corresponds to those of each of the Faraday cups arranged at 1.5 mm intervals. The figures show the sharp edges of the signals, as expected, from the beam restricted of limiter 2. From fig. 4 it is seeen that the double peaking of the signal occurs for the higher acceleration voltage, which means there is a focusing effect. In fig. 5 it is seen that this focusing effect also occurs for high currents, because the intensity of the signal increases as the acceleration voltage increases. From the comparison of signals in fig. 4 and fig. 5, we conclude that beam uniformity is improved by increasing the current.

4. Conclusion

High current aluminum (110 mA) and chromium (95 mA) ion beams were extracted from the multicusp ion source The impurities contained in the beam were within 1%, and most of the beam was singly-charged and doubly-charged ions In the case of aluminum ions the proportion of singly-charged ions could be enhanced up to 96%.

As a result of an ion beam accelerated by using the single gap acceleration column, 50 mA of aluminum ions of 90 keV were obtained on the beam target Then,

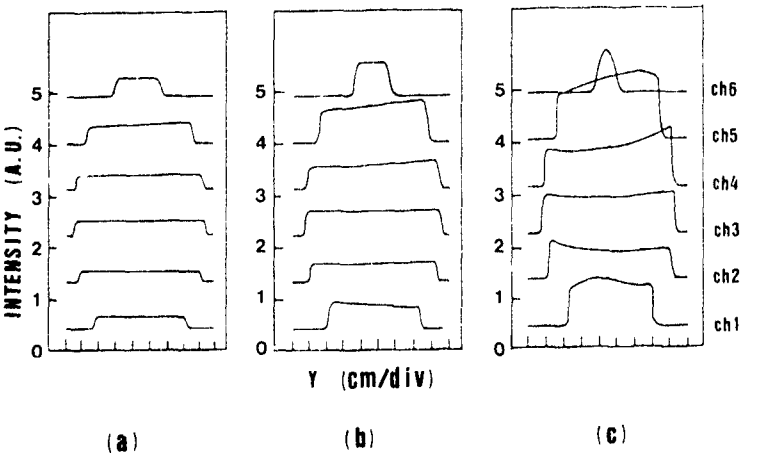

Fig. 5 Spatial profile of the accelerated aluminum ion beam Symbols "ch$n$" denote the nth Faraday cup of profile monitor (a) $V_{acc} = 30$ kV, (b) $V_{acc} = 50$ kV, (c) $V_{acc} = 70$ kV ($I_{acc} = 50$ mA, $d = 65$ mm, $P = 1.8 \times 10^{-4}$ Pa).

the transport efficiency in the whole system $\eta(=\eta_1 \times \eta_2)$ was about 62%. From the spatial profile measurement, the focusing effect of the acceleration column was observed and it was found that beam uniformity was improved by an increase of the beam current.

Acknowledgement

This work was performed under the Research and Development Program on "Advanced Material Processing and Machining Systems", conducted under a program set by the New Energy and Industrial Technology Development Organization.

References

[1] U. Bernabai, M. Cavallini, G. Bomara, G. Dearnaley and M.A. Wilkins, Corros Sci 20 (1980) 19
[2] M Iwaki Proc. Int Engineering Congress ISIAT '83 and IPAT '83, Kyoto (1983) p 1793.
[3] Y. Okabe, M Iwaki, K. Takahashi, S Numba and K Yoshida, ibid., p. 1811
[4] T Hioki, Proc. 10th Symp. ISIAT '86 Tokyo (1986) p 547
[5] N. Sakudo, Proc. 9th. Symp ISIAT '85, Tokyo (1985) p 1.
[6] I.G. Brown, J E. Calvin, R.A. Macgill and F J Paoloni, Rev Sci Instr 61 (1990) 577.
[7] B Torp, B R. Nielsen, D.M. Ruck, H. Emig, P Spudtke and B.H. Wolf, Rev Sci. Instr 61 (1990) 595.
[8] H. Inami, F. Fukumaru, Y Inouchi, D. Sato, K. Tanaka and K. Matsunaga, Nucl. Instr and Meth. B37/38 (1989) 198
[9] Y Inouchi, H. Tanaka, H Inami, F. Fukumaru and K. Matsunaga, Rev. Sci. Instr 61 (1990) 538.

Nuclear Instruments and Methods in Physics Research B55 (1991) 374–378
North-Holland

Beam optics research for a 600 keV heavy ion implanter

Zhao Qihua [1], Jiang Xinyuan and Lin Chenglu

Shanghai Institute of Metallurgy, Academia Sinica, 865 Changning Road, Shanghai 200050, People's Republic of China

Pierre Tanguy

Laboratoire Théorie des Systèmes Physiques, Université de Rennes I, Campus de Beaulieu, 35042 Rennes-Cedex, France

The beam optics research for a high energy (over 600 keV), high mass resolving power (over 210) and very high beam transportation efficiency (over 85%) ion implanter is described. The analytical equation for a constant gradient accelerating tube is given, and the beam optics design has been carried out taking into consideration the space-charge effect in the accelerating tube and a second-order aberration in the analyzing magnet. The ion beam was successfully transported over 19 m, and the beam current on the implantation target for Mg^+ (total), Ar^+, P^+, and Cd^+ (total) was $\geqslant 50$, 200, 100 and $\geqslant 50$ μA, respectively, at 630 keV.

1. Introduction

Research into the application of ion implantation commenced at the Shanghai Institute of Metallurgy 20 years ago. During this period, a 200 keV ion implanter for semiconductors as well as for RBS (Rutherford backscattering spectroscopy) was built, but the old machine cannot satisfy further developments in research, so we decided to build a (1) high energy (over 600 keV), (2) whole mass range (1–210 amu), (3) high mass resolving power (over 210), (4) high beam current stability and high energy stability (less than 10^{-4}), and (5) high beam transportation efficiency implanter. In addition, this implanter can be used both for ion implantation (including isotopic element ion implantation) and for ion beam analysis (i.e., RBS channeling) [1].

The scheme of pre-acceleration and post-analysis was chosen so that the high resolving power magnet (deflecting radius of 1200 mm) could be placed on the ground. The beam is extracted from a Nielsen-type ion source, focused by an einzel lens, and then accelerated and analyzed. In this scheme the extracting energy (30 keV) section is only 682 mm long. A magnetic switch is used for deflecting the beam into any one of five beam lines. Fig. 1 shows the general layout of the 600 keV research heavy ion implanter.

[1] Present address: Institute of Information Display and Transducer, Shanghai Jiao Tong University, Shanghai 200030, People's Republic of China

2. Optics

2.1. Optics of the accelerating system

At first, we used a first-order beam transportation matrix (5×5) to calculate the beam envelope of the whole machine. But the low energy (less than 200 keV), heavy ions (e.g., $^{208}Pb^+$, $^{209}Bi^+$) and strong beam current (500 μA) affect the beam transportation. So the space-charge effect was considered in the accelerating system. The accelerating tube is composed of four working sections with a total length of 1760 mm. The dis-

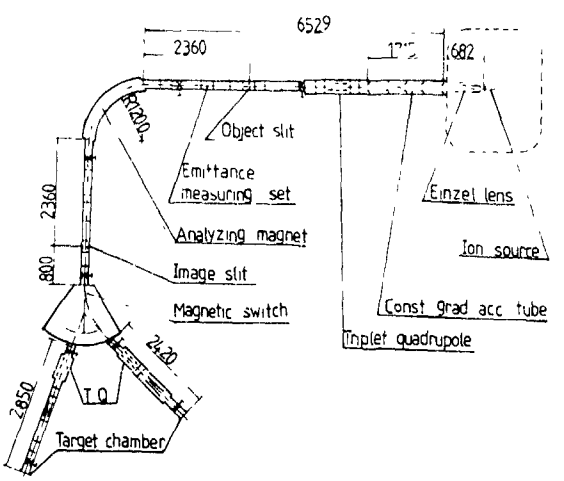

Fig. 1. General layout of the 600 keV heavy ion implanter.

0168-583X/91/$03.50 © 1991 – Elsevier Science Publishers B.V (North-Holland)

tance between the object waist of the accelerating tube and the entrance of the triplet electrostatic quardrupole lens is defined as the accelerating system.

2.1 1. The potential equation of the rotationally symmetric constant gradient accelerating tube

In order to increase the accuracy of the calculation of the accelerating system, an analytical formula of the potential on the axis of the rotationally symmetric accelerator tube was derived. The schematic diagram of accelerator tube is shown in fig. 2, where $E_0 = (U_f - U_0)/L$, the origin is at the entrance of accelerator tube, L is the length and a is the radius of the accelerator tube, U_0 is the potential before acceleration, and U_f is the potential after acceleration.

Simply the electrical potential can be obtained through the consideration of the entrance thin lens model, constant gradient accelerating field and exit thin lens model. The focal length can be calculated from the Davisson–Calbick equation. In practice, however, there is a fringing electrical field at the entrance or the exit of accelerating tube. The potential equation describing the system should consider the boundary conditions below:

$$U(0, r \geq a) = U_0, \quad U(L, r \geq a) = U_f,$$
$$E(z = -\infty) = 0, \quad E(z = \infty) = 0. \tag{1}$$

Through consideration of the entrance and exit fields and solving the Laplace equation, the approximate analysis formula on the axis of the rotational symmetric accelerating system is:

$$U(z) = \tfrac{1}{2}(U_0 + U_f) + (E_0/\pi) \times \left(z \tan^{-1}(z/a) - (z - L)\tan^{-1}((z - L)/a)\right) \tag{2}$$

In our 600 keV heavy ion implanter, the length of the accelerating tube is 1715 mm, and radius $a = 57$ mm.

2 1.2 Space charge effects in the accelerating system

Tanguy has set up a numerical method [2] for solving aberrations and space charge problems in beam transportation systems, and established a computer program

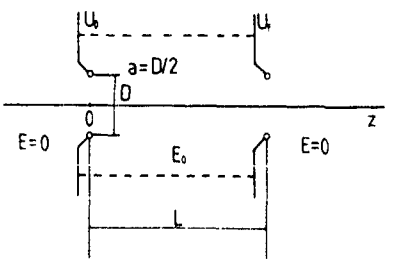

Fig. 2. Schematic diagram of the constant gradient accelerating tube.

called REVØL, in which the beam was considered as a nonuniformity distribution, e.g., a parabolic distribution in the present case. From the dynamical equations

$$m(d^2x/dt^2) = qE_{xc} + F_x(x, y),$$
$$m(d^2y/dt^2) = qE_{yc} + F_y(x, y), \tag{3}$$

where the E_{xc} and E_{yc} are contributed by the space charge, and:

$$F_x = -q(\delta U/\delta x), \quad F_y = -q(\delta U/\delta y). \tag{4}$$

We put several thousand ions (e.g. 3000–7000 ions) in the simulation. If $I(r)$ is the beam current for $r \leq R$:

$$E_{rc} = (1/(\epsilon_0 r))\int_0^r r\rho(r)\,dr = I(r)/(2\pi\epsilon_0 rv) = (I/(2\pi\epsilon_0 rv))(I(r)/I), \tag{5}$$

Where I = beam current. If we take N ions for a simulation, we number them from the beam centre to the outside, the ion number increasing with increasing radius. So there are j ions within the area $r \leq r_j$, $I(r)/I = j/N$, thus, from eq. (5):

$$E_{xc} = \left(xI/\left(2\pi\epsilon_0 r_j^2 v\right)\right)(j/N),$$
$$E_{yc} = \left(yI/\left(2\pi\epsilon_0 r_j^2 v\right)\right)(j/N), \tag{6}$$

The beam simulation is initiated by the experiments and Monte Carlo methods [3]. From the experiment it is found to be a parabolic distribution, also satisfying the equation:

$$x^2/\overline{X}^2 + x'^2/\overline{X}'^2 + y^2/\overline{Y}^2 + y'^2/\overline{Y}'^2 \leq 1. \tag{7}$$

We calculated

$$x_j(z_0 + kh), \quad x_j'(z_0 + kh),$$
$$y_j(z_0 + kh), \quad y_j'(z_0 + kh), \qquad j = 1, 2, \ldots, N,$$

step by step (where z_0 is initial position, h is step length and $k = 1, 2, \ldots$), the beam distribution at position $(z_0 + kh)$ can be given, we can have the rms beam radius X, Y and rms beam emmitance ϵ_x, ϵ_y:

$$x\text{-direction: } \overline{X} = 2\sqrt{\overline{X^2}}, \quad \epsilon_x = 4\left(\overline{X}^2\overline{X}'^2 - (\overline{XX}')^2\right)^{1/2},$$
$$y\text{-direction: } \overline{Y} = 2\sqrt{\overline{Y^2}}, \quad \epsilon_y = 4\left(\overline{Y}^2\overline{Y}'^2 - (\overline{YY}')^2\right)^{1/2} \tag{8}$$

The accuracy of the calculations by the REVØL program were greatly improved compared to the K–V distribution [4]. We also developed a much simpler envelope equation [5] and a transfer matrix method [6] for heavy ion beam acceleration in a rotationally symmetric field. The computer programs are CP600M and INTEFLOW. These two computer program CP600M and INTEFLOW were written and compared with REVØL. The results yield good agreements, but the REVØL program can give more information as it in-

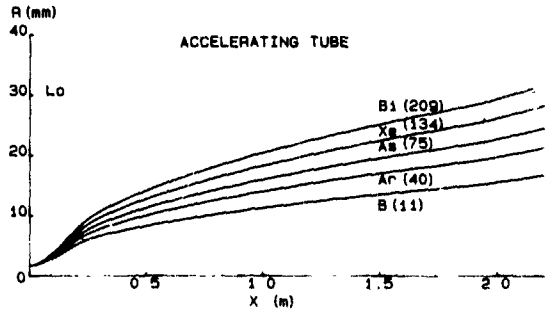

Fig 3 Beam envelope of a current of 300 μA, accelerated from 30 to 600 keV, for $^{11}B^+$, $^{40}Ar^+$, $^{75}As^+$, $^{134}Xe^+$ and $^{209}Bi^+$ ions $R_0 = 1.7$ mm, $\epsilon = 34$ mm mrad, $L_0 = 230$ mm

cludes beam cross section, beam emittance and density of particles in the beam cross section at the assigned position of the beam line. Fig. 3 is the beam envelope of $I = 300$ μA, for the mass of $^{11}B^+$, $^{40}Ar^+$, $^{75}As^+$, $^{134}Xe^+$ and $^{209}Bi^+$. The beam transportation was simulated from the object waist of the accelerating tube, it is 230 mm before the accelerating, and the beam radius is 1.7 mm (90%) with a beam emittance of 34 mm mrad (30 keV). The beam current can be changed from 100–500 μA.

Referring to the results of the experiment, it was defined that the space charge effect should only be considered when the ion energy was less than 200 keV, and the first-order beam transportation matrix should be valid when the ion energy was higher than 200 keV

2.2 Optics of the mass analyzing magnet

2.2.1 The mass analyzing magnet

The magnet with the radius $R = 1200$ mm and pole gap $g_0 = 40$ mm deflects the ion beam 90°. The test results show that the magnet induction can reach 18 kG, and non-homogeneity of the magnetic field is less

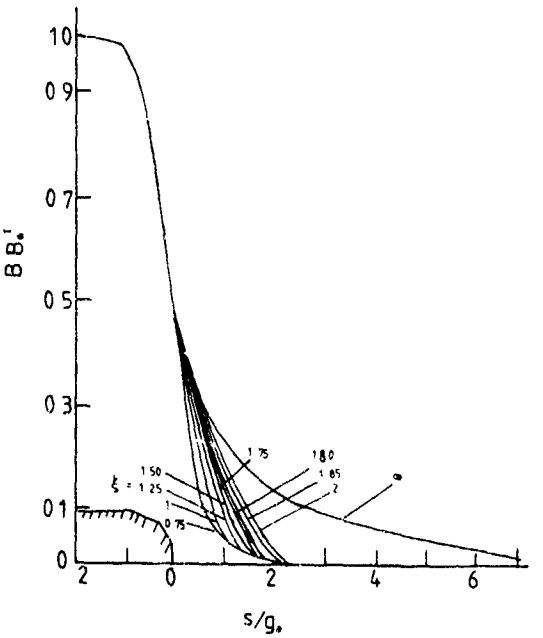

Fig 4 Distribution of the extended fringing field at the magnet exit

than $\pm 3 \times 10^{-4}$ when the magnetic induction is less than 10.8 kG and the homogeneity width along the radius is 60 mm The test results also show that the entrance fringing field is the same as the exit fringing field. Fig. 4 is the distribution of the extended fringing fields of the exit edges, where $h(s) = B(s)/B_0$, ξ is the distance between magnet contour and shield ($\xi = 0.75$, 1, 1.25, 1.5, 1.75, 1.8, $2g_0$ and ∞), s is the distance between the magnet contour and the testing spot (the unit is g_0). B_0 is the magnet induction in the uniform region. From the experimental data, the virtual field boundaries of the extended fringing fields S_0, and the correction coefficients I_1 and I_2 can be obtained by

Table 1
Variations of S_0, I_1 and I_2 at different magnetic inductions ($\xi = 1.80 g_0$, $g_0 = 40$ mm)

B_0 [G]	4000	6000	8000	10000	11500	13000	15000
S_0 [g_0]	0.117	0.116	0.112	0.111	0.112	0.111	0.111
I_1	0.310	0.329	0.335	0.331	0.338	0.325	0.330
I_2	0.445	0.451	0.451	0.451	0.451	0.450	0.452

Table 2
Variations of S_0, I_1 and I_2 at different magnetic inductions ($\xi = 1.85 g_0$, $g_0 = 40$ mm)

B_0 [G]	4000	6000	8000	10000	11500	13000	15000
S_0 [g_0]	0.140	0.139	0.131	0.133	0.313	0.133	0.135
I_1	0.318	0.317	0.323	0.321	0.327	0.317	0.335
I_2	0.451	0.451	0.452	0.452	0.453	0.453	0.458

numerical integration methods [7]. For our implanter, the magnetic shield must be at $\xi = 1.80$–$1.85 g_0$, i.e., the virtual field boundary is $0.125 g_0$ (5 mm). Tables 1 and 2 show S_0, I_1 and I_2 for different values of magnetic induction of $\xi = 1.80$ and $\xi = 1.85 g_0$. Although the magnet induction changes from 4 to 15 kG, the variation of the virtual field boundary S_0 is less than $0.006 g_0$ (0.24 mm), and the I_1 and I_2 are less than 0.028 and 0.006 respectively, that is to say: the ion beam may be moved less than 0.03 mm at the deflecting plane and the image position may be changed less than 4 mm.

2.2.2. First- and second-order aberrations

From experimental results, we calculated the first- and second-order aberrations of the magnet to satisfy our implanter. Fig. 5 shows the beam deflecting system, the horizontal plane is the bending plane.

In order to focus the ion beam at the image slit, with $\ell_H = \ell_V = \ell_2$ (H = horizontal, V = vertical), and the magnet object distance ℓ_1 given, the image distance can be calculated as below [7]:

$$\ell_H = \frac{(R + \ell_1 \tan\alpha)}{(\ell_1/R - \tan\beta - \ell_1 \tan\alpha \tan\beta/R)},$$

$$\ell_V = \left(\left[\ell_1(1 - \pi(\tan\alpha_V)/2) + \pi R/2\right]\right) \times \left(\left\{\left((\ell_1/R)\left[\tan\alpha_V + (1 - \pi(\tan\alpha_V)/2)\tan\beta_V\right] - 1 + \pi(\tan\beta_V)/2\right\}\right)^{-1} \quad (9)$$

The image divergence with the changes of object distance ℓ_1 is $\delta(\ell_H - \ell_V)/\delta\ell_1$. If the image dispersion $(\ell_H - \ell_V)$ is minimized, the ℓ_1 should be satisfied by the equation below:

$$\ell_1 = \left[R(\tan\beta + \pi(\tan\beta_V)/2 - 1)\right] \times \left[(1 - \tan\alpha_V - \tan\beta_V - \tan\alpha\tan\beta + \pi(\tan\alpha_V \tan\beta_V)/2)\right]^{-1}. \quad (10)$$

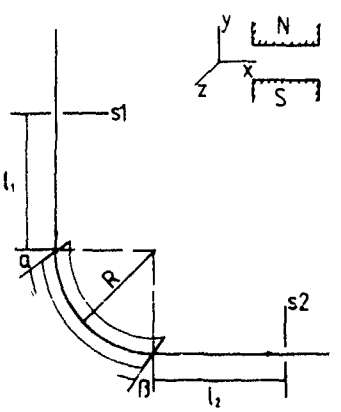

Fig. 5. Magnet deflecting and analyzing system.

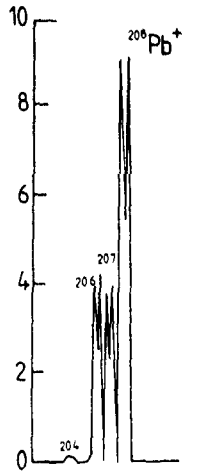

Fig. 6 Mass spectrum of Pb^+.

Consider the mass resolving power and beam acceptance [8]:

$$\ell_1 = R/(1 - \tan\alpha) \quad (11)$$

From eqs. (9), (10) and (11), we can get the results For a symmetric magnet, $\alpha = \beta$, $\alpha_V = \beta_V$, we can have:

$$\tan\alpha + \tan\alpha_V = 1. \quad (12)$$

(a) If analyzing the magnet system without considering the extended fringing field, $\alpha = \alpha_V$, $\beta = \beta_V$, $\tan\alpha = \frac{1}{2}$, $\alpha = 26°34'$, $\ell_1 = \ell_2 = 2R$

(b) For our magnet, $\tan(\alpha - \psi) = \tan\alpha_V$, $\psi = (I_2 g_0/R)(1 + \sin^2\alpha)/\cos^3\alpha$;

$\xi = 1.8 g_0$, $\alpha = 27\,145°$, $\ell_1 = \ell_2 = 2.052R$,

$\xi = 1.85 g_0$, $\alpha = 27.149°$, $\ell_1 = \ell_2 = 2.056R$.

The second-order aberration of the magnet was calculated by the TRANSPORT [9] computer program. The results of the experiment and calculation show that, if the ion beam radius at the object slit is 1.04 mm and the beam emittance is 7.38 mm mrad, taking the second-order aberration effects into consideration, α is 27.13°, and the beam radius at the deflecting plane is 1.08 mm but that at the vertical plane 1.31 mm. The second-order aberration can be overcome by putting a concave curvature with radius 1443 mm at the exit contour of the magnet, the beam radius at the deflecting plane will be 1.08 mm and that at the vertical plane will be 1.07 mm.

3. Results

The ion beam is transported with high efficiency through a 19 m long beam line. The typical result of ion beams for Ar^+ at 630 keV is 165 μA near the object slit, 145 μA near the image slit and 140 μA at the target.

The beam transportation efficiency of the whole machine is over 85%. The good beam quality and the high stability of all the power supplies make the long time stability of the beam better than 100 μA ± 2.5% per 71 min, at 630 keV, recorded by an $X-Y$-recorder. Fig. 6 is the mass spectrum of Pb^+ with the $^{208}Pb^+$ beam current near 10 μA, heavy element isotope ion implantation can be done. The beam current was not very high on the target because we used the Nielsen-type ion source and the extracting beam current was limited. But the implanter was also designed for strong beam current, even up to 1–3 mA.

References

[1] Jiang [illegible] Yuan, Lu Shi Wan and Shi Zhi Zu, Nucl. Instr and Meth. B21 (1987) 310.
[2] P. Tanguy, Proc. Proton Linear Accelerator Conf., Batavia, 2 (1970) 771.
[3] B. Bru and M. Weiss, CERN/MPS/LIN 74-1.
[4] I.M. Kapchinskij and V V. Vladimirskij, Proc. Int. Conf on High Energy Accelerators (CERN, 1959) p. 274.
[5] Jiang Bin Yao, P. Tanguy and Xia Jin Zhi, Nucl. Instr. and Meth. 213 (1983) 179.
[6] Yu Qing Chang, Chin J Nucl Phys. 3 (1981) 261.
[7] P. Septier, Focusing of Charged particles, vol 2 (Academic Press, New York, 1967) p 239
[8] Lai Wei Chuan and Xu Senlin, Nucl Techniques (China) 3 (1982) 21.
[9] SLAC Report, No 91 (1970)

Nuclear Instruments and Methods in Physics Research B55 (1991) 379–385
North-Holland

Section V. Advanced machine technologies

Ion implantation challenges in the drive towards 64 Mb and 256 Mb memory cell type devices *

Alan D. Giles
Applied Materials, Foundry Lane, Horsham, West Sussex RH13 5PY, UK

Anton van der Steege
Philips Components Nijmegen, Gerstweg 2, 6534 AE Nijmegen, The Netherlands

Ion implantation techniques will be critical in the production of evermore complex devices, with major challenges for the device designer in utilising available techniques and those that are potentially available. Equally difficult challenges face the equipment designer in judging which technologies are required for future devices and welding these requirements into a reliable, production-worthy fabrication tool, capable of meeting or exceeding the automation and up-time expectations of the wafer fabrication managers. High yield and consistent performance on the wafer continue to be paramount. This paper will review these challenges from the equipment suppliers' viewpoint and in particular the new technology needs and cost of ownership issues.

1. Introduction

This conference series serves as a unique forum for discussion of the technological issues involved in the design, manufacture and utilisation of ion implantation technology. In previous meetings, a wide variety of issues have been reviewed, ranging from advanced process requirements to new machine technology to process and yield issues such as particle control and photoresist processing [1–4]. The goal of this paper is to step somewhat beyond the direct consideration of process performance of ion implantation systems and to consider the special challenges of reliability and automation in advanced IC production environments.

2. Technological challenges

Ion implantation continues to be driven by the requirements for fabrication of ULSI devices with feature sizes in the range of 0.3 to 0.5 μm. In addition to such process concerns as particles and tight dose and energy control, another major force is the steady increase in the number of implant steps which are required to fabricate an advanced IC device. The shift in process technology from NMOS for 64k DRAMs to twin-well BiCMOS for 64M DRAMs has brought about a tripling of the number of implant steps (see fig. 1).

In addition, the energy and beam current range continues to expand (see fig. 2). The central process range of "routine" ion implantation, from a few keV to approximately 200 keV in energy and beam currents ranging from a few μA to approximately 30 mA, has recently been expanded to the use of MeV implanters for DRAM production [4]. The site for this conference, the University of Surrey, has been the source of much pioneering work in extending upwards the dose and beam current capabilities for direct fabrication of buried dielectric layers. This conference will also feature work done in the use of low-energy (1 eV to approximately 0.5 keV) ions for deposition and formation of shallow junctions [5,6].

The increased complexity of the topography of advanced IC designs has resulted in a new emphasis on the control and choice of beam incidence angle. The need to fabricate symmetric junctions for self-aligned structures such as source/drains and emitters has driven the shift in implant incidence angle from the approximately 7° tilt, which was characteristic of most of the processes in the last decade, to normal-incidence orientations. Recent developments in the use of high-angle (> 7° tilt) implantation have opened the exploration of a wide range of applications (see fig. 3).

The critical nature of process and yield issues, such as control of surface charging effects and particle levels, can be clearly seen in the increased number of papers on these topics which are in these proceedings. Another measure of these topics is the number of times an issue

* Invited paper.

0168-583X/91/$03.50 © 1991 – Elsevier Science Publishers B.V. (North-Holland)

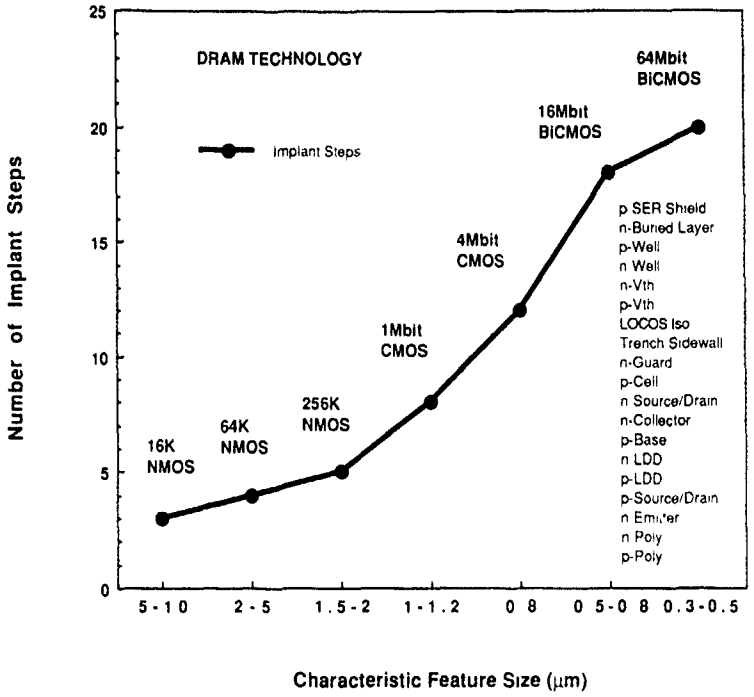

Fig 1 Process complexity

is the focus of a "users group" meeting, such as the established groups in Silicon Valley and Europe. As indicated in fig 4 [7], beyond the key focus on charging issues, the areas of concern in the use of ion implantation technology in IC fabrication includes a host of topics with relatively even emphasis

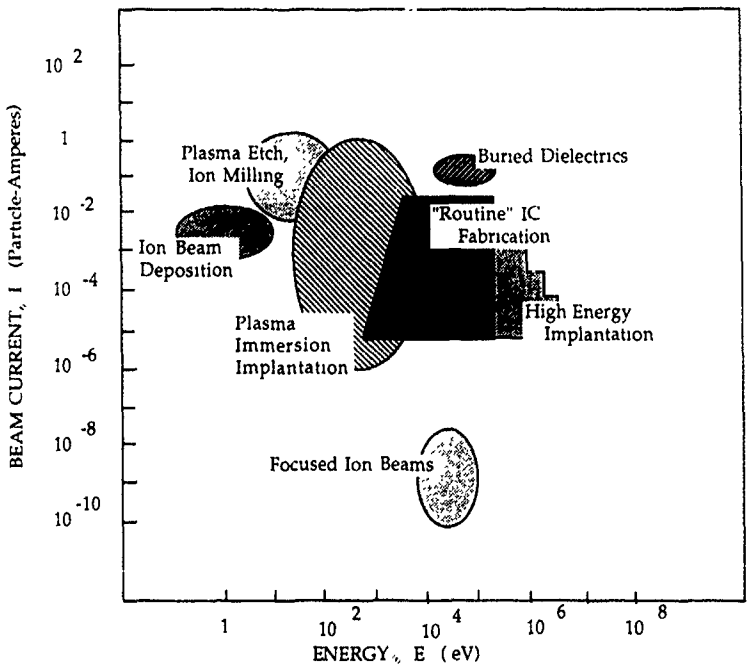

Fig. 2. Ion beam processing

3. Reliability and automation

Many of the papers in this conference are focused on "technology challenges" in the process performance area. Perhaps an even greater challenge facing the implant equipment manufacturer is the need to meet unheralded levels of equipment reliability in the coming decade. It is worth examining the background to this demand.

It is well known that the driving force behind the growth of the semiconductor industry has been its ability to maintain costs per chip, whilst increasing memory capacity fourfold with each new generation of memory device. This has been achieved by:

(1) shrinking geometries through improved lithography and other design advances,
(2) increasing yield to levels in excess of 90% on some established processes, and
(3) increasing wafer size up to 200 mm diameter.

It is unlikely that the same rate of economic progress can be achieved by extrapolating the three areas above. New areas of rapid improvement will be necessary if the economic drive to technological change in the industry is to be maintained.

One such area is equipment utilisation. For ion implanters utilisation levels of around 50% are often reported in production environments. Increasing these utilisation levels to 80% or 90% would have huge cost benefits to the device manufacturer in terms of savings in equipment capital and running costs as well as reduced clean-room areas. This saving may be the critical area which will make 64 Mb DRAM memory and similar technologies viable and it will be necessary to substantially improve the reliability and hence the utilisation of equipment.

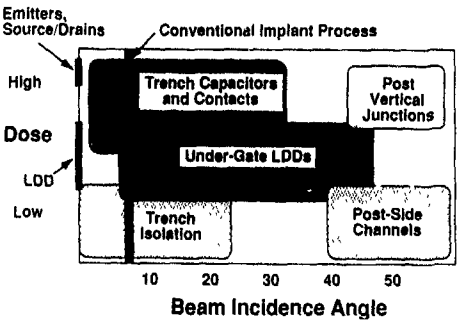

Fig 3. Tilt angle: the new phase space.

Fig. 5 defines up-time and reliability based on SEMI standards and adapted for the implant situation. The equipment manufacturer focuses on equipment up-time, mean time between failures (MTBF) and mean time to repair (MTTR) whereas the fabrication manager concentrates on all the factors leading to improved utilisation.

Before we look at the reliability of equipment in detail we must also consider other changes besides "process" issues which will have an impact on the reliability challenge over the next five years. Fig. 6 shows some of the general trends in equipment requirements from 1982 to 1994 when production of 64 Mb DRAM devices is expected to commence.

The need to achieve utilisation levels of 80% to 90% in 1994 dictates tough equipment reliability challenges and these are outlined in the road map shown in fig. 7.

At present, mean time between failures (MTBF) is typically between 50 and 100 hours on production ion implant systems. This drives equipment-dependent up-times in the area of 80–90%. Availability, which allows for down-time due to facilities, engineering and equip-

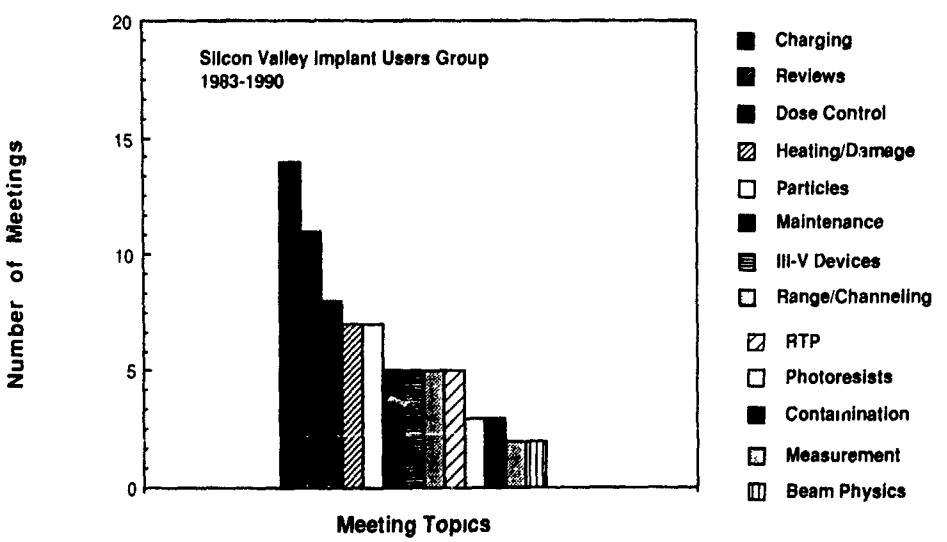

Fig. 4. Distribution of meeting topics for the Silicon Valley Implant Users Group for the years mid-1983 to mid-1988

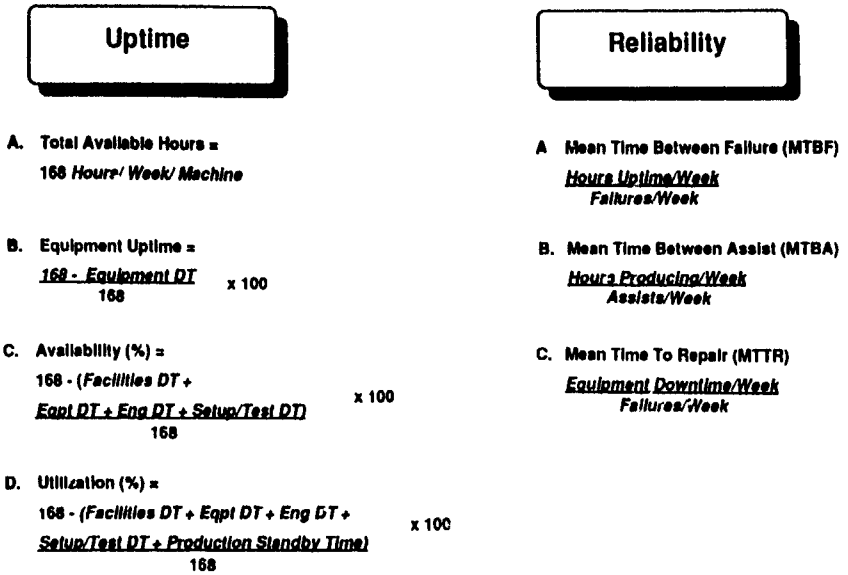

Fig. 5. Definition of terms

ment requalification, is typically 5% lower at the 75–85% level. The unpredictability of machine availability forces the device manufacturer to have some redundancy in his capacity planning. This leads to reduced levels of production efficiency with which he can use his machines and an upper limit of approximately 70% is typical. This drives utilisation levels in the 40–60% range.

Given an equipment MTBF capability of 100 hours it is necessary to install a vigorous system management regime to maintain high availability levels. This is illustrated schematically in fig. 8. Failure to provide

1982	1988	1992	1994
64 K Memory	256 K Memory	16M Bit Memory	64M Bit Memory
Min Feature	Min Feature	Min Feature	Min Feature
2.5 Micron	1 5 Micron	0 6 Micron	0 5 Micron
Killer Defect	Killer Defect	Killer Defect	Killer Defect
>0.7 Micron	>0 3 Micron	>0.1 Micron	>0.05 Micron
Reliability	Reliability	150 Hours	200 Hours
(Uptime<50%	(MTBF, MTTR)	(MTBF)	(MTBF)
Manual Wafer Handling	Cassette-to-Cassette	Transaction Processing	
Atmospheric Loading	Vacuum Load Locked	Self Cleaning Process	No Need for Self Cleaning
Equipment In Cleanroom	Bulkhead Mounted	Cleanroom?	Cleanroom?
Programme Sequencing	Distributed Computers	Networked Factory Contro'	Fully networked factory plan/ controlling
Timed Process	Automatic Endpoint	Expert System Process Mgmt	Dynamic "smart" Factory Mgmt
Test Point	Limited Automatic Diagnosis	Expert System Remote Diagnosis	In-process Measurement and Diagnosis

Fig. 6. Semiconductor manufacturing equipment reliability (increasing application and feature complexity).

	1988 - 90	1991- 92	1993 - 94
Utilization	40% - 60%	60% - 80%	80% - 90%
Production Efficiency	55% - 70%	70% - 90%	90% - 93%
Availability	75% - 85%	85% - 90%	90% - 97%
Uptime	80% - 90%	90% - 99%	99 + %
MTTR	3 - 8 Hrs	1.5 - 2 Hrs	0.5 - Hrs
MTBF	100 - 150 Hrs	200 - 250 Hrs	>500 Hrs

Fig. 7. Equipment reliability challenges

adequate documentation or spare parts can be equally disastrous to equipment availability levels as a modest decline in MTBF. This is of course true of any given level of MTBF for a machine and as it may be argued that only marginal improvement in MTBF can be obtained with any particular design of machine, in the short term focus should be on system management improvement opportunities.

However, failure to focus on MTBF issues will lead the equipment manufacturer down a blind alley. The main way to improve reliability and therefore lower the cost of ownership is to prevent the machine failing. As this is achieved the requirement for other system management factors will become relatively less important

We can see in fig. 7 that over the next five years the challenge is to achieve utilisation levels as high as 90%. This dramatic doubling of the present utilisation levels will be needed if the continuing cost performance ratio

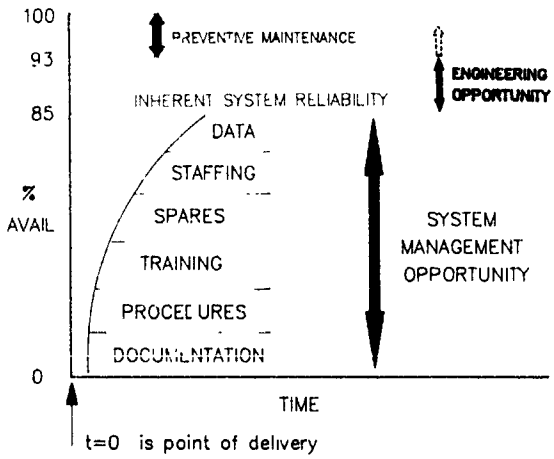

Fig. 8. System management – the potential

for memory devices is to be maintained. Looking at other industries it is also clear that the present level of equipment availability is not acceptable for a mature industry and that higher utilisation and therefore reliability levels are inevitable and the only question is how these can be made economically viable.

MTBF requirements exceeding 500 hours and MTTR of less than one hour drive a whole new set of challenges, especially when considered against the backdrop of increasing system design complexities and automation. Common tools used by equipment designers include the following:

(1) *System modelling*. Fig. 9 shows a modular approach to reliability modelling where a total MTBF in excess of 500 hours is stipulated with scheduled maintenance of less than 5%. This dictates design parameters for each module in terms of reliability. Although some of these MTBF numbers seem extraordinarily high, they are necessary if future devices are to be economically viable. Hence the system designer may be forced to use redundancy or very specific preventive maintenance schedules as is common practice in the aircraft industry

(2) *Continuous improvement programmes*. Close customer relationships are needed to effectively feed back reliability problems to the manufacturer in a digestable fashion. Root-cause analysis and a subsequent maintenance procedure change or design change are required to close the loop. All manufacturers have such programmes and the issue is how can they be made more effective. Pareto charts (fig. 10) are commonly used to give rank priority to reliability issues and these are based on accurate customer feedback.

Undoubtedly 500 h MTBF systems will be developed if they are economically feasible, both for the semiconductor device manufacturer and the equipment manufacturer. Unfortunately, to date, implant equip-

RANDOM FAILURES

Module	Sub module	MTBF	MTTR	DOWNTIME/ 100 HRS
Beamline	Sub total	1200	9	0.74
Processor	Sub total	3000	9	0 30
Vacuum	Sub total	2222	8	0 35
	Sub total	3279	5	0.16
Complete Control System	**TOTAL**	**520**	**8**	**1.55**

SHEDULED MAINTENANCE

Acuvity name	MTBS	MTTS	SCHEDULED DOWNTIME
Ion source and extraction service	75	2 00	2.67
Graphite service	4000	4 00	0.10
Gas bottle change	2000	4.00	0.20
Cryo regeneration	250	2 00	0.80
Wafer handling check	1000	1 00	0 10
Flood gun replacement	500	2 00	0 40
Heat sink inserts	2000	4.00	0 20
Vacuum full service	4000	16 00	0 40

SUMMARY		Failure Rates	
Availability	94 0%	% Beamline	64 0%
Scheduled downtime	4 9%	% Processor	9 4%
MTBF	520 4 HRS	% Vacuum	24 2%
MTTR	8.1 HRS	% Control	2.5%

Fig 9 Reliability model PI9200.

ment manufacturers have not enjoyed a universally successful profitability track record. It is also not clear what costs will be involved in creating a 500 h MTBF tool which has the self-diagnosis capability to allow an MTTR of less than 1 h, coupled with the spare-parts investment and logistics to allow any repair to take place in that time frame. Yet it is clear that just the reliability challenges set out for the next five years will require significant investment and change.

4. Conclusion

This paper has set out some of the process performance challenges faced by the implant community. It has also focused on the significant reliability challenge faced by the equipment manufacturer driven by the need of the industry to increase utilisation levels to remain viable. It is evident that the equipment supplier and user will need to work together in closer partnership if we are to succeed in the development of more automated yet more reliable ion implant systems. The trade-offs in terms of initial capital cost, operating cost and reliability will need to be understood by both parties. One scenario is that a higher capital cost system but with dramatically improved reliability will show huge cost-of-ownership savings. The details of this equation need to be well tested and accepted by both user and manufacturer.

One final concern is over another partnership or lack

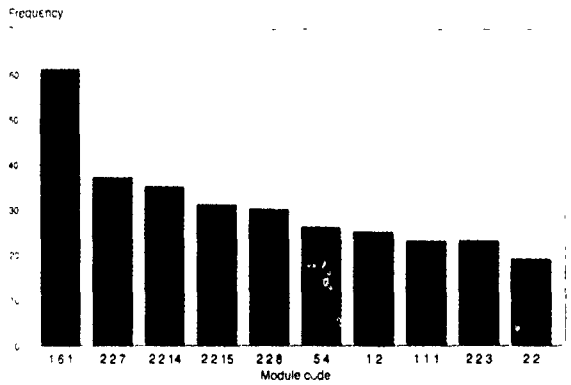

Fig 10. Pareto of top-ten failures areas from April 1 to July 1, 1990.

of it. Until now the major western government-sponsored groups, at least, such as Sematech and JESSI, have seen ion implantation as a mature and relatively unchallenging sector of the semiconductor processing field. The number and range of challenges presented at this conference suggest that this attitude is a mistake and we, as a group, should lobby to rectify this ill-informed conclusion.

References

[1] P.R. Hanley, in: Ion Implantation Equipment and Techniques, eds. H. Ryssel and H Glawischnig, Springer Series in Electrophysics, vol. II (1983) p. 2.
[2] M I Current, Nucl. Instr. and Meth. B6 (1985) 9
[3] T C. Smith, Nucl. Instr. and Meth. B21 (1987) 90.
[4] Y. Akasaka, Nucl. Instr and Meth. B37/38 (1989) 9.
[5] N W. Cheung, these Proceedings (8th Int Conf. on Ion Implantation Technology, Guildford, UK, 1990) Nucl. Instr. and Meth B55 (1991) 811
[6] I. Yamada, these Proceedings, ibid , p. 544
[7] M I Current, C.B Yarling and W.A Keenan, Ion implantation diagnostics and process control, Ion Implantation Science and Technology, 2nd ed (Academic Press, 1988) p 378
[8] M I. Current and W. Weisenberger, Solid State Technol 29 (2) (1986)

Nuclear Instruments and Methods in Physics Research B55 (1991) 386–392
North-Holland

Development of ion implantation equipment in the USSR *

A.F. Vyatkin [a], V.V. Simonov [b] and A.I. Kholopkin [b]

[a] *Institute of Microelectronics Technology and High Purity Materials, Academy of Sciences of the USSR, 142432 Chernogolovka, Moscow District, USSR*

[b] *"Vakuumashpribor" Scientific Industrial Corporation, Moscow, USSR*

A retrospective review of the development of ion implantation equipment in the USSR is presented and modern design philosophies are highlighted. The main developments made by Soviet scientists in the field of ion implantation over the past 30 years are reviewed

1. Introduction

Ion implantation into semiconductors started to develop in the USSR, as in some developed western countries, in the 50s and early 60s. It has its origin in semiconductor physics and physics of atomic collisions in solids. In 1952 at the Leningrad Physico-Technical Institute, M.M Bredov observed the change of the conductance type in p-type germanium upon Li^+ ion irradiation. In 1961 at the ion bombardment laboratory of the Kurchatov Institute of Atomic Energy, V.M. Gusev and M.I Guseva obtained p–n junctions with good rectification properties when irradiating silicon with ions of III and V group elements These and subsequent works demonstrated the possibility of introducing ion implantation into semiconductor device technology which called, in its turn, for development of appropriate industrial equipment.

Ion implantation technology was first extended to the high-volume production of switching pin-diodes, solar cells and bipolar transistors. These devices are distinguished by the presence of highly doped n- and p-layers. Hence, the first generation of implanters brought to the commercial level in 1966 features comparatively high ion currents (up to 10 mA) and an energy up to 100 keV. The machines of this series, namely, "ILU-1", "ILU-2", "ILU-3", developed at the Kurchatov Institute afforded high-efficiency implantation of a wide variety of ions. By way of example, in solar cell production the capacity of the "ILU-2" machine equipped with a conveyer-type sample holder system reached 0.5 m^2 per 100 min.

The ILU-machines belong to the first generation of Soviet-developed implanters. Among these are also Vesuvius machines developed at the Vacuum Institute by V.A. Simonov and coworkers. The Vesuvius-1 machine produced in 1969 showed the following parameters: ion current up to 100 μA, ion energy up to 200 keV, nonuniformity and nonreproducibility of dose < 2.56%, mass resolution $M/\Delta M > 100$ and an electrostatic scanning system.

2. Commercial ion implantation machines

The design and production of ion implantation machines in the USSR passed through four generations of machines classified into three groups according to application: (1) low-dose (medium-current) machines, (2) high-current machines, and (3) high-energy machines. The succession of generations is most fully represented by the Vesuvius accelerators which dominated the Soviet market for almost 20 years.

Hundreds of Vesuvius machines are now operating in the USSR (table 1) [1]. The table illustrates the evolution of commercial implanters. For many years Vesuvius-3 was the most popular among low-dose machines. It is a double target chamber with a mechanical scanning system of the drum type and electrostatic scanning. Developed in 1974, this machine provided an efficiency up to 300 wafers per hour from 1.5 in to 4 in. in diameter with sufficiently low nonuniformity of dose (2%) and an energy of 150 keV. Boron, phosphorus and arsenic ion currents reached 1 mA.

For quite a time in the field of high current machines the main emphasis was on plants with combined mechanical and electromagnetic scanning. The Vesuvius-4 and Vesuvius-8 machines of the 70s and their versions were produced with beam post-acceleration and a high-voltage target chamber.

The main trend in the development of Soviet ion implantation equipment was to smaller size and higher

* Invited paper.

0168-583X/91/$03.50 © 1991 – Elsevier Science Publishers B.V (North-Holland)

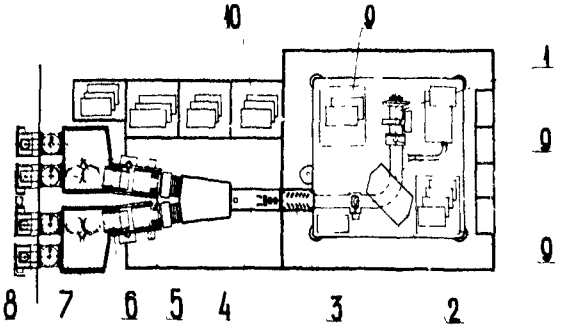

Fig 1 Schematic diagram of the Vesuvius-17 machine: (1) ion source, (2) analyzing magnet, (3) accelerated tube, (4) deflection and scanning system; (5) quadrupole lens, (6) wafer, (7) load/unload system, (8) vacuum load lock system, (9) high voltage power supplies and control blocks, and (10) control cabinet of the target chamber

efficiency. In the last decade the efforts have been concentrated on the qualitative parameters, namely, doping uniformity, full automatization, lower particle contamination. The modern Soviet–Czechoslovak Vikhr high-current machine utilizes nine locally distributed noise-immune microprocessors. Nine 6 in. wafers are mounted onto a spinning disk and two-coordinate mechanical scanning ensures an efficiency of 100 wafers per hour at a dose of 6×10^{15} cm^{-2}. The particle contamination is 0.15 particles per cm^2 at a particle diameter less than 0.25 μm, the doping nonuniformity being $< 0.75\%$. The cryogenic high vacuum pumping system, and the compatibility with clean rooms of class 10 enable the Vikhr machine to be used in the technological process of the production of 1–4 Mbit VLSI.

The Vesuvius-17 medium current machine is designed for implantation of VLSI, ultrahigh speed IC and ULSI. This fully automatic unit affords implantation of 10–200 keV B^+, P^+ As^+ ions at a maximum ion current of 3 mA. Each 150 mm wafer is alternately treated in one of the two chambers with an electrostatic deflection and scanning system. Wafers are loaded and unloaded in a vacuum from cassettes coming into the chamber through a vacuum lock. This enables the particle contamination to be lowered and the efficiency to be increased to 300 wafers per hour. The Vesuvius-17 machine schematic is shown in fig. 1. Commercial production is planned for 1991.

3. Special-purpose implanters

3.1. High-energy machines for ion implantation

The Vesuvius-9 high-energy machine for ion implantation was developed in 1980. In this machine both the ion source and the target chamber are at a high potential whilst the mid-point of the accelerator is at ground potential. This permits obtaining 600 keV singly charged ions, 1200 keV doubly charged ions and 1800 keV triply charged ions at a maximum power supply voltage of 300 kV. One of the Vesuvius-9 versions had a capacity up to 2.1 meV at a total accelerating voltage of 700 kV and generated P^{2+} ion currents up to 1 mA and P^{3+} ion currents up to 300 μA. The machine employed two-stage acceleration, two-coordinate mechanical scanning of the sample holder and a Makov-type ion source. The large size prevented extension of the machine to

Table 1
Ion implanters of the "Vesuvius" family

Model name	Year of issue	Ion energy [keV]	Ion current [mA]		Wafer diameter [in]	Nonuniformity and nonreproducibility of dose [%]	Maximal productivity [wafers/h]
			B^+	P^+, As^+			
Vesuvius-1	1969	10 - 200	0.2	0.3	2,3	2	50
Vesuvius-2	1972	15 - 150	0.2	0.5	2,3	4	50
Vesuvius-3	1974	15– 150	0.3	0.9	2,3,4	2	50
Vesuvius-4M	1974	15– 100	1.0	2.0	2,3	4	100–300
Vesuvius-5	1976	15- 140	1.0	2.0	3,4	4	40
Vesuvius-7M	1978	15 - 100	0.3	0.3	3,4	1.5	40
Vesuvius-8M	1981	15 - 100	2.0	5.0	3,4	2	200
Vesuvius-9 [a]	1980	100- 1300	0.3	0.8	2,3,4	2	80
Vesuvius-12M	1985	10– 100	2.0	5.0	4,5	1.5	20
Vesuvius-13M	1984	10– 200	1.0	1.2	4,5	1	50
Vesuvius-15 [a]	1987	20– 600	0.5	1.0	4,5,6	1	200
Vikhr	1989	10– 200	3.0	8.0	4,5,6	0.75	50–200
Vesuvius-17 [b]	1990	10– 200	2.0	3.0	4,5,6,8	0.75	120

[a] Doubly and triply charged ions are used.
[b] Commercially available from 1991.

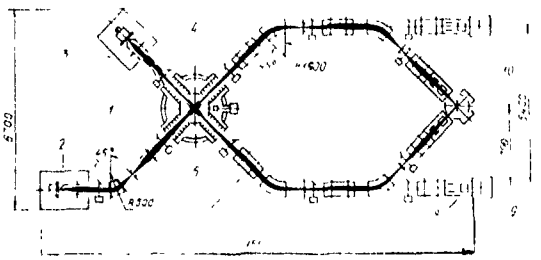

Fig. 2. Component layout of the UKP-2-1 machine: (1) high-voltage structure, (2) injector 1, (3) injector 2, (4) neutralizer, (5) Faraday cup, (6) quadrupole doublet, (7) analyzing magnet, (8) electrostatic scanner, and (9,10) target chambers

high-volume production Now its small-size prototype, 600 keV Vesuvius-15, comes in two versions: for A^{III} and B^{V} doping with controlled heating of 3-in. and 4-in. wafers, and for doping 4-in. and 5-in. silicon wafers with the use of cooling. The high vacuum pumping using turbomolecular pumps, triple beam "separation" by means of distributed mass-separators, a special target chamber with horizontal transport and wafer clamping and the possibility of operation over a wide range of ion mass and energy make Vesuvius-15 an all-purpose machine for ultrahigh speed IC fabrication.

The development of the high-energy Vesuvius-19 machine is being completed at Vakuumashpribor Scientific Industrial Corporation. It is designed in two versions: (a) with linear ion acceleration, employing a small-size high-voltage terminal (up to 1.5 MV) isolated by compressed gas (SF_6), (b) with rf linear ion acceleration up to 4 MeV.

In 1989 the UKP-2-1 high-energy machine designed at the Efremov Research Institute of Electrical and Physical Equipment (Leningrad) was put into operation at the Alma-Ata Institute of Nuclear Physics. This tandem-type heavy ion accelerator features the following parameters:

Ion energy (single-charge):	0.4–2.0 MeV
Energy stability:	0.05%
Beam current.	up to 50 μA
Ion mass range:	1–250 amu.

The accelerator is shown schematically in fig. 2. Two acceleration tracks based on a single high-voltage power supply enable both separate and simultaneous implantation of ions into the target. Moreover, the system allows concurrent implantation of heavy ions and analysis in the Rutherford backscattering mode.

Table 2 lists some parameters of ion beams produced by this accelerator

R&D in the field of ion implantation at very high energies is being carried out on the accelerator of the International Joint Institute of Nuclear Research in Dubna. Experiments with ion energies from ten to hundreds of mega-electronvolts are being carried out as a cooperative endeavor between specialists in material science and specialists in nuclear physics

At the Obninsk Physico-Energetic Institute the experiments on heavy-ion implantation are performed on an accelerator with an ion energy up to 5 Mev.

The Priz-500 small-size high-voltage vertical accelerator was developed at the Institute of Nuclear Physics of the Siberian Branch of the USSR Academy of Sciences in the second half of the 80s. It is designed for proton implantation at a H^+ beam current of 0.1 mA and is used for proton induced isolation of gallium-arsenide based IC devices.

The LUI-700 machine was also designed at the Institute of Nuclear Physics in 1987–1989 for 700 keV B^+, P^+, As^+ ion implantation at an ion current of 0.5 mA.

3.2. Analytical machines

As in the countries with advanced R&D in nuclear physics, the first analytical works in the USSR using high-energy ion beams were performed on vertical electrostatic Van de Graaff accelerators At present such analytical centres are run at the Moscow Institute of Nuclear Research, at the Institute of Nuclear Physics of the Moscow State University, at the Kharkov Physico-Technical Institute of the Ukraine Academy of Sciences and at the Tomsk State University. In the middle of the 80s the Sokol-3 analytical complex was developed at the Kharkov Physico-Technical Institute employing a horizontal electrostatic accelerator. The main technical characteristics of the machine are as follows:

(1) Ion energy:	0.3–2.0 MeV
(2) Beam energy homogeneity $\Delta E/E$.	< 0.04%

Table 2
Ion beam currents for 1 MV terminal voltage (UKP-2-1)

Injected particles	Ion species	Beam current [mA]	Energy [MeV]
H_1^-	H_1^+	54	2.0
$^4He^0$	$^4He^+$	1.7	1.0
	$^4He^{2+}$	0.04	2.0
$^{12}C^-$	$^{12}C^+$	0.5	2.0
$^{16}O^-$	$^{16}O^+$	3.9	2.0
	$^{16}O^{2+}$	3.1	3.0
	$^{16}O^{3+}$	0.06	4.0
$^{40}Ar^0$	$^{40}Ar^+$	1.8	1.0
	$^{40}Ar^{2+}$	0.1	2.0
	$^{40}Ar^{3+}$	0.02	3.0
$^{61}Cu^- + ^{63}Cu^-$	$^{63}Cu^+/^{65}Cu^+$	2.2/0.5	2.0
	$^{63}Cu^{2+}/^{65}Cu^{2+}$	2.8/0.5	3.0
	$^{63}Cu^{3+}/^{65}Cu^{3+}$	0.4/0.05	4.0
	$^{63}Cu^{4+}/^{65}Cu^{4+}$	0.004/–	5.0
$^{197}TaO^-$	$^{181}Ta^+$	0.09	2.0

(3) Ion current. 1×10^{-3}–50 μA
(4) Ion type. H^+, D^+, $^4He^+$, $^4He^{2+}$
(5) Beam current stability: 5–7%
(6) Gas pressure in the tank: 5 atm

This machine made it possible to apply the techniques of Rutherford backscattering with channeling, nuclear resonance reactions and proton induced X-ray emission. Several machines are now operating in industry and at the Institutes of the USSR Academy of Sciences.

3.3. Ultrahigh-current machines

Ultrahigh-current machines are designed for ion synthesis of materials and, in particular, for fabrication of buried isolated layers in silicon when producing silicon-on-insulator structures. Among these is the Vesuvius-20 machine. Its main technical characteristics are listed below:

(1) Ion type: N^+ and O^+
(2) Ion energy: up to 300 keV
(3) Ion beam current. up to 200 mA
(4) Nonuniformity and nonreproducibility of dose: < 5%
(5) Target temperature range upon irradiation 100–800 °C
(6) Target temperature maintenance ±5 °C

An UHF ion source and a magnetron-type ion source with a rhenium cathode have been designed for the Vesuvius-20 machine. Mass-production is planned for 1992.

The Implant-500 and Quartz ultrahigh current machines have been developed at the Leningrad Institute of Electrophysical Apparatuses on the basis of high-voltage air-insulated accelerators. The main characteristics of the machines are as follows.

	Implant-500	Quartz
(1) Energy [keV]	50–500	100–250
(2) Beam current [mA]	0.05–5	10–100
(3) Ion mass [amu]	1–200	1–32

3.4. High-current low-energy machines

Along with the conventional designs of ion accelerators, novel implanters are being developed. Among them are three types of machine distinguished by the absence of ion separation.

The Granat pulsed ion implantation machine has evolved from collaboration between the Moscow Technico-Physical Institute, the Elkor enterprise, the Vakuumashpribor scientific industrial corporation and the Saratov Elmash industrial corporation (fig. 3). The machine is intended for implantation of low and medium ion doses into semiconductors and other materials.

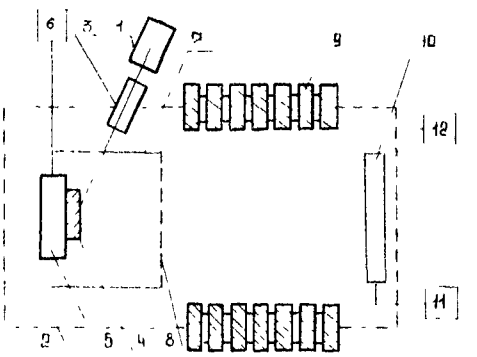

Fig. 3 Schematic diagram of the Granat machine (1) laser, (2) vacuum chamber, (3) optical system, (4) target, (5) movable target stage, (6) control system formation of target stage, (7) ionization chamber, (8) grid, (9) acceleration tube, (10) wafer holder, (11) dose control system, and (12) vacuum chamber

The Granat machine utilizes a laser-plasma ion source that affords evaporation and ionization of any solid material (Sb, As, Al, Ta, Cr, etc.). The noncontaminating nature of laser radiation and purity of the target materials to be doped eliminates the need for an ion beam separation system. The design of the ion source also enables high-homogeneity implantation over a large area without using an ion beam scanning system. This is a single-wafer machine which can be operated in manual and automatic modes. It may be used to obtain specified properties in solid state materials used in microelectronics technology and as a R&D machine in other fields.

The powerful pulse of laser radiation is focused on a target made of doping material. The latter evaporates to dissociate into ions. This laser generated plasma then expands in the source region. The system of ion beam generation and acceleration divides the laser plasma into the ion and electron components to form a slightly divergent ion beam and accelerates it to the required energy. Samples are continuously fed into the implantation zone via the single wafer handling system.

Technical characteristics:

Ion energy: 10–40 keV
Medium ion current: 100–300 μA
Implantation nonuniformity. 4%
Diameter of doped wafers: up to 100, 125, 150 mm
Capacity at a dose of 1×10^{14} cm^{-2} 80 wafers/h
Limiting residual pressure in the working chamber: 2.5×10^{-5} Pa
Pumping system: oil-free
Overall dimensions: $1800 \times 900 \times 2300$ mm^3
Weight: 1800 kg

The Titan machine has been developed at the Institute of High-Current Electronics of the Siberian Branch of the USSR Academy of Sciences from a pulse source generating different gas ions and ions of any conducting materials (metals, alloys, etc.).

The operation principle of the machine is based on simultaneous or sequential ignition of two forms of arc discharge with a common hollow anode. A constricted arc discharge with a cold cathode ensured the gas ion current component and initiates a vacuum arc which is a solid state ion source. This means that two-component ion flow generation is feasible.

Main parameters of the Titan source:

Accelerating voltage:	20–100 kV
Gas ion current:	up to 250 mA
Solids ion current:	up to 500 mA
Pulse duration:	400 μs
Pulse frequency:	up to 50 s^{-1}
Beam size:	250 cm
Nonuniformity of ion current density:	no more than +15%
Time of continuous operation with the same cathode:	35 h
Lifetime with gas ions.	100 h
Time to reach a dose of 10^{17} ion/cm^2:	10–20 min

The Vita ion plasma machine has been designed at the Kurchatov Institute. Its vacuum chamber houses a low energy ion plating system (IPS) and a low energy ion implantation system (IIS). This combination makes possible different technological operations:

- Plasma beam cleaning of surface areas
- Layer deposition.
- 40 keV ion implantation.
- A combination of these operations.

Technical characteristics of the Vita machine:

Implanted 40 keV ions:	He^+, Ar^+, Kr^+, Xe^+, N^+, CO^+, O^+, BF^+, Mg^+, Ca^+, Si^+, Al^+, P^+, Cu^+, Cs^+, S^+, Zn^+, Ge^+, Pd^+, Cd^+, In^+, Ag^+, Sn^+, Yb^+, Au^+, Pb^+
Energy of implanted ions of	
- the IIS:	up to 40 keV
- IPS (Ar, N, Xe).	from 250 to 400 eV
Total ion beam current	
- IIS:	from 5 to 20 mA
- IPS:	from 1 to 2.5 A
Beam size:	150 × 200 mm^2

3.5. Ion projection lithography machine

The ion projection lithography machine is being devised at the Vakuumashpribor scientific industrial corporation for application in short-cut resistless VLSI technology (fig. 4).

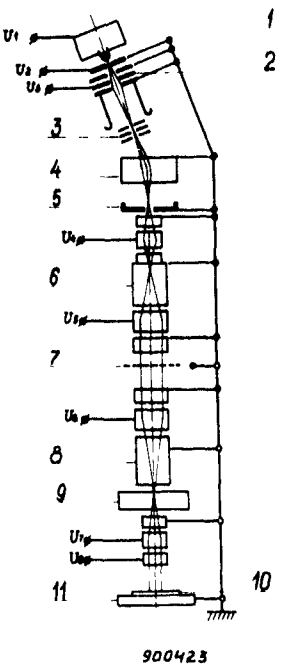

Fig. 4. Schematic diagram of the ion projection lithography machine: (1) ion source, (2) extraction system, (3) lenses, (4) analyzing magnet, (5) slit, (6) condenser lens, (7) silicon stencil mask, (8) projected lens, (9) alignment system, (10) wafer, and (11) wafer stage.

The design utilizes original designs of all the key elements, namely:

- Ion optical system,
- High brightness sources for different types of ions;
- Design and technology of reticles with high ion erosion resistance;
- Image alignment system,
- Image correction system.

The machine features the following parameters:

- Scale of image transfer from 3 : 1 to 10 : 1;
- 0.2 μm resolution over an area of 10 × 10 mm^2;
- liquid metal sources with needle electrodes made from tungsten, boron nitride and glassy carbon produce B^+, P^+, Pt^+, etc. with an ion beam current in the range 5–60 μA,
- duoplasmatron ion sources produce inert gas ions, N^+, H^+ with an ion current up to 100 μA.

Reticle parameters:

- thickness:	0.2–4.5 μm
- size of reticle field:	up to 45 × 45 mm
- minimum hole size:	1 μm
- accuracy of pattern registration:	< 0.15 μm
- ion erosion resistance of reticles:	> 10^{19} ion/cm^2

Along with its application to resistless technology, i.e. direct ion implantation through the mask, this ma-

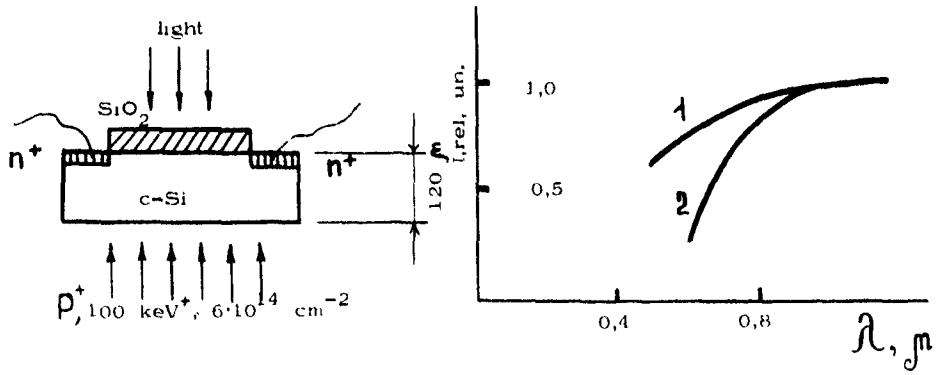

Fig 5 (a) Scheme of the long-range effect of ion implantation (b) Spectral dependence of photoconductivity current: (1) reference sample; (2) P^+ ions implanted from the back side of the sample

chine can be used to advantage in the lithography processes on different types of resists including "dry" resists.

4. Contribution of Soviet scientists to the art of ion implantation

The achievements in ion implantation machine development as well as the high level of knowledge in the field of solid state physics and materials science have enabled Soviet scientists to make a significant contribution to the understanding of the processes related to ion implantation into solids.

Besides the aforementioned pioneering works done in the area of ion implantation, the results obtained in different scientific institutions of the USSR rank among the most remarkable. Some of the results are the following.

The possibility, in principle, of synthesizing new phases containing irradiated target atoms and implanted atoms was demonstrated in 1961 [2]. Semiconductor cadmium telluride compound was synthesized in 1967 [3]. Tellurium films 0.1 μm thick were irradiated with 5–15 keV cadmium ions at a dose of 2×10^{15} ions cm^2. High-energy electron diffraction analysis and photoconductivity measurements point unambiguously to formation of CdTe

Consistent investigations of the mechanism of accelerated ion–solid interactions have led to the development of the physical models of the formation of randomly damaged regions and damaged surface layers [4]. The models are based on the idea of vacancy–interstitial space separation which provides accumulation of defects of one type to concentrations required to change the single crystal to the amorphous state. In the opposite case annihilation of defects results in saturation of the defect accumulation process at low concentrations.

In 1973 the studies of silicon amorphization revealed that epitaxial recrystallization occurs under certain conditions when the dose of silicon(III) irradiation is increased above the critical amorphization value [5]. It was particularly shown that at room temperature the effect of epitaxial recrystallization of Si(III) is observed upon P^+ ion irradiation at doses $> 10^{16}$ ions/cm^2 and ion current densities < 5 μA/cm^2. This effect, now

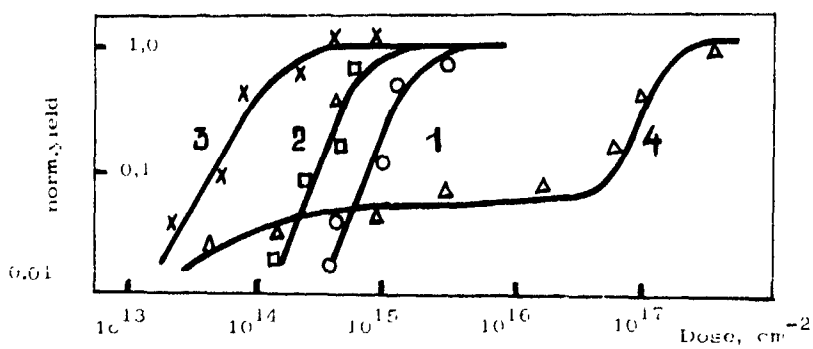

Fig 6 Backscattered ion yield as a function of 80 keV Ne^+ ion implantation dose at room temperature in: (1) pure Si(100); (2) B^+ doped Si (100), B concentration 2×10^{21} cm^{-3}, (3) As^+ doped Si (100), total concentration 2×10^{21} cm^{-3}

known as ion-beam induced solid phase epitaxial growth (IBIEG), was called the large-dose effect.

The problems of semiconductor crystal structure reconstruction and electrical activation of interstitial impurities calls for physical investigations of these processes and development of appropriate technology. For instance, laser pulse annealing of radiation damage was studied at the Kazan Physico-Technical Institute in 1974 and then at the Institute of Semiconductor Physics of the Siberian Branch of the USSR Academy of Sciences in 1975 [6,7]. It was shown that a single pulse of the solid-state laser with a pulse duration of 30 ns and a pulse energy of 0.1 J focused into a 15 mm spot is sufficient for the annealing of radiation damage in implanted layers and producing a high-level carrier concentration both in Si and GaAs.

In the late 60s and early 70s a group of scientists of the Gorki Physico-Technical Research Institute headed by P.V Pavlov discovered the so-called long-range effect, i.e. the change in the semiconductor properties at distances exceeding considerably the range of bombarding ions [7]. Later the effect was studied in detail in ref [9]. Its essence is illustrated by the scheme of the experiment and the experimental spectral dependence of photoconductivity shown in fig. 5.

Another example of this kind is the discovery of the impurity amorphization effect which is described comprehensively in paper [10]. The essence of the effect is vividly shown in fig. 6.

At present, the engineers designing ion implantation equipment work in collaboration with the scientific institutions engaged in investigations of the physical processes of the ion–solid interactions The most active among them are: the Institute of Semiconductor Physics of the Siberian Branch of the USSR Academy of Sciences, the Lebedev Physical Institute of the USSR Academy of Sciences, the Institute of Microelectronics Technology and High-Purity Materials of the USSR Academy of Sciences, the Leningrad Polytechnical Institute, the Byelorussia State University, the Institute of Electronics of the Uzbek Academy of Sciences, the Institute of Nuclear Physics of the Kazakh Academy of Sciences, the Kaunas Polytechnical Institute, the Gorki Physico-Technical Research Institute, and the Kazan Physico-Technical Institute.

References

[1] V V Simonov, A A Kornilov, A.V. Shashelev and E V Shokin, in. Ion implantation Equipment (Radio and Communication, Moscow, 1988).
[2] M I Guseva and B.V Aleksandria, Zh. Tekh Fiz 31 (1961) 867
[3] A.E. Gorodetskii, G A. Kachurin, N.B. Pridachin and L S Smirnov, Fiz Tekh. Poluprovodn 2 (1967) 136.
[4] N.B. Pridachin and L S Smirnov, Fiz Tekh Poluprovodn. 5 (1973) 166
[5] N N Gerasimenko, A.V Dvurechenskii, S.I. Romanov and L.S. Smirnov, Fiz Tekh Poluprovodn (1973) 2195.
[6] I.B. Khaibullin, E I Shtyrkov, M.M. Zaripov, M.F Galyautdinov and R.M Bayazitov, VINITI, No 2661-74, M., 32
[7] G.A. Kachurin, N.B Pridachin and L S Smirnov, Fiz Tekh Poluprovodn 9 (1975) 1428.
[8] G.N. Uspenskaya, N N Abramova, D.I Tetelbaum, E I Zorin and P V Pavlov, in: Physical Fundamentals of Ion-beam Implantation (Gorki, 1972) p. 96, in Russian
[9] V.G. Goryachev, L N Marenina and V N Modkovich, in Radiation Effects in Semiconductor Systems, (Izd KIYaN AN USSR, Kiev, 1977) p. 26
[10] A.V Dvurechenskii, R Groetzschel and V P Popov, Phys. Lett A116 (1986) 399

Nuclear Instruments and Methods in Physics Research B55 (1991) 393–397
North-Holland

The Nissin NH-20SP medium-current ion implanter

N. Nagai, T. Kawai, M. Nogami, T. Shin'yama, T. Yuasa, Y. Kibi, H. Kawakami, K. Nishikawa and M. Isobe

Nissin Electrical Co Ltd, Ion Equipment Division, 575 Kuze Tonoshiro-cho, Minami-ku, Kyoto, Japan

The NH-20SP medium-current ion implanter has been developed to meet the needs of advanced ULSI fabrication processes The NH-20SP has the following features: (1) parallel-beam implantation, (2) 8 in wafer compatible, (3) precise dose-uniformity control, (4) in-situ parallelism and uniformity monitor, (5) large-tilt-angle implantation, (6) step wafer-rotation during implantation. The NH-20SP employs a hybrid scan system. The horizontal parallel-beam sweep is accomplished with two sets of electrostatic electrodes A wafer is scanned vertically by a swing-arm scan mechanism A digital beam sweep system controls the dose uniformity across the wafer Implant dose uniformity is achieved by adjusting the speed of the vertical wafer motion The swing-arm scan mechanism provides a large-tilt-angle implantation and stepwise rotation of the wafer during implantation In this paper an overview of these features will be given and performance data will be presented

1. Introduction

The NH-20SP medium-current ion implanter has been developed to meet the needs of advanced ULSI fabrication processes (figs. 1 and 2). The implanter provides parallel-beam implantation, 8 in wafer processing, precise dose and uniformity control, large-tilt-angle and step-rotational implants for novel ULSI processes.

The NH-20SP employs a hybrid scan system. A hybrid scan system sweeps an ion beam in one direction and translates a wafer in another. In NH-20SP, a horizontal parallel-beam sweep is accomplished with a digitally controlled electrostatic electrode. A wafer is scanned

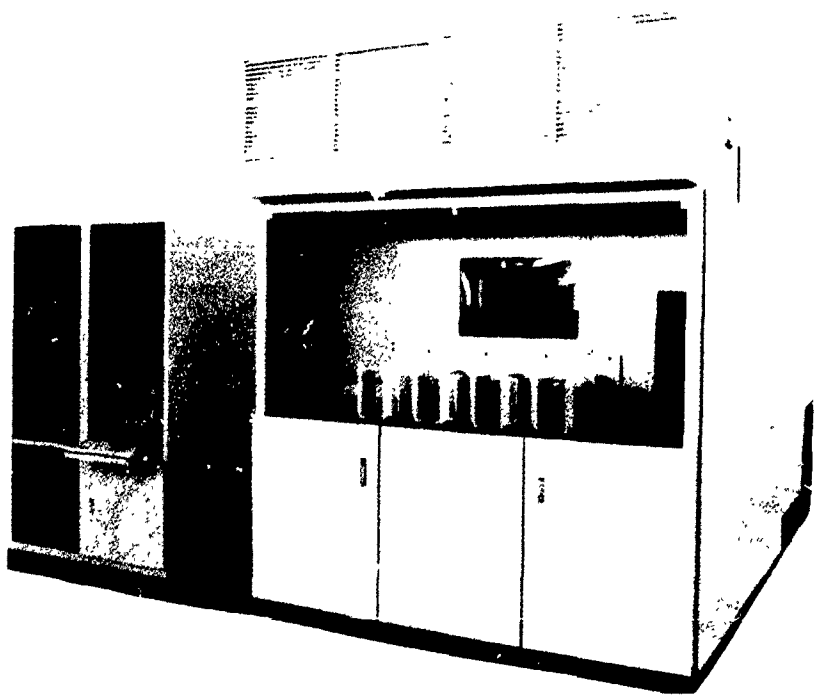

Fig. 1. Photograph of the NH-20SP

0168-583X/91/$03.50 © 1991 – Elsevier Science Publishers B V (North-Holland)

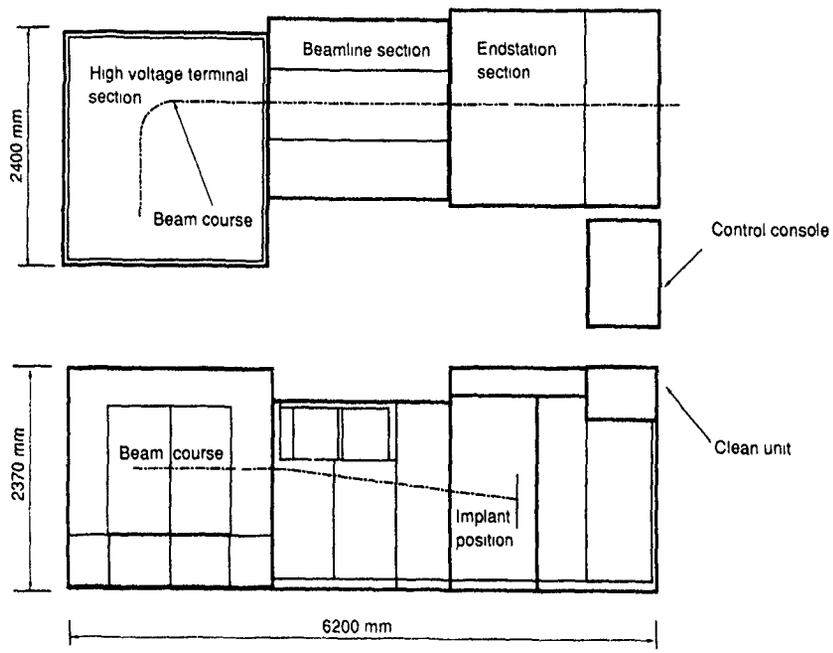

Fig. 2. Overall plane view of the NH-20SP medium-current ion implanter.

vertically by a swing-arm scan mechanism and the scanning speed is controlled to perform uniform implantation

2. Beam line (parallel-beam generation)

In the NH-20SP, an ion beam is swept electrostatically The frequency of the horizontal beam sweep is 1 kHz. Fig. 3 shows a schematic view of the beam line. The ion beam, after being mass-analyzed and post-accelerated, is swept horizontally by the H1 electrode. The V electrode bends the ion beam downwards to eliminate neutrals and other unnecessary components such as charge-transferred ions and dissociated molecules. In the case of a 50 keV BF_2^+ implant (30 kV extraction, 20 kV post-acceleration), the vertical separation between BF_2^+ and BF^+ – which is dissociated

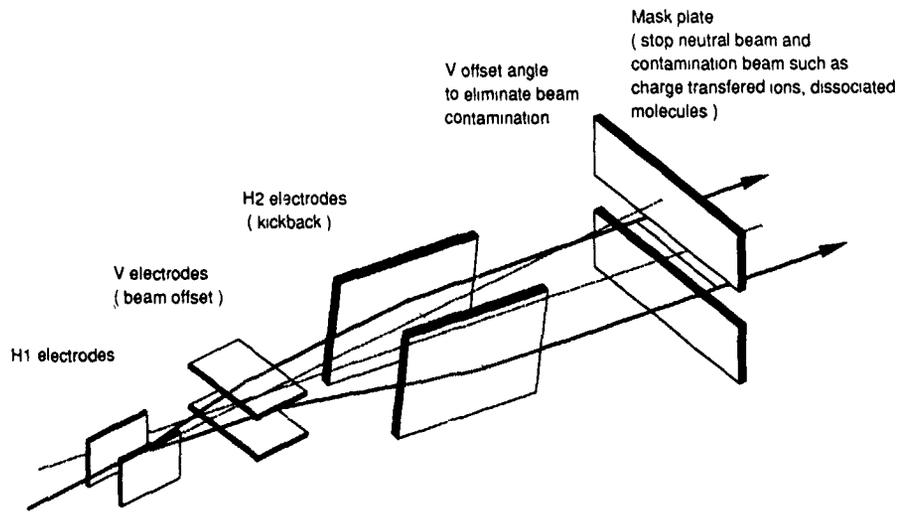

Fig. 3. Schematic view of the beam line

from BF_2^+ after mass analysis – is about 60 mm at the mask. This is sufficient to eliminate contaminants. The H2 electrode kicks back the ion beam to make a so-called parallel swept beam. This simple beam-sweeping system provides a good parallel beam at the target. Measurements of the beam entrance angle at the surface of the wafer show that the angle variation over an 8 in. wafer is less than 0.5°.

The sweep-voltage waveform applied to the H1 and H2 electrodes is generated by a digital-waveform generator, which we call a waveform controller. The beam-sweep waveform is generated to get uniform beam-sweep speed over the entire wafer surface.

In the near future, the beam profile or beam current density distribution will be considered as important implant parameters to perform high-quality implantation even for a medium-current ion implanter. The NH-20SP provides the means of monitoring both the horizontal and the vertical beam profile. In the NH-20SP, an ion beam can be swept vertically by the V electrode. To get a beam profile, select one of the multislit Faradays and measure the beam current as the beam is swept horizontally or vertically by varying the horizontal and vertical sweep voltages.

3. Implant control system

The mechanical scan is accomplished with a swing-arm scan mechanism. In this system, vertical wafer motion is achieved by combination of two circular motions (fig. 4).

The platen is swung up and down like a pendulum by the M2 direct-drive (DD) motor and the wafer on the platen is spun by the M3 DD motor (not shown in fig 4). The M2 and M3 motors are controlled to move

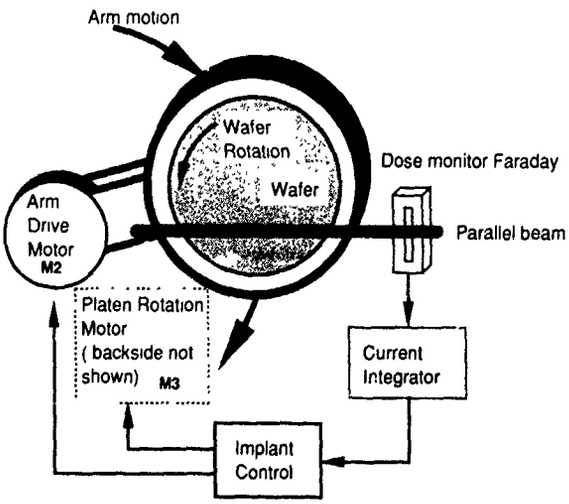

Fig. 4 Block diagram of the implant control system.

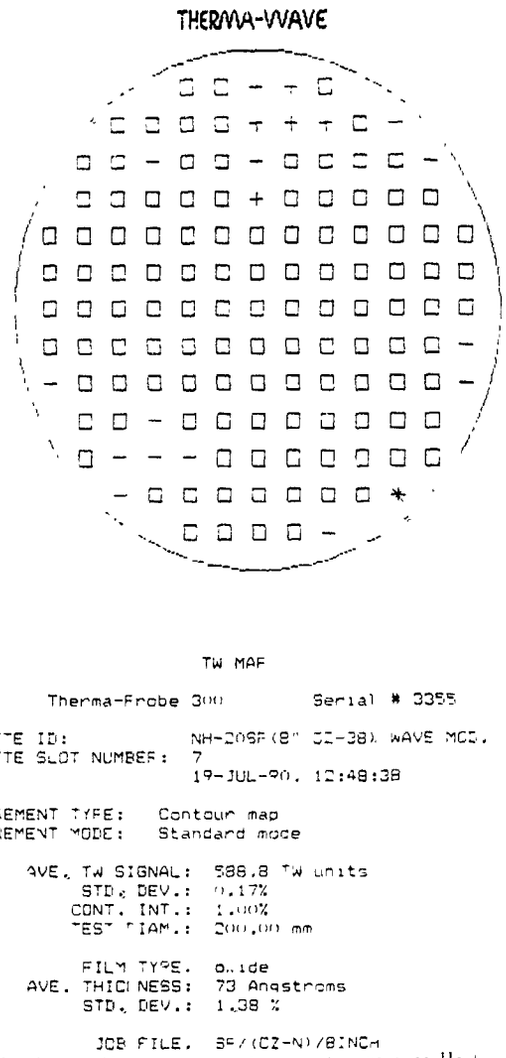

Fig 5. Implant uniformity on an 8 in wafer 30 keV $^{11}B^+$, dose = 10^{13} n/cm^2, implant time = 13.3 s, tilt angle = 0°

in the same speed and in opposite direction. As a result, the angular motion of the wafer caused by the swing arm is canceled and the direction of the wafer is fixed against the ion beam.

Fig. 4 shows the block diagram of the implant control system. To implant the desired dose over a wafer, the NH-20SP controls the speed of the swing-arm motion as a high-current mechanical scan implanter. The implant controller drives the M2 and M3 motor to make the ratio of the wafer's vertical speed to the beam current the same at any position The beam current is measured by the dose monitor Faraday at every beam sweep. If the measured beam current is smaller than a predetermined value, the implant controller slows down the swing-arm motion in order to achieve the required dose. When the beam current is larger than the maxi-

mum value, the beam sweep is suspended and it resumes when the beam current becomes allowable.

The parallel swept beam is exposed on the wafer at every 0.5 mm step at maximum vertical scan speed (1 Hz). Fig. 5 shows a typical implanted contour map.

4. In-situ parallelism and uniformity monitor

The horizontally swept beam is monitored by multislit Faradays. The Faradays are situated before (front) and after (back) the implant position. The front multislit Faraday is located at a different vertical offset angle position, and the back multislit Faraday is on the beam course.

The waveform controller which outputs the sweep voltage, monitors the beam current collected by each Faraday during beam sweeping. The controller detects the current peak of the beam for one of the multislit Faradays and memorizes the output voltage. As the horizontal position of each Faraday is fixed, the beam position as a function of the sweep voltage is obtained by performing this procedure for all Faradays. The beam position as a function of sweep voltage is measured at the front and back Faraday position. The beam flight path is determined using those two data. In this manner, beam parallelism is monitored and interlocked.

To get uniform implantation on a wafer, an ion beam must be swept over the wafer at a constant speed. The ion beam position data, measured by the "before" and "after" Faradays, can tell the beam-sweep speed over the wafer. The implant uniformity can be predicted using the position versus the sweep voltage data. By adjusting the beam-sweep waveform so as to get a uniform beam-sweep speed over the wafer, in-situ uniformity control is achieved. To take account of the response of the high-voltage amplifier that outputs the beam-sweep voltage, an ion beam is swept in a modified waveform and the beam position data are measured again. This procedure (iteration) is repeated until the waveform converges within a given uniformity.

5. Endstation

The NH-20SP has a dual platen system equipped with a spinning platen and with a variable-tilt-angle mechanism (VTAM [1]). A pick-and-place mechanism and back-side contact are aspects of our concept of wafer handling. Fig. 6 is a schematic of the endstation seen from above.

Wafer cassettes, based on the SEMI standard are located at 900 mm above the floor. A wafer is picked up by a loader vacuum chuck and the loader robot is

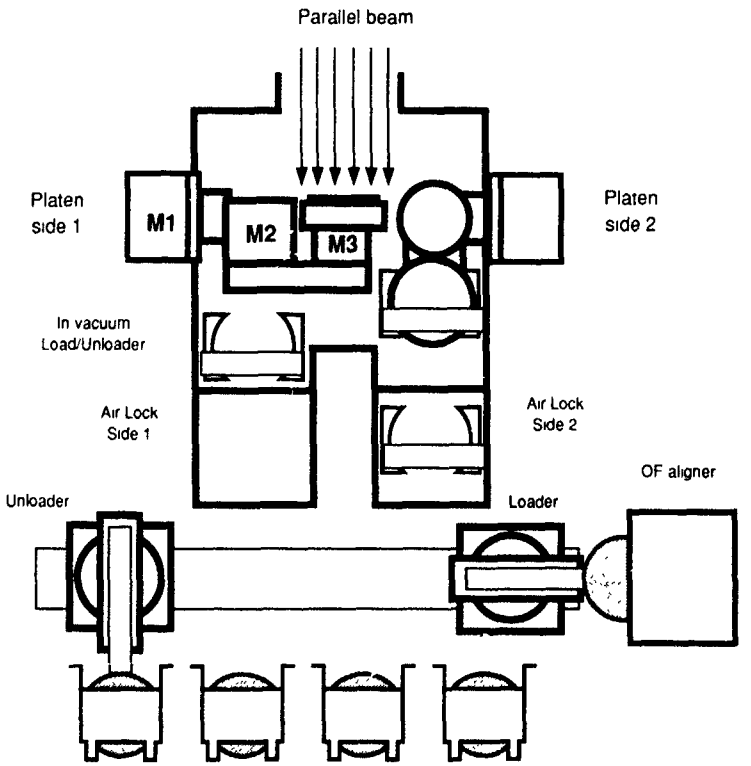

Fig. 6. Schematic view of the endstation, top view

moved to an OF ("flat" orienter) aligner by a linear motor. When the OF or notch direction is optically aligned, the wafer is placed at one side of an air-lock chamber, which is evacuated by a dry pump first, followed by a turbomolecular pump (TMP) directly mounted on the air-lock chamber. When the pressure of this chamber is at high vacuum, a gate value is opened and the wafer is lifted by an in-vacuum wafer-load transfer arm and brought to the platen. At the same time, an implanted wafer is returned to the air-lock chamber by the in-vacuum wafer-unload transfer arm. When venting of this chamber is completed, the implanted wafer is picked up by an unloader robot and returned to the wafer cassette.

The M1 motor moves the platen to a given tilt angle. The tilt angle is the same as the rotational angle of the M1 motor, and is variable from 0° to 60°.

The orientation of the wafer is set by the M3 motor at the beginning of an implantation. The presettable angle runs from 0° to 359°.

During implantation the M3 motor can rotate the wafer to change the "flat" orientation when the wafer is at the over-scan position This means that the direction of the wafer relative to the beam-sweep plane can be changed. Such a procedure is called step-rotational implant. The step division number is selectable from 1 to 99 for an implant The tilt angle can also be varied at the same time. As a result, a combination of changes of the tilt angle and step-division number during implantation is possible.

As the NH-20SP employs a dual-platen system, customers can process two different sizes of wafers at the same time.

6. Conclusion

A new medium-current ion implantation system, the NH-20SP, has been developed. It can generate a parallel ion beam in order to overcome problems due to the nonparallelism of the beam, such as the asymmetry characteristics and shadow effect, which are inherent to an ordinary electrostatic scanning system. Beam parallelism and dose uniformity are optimized by an in situ monitoring system consisting of two multislit Faradays The system can cope with an 8 in. wafer which is thought to be a standard in the next-generation systems with dual-platen scheme.

References

[1] Y Tamura, M Nogami, M Tanaka, T Maeda, H. Kumasaki and S Tamura, Nucl Instr and Meth. B37/38 (1989) 618.

Nuclear Instruments and Methods in Physics Research B55 (1991) 398–407
North-Holland

A high-current ion implanter system

M. Nasser-Ghodsi, M. Farley, J. Grant, D. Bernhardt, M. Foley, S. Holden, T. Bowe, C. Singer, K. Dixit and G. Angel

Eaton Corporation, Semiconductor Equipment Division, 108 Cherry Hill Drive, Beverly, MA 01915, USA

The important issues in the design and development of the Eaton NV20A high-current ion implantation system are discussed The control system is based on a Sun Microsystems workstation connected through an Ethernet to a multiprocessor controller. The software is based on an object-oriented environment with a layered operator interface design An adaptive robotics-based wafer handling system, and clampless wafer holding allow for high throughput with good particulate performance The modular design of the beam optics add to system versatility

1. Introduction

Since the development of the Nova NV10-80 pre-deposition implantation system in 1978–1979 [1], Eaton Ion Beam Systems Division has continued to evolve the high-current technology to meet the semiconductor industry needs. The first major deviation from the special purpose low-energy (Pre-Dep™) machines was the

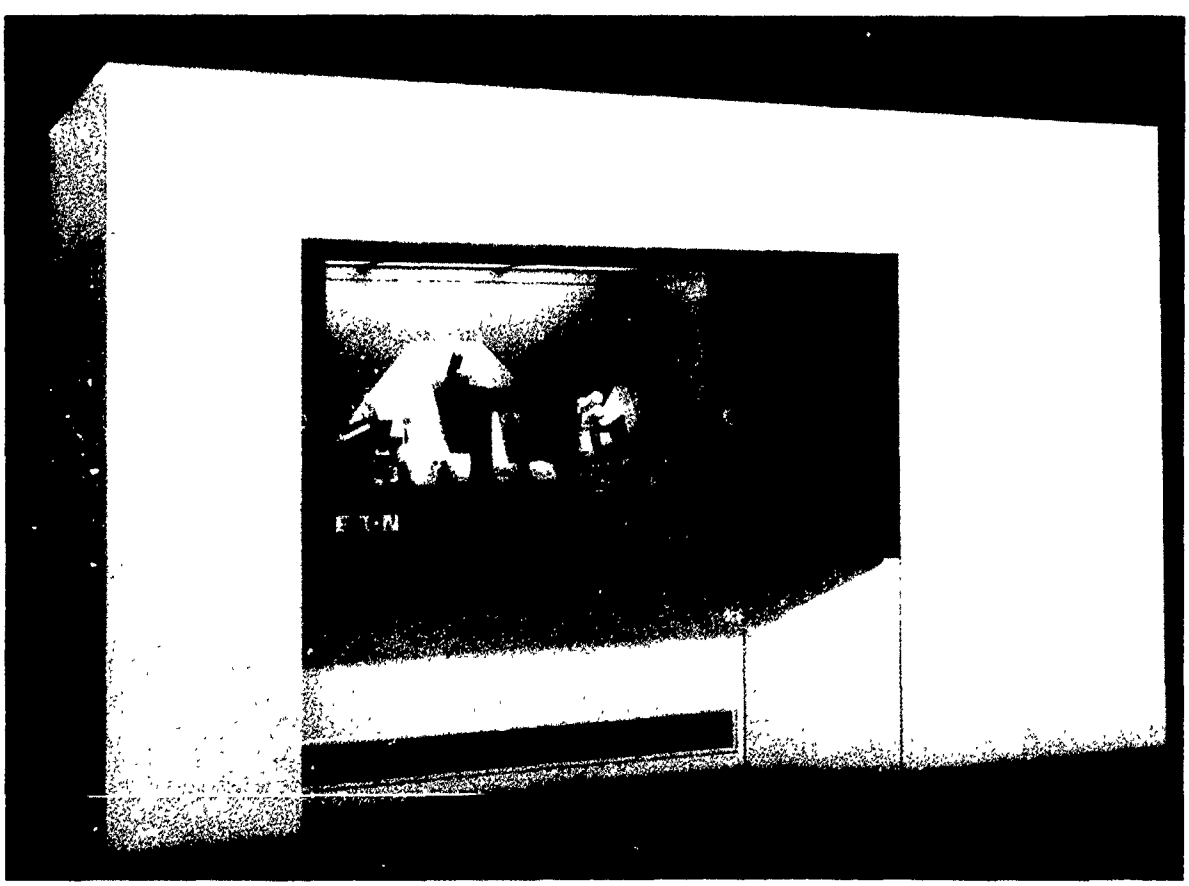

Fig. 1. Photograph of the NV-20A high-current ion implantation system

0168-583X/91/$03.50 © 1991 – Elsevier Science Publishers B.V. (North-Holland)

NV10-160 [2] which covered a much wider range of implant energies and doses. This equipment evolution continued with the development of the NV 20-200 which was designed to meet 200 mm wafer handling requirements as well as the requirements for wider energy and dose ranges. Ultimately, this machine met with limited success due to the lack of a sophisticated automation package, its small 25 wafer batch capacity, and its low mechanically limited throughput. To address these needs, the NV20A (fig. 1) was designed to include an advanced automation package, a large implant batch capacity, and an increase in mechanically limited throughput. There are now fourteen of these systems in operation and positive performance results are beginning to emerge. This paper describes some of the design features of this system was well as some early performance characteristics.

The key performance specifications are listed in table 1.

Table 1
Key performance specifications

Energy range.	5–200 keV	
Wafer charging:	±10 V maximum	
Variable implant angle.	0–10° recipe selectable	
Throughput:	Wafer size	Wafers/h
	100 mm	200
	125 mm	200
	150 mm	196
	200 nm	160
Dose control		Specification
	Range	10^{11}–10^{17}
	Uniformity	$\sigma \leq 0.5\%$
	Run to run	$\sigma \leq 0.5\%$
Particulate control·	Size	Specification
	≥ 0 5 μm	≤ 0.025/cm^2
	≥ 0 3 μm	≤ 0 050/cm^2

Beam current [mA]·

Energy [keV]	B^+	P^+	As^+	Sb^+
10	2.5	5 0	5 0	
20	7.0	10 0	10.0	
40	8.0	20 0	20 0	10 0
60 to 200	8.0	20 0	20.0	10 0
	B^{2+}	P^{2+}	As^{2+}	
to 400 keV	0 25	1 5	1 5	

2. Beam generation and transport

The NV20A beam generation and transport system (fig 2) includes the ion source, extraction electrodes, mass analysis magnet, post-acceleration tube and electron shower for beam neutralization. The basic optical design is taken from the NV10 [1] with only minor changes to accommodate a larger beam envelope. The vacuum system and beamline envelope is designed for optimum control of pressure along the entire beam path. Measured beam currents are shown in table 2.

2 1 *Ion source*

The ion source is a Bernas type with a repeller mounted opposite the filament to enhance electron life-

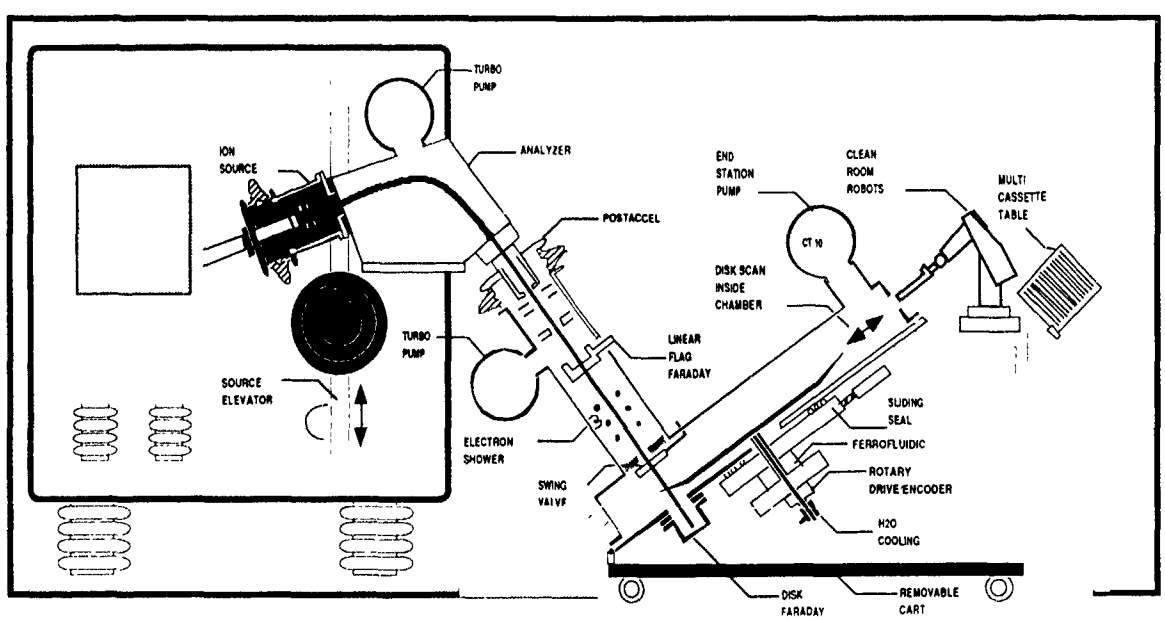

Fig 2. NV-20A beamline schematic.

time in the source plasma. This source routinely yields B to BF_2 fractions of greater than 1 and has a lifetime of greater than 85 hours, limited only by metallic plating of the filament insulators. Versions of this source made of tantalum as opposed to molybdenum have been demonstrated to have no measurable Mo^{2+} cross contamination in BF_2^+ implants. The source has an elliptically shaped slit aperture with special shaping designed to eliminate unwanted focusing and resulting hot spots in the beam density profile.

2.2 Extraction system

The extraction electrode was designed to cover a wide dynamic range of current and energy by placing two apertures on a single accel/decel electrode configuration (fig. 3). One of the apertures is optimized for 5 to 40 keV while the other is optimized for 20 to 80 keV, providing good energy range overlap. The traditional adjustments, x, y, and z, are accomplished using mechanical linkages coupled through vacuum feedthroughs, while the selection of apertures is accomplished by moving the electrode assembly in one step. The pitch of the step is equal to the aperture spacing, thus assuring alignment when changing between apertures.

2.3. Electron flood system

The electron shower system (fig. 4) is designed to produce electrons within the potential well of the ion

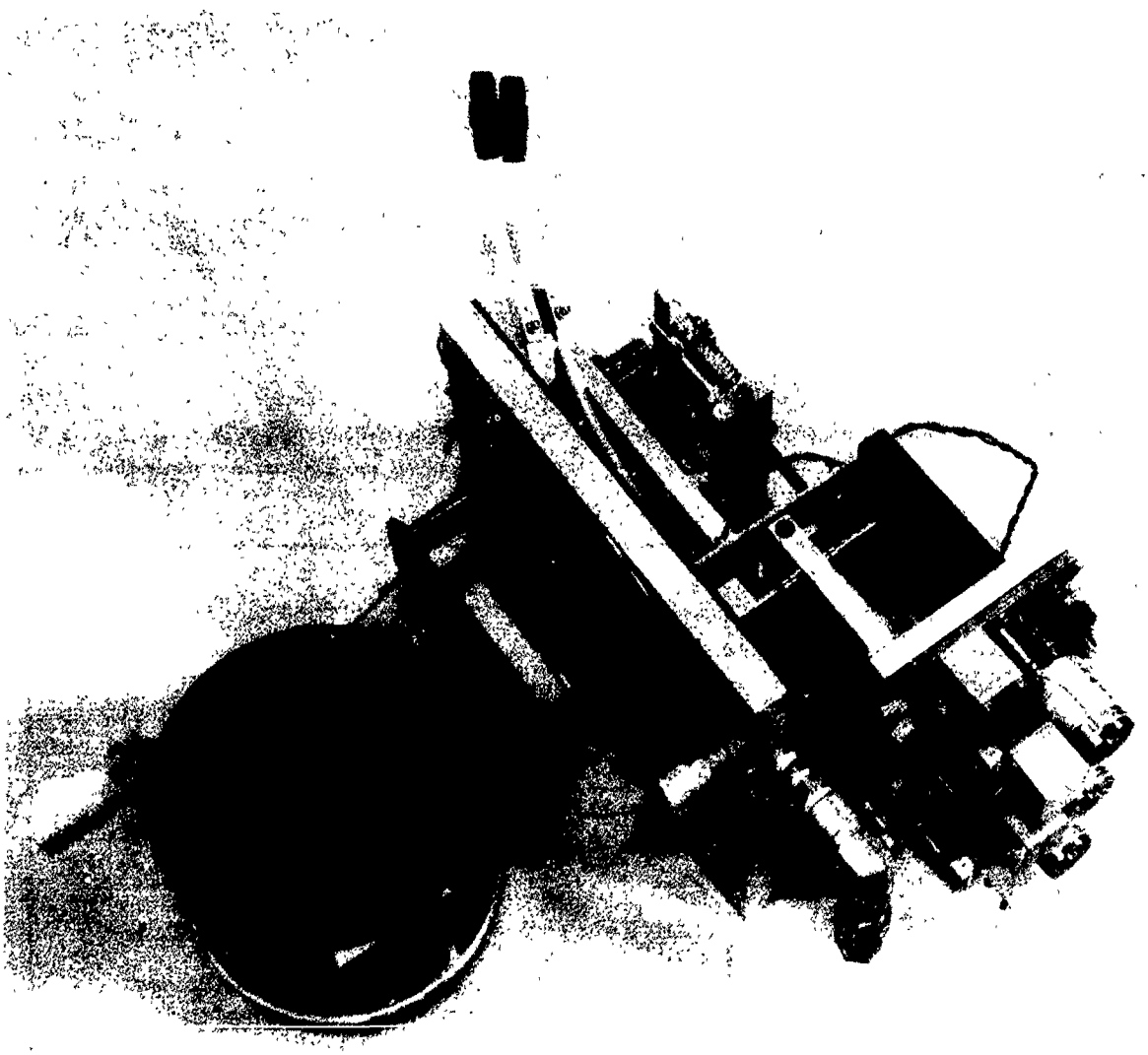

Fig. 3. Photograph of the dual aperture extraction electrodes

Table 2
Beam current vs energy performance

Energy [keV]	Beam current [mA]		
	As^+	P^+	B^+
5	1.0 [a]		2.2 [a]
10	5.75 [a], 3.0	7.5 [a]	6.0 [a]
15	10.5 [a]	9.5 [a], 7.5	8.0 [a]
20	12.0 [a], 8.0	12.5 [a], 11.0	9.5 [a]
25	15.0 [a]	14.0 [a], 14.0	11.0 [a]
30	16.8 [a], 18	20.0 [a], 18.5	11.0 [a]
40	22	24.0	
50	30	27.0	
60	30	28.5	
70	> 30	28.0	
80	> 30	28.0	

[a] Measurements using the low-energy aperture.

beam. In principle, low energy electrons generated in the potential well will escape primarily through the ends of the beam. A suppression ring encircling the beam upstream of the shower prevents the loss of electrons to the upstream regions, leaving only the region between the shower and the wafer surface for electron loss.

The shower is designed to confine 300 eV primary electrons to oscillate back and forth through the ion beam, which will enhance the probability of ionizing collisions between the primary electrons and the residual gas atoms. An inert gas is fed into the shower region to maintain a constant production rate of electron–ion pairs. Since the shower is completely enclosed with only small entrance and exit apertures, it is effectively differentially pumped by the beamline and endstation region vacuum systems. This allows for a relatively high gas pressure within the shower which is used to increase the ionization frequency. Measurements have shown that the average number of primary electron passes through the shower is five, which provides an approximated 50 cm electron path length. With an ionization cross section of 2×10^{-16} cm^2, a pressure of 1.5×10^{-4} Torr, and a primary current of 400 mA, this shower can produce an ionization current of 20 mA. This current, in addition to secondary electrons produced from the shower grid, is sufficient for controlling wafer surface potentials during high-current ion implantation.

3. Wafer handling and implant control

The wafer handling for the NV20A is designed to accommodate large batch sizes while maintaining high wafer throughput. In addition to a reusable 25 wafer dummy fill capacity, the maximum number of 25 wafer batches that can be loaded at one time are 4, 5, 6, and 7 for 200, 150, 125, and 100 mm wafers, respectively. Each of the 25 wafer batches can be processed with different process recipes under fully automated control. Process recipes can also be chained together to accommodate multiple implant parameters on a single implant batch. An example of this application would be implants with multiple energies to control junction depth and dose profiles.

3.1. Wafer handler description

At the heart of the wafer handling system (fig. 5) is a pair of Puma 260C six-axis robots fitted with vacuum chucks which are used to gently move wafers from cassettes through a laser beam flat-notch aligner and into one of two 25 wafer buffer cassettes. The wafers

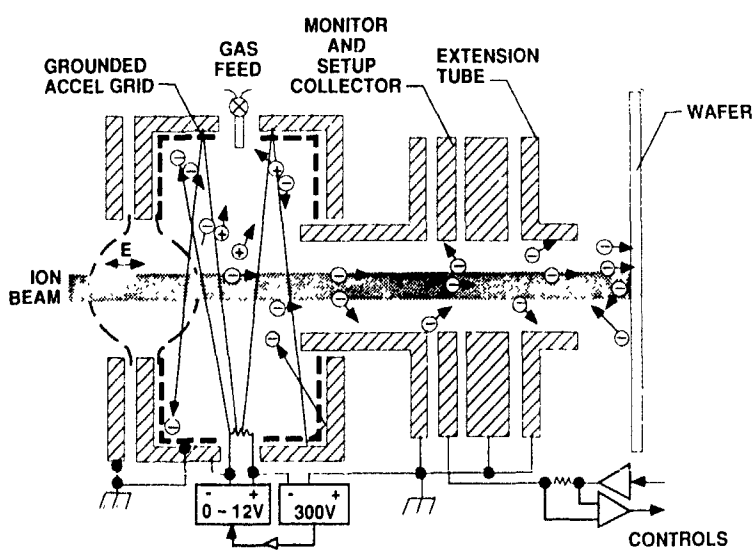

Fig. 4. NV-20A electron shower system

are then loaded onto a 1 m diameter disk (fig. 6) prior to implantation. Once the wafers have been implanted, they are removed from the disk and placed back into their original cassette with slot-to-slot integrity maintained. Wafers are sensed throughout the handling sequence by means of vacuum sensors connected to each of the vacuum chucks. The multiple cassette table, on which cassettes are loaded, is moved laterally to position cassettes at a single access point. A sonic transducer located below this access point accurately locates the next available wafer within a cassette to eliminate the need for time-consuming search algorithms involving the robot arms. The system also has the capability of detecting cross threaded wafers within a cassette, which will prevent wafer breakage if such an event occurs. The entire wafer handling environment is enclosed within a closed circuit laminar flow system with ULPA filters (fig. 7). The performance in the wafer handling area approaches class 1 when bulkhead mounted into a class 10 clean room.

The wafer handling sequence consists of two distinct periods in which the two robots are used; the first period is for buffering wafers while an implant sequence is conducted, the second period is for loading and unloading wafers from the disk between implants. Loading and unloading of cassettes is accomplished with random access through a single load door located in front of the machine.

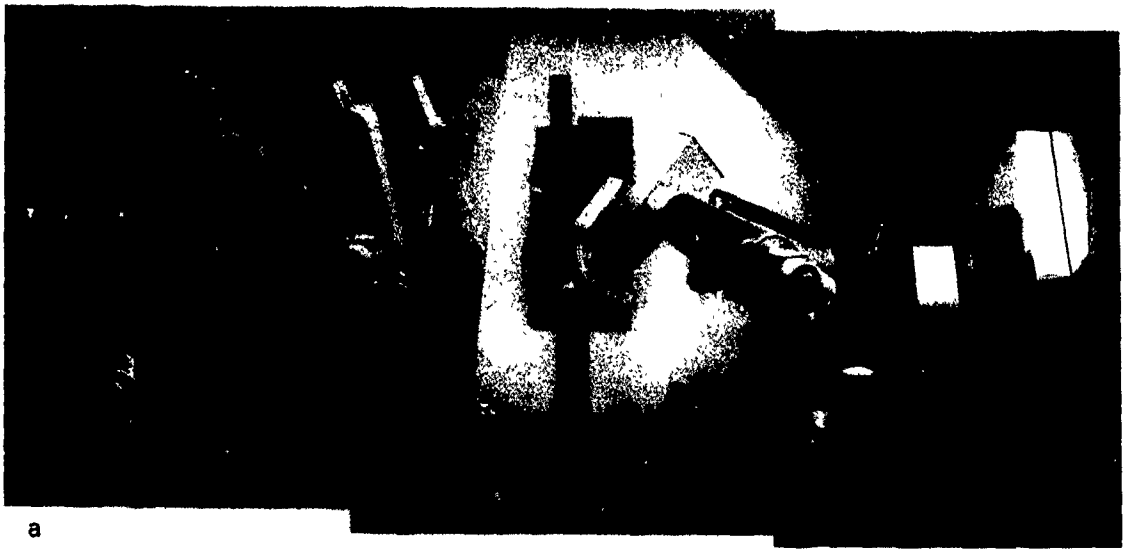

a

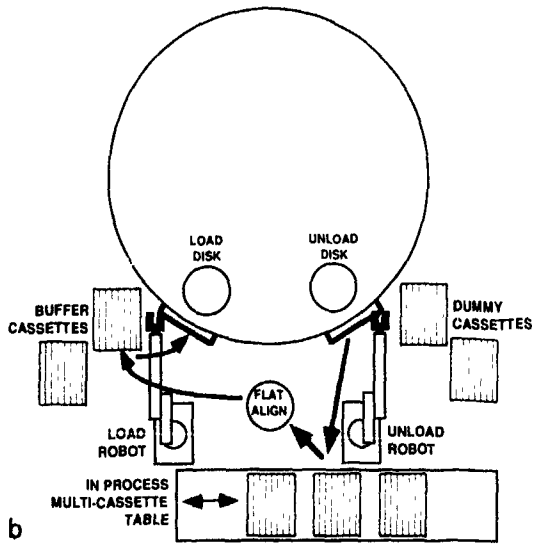

b

Fig 5. (a) Photograph of the NV-20A wafer handler (front view). (b) Schematic of the NV-20A wafer handling system.

3.2 Dose control system

The dose control system is an improved version of the one used on the NV10 [4]. Wafers are located on the perimeter of the disk, into which five radially oriented slots are cut. The disk spins at 1200 rpm while it is translated up and down to cause the beam to scan across the wafers in the perimeter. The beam current pulses transmitted through the slot and into the disk Faraday are integrated to arrive at the one-dimensional dose rate in the wafer plane. This measurement is used to control the translation velocity in the radial (control) direction, which provides for uniform dose across the scanned implant area. The number of up and down scans and radial velocity constants determine the final dose received by the wafers.

3.3. Beam profile monitor

Twenty small apertures are located in the perimeter of the implant disk, each of which has a unique angular and radial location on the disk surface. At the beginning of an implant, the intensity–time profile of the beam current transmitted through each of these small apertures is measured. This provides a beam density profile with a resolution of about 2.5 mm.

3.4. Differential current measurement

To improve the overall accuracy and linearity of the dose control system, a differential current measurement technique (fig. 8) is employed. The current pulse transmitted through the dose control slit is integrated for a

Fig. 6. Photograph of the NV-20A disk cart assembly

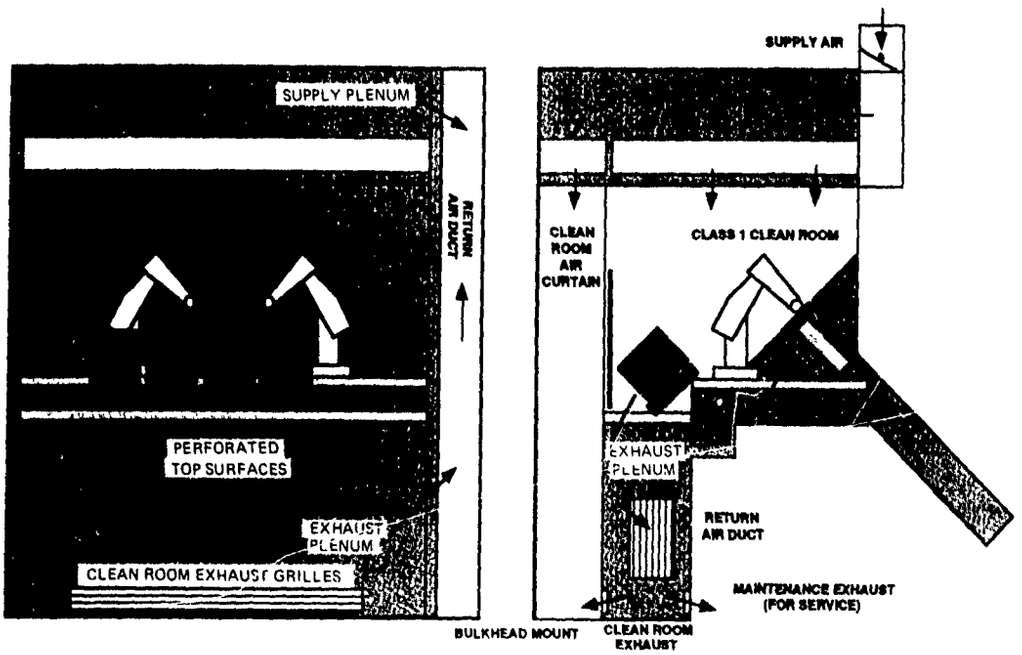

Fig. 7 NV-20A laminar flow system

fixed period of time, after which a dark current measurement is made for an identical period of time. The difference between the two integrations is the true beam current less all instrument offsets and Faraday leakages. This technique, in combination with the low tolerances of range resistors in the instrument, results in a monotonic measurement and control of dose over the entire measurement range of the instrument.

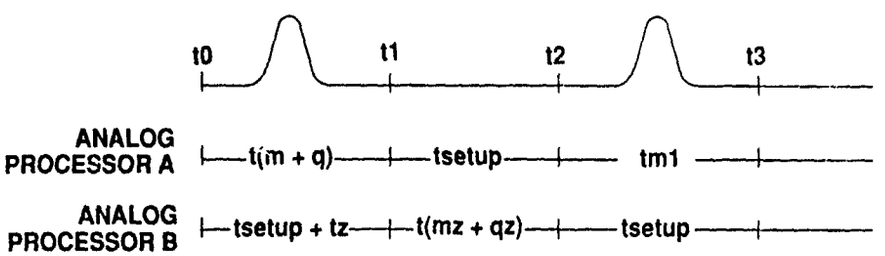

t(m + q) = measurement and quantization of beam current
tsetup = time to set up & zero the analog processor
t(mz + qz) = measurement & quantization of all leakage & offset currents
t1 - t0 = t2 - t1

$$Qb = \int_{to}^{t1} Ibd\,t - \int_{t1}^{t2} I_{Ofs}dt$$

Offsets & leakage currents are cancelled

Fig 8. Dose control integrator timing

4. Control system

The NV20A control system, shown schematically in figs. 9 and 10, is designed around a generic architecture which can be applied to all Eaton IBSD products. The user interface is a Sun Microsystems color graphic workstation with a keyboard and mouse. This system is also compatible with touch screen and trackball interfaces. The Sun system computer is connected through a fiber optic Ethernet to a VME Bus cell controller. The cell controller is connected through high-speed fiber optic serial loops to each of the specialized I/O modules or device interfaces. Included in the Sun package is a 105 Mb disk drive with tape back-up, which houses all of the operating software plus the implant data files as well as the alarm history.

4.1 Control description

The control system software (fig. 11) is an object-oriented multiply layered communications network. Modules communicate to one another and the database by way of a messaging system. At the top of the layer is the user interface which communicates directly with the system database and the control applications software. The user interface software is based on Motif which runs on X-windows which minimized the software development task. Access to screens and applications is controlled by a password management system. At present, there are three basic levels of access: Supervisory, Maintenance, and Operator. Customized access can be programmed for any individual at the supervisory level.

The system database resides in the cell controller in battery backed RAM. An image of all I/O points and values is stored in the database for use by applications and communications layers of software. The applications software uses the database parameters to make control system decisions as well as to change output parameters. The communications layer manages the I/O tasks. In most case, the device interfaces simply transfer I/O information. There are, however, a few real-time control applications that cannot tolerate the communi-

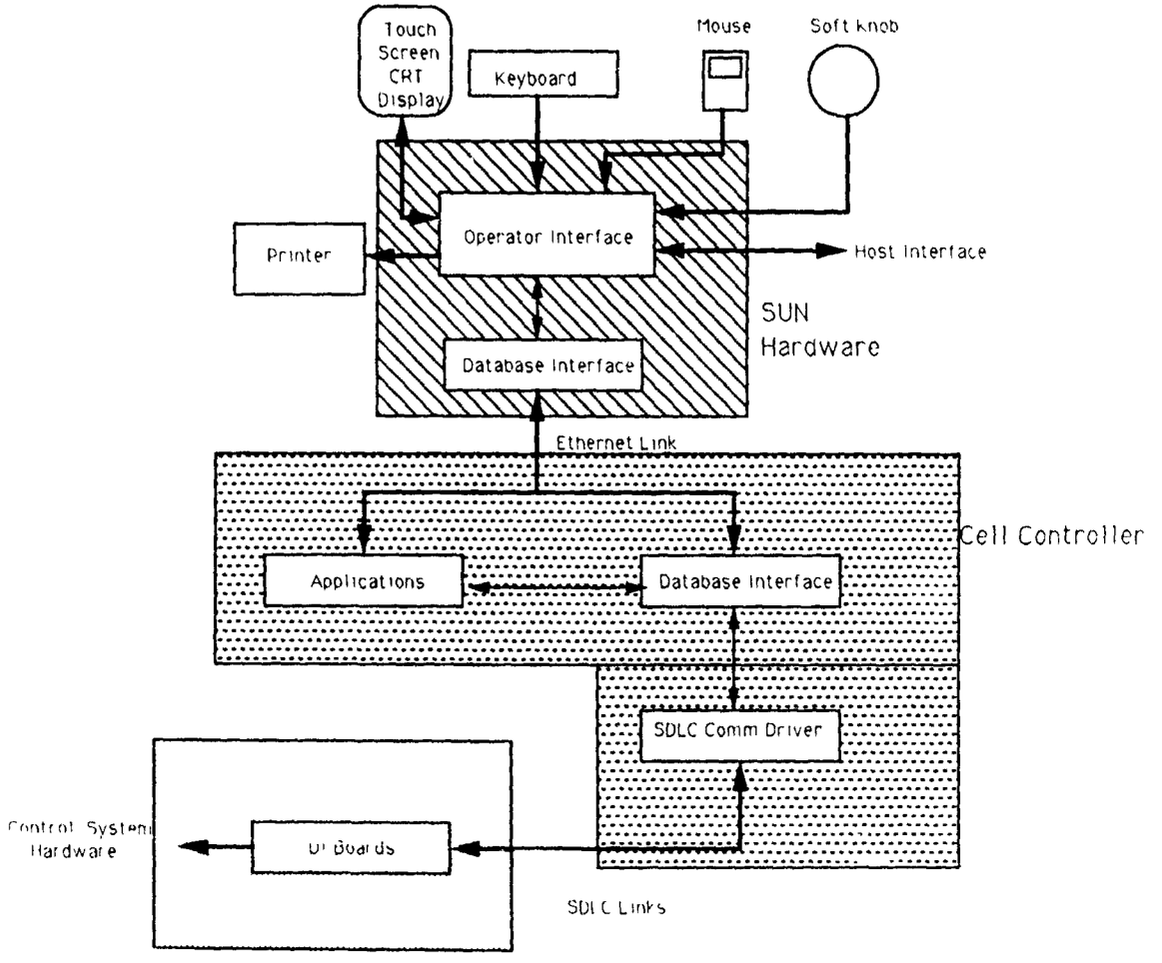

Fig. 9. Control system software data flow.

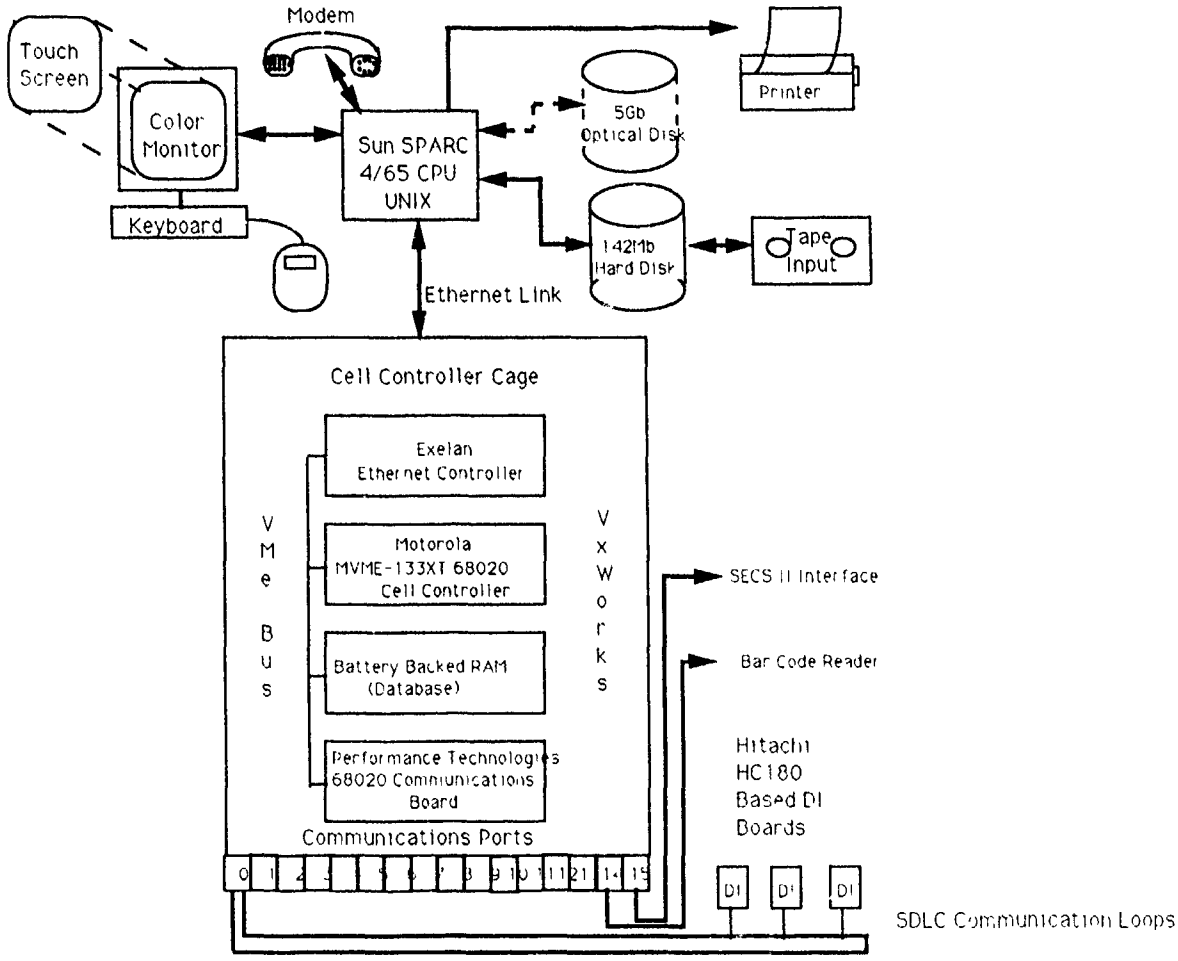

Fig 10 Generic control system architecture

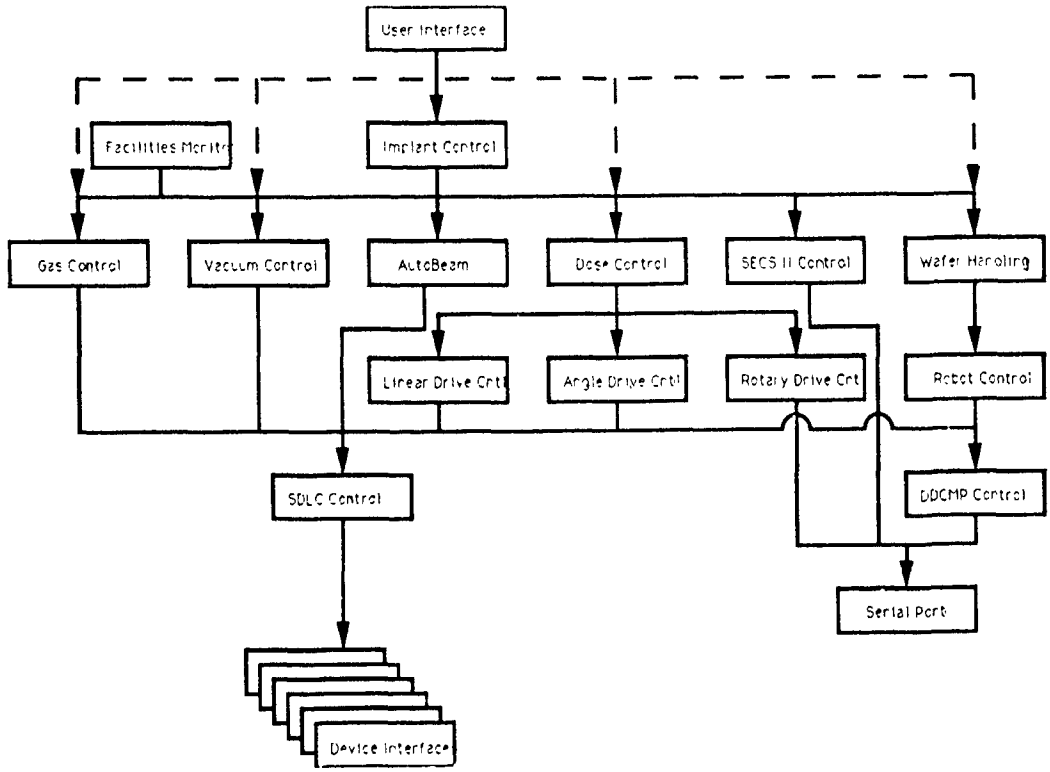

Fig. 11 NV-20A control system hierarchy

cations delays and these applications reside at the device interface layer.

Acknowledgements

The authors would like to acknowledge the many individuals on the team who contributed to the design, development and delivery of the NV20A. We would also like to thank Kelly Morrisey and Dan Ferrin of our Technical Publications Department for their hard work in producing this and many other manuscripts and illustrations under an extremely tight schedule. And finally, we would like to express out appreciation for the confidence our first few NV20A customers have shown in our design and manufacturing team.

References

[1] G. Rydıng, Springer Series in Electrophysics, vol. 2 (Springer, Berlin and New York, 1983).
[2] P H. Rose, R Faretra and G Rydıng, Nucl. Instr and Meth. 86 (1985) 27.
[3] V Benveniste, Nucl. Instr. and Meth. B21 (1987) 366
[4] G Rydıng and M. Farley, Inst. Phys. Conf. Ser 54 (1981) 100

Nuclear Instruments and Methods in Physics Research B55 (1991) 408–412
North-Holland

Mechanically scanned ion implanters with two-axis disk tilt capability

T. Tamai
Sumitomo Eaton Nova Corporation, Toyo-shi, Ehime Pref., Japan

M. Diamond
Eaton Corp. Semiconductor Equipment Division, 2433 Rutland Drive, Austin, TX 78758, USA

B. Doherty and P. Splinter
Eaton Corp. Semiconductor Equipment Division, 108 Cherry Hill Drive, Beverly, MA 01915, USA

New techniques for high-density circuit integration require parallel scanning in combination with the ability to reposition the circuit devices during implantation. A new family of high- and medium-current implanters utilizing a common end-station concept has been developed in a cooperative effort of design groups in Japan, Massachusetts and Texas. The new family utilizes rotating-disk, mechanically scanned batch processing with vacuum-lock wafer loading and unloading. A small, high-speed robot performs the in-air handling associated with loading the vacuum lock. The disk has a gimbal mount which permits two-axis tilting of the disk during implantation. Construction details and process capabilities of this implanter family are described and discussed.

1. Introduction

Eaton has recently introduced a new family of implanters which is truly international in design and manufacture. The machines are available in two basic types, the NV-GSD high-current model (80 and 160 kV versions) and the NV-8200GD medium-current model.

Both implanters are high-volume manufacturing tools designed to be compatible with some of the newer processes which require variable tilts and repositioning. In such applications this family of implanters can simulate wafer rotation for implanting the walls of a trench structure.

2. Design methodology

These ion implanters are not simply machines that were designed in one place and manufactured in another place. Design teams in Austin, TX, Beverly, MA and Toyo, Japan have cooperated to design these implanters, including associated control software. As a part of the design process, engineers from each of the sites involved met to agree upon the form and features of the new implanters.

The design concept was for a family of implanters with a "common process interface", that is, a common mechanical interface and common recipe of parameters, such that a user who has one machine and requires the other would automatically be familiar with many of the operational characteristics. As an example, a robotic interface designed to work with a high-current system would work equally well with a medium-current system. Another benefit is interchangeability of parts used in both machines, which reduces the required spare parts and maintenance training.

Eaton Corporation and its Japanese affiliate, Sumitomo Eaton Nova, are well established implanter manufacturers. The design strategy included use of past design experience and proven, existing hardware in the new implanters. The terminal section of both models derives from American designs and the end stations from Japanese designs. Sumitomo Eaton Nova produces the NV-10SD-80 and the NV-10SD-160 implanters in Japan. These implanters are based on the Eaton, Beverly Plant NV-10-80 and NV-10-160 terminal sections and a Sumitomo Eaton Nova end station. The NV-8200GD/NV-GSD designs are the next steps in the evolution of Sumitomo Eaton Nova's end-station designs coupled with improvements to the Eaton, Beverly Plant terminal section (NV-10/NV-20) and the Eaton, Austin Plant terminal section (NV-6200A). The improvements in end-station design include single-robot handling, two-axis tilt and vacuum-load-lock wafer handling.

0168-583X/91/$03.50 © 1991 – Elsevier Science Publishers B.V. (North-Holland)

3. Construction details

3.1. End station

Both implanters are two-axis, mechanically scanned batch systems. The scan axes are rotary and vertical, with servodrives used for both axes. The rotary axis is operated at constant speed, while the vertical axis speed is dependent on beam current and vertical position. The mechanical implementation of the vertical scan is slightly different on the high- and the medium-current implanters due to the difference in the mass of the disk and disk housing. The high-current mechanics incorporates a pneumatic spring but the medium-current does not. There is also some difference in the mounting arrangement of the servomotor and lead screw. The vertical drive moves the plate carrying the rotary drive motor and the bearing set for the disk. Vacuum sealing between this plate and the disk chamber is provided by a series of progressively pumped sliding seals.

The medium-current disk is smaller and therefore holds fewer wafers. By changing the disk and wafer handling fixtures (buffer cassettes, in-vacuum handling arm, etc.), wafer sizes between 4 in. (100 mm) and 8 in. (200 mm) can be accommodated. Table 1 is a comparison of the NV-8200GD and NV-GSD disks.

The rotating disk is composed of bolted-together "segments", as opposed to a cast one-piece construction. This machined structure is more uniform than a casting. The wafer platens are machined as part of the "segments". Cooling during implant is provided by a water-cooling circuit which runs through the disk and into the platens. The platens are coated with an RTV material to insure good heat transfer from the wafer.

Table 1
Comparison between the NV-GSD and NV-8200GD disks

	NV-GSD	NV-8200GD
Disk diameter [m]	1.10	0.78
Wafer size [mm]	Batch size [wafers]	
	NV-GSD	NV-8200GD
100	25	20
125	20	15
150	17	13
200	12	9

Because the disk is designed to be clampless with wafers held flat against their platens, there is no angle variation due to bowing of the wafers. Also, there is no shadowing of the wafer by a clamp or sputtering of the clamp material onto wafers.

Both the NV-8200GD and NV-GSD models offer two-axis tilting of the disk. The NV-8200GD is capable of $\pm 15°$ tilt and the NV-GSD of $\pm 11°$ tilt. The tilt mechanism consists of a two-axis gimbal, with pivots centered on the beam path. The tilt drive consists of two servomotors operating through lead screws. A bellows is used between the beam line and disk housing to provide the compliance required for the disk housing motion with respect to the beamline. The ability to tilt

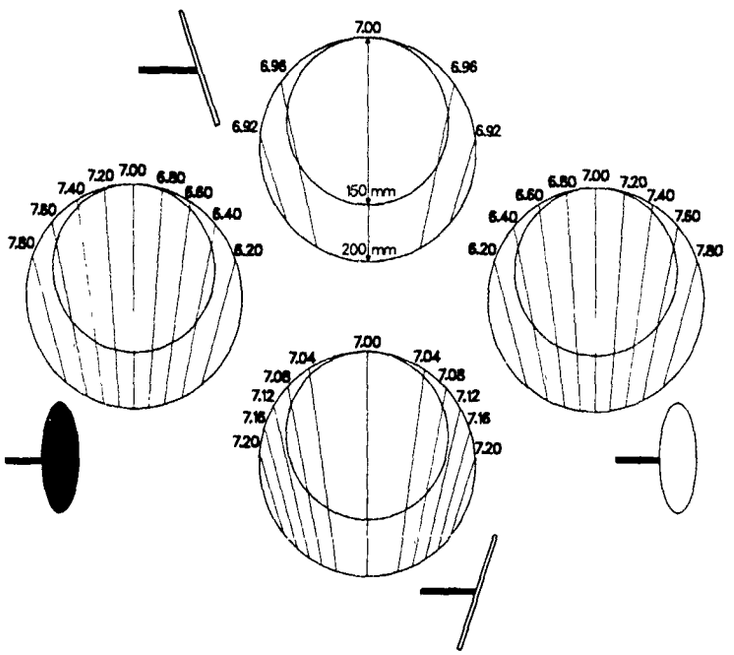

Fig 1. Angular deviation contours.

allows the implanter to perform simulated quadrant or octant implants. The implanter only achieves parallel scan when the spin axis is parallel to the beam axis [1]. For all other tilt settings, there is a small angular deviation, which depends on the tilt setting and the beam position on the wafer. Fig. 1 is a set of tilt-angle maps for a 7° quadrant implant performed on the NV-8200GD. The inner circles represent 6 in. (150 mm) wafers and the outer ones represent 8 in. (200 mm) wafers. This illustrates that the worst deviation for a 8 in (200 mm) wafer is 0.8°, although this only occurs in a small area. The worst deviation for the NV-GSD, under the same conditions, is about 1°.

The chamber is a machined aluminum clam-shell design, hinged on one edge and held together on the other with quick-release clamps. The chamber is designed so that it may be opened quickly for maintenance by releasing the clamps and several pipe unions.

An electron shower system controls wafer surface charging by supplying low-energy electrons which can be trapped by the ion beam and reduce the potential resulting from the space-charge distribution of the beam. Argon gas may be fed to the shower to enhance the production of low-energy electrons within the beam These low-energy electrons are produced when the argon gas molecule is ionized by collisions with either primary electrons from the shower or ions within the beam. Cylindrical tubes encircle the beam downstream of the shower to prevent high-energy electrons from reaching the wafer surface in the region outside the beam cross section. To prevent the stripping of space-charge neutralizing electrons upstream of the shower, a negatively biased aperture is located near the electron shower. This aperture creates a negative potential near the beam

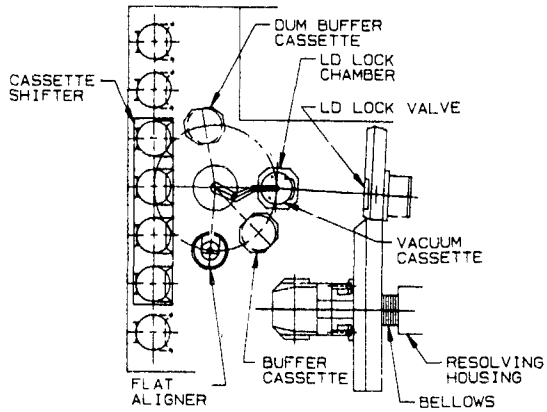

Fig 2. End-station wafer handling

which prevents diffusion of the upstream electrons to the downstream region.

Both machines use the same wafer-handling scheme and much of the same hardware (see fig. 2). Up to four cassettes may be loaded on the cassette shifter, which positions the cassette in use in front of the wafer-handling robot. The robot is a three-axis dc servo, the axes being radial motion, rotation and elevation The robot takes the wafer from the input cassette and then places it on the flat finder station. After orientation the robot moves the wafer to the buffer cassette. All handling is from the back side of the wafer using a vacuum pick

The process of orienting and moving wafers to the buffer cassette takes place while wafers are being exchanged between the load-lock cassette and the disk. If not enough wafers are available to fill the buffer cassette, wafers from the dummy cassette are used

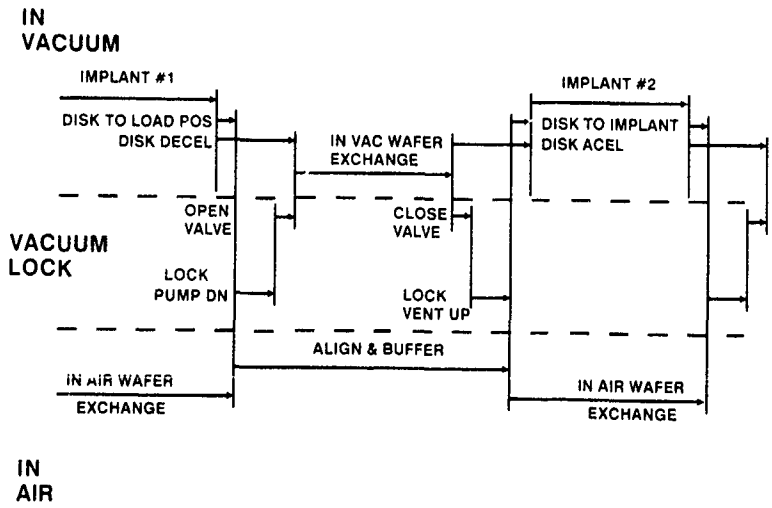

Fig 3 Implant and wafer-handling timing

The vacuum load-lock cassette assembly consists of an elevator cassette within an aluminum housing. This assembly has two axes of servo-motion. One axis is used to retract the cassette into the housing. The other axis is operated to move the assembly to a horizontal position. In this position the housing will line up with the load-lock valve on the process chamber. A short-stroke cylinder then pushes the housing against the load-lock valve chamber, forming a vacuum seal. The load-lock housing can then be evacuated and the load-lock valve opened. After the load-lock valve is opened, the cassette is moved into the load-lock chamber and indexed to align the wafers with the in-vacuum handling arm.

The in-vacuum handling arm moves wafers from the vacuum load-lock cassette to the in-vacuum wafer holder located within the process chamber. It also returns wafers from the disk to the load-lock cassette. The in-vacuum wafer holder positions the wafers on the disk. Parallel operation of the handling arm and wafer holder affect the rapid wafer handling needed to produce the high throughput desired.

The timing of the entire load/implant/unload sequence is shown in fig. 3. For clarity, the drawing is broken into three sections: in-air, vacuum lock and in-vacuum. The implanted wafers in the vacuum cassette are exchanged for new ones while the implant is in progress. Likewise, the robot orients the wafers and places them in the buffer cassette while the in-vacuum exchange is taking place between the vacuum cassette and the disk The orient and buffer process has been designed to be faster than the in-vacuum handling, therefore the implant process is not delayed due to slow in-air handling.

The disk chamber remains under vacuum except during maintenance. This reduces the load on the pumping system and reduces the probability of particles entering the chamber. Also, the load lock can be pumped and vented slowly to avoid moving particles while not adversely affecting throughput Another benefit of keeping the chamber and disk under vacuum is that the potential for run-to-run dose shifts, caused by outgassing of water vapor is reduced. The in-vacuum handling, while sometimes viewed as a potential problem, has been thoroughly tested and the system has been conservatively rated at a wafer breakage rate of 1 : 25 000 and a mishandling rate of 1 : 5 000. We are continuing to test the handling system to improve the handling specification

Several other features have been implemented to help reduce particulates. The disk chamber and load lock all have machined, polished, nonporous surfaces, to reduce the probability of particles adhering. An automatic disk-cleaning system is incorporated into the disk chamber to aid in removing beam-generated or

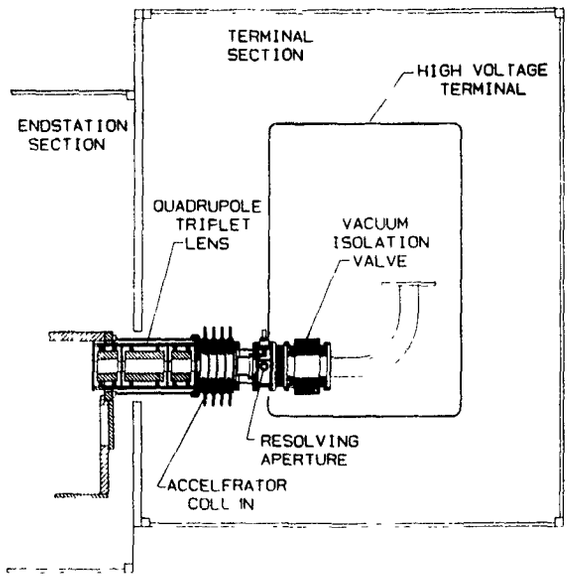

Fig 5 NV-8200GD terminal section.

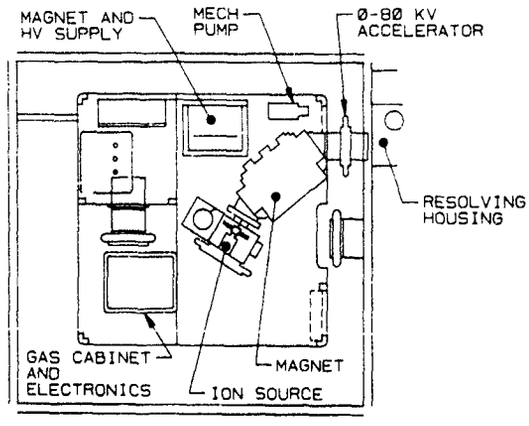

Fig 4 NV-GSD terminal section

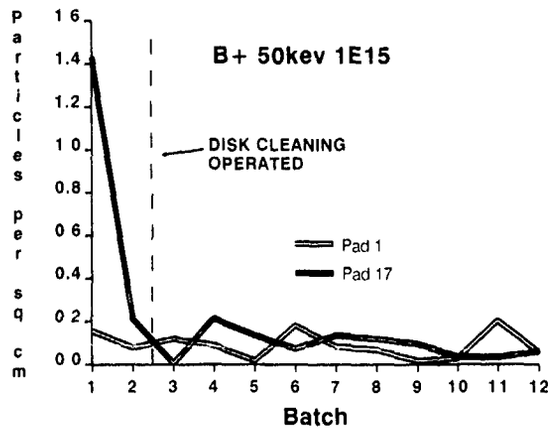

Fig. 6 Particles vs batch.

Table 2
Comparison between the NV-GSD and NV-8200GD terminal sections

	NV-GSD	NV-8200GD
Source type	Enhanced Bernas	Modified Freeman, STD or SKM
Vaporizers	2	1
Gasses	4	4 (1 inert)
Max energy (single charge) [keV]	160 (180 opt)	200
Extraction [kV]	up to 80 (90 opt)	up to 20
Magnet [deg]	70	90
B^+ current [mA]	7	2
P^+ current [mA]	15	3
P^{2+} current	nA	0.4 mA

beam-generated or beam-transported particles This system sequentially vents and roughs the chamber to dislodge and sweep away loose particles.

3 2 Terminal section

The terminal section and beam-line section for these implanters are modified versions of the terminal sections used on the be NV-10 high-current system and the NV-6200A medium-current system.

The NV-GSD terminal section (fig. 4) consists of an enhanced Bernas source with dual vaporizers and an external gas-feed system. The selectable extraction slit and adjustable electrode position allow the source to be optimized for performance across a wide range of energies. The extraction voltage can be varied between 5 and 80 kV. An additional post-analysis accelerator capable of 0–80 kV (90 kV optional) can be added to increase the beam energy up 160 keV (180 keV optional)

The NV-8200GD terminal section (fig. 5) utilizes a modified Freeman source which incorporates a single vaporizer The extraction voltage is typically 20 kV. This, coupled with a post-analysis acceleration of up to 180 kV, can produce energies of up to 200 keV for singly charged species. Several modifications have been made to the terminal section for use in the NV-8200GD system A four-gap accelerator tube is used, which has better low-energy transport than previous designs After acceleration, the beam is focused using an electrostatic triplet quadrupole lens. Table 2 summarizes the differences between the NV-8200GD and NV-GSD terminal sections.

Table 3
Implanter throughput

	100 mm	125 mm	150 mm	200 mm
NV-GSD				
Wafers per hour	247	243	235	215
In-air exchange [s]	140	112	95	67
NV-8200GD				
Wafers per hour	238	228	220	196
In-air exchange [s]	112	84	72	50

4. Performance

This section details some of the performance characteristics of the NV-GSD and NV-8200GD implanters The data are from tests run as part of the performance verification of the design. The use of active cooling and a closed-loop chiller maintains a constant disk temperature during implantation The wafer temperature stays below 100°C for 1.6 kW of incident beam power.

Fig 6 is a demonstration of the effects of opening the process chamber and running the disk-cleaning system. Particle-added counts are displayed for the first and seventeenth wafer pad. The number of counted particles increased dramatically after the chamber had been opened and then fell rapidly after several implants were performed. After the cleaning process, the number of particles fell to a level even lower than before the chamber was opened. The implanter specification calls for 0.1 cm^{-2} at 0.3 μm or larger After disk-cleaning, the ten test implants show an average of 0.088 particles per cm^2 added.

Implant uniformity tests were run under a variety of operating conditions. In all cases the specified uniformity of 0 5% is exceeded.

Wafer throughput for both models and different size wafers are shown in table 3. The throughput rates are based on the mechanical wafer-handling rates and assume that the implant time is equal to the time it takes the in-air handling robot to exchange the wafers in the vacuum cassette. For implants where the implant time exceeds in-air exchange times, the throughput will be less The numbers shown reflect design limits. The specifications are slightly more conservative.

References

[1] A Ray and J. Dykstra, these Proceedings (8th Int Conf on Ion Implantation Technology, Guildford, UK, 1990) Nucl Instr and Meth B55 (1991) 488
[2] B J. Doherty and D J McCarron, Nucl Instr and Meth B37/38 (1989) 559

Nuclear Instruments and Methods in Physics Research B55 (1991) 413–416
North-Holland

Charge neutralisation in the PI9000 series implanters

M.T. Wauk [1], N. White, B. Adibi, M. Current and J. Strain
Applied Materials, Implant Division, Foundry Lane, Horsham, West Sussex, RH13 5PY England

The relationship between ion implantation system parameters, charge indications from a system charge sensor and various wheel current measurements, and the yield of devices have been investigated. It is found that beam balanced-charge conditions, as determined by either charge levels on dielectric films or by wheel current measurements, occur at consistent values of flood gun setting This paper describes the charge control system design, the exploration of several charge measurements to determine effective control variables, and a new closed loop charge control system

1. Introduction

Charge buildup in advanced CMOS devices, especially DRAMs, has become one of the most important and critical factors in ion implantation as the device densities increase. The complex conditions present in the ion beam environment require that we play close attention to the detailed conditions of beam ions and electron transport to the wafer, to ensure that low-energy electrons equalise charge to lower and lower residual charge levels.

2. Charge control system description

The PI9000 system design has been described before [1] The flood gun design employed in the PI9000 consists of a negatively biased tungsten filament heated with dc current to thermionic emission temperature, with a grounded spiral tungsten wire grid surrounding the filament to accelerate the electrons in a normal direction away from the filament.

Electron transport is enhanced by the use of a low background pressure of argon gas. The argon flow is set by means of a mass flow controller. Base vacuum level was maintained below 5.0×10^{-7} mbar. The function of the argon is to:

(a) reduce electron space charge effects, which otherwise severely limit electron current,
(b) provide a weak plasma in the beam/wafer region,
(c) reduce electron energy.

This then provides current at a low bias voltage. The beam size depends on species, energy and beam current; however it is generally as large as 65 mm wide to give low charge buildup in each pass through the ion beam.

The gun is positioned vertically near the horizontal ion beam. There is an aperture separating the gun from the wafers, which serves to reduce the exposure of the wafers to direct line-of-sight electrons and also to reduce the gas load to the target chamber. This design uses the primary electrons directly, rather than the secondary electrons from an intermediate surface, avoiding the repeatability problems of secondary emitting surfaces and the reflected primary energy electrons. The bias voltage is typically in the range of 60 to 90 V to achieve 200 mA Fig. 1 shows the bias voltage versus emission for various argon gas flows Flood gun emis-

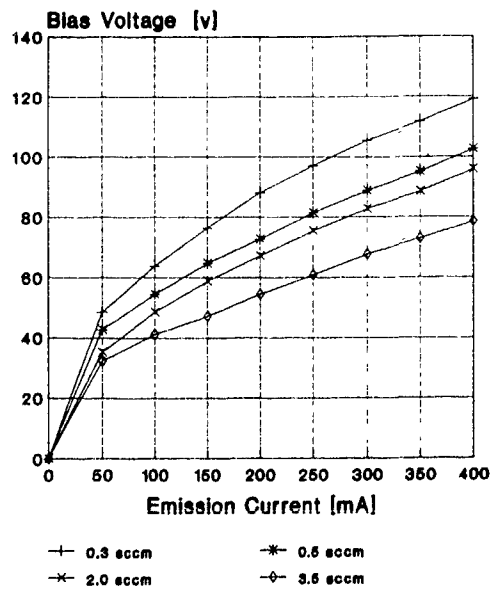

Fig 1 Measured bias voltage versus flood gun emission current, for various values of argon flow

[1] Present address: Applied Materials (Japan), 14-3 Shimizumi, Narita, Chiba 286, Japan.

0168-583X/91/$03.50 © 1991 – Elsevier Science Publishers B V (North-Holland)

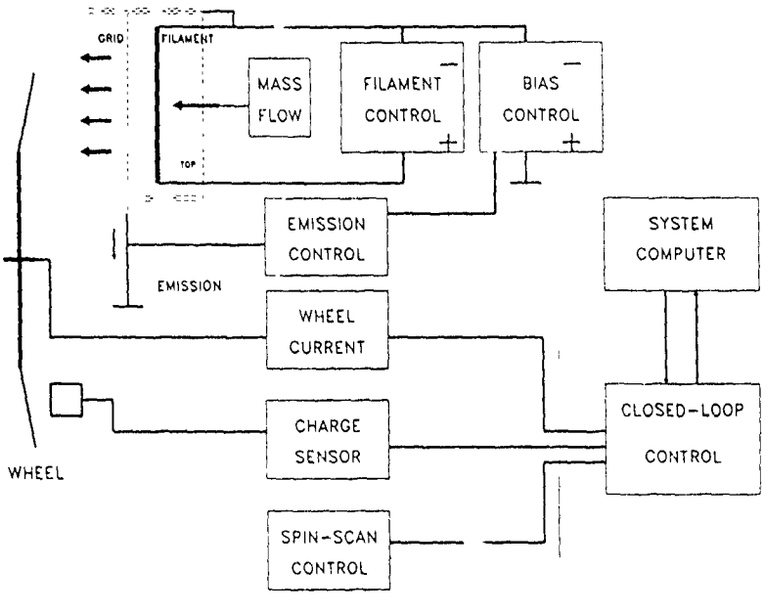

Fig 2. Block diagram of PI9200 charge control system

sion is the current leaving the flood gun body, and is in the range of 0–400 mA. Electron current to the wheel is a fraction of the emission, typically 15–50 mA at an emission of 200 mA, depending on conditions. Although, in principle, the electron energy can be as high as the bias voltage, actually the electrons reaching the wafers have energy much lower than this [2] for two reasons:

(a) the weak plasma in the region of the beam and wafer randomises the electron energies, and
(b) the geometric restrictions of the final beam aperture prevent direct line transport normal to the wafer.

The magnetic field in the region between the flood gun and the wafer is very low to avoid unwanted electron trajectories

Fig. 2 shows a block diagram of the charge control system used in the PI9000. The filament bias voltage is servo controlled by the electronics to produce the emission current requested by the system computer. This servo has a relatively high frequency response, to accommodate any pressure variations during implantation. All parameters are controlled and monitored by the system computer, which also turns the gun emission off briefly at the end of each scan for the beam current (dose) measurement. The interlocks halt the implant in the event of flood gun emission failure

3. Wheel current measurements

Although the spinning wheel in this system is always earthed, it can be electrically isolated for the measurement of total ion and electron current. The wheel is not a solid disk, but is designed to expose only the silicon wafers to the beam, in order to reduce cross-contamination. Consequently, the wheel current signal changes as the wheel is scanned. Values are measured at mid-scan when the wafers are centred on the beam. Fig. 3 shows a typical measurement of wheel current with ion beam, on bare wafers. In principle, this current includes a contribution from secondary electrons produced by ion bombardment of the wafers; however, this is usually less than 10%. The current with beam only is generally within 10–15% of the real ion current.

The wheel current measurement, as well as the charge sensor voltage, provides a measure of implant conditions that can be correlated with the device yield [3]. It

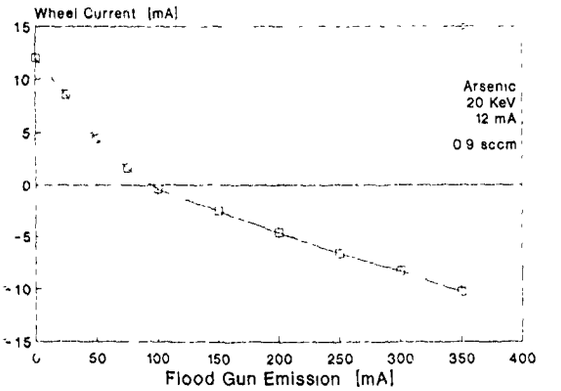

Fig. 3. Total wheel current versus flood gun emission current, with arsenic, 20 keV, 12 mA beam. Wafers are bare, p-type.

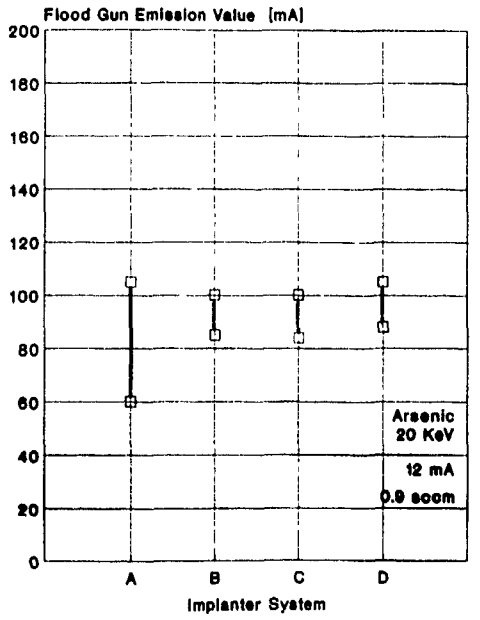

Fig 4 Comparison of several different systems of flood gun emission current for zero wheel current, arsenic, 20 keV, 12 mA.

also is found to give an indication of system overall configuration and performance, and is therefore used as a standard test for system qualification. As seen in fig. 3, the wheel current with beam is zero at an emission value of approximately 90 mA. Fig 4 shows the data for zero crossing emission values for four field systems measured under the same conditions, showing good system-to-system repeatability. Zero current generally occurs at 80–100 mA for a 12 mA beam.

4. Charge sensor measurements

A charge sensor is included in the system to measure charge potential appearing on implanted wafers. This sensor consists of a capacitively-coupled 10 mm diameter disk connected to a shielded operational-amp, the output of which is either viewed on an oscilloscope or sampled in the closed loop control system described below The charge sensor is mounted on the scanning arm supporting the wheel so it always indicates charge in the centre of each wafer As the wheel is scanned, the charge signal is observed. Generally a maximum is observed at mid-scan (wafers centred on the beam) and a minimum is observed near the beam edges Both maximum and minimum signals are plotted in fig. 5. Note that the charge becomes negative over the entire scan above an emission of 50 to 100 mA.

It is found that device damage often occurs when the charge signal maximum is positive. The device yield is generally highest at or above the point of neutral charge or wheel current, which is ranging from 50 to 300 mA [3–5]. This means that high yield for some devices is obtained in regions of significant negative wheel current and negative charge voltage, while others cannot tolerate such overflooding

5. Closed loop charge control system (CLC)

Because of the increasingly thin gate oxides and complexity of modern devices, a flood gun closed loop control system can provide many advantages. The system employed here is designed to:

(1) provide automatic feedback control of flood gun emission to maintain the conditions within selectable limits throughout the implant,
(2) provide system interlocks to detect and render harmless any system faults, and
(3) monitor charging conditions and provide lot tracking data

Fig. 6 shows a block diagram of the closed loop control system. It is designed to accept both wheel current and charge voltage sensors. Both signals are sampled on a particular (recipe selectable) wafer at a particular point during each scan, and this is compared to programmable limits in the recipe, and one of them (recipe selectable) is then used to alter the flood gun emission to give any desired but constant wheel current or charge signal The implant is interlocked subject to

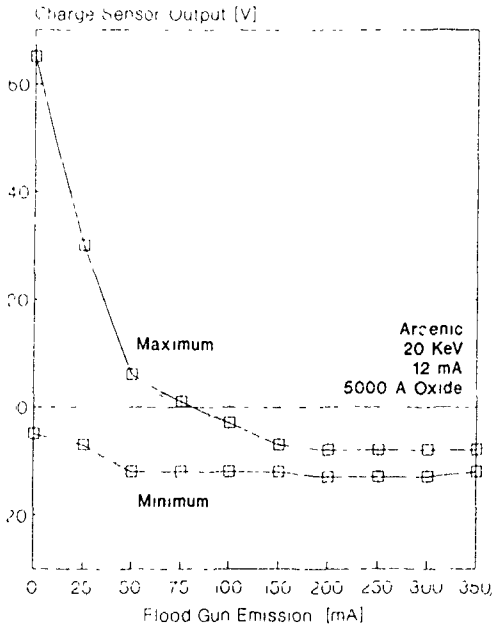

Fig. 5 Charge voltage versus flood gun emission current, measured with system charge sensor, with arsenic, 20 keV, 12 mA beam Wafer is oxidised to 500 nm

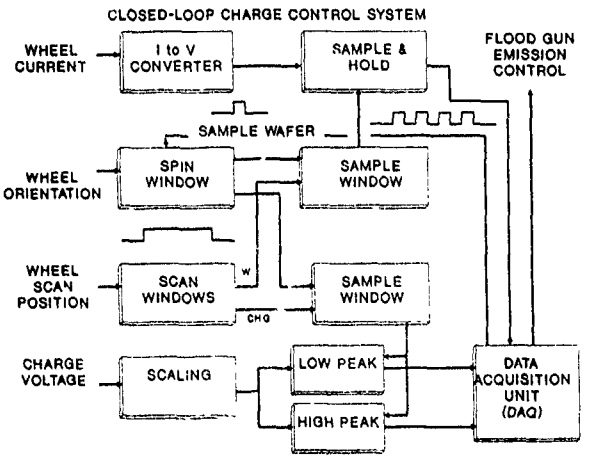

Fig 6. Block diagram of PI9200 closed loop charge control system.

numerous programmable limits on emission, bias voltage, sampled signal, etc. If the flood gun fails at any time, the implant is halted immediately.

It is observed that the implant conditions represented by wheel current or charge signal vary during the course of the implant enough to affect the device yield. This variation occurs in the first few scans due to adsorbed air and water vapour released by the ion beam, and also, with photoresist-coated wafers, due to hydrogen evolution. A closed loop system such as described above can significantly reduce these effects

6. Summary

We have described the design of a system for an effective control of charge buildup in sensitive devices, and shown that both wheel current and charge voltage measurements are effective tools in adjusting and monitoring a system in production. A closed loop control system for automatic feedback control of flood gun emission was also described.

Acknowledgements

There are many people in the Implant Division who have dedicated themselves to this work. The authors wish to acknowledge the efforts of N. Underwood, who designed the flood gun electronics system, T. Renau, who designed the original flood gun, B. Woods, N. Bright, I. Joyce and T. Marin, who designed and developed the closed loop control system, and C. Knowler, who has made most of the system measurements reported here.

References

[1] M.T. Wauk and A.D Giles, Proc 7th Int Conf on Ion Implantation Technology, Kyoto, Japan, 1988, Nucl. Instr. and Meth B37/38 (1989) 442
[2] J A Strain, R. Woodward and N.R. White, these Proceedings (8th Int. Conf. on Ion Implantation Technology, Guildford, UK, 1990) Nucl. Instr. and Meth. B55 (1991) 97
[3] B Adibi and M.T Wauk, presented at the 8th Int. Conf on Ion Implantation Technology, Guildford, UK, 1990
[4] J Alvis, E Nangle and M I. Current, ibid.
[5] J Horvath, S Edel and S Moffatt, ibid , p. 154

Nuclear Instruments and Methods in Physics Research B55 (1991) 417–422
North-Holland

Parallel beam ion implanter: IPX-7000

Y. Mihara, K. Niikura, O. Tsukakoshi and Y. Sakurada
ULVAC Japan Ltd., 2500, Hagisono, Chigasaki, Kanagawa 253, Japan

As the wafer size increases from 6 to 8 in. and device integration develops into 4 and 16 Mbit levels, the ability to provide parallel beam ion implantation becomes more important. The parallel beam ion implanter, IPX-7000, has been developed by ULVAC Japan Ltd. ULVAC's parallel beam scan system has eliminated all mechanical scan drives and has replaced them with electrical scanning by multipole parallel scanner. This paper describes the basic principle of our parallel scanning system and the performance of the IPX-7000.

1. Introduction

Since the first appearance of medium current ion implanters, their basic technology has remained unchanged, but various improvements have been made in the design of endstations for better reliability and throughput and to reduce particle contamination. As the wafer size increases from 6 to 8 in. and device integration develops into 4 and 16 Mbit levels, the conventional beam scanning ion implanter encounters difficulties such as the device asymmetry problem and the shadow effect caused by different beam incident angles between the wafer center and edge.

ULVAC has developed a next generation medium current ion implanter, IPX-7000 series, with parallel beam scan technology and solved these problems. ULVAC's parallel beam scan system uses the unique and complete parallel scan method with electrostatic scanning and it eliminates the mechanical scan drives.

2. System configuration

The IPX-7000 series is a successor of field-proven medium current ion implanters, with a new parallel beam scan system. This means that it has the same configuration as our enhanced medium current implanter, I-7000 series, which features improved maintainability, safety and ease of operation.

Fig. 1 shows the schematic drawing of the IPX-7000 series. It has the same post-acceleration system of the medium current ion implanter, I-7000 series, but includes two sets of multipole electrostatic parallel scanners to create the parallel beam. This system con-

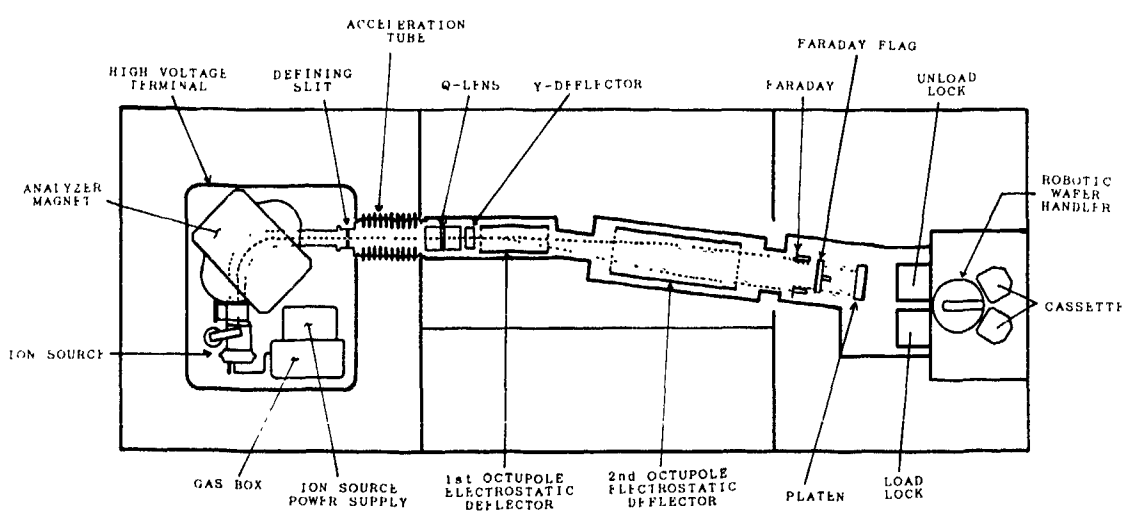

Fig. 1 Schematic drawing of the IPX-7000

0168-583X/91/$03.50 © 1991 – Elsevier Science Publishers B.V. (North-Holland)

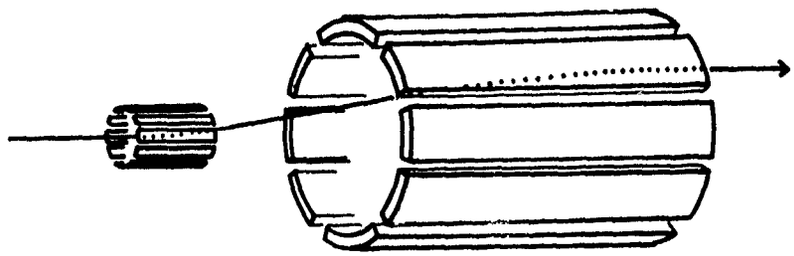

Fig. 2. A parallel scanner.

figuration makes it possible for the implanter to have any type of endstation designed for a conventional medium current ion implanter.

3. Parallel scanner

An orthodox method to perform parallel scanning would be a scanner comprising two sets of parallel-plate deflectors. At a glance, insurmountable difficulties with this parallel-plate deflector system are clear. With a parallel-plate deflector, the available scan region is narrowed due to the disturbance of the electric field at the edge portion. The width of the parallel-plate scanner is necessitated to be at least $2W$ for its gap of W, considering the half-gap disturbance of the electric field uniformity at both edges. The size of the electrode plates of the parallel-plate scanner would then necessarily be at least 50 cm × 100 cm, thus making the system huge. Since the electric capacitance between the electrode and vacuum chamber would be more than 200 pF, this would cause serious difficulties in the design of the precise power supply system. This is because the distortion of triangular waveforms of negative feedback power amplifiers depends on the product FCR, where F is the frequency of the scanning voltage waveform, C is the capacitance of the load and R is the output impedance of the amplifier.

ULVAC has solved these difficulties by employing two octupole electrostatic deflectors of configuration geometrically similar to a parallel scanner. The first octupole deflects the post-accelerated ion beam whereas the second octupole corrects for this deflection of the ion beam making it a parallel beam with a definite direction so that a parallel beam scans over the wafer.

The principle of this "octupole parallel scan" is as follows. Shown in fig. 1, the post-accelerated ion beam is bent about 7° to eliminate neutral particles and is also deflected by the first octupole electrostatic deflector. The second octupole deflects the ion beam in the opposite sense and makes it parallel to the optical axis. The second octupole electrostatic deflector is disposed co-axially along the beam axis at the rear of the first octupole, and the corresponding electrodes of the first and the second octupole deflectors are aligned to each other as shown in fig. 2 (the 7° deflection is not shown in the figure).

The first and the second octupole electrostatic deflectors comprise eight electrodes respectively. Each of the electrodes is electrically connected as shown in fig. 3 and supplied with scanning voltages by eight power sources each of which generates an electrostatic deflecting voltage and constitutes a scanning control system.

The raster scanning component of the parallel scanner is discussed but the 7° deflection is not included in the following discussion. It is assumed, as shown in fig. 4, that the diameter and the length of the first octupole are d_1 (cm) and L_1(cm), respectively, the diameter and the length of the second octupole are d_2(cm) and L_2(cm), respectively, and the distance between the first and the second deflector is L(cm). The

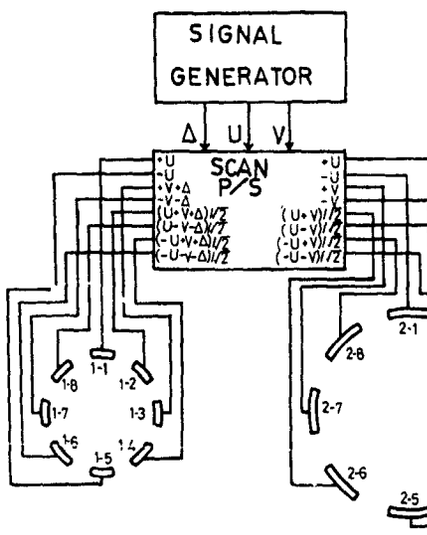

Fig. 3. Circuit diagram of the parallel scanner. Δ: dc offset voltage; U, V: raster scanning voltages.

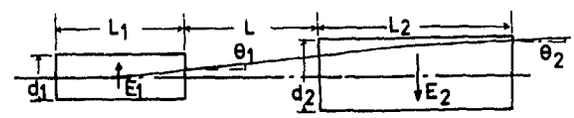

Fig. 4. The parallel octupole scanner configuration.

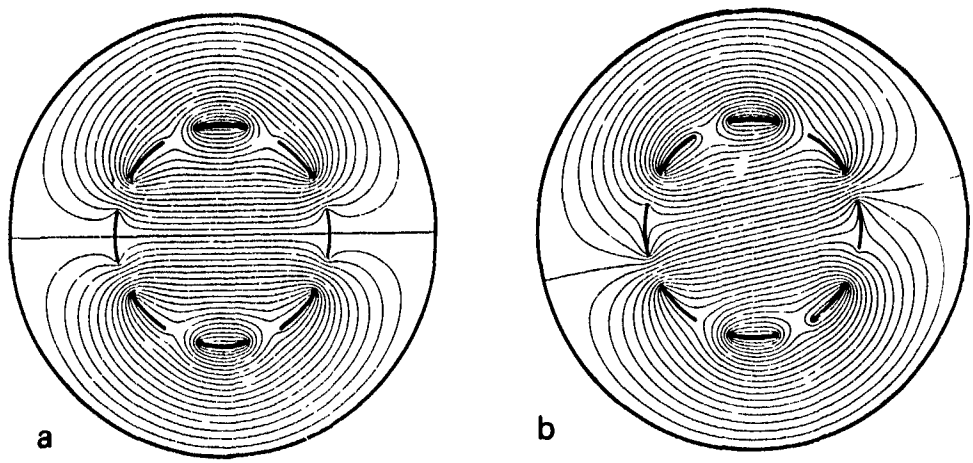

Fig 5 Equipotential lines of the octupole scanner calculated by FEM (a) at 90° deflection, (b) at 102.5° deflection

electric fields in the first and the second deflector at the moment considered are E_1(V/cm) and E_2(V/cm), respectively. The electric fields E_1 and E_2 are assumed as parallel and opposite in direction. The exit angle of θ_1 at the outlet sides of the first octupole is

$$\tan\theta_1 = E_1L_1/2U_0, \quad (1)$$

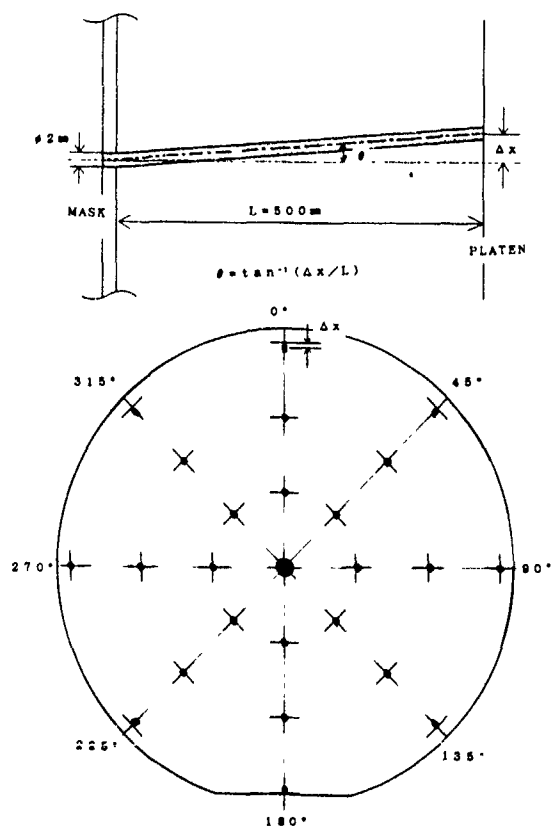

Fig 6. Parallelism measurement.

and θ_2 for the second octupole is

$$\tan\theta_2 = E_1L_1/2U_0 - E_2L_2/2U_0. \quad (2)$$

Here, U_0(eV) is the beam energy at the entrance of the first deflector. In this case, if the relation

$$E_1L_1/2U_0 = E_2L_2/2U_0,$$

namely,

$$E_1L_1 = E_2L_2, \quad (3)$$

is satisfied, it follows that $\tan\theta_2$ is null, and the conditions for the parallel sweeping can be realized. If the first and the second octupole are similar in configuration, and when a voltage U is applied to the electrode (1-1) of the first octupole and to the electrode (2-5) of the second octupole, a voltage V to the electrodes (1-3) and (2-7), and a voltage $(U+V)/\sqrt{2}$ to (1-2) and (2-6), and so on (see fig. 3), the electric fields E_1 and E_2 produced in the first and the second octupole, respectively, are parallel to each other but opposite in direction, and are represented by the following equations:

$$E_1 = k\sqrt{(U^2+V^2)}/d_1,$$

$$E_2 = k\sqrt{(U^2+V^2)}/d_2 \quad (4)$$

As the first and the second deflector are similar in configuration, the following relation is obtained:

$$L_1/d_1 = L_2/d_2. \quad (5)$$

From eq. (4) the following equation is obtained:

$$E_1d_1 = E_2d_2 = k\sqrt{(U^2+V^2)}. \quad (6)$$

From eqs. (5) and (6), the following relation is obtained.

$$E_1L_1 = E_2L_2.$$

Thus the parallel sweeping condition of eq. (2) is satisfied.

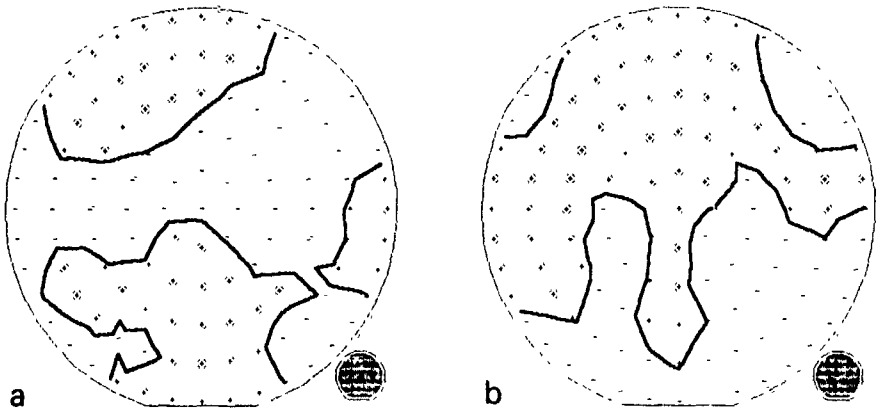

Fig 7. Sheet resistance map of 100 keV $^{31}P^+$, 1×10^{14} ions/cm^2 implant on 150 mm bare silicon wafers at 7° tilt angle (a) Without rotation, $\sigma/\rho_s = 0.455\%$, (b) with rotation (60 rpm), $\sigma/\rho_s = 0.298\%$.

The electrode structure has been optimized by extensive computer simulation. Fig 5 shows computer-simulated equipotential lines in an octupole electrostatic deflector for the deflection directions of 90° and 102.5°. The diagram shown in fig. 5b is the case that the voltages U and V are selected to rotate the electrical field by 12.5° from fig. 5a. The deflection angle of the beam is easily controlled by means of changing the applied voltages of electrodes. For any value of the deflection angle, the octupole electrostatic deflectors can produce a uniform electric field which prevails over a range of 70% of the diameter in the deflection direction

4. Performance results

4.1. Parallelism measurement

The parallelism of the scanned beam on a 6 in wafer was measured by placing a 6 in. mask plate with 2 mm holes at 25 mm space at a distance of 500 mm from the platen as shown in fig 6. The mask plate is set perpendicular to the optical axis, and a white flat paper is placed on the platen holder at 0° implant angle. A 200 μA, 115 keV Ar^+ beam was scanned over the mask plate with the octupole parallel scanner for several minutes to make a brown burned mask pattern on the paper. The parallelism of the beam is measured by comparing the location of burned spots on the paper with the pattern of the mask plate. The maximum deviation from the exact parallelism was 0.2° at the circumference.

4.2. Uniformity

The IPX-7000 has a specification for uniformity of $\sigma/\rho_s < 0.75\%$ whithout wafer rotation and $\sigma/\rho_s < 0.5\%$ with continuous wafer rotation, where σ is the standard deviation of the sheet resistance for one wafer and ρ_s is the average value of the sheet resistance for that wafer A typical example is shown in fig 7 for a 100 keV $^{31}P^+$ beam at a dose of 1×10^{14} ions/cm^2 on a 150 mm bare wafer at 7° implant angle The sheet resistance map was measured after a 900°C$_2$ 30 min anneal with the four-point probe.

4.3 Beam measurement

The beam measurement depends on its endstation type Basically, it is the same as that of the conventional medium current ion implanter There are two methods to measure the dose One is the common way which measures the dose directly by putting the wafer at the end of the electrically isolated Faraday-cup In the other method the dose is monitored by an additional Faraday system in the periphery of the platen. The total

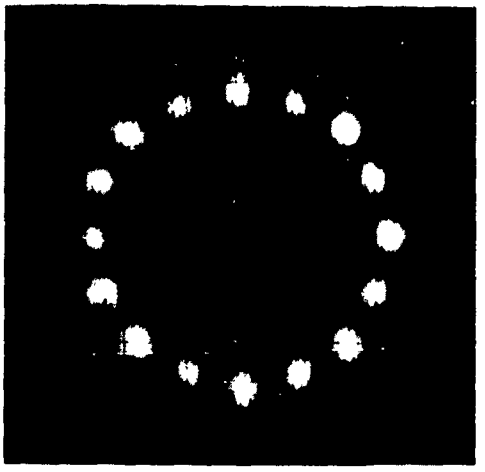

Fig. 8. Parallel monitor.

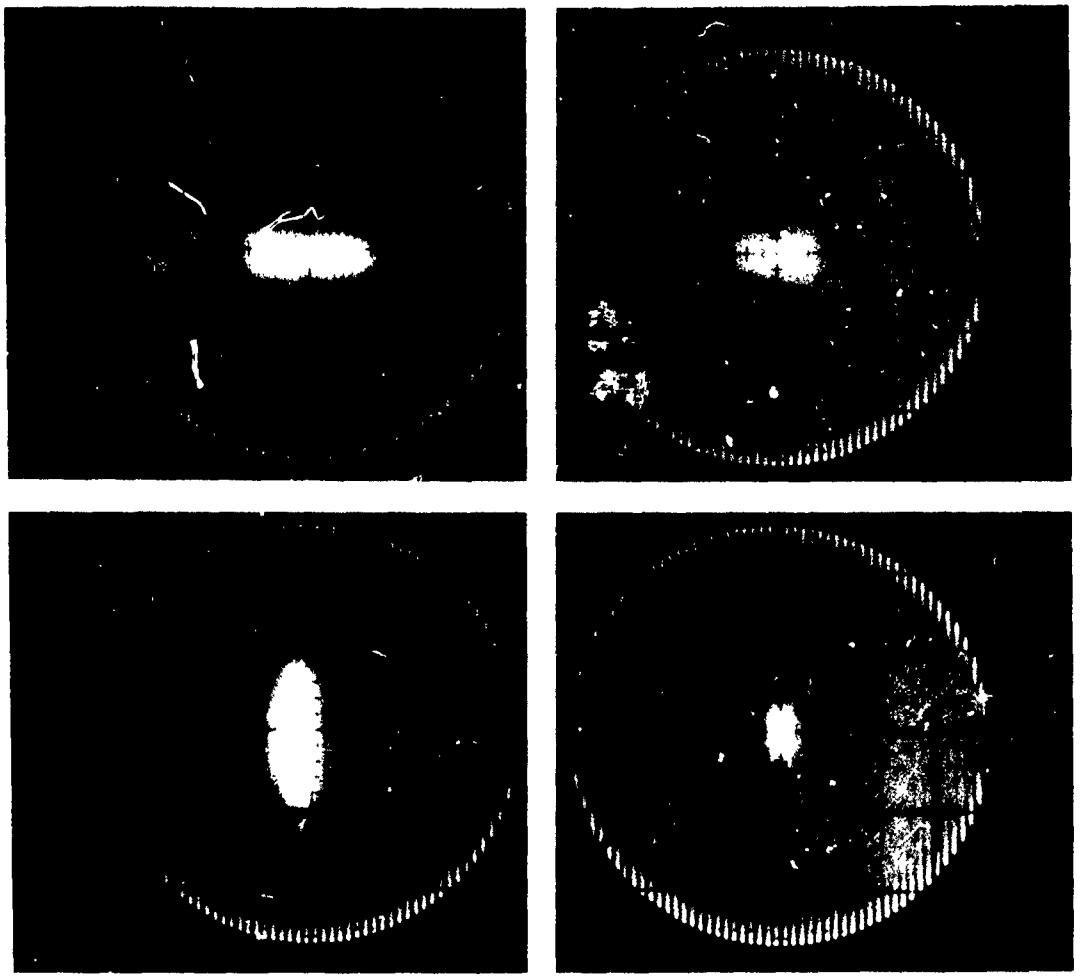

Fig. 9 Beam spot monitor

dose on the wafer is calculated from the accumulated beam current of the additional Faraday system In this case the wafer is located at the ground level potential. In both cases, convenient monitoring is available to check the beam parallelism on the oscilloscope (fig 8). The 16 spots in the picture are the beam spots reaching through doubly aligned 1 mm diameter apertures located around the mask Also, another convenient feature is available to check the shape of the beam spot Fig 9 displays the various shapes of the beam spot when the voltages of the Q-lens are adjusted.

4 4 Particulate

As stated in the system configuration, the end-station of IPX-7000 is the same as that of the other medium current ion implanters which use vacuum locks with cassette-to-cassette loading. The wafers are handled gently with a beltless transfer system in air and with a swing arm mechanism in the vacuum The specification of the particulates is a maximum of 30 particles of 0.3 μm or more on a 6 in. wafer According to the field data, it is around 10 particles of 0 3 μm or more on a 6-in wafer

5. Control system

The machine is operable with the control of a computer with the following features.

(a) The system is fully automated in vacuum sequence, ion source adjustment, beam adjustment and ion implantation

(b) The instrumental conditions can be comprehended at a glance on an easy-to-see monitor display.
(c) Automatic beam adjustment has the capability to optimize the waveform of the beam scan. Besides, a learning function is incorporated for automatically memorizing the parameters necessary for waveform adjustment.
(d) Even a novice can operate the implanter by a convenient interactive entry method.
(e) The data logging function stores the process data required for product and process control.
(f) Maintenance information is offered to facilitate maintenance of the implanter.
(g) Operation is completed just by inputting the recipes.
(h) Communication with the host computer system is available.

Nuclear Instruments and Methods in Physics Research B55 (1991) 423–427
North-Holland

A system and performance overview of the EXTRION 220 medium-current ion implanter

Michael W. Pippins

Varian Ion Implant Systems, Blackburn Industrial Park, Gloucester, MA 01930, USA

The EXTRION 220 was the first parallel scan/200 mm serial medium-current ion implanter introduced to the market (May of 1987) Since 1987, the EXTRION 220 has been utilized in advanced device development and production Performance enhancements developed for advanced applications in the areas of particulate reduction and beam purity are discussed The paper begins with a description of the basic EXTRION 220 design.

1. Introduction

The EXTRION 220 was introduced in May of 1987 as the first parallel scan serial medium-current ion implanter. Since 1987, more than thirty systems have been shipped into development and production applications The basic EXTRION 220 design is reviewed in this paper along with performance enhancements in the areas of particle and energy contamination.

2. A description of the EXTRION 220 medium-current ion implanter

The EXTRION 220 is a serial medium-current ion implanter which utilizes a hybrid scanning system to create a parallel beam capable of uniformly implanting wafers from 100 mm to 200 mm in diameter A parallel beam is electrostatically scanned in the *X*-axis (horizontal) at 1 kHz while the platen is mechanically scanned in the *Y*-axis (vertical) at 0.5 Hz A fixed Faraday is positioned at one side of the moving platen. This Faraday samples the ion beam once every millisecond during the electrostatic scan of the parallel beam. Fig. 1 illustrates this hybrid scanning technique.

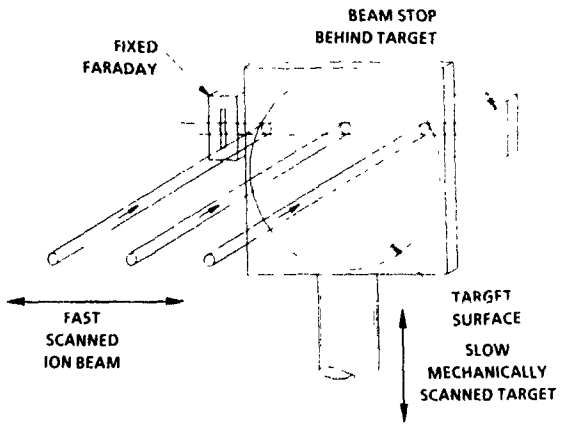

Fig. 1 Schematic of the hybrid scanning method

2.1 Beamline

Fig 2 illustrates the beamline layout for the EXTRION 220 The system utilizes a Freeman ion source to extract the ion beam at variable energies up to 40 keV The beam is mass analyzed with a 100° magnet prior to being focused and scanned.

Conventional medium-current implanters accelerate the ion beam to the final energy between the analyzer magnet and the focusing elements. However, the EXTRION 220 utilizes a post acceleration technique which focuses and scans the beam, at extraction potential, prior to acceleration Because the beam is at extraction potential (low energy), focusing can be performed with a magnetic quadrupole doublet which is external to the beamline. This magnetic quadrupole is highly reliable and eliminates the multiple high-voltage feedthrough of the conventional electrostatic focusing plates Electrostatic scanning is performed in the horizontal axis with a unipolar deflector. A significant gain in low-energy beam current is obtained via the post acceleration technique The beam current specification for 5 keV B^+ is 500 μA, which can be compared to less than 50 μA for some conventional designs.

2.2 Parallel scan

The horizontal scan of the EXTRION 220 is achieved by the combination of an electrostatic deflector and a non-uniform field dipole magnet. This dipole magnet has been designed to convert the angular electrostatic

0168-583X/91/$03.50 © 1991 – Elsevier Science Publishers B V. (North-Holland)

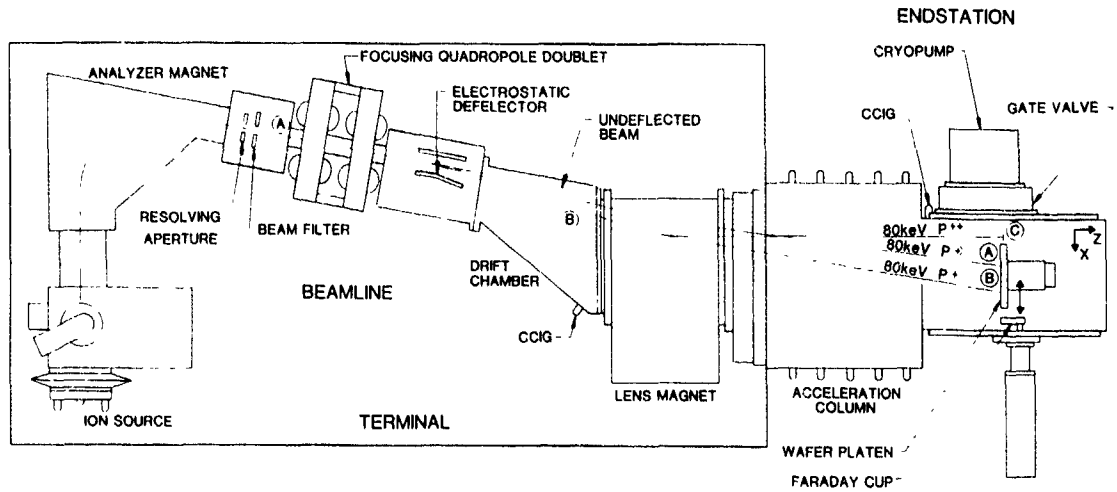

Fig 2 EXTRION 220 beam line layout with ion trajectories ($^{2+}$ beam is labeled C, and $^{+}$ contaminant beams are labeled A and B).

scan into a parallel scan by varying the magnet field. The accuracy of beam parallelism has been measured by utilizing two plates containing identical patterns of vertical slits installed in the EXTRION 220 endstation. The first plate is fixed in the endstation. The second plate, separated by a fixed distance from the first, can be manipulated in the X-axis with a micrometer screw. A beam transmitted through the pair of slits can be measured with a Faraday plate. This test configuration is illustrated in fig. 3. An ion beam can be steered through the slits in the first plate by varying the dc voltage on the electrostatic deflector. The second plate can then be moved to a position which maximizes the beam transmission to the Faraday plate. The parallelism of the beam can be measured as a function of the position of the second plate and the relative movement required to optimize transmission [1].

Measurements have been made for 40 keV As^+ and B^+ using this measurement technique. Fig. 4 illustrates that the beam deviation for B^+ across a 200 mm wafer field is $< 0.4°$, and the deviation for As^+ across a 200 mm water field is $< 0.3°$.

After the beam has been analyzed, focused, scanned and corrected to parallel, it is accelerated up to 200 keV with a large slotted column This column has been designed to maximize the vacuum conductance (the internal dimensions are 16 in. in width and 3 in. in height). This design eliminates many vacuum problems

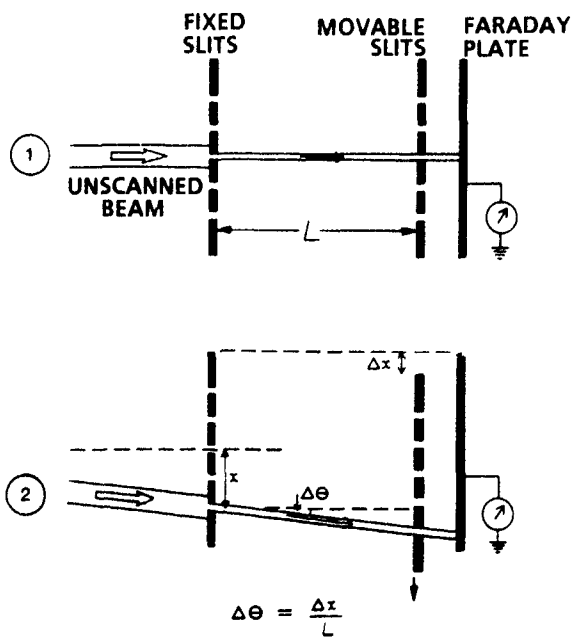

Fig. 3. Method used to measure deviation of beam scan from parallel.

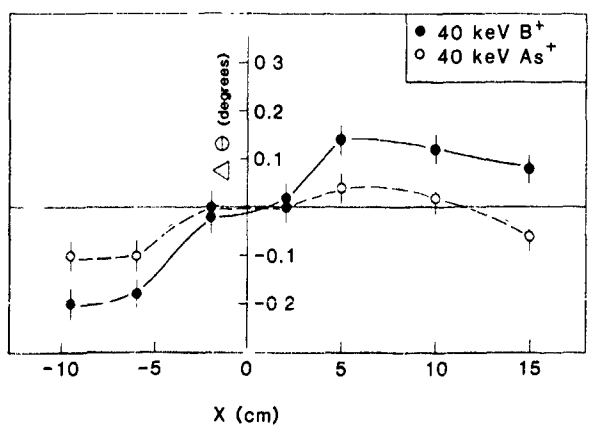

Fig 4. Deviations from parallelism of 40 keV B^+ and As^+.

associated with poor conductance of previous column designs.

2.3 Dosimetry

The dosimetry system of the EXTRION 220 samples the beam every millisecond as the beam is overscanned in the X-axis into a fixed Faraday, see fig. 1. This measurement technique allows the dosimetry system to correct any changes in beam current during implant by varying the scan rate of the electrostatic deflector [2].

2.4 Endstation

The endstation of the EXTRION 220 has been designed to perform all wafer handling in the high vacuum environment. Fig. 5 illustrates the endstation layout. Cassettes are first loaded into the elevator chambers and are pumped to high vacuum with two cryopumps. The elevators function as loadlocks and are the only chambers in the endstation that are routinely vented and pumped down. After the elevators have been pumped down to high vacuum, the isolation valves open and the elevators are exposed to the wafer handler and target chamber.

All wafer handling in the EXTRION 220 is performed with a backside pick-and-place technique, utilizing two wafer handlers which work simultaneously during implant. Linear movement of the wafer handler is used to transport the wafers from the cassettes to the orient/centering station. A rotary motion of the same wafer handler is utilized to precisely place the wafer on the platen after orientation.

The EXTRION 220 utilizes a single platen design which is capable of implant tilt angles from 0 to 90°. The tilt angle is achieved by rotating the platen on a 45° head shaft as illustrated in fig. 6. Once the wafer has rotated to the desired tilt angle, mechanical scanning begins. Wafers can be rotated, in discrete steps, during implant with the rotating platen. The linear movement of the mechanical scan is driven by a linear stepper motor in combination with an air bearing. Vacuum sealing of this air bearing is achieved by means of a series of empty groove differentially pumped stages. This non-contact mechanism is maintenance free and extremely reliable [3].

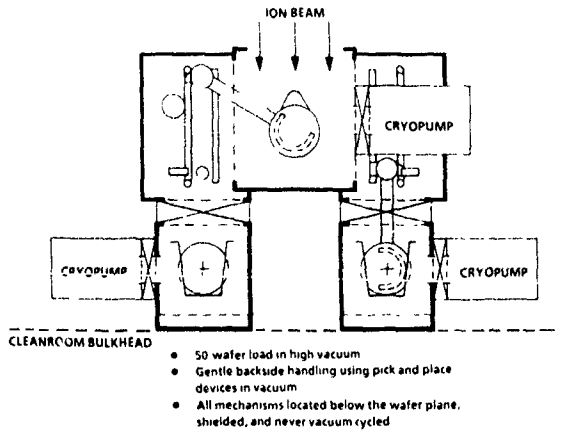

Fig 5 Schematic of the EXTRION 220 endstation.

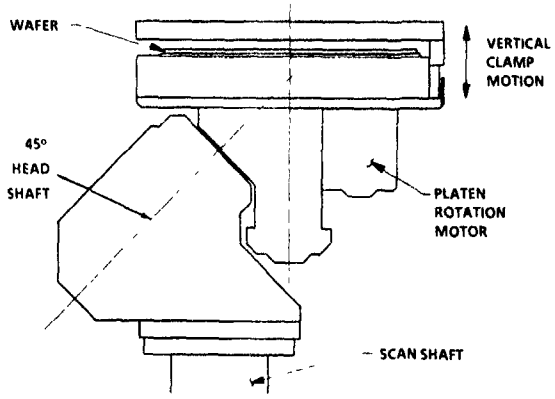

Fig 6 EXTRION 220 rotating platen

3. Contamination

A key technical challenge for ion implanters in the 1990s will be contamination control. As device geometries shrink to levels unimaginable just a few years ago, the impact of contamination in the form of particles, metals and energy will require better control on ion implanters. Varian has implemented development programs in strategic contamination areas in order to satisfy the contamination requirements for present and future applications.

3.1. Particles contamination

Extensive engineering effort has gone into the reduction of particle contamination in conventional medium-current implanters where wafer handling is performed in atmosphere and each wafer was individually pumped and vented [5]. Even though progress was made, it was determined by the EXTRION 220 design team that present and future requirements in the area of particulate control warranted a fundamental concept change. Thus, the EXTRION 220 was designed with high vacuum wafer handling techniques [4].

The basic design philosophy of the EXTRION 220 endstation has been selected as based on the reality that complete elimination of all potential particle sources in the endstation is not economically feasible today. Instead, the EXTRION 220 has been designed to mini-

mize and strategically locate all particle sources in a controlled (high vacuum) environment.

The basic design philosophy of the EXTRION 220 is summarized below:

(1) Two cassettes of wafers will be pumped down and vented as a batch.
(2) All wafer handling will be performed in the high-vacuum environment.
(3) Handling of the wafer will be performed with backside pick-and-place techniques.
(4) All handling mechanisms will operate below the wafer plane.
(5) The handler and process chambers will remain in a high-vacuum environment during normal operation

Extensive particle measurements on the EXTRION 220 indicate that the majority of particles are added during the elevator (or loadlock) vent cycle [4]. Thus, engineering programs have been implemented to improve particulate performance during the vent cycle.

The results of implementing a point of use filter and a polished baffle below the vent port are promising. As fig. 7 illustrates, in a 200 mm production environment which operates 168 hours per week, the average number of 0.3 μm particles (and larger) added during a four-day experiment was 4.6 (0.016 particles per cm^2). There were no unusual cleaning procedures performed during this test, and both bare and resist wafers were implanted. This is well below the EXTRION 220's specification of 0.05 particles per cm^2 at 0.3 μm and larger. While further particle reduction programs are planned to satisfy the coming 0.2 μm requirements, the initial 0.3 μm data verifies the performance of the EXTRION 220 design philosophy.

3.2 Energy contamination

Doubly charged ion beams are utilized in many applications to extend the energy range of implanters. A potential disadvantage of doubly charged beams is energy contamination where the beam contains ions with different energies from the main beam. Energy contamination results in changes in uniformity and dosimetry problems [6].

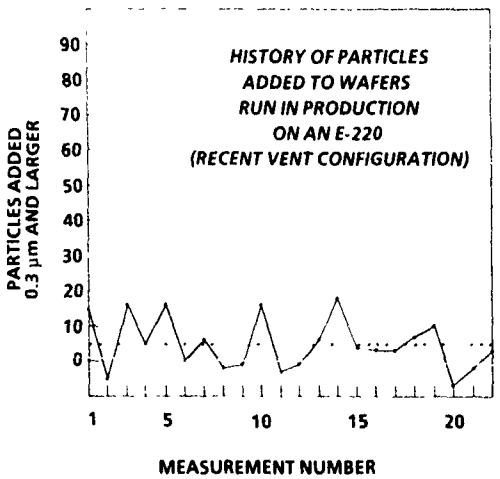

Fig. 7. Particles added on 200 mm wafers in production environment.

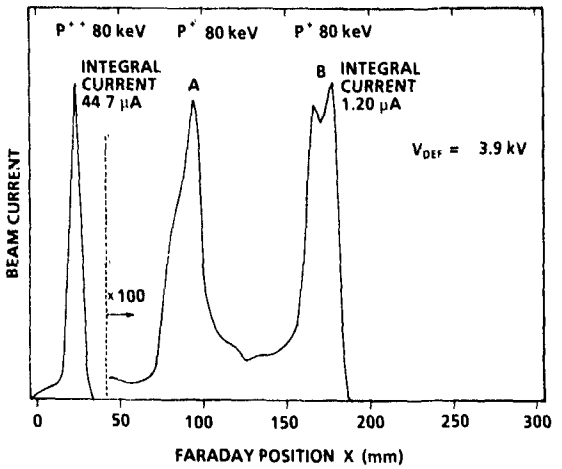

Fig. 8. Beam current measurement as a function of Faraday position. Doubly charged main beam and singly charged contaminant beams A and B are shown

A technique to measure energy contamination, prior to implanting, has been developed on the EXTRION 220. Energy contamination is caused by interaction of residual gas molecules and the ion beam. As fig. 2 illustrates, there are three sections in the EXTRION 220 beam line where charge exchange occurs (A, B, and C). The contaminant beams, that are created in these areas, have a higher magnetic stiffness than the main beam [7]. Thus, the contaminant beams will be deflected less than the main beam in the dipole magnet as fig. 8 illustrates.

The fixed Faraday can be translated across the X-axis of the end station to measure both the doubly charged and the singly charged contaminate ion beams. The relative amount of energy contamination (EC) as a percentage of particles can be calculated with the following formula [7]

$$EC = \frac{I^+}{(I^{2+} - I^+)/2} \times (100\%) \qquad (1)$$

Thus, the EXTRION 220 can measure energy contamination (on-line) prior to implantation. Energy contamination has been measured at less than 2% (by particle with vaporizer source) on the EXTRION 220 with this technique [7]. This technique will be integrated into a future version of the standard EXTRION 220 software

4. Summary

The EXTRION 220 was the first parallel scan serial medium-current implanter on the market. With more

than thirty systems in the field, many in advanced development, extensive application experience has been obtained. Experience in advanced applications has driven application and performance enhancements in the areas of particle and energy contamination.

References

[1] R E Kaim and P.F.H.M van der Meulen, these Proceedings (8th Int. Conf. on Ion Implantation Technology, Guildford, UK, 1990) Nucl Instr. and Meth B55 (1991) 453.

[2] D.W Berrian, R E. Kaim and J.W. Vanderpot, Proc. 7th Int. Conf on Implantation Technology, Kyoto, Japan, 1988, Nucl. Instr. and Meth. B37/38 (1989) 518.

[3] J D. Pollock, R.W. Milgate, R.F. McRay and R.E. Kaim, Proc. 7th Conf. on Ion Implantation Technology, Kyoto, Japan, 1988, Nucl. Instr. and Meth B37/38 (1989) 576.

[4] R. Milgate and J. Pollock, these Proceedings (8th Conf. on Ion Implantation Technology, Guildford, UK, 1990) Nucl Instr. and Meth. B55 (1981) 66

[5] R. Milgate and R. Simonton, Nucl. Instr. and Meth B21 (1987) 383.

[6] R. Simonton, M. King and D.E. Kamenitia, Nucl Instr. and Meth. B37/38 (1989) 616

[7] P.F H.M. van der Meulen, S. Mehta and R.E Kaim, these Proceedings (8th Conf. on Ion Implantation Technology, Guildford, UK, 1990) Nucl. Instr. and Meth. B55 (1991) 45

Nuclear Instruments and Methods in Physics Research B55 (1991) 428–433
North-Holland

Advances in the Extrion 1000 and XP Series high-current ion implantation systems

M. Harris

Varian Ion Implant Systems, Gloucester, Massachusetts 01930, USA

During the past decade, ion implantation systems have evolved from labor-intense, novel machines in the manufacturing environment to automatic, highly productive manufacturing tools. Performance advances have been made in several areas: wafer charging, high-energy operation, BF_2^+ dissociation, reliability and automation of the machine and information transfer to the host computer. The changes and improvements in these areas are discussed for the Varian High Current XP Series and the EXTRION 1000 ion implantation systems

1. High Current XP Series

The High Current XP Series of implanters has four models differentiated by maximum energy: 80XP, 120XP, 160XP, and 180XP. The four models are basically similar, with small differences to produce the different energy levels. Beam generation begins with a standard hot-filament ion source which, coupled with preanalysis acceleration, produces 10 mA of arsenic and phosphorus beam current and 5 mA of boron beam current. The beam scanning is a hybrid type which magnetically moves the beam in the horizontal plane at the slow scan speed and mechanically moves the wafer in the vertical plane at the fast scan speed. A neutral trap is a unique feature of the scanning system and helps ensure high-purity beams. A Faraday system, described by Outcault et al. [1], provides dose and uniformity control as well as an effective environment for wafer charge neutralization. The versatile Robotic Loading System (RLS-200), a second-generation wafer handling system, safely delivers the wafer to the disc using simple motions and positive wafer positioning.

The High Current XP Series evolved over several years from the "Ten" Series as Varian supported over 420 systems in the production environment. Advances in techniques, technology, and designs continue to be made by the Varian engineers. Four areas of advancement will be described here: wafer charging, ion source lifetime, 180 keV operation, and Auto Sequence software.

1.1 Wafer charging

The evolution of wafer charge control in the High Current XP Series is well documented in other papers [2,3]. These papers describe the use of a hot filament with an extraction grid assembly to focus and extract a large quantity of primary electrons. The primary electrons impact the aluminum Faraday wall producing copious quantities of low-energy, secondary electrons. These secondary electrons then neutralize the charges on the wafer surface, both directly and by neutralizing the beam. This system used a constant primary emission current which was empirically determined for each device type. While successful at improving yields, this design did not automatically respond to variations in device wafers due to photoresist and oxides. Also, changing machine parameters such as system pressure and beam spot size were not totally accounted for with a constant emission current.

The latest advance by Varian engineers is the Auto Emission Flood system for the High Current XP Series. The core of this newest flood system is the "closed-loop" control of the primary emission current (fig. 1) in response to changing conditions on the wafer surface. The primary emission current is regulated to balance the net current flow to the disc. A process engineer can set the net disc current to 0 mA and the primary emission current will be increased or decreased automatically to keep the net disc current nulled. The net disc current can be set for each device type, but this is usually within the window of -2 to $+1$ mA.

A *Q*-Monitor for wafer charge sensing is also available on the High Current XP Series. This feature allows the process engineer to establish an understanding of the wafer charge level during the implant. A capacitive sensor picks up the charge on the wafer surface as it rotates by on the disc. The charge is fed out of the end station chamber, amplified and displayed on a storage oscilloscope. Calibration of the *Q*-Monitor with a fixed, known voltage allows the user to determine the relative charge developed by the beam on the device wafer. A more detailed discussion of the wafer charging system can be found in Mehta et al. [4].

0168-583X/91/$03.50 © 1991 – Elsevier Science Publishers B.V. (North-Holland)

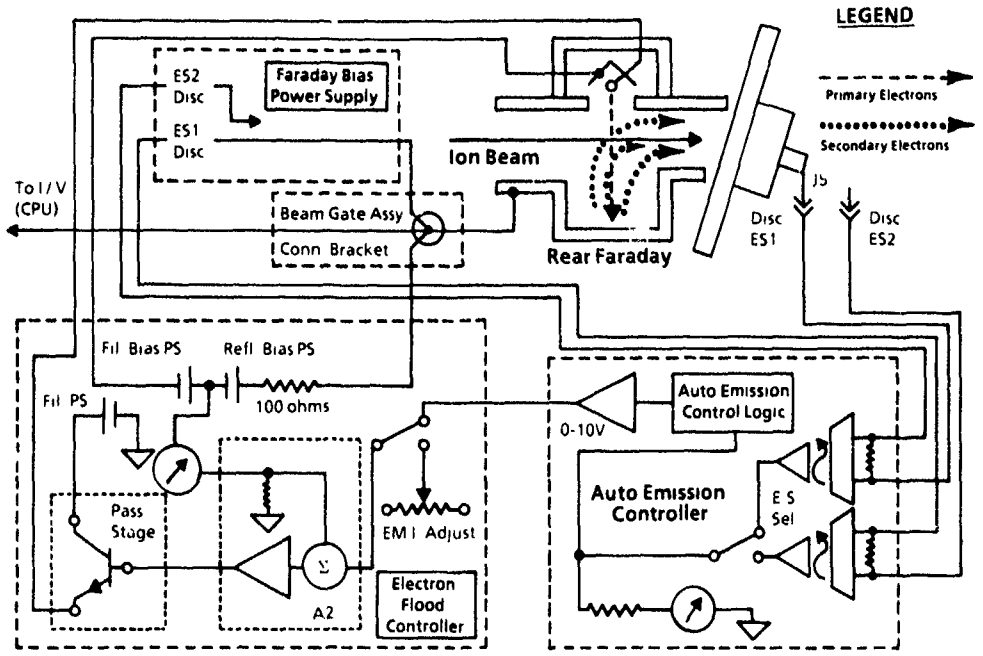

Fig. 1. Auto emission flood control schematic

1.2 180 keV operation

The High Current XP Series of implanters has been extended to include a model with a top energy of 180 keV. The design changes to the 160XP were straight-forward and included the Shikoku high-voltage power supply, corona rings on the acceleration column, and a stainless-steel gas box with 4 in. radii. In the 161–180 keV energy range, the beam specifications are 5 mA of arsenic and phosphorus, and 2 mA of boron The extra energy capability allows process engineers more flexibility in assigning implants to the High Current XP Series.

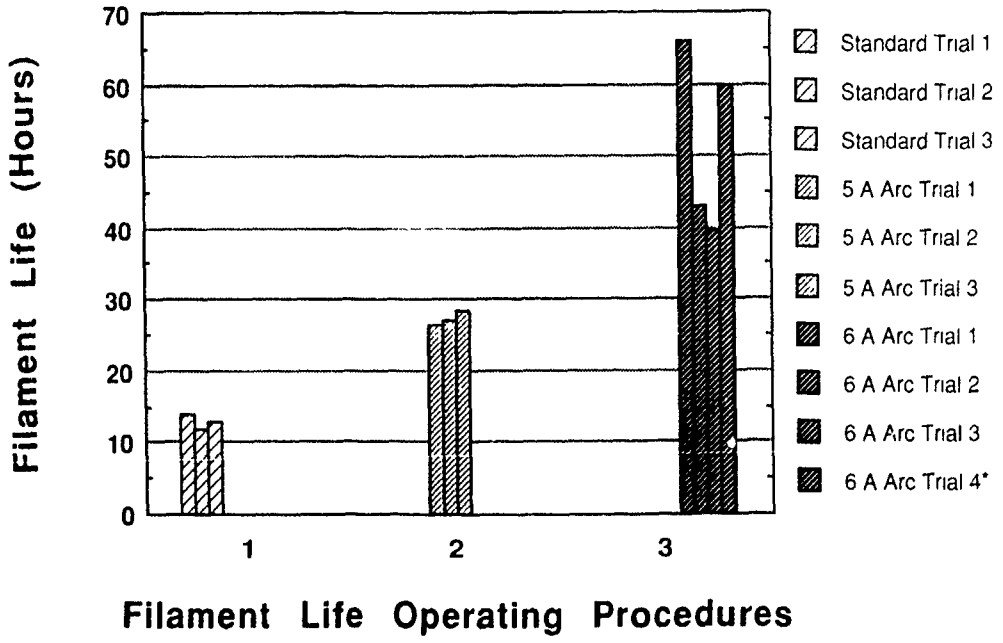

Fig 2 Source life results for testing with a 5 mA B^+ ion beam.

1.3. Ion source lifetime

The ion source lifetime of the High Current XP Series implanter has been improved by a factor of 2 for standard high-current operation and by a factor of 4 for a nonstandard hardware configuration. The nonstandard hardware increased lifetime from a standard of 12–14 h to an average of 55 h for a boron, 5 mA beam current at 100 keV. The limited filament lifetime of the Freeman source is due to the high plasma densities near the filament. In order to improve the filament lifetime, either the plasma density must be reduced, or the sputtering rate per plasma ion striking the filament must be reduced. By reducing the arc voltage of the discharge, the sputtering coefficient for incoming ions can also be reduced. Calculations showed that a change of ion energy in a BF_3 discharge from 120 to 60 V results in a tenfold reduction in the sputtering rate. Fig. 2 is a graph illustrating the improvements in source lifetime. For a complete description of this work, refer to Walther and Outcault [5].

1.4. Auto Sequence

Auto Sequence is a software program that automatically ties in the end station selection and wafer exchange procedures with implanting, making the machine capable of complete "hands-off" operation. Once Auto Sequence is engaged, the only human intervention required is the replacement of wafer cassettes. Auto Sequence is engaged by depressing one or both of the "load" buttons on the operator control panel. Once engaged, the implanter begins to process wafers from initial loading to implant and on through wafer exchange until all available wafers are processed. As long as wafers are supplied to the loading system, the process continues. The user has the option of choosing automatic or manual beam setup, and automatic or manual implant start.

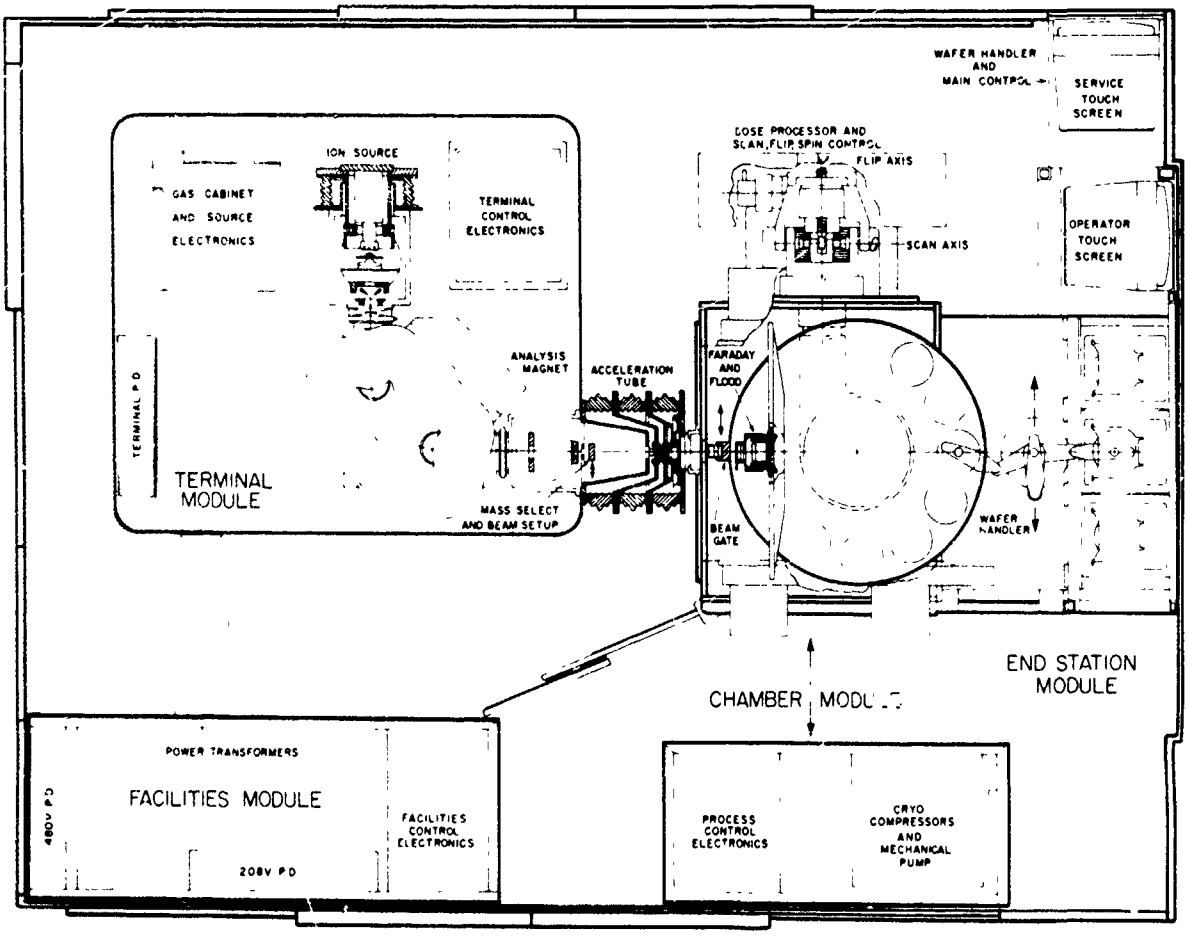

Fig. 3. Extrion 1000 layout.

2. Extrion 1000

The Extrion 1000 is a new batch ion implantation system utilizing post-analysis acceleration, load-locked, horizontal, wafer handling, and dual mechanical scanning. Special features and an advanced control system allow for real-time process control, adaptive control techniques, and extensive built-in diagnostic and failure prevention capability. Process flexibility is attained through control over wafer orientation (0°–360°), adjustable implant angle (0°–10°) without breaking vacuum, wide energy range (2–200 keV), and easy wafer size change. High beam current capability and an efficient wafer handler result in production throughput of 180 wafers per hour at low dose, and usable high dose throughput at doses over 10^{16}. Designs for minimum parts count, extensive use of modular systems, software self-analysis, adaptive control techniques, conservative component rating, and life testing were used to make for a reliable and maintainable system [6].

The Extrion 1000 was designed to meet the several challenging requirements from the ever changing semiconductor processes (fig. 3). The ion source is a cusp-type design to optimize dopant species output with good lifetime. A triple crucible vaporizer uses commercially available halogen lamps to heat the three crucibles. The beam is extracted using a 60 keV potential. Immediately following the extraction electrode, a remotely controlled variable slit can throttle the beam for stable and reliable production of a very low beam current. Mass analysis is performed in a 90° magnet which is pumped by a Varian VHS 250 diffusion pump at the source and a 1000 l/s turbomolecular pump mounted at the mass selection slit preceding the acceleration tube. The acceleration tube is a high-conductance design with integral strong focussing. This is especially useful in controlling low energy transport at high beam currents [7].

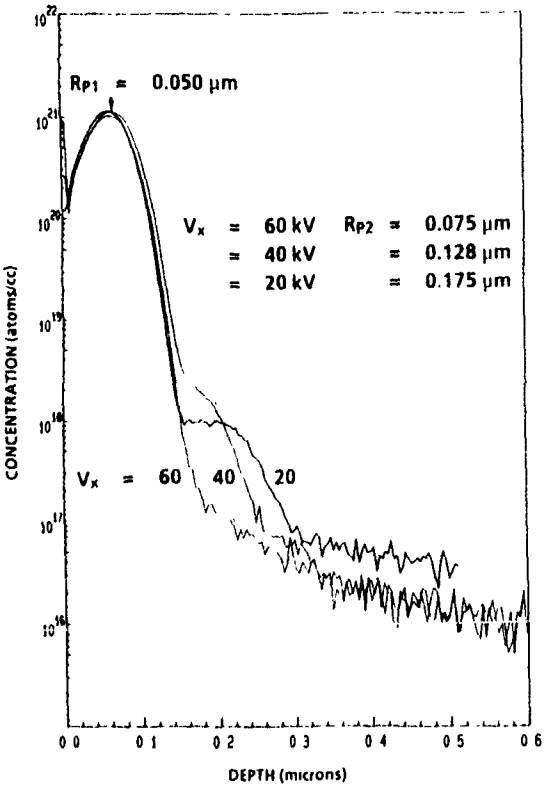

Fig 4. The effect of extraction energy on BF_2^+, 5×10^{15}, 70 keV implants.

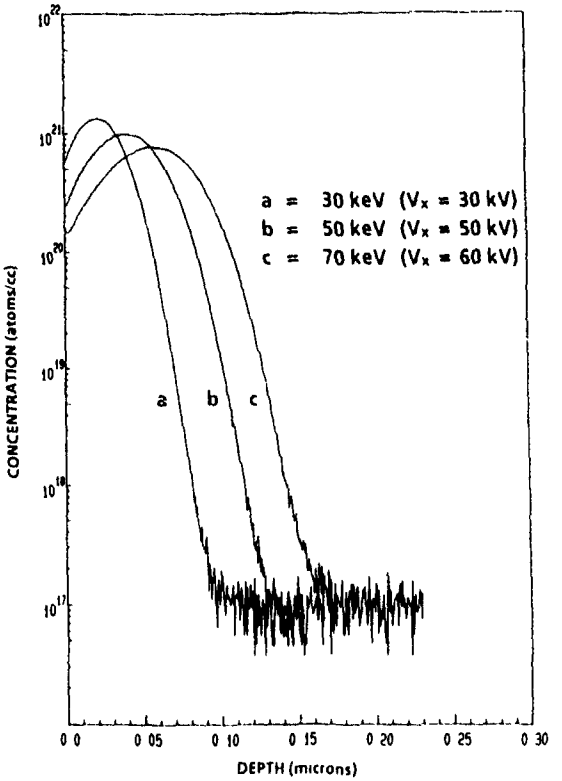

Fig. 5. BF_2^+, 5×10^{15} implants with the extraction energy equal to the implant energy or at maximum extraction energy.

The dosimetry system features real-time dose control. A Faraday system mounted in front of the wafers is used to collect beam current and secondary electrons while retaining the electron flood wafer neutralization electrons. Extensive pumping in the process chamber minimizes neutral production, and a combination of dual bias electrodes and a magnetic barrier assures good performance under photoresist outgassing conditions [8].

The Extrion 1000 end station utilizes three independently operated vacuum load locks to introduce semi-standard plastic cassettes into the vacuum exchange end

station. The load locks also serve as elevators to permit wafer picking in the horizontal plane. Wafers are placed onto a horizontal disc via a two-pivot robotic arm. Before the transfer to the disc takes place, corrections are made for orientation and centering. Once a full batch of wafers is exchanged, the disc rotates up to the vertical position for implant. High-speed scanning is accomplished by disc rotation at 1200 rpm. Slow scan speed is done by rotating the scan arm about a remote pivot point located in atmosphere. The end station maintains slot-to-slot and cassette-to-cassette integrity [9].

2.1. Control of BF_2 dissociation

Over the last several years, BF_2^+ ions have been commonly used in the formation of shallow P-type ion implanted layers. The earliest applications of BF_2^+ were driven by the higher beam currents available for BF_2^+ versus those achievable for the equivalent energy B^+ implant which is 11/49 of that required for BF_2^+. As time progressed, commercially available ion implanters started to provide increasingly higher beam currents of low-energy boron, but the demand for BF_2^+ implants remained high and it now appears that BF_2^+ will continue to be the species of choice in the fabrication of shallow P^+ junctions or the next generation of devices.

The literature cites several possible reasons for the continued popularity of BF_2^+, however, there also have been disadvantages to using BF_2^+. The major disadvantage has been associated with the structure in the boron profile as seen by SIMS, which extends the depth of the implant far beyond the desired value, compromising the integrity of a shallow junction. The Extrion 1000 uses an extraction energy of 60 keV to avoid this problem. Fig. 4 dramatically illustrates the effect of the extraction voltage on the boron profile. As the extraction energy is decreased, an energy contaminant is observed at increasingly larger depths. As can be observed, an extraction energy of 60 keV provides a clean profile and therefore a good junction for shallow implant devices.

Another approach to solving this problem is to do the implants with the extraction energy equal to the

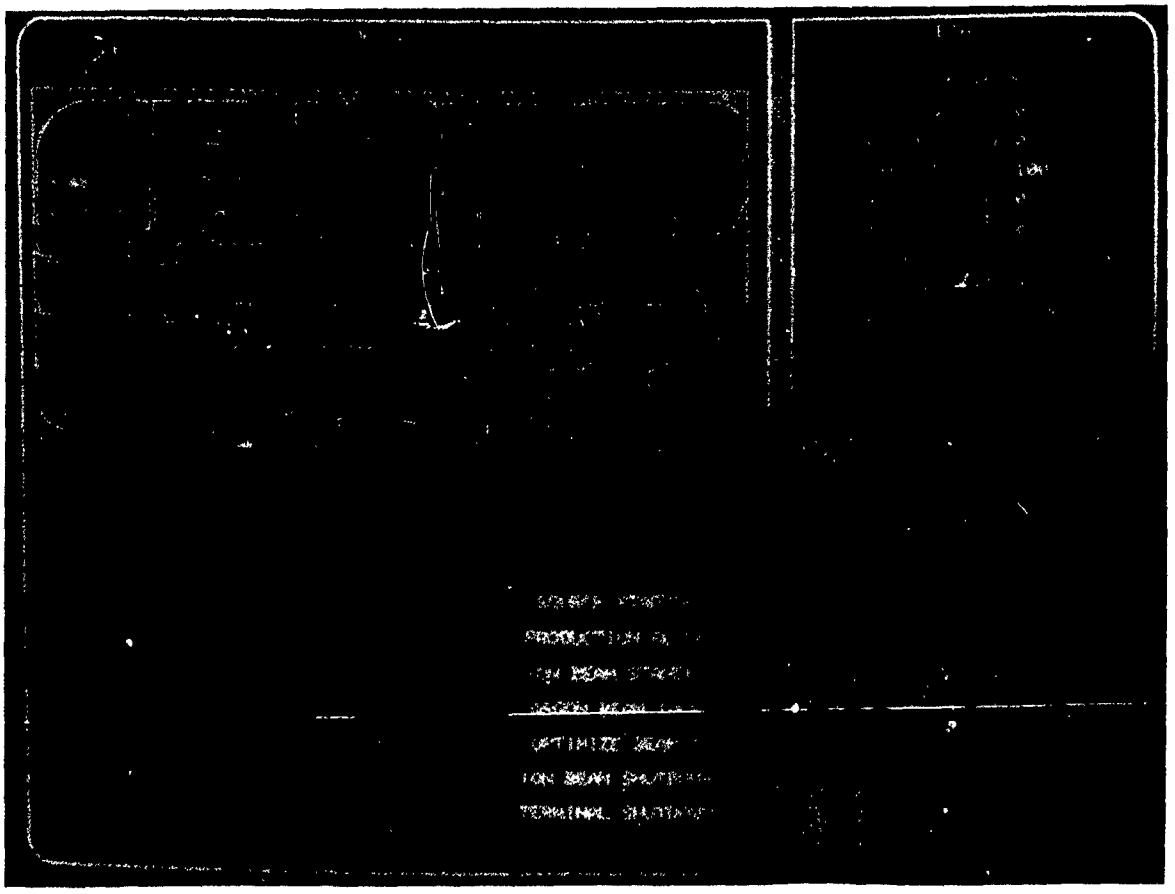

Fig. 6. Automatic ion beam control screen.

Table 1
Extrion 1000 low-dose uniformity data using thermal-wave measurements; oxide thickness 250 Å, implant angle 7°, orientation: flats to outside of disc

Run no.	Ion	Energy [keV]	Dose	Current [μA]	Thermal wave (av.)	T.W. (σ (%))
1	B^+	60	2.5×10^{11}	1.5	239.5	0 21
					238.7	0.18
2	B^+	60	2.5×10^{11}	1.5	240.1	0 19
					235.8	0 18
3	B^+	60	2.5×10^{11}	1.5	234.2	0 18
					232.0	0.32
4	B^+	60	2.5×10^{11}	1.5	239 2	0.19
					243.6	0.18
5	B^+	60	2.5×10^{11}	1.5	239.8	0.14
					241.5	0.17

implant energy (drift mode or single-stage acceleration) or with the extraction energy as large as possible. Fig. 5 contains examples of SIMS profiles from 30, 50, and 70 keV BF_2 implants using extraction energies of 30, 50, and 60 keV respectively. The profiles are clean with no discernible energy contaminant peaks. For an in-depth discussion of this subject see Downey and Liebert [10].

2.2. Automation

The Extrion 1000 has four levels of software control: manual, automatic, one button, and lights out. The three basic screens needed to operate the implanter are the ion beam tuning screen, the wafer handling screen, and the process control screen. In the manual software level, the operator has detailed control over the operation of the machine. The operator can adjust arc voltage and arc current as well as load wafers from a chosen cassette to selected locations on the disc. In the automatic software level (fig. 6), the operator has control of higher-level beam functions like source startup, production setup, and ion beam shutdown. Wafer handling in the automatic level consists of auto wafer exchange or starting the scheduler program. The scheduler program is a supervisory program which controls movement of wafers through these steps: roughing of the load lock, initialization of the cassette, loading the wafers on the disc, implanting the wafers, unloading the wafers into the original cassette and slot, and venting the load lock. The one button and lights out software levels are complete, but depend on user host computer inputs to become operational.

2.3. Universal implanter

The Extrion 1000 was primarily designed as a high-current implanter, however, provisions were made for providing a large dynamic range to be compatible with low implant doses. The variable slit in the source area and a tight Faraday design allow low-dose implants to be performed within process control windows. Table 1 shows data from boron, 2.5×10^{11}, 60 keV, implants with excellent uniformities of 0.14–0.32% as measured by thermal-wave techniques.

3. Conclusion

Performance advances have been discussed for the High Current XP Series implanters and the Extrion 1000 implanter. These advances will keep the implanters capable of meeting the most stringent requirements of today's semiconductor processing needs.

References

[1] R Outcault, C. McKenna, T Robertson and L. Biondo, Proc. 6th Int. Conf. on Ion Implantation, 1986, Varian SEG Report No. 116 (1986) p 5–8
[2] S. Felch, B Basra and C McKenna, Microelectronic Manufacturing and Testing, Varian SEG Report No. 153
[3] C. McKenna, B. Pedersen, J.K Lee, R. Outcault and S Kikuchi, Proc 7th Int Conf on Ion Implantation, 1988, Varian SEG Report No 165 (1988) p 492
[4] S Mehta, R. Outcault, C. McKenna and A. Heinonen, these Proceedings (8th Int. Conf on Ion Implantation Technology, Guildford, UK, 1990) Nucl Instr and Meth. B55 (1991) 457.
[5] S Walther and R. Outcault, these Proceedings (8th Int. Conf. on Ion Implantation Technology, Guildford, UK, 1990) Nucl. Instr and Meth B55 (1991) 465.
[6] R. Liebert, S Satoh, A. Delforge and E Evans, Proc. 7th Int Conf. on Ion Implantation Technology, 1988, Varian SEG Report No. 169 (1988) p. 464.
[7] S. Satoh, T Sakase, E. Evans and R Liebert, Proc 7th Int. Conf. on Ion Implantation Technology, 1988, Varian SEG Report No 161 (1988) p. 612.
[8] R. Liebert, S. Satoh, A. Delforge and E. Evans, Nucl. Instr. and Meth. B37/38 (1989) 464.
[9] R. Hertel, A Freytsis, E. Mears and A. Delforge, Proc. 7th Int. Conf on Ion Implantation Technology, 1988, Varian SEG Report No. 159 (1988) p 580.
[10] D. Downey and R. Liebert, these Proceedings (8th Int. Conf on Ion Implantation Technology, Guildford, UK, 1990) Nucl Instr. and Meth. B55 (1991) 49

Nuclear Instruments and Methods in Physics Research B55 (1991) 434–438
North-Holland

The beam performance of the Genus G-1500 ion implanter

N. Tokoro, J.P. O'Connor, A. Renau and M.E. Mack

Genus Incorporated, Ion Technology Division, 4 Mulliken Way, Newburyport, MA 01950, USA

The current ion beam performance of the Genus G-1500 MeV ion implanter is described in this paper. Substantial improvements of beam currents have been realized by modification of the hot-cathode PIG source used on the ion implanter. Approximately 250 μA of $^{11}B^-$ and 1100 μA of $^{31}P^-$ are routinely achieved at the injector Faraday cup of the G-1500 system. Typical maximum beam currents of boron and phosphorus on target are ~110 μA and ~350 μA, respectively. Recent results of acceleration of carbon, oxygen and silicon are also described. Finally, the result of unique neutral-hydrogen-molecule injection into the tandem accelerator to obtain H^+ on the target is given in this paper.

1. Introduction

The high-energy ion implantation process has become increasingly important as one of the key technologies in the fabrication of most advanced VLSI [1]. Since the first shipment of the G-1500 MeV ion implanter in early 1988, it has been widely accepted as a production machine for low- and medium-dose applications at energy ranges from 40 to 3000 keV. Moreover, Genus has made a continuous effort to improve beam current output and stability, as well as source lifetime, to further enhance the utility of the G-1500 MeV ion implanter in a production environment.

The results which are given in this paper have been obtained as a result of this effort

2. The modification of the ion source

In fig. 1, the hot-cathode PIG source used on the G-1500 MeV ion implanter is shown with the vaporizer assembly. This hot-cathode PIG source has a circular extraction aperture instead of the more usual ribbon shape, mainly because the beam needs to go through a cylindrical stripper canal in the tandem accelerator. Since a detailed discussion of the ion source and beam optics was given in previous papers [2–4], only the recent source modifications will be described here. A primary goal of this effort has been to increase boron beam current since in the initial Genus source boron current was relatively low.

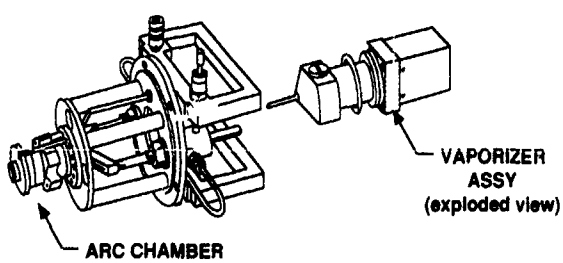

Fig 1. Axial hot-cathode PIG ion source of the G-1500 MeV ion implanter.

Basic modifications of the source are as follows:

(1) the material of the extraction cap was changed from molybdenum to mild steel to increase the magnetic field in the vicinity of the plasma extraction area to enhance dissociation of BF_3 molecules;
(2) the material of all insulators in the arc chamber was changed from alumina to boron nitride because a considerable amount of contamination of oxygen and aluminum ions into the source plasma, most likely generated by an interaction of excited fluorine and alumina, was found to reduce the fraction of boron beam current relative to the extracted beam current;
(3) the anticathode which is the base of the arc chamber is now made of boron nitride instead of molybdenum, resulting in the plasma being repelled toward the extraction region and generating higher plasma density in the extraction region;
(4) the anode shape was modified to reduce the metal surface area significantly, resulting in a longer lifetime due to less interaction between the source plasma and the anode surface which creates flakes inside the arc chamber.

Based on these source modifications, all available beam currents have been increased and the beam output of boron has been nearly doubled.

Source lifetime has been measured at Genus in our source test stand as well as at customer sites. Many

0168-583X/91/$03.50 © 1991 – Elsevier Science Publishers B.V. (North-Holland)

customers report more than 150 hours of source lifetime when the source is operated continuously.

3. The beam performance

3.1. Boron, phosphorus and arsenic

Measured beam currents of boron, phosphorus and arsenic using the present source are shown in table 1 as a function of beam energy.

3.1.1 Boron

As can be seen in table 1, approximately 100 μA of boron is available at a broad energy range from 200 to 2400 keV in the G-1500 MeV ion implanter. The maximum beam transmission of boron through the system was found to be approximately 50%. In fig. 2, a 2 h boron beam stability run at 1.6 MeV is shown. In this case, the beam current on the target was 81.0 μA at the beginning of this run and it ended at 83.7 μA, and five source-related glitches were observed. This data is consistent with the Genus specification of less than 10 sparks per hour and with a variation of less than 10% of the beam current over two hours.

3.1.2 Phosphorus

More than 300 μA of phosphorus is now easily achievable on the G-1500 MeV ion implanter with either the combination of the present source and vaporizer, or phosphine gas. With this level of beam current, the full mechanical wafer throughput, for example 140 wafers per hour with a 150 mm wafer size, can be met up to the high dose range of 10^{13} cm^{-2}.

3.1.3 Arsenic

Since arsenic is not widely used as a dopant for MeV implant processes because of its large stopping power and reduced penetration into the crystal, the beam performance of arsenic with the present source has not been fully evaluated, but a maximum beam current of 200 μA has been verified. In addition, low-energy arsenic beam performance was recently confirmed. Previously, based on the semi-empirical formula of the charge-state fractions by Greenway [5], the arsenic beam current was not specified at an energy range lower than 500 keV.

For arsenic in the stripper canal region, based on the direct Coulomb ionization scheme, one would not expect multiple ionization of both target and projectile at a lower collision velocity. For example, the velocity of arsenic at the stripper canal is less than the equivalent velocity of 2 keV/amu to obtain a final energy on target of less than 200 keV. So, one may not expect multiple electron stripping at this velocity range. However, it is well known that molecular autoionization and dynamical effects [6] are very important ionization mechanisms especially for heavy-ion–atom collision systems in the low-velocity region in which a quasimolecule is formed during the collision. This mechanism of ionization in the low velocity region may be one of the major reasons why low-energy arsenic is still obtainable on the tandem system with normal operation.

However, Genus is also investigating another approach to enhance beam usability on the tandem system at the lower-energy side, using negative ions directly. Details of this are described in an accompanying paper [7].

3.2 Carbon, oxygen and silicon

Feasibility studies for carbon, oxygen and silicon have been done because these ions are also important for both Si and GaAs devices. CO_2 gas was used to generate carbon and oxygen ions, and SiF_4 was used to generate Si ions. Measured beam currents of carbon, oxygen and silicon are also given in table 1 as a function of beam energy.

3.2.1 Carbon

In fig. 3, the mass spectrum with CO_2 gas running is shown. In this case, 146 μA of $^{12}C^-$ was injected into the tandem system. The beam transmission through the system was found to be 30–35% for carbon charge state 1 which is approximately 10–15% lower than that of boron, and charge state 2 is about the same. Since one may be able to compare carbon and boron almost directly at the same energy because of a mass difference of only 9%, this fact may be attributed to the difference of electron affinity and the first ionization potential of carbon and boron. The sum of the electron affinity and the first ionization potential for carbon is 12.52 eV, whereas that of boron is only 8.57 eV.

Since the extraction voltage was 30 kV in this case, and can be increased up to 40 kV, one may be able to increase the beam current substantially, even though the charge-transfer efficiency is slightly decreased at 40 keV [8]. In addition, the use of CO gas as a source feed material would be expected to give a better carbon ion fraction and higher beam current on target than CO_2.

3.2.2. Oxygen

Approximately 120 μA of $^{16}O^-$ was injected with CO_2 as the source gas. As can be seen in fig. 3, an oxygen peak which originates from CO^+ ion dissociation inside the Mg charge-exchange canal has a much higher contribution because the doubly charged transfer cross section of oxygen with magnesium increases steeply as the collision energy decreases in the energy region of several tens of keV [8]. Thus, if this peak was chosen to inject into the G-1500 system, the oxygen beam current in table 1 will be nearly doubled

Table 1
Measured G-1500 beam currents [particle μA]

	Energy [keV]						
	40	100	150	200	500	800	1100
^{11}B	12	27	42	83	105	112	105
^{31}P	42	112	188	212	296	325	316
^{75}As	16	37	42	101	93	138	190
^{12}C	–	–	–	38	50	53	49
^{16}O	10	–	–	25	32	35	37
^{28}Si	–	–	–	36	45	44	41 (45)
	Energy [keV]						
	1400	1500	1600	1700	2000	2400	3000
^{11}B	93	–	–	94	101	111	19
^{31}P	271	–	–	232	244	283	111
^{75}As	200	–	–	201	72	80	15
^{12}C	–	45	–	–	39	41	8
^{16}O	–	32	–	–	25	26	8
^{28}Si	36 (52)	–	32 (53)	–	58	61	20

3.2.3. Silicon

A significant advantage of the G-1500 system in comparison with standard low-energy ion implanters, related to silicon, is beam purity. Because there are two steps of charge-transfer processes, one being negative-ion formation by the Mg cell and the other being the electron-stripping process by the N_2 stripper canal, it is most unlikely that an N_2 molecule reaches the target, so ^{28}Si can be used instead of ^{29}Si.

The numbers which are given in parentheses in table 1 were obtained with charge state 2. If the beam transmission of phosphorus and silicon were compared as boron and carbon above, one notices that silicon makes a much more significant contribution in charge state 2 at this energy range, probably due to the lower first and second ionization potentials of silicon compared to those of phosphorus.

4. Neutral hydrogen injection

Historically, protons have been used for applications to form defect layers deep inside crystals. A disadvantage related to protons on the tandem system is its very small double-electron-capture cross section ($\sigma_{+1,-1}$) at several tens of keV. One of the ways to circumvent

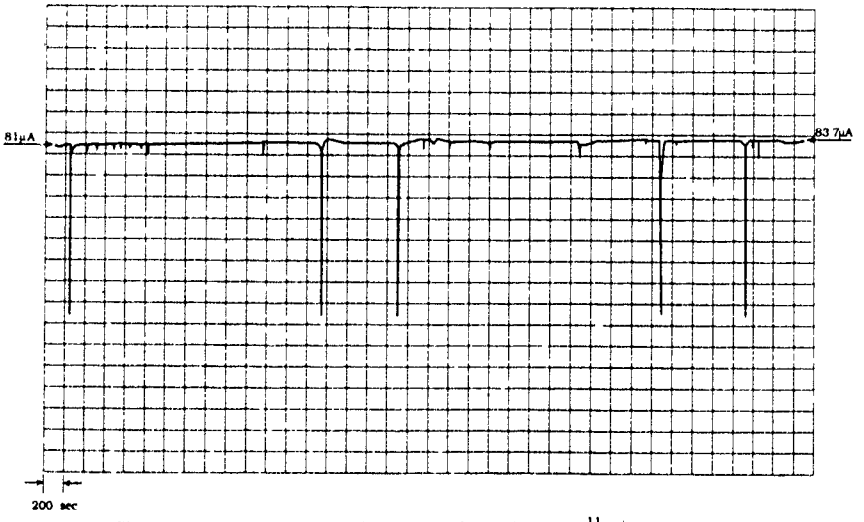

Fig. 2. Two hour beam stability run with ~ 80 μA of $^{11}B^+$ at 1.6 MeV.

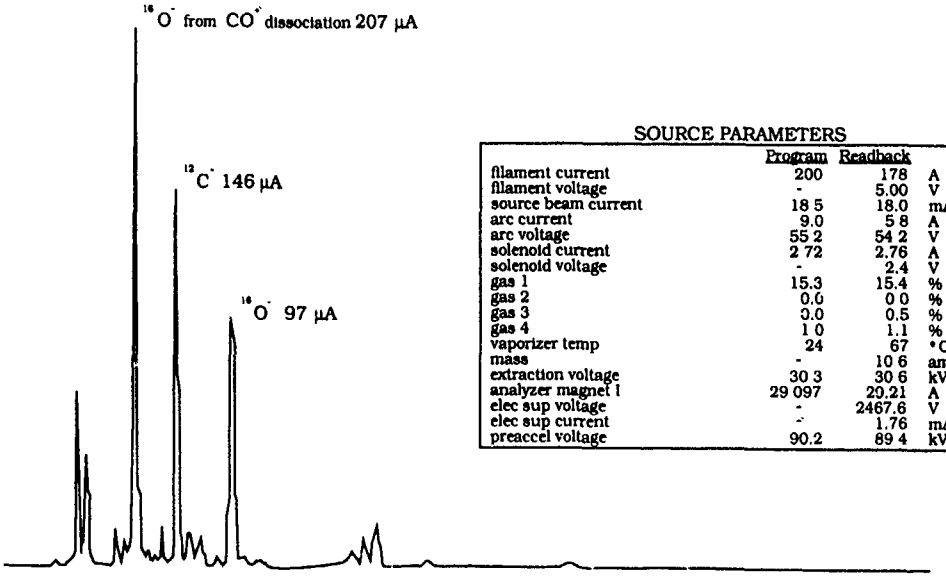

SOURCE PARAMETERS

	Program	Readback	
filament current	200	178	A
filament voltage	-	5.00	V
source beam current	18 5	18.0	mA
arc current	9.0	5 8	A
arc voltage	55 2	54 2	V
solenoid current	2 72	2.76	A
solenoid voltage	-	2.4	V
gas 1	15.3	15.4	%
gas 2	0.0	0 0	%
gas 3	0.0	0.5	%
gas 4	1 0	1.1	%
vaporizer temp	24	67	°C
mass	-	10 6	amu
extraction voltage	30 3	30 6	kV
analyzer magnet I	29 097	29.21	A
elec sup voltage	-	2467.6	V
elec sup current	-	1.76	mA
preaccel voltage	90.2	89 4	kV

Fig. 3. Mass spectrum at the low-energy Faraday cup with CO_2 gas

this problem is to use a combination of the H_3 molecular ion as a projectile and an H_2 gas cell [9]. In this work, a unique method of injection of the neutral hydrogen molecule into the tandem system has been developed to obtain H^+ on target for the first time.

With this method of neutral beam injection, a positive beam is extracted from the source and mass-analyzed by the 90° magnet. After mass analysis but before the entrance of the tandem accelerator, the positive beam is converted into a neutral beam by passing through a gaseous target which is introduced via a leak valve and effused towards the beam. For the hydrogen molecule ion, hydrogen-molecule gas was chosen as a neutralizer. Then, the neutralized beam is injected towards the high-voltage terminal with the energy of the extraction voltage. During operation the preacceleration voltage of the injector is shut off and grounded. When the neutral beam reaches the high-voltage terminal of the tandem system, a portion of beam is ionized by collisions with the stripper gas inside the canal, then repelled to the ground potential. Hence, the final energy of the injected beam is primarily the sum of the extraction voltage plus the terminal voltage. Although one loses the energy doubling of normal tandem operation, this method is still attractive, because no negative-ion formation is needed. Principally, species like nitrogen and other inert gases which do not have a stable negative binding state can still be accelerated up to high voltage on the terminal.

Very preliminary results of neutral hydrogen molecule injection are shown in table 2. In this case, approximately 3.' mA of the positive hydrogen molecule ion was extracted, and about 40% of it was neutralized by hydrogen gas which was introduced at the low-energy pumping box. As a result of collisions between neutral hydrogen molecules and nitrogen molecules, protons whose momentum is half that of initially injected neutral molecules were produced at the accelerator terminal and repelled to the ground potential.

It should be emphasized that this result was obtained without any modifications to optimize this neutral-beam injection method. Further, it should be mentioned that an actual device implant has been done with this method with good results.

Table 2
Measured H^+ beam current with a method of neutral-beam injection

Energy [keV]	62	120	170	220	270	320	370
H^+ beam current [μA]	35	38	35	33	30	29	28

5. Conclusion

The current beam performance on the G-1500 MeV implanter with the modified axial hot-cathode PIG source is described in this paper. More than 100 μA of boron and 300 μA of phosphorus are available on the G-1500 MeV ion implanter. Also the results of studies of C, O and Si and the unique method of neutral-beam injection are given in this paper.

Further efforts to improve the beam performance of the implanter continue, such as adopting a three-axis manipulator for the beam extraction system which will enable us to control beam optics for a wider variation of plasma densities and extraction voltages.

References

[1] Y. Matsuda, K. Tuskamoto, M Inuishi, M. Shimizu, M. Asakura, K Fujishima, J. Komori and Y. Akasaka, Extended Abstracts of the 19th Conf. on Solid State Devices and Materials, Tokyo, 1987, p. 23

[2] N. Turner, K H Purser and M. Sieradzki, Nucl. Instr. and Meth. B21 (1987) 285

[3] N. Turner, N. White, J.P. O'Connor and K.H. Purser, Proc ISIAT '87, Tokyo.

[4] J.P. O'Connor, N. Tokoro, J Smith and M. Sieradzki, Nucl. Instr. and Meth. B37/38 (1989) 478.

[5] T. Greenway, private communication.

[6] N. Tokoro, S Takenouchi and N. Oda, Phys. Rev. Lett 51 (1983) 1255.

[7] J.P. O'Connor, M.E. Mack, A Renau and N. Tokoro, these Proceedings (8th Int. Conf on Ion Implantation Technology, Guildford, UK, 1990) Nucl. Instr and Meth B55 (1991) 207.

[8] A.S. Schlachter and T.J. Morgan, Proc. 3rd Int Symp. on Production and Neutralization of Negative Ions and Beams, BNL, 1984, AIP Conf. Proc. 3 (1984) 149

[9] N.B Brooks, P H. Rose, A.B Wittkower and R P. Bastide, Nucl Instr. and Meth. 28 (1964) 315.

Nuclear Instruments and Methods in Physics Research B55 (1991) 439–442
North-Holland

Vacuum system design for ion implanters

D.J. Hucknall
Leybold Ltd., London SW17 7AB, UK

M. Kuhn
Leybold AG, W-5000 Cologne 51, Germany

The demands on the vacuum pumping system for ion implanters are great, particularly with those used for substrate doping in the semiconductor industry. The pumps must generate and maintain contamination-free conditions at appropriate pressure levels and be capable of handling efficiently a range of highly reactive gases and products Based on experience with some commercial ion implanters, the behaviour of conventional pumping systems will be reviewed and the use of newer types of pumps on ion implanters will be discussed.

1. Introduction

Ion implantation is a versatile and highly-controllable technique for the modification of surfaces and the synthesis of buried layers. In the manufacture of semiconductor devices, it is now the established technique for substrate doping [1]. Advanced CMOS devices may require up to eleven implants [2] ranging from low energy implantation to the ion beam synthesis of buried insulator layers which requires high beam currents. A range of commercial implanters is available which can provide ion doeses in the range 10^{10} to 10^{19} cm^{-2} at energies up to 200 keV. For semiconductor purposes, they are required to produce a range of species efficiently and to yield products accurately dosed over large target areas. This imposes considerable demands on the ion optical, electronic and vacuum systems [2,3]. The present paper reviews the behaviour of conventional pumping systems on commercial ion implanters for substrate doping in the semiconductor industry. It is

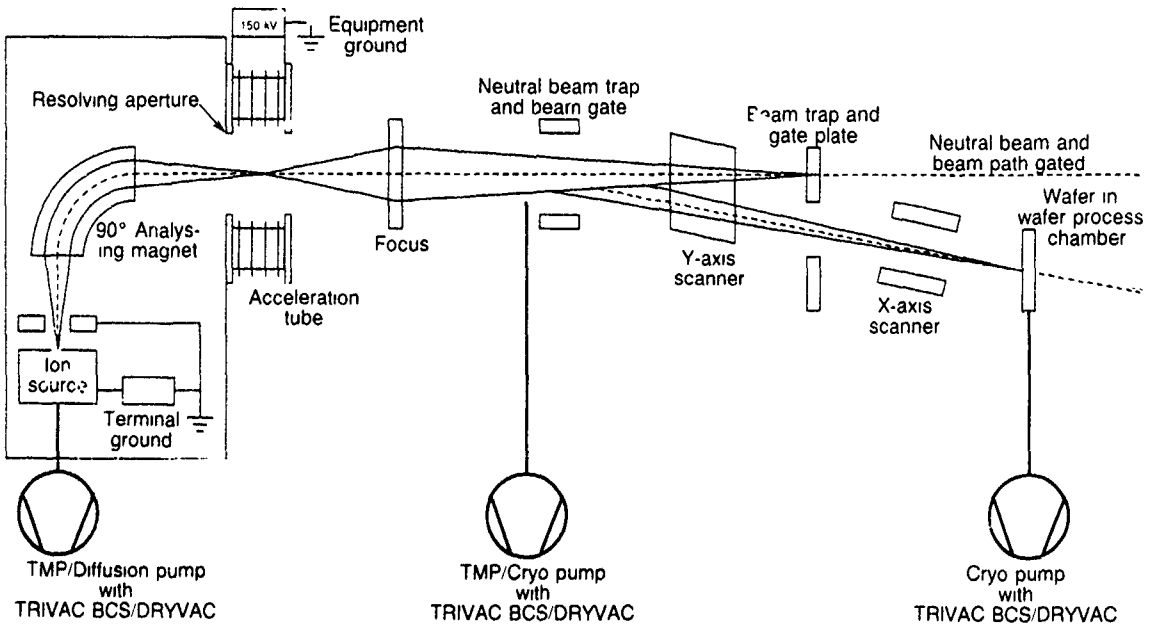

Fig. 1. Configuration of a typical 200 keV ion implanter.

0168-583X/91/$03.50 © 1991 – Elsevier Science Publishers B V. (North-Holland)

based on experience with machines from various manufacturers (Applied Materials, Eaton Nova, Varian). The use of newer types of pumps will also be discussed.

2. Ion implanters

Ion implantation involves the generation of ionized species from a suitable gas or vapour source and their extraction and acceleration towards the target. Conventional implanters for semiconductor processing are dedicated machines, optimized to implant B, P and As with limited beam energy. They consist of several subsystems (source, extraction/acceleration areas, target chamber (see fig. 1)) and although the vacuum levels within these systems may be different, the demands on the vacuum pumps can be equally great. Contamination-free conditions must be generated and maintained and the pumps must be capable of efficiently handling a range of highly reactive (including toxic and corrosive material) gases and products. Additional problems which arise with semiconductor implanters include charging, contamination due to sputtering and the rapid evolution of hydrogen from the substrates [1].

3. Subsystems

3.1. Ion source

The ion source is the critical component in implanters; a beam of poor emittance cannot be rectified elsewhere in the system. In the source, pressure must be maintained in the range 10^{-2} to 10^{-4} mbar in the presence of gases such as BF_3, PH_3, AsH_3 (for Si implantation) or SiF_4, SiH_4, H_2Se (for implantation of III–V compounds). Without exception, these compounds are highly toxic Some (BF_3, SiF_4) are corrosive, yielding HF in the presence of moisture, whilst others (PH_3, SiH_4, H_2Se) are spontaneously flammable [4]. Particulates may also be generated due to the reaction of some of the gases (BF_3, PH_3) with adsorbed oxygen-containing species. A further problem can arise because of the intense electromagnetic fields (associated with the ion extraction and analysis systems) to which the pumps are subjected.

In the ion source, argon gas may be used under certain circumstances until source conditions have stabilized and the large gas load presented to the system demands a high pumping speed. Combinations of oil-sealed, two-stage rotary vane pumps (volume rate of flow, 40–70 $m^3\ h^{-1}$) with either diffusion pumps (~ 5000 $l\,s^{-1}$) or turbomolecular pumps (~ 1000 $l\,s^{-1}$) are typically used to evacuate the source. The backing pump is the critical component in this configuration since the performance of the system depends on its efficiency. An adequate supply of oil having the correct properties is essential for normal pump operation. Because of the presence of high concentrations of both aggressive gases and solid particles, appropriate measures must be taken to protect the pump fluid and to monitor automatically important parameters such as oil level and pressure, temperature, etc., in order that impending malfunctions can be picked up.

Normal hydrocarbon-based pump fluids are rapidly destroyed by the effects of the compounds indicated and it is necessary to use more stable compounds. Perfluoroalkyl- (PFAPE) and perfluoropolyethers (PFPE) are widely used on account of their relative chemical inertness. They are, however, decomposed in the presence of Lewis acids (e.g. BF_3), at normal pump operating temperatures (70–80°C). Although hydrocarbon-based fluids, doubly-distilled to remove susceptible components, ("white oils"), can be used, it has been shown (see, for example, ref. [5]) that PFPEs can also be used if a suitable oil filter is fitted to remove Lewis acids. Filters containing activated alumina incorporated within the oil circulation system of the pump are effective adsorbants for a range of compounds. Particulates may be removed using other appropriate filters. Since pump fluids can dissolve large amounts of gas, including hydrofluoric acid, considerable care must be exercised in the handling and disposal of used filters and oil. The problems associated with arsenic compounds are particularly severe.

Easily hydrolyzed gases such as BF_3 and SiF_4 can cause severe corrosion problems in vacuum systems and the ingress of water vapour must be prevented. Apart from system leaks, back-diffusion of ambient air from the exhaust lines is the main source of moisture. This can largely be prevented by the incorporation of a moisture barrier system [6] in the exhaust. Water vapour from other sources can be minimized by ensuring an overall leak-tightness for the system to $< 10^{-5}$ mbar $l\,s^{-1}$ at the normal working temperature. The continuous admission of an inert gas (e.g. N_2) to both the pump housing and the pump chamber itself, through the gas ballast, is invaluable in these circumstances. Not only does this inhibit the back-diffusion of water vapour but it also reduces considerably the accumulation of reactive and toxic gases in the pump. Finally, in order to remove small amounts of lubricant entrained in the gas leaving the oil-sealed pump, exhaust filters are fitted. By removing and returning lubricant to the pump, the consumption of oil is minimized. Removal is not complete, however, and traces may pass to the exhaust gas where they can adversely affect the clean-up devices.

The efficiency of an oil-sealed pump fitted with complex protective devices (see fig. 2) can only be maintained if the state of the pump is closely monitored. Sensors are therefore fitted that check the following:

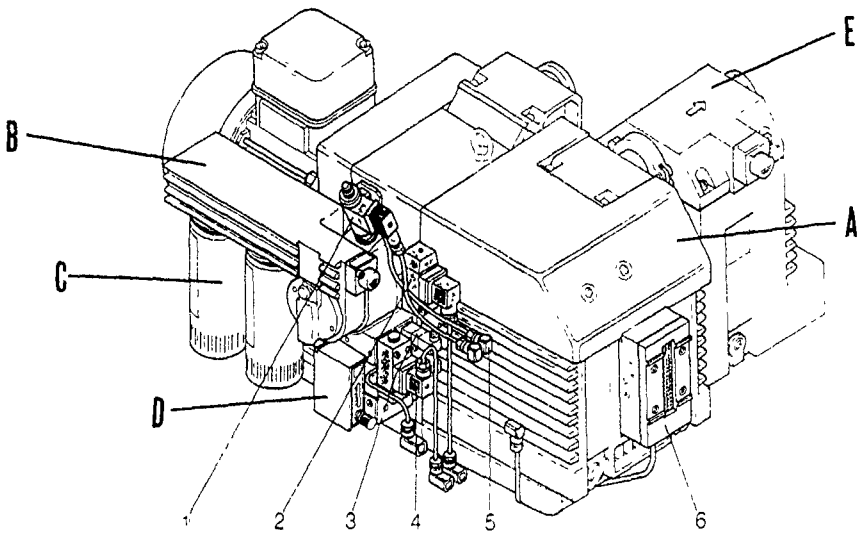

Fig. 2 Diagram of a protected two-stage, oil-sealed rotary vane pump. (A) Pump; (B) chemical/physical filter system; (C) filters; (D) inert gas supply, (E) exhaust filter. Protection system: (1) pressure difference switch (filter); (2) oil pressure switch; (3) inert gas flow switch; (4) pressure switch; (5) connection to thermal switch (oil temperature), (6) float switch (oil level).

(i) pump temperature,
(ii) lubricant level and temperature,
(iii) inert gas flow,
(iv) the condition of both the oil and exhaust filters.

Any deviation from permitted limits is immediately indicated With such modifications, oil-sealed rotary vane pumps will perform with great reliability. Indeed, a recent routine examination of such a pump after six months use on an ion implanter revealed its excellent overall condition.

The cost of maintenance of an oil-sealed pump fitted with complex oil filtration and monitoring systems is high. Moreover misused or inadequately trapped, these pumps can cause significant contamination of the vacuum system. Because of this, considerable effort has been expended on the development of so-called dry pumps [7] in which the pumped gases are compressed in a sealant-free chamber. Such pumps are available commercially and are based on multi-stage Roots- or claw-type impellers. A four-stage claw-type dry pump typically has a maximum pumping speed of 100 $m^3\ h^{-1}$ at ~ 1 mbar and an ultimate pressure of approximately 10^{-2} mbar. Lubricants are present, of course, in the gear and bearing areas but they are separated from the pump chamber by shaft seals. N_2 may be admitted to the separate pump stages in order to improve gas flow through the pump. This also inhibits water back-diffusion but transports solids to the exhaust gas purification system where they may cause problems.

The use of dry vacuum pumps as replacements for oil-sealed rotary pumps on various parts of implanters, including the ion source, is relatively recent. Experience is consequently limited. It appears, however, that they perform efficiently with long up-times and consequent low maintenance costs.

Diffusion pumps are used extensively to evacuate implanter ion sources but they may cause problems due to back-streaming. Further, the pump fluid used must be compatible both with the process gas and the sealant in the backing pump. For these reasons, diffusion-pumped systems will probably not meet future demands for cleanliness and will become unacceptable.

Turbomolecular pumps, when correctly used, produce clean, high vacua. They can also tolerate high gas throughputs [8]. The rotor support bearings are critical to pump operation and, in the presence of corrosive gases and particulates, failure can occur This problem has largely been eliminated by the use of a purge gas system whereby a gas such as N_2 is admitted to the motor housing in such a way that there is a continuous flow of gas to the forevacuum port of the turbomolecular pump. By correct adjustment of the purge gas flow (using helium as a tracer and a quadrupole mass spectrometer as the sensor) ingress of corrosive material and solids can be prevented.

3.2. Beam line

The ion beam, having left the acceleration tube, must be focussed and shaped before entering the target area. In this region, pressures below 10^{-7} mbar are required. Undesirably high pressure in the beam line can lead to ion neutralization, recombination [3] and other side reactions such as dissociation (mainly of BF_2).

These effects increase the energy contaminants in the beam and effect the implant profile. Further, deflexion can cause sputtering in the beam line and subsequent contamination. Sputtering may occur at the resolving slit, defining apertures, etc.

Because of their cleanliness and ability to produce low pressure, turbomolecular pumps or cryopumps are preferred in this area. Cryopumps are entrapment pumps in which gases are held on surfaces maintained at approximately 10 and 80 K. The mechanism of trapping depends on the gas. It usually involves cryocondensation (multilayers formed) or cryosorption (a monolayer is formed on an adsorbate such as charcoal). H_2, for example, is pumped by cryosorption at ~ 10 K. Cryopumps have the highest speed for a given inlet port diameter of all the high vacuum pumps. A possible disadvantage, however, is that their pumping capacity is eventually reached and regeneration must be performed. Electrical heaters can be used to shorten regeneration time but it still involves ~ 5 h down-time. Evolved gases are usually removed by a suitable backing pump.

3.3 Target area

Maintenance of pressure in the range 10^{-7} to 10^{-11} mbar is essential since beam broadening and charge exchange with neutrals can lead to dose error The main gas sources in this region are:

(i) large amounts of H_2 released due to the interaction of the ion beam with the wafer photoresist;
(ii) water vapour introduced by wafer handling.

A *rapid* pressure rise (up to 10^{-3} mbar in a few seconds) can occur due to hydrogen evolution and it must be dealt with quickly. Cryopumps are excellent pumps for both H_2 and water vapour and are widely used. Their capacity for hydrogen is limited, however, by the area of cryosorbent surface available and regeneration will be necessary at intervals. Modifications have been made to standard pumps by increasing the charcoal loading and hence the capacity for H_2. In this way, the up-time is increased significantly.

Recently, it has been suggested that an alternative to the cryopump for use in the target area would be a turbomolecular pump fitted with a cryobaffle (at ~ 77 K). The baffle would have a high pumping speed and capacity for water whilst the turbomolecular pump can deal with H_2.

4. Summary

Vacuum systems currently used on ion implanters have been reviewed. On the ion source combinations of diffusion and suitably-protected oil-sealed rotary pumps are usual. On the beam line and target area, cryopumps are used. Due to the accelerating trend towards cleaner and more efficient systems, turbomolecular pumps, inevitably backed by "dry" vacuum pumps, are being increasingly applied. Nitrogen-purged turbomolecular pumps are suitable for the ion source and, fitted with a cooled baffle to increase pumping speed for water, they may eventually replace cryopumps in the beam and target areas.

References

[1] D Aitken, Vacuum 39 (1989) 1025
[2] D. Aitken, Vacuum 36 (1986) 953.
[3] D.G Armour, Vacuum 37 (1987) 423
[4] P. Duval, High Vacuum Production in the Microelectronics Industry (Alcatel/Elsevier, Amsterdam, 1988)
[5] P. Bachmann and M Kuhn, Vacuum (in press).
[6] L Arndt, P Bachmann, H.-P. Berges, W Leier and D. Varberg, US Patent 4612957 (1976)
[7] H -P Berges and D G Goetz, Vacuum 38 (1988) 761
[8] D.J Hucknall and D G. Goetz, Vacuum 37 (1987) 615.

Nuclear Instruments and Methods in Physics Research B55 (1991) 443–447
North-Holland

The Nissin PR-80A high current ion implantation system

T. Kawai, M. Chohtokudani, M. Naito, T. Hiramatsu, M. Sasaki, T. Sunouchi, Y. Nishigami, T. Matsumoto, M. Nakaya and M. Nakazawa

Nissin Electric Co., Ltd., Ion Equipment Division, 575 Kuze Tonoshiro-cho, Minami-ku, Kyoto, Japan

The PR-80A has been developed form its original model PR-80, featuring a fully automated beam shaping system for the reduction of charging on wafers. The beam shaping control has been realized by sophisticated integration of such improved components as an ion source, an extraction electrode system, a mass analyzing system, and a machine controller. The ion source and extraction electrode system has been designed to ensure the precise and reproducible settings. The mass analyzing system has a mechanism which automatically adjusts the exit pole-face angle according to an implant recipe. The machine controller sets the beam shape by varying the extraction gap and the arc current, adjusting the normalized perveance of the ion source. The beam shape is monitored by the beam profile monitor. The system is interlocked when a beam has an unacceptable width, peak density or offset in position. The performance of the PR-80A's endstation is also described.

1. Introduction

Wafer charging is widely acknowledged as one of the most crucial problems which degrade the performance of a high current ion implantation system. Various types of electron shower system have been proposed [1–3] and have proved to be useful, but they are not necessarily satisfactory. For instance, the yield of IC varies day to day even in the same implanter settings. We suspect that one of the major causes of the poor reproducibility is the day-to-day variation of the beam shape or current density profile on the wafer.

The PR-80A has been developed from its original model PR-80 [4], featuring a fully automated beam shaping system for the reduction of charging from the viewpoint mentioned above. Using this technique, the PR-80A provides a fixed flattened beam density profile at the target, independent not only of the operator skill but also of the process recipes such as ion species, energy, beam current, etc.

Another major feature of the machine is its endstation, which satisfactorily meets the user requirements of low particle performance, factory automation compatibility, and higher availability including ease of maintenance. In this paper, we describe these features.

2. System configuration

Fig. 1 shows the overall view of the PR-80A. The footprint is reduced to three-fourths of the PR-80's without lessening the accessibility to the components. The endstation has been changed from the dual chamber to a single chamber concept. The components for the beam generation and transport have been improved to obtain "good beam profile" at the target, without altering the outer view.

3. A fully automated beam shaping system

There are many factors which influence the beam shape at the target. These are classified into 4 groups.

group 1: parameters of the ion source;
group 2: parameters of the analyzing magnet;
group 3: parameters of the space charge effect along the beam transport line;
group 4: parameters of the apertures set in the beam line.

3.1 Parameters in group 1

The elements of group 1 are the normalized perveance P_N, the alignment and the shape of electrodes for beam extraction, the source magnet current, and the time-varying factors such as the filament diameter and the accumulation of the sputtered material in the arc chamber and so on. Among these, the normalized perveance P_N, which is a function of the extracted beam current, extraction voltage, extraction gap and extracted ion species, is the most critical factor [5], because the extracted beam divergence is determined approximately by P_N only. Therefore the fully automated beam setup procedure is carried out to adjust P_N to an appropriate reference value which is registered in a tabulated form in the machine controller and is automatically selected according to the recipes. For the desired beam current, energy and mass number, the reference value of P_N

0168-583X/91/$03.50 © 1991 – Elsevier Science Publishers B.V. (North-Holland)

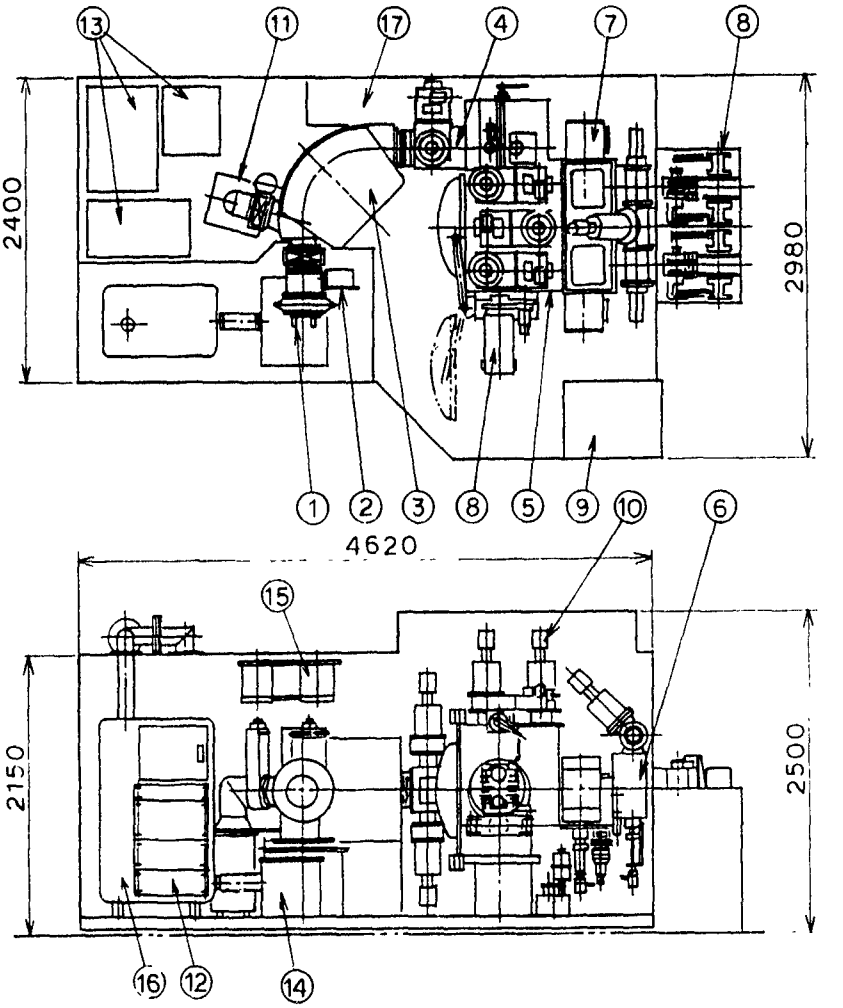

Fig 1 Plan and side views of the PR-80A (1) Ion source, (2) driving system for ex electrode, (3) analyzing magnet, (4) Faraday chamber, (5) disk chamber, (6) air-lock room, (7) wafer stocker, (8) driving disk system, (9) control console, (10) cryopump, (11) oil diffusion pump, (12) ion source power supply, (13) distributor, power supplies and controllers, (14) insulating transformer, (15) extraction power supply, (16) source gas box, and (17) cooling system

designates a certain value of the extraction gap. When the designated value of the gap cannot give the reference value of P_{N_2}, the gap is automatically re-adjusted, keeping the beam current at the desired value and varying the arc current when needed.

The alignment of the extraction electrodes including the arc chamber slit mainly governs the direction of the extracted beam and consequently the location of the beam at the target. In order to direct the beam at a fixed position on the target, the alignment should be done very accurately with precise reproducibility, especially when reassembling the electrode system for maintenance. The ion source system has been renovated as follows. A new driving mechanism for the extraction electrode adopts the double eccentric gear. A jig is provided for assembling the ion source. Alignment pins for mounting the ion source to the base flange and the electrodes to the base plate are built in the stuctures. The accuracy of setting the electrodes is reproducibly obtained as shown in table 1. In the automatic beam setup, the transverse location and the tilt angle of the extraction electrode is set in advance at the prescribed value, and readjusted at the optimum value to get a maximum beam current.

The shape of the extraction electrodes has been modified to get the beam uniform in the vertical direction at the target. The curvature of the arc chamber slit in the vertical direction is made large, so that the

Table 1
Summary of the components and their performances of the fully automated beam shaping system

No.	Components	Performances
1	Ion source	Setting accuracies
	Extractor	(a) Transverse location: $\leq \pm 0.05$ mm
	Positioning system	(b) Tilt angle: $\leq \pm 0.1°$
		(c) Gap length: $\leq \pm 0.25$ mm
		(d) Twist angle: $\leq \pm 0.2°$
	Curved arc-chamber slit	Vertically extended beam shape
2	Analyzer magnet & slits	Automated setup of β angle Beam transmission optimized
3	Machine controller	(a) P_N set up & adjust (b) P_N check (c) Interlock with source parameter (d) Compatible with batch implant
4	Beam profile monitor	Monitor and judge the width, offset, and density of beam

vertical crossover point of the beam goes downstream in the waveguide chamber. This results in the vertical extension of the beam at the target.

The source magnet current affects the direction of the extracted beam. In the fully automatic beam shaping operation, this is set at a fixed value depending on the mass number.

Time-varying factors in the ion source might influence the beam shape. In order to avoid this, we chose a rather small value of P_N, around 0.3, which keeps the flattened beam profile at the target within good tolerance.

3.2. Parameters in groups 2 and 3

The beam exit angle to the face of the magnetic pole edge can be varied automatically according to the recipe so as to compensate the influence of the space charge effect upon the beam focal point. If the implant is done at a lower energy, a higher mass, or a higher current, the beam focal point would go downstream due to its space charge effect and the beam cross section at the target would change to a smaller size.

3.3. Parameters in group 4

The size and location of the analyzing slit as well as of the beam defining slit have been optimized experimentally so as to obtain a wider beam on the wafer without worsening the beam transmission substantially.

3.4. The beam profile monitor (BPM)

The endstation is equipped with an in situ beam profile monitor. This monitor comprises of small multi-Faraday cups aligned in vertical and horizontal directions, a current sensing amplifier, a CRT display and a logic circuit to monitor the beam shape and judge whether it is allowable for implantation. The criteria are the peak current density, beam width and height, and the location of the beam. When they are satisfied the logic circuit generates a "go signal" to start implantation at each batch.

3.5. Performance of the fully automated beam shaping system

Fig. 2 outlines the general flow of the fully automated beam shaping control, which is performed by a machine controller. A typical beam shape indicated on the CRT is shown in fig. 3. Two photos in fig. 3 show that the controlled beam shape (a) is much more uniform than the uncontrolled one (b).

This system realizes a wide and uniform beam cross section in the operational region as shown in fig. 4. In this region, a beam width above 60 mm, a height above 140 mm and a local peak density below 0.3 mA/cm^2 are obtainable. Table 1 summarizes the components, and their performances, of the fully automated beam shaping system. The effect of the fully automated beam shaping control upon the wafer charging was examined using the failure ratio (fraction defective) of a 4M DRAM gate oxide layer due to the implant and the result is very attractive, as shown in fig. 5 for the As^+, 35 keV, 3×10^{15}/cm^2 implant.

4. Endstation performance

The target chamber is equipped with five 8-in. cryopumps; only three of those are selected at a time to evacuate the target chamber. This substantially

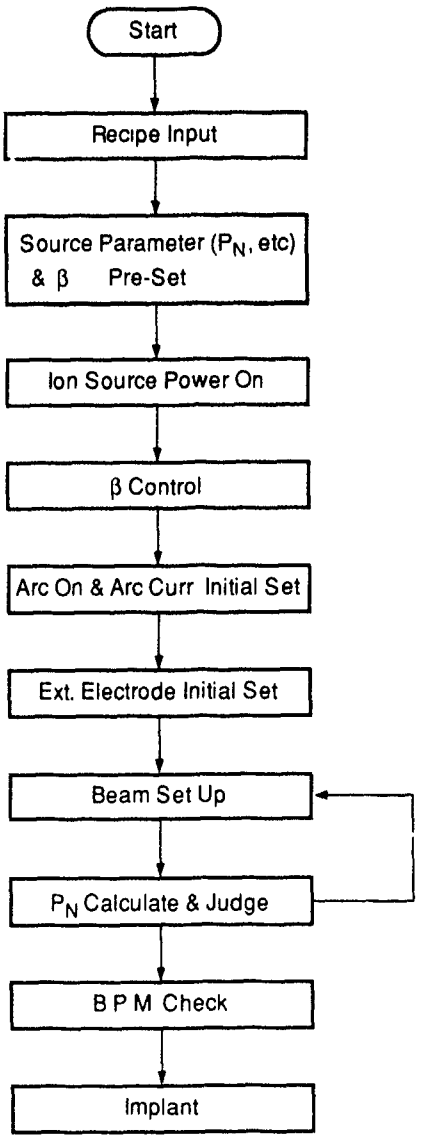

Fig. 2. Flow diagram of the fully automated beam shaping control system.

eliminates the nonavailability of the machine due to the maintenance needed for the regeneration of the cryopumps. One cryopump exclusively evacuates the load lock room for the wafer cassette. To ease the maintenance, the target chamber has six lids, dedicated respectively to the Faraday chamber, the disk, the beam profile monitor, the robotic arms, and the two wafer stockers.

Fig. 6 shows the schematic inside view of the target chamber. A single wafer disk, which can automatically change the implant angle up to 10° according to the recipe, is housed in vacuum all the time. The spinning speed is 1500 rpm maximum. Wafers are handled with

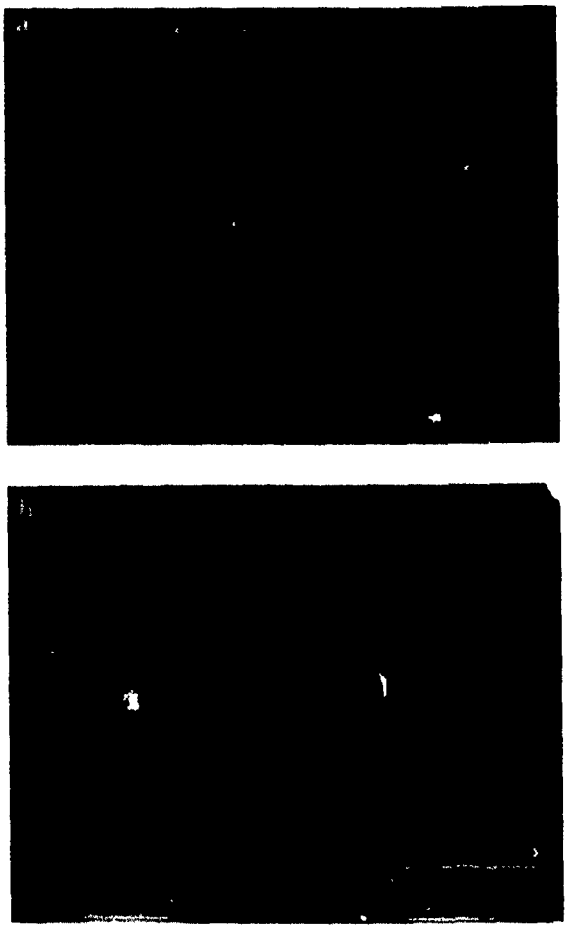

Fig. 3. Horizontal cross-sectional beam profile for As^+, 35 keV, 8 mA Spacing between the sensors is 6 mm. (a) The controlled beam; (b) the uncontrolled beam. The amplification factor of (a) is 2.5 times that of (b).

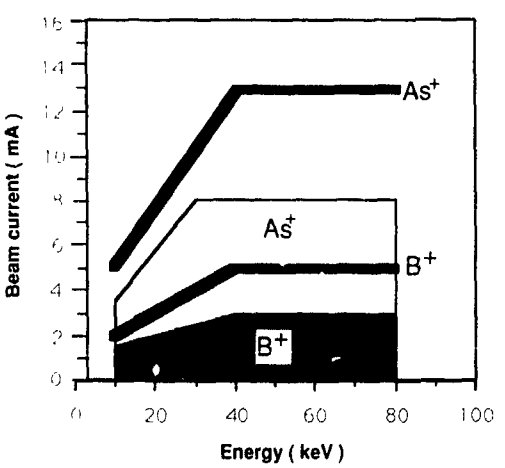

Fig. 4. PR-80A performance diagram in the fully automated operation: The thick lines indicate the maximum beam currents. A "good" uniform beam is guaranteed in the shaded region.

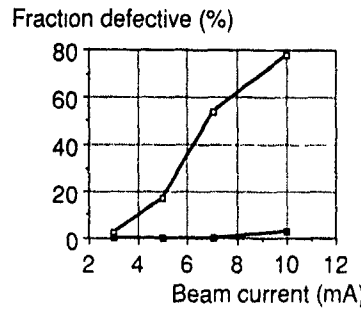

Fig. 5. Comparison of fraction defectives between the fully automated beam shaping control system (■) and the conventional (□) (no control system). The implant condition is As^+, 35 keV, $3\times10^{15}/cm^2$.

the robotic arm, which has been successfully used in the Nissin NH-20SR [6]. The wafer handling system has two operation modes; one is of the same cassette same-slot operation compatible for ASIC processing and the other is o. .e cassette to another cassette mode for high throughput. The cassette loader is optionally provided to be integrated with the cassette carrying robot in a factory automation system. The cassette loader transfers wafers between the cassette carried by the factory robot and the specifically surface-treated cassette. After completion the cassette loader also transfers the special

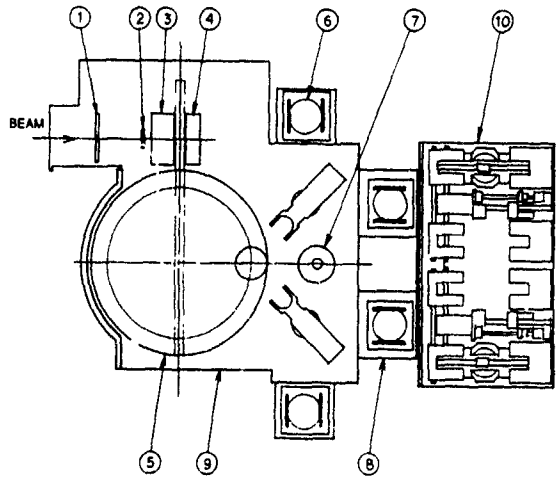

Fig. 6. Schematic inside view of the target chamber (1) Analyzing slit, (2) defining slit, (3) Faraday cup, (4) beam catcher and beam profile monitor, (5) disk, (6) wafer stocker, (7) OF aligner, (8) air-lock chamber, (9) disk chamber, and (10) cassette.

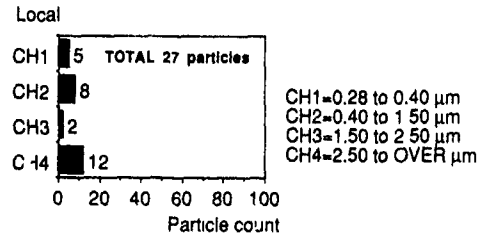

Fig. 7. Particulation of the PR-80A after As^+, 50 keV, $1\times10^{16}/cm^2$ implant

cassette to the load rock room. The use of the robotic arm and the special cassette keeps the particulation on wafer at a very low level, around 0.15 particles/cm^2 for 0.3 μm or higher. Fig. 7 shows typical particulation data after the As^+, 50 keV, $1\times10^{16}/cm^2$ implant.

5. Summary

The fully automated beam shaping system provides a very promising method for the reduction of wafer charge-up. Further study is scheduled to be done in combination with the electron shower system. This study will enable us to find more effective use of the electron shower system so that the usefulness of the beam shaping system will be more appreciated. PR-80A is easily interfaced to a host computer and in its fully automated mode the machine is integrated into a human-free factory automation system to comply with more stringent IC process environment.

References

[1] N Nagai, T. Kawai, M Naito, Y Nishigami, H Fujisawa and K. Nishikawa, Nucl. Instr and Meth B37/38 (1989) 572.
[2] M.E. Mack, ibid., p 472.
[3] C M. Mckenna, B.O. Pedersen, J K Lee, R F Ouitcault and S. Kikuchi, ibid., p. 492.
[4] T. Kawai, M. Naito, M Nogami, T Kinoyama, N. Nagai and H Fujisawa, Nucl. Instr and Meth. B21 (1987) 239.
[5] M. Tanjo, S. Fujiwara, M. Sakamoto and M. Naito, these Proceedings (8th Int. Conf. on Ion Implantation Technology, Guildford, UK, 1990) Nucl. Instr. and Meth. B55 (1991) 86
[6] Y. Tamura, M Nogami, M. Tanaka, T Maeda, H. Kumasaki and S. Tamura, Nucl. Instr. and Metn B37/38 (1989) 620

Nuclear Instruments and Methods in Physics Research B55 (1991) 448–452
North-Holland

System and process enhancements of the Applied Materials Precision Implant 9200

P.R. Jaffe and K.P. Fairbairn

Applied Materials Implant Division, Foundry Lane, Horsham, West Sussex RH13 5PY, UK

The Applied Materials PI9000 high current ion implanter was first introduced to the market in September 1985, and the 200 mm compatible system, together with a number of additional developments, was introduced, as the PI9200, in April 1988. Since that time the system has been further developed and refined to meet users' ever increasing requirements. This paper presents an overview of the present system with details on a number of recent product enhancements

1. Introduction

The Precision Implant 9200 is a new generation general purpose ion implantation system for fully automated high productivity operation over a wide range of beam energies, currents and implant species. Since introduction in 1985 it has become well established worldwide and has repeatedly proven itself as a valuable production tool, noted for its excellent performance in areas of uniformity, consistency, purity, wafer

Table 1
PI9200 system specifications

Energy range [keV]	5–180 keV			
Dose range [cm^{-2}]	1×10^{11}–1×10^{17}			
Wafer size [mm]	100	125	150	200
Batch size	25	25	25	17
Maximum throughput [w/h]	> 200	> 200	> 200	> 150
Throughput for 5×10^{14} @ 20 mA	> 200	> 200	> 200	> 150
Throughput for 1×10^{16} @ 27 mA	87	87	87	56
Particulates	mean level: 0.05 cm^{-2} for $\geq$ 0.5 μm particles			
Uniformity (1 sigma)	≤ 0.5% for doses $>1\times10^{15}$ cm^{-2}			
	< 0.75% for doses $>1\times10^{13}$ cm^{-2}			
	< 1.0% for doses $>1\times10^{13}$ cm^{-2}			
Wafer temperature	< 50 °C at 3600 W			
Size, system	5145 × 3156 mm or 1.69 × 10.2 ft			

Ion energy [keV]	Ion current [mA]			
	B^+, BF_2^+	P^+	As^+	Sb^+
5	2.5	–	–	–
10	5	8	8	4
20	10	27	27	9
25 [a]	8	14	12	9
30	10	16	14	10
40	10	27	20	10
50	10	27	27	10
60	10	27	27	10
80	10	27	27	10
100	10	27	27	10
120	10	27	27	10
140	10	20	20	10
160	10	15	15	10
180	10	10	10	–

[a] Post-acceleration power supply (high voltage) is switched on at 20 keV.

0168-583X/91/$03.50 © 1991 – Elsevier Science Publishers B.V. (North-Holland)

temperature and throughput [8,9]. It has been subject to continuous evolution as the state of the art improves, such as the 200 mm capability and new computer control which have already been well documented [1]. Over the past two years further developments have been carried out in all areas of the implanter, including the beamline and wafer handling.

The Precision Implant 9200 is a fully automated system designed for minimal operator intervention. It can handle wafer sizes from 100 to 200 mm diameter, and implant at up to 27 mA in practice with beam energies between 5 and 180 keV. Table 1 shows the PI9200 system specification.

A number of enhancements have been made to the Precision Implant 9200 recently, which are described in the following sections.

2. Automated variable implant angle

The two-axis mechanical scanning of the PI9200 ensures excellent implant uniformities, see table 1, and the large wheel/fast spin configuration minimises the instantaneous beam pulse per wafer pass. This ensures minimal wafer power loading and charging effects. A variable tilt axis has been added to provide a variation in implant angle, from 0° to 7°, which enables gate overlap low dose drain implants and accurate implant control of trench sidewalls. The implant angle is selectable from the system software and can be programmed into the process recipe. An angle change now takes just ten seconds, whereas previously the vacuum seal had to be broken and mechanical components exchanged in order to change the implant angle. The new design utilises a pivot axis within the scan arm which enables the whole wheel to swivel with respect to the beam. This is described in greater detail in ref. [2].

3. Wafer orientation

Fully automated wafer orientation is now possible for angles between 0° and 360°. Most angles are available by orientation within the vacuum loadlock using one of two types of wafer orientation systems. Each is retrofittable to the cassette indexer, one design being suitable for flatted wafers, and another for notched wafers The wafer flat orienter uses rollers to align all the flats simultaneously, whereas the notch orienter rotates each wafer in turn using an optical sensor to detect the notch. In either case the software automatically rotates the wafers from this reference position to the desired angle. Where possible this orientation sequence is carried out during the implant of a previous batch so that throughput is not affected. Full consideration to particle performance was addressed in these designs so that the excellent performance of the whole wafer loading cycle was maintained.

4. Automation

The mature automation software, yet with state-of-the-art features, ensures both system and process reliability and flexible manufacturing operation. The light-pen controlled software automation eliminates operator error, performs beamline set-up, monitors all operations and provides extensive self-diagnostic routines and numerous process integrity checks. An RS-232C interface and SECSII option allow a host computer interface, and a modem link option permits remote diagnostic service support and remote terminal monitoring of implanter performance.

Automation has recently been extended to the facility for robotic loading of wafer cassettes by a new design of loadlock called the robotic interface. This loadlock is readily interfacable to a customer supplied robotic cassette load/unload facility for full factory automation implementation. This is achieved by using a larger loadlock door opening, an automatically open/close and sealing loadlock door, horizontal cassette load stations and a new cassette sensor.

5. Maintenance

The Precision Implant 9200 system uses two CTI 10 cryopumps, to pump the process chamber/wafer loader chamber and the beamline/differential pumping (DP) box. The side cryopump is readily accessible for servicing, however, the rear cryopump is at the centre of the system and is less readily accessed. Since it may be necessary to remove/replace the rear cryopump for servicing every six to twelve months, a lift has been designed into the enclosure roof in order to ease the removal of this pump and reduce the service time.

The lift consists of a band around the pump connected to a ratcheted manual drive, all slung from a permanently roof-mounted monorail. The monorail runs from the installed position of the cryopump to the rear exit of the system, between the cleanroom wall and the beamline ground enclosure. Use of the lift reduces the removal/replacement time from 3-4 hours to 30 minutes, and may be accomplished by one person rather than the two to three people previously required. This improves the tendency to regularly service the pumps rather than delay and risk inferior processing.

In addition, flanges have been added to the source and to the flight tube, allowing simpler maintenance and more effective cleaning.

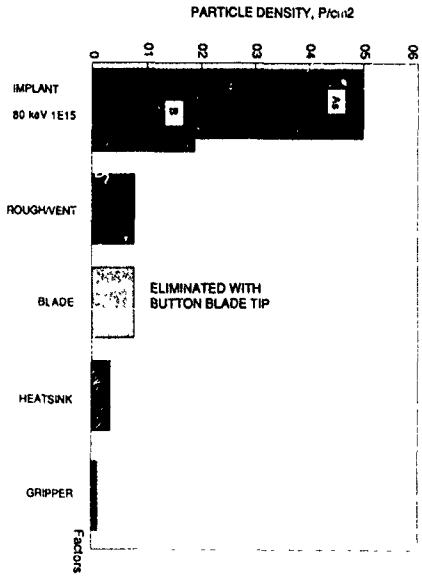

Fig. 1 A Pareto analysis of particulate addition at $> 0.5\ \mu m$ diameter in the PI9200, for various parts of the implanter.

6. Freon-free cooling system

The freon-free cooling system is a new heat exchanger which circulates deionised water coolant through the PI9000/9200 system and extracts the heat to the factory water supply which is then flowed out to the drain. The previous heat exchanger used three recirculating cooling circuits, one employing freon as the cooling medium and two using deionised water (in addition to the mains water cooling to the isolation transformer and the source diffusion pump). The new system uses only one recirculating cooling circuit which employs deionised water as the coolant.

The freon-free cooling system can be retrofitted to early PI9000/9200 systems which are still using the freon-based heat exchanger.

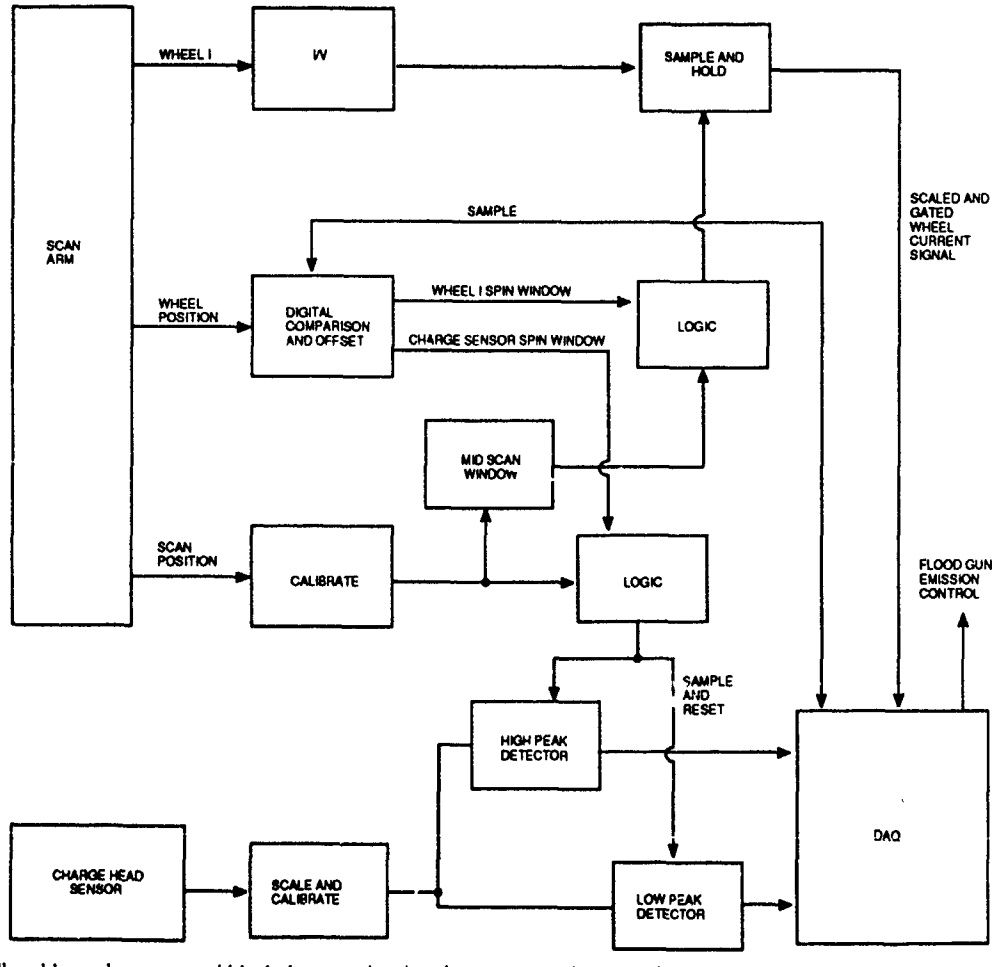

Fig. 2 Closed loop charge control block diagram showing the interaction between the detected charge and the flood gun emission.

7. Particulates

In the interest of minimising particulate contamination, the Applied Materials PI9000 Implanter Series uses a loadlock to transfer wafers under vacuum into the process chamber of the system. This has been assessed in detail and results are presented in fig. 1. It was found that a total wafer handling cycle added on average two particles > 0.5 μm to a 150 mm wafer with the loadlock rough and vent being the main contributor. The main cause of this was a shock wave generated by the crossover between the slow and fast roughing cycles [1]. This was addressed by throttling the pneumatics which open the valve, thus ensuring a smooth transition and eliminating the shock wave.

It is now possible to polish the cast heatsink paddles to a mirror finish to ease the cleaning of the wheel, and prevent it from retaining deposits. The polishing process was developed over several iterations to optimise the finish while introducing no new contaminants into the surface. Electron microscopy and X-ray analysis were used in the development to check the quality of the polished surface.

Beamlines can account for 60 to 90% of defect density [3]. It was found that particulate levels in the PI9200 increased with implant energy and dose, and it was thought that this was due to condensation effects [4]. However, further work has shown that materials in the beamline may be responsible and that paticles can actually be transported by beam impact and charge effects onto the wafers [6]. This has been addressed by changing the specification of parts of the beamline to improved materials. This has resulted in a significant reduction in beamline conditioning time and an improvement in beamline generated particulate levels.

Real time monitoring of particulates was required in order to improve our understanding of the beamline particulate contribution. Commercially available in situ monitors were limited in their performance by the size, velocity and density of the particles to be detected. For this reason Applied Materials has developed its own monitor, capable of measuring particle sizes down to > 0.22 μm [5]. The monitor uses a laser beam focussed to 3 mm^2 with highly sensitive photodetection equipment. It was developed in a comprehensive programme both in the laboratory using latex spheres and in PI9200s. It is now used to optimise the autoclean cycle, maintaining low particulate levels while minimising downtime for maintenance. A closed loop particle control is now being developed to incorporate particulate levels in the automatic software.

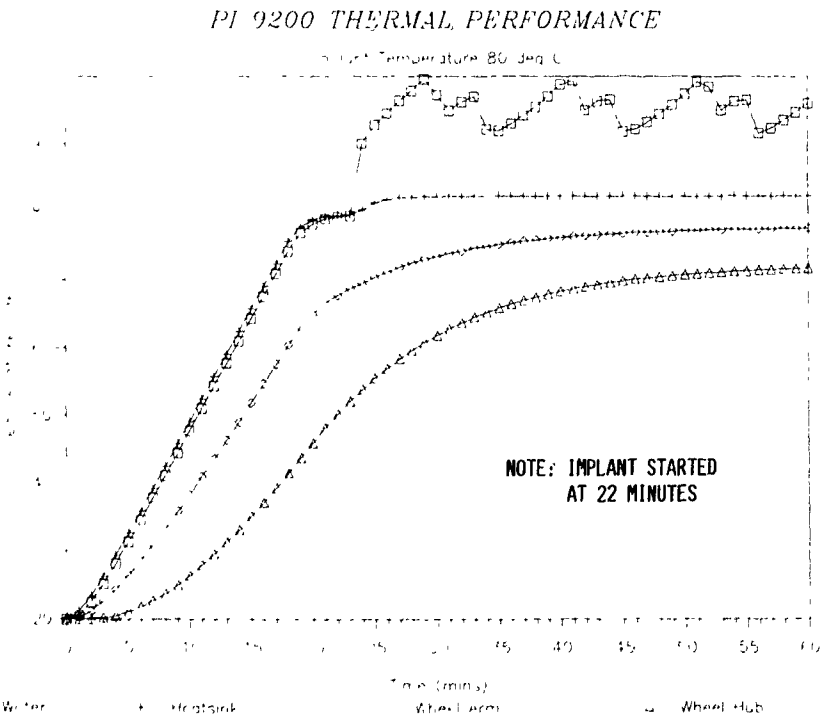

Fig. 3. Thermal performance graphs during warm-up of the heated process wheel system, showing initial heating prior to implant followed by a 120 keV 17 mA As^+ high dose implant. Curves are calculated for the wafer, heatsink, wheel arm and hub.

8. Closed loop charge control

Charge build-up in advanced CMOS devices, especially DRAMs, has become one of the most important and critical factors in ion implantation as device densities increase. The complex interactions present in an ion beam environment require that we pay increasingly close attention to the detailed conditions of electron transport to the wafer, to ensure that low energy electrons equalise ion charge to lower and lower residual charge levels.

An investigation has been carried out on the relationship between system configurations and adjustable parameters, charge indications from the system charge sensor and various wheel current measurements and the yield of devices. To provide automatic control of flood gun emission for optimum yield, a new closed loop control system has been developed based on these measurements This has been found to be very effective in compensating for time-varying charging effects, monitoring all implanter sub-systems and providing lot tracking data on charging conditions. Beam-balanced charge conditions can easily be determined by either charge levels on dielectric films or by wheel current measurements. It is found that devices exhibiting sensitivity to charge damage have the highest yield under conditions of balanced charge and also into the region of significantly negative wheel current or measured charge [7]. Both the wheel current and output from the charge head sensor are constantly monitored. Either may be used as basis for the control, which adjusts the flood gun emission current to maintain constant conditions. The flood gun can be fitted to all PI900/9200 systems and is essentially a controllable thermionic valve, which directs a flood of low energy electrons towards the wafer. It is controlled by both bias voltage and argon gas pressure. A mass flow controller provides the gas flow which allows the bias voltage to be reduced for the same emission current. A block diagram of the control is shown in fig. 2.

9. Heated wheel

The PI9200 system has been designed to enable high beam current implants at low wafer temperatures, to preserve the integrity of photoresists and prevent lattice damage. Typically the temperature of wafers does not exceed 50 °C, achieved by conducting heat from the backside of the wafer via an elastomer. The clampless, planar design uses centrifugal force to provide the contact area required for this conduction while not shadowing the wafer itself. Recent advances have enabled the implanter to circulate coolant at a range of temperatures from 20 to 80 °C, selectable on the heat exchanger. This enables hot implants where the maximum wafer temperature is 100 °C, which improves the removal of any remaining water vapour from the wafer surface (see fig. 3). The redesign addresses all areas of thermal expansion and replaces components which are not suitable for the higher temperatures.

10. Conclusion

Data has been presented on the last two years of field experience of the PI9200 ion implantation system, concentrating on areas of system evolution and performance.

Acknowledgement

I would like to thank all members of Applied Materials for their contributions, and our many customers for their help in the development of the PI9200.

References

[1] K. Fairbairn, Nucl. Instr. and Meth B37/38 (1989) 596.
[2] P. Edwards and M. Current, presented at the 8th Int. Conf on Ion Implantation Technology, Guildford, UK, 1990.
[3] T Hattori and S. Koyata, Detection and identification of process equipment – generated particles for yield improvement, Proc Microcontamination Conf. and Exposition, Santa Clara, CA, 1988, p. 1
[4] J. Strain et al., Microcontamination (May 1989) 47
[5] S Leung et al, these Proceedings (8th Int. Conf. on Ion Implantation Technology, Guildford, UK, 1990) Nucl Instr. and Meth. B55 (1991) 35
[6] H. Ito, private communication.
[7] M. Wauk, these Proceedings (8th Int. Conf. on Ion Implantation Technology, Guildford, UK, 1990) Nucl. Instr. and Meth. B55 (1991) 413.
[8] M.T. Wauk, Nucl Instr. and Meth B21 (1987) 280
[9] M.T. Wauk and A D Giles, Nucl. Instr and Meth. B37/38 (1989) 442.

Nuclear Instruments and Methods in Physics Research B55 (1991) 453–456
North-Holland

The EXTRION 220 parallel scan magnet

R.E. Kaim and P.F.H.M. van der Meulen
Varian Ion Implant Systems, Gloucester, Massachusetts 01930, USA

The design of the EXTRION 220 nonuniform field angle correction magnet is described. Implementation of the design is checked by making field maps of each magnet. The accuracy of beam parallelism has been verified by measuring the angular deviation of ion beam trajectories over the scanning width. It is shown that even small parallelism errors can have an effect on sheet resistance uniformity of high tilt angle implants.

1. Introduction

Beam scanning in the EXTRION 220 is achieved by the combined action of an electrostatic deflector and a rectangular dipole magnet [1]. The field of the magnet varies in such a way as to convert the electrostatic angular scan into a one-dimensional parallel scan. In this paper the design, construction and testing of the nonuniform field magnet are discussed.

2. Magnet design

Fig. 1 shows the geometrical layout of the magnet and electrostatic deflector. In designing the magnet, the following assumptions were made:

(i) The magnetic field in the x direction must vary as

$$B(x) = B_0(1 + ax + bx^2), \tag{1}$$

where a and b are constants to be determined.

(ii) The effective width of the magnetic field in the z direction is constant for all values of x.

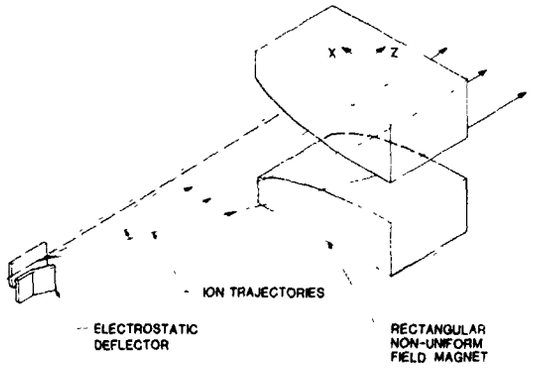

Fig 1 Schematic of E-220 parallel beam scanning

The values of the constants a and b in eq. (1) were determined using the computer program RAYTRACE [2] which calculates the trajectories of charged particles in the presence of magnetic or electrostatic fields. The calculation was performed for the three trajectories shown in fig. 1, corresponding to the center and sides of the scan for a 200 mm wafer. Values of a and b were varied iteratively in order to minimize the deviation from the z direction of all three trajectories emerging from the magnet.

Since the field inside a magnet is inversely proportional to the pole gap, the required pole curvature is governed by the equation

$$D(x) = \frac{D_0}{1 + ax + bx^2}, \tag{2}$$

where $D(x)$ is the pole gap

3. Effective field boundary

The difficulty with the design procedure outlined above is its assumption that the "magnetic width", or distance between effective field boundaries on each side of the poles, does not vary with x. The effective field boundary (EFB) is a measure of how much the magnetic field extends beyond the edge of the poles (see fig. 2). The distance to the EFB is given by

$$L(x) = \frac{\int_0^\infty B(x, z)\,\mathrm{d}z}{B(x, 0)} \tag{3}$$

Fig. 3a shows the expected effective field boundaries for the magnet depicted in fig. 1. The distance from the pole edge to the EFB is roughly proportional to the pole gap [3], which means that the magnetic width is largest where the least deflection is required. Under these conditions the pole shape of eq. (2) cannot produce the required parallel beam.

0168-583X/91/$03.50 © 1991 – Elsevier Science Publishers B.V. (North-Holland)

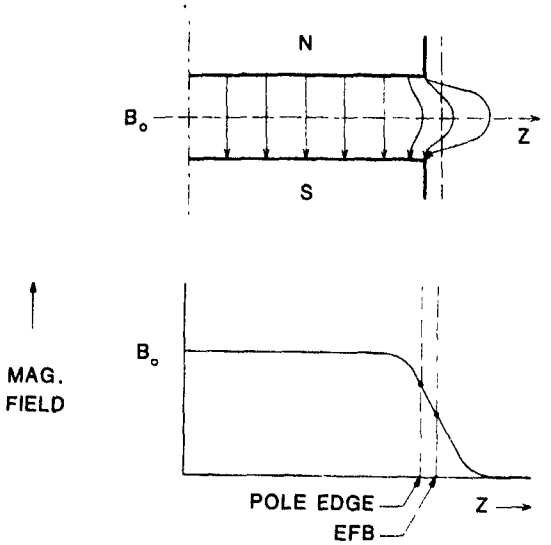

Fig. 2 Concept of effective field boundary

To correct for the "bulging" of the effective field boundaries, the magnet design incorporates field clamps whose purpose is to constrain the fringing fields. The field clamps consist of four flat plates fixed to the top and bottom return yokes on either side of the magnet. The effect of the clamps is to create a reversed magnetomotive force which constrains the magnetic field to very low values between each clamp pair, and thereby pushes the effective field boundaries closer to the poles. The goal is to achieve perfectly straight and parallel EFBs as shown in fig. 3b, so that the RAYTRACE calculation becomes valid and a parallel beam is produced. The extent to which the EFBs deviate from their desired location determines the accuracy of the beam parallelism achieved with the magnet.

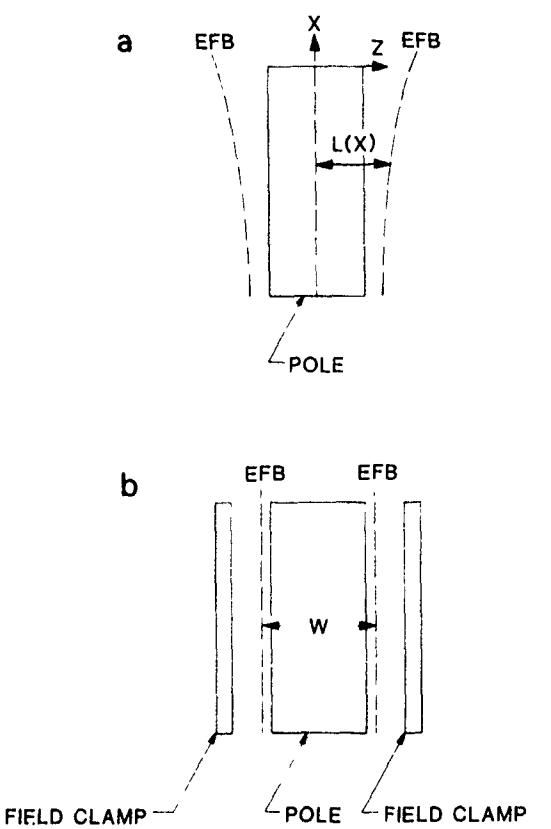

Fig. 3. Effective field boundaries (a) with magnet as shown in fig 1, and (b) with addition of field clamps

4. Magnetic field measurements

In order to minimize the deviation of the EFB from its desired location, the gap between the field clamp plates has to be varied along the x direction – the smaller the gap the more the EFB is pushed in towards the pole edge. The optimum shape of the clamp plates was determined empirically for the first magnet by machining the clamps, measuring the resultant change in the EFB profile, and repeating the process until the deviation was sufficiently small.

For all subsequent magnets, the most critical measure of reproducibility and accuracy is the location of the EFBs. For each magnet the EFBs are measured, and the deviations from the design are required to be within limits which ensure that the specified beam parallelism will be achieved. Fig. 4 shows the longitudinal deviation of the magnetic width, W, for a sample of five magnets. The measurements were made at 25% and 100% of the maximum field, and it can be seen that the width

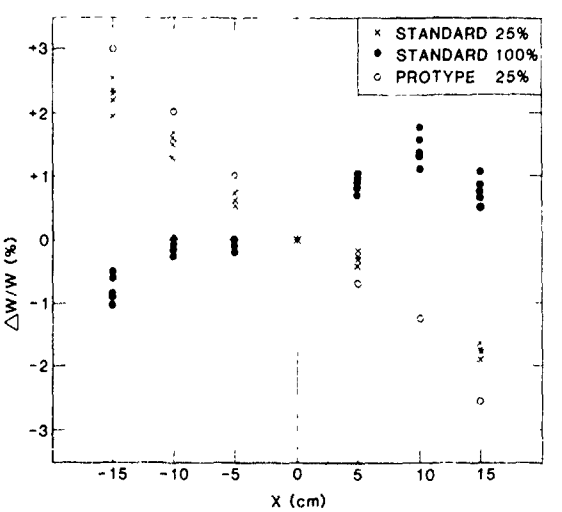

Fig. 4 Deviation of magnetic width as a function of x. Measurements were made for five standard magnets and one prototype magnet at 25% and 100% of maximum field

depends on the field strength, illustrating the nonlinear nature of the magnetic effects causing deviation of the EFB. Nevertheless, these effects are reproducible from magnet to magnet, and amount to a few percent at most. Also shown at 25% field is the result for a prototype magnet which has different yoke and clamp dimensions from the later magnets.

Another magnetic field measurement which is performed on each magnet is a check of the conformance to eq. (1) by measuring the field as a function of x at the line $z = 0$. The deviation from eq. (1) is required to be less than 0.5% over the working length of the magnet.

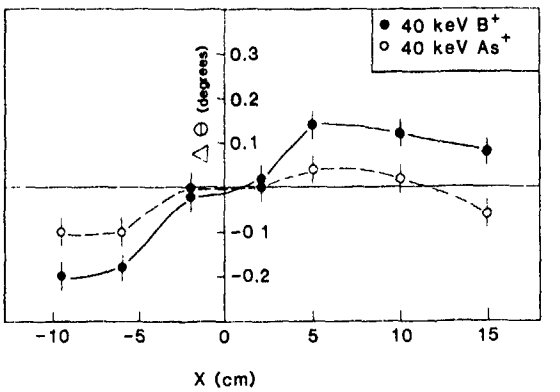

Fig. 6 Deviations from parallelism of 40 keV B and As (standard magnet)

5. Beam parallelism measurements

Once a magnet has been installed on the implanter, the accuracy of the beam parallelism can be measured in a number of ways. The most accurate method is illustrated in fig. 5: two plates containing identical patterns of vertical slits are installed a fixed distance apart in the E-220 end station. The second plate is movable with a micrometer screw, and beam current transmitted through any pair of slits can be measured with a Faraday plate. Using dc voltage on the electrostatic deflectors, the beam is steered sequentially through each slit in the first plate. The second plate is then moved to a position which maximizes beam transmission to the Faraday plate, and the relative movement required provides a measure of the deviation from parallelism as a function of the position x of the first slit. Fig. 6 shows measurements made for 40 keV B^+ and As^+, corresponding to low and high values of magnetic field. The deviations from parallelism are larger for B^+ than for As^+, which is in agreement with the deviations of the magnetic width measurements shown in fig. 4.

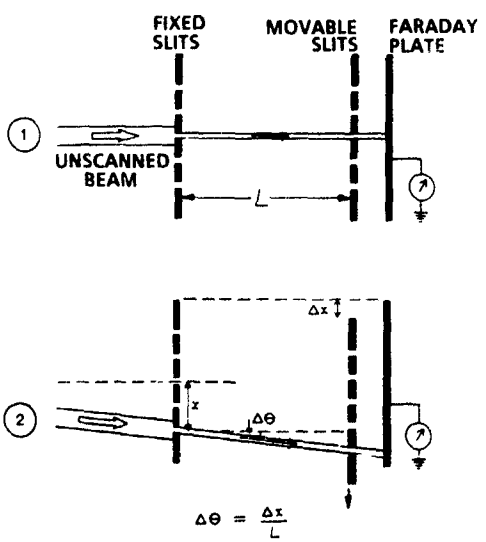

Fig 5. Method used to measure deviation of beam scan from parallelism.

6. High tilt angle uniformity

There is a recent trend in ion implantation towards use of large tilt angles (60° or more) For such large angles, errors in beam parallelism can cause degradation of the implant uniformity: for a tilt angle θ and beam parallelism error $\delta\phi$ over the wafer diameter, the fractional change in dose from the center to the edge of the wafer is given by [4]

$$\Delta = 2 \tan\theta \tan\delta\phi. \quad (4)$$

It has been found that the inferior low-field performance of the prototype magnet (see fig. 4) causes a noticeable degradation of the uniformity of high tilt angle boron implants. Fig. 7 illustrates the result of an

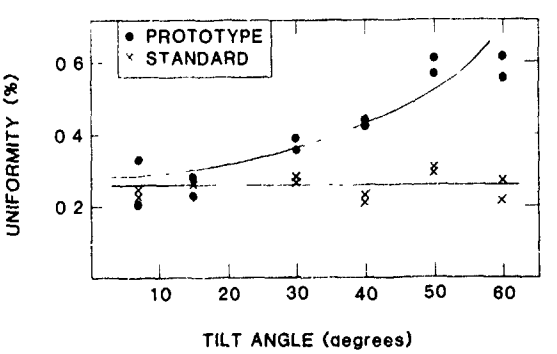

Fig. 7 Implant uniformity as a function of tilt angle

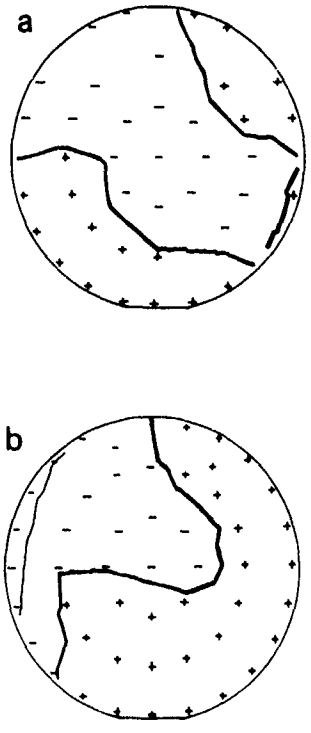

Fig. 8 Sheet resistance maps for implants at 50° tilt (boron, 124.5 keV, 1.56×10^{14} ions/cm^2): (a) standard magnet (standard deviation, 0.31%), (b) prototype magnet (standard deviation: 0.58%)

experiment in which wafers were implanted with boron at different tilt angles, but with the same effective dose and beam energy (i.e. corrected by a factor $1/\cos\theta$). The uniformity worsens with increasing tilt angle for the prototype magnet, but the effect is not apparent for an implanter using a magnet of the final design type. In fig. 8 sheet resistance maps at 50° tilt are compared for the two magnets. Here it is seen that the degradation of uniformity for the prototype occurs in the direction of the horizontal beam scan, which is consistent with the effect of beam parallelism error.

7. Conclusion

Measurements of the magnetic width provide an effective way to assure the accuracy and reproducibility of parallel scan magnets for the E-220. The parallelism may also be directly checked with an ion beam. Uniformity of high tilt implants can be a sensitive indicator of parallelism.

References

[1] D.W. Berman, R.E. Kaim, J.W. Vanderpot and J.F.M. Westendorp, Nucl. Instr. and Meth. B37/38 (1989) 500.
[2] S. Kowalski and H.A. Enge, RAYTRACE, 1985
[3] H.A. Enge, Rev. Sci. Instr. 35 (1964) 278
[4] J.H. Keller, Radiat. Eff. 44 (1979) 71

Nuclear Instruments and Methods in Physics Research B55 (1991) 457–464
North-Holland

Improved wafer charge neutralization system in Varian high current implanters

S. Mehta, R.F. Outcault, C.M. McKenna and A. Heinonen
Varian Ion Implant Systems, Blackburn Industrial Park, Gloucester, MA 01930, USA

Control of wafer charging during high current implantation plays a key role in achieving higher device yields. As certain device dimensions shrink with a corresponding reduction in gate oxide thicknesses, their sensitivity to charging increases. This characteristic of devices, compounded with the increasing beam currents available in commercial high current implanters (up to 25 mA or more), poses critical challenges to techniques used for wafer charge control during implantation.

In this paper, we will present the key features of an auto emission flood control system which holds the disc current constant at a desired setting, and minimizes any charge fluctuations on the wafer in real time. The features of this system were compared to those of "no electron flood" and "constant emission flood system" using a variety of wafers (e.g., bare, poly-Si, poly-Si-on-oxide and photoresists, etc.) In all cases, the charging characteristics of each wafer were monitored in real time using a capacitive charge collecting device. Correlations between disc current, flood emission current and the charge collectors response were used to demonstrate the merits of the auto emission flood control system. In addition, the flood gun options available on the XP series of high current implanters, including the features of the charge collecting device, will be presented

1. Introduction

Wafer charging, a major yield limiting factor in high current implantation, has always been an area of concern for device manufacturers. In recent years, several studies have been conducted on this particular aspect of ion implantation by both the device engineers and by equipment manufacturers [1–3]. Although several techniques for charge neutralization in high current implanters have been commercialized, none of the methods has been designed to take into account changing conditions of pressure and electron population within the Faraday in the immediate vicinity of the wafer. Today, the higher beam currents for enhancing throughput and the increasingly sensitive, complex device structures with reduced gate-oxide thicknesses make it even more necessary to have a charge control system that will continuously respond to these changing conditions during the implantation process. Also, the Faraday and electron flood systems have to be designed to prevent any electron leakage, so as not to affect dose measurement.

The objectives of this paper are to present the features of an auto emission electron flood control system employed on the Varian XP series of high current implanters. This system regulates the net charge on the disc (wafer) during the entire length of the implantation process. The features of a charge collecting device (Q-Monitor) mounted in the end station chamber will be also be presented. The real-time charge signals measured by this device will be used to demonstrate the charge controlling features of the electron flood system under a variety of pressure and implant conditions. In addition, the effects of the auto emission system on the yield of a variety of charge-sensitive device structures under several implant conditions will be presented.

An evolution of the Varian high current implanters has occurred over the last ten years. Since the commercial realization of the 80-10 ion implanter in 1980, the XP series of high current implanters (80/120/160 and 180XP) have subsequently been introduced with advancements over their respective previous models. One of the areas of continued improvement has been the Faraday and wafer-charge control systems [3,4]. While these systems have been designed for the XP series of implanters, they can be retrofitted to some of the earlier models as well. The new machines incorporate the auto emission control system (which controls the disc current), and the Q-Monitor (which picks up real-time charge signals from wafers by capacitive pick-up).

2. Flood systems and their characteristics

Faraday systems are employed in ion implanters to monitor and control the dose of the implanted species. The prime function of the Faraday is to count the ions implanted, without affecting the beam characteristics [5]. The schematics of the Faraday system for 80/120/160-10 models and the XP models are shown in figs. 1a and b respectively, including the corresponding electron flood guns. The transition from the original

0168-583X/91/$03.50 © 1991 – Elsevier Science Publishers B.V. (North-Holland)

design to that of the XP occurred in several sequences described elsewhere [3,4]. Primary electrons from an electrically heated filament are injected into the Faraday, and strike the opposite wall of the Faraday cage to produce secondary electrons with a dominantly Maxwellian distribution, which in turn are used for beam and surface-charge neutralization.

In all the systems described above, a fixed emission current was used to generate electrons from the filament. The appropriate emission level was determined empirically for each device type depending on its charge sensitivity and the implant conditions. Although very repeatable in its operational characteristics, such a system did not provide any automatic response to the constant variations taking place in the Faraday during the implant, e.g.: pressure changes due to photoresist outgassing, device variables (oxide thickness etc.), position of the beam during scan (on wafer, off wafer) and other factors such as beam spot size and space-charge conditions of the beam.

In order to account for all the above mentioned variables, the latest charge control system, "auto emission control flood system", was developed for the 80/120/160-10 and the corresponding XP series of implanters. In this system, the disc current signal is used as an input to the flood control regulation system. The control system varies the flood gun emission current as required, to regulate the disc current. As the conditions in the Faraday change, the emission current is also adjusted, which in turn produces a resultant change in the secondary electron current to the disc. Thus, the disc current can be held steady despite the changing conditions in the Faraday. The operator has the option to choose the desired disc current setting for any given implant. The optimum disc current depends on the device type and the implant conditions, as will be shown later. In fig. 2, the characteristics of the auto emission system have been compared with those of a fixed emission flood system for a high current arsenic implant run on a disc load of wafers, among which were several coated with photoresist. The scan waveform, disc current, emission current and the end station pres-

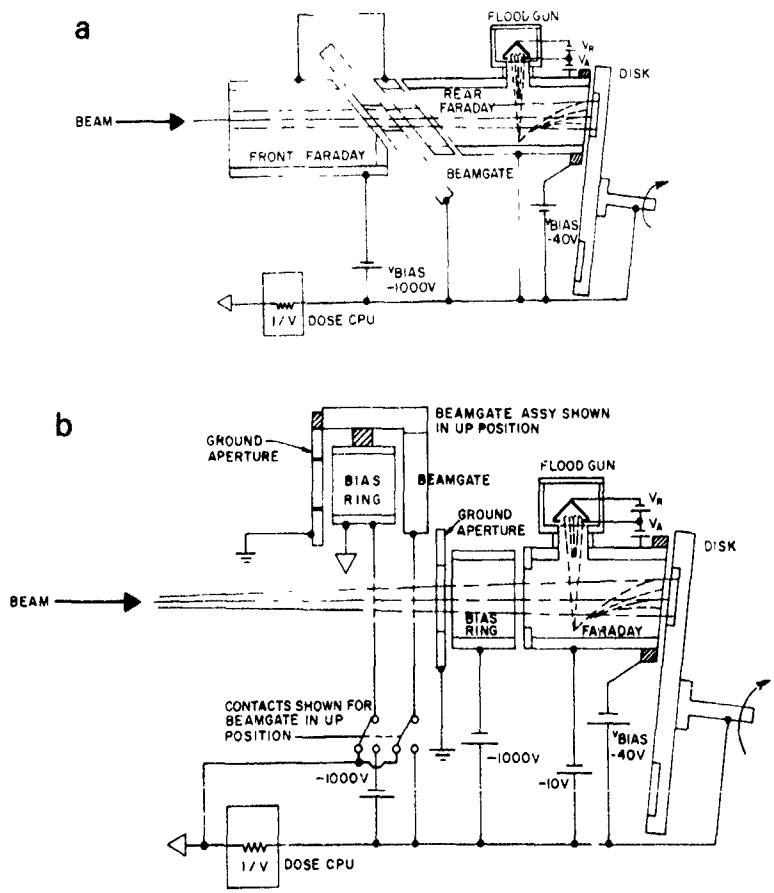

Fig. 1. Schematics of the Faraday and the associated flood gun systems for the Varian high current implanters (a) 80/120/160-10 systems and (b) 80/120/160/180XP systems.

sure have all been plotted for the implant in question. In the fixed emission flood system, the emission level stays constant through the entire implant process.

When charge-sensitive devices are being implanted, the combined effect of the fixed emission flood, beam interaction with the residual gas and the disc during the

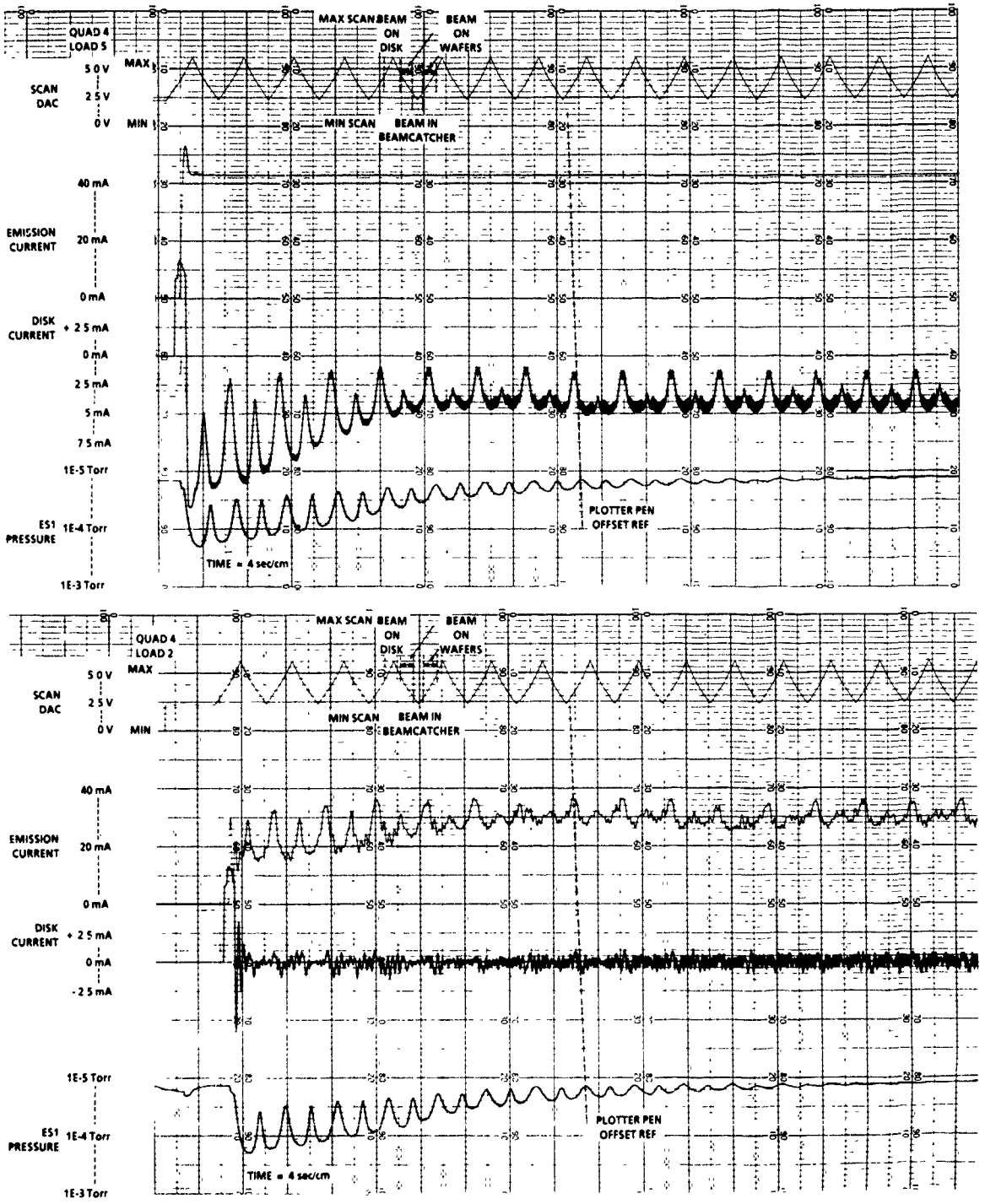

Fig. 2 Characteristics of the "auto emission control system" ($I_{disc} = 0$ mA) compared with those of "fixed emission system" for an arsenic, $5 \times 10^{15}/cm^2$, 60 keV implant under varying conditions of pressure caused by photoresist outgassing.

scan process can overflood the Faraday with electrons, thereby increasing the risk of device damage due to negative-charge effects. The same is not true for the auto emission control system. As the pressure in the end station rises during the initial stages of the implant due to photoresist outgassing, the beam interactions with the gas molecules create more electrons in the Faraday. In order to maintain a steady disc current (0 mA in this case), the control system responds accordingly and reduces the level of emission current. As the vacuum improves, the requirement for more electrons is met by the control system with greater emission current. The electron requirements related to beam position during scan are also illustrated in fig. 2. Once the photoresists has been fully carbonized, the outgassing rate drops as indicated by the stabilization of pressure. Consequently, the flood emission current also stabilizes to maintain the desired disc current value.

3. Q-Monitor

Recently, some attempts have been made to directly sense charge build-up on the wafers by using real-time charge monitors as accessories to wafer charge control systems [6]. These systems use the phenomenon of capacitive coupling between the wafers and the charge pick-up device. Varian has introduced such a system, the Q-Monitor, for the XP series of high current implanters. A design schematic of the same is depicted in fig. 3. The carefully positioned device capacitively picks up the wafer surface-charge. This charge signal is then displayed on a storage oscilloscope and can be plotted on an $X-Y$ chart recorder to assist in data analysis. Calibration of the Q-Monitor with a fixed, known voltage allows the user to determine the relative charge (or some function of it!) developed on the wafers during the implant process. Further work to improve upon this first design is in progress. There are some concerns about the ability of this device to provide a measure of the absolute charge on the wafer due to charge decay that may occur before the wafer reaches the sensor position and to the consistency of its sensitivity being affected by variations in the sensor–wafer separation. However, this device in its present configuration can assist the user in evaluating the relative charge phenomenon taking place in real time on the wafers and therefore provide valuable assistance in the optimization process without the risk of using many wafers.

4. Experimental

All charging tests conducted for this investigation were run on a Varian 160XP high current ion implanter

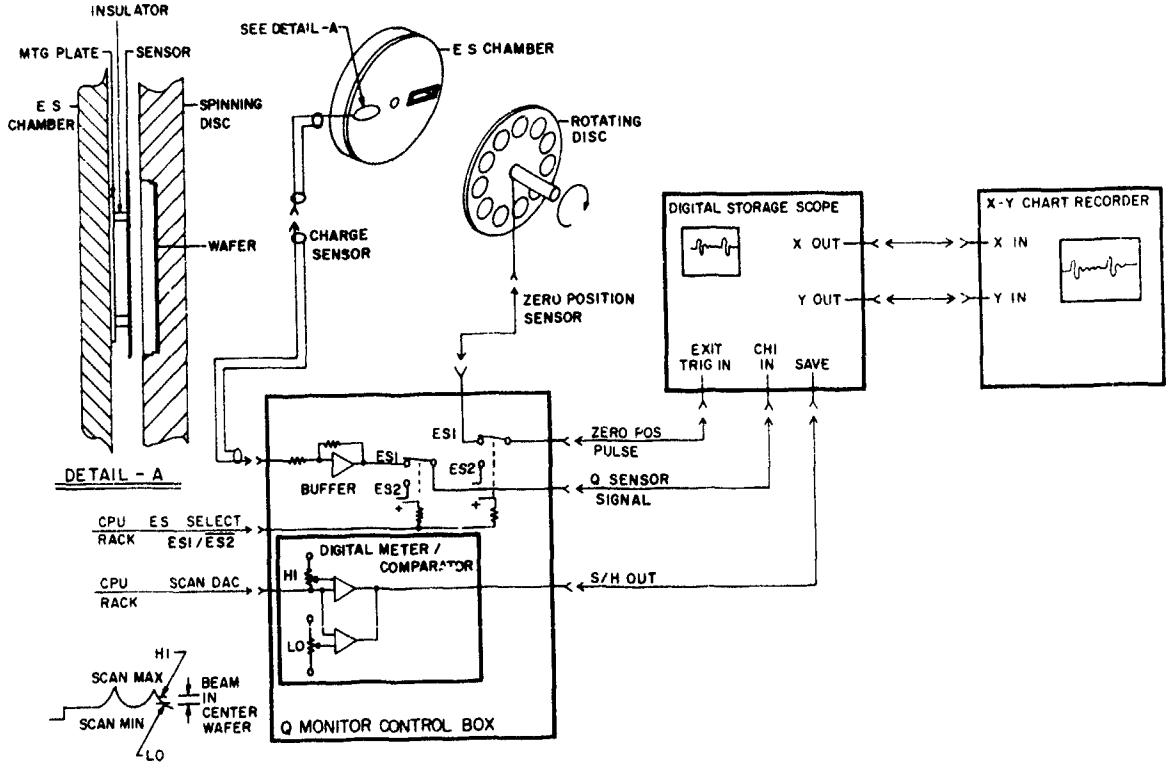

Fig. 3. A schematic design of the Q-Monitor system for the Varian XP series of high current implanters.

equipped with the auto emission flood control system and Q-Monitor. In order to demonstrate the characteristics of these systems, the effects of several implant parameters such as ion species, end station pressure and electron flood conditions, on the yield of several charge monitor wafers were studied. In addition, the effects of the presence of photoresist wafers upon yield of the devices was also studied. Table 1 summarizes the test matrix used in this study.

Test vehicles used were state-of-the-art MOS structures with gate oxide thicknesses of 235 Å, 180 Å and 80 Å, fabricated on 150 mm silicon wafers with a high charge multiplier ratio. Breakdown measurements were done on the 235 Å and 80 Å devices. Charge-to-breakdown measurements were done on the 180 Å oxide set of devices fabricated at Varian. The criterion for breakdown was defined as the voltage where 1 μA of current was detected through the oxide.

5. Results and discussion

Typical p^+ and n^+ source/drain implants were used for this investigation. For the p^+ implant, BF_2 ions with 50 keV energy were implanted into the test wafers to a dose of $5 \times 10^{15}/cm^2$ at 6.5 mA of beam current in the "decel mode" of operation. The n^+ implant consisted of arsenic ions with 60 keV energy implanted to the same dose at 9.3 mA of beam current in the "accel mode" of operation.

Device yields for the 80 Å and 235 Å oxide devices implanted under several electron flood conditions are shown in figs. 4 and 5 for the two respective implant species. The control wafers, which received no implant, had 100% yield for both oxide thicknesses, indicating good process control in the fabrication of the devices. On the other hand, wafers implanted without any electron flood showed poor yields for both species, clearly demonstrating the need for charge neutralization.

It is also observed that the device yields for the arsenic-implanted wafers were in general much higher than those obtained with BF_2 implants. The reason for the observed disparity in yield between the two cases under consideration is not clear. Recently, some studies [7,8] have shown that, although small amounts of fluorine introduced into the gate-oxide improve the interface quality, large amounts can have a detrimental effect on the electrical integrity of the oxide The beam

Table 1
Experimental text matrix

Test ID	Test device ID			Electron flood conditions	Status of other sites	Other remarks
	235 Å ox	Var ox	80 Å ox			
BF_2, $5\times10^{15}/cm^2$, 50 keV						
Q1-L1	18	K-19	10	no flood	bare Si	
Q1-L2	23	K-15	18	$I_{disc} = 0$ mA	bare Si	
Q1-L3	21	K-17	06	$I_{disc} = -2$ mA	bare Si	
Q1-L4	20	K-4	23	$I_{disc} = +1$ mA	bare Si	
Q1-L5	07	K-5	12	$I_{em} = 33$ mA	bare Si	
Q2-L1	01	K-8	13	no flood	photoresist	
Q2-L2	22	K-14	02	$I_{disc} = 0$ mA	photoresist	
Q2-L3	16	K-24	08	$I_{disc} = -2$ mA	photoresist	
Q2-L4	15	K-13	09	$I_{disc} = +1$ mA	photoresist	
Q2-L5	24	K-34	24	$I_{em} = 33$ mA	photoresist	
As^+, $5\times10^{15}/cm^2$, 60 keV						
Q3-L1	12	K-37	07	no flood	bare Si	
Q3-L2	11	K-10	04	$I_{disc} = 0$ mA	bare Si	
Q3-L3	14	K-12	05	$I_{disc} = -2$ mA	bare Si	
Q3-L4	09	K-06	03	$I_{disc} = +1$ mA	bare Si	
Q3-L5	08	K-16	14	$I_{em} = 45$ mA	bare Si	
Q4-L1	10	K-11	11	no flood	photoresist	
Q4-L2	03	K-36	16	$I_{disc} = 0$ mA	photoresist	
Q4-L3	06	K-9	15	$I_{disc} = -2$ mA	photoresist	
Q4-L4	05	K-32	01	$I_{disc} = +1$ mA	photoresist	
Q4-L5	04	K-20	17	$I_{em} = 45$ mA	photoresist	
P1-L1	12	K-7	-	$I_{em} = 45$ mA	bare Si	5.4×10^{-5} Torr
P1-L2	13	K-35	-	$I_{disc} = 0$ mA	bare Si	5.4×10^{-5} Torr
P2-L2	14	K-33	-	$I_{em} = 45$ mA	bare Si	1.4×10^{-4} Torr
P2-L2	08	K-18	-	$I_{disc} = 0$ mA	bare Si	1.4×10^{-4} Torr

density itself can also affect device yield, however, in this study the difference in the beam densities for BF_2 and arsenic implants was not significant enough to cause the large difference in yield for the two cases. Therefore, the relative contribution of the individual beam densities to the observed yield differences is not clear.

Of all the BF_2 implants, regardless of the flood condition employed, the yield for the 80 Å oxide device was the highest (52.2%) when the disc current was held at 0 mA by the auto emission flood control system, and with no photoresist wafers present. However, when fixed emission flood is used, the yield drops tremendously (25.4%), demonstrating the high charge-sensitivity of the thin gate-oxide device structure used in this study. The drop in yield in the case of fixed emission flood is most likely due to overflooding of electrons that result in negative charge damage of the oxide.

This finding is substantiated by the results obtained on the 235 Å oxide device under similar implant and electron flood conditions. Since the oxide is thicker in this case and therefore less charge sensitive, the effect of overflooding *without* photoresist wafers is not significant. However, the effect is more pronounced in the case of implants run *with* photoresist wafers present. Outgassing from the photoresist raises the end station pressure, thereby increasing the production of electrons by the beam interaction with the gas molecules. Since the electron population is enriched, the negative charging damage causes the yield to drop more significantly. When the disc current is maintained at 0 mA by the auto emission flood system the yield *improves to 100%* for the 235 Å oxide device. Fig. 6 illustrates the above phenomenon by Q-Monitor signals for a BF_2 implant run under different flood conditions with photoresist wafers present. It is worth noting that the charge signals with $I_{disc} = 0$ mA are completely suppressed regardless of the conditions, thereby demonstrating the excellent control characteristics of the auto emission flood system.

Q_{bd} measurements [9] were made on the corresponding Varian test wafers for all implants of table 1. For arsenic implants, the Q_{bd} peaks for the implants *with* photoresist occur at 30–32 C/cm^2 while for *non*-photoresist implants, the peaks are at 29–30 C/cm^2. This indicates that the presence of photoresist creates positive charging effects as one would expect. Similar effects of photoresist have been observed by other workers as well [10]. It is also observed that the presence of photo-

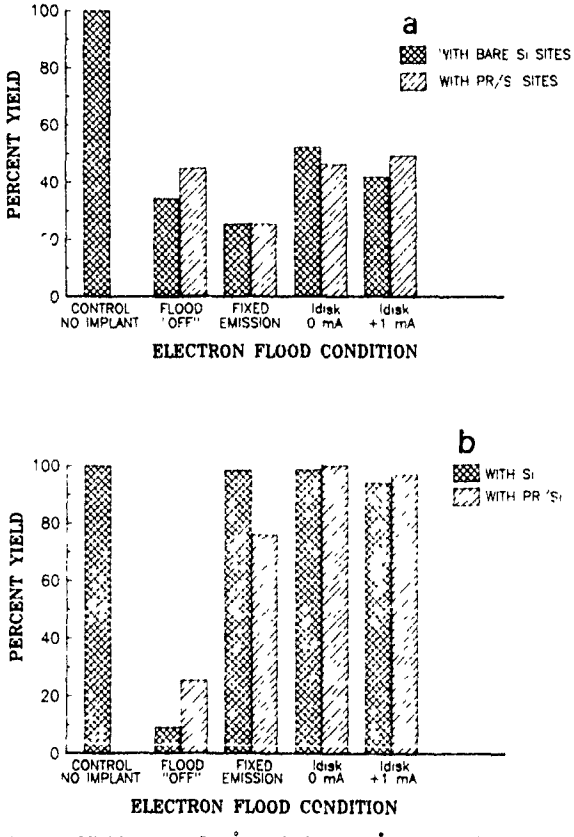

Fig 4. Yield of (a) 80 Å and (b) 235 Å gate-oxide devices implanted with BF_2^+, 5×10^{15}/cm^2, 50 keV at 6 6 mA of beam current, under various electron flood conditions

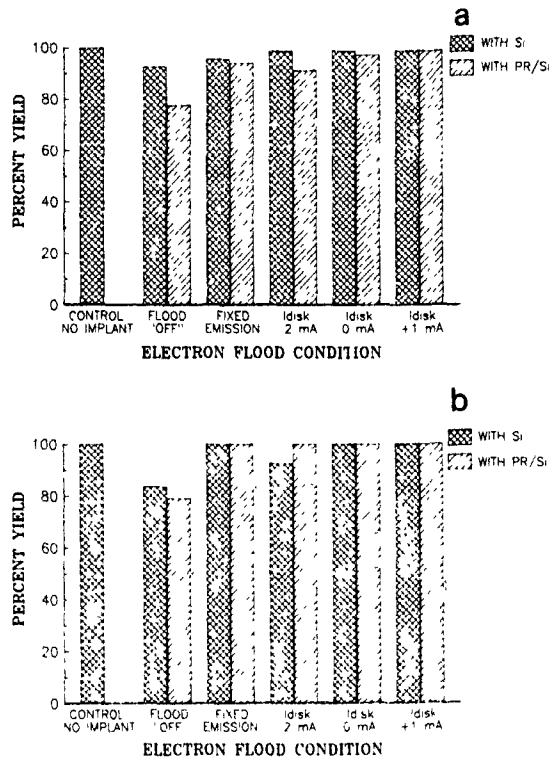

Fig 5 Yield of (a) 80 Å and (b) 235 Å gate-oxide devices implanted with As^+, 5×10^{15}/cm^2, 60 keV at 9 30 mA of beam current, under various electron flood conditions.

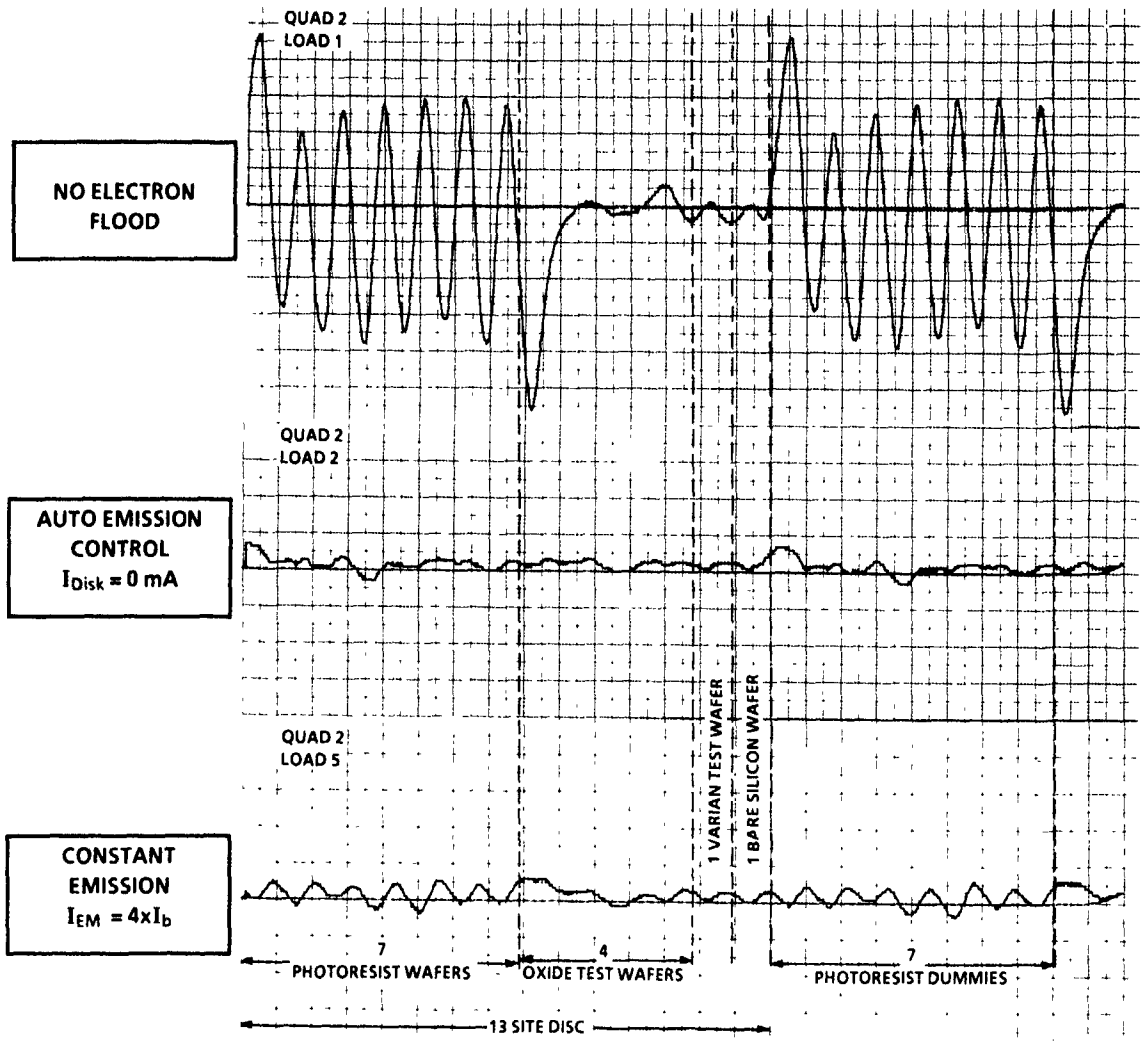

Fig. 6 Q-Monitor signals for a BF_2 implant with photoresist wafers present, recorded under conditions of (a) no electron flood, (b) I_{disc} = 0 mA with auto emission control flood and (c) fixed emission electron flood.

resist had little effect on the Q_{bd} value for the BF_2 implants.

While the effects of various electron flood conditions have been investigated as a function of changing pressure conditions caused by the photoresist wafers, additional tests were done to compare the effects of the "fixed emission" and the "auto emission" electron flood systems on device yield, under constant pressure conditions maintained through the length of the entire implant. Tests were done for the arsenic implant under two different pressure conditions and the yields for the 235 Å oxide device were compared for the two electron flood systems. The results are summarized in table 2.

Table 2
Effect of end station pressure on the yield of a 235 Å oxide device under different electron flood conditions. Implant: arsenic, $5\times10^{15}/cm^2$, 60 keV, I_{beam} = 9 30 mA.

Test ID	Device ID	Electron flood conditions	ES pressure [Torr]	Device yield [%]
P1-L1	12	I_{em} = 45 mA	5.4×10^{-5}	100
P1-L2	13	I_{disc} = 0 mA	5.4×10^{-5}	100
P2-L1	11	I_{em} = 45 mA	1.4×10^{-4}	95.5
P2-L2	08	I_{disc} = 0 mA	1.4×10^{-4}	100

Under both conditions of pressure tested, the yield is maintained at 100% with the auto emission system holding the disc current at 0 mA. However, a slight drop in yield occurs at the higher of the two pressure conditions (1.4×10^{-4} Torr) when the fixed emission flood is used. As explained earlier, this drop in yields is attributed to negative charging caused by the increased

electron population resulting from the ion beam interaction with the gas molecules. This effect was substantiated by the slight negative shift observed in the Q_{bd} peak of the Varian oxide sample also run together with the test in question. Although one can argue that the observed drop in yield is rather small, this effect will be more pronounced in thinner oxides due to their high sensitivity towards charging, as has been explained earlier.

In addition, sheet resistance monitor wafers implanted with all the tests showed excellent uniformity and repeatability regardless of the implant, pressure and electron flood conditions employed. These results indicate that the Faraday system is well designed so as to prevent any electron leakage and that the electron flood characteristics do not degrade the accuracy of the dose measurement system.

6. Conclusions

The merits of the control characteristics of the auto emission control electron flood system for the XP series of Varian high current implanters have been demonstrated on state-of-the-art charge-monitor wafers under several conditions of implantation.

The introduction of the Q-Monitor as an added accessory to the auto emission system represents a step towards a better understanding and more localized control of wafer charging. The information provided by the combination of the above systems will allow the users to optimize the charge control conditions in a more efficient and cost-effective manner.

Acknowledgements

The authors wish to thank Larry Gering for the invaluable assistance in the successful running of the tests under limited time conditions. Many thanks to Aki Ueda of Motorola Inc. for his guidance and valuable assistance in data analysis. Thanks are due to Susan Felch and Juanita Sonico of Varian for Q_{bd} tests and data analysis. We are also grateful to Ron Eddy of Varian for many helpful discussions and to Pam Mansfield for the artwork and Peter Bradford for preparation of the final manuscript.

References

[1] N. Nagai, T Kawai, M. Naito, Y. Nishigami, H. Fijisawa and K. Nishikawa, Nucl Instr. and Meth B37/38 (1989) 572.
[2] M.E. Mack, Nucl. Instr. and Meth B37/38 (1989) 472.
[3] C.M. McKenna, B O Pedersen, J K Lee, R.F. Outcault and S Kikuchi, Nucl. Instr. and Meth. B37/38 (1989) 492
[4] R.F Outcault et al , Nucl. Instr. and Meth. B21 (1987) 354
[5] H Glawischnig and K. Noack, in Ion Implantation Science and Technology, ed. J F. Ziegler (Academic Press, 1984)
[6] B.J. Doherty and D J. McCarron, Nucl. Instr and Meth B37/38 (1989) 559.
[7] W. Ting, G.Q Lo and D.L. Quong, SRC publication, private communication, June 1990
[8] T.P. Ma, SRC Publications, private communication, June 1990
[9] S Felch, S. Mehta, S Kikuchi and S Kitahara, these Proceedings (8th Int. Conf on Ion Implantation Technology, Guildford, UK, 1990) Nucl Instr and Meth B55 (1990) 82
[10] A. McCarthy and W Lukaszek, Stanford CIS Annual Report for SRC (1989)

Nuclear Instruments and Methods in Physics Research B55 (1991) 465–468
North-Holland

Operating procedure for improving ion source lifetime for the 80-180XP ion implanter

S.R. Walther and R.F. Outcault

Varian Ion Implant Systems, Blackburn Industrial Park, Gloucester, MA 01930, USA

The limited lifetime of the Freeman ion source filament has been the cause of equipment downtime, for filament replacement, in the use of high current ion implanters. The ion source lifetime of the 160XP ion implanter has been improved by a factor of four for high current operation, where source lifetime, especially with boron, has been very limited. The key to obtaining this result is a reduction of physical sputtering of the tungsten filament. This is achieved by minimizing the arc voltage used by the ion source, while still delivering the same boron performance. The reduction in filament wear is also applicable to other dopants, and has been demonstrated with arsenic. Calculations of the sputtering rate, as a function of arc voltage, are consistent with the improvement in filament lifetime noted experimentally and imply that further improvements may be possible.

1. Introduction

The limited ion source lifetime of the Freeman ion source used on the 80-180XP ion implanter [1] has been a problem, contributing to the overall downtime of the machine. This is particularly true during high current $^{11}B^+$ ion beam operation. To address this issue, it is important to know the mechanisms by which the source filament is eroded. The most likely mechanism is sputtering of the filament material by plasma ions. The rate at which this process progresses is determined by the plasma density (roughly proportional to the discharge power) and the arc voltage (which determines the plasma ion energy, along with a small contribution from the plasma potential). A second mechanism that reduces filament life is cycling of the source on and off. Although it is not completely understood, the filament appears to fail prematurely when subjected to complete thermal cycling (the source is allowed to cool and is then restarted).

The Freeman ion source [2] has been used for many years in the ion implantation industry. The use of the externally generated axial magnetic field, in combination with the magnetic field produced by the filament itself, provides the electron confinement for the discharge. The electrons emitted from the filament have a cycloidal orbit [3] in the region near the filament. This results in a substantial plasma density gradient between the filament and the ion extraction slot of the ion source. The limited filament lifetime of the Freeman source is due to the high plasma densities near the filament. In order to improve the filament lifetime, either the plasma density must be reduced, or the sputtering rate per plasma ion striking the filament must be reduced. Unfortunately, reducing the plasma density also reduces the beam current available and is therefore unacceptable.

It is well known that lowering the arc voltage of the discharge increases the source lifetime by reducing sputtering. The improvement in filament life is due to the much lower sputtering coefficient for incoming ions at reduced arc voltages, as well as the reduction in plasma density. The sputtering coefficient is a very strong function of the ion energy (arc voltage). The rate can be calculated using an empirical relation [4], given below, as a function of ion mass (m_1), target atom mass (m_2), ion energy (W), and the surface binding energy (W_b) of the filament material. A value of 8.4 eV is used here for the W_b of tungsten. The ion energy (W) is given approximately by the sum of the arc voltage and the plasma potential:

$$\text{Rate} = 0.0064 m_2 \beta^{5/3} (W/W_{th})^{1/4} (1 - W_{th}/W)^{7/2},$$

where β is given by $4m_1m_2/(m_1 + m_2)^2$, and W_{th} is given by $W_b/\beta(1 - \beta)$, for $m_1/m_2 \leq 0.3$, or $8W_b(m_1/m_2)^{2/5}$ for $m_1/m_2 > 0.3$.

In the case of boron, the discharge contains B^+, F^+, BF^+, and BF_2^+ as the dominant ion species in the plasma. The minor difference in sputtering yield of $^{10}B^+$ (versus $^{11}B^+$) is neglected here. The ion beam fractions of the different species were measured on numerous occasions for high current boron operation. An average of 33% B^+, 21% F^+, 11% BF^+, and 35% BF_2^+ was used to model the discharge, even though there is some variation over time and from one test to another. The sputtering rate for each species was calculated and summed. Fig. 1 shows the relative sputtering rate as a function of ion energy for a tungsten filament in a BF_3 discharge. This graph details the significance of the arc voltage to the sputtering rate. A change of ion

0168-583X/91/$03.50 © 1991 – Elsevier Science Publishers B V. (North-Holland)

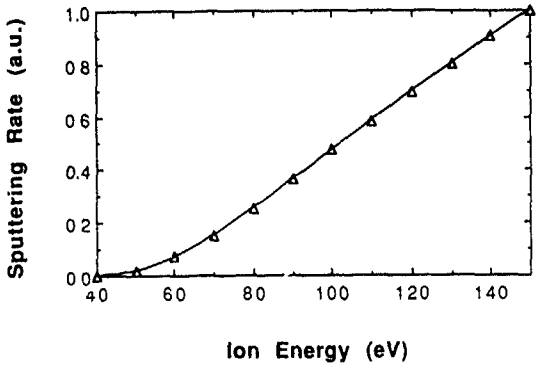

Fig 1 Calculated physical sputtering rate versus ion energy for a BF_3 discharge.

energy from 120 to 60 V results in a tenfold reduction in the sputtering rate. To arrive at an actual rate, the results must be multiplied by the local current density of the plasma. If this value is known, the erosion due to physical sputtering of the filament as a function of time, and hence filament lifetime, can be calculated.

2. 160XP lifetime experiments

Initial testing was conducted to determine the actual source lifetime using standard operating procedures, which specify an arc voltage c. ~ 120 V, while the arc current is used as a free parameter to adjust the beam current. The implanter was operated at a constant 5 mA of $^{11}B^+$ beam current (100 keV beam energy) in the end station, since 5 mA $^{11}B^+$ can be achieved immediately and maintained over the course of the test. In this case, the source lifetime was between 12 and 14 h during standard operation, with no thermal cycling of the ion source. Lifetime is defined here as the actual operating time during which the source is producing the specified $^{11}B^+$ ion beam, until the filament fails.

To determine if higher arc currents and lower arc voltages would improve source life, a production machine was operated at a constant 5 A of arc current, normally the upper limit for this parameter, and the arc voltage was varied in a manner to maintain the constant 5 mA of $^{11}B^+$ ion current. The use of the larger arc current allowed a reduction in the arc voltage, while still providing the same performance. These tests lasted several days, which included cycling the source on and off, with the result of a source life of *27 h*. The test was repeated twice to confirm this, and lifetimes of 26.5 and 28.5 h were obtained. This includes the effect of the source cycling on and off, where the filament often fails even though the diameter is relatively large. This premature filament failure is most likely caused by mechanical stresses induced by rapid thermal expansion and contraction of ion source parts during startup and shutdown. This can be alleviated through continuous operation of the ion source. The arc voltage was reduced to 60 V towards the end of these tests as the filament became thinner.

Additional testing was undertaken, using a constant 6 A arc current and 24 h/d operation, to determine if further improvements in source life were possible. It should be noted that operation at 6 A of arc current exceeds the rated power supply capacity and is not recommended. The results of these tests show the impact a large reduction in arc voltage and continuous operation can achieve. Source lifetimes of 66, 43, 39.5, and 60+ h were attained during operation at 5 mA of $^{11}B^+$ current. The 60 h test was terminated, due to personnel constraints, before the filament failed. The true filament life for that test is estimated to be $\geq$ 75 h using an extrapolation based on the filament current.

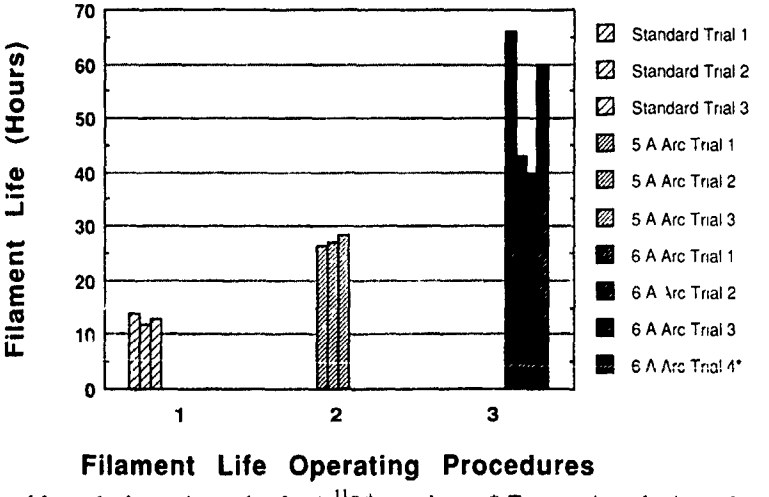

Fig. 2. Source life results for testing with a 5 mA $^{11}B^+$ ions beam. * Test terminated prior to filament failure.

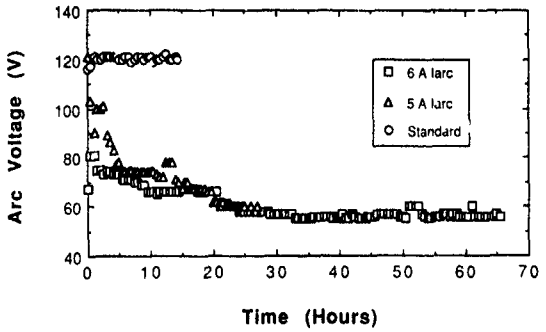

Fig. 3 Arc voltage as a function of time for the three cases tested

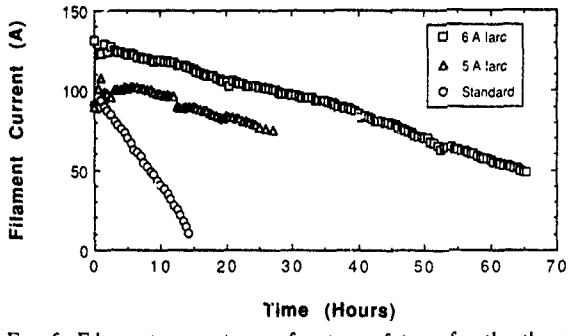

Fig. 5. Filament current as a function of time for the three cases tested.

Fig. 2 is a graph illustrating the improvement in source life obtainable by reducing the arc voltage, while producing the same beam current for three cases: (1) standard operation, (2) 5 A arc current operation, and (3) 6 A arc current operation. It should be emphasized that high current boron operation ordinarily represents the worst case for source lifetime.

These experiments have demonstrated that operation of the 160XP at reduced arc voltages and higher arc currents than are currently standard has substantially improved the source lifetime during high current BF_3 operation, when source life is a serious problem. This is due to a reduction in filament sputtering by plasma ions at the lower arc voltages. Fig. 3 shows the arc voltage used as a function of time for the three cases tested. The major difference is the lower arc voltage used, when the arc current is maintained at a constant value. Arc current for the three cases is detailed in fig. 4. The relative rate of filament wear for these three cases can be judged from the slope of the filament current as a function of time, shown in fig. 5. This indicates the improvement due to the reduction in arc voltage used. Operation at a constant 5 A of arc current resulted in a 2 times improvement in source life versus standard operation. If the effect of thermal cycling of the source is accounted for, the real improvement is even larger. For continuous operation at 6 A of arc current, a source lifetime of ~ 4 times (an average lifetime of over 52 h) that attained during standard operation was achieved

Using the measured arc voltages, and assuming a plasma potential of 5 V, the filament lifetime results are compared with physical sputtering theory. Fig. 6 uses the standard 120 V arc data to determine a plasma density consistent with the measured 13 h lifetime. The data from the 66 h 6 A arc test was then modeled for comparison. The experimental values of the final filament radii are denoted by solid triangles on the graph. The theory predicts a somewhat lower wear rate (larger radius) than that found experimentally. However the predicted lifetime, determined by extrapolating the physical sputtering model, was ~ 6 × the standard value (~ 84 h), versus the actual value of ~ 5 × (66 h) This represents relatively good agreement, considering the strong dependence of sputtering rate on ion energy and the assumptions made regarding plasma density and potential. This result does not rule out chemical effects, since chemically enhanced physical sputtering could also be taking place. This process would have a similar dependence on ion energy as physical sputtering, but the rate would be increased through a chemical reaction on the filament surface.

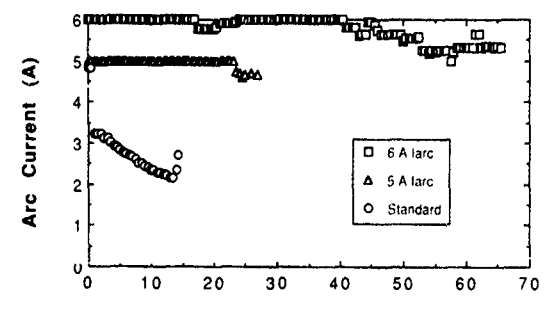

Fig. 4. Arc current as a function of time for the three cases tested.

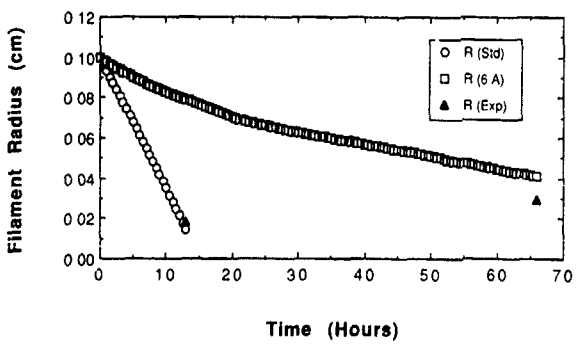

Fig. 6 Calculated filament radius versus time using the physical sputtering model.

3. Operation with arsenic

While improving the source life for boron operation is critical overall, it is certainly advantageous to be able to extend these results to other species such as arsenic and phosphorous. Given the long lifetimes expected, testing until filament failure is not feasible. Instead the rate of filament wear is measured based on operation for 10 h continuously at maximum beam. Two trials, for both standard operation and extended life operation, have been completed for arsenic using arsine gas. It was expected that there would be little improvement in life due to the already low arc voltage (55–65 V) which is standard. However, the results show that reducing the arc voltage further does provide a significant reduction in filament wear. Fig. 7 shows the filament current as a function of time for the case of standard operation (constant 65 V arc voltage) and extended life operation (constant ~ 35 V arc voltage), which used the lowest arc voltage possible from the power supply. The rate of filament wear can be roughly judged by the slope of the data points. It is clear that the rate of wear is much lower at the reduced arc voltage, which is consistent with physical sputtering as the dominant wear mechanism. This is also born out by the filament diameters at the end of the test. The measured filament diameters after these tests were 1.45 and 1.60 mm for standard operation, and 1.93 and 1.96 mm for the test conducted at low arc voltages. As usual, the initial filament diameter was 2.03 mm.

Fig. 8 details the relative sputtering yield for As^+ as a function of ion energy, calculated in the same manner as fig 1. It is apparent that a reduction in arc voltage to 35 V from 65 V still provides a substantial reduction in sputtering yield. In fact, only a reduction to a voltage under ~ 50 V appears to be necessary. Similar results are expected for operation with phosphorous and other dopants Hence, there is now reason to believe that the strategy of reducing are voltages to improve source life will be applicable to all dopant gases including operation with a vaporizer.

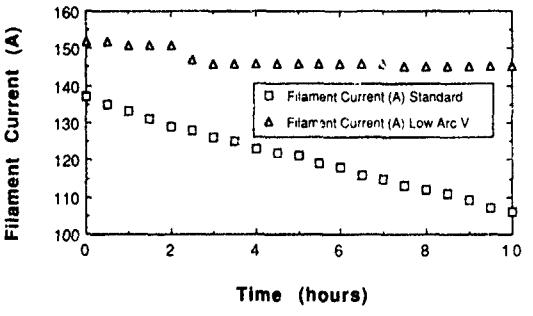

Fig. 7. Filament current versus time for standard and for extended life operation.

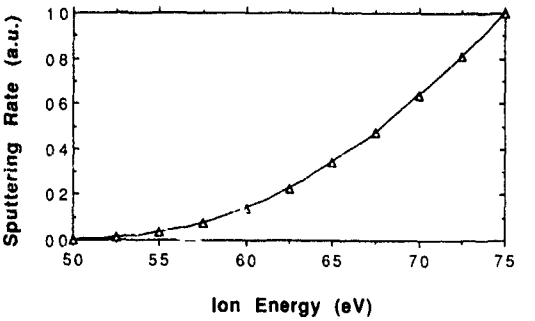

Fig. 8. Calculated physical sputtering rate versus ion energy for an arsenic discharge

4. Conclusion

Filament lifetime for high current boron operation has been improved by an average of a factor of 4, by reducing the arc voltage, with no loss of performance. This filament lifetime improvement is also applicable to other dopants and has been demonstrated during operation with high current As^+ ion beams at reduced arc voltages. The dominant filament wear mechanism is physical sputtering; in the case of boron, chemically enhanced physical sputtering is also a possibility. In general and particularly for high current operation, the new operating procedure [5], utilizing a reduction in arc voltage, will result in a substantial decrease in implanter downtime. These results have been verified through over 500 h of tests on production model 160XP ion implanters.

Future work will expand these results to include other dopants, and to determine the effect on filament life during low and medium current operation. Although physical sputtering has been determined to be the dominant filament wear mechanism, in the case of BF_3 operation more work should be done to ascertain whether this is chemically enhanced. Automation software to incorporate these improvements to the operating procedure must be developed in order to provide the most flexibility to the user. Further improvements in filament life, particularly during high current boron operation, are possible with a hardware upgrade to increase the power supply capacity

References

[1] R Liebert, B. Pedersen, C Ehrlich and W. Callahan, Nuc. Instr. and Meth. B6 (1985) 16
[2] J H. Freeman, Nuc. Inst and Meth. 22 (1963) 306.
[3] H. Hinkel, Nuc Instr. and Meth. 139 (1976) 1.
[4] M.D Gabovich, N.V Pleshivtsev and N.N Semashko, Ion and Atomic Beams for Controlled Fusion and Technology (Consultants Bureau, New York, 1989)
[5] S R Walther and S. Hays, Varian Associates Product Support Bulletin (January, 1991)

Nuclear Instruments and Methods in Physics Research B55 (1991) 469–472
North-Holland

Particulate performance for robotics-based wafer handling ion implant system

M. Nasser-Ghodsi, D. McCarron, M. Folev, S. Holden, D. Veinbachs, S. Mooney and S. Ward
Eaton Corporation, Semiconductor Equipment Division, 108 Cherry Hill Drive, Beverly, MA 01915, USA

The continued reduction in design geometries has lead to manufacturing sensitivity to particulate generation in each manufacturing step. The NV20A developed an adaptive wafer handling system for in-air wafer motion. This paper will discuss the development criteria and particulate measurement results from experiments with the system. Origins of particulates are identified as each step in the implant process is independently measured.

1. Introduction

The Eaton NV20A high-current ion implanter is designed to provide in-air wafer handling compatible with class 1 environments. High throughput, reliable wafer handling is achievable while maintaining the level of 0.5 μm and greater particles below 0.025 cm^{-2}. At the heart of the system are two commercially available cleanroom-compatible robots. The robots provide clean, accurate pick and place movement of the wafers through the system. The layout of the endstation provides ease of service without compromising performance.

2. System overview

In order to successfully incorporate a wafer handling system into a class 1 environment, the airborne particle level must be maintained below 1 particle/ft^3 for 0.5 μm particles. To accomplish this, only cleanroom-compatible components are used in the endstation. The endstation enclosure is stainless steel with a high-efficiency grid table top, allowing constant laminar flow through the wafer handling area. A large Lexan window is placed on the front of the system to allow visual observation of the wafer handling sequence.

Wafer cassettes are added through an automatic door in the Lexan window. Maintenance access is through two doors on either side of the endstation. Maintaining balanced air pressure between the endstation and the fab is critical in maintaining laminar air flow in and around the system. A simple system of louvers is used to maintain pressure equilibrium between the endstation and fab when the cassette door is opened. These same louvers are used to balance the air pressure when the maintenance panels are open, exposing the endstation to the area behind the clean room wall.

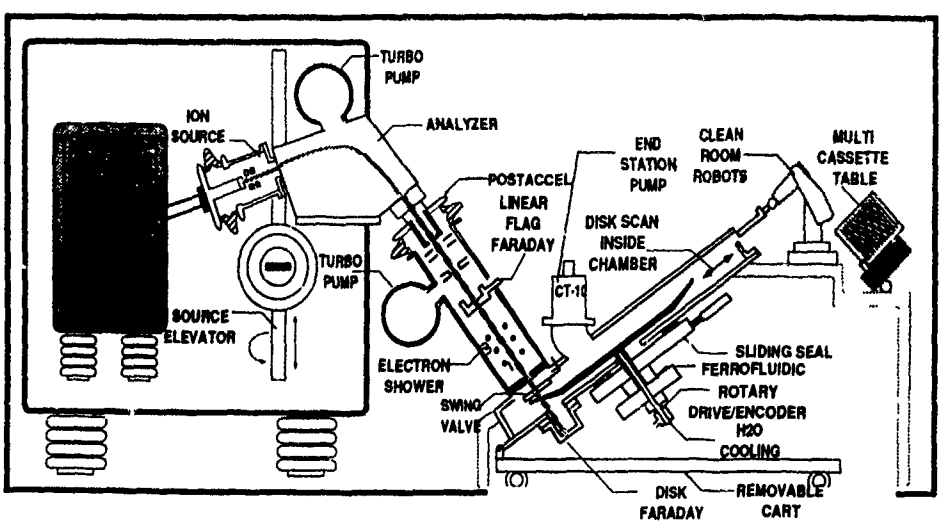

Fig. 1. NV20A system schematic.

0168-583X/91/$03.50 © 1991 – Elsevier Science Publishers B.V. (North-Holland)

Cleanroom-compatible robots are used to transfer wafers through the system. Because all wafer handling is performed at atmospheric pressure, backside vacuum chucks can be used for wafer transport; vacuum sensors are utilized for wafer position verification. Positive wafer sensing allows the NV20A control system to identify and track each wafer, with this information being displayed via a continuously updated wafer map [1].

3. System development

The early development effort to create a clean and reliable wafer handling system for the NV20A centered around the application of cleanroom-compatible robots to the existing NV20 disk and chamber geometry [2], fig. 1. The construction of the test stand was based upon well-defined objectives:

(1) Reduced particulate generation from in-air wafer handling.
(2) Improved wafer throughput.
(3) Class 1 operation.
(4) Application of commercially available six-axis robots for configuration flexibility and optimization potential.
(5) Staging of multiple cassettes for reduced operator interaction.
(6) Selectable slot-to-slot wafer positioning integrity.
(7) Reduced service time to within two hours.
(8) Ease of reconfiguration for different wafer sizes, 100 to 200 mm.

The development base consisted of two Westinghouse/Staubli 260 series arms mounted on an NV20 endstation frame equipped with process chamber and spinning disk. Tooling was designed for 200 mm wafers, assuring adequate clearance for smaller wafers (fig. 2). Supervisory control of the robots was through a host computer via RS232 links with DEC DDCMP protocol and VALII based software. Wafer handling vacuum functions operated through the robot controllers via a remote I/O module.

During the initial testing, 250 000 wafers were cycled through the test stand. Several of the test runs cycled more than 20 000 wafers between assists [3] with one run handling 50 000 wafers through the system without an assist. This testing confirmed the inherent reliability of the design. Subsequent tests were designed to characterize the particulate performance of a system in a manufacturing environment.

4. NV20A particle characterization

In order to fully understand the root cause of equipment-generated particles in a multi-component system, the particle contribution of each component must be characterized. Four distinct components comprise the steps what a wafer experiences when being processed in the NV20A. The four components are: wafer handling, vacuum and vent cycling, disk spin, and implant. Fig. 3 graphically represents this component breakdown.

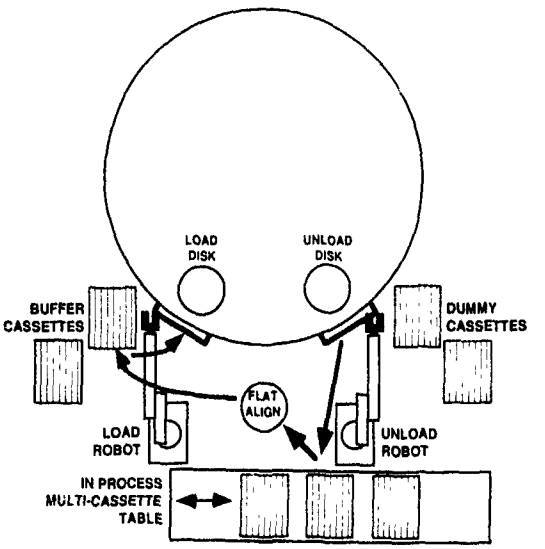

Fig. 2. NV20A wafer handling subsystem.

The data presented was taken over the period of four weeks from a machine used in a production facility. One day each week was set aside in order to perform these engineering tests. Prior to testing, the system was brought up from a cold start with a 100 keV, 10 mA Ar^+ beam run for twenty minutes.

The experiment was designed to be able to detect a difference of one in the mean number of particles added with 90% confidence [3–5]. To accomplish this, for each of the components tested, ten consecutive runs were made with 150 mm monitor wafers. Fifteen wafers were used per run; the measurements from all fifteen wafers were used to determine a run average. The wafers were measured before and after run on a Tencor 5200. The

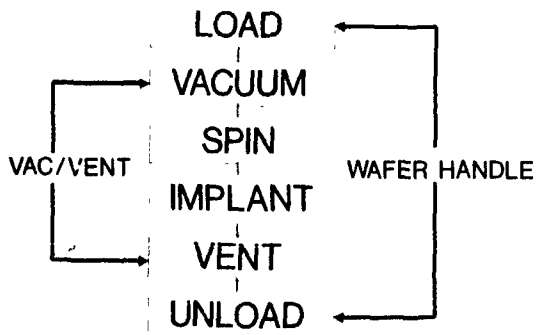

Fig. 3. NV20A wafer handling component breakdown.

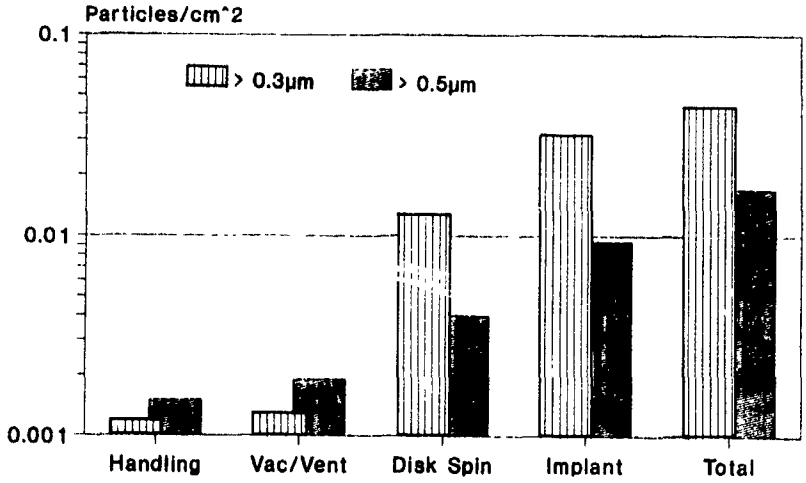

Fig. 4. Particles per wafer pass.

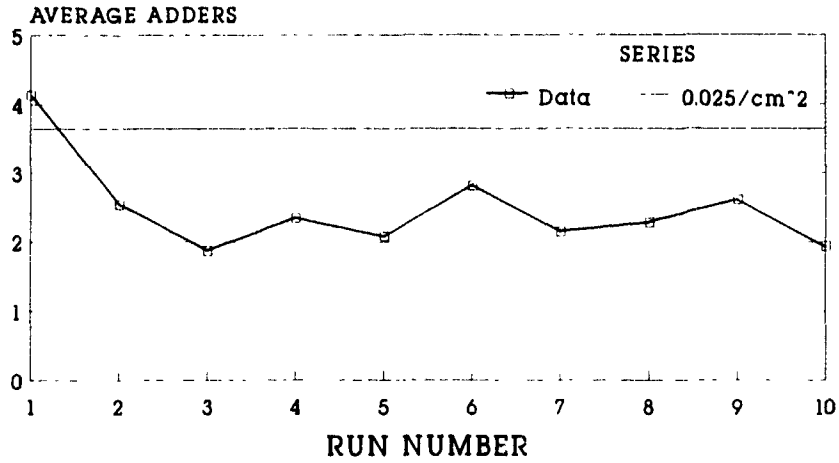

Fig. 5 Particles added > 0.5 μm.

particle counts were binned according to size: 0.3 to 0.5 μm, 0.5 to 1.0 μm and 1.0 to 5.1 μm. A 7 mm edge exclusion was used, making the total scanned area of the wafer 145 cm^2.

The wafer handling sequence involved removing wafers from a cassette, orienting the flat, buffering the wafers, loading the wafers onto the implant disk, removing the wafers from the disk and placing them back into the cassette.

For wafer handling and vacuum cycle, the wafers were loaded onto the disk as mentioned above but, before being removed, are subjected to a vacuum/vent cycle. During the vacuum cycle, the process chamber pressure is brought to 1×10^{-5} Torr prior to venting. Differential venting was used [6]; the total vent time to atmosphere averaged 20 s.

For testing the particles added during the spin cycle, after the process chamber was brought into high vacuum, the disk was spun at 1200 rpm for 3 min. The spin sequence was then stopped, the chamber vented and the wafers removed. For the implant sequence, a 100 keV,

Table 1
Subsystem particulate contribution

Component	Added particles [cm^{-2}]	
	0.3–0.5 μm	> 0.5 μm
Wafer handling	0.0012	0.0015
Vac/vent	0.0013	0.0019
Spin	0.0128	0.0040
Implant	0.0316	0.0094
Total	0.0469	0.0168

10 mA argon beam was implanted at a dose of 1×10^{15} ions/cm^2.

5. Results

Fig. 4 and table 1 present the summarized results of the testing. The results are presented in a manner which shows the particle contribution of each component of the implant sequence. The total particles added per pass through the system is then the total of each of the individual contributions. This value is shown in the row marked "total".

This data indicates that the wafer handling in air and the vacuum/vent cycle combined to add less than 0.5 particles per 150 mm wafer. Because the experiment was designed with a sensitivity of detecting a mean change of greater than one particle per wafer pass, the particles added during the wafer handling and vacuum/vent cycle cannot be separated from the measurement noise and experiment error.

The spin cycle accounts for roughly one quarter of the particles added to the wafers. The majority of the particles added are the result of the implantation step. The number of particles detected are well within the sensitivity of the experiment and a clear distinction can be made between the spin and implant sequences.

The specification for the NV20A is less than 0.025 cm^{-2} greater than 0.5 μm diameter. The average for the ten runs made, 0.0168 cm^{-2}, is well within these specification limits. Fig. 5 shows the average number of adders (> 0.5 μm) per run for all ten runs of the complete implant sequence. It is seen that, with the exception of the first run, all runs were within the specified limits and that the run to run repeatability is quite good, $\sigma = 0.66$ adders for all ten runs. This good repeatability is due largely to careful experimental setup and performing the test implants under identical beam conditions. By performing tests in this fashion, the experimenter is assured of accurate results with a minimal number of repetitions.

6. Conclusion

The data presented in this paper confirms that the design objectives of the NV20A wafer handling system have been met. The low number of particles added during the wafer handling and vacuum/vent cycling indicate that in-air wafer handling system is capable of providing state-of-the-art particle performance, while providing ease of operation and maintenance.

References

[1] M. Nasser-Ghodsi, T. Bowe, D. Bernhardt, S. Holden, M. Foley, M. Farley and J. Grant, these Proceedings (8th Int. Conf. on Ion Implantation Technology, Guildford, UK, 1990) Nucl. Instr. and Meth. B55 (1991) 398

[2] C. Taylor, P. Splinter, A. Weed, J. Grant and S. Holden, 6th Int. Conf. on Ion Implantation Technology, Berkely, USA, 1986) Nucl. Instr. and Meth. B21 (1987) 224

[3] F. Tardiff, H. Paris and J. Daval, Microcontamination 8(4) (1990) 21

[4] T. Bedini, C. Pellett, J. Todoroff and J. Turner, Microcontamination 7(10) (1989) 54

[5] G. Box, W. Hunter and J. Hunter, Statistics for Experimenters (Wiley, 1978).

[6] P. Sferlazzo, D. Stone, J. Jost and M. Mack, Aerodynamic Transport in Ion Implanters, Proc. Semicon East Technical Conf., 1989

Nuclear Instruments and Methods in Physics Research B55 (1991) 473–477
North-Holland

Initial performance results from the NV1002 high energy ion implanter

E. McIntyre [a], D. Balek [a], P. Boisseau [b], A. Dart [a], A.S. Denholm [a], H. Glavish [c], C. Hayden [a], L. Kaminski [a], B. Libby [a], N. Meyyappan [a], J. O'Brien [a], F. Sinclair [a] and K. Whaley [a]

[a] *Eaton Corporation, Semiconductor Equipment Division, 108 Cherry Hill Drive, Beverly, MA 01915, USA*
[b] *PTC Inc., 259 Bishop's Forest Drive, Waltham, MA 02154, USA*
[c] *GMW Assoc., 1060 Lakeview Way, Redwood City, CA 94062, USA*

The Eaton NV1002 is a high energy ion implanter with beam current capability greater than 1 mA. Acceleration to energies between 80 and 2000 keV is achieved with a variable phase linear accelerator (linac). The first production NV1002 is being tested, and the initial results are reported. Currents of 1–2 mA can be generated over an energy range of 40–1000 keV for boron, phosphorus, and arsenic. Useful currents are available at energies as low as 10 keV, and using doubly charged ions, as high as 2 MeV. Considerations for a commercial implanter such as ease of operation are discussed. Analyses of implanted wafers are presented, demonstrating uniformity, correct implant depth profiling, and freedom from contamination

1. Introduction

Several years ago, Eaton initiated a study to determine the best method for generating high energy ions for ion implantation. It was concluded that rf linear acceleration was the preferred approach because it allowed the use of all relevant dopants, was flexible in energy, and was simple to operate. During the course of the study, the variable phase linear accelerator concept was developed [1]. Major advantages over the alternative dc approaches exist since there are no voltages in the linac system above 80 kV and a conventional ion source can be used. Also, since the linac block is at ground potential, access is easy all along its length for pumping and the control of beam optics. These considerations led to the rapid development of the NV1000 implanter, which has been a technically successful system capable of generating beam currents up to 1 mA [2] Subsequently, it was recognized that several improvements could be made to reduce the machine footprint and increase beam current capability. This led to the development of the NV1002.

The NV1002 linac has been designed primarily to accelerate singly charged ions in the mass range from 11 to 75 amu. It is, however, useful outside that range, though with lesser acceleration capability. For example, H^+ should be accelerated to > 500 keV, and since doubly charged ions behave in the linac like particles of half their mass, ions up to Sb^{2+} are also accelerated. The NV1002 uses the same sources as Eaton's other implanters, and utilizes the Eaton NV20A robotic endstation. The automated software control of the source, injector, linac and robotics is consistent with the generic system developed for the NV20A. Such cross-model commonality has obvious advantages. The NV1002 combines high energy (1 MeV) and low energy (10–80 keV) performance in a single machine. This article presents results from the initial performance tests of the first installed NV1002.

2. Beam current and energy capabilities

The principle of rf linear acceleration with variable phase control and the design of the NV1002 have been described earlier [3–5]. The present design specifications of the NV1002 include an energy range of 80–1000 keV for singly charged ions, current capability of 1 mA, and mass acceptance from B^{2+} to Sb^{2+}. These goals have been achieved and in some cases surpassed. Information from the initial tests are summarized below, beginning with the low energy range which uses only the dc injector stage of the system.

In the energy range below 80 keV, the NV1002 performance is similar to that of a conventional medium-current ion implanter. The ion beam is accelerated to final energy in the dc injector stage of the machine. The beam passes through the linac with all of the rf cavities off. Radial focussing through the linac is maintained using the small electrostatic quadrupole lenses which are between each cavity.

For energies from 10 to 80 keV sufficient current is always available from the injector to optimize transmission through the linac. Maximum beam currents are limited by increased space charge effects in the linac

0168-583X/91/$03.50 © 1991 – Elsevier Science Publishers B.V. (North-Holland)

which cannot be overcome by the electrostatic quadrupoles. For a given beam energy E_{beam} and ion mass M_{ion}, these space charge effects lead to final beam currents that vary more or less in accordance with $(E_{beam}^{3/2}/M_{beam}^{1/2})$. A series of beam tests were performed on the first NV1002. At each of several energies, and for three different ion species, the current injected into the linac was increased until no substantial increase in final transmitted current was observed. While there is more testing to be done, the currents observed to date increase as expected and are displayed in fig. 1.

Ion energies above 80 keV are achieved through the use or one or more of the twelve cavities of the rf linac. The first cavities are used to form the 80 keV injected dc beam into ion "bunches" at the fundamental operating frequency of the machine (6.78 MHz). In the simplest bunching scheme, the conversion of the dc beam into bunches is done with a typical efficiency of about 25%. This bunching/transmission efficiency (ϵ) is defined as the ratio of the total beam current at the entrance of the linac to the final accelerated and energy-analyzed beam current delivered to the endstation. The ratio reflects the capture efficiency of the bunching cavities, limitations on the focussing power of the quadrupole lenses and beam dynamical losses along the linac. In some instances it includes a small beam loss due to mechanical collimators at the linac entrance. In practice, these efficiencies for the NV1002 vary from 20–35%. The determination of optimized acceleration parameters (namely phases and voltage amplitudes for each cavity and quadrupole voltage settings) for the NV1002 has been made using our simulation program

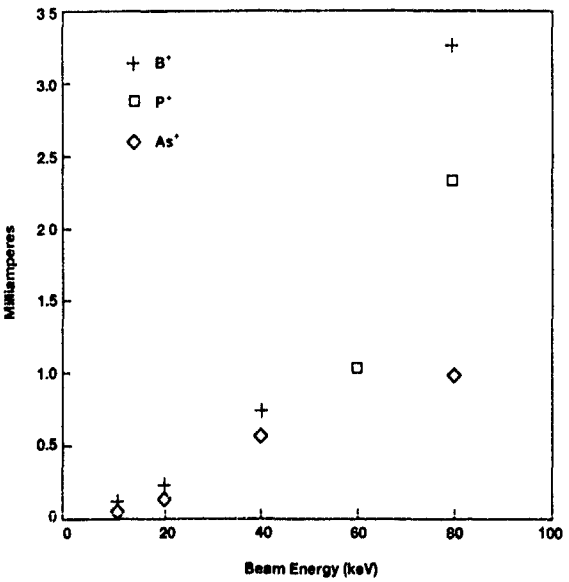

Fig 1. The beam intensities (mA) of B^+, P^+ and As^+ delivered through the linac in low energy dc mode.

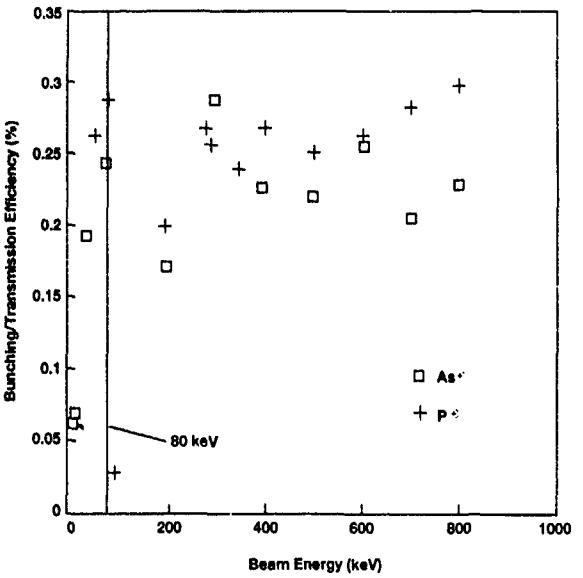

Fig. 2. The bunching/transmission efficiency (ϵ) of the linac as a function or energy from 10 to 800 keV. Below 80 keV, the transmission rises to almost 30% Above 80 keV, the transmission falls but recovers at about 200 keV, and remains essentially constant.

LINAC [2]. Data sets of the acceleration parameters are available for a wide range of species and energy and are stored for immediate recall in the control system. Additional bunching techniques are being developed to capture more of the dc beam. Higher bunching capture efficiency will be useful when the optimization of doubly charged ion currents is investigated.

In the energy range just above 80 keV, where rf acceleration begins, the maximum current transmitted through the operating linac drops below the maximum current transmitted in the 80 keV dc mode. This effect is clearly seen in fig. 2 for P^+ and As^+ beams and is due to the bunched nature of the rf beam, where the increased peak space charge density reduces transmission through the linac because of radial expansion of the bunches. Above 200 keV, the increased beam energy compensates for the high peak currents. In this higher energy range the maximum current limits remain fairly flat up to the highest energy of the machine, because the amount of charge which can be accommodated in a single beam pulse (and thus the current) is determined in the bunching process early in the linac. Fortunately, two techniques should allow significantly improved transmission in the 80 to 200 keV range. First, acceleration of doubly charged ions in the dc mode can provide relatively high currents up to 160 keV. Second, operation of the linac in an accelerate/decelerate mode may allow beams with energy greater than 200 keV to be decelerated at the end of the linac into the 80–200 keV

range. The accel/decel mode has not been demonstrated to date and the outcome is likely to be dependent on the final energy spread that is acceptable.

The first NV1002 has not yet been fully characterized, however table 1 shows the results of initial measurements for a variety of ions and energies. The injected and transmitted current, as well as the bunching/transmission efficiency (ϵ) is shown. It should be noted that in most cases listed here, the injected current was not maximized, so that the table does not represent the maximum performance of the machine. Singly charged As^+ beams of about 450 μA have been generated from 200 to 800 kev. This As^+ data was collected with a relatively low injected current and higher transmitted values are obtainable with higher injected currents. B^+ beams of at least 1 mA were produced at 500 and 950 keV and 1.5 mA was produced at 800 keV. Singly charged phosphorus beams of at least 1 mA and ranging up to 1.8 mA have been generated in the 400 to 1000 kev range. Although the general current specification of the NV1002 is 1 mA, the goal has been to develop stable 2 mA beams over a broad range of species and energies. A 2 mA beam of N_2^+ has been produced. At 770, 880 and 1000 keV, stable P^+ beams up to 1.8 mA were generated by increasing the injected current. At these high currents (and corresponding high injected currents) transmission efficiency drops significantly and loading on the electrostatic quadrupole supplies becomes significant. (Compare the transmitted currents for 4.75 and 10 mA of injected P^+). Achievement of 2 mA capability in normal operation will require modification of injection optics and an increase in the power handling capabilities of the quadrupole lenses. Finally, the use of doubly charged ions allows acceleration to energies above 1 MeV. Currents of 450 charge μA of 1.9 MeV P^{2+} and 100 charge μA of 1.4 MeV B^{2+} have been produced

Table 1
Initial results of injected and transmitted currents for a variety of species and energies. In many cases more transmitted current could be obtained by increasing the injected current. Note that results for P^{2+} and B^{2+} are given in charge mA

Species	Energy [keV]	Injected current [mA]	Transmitted current [mA]	B/T efficiency (ϵ)
B^+	200	4 52	0.83	0.18
B^+	500	4 16	1.02	0 24
B^+	800	4 12	1.03	0.25
B^+	800	–	1 5	–
B^+	950	–	1 08	–
P^+	200	2.6	0 527	0.20
P^+	280	2 47	0 666	0.27
P^+	300	2.5	0.650	0.26
P^+	350	2 90	0 702	0.24
P^+	400	4 37	1 19	0.27
P^+	500	5 5	1.1	0.20
P^+	600	–	1 0	–
P^+	770	5.7	1.37	0 24
P^+	800	4 4	1 1	0.25
P^+	880	9.1	1.88	0.20
P^+	900	–	1.00	–
P^+	1000	4.75	1.28	0.27
P^+	1000	10 0	1 8	0.18
As^+	200	1.98	0 350	0.17
As^+	300	1.99	0 580	0 29
As^+	400	2.4	0.500	0.21
As^+	500	2.0	0.442	0.22
As^+	600	2.0	0.516	0 26
As^+	700	2.0	0.416	0.21
As^+	800	2.06	0.466	0.23
Ar^+	1000	–	1.0	–
N_2^+	464	7.25	2.0	0.28
P^{2+}	1900	–	0.450	–
B^{2+}	1400	–	0.100	–

3. Linac operation

At full energy, all twelve acceleration stages of the linac are under power. Each stage requires three control parameters. rf voltage, rf phase, and electrostatic quadrupole voltage. Thus for a given ion species and final energy, there are as many as 36 parameters to be set for proper operation. These parameters constitute a Linac Data Set. The NV1002 control system contains data sets for boron, phosphorus, and arsenic for energies from 100 to 1000 keV in 100 keV increments. Data sets at intermediate energies may be generated in a few minutes by manual adjustment of the machine parameters and then added to the database. In normal operation, the source/injector stage and linac are ramped to the desired settings simultaneously. The dc beam is injected into the linac, and high energy beam current is observed in the final Faraday cup. If source parameters and total current are similar to the conditions under which the stored data set was originally created, > 90% of the optimized beam current is typically available without fine tuning. Linac fine tuning to optimize final current is fully automated, allowing peak beam currents to be achieved in 1–2 min.

From the experience with the NV1000 linac and through the use of many proven NV20A components and subsystems, the NV1002 should be a very reliable implanter. The first period of operation is confirming this belief.

4. Implanted wafer analysis

Good implant uniformity is a critical feature of any implanter. As a check on uniformity, implants were done on 200 mm wafers with 1.2 mA of 900 keV P^+. Wafers were dosed to 5×10^{13} cm^{-2} using a tilt of 7° and a twist of 0°. Fig. 3 shows a contour map of resistivity obtained from a Prometrix Omnimap RS2O for a preamorphized wafer. This shows excellent uniformity, with $\sigma < 0.5\%$. Additionally, the mean sheet resistivity is as expected for the dose. The implant depth profile was examined through spreading resistance measurements as well as via SIMS (secondary ion mass spectrometry) analysis. Fig. 4 is a spreading resistance measurement for a wafer implanted with 500 keV B^+. The peak of the concentration curve is just over 1 μm, consistent with theoretical and measured ranges of 500 keV B^+ [6]. Fig. 5 is a SIMS analysis of a 500 keV P^+ implant. It has a peak concentration at a depth of about 0.6 μm and a straggling width near 0.17 μm. This is consistent with measured values [6] of straggling. Wafers were also analyzed for impurities. Fig. 6 shows SIMS analysis of a wafer implanted with 1.4 MeV B^+ for the presence of B, Na, Al, Cr, Fe and Mo. The concentrations measures are accurate to about 20% and the depth to within 10%. All the impurities are small, have a flat

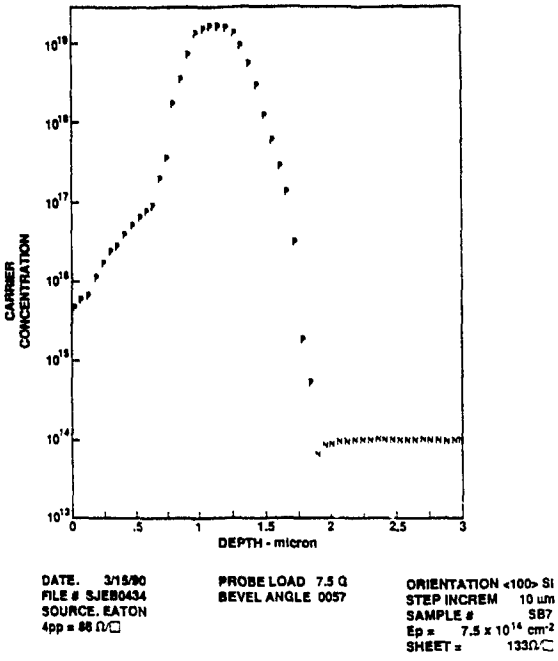

Fig 4. A spreading resistance measurement for a 500 keV B^+ implant

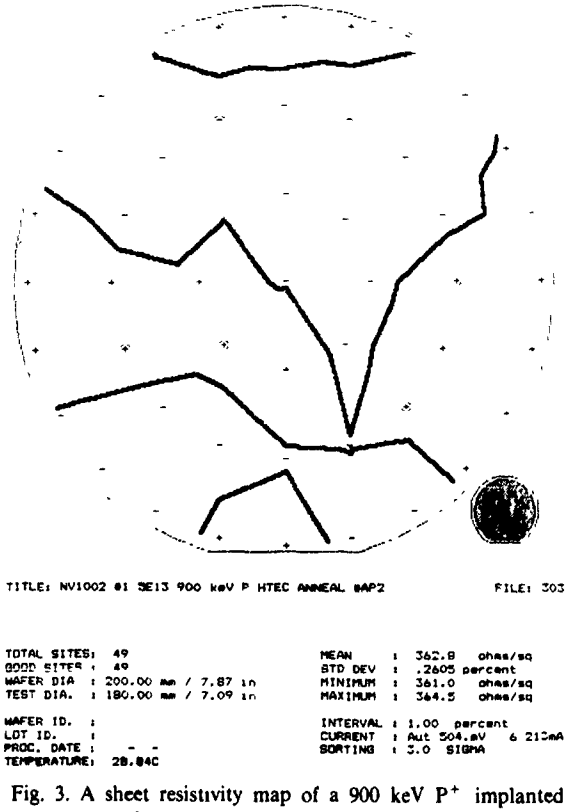

Fig. 3. A sheet resistivity map of a 900 keV P^+ implanted wafer. Uniformity is good with $\sigma \leq 0.5\%$

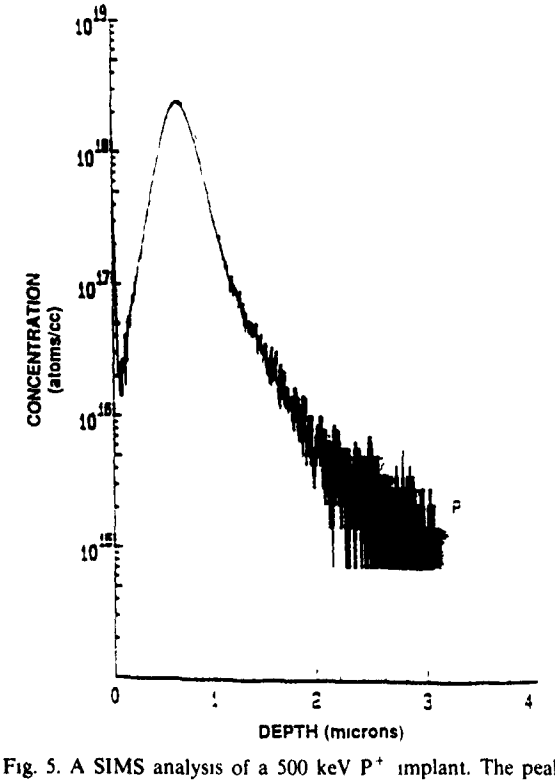

Fig. 5. A SIMS analysis of a 500 keV P^+ implant. The peak concentration is near 0.6 μm.

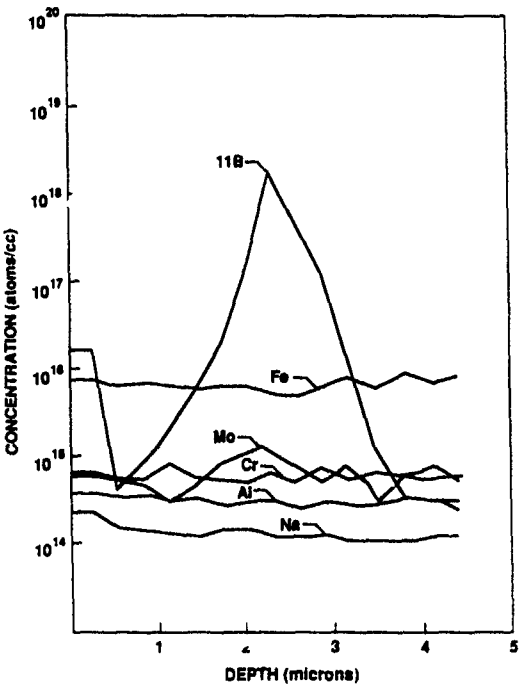

Fig. 6 A SIMS analysis of a 1400 keV B^+ implant. Contamination is low

distribution in depth (and are probably dominated by instrumental backgrounds). The peak of the boron distribution is just over 2 μm deep, again consistent with measured and calculated values [6].

Such low contamination might be expected. The injector stage mass analysis prevents unwanted species from entering the linac. The linac itself has mass selectivity. Injected contaminants as well as contaminants created in the linac will be out of phase and gain little energy. Finally, the 51° post acceleration energy analysis will refine the mass purity further.

5. Conclusions

The NV1002, an rf linac based implanter, is a robust, flexible, and simple to operate tool for high energy implantation. It has been demonstrated to generate milliampere beams of boron to arsenic in the MeV energy range. Low energy capability below 80 keV is similar to standard medium current implanters. Uniform, low contamination implants of the expected depth profile have been generated. Because of scheduling considerations, there was no prototype for the NV1002 and the first system to be made was recently shipped. Its initial performance characteristics are very encouraging and final testing will determine the full power of the NV1002.

References

[1] H.F. Glavish, A. S. Denholm and G.K Simcox, US Patent 4667111, 1987.
[2] H.F. Glavish, D. Bernhardt, P.Boisseau, B. Libby, G. Simcox and A.S. Denholm, Nucl Instr. and Meth B21 (1987) 264.
[3] H.F. Glavish, Nucl. Instr and Meth. B21 (1987) 218.
[4] J P. Boisseau, A.S. Denholm, H.F Glavish and G Simcox, Mater. Sci. Eng. B2 (1989) 223.
[5] P.Boisseau, A Dart, A.S Denholm, H.F Glavish, B.Libby, G. Simcox, Nucl Instr. Meth. B37/38 (1989) 591.
[6] J.F. Zeigler, J.P Biersack and U Littmark, The Stopping and Range of Ions in Solids (Pergamon, New York, 1984)

Nuclear Instruments and Methods in Physics Research B55 (1991) 478–481
North-Holland

A versatile ion implanter for planar and 3D device construction

Jerald P. Dykstra, Andy M. Ray and Robert B. Simonton
Eaton Corporation, Semiconductor Equipment Division, 2433 Rutland Drive, Austin, TX 78758, USA

The ever increasing demand for smaller devices is creating a new set of performance and reliability problems. Overcoming these problems requires sophisticated device structures incorporating advanced knowledge of device physics coupled with improved process uniformity and precision. Fabrication of such structures in silicon and compound semiconductors is generating demands for new process technology. An ion implanter has been designed specifically for improvement of process control and construction of advanced three-dimensional device structures. The instrument uses a programmable goniometer as the target positioning system. This versatile end station, combined with a sophisticated automation and control system, is designed to meet the emerging requirements for flexible target positioning and repositioning for both planar and 3D structures. Details of the design of this new ion implanter are described and performance specifications are presented.

1. Introduction

Recent trends toward denser circuit designs have resulted in the development of 3D circuit structures to augment planar technology. These challenges of modern integrated device technology also present challenges to designers of semiconductor manufacturing equipment. Eaton Corporation has developed an ion implanter specifically designed to provide superior performance in many of the areas related to the new technologies. Implanter improvements which facilitate construction of 3D devices also result in improved process control for planar devices, especially implant uniformity and reduced variability from channeling effects.

2. Modern semiconductor device technology

An increasing variety of 3D devices are being developed to make more efficient use of semiconductor surface area or to provide enhanced device performance. A literature survey [1] has disclosed a growing variety of active 3D devices constructed on the sidewalls of trenches or islands created by etching processes. Implantation doping of such devices requires inclining the wafers at substantial angles with respect to the incident ion beam and rotating the wafer during implantation.

Besides active 3D devices, a wide variety of applications for implanting isolation trenches and trench capacitor walls have been identified [2,3]. These typically require tilt angles of 4° to 20° (depending on the trench aspect ratio) and continuous or quadrant rotation for complete coverage.

For very narrow trenches, grazing-angle implants which do not directly illuminate the entire depth of the trench can be effective because of reflection of the incident beam into the deeper portions of the trench [2]. In fact, forward scattering of dopant to the bottom of deep trenches must be compensated to achieve uniform doping of trench sidewalls. Fig. 1 illustrates the problem. Implant a, a grazing implant intended to illuminate the sidewalls and bottom, results in considerable forward scattering and poor sidewall doping. The bottom is more heavily doped than the sidewalls. Implant b is performed at a higher tilt angle, which results in less forward scattering and greater sidewall penetration. At a still greater tilt angle, implant c completes the doping of the upper portions of the sidewalls with very little additional scattering to the deeper portions. The multi-tilt process results in a uniformly implanted trench and reduces sensitivity to sidewall angle and scan angle variations. Distributing dopant around all sides of the trench requires rotation or rotational repositioning.

Very-small-scale planar devices suffer from bothersome hot-carrier effects, subthreshold conduction, threshold voltage shifts, and punchthrough phenomena. New implant techniques to fabricate small-scale planar devices with immunity to these effects have been described [4,5]. The methods called LATID (large-angle tilt implanted drain) and LATIPS (large-angle tilt implanted punchthrough stopper) both require large tilts (25°–45°) and rotation or repositioning during the implant.

The down-scaling of device dimensions requires shallower junction depths accompanied by somewhat higher threshold adjustment doses. This results in greater sensitivity of threshold voltage to the shape of the dopant profile. The simultaneous increase in critical channeling angles resulting from the use of lower-energy implants for threshold shift implants has compounded the difficulties of producing uniform V_{th} distributions with

0168-583X/91/$03.50 © 1991 – Elsevier Science Publishers B.V. (North-Holland)

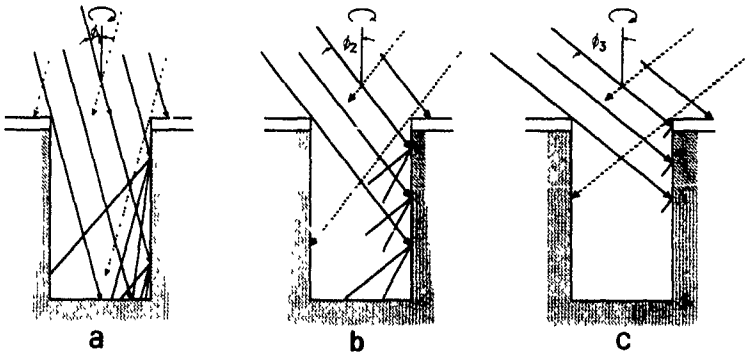

Fig. 1 Trench sidewall doping: multiple tilt implant steps a, b and c contribute to improved sidewall doping uniformity See text for details.

cost-effective electrostatically scanned medium-current ion implanters. These effects can be even more pronounced in high-Z substrates such as GaAs and other compound semiconductors, since higher-Z substrates exhibit larger critical angles for channeling. Junction depth variation due to channeling and other residual non-uniformities such as dopant gradients due to wafer tilt or uncorrected scanner non-uniformities can be reduced by performing multiple implant segments with wafer repositioning between segments. When optimal anti-channeling tilt and twist angles have been chosen this can be effected by implanting a fraction of the dose in each of the symmetric lattice orientations. For ⟨100⟩ materials this requires four partial implants, and for ⟨111⟩, three. Dramatic additional improvement in areal and depth uniformity results from the averaging effects produced when wafers are continuously rotated during implantation [6]

3. A versatile new ion implanter

Eaton has developed a highly automated new medium-current ion implanter. It has been optimized for doing a broad range of low- and medium-dose implants including the emerging implants requiring versatile target positioning capabilities. This implanter, Eaton model NV-6200AV, is based upon the design of the successful NV-6200A and uses that machine's field proven high-voltage terminal, beam line and control system. To this basic tool has been added a new end station having a wafer-holding target block which is a fully programmable goniometer. The target goniometer is capable of presenting the wafer to the ion beam in any combination of tilt and twist within its range. It is further capable of repositioning the target during the implant, either in discrete steps, or in continuous motions. Since the system is designed as a production tool, it is capable of doing implants requiring complex positioning at high throughputs. The system provides high-speed electrostatic scanning, cassette-to-cassette automatic handling and single-wafer serial processing. Table 1 summarizes a few key specifications of the Eaton model NV-6200AV ion implanter.

Fig. 2 shows the mechanical construction of the goniometer stage and positioning system. The target is shown in its horizontal, wafer loading/unloading position. From this position it rotates 90° about its tilt axis to reach the 0° tilt implant position. The tilt drive is a worm-and-gear drive. A drive train transmits the target rotary motion through the hollow interior of the yoke. The yoke interior is hermetically sealed from the implant vacuum chamber to isolate particles generated in the drive mechanisms from the process chamber. Ferro-fluidic feedthroughs couple all target positioning motions into the vacuum chamber to increase reliability and to minimize maintenance. Pick-and-place robotic arms (not shown) move wafers through vacuum locks and load and unload the platen. This method of gentle, low particulate handling was first introduced in the Eaton model NV-6200 implanter, and now enjoys wide acceptance as a reliable, minimum-contamination, technique.

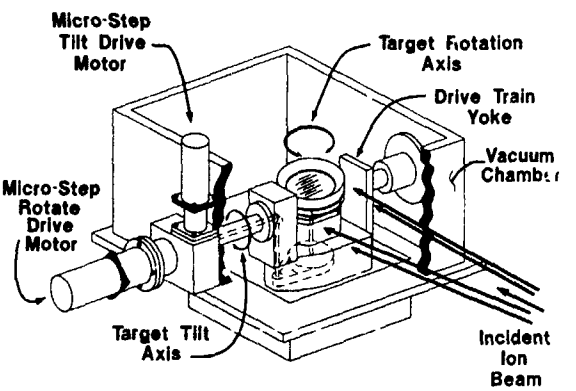

Fig. 2. NV-6200AV end-station target goniometer motions and drive-train arrangement.

Table 1
NV-6200AV implanter specification summary

Ion beam energy range:	5 to 200 keV for singly charged ions	
Maximum scanned beam currents:	Species	Beam current [μA]
	B^+	700 (1000 [a])
	P^+	1700
	As^+	1400
	B^{2+}	25 [a]
	P^{2+}	300 [a]
	As^{2+}	300 [a]
Throughput, 10 s implants:	Continuous rotation, ⩾ 200 wafers per hour	
	Quadrant rotation with beam gating between steps, ⩾ 170 wafers per hour	
Water flat positioning:	Variable, fully programmable, 0–(360 ± 2)°	
Water tilt:	Variable, fully programmable, 0–(60 ± 0.5)°	
Water repositioning:	Up to 15 discrete positioning steps per implant	
Water sizes	3 in. to 150 mm	
Particulate contamination.	Adds (statistical mean) ⩽ 0.12 particles ⩾ 0 3 μm/cm^2	
Dose uniformity:	σ ⩽ 0.5% for single-position implants	
	σ ⩽ 0.35% for implants with rotation	

[a] Requires an optional high-efficiency ion source.

The implanter automation system performs automatic source and beam-line setup and tuning across a wide range of implant conditions. Process specifications can be stored and recalled by the system's fixed disk storage or downloaded from a remote host. All ion-beam, dose and wafer-motion control information can be pre-stored in process recipe records. During production, the implanter is operated automatically by a remote host using the SECS II communication protocol, or operated locally in either manual or automatic modes. The operator interface for local operation is a large (48 cm), high-resolution color CRT with an infrared touch-sensitive screen. Fiber-optic interfacing isolates and protects the system control computer from electrical transients.

4. Scanning and target control

A digital scan generator synthesizes complex scan waveforms at high speed to automatically compensate system scan non-uniformities or the effects of large or varying tilt angles. The scanning method is high-speed electrostatic X–Y scanning of approximately 2.7 kHz, each axis. Because of the high-speed scan, continuous rotation of the target during implant is possible without risk of loss of implant uniformity due to spatial beat frequencies between the scan and rotation frequencies, as occurs in mechanically scanned systems.

Target rotation during the implant can be continuous or can consist of up to 15 discrete repositioning steps. Target tilt is also programmable in up to 15 discrete steps. Each stored process recipe contains control instructions for ion-beam setup, operating parameter limits, and target positioning for up to 15 implant segments. For each implant segment the process engineer can independently specify tilt angle, flat orientation, implanted dose and amount of continuous rotary motion during the implant segment. At tilt angles above a few degrees the cosine dependence of implanted dose to tilt angle becomes significant This dependence is a geometric effect resulting from the foreshortening of the tilted wafer with respect to the beam. The dose control system automatically compensates the beam fluence to provide accurate doping.

Fig. 3 schematically illustrates the patented [7] method for rotary motion control. The target Faraday enclosure collects the incident beam for dosimetry purposes. A digital packet integrator digitizes the beam current and emits a step pulse each time it integrates a precalculated charge packet, P:

$$P = D/Sn,$$

where D is the total desired dose for the segment, S the number of target steps per degree of rotation (approximately 56), and n the number of degrees of rotation desired during the segment. As the incident beam current fluctuates, the angular velocity of the target varies proportionately, assuring that the implanted dopant is uniformly distributed with respect to angular position on the wafer. The method also assures that the implanted dose can be distributed over a precise number of revolutions of the target. Older implant systems having continuous rotation capability have used high speed free spinning rotation without synchronization to the implanted beam. In such systems, unless the number of free spinning revolutions is high, considerable non-uniformity results from failure to illuminate all sides of

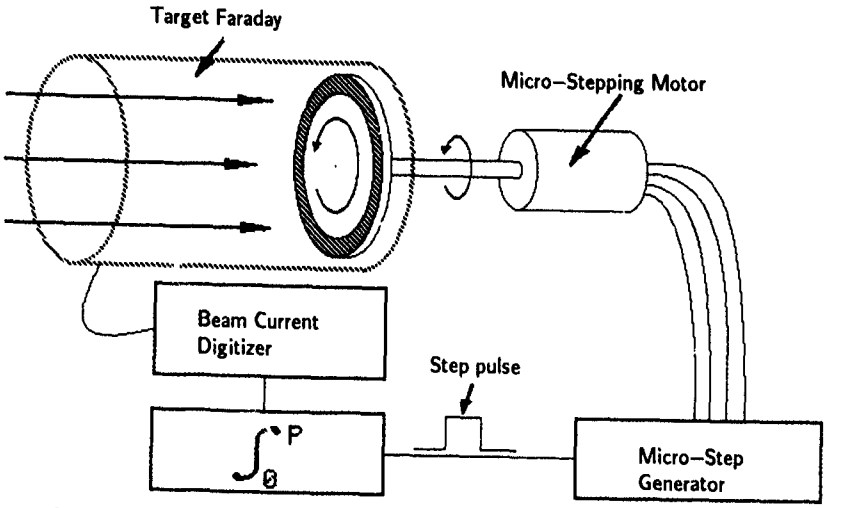

Fig. 3. Digital servo-controlled target rotation synchronizes motion to ion beam.

the three-dimensional structures equally because of end effects from beam gating. Since rotary velocities should be low to avoid spatial beat frequencies between scan and rotation frequencies, free spinning systems must trade off between throughput and uniformity. Servoing the rotary motion to the beam avoids this tradeoff.

5. Uniformity results

Fig. 4 shows typical implant uniformity results obtained with the NV-6200AV implanter. The 1% contour interval maps are from thermally modulated conductivity measurements obtained using a Therma-Wave, Inc. model TP-300 laser measurement system. The Therma-Wave measurement technique exhibits depth-weighted sensitivity and is therefore quite sensitive to channeling effects. Implants were of 10 s duration at $^{11}B^+$ doses of 5×10^{11} ions/cm^2 into 150 mm diameter, ⟨100⟩ bare (oxide-free) silicon wafers at 100 keV energy. The implant tilt angle was 7°. Because of the low dose and absence of an amorphous oxide layer, this implant is very susceptible to the effects of channeling due to implant angle variation in electrostatically scanned systems. Two wafers are shown. Wafer a was positioned with an initial 23° rotational alignment, but implanted in four segments (1/4 of the total dose given at each segment) with 90° additional rotation between each of the segments. Wafer b had an initial flat orientation of 23° and was rotated through 360° during the implant using uniform continuous motion synchronized to the beam. Wafer a shows that even with discrete repositioning during implantation, residual channeling effects result in some nonuniformity of junction depth. However, in wafer b we see that continuous rotation provides the equivalent of randomized implant direction, with resultant reduction of channeling effects below measurable limits.

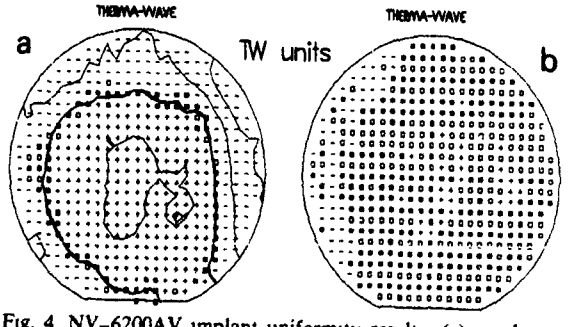

Fig. 4. NV-6200AV implant uniformity results: (a) quadrant implant (4× repositioned, σ = 0.88%), (b) continuous rotation (σ = 0.18%). See text for details.

References

[1] R. Simonton and F Sinclair, Emerging Ion Implantation Processes for the 1990's (Eaton Corp. Tech. Pub., Austin, TX, 1989).
[2] G. Fuse, H. Umimoto, S. Odanaka, M Wakabayashi, M. Fukumoto and T Ohzone, J. Electrochem. Soc 133 (1986) 996.
[3] G Fuse, M Fukumoto, A. Shinohara, S. Odanaka, M Sasago and T Ohzone, IEEE Trans. Electron Devices ED-34 (1987) 356.
[4] T. Hori and K. Kurimoto, IEEE Electron Device Lett 9 (1988) 300.
[5] T. Hori and K. Kurimoto, IEEE Electron Device Lett. 9 (1988) 641.
[6] R. Simonton, D. Kamenitsa and A. Ray, these Proceedings (8th Int. Conf. on Ion Implantation Technology, Guildford, UK, 1990) Nucl. Instr and Meth B55 (1991) 188.
[7] J. Dykstra and A. Ray, US Patent 4929840 (1990).

Nuclear Instruments and Methods in Physics Research B55 (1991) 482–487
North-Holland

Simulation of the geometrical characteristics of a mechanically scanned high current implanter

Frank Sinclair
Eaton Corporation, Beverly, MA 01915, USA

An understanding of the geometrical properties of the implantation process is essential for the optimization of dose control algorithms and for control of channeling effects. The EATON mechanically scanned implanters use a closed loop dose measurement system to control the scan speed in the slow direction. The input for this is provided by a measurement of the beam through a rectangular slot in the disk. Analytical calculations of the approximations involved in this approach become prohibitively complicated when one wishes to consider all possible beam shapes, angular spreads and disk geometries For this reason, we have implemented a computer program which uses a simple approach based on a Monte Carlo simulation of the implant process. The results show that the basis of the control algorithm is sound, leading to deviations of less than 0.3% across a 150 mm wafer for all plausible beam geometries. Another feature of this approach is that it allows easy calculation of the angle with which the ion beam penetrates the wafer or other geometrical considerations

1. Introduction

Mechanically scanned batch high current ion implanters typically mount the wafers on a rotating disk which is also translated in a linear motion past a steady beam of high energy ions. The dose and uniformity of the implant is controlled by adjusting the speed of the linear scan. One essential feature of this adjustment is that it must compensate for changes in the beam current. Despite all the advances in this approach, nonuniformities due to the failure of some part of the system do occur, and some nonuniformity may also be introduced in the design of the equipment.

There have been several observations of very linear dose gradients on wafer maps where the delivered dose was several percent lower at the point on the wafer furthest from the center of the spinning disk, and rising monotonically towards the center. In some cases the elimination of this gradient has only been achieved by the implementation of a software program that compensated heuristically for the observed gradient.

Many possible explanations for the origin of these gradients have revolved around the geometrical assumptions implicit in the dose control algorithm. Because the general three-dimensional geometrical problem is a very complicated situation, it is very difficult to justify all the assumptions by analytical argument. We therefore decided that it might be useful to undertake a simulation of the dose control system so as to evaluate these geometrical issues without invoking any debatable analytical approximations.

This report is a description of the computer program written to address these issues and some of the results of the calculations. In summary, the conclusion is that with the dose control algorithm as implemented on Eaton implanters, none of the expected ranges of beam current distributions should produce a gradient of more than about 0.5% across a 15 cm wafer. This is significantly less than has been observed on several instances, and suggests that other mechanisms are responsible for the observed effects. The approach to the simulation of the geometrical characteristics of an implanter however, has other applications and may be useful in simulating several process issues.

2. The dose control algorithm

The fundamental operation of the dose control algorithm is based on the use of a rectangular slit in the disk [1,2]. The fraction of the beam current that passes through the slot is measured by a Faraday behind the disk which measures the beam as it passes through the slit, and the slow scan advances at a velocity proportional to this current. The justification for this algorithm can be appreciated by considering the dose distribution $D_1(y)$ deposited in one pass by a beam with a current density $J(x', y')$ traveling at a velocity v in the x-direction:

$$D_1(y) = \frac{1}{v}\int J(x', y')\,\mathrm{d}x'. \qquad (1)$$

0168-583X/91/$03.50 © 1991 – Elsevier Science Publishers B.V. (North-Holland)

The charge deposited into a slit of width s in the plane of the wafer is given by:

$$Q = \frac{s}{v}\int\int J(x', y')\,dx'\,dy' = s\int D_1(y)\,dy. \quad (2)$$

If we now carry out many passes in the fast scan direction, each displaced by a distance δy in the slow scan direction, the final dose to every point on the wafer is given by:

$$D(y) = \sum_i D_i(y + i\delta y). \quad (3)$$

In the limit of small δy, $D(y)$ becomes perfectly constant and can be expressed as an integral:

$$D = \frac{1}{\delta y}\int D_1(y)\,dy = \frac{Q}{s\delta y}. \quad (4)$$

Thus a uniform implant can be achieved by displacing the beam a distance $\delta y = Q/Ds$ in the y direction between passes. Notice that this derivation is applicable to any general shape of the beam current distribution and at any velocity for the fast scan. It does, however, assume that the fast scan and slow scan directions are orthogonal and that the slit has a constant width in the fast scan direction.

In the context of a rotating disk ion implanter, if the wafer passes through the beam at a frequency f, the rotation frequency of the disk, the ideal slow scan velocity is given by $u = \delta y f = Qf/Ds$. If several passes are used, the velocity is appropriately scaled for the number of passes over any given point on the wafer. This application of the general formula does not allow for the fact that the fast scan direction is not linear and thus may not be perpendicular to the slow scan direction at some off axis points in the beam, nor does it allow for the position of the slit in a plane different from that of the wafer. These deviations from the ideal case make an analytical approach to calculating the dose on the wafer for a given control algorithm very difficult, and we have therefore developed a computer program to understand the effects of a given algorithm.

3. Monte Carlo program

We selected a Monte Carlo approach based on the calculation of the trajectories of discrete particles rather than the alternative of the numerical integration of three-dimensional vector fields. The program is called MIKADO, loosely standing for Monte Carlo dose analysis. The Monte Carlo approach allows easy visualization of what is happening in the simulation by use of a simple subroutine that displays a projection of the important coordinates in any of the three principal directions. This approach also decouples the various geometrical issues, making it quite easy to change the

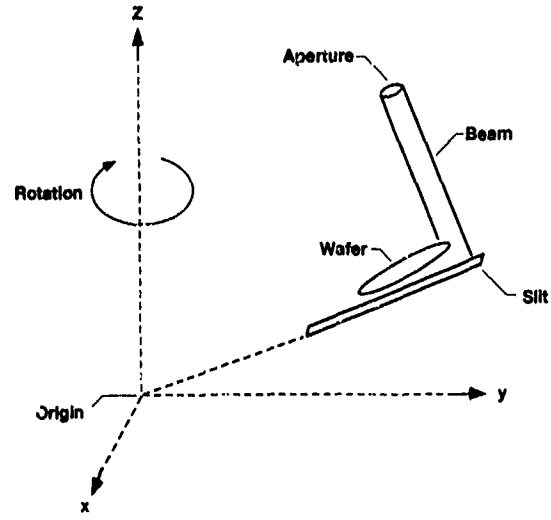

Fig. 1 Diagram showing the geometrical elements simulated in the program MIKADO.

orientation of the beam or the slit in the program, or to add other objects as desired.

The main elements of the geometrical model are illustrated in fig. 1. The coordinate system is fixed with the z-axis parallel to the rotation axis of the disk. The origin of the coordinate system is at the apex of the cone formed by the sweep of the slit in the disk at the starting slow scan position. The wafer is radially centered in the span of the slit rotated by 15°, and elevated by a small amount in the z-direction.

The beam is defined by specifying a circular aperture, a mean direction and a divergence. Since MIKADO assumes that the beam is made up of a large number of discrete particles that travel in straight lines, the program selects a random point within the circular aperture and uses this as the starting point of the particle's path. The propagation direction is then set to be a unit vector in the mean beam direction plus a vector given by a product of the selected divergence and the relative position of the starting point within the aperture.

The program then calculates the interception of the particle path with the plane of the slit, and if it passes through the rectangular slit aperture the program assumes that it will enter the disk Faraday and thus increments a simulated disk Faraday charge (Q) by one. Similarly the interception with the plane of the wafer is calculated, and if it falls within the circle of the wafer, a two-dimensional dose matrix is incremented.

After an adjustable number of particles have been propagated in this manner, the disk is rotated, and new positions for the slit and the wafer are calculated and can be displayed on the screen. This sequence repeats until both the slit and the wafer have passed the beam. At this point, the y position of the disk is incremented

by an amount given by $\delta y = Q/Ds$ where D is the target dose (in particles/cm^2) and s is the slit width (cm). The simulation only does a single slow scan in y and only considers singly charged species.

The program was executed in compiled Basic on a 386 personal computer with a math coprocessor and compared to a real implant, the effective beam current is tiny. It can calculate about 1000 particle trajectories per second, about 10^{14} less current than a real implanter. Because the particles are randomly distributed within the confines of the beam, the final dose uniformity is governed by Poisson statistics. An overnight simulation can build up to a dose of about 1×10^5 cm^{-2} and this gives an accuracy of about 0.4% in the dose. An average of five such runs reduces the purely Poisson spread to below 0.2%, sufficient for the problem at hand.

4. Simulation results

Fig. 2 shows a photograph of the screen during the execution of the program, about half way through an implant. The wafer (in pink) and the slit (orange) are shown superimposed for a sequence of angular rotations of the disk. The lines traced by the beam particles are shown in red, with their intersections with the wafer in pink. The accumulating dose matrix is overlaid in red and blue, showing the total dose for each square centimeter on the wafer. In this case the target dose was 100 cm^{-2} for illustrative purposes. Fig. 3 is a photograph of the completed run shown in fig. 2. The top array shows the final accumulated dose matrix. Notice that the variation from the target dose is dominated by Poisson statistics in this low dose test. Runs to higher doses are needed to show small deviations from the target dose. The lower array shows the average angle of implanted ions measured in terms of the deviation from the wafer normal in the x-direction. In this case the random nature of the program has very little effect and the systematic variation in angle is readily apparent.

Fig. 4 shows a comparison of the dose offsets and gradients produced by various deviations from the ideal geometry. The horizontal axis represents a "top to bottom diameter scan" of a wafer in the usual orientation, with the edge of the wafer closest to the outer

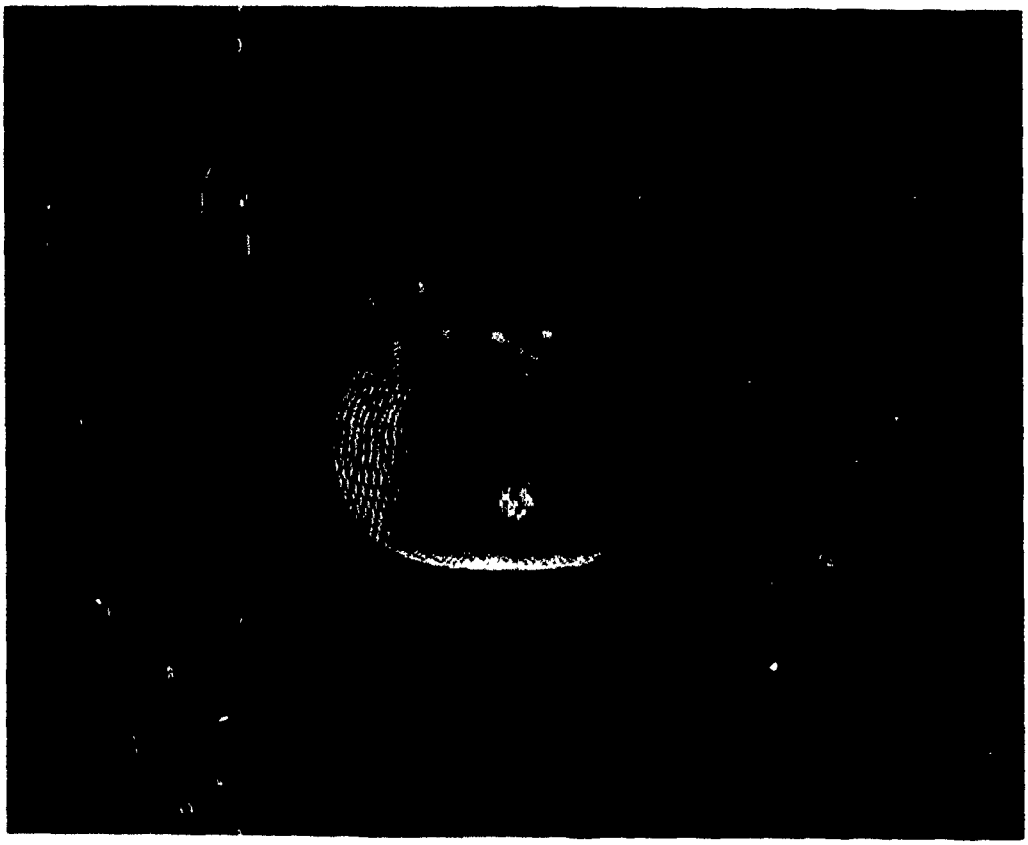

Fig. 2. Photograph showing the screen during the execution of the program, about half-way through an implant. The wafer and slit are shown at several angular positions. The accumulating dose matrix is overlaid.

radius of the disk corresponding to $y = -7$ cm, and the inner edge at $+7$ cm. All these simulations were run with a 1 cm^2 bin size, and bins within the circular wafer were averaged across the wafer in the x direction to give the y dependence shown. The vertical axis is the dose relative to a target dose of 100000 particles/cm^2.

The line labeled "nominal NV20A", was calculated assuming a 1 cm diameter parallel beam, incident at 6° to the z-axis in the y–z-plane. The line labeled Div = 0.3R was calculated using a very widely divergent beam, such that particles emerging from the edge of the aperture had an angle of 0.3 rad (17°) with respect to the beam direction. The last point in this data set has been omitted because a sufficient overscan length was not allowed for, and this resulted in a significant underdosing at the last point. The line labeled BeamDia = 5 cm was calculated with a zero divergence, but a beam spread out uniformly over a circle with a 5 cm diameter. All three of these conditions produced essentially identical results: a net overdosing of about 0.4% and no significant gradient (less than maybe 0.2% edge to edge).

The upper line, labeled offset = 5 cm was calculated by displacing a 1 cm diameter beam 5 cm in the x-direction, so that it no longer lies in the plane formed by the axis of rotation and the y scan direction. As can be seen this last condition produces a larger average overdosing and a significant gradient, overdosing at the inner radius of the disk. The total gradient simulated is about 1% edge to edge, leading to a standard deviation of the dose of about 0.4%. In an NV20A implanter, the maximum opening of the disk Faraday is about 4 cm from the middle, making this amount of deviation impossible.

5. Analytical approximations

After observing these effects, it seemed that it might be useful to revisit the simplest analytical models of the geometrical situation to see if they might elucidate the deviations observed. The two smooth lines in fig. 4 are based on very simple calculations. The lower one is due to the angle with which the beam strikes the disk in combination with the height difference between the wafer and the slit, as illustrated in fig. 5. This results in a difference between the radius at which the beam

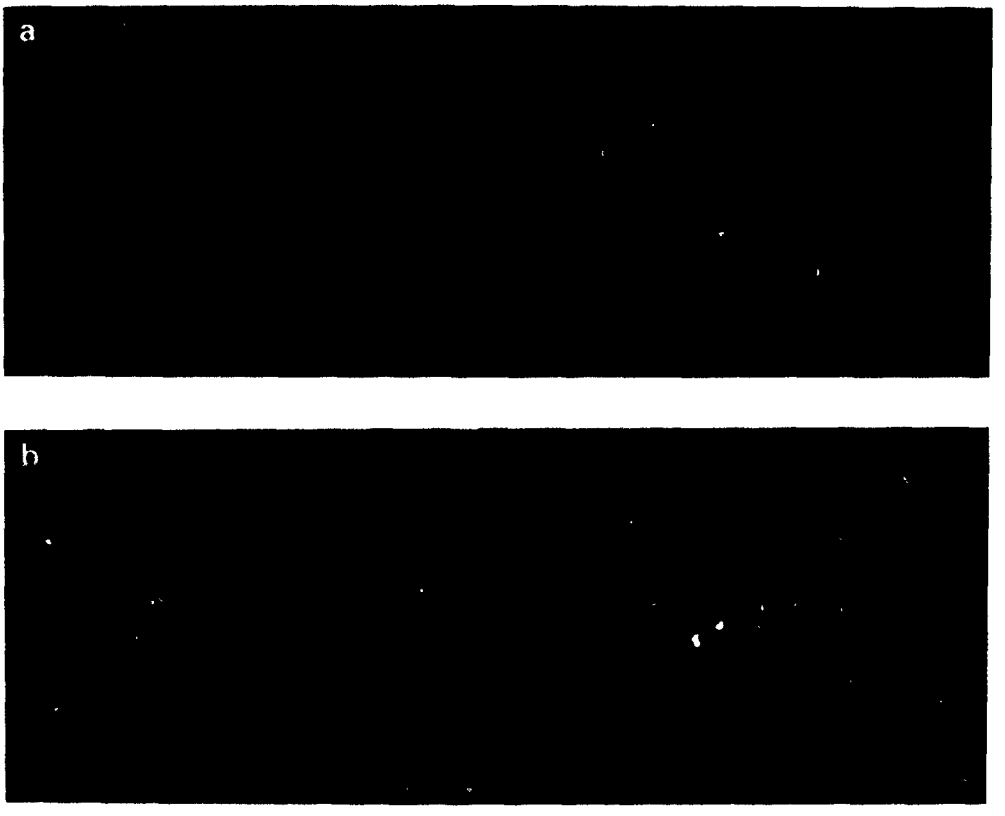

Fig. 3. Photograph of the calculated output at the completion of the simulation. The top array (a) shows the final accumulated dose matrix, while the lower array (b) shows the average angle of implanted ions measured in terms of the deviation from the wafer normal in the x-direction.

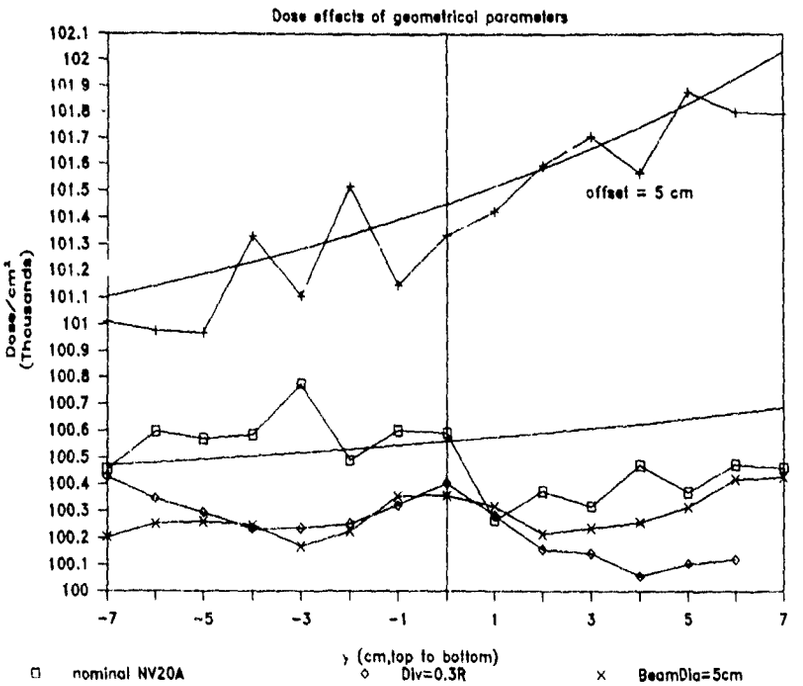

Fig 4. Dose simulation results with a target dose of 1×10^{5} cm^{-2} plotted as a function on radial position on the wafer. Several deviation-from ideal geometry were considered, but none produced a dose gradient that would lead to a standard deviation of the dose of more than 0.5%.

strikes the slit in comparison to that at the wafer, producing a dose shift given by $D' = D(R + h\theta)/R$ (where D is the target dose, R is the radius at the wafer and h is the vertical displacement from wafer to slit). The value used for h in the simulation was 2 cm, although in a standard NV20A the actual value is smaller, 1.25 cm.

The upper smooth curve in fig. 4 is a first-order analytical approximation for the effects of an x-direction offset, as illustrated in fig. 6. If the beam is

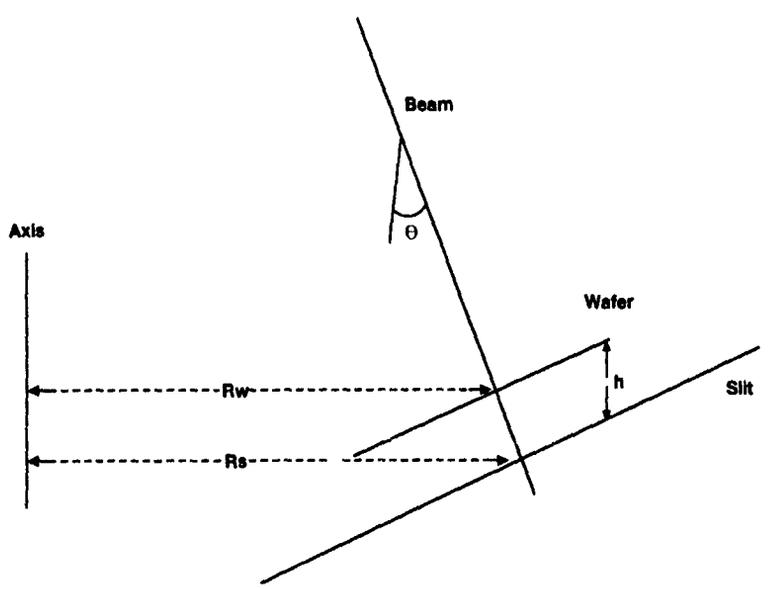

Fig. 5. Diagram showing the effect of the displacement of the wafer from the plane of the slit, in combination with a beam incident at an angle to the axis of rotation.

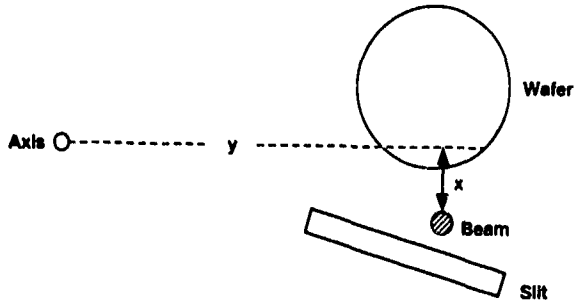

Fig. 6. Diagram showing the effect of a beam significantly displaced from the $y-z$-plane.

displaced by a distance x, the actual radial position is given by $R' = \sqrt{(R^2 + x^2)}$. This results in an overdosing that can be calculated as $D'' = D' \times \sqrt{(R^2 + x^2)}/R$. This line follows the results of MIKADO quite closely although it was calculated with no adjustable parameters, and gives confidence that the simplified algebraic form is sufficiently accurate to analyze the real situation.

6. Other applications

The simulation of process equipment with any given set of assumptions aimed at elucidating specific questions often allows the evaluation of many important process issues [3]. In this case, the angle with which ions strike the surface of the wafer were easily extracted from the geometrical model, as shown in fig. 3. This can facilitate the understanding of the effects of differential channeling across the face of the wafer.

It might also be possible to extend the veracity of the simulation to take into account more complex ion trajectories, under the influence of electrostatic or magnetic fields, or to allow for the effects of beam neutralization by collisions with residual gases.

7. Conclusions

It seems that within the assumptions built into this simulation (straight line particle paths, beam geometry independent of y-scan position, no charge neutralization, etc.) no plausible beam geometry leads to a significant dose nonuniformity and simple first-order analytical approximations are sufficient to estimate the magnitude of the effects revealed by the simulation. The explicit simulation of the geometrical characteristics of a high current implanter has already been used to calculate other effects that can effect the implant process, and could easily be used as a design tool to investigate novel dose control algorithms.

References

[1] G. Ryding, US Patent 4234797 (1980)
[2] G. Ryding and M Farley, Inst Phys Conf Ser. 54 (1980) 100.
[3] A.M. Ray and J.P. Dykstra, these Proceedings (8th Int Conf. on Ion Implantation Technology, Guildford, UK, 1990) Nucl. Instr and Meth B55 (1991) 488.

Nuclear Instruments and Methods in Physics Research B55 (1991) 488–492
North-Holland

Beam incidence variations in spinning disk ion implanters

Andy M. Ray and Jerald P. Dykstra
Eaton Corp Semiconductor Equipment Division, 2433 Rutland Drive, Austin, Texas 78758, USA

Recent trends in high density semiconductor processing technology are resulting in increasingly stringent requirements for spatial uniformity of beam incidence upon the wafer, as well as greater versatility in controlling the angles of wafer tilt and twist. These requirements have resulted in the production of a new generation of spinning disk mechanical scanning implanters capable of easily varying wafer tilt, including repositioning during implant. Greater versatility has also increased the difficulty in visualizing beam incident angle (tilt and twist) variations. A generalized model for calculating these variations is derived and presented. Graphs generated by the model may be used to evaluate various configurations of commercially available spinning disk mechanically scanned batch ion implanters.

1. Introduction

Due to the space charge limitation of electrostatic elements, the design of equipment capable of high current ion implantation into semiconductors has generally depended on mechanically scanning the wafer in front of a stationary ion beam. Additionally, the need to minimize wafer heating has dictated batch processing. Although other configurations exist, such as carousels, most equipment now depends on the familiar spinning disk in combination with a slow mechanical scan.

Previous generation designs generally consisted of a disk with a domed pedestal support for the wafer and a device for holding the wafer in place and to allow contact cooling. Wafer tilt was commonly 7° to minimize channeling, although 0° was sometimes used to reduce shadowing effects. Wafer tilt was varied by changing the angle of the wafer pedestal. In these designs, the spin axis of the disk was usually parallel to the central ray of the ion beam, which, as will be shown later, results in no tilt or twist variations across the wafer.

Concerns for particulate contamination have resulted in incorporation of centrifugal clamping, generally known in the industry as clampless cooling [1]. This technique uses small fingers or paddles to hold the wafer in place until the disk is spinning. During the actual implant, centrifugal forces hold the wafer in place and provide the pressure required for contact cooling. This centrifugal force is proportional to the sine of the pedestal angle, and, since the force vanishes at 0°, manufacturers have devised various methods of modifying scan systems to allow clampless cooling for 0° implants. These modifications have inevitably resulted in the spin axis of the disk being nonparallel to the ion beam.

The advent of three-dimensional circuit device structures, such as trenches, has resulted in an increased interest in varying the tilt and twist during the implant. Continuous wafer rotation during the implant, discrete rotations during or between steps, and implants consisting of several steps at different tilts may be required to provide wall coverage for three-dimensional devices. To answer this challenge, recent designs have focused on providing the flexibility of programmable tilt and twist [2]. Again, this increase in flexibility has occurred at the expense of increasing the angle between the spin axis and the ion beam.

2. Tilt/twist definitions

The wafer tilt and twist are traditionally defined as the ϕ and θ angles of a beam vector relative to a spherical coordinate system located at the wafer surface (fig. 1). The ion beam is denoted as V and a local wafer coordinate system defined by the orthogonal vectors W_x, W_y, and W_z. The orientation of this coordinate system to the physical surface of the wafer is arbitrary; for convenience, the W_y-axis is parallel to the wafer major flat and it is assumed that the wafer is loaded with the flat towards the center of the disk.

The above definitions of tilt and twist are very useful when considering channeling effects by using a stereographic projection [3]. However, in some cases, it may be also useful to know the angles between the beam vector and the W_x–W_z- and W_y–W_z-planes, denoted respectively by A and B, since these planes may represent physical structures on the wafer, as, for example, in a trench device, where a side wall implant might be more sensitive to changes in one of these angles than

0168-583X/91/$03.50 © 1991 – Elsevier Science Publishers B.V. (North-Holland)

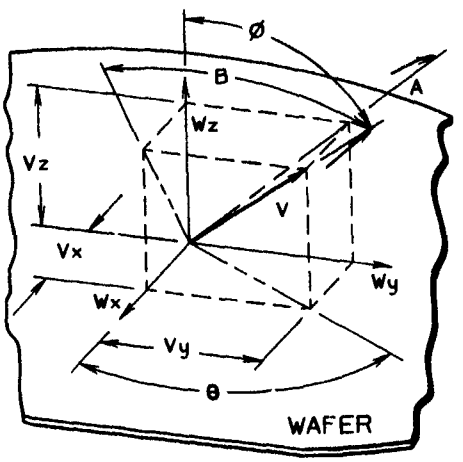

Fig. 1 Definition of a local wafer coordinate system (W_x, W_y, W_z) located at the wafer surface and the relationship of the beam vector, V, to the wafer coordinate system.

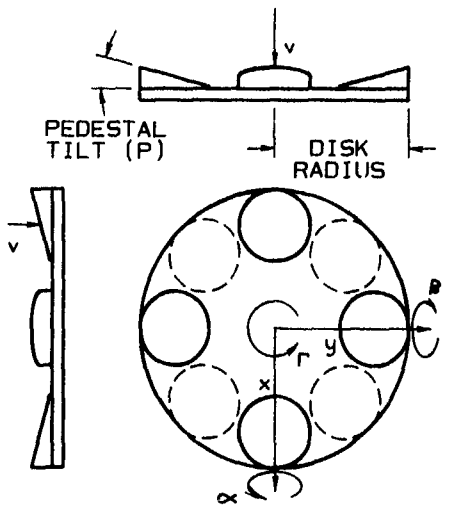

Fig. 2. Definition of a global coordinate system (x, y, z), aligned with the disk surface prior to rotation, and the relationship of the beam vector, V, to the global coordinate system The three possible disk rotation angles, α, β, and γ, and the pedestal tilt angle, P, are defined as shown.

the other. Both sets of angles will be presented for convenience.

If one defines V as a unit vector, then, by inspection of fig. 1, the following may be stated:

$\theta = \arctan(V_y/V_x)$: twist angle
$\phi = \arccos(V_z)$: tilt
$A = \arcsin(V_x)$: beam to W_y–W_z-plane
$B = \arcsin(V_y)$: beam to W_x–W_z-plane

3. Disk description

The disk is initially assumed to be aligned with the global (x, y, z) coordinate system. In the general case, the disk has three degrees of freedom, denoted by α, β and γ. The beam vector is aligned with the z-axis. By inspection of figs. 1 and 2, the following may be stated:

$$V = \begin{pmatrix} 0 \\ 0 \\ 0 \end{pmatrix}, \quad W_x = \begin{pmatrix} \cos P \\ 0 \\ -\sin P \end{pmatrix}, \quad W_y = \begin{pmatrix} 0 \\ 1 \\ 0 \end{pmatrix},$$

$$W_z = \begin{pmatrix} \sin P \\ 0 \\ \cos P \end{pmatrix}.$$

The disk radius is not generally the same for various pieces of equipment. However, if the batch size (n) and wafer size are known, the radius may be estimated by the following formula:

$$\text{Disk}_{\text{dia}} \approx \text{Wafer}_{\text{dia}} + (\text{Wafer}_{\text{dia}} + k)/\sin 180°/n,$$

where k is the mean linear clearance between wafers.

It will also be necessary to know the amount of disk spin, γ. The rotation angle, γ, required to move the beam from the center to the extreme edge of the wafer may be found from fig. 3, as a function of disk radius and wafer diameter.

4. Method of analysis

The general solution algorithm consists of rotating the wafer coordinate system by the three possible disk rotations, calculating the components of the beam vector relative to the wafer coordinate system, and using

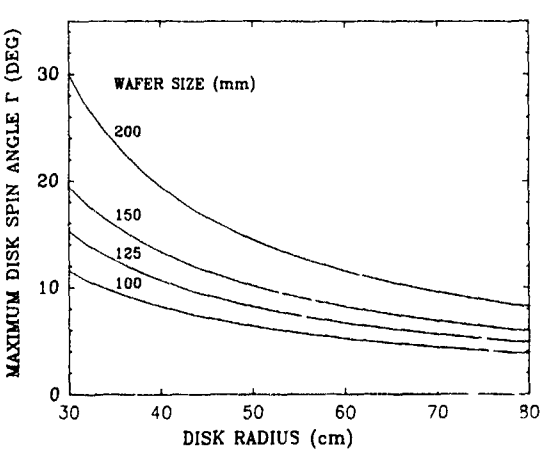

Fig. 3. Approximate value of the disk spin angle, γ, required to move the beam from the center to the edge of the wafer, as a function of disk radius and wafer size. The largest tilt and twist variations will normally occur at the edge of the wafer, corresponding to this value of γ.

these components to calculate the various tilt and twist angles by the equations listed above.

The rotated wafer unit vectors, denoted by W', may be calculated by the direction cosines of the rotated coordinate systems, as follows [4]:

$$\begin{pmatrix} W_x' \\ W_y' \\ W_z' \end{pmatrix} = R_3 \times R_2 \times R_1 \times \begin{pmatrix} W_x \\ W_y \\ W_z \end{pmatrix},$$

where R_3, R_2, and R_1 are the rotation matrices of the disk rotations γ, β, and α, respectively. Table 1 states the generalized transform matrix R, as well as the components of the rotated wafer unit vectors.

The required components of V relative to the rotated wafer axis may be calculated by evaluating the dot product of V with each of the three wafer unit vectors. However, the definition of V as a unit vector along the z-axis greatly simplifies this process, the dot products may be read directly as the third term of each wafer unit vector, and, therefore, the various tilt and twist angles may be calculated directly from their respective definitions and table 1.

5. Examples

The numerical evaluation of the various tilt and twist angles, while certainly possible, is not a trivial task. However, additional information may be gained by considering some special cases.

5.1. $\alpha = \beta = 0$

This is the previously mentioned special case of the spin axis parallel to the beam axis. In this case, the wafer unit vectors reduce to:

$$W_x' = \begin{pmatrix} \cos P \cos \gamma \\ \cos P \sin \gamma \\ -\sin P \end{pmatrix}, \quad W_y' = \begin{pmatrix} -\sin \gamma \\ \cos \gamma \\ 0 \end{pmatrix},$$

$$W_z' = \begin{pmatrix} \sin P \cos \gamma \\ \sin P \sin \gamma \\ \cos P \end{pmatrix}.$$

The resultant beam incidence angles are:

$$\phi = \arccos(\cos P) = P, \quad A = \arcsin(-\sin P) = P,$$
$$\theta = \arctan(0/(-\sin P)) = 0, \quad B = \arcsin(0) = 0.$$

As expected, none of the tilt or twist angles are functions of the disk rotation, Γ, and no tilt or twist variations will occur during the implant.

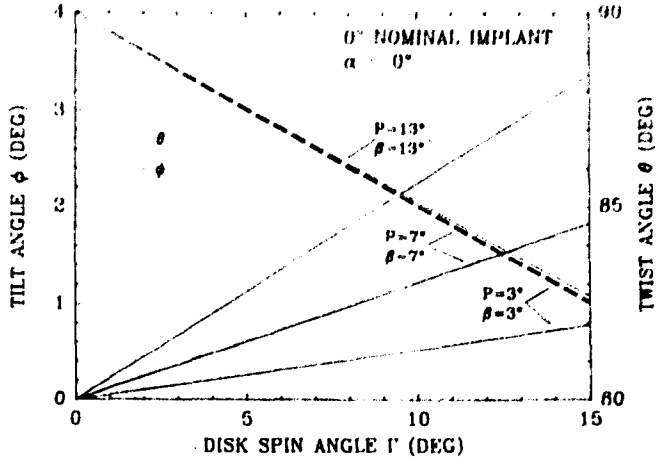

Fig. 4. Values for the tilt and twist angles, ϕ and θ, for a nominal 0° implant as a function of the disk spin angle, γ, disk rotation about the horizontal axis, β, and the angle of the wafer pedestal, P.

Table 1
Generalized rotation matrix for the allowable disk rotations (R) and the components of the wafer coordinate system after multiplication by the generalized rotation matrix (W_x, W_y and W_z)

$$R = \begin{pmatrix} \cos\gamma\cos\beta & -\sin\gamma\cos\beta & -\sin\beta \\ \cos\alpha\sin\gamma + \sin\alpha\cos\gamma\sin\beta & \cos\alpha\cos\gamma - \sin\alpha\sin\beta\sin\gamma & \sin\alpha\cos\beta \\ -\sin\alpha\sin\gamma + \cos\alpha\cos\gamma\sin\beta & -\sin\alpha\cos\gamma - \cos\alpha\sin\beta\sin\gamma & \cos\alpha\cos\beta \end{pmatrix}$$

$$W_x = \begin{pmatrix} \cos P\cos\gamma\cos\beta + \sin P\sin\beta \\ \cos P\cos\alpha\sin\gamma + \cos P\sin\alpha\cos\gamma\sin\beta - \sin P\sin\alpha\cos\beta \\ -\cos P\sin\alpha\sin\gamma + \cos P\cos\alpha\cos\gamma\sin\beta - \sin P\cos\alpha\cos\beta \end{pmatrix}$$

$$W_y = \begin{pmatrix} -\sin\gamma\cos\beta \\ \cos\alpha\cos\gamma - \sin\alpha\sin\beta\sin\gamma \\ -\sin\alpha\cos\gamma - \cos\alpha\sin\beta\sin\gamma \end{pmatrix}$$

$$W_z = \begin{pmatrix} \sin P\cos\gamma\cos\beta - \cos P\sin\beta \\ \sin P\cos\alpha\sin\gamma + \sin P\sin\alpha\cos\gamma\sin\beta + \cos P\sin\alpha\cos\beta \\ -\sin P\sin\alpha\sin\gamma + \sin P\cos\alpha\cos\gamma\sin\beta + \cos P\cos\alpha\cos\beta \end{pmatrix}$$

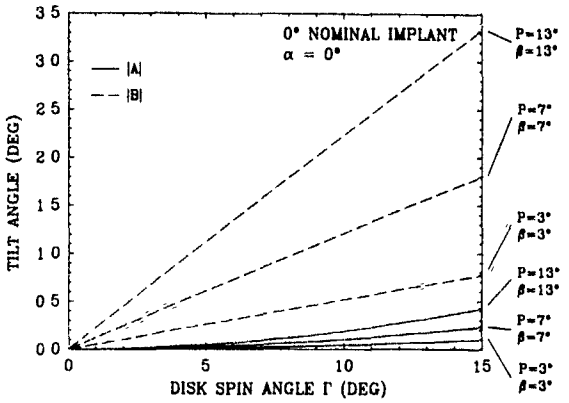

Fig 5. Values for the tilt angles to the W_x-W_z- and W_y-W_z-planes, A and B, for a nominal 0° implant as a function of the disk spin angle, γ, disk rotation about the horizontal axis, β, and the angle of the wafer pedestal, P.

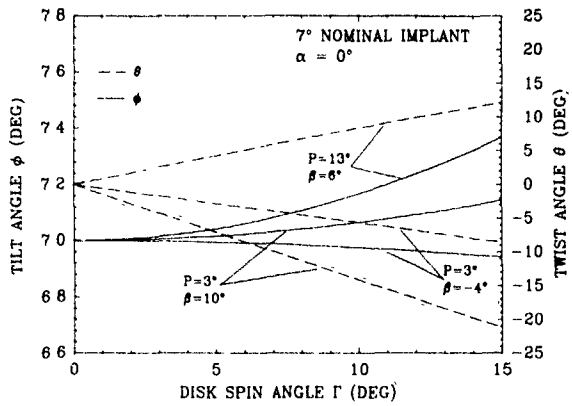

Fig. 6 Values for the tilt and twist angles, ϕ and θ, for a nominal 7° implant as a function of the disk spin angle, γ, disk rotation about the horizontal axis, β, and the angle of the wafer pedestal, P.

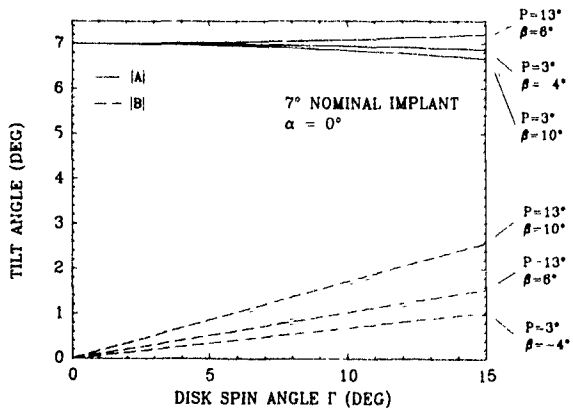

Fig. 7. Values for the tilt angles to the W_x-W_z- and W_y-W_z-planes, A and B, for a nominal 7° implant as a function of the disk spin angle, γ, disk rotation about the horizontal axis, β, and the angle of the wafer pedestal, P.

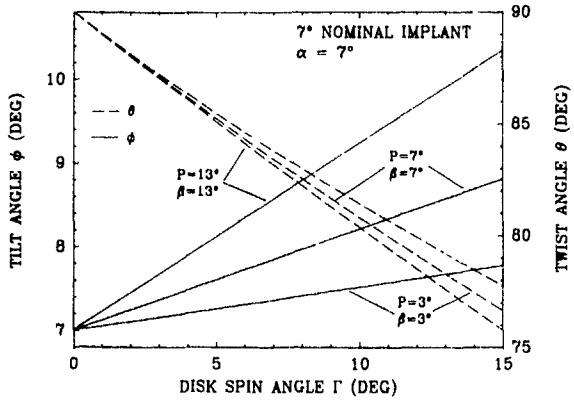

Fig 8. Values for the tilt and twist angles, ϕ and θ, for a nominal 7° implant as a function of the disk spin angle, γ, disk rotation about the horizontal axis, β, and the angle of the wafer pedestal, P. In this case, β is equal to P and the tilt angle is due to the disk rotation about the vertical axis, α, as would be necessary to vary the wafer twist by 90° for a quadrant rotation implant

5.2. $\alpha = 0$, $\beta \neq 0$

Figs. 4–7 depict typical tilt and twist variations for 0° and 7° implants; additional tilt angles may be calculated by table 1 and the angle definitions.

One may conclude from these graphs that a smaller pedestal angle will result in smaller variations of tilt angles, however, this may not be true in the general case. For example, for both of these tilts a 3° pedestal exhibits a lower variation, but that is due to the fact that this pedestal angle produces the smallest disk spin axis rotation to achieve 0 and 7° implants. If one were

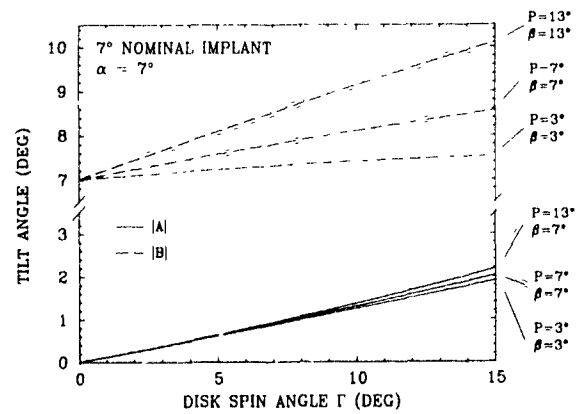

Fig. 9 Values for the tilt angles to the W_x-W_z- and W_y-W_z-planes, A and B, for a nominal 0° implant as a function of the disk spin angle, γ, disk rotation about the horizontal axis, β, and the angle of the wafer pedestal, P. In this case, β is equal to P and the tilt angle is due to the disk rotation about the vertical axis, α, as would be necessary to vary the wafer twist by 90° for a quadrant rotation implant.

V. MACHINES

interested in, for example, 0 and 14° implants, a pedestal angle of 7° might produce the lowest average variation of both implants.

5.3. $\alpha \neq 0$, $\beta \neq 0$

Figs. 8 and 9 depict the tilt and twist variations for a 7° implant formed by a compound rotation of the disk spin axis. Comparison of these graphs to figs. 6 and 7 show that this method consistently exhibits more variation than the corresponding angle produced by only one disk rotation. Again, this is due to the larger angle between the spin axis and the beam vector produced by the compound rotation.

6. Summary

The requirements of programmable tilt, programmable twist, and clampless cooling for 0° implants have produced a new generation of spinning disk ion implanters. However, these performance improvements have complicated the process of visualizing the tilt and twist angles of the ion beam to the wafer. We have presented an analysis that may be used by both users and manufacturers to understand the effects of the various possible machine configurations.

References

[1] V. Benveniste, Nucl. Instr. and Meth. B21 (1986) 366.
[2] T. Tamai, M. Diamond, B. Doherty and P. Splinter, these proceedings (8th Int. Conf. on Ion Implantation Technology, Guildford, UK, 1990) Nucl. Instr. and Meth. B55 (1991) 408.
[3] R. Simonton, D. Kamenitsa and A. Ray, ibid., p. 188.
[4] J. Gere and W. Weaver, Matrix Algebra for Engineers (Nostrand, Princeton, 1965).

Nuclear Instruments and Methods in Physics Research B55 (1991) 493–501
North-Holland

The MeV ion implantation system "RFQ-1000" and its applications

Akira Hirakimoto, Hiroaki Nakanishi and Masatoshi Asari
Shimadzu Corporation, Nakagyo-ku, Kyoto, 604, Japan

Advanced VLSI devices are nowadays required to raise switching speed, to improve noise immunity and to minimize chip size. Presently, MeV ion implantation attracts much technological attention in the field of VLSI fabrication, because it is expected to be one of the most feasible solutions to those demanding requirements. In order to realize such prospective expectations, an RFQ (radio-frequency quadrupole) accelerator was applied for the first time to the field of ion implantation and a MeV ion implantation system "RFQ-1000" has been developed. First, we briefly refer to the background of the system development, putting emphasis on the RFQ. Next an outline is given of the system configuration and features. Following, detailed performances of the system are described, i.e., beam current capability, energy variability, dose uniformity, particle performance and so on. Then we move onto the viewpoint of applications. The current status of device applications by the MeV ion implantation are briefly reviewed. Finally future applications of the system to the field of compound semiconductors and to the surface modification of materials are presented.

1. Introduction

The necessity of MeV ion beams has expansively increased in the field of ion implantation because many innovative applications [1] have been evaluated to be highly promising. Since these applications require a beam current as high as several hundred microamperes for achieving reasonable throughput, current capability turns out to be a critical issue. Existing systems for MeV implantation, however, set a limit on the current capability, because their acceleration methods remain conventional electrostatic types.

Thus we aimed at the development of a both high-energy and high-current implantation system [2], whose kernel is the latest linear accelerator, RFQ (radio-frequency quadrupole). One of the most attractive and outstanding features of the RFQ is its capability of accelerating ion beams in excess of several milliamperes up to energies in the MeV range. This capability is based upon the fact that the RFQ utilizes its intense rf electric field for focusing and accelerating ions simultaneously [3,4].

Most RFQ machines, however, accelerate the ions of neither boron nor phosphorus, but of hydrogen. The main reason for this is the difficulty in the focusing control of heavy ion acceleration, because the focusing force is inversely proportional to the mass of the projectile ion. There is, furthermore, a severe drawback that the output energy of the RFQ, similar to other types of linear accelerators, is said to be invariable without change of the resonant frequency. It goes without saying that the energy variability is indispensable to the ion implantation because the control of ion implanting depth is realized by the energy variability. A straightforward solution is of course a variable frequency RFQ. But it is scarcely a practical proposal, because a change of the resonant frequency causes troublesome complications of RFQ structures and rf power supply circuits, which result in a severe rise of total cost. This drawback and the difficulty have been critical barriers to the application of the RFQ to the field of ion implantation.

Shimadzu, with the aid of computer simulations and experimental studies, has successfully developed a variable energy RFQ without change of the resonant frequency, capable of accelerating heavy ions. Preliminary explanation to the variability will be given in section 3.2. Other parts of the system have also been developed, such as an injector supplying high current beams into the RFQ and an endstation processing silicon wafers in a superclean environment. Many advantages compared with conventional high energy implantation machines are stated in ref. [2].

2. System configuration and features

A bird's-eye view of an "RFQ-1000" layout example is shown in fig. 1 (top). The system consists of three parts as shown in fig. 1 (bottom) and mentioned below.

2.1 Injector

In order to satisfy the acceptance conditions of the present RFQ, the emittance value of the ion source is strictly required to be less than 100π mm mrad. If the emittance value exceeds the permissible level, a considerable number of ions will collide with the accelerating electrodes of the RFQ, namely vanes, and will damage

0168-583X/91/$03.50 © 1991 – Elsevier Science Publishers B.V. (North-Holland)

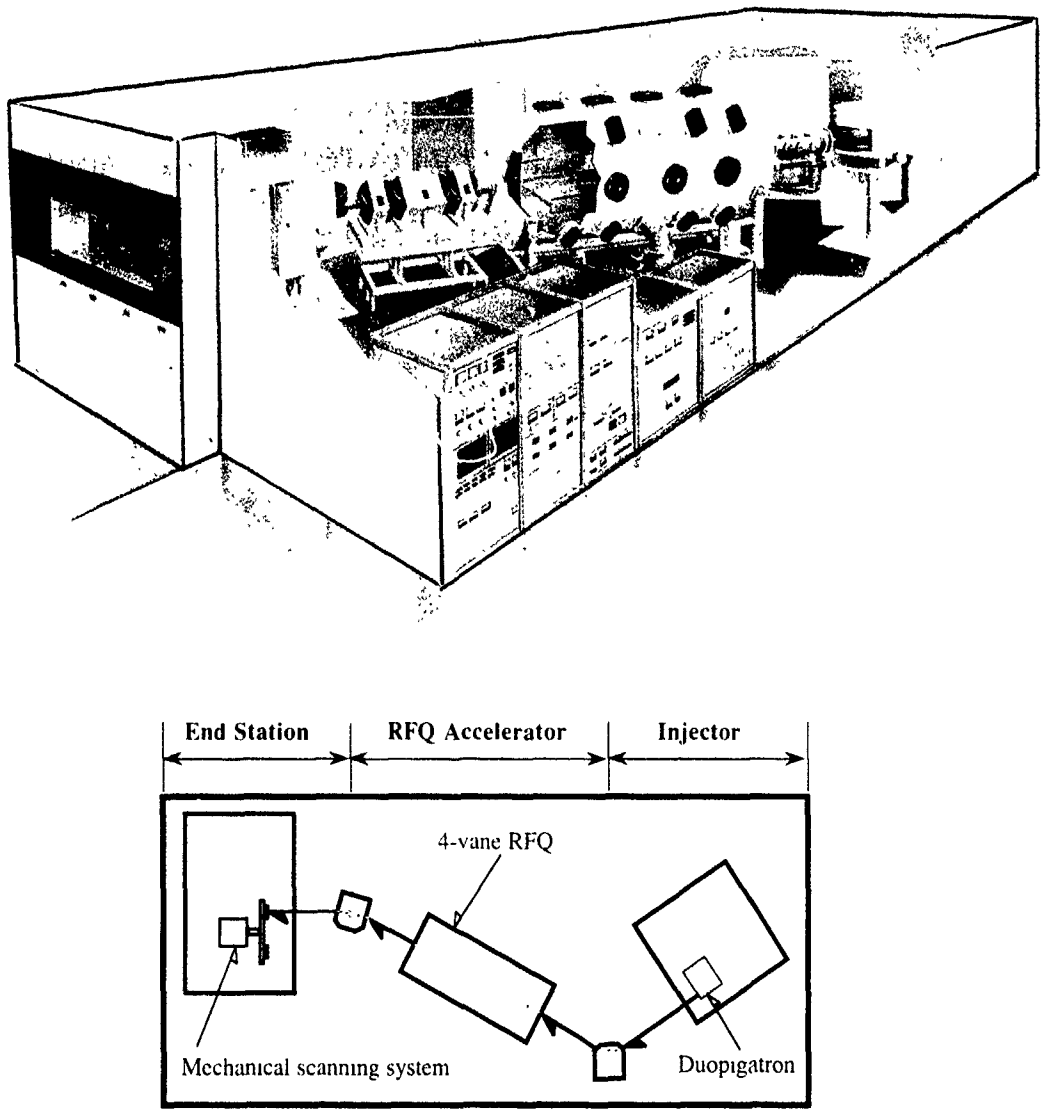

Fig. 1. Shimadzu MeV ion implantation system RFQ-1000. Top: bird's-eye view Bottom: system diagram

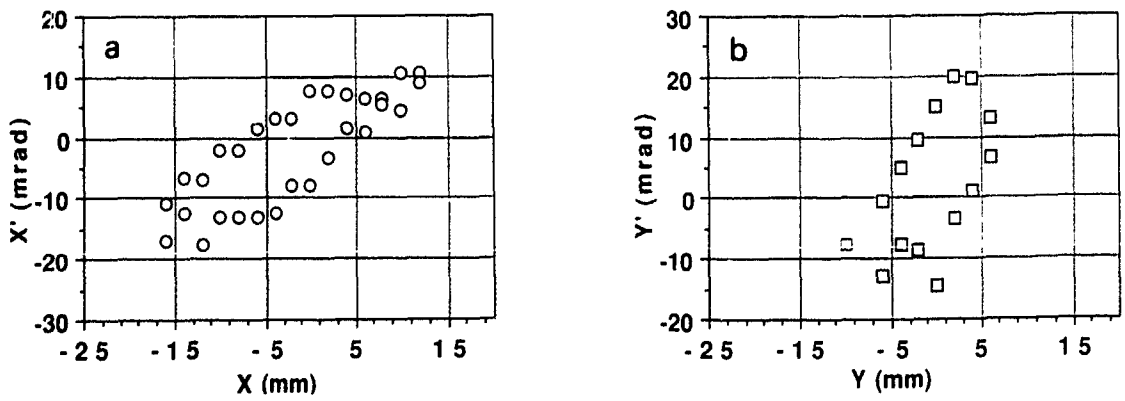

Fig. 2. Measured emittance of boron beam. (a) x-axis emittance, $E_x = 84.4\ \pi$ mm mrad. (b) y-axis emittance, $E_y = 77.4\pi$ mm mrad.

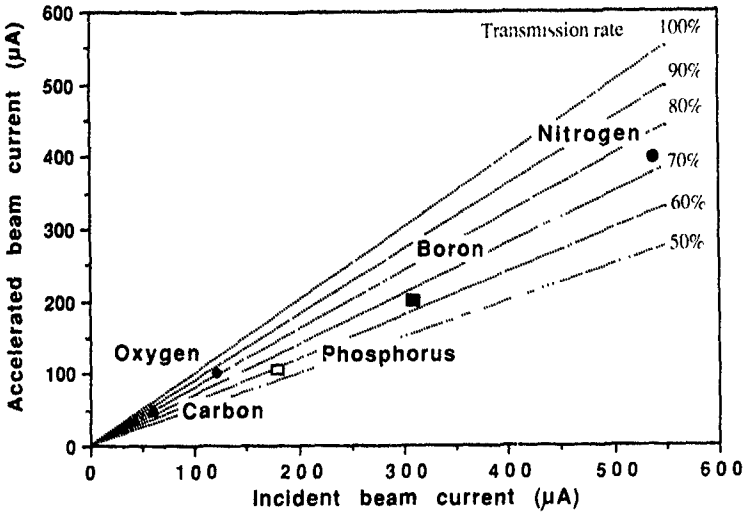

Fig. 3. Beam current capability. The transmission rate is shown at right-hand side of the figure

them. Needless to say, a high current capability is another requirement. In order to fulfill these two contradicting requirements, a duopigatron-type ion source [5] has also been developed in expectation of its high brightness characteristics. This new type of ion source [6] generates ion beams of boron, phosphorus, nitrogen, carbon, oxygen and so on. These heavy ions are preaccelerated to 5 keV/amu by using a dc power supply with a maximum terminal voltage of 100 kV. Before being injected into the RFQ, ions are mass-separated by a bending magnet with an angle of 60°. A typical emittance measurement of a boron beam at a current of several hundred microamperes is shown in fig. 2.

Table 1
System specification

Maximum output energy, and (preliminary) beam current	
for boron	1.0 MeV, ≥ 200 μA
for nitrogen	1.2 MeV, ≥ 400 μA
for phosphorus	2.8 MeV, ≥ 100 μA
Energy variable range	50–100%
RFQ resonant frequency	70.0 MHz
Vane length	1850 mm
Rf power required	25 kW max
Space charge limited current	7.8 mA
Transmission rate	84%
Wafer capacity	19 wafers for 100 mm, 15 for 125 mm, 13 for 150 mm
Throughput (preliminary)	120 wafers/h for 100 mm, 110 for 125 mm, 100 for 150 mm
Wafer temperature	≤ 100 °C
Dose uniformity	≤ 1%
Particle	≤ 0.05/cm^2 (particle size ≥ 0.5 μm)

2.2. RFQ

The four-vane type RFQ is designed for accelerating injected ions up to an MeV energy range [2]. In design procedures of the RFQ beam dynamics, we found the possibility of energy variability without change of the resonant frequency. Up to the present, the ion energies can be discrete variable in the range of 50–100% of the maximum designed value (for boron: 0.50–1.00 MeV, for phosphorus: 1.4–2.8 MeV), and we obtain about five discrete values in these ranges. The transmission rate (the ratio of accelerated beam current to the incident one, see fig. 3) lies between 60 and 70%. Though the difference between the experimental values and the calculated 84% [2] is still open to discussion, we suppose that it is due to some misadjustment of the beam optical conditions.

2.3. Endstation

The endstation contains a mechanical wafer scanning system, a precise dose control electronics and a reliable vacuum system. In the batch processing mode, the endstation accommodates 100-, 125-, or 150-mm wafers with a capacity of 19, 15 or 13, respectively. To prevent particle contamination, the silicon wafers are transported back and forth between a processing chamber and a pair of loadlocks with in-vacuum wafer handling robotics. Also the endstation is equipped with a HEPA-filtered air ventilation system. For protection against beam-induced sputtering contaminations, amor-

phous-silicon coatings are applied to the areas of beam bombardment.

3. System performance

System specifications of the RFQ-1000 are listed in table 1. Of the listed performances, some brief reviews are given below with respect to key parameters from a user's point of view.

3.1. Beam current capability

The present system has a superior current capability of the MeV range, because of simultaneous rf-focusing and rf-accelerating features. We have achieved a boron beam current at an energy of 1.0 MeV above 200 μA, and have already confirmed that the nitrogen beam current at 1.2 MeV exceeds 400 μA. Up to the present, we estimate that the accelerating beam current is mainly limited not by the RFQ but by the ion source, because

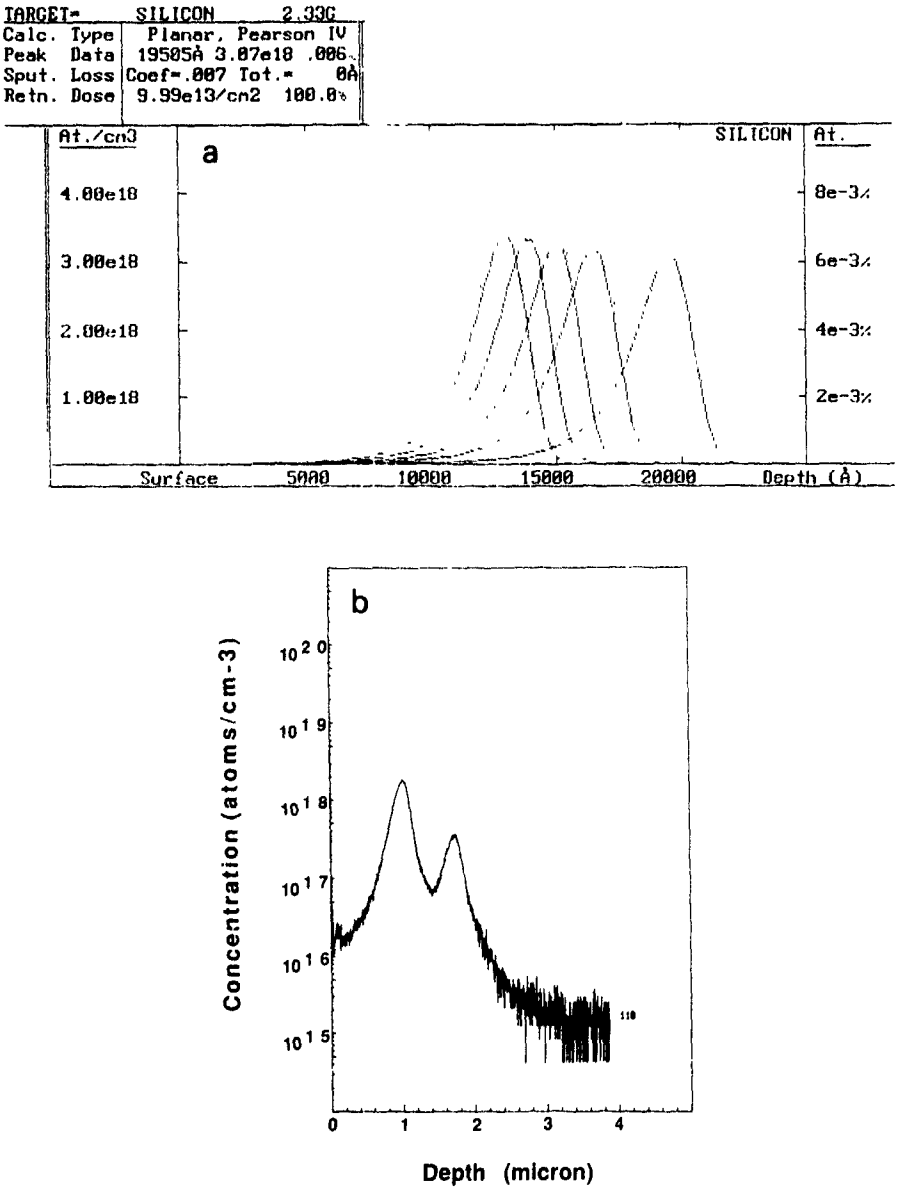

Fig. 4. Energy variability of the RFQ-1000. (a) Implant profile simulation of discrete-variable energy. Ion: ^{11}B, energy: 0.5–1.0 MeV, dose: 1×10^{14} ions/cm^2. (b) Implant profile of ^{11}B into Si measured by SIMS. Ion: ^{11}B, energy: 0.5 MeV, dose: 6×10^{13} ions/cm^2. Ion: ^{11}B, energy: 1.0 MeV, dose: 1×10^{13} ions/cm^2.

the space-charge limited current of the RFQ is calculated theoretically to be as high as 7.8 mA [2]. The schedule for beam enhancement up to 1000 μA including tune-up of the ion source is now in progress. In fig. 3 the latest beam current performances are shown.

3.2. Energy variability

The energy variability of the RFQ is, as mentioned above, an unavoidable problem. Instead of a variable frequency RFQ, a fixed frequency RFQ with discrete variability of energy is realized. The method to vary output energy is to modify somehow the RFQ electric field, for example, by a decrease of vane voltage compared with the designed value. This practical method is based on the inherent characteristics of the RFQ beam dynamics, i.e., the strong focusing capability, and is not applicable to other linear accelerators.

A preliminary explanation to the energy variability is the following. The decrease of vane voltage causes some deviation of the synchronous acceleration condition and results in a decrease of ion energy gain. The focusing force of the RFQ, in the meanwhile, interacts all along the ion passage and can keep most of the ions in a stable bunching bucket, even if the vane voltage is less than the designed value. Therefore, the focusing force prevents swift losses of injected ions during the acceleration and most of ions can survive to reach the outlet of the RFQ. Consequently, the output energy of projectile ions is shifted to a lower value. The discreteness of the output energy is simulated by a computer code, but a complete physical theory is left to be developed because of its excessive complexity.

On the other hand, the focusing force of a conventional Alvarez-type linear accelerator interacts only in the drift-tube and cannot converge the ions when the synchronous condition is deformed even slightly. Therefore, the decrease of drift-tube electrode voltage results in rapid beam divergence.

The energy variability of the RFQ is demonstrated in fig. 4, showing the depth profile of ion implantation at an energy of 0.5 MeV and a subsequent one at 1.0 MeV of boron-11 measured by SIMS (secondary ion mass spectroscopy).

3.3. Dose uniformity

Dose uniformity is one of the most important performances in a production implantor. The RFQ-1000 has at present a specification for dose uniformity $\sigma/X \leqslant 1.0\%$, where σ is the standard deviation and X the

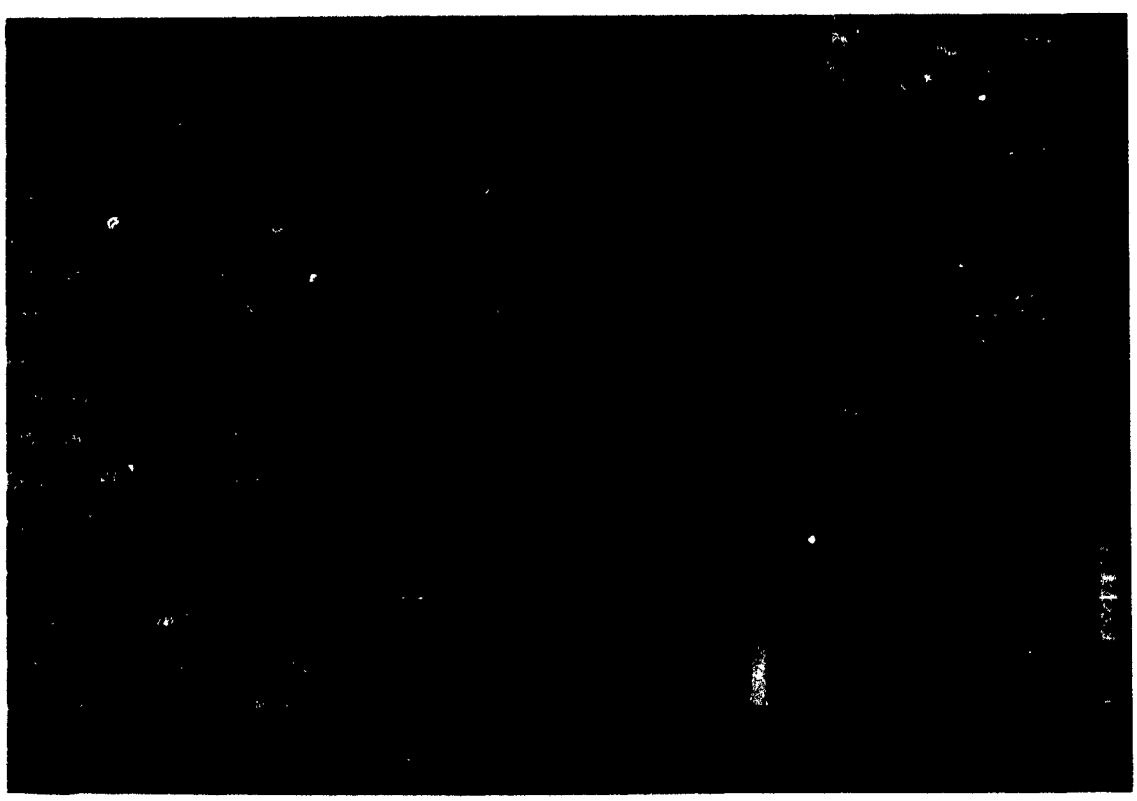

Fig. 5. Dose uniformity showing a typical value of $\sigma/X = 0.69\%$. Ion: ^{31}P, energy: 2.8 MeV, dose: 2×10^{13} ions/cm^2.

average dose. As shown in fig. 5, improved results as low as 0.7% are regularly achieved by a mechanical wafer scanning system, composed of a high-speed spinning disk (800–1000 rpm) and a parallel scanning mechanism whose speed is servo-controlled according to the beam current and the scan position of the beam.

3.4. Particle performance

Requirements for the prevention of particle contamination come to be more and more demanding as device integration progresses. In the present system, a pair of loadlocks and wafer handling robotics in the vacuum ensure the specification of 0.05 particle/cm^2 (particle size $\geqslant 0.5$ μm). In order to check the specification, a number of particle measurements by a laser particle monitor were carried out, before and after the implantations of 1.0 MeV boron at a dose of 2×10^{14} ions/cm^2. We found that added particle counts were less than 10 in a 150-mm wafer.

3.5. Metal contamination

Metal contamination is a rising problem for advanced VLSI, especially in CCD and megabit DRAM. In order to check for heavy metal contamination at the wafer surface, we used TXRF (total X-ray reflection fluorescence) analysis [7]. In TXRF, X-rays are incident on the wafer at a glancing angle so that the condition for total reflection may be satisfied. Therefore, only the near-surface region of the wafer is excited, and fluorescence X-rays emitted from contaminants are detected. The detection limits lie on the order of 10^{11} atoms/cm^2. Two TXRF measurements were carried out: one sample was a control wafer as received from a vendor and the other was implantated with 1.2 MeV nitrogen at a dose of 3×10^{16} ions/cm^2. The results showed that heavy metal contaminants were under the detection limits, except zinc which was detected as high as 2.8×10^{12} atoms/cm^2 but was supposed to be an initial contaminant, because its peak height was the same in the wafer from a vendor. Needless to say, we used SIMS measurements with oxygen flooding in order to check for aluminum and other light metals undetectable by TXRF. There was no evident contamination of those light metals. From the obtained results, we confirm that amorphous-silicon coatings on the area of beam bombardment are effective for the prevention of sputtered foreign materials.

3.6. Vacuum performance

Due to the outgassing of photo-resist bombarded by energetic ions, the pressure in the processing chamber rises sharply. This is of great concern because dose errors will occur when ions are neutralized to a significant extent. In particular, the outgassing becomes more serious with increasing ion energies. In order to measure the vacuum performance, the following experiment was carried out. After 150-mm wafers were coated with a positive photo-resist OFPR-800 with a thickness of 5 μm (slightly deeper than projectile ranges of MeV) and baked at 130 °C, they were bombarded by 1.2 MeV nitrogen at a current of 200 μA. In fig. 6 the vacuum performance is shown, which indicates the present vacuum system is by no means inferior to other implantation systems [8]. Residual gasses were analyzed simultaneously by a quadrupole mass spectrometer and hydrogen was extremely dominant, as reported in ref. [9]. An investigation of dose error occurrence is now being carried out.

4. Applications

4.1. Silicon semiconductor devices

Principal applications, based on deep implantation, have many advantages in VLSI fabrications. Detailed

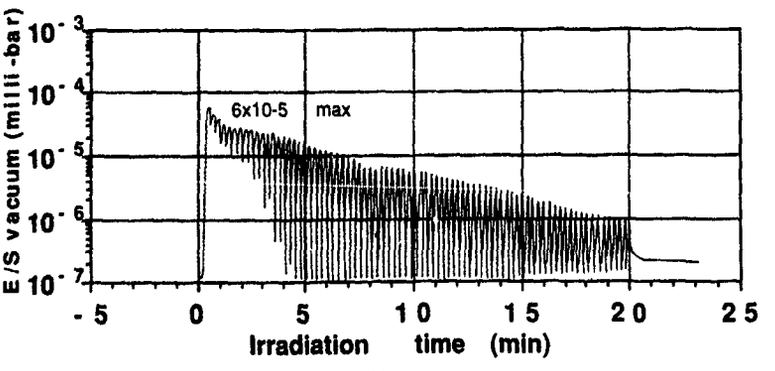

Fig. 6. Vacuum performance with photo-resist outgassing. Ion: ^{14}N, energy: 1.2 MeV, dose: 5×10^{14} ions/cm^2, current: 200 μA, irradiation time: 20 min. Resist: OFPR-800, thickness: 5 μm, bake temp.: 130 °C.

descrip'ions are given in ref. [10]. We now briefly review the current status of silicon semiconductor applications.

Typical low and medium dose applications below 10^{14} ions/cm^2 are retrograde wells and ROM late programmings. At these dose levels the crystalline defects caused by the implantation can be annealed out to a sufficient extent. Accordingly, low and medium dose device applications are highly promising and some of them have come to be on the production line.

Major high dose applications above 10^{14} ions/cm^2

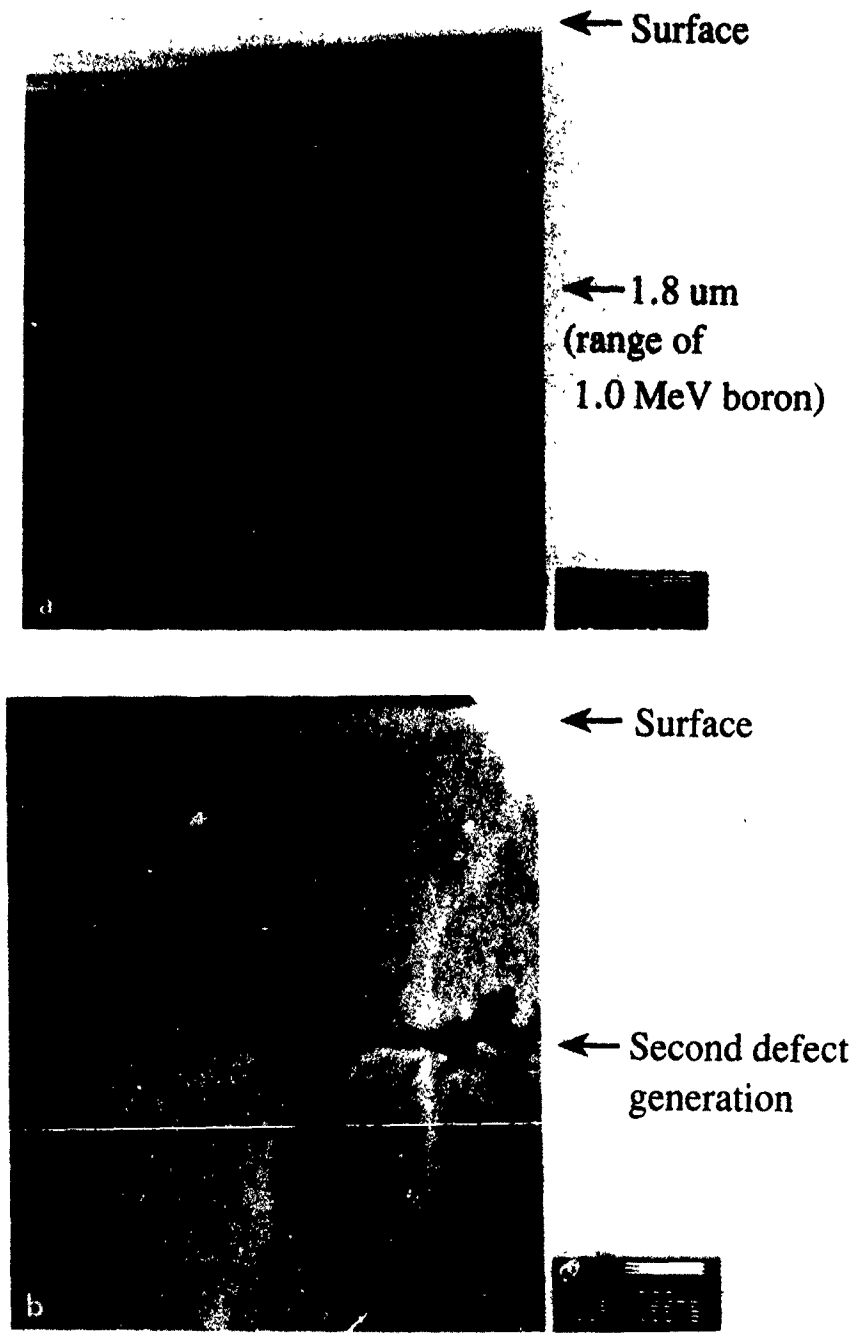

Fig. 7. Cross-sectional TEM micrographs and spreading resistance profile. (a) TEM micrograph as implanted in Si⟨100⟩. Ion: ^{11}B, energy: 1.0 MeV, dose: 2×10^{14} ions/cm^2. (b) TEM micrograph after furnace anneal, showing secondary defect generation. Temperature: 900 °C, time: 15 min, ambient: N_2. (c) Spreading resistance profile (following page).

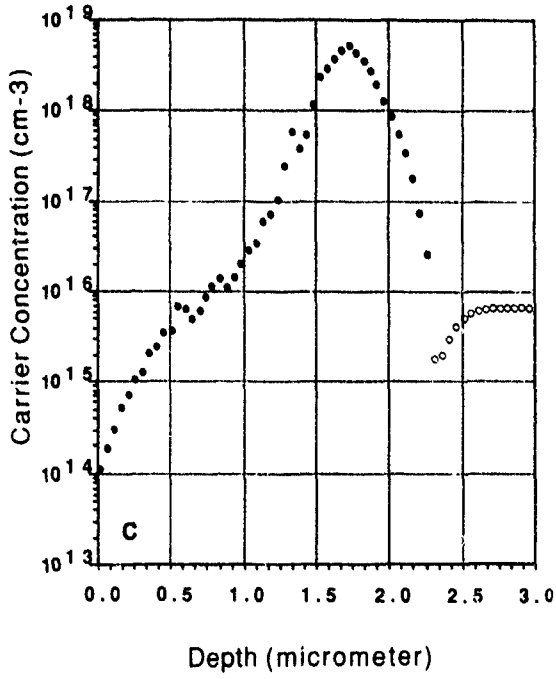

Fig. 7. (continued).

are buried shield layers for soft-error protection and subcollector formations for bipolar transistors. Annealing methods for reducing crystalline defects are not yet established, compared with those of low and medium dose applications. In fact, a conventional furnace anneal sometimes causes second defects which can be observed by cross-sectional TEM (transmission electron microprobe) as shown in fig. 7b. Some dislocation loops and line-like defects are extended along the direction of the ⟨111⟩ axis. It was found that these defects do not disappear even at an anneal temperature as high as 1250 °C. Thus electric properties, such as reverse leakage

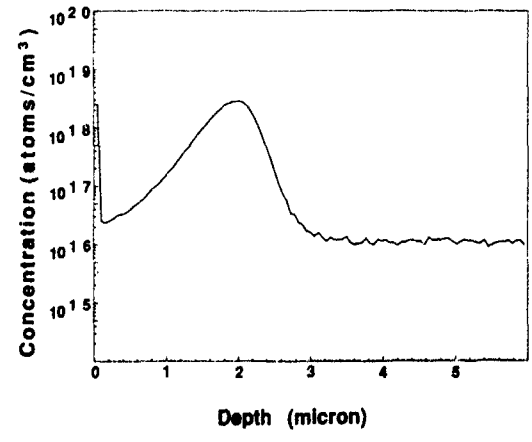

Fig. 8. Implant profile of ^{24}Si into GaAs measured by SIMS. Ion: ^{24}Si, energy: 2.5 MeV, dose: 3×10^{14} ions/cm^2.

current and breakdown voltage, are considerably degraded. In order to check these properties, it is necessary to fabricate some types of diodes. First of all, a measurement of the spreading resistance profile was carried out as shown in fig. 7c. From the result, we estimate that the activation rate is between 60 and 70%. Some candidates for novel solutions to the degradations caused by those defects are an RTA (rapid thermal anneal) [11] and a proximity gettering [12] by high energy carbon or oxygen implantation. Many investigations are focused on these problems and a breakthrough is strongly desired.

4.2. Compound semiconductor devices

Diffusion processes, such as thermal drive-in, are widely used for silicon device fabrications. In the III–V-group compound semiconductors, on the other hand, the application of diffusion processes is generally supposed to be impossible, since the temperature of evaporation in the V-group is considerably lower than that of thermal diffusion processes. Therefore, high energy ion implantation with moderate thermal annealing is a principal and practical dopant feeding technology. With the present RFQ and a projecting ion source for indispensable dopants such as beryllium and silicon, it is expected to contribute to the development of III–V-group compound semiconductor devices, for example, a super-high-speed mixer diode [13] and an OEIC (opto-electronic integrated circuit). A preliminary experiment of silicon implantation into gallium arsenide by the RFQ-1000 was performed as shown in fig. 8. Conventional tandem accelerators, on the other hand, have a critical limitation for compound semiconductor applications because they can only accelerate negative ions, and these ions of beryllium can be hardly produced due to its small electron affinity.

4.3. Surface modification of materials

Surface modification technology [14] is intended to improve wear resistance, hardness and other properties by implanting ions into metals and other materials. Hitherto, because of the energy limitation, the modified layer was limited only to the outermost surface, and its durability was not sufficient. Since the present system has a capability of deep implantation, a possibility of overcoming the limitation is expected. Presently, the most practically used ion with excellent results is nitrogen which has a small value of electron affinity. Thus tandem accelerators also have a critical limitation for surface modifications. In the present system, a half-milliampere beam of nitrogen is almost achieved. With the aid of the aircraft equipment division of Shimadzu, we are now researching some aero-space applications. One of them is a durability improvement of valves for rockets

and satellites, where conventional surface treatments are not available.

5. Conclusion

In the present report, the current status of the RFQ-1000 is briefly described. The system consists of three parts, i.e., an injector with duopigatron ion source, an RFQ accelerator with variable energy capability and an endstation with clean wafer processing. The system performances are quite suited to the fabrication of advanced VLSI devices. Compound semiconductor fabrications and surface modifications will also be promising application fields in the near future. The versatility of the present system will remain to be of importance in these fields.

Acknowledgements

The authors would like to acknowledge Dr. M. Sakisaka, Professor Emeritus of Kyoto University, for his valuable discussions and constant encouragement.

References

[1] M.I. Current, R.A. Martin, K. Doganis and R.H. Bruce, Semicond. Int. (1985) 106.
[2] A. Hirakimoto, H. Nakanishi, H. Fujita, I. Konishi, S. Nagamachi, H. Nakahara and M. Asari, Nucl. Instr. and Meth. B37/38 (1989) 248.
[3] R.H. Stokes, K.R. Crandall, J.E. Stovall and D.A. Swenson, IEEE Trans. Nucl. Sci. NS-26 (1979) 3469.
[4] R.H. Stokes and T.P. Wangler, Ann. Rev. Nucl. Part. Sci. 38 (1988) 97.
[5] M.R. Shubaly, IEEE Trans. Nucl. Sci NS-30 (1983) 1399.
[6] S. Nagamachi, Y. Takami and M. Asari, Proc. 12th Symp. on Ion Sources and Ion Assisted Technology 89 (Ionics) p. 75.
[7] R.S. Hockett, Proc. Soc. Photo-opt. Instr. Eng. 1186 (1989) 10.
[8] J.P. O'Connor and J.T. Riley, Mater. Sci. Eng. B2 (1989) 177.
[9] T.C. Smith, Ion implantation Science and Technology (Academic Press, 1988) p. 345.
[10] J. Middelhoek, Mater. Sci. Eng. B2 (1989) 15.
[11] M. Tamura, N. Natsuaki, Y. Wada and E. Mitani, Nucl. Instr. and Meth. B21 (1987) 438.
[12] N.W. Cheung, C.L. Liang, B.K. Liew, R.H. Mutikainen and H. Wong, Nucl. Instr. and Meth. B37/38 (1989) 941.
[13] H.B. Dietrich, Proc. Soc. Photo-opt. Instrum. Eng. 530 (1985) 30.
[14] P. Sioshansi, Nucl. Instr. and Meth. B37/38 (1989) 667.

Nuclear Instruments and Methods in Physics Research B55 (1991) 502–505
North-Holland

A 500 keV ion accelerator with two types of ion source

Y. Agawa [b], M. Takai [a], S. Namba [a], T. Uchiyama [b], R. Fukui [b] and H. Yamakawa [b]

[a] *Faculty of Engineering Science and Research Center for Extreme Materials, Osaka University, Toyonaka, Osaka 560, Japan*
[b] *ULVAC Japan Ltd., Chigasaki, Kanagawa 253, Japan*

A 500 keV ion accelerator system equipped with a DISKTRON high voltage generator and two types of ion source has been developed to provide ion beams for RBS analysis with microbeams and surface modification. H^+ and He^+ beams focused to less than 1 μm with a voltage stability of less than 10^{-4} have been obtained in a microbeam line. P^+, As^+ and other heavy ion beams of sufficient intensity for surface modification are also obtained. Uniformities of P^+ and As^+ ions implanted into a 2 in. Si wafer were evaluated to be 1.5% and 1.2%, respectively.

1. Introduction

Recently, an ion microbeam technique has been widely required in microprocessing of semiconductor devices. Ion beams of less than 1 μm have been applied to ion beam analysis as well as ion implantation. In research work it is preferred that the analysis and modification are performed with a single apparatus. It is not easy, however, to construct a high voltage generator which is capable of satisfying these two aims. The ion beam analysis requires voltage stability rather than higher current. On the other hand, surface modification requires higher current, at least a few hundred μA.

"DISKTRON" [1], a rotary-disk type high voltage generator is quite suitable for this purpose due to its excellent output performance. The maximum voltage and current of the DISKTRON are 500 keV and 2 mA, respectively, with a voltage stability as low as 1×10^{-4}. A 500 keV ion accelerator equipped with the DISKTRON and two types of ion sources has been developed to provide ion beams for surface analysis and modification [2,3]. A duoplasmatron ion source, which can produce H^+ and He^+ of up to 50 μA, provides beams to a microbeam line for the surface analysis [4,5]. The other is a conventional Freeman type which provides a few hundred μA of P^+, As^+ and other heavy ions for surface modification.

In this paper, two kinds of performances are presented for application of the 500 keV ion accelerator. One is the RBS mapping [6] with microbeams of less

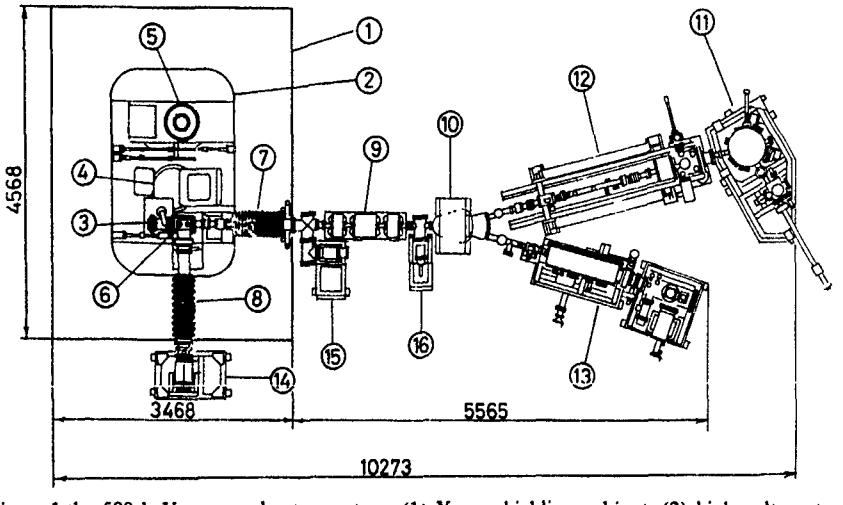

Fig 1. Schematic view of the 500 keV ion accelerator system: (1) X-ray shielding cabinet, (2) high voltage terminal box, (3) ion source, (4) DISKTRON high voltage generator, (5) ac power supply, (6) einzel lens, (7) acceleration tube, (8) vacuum-pumping tube, (9) magnetic quadrupole lens (triplet), (10) switching magnet, (11) MEIS ultra high vacuum chamber, (12) microbeam line, (13) implantation beam line, (14–16) turbomolecular pumping units.

0168-583X/91/$03.50 © 1991 – Elsevier Science Publishers B.V. (North-Holland)

than about 1 μm on the target in microbeam line and the other is the evaluation of uniformity of P and As implanted at 500 keV into Si wafers.

2. Apparatus

The system consisting of a 500 keV ion accelerator, a microbeam line, an ultra high vacuum (UHV) target chamber and an implantation beam line is schematically shown in fig. 1. Details of the 500 keV ion accelerator and the microbeam line have been described elsewhere [2,3]. The accelerator system, consisting of a high voltage generator, an ac power supply and a high voltage terminal, is isolated in an X-ray shielding cabinet of 4.5 m × 3.5 m and 2.9 m in height. This system is very compact as compared with other conventional ones of the same voltage standing in open air. Two types of ion sources are installed in the high voltage terminal. Ion beams are extracted from the ion sources at a maximum voltage of 30 kV and are focused at the entrance of an acceleration tube by an einzel lens. After acceleration of up to a voltage of 500 kV, the ion beams are focused again by a triplet Q-magnetic lens and deflected by a switching magnet to one of the two beam lines. H^+ or He^+ beam is introduced into the microbeam line aligned 15° to the left of the primary beam axis. The beam spot size on a target can be focused down to less than 1 μm and RBS mapping is measured. The detailed procedures of the RBS mapping measurement have been given elsewhere [6–8]. Furthermore, medium energy ion-scattering spectroscopy (MEIS) [9] can be applied to the investigation of crystalline structures of solid surfaces in the UHV chamber downstream of the microbeam line. The toroidal electrostatic analyzer equipped with a position sensitive detector (PSD) and microchannel plate (MCP) is set up in the chamber to provide measurements with high energy and angular resolutions. It has been proved that the MEIS system combined with the microbeam is a particularly powerful technique to observe crystalline behavior at atomic levels in an area of the order of a μm.

The ion beams introduced into the implantation beam line are electrically scanned over a 2 in. wafer by the X–Y deflection plates. The scanning frequency of the X and the Y direction is 76.6 and 833 Hz, respectively. In order to prevent wafers from being contaminated by the environment, the target chamber can be pumped to less than 3×10^{-10} Torr. A target wafer is located on each side of a hexagonal carrousel except for one side where a beam monitoring system is mounted. The beam monitoring system is composed of two coaxially separated Faraday cups, a main peripheral and a small central one. In order to get uniform scanning of the beam, the ion source parameters are adjusted by monitoring the current signal from the Faraday cups until a clear trapezoidal waveform appears on an oscilloscope [2]. Then the carrousel is turned around to expose the wafer to the beam.

3. Results and discussion

Stability of the acceleration voltage of the DISKTRON at 470 kV and the He^+ beam current measured by a Farraday cup just behind the switching magnet during one-hour operation are shown in fig. 2. The beam energy was 500 keV (470 keV acceleration plus 30 keV extraction). The beam current stability was better than about 1% and the accelerating voltage stability (dV/V) is around 2×10^{-4}. An RBS mapping image for a test sample with 30 nm thick Au island patterns (10 μm × 10 μm) with a periodicity of 10 μm is shown in fig. 3. In this experiment, the spot size of the ion beam on target was adjusted to about 1 μm with a beam current of 10 pA. The energy window for RBS signals

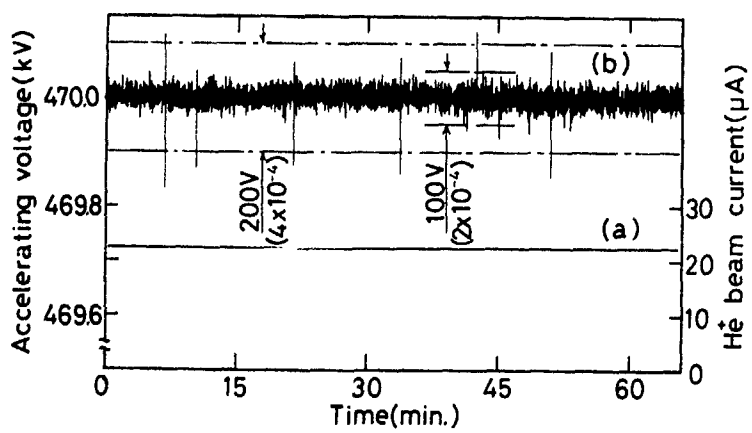

Fig. 2. Beam stability: (a) beam current and (b) accelerating voltage at $V = 470$ kV with ion beam. He^+ ion energy: 500 keV; ion extraction voltage: 30 kV.

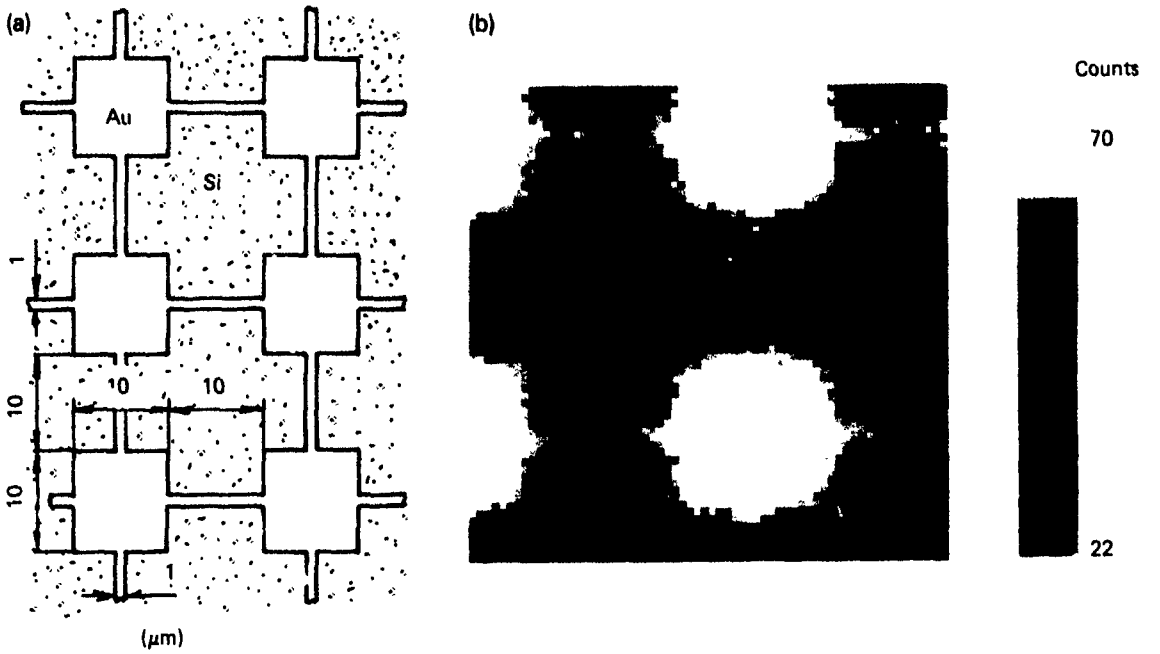

Fig. 3. (a) A schematic of the test sample (the pattern of Au islands with Au connecting stripes on silicon) and (b) corresponding RBS mapping image. Ion: He^+, beam energy: 400 keV, specimen $t \approx 30$ nm.

was adjusted to Au signals by a single channel analyzer. The color in the figure corresponds to the backscattered yield from Au islands. The pattern of Au islands along with Au connecting lines with a width of 1 μm is clearly observed in this RBS mapping image. These results indicate that the accelerator can provide a sufficiently stable ion beam into the microbeam line [7].

Table 1 shows the ion species and the amount of beam current measured by the main Faraday cup set at the end of implantation beam line. These ion species were chosen for research work not only on semiconductor fabrication but also for surface modification of solid materials. A boron (B^+) beam was obtained by ionizing BF_3 gas. A gold ion (Au^+) beam is obtained by sputtering with ions such as Ar^+ and ionizing in the arc chamber. The other ions were obtained by vaporizing the solid material in an oven and ionizing in the arc chamber. As shown in table 1, a beam current comparable with other medium current implanters can be obtained in this implantation system. The vacuum in the target chamber was kept at less than 1×10^{-7} Torr on irradiating the target with 220 μA As^+ at 200 keV.

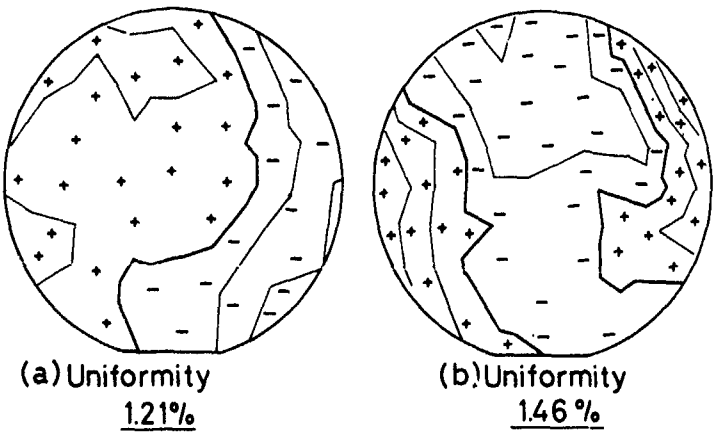

Fig. 4. Wafer contour maps showing average sheet resistance and sheet resistance uniformity: (a) As^+, $1 \times 10^{15}/cm^2$, (b) P^+, $1 \times 10^{15}/cm^2$. As^+ and P^+ are implanted into a 2 in. silicon wafer at 500 keV.

Table 1
List of the maximum beam current, beam energy, state of the source materials and vapor pressure by which the maximum beam current was obtained for each species

Ion species	Beam current [μA]	Beam energy [keV]	State	Temperature [°C]
Cr^+	12	200	solid: $CrCl_3$	631
Cd^+	195	200	solid: Cd	357
Au^+	16	200	solid: Au	
P^+	300	200	solid: P	428
	195	500		
As^+	300	200	solid: As	377
	165	500		
B^+	100	200	gas: BF_3	
	10	500		

Wafer contour maps showing average sheet resistance and sheet resistance uniformities in the case of P and As implanted at 500 keV into 2 in. Si wafers are shown in fig. 4. The wafers were set up on the holders with a tilt angle of 7°. The measurement of sheet resistance was made by using PROMETRIX Omni Map RS30 after annealing at 1000°C.

The uniformities in the case of P and As were evaluated to be 1.5% and 1.2%, respectively. Consequently, the performance of this implantation system coupled to the accelerator is comparable with that of other existing high energy implantation systems.

4. Conclusion

A 500 keV ion beam accelerator system equipped with a DISKTRON high voltage generator and two types of ion source has been developed to provide ion beams for surface analysis and modification. The results obtained in the performance test are as follows:

(1) A He^+ beam current of more than 20 μA has been obtained at 500 keV. The stability of the beam current and acceleration voltage were less than 1% and 2×10^{-4}, respectively. When the beams were introduced into the microbeam line, the beam spot on target was focused down to less than 1 μm. Observed RBS mapping images clearly showed the connecting Au stripe of 1 μm, which revealed the high stability of the microbeam.

(2) In the case of the implantation beam line, several hundred μA of beam current has been obtained for P^+ and As^+ in energy ranges up to 500 keV. Sufficient beam current for surface modification has been obtained for other metal ions. When P^+ and As^+ are implanted into a 2 in. Si wafer at 500 keV, the uniformities were evaluated to be 1.5 and 1.2%, respectively.

The results of the performance test proved that this accelerator is satisfactorily applicable to surface analysis and modification.

Acknowledgements

The authors wish to express sincere thanks to K. Kawasaki of Osaka University, and K. Ishibashi of Kobe Steel, Ltd., for their help during the experiment. We also wish to thank T. Takakuwa of ULVAC Japan, Ltd., for his devoted help and valuable discussion.

References

[1] A. Iosoya, Y. Miyake, K. Takagi, T Uchiyama, K. Yui, R. Kikuchi, S. Komiya and C. Hayashi, Nucl. Instr. and Meth. B6 (1985) 250.
[2] Y. Agawa, T. Uchiyama, A. Hoshino, H. Tsuboi, R. Fukui, K. Takagi, H. Yamakawa, T. Matsuo, M. Takai and S. Namba, Nucl. Instr. and Meth. B45 (1990) 540.
[3] Y. Mihara et al., Nucl. Instr. and Meth. B37/38 (1989) 609.
[4] M. Takai, T. Matsuo, S. Namba, K. Inoue, K. Ishibashi and Y. Kawata, Nucl. Instr. and Meth. B37/38 (1989) 260.
[5] M. Takai, T. Matsuo, A. Kinomura, S. Namba, K. Inoue, K. Ishibashi and Y. Kawata, Nucl. Instr. and Meth. 345 (1990) 533.
[6] A. Kinomura, M. Takai, K Inoue, K. Matsunaga, M. Izumi, T. Matsuo, K. Gamo, S. Namba and M. Satou, Nucl. Instr. and Meth. B33 (1988) 862.
[7] Y. Agawa, M. Takai, K. Ishibashi, K. Hirai and S. Namba, Jpn J. Appl. Phys. 29 (1990) L1011.
[8] M. Takai, Y. Agawa, K. Ishibashi, K. Hirai, S. Namba, K. Inoue and Y. Kawata, 2nd Int. Conf. on Nuclear Microprobe Technology and Applications, Melbourne, Australia, 1990, Nucl. Instr. and Meth. B54 (1991) 279
[9] T. Koshikawa, R. Kikuchi, K. Takagi, T. Uchiyama, Y. Mihara, Y. Agawa, S. Matsuura, E. Inuzuka and T. Suzuki, Nucl. Instr. and Meth. B33 (1988) 623.

Nuclear Instruments and Methods in Physics Research B55 (1991) 506–510
North-Holland

A broad-beam, high-current metal-ion implantation facility

I.G. Brown, M.R. Dickinson, J.E. Galvin, X. Godechot [1] and R.A. MacGill
Lawrence Berkeley Laboratory, University of California, Berkeley, CA 94720, USA

We have developed a high-current metal-ion implantation facility with which high-current beams of virtually all the solid metals of the periodic table can be produced. The facility makes use of a metal-vapor vacuum-arc ion source which is operated in a pulsed mode, with 0.25 ms pulse width and a repetition rate up to 100 pps. Beam extraction voltage is up to 100 kV, corresponding to an ion energy of up to several hundred keV because of the ion charge-state multiplicity; beam current is up to several amperes peak and around 10 mA time-averaged delivered onto target. Implantation is done in a broad-beam mode, with a direct line-of-sight from ion source to target. Here we describe the facility and some of the implants that have been carried out using it, including the "seeding" of silicon wafers prior to CVD with titanium, palladium or tungsten, the formation of buried iridium silicide layers, and actinide (uranium and thorium) doping of III–V compounds.

1. Introduction

Metal-ion beams of high intensity have traditionally been somewhat more difficult to produce than beams of gaseous ions, and this has been an experimental inconvenience and an impedance to the development of metal-ion implantation applications. With the development of the MEVVA (metal-vapor vacuum-arc) ion source [1–6], however, metal-ion beams of exceptionally high intensity have become available, providing a means for carrying out a wide range of metal-ion implantations. The source has been operated with 48 of the solid metallic elements of the periodic table and with a range of alloys and compounds. The beam ions are typically multiply ionized with a spectrum of charge states from 1 to 5.

Several versions of the MEVVA ion source have been developed and their operation and performance has been described previously [1–6]. The implanter makes use of the MEVVA-V source version. This embodiment is a broad-beam multicathode ion source. The extractor grids are 10 cm in diameter, and this is thus also the beam maximum initial diameter. The multicathode assembly houses 18 separate cathode materials, between which one can switch simply and quickly. This source has been described in more detail in refs. [4,5]. A photograph of the partially disassembled source showing the multicathode feature and the large-area extractor is shown in fig. 1. In typical operation the source is pulsed at a rate of several tens of pulses per second. For our standard pulse length of 250 μs, a repetition rate of 40 pps corresponds to a duty cycle of 1%, and the mean beam current is then 1% of the peak (pulse) beam current. The pulsed operation of the source described here is not inherent to the MEVVA technology, but is simply a legacy from its accelerator-based lineage; a version capable of delivering up to several amperes of dc metal-ion beam current has been tested and is in development.

2. Description of the facility

Implantation is done in a broad-beam mode, without magnetic analysis of charge-to-mass beam components, and the ion trajectories are line-of-sight from ion source to target. The high ion-beam charge density demands a very high degree of space-charge neutralization of the beam, and any attempt at magnetic analysis would cause a major perturbation to the neutralizing electrons and disturb or destroy the neutralization, with consequent space-charge blowup and loss of beam. However, the MEVVA ion beam is particularly pure, containing a high fraction of just the wanted metal-ion species; this is because the plasma is formed solely from the cathode material where the cathode spots of the vacuum arc are active, and there is no carrier gas. Thus implantation in a non-mass-analyzed mode for many purposes (but not all) poses no problems.

The vacuum pressure during implantation is typically in the low-to-mid 10^{-6} Torr range. The target to be implanted is introduced into the vessel through an air lock and the turn-around time between target changes can be as short as a matter of minutes. The

[1] On leave to Lawrence Berkeley Laboratory from SODERN, present address: SODERN, 1 Ave. Descartes, 94451 Limeil-Brevannes, France. Supported by a grant from the French Ministère des Affaires Etrangères, Bourse Lavoisier, and a grant from SODERN.

0168-583X/91/$03.50 © 1991 – Elsevier Science Publishers B.V. (North-Holland)

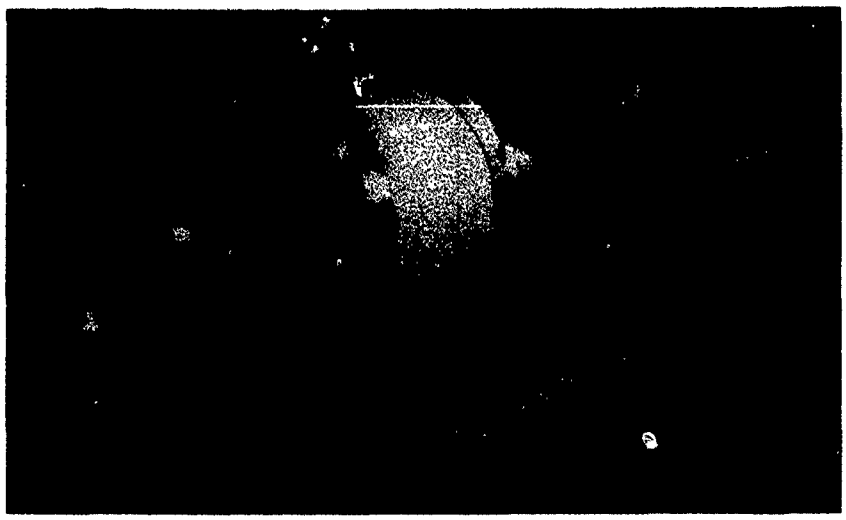

Fig. 1. The MEVVA-V ion source, partially disassembled to show the multiple-cathode feature (holds 18 separate cathodes) and the large beam-formation electrodes.

target is mounted on a water-cooled holder suspended from a vertically moving shaft; the source-to-target distance is 65 cm. A magnetically suppressed Faraday cup with a 5 cm diameter entrance aperture can be inserted into the beam immediately in front of the target. The beam current can thus be adjusted prior to implantation and the number of beam pulses required to accumulate the required dose can be calculated. The overall setup is shown in fig. 2. An example of the implanter beam current performance for the case of a titanium beam is shown in fig. 3. Here the beam-pulse current density delivered onto target is plotted as a function of extraction voltage for a range of different arc currents. The peak ion-beam current density is as high as 20 mA/cm^2, and the time-averaged current density up to approximately 1% of this.

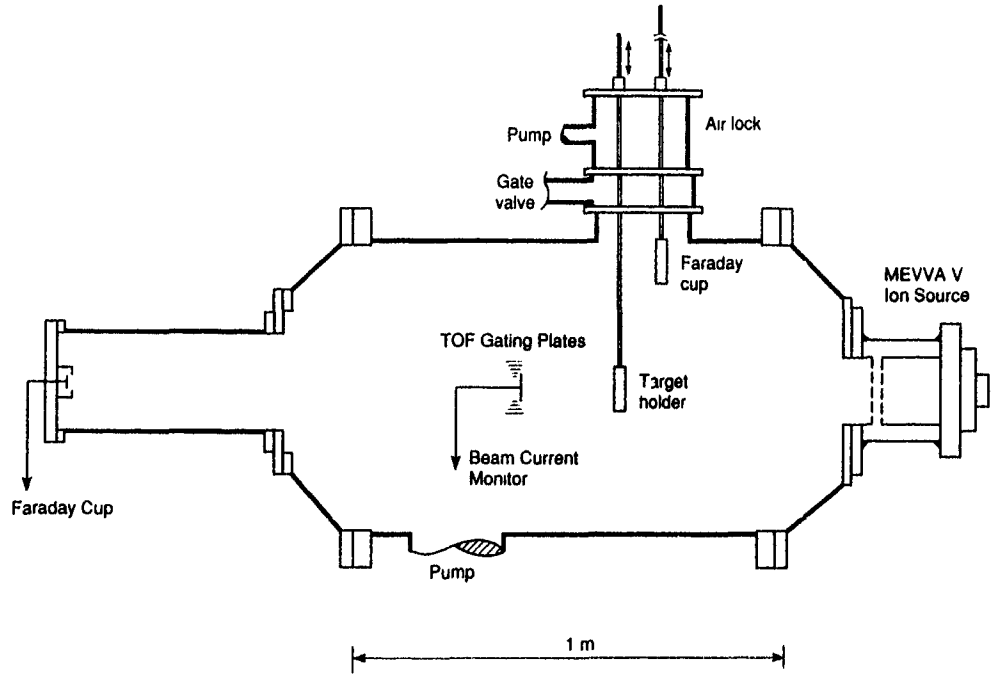

Fig. 2. Schematic of the experimental facility.

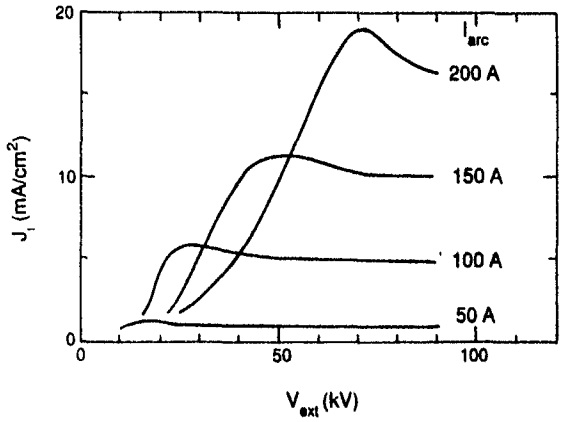

Fig. 3 Measured ion-current density as a function of extraction voltage for several arc currents; titanium beam.

The ion-beam charge-state distribution can be measured using a time-of-flight diagnostic. The detector measures the electrical current in the different Q/A states and provides a good measurement of the ion composition of the extracted ion beam. The time-of-flight system has been described in more detail in ref. [7]. An oscillogram of the time-of-flight charge-state spectrum for an Ir ion beam is shown in fig. 4.

Beam is extracted typically at 50–75 kV, and the maximum voltage at which we have operated is 110 kV. Since the ion charge-state distribution contains multiply ionized species with charge state up to about $Q = 5+$ for some metals and with mean charge state of typically $\overline{Q} = 2+$ to $3+$, the mean energy of the beam ions produced can be 200–300 keV with components as high as 500 keV.

Cathode materials, and thus ion beams, with which we have operated include: Li, C, Mg, Al, Si, Ca, Sc, Ti, V, Cr, Mn, Fe, Co, Ni, Cu, Zn, Ge, Sr, Y, Zr, Nb, Mo, Pd, Ag, Cd, In, Sn, Ba, La, Ce, Pr, Nd, Sm, Gd, Dy, Ho, Er, Yb, Hf, Ta, W, Ir, Pt, Au, Pb, Bi, Th and U [8,9].

Fig. 4. Time-of-flight charge-state spectrum for an iridium beam. The peaks correspond to $Q = 1+$ (far right), $2+$, $3+$ (maximum), $4+$ and $5+$, right to left.

Compound and alloy cathode materials have also been investigated [10] and mixed-composition beams can be produced.

3. Some implantations

The facility has been used for exploratory research for a variety of different ion-implantation applications, including semiconductor, superconductor and metallurgical applications. Although the fundamental characteristics of the MEVVA ion beam make the source not ideal for a simple retrofit to traditional semiconductor implanters, the MEVVA implanter can be a valuable tool for specialized or unique implants into semiconductors, especially in a research mode.

The requirements of future interconnect densities in VLSI devices have led to the development of new multilevel interconnect technologies. One such technique involves forming interconnects by selectively depositing tungsten into oxide channels which have been implanted with silicon. However, a high Si dose is required to initiate the selective deposition of W on oxide. In this work [11] the selective deposition of W on oxide that has been implanted with W was investigated. W implants were done at 137 keV. We found that a concentration of less than only 7.3×10^{20} cm^{-3} of implanted W is needed for the nucleation process, to be compared with a minimum Si concentration of 7.3×10^{21} cm^{-3} required to nucleate W on oxide when Si is the implanted species. We are indebted to Drs. Nathan Cheung and colleagues (University of California at Berkeley), Simon Wong (Stanford University) and David Thomas (Cornell University) for their lead collaboration in this research. This work is being continued using other implant species including Ti, Cu and Pd; see an accompanying paper [12] for more details.

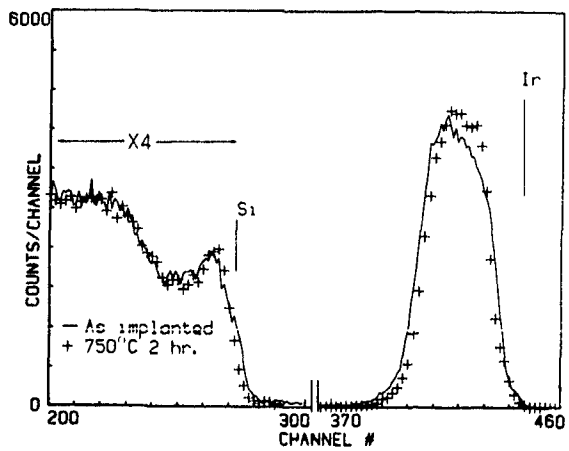

Fig. 5. Iridium-implanted silicon: RBS spectra of the samples with medium dose, (7×10^{16} cm^{-2}), as-implanted and after annealing at 750 °C for 2 hours.

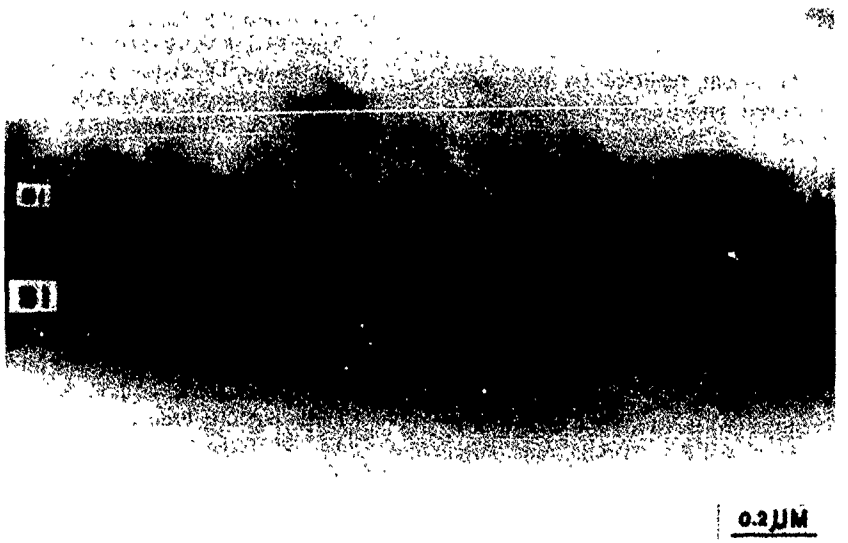

Fig. 6. Cross-sectional TEM micrograph of buried $IrSi_3$ layer.

Uranium and thorium impurities are known to be sources of soft errors in semiconductor memory devices, and this has motivated the implantation of U and Th into Si for some fundamental studies of diffusion. We are indebted to Dr. Fred Stevie and colleagues from ATT/Bell Laboratories for lead collaboration in this work; the results have been reported in detail in refs. [13,14]. We implanted U and Th into Si wafers at a mean energy of 185 keV (U) and 205 keV (Th) and to doses of 1.2×10^{14} cm^{-2} (U) and 4.0×10^{14} cm^{-2} (Th), respectively. RBS and SIMS were used to obtain the depth profiles. The U and Th follow the anomalous diffusion behavior that is also seen for Al and Ag in Si at low temperatures, in that the implants migrate to two regions – the surface and the amorphous/crystalline interface.

Actinides are good candidates for active ions in electro-optic materials due to the numerous sharp emissions covering a broad spectral range. Applications include non-silica-based fiber optics and light-emitting junction diodes. We implanted uranium into the III–V semiconductors GaAs and InP at a mean ion energy of 131 keV and to a dose of approximately 4×10^{13} cm^{-2}; the implanted samples were annealed at 640–850 °C. Characteristics of the emission lines found are described fully in ref. [15]. We are indebted to Dr. Gernot Pomrenke, of Wright Patterson AFB (present address AFOSR Washington), and colleagues for their lead collaboration in this work.

We have investigated the formation of $IrSi_3$ layers buried in ⟨111⟩ silicon. The layers were formed by iridium ion implantation with a mean beam energy of 130 keV and at doses ranging from 2×10^{16} to 1.5×10^{17} cm^{-2}. The formation of the $IrSi_3$ phase was realized after annealing at temperatures as low as 500 °C. A continuous $IrSi_3$ layer about 200 Å thick, buried under 400 Å Si, was formed. Radiation damage, and the effects of the implant dose on phase formation, interface morphology and implanted atom redistribution were investigated. It was determined that a critical minimum dose of 3.5×10^{16} cm^{-2} was necessary for the formation of a continuous buried layer after annealing, while implant doses over 8×10^{16} cm^{-2} resulted in the formation of an $IrSi_3$ layer on the surface due to excessive sputtering of Si by the Ir ions. Fig. 5 shows the RBS spectra of samples implanted at a medium dose of 7×10^{16} cm^{-2}, before and after annealing at 750 °C for 2 hours. Fig. 6 shows a cross-sectional TEM micrograph of this sample; note the sharpness of the interfaces between the buried silicide layer and the surface and substrate Si. We are indebted to Dr. Kin Yu and colleagues at LBL for their lead collaboration in this work; this research has been reported in detail in ref. [16].

4. Conclusions

The MEVVA implantation facility provides a unique tool for carrying out metal-ion implantation experiments; a wide range of metallic ion species can be produced and delivered onto target. The implanter operates in a broad-beam, non-mass-analyzed mode, and the beam current is pulsed with a maximum beam current of about 1 A and a mean current of about 10 mA. Ion energy can be varied up to several hundred keV.

Acknowledgements

The various implantations reported on here were carried out collaboratively and we are grateful to our colleagues as referred to in the text. This work was supported by the U.S. Army Research Office and the Office of Naval Research under Contract no. ARO 116-89 and by the Department of Energy under Contract no. DE-AC03-76SF00098.

References

[1] I.G. Brown, in: The Physics and Technology of Ion Sources, ed. I.G. Brown (Wiley, New York, 1989) p. 331.
[2] I.G. Brown, J.E. Galvin and R.A. MacGill, Appl. Phys. Lett 47 (1985) 358.
[3] I.G. Brown, J.E. Galvin, B.F. Gavin and R.A. MacGill, Rev Sci. Instr. 57 (1986) 1069.
[4] R.A. MacGill, I.G. Brown and J.E. Galvin, Rev. Sci. Instr 61 (1990) 580.
[5] I.G Brown, J.E. Galvin, R A MacGill and F.J Paoloni, Rev Sci. Instr. 61 (1990) 577.
[6] I.G. Brown, J.E. Galvin, R.A. MacGill and R.T. Wright, Appl. Phys. Lett. 49 (1986) 1019.
[7] I.G. Brown, J.E. Galvin, R.A. MacGill and R.T. Wright, Rev. Sci. Instr. 58 (1987) 1589.
[8] I.G. Brown, B. Feinberg and J.E. Galvin, J. Appl. Phys. 63 (1988) 4889.
[9] X. Godechot and I.G. Brown, to be published.
[10] J. Sasaki and I.G. Brown, J. Appl. Phys. 66 (1989) 5198.
[11] D.C. Thomas, N.W. Cheung, I.G. Brown and S.S. Wong, Mater. Res. Soc. Symp. Proc. VLSI V (1990) 233.
[12] X.Y. Qian, M.H. Kiang, N.W. Cheung, M.A. Lieberman, I.G. Brown, X. Godechot and K.M. Yu, these Proceedings (8th Int. Conf. on Ion Implantation Technology, Guildford, UK, 1990) Nucl. Instr. and Meth. B55 (1991) 893.
[13] A.J. Filo, F.A. Stevie, P.M. Kahora, V.C. Kannan, R. Singh and I.G. Brown, submitted for publication in J. Vac. Sci. Technol.
[14] V.C. Kannan, A.J. Filo and I.G. Brown, presented at the 12th Int. Congr. for Electron Microscopy, Seattle, WA, USA August 13–18, 1990.
[15] G.S. Pomrenke, R.L. Hengehold, Y.K. Yeo, I.G. Brown and J.S. Solomon, J. Appl Phys. 67 (1990) 2040.
[16] K M. Yu, B. Batz, I.C. Wu and I.G. Brown, Mater Res. Soc. Symp Proc 147 (1989) 229.

Nuclear Instruments and Methods in Physics Research B55 (1991) 511–516
North-Holland

A versatile WIBS 200 kV ion implanter for materials modification

P. Bond, D. Duckworth, R.G. Elliman [1], R. Henshaw, S.T. Johnson, M.C. Ridgway [1], R.P. Thornton and J.S. Williams [1]

Microelectronics and Materials Technology Centre, Royal Melbourne Institute of Technology, Melbourne, 3000 Australia

P. Byers

Whickham Ion Beam Systems, Sedgefield, TS21 3EB, UK

D.J. Chivers

AEA Industrial Technology, Harwell, OX11 ORA, UK

The Whickham Ion Beam Systems 200 kV ion implanters at the Royal Melbourne Institute of Technology and at Harwell are used for a wide range of materials modification applications covering semiconductor devices, metals, polymers, insulators and industrial components. In particular, this paper describes flexible features of the prototype RMIT machine, concentrating on the scanning and endstation arrangements. Selected applications are reviewed, with particular attention given to variable temperature implantations into semiconductors.

1. Introduction

Ion implantation is a powerful method for modifying the near-surface properties of materials. Diverse applications include controllably altering the electrical, physical, chemical, mechanical and optical properties of semiconductor devices, metals, polymers and ceramics [1]. Ion implanters which cater for such diverse research applications must be extremely flexible. For example, ion beams of all elements in the periodic table are desirable, doses can cover the range $10^9\,cm^{-2}$ to greater than $10^{18}\,cm^{-2}$, sample sizes are variable, necessitating versatile beam scanning and sample manipulation capabilities, and sample temperatures during implantation often need to be varied from well below room temperature to several hundred degrees centigrade. This paper describes certain features and applications of the prototype 200 kV Whickham Ion Beam Systems (WIBS) ion implanters at the Royal Melbourne Institute of Technology and at Harwell. These machines cater for diverse research and precommercial applications involving ion beam modification of materials.

[1] Also: Department of Electronic Materials Engineering, Australian National University, Canberra, 2600 Australia.

2. Machine specifications and features

Fig. 1 illustrates the modular design and layout of the present commercially available WIBS 200 kV ion implanter, but the basic features are similar on the prototype RMIT and Harwell machines. The basic ion implanter features two-stage acceleration with practical ion source beam extraction from 5–50 kV and post acceleration from 0–150 kV. General details of the ion implanter have been described elsewhere [2] and will not be covered in detail here.

Briefly, three ion sources are available, all based on the Freeman-type source [3]: (i) a gas source, (ii) a furnace source for solid materials operating up to 1150 °C, and (iii) a sputter probe source for high melting point materials. These sources are mounted into a large ion source chamber providing ease of access and source interchangeability. Collectively, these Freeman-type sources can provide ion beams of all species in the periodic table at analysed beam currents exceeding 1 mA for most species, as indicated earlier [4]. Specific performance details of the Whickham–Freeman sources used in this study, particularly the sputter source, will be published elsewhere.

Fig. 2 is a simple schematic of the beam optics and transport up to the single-gap post acceleration lens. The natural focal point of the beam (in the horizontal

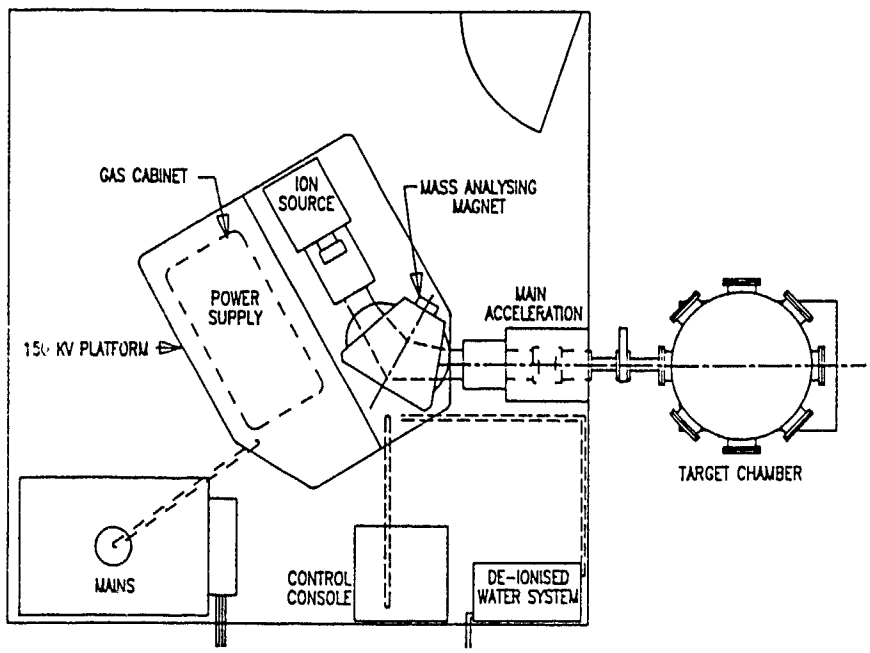

Fig. 1 Modular layout of the WIBS 200 kV ion implanter. This relates specifically to the present commercial machine but the features are the same as those on the RMIT and Harwell machines

plane) is at the entrance aperture of the post acceleration lens. However, a double focusing, 60° magnet with externally adjustable pole tips allows the focal length to be increased (up to about 5 m) as desired [2]. Such an arrangement can provide analysed beams of > 250 amu at 50 keV with excellent mass resolution ($M/\Delta M$ up to

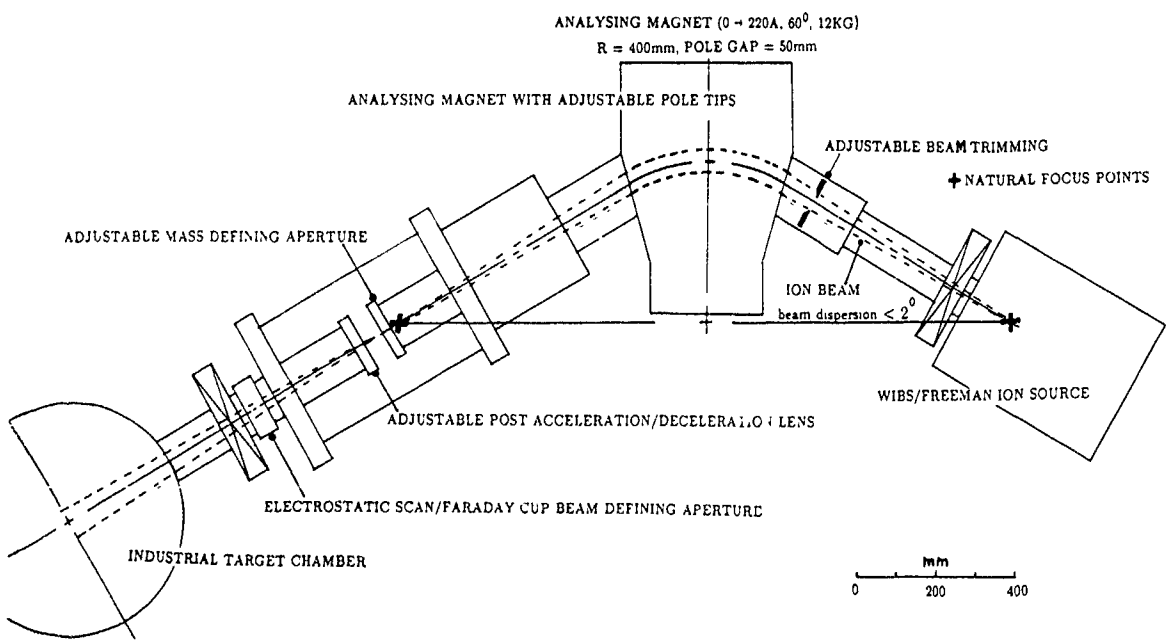

Fig. 2. Beam optics and beam transport showing variable post acceleration lens and defining aperture on the RMIT machine.

2000). The RMIT post acceleration lens has an externally variable entrance slit in the horizontal plane from 0–5 mm, with a fixed vertical slit of 40 mm. This flexibility allows optimum beam current, mass resolution and focusing to be obtained under all conditions involving low or high post acceleration potentials and for all mass species. Operation and optics of the magnet and post acceleration system is essentially similar to that described previously [2,3].

3. Scanning and endstation arrangements

The RMIT machine incorporates two types of scanning (electrostatic and mechanical) and two implantation endchambers in series; one principally for large area industrial components and one for small area research samples. Fig. 3 shows a plan-view of the industrial chamber and both the electrostatic and mechanical scanning arrangements.

The RMIT industrial chamber uses a 16×16 cm^2 x–y mechanical stage. When this stage is being used, the x–y electrostatic scan plates are removed to allow the full 40–50 mm high beam to impinge on the target plate. A fixed beam defining aperture block is mounted in front of the moving x–y stage. Beam currents on target of up to 15 mA (e.g., for gas species such as Ar^+ and N^+) have been obtained in this system.

An x–y mechanical stage is currently being developed at RMIT to provide target cooling. This uses flexible heat pipes connected to a heat exchanger mounted external to the vacuum system. Measurements of the performance (e.g., cooling efficiency) of this system are currently in progress. The dose uniformity achieved with the (uncooled) mechanical stage over an area of 12×12 cm^2, as measured by Rutherford backscattering, can be better than 3%.

For implantation in the research chamber the electrostatic scan system is used. In this case, the beam is defined by a water cooled aperture (2×1 cm^2) immediately in front of the x-plates (fig. 3). The implant area is defined by x–y variable slits at the entrance to the research chamber which is offset about 2° in the horizontal plane to effectively provide a neutral trap (fig. 3). The beam is steered onto the x–y defining slits and overscanned to provide a maximum scan area of 5×5 cm^2.

The research chamber arrangement is shown in plan-view in fig. 4. It incorporates a sample holder with two degrees of freedom (translation over 15 mm and rotation through 360°) allowing many small research samples to be loaded at the one time for individual implantation. A variety of sample holders are available to achieve constant implant temperatures (liquid nitrogen cooled and between 0–900 °C). A fixed, liquid-nitrogen-cooled shield surrounds the target to reduce hydrocarbon contamination. This cold shield also serves as a secondary electron shield when biased to −300 V. Magnetic suppression is also used at the entrance to the research chamber. The dose uniformity provided by the

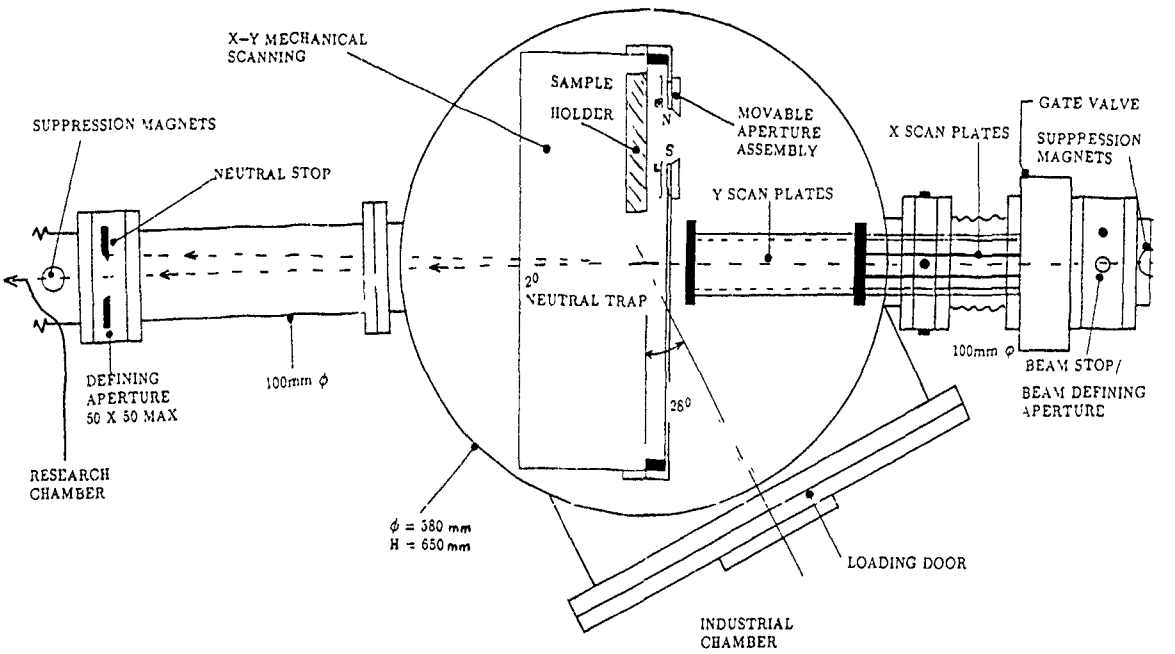

Fig. 3. The RMIT industrial chamber (plan-view) showing both electrostatic and mechanical x–y scanning systems The research chamber (fig. 4) is mounted in series and utilizes the electrostatic scanning system.

electrostatic scan arrangement can be better than 3% as measured by subsequent Rutherford backscattering analysis. However, the available electrostatic scan area currently is limited in the prototype RMIT system when higher ion energies (> 100 keV) are used. In such cases, and when large scan areas (5×5 cm^2) are required, it is not possible in the present system to completely eliminate a possible neutral beam component, necessitating very good beam line and chamber vacuum. These limitations are currently being addressed.

Also shown in fig. 4 is the provision of in situ diagnostics consisting of: (i) time resolved reflectivity (TRR) from the sample surface during implantation to dynamically detect amorphization, phase changes and compound formation; a He–Ne laser is used as the optical source; (ii) a low energy Rutherford backscattering (RBS) arrangement (shown in side-view in the inset of fig. 4). This latter arrangement allows doubly-charged He ions to be used for monitoring composition and depth profile changes during implantation. The performance and application of the in situ diagnostic facilities will be published elsewhere [15].

4. Selected applications

Table 1 illustrates some applications pursued to date on the RMIT WIBS 200 kV ion implanter. Semiconduc-

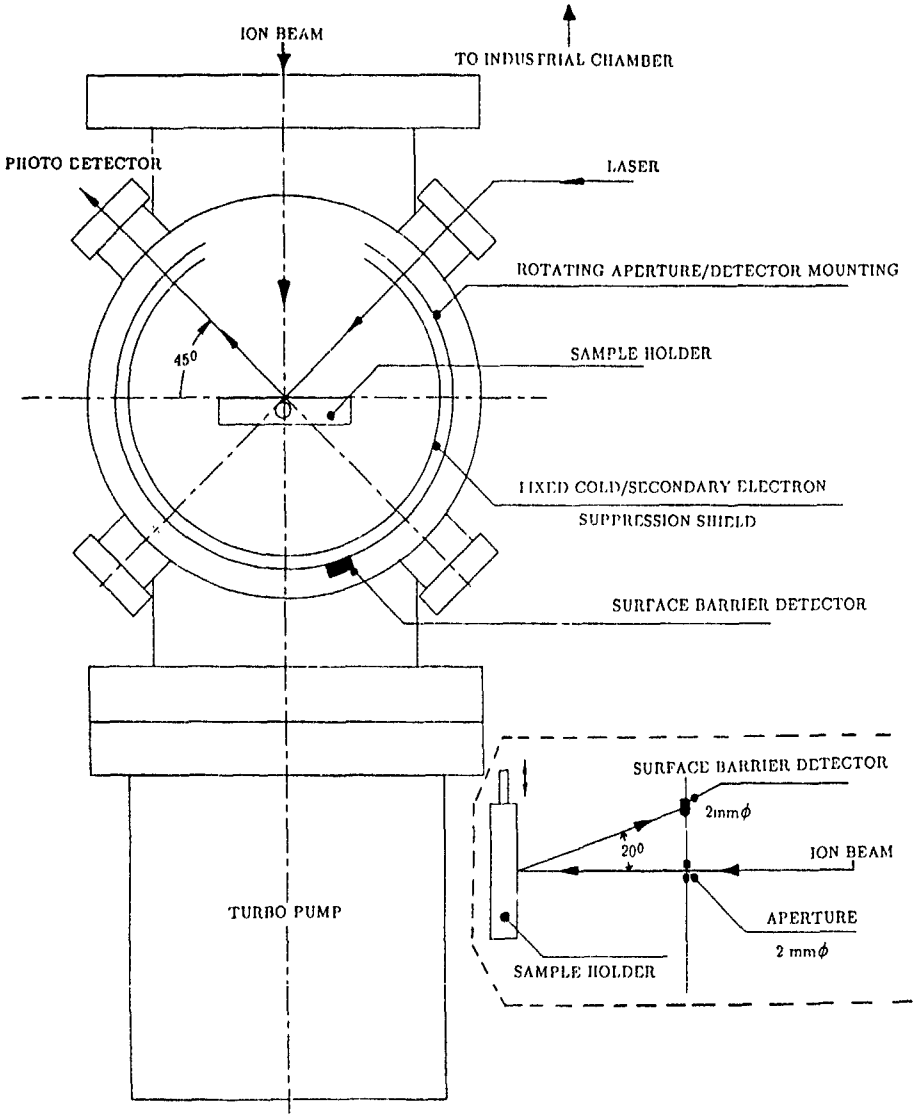

Fig. 4. The RMIT research chamber (plan-view) showing in situ laser reflectivity and Rutherford backscattering (RBS) systems. The inset (side-view) shows the RBS geometry.

tor applications include very low to medium doses for doping requirements in Si and GaAs [9], high doses for studies of damage [6] and phase transformations [5,7], very high doses for buried oxide [8] and other compound formation applications and implantation of inert species for isolation of GaAs structures [10]. Most of these semiconductor applications have utilized small implant areas, where implant dose accuracy and uniformity of better than 3% can be achieved with care during the implantation.

Another class of semiconductor applications has involved variable temperature implantation at either −196 °C or from 0–500 °C to either introduce damage (i.e., amorphization) or induce damage removal (i.e., crystallization). These studies first involve the amorphization of the near-surface of semiconductors by low energy ions at low temperatures, then the subsequent irradiation of such layers with high energy ions at high temperatures to induce crystallization. Recent experiments have involved epitaxial Ge–Si alloys and silicides on Si [11,12]. Fig. 5 shows the experimental arrangement for both amorphizing and recrystallizing such layers using ^{28}Si or ^{29}Si ions from the RMIT WIBS 200 kV ion implanter. Fig. 6 shows RBS and ion channeling spectra illustrating the epitaxial crystallization of amorphous $Ge_{0.2}Si_{0.8}$ layers using Si ions at an effective energy of 300 keV and with the sample held at 275 °C. The extent of epitaxial growth is roughly proportional to the Si^{2+} ion dose [11].

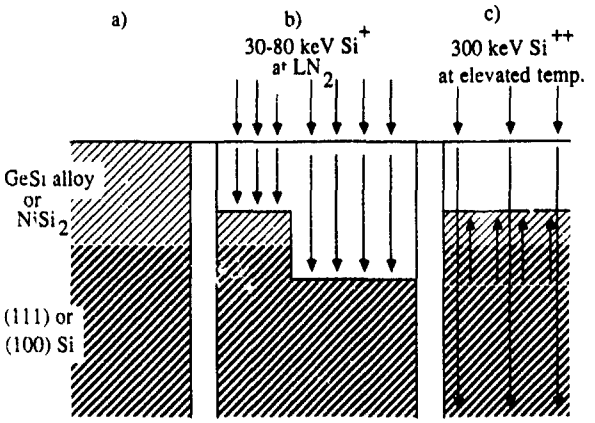

Fig. 5. Schematic illustration of beam annealing of epitaxial Ge–Si alloys and $NiSi_2$ layers on (100) or (111)Si. (a) The initial epitaxial layer structure (~ 1000 Å thick) (b) Amorphization schedule. (c) Beam annealing at elevated temperature

Also illustrated in table 1 are implantation into Ni-based alloys for corrosion resistance, activation (i.e., bond breaking) of polymer surfaces using low energy gaseous ion bombardment, the amorphization of sapphire [14], and implantation studies of diamond (for hardness improvement) by C and N bombardment at temperatures up to 900 °C. Finally, industrial applications have included the bombardment of burner tips and stainless steel dies to improve working lifetimes of

Table 1
Selected applications which have been pursued on the RMIT WIBS 200 kV ion implanter

Target	Implant species	Implant temperature	Dose range [cm^{-2}]	Application
Silicon	P, B	15 °C	10^{11}–10^{12}	MOS threshold adjustment
	In, Sn, Ga, Sb, Bi, etc	−196–400 °C	10^{14}–5×10^{16}	high dose studies [5]
	^{28}Si or ^{29}Si	−196 °C	10^{14}–10^{17}	amorphization/damage studies [6]
	^{119}Sn	−196 °C	10^{16}	Mossbauer studies [7]
	O, C or N	variable	~10^{18}	oxide, carbide, silicide formation [8]
Gallium arsenide, III–V structures	^{29}Si, Mg, etc	variable	variable	doping for n-, p-layers/contact [9]
	H, He, O	variable	variable	device isolation [10]
Ge–Si alloy heterostructures	^{28}Si, ^{29}Si	−196 °C	10^{14}–10^{15}	amorphization
	high energy ^{29}Si	200–400 °C	10^{15}–10^{17}	beam-induced crystallization [11,12]
Ni, NiSi alloys	Mg, Ni, Si, Kr	15 °C	10^{15}–10^{17}	high temperature corrosion resistance
Various polymers	He, O, Ar	15 °C	10^{12}–10^{17}	doping and surface activation
Diamond	C, N	15–900 °C	10^{14}–10^{18}	damage studies [13]
Sapphire	O, In, Pb	−196–15 °C	10^{13}–10^{16}	amorphization, damage, crystallization [14]
Cu–Be components	N, Cr, Ti	nominally 15 °C	~10^{17}	reduce pitting corrosion
Stainless steel components	N	nominally 15 °C	10^{17}–10^{18}	improved hardness, wear resistance

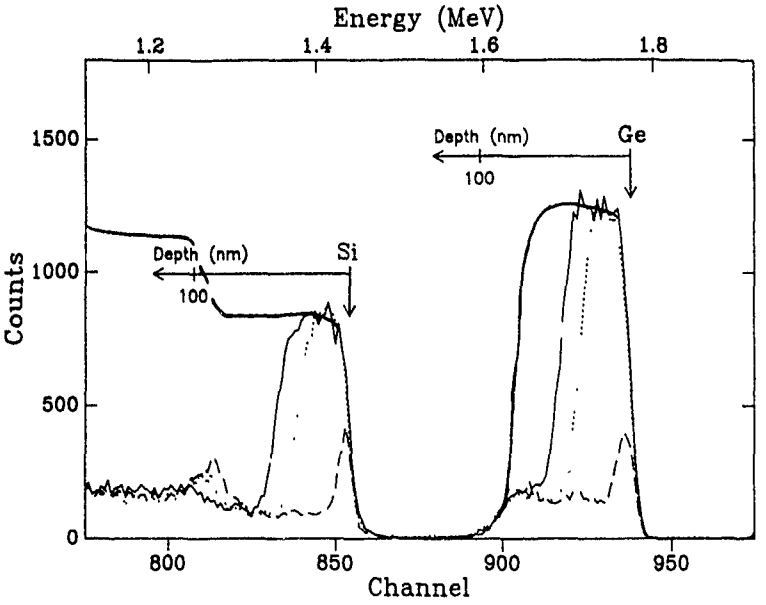

Fig. 6. Rutherford backscattering and channeling spectra (2 MeV He) from a $Ge_{0.2}Si_{0.8}$ layer amorphized to form a layer ~ 400 Å thick and then beam annealed at 275 °C with 300 keV Si^{2+} ions. The spectra correspond to the initial amorphous layer (thin solid curve), partial annealing (dashed curve) and full annealing (dotted curve) The thick solid curve is a random spectrum

such components. These latter applications have involved the use of x–y mechanical scanning. Many of the non-semiconductor applications, particularly those involving large area ($\geq 3 \times 3$ cm^2), have not required absolute dosimetry or high dose uniformity. However, current developments are in train at RMIT to ensure dosimetry and uniformity to acceptable levels for large area implants. The Harwell implanter (and indeed the current commercial WIBS machines) do not suffer from such limitations.

5. Conclusion

The WIBS 200 kV ion implanter is a flexible, user friendly R&D machine for materials modification. Scanning and endstation arrangements on the prototype RMIT machine have been described which enable both research and precommercial component implantations of many elements to be undertaken into a wide range of material types and sample sizes.

Acknowledgements

The Australian Research Council, the Victorian Government and the Special Research Centres Scheme are acknowledged for financial support of this project.

References

[1] J.S Williams, Rep. Prog. Phys 49 (1986) 491
[2] P. Byers, P. Bailey, P A Judge and D.G. Armour, in. 1st Nat. Conf on the Application of Ion Plating and Implantation to Materials, ASM Mater. Technol. Ser. 8504-001 (1985).
[3] J.H. Freeman, AERE Report R6254 (1970).
[4] J.H Freeman, D J Chivers, G A. Gard and W Temple, Nucl Instr and Meth 145 (1977) 473
[5] J.S. Williams, R.P Thornton, R.G. Elliman, Y.H Li and A.P. Pogany, Mater Res Soc. Symp Proc. 157 (1990) 629.
[6] J S. Williams, K.T Short, R G Elliman, M.C Ridgway and R Goldberg, Nucl. Instr and Meth. B48 (1990) 431
[7] R.P Thornton, R G Elliman and J.S. Williams, J Mater Res. 5 (1990) 1003
[8] M.C Ridgway, R Loccisano, J.S. Williams, A P Pogany and D.K. Sengupta, Mater Lett. 10 (1990) 156
[9] S.T. Johnson, J S Williams, E. Nygren and R.G Elliman, J. Appl. Phys 64 (1988) 6567.
[10] J.S. Williams, R G. Elliman, S T Johnson, D K Sengupta and J M. Zemanski, Mater. Res. Soc. Symp Proc. 144 (1989) 355.
[11] R.G. Elliman, M C Ridgway, J S Williams and J.C Bean, Appl. Phys. Lett. 55 (1989) 843.
[12] M C Ridgway, R.G. Elliman and J S Williams, Nucl Instr. and Meth. B48 (1990) 453
[13] D. McCullock and S. Prawer, Mater Res Soc. Symp. Proc. 157 (1990) 825.
[14] W. Zhou, D.X. Cao and D.K Sood, Mater. Res Soc Symp Proc. 157 (1990) 543.
[15] M C Ridgway, S.T. Johnson, D. Duckworth, J.S. Williams, P. Bond, P. Byers and D.J Chivers, Nucl. Instr and Meth. (1991) in press.

Nuclear Instruments and Methods in Physics Research B55 (1991) 517–521
North-Holland

The phased linear scanner

Derek Aitken
Superion Limited, 10 St Leonard's Road, Surbiton, Surrey KT6 4DE, UK

The potential demand for high- and low-dose ion implantation into large substrates, created by flat-panel display and similar technologies, has highlighted the need for a suitable mechanical parallel-scanning technique. The phased linear scanner (PLS) concept is described and the advantages over other mechanical scanning techniques for large-substrate implantation are discussed. The application of PLS to high-throughput production machines is described.

1. Introduction

The phased linear scanner is a result of the increasing demand for an end station suitable for high- and low-dose ion implantation of large substrates, i.e., substrates significantly larger than a 200 mm wafer. It also fulfils the common requirement for a parallel scan.

Existing scanning techniques can be divided into three different types:
(a) X–Y beam scanning,
(b) hybrid scanning, and
(c) X–Y mechanical target scanning.

Beam scanning is widely used for low- and medium-current ion implantation into silicon wafers. The beam current that can be electrostatically scanned is limited by space-charge considerations to approximately 1 mA. X–Y parallel electrostatic scanning is difficult to achieve and is not appropriate for large substrates. Magnetic scanning does not suffer from the space-charge beam-current limitation, but hysteresis, eddy currents and physical size problems limit the practical usefulness of either conventional or parallel X–Y magnetic scanning. Some of the geometrical problems in parallel-scanning systems can be minimised by scanning the beam in one plane only, the slow scan being achieved by mechanical target scanning (hybrid scanning).

The most suitable technique, particularly when high doses are required, is X–Y mechanical scanning as used in existing high current machines. The problem with existing mechanical scan techniques is that they are large for 200 mm wafers and become excessively large for larger substrates. This is true for both spinning-disc and racetrack carousel designs because geometric considerations require minimum batch sizes of 8–10 substrates. The only mechanical scan technique to be attractive for small batch sizes is the reciprocating linear mechanical scan, but this technique is inherently slow because of the conflict between scan speed and reversal time imposed by the need to reverse the scan direction at the end of each fast scan. The limitations of conventional linear mechanical scanning have been overcome by a technique called "phased linear scanning".

2. Linear scanning

With a single-target oscillatory linear scan there is a fundamental conflict between scan speed (in the fast scan direction) and reversal time. As simple harmonic reversal is a convenient option, the first question to be asked is whether there is an optimum relationship between scan speed and SHM reversal time, i.e., a condition for maximum scan frequency.

Let the linear-scan distance be s, the reversal distance r (corresponding to the radius of the SHM circle) and the maximum acceptable reversal acceleration a. Then the frequency f is

$$f = \frac{(ar)^{1/2}}{2(s + \pi r)}$$

For maximum frequency, $\mathrm{d}f/\mathrm{d}r = 0$ and $r = s/\pi$. Therefore the maximum frequency is achieved when the linear-scan time and the reversal time are equal.

3. Phased linear scanning

Phased linear scanning (PLS), in its simplest form, scans two substrates along parallel tracks. The linear-scan time and the reversal time are approximately equal; while one substrate is being scanned through the beam, the other is being decelerated to rest and then accelerated to full scan speed in the opposite direction. There is always at least one substrate moving at full scan speed. The two substrates are therefore given identical mechanical scan movements but the two motions are out of phase; hence the name "phased linear scan". The

0168-583X/91/$03.50 © 1991 – Elsevier Science Publishers B.V. (North-Holland)

generous time available for reversal means that high scan speeds can be achieved with modest reversal acceleration. PLS is used for the fast scan; the slow scan is a conventional mechanical scan.

Fig. 1 shows a schematic of a PLS system driven by a racetrack mechanical driver. The linear movement and SHM reversal of the followers driven by the two pins moving round the racetrack at a constant speed are transferred to the two substrates moving along parallel scan tracks in the target chamber. The scan-track unit moves vertically to give the slow scan component of the mechanical scan.

The sequence of PLS movement along the scan track during reversal is shown in fig. 2. The target represented by solid lines will be called target 1 and the target represented by dotted lines target 2. In position |1| the two substrates are positioned symmetrically about the beam and are both moving at full speed to the left (as indicated by the solid and dotted arrows); in position |2| target 1 has cleared the beam and is about to start reversal; in position |3| target 1 is halfway through reversal and is stationary, while target 2 is moving to the left at full speed through the beam; in position |4| both substrates are clear of the beam, target 1 moving at full speed to the right and target 2 at full speed to the left, in position |5| target 1 is moving to the right at full speed through the beam, while target 2 is halfway through reversal and is stationary; in position |6| target 2 is just entering the beam and both substrates are moving to the right at full speed; etc.

It will be noticed that the linear-scan distance and the reversal distance round the semicircular part of the racetrack driver are not equal; the racetrack reversal distance is equal to the distance between the centre lines of the two targets; the linear-scan length is increased to allow for the width of the beam. Except for a brief instant at the overscan position |4|, there is always at least one of the two targets passing through the beam.

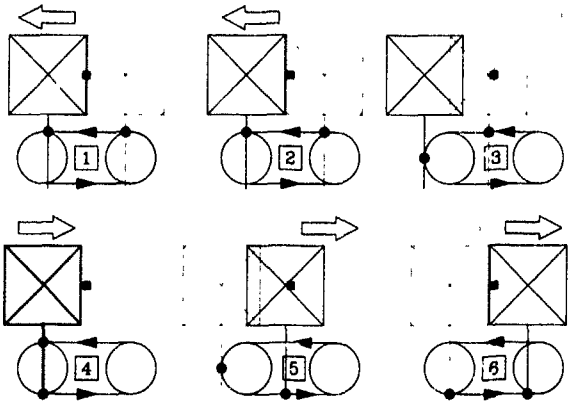

Fig. 2. PLS reversal sequence.

4. PLS with more than two substrates

So far only the two-target situation has been considered. If the number is larger than two, the reversal time can be increased relative to the linear-scan time and higher scan speeds achieved for a particular reversal acceleration value.

Fig. 3 shows PLS phase diagrams for one to six targets. Each phase diagram is effectively a simplified representation of the racetrack driver with the racetrack represented by a circle; the linear portion is that in the cross-hatched box (representing the ion beam) and the reversal portions outside the box. For simplicity the

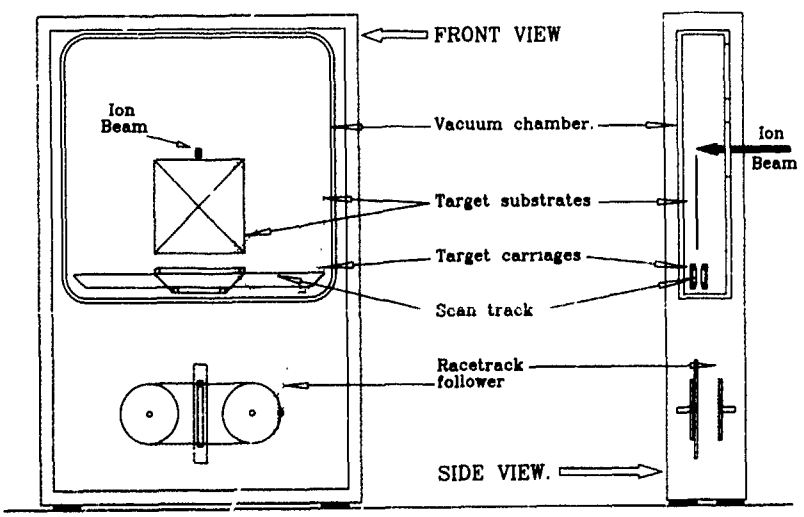

Fig. 1 The phased linear scanner.

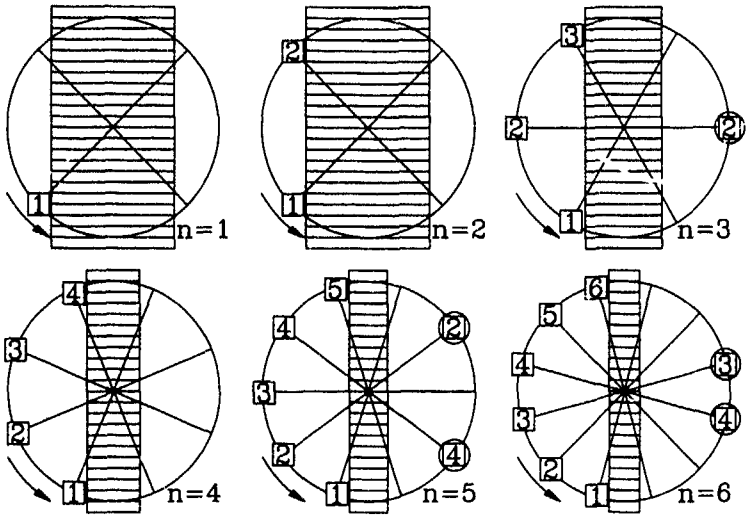

Fig. 3. PLS phase diagrams.

linear-scan distance and the distance between targets are shown as being equal so that the diagram can be divided into a number of equal sectors.

The targets are represented by numbered squares travelling round the circumference at a constant speed in the anticlockwise direction. Each diagram shows target |1| about to pass through the beam (i.e., through the linear-scan portion) from left to right at the bottom of the diagram.

For a single target ($n = 1$) the target passes through the beam from left to right, reverses while clear of the beam and then passes through the beam from right to left, etc. Maximum scan frequency is obtained when linear-scan and reversal times are equal. This gives a nominal 50% beam utilization.

The two-target situation ($n = 2$) has already been described. Note that it is a batch sequence (a pair of targets pass through the beam with a nominal small gap between them). For three targets there are two options. Either the three targets pass through the beam from left to right in succession, followed by the three passing through the beam from right to left (batch sequence). Alternatively the position for target |2| can be that represented by the square and circle (on the other end of the diameter); targets now pass through the beam alternately in opposite directions. The practical advantage of the latter is that it is a mechanically better balanced sequence; the disadvantage is that it is less efficient because overscan clearance is required around each target whereas the batch approach only requires overscan around the group of targets (with nominal small gaps in between). The available reversal time is double that of the two-target situation; therefore the reversal acceleration is halved or the speed can be increased by $\sqrt{2}$ for the same maximum acceleration (SHM maximum acceleration is v^2/r).

The four-target system will logically be the batch sequence shown in the $n = 4$ diagram. The opposite end of the diameter is available for each target but no regular sequence is available for a value of n that is not divisible by an odd number. The reversal time is three times that of the linear scan time and the speed can be increased by $\sqrt{3}$ for a particular maximum acceleration value compared with two-target system.

The five-target situation is similar to $n = 3$ (i.e., two logical options) and the available scan speed is double that of the two-target system. The six-target system is similar to $n = 4$ except that as $n = 6$ is divisible by an odd number then a hybrid batch sequence is available (three batches of two). A similar situation arises with $n = 10$ (five batches of two).

It is worth noting that the $n = 4$ and $n = 6$ situations are different to a double-width target holder taking two targets in the $n = 2$ and $n = 3$ modes; the total scan amplitude (determining one dimension of the target chamber) is less for $n = 4$ and $n = 6$ and the available scan speed is larger.

5. Multiple PLS

The previous section has looked at increasing the number of targets in the system by increasing the number of targets involved in the PLS sequence. A very attractive practical alternative is to stack PLS scan systems behind each other and to use an alternate sequence of slow scan cycles.

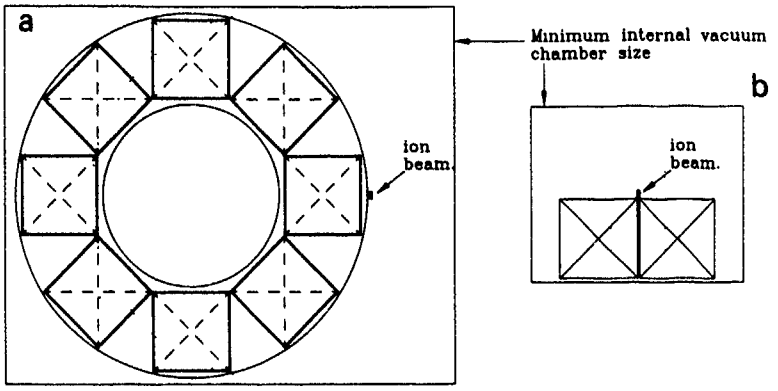

Fig. 4. End stations for large-substrate implantation: (a) spinning-disc end station, (b) PLS end station.

The simplest and most attractive combination being considered is to stack up to six two-target PLS modules behind each other. The main motive is to increase the throughput by reducing the number of vent/unload/load/pump cycles and to reduce wafer heating by increasing the implant area. A very important consequence of using one or more two-target PLS modules is the ability to park the targets in position |4| in fig. 2; when the targets are parked behind each other in this way they can be unloaded and loaded each in a single operation. Another important consequence is that although there may be (say) twelve targets in the batch, only two are being implanted at any one time (because of sequential slow scans) and therefore only two of the twelve targets would be affected by the discontinuity caused by a beam failure during implant.

6. Comparison of scan techniques for large substrates

The primary advantage of PLS is its ability to allow an efficient implant of large substrates in a small system. As a result it is easily retrofittable to existing implanter systems. The most suitable alternative mechanical scan technique is the conventional spinning disc; that is, conventional in principle if not in size. The size issue is illustrated in fig. 4. The spinning disc is shown with eight substrates. This is probably the smallest practical number; the issues are the following.

(a) *Scan efficiency*: with eight substrates the geometry is such that for a 40 mm × 20 mm beam onto 360 mm square substrates (a typical requirement) the beam spends 38% of the scan cycle hitting the beam stop. The size of the system decreases as the batch size decreases, but the beam utilization gets rapidly worse.

(b) *Fast scan speed as a function of radius*: for eight substrates the scan speed on the outside of the disc is double that on the inner radius. This ratio is possibly dangerous at this level as it could cause an annealed implant property drift (at high beam currents) from one side of the substrate to the other; a smaller batch size makes the situation worse.

If the systems in fig 4 were for 360 mm square substrates, the minimum internal dimensions of the spinning disc vacuum chamber would be 2.2 m by 1.75

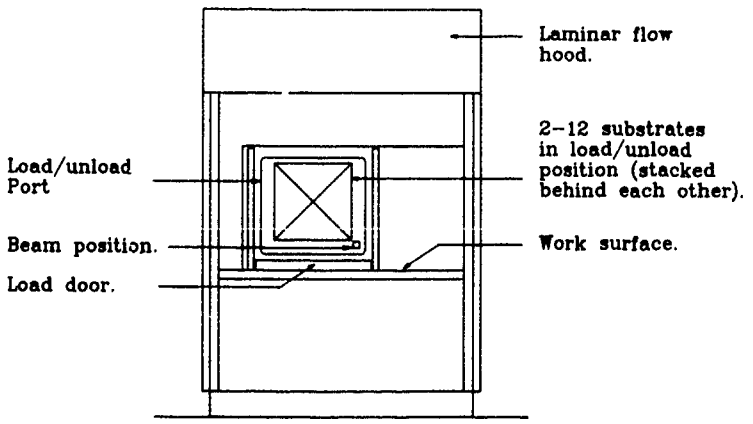

Fig. 5. Autoload PLS.

m, whereas the PLS would be 1.0 m by 0.8 m. The weight and cost of these small-depth vacuum chambers is very sensitive to these dimensions and is relatively insensitive to the depth dimension while it remains small (say, less than $\frac{1}{2}$ m).

7. PLS systems for large-substrate implant

The design and performance of a PLS end station will depend on a number of details:

(1) the substrate size and batch size,
(2) beam current, beam power and implant dose,
(3) maximum allowable substrate temperature,
(4) maximum allowable reversal acceleration,
(5) required throughput, and
(6) manual or automatic loading.

Fig. 5 shows an autoload system for substrates up to 500 mm square. For production systems it is likely to be a multiple PLS (MPLS) system with up to six two-substrate PLS modules (i.e., up to a twelve substrate load) stacked behind each other. The depth of the chamber for a twelve substrate system would be approximately 40 cm; only the small dimension of the system increases as the batch size increases. The substrates (up to twelve substrates stacked behind each other) are loaded and unloaded each in a single operation through a minimum-size gate-valve-type loading door using a robot or a dedicated autoloader, the loading being carried out in position |4| in fig. 3 with the vertical scan in the upper position.

8. Summary

The phased linear scanner is the ideal end station for large-substrate ion implantation. It is easily retrofitted to existing medium- or high-current ion implanters and its small footprint generally results in a reduction in the size of the total system. The manual-load PLS is ideal for R & D and pilot-production requirements, and the autoload MPLS for production facilities.

Nuclear Instruments and Methods in Physics Research B55 (1991) 522–526
North-Holland

A universal sample manipulator with 50 kV negative bias

M.J. Kenny, L.S. Wielunski, M.D. Scott, R.A. Clissold, D. Stevenson and G. Baxter
CSIRO, Division of Applied Physics, Private Mail Bag 7, Menai, NSW 2234, Australia

A manipulator incorporating a number of novel features has been built for a research ion implanter. The system is designed to enable uniform dose implantation of both planar and nonplanar surfaces by incorporating one translational and two rotational degrees of freedom. Negative target bias of up to 50 kV may be applied to the target, thus increasing the ion energy by this amount. The target chamber and all external manipulator controls are grounded. With the exception of the high voltage power supply, cable and feedthrough, all high voltage components are within the vacuum system. A secondary electron suppression cage which can be held at a negative bias of up to 60 kV relative to the chamber (i.e. 10 kV relative to the manipulator) surrounds the manipulator. Performance has been evaluated using ^{15}N ions and nuclear reaction analysis through $^{15}N(p,\alpha)^{12}C$ to profile ion concentrations for dose uniformity and for ion depth at elevated target potentials.

1. Introduction

One of the more significant practical uses of ion implantation is in reducing wear between surfaces. Typically these may be tool bits, dies or bearing surfaces and are frequently nonplanar in shape with cylindrical, conical or spherical surfaces. In order to implant the surface with a uniform dose over its entire area, it is necessary to move the sample in the ion beam so that all parts of it are exposed into the beam uniformly. Conventional ion implantation is a line-of-sight process. To produce a uniform implant on a planar sample requires either electrostatic scanning of the beam, mechanical scanning of the sample or a combination of both. More complex nonplanar surfaces require both rotation and translation.

The thickness of the modified layer produced in ion implantation for a given substrate and ion species is dependent on ion energy. Typically for 50 keV nitrogen ions implanted in steel, this layer extends from the surface to a depth of about 70 nm. Although improved wear resistance may be obtained under these conditions, breakthrough of the layer is catastrophic. Therefore it is desirable to produce a thicker modified layer by implanting at higher ion energy. It may be necessary to implant at more than one energy to create a thicker treated layer which begins at the surface. This is not usually the case for an implant energy < 200 keV.

Our implanter is a 50 kV unit with a single stage of acceleration from the ion source. In general the energy range of an implanter may be extended in various ways such as:

(i) Acceleration after initial extraction, but before the analyser magnet.
(ii) Analyser magnet at elevated potential and subsequent acceleration.
(iii) Target at negative potential.

Each of these has advantages and disadvantages. Acceleration prior to the analyser magnet means that the magnet must handle the higher energy and is considerably larger and more expensive. Acceleration after the analyser magnet requires the magnet and its power supplies to be at high potential and creates problems with insulation and the vacuum system – the ion source is at a potential of 50 kV with respect to the magnet and up to 100 kV with respect to ground. If the target chamber is raised to negative potential, it requires large insulators with clearances in the range 75–100 mm, insulation of the pumping system and a safety cage surrounding the high voltage components. There are also difficulties in monitoring beam current and sample temperature.

The technique of obtaining additional energy by negative target bias is well established [1,2], but the approach has been to raise the whole target chamber to high voltage. We have used an alternative approach by raising only the target and its holder to the elevated potential with the chamber and vacuum system remaining at ground potential. A high voltage vacuum feedthrough is used to bias the target. Because of the high dielectric strength of the vacuum, insulation gaps of 15 to 20 mm are adequate within the vacuum chamber and the whole system is very much simplified.

An advantage of the target bias approach over the pre-analyser magnet acceleration is that the high voltage power supply needs only to provide a current appropriate to that on the target (in this case typically 100 μA) and hence is more compact and less power consum-

0168-583X/91/$03.50 © 1991 – Elsevier Science Publishers B.V. (North-Holland)

ing than a supply which would have to handle the entire current output of the ion source (2 mA or more).

2. Manipulator

The manipulator (shown schematically in fig. 1 and as a photograph in fig. 2) is designed to hold a sample up to 50 mm diameter and to provide unlimited rotation about one of its axes. This axis can be aligned parallel to the ion beam or tilted in a controllable manner up to 150° from this direction. The whole asssembly can be translated in a direction normal to the ion beam by up to 100 mm to allow implantation of objects up to this length and/or introduction of beam monitoring devices for diagnostics and integration. Three UHV rotary feedthroughs are mounted on a 20 cm OD flange. Through a system of reduction gears, these control the translation and rotations. The feedthroughs are driven by stepping motors controlled from an IBM PC XT type computer using a program written in-house.

The translational movement allows the sample to be moved out of the beam and the introduction of a beam monitoring unit in the form of a graphite block with a vertical slot 20 mm × 0.8 mm and a 45° diagonal slot 45 mm long. With the block set at the appropriate position, the beam can pass through the vertical slot to a Faraday cup mounted behind the manipulator. This is used to monitor the horizontal distribution of the beam and to integrate the total current. As the diagonal slot is moved through the beam, the Faraday cup samples the beam current as a function of time. This gives a measure of beam distribution in the vertical direction.

The computer program is written to allow a prescribed number of revolutions at a given sample tilt, then to move the sample out of the beam and check the beam current and uniformity. If the latter are within predetermined limits, the sample is moved back into place and the implant continues. Alternatively the beam current conditions or the implant time are adjusted to attain the prescribed dose.

3. High voltage system

Mechanical connections from the UHV rotary feedthroughs are through insulated gear wheels and drive connectors, all capable of withstanding at least 60 kV in vacuum. The carrier mechanism is supported by teflon insulators. These are seen in fig. 2.

With a negatively biased target, a significant number of secondary electrons are emitted when the beam hits the target and these flow away from the target to ground. This causes errors in beam current integration and an unnecessary large current drain. To overcome this problem, the sample holder is surrounded by a screen cage mounted inside the chamber and supported by 20 mm long ribbed teflon high voltage insulators. A second high voltage power supply and high vacuum feed through insulator are used to maintain the cage at a negative potential of several thousand volts relative to the target. Secondary electrons emitted from the target are repelled by this negative potential and are trapped within the cage. The power supply for this screen is capable of 60 kV, to enable the full 50 kV bias to be applied and at the same time to provide adequate suppression of the secondary electrons.

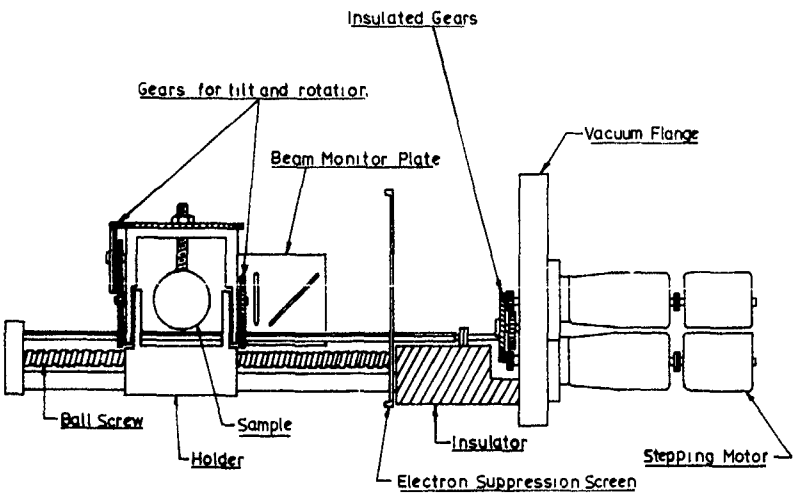

Fig. 1. Schematic layout of the manipulator showing rotational and translational movements and insulators

The screen has shaped entry and exit ports for the beam and target manipulator. When the sample holder is moved at right angles to the beam so that its vertical slot is aligned with the beam entry and exit ports, the beam passes through to a grounded Faraday cup, for monitoring. This overcomes the problem encountered with previous target bias systems [1,2] where beam monitoring is not practical. Fig. 3 is a photograph of the screen and fig. 4 is a schematic of all voltages from ion source through to Faraday cup.

It is desirable to maintain high vacuum within the chamber to give maximum insulation. Typical pressure without beam is < 100 μPa. This rises to 1 mPa with beam on. The high voltage is interlocked mechanically and electrically and also with the vacuum system to prevent breakdown or contact with high voltage when loading or unloading samples.

4. Performance

4.1. Manipulator

Manipulator operation was first tested without target bias. A number of spherical samples were implanted with doses of order 5×10^{16} nitrogen ions cm^{-2}. Each sample was held on a stem (nominal south pole) and implanted from the north pole to 45° south. During implanting the sample was continuously rotated about its axis at two revolutions per minute. The beam size was 25 mm high and 3 mm wide. Vertical height of the beam is controlled by electrostatic scanning and can be varied from 10 to 30 mm. The surface area presented to the beam varies with latitude, being greatest at the equatorial region and least at the pole. The times at which changes in tilt angle were made were adjusted to allow for this and hence provide reasonably uniform dose per unit area. When the polar region is being implanted, any misalignment of the beam relative to the pole could result in the polar region receiving no dose at all. To overcome this, the sample is translated back and forth by several mm during implantation of this region.

Dose uniformity was measured by placing a 5 mm wide stainless steel strip around a ball, passing from south through the north pole and back to south again. After implanting the whole assembly with ^{15}N ions, the strip was removed and the nitrogen dose measured at nine places along the strip using nuclear reaction analysis with the reaction $^{15}N(p,\alpha)^{12}C$ employing 1.0 MeV protons from a Van de Graaff accelerator. The 4.3 MeV

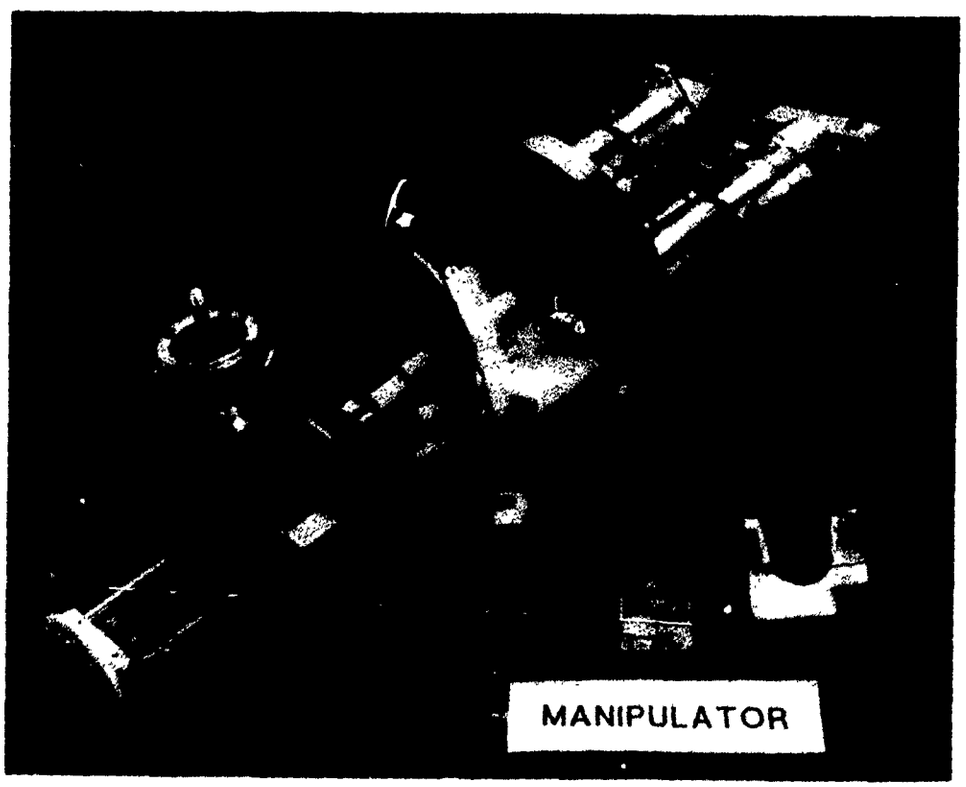

Fig. 2. Manipulator.

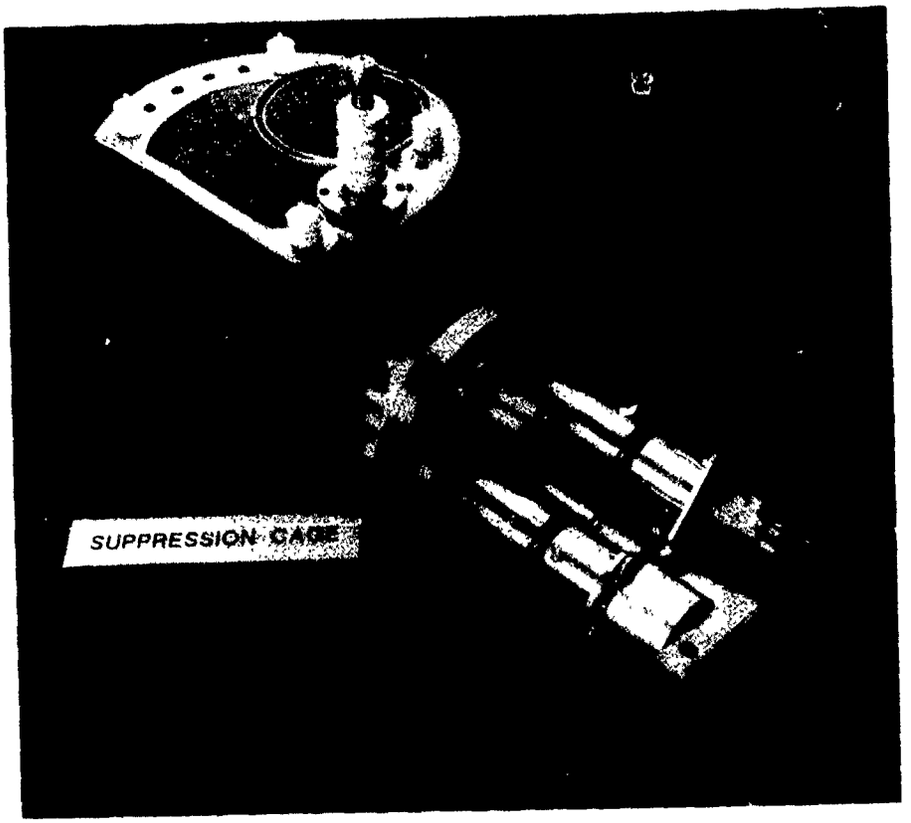

Fig. 3. Electron suppression cage.

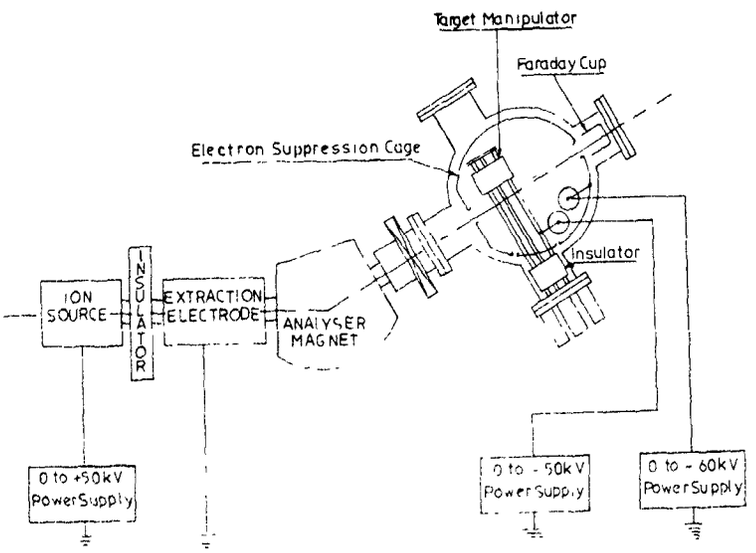

Fig. 4. Schematic of voltage levels from ion source to Faraday cup

α-particles are readily distinguished above background. It is preferable to use ^{15}N rather than ^{14}N because the cross section for profiling ^{15}N using this reaction is thirty times greater than the cross section for $^{14}N(d,\alpha)^{12}C$ which is the reaction used to profile ^{14}N. The measurements showed uniformity of dose was within 25%. Better dose uniformity can be obtained by improving beam position and reducing beam height.

The manipulator can accommodate a variety of sample shapes and sizes. For example five planar samples can be mounted on a cube shaped holder. The first sample is implanted using a vertical electrostatic scanner and horizontal movement to provide uniform dose over its area and then a 90° rotation is used to align the second, third and fourth samples. A 90° tilt aligns the fifth face. Complex shapes are implanted using an appropriate combination of the translation, tilt and rotational movements.

4.2 Target bias

Measurements have been made with 47 kV target bias and a screen bias of 55 kV. With bias applied, current on the sample cannot be read directly. Therefore it is necessary to periodically translate the sample horizontally until the beam monitoring slot is aligned with the beam. The beam then passes through this slot and the exit port of the supression screen to the Faraday cup at the back of the chamber where it can be monitored

Performance was evaluated by implanting glassy carbon samples with ^{15}N ions at 50 keV energy (no bias), then with 47 kV bias giving a beam energy of 97 keV. The expected ranges of 50 and 97 keV ^{15}N ions in glassy carbon as calculated using TRIM-89 are respectively 129 and 247 nm. Nuclear reaction analysis was then used to obtain the depth distribution of the implanted ions in each case Fig 5 shows the relevant parts of the α-particle spectra obtained from the reaction $^{15}N(p,\alpha)^{12}C$ using 1 0 MeV protons and the depth profiles derived from it. For the 97 keV situation, the

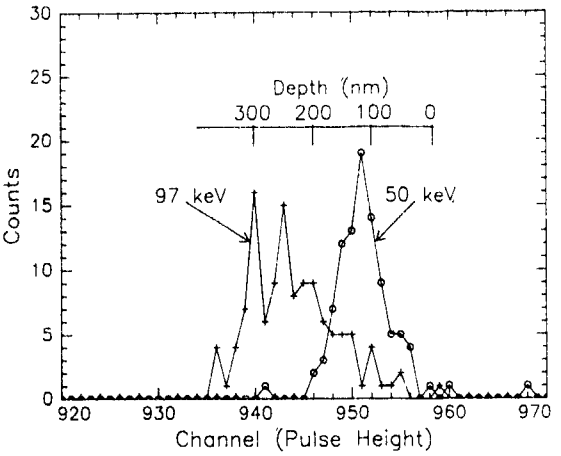

Fig. 5 Depth profiles of ^{15}N implants in glassy carbon at 50 and 97 keV

lower α-particle energy corresponds to the increased range of these ions. The observed depths of 112 ± 15 and 228 ± 20 nm agree well with the calculated ranges

5. Conclusion

For research areas where a variety of different shapes may need to be implanted, this design offers considerable flexibility for samples to be implanted with a uniform dose. At the same time, a novel approach to negative target bias enables implant energy (and hence thickness of modified layer) to be increased without expensive hardware additions.

References

[1] J G Bannenberg, Radiat Eff 44 (1979) 3.
[2] P. Byers, P. Bailey, P.A. Judge and D G. Armour, Ion Implanters and Ion Sources, American Society for Metals, Met. Mater. Technol. Ser . 8504-001 (1985)

Nuclear Instruments and Methods in Physics Research B55 (1991) 527–532
North-Holland

Computer modelling for ion-beam system design

Hiroyuki Ito and Nicholas R. White
Applied Materials Implant Division, Horsham, West Sussex RH13 5PY, UK

The design of ion-beam transport systems based on computer modelling is discussed and some typical examples are presented Integrated modelling work involves beam envelope programs to design overall systems, Poisson or Laplace solutions to calculate electric and magnetic fields in the system, ray-trace programs to see the collective movement of charged particles, plasma solutions for the consideration of the target environment and plasma-simulation programs to predict possible microscopic interactions between charged species and the fields Experimental checks to assure the performance of the beam-line components are also given and explained These are used as a means of making more accurate predictions in the future.

1. Introduction

Ion-beam transport systems and beam-optics calculations have been developed largely in nuclear physics and other related fields [1]. As semiconductor device structures increase in complexity, tight control of the ion-beam conditions becomes more important in ion implantation doping processes [2] The main concerns are the beam current extracted and transferred at a certain energy through the system, beam divergence, mass resolution and the beam-plasma conditions in the target region. Fig. 1 shows which design tools are used for which parts of the beam line, and the physics to be considered [3–5].

It is always important to ensure that the modelling can closely follow the real situation so that design work based on these predictions is sufficiently reliable. Associated experiments should be performed to check the agreement with the theoretical models. The results help determine the conditions under which the programs are valid and can suggest further improvements in calculation.

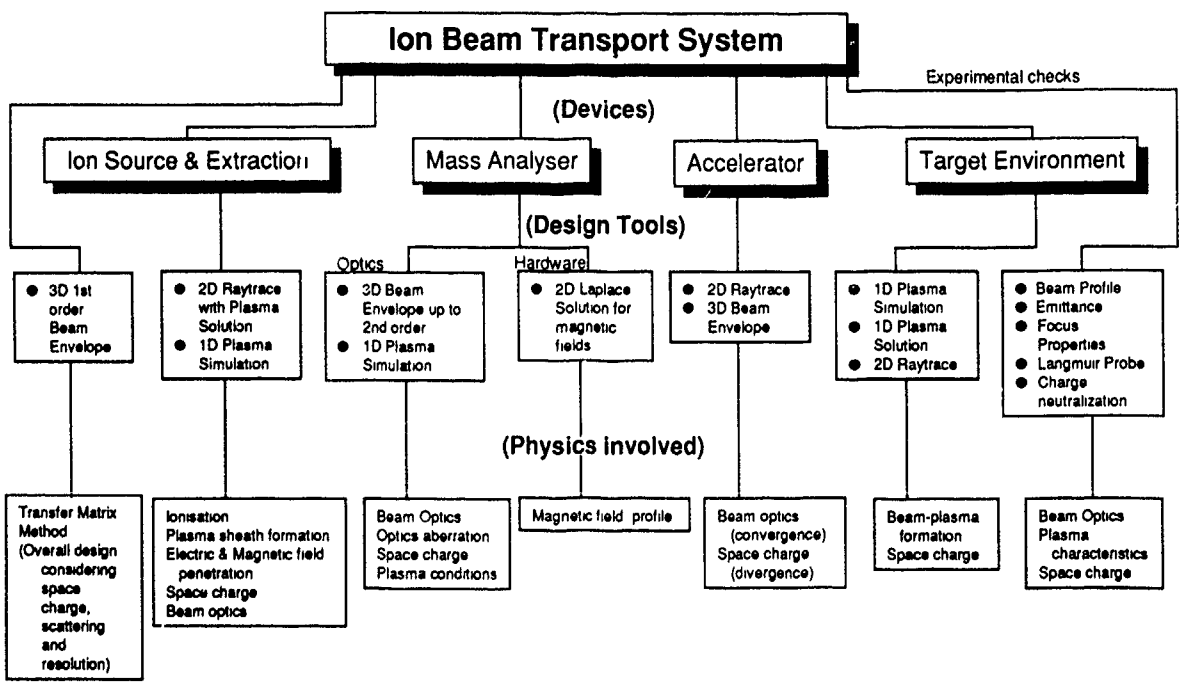

Fig. 1 System overview System devices, computer design tools and the physics involved in the modelling are shown

0168-583X/91/$03.50 © 1991 – Elsevier Science Publishers B V (North-Holland)

2. Overall system design

For an ion implantation beam line, as with any ion-beam system, the whole system should first be designed to a first-order approximation according to the desired specification. The main concerns at this stage are: (1) energy range, (2) beam current with species and associated energy range, (3) beam dimensions and divergence, (4) mass resolution and (5) overall system dimensions and interface to other systems.

There are some physical limits which might not allow a theoretical model to be realised, such as the minimum gap between acceleration electrodes. These constraints can give a certain conflict with the ideal design and the best possible solution should be sought by considering other changeable parameters of the related devices. A design tool used for this purpose is an interactive 3D first-order beam-envelope program based on the transfer-matrix method [6] called OPTICIAN [7], which calculates the coordinates of the beam envelope through the system.

Beam coordinates are composed of spatial coordinates x and y (having z coincide with the central ray), divergence, path-length spread and momentum spread. The first-order FWHM mass-resolving power can be derived from the dispersion element of the transfer matrix Fig. 2 shows a hypothetical ion-implanter beam line which can bend a 60 keV As^+ beam through 90° and accelerate it to 90 keV onto the target. The tightly controlled point-to-point focus between the entrance and the end of the drift element 5 can be seen.

One of the additional features implemented into OPTICIAN is that space-charge effects including neutralisation are considered [8]. These give rise to radial electric fields. The potential difference between the beam centre and the plasma sheath is assumed to be $T_e/2$ (T_e is the electron temperature) based on stable plasma-sheath formation [9], and the resultant electric field can cause positive ions to drift outward. No space-charge neutralisation is assumed in accelerator tubes, so defocussing can be strong.

The validity of first-order calculations is limited, and second-order aberrations may cause large errors, for example in the determination of mass resolution. The differences which appear in second order should be minimised to achieve performance close to the first order (see section 4).

3. Ion-source and extraction system

The ion source and its extraction-system requirements need to be specified as follows: (1) extraction energy range, (2) beam current and density range. (3) ion species, (4) beam dimensions and divergence and (5) optics control over the operation range.

There are many important parameters which affect the performance of this system, such as ion mass, electron temperature, ion density in the source chamber, electrode geometry and space charge. The maximum current extracted through the system, for example, is limited by several relations shown below [10]. The number of ions leaving the plasma cannot exceed the value determined by the product of the Bohm velocity and the ion density given by

$$J_p = c_p n_i T_e^{1/2} m_i^{-1/2}, \tag{1}$$

where J_p is the current density at the plasma sheath, c_p a constant, n_i the ion density at the plasma sheath, T_e the electron temperature and m_i the mass of the ion. The beam current extracted through the electrodes is also limited by the space-charge effect, expressed by

$$J_s = c_s d^{-2} m_i^{-1/2} V^{3/2} f_s, \tag{2}$$

where J_s is the current density at extraction, d the extraction sheath distance, c_s a constant, V the extraction voltage and f_s the space-charge neutralisation factor For systems in which the extraction energy is high

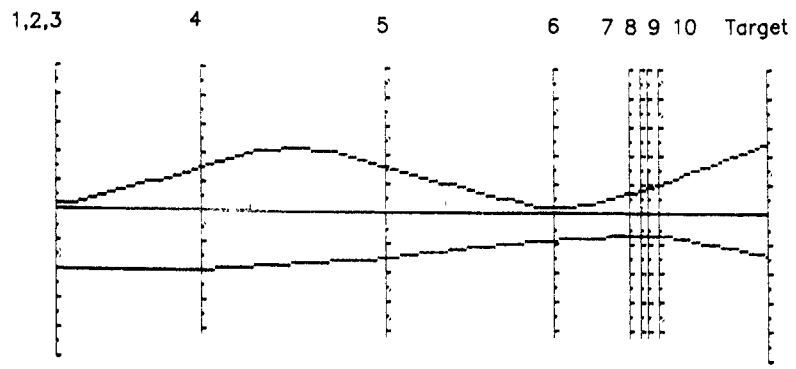

Fig 2 Ion-beam transport system of a 300 mm radius 90° bending magnet, with 60 keV extraction and 30 keV post-acceleration using an As^+ beam, modelled by the 3D first-order beam envelope program OPTICIAN [7]. (1) Source, (2) lens, (3) drift, (4) magnet, (5, 6) drift, (7–9) accelerator and (10) drift.

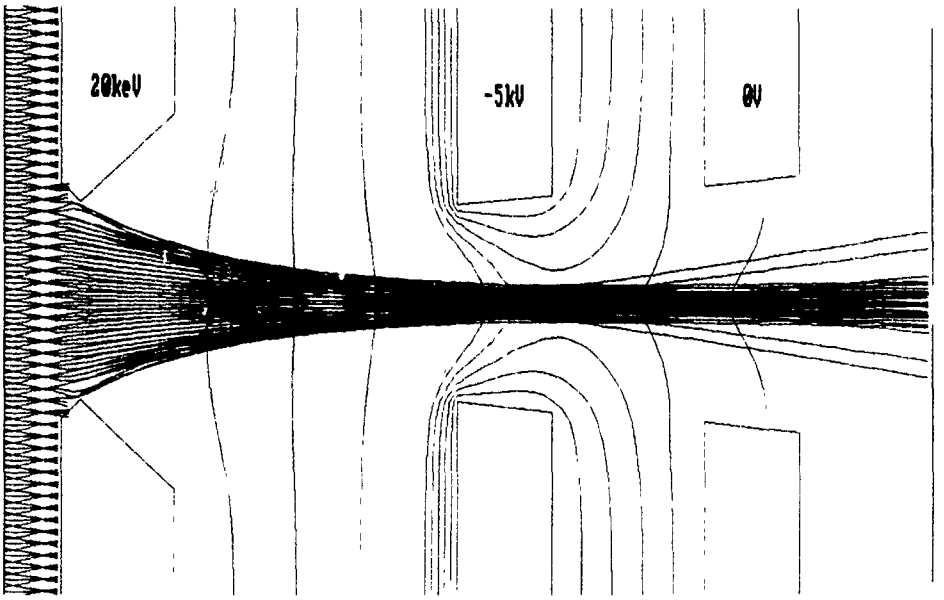

Fig. 3 Ion-source and extraction system composed of source chamber, suppression electrode and ground electrode, modelled by the 2D ray-trace program SORCERY [7] The potential is 20 kV at the source front plate (left), −5 kV at the suppression electrode (middle), 0 V at the ground electrode (right), and the ion species is Ar^+

($\gtrsim$ 10 keV), the beam divergence is usually dominated by the optical properties of the extraction system [11], rather than the thermal motion of the ions which causes momentum spread.

The main tool used to design the extraction region is a 2D ray-trace program called SORCERY [7]. The program traces particle trajectories solving Poisson's equation by the finite-element method, assuming a Boltzmann distribution of electrons inside the plasma. Each particle trajectory is integrated using the Runge–Kutta method. The plasma boundary adopts a shape satisfying eq. (2). The performance of any ray-trace programs should be equivalent regardless of the differences in trajectory integration as long as the calculation of the field is sufficiently accurate [12].

2D raytrace programs are extremely useful to display the electrostatic lens formation around the beam extraction area. As can be seen in fig. 3 (double-electrode extraction system: one to suppress the electron backstreaming, and another to define the final energy), the electric field along the plasma sheath converges the ions toward the axis, then the beam passes through a divergent lens formed around the extraction electrodes. The combination of these two lenses determines the beam formation

4. Mass analyser

The first-order design of the mass analyser is assumed to have been done in the overall system design explained in section 2, which would give the first-order parameters such as bending radius, bending angle, magnetic field strength, field index, pole face angles and positions of the foci.

A 3D second-order beam-envelope program called TRANSPORT from SLAC [13] is then used to check the first-order design and to perform second-order optimisation. The method of second-order calculation is also based on transfer matrices which now contain second-order terms The results are affected by such variables as the quadratic field coefficient ϵ and the entrance and exit pole-face curvatures. Beam growth caused by the magnet aberration is minimised by changing the second-order variables. If these parameters are not considered, the aberration tends to give a crescent shape to the output of a ribbon beam

The effects of the fringing field are taken into account in terms of field integrals I_1 and I_2 [14] which give corrections to the central ray displacement and the focal power in the non-dispersion plane, respectively. These are zeroth- and first-order constraints, but require accurate calculations to determine the entrance and exit pole geometry.

The actual pole shape can be designed by solving the Laplace equations assuming the magnetic scalar potential is valid between the poles. 2D ray-trace programs can be used as a Laplace solver. The pole radial cross section determines the value of ϵ and the entrance and exit pole shapes determine I_1 and I_2.

Fig. 4 shows the equipotential plot in the plane of the magnet pole cross section. The field near the edge of

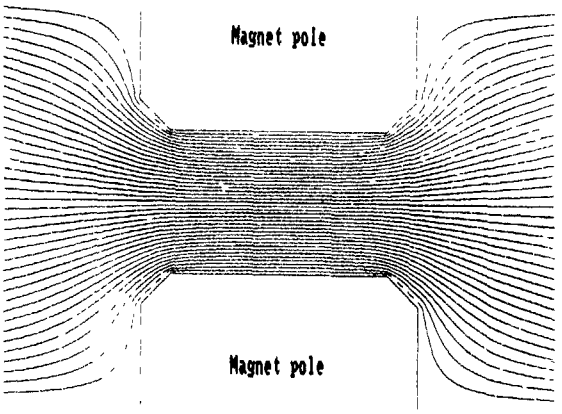

Fig. 4 Equipotential plot in the plane of the magnet pole cross section, obtained as a 2D Laplace solution using SORCERY

the pole decreases as the gap between potential lines increases. The field profile along the beam axis showing the effect of the fringing field is plotted in the left half of fig. 5. Similarly the effect of ϵ on the radial profile is shown in the right half of fig 5.

5. Acceleration tubes

To design acceleration (or deceleration) systems, energy range, beam dimensions and optics control, balancing focal power against space charge, should be considered. The field inside the acceleration tubes forms a convergent lens and the effect is increased as the acceleration energy is increased. If the energy is high, the beam can be focussed to a very small size, making the beam current density high, which may aggravate problems such as charging up on the semiconductor wafers [15]. If, on the other hand, the energy is low, space-charge blow-up would play a more dominant role, making the optics control very difficult. 2D ray-trace programs are again effectively used for this design. The field lens formation is easily seen from the equipotential lines. OPTICIAN can also be used to see the macroscopic character since it approximates the space-charge effect in the acceleration tube.

6. Target environment (wafer chamber)

The requirements of each beam transport system strongly depend on the actual processes in the target chamber and its environment. The process-related problems, such as "wafer charging" mentioned in the previous section, are getting more and more subtle as complex submicron structures are developed with increasing sensitivity to the environment. In the target chamber the ion beam will collide with neutral gas, creating ions which then form a beam-plasma together with the

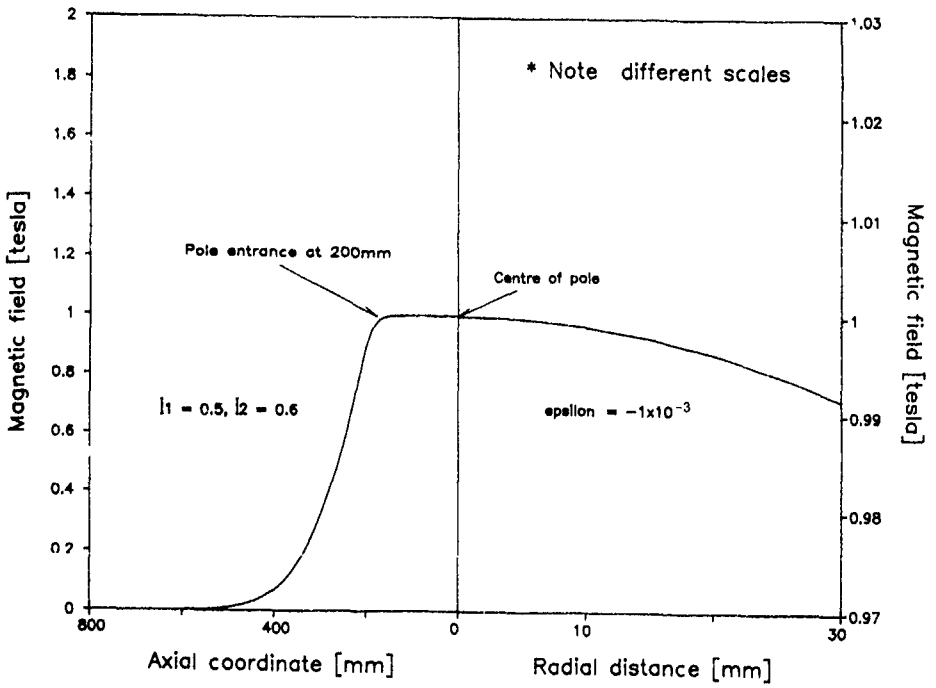

Fig. 5. Magnetic field profile in the median plane. The left-hand side shows the field along the beam axis The extended fringing field is clearly seen in the region outside the pole. The right-hand side shows the field along the radial direction. The field is maximum at the centre and decreases outward, as can be seen in fig. 4.

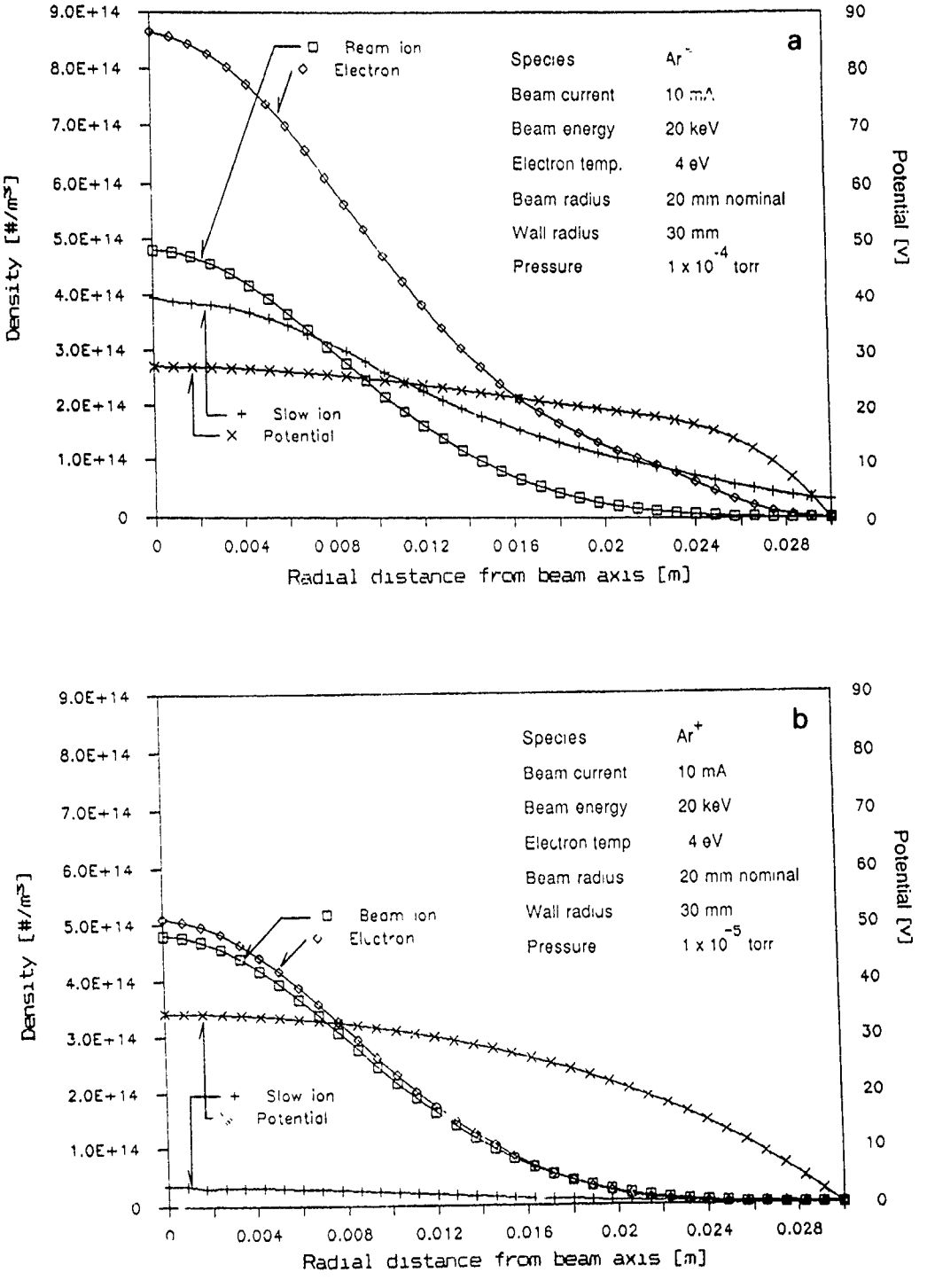

Fig. 6 (a) Radial distribution of the beam plasma at 1×10^{-4} Torr assuming a 4 eV electron temperature, modelled by a 1D plasma solution [16]. The density of each species and the potential are expressed in terms of the number per cubic metre and volts, respectively. A well-defined plasma around the ion beam with a small Debye length is seen. (b) Radial distribution of the beam plasma at 1×10^{-5} Torr at the same electron temperature of 4 eV. The field penetration is much greater than that in (a), reflecting the fact that the Debye length is now large due to the decrease in plasma density Further data are: 20 keV beam energy, 20 mm nominal beam radius and 30 mm wall radius.

trapped electrons inside its potential well [8,16]. All of these processes need to be understood.

In terms of the computer modelling, some simulation programs have been intensively developed by plasma physicists in recent years [17,18]. A 1D plasma solution [16] is one of the tools used to see the radial distribution of each particle species and the potential, electric field and particle flux in the beam-plasma in the steady state This program solves Poisson's equation with the continuity equation based on the finite difference method. Ionisation and charge-exchange collisions are taken into account, and up to two Maxwellian distributions of electron species can be calculated at different temperatures. A well-collimated cylindrical beam is assumed and cold ion species created from neutrals drift along the field. Figs. 6a and b are examples of the results. The former presents the well-defined plasma around the beam with a small Debye length at a pressure of 10^{-4} Torr, and the latter shows the relatively large field penetration across the system at the lower pressure of 10^{-5} Torr.

A real-time simulation is the 1D plasma simulation program called the PDX1 series, developed by the Plasma Theory and Simulation Group at the University of California at Berkeley [19]. This program solves Poisson's equation together with the external circuit connected to the system boundary based on the particle in cell method, and advances particles in real time by applying the Lorentz force. Particle collisions resulting in excitation, charge exchange and ionisation are also implemented by the Monte Carlo method. By using this program, the effects of a potential applied in a short time ($\sim 1\ \mu s$) on one side of the electrodes, for instance, can be evaluated effectively.

7. Experimental checks

The main purposes of experimental checks are (1) to check whether the performance of devices is close enough to that predicted by the model, and (2) derive any possible suggestions which can be implemented into the modelling procedure for future improvement. For example:

(1) *Beam profile*. Beams are basically better if symmetric and uniformly distributed along the axes in the plane of the cross section. Some commercial beam profilers are available to measure the distribution.

(2) *Focal point*. The focal point must be well defined to ensure high resolution. It can be found by making a beam burn on a tantalum plate placed in the beam at a shallow angle, or by viewing directly through a window near the focus.

(3) *Langmuir probe*. Electron temperature and plasma densities are important parameters in understanding the plasma character around the beam Langmuir-probe techniques are widely used to obtain these values [20].

8. Conclusion

Ion beam transport systems can be modelled accurately by computer if the physics involved in each component is properly considered. This gives great advantages in speeding up development, reducing costs and understanding the system performance

References

[1] K.L. Brown, R. Belbeoch and P. Bounin, Rev. Sci Instr 35 (1964) 481
[2] M E Mack, G Ryding, D.H Douglas-Hamilton, K Steeples, M Farley, V Gillis, N White, A Wittkower and R. Lambracht, Nucl Instr and Meth B6 (1985) 405
[3] K L. Brown, Advanced Particle Phys. 1 (1967) 71
[4] D C Carey, Fermilab Report No NAL-64 (1971).
[5] A J T Holmes, Phys Rev A19 (1979) 389
[6] A.P Banford, The Transport of Charged Particle Beams, (E & F N. Spon, London, 1966)
[7] N R White, Nucl. Instr and Meth B21 (1987) 339
[8] N R White, these Proceedings (8th Int Conf on Ion Implantation Technology, Guildford, UK, 1990) Nucl Instr and Meth B55 (1991) 287.
[9] F F. Chen, Introduction to Plasma Physics and Controlled Fusion, (Plenum, New York 1984).
[10] J Ishikawa, Ion Source Technology (Ionics, Japan, 1986) p 178.
[11] N R White and A S Devaney, Proc 12th Symp on ISIAT '89, Tokyo, 1989, p 111
[12] P Spadtke, The Physics and Technology of Ion Sources, (Wiley, New York, 1989) p 107.
[13] K.L Brown, F Rothacker, D.C Carey and Ch Iselin, CERN Report 80-04 (1980)
[14] H.A Enge, Rev Sci Instr 35 (1964) 278
[15] M I Current, A. Bhattacharyya and M Khid, Nucl Instr and Meth B37/38 (1989) 555
[16] H. Ito, Steady-state beam plasma solution, Internal Report, Applied Materials, UK (1990)
[17] C.K. Birdsall and A B Langdon, Plasma Physics via Computer Simulation (McGraw-Hill, 1985)
[18] R W. Hockney and J W. Eastwood, Computer Simulation Using Particles (Hilger, 1988)
[19] J P Verboncoeur and V. Vahedi, Proc 13th Numerical Simulation Conference, Santa Fe, NM, USA, 1989.
[20] J.A Strain, Y. Tanaka, N.R White and R Woodward, these Proceedings (8th Int. Conf. on Ion Implantation Technology, Guildford, UK, 1990) Nucl. Instr. and Meth B55 (1991) 97.

Nuclear Instruments and Methods in Physics Research B55 (1991) 533–543
North-Holland

Section VI. Materials Science

Amorphous Si – the role of MeV implantation in elucidating defect and thermodynamic properties *

J.M. Poate, S. Coffa [1], D.C. Jacobson and A. Polman
AT&T Bell Laboratories, Murray Hill, NJ 07974, USA

J.A. Roth and G.L. Olson
Hughes Research Laboratories, Malibu, CA 90265, USA

S. Roorda and W. Sinke
FOM Instituut voor Atoom- en Molecuulfysica, Kruislaan 407, 1098 SJ Amsterdam, The Netherlands

J.S. Custer and M.O. Thompson
Cornell University, Ithaca, NY 14853, USA

F. Spaepen and E. Donovan [2]
Harvard University, Cambridge, MA 02138, USA

The role of MeV implantation in producing thick amorphous Si layers has been central in elucidating several of its properties. The recent use of MeV Si beams to produce very pure layers will be reviewed. The kinetics of solid-phase epitaxy have been measured for amorphous Si layers up to 5 μm thick and the activation energy found to be 2.70 ± 0.02 eV. Calorimetry measurements of such thick layers show an interfacial heat release due to crystallization of 13.4 ± 0.7 kJ/mol and a homogeneous heat release of 5.1 ± 1.2 kJ/mol. This homogeneous heat release, associated with relaxation, is due to the annihilation of defects in the amorphous structure. These defects have been studied by ion-bombarding 500°C annealed amorphous and single-crystal Si. The formation and annihilation properties of the defects in these two states are intriguingly similar. Defects saturate in previously annealed a-Si at ion doses ~ 0.02 dpa. The presence of the defects is also manifested in measurements of the density of amorphous Si which is $(1.8 \pm 0.1)\%$ less dense than the crystal. The diffusion and solubilty of Cu, Zn, Pd, Ag, Pt and Au have been measured in amorphous Si and found to be very sensitive to defect population. The various experiments show that the intrinsic defect level in amorphous Si is 1–2 at %.

1. Introduction

Understanding the structure and properties of amorphous (a)-Si is a scientific challenge of some complexity [1]. Much progress has been made in the study of hydrogenated a-Si because of its technological importance. The study of a-Si formed by ion implantation has historically had very different driving forces. Interest has focussed on recrystallization phenomena because of the need to remove all damage and incorporate dopants on lattice sites. Important phenomena were discovered in these studies such as solid-phase epitaxy. This review will detail our recent experimental studies of the formation and properties of amorphous (a)-Si formed by MeV implantation. The question should be asked what special significance there is to producing micron thick amorphous layers by MeV beams rather than the thinner layers, typically 0.1 μm, produced in the usual low-energy implantation machines. The answer lies in the fact that the extra dimension permits better measurement of the following properties.

Four specific areas will be discussed:

(a) *kinetics* of solid-phase epitaxy of 5 μm thick layers where the behavior mimics that of much thinner layers but a novel ambient annealing effect has been observed,

* Invited paper

[1] Permanent Address: University of Catania, Catania, Italy

[2] Permanent Address: Naval Research Laboratory, Washington, DC, USA

(b) *calorimetry* studies of heat release of a-Si layers where the relaxation process has been identified in terms of defect annihilation,
(c) *density* measurements of a-Si where the role of defects are investigated, and finally
(d) *diffusion* studies where considerable progress has now been made in identifying diffusing species in a-Si and the role defects play in the diffusion mechanisms.

The a-Si layers described in these experiments were formed by ^{28}Si implantation using the National Electrostatics Corporation 1.7 MV tandem accelerator at AT&T Bell Laboratories.

2. Kinetics of solid-phase epitaxy

It is well established that a-Si layers formed by ion implantation into single-crystal (c) substrates can be crystallized epitaxially in the solid phase [2]. The kinetics of solid-phase epitaxy (SPE) have been extensively studied on amorphous layers less than 500 nm thick using time-resolved reflectivity (TRR) measurements [2], and it has been shown that SPE in these layers is characterized by an activation energy of 2.7 eV. The study of SPE in much thicker layers has recently become possible with the advent of MeV ion-implantation methods capable of producing high-purity a-Si films with thicknesses exceeding 5 μm. In order to monitor the location of the c/a interface during SPE and to accurately measure epitaxial growth rates in these layers, the TRR technique has been extended to infrared wavelengths where a-Si is nearly transparent, thus avoiding the thickness limitation imposed by absorption in the visible-wavelength region. In this way the SPE kinetics of very thick layers can be monitored [3].

The a-Si layers were prepared as follows. The Si single-crystal substrates were contacted to an LN_2-cooled stage during implantation. Uniform amorphous layers of various thicknesses were prepared by multiple MeV implants of ^{28}Si with overlapping damage profiles. The implantation schedules used to form layers of several different thicknesses are given in table 1. SPE kinetics measurements were conducted both in vacuum ($P < 5 \times 10^{-7}$ Torr) and in air. Fig. 1 shows the reflectivities measured at $\lambda = 1.15$ μm and $\lambda = 0.633$ μm during SPE growth of a 4.16 μm thick film heated to 625 °C in vacuum. The $\lambda = 1.15$ μm trace exhibits uniformly spaced oscillations throughout the entire growth period, indicating that the velocity of the c/a interface is constant through the film. Additionally, aside from minor fluctuations, the amplitude of oscillations observed in this in situ interferometry measurement equals the value expected for an ideal film having perfectly flat and parallel interfaces. The excellent interference contrast throughout the growth also implies that competing effects such as nucleation and growth of polycrystalline material or twin formation do not occur. The oscillation amplitude increases gradually with time during SPE due to reduced attenuation as the a-Si layer gets thinner. Due to the much stronger optical absorption in a-Si at $\lambda = 0.633$ μm, oscillations in the TRR data at this wavelength are only evident during the latter stages of growth. The temperature dependence of the SPE growth rate for 2.2 μm thick a-Si films is given in fig. 2. Fitting the data to an Arrhenius expression for the SPE rate $r = r_0 \exp(-E_a/kT)$ yields the value 2.70 ± 0.02 eV for the activation energy E_a. This is in excellent agreement with the 2.68 ± 0.05 eV activation energy found earlier for self-ion-implanted 300 nm films [2] and with the value 2.71 ± 0.05 eV for a-Si films formed by evaporation in ultrahigh vacuum [2]. To test whether the SPE rate in very thick a-Si layers is sensitive to the total amount of displacement damage caused by ion implan-

Table 1
Ion implantation conditions used to form thick a-Si layers. Implants were performed with the sample at 77 K. Thicknesses listed here were determined from TRR data. From Roth et al [3]

a-Si thickness [a] [μm]	^{28}Si energy [MeV]	dose [10^{15} cm^{-2}]
0.9	0.5	5
1.4	1.0	5
2.2	2.0	5
3.0	3.5	6
3.7	5.0	7
4.3	6.5	8

[a] A uniform amorphous layer of a particular thickness is obtained by using all of the implants up to and including the one listed for that thickness.

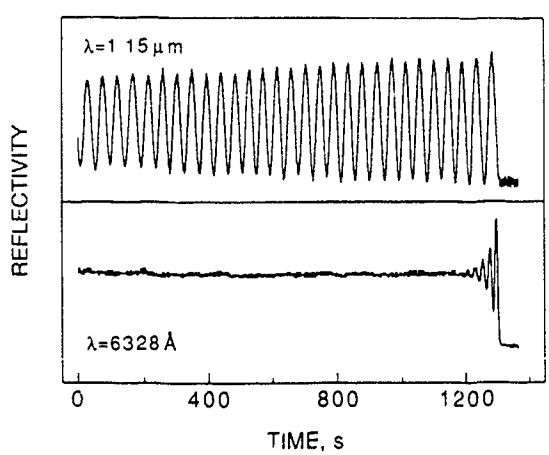

Fig. 1. Time-resolved reflectivity data at $\lambda = 1.15$ and $\lambda = 0.633$ μm for SPE growth of 4.16 μm thick, ion-implanted a-Si at 625 °C in vacuum. From Roth et al [3].

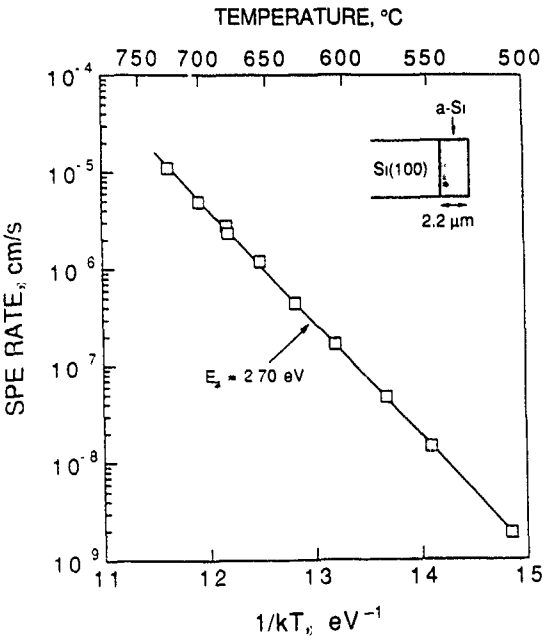

Fig 2 Arrhenius plot showing the temperature dependence of the SPE rate in a 2.2 μm thick a-Si film formed by MeV ion-implantation The solid line is a least-squares fit of the data to the expression $r = r_0 \exp(-E_a/kT)$ From Roth et al. [3]

tation, the rate was also measured in samples implanted at doses more than 1000 times above the threshold required to create an amorphous layer. The threshold dose for forming a thin, buried amorphous layer at 77 K using 1 MeV ^{28}Si irradiation is 2×10^{14} cm^{-2}. Previously amorphized films 2.2 μm thick were implanted with 1 MeV ^{28}Si ions at doses up to 2×10^{17} cm^2 in order to create an extra damage distribution peaked near the middle of the original amorphous layer. The SPE rate as a function of interface position was accurately measured, and no difference due to the extra implant was observed. It is interesting that the SPE rate does not change over this wide range of implant conditions, suggesting that the state of a-Si once formed is insensitive to additional ion bombardment.

The uniformity of the oscillation period in the TRR data in fig. 1 indicates that SPE occurs at a constant rate over distances greater than 4 μm when annealing is performed in vacuum. A marked deviation from this behavior is observed, however, when a-Si specimens are heated in normal room air. At depths approximately 1 μm from the surface the regrowth velocity is seen to decrease by as much as 40%. This effect has been correlated with the presence of water vapor in the annealing ambient and the growth of a surface oxide. The only impurities detected in the a-Si are hydrogen. These results indicate that atomic H is formed as a by-product of the oxidation of the a-Si during annealing in the presence of water vapor [4] (Auger analysis showed that a thick (~ 5 nm) native oxide forms on a-Si during annealing in air). Once H is formed at the SiO_2/a-Si interface, it can diffuse rapidly [5] into the a-Si and attach to dangling bonds [6]. The solubility of H in c-Si is much lower than in a-Si due to the absence of defect sites, thus explaining why H is not seen in fully recrystallized layers.

The possibility that H affects the SPE rate is very intriguing since H is known to passivate dangling bonds in both deposited [6] and ion-implanted [7] a-Si films. Several different defect-based models involving dangling bonds [8], vacancies [9] and floating bonds [10] have been proposed for the mechanisms of SPE but no experimental data have been available to discriminate between the different defects. An understanding of the effect of H on the crystallization process should help contribute to the development of a microscopic model for SPE in a-Si.

3. Heat release, relaxation and defects

Our original experiments [11] on the formation of μm thick a-Si layers by MeV inert gas atoms produced enough material to measure the heat of crystallization, ΔH_{ac}, by differential scanning calorimetry (DSC). The heat of crystallization, 12.0 ± 0.7 kJ/mol, was used to estimate from free-energy consideration, the melting temperature of a-Si; a first-order phase transition. This estimate of the reduction, ~ 250 °C, in melting temperature beneath the crystal melting temperature was confirmed by direct measurement [12] of the reduction, 225 ± 25 K. Some questions remained, however, concerning the state of the amorphous phase and the nature of the amorphous-to-crystal transition. The crystallization velocity was determined from the DSC net power signal. The definitive TRR [2] study of interface velocities gave values of velocity that were lower in magnitude and had a higher activation energy than those obtained from the DSC study Second, the relative values of ΔH_{ac} for a-Ge and a-Si were surprisingly close: 11.5 and 12.0 kJ/mol, respectively. If ΔH_{ac} arises only from relief of bond angle distortions of the connected random network, ΔH_{ac} should scale with the force constants for the distortion, which are 15–20% higher in Si than Ge [11].

The most obvious difference between the a-Ge and a Si data was a low-temperature heat release, clearly measured in Ge but not seen in Si. This release was mostly homogeneous in nature, and not primarily associated with interface motion. For a-Ge the homogeneous heat release was determined to be 6 kJ/mol over the range 400–600 K. In the case of a-Si, where higher temperatures made the base line curvature problems more severe, the net DSC signal below the crystalliza-

tion peak varied between endothermic and exothermic, indicating a much smaller homogeneous release. Nevertheless, annealing-induced relaxation effects on the optical properties such as the width of the Raman transverse optical band [13] or the infrared indices of refraction [14,15] have been observed in both a-Ge and a-Si. The situation has been clarified by the recent DSC measurements of Roorda et al. [16] of a low-temperature heat release from a-Si formed by Ar and Si implantation. They measured a homogeneous heat release of 3.7 ± 0.2 kJ/mol and an interfacial heat release $\Delta H_{ac} = 11.7 \pm 1.0$ kJ/mol. These important findings were confirmed [17] by using the 2.2 μm thick layers described in the previous section.

Fig. 3 shows DSC scans for as-implanted (lower) and samples that had been preannealed in a furnace at 525, 670 and 820 K, respectively. Two regimes are seen: at high temperature crystallization dominates, and over the entire 400 K lower-temperature region a fairly uniform release occurs. Samples that were preannealed show no heat release below the preannealing temperature, similar to the earlier observations in Ge. Since no motion of the a–c interface was observed by RBS after the 525 and 670 K anneals, the low-temperature signal corresponds to a one-time homogeneous heat release in the bulk of the a-Si. The kinetic parameters for crystallization can be determined directly from an Arrhenius plot for the high-temperature DSC signal that gives crystallization velocity and has an activation enthalpy of 2.62 eV. This is in excellent agreement with the TRR measurements. By fitting an exponential with the appropriate activation enthalpy to the data down to the base line and integrating under this curve, the heat of crystallization, without any contribution from the homogeneous heat release, was determined. The average value from the measurements is 13.4 ± 0.5 kJ/mol. The average value of the remaining part, corresponding to the homogeneous heat release, is 5.1 ± 1.2 kJ/mol. The estimated error, taking into account all possible systematic errors, is ~ 6%. This gives as the new value of the heat of crystallization of a-Si: $\Delta H_{ac} = 13.4 \pm 0.7$ kJ/mol. This is ~ 10% higher than the earlier value, which was obtained by drawing a base line from the crystallized region to the onset of the peak and hence was an underestimate. That the new value of ΔH_{ac} for Si is higher than that for Ge is in better agreement with the relative values of the force constants for bond bending. It also explains why the earlier velocity data differed from the TRR data.

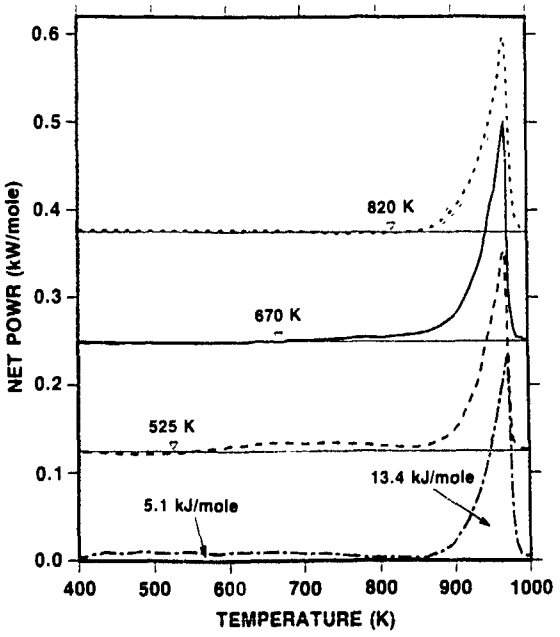

Fig. 3. DSC signals with base lines subtracted. The lower signal shows the as-implanted sample, the other three show samples that had been annealed in a furnace at 525, 670 and 820 K, respectively. The high-temperature part of the signal (crystallization) was fit to an exponential with an activation energy of 2.62 eV and was integrated to give an enthalpy of crystallization of 13.4 kJ/mol. From Donovan et al. [17].

The observation of the low-temperature release in a scanning experiment, such as that of fig. 3, depends sensitively on the stability of the base line. It was therefore useful to perform isothermal experiments, since the base line is always a simple horizontal line (constant). A monotonically decreasing exothermal signal was observed in all cases [17,18]. This unambiguously confirms the existence of a low-temperature heat release. The data were fit with an exponential decay with typical delay times of 100 s. The fact that the low-temperature heat release was not observed in the earlier experiments was probably due to the inherent difficulties in background subtraction; the DSC technique was improved in the later measurements.

The question remains as to the physical mechanisms of the low-temperature release. In recent years there has been much discussion of the physical changes observed during annealing of a-Si without crystallization. This relaxation process had been interpreted in terms of changes in average bond angle distortion [13,14]. Our experiments [18–20] have resolved some of these issues. It was postulated that relaxation is primarily defect annealing. This postulate was checked by introducing defects by ion bombardment into annealed or relaxed a-Si, the samples being annealed at 500°C. Equivalent doses were also introduced into c-Si. The annealing characteristics, determined by calorimetry, of bombardment damage in relaxed a-Si and in c-Si were compared directly. Fig. 4 shows the low-temperature DSC traces of (a) well-relaxed a-Si and (b) c-Si, after irradiation with He^+ ions for a range of ion fluences. The curves for ion doses resulting in less than 0.03 displacements per atom (dpa) did not differ significantly from the

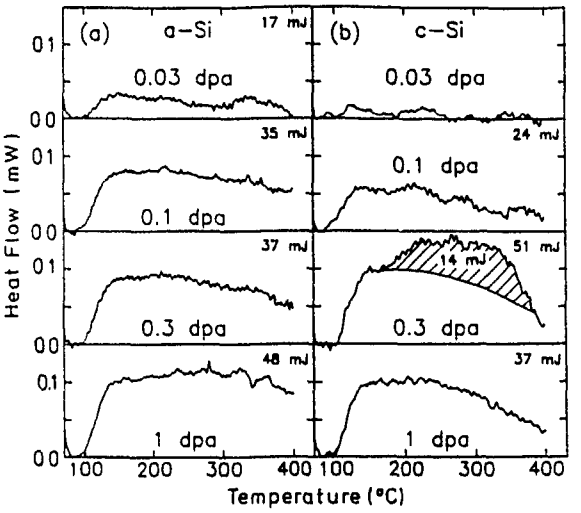

Fig. 4 Low-temperature DSC difference traces for (a) well-relaxed a-Si and (b) c-Si, after bombardment with keV He^+ ions The hatched area is discussed in the text. The values of the integrated heat release are shown From Roorda et al [18,20]

zero-signal base line and are not shown The curves for 0.03 to 1 dpa a-Si (fig. 4a) deviate clearly from the base line, and show a heat release similar to that observed when as-implanted a-Si is ramp heated for the first time [16,17]. Saturation occurs between 0.03 and 0.1 dpa. Thus, bombardment with He^+ ions yielding 0.03 (or more) dpa in well-relaxed a-Si results in "de-relaxation" of the a-Si, i.e., the a-Si returns to the unrelaxed state which cannot be distinguished from as-implanted a-Si.

For c-Si (Fig. 4b), the curve for 0.03 dpa is not significantly different from the base line but the curve for 0.1 dpa indicates a heat release which is qualitatively similar to the signal from a-Si. This sample contains damage which has been identified, on the basis of RBS and TEM results, as a distribution of point defects and small point-defect clusters After the DSC analysis to 400°C the damage has disappeared leaving a perfect crystal It is concluded, therefore, that the heat release for the 0.1 dpa c-Si is due to annihilation of point defects and small point-defect clusters only These point defects seem to anneal out continuously over a range of temperatures, as opposed to annealing kinetics dominated by only a few processes. Such annealing behavior implies a zoo of point defects in irradiated c-Si, with a large number of routes to annihilation. The area under the curve for 0.1 dpa c-Si corresponds to the total amount of heat released, this is 30% less than from 0.1 dpa a-Si. Combining the number of displaced atoms with the integrated heat release gives 0.56 eV per displaced atom. This may serve as an estimate of the stored energy per defect, but it is emphasized that the number of displaced atoms as determined by RBS is not necessarily equal to the number of point defects. For 1 dpa the signal from c-Si resembles that from a-Si, b with somewhat reduced magnitude. In fact, this is the dose where the sample has just been made amorphous and the DSC signal is due to relaxation of this as-implanted a-Si.

The curve for 0.3 dpa c-Si, which contains bands of extended defects and/or amorphous zones, differs from all other curves: a heat release can be seen which is larger than any other. Moreover, this curve is qualitatively different because above 180°C an extra heat release begins (hatched area), which can be understood in terms of recrystallization of amorphous zones at anomalously low temperatures. The assumption is made that the heat release from 0.3 dpa c-Si is a linear superposition of annihilation of point defects (i.e., 0.56 eV/displaced atom) and heat release from crystallization and relaxation of amorphous zones (0.12–0.16 eV/atom [16,17]). The contribution from point defect annihilation should have the same onset and form as that from 0.1 dpa c-Si. The hatched area corresponds, therefore, to heat release from amorphous zones. From the measured heat release, the hatched area in fig. 4 would then correspond to $(8.2–6.2) \times 10^{17}$ atoms/cm^2 and the remaining area to 4.6×10^{17} displaced atoms/cm^2, thus giving a total number of $(1.3–1.1) \times 10^{18}$ displaced atoms/cm^2. This number is in good agreement with the channeling estimate of 1.3×10^{18} cm^{-2}. It is remarkable that the onset of epitaxial recrystallization in the 0.3 dpa c-Si occurs at 180°C, but recrystallization of small amorphous zones at these low temperatures has been reported before [21] One possible reason for this phenomenon is that these small amorphous zones are embedded in a sea of defects which can enhance crystallization.

These collisional and defect ideas have been checked by bombarding relaxed a-Si with MeV C, Si and Ge ions [18,19] and examining the a-Si with Raman spectroscopy The transition from the relaxed to unrelaxed state occurs for ion doses on the order of 0.02 dpa irrespective of the mass of the projectile. Therefore it can be concluded that the phenomenon of de-relaxation by ion beams is due to the introduction of defects by nuclear collision. The similarity of the calorimetry data of fig 4 strongly supports the contention that the zoos of defects introduced into a- and c-Si by ion bombardment are similar. Moreover, their annihilation properties are very similar. These similarities seem to be confirmed by the following observation.

A rough estimate of the defect densities involved in structural relaxation can be made by comparing the stored energy per displaced atom in c-Si determined from fig. 4b (0.56 eV) with the integrated heat release from 0.03 and 0.1 dpa a-Si (fig. 4a). Under the assumption that the average heat release from one annihilation event in a-Si is equal to that in c-Si, this yields defect

densities of 3.5 and 7.3 at.% in 0.03 and 0.1 dpa a-Si, respectively. It must be kept in mind that this analysis relies on a RBS and channeling measurement of the number of displaced atoms in 0.1 dpa c-Si which is not necessarily equal to the number of defects. Nevertheless, the agreement of this estimate of the defect density in a-Si with the Monte Carlo calculations is striking.

4. Density and defects

The density of a solid can give important clues regarding defect density. Moreover, in light of the previous discussion, it is interesting to measure the density in both the relaxed and unrelaxed configuration. The density of a-Si relative to the crystal, for example, has been a source of much debate. Early X-ray diffraction data indicated an amorphous density as much as 10% below [22] that of the crystal, although this was attributed to the presence of voids in the vapor-deposited films. Brodsky et al. [23] interpreted Rutherford-backscattering measurements in combination with surface profilometry to conclude that a-Si could be up to 1% denser than c-Si, although the measured density of their electron-beam-deposited a-Si films was 3% less dense than c-Si. Direct density measurements using weighing and interferometry of a-Ge deposited at the highest possible temperature indicated a density 1% higher than c-Ge [24]. Computer models of the structure of a-Si, assuming a continuous random network (CRN) without point defects, predict that the amorphous phase should be 3.4% more dense than the crystal [25]. Attempts to estimate the density of a-Si using molecular dynamics simulations have lead to results on either side of c-Si [26]. Recent experimental results on thin implanted layers indicate an a-Si density between 1.7 and 2.3% less than the crystal [27].

The availability of the high-energy Si ion beams has made it possible to produce thick, well characterized amorphous layers whose density can be accurately measured [28,29]. Alternating stripes of a-Si (~ 300 μm) and c-Si (~ 100 μm) were produced by MeV Si ion implantation through a steel mask into ⟨100⟩ Si. The relative density was then determined by measuring the physical step height at the lateral a–c-Si boundary. The implants were performed at a series of energies from 0.5 to 8.0 MeV with irradiation conditions chosen to ensure complete amorphization to the surface. All irradiations, except one, were performed with samples heat-sunk with vacuum grease to a copper block held at liquid-nitrogen temperature. The measured temperature rise during similar irradiations was less than 20°C. A single sample was irradiated at room temperature, again heat-sunk to the block, to check for density variations caused by the implant conditions. A wider range of a-Si thicknesses was obtained by partially recrystallizing the layers at 500°C in a vacuum annealing furnace with a base pressure of ~ 10^{-7} Torr. In addition, a section of each sample was thermally relaxed by annealing for one hour at 500°C.

The areal densities (at/cm^2) of the a-Si layers were measured by RBS in the channeling configuration using 3 MeV ^{4}He. Areal density can be converted into a film thickness using the density of a-Si (~ 4.9×10^{22} at/cm^3). The maximum observable depth is limited by dechanneling in the a-Si to ~ 2.8 μm. The conversion of energy loss to areal density depends on the stopping powers for ^{4}He; however, two accepted sets of experimental measurements differ by up to 6% from each other [30,31]. Since this conversion represents a systematic error substantially larger than any other errors in the measurement, results are presented using both sets of stopping powers. Amorphous thicknesses between ~ 2.8 μm and 3.4 μm were estimated by measuring the thickness after partial solid-phase epitaxy. The resulting annealed thickness was extrapolated back to obtain the original as-implanted thickness using the measured epitaxial crystallization kinetics [3]. Surface profiles of the alternating a-Si and c-Si lines were obtained for each sample using a Tencor Instruments Alpha-step 200 surface profilometer calibrated with an NIST traceable standard. Typical scans are shown in fig. 5a for an as-implanted layer of 2.1 μm and for other thicknesses obtained by SPE from this implant set. Fig. 5b shows the corresponding RBS channeling spectra for these samples. Prior to determining the density difference, a small correction must be applied to the measured step heights to account for the Si implanted and sputtered [32] during amorphization. For example, at

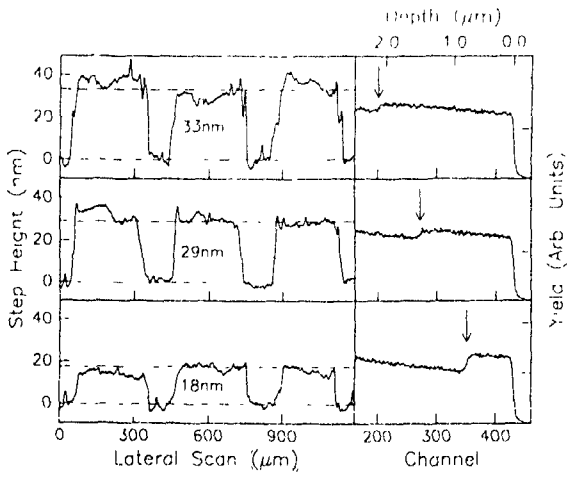

Fig. 5 (a) Surface profilometer traces of 2.1, 1.5 and 0.8 μm thick a-Si layers produced by 0.5–2.0 MeV series implants and epitaxial recrystallization. (b) Channeling spectra of samples shown in (a). The a-Si thicknesses are indicated. From Custer et al [29].

2.0 MeV the implanted material adds 1.0 nm while sputtering removes 0.15 nm, giving a net addition of 0.85 nm.

Converting the measured step heights into a density difference requires knowledge of how the volume change is accommodated. The volume increase from c-Si to a-Si can be accommodated in several ways; a-Si can be formed with built-in stress, the substrate can plastically deform, or the a-Si can plastically deform. Measurements on laterally continuous 1 μm a-Si layers demonstrate that the volume change is primarily accommodated by a vertical strain with the in-plane strain less than 1% of the total strain [33]. This indicates that a-Si deforms plastically during formation by ion implantation. In the constrained geometry of these experiments, plastic deformation of the a-Si occurs for implants below 5 MeV and the entire volume change is exhibited as a vertical expansion. Below 5 MeV, little deformation of the surrounding c-Si is observed. However, for the higher-energy implants, plastic deformation of the constraining c-Si can be readily observed

Step height data from samples implanted up to 5 MeV are shown in fig. 6 versus the areal densities of the a-Si layers As-implanted samples are shown by the open circles and partially recrystallized or relaxed samples by filled squares. Within the error bars, step heights

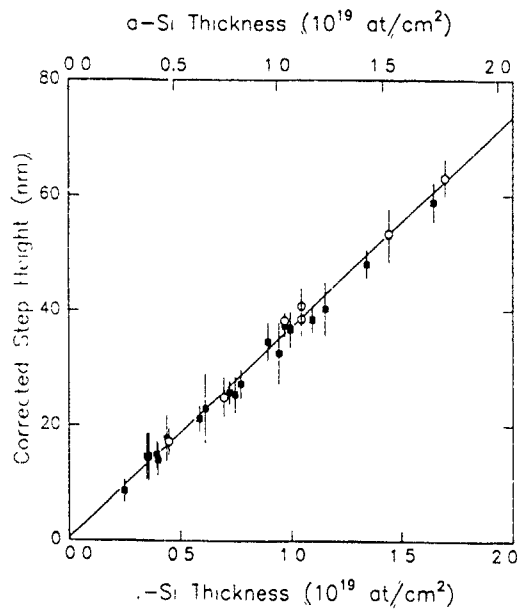

Fig. 6 Corrected step height vs a-Si areal density for as-implanted samples (open circles) and annealed samples (filled squares) of all implant series from 0.5 to 5.0 MeV. The areal density was obtained using the stopping powers of either Ziegler [30] (bottom axis) or Santry and Werner [31] (top axis). The solid line shows the step height expected for a 1.73% density difference (Santry and Werner values). From Custer et al. [29].

measured for the room temperature implanted sample were identical to those measured on samples implanted at liquid-nitrogen temperature. In addition, no differences in density could be detected between unrelaxed, relaxed or regrown samples, nor between samples implanted at any energy up to 5 MeV. Converting the areal density (using stopping powers of ref. [31]) to a-Si thickness and fitting a least-square line (with consideration for the individual error bars) through all the data yields a density difference of (1.74 ± 0.06)%. Fitting only as-implanted (unrelaxed) samples, the density difference is (1.79 ± 0.13)% while for annealed (i.e., relaxed) samples it is (1.70 ± 0.07)%. Considering the relative and absolute uncertainties in the stopping power measurements, an average value of (1.8 ± 0.1)% is the best estimate of the difference between the a-Si and c-Si densities. Very recent wafer-curvature experiments [34] have shown that the a-Si densifies by 0.15% on annealing to 500°C.

These measurements therefore raise several intriguing issues. First, the sign of the density difference is the opposite of that predicted by fully coordinated CRN models [25] This means that defects have to be introduced into the CRN to make a realistic model. Moreover, the density change on annealing is very small even though the relaxation or annealing process discussed in the previous section consists of the annihilation of large defect populations. These results should give important clues as to the fundamental nature of the defects.

5. Diffusion and defects

The study of diffusion mechanisms can be a critical probe of the atomic structure of a solid Little is known about diffusion in a-Si In our earlier studies [35,36] it was established that Cu, Ag and Au are fast diffusers in a-Si and moreover there was a remarkable correlation between diffusion in a- and c-Si. This correlation is shown in fig. 7 for Au [36]. Why there is such a correlation in absolute magnitude and activation energy is an intriguing puzzle. It can be generally stated [37] however, that the fast diffusers in c-Si, with interstitial components, are fast diffusers in a-Si and that the slow, substitutional, diffusers in c-Si exhibit similar behavior in a-Si. The solubility of fast diffusing species in a-Si was also found to be at least six orders of magnitude greater than their solubility in c-Si

Recent experiments by us [38,39] throw light on the diffusion mechanisms A systematic study [38] of impurities implanted in thick a-Si layers has revealed more diffusing species (Zn, Pd and Pt), as shown in fig. 8. It should be noted that Cu and Pd are pure interstitial diffusers in c-Si while the remaining species are hybrid diffusers, i.e., they diffuse interstitially but exchange with substitutional sites As was discussed in the previ-

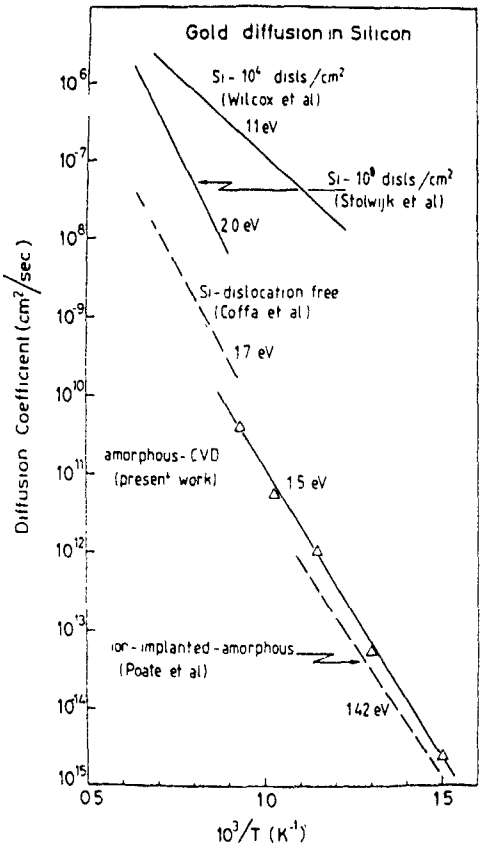

Fig 7 Diffusion coefficients vs temperature for Au implanted a-Si and ion-implanted a-Si For comparison the diffusion coefficients in dislocation-free single-crystal Si and dislocated Si are shown. From Calcagno et al [36]

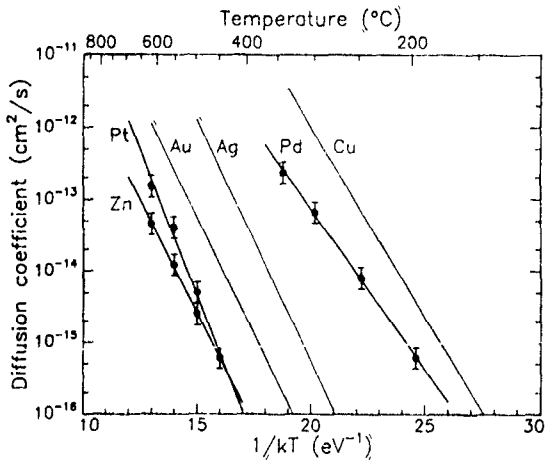

Fig. 8 Diffusion coefficients of implanted metallic impurities in a-Si. Diffusion was measured by RBS techniques in thick as-implanted a-Si. From Coffa et al. [38].

ous sections, a-Si contains a high density of defects whose population can be reduced by annealing. The effect of these defects on diffusion is dramatically demonstrated in the following experiment [39]. It is known that the fast diffusing impurities such as Cu can be trapped or gettered at defects in c-Si. Analogous behavior is shown here for Cu in a-Si.

Amorphous Si layers, 2.2 μm thick, were prepared in the as-implanted and also in the relaxed 500°C annealed state. The samples were then implanted with 200 keV Cu ions to a dose of 5.5×10^{15} ions/cm^2. The diffusion of Cu in all samples was then studied following thermal treatment at various temperatures ranging from 150 to 270°C, for times between 20 min and 104 h (the terminology "annealing" refers to heating of the a-Si at 500°C for 1 h and "thermal treatment" to the subsequent heating used to induce the Cu diffusion). The Cu concentration profiles were measured using 4 MeV $^4He^{2+}$ backscattering with a scattering angle of 125°. Fig. 9 shows Cu RBS spectra of the unannealed and annealed samples, before and after thermal treatment for 4 h at 221° C. As can be seen, the as-implanted Cu profile peaks at ~ 100 nm below the surface. The peak Cu concentration amounts to 0.7 at.%. After thermal treatment on the unannealed sample, significant

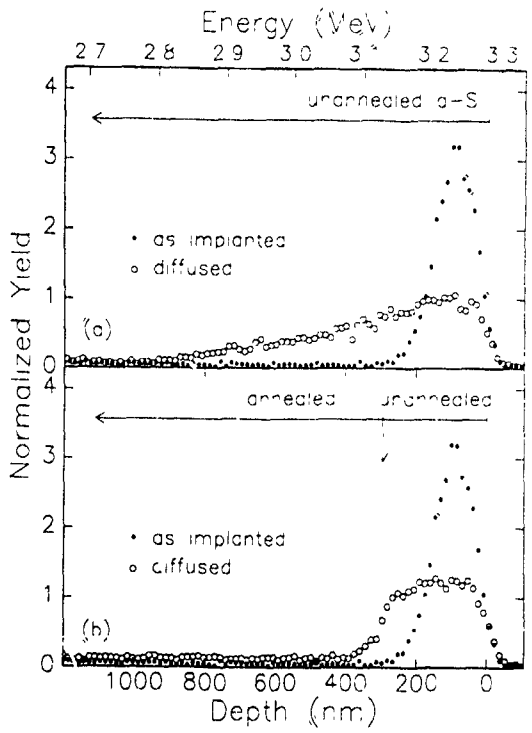

Fig 9 Backscattering spectra of two types of Cu implanted a-Si samples before and after thermal treatment at 221° C for 4 h (a) unannealed a-Si, (b) double-layer of annealed and unannealed a-Si From Polman et al [39].

in-diffusion of Cu is observed (fig. 9a) with diffusion distances in agreement with parameters previously measured [35].

An entirely different diffusion behavior is observed in the annealed sample (fig. 9b). A uniform Cu concentration is observed in an approximately 300 nm thick surface layer, and a low-concentration Cu tail is observed in the deeper-lying annealed layer. The interface between the two concentration regions coincides with the end of range of the Cu implant, which has returned the 300 nm thick surface region to the as-implanted, unannealed state. The diffused Cu concentration in the 300 nm surface layer in fig. 9b is higher than in the corresponding region in fig. 9a. This indicates that during diffusion, Cu is partially reflected at the interface between annealed and unannealed a-Si. Such behavior is characteristic for solute partitioning at a phase boundary. The ratio between the Cu levels in the two a-Si phases can then be interpreted as a partition coefficient (k), and amounts to $k = 9 \pm 1$ in this case A diffusion experiment has also been performed in a similar structure as in fig. 9b produced by half the Cu fluence, giving a value of $k = 10 \pm 2$. The discontinuity in the Cu profile is quite abrupt. This abruptness can be understood from the fact that at the end of range the damage (dpa) profile of the Cu implant is a rapidly decreasing function of depth, resulting in a sharp phase boundary between unannealed and annealed a-Si. The Cu tail in fig. 9b extends deeper than that in fig. 9a, indicating that the diffusion coefficient in annealed a-Si is higher than in unannealed a-Si.

Additional studies were performed to determine diffusion and partition coefficients over a wide temperature range Fig 10 shows a Cu concentration profile in the annealed/unannealed layer structure after thermal treatment at 170°C for 20.5 h. It also shows results of numerical calculations of the Cu profile taking into account total reflection at the surface and partitioning at the annealed/unannealed interface. The line represents a best fit, obtained using $k = 7$ and a ratio of 2 between the diffusion coefficients in annealed and unannealed a-Si. In additional experiments it was found that, within the error bars, the partition coefficient was not very sensitive to the diffusion time and temperature in the temperature range between 150 and 270°C, an average of $k = 8.2 \pm 1.3$ was obtained. Also, it was found that the partition coefficient is smaller for samples in which the a-Si is annealed at a lower temperature, i.e., more defects in the starting material.

Fig 11 summarizes the measured Cu diffusion coefficients in annealed a-Si in the temperature range 150–270°C in an Arrhenius fashion. The data from our earlier study on diffusion in unannealed a-Si are also shown [35]. These data are in agreement with coefficients found for the unannealed layer in the simulations described above. As can be seen, in the temperature

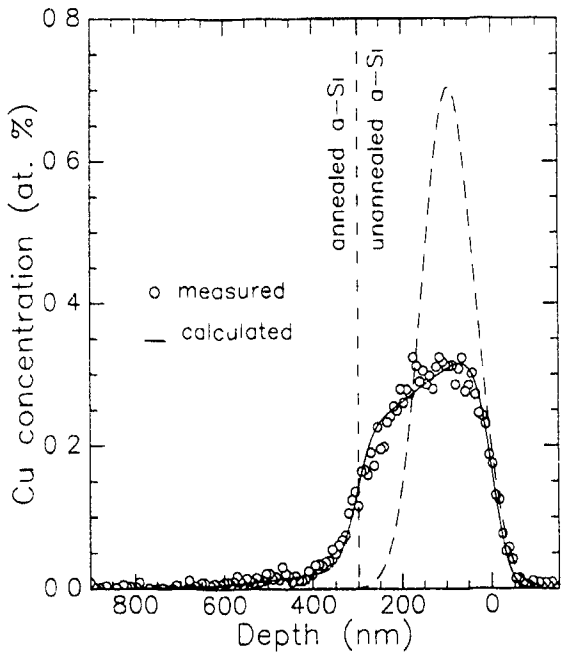

Fig 10 Cu concentration as a function of depth in an unannealed/annealed double-layer structure after thermal treatment at 170°C for 20.5 h (circles) The dotted line is the as-implanted profile, the drawn line is a fit using numerical simulation of diffusion and solute partitioning. From Polman et al [39].

range studied, the diffusion rate in annealed a-Si is a factor 2–5 higher than in unannealed a-Si. It should be pointed out that this behavior is opposite to that seen in the annealing of metallic glasses where the diffusivity decreases with annealing [40]. However, the defect annealing process in a-Si would appear to be quite different from that of a glass. The diffusion activation energy (E) in annealed a-Si is not significantly different than in unannealed a-Si ($E = 1.39 \pm 0.15$ eV vs $E = 1.25 \pm 0.04$ eV, respectively).

These Cu data show quite strikingly the role which defects can play in the a-Si structure. To first order, if it is assumed that Cu concentrations are correlated with defect concentrations, the data would imply that the defect concentration in the annealed material is one order of magnitude lower than that in the as-implanted, unannealed material. However, even in the annealed a-Si the Cu concentration is relatively high. The correlation of Cu concentration or solubility with defect concentration is plausible and leads to an interesting observation. The flat-topped Cu profile would indicate that the defects introduced by the Cu implantation are saturating over a distance of some 300 nm from the surface. Moreover, these defects influence the diffusion rate (fig. 11). Assuming that Cu is an interstitial diffuser in a-Si and is trapped at defect sites, then the diffusion

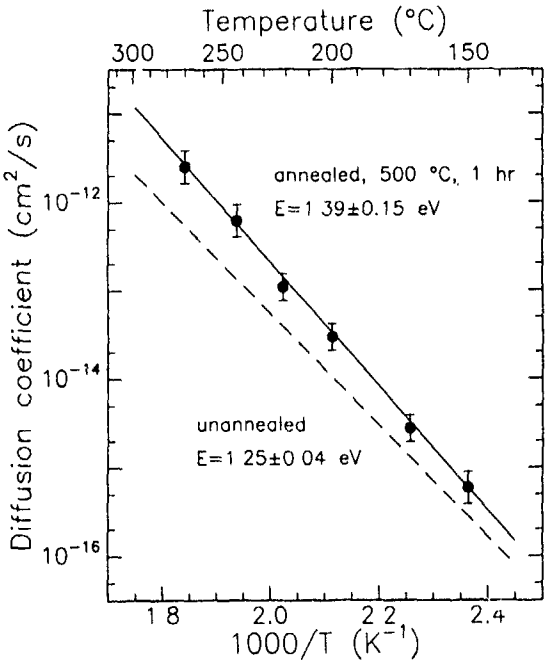

Fig 11 Cu diffusion coefficients in a-Si annealed at 500°C for 1 h (circles) The drawn line is an Arrhenius fit to the data Data from our earlier study [35] for unannealed a-Si are also indicated (dashed line) From Polman et al [39]

coefficient will increase for lower defect concentrations, as is observed. Experiments are in progress to correlate the diffusion of some of the other species shown in fig. 8 with defect concentrations.

6. Conclusions

The experiments described here have solved some old puzzles and raised more questions regarding a-Si. The role of defects is seen to be crucial. Relaxation has been identified as a defect annealing process but even in the well-relaxed state the defect population is high. The diffusion of impurities is strongly influenced by defects and the fast diffusers such as Cu are remarkably sensitive markers of these defects. One message that comes through strongly from these data is that many of the defect production, annealing processes, impurity diffusion and solubility phenomena in a-Si can be thought of in terms of c-Si with a high defect population. The atomistic nature of these defects, however, has not been identified.

References

[1] J.M. Poate, in: Amorphous Si and Related Materials, vols. A and B, ed. A Fritsche (World Scientific, New Jersey, 1989) p. 149.
[2] G.L. Olson and J.A. Roth, Mater. Sci. Rep. 3 (1988) 1
[3] J A. Roth, G.L. Olson, D C Jacobson and J M. Poate, Appl. Phys. Lett. 57 (1990) 1340
[4] A.G Revesz, J. Electrochem. Soc 126 (1979) 122
[5] D.E. Carlson and C W. Magee, Appl. Phys. Lett. 33 (1978) 82.
[6] P.G. LeComber, A. Madan and W E Spear, J Non-Cryst Solids 11 (1972) 219
[7] H.J. Stein and P.S Peercy, Appl Phys. Lett. 34 (1979) 604.
[8] F. Spaepen and D. Turnbull, in; Laser-Solid Interactions and Laser Processing, eds. S.D Ferris, H J. Leamy and J.M. Poate (AIP Press, New York, 1978) p 73.
[9] L Csepregi, R.P. Kullen, J.W. Mayer and T.W Sigmon, Solid State Commun. 21 (1977) 1019.
[10] S.T. Pantelides, Mater. Res. Soc. Symp. Proc 100 (1988) 387.
[11] E P. Donovan, F. Spaepen, D. Turnbull, J M Poate and D.C Jacobson, J Appl Phys. 57 (1985) 1795
[12] M O. Thompson, G J. Galvin, J W Mayer, P.S Peercy, J M. Poate, D.C. Jacobson, A G. Cullis and N.G Chew, Phys. Rev. Lett. 52 (1984) 2360, and unpublished data
[13] W.C Sinke, S. Roorda and F Saris, J. Mater Res 3 (1988) 1202.
[14] G K. Hubler, E.P Donovan, K.W. Wang and W.G. Spitzer, Proc. SPIE 350 (1985) 222
[15] E.P Donovan, G K. Hubler and C.N Wadell, Nucl Instr. and Meth. B19 (1987) 590
[16] S. Roorda, S Doorn, W.C Sinke, P M L O. Scholte and E. van Loenen, Phys Rev Lett. 62 (1989) 1880
[17] E.P Donovan, F. Spaepen, J.M. Poate and D C Jacobson, Appl Phys Lett 55 (1989) 1516, and unpublished data
[18] S. Roorda, Ph.D Thesis (University of Utrecht and FOM-Instituut, Amsterdam, 1990)
[19] S. Roorda, J.M. Poate, D.C Jacobson, S Dierker, B.S Dennis and W C Sinke, Appl Phys Lett 56 (1990) 2097
[20] S. Roorda, J M Poate, D.C Jacobson, D J Eaglesham, B D. Dennis, S Dierker, W C Sinke and F. Spaepen, Solid State Commun 75 (1990) 197
[21] M O Ruault, J Chaumont and H Bernas, Nucl Instr and Meth 209/210 (1983) 351.
[22] S.C. Moss and J.F Graczyk, Phys. Rev Lett 23 (1969) 1167.
[23] M.H. Brodsky, D. Kaplan and J F Ziegler, Appl Phys Lett 21 (1972) 305.
[24] T M. Donovan, E.J Ashley and W E. Spicer, Phys. Lett. 32A (1970) 85.
[25] F Wooten and D Weaire, Solid State Phys 40 (1987) 1.
[26] W.D. Luedtke and U. Landman, Phys. Rev. B40 (1989) 1164
[27] W G Spitzer, G.K Hubler and T.A Kennedy, Nucl Instr. and Meth 209/210 (1983) 309
[28] J.S. Custer, Ph D Thesis (Cornell University, Ithaca, NY, 1990).
[29] J.S. Custer, M.O. Thompson, D C Jacobson J.M Poate, S Roorda, W.C. Sinke and F. Spaepen, Appl. Phys Lett, in press
[30] J. F. Ziegler, He Stopping Powers and Ranges in all Elemental Matter (Pergamon, New York, 1978).
[31] D.C. Santry and R.D. Werner, Nucl. Instr and Meth. 159 (1979) 523.

[32] P. Sigmund, Phys Rev. 184 (1969) 383
[33] C.A. Volkert, Mater. Res Soc Symp. Proc. 157 (1990) 635
[34] C A Volkert, unpublished data.
[35] J.M Poate, D.C. Jacobson, J.S Williams, E.G. Ellman and D.O. Boerma, Nucl. Instr. and Meth. B19/20 (1987) 480.
[36] L. Calcagno, S U. Campisano and S Coffa, J. Appl. Phys. 66 (1989) 1874.
[37] J M. Poate, D.C Jacobson, F Priolo and M O. Thompson, Mater Res. Soc. Symp. Proc. 128 (1989) 533
[38] S Coffa, D.C Jacboson, J.M Poate, W. Frank and W. Gustin, to be published.
[39] A Polman, S. Coffa, D.C Jacobson, J.M. Poate, S. Roorda and W Sinke, Appl Phys Lett 57 (1990) 1230.
[40] H.S. Chen, L.C. Kimerling, J.M. Poate and W.L. Brown, Appl Phys Lett 32 (1978) 461

Nuclear Instruments and Methods in Physics Research B55 (1991) 544–549
North-Holland

Recent progress in depositing epitaxial metal films by an ionized cluster beam *

Isao Yamada

Ion Beam Engineering Experimental Laboratory, Kyoto University, Sakyo, Kyoto 606, Japan

Epitaxial Al films have been deposited by ICB equipment on room temperature Si substrates. The equipment available for forming Al epitaxial and single crystal films has been discussed Epitaxial Al films can also be deposited on various semiconductor and insulator substrates such as Ge, GaAs, CaF_2 and sapphire at room temperature. Application of epitaxial Al film to VLSI has been proposed Deposited Al films are thermally and electrically stable. The prospect of VLSI application of epitaxial Al films is shown

1. Introduction

Future semiconductor devices will require a process technology capable of providing high quality semiconductor, dielectrics and metals. Silicon growth has already been established and near-perfect crystals can be provided Combined with ion implantation technology, the semiconductor substrate could be well tailored to achieve superior device and circuit performance [1]. Ion implantation technology has been successfully applied to the semiconductor material processing. On the other hand, little attention has been paid to metal film deposition processes by which the crystalline state of the depositing films on the semiconductor or dielectric substrate can be controlled.

Metal films play important roles in the performance of a VLSI circuit [2]. Gate, contact and via fill metallization applications bring various requirements on film quality and the deposition methods. These films can be deposited using various deposition techniques such as physical, or chemical vapor deposition. Among those deposition techniques, the ICB deposition technique, which is one of the low energy ion assisted deposition techniques, was found to provide a better control of the crystalline state of the deposited metal films. The basic mechanism of cluster formation is described elsewhere [3]. It is suggested that typical clusters may be quite large, containing 500–1000 loosely bound atoms. However the size and size distribution of metals have not been studied in this paper.

In 1984, we have demonstrated that epitaxial Al films could be grown by ICB on room temperature Si substrates in spite of the large lattice misfit of 25% [4]. A remarkable feature concerning these results is that the interface between Si and Al is very sharp and has no transition layer. The film surface is very smooth. The atomic resolution cross-sectional micrograph indicated that the Al layer, having its inherent lattice constant, grows directly on the Si substrate surface without distortion of the atomic arrangement at the interface [5]. These films have high thermal stability [6], are resistant to electromigration, and provide good step coverage [7]. The metallization is one of the most important factors in VLSI technology, which determines the device performance and gives the limiting factor of the device density. The ICB deposition technique for epitaxial film formation could be valuable to extend device density of VLSI

Several reports on the epitaxial growth of Al films have recently been published. By electron beam evaporation in a UHV chamber, epitaxial growth of Al on Si(111), (100) and (110) substrates at 300 °C depositions have been observed [8]. High oriented Al films were observed on Si(511), (411) and (311) substrates. The film surface on Si(111) has a highly reflective appearance, even though many sharp protrusions existed on the surface In other Si substrate cases of (100), (110), (511), (411) and (311), Al surfaces showed a rough and milky appearance, and many islands with a different morphology could be observed. The paper also reports that Si diffusion into growing Al film from the interface was studied by SIMS analysis A CVD method names as gas-temperature-controlled CVD has been proposed [9]. Tri-isobutyle aluminum (TIBA) is heated to 230 °C and introduced into the reaction chamber with Ar. The deposition was made on 400 °C Si substrates. Epitaxial relations obtained on different substrate orientations are as follows; Al(100)/Si(100), Al(100)/Si(111), Al(111)/Si(111) and Al(110)/Si(511).

* Invited paper.

0168-583X/91/$03.50 © 1991 – Elsevier Science Publishers B.V. (North-Holland)

Al epitaxial deposition was also reported by the bias-sputtering method [10]. In this case, epitaxial relations of Al(111)/Si(111) and Al(111)/Si(100) have been reported.

This paper is a survey of the results of epitaxial deposition of metal films on room temperature substrates by ICB techniques. The survey includes development of ICB equipment, study of the film formation processes and the consequent film characteristics. A prospect of epitaxial metal films for VLSI applications is also discussed.

2. Equipment development

Several ICB systems are commercially available. Fig. 1 shows a typical UHV type ICB system. The chamber is fitted with three or four ICB sources depending on the film composites. The systems are generally equipped with a substrate holder, a substrate heater, a beam shutter, substrate temperature thermocouples, and a film thickness monitor. Options include a substrate rotator, a vacuum load lock unit, and a reactive gas controller. The pumping package can be based on a sorption pump, a turbo pump, a cryo pump and an ion sputter pump.

Among active developments of ICB equipment in Japan, an important project is being undertaken. This is a large scale research of AMMTRA (Advanced Material-Processing and Machining Technology Research Association) which is built under the Agency Technology of the Ministry of International Trade and Industry (MITI). The project includes the development of an ICB apparatus system with a high deposition rate and a large substrate size deposition. The goal of the deposition rate is 1 μm/min for the Al deposition. Special effort has been made in order to create an extremely uniform ion beam density distribution at the substrate surface by using conical multi-nozzles.

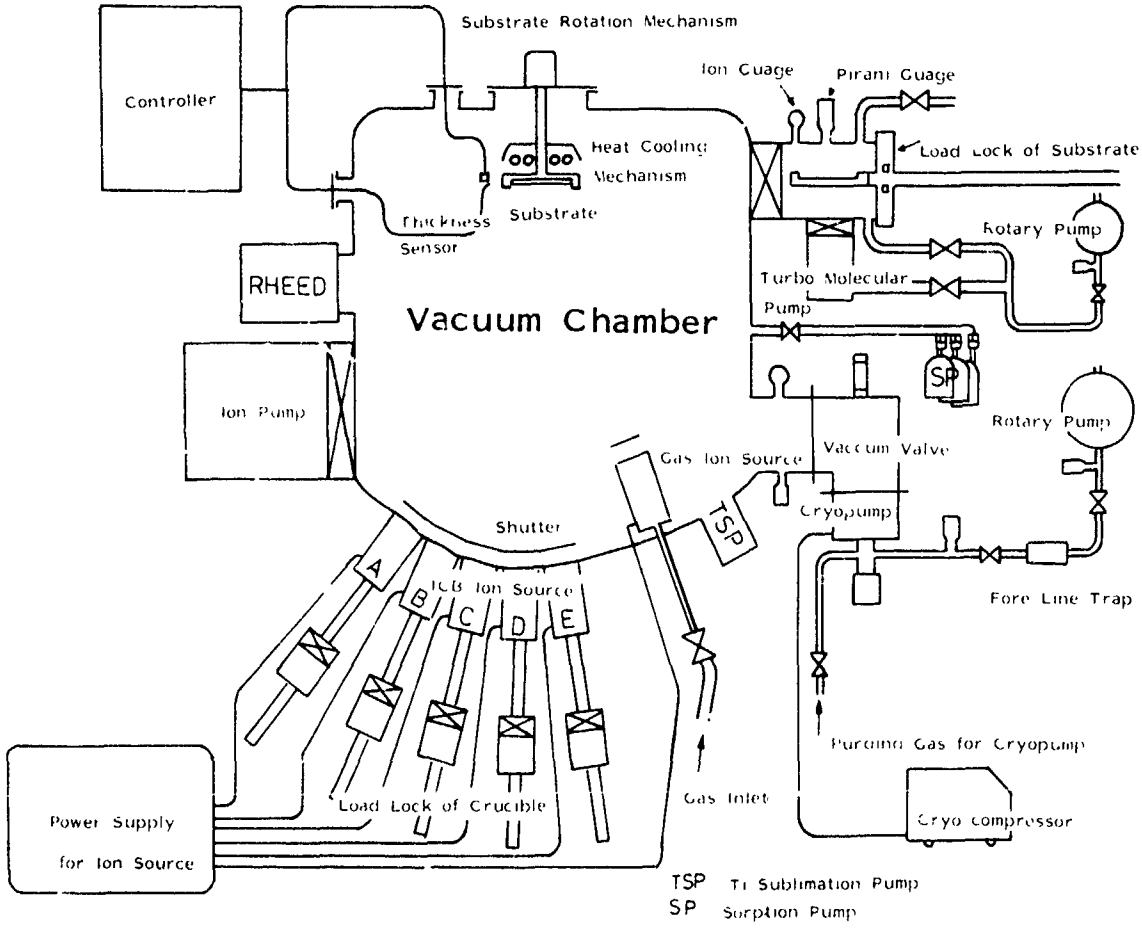

Fig. 1. Schematic layout of the UHV type ICB equipment

3. Film formation characteristics

Two important effects of ion bombardment on the film formation processes at the initial stage of the deposition have been experimentally observed [11]. These are the enhancement of nucleation site formation and the adatom migration. A small amount of silver was deposited on amorphous carbon films and was observed by TEM. The ion bombardment increases the density of the nucleation sites. TEM images of the deposits showed small islands dispersed uniformly over the substrate. The maximum island concentration tends to occur at a smaller incident quantity at higher acceleration voltages. Fig. 2 shows the island concentration as a function of incident quantity of silver for different deposition conditions. These results suggest that the ion bombardment can influence the formation of uniform nucleation sites and the enhancement of the coalescence process

The migration of Al atoms on Si[12] and on SiO_2[13] surfaces has been studied. Al was deposited on Si(111) substrates through a stainless steel mask slit, 50 μm wide and 100 μm long at the substrate temperature range of RT–400 °C. The size and the shape of islands are different at different distance from the mask edge Diffusion distances as large as 13 to 17 μm were obtained even at the substrate temperature of 50 °C. Fig 3 shows the result of the diffusion distance measurement on SiO_2 substrates It is seen that the diffusion distance of Al increases as the acceleration voltage increases at low substrate temperatures. This tendency continued to 200 °C, but the order was reversed at 400 °C. The measurement on a Si substrate indicated a similar tendency. It is likely that this reversal was caused by an increased re-evaporation rate at the high acceleration voltage and temperature

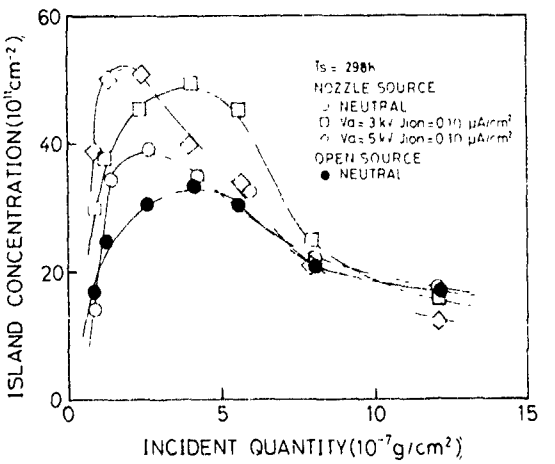

Fig 2 Island concentration change as a function of deposits for different deposition conditions.

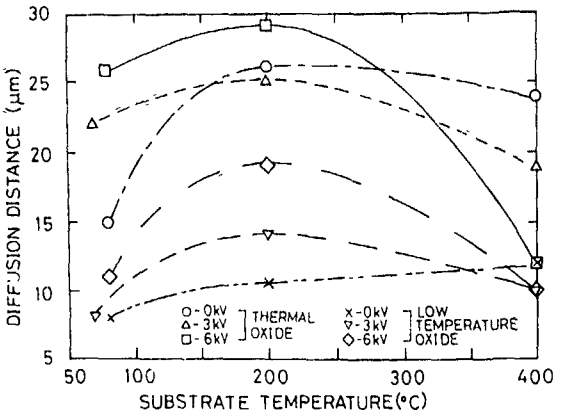

Fig. 3 Surface diffusion distance of Al on two kinds of SiO_2 substrate as a function of ion acceleration voltage and surface temperatures

Metal film on semiconductor or insulator substrates grows usually three-dimensionally (Volmer–Weber growth type) by conventional vacuum deposition. In the case of ICB, AES and SEM studies have shown that there is a transition from three-dimensional growth to two-dimensional growth at high acceleration voltages [14]. Due to the difference in escape depth of these Auger electrons, measurement of the signal ratio can tell whether the growth morphology is three-dimensional or two-dimensional at the initial stage of the deposition Fig. 4 shows the ratio of peak-to-peak intensities of the Auger signals corresponding to Al_{KLI} (1396 eV) and Al_{LVV} (68 eV) transitions as a function of

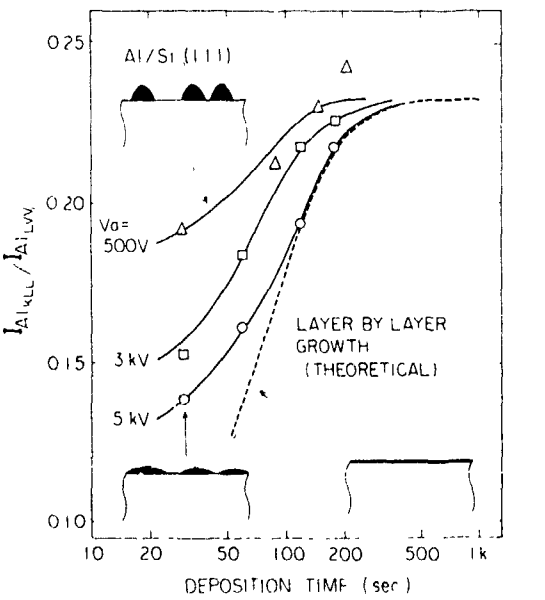

Fig 4. Ratio of Al_{KLI} to Al_{LVV} Auger signal peak intensity shown as a function of deposition time

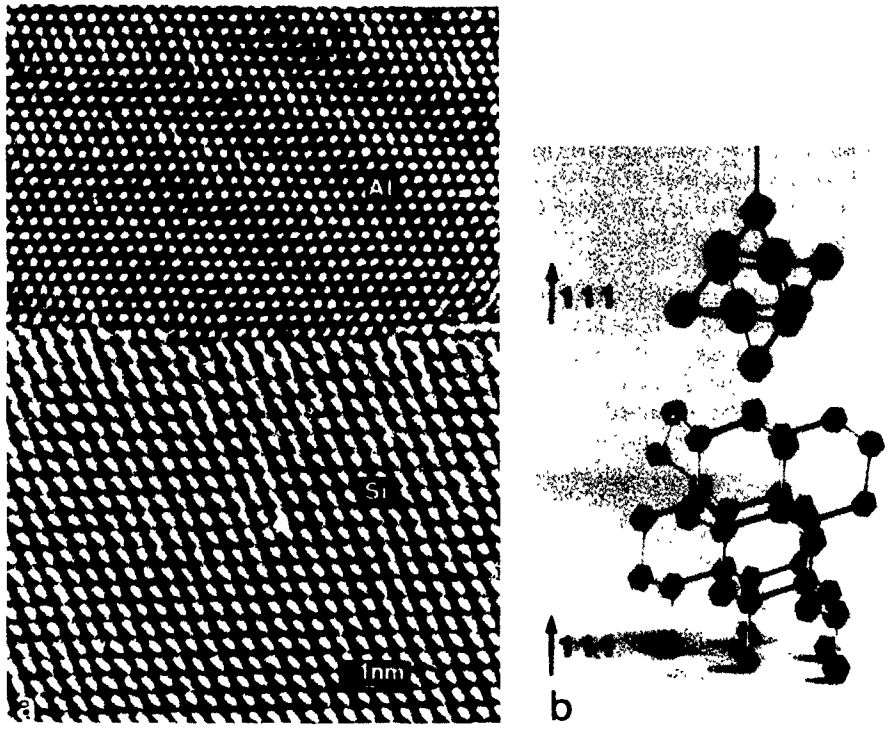

Fig 5 (a) TEM micrograph of an epitaxial grown Al film on a Si substrate The micrograph shows that the single crystal Al (fcc) film is grown on Si(111) substrate at room temperature (b) Model of the atomic arrangement of Al(111) on Si(111), showing that the fcc structure of Al cannot match to the diamond structure of Si

deposition time for Al films grown on room temperature Si substrates at different acceleration voltages The figure shows that the growth process approaches to the layer-by-layer growth (Frank–van der Merwe growth type) by increasing the acceleration voltage

Above-mentioned ion bombardment effects could be effective for the epitaxial growth of metal films on semiconductor substrates in spite of the large lattice misfit of 25% [4]. Fig 5 shows a TEM micrograph at the interface of Si substrate and the grown film The micrograph shows the realization of the epitaxial growth of an Al film on a Si substrate. The number of lattice defects at the interface seems to be very small· because appreciable change of the Schottky barrier height as a function of the annealing temperature up to 550°C could not be seen [15]. A model of atomic arrangement of Al(111) on Si(111) is also shown in the figure. The model shows that the fcc structure of Al cannot match

Table 1
Lattice constant (a), crystal structure, and lattice misfit (δ) for Al films (fcc, $a = 4.049$ Å) on various substrates The type of matching to accommodate the lattice misfit, and the resulting lattice misfit (Δ) for this match are also indicated for the specific substrate plane

Substrate	a [Å]	Structure	δ with Al [%]	Plane	Matching	Δ [%]
Si	5.428	diamond	−25 4	(111)	3·4 match	−0.5
				(100)	$d_{Al(001)}$ to $d_{Si(011)}$	5.5
CaF_2	5.463	flourite	−25 9	(111)	3.4 match	−1 2
				(100)		
Ge	5.658	diamond	−28 4	(111)	5.7 match	0 2
				(100)	$d_{Al(010)}$ to $d_{Ge(011)}$	1 2
GaAs	5 653	zincblende	−28 4	(100)	$d_{Al(010)}$ to $d_{GaAs(011)}$	1 3
Sapphire	4 759	hexagonal	−14 9	(0001)	Al to Al match	4 0

to the diamond structure of Si. Epitaxial deposition of Al films on Si(100) has also been made. The film consists of the bicrystal, Al(110) and Al(110)R which is rotated 90° to Al(110). A great number of detailed studies have been made to analyze the crystalline structure and the interface by in situ electron diffraction [4], RBS [15], normal TEM [16], and atomic resolution TEM [5]. A remarkable feature concerning these results is that the interface between Si and Al is very sharp and has no transition layer. The atomic resolution cross-sectional micrograph indicated that the Al layer having its inherent lattice constant grows directly on the Si substrate surface without distortion of the atomic arrangement at the interface. No damage caused by ICB bombardment is seen at the interface. Epitaxial Al films can also be grown on CaF_2, Ge, GaAs and sapphire substrates [6]. Table 1 summarizes these results. In any case, the explicit lattice misfit is extremely large for simple epitaxy. Our study has shown, however, that epitaxial metal films can be grown even for these combinations by forming atomic coincidences either by a superlattice or by a suitable crystal plane. In some cases, complicated island growth whose crystal orientation is quite different from that of the final film is found.

4. Prospective applications of epitaxial metal films to VLSI

The progress of VLSI has been achieved by a reduction in lithographic dimensions coupled with a corresponding decrease in vertical dimensions. The ion implantation technology is contributing to further achieving the shallow junction. This development has placed severe demands upon semiconductor metallization Aluminum metallization has been widely used for contact electrodes and interconnects However, many problems associated with the electromigration lifetime, the contact stability, the corrosion resistance, and the multilevel capability have arisen according to the reduction of the device size.

The use of single crystal or epitaxial aluminum films has been proposed in order to break the integration threshold of VLSI circuits. Fig. 6 shows the comparison between characteristic features of epitaxial single crystal film and polycrystal films. The illustration shows that the epitaxial film could be stable to the heat cycle and the corrosion which might occur by the residuals of some chemical after etching through the grain boundary Problems related to the electromigration and stress migration could be eliminated because those problems are related to the characteristics of the grain boundary. Several unique characteristics of single or epitaxial cycle Al films are summarized [6].

Interdiffusion – It is commonly recognized that in the integrated circuits structure, the diffusion of Si in pure Al films is enhanced by the polycrystalline nature and imperfections of the Al film. For an annealing time of 30 min and temperatures of 550 °C, the diffusion length for Si in thin Al film is reported to be 83 μm ($D = 3.5 \times 10^{-8}$ cm^2/s) [17]. The Si solubility at 500 °C is about 0.9%. The Auger analyzer could have a detection limit of 0.1% of Al in Si. However, in both epitaxial Al films deposited on Si(111) and Si(100) substrates, detectable amounts of Si could not be seen after the annealing at 500 °C. Though the Al film on Si(100) is an epitaxial film with two microcrystals, the results were similar with that of single-crystal Al on the Si(111) substrate.

Morphology – Changes in the morphology of the surface and the interface after annealing at 550 °C for 30 min were examined by SEM. No annealing hillocks or valleys can be seen on the surface of the epitaxial Al film. At the interface of the sample prepared by conventional vacuum deposition, there are many deep pits and undu-

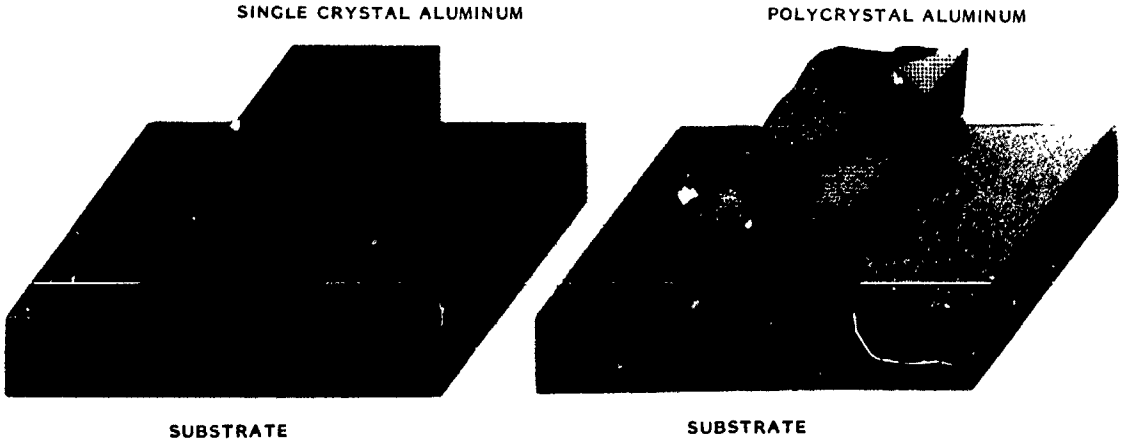

Fig. 6 Illustration of (left) an epitaxial single crystalline Al film on Si substrate and (right) polycrystal films on Si substrate

lations caused by so-called alloy penetration, while no irregularity can be seen at the interface of the ICB deposited sample.

Contact – In conventional metallization techniques, recrystallization of Si that has been dissolved in Al causes such problems as an increase in contact resistance on n-Si and an increase of the barrier height of Al/n-Si junctions. Schottky contact characteristics were studied for the epitaxial Al films. Al/n-Si (0.7 Ω cm) junctions of 1 mm diameter were fabricated and the current density–voltage (J–V) characteristics were measured before and after annealing at 450, 500, and 550 °C. The barrier height and the n value are around 0.73 eV and 1.17, respectively. Changes in the barrier height and the n value are 0.03 eV and 0.02, respectively, while in the case of the Al–Si junction fabricated by conventional deposition techniques, changes of more than 0.1 eV and 0.1, respectively, have been reported [15]. It is thought that the dissolution and/or the recrystallization of Si are suppressed in the epitaxial Al films.

Electromigration – The electromigration of an epitaxial Al(111) film on Si(111) has been tested. A 400 nm thick film was chemically etched to 10 μm wide, 1000 μm long strips. When they were applied with a current of 10^6 A/cm^2 at 250 °C, there was no change in resistance even after 400 h of operation, as opposed to sputtered Al films, which normally fail at 10^6 A/cm^2 after 20 h [7]. The electrical resistivity of 2.7 μΩ cm for the 400 nm thick film is comparable to the bulk value.

5. Conclusions

Characteristics of Al epitaxial film have been discussed in terms of the application to VLSI metallization. The film surface is atomically flat and the interface is also flat. No ion bombardment damage could be seen near the interface in the Si substrate. The films can be deposited stably by the UHV type system. However, there are still many unanswered questions regarding the fundamental phenomena underlying the ICB technique. Our effort will be continued to make the technology clear.

References

[1] Y. Akasaka, Nucl Instr. and Meth B37/38 (1989) 9
[2] D.M. Brown, M Ghezzo and J M Pimbley, Proc. IEEE 74 (1986) 1678
[3] I. Yamada, H. Usui and T. Takagi, J. Phys Chem 91 (1987) 2463.
[4] I. Yamada, H Inokawa and T. Takagi, J. Appl. Phys 56 (1984) 2746.
[5] I. Yamada, H. Usui, S. Tanaka, U Dahmen and K.H. Westmacott, J. Vac. Sci. Technol. A8 (1990) 1143
[6] I. Yamada and T Takagi, IEEE Trans Electron Devices ED-34 (1987) 1018.
[7] I Yamada, H Usui and R.E. Hummel, Proc 1st Int Symp on Advanced Materials for ULSI, vol 88-19 (Electrochemical Soc., Pennington, NJ, 1988) p. 217.
[8] K. Aizawa, H Okabayashi and A Tanikawa, Symposium Record on Semiconductor and Integrated Circuits Technology, Vol 37 (1989) 85, in Japanese
[9] T Kobayashi, A Sekiguchi, N Hosokawa and T Asamaki, Mater. Res. Soc. Symp Proc 131 (1989) 363.
[10] T Ohmi, H Kuwabata, T Shibata, N Kowata and K Sugiyama, Proc. 5th Int. VLSI Multilevel Interconnection Conf., Santa Clara (Institute of Electrical and Electronics Engineers, New York, 1988) p 446
[11] I. Yamada, Appl Surf. Sci 43 (1989) 31
[12] L L Levenson, M Asano, T Tanaka, H Usui, I Yamada and T Takagi, J Vac. Sci Technol A6 (1988) 1552
[13] L L Levenson, A B. Swartzlander, A Yahashi, H Usui and I. Yamada, J Vac. Sci Technol A8 (1990) 1147
[14] I. Yamada, Mater Res Soc. Symp Proc 128 (1989) 113
[15] I Yamada, C J Palmstrøm, E. Kenneky, J W Mayer, H Inokawa and T Takagi, Mater Res. Soc Symp. Proc 37 (1985) 401.
[16] I Yamada, Nucl. Instr and Meth B37/38 (1989) 770
[17] T.M Reith and J D Schick, Appl. Phys Lett 25 (1974) 524

Nuclear Instruments and Methods in Physics Research B55 (1991) 550–554
North-Holland

BF_2^+ implantation in predamaged Si with Ge^+ or Si^+ at doses lower than amorphization

Masataka Kase, Mami Kimura, Yoshio Kikuchi, Haruhisa Mori and Tsutomu Ogawa
Electronics Devices Group, Fujitsu Limited, 1015 Kamikodanaka, Nakahara, Kawasaki 211, Japan

The B diffusion dependence on the preimplantation energy and dose of Ge^+ or Si^+ was studied Boron-enhanced diffusion is reduced by moderate lattice disorder below amorphization The residual damage was examined by cross-sectional transmission electron microscopy, which indicated that amorphization causes the formation of extended defects A gate-controlled diode was designed and fabricated for the evaluation of preimplanted layer The dependence of the leakage current on the preimplantation dose indicates that no serious defects are caused by Ge^+ implantation at 40 keV and 5×10^{13} cm^{-2} or Si^+ at 40 keV and 2×10^{14} cm^{-2}

1. Introduction

Ultralarge-scale integration (ULSI) fabrication processes require p^+n junctions shallower than 100 nm with good uniformity and repeatability. Ion implantation has been used in fabricating doped layers due to its controllability, but implanted B^+ has a longer projected range and a higher diffusivity than As or Sb. Even if BF_2^+ implantation is used, it is impossible to make p^+n junctions shallower than 100 nm because of the channeling tail. A preamorphization technique involving the amorphization by Si^+ or Ge^+ implantation prior to B^+ or BF_2^+ implantation [1,2] has been quite successful in eliminating the channeling tail [3–5].

There are two problems with this technique. One is an anomalously rapid diffusion of boron in the initial stage of rapid thermal processes [3] and low-temperature processes [4]. This problem originates from the presence of abundant self-interstitials and vacancies generated by preamorphization and annealing. The other problem concerns with the formation of defects induced by preamorphization. These cannot be removed by high-temperature annealing [5] Many researchers have investigated the influence of the amorphization on the impurity diffusion and on the residual damage.

The conditions of preimplantation, prior to donor or acceptor ion implantation, must be optimized to eliminate both the channeling tail and the previously mentioned phenomena. We reported [6] that the doses for eliminating the channeling tail are 25% of the doses for full amorphization. RBS analysis indicates that the layers preimplanted with the optimum dose contain 60% of silicon on irregular sites.

In this paper, we describe the B diffusion at various preimplantation conditions including moderate lattice disorder below amorphization. We evaluate the residual defects using a cross-sectional transmission electron microscope (XTEM) and gate-controlled diodes with lightly doped layers [7].

2. Experiments

Czochralski-grown ⟨100⟩-oriented n-type silicon wafers with a resistivity of 10 Ω cm were implanted with Ge^+ or Si^+. Implantation was done with a current density below a few μA/cm^2 to avoid beam heating annealing. Then BF_2^+ was implanted at 10 keV with 3×10^{13} cm^{-2} and the samples were annealed in nitrogen at 800°C for 30 min. We studied the B profiles with a secondary ion mass spectroscope (SIMS), the lattice disorder with a grazing exit Rutherford backscattering spectroscope (RBS) and the residual damages with an XTEM

Gate-controlled diodes were fabricated on a Czochralski-grown ⟨100⟩-oriented n-type silicon wafer with a resistivity of 1 Ω cm. The round diode was ringed by n-poly silicon gate having 1200 μm inner diameter. Ge^+ or Si^+ was implanted at 40 keV with several doses through a thermally-grown 10 nm screening oxide. For the p^+ layer, B^+ was implanted at 10 keV with 3×10^{13} cm^{-2}. The samples were annealed at 800°C for 10 min in nitrogen. Contact areas were opened and the aluminium electrodes were fabricated. The leakage current was measured with an HP4145A semiconductor parameter analyzer.

When the Si surface under the gate is accumulated by the controlled gate bias, the leakage current is mainly due to the bulk generation current corresponding to the amount of the generation–recombination (G–R) centers in the depletion region [7]. We can evaluate the damage induced by preimplantation quantitatively because the

0168-583X/91/$03 50 © 1991 – Elsevier Science Publishers B.V. (North-Holland)

depletion layer extends into the preimplanted layer due to the low B concentration.

3. Results and discussions

3.1. Boron diffusion dependence on the preimplantation energy

Fig. 1 shows the B profile dependence on preimplantation energy. BF_2^+ was implanted at 10 keV with a dose of 3×10^{13} cm^{-2}, with Ge^+ preimplantation at 40 or 130 keV with a dose of 2×10^{14} cm^{-2}. The solid line is the as-implanted B profile in either 40 or 130 keV Ge^+ preimplants to prevent the channeling tail. The dashed lines are B profiles after annealing at 800 °C for 30 min. Transient enhanced diffusion is observed in the 40 keV preimplanted sample (short dashed line), originating from self-interstitial diffusion. In the 130 keV preimplanted sample, the B diffusion is retarded in the vacancy-rich region caused by the amorphous/crystalline (A/C) interface defects [3].

3.2 Boron diffusion dependence on the preimplantation dose

We studied the boron profile dependence on the preimplantation dose, focusing on the transition region from the crystalline to the amorphous. BF_2^+ was implanted at 10 keV with a dose of 3×10^{13} cm^{-2} in wafers preimplanted with Si^+ at 40 keV and at doses of 2.3×10^{14}, 3.0×10^{14}, 3.3×10^{14}, or 4.0×10^{14} cm^{-2}. Si^+ preimplantation with a dose of 4×10^{14} cm^{-2} was found to prevent the channeling tail [6]. The RBS analysis shows that the Si^+ preimplanted layers contain displaced lattice site silicon atoms whose amounts increase with the dose as indicated by the χ values shown in table 1. Fig. 2 shows the 800 °C 30 min annealed B profiles dependent on the preimplantation dose. As-implanted B profiles have the same profile (the solid line). In the 2.3×10^{14} cm^{-2} preimplanted sample (line 1), B diffusion is very fast. When the preimplantation dose increases slightly, that is, the Si lattice is disordered moderately, the mobility of B decreases (lines 2 and 3). If the fraction of irregular site silicon atoms increases to near 100%, the B diffusion is retarded similar to the behavior in the presence of an amorphous layer (line 4) [3].

Table 1
Dependence of the concentration of irregular site silicon atoms, χ_{max} (%), on Si^+ preimplantation dose

Si^+ dose [cm^{-2}]	χ_{max} [%]
2.3×10^{14}	20– 25
3.0×10^{14}	30– 40
3.3×10^{14}	30– 50
4.0×10^{14}	40–100

The rapid diffusion of B was induced by the preimplantation with a lower dose than amorphization. In amorphized samples, a vacancy-rich region is generated at the original amorphous region, and an interstitial-rich region is formed below the original A/C interface. When the B extends to the interstitial-rich region, the diffusion is very fast [3]. In samples preimplanted with a lower dose than amorphization, an interstitial-rich region is generated in the preimplanted region, similar to the region below the A/C interface in the amorphized sample. This mechanism has not yet been experimentally verified.

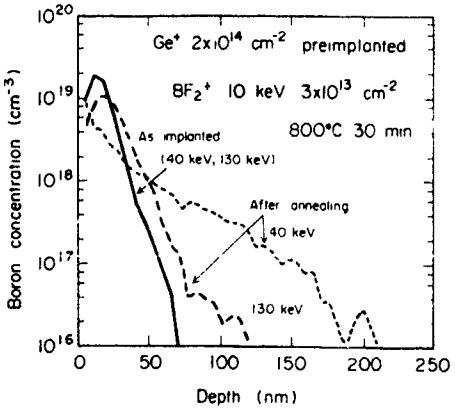

Fig. 1. SIMS boron profiles of samples implanted with 3×10^{13} cm^{-2} BF_2^+ at 10 keV in Ge^+ preamorphized silicon before and after annealing at 800 °C for 30 min.

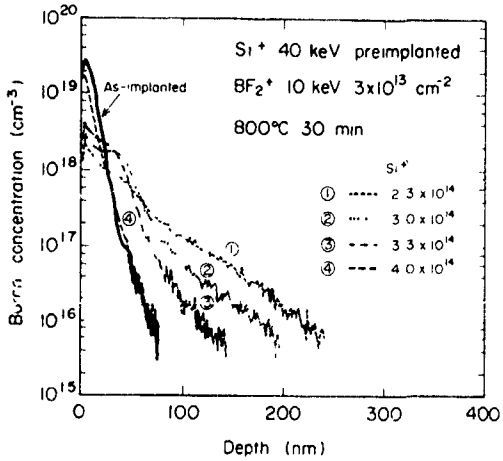

Fig. 2. SIMS boron profiles of samples implanted with 3×10^{13} cm^{-2} BF_2^+ at 10 keV in Si^+ preimplanted silicon before and after annealing at 800 °C for 30 min.

3 3 XTEM analysis of the residual defects

Fig. 3 shows XTEM micrographs of the gate edge implanted with Ge^+ at 130 keV and at a dose of 2×10^{14} cm^{-2}. Fig. 3a shows that crystalline regions remain at the surface while a 80-nm-thick amorphous layer is formed. After annealing at 800 °C for 30 min, defects like grain boundaries are observed at a depth of 60 nm and below the gate edge. The grain-boundary-like defect at a depth of 60 nm originates from the encounter of the upward solid phase epitaxy (SPE), and downward SPE from the surface crystalline islands. The gate edge one originates from the encounter of upward and lateral SPE. To prevent the defect at a depth of 60 nm, high-dose or multiple implantation might completely eliminate surface crystalline islands. However, gate edge defects like grain boundaries cannot be eliminated [5]. Fig. 4 shows an XTEM micrograph of the Ge^+ im-

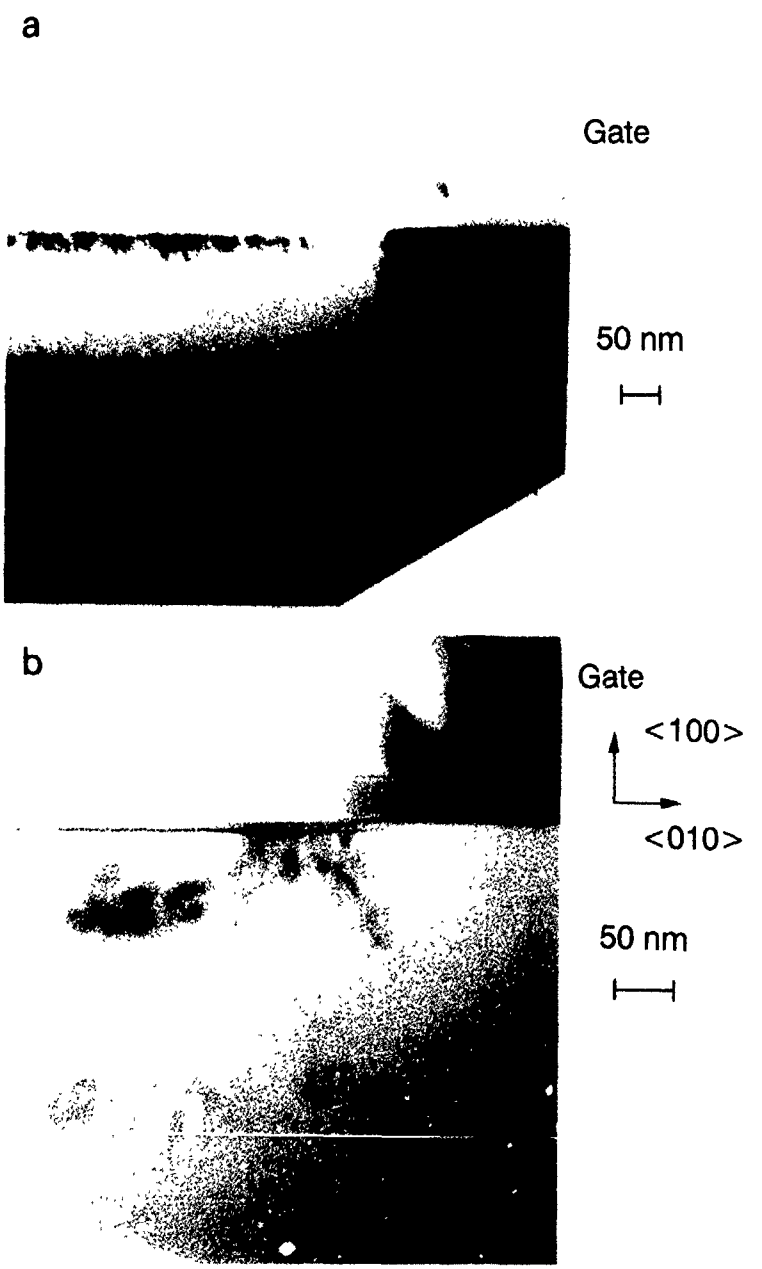

Fig 3. Cross-sectional TEM micrographs of a gate edge amorphized by Ge^+ at 130 keV with 2×10^{14} cm^{-2} before (a) and after (b) annealing at 800 °C for 30 min.

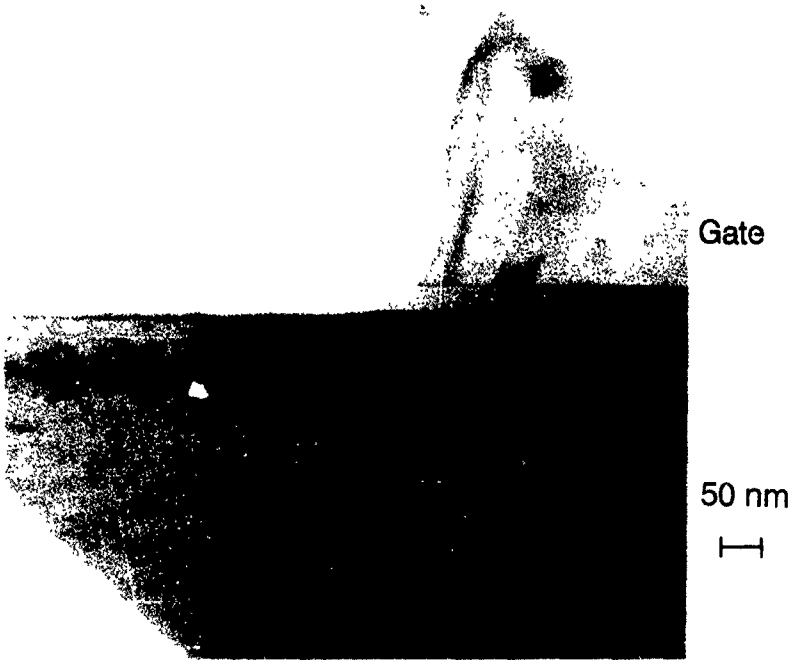

Fig 4 Cross-sectional TEM micrograph of a gate edge amorphized by Ge^+ at 40 keV with 5×10^{13} cm^{-2} after annealing at 600 °C for 30 min

planted sample at 40 keV and at a dose of 5×10^{13} cm^{-2} and annealed at 600 °C for 30 min. This shows that neither grain-boundary-like defect nor any serious defect remains because amorphization does not occur.

3.4. Analysis of residual defects using a gate-controlled diode

We studied the characteristics of gate-controlled diodes with various preimplantation conditions. The samples were preimplanted with Ge^+ at 40 keV and doses ranging from 5×10^{13} to 8×10^{14} cm^{-2} or with Si^+ at 40 keV and doses ranging from 2×10^{14} to 2×10^{15} cm^{-2}. Leakage current was measured at a fixed gate bias (1 V) to accumulate charges in the silicon surface under the gate, to show dependence on the preimplantation dose (fig. 5). The leakage current depends strongly on the preimplantation doses of both Ge^+ and Si^+ preimplantations. The leakage currents of samples implanted with Ge^+ at 5×10^{13} cm^{-2} or with Si^+ at 2×10^{14} cm^{-2} are the same as those of not preimplanted samples. This shows that defects are annealed out in the lower dose preimplantation. Preimplantations with these doses eliminate both the residual defects and the channeling tail, but to prevent the enhanced diffusion, the moderate disordered layer is the key. The Ge^+ preamorphization (2×10^{14} cm^{-2}) cannot be used for low-temperature annealing due to the leakage current.

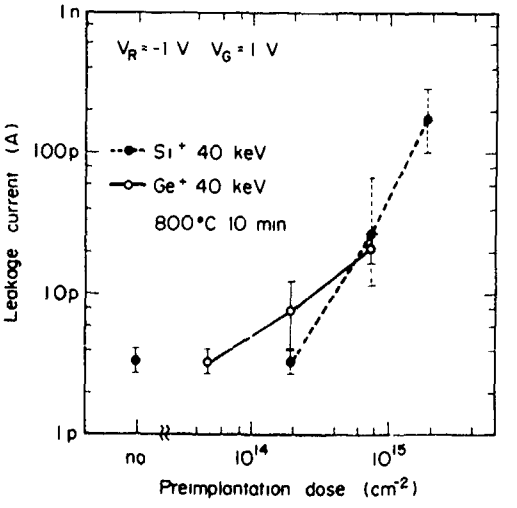

Fig. 5 The leakage current of gate-controlled diodes as a function of preimplantation dose.

4. Summary

We studied the B diffusion dependence on preimplantation energy and dose. Boron-enhanced diffusion is reduced by moderate lattice disorder below amorphization. The residual defects were examined by XTEM, which indicated that amorphization induces serious defects (the grain-boundary-like defects). We proposed the best design of the gate-controlled diode for the evaluation of preimplantation. The dependence of the leakage current on the preimplantation dose indicates that no serious residual defects are caused by Ge^+ implantation at 40 keV with 5×10^{13} cm^{-2} or Si^+ at 40 keV with 2×10^{14} cm^{-2} after 800 °C annealing. Preimplantation below the amorphization dose results in no grain-boundary-like defects and low leakage currents. To prevent enhanced diffusion, the moderate disordering preimplantation is the key

Acknowledgement

We would like to thank M. Yoshida for his support

References

[1] A.C Ajmera and G A Rozgonyi, Appl Phys. Lett 49 (1986) 1269
[2] M.Y Tsai and B G Streetman, J. Appl Phys 50 (1979) 183
[3] T O. Sedgwick, A E. Michel, V.R. Deline, S A Cohen and J B. Lasky, J Appl. Phys. 63 (1988) 1452.
[4] R B. Fair, Nucl. Instr. and Meth B37/38 (1989) 371.
[5] M Horiuchi, M. Tamura and Y Kamamoto, J Appl Phys. 65 (1989) 2238.
[6] M. Kase, M. Kimura, H Mori and T. Ogawa, Appl Phys. Lett. 56 (1990) 1231
[7] A.S. Grove and D J Fitzgerald, Solid-State Electron 9 (1966) 783.

Nuclear Instruments and Methods in Physics Research B55 (1991) 555–560
North-Holland

Formation of thin silicon films using low energy oxygen ion implantation

A.K. Robinson [a], C.D. Marsh [c], U. Bussmann [a], J.A. Kilner [b], Y. Li [b], J. Vanhellemont [d], K.J. Reeson [a], P.L.F. Hemment [a] and G.R. Booker [c]

[a] *Department of Electronic and Electrical Engineering, University of Surrey, Guildford, Surrey, GU2 5XH, UK*
[b] *Department of Materials, Imperial College, London SW7 2BP, UK*
[c] *Department of Metallurgy & Science of Materials, University of Oxford, OX1 3PH, UK*
[d] *InterUniversity Micro-Electronics Centre (IMEC), Kapeldreef 75, B-3030 Leuven, Belgium*

SIMOX (separation by implanted oxygen) is an established technique to produce device worthy silicon-on-insulator structures Current interest in thin film fully depleted CMOS devices in SIMOX material has placed emphasis on producing silicon overlayers of 100 nm thickness or less Thin film SIMOX substrates have been prepared using halogen lamps, to preheat and provide background heating during oxygen ion implantation in the relatively low energy range 50–140 keV The resulting structures have been studied by RBS, cross-sectional TEM and SIMS. This paper reports on the crystalline quality of the silicon overlayers and discusses the viability of low energy oxygen implantation to produce thin film SIMOX structures suitable for VLSI device fabrication

1. Introduction

D vice-worthy silicon on insulator structures formed on SIMOX material, are usually implanted with 200 keV oxygen ions in silicon and a typical implantation dose is 1.8×10^{18} O^+/cm [1]. This clean, reproducible, implantation process results in 300 nm of silicon overlaying an oxide layer of 400 nm [2]. For fully depleted devices, silicon overlayers of 100 nm thickness are required [3]. Thinner silicon overlayers can be achieved by thermal oxidation and chemical etching of thick silicon layers. An alternative method is to implant lower energy oxygen ions into the silicon and thereby reducing the projected range of the ions, hence, the synthesis of the buried oxide occurs closer to the surface. Once the oxide is formed, its thickness increases at the expense of the silicon overlayer [4]. Therefore, a thinner silicon overlayer can be achieved by controlling the ion energy and the implantation dose.

Experiments to evaluate the quality of thin film SIMOX substrates prepared by O^+ implantation in the energy range 50 to 140 keV are being carried out using a heated halogen lamp sample holder, which enables an implantation temperature of $680 \pm 10\,^{\circ}C$ to be maintained. As a consequence, the implantation beam current and power loading of the wafer are now less critical parameters in the production of the substrate. The aim of this paper is to report on the thickness of the layers formed and the crystalline quality of the thin silicon overlayers produced using this method.

2. Experimental details

Square areas of 6.25 cm^2 in the centre of bulk silicon (100) wafers were implanted with molecular oxygen ions (O_2^+) in the energy range 50 to 140 keV at a temperature of $680 \pm 10\,^{\circ}C$. Implantation temperatures were

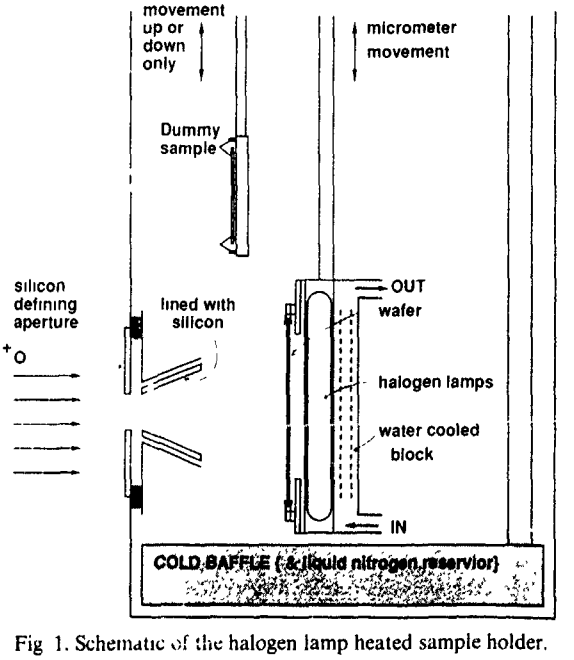

Fig 1. Schematic of the halogen lamp heated sample holder.

0168-583X/91/$03 50 © 1991 – Elsevier Science Publishers B V (North-Holland)

maintained by halogen lamps fitted behind the wafer in the sample holder. The schematic in fig. 1 shows the sample holder, and the implantation conditions of the nine wafers produced are shown in table 1. Wafers 1 to 5 were implanted with 70 keV oxygen ions and wafers 6, 7, 8 and 9 were implanted with 140, 90, 50 and 200 keV oxygen ions respectively.

Three different doses of O^+ have been implanted into different areas on each wafer by linear movement of the wafer during the implantation process. Subsequently, wafers 2–4 were capped with a deposited ≈ 500 nm oxide layer and annealed at 1405 °C for 30 min [5].

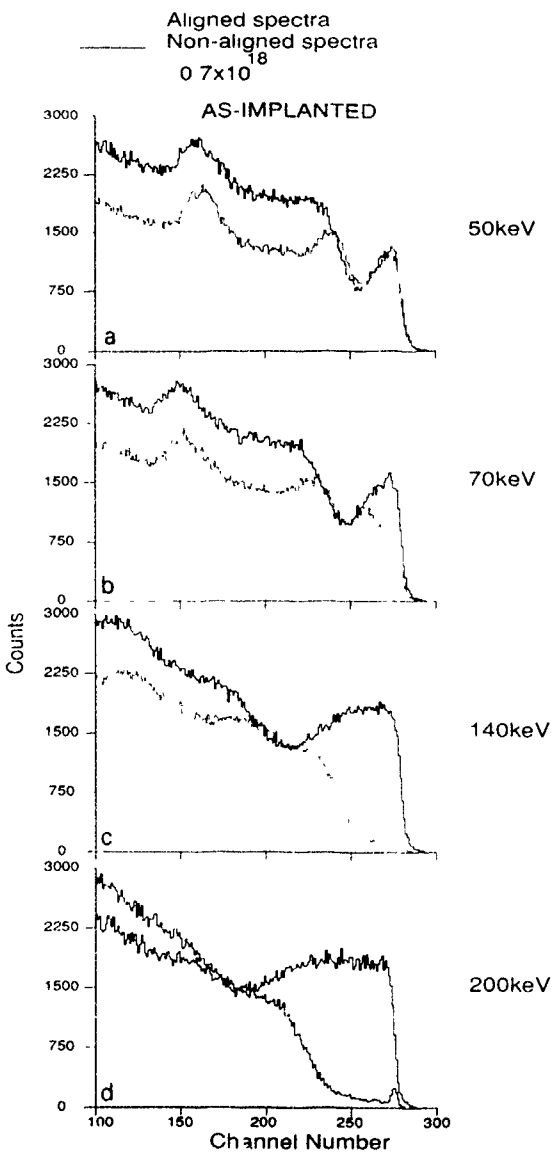

Fig. 2. "As-implanted" RBS spectra for wafers 8, 5, 6 and 9 implanted with O^+ at energies of 50, 70, 140 and 200 keV, respectively.

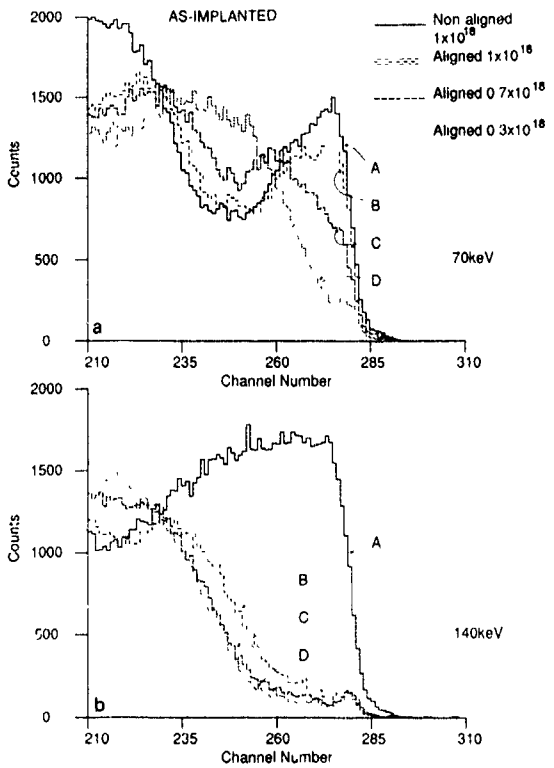

Fig 3 Aligned "as-implanted" RBS spectra from wafers 5 and 6 implanted with doses of 0 3, 0.7 and 1×10^{18} O^+/cm^2 together with a non-aligned spectrum from a sample implanted with 1×10^{18} O^+/cm^2.

Wafers 6–8 were cleaved into small samples before capping and were annealed in a tube furnace at 1320 °C for two hours. Rise and fall ramp rates were 10 °C/min from and to room temperature, with an anneal ambient of flowing nitrogen. RBS analysis of the capping oxide layer performed before and after the anneal showed the oxide to be clean and intact.

The resulting structures have been studied by Rutherford backscattering (RBS) and channelling techniques using a 1.5 MeV $^4He^+$ beam with a backscattering angle of 160°. Samples were also analysed by XTEM and SIMS. Non-destructive spectroscopic ellipsometry has been used to calculate the thickness of the silicon overlayers and the buried oxide layers for selected samples. RBS, SIMS and XTEM analysis, together, give information on the crystalline quality, oxygen concentration and oxygen depth distribution.

3. Results

Fig. 2a–d shows normalised RBS non-aligned and aligned spectra from four "as-implanted" wafers implanted with a dose of 0.7×10^{18} O^+/cm^2 at energies of

Table 1
Implantation, anneal conditions and analysis techniques

Wafer number	Dose [1×10^{18} O^+/cm^2]	Energy [keV]	Anneal conditions	Analysis techniques
1	1	70	–	RBS XTEM
2	0.3, 0.7, 1	70	1405 °C, 30 min	RBS, XTEM
3	0.3, 0.7, 1	70	1405 °C, 30 min	ellipsometry
4	0.3, 0.7, 1	70	1405 °C, 30 min	XTEM
5	0.3, 0.7, 1	70	–	RBS, XTEM
6	0.3, 0.7, 1	140	(a) 1320 °C, 2 h (b) as-implanted	RBS, SIMS
7	0.3, 0.7, 1	90	(a) 1320 °C, 2h (b) as-implanted	RBS, SIMS
8	0.2, 0.5, 0.7	50	(a) 1320 °C, 2h (b) as-implanted	RBS, SIMS
9	0.3, 0.7, 1	200	–	RBS

50, 70, 140 and 200 keV, respectively. The spectra indicate that the buried oxide is located closer to the surface if lower energies are used. Fig. 2d also shows a χ_{min} value of 4.6% indicating that a good quality silicon overlayer is maintained during the implantation process. However, as the energy is lowered, the oxygen profile shifts towards the surface leading to a reduction of the crystalline quality of the silicon overlay.

The aligned, as-implanted, spectra for 0.3 (B), 0.7 (C) and 1×10^{18} O^+/cm^2 (D) doses implanted with energies of 70 and 140 keV are shown in fig. 3a and b, respectively, together with a corresponding non-aligned spectra (A) from the highest dose. With increasing dose for the 70 keV energy implants there is a degradation in the crystalline quality of the silicon overlay which is seen from the increasing χ_{min} values of 16%, 50% and 82% for D, C and B, respectively. In fig. 3b the spectra from wafer 6 implanted with the same doses but at the higher energy of 140 keV, show little change in the crystalline quality of the surface with χ_{min} for B, C and D having values of 8, 5.5 and 4.3%, respectively.

Fig. 4 shows a cross sectional TEM micrograph from an unannealed sample prepared from wafer 1 after implantation of 70 keV to a dose of 1×10^{18} O^+/cm^2. The "as-implanted" microstructure is superior to that found in samples prepared previously using only beam heating during the implantation [6]. The laminar struc-

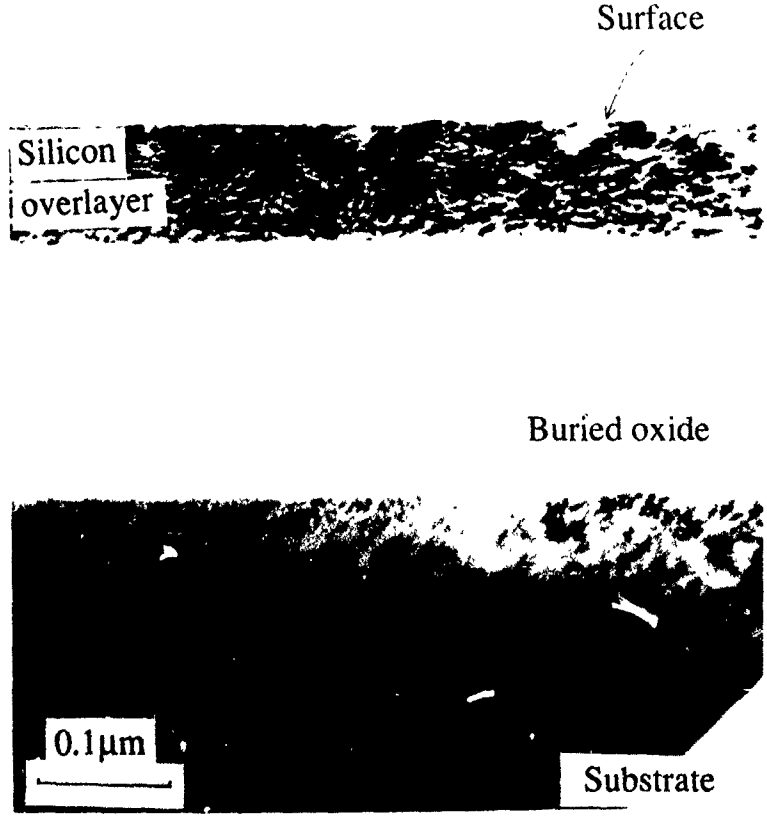

Fig. 4. Cross-sectional XTEM micrograph showing the as-implanted structure prepared from wafer 1, which was implanted with a dose of 1×10^{18} O^+/cm^2 and energy of 70 keV

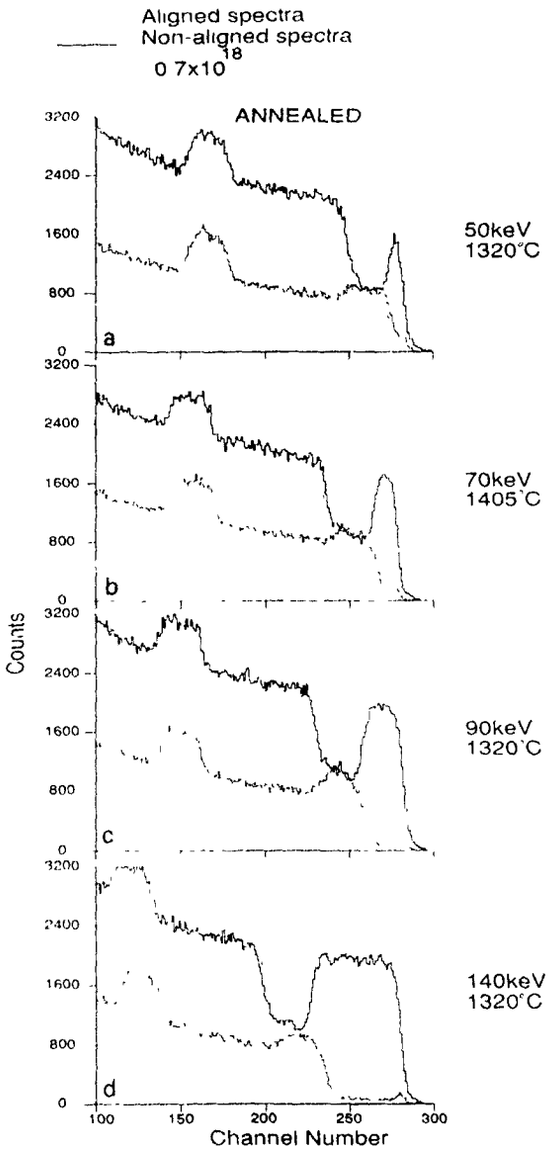

Fig 5 Aligned and non-aligned RBS spectra from annealed wafers 8, 5, 7 and 6 implanted with O^+ at energies of 50, 70, 90 and 140 keV, respectively

tures observed in the silicon overlay are assumed to be due to SiO_2 precipitates. No ordering in these structures is observed, unlike the ordered SiO_2 precipitates reported by van Ommen [7]. Defects on the silicon {311} and {111} lattice planes are also evident near the SiO_2/substrate interface.

Fig. 5 shows typical RBS non-aligned and aligned spectra from the annealed samples from wafers 2, 6, 7 and 8. The non-aligned spectra indicate the variation in the silicon overlayer and buried oxide thicknesses and the results are summarised in table 2. Also tabulated is the thickness of the layers as predicted by IRIS [8], a computer program which simulates high dose oxygen profiles before and after high temperature annealing, plus additional thickness data from XTEM and spectroscopic ellipsometry analyses.

Comparison of the non-aligned, experimental spectra, with simulated RBS spectra (not shown) indicates that for the sample implanted with a dose of 1×10^{18} O^+/cm^2 and energy of 70 keV a layer of stoichiometric SiO_2 is formed. In this sample, the buried oxide has formed abrupt interfaces and there is no evidence of oxide precipitates in the silicon overlayer. The abrupt interfaces have also been confirmed by spectroscopic ellipsometry. However for doses of 0.3 and 0.7×10^{18} O^+/cm^2, the buried oxide contains excess silicon. For wafer 8 (lowest implantation energy) the RBS simulations indicate that the silicon overlayer still contains oxygen even after the high temperature anneal. It is assumed that these effects are due to crystalline silicon inclusions in the buried oxide and due to oxide precipitates within the silicon overlayer [9]

Fig. 6a shows a XTEM micrograph for a sample from wafer 5 (0.7×10^{18} O^+/cm^2) which confirms that after annealing, the excess silicon in the buried oxide is in the form of crystalline inclusions These inclusions appear to be distributed throughout the oxide layer with a greater proportion being located near the lower SiO_2/Si interface rather than the upper interface. The threading dislocation density obtained from plan-view TEM in this sample was found to be $\approx 10^9/cm^2$ The micrograph in fig. 6b is from a sample implanted with a dose of 1×10^{18} O^+/cm^2 from wafer 4, which was also annealed at 1405 °C. The silicon overlay is seen to be of good crystalline quality containing some threading dislocations. The synthesised buried oxide has abrupt interfaces and contains small crystalline silicon inclusions near the lower interface with many of these inclusions in contact with the substrate

4. Conclusions

(1) SIMOX material has successfully been produced with low energy oxygen ions implanted at elevated implantation temperature of 680 ± 10 °C.

(2) Device quality silicon overlayers of various thicknesses (less than 100 nm) have been produced with uniformly thick buried oxides. For any oxygen dose of 1×10^{18} O^+/cm^2 and energy of 70 keV, after annealing, the RBS results indicate that the buried oxide has abrupt planar interfaces and is of uniform thickness (240 nm). The silicon overlay was found to be 50 nm thick and of good silicon crystalline quality, which has been confirmed by XTEM analysis and spectroscopic ellipsometry However, for lower doses, XTEM analysis

Table 2
Thickness of the silicon overlay and the buried oxide determined using RBS, XTEM, spectroscopic ellipsometry and SIMS Also predicted thicknesses from IRIS [5]

Energy [keV]	Dose [1×10^{18} O^+/cm^2]	RBS thicknesses accuracy ±17 nm [nm]		IRIS simulation [nm]		Other [nm]	
		Si	SiO_2	Si	SiO_2	Si	SiO_2
50	0.7	45	150	50	140	60 [c]	170 [c]
70	0.7	80	182	100	140	75 [a]	140 [a]
90	0 7	145	160	160	140		
140	0 7	386	160	260	140	270 [c]	145 [c]
70	1	50	240	60	210	52 [b]	200 [b]
						49 [a]	195 [a]
140	1	300	240	215	215		
200 [d]	1 8	300	400	230	385		

[a] XTEM. [b] Ellipsometry. [c] SIMS ±5% [d] From ref [1]

confirms the synthesised oxide contains many small, crystalline silicon inclusions.

Acknowledgements

The authors thank R. Chater for performing the 1320 °C anneals and G Celler for the 1405 °C anneals. Thanks are extended to N. Hatzopoulos and V. Starkov and also to the staff at the D R. Chick laboratory, R. Watt, M. Chapman, M. Browton, J Mynard and A. Cansell for their assistance during the implantation and RBS analysis. This work is in part funded by the UK. Science and Engineering Research Council.

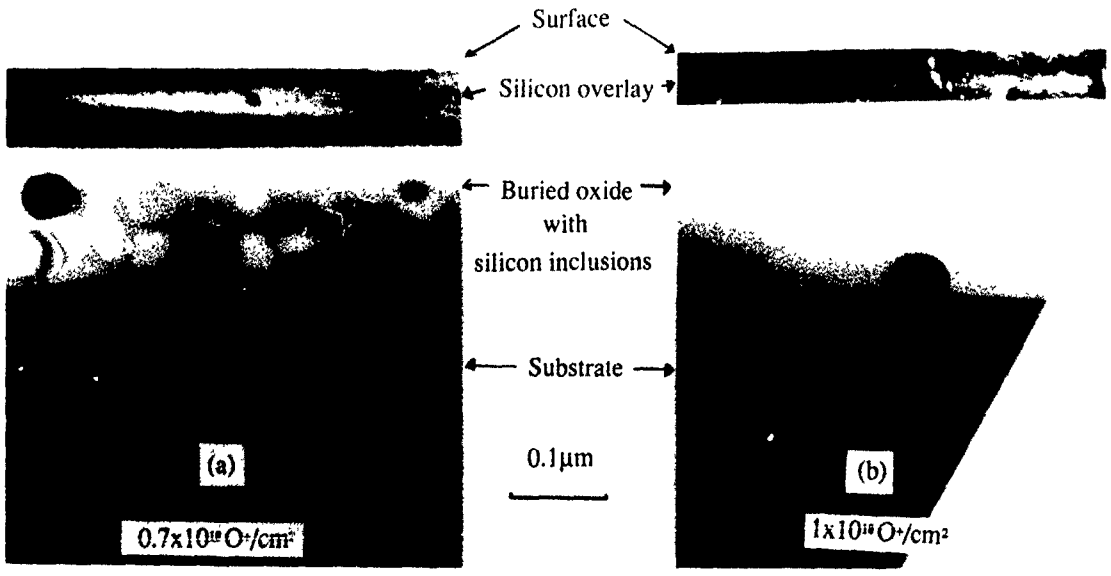

Fig. 6. Two cross-sectional XTEM micrographs, (a) an annealed sample from wafer 2 implanted at 70 keV with a dose of 0.7×10^{18} O^+/cm^2. This micrograph shows a uniformly thick buried oxide layer containing silicon inclusions, and (b) a sample implanted at the same energy and annealed under the same conditions but with a dose of 1×10^{18} O^+/cm^2. For the larger dose the density of silicon inclusions in the buried oxide is much reduced

References

[1] J.R. Davis, A.E. Glaccum, K. Reeson and P. Hemment, IEEE Electron. Device Lett EDL-7 (1986) 570.
[2] C D. Marsh, J.L. Hutchinson, G R. Booker, K.J Reeson, P.L.F. Hemment and G. Celler, Inst. Phys. Conf. Ser 87, section 6 (1987) 409
[3] J.-P. Colinge, IEEE Circuits and Devices Mag. 3(6) (1987) 16
[4] R. Chater, J.A. Kilner, P.L.F Hemment, K.J Reeson and R F. Peart, Semiconductor Silicon 1986, vol 86-4 (Electrochemical Soc., 1986) p 652.
[5] G.K. Celler., P.L.F. Hemment, K.W. West and J M. Gibson, in: Semiconductor-On-Insulator and Thin Film Transistor Technology, eds. A Chiang, M.W. Geis and L Pfeiffer, Mater. Res Soc. Symp Proc. 53 (1986) 227
[6] K.J. Reeson et al., Microelectronics Eng. 8 (1988) 163.
[7] V. Ommen, Nucl. Instr and Meth. B39 (1989) 194
[8] U. Bussmann, A.K. Robinson and P.L.F. Hemment, these Proceedings (8th Int. Conf on Ion Implantation Technology, Guildford, UK, 1990) Nucl. Instr and Meth. B55 (1991) 852.
[9] S J. Krause, C.O. Jung, T.S. Ravi, S.R. Wilson and D E Burke, Mater Res. Soc. Symp. Proc 107 (1988) 93

Nuclear Instruments and Methods in Physics Research B55 (1991) 561–564
North-Holland

Measurements and applications of high energy boron implants in silicon

A. La Ferla
Istituto di Metodologie e Tecnologie per la Microelettronica, c/o Dip di Fisica, Università di Catania, Catania, Italy

E. Rimini
Dipartimento di Fisica, Corso Italia 57, 95129 Catania, Italy

A. Carnera and A. Gasparotto
Dipartimento di Fisica, via Marzolo 8, 35131 Padova, Italy

G. Ciavola
Laboratorio Nazionale del Sud, via S. Sofia, 95100 Catania, Italy

G. Ferla
SGS-Thomson, Stradale Primosole 50, 95100 Catania, Italy

Boron ions were implanted into high resistivity Si wafers at energies in the 15–50 MeV range and doses in the 10^{11}–10^{16} cm^{-2} range. The distribution of the implanted ions was analyzed by spreading resistance profilometry and for the high fluences by secondary ion mass spectrometry. Some samples were implanted with the beam normal to the wafer surface to study the channeling effect in a pure electronic stopping power regime of slowing down. The experimental measurements of the projected ranges and of the stragglings are compared with calculations based on the usual LSS and Bethe–Bloch formulas for the stopping power. This classic approach justifies quantitatively the distribution for the samples implanted in a random direction. The I–V characteristic of a diode performed by multiple energy boron implants of 15, 22 and 50 MeV is presented. The obtained breakdown voltage, 5×10^{3} V, represents a possible application of the high energy implants.

1. Introduction

In the last few years interest in MeV implants has arisen because of the large field of technological applications. MeV implants are mainly used for the formation of deep p–n junctions [1–3] without the traditional predep and drive-in process that requires thermal treatments at high temperatures and for long times. Using these high energies the near-surface region remains practically free of damage and dopants. This is a very important advantage in the formation of deep wells. While for the 1–2 MeV implants a lot of measurements have been reported [4–6], for energies of tens of MeV only a few studies on the ion distribution are reported in the literature [7,8]. For energies in the 10–100 MeV range a description of the concentration profile in terms of several moment parameters is not reasonable, in contrast with the 1–2 MeV implant case. The ion distribution is characterized by a narrow peak located at a depth determined by the electronic stopping power and by a low concentration surface front tail associated with large-angle single scattering events [9,10].

We report an experimental investigation of the range distribution for random and channeling high energy boron implantation. The experimental analysis is made by spreading resistance profilometry (SRP) to determine the carrier distribution and for the first time by secondary ion mass spectrometry (SIMS) to obtain the chemical boron profile.

An application of the high energy boron implants is also presented. These implants were used to fabricate a diode with a breakdown voltage near the limiting value characteristic of a parallel plane structure.

2. Experimental

⟨100⟩ and ⟨111⟩ oriented silicon wafers were implanted with boron ions in the 15–50 MeV energy

0168-583X/91/$03.50 © 1991 – Elsevier Science Publishers B.V (North-Holland)

range. Doses used were in the range between 10^{11} and 10^{16} cm^{-2}. The n-type silicon substrates of $\sim 10^3$ Ω cm were floating zone (FZ) grown and doped by neutron transmutation to a phosphorus concentration of $\sim 5 \times 10^{12}$ cm^{-3}. The boron implants were performed with the high voltage tandem accelerator of the National Laboratory of the South in Catania. Some samples were implanted with the beam normal to the silicon surface to study the channeling effect. To ensure a reasonable uniformity of dopant the boron beam was defocused and the implanted area defined by a 2×4 mm^2 rectangular window. The boron current was in the 10–100 nA range.

The hole and ion profiles were determined by spreading resistance and secondary ion mass spectrometry, respectively. A thermal process at 950 °C for 1 h was performed in an N_2 ambient to ensure the electrical activation in all samples without substantial diffusion. This thermal process is necessary for the SRP measurements. This technique allows carrier measurements at concentrations as low as 10^{13}–10^{14} cm^{-3} typical of that in the front tail.

Using the same material a family of diodes was constructed. Every diode was multiply implanted with boron at energies of 22, 35 and 50 MeV using circular masks of decreasing diameter; 7, 5 and 3 mm respectively. In addition an area of 9 mm in diameter was implanted with a low energy B^+ process: 80 keV, dose $= 3 \times 10^{11}$ cm^{-2}.

The implanted dose should be of low value so that the doped regions can be easily depleted under the reversely biased condition. In this case the electric field can reach the maximum allowed value before the heavily p-doped surface region be completely depleted. The maximum electric field before breakdown, which occurs by the avalanche impact ionization mechanism, is called the critical electric field, E_c and it amounts to 15.4 V μm^{-1}. Details on the diode construction have been already reported [11] but in the first experiment no field plate was used.

3. Results: analysis of high energy boron distributions

The distribution of 50 MeV B^+ ions implanted in silicon is peaked at a depth of about 86 μm [9,10]. Clearly a usual SIMS analysis cannot be performed and it was done on beveled samples as shown in fig. 1. A 1 μA oxygen beam was rastered over an area of 150 × 150 μm^2 on different points of the beveled sample. The lapped surface of the implanted sample is mounted perpendicular to the secondary ions beam direction of detection. By means of micrometric screws driven by stepping motors the rastered zone is centered in different points of the concentration distribution and just a few microns in depth are analyzed. Moving the sample in different positions the whole concentration profile is reconstructed. Only the secondary boron ions coming from the middle of the rastered area are detected and the depth resolution is determined from this area. The distribution around the peak, where the concentration changes three or four orders of magnitude in a few microns, was measured with a depth resolution of about 200 nm.

Carrier and boron atom profiles are shown in fig. 2 for a 50 MeV, 4×10^{16} cm^{-2} B implanted into a ⟨100⟩ Si sample. The boron beam was normal to the target surface. The two distributions obtained by these different techniques are quite similar. The SIMS distribution is slightly narrower than the SRP one. Probably this is due to the computer code used for the conversion from the resistance data to the carrier profile [12].

The boron concentration profile is characterized by a long near-surface tail caused by the rare elastic nuclear scattering events a narrow peak due to the large number of ions that slow down by electronic scattering and an asymmetric concentration fall. This is probably due to the channeling effect. In fact the projected range, R_p, corresponds to a depth where the boron ions stop after slowing down by electronic losses and it is well predicted by the classical formulas valid for an amorphous material. Depths greater than R_p corre-

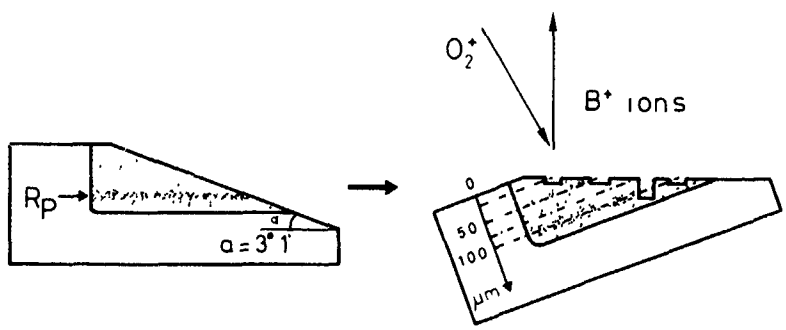

Fig. 1. Geometry adopted for SIMS-depth profiling in beveled samples.

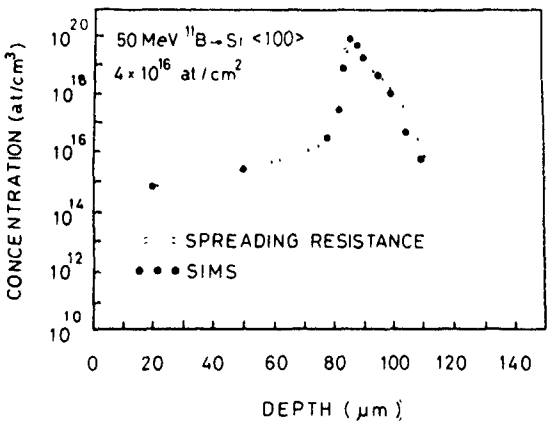

Fig 2. Concentration profiles of a ⟨100⟩ Si sample implanted with 50 MeV B, 4×10^{16}/cm^2 normal to the sample surface. SRP (· · ·) and SIMS (●) measurements.

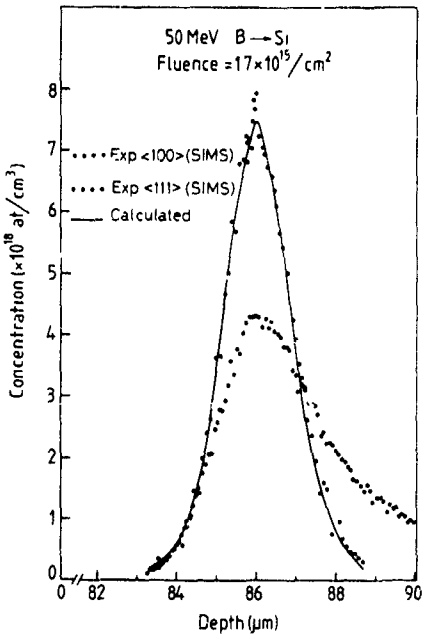

Fig 3. SIMS profiles of 50 MeV Boron implanted in ⟨100⟩ (○) and ⟨111⟩ (●) Si samples, with the boron beam impinging normally to the sample surface A calculated profile is also shown

spond to ions that have experienced a lower stopping power during part of their trajectory, as for channeled ions. Because of the large B^+ beam divergence in our experiment a quantitative determination of the channeled ion distribution is not feasible at this moment. By the analysis of R_{MAX} (depth where the B concentration is reduced to 1% of the peak value) as a function of the implant energy it is found that the channeled ions experience in average an electronic stopping power 25% lower than that of a random medium.

For comparison a ⟨111⟩ Si sample, was also implanted with 50 MeV, 1.7×10^{15} B^+ cm^{-2}. This sample is cut 1–2° off axis and because the critical angle for channeling at the energy of 50 MeV is ~0.5° [13] directional effects are practically avoided The SIMS profile is shown with a linear scale in fig. 3 together with the boron normalized distribution obtained for the ⟨100⟩ sample. The channeling effect appears evident In the same figure, as a full line, the single scattering

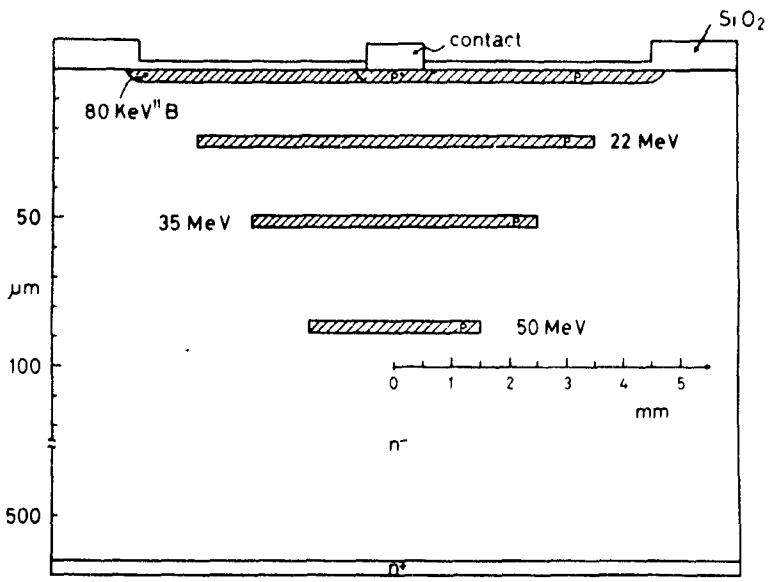

Fig 4. Schematic cross section of the diode structure with the depth locations of the boron implants. The horizontal and the vertical dimensions are not to scale

simulation convoluted with the electronic straggling [14] is shown. The calculated profile is in good agreement with the experimental one without directional effect.

4. High breakdown voltage diode: an application of MeV B implants

The avalanche impact ionization process responsible for diode breakdown is determined by the curvature of the doped device regions. To increase the breakdown voltage toward the limiting value of a parallel plane structure it is necessary to have a high curvature radius extending laterally the depleted regions. This goal was obtained by using multiple high energy boron implants: 22, 35 and 50 MeV in regions of decreasing diameter to have a structure designed like a "funnel". The diode design is presented in fig. 4. With this geometry each p-type region works as a field plate for the other p-type deeper regions and when the device is reversely biased the depleted regions extend laterally more and more as the diode surface is approached, so the curvature radius is considerably increased.

The E_c value for our substrate doping is 15.4 V/μm The ideal breakdown voltage value for a plane structure $p-n-n^+$ uniformly doped and with a depth junction of 100 μm is 6500 V This value is critically determined from the wafer thickness, 520 μm.

In fig. 5 the reverse current–voltage characteristic is shown, the breakdown occurs at $\sim 5 \times 10^3$ V. Solving numerically the Poisson equation with the experimental boron concentration profile, as obtained by SRP measurements, it was possible to determine that a partial depletion of the surface 80 keV B implanted region is responsible for the breakdown voltage value. To reach the ideal breakdown voltage it would be necessary to control also the curvature of the near-surface region by means of a floating field plate.

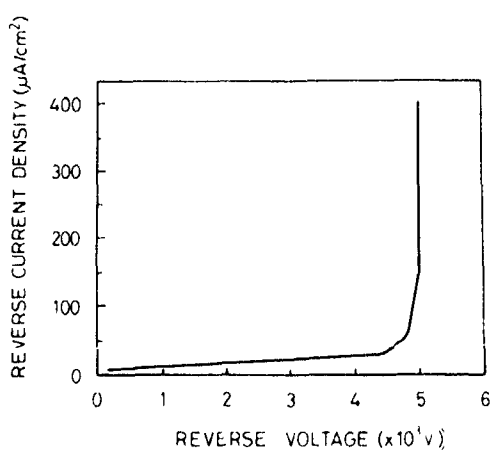

Fig. 5. Current–voltage characteristic for a reverse bias of the diode.

5. Conclusions

Very high energy boron implanted distributions have been experimentally studied using two different techniques: spreading resistance profilometry and secondary ion mass spectrometry. Channeling effects must be considered also at these energies where the slowing-down processes are purely electronic to justify the concentration profile shape when the B beam is normal to the sample surface. In particular in this case a ~25% reduction in the electronic stopping power was evaluated in comparison, with that experienced in an amorphous medium.

Avoiding the channeling effect the distribution can be quantitatively approximated by a theoretical distribution based on single scattering and LSS–Bethe–Bloch approximation for the electronic stopping power, while the experimental straggling is well fitted by a pure electronic straggling.

As an application of these high energy implants a family of diodes was constructed. Multiple MeV B implants were employed to obtain a "funnel" design of the structure to increase the effective curvature radius of the doped regions. A breakdown voltage of $\sim 5 \times 10^3$ V was obtained, this value is ~75% of the ideal calculated breakdown voltage of a $p-n-n^+$ plane structure.

References

[1] D Pramenik and M I Current, Solid State Technol. 5 (1984) 211.
[2] P F Byrne, N.W Cheung and D.K. Sadana, Thin Solid Films 95 (1983) 363
[3] A.N Saxena and D Pramenik, Mater. Sci Eng B2 (1989) 1
[4] N W Cheung, C.L. Liang, B K Liew, R H Mutikainen and H. Wong, Nucl. Instr Meth. B37/38 (1989) 941.
[5] R J. Schreutelkamp, J.R Liefting, P.M. Zagwijn, W X Lu and F W Saris, Nucl. Instr Meth B48 (1990) 448
[6] B.X. Zhang, Z L Wang, R J. Schreutelkamp, F.W Saris, A Y Du and Q Li, Nucl Instr and Meth. B48 (1990) 425
[7] W.R. Fahrner, D Braunig, M Knoll and J R. Laschinski, in: Semiconductor Processing, ed D.C. Gupta, ASTM Spec Techn. Publ vol. 850 (1984) p 77.
[8] G Bardos, Radiat Eff 105 (1988) 191
[9] A La Ferla, E. Rimini, G. Ciavola and G. Ferla, Nucl. Instr. and Meth. B37/38 (1989) 951.
[10] A La Ferla, A. Di Franco, E Rimini, G. Ciavola and G Ferla, Mater Sci Eng. B2 (1989) 69.
[11] A. Di Franco, A La Ferla, E Rimini, G. Ciavola, G Ferla, Semicond Sci. Technol. (1990) in press
[12] S.C. Choo, M.S. Leong, H L Hang, L. Li and L.S Tan, Solid-State Electron. 20 (1977) 460.
[13] J. Lindhard, K. Dan Vidensk. Selsk. Mat. Fys Medd 34 (1965) no. 14.
[14] J.P. Biersack, private communication.

Nuclear Instruments and Methods in Physics Research B55 (1991) 565–568
North-Holland

Ultra low energy (100–2000 eV) boron implantation into crystalline and silicon-preamorphized silicon

A. Bousetta, J.A. Van den Berg, R. Valizadeh and D.G. Armour
Department of Electronic and Electrical Engineering, University of Salford, Salford, M5 4WT, UK

P.C. Zalm
Philips Research Laboratories, PO Box 80 000, 5600 JA Eindhoven, The Netherlands

Very low energy (<1 keV) B^+ ion implantation has been carried out on both crystalline and silicon-preamorphized silicon. The amorphous layer depth was determined using Rutherford backscattering analysis (RBS). The penetration depth and channelling tail of B^+ ions into silicon was studied as a function of ion energy (100–2000 eV) and low temperature regrowth/annealing ($T < 600\,^\circ C$), using secondary ion mass spectroscopy (SIMS). These studies also involved low energy (40–60 eV) ion beam deposition (IBD) of 10–20 nm isotopic $^{28}Si^+$ cap layer at room temperature to enable accurate SIMS depth profile measurements to be carried out. The results show the extent of the channelling tails at these low energies and indicate that sub 40 nm p^+–n junctions with estimated carrier concentrations as high as 10^{20} cm^{-3} can be obtained.

1. Introduction

Fabrication of shallow p^+–n junctions with profile abruptness in the 10 nm/decade range is desired for the miniaturization of conventional and novel devices based on multilayer structures. Among the acceptor impurities, boron is most widely used in silicon device technology. However, boron is not easily evaporated from a usual Knudsen cell, because of its high evaporation temperature (1200–2000 °C). In recent years, to overcome such problem, low energy ion implantation during silicon MBE has become widely used [1–3]. Even so, shallow p^+–n junctions are still difficult to manufacture, because the common p-type dopant, B, channels easily in the silicon lattice which sets a lower limit to the formation of shallow B profiles [4–6]. Different approaches have been made to minimize the channelling in crystalline silicon when implanted with ions at energies higher than 10 keV. The more commonly used one is to tilt the substrate 7° off normal incidence with an arbitrary azimuthal rotation angle [7]. However to obtain shallow junctions in the 50 nm region or below, much lower ion energies must be used (< 2 keV). In this case the channelling tails of implanted light atoms such as boron may be expected to remain a major problem since the critical angles for channelling become sufficiently large for ions to be scattered into the open Si channels regardless of the substrate tilt [8]. Another useful technique is to preamorphize silicon (usually with group IV ions: Si or Ge) before the B^+ and/or BF_2^+ implantation [9,10]. Although heavier atoms such as Ge and Ga might have advantages over Si to obtain full amorphization, they can produce additional damage [11,12] which will affect the minority carrier lifetime of such shallow junctions [11]. Thus preamorphization with silicon itself is preferred. It has also been shown that silicon preamorphized via self ion implantation provides full dopant activation at a lower annealing temperature [13] and consequently the high temperature annealing (1000–1100 °C) required for device quality, which result in much deeper junctions [14], might not be necessary.

In this work, a combination of very low energy boron implantation (100–2000 eV) and low temperature (< 600 °C) in situ silicon regrowth has been used to investigate the effect of preamorphization on the boron distribution at these low energies and to obtain p^+–n junctions with depths as shallow as 40 nm and below.

2. Experimental procedure

A series of phosphorus-doped (5–7 and 200–500 Ω cm) Si(100) wafers were implanted with B ions at energies between 100 and 2000 eV using a low energy implanter [15]. Preamorphization was carried out using Si ion bombardement. The depth of the resulting damaged region was determined using Rutherford backscattering spectrometry (RBS)/channelling with a 2 MeV He^+ ion beam. Recrystallization of the amorphous layer and/or dopant activation was done in situ by annealing at 550 °C for 20 min. All samples were stripped of their oxide layers by immersion in a hydro-

0168-583X/91/$03.50 © 1991 – Elsevier Science Publishers B.V (North-Holland)

fluoric acid solution followed by a deionised water rinse and were finally dipped in methanol and dried. In situ thermal cleaning at 850–900 °C for 20 min, was carried out before implantation. The system base pressure was 2×10^{-10} mbar, and during implantation the pressure increased to 10^{-9} mbar. Preamorphization of the sample was achieved using a 10 keV $^{28}Si^+$ beam at a dose of 5×10^{15} cm^{-2}. The ion beam current density was below 0.6 μA cm^{-2} which prevented sample heating during amorphization

In order to make accurate comparisons between B implants into preamorphized and crystalline Si, only half of the sample was bombarded by Si by moving the target partly out of the rectangular cross section Si beam after which the whole sample was B implanted. This novel approach minimizes the possible causes of misinterpretations so that the influence of preamorphization on dopant channelling and/or dopant diffusion can be clarified.

Boron ^{11}B was implanted at several energies ranging from 100 eV to 2 keV and at dose levels from 2×10^{13} to 1×10^{15} cm^{-2}. The B beam current density was about 0.08 μA cm^{-2}. The ion beam width and heigh were 1 and 2 cm respectively. Following boron implantation, in situ thermal annealing at 550 °C was used for 20 min to regrow the crystal by solid phase epitaxy (SPE) [13] and remove the damage created by both Si and B implantations. Finally the samples were covered by a 10–20 nm isotopic ^{28}Si cap layer grown at room temperature (RT) by ion beam deposition (IBD) [16,17] at a energy in the range of 40–60 eV. This technique allows the equilibration of the altered layer in SIMS due to oxygen bombardement which is necessary to give high constant ion yields, prior to the erosion reaching the original surface. This latter is marked by the onset of the ^{30}Si signal. This procedure enables measurements of shallow profiles to be obtained without distortion due to matrix effects.

3. Results and discussion

Fig. 1 shows an aligned RBS spectrum obtained for two different samples implanted with 10 keV $^{28}Si^+$ to doses of 1×10^{15} and 5×10^{15} cm^{-2}. The surface peak height reaches the silicon random level confirming that a complete and continuous amorphous layer was obtained for both bombardments. Some carbon and oxygen are also present at the surface. These contaminants are mainly produced during the transfer and RBS analysis of the sample rather than during implantation. From the RBS spectrum the thickness of the amorphous layer was estimated to be 25 and 18 nm for higher and lower doses, respectively. Since all boron implants were carried out in samples preamorphized with the higher silicon dose (5×10^{15} cm^{-2}), the preamorphized depth

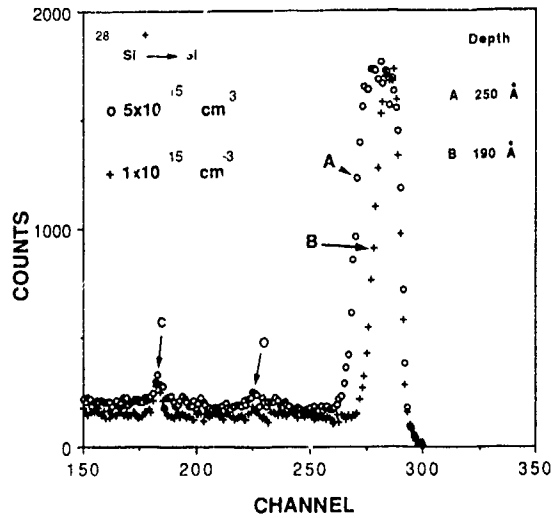

Fig. 1. RBS spectra obtained from two samples preamorphized by silicon ion implantation at 10 keV and doses of 5×10^{15} cm^{-2} (sample A) and 1×10^{15} cm^{-2} (sample B)

layer was sufficient to contain the entire range of the implanted boron, thus eliminating boron channelling [18].

Figs 2, 3 and 4 show the boron profiles obtained, using a Cameca IMS 4f at 2 keV primary O_2 ions and 0.1 μA, on both amorphous and crystalline silicon for samples implanted with B^+ at various energies and doses. In some samples (see fig. 3), a variation in the thickness of the silicon cap layer does exist as a consequence of a nonuniformity of the Si beam during capping. This does not affect the determination of the interface which is characterized by the appearance of the ^{30}Si signal. As shown in fig. 2, for a 2 keV boron implant, the effect of channelling into the crystalline

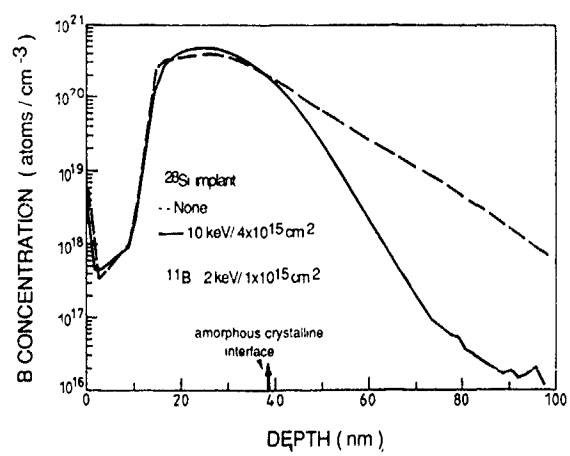

Fig. 2. SIMS profiles of B-implanted sample (1×10^{15} cm^{-2} at 2 keV) with (solid line) and without (dashed line) Si preamorphization.

Table 1
Comparison between the experimental projected range R_p and the calculated one, using PRAL [19], at low energy boron implantation

B energy	R_p [Å]	
	calculated [19]	experimental
200 eV	18	55
500 eV	33	60
1 keV	54	85
2 keV	94	137

silicon (dashed line) is as expected, far more significant than in the preamorphous region (solid line) and the broad, long tailed implant distribution is characteristic of channelling effects seen at higher energies. The depth of the junction defined at the background concentration of 1×10^{16} cm^{-3} for the amorphous region is approximately half that in the crystalline one. In table 1 the present experimental values of R_p are reported (R_p is the boron projected range). These values are rather large compared to the calculated one using PRAL [19] and the difference increases at lower energy. One possible reason for this lack of agreement is that the physical basis of fast simulation codes used in PRAL becomes less realistic at low energies. However, defect-related diffusion process may also be important in determining the form of the boron distribution in both the initially crystalline and preamorphous samples and may distort the effects of channelling. In the preamorphized samples, no boron channelling would be expected. During post implantation annealing, even though SPE does not lead to redistribution of the implant, the remnant damage close to the surface, may affect the final boron distribution. This damage has been reported by Mazzone [20] and Servidori and co-workers [21] who identified it as a vacancy-rich region. Incomplete annealing of very low energy damaged silicon has also been investigated by Al-Bayati and co-workers [22] who observed highly stable, near-surface damage following annealing at temperatures up to 900 °C. The precise contribution of defect-related diffusion is difficult to assess but the main features of the data shown in figs. 3 and 4 can be explained in terms of channelling effects. At the low energies used, the large critical angles for channelling, which would enhance the effect, are compensated by the large scattering cross sections which would tend to lead to rapid de-channelling. Hence in view of these cross sections it is expected that ions incident on either the crystalline or amorphous samples would initially have similar scattering probabilities. Thus the range distributions close to the surface would be the same as is observed. However, for the crystalline sample, ions incident close to the centre of channels may travel a considerable distance before de-channelling because of the large effective critical angles, i.e., they may be hyperchannelled. These particles are not stopped in the immediate subsurface region and the observed depth distribution would fall below that for the amorphous sample. This contrasts with the conventional, high energy situation. In fig. 2, the smaller critical angles lead to more uniform de-channelling with depth and a channelled range distribution which is always broader than that for the amorphous target. The channelled particles in the low energy situations are eventually stopped at greater depths and make up the observed tails in the distributions which extend beyond the range in the amorphous material.

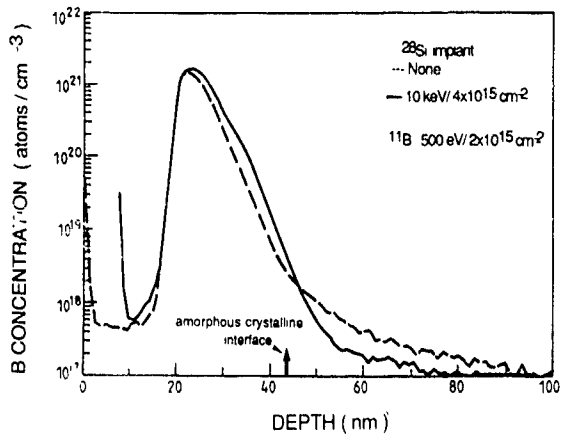

Fig. 3. SIMS profiles of B-implanted sample (2×10^{14} cm^{-2} at 500 eV) with (solid line) and without (dashed line) Si preamorphization

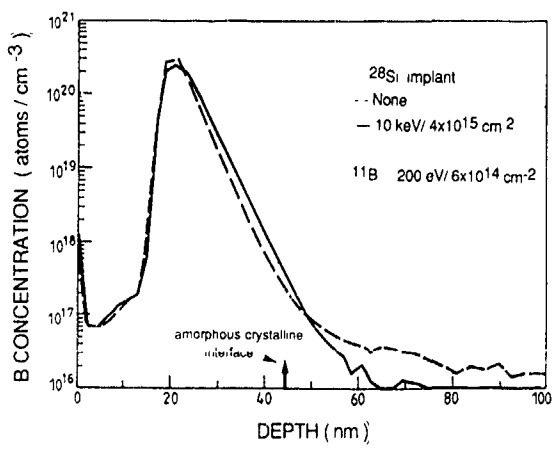

Fig. 4. SIMS profiles of B-implanted sample (6×10^{14} cm^{-2} at 200 eV) with (solid line) and without (dashed line) Si preamorphization

4. Conclusion

It is shown in the present results that preamorphization is not an important process in reducing the junction depth at very low boron energies (< 500 eV). This is different from the situation observed at 2 keV and at the much higher energies reported in the literature [10,18,23] where preamorphization leads to a significant reduction. It is also shown that shallow p^+–n junctions with 20 nm full width at half maximum (FWHM) are obtained. Using a four-point probe sheet resistance measurement on similar samples with no Si cap layer and annealed at 600 °C for 20 min, a carrier concentration of 10^{20} cm^{-3}, estimated from a sheet resistance of 750 Ω/□ [24], was obtained. This value was an average of four measurements taken on different spots of the 1 cm^2 sample. Differences between these measurements were less than 10%.

Despite the shallow p^+–n junctions obtained, a small percentage of the dopant particles introduced at low energies do penetrate to depths significantly beyond the mean projected range. For 200 eV B bombardment, dopant concentration in excess of 10^{16} cm^{-3} persist at depths greater than 80 nm. To date the data cannot confirm the mechanism by which the particles reach this depth but channeling rather than some form of radiation enhanced diffusion either during implantation or annealing is considered to be the most probable explanation.

References

[1] Y. Ota, J Appl Phys 51 (1980) 1102.
[2] H Sigiura, J Appl Phys. 51 (1980) 2630
[3] Y Ota, Thin Solid Films 106 (1983) 3
[4] T M Liu and W.G. Oldham, IEEE Electron Device Lett. EDL-4 (1983) 59
[5] E. Ganin, B. Davari, D. Harane, G Scilla and G.A. Sai-Halasz, Appl Phys. Lett. 54 (1989) 2127.
[6] R Koshke and K Ehinger, Nucl. Instr. and Meth. B37/38 (1989) 823
[7] K. Cho, W.R Allen, T G. Finstad, W K Chu, J Liu and J.J. Wortman, Nucl. Instr. and Meth. B7/8 (1985) 265.
[8] P. Blood, G. Dearnaley and M.A. Wilkins, J Appl. Phys 45 (1974) 5123
[9] B Y. Tsaur and C.H Anderson Jr, J. Appl. Phys. 54 (1989) 6336.
[10] M C. Ozturk, J J. Wortman and R.B. Fair, Appl. Phys Lett. 52 (1988) 963
[11] A.C Ajmera and G A Rozgoni, Appl Phys Lett. 49 (1986) 1269.
[12] P. Mei, B. Jalali, E.S. Yang, N.G Stoffel and D L. Hart, Appl Phys. Lett 56 (1990) 1362.
[13] M.Y Tsai and B G Streetman, J Appl Phys 50 (1979) 183.
[14] C.M. Lin, A J Sleckl and T P. Chow, Appl. Phys Lett 54 (1989) 1790
[15] D G Armour, P. Bailey and G Sharples, Vacuum 36 (1986) 769
[16] P C. Zalm and L J Beckers, Appl. Phys Lett 41 (1982) 167
[17] R.A Zuhr, B R. Appleton, N Herbots, B C Larson, T.S. Noggle and S.J. Pennycook, J Vac Sci Technol. A5 (1987) 2135.
[18] A.E Michel, W Rausch and P A Ronsheim, Appl. Phys. Lett 51 (1987) 487
[19] J P. Biersack and J F Ziegler, in Ion Implantation Techniques, eds H Ryssel and J H Glawishnig. Springer Ser in Electrophysics, vol 10, (1982) p 157
[20] A M Mazzone, Phys Status Solidi A95 (1986) 149
[21] M. Servidori, R. Angelucci, F Cembali, P Negrini and S Solmi, J. Appl. Phys 61 (1987) 1834
[22] A H. Al-Bayati, K.G Orrman-Rossiter and D.G. Armour, to be published
[23] R.G. Wilson, J. Appl Phys 54 (1983) 6879.
[24] A. Bousetta, J A. Van den Berg and D G. Armour, unpublished

Nuclear Instruments and Methods in Physics Research B55 (1991) 569–572
North-Holland

Shallow junction formation by dual Ge/B, Sn/B and Pb/B implants

V. Hašlar [a], P. Seidl [a], P. Hazdra [b], R. Gwilliam [c] and B. Sealy [c]

[a] *Ion Implantation Laboratory, Czech Technical University Prague, Suchbátarova 2, 166 27 Praha 6, Czechoslovakia*
[b] *Department of Microelectronics, Czech Technical University Prague, Suchbátarova 2, 166 27 Praha 6, Czechoslovakia*
[c] *Department of Electronic and Electrical Engineering, University of Surrey, Guildford, Surrey GU2 5XH, UK*

Shallow p^+n junctions were produced in silicon by dual Ge/B, Sn/B and Pb/B implants followed by RTA or FURIA annealing. Electrical properties (sheet-resistance and I–V characteristics) of fabricated shallow junctions were investigated for each of the preamorphizing elements and different types of annealing. The analytical techniques used include DLTS as well for monitoring the defect structure in the vicinity of the junction. The results are discussed for different amorphizing and annealing conditions from the viewpoint of literature data.

1. Introduction

Shallow source/drain junctions are one of the key requirements for VLSI technologies as a result of so-called scaling laws. At present ion implantation is the best controlled technique for semiconductor doping and its use for shallow junction formation has been extensively studied during the last decade. The attention has been paid especially to shallow p^+n junctions which are difficult to form due to the significant channeling of boron at low energies [1]. One approach to the problem is to replace boron by molecular or heavy ions such as BF_2^+ [2] and Ga^+ [3]. Another way is to amorphize the substrate by an implantation of heavy ions prior to the boron implantation [4]. The major problem in this technique is the presence of various classes of implantation defects which may enhance boron diffusion [5] and strongly affect the electrical properties of the junction [6]. Obvious candidates for preamorphization in silicon were the elements from group IV of the periodic table: Si and later Ge [6–8]. More recently Sn^+ preamorphization has been examined [9,10] with very good results in terms of the magnitude of reverse leakage currents. An explanation of the results was given in ref. [10] by the suppression of the generation efficiency for centers close to the junction in the moderately lightly doped substrates.

The aim of this paper is to compare the effect of preamorphization by three different elements (Ge, Sn, Pb) from the viewpoint of electrical properties. The conditions of preamorphization were chosen to be practically identical in terms of amorphous layer depths.

2. Experimental

The substrate used was CZ n-Si with a resistivity of 3.5–5.5 Ω cm and ⟨100⟩ orientation. A thick (450 nm) oxide film was grown in wet oxygen on the surface of the wafer. The windows for five different diode structures of areas ranging from 2.6×10^{-4} to 34.2×10^{-4} cm^2 with perimeters from 0.064 to 0.234 cm were opened in the oxide by photolithography. After cleaning and growing of 15 nm thick thermal screening oxide, preamorphization was carried out with the parameters given in table 1. The parameters were determined on the basis of optimum Ge preamorphization for 10 keV boron implantation as given by Ozturk et al. [11], using the empirical recipe of Thornton et al. [12] for a safe amorphization dose and the depth of the amorphous layer, and verified by the Monte Carlo simulation program TRIM 88 [13]. According to TRIM 88 the thickness of the amorphous layer in silicon should be within 75–85 nm for all three implants. After preamorphization $^{11}B^+$ was implanted at 10 keV at a dose of 1×10^{15} cm^{-2}. The implantations were done at a tilt angle of 7° and the implanter beam current was kept below 1 μA/cm^2. Three types of annealing were used: (1) RTA (1050 °C/10 s, see ref. [11]), (2) two-step (2ST) anneal-

Table 1
The parameters of preamorphizing implants (E: ion energy, N_D: implanted dose, R_p and δR_p mean projected range and standard projected deviation, respectively, after the removal of screening oxide)

Ion	E [keV]	N_D [10^{15} cm^{-2}]	Measurement (SIMS)		Simulation (TRIM 88)	
			R_p [nm]	δR_p [nm]	R_p [nm]	δR_p [nm]
$^{74}Ge^+$	70	1	37	31.6	38.2	18.5
$^{120}Sn^+$	98	1	37.5	20	38.5	14.9
$^{208}Pb^+$	150	0.7	47.2	16.1	43.3	12.6

0168-583X/91/$03.50 © 1991 – Elsevier Science Publishers B.V. (North-Holland)

ing (furnace: 550 °C/30 min + RTA · 1050 °C/10 s) and (3) FURIA (furnace rapid isothermal annealing) at 1050 °C for 10 s. The annealing was performed in a nitrogen ambient. The SHS 1000 AST system was used for RTA with a mean ramp rate of 120 °C/s. Before the measurements the screening oxide was removed and the diode structures were contacted by a tungsten tip. The I–V characteristics were measured by an HP 4140B pA-meter and for DLTS measurements a DLS-82E SemiTrap spectrometer was used at standard conditions (frequency 480 Hz, temperature ranging from 78 to 350 K).

The samples used for SIMS and sheet-resistance measurements were prepared analogically without any patterning. SIMS profiles were measured with the CAMECA system using bombardment by 10 and 15 keV O^+ and 5 keV Cs^+ primary beams.

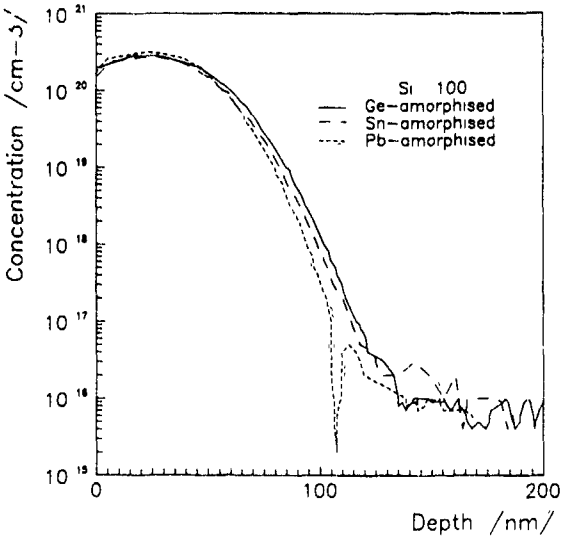

Fig 1 SIMS profiles of as-implanted boron (10 keV, 1×10^{15} cm^{-2}) for different types of preamorphizations

3. Results and Discussion

The as-implanted profiles of boron for all three types of amorphizations as measured by SIMS after the removal of screening oxide are shown in fig 1 and the corresponding profile parameters are given in table 2. According to TRIM 88 R_p and δR_p in silicon are equal to 29.6 and 21.4 nm, respectively, which is in good agreement with the results of ref. [11].

Areal junction leakage densities I_A at −5 V were obtained by plotting the reverse current against the junction area. The standard deviation of I_A was found to be within 30% of the mean value across the wafer. The areal leakage values together with the corresponding sheet resistance are given in table 3.

The C–V measurements at room temperature did not reveal any influence of different types of preamorphizations and annealings on carrier concentration in depths of more than 0.6 μm below the junction. The DLTS spectra of samples after 2ST annealing and RTA measured to 0.85 μm beyond the junction position showed minority carrier traps in the concentration of $\sim 10^{13}$ cm^{-3} (fig. 2) associated probably with the deep donors. In the case of FURIA the shape of the DLTS spectra is slightly different (see fig. 3), the concentration of deep donors being lower by one order of magnitude. The complexity of the DLTS spectra suggests that the origin of DLTS signal is caused by defect clusters rather than by isolated defects. In Pb^+ amorphized samples an electron trap emission peak was detected at 85 K (activation energy 0.17 eV, capture cross section 6×10^{-19} cm^{-2}) with the concentration profile extending to 1.5 μm below the junction. According to ref. [14] this

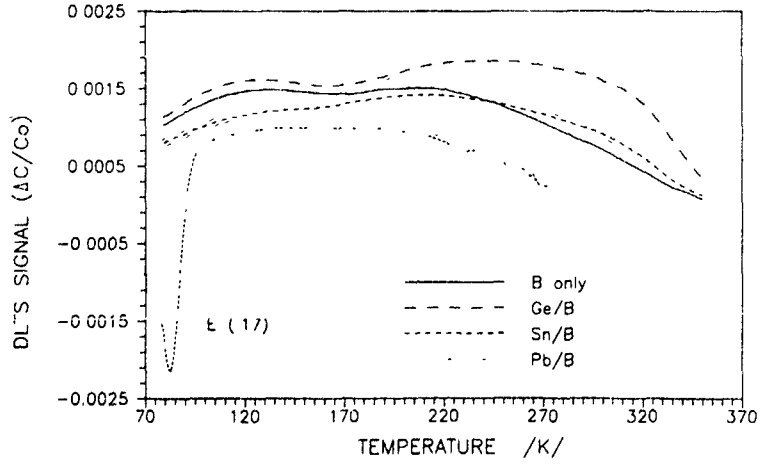

Fig. 2 DLTS spectra of RTA annealed samples (1050 °C/10 s in nitrogen); reverse bias −0.4 V, filling pulse 10 mA/100 μs

Table 2
The parameters of as-implanted boron profile in silicon determined by SIMS for different amorphization conditions

Amorphization	R_p [nm]	δR_p [nm]
Ge	26.4	22
Sn	25	15.6
Pb	22 2	15.1

Table 3
The values of areal leakage current density I_A and sheet resistance $R_\square$ for different annealing conditions

Amorphization	Annealing	I_A [nA/cm^2]	$R_\square$ [Ω/□]
Non.	2ST	9	108
	RTA	15	107
	FURIA	1.1	493
Ge	2ST	18	109
	RTA	14	110
	FURIA	1.3	126
Sn	2ST	7.6	115
	RTA	7.0	114
	FURIA	2 3	146
Pb	2ST	170	120
	RTA	160	117
	FURIA	50	221

peak corresponds to the lead acceptor level in Si. This finding is consistent with the depth profiles of Pb and B in RTA samples (fig 4).

The given results indicate that there is no significant difference between 2ST annealing and RTA. In addition, B and Ge/B implants have comparable values of I_A and $R_\square$, suggesting that the properties of Ge/B samples may not be influenced primarily by preamorphization but more probably by annealing The moderate decrease of I_A in the Sn/B set compared to

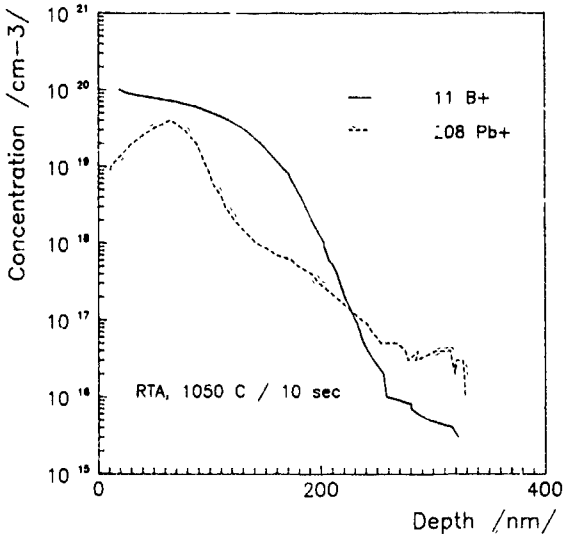

Fig 4. SIMS profiles of $^{11}B^+$ and $^{208}Pb^+$ after RTA (1050 °C/10 s in nitrogen)

the Ge/B results could be due to more pronounced free-hole suppression of generation current [10] or more complete defect removal. The first possibility supposes enhanced boron movement already described in Sn-implanted samples [10] which could be verified only by the junction depth measurements. The same reason can explain the low values of leakage current density for FURIA samples. This viewpoint is supported by the considerable boron diffusion in Pb/B samples during RTA (fig 4): using a background concentration of 1×10^{16} cm^{-3} the junction depth is 260 nm, while in Ge/B samples under the same experimental conditions the junction depth is reported to be only about 200 nm [11] The leakage current in Pb/B samples is probably increased by the lead profile extending deeply beyond

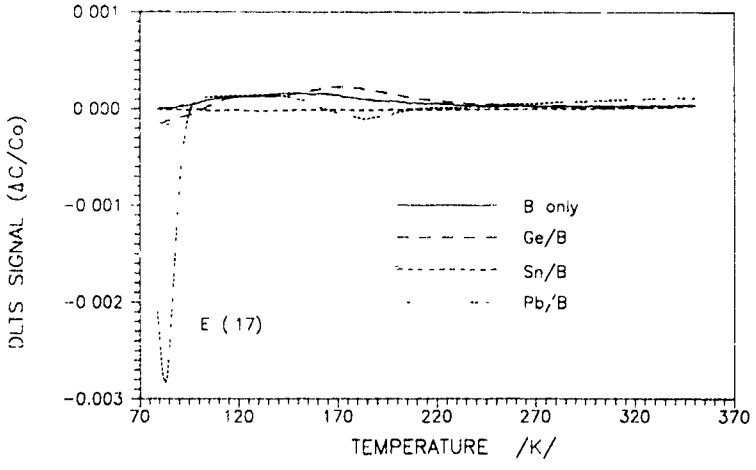

Fig. 3 DLTS spectra of FURIA annealed samples (1050 °C/10 s in nitrogen), reverse bias −0.4 V, filling pulse 10 mA/100 μs

the boron junction. Thus it seems that higher R_s-values in Sn- and Pb-implanted samples can only hardly be explained by the lower junction depth but rather by the lower dopant activation (this is the case of the non-pre-amorphized FURIA annealed sample where the preliminary results of electrochemical profiling revealed considerably lower surface concentration) or higher defect concentration in the p^+ layer (the effect of low solubility of Sn and Pb in silicon combined with the possible effect of recoiled oxygen from the screening oxide).

Acknowledgements

The authors wish to thank Ing. P. Kalina from Tesla VUST for diode fabrication. Special thanks are due to Ing. M. Šumbera and Ing. V. Tesař from Tesla Rožnov who carried out both RTA and FURIA.

References

[1] K. Cho, W.R. Allen, T.G. Finstad, W.K. Chu, J. Liu and J.J. Wortman, Nucl. Instr. and Meth. B7 (1985) 265

[2] I.-W. Wu, R.T. Fulks and J.C. Mikkelsen, Jr., J. Appl. Phys. 60 (1986) 2422.

[3] C.-M. Lin, A.J. Steckl and T.P. Chow, Appl. Phys. Lett. 54 (1989) 1790

[4] B.-Y. Tsaur and C.H. Anderson, Jr., J. Appl. Phys. 54 (1983) 6336

[5] R.B. Fair, Nucl. Instr. and Meth. B37/38 (1989) 371

[6] S.D. Brotherton, J.P. Gowers, N.D. Young, J.B. Clegg and J.R. Ayres, J. Appl. Phys. 60 (1986) 3567

[7] J.R. Ayres, S.D. Brotherton, J.B. Clegg and A. Gill, J. Appl. Phys. 62 (1987) 3628

[8] A.C. Ajmera and G.A. Rozgonyi, Appl. Phys. Lett. 49 (1986) 1269.

[9] M. Delfino, A.E. Morgan and D.K. Sadana, Nucl. Instr. and Meth. B19/20 (1987) 363.

[10] J.R. Ayres, S.D. Brotherton, J.B. Clegg, A. Gill and J.P. Gowers, Semicond. Sci. Technol. 4 (1989) 339

[11] M.C. Ozturk, J.J. Wortman, C.M. Osburn, A. Ajmera, G.A. Rozgonyi, E. Frey, W.-K. Chu and C. Lee, IEEE Trans. Electron Devices 35 (1988) 659

[12] J. Thornton, P.L.F. Hemment and I.H. Wilson, Nucl. Instr. and Meth. B19/20 (1987) 307

[13] J.P. Biersack and L.G. Haggmark, Nucl. Instr. and Meth. 174 (1980) 257

[14] W. Fahrner and A. Goetzberger, Appl. Phys. Lett. 21 (1972) 329

Nuclear Instruments and Methods in Physics Research B55 (1991) 573–575
North-Holland

Sublimation and diffusion of arsenic implanted into silicon at rapid electron beam annealing

R. Grötzschel
Central Institute of Nuclear Research, Rossendorf, Germany

V.A. Kagadey and N.I. Lebedeva
Institute of Semiconductor Devices, Tomsk, USSR

D.I. Proskurovsky
Institute of High Current Electronics, Tomsk, USSR

Properties of silicon layers implanted with As^+ ions (100 keV, 10^{16} cm^{-2}) through 30 nm SiO_2 film and annealed in vacuum by means of a 15 s duration electron beam were studied using Rutherford backscattering plus channeling and electrical measurements. The influence of the irradiation conditions on As activation, diffusion and sublimation, as well as on the crystal structure perfection of the samples are discussed. Results have been obtained which testify to As sublimation and diffusion in connection with its deactivation in the area of realization of an electrically active As nonequilibrium concentration.

1. Introduction

It is established [1–4], that the annealing of implanted layers of Si⟨As^+⟩ using pulse annealing (10 ns–1 μs) or certain conditions of rapid thermal annealing (RTA) result in the realization of a nonequilibrium concentration of electrically active As. However, further thermal treatments (as well as RTA duration increase) result in an impurity deactivation and the obtaining of an equilibrium concentration value (3×10^{20} cm^{-3} at 1370 K). When the As concentration, as implanted, in a distribution maximum exceeds $N_{max} = 4 \times 10^{20}$ cm^{-3}, an enhanced As diffusion into the Si bulk is observed during a photon annealing process (PA), but no As sublimation occurs usually [3]. Whereas, using an electron beam annealing (EBA), one does not observe considerable As atom diffusion into the bulk, as a rule, and a certain part of these atoms sublimate [4]. This report is devoted to elucidating the reasons for the aforesaid peculiarities in the As atom behaviour in Si at EBA, as well as to investigate possible connections between the deactivation, sublimation and impurity diffusion processes.

2. Experimental

(100) Si was implanted with As^+ ions ($E = 100$ keV, $\mathcal{D} = 1 \times 10^{16}$ cm^{-2}, $N_{max} = 1.5 \times 10^{21}$ cm^{-3}) through an SiO_2 film (30 nm). The annealing of samples was made by a 15 s duration electron beam. The temperature of the samples reached $T_{max} = 1400$ or 1490 K. The dwell time at these temperatures was 5 s. Two sample pairs were irradiated simultaneously. The film was previously removed from the surface of one sample pair and preserved on the other one to capsulate surfaces at the annealing. One sample from each pair was irradiated from the implanted layer (front to beam) and the other from the back side (back to beam). The samples were investigated by the Van der Pauw method and Rutherford backscattering spectroscopy (RBS) plus channeling of He^+ ions (1.7 MeV).

3. Results

The analysis of RBS spectra yielded the values of $\chi_{min} \sim 0.04$ at $T_{max} = 1400$ K, and 0.03 at $T_{max} = 1490$ K. These values of χ_{min} show the high quality of the crystal structure in the recrystallized layer. Besides, the quality of the crystal structure does not depend on the direction of irradiation as well as the presence of an SiO_2 cap layer, being only determined by the annealing temperature.

After the annealing at $T_{max} = 1400$ K only 50–60% of the As atoms being in substituting positions are electrically active, so the decrease in electrical activation at this temperature can be partially associated with the

0168-583X/91/$03.50 © 1991 – Elsevier Science Publishers B.V (North-Holland)

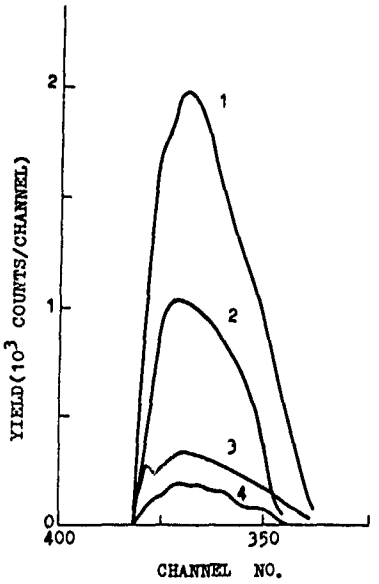

Fig. 1 RBS and channeling spectra of As implanted Si irradiated from the implanted layer: (1,3) with SiO_2, (2,4) without SiO_2; (1,2) random, (3,4) aligned. $T_{max} = 1490$ K

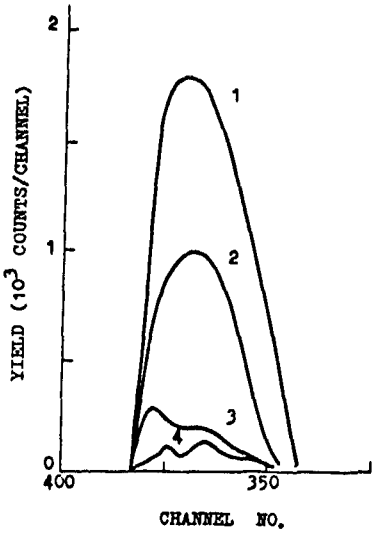

Fig. 2. RBS and channeling spectra of As implanted Si irradiated from the back wafer side. (1,3) with SiO_2, (2,4) without SiO_2; (1,2) random, (3,4) aligned $T_{max} = 1490$ K.

formation of either impurity–defect complexes [1] or coherent precipitates [2]. Moreover, the area density of the interstitial As in the samples after the annealing at $T_{max} = 1400$ K under the SiO_2 cap (4×10^{15} cm^{-2}) considerably exceeds the corresponding As concentration in noncapsulated samples (0.45×10^{15} cm^{-2}). These data coincide with our previous data [4] and they confirm the fact that As^+ deactivation connected with As displacement into the interstices is also realized. If the SiO_2 film impedes the following sublimation of the As atoms from Si, their amount in channels is increased, RBS and He^+ ion channeling testify to that fact. We also think that no As atoms from the Si near-surface region go out onto the surface and sublimate, but only those from the interstices.

The RBS spectra characterizing the depth distribution of As atoms in Si wafer are depicted in figs. 1 and 2. The results obtained from the analysis of these spectra are presented in table 1. Comparison of the values of N_s and N_f show that after the annealing at $T_{max} = 1490$ K all the As atoms in substituting positions are electrically active. So at this temperature the deactivation mechanism connected with the As atom displacement into the interstices may be considered to be dominating. In this case, after the annealing under the SiO_2 cap layers, as electrical activity reaches about 90% of the implanted As dose, while at the annealing without SiO_2, it decreases to 45% with 55% implanted ions sublimating. The sublimation intensity is considerably decreased by the SiO_2 film capsulation. Moreover the intensity of sublimation is affected by the radiation direction: the amount of sublimated As atoms is smaller for samples irradiated from the implanted layer side. This effect is more noticeable for the SiO_2 capsulated samples. This can be explained by the formation of a thin film of

Table 1
Data of RBS and channeling spectra and Van der Pauw measurements of As implanted Si ($T_{max} = 1490$ K). N_r and N_a are the random and aligned area density of As atoms, respectively; $f = (1 - \chi_{As})/(1 - \chi_{min})$ is the fraction of As atoms on lattice sites; $N_f = N_r f$ is the density of As atoms on lattice sites, N_{subl} is the sublimated density of As atoms; N_s is the sheet carrier concentration.

Irradiation conditions	N_r [$\times 10^{15}$ cm^{-2}]	N_a [$\times 10^{15}$ cm^{-2}]	f	N_f [$\times 10^{15}$ cm^{-2}]	N_{subl} [$\times 10^{15}$ cm^{-2}]	N_s [$\times 10^{15}$ cm^{-2}]
With SiO_2						
front to beam	9.4	1.3	0.89	8.8	0.6	8.4
back to beam	8.1	1.0	0.91	7.6	1.9	9.1
Without SiO_2						
front to beam	4.1	0.7	0.86	3.7	5.9	4.5
back to beam	3.9	0.4	0.92	3.6	6.1	4.9

polymerized oil from the residual atmosphere on the surface irradiated by the electron beam. Perhaps this film covers the defects in the SiO_2 cap layer formed due to the As^+ implantation, thus resulting in As loss minimization from 19 to 6% of the implanted As dose.

The diffusion of As is also dependent on the conditions on the implanted layer surface. At the presence of the SiO_2 film at $T_{max} = 1490$ K, an enhanced As diffusion in the Si bulk is observed, the diffusion coefficient being $\mathcal{D} = 3.6 \times 10^{-12}$ cm^2/s. This $\mathcal{D}$ value is within the range of $\mathcal{D} = (2.4\text{–}12) \times 10^{-12}$ cm^2/s, determined in experiments on the photon annealing of similar samples [5]. At the same time the diffusion of As into the bulk is much weaker at the annealing of uncapsulated samples ($\mathcal{D} = 1.3 \times 10^{-12}$ cm^2/s).

4. Discussion

There are some different models [6–8] and their modifications explaining the mechanism of the enhanced impurity diffusion at RTA. The results we have obtained by RTA are in favour of the interstitial mechanism of diffusion, whereby substitutional dopant atoms are displaced from site to site by passing interstitials [8] (relay-race mechanism).

The spectra analysis of RBS and channeling of He^+ ions show that in $Si\langle As^+\rangle$ samples, being in a thermodynamical equilibrium state, the ratio of the As concentration in the interstitial state to that in the substituting state (at $\chi_{min} \leq 0.04$) is within the range of 0.01–0.1.

The deactivation of the impurity in the samples implanted with a large dose of As^+ results in the appearance of a non-equilibrium As excess in the interstices, which has a tendency of being "dispersed". If sublimation is possible, the above-mentioned ratio at the surface is sharply diminished and there occurs a replenishment of the near-surface region by the interstitial atoms using the relay-race-mechanism As a result the flux of excessive interstitial As atoms moves toward the surface. If the surface is capsulated this ratio is not diminished there by the sublimation and, with the As reactivation at the surface being excluded due to the As active concentration relaxed to the equilibrium value, it is thermodynamically more efficient for nonequilibrium interstitial As atoms appearing at deactivation to diffuse into the Si bulk. It is in this case that we observe the enhanced As diffusion with the diffusivity exceeding many times the equilibrium value (defined by a vacancy mechanism) for these temperatures. The necessity of the realization of the above-mentioned ratio results in the interstitial As atoms reactivating in the Si bulk. This process increases the As electrical activity in the SiO_2 capsulated samples.

Thus the peculiarities in the behaviour of As atoms in $Si\langle As^+\rangle$ at the PA and EBA in similar regimes are defined by different conditions, realized on the implanted layer surface, as far as at the photon annealing, even when the samples are not previously capsulated, a SiO_2 film of ~ 10 nm is formed on the Si surface, which prevents As sublimation

References

[1] A Lietoila, J Gibbons and T W Sigmon, Appl. Phys Lett. 36 (1980) 765.
[2] V P Popov, A V. Dvurechenskii, B P Kashnikov and A I Popov, Phys Status Solidi A94 (1986) 569
[3] A Nylandsted, O. Larsen and V E Borisenko, Appl Phys A33 (1984) 51.
[4] V.S Budishevsky, R. Grotzschel, V A Kagadei, N.I Lebedeva, D I. Proskurovsky and E B Yankelevich, Phys Res. 8 (1988) 262
[5] J. Narayan and O W Holland, J. Appl Phys 56 (1984) 2913.
[6] M. Servidori and S Solmi, J Appl Phys 65 (1989) 98
[7] R Kalish, T O Sedgwick and S. Maden, Appl Phys. Lett 44 (1984) 107
[8] S J Pennycock, J. Narayan and O W Holland, J Electrochem Soc. 132 (1985) 1962.

Nuclear Instruments and Methods in Physics Research B55 (1991) 576–579
North-Holland

Thermal-annealing effects on the structural and electrical properties of heavy-ion-implanted silicon layers

Jumana Said and Gérard Ghibaudo

Laboratoire de Physique des Composants à Semiconducteurs, CNRS (UA 840), 23 rue des Martyrs, BP 257, 38016 Grenoble Cedex, France

Iannis Stoemenos

Department of Physics, University of Thessaloniki, Thessaloniki, Greece

Peter Zaumseil

Akademie der Wissenschaften der DDR, Institute für Halbleiterphysik, Körsing Strasse 2, 1200-Frankfurt/Oder, Germany

A study is made of the thermal-annealing effects on the electrical and structural properties of heavily damaged silicon layers induced by high-dose arsenic implantation. The combination of electrical, transmission-electron microscopy (TEM) and triple-crystal X-ray diffraction (TCD) measurements allows us to separate the existence of a local impurity-activation process from the amorphous–crystal transformation The local process occurs in the highly damaged surface layer induced by the arsenic implantation and is efficient well below the solid-phase epitaxy transition temperature. It is suggested that point-defect migration should play an important role in the electrical-impurity activation at low annealing temperatures

1. Introduction

In recent years ion implantation in semiconductors has received great attention. Especially, this process provides doping techniques with several potential advantages over standard methods used in device fabrication Inherent in the implantation process is the possibility of introducing a wide range of atomic species into a variety of substrates and avoiding certain undesirable effects that accompany the classical high-temperature diffusion process. However, ion implantation has the serious disadvantage of creating a large amount of defects and even surface amorphization of the target material [1]. All the defects introduced during the ion implantation considerably alter the electrical properties of the semiconductors and have to be removed by subsequent thermal annealing in order to enable the implanted atoms to take a substitutional lattice site and, thereby, achieve a complete electrical activation of the dopants.

Details concerning the post-implantation thermal treatments have been reported for most of the common silicon dopants; however, there is considerable confusion about the mechanisms by which the impurities are electrically activated and the surface layer reconstructed.

In this work, electrical and physical characterization methods were used to investigate separately the roles of these two distinct processes.

2. Experimental

Samples were realized on 3.9 Ω cm ⟨100⟩ p-type silicon substrate. Prior to implantation, the wafers were provided with a 40 nm thick SiO_2 thermally grown passivating layer. Arsenic implantation was performed at room temperature, at various doses and energies (10^{13} to 8×10^{15}, As^+/cm^2 150–200 keV). After implantation, the samples were furnace-annealed in flowing nitrogen under different conditions (temperature: 200–1100 °C, duration: 0–120 min). The spreading-resistance measurements were carried out on ASR-100B equipment made by Solid State Measurements, Inc. The resistivity profile was obtained from the gross spreading-resistance curve by applying the local-slope approximation of the Dickey model [2]. The characterization of the lattice defects induced in highly arsenic-implanted samples and their evolution after annealing was made by triple-crystal X-ray diffraction (TCD) and transmission electron microscopy (TEM) experiments. From the former technique, the nature and depth posi-

0168-583X/91/$03.50 © 1991 – Elsevier Science Publishers B.V. (North-Holland)

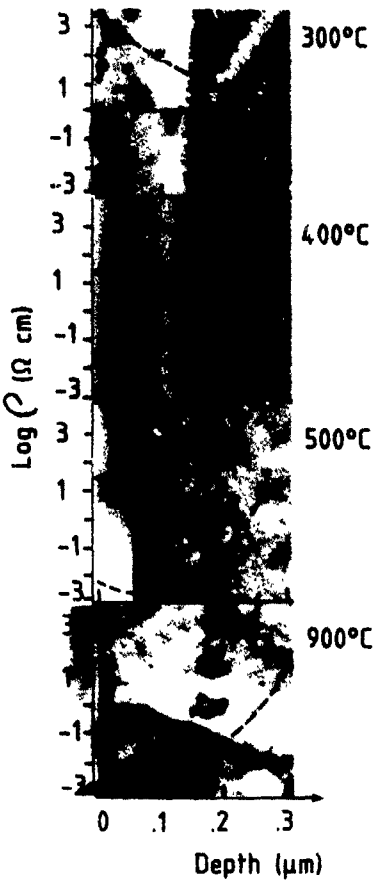

Fig 1 Resistivity profiles and TEM micrographs as obtained after various isochronal (1 h) anneals (2×10^{14} As^+/cm^2, 200 keV)

tion of the residual strain were determined by the analysis of the rocking curves obtained by using a standard (n, $-n$, n) parallel geometry [3]. Cross-sectional TEM observations were realized to obtain the spatial extent of the defected region and the amoprhous-layer thickness at the surface of the implanted sample both before and after thermal annealing. In addition, in situ TEM micrographs were elaborated in order to investigate the kinetics of the recrystallization by solid-phase epitaxy

3. Results and analysis

In fig. 1 resistivity profiles are superimposed on TEM micrographs obtained for a n + /p sample implanted at 2×10^{14} As^+/cm^2 and isochronally annealed (1 h) at different temperatures. After annealing, the surface resistivity of a low-temperature annealed sample (400 °C, 1 h) drops by more than 7 decades, though the surface layer is still amorphous. Furthermore, in spite of the sharp a–c interface, no resistivity discontinuity does appear and the recrystallization of the amorphous layer seems to be independent of the dopant electrical activation.

The above results, correlated with the sheet-resistance data of ref. [4], lead us to conclude that this decrease of the surface resistivity occurs at an annealing temperature around 420–430 °C mainly because of the electrical activation of the majority of the impurity atoms within a highly damaged surface region (100 nm thick in the case of the sample shown in fig. 1).

Thus we suggest that a local impurity activation occurs both in the crystalline and in the amorphous regions via a local reconstruction process. Therefore, the resistivity $\rho(x)$ can be described by an exponential kinetics function of the annealing time t as [4]

$$\rho(x,t)=\rho_f(x)+[\rho_i(x)-\rho_f(x)]\exp[-t/\tau(x)], \tag{1}$$

where $\rho_f(x)$ and $\rho_i(x)$ are, respectively, the final and initial values of $\rho(x)$ and $\tau(x)$ is the relaxation time constant of the local electrical activation process at depth x. In practice, $\rho_f(x)$ is given by the resistivity profile of a well-annealed sample and $\rho_i(x)$ by that of an unannealed one. In this context, $\tau(x)$ can be represented by an expression of the form [5]

$$\tau(x)=\frac{\epsilon kT_a}{4\pi q^2}\,\frac{1}{D(x)N(x)}, \tag{2}$$

with

$$D(x)=D_0(x)\exp\left[\frac{-E_a(x)}{kT_a}\right], \tag{3}$$

where $D(x)$ and $N(x)$ are, respectively, the diffusivity and concentration of the point defects ensuring the electrical activation of the impurities, ϵ is the dielectric constant, q is the absolute electron charge and k is the Boltzmann constant.

The activation energy E_a has been determined experimentally by a proper analysis of the Arrhenius plot of the quantity

$$Q(x)=[\rho_i(x)-\rho_f(x)]/[\rho(x)-\rho_f(x)]. \tag{4}$$

As a result, E_a is found to be weakly depth-dependent, always smaller than 0.8 eV and independent of the annealing duration (fig. 2), confirming, therefore, the consistency of the kinetics model of eqs. (1)–(3) with regard to its time dependence.

Likewise, the variation of the relaxation time constant with depth, $\tau(x)$ has also been deduced (fig. 3). $\tau(x)$ essentially increases when going from the surface towards the substrate. This feature is also consistent with the adopted local relaxation process in which is shown that the relaxation time constant is inversely proportional to the diffusivity and the concentration of the point defects involved in the doping activation.

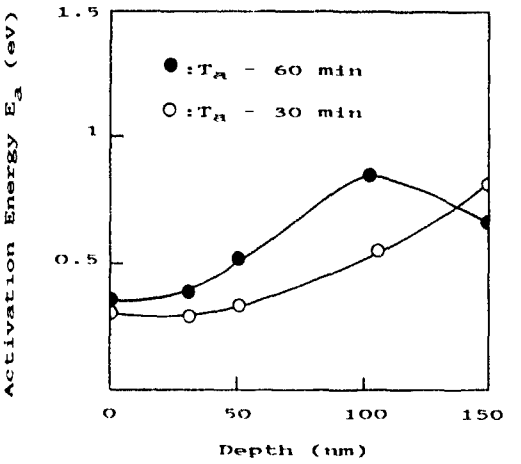

Fig. 2. Variations of activation energy E_a with depth for samples implanted at 5×10^{14} As^+/cm^2 and annealed during 30 and 60 min.

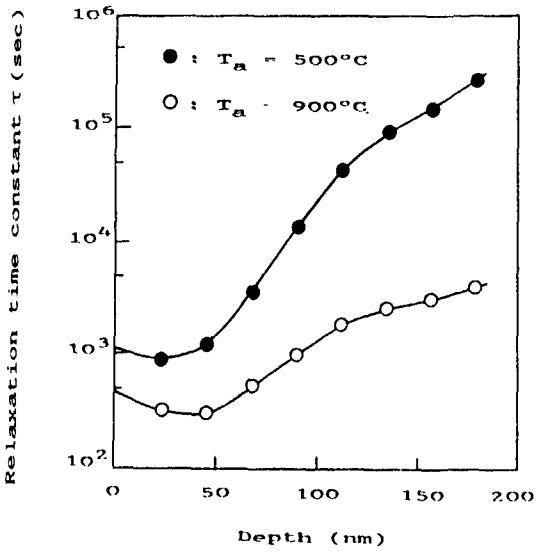

Fig. 3. Variations of the relaxation time constant τ with depth for samples implanted at 5×10^{14} As^+/cm^2 and isochronally annealed (1 h) at 500 and 900 °C

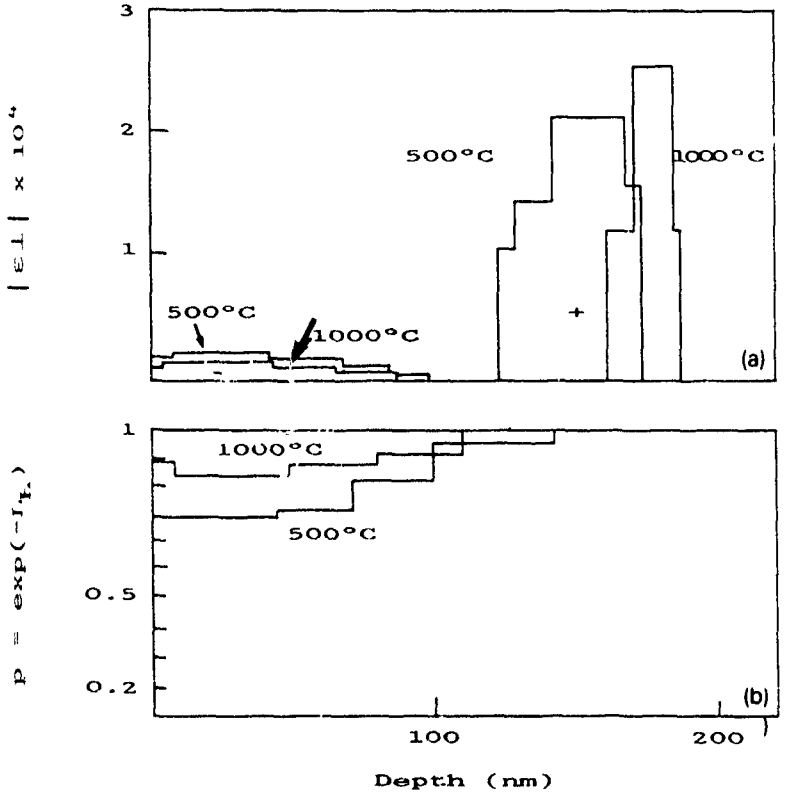

Fig. 4. Mechanical relative strain (a) and the Debye-Waller factor (b) profiles as obtained by TCD measurements for samples implanted at 1×10^{15} As^+/cm^2 and isochronally annealed at 500 and 1000 °C.

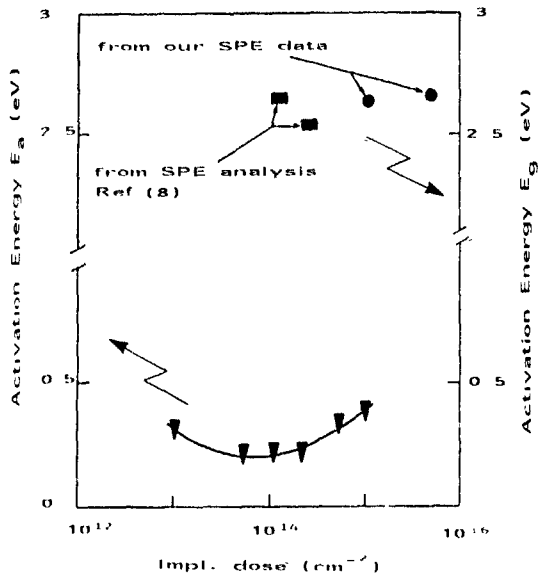

Fig 5 Activation energy variations with the implantation dose E_a as obtained from our resistivity data (depth = 80 nm) and E_g from SPE studies

Besides, triple-crystal X-ray diffraction experiments conducted on the same samples enable us to show the depth distribution of both components of lattice strain normal to the surface (ϵ) and static atomic disorder through the Debye-Waller factor $P = \exp(-L_H)$ (L_H is the mean-square displacement of the atoms from their lattice site) induced by arsenic implantation. Fig. 4 shows the results of TCD analysis for a low-temperature annealed sample and a well-annealed one. It must be pointed out that, since the tetrahedral radius of arsenic is nearly the same as that of silicon, substitutional arsenic does not change the lattice constant of the implanted layer. Therefore, the TCD data are actually indicative of the lattice distortion due to the implantation-induced defects. In particular, the negative surface strain is likely related to an excess of vacancies while the positive strain is associated with an excess of interstitials.

Moreover, the comparison of the values of the activation energy of fig. 2 with those of the usual point-defect migrations (0.25 eV for a vacancy–interstitial pair, 0.51 eV for a silicon interstitial, 0.8 eV for a vacancy–As^+ complex and 0.33 eV for a vacancy) [6,7] suggests that the migrating species involved in the activation process should be associated with a vacancy and/or an interstitial diffusion. More precisely, in view of the evolution of $E_a(x)$ it can be concluded, in agreement with the TCD data, that vacancy-like defects are presumably the dominant species in the first 100 nm, while interstitials seem to prevail above 100 nm.

Besides, fig. 5 displays the values of the activation energy both of the relaxation time constant associated with the electrical local activation process and of the regrowth velocity corresponding to the recrystallization mechanism as obtained from our TEM analysis and from the literature [8]. It is clear from fig. 5 that the activation energies deduced from our resistivity data, $E_a = 0.1$–0.5 eV, are in any case much smaller than those for a regrowth process, $E_g = 2.5$–2.7 eV. In the former case, the electrical activation of the impurity undergoes via a low energy consumming mechanism whereas, in the latter one, the solid-phase epitaxy involves a higher-energy-consuming process in which the reordering at the interface requires the breaking of silicon bonds [9].

4. Conclusion

It has been shown that the dopant electrical activation in highly doped arsenic implanted silicon is independent of the reconstruction mechanism occurring by solid-phase epitaxy. In contrast, the impurity activation process has been shown to be satisfactorily described by a local relaxation model in which the relaxation time is inversely proportional to the diffusivity and the concentration of the point defects leading to the dopant incorporation. Regarding the values of the activation energies found for this process, it is suggested that the migration of vacancies and/or silicon interstitials presumably plays a prevailing role in the impurity activation process.

References

[1] F.F. Morehead, B.L. Crowder and R.S. Title, J. Appl. Phys. 43 (1971) 1112
[2] J.R. Ehrstein, in: Non Destructive Evaluation of Semiconductors Materials and Devices, ed. J.N. Zemel (Plenum, New York, 1978) p. 36
[3] M. Servidori, R. Angelucci, F. Cembali, P. Negrini, S. Solmi, P. Zaumseil and U. Winter, J. Appl. Phys. 61 (1987) 1834.
[4] C. Christofidès, G. Ghibaudo and H. Jaouen, J. Appl. Phys. 65 (1989) 4840.
[5] C.S. Fuller, in: Defects Interaction in Semiconductors, ed. N.B. Hannay (Reinhold New York, 1959) chap. 5, p. 209
[6] B. Boltaks, in: Diffusion et Défauts Ponctuels dans les Semiconducteurs (Mir, Moscow, 1977).
[7] G.D. Wattkins, in: Deep Centers in Semiconductors, ed. S.T. Pantelidis (Gordon and Breach, 1986) chap. 3, p. 166.
[8] I. Suni, G. Göltz, M.G. Grimaldi and M.A. Nicolet, Appl. Phys. Lett. 40 (1982) 269.
[9] J. Narayan, J. Appl. Phys. 53 (1982) 607

Nuclear Instruments and Methods in Physics Research B55 (1991) 580–584
North-Holland

Epitaxial regrowth and lattice location of indium implanted in arsenic-preamorphized silicon

E. Alves and M.F. Da Silva
Departamento de Física, Instituto de Ciências e Engenharia Nucleares, LNETI, 2685 Sacavém, Portugal

J.C. Soares and A.A. Melo
Centro de Física Nuclear da Universidade de Lisboa, Av Prof Gama Pinto 2, 1699, Lisboa, Portugal

J. May
Faculty of Electrical Engineering, Technical University, Praha 6, Czechoslovakia

V. Haslar and P. Seidl
Ion Implantation Laboratory K334 FEL CVUT, Praha, Czechoslovakia

U. Feuser and R. Vianden
Institut für Strahlen und Kernphysik der Universität, Nussallee 14–16, W-5300 Bonn, Germany

The ion implantation of indium in silicon has been carefully studied using ion beam analysis techniques and hyperfine interactions. The perturbed angular correlation (PAC) method provides an internal monitoring of the epitaxial regrowth and gives information about the annealing process. In the present work results are presented on the behaviour of the epitaxial regrowth, diffusion and lattice location of indium implanted in silicon and in arsenic-preamorphized silicon. Half of each of (100) and (111) oriented silicon wafers have been preamorphized using a 10^{15} As^+ ions/cm^2 fluence. The whole wafer was subsequently implanted with the same fluence of In^+ ions. Both types of crystals have been furnace-annealed in vacuum and studied using the RBS/channeling technique. Some of the crystals were later implanted for hyperfine-interaction studies using the PAC technique with a low dose of the ^{111}In isotope. Different results are obtained for the lattice location, diffusivity and damage annealing in both halves of the wafers. Evidence is shown for the out-diffusivity of indium in the indium-implanted silicon crystals and for indium/arsenic pair formation in the preamorphized samples. This latter effect inhibits the out-diffusivity of the indium atoms and enhances their substitutionality in the silicon lattice.

1. Introduction

Low- and high-dose indium-implanted silicon crystals have been recently studied [1–4], using different techniques and a great variety of annealing treatments. These studies are important to understand the doping process and to learn how to produce shallow p^+ layers for applications in the production of very-large-scale integrated circuits. Previous results have shown that high-dose In-implanted silicon undergoes a polycrystalline phase transformation accompanied by a significant indium redistribution at temperatures below those at which the solid-phase epitaxial regrowth proceeds [2]. Studies on the regrowth behaviour of In-implanted silicon crystals with both the Rutherford backscattering (RBS)/channeling and perturbed angular correlation (PAC) techniques showed that only a small fraction of indium atoms can be incorporated in regular silicon lattice sites after appropriate annealing treatments [4]. This fraction is strongly dependent on the crystal type, annealing treatment and crystal orientation.

Indium is one of the best probes for hyperfine-interaction studies, which are very sensitive to the near surroundings of the indium ions. Defects can be detected and characterized and their activation energies measured using these techniques [3–6]. Wichert and Swanson showed that indium can form pairs in silicon with the group V elements. The pairs are identified by a characteristic frequency which is the signature of the pair formation. The amplitude of this frequency gives

0168-583X/91/$03.50 © 1991 – Elsevier Science Publishers B.V (North-Holland)

information about the number of pairs thus formed. In this way, the activation energies for pair formation and breaking are obtained.

In the present work, results of a comparative study, using RBS/channeling and PAC techniques, for (100) In-implanted silicon and In-implanted silicon pre-amorphized with arsenic ions are given and discussed. The (100) preamorphized samples show a significant enhancement of the In solid solubility. The hindrance of indium out-diffusion is proposed in this work to be due to the In–As pair formation. The RBS results indicate that almost all the indium ions are substitutional in the silicon lattice. However, from the PAC data only about 30% of the In ions show the characteristic frequency of the In–As pair.

2. Experimental procedures

Boron-doped (100) and (111) silicon wafers have been $^{115}In^{+}$-implanted with a dose of 1×10^{15} cm^{-2} and an energy of 66 keV. Half of each wafer has been previously amorphized with the same dose of $^{75}As^{+}$, selecting the energy of 53 keV in order to obtain the overlap of the implanted profiles for both As^{+} and In^{+} ions. Samples of 1 cm^2 have been cut from these wafers for RBS/channeling and furnace-annealing experiments. One of these (100) samples has been post-implanted with radiative $^{111}In^{+}$ ions with a dose of the order of 10^{12} cm^{-2} for PAC measurements. Samples implanted with In in crystalline and in As-preamorphized silicon have been analysed before and after furnace annealing in the range of 550–750 °C. Some of these samples have been further annealed at 900 °C. The pressure was kept in the range of 10^{-7} mbar during the annealing treatment.

RBS/channeling analyses were done using the 1.6 MeV collimated He^{+} beam of the Van de Graaff accelerator of LNETI, Sacavém. Backscattered particles were detected with both an annular and standard surface-barrier detector placed at scattering angles of 180° and 140° and with an energy resolution of 18 and 13 keV, respectively. Channeling angular scans were done using a two-axis goniometer. The back sides of the samples were used to orient the crystals in order to avoid unnecessary radiation damage before the start of the RBS/channeling measurements. The effect of the analysing beam has been controlled by comparing the aligned spectra at the beginning and at the end of the angular scans.

The PAC measurementes were carried out after the implantation of the radioactive isotope and after subsequent annealing at 650 °C. During annealing the sample was sealed in vacuum in a quartz tube.

3. Results and discussion

Fig. 1a shows random and ⟨111⟩ aligned spectra of the As- and In-implanted (100) silicon wafer after different annealing treatments. For comparison the aligned spectrum taken in an unimplanted zone is included. It is clear that at the surface an amorphous layer with a thickness of 750 Å has been formed due to the implantation. A mean projected range (R_p) of 400 Å and a standard deviation (ΔR_p) of 300 Å has been measured for In and As profiles in agreement with TRIM code

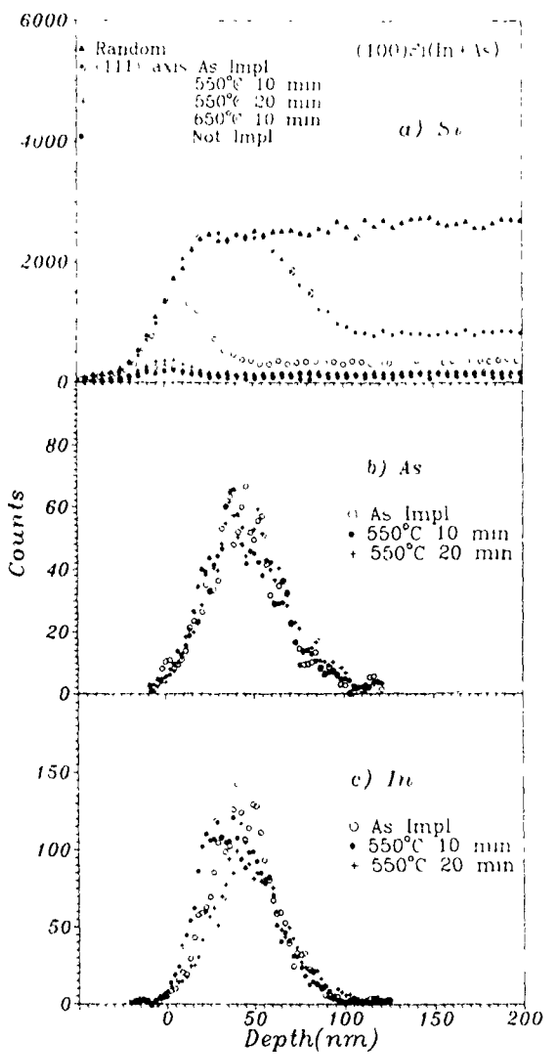

Fig. 1. (a) RBS spectra showing the recovery of the amorphous layer after the annealings referred to in the figure. (b) Depth profile of As as-implanted and after annealing at 550 °C during 10 and 20 min. The profile after 20 min annealing at 550 °C does not change if we increase either the annealing time or the temperature up to 650 °C (c) The same as in (b) but for In

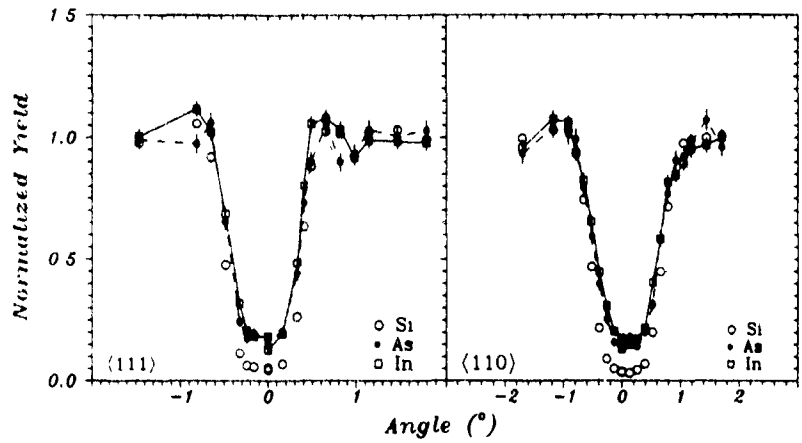

Fig 2 Angular scans along the ⟨111⟩ and ⟨110⟩ directions for the preamorphized (100) Si crystal after the annealing at 650 °C during 10 min. The lines were drawn to guide the eye

calculations. The data show a partial recovery of the damage after the annealing at 550 °C during 10 min. The complete recovery is reached after 20 min at this temperature This result can also be achieved with annealing at 650 °C for 10 min. The regrowth velocity at 550 °C is greater than 60 Å min^{-1}, in agreement with previous results obtained in compensated implants [7,8]. Figs. 1b and 1c show the evolution of the As and In profiles after the isothermal annealing at 550 °C. After the first annealing the amount of As and In ions remains constant, but, after the second annealing about 25% of In atoms were lost. The In loss is clearly seen in fig. 1c and explains the complete recovery of the silicon surface.

Fig 2 shows the In and As ⟨111⟩ and ⟨110⟩ angular scans after annealing at 650 °C. In both scans the substitutionality is greater than 90%. Fig. 3 shows the angular scans of one sample annealed during 60 min at 550 °C followed by 30 min at 900 °C. The increase of the minimum yield for the implanted ions shows that some In and As leave the silicon lattice sites. The evolution of the substitutional fraction of In and As for different isochronal annealings of 10 min from 550 °C up to 750 °C is displayed in fig. 4a. The maximum substitutionality takes place after annealing at 600 °C. The evolution of the retained dose for both ions after the same annealing treatments is shown in fig 4b. A loss of In of about 25% is measured at annealing temperatures starting at 600 °C while the As content remains constant. The same loss of In has been observed during the 20 min annealing at 550 °C

Fig. 5 presents the results of PAC experiments for the sample, post-implanted with radioactive In, as-implanted and after annealing at 650 °C for 10 min. The

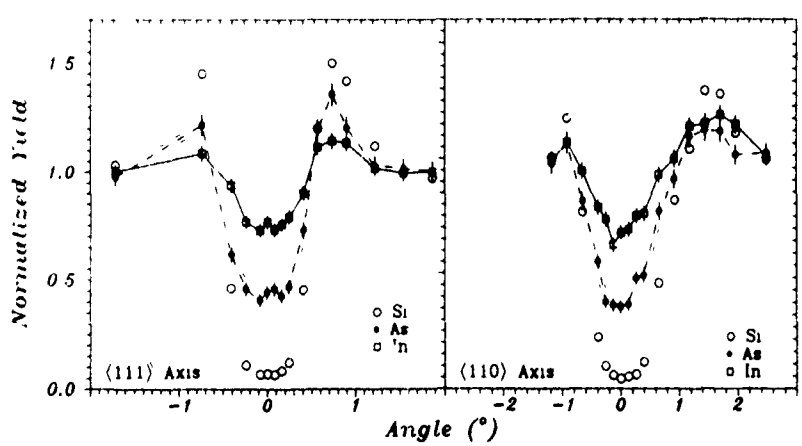

Fig. 3. Angular scans along the ⟨111⟩ and ⟨110⟩ directions for the preamorphized (100) Si crystal annealed at 550 °C for 10 min followed by 30 min at 900 °C. The lines were drawn to guide the eye.

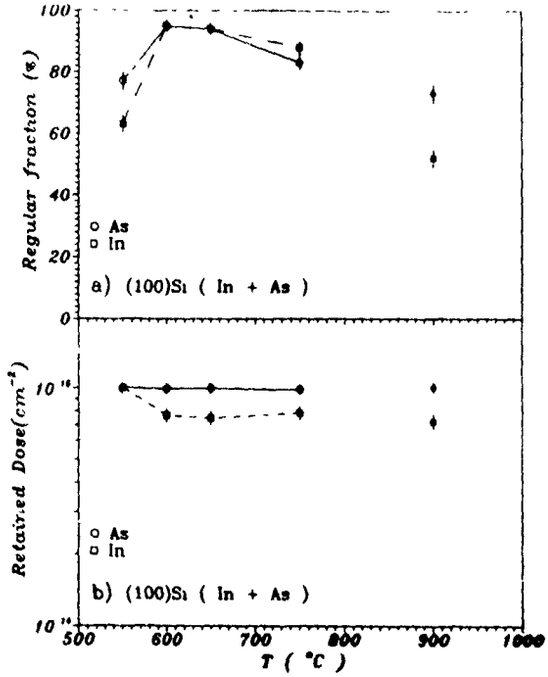

Fig. 4 (a) Evolution of In and As regular fraction for isochronal annealings of 10 min. The same fraction was measured for both the ⟨111⟩ and ⟨110⟩ directions. The full dots were obtained for a sample annealed at 550 °C for 20 min followed by 5 min at 900 °C. (b) Evolution of the In and As retained dose for the same annealing procedure The lines were drawn to guide the eye.

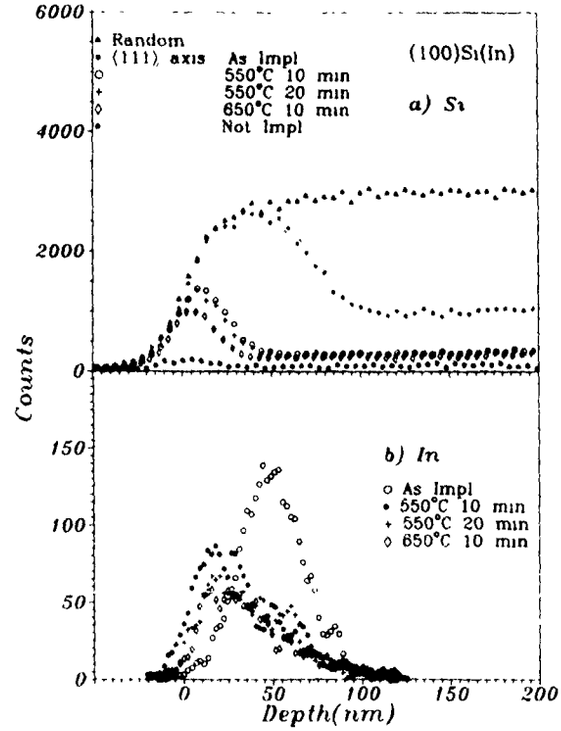

Fig. 6. (a) RBS spectra showing the regrowth of the amorphous layer for In implanted in crystalline (100) Si after the annealing steps inserted in the figure (b) The depth profile of In as-implanted and after the same annealing treatments

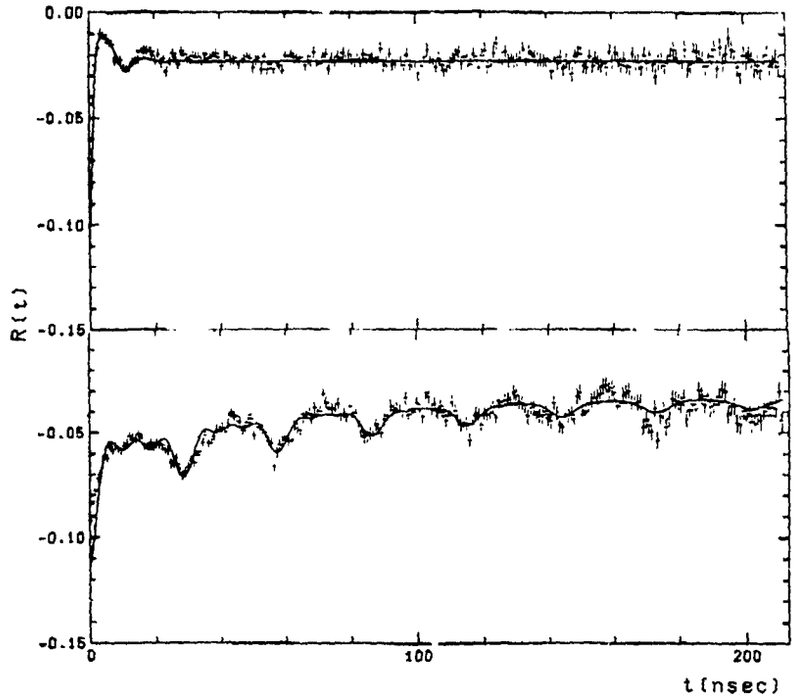

Fig. 5. PAC results showing the frequency distribution observed after the implantation of $^{111}In^{+}$ in As-preamorphized (100) Si (upper part) and a well defined frequency of 229 MHz observed after the annealing at 650 °C for 10 min (lower part).

frequency distribution observed after the implantation shows that the hyperfine-interaction probe is in an amorphous surrounding in agreement with the RBS/channeling data. After the annealing a sharp frequency appears indicating the reorganization of the indium within the surrounding crystal, also in agreement with the channeling data which clearly show epitaxial regrowth at this temperature. In this work we observe the same frequency previously reported in ref. [3]. The amplitude of the perturbation function, however, corresponds only to 30% of the In atoms forming pairs with As. From the remaining fraction, 30% of In atoms can be described by a broad frequency distribution centered in a higher frequency. The 40% of the In atoms which do not sense any field gradient are probably in a cubic surrounding formed by silicon atoms

A completely different behavior has been observed and is shown in figs. 6a and 6b with the In-implanted crystalline (100) Si. In agreement with previous experiments [4] we observe that within 200 Å from the surface the regrowth is appreciably retarded due to In segregation. The maximum In fraction in regular lattice sites is obtained after annealing at 550 °C and decreases above

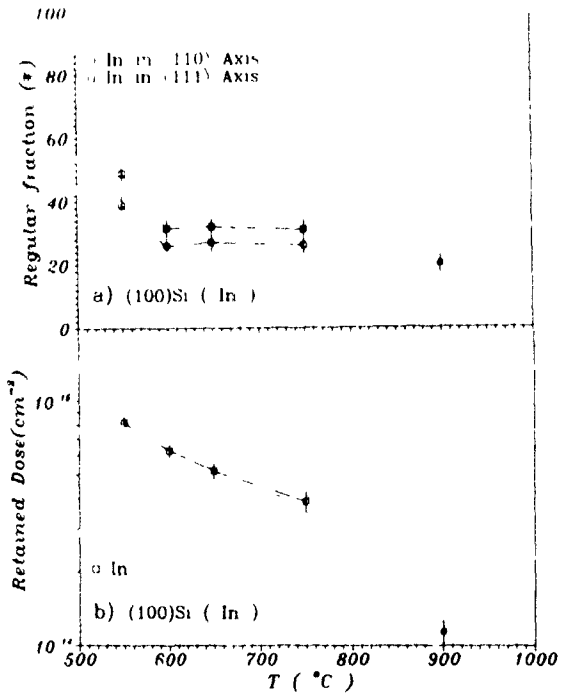

Fig. 7. (a) Evolution of In regular fraction for isochronal annealings of 10 min. The difference in the minimum yield in the ⟨111⟩ and ⟨110⟩ directions implies that some of the In is located in the interstitial tetrahedral site. The full point was obtained for a sample annealed at 550 °C for 20 min followed by 5 min at 900 °C (b) Evolution of the In-retained dose for the same annealing procedure The lines were drawn to guide the eye.

this temperature as is shown in fig. 7a. Also, the loss of In starts after the first annealing at 550 °C and increases with the temperature (fig. 7b).

Similar studies carried out with (111) samples show that the regrowth process stops after the amorphous–crystalline interface reaches the maximum concentration of the dopant profile. Only a small amount of In or In and As are incorporated in regular sites in the regrown part of the amorphous layer.

4. Conclusions

The first conclusion of this systematic study is related to the In fraction in regular lattice sites. In fact, with the implantation of In in crystalline (100) Si the highest fraction in regular lattice sites is about 50% which corresponds to a concentration of 3×10^{19} cm^{-3}. This fraction decreases with a small increase of the temperature which indicates that indium precipitates very easily. On the other hand, the system can be stabilized by a previous implantation of As ions. In this case the fraction of In in substitutional sites is about 95%. This fraction gives a concentration of 2×10^{20} cm^{-3} which is about 300 times the solid solubility of In in silicon (8×10^{17} cm^{-3}) in the temperature range of 550–650 °C. However, with the increase of the temperature part of the In and As atoms leaves the substitutional sites The results show therefore that the high solubility is related to In- As pair formation This mechanism will also be responsible for the hindrance of the In out-diffusion. It is not yet clear if all indium atoms form pairs with arsenic atoms. Further studies of the electrical properties of these samples are in progress in order to answer this question.

References

[1] S Y Shiryaev, A N Larsen and W Safronov, J Appl Phys 65 (1989) 4220
[2] E. Nygren, A P Pogany, K T Short, J S Williams R G Elliman and J M. Poate, Appl Phys. Lett 52 (1988) 439.
[3] Th. Wichert and M.L. Swanson, J. Appl Phys 66 (1989) 3026
[4] E. Alves, M.F Da Silva, A A. Melo, J C Soares, U Feuser and R Vianden, Mater. Sci. Eng B4 (1989) 189.
[5] Th. Wichert and E Recknagel, Microscopic Methods in Metals, ed U Gonser (Springer, Berlin, 1986) p. 317
[6] G. Weyer, in: Nuclear Physics Applications on Materials Science, eds E. Recknagel and J C Soares (Kluwer, Dordrecht, 1988) p 167
[7] A. Lietoila, A. Wakita, T W. Sigmon and J.F. Gibbons, J Appl. Phys. 53 (1982) 4399
[8] J S. Williams and K T Short, Nucl Instr. and Meth. 209/210 (1983) 767.

Nuclear Instruments and Methods in Physics Research B55 (1991) 585–588
North-Holland

Effect of SiN_x coating in lateral solid phase epitaxy of implanted amorphous Si films

Hiroshi Ishiwara and Kazuichi Fukao

Research Laboratory of Precision Machinery and Electronics, Tokyo Institute of Technology, 4259 Nagatsuda, Midoriku, Yokohama 227, Japan

The effect of a SiN_x coating was investigated in lateral solid phase epitaxy (L-SPE) of implanted amorphous Si (a-Si) films. It was found that the L-SPE growth rate decreased with increasing thickness of the SiN_x film. The internal stress of a-Si films derived from the change of the growth rate was on the order of 5×10^9 dyn/cm^2. A model to explain these phenomena is presented.

1. Introduction

Lateral solid phase epitaxy (L-SPE) of amorphous Si (a-Si) films deposited on selectively oxidized Si wafers [1–4] is one of the most promising silicon-on-insulator (SOI) technologies suitable for the fabrication of three-dimensional integrated circuits (3D-ICs), since the process temperature of this method is as low as 600°C [1]. This method has another advantage that a multilayered structure of a-Si and SiO_2 films can be crystallized simultaneously from a common seed region by a single heating process, without deforming the impurity profiles in the a-Si films. Thus, the L-SPE method has a potential to provide a new fabrication process for 3D-ICs which is superior to the conventional layer-by-layer process.

In the simultaneous L-SPE growth of multilayered structures, however, there is a possibility that the growth characteristics of a-Si films in the lower levels are deteriorated by the mechanical and/or thermal stress from the overlayers. So far, we have shown that the effect of a SiO_2 coating is not a large problem, even if a 1.8 μm thick SiO_2 film is deposited on an a-Si film [5]. In the practical 3D structure, however, the effect of the overlayers is considered to be stronger, since they are composed of a stacked structure of Si and SiO_2 films. Therefore, in this paper, we further investigate the effect of the overlayers in a more realistic structure, that is, a-Si films are coated with harder SiN_x films and the L-SPE growth characteristics are measured.

2. Experimental procedures

SiO_2 films about 50 nm thick were thermally grown on Si(100) wafers and stripe-shaped seed regions were formed parallel to the ⟨011⟩ direction by etching of the films. The wafers were then chemically cleaned, dipped in RCA solution to form thin chemical oxide films, and mounted in an ultrahigh vacuum (UHV) chamber whose base pressure was about 1.3×10^{-7} Pa. After thermal cleaning at 800°C for 30 min, a-Si films about 400 nm thick were deposited at room temperature and the samples were in situ annealed at 500°C for one hour for densification of the a-Si films. The annealed samples were taken out from the chamber and P ions were implanted in some of these samples, since P atoms doped in an a-Si film are known to enhance the growth rate and to expand the L-SPE region [2]. The implantation energy and dose were determined so that the profile was almost flat near the surface of the film and its concentration was about 3×10^{20} cm^{-3}. Under these conditions, the thickness of the P-doped region where the concentration is higher than 1×10^{20} cm^{-3} is about 290 nm.

Then, SiN_x films were deposited on both undoped and P-doped a-Si films by plasma-enhanced chemical vapor deposition (PCVD) at 400°C. The thicknesses of the films were 1.2 μm (sample P1) and 2.4 μm (sample P2). In some samples, a part of the SiN_x films was etched prior to the L-SPE annealing, in order to check for degradation of a-Si films during the deposition process of SiN_x. The sample structure is schematically shown in fig. 1. The samples were finally furnace-an-

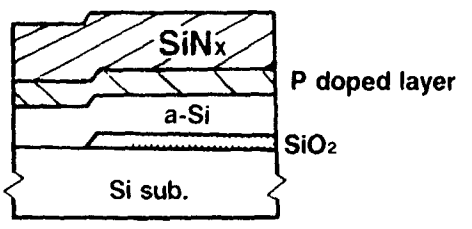

Fig 1. A schematic drawing of the sample structure

0168-583X/91/$03.50 © 1991 – Elsevier Science Publishers B.V. (North-Holland)

nealed in a dry N_2 atmosphere to induce L-SPE. The L-SPE characteristics were investigated by Nomarski optical microscopy.

3. Results

Fig. 2 shows the annealing time dependence of the L-SPE length along the ⟨010⟩ direction at 600°C in undoped and P-doped samples. In this figure, the open circles show the characteristics in a part of the P1 sample where the SiN_x film was etched off. We can see from this figure that the growth rate in the P-doped samples decreases with increasing thickness of the SiN_x films. The results for the undoped samples (closed circles and triangles) show the same tendency. It was found that the characteristics of the open and closed circles in the figure were almost the same as those of uncoated a-Si films. Thus we can say that the degradation of the growth rate is not due to the deposition process of the SiN_x film, but it is due to existence of the film itself. We can also see from fig. 2 that the random crystallization time at which about 2/3 of the a-Si film is occupied by polycrystalline grains becomes longer with increasing thickness of the SiN_x film. As a result, the L-SPE growth length from the seed edge is virtually independent of the thickness of the SiN_x film.

The detailed growth characteristics at the initial stage are shown in fig. 3. We can see from this figure that the initial growth length on {110} facets [3] becomes shorter as the SiN_x film is made thicker. Since the crystalline quality of the film is known to be better in the {110} facet growth region, we conclude from this result that the L-SPE characteristics of a-Si films degrade by deposition of SiN_x overlayers. It was also found from these experiments that the size of {111} facets, which appear at the growth front as a zig-zag pattern, is much larger in the uncoated region, when it is compared at the same L-SPE length. However, the origin of this phenomenon is not well understood at present.

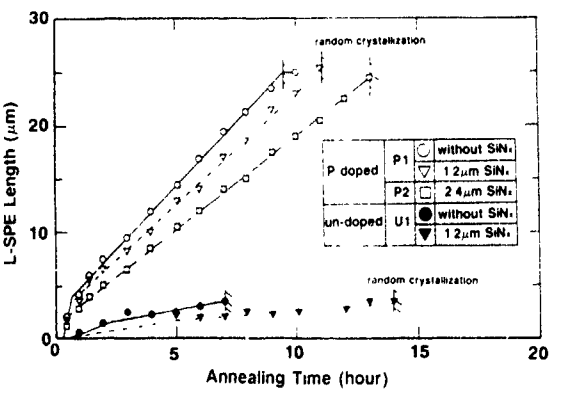

Fig. 2. L-SPE characteristics of the undoped and P-doped samples with and without SiN_x coating.

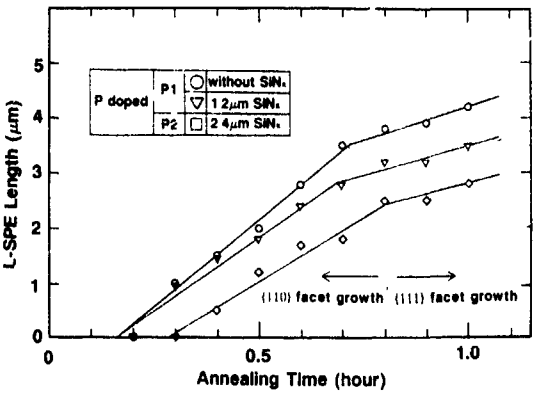

Fig. 3. The initial growth characteristics of the P-doped samples

4. Discussion

It was found from figs. 2 and 3 that the growth rates on both {111} and {110} facets were decreased with an increase of the SiN_x film thickness. It was also found from Nomarski optical microscopy that the growth rate of polygrains was decreased similarly. These results are different from our previous result for the SiO_2 coating [5]. We speculate that this difference is due to the internal stress of the a-Si film, that is, the stress is greater in a-Si films coated with SiN_x films because of

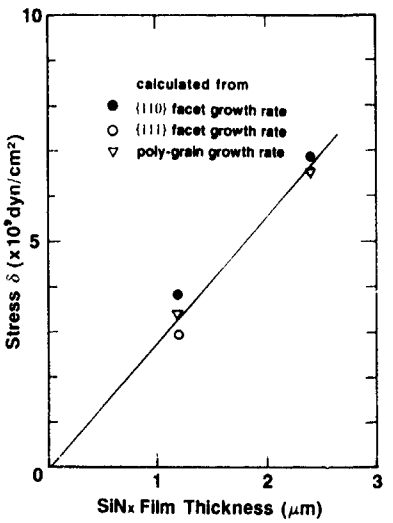

Fig. 4. Variation of the internal stress in a-Si films with the SiN_x film thickness. The values are derived from the growth rate of polygrains as well as the L-SPE growth rate on {110} and {111} facets

their mechanical hardness, and the stress effect degrades the L-SPE characteristics.

Concerning the pressure effect of the SPE growth rate, a few experimental results have been reported [6,7] and the growth rate v at pressure p and temperature T is known to be expressed by the following equation:

$$v = v_0 \exp\{-(E_a + P\Delta V)/RT\}, \quad (1)$$

where v_0 is a constant, E_a is the activation energy, ΔV is the activation volume and R is the gas constant. The reported ΔV value is -3.3 cm^3/mol for vertical SPE of an implanted a-Si layer at 550 °C [7]. In the following, we assume the same value for L-SPE at 600 °C. Fig. 4 shows the variation of stress in a-Si films as a function of the SiN_x film thickness, which was derived from the growth rate using eq. (1). In this figure, the inherent stress existing in the uncoated film is assumed to be zero. We can see from this figure that the internal stresses derived from various growth rates are consistent with one another and that they are on the order of 5×10^9 dyn/cm^2.

In order to explain the origin of the internal stress in fig. 4, thermal stress due to the different expansion coefficients was measured using a bimetal structure of a SiN_x film and a single-crystal Si substrate. In this experiment, the temperature dependence of the bending angle of the sample was determined from movement of a reflected spot of a He–Ne laser. Fig. 5 shows a typical result of the temperature dependence for a bimetal structure with a 2.4 μm thick SiN_x film. We can see from this figure that the internal stress around 600 °C is much smaller than the value in fig. 4. This result shows that the experimental value of the internal stress cannot be explained by a simple bimetal structure.

Finally, we propose a model to explain the above experimental results. This model is schematically shown in fig. 6 for the case of grain growth from a single nucleus. In an uncoated a-Si film as shown in (a), the

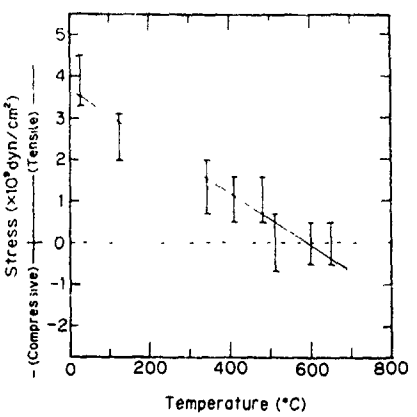

Fig. 5. Temperature dependence of the internal stress in a bimetal structure of SiN_x and Si.

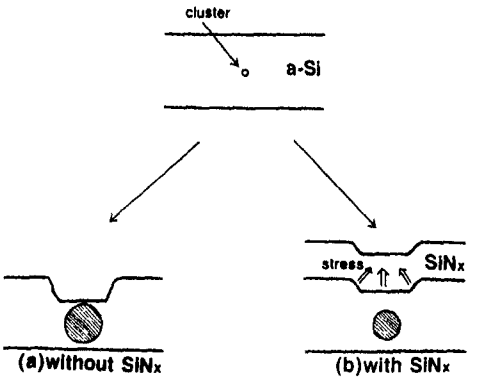

Fig. 6. A schematic drawing of the stress model.

film thickness decreases freely as the crystallite grows. On the other hand, if the a-Si film is coated with a hard film like SiN_x as shown in (b), free shrinkage of the film is prevented and a tension is generated around the crystallite. Thus, the growth rate of the crystallite is decreased, as can be seen from eq. (1). Similar tension is expected to be generated at the growth front of L-SPE, when an a-Si film is coated with a hard film. In this model, an internal stress is generated around the crystallized region, even if no stress appears in the bimetal structure. Therefore, this model seems to be suitable to explain the experimental results which we have obtained, although we have not yet checked its validity quantitatively.

5. Summary

We investigated lateral solid phase epitaxy (L-SPE) of amorphous Si films which were coated with SiN_x films. The main results obtained are summarized as follws.

(1) Both L-SPE growth and grain growth rates decrease with increasing thickness of the SiN_x film.
(2) The initial growth region on {110} facets, where the crystalline quality of the film is superior, becomes narrow with increasing thickness of the SiN_x film.
(3) The internal tension stress derived from the change of the growth rate was about 5×10^9 dyn/cm^2. This value is much larger than the experimental value derived from a simple bimetal structure of a SiN_x film and a Si substrate.
(4) A qualitative model to explain the experimental results was proposed.

Acknowledgement

The authors gratefully acknowledge useful discussion with Prof. S. Furukawa.

References

[1] H. Ishiwara, H. Yamamoto, S Furukawa, M. Tamura and T. Tokuyama, Appl. Phys. Lett. 43 (1983) 1028.
[2] H. Yamamoto, H. Ishiwara and S. Furukawa, Appl Phys Lett. 46 (1985) 268.
[3] H. Yamamoto, H. Ishiwara and S Furukawa, Jpn J. Appl. Phys. 24 (1985) 411
[4] H. Yamamoto, H. Ishiwara and S. Furukawa, Jpn. J. Appl Phys. 25 (1986) 667.
[5] H Ishiwara, N. Tomita, T. Dan and S Furukawa, Nucl Instr. and Meth. B39 (1989) 393.
[6] E. Nygren, M.J. Aziz, and D Turnbull, Appl Phys. Lett. 47 (1985) 232.
[7] G.Q. Lu, E Nygren, M.J. Aziz and D. Turnbull, Appl Phys. Lett 54 (1989) 2583

Nuclear Instruments and Methods in Physics Research B55 (1991) 589–592
North-Holland

Near-surface damage created in silicon by BF_2^+ implantation

Li Xiaoqin, Lin Chenglu, Yang Genqin, Zhou Zuyao and Zou Shichang

Ion Beam Laboratory, Shanghai Institute of Metallurgy, Academia Sinica, Shanghai 200050, People's Republic of China

The near-surface damage in silicon induced by the bombardment of 147 keV BF_2^+ has been investigated by 2 MeV He^+ Rutherford-backscattering spectrometry The implantation was carried out at room temperature with the ion doses ranging from $\sim 10^{13}$ to $\sim 10^{16}$ cm^{-2}. The radiation damage was compared with corresponding B^+ and F^+ atomic-ion implantation A damage enhancement at the surface region of the silicon implanted with BF_2^+ has been observed and it is attributed to the multiple-collision effect between molecular ions and host atoms.

1. Introduction

BF_2^+ implantation is commonly used in the boron doping process, as the dissociation of the BF_2^+ ion upon its initial scattering events gives a lower-energy boron atom. In addition, the fluorine ion is relatively heavy and is therefore able to generate an amorphous zone which contains most of the boron so that low-temperature solid-phase epitaxy can be used to produce doped layers without appreciable atomic diffusion. However, the bombardment of molecular ions such as BF_2^+ will result in distinctive damage and annealing behavior, which may be interesting for both technical applications and fundamental studies of atomic collision in solids These molecular effects were generally explained by "spike effects" [1] in the overlap region of cascade volumes generated by the atomic species of the molecular ion when it penetrated into the target. In most previous studies, to understand the microscopic events of spike effects, diatomic implants were used [2] to show the existence of a "damage-enhancement" effect in Si and Ge This effect is related to ion species, energy and target temperature [3]. Grob et al. [4] reported the damage-enhancement effect in silicon induced by BF_n^+ and PF_n^+ implants and accounted for it in terms of the overlap probability of two or three subcascades. In our recent work, a strong damage enhancement at the surface of crystalline silicon created by P_2^+ bombardment has been pointed out [5]

The aim of this work is to demonstrate the molecular effect in the near-surface region induced by BF_2^+ implantation. To this purpose, high-resolution Rutherford-backscattering spectrometry (RBS) with the channeling technique has been employed.

2. Experimental

Etch-polished ⟨100⟩ oriented n-type Si wafers were bombarded at room temperature using an ULVAC IM-200M implanter The projectile energy was chosen as 3 keV/amu, i.e., 147 keV for BF_2^+, 57 keV for F^+ and 33 keV for B^+, so that the surface damage peak could be distinguished from the buried one The doses of BF_2^+ ions ranged from 5×10^{13}–5×10^{15} cm^{-2}. All implantations were performed 7° away from the surface normal of the wafers in order to minimize the channeling effect. In each atomic–molecular-ion comparison, the atomic flux and fluence were kept constant.

The number and depth distribution of displaced silicon atoms were extracted from the aligned 2 MeV He^+ backscattering spectra. The depth resolution of the detection system was greatly improved by using a grazing-angle detector geometry (scattering angle $\theta = 97°$).

3. Results and discussion

A typical set of RBS spectra of BF_2^+-implanted silicon is indicated in fig. 1. Two damage peaks in the figure are clearly separated as the incident ion energy is high enough. One peak is buried at a position corresponding to the nuclear energy-deposition peak R_D (about 1100 Å deep from the surface estimated by the WSS theory) while the other peak appears at the top surface of the sample. Disordered atoms in both damage regions increase with increasing ion doses The surface damage peak exists at a rather low dose, e.g 5×10^{13} ions/cm^2, while the buried peak cannot be defined until the dose is up to 10^{15} ions/cm^2.

Fig. 2 illustrates a comparison of the damage behaviors of molecular BF_2^+ implants and dually implanted atomic ions of F^+ and B^+. In fig. 2, one can see that the damage enhancement induced by molecular ions is quite different in the two damage regions. Two buried damage peaks in fig. 2 are almost coincident with each other while a striking damage enhancement takes place at the surface of the sample bombarded with BF_2^+. Generally,

0168-583X/91/$03.50 © 1991 – Elsevier Science Publishers B V (North-Holland)

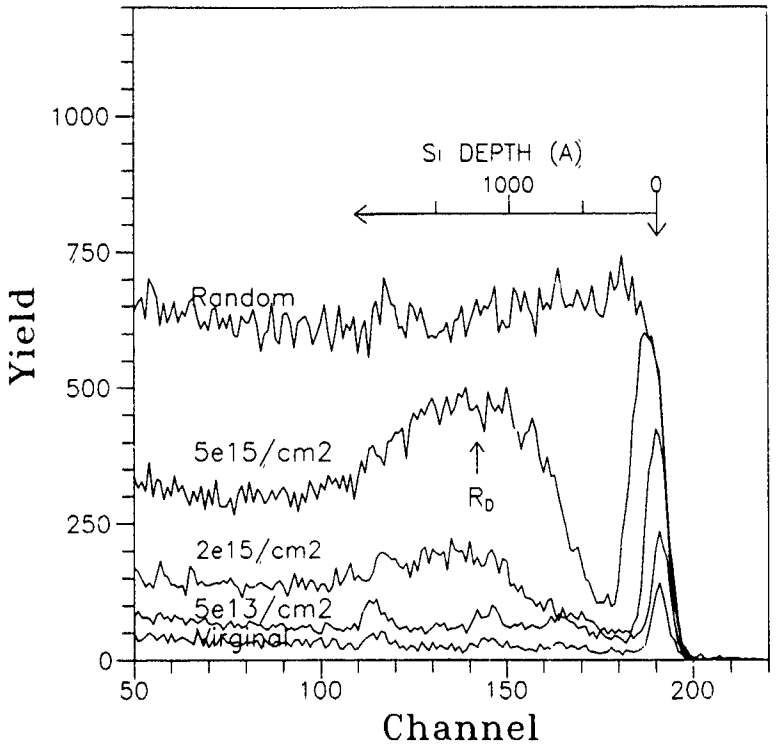

Fig. 1 Aligned spectra of ⟨100⟩ silicon implanted with BF_2^+ at room temperature at an energy of 3 keV/amu.

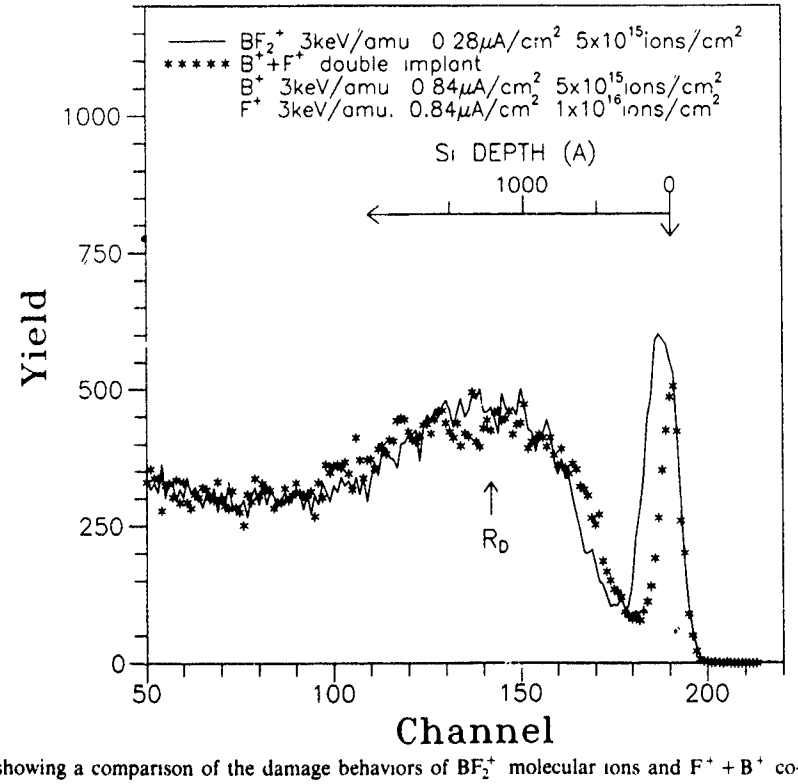

Fig. 2. RBS spectra showing a comparison of the damage behaviors of BF_2^+ molecular ions and $F^+ + B^+$ co-implants in silicon at room temperature.

the damage enhancement in the buried region can be explained in terms of overlap of two or three collision cascades generated by every atomic species of the molecular ion because of the nonlinear dependence of damage creation on the nuclear energy-deposition density. When the initial energy of BF_2^+ is increased, the damage enhancement factor F_D – defined as the ratio of total number of displaced target atoms for molecular ($N_D[BF_2]$) to atomic ($N_D[F + B]$) ion bombardment, i.e., $F_D = N_D[BF_2]/N_D[F + B]$ – will decrease [4]. This is because at high energy, the cascade volume generated by fluorine or boron implants becomes large and the nuclear energy deposition in the cascade volume is diluted. At an incident energy of 3 keV/amu for BF_2^+, the value of F_D calculated from the buried damage region is almost equal to 1, which is coincident with the results of ref. [4].

Fig. 3 indicates that F_D, calculated from the surface damage peak, varies as a function of ion dose. Even at a higher dose of 5×10^{15} ions/cm^2, F_D is as large as 1.6, and the damage enhancement effect becomes even more striking as the dose decreases. Considering that the damage creation rises with the increase in nuclear stopping power dE/dx, a heavy ion will generate much more displaced host atoms than a light one. Although the chemical bond of BF_2^+ will be broken as soon as it enters the solid target, the fluorine and boron atoms will keep their relative positions and flight forward together until one of them encounters a large-angle scattering. When all atomic species of the molecular ion are flighting together, the binary-collision model would be invalid to describe the collision process between the flighting atomic species and target atoms, hence a multiple collision model should be considered. But a practical evaluation of this model will be very complicated. In a rough exploration, the surface-damaging behavior of BF_2^+ can be considered to be approximately like that of V^+ or Ti^+. Table 1 lists the nuclear stopping power dE/dx for 3 keV/amu V^+, Ti^+, F^+ and B^+ ions in silicon. The dE/dx of V^+ is greater by a factor of 2 than the sum $2dE/dx(F^+) + dE/dx(B^+)$, which is

Table 1
Nuclear stopping power dE/dx calculated by TRIM

ion	Mass [amu]	Z	Energy [keV]	dE/dx [eV/Å]		
				Electronic	Nuclear	Total
B	11	5	33	12.57	5.388	17 91
F	19	11	57	22 83	14 61	37.44
Ti	48	22	144	37.80	60.68	98.48
V	51	23	153	37.65	65.00	102 6

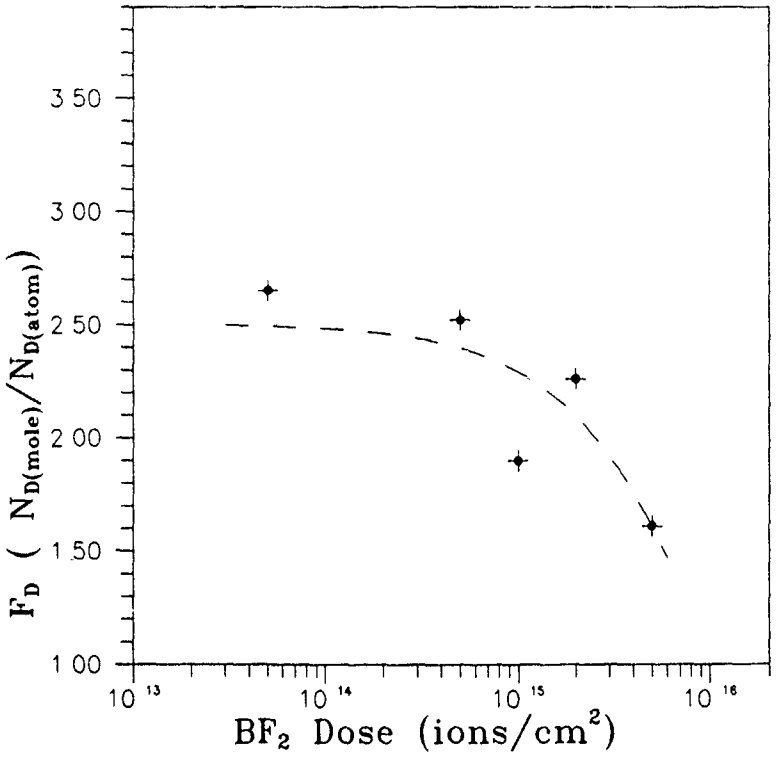

Fig. 3 Plot of the enhancement factor F_D calculated from the near-surface peak as a function of the 3 keV/amu BF_2^+ dose implanted at room temperature.

almost corresponding to the average damage enhancement factor F_D demonstrated in fig. 2. The estimation above reveals that the multiple collisions between all atomic species of the BF_2^+ and the host silicon atoms play a dominant role in generating the excess damage at the top surface region.

In summary, we have compared the damage behavior of the molecular BF_2^+ ions with that of $F^+ + B^+$ implants in silicon at an energy of 3 keV/amu. A striking damage enhancement is observed at the surface of the sample bombarded with BF_2^+, and it is attributed mainly to the multiple collisions between atomic species of the molecular ion and target atoms.

References

[1] P. Sigmund, Appl Phys Lett. 25 (1974) 164.
[2] D A Thompson, R.S. Walker and J A Davies, Radiat. Eff. 32 (1977) 135.
[3] Fang Ziwei, Lin Chenglu and Zou Shichang, Mater. Res. Soc Symp. Proc. 100 (1987) 255
[4] A Grob, J J. Grob and A. Golanski, Nucl. Instr. and Meth. B19/20 (1987) 55.
[5] Yang Genqing, Lin Chenglu, Fang Ziwei, Zhou Zuyao and Zou Shichang, Mater. Res. Soc Symp Proc. (1989) in press

Nuclear Instruments and Methods in Physics Research B55 (1991) 593–597
North-Holland

Custom profiles by automated multi-step implantation

J. Philip Crook [a], Michael I. Current [b], Babak Adibi [c], S. Leung [c] and L.A. Larson [d,1]

[a] *National Semiconductor, Puyallup, WA 98374, USA*
[b] *Applied Materials, Santa Clara, CA 95054, USA*
[c] *Applied Materials, Horsham, West Sussex, RH13 5PY, England*
[d] *National Semiconductor, Santa Clara, CA 95051, USA*

Multi-step implants using F as a preamorphizing species for the formation of shallow p^+ source/drain junctions are investigated. SIMS, RBS and SRP data are combined to optimize process equivalents to 50 and 25 keV BF_2 implants. Incorporation of a dual implant sequence into a single, chained recipe and device results for a 1 Mbit SRAM are discussed.

1. Introduction

The scaling requirements for CMOS devices with gate widths of ≈ 0.5 μm call for junction depths of ≈ 0.1 μm for both the p^+ and n^+ source/drain regions [1]. Control of B channeling and diffusion for p^+ junctions is particularly challenging [2,3]. The usefulness of an initial preamorphization implant to suppress channeling effects has been shown for BF_2 implants with energies as low as 5 keV [4], for B energies as low as 1 keV [5] and for "plasma immersion" implants using a mixed BF_3-fed discharge with a wafer bias of ≈ 1 keV [6].

Although most of the work with preamorphization implants have used Si or Ge as the amorphizing species, there are numerous practical difficulties with adapting these processes to production environments. In addition to the development of efficient source plasmas for these ions and the need to control wafer temperature during implantation, there are severe constraints on the mass resolution limits. For example, ^{29}Si is often used rather than the more abundant ^{28}Si to avoid contamination of the ion beam by N_2^+ or CO^+. However, ^{29}Si can be contaminated by $(^{10}B^{19}F)^+$ if there is residual BF_3 gas leaking into the source area [3]. Si and Ge are also inconvenient species for preamorphization in production environments since they require a source retuning step before the implantation of dopants ions.

Fluorine, since it can be extracted from the same BF_3-fed plasma as is used to supply B or BF_2 for the doping implant, is a more attactive species for damage and amorphization implants since little or no source retuning is required for dual-step implants. Flourine has been used to suppress channeling and to achieve good electrical activation with low temperature anneals [7,8]. The specific goals of this work were to develop a source/drain implant process with F as a preamorphizing species utilizing the automation features of an advanced ion implantion system.

2. Dose optimization

The optimization of the F dose was the first step in the development process. High levels of residual F from high-dose BF_2 implants have been associated with dopant deactivation [9,10], defect decoration and pinning [11,12], anomalous diffusion effects [13–16], degradation of oxides [17,18] and formation of gas-filled voids [19–21]. Tests of preamorphization with F at doses of 10^{16} F/cm^2 resulted in significantly higher leakage currents and defect levels than junctions amorphized with Si or Ge ions [22]. Studies have indicated that Ge doses as low as 5×10^{13} ions/cm^2 can suppress B channeling effects [23,24] All indications, including the desire for short implantation times, favor the use of F doses that are significantly lower than the equivalent dose from a BF_2 implant.

2.1. Experimental conditions

In order to develop an "xFB" equivalent to a generic 50 keV BF_2 source/drain implant step, it was decided to increase the F energy to 39 keV, twice the equivalent energy for the molecular implant. This was done to ensure that the B implant depth was shallower than the thickness of the amorphous layer [7] and to take advantage of reported conditions for reduced diffusion and defect effects [8]. Preamorphization implants were done for doses ranging from 10^{14} to 10^{16} F/cm^2. Boron

[1] Present address: Sematech, Austin, TX 78741, USA.

0168-583X/91/$03.50 © 1991 – Elsevier Science Publishers B.V. (North-Holland)

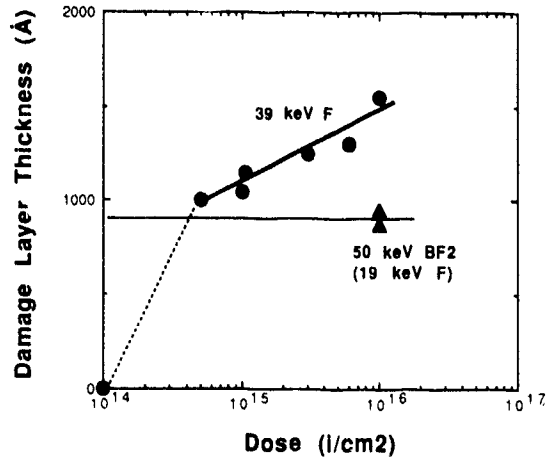

Fig. 1 Dependence of amorphous layer thickness, as measured by grazing-angle RBS, on dose for 39 keV F and 50 keV BF_2 implants into Si(100)

implants were done at 11 keV over a dose range between 1 to 5×10^{15} B/cm^2. Comparisons were also made with 50 keV BF_2 implants

2.2 Amorphous layer thickness

The thickness of the amorphous layer was determined by the depth at which the grazing-angle RBS signal was at 50% of the amorphous and random orientation level. The thickness of amorphous layer (fig. 1) grew steadily for doses above 5×10^{14} F/cm^2. An amorphous layer was not seen in the RBS analysis for the 10^{14} F/cm^2 implant.

2.3. Boron profiles

The B profiles for the 11 keV implants were identical for F doses from 5×10^{14} to 10^{16} F/cm^2 and showed no channeling effects (fig. 2). These B profiles were slightly deeper than a Monte Carlo range calculation (TRIM-84 [25]) and shallower than direct 11 keV B implants into Si(100) and 50 keV BF_2 implants. For a F preamorphization dose of 10^{14} F/cm^2, strong channeling effects were evident in the the 11 keV B profile.

3. Process qualification and device testing

The *x*FB process was adapted to a 1 Mbit SRAM process with gate feature sizes of 0.8 μm [26]. Results for *x*FB implants of 11 keV B implants after 50 keV F preamorphization implants at doses of 5×10^{14} and 10^{15} F/cm^2 were compared with the 50 keV BF_2 implants.

3.1 Boron profiles

The as-implanted profiles closely resembled the results from the F dose optimization studies (fig. 3). The *x*FB profiles closely followed TRIM-84 results from a 10^5 Monte Carlo run for both F doses, indicating that

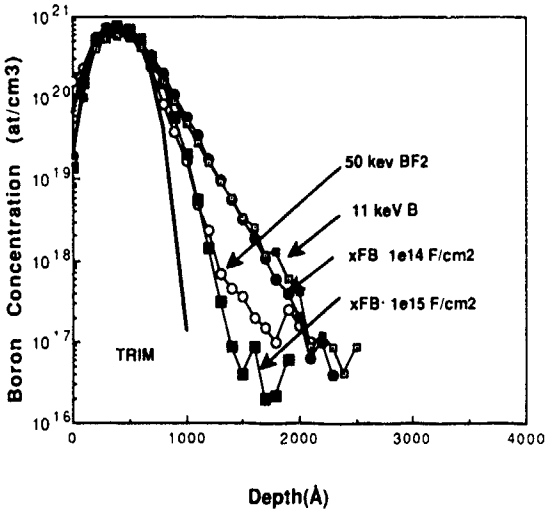

Fig. 2. As-implanted atomic concentration B profiles for direct 11 keV B implants into Si(100) and after 39 keV F preamorphization implants at doses of 10^{14} and 10^{15} F/cm^2 The B dose was 5×10^{15} B/cm^2. Note the strongly channeled character of the B profile for the lower F preamorphization dose. A 50 keV BF_2 implant and a TRIM-84 simulation for 11 keV B are also shown.

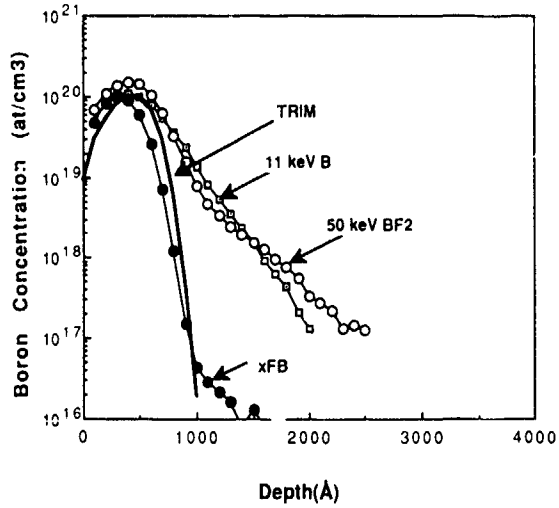

Fig. 3. As-implanted atomic concentration B profiles for 11 keV implants at a dose of 10^{15} B/cm^2 for direct implants into Si(100) and after 50 keV F preamorphization implants at doses of 5×10^{14} and 10^{15} F/cm^2. A 50 keV BF_2 implant and a TRIM-84 simulation for 11 keV boron are also shown.

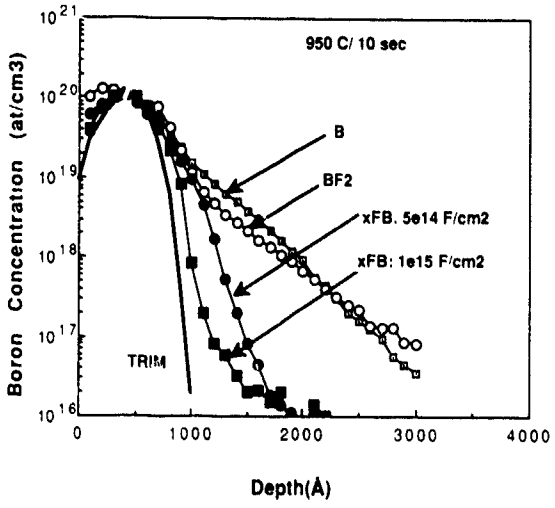

Fig. 4. Atomic concentration B profiles after an anneal of 950 °C for 10 s The implantation conditions were the same as in fig. 3

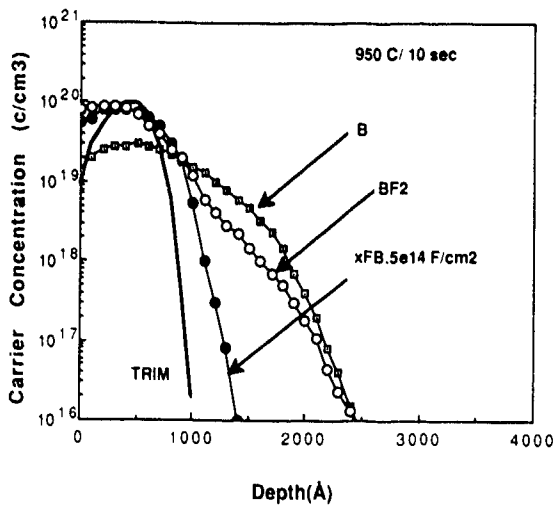

Fig. 5. Carrier concentration profiles after an anneal of 950 °C for 10 s The implantation conditions were the same as in fig. 3

an adequate degree of amorphization was achieved. Both B and BF_2 implants showed strong channeling effects under direct implantation conditions.

After an anneal cycle of 950 °C for 10 s, the *x*FB implants continued to give significantly shallower profiles and junction depths (fig. 4). The B profile for the F dose of 5×10^{14} F/cm^2 diffused deeper than the 10^{15} F/cm^2 case [13,14]. The carrier concentration profiles (fig. 5) follow the trends in the atomic profiles.

3.2 Electrical results

The electrical characteristics are summarized in table 1 After a test anneal of 950 °C for 10 s, the *x*FB implants had a higher sheet resistance than the BF_2 splits, which is characteristic of shallower junctions for the *x*FB process. The relatively low activation levels in the directly implanted B profile (fig. 5) are consistent with the high sheet resistance for this junction.

The p^+ source/drain resistance of the 40×0.8 μm transistors after the full SRAM process was lower for the *x*FB splits. The SRAMs were full functional with similar speed and leakage current characteristics for all of the process variations tested. The other significant shifts were a 0.1 V shift in the threshold voltage and a 1 mA drop in the source/drain saturation current with the *x*FB splits in comparison to the BF_2 implants.

4. Chained recipes

The system automation on the PI9200 allows for direct processing of up to 10 implants in a sequence [27]. The process recipes for the preamorphization and

Table 1
Electrical characteristics

	Implant Process			
	50 keV F 5×10^{14} F/cm^2; 11 keV B 10^{15} ions/cm^2	50 keV F 10^{15} F/cm^2, 11 keV B 10^{15} ions/cm^2	50 keV BF_2 10^{15} ions/cm^2	11 keV B 10^{15} B/cm^2
950 °C/10 s anneal				
Junction depth [μm]	0.14	– [a]	0 25	0.26
Sheet resistance [Ω/□]	143	– [a]	127	287
1 Mbit SRAM process (40×0 8 μm test structure)				
p^+ S/D sheet resistance [Ω/□]	157	158	171	– [a]
Threshold voltage [V]	−0 89	−0.91	−0.81	– [a]
S/D saturation current [mA]	8.7	9 1	9.8	– [a]

[a] No data.

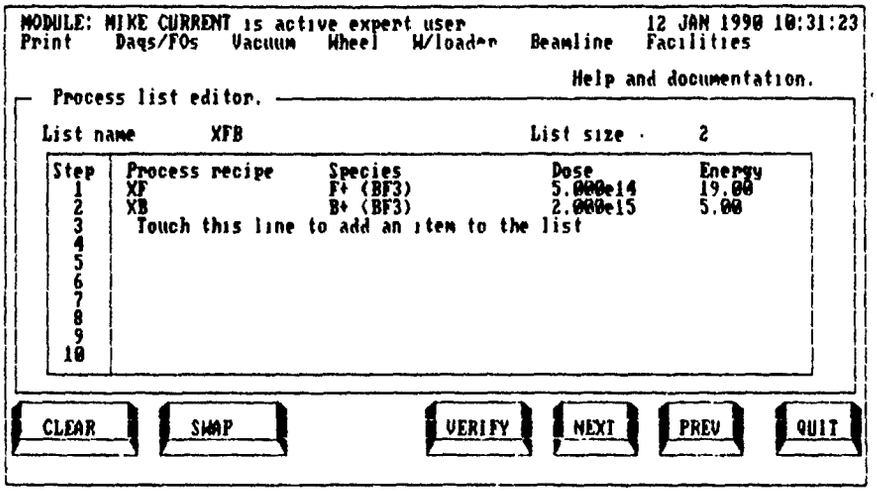

Fig. 6. Process list editor screen showing a chained recipe called "XFB" comprised of a 19 keV F preamorphization implant at a dose of 5×10^{14} F/cm^2 followed by a 5 keV B implant at a dose of 2×10^{15} B/cm^2.

dopant implants are combined from separate recipes in the system library under a new process name as a "list" (fig. 6). In a chained sequence, wafers are loaded onto the implant wheel from a loadlock chamber which holds the wafer cassettes while the source and beamline are tuned to the conditions specified in the first process recipe. After the first implant is completed, the system retunes to the second recipe while the wafers are held on the implant wheel under vacuum. This sequence can be elaborated to allow for multiple implants for each of the preamorphizing and dopant functions. This level of automation allows for the introduction of multiple implant processes into production environments with no increase in operational complexity.

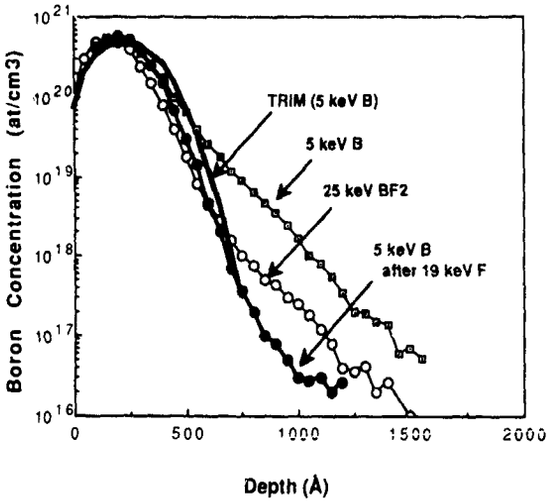

Fig. 7. As-implanted atomic concentration B profiles for 5 keV implants at a dose of 2×10^{15} B/cm^2 for direct implants into Si(100) and after a 19 keV F preamorphization implant at a dose of 5×10^{14} F/cm^2. A 25 keV BF_2 implant and a TRIM-88 simulation for 5 keV boron are also shown.

5. 5 keV boron profiles

A series of chained implants was done with a F preamorphization implant at 19 keV at a dose of 5×10^{14} F/cm^2 followed by a 5 keV B implant at a dose of 2×10^{15} B/cm^2. Direct implants of 5 keV B and 25 keV BF_2 were also tested. The B beam current at 5 keV was 2.3 mA after a 5 min automatic tuning cycle. The F preamorphization resulted in a 40% reduction in the depth of B penetration at a dopant concentration of 10^{17} B/cm^3 compared to the direct 5 keV B (fig. 7).

6. Summary

Profile analysis and process tests have shown F to be a useful species for preamorphization for formation of shallow p^+ source/drain junctions. The dual implant process has been shown to be compatible with an advanced SRAM process with minor alterations in product characteristics. The shallow junction depths which can be achieved with the xFB approach provide an attractive base for process shrinks for higher performance devices. Utilization of the chained recipe capability of an automated implanter allows for a low-risk implementation of this process into a production environment.

Acknowledgements

The authors wish to acknowledge many useful discussions during the development of this work, in par-

ticular B. Landau, T. Kay, R. Johnston and L. Coonce of National Semiconductor, M.T. Wauk, N. Ohno and N. White of Applied Materials, H. Mori of Fujitsu and J. Alvis of Motorola. We thank R. Brennan of Solecon Labs, San Jose for providing the SRP analysis. The SIMS and RBS analysis were done by Gayle Lux and Scott Baumann of Charles Evans and Associates, Redwood City.

References

[1] Y Akasaka, Nucl. Instr. and Meth. B37/38 (1989) 9.
[2] M Miyake, T. Kobayashi and Y. Okazaki, IEEE Trans Electron. Devices ED-36 (1989) 392.
[3] I.-W. Wu, Solid State Phenomena 1-2 (1988) 159.
[4] G A. Ruggles, S -N. Hong, J.J. Wortman, M. Ozturk, E R. Myers, J J. Hren and R.B. Fair, Mater. Res. Soc. Proc 128 (1989) 611
[5] S H. Hong, G A. Ruggles, J.J Paulos, J.J Wortman and M C Ozturk, Appl. Phys Lett. 53 (1988) 1741
[6] X.Y. Qian et al., these Proceedings (8th Int Conf on Ion Implantation Technology, Guildford, UK, 1990) Nucl. Instr. and Meth. B55 (1991) 821
[7] B. Baisse, A M. Cartier, P Spinelli and M Buel, Nuc Instr. and Meth. B21 (1987) 493
[8] S Ando, H Horie, M Imai, K Oikawa, H Kato, H Ishiwari and S Hijiya, IEEE Symp. on VLSI, Hawaii, USA, 1990.
[9] S P Wong, M C. Poon, H.L Kwok and Y W Lam, J Electrochem. Soc. 133 (1986) 2172
[10] O W Holland, J.R Alvis and C Hance, SPIE Proc 797 (1987) 14
[11] R.G Wilson, J Appl Phys. 54 (1983) 6879
[12] S Prussin, D I Margolese, R.N Tauber and W B Hewitt, J Appl. Phys 56 (1984) 915.
[13] K. Ohyu, T Itoga and N. Natsuaki, in: 20th Symp on Ion Implantation and Submicron Fabrication, RIKEN Symp. (1989) 149.
[14] J Kato, J. Electrochem. Soc. 137 (1990) 1918.
[15] F.K. Baker, J.F. Pfiester, T.C. Mele, H.-H Tseng, P J Tobin, J.D. Hayden, C.D Gunderson and L.C Parrillo, IEEE Int. Electron Device Meeting, Washington DC, USA, 1989 (IEDM-89) p. 443
[16] J.M. Sung, C.Y. Lu, M.L Chen, S.J Hillenius, W S. Lindenberger, L. Manchanda, T.S. Smith and S J. Wang, ibid., p. 447.
[17] K.W. Teng, H.H. Tsong, B.Y. Nguyen and F T. Liou, Electochem. Soc. Abstr. 87-1 (1987) 328.
[18] P.J. Wright and .I. Saraswat, IEEE Trans. Electron Devices 36 (1989) 879.
[19] C.W. Nieh and L.J. Chen, Appl. Phys. Lett 48 (1986) 1528.
[20] L J Chen, C W. Nieh and C H. Chu, Solid State Phenomena 1-2 (1988) 45.
[21] G.E. Pike, M.J. Carr, W.K. Shubert, C R Hills, G.C Nelson and P J. McWhorter, Mater Res. Soc Proc 138 (1989) 227
[22] C P Wu, J.T. McGinn and L R. Hewitt, J Electron Mater. 18 (1989) 721.
[23] M Kase, M. Kimura, H Mori and T. Ogawa, Appl. Phys Lett. 56 (1990) 1231.
[24] T Takeda, S. Tazawa and A. Yoshii, IEEE Trans. Electron Devices ED-33 (1986) 1278.
[25] J.F Ziegler, J.P Biersack and U Littmark, The Stopping and Range of Ions in Solids, vol 1 (Pergamon, 1985)
[26] W R. Burger, C Lage, T. Davies, M. DeLong, D Haueisen, J Small, G. Huglin, B Landau, F Whitwer and B Bastini, IEEE Int. Electron Device Meeting, Washington DC, USA, 1989 (IEDM-89) p. 421
[27] I. Joyce, C Lowrie, N Bright and B. Beeston, presented at the 8th Int Conf. on Ion Implantation Technology, Guildford, UK, 1990

Nuclear Instruments and Methods in Physics Research B55 (1991) 598-601
North-Holland

The annealing behaviour of ion-implanted Si studied using time-resolved reflectivity

R.P. Thornton, Y.H. Li, R.G. Elliman and J.S. Williams [1]

Microelectronics and Materials Technology Centre, RMIT, Melbourne 3000, Australia

The annealing behaviour of ion-implanted Si has been studied using time-resolved reflectivity (TRR) Various regimes have been identified which depend upon the implanted species and dose, the substrate orientation and the annealing temperature At low doses, electrically active impurities, such as Sb, enhance the regrowth rate in ⟨100⟩ orientated Si. In ⟨111⟩ Si, the presence of low concentrations of certain impurities, such as Sb, Ga and Sn, also affects the degree of twinning which accompanies epitaxial regrowth. At higher doses of impurities, the regrowth rate of ⟨111⟩ and ⟨100⟩ Si is retarded and some impurities are seen to segregate at the amorphous–crystalline interface Further increasing the dose provokes a dramatic phase transition to fine grain polycrystalline Si for the low melting point impurities, occurring typically 250°C below temperatures where epitaxial crystallisation is observed

1. Introduction

Since the advent of ion implantation as a method for doping Si with electrically active impurities, there has been considerable interest in the annealing behaviour of implantation-induced amorphous Si These studies have mainly concentrated on Si of (100) orientation, and the epitaxial recrystallisation kinetics for intrinsic and doped amorphous Si have been measured over a wide temperature range [1] In contrast, there has been little work reported on the effect of impurities on the regrowth of (111) Si, owing to the poor quality of recrystallised layers characterised by the formation of twins However, it was shown recently that implanted Sn can have a beneficial effect on the quality of the regrowth of (111) orientated Si [2]

In this study the effect of impurities on the regrowth behaviour of (100) and (111) orientated Si is compared This paper concentrates on the behaviour of Sb-implanted Si.

2. Experimental

Both (100) and (111) Si were implanted with doses of Sb, and Si in the range 1×10^{15} to 1×10^{16} cm^2 using a Whickham 200 keV ion-implanter. The samples where held at −196°C during implantation The dose and amorphous layer thickness was measured by Rutherford backscattering and channeling (RBS-C). The samples were annealed in air on a temperature-controlled hot block and the regrowth kinetics were monitored during annealing using time-resolved reflectivity (TRR) The samples were then analysed once again using RBS-C to determine the degree of recrystallisation. Selected samples were then prepared for plan-view transmission electron microscopy (TEM).

3. Results and discussion

Figs 1a and b compare typical TRR spectra for intrinsic and Sb implanted (100 keV, 9×10^{16} Sb/cm^2) (100) Si annealed at 600°C Fig 1c shows the derived regrowth rate for the Sb-implanted case Initially, the Sb causes an enhancement in the regrowth rate, but as the interface passes through the region of high Sb concentration, the rate is retarded to a value below that of intrinsic Si. It remains retarded as the growth continues towards the surface. Fig 2 indicates that the Sb is highly substitutional after the recrystallisation and that the Sb profile is unaffected by the regrowth Retardation is also observed for samples implanted with Sn [3], As [1], In [4] and Pb [4].

No appreciable interface segregation or "push-out" of the implanted impurity is observed for Sb or Sn during the regrowth retardation phase. However, segregation has previously been reported for both In- and Pb-implanted Si during the retarded phase of the growth [4]. The rate observed for Sb and Sn-implanted Si is somewhat surprising as changes in the regrowth rate would be expected to follow the unchanged concentration profile of the implanted impurity. Olson and Roth have reported similar asymmetric growth rate behaviour for As-implanted Si, and speculated that defects gener-

[1] Also Department of Electronic Materials Engineering, R.S.Phys.S., ANU, Canberra, Australia.

0168-583X/91/$03 50 © 1991 – Elsevier Science Publishers B V (North-Holland)

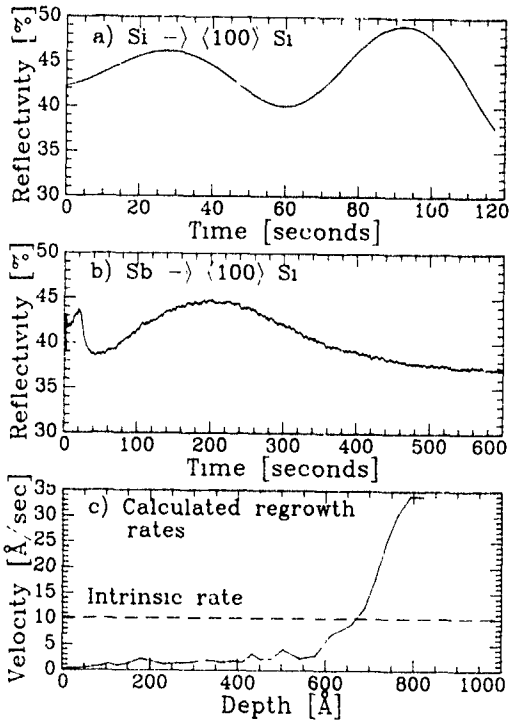

Fig 1 TRR spectra, (a) simulated for 600°C, 1200 Å amorphous layer on (100) Si, (b) for 9×10^{15} Sb/cm^2, 100 keV, annealed at 600°C, (c) calculated regrowth rates for intrinsic and Sb-implanted Si from the above data

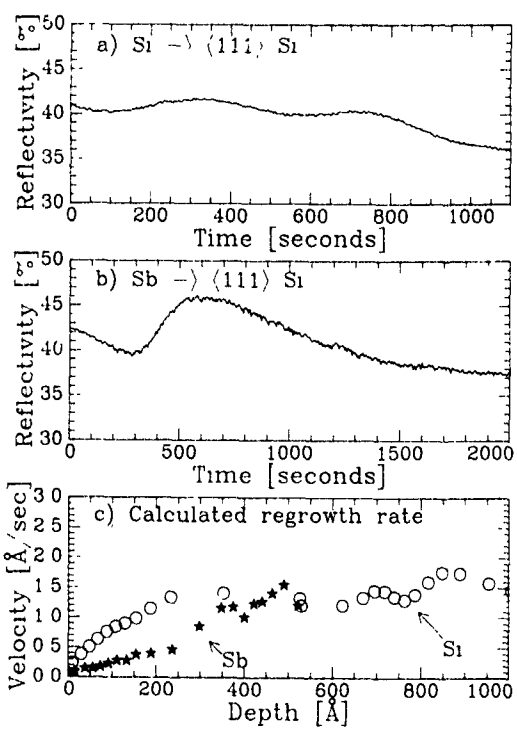

Fig 3 TRR spectra for (a) ⟨111⟩ Si implanted with 75 keV, 1×10^{15} Si/cm^2, annealed at 620°C, (b) 1×10^{15} Sb/cm^2, 100 keV, annealed at 600°C, (c) calculated regrowth rates for intrinsic (○) and Sb-implanted (★) Si from the above data

ated at the peak of the impurity profile influence subsequent growth [1] Further studies are underway to clarify the mechanism for retarded epitaxy.

The presence of impurities in (111) Si has been shown to have an effect on the quality of the recrystallised material and on the regrowth rate of Si [2]. Figs. 3a

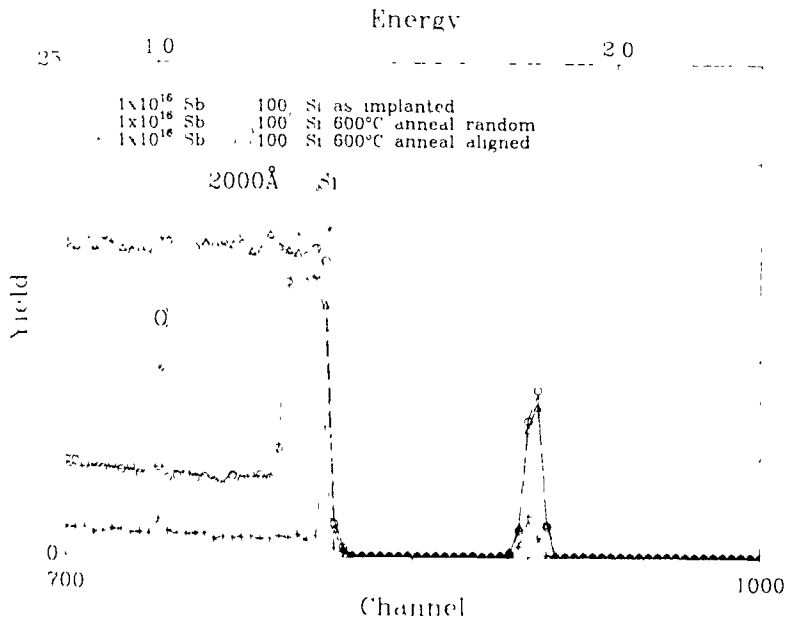

Fig 2 RBS spectra of 100 keV, 9×10^{15} Sb/cm^2 implanted Si, before and after annealing at 600°C, using 2 MeV He^{2+} with a scattering angle of 98°

and b show TRR spectra for annealing at 620°C of both impurity-free and 1×10^{15} cm^{-2}, 100 keV Sb-implanted amorphous layers on (111) Si. The regrowth of (111) Si is characterised by the generation of stacking faults and twins that effectively convert (111) directions to (511) directions [5]. Since (511) Si regrows at a faster rate than (111) Si [6], the interface becomes rough during epitaxial regrowth. This loss of interface planarity can be detected by TRR as a loss of contrast in the reflected signal [7]. Such behaviour is clearly seen in fig. 3 (cf. fig. 1a). Indeed the amplitude of the reflectivity oscillations is much greater in the case of the Sb-implanted sample (fig. 3b) than for the Si-implanted sample (fig. 3a); this indicates a smoother regrowth interface for the Sb-implanted case. This phenomenon is also observed for Ga, In, Bi, and Sn, but is most pronounced for Sb. The derived regrowth rates for the impurity-free and Sb-implanted samples are shown in fig. 3c. The loss of contrast in the TRR signal makes calculation of the regrowth rate more difficult, resulting in an increased scatter of the data points. Nevertheless, it is clear that both samples exhibit retarded growth in the near-surface region, although the retardation effect appears to be greater for the Sb-implanted sample

The RBS-C spectra in fig. 4 for Si- and Sb-implanted Si after annealing clearly show that the level of residual defects remaining in the Si after regrowth is less for the Sb-implanted case than for the impurity-free case. This may indicate that Sb restricts the formation of twins during regrowth. Plan-view TEM of the Si-implanted and the Sb-implanted samples indicate that twins are present in both cases after annealing, but it is difficult to accurately measure the twin concentration in each case. However, when combined with the channeling data, it is clear that the number of twins in the Sb-implanted sample is reduced relative to the impurity-free sample. Table 1 summarises the level of residual disorder (as measured by the near-surface channeling yield, χ_{min}) for a range of different impurities, indicating that less defective regrowth is also obtained in these cases. Note that Ga enhances the growth rate and is pushed out during epitaxy, whereas Sb and Sn retard epitaxy and retain their implanted distribution.

Table 1
Summary of residual damage seen after annealing of (111) Si implanted with various impurities

	χ_{min}	SPEG rate change	Push-out
Si	46%	-	-
Sb	10%	retarded	no
Ga	23%	enhanced	yes
Sn	38%	retarded [a]	no

[a] See ref. [2].

The mechanism for this impurity-induced improvement in the regrowth quality in (111) Si is not clear Since similar behaviour is observed for group III, IV and V impurities, it would seem to indicate that the reduced twinning is not purely an electronic effect. However, electrical dopants do seem to effect a greater reduction in the number of twins produced.

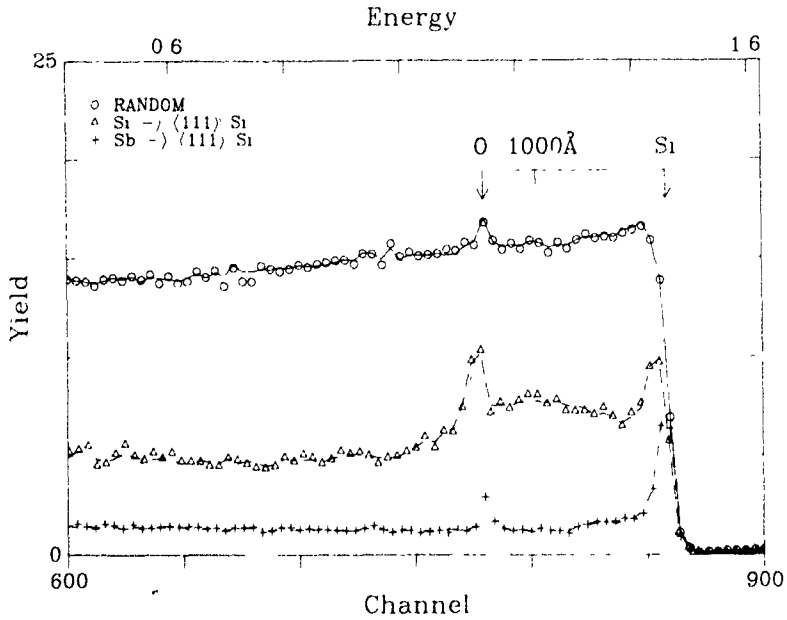

Fig 4. RBS spectra of the Si- and Sb-implanted samples, shown in fig 3, after annealing, using 2 MeV He^{2+} with a scattering angle of 98°

4. Conclusion

Two interesting regrowth observations in high-dose ion-implanted Si have been reported. First, it was shown that the presence of high concentrations of Sb can retard the regrowth rate of (100) Si without any noticeable segregation or push-out taking place. Furthermore, the retardation persists to the surface, and the growth rate does not follow the impurity concentration profile. Second, the presence of ion-implanted impurities can have a beneficial effect on the quality of recrystallised (111) Si by reducing the twin density.

Acknowledgements

We acknowledge the Commonwealth Special Research Centres Scheme, the Australian Research Council and the Victorian State Government for financial support. One of us (RPT) acknowledges the award of a Commonwealth Postgraduate Research Award.

References

[1] G L. Olson and J.A. Roth, Mater Sci Rep. 3 (1988) 1.
[2] R.P. Thornton, R.G. Elliman and J.S. Williams, Nucl. Instr. and Meth B37/38 (1989) 387
[3] R.P Thornton, R.G. Elliman and J.S Williams, J. Mater. Res. 5 (1990) 1003
[4] J.M. Poate and J S Williams, Ion Implantation and Beam Processing (Academic Press, 1984)
[5] M.D. Rechtin, P.P. Pronko, G. Foti, L Csepregi, E F Kennedy and J.W. Mayer, Philos. Mag. A37 (1978) 605.
[6] L Csepregi, E.F. Kennedy, J W. Mayer and T.W Sigmon, J Appl. Phys 49 (1978) 3906
[7] C. Licoppe, Y I Nissim, C Meriadec and P. Rauz, J Appl Phys 60 (1986) 1352.

Nuclear Instruments and Methods in Physics Research B55 (1991) 602–606
North-Holland

MeV ion-beam annealing of semiconductor structures

J.S. Williams [1], M.C. Ridgway, R.G. Elliman [1], J.A. Davies [2], S.T. Johnson [1] and G.R. Palmer [3]

Department of Electronic Materials Engineering, Research School of Physical Sciences, Australian National University, Canberra 2600, Australia

MeV heavy-ion beams have been used to induce epitaxial crystallization of amorphous Si, GaAs, InP, Ge–Si alloy and metal silicide layers. In all cases, the crystallization kinetics and the quality of the recrystallized layers have been compared with thermal-annealing behaviour. The most striking differences between the two annealing regimes (thermal and ion beam) have been observed for InP and high-dose In-implanted Si, where ion-beam annealing at low temperatures results in more extensive and higher-quality epitaxy than that achieved by thermal annealing.

1. Introduction

MeV ion implanters are receiving increasing attention for a wide range of semiconductor applications. These include the formation of buried compounds such as silicides and oxides, dopant implants for deep junctions and conducting layers, isolation of III–V semiconductor structures, production of doped amorphous layers for subsequent study of diffusion and crystallization, and for inducing controlled epitaxial crystal growth of pre-existing amorphous layers at low temperatures. It is this last application that is the subject of this paper.

Amorphous Si layers produced in crystalline Si by ion implantation have been shown to recrystallize epitaxially during subsequent MeV ion irradiation at temperatures as low as 150 °C [1]. Under these conditions, the crystallization rate is controlled by the nuclear energy deposition rate at the amorphous–crystalline (a-c) interface and has only a small dependence on temperature (activation energy ~ 0.24 eV). Furthermore, the ion-beam-induced crystallization process is relatively insensitive to impurities within the amorphous layer [1]. This opens up the possibility of inducing epitaxial growth in cases where high impurity concentrations impede conventional thermally induced epitaxy [2].

Ion-beam-induced epitaxial crystallization has also been demonstrated in GaAs [3] and, more recently, in amorphous Ge–Si alloys [4] and $NiSi_2$ [5] grown epitaxially on Si. In this paper, we report on an extension of our MeV ion-beam-induced crystallization studies, particularly into InP, $CoSi_2$ and high-dose-implanted Si. The crystallization kinetics and the quality of crystallization are compared for the various systems.

2. Experimental

The experimental sequence for the present studies is shown schematically in fig. 1. For high-dose Si studies, (100) Si wafers were first implanted with 100 keV In

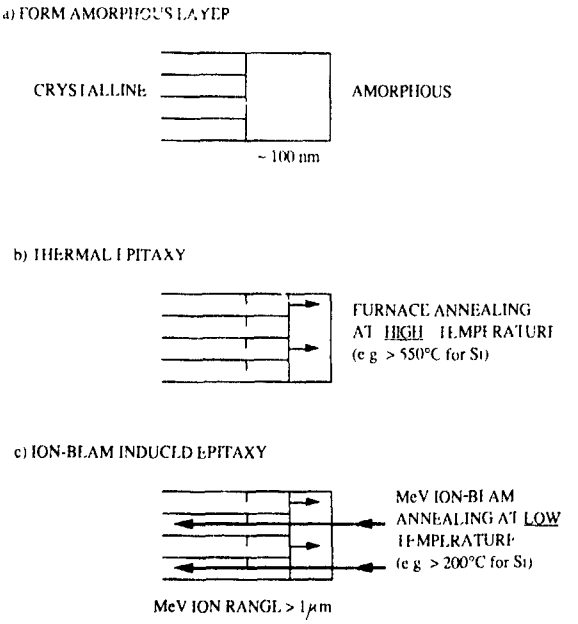

Fig. 1. Schematic illustration of epitaxial crystallization of (a) an initial surface amorphous layer, (b) by thermal annealing and (c) MeV ion-beam annealing.

[1] Also: Microelectronics and Materials Technology Centre, Royal Melbourne Institute of Technology, Melbourne, 3000, Australia.

[2] Permanent address: Department of Engineering Physics, McMaster University, Hamilton, Ontario, Canada.

[3] Present address: Physics Department, Queen's University, Kingston, Ontario, Canada.

0168-583X/91/$03.50 © 1991 – Elsevier Science Publishers B.V. (North-Holland)

ions to a dose of 2.4×10^{15} cm^{-2} with the samples held at -196 °C. The resultant amorphous layers were ~ 100 nm thick (fig. 1a). Amorphous layers (20–100 nm thick) were formed in (100) GaAs and InP wafers by implanting with 15–50 keV ^{28}Si, ^{29}Si or ^{31}P ions to doses of ~ 10^{15} cm^{-2}.

For multilayer structures, Ge–Si alloys and Ni and Co silicide layers were initially grown epitaxially on either (100) or (111) Si substrates as described elsewhere [4,6]. These layers were then implanted with 30–100 keV ^{28}Si ions to form amorphous layers, either confined to the alloy layer or extending into the underlying Si substrate. All implantations were performed with a Whickham Ion Beam Systems 200 kV high-current ion implanter.

Following amorphization, some samples were mounted on a resistively heated hot stage and annealed in air at temperatures between 60 °C and 650 °C depending on the substrate type. During annealing, a 633 nm He–Ne laser was incident on the sample and changes in the reflected light intensity were monitored with a photodiode. This time-resolved reflectivity (TRR) technique, described elsewhere [7], is a convenient method for measuring the thermally induced epitaxial growth kinetics (fig. 1b). For ion-beam-induced epitaxy, samples were irradiated with Ne^+, Ar^+ and Si^+ ions at energies between 300 keV and 1.5 MeV whilst the sample temperature was held constant between 15 °C and 400 °C depending on substrate type. An in situ TRR arrangement was also used to monitor the extent of epitaxy (fig. 1c) during ion irradiation

Following either thermally induced or ion-beam-induced epitaxy, samples were analyzed by Rutherford backscattering and channeling (RBS-C) and selected samples were examined by transmission electron microscopy (TEM) techniques. This paper concentrates on RBS-C to monitor regrowth quality and TRR to measure crystallization kinetics.

3. Results and discussion

Indium-implanted Si samples were irradiated with 1.5 MeV Ar^+ ions at 200 °C, 300 °C and 400 °C. In situ TRR was used to monitor the progress and quality of ion-beam-induced epitaxial growth by observing the amplitude of oscillations in the reflected light intensity [7]. For irradiation at 400 °C, TRR indicated that epitaxy of the original ~ 100 nm thick amorphous layer proceeded at a constant rate until the a–c interface approached within ~ 40 nm of the surface. Thereafter, the TRR signal changed abruptly in a manner indicative of an amorphous-to-polycrystalline phase transformation, as previously observed for thermal annealing of high-dose In-implanted Si [2]. Ion-channeling spectra confirmed that epitaxial growth had been arrested ~ 40 nm from the surface. Fig. 2a shows schematically the RBS profile for as-implanted In (dashed curve) compared with that obtained following the 400 °C Ar^+ irradiation (solid curve). The latter profile is essentially similar to behaviour previously observed for thermal annealing. The implanted In is segregated towards the surface (at the a–c interface) and is then redistributed within the near-surface layer which has transformed to polycrystalline Si and hence not undergone epitaxial growth. However, compared with previous studies of thermal annealing at 525 °C [2], the extent of epitaxial recrystallization appears to be greater for the 400 °C ion-beam anneal. There is also less In redistribution within polycrystalline Si after ion-beam annealing, presumably as a consequence of the lower annealing temperature.

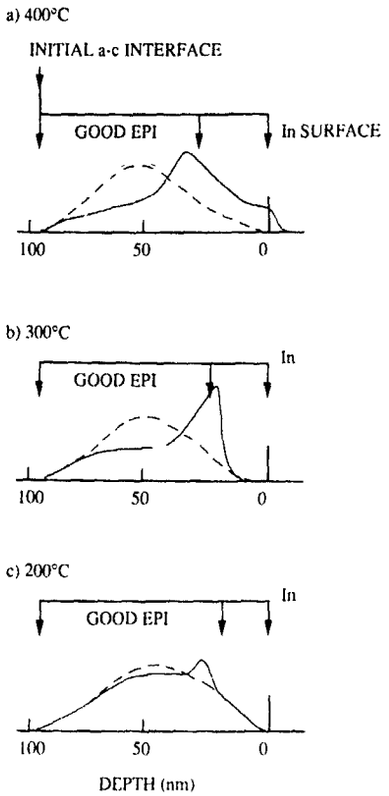

Fig. 2 Schematic In profiles obtained from RBS spectra. Solid curves indicate In profiles following ion-beam annealing with 1.5 MeV Ar^+ ions at (a) 400 °C, (b) 300 °C and (c) 200 °C. The as-implanted profiles are shown by the dashed curves and the extent of Si epitaxial growth with respect to the In depth distribution is also indicated.

Ion-beam annealing at 300 °C produced more extensive epitaxy before the TRR signal departed from regular oscillatory behaviour. In this case, the TRR signal did not show an abrupt change indicative of a sudden polycrystalline phase transformation; rather, it changed

slowly to a near-constant level. The RBS profile of the In (fig. 2b) also showed differences from that in fig. 2a. At 300 °C, a clear In segregation peak at the a–c interface accompanies epitaxy. It appears that an amorphous-to-polycrystalline transformation has been initiated within the surface amorphous layer but is incomplete. Consequently, In has not yet redistributed throughout this surface layer.

At 200 °C, the ion-beam annealing behaviour is again different. Epitaxy proceeds towards the surface but TRR indicates extremely slow (retarded) growth as the a–c interface proceeds to within 30 nm of the surface. In fact, the growth could not be completed in a reasonable time under the Ar^+ bombardment conditions used. Furthermore, the In profile following 200 °C beam annealing (fig. 2c) indicates much less segregation than that at higher ion-beam annealing temperatures. In this case, the near-surface layer appears not to have transformed to a polycrystalline layer.

More detailed analysis of ion-beam-annealed layers of high-dose In-implanted Si will be presented elsewhere, including TEM measurements. However, some important features are clear from the present preliminary study:

(i) lower ion-beam annealing temperatures favour epitaxy over the competing amorphous-to-polycrystalline transformation;

(ii) less In is segregated at the advancing amorphous-to-crystalline interface as the ion-beam annealing temperature is lowered.

These observations suggest that In diffusion in amorphous Si (the proposed initiating factor in the thermally induced phase transformation and In interface segregation [2]) is less pronounced during ion-beam annealing than during thermal annealing at higher temperatures. Thus, ion-beam annealing at low temperatures may offer the prospect of improved crystal growth of Si amorphous layers implanted with high doses of impurities.

Fig. 3 shows RBS-C spectra indicating the quality of recrystallization achieved in GaAs following both furnace and ion-beam annealing. Previous studies [3] have shown that furnace annealing (at 250 °C) initially induces good quality epitaxy, but severe twinning occurs

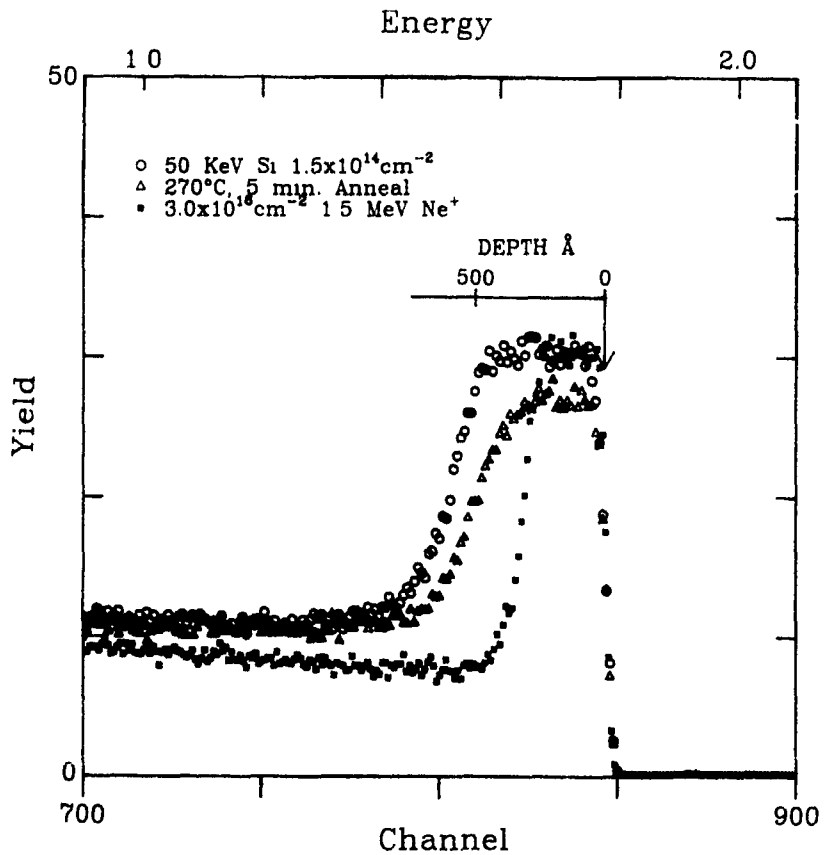

Fig. 3. RBS-C spectra illustrating the extent of epitaxial growth following thermal annealing at 270 °C (Δ) compared with partial epitaxy during ion beam annealing with 1.5 MeV Ne^+ at 75 ° (■). The final spectrum (○) corresponds to the starting material with an ~ 650 Å amorphous surface layer

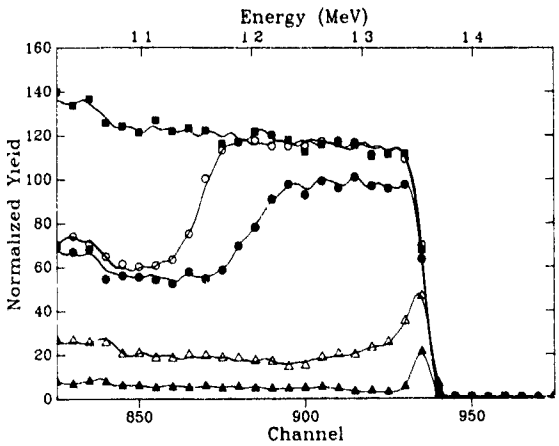

Fig 4. RBS-C spectra illustrating the quality of crystallization of a ~100 nm amorphous layer on (100) InP (○) during furnace annealing at 260°C (●) compared with ion-beam annealing with 1.5 MeV Ar^+ at 145°C (△) A virgin InP spectrum is also shown (▲).

as the growth proceeds towards the surface. The behaviour indicated in fig. 3 is consistent with such a growth process. As shown in fig. 3, ion-beam annealing with 1.5 MeV Ne^+ at 75°C results in more extensive epitaxy than furnace annealing. In this case, the amorphous GaAs has only been partly recrystallized and about half of the layer remains amorphous. Higher-dose Ne^+ irradiation leads to a breakdown in epitaxy and eventually results in extensive near-surface damage which could originate from ion-beam-induced dissociation of GaAs.

In contrast to GaAs, fig. 4 shows that InP exhibits much improved epitaxy under ion-beam annealing (1.5 MeV Ar^+ at 145°C) compared with furnace annealing at 260°C. TEM suggests that twinning is suppressed during ion-beam annealing at low temperatures, consistent with the low levels of residual disorder as measured by RBS-C [8]. Furthermore, TRR spectra imply that the planarity of the crystallization front is much better for InP than for GaAs. This may account for, or be a consequence of, the reduced twinning.

Table 1 summarizes the ion-beam annealing behaviour for various semiconductor structures compared with furnace annealing. As indicated in figs. 2, 3 and 4, low-temperature ion-beam annealing can have advantages over furnace annealing in terms of improved epitaxy for high-dose-ion-implanted elemental semiconductors and for compound semiconductors. For Ge–Si alloys on (100) Si, our previous ion-beam studies [4] have shown that high-Ge-content amorphous layers (exceeding 20%) can be recrystallized epitaxially in a layer-by-manner from the underlying Si substrate Such behaviour cannot be achieved by furnace annealing since the crystallization temperatures of Si and the Ge-rich alloy are very different. The initial result of furnace annealing in 50% Ge-rich layers is a polycrystalline alloy layer. In addition, ion-beam annealing forms strained Ge–Si alloy layers on Si when the Ge content is < 30%, similar to the behaviour in the MBE grown starting material. There are also indications from other workers [9,10] that different (both higher and lower) strain levels can be sustained in annealed layers than in initial layers grown by molecular beam epitaxy.

For silicide layers on Si (111), both amorphous $NiSi_2$ [5] and $CoSi_2$ can be epitaxially recrystallized using

Table 1
Comparison of the epitaxial growth kinetics and growth quality of a number of semiconductor structures annealed thermally and with MeV ion beams

Sample	Furnace annealing		Ion-beam annealing		Advantages of ion-beam annealing
	Temp. [°C]	E_{act} [eV]	Temp [°C]	E_{act} [eV]	
Si (100)	≥ 550	2.7 [11]	≥ 200	0.2–0.3 [1]	Less sensitive to impurity effects
Ge (100)	≥ 330	2.0 [12]	≥ 150	0.2–0.3 [10]	Similar to Si
Si–Ge on Si (100)	330–550	1.8–2.7	≥ 200	0.2–0.3 [10]	Improved epitaxial growth for high Ge content alloys on Si, preserves strained layers
GaAs (100)	≥ 250	1.6 [13]	≥ 75	~ 0.17 [3]	Slightly improved growth but dislocations introduced
InP (100)	≥ 200	1.6 [8]	≥ 150	0.15 [8]	Greatly improved growth but dislocations introduced
$NiSi_2$ on Si (111)	≥ 80	1.1 [6]	≥ 0	0.26 [5]	Can induce epitaxial growth but also high levels of ion-beam-induced defects
$CoSi_2$ on Si (111)	≥ 100	1.2 [6]	≥ 40	0.21 [14]	

ion-beam irradiation at temperatures below 50 °C. This results in amorphization of underlying Si, leading to crystalline Si/amorphous Si/crystalline silicide structures. The quality of recrystallized silicide layers is not as good as those obtained using furnace annealing as a result of ion-beam-induced defects [5].

Table 1 also includes the activation energies for both thermal and ion-beam-induced epitaxy for the various structures listed. It is significant to note that, in all cases, the activation energy for ion beam annealing is 1/5 to 1/10 of the value for thermal annealing. As indicated earlier [1,3] this suggests that the ion beam introduces, athermally, preferred growth (nucleation) sites at the a–c interface, which constitute the high-energy component of the thermal activation energy. It is interesting that the silicides, which are metallic layers, also exhibit the same low activation energy for ion-beam-induced epitaxy as do the semiconductor layers. This may reflect the covalent nature of bonding in metal silicides.

4. Conclusions

The conclusions from this study of MeV ion-beam-induced crystallization of semiconductor structures are as follows:

(i) the lower temperatures afforded by ion-beam-induced epitaxy can be used to suppress In diffusion, interface segregation and polycrystalline phase transformations in high-dose In-implanted Si;

(ii) ion-beam annealing can lead to dramatically improved epitaxy (and reduced twinning) in the case of InP;

(iii) amorphous Ge–Si alloys of high Ge content on (100) Si can be successfully recrystallized epitaxially using ion beams, compared with poor-quality thermally induced crystallization; and

(iv) in all cases, even for metal silicides, the activation energies for ion-beam-induced epitaxy are 5 to 10 times lower than those for thermal epitaxy.

Acknowledgement

The Special Research Centres Schemes and the Australian Research Council are acknowledged for financial support.

References

[1] R.G. Elliman, J S Williams, W.L. Brown, A Leiberich, D.M. Maher and R V Knoell, Nucl Instr and Meth B19/20 (1987) 435.

[2] E Nygren, J C. McCallum, R Thornton, J.S. Williams and G L Olson, Mater. Res Soc Symp Proc 100 (1988) 405.

[3] S.T. Johnson, J.S. Williams, E Nygren and R.G. Elliman, J Appl Phys. 64 (1988) 6567

[4] R G. Elliman, M.C Ridgway, J S. Williams and J C Bean, Appl Phys. Lett 55 (1989) 843

[5] M C Ridgway, R G. Elliman and J.S Williams, Appl Phys. Lett 56 (1990) 2117

[6] M.C. Ridgway, R.G Elliman, R.P Thornton and J S. Williams, Appl Phys. Lett 56 (1990) 1992.

[7] G.L Olson, S A. Kokorowski, R.A MacFarlane and L D Hess, Appl. Phys. Lett 37 (1980) 1019.

[8] M C Ridgway, G R. Palmer, R G Elliman, J.A. Davies and J.S. Williams, Appl Phys Lett (1991) in press

[9] B T Chilton, B J Robinson, D A Thompson, T.E. Jackman and J -M Baribeau, Appl Phys. Lett 54 (1989) 42.

[10] A Yu, Ph.D. Thesis, Cornell University (1989)

[11] G.L. Olson and J A Roth, Mat. Sci. Rep. 3 (1988) 1

[12] L. Csepregi, R P Kullen, J W. Mayer and T W. Sigmon, Solid State Commun 21 (1977) 1019

[13] C. Licoppe, Y.I Nissim and C Meriadec, J. Appl Phys 58 (1985) 3094

[14] M.C Ridgway, R.G. Elliman and J S. Williams, Mater. Res Soc Symp. Proc 157 (1990) 131

Nuclear Instruments and Methods in Physics Research B55 (1991) 607–610
North-Holland

Distribution of paramagnetic defects formed in silicon by MeV ion implantations

Y. Yajima, N. Natsuaki [1], K. Yokogawa and S. Nishimatsu
Central Research Laboratory, Hitachi Ltd, Kokubunji, Tokyo 185, Japan

Two different types of paramagnetic centers in silicon, Si-P3 (neutral {110} planar tetravacancies) in a well defined crystalline structure and point defects with poorly defined local structure in substantially damaged crystalline environments, formed by 3 MeV phosphorus and silicon ion implantations up to a dose of 1×10^{14} cm^{-2} have been compared both in the dose dependence of area densities and in depth profiles. When the dose reaches to 1×10^{14} cm^{-2}, the area density of Si-P3 starts to saturate while that of "indefinite" point defects keeps increasing. Also at this dose, the mean concentration of Si-P3 decreases as a function of depth from the surface whereas that of "indefinite" point defects increases. These results are discussed in terms of a damage overlap model in conjunction with a Monte Carlo simulation of lattice disorder.

1. Introduction

Ion implantation in the MeV region is a promising new doping technique that would make it possible to fabricate novel semiconductor device structures [1,2]. Accordingly, there is a growing interest in the effects of MeV ion bombardments on the crystalline state of substrate semiconductors [3–7].

We have previously reported the results of EPR (electron paramagnetic resonance) investigation on 3 MeV phosphorus ion implantation into silicon [8]. EPR measurements at room temperature in conjunction with successive removal of sample surfaces have revealed that:

(1) implantation of 10^{14} cm^{-2} ions results in the preferential formation of Si-P3 (neutral {110} planar tetravacancies [9,10]);
(2) these Si-P3 are embedded in a well-defined crystalline region retaining the original lattice structure and orientations;
(3) their density decreases in going from the surface toward the buried phosphorus-rich layer;
(4) in addition to sharp Si-P3 lines, a broad and slightly anisotropic resonance appears.

The above broad resonance has been attributed to the dangling-bond-type point defects with poorly defined local structure located in crystalline environments that are substantially damaged, but not fully randomized nor amorphized, by the ion impact. Paramagnetic centers in this heavily damaged region are not likely to give EPR lines with narrow linewidths and definite anisotropy just like those of Si-P3, since orientations of local lattice structure deviate around the mean, perhaps original, orientations. Therefore, we can say that Si-P3 and these "indefinite" point defects are not coexistent. They are separated in regions different from each other in terms of the extent of lattice disorder. Accordingly, the spatial distribution of Si-P3 and "indefinite" point defects should reflect the distribution of lightly damaged and heavily damaged crystalline regions, respectively.

We have thus compared the depth profiles of Si-P3 and "indefinite" point defects as well as the dose dependence of their area densities in order to elucidate how the crystalline disorder develops with the MeV ion bombardments.

2. Experimental

Details of experimental procedures have been described previously [8]. Here we only summarize the points essential for the discussion that follows.

Samples were prepared from high-resistivity (500–2000 Ω cm) FZ silicon wafers. Ion implantations were performed under nonchanneling conditions at temperatures between 50 °C and room temperature. Temperature rise of samples prior to the measurements was carefully avoided. EPR measurements were carried out at room temperature on an X-band EPR spectrometer. The absolute numbers of paramagnetic species were determined only within the accuracy of a factor 5. During the process of surface stripping for the depth profile analysis, surface roughness gradually increased because of etching-rate inhomogeneity. This allowed the determination of only the approximate profiles. The

[1] Present address: Device Development Center, Hitachi Ltd., Ome, Tokyo, Japan.

0168-583X/91/$03.50 © 1991 – Elsevier Science Publishers B.V. (North-Holland)

attempt to obtain the depth profile in the region deeper than about 2.5 μm from the original surface was hampered, since the decrement of EPR intensity at each step of surface removal became comparable to the noise level of the signal in this region.

3. Results and discussion

EPR spectra of silicon implanted with 1×10^{14} cm^{-2} phosphorus ions at 3 MeV are compared with corresponding simulated Si-P3 spectra in fig. 1. Sharp lines are readily attributed to Si-P3. Their systematic angular variation relative to the original crystal axes as well as the narrow line profile indicates that these Si-P3 are embedded in a well defined crystalline region where the lattice structure and orientations remain unaffected by the ion bombardments.

The broad resonance overlapping with Si-P3 lines exhibits a slight but obvious anisotropy. This resonance looks "sharpest" when the external static magnetic field, B, is parallel to one of the ⟨100⟩ axes. Regardless of the type of g tensor involved, a cubic lattice structure renders the highest degeneracy of the effective g value when $B \parallel \langle 100 \rangle$. Paramagnetic species giving rise to this broad anisotropic resonance are thus supposed to exist in substantially damaged, but not fully randomized, crystalline environments in which lattice orientations deviate around the original ones. The anisotropy also indicates that these paramagnetic species favor some specific local structure, but it might not be so definite as that of Si-P3. They are thus referred to as "indefinite" point defects hereafter.

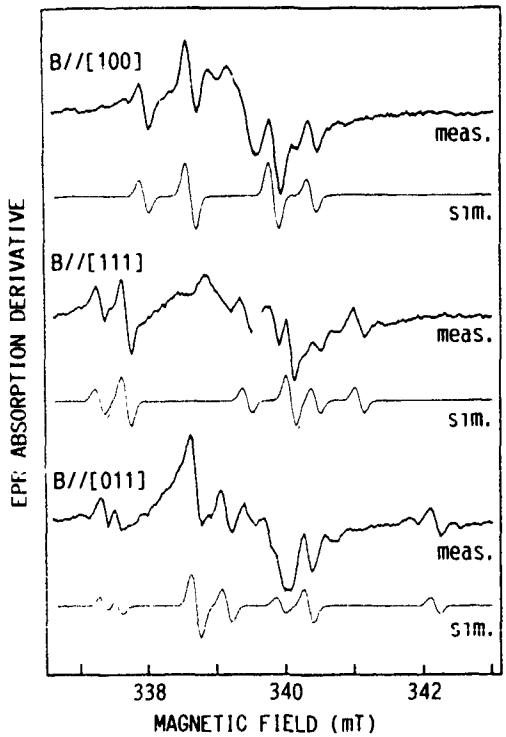

Fig. 1. Room-temperature EPR spectra at 9.530 GHz of silicon implanted with 3 MeV phosphorus ions to a dose of 1×10^{14} cm^{-2} (upper), and simulated Si-P3 spectra (lower).

The above observation suggests that Si-P3 and indefinite point defects are not coexistent in the same region, but are distributed separately in different regions. Therefore we classify damaged regions into two categories, lightly damaged regions and heavily damaged regions. EPR measurements facilitate the probing of the former through the sharp lines of Si-P3 and of the latter through the broad anisotropic resonance of indefinite point defects.

Area densities of Si-P3 and indefinite point defects formed by 3 MeV phosphorus ion implantation at a dose of 1×10^{14} cm^{-2} and 3 MeV silicon ion implantations at lower doses are plotted together in fig. 2a

Here we only discuss the dose dependence by referring to the fact that the experimental accuracy in this work is not sufficient to distinguish the mass and atomic number differences between phosphorus and silicon ions. This is justified in a more quantitative manner by standard LSS calculations of nuclear stopping power (fig. 3). It is seen that experimental values should be determined with an accuracy of at least 15% for an investigation in which the difference between 3 MeV phosphorus and 3 MeV silicon ion implantations is to be discussed. This is not the case in the present work.

An advantage, of which we make much use here, of comparing phosphorus ion implantation with silicon ion implantation is that one can rule out the impurity-driven effect, if any, even when one discusses the results of phosphorus ion implantation.

Returning to fig. 2a, one recognizes that the density of Si-P3 tends to saturate when the dose reaches 1×10^{14} cm^{-2}, while that of indefinite point defects keeps increasing. This is an indication of damage overlap; subsequent ions cause new damage in the lightly damaged region formed by the preceding ion. This multiple overlap of damage alters lightly damaged regions into heavily damaged regions where well behaved Si-P3 can no longer survive.

Depth profiles of Si-P3 and indefinite point defects formed by 1×10^{14} cm^{-2} 3 MeV phosphorus ions shown in fig. 4 also support this view. The decrease of Si-P3 and the increase of indefinite point defects in going from the surface to the buried phosphorus-rich layer again suggest that the lightly damaged region is depleted with the growth of the heavily damaged region.

For further analysis we develop a model. We aim at constructing a model which reproduces essential features of the dose dependence of integrated area densi-

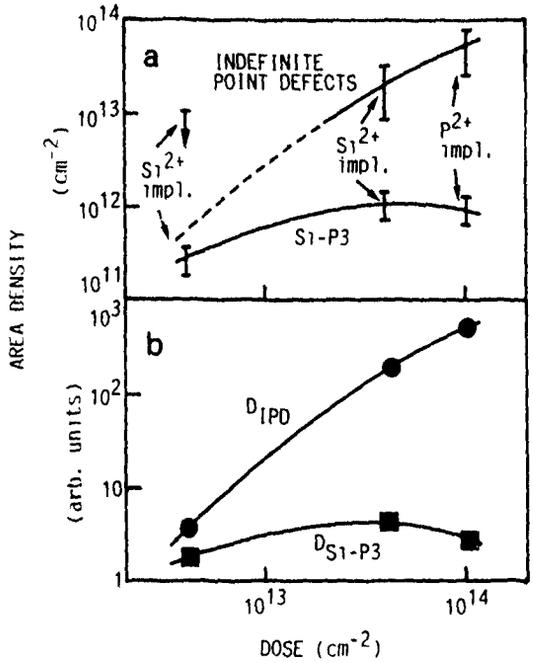

Fig 2. (a) Area densities of Si-P3 and indefinite point defects formed in silicon by 3 MeV phosphorus and silicon ion implantations at different doses. At a dose of 4×10^{12} cm^{-2} only the upper limit has been determined for the area density of indefinite point defects because of the broad line profile together with its substantial overlap with Si-P3 lines and with a signal presumably arising from sample edges (b) Calculated dose dependence of $D_{Si\,P3}$ and D_{IPD}. See text for their definitions

ties and the depth profiles of the two types of defects in as simple a way as possible

We first make an assumption that each incident ion, if fully isolated from others, creates what we refer to

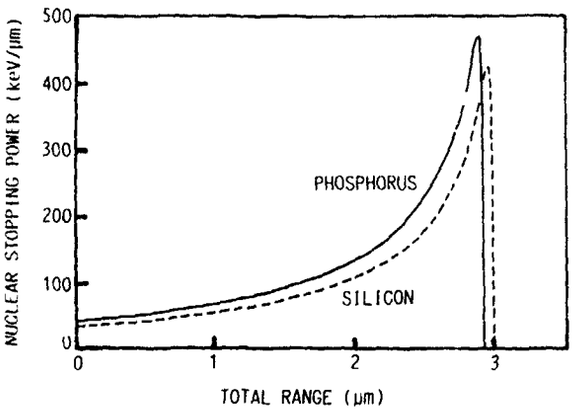

Fig 3. Calculated nuclear stopping power as a function of *total* range The universal nuclear stopping function proposed in ref. [11] has been employed in the calculation

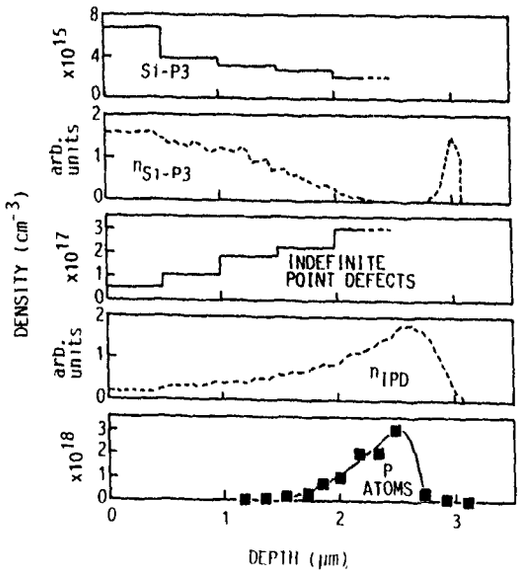

Fig 4 Approximate depth profiles of Si-P3 and indefinite point defects (solid lines). The profile of Si-P3 was taken from ref [8] Also shown are the calculated depth profiles of $n_{Si\,P3}$ and n_{IPD} defined in the text (dashed lines) The phosphorus atom distribution is also shown for comparison.

here as a lightly damaged region Accordingly, a heavily damaged region appears only at a multiple overlap of lightly damaged regions. In addition, Si-P3 are assumed to be distributed uniformly in the lightly damaged region. We then introduce an overlapping factor, F, as $F = Nf$, where N and f denote, respectively, the number of ions passing through a volume element of the target material, and the volume fraction of damaged region induced in this volume element by the passage of each ion. In the situation of ion implantation which we are dealing with, the overlapping factor F becomes proportional to the total dose through N, and depends on the depth from the surface through f. The depth dependence of F arising from the nonuniformity of the damage profile merits particular attention. Although frequently neglected, this is crucial to a model attempting to interpret the depth distribution of defects.

One then obtains a set of equations for V_i ($i \geqq 1$), the volume fraction of lightly damaged region subjected to i times overlap, and V_0, the volume fraction of undamaged region,

$$dV_0/dF = -V_0,$$

$$dV_i/dF = -V_i + V_{i-1} \quad (i \geqq 1).$$

One immediately gets, under the conditions $V_0 = 1$, $V_1 = V_2 = \ldots = 0$ at $F = 0$, namely no damage before implantation,

$$V_0 = \exp(-F),$$

$$V_i = \exp(-F)F^i/i! \quad (i \geqq 1)$$

If the damage overlap of any multiplicity results in the formation of a heavily damaged region, and if the concentration of indefinite point defects in the heavily damaged region is proportional to the multiplicity of the overlap, the concentration of Si-P3, $n_{\text{Si-P3}}$, and that of indefinite point defects, n_{IPD}, are:

$$n_{\text{Si-P3}} = kV_1 = kF\exp(-F),$$

$$n_{\text{IPD}} = k'(2V_2 + 3V_3 + \ldots) = k'F[1 - \exp(-F)],$$

where the proportionality constants k and k' are in general different from each other. Since we are not interested in absolute concentrations of Si-P3 and indefinite point defects, these proportionality constants are not detrimental. This formalism is similar to that employed in the analysis of amorphization based on the overlap of damage clusters [12,13].

Integration of $n_{\text{Si-P3}}$ and n_{IPD} in terms of depth, z, yields integrated area densities, $D_{\text{Si-P3}}$ and D_{IPD}, respectively

$$D_{\text{Si-P3}} = \int_0^\infty n_{\text{Si-P3}}(z)\,\mathrm{d}z,$$

$$D_{\text{IPD}} = \int_0^\infty n_{\text{IPD}}(z)\,\mathrm{d}z. \qquad (1)$$

Except for unimportant proportionality factors, k and k', this model depends on a single parameter, F. It is, however, impossible to determine F by any experimental means available. As a practical compromise, we assume that F is proportional to the density of displaced lattice atoms per unit ion dose, n_{DLA}, which is, of course, dependent on the depth from the surface,

$$F = cI_{\text{ion}}n_{\text{DLA}},$$

where the incident ion dose is denoted by I_{ion}, and the proportionality constant, c, is chosen so that it reproduces experimental results satisfactorily. The value of n_{DLA} at each depth is readily available from a Monte Carlo simulation [14]. Then integrated area densities are obtained by carrying out the integrations (1) numerically.

The dose dependence of $D_{\text{Si-P3}}$ and D_{IPD} in which c is set to 1.8×10^{-21} cm^3 is shown in fig. 2B. It agrees well with the corresponding dose dependence of Si-P3 and indefinite point defect area densities (fig. 2a).

Depth profiles of $n_{\text{Si-P3}}$ and n_{IPD}, based on the same value of c, are illustrated in fig. 4 together with the experimentally determined depth profiles of Si-P3 and indefinite point defects. Considering the poor depth resolution of the experiment and the simplicity of the model adopted here, the agreement should be regarded as satisfactory.

The profile of $n_{\text{Si-P3}}$ in the deep region where experimental data are no longer available is worth mentioning. The peak appearing in the $n_{\text{Si-P3}}$ profile in the region behind the phosphorus-rich layer is a natural consequence of the model employed here. Our model correlates ion bombardments with the resultant lattice damage only by the energy conveyed by the incident ions and dissipated through nuclear processes. The role of knocked-on lattice atoms, for instance, is not taken into account, although it has been pointed out that a substantial amount of knocked-on lattice atoms accumulates in the region where $n_{\text{Si-P3}}$ based on our model gives a peak [15]. This behavior of knocked-on lattice atoms might argue against the existence of a dense Si-P3 layer behind the phosphorus-rich layer, since knocked-on lattice atoms possibly at interstitial positions could easily annihilate vacancy-type defects like Si-P3.

Although the details still remain open for further investigation, experimental results and their analyses based on the simple model presented here clearly manifest the important role of damage overlap in the formation of lattice disorder prior to amorphization.

Acknowledgement

The authors would like to thank Dr. T. Ishitani for helpful comments on computational methods of ion-induced damage.

References

[1] D. Pramanik and M. Current, Solid State Technol. 27 (1984) 211.
[2] J.F. Ziegler, Nucl. Instr. and Meth. B6 (1985) 270.
[3] P.F. Byrne, N.W. Cheung and D.K. Sadana, Appl. Phys. Lett. 41 (1982) 537.
[4] M. Tamura, N. Natsuaki, Y. Wada and E. Mitani, J. Appl. Phys. 59 (1986) 3417.
[5] A.K. Rai, J. Baker and D.C. Ingram, Appl. Phys. Lett. 51 (1987) 172.
[6] W. Skorupa, E. Wieser, R. Groetzschel, M. Posselt, H. Buecke, A. Armigliato, A. Garulli, A. Bever and W. Markgraf, Nucl. Instr. and Meth. B19/20 (1987) 335.
[7] O.W. Holland, M.K. El-Ghor and C.W. White, Appl. Phys. Lett. 53 (1988) 1282.
[8] Y. Yajima, N. Natsuaki and S. Nishimatsu, Materials Science Forum 38–41 (1989) 1227.
[9] W. Jung and G.S. Newell, Phys. Rev. 132 (1963) 648.
[10] J.W. Corbett, Electron Radiation Damage in Semiconductors and Metals (Academic, New York, 1966) p. 82.
[11] J.F. Ziegler, J.P. Biersack and U. Littmark, The Stopping and Range of Ions in Solids (Pergamon, New York, 1985) pp. 50–53.
[12] J.F. Gibbons, Proc. IEEE 60 (1972) 1062.
[13] J.R. Dennis and E.B. Hale, J. Appl. Phys. 49 (1978) 1119.
[14] T. Ishitani, A. Shimase and S. Hosaka, Jpn. J. Appl. Phys. 22 (1983) 329.
[15] T. Ishitani, Jpn. J. Appl. Phys. 29 (1990) 162.

Nuclear Instruments and Methods in Physics Research B55 (1991) 611–614
North-Holland

Evolution of low-fluence heavy-ion damage in Si under high energy ion irradiation

A. Battaglia [a], F. Priolo [b], C. Spinella [a] and E. Rimini [b]

[a] *Istituto di Metodologie e Tecnologie per la Microelettronica, CNR Corso Italia 57, 195129 Catania, Italy*
[b] *Dipartimento di Fisica, Corso Italia 57, 195129 Catania, Italy*

The annealing of low-fluence heavy-ion damaged Si crystals induced by ion assisted treatments is reported. Damage was produced by 150 keV Au implantations at a dose of 2×10^{13} ions/cm^2 onto ⟨100⟩ oriented Si single crystals and resulted in small amorphous-like regions surrounded by crystal material. The interaction of these damaged structures with defects induced by energetic ions (600 keV Kr^{2+}) was investigated. Kr post-irradiation resulted in either damage accumulation or annealing, depending on the substrate temperature. A transition temperature of about 420 K was found between these two different regimes. Ion-assisted processes are discussed and explained on the basis of the damage morphology.

1. Introduction

The epitaxial recrystallization of continuous amorphous Si (a-Si) layers under both thermal [1] and ion-assisted [2,3] treatments has been the subject of extensive investigations during the last decade. Thermal heating of a-Si layers onto single crystal substrates results in layer-by-layer growth at temperatures above 750 K. At lower temperatures, however, the process is kinetically inhibited and the amorphous phase exists under metastable conditions. In the temperature range between 400 and 650 K epitaxial recrystallization can also occur if stimulated by ion beam irradiation [2,3]. This process has been attributed [4,5] to the generation of a non-equilibrium defect concentration which enhances the kinetics of the phase transition. Moreover, as soon as the temperature is further decreased the process can be reversed and ion irradiation can produce a layer-by-layer amorphization [6].

Heavy-ion damaging of Si crystals at low doses is not able to fully amorphize a surface layer and produces instead several damage clusters embedded in a crystal matrix. The nature and annealing behavior of these clusters raised great interest in the last years [7–10]. The question concerning the "amorphicity" of these clusters, however, is still unresolved.

In this paper we have studied the evolution of low-dose Au damaged regions in Si under ion-assisted treatments, in order to investigate the difference, if any, with the behavior of continuous amorphous layers and to obtain a better understanding on the morphology of this damage.

2. Experimental

⟨100⟩ oriented Si single crystals were predamaged by 150 keV Au implantations at a dose of 2×10^{13} ions/cm^2 and at an average current density of 5 nA/cm^2. Au implantations were performed maintaining the samples either at room temperature (RT) or at 77 K (LN_2T) by means of a liquid nitrogen cooled sample holder. Fig. 1 shows 2.0 MeV He^+ Rutherford backscattering (RBS) spectra in random (continuous line) and with the He^+ beam aligned along the ⟨100⟩ direction, for the as-implanted samples. A grazing angle detection was used to enhance the depth resolution. Open circles refer to

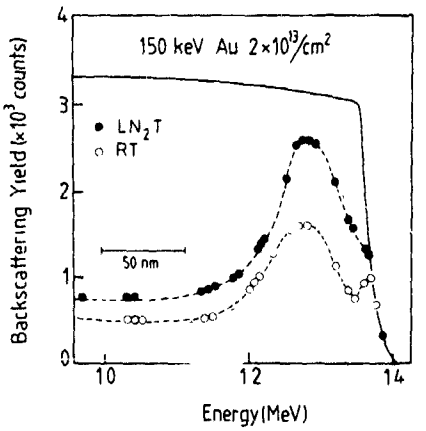

Fig. 1. RBS spectra in random (continuous line) and in channeling along the ⟨100⟩ direction (symbols) for Au damaged Si single crystals at LN_2T (closed circles) and at RT (open circles).

0168-583X/91/$03.50 © 1991 – Elsevier Science Publishers B.V. (North-Holland)

samples damaged at RT, closed circles to those damaged at LN_2T. In both cases a damage peak at a depth of 40 nm is present. From an analysis of these spectra we can estimate that the total number of displaced Si atoms per unit area is about 9×10^{16} at./cm^2 for RT damaged samples and 1.4×10^{17} at./cm^2 for LN_2T damaged samples, i.e., about 4500 and 7000 atoms per collision cascade respectively. We can correlate this difference to dynamic annealing processes which occur already during RT implantations. This result is in qualitative agreement with the amorphization model proposed by Morehead and Crowder [11] where the size of stable amorphous clusters formed around a given ion track strongly depends on the substrate temperature

The morphology of RT as-damaged samples has been also investigated by plan-view transmission electron microscopy (TEM), as shown by the image in fig. 2 Bright regions represent undamaged crystal material, black dots are associated to clusters of defects, whilst the diffused grey regions are probably composed by amorphous material. The presence of the amorphous phase is confirmed by the diffraction pattern shown as an inset in the same figure.

Ion-assisted treatments were performed on RT damaged samples by irradiation with a 600 keV Kr^{2+} beam at different doses and for different substrate temperatures in the range 350–500 K. The beam was electrostatically scanned onto a 1 in diam sample area and the average dose rate was maintained at 1×10^{12} ions/cm^2 s

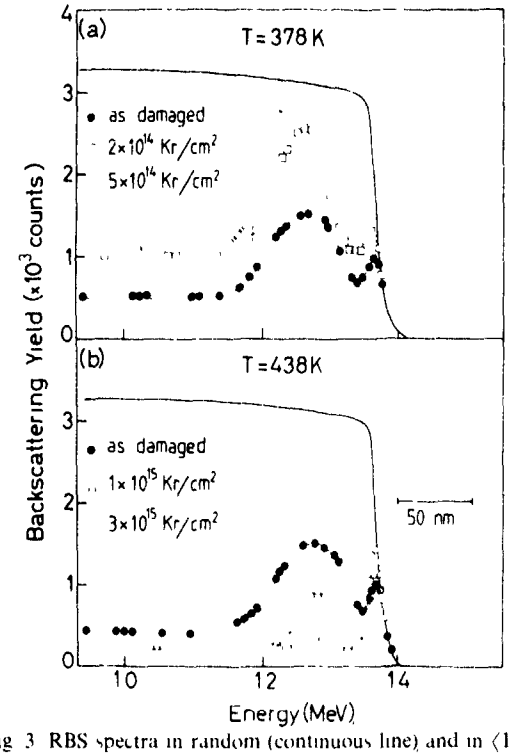

Fig 3 RBS spectra in random (continuous line) and in ⟨100⟩ aligned direction of Au damaged Si crystals before and after post-irradiation with 600 keV Kr ions Spectra refer to irradiation performed at a substrate temperature of (a) 378 K, and (b) 438 K at different Kr doses

3. Results and discussion

Fig. 3 shows the RBS spectra in random (continuous line) and with the He beam aligned along the ⟨100⟩ direction (symbols), before and after Kr irradiations at different doses and for different substrate temperatures. At a temperature of 378 K (fig 3a) an increase of the damage peak, corresponding to disorder accumulation, is observed At a dose of 5×10^{14} ions/cm^2 a continuous amorphous layer is obtained. A completely opposite behavior is shown in fig. 3b where at a substrate temperature of 438 K the damage peak is seen to decrease, i e, a reordering of the displaced atoms is taking place

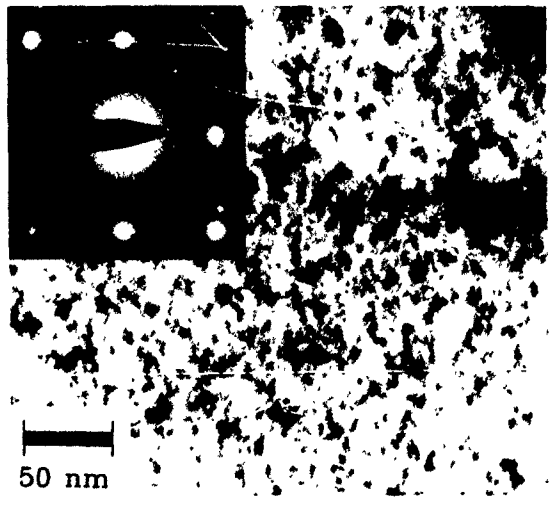

Fig. 2 TEM plan-view micrograph of RT Au damaged samples The diffraction pattern is shown as an inset

The structure of both unirradiated as-damaged samples and Kr irradiated samples was investigated by cross-sectional TEM analyses. Fig 4a shows the morphology of the non-irradiated as-damaged sample. At a depth of about 40 nm damage structures are present. The darker areas can probably be attributed to clusters of defects which are generated at the boundaries of the Au collision subcascades whilst the grey regions are amorphous. This picture is consistent with the plan-view image shown in fig. 2 In fig. 4b the effect of Kr post irradiation on the damaged samples at a temperature of 378 K and, at a dose of 5×10^{14} ions/cm^2 (RBS spectrum in fig. 3a) is clearly shown. A continuous amorphous layer, with a wavy interface is present. The c–a interface is composed by a band of defects (darker

regions) accumulated during Kr irradiation and swept on the border during the growth of the amorphous layer Fig 4c, finally, shows the damage morphology in

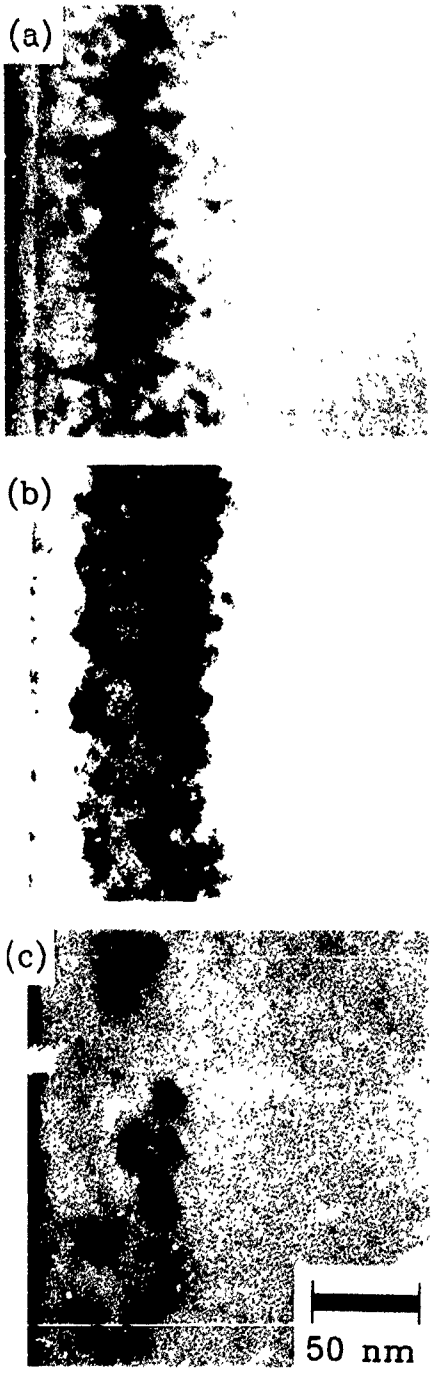

Fig. 4. TEM cross-sectional images of Au damaged samples (a) before and (b) after 600 keV Kr irradiation at 378 K to a dose of 5×10^{14} Kr/cm^2 and (c) at 438 K to a dose of 3×10^{15} Kr/cm^2

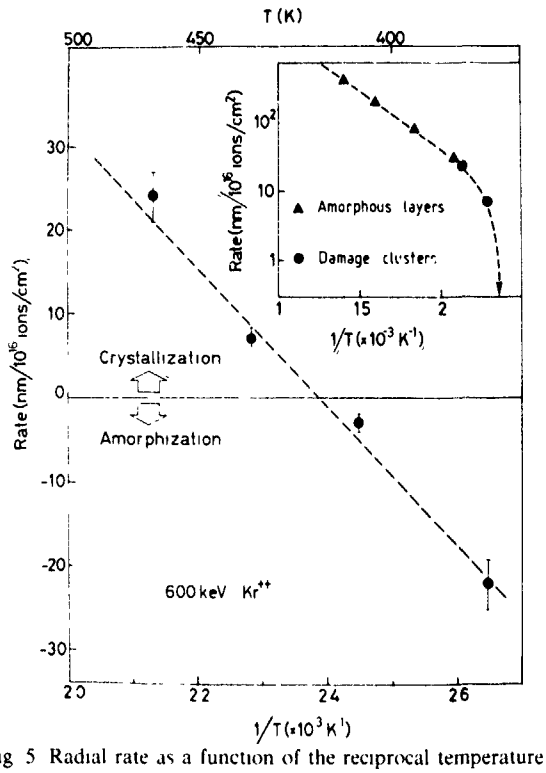

Fig 5 Radial rate as a function of the reciprocal temperature (on a linear scale) The transition temperature between the amorphization regime and the crystallization regime corresponds to a null rate In the inset, in a logarithmic plot, the annealing rate of isolated damage clusters (closed circles) is shown together with the ion-induced epitaxial crystallization rate of continuous amorphous layers (triangles)

the samples after Kr irradiation at a temperature of 438 K and at a dose of 3×10^{15} Kr/cm^2 (RBS spectrum in fig. 3b). Amorphous regions are not present, few residual damage clusters (dislocation loops) can be evidenced within a good quality single-crystal matrix. This residual damage being below the detection limit was not observed by channeling mesurements.

The kinetics of damage accumulation or annealing under ion beam irradiation has been characterized in some details as a function of the substrate temperature In fig. 5 we report the measured value for the radial rate of crystallization or amorphization, k, as a function of the reciprocal temperature These values are extracted from fits to the experimental channeling data assuming that the pre-existing amorphous-like regions have an almost spherical shape and that they shrink or grow linearly along the radius with the irradiating dose, with a radial rate independent of the clusters dimension. The error bars in the experimental points refer to the uncertainty due to the fits (±10%). The two regimes, amorphization and crystallization, are well separated by the horizontal line, and a transition temperature of 420

K is measured at a dose rate of 1×10^{12} Kr/cm^2 s. This value is in good agreement with the one observed during ion-beam induced layer-by-layer crystallization [6]. In the inset of fig. 5 the values for the crystallization rate of damage clusters (circles) and continuous surface amorphous layers (triangles) irradiated under identical conditions are compared. It should be noted that the two sets of data correlate to one another very well; as soon as the transition temperature is approached we can observe a sudden decrease of the curve towards zero. This behavior is well-known for ion-beam induced epitaxy and has been attributed [4,5] to a balance between an athermal amorphization term and a temperature-dependent crystallization term. As soon as the temperature is lowered the crystallization rate decreases and the athermal amorphization regime becomes suddenly important producing the sharp fall in the net rate

In conclusion we have studied the annealing behavior of low-fluence heavy-ion damage in Si under ion-assisted treatments. Ion beam irradiation of this damage can produce either crystallization or amorphization depending on the substrate temperature. The strong similarities between this behavior and that observed for planar c–a interfaces support the idea that these damage structures are composed mainly by amorphous material

Acknowledgements

We wish to acknowledge Mr. O. Parasole and Mr. A. Marino for technical assistance. This work was supported in part by Progetto Finalizzato Materiali e Dispositivi per l'Elettronica a Stato Solido, CNR, and in part by the Esprit Project 2016 TIP BASE.

References

[1] G.L. Olson and J A. Roth, Mater Sci. Rep. 3 (1988) 1.
[2] J.S. Williams, R.G. Elliman, W.L. Brown and T.E. Seidel, Phys. Rev Lett 55 (1985) 1482.
[3] F. Priolo, A La Ferla and E Rimini, J. Mater. Res 3 (1988) 1212.
[4] K.A Jackson, J. Mater. Res. 3 (1988) 1218.
[5] F Priolo, C Spinella and E Rimini, Phys. Rev B41 (1990) 5235
[6] J. Linnros, R.G Elliman, W L. Brown, J. Mater. Res. 3 (1988) 1208.
[7] L M Howe and M H Rainville, Nucl Instr and Meth 182/183 (1981) 143
[8] D A Thompson, A. Golanski, H.K Haugen, L M Howe and J A Davies, Radiat. Eff. Lett 50 (1980) 125.
[9] L M. Howe and M H. Rainville, Nucl Instr. and Meth B19/20 (1987) 61
[10] A Battaglia, F Priolo, E. Rimini and G. Ferla, Appl Phys. Lett 56 (1990) 2622.
[11] F.F. Morehead and B L Crowder, Radiat. Eff 6 (1970) 27.

Nuclear Instruments and Methods in Physics Research B55 (1991) 615–619
North-Holland

Channeling implantation of B and P in silicon

R.J. Schreutelkamp, V. Raineri [1] and F.W. Saris
FOM Institute for Atomic and Molecular Physics, Kruislaan 407, 1098 SJ Amsterdam, The Netherlands

R.E. Kaim, J.F.M. Westendorp [2] and P.F.H.M. van der Meulen
Varian/Extrion Division, 123 Brimbal Avenue, Beverly, MA 01915, USA

K.T.F. Janssen
Philips Research Laboratories, P O. Box 80000, 5600 JA Eindhoven, The Netherlands

Highly uniform profiles of B and P ions have been obtained by channeling implantations in 150 mm diameter Si(100) wafers. Large differences in penetration depth, doping depth profiles and implantation damage are observed between implantations under channeling and random conditions for a wide range of doses and ion energies using Rutherford backscattering spectrometry, cross-sectional transmission electron microscopy and secondary-ion mass spectrometry

1. Introduction

Channeling implantation offers several advantages over conventional ion implantation [1]. When the ion beam is aligned along one of the major axes of a crystal less damage is created and the penetration depth of the ions is considerably larger However, applying the channeling technique requires a high degree of uniformity which has prevented the use of channeling implantation in conventional ion implanters Recently a new ion implanter, the Varian 220, has been introduced which has the potential to successfully perform channeling implantation on wafers as large as 200 mm. The beam is scanned by means of a combined electrostatic/mechanical scan system [2]. In the horizontal direction the beam is scanned electrostatically; a parallel scan is achieved by means of a nonuniform dipole magnet [3]. The wafer is mechanically translated vertically [4]. The application of this parallel beam scan has already been shown to be useful for the formation of high-quality trench sidewalls for VLSI manufacturing [5].

In this paper we present an overview of doping depth profiles obtained by channeling implantations of B^+ and P^+ ions in 150 mm silicon wafers for various energies and doses. A comparison is made between channeled and random conditions. Furthermore, the differences in damage both before and after thermal annealing are investigated

2. Experimental

Implantations were performed with a Varian/Extrion 220 medium-current ion implanter at Varian/Extrion [2]. Boron was implanted in 1–2 Ω cm, n-type Czochralski-grown 150 mm silicon wafers of (001) substrate orientation along channeling and random directions at energies ranging from 5 to 380 keV and doses from 1×10^{12} to 2×10^{15} cm^{-2}. Phosphorus implantations were done in 1 Ω cm, p-type Czochralski-grown silicon wafers at an energy of 100 keV and doses between 1×10^{13} and 1×10^{15} cm^{-2} The channeling implantations were done along [001], while the random direction corresponded to a tilt of 10° off normal and a twist of 15° with respect to the flat positioned horizontally.

Rapid thermal annealing (RTA) was done in an AG Associates Heatpulse 410 rapid thermal processor under a continuous Ar flow. Conventional anneals were done in a vacuum furnace with a base pressure $< 10^{-7}$ Torr. Secondary-ion mass spectrometry (SIMS) analysis was used to determine the boron and phosphorus profiles The SIMS measurements were carried out with a Cameca IMS 3f or 4f instrument. For P-implanted samples a 14.5 keV Cs^+ primary beam was used. The 5 and 10 keV B profiles were measured using a primary beam of 3.0 keV, 0.25 μA O_2^+ in an oxygen ambient in

[1] Permanent address University of Catania, Corso Italia 57, 95100 Catania, Italy
[2] Permanent address: ASM International, P O Box 100, 3720 AC Bilthoven, The Netherlands

0168-583X/91/$03.50 © 1991 – Elsevier Science Publishers B.V (North-Holland)

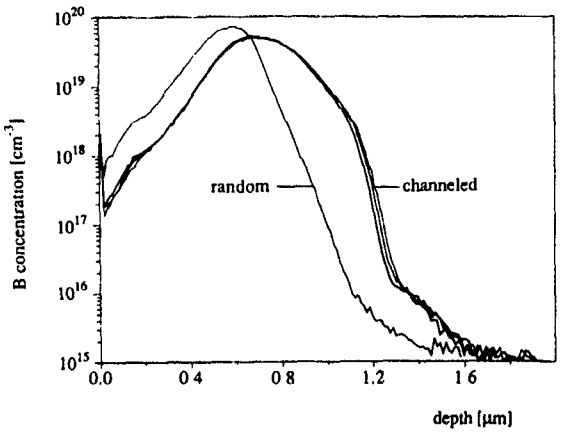

Fig. 1. Doping profiles measured with SIMS for 200 keV B^+ 2×10^{15} cm^{-2} channeling and random implantations. For the channeling implantation profiles are shown from two spots on opposite sides of a 150 mm wafer and at one spot in the center

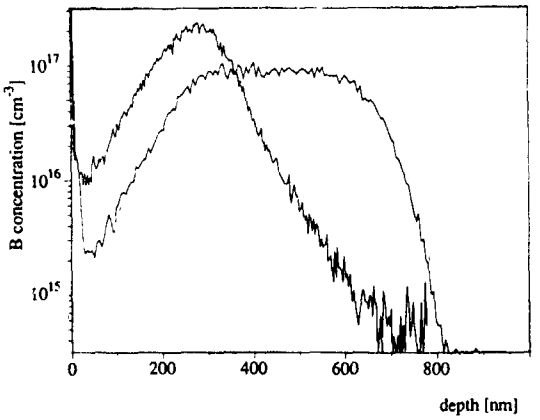

Fig 3 Boron depth profiles for 80 keV 4×10^{12} cm^{-2} implantations under channeling and random conditions are compared

order to resolve the near-surface part of the profile ($p(O_2) = 2\times10^{-5}$ Torr). For higher-energy B-implanted samples a primary beam of 6 5 keV, 0.7 μA O_2^+ was used. The scanned area was 250×250 μm^2 and the diameter of the analyzed area was $\varnothing = 60$ μm.

3. Results

3 1 Boron implantations in Si(100)

Fig. 1 compares the doping profiles of 200 keV 2×10^{15} cm^{-2} ^{11}B ions implanted in Si(100) under channeling and random conditions. The three channeled doping profiles shown were measured at three different spots across a 150 mm Si wafer along a line parallel to the horizontal electrostatic scan. One spot was in the center, while the other two spots were at opposite sides of the wafer. The maximum penetration depth of the channeling implantations was $R_{max} = 1.23$ μm, in excellent agreement with the calculated value of $R_{max} = 1.22$ μm based on the modified Firsov theory [6]. The maximum penetration depth is defined as the depth required to stop all but 1% of the particles [7]. The critical angle for channeling of 200 keV B ions is ≈ 2°; earlier, we have found that an angular variation of 1° has a significant influence on the resulting doping depth profile [8]. Since we do not observe a difference in the B profile at the three spots this means that well channeled conditions were maintained across the wafer. The uniformity has also been checked for various ion species, implantation energies and doses using sheet-resistance measurements and RBS [9,10]. For all channeling implants we found the peak of the doping depth profiles to be uniform within 1%.

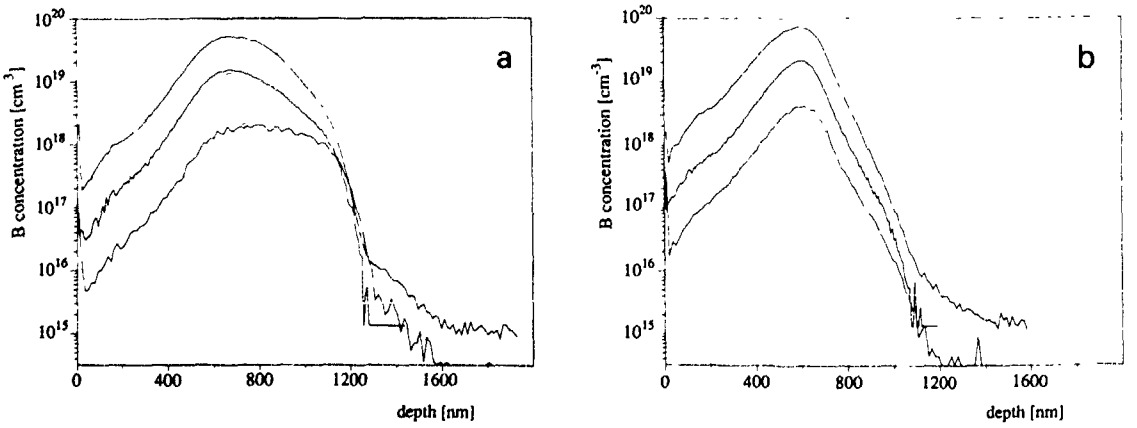

Fig. 2. Boron profiles for 200 keV implantations at doses of 1×10^{14}, 5×10^{14} and 2×10^{15} cm^{-2} under channeling (a) and random (b) conditions.

Fig. 2 shows the doping depth distributions for several 200 keV ^{11}B doses under channeling and random conditions. The doses shown are 1×10^{14}, 5×10^{14} and 2×10^{15} cm^{-2}. Implantation of 1×10^{14} cm^{-2} under channeling condition results in a constant doping level of 2×10^{18} cm^{-3}. The depth doping profiles obtained after the implantations of 5×10^{14} cm^2 and 2×10^{15} cm^{-2} are peaked at 0.69 μm, close to the projected range $R_p = 0.59$ μm for implantation under random condition. These results show that the difference between channeling and random implantations is no longer pronounced above a dose of 1×10^{14} cm^{-2} owing to dechanneling from the buildup of disorder as the dose is increased.

In fig. 3 the depth profiles for channeled and random implants of 80 keV 4×10^{12} cm^{-2} B^+ ions are compared. A nearly Gaussian profile peaked at 0.28 μm results after a random implant in good agreement with the projected range calculated by TRIM [11] of 0.26 μm We observe that the B profile has a tail at the substrate side of the wafer apparently caused by channeling effects in crystalline Si, as was pointed out by Hofker et al. [12]. A flat doping depth profile results for the channeled implantation. The B concentration beyond the maximum penetration depth falls off at 21(2) decades/μm, much sharper than for the random implants The maximum B penetration depth of 0.74 μm is in excellent agreement with the calculated value of 0.77 μm based on the modified Firsov theory [6].

Fig 4 shows the doping depth distributions for channeled implantations of B at energies ranging from 5 to 380 keV All doping profiles were normalized to a dose of 1×10^{13} cm^{-2}. The actual dose ranged from 2×10^{12} to 2×10^{14} cm^{-2}. The influence of the energy on the shape of the resulting depth doping profiles is clearly

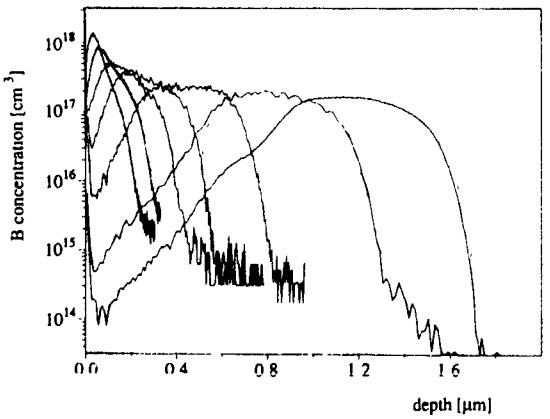

Fig. 4 The energy dependence of B depth profiles resulting from channeling implants at energies of 5, 10, 20, 40, 80, 200 and 380 keV. All doping depth profiles were normalized to a dose of 1×10^{13} cm^{-2}. The decay in B concentration at R_{max} is 23(2) decades/μm independent of energy.

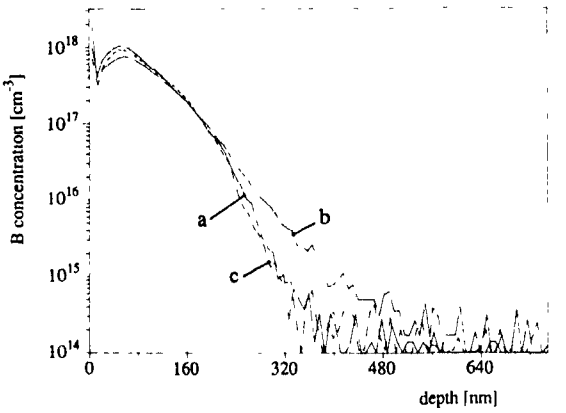

Fig 5 Transient diffusion is illustrated for an implantation of 10 keV 1×10^{13} cm^{-2} B^+ ions in silicon The as-implanted profile is referred to as (a) while the profile after RTA showing transient diffusion is referred to as (b) When the sample is post-amorphized with Ge^+ ions prior to annealing transient diffusion is avoided (c)

illustrated. The profile is flat for the highest implantation energies and becomes more and more sharply peaked as the implantation energy is lowered. However, the decrease in B concentration at the maximum penetration depth is nearly constant with energy, roughly 23(2) decades/μm.

The effect of RTA anneals on the B profile is shown for a channeling implantation of 10 keV 1×10^{13} cm^{-2} in fig. 5. Transient diffusion of the B profile tail is observed after annealing at 900°C for 10 s To prevent transient diffusion, samples were implanted with Si^+ or Ge^+ ions prior to annealing to form a 0 5 μm amorphous layer [13]. The B profile is completely incorporated in the amorphized layer. Annealing at 550°C for 5 h in vacuum followed by RTA at 900°C for 10 s results in

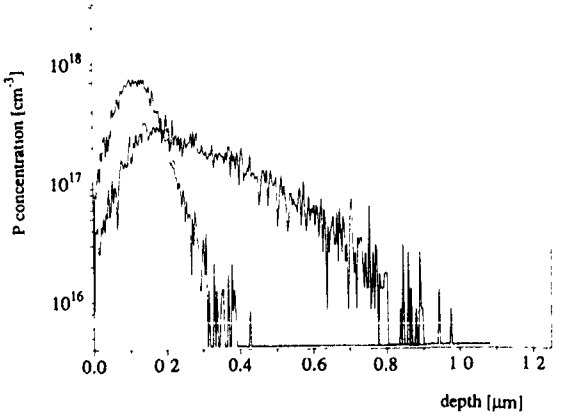

Fig. 6. Comparison of P depth profiles resulting from 100 keV 1×10^{13} cm^{-2} implantations under channeling and random conditions.

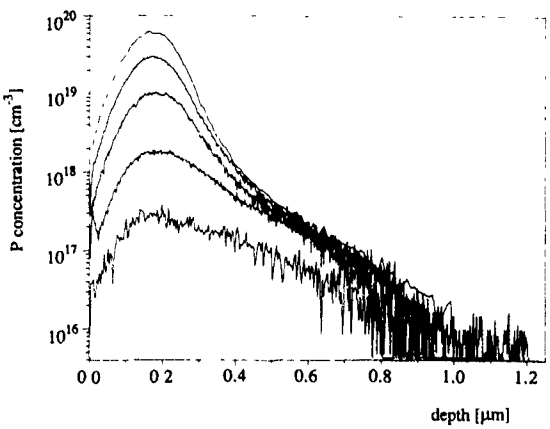

Fig 7 Phosphorus depth profiles for implantations at 100 keV of 1×10^{13}, 5×10^{13}, 2×10^{14}, 5×10^{14} and 1×10^{15} cm^{-2}. Above 5×10^{13} cm^{-2} the number of P ions incorporated in the deep tail saturates and a strong increase in P concentration is observed around a depth of 190 nm

the profile labeled (c). Clearly, post-amorphization eliminates the transient diffusion and a profile with a steep B falloff results.

3.2. Phosphorus implantations in Si(100)

Fig. 6 compares random and channeled implants of 100 keV 1×10^{13} cm^{-2} ^{31}P. A Gaussian profile peaked at 113 nm results for the random implant, in excellent agreement with TRIM [11] calculations. The channeling implantation leads to a doping profile extending to 0.8 μm.

The dose dependence of channeled implants of 100 keV ^{31}P are shown in fig. 7 for doses from 1×10^{13} to 1×10^{15} cm^{-2}. All profiles show the deep tail of well-channeled ions. The number of P ions in the deep tail saturates at a dose of 5×10^{13} cm^{-2} as the dechanneling probability increases with increasing damage in the silicon. Above 5×10^{13} cm^{-2} a strong increase in the P concentration is observed around a depth of 190 nm, which is more than 1.5 times the projected range of $R_p = 115$ nm for 100 keV P$^+$ ions under random condition.

The difference in damage produced by random and channeled implantations of 100 keV 2×10^{14} cm^{-2} P$^+$ ions has been studied using RBS in the (001) channeling configuration Results are given in ref. [15]. The damage profile of the random implant peaks at a depth of 100 nm, which is consistent with a TRIM [11] calculation for 100 keV P$^+$ into amorphous silicon, while for the channeling implant the damage peaks at roughly 165 nm. The total damage level is significantly lower for the channeled implant as shown by quantitatively comparing the total number of displaced silicon atoms in both cases. Using the method of Chu et al. [14] the number of displaced atoms has been estimated to amount to 1.1×10^{17} cm^{-2} vs 3.4×10^{17} cm^{-2} for the channeling and random implantations, respectively. After annealing in vacuum at 900°C for 15 min we observe in both samples a band of dislocation loops at a depth of 110 and 160 nm for the random and channeling implants, respectively. The positions of the bands of dislocation loops correspond to the peak positions of the damage distributions. The concentration of dislocation loops is considerably lower for the channeled implant

4. Conclusion

Extremely good uniformity has been achieved for channeling implantations in wafers up to 150 mm diameter. The combined effects of wafer orientation, beam parallelism and beam divergence result in angle deviations smaller than the critical angles for the ion species considered For both B$^+$ and P$^+$ ions we observe a significant increase in the penetration depth. However, above a critical dose the difference between channeling and random implantations is no longer pronounced due to dechanneling by built-up disorder. The critical dose is 1×10^{14} cm^{-2} for 200 keV B$^+$ ions and 5×10^{13} cm^{-2} for 100 keV P$^+$ ions. Flat doping profiles up to 10^{17} cm^{-3} extending to a depth of 1–1.5 μm can easily be achieved by modest energy (100–200 keV) channeled implants of both B and P. Comparable profiles can be obtained only by multiple conventional (random) implantations at considerably higher energies The strong reduction of nuclear interactions for channeled ions leads to reduced ion range straggling, and a consequently steep falloff in the B concentration on the substrate side of the doping profile. In addition, channeled implants result in a strong reduction in both implant damage and, the density of secondary defects formed during thermal annealing

Acknowledgements

This work is part of the research program of the Stichting voor Fundamenteel Onderzoek der Materie and was made possible by financial support from the Nederlandse Organisatie voor Zuiver Wetenschappelijk Onderzoek and from Varian/Extrion (USA) We gratefully acknowledge J.S. Custer (FOM) for carefully reading the manuscript

References

[1] H. Nishi, T. Inada, T. Sakurai, T Kaneda, T Hisatsugu and T Furuya, J Appl Phys. 49 (1978) 60
[2] D W Berrian, R.E Kaim, J.W. Vanderpot and J F M. Westendorp, Nucl. Instr and Meth. B37/38 (1989) 500

[3] D.W. Berman, R.E. Kaim and J.W. Vanderpot, Nucl. Instr. and Meth. B37/38 (1989) 518.
[4] J.D. Pollock, R.W. Milgate, R.F. McRay and R.E. Kaim, Nucl. Instr. and Meth. B37/38 (1989) 576.
[5] R. Kokaschke, R.E. Kaim, P.F.H.M. Van Der Meulen and J.F.M. Westendorp, IEEE Trans. Electron Devices 37 (1990) 1052.
[6] O.B. Firsov, Sov. Phys. JETP 36 (1959) 1076.
[7] E.V. Kornelsen, F. Brown, J.A. Davies, B. Domeij and G.R. Piercy, Phys. Rev. 136 (1964) A849.
[8] R.J. Schreutelkamp, F.W. Saris, J.F.M. Westendorp, R.E. Kaim, G.B. Odlum and K.T.F. Janssen, Mater. Sci. Eng. B2 (1989) 139.
[9] J.F.M. Westendorp, R.E. Kaim, J.W. Vanderpot, G.B. Odlum, R. Schreutelkamp and F.W. Saris, Solid State Techn. 31 (1988) 53.
[10] J.F.M. Westendorp, R.E. Kaim, G.B. Odlum, R. Schreutelkamp, F.W. Saris and K.T.F. Janssen, Nucl. Instr. and Meth. B37/38 (1989) 357.
[11] J.P. Biersack and L.G. Haggmark, Nucl. Instr. and Meth. 174 (1980) 257.
[12] W.K. Hofker, H.W. Werner, D.P. Oosthoek and H.A.M. de Grefte, Radiat. Eff. 17 (1973) 83.
[13] For details about the post-amorphization implants see R.J. Schreutelkamp, W.X. Lu, F.W. Saris, K.T.F. Janssen, J.J.M. Ottenheim, R.E. Kaim and J.F.M. Westendorp, in Beam-Solid Interactions: Physical Phenomena, eds. P. Borgesen, J.A. Knapp and R.A. Zuhr (Mater. Res. Soc. Proc. 157, Boston, MA, 1989).
[14] W.K. Chu, J.W. Mayer and M.-A. Nicolet, Backscattering Spectrometry (Academic Press, New York, 1978).
[15] V. Raineri, R.J. Schreutelkamp, F.W. Saris, R.E. Kaim and K.T.F. Janssen, presented at IBMM 1990.

Nuclear Instruments and Methods in Physics Research B55 (1991) 620–624
North-Holland

Annealing behavior of dislocation loops near the projected ion range in high-dose As^+- and P^+-implanted (001) Si

S.N. Hsu and L.J. Chen

Department of Materials Science and Engineering, National Tsing Hua University, Hsinchu, Taiwan

The annealing behavior of dislocation loops near the projected range (R_p loops) in (001) Si implanted by 150 keV As^+ and 65 keV P^+ to a dose of 5×10^{15} cm^{-2} has been studied by both plane-view and cross-sectional transmission electron microscopy and Rutherford-backscattering spectrometry. The annealing behavior of R_p loops in single- and two-step annealed samples and in sample with an oxide capping layer were found to be consistent with the suggestion that their formation is related to the agglomeration of self-interstitials mediated by the presence of a high concentration of electrically inactive arsenic or phosphorous atoms. However, the R_p loops were found to be more prone to be annealed out in P^+-implanted than in As^+-implanted (001) Si.

1. Introduction

Recent developments in the downscaling of microelectronic devices have resulted in the adoption of ion implantation as the doping technique for the high-dose sections of devices in addition to its established use for the implants in low-dose sections [1]. In high-dose implantation, the concentrations of dopant may exceed its equilibrium solid-solubility limit. Previous studies have suggested that the retarded amorphous/crystalline (a/c) regrowth rate, poor-quality epitaxial growth and concentration-dependent precipitation effects may well be related to solid-solubility limits for the implanted impurity in silicon [2,3].

Arsenic and phosphorous have been used as the main n-type dopants in silicon devices. Owing to the difference in solubility, diffusivity and atomic size between As and P atoms, the annealing behaviors of As^+- and P^+-implanted silicon are expected to be different. Discrete layers of defect clusters were observed to form at a depth matching the projected range (R_p) of As and the original a/c interface in high-dose As^+ and P^+ implantation and annealed samples [4,5]. Recently, the formation of a two-layer structure and the inhibition of the formation of R_p loops were observed in 80 keV, 1×10^{16} and 2×10^{16}/cm^2 As^+-implanted (001) Si, respectively [6]. The results indicated that the formation of R_p loops is likely to be due to the agglomeration of self-interstitials mediated by the presence of a high concentration of electrically inactive As in the local region. As the concentration of arsenic exceeds a critical value, loops were inhibited to form. In view of the new insight gained on the point-defect migration and agglomeration, a detailed study of the annealing behavior of the R_p loops has been carried out. In this paper, we report the results of a study of the formation and growth of the R_p loops in high-dose As^+- and P^+-implanted silicon by both plane-view and cross-sectional transmission electron microscopy (XTEM) and by Rutherford-backscattering spectrometry.

2. Experimental procedures

Single-crystal, 3–5 Ω cm, phosphorous-doped (001) Si wafers were implanted with 65 keV P^+ and 150 keV As^+ to a dose of 5×10^{15} cm^{-2} at room temperature. Almost all samples were annealed isothermally in a dry-nitrogen flowing diffusion furnace at temperatures ranging from 500 to 1000 °C. In order to find out the interrelationship between the growth of residual defects and the diffusion of dopants, some samples were first annealed at 900 °C followed by a 500 °C annealing. The annealing time was 0.5 h at each temperature unless specified otherwise. High-purity nitrogen gas was first passed through a titanium getter tube, maintained at 800 °C, to reduce the O_2 content. To find out whether the outdiffusion of As will significantly influence the evolution of microstructures, a 130 nm thick protective oxide layer was deposited on some of the implanted samples by electron beam evaporation to prevent outdiffusion of As during annealing. For short-time annealing, rapid thermal annealing with a graphite heater in Ar ambient was also performed. For a typical thermal cycle, a ramp-up time of about 10 s and a cooling rate of about 100–200 °C/s were used. The temperature of the samples during annealing was constantly measured by a thermocouple attached to the samples. A JEOL-200CX scanning transmission electron microscope operating at 200 kV was used for TEM examinations.

0168-583X/91/$03.50 © 1991 – Elsevier Science Publishers B.V. (North-Holland)

Rutherford-backscattering spectrometry with 2 MeV He^+ ions was used to measure the depth profile of As. The backscattered ions were collected at a scattering angle of 160° from the incident beam direction.

3. Results and discussion

3.1 As^+-implanted (001) Si

Amorphization of the surface layer to a depth of about 200 nm was found in as-implanted samples. Solid phase epitaxial growth (SPEG) was completed after annealing at 470 °C for 4 h and was near completion after annealing at 500 °C for 2 h. An example is shown in fig. 1. The regrowth layer was observed to be essentially defect-free.

The SPE regrowth of the amorphous layer was found to be complete after 550 °C annealing for 15 min. No R_p loops were evident. However, the R_p loops were observed in samples annealed at 550 °C for 20 min. The density and the average size of the R_p loops were found to decrease and increase with annealing temperature, respectively, in 500–900 °C annealed samples. The R_p loops were found to form in samples annealed at 800 °C for a time as short as 1 s. Examples are shown in figs. 2a–e. The dislocation loops were analyzed to be interstitial in nature with $\frac{1}{3}\langle 111\rangle$ or $\frac{1}{2}\langle 110\rangle$ Burgers vectors. The R_p loops appeared to be rather stable in samples

Fig. 1. Weak-beam dark-field (WBDF) image of cross-sectional (cs) view of an As^+-implanted sample annealed at 500 °C for 2 h.

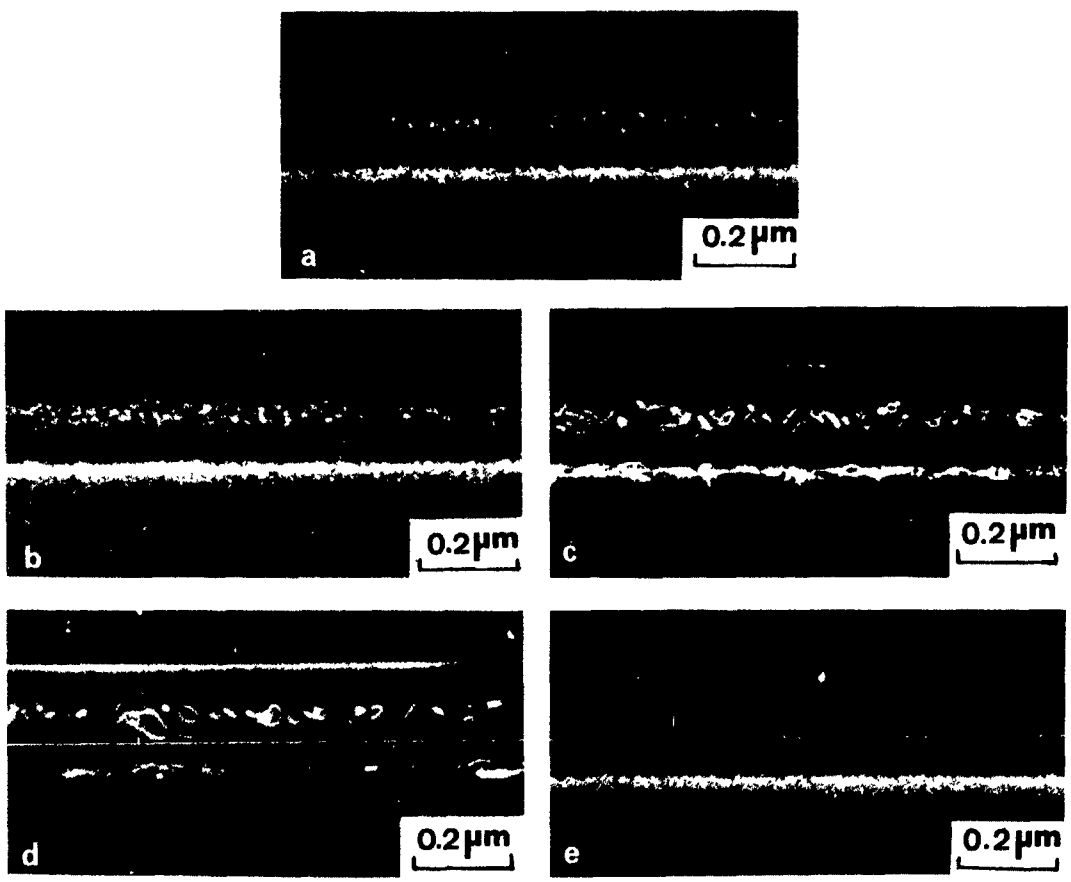

Fig. 2. WBDF images of As^+-implanted samples annealed at (a) 600 °C, (b) 700 °C, (c) 800 °C and (d) 900 °C for 0.5 h, and (e) at 800 °C for 1 s, cross-sectional view.

Fig. 3. WBDF image of an As^+-implanted sample annealed at 1000 °C for 0.5 h, cross-sectional view.

Fig. 5. WBDF image of an as-P^+-implanted sample.

annealed at 700 and 800 °C since they were still present after annealing for 4 and 8 h, respectively. The R_p loops were still present in samples annealed at 900 °C for 1 h.

The two-band structure of defects was no longer evident in the 1000 °C annealed samples as seen in fig. 3. A low density of dislocations was observed to be distributed from the surface to a depth of about 400 nm from the surface. The dislocations were identified to be of mixed type with $\frac{1}{2}\langle 110\rangle$ Burgers vectors.

In samples annealed first at 900 °C followed by annealing at 500 °C for 2 h, the density and the average size of the R_p loops were found to be lower and larger, respectively, than those in 900 °C annealed samples (see fig. 4). The microstructures were found to be not significantly different between samples with and without a protective oxide layer and annealed at 800 or 900 °C. The observation indicated that outdiffusion of As during the annealings at 800–900 °C did not induce significant change in the microstructures.

3.2 P^+-implanted (001) Si

A 140 nm thick implantation amorphous layer was found in as-implanted samples as shown in fig. 5. The a/c interface was observed to be rather flat with undulation about 5 nm in amplitude. Two discrete layers of defects, one near the R_p and the other around the original a/c interface, were found in the 600–800 °C annealed samples. The Burgers vectors of the loops were identified to be either $\frac{1}{2}\langle 110\rangle$ or $\frac{1}{3}\langle 111\rangle$ with the perfect loops being predominant. The average size and the density of the dislocation loops near R_p were found to increase and decrease with annealing temperature, respectively. In samples annealed at 900 °C, no R_p loops were observed. The dislocation loops around the R_p were analyzed to be interstitial in nature. The R_p loops in P^+-implanted samples were similar to those in 150 keV As^+-implanted samples. However, the R_p loops in As^+-implanted samples were preserved at 900 °C as shown in the previous section. After 1000 °C annealing, neither the R_p loops nor the defects around original a/c interface were observed. However, dislocations, relatively large in size and very low in density, were found to be distributed to a depth of about 340 nm from the surface. Examples are shown in fig. 6.

Fig. 4. WBDF image of a sample annealed at 900 °C for 0.5 h followed by annealing at 500 °C for 2 h.

The occurrence of R_p loops in high-dose As^+-implanted silicon annealed at 600 °C was previously found [4,6]. In the present study, the absence of observable R_p loops in samples annealed at 500 °C for 2 h and at 550 °C for 15 min is likely due to the low diffusivity of As and/or Si self-interstitials at these temperatures. In samples annealed at 550–900 °C, the density and the size of R_p loops were found to decrease and increase with annealing temperature, respectively. The R_p loops were also observed in samples annealed at 500 °C for 20 min and at 800 °C for a time as short as 1 s. The annealing behaviors of R_p loops were found to be consistent with the suggestion that the formation of the R_p loops is due to the agglomeration of self-interstitials mediated by the presence of a high concentration of electrically inactive As [7].

The annealing behavior of R_p loops in 900–500 °C two-step annealed samples and in samples with an oxide capping layer seemed to render further support to the suggestion that As diffusion is not the dominant factor in influencing the growth of dislocation loops near R_p at 500 °C. In samples first annealed at 900 °C followed by a further annealing at 500 °C for 2 h, RBS data showed that the As profile remained the same as that of the 900 °C annealed samples. However, the average size and the number density of R_p loops were

considerably larger and lower, respectively, than those in single-step annealed samples. It is known that little diffusion of both Si and dopants occurred during solid-phase epitaxial growth of Si at 500 °C. The coarsening of defects in 900–500 °C two-step annealed samples is attributed to the enhanced diffusion owing to the presence of defects formed at 900 °C during a further 500 °C annealing. A previous study indicated that the diffusion rate of Si self-interstitials is generally higher than that of As interstitials in silicon [8].

In As^+-implanted (001) samples, the R_p loops were found after annealing at a temperature as high as 900 °C. However, in P^+-implanted samples, the R_p loops were observed only in samples annealed at a temperature up to 800 °C for (001) samples and 700 °C for (011) Si. As discussed by Pennycook and Culbertson, the group V dopants serve to trap interstitials. The interstitials are released during solid-phase epitaxial regrowth to form a band of extended defects [7]. It is conjectured that a higher concentration of vacancies was emitted during dissolution of clusters for P^+ implantation owing to the relatively small size of P compared to the As atoms.

4. Summary and conclusions

Both plane-view and cross-sectional TEM as well as RBS spectrometry have been applied to study the annealing behavior of R_p loops in post-implantation annealed (001) Si irradiated by 150 keV As^+ and 65 keV P^+ to a dose of 5×10^{15} cm^{-2}. Factors influencing the formation and growth of the R_p loops, such as annealing temperature and time, single- and two-step annealings as well as substrate orientation, have been investigated.

For As^+-implanted samples annealed at 550–900 °C and P^+-implanted samples annealed at 600–800 °C, the average size and density of defect clusters were found to increase and decrease with annealing temperature, respectively. The R_p loops were annealed out following 1000 and 900 °C annealing for As^+- and P^+-implanted samples, respectively. The annealing behaviors of R_p loops in As^+- and P^+-implanted samples are consistent with the suggestion that they are induced by the agglomeration of self-interstitials mediated by the presence of a high concentration of electrically inactive As.

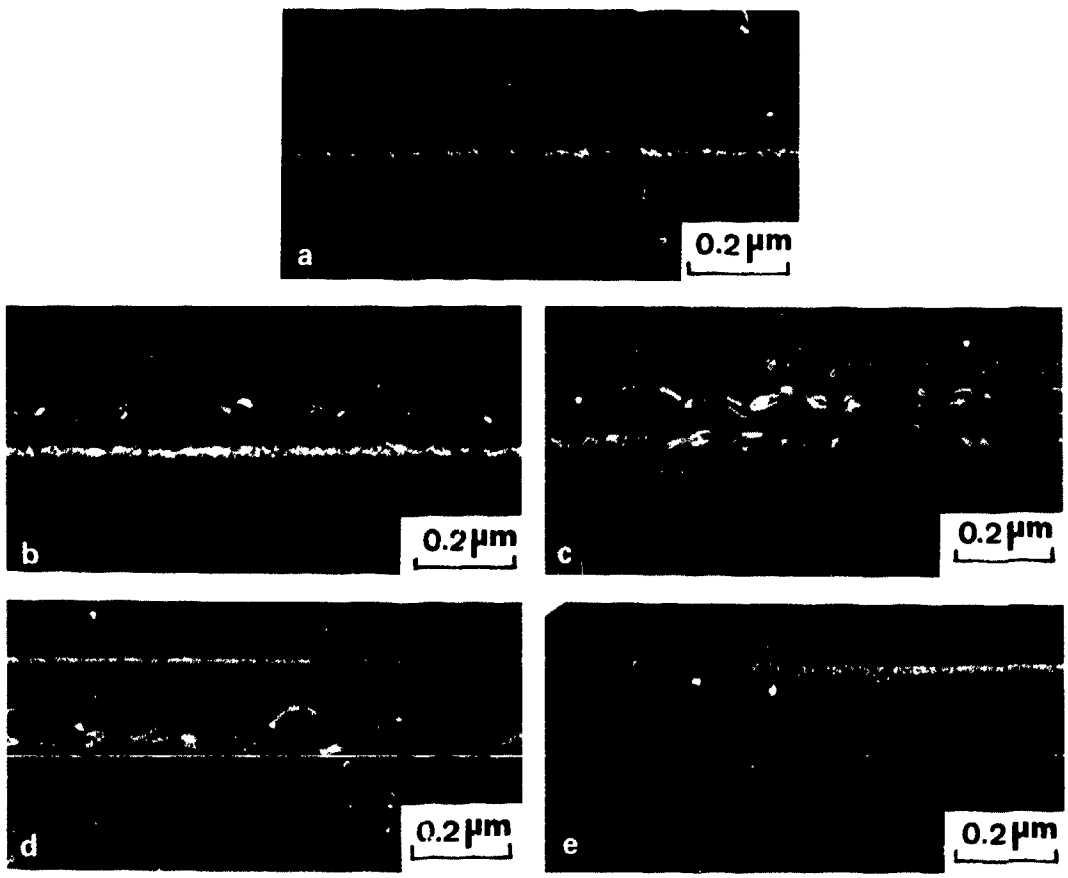

Fig. 6 WBDF images of P^+-implanted samples annealed at (a) 600 °C, (b) 700 °C, (c) 800 °C, (d) 900 °C and (e) 1000 °C for 0.5 h, cross-sectional view

Acknowledgement

The research was supported by the Taiwan National Science Council.

References

[1] D.G Beanland, in Ion Implantation and Beam Processing, eds J.S. Williams and J.M Poate (Academic Press, Sydney, 1984) p 261
[2] J.M. Poate and J.S Williams, ibid., p. 13
[3] G.L Olson and J.A. Roth, Mater Sci Rep. 3 (1988) 1.
[4] N.R. Wu, D.K. Sadana and J Washburn, Appl. Phys Lett. 44 (1984) 782.
[5] S.N. Hsu and L.J. Chen, Appl Phys. Lett 55 (1989) 565.
[6] S.N. Hsu and L.J. Chen, Appl Phys Lett 55 (1989) 2304.
[7] S.J. Pennycood and R.J. Culbertson, Mater Res. Soc Symp. Proc. 52 (1986) 37
[8] T.E. Seidel, D.J. Lischner, C.S Pai, R.V. Knoell, D.M. Maher and D.C. Jacobson, Nucl Instr. and Meth B7/8 (1985) 251

Nuclear Instruments and Methods in Physics Research B55 (1991) 625–629
North-Holland

Activation of shallow implants in Si by pulse laser irradiation

W. Wesch, T. Bachmann, G. Götz, F. Hagemann and A. Heft

Friedrich-Schiller-Universität Jena, Institut für Festkörperphysik, Max-Wien-Platz 1, D(O)-6900 Jena, Germany

The use of a KrF excimer and a Nd-glass laser for the annealing of shallow implanted Si layers is studied. Due to the different absorption lengths of the two lasers, optimum electrical parameters are obtained in different regions of the laser energy density (in the case of 100 nm thick amorphous layers at $E_L \approx 1.2$ J/cm^2 for the UV laser, at $E_L \approx 2.8$ J/cm^2 for the IR laser). It is shown that SiO_2 structural edges are not influenced by the laser beam up to an energy density of about 4.5 J/cm^2. At low energy densities the maximum melting depth is in good accordance with values determined by means of heat-flow calculations. The deviations at higher energy densities are discussed. At the laser energy densities $E_L = 2$ J/cm^2 (UV laser) and 3 J/cm^2 (IR laser) the surface temperature is sufficiently below the vaporization temperature of silicon.

1. Introduction

The development of microelectronic devices with increasingly higher packing densities and faster switching speeds is connected with decreasing lateral and vertical dimensions of the device structures. Especially the depth of pn junctions in a submicron device technology reduces to values remarkably below 200 nm. To produce such structures a special low-energy ion implantation equipment as well as unconventional annealing techniques are necessary. A peculiarity of low-energy implantation of light ions, as for instance boron as a technologically important p-dopant in Si, is to produce an amorphous layer before the dopant implantation to suppress channeling pronounced at low energies. To recrystallize the amorphous layers, rapid thermal annealing (RTA) using optical furnaces or graphite heaters [1,2] is widely used. However, solid-phase epitaxial processes are always connected with the occurrence of a defect band remaining in the region of the amorphous–crystalline interface. Therefore, the implantation conditions have to be chosen so that this defect band lies far behind the pn junction or before the end of range of the dopant atoms. But in the latter case channeling effects in the tail of the range of implanted atoms may shift the pn junction to larger depths. This problem can be overcome if the layers are annealed by liquid-phase epitaxy using nanosecond laser pulses. In this case the laser density must be chosen so that the melt front penetrates the amorphous–crystalline interface and the defective region behind the interface to anneal the point defects located there. For this process principally lasers can be used which emit light from the ultraviolet up to the near-infrared wavelength region. Whereas infrared lasers have the advantage of selective melting of amorphous and heavily damaged areas, visible and ultraviolet lasers because of their short wavelength and the improved energy deposition should be favoured for producing extremely shallow pn junctions [3,4]. In order to test the applicability of selectively and unselectively acting lasers for the annealing of shallow implants in Si, we have made a comparative study using a KrF excimer and a Nd-glass laser.

2. Methods

Sb^+ ions (energies between 11 and 65 keV, ion fluence of 1×10^{15} to 5×10^{15} cm^{-2}) and B^+ ions (energies of 7 and 11 keV, ion fluence of 1.2×10^{15} cm^{-2}) were implanted at room temperature into p- and n-type ⟨100⟩ silicon, respectively. To prevent channeling effects, in the case of boron implantation the samples were preamorphized by implanting 1×10^{15} Ge^+/cm^2 with 30, 60 or 90 keV, by which 60, 100 or 130 nm thick amorphous layers were generated. In the case of Sb-implantation, amorphous layers with thicknesses between 25 and 88 nm were produced. The implanted samples were annealed with 40 ns pulses from a homogenized Nd-glass laser ($\lambda = 1064$ nm, energy density in the region from 0.5 to 5.0 J/cm^2; the homogeneization system is described in ref. [5]) and with 35 ns pulses from a KrF excimer laser ($\lambda = 248$ nm, energy density in the region from 0.2 to 1.7 J/cm^2 [4]).

The recrystallization of the implanted layers was investigated by means of the RBS/channeling technique using 1.4 MeV He^+ ions. A glancing-angle geometry (backscattering angle $\theta = 100°$) was used to improve the depth resolution [6]. From the redistribution of the Sb atoms during the melt the melting depth was estimated, and the percentage of substitutionally incor-

0168-583X/91/$03.50 © 1991 – Elsevier Science Publishers B.V. (North-Holland)

porated atoms was determined from the relation between random and aligned yield of the Sb distribution [6]. Depth distributions of boron atoms were determined by means of SIMS analysis using CAMECA equipment. The measured dopant distributions are compared with those calculated by means of the TRIM Monte Carlo code [7]. Furthermore, calculations of the melting behaviour were carried out using the computer programme HEAT 248 [8].

By combined Hall-effect and sheet-resistivity measurements in van der Pauw geometry, sheet resistivity as well as effective values of carrier concentration and mobility were determined.

3. Results and discussion

The difference in the absorption length of the light emitted from the two lasers used ($\lambda = 1064$ nm: $\alpha^{-1} \simeq 1$ μm for amorphous Si, $\lambda = 248$ nm: $\alpha^{-1} \simeq 5$ nm for crystalline and amorphous Si) is connected with differences in energy deposition. To melt a given layer thickness, the laser energy density to be used should be remarkably higher for infrared radiation compared to ultraviolet light. To study the melting behaviour of 100 nm thick amorphous Si layers induced by the two lasers, in a first step heat-flow calculations were carried out. Fig. 1 shows the melting depth s as well as the temperature near the surface, T_{surf}, as a function of time. Due to the different absorption lengths the time difference between beginning of the laser pulse and melting is different for the two wavelengths (figs. 1a, c). For sufficiently high laser energy densities the melt front penetrates the amorphous–crystalline interface and reaches a maximum value s_{max} after a certain time which depends on the wavelength and the energy density (shown in figs. 1a, c). It is obvious, that for the wavelength $\lambda = 248$ nm an energy density of 1.2 J cm^{-2} is sufficient to melt a layer of 200 nm which is twice the thickness of the amorphous layer (fig. 1a). On the other hand, for the melt of a 150 nm thick layer with the infrared laser a laser energy density of 1.6 J cm^{-2} is necessary (fig. 1c). Just as the position of the melt front, the surface temperature also increases with time up to a maximum value (fig. 1b, d). A comparison of the surface temperatures obtained with the two lasers shows, that the same maximum value of $T_{surf} \simeq 2700$ K is reached with $E_L = 2.0$ J cm^{-2} of the UV-laser and with $E_L = 3.0$ J cm^{-2} of the IR-laser. It is worth to note that at $E_L = 3.0$ J cm^{-2} the maximum surface temperature is still sufficiently below the vaporization temperature of silicon ($T_v = 2903$ K).

The calculated maximum melting depths s_{max} are depicted in fig. 2 as a function of the laser energy density E_L. After the melt front has penetrated the amorphous–crystalline interface, s_{max} increases linear

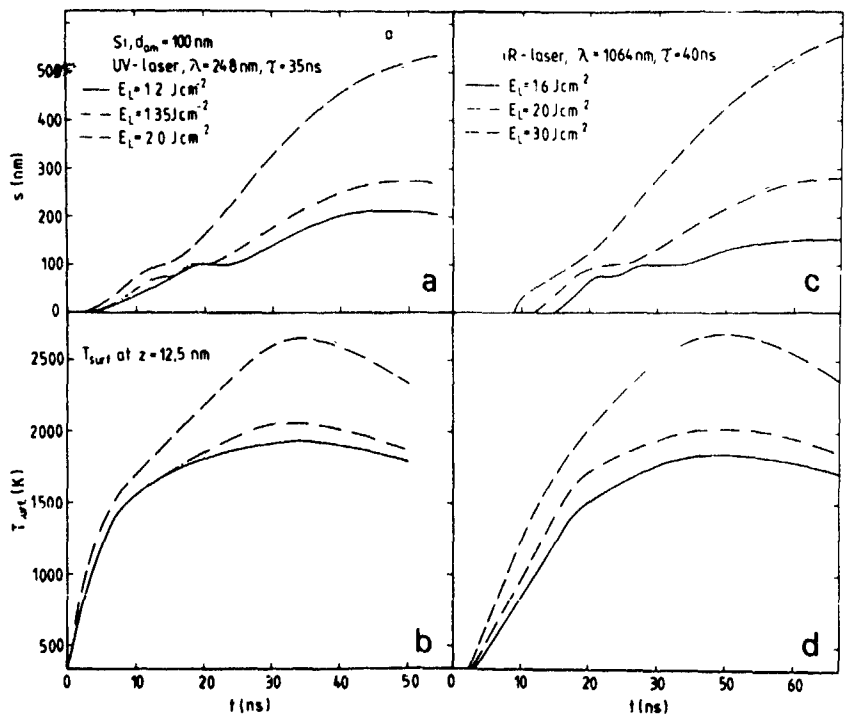

Fig. 1. Calculated melting depth s (a, c) and surface temperature T_{surf} (b, d) for annealing of 100 nm thick amorphous Si layers with a KrF excimer laser (a, b) and a Nd-glass laser (c, d) as a function of time.

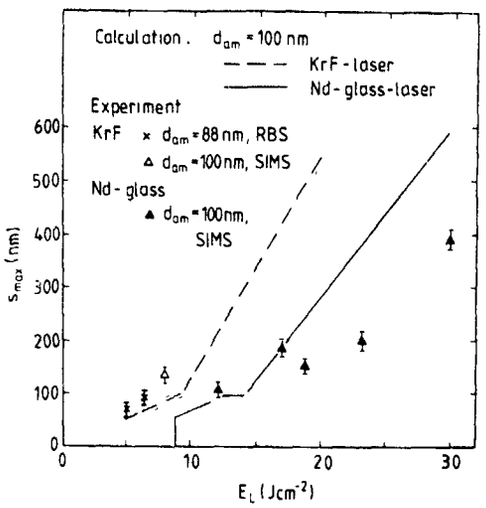

Fig 2 Calculated (curves) and measured (points) values of the maximum melting depth s_{max} for 100 nm thick amorphous Si layers as a function of the laser energy density E_L

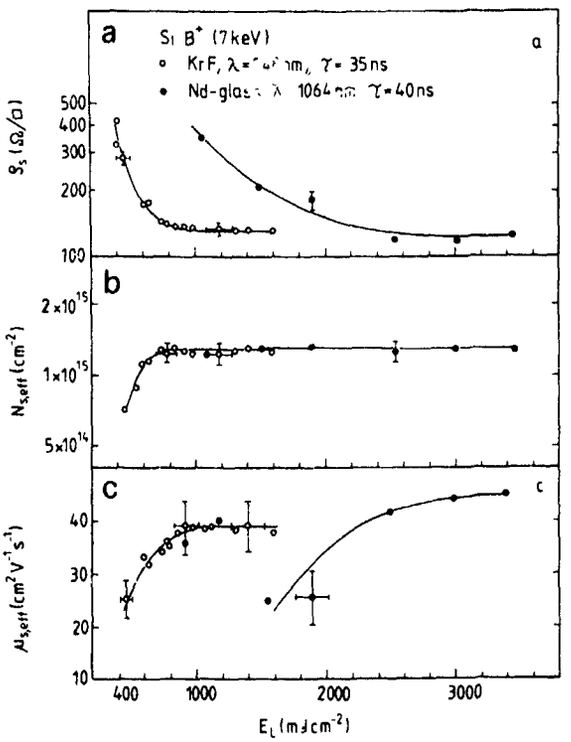

Fig. 4. (a) Sheet resistivity ρ_s, (b) effective carrier concentration $N_{s\,eff}$ and (c) effective sheet mobility $\mu_{s\,eff}$ for KrF excimer (open circles) and Nd-glass (dots) laser-annealed Si layers as a function of the laser energy density

with the laser energy density. To melt a fixed layer thickness, with the infrared laser a 1.5 times higher laser energy density is necessary than in the case of the ultraviolet laser

The investigation of the recrystallization by means of the channeling–RBS technique shows, that 100 nm thick amorphous layers are completely recrystallized (i.e., the

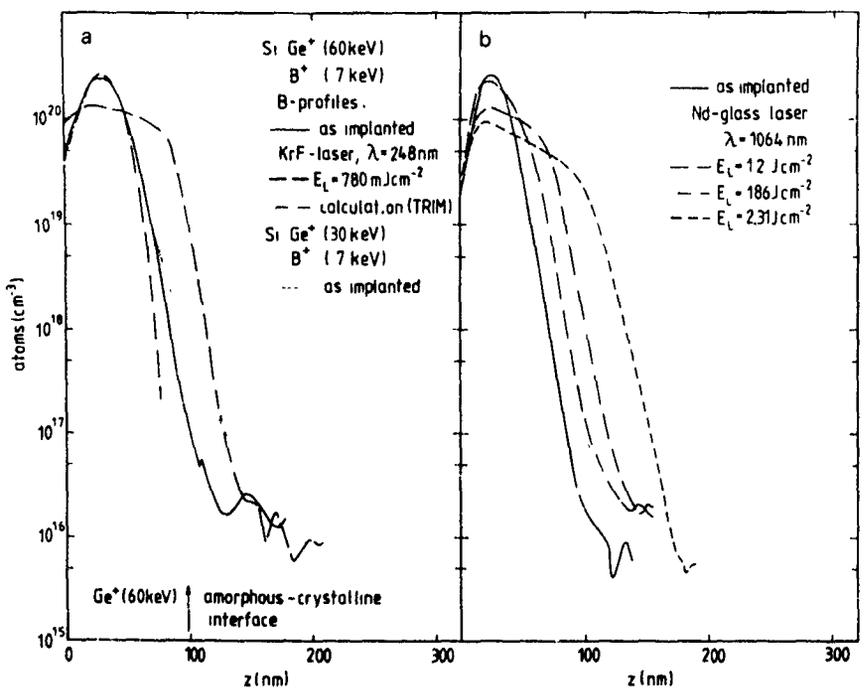

Fig. 3 SIMS profiles of the boron distribution after 7 keV B$^+$ implantation into Ge$^+$-preamorphized Si and laser annealing with (a) a KrF and (b) a Nd-glass laser.

melt front has penetrated the amorphous–crystalline interface) at the laser energy densities $E_L \simeq 780$ mJ/cm^2 in the case of UV-laser annealing [4], and at $E_L \simeq 1.2$ J/cm^2 for IR-laser annealing. In fig. 2 experimental s_{max}-values determined from RBS spectra (redistribution of Sb atoms) or from SIMS profiles are included. At low energy densities the theoretical and experimental values are in fairly good agreement. However, for higher energy densities, if part of the crystalline substrate is molten, remarkable deviations occur. These deviations may result from different reasons. First, because of the detection limit of the RBS technique ($\simeq 10^{19}$ at./cm^3), the determination of the maximum melting depth from the redistribution of heavy atoms may lead to an underestimation of s_{max}. Second, for laser energy densities in the order of $E_L \geq 3$ J/cm^2 the diffusion length of boron is remarkably lower than the thickness of the amorphous layer (with the diffusion coefficient $D_l = 2.4 \times 10^{-4}$ cm^2/s^1 and a melting time of $\simeq 100$ ns the diffusion length is $L \simeq 50$ nm), so that the determination of s_{max} from the boron profiles determined by SIMS is doubtful at high laser energy densities. And last, but not least, the uncertainty of some parameters used for the calculation may lead to a systematic error of the calculated curves. For example, the assumption of a higher reflectivity and specific heat of the liquid silicon would cause a lower energy deposition and a decrease of s_{max} and T_{surf} at the same energy density.

The boron profiles determined by means of SIMS are illustrated in fig. 3. It can be seen that for 7 keV B^+ implantation the preamorphization by 60 keV Ge^+ ions gives good results (no pronounced tail in boron distribution, fig. 3a [4]). Laser annealing with both wavelengths leads to a broadening of the boron distribution with an abrupt decrease of the boron concentration within the region of maximum melting depth.

The recrystallization of the implanted layers is connected with the substitutional incorporation of the dopants (for $\lambda = 248$ nm a substitutional Sb fraction of 99% was determined at $E_L = 780$ mJ/cm^2 [4]) leading

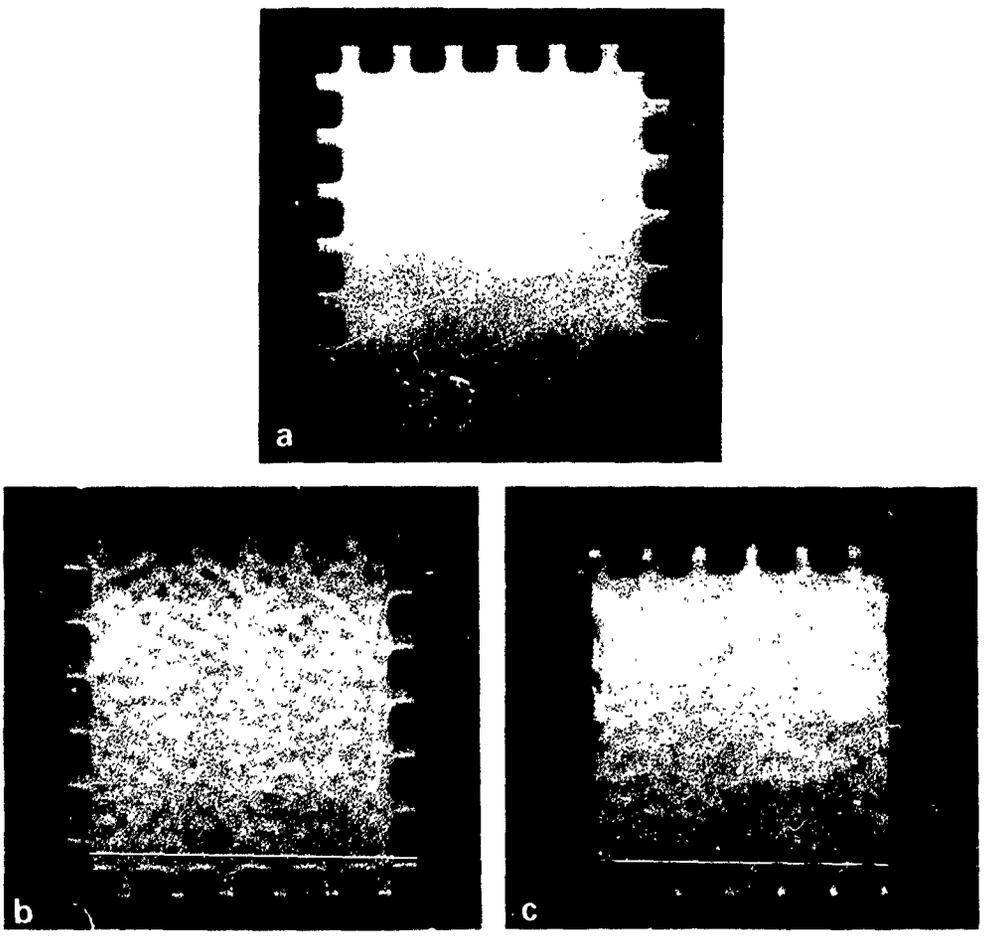

Fig. 5 Optical micrographs of SiO_2 structural edges after irradiation with pulses from a Nd-glass laser (laser energy densities (a) $E_L = 3.11$ J/cm^2, (b) 4.24 J/cm^2 and (c) 4.95 J/cm^2)

to a steep descent of the sheet resistivity ρ_s (see fig 4a). For the KrF laser irradiation a constant value $\rho_s \approx 130$ $\Omega/\square$ is reached at $E_L \approx 800$ mJ/cm^2, for the Nd-glass laser-irradiated samples $\rho_s \approx 120$ $\Omega/\square$ is obtained at $E_L \approx 2.6$ J/cm^2, indicating a good electrical activation of the layers. According to that, in the same region of the energy density the sheet carrier concentration reaches its maximum value $N_{s\,eff} \approx 1.2 \times 10^{15}$ cm^{-2} (see fig 4b). A comparison with the effective carrier mobility, however, shows that to obtain maximum mobility, higher energy densities are necessary: for the KrF laser about 1.2 J/cm^2, for the Nd-glass laser about 2.8–3.0 J/cm^2 (fig 4c) This means that layers at least twice as thick as the amorphous layer have to be molten to obtain optimum electrical parameters.

A key problem of laser annealing via the liquid phase, especially at higher energy densities, is the influence on structural edges. Therefore, we have investigated the influence of Nd-glass laser irradiation on SiO_2 structures. Fig. 5 shows optical micrographs of SiO_2 edges irradiated with 3.11, 4.24 and 4.95 J/cm^2, respectively. Whereas at 3.11 and 4.24 J/cm^2 no modification of the edges can be observed, at 4 95 J/cm^2 the window of the laser energy density is exceeded Similar results are obtained at microstructures From these results it can be concluded that Nd-glass laser energy densities up to about 4.5 J/cm^2 do not influence SiO_2 structures on implanted Si layers

4. Summary

Shallow dopant profiles in the order of 100–200 nm can be produced by ion implantation and laser annealing of amorphous Si layers. The use of ns laser pulses gives the possibility to melt a thin surface layer and to activate the implanted ions in this region. Whereas by a Nd-glass laser an energy density of 2.8–3 0 J/cm^2 yields maximum carrier concentration and carrier mobility, by using an excimer laser the same results are already achieved for 1 2 J/cm^2 By these laser energy densities layers twice the thickness of the amorphous layers were molten. The investigation of structural edges indicates that laser energy densities up to about 4.5 J/cm^2 can be used. Therefore, also with the Nd-glass laser the formation of pn junctions with depths below 200 nm should be possible. The theoretical simulation of the melting process gives a fairly good agreement with experimental values for low energy densities, whereas for high laser energy densities ($E_L \geq 1.5$ J/cm^2) remarkable differences exist. Explanations for these deviations are the detection limit of the analysing method (RBS, differences between molten depth and concentration pro file of dopants due to short diffusion length) and the uncertainty of the optical and thermodynamical parameters of liquid silicon

Acknowledgement

The authors wish to thank M Trapp, Werk fur Fernsehelektronik Berlin, for carrying out the SIMS measurements

References

[1] A L Butler and D J Foster, IEEE Trans Electron Devices ED-32 (1986) 335
[2] C Hill, Nucl Instr and Meth B19/20 (1987) 348
[3] J Narayan, C W White, M J. Aziz, B Stritzker and A Walthuis, J Appl. Phys 57 (1985) 564
[4] W. Wesch, T Bachmann and F Hagemann, Nucl. Instr and Meth B53 (1991) 173
[5] M Wagner, A Witzmann, H -D Geiler and K -H Heinig, Appl Surf Sci 43 (1989) 260
[6] G Götz and K Gartner (eds), High Energy Ion Beam Analysis of Solids (Akademie-Verlag, Berlin, 1988)
[7] J F Ziegler and J P Biersack, The Stopping and Range of Solids (Pergamon, New York, 1985)
[8] D Stock, private communication

Nuclear Instruments and Methods in Physics Research B55 (1991) 630–632
North-Holland

Centers of spin-dependent recombination in structures formed by N^+ ion implantation into Si

A.A. Karanovich, A.V. Dvurechenskii, I.E. Tyschenko and G.A. Kachurin
Institute of Semiconductor Physics, Novosibirsk 90, USSR

Spin-dependent recombination (SDR) measurements have been made on (100) and (111) n- or p-type silicon wafers implanted with 135 keV N^+ ions in the dose range $D = 5\times10^{15}$–10^{18} cm^{-2} at an implantation temperature in the range of T_i = 700–1000 °C or at room temperature with subsequent annealing at T_a = 500–1200 °C for two hours. For $T_i > 800$ °C and $D > 5\times10^{16}$ cm^{-2} an intensive anisotropic spectrum was observed. Its $\hat{g}$-tensor parameters ($g_{\parallel} = 2.0010 \pm 0.0005$; $g_{\perp} = 2.0080 \pm 0.0005$; $g_{\parallel} \parallel \langle 111 \rangle$) coincide with those of P_{bO} or P_{bN} spectra – the signal at the boundary between silicon and buried precipitates of crystalline Si_3N_4. For $T_i < 750$ °C or $D < 10^{16}$ cm^{-2}, as well as for room-temperature implanted and 1200 °C annealed samples, only a single isotropic line was observed. This signal was found to consist of two lines, which are characterized by different relaxation times. These two components of the isotropic signal are supposed to correspond to Si dangling bonds at dislocations and at the Si/amorphous SiN_x interface. It was concluded that the formation and growth of crystalline Si_3N_4 precipitates are stimulated by ion irradiation.

Among SOI technologies the formation of buried insulating layers by N^+ or O^+ ion implantation is the favored technique. In order to obtain good SOI structures, the dependence of their properties on the production regime should be known. Defects in SOI structures with buried Si_3N_4 layers were investigated by electron paramagnetic resonance (EPR) in ref. [2]. An isotropic signal was observed ($g = 2.0039 \pm 0.0002$), which is believed to arise from the silicon dangling bonds in buried amorphous nitride layers.

In the present work a method of spin-dependent recombination (SDR) of excess carriers [3–5] was used to study the defect structure in silicon implanted with N^+ ions. The SDR technique has a number of advantages compared to the EPR measurements. Firstly, the sensitivity of SDR signal detection is independent of the number of centers as long as they dominate the recombination process. This makes it possible to carry out SDR investigations of effects in thin silicon films (for example, in SOI structures) where EPR measurements are hard to perform because of the sensitivity limitation. The second advantage is concerned with the selectivity of this method: the SDR signal of defects in SOI structures is observed only in the silicon layer, while in EPR the defects localized in the insulator or in the substrate are observed as well.

Structures formed by N^+ ion implantation (E = 135 eV, dose $D = 5\times10^{15}$–10^{18} cm^{-2}) into substrates of n- or p-type {111} or {100} silicon were investigated. The irradiation was carried out in two ways: (i) implantation into a hot target (T_i = 500–1000 °C) and (ii) room temperature irradiation followed by annealing at T_a = 500–1200 °C for two hours. The implanted layers are characterized by n-type conductivity (apparently due to the nitrogen atoms [1]), therefore p-n-junctions were formed when p-type silicon substrates were used. For control measurements n-Si implanted with B^+ (E = 60 keV, $D = 10^{15}$ cm^{-2}, T_i = 20 °C plus annealing at T_a = 900 °C for two hours) and p-type Si irradiated by P^+ (E = 100 keV, $D = 10^{16}$ cm^{-2}, T_i = 900 °C) were used.

The photoconductivity of the implanted layers, voltage or photovoltage on p-n-junctions (formed by N^+ implantation into p-type wafers) were measured to record SDR spectra in the X-band of an EPR spectrometer (frequency f = 9 GHz, klystron power ~ 250 mW). Illumination with white light was provided by a 100 W tungsten lamp. Modulation of the magnetic field (f = 0.3–100 kHz) or microwave power (f = 1 kHz) was used. The measurements were made at room temperature.

It was found that the shape and intensity of the observed signals were independent of the registration technique and were determined by the dose and the implantation (annealing) temperature. The relative intensity of the SDR effect $\Delta A/A$ (A = the measured value, ΔA = its change at resonance) was varied in the range $(1–3)\times10^{-5}$.

For an irradiation temperature $T_i > 800$ °C and dose $D > 5\times10^{16}$ cm^{-2}, an intense anisotropic spectrum was observed (fig. 1). The angular dependence of the lines in the observed spectrum with $\boldsymbol{B}$ in the (011) plane (fig. 2) corresponds to a defect with electronic spin $S = 1/2$

0168-583X/91/$03.50 © 1991 – Elsevier Science Publishers B.V. (North-Holland)

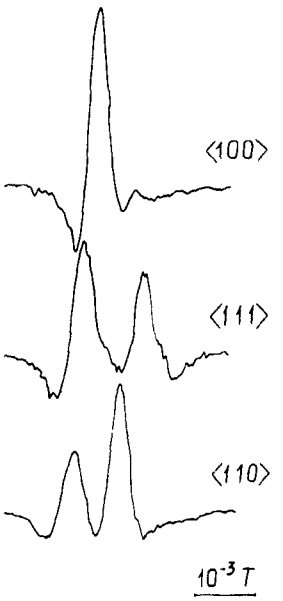

Fig 1 Spin-dependent photoconductivity spectra (second derivative) in structures formed by nitrogen ion implantation ($E = 135$ keV, dose $D = 5 \times 10^{16}$ cm^{-2}, $T_i = 850$ °C) into p-type {100} silicon substrates at different orientations of the magnetic field Frequency of magnetic field modulation $f = 35$ kHz, measurements at room temperature (RT)

and axially symmetrical $\hat{g}$-tensor (the principal values are $g_{\parallel} = 2.0010 \pm 0.0005$, $g_{\perp} = 2.0090 \pm 0.0005$, $\boldsymbol{g}_{\parallel} \parallel \langle 111 \rangle$).

For lower doses ($< 10^{16}$ cm^{-2}) or lower temperatures (< 750 °C) an anisotropic spectrum was absent and only a single isotropic line ($g = 2.0035 \pm 0.0005$) was observed. Just such a spectrum was observed in our samples after room temperature implantation followed by annealing up to $T_a = 1200$ °C.

The $\hat{g}$-tensor parameters of the discovered anisotropic defect coincides with those of defects at Si/SiO_2 (spectrum P_{bO} [6]) or Si/Si_3N_4 (spectrum P_{bN} [7]) interfaces. These defects are believed to be related to the dangling Sp^3 bonds located on interfacial Si atoms which are backbonded to three Si atoms in the bulk [7]. Such dangling bonds at the boundary between silicon and buried precipitates of crystalline Si_3N_4 (the formation of which was proved in ref. [8]) or at the Si/natural SiO_2 interface could be responsible for the observed anisotropic spectrum In the latter case, however, the P_{bO} spectrum would be observed independently of the type of implanted ion. But our experiments show that p-n-junctions formed by B^+ or P^+ implantation give a single isotropic line only ($g = 2.0040 \pm 0.0005$). Just such a SDR signal was observed in silicon with dislocations [4,5] and, therefore, it is reasonable to conclude that the observed isotropic signal in our case is due to dislocation loops, which are known to exist in implanted layers under the implantation conditions used [9]. Moreover, if the observed anisotropic signal is caused by the planar Si/SiO_2 interface, then the spectrum from the {111} surface would consist of a single line [6] (because all the dangling bonds have the same orientation), while in our case several lines are observed in the spectrum simultaneously Therefore, the observed anisotropic signal is caused by defects at the considerably nonplanar Si/Si_3N_4 interface

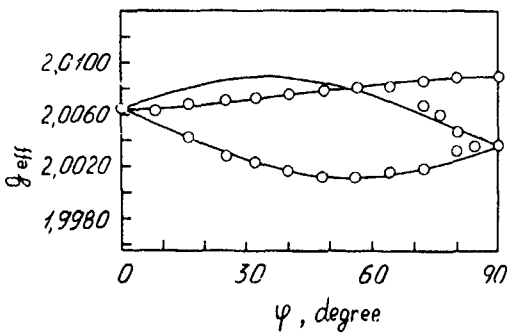

Fig 2 The angular dependence of g-factor effective values of the observed spectrum lines with the magnetic field B in the {110} plane. Points refer to the experimental values, solid lines to computations

It was found that the form of isotropic signal depends on the modulation frequency and phase of the lock-in detector (fig. 3). From the analysis of this dependence we conclude that the observed isotropic signal consists of at least two lines (with identical g-factors but different line widths ($\Delta B_1 = (14 \pm 3) \times 10^{-4}$ T, $\Delta B_2 = (7 \pm 2) \times 10^{-4}$ T), which are characterized by different relaxation times This difference in the relaxation times leads to the appearance of a distinction between the two SDR signal phases with respect to the phase of the modulation signal. This phase difference depends on the implantation and annealing conditions and is varied in the range $\Delta\phi = 5$–50° at a modulation frequency $f = 35$ kHz. Such a value of $\Delta\phi$ corresponds to typical relaxation times $\tau \sim 10^{-5}$ s It is unlikely that such a long τ is concerned with a spin–lattice relaxation time because the latter is usually much shorter at room temperature. Therefore we suppose that the relaxation time is determined by the recombination time of excess carriers and the two components of the isotropic signal are caused by identical defects localized in two distinct environments. These regions differ by the recombination time of excess carriers. According to the g-factor, the observed signal is quite similar to the spectrum of amorphous silicon or dislocations in silicon. Therefore, it is reasonable to suppose that the Si dangling bonds at the dislocations and at the Si/amorphous SiN_x interface are responsible for the two components of the isotropic spectrum

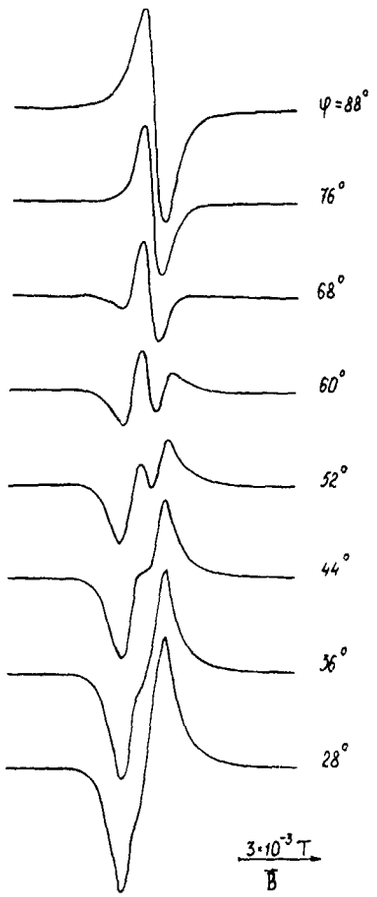

Fig. 3 Modification of the isotropic spectrum shape when the phase of lock-in detector is changed. RT, $T_a = 500\,^\circ$C, the magnetic field modulation frequency $f = 35$ kHz

The P_{bN} spectrum was not observed in our samples after room temperature implantation and subsequent annealing up to $T_a = 1200\,^\circ$C, while the implantation into a hot target leads to the appearance of the P_{bN} spectrum at temperatures as low as $T_i = 800\,^\circ$C. These experimental results confirm the conclusion [10] that the formation and growth of crystalline Si_3N_4 precipitates are stimulated by ion irradiation.

Thus, by means of the SDR technique, two types of spectra in SOI structures formed by N^+ ion implantation were found: (i) an isotropic signal consisting of two lines, which are characterized by different relaxation times and are apparently caused by Si dangling bonds at dislocations and at the Si/amorphous nitride interface, and (ii) an anisotropic spectrum P_{bN}, which is believed to arise from dangling bonds located on an Si atom backbonded to three Si atoms in the bulk and localized at the boundary between Si and crystalline Si_3N_4 precipitates. The formation and growth of Si_3N_4 precipitates are stimulated by ion irradiation.

References

[1] K J Reeson, Nucl Instr and Meth B19/20 (1987) 269
[2] A Hobbs, R C Barklie, P L F Hemment and K. Reeson, J. Phys. C19 (1986) 6433.
[3] D. Lepin, Phys. Rev B6 (1972) 436
[4] F.I Borisov, V I. Strikha and O V. Tretiak, Fisika i Tekh Poluprovodn 15 (1981) 1978 [Sov Phys -Semicond].
[5] I Solomon, Solid State Commun 20 (1976) 215
[6] E H Poindexter, P J. Caplan, B E Deal and R.R Razouk, J Appl Phys 50 (1979) 5847
[7] A Stesmans and G. Van Gorp, Phys Rev B39 (1989) 2864.
[8] G A. Kachurin, I E Tyschenko, V P Popov, S A Tiys and A E. Plotnikov, Fisika i Tekhn Poluprovodn. 23 (1989) 434 [Sov Phys -Semicond.]
[9] G A. Kachurin, L I Fedina and I E. Tyschenko Poverkhnost 1 (1990) 72
[10] G A. Kachurin, I E Tyschenko, F T Plotnikov and V P Popov, 3rd Int Conf on Energy Pulse and Particle Beam Modification of Materials, Dresden, Germany, 1989, Abstracts p 8 09

Nuclear Instruments and Methods in Physics Research B55 (1991) 633–636
North-Holland

Anomalous redistributions of As and Sb atoms in As-implanted Sb-doped Si and Sb-implanted As-doped Si during annealing

Katsuhiro Yokota [a], Hiroshi Furuta [a], Shinji Ishihara [b] and Itsuro Kimura [b]

[a] *Faculty of Engineering, Kansai University, Suita, Osaka 564, Japan*
[b] *Research Reactor Institute, Kyoto University, Kumatori, Sennan-gun, Osaka 590-04, Japan*

Sb^+ ions were implanted into heavily As-doped bulk silicon and As^+ ions were implanted into heavily Sb-doped bulk silicon Subsequent high-temperature annealing indicated the loss of Sb atoms For the samples implanted with antimony the amount of lost Sb depends on the implanted dose In comparison, the arsenic concentration in both samples remained constant and no abnormal loss of arsenic was evident during the high-temperature anneal

1. Introduction

Ion implantation as a conventional doping technique requires high-temperature annealing to restore the destroyed crystal lattice and to electrically activate the implanted dopants. The implanted dopants will redistribute to a profile which can be determined by the diffusion of a limited-source during annealing However, the dopants induce stress in the Si crystal since the atomic radius of the dopant atoms differs from that of Si [1] This stress results in a significant effect on the dopant diffusion and the solid solubility of the impurities [2]

In many cases the impurities are implanted with low doses. The differences in the atomic radii are not a serious problem during annealing since the concentration of the dopant is low. However, the behavior of B, P and As in heavily doped Si during annealing is complicated, as the diffusion coefficient of the dopant depends on its concentration.

The interest in this subject is whether or not the differences in the atomic sizes of Si and impurities really affect the redistributions of the dopants in Si during annealing. We reveal in this paper that the redistributions of the dopants in As-implanted Sb-doped Si and Sb-implanted As-doped Si during annealing depend highly on the radius of the implanted ion and the solid solubility

2. Experiments

Heavily Sb-doped Czochralski (100) Si wafers with a concentration of 0.8×10^{19} cm^{-3} and heavily As-doped Czochralski (100) Si wafers with a concentration of 2×10^{20} cm^{-3} were used for the experiments. 50 keV As^+ ions were implanted into the Sb-doped Si wafers at doses in the range 1×10^{14}–1×10^{16} As^+ cm^{-2} This sample is referred to as Si(Sb–As). Also, 70 keV Sb^+ ions were implanted into the As-doped Si wafers at doses in the range 1×10^{14}–1×10^{16} Sb^+ cm^{-2}. This sample is referred to as Si(As–Sb). The incident direction of the ion beam was misaligned by 7° from the (100) crystal axis to minimize the channeling effect. The implanted samples were annealed in flowing Ar gas at a temperature of 1000 °C for 30 min. The ellipsometric thickness of native oxide films grown on silicon wafers was about 2.5 nm.

To confirm the results for Si(As–Sb) and Si(Sb–As), the following experiments were performed. First, 70 keV Sb^+ ions were implanted into B-doped Czochralski (100)Si wafers with a concentration of 3×10^{19} cm^{-3}, at a dose of 1×10^{15}–1 Sb^+ cm^{-2}. The sample is referred to as Si(B–As). Secondly, 50 keV As^+ ions were implanted into P-doped Czochralski (100)Si wafers with a concentration of 3×10^{19} cm^{-3}, at a dose of 1×10^{15}–1 As^+ cm^{-2}. The sample is referred to as Si(P–As) Thirdly, 40 keV Ar^+ ions were implanted into Sb-doped Czochralski (100)Si wafers with a concentration of 0.8×10^{19} cm^{-3} and As-doped Czochralski (100)Si wafers with a concentration of 2×10^{20} cm^{-3}, at a dose of 1×10^{15} Ar^+ cm^{-2} These samples are referred to as Si(Sb–Ar) and Si(As–Ar), respectively The Si wafers were annealed in flowing Ar gas at 1000 °C for 30 min.

The annealed samples were activated in a neutron flux of 2.8×10^{13} cm^{-2} s^{-1} for 1 h. Some of the As and Sb converted into the radio-isotopes of ^{76}As and ^{122}Sb, respectively. A thickness of 10 nm was removed successively from the sample surfaces by repeating anodic oxidation and oxide removal by HF diluted with water. Depth profiles of the As and Sb concentrations in Si were obtained by measuring the radiation emitted from

0168-583X/91/$03.50 © 1991 – Elsevier Science Publishers B.V. (North-Holland)

the radioactive isotopes of ^{76}As and ^{122}Sb in the HF solutions The radiation was measured using an NaI(Tl) scintillation counter and a 1024-channel pulse-height analyzer. The system was calibrated by measuring the radiation emitted from standard samples of ^{76}As and ^{122}Sb.

The γ-ray spectrum from ^{76}As was in the same energy region as that from ^{122}Sb. The energy of the dominant radiation from ^{76}As is 0.56 MeV and that from ^{122}Sb is 0.564 MeV. Time decay curves of the radiations were measured to separate the γ-ray spectrum The half-life of ^{76}As is 26 4 h and that of ^{122}Sb is 64.3 h.

3. Results and discussion

Fig. 1 shows the concentration profiles of Sb and As in Si(Sb–As) annealed at a temperature of 1000 °C for 30 min as a function of the implanted dose The larger the arsenic dose, the deeper the As has diffused in the Sb-doped sample The depth where the concentration of the As is reduced by an order of magnitude from its peak concentration became deeper with the increase of implanted dose It was 85 nm for a dose of 1×10^{14} cm $^{-2}$, 115 nm for a dose of 1×10^{15} cm^{-2}, and 265 nm for a dose of 1×10^{16} cm^{-2}. The diffusion coefficient of As in Si at 1000 °C increases with the increase of As concentration It reaches a maximum value of 5×10^{-14} cm^2 s $^{-1}$ at an As concentration of 3×10^{20} cm $^{-3}$, and then decreases [3]. At high concentrations of As, i e above 10^{20} cm $^{-3}$, it is believed that arsenic can form clusters [4], which are immobile below 1000 °C. However, the diffusion of As in Si(Sb–As) implanted with As at a dose of 1×10^{16} cm $^{-2}$ after annealing at 1000 °C for 30 min was compared with that in As-implanted p-type Si after annealing at 1000 °C for 20 min [5] The distribution of As in Si(Sb–As) was shallower than that in both Si(B–As) and Si(P–As) shown in fig 3b. The redistribution profile of As in the Si(B–As) was the same , that in the Si(P–As). This indicates that the n-type or p-type nature of the substrate had no effect on the redistribution of the implanted arsenic Thus, the anomalous redistribution profiles of As in Si(Sb–As) and Si(As–Sb) may be caused by the differences in the atomic sizes of impurities and Si atoms. A similar profile of antimony has been obtained in Ga-implanted Sb-doped Si covered by native oxide films after being annealing at 950 °C for 30 min [6]. However, the profile differs from that of antimony in silicon with a capping layer [7] This seems to be because the native oxide films are much thinner than the capping layer and their physical and chemical properties differ considerably from those of thermally grown silicon oxide

A large amount of Sb in Si(Sb–As) with the As concentrations of 1×10^{14} and 1×10^{15} cm $^{-2}$ was lost from the surface into the atmosphere during annealing The number of lost Sb atoms increased proportionally to the implanted dose The profile of the Sb is described by the equation $N_{Sb} = 8 \times 10^{18}$ (cm $^{-3}$) $- 0.043 N_{As}$ for the sample implanted with arsenic at a dose of 1×10^{14} cm $^{-2}$ The profile of antimony in all regions in silicon, except the near surface of the sample implanted with arsenic at a dose of 1×10^{15} cm $^{-2}$, is described by this equation Here, N_{Sb} is the Sb concentration and N_{As} is the As concentration. The Sb concentration in Si(Sb–As) is 8×10^{18} cm $^{-3}$ The value of 0 043 agrees with the value calculated from the relation $(1 - (d_{As}/d_{Si})^3)/(1 - (d_{Sb}/d_{Si})^3)$ [1], where d is the atomic size Thus, this latter equation implies that the stress induced by the As^+ implantation is released by losing Sb from Si into the atmosphere However, the redistribution of Sb in Si(Sb–As) with an As concentration of 1×10^{16} cm $^{-2}$ did not follow the former equation The stress release caused by the Sb loss seems not to occur in this sample since the stress due to As incorporation is much larger than the stresses induced by the Sb

Fig 2 shows the concentration profiles of As and Sb

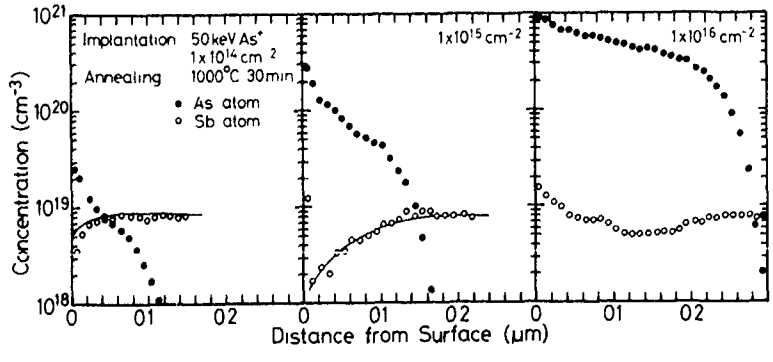

Fig 1 Concentration profiles of Sb and As in Si(Sb–As) annealed at a temperature of 1000 °C for 30 min as a function of the implanted dose Solid lines show the concentration of Sb remaining in Si after annealing This is represented by the equation $N_{Sb} = 8 \times 10^{18}$ (cm $^{-3}$) $- 0.043 N_{As}$, approximately, in silicon implanted with doses of 1×10^{14} and 1×10^{15} As^+ cm $^{-2}$

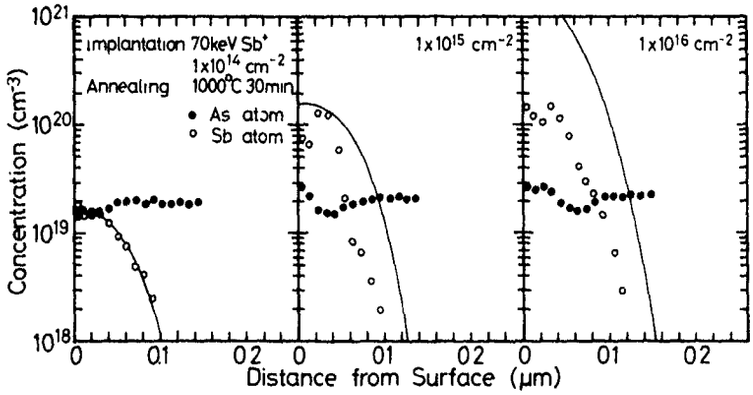

Fig 2 Concentration profiles of As and Sb in Si(As–Sb) annealed at a temperature of 1000 °C for 30 min as a function of the implanted dose of As ions The solid line represents the profile calculated from a solution for limited-source diffusion [4].

in Si(As–Sb) annealed at a temperature of 1000 °C for 30 min as a function of the implanted dose. The solid line in this figure represents the profile calculated from a solution for limited-source diffusion [8] The diffusion of Sb is retarded in Si(As–Sb) with the increase of the Sb dose. A large loss of Sb atoms during annealing must be noted in addition to the retarded diffusion, compared to the calculated profile The number of lost Sb atoms increased with the increase of dose

The experimental results for the Sb^+-implanted samples are shown in fig 3a The diffusion of Sb in annealed Si(P–Sb) is retarded slightly compared to the curve calculated from the solution for limited-source diffusion [8]. However, the retardation of the diffusion was smaller than that in Si(As–Sb) The atomic size of P is smaller than that of Si by 0 07 nm [9] Thus, the stress induced by the incorporation of Sb ions is compensated by that induced by P doped into Si and the redistribution profile of Sb in Si(P–Sb) compares with the calculated curve.

The experimental results for As^+ implanted in B- and P-doped silicon are shown in fig. 3b The redistribution profile of As in Si(P–As) agrees with that of As in Si(B–As). The redistribution profile of As is independent of the background impurity in Si although the atomic size of B differs slightly from that of P This implies that the n-type or p-type nature of the substrate had no effect on the redistribution of the implanted arsenic The stress induced by the As ion implant is compensated by that induced by boron and phosphorus Thus, the larger stress induce by ion implantation causes the anomalous redistributions of As and Sb in both Si(Sb–As) and Si(As–Sb)

The experimental results for Ar^+-implanted silicon are shown in fig. 3c. The redistribution of As in Si(As–Ar) and of Sb in Si(Sb–Ar) occurred even after high-

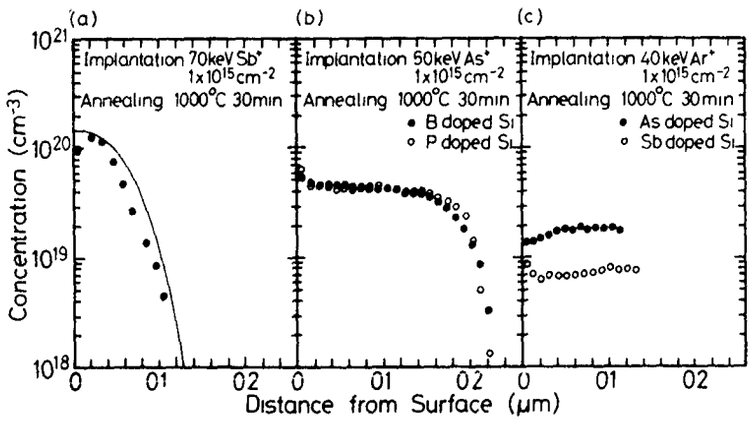

Fig 3 (a) Concentration profiles of Sb in Si(P–Sb) annealed at a temperature of 1000 °C for 30 min The solid line represents the profile calculated from a solution for limited-source diffusion [4] (b) Concentration profiles of As in Si(B–As) and Si(P–As) annealed at a temperature of 1000 °C for 30 min (c) Concentration profiles of As in Si(As–Ar) and Sb in Si(Sb-Ar) annealed at a temperature of 1000 °C for 30 min

temperature annealing. The implantation of argon damages the Si at this high dose and destroys the Si lattice. The destroyed Si lattices recover at temperatures as low as 500 °C [10]. The annealing temperatures in these experiments were much higher. That is, the anomalous redistributions in figs. 1 and 3 are not caused by the mechanism of impurity segregation at the moving amorphous-crystalline boundary as it moves towards the surface during regrowth [11].

However, the anomalous redistribution of implanted antimony in Si(As-Sb) cannot be considered to be caused only by the stress induced by the incorporation of impurities. That is, the concentration of Sb remaining in Si(As-Sb) after annealing was limited to about 1.4×10^{20} cm^{-3} for samples implanted with a dose of 1×10^{15}–1×10^{16} Sb^+ cm^{-2}, as shown in fig. 2. This concentration compares approximately with a solid solubility of 8×10^{19} cm^{-3} [12] for antimony-implanted silicon. On the other hand, the distribution of As in Si(As-Sb) was scarcely modified by annealing in comparison to the anomalous redistribution of Sb in Si(Sb-As) during annealing. The solid solubility of As in Si is 2×10^{21} cm^{-3} [8]. The difference in the distributions of the Sb profile in Si(Sb-As) and the As profile in Si(As-Sb) may be explained by the difference in the solid solubilities of As and Sb in silicon.

5. Conclusion

The diffusion of As in Si(Sb-As) was retarded compared to that in both Si(B-As) and Si(P-As) wafers. In both Si(Sb-As) and Si(As-Sb) no significant loss of arsenic occurred during annealing. The retarded diffusion of arsenic was caused by the larger stress induced by the As ion implantation. The majority of the Sb atoms in Si(Sb-As) and Si(As-Sb) was lost into the atmosphere during annealing. To release the stress induced by ion implantation an unusual redistribution of the Sb atoms took place, aided by the low solid solubility of antimony in silicon. In Si(Sb-As) with an As concentration of 1×10^{16} cm^{-3}, the redistribution of the Sb atoms did not occur because the stress induced by As is much larger than that induced by Sb.

References

[1] K. Yagi, N. Miyamoto and J. Nishizawa, Jpn. J. Appl. Phys. 9 (1970) 246
[2] C.P. Flynn, Point Deffects and Diffusion (Clarendon, Oxford, 1972) chaps. 3 and 9
[3] T.L. Chiu and H.N. Ghosh, IBM J. Res. Dev. 15 (1971) 472
[4] J.C.C. Tsai, in: Diffusion in VLSI Technology, ed. S.M. Sze (Wiley, New York, 1983)
[5] K. Tsukamoto, Y. Akasaka and K. Kijima, Jpn. J. Appl. Phys. 19 (1980) 87
[6] K. Yokota, H.I. Furuta, S. Ishihara and I. Kimura, J. Appl. Phys. 68 (1990) 5385
[7] T.E. Seidel and A.U. MacRae, Trans. Metall. Soc. AIME 25 (1969) 491.
[8] S.M. Sze, Semiconductor Devices Physics and Technology (Wiley, New York, 1985) p. 418
[9] H.F. Wolf, Silicon Semiconductor Data (Pergamon, Oxford, 1969) p. 150
[10] L. Czepregi, E.F. Kennedy, J.W. Mayer and T.W. Sigmon, J. Appl. Phys. 49 (1978) 3906.
[11] J.S. Williams and K.T. Short, Metastable Phases by Ion Implantation (North-Holland, Amsterdam, 1982) p. 131
[12] F.A. Trumbore, Bell Syst. Tech. J. 39 (1960) 205

Nuclear Instruments and Methods in Physics Research B55 (1991) 637–641
North-Holland

The influence of implantation temperature and subsequent annealing on residual implantation defects in silicon

P. Hazdra [a], V. Hašlar [b] and M. Bartoš [b]

[a] *Department of Microelectronics, Faculty of Electrical Engineering, Czech Technical University, Suchbátarova 2, 166 27 Prague 6, Czechoslovakia*
[b] *Ion implantation Laboratory, Faculty of Electrical Engineering, Czech Technical University, Suchbátarova 2, 166 27 Prague 6, Czechoslovakia*

The implantation of $^{28}Si^{+}$ ions at different substrate temperatures ranging from 120 to 820 K into shallow $p^{+}n$ junction structures was used for the study of ion implantation defects in n-type Si. The stability of the created defects was investigated using isochronal furnace annealing in the temperature range 370–820 K. The results of DLTS measurements were compared with measured reverse I–V characteristics. The results show the dominant role of thermally stimulated dissociation and the production of secondary defects involving vacancies. These processes are significantly influenced both by implantation temperature and by the subsequent transient to room temperature.

1. Introduction

Contemporary trends toward VLSI and ULSI devices have increased the importance of investigating low-dose ($< 10^{12}$ cm^{-2}) ion-implantation residual defects. The reason for this is the necessity to completely remove these defects and an antagonistic industry trend towards lower temperature processing. On the other hand, the importance of controlled introduction of defects for local control of semiconductor microphysical parameters is increasing [1]. In this case attention is paid to the influence of implantation conditions on defect production and stability.

Investigations in this field [1–5] have been focused in the last decade on the identification of the defects produced, their concentration profiles, stability and the influence of implantation dose and substrate quality parameters on individual defect production. The results [2,3] show a similarity in the nature of defects produced by implantation and electron irradiation [5]. The point defects, such as divacancies (V_2), vacancy–oxygen pairs (VO – "A" center), vacancy–phosphorus pairs (VP – "E" center) and CVO, CVB, C_iC_s complexes could be considered as the most important. Less attention has been paid to the influence of implantation temperature on implantation defect generation. The works investigating substrate temperature influence on electron-irradiation defect production (e.g. ref. [6]) are only available.

In this paper the influence of implantation temperature on implantation defect production and stability was studied. Deep-level transient spectroscopy (DLTS) [7] was used to identify the defects created. The results were correlated with the electrical parameters of the investigated structures, represented by reverse I–V characteristics.

2. Experiment

Phosphorus-doped n-type silicon wafers with a shallow donor concentration of about 1.3×10^{15} cm^{-3} and ⟨100⟩ orientation were used in the experiment. The concentration of residual impurities declared by the manufacturer was lower than 1×10^{18} cm^{-3} in the case of oxygen and around 10^{16} cm^{-3} for carbon. The fabrication of test diode structures was performed by shallow implantation of $^{49}BF_2^{+}$ complex at 10 keV and with a total dose of 5×10^{15} cm^{-2} at 300 K through 550×550 μm windows created in the oxide layer. The implant was then annealed for 30 min at 1073 K in an N_2 atmosphere. According to SUPREM II simulation, the resulting junction depth should be about 160 nm. Back ohmic contact was produced by shallow PSG diffusion. The mean value of the leakage current I_{ro} (-5 V) measured for 5 V reverse bias was 4.5 ± 0.3 pA. In the next step the wafers were implanted by 160 keV $^{28}Si^{+}$ (1×10^{11} cm^{-2}) at twelve different substrate temperatures ranging from 120 to 820 K with a dose rate of 1×10^{9} cm^{-2} s^{-1}, so that only radiation defects were created by ion implantation. The temperature was measured by a thermocouple mounted on the wafer holder on the back of the wafer and stabilized to within ± 3 K of the desired value. After implantation spontaneous

0168-583X/91/$03.50 © 1991 – Elsevier Science Publishers B.V. (North-Holland)

transient to room temperature followed and reverse I–V characteristics were immediately measured using an HP 4140B pA-meter. Capacitance DLTS measurements using a DLS-82E spectrometer and a multichannel DLTS system based on an HP 4280A 1 MHz capacitance meter were performed in the temperature range 80–300 K with rate windows of 20 μs–1 s and with majority as well as minority carriers filling pulse excitation. Subsequent 30 min isochronal furnace annealing in an N_2 atmosphere and in a temperature range of 370–820 K was performed for each set of samples implanted at a different temperature. After that DLTS and I–V measurements were repeated.

3. Results

Typical DLTS spectra of unannealed samples implanted at 120, 220 and 820 K are shown in fig. 1. DLTS spectra of all the samples were measured under equivalent conditions with current pulse excitation (10 mA, 400 μs) A total of three electron traps, E1–E3, and ten hole traps, H1–H10, were observed Identification parameters of these levels obtained by isothermal and multichannel DLTS measurements are presented in table 1 which also includes the thermal stability of defects for an implantation temperature of 300 K. The influence of implantation temperature and the temperature of subsequent annealing on the DLTS signal of the most important levels is shown in fig. 2 (E1 level – VO), fig. 3 (E3 – V_2 and VP), fig. 4 (H3 – CVO) and fig 5 (H5). Concentration profile measurements of E1 and E3 levels showed that the width of the profiles is about a factor of 2 wider than the primary defect profiles calculated by the Monte Carlo full-cascade simulation code TRIM [9] The influence of implantation temperature

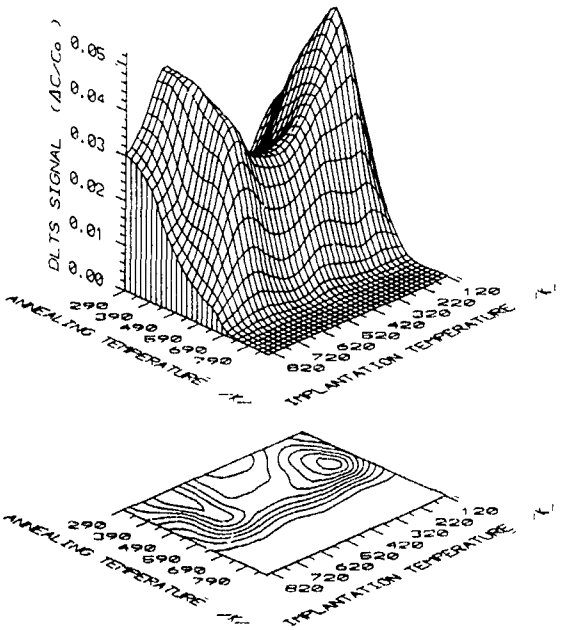

Fig. 2 Level E1 (V O pair) DLTS signal dependence on implantation and annealing temperature.

and the temperature of isochronal annealing on the reverse current I_r (-5 V) is shown in fig. 6 in the form of a ratio of the measured current I_r and the mean value of the leakage current I_{ro} of unimplanted diodes.

4. Discussion

DLTS spectra of unannealed Si^+ implanted samples with typical defect levels labeled E1, E3 and H3 are generally comparable to those observed in the same material after implantation with different ions (e.g

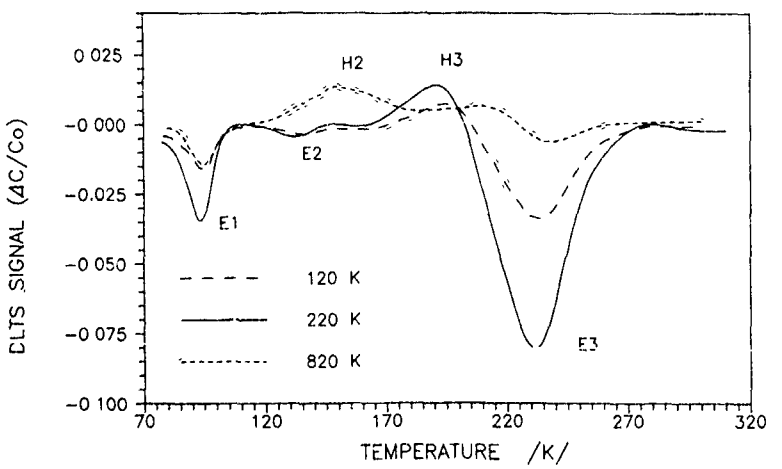

Fig. 1 DLTS spectra of unannealed p^+n diodes implanted by $^{28}Si^+$ ions at 120, 220 and 820 K, current pulse excitation (10 mA, 400 μs), rate window 260 s^{-1}

Table 1
Deep-level identification parameters and tentative interpretation

Level	Energy level [eV]	Cross section [m^2]	Occurrence	Interpretation	Ref.
E1	$E_c - 0.18$	2×10^{-18}	$T_a < 620$ K	VO(0/−)	[1,3,5]
E2	$E_c - 0.23$	1×10^{-19}		V_2(−/−−)	[1,3,4]
E3	$E_c - 0.41$	1×10^{-19}	$T_a < 570$ K	V_2(0/−)	[1–4,5]
			$T_a < 420$ K	VP(0/−)	[1–4,5]
H1	$E_v + 0.18$	1×10^{-20}	$T_a < 570$ K	V_2(+/0)	[3,5]
H2	$E_v + 0.29$	3×10^{-18}	$T_a < 620$ K	OVB	[3,5]
H3	$E_v + 0.38$	3×10^{-18}	$T_a < 570$–620 K	CVO	[3,5]
H4	$E_v + 0.20$	5×10^{-19}	$420 < T_a < 770$ K	?	[3]
H5	$E_v + 0.36$	3×10^{-19}	$570 < T_a < 720$ K	C_iC_s?	[3,5]
H6	$E_v + 0.23$	4×10^{-19}	$570 < T_a < 820$ K	?	
H7	$E_v + 0.11$	8×10^{-21}	$670 < T_a < 820$ K	?	
H8	$E_v + 0.29$	1×10^{-20}	$670 < T_a < 820$ K	?	
H9	$E_v + 0.45$	4×10^{-18}	$670 < T_a < 820$ K	?	
H10	$E_v + 0.56$	8×10^{-18}	$670 < T_a < 820$ K	?	

$^1H^+$, $^4He^+$, $^{11}B^+$, $^{29}Si^+$, $^{31}P^+$, $^{32}S^{7+}$, $^{79}Br^{8+}$, $^{127}I^{10+}$) [1–4] or after electron bombardement [5] A tentative interpretation of the identified defects is presented in table 1 It is based on a comparison of deep-level parameters, implantation-temperature dependence and stability with results of previous works in this topic [1–5]. In the case of the E3 ($E_c - 0.41$ eV) level, two distinct defects – divacancy (V_2) and phosphorus–vacancy pair – contribute together to the observed DLTS signal. The relative numbers of these defects may be found from fig. 3 according to their thermal stability ($V_2 < 570$ K, VP < 420 K). The dominant defects created after implantation of Si^+ into n-type Si are divacancies, VO and VP pairs and CVO complexes. Hole traps H4 to H10 are connected with defect complexes created at higher implantation and annealing temperatures (fig. 6) and their nature is still unknown.

The dominant influence of the E3 level on the magnitude of diode reverse currents can be estimated by

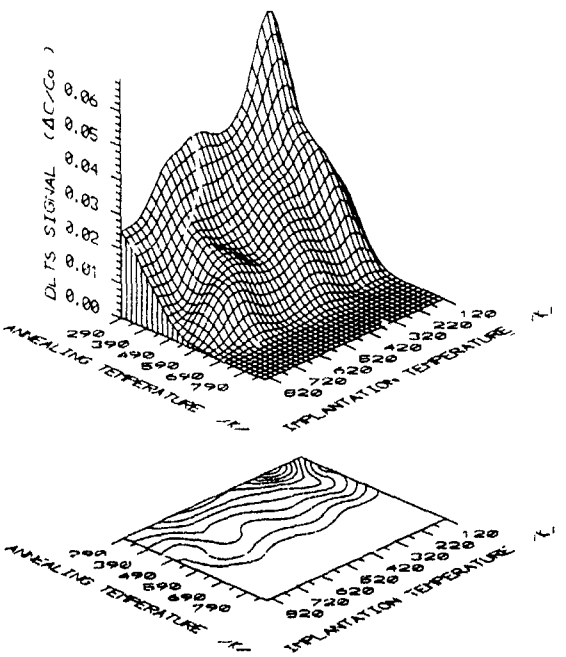

Fig. 3. Level E3 (V_2 and VP pair) DLTS signal dependence on implantation and annealing temperature.

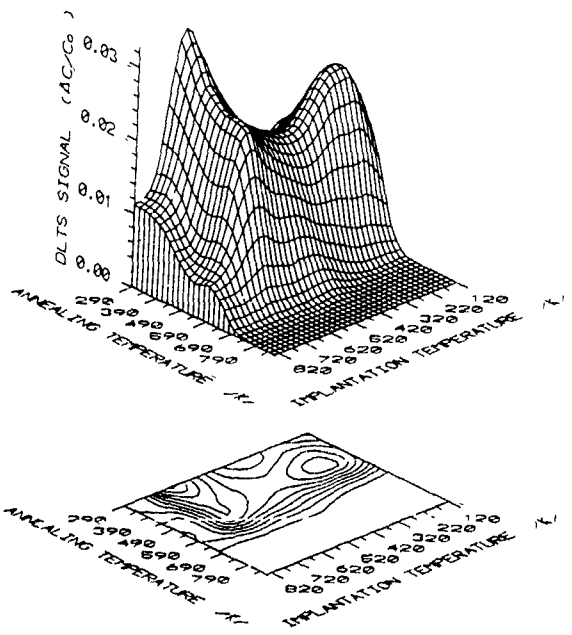

Fig. 4 Level H3 (CVO complex) DLTS signal dependence on implantation and annealing temperature.

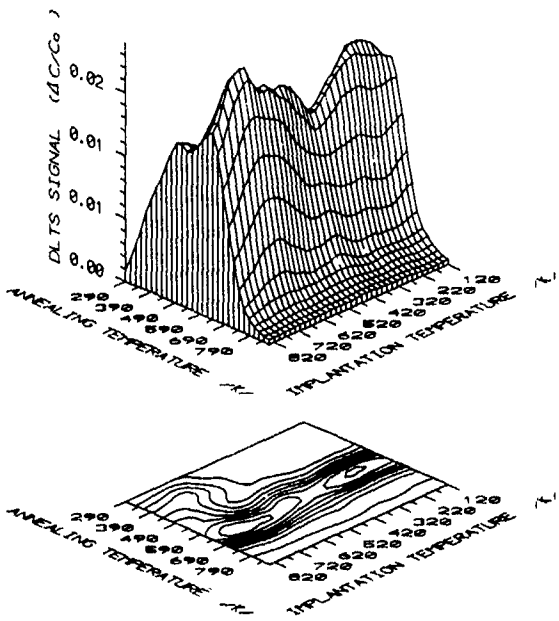

Fig 5 Level H5 DLTS signal dependence on implantation and annealing temperature

comparing the dependences in fig. 3 and fig. 6. However, simulation of the obtained results using a one-dimensional device simulator HAHA [10], involving implementation of the measured DLTS data, shows the

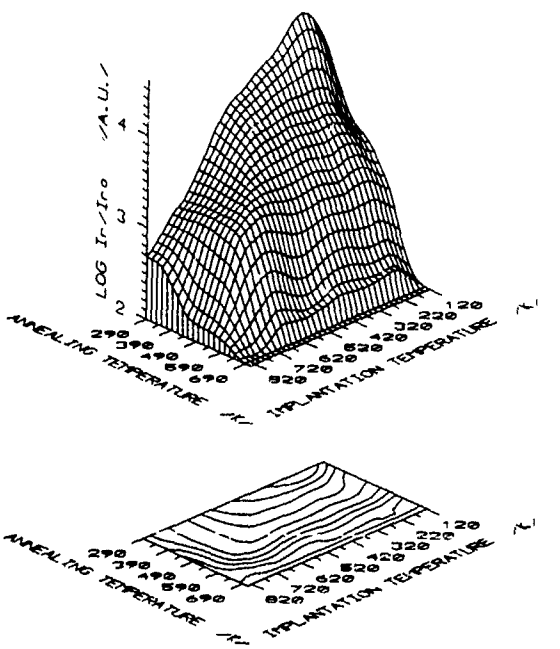

Fig 6 Diode reverse-current dependence on implantation and annealing temperature

crucial role of mutual coupling between level E3 and H3 on charge transport between bands and as a consequence on the reverse current. Consideration of the multilevel generation model without coupling leads to unrealistic values of deep-level concentrations

The role of implantation temperature on implantation defect generation can be resolved by considering the separate defect concentration dependences (figs. 2–6). The increase of diode reverse current for implantation temperatures lower than 220 K may be connected with enhancement of the generation of secondary stable defect (V_2, VP, etc.) due to the liberation of free vacancies [8]. The gradual decrease in the temperature range 270–570 K is caused by successive annealing of VP pairs. A sharp decrease at 720 K is connected with the generation decrease of stable secondary defects, e.g., V_2, VO and CVO. The occurrence of defects in a temperature region higher than the annealing temperature of a given defect (see, e.g., fig. 2) is at variance with results of ref. [6], in which the influence of substrate temperature on radiation-defect production generated by electron irradiation was investigated. This may be caused by a process of primary-defect reaction and secondary-defect creation and annihilation during spontaneous cooling of the sample. The greatest unstability of secondary defects for implantation temperatures near 270 K is due to the low annealing temperature of VP pairs, which are mainly generated near this temperature. Phosphorus–vacancy-pair decomposition near 420 K leads to free-vacancy release, and an increasing number of free vacancies stimulates further production of stable vacancy–impurity complexes so that negative annealing of these defects at 370–550 K may be observed (see figs 2 and 4) High stability of implantation defects is achieved at implantation temperatures above 670 K, at which unstable VP pairs are not generated. Similarly, concentration-profile measurements of VO and V_2 + VP defects show good stability of their damage profiles when implantation temperatures higher than 670 K are used.

5. Summary

DLTS and reverse I–V characteristics measurements have been used to investigate the influence of implantation temperature on ion-implantation-defect generation in shallow p$^+$n diode structures, and the crucial mechanisms of defect production have been determined. The highest production rate, but the worst defect stability, is achieved by selecting an implantation temperature in the 200–300 K region. Utilization of implantation temperatures higher than 670 K increases defect stability.

References

[1] A Hallén, Ph D Thesis, Acta Universitatis Upsaliensis (Uppsala, 1990)
[2] K L Wang, Appl. Phys Lett. 36 (1980) 48
[3] J R Troxell, Solid-State Electron 26 (1983) 539
[4] J Krynicki, J C Muller, P. Siffert, I Brylowska and P Paprocki, Phys Status Solidi A100 (1987) 48.
[5] L C Kimerling, in. Radiation Effects in Semiconductors 1976, eds N.B. Urli and J V Corbett, Inst Phys Conf. Ser 31 (1977) 221
[6] L.S. Milevsky and T A Pagava, Phys Tech Semicond. 10 (1976) 1287
[7] D V Lang, J Appl Phys 45 (1974) 3023
[8] J. Bourgoin and M Lanoo, Point Defects in Semiconductors II, (Springer, Berlin, 1983)
[9] J P Biersack and L G Haggmark, Nucl Instr and Meth 174 (1980) 257
[10] P Hazdra and M Hatle, Solid-State Electron., to be published

Nuclear Instruments and Methods in Physics Research B55 (1991) 642–646
North-Holland

Some properties of amorphous silicon produced by helium ion implantation

A.V. Buravlyov, A.F. Vyatkin, V.K. Egorov, V.V. Kireiko and A.P. Zuev

Institute of Microelectronics Technology and High Purity Materials, Academy of Sciences of the USSR, 142432 Chernogolovka, Moscow District, USSR

The properties of silicon damaged layers obtained by 100 and 50 keV helium ion irradiation at room temperature have been studied. At irradiation doses of 5×10^{16} cm^{-2} the yield of scattered ions at the depth of maximum damage distribution in the Rutherford backscattering spectra (RBS) corresponded to the yield for the random spectrum. In as-implanted samples the value of the electron spin resonance (ESR) signal with $g = 2.0055$ characteristic of amorphous silicon did not exceed the background level of the spectrometer. Further isochronal annealing from room temperature to 600°C revealed that beginning from 180°C there occurs an ESR signal, the value of which increases up to 300°C, and decreases to zero at 450°C. The backscattering spectra in this case exhibit significant changes, suggesting the abnormal character of annealing of the amorphous layer. This paper presents an analysis of the observed variations of the ESR signal and the RBS spectra.

1. Introduction

Formation of amorphous layers upon ion implantation of semiconductors is either an inevitable result of the formation of highly doped regions [1] or a process specially performed to fabricate regions of semiconductor materials with given properties (for instance, saturated solid solutions [2], shallow p–n transitions [3], etc.). Therefore, the amorphization process is of interest, i.e., the crystal–amorphous state phase transition (c–a transition), as well as the reverse process, i.e. solid phase epitaxial growth from the amorphous phase (a–c transition). Over the recent decade intense investigations of these processes allowed for establishing their mechanisms which served as the basis for development of some models of a–c transitions [4,5].

In most models the decisive influence of point defects on the parameters of the processes is emphasized. In particular, practically all the models of ion-beam induced epitaxial growth (IBIEG) are based on the a–c transition being induced by radiation damage formed upon irradiation in the vicinity of the a–c interface. However, the mechanism of the influence of point defects and each specific type of defect on a–c transitions has yet to be studied.

In ion implantation the atomic structure of the damaged layer is generally characterized by the presence of a great number of different defects, both simple and complex ones. For this reason, in the processes related to defect-structure relaxation it is difficult to isolate the role of a particular type of defect. Implantation of silicon with light ions at low dose rates is accompanied with the formation of simple point defects or their mobile complexes [6,7]. Therefore, in the present work an attempt has been made to estimate the role of radiation-induced simple point defects during amorphization and crystallization of silicon.

2. Experimental

N-type (100) Si wafers with a resistivity of 10 Ω cm were irradiated at room temperature by a scanning beam of 50 and 100 keV He^+ ions at a dose of 5×10^{16} ion/cm^2. Subsequent to implantation the wafers were cut into separate samples that were subjected to 30 min isochronal annealing from room temperature to 600°C. After each stage of annealing one sample was selected to record the ESR and RBS spectra. Some samples were investigated by cross-section transmission electron microscopy.

3. Results

Fig. 1 shows RBS spectra taken in the channeling direction for the [100] samples in question. It is easily seen that in both cases 50 and 100 keV He^+ ion implantation (figs. 1a and b, respectively) at a dose of 5×10^{16} ion/cm^2 leads to formation of a region whose level of radiation damage coincides with that of random spectra. This region is formed near the maximum of the damage distribution. No appreciable accumulation of defects occurs in the crystal area located between the buried amorphous layer and the surface. The defect

0168-583X/91/$03.50 © 1991 – Elsevier Science Publishers B.V. (North-Holland)

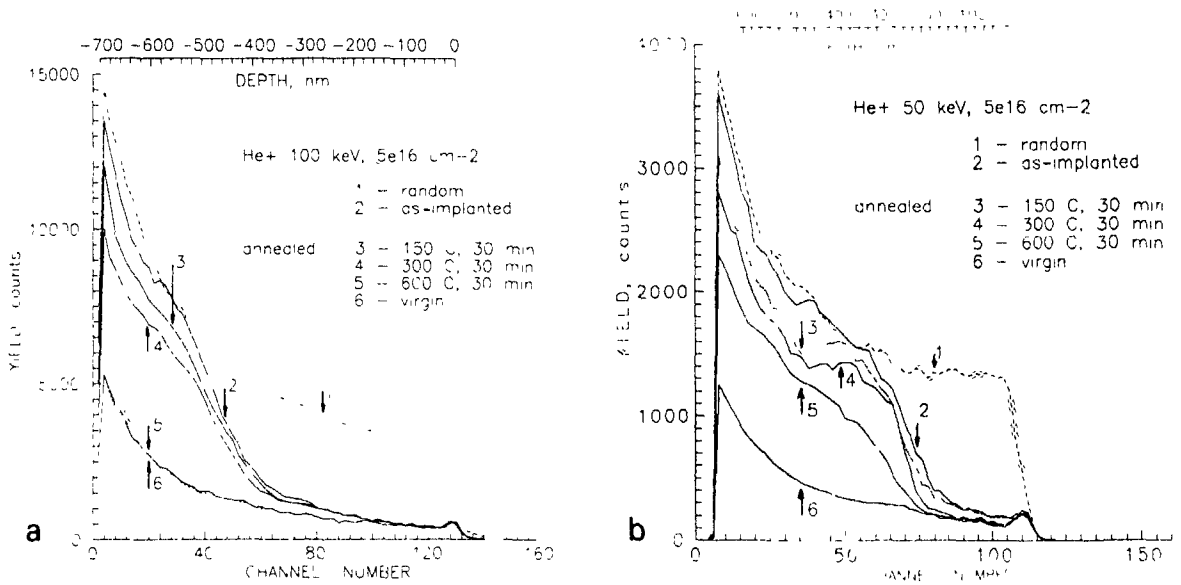

Fig 1 Rutherford backscattering spectra taken in the direction of channeling of [100] silicon samples implanted with (a) 50 keV, and (b) 100 keV helium ions at a dose of 5×10^{16} cm^{-2}, at room temperature and annealed at 150, 300, 450 and 600 °C

density near the amorphous layer decreases rapidly to that of the virgin crystal. Yet, the ESR spectra of such samples do not exhibit any significant concentration of paramagnetic centres with a g-factor equal to 2.0055 which are always indicative of the amorphous state in silicon [8,9] (fig 2).

Annealing of samples to 180 °C does not bring about any perceptible changes in the ESR spectra At temperatures > 150 °C there occurs partial annealing of radiation damage involving a decrease of the ion yield in the RBS spectra to values much less than the level of the random spectrum The ESR spectrum of the same sample shows a peak with $g = 2.0055$ after annealing at 180 °C. As the annealing temperature is increased to 450 °C, the RBS spectra exhibit a monotonic decrease in the backscattered ion yield. Treatment of 100 keV He^+-implanted samples at 600 °C results in practically complete annealing of defects and their RBS spectrum does not differ from that of unimplanted silicon. In the 50 keV He^+-implanted samples annealed at 600 °C a great number of defects remain at the He^+ ion projected range which may be due to the formation of microcavities filled with gaseous helium In the ESR spectra the signal for $g = 2.0055$ increases with temperature up to 300 °C and then decreases monotonically to zero at 450 °C for both types of samples. The ESR signal of the 50 keV He^+-implanted samples exceeds by 30% the signal of the 100 keV He^+-implanted samples This excess agrees with the corresponding difference in radiation damage density in the energy deposition maximum calculated for the case of 50 keV and 100 keV He^+ implantation according to ref [10] (fig 3) Fig. 4 shows a TEM microphotograph of the cross-section of the 100 keV He^+-implanted sample. The surface exhibits an amorphous region obtained by subsequent 100 keV argon ion implantation at a dose of 1×10^{15} cm^2 The contrast and size of the amorphous region served as a reference when estimating the damaged area upon He^+ implantation. It is also seen that the damaged area is localized close to the projected range of 100 keV He^+ ions, i.e , at a depth of 0.56 μm.

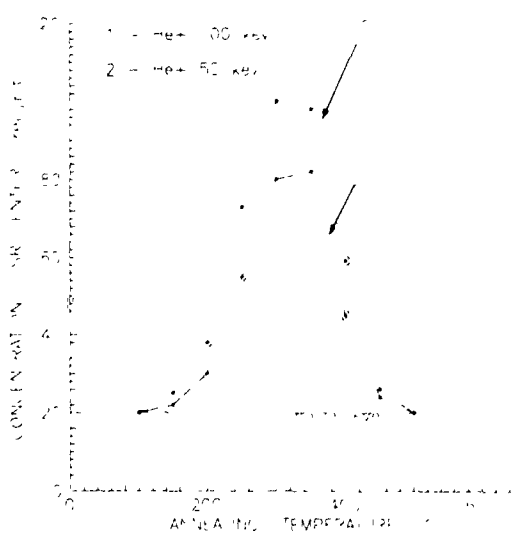

Fig. 2 ESR signal of silicon samples implanted with 50 keV (curve 1) and 100 keV (curve 2) helium ions at a dose of 5×10^{16} cm^{-2} at room temperature as a function of annealing temperature

4. Discussion

The irradiation dose of 5×10^{16} ion/cm^2 used for implantation at room temperature is optimal from the viewpoint of introducing the maximum number of defects into silicon which does not lead to irreversible changes in its structure. Yet, this dose is below the practical dose of the formation of helium-filled gas bubbles (cavities, pores) [11]. It is known [12] that helium irradiation at liquid-nitrogen temperature produces amorphization of silicon at the end of the ion projected range (R_p) even at a dose of 2×10^{16} ion/cm^2. According to ref. [13], this dose corresponds to the number of collision-induced displacements per atom (dpa) which is equal to 1 dpa. It is clear that the number of primary point defects occurring in nuclear collisions upon helium ion irradiation of silicon at room temperature and a dose of 5×10^{16} ion/cm^2 is at least no less than that for the implantation conditions [12]. However, at room temperature the irradiation effect is less pronounced as regards the amorphous layer formation. Comparison of the RBS spectra for our irradiation conditions and those of ref. [12] shows that at room temperature and a dose of 5×10^{16} ion/cm^2 the amount of radiation damage accumulated in the sample corresponds to the number of defects accumulated in the sample upon irradiation at liquid-nitrogen temperature and a dose of 6×10^{15} ion/cm^2. This means that about 10% of the defects generated by helium ion bombardment at room temperature are effective for radiation damage accumulation and 90% of the defects annihilate and partially form a defect-background in the crystal. This proves that helium irradiation of silicon generates chiefly simple point defects since only the latter show sufficient mobility in silicon at room temperature [14] and, hence, may effectively annihilate when moving in the crystal.

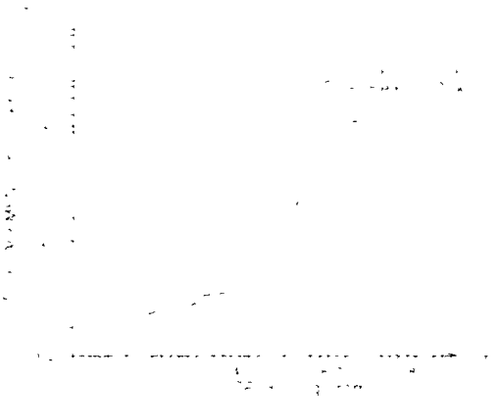

Fig. 3. Profiles of energy loss density for 50 keV (curve 1) and 100 keV (curve 2) He^+ ions in silicon. Implantation dose 5×10^{16} cm^{-2}.

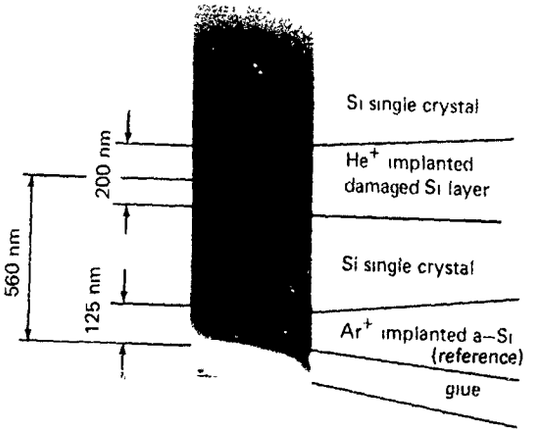

Fig. 4. Electron microscopy microphotograph of the cross section of the silicon sample implanted with 100 keV He^+ ions at a dose of 5×10^{16} cm^{-2} at room temperature. The surface was implanted with 100 keV Ar^+ ions at a dose of 1×10^{15} cm^{-2}.

Analysis of the RBS and ESR spectra enables us to conclude that helium ion irradiation of silicon under the foregoing conditions produces an unusual buried amorphous silicon layer whose properties are different from those of conventional amorphous layers. First, the as-implanted amorphous layer is free of isotropic paramagnetic centres ($g = 2.0055$). Second, this layer is very unstable as the material is transformed even at 150 °C, which is reflected in the RBS spectra as a decrease in the backscattered ion yield. This pattern of changes in the spectrum is greatly different from that observed on annealing of implanted amorphous layers when their thickness decreases as a result of solid phase crystallization on two a–c interfaces. The recrystallized regions in that case are marked by a high crystal-structure perfection which manifests itself in a decreased yield of backscattering ions.

The RBS spectra observed in as-implanted samples and their behaviour on annealing as well as the appearance of the ESR spectra suggest the following model of the structure of the damaged layer and its changes on annealing.

Ion irradiation produces a damaged layer at the depth of the helium projected range. The structure of the layer is amorphous from the standpoint of ion backscattering. The atomic structure of amorphous silicon is known to differ depending on the annealing temperature [12,15], the mass of the amorphization-producing ions [16] and the substrate temperature during vacuum deposition of the amorphous layer [17]. In this case it should be assumed that the layer is inhomogeneous and contains fully and partially damaged regions (see fig. 5). The structure of both regions is rearranged with an increase in temperature accompanied with increasing mobility of defects. For instance, in amorphous

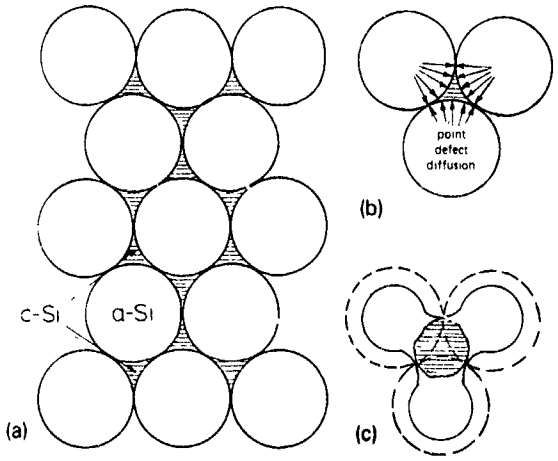

Fig 5 Schematic diagram of the silicon region obtained by 100 keV He^+ ion implantation at a dose of 5×10^{16} cm^{-2} and its evolution on annealing

regions the defects migrate and sink to the a–c interface which leads to the induced crystallization of the amorphous regions of the damaged layer [4] This reduces the amount of the amorphous material in the layer The process proceeds in the whole volume of the damaged layer and in the RBS spectra it shows up as a decrease in the backscattered ion yield throughout the whole damaged layer Such an a–c transition appears to be feasible even at temperatures close to room temperature and in this respect it is analogous to the known processes of ion beam-induced epitaxial growth (IBIEG) [13] Obviously, in the case under consideration the conditions for realizing an a–c transition are similar to those for IBIEG Indeed, the concentration of defects in the amorphous regions should be comparable to their concentration in the amorphous phase during IBIEG. The interface is fairly long whilst the diffusion distances are small, i.e., the defect-flux onto the a–c interface is likely to be substantial

Escape of defects from the amorphous regions causes rearrangement of the atomic structure Annealing at 200 °C produces an amorphous structure incorporating isotropic paramagnetic centres with $g = 2.0055$ A similar effect was observed for the same doses of He^+ ions implantation of silicon [19]. The number of paramagnetic centres in the material increases up to 300 °C and then decreases This decrease in paramagnetic centre concentration at $T > 300$ °C may occur as a consequence of two processes: (a) a decrease of the total share of amorphous regions in the layer as a result of the a–c transition; (b) the annealing of paramagnetic centres (i e., further rearrangement of the structure of amorphous regions) typical of this temperature range [20,21]. Relaxation of amorphous material structure with increasing temperature is an established experimental fact [12,15]. For instance, in ref. [12] anomalies were observed in defect-structure relaxation when annealing silicon crystal regions from 180 to 400 °C in which the degree of He^+-irradiation-induced damage was close to the amorphous state, but did not reach it. This temperature range coincides with that revealed in the present work when the samples exhibit the ESR signal. In ref. [12] it was suggested that the effect observed might be caused by the recrystallization of small amorphous zones in the heavily damaged crystal material.

This conclusion is confirmed by the following estimates. In refs. [12,15] it was shown that mobile defects are characteristic of the amorphous silicon structure. They are completely annealed at 500 °C for 45 min, the material remaining in the amorphous "well-relaxed" state. Repeated He^+-irradiation of relaxed amorphous silicon at a dose of > 0.03 dpa brings it back to the initial state characteristic of the as-implanted sample Let the He^+ ion irradiation of amorphous silicon induce mainly simple point defects. Then, as an upper estimate, we may assume that the irradiation dose indicated generates $3\times10^{-2}\times5\times10^{22} = 1.5\times10^{21}$ defects/cm^3 Assuming also that occurrence of a single intrinsic point defect on the a–c interface stimulates rearrangement of ~ 30 atoms of the amorphous phase into a crystal, it is clear that the number of defects stored in the amorphous regions is sufficient for recrystallization of the greater part of the amorphous silicon into a crystal Thus, when the a–c system is not under ion-irradiation conditions, point-defect enhanced a–c transition can be realized at low temperatures

5. Conclusion

He^+ ion irradiation of silicon at room temperature at a dose of 5×10^{16} cm^{-2} leads to formation of a buried amorphous layer at the depth of the maximum damage distribution

The structure of the amorphous layer is not homogeneous It incorporates amorphous silicon regions and heavily damaged crystalline silicon The structure of the amorphous silicon regions is characterized by the absence of the isotropic paramagnetic centres. Annealing of samples with a buried amorphous layer results in epitaxial recrystallization of the amorphous regions on the a–c interfaces at abnormally low temperatures 150–400 °C. In this case the a–c transition is enhanced by the flow of defects from the bulk of the amorphous regions onto the a–c interface Escape of defects from the amorphous regions is accompanied by the rearrangement of the amorphous structure and the occurrence of isotropic paramagnetic centres As annealing temperature increases above 300 °C, the amount of the amorphous phase decreases at the expense of the a–c transition which is followed by a decrease in the num-

ber of paramagnetic centres in the sample. At 400–450 °C the a–c transition is completed.

References

[1] J Mayer, L. Erikson and J. Devis, in Ion Implantation in Semiconductors, (Academic Press, New York, 1970).
[2] J Narayan, O.W. Holland and B.R. Appleton. J. Vac. Sci Technol B1 (1983) 871.
[3] T.E. Seidel, R.V. Knoell, F.A. Stevie, G. Poli and B Schwartz, in: VLSI Science and Technology, vol 84-7, eds K.E Bean and G A. Rozgonvii (The Electrochem Soc., 1984) p. 201
[4] A F Vyatkin, Surface, to be published, in Russian.
[5] G L Olson and J.A. Roth, Mater. Sci. Rep. 3 (1988) 1.
[6] D A. Thompson, A Golanski, K.H Hangen, D.V Stevanovic, G Garter and C.E Christodoulides. Rad Effects 52 (1980) 69
[7] R.G Elliman, S T Johnson, A P Pogany and J.S Williams, Nucl. Instr and Meth B7/8 (1985) 310
[8] B L Crowder, R S. Title, M N. Brodsky and G.D Petit, Appl. Phys. Lett 16 (1970) 205
[9] N.N Gerasimenko, A V Dvurechenskii and L.S. Smirnov, Fiz Tekh Poluprovodn 5, 1700 (1971)
[10] J F Ziegler, J P. Biersack and U. Littmark, In: The Stopping and Range of Ions in Solids, (Pergamon, New York, 1985)
[11] E. Kotai, F. Paszti, A. Mannaba, G Mezey, J. Gynlai, A. Barna, P Barna and G. Radnoczi, Nucl Instr and Meth. B19/20 (1987) 312
[12] S. Roorda. J.M Pate, D.C. Jacobson, D.J. Eaglesham, B.S. Dennis, S Dierker, W C. Since and F Spaepen, Phys Rev. Lett , to be published.
[13] J.P. Biersack and L.J. Haggmark, Nucl. Instr. and Meth. 174 (1980) 257
[14] P M Fahey, P B. Griffin and J D Plammer, Rev. Mod Phys. 61 (1989) 289
[15] S Roorda, W.C Sinke, J M Poate, D C Jacobson, S. Dierker, B S. Dennis, D.J Eaglesham and F. Spaepen, Mater. Res Soc Symp Proc 157, to be published
[16] O W. Holland, D. Fathy and J. Narayan, Nucl. Instr. and Meth. B10/11 (1985) 565.
[17] A.F Vyatkin, L.E Farber, A.S. Avilov and S N Orekhov, Thin Solid Films 183 (1989) 357.
[18] J. Linnros, Ph.D Thesis (Chalmers University of Technology, Göteborg, 1985)
[19] Yu. V. Gorelkinskii, V N. Nevinnyi and A A Kim, Phys Stat. Sol 130 (1985) K51
[20] A.V Buravlyov, A G Italyantsev, Z Ya Krasnobayev, V N Mordkovich and A F Vyatkin, Nucl Instr and Meth B39 (1989) 386.
[21] P A Thomas, M H. Brodsky, D. Kaplan and D. Lepine, Phys. Rev B18 (1978) 3913

Nuclear Instruments and Methods in Physics Research B55 (1991) 647–649
North-Holland

Electrical activation process of erbium implanted in silicon and SIMOX

Y.S. Tang [1] and B.J. Sealy

Department of Electronic and Electrical Engineering, University of Surrey, Guildford, Surrey GU2 5XH, UK

The electrical activation mechanism of erbium implanted in silicon and SIMOX (separation by implanted oxygen) following different annealing processes is studied by using the Van der Pauw technique in combination with photoluminescence and Rutherford backscattering angular scanning measurements. The results show that the activation of the erbium is related to the lattice configuration. In the case of conventional furnace annealing, the activation corresponds to an occupation of erbium on substitutional lattice sites, but in the case of rapid thermal annealing, it corresponds to the occupancy of both interstitial with a tetrahedral (Td) symmetry and substitutional lattice sites. The transfer of interstitial erbium to substitutional sites corresponds to an electrical deactivation process due to partial compensation of the n-type and p-type carriers produced by the two different electrically active erbium sites.

1. Introduction

The rare earth element erbium implanted in semiconductors such as silicon and III–V compounds has been extensively studied by several groups [1–11] due to its promising applications in optical fibre telecommunications engineering. Most of the studies have concentrated on the luminescence and structural configurations of the erbium. It was found that sharp luminescence peaks resulting from the internal transitions between the weakly crystal field split spin–orbit levels $^4I_{13/2} \rightarrow {}^4I_{15/2}$ of Er^{3+} ions were observed, which are independent of the substrates and environmental temperature, and are only decided by the lattice positions of Er^{3+} ions in the host materials. For erbium implanted in silicon, we reported the isotopic effect of Si on the luminescence properties of the erbium implants [6] and found that the preferential lattice sites of erbium in silicon are those having tetrahedral symmetry [7], but it is very difficult to keep the erbium from escaping to the sample surface due to its limited solid solubility, which restricts the luminescence efficiency of this kind of material. To solve this problem, we studied erbium implanted in silicon-on-insulator (SOI) made by a separation-by-implanted-oxygen (SIMOX) technique [9,10]. It is expected that the radiation damage in the silicon overlayer of the SIMOX material will trap the erbium atoms and reduce the amount of out-diffusion compared with results from conventional silicon wafers. The studies on the luminescence and regrowth of the implantation-induced amorphous silicon overlayer show that this is indeed an effective way to avoid erbium out-diffusion and to enhance the luminescence efficiency of the material. In this paper, we report the electrical activation process of erbium implanted in silicon and SIMOX following different annealing processes by using the Van der Pauw technique in combination with photoluminescence and Rutherford backscattering angular scanning measurements. The activation mechanism is also discussed in detail in the text.

2. Experimental details

The samples were prepared by 250 keV $^{166}Er^+$ implanted in both bulk silicon and the silicon overlayer of a SIMOX structure with a projected range of about 90 nm. The doses were between 10^{13} and 10^{15} cm^{-2}. To activate the implants, the samples were annealed in a temperature range of 600 to 1100 °C in a dry nitrogen atmosphere. During the annealing process, both conventional furnace annealing (FA) and rapid thermal annealing (RTA) using a graphite strip heater were employed.

To measure the electrical activation process of the erbium implants, the Van der Pauw technique was used. Both photoluminescence and Rutherford backscattering angular scanning were utilized to determine the lattice configuration related to the activation mechanism of the erbium implanted in the above samples. A detailed description of the measurements has been published elsewhere [7–9].

[1] Present address: Department of Electronics and Electrical Engineering, University of Glasgow, Glasgow G12 8QQ, UK.

0168-583X/91/$03.50 © 1991 – Elsevier Science Publishers B.V. (North-Holland)

3. Results and discussion

As reported before [7], the number and energies of the photoluminescence peaks of erbium implanted silicon and related materials reflect the structural symmetric information of Er^{3+} ions in the silicon lattice. When the erbium ions occupy tetrahedral symmetric lattice sites (substitutional or interstitial), five distinct luminescence peaks can be observed, while erbium ions which occupy lattice sites having lower symmetry give rise to eight luminescence peaks. In the first case, the most intense peak locates at about 1.538 μm, while in the latter case, at 1.541 μm. These results were confirmed by further Rutherford backscattering angular scanning measurements [8]. For those samples with five distinct luminescence peaks, it was found that most of the erbium atoms occupy substitutional lattice sites when annealed in a conventional furnace at a relatively high temperature. However, the erbium atoms locate at interstitial sites having tetrahedral symmetry when rapid thermal annealing was applied. At lower annealing temperatures, the erbium implants are randomly located and they are independent of the annealing method used.

The above discussion has concentrated on the silicon samples for which a combination of both photoluminescence and Rutherford backscattering angular scanning techniques was used to determine the lattice locations of the erbium ions in the host material [8]. In the following, we choose erbium-implanted SIMOX to study the electrical activation process and its structural configuration related activation mechanism.

As shown in fig. 1, for the samples annealed in a conventional furnace for 30 min, the sheet resistance gradually decreased with increasing annealing temperature and then remained at a constant value in the temperature range of 600–1000 °C, which corresponds to an electrical activation of the implanted erbium. In

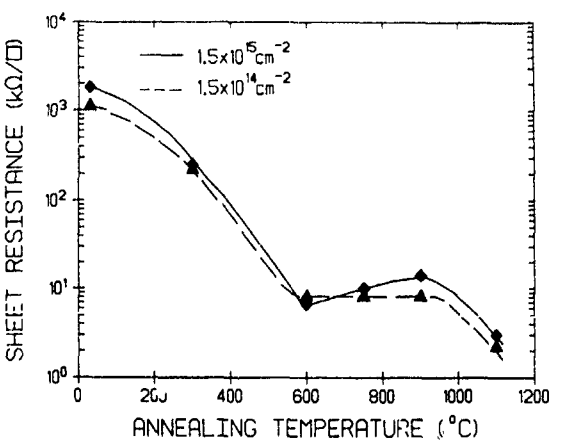

Fig 1 The furnace annealing temperature dependence of sheet resistance for erbium-implanted SIMOX structures

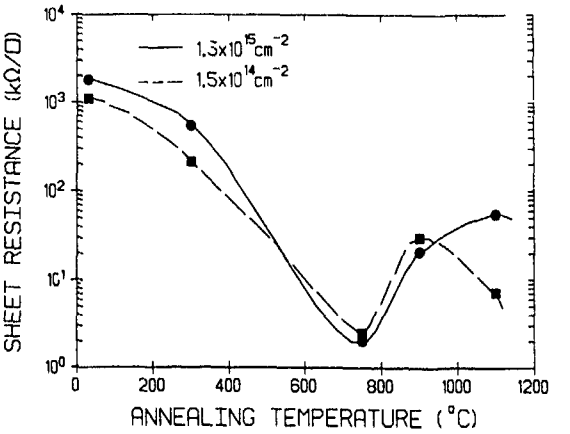

Fig. 2. The relationship between sheet resistance and the annealing temperature for the rapid thermal annealed erbium-implanted SIMOX samples

the photoluminescence measurements on the same samples, we find that the most intense peak locates at 1.538 μm when the annealing temperature is above 600 °C while it is shifted to 1.541 μm when the annealing temperature is below 600 °C, which means that the erbium implants occupy random positions at first and then move to thermally more stabilized tetrahedral symmetric sites as the annealing temperature rises. Similar to that reported in ref. [8], Rutherford backscattering angular scanning measurements suggest that these tetrahedral symmetric lattice sites are substitutional rather than interstitial.

Fig. 2 shows the relationship between the sheet resistance and the rapid thermal annealing temperature for 10 s anneals. With increasing annealing temperature, the sheet resistance decreases to a minimum at about 750 °C, and then goes through to a maximum before decreasing again. Obviously, the increase in sheet resistance corresponds to an electrical deactivation process What is interesting is that during the photoluminescence measurements, this deactivation region corresponds to the appearance of both the 1.538 and the 1.541 μm peak, which indicates that the erbium implants occupy both tetrahedral and lower symmetric lattice sites (or random locations) in the silicon overlayer in SIMOX structures, while on both sides of the region, only one luminescence peak (1.538 μm) was observed, which, according to what we discussed above, represents an occupation of the erbium on substitutional or interstitial lattice sites having tetrahedral symmetry. According to further Rutherford backscattering angular scanning measurements on those samples, it was found that on the lower annealing temperature side of this deactivation region, the activation is due to the occupation of most of the erbium implants on the interstitial lattice sites, but on the other side of the

region, the reactivation process is associated with the erbium occupying more stable substitutional lattice sites.

Based on the above discussion, we find a correlation between the electrical activation and lattice configuration of the implanted erbium through using a combination of photoluminescence and Rutherford backscattering angular scanning measurements, which suggests one kind of special electrical activation mechanism for the erbium-implanted silicon and related materials. We explain the experimentally observed results as follows:

In conventional furnace annealing, the electrical activation of the implanted erbium means, as usual, the occupation of the implanted atoms on substitutional lattice sites; but in the case of rapid thermal annealing, the situation is different from what happened in the furnace annealing case. With increasing rapid thermal annealing temperature, most of the randomly located erbium atoms will firstly be activated to interstitial sites with tetrahedral symmetry, which corresponds to the first sheet resistance valley in fig. 2, and act as donors in the material, but the energy transfer is still not enough to place most of the implants on to the thermally more stable substitutional lattice sites. With a further increase in the annealing temperature, the erbium on the relatively unstable interstitial lattice sites will be shifted to the most stable sites, i.e. substitutional lattice sites, where the implants act as acceptors [2] and are electrically activated again. The transfer of the interstitial erbium with tetrahedral symmetry to substitutional lattice sites corresponds to an unusual deactivation process in the sheet resistance measurements and is just a compensation effect, as shown in fig. 2

A similar process was also observed in erbium-implanted silicon samples following similar annealing treatments.

4. Conclusion

In conclusion, we report a study on the electrical activation process of erbium implanted in silicon and SIMOX structures. It was found that the electrical activation mechanism for erbium-implanted silicon and related materials is related to the structural configuration. The electrial activation of the erbium corresponds to an occupation of the implants on tetrahedral symmetric lattice sites (both substitutional and interstitial); and the transfer of the erbium from tetrahedral interstitial sites to substitutional ones is just a donor-to-acceptor transition process and corresponds to a deactivation process in the electrical activation measurements.

Acknowledgements

The authors thank P.L F. Hemment for supplying the SIMOX substrate and are grateful to W. Gillin, J.P. Zhang and the staff of the D.R. Chick Laboratory of the University of Surrey for their help with the experiments.

References

[1] H Ennen, J Schneider, G Pomrenke and A Axmann, Appl. Phys Lett 43 (1983) 943
[2] H Ennen, G Pomrenke, A Axmann, K Eisele, W. Haydl and J. Schneider, Appl Phys Lett. 46 (1985) 381
[3] G S Pomrenke, H. Ennen and W Haydl, J Appl Phys 59 (1986) 601
[4] H. Ennen, J Wagner, H D Muller and R S Smith, J Appl Phys 61 (1987) 4877
[5] K Uwai, H. Nakagome and K. Takahei, Appl Phys Lett 50 (1987) 977.
[6] Y S. Tang, Phys Stat Sol (b)156 (1989) K153
[7] Y S Tang, K C. Heasman, W P Gillin and B J Sealy, Appl Phys Lett 55 (1989) 432
[8] Y S. Tang, Z Jingping, K C Heasman and B J Sealy, Solid State Commun 72 (1989) 991
[9] Z. Jingping, Y S. Tang, P L F Hemment and B.J Sealy, Nucl. Instr. and Meth B47 (1990) 155
[10] Y S Tang and Z Jingping, J Cryst Growth 100 (1990) 681
[11] Y S Tang and B J. Sealy, J Appl Phys. 61 (1990)

Nuclear Instruments and Methods in Physics Research B55 (1991) 650–654
North-Holland

Isotope effects for ion-implantation profiles in silicon

B.G. Svensson and B. Mohadjeri

The Royal Institute of Technology, Solid State Electronics, P O Box 1298, S-164 28 Kista-Stockholm, Sweden

Isotope shifts of ion-implantation profiles for ^{6}Li and ^{7}Li, ^{10}B and ^{11}B, ^{16}O and ^{18}O, and ^{116}Sn and ^{124}Sn in silicon have been investigated at energies between 10 and 400 keV. Monte Carlo simulations as well as numerical calculations applying Boltzmann's transport equation yield a reverse isotope shift at high enough energies, i.e., the implantation energy of the heavier isotope should be *lower* than that of the lighter one to obtain identical depth profiles. This effect is attributed to a larger electronic stopping cross section S_e for the lighter isotope at a given energy in the range where S_e is roughly proportional to the ion velocity v and dominates the slowing-down process. Moreover, also at low enough energies where the stopping is predominantly nuclear and screening effects are important, a small reverse isotope shift is predicted since the nuclear stopping cross section S_n is approximately proportional to v^a with $a > 0$ for energies below the maximum of S_n. Experimental support for the theoretical predictions is provided by range data for Li and B obtained by secondary-ion mass spectrometry (SIMS). SIMS has proven to be a suitable analysis technique with respect to isotope effects because of its good depth and mass resolution, and a reverse isotope shift is clearly resolved for both Li and B at energies above 100 keV.

1. Introduction

Implantation of isotope ions of the same element is frequently used in various types of experiments, e.g., diffusion mechanism studies, identification of impurity-related point defects, and analysis of impurity distributions and buried layers by nuclear-resonance techniques. In order to produce identical as-implanted isotope depth profiles the implantation energy is normally adjusted in such a way that the value of keV per atomic mass unit (amu) of the projectiles is kept constant. However, in the energy range where electronic stopping dominates the slowing-down process and the corresponding stopping cross section S_e is roughly proportional to the ion velocity v the implantation energy of the heavy isotope should be reduced in comparison with that of the light isotope (not increased as suggested by a constant value of keV/amu) in order to obtain identical depth distributions. At a given bombardment energy E, the velocity v of the heavy isotope is lower than that of the light one, and consequently, the heavy projectile penetrates further and exhibits a deeper profile.

Some controversy has existed in the literature about the isotope shift of the experimental depth profiles for $^{10}B^{+}$ and $^{11}B^{+}$ ions: Ohmura and Koike [1] applied capacitance–voltage (C–V) measurements for analysis of the profiles and despite a considerable scatter in their data, they concluded that the ^{10}B distributions were shallower than those of ^{11}B. Vaidyanathan et al. [2] argued, however, that the accuracy of the C–V data in ref. [1] was not sufficient to properly distinguish between the differences in projected range R_p of the profiles. They claimed that the observed separation was well within the experimental error introduced by the uncertainties in the metallization area and by the zero-Debye-length approximation. Ryssel et al. [3] compared the ranges measured by the ^{10}B(n, α)^{7}Li reaction with that obtained from Hall-effect and sheet-resistivity measurements for ^{10}B and ^{11}B; the range and straggling data were identical for the two isotopes. Thus the results from these electrical studies are contradictory, suggesting that the depth resolution is too poor to make any definite conclusions, and methods with better resolution are required [2]. Secondary-ion mass spectrometry (SIMS) has recently been demonstrated to be highly applicable for this purpose, and a reverse isotope effect was clearly resolved for ^{10}B and ^{11}B at energies above 100 keV [4,5]. Projected range values extracted from the measured profiles were compared with calculations, and the experimental isotope shift showed reasonable agreement with the theoretical predictions [5].

In this work, calculations of the isotope shift have been carried out for a variety of dopant and impurity elements encountered in silicon technology, e.g., ^{6}Li and ^{7}Li, ^{10}B and ^{11}B, ^{16}O and ^{18}O and ^{116}Sn and ^{124}Sn. Two types of calculations have been performed; Monte Carlo simulations using the transport of ions in matter (TRIM) code originally developed by Biersack and Haggmark [6] and a numerical solution derived from Boltzmann's transport equation. Experimental support for the validity of the theoretical results is provided by SIMS data for lithium and boron implantation profiles. The numerical values for the shift are presented in the form

0168-583X/91/$03.50 © 1991 – Elsevier Science Publishers B.V. (North-Holland)

of graphs and can be used by other authors in order to obtain identical as-implanted isotope depth profiles.

2. Calculations

Two sets of range calculations were performed:

(i) Monte Carlo simulations were carried out utilizing the TRIM code originally compiled by Biersack and Haggmark [6] (version-89). More than 15000 runs (ions) were undertaken for every profile to obtain good statistics, and a displacement energy threshold of 13 eV was assumed.

(ii) On the basis of transport theory Lindhard et al. [7] derived an equation for the spatial averages (moments) of the ion depth distribution. This equation generally has to be solved numerically, and we applied a modified version of the computer code COREL, originally written by Brice [8]. The elastic interaction was described by the differential scattering cross section according to Wilson, Haggmark and Biersack [9] (WHB-77). A velocity-proportional electronic stopping cross section S_e was assumed; the proportionality constant k was considered as a fitting parameter with respect to experimental range data for the studied ions

3. Experiment

Czochralski silicon samples grown in the ⟨111⟩ direction and doped with phosphorus (3 Ω cm) were implanted with lithium or boron ions to a dose of 1×10^{15} cm^{-2} or 2×10^{14} cm^{-2}, respectively. Implantation energies in the range of 50 to 250 keV were used, and the samples were sequentially bombarded with $^{7}Li^{+}$ and $^{6}Li^{+}$ ions or $^{11}B^{+}$ and $^{10}B^{+}$ ions. The implantations were carried out at nominal room temperature; a low ion-current density was used (≤ 1 $\mu A/cm^2$) to avoid beam-heating effects, and the samples were tilted 7° with respect to perpendicular incidence to diminish the influence of channeling

SIMS analysis of the implanted distributions was performed by a Cameca IMS 4f microanalyzer. A primary beam of $^{32}O_2^{+}$ ions with a net impact energy of 8 keV and an angle of incidence of 39° (with respect to perpendicular incidence) was rastered over an area with a size of 300×300 μm^2. Positive secondary ions were collected from the central region of the sputtered crater, and the diameter of the analysed area was 60 μm. The erosion rate during profiling was ~ 10 Å/s; the crater depths were measured by an Alpha step 200 stylus profilometer.

4. Results

Fig. 1 shows the measured depth profiles of ^{6}Li and ^{7}Li for an implantation energy of 250 keV: a shift between the two distributions is clearly resolved, and the ^{6}Li profile has its peak at ~ 0.94 μm versus ~ 1.00 μm for ^{7}Li, i.e., the lighter isotope occurs at *shallower* depths. In this context it must be pointed out that Li diffuses rapidly in crystalline silicon [10], but no effects on the recorded distributions were observed. The implanted region is damaged to a certain extent, and the interaction of Li with defects in the silicon lattice reduces the diffusion rate by several orders of magnitude [10].

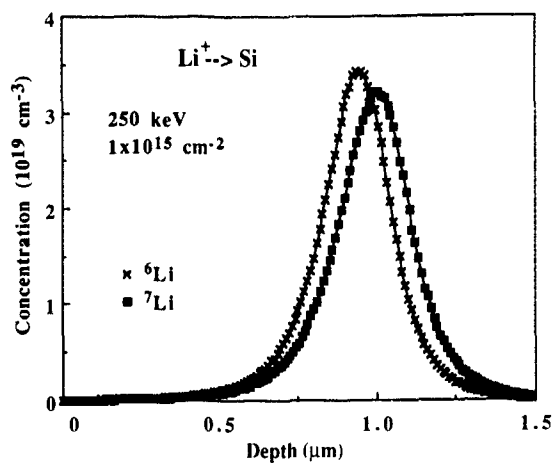

Fig 1 SIMS-measured depth distributions of ^{6}Li and ^{7}Li in silicon The implantations were performed using an energy of 250 keV and a dose of 1×10^{15} cm^{-2}.

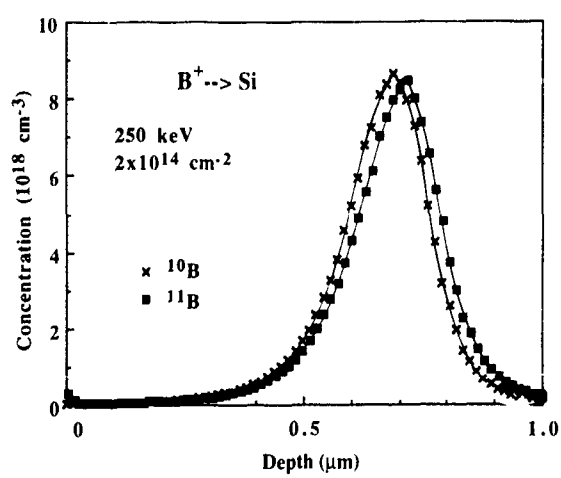

Fig 2 SIMS-measured depth distributions of ^{10}B and ^{11}B in silicon The implantations were performed using an energy of 250 keV and a dose of 2×10^{14} cm^{-2}

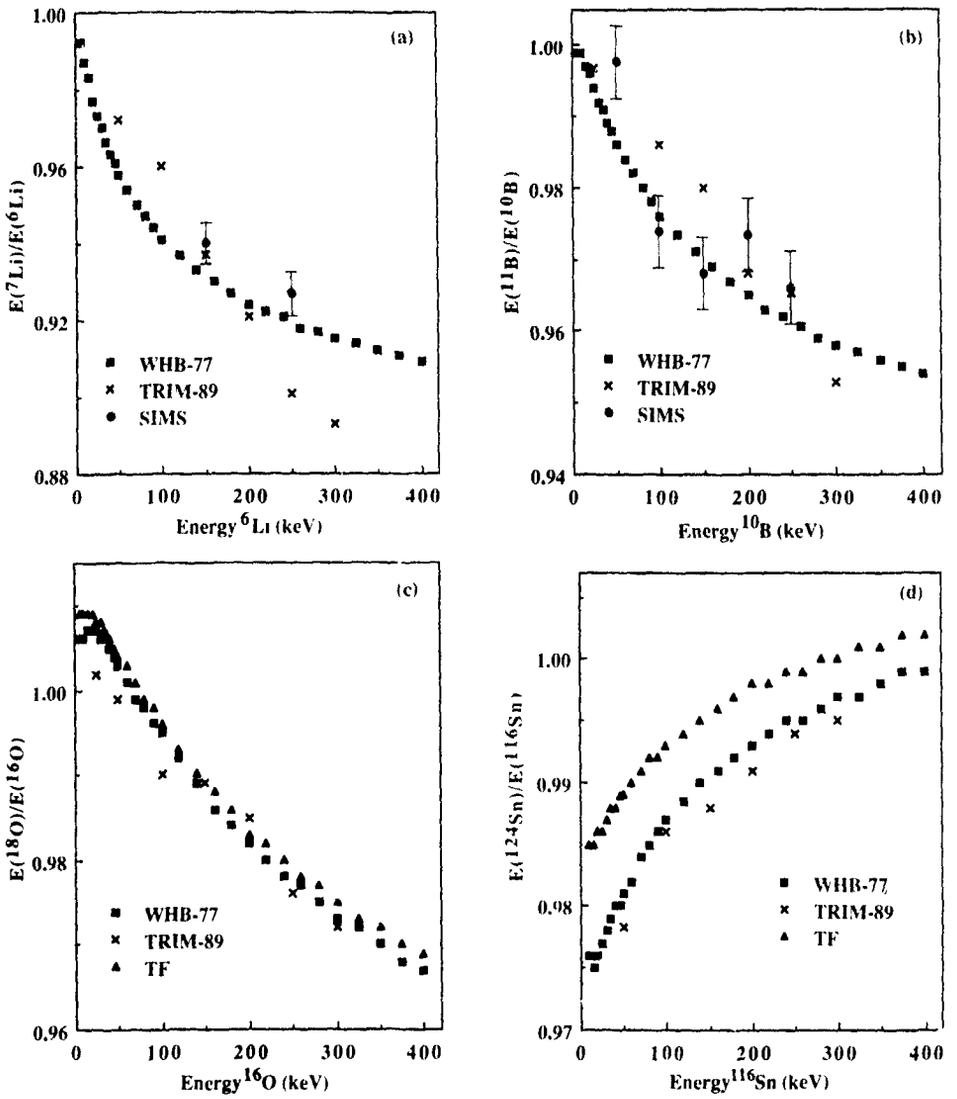

Fig 3 (a) The ratio $E(^7Li)/E(^6Li)$ for profiles with identical projected range as a function of the implantation energy for ^{6}Li Error bars on the SIMS data indicate a relative accuracy of 1% (b) The ratio $E(^{11}B)/E(^{10}B)$ for profiles with identical projected range as a function of the implantation energy for ^{10}B Error bars on the SIMS data indicate a relative accuracy of 1% (c) The ratio $E(^{18}O)/E(^{16}O)$ for profiles with identical projected range as a function of the implantation energy for ^{16}O (d) The ratio $E(^{124}Sn)/E(^{116}Sn)$ for profiles with identical projected range as a function of the implantation energy for ^{116}Sn

In fig. 2 similar data are presented for 250 keV boron ions [5]; the ^{10}B profile has its maximum at ~ 0.69 μm versus ~ 0.72 μm for ^{11}B.

In fig. 3a the ratio $E(^7Li)/E(^6Li)$ is plotted as a function of $E(^6Li)$ for isotope profiles with identical projected range R_p. The experimental values obtained by SIMS are compared with results from the two sets of computations which show a decrease with increasing energy. At $E(^6Li) = 200$ keV both calculations predict a reduction of $E(^7Li)$ by ~ 8% (184 keV) in order to obtain profiles with equal R_p. However, for $E(^6Li) <$ 200 keV, TRIM-89 yields larger values than the transport calculations while the opposite holds above 200 keV In the transport calculations k was put equal to $1.4k_L$ which was found to give a reasonable agreement with the absolute R_p-values extracted from the SIMS distributions; k_L denotes the estimate given by Lindhard and Scharff [11].

In fig. 3b an analogous plot is given for boron, using $k = 1.3k_L$ in the transport calculations. $E(^{11}B)/E(^{10}B)$ is higher than the corresponding values for Li but shows a similar energy dependence with a correction of ~ 4%

at 250 keV. Also for boron, TRIM-89 predicts a relatively weak decrease at low energies (< 150 keV) but a more pronounced effect at higher energies.

For oxygen the two sets of calculations give essentially identical results, fig 3c, and also the difference between the elastic interaction potentials according to Lindhard et al. [12] (Thomas Fermi (TF) model) and WHB [9] is found to play only a minor role. The ratio $E(^{124}\mathrm{Sn})/E(^{116}\mathrm{Sn})$ depends, however, more strongly on the nuclear stopping cross section S_n and is shifted to somewhat higher values by the larger interaction according to the TF model, fig 3d. Moreover, in contrast to the previous results in figs. 3a-c, $E(^{124}\mathrm{Sn})/E(^{116}\mathrm{Sn})$ increases with energy and is close to 1 at 400 keV. For both O and Sn, k was put equal to k_L in the transport calculations.

5. Discussion and conclusions

A reverse isotope shift of the experimental depth profiles for Li and B is clearly resolved at 250 keV, i.e., the lighter isotope exhibits a shallower profile. In order to eliminate any artifacts because of erosion rate variations during profiling, limited accuracy of crater-depth determination and sequential registration with respect to sputtering-time results from three different measurements were compared. In the first run both isotopes (^{6}Li and ^{7}Li or ^{10}B and ^{11}B) were recorded while in the second and third runs only one single isotope was monitored. The absolute range values extracted from the corresponding profiles are identical within less than 1%, and SIMS is concluded to be a suitable technique with a high enough depth resolution to resolve relative isotope shifts in R_p larger than ~1%. A detailed discussion of the requirements for accurate SIMS analysis and the possible role of mass fractionation, sputtering-induced profile broadening and shift, etc., is given in refs. [4,5].

A channeling tail was observed in some samples, the tail occurred at about two orders of magnitude below the peak concentration and did not significantly influence the R_p-values utilized in figs. 3a–b. However, for the higher-order moments an increasing influence was found, and for a proper determination of the skewness, kurtosis, etc., amorphous samples are required.

The values of $E(^7\mathrm{Li})/E(^6\mathrm{Li})$ and $E(^{11}\mathrm{B})/E(^{10}\mathrm{B})$ deduced from the SIMS data to obtain profiles with identical R_p show a reasonable agreement with those estimated by the theoretical models, figs 3a, b. Both sets of calculations predict a decreasing ratio with increasing implantation energy for Li, B and O. For these ions electronic stopping dominates, and the calculated ratio decreases with energy because of the increasing relative importance of S_e, which is roughly proportional to the ion velocity v. At a given bombardment energy v(heavy isotope) < v(light isotope) and consequently the energy of the heavy isotope ion should be reduced. If S_n is neglected and $S_e = kv^p$ an asymptotic value of $(M_{\mathrm{light}}/M_{\mathrm{heavy}})^{p/(2-p)}$ is predicted for E(heavy)/E(light), i.e., 6/7, 10/11 and 16/18 for Li, B and O, respectively, if $p = 1$ (M denotes the ion mass). The TRIM results for Li and B suggest a more linear decrease of the energy ratios than that extracted from the transport calculations, this is due to different estimates of S_e as a function of E. TRIM-89 assumes a non-velocity-proportional dependence, and in particular, the ratio S_e(light)/S_e(heavy) varies with E; it is smaller than $(M_{\mathrm{heavy}}/M_{\mathrm{light}})^{1/2}$ at low energies (≤ 150 keV) and larger at high energies.

For the Sn ions the stopping is predominantly nuclear in the studied energy range, and S_n has its maximum at $E \sim 160$ keV, the relative contribution of S_e to the total stopping cross section is only ~20% at 400 keV. The ratio $E(^{124}\mathrm{Sn})/E(^{116}\mathrm{Sn})$ increases with energy and becomes gradually larger than 1, as expected when an unscreened Coulomb interaction dominates. However, screening is important at low energies, and as a result, a ratio smaller than 1 occurs. If $M_{\mathrm{ion}} \gg M_{\mathrm{target\,atom}}$ it can be shown that S_n is proportional to v^{2-4m} where m is the exponent in the power approximation of the screening function [12,13]. For energies below the maximum of S_n, $m < \frac{1}{2}$, and thus a reverse isotope shift holds in this regime. At high enough energies where Rutherford scattering takes place, $m = 1$ and the sign of the resulting isotope shift is determined by the relative influence of S_n versus S_e.

The numerical values given in figs 3a–d can, hopefully, be used by other authors if isotope profiles with identical R_p are desired. Finally, it should be pointed out that both sets of calculations used here are based on theoretical models containing a number of inherent approximations; e.g., binary collisions are assumed and many-body effects are neglected, S_e is treated as a friction-like force and electron straggling is omitted, a screened elastic Coulomb interaction is applied and correlation with electronic scattering is neglected, which must be considered in detail to obtain isotope shift data accurate within a few percent for higher-order moments (skewness, kurtosis, etc.).

Acknowledgements

Financial support was received from the Swedish Natural Science Research Council and the Swedish Board for Technical Development.

References

[1] Y. Ohmura and K. Koike, Appl. Phys. Lett. 26 (1975) 221.
[2] K.V. Vaidyanathan, P.K. Chatterjee and B.G. Streetman, Appl. Phys. Lett. 27 (1975) 648.

[3] H Ryssel, H. Kranz, K. Müller .A Henkelmann and J.P. Biersack, Appl. Phys. Lett. 30 (1977) 399.
[4] P C. Zalm, G.M. Fontijn, K.T.F Janssen and C.J. Vriezema, Nucl. Instr. and Meth. B42 (1989) 397
[5] B G. Svensson, J.T Linnros and G Holmén, J Appl Phys. 68 (1990) 73.
[6] J P Biersack and L.G. Haggmark, Nucl. Instr. and Meth 174 (1980) 257.
[7] J Lindhard, V Nielsen, M. Scharff and P.V. Thomsen, K. Dan Vidensk Selsk. Mat Fys Medd. 33(14) (1963).
[8] D.K. Brice, Sandia Lab. Res. Rep SAND75 (July 1977) No. 0622.
[9] W.D. Wilson, L.G Haggmark and J P. Biersack, Phys Rev. B15 (1977) 2458.
[10] L T. Canham, in: Properties of Silicon, EMIS Data Reviews 4 (Inspec, London, 1988) p 455.
[11] J. Lindhard and M. Scharff, Phys Rev. 124 (1961) 128.
[12] J Lindhard, V Nielsen and M. Scharff, K. Dan. Vidensk Selsk Mat Fys. Medd. 36(10) (1968).
[13] K B. Winterbon, P Sigmund and J B. Sanders, K. Dan Vidensk Selsk Mat. Fys Medd. 37(14) (1970).

Nuclear Instruments and Methods in Physics Research B55 (1991) 655–660
North-Holland

The enhanced diffusion of boron in silicon after high-dose implantation and during rapid thermal annealing

F. Marou [b], A. Claverie [a], Ph. Salles [a] and A. Martinez [b]

[a] *CEMES-LOE/CNRS, 29, rue Jeanne Marvig, 31055 Toulouse Cedex, France*
[b] *LAAS/CNRS, 7, avenue du Colonel Roche, 31077 Toulouse Cedex, France*

In this paper we have studied the diffusion of boron in silicon after high-dose implantation (50 keV, 5×10^{15} ions/cm^2) and during rapid thermal annealing at 1100°C, under nitrogen gas. We confirm that some enhanced as well as "anomalous" diffusion takes place during the early stage of annealing and that this phenomenon must be related to the defects generated by ion implantation Experiments were performed on companion samples by SIMS, XTEM and resistivity methods "Damage" calculations were obtained by running the computer code LUPIN to generate the defect profile (displacements) due to the bombardment For samples which were subjected to increasing annealing periods (1 s, 3 s, 5 s, etc.) the dopant profile can be simulated only when assuming a phenomenological *depth-dependent* diffusion coefficient which is always many times higher than according to the "classical" theory The discussion is conducted by comparing the depth variation of the diffusion coefficient with the position and density of the extended defects seen by XTEM We show that the formation of a dense band of dislocations and loops around the boron projected range (within 1 s at 1100°C) corresponds to the ejection and clustering of Si interstitials due to the activation of boron For larger annealing times, boron diffusion is dependent on the motion of these interstitials emitted from the extended defects until they dissolve into the bulk These experiments clearly evidence the role played by Si interstitials and lead us to reject the idea that the "collisional" damage is responsible for the enhanced diffusion of boron in silicon

1. Introduction

The elaboration of MOS or bipolar circuits for VLSI technology requires the production of highly doped shallow junctions in the near-surface layer of silicon. Moreover, this layer should be free of defects. Ion implantation is the usual process to introduce to low depths and with a good precision a known amount of dopant impurities. Unfortunately, annealing of the material is necessary to activate the dopant on substitutional sites and to restore the crystalline quality of the layer. This annealing stage is detrimental to the production of shallow and sharp junctions when conducted with the conventional furnace processes because of the long times needed and hence to the subsequent redistribution of the dopant which inevitably occurs.

Appearing recently as an alternative process, rapid thermal annealing (RTA) involves a temperature and time of typically about 1100°C and 5 s, respectively. Thus, RTA seems to offer a compromise between a complete removal of implantation damage and a negligible dopant redistribution.

First experiments in that field have shown that for boron-implanted silicon, the diffusion is drastically enhanced during the early stage of annealing with respect to what is predicted by the theory of "classical" diffusion. For an explanation of this "anomalous" diffusion of implanted boron two mechanisms were proposed. The first is that the enhanced diffusion is caused by the fast diffusing interstitial boron in the tail region [1]. The other suggests that the anomalous diffusion is due to point defects introduced by ion implantation. Cho et al [2], Michel et al. [3], Servidori et al. [4] and more recently Bao et al. [5] have provided new evidence for this mechanism. All these results are in accordance with the hypothesis initially proposed by Fair et al. [6] after comparison with the XTEM results obtained by Sadana et al [7].

Anyway, the point which remains unclear is what are "ion-implantation defects" and what is the nature and origin of the point defects responsible for the enhancement of diffusivity Thus, we believe that a complete study including the chemical, structural and electrical aspects should in principle be able to lead to a better understanding of this phenomenon.

In this paper we have studied the diffusion of boron after high-dose implantation (5×10^{15} ions/cm^2, 50 keV) and during rapid thermal annealing (RTA) at 1100°C by SIMS, XTEM and resistivity methods. We confirm that some enhanced as well as "anomalous" diffusion takes place during annealing The discussion is conducted by comparing the *depth variation of the diffusion coefficient* with the position and density of the extended defects revealed by XTEM. It is shown that Si interstitials play a key role in the enhanced diffusion. These experiments when compared to the damage calcu-

0168-583X/91/$03 50 © 1991 – Elsevier Science Publishers B.V. (North-Holland)

lations lead us to reject the idea that the "collisional" damage is responsible for the enhanced diffusion of boron.

2. Results

2.1 "Damage" defects

The slowing-down process of a boron ion is typical of a "light"-ion (low-mass, high-energy) implantation in silicon. In fig. 1 we have represented the results of damage calculations as given by the LUPIN code [8–10]. $E_{p,n}$ and E_e are the energy losses of the incident particle through nuclear and electronic interactions, respectively. After energy transport by the cascades (recoil displacements), the energy received by the target through Si–Si or B–Si nuclear interactions is called the "damage" energy E_d and is shown in the same figure. This is a calculation of interest because in a good approximation (for boron), the number of defects (Frenkel pairs V–I) generated by one "average" ion is proportional to E_d, following the Kinchin and Pease relation [11]:

$N_d = 0.42 E_d / E_s$.

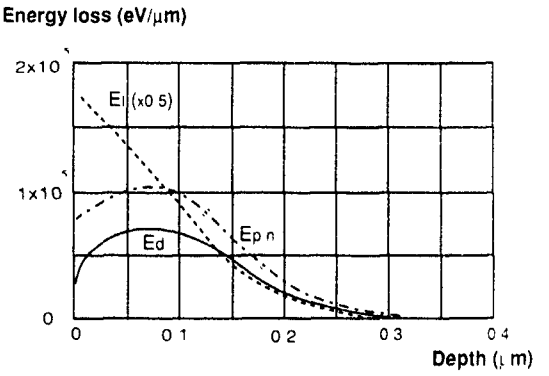

Fig. 1. Energy losses of the incident-particle and damage energy received by the target atoms for 50 keV boron incident on silicon

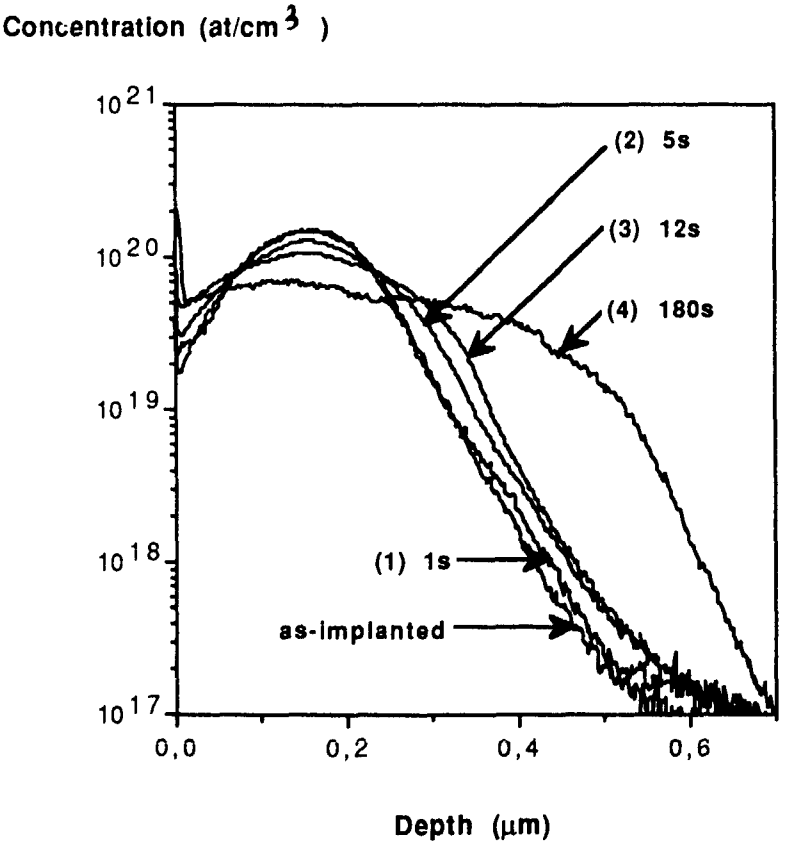

Fig 2. SIMS profiles of the samples implanted with 50 keV boron ions at a dose of 5×10^{15} ions/cm^2 and subsequently annealed by RTA.

where E_s stands for a threshold for displacement and is usually taken in the 10–15 eV range. For the present purpose, we shall remember that the depth distribution of the displacement defects initially created by the bombardment is described by the function $E_d(x)$.

2.2. Boron profiles

The results we have obtained by SIMS are represented in fig. 2. It is to be noted that a dose of 5×10^{15} ions/cm^2 corresponds to a maximum concentration of about $1-2 \times 10^{20}$ atoms/cm^3, just below the solubility limit of boron in silicon, in the case of an as-implanted sample. It is then expected that the anomalous diffusion will be easily seen under this condition. The general profile is in general accordance with the TRIM results [12] as well as with the table of Gibbons et al. [13] in spite of a strong tail due to boron channelling.

The general behaviour of boron diffusion during RTA at 1100 °C is as follows:

- At the beginning (curve 1) boron atoms seem to be more mobile in the tail of the profile and in the near-surface region than around R_p;
- after some more seconds (curve 2), this behaviour seems to reverse because the asymmetry of the profile is less than noted previously;
- this is confirmed on curve 3 where it is obvious that boron atoms diffuse more easily in the peak region;
- finally, after some minutes the profile is stabilized and its evolution is in accordance with the "classical" diffusion theory [14,15].

Table 1
Resistivity measurements (four-point-probe method) on the samples implanted with boron at 50 keV and 5×10^{15} ions/cm^2 as a function of annealing time The minimum $R_\square$ attainable is about 30 Ω/□ after 12–15 s which corresponds to 100% activation

t [s]	0	1	5	12
$R_\square$ [Ω/□]	70	71	34	31

In order to reach a better understanding of this complicated phenomenon, we have adapted the well-known computer code SUPREM [14] based on the resolution of modified Fick's laws (including a concentration dependence) but injecting a phenomenological depth-dependent diffusion coefficient in this simulation. The results are shown in fig. 3 where we have also plotted the "classical" or "normal" diffusion coefficient for comparison. The first conclusion is that boron diffusion is strongly enhanced with respect to classical diffusion It is also clearly evident that in a first period (≈ 5 s), boron diffusion is enhanced in the near-surface as well as in the tail region, while with increasing time this phenomenon reverses and the fast diffusing boron is situated around the peak (R_p). It should also be noticed that the diffusion anomalies do not fit to the damage profile, but to the boron profile itself.

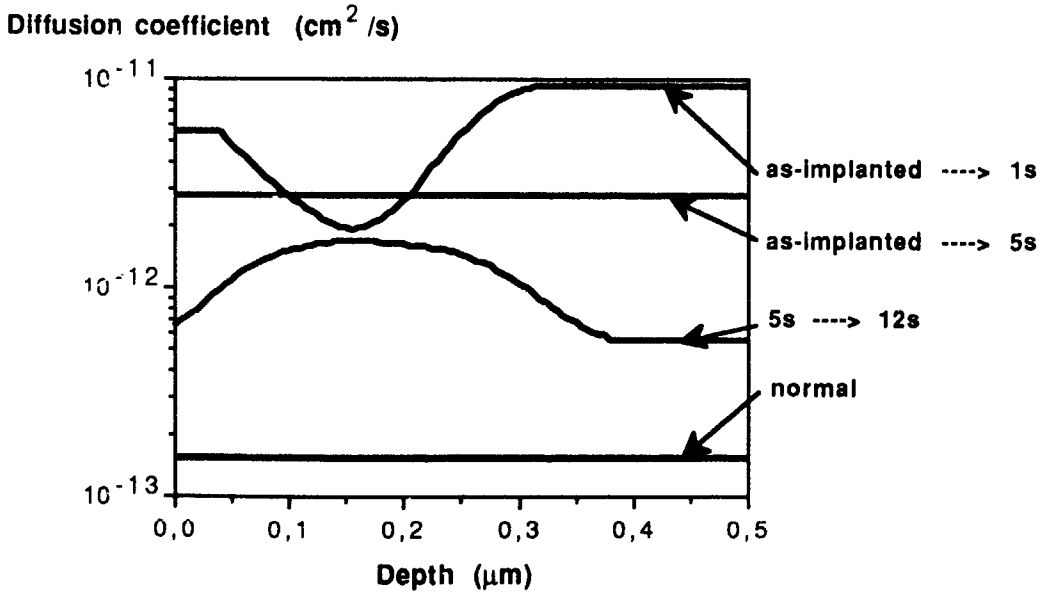

Fig. 3 Depth variations of the phenomenological diffusion coefficients needed for simulating the time evolution of the experimental SIMS profiles.

2.3. Resistivity measurements

The results of the four-probe measurements are presented in table 1. It is known that about 30% of boron atoms are activated in the as-implanted state [16]. A 1 s RTA does not seriously affect this proportion, while a 5 s RTA activates almost all boron atoms. Finally, 12 s are needed to obtain the maximum activation corresponding to $R_{\square} \approx 30\ \Omega/\square$.

2.4. XTEM characterization

This structural analysis was conducted on the same specimens as used for SIMS and electrical measurements. Micrographs obtained by XTEM in the BF mode are shown in fig. 4. For imaging, the strong 220 beam was excited resulting in a two-beam condition. As already reported, the as-implanted sample exhibits small defects, probably interstitial loops, centered on the boron profile. After 1 s RTA, these loops coalesce and form bigger loops easily observable by TEM, roughly on the same profile. With the increasing annealing time, these defects increase in size and decrease in number as expected. Finally, after a few minutes most of the defects have disappeared and only some dislocations are visible.

3. Discussion

It is possible to discuss and propose an explanation of the behaviour of anomalous diffusion by combining the results obtained through different experiments. We now review the phenomenon step by step.

(1) As-implanted state. Immediately after implantation one-third of the boron atoms are on substitutional positions and the same amount of Si atoms are in interstitial positions [16]. Because these Si-I's are highly mobile and unstable at RT, they agglomerate in the form of small dislocation loops at depths where their concentration is high, i.e. in the region centered around R_p, the depth position corresponding to the maximum boron concentration [17,18].

(2) $0 < t < 1$ s In a very short time, these defects precipitate to form dislocations and loops of bigger sizes. Moreover, it is possible that during that stage some boron atoms are trapped by Si-I's to form complex agglomerates [19,20]. Note that the activation of boron does not take place during this annealing period and that the number of Si-I available in the network does not increase from 0 to 1 s. The regions where the diffusion phenomenon reaches a maximum are at the borders of the defective region. This is probably be-

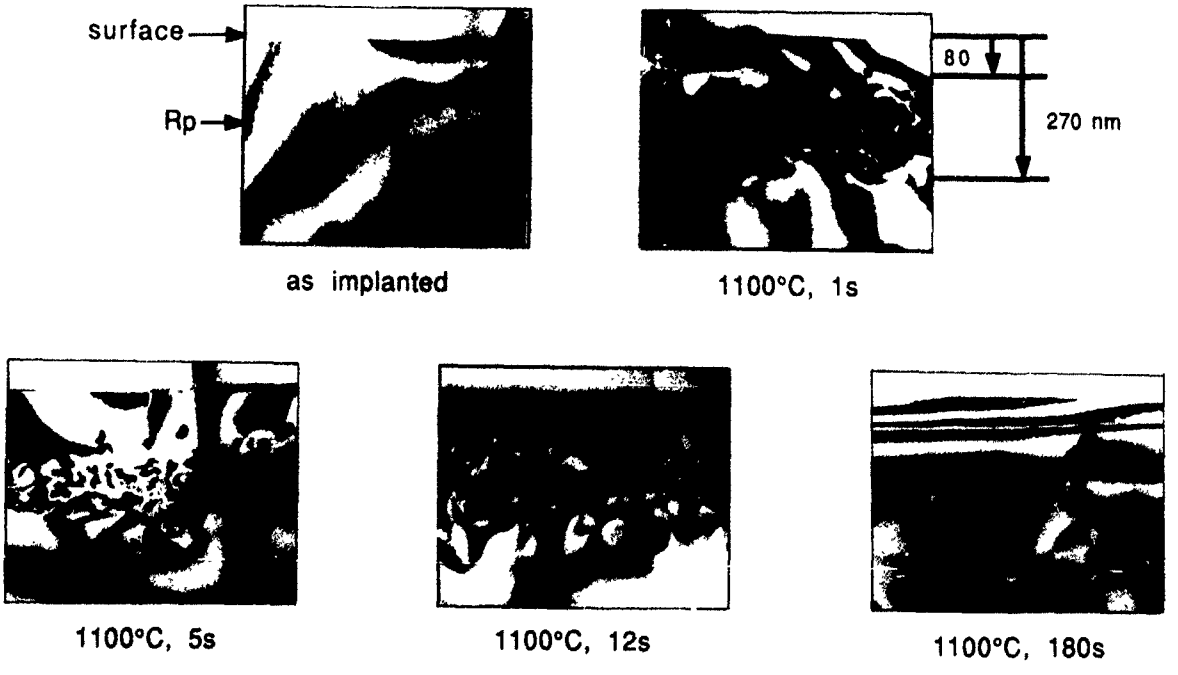

Fig. 4. XTEM images (CC 220) showing the structural evolution of the samples after RTA at 1100 °C. Note the presence of dislocations and loops centered around R_p.

cause only there the Si-I and boron atoms can diffuse without being trapped by the extended defects.

(3) $t \approx 1$ s. When the temperature is high enough, dislocation loops emit a great number of Si-I's in all directions of the crystal. Within this volume, the defect concentration is so high that boron and silicon atoms seem immobile. Any interstitial atom emitted from a dislocation will be soon trapped by another defect. The dissociation of agglomerates may not be possible under these conditions and this may explain the electrical measurements showing that activation of boron has not been reached at this stage. On the other hand, in the two regions separating the defective material from the perfect crystal, Si-I atoms which are injected toward the surface or toward greater depths have a low probability to be trapped by extended defects so that they can diffuse over larger distances before stabilization on a free substitutional position. These high fluxes of Si-I's emitted from the defective region to the surface and to greater depths are then suspected to be responsible for the enhanced diffusion of boron in the tail of the distribution and in the near-surface region.

(4) 1 s < t < 12 s After some more seconds, the maximum activation has been reached. One can suppose that almost all boron atoms which were trapped around R_p have been free and finally put on a substitutional position. TEM has evidenced the reduced number of extended defects at this stage. This is why boron diffusion is now possible in the peak region. Si-I atoms emitted from the loops can diffuse in the central region before being trapped by another defect and this is consistent with the variation of the diffusion coefficient. On the contrary, there are not enough defects to produce a high flux of Si-I's toward the surface and to greater depths. It is therefore logical to check that the diffusion coefficient is decreasing so as to reach the normal values in the tail and surface region. It is also important to note that from 5 to 12 s while almost all boron atoms are on substitutional positions, the diffusion is still enhanced. This evidences that the "anomalous" diffusion is not purely related to interstitial diffusion.

(5) t > 12 s. Finally, for large annealing times boron diffusion becomes homogeneous in depth and "classical" over the whole profile. This must be connected to the disappearance of the extended defects as checked by XTEM.

4. Summary and conclusions

The diffusion during RTA of boron implanted into silicon cannot be described by the classical diffusion theory. This "anomalous" diffusion is a transient (few seconds) and enhanced phenomenon whose important characteristic is to be depth-dependent. Combining the experimental characterizations by XTEM, SIMS and four-point-probe measurements and the damage calculations provides the following information:

- the structural defects seen in both as-implanted and annealed materials are centered around R_p, the maximum of boron concentration where diffusion anomalies occur;
- these defects are not a result of displacement damage (nuclear collision) but of boron activation through a kickout mechanism;
- these defects are mainly interstitial dislocation loops of Si. These Si atoms are ejected during boron activation and then agglomerate to form bigger loops;
- kinetics of dissolution of these defects when compared to the behaviour of the "anomalous" diffusion suggests that the enhanced phenomenon is due to a high flux of Si interstitials which may (or may not) escape from the defect-rich region during dissolution (depending on the density of these defects),
- it is also to be noted that the enhanced diffusion affects also the active boron, i.e. the boron atoms on substitutional sites; a strong coupling between Si-I and B-(sub) along with a fast diffusion of this pair might be able to describe the generally observed "anomalous" diffusion of boron in silicon during RTA.

Acknowledgement

This work was partly supported by a grant from the French GCIS.

References

[1] L.C. Hopkins, T.E. Seidel, J.S. Williams and J.C. Bean, J. Electrochem. Soc. 50 (1987) 416
[2] K. Cho, M. Numan, T.C. Finsdtad, W.K. Chu, J. Liu and J.J. Wortman, Appl. Phys. Lett. 47 (1985) 1723
[3] A.E. Michel, W. Rausch, P.A. Ronsheim and R.H. Kastl, Appl. Phys. Lett. 50 (1987) 416
[4] M. Servidori, Z. Zourek and S. Solmi, J. Appl. Phys. 62 (1977) 1723
[5] X. Bao, Q. Guo, M. Hu and D. Feng, J. Appl. Phys. 66 (1989) 1475
Q. Guo, X. Bao, J. Hong, Y. Yvan and D. Feng, Appl. Phys. Lett. 54 (1989) 1433.
[6] R.B. Fair, J.J. Wortman and J. Liu, J. Electrochem. Soc. 131 (1984) 2387
[7] D.K. Sadana, J.C. Shatas and A. Gat, Inst. of Phys. Conf. Series (Inst. of Phys., London, 1983)
[8] C. Vieu, A. Claverie, J. Faure and J. Beauvillain, Nucl. Instr. and Meth. B28 (1987) 229
[9] A. Claverie, C. Vieu and J. Beauvillain, Appl. Surf. Sci. 43 (1989) 106

[10] C. Vieu, A. Claverie, J. Faure and J Beauvillain, Nucl. Instr. and Meth. B36 (1989) 137.
[11] G.H. Kinchin and R.S. Pease, Rep. Prog. Phys. 18 (1955) 1.
[12] J.P Biersack, Nucl. Instr. and Meth. B19/20 (1987) 32
[13] J.F Gibbons, W.S. Johnson and S.W. Mytroie, Projected Range Statistics, 2nd ed. (Stroudsburg, Pennsylvania, 1975).
[14] D.A. Antoniadis, S.E. Hansen and R W. Dutton, SUPREM II notice, Army Research Office Contract DAAG-29-77-C 006, technical report no. 5019-2 (1978).
[15] D.A Antoniadis, A G. Gonzalez and R W. Dutton, J. Electrochem. Soc 125 (1978) 813.
[16] D. Fink, J.P. Biersack, H.D. Cortanjen, F. Jahnel, K. Muller, H. Ryssel and A. Osei, Radiat. Eff 77 (1983) 11.
[17] J Narayan and O.W. Holland, J. Appl. Phys. 58 (1984) 2913.
[18] J Narayan and K Jagannadham J Appl. Phys. 62 (1987) 1694.
[19] T.O. Sedgwick, A.E. Michel, U.R Deline, S.A. Cohen and J.B Lasky, J. Appl. Phys. 63 (1988) 1452
[20] A.E Michel, M. Numan and W.K. Chu, Appl. Phys. Lett 53 (1988) 851.

Nuclear Instruments and Methods in Physics Research B55 (1991) 661–665
North-Holland

Channeling implants of boron in silicon

V. Raineri, G. Galvagno and E. Rimini
Dipartimento di Fisica, Università di Catania, Corso Italia 57, Catania, Italy

A. La Ferla and S. Capizzi
Istituto di Metodologie e Tecnologie per la Microelettronica, c/o Dip. Fisica, Università di Catania, Italy

A. Carnera
Dipartimento di Fisica, Università di Padova via Marzolo 8, Padova, Italy

G. Ferla
ST Microelectronics, Stradale Primosole 50, Catania, Italy

80 keV B^+ ions were implanted in ⟨100⟩ Si with a high current implanter. The wafers were irradiated at 0° and 7°. The feasibility of the 0° implants was checked testing the influence of several geometrical parameters, such as the twist angle and the flex angle, on the shape and uniformity of the ion depth distributions. The damage generated by a high-fluence B^+ implant was lower for the 0° implanted samples and the disorder evolution was analyzed after different annealing processes were performed in the 600–1200°C temperature range. Agglomeration and dissolution of extended defects in the 0° implanted samples occurs at temperatures 100°C lower than those in the 7° implanted samples.

1. Introduction

In the last years the shrinkage of device dimensions with the increasing use of three-dimensional structures has determined the use of implants performed with the beam direction normal to the wafer surface (0° implants) in VLSI technology. This implantation condition avoids the right–left asymmetry, which results from the usual 7° tilted implantation on masked wafers [1–3]. Channeling phenomena can arise in silicon wafers cut with a tolerance of +0.5° with respect to the main axis [4].

The lower influence of nuclear phenomena in the slowing-down process of channeled ions reduces the displaced target atoms and thus the lattice damage of the as-implanted wafer. This can be another important aspect of the 0° implants.

In this work we report the characterization of the depth distribution and of the disorder annealing of boron implanted in silicon using the 0° wafer holder of the high-current implanter Eaton Nova NV80. The influence of several geometrical parameters as well as the damage evolution after thermal treatments is investigated by comparing the samples implanted with the 0° holder to those with the usual 7° tilting angle holder. We also report the results of a computer calculation obtained using the Marlowe code on the 0° implants [5].

2. Experimental

80 keV boron ions were implanted in ⟨100⟩ n-type 5 in. Si wafers of 1.5 Ω cm resistivity with the high-current Eaton Nova NV 80. The adopted fluence was in the range of 1×10^{14}–2×10^{15}/cm^2 and all implants were performed at room temperature. The boron beam is mechanically scanned over the wafers during implantation and two wafer holders are used to keep the silicon samples at a tilt angle of either 7° or 0° between the ion beam and the normal to the wafer surface. To improve wafer cooling and good heat transfer characteristics a flex angle of 0.2° is designed on the wafer support; the beam divergence is estimated to be lower than +0.5°.

The boron depth distributions were analyzed by secondary-ion mass spectrometry and compared with the carrier distributions obtained by cycles of resistivity and Hall-effect measurements, followed by anodic oxidation and oxide stripping on samples designed with Van der Pauw geometry.

0168-583X/91/$03.50 © 1991 – Elsevier Science Publishers B.V. (North-Holland)

The dopant activation of the as-implanted samples was obtained by a rapid thermal annealing at 1000 °C for 10 s under a N_2 flow. This process has no effect on boron diffusion. To study the damage evolution of the high-fluence implanted samples, different annealing treatments were performed either in a furnace under vacuum in the 600–900 °C temperature range for 30 min, or in a rapid thermal annealer under nitrogen flux in the 1000–1200 °C range for 10–30 s. All these processes were simultaneously performed for the 0° and 7° tilt angle implanted samples. The residual damage was investigated by Rutherford backscattering spectrometry, a channeling technique with 2 MeV He^+ ions.

3. Results and discussion

In fig. 1a chemical and electrical profiles of 80 keV, $1 \times 10^{14}/cm^2$ B^+ implanted Si are shown for the two tilting-angle implants. The samples were annealed at 1000 °C for 10 s. The agreement between the distributions of ions and holes indicates a good activation of the implanted boron after this thermal treatment. RBS-channeling measurements also revealed no detectable damage within the technique sensitivity.

The 0° tilt angle implantation profiles show the influence of the channeling effect, i.e. they are deeper with a peak shift from 0.25 to 0.3 μm and a low-gradient exponential tail. The maximum penetration depth for the 0° profile is about 0.8 μm, which is in good

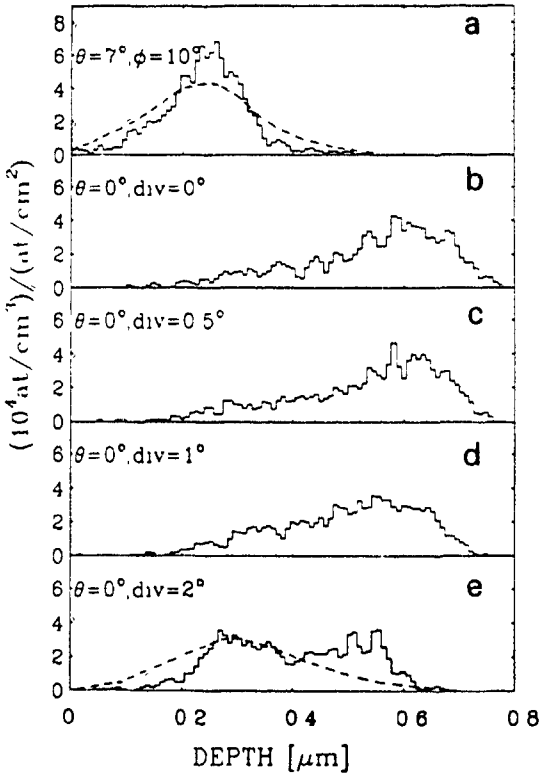

Fig. 2. Depth distributions of 80 keV B^+ in ⟨100⟩ Si obtained with 1000 particles in the Marlowe simulation. The ions were incident at 7° (a) and 0° (b–e). In the last case different angular beam divergences were considered. The dashed lines in (a) and (e) are the SIMS profiles.

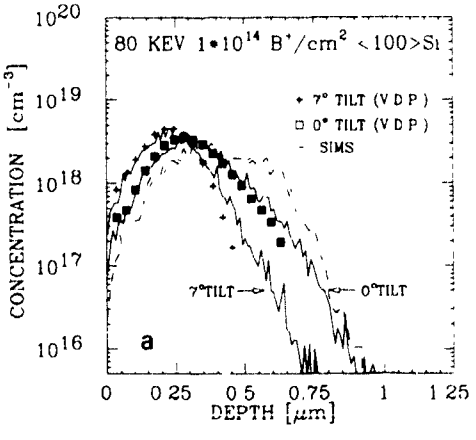

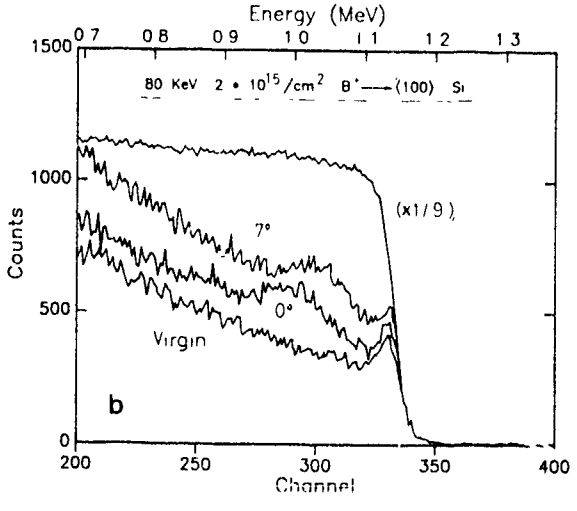

Fig. 1. (a) Carrier and chemical concentration profiles for 7° and 0° boron implants into a ⟨100⟩ silicon target at a fluence of $1 \times 10^{14}/cm^2$. For comparison, the SIMS profile of the same implant in under perfect channeling conditions is shown as a dashed line. (b) Aligned yields of 2.0 MeV He^+ backscattered from Si samples implanted at 80 keV, $2 \times 10^{15}/cm^2$ with a tilt angle of 0° and 7°, respectively. For comparison the yield of an unimplanted sample is also shown.

agreement with the depth where the ions stop after only electronic losses. To evaluate the percentage of channeled ions we have shown in the same figure the SIMS profile of 80 keV, $1 \times 10^{14}/cm^2$ B^+ implanted under controlled channeling conditions. This implant was performed in a research machine where a perfect orientation of the Si sample under the B^+ beam was obtained by a previous alignement using 700 keV H_2^+ backscattering. In this case the boron profile is broader but the R_{max} value is the same as that of the 0° distribution, evidencing that no misalignments are present in the 0° geometry but that the beam divergence causes a high number of dechanneled particles.

To evaluate the influence of beam divergence on the boron depth distributions, we have performed some Monte Carlo simulations with the Marlow code. This computer program allows the simulation of the 0° implant, taking into account the single-crystal Si structure, an impact parameter dependent formula for the electronic stopping power, several geometrical parameters and the thermal vibrations of the lattice atoms. In fig 2 the depth distributions of 80 keV B^+ ions impinging along the ⟨100⟩Si axis computed with 1000 particles are shown for several parameters. The sequence b–e shows the influence of the angular beam spread: a divergence higher than 0.5° greatly modifies the distribution, although this value is lower than the critical angle for channeling. The ion trajectories depend in fact upon the impact parameter and the ion path direction. On increasing the angle between the axis and the ion direction, the particles experience higher multiple scattering by electrons and thermal vibrations, so the dechanneling rate increases and a broader distribution is obtained.

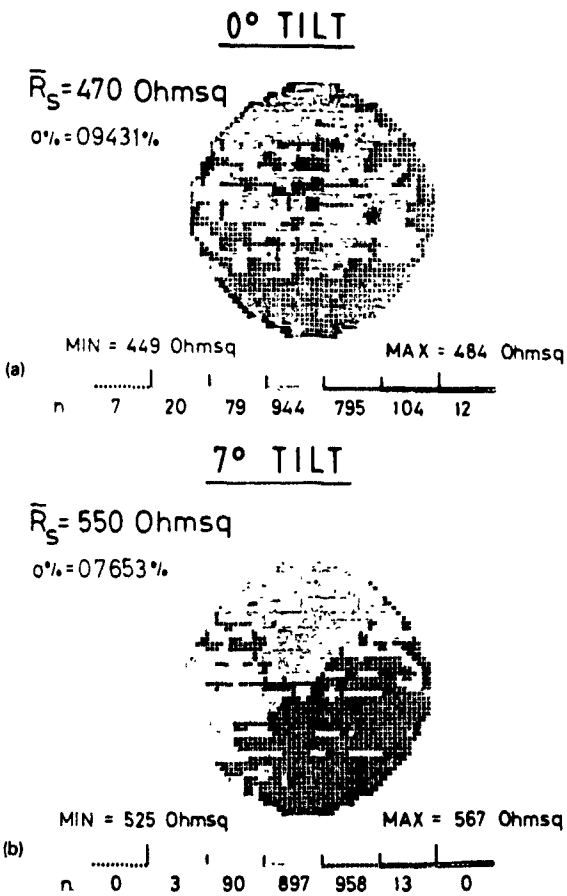

Fig. 3. Sheet resistance maps for 0° (a) and 7° (b) 80 keV, $1 \times 10^{14}/cm^2$ boron implants into ⟨100⟩ silicon. The sheet resistance is measured at 500 spots on the wafer

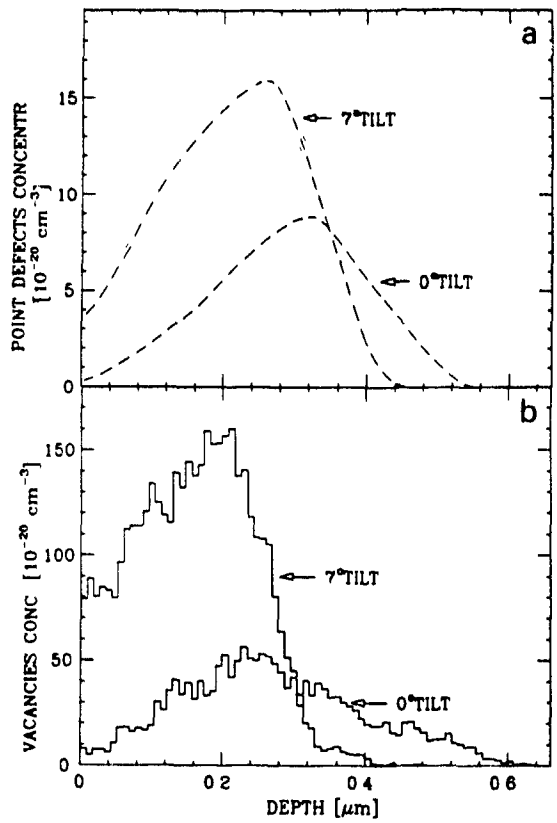

Fig 4 (a) Point defect distributions from the RBS spectra for the samples implanted at 0° and 7° tilt angle. (b) Vacancy distributions computed by the Marlowe code for the two implantation conditions for 0° and 7° tilt angles

The sheet resistance maps of the two 0° and 7° tilt angle implanted wafers are presented in fig. 3. The lower value of the average sheet resistance in the 0° implanted wafer, about 15%, is due to the lower peak concentration and to the higher carrier mobility as evidenced by the Hall measurements. The higher standard deviation (0.94% as opposed to 0.77%) indicates a larger nonuniformity in junction depth for the wafer implanted with the 0° geometry. A detailed analysis of

the carrier profiles performed in different regions of the wafer evidences a small difference in junction depth between samples cut from the center and those from the border of the wafer. This phenomenon is not seen in the 7° implanted wafer and must be attributed to the flex angle: because the channeling critical angle for 80 keV B in ⟨100⟩ Si is 2.87° the flex angle does not disturb the 7° boron profiles but becomes crucial for the 0° implants.

Increasing the 80 keV B^+ fluence to $2 \times 10^{15}/cm^2$, the shapes of the ion profiles change due to a damage effect. The SIMS spectra show a shift in the projected range between the two geometries, but in the 0° case the channeled fraction of ions is reduced with respect to low-fluence implants. The $2 \times 10^{15}/cm^2$ implant introduces a lot of disorder in the Si single crystal, and thus impinging ions are prevented from channeling. The distribution of displaced silicon atoms, as extracted from the RBS spectra (fig. 1b), is shown in fig. 4a and, for comparison, in fig. 4b the vacancy distribution obtained by the Marlowe simulation for the two geometries is plotted. The calculated profiles include all the generated vacancies without taking into account close pairs recombination between vacancies and interstitials [6]. The agreement between the experimental and the computed distributions of displaced atoms is then only qualitative: evidently a large number of the generated vacancies can recombine with interstitials in sites farther than neighbouring sites.

The annealing of disorder produced by the 0° and 7° implants was investigated in the 600-1200°C temperature range. The sequence of the channeling spectra reported in fig. 5 refers to some of the performed annealings.

The evolution and the removal of the damage is the same for both wafers, but the temperatures that char-

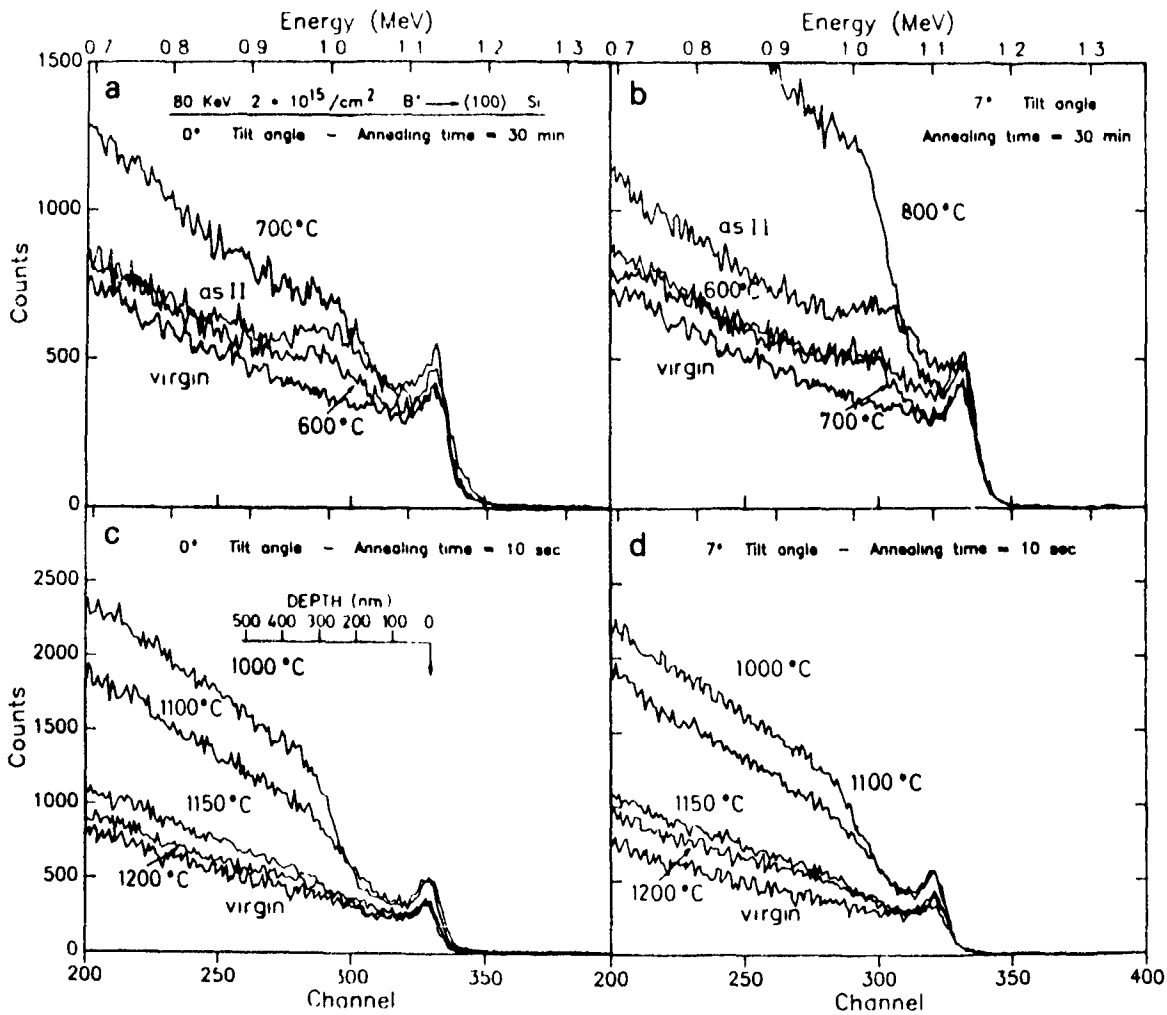

Fig 5 Aligned yields of 2.0 MeV He^+ backscattered from Si samples implanted with 80 keV, $2 \times 10^{15}/cm^2$ B^+ ions at 0° (a, c) and 7° (b, d) as a function of several thermal treatments.

acterize each phenomenological step are different. It is possible to distinguish three regimes of evolution of the as-implanted damage: first, a partial removal of point defects or small clusters with a consequent reduction in the aligned yield; then, at higher annealing temperatures, the agglomeration of point defects into extended defects, such as dislocation loops, with a dramatic increase in the dechanneling yield; and finally, the annealing of the extended defects. Because the as-implanted materials is less damaged when the ion beam impinges normally on the wafer surface, these annealing regimes are characterized by a lower threshold temperature for the 0° geometry: a 700°C–1/2 h annealing already induces the agglomeration of point defects (whereas a temperature of 800°C is necessary for the 7°-implanted sample) and a temperature of 1000°C is enough to start the dissolution of extended defects (cf. 1100°C for the 7° case). After annealing at 1200°C for 10 s, the material is nearly defect-free from the channeling-RBS point of view, but the annealing efficiency seems better for the 0° wafer.

4. Conclusion

Implants performed with a high-current implanter have been studied for a 80 keV B^+ beam impinging normally on the ⟨100⟩ silicon surface. The onset of channeling effects allows the control of several geometrical parameters to obtain the uniformity and the reproducibility of the dopant distributions in different points on the same wafer and from wafer to wafer. Angles such as the beam divergence or the flex angle are critical even if they are smaller than the critical angle of channeling.

On increasing the boron fluence, a nonlinearity between the channeled fraction of ions and the dose is noticed. This is a damage effect. The lower point-defect density in the 0° implanted sample results in a 100°C shift in the temperature necessary to agglomerate and subsequently dissolve the extended defects. The Marlowe code is a convenient tool to simulate the 0° implant conditions.

References

[1] V G K Reddi and J D Sansbury, J Appl. Phys 44 (1973) 2951
[2] H Nishi, T Inada, T Sakurai, T Kaneda, T. Hisatsugu and T. Furuya, J. Appl. Phys 49 (1978) 608.
[3] R.J Schreutelkamp, F.W. Saris, J F Westendorp, R.E Kaim, G B Odlum and K T F Janssen, Mater Sci Eng B2 (1989) 139.
[4] J Lindhard, K. Dan. Vidensk Selsk Mat.-Fys Medd. 34 (no. 14) (1965).
[5] M.T Robinson and I M. Torrens, Phys. Rev B9 (1974) 5008.
[6] Marlowe User's Guide, version 12 (1985).

Nuclear Instruments and Methods in Physics Research B55 (1991) 666–670
North-Holland

Calculation of channeling effects in ion implantation

J. Bausells, G. Badenes and E. Lora-Tamayo

Centro Nacional de Microelectrónica (CSIC), Campus Universitat Autònoma de Barcelona, 08193 Bellaterra, Spain

Channeling effects during ion implantation in silicon are calculated in this work by using a modified version of the TRIM Monte Carlo code. As the direction of motion of each ion is known during its movement inside the target, an ion can be considered to enter into a channel when its direction of motion is aligned with a channel axis within a critical angle. Simple models are used for ion movement and stopping along channels. Range distributions including channeling effects are obtained with a shorter computation time than with amorphous TRIM calculations. Good agreement is obtained with experimental profiles implanted at low energies into tilted silicon.

1. Introduction

The current trend towards device dimensions reduction in semiconductor manufacturing makes a precise control of ion-implanted dopant profiles necessary. This need is increased by the use of rapid thermal annealing techniques, that produce a very low dopant diffusion.

Ion implanted profiles in amorphous targets can be accurately calculated. The first unified theory of range distributions was developed by Lindhard, Scharff and Schiott [1] and provides the moments of the range distribution, from which the distribution itself can be obtained. The moments method of solving the transport equation was modified and applied by many workers [2–5]. Monte Carlo calculations such as the TRIM code [6,7], and the numerical calculation of the Boltzmann transport equation [8] have also been used and provide very accurate results.

Range distribution calculations in crystalline targets are more difficult due to channeling effects. Ions moving along a channel direction lose much less energy per unit path length than ions moving in a random direction, giving rise to channeling "tails" in range distributions. Much work has been devoted to the theory of ion motion inside channels [9–14]. Calculations of range distributions including channeling effects have used [15] Monte Carlo methods, such as the MARLOWE [16] code, that includes the crystalline structure of the target, but needs a great amount of computation time. By using the numerical integration of the Boltzmann transport equation (BTE), Giles and Gibbons [17] have been able to calculate range distributions for ions implanted into misaligned crystalline targets.

Monte Carlo calculations of ion implantation effects have the advantage of allowing a rigorous treatment of elastic scattering, explicit consideration of surfaces and interfaces, an easy determination of energy and angle distributions and, especially, a straightforward control of the physics involved in the ion motion. The method follows the motion of a large number of individual ions inside the target until they come to rest. Although it is a time-consuming procedure there are very efficient implementations, such as the TRIM code [6,7], developed for amorphous targets, that uses an accurate analytic scheme for nuclear scattering integrals. The knowledge of the direction of motion of each ion after each elastic collision, however, offers the possibility of considering the ion to enter a channel when its direction is aligned with a crystal channel direction. In this work we use this concept in a modified version of the TRIM code to calculate ion-implanted range distributions with channeling effects. Simple models are used to calculate the ranges of channeled ions. We will restrict ourselves to low energy ($E_0 < 25$ keV/amu) implantations into (100) silicon substrates with the ion beam entering the target near the normal direction. Then only the ⟨100⟩ axial channel and the major planar channels containing that axial channel, i.e., {100} and {110}, will be considered.

2. Formalism

A model based on the TRIM85 [6,7] Monte Carlo code will be used to calculate channeling effects in ion implantation. In the TRIM code an ion travels, during its movement inside the solid, in free-flight paths between elastic collisions with the crystal atoms. In these free-flight paths it loses energy by inelastic electronic stopping. As the direction of these paths in space is known, we will consider an ion to enter into a channel when its direction of motion is aligned with a channel direction within a critical angle ψ_c. For the critical

0168-583X/91/$03.50 © 1991 – Elsevier Science Publishers B.V. (North-Holland)

angles we have used the standard expression for the low energy range:

$$\psi_c = \left(\frac{\sqrt{1.5}\, a\psi_1}{d}\right)^{1/2}, \quad \psi_1 = \left(\frac{2Z_1Z_2e^2}{dE}\right)^{1/2}, \tag{1}$$

for axial channeling [9,13], where Z_1 and Z_2 are the atomic numbers of the incoming ion, of energy E, and an atom of the target, a is the screening length, e is the electron charge, d is the spacing between two atoms in a channel row, and

$$\psi_c = F_{ps}\left(\frac{b_{min}}{a}, \frac{d_p}{a}\right)\psi_a, \quad \psi_a = \left(\frac{2\pi Z_1Z_2e^2aNd_p}{E}\right)^{1/2}, \tag{2}$$

for planar channeling, where d_p is the spacing between atomic planes, N is the atomic density of the target, and $F_{ps}(x, y)$ is a function with values typically between 0.5 and 1 [13]. Not all the ions that are aligned with the channel directions will be channeled, however, due to the blocking effect of the channel walls. An estimation of this effect can be obtained from the distance b_{min} of closest approach to the channel wall for an ion which travels at the critical angle at the center of the channel [17]. Ions moving closer than b_{min} to a channel wall will be scattered out of the channel. This defines a blocking area in a plane perpendicular to the rows or planes that gives the probability that an aligned ion enters a channel.

We will use a simple model to describe the ion motion within a channel and to calculate the range of a channeled ion, in order to show that useful results can be obtained with this method. A more accurate description is left for future work. When an ion has entered a channel, it follows an oscillatory motion between the channel walls [11], which will be described by static continuum potentials. If we use the universal interatomic potential of Biersack and Ziegler [7,18], which is used in the TRIM code and has the same analytical form as the Molière potential, to calculate the continuum potentials, we get [10,13]:

$$V_{RS}(b) = \frac{2Z_1Z_2e^2}{d}\sum_{i=1}^{4}\alpha_i K_0\left(\frac{\beta_i}{a}b\right),$$
$$V_{PS}(b) = 2\pi Nd_pZ_1Z_2e^2a\sum_{i=1}^{4}\frac{\alpha_i}{\beta_i}\exp\left(-\frac{\beta_i}{a}b\right), \tag{3}$$

where the subscript RS is used for axial channeling and PS for planar channeling, b is the distance to the row or plane, $K_0(x)$ is the modified Bessel function, and α_i and β_i are the potential coefficients [7]. The contributions from several rows or planes are added to obtain the continuum potential. From the continuum potentials the distance b_{min} can be obtained as a function of the angle α between the initial ion motion and the channel axis. The amplitude of the ion oscillatory movement is then given by $r_{max}(\alpha) = \frac{1}{2}d_0 - b_{min}(\alpha)$, where d_0 is the channel width. As the ion moves inside the channel, it loses energy by electronic stopping. We will not consider dechanneling effects due to lattice defects or thermal vibrations of the crystal atoms. Therefore, an ion that enters into a channel will continue travelling in that channel until it loses all its energy. The range of such an ion will be calculated from the ion stopping power inside the channel. The channel electronic density at a distance b from the channel wall can be calculated from the solid-state atomic charge distributions calculated by Ziegler et al. [7]. A local-density approximation is then used to calculate the ion electronic stopping. The electronic stopping power S_{Z_1} of an ion of atomic number Z_1 is related to the proton stopping power S_p at the same velocity by [19]:

$$S_{Z_1} = (Z_1^*)^2 S_p, \tag{4}$$

where Z_1^* is the ion effective charge that, at low and moderate velocities, oscillates with Z_1 [20,21]. The stopping power of a low-velocity ion is proportional to its velocity v [21,22]. Accurate values of S_p and Z_1^* at low velocities in an electron gas can be calculated by the density functional formalism [23] We have used the results of Echenique et al. [24] to calculate the stopping power function [14] $S_{Z_1}(b)/v$ from eq. (4) and from the channel electron densities. In fig. 1 we show the electron density and the stopping power function for boron ions in axial and planar channels in silicon The values of stopping calculated in this way for well-channeled boron ions in silicon axial channels agree very well with Eisen's [20] experimental results.

The average electronic stopping in the channel direction for an ion entering the channel at an angle α at the

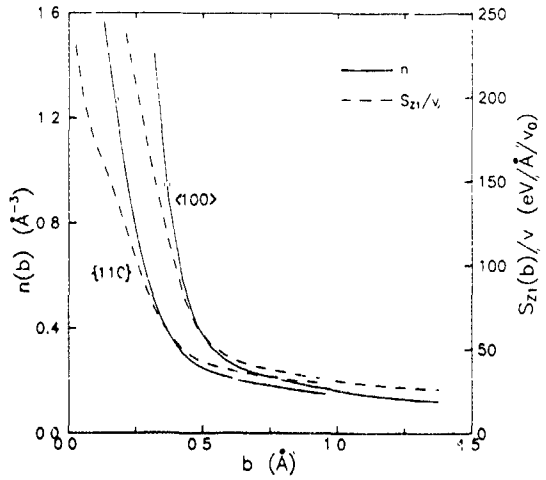

Fig. 1. Electron density and stopping power function for boron ions in static axial ⟨100⟩ and planar {110} channels in silicon.

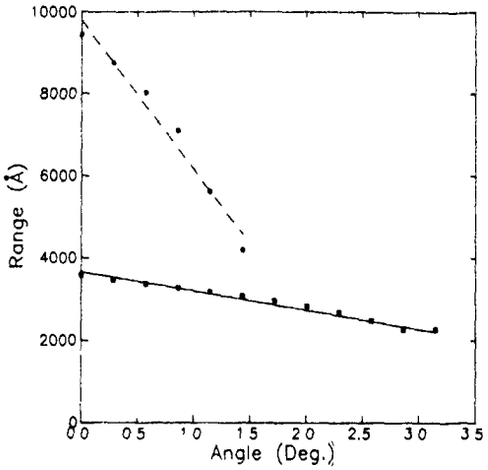

Fig 2. Range of a boron ion channeled in a planar {110} channel in silicon, as a function of its initial angle with respect to the channel axis, calculated with eq. (7) (■: initial ion energy, 10 kev; ●: initial ion energy, 70 keV). The solid and dashed lines are the approximations given by eq. (8) at the same initial ion energies.

channel center, can then be calculated, by assuming an harmonic oscillatory motion, from [11,14];

$$\left\langle \frac{S_e}{v}(\alpha) \right\rangle = \frac{1}{2\pi}\int_0^{2\pi} \mathrm{d}x \, \frac{S_{Z_1}}{v}[r_{\max}(\alpha)\sin x]. \qquad (5)$$

Then the stopping power as a function of the ion energy is given by:

$$S_e(\alpha, E) = \left\langle \frac{S_e}{v}(\alpha) \right\rangle \sqrt{\frac{2E}{M_1}}, \qquad (6)$$

where M_1 is the ion mass. From this value of the stopping power, the range of a channeled ion can be roughly estimated as

$$R(\alpha, E) = \int_0^L \frac{\mathrm{d}E'}{S_e(\alpha, E')} = \sqrt{2M_1 E}\left\langle \frac{S_e}{v}(\alpha) \right\rangle^{-1};$$
$$0 \le \alpha \le \psi_c, \qquad (7)$$

where E is the ion energy when it enters the channel. The function $R(\alpha, E)$ can be fitted to a very good approximation, for both axial and planar channeling, by a linear equation of the form

$$R(\alpha, E) = -AE\alpha + R_{\max}(E), \qquad (8)$$

as is shown in fig. 2, where $R_{\max}(E)$ is the channeled ion maximum range, corresponding to eq. (7) for $\alpha = 0$. The minimum range of a channeled ion will then be given by $R_{\min}(E) = R(\psi_c, E)$.

An ion entering a channel at an angle α will only have a range $R(\alpha, E)$ if it is initially at the center of the channel. Otherwise it will have closer encounters with the channel walls and will suffer a higher stopping. In particular, an ion entering the channel perfectly aligned will have a range $R_{\max}(E)$ if it is at the center of the channel and will be scattered to a critical angle trajectory and have a range $R_{\min}(E)$ if it is at a distance $r_{\max}(\alpha)$ from the center of the channel. In our calculation we have assumed a uniform range probability distribution between $R_{\min}(E)$ and $R(\alpha, E)$ for an ion entering the channel at an angle α. Therefore only a few ions will travel a distance close to $R_{\max}(E)$.

Range distributions including channeling effects are thus calculated as follows: after an ion has entered the target, its trajectory is followed as in the standard TRIM code. After each elastic collision with a target atom, the direction of the ion motion is compared with the axial and planar channel directions considered. If it is close to any of them within its critical angle, the ion is considered to be channeled (taking into account the channeling probabilities discussed above) and its range within the channel is calculated using eq. (8). This is added to the ion position when it entered the channel and the final ion position is obtained. As the range of an ion that enters a channel is calculated analytically, the computation time for a channeled calculation is lower than that for an amorphous TRIM profile determination.

3. Results

We have calculated range distributions for boron ions implanted into crystalline silicon tilted 7°, which is one of the most common situations in standard implants to avoid direct ion channeling. As eq. (7) provides only a first-order estimate of the range of channeled ions, the value of the stopping power of a well channeled ion $\langle S_e(0)/v \rangle$, has had to be increased by a factor 1.7 in eq. (8) in order to obtain a good agreement with experiments. The value of A in eq. (8) is not critical because it determines mainly the near surface portion of the channeling distribution, which is hidden under the main amorphous peak [17]. Best results are obtained with a value of A that makes $R_{\min}(E)$ to be near zero.

Especially for low-energy implantations, almost all ions are aligned with a planar channel within the critical angle at some time of their trajectory. This means that our calculation would not produce the random peak of the range distribution. This is a consequence of neglecting any dechanneling effects in our model. This effect can be taken into account by reducing the probability that an aligned ion enters a planar channel to a value lower than its purely geometrical value discussed above.

In fig. 3 we show the results for a 10 keV boron implantation into 7° tilted silicon compared with experimental measurements [25]. The amorphous calculation from the standard TRIM code and the BTE results of Giles and Gibbons [17] are also shown. It can be seen

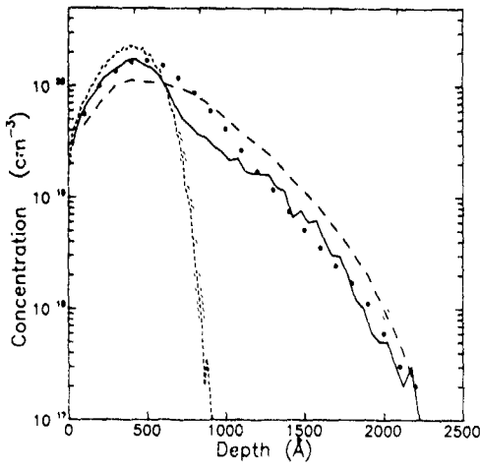

Fig 3 10 keV boron implanted into 7° tilted silicon with a dose of 1×10^{15} cm^{-2}. Points: experimental result; solid line: this work; dashed line: BTE result of Giles and Gibbons [17]; dotted line: amorphous calculation

that the amorphous calculation is very different from the experimental profile. Our result shows a better agreement in the tail region with the experimental profile than the BTE calculation for a 7° tilted target, that follows the experimental well-aligned (0° tilt) implantation profile [17].

In fig. 4 the results for a 60 keV boron implantation into 7° tilted silicon are shown, and are compared with experimental results [26] and the amorphous calculation. Our result follows reasonably well the experimental profile, although its tail region tends to the values expected for a well-aligned range distribution.

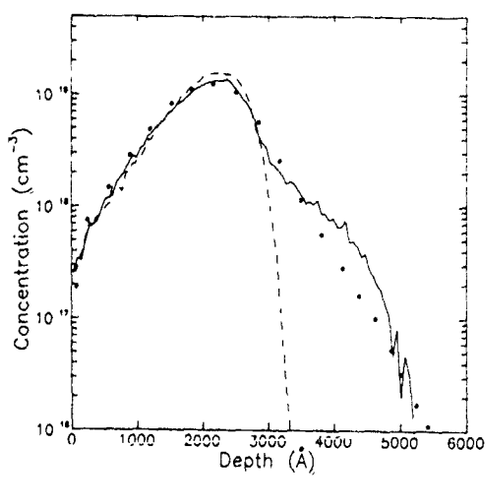

Fig. 4. 60 keV boron implanted into 7° tilted silicon with a dose of 2×10^{14} cm^{-2}. Points: experimental result; solid line: crystalline calculation; dashed line: amorphous calculation.

It should be noted that the method can also be applied in a straightforward way to multilayer targets such as for implantations through screening oxides.

4. Conclusions

Channeling effects in ion implantation in silicon have been calculated by using a modified version of the TRIM Monte Carlo code. An ion is considered to enter into a channel when it is aligned with the channel direction. The range of the ion within the channel is calculated by using a simple model based on a local-density approximation and density-functional electronic stopping results. Computation time is lower than that needed by the standard amorphous TRIM code. Good agreement has been obtained with low-energy profiles implanted into 7° tilted silicon. Further progress can be made by using a more accurate description of the range of channeled ions, including dechanneling effects.

References

[1] J Lindhard and M Scharff, Phys. Rev 124 (1961) 128; J. Lindhard, M Scharff and H.E. Schiott K. Dan. Vid Selsk. Mat Fys Medd 33 (1963) no 14
[2] J.B. Sanders, Can J Phys. 46 (1968) 455
[3] D.K. Brice, Appl Phys. Lett 16 (1970) 3
[4] K.B. Winterbon, Radiat Eff 13 (1972) 215.
[5] U. Littmark and J.F Ziegler, Phys Rev A23 (1981) 64.
[6] J P. Biersack and L.G Haggmark, Nucl Instr. and Meth. 174 (1980) 257
[7] J F. Ziegler, J.P Biersack and U. Littmark, The Stopping and Range of Ions in Solids, vol. 1 of: The Stopping and Ranges of Ions in Matter, ed J F Ziegler (Pergamon, New York, 1985)
[8] L.A Christel, J.F. Gibbons and S. Mylroie, J. Appl Phys. 51 (1980) 6176
[9] J. Lindhard, K Dan. Vid. Selsk Mat. Fys. Medd 34 (1965) no 14.
[10] B.R. Appleton, C Erginsoy and W.M Gibson, Phys Rev. 161 (1967) 330.
[11] M T Robinson, Phys. Rev. 179 (1969) 327
[12] J H. Barrett, Phys Rev B3 (1971) 1527
[13] D S. Gemmell, Rev. Mod. Phys. 46 (1974) 129
[14] Y H. Ohtsuki, Charged Beam Interactions with Solids (Taylor and Francis, London. 1983)
[15] J.S. Moore and G.R Srinivasan, J. Electrochem. Soc 135 (1988) 2034
[16] M T. Robinson and I.M Torrens, Phys Rev B9 (1974) 5008
[17] M.D. Giles and J.F. Gibbons, IEEE Trans. Electron Devices ED-32 (1985) 1918.
[18] W.D. Wilson, L.G. Haggmark and J.P Biersack, Phys Rev B15 (1977) 2458.
[19] W. Brandt, in: Atomic Collisions in Solids, vol 1., eds. S. Datz, B.R. Appleton and C.D. Moak (Plenum, New York, 1975) p. 261

[20] F.H. Eisen, Can. J. Phys. 46 (1968) 561.
[21] P.M. Echenique, Nucl. Instr. and Meth. B27 (1987) 256.
[22] J. Lindhard and A Winther, K. Dan. Vid. Selsk. Mat. Fys. Medd. 34 (1964) no. 4
[23] P M. Echenique, R.M. Nieminen and R.H Ritchie, Solid State Commun. 37 (1981) 779.
[24] P.M. Echenique, R.M. Nieminen, J.C Ashley and R H. Ritchie, Phys. Rev. A33 (1986) 897
[25] W. Wach and K Wittmaack, Nucl. Instr. and Meth. 194 (1982) 113
[26] A.E Michel, W. Rausch, P.A. Ronsheim and R.H. Kastl, Appl. Phys Lett. 50 (1987) 416

Nuclear Instruments and Methods in Physics Research B55 (1991) 671–675
North-Holland

Molecular complexes on implanted surfaces: unenhanced surface Raman study

M.S. Mathur, J.S.C. McKee and C.B. Kwok
Department of Physics, University of Manitoba, Winnipeg, R3T 2N2, Canada

The bombardment of surfaces by gaseous ions often results in the formation and adsorption of molecular complexes Conventional characterization techniques involving low energy electron beams cause desorption of these complexes. The characterization of ion implanted surfaces is undertaken at the University of Manitoba in association with the University of Kentucky by the technique of unenhanced surface Raman scattering with which it is possible to identify the complexes formed as a result of implantation of gaseous ions in various substrates.

1. Introduction

The bombardment of a solid surface by energetic ions often results in the retention of some of the incident ions by the lattice of the solid target In understanding the processes involved in the implantation and post-implantation behaviour of the gaseous atoms in solids, certain assumptions are made·

(1) Collision between substrate and gaseous atoms are the main source of energy loss, and this transfer of energy results in some damage to the solid.
(2) Retention and release are governed by trapping at the damage site and by the recombination of molecules at the surface.
(3) Formation of new molecular complexes on the implanted surface is due to the rearrangement of chemical bonds.

Conventional characterization techniques involving low energy electron beams (SIMS, Auger, LEED, etc.) cause desorption of these complexes and prove somewhat ineffective (complexes formed are often lost before the measurements commence).

2. Experimental

A linear ion accelerator employing a duo-plasmatron ion source is used as a 30–120 keV ion implanter. In order to achieve good vacuum a clean environment is maintained around the target area, and to prevent the deposition of pump oil a liquid nitrogen cooled jacket surrounds the target. A computer controlled beam scanning mechanism is used to deflect the ion beam across the target surface. In this way uniform implantation is achieved.

Raman studies of ion implanted samples were performed using a surface Raman facility at the University of Kentucky. The samples were mounted in a special mount designed to eliminate reflected light which otherwise would enter the monochromator (fig. 1), and the 5145 Å line from an Ar^+ laser is allowed to illuminate a small part of the implanted area. Using the standard 90° geometry for Raman scattering, scattered radiation is collected by a specially designed optical collection system. A cylindrical lens is used to transfer Raman scattered radiation to the entrance slit of a Spex 1403 0.85 m double monochromator. ECG and OMA data acquisition systems are used to collect, store and analyze the Raman activity on the surface. The average dark

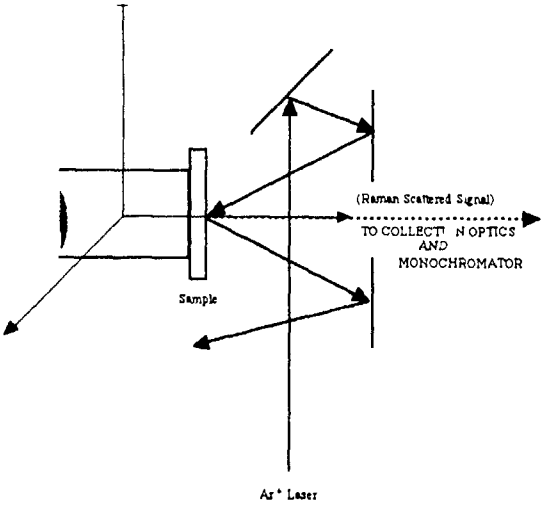

Fig. 1. Schematic diagram of the sample mounting arrangement for Raman characterization.

0168-583X/91/$03.50 © 1991 – Elsevier Science Publishers B.V. (North-Holland)

noise of the cooled photomultiplier duri a 2 s step was on the order of 2 counts. Signals significantly higher than the background mentioned earlier are taken as real.

Inelastic light scattering is a second-order process [1] and the corresponding scattering cross section is quite small (approximately 10^{-34} m^2 molecule-steradian typically) and normally the counting rates for the absorbed species are prohibitively small for routine surface studies. However, with a system dedicated to the study of Raman spectra from low polarizability molecules adsorbed onto a poor Raman signal enhancer [2], we have been successful in the characterization of various complexes on a variety of surfaces.

3. Results and discussion

3.1. Graphite surface implanted with D_2^+ (30 keV D_2^+, fluence 10^{17} ions/cm^2)

The Raman activity on the surface of the implanted graphite is evidenced by the presence of bands at 208, 225, 850, 890, 919, 990, 1034, 1046, 1060, 1085, 1095, 1135, 1156, 1185, 1207, 1280, 1290, 1306, 1330, 1348, 1495, 1530, 1550 and 1560 cm^{-1} as shown in fig. 2a–i. It is true that all these bands are very weak and require very patient and special attention, but nonetheless they are there. Dark noise during the 2 s/step is of the order of five counts. Only those signals significantly higher than the dark noise level are considered. The presence of two Raman bands at 1550–1560 cm^{-1} and 1348 cm^{-1} indicates that the surface is polycrystalline in nature, which can be expected from the ion bombardment on graphite surface. Tunistra and Koening [3] have reported a polycrystalline band at 1355 cm^{-1} and have attributed it to the particle size effect, which results in a change in the selection rule for Raman activity of certain phonons that were inactive in the infinite lattice. In other words, the 1348 cm^{-1} band is due to A_{1g} mode of small crystallites or to the boundaries of large crystallites. The 1550–1560 cm^{-1} doublet is characteristic of crystallinity in graphite. The C–C stretching vibration in hydrogen ion and deuterium ion implanted graphite occur around 993 and 852 cm^{-1} respectively [4] and our 990 and 850 cm^{-1}

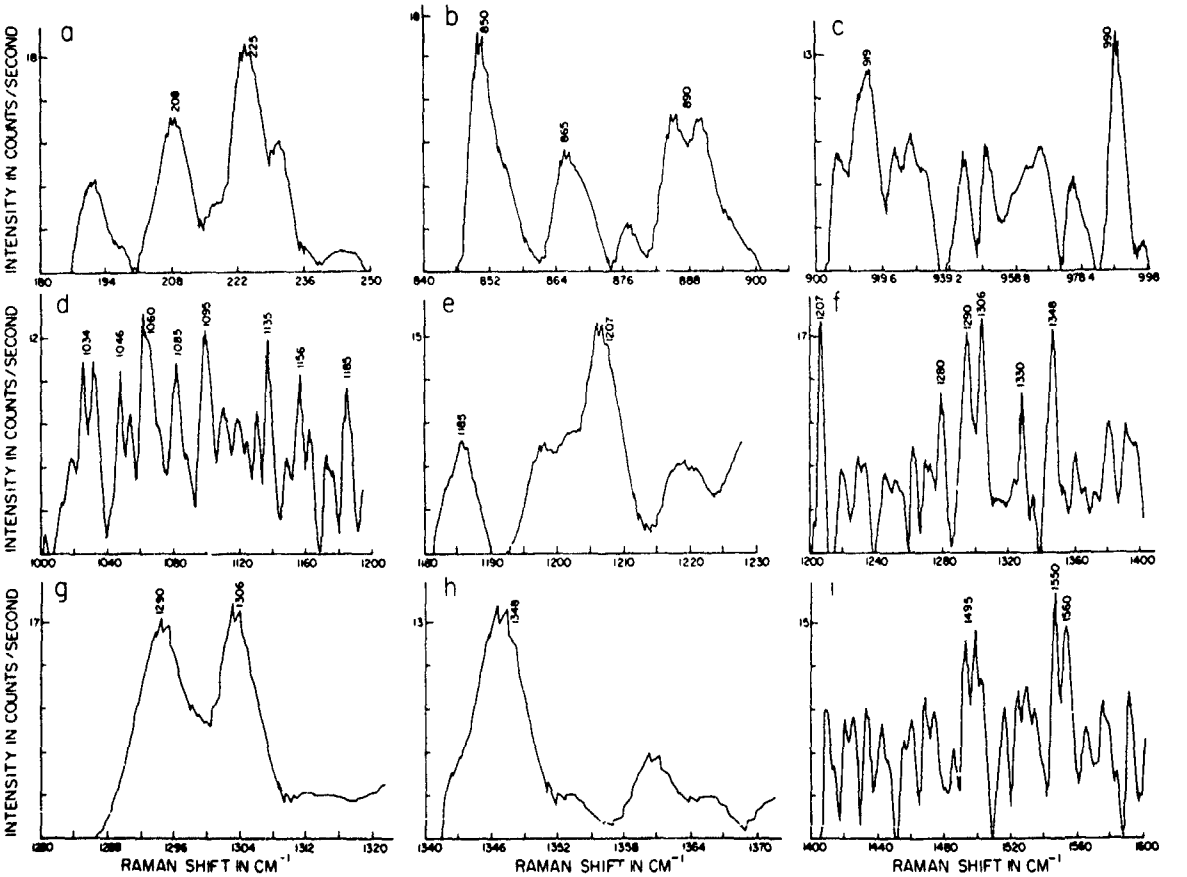

Fig. 2. Surface Raman spectra of a 30 keV D_2^+ implanted graphite surface. The entrance slit width was 100 μm, intermediate slit 100 μm, and exit slit 100 μm. For (a)–(c) the laser power was 800 mW and for (d)–(i) the laser power was 950 mW.

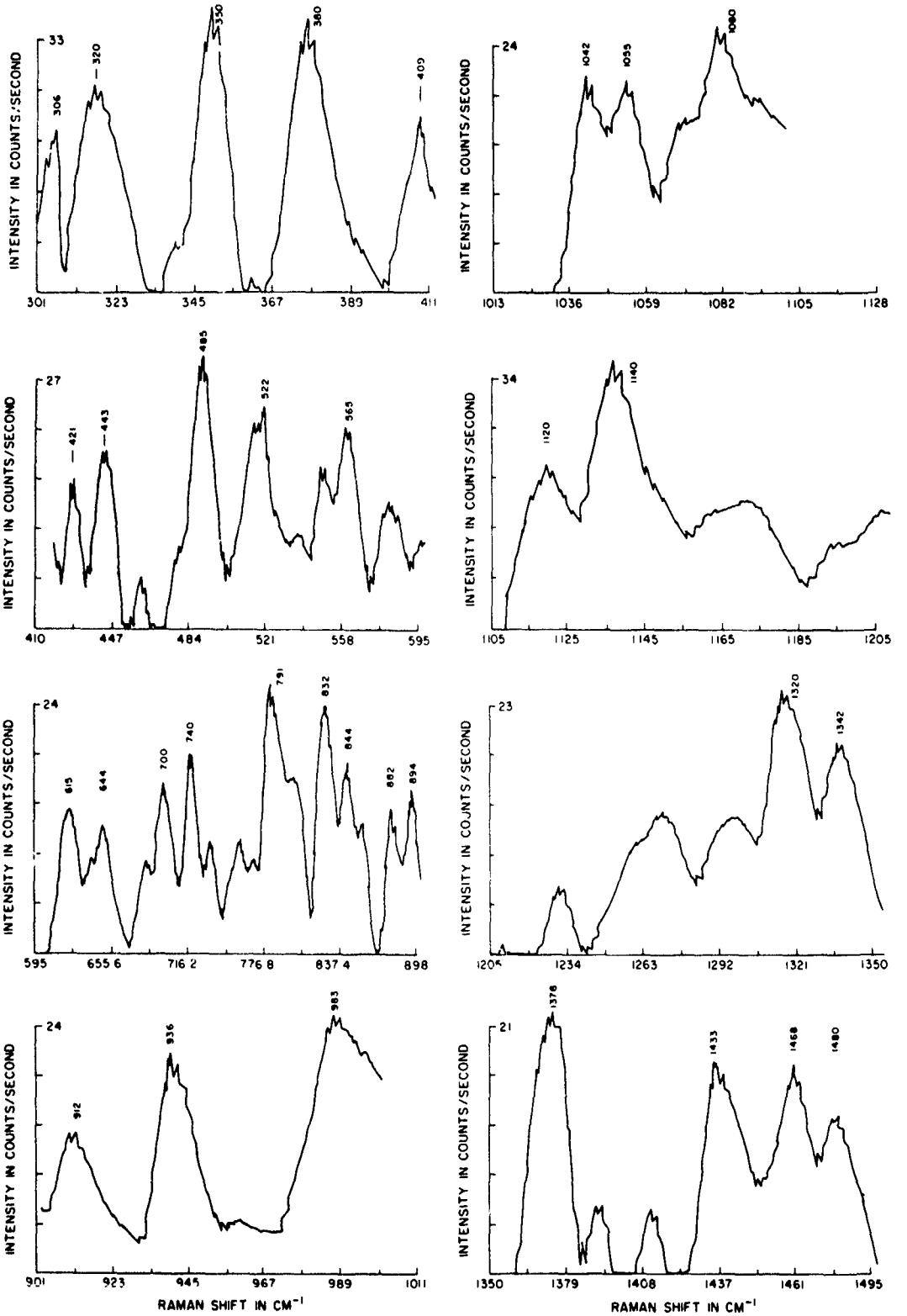

Fig 3. Surface Raman spectra of a 30 keV $^{16}O_2^+$ and $^{14}N_2^+$ implanted p-type silicon surface. The entrance slit width was 250 μm, intermediate slit 100 μm, and exit slit 250 μm. Laser power was 500 mW. Dark noise during a 5 s step was on the order of nine counts

Raman bands are in close proximity. Additional bands at 208, 225, 865, 890, 919 and 1055 cm^{-1} suggest the possibility of some other complexes of the type C_3H_8 and C_3D_8 being formed where C–C–C bending and twisting vibrations occur below 500 cm^{-1}. Pitzer [5] has reported one such band at 202 cm^{-1} and the 208–255 cm^{-1} doublet in our study is in good agreement with it. C–C stretching vibrations occur around 900 cm^{-1} in such complexes and the observed 865 and 890 cm^{-1} Raman bands could be assigned to these stretchings. The region between 900–1200 cm^{-1} is where most of the CH_3 and CH_2 (or CD_3 and CD_2) rocking and twisting vibrations are expected to be active, the 919 and 1060 cm^{-1} bands in our study are certainly well within this region of activity. Thus we have been able to detect the adsorbed carbon–hydrogen complex on the surface by the surface Raman technique [6].

3.2 Silicon surface bombarded with $^{16}O_2^+$ and $^{14}N_2^+$ (30 keV $^{16}O_2^+$ and $^{14}N_2^+$, fluence 10^{18} ions/cm^2)

The bombardment of crystalline silicon by a heavy dosage of ions ($\geq 10^{15}$ ions/cm^2) results in the formation of a thin continuous layer of amorphous silicon (a-Si) on the crystalline surface as is evidenced by the presence of a crystalline silicon peak at 522 cm^{-1} as well as an a-Si peak at 480 cm^{-1} in the Raman spectrum This combination of amorphous and crystalline silicon has been subjected to both $^{16}O_2^+$ and $^{14}N_2^+$ bombardment, and the surface Raman spectra of $^{16}O_2^+$ and $^{14}N_2^+$ implanted silicon are displayed in fig 3a–h The 405 and 522 cm^{-1} Raman bands confirm the existence of an amorphous silicon layer on the crystalline silicon surface. Our 308 cm^{-1} Raman band is equivalent to the 300 cm^{-1} longitudinal acoustical (LA) mode of a-Si as observed by Smith et al. [7]. The 615 and 983 cm^{-1} bands are the overtones of 308 and 485 cm^{-1} Raman bands respectively The IR spectra of $^{14}N_2^+$ and $^{16}O_2^+$ implanted silicon indicates two absorptions at 1036 and 800 cm^{-1} [8] which were attributed to Si–O and Si–N stretchings in the ion beam synthesized SiO_2 and Si_3N_4 layers In our study these stretchings appear at 1055 and 832 cm^{-1}, confirming the presence of both SiO_2 and Si_3N_4 on the $^{16}O_2^+$ and $^{14}N_2^+$ implanted silicon surface. The bombardment of p-type silicon with $^{16}O_2^+$ and $^{14}N_2^+$ results not only in the formation of an amorphous silicon layer but in various complexes of silicon, oxygen, and nitrogen in addition to the complexes of boron, oxygen and nitrogen (as evidenced by the presence of 740 cm^{-1} totally symmetric and 1480 cm^{-1} asymmetric longitudinal vibration of linear BO_2^- as well as 1378 cm^{-1} strong Raman band due to BN^-), boron being the p-type impurity in the silicon. The simultaneous formation of SiO_2 and Si_3N_4 supports the synthesis of an oxinitride $Si_xO_yN_z$ layer. Complexes of the type SiO_3^{2-}, B_2O_3, BO_2^- and BN^- have also been detected in the surface Raman spectrum shown in fig. 3. In addition, the synthesis of NO_2^- and its adsorption on the silicon surface has been demonstrated [9]

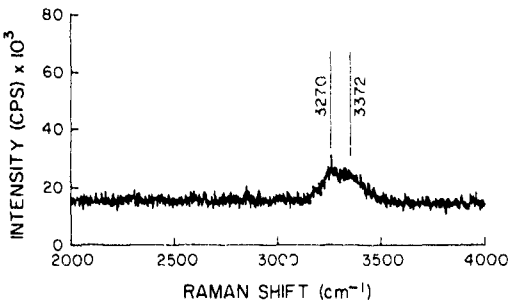

Fig 4. Raman spectrum of a 60 keV H_2^+ bombarded surface of TiC The entrance slit width was 80 μm, intermediate slit 80 μm, and exit slit 80 μm Laser power was 500 mW Total data acquisition time was 6 h comprising multiple scans with 2 s steps.

3.3 Carbon–hydrogen activity on a TiC surface implanted with H_2^+ (60 keV H_2^+, fluence 10^{17} ions/cm^2)

Presented in fig 4 is the Raman scattered signal accumulated over a period of 6 h from the surface of TiC bombarded with 60 keV H_2^+ to a fluence of 10^{17} ions/cm^2 A doublet with its component Raman bands at 3270 and 3372 cm^{-1} is the observed Raman signal. Gaseous methane (CH_4) has been studied extensively [10] and the Raman spectrum is known to contain two active fundamentals at 2914.2 and 3022.0 cm^{-1}. Dennison [11] also calculated the zero-order frequencies from the observed fundamentals. He obtained for CH_4 (in cm^{-1}) $\omega = 3029.8$ and $\omega_2 = 3156.9$, respectively. Raman bands observed by us have slightly higher shifts than the Raman bands of pure CH_4 gas. Then, too, the CH_4 adsorbed on a TiC surface with dissociated Ti atoms in the vicinity is different from an isotropic CH_4 gas. It is likely that in our situation some impedance is offered to the CH_4 molecules in their vibration, and this in turn can result in the damping of the vibrational frequencies. Fournier et al. [12] suspect that H being chemically active links to Ti, but the affinity of carbon for hydrogen is well known and the possibility of C–H bonding is much stronger. Our observations confirm this fact and suggest that the rearrangement of chemical bonds between the impinging hydrogen ions and the dissociated carbon atoms at the TiC surface results in the formation of carbon–hydrogen complexes.

The above observations clearly illustrate the versatility of the unenhanced surface Raman scattering technique in the detection and characterization of various complexes formed on the implanted surfaces.

Acknowledgements

The authors are grateful to the staff of the Materials Characterization Centre at the University of Kentucky for allowing us the use of their unenhanced surface Raman facility. Graduate student support for one of us (C.B. Kwok) by Manitoba Hydro is gratefully acknowledged.

References

[1] G Baym, Letters on Quantum Mechanics (Benjamin, New York, 1974).
[2] K.A. Arunkumar, H A Marzouk and E B Bradley, Rev. Sci Instr 56 (1984) 905.
[3] F Tunistra and J L Koening, J Chem. Phys 53 (1970) 1126
[4] S Bhagwantam, Indian J Phys 6 (1938) 718; F. Stilt, J. Chem Phys 7 (1939) 297
[5] S.K Pitzer, J Chem. Phys. 12 (1944) 310
[6] M.S. Mathur, V P. Derenchuk and J S.C McKee, Can. J. Phys. 62 (1984) 3.
[7] J.E. Smith, Jr, M.H. Brodsky, B.L. Crowder, M I. Nathan and A. Pinezuk, Phys. Rev Lett 26 (1971) 642.
[8] A D. Yadav and M.C. Joshi, Thin Solid Films 91 (1982) 45.
[9] M.S Mathur, V P Derenchuk and J S.C McKee, Can J. Phys. 62 (1984) 201.
[10] R.G. Dickerson, R.T Dillon and F Rasetti, Phys. Rev 34 (1929) 582
[11] D M. Dennison, Rev. Mod. Phys 12 (1940) 175.
[12] D. Fournier, M.O. Ruault and R.G. Saint-Jacques, Nucl. Inst. and Meth B19/20 (1987) 559

Nuclear Instruments and Methods in Physics Research B55 (1991) 676–680
North-Holland

A new method to calculate range and damage distributions by direct numerical solution of Boltzmann transport equations

M. Posselt

Central Institute for Nuclear Research, Rossendorf, PF 19, D(O)-8051 Dresden, Germany

We have developed a new method to determine depth distributions of implanted ions, recoiled target atoms and energy deposition in amorphous targets. Our procedure is based on the direct numerical solution of one-dimensional linearized Boltzmann transport equations for the scalar fluxes of the ions and the recoils. The profiles calculated by the new method are compared with range distributions obtained from TRIM Monte Carlo simulations. Our program BOTE is up to two orders of magnitude faster than the TRIM calculations.

1. Introduction

In the framework of the linear cascade theory [1] the ballistic processes occurring in solids during ion implantation are described by two alternative procedures: (i) "static" Monte Carlo simulations (e.g. TRIM [2]) and (ii) linearized Boltzmann transport equations (LBTE) [1,3–4]. The LBTE are linear partial integro-differential equations for the statistical distribution functions of the particles moving in ion-beam-induced collision cascades. The method of the LBTE is not so general and versatile as the Monte Carlo simulations. However, it yields ion range distributions, recoil range profiles, etc. by the solution of equations, not by statistical experiments. Therefore, in many applications the computing time is shorter than in the case of Monte Carlo simulations.

In the last ten years several methods for a direct calculation of the profiles by the LBTE have been proposed [5–10]. Most of the works consider a one-dimensional geometry. In contrast to the well-known LSS(WSS) theory [11,12] which yields the statistical moments of the range and damage distributions, these procedures can be applied to multilayer targets frequently used in modern ion beam technologies.

In section 2 of the present work the general form of the one-dimensional LBTE is briefly elucidated. In section 3 we develop a new efficient method to calculate the depth distributions of implanted ions, recoiled target atoms and energy deposition by direct numerical solution of the LBTE. This procedure is applied to characteristic examples of ion implantation. The results are compared with profiles obtained from TRIM Monte Carlo simulations (section 4).

2. One-dimensional Boltzmann transport equations

In the case of a one-dimensional planar geometry with normally incident ions, the statistical distribution function of the particles depends only on three variables: (i) the depth coordinate x, (ii) the energy E and (iii) the cosine of the angle θ between the direction of motion of the particles and the x-axis, $\eta = \cos\theta$. The LBTE for the scalar flux $f_1(x, E, \eta)$ of the ions is given by

$$\eta(\partial f_1/\partial x) = I_1(f_1) = I_{\mathrm{In1}}(f_1) + I_{\mathrm{In2}}(f_1) + I_{\mathrm{Ie}}(f_1). \tag{1}$$

I_1 consists of three parts. The first term describes the elastic atomic scattering for energy transfers T above a certain threshold $T_{\min}$:

$$I_{\mathrm{In1}}(f_1) = N\int_{\substack{T' > T_{\min} \\ E + T' = E'}} \mathrm{d}\sigma_{11}(E' \to E, \eta' \to \eta) \times f_1(x, E', \eta') - N\int_{\substack{T'' > T_{\min} \\ E = E'' + T''}} \mathrm{d}\sigma_{1T}(E \to E'', \eta \to \eta'') \times f_1(x, E, \eta). \tag{2}$$

N and $\mathrm{d}\sigma_{1T}$ are the particle density of the target atoms and the differential scattering cross section of the collisions between the incident ions and the target atoms, respectively. The first and the second integral in eq. (2) are called "gain" and "loss" terms, respectively. For "soft" atomic collisions with energy transfers below

0168-5 '3X/91/$03.50 © 1991 - Elsevier Science Publishers B.V. (North-Holland)

T_{min}, the change of the direction of motion of the projectiles can be neglected. In this case we obtain

$$I_{ln2}(f_l) = (\partial/\partial E)[NS_n(T_{min}, E)f_l],$$

$$S_n(T_{min}, E) = \int_{\substack{T'<T_{min} \\ E+T'=E'}} d\sigma_{lT}(E' \to E)T'. \quad (3)$$

The electronic stopping acts as a continuous friction force. $I_{le}(f_l)$ is given by

$$I_{le}(f_l) = (\partial/\partial E)[NS_e(E)f_l], \quad (4)$$

where S_e is the electronic stopping cross section. I_{ln2} and I_{le} are so-called "drift" terms. The scalar flux f_l must obey the following boundary condition:

$$\begin{aligned} &\eta \geq 0: \quad f_l(0, E, \eta) \sim \delta(\eta - 1)\delta(E - E_0), \\ &\eta < 0: \quad f_l(\infty, E, \eta) = 0. \end{aligned} \quad (5)$$

E_0 is the incidence energy of the ions. δ denotes Dirac's delta function. The LBTE for the scalar flux $f_T(x, E, \eta)$ of the target atoms is similar to that of the ions. Additionally, this LBTE contains a "source" term which describes the generation of moving target atoms by collisions with incident ions.

The ion range distribution $F_l(x)$ and the recoil range profile $F_T(x)$ can be determined using the solutions f_l and f_T of the LBTE for the ions and the target recoils, respectively:

$$F_l(x) = \lim_{E \to E_c} \frac{\int d\eta f_l(x, E, \eta)}{\int dx\, d\eta f_l(x, E, \eta)}, \quad (6)$$

$$F_T(x) = \lim_{E \to E_c} \frac{\int d\eta f_T(x, E, \eta)(m_T/m_l)^{1/2}}{\int dx\, d\eta f_l(x, E, \eta)}. \quad (7)$$

Below the cutoff energy E_C we assume the particles to be stopped. m_l and m_T are the masses of the ion and the target atom, respectively. If we neglect the energy transport by the recoiled target atoms, the profiles of energy deposition $F_D(x)$ are obtained from

$$F_D(x) = E_0 \frac{\int D(E, \eta)(f_l(x, E, \eta)|\eta|)\, dE\, d\eta}{\int D(E, \eta)(f_l(x, E, \eta)|\eta|)\, dE\, d\eta\, dx}, \quad (8)$$

where $D(E, \eta)$ denotes the energy deposition of a particle moving with an energy between E and $E + dE$ and a direction cosine between η and $\eta + d\eta$ within the depth interval dx. The number of particles incident in that depth interval is given by $f_l(x, E, \eta)|\eta|\, dE\, d\eta$. Therefore, $\int D(E, \eta)(f_l(x, E, \eta)|\eta|)\, dE\, d\eta$ is proportional to the whole energy deposition in dx. The profile of nuclear energy deposition $F_{Dn}(x)$ is determined by eq. (8), inserting

$$D(E, \eta) = N \int_{E+T'=E'} d\sigma_{lT}(E' \to E) q(T')(dx/|\eta|). \quad (9)$$

A certain part of the energy transfer T' of the particles contributes to nuclear energy deposition. It can be obtained by the known approximation of Robinson [13]:

$$q(T') = T'/\left(1 + k_d\left(\epsilon_d + 0.4\epsilon_d^{3/4} + 3.4\epsilon_d^{1/6}\right)\right), \quad (10)$$

$$k_d = 0.1334 Z_T^{2/3} m_T^{-1/2}, \quad \epsilon_d = 0.01024 Z_T^{-7/3} T', \quad (11)$$

where Z_T is the atomic number of the target. The distribution of the electronic energy deposition $F_{De}(x)$ is calculated by eq. (8) using

$$D(E, \eta) = N\left[S_e(E) + \int_{E+T'=E'} d\sigma_{lT}(E' \to E)(T' - q(T'))\right] \times (dx/|\eta|). \quad (12)$$

The relations (1)–(12) can be easily generalized to multicomponent and multilayer targets. In the latter case, the particle density and the differential scattering cross section – as functions of the target atomic number and mass – show discontinuities at the interface between the two layers.

3. Direct numerical solution

In the last decade several methods for solving the one-dimensional LBTE have been published. A short overview is given in refs. [1,3]. In general these methods are either special approximation procedures which are employed to treat the LBTE in particular cases [8,9] or numerical calculation schemes derived in a more or less intuitive way [5–7]

Our aim was to develop a new method of solution which satisfies the following conditions: (i) It is based on a consistent derivation from the LBTE. (ii) The method is not limited to a special class of ion–target combinations or to a certain range of implantation energies. (iii) The procedure is applicable to multicomponent and multilayer targets. (iv) The method yields ion range distributions, profiles of recoil implantation and energy deposition distributions. (v) The numerical solution of the LBTE for the scalar fluxes of the incident ions and the target recoils is performed directly using an explicit iteration scheme with finite differences.

In the following we elucidate some details of our procedure. At first we consider the LBTE for the scalar flux f_I of the incident ions. In general, the differential scattering cross section $d\sigma_{IT}$ in the first integral of eq. (2) ("gain" term) is written in the following form:

$$d\sigma_{IT}(E' \to E, \eta' \to \eta) = d\sigma_{IT}(E' \to E)\delta(e'e - \cos\vartheta(E', E)) \times d\eta'\, d\varphi'/4\pi. \quad (13)$$

The differential cross section $d\sigma_{IT}(E' \to E)$ is given by

$$d\sigma_{IT}(E' \to E) = \pi a_s^2 f(t'^{1/2})/(2t'^{3/2})\, dt', \quad (14)$$

with

$$t' = (C_F^2 E' T')/\gamma, \quad E' = E + T',$$

$$C_F = a_s m_T/(Z_I Z_T e^2 (m_I + m_T)) \quad \text{and}$$

$$\gamma = 4m_I m_T/(m_I + m_T)^2, \quad (15)$$

where Z_I is the atomic number of the projectile. Different relations for the screening length a_s and the scattering function f are known for special interatomic potentials. In the delta function of eq. (13), e' and e are vectors characterizing the directions of motion of the projectile before and after the collision, respectively. The scalar product $e' \cdot e$ must be equal to the cosine of the laboratory scattering angle ϑ which is a known function of E and T'.

The product $e' \cdot e$ does not depend only on the direction cosines η' of e' and η of e with respect to the x-axis but also on the azimuthal angle φ'. Since in the first integral of $I_{In1}(f_I)$ the scalar flux depends on η' but not on φ', one has to integrate the delta function with respect to φ'. We succeeded in performing the integration analytically by the solution of a spherical trigonometry problem. This was the crucial step in the elaboration of our new method of direct numerical solution. The result of somewhat lengthy calculation is [14]

$$a(E, \eta, E', \eta') = \int_0^{2\pi} \delta(e' \cdot e - \cos\vartheta(E', E))\, d\varphi'/2\pi = \left\{\theta\left[\sin\vartheta(1-\eta'^2)^{1/2} + \eta - \eta'\cos\vartheta\right] \times \theta\left[\sin\vartheta(1-\eta'^2)^{1/2} - \eta + \eta'\cos\vartheta\right]\right\} \times \left\{\pi\left[\sin^2\vartheta(1-\eta'^2) - (\eta - \eta'\cos\vartheta)^2\right]^{1/2}\right\}^{-1}, \quad (16)$$

θ denotes the Heavyside theta function. Finally, we obtain the following expression for $I_{In1}(f_I)$:

$$\frac{C_X C_E^2}{\gamma} \int_{T_{min}}^{\min[(\gamma/(1-\gamma))E,\, E_0 - E]} dT'(2T' + E)\frac{f(t'^{1/2})}{(2t'^{3/2})} \times \int_{-1}^{1} d\eta'\, a(E, \eta, E + T', \eta') f_I(x, E + T', \eta') - \frac{C_X C_E^2 E}{\gamma} \int_{T_{min}}^{\gamma E} dT'' \frac{f(t''^{1/2})}{(2t''^{3/2})} f_I(x, E, \eta), \quad (17)$$

with $C_X = \pi a_s^2 \gamma N$.

The expression $I_{In2}(f_I)$ can be transformed into

$$I_{In2}(f_I) = (C_X/C_E)(\partial/\partial E) \times \left[(T_{min}/\gamma E)^{1/2} S_n(C_F(E T_{min}/\gamma)^{1/2}) \times f_I(x, E, \eta)\right]. \quad (18)$$

The function S_n is the reduced (dimensionless) nuclear stopping cross section [2].

The LBTE for the scalar flux of the target recoils can be treated in a similar manner. In particular we have to consider the "source" term describing the generation of moving target atoms by the energy transfer from incident ions. The generalization to multicomponent targets leads to further "source" terms characterizing the generation of target recoils of a given sort by moving target atoms of another type.

Similar to other methods for solving the LBTE in this work, we only consider the motion of particles with $\eta \geq 0$ ("forward" direction). Particles with $\eta < 0$ are assumed to be stopped. Since the direction of ion incidence is $\eta = 1$, this approximation is mostly sufficient to calculate ion range distributions. It can also be used in the evaluation of profiles for the recoil implantation in layered targets, since these profiles are mainly determined by high-energy recoils. The scalar flux of the high-energy recoils shows a dependence on η which is similar to that of the scalar flux of the incident ions [15]. In the case of the implantation of light ions into very heavy targets, e.g. B^+ into Au on Si, the above approximation is not applicable. Then, the so-called "multipass" method [6,1] must be employed. In this procedure the motion of the particles with $\eta < 0$ ("backward" direction) is taken into account approximately.

With the approximation mentioned above and $I_{In1}(f_I)$ from eq. (17), $I_{In2}(f_I)$ from eq. (18), $I_{Ie}(f_I)$ from eq. (4) and similar terms for the LBTE for the scalar flux of the recoils, the further numerical treatment is evident. We have developed the computer program BOTE (BOltzmann Transport Equations) using an explicit iteration scheme with finite differences Δx, ΔE and $\Delta\eta$ with $T_{min} = E_C = \Delta T = \Delta E$. The stability of the iteration is determined by the "drift" terms. If the

electronic stopping dominates, ΔE and Δx have to be small to give sufficiently precise results. However, this may lead to a considerable computing time since for every depth step Δx the "gain" and the "source" terms must be calculated by numerical integrations with respect to E and η. To save computing time we employ the following procedure: The calculations are performed on a three-dimensional point grid (x, E, η) with a "fine structure" characterized by Δx, ΔE and $\Delta\eta$ and a "coarse structure" characterized by $\delta x = m_x \Delta x$, $\delta E = m_E \Delta E$ and $\Delta\eta$. A new calculation of the integrals is carried out only at the points of the "coarse structure". A further method to save computing time is the use of variable depth steps Δx. They are chosen as functions of the "friction" forces in the "drift" terms. Typical values used in our calculations are Δx: 100–10000 intervals, ΔE: 10–200 intervals, $\Delta\eta$: 5–20 intervals, m_x: 1–50 and m_E: 1–20.

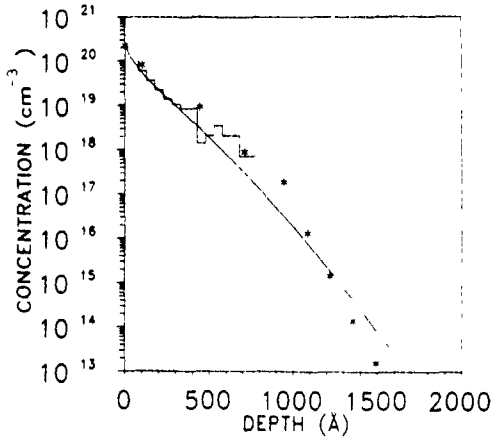

Fig. 2. Recoil range profile (Co in Si) for 150 keV Ar^+ implantation (10^{15} cm^{-2}) into Co (520 Å)/Si. Experimental data from ref. [17]

4. Results and discussion

Figs. 1a and b show ion range and energy deposition distributions obtained from direct numerical solution of the LBTE by the program BOTE (curves) and from TRIM Monte Carlo simulations (histograms). For both procedures we have used similar physical inputs. In particular, the nuclear atomic scattering is described by the "universal" potential [2] and the electronic energy loss is given by the combination of the Lindhard–Scharff and the Bethe–Bloch formulae [2]. In the calculation of the energy deposition profiles (fig. 1b) we have assumed that the energy transport by the target recoils can be neglected. The agreement of the distributions calculated by BOTE with the histograms simulated by TRIM is rather good In fig. 1a experimental data from the literature are shown for comparison [16]. Fig. 2 illustrates an example of recoil implantation The agreement between the curves obtained by BOTE with the histograms calculated by TRIM and with the experimental data [17] is satisfactory Using our program BOTE we can easily calculate the concentration profile over seven orders of magnitude. In the case of the TRIM program this is only possible by a time-consuming simulation of 10^6 to 10^7 particle histories. In the examples discussed above, the program BOTE is about 10 to 100 times faster than corresponding TRIM simulations with 10000 particle histories. Further examples of range distributions calculated by BOTE are given in refs. [3,4].

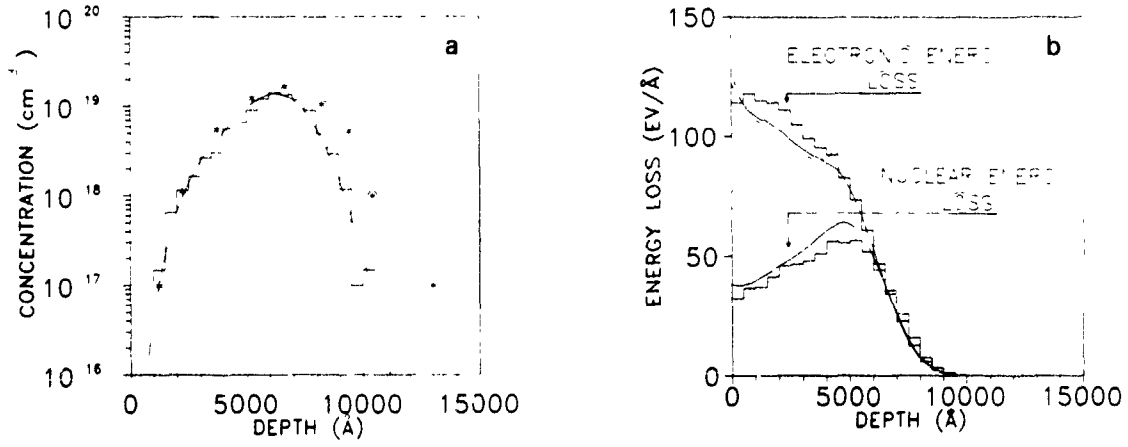

Fig 1. Range (a) and energy deposition (b) profiles for 1 MeV As^+ implantation (5×10^{14} cm^{-2}) into Si Experimental data from ref. [16].

5. Conclusions

A new effective and general method to calculate one-dimensional ion range distributions, profiles of recoiled target atoms and energy deposition distributions by direct numerical solution of the one-dimensional LBTE have been proposed. The method has two advantages: (i) It is based on a consequent derivation from the LBTE, and (ii) it is not limited to special applications. The procedure is up to two orders of magnitude faster than TRIM Monte Carlo simulations.

References

[1] M Posselt, Phys. Status Solidi (a) 112 (1989) 263.
[2] J.F Ziegler, J.P. Biersack and U. Littmark, The Stopping and Range of Ions in Solids (Pergamon, New York, 1985).
[3] M. Posselt, Proc. 3rd Int. Conf. on Energy Pulse and Particle Beam Modification of Materials (EPM'89), Dresden, September 1989, in: Physical Research, vol. 13, eds. K Hohmuth and E. Richter (Akademie-Verlag, Berlin, 1990) p. 81.
[4] M. Posselt, to be published in Vacuum (1990).
[5] L.A. Christel, J.F. Gibbons and S.W. Mylroie, J. Appl. Phys. 51 (1980) 6176.
[6] M.D. Giles and J.F. Gibbons, Nucl. Instr. and Meth. 209/210 (1983) 33.
[7] D.G. Ashworth, M. Moulavi-Kakhi and K.V Anand, J Phys. C17 (1984) 2449
[8] G. Bardos, Phys. Lett A119 (1987) 415.
[9] Luo Zengming and Wang Shiming, Phys. Rev. B36 (1987) 1885.
[10] Yu.D Lizunov and A.I. Ryazanov, Radiat. Eff. 107 (1989) 185.
[11] J. Lindhard, M. Scharff and H.E. Schiott, K. Dan. Vidensk. Selsk. Mat.-Fys. Medd. 33 (1963) no. 14.
[12] K.B. Winterbon, P. Sigmund and J.B. Sanders, K. Dan Vidensk. Selsk. Mat.-Fys. Medd. 37 (1970) no. 14.
[13] M.T. Robinson, Nuclear Fission Reactors (British Nuclear Energy Society, London, 1970) p. 364.
[14] M. Posselt, Annual Report, ZfK-621 (Central Institute for Nuclear Research, Rossendorf, 1986) p 63.
[15] M. Posselt, Nucl Instr. and Meth. B36 (1989) 420.
[16] M. Tamura, N. Natsuaki, Y. Wada and E Mitani, Nucl. Instr. and Meth. B21 (1987) 438.
[17] H.L. Kwok, Solid State Phenomena 1/2 (1988) 195

Nuclear Instruments and Methods in Physics Research B55 (1991) 681–685
North-Holland

Transport-theoretical studies of static and dynamic recoil mixing

J.J. Jimenez-Rodriguez [a], I. Abril [b], J.A. Peinador [a] and A. Gras-Marti [b]

[a] *Departamento de Electricidad y Electrónica, Facultad de Fisicas, Universidad Complutense, E-28040 Madrid, Spain*
[b] *Departament de Fisica Aplicada, Universitat d'Alacant, Apt. 99, E-03080 Alacant, Spain*

The introduction by ion bombardment of atomic species ("impurities") into a substrate can be performed in direct (or ion implantation) and indirect modes. The indirect or recoil implantation mode involves generating an impurity layer on top of the substrate, and bombarding the sample with some energetic ions. In the *dynamic* recoil-mixing mode one compensates, via simultaneous deposition of impurity atoms, the erosion of the surface layer by sputtering. We shall analyze the static and dynamic recoil-mixing modes with a theoretical formalism that describes the impurity and matrix concentration depth-profile evolution with bombarding ion fluence, accounting for atomic mixing, surface erosion, surface-barrier effects and matrix relaxation. The potentiality of the theoretical approach to obtain detailed recoil-mixing profiles and yields will be shown.

1. Introduction

The implantation of atomic species, which we shall call the *impurities*, into a substrate can be performed in direct and indirect modes. The direct mode of implantation requires the possibility to generate an impurity ion beam. The indirect or recoil implantation mode of operation involves producing an impurity layer on top of the substrate. Bombarding the sample with some energetic (usually inert) ions produces then the desired impurity implantation effect. This constitutes the static recoil implantation or recoil-mixing mode.

A *dynamic* improvement over conventional recoil implantation was introduced by Colligon et al. [1–3] and also investigated by other groups [4,5]. In this mode, the erosion of the surface layer by sputtering is compensated via simultaneous deposition of the impurity atoms, so that the impurity layer thickness remains constant at all ion fluences. The technique is known as dynamic recoil mixing (DRM). We shall stick to that terminology in this communication, although dynamic recoil implantation might be preferred [6] if one leaves the term mixing for the (more general) atomic relocation processes and implantation for a specific application.

The pros and cons of the DRM technique in comparison with direct ion implantation or with the static mode have been discussed at length and proven experimentally [1–3]. In brief, recoil-mixing profiles usually peak at the surface and decrease monotonically away from it. In contrast, direct ion implantation profiles have a more or less Gaussian shape [7]. Furthermore, less irradiation damage is obtained in the dynamic than in the static indirect mode of implantation. However, an etching of the remaining surface layer may be required before the recoil-implanted sample is used. The DRM technique has been used to evaluate mixing parameters [8] and also in adhesion studies of films to substrates [9]. The static recoil-mixing mode is usually employed with higher energy ions and larger layer thicknesses ($\approx$ 50–100 keV, 100–700 Å) than the dynamic mode ($\approx$ 5 keV, 25 Å). Estimates of static recoil-mixing profiles and yields are available [10,11]. Theoretical efforts to quantify and parameterize the DRM technique, however, have concentrated on computer simulations of transmission sputtering [3,8,12].

We shall study the dynamic and static recoil-mixing techniques using a powerful theoretical formalism [13–17] that accounts for concentration depth-profile evolution with ion fluence in irradiated polyatomic targets, including atomic relocation by collisional mixing, sputtering depletion of the target, surface-barrier effects and homogeneous matrix relaxation. Recoil concentration profiles and recoil yields in both static and dynamic configurations shall be obtained via numerical solution of the appropriate integro-differential equations. The model can equally be applied to analyze ion assisted deposition during ion bombardment [18].

Next we briefly set the theoretical stage, and in section 3 we present and discuss some results. The model used in the calculations is applicable in situations where temperature-dependent effects are not expected to contribute significantly to the mixing profiles.

2. Model

The balance equation derived in ref. [15] for the evolution with ion fluence of the composition of sputtered polyatomic targets, has been used to analyze

0168-583X/91/$03.50 © 1991 – Elsevier Science Publishers B.V. (North-Holland)

desorption by ion bombardment [14] and depth profiling via sputtering [15]. The formalism is explained in detail elsewhere [16], so here we only give the background. The effect of atomic species relocation by ion bombardment is contained in the relocation operators L_i [13,16,17]. These are expressed [19,20] in terms of the relocation cross section $d\sigma_i(x, z)$, which is defined [19] so that $\Delta\phi\, d\sigma_i(x, z)$ is the probability that an atom of species i is relocated from a depth x in the target, to a layer $(x+z, dz)$ after an ion fluence $\Delta\phi$. In refs. [14,17] one can find the relocation operators L_i specified for the contribution of cascade-mixing and recoil-mixing processes. The recoil-mixing mechanism describes the relocation of impurity and substrate atoms in direct collisions with incident ions. The cascade-mixing mechanism refers to the relocation of atoms participating in cascades developed in the target by energetic ions and energized recoils. We use analytical expressions for the relocation cross section [13,16,21].

Consider a bilayer system consisting of a layer of material 1 and thickness X, on top of a substrate of material 2. The plane $x = 0$ is always kept at the target surface. Let α_1 and α_2 be the fractional volume concentrations of species 1 and 2 in the target. They are given by $\alpha_i = N_i\Omega_i$ in terms of the effective atomic volume Ω_i and the atomic density N_i associated with the species i. The variation of these concentration at each depth x and each ion fluence ϕ, after a fluence increment $\Delta\phi$, can be expressed as [13]:

$$\Delta\alpha_i(x, \phi) = \Delta\phi\Big\{ L_i\alpha_i(x, \phi) - \frac{\partial}{\partial x}\Big[\alpha_i(x, \phi)\int_0^x dx' h(x', \phi)\Big] + v\,\delta(x)\delta_{i1}\Big\}, \quad (1)$$

where $i = 1$ or 2, $\delta(x)$ is Dirac's delta, δ_{ij} is Kronecker's delta, and $h(x, \phi)$ is a relaxation function to be specified below. The first term in the RHS of eq. (1), $L_i\alpha_i(x, \phi)$, describes atomic relocation by collisional mixing; the second term accounts for surface recession due to sputtering and homogeneous target relaxation; and the last term in this equation takes into account the simultaneous deposition of impurity material (δ_{i1}) over the target ($\delta(x)$), while one bombards the solid with energetic ions. This is a source term, accounting for the eventual replenishment of the impurity material as the surface is eroded. The surface erosion speed v is defined as the surface-layer thickness eroded per unit fluence, $v = dx/d\phi$. To describe the static recoil mixing mode we need remove the last term in eq. (1).

Our calculations include explicitly the effect of the target surface barrier through the relocation operator [14–17]; those particles with insufficient kinetic energy, in the direction of the surface normal, to overcome the surface planar potential barrier are accounted for. This surface effect is not considered in refs. [13,21]. One can also incorporate easily in eq. (1) the effect of the implant concentration profile [16], but this will be left out in the following calculations, in order to simplify the discussion.

The recession of the surface due to sputtering of species i is calculated as

$$v_i = \int_0^\infty \alpha_i(x, \phi)\sigma_i^s(x, \phi)\, dx, \quad (2)$$

where the sputtering cross section σ^s is closely related [14,16] to the relocation cross section. In fact, it corresponds to a relocation past the surface, from any depth x inside the solid. After a fluence $\Delta\phi$, a layer of thickness $\Delta X = v\,\Delta\phi$ is eroded away. In the ordinary mode of static recoil-mixing experiments, the surface layer will be reduced to a thickness $X - \Delta X$. For the constant layer-thickness mode of recoil implantation operation (DRM), we compensate the sputtering effect by introducing a layer of thickness ΔX at the surface of the target after each fluence increment $\Delta\phi$, and we solve numerically the balance eq. (1).

Two *dynamic* recoil-mixing modes will be modeled theoretically. In mode 1, DRM1, we replenish the eroded surface layer with impurity atoms in the same amount that impurities are lost by sputtering. In the second model DRM2, we replenish the eroded surface layer with impurity atoms in an amount which coincides with the number of impurity *and* substrate atoms that have been sputtered away. This second dynamic mode is closer to the experimental situation, where the total (layer plus substrate) mass loss is monitored by means of a quartz microbalance [1–3].

The relaxation function, $h(x, \phi)$ in eq. (1) is usually specified by assuming that the target relaxes homogeneously, after each ion fluence increment, to a constant volume concentration. This means that the atomic density of the target is not constant in the solid [13–17]. The relaxation model adopted in the present calculations is similar to the one used in dynamic Monte Carlo simulations of high-fluence effects during ion bombardment [22,23]. The atomic species are assigned an effective atomic volume equal to the reciprocal standard density of the corresponding homogeneous medium. For instance, for the system Al/Si that we study in the next section, these atomic volumes are 20 Å^3 for Si and 16.6 Å^3 for Al. When, during the evolution of target concentrations by irradiation, local over- or under-densities are generated, the expansion or contraction via relaxation or packing is performed in a given depth interval so that the existing atoms in that interval are allowed to occupy their "standard" volumes.

The integro-differential eq. (1) is solved numerically using a finite-difference method for static and dynamic

recoil-mixing techniques. Some results are presented in the following section.

3. Results and discussion

The theoretical model outlined above can be applied in a most straightforward manner when the masses of the atomic species involved do not differ much, and we shall consider such a situation in order to test the code. In this particular case, the target can be treated as monoatomic for the slowing down of the particles. Also, the relocation operators will not depend on the atomic concentration in the target, and they are similar, i.e., $L_1 \approx L_2 \approx L$. And then, the relaxation operator will be $h(x) \approx L(x)$. Therefore, in this limit the balance eq. (1) is linear. Experiments, on the other hand, where depth analysis techniques such as RBS are used [3,4,8,18], require a wide difference in the atomic masses of the target constituents. Comparison of theoretical predictions with actual experiments is under way and will be reported elsewhere. As an example of model calculations, we consider a bilayer consisting of a 10 Å thick Al film on top of a Si substrate, the system being bombarded with 5 keV Ar ions. We shall compare the dynamic and the static modes of recoil mixing for this system. In the analysis of recoiling particles leading to ejection through the target surface, we use the surface binding energy of aluminum at all ion fluences. This overestimates the sputtering yield of silicon atoms.

Fig. 1 shows the impurity, Al, recoil-mixing depth profiles obtained in the static mode, i.e., for a given initial 10 Å layer of Al and an ion fluence $\phi \approx (2\text{–}10) \times 10^{14}$ cm^{-2}. The amount of Al in the layer decreases rapidly for increasing fluence, and more Si atoms show up close to the surface. Notice the long tails in the concentration profiles of Al extending deep into the substrate, due to the operation of the recoil implantation and cascade mixing mechanisms mentioned before, which push impurity atoms towards the bulk of the substrate. The initial layer becomes only slightly narrower upon irradiation. Due to the relaxation mechanism assumed, namely volume conservation, and because the Si atoms have a larger atomic volume, the reduction in the initial layer thickness due to Al sputtering is compensated by a layer thickness increase due to the arrival of Si atoms relocated from the bulk. The net result is then that the layer thickness remains almost constant at 10 Å, up to a fluence where the location of the interface fades away (at $\phi > 10^{15}$ cm^{-2})

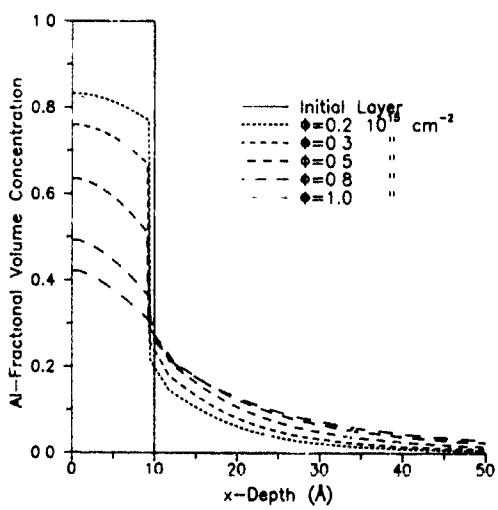

Fig. 1. Impurity concentration profiles at different ion fluences, ϕ, for 5 keV Ar^+ bombardment of an Al/Si sample. The initial layer thickness is 10 Å. There is no replenishment of sputtered material (static mode)

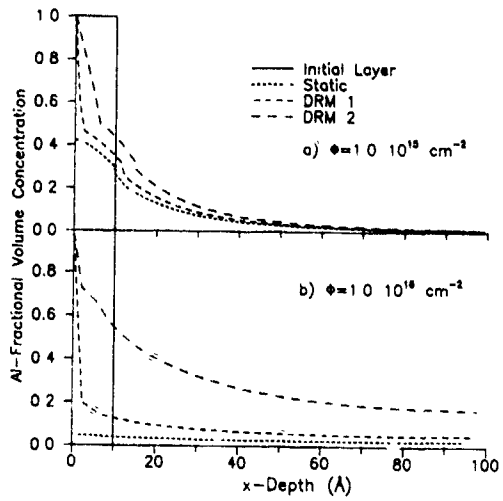

Fig. 2 Impurity concentration profiles for the three recoil-mixing modes discussed in the text and two ion fluences, for 5 keV Ar^+ bombardment of an Al/Si sample The initial layer thickness is 10 Å

We compare in figs. 2a and b the three modes of recoil-mixing operation, static, DRM1 and DRM2, in terms of the depth profiles of the impurities at two ion fluences, for the same system as in fig. 1. With increasing fluence there is, in the three modes investigated, a rapid decrease of the profile in the interface region. The overall decrease of the Al profile with ion fluence is very strong in the static and DRM1 calculation, and for both cases, at $\phi > 10^{16}$ cm^{-2} the maximum Al concentrations is below 10% at any point beyond the initial location of the interface. Note again the appearance of long tails in the impurity concentration as the fluence increases.

In considering the two basic mechanisms of atomic mixing that contribute to the recoil implantation of the impurity atoms, one may add that the recoil-mixing

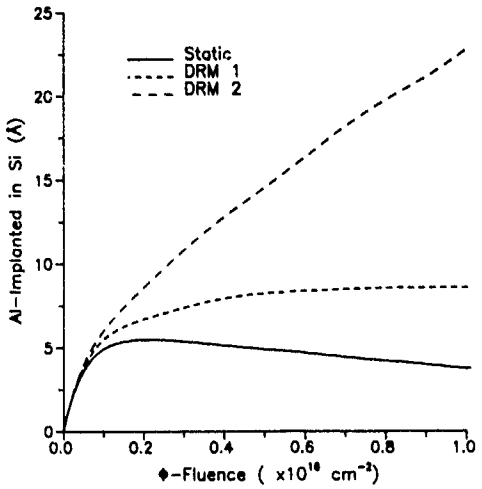

Fig 3 Integrated amount of impurity atoms recoil implanted past the interface, $\int_{x_0}^{\infty} \alpha_{Al}\, dx$, as a function of ion fluence for 5 keV Ar^+ bombardment of an Al/Si sample. The initial layer thickness is 10 Å The three recoil-mixing modes are described in the text

mechanism mainly contributes to the tails of the profiles at large depths. On the contrary, the cascade-mixing mechanism provides the major contribution to the calculated profiles close to the interface. It is very simple to observe this in the calculations, by switching off the relocation mechanisms one at a time.

Not shown in fig. 2 is that for intermediate ion fluences the DRM1 mode gives rise to a depth profile that rapidly becomes quasi-stationary: there are no important changes in the shape nor in the value of the concentration of Al versus depth. However, as seen in fig. 2, the concentration of Al in the DRM2 mode increases with fluence: the tail becomes less steep at large depths, and nearly constant up to depths commensurate with the range of the bombarding ion. At an ion fluence of 10^{16} cm^{-2} the mixed Al–Si region contains about 30% of Al.

The steeply rising part of the DRM profiles that appears in fig. 2, very close to the surface, is due to the replenishment of the surface layer by simultaneous deposition. The nearby bump, more pronounced in fig. 2a, is a reminiscence of the structure of the initial step. Anyway, these two are details extending only a few Å within the monolayer range, and the discontinuities are a consequence of the numerical procedure.

Fig. 3 shows the integrated amount of recoil implanted material, versus ion fluence, for the three recoil implantation modes mentioned before and for the same ion–target system. This result was obtained by integration of profiles like those shown in fig. 2, for impurities located beyond a depth x_0 that specifies the interface position at fluence ϕ. In actual experiments the position x_0 of this interface is not well defined [10] and some criterion has to be introduced. From an experimental viewpoint [1–3], and for the DRM2 mode, it appears simpler to consider that the amount of impurities missing from the impurity layer (with the initial thickness) corresponds to the total amount of recoil implanted atoms [24]. In the calculations reported here, x_0 is defined as:

$$x_0 = X - \int_0^{\phi} v(\phi')\, d\phi', \tag{3}$$

where X is the initial layer thickness, and the erosion rate $v(\phi)$, given by eq. (2), depends on the recoil implantation mode considered. For the static mode the erosion rate of the impurity atoms has to be taken into account, and $v = v_{Al}$. Naturally, $v = 0$ for the DRM1 mode. For the DRM2 mode, however, the negative of the erosion rate of the substrate atoms enters $v = -v_{Si}(\phi)$, and depends on the ion fluence.

As one can see in fig. 3, up to ion fluences $\phi \approx 5 \times 10^{14}$ cm^{-2} there are no significant differences in the total amount of Al recoil-mixed among the three recoil-mixing modes, since the total amount of sputtered material is small. For larger fluences, in the static mode, the amount of impurity atoms remaining in the target decreases with fluence. On the other hand, the integrated recoil yield saturates to a constant value in the DRM1 mode, i.e., the amount of Al atoms in the target reaches a steady state. Contrarily, in the DRM2 mode, the Al concentration steady increases with ion fluence for a wider fluence interval. This behavior has been actually seen in the experiments [3], and reflects the fact that the amount of Al introduced into the target is larger than the amount sputtered away. Eventually, the integrated yield also saturates in the DRM2 mode of operation.

The slope of the curves in fig. 3 is related to the recoil yield, or number of recoil-implanted atoms per bombarding ion,

$$Y_R = \frac{d}{d\phi} \int_{x_0}^{\infty} \alpha_{Al}\, dx. \tag{4}$$

At low fluence, $Y_R \approx 3$, the same value for the three modes. The largest rate of recoil implantation occurs at low fluence, when the total amount of Al in the layer is maximum. For the static mode at high fluences, there is a transition to a negative value of the recoil yield, whereas $Y_R \approx 0$ for DRM1, since the amount of sputtered Al coincides with the amount of deposited impurity atoms. At high fluences, in the DRM2 mode, one still has a recoil yield $Y_R \approx 2$, i.e., one ion is able to introduce indirectly two recoils into the substrate.

The calculations discussed here were done for a thin (10 Å) layer, in order to keep the amount of computing time low. In this way, the effects are observed without having to go to very high fluences. We have done the

calculations for a thicker layer (60 Å) and the overall trends are similar to those discussed here, although naturally the absolute quantities vary. One can, however, scale the present results to other ion energies and layer thicknesses by using the energy deposition function F_D [25]. So, for example at 100 keV and for ~ 600 Å films, there is more mixing in the neighborhood of the interface, where F_D is at a maximum.

4. Conclusions

The general theoretical framework describing the composition of irradiated polyatomic targets is capable of providing detailed insight into the recoil-mixing technique. Further investigations of the predictions of the model for actual experimental arrangements are under way. It is of interest, for example, to analyze both theoretically and experimentally an extended version of the dynamic mode DRM2, whereby the amount of replenished impurities is larger than the amount of sputtered atoms. Maybe one could then increase the value of the recoil yield at high fluences.

Acknowledgements

This work has received support from the Spanish DGICyT (projects number PS88-0066 and PS89-0088). Discussions with Prof. G. Carter, Prof. J. Colligon, Dr. H. Kheyrandish and Dr. R.P. Webb were facilitated by The British Council support via an Academic Link.

References

[1] W A Grant and J.S. Colligon, Vacuum 32 (1982) 675.
[2] J.S. Colligon, Mater. Sci Eng 69 (1985) 67,
J S. Colligon and A E Hill, Vacuum 35 (1985) 508.
[3] P Argyrokastritis, D S Karpuzov, J S. Colligon, A.E. Hill and H. Kheyrandish, Philos Mag A49 (1984) 547.
[4] J. Budinavicius, L Pranevicius and S Tamulevicius, Phys. Status Solidi A114 (1989) k25
[5] F Yucai, Y. Dawei, L. Wenzhi and W. Yuntao, Vacuum 39 (1989) 255.
[6] A. Gras-Marti and U. Littmark, in: Materials Modification by High-fluence Ions Beams, eds. R. Kelly and M.F. da Silva, NATO ASI Series E 155 (1989) p 257.
[7] K. Paprocki and I. Brylowska, Phys. Status Solidi A94 (1986) 391.
[8] H. Kheyrandish, J.S. Colligon, D.S. Karpuzov, N.A.K. Hussein, Thin Solid Films 170 (1989) 127.
[9] N.A.G. Ahmed and J S. Colligon, Vacuum 38 (1988) 83
[10] A. Gras-Marti, Phys. Status Solidi A76 (1983) 621;
I Abril, R. Garcia-Molina and A Gras-Marti, Phys. Status Solidi A96 (1986) 161.
[11] K. Paprocki, I. Brylowska and W. Syszko, Appl. Phys. A45 (1988) 109;
K. Paprocki and I. Brylowska, Radiat. Eff. Lett. 87 (1985) 63;
K. Paprocki, I. Brylowska, W. Andra and J. Krynicki, Phys Status Solidi A112 (1989) 301.
[12] D.S. Karpuzov, J.S. Colligon, H. Kheyrandish and A E Hill, Nucl. Instr. and Meth. B6 (1985) 474.
[13] P. Sigmund, A. Oliva and G Falcone, Nucl Instr and Meth. 194 (1982) 541.
[14] J A. Peinador, I. Abril, J.J. Jimenez-Rodriguez and A Gras-Marti, Nucl. Instr. and Meth. B48 (1990) 589.
[15] J A Peinador, I Abril, J J. Jimenez-Rodriguez and A. Gras-Marti, Surf Interf. Analysis 15 (1990) 463.
[16] J.A. Peinador, I. Abril, J J Jimenez-Rodriguez and A. Gras-Marti, to be published.
[17] J.A. Peinador, I. Abril, J.J Jimenez-Rodriguez and A. Gras-Marti, Vacuum 39 (1989) 695
[18] J P. Budinavicius, L J. Pranevicius and S.J Tamulevicius, Mater Sci. Eng. A115 (1989) 193
[19] P Sigmund and A Gras-Marti, Nucl. Instr and Meth 182/183 (1981) 25, Nucl Instr. and Meth. 168 (1980) 389
[20] A. Gras-Marti and P. Sigmund, Nucl. Instr and Meth 180 (1981) 211
[21] U. Littmark and W O. Hofer, Nucl Instr. and Meth. 168 (1980) 329;
U. Littmark and W.O Hofer, in: Topics in Current Physics, ed. H. Oechsner (1984) chap 8
[22] W. Möller, in. Materials Modification by High-fluence Ion Beams, eds. R. Kelly and M.F. da Silva, NATO ASI Series E 155 (1989) p. 151
[23] A Schönborn, N Hecking and E.H Te Kaat, Nucl Instr. and Meth B43 (1989) 170.
[24] H Kheyrandish, private communication.
[25] K.B Winterborn, P Sigmund and J B. Sanders, K Dan Vidensk Selsk. Mat. Fys. Medd 37 (1970) no 14

Nuclear Instruments and Methods in Physics Research B55 (1991) 686–690
North-Holland

High-dose oxygen implantation into silica

R.J. Chater and J.A. Kilner
Department of Materials, Imperial College, London SW7 2BP, UK

K.J. Reeson, A.K. Robinson and P.L.F. Hemment
Department of Electronic and Electrical Engineering, University of Surrey, Guildford, Surrey GU2 5XH, UK

High doses of the stable oxygen-18 tracer isotope have been implanted at 200 keV into thick thermal oxide on silicon to study oxide sputtering in conditions similar to the formation of isolated silicon device islands by SIMOX. Final tracer distributions were obtained by secondary ion mass spectrometry confirming the high mobility of oxygen within the silica, diffusion coefficient 1.7×10^{-12} cm^2 s^{-1}, with rapid desorbtion of excess oxygen from the top silica surface after perfect isotopic exchange as the oxide layer remains at the stoichiometry of SiO_2

1. Introduction

Silicon-on-insulator (SOI) structures may be formed by high-dose ion implantation of energetic oxygen ions into silicon held at elevated temperatures (SIMOX), followed by a subsequent anneal. This process is actively being developed for future small-geometry integrated circuitry to exploit its potential advantages over bulk silicon in radiation hardness and higher switching speeds SIMOX technology has recently been extended to achieve both vertical and lateral isolation of silicon device islands in a single implantation step or total dielectric isolation (TDI) [1]. Prior to implantation a silica masking layer is grown or deposited in which windows are opened to define the silicon device islands. In the masked regions, with the correct thickness of surface silica, the incoming oxygen ions penetrate below the mask and into the underlying silicon where the buried oxide layer is synthesized. It has been found that the masked region is eroded at a much faster rate than the window region so that the mechanism of buried layer formation for these two regions is different [2].

In the experiments reported in this work, high doses of the stable tracer isotope ^{18}O at 200 keV were implanted into thick silica mask layers (thick thermal oxide) on silicon. The thickness of the silica mask, 1800 nm, was chosen to be much greater than the total range of the oxygen, approximately 600 nm. Implantations were performed at a sample target temperature of ~ 500 °C using beam heating to re-create SIMOX and TDI fabrication conditions and study the sputtering of the mask material. The final tracer ^{18}O distributions were obtained by secondary ion mass spectrometry (SIMS). Thus we have been able to compare the implanted and unimplanted regions of the thermal oxide with respect to the buildup of ^{18}O and oxygen mass transport in the silica as the surface of the mask recedes by sputtering.

2. Experimental

A device grade 3 inch n-type wafer (P-doped, 14–26 Ω cm) was thermally oxidized in wet conditions to a thickness of 1.2 μm and a further 0.6 μm of SiO_2 was deposited by a low-temperature deposition technique. The oxidized wafer was then densified by annealing at 1300 °C in flowing argon/5% oxygen mixture atmosphere for several hours. The resulting structure, 1.88 μm of oxide on silicon was used as the starting material for oxygen-18 implantations with the 500 keV heavy ion implanter at the University of Surrey. To minimise conductive heat losses the wafer was thermally isolated from the sample holder by means of small silicon tips [3]. Implanter beam currents of (60 ± 2) μA, instantaneous current density ~ 0.1 mA/cm^2 and power density ~ 40 W/cm^2 were used to raise and maintain the wafer temperature to (580 ± 20) °C [3]. The central area (25 mm × 25 mm) of the wafer was uniformly implanted with 400 keV, $^{18}O_2^+$ ions by raster scanning the implanter beam to total atomic doses in the range 5×10^{16} to 1.8×10^{18} ^{18}O/cm^2, see table 1. No compensating electron flux was applied separately during implantation although secondary electrons generated in the vicinity of the target were redirected on to the target by local suppression electrodes.

After implantation the wafers were cut into small samples and the ^{18}O and ^{16}O distributions measured

0168-583X/91/$03 50 © 1991 – Elsevier Science Publishers B V. (North-Holland)

using an Atomika SIMS at Imperial College. The samples were sputtered using a 10 kV Xe^+ primary beam at normal incidence to produce a 600 μm × 600 μm square crater. The intensities of the $^{16}O^-$, $^{18}O^-$ and $^{28}Si^-$ negative secondary ions from the central 6% of the crater were monitored sequentially during sputtering. Charge compensation at the surface of the sputtered crater was achieved using a coincident 400 V, 5 μA electron flood. This value, which represents an electron current density of less than 1 mA cm^{-2}, was chosen to avoid reduction of the silica by decomposition and oxygen desorption [4]. Finally, the depth of the crater was measured by the stylus-based TALYSTEP instrument and the sputter time scale directly converted to sputter depth.

The oxygen isotope profiles are presented as their respective O/Si intensity ratios, which removes the effect of any charging over a large range of energies (~ 40 V) [5]. The ratio of the ^{18}O intensity to the total oxygen intensity ($^{18}O + ^{16}O$), the ^{18}O isotopic ratio, also removes the effect of charging and oxygen yield enhancement of negative ions because these phenomena are the same for both isotopes at each point in the profile. The isotopic ratio profiles are used for comparisons between samples of different total oxygen doses and for estimations of the retained oxygen dose in the surface layer. Because the original oxide contains ^{18}O at the natural abundance level of 0.0020 prior to implantation, calculations using the isotope ratio profile plots have this natural abundance level subtracted in this study of the implanted ^{18}O atoms.

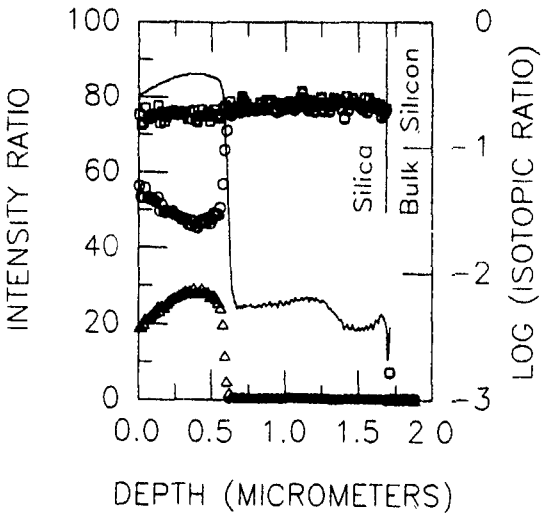

Fig. 1. SIMS oxygen depth profiles of ^{16}O (○), ^{18}O (△) and $^{16}O + ^{18}O$ (□) from sample K207 implanted with 1.1×10^{18} $^{18}O^+/cm^2$. The ^{18}O isotopic ratio (———) shown is derived from these profiles.

3. Results and discussion

3.1 Oxide sputter-rate

In fig. 1 the ^{18}O and ^{16}O concentration depth profiles are shown for the sample implanted with the dose of 1.1×10^{18} $^{18}O/cm^2$. Fig. 1 includes the plot of the total oxygen ($^{18}O + ^{16}O$) depth profile which allows the thickness of the remaining oxide to be readily determined and also the oxygen-18 isotopic ratio profile within the thermal oxide surface layer. For each of the implantation doses given in table 1, the thickness of the surface oxide sputtered away can be determined by comparison with the unimplanted reference using the thermal oxide–silicon interface as the reference marker. This data is plotted in fig. 2 with data from ref. [2] obtained under similar implantation conditions but using a marker position that was *within* the ^{18}O implantation profile. Both sets of data essentially confirm the sputtering coefficient of 1.1 atoms per incident particle of 200 keV oxygen ions in SiO_2, assuming a density of 2.3 g cm^{-3}. Computer simulations [2] which consider only the kinetics of sputtering give a value of 0.38 atoms/incident ^{16}O ion. The higher experimental value which has been confirmed in this work is assumed to be

Table 1
Implantation history and tabulated results derived from SIMS depth profiles for each of the samples

Sample identity	Nominal dose [$^{18}O/cm^2$]	Oxide lost [μm]	Interface [a] depth, width [μm]	Retained dose [b] [$^{18}O/cm^2$]
K207, unimplanted	0	0	–	–
K207	5.0×10^{16}	0.071	–	1.3×10^{16}
K260	4.0×10^{17}	0.096	0.569, 0.034	3.5×10^{16}
K207	4.5×10^{17}	0.049	0.590, 0.027	3.7×10^{17}
K207	7.0×10^{17}	0.118	0.584, 0.034	6.2×10^{17}
K260	1.1×10^{18}	0.180	0.583, 0.027	9.2×10^{17}
K260	1.4×10^{18}	0.233	0.580, 0.035	9.9×10^{17}
K260	1.8×10^{18}	0.280	0.585, 0.033	1.1×10^{18}

[a] Measured dose assumes an oxide density of 2.3 g cm^{-3}
[b] Depth measured at the 50% down point and width between the 75 and 25% down points on the isotopic ratio curve.

due to chemical processes which are enhanced at the implantation temperature of ~ 500 °C. The comparable sputter coefficient for silicon, appropriate to the window region in TDI is 0.2 atoms per incident ion, that is one fifth smaller.

3.2. ^{18}O implantation profile in silica

The isotopic ratio profile of the implanted ^{18}O for the lowest implant dose of 5×10^{16} $^{18}O/cm^2$ is shown in fig. 3 to be a skew Gaussian with a background level of 0.0020 corresponding to the natural abundance of ^{18}O. The peak of the distribution R_{MAX}, is at 443 nm. This low-fluence ion implantation profile was simulated using the PC-based TRIM88 code [6] and detailed calculations with full target damage cascades. The same R_{MAX} is obtained if the silica target density is set to the rather high value of 2.5 g cm^{-3} when $R_p = 400$ nm and straggling = 83 nm. The total range of oxygen is 600 nm, slightly shorter than experiment.

3.3 ^{18}O buildup in the surface layer

The isotopic ratio profile for one of the samples is shown in fig. 1 and represents the measured fraction of the network of oxygens in the surface oxide that is now oxygen-18 atoms. This profile is one of the series shown

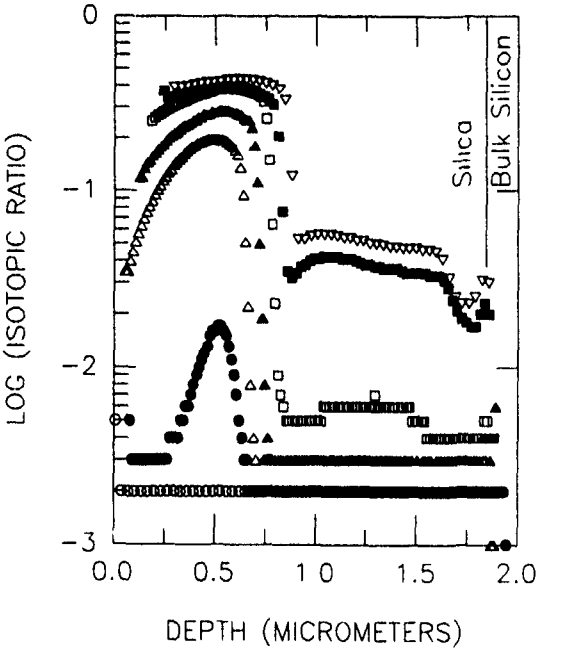

Fig. 3. The ^{18}O isotope ratio profiles for the samples implanted with the doses of ^{18}O listed in table 1; unimplanted (○), 5×10^{16} (●), 4.5×10^{17} (△), 7×10^{18} (▲), 1.1×10^{18} (□), 1.4×10^{18} (■), 1.8×10^{18} (▽) The profiles are offset by the corresponding thermal oxide lost as listed in table 1

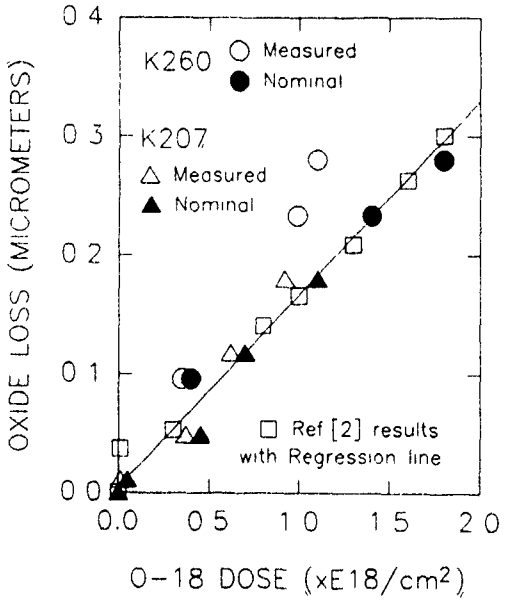

Fig. 2. Sputtered oxide lost from the thermal oxide surface due to ^{18}O implanted at 200 keV. These results, given in table 1, are plotted for the nominal ^{18}O dose (●, ▲) and the retained ^{18}O as a dose (○, △) Comparable nominal dose results from ref. [2] are also plotted (□) with their first order regression line fit (———).

in fig. 3 which includes all the implantation doses listed in table 1 except K260, dose 4E17 $^{18}O/cm^2$ which has been omitted for clarity. The same position for the thermal oxide–bulk silicon interface on the x-axis in fig. 3 has been achieved by plotting the ^{18}O isotopic ratio profile with a depth offset of the corresponding oxide thickness lost for each implantation dose.

Samples with doses 4.5×10^{17} $^{18}O/cm^2$ and above are substantially broadened particularly towards the surface where the TRIM88 simulation, used in section 3.2, gives a peak in the damage distribution. The surface layer containing the implanted ^{18}O is characterised by a well-defined thickness (582 ± 6) nm corresponding to the ^{18}O total range, see section 3.2 above, and an interface width of (32 ± 3) nm, see table 1. The nature of the interface is seen to be established for doses of 4.5×10^{17} $^{18}O/cm^2$ and above in contrast to the surface isotopic ratio which has only risen to 0.03 for this dose compared to a uniform level of 0.43 for samples with the highest doses. This is similar to the case of TDI formation in the mask region [2] where internal oxidation of the bulk silicon is taking place preferentially at the lower interface in contrast to normal SIMOX formation in the window region where internal oxidation takes place at the upper interface [7]. This is also attributed in ref. [2] to the rapid erosion of the mask oxide in contrast to the erosion rate for silicon.

3.4. ^{18}O Diffusion in the silica

The broadening apparent in the surface layer of width approximately equal to the total range of ^{18}O in silica, see fig. 3, is due to radiation-enhanced diffusion of oxygen primarily towards the surface. This is consistent with buried oxide layer growth for SIMOX [7] with high-energy oxygen implantation into silicon and at low energies in the formation of surface layers with normal incidence oxygen primary ions in SIMS [8]. For the implantation dose of 1.1×10^{18} ^{18}O isotope ratio has become approximately constant over a characteristic diffusion length, x, of 402 nm (implanted surface layer thickness–surface recession for that dose, table 1) in a time, t, of 160 min. Using $x^2 = Dt$, the radiation-enhanced diffusion coefficient, D, is 1.7×10^{-12} cm^2 s^{-1}, which is in fair agreement with experimental values found for low-energy surface oxide formation, 10^{-14} cm^2 s^{-1} [8] and very similar to the value, $\geqslant 10^{-12}$ cm^2 s^{-1}, used satisfactorily in continuity equation models of SIMOX formation by Jager et al. [9]. This experiment has provided an estimate for D in a situation free of oxide layer growth and oxidation or the proximity of an SiO_2/Si interface in contrast to previous estimates [7,8].

The region of the thermal oxide below the implant range of ^{18}O ions has uniformly increased in ^{18}O content, ~ 30 times above the natural abundance level for the highest doses except in a layer of width ~ 250 nm next to the SiO_2/Si interface, see fig. 3. A possible mechanism for this uniform increase is a radiation-induced enhancement of oxygen diffusion and exchange in the network of the silica.

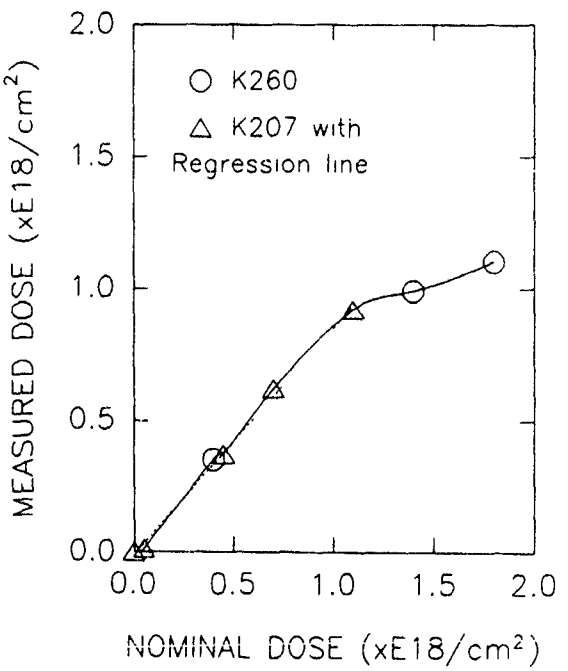

Fig. 4. The retained ^{18}O in the surface implanted layer as an equivalent dose determined from SIMS measurements for nominal ^{18}O-implants at 200 keV into thick thermal oxide on silicon.

3.5. Silica stoichiometry

In fig. 1 the total oxygen signal remains constant to within ±5% throughout the whole thickness of the silica to the SiO_2/Si interface. The total oxygen to silicon ratio is the same for both the ^{18}O-implanted region and the unimplanted region which has provided an in situ oxygen/silicon reference signal during the same SIMS analysis. This result is typical of all of the doses listed in table 1. This is because of the high mobility of oxygen in the ^{18}O-implanted layer and the rapid out-diffusion of any excess oxygen through the surface by desorbtion. Also this result indicates that the implanter conditions chosen did not cause substantial reduction of SiO_2 by preferential oxygen loss [4] to a depth greater than 5 to 10 nm. See the experimental section 2 above.

3.6. Retension of the ^{18}O-implanted dose in the silica

Choosing a density of 2.3 g cm^{-3} for the whole of the silica layer, the area under the ^{18}O isotopic ratio curves of fig. 3 represents the retained dose of ^{18}O in the ^{18}O-implanted surface layer. The dose measured in this way for each of the nominal doses is tabulated in table 1 and plotted in fig. 4. The line drawn through all the points in fig. 4 deviates from the regression curve fitted to the lowest doses between the nominal doses of 0.7 and 1.1×10^{18} ^{18}O/cm^2. Below a nominal dose of 7×10^{18} all the ^{18}O is retained in the ^{18}O-implanted surface oxide layer whilst the layer has remained stoichiometric SiO_2, see section 3.5 above. Thus an equivalent dose of ^{16}O is desorbed from the surface together with oxygen desorbed and sputtered due to the recession of the oxide surface, mainly ^{16}O. This result is similar to a conclusion drawn in a previous experimental study by Kilner et al. [10] on buried oxide formation, viz. perfect isotopic exchange within the buried layer. For the nominal dose of 1.1×10^{18} ^{18}O/cm^2 and above, fig. 3 indicates that the retained doses tend in our experiment to a saturation level of approximately 1×10^{18} ^{18}O/cm^2. In this case the incoming ^{18}O ion is increasingly likely to exchange with a previously implanted ^{18}O atom incorporated into the network of oxygens of the silica. Also, from fig. 3, the surface concentration of ^{18}O in the silica rises so that a substantial fraction of sputtered oxide includes network oxygens that are implanted ^{18}O atoms.

4. Conclusions

^{18}O implants into silica surface layers on silicon have provided a detailed insight into the mass transport of oxygen and sputtering of SiO_2 for implantation conditions which are used for buried oxide layer formation in a target *free of oxide layer growth or oxidation*:

(1) The oxygen mobility is high, $D = 1.7 \times 10^{-12}$ cm^2 s^{-1}, with rapid out-diffusion of excess oxygen through the surface.
(2) The stoichiometry of the silica surface layers was found to remain as SiO_2.
(3) The sputter-rate of the silica is confirmed to be high at 1.1 atoms per incident particle.
(4) Perfect oxygen isotopic exchange was found for these surface silica layers in common with buried oxide layer formation.

Acknowledgements

The authors would like to thank the staff of the Accelerator Laboratory at the University of Surrey for their assistance in performing the implantations and Dr J.R. Davis, BTRL, Martlesham Heath, UK for providing the starting material. This work is in part supported by the UK SERC.

References

[1] P.L.F. Hemment, A.K. Robinson, K.J. Reeson, J.R. Davies, J.A. Kilner, R.J. Chater and J. Stoemenos, Mater. Res. Symp. Proc. 107 (1988) 87.
[2] P.L.F. Hemment, K.J. Reeson, A.K. Robinson, J.A. Kilner, R.J. Chater, C. Marsh, K.N. Christensen and J.R. Davis, Nucl. Instr. and Meth. B37/38 (1989) 766.
[3] P.L.F. Hemment, E.A. Maydell-Ondrusz, K.G Stephens, J. Butcher, D. Ioannou and J. Alderman, Nucl. Instr. and Meth. 209/210 (1983) 157.
[4] S. Thomas, J. Appl. Phys. 45 (1974) 161.
[5] J.A. Kilner, R.J. Chater, P.L F. Hemment, R.F. Peart, E.A. Maydell-Ondrusz, M.R. Taylor and R.P. Arrowsmith, Nucl. Instr. and Meth. B7/8 (1985) 293
[6] J.F. Ziegler, J.P. Biersack and U. Littmark, in: The Stopping and Ranges of Ions in Solids, vol. 1, ed J.F. Ziegler (Pergamon, New York, 1985).
[7] R.J. Chater, J.A. Kilner, P.L.F Hemment, K.J. Reeson and R.F. Peart, in: Semiconductor Silicon 1986, vol. 86-4, eds. H.R. Huff, T. Abe and B. Kolbesen (Electrochem. Soc. Boston, 1986) p. 652
[8] S.D. Littlewood and J.A. Kilner, J. Appl Phys. 63 (1988) 2173.
[9] H.U. Jager, J.A. Kilner, R.J. Chater, P.L.F. Hemment, R.F. Peart and K.J. Reeson, Thin Solid Films 161 (1988) 333.
[10] J.A. Kilner, R.J Chater, P.L.F Hemment, R.F. Peart, E.A. Maydell-Ondrusz, M R. Taylor and R P Arrowsmith. Nucl. Instr. and Meth B7/8 (1985) 293

Nuclear Instruments and Methods in Physics Research B55 (1991) 691–696
North-Holland

The study of $Si_{0.5}Ge_{0.5}$ alloy implanted by high dose oxygen

J.P. Zhang [1], P.L.F. Hemment, U. Bussmann and A.K. Robinson
Department of Electronic and Electrical Engineering, University of Surrey, Guildford, Surrey GU2 5XH, UK

J.E. Castle, H.D. Liu and J.F. Watts
Department of Materials Science and Engineering, University of Surrey, Guildford, Surrey GU2 5XH, UK

S.M. Newstead, A.R. Powell, T.E. Whall and E.H.C. Parker
Department of Physics, University of Warwick, Coventry CV4 7AL, UK

The effects of high dose O^+ implantation into a $Si_{0.5}Ge_{0.5}$ alloy, studied by Rutherford backscattering, infrared spectrophotometry and X-ray photoelectron spectroscopy, are reported for the first time. The alloy layers were prepared by molecular beam epitaxy (MBE) when a thick (900 nm) film of $Si_{0.5}Ge_{0.5}$ alloy followed by a 75 nm top Si layer was grown on a n-type (100) Si ($\rho = 5$–20 Ω cm) substrate. This material was, subsequently, implanted with doses of 0.6×10^{18} O^+ cm^{-2}, 1.2×10^{18} O^+ cm^{-2} and 1.8×10^{18} O^+ cm^{-2} at an energy of 200 keV with a substrate temperature of about 500 °C. Selected samples have been annealed in flowing nitrogen at temperatures of 800 °C, 900 °C or 1000 °C for 1 h. The redistribution of the implanted oxygen and the composition of the resulting structure has been investigated before and after thermal treatment.

The results show that Si–O and Ge–O compound formation depends strongly on the dose of oxygen and annealing temperature. Most of the implanted oxygen reacts with Si to form SiO_2. The Ge–O bonding was only observed in the buried oxide layer where the concentration of oxygen atoms was saturated. In the high dose sample and at the highest annealing temperature the SiO_x converted to stoichiometric SiO_2 with this dielectric also containing some Ge and GeO_x ($x \le 2$) trapped in the silicon dioxide layer. With increasing anneal temperature decomposition of Ge–O bonding was observed and, generally, Ge atoms were found to be rejected from the oxide and segregated in the alloy layers above and below the buried oxide. The different behaviours of the Si and Ge atoms can be described in terms of the thermodynamics of the systems.

1. Introduction

SIMOX (separation by implanted oxygen) is one of the most promising manufacturing approaches for the production of silicon on insulator (SOI) substrates. Review papers on this topic can be found in reference [1]. Although O^+ implanted silicon structures have been extensively investigated [2,3], little work has been reported on SiGe alloy substrates. Currently, Si–Ge heterostructures are of much interest as a material for advanced devices. In this paper the effects of high dose oxygen implantation of $Si/Si_{0.5}Ge_{0.5}/Si$ heterostructures is reported. This subject will be addressed by studying the redistribution and chemical bonding of the implanted oxygen before and after annealing by Rutherford backscattering (RBS), ion channeling, infrared (IR) transmission spectroscopy and X-ray photoelectron spectroscopy (XPS).

[1] Permanent address. Institute of Semiconductors, Academia Sinica, PO Box 912, Beijing 100083, People's Republic of China.

2. Experimental

The samples were prepared by molecular beam epitaxy (MBE). First, a Si buffer layer was grown on a (100)n-type Si ($\rho = 5$–20 Ω cm) substrate followed by a 900 nm $Ge_{0.5}Si_{0.5}$ layer and terminated with a Si capping layer with a thickness of 75 nm. The wafers were implanted with O^+ ions at an energy of 200 keV with doses of 0.6×10^{18}, 1.2×10^{18} and 1.8×10^{18} cm^{-2} hereafter referred to as low, medium and high doses. The choice of ion energy and layer thicknesses ensure that the majority of the implanted oxygen ions ($R_p =$ 4200 Å) came to rest in the SiGe alloy. The wafer temperature during implantation was about 500 °C. Details of the implantation procedure have been previously reported [4]. The annealing in flowing nitrogen was carried out at temperatures of 800, 900 and 1000 °C for 1 h, as shown in table 1. Rutherford backscattering with an analysing beam of 1.5 MeV $^4He^+$ and a scattering angle of 160° was used to determine the composition and thicknesses of the implanted layers. The formation of silicon dioxide and bonding of oxygen atoms were

0168-583X/91/$03.50 © 1991 – Elsevier Science Publishers B.V. (North-Holland)

Table 1
Sample structure: 75 nm Si top layer/900 nm $Si_{0.5}Ge_{0.5}$ alloy/Si substrate; RBS spectrum a

Oxygen dose [10^{18}/cm^2]	Annealing temperature [°C]	Method of measurement	Identity of RBS spectrum
0.6	as implanted	RBS, IR	b
	800	RBS, IR	
	900	RBS, IR	
	1000	RBS, IR	
1.2	as implanted	RBS, IR	c
	800	RBS, IR	e
	900	RBS, IR	f
	1000	RBS, IR	g
1.8	as implanted	RBS, IR and XPS	d
	800	RBS, IR and XPS	h
	900	RBS, IR	i
	1000	RBS, IR and XPS	j

confirmed by IR spectroscopy, using a Perkin-Elmer 577 grating Spectrophotometer. For some selected samples the O–Si and O–Ge bonding was also studied by XPS analysis using a VG Scientific ESCALAB MkII system with a vacuum better than 3×10^{-10} mbar. Al Kα radiation (1486.6 eV) was used as the X-ray source and an Ar^+ sputtering system at 3 keV was used for depth profiling.

3. Results and discussion

3.1. As implanted samples

Fig. 1 shows a series of random RBS spectra from samples before and after implantation. The positions of the signals from surface atoms of Si and Ge are marked on the figure. The curve (a) shows a spectrum from a sample before O^+ ion implantation. The signals from Si and Ge within the $Si_{0.5}Ge_{0.5}$ matrix are between channels 138–267 and 226–380, respectively. As a consequence of the thickness of the SiGe alloy the Si signal is partially overlapping the Ge signal between channels 226 and 267. The peak "A" between channels 267–279 on the Ge signal is due to the Si top layer. Curves (b), (c) and (d) are random spectra from the low, medium and high dose samples. By comparing these spectra with curve (a), a reduction in area of peak "A" and a movement of the high energy edge of the Ge signal to higher channel numbers can be observed. This is due to the sputter erosion of the Si cap which depends on the

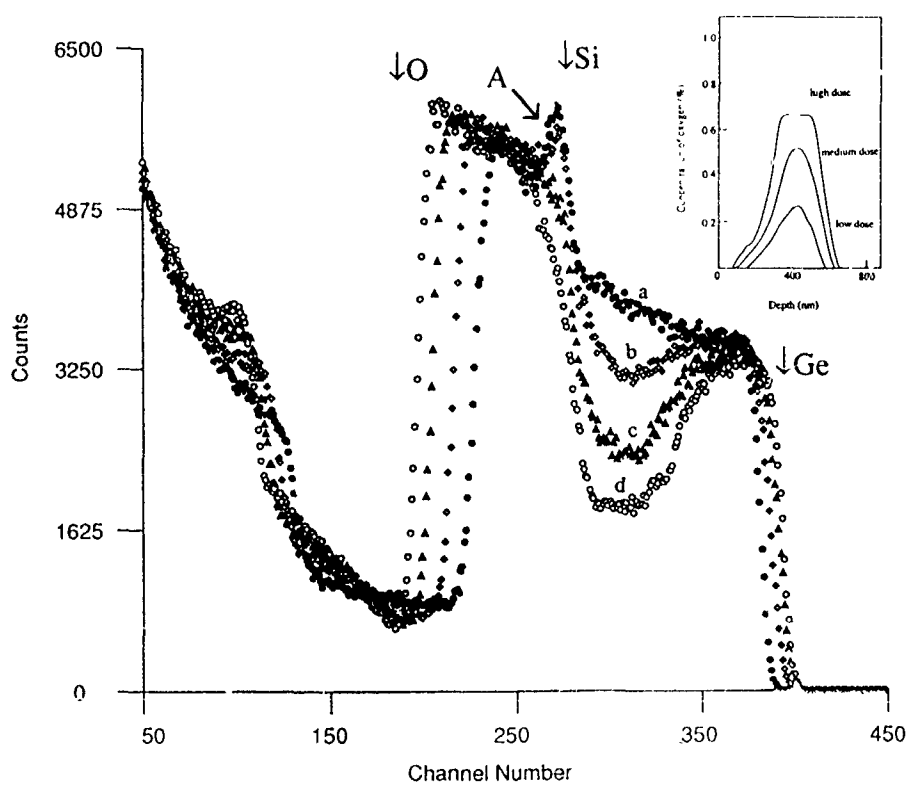

Fig. 1. Random RBS spectra of the Si/SiGe/Si substrate implanted with O^+ ions at an energy of 200 keV, (a) as implanted, (b) 0.6×10^{18} cm^{-2} (low dose sample), (c) 1.2×10^{18} cm^{-2} (medium dose sample), and (d) 1.8×10^{18} cm^{-2} (high dose sample)

implanted O^+ dose. For the low dose sample (curve (b)) it is found that about 40 percent of the Si top layer has been sputtered away whilst for the medium dose sample less then 10 nm of the Si film remains. These losses of Si correspond to a sputtering rate of about 0.26 Si atom/O ion. For the high dose sample the edge of Ge signal is at channel 395 indicating that the Ge atoms are at the surface thus confirming that all of the top silicon layer has been removed by sputtering. The yield deficiency between channels 280–380, which develops with increasing dose, is due to the displacement of Ge atoms from the oxygen region. The shape of the dips gives a quantitative approximation of the oxygen depth distributions which are shown in the inset in fig. 1. These profiles show a similar dose dependence to distributions reported previously [5] for O^+ implantation into bulk Si. For the high dose sample saturation of the oxygen concentration is observed. This effect is only found in regions of the structure where the constituents are in the ratio Si : Ge : O about 1 : 1 : 4 with an uncertainty of about 15% and occurs within the buried layer of thickness 200 nm at a depth of 450 nm beneath the surface. This is in agreement with the TRIM simulations and indicates that oxygen is redistributed during the implantation, as observed in SIMOX material [1]. Analysis of RBS ion channelling spectra shows that the fraction of displaced atoms in the $Si_{0.5}Ge_{0.5}$ overlayer increases with increasing doses.

The optical transmission of the implanted samples was measured in the wave number range from 4000 to 200 cm^{-1} using as a reference a sample from the same wafer but without implanted oxygen. Fig. 2 shows transmission spectra from implanted samples in which three absorption bands due to the vibrational modes of the Si–O–Si local bonding unit at 1000 to 1100 cm^{-1}, about 800 cm^{-1}, and 450 cm^{-1} are evident. The position of each of the three bands shifts to larger wavenumber with increasing dose of implanted oxygen. This data is qualitatively similar to earlier studies [6] of bulk Si implanted with oxygen doses greater than 1×10^{18} cm^{-2}. In order to have a more detailed discussion of these effects we concentrate on the dominant band in the 1000 to 1100 cm^{-1} region due to the asymmetric stretching vibration. For reference the dashed curve shown in the figure is from SiO_2 with a thickness of 400 nm grown on bulk Si by dry oxidation at 1000 °C. The implanted SiGe samples all exhibit absorption at a lower wavenumber which is indicative of the existence of sub-oxides (SiO_x with $x < 2$) or to compressive stress as found in l v temperature thermal oxides [7]. Within our experimental sensitivity we observed no evidence for Ge–O bonding using this IR technique.

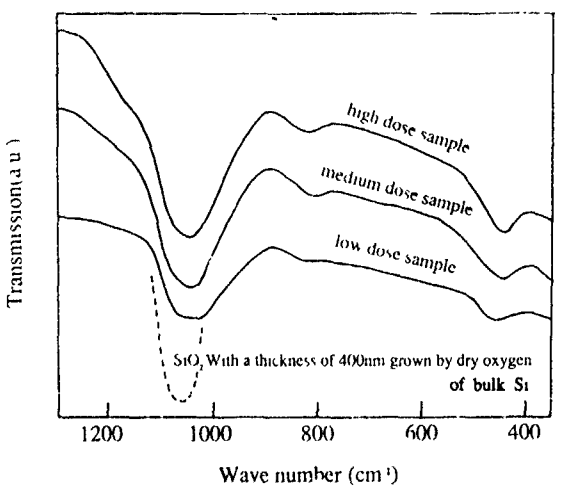

Fig 2 Transmission spectra from implanted samples.

Photoelectron spectroscopy analysis was carried out on the as-implanted high dose sample and the results are reported in detail in reference [8]. The analysis agrees qualitatively with the RBS and IR results although XPS suggests that the saturated region contains a somewhat higher proportion of Si than determined by RBS, having a composition of 2 : 1 : 4 (±15%). Within the saturation region of the buried oxide layer about 90% of the Si atoms are bonded to oxygen to form SiO_2 and the remaining atoms are bounded to form SiO_x, where $x < 2$. Within this region, with about 14% atomic Ge, less than half of the Ge is bonded to oxygen atoms to form GeO_2 and only a small proportion is partially bonded to form GeO.

In common with SIMOX material [1] the synthesis of a buried oxide layer in the alloy $Si_{0.5}Ge_{0.5}$ will be controlled by the processes of sputtering, swelling and diffusion. As discussed by Van Ommen [9] the presence of point defects, resulting from oxygen ion damage (generation of Frenkel pairs) and the reaction of the implanted oxygen with the matrix atoms, will control the evolution of the buried oxide. In the case of SiGe alloys the situation is more complicated as it is necessary to consider the two reactions:

$$2Si_{sub} + 2O_{int} \rightleftharpoons (SiO_2) + Si_{int}, \quad (1)$$

$$2Ge_{sub} + 2O_{int} \rightleftharpoons (GeO_2) + Ge_{int}, \quad (2)$$

where the subscripts "sub" and "int" indicate substitutional and interstitial lattice positions. From a knowledge of the heat of formation and dissociation of SiO_2

Table 2
Standard heat of formation and heat of decomposition

Substance	Standard heat of formation at 25 °C [kcal/g mol]	Heat of decomposition [kcal]
SiO_2 (glass)	−202 5 [10]	210 [11]
GeO_2 (glass)	−128 3 [10]	129 [11]

and GeO_2, shown in table 2 [10,11] it may be concluded that SiO_2 is the more stable of the two oxides and that the O/Si reaction will dominate with eq. (1) tending to the right hand side for the system to accommodate the implanted oxygen [9]. Consideration of mass action shows that eq. (2) will tend in the opposite direction due to the reduced concentration of O_{int} following the preferential formation of SiO_2. However, it must be remembered that inferences drawn from equilibrium dynamics can only provide pointers to the way in which a system

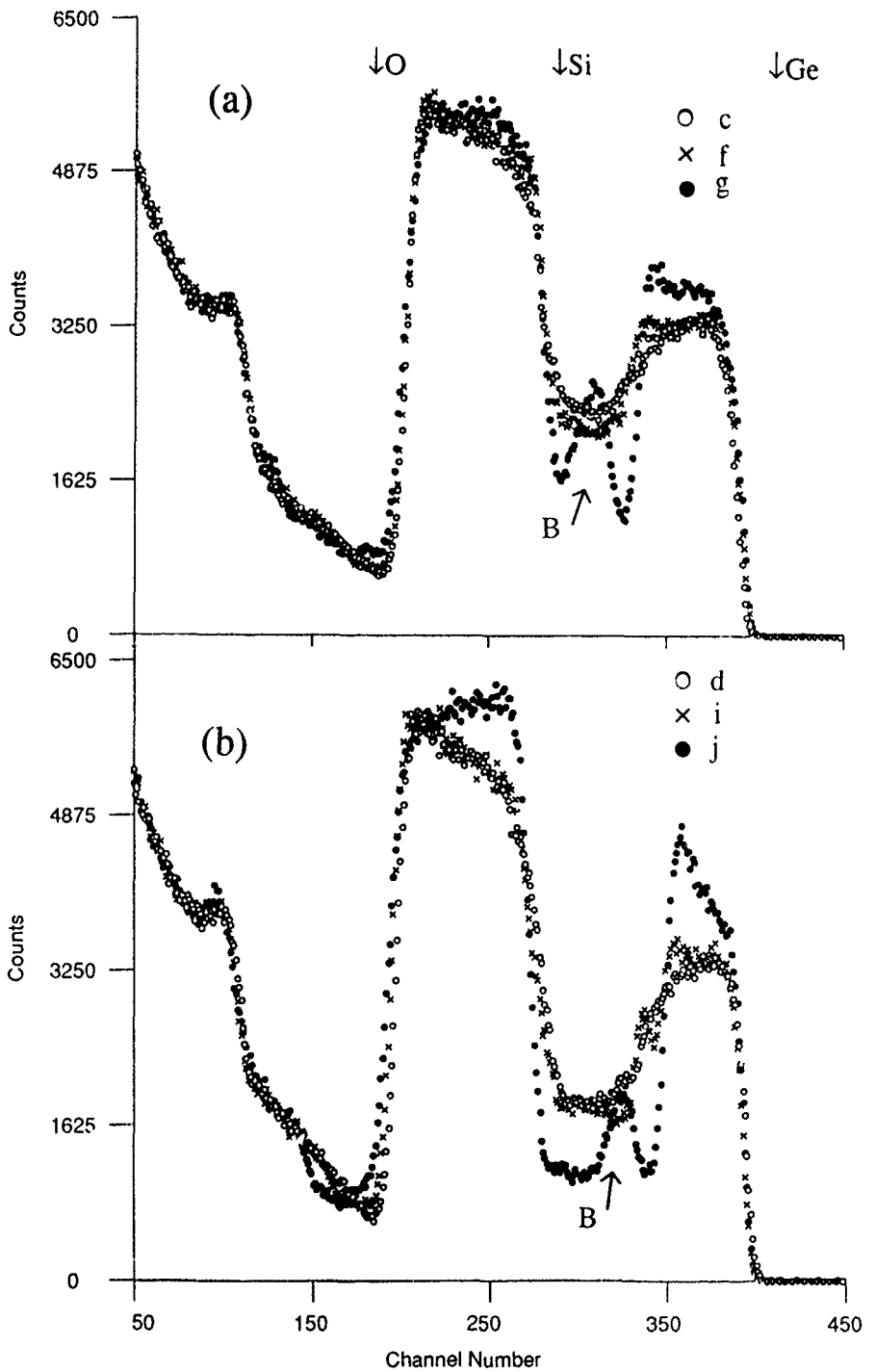

Fig. 3. (a) RBS spectra of medium dose sample. (b) RBS spectra of high dose sample.

will respond under ion bombardment. In this case the low heat of decomposition of GeO_2 compared to SiO_2 also favours a low concentration of GeO_2, as observed experimentally. Additionally the rate of formation of the two oxides, which will be enhanced by the high density of point defects created by the oxygen ions, will be dependent upon the relative concentrations of incompletely oxidized Si and Ge atoms. Thus the relative concentration of the oxides of Si and Ge in the implanted sample may be expected to have a dependence upon the oxygen ion dose. This dependence was indeed observed at the oxide layers in the low and medium dose samples were found to consist predominantly of SiO_2 with no evidence (from the IR analysis) for the existence of Ge–O bonding. This observation in samples implanted at 500 °C is consistent with the work of Ravindra et al. [12] who reported the absence of Ge–O bonding in bulk Ge implanted at 370 °C with 2×10^{15} cm^{-2} at 180 keV. In contrast, SiGe samples implanted with the high dose of oxygen, which resulted in complete or partial oxidation of all of the Si atoms within the saturation region, showed strong evidence (XPS) for the existence of GeO_x ($x \leq 2$).

3.2. Annealed samples

The detailed behaviour of the implanted samples during high temperature annealing was found to be highly dependent upon O^+ dose and annealing temperature. Figs 3a and b show RBS spectra from medium and high dose samples after annealing at 900 and 1000 °C. It is evident that little mass transport of oxygen, which can be inferred from the yield deficiency in the Ge part of the spectrum, has occurred during anneals up to 900 °C. In contrast IR analysis (spectra not shown) indicates that significant local bond rearrangement occurs at this temperature leading to the formation of stoichiometric SiO_2. This is confirmed by XPS [8] which shows bond reordering to be most pronounced in the high dose sample. Further, the intensity of the GeO_x signal decreases with increasing temperature indicating that oxygen is preferentially bonding to Si to form SiO_2 (as discussed in section 3.1 eqs. (1) and (2)).

Inspection of RBS spectra from samples annealed at 1000 °C for 1 h (curves g and j) show that the samples undergo significant reordering at this temperature with the formation of relatively abrupt SiGe/oxide interfaces and strong segregation of Ge atoms to the SiGe alloy above and below the oxide layer where the local volume concentration of Ge rises above the original 50% atomic to the higher value of 59% atomic. The average composition of the buried layer in the high dose sample (Si : Ge : O) is about 1 : 0.3 : 2. XPS analysis [8] indicates that the Si atoms are now fully bonded with oxygen to form stoichiometric SiO_2 whilst the concentration of GeO_2 is decreased. The volume concentration of GeO is little changed during the anneal at high temperature. The presence of peak "B" in the RBS spectra from both the medium and high dose samples is evidence for Ge segregation within the buried oxide layer. XPS shows that most of Ge within the oxide layer (mainly SiO_2) is metallically bonded and therefore it is postulated that the entrapped Ge is in the form of precipitates which are dispersed throughout a matrix of SiO_2. Peak "B" would then be due either to an enhanced concentration of precipitates or to larger precipitates which are localized near the centre of the oxide layer. Similar structures are found in SIMOX samples [1] and have been reported by Celler and Trimble [13] for As in SiO_2.

The anneal temperature dependence of the position and peak width of the principal absorption band is shown in fig. 4. For all samples these parameters show a shift with increasing anneal temperature which is indi-

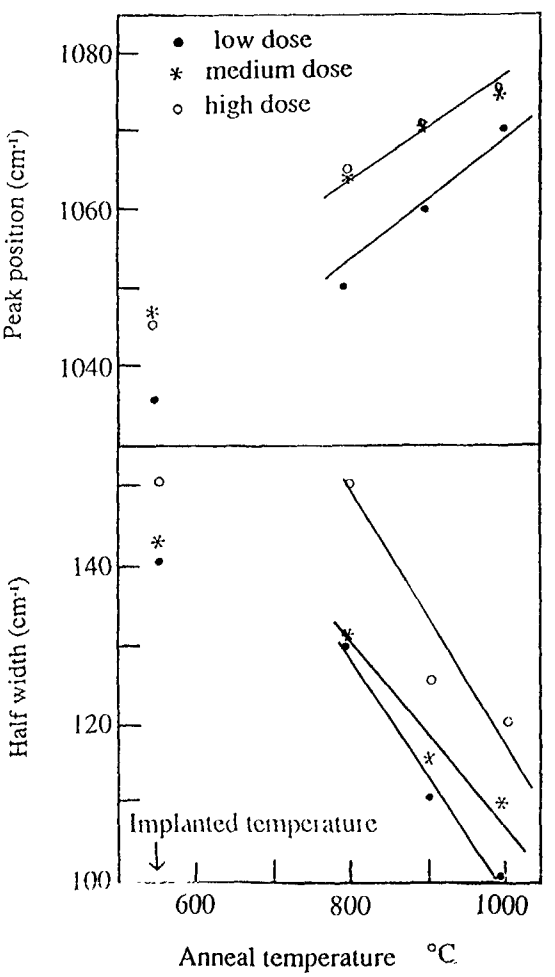

Fig 4. The IR result of the annual temperature dependence of the position and peak width of the principal absorption bond

cative of reducing stress and an increasing proportion of stoichiometric SiO_2. However for all samples the signals fail to achieve values appropriate to a thermal oxide grown on bulk Si. The discrepancy is most pronounced in the high dose samples.

The reordering during the 1000 °C anneal of these SiGe structures is dominated by the net thermally driven segregation of oxygen to the buried oxide layer [1] which results in a reduction in the density of Ge atoms from 25% atomic (as implanted) to 10% atomic (annealed at 1000 °C for 1 h). As is the case with SIMOX (Si/O) samples this reordering may be described in terms of the system moving to minimise the interface energy associated with oxide precipitates [9], which XPS shows for both systems consist of stoichiometric SiO_2.

The reduced density of Ge atoms in the buried layer after annealing arises from the relative thermal instability of oxides of Ge which was observed in bulk Ge by Sjoreen et al. [14] who found that an anneal at 650 °C for 30 min was sufficient to cause the decomposition of a synthesised oxide with a total loss of oxygen from the samples. For SiGe samples the presence of Si acts as a trap for the implanted oxygen due to the thermodynamically driven preferred formation of stoichiometric SiO_2 (table 2). However the low solubility of Ge in SiO_2 leads to rejection of Ge atoms from the synthesised oxide. With the absence of data following extended anneals (> 1 h at 1000 °C) it is not known whether the observed composition (14% atomic Ge) is the equilibrium value or a metastable composition. Whatever the case it is evident from XPS analysis that the Ge is predominantly metallically bonded and must exist as inclusions within the SiO_2 matrix. The segregation of metallically bonded Ge has been previously observed [15] during dry oxidation of $Si_{0.5}Ge_{0.5}$ when Ge atoms are found to be trapped within the growing SiO_2 layer during the initial stage of oxidation (linear region). The behaviour of implanted metallic impurities has been studied by several authors [16,17] who also have proposed that the observed segregation is due to a thermodynamic driving force arising from differences in the enthalpies of formation of the relevant oxides. Kilner [17] finds that those elements with a large positive enthalpy of formation with respect to SiO_2 are strongly segregated. The data reported here for O^+ implanted SiGe alloy is consistent with his findings and supports our premise that the system is driven by chemical thermodynamics.

4. Conclusion

The composition and structure of an $Si_{0.5}Ge_{0.5}$ alloy implanted with high doses of O^+ ions is reported. In common with bulk Si, the formation of a buried oxide layer in an SiGe alloy is found to be controlled by sputtering, swelling and diffusion. The dominant component of the buried layer is silicon dioxide. Oxygen atoms are redistributed at elevated temperatures and trapping and segregation of Ge is observed at an anneal temperature of 1000 °C. These effect can be attributed to chemical thermodynamics.

Acknowledgement

The authors thank the staff of the DR Chick Accelerator Laboratory, University of Surrey for assistance in carrying out these experiments and acknowledge the value of discussion with J.A. Kilner. This work is supported in part by the UK Science and Engineering Research Council.

References

[1] See: Proc 4th Int Symp on Silicon-on-Insulator Technology and Devices, Montreal, Canada, 1990, vol 90-6, ed D.N Schmidt (Electrochem Soc., USA, 1990).
[2] K.J Reeson et al., Microelectron Eng 8 (1988) 163.
[3] P L.F Hemment, K.J. Reeson, A K Robinson, J.A. Kilner, R.J. Chater, C D. Marsh, K.N Christensen and J R Davis, Nucl. Instr and Meth B37/38 (1989) 304
[4] P L.F. Hemment, E A Maydell-Ondrusz, K.G Stephens, J.B Butcher, D Ioannou and J Alderman, Nucl Instr and Meth. 209/210 (1983) 157
[5] J A Kilner, R J Chater. P.L.F. Hemment, R F Peart, E.A. Maydellondrusz, M.R Taylor and R P. Arrowsmith, Nucl Instr and Meth B7/8 (1985) 293
[6] J Dylewsk and M.C Joshi, Thin Solid Films 35 (1976) 327
[7] G. Lucovsky, M.J. Manitini, J K Srivstava and E A. Irene, J. Vac Sci Technol B4 (1987) 530
[8] J.E Castle et al., these Proceedings (8th Int. Conf. on Ion Implantation Technology, Guildford, UK, 1990) Nucl Instr. and Meth. B55 (1991) 697
[9] A H. Van Ommen, Nucl. Instr and Meth B39 (1989) 194
[10] R.C. West, Handbook of Physics and Chemistry, 56th ed. (CRC Press, Ohio, 1976).
[11] G.V Samsonov (ed.), The Oxide Handbook (Plenum, New York, 1982).
[12] N.M. Ravindra, T Fink and W. Savin, T P Sjoreen, P.L. Pfeffer, L G Yerke, R T Lareau, J.G. Gualtieri and R. Lux, Nucl Instr. and Meth B46 (1990) 409
[13] G K. Celler and L E. Trimble, Appl Phys. Lett 53 (1988) 2492
[14] T.P. Sjoreen, N M Ravindra, M.K. El-Ghor and D Fathy, Mater. Res. Soc Symp Proc 107 (1988) 137.
[15] P.L F. Hemment, J.P Zhang, S M. Newstead, A.R Powell, T.E Whall and E.H.C. Parker, to be submmited
[16] V.R Deline, W. Reuter and R Kelly, in. Secondary Ion Mass Spectrometry SIMS V, ed. A Benninghoven (Springer, Berlin, 1986) p 229.
[17] J A Kilner, Proc. 4th Int. Symp on Silicon-on-Insulator Technology and Devices, Montreal, Canada 1990, vol 90-6, ed. D.N Schmidt (Electrochem. Soc., USA, 1990)

Nuclear Instruments and Methods in Physics Research B55 (1991) 697–700
North-Holland

An investigation of $Si_{0.5}Ge_{0.5}$ alloy oxidation by high dose oxygen implantation

J.E. Castle, H.D. Liu and J.F. Watts
Department of Materials Science and Engineering, University of Surrey, Guildford, Surrey GU2 5XH, UK

J.P. Zhang, P.L.F. Hemment, U. Bussmann and A.K. Robinson
Department of Electronic and Electrical Engineering, University of Surrey, Guildford, Surrey GU2 5XH, UK

S.M. Newstead, A.R. Powell, T.E. Whall and E.H.C. Parker
Department of Physics, University of Warwick, Coventry CV4 7AL, UK

An attempt to implant a high dose (up to $1.8\times10^{18}\,cm^{-2}$) of O^+ ions into a $Si_{0.5}Ge_{0.5}$ alloy grown by molecular beam epitaxy (MBE) was made in this work, and the oxidation of the alloy by the implantation before and after thermal treatment was studied using X-ray photoelectron spectroscopy (XPS). The changes of the composition distribution in the sample were observed from the XPS depth profiles. The chemical states of Si and Ge as well as the location of their oxides were obtained from the spectrum fitting. The results indicate that compared to the implantation made on single crystal Si or Ge, this alloy seems to have more in common with the bulk Si and the reason is attributed to the different reactivities between Si and Ge with oxygen and the different stabilities of their oxides. A possible way to improve the experiment to achieve the SIMOX (separation by implanted oxygen) structure in this material is also suggested.

1. Introduction

Synthesizing silicon dioxide by implanting high-dose oxygen ions into bulk silicon wafers is a very promising technique for forming silicon-on-insulator (SOI) structures [1–3]. By annealing the wafers afterwards at high temperature, usually over 1000 °C, a layer of stable high quality dielectric, i.e., SiO_2, can be achieved in the oxygen buried region to eliminate those unwanted resistive and capacitive loads produced by the thick slab of silicon underneath. In the meantime the lattice damage induced by the implantation is restored and the defects within the oxygen projected range are annihilated owing to the high temperature annealing.

This technology, separation by implanted oxygen (SIMOX), has the strength that ion-beam processing is predictable, transferable and easy to control. In recent years a considerable number of investigations have been made and though in practice there are still some potential problems to be solved [2], the benefits of using this material have been demonstrated by many research laboratories [4–6].

On the other hand there are relatively few studies of Si/Ge heterostructures and SiGe alloys processed in this way, which can be very useful materials for applications in opto-electronics. Consequently an attempt has been made in our recent research [7] to implant a high dose of O^+ ions into a Si/Ge/Si heterostructure. The results from X-ray photoelectron spectroscopy (XPS), Rutherford backscattering (RBS) and infrared (IR) transmission spectroscopy show that the Ge in the middle layer mixed with Si on each side during the implantation and diffused further into the Si layers after the annealing, which resulted in its interfaces with Si becoming quite obscure. For this reason we report in this paper an investigation on high-dose oxygen implantation into a $Si_{0.5}Ge_{0.5}$ alloy. XPS was employed to provide the information of the formation and the characters of the Si–O and the Ge–O bonding as well as the composition profiles. In addition, the samples were also studied with RBS, channelling and IR and the results from this part of the investigations will be discussed in detail in another paper in these proceedings [8].

2. Experimental

The samples used for this study were first prepared by molecular beam epitaxy (MBE). Based on a well grown Si buffer layer on an n-type (100) silicon ($\rho \approx 15\ \Omega\,cm^{-1}$) substrate, a 900 nm thick film of $Si_{0.5}Ge_{0.5}$ alloy with a 75 nm Si cap on the top was grown.

0168-583X/91/$03.50 © 1991 – Elsevier Science Publishers B.V. (North-Holland)

To achieve the SIMOX structure, this material was then implanted with a dose of 1.8×10^{18} cm^{-2} O^+ ions at 200 keV. During the implantation the temperature of the target rose to about 550 °C due to the ion beam current. Because the wafer was mounted on small silicon tips, conductive heat loss was minimized and therefore the substrate was maintained around 550 °C, which is known to be good for lattice restoration. Annealing was accomplished by keeping the sample in a dry nitrogen atmosphere in a quartz tube furnace at 1000 °C for one hour.

XPS analysis was carried out with a VG Scientific ESCALAB MkII system equipped with a concentric hemispherical analyser (CHA). Al Kα radiation (1486.6 eV, 10 kV, 20 mA) was used as the X-ray source, and the analyser operating in the CAE mode at a pass energy of 50 eV for a survey spectrum and at 20 eV for the high resolution spectra of individual elements. An ion gun (VG Scientific AG21) operating at 3 kV in the focussed mode was employed as the bombardment beam (Ar^+) for depth profiling, and a target current of 15 μA was obtained. The etch rate was found to vary with the sample composition. For the implanted samples, an average erosion rate of 2.0(±15%) nm/min was estimated. The base pressure was maintained at better than 3×10^{-10} mbar and the argon gas pressure during profiling was kept at 1×10^{-7} mbar.

3. Results and discussion

Fig. 1 Shows the XPS depth profile for the sample cut from the wafer before the implantation. The result confirms that this alloy is $Si_{0.5}Ge_{0.5}$ and there is no preferential sputtering for this material during the Ar^+ etching.

The results of the XPS depth profiles from the implanted sample before and after the thermal treatment are presented in fig. 2 and fig. 3 respectively. These curves show the integral amount of each element, in all its forms. It can be seen from fig. 2 that the distribution of the composition in the sample has changed dramatically after the implantation. In comparison with fig. 1, the top Si layer of the sample has been removed because of the oxygen sputtering during the implantation. There is a plateau region of the oxygen distribution around the etch time of 200–350 min, within which the Si is nearly twice as much as the Ge whereas beyond this region a Ge-rich layer shows up. After the annealing this Ge segregation becomes much more distinct (fig. 3). In particular, on the side near to the sample surface the gradient of Ge is much greater than that of Ge close to the Si buffer layer, and the ratio of Ge to Si is about 2. On the contrary, the Si in the plateau region of the oxygen is increased.

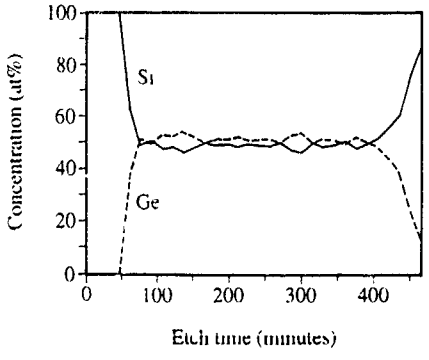

Fig. 1 XPS depth profile for the unimplanted sample. The result confirms that this alloy is $Si_{0.5}Ge_{0.5}$ and there is no preferential sputtering for this material during the Ar^+ etching

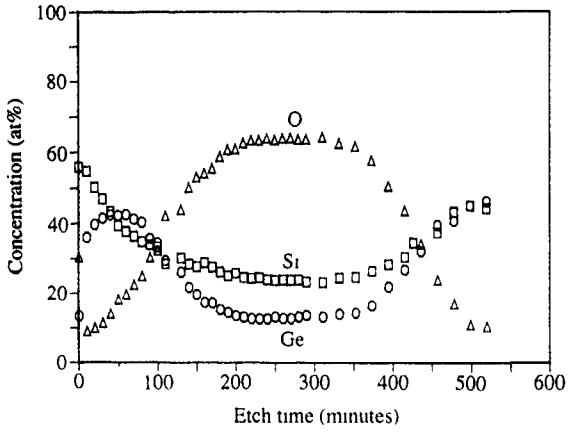

Fig. 2. XPS depth profile from the as-implanted sample without annealing. The implantation was performed at 200 keV with a dose of 1.8×10^{18} cm^{-2} O^+ ions.

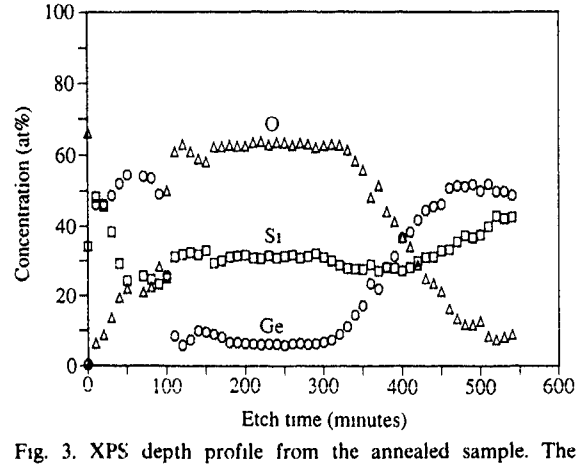

Fig. 3. XPS depth profile from the annealed sample. The thermal treatment was carried out in a quartz tube furnace at 1000 °C in a dry nitrogen atmosphere for one hour.

It is generally agreed [1,2] that for the SIMOX structure achieved on Si single crystals, the implanted oxygen has a skew Gaussian profile but once the dose of O^+ ions in the peak approaches the value for stoichiometric SiO_2 (a volume concentration of 2.2×10^{22} O^+ cm^{-3}, corresponding to a value about 1.4×10^{18} O^+ cm^{-2}), a thin layer of SiO_2 will be formed. The increasing dose of oxygen afterwards only favours the growth of this SiO_2 film and hence an oxygen saturated region appears, which results in the distribution of the oxygen becoming top flat in shape. Consequently the original peak shape can not be observed. Again this is true for the $Si_{0.5}Ge_{0.5}$ alloy. In the plateau region of the oxygen distribution (fig. 2), the proportion of O to Si is approximate to 2.74, much higher than the value for stoichiometric SiO_2. Therefore, the concentration of the oxygen in this region is also saturated and its profile has the similar top-flat shape.

The changes of the chemical states inside the sample for both cases, before and after annealing, are also observed from the XPS spectra. In order to view these changes clearly, a series of spectrum fittings for each of the above cases have been made using the method of least squares. Results presented in the normalized profile form are shown in fig. 4 (as-implanted) and fig. 5 (after annealing).

Fig. 4 shows that in the oxygen saturated region more than 90% of the Si has converted to SiO_2, while SiO_x ($0 < x < 2$) mainly exists at the Si/SiO_2 interfaces. A part of the Ge also forms GeO_2 in this region, but compared to the SiO_2, the amount of the GeO_2 is less and distributes in a smaller area. Again a little GeO_x ($0 < x < 2$) is found at the Ge/GeO_2 interfaces.

After the annealing all the Si in that oxygen saturated region is converted to SiO_2 and the Si/SiO_2 interfaces, especially on the side towards to the surface, become

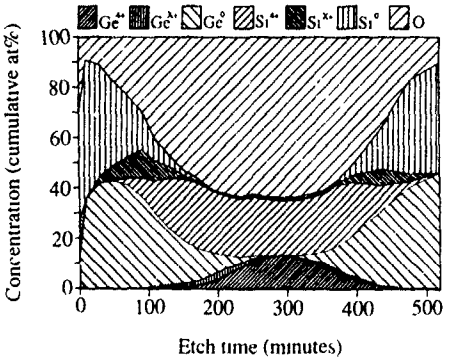

Fig. 4 XPS depth profile in the normalized form for the as-implanted sample The profile is made by a series spectrum fittings with the method of the least square procedure. The purpose of using this normalized form lies in that it has the advantage to show the chemical states of the different components in one diagram without curve overlap

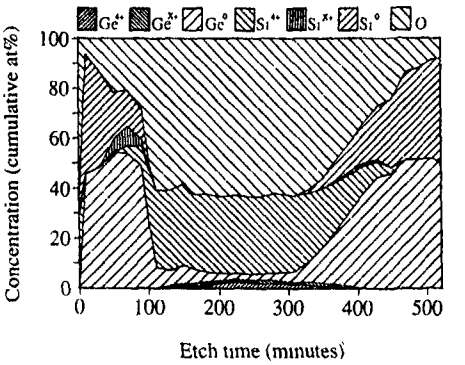

Fig. 5 XPS depth profile in the normalized form for the annealed sample obtained in the same way as mentioned in fig 4.

much sharper. As a result, only a little SiO_x remains at these interfaces. Unlike the SiO_2 the ratio of the GeO_x to GeO_2 is increased after annealing though the total amount of Ge in oxide form reduces.

From previous work on SIMOX, Sjoreen et al. [9], wishing to achieve the germanium-on-insulator (GOI), implanted high dose O^+ ions into a Ge single crystal. This attempt seems not to have been successful because the oxygen implanted Ge only contained GeO_x ($0 < x < 2$) instead of forming GeO_2. Furthermore, the buried oxygen layer was gone after the annealing at 650°C and all that remained was a damaged Ge substrate.

Unlike the case that they reported, SiGe alloy used in this experiment shows its quite different behaviour. The existence of the Si leads to the formation of SiO_2 after the oxygen was implanted and the Si–O bond in the SiO_2, due to its high chemical stability, fixed oxygen in its buried area As shown in fig. 4, in the oxygen saturated region SiO_2 is the main component and Si^0 is close to zero. Therefore the equilibrium $Si + 2O \rightleftharpoons SiO_2$ (the standard free energy of formation $\Delta G_{298} = -850.7$ kJ mol^{-1} [10]) is almost to the right hand side and O is in excess. On the other hand, as it is known that the reactivity of Ge towards oxidation is much less than that of Si [10,11], most of the Ge, being larger than Si, had to be rejected from this oxygen saturated region because of its lack of solubility in SiO_2. The remaining small part of Ge was then in equilibrium with the excess O according to $Ge + 2O \rightleftharpoons GeO_2$ ($\Delta G_{298} = -497.1$ kJ mol^{-1} [10]), but both Ge and GeO_2 are present and the concentration of GeO_2 has a profile expected for O. Thus the reaction is controlled by the local oxygen concentration and the oxygen activity is revealed by ratio $[GeO_2]/[Ge]$ in the light of mass action equilibrium. At the shoulders of the plateau the equilibria $Ge + GeO_2 \rightleftharpoons 2GeO$ and $Si + SiO_2 \rightleftharpoons 2SiO$ determine the oxygen concentration as all three species are present.

However, the growth of the oxide film thickness intensified the oxygen diffusion and hence the oxidation process concurrent with implantation was arrested. The approach to oxidation equilibrium can be regenerated by thermal treatment: transport through the oxide layers resumed and more SiO_2 formed. The increasing ratio of GeO_x to GeO_2 is attributed to the fact that the annealing favours the Ge suboxide states [11] which have a greater free energy of formation than GeO_2. For this reason, it is expected that by increasing the annealing time and temperature the amount of SiO_2 will increase further while less Ge will remain in that region and eventually a layer of film containing only SiO_2 will be formed. This goal may also be reached, in another way, by reducing the proportion of Ge to Si in the alloy.

4. Conclusions

The behaviour of the $Si_{0.5}Ge_{0.5}$ alloy after the implantation of a high dose of oxygen appears to have more in common with that of the bulk Si rather than the Ge. The implanted oxygen tends to bond Si as SiO_2, whereas Ge is found to be rejected from the oxide and to pile up at the Si/SiO_2 interfaces except that a little Ge with its oxides remains in the oxygen saturated region. Annealing up to 1000 °C favours the formation of SiO_2 but reduces the amount of GeO_2, which leads to more Ge to be repelled from that region. Perhaps a SIMOX, having the structure of Si_xGe_{1-x} on SiO_2, could be achieved by either reducing the ratio of Ge to Si in the alloy or increasing the annealing time and temperature, or both.

Acknowledgements

The authors are grateful to the D.R. Chick Laboratory of the University of Surrey for help with the implantation. This work is supported in part by the U.K. Science and Engineering Research Council. One of us, H.D. Liu, acknowledges VG Scientific Ltd. for a scholarship.

References

[1] P.L.F Hemment and K.J. Reeson, Phys. World 2(6) (1989) 39.
[2] G.K. Celler, Solid State Technol. 3 (1987) 93
[3] P.L.F. Hemment, Proc. Mater. Res. Soc. Symp. 53 (1986) 207
[4] J.P. Colinge, K. Hashimoto, T Kamins, S.Y. Chiang, E.D. Liu, S Peng and P. Rissman, IEEE Electron Device Lett. EDL-7 (1986) 279.
[5] B.Y. Tsaur, V J Sferrino, H K. Choi, C.K. Chen, R.W. Mountain, J.T Schott, W.M. Shedd, D C. LaPierre and R. Blanchard, IEEE Trans. Nucl. Sci. NS-33 (1986) 1372
[6] G.E. Davis, L.R Hite, T.G.W Blake, C.E. Chen, H.W. Lam and R. DeMoyer, IEEE Trans. Nucl Sci. NS-32 (1985) 4432.
[7] J.E. Castle, H.D. Liu, J F. Watts, J P. Zhang, Y S. Tang, P L.F. Hemment, S M. Newstead, A.R Powell, T.E Whall and E.H.C Parker, submitted to J. Phys. D
[8] J.P Zhang et al , these Proceedings (8th Int. Conf on Ion Implantation Technology, Guildford, UK, 1990) Nucl Instr. and Meth. B55 (1991) 691.
[9] T.P. Sjoreen, N.M. Ravindra, M K. El-Ghor and D. Fathy, Mater. Res. Soc Symp. Proc. 107 (1988) 137
[10] G.W C Kaye and T.H. Laby, Tables of Physical and Chemical Constants, 14th ed (Longman, London, 1975).
[11] D. Schmeisser, R.D Schnell, A Bogen, F J Himpsel and D Rieger, Surf. Sci 172 (1986) 455

Nuclear Instruments and Methods in Physics Research B55 (1991) 701–704
North-Holland

Amorphisation and solid phase epitaxial regrowth of the silicon overlayer in SIMOX structures

V.V. Starkov [a], P.L.F. Hemment [b] and A.F. Vyatkin [a]

[a] *Institute of Problems of Microelectronics Technology and High Purity Materials, Academy of Sciences of the USSR, 142432 Chernogolovka, Moscow District, USSR*

[b] *Department of Electronic and Electrical Engineering, University of Surrey, Guildford, Surrey GU2 5XH, UK*

In order to study the kinetics of amorphisation and regrowth in SIMOX material, device grade SIMOX wafers were implanted with 80 and 150 keV $^{28}Si^+$ ions at room temperature over the dose range 1×10^{14} to 5×10^{15} cm^{-2}. Bulk silicon control samples ((100), 17 Ω cm) were implanted at the same time under similar conditions. Subsequently these samples were annealed at temperatures of up to 550 °C. The regrowth kinetics were studied using 1.5 MeV He^+ Rutherford backscattering and channeling and in this paper a comparison of the regrowth in bulk silicon and in SIMOX is reported.

1. Introduction

The end goal of forming a SIMOX structure is to obtain a perfect single-crystal silicon layer, with bulk-like electrical properties, above the isolated SiO_2 layer. Very few studies have been devoted to investigations of the properties of the top silicon layer in SIMOX material. (See, e.g., refs. [1–3]). It is clear, that this silicon overlayer will be subjected to various technological treatments when producing devices therein. Particularly, the technique of creating a preamorphised silicon layer before B^+ or P^+ ion implantation is a well-established method of eliminating unwanted channelling during shallow junction formation. A dual implantation and annealing procedure [4] could also be utilised to improve the crystal perfection. Therefore, the study of the kinetics of silicon amorphisation and solid phase epitaxial regrowth is not only of fundamental interest, but is required if the benefits of using SIMOX substrates are to be fully exploited.

2. Experimental

In order to study the kinetics of amorphisation and regrowth in SIMOX material, device grade wafers were implanted with 80 and 150 keV $^{28}Si^+$ ions at room temperature over the dose range 1×10^{14} to 5×10^{15} cm^{-2}. Bulk silicon control samples ((100), 17 Ω cm) were implanted at the same time under similar conditions. SIMOX substrates were obtained by 200 keV $^{18}O^+$ ion implantation into device grade single crystal (100) silicon wafers at a dose of 1.8×10^{18} cm^{-2} followed by annealing at 1300 °C for 5 h. In order to investigate the solid phase epitaxial regrowth kinetics, these samples were subsequently annealed over the temperature range of 470–530 °C. The regrowth and amorphisation kinetics were studied using 1.5 MeV He^+ Rutherford backscattering and channelling.

3. Results and discussion

Channelling RBS spectra taken from a SIMOX sample (top) and a sample of bulk Si crystal (bottom) are presented in fig. 1. The channels about 270–230, 230–170 and 140–90 in fig. 1(top) correspond to ion scattering from the surface silicon layer, silicon atoms in amorphous SiO_2 and oxygen atoms in SiO_2, respectively.

There is no difference in amorphisation kinetics between the two types of samples when the implantation dose exceeds 1×10^{15} cm^{-2} (fig. 1). However, the amount of defects in the damaged layer is different when the dose is equal to 3×10^{14} for 80 keV Si^+ implantation and within the range of 6×10^{14} to 1×10^{15} for 150 keV Si^+ implantation (figs. 1 and 2). We find that accumulation of defects in SIMOX samples proceeds more slowly. A continuous amorphous layer growing from the sample surface is formed in the bulk silicon sample for doses $>6\times10^{14}$ cm^2 for 80 keV Si^+ implantation. In the SIMOX samples this amorphous layer is formed for doses $>9\times10^{14}$ cm^2. Upon 150 keV Si^+ implantation the buried amorphous layer reaches the sample surface at a dose of 3×10^{15} cm^2 for both types of samples. In all the cases of implantation, excluding 150 keV Si^+ implantation at doses $>1\times10^{15}$ cm^{-2}, a crystalline layer existed between the buried

0168-583X/91/$03.50 © 1991 – Elsevier Science Publishers B.V. (North-Holland)

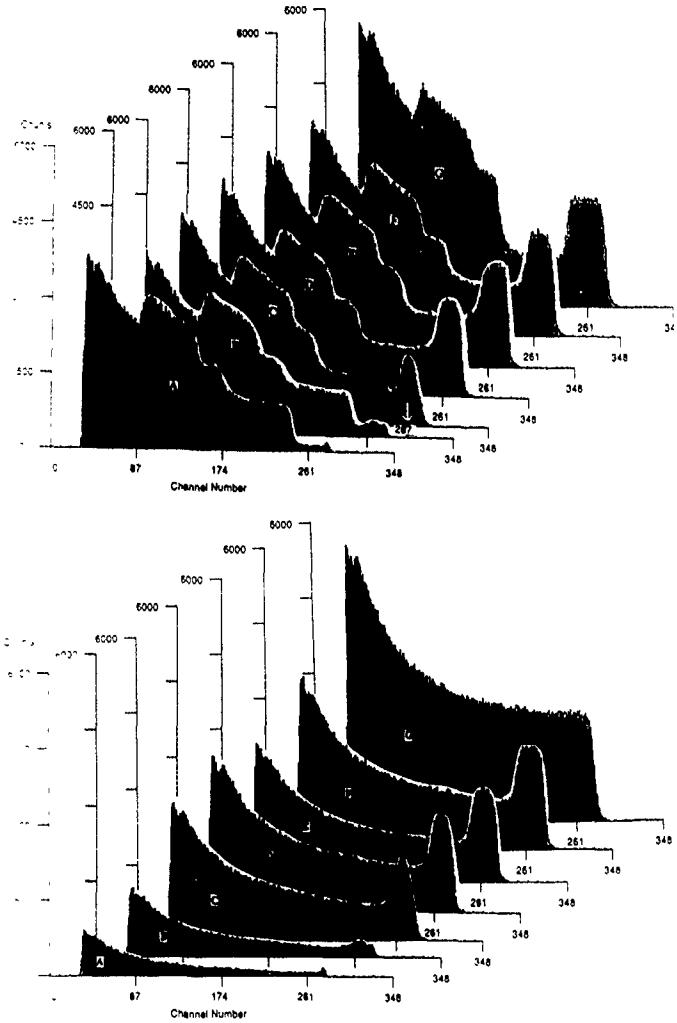

Fig. 1 Rutherford backscattering and channelling spectra taken from (top) SIMOX structures, and (bottom) bulk silicon samples for various doses of 80 keV Si^+ ion implantation. (A) virgin; (B) 1×10^{14} cm^{-2}; (C) 3×10^{14} cm^{-2}; (D) 6×10^{14} cm^{-2}; (E) 9×10^{14} cm^{-2}; (F) 1.2×10^{15} cm^{-2}. (G) Nonchanneling spectra.

silicon dioxide layer and the amorphous one. This layer serves as a seed for crystallisation during subsequent annealing.

In our investigations of the regrowth kinetics of the amorphous and damaged layers in the temperature range 470–530 °C, we have found a different behaviour for the two groups of samples.

The first group consists of samples with a buried amorphous layer and is characterised by a regrowth rate which is twice as high as that for the samples with a continuous amorphous surface layer. This is quite understandable. For the samples with a surface amorphous layer the regrowth rate is slightly less for SIMOX samples (~ 15% less) than that for bulk silicon samples.

The experimental data obtained show that the rates of both phase transitions, namely, crystal–amorphous phase (c → a transition) and amorphous phase–crystal (a → c transition) depend on the properties of the silicon overlayer and the nearness of the $Si–SiO_2$ interface. However, this influence is not very dramatic.

To understand the influence of the $Si–SiO_2$ interface on the a ⇌ c transition rate one should bear in mind the following facts. It is known [5] that accumulation of silicon interstitials takes place near the $Si–SiO_2$ interface during high-temperature annealing. This is a result of the internal oxidation process. The diffusion mobility of interstitials is rather high even at room temperature [6].

According to the model developed in [7], the rate of the c → a transition under the ion irradiation conditions is limited by the vacancy-type defect flux onto the a–c interface from the crystal side (fig. 3). When the SIMOX structure is irradiated by silicon ions, the number of vacancy-type defects coming onto the c–a interface is

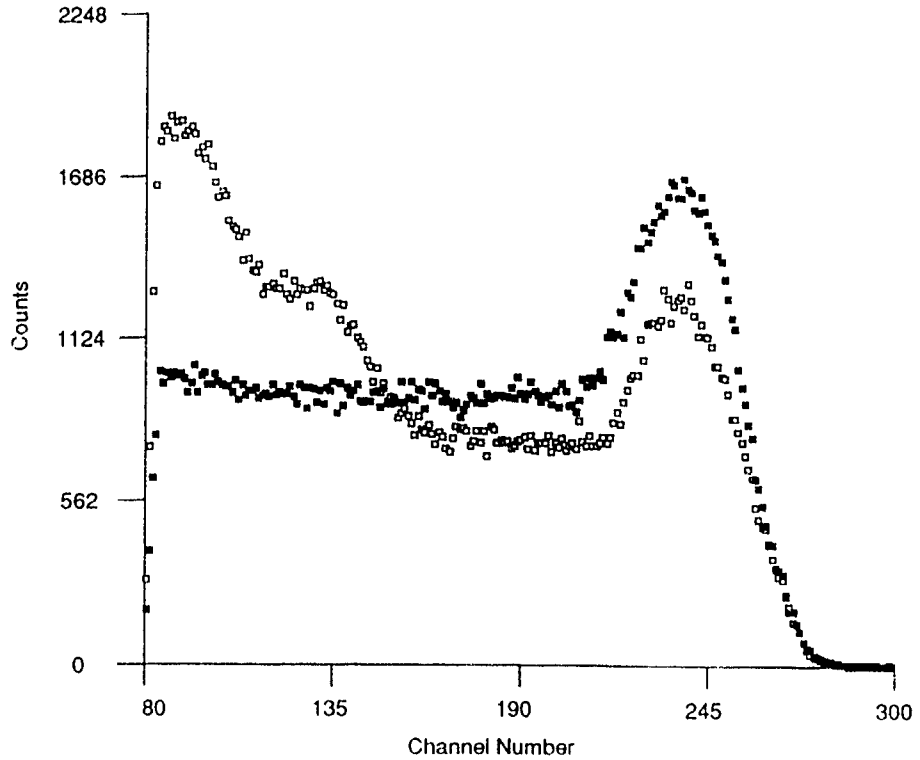

Fig 2 Channelling spectra taken from SIMOX (□) and bulk silicon (■) samples for 150 keV Si^+ ions implanted at a dose of 6×10^{14} cm^{-2}.

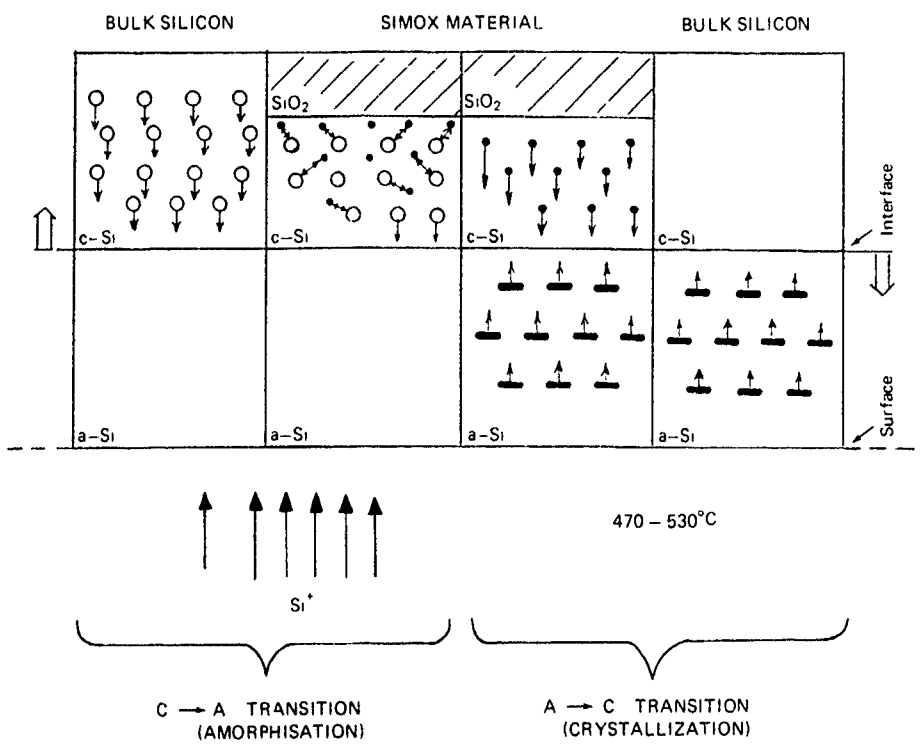

Fig. 3 Illustration of the influence of the excess interstitial flux on a ⇌ c transitions (○) Ion beam produced vacancies; (●) extra interstitials, (▬) native interstitials of a-Si

less in comparison with bulk silicon irradiation because some of them are annihilated by interactions with excess interstitials. This results in a decrease of the amorphisation rate in the SIMOX samples as compared to the that in the bulk silicon samples which are free from extra silicon interstitials. It is suggested that the equalisation of amorphisation rates for both types of materials, at larger irradiation doses, is due to the exhaustion of excess mobile interstitials.

The difference in the value of the limiting irradiation dose at which the difference in the amorphisation rate between the SIMOX and bulk silicon samples still exists can be explained within the framework of the foregoing model. Indeed, the a - c interface is located closer to the $Si-SiO_2$ interface for 150 keV Si^+ irradiation than in the case of 80 keV Si^+ ion bombardment. This leads to more effective annihilation of defects in the first case providing a delay in the movement of the a–c interface to larger irradiation doses.

According to ref. [7] the factor limiting the a → c transition is the interstitial-type defect flux onto the a–c interface from the amorphous phase side. This suggests that at the temperature of the a → c transition (470 to 530 °C in the present work) an excess number of interstitials are released from complexes where they are bound at room temperature. The flux of these defects, directed onto the a–c interface from the crystal side, will compensate the flux of interstitials from the amorphous phase side and, hence, decrease the rate of the a → c transition.

4. Conclusions

(1) The $Si-SiO_2$ interface affects the rate of a ⇌ c transitions.
(2) This influence is due to the flux of excess interstitials directed onto the a–c interface from the crystal region located near the $Si-SiO_2$ interface.
(3) The experimental data obtained gives additional evidence of the influence of the point-defect flux on the parameters of amorphisation and solid phase epitaxial crystallisation.

References

[1] G.A Rozgonyi, Z.J. Radsimski, T Higuchi, B L Jiang, D.M. Lee, T. Zhou, D. Schmidt, J. Blake, Appl Phys Lett 55 (1989) 586.
[2] P.L.F. Hemment, E A Maydell-Ondrusz, K.G. Stephens, Electron Lett 19 (1983) 483.
[3] F Ferrieu, D.P Vu, C. D'Anterroches, J.C Oberlin, S Maillet, J.J. Grob, J. Appl. Phys. 62 (1987) 3458
[4] M.A. Parker, R. Sinclair and T. Sigmon, Mater Res. Soc. Symp. Proc 37 (1985) 211
[5] C.J. Griffin, J.A. Kilner, R.J. Chater, A. Staton-Bevan, K.J. Reeson, P L.F. Hemment, J R. Davis, Nucl Instr and Meth. B39 (1989) 215, and ref. [3] therein.
[6] P.M. Fahey, P.B. Griffin and J.D Plummer, Rev Mod. Phys. 61 (1989) 289
[7] A.F Vyatkin, Surface, in press, in Russian

Nuclear Instruments and Methods in Physics Research B55 (1991) 705–709
North-Holland

The IR properties in SOI wafers formed by oxygen implantation into silicon

Lu Diantong [a], Zheng Lirong [b], Wang Zhonglie [a] and P.L.F. Hemment [c]

[a] *Institute of Low Energy Nuclear Physics, Beijing Normal University, Beijing 100875, People's Republic of China*
[b] *Department of Physics, Shantou University, Shantou 515063, Guangdong, People's Republic of China*
[c] *Department of Electronic and Electrical Engineering, University of Surrey, Guildford, Surrey GU2 5XH, UK*

SOI (silicon-on-insulator) structures have been formed by high dose ($1.8–2.0\times10^{18}$ O^+ cm^{-2}) O^+ implantation into n-type (100) Si samples at 200–350 keV, after the different annealing methods. The SOI structures were evaluated by means of infrared absorption spectroscopy (IR) and electron paramagnetic resonance spectroscopy (EPR). After one-step high-temperature annealing, the buried SiO_2 layers in SOI wafers became amorphous. There are three major characteristic peaks in the IR spectra which are the same as those of the thermal SiO_2 film. The three absorption coefficients were calculated. A new nondestructive method to determine the thickness of a buried SiO_2 layer in the SOI wafers is suggested by using IR spectra without destruction of the wafers. After two-step annealing, the results of IR and EPR measurements proved that a crystalline buried SiO_2 layer in the SOI wafer was obtained. The vibration of the Si–Si band in this SOI wafer is much stronger than that in one-step annealed SOI wafers and the CVD SiO_2 and the thermal SiO_2 film. The absorption coefficient of the Si–Si band in this SOI wafer is about four times of that in the amorphous SiO_2 wafers.

1. Introduction

There is increasing interest in making silicon-on-insulator (SOI) structures by high dose oxygen implantation into Si. SOI wafers may someday replace SOS (silicon-on-sapphire) to make the high speed CMOS circuits and radiation hardened devices [1].

Properties of SOI structures fabricated by different procedures have been reported in many papers mostly by RBS (Rutherford backscattering spectroscopy), TEM (transmission electron microscopy) and SIMS (secondary ion mass spectrometry) techniques [2–6]. We have evaluated some SOI materials by RBS, SR (spreading resistance), EPS (elliptical polarization spectroscopy) and IR absorption spectroscopy [7].

In this study, we mainly use IR spectra to analyse the structural change of buried SiO_2 layers in SOI wafers made after the different annealing methods. Based on the results of IR spectra, we recommend a new nondestructive method of determining the thickness of a buried SiO_2 layer in the SOI wafer without destruction of the sample.

2. Experimental procedure

Five Ω-cm n-type Si wafers with (100) orientation were implanted with an oxygen dose of $1.8–2.0\times10^{18}$ O^+ cm^{-2} at 200–350 keV. During the implantation, the wafer temperature was kept constant between 80 and 450 °C by adjusting the O^+ beam current between 40 and 300 μA in the implanted area of (2×2)–(4×4) cm^2. The implanted wafers were annealed by a furnace or by rapid lamp annealing equipment or by both of them at 600–1300 °C for 30 s–2 h in a N_2 atmosphere.

The SOI wafers were examined by IR and EPR measurements, before and after various annealing conditions. Fourier-transform infrared spectroscopy was used for IR spectra in the energy range from 400 to 1400 cm^{-1}. The surface of the buried SiO_2 layer in wafer no. 45-1 was exposed by plasma-etching the overlaying Si layer. The thickness of buried oxide layer was measured by ellipsometry. We have calculated the absorption coefficients from the IR spectra and the thickness of the buried SiO_2 layer. Using our experimental data, the thickness of the buried SiO_2 layer in a SOI wafer will be determined without destroying the SOI sample.

3. Results and discussion

The spectrum of the unimplanted surrounding region was used as a reference background to determine the IR spectra of SOI wafers. Data from IR spectra of CVD SiO_2 and thermal SiO_2 films were compared with our results to help define the structure of buried SiO_2 layers in the SOI wafers.

Fig 1 shows the IR spectra of the samples implantated with 2.0×10^{18} O^+ cm^{-2} at 200 keV at the

0168-583X/91/$03.50 © 1991 – Elsevier Science Publishers B V. (North-Holland)

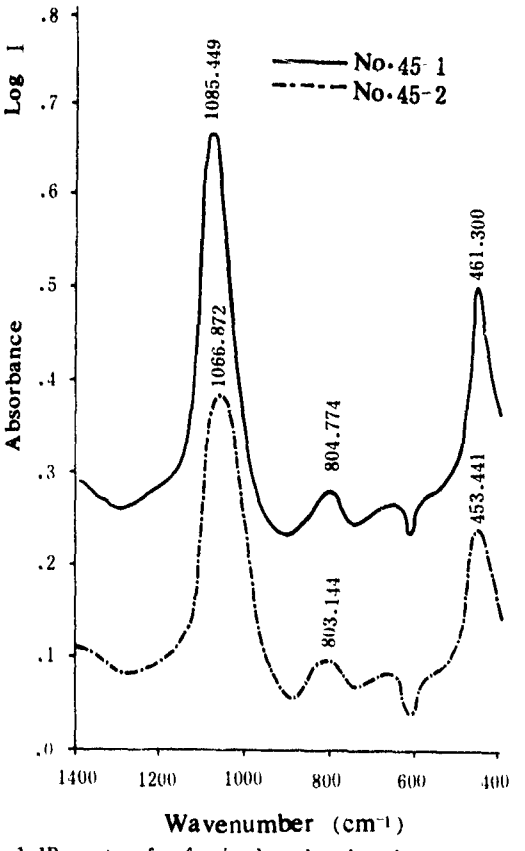

Fig. 1. IR spectra of wafers implanted at the substrate temperature 300 °C with 2.0×10^{18} O^+ cm^{-2} at 200 keV. No. 45-2 was the as-implanted wafer; no. 45-1, the same wafer annealed at 1200 °C for 2 h in a N_2 atmosphere.

substrate temperature 300 °C. Wafer no. 45-1 was annealed at 1200 °C for 2 h in a N_2 atmosphere, no. 45-2 was non-annealed.

Fig. 2 shows the IR spectra from the CVD SiO_2 and the thermal SiO_2 (dry O_2, 2 h plus wet O_2, 4 min) films.

There are three major peaks in the energy range of 400–1400 cm^{-1}. The first peak P_1 (around 1085 cm^{-1}) is the well-known Si–O stretching vibration mode; the second peak P_2 (around 805 cm^{-1}) the Si–Si stretching vibration mode; and the third peak P_3 (around 460 cm^{-1}) the Si–O–Si bending vibration mode [8,9]. After high-temperature annealing (HTA), the three peaks moved to higher wavenumbers and became narrow in the IR spectra of SOI wafers. The positions and shapes of the IR spectra of SOI wafers after HTA are nearly the same as that of the thermal SiO_2 film [10,11]. This indicates that the thermal energy caused oxygen rearrangement, structural changes in the silica networks and reduced the lattice strain introduced by oxygen implantation. Angular reorientation of the Si–O–Si center and futher condensation of the Si–O chains are possibilities of these structural changes [12].

The infrared transmission minima in the SiO_2 film obey the Lambert–Bouguer law:

$$A = \log(I_0/I) = 0.434\alpha t, \quad (1)$$

where A is the absorbance or optical density at the minimum; I_0 and I, the incident and transmitted intensities, respectively; α is the absorption coefficient and t, the sample thickness [12]. This property will be utilized as a nondestructive method of determing the thickness of a buried SiO_2 layer in SOI wafers by IR absorption spectroscopy, if the absorption coefficients of a buried SiO_2 layer are obtained. After plasma-etching the surface Si layer in the SOI wafer with CF_4 gas, the thickness of the buried SiO_2 layer (t_0) was measured by an ellipsometer. The thickness of the buried SiO_2 layer t_0 and the absorption coefficients α from this study and ref. [12] are shown in table 1.

Fig. 3 gives the IR spectra from wafers implanted only in the center part (2×2 cm^2) with 2.0×10^{18} O^+ cm^{-2} at 200 keV. Oxygen implantation was performed

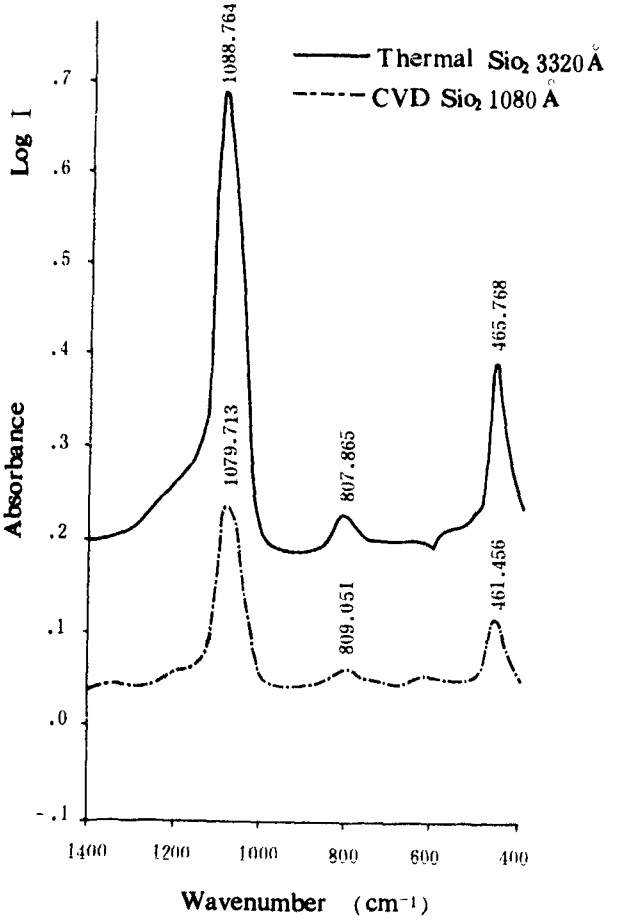

Fig. 2. IR spectra from the CVD SiO_2 film (1000 °C, 20 min) and the thermal SiO_2 film (dry O_2, 1100 °C, 2 h plus wet O_2, 4 min).

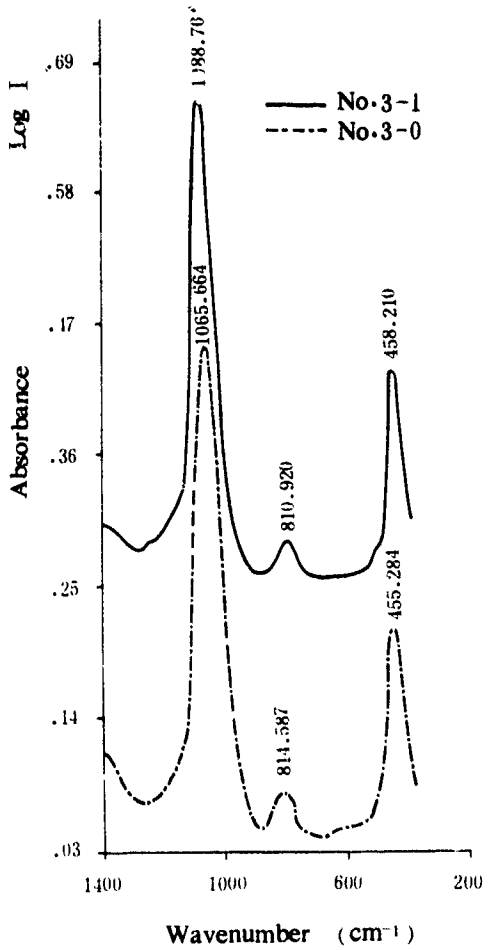

Fig 3 IR spectra from the wafers implanted at the substrate temperature 450 °C with 2.0×10^{18} O^+ cm^{-2} at 200 keV. No 3-0 is the as-implanted wafer, no 3-1 is the same wafer annealed at 1200 °C for 30 s by rapid lamp annealing equipment

at the substrate temperature 450 ± 10 °C by controlling the O^+ beam current 250–270 μA in the implanted area 2×2 cm^2. No. 3-0 is the as-implanted wafer; no. 3-1 is the same wafer annealed at 1200 °C for 30 s in a rapid lamp annealing equipment. By comparing fig. 3 with fig. 2, we notice that the structure of the buried SiO_2 layer after HTA (no. 3-1) appears to be very close to the thermal SiO_2 film. The thickness of the buried SiO_2 layer, t_0, in wafer no. 3-1 was calculated by using eq. (1) and the absorption coefficients in table 1.

$t_0 = 2.303\,(A/\alpha) = 4025$ Å in wafer no. 3-1.

The concentration of oxygen atoms N_0 is between 4.37 and 4.56×10^{22} O^+ cm^{-3} in the thermal SiO_2 films [12]. To form the buried SiO_2 layer in wafer no. 3-1, the actual dose ϕ_0 was estimated:

$\phi_0 = N_0 t_0 = 1.84\times10^{18}$ O^+ cm^{-2}.

Fig. 4 is the IR spectra from the wafers implanted with 1.8×10^{18} O^+ cm^{-2} at 350 keV at room temperature. No. 1-0 is as-implanted; no. 1-1, the same wafer annealed at 600 °C for 5 h and no. 1-2 is the same wafer annealed by a two-step process: (1) at 600 °C for 5 h in a furnace, and (2) at 1200 °C for 30 s in rapid lamp annealing equipment. From the IR spectrum of water no. 1-2, we know that the structure of buried SiO_2 layer in this two-step annealed wafer is very different from that in the CVD SiO_2, the thermal SiO_2 and the buried SiO_2 layers in the SOI wafers before or after

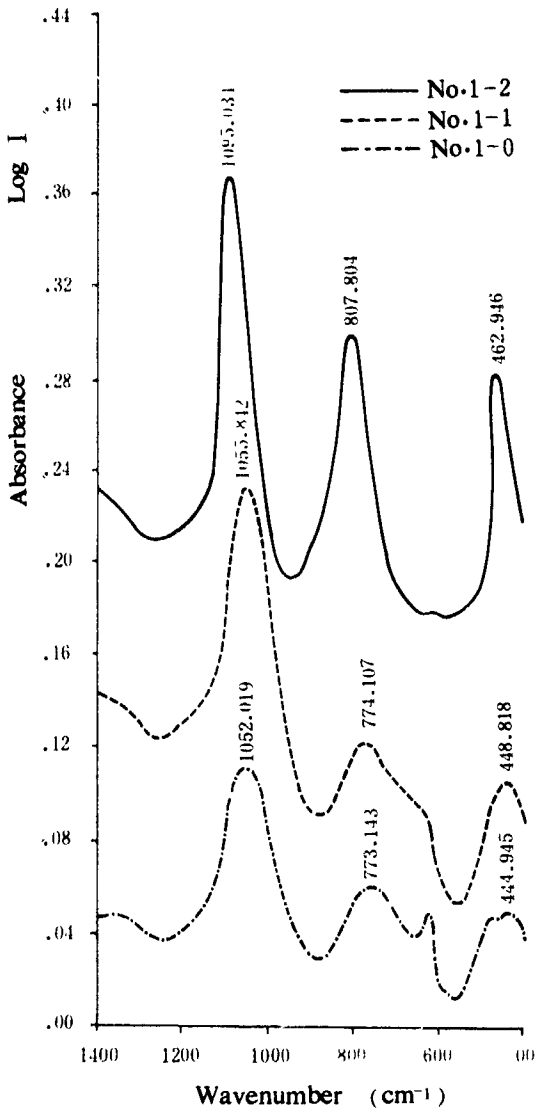

Fig. 4. IR spectra of wafers implanted with 1.8×10^{18} O^+ cm^{-2} at 350 keV at room temperature. No. 1-0 is the as-implanted wafer; no. 1-1 is the same wafer annealed at 600 °C for 5 h in a furnace; no. 1-2 is the same wafer annealed by a two-step process: (1) at 600 °C, 5 h, in a furnace, (2) at 1200 °C, 30 s, in rapid lamp annealing equipment.

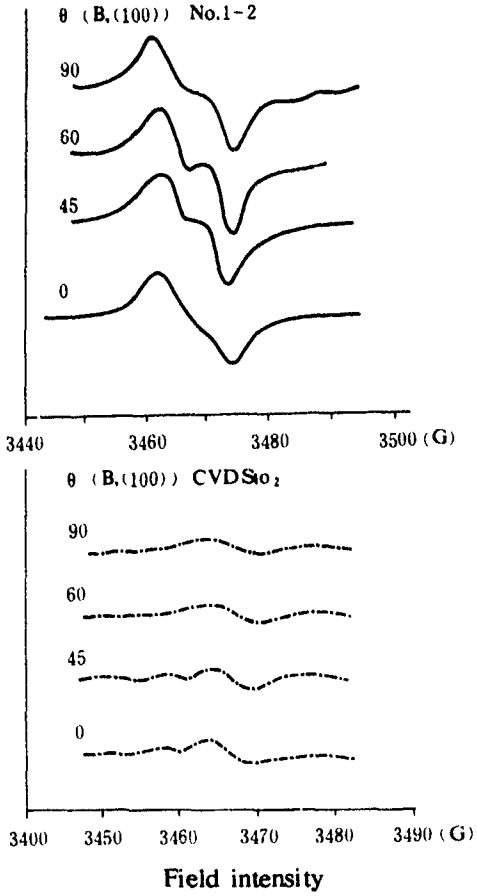

Fig 5 EPR results from wafer no. 1-2 implanted with 1.8×10^{18} O^+ cm^{-2} after two-step annealing and CVD SiO_2 wafer with 1080 Å. The EPR of no 1-2 changes with the angle θ (B, (100)) and that of CVD SiO_2 wafer stays the same while the angle θ (B, (100)) is changing

one-step annealing. This buried SiO_2 layer in wafer no. 1-2 does not look like any amorphous film.

Fig. 5 is the EPR results of the wafer no. 1-2 implanted with 1.8×10^{18} O^+ cm^{-2} after the two-step annealing and the CVD SiO_2 sample with 1080 Å. The EPR of no. 1-2 depends on the angle between the magnetic field B and the ⟨100⟩ orientation. The EPR of CVD SiO_2 wafer does not change when the angle $\theta(B$, (100)) is changed.

The results of EPR proved that the buried SiO_2 layer in no. 1-2 became a kind of crystalline structural layer (perhaps β-quartz). The vibration of the Si–Si band in this buried SiO_2 layer is much stronger than that in one-step annealed SOI wafers and the CVD SiO_2 and the thermal SiO_2 films. The absorption coefficient of the Si–Si band in this SOI wafer is about four times of that in the amorphous SiO_2 layers. The peak P_2 at 807 cm^{-1} is associated with an oxygen–vacancy complex [O–V], which forms due to thermal redistribution of both silicon vacancies and interstitial oxygen [13].

4. Conclusion

SOI structures have been prepared by implanting high dose oxygen into Si at 200–350 keV after various annealing conditions.

A. The structure of the buried SiO_2 layer in SOI wafers implanted at the higher substrate temperature (300–450 °C) is similar to that of the CVD SiO_2 film. The three major peaks of the IR spectra occur at lower frequencies and have larger half-band widths, implying that the atomic arrangement is more irregular than that in thermally grown SiO_2 film.

B. After HTA, the three major peaks (especially P_1) show a positive frequency shift accompanied by an increase in absorbance at the band maximum. This means that the shifts to higher frequency and narrowing of the half-band widths are merely a manifestation of structural changes in the silica network brought about by thermal annealing.

C. The coefficients of buried SiO_2 layers in SOI wafers before and after annealing have been calculated, which are a good agreement with that of the CVD SiO_2 and the thermal SiO_2 films, respectively. We have put

Table 1
Absorption coefficients calculated from the IR spectra of SOI wafers and other SiO_2 films

Wafer	Annealed	t_0 [Å]	Mode Si–O		Mode Si–Si		Mode Si–O–Si	
			Peak [cm^{-1}]	α_1 [cm^{-1}]	Peak [cm^{-1}]	α_2 [cm^{-1}]	Peak [cm^{-1}]	α_3 [cm^{-1}]
No 45-2	no	3193	1067	2.49×10^4	903	0.285×10^4	454	1.27×10^4
No. 45-1	1200 °C, 2 h	3256	1085	3.10×10^4	805	0.344×10^4	461	1.30×10^4
CVD SiO_2	1000 °C, 20 min	1080	1079	3.09×10^4	809	0.299×10^4	461	1.43×10^4
Thermal SiO_2	dry O_2, 1100 °C, 2 h; wet O_2, 4 min	3320	1089	3.45×10^4	808	0.257×10^4	466	1.19×10^4
CVD SiO_2 [12]			1060	2.56×10^4	800	0.250×10^4	440	0.76×10^4
Thermal SiO_2 [12]			1085	3.20×10^4	805	0.345×10^4	460	1.08×10^4

forward a new nondestructive method for determining the thickness of buried SiO_2 layers in the SOI wafers by IR spectra.

D. After two-step annealing, the buried SiO_2 layer turned into a kind of SiO_2 crystalline structure. The absorbance of the Si–Si band vibration is much stronger than that in the amorphous SiO_2 films.

Acknowledgement

The authors thank Chen Ruyi for carrying out the implantation.

References

[1] K. Hashimoto, T.I. Kamins, K.M. Cham and S.Y. Chiang, IEDM 85, p. 672.
[2] P.L.F. Hemment, E. Maydell-Ondrusz and K G. Stephens, Nucl. Instr. and Meth. 209/210 (1983) 157.
[3] F. Namavar, I.I. Budnick, F.H Sanchez and H.C Harden, Mater. Res. Soc. Symp. Proc. 45 (1986) 317.
[4] P.L.F. Hemment, R.F. Pearse, M.F. Yao, K.G. Stephens, R.J. Chater and J.A. Kilner, Nucl Instr. and Meth. B6 (1985) 292.
[5] G.K. Celler, P.L.F. Hemment, K.W. West and J.M. Gibson, Appl. Phys. Lett. 48 (1986) 532
[6] K.J. Reeson, Nucl. Instr. and Meth. B19/20 (1987) 269.
[7] Lu Diantong, Lu Wuxing and Wang Zhonglie, Vacuum 39 (1989) 219.
[8] N. Nagasima, Jpn. J. Appl. Phys. 9 (1970) 879.
[9] N. Nagasima, J. Appl. Phys 43 (1972) 3378.
[10] J.E. Dial, R.E. Gong and J.N. Fordemwalt, J. Electrochem. Soc. 115 (1968) 326.
[11] W.A. Pliskin and H.S. Lehman, J. Electrochem. Soc. 112 (1965) 1013.
[12] Joe Wong, J. Electron. Mater. 5 (1976) 113.
[13] M.J. Kim, D.M. Brown and M. Garfinkel, J. Appl. Phys. 54 (1983) 1191.

Nuclear Instruments and Methods in Physics Research B55 (1991) 710–713
North-Holland

Raman measurement of local SOI structure by SIMOX

K. Kato [1], M. Takai and S. Namba

Faculty of Engineering Science and Research Center for Extreme Materials, Osaka University, Toyonaka, Osaka 560, Japan

R. Schork and H. Ryssel

Lehrstuhl für Elektronische Bauelemente, Universitat Erlangen – Nürnberg, Fraunhofer AIS, Artilleriestrasse 12, D8520 Erlangen, Germany

Oxygen ions were implanted at an energy of 150 keV with a dose of 1.5×10^{18} cm^{-2} in silicon through an aperture to form locally buried insulating layers. Raman microprobe measurement was performed to investigate the influence of the locally buried insulating layer on the top silicon layer at the boundary region between local SOI and unimplanted layers. Single-crystalline silicon layers on buried insulating layers after annealing at 1000–1300 °C were found to have tensile stresses, whereas compressive stresses were induced in the unimplanted region near the boudary. The tensile stresses existing in the SOI region were almost relieved after annealing at 1300 °C. The compressive stresses in the unimplanted region disappeared after annealing at 1300 °C.

1. Introduction

There has been increasing interest in single-crystalline silicon-on-insulator (SOI) structures because of many potential advantages over bulk silicon [1–3]. Local SOI structures have attracted attention for forming an insulating layer under the source and drain of the transistor to minimize the stray capacitance. Thus, experiments and computer simulations have been performed to achieve not only vertical but also lateral isolations by SIMOX [4–7]. In some cases, device performance can be enhanced by limiting the spatial extent of the buried oxide layer only under the source and drain region [6]. However, few have investigated the boundary region between locally buried insulating and unimplanted layers.

The problem of SOI structures by SIMOX is that the single-crystalline silicon layer on a buried insulating layer contains a high density of dislocations and tensile stress [8,9]. SOI structures by SIMOX have recently been extensively investigated, cross-sectional transmission electron microscope (TEM) or Rutherford backscattering (RBS) measurements being performed mainly to investigate the crystallinity of the top silicon layer of this structure [8–10]. Cross-sectional TEM measurements require special sample preparation and, hence, are destructive methods. Although RBS provides the crystallinity of the top silicon layer and stoichiometric information on underlying insulating layers nondestructively, it induces radiation damage. Raman scattering spectroscopy, on the other hand, can measure the sample completely nondestructively at room temperature and does not need special conditions such as a vacuum [8,9].

In this paper, the influence of the locally buried insulating layer on the top silicon layer at the boundary region between local SOI and unimplanted layers was investigated using Raman microprobe measurement.

2. Experimental procedures

Oxygen ions were implanted to the center of a (100)-oriented 3 in. single-crystalline silicon wafer at an energy of 150 keV with a dose of 1.5×10^{18} cm^{-2} through a circular aperture. The diameter of the aperture is 50 mm. The wafer temperature during implantation was controlled at 600 °C by a radiation heater with seven halogen lamps located at the back side of the wafer with a 10 mm gap as described elsewhere [10]. The annealing was performed in a nitrogen atmosphere at temperatures from 1000 °C to 1300 °C. A SiO_2 capping layer was used during annealing as a protective layer.

Microprobe Raman scattering spectroscopy with a laser beam spot diameter of 1.2 μm was used to locally measure the crystallinity and residual stress in a top silicon layer on buried insulating layers and boundary layers to unimplanted regions. The relative peak position of Raman signals can be determined with an accuracy of about 0.1 cm^{-1}. The experimental arrangement has been described in detail elsewhere [11]. The 488 nm line of an Ar-ion laser with a penetration depth of

[1] On leave from: Central Research Laboratory, Glory Ltd., Himeji, Hyogo 670, Japan

0168-583X/91/$03.50 © 1991 – Elsevier Science Publishers B V. (North-Holland)

about 500 nm in silicon was used to excite the sample. The laser power was about 5 mW on the sample surface. From the intensity ratio of Stokes to anti-Stokes, the sample heating which causes the frequency change was not found [12].

3. Results and discussion

Fig. 1 shows the schematic of the local SOI and its boundary. Oxygen atoms implanted locally diffuse towards the buried insulating layer at a high annealing temperature because oxygen has a high diffusion coefficient in SiO_2 [10]. The crystallinity and the stress distribution of this boundary was locally investigated.

Fig. 2 compares the Raman spectra at the center of local SOI structures after various annealing conditions, and for bulk silicon. The Raman spectrum after annealing at 1000 °C has a broad peak shifted to lower wave numbers by 2.2 cm^{-1} from the Raman peak of bulk silicon centered at about 520 cm^{-1}. The peak shift and broadening of the spectra are relieved after high-temperature annealing. Table 1 summarizes the Raman scattering measurement at the center of local SOI structures for various annealing conditions. The peak shift can be considered as the effect of stress [8]. The stress induced in this local SOI structure is at first considered as the effect of the difference in the thermal expansion coefficient between top silicon and buried insulating layers. The stress induced by the difference of the thermal expansion coefficient is calculated to be 3.5–4.4 kbar for a temperature difference of 1000–1300 °C. Values for the stress at the center of the local SOI structure derived from the shift of Raman spectra are 0.3–5.7 kbar [13]. Thus the results of thermal expansion calculations are not in good agreement with the stress

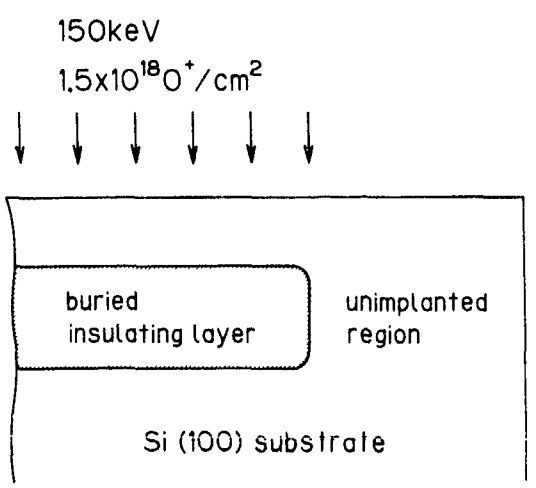

Fig. 1. Schematic of the boundary region of a local SOI structure.

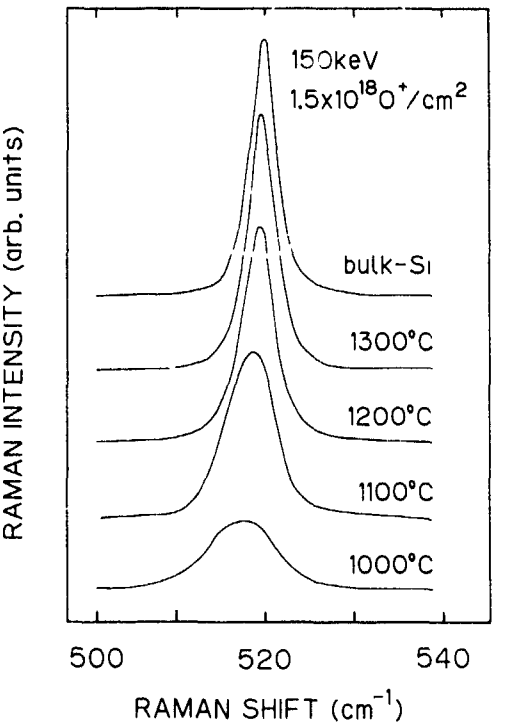

Fig. 2 Raman spectra at the center of local SOI structures after various annealing conditions, and of bulk silicon

derived from Raman shifts. Another possible reason for the Raman shift is that it is also due to oxide precipitates which create a volume expansion in the top silicon layer [8,9]. Such precipitates diffuse towards the buried insulating layer by higher-temperature annealing, and almost all precipitates diffuse to the insulating layer after annealing at 1300 °C [10]. As a result, the shift and half-width (FWHM) of the spectra decreased with an increase in annealing temperature.

Fig. 3 shows a two-dimensional mapping of the peak shift and half-width of Raman scattering spectra of local SOI structures annealed at 1100 °C. In the region of a single-crystalline silicon layer on a buried insulating layer there is a peak shift to lower wave numbers of about 1.3 cm^{-1} from the Raman peak of bulk silicon, and the half-widths of the spectra are about 5.6 cm^{-1},

Table 1
A comparison of Raman data at the center of a local SOI after annealing at various conditions

Annealing temperature [°C]	Width [cm^{-1}]	Shift [cm^{-1}]
1000	8.5	2.1
1100	5.6	1.4
1200	4.2	0.5
1300	3.5	0.3

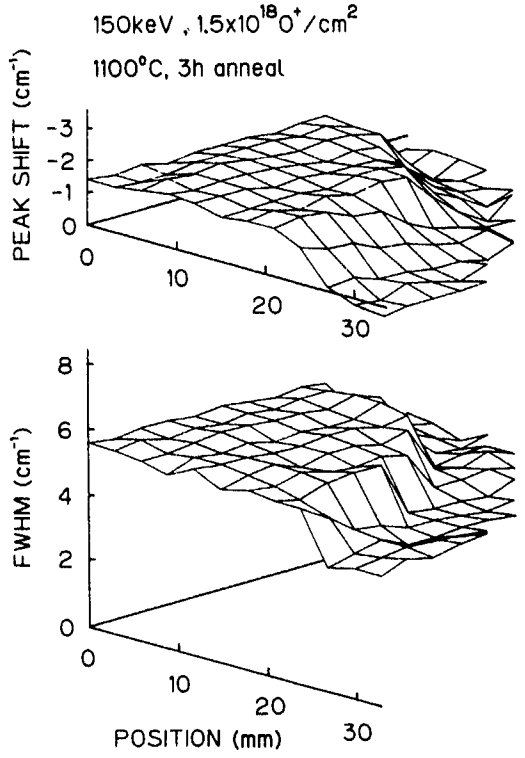

Fig 3 Two-dimensional mapping of the peak shifts and half-widths of Raman scattering spectra for a local SOI structure after annealing at 1100 °C.

whereas in the unimplanted region the peak is shifted to higher wave numbers by about 0.6 cm^{-1}, and the half-widths of the spectra also change to the smaller values of about 4.5 cm^{-1}. In the whole region of a single-crystalline layer on a buried insulating layer, there is a tensile stress of about 3.2 kbar. The tensile stress existing in the single-crystalline layer on the buried insulating layer induces a compressive stress of about 1.5 kbar in the unimplanted region.

Fig. 4 shows two-dimensional mapping of the peak shift and half-width of Raman scattering spectra of local SOI structures annealed at 1300 °C. The peak shift in the SOI region drastically decreased to 0.3 cm^{-1}, while that in the unimplanted region became zero. The half-width of the Raman peak is almost the same as for the bulk silicon (3.5 cm^{-1}) throughout the wafer. The tensile stress existing in the single-crystalline layer on the buried insulating layer relieved to about 0.3 kbar after annealing at 1300 °C. The compressive stress in the unimplanted region disappeared after annealing at 1300 °C. From the results of fig. 3 and fig. 4, we see that the tensile stress that existed throughout the single-crystalline silicon layer on the buried insulating layer is relieved by annealing at 1300 °C. The decrease in stress in the top silicon layer of the SOI region causes the disappearance of the compressive stress in the unimplanted region after annealing at 1300 °C.

In order to examine the boundary region for various annealing temperatures more exactly, the sample was measured from the center to the edge of a wafer in detail. Fig. 5 shows the change of the peak shift and the half-width of Raman spectra as a function of position from the center of the local SOI structure. In the region of the single-crystalline layer on the buried insulating layer (position from 0 mm to 25 mm), Raman spectra have constant peak shifts with constant half-widths almost independent of position after annealing at 1000–1300 °C. The shifts and half-widths of the spectra decreased with an increase in annealing temperature. The reason of stress in the SOI region can be considered to be the oxide precipitates in the top silicon layer as mentioned above. Such precipitates diffuse towards the buried insulating layer by higher-temperature annealing, and are extinguished after annealing at 1300 °C. As a result, the tensile stress existing throughout the single-crystalline silicon layer on the buried insulating layer is almost relieved after annealing at 1300 °C. It should be noted that the peak shift and half-width of the Raman spectra in the unimplanted region were affected by implantation: the peak in this region shifts to higher

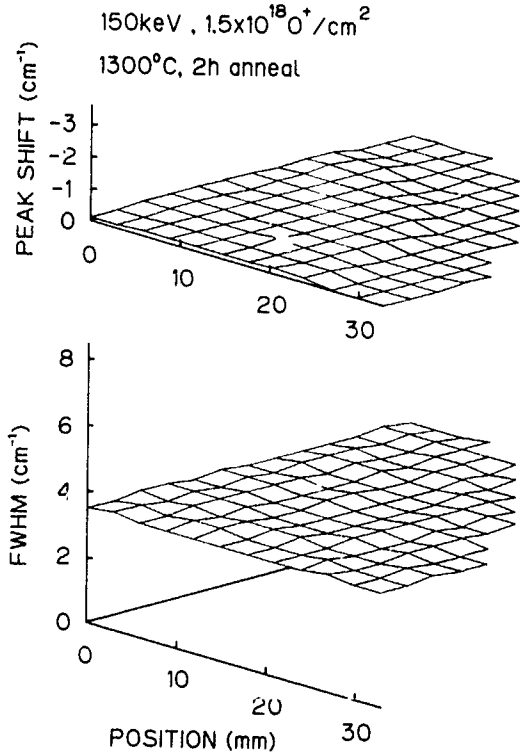

Fig. 4. Two-dimensional mapping of the peak shifts and half-widths of Raman scattering spectra for a local SOI structure after annealing at 1300 °C

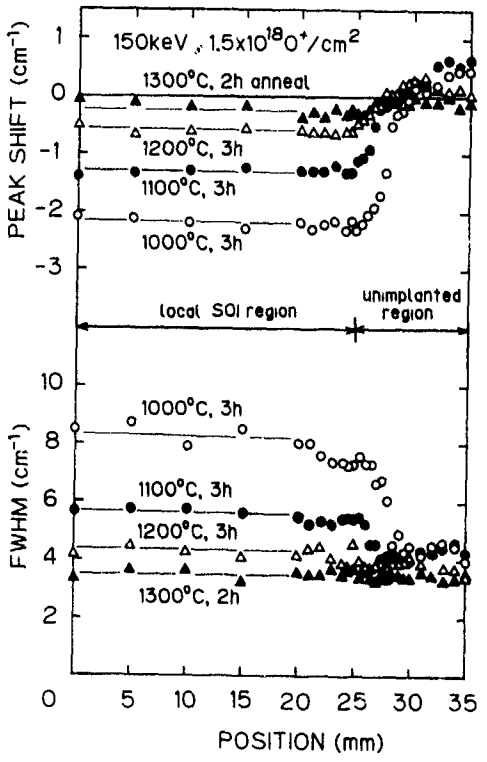

Fig. 5 Peak shifts and half-widths of Raman scattering spectra for local SOI structures after annealing at various conditions.

wave numbers and the half-width slightly broadens. These results indicate that the stress caused by the local SIMOX process in the implanted region affects the unimplanted region, where a compressive stress (i.e., peak shift) and crystalline degradation (i.e., half-width broadening) are induced. Such influences are mostly removed by annealing at 1300 °C.

4. Conclusions

Local SOI structures were produced to form buried insulating layers locally. Raman microprobe measurement was performed to investigate the influence of the locally buried insulating layer on the top silicon layer in the boundary region. Single-crystalline silicon on buried insulating layers after annealing at 1000–1300 °C was found to have tensile stresses of 0.3–5.7 kbar independent of the position. The tensile stresses existing in the SOI regions caused compressive stresses of 1.0–1.6 kbar in the unimplanted regions after annealing at 1000–1200 °C, and the compressive stress disappeared after annealing at 1300 °C.

Acknowledgements

This work was partly supported by the Izumi Science and Technology Foundation. One of the authors (K.K.) thanks K. Onishi and S. Naito who gave him (K.K.) a chance to visit Osaka University for two years.

References

[1] J.P. Colinge, IEEE Electron Device Lett. EDL-7 (1986) 244.
[2] W.A. Krull, J.F. Buller, G.V Rouse and R.D Cherence, IEEE Circuits and Device Mag. 3 (1987) 20.
[3] J.P Colinge, IEEE Circuits and Device Mag. 3 (1987) 16
[4] P.L.F Hemment, K J Reeson, A.K Robinson, J A. Kilner, R.J. Chater, C.D Marsh, K.N. Christensen and J.R Davis, Nucl. Instr and Meth B37/38 (1989) 766.
[5] J.R. Davis, A. Robinson, K.J. Reeson and P L.F Hemment, Appl. Phys. Lett 51 (1987) 1419
[6] T.I Kamins, P.J Marcoux, J L. Mol and L.M. Roylance, J. Appl Phys 60 (1986) 423.
[7] U Bussmann and P L F. Hemment, Nucl. Instr and Meth. B47 (1990) 22.
[8] M. Takai, H. Ryssel, R Shork, N Ueyama, T Minamisono and S Namba, Nucl. Instr and Meth B39 (1989) 400.
[9] A H.V. Ommen, Nucl Instr. and Meth. B39 (1989) 194
[10] R. Shork, H. Ryssel and C. Dehm, Nucl. Instr. and Meth. B39 (1989) 220.
[11] M. Takai, H Nakai, S Nakashima, T Minamisono, K. Gamo and S. Namba, Jpn J. Appl Phys 24 (1985) L755
[12] T.R. Hart, R.L. Aggarwai and B. Lax, Phys Rev B1 (1970) 638.
[13] T. Englert, G. Abstreiter and J Pontcharra, Solid-State Electron 23 (1980) 31

Nuclear Instruments and Methods in Physics Research B55 (1991) 714–717
North-Holland

Raman scattering and photoluminescence analysis of SOI/SIMOX structures obtained by sequential implantation and annealing correlated with cross sectional TEM

A. Pérez [a], J. Portillo [a], A. Cornet [a], J. Jiménez [b], J.R. Morante [a], P.L.F. Hemment [c] and K.P. Homewood [c]

[a] *Càtedra d'Electrònica, Facultat de Física, Universitat de Barcelona, Avda. Diagonal 645–647, 08028-Barcelona, Spain*
[b] *Departamento de Física de la Materia Condensada, Universidad de Valladolid, Po de la Magdalena SN, 47011-Valladolid, Spain*
[c] *Department of Electronic and Electrical Engineering, University of Surrey, Guildford, Surrey, GU2 5XH, UK*

In this paper we describe the analysis by Raman scattering and photoluminescence spectroscopy of silicon-on-insulator (SOI) structures obtained by sequential implantation and annealing (SIA) TEM observations have allowed correlation of the tensile strain observed from the Raman spectra obtained with excitation wavelengths higher than 488 nm and the D bands from the photoluminescence spectra to the presence of a region with precipitates and dislocations close to the buried oxide. Likewise, the comparison between the Raman spectra obtained with lower wavelength (457.9 nm) from SIA samples and from equivalent ones obtained by a single implantation and anneal, has corroborated the higher quality of the surface silicon layer from the SIA structure

1. Introduction

Raman scattering and photoluminescence spectroscopy are techniques which have special interest when characterizing semiconductor materials for microelectronic applications. This is due to their nondestructive character, as well as their suitability for the study of thin layered structures, such as silicon-on-insulator (SOI) substrates. Between the different techniques for formation of these substrates, SIMOX (separation by implanted oxygen) appears to be the leading one [1,2]. Analysis carried out on these structures using the above techniques have been already reported by different authors [2–5]. They have observed from their measurements the existence of a tensile strain in the top silicon layer, as well as its possible recovery by high temperature anneal (HTA) stages.

In this work we have performed an analysis by Raman scattering and photoluminescence techniques of SOI/SIMOX structures which, unlike those previously reported, have been obtained by sequential implantation and annealing (SIA). SIA constitutes one of the more interesting methods of production of high quality SOI material [1,2]. The substrates obtained by this method have defect densities several orders of magnitude lower than those obtained by a single implant and anneal. However, the mechanisms related to the defects and their dependence on the technological parameters are not well known, which gives a strong interest in the characterization of these structures and comparison with the substrates formed by conventional processing (single implant and anneal).

Raman scattering measurements have been obtained using different excitation wavelengths. This has allowed information about the structure of the different regions of the material to be obtained, and the presence of strain for different penetration depths to be detected. By correlating these data with the microscopic structure of the material (observed by cross sectional TEM) it is possible to determine the contribution of each region to the measured spectra, which constitutes relevant information for the analysis of the transport properties of the devices built in these materials

2. Results and discussion

SIMOX wafers were produced by Ibis Technology Corp. [6]. Two different sets of samples were measured which, according to their preparation, were labelled SS and SIA. The SS samples were made by a single step oxygen implantation at an energy of 200 keV and a dose of 1.7×10^{18} cm^{-2}. During implantation the substrate was held at a temperature of 640 °C. Subsequently, samples were annealed at a temperature of 1300 °C for 6 h. The SIA samples were obtained by implanting one third of the total dose at 640 °C after which the wafer was annealed at 1300 °C for 2 h. This cycle was carried out three times to give a total dose of

0168-583X/91/$03.50 © 1991 – Elsevier Science Publishers B.V. (North-Holland)

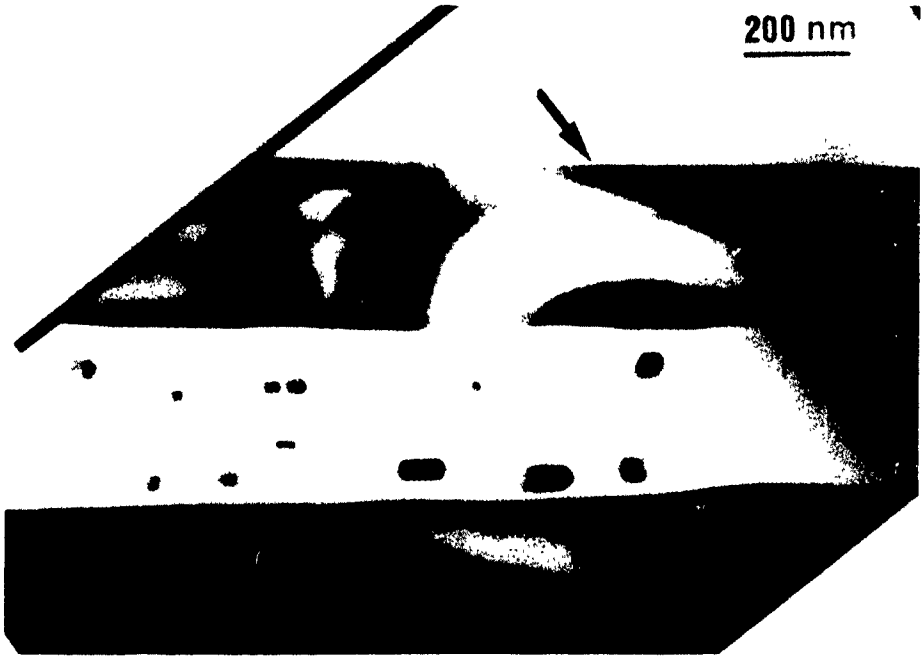

Fig. 1. Cross section image of SS sample. The arrow indicates the upper surface

1.5×10^{18} cm^{-2} and a total annealing time of 6 h at 1300 °C.

The observation of the samples by cross sectional TEM has revealed the existence of significant differences between the SS and SIA structures. The cross section structure of the SS samples is shown in fig. 1. It is formed by a top silicon layer free of SiO_2 precipitates and a buried oxide layer with silicon islands. We have not been able to detect the presence of dislocations in the top layer. The thickness of these layers (observed along 2 μm of the structure) are about 295 and 310 nm, respectively. In the case of the SIA sample (shown in fig. 2), the structure has three different regions: the first one is a 235 nm thick silicon layer free of precipitates and dislocations. Below this layer there is a region of silicon with oxide precipitates and dislocations, with an average thickness about 200 nm, and the buried oxide layer. The upper interface of this layer is very wavy, due to the coalescence of some of the precipitates The total structure has a thickness of about 650 nm.

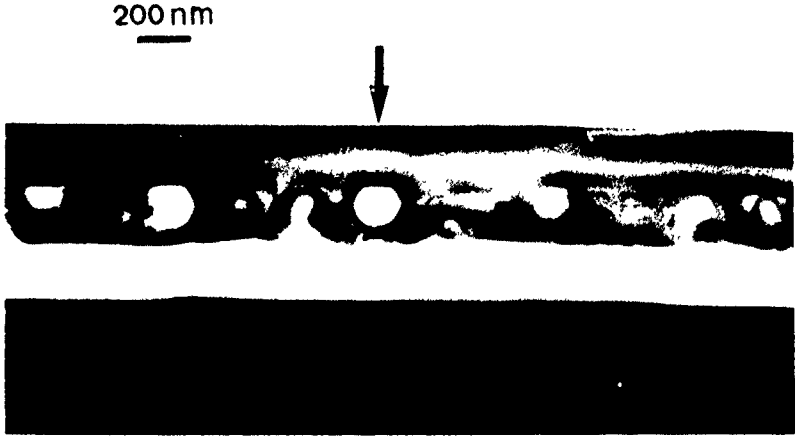

Fig. 2. Cross section image of SIA sample The arrow indicates the upper surface.

Raman scattering measurements have been performed with a DILOR XY spectrometer. The samples were excited with the 457.9, 488 and 514 nm lines from an Ar^+ laser. For these lines, the penetration depths for the scattered light have been estimated to be approximately 300, 600 and 800 nm, respectively [7]. Detection has been made using the multichannel mode with photon counting electronics. Moreover, all the spectra have been compared to these obtained under the same conditions in bulk silicon.

Fig. 3 shows the spectra obtained from the different samples with an excitation wavelength of 457.9 nm. In this figure the intensity is normalized to the maximum value. These spectra show a shift towards the low frequencies and a symmetric broadening in relation to that obtained in bulk silicon. This indicates that these layers are under a tensile strain. The symmetrical shape of the lines confirms the crystalline nature of the layers, and their broadening points to the existence of a distribution of strains. No amorphous-like bands are observed. Moreover, the spectra from SS samples present higher shifts and broadenings of the Raman lines than those from SIA samples. This points to the existence of a higher tensile strain in the surface region of the SS structure in relation to the SIA one.

The results obtained using excitation wavelengths of 488 and 514 nm show a different behaviour. In fig. 4 the spectra measured for a wavelength of 514 nm are plotted. In this case, the higher shifts and broadenings occur in the SIA structure. Moreover, the spectra obtained for this structure show a small contribution in the higher frequencies side, which indicates the presence in the SIA sample of a compressive stress.

The increase in the shift and the broadening of the Raman lines from SIA samples as the penetration depth increases is in agreement with the observations of Olego et al. [4] and Takahashi et al. [7] from SS samples. These authors correlated the strain in the top silicon layer with

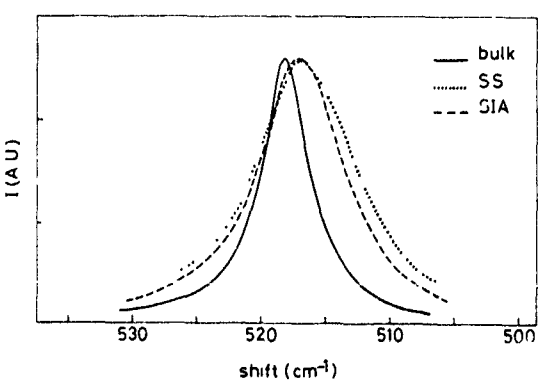

Fig. 3 First-order Raman spectra obtained from the different samples with an excitation wavelength of 457.9 nm. The Raman intensities are normalized ($I_{max} \approx 1$ for every sample).

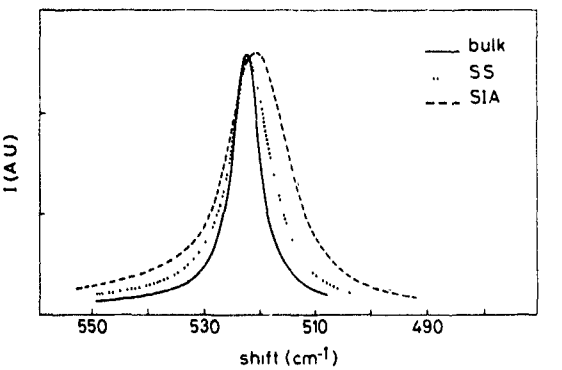

Fig. 4 First-order Raman spectra obtained with an excitation wavelength of 514 nm. The Raman intensities are normalized

the presence of oxide precipitates. As the penetration depth increases, the contribution to the spectra of the region with precipitates and dislocations increases. However, from the measurements carried out with the lower penetration depth we observe a lower strain in the SIA structure than in the SS one (free of oxygen precipitates). This gives a strong indication about the higher quality of the surface region of the SIA structure (free of precipitates and dislocations). According to this, higher mobility values (closer to those of bulk silicon) are to be expected in the surface region of the SIA sample. The small compressive strain component found for higher penetration depths could be due to the existence of a higher compressive strain below the buried layer (similar to that observed in as-implanted structures [2]) or maybe in the silicon regions below the precipitates.

The higher quality of the SIA structure has been corroborated by photoluminescence (PL) measurements. These measurements have been made over the energy range 0.750 to 1.160 eV. The sample has been excited with the 514 nm line from the Ar^+ laser The temperature of the sample has been estimated to be 25 K. The spectral response was determined with a grating monochromator (Jobin–Yvon, model HR2) with a resolution of 13 Å/mm, using a cooled InAs detector and a conventional lock-in amplifier. The spectra were normalized to compensate for the detector response.

Fig. 5 shows PL spectra from SS (curve a) and SIA samples (curve b). Both curves show a peak located in the near band-gap region which is due to the recombination of intrinsic excitons. The intensity of this peak in the SIA sample is a factor of 2 greater than in the SS sample, indicating a larger number of non-radiative defects in the single implant material, which is in agreement with the lower strain observed in the top Si layer of the SIA material.

Moreover, the spectrum from the SIA sample shows at lower energies the presence of broad defect related

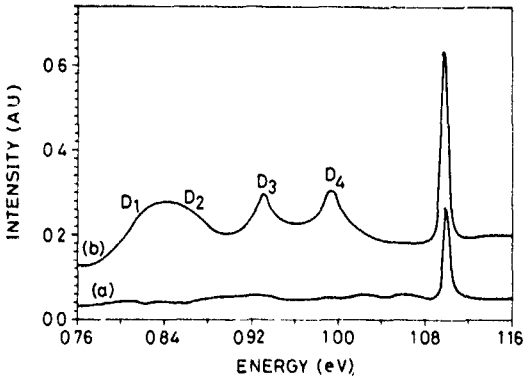

Fig 5 PL spectra obtained from (a) SS and (b) SIA samples.

peaks labelled D_1, D_2, D_3 and D_4. Their positions fall within the range of energies previously reported by Duncan et al. [8], namely, 0.802 to 0.814 eV, 0.862 to 0.875 eV, 0.930 to 0.948 eV and 0.992 to 1.000 eV. The broadest peak, which appears at the lowest energy, includes the D_1 and D_2 bands. These peaks were first observed in plastically deformed silicon, and are believed to be related to dislocations [8]. They have been observed also in bulk silicon in which oxygen is known to have precipitated and in SS SIMOX material [5,8,9]. In this latter case, the width of the D lines was found to be much broader than in the plastically deformed samples. Drozdov et al. [10] have reported that a high oxygen concentration can increase considerably the width of the D lines, specially if the samples are cooled down slowly from high temperatures to produce a high concentration of oxygen precipitates. According to this, Weber et al. [5] have attributed this broadening of the D lines to inhomogeneous strains in the layers, determined by the presence of oxygen precipitates. So, the broad bands from the SIA samples (curve b) would be due to excess oxygen in these samples, maybe as oxygen precipitates The appearance of the D bands in the PL spectrum is consistent with the observation by TEM of dislocations in the second region of the SIA structure pinned to the precipitates.

3. Conclusions

From cross sectional TEM analysis of both sets of samples we have deduced the high morphological quality of the studied structures. In both cases we have observed the existence of a Si surface layer free of dislocations within the resolution of our observations (about $10^7\,cm^{-2}$). However, the characterization of the samples by Raman scattering and photoluminescence spectroscopy has allowed demonstration of the better quality of the top silicon layer free of precipitates from the structure obtained by sequential implant and annealing and showing a lower strain and a lower concentration of defects such as non-radiative recombination centers, in relation to the SS substrate.

The presence of a layer of SiO_2 precipitates close to the buried oxide with dislocations pinned to them determines a higher tensile strain in this region, which is observed by the shifts and broadenings of the Raman peaks, as well as the appearance of the D bands in the PL spectra. A similar structure has been observed by Hill et al. [11] from SIA samples implanted at 150 keV. The cause of these precipitates is not clear. It seems to be related to initial wafer conditions affecting the oxygen precipitation. In any case, they indicate the need for an optimization of the technological parameters related to the SIA process.

References

[1] J.C. Sturm, C K Chen, L Pfeiffer and P.L.F Hemment (eds.), Silicon on Insulator and Buried Metals in Semiconductors, Mater Res Soc. Symp. Proc 107 (Mater Res Soc., Pittsburgh, 1988).
[2] A H. Van Ommen, Proc. 6th Int Conf Ion Beam Modification of Materials, Nucl. Instr and Meth B39 (1989) 194.
[3] G. Harbecke, E F Steigmeier, P L F Hemment and K.J. Reeson, Semicond. Sci Technol 2 (1987) 687
[4] D.J Olego, H. Baumgart and G.K. Celler, Appl Phys Lett 52 (1988) 483.
[5] J. Weber, H Baumgart, J Petruzzello and G K Celler, Mater Res. Soc Symp Proc 107 (1988) 117.
[6] IBIS Technology Inc., Cherry Hill Drive, Danvers, MA-01923, USA
[7] J. Takahashi and T. Makino, J. Appl Phys. 63 (1989) 87
[8] W.M. Duncan, P H. Chang, B Y Mao and C.E. Chen, Appl Phys. Lett 51 (1987) 773
[9] S.T. Davey, J.R. Davis, K.J. Reeson and P L F Hemment, Appl. Phys. Lett. 52 (1988) 465.
[10] N A Drozdov, A.A Patrin and V T. Tkachev, Phys. Status Solidi A64 (1981) K63
[11] D Hill, P. Fraundorf and G. Fraundorf, J Appl Phys. 63 (1988) 4933

Nuclear Instruments and Methods in Physics Research B55 (1991) 718-724
North-Holland

Microscope-spectrophotometric analysis to determine the origins of the colour variations on SIMOX wafers

Karen J. Reeson [a], Alan J. Criddle [b], Peter Pearson [c], Richard J. Chater [d], Kim Christensen [e], John Alderman [c], G. Roger Booker [e] and John A. Kilner [d]

[a] *Department of Electronic and Electrical Engineering, University of Surrey, Guildford, Surrey, GU2 5XH, UK*
[b] *Department of Mineralogy, Natural History Museum, Cromwell Rd., South Kensington, London, SW7 5BD, UK*
[c] *Plessey Research (Caswell Ltd.), Caswell, Towcester Northants, NN1 8EQ, UK*
[d] *Department of Materials, Imperial College, Prince Consort Rd., London, SW7 2BP, UK*
[e] *Department of Materials, University of Oxford, Parks Rd., Oxford, OX1 3PH, UK*

Reflectance measurements using microscope-spectrophotometry have been undertaken to determine the origin of the colour rings on SIMOX wafers. When these measurements are correlated with the results from cross sectional transmission electron microscopy (XTEM) and secondary ion mass spectrometry (SIMS) it is found that normal incidence reflectance is extremely sensitive and closely related to changes in the microstructure of the specimen. In addition, the increasing transparency of silicon to visible light, with increasing wavelength, means that the structure can be effectively probed to different depths, simply by changing the wavelength. These data have been used to establish optical models which enable the computed data to be fitted with the experimental measurements, and vice versa. Thus the microstructure of a SIMOX specimen may be predicted simply from the dispersion of its reflectance. As this is a fast and contactless technique it has potential applications for the nondestructive testing and mapping of SIMOX substrates.

1. Introduction

The fabrication of buried oxide layers, in silicon, by high dose oxygen implantation (SIMOX) is one of the leading silicon on insulator (SOI) technologies, which is now being actively developed for current and future generations of fast, radiation tolerant silicon integrated circuits [1]. As SIMOX moves from the research environment into the production stage, however, it is essential that a quick contactless technique is developed for nondestructively evaluating the wafers, prior to costly device fabrication.

Previous optical studies [2–7] principally using ellipsometry [3–5,7] have established that optical measurements can be used to characterise SOI substrates. However, as ellipsometric measurements are made at oblique incidence (at angles close to the critical angle, typically 70–75°), the measurements are highly susceptible to surface films and roughness [8]. Although it has been possible to obtain extremely good fits between the measured ellipsometric data and computer simulations of the structure, this method is extremely costly in terms of computer time and also requires a degree of foreknowledge about the structure under investigation. Another disadvantage of ellipsometry is that the size of the beam spot on the sample is large (typically several millimetres) hence it is insensitive to local structural variations which will tend to be averaged. Although attachments are available to reduce the spot size on commercial ellipsometers, in practice their use is fraught with problems, since the large cone angle introduces large uncertainties in the absolute determination of the angle of incidence and consequently puts very large error bars on the optical measurements. For these reasons ellipsometry is not a good technique for nondestructive wafer mapping.

In the past, reflection spectrometry has been recognised as a means of rapidly determining the thickness of the superficial silicon layer of SIMOX substrates, but it has been claimed that its uses are restricted to single phase systems, with abrupt interfaces, over a limited thickness range [4,5,7]. Our experience in mineralogical applications of the technique suggested that these claims were erroneous and it was our belief that accurate normal-incidence reflectance measurements would prove at least as successful as ellipsometric measurements in the characterization of SIMOX substrates. We also realised that construction of the fitting algorithm would be slightly simpler at normal incidence and that the measurements would not be so susceptible to the effects of surface films and roughness. In addition, by using microscope-spectrophotometry we had the potential of measuring very small areas (down to ≈ 1 μm) which makes the technique ideal for wafer mapping. In order to rigorously test the use of microscope-spectrophotometry in the characterisation of SIMOX samples, a

0168-583X/91/$03.50 © 1991 – Elsevier Science Publishers B.V. (North-Holland)

non-ideal specimen was deliberately chosen. This specimen, implanted at the University of Surrey, had a number of thin and well defined colour rings around the edges of the implanted area. We believed that these colour rings resulted from local changes in the microstructure, due to a temperature gradient of some 25–50 °C acorss the implanted area during implantation [9–10]. However, prior to this study, we had not systematically investigated the structure to see if this belief was true.

2. Experimental

A 3 inch device grade p-type (B doped 17–23 Ω cm) wafer was implanted with 200 keV oxygen ions to a dose of 1.8×10^{18} O^+ cm^{-2} at a substrate temperature of ≈ 560 °C. To minimise conductive heat losses the wafer was isolated from the sample plate by means of small silicon tips and heated solely by the ion beam. In order to ensure that the dose was constant across the implanted area the beam was overscanned. After implantation, the wafer was capped with 5000 Å SiO_2 and half of it was annealed in a furnace at 1300 °C for 5 h in a flowing nitrogen ambient. After annealing the wafer was measured using microscope-spectrophotometry, XTEM and SIMS.

2.1 Microscope-spectrophotometry

The technique of normal-incidence specular reflectance measurement with the polarising reflected-light microscope-spectrophotometer is routinely applied for identification purposes in mineralogy, where it has been described by Criddle [11,12], Piller [13] and Reeson [14]. For this reason, only a very brief summary is given here: in this study a Zeiss MPM03 microscope-spectrophotometer at the Natural History Museum, London, was used to measure the spectral reflectance from 400 to 700 nm in plane (or linearly) polarised light, relative to a precalibrated WTiC reflectance standard:

$$R_{\text{specimen}} = R_{\text{standard}} \times P_{\text{specimen}}/P_{\text{standard}}, \quad (1)$$

where R is the reflectance of the specimen/standard at a given wavelength, and P is the photometer response for the specimen/standard at a given wavelength.

Modulated light from a stabilised tungsten–halogen source was reflected onto the surface of the specimen and standard with a 45° plane-glass reflector. The effective numerical aperture of the ×4 objective was adjusted with the illuminator aperture diaphragm to 0.03 to provide a maximum cone angle of 1–2° and measurement of the levelled specimen and standard was made semi-automatically by step scanning with a motorised continuous line-interference filter (bandwidth 12 nm).

Fig. 1 shows the reflectance dispersion spectra, for five different regions across the SIMOX specimen, designated E1 to E5 (inset fig. 1). From the inset in fig. 1 we can see that region E5 lies near the centre of the implanted area (a mauve colour) region E4 is still in the mauve region but closer to its edge, region E3 lies just within an outer emerald ring, region E2 lies at the interface between the emerald ring and the outermost gold ring and region E1 lies within this outer gold ring (adjacent to the implant edge). From fig. 1 we can see that there are large changes in the reflectance dispersion as one traverses from region E5 to region E1. It should also be noted that, as silicon becomes increasingly transparent with increasing wavelength, these spectra also give us an appreciation of microstructural changes within the specimen with depth. To understand the microstructural features which are giving rise to the optical spectra, we used XTEM and SIMS to probe areas analogous to those used in the optical measurements.

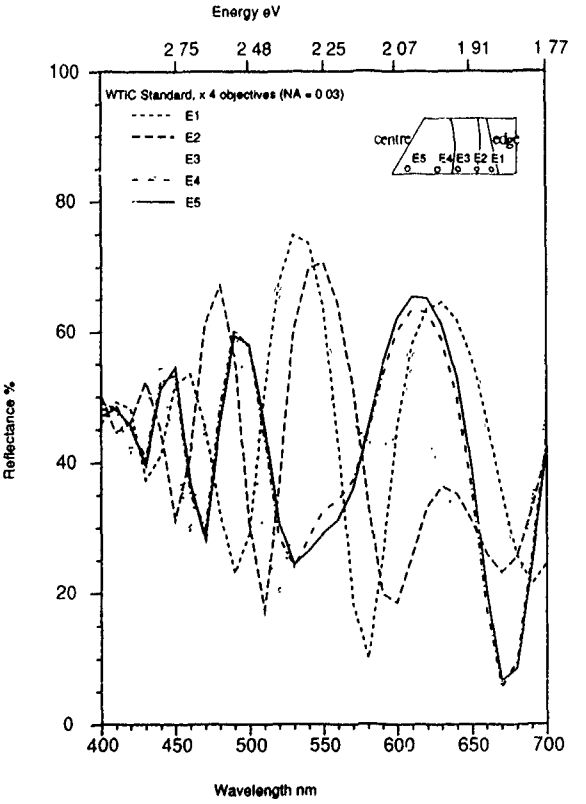

Fig. 1 Reflectance spectra, for five different regions across a SIMOX wafer The positions of these regions with respect to the implanted area are also shown

2.2. XTEM and SIMS measurements

Fig. 2 shows XTEM micrographs for regions E1 to E5. Comparison of the XTEM and SIMS data (fig. 2 and table 1) shows that the microstructure changes significantly from the centre of the wafer to the edge. At the centre of the implanted area (region E5), the structure essentially consists of a layer of high quality single crystal silicon, with a low oxygen content ($\sim 10^{18}$ O cm^{-3}) $\approx$ 2550 Å thick overlying a buried layer of SiO_2 ($\approx$ 3750 Å thick) which contains a number of single crystal silicon islands, mostly situated near the lower interface of the oxide and having the same, or nearly the same orientation as the substrate. The structure of region E4 is similar to that of region E5, except that now a few single crystal silicon islands are observed at the upper, as well as at the lower Si/SiO_2 interface. In region E3, even more silicon islands are observed near the upper Si/SiO_2 interface. The increased concentration of silicon within the oxides serves to increase its thickness and consequently the thickness of the silicon overlayer is reduced. Examination of the silicon islands at the upper oxide interface, now reveals them to be polycrystalline in nature, which indicates that they crystallised from a region of amorphous silicon (of which, more later). Progressing to region E2 we find that the size and density of the polycrystalline silicon islands, at the upper oxide interface, has increased still further and that some very small polycrystalline islands are now detected at the lower oxide interface. This trend is continued in region E1 and as successively more silicon is incorporated into the oxide, its thickness increases at the expense of that of the silicon overlayer. The effects described above are shown schematically in

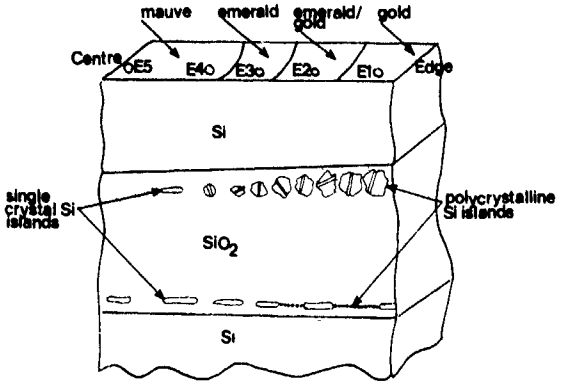

Fig. 3. Schematic showing effects of variations in the microstructure from regions E1–E5

fig. 3. Examination of the SIMS profiles for regions E5–E2 (not shown) reveals that there is a reduction in the oxygen secondary ion yield in the region corresponding to the silicon islands. We have used this effect to accurately pinpoint regions in the oxide where the silicon content is high.

3. Optical modelling

The analysis of light reflected specularly from multilayer structures requires a foreknowledge of the materials through which the light is propagated [15]. A suitable optical model must be constructed as a framework into which the optical properties and the thickness of the various films are fitted. Layers which are optically homogeneous, and which are bounded by abrupt,

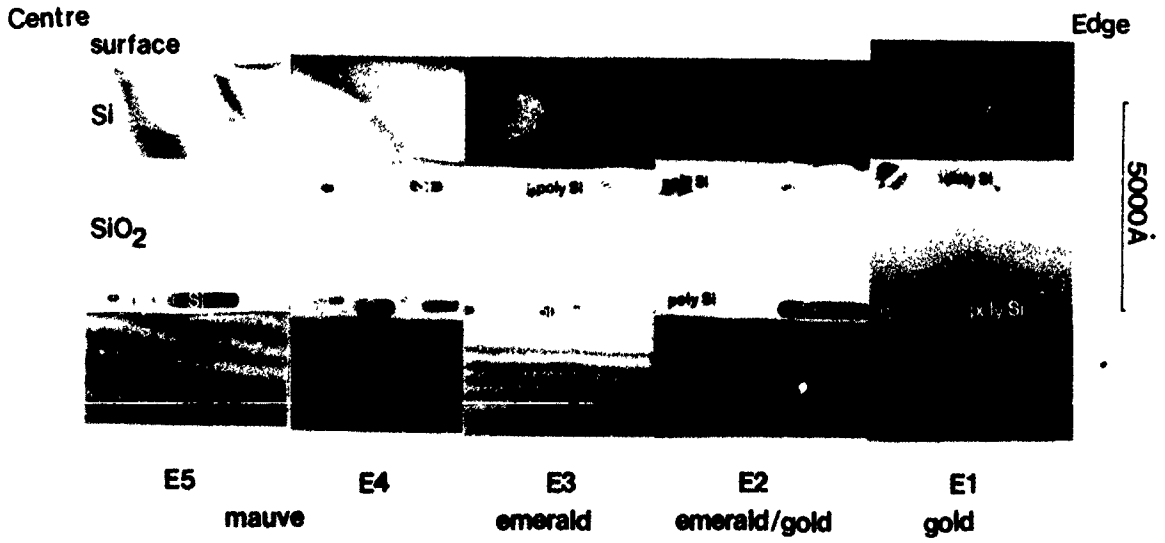

Fig. 2 XTEM micrographs for regions E1–E5.

Table 1
Comparison of layer thicknesses obtained from microscope-spectrophotometry, XTEM and SIMS

Layer no. [a]	E5			E3			E1	
	XTEM [Å]	S [b] [Å]	SIMS [Å]	XTEM [Å]	S [b] [Å]	SIMS [Å]	XTEM [Å]	S [b] [Å]
1		20			20			20
2	2516 ± 62	2600	2870	2610 ± 61	2500	2670	2270 ± 21	2290
3	471 ± 51	420		471 ± 108	420	430	220 ± 85	200
4	0	0		280 ± 77	200 $vf = 0.3$ [c]	330	628 ± 151	620 $vf = 0.4$ [c]
5	2615 ± 61	2700	2770	2640 ± 65	2600	2250	2814 ± 91	2850
6	360 ± 84	280 $vf = 0.25$ [c]	390	256 ± 77	280 $vf = 0.3$ [c]	340	105 ± 42	100 $vf = 0.3$ [c]
7	178 ± 75	250	290	237 ± 66	250	250	313 ± 26	250

[a] Layer 1 = native oxide on surface, layer 2 = silicon overlayer, layer 3 = SiO_2, layer 4 = silicon islands in SiO_2, layer 5 = SiO_2, layer 6 = silicon islands in SiO_2, layer 7 = SiO_2.
[b] S = simulated data.
[c] vf = volume fraction of silicon in oxide layer.

smooth and parallel interfaces are completely characterised by the layer thickness and its complex refractive index, N, where:

$$N = n - ik, \tag{2}$$

with the real part of the refractive index (n) having its usual meaning and k as the extinction (or absorption) coefficient. For discontinuous films, such as the silicon islands frequently observed after annealing ion implanted materials, a suitable approximation to a homogeneous film must be found, if the classical equations which quantify the nature of reflected light are to be used. A frequently used model for such composite materials is the Bruggeman effective medium approximation [16] in which the optical properties of the impurity and host phases are combined to produce a new phase with homogeneous effective properties. This model has been verified experimentally for physically mixed composite phases in which the impurity particles are smaller than the wavelength of the incident light. The effective phase may be described by a thickness and volume fraction of the impurity phase in the host.

Based on extensive TEM studies, the simplest model that accurately describes SIMOX materials requires seven layers (including a native or capping oxide layer) two of which are composite phases. To derive layer thickness and optical properties of such multi-layer structures, numerical inversion techniques must be used to solve the classical reflectance equations. A sensible strategy, before attempting the multi-dimensional fitting of layer thicknesses and volume fractions, is to test the validity of the proposed optical model. This has been achieved by using measurements of layer thickness (from

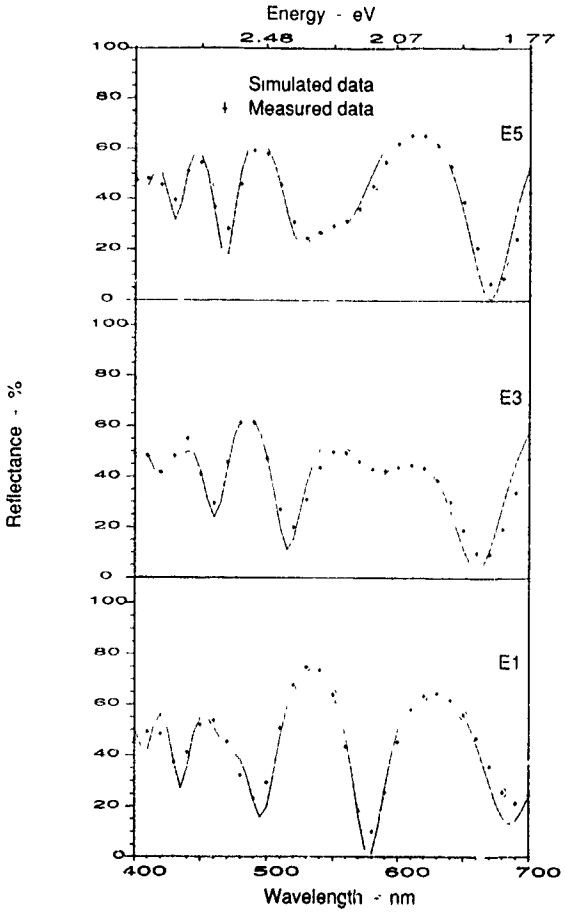

Fig. 4 Comparison of measured and simulated optical data for regions E5, E3 and E1.

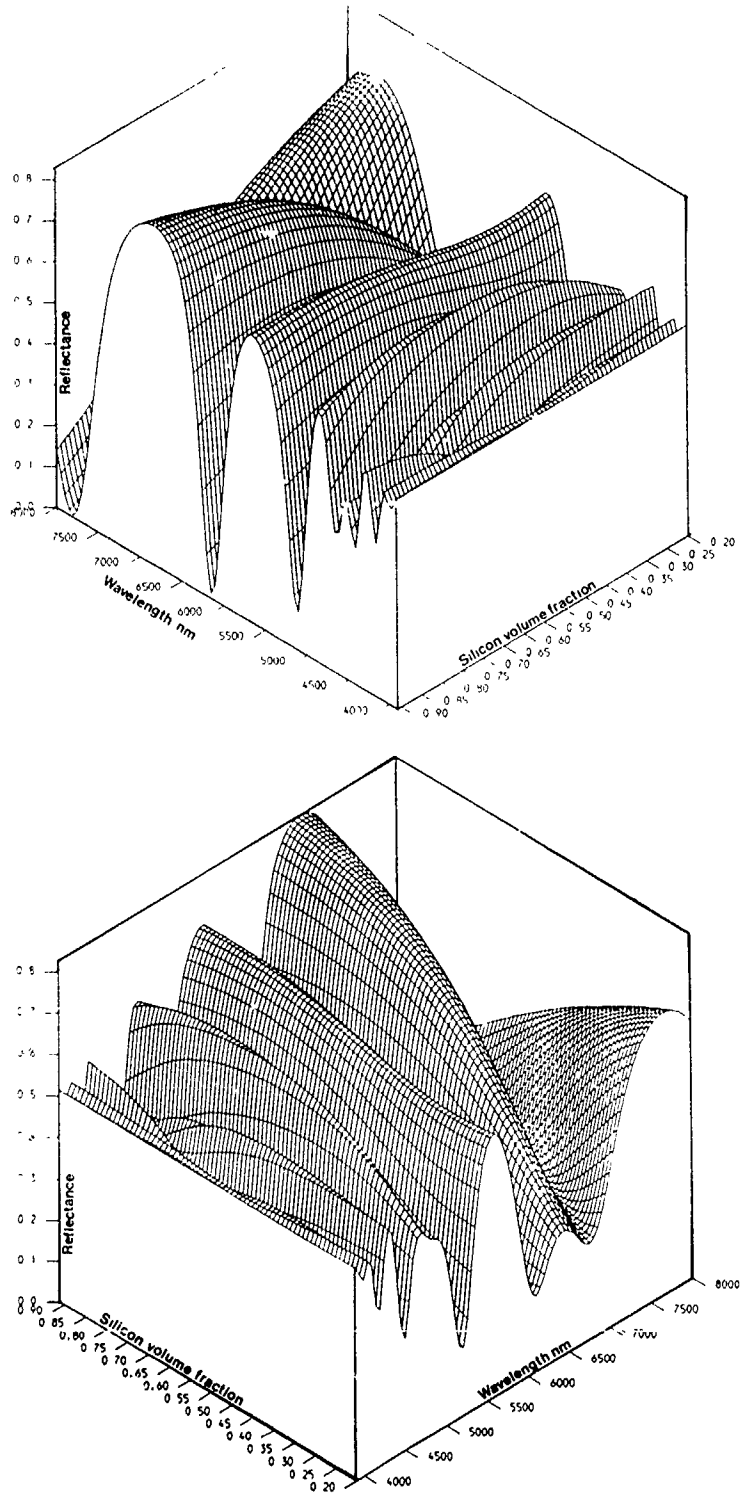

Fig. 5. Computer simulation showing how the percentage of silicon islands in the buried oxide layer affects the reflectance dispersion.

XTEM examinations of sections of the wafer where reflectance spectra had been previously collected) as a set of starting parameters for reflectance simulation. By varying the thicknesses and volume fractions of the layers defining the optical model it has been possible to obtain very good agreement between the experimental and simulated spectra, this is shown in fig. 4 for regions E1, E3 and E5, the thicknesses of the layers determined by the simulation and XTEM and SIMS are shown in table 1.

Although the parameters found in these simulations have not been optimised, the validity of the optical model has been demonstrated. Multi-dimensional function minimisation routines are being developed, which we believe will enable the quality of SIMOX materials to be rapidly and nondestructively mapped In fig. 5 we show simulated spectra, in which the percentage of silicon islands within the buried oxide layer has been varied. Examination of fig. 5 reveals the sensitivity of microscope-spectrophotometry to the presence of silicon islands and highlights its nondestructive capabilities

4. Formation of silicon islands in SIMOX structures

The presence of single crystal silicon islands at the lower SiO_2/Si interface in SIMOX specimens, after high temperature annealing has been reported by many authors [17–25]. Here, the general consensus of opinion is that these islands (or boats) are the vestige of the rather ragged lower interface resulting from implantation During annealing the oxide layer grows, and its interfaces become more planar, causing small islands of silicon near the lower oxide interface to be pinched off and trapped within the oxide layer Since the diffusion of silicon in SiO_2 is extremely low [26] these islands remain imprisoned in the oxide after annealing and, in general, have the same orientation as the silicon substrate from which they are derived. The slight misorientation of some of the islands with respect to the substrate is thought to result from the viscous flow of the oxide, during high temperature annealing, which causes some of the islands to be rotated slightly off axis.

The presence of silicon islands, especially polycrystalline ones, at the upper oxide interface, in SIMOX specimens has been reported by far fewer authors [23–25] It is thought that these polycrystalline islands are formed when areas of amorphous silicon recrystallise during high temperature annealing. This hypothesis is strengthened by the fact that the region in which the polycrystalline islands are formed coincides with the predicted peak of the damage distribution for 200 keV oxygen ions. The reason why amorphous silicon is produced in some parts of the implanted region and not in others is not fully understood but must be related to the local implantation temperature. In two earlier studies [9,10] we have found that there is a decrease in temperature of some 30 to 50 °C from the centre of the implanted region to the edge

5. Conclusions

We have shown that microscope-spectrophotometry is an extremely valuable technique for the nondestructive evaluation of SIMOX wafers. Not only because it can be accurately used to probe small areas and therefore analyse local changes in the microstructure, but also because it enables us to establish optical models which can aid in the deconvolution of complex multilayer structures, without the need for fudge factors and hours of computer time. The uses of microscope-spectrophotometry in microelectronics extend well beyond the realm of SIMOX and we are currently studying a variety of complex multi-layer structures in order to gain a better insight into their optical and microstructural properties.

Acknowledgements

This work is partially funded by the Procurement Executive Ministry of Defence (RSRE) under contract RP9-341.

References

[1] P L F Hemment and K J. Reeson, Phys World 2 (1989) 39
[2] T I Kamins and J.P Colinge, Electron Lett 22 (1986) 1236
[3] P. Dutta, G A Candela, D Chandler-Horowitz, J E Marchiando and M C. Peckerar, J Appl. Phys 64 (1988) 2754
[4] J Vanhellemont, H Maes and A De Veirman, J Appl Phys. 65 (1989) 4454
[5] J Vanhellemont and H. Maes, Mater Sci. Eng B5 (1990) 301
[6] S N. Bunker, P Sioshansi, M. Sanfacon, A Mogro-Campero and G A Smith, Nucl Instr and Meth B21 (1987) 148
[7] J Vanhellemont, H Maes and A De Veirman, to be published in Vacuum
[8] T Smith, J Electroanal Chem 150 (1983) 277.
[9] J.R Davis, M R. Taylor, G D T Spiller, P J Skevington and P L.F Hemment, Appl Phys Lett 48 (1986) 1279
[10] G. Harbeke, E.F Steigmeir, P.L F Hemment, K.J Reeson and L. Jastrzebski, Semicond Sci. Technol 2 (1987) 687
[11] A.J Criddle, in Advanced Microscopic Studies of Ore Minerals, eds. J L Jambor and D J. Vaughan, MAC/COM short course 17 (1990) 1

[12] A J. Criddle, in: Advanced Microscopic Studies of Ore Minerals, eds. J.L Jambor and D.J Vaughan, MAC/COM short course 17 (1990) 135
[13] H. Piller, Microscope Photometry (Springer, Berlin, 1977).
[14] K J. Reeson, Microreflectance and Ellipsometric Studies of the Polished Surfaces of some Minerals, Ph.D. thesis (CNAA, 1987).
[15] R.M A Azzam and N.M. Bashara, Ellipsometry and Polarised Light (North Holland, Amsterdam, 1977).
[16] D.E Aspnes and J.B. Theeten, Phys. Rev B20 (1970) 3292.
[17] C Jaussaud, J. Stoemenos, J. Margail, M. Dupuy, B. Blanchard and M Bruel, Appl Phys. Lett. 46 (1985) 1046.
[18] G.K Celler, P.L.F Hemment, K.W. West and J M Gibson, Appl Phys Lett. 48 (1986) 532
[19] A H. van Ommen, B H Koek and M.P.A Viegers, Appl. Phys Lett. 49 (1986) 628
[20] R.J. Chater, J.A. Kilner, E Schied, S. Christoloveanu, P L.F. Hemment and K.J. Reeson, Appl. Surf Sci. 30 (1987) 390.
[21] C Jaussaud, J. Margail, J Stoemenos and M. Bruel, Mater. Res. Soc. Proc. 107 (1988) 17
[22] S Krause, C O Jung, T.S Ravi, S.R Wilson and D.E Burke, Mater Res. Soc. Proc. 107 (1988) 93.
[23] P D Augustus, Mater. Res. Soc. Meeting (Boston, MA, USA, Dec. 1987)
[24] J. Margail, Realisation de structures silicum sur insolant (SSI) par implantation d'ions oxygene, SIMOX. Ph D Thesis (Grenoble University, Grenoble, 1987)
[25] K.J. Reeson et al., Microelectron Eng 8 (1988) 163.
[26] G Brebec, R. Seguin, J Bevenot and C. Martin, Acta Metall. 28 (1980) 327

Nuclear Instruments and Methods in Physics Research B55 (1991) 725–729
North-Holland

Thermal-wave measurements of high-dose ion implantation

Michael Taylor, Kurt Hurley, King Lee, Mark LeMere and Jon Opsal
Therma-Wave, 47320 Mission Falls Court, Fremont, CA 94539, USA

Tim O'Brien
Micron Technology Inc., 2805 East Columbia Road, Boise, ID 83706, USA

Thermal-wave measurements of high-dose ion implantation into silicon have been characterized In order to evaluate this technique for use in production as an ion-implant monitor, correlations were performed between thermal-wave and four-point-probe sheet-resistance measurements on test wafers. On device wafers, thermal-wave measurements were correlated to contact resistance on resistor test structures.

1. Introduction

Thermal-wave measurements are commonly used to characterize and monitor ion implantation at low and medium doses [1–3]. This technique has advantages over other methods because it is nondestructive and may be used directly on product wafers Until recently, thermal-wave measurements had a practical upper application limit of about 1×10^{15} ions/cm^2. This is because implants at higher doses from a subsurface amorphous layer that causes a nonmonotonic behavior of the thermal-wave signal. A recently developed capability for thermal-wave measurements now extends the measurable dose range to 2×10^{16} ions/cm^2

To evaluate the effectiveness of this technology for production monitoring of high-dose ion implantation, we performed a series of studies to determine the repeatability of the technique and to correlate thermal-wave measurements of dose with other established techniques We also present data correlating dose measurements with electrical test data on actual device wafers.

2. Technology

The thermal-wave measurement technique employs two low-power laser beams focused to a 1 μm spot on the sample surface. A simplified schematic of the system is shown in fig 1. Absorption of light from an intensity-modulated Ar-ion "pump" laser generates thermal and plasma waves within the surface region of the wafer. These waves are detected by the HeNe laser

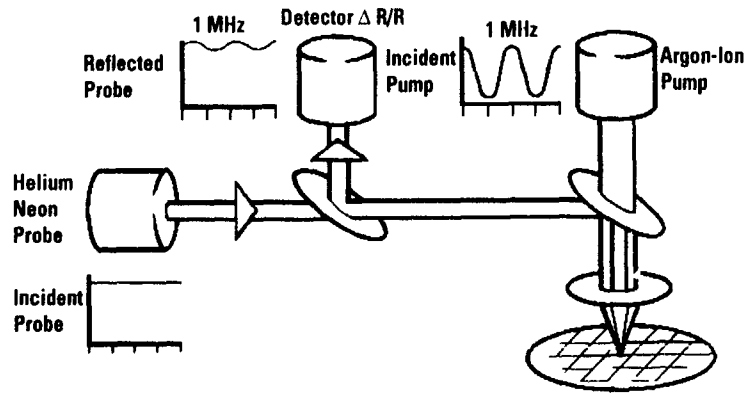

Fig 1 Thermal and plasma waves are generated and detected by two low-power nondestructive laser beams focused to a 1 μm diameter spot on the sample surface Absorption of light from an acousto-optically modulated (1 MHz) argon-ion pump laser generates thermal and plasma waves within the surface region of the sample. These waves are detected by the helium neon probe laser through the pump-induced modulation of the sample reflectivity or other material characteristics

0168-583X/91/$03 50 © 1991 – Elsevier Science Publishers B.V (North-Holland)

"probe" through the modulation of the sample reflectivity. The modulation $\Delta R/R$ is defined as the thermal-wave (TW) signal. The effects of the thermal and plasma waves on the silicon reflectivity is very sensitive to the presence of crystalline disorder created in the surface region of the wafer by the ion-implantation process [4]. Therefore, the thermal-wave signal can be directly correlated to the ion implantation dose in crystalline silicon.

3. High-dose ion implantation

A layer of amorphous silicon will be produced when crystalline silicon is implanted at a high dose with sufficient energy. For example, arsenic implants will cause amorphization at doses greater than about 1×10^{14} ions/cm^2 for energies above 10 keV. The thickness of the amorphous layer increases with dose for a fixed energy and conversely, increases with energy for a fixed dose

Calculations of dc laser reflectivity and modulated reflectance (TW signal) from an amorphous layer on a crystalline silicon substrate have been performed previously [5,6] As seen there, the modulated reflectance and dc reflectivity show an interference behavior with increasing amorphous thickness. Because of the non-monotonicity of the modulated reflectance signal, a simple correlation to dose is not possible (fig. 2). Therefore, in order to extract dose from modulated reflectance and dc reflectivity measurements, a model calculation must first be performed to determine the thickness of the amorphous layer. The amorphous-layer thickness is then a monotonically increasing function of dose, and a simple calibration can be made between the two

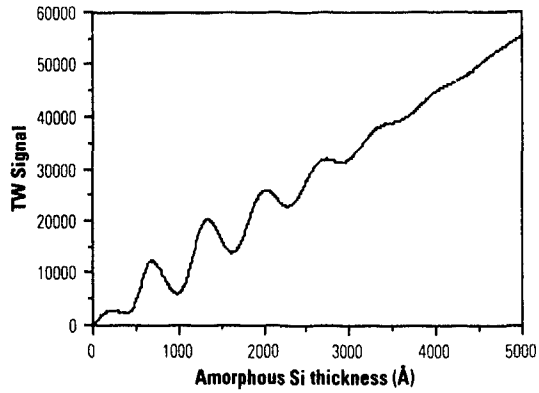

Fig. 2 High-dose ion implantation results in the formation of a subsurface amorphous silicon layer in crystalline silicon The modulated reflectance signal (thermal-wave signal) demonstrates an interference behavior as function of increasing amorphous-silicon thickness

4. Experimental results and discussion

We examined the capabilities of the high-dose thermal-wave measurement technique utilizing a commercially available Therma-Probe 300 system (Therma-Wave). Experiments were performed to determine the repeatability of the measurement technique and correlation to existing monitoring techniques. Additional studies were conducted to determine the sensitivity of the thermal-wave technique to electrical-device parameters on product wafers.

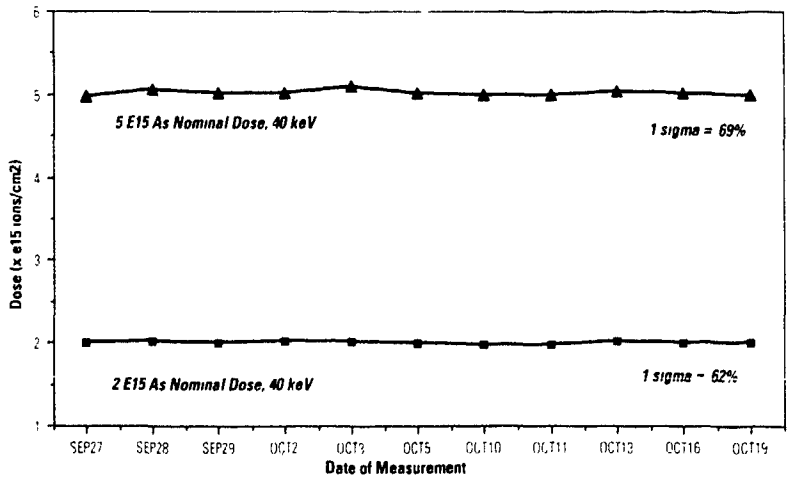

Fig 3 Two wafers were measured repeatedly over a period of approximately three weeks The $\pm 1\sigma$ dose repeatability is better than 1% in both cases.

In order to measure the repeatability of the method, a calibration was performed for an arsenic implant at 40 keV. Two wafers (2×10^{15} and 5×10^{15} ions/cm^2) were measured repeatedly over a period of approximately three weeks. Fig. 3 shows the result of dose measurements. In both cases the measurements demonstrated better than 1% (1σ) dose repeatability over the measurement period. This is significantly smaller than the 10–20% dose limit specification for many high-dose implant processes.

A correlation was performed between the thermal-wave measurement of dose and four-point-probe sheet-resistance measurements. Each day an implant monitor wafer was implanted under the same conditions. A thermal-wave measurement was performed before the wafer was furnace-annealed and measured on the four-point probe. This comparison was performed over a period of about one month. The results of the measurements are shown in fig. 4 As expected, the sheet-resistance and thermal-wave dose measurements show an anticorrelation, since the sheet resistance drops as the dose rises

Fig. 5 shows the thermal wave measurement of dose plotted against sheet resistance Even though the total variation in the dose is relatively small, a correlation to sheet resistance can be discerned with a correlation coefficient of 0 77 Comparisons between thermal-wave measurements and four-point-probe measurements of sheet resistance are instructive, but must be analyzed with caution. Thermal-wave measurements are made directly after ion implantation with no intervening process steps. Sheet-resistance measurements are made after the implanted species is activated through a high-temperature anneal Therefore, the sheet-resistance uniformity may be affected by the uniformity of activation during the anneal Also, some diffusion (redistribution)

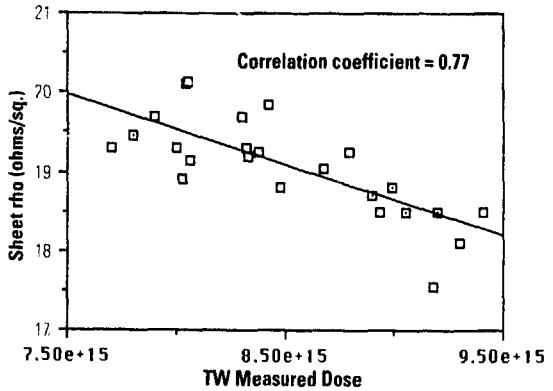

Fig. 5 Comparison of thermal-wave measurements with sheet-resistance maps for an implanter stability monitor demonstrates good correlation. Some variation between the two measurement techniques is expected since the sheet-resistance maps involve an extra anneal step that introduces another parameter into the experiment

of the implanted species may take place during anneal. Finally the spatial resolution of the two techniques are quite different. Thermal-wave measurements are made with a spatial resolution on the order of 1 μm, whereas four-point-probe sheet-resistance measurements average the data over an area of about 1 cm.

Fig. 6 shows a comparison of thermal-wave dose maps and four-point-probe measurements taken on the same test wafer In this case the standard deviations of the two maps match quite closely. Again, as with the trend data, the contours reverse since a higher dose corresponds to a lower sheet-resistance value

Since the thermal-wave measurement is used to predict and control electrical parameters on actual devices, it is important to characterize the correlation of dose

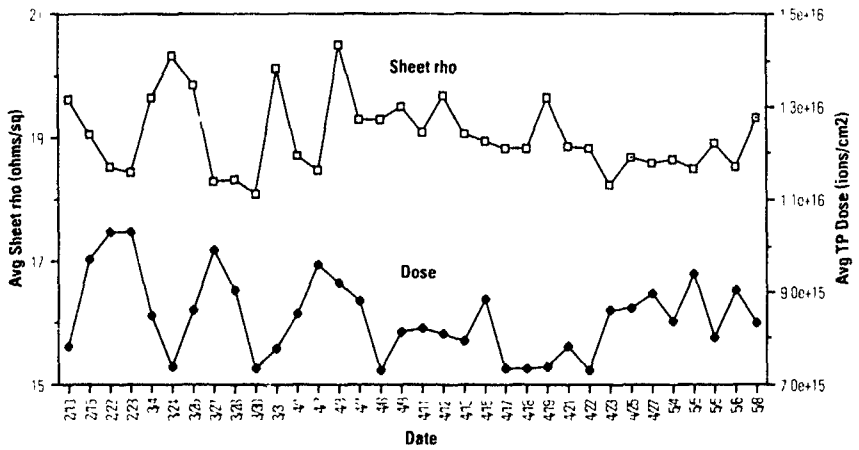

Fig 4 Process-stability trend data was collected by thermal-wave measurements of dose and simultaneously by a four-point probe One wafer per day was implanted and measured on both systems The trends appear as a mirror image since the sheet resistance decreases as dose increases

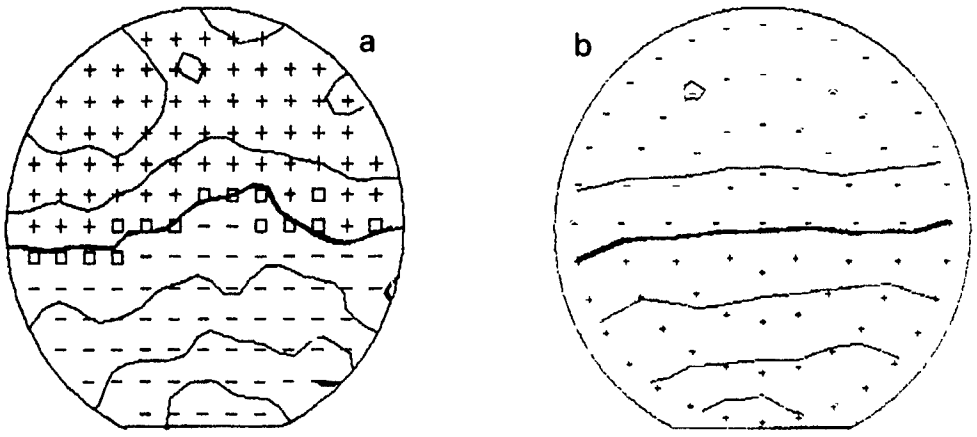

Fig. 6. Comparison of the actual maps measured on the same implant monitor wafer, 30 keV arsenic; (a) 9.94×10^{15} ions/cm^2, 1 61% standard deviation, 1 0% contour interval; (b) 19 1 Ω/□, 1 56% standard deviation, 1 0% contour interval The contours reverse since a higher dose corresponds to a lower sheet-resistance value

measurements to electrical test parameters This was done by implanting a series of device wafers at different doses, performing a thermal-wave measurement on the wafers directly after implantation, and comparing these measurements to electrical parameters on the completed devices.

The device wafers were implanted at five different doses: target dose, +7%, −7%, +15% and −15%. The implant was arsenic with a nominal dose of 9×10^{15} ions/cm^2 with a nominal beam current of 5 mA performed on a Varian 120-10 implanter. No screen oxide was used. Measurements were performed on the wafers at three locations, top, center and bottom.

After completing the measurements, the wafers were sent on to complete the manufacturing process. Electrical measurements were made on simple resistor test structures to determine the implanted dose The results are plotted in fig. 7. A clear dependence can be seen of contact resistance on thermal-wave measured dose. The significant scatter of the data in contact-resistance readings for each dose grouping may be attributable to critical-dimension (CD) variations in the resistor test structures.

There is a group measurements at approximately 1.1×10^{16} that do not correspond to a particular implant target dose. These points do lie in a smooth line with the other data points with respect to contact resistance. This indicates that these measurements actually represent areas of the wafer that received a substantially different dose from the implant target.

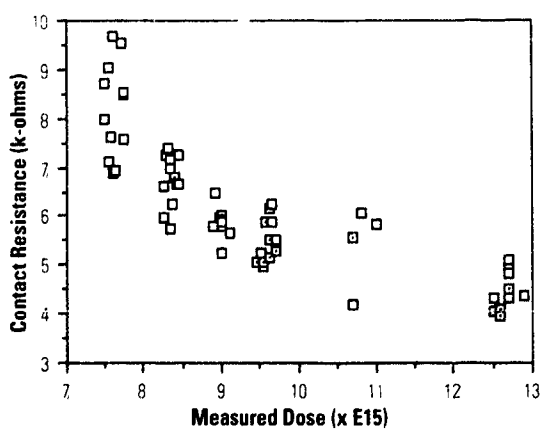

Fig. 7 Correlation of contact resistance to thermal-wave-measured dose on device structures on product wafers.

5. Conclusions

We have demonstrated the capabilities of the thermal-wave measurement technique to monitor high-dose implants on test and device wafers. The results have been correlated to sheet-resistance measurements for test wafers. On device wafers, we have correlated the thermal-wave measurements to electrical-device parameters. The repeatability of the measurement technique was demonstrated to be superior to the typical dose ranges of most high-dose implant processes.

Acknowledgement

The authors wish to thank Mike O'Connor for helping provide the experimental results on four-point-probe and electrical-test correlations

References

[1] W.L. Smith, A Rosencwaig, D L Willenborg, J Opsal and M W. Taylor, Solid State Technol. 29 (1) (1986) 85.
[2] R Martini, C. Whichard, W.L. Smith and M W Taylor, Solid State Technol 30 (5) (1987) 89.
[3] W.L. Smith, A Rosencwaig and D. Willenborg, Appl Phys Lett 47 (1985) 584
[4] A Rosencwaig, J. Opsal, W L Smith and D L Willenborg, Appl. Phys. Lett 46 (1985) 1013
[5] S. Wurm, P Alpern, D. Savignac and R Kakoschl ppl Phys A47 (1988) 147
[6] J Opsal, in: Review of Progress in Quantitative Nondestructive Evaluation, vol 8B, eds D O. Thompson and D E. Chimente (Plenum, 1987) p. 1241

Nuclear Instruments and Methods in Physics Research B55 (1991) 730-733
North-Holland

Optical characteristics of multi-layer structures formed by ion beam synthesis and their computer simulation

Yuehui Yu, Chenglu Lin, Xianghuai Liu and Shichang Zou

Ion Beam Laboratory, Shanghai Institute of Metallurgy, Academia Sinica, Shanghai 200050, People's Republic of China

P.L.F. Hemment

Department of Electronic & Electrical Engineering, University of Surrey, Guildford, Surrey GU2 5HX, UK

Layered structures such as silicon on insulator (SOI), and Si_3N_4 on silicon have been synthesized by different ion beam techniques and investigated by infrared (IR) reflection and absorption, Auger electron spectroscopy (AES) and cross-sectional transmission electron microscopy (XTEM). Buried SiO_2, Si_3N_4 and SiO_xN_y layers in silicon have been formed by oxygen (200 keV, 1.8×10^{18} O^+/cm^2) or nitrogen (190 keV, 1.8×10^{18} N^+/cm^2) implantation and by dual implantation of oxygen (200 keV, 1.8×10^{18} O^+/cm^2) and nitrogen (180 keV, 4×10^{17} N^+/cm^2) into silicon and annealing at different temperatures. Silicon nitride films with a stoichiometric ratio of Si_3N_4 have been synthesized by ion beam enhanced deposition (IBED). Infrared reflection spectra in the wavenumber range 1700–5000 cm^{-1} were measured for the SOI structures and Si_3N_4 films on silicon. Refractive index profiles of the SOI structures and Si_3N_4 films on silicon were obtained by computer simulation of the IR reflection interference spectra. In-depth composition profiles of the Si_3N_4 film on silicon have been correlated with its refractive index profiles using the Lorentz–Lorenz equation. The results of IR analysis are in agreement with AES and XTEM results.

1. Introduction

The synthesis of silicon on insulator (SOI) structures by ion implantation for very large scale integrated (VLSI) circuits has received considerable attention in recent years [1]. The technique of ion implantation is currently being developed to form SOI structures with a high-quality, single-crystal silicon layer on an insulating layer. Until now SOI structures have mainly been formed by oxygen or nitrogen implantation and investigated by transmission electron microscopy (TEM), secondary ion mass spectroscopy (SIMS) and Rutherford backscattering spectroscopy (RBS) [2,3]. Silicon nitride films with high thermal and chemical stability can be used as an important dielectric layer in electronics components [4]. Such films can be obtained by ion beam enhanced deposition (IBED) which is a combination of ion implantation and physical vapor deposition (PVD). The films synthesized by IBED have the advantage of a sufficient adhesion to the substrate, and easier control of the chemical composition and thickness of the film. Silicon nitride films have been synthesized by IBED and investigated by TEM and RBS. In this paper, we report on the optical characterization of films with a layered structure such as SOI, and silicon nitride films formed by different ion beam techniques. The refractive index profiles of SOI structures formed by ion implantation and annealing at high temperature, the structure of the buried layer, profiles of silicon nitride films synthesized by IBED and the width and shape of the transition region were investigated by the best fitting process for the IR reflection spectra. The relationships between the IR reflection spectra and the SOI structures, the IBED silicon nitride film structures were also obtained by a theoretical analysis. Refractive index and composition of the IBED silicon nitride film have been correlated using the Lorentz–Lorenz equation.

2. Experimental

n-type ⟨100⟩ Si, with a resistivity of ~ 10 Ω cm, was implanted with oxygen (1.8×10^{18} O^+/cm^2, 200 keV) or nitrogen (1.8×10^{18} N^+/cm^2, 190 keV), or first oxygen (1.8×10^{18} O^+/cm^2, 200 keV) and then nitrogen (4×10^{17} N^+/cm^2, 180 keV). During implantation, the wafer was maintained at 500–550 °C. After implantation, thermal annealing was used in order to allow for solid-phase epitaxial regrowth of the top silicon layer and for formation of the buried layer. The samples formed by nitrogen implantation and by dual implantation of oxygen and nitrogen were annealed at 1200 °C for 2 h. The samples implanted with oxygen were annealed at 1300 °C for 5 h. Deposition of silicon nitride films was carried out on an Eaton Z-200 ion beam

0168-583X/91/$03.50 © 1991 – Elsevier Science Publishers B.V. (North-Holland)

enhanced deposition system. Silicon wafers were used as substrates. High purity Si and N_2 gas were used as source materials of electron beam evaporation and implantation. During silicon film growth, 40 keV nitrogen ions with a ratio of $N^+/N_2^+ = 3/4$ were implanted into the silicon film and silicon nitride films were formed.

Infrared reflection measurements were made at room temperature by means of a Perkin-Elmer 983 double beam spectrometer for the frequency range 1700-5000 cm^{-1}. The quoted accuracy of the Perkin-Elmer is ±1% in absolute reflection. The reflections were measured with the beam at near-normal incidence to the implanted surface. Multiple reflections between the front and rear surfaces were eliminated by the lapped back surface. The SOI structures and the silicon nitride films were also measured by using RBS and channeling-effect techniques, TEM and AES.

3. Results and discussion

3.1 IR reflection interference analysis and optical effects of SOI structures

Fig 1 shows the infrared reflection spectra (solid line) for the SOI structures formed by (a) oxygen (1.8×10^{18} O^+/cm^2, 200 keV) implantation and annealing at 1300 °C for 5 h, (b) nitrogen (1.8×10^{18} N^+/cm^2, 190 keV) implantation and annealing at 1200 °C for 2 h, or (c) first oxygen (1.8×10^{18} O^+/cm^2, 200 keV) and then nitrogen (4×10^{17} N^+/cm^2, 180 keV) implantation and annealing at 1200 °C for 2 h The interference effects observed in fig 1 are caused by refractive index changes in the buried layer The RBS and AES analyses show that there is a defective top silicon layer which extends from the surface down to the buried layer after high temperature annealing, the interfaces of top silicon-buried layer and buried layer-substrate are steep and there is an internal nitrogen-rich thin layer in the buried nitride layer. The AES and IR absorption analyses also show that there is the thin oxynitride layer at the wings of the buried oxide layer for the SOI structure formed by dual implantation of oxygen and nitrogen

A theoretical model was established through a consideration of the optical properties of the top silicon layer and the buried layer. A computer code was established to calculate the interference at normal incidence in reflection (R) from a multi-layer thin film model [5] The code computes R for an arbitrary number of layers having index of refraction n_j, extinction coefficient K_j and layer thickness d_j. The top silicon layer of the SOI structure was taken as one uniform layer of index n_0 and thickness D_0. The buried layer was taken as one uniform silicon oxide layer or silicon nitride layer with an internal porous nitrogen-rich thin layer, one uniform silicon oxide layer in the the middle part of the buried

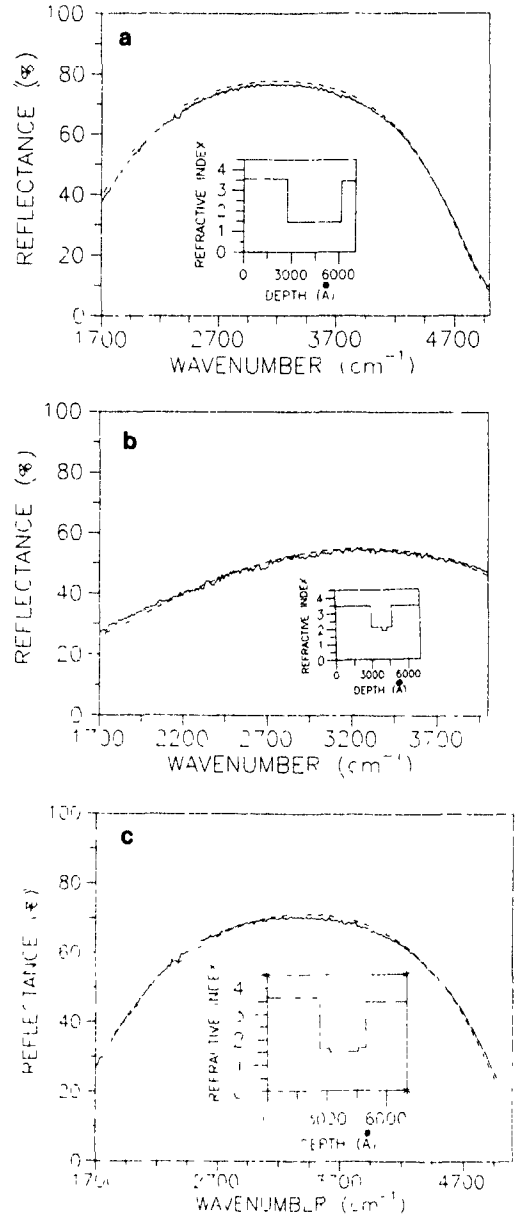

Fig 1 IR reflection spectra of SOI structures formed by (a) oxygen (200 keV, 1.8×10^{18} O^+/cm^2) implantation and annealing at 1300 °C for 5 h, (b) nitrogen (190 keV, 1.8×10^{18} N^+/cm^2) implantation and annealing at 1200 °C for 2 h, and (c) first oxygen (200 keV, 1.8×10^{18} O^+/cm^2) and then nitrogen (180 keV, 4×10^{17} N^+/cm^2) implantation and annealing at 1200 °C for 2 h Both experimental spectra (solid lines) and the best fitting curve (dashed curves) are shown The inset shows the refractive index profiles of the SOI structures

layer and two uniform thin oxynitride layers at the interface of the buried layer The extinction coefficients are zero for the wavenumber range 1700–5000 cm^{-1} The experimental reflection spectrum was fitted by using the computer code which adjusted the values of parame-

ters of the multi-layer thin film model to minimize the reduced chi-square. The dashed curves in fig. 1 are the results of the fitting of the reflection spectra using the theoretical model. The insert shows the refractive index profiles of the SOI structures. In fig. 1, it is seen that the sample of both oxygen and nitrogen implanted silicon after annealing at 1200 °C for 2 h results in a continuous buried layer with silicon oxide in the middle part of the buried and the two thin oxynitride layers at the interfaces. The thicknesses of the top silicon layer and the buried layer are 2650 and 2300 Å, respectively Variations in IR reflection spectra caused by deviation in the parameters of SOI structures away from the best fitting parameter set in fig. 1 were observed by theoretical calculation. The results indicate that the IR reflection spectra are sensitive to the parameters of the theoretical model.

3.2 IR reflection interference analysis and optical effects of the IBED silicon nitride film

Fig. 2 shows the infrared reflection spectra for the silicon substrate and the silicon nitride film deposited on silicon by IBED. As a result of RBS and AES analysis, there is a thin top silicon-rich layer on the surface of the silicon nitride film formed by IBED. The infrared absorption analysis proves that silicon nitride films deposited on silicon by IBED are stoichometric Si_3N_4 films. The AES analysis shows that there is a smooth transition region between the silicon nitride layer and the silicon substrate. A theoretical model was established through consideration of all the effects discussed above In this model, the transition region is approximated by I layers of equal thickness D with n_j,

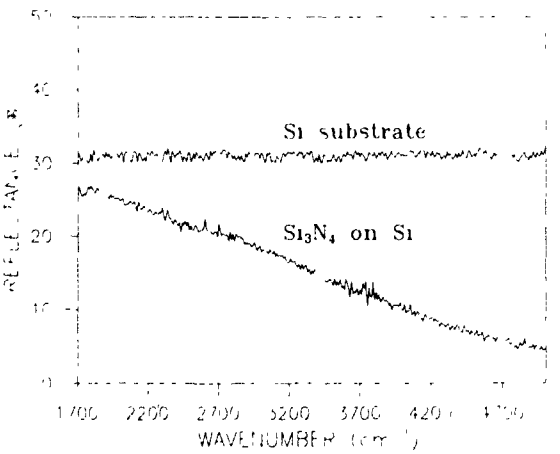

Fig. 2 IR reflection spectra of a silicon substrate and of a silicon nitride film deposited on silicon.

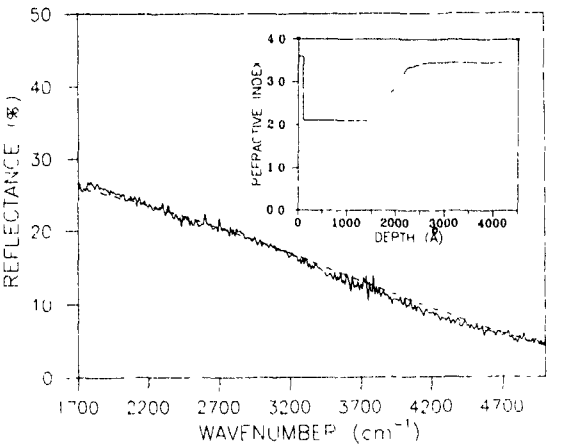

Fig. 3 Both the experimental spectrum (solid line) and the best fit curve (dashed line) of a silicon nitride film deposited on silicon are shown The inset shows the refractive index profile of the silicon nitride film deposited on silicon

the index of refraction of the jth layer, given by a half Gaussian distribution of the form:

$$n_j = n_S + (n_B - n_S)\exp\left\{-[(j-1)D]^2/(2\,\Delta R_p^2)\right\},$$

where n_B is the index of refraction of the silicon nitride layer, n_S is the refractive index of the silicon substrate and ΔR_p is the standard deviation. The extinction coefficients are zero for the wavenumber range 1700–5000 cm^{-1} A computer code was established to calculate the interference at normal incidence in reflection (R) from a multi-layer thin film model described above.

Fig. 3 shows the infrared reflection spectra (solid line) for the silicon nitride film deposited on silicon by IBED. The dashed curve is the result of fitting the reflection spectrum using the theoretical model Also shown is the refractive index profile of the IBED film as the fitting function in fig. 3. In fig. 3, it is seen that the structure of the silicon nitride film deposited on silicon consists of a smooth transition region between the deposited film and the silicon substrate. The thickness of the silicon nitride layer and width of the transition region are 1300 and 1000 Å, respectively.

The large changes observed in the refractive index of the IBED silicon nitride film shown in fig. 3 appear to be associated with changes in the microstructure The model to predict the refractive index of the silicon nitride film formed by IBED was constructed using the results analyzed above which show that the silicon nitride film is a mixture of Si_3N_4 and pure Si. If x is the atomic ratio of Si and Si + N is determined by quantitative AES analysis while sectioning through the silicon nitride film, the Lorentz–Lorenz equation is given:

$$(n^2 - 1)/(n^2 + 2) = \tfrac{4}{3}\pi N_{Si_xN_1}\alpha_{Si_xN_1}$$

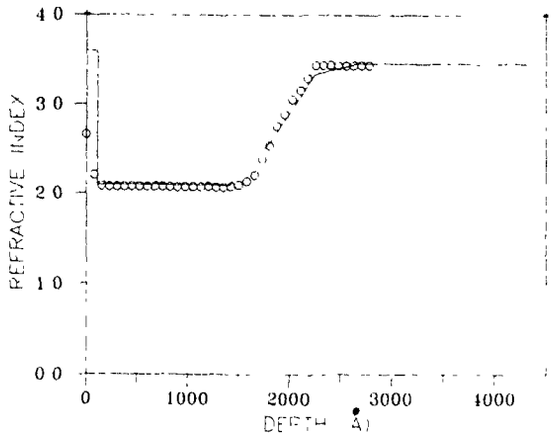

Fig 4 Refractive index profile of silicon nitride film deposited on silicon. Both the refractive index profile (solid line) determined by fitting the interference spectrum and that calculated by using the Lorentz–Lorenz equation (○) are shown for comparison

where $N_{Si_xN_{1-x}}$ is the atom density of the mixture Si_xN_{1-x}, and $\alpha_{Si_xN_{1-x}}$ is the polarizability for the mixture Si_xN_{1-x}. $\alpha_{Si_xN_{1-x}}$ was taken as

$$\alpha_{Si_xN_{1-x}} = \tfrac{1}{3}(7x-3)\alpha_{Si} + \tfrac{7}{3}(1-x)\alpha_{Si_3N_4},$$

where α_{Si} is the polarizability for Si (3.47×10^{-24} cm^3) and $\alpha_{Si_3N_4}$ is the polarizability for Si_3N_4 (9.24×10^{-24} cm^3).

The Lorentz–Lorenz equation can be used to compute the refractive index $n(x)$. The results of these calculations are presented in fig. 4. There is good agreement with the refractive index profile obtained by computer fitting the IR reflection spectrum of the silicon nitride film.

4. Conclusion

Layered structure films such as SOI, and silicon nitride films have been synthesized by different ion beam techniques and investigated by RBS, AES and IR absorption and reflection spectroscopy. Computer simulation of the reflection interference spectrum has been proven to be an effective method for the analysis of layered structures formed by different ion beam techniques. The parameters for the SOI structures and the IBED silicon nitride films deposited on silicon, such as the thickness of the top silicon layer, the buried layer and width of the transition region between the IBED silicon nitride film and the silicon substrate were obtained in this manner

References

[1] J Davis, IEE Tutorial Meeting on SOI Current Status and Future Potential (London, 1987)
[2] P L F Hemment, Mater. Res Soc Symp Proc. 53 (1986) 207
[3] K.J Reeson, Nucl. Instr and Meth B19/20 (1987) 269.
[4] J Wang, J Electron Mater 5 (1976) 113
[5] O.S. Heavens, Optical Properties of Thin Solid Films (Academic Press, New York, 1955).

Nuclear Instruments and Methods in Physics Research B55 (1991) 734–737
North-Holland

Buried insulator formation by nitrogen implantation at elevated temperatures

N. Hatzopoulos, U. Bussmann, A.K. Robinson and P.L.F. Hemment
Department of Electronic and Electrical Engineering, University of Surrey, Guildford, Surrey GU2 5XH, UK

Buried silicon nitride layers can be synthesized by high dose nitrogen implantation into silicon To investigate temperature effects, 200 keV N^+ implantations into silicon were performed with doses of 0 35 to 1.05×10^{18} N^+ cm^{-2} A first set of samples was implanted at 500 °C, using ion beam induced heating only For the second set, a new sample holder provided constant background heating of the wafer maintaining it at a constant temperature of 670 ± 10 °C by halogen lamp irradiation Two hour anneals were carried out in flowing nitrogen at temperatures between 700 and 1200 °C in 100 °C steps Rutherford backscattering measurements were performed in order to assess the quality of the silicon top layers It is concluded that constant background heating leads to a major improvement of the crystalline quality for all implantation doses and for annealing temperatures up to 1100 °C

1. Introduction

One way to produce SOI (silicon-on-insulator) structures by ion beam synthesis is to implant nitrogen ions into silicon to form a buried nitride layer, known by the acronym SIMNI (Separation by IMplantation of NItrogen) [1]. In comparison to the formation of SIMOX (Separation by IMplantation of OXygen) substrates [2], lower doses of ions are required to synthesize the nitride layer. In addition lower anneal temperatures are adequate for complete segregation of the nitrogen atoms to the nitride layer [3].

The formation of SIMNI structures is a two-step procedure; the implantation of a high dose of nitrogen into silicon is followed by a high temperature annealing stage The implantation has to be performed at temperatures $T_i > 350$ °C to give a device quality silicon top layer [4] Common nitrogen implantation temperatures are in the range 420–520 °C.

In this paper the crystalline quality of wafers implanted with the heated sample holder ($T_i = 670$ °C) is compared to that of wafers implanted using beam heating only ($T_i = 500$ °C)

2. Experiment

Molecular nitrogen (N_2^+) was implanted into device grade (100) silicon wafers using the 500 kV high current implanter at the University of Surrey. The energy of the incident N_2^+ ions was 400 keV and the doses of 0.35, 0.70 and 1.05×10^{18} N^+ cm^{-2} are designated low, medium and high doses.

Two series of implantations were performed. For the first series (set 1) the wafer rests on three silicon tips, which ensure thermal isolation of the sample from the mounting plate [5]. The implantation starts at room temperature, using a beam current of 60 μA, and after one to two minutes an equilibrium implantation temperature of 500 ± 30 °C is reached as a result of ion beam induced heating only.

The second implantation series (set 2) was performed at 670 ± 10 °C using a heated sample holder [6] in which halogen lamps provide constant background heating to preheat and maintain the sample at an elevated temperature. The advantages of using halogen lamps include a higher implantation temperature as well as preheating of the wafer prior to the start of the implantation process

On each wafer the implanted area of 2.5×2.5 cm^2 was cleaved into small samples which were annealed in a dry nitrogen atmosphere for 2 h, covering the temperature range from 700 to 1200 °C in 100 °C steps. The as-implanted and annealed samples were analysed by Rutherford backscattering (RBS) and ion channeling of 1.5 MeV helium ions and cross-sectional transmission electron microscopy (XTEM).

3. Results and discussion

3.1 As-implanted samples

Figs. 1a, b and c show the aligned RBS spectra for as-implanted samples from set 1 (curves (ii)) and set 2 (curves (iii)) and for samples annealed at 1200 °C from

0168-583X/91/$03.50 © 1991 – Elsevier Science Publishers B V (North-Holland)

set 1 (curves (iv)) and set 2 (curves (v)), together with the random spectra for the 1200 °C annealed samples from set 2 (curves (i)). For both sets the dose of 0.35 ×

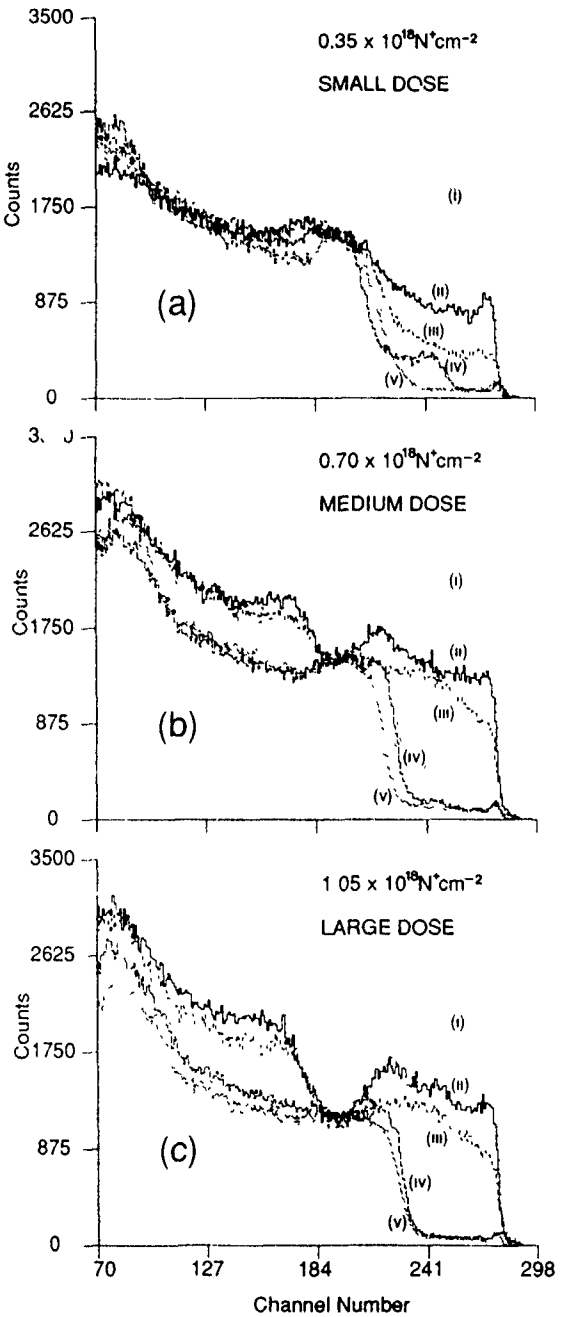

Fig. 1. RBS spectra from samples implanted with (a) 0.35×10^{18} N^+ cm^{-2}, (b) 0.70×10^{18} N^+ cm^{-2} and (c) 1.05×10^{18} N^+ cm^{-2} without (set 1) and with (set 2) background heating. Curves: (i) set 2, random, annealed at 1200 °C; (ii) set 1, channelled, as-implanted; (iii) set 2, channelled, as-implanted, (iv) set 1, channelled, annealed at 1200 °C; (v) set 2, channelled, annealed at 1200 °C.

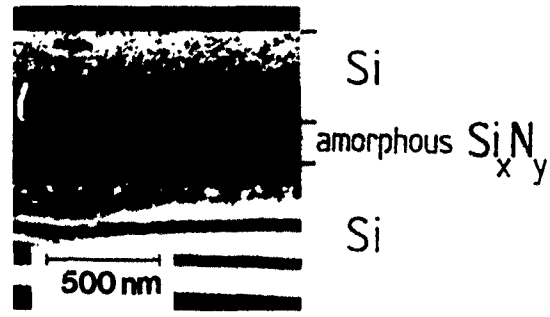

Fig. 2 Dark field XTEM micrograph of a unannealed sample implanted with 1.05×10^{18} N^+ cm^{-2} using constant background heating ($T_i = 670$ °C).

10^{18} N^+ cm^{-2} (Fig. 1a) produces the least damage in the top silicon layer. Comparing the two sets it is obvious that for set 2 samples (curves (iii), background heating), the silicon top layer is of better quality for all doses. The higher temperature leads to an improved crystalline structure after the implantation due to self annealing during the implantation. The most pronounced improvement is seen for the smallest dose.

XTEM investigations have been performed in order to compare the stucture of implanted samples from set 1 and set 2 for the highest dose. In both cases, the nitride layer is amorphous but precipitation above and below the buried nitride layer is more pronounced in the sample from set 2 (fig. 2) These precipitates are believed to consist of amorphous nitride which formed during the implantation at the higher T_i.

3.2. Annealed samples

3.2.1 Small dose (0.35×10^{18} N^+ cm^{-2})

For the beam heated samples (set 1), increasing the anneal temperature improves the crystallinity of the silicon overlayer. This is evident from the χ_{min} values (ratio of minimum channelling yield and random yield in the near surface region) of 43, 14, 8 and 4% in samples annealed for 2 h at 700, 900, 1100, and 1200 °C, respectively.

For the samples annealed at 1200 °C, RBS spectra showed an anomalous dechannelling occuring at a depth of 150 nm. This dechannelling may be a result of residual damage or the presence of nitrogen in the form of precipitates.

Samples implanted using constant background heating (set 2), which were annealed over the same temperature range, showed a 50% reduction in the channelling yield at the relatively low anneal temperature of 700 °C. Higher anneal temperatures result in good crystalline quality silicon top layer with a χ_{min} value of 4%.

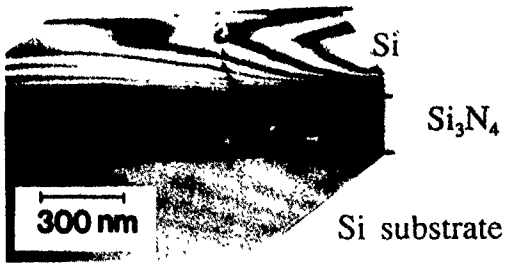

Fig. 3. XTEM micrograph of a sample implanted with 1.05×10^{18} N^+ cm^{-2} and annealed at 1200 °C for 2 h. Implantation conditions as in fig. 2.

3.2.2 Medium dose (0.70×10^{18} N^+ cm^{-2})

In both set 1 and set 2 samples, gradual improvement of the crystalline quality in the near surface region is observed during anneals between temperatures of 700 and 1100 °C. During the 1200 °C anneal the silicon overlayer recovers fully (fig. 1b, curves (iv) and (v)). For all anneal temperatures RBS analysis shows a reduced number of defects in the Si overlayer for samples from set 2 The silicon overlayer thickness of samples annealed at 1200 °C is found to be greater in the sample implanted with background heating (300 nm) than in the sample implanted without external heating (290 nm).

3.2.3. Large dose (1.05×10^{18} N^+ cm^{-2})

The channelled RBS spectra from as-implanted and annealed samples from set 1 and set 2, over the anneal temperature range 700 to 1200 °C indicate similar improvements in the crystalline quality of the top silicon layer as for samples implanted with the medium dose. Again for the samples annealed at 1200 °C, the silicon overlayer thickness is greater for the sample implanted with background heating (fig. 1c, curves (iv) and (v)). Shown in fig. 3, is a typical XTEM micrograph of the 1200 °C annealed sample from set 2. The estimated density of threading dislocations is $? \times 10^7$ cm^{-2}. Furthermore the dislocation density in the silicon overlayer for the set 1 samples (not shown) was found to be about 10^{10} cm^{-2}.

The anneal temperature dependence of the values of χ_{min} for all samples is shown in fig. 4 It can be seen that the χ_{min} values after the 1200 °C anneal coincide for set 1 and set 2 samples, indicating the good quality of the near surface region of the silicon overlayer. However XTEM investigations indicated that the threading dislocations density was higher by about three orders of magnitude for the set 1 samples.

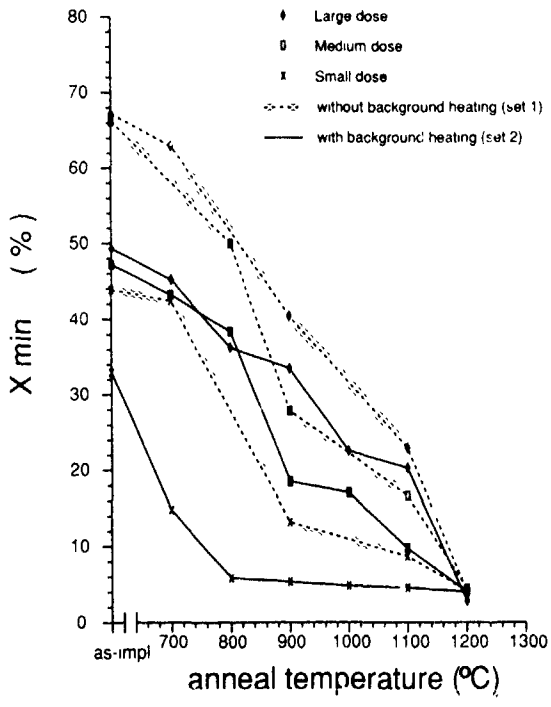

Fig. 4. Comparison of the anneal temperature dependence of x_{min} (ratio of the minimum channelled yield and random yield in the near surface region) for samples implanted without (set 1) and with (set 2) background heating.

4. Conclusions

(i) Constant background heating providing sample preheating and a higher implantation temperature leads to an improved crystalline quality in the top layer of silicon of the SIMNI structures in the as-implanted as well as in the annealed samples for $T_a < 1200$ °C.

(ii) Implantation with constant background heating at ≈ 670 °C leads to a thicker silicon overlayers (300 nm) after the 1200 °C anneal with a dislocation density three orders of magnitude lower than those implanted using beam heating only.

(iii) An annealing temperature of 1200 °C is required in order to achieve a low defect density, precipitate-free silicon overlayer.

Acknowledgements

The authors would like to acknowledge the contributions made by Prof. J Stoemenos, University of Thessaloniki, Greece, who provided most of the XTEM micrographs, as well as the staff of the D.R Chick Laboratory, University of Surrey, for their technical assistance during the implantations and RBS analysis. This work was supported in part by the UK Science and Engineering Research Council.

References

[1] K J Reeson, Nucl Instr and Meth. B19/20 (1987) 269
[2] P L F Hemment, Mater Res. Soc Symp. Proc. 53 (1986) 207.
[3] L. Nesbit, S. Stiffler, G Slusser and H. Vinton, J. Electrochem Soc 132 (1985) 2713
[4] G. Zimmer and H Vogt, IEEE Trans Electron. Devices ED-30 (1983) 1515
[5] P.L.F. Hemment, E. Maydell-Ondrusz, K G. Stephens, J. Butcher, D. Ioannou and J Alderman, Nucl. Instr. and Meth. 209/210 (1983) 157.
[6] A K. Robinson, C.D. Marsh, U Bussmann, J.A Kilner, Y Li, J. Vanhellemont, K J Reeson, P L F Hemment and G.R. Booker, these Proceedings (8th Int. Conf. on Ion Implantation Technology, Guildford, UK, 1990) Nucl. Instr and Meth. B55 (1991) 555.

Nuclear Instruments and Methods in Physics Research B55 (1991) 738–741
North-Holland

Studies on $Si^+ + B^+$ dual implantations into the top silicon layer of SIMNI material

Shunkai Zhang, Chenglu Lin, Zuyao Zhou and Shichang Zou

Ion Beam Laboratory, Shanghai Institute of Metallurgy, Academia Sinica, Shanghai 200050, People's Republic of China

SIMNI material was formed by N^+ implantation into crystalline silicon wafers at 170 keV with a dose of 1.8×10^{18} cm^{-2} and annealing at 1200 °C for 2 h. The top silicon of these SIMNI wafers was amorphized at different depths by Si^+ implantation at three conditions. (1) 25 keV, 5×10^{15} cm^{-2}, (2) 140 keV, 5×10^{15} cm^{-2}, (3) 25 keV, 5×10^{15} cm^{-2} + 80 keV, 5×10^{15} cm^{-2} + 140 keV, 5×10^{15} cm^{-2}. Then the three groups of SIMNI wafers and another group with no implantation by Si^+ were implanted by B^+ at 25 keV with a dose of 1×10^{15} cm^{-2}, and annealed at a series of temperatures for 30 min. Glancing RBS/C measurement shows that an epitaxial regrowth toward the surface or the inner part of the top silicon exists for the samples in group (1) and (2), respectively, with increasing annealing temperature. No epitaxial regrowth exists for the samples in group (3). Raman measurement shows that a phase transformation from amorphized silicon to polysilicon exists for the top silicon of samples in group (3) when the annealing temperature is increased from 500 °C to 600 °C. SRP measurement shows that $Si^+ + B^+$ dual implantations are able to increase the activation rate of boron in the top silicon of SIMNI material.

1. Introduction

Up to now, many studies have been done on the formation mechanism of SOI material formed by ion implantation, the dependence of its microstructure and properties on implantation and annealing conditions and its application in device fabrication [1–7]. However, the implantation damage and annealing behavior of top silicon in SIMNI (Separation by IMplanted NItrogen) or SIMOX (Separation by IMplanted OXygen) materials have not been studied much, although this is of great importance for the application of SIMNI or SIMOX materials in device fabrication. In this paper, Si^+ was implanted into the top silicon of SIMNI wafers at three different conditions. Then these wafers and those of another group with no implantation of Si^+ were implanted by B^+. Glancing Rutherford backscattering and channeling (RBS/C) and Raman measurements were used to investigate the implantation damage and annealing behavior of the top silicon in SIMNI material. Spreading resistance probe (SRP) measurements were used to characterize the activation of boron in the top silicon of SIMNI. The results indicate that the implantation damage and annealing behavior and activation of boron differ from each other with different implantation conditions.

2. Experiment

Clean surface n-type ⟨100⟩ crystalline silicon wafers with a resistivity of about 10 Ω cm were implanted by N^+ at 170 keV with dose of 1.8×10^{18} cm^{-2}. During implantation, the wafers were heated by the incident

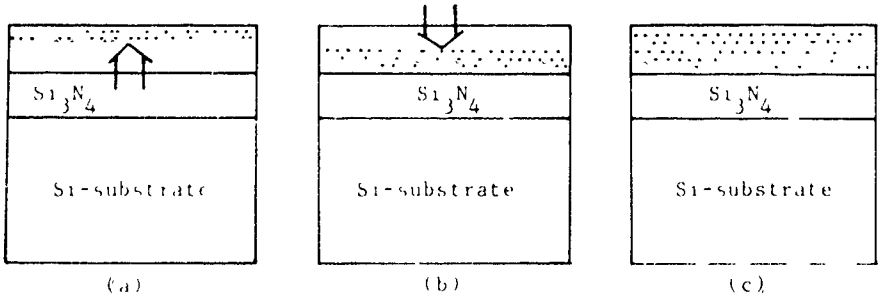

Fig. 1. Diagram of epitaxial regrowth after annealing of SIMNI samples implanted by Si^+ at different depths. (a) Si^+ 25 keV, 5×10^{15} cm^{-2} + B^+ 25 keV, 1×10^{15} cm^{-2}, (b) Si^+ 140 keV, 5×10^{15} cm^{-2} + B^+ 25 keV, 1×10^{15} cm^{-2}, (c) Si^+ 25 keV, 5×10^{15} cm^{-2} + 80 keV, 5×10^{15} cm^{-2} + 140 keV, 5×10^{15} cm^{-2} + B^+ 25 keV, 1×10^{15} cm^{-2}.

0168-583X/91/$03.50 © 1991 – Elsevier Science Publishers B.V. (North-Holland)

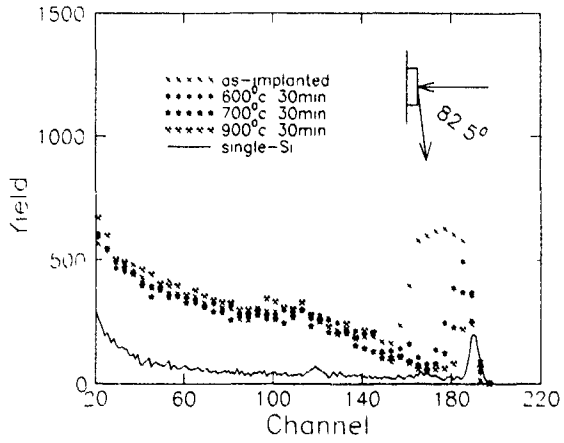

Fig 2 RBS/C spectra of SIMNI material implanted by Si^+ at 25 keV, 5×10^{15} cm^{-2} and B^+ at 25 keV, 1×10^{15} cm^{-2}

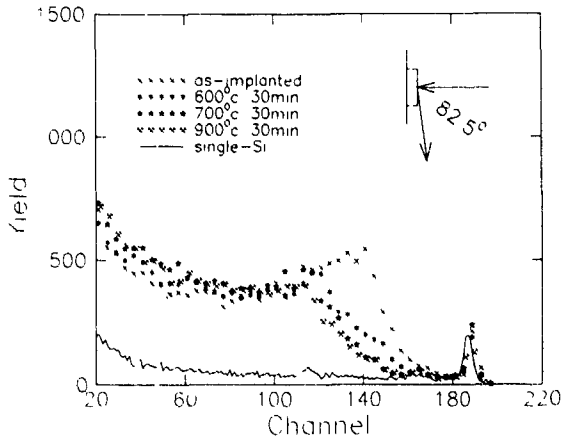

Fig 3 RBS/C spectra of SIMNI material implanted by Si^+ at 140 keV, 5×10^{15} cm^{-2} and B^+ at 25 keV, 1×10^{15} cm^{-2}

beam and the temperature of the wafers was kept at about 500 °C. Then these wafers were annealed at 1200 °C for 2 h in a dry N_2 ambient, and SIMNI wafers with a top layer of silicon of about 250 nm were obtained. Si^+ was implanted into the top silicon of these SIMNI wafers at three different conditions to amorphize the top silicon at different depths (see fig. 1). (1) 25 keV, 5×10^{15} cm^{-2}; (2) 140 keV, 5×10^{15} cm^{-2}; (3) 25 keV, 5×10^{15} cm^{-2} + 80 keV, 5×10^{15} cm^{-2} + 140 keV, 5×10^{15} cm^{-2}. Then these three groups of samples and another group with no implantation of Si^+ were implanted by B^+ at 25 keV with a dose of 1×10^{15} cm^{-2}. For each group, annealing at a series of temperatures ranging from 500 °C to 900 °C for 30 min was done, and glancing RBS/C measurements were performed with an incident beam of He^+ at the energy of 2 MeV. Raman backscattering measurements were done by a RAMANLOG-5 spectrometer with the wavelength of the incident light at 488 nm. SRP measurements were carried out by ASR-100C/2.

3. Results and discussion

Fig. 2 shows glancing RBS/C spectra for the samples in group (1). Because of the relatively low energy of Si^+ implantation, a thin layer of amorphous silicon existed near the surface of the top silicon before annealing. Below the amorphous silicon layer, there is a layer of crystalline silicon with damage created by B^+ implantation. With increasing annealing temperature, an epitaxial regrowth toward the surface of the top silicon takes place. After annealing at 900 °C for 30 min, the thin amorphous top silicon recrystallized into crystalline silicon with a minimum yield χ_{min} [8] of 7.6%. This value is slightly higher than that of crystalline silicon. Also, the point defects created by B^+ implantation might grow into second-order defects during annealing and they could not be annealed out at 900 °C for 30 min. Raman measurements of samples in group (1) demonstrated that the amorphous silicon phonon peak that existed before annealing disappears after annealing at 600 °C for 30 min. Since the amorphous layer near the surface of the top silicon is thin, the incident light can penetrate through the amorphous layer on to the crystalline silicon area below. So a small phonon peak exists at about 520 cm^{-1}. It became more and more intense during annealing with increasing annealing temperature.

Fig. 3 shows the glancing RBS/C spectra for samples in group (2). An epitaxial regrowth toward the interface between the top silicon and the buried insulator layer exists during annealing with increasing annealing temperature. After annealing at 900 °C for 30 min, the minimum yield for the thin layer near the surface of

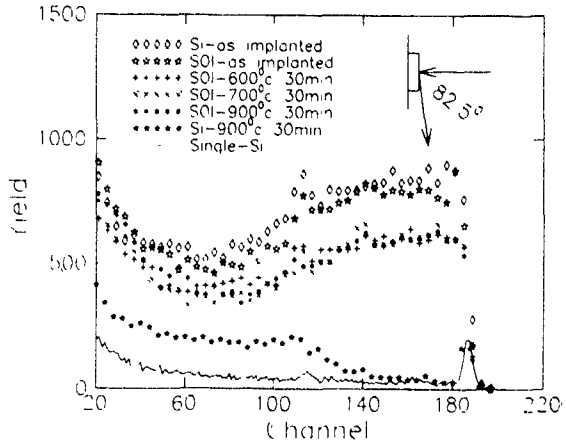

Fig 4 RBS/C spectra of SIMNI material implanted by Si^+ at 25 keV, 5×10^{15} cm^{-2} + 80 keV, 5×10^{15} cm^{-2} + 140 keV, 5×10^{15} cm^{-2} and B^+ at 25 keV, 1×10^{15} cm^{-2}.

the top silicon was reduced to 4.7%. It reached that level for crystalline silicon. So the arrangement of silicon atoms in the thin top layer seems to be perfect. However, some of its properties may not be the same as those for crystalline silicon. Also, the abrupt front interface was destroyed by Si^+ implantation and its gradient became lower after annealing at 900 °C for 30 min. Therefore, implantation into the front interface should be avoided in order to keep the interface abrupt. Raman measurement for the samples in group (2) indicated that no amorphous silicon phonon peak appeared, and the phonon peak at about 520 cm^{-1} became more and more intense with increasing annealing temperature.

Raman spectroscopy measurement is an effective way to detect a phase transformation. Fig. 4 and fig. 5 are glancing RBS/C and Raman spectra, respectively, for the samples in group (3). Before annealing, the whole top silicon was amorphized by Si^+ implantation, and only the amorphous silicon phonon peak was observed (see fig. 5 (a)). After annealing at 500 °C for 30 min, no change was observed from the Raman measurement (see fig. 5 (b)). But after annealing at 600 °C for

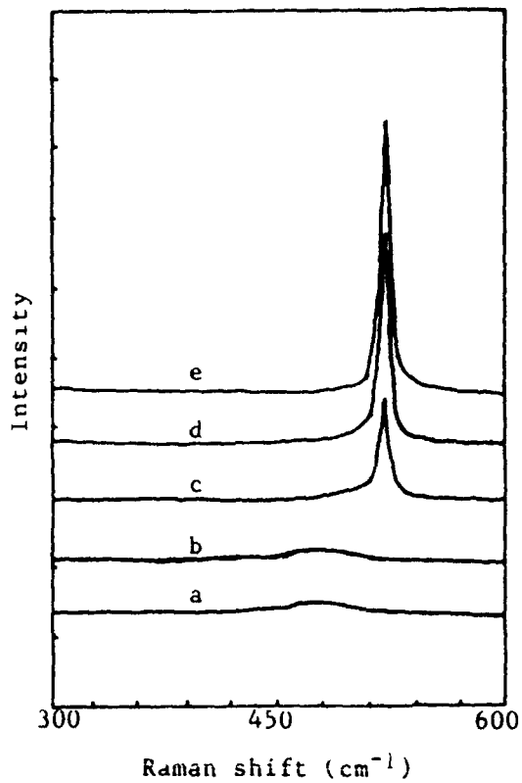

Fig. 5 Raman spectra of SIMNI material implanted by Si^+ at 25 keV, 5×10^{15} cm^{-2} + 80 keV, 5×10^{15} cm^{-2} + 140 keV, 5×10^{15} cm^{-2} and B^+ at 25 keV, 1×10^{15} cm^{-2}, annealed at different temperature. (a) as-implanted; (b) 500 °C, 30 min, (c) 600 °C, 30 min, (d) 700 °C, 30 min; (e) 900 °C, 30 min

Table 1
Activation rate of boron in SIMNI material implanted by Si^+ at different conditions followed by B^+ implantation at 25 keV, 1×10^{15} cm^{-2}, annealed at 900 °C for 30 min

Material	Si^+ energy [keV]	Si^+ dose [$\times10^{15}$ cm^{-2}]	Activation rate of boron [%]
SIMNI	–	–	25
	25	5	38
	140	5	50
	25 + 80 + 140	5 + 5 + 5	5
⟨100⟩-Si	–	–	75

30 min, a phonon peak at about 520 cm^{-1} appeared. It indicated that the top amorphous silicon was recrystallized into polysilicon or crystalline silicon. That is, a phase transformation from amorphous silicon to polysilicon or crystalline silicon took place With increasing annealing temperature, this peak became more and more intense. In fig. 4, it is shown that after annealing at 600 °C for 30 min, the channeling yield decreases a little. It cannot decrease more with the annealing temperature increasing further (see the following explanation). After annealing at 900 °C for 30 min, the minimum yield was much higher than that of crystalline silicon. That means, the top amorphous silicon was not recrystallized into crystalline silicon. Therefore, combined with the Raman measurement results described above, it can be concluded that a phase transformation from amorphous silicon to polysilicon took place for the samples in group (3) when the annealing temperature was increased from 500 to 600 °C. This led to the channeling yield decreasing a little. With further increasing of the annealing temperature, there is only an increase in grain size of the top polysilicon. So, the channeling yield can not decrease any more.

Table 1 shows the results of boron activation in the top silicon layer (SIMNI) in comparison to that in bulk silicon obtained by SRP measurements. It can be seen that the activation rate of boron in the top silicon layer of the SIMNI material is much lower than that in crystalline silicon, whether $Si^+ + B^+$ dual implantations were used or not. This might result from the lower mobility of carriers in the top silicon layer of SIMNI material. But in the conversion of the spreading resistance depth profile into the carrier concentration depth profile, only the carrier mobility of standard single silicon samples was used. Therefore, there may be a difference between the actual activation rate of boron in the top silicon layer (SIMNI material) and that given in table 1. However, the relative trend is right, and from table 1, it is shown that $Si^+ + B^+$ dual implantations into the surface area or the front interface area can increase the activation rate of boron in the silicon of the SIMNI material. It is estimated that some of the defects

in the top silicon layer, for example deep level defects, may diffuse into the amorphous area created by the Si^+ implantation and be annealed. So the activation rate of boron can be increased. Because the quality of the silicon layer near the surface is more perfect than that near the front interface, the amorphization of the interface region can increase the activation rate more than surface amorphization can.

References

[1] I H Wilson, Nucl Instr and Meth. B1 (1984) 331.
[2] O W Holland, T P Sjoreen, D. Fathy and J Narayan, Appl. Phys Lett 45 (1984) 1081.
[3] P.L F. Hemment, Mater. Res. Soc Symp Proc. 53 (1986) 207.
[4] K.J Reeson, Nucl Instr and Meth B19/20 (1987) 269.
[5] J. Blez and E.H. Tekaat, Nucl. Instr and Meth. B19/20 (1987) 279.
[6] G. Zimmer and H. Vogt, IEEE Trans Electron Devices ED-30 (1987) 291.
[7] B.Y Mao, R. Sundaresan, C.E. Daniel Chen, M Matloubian and G Pollack, IEEE Trans Electron Devices 35 (1988) 629
[8] W K. Zhu and J.W Mayer, Backscattering Spectrometry (Academic Press, 1978) p 236.

Nuclear Instruments and Methods in Physics Research B55 (1991) 742–745
North-Holland

SOI structure formed by 95 keV N_2^+ and N^+ implantation and epitaxial growth

Lin Chenglu [a], Li Jinghua [b], Zhang Shunkai [a], Yu Yuehui [a] and Zou Shichang [a]

[a] *Ion Beam Laboratory, Shanghai Institute of Metallurgy, Academia Sinica, Shanghai 200050, People's Republic of China*
[b] *Changzhou Semiconductor Factory, Jiangsu 213001, People's Republic of China*

N-type ⟨100⟩ Si wafers were implanted with 95 keV, $(0.1–1)\times10^{18}$ cm^{-2} N_2^+ and N^+ and a beam current of 6 mA by using an ion implanter without mass analysis. The waters were maintained at 500 °C during implantation After implantation the samples were annealed at 1200 °C for 2 h and underwent vapor-phase epitaxial growth. The experimental results showed that the thicknesses of the top silicon layer with a minimum channeling yield of 5% are 0 3–1 μm and the thicknesses of buried Si_3N_4 layer are 170–200 nm The buried silicon nitride layer consists of polycrystalline α-Si_3N_4 and nitrogen-rich nitride The Si–Si_3N_4 interface is extremely abrupt, and the spreading resistance depth distribution is uniform in the top silicon layer The results indicate that this method is an effective technology for forming cheap SOI material

1. Introduction

Various techniques are currently being developed to form SOI structures. One of the most promising techniques for producting device-worthy SOI structures is SIMOX or SIMNI (separation by implanted nitrogen). However, the rapid development of SOI technology has been hindered by the limited supply of substrate due to very long implantation times using presently available implanters. In most cases, to produce a buried layer of oxide or nitride, the ratio $R_p/\Delta R_p$ should be greater than about three For both oxygen and nitrogen in silicon this corresponds to a implantation energy greater than 100 keV [1].

In this work, we report the use of 95 keV N_2^+ and N^+ implantation by using an ion implanter without a mass analysis stage and subsequent vapor-phase epitaxial growth to check whether good quality SOI structures can still be formed or not

2. Experimental

N-type ⟨100⟩ silicon wafers with a resistivity of about 10 Ω cm were implanted with 95 keV N_2^+ and N^+ (60% N_2^+, 40% N^+) with a beam current of 6 mA and doses from 1×10^{17} cm^{-2} to 1×10^{18} cm^{-2} using an un-analysed beam of nitrogen ions The wafers were maintained at 500 °C during implantation. After implantation, the samples were annealed at 1200 °C for 2 h with 300 nm of deposited SiO_2 as an encapsulant. After removing the SiO_2 cap, the samples underwent vapor-phase epitaxial growth with the reaction $SiCl_4 + 2H_2 \rightarrow Si + 4HCl$ at 1200 °C in a horizontal inductive graphite furnace [2]. The rate of growth was about 0 25 μm/min. The time of the vapor-phase epitaxial growth was from 1 to 4 min. To achieve a low impurity concentration for the epitaxial layer, PCl_3 carried by H_2 was mixed with $SiCl_4$ during reaction.

Rutherford backscattering and channeling (RBS/C) techniques with 2 MeV He^+ were used to assess the nitrogen profile and radiation damage remaining in the top silicon layer. Transmission electron microscopy (TEM) was used to study the microstructure of the SOI samples Infrared (IR) absorption and reflection measurements were made at room temperature by means of a 7199-C single beam spectrometer over the frequency range 400–1400 cm^{-1} and a Perkin–Elmer 983 double beam spectrometer over the frequency range 1500–5000 cm^{-1} Spreading resistance probes (SRP) were used to measure the electrical properties.

3. Results and discussion

Fig 1 shows the RBS/C spectra of SIMNI formed by N_2^+ and N^+ implantation at 95 keV with a total dose of 4×10^{17} cm^{-2} after annealing at 1200 °C for 2 h and vapor-phase epitaxial growth It is found that the thicknesses of the top silicon layer and buried nitride layer are 350 and 170 nm, respectively. The minimum channeling yield (X_{min}) of the top silicon layer in the RBS/C spectra is 5%, which approaches the value of bulk single-crystal silicon.

Fig. 2 is the IR transmission spectra of the SIMNI samples. The IR spectrum of the as-implanted sample is

0168-583X/91/$03 50 © 1991 – Elsevier Science Publishers B.V (North-Holland)

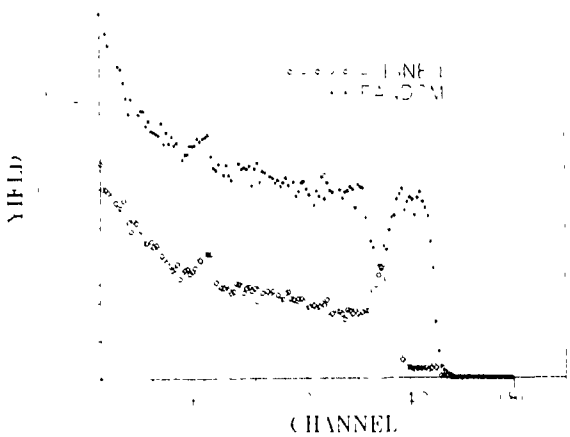

Fig. 1 RBS/C spectra of a SIMNI sample implanted with 95 keV N_2^+ and N^+ with a total dose of 4×10^{17} cm^{-2}

relatively weak and rather broad because of the small amount and random distribution of the Si–N stretch bands which shows a typical absorption curve of amorphous silicon nitride After annealing, the curve of amorphous nitride splits into a few peaks, and the peak

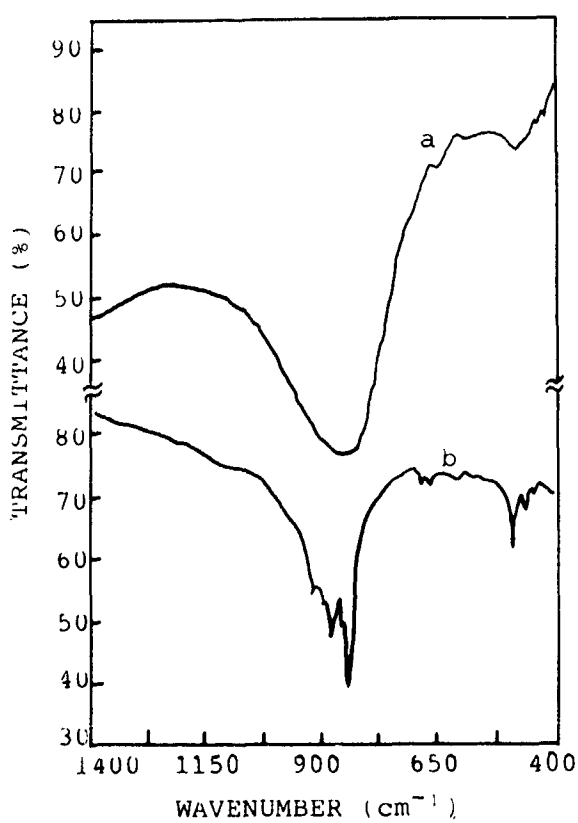

Fig 2 IR transmission spectra of SIMNI samples: (a) as-implanted, (b) after annealing at 1200 °C for 2 h.

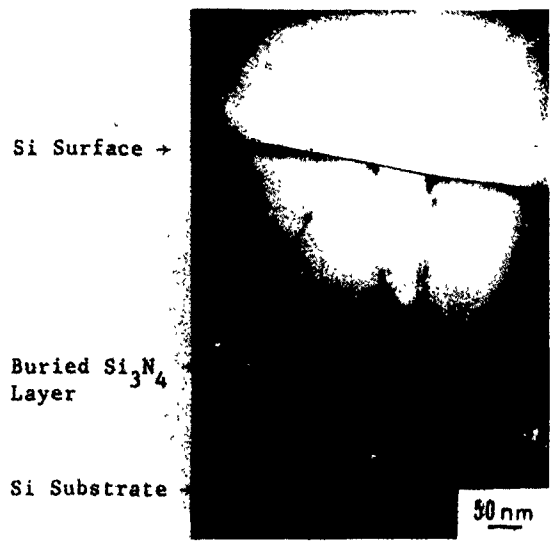

Fig 3 Cross-sectional TEM photograph of a SIMNI sample after epitaxial growth.

positions coincide with the absorption peaks of α-Si_3N_4 reported by Wada et al. [3]

Fig. 3 shows a cross-sectional TEM photograph of a SIMNI sample with a total implantation dose of 4×10^{17} cm^{-2} N_2^+ and N^+ It can be seen clearly that the cross section of the sample consists of the top single-crystal silicon layer with a few defects and the buried silicon nitride layer. If the implantation dose is above the critical dose (N_c, i.e., the dose required to directly form the stoichiometric compound Si_3N_4 at the peak of the nitrogen depth distribution) the buried silicon nitride layer consists of polycrystalline nitride and porous nitrogen-rich nitride in the middle of polycrystalline nitride A high resolution TEM micrograph of the buried silicon nitride showed that the crystal structure of the polycrystalline nitride is trigonal α-phase Si_3N_4 with cell dimensions $a = 0.781$ nm and $c = 0.559$ nm.

The above experimental results show that the SIMNI materials with a good quality top silicon layer can be formed by using 95 keV N_2^+ and N^+ implantation, annealing, and epitaxial growth. However, the key problem, which has a great influence upon the quality of SIMNI material, is the selection of the implantation conditions. Fig 4 shows the depth distributions of implanted nitrogen ions and the number of total recoil atoms for 95 keV N_2^+ implantation into silicon by TRIM'88 computer simulation. It indicated the R_p and ΔR_p of 95 keV N_2^+ ions in Si to be 126 and 41 nm, respectively, and the distribution of the recoil atoms extends to the surface. So, in order to obtain SIMNI material with a thin surface silicon layer, which is a seed crystal during epitaxial growth, we must carefully select the implantation condition. From the present work, the

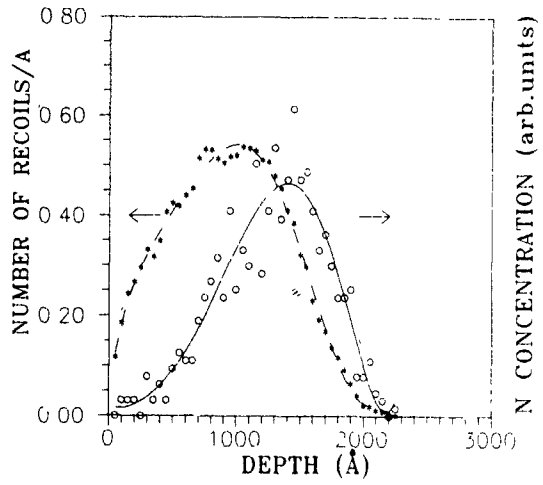

Fig 4. The depth distributions of R_p and the number of total recoil atoms for 95 keV N_2^+ implantation into silicon

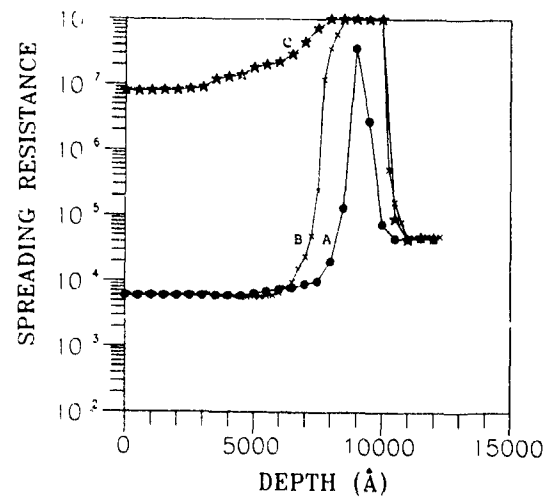

Fig 6 Spreading resistance vs depth by SRP measurements for SIMNI samples with implantation doses (A) 1×10^{17} cm^{-2}, (B) 4×10^{17} cm^{-2} and (C) 1×10^{18} cm^{-2}

critical dose value for formation of a SIMNI structure at 95 keV N_2^+ and N^+ implantation is 3.2×10^{17} cm^{-2}. In order to form a buried and continuous Si_3N_4 layer, the doses were chosen to be larger than the critical value. Fig. 5 shows the IR reflection spectrum of SIMNI implanted by 95 keV N_2^+ and N^+ with a total dose of 4×10^{17} cm^{-2} after annealing at 1200 °C for 2 h. The dashed curve is the result of fitting the reflection spectrum using a theoretical model described in our previous paper [4]. It is seen that the SIMNI structure consists of a thin crystal top silicon layer and a buried silicon nitride layer.

Fig 6 shows the spreading resistance versus depth distributions for three SIMNI samples with different implantation doses: (A) 1×10^{17} cm^{-2}; (B) 4×10^{17} cm^{-2}; (C) 1×10^{18} cm^{-2} In fig. 6 (curve A), it is found that the spreading resistance versus depth distribution in the top silicon layer is uniform, but there is not an insulating buried layer. Fig. 6 (curve B) shows the spreading resistance profile in the top silicon layer is uniform, and there is a high resistance insulating buried layer. Fig. 6 (curve C) indicates that for this high dose the top silicon layer has a high resistance. TEM analysis shows that the top silicon layer, in this case, is polycrystalline silicon

The above results show that the implantation dose is an important parameter for the formation of SIMNI material. If the dose is too low, the buried silicon nitride cannot be formed. However, if the dose is too high, the surface layer of silicon is heavily damaged during implantation After annealing and epitaxial regrowth, a top polycrystalline silicon layer was obtained

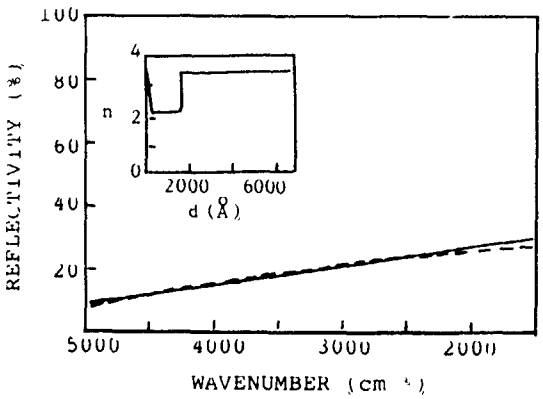

Fig 5. IR reflection spectrum of a SIMNI sample Both the experimental spectrum (solid line) and the best fit curve (dashed line) are shown for comparison. The insert shows the deduced refractive index profile of the SIMNI sample.

4. Summary

Using N_2^+ and N^+ implantation with an energy as low as 95 keV, high temperature annealing and vapor-phase epitaxial growth of a Si layer, enables SIMNI structures with top crystal silicon layer and buried silicon nitride layer to be formed.

In order to obtain good SIMNI material, the ion implantation dose is an important parameter, which has a great influence upon the quality of the top silicon layer.

The method reported in this paper is an effective technology for forming cheap SOI material.

References

[1] C.G. Tuppen, M R. Taylor, P L.F Hemment and R P Arrowsmith, Thin Solid Films 131 (1985) 475.
[2] Lin Chenglu, Li Jinghua, Fang Ziwei and Zou Shichang, Chin. Semicond. 10 (1989) 229.
[3] N Wada, S.A Solin, J. Wong, S. Prochazka, J Non-Cryst Solids 43 (1981) 7.
[4] Yu Yuehui, Fang Ziwei, Lin Chenglu and Zou Shichang, Mater Lett. 8 (1989) 95

Nuclear Instruments and Methods in Physics Research B55 (1991) 746–749
North-Holland

The effects of epitaxy and oxidation on the properties of SIMNI and SIMOX materials

Li Jinhua [a], Lin Chenglu [b], Lin Zhixing [b], Jin Yuqing [a] and Zou Shichang [b]

[a] *Changzhou Semiconductor Factory, Jiangsu 213001, People's Republic of China*
[b] *Ion Beam Laboratory, Shanghai Institute of Metallurgy, Academia Sinica, Shanghai 200050, People's Republic of China*

SIMNI and SIMOX samples were subjected to burial by epitaxial growth of Si (1200 °C), oxidation (900–1180 °C, in O_2 or H_2/O_2) and baking (1200 °C, in H_2) to investigate in the changes in the properties of their surface and buried layers. The results of RBS/C and ASR pointed out that the minimum channelling yield of the top silicon layer of SIMNI decreased from 10% before epitaxy to 3.4% after epitaxy, while no properties of the SIMNI structure either in the remaining Si top layer or in the buried layer were changed during oxidation. The SIMOX structure without enough annealing would become damaged as a result of baking in H_2 at high temperature.

1. Introduction

Since 1978, many studies on SIMOX (separation by implanted oxygen) and SIMNI (separation by implanted nitrogen) material and SOI devices have been reported [1–5]. The process stability of these two structures is not reported frequency. We have investigated the effects of device processing, including oxidation, epitaxy and treatment with different atmospheres on the SIMOX and SIMNI structures. In this paper, some interesting results will be presented.

2. Epitaxy

In order to overcome the effect of the limited projected range due to the ion energy used in the experiment, i.e., to increase the thickness of the surface silicon layer, epitaxial growth of a covering Si layer was carried out using the reaction $SiCl_4 + 2H_2 \rightarrow Si + 4HCl$ at 1200 °C. Usually, baking the wafer in H_2 for 3–5 min was needed before epitaxy. The results of automatic spreading resistance (ASR) measurement before and after epitaxy are shown in figs. 1 and 2. The SIMNI and SIMOX samples were formed by 170 keV implantation with a dose of 1.4×10^{18} cm^{-2} and annealed in N_2 at 1200 °C for 2 h. After epitaxy for SIMNI samples, the thickness of the buried layer with high resistivity was decreased from 3400 to 2800 Å. The interface between top and buried layers became more abrupt, the transition region was decreased remarkably and the electrical properties became more uniform in the top silicon layer than before epitaxy. These effects can be seen in fig. 1. Fig. 2 illustrates that the epitaxy, including the pre-baking, not only makes the thickness of the high resistivity region in SIMOX increase, but also affects the carrier concentration of the top silicon layer. If the SIMOX is annealed with a SiO_2 gap, the high resistivity region is thicker and the carrier concentration of top silicon is lower than for one annealed without capping.

The influence of epitaxy on the perfectness of the top crystal silicon layer of SIMNI can be seen in fig. 3. Before and after epitaxy, the minimum channelling yields of the SIMNI samples were about 10 and 3.4%, respectively. This means that the perfectness of the top crystal silicon layer of SIMNI samples having undergone epitaxy is improved significantly.

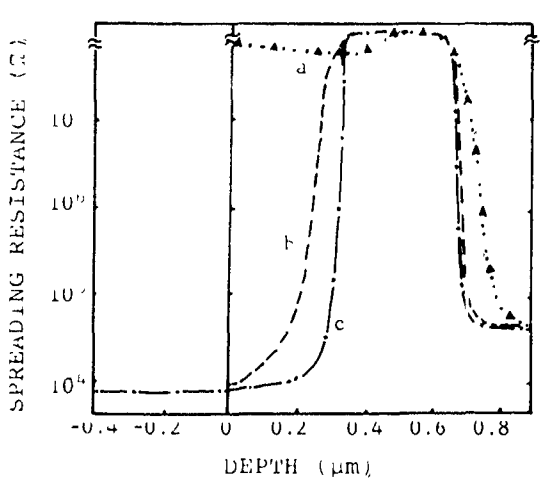

Fig. 1. ASR results of SIMNI samples. Energy 170 keV, dose 1.4×10^{18} cm^{-2}, annealing temperature 1200 °C, in N_2, for 2 h. Curve a: as implanted; curve b: after annealing; curve c: after epitaxy.

0168-583X/91/$03.50 © 1991 – Elsevier Science Publishers B.V. (North-Holland)

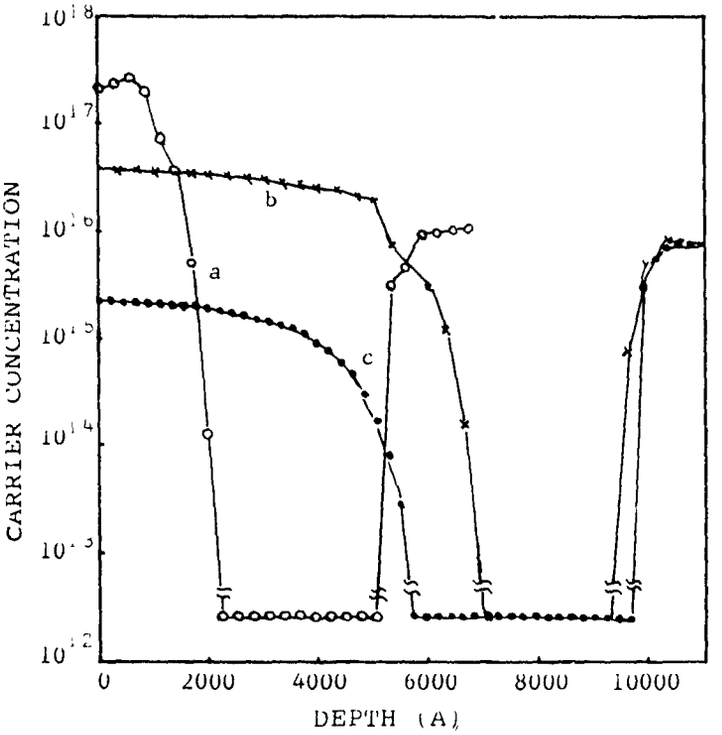

Fig 2 ASR results of SIMOX samples. Energy 170 keV, dose 1.4×10^{18} cm^{-2}, annealing temperature 1200 °C, in N_2, for 2 h Curve a after annealing with a 3000 Å SiO_2 cap; curve b after epitaxy (annealed without SiO_2 cap), curve c after epitaxy (annealed with 3000 Å SiO_2 cap)

3. Oxidation

The oxidation rates of the top silicon layer of SIMOX and of SIMNI have been studied by the present authors [6] Values are near the rate for perfect crystalline silicon In order to know the carrier concentration of the surface layer and the change in the buried layer after oxidation, the SIMNI samples were oxidized in O_2 or H_2/O_2 at 900-1180 °C. The measured carrier concentration profiles are shown in fig. 4 The carrier concentration of the top silicon, the thickness of the buried Si_3N_4 layer and the properties of the interface were not changed after oxidation when the oxidized layer was 3400 Å (fig. 4c) or 7400 Å (fig. 4d) thick. In the case where the advancing edge of the oxidized layer met the buried layer (fig 4b), it became thinner due to oxidation

Thus, the electrical properties of the SIMNI structure, shown in fig 4, were stable in all cases.

4. Baking in H_2

After SIMNI and SIMOX samples were put into an epitaxial deposition furnace to bake in a H_2 atmosphere for ten minutes, a few points appeared on the surface of the SIMNI sample (fig 5b), but dense round patterns

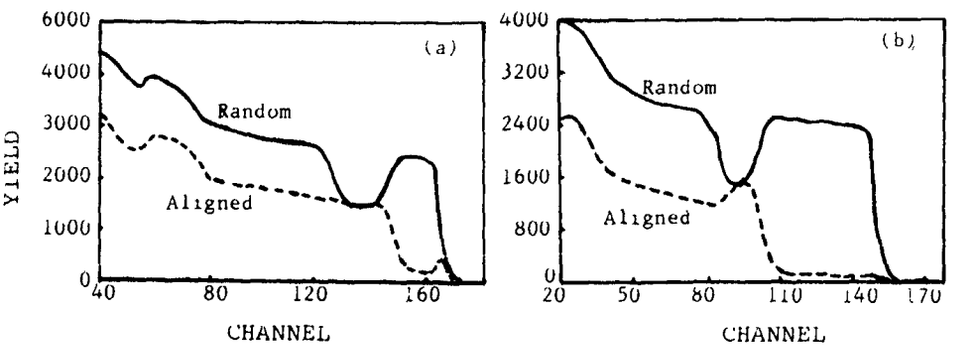

Fig. 3 RBS/C results of SIMNI samples (a) after annealing, (b) after epitaxy

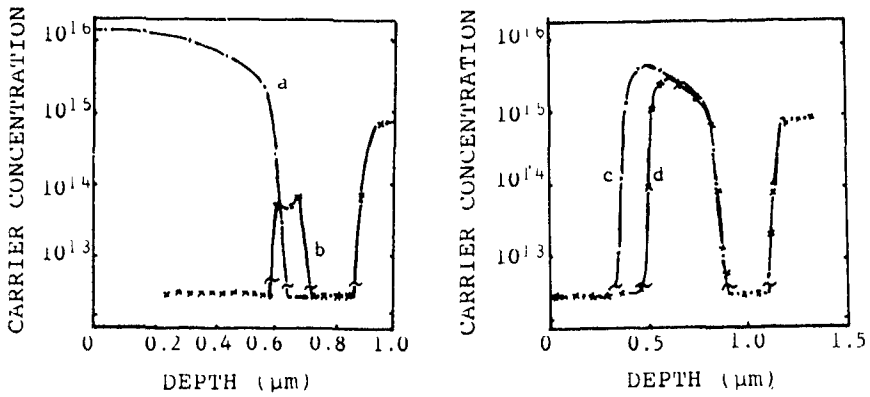

Fig. 4. ASR results of oxidation of SIMNI samples. Curve a. before oxidation; curve b. oxidized to the buried layer, curve c oxidized, 3400 Å SiO_2, curve d oxidized, 7400 Å SiO_2

showed on the SIMOX (fig. 5a). The results of ASR for SIMNI (fig. 6a, b) were identical to those for samples having undergone epitaxy (fig. 1b, c) The top crystal silicon layer of SIMOX had become damaged and showed high resistivity (fig. 6d).

5. Discussion

The interesting results presented in this paper were reproducible but a full explanation is not yet available The following comments may be made.

(1) In general, to eliminate the oxide precipitate, an annealing temperature of 1300 °C is needed for the SIMOX structure [3]. Celler et al. have pointed out that when this temperature is raised to 1405 °C [7], the oxide precipitates can dissolve substantially. Because of the limit in annealing equipment in the present case, it is sure that there must be a high density of oxide precipitates and defects in the surface silicon layer annealed at 1200 °C only. Besides, hydrogen is an active element with a high diffusion coefficient. When a SIMOX sample is baking at 1200 °C in H_2, hydrogen atoms could enter into the top silicon layer quickly and could cause precipitates and dislocations within the top silicon layer to migrate and spread. If the baking time is long enough, the whole crystal silicon layer would become damaged (see ASR results in fig 6d) some square form dislocations can be seen at the surface of the SIMOX sample [8]. If the baking time is not long enough (e.g., for epitaxy 3–5 min were required to raise the temperature

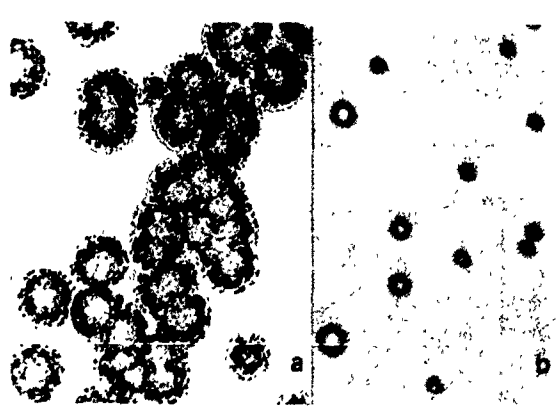

Fig. 5. Optical microscope photograph of SIMOX and SIMNI samples baking temperature 1200 °C, in H_2, for 10 min (a) SIMOX, magnified 350 times, (b) SIMNI, magnified 30 times

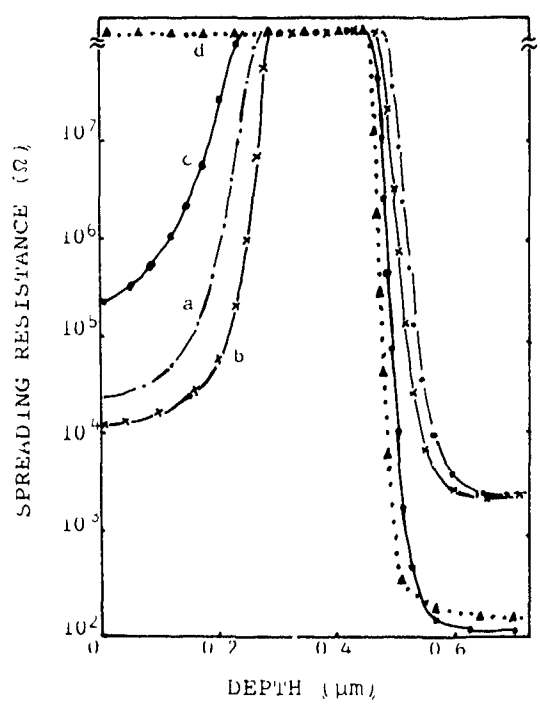

Fig. 6. ASR results of SIMOX and SIMNI samples baked in H_2 for 10 min at 1200 °C Curve a: before baking (SIMNI), curve b· after baking (SIMNI), curve c. before baking (SIMOX); curve d: after baking (SIMOX)

in H_2) the oxide precipitates and dislocations cannot spread up to the surface. This means the high resistivity region would spread to some degree (fig. 2c). It is clear that the high resistivity region seen by ASR measurements is not equivalent to buried SiO_2 in this case, but is due to the buried SiO_2 layer (insulator) and damaged silicon layer (absence of free carriers). The transition of the top silicon layer from crystal to damaged state starts from the front interface of the SIMOX structure.

(2) If the SIMOX sample was annealed without a SiO_2 cap as a shield, a compact buried SiO_2 layer was formed in which the density of implanted oxygen reached the stoichiometry of SiO_2. The implanted oxygen would diffuse out of this region mostly during annealing. The thickness of the buried layer was thus less, the density of oxide precipitate was lower, and the concentration of free carriers was higher (fig. 2b). If the sample was annealed with a SiO_2 cap, the most oxygen atoms from the stoichiometric region would remain at the top layer. An oxide layer enriched in silicon would be formed at the region nearby the buried SiO_2. Other oxygen atoms in the top layer would form some precipitates. Then, the concentration of free carriers would be decreased and the transition region would spread Therefore, the thickness of the high resistivity layer of fig. 2a is larger than that in fig. 2b. At high temperatures in a hydrogen atmosphere, the enriched silicon oxide layer would be dissolved by hydrogen, and the bottom of the top silicon layer would be damaged quickly Finally, the high resistivity layer was spread out from one of fig. 2a to one of fig 2c (from ASR measurements after epitaxy). RBS analysis indicated that the high resistivity region was partly removed and the oxygen density of the top silicon layer was increased after baking for a longer time in H_2 [8]

(3) After epitaxy of the SIMNI, the thickness of the buried layer and transition region were reduced. This may be explained by the role of hydrogen. In order to get a uniform epitaxial layer, a period of 3-5 min was taken to raise the temperature of the wafer to 1200°C in H_2 before epitaxy. During this time, hydrogen atoms could enter into surface layer and up to the transition region, to combine with the dangling bonds of silicon The carrier concentration would be greatly increased and the high resistivity region reduced after epitaxy Based on such a mechanism, the front interface would be abrupt and the buried layer reduced (figs. 1c and 6b)

Because the annealing condition (1200°C, 2 h, in N_2) is enough to form a SIMNI structure of good quality [5], there are few defects within the top crystal silicon layer. The density of defects driven to the surface by hydrogen in SIMNI is lower than that for SIMOX on baking.

(4) With a surface crystal silicon layer of high quality the epitaxial layer on SIMNI has a quite low channelling yield (fig. 3). We imagine there might also be an inward epitaxy, which proceeds as a result of the participation of hydrogen and has the benefit of improving crystal perfectness. This occurred while the outward epitaxial growth was proceeding. The effect certainly reduces the channelling yield.

6. Conclusion

The oxidation of the top crystal silicon layer in O_2 or H_2/O_2 at 1180°C, basically does not affect the electrical properties of the surviving top crystal silicon layer, the buried layer and the interface for a SIMNI structure. Based on these results and a previous study on oxidation of SIMOX [6], it could be seen that SIMNI and SIMOX structures have a good process stability for SOI device fabrication at 900–1180°C. Baking for a shorter period in H_2 at 1200°C has no effect on SIMNI layers, evidently, but it could cause the defects to spread outward and a thickening of the layer with high resistivity for SIMOX. If this baking were prolonged to ten minutes, the whole top c-Si layer became damaged. The reason might be the migrating and spreading of the remaining oxide precipitates and defects. Finally, good surface layers with lower channeling yields and uniform electrical properties could be achieved for a SIMNI structure annealed enough, and undergoing epitaxy. The hydrogen atmosphere could improve crystal perfection even at 1000°C [8]

References

[1] K Izumi, M Doken and H. Ariyoshi, Electron Lett 14 (1978) 593
[2] G. Zimmer and H Vogt, IEEE Trans. Electron Devices ED-30 (1983) 1515
[3] K.J Reeson, Nucl Instr and Meth B19/20 (1987) 269
[4] J R. Davis, A K Robinson, K J Reeson and P.L.F. Hemment, Appl Phys Lett 51 (1987) 1419.
[5] R Schork, H. Ryssel and C Dehm, Proc 6th Int. Conf. on Ion Beam Modification of Materials, Tokyo, Japan, 1988, Nucl. Instr. and Meth B39 (1989) 220
[6] Lin Chenglu, Yu Yuehui, Zhang Shunkai, Fang Ziwei, Li Jinhua and Zou Shichang, Proc 2nd Int Conf on Solid State and Integrated Circuit Technology, Beijing, 1989, ed Mo Bangxian (International Academic Publishers, Beijing, 1989) p 420
[7] G A Celler, P L F Hemment, K W. West and J M. Gibson, Appl Phys Lett 48 (1986) 532
[8] Li Jinhua, Lin Chenglu, Lin Zhixing and Zou Shichang, IBMM'90, to be published

Nuclear Instruments and Methods in Physics Research B55 (1991) 750–753
North-Holland

The peculiarities of the new phase formation by O^+ ion implantation into silicon under thermo-ionization excitation

A.I. Belogorokhov, A.B. Danilin, Yu.N. Erokhin, A.A. Kalinin, V.N. Mordkovich, V.V. Saraikin and I.I. Khodos

Institute of Problems of Microelectronics Technology and High Purity Materials, 142432 Chernogolovka, Moscow Region, USSR

Investigations were conducted on implanting oxygen at doses much smaller than the stoichiometric dose into a heated silicon substrate. Interstitial radiation defects, which lie at depths exceeding the ion projected range, are shown to getter the oxygen. An additional photoionization during implantation increases the mobility of point defects in the Si surface layer, thus enhancing diffusion of some oxygen atoms to the surface. Subsequent oxygen outdiffusion during a post-implantation heat treatment accelerates the annealing of radiation defects and facilitates the formation of SiO_2 phase precipitates. The VO and VO_2 complexes were detected in samples subjected to implantation at 300 °C.

1. Introduction

It has been established [1] that radiation defects play a decisive part in heterogeneous formation of dielectric phase nuclei in silicon when substoichiometric doses of ion synthesis are employed. In turn, an additional photoexcitation during ion implantation influences markedly the defect formation in the irradiated silicon [2,3]. Heating of the substrate during implantation accelerates the defects–impurity reaction. Besides, such heating makes it possible to exclude amorphization of silicon surface layers when structures with new phase buried layers are produced.

The aim of the present paper is to study how thermo-ionization excitation affects the initial stage of the ion synthesis of silicon dioxide, when radiation defects play a major part in the phase formation.

Oxygen ions were implanted into n-type silicon, 4.5 Ω cm, orientation (100). The energy of the ions was 150 keV, and the dose 1.7×10^{16} ions/cm^2. The ion current density did not exceed 0.5 μA/cm^2. The substrate temperature during implantation for the two groups of samples was 300 °C and 500 °C, respectively, and was monitored by a thermocouple. The faces of some samples from both groups were irradiated during implantation by a high-pressure mercury lamp with a power density of 60 mW/cm^2. Control samples were subjected to implantation without additional photoexcitation. After implantation, a part of each sample was annealed at 1000 °C for 5 min. The ion-doped layers were investigated by IR spectrometry, SIMS and TEM methods.

2. Basic results and discussion

Fig. 1 demonstrates that the concentration profiles for oxygen atoms are anomalously deep (with a peak at a depth of approximately 0.5 μm) while the projected range (R_p) for oxygen ions at an energy of 150 keV is 0.36 μm [4]. A comparison of SIMS and TEM data (figs. 1 and 2) indicates that the concentration profile of oxygen atoms in silicon is governed by the distribution of interstitial radiation defects. Such behaviour of oxygen is consistent with the following available data:

(1) interstitial radiation defects are observed at depths exceeding R_p [5];
(2) implantation into a heated substrate leads to the formation of thermostable interstitial defects whose size increases and density decreases with implantation temperature [6], and
(3) interstitial radiation defects are an effective sink for some reactive impurities including oxygen [7].

IR transmission spectra of the oxygen-implanted samples (fig. 3) are rather complex which probably indicates that there can be a large number of states in which oxygen exists in the system supersaturated by interstitial radiation defects. Proceeding from the shape of the spectrum, it can be concluded that it corresponds to quartz inclusions in a highly imperfect silicon matrix [8].

Fig. 3a demonstrates that oxygen ion implantation at 300 °C leads to the formation of a defect layer closely resembling an amorphous one. Besides, the spectra in fig. 4 exhibit absorption lines indicating the presence of VO and VO_2 complexes in the layer [7]. The increase in

0168-583X/91/$03.50 © 1991 – Elsevier Science Publishers B.V. (North-Holland)

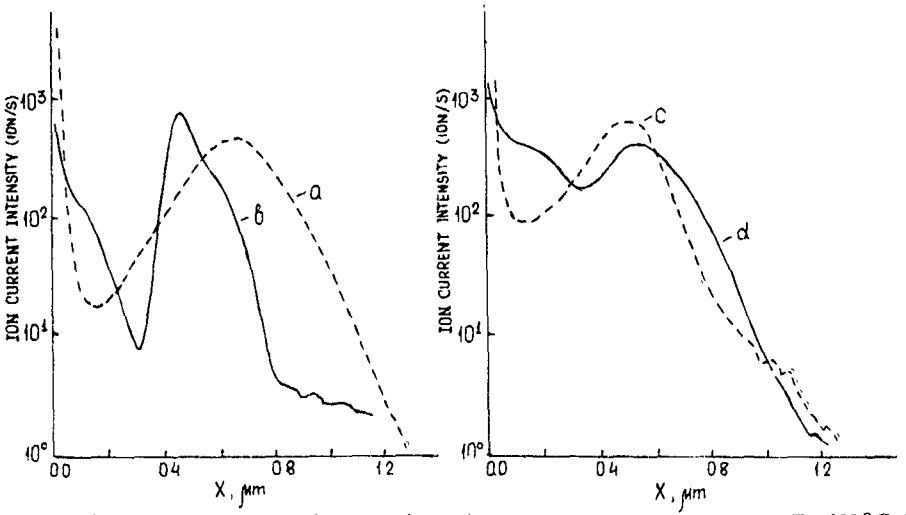

Fig 1 Concentration profiles for oxygen atoms in silicon (a) the implantation at a substrate temperature $T = 300\,^\circ$C, (b) $T = 300\,^\circ$C with additional photoexcitation, (c) $T = 500\,^\circ$C, and (d) $T = 500\,^\circ$C with additional photoexcitation

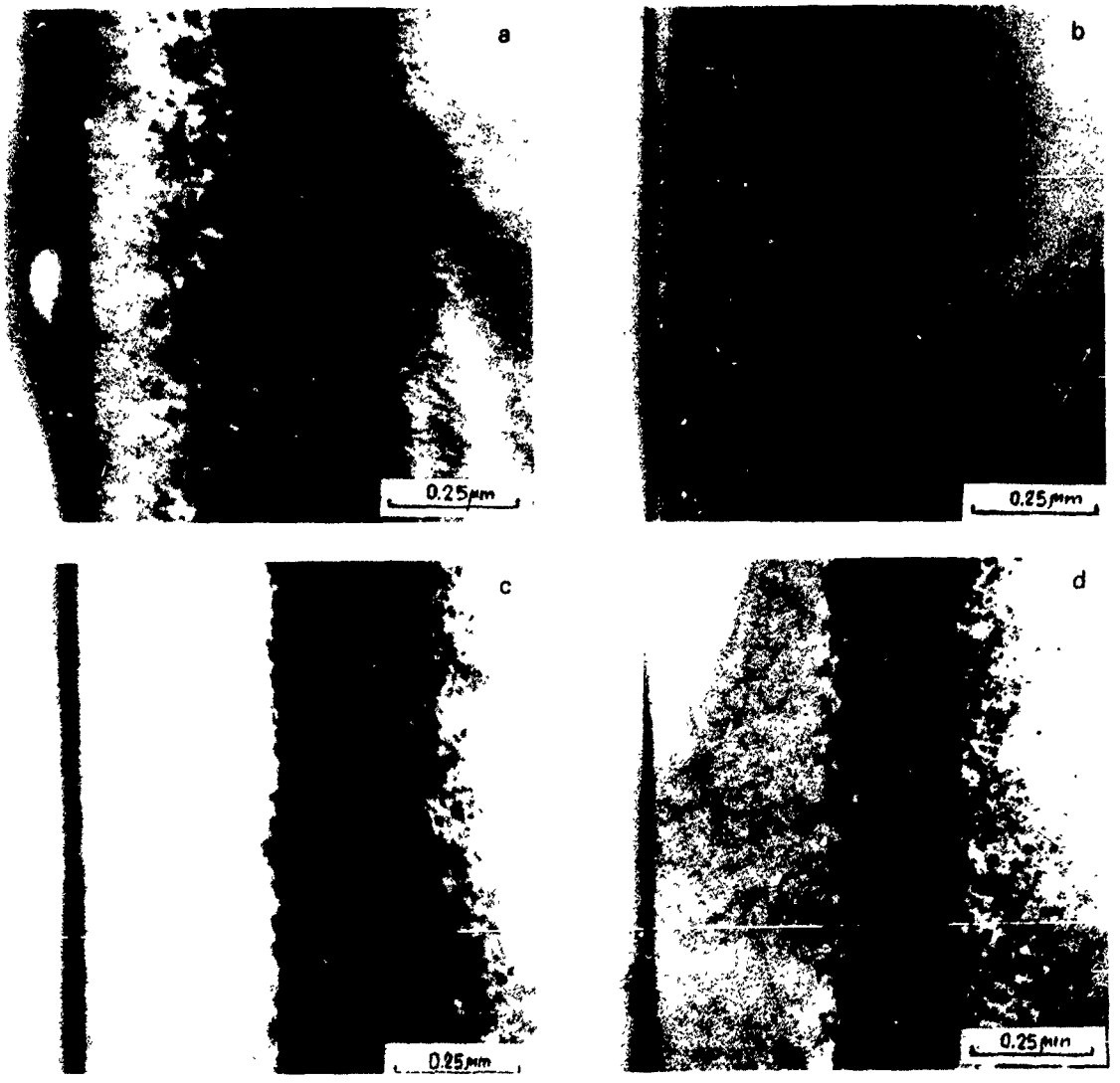

Fig. 2. Photomicrographs of sample cross sections (the notation is the same as in fig. 1)

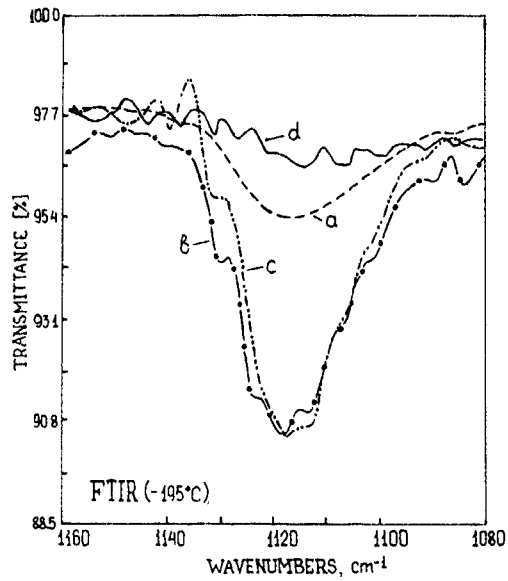

Fig 3 IR transmittion spectra of samples subjected to implantation by oxygen (the notation is the same as in fig 1)

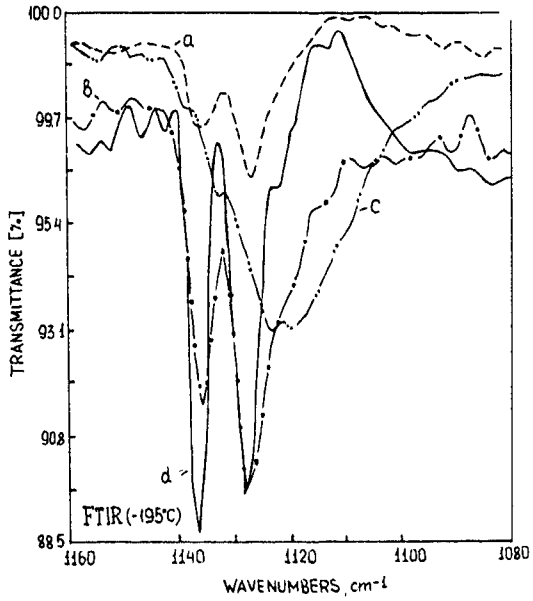

Fig 5 IR spectra of samples subjected to implantation by oxygen and annealing (the notation is the same as in fig 1)

the implantation temperature to 500 °C, as well as the additional photoexcitation, enhances the optical activity of the implanted oxygen (fig. 3b and c). At the same time, the spectrum itself changes which points to the fact that some ordering takes place in the radiation defect system. The concentration profiles of oxygen atoms also change (see fig. 1). The additional photoexcitation for the 500 °C implantation drastically reduces optical activity of the implanted oxygen. This reduction in optical activity can only be attributed to the emergence of dislocation-type defects and the precipitation of a sizeable part of the implanted oxygen on them [9]. Another feature of implantation under additional photoexcitation is a significant enrichment of the silicon surface layer in oxygen (see fig. 1). The oxygen atom distribution in the surface layer suggests that in this layer point defects exist due to the thermo-enhanced diffusion of oxygen atoms to the surface. The annealing of the samples subjected to implantation at 300 °C

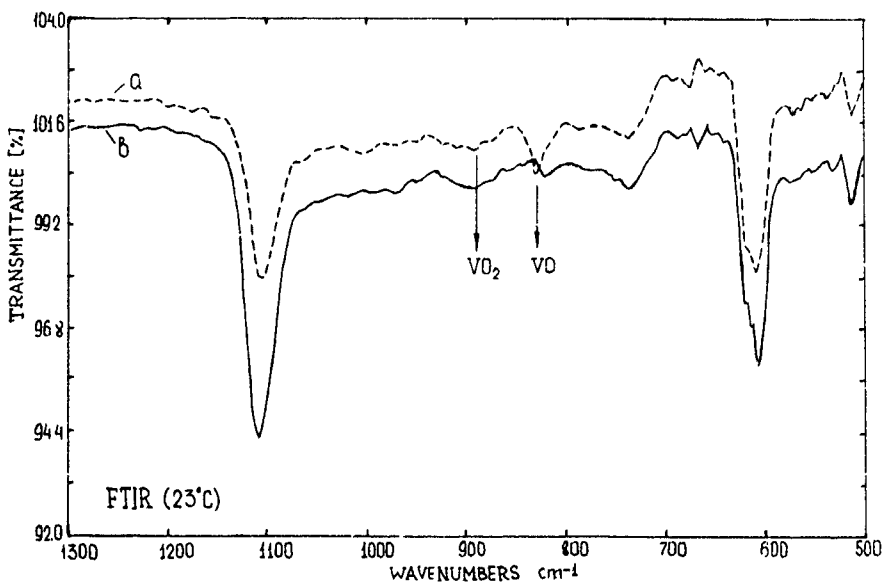

Fig. 4. IR transmittion spectra of samples subjected to implantation at (a) 300 °C and (b) 500 °C.

Fig 6 A TEM photomicrograph of a sample subjected to implantation at a substrate temperature of 500° with additional photoexcitation

without additional photoexcitation does not noticeably affect the optical activity of the oxygen (fig. 5a). This can be attributed to a high density of radiation defects in the layer. The emergence of two characteristic lines in the absorption spectrum is caused by significant structural ordering. The 1128 cm^{-1} absorption line is due to oxygen dissolved in silicon [10]. As regards the 1136 cm^{-1} line, there are two explanations. The first [10] also ascribes the line to the interstitial oxygen forming two bonds with neighbouring silicon atoms The second [11] attributes this line to SiO_2 phase precipitates. The annealing of the samples subjected to implantation at 500 °C does not influence significantly the IR transmission spectra (fig 5c), which indicates a high thermal stability of interstitial defect system supersaturated by oxygen The additional photoexcitation of the substrate surface during implantation considerably increases the structural perfection of the ion-doped layer, with both lines, 1128 cm^{-1} and 1136 cm^{-1}, clearly observed (fig. 5d). At an implantation temperature of 500 °C, the 1136 cm^{-1} line dominates. Electron microscopy data (fig. 6) indicate that this line is due to SiO_2 precipitates.

Thus, the main result of the additional photoexcitation is an enhanced reactivity of the implanted oxygen This effect is evidently connected with a general decrease in the thermal stability of the system of interstitial radiation defects, which is due to the outdiffusion of some of the implanted oxygen The oxygen outdiffusion during annealing is, in turn, a result of a photoexcitation-enhanced radiation-stimulated diffusion of oxygen atoms to the surface in the process of implantation.

References

[1] A.B Danilin and V.N Mordkovich, Abstracts of the EPM-89 3rd Int Conf. on Energy Pulse and Particle Modification of Materials, 1989, Dresden, Germany, p. 8 03
[2] Yu.N Erokhin, A G Italyantsev and V N. Mordkovich, Pis'ma Zh. Tekh. Fiz 9 (1989) 835
[3] A B. Danilin, Yu N Erokhin and V N Mordkovich, Pis'ma Zh. Tekh Fiz 21 (1989) 1
[4] A.F. Burenkov, F F Komarov, M A. Kumakhov and M M. Temkin, Tablitsi Parametrov Prostranstvennogo Raspredelenia Ionno-Implantirovannykh Primesey (Izdatelstvo BGU, Minsk, 1980) p 352
[5] N N. Gerasimenko, Proc. 2nd USA–USSR Seminar on Ion Implantation, Puschino, 1979 (Institute of Semiconductor Physics, Siberian Branch of the USSR Academy of Sciences, Novosibirsk, 1979) p 352.
[6] M. Hirata and H Saito, J Phys Soc Jpn 27 (1969) 405
[7] K Sumino, 2nd Int Autumn Meeting Proc. Gettering and Defect Engineering in Semiconductor Technology (GADEST 87), Garzau, Germany, 1987 (Akad. Wissenschaften DDR, Frankfurt (Oder), 1987) p. 218
[8] S L. Olimpiev and V A Sutyagin, Fizika Poluprovodnikov 16, no 12 (1982) 221
[9] S Lederhandler and J R Patel, Phys Rev. 108 (1957 239
[10] R C Newman, Infra-Red Studies of Crystal Defects (Taylor & Francis, London, 1973) p 187
[11] F N Komarova, V.N Mordkovich, E M. Temper and V A Kharchenko, Fizika Poluprovodnikov 10, no 2 (1976) 320

Nuclear Instruments and Methods in Physics Research B55 (1991) 754–757
North-Holland

SOI structures produced by oxygen ion implantation and their annealing behaviour

Zheng Lirong

Department of Physics, Shantou University, Shantou 515063, Guangdong Province, People's Republic of China

Lu Diantong and Wang Zhonglie

Institute of Low Energy Nuclear Physics, Beijing Normal University, Beijing 100875, People's Republic of China

Zhang Bei

Department of Physics, Beijing University, Beijing, People's Republic of China

P.L.F. Hemment

Department of Electronic and Electrical Engineering, University of Surrey, Guildford, Surrey GU2 5XH, UK

SOI (silicon on insulator) samples were produced by large dose ($1.8–2.5\times10^{18}/cm^2$) oxygen ion implantation into n- and p-type (100) silicon wafers at an energy of 360–400 keV, after different annealing methods. The SOI structures were measured by IR (infrared) absorption spectroscopy and Hall-effect measurements. After high temperature annealing (1300 °C, 30 min–8 h), we obtain excellent quality SOI films, both the top crystal silicon and the buried SiO_2 layer. After a long-time anneal (at 1300 °C), the carrier concentration (electrons) becomes lower and the Hall mobility is higher at 120–300 K in the top silicon.

1. Introduction

Ion beam synthesis has been used to form high quality SOI films for applications to small geometry and radiation-resistant MOS integrated circuits. Properties of SOI wafers formed by different procedures have been reported in some papers mostly by RBS (Rutherford backscattering spectroscopy), TEM (transmission electron microscopy) and SIMS (secondary ion mass spectrometry) techniques [1–5]. We evaluated some SOI films by RBS, SR (spreading resistance) and IR absorption spectroscopy [6]. In this paper, we present (a) a new method to measure the thickness of the buried SiO_2 layer in SOI samples with the SiO_2 mask patterns on the top silicon surface by the IR absorption spectroscopy, and (b) the electrical properties of the top silicon layer in SOI wafers by Hall-effect measurements. The influence of the implantation oxygen-related donors on the carrier concentration and Hall mobility will be discussed.

2. Experimental sample preparation

2.1. IR measurement samples

For the substrate silicon we used: p-type Si(100), 15.9–23.0 Ω-cm, implanted at 400 keV with 1.8×10^{18} O^+ cm^2. This sample was cut into two pieces, UK 1 and UK 2. UK 1 was annealed at 1300 °C for 30 min by infrared anneal equipment in a N_2 atmosphere.

2.2 Hall-effect measurement samples

N-type Si(100), 4–8 Ω-cm was used as the substrate wafers, implanted at 360 keV with $2.5\times10^{18}O^+/cm^2$ at a substrate temperature of 500 °C. Then the wafer was cut into a few squares (6×6 mm^2). Samples 10-2H, 10-4H, 10-6H and 10-8H were annealed in a furnace at 1300 °C for 2, 4, 6 and 8 h, respectively, in N_2 atmosphere. The four angle areas of samples were implanted by phosphorous at 60 keV with $5\times10^{15}/cm^2$, then annealed at 1000 °C for 10 s by a lamp rapid anneal equipment in a N_2 atmosphere. Good ohmic contacts were formed at the angle ends for Hall-effect measurements.

3. Results and discussion

3.1. IR absorption spectroscopy

Fig. 1 is a part of the photograph in samples UK1 and UK 2. Some parts of the SiO_2 mask patterns were broken and sputtered away after the oxygen implantation. The mask pattern area is 0.373 of the total area

0168-583X/91/$03.50 © 1991 – Elsevier Science Publishers B.V. (North-Holland)

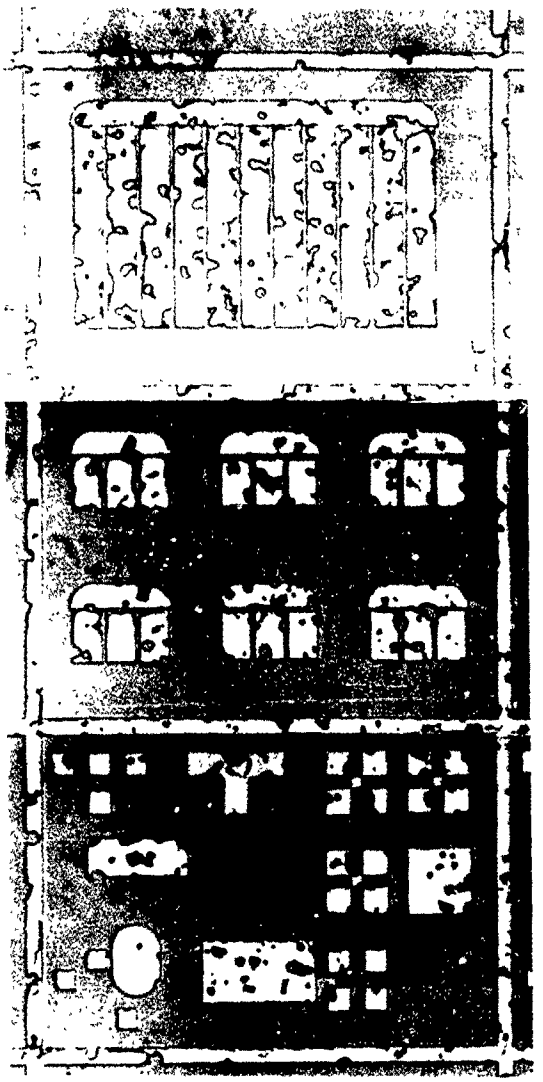

Fig 1. Part of a photograph of SOI samples UK 1 and UK 2 with SiO_2 mask patterns. The mask pattern area and the implantation area are 0.373 and 0.637 of the total area, respectively The thickness of the SiO_2 mask layer is 11026 Å.

and the implantation area is 0.637 of the total area on the samples UK 1 and UK 2.

Fig. 2 shows the IR spectra from the samples UK 1 and UK 2. There are three major peaks in the IR spectra. The first peak P_1 (1069–1090 cm^{-1}) is the well-known Si–O stretching vibration mode, the second P_2 (810–811 cm^{-1}) Si–Si stretching vibration mode and the third P_3 (457–461 cm^{-1}) Si–O–Si bending vibration mode [6]. After high temperature annealing, the peaks P_1 and P_3 moved to higher wavenumbers and became larger in the absorbance. This means that the thermal energy caused oxygen rearrangement and structural changes in the SiO_2 network.

The infrared transmission minima in SiO_2 films obey the Lambert–Bouguer law:

$$A = \log(I_0/I) = 0.434\alpha t, \quad (1)$$

where A is the absorbance at the minimum, I_0 and I the incident and transmitted intensities, respectively, α the absorption coefficient, and t the sample thickness This property will be utilized as a nondestructive method of determining the thickness of buried SiO_2 layers in SOI wafers by IR absorption spectroscopy. In our case, the absorbance A is composed of 0.373 A_0 and 0.627 A_1, where A_0 is the absorbance of the mask CVD SiO_2, with thickness 11026 Å, A_1 is the absorbance of the buried SiO_2 layer with the thickness t_1.

$$A = 0.373A_0 + (1 - 0.373)A_1, \quad (2)$$

$$A_0 = 0.434\alpha t_0, \quad (3)$$

$$A_1 = 0.434\alpha t_1. \quad (4)$$

Before and after high temperature annealing, the absorption coefficients of the mask CVD SiO_2 are 2.56×10^4/cm and 3.20×10^4/cm, and the coefficients of buried SiO_2 are 2.39×10^4/cm and 3.10×10^4/cm, respectively, which were reported in our earlier work [6] We can obtain the absorbance A from experiments in fig. 2, so the buried SiO_2 thicknesses t_1 were calculated

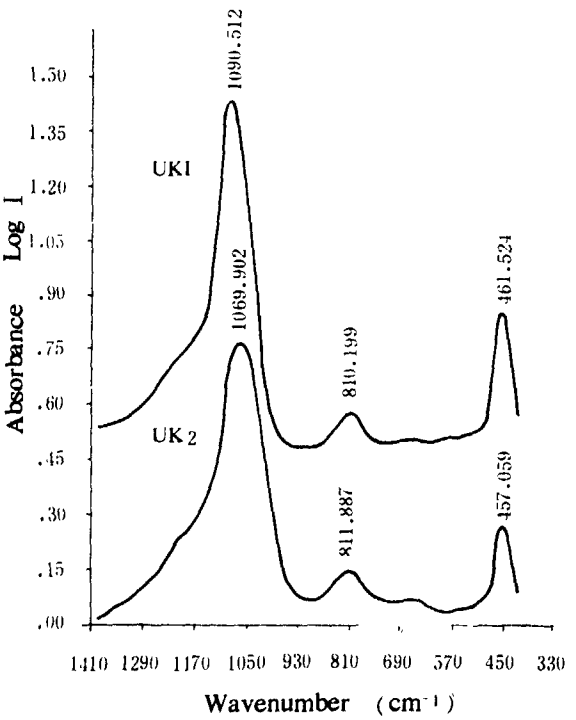

Fig. 2 IR spectra of the samples UK 1 and UK 2 with SiO_2 mask patterns, thickness 11026 Å, implanted at 400 keV with $1.8 \times 10^{18}/cm^2$. UK 2, as implanted, UK 1, annealed in an infrared furnace at 1300 °C for 30 min.

Table 1
The thickness of buried SiO_2 before and after anneal

Sample no	Energy [keV]	Dose [O^+/cm^2]	Annealing	A	A_0	A_1	t_1 [Å]
UK 2	400	1.8×10^{18}	none	0.7324	1 225	0.4394	4235
UK 1	400	1.8×10^{18}	1300 °C, 30 min	0.9443	1.4834	0.6236	4635

from eqs (2), (3) and (4), which are given in table 1. We can get the theoretical thickness of the buried SiO_2:

$$t = \frac{\text{dose}}{N_0} = \frac{1.8\times10^{18}\,O^+/cm^2}{4.37\,O^+/cm^3} = 4119\ \text{Å}.$$

This is a good agreement with our experimental results. After high temperature annealing, the thickness of the buried SiO_2 layer became larger than that before annealing. This indicates that the implanted oxygen has the tendency to move towards the buried layer and form the SiO_2 layer during the high temperature anneal.

3.2. Hall-effect measurement results

The Van der Pauw method was used to measure the Hall-effect in the temperature range 77–300 K. The thickness of top silicon layer in samples 10-2H–10-8H was measured by SR measurements.

Fig. 3 illustrates Hall mobility variation with the temperature. The Hall mobility decreased with increasing temperature (77–300 K) as shown in table 2.

The higher value of Hall mobility in sample 10-8H is due to the SOI film after the long time, high temperature anneal (1300 °C, 8 h), and the top silicon becoming a better quality. Above 130 K the mobility dependences: $\mu_H \sim T^{-2.04}$ in sample 10-8H and $\mu_H \sim T^{-2.71}$ in sample 10-2H are close to the theoretical expectation. $\mu_H \sim T^{-1.5}$. This indicates the dominant scattering to be the acoustic phonon scattering.

Fig. 4 is the electron carrier concentration as a function of the reciprocal temperature in samples 10-2H and 10-8H. The carrier concentration increases with the increase of temperature. The carrier concentration is 4.6×10^{18}–$5.0\times10^{18}/cm^3$ at 77–300 K in sample 10-2H and 4.5×10^{17}–$1.8\times10^{18}/cm^3$ at 77–300 K in sample 10-8H. The average carrier concentration is much higher than that in the substrate Si: $\sim 10^{15}/cm^3$. This means that a new donor with high concentration was formed in

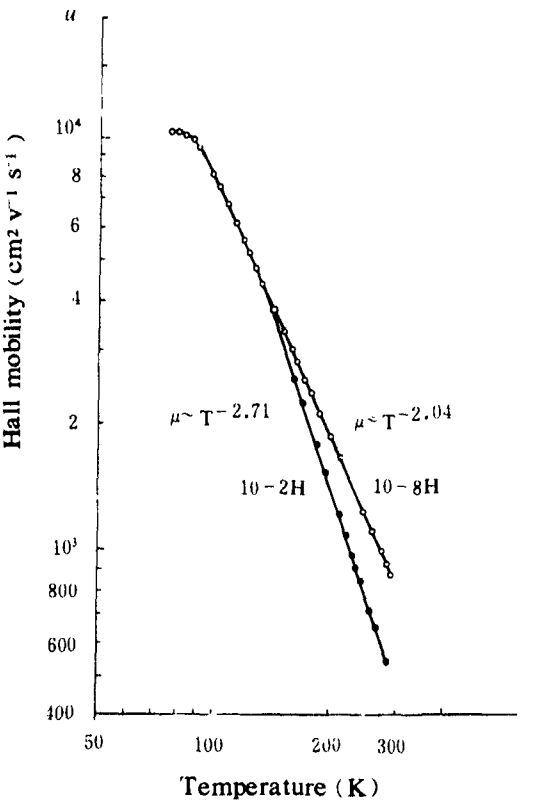

Fig. 3. Hall mobility vs temperature for the top silicon in SOI samples 10-2H and 10-8H, implanted at 360 keV with 2.5×10^{18} O^+/cm^2, annealed at 1300 °C for 2 and 8 h, respectively.

Table 2
Hall mobility vs temperature

Sample	μ [cm^2/V s]					
	T = 77 K	T = 100 K	T = 150 K	T = 200 K	T = 250 K	T = 300 K
10-2H	8960	5991	3064	1354	848	543
10-8H	10103	6185	3369	1851	1245	876

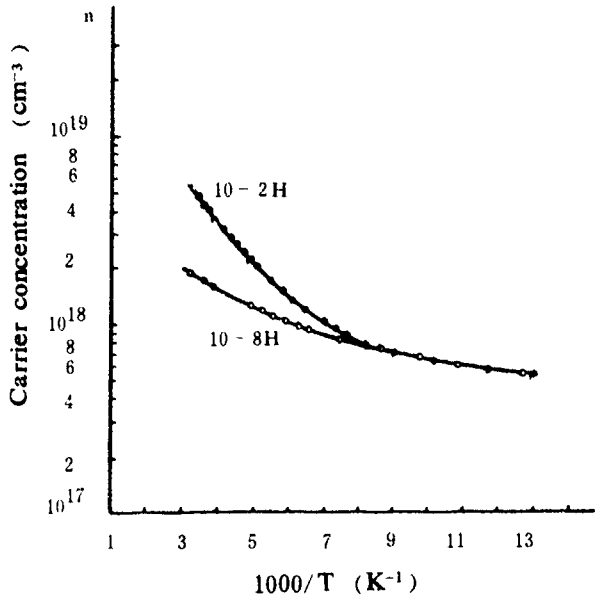

Fig. 4 Carrier concentration (electron) as a function of reciprocal temperature for samples 10-2H and 10-8H.

the top silicon layer of SOI samples. But after a long time, high temperature anneal, the number of implanted-oxygen related donors decreased, so the electron concentration in sample 10-8H is lower than that in sample 10-2H

4. Conclusion

(1) A new method to determine the thickness of a buried SiO_2 layer in SOI samples with SiO_2 mask patterns, before and after oxygen implantation, by IR absorption spectroscopy has been reported. The experimental result is in good agreement with the theoretical result.

(2) The Van der Pauw technique was used to analyze the electrical properties of the top silicon layers in SOI samples. After the long time, high temperature anneal, the Hall mobility becomes higher and the electron carrier concentration is lower in sample 10-8H, because of the decrease of the implanted oxygen (new donor) in the top silicon layer.

Acknowledgements

The authors thank Chen Ruyi for carrying out the oxygen implantation

References

[1] N Nagasima, J. Appl. Phys. 43 (1972) 3378
[2] K Nashimoto, T I Kamins, K.M. Chan and K Kajiyama, Jpn J Appl Phys 20 (1981) L909
[3] P L F Hemment, E Maydell-Ondrusz and K G Stephens, Nucl Instr and Meth 209/210 (1983) 157
[4] G K Celler, P L F Hemment, K W West and J M Gibson, Appl Phys Lett 48 (1986) 532
[5] K J Reeson, Nucl Instr and Meth B19/20 (1987) 269
[6] Lu Diantong et al., Vacuum 39 (1989) 219

Nuclear Instruments and Methods in Physics Research B55 (1991) 758–762
North-Holland

Radiation damage in As^+ implanted $TiSi_2$ films

C.T. Hsu, C.J. Ma and L.J. Chen

Department of Materials Science and Engineering, National Tsing Hua University, Hsinchu, Taiwan

Radiation damage in C54-$TiSi_2$ film implanted by 80 keV, 5×10^{15} cm^{-2} As^+ has been studied by both cross-sectional and planview transmission electron microscopy as well as by four-point probe resistivity measurements. Phase reversion from C54-$TiSi_2$ to C49-$TiSi_2$ was observed in as-implanted samples. The electrical resistivity of implanted samples was found to decrease with annealing temperature and time. Phase transition from C49-$TiSi_2$ to C54-$TiSi_2$ and decrease in the density of residual defects were found to correlate with the decrease in electrical resistivity.

1. Introduction

Ion implantation has become a standard technique to dope silicon for micro-electronics applications. The ability to anneal implantation damage and activate the dopants is crucial to the successful utilization of the technique [1]. It has been reported that residual defects would cause excess leakage current. The performances of devices are very sensitive to the residual defects in the active layer. The redistribution of dopants after annealing is also of major concern in device applications. For VLSI circuits with a feature size below one micron, a concomitant scaling of device geometries in both vertical and lateral dimensions is required. The reduction in vertical direction imposes a shallow junction limit in depth to about 0.1 μm or less [2].

In order to form a shallow junction and, at the same time, minimize the damage in silicon, an alternative approach to form silicide prior to junction formation has been adopted. The process involves the implantation of dopant into the silicide layer followed by annealing to drive the dopant species into the silicon substrate [3–5]. It was suggested that an additional advantage of the process is to reduce the probability of short-circuiting the junction due to the roughness of the silicide, since the diffusion front precedes the silicide/Si interface by a nearly constant distance. Subsequent studies showed that the process is a promising one for shallow junction formation in VLSI circuits subjected to the limitation imposed by a number of factors such as the solubility and diffusivity of various dopants in silicides and compound formation.

One of the problems that may be encountered in the implantation of dopants into silicide is the radiation damage of the silicides. Radiation damage in silicide may result in considerable changes in the properties of silicides. Radiation damage in Si, GaAs, and a large number of metals and alloys have been extensively studied [1]. However, relatively little attention was paid to the study of radiation damage in silicides. In the paper, we report the results of a structural and electrical investigation of radiation damage in a C54-$TiSi_2$ layer. We note that C54-$TiSi_2$ is a primary candidate material for self-aligned silicidation in submicron devices.

2. Experimental procedures

Single-crystal, boron-doped, 10–20 Ω cm resistivity, 4 in. diameter, (111)-oriented silicon wafers were used in this study. The wafers were first cleaned chemically by a standard procedure followed by a diluted HF dip immediately prior to loading into an electron gun evaporation chamber. Thin Ti films, 40 nm in thickness, were evaporated by electron beam evaporation. A 30 nm thick amorphous silicon capping layer was then deposited on Ti thin films to protect the films from oxidation during the subsequent heat treatments. The deposition rate was kept to be about 0.1 nm/s. The silicidation was conducted in a flowing-nitrogen diffusion furnace at 800°C for 120 s or 1 h. The cleaned wafers with a silicide layer were implanted by 80 keV As^+ to a dose 5×10^{15} cm^{-2}. The ion beam current density was controlled to be less than 10 μA/cm^2. The

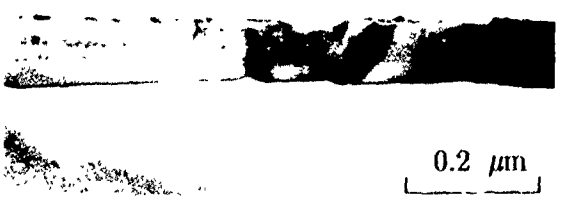

Fig. 1. Bright field (BF) micrograph of a cross-sectional sample showing a $TiSi_2$ layer on silicon.

0168-583X/91/$03.50 © 1991 – Elsevier Science Publishers B.V. (North-Holland)

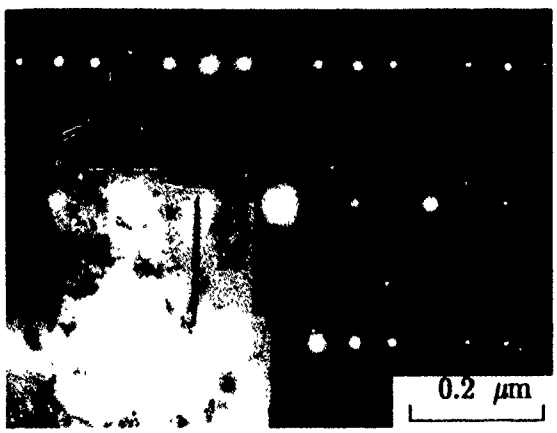

Fig. 2. Overlapping diffraction pattern and direct image showing the (200) habit plane of polytypes.

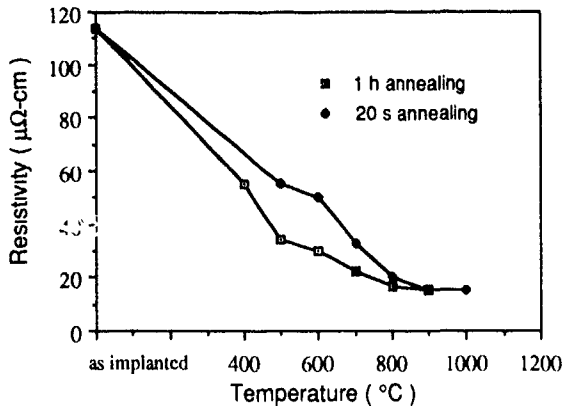

Fig. 4. Resistivity vs annealing temperature data.

wafers were water-cooled during implantation to minimize the self annealing effect. The normals of specimens were tilted 7° off the incident ion beam direction to alleviate the channeling effect. The choice of the ion energy was based on the consideration to create a defected surface layer and, at the same time, not to allow the dopants to penetrate through the silicide layer. The projected ion range and straggling in the $TiSi_2$ film were calculated to be about 36.9 and 14.5 nm, respectively [6].

For diffusion furnace annealing, high purity N_2 gas was first passed through a titanium getter tube maintained at about 800 °C to reduce the oxygen content. The samples were annealed at 400–1000 °C. The annealing time at each temperature was either 20 s or 1 h. A four-point probe was used to measure the sheet resistance. A Rigaku X-ray diffractometer and a JEOL-200 CX transmission electron microscope (TEM) were used to to detect the phase formed and characterize the microstructures.

3. Results and discussion

C54-$TiSi_2$ was found to be the only phase present in samples annealed at 800 °C. The average grain sizes of C54-$TiSi_2$ were measured to be 1 and 2 μm for samples annealed for 20 s and 1 h, respectively. An example is shown in fig. 1. The resistivity of the $TiSi_2$ layer was about 14 μΩ cm for both sets of samples. Polytypes were observed in the silicide layers. The habit plane of the polytypes was identified to be (002). An example is shown in fig. 2.

No amorphous layer was formed as inferred from TEM observation. A two-layer structure was evident in the $TiSi_2$ thin film. The upper layer was identified to be C49-$TiSi_2$. Examples are shown in fig. 3. The lower layer remained to be C54-$TiSi_2$. However, a high density of polytypes was found to extend upward from the layer. C49-$TiSi_2$ was also evident in planview samples. Heavily damaged regions were observed.

For as-implanted samples, the resistivity was increased to 115 μΩ cm. Fig. 4 shows the resistivity versus annealing temperature data. The resistivity was generally found to decrease with annealing temperature. In samples annealed at 500–700 °C, prolonged annealing was found to lower the resistivity considerably. The electrical conductivity was found to be fully recovered in samples annealed at 800 °C for 1 h. For 20 s annealing, higher temperature (900 °C) annealing was required for the resistivity to decrease to 14 μΩ cm, the resistivity value of the unimplanted silicide.

After 400 °C annealing for 1 h, the lower C54-$TiSi_2$ layer was found to grow into the upper damaged layer

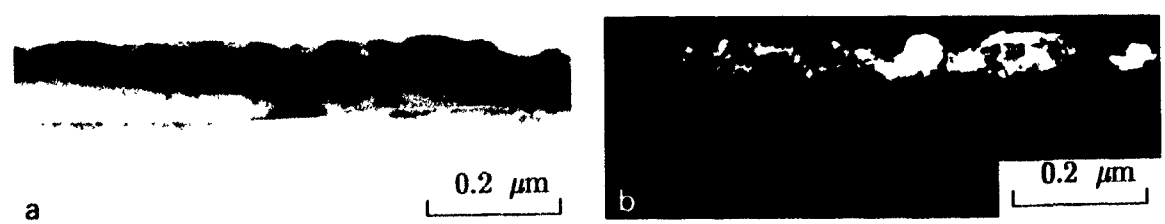

Fig. 3. (a) Bright field (BF) micrograph of as-implanted sample. (b) Dark field (DF) micrograph. The bright region corresponds to C49 $TiSi_2$.

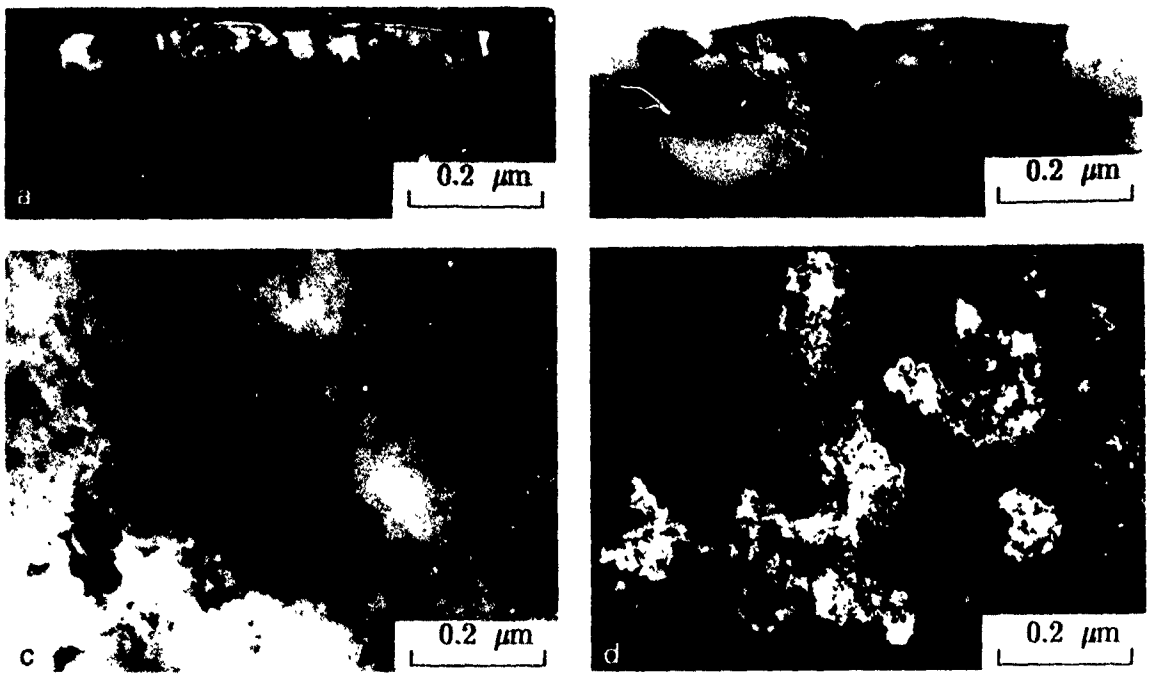

Fig 5 (a) Dark field, and (b) bright field cross-sectional micrographs (c) Bright field, and (d) dark field, planview The bright regions correspond to C49–$TiSi_2$, 400 °C annealed.

The interface between C54 and C49 grains appeared to be very uneven in cross-sectional (c-s) micrographs. Examples are shown in fig. 5. After annealing at 500 °C, the two-layer structure remained. C49-$TiSi_2$ was also found in the upper layer. The density of defect clusters was found to decrease with annealing time

In the sample annealed at 600 °C for 20 s, C54-$TiSi_2$ was found to grow into the upper layer from the lower layer Examples are shown in fig. 6. The C49-$TiSi_2$ was also seen in the film. From the planview observation, the highly damaged region was identified to be of C49-$TiSi_2$ structure. On the other hand, the regrown C54-$TiSi_2$ region was found to be relatively low in density of damage clusters. The C49 to C54 transformation in damaged regions was evident after annealing for 1 h. The areal fraction of regrown C54-$TiSi_2$ region was found to increase with annealing time from planview observation. Polytypes were found to form in the regrown layer. Similar to those found in the unimplanted samples, the habit plane was identified to be (002). For damaged regions not involving the formation of C49 grains, no polytypes were observed in the regrown layer. Instead, dislocations and moiré fringes were found.

After annealing at 700 °C for 20 s, the two-layer structure was still evident. The heavily damaged region was found to correspond to C49-$TiSi_2$ The areal fractions of C54-$TiSi_2$ regions which exhibited little damage were found to be higher than those in 600 °C annealed samples. After 1 h annealing, the density of dislocations was found to be lowered considerably. The Burgers

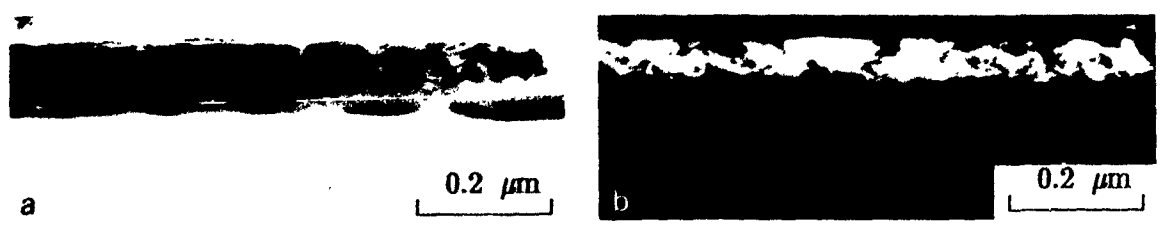

Fig 6 Cross-sectional micrographs, 600 °C, 20 s. (a) Bright field, (b) dark field. The bright region corresponds to C54-$TiSi_2$

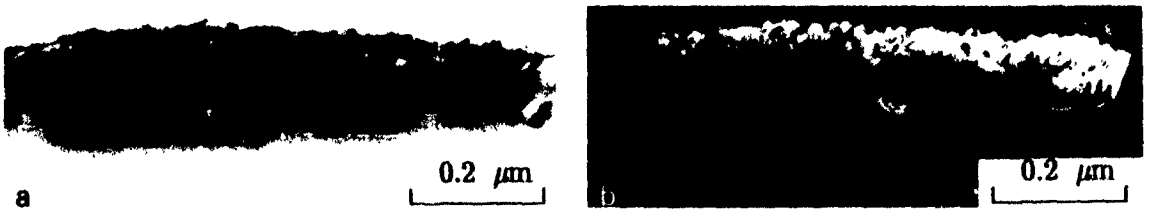

Fig. 7. Cross-sectional micrographs, 800 °C, 20 s. (a) Bright field, (b) dark field. The bright region corresponds to C49-$TiSi_2$.

vectors of the dislocations were identified to be along ⟨111⟩ of the C54 structure. The two-layer structure was no longer evident.

In samples annealed at 800 °C for 20 s, the two-layer structure was less obvious than those in samples annealed at lower temperature. Examples are shown in fig. 7 However, a heavily damaged region was still evident in the planview micrograph. The region was identified to be of C49 structure. The areal fraction of the C54-$TiSi_2$ phase was measured to be more than 90%. After 1 h annealing, only the C54-$TiSi_2$ phase remained. However, polytypes were still present. The density of dislocations was also found to be lower than that in 20 s annealed samples.

After annealing at 900 °C for 20 s, the two-layer structure was not found. Planview micrographs revealed that heavily damaged regions were no longer present. Only C54-$TiSi_2$ was found as the annealing temperature was at or higher than 900 °C. Examples are shown in fig 8.

For 80 keV As^+ implanted silicon to a dose of 5×10^{15} cm^{-2}, the surface layer was found to be amorphous. In contrast, no amorphous layer was formed in $TiSi_2$ samples implanted under the same condition. $TiSi_2$ is known to be metallic [7]. Covalent bonds in semiconductors are directional. The breaking of highly ordered bonds in these materials by ion implantation tended to amorphize the surface layer relatively easily On the other hand, amorphization in metallic materials is relatively difficult to achieve. The heat of formation of $TiSi_2$ is -134 kJ/mol [8], which implied that the Ti–Si bond is stronger than the Si–Si bond. Maenpaa et al. reported that Pd_2Si could not be made amorphous up to a dose of about 10^{17} Ar^+ cm^{-2}. An XTEM study showed that a $NiSi_2$ layer did not become amorphous up to a dose of 1×10^{16} Si^+ cm^{-2} [9].

The C49 phase was found to form in the surface layer. Both the effects of dopant and radiation damage may play a role in transforming the damaged C54 layer into a C49 layer. Beyers et al. [10] studied titanium disilicide formation on a heavily doped Si substrate. For heavily As-doped substrates (3×10^{22} As cm^{-3}), the C49- to C54-$TiSi_2$ transformation temperature was increased to 850 °C. Van Ommen et al. [11] found that samples after As^+ implant were observed to have broadened peaks of the C54 phase in X-ray diffraction spectra. The C49 phase was detected to form in samples annealed at lower temperatures (600 or 700 °C). The phase was found to disappear after annealing at 800 °C for 30 min. It seemed that As atoms stabilized the C49 phase in a $TiSi_2$ film with As^+ implant. Gas et al. concluded that As diffused through a $TiSi_2$ film very fast by moving as substitutional atoms on the silicon sublattice sites [12,13]. The size of the As atom (1.18 Å) is slightly larger than that of a Si atom (1.17 Å). The C49 phase is packed less densely (density = 3.85 g/cm^3) than the C54 phase (density = 4.126 g/cm^3). It may be reasoned that if silicon-sublattice sites were replaced by As atoms, the C49 phase, with a more loosely packed structure, would be more stable than the C54 structure at temperatures lower than 200 °C during high beam current ion implantation with sufficient water cooling.

The C49 phase was found to be prone to misplace one atomic layer along the [010] direction. If the frequency of misplacement was high, a one-directional high-density disorder structure may be produced. The

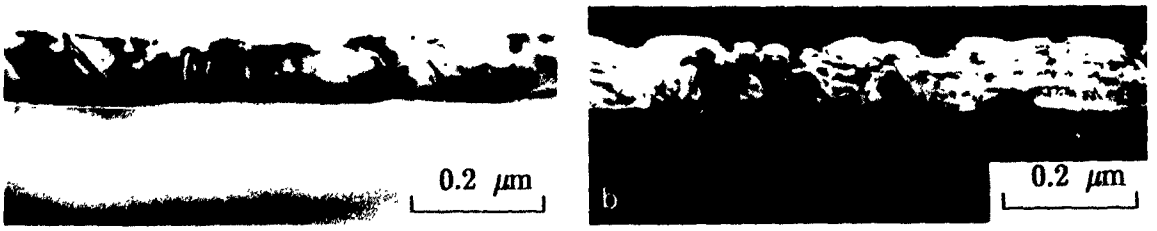

Fig. 8 Cross-sectional micrographs, 900 °C, 20 s. (a) Bright field, (b) dark field. The bright region corresponds to C54-$TiSi_2$.

presence of a high density of polytypes was correlated to the high resistivity value (≈ 96 μΩ cm). In contrast, stable C54-$TiSi_2$ shows clean and almost defect-free microstructures and was correlated to a relatively low electrical resistivity value (≈ 20 μΩ cm) [14,15].

4. Summary and conclusions

Radiation damage in C54-$TiSi_2$ implanted by 80 keV, 5×10^{15} cm^{-2} As^+ has been studied by both cross-sectional and planview TEM as well as by four-point probe resistivity measurement.

Phase reversion from C54-$TiSi_2$ to C49-$TiSi_2$ was observed in as-implanted samples. The electrical resistivity of implanted samples was found to decrease with annealing temperature and time. After annealing at 800 °C for 1 h or at 900 °C for 20 s, the conductivity of the $TiSi_2$ layer was found to fully recover to its pre-implantation value. The phase transition from C49-$TiSi_2$ to C54-$TiSi_2$ and the decrease in the density of residual defects were found to correlate with the decrease in electrical resistivity.

Acknowledgement

This research was supported by the Republic of China National Science Council.

References

[1] J.S. Williams and J.M. Poate, in: Ion Implantation and Beam Processing, eds. J.S. Williams and J.M. Poate (Academic Press, Sydney, 1984) p. 1.
[2] S.M. Sze, VLSI Technology (McGraw-Hill, New York, 1988)
[3] D.L. Kwong, Y.H Ku, S.K. Lee, E. Louis and N.S. Alvi, J. Appl. Phys 61 (1987) 5084.
[4] V. Probst, H. Schaber, P. Lippens, L Van den Hove and R. De Keersmaecker, Appl. Phys. Lett 52 (1988) 1803.
[5] K.J. Barlow, Electron. Lett 24 (1988) 949.
[6] J.F. Ziegler, J.P. Biersack and U. Littmark, The Stopping and Range of Ions in Solids, vol. 1 (Pergamon, New York, 1984).
[7] V. Malhotra, T.L. Martin and J.E. Mahan, J. Vac. Sci. Technol B2 (1984) 10.
[8] M.A. Nicolet and S.S. Lau, in: Materials and Process Characterization, eds. N.G. Einspruch and G.B Larrabee (Academic Press, New York, 1983) p. 329.
[9] M Maenpaa, L.S. Hung and M A Nicolet, Thin Solid Films 87 (1982) 277.
[10] R. Beyers, D Coulman and P. Merchant, J. Appl Phys 61 (1987) 5110
[11] A.H. van Ommen, H J W. van Houtum and A.M.L. Theunissen, J Appl. Phys. 60 (1986) 627.
[12] P Gas, V. Deline, F.M d'Heurle, A. Michel and G. Scilla, J Appl. Phys. 60 (1986) 1634.
[13] P. Gas, G. Scilla, A Michel, F K LeGoues, O. Thomas and F.M. d'Heurle, J. Appl. Phys 63 (1988) 5335.
[14] M.S. Fung, H.C Cheng and L J Chen, Appl Phys Lett 47 (1985) 1312.
[15] T.C Chou, C.Y Wong and K.N. Tu, J. Appl Phys 62 (1987) 2275

Nuclear Instruments and Methods in Physics Research B55 (1991) 763–768
North-Holland

Comparison of models for the calculation of ion implantation moments of implanted boron, phosphorus and arsenic dopants in thin film silicides

P.D. Cole [a], G.M. Crean [a], J. Lorenz [b] and L. Dupas [c]

[a] *NMRC, Lee Maltings, Prospect Row, Cork, Ireland*
[b] *FhG-AIS, Artilleriestrasse 12, Erlangen W-8520, Germany*
[c] *IMEC, Kapeldreef 75, Leuven B-3030, Belgium*

The accurate prediction of dopant ion implantation profiles both before and after thermal processing is becoming increasingly critical in the design of ultra-large scale integration (ULSI) sub-micron devices. In this paper, the ion implantation moments of boron, phosphorus and arsenic dopants implanted into thin film titanium, tungsten and cobalt silicides are calculated using Monte Carlo, Boltzmann transport equation and look-up table approaches. Four ion implantation simulators are evaluated the TRansport of Ions in Matter (TRIM89) Monte Carlo code, RAMM and SUPREM-3 transport equation codes and PREDICT-1.4 which relies on look-up tables for its calculations. Theoretical results are subsequently compared with experimentally measured boron, phosphorus and arsenic range and straggle parameters in thermally reacted titanium silicide thin films obtained using secondary ion mass spectroscopy (SIMS) and Rutherford backscattering spectrometry (RBS). Ion implantation energies were varied from 20 keV to 160 keV. It is demonstrated that SUPREM-3 and PREDICT-1.4 ion implantation codes do not at the present time accurately calculate the ion implantation moments of dopants implanted into the silicides investigated. However the overall correlation between TRIM, RAMM and the experimental data presented is very good. The ion implantation models in TRIM and RAMM could be employed as preprocessors in a more general ULSI sub-micron process simulator capable of modelling a doped silicide fabrication technology

1. Introduction

Lateral and vertical shrinkage of device dimensions in metal oxide semiconductor (MOS) ultra-large scale integrated (ULSI) circuits, poses significant semiconductor fabrication manufacturing challenges. In particular, optimized shallow junction fabrication techniques are required to form junctions, with depths of less than 1000 Å for a 0.25 μm CMOS technology. The accurate prediction of dopant ion implantation profiles both before and after thermal processing is therefore becoming increasingly important in the design of sub-micron microelectronic devices [1]. One novel process fabrication technique under intensive investigation for very shallow junction fabrication, is dopant diffusion from an ion implantation doped silicide source [2]. This has the advantages of minimising implant channeling and lattice damage in the silicon substrate and also of trapping contaminants associated with the ion beam in the silicide. While a number of ion implantation models exist for modelling the interaction of the dopant within the thin film silicide on silicon structure, the accuracy of these models, which is determined by the mathematical approach employed and the material properties incorporated into the simulation program, are not well documented. The objective of this work is to evaluate the ion implantation models currently available for this simulation task via a comparison of experimental and theoretical results for ion implantation into three technologically relevant silicides.

2. Modelling

The range and straggle moments of boron, phosphorus and arsenic ion implantations into titanium, cobalt and tungsten silicides are calculated using the TRIM Monte Carlo code [3], the RAMM [4] and SUPREM-3 [5] transport codes. Boron, phosphorus and arsenic implantation moments into titanium and cobalt silicides are also calculated using the PREDICT-1.4 simulator [6]. The densities of titanium, cobalt and tungsten silicides were 4.02 g/cm^3, 4.9 g/cm^3 and 9.4 g/cm^3, respectively [7]. We consider a thin film silicide on silicon substrate. The thickness of the silicide film was fixed at 2500 Å to ensure that the ion implant did not penetrate the silicide/silicon interface. One should note that the ion implantation models investigated in this work treat the target materials as amorphous. For the TRIM Monte Carlo code, 2000 ion histories were followed for each calculation. In order to determine the effect of increasing the number of ion histories on the calculated moments, a number of simulations were performed using 2000 and 10000 ion histories [8]. Negliga-

0168-583X/91/$03.50 © 1991 – Elsevier Science Publishers B.V. (North-Holland)

ble variation was noted in the range and straggle data extracted from these profiles.

3. Experimental

Both n-type (2–4 Ω cm) and p-type (16–20 Ω cm) single crystal (1 0 0) silicon substrates were used as the starting materials. The substrates were chemically cleaned and etched in dilute HF immediately prior to loading into a sputter deposition chamber. The wafers were then RF etched and baked at a temperature of 250 °C. 280 nm of Ti was sputtered onto the silicon wafers with subsequent annealing using a conventional two-stage anneal at temperatures of 550 and 800 °C respectively in a high purity (≤ 5 ppm moisture and O_2 concentration) nitrogen purged furnace. The final sheet resistance of the fully reacted silicide layers was 0.5 Ω/□.

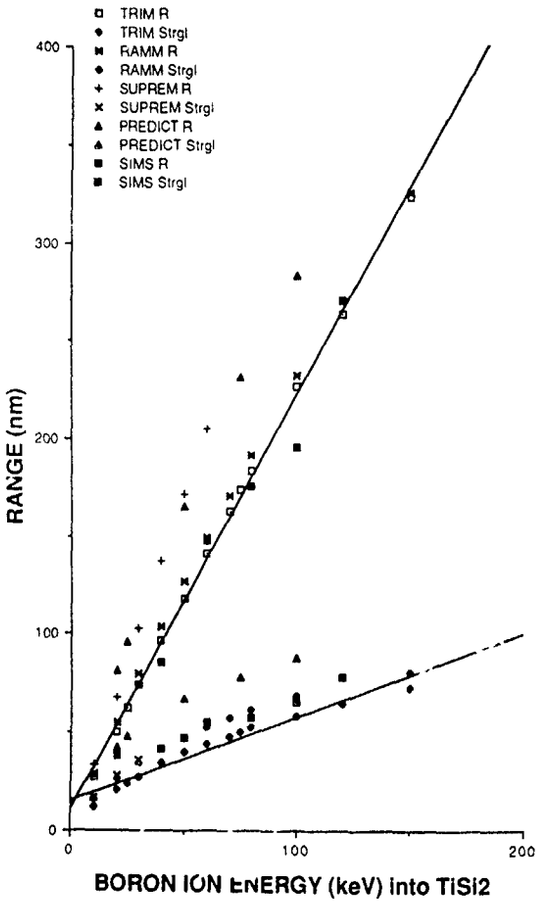

Fig. 1. Measured and simulated range and straggle moments of boron ions implanted into titanium silicide as a function of ion implant energy. Experimental data was obtained by means of SIMS analysis. Calculated data was obtained using the TRIM, RAMM, SUPREM-3 and PREDICT-1.4 simulation codes.

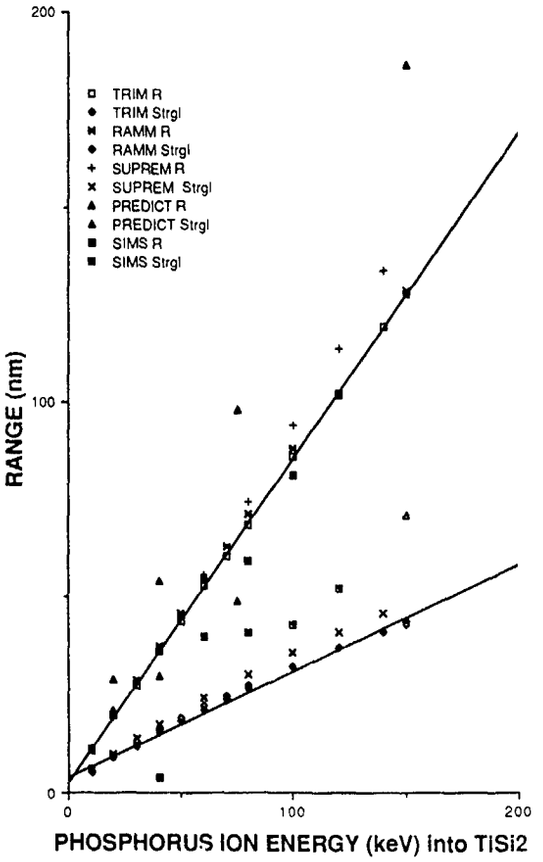

Fig 2 Measured and simulated range and straggle moments of phosphorus ions implanted into titanium silicide as a function of ion implant energy. Experimental data was obtained by means of SIMS analysis. Calculated data was obtained using the TRIM, RAMM, SUPREM-3 and PREDICT-1 4 simulation codes

Boron, phosphorus and arsenic ions were implanted into the thin film titanium silicides at nominal room temperature. The ion implant energies ranged from 20–120 keV, 40–120 keV and 20–160 keV for the boron, phosphorus and arsenic dopants, respectively. A dose of 1×10^{15} atoms/cm^2 was implanted in all cases, and the ion beam current was maintained at 20 μA.

RBS measurements were obtained using a 1.5 MeV He beam. Samples were analysed with the beam at both normal incidence and at an angle of 35° (exit beam 55° with a scattering angle of 160°). The accuracy of the RBS depth scales depend upon the accuracy of the energy loss factors used. These are known to better than 10%. The SIMS characterisation was performed using a Cameca IMS 3f dynamic SIMS system employing Cs^+ bombardment to avoid any change in erosion rate between the silicon and the silicide film. Depth scales were obtained by measuring the crater depths using optical interference microscopy, the absolute accuracy of which

is approximately 30 nm, the duration of each profile scan remained constant.

4. Results and discussion

Figs. 1–8 show measured (for titanium silicide), and calculated range and straggle parameters for boron, phosphorus and arsenic ions implanted into titanium, cobalt and tungsten silicides as a function of ion implantation energy (As ions implanted into WSi_2 not included). The fitted lines on all graphs are the TRIM range and straggle data.

It can be seen from figs. 1–3 that there is excellent agreement between the ion implantation moments extracted from the TRIM simulation data and the experimental results for boron, phosphorus and arsenic ions implanted into titanium silicide. The boron and phosphorus experimental data (figs. 1 and 2) were determined using SIMS analysis while the arsenic experimental range and straggle data was extracted from RBS profiles (fig. 3). Deviations in agreement between the RBS and SIMS data were noted. These differences can arise from a number of different factors including the method of depth calibration, the correction of SIMS artefacts, e.g., differential shift [9] and the choice of analytical function to which the experimental profiles are fitted. A detailed discussion of the experimental results shown on figs. 1–3 has already been presented [10].

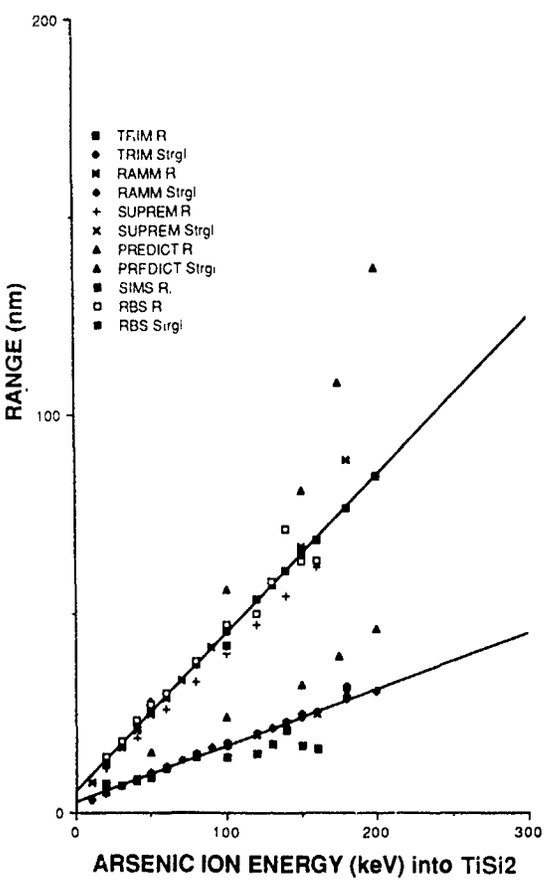

Fig 3 Measured and simulated range and straggle moments of arsenic ions implanted into titanium silicide as a function of ion implant energy. Experimental data was obtained by means of SIMS and RBS analysis. Calculated data was obtained using the TRIM, RAMM, SUPREM-3 and PREDICT-1.4 simulation codes.

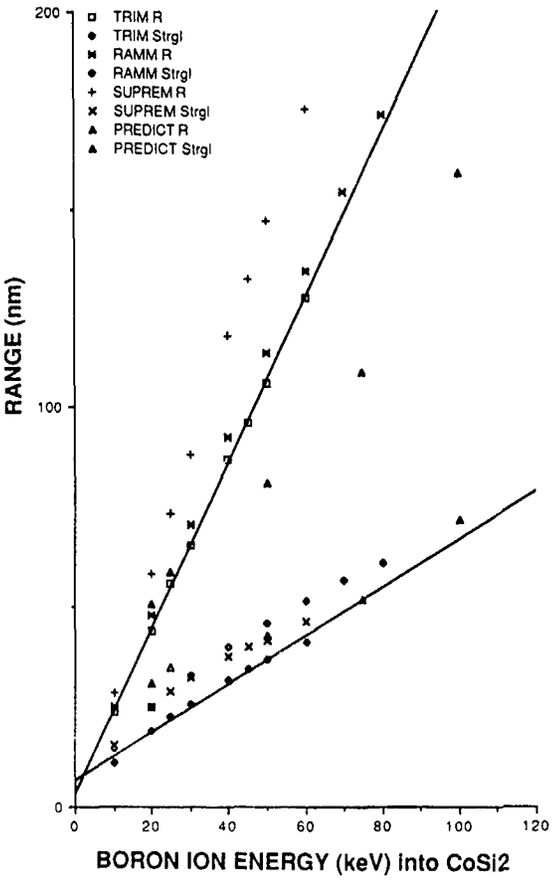

Fig. 4 Simulated range and straggle moments of boron ions implanted into cobalt silicide as a function of ion implant energy Calculated data was obtained using the TRIM, RAMM, SUPREM-3 and PREDICT-1 4 simulation codes

Figs. 1–8 show that the TRIM and RAMM simulation results for the range and straggle moments of implanted boron, phosphorus and arsenic ions into titanium, cobalt and tungsten silicides, are in very good agreement. However, the SUPREM-3 simulation results differ significantly from those of TRIM (figs. 1–8). For the case of the boron implantation into cobalt silicide (fig. 4), SUPREM-3 overestimates the range and strag-

gle parameters of the implant by comparison with the data obtained from TRIM (fitted lines). In fig. 6, for the arsenic implantation into cobalt silicide, SUPREM-3 underestimates the range and straggle parameters of the implant by comparison with the TRIM data (fitted lines). The results of the SUPREM-3 simulations imply that the nuclear and electronic stopping powers incorporated into the SUPREM-3 program are at variance with those incorporated into both the TRIM and RAMM simulation codes.

PREDICT-1.4 ion implantation moments do not exhibit good agreement for dopant ions implanted into titanium silicide when compared with the experimental results obtained (see figs. 1–3). Moreover PREDICT-1.4 does not show good agreement with the ion implantation moments extracted from the TRIM or RAMM theoretical simulations. A possible explanation for this is that as PREDICT-1.4 is using look-up tables of experimental data obtained from SIMS and RBS as-implanted profiles for its calculations [6], there may be inconsistencies with the manner in which the data was

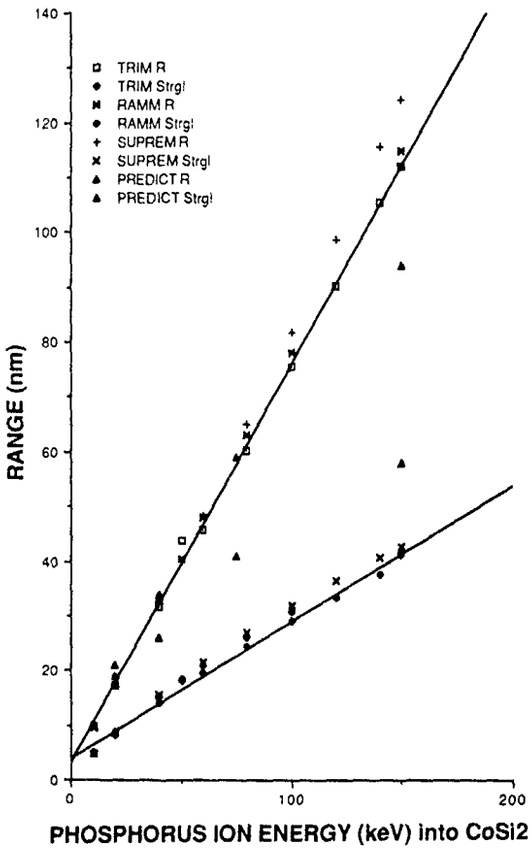

Fig. 5. Simulated range and straggle moment of phosphorus ions implanted into cobalt silicide as a function of ion implant energy Calculated data was obtained using the TRIM, RAMM, SUPREM-3 and PREDICT-1.4 simulation codes.

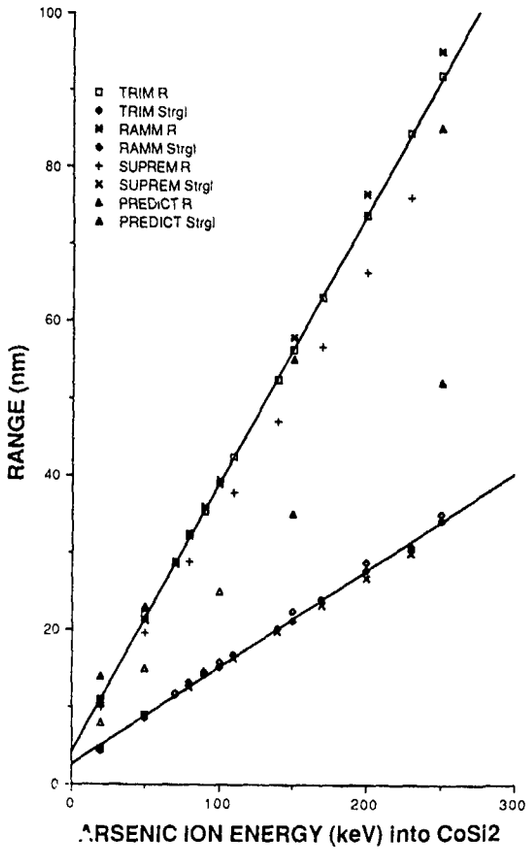

Fig 6. Simulated range and straggle moments of arsenic ions implanted into cobalt silicide as a function of ion implant energy Calculated data was obtained using the TRIM, RAMM, SUPREM-3 and PREDICT-1 4 simulation codes

obtained as a result of the difficulties that are associated with the characterisation of these techniques.

5. Conclusions

The ion implantation ranges of boron, phosphorus and arsenic dopants in thermally reacted titanium silicide thin films on silicon (100) have been determined experimentally using SIMS and RBS analysis. Experimental ion range measurements have been compared with simulated data using the TRIM Monte Carlo code, the RAMM and SUPREM-3 transport codes and PREDICT-1.4. The overall correlation between TRIM, RAMM and the experimental data is very good. The ion implantation models utilised in SUPREM-3 and PREDICT-1.4 simulators do not appear at the present time to be accurate for calculating the ion implantation moments of dopants implanted into the silicides investigated.

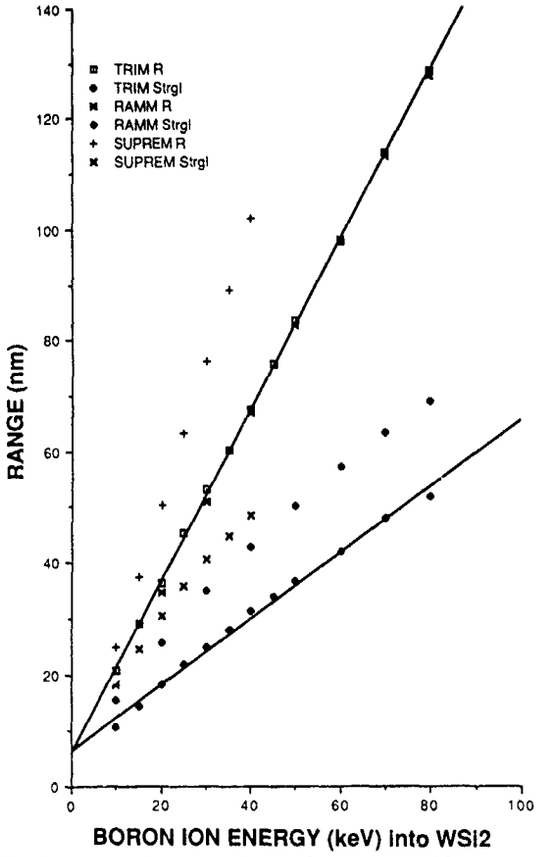

Fig 7 Simulated range and straggle moments of boron ions implanted into tungsten silicide as a function of ion implant energy Calculated data was obtained using TRIM, RAMM and SUPREM-3 simulation codes

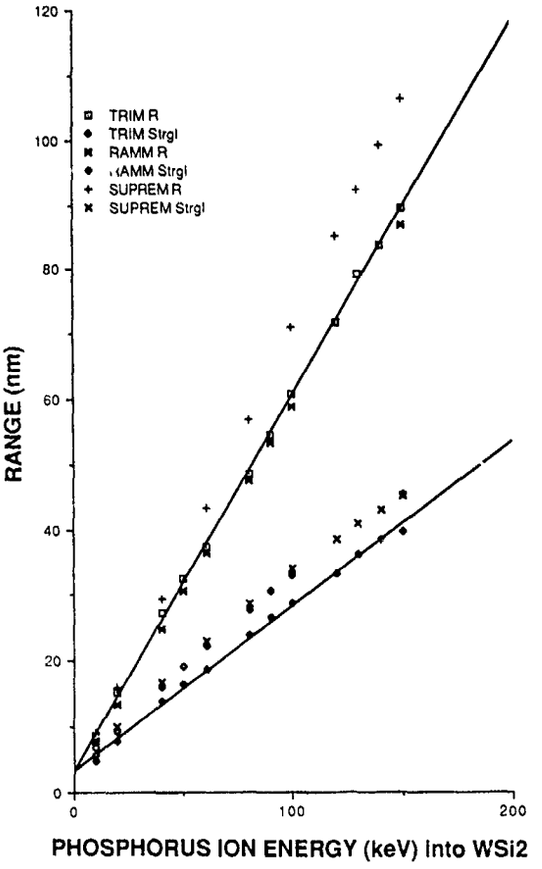

Fig. 8 Simulated range and straggle moments of phosphorus ions implanted into tungsten silicide as a function of ion implant energy Calculated data was obtained using the TRIM, RAMM and SUPREM-3 simulation codes

Based on the above results, TRIM or RAMM are suitable modelling tools for the initial step in the process simulation of an ion implanted doped silicide technology. Such codes could subsequently be employed as preprocessors in a more general ULSI sub-micron process simulator capable of modelling a doped silicide fabrication process.

Acknowledgements

The authors gratefully acknowledge the considerable assistance of S. Edwards in helping to run the SUPREM-3 code. We acknowledge the assistance of the NMRC fabrication staff in preparing the ion implanted titanium silicide films. We also thank A. Mathewson for his critical reading of this paper. One of the authors (P.D. Cole) would like to thank the the NMRC for the award of a research studentship. This work was partially funded by the European Community under ESPRIT project 2197 "Simulator for Technology Optimization in Research and Manufacture (STORM)".

References

[1] J Lorenz, A Barthel, L. Gong, H Ryssel and R.J. Wierzbicki, Proc 6th Int Symp on Silicon Mater. Sci and Techn., eds. H.R. Huff and K.G. Barraclough, Electronics and Dielectrics and Insulation Divisions, Proc. vol. 90-7 (Electrochem. Soc, 1990) p 538.

[2] D.L. Kwong, Y H. Ku, S.K. Lee, E. Louis, N.S. Alvi and P. Chu, Appl Phys. 61 (1987) 5084

[3] J.P. Biersack and L.G. Haggmark, Nucl. Instr. and Meth. 174 (1980) 257

[4] J. Lorenz, J. Pelka, H. Ryssel, A. Sachs, A Seidl, M. Svoboda, IEEE Trans. Electron Devices ED-32 (1984) 1977

[5] SUPREM-3 is a 1D process analysis program from Technology Modeling Associates, Inc, Menlo Park, CA, USA.

[6] PREDICT-1.4, Process Estimator for the Design of Integrated Circuit Technologies. Microelectronics Center of North Carolina, Research Triangle Park, NC, USA.
[7] M.A Nicolet and S.S. Lau, in: VLSI Electronics Microstructure Science, vol 6, eds. N G Einspruch and G B. Larrabee (Academic Press, 1983) chap. 6
[8] P.D Cole and G.M. Crean, First Periodic Progress Report, ESPRIT Project 2197 (1989).
[9] K Wittmaack and W Wach, Nucl. Instr. and Meth. 191 (1981) 327.
[10] G.M. Crean, P D Cole and C. Jeynes, Solid State Electron. 33 (1990) 655.

Nuclear Instruments and Methods in Physics Research B55 (1991) 769–772
North-Holland

Ion beam synthesis of cobalt silicide: effect of implantation temperature

E.H.A. Dekempeneer, J.J.M. Ottenheim, D.E.W. Vandenhoudt, C.W.T. Bulle-Lieuwma and E.G.C. Lathouwers

Philips Research Laboratories, PO Box 80000, 5600 JA Eindhoven, The Netherlands

In order to understand the physical processes which occur during ion beam synthesis of $CoSi_2$, we have studied the effect of implantation temperature. The experiment consisted of 170 keV Co implantations (dose = 1.7×10^{17} ions/cm^2) in Si(100) targets at temperatures varying between 250°C and 500°C. Both as-implanted and annealed samples have been analyzed by several techniques, such as cross-section transmission electron microscopy, X-ray diffraction, Rutherford-backscattering spectrometry and the four-point probe technique. Our data indicate that an optimum implantation temperature interval exists where pinhole-free buried layers of $CoSi_2$ can be synthesized. Outside this interval, the evolution of the precipitate size distribution and/or strain situation in the as-implanted state effectively reduce the necessary depth variation in precipitate stability.

1 Introduction

Ion beam synthesis (IBS) of $CoSi_2$ refers to a process in which a buried epitaxial silicide layer in silicon is formed after annealing of a high-dose Co implantation in Si [1]. Typically, the implantations are carried out at elevated temperatures T_i (300–500°C) to anneal out the radiation damage [1–4]. It has indeed been observed that when near-surface amorphization occurs during Co implantation, annealing will result in large amounts of silicide being segregated at the surface. However, at present, no clear treatment has been presented on the influence of varying the implantation temperature in a region above this lower limit where amorphization occurs. Given the fact that already at 600°C sharpening of the Co distribution has been observed (often it is the first step in the subsequent anneal treatment), one may expect that varying the implantation temperature from 300°C up to 500°C will significantly affect the microstructure in the as-implanted state, and hence also the structure after annealing. It may also be anticipated that, since the diffusion of Co atoms is expected to play an important role, the implantation time, and therefore ion-beam current density, may be an important parameter.

In the present work we study these influences by looking at the microstructure of the implanted material before and after annealing.

2. Experiment

Co ions were implanted into Si(100) 4 in. wafers at different implantation temperatures between 250°C and 500°C, with an energy of 170 keV and a dose of $(1.7\pm0.1)\times10^{17}$ ions/cm^2 (table 1). The surface normal was tilted by 7° with respect to the incident beam direction to reduce channeling effects. The implantation temperature T_i was controlled by external heating. Beam heating effects are expected to raise the sample temperature by no more than 40°C. Above 350°C the external heat source consisted of a matrix of seven halogen lamps irradiating the target from the rear. At lower implantation temperatures, the samples were clamped onto an Al holder against a solid Cu block provided with resistive heating. Two series of implantations were carried out (set 1 and set 2, see table 1) which differ by the beam current density (1.6 and 3 μA/cm^2, respectively). During the 500°C and 425°C implantations of set 1, the ion source dropped out for some period of time, thereby extending the effective implantation time by 10% and 30%, respectively.

Table 1
Experimental details giving the implantation temperature (T_i), total ion dose as measured by RBS (Φ), ion beam current density (I) and total implantation time (S)

T_i [°C]	Set 1			Set 2		
	Φ [cm^{-2}]	I [μA/cm^2]	S [h]	Φ [cm^{-2}]	I [μA/cm^2]	S [h]
500	1.8×10^{17}	1.6	5.5[a]	1.75×10^{17}	3	2.7
425	1.8×10^{17}	1.6	6.5[a]	1.75×10^{17}	3	2.7
350	1.55×10^{17}	1.8	4	1.75×10^{17}	3	2.7
290	1.6×10^{17}					
250	1.6×10^{17}					

[a] Includes downtime of the ion source.

0168-583X/91/$03.50 © 1991 – Elsevier Science Publishers B.V (North-Holland)

The post-implantation anneal treatments were carried out in a heat-pulse 610 (AG) furnace, in the sequence 30 min 600°C + 30 min 1000°C in flowing N_2 ambient.

Both as-implanted and annealed specimens have been analyzed in cross section by conventional transmission electron microscopy (XTEM), X-ray diffraction (XRD) and Rutherford-backscattering spectrometry (RBS) using a 2 MeV He^+ beam. The resistivity of the layers was measured by the four-point probe technique.

3. Results

First, let us concentrate on the as-implanted state of set 1. Fig. 1 shows bright-field XTEM images for T_i = 425°C and 500°C. Large differences can be seen, both in size and shape of the $CoSi_2$ precipitates. At 425°C, the precipitate size varies strongly with depth in a way that is logically linked with the implantation depth profile: small precipitates in the front and back tail, and larger ones near the peak of the distribution. At 500°C all precipitates have become appreciably larger and highly facetted, predominantly along the {111} planes. The gradient in the size distribution is also less pronounced. XTEM was also carried out on the 350°C implantation (not shown). This sample exhibits a microstructure similar to the 425°C implantation, but with the precipitates, on average, being still somewhat smaller and more circular in shape. Together with these variations in size and shape as function of temperature, we also observe large differences in the strain situation of these precipitates. Previous work [5] has indicated that the $CoSi_2$ lattice in the as-implanted precipitates is compressed in a direction normal to the surface. This was explained as being a result of a tetragonal distortion of the $CoSi_2$ lattice which tries to match the larger Si lattice parallel to the surface. Our XRD data in fig 2 show that this compression varies in magnitude as a function of implantation temperature. With increasing implantation temperature, the precipitates become more and more relaxed. Obviously, strain relaxation is correlated with the precipitates becoming larger and highly facetted and is due to the formation of misfit dislocations [6]. The smaller strain relaxation observed for set 2 can be explained by the fact that, due to the shorter implantation time, precipitates had less time to grow. The relaxation of strain, and hence, the reduction of deformation energy with increasing implantation temperature is important because it renders the precipitates more stable [7]. As we will show now, this increased stability has important consequences for the subsequent anneal treatment.

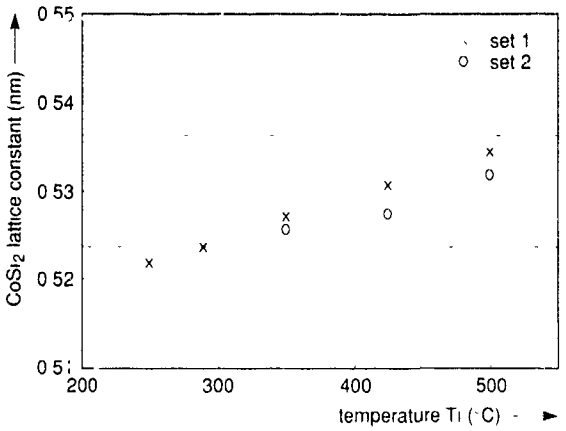

Fig 2 XRD measurements on as-implanted samples (set 1 and set 2) of the $CoSi_2$ lattice constant perpendicular to the surface as function of implantation temperature. The upper dashed line indicates the value for $CoSi_2$ powder. The lower dashed line gives the value calculated for tetragonally distorted precipitates that fully match the Si lattice parallel to the surface, assuming conservation of cell volume.

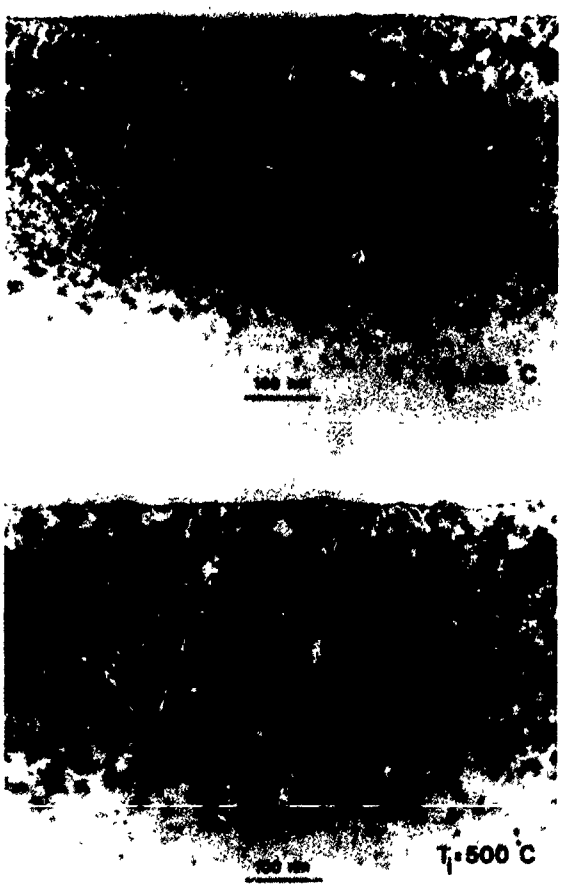

Fig. 1 Bright-field XTEM images of as-implanted samples (set 1) for different implantation temperatures.

Fig. 3 shows bright-field XTEM images of annealed samples of set 1 for four different implantation temperatures. Clearly, the 350°C implantation yields the best pinhole-free buried silicide layer. Apparently, the number of threading dislocations in the top silicon film is simultaneously reduced to a minimum. The damage level in the top Si layers was also directly measured by channeling RBS along the Si ⟨100⟩ direction. As expected from the XTEM results, the lowest minimum yield value was obtained for the 350°C implantation ($\chi_{min} = 6\%$). The 250°C, 290°C (not shown) and 425°C implantations contain a lot of pinholes which can be recognized because of their facetted character. The worst case is clearly the 500°C implantation, where no layer formation occurs at all. Instead, large isolated precipitates reaching up to the surface are formed.

For $T_i \geq 425$°C, these observations can be explained by the fact, that in the as-implanted state, the gradient in precipitate size over the implanted depth gradually becomes smaller with increasing T_i. Correspondingly, precipitates in the tails increase their stability with respect to the precipitates near the peak of the implantation profile. This hinders the buried layer formation process because the difference in precipitate stability happens to be the driving force for Co atoms to diffuse from the tails towards the peak of the implantation profile. Note that based on the principle of minimization of interface energy alone, a simple calculation of the total interface area shows that, instead of a buried layer, a series of large isolated precipitates becomes energetically more favourable as soon as their radius becomes larger than a certain critical radius R_c. For spherical precipitates and a dose of 1.7×10^{17} ions/cm^2, $R_c \simeq 1000$ Å. This picture is close to what we observe for the 500°C implantation (fig. 3).

For $T_i \leq 290$°C, again pinholes are formed. In order to understand the reason for this, it is interesting to make a comparison with the strain–dose relationship

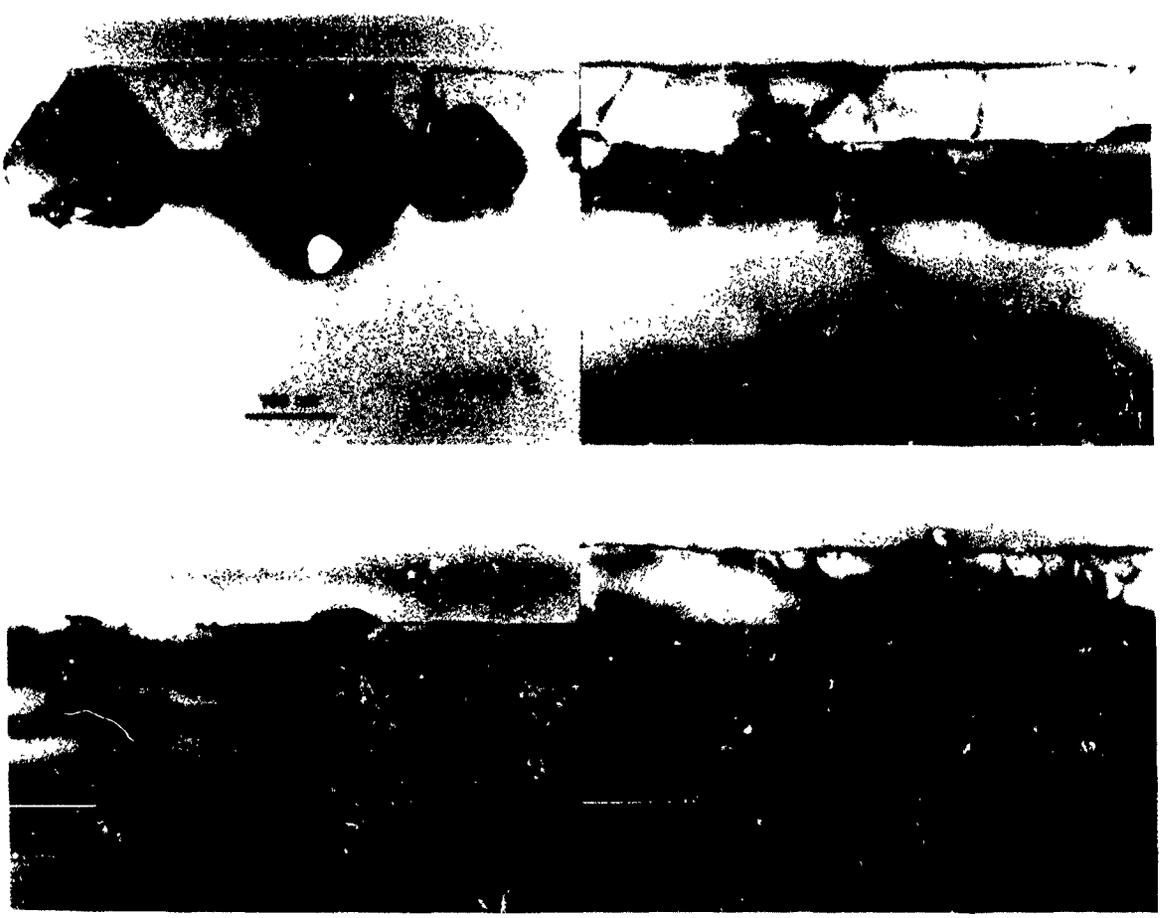

Fig. 3 Bright-field XTEM images of annealed samples (set 1) for different implantation temperatures. Top left: $T_i = 500$°C; top right: $T_i = 425$°C, bottom left: $T_i = 350$°C; bottom right: $T_i = 250$°C.

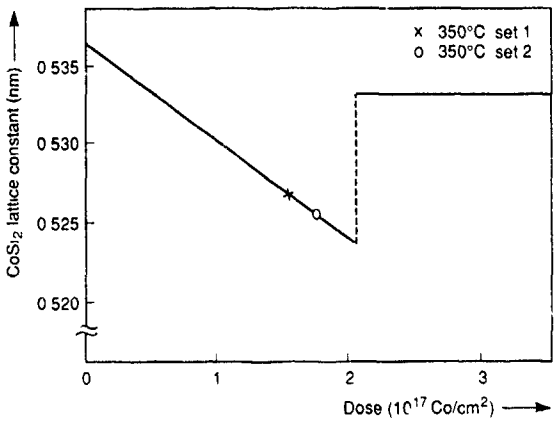

Fig 4. Dose dependence, for 170 keV Co implantations, of the perpendicular lattice constant of $CoSi_2$ precipitates in the as-implanted state (for implantation conditions which, upon annealing, result in pinhole-free buried layer formation) The drawn line is from ref [2]

measured in ref. [2]. In the experiments of ref. [2], implantation conditions were such that for doses above the critical dose, a pinhole-free buried layer was synthesized. Fig. 4 shows that there is good agreement, regarding the strain in the as-implanted state, between their experiment and our 350°C data (which also yields a pinhole-free silicide layer). This consistency supports again the idea that the strain in the as-implanted state largely determines its behaviour during the anneal treatment. To explain their data, the authors of ref. [2] proposed a model in which the perpendicular contraction of the $CoSi_2$ precipitates was partly counteracted by the surrounding strained Si matrix itself. Returning to our data in fig. 2, the increased distortion of precipitates for $T_i \leq 290$°C might therefore be indicative of the fact that the Si matrix around the precipitates tends to relax, possibly because too much damage is being introduced This relaxation is a possible cause of the observed reduced efficiency of buried layer formation, because it increases the precipitate stability. However, at present this is rather speculative since we have no direct measurement of the strain in the Si matrix. Raman measurements were performed, but the observed shift and broadening of the Raman line could also be explained by the microcrystalline nature of the as-implanted state [8].

Concerning the influence of implantation time, our room-temperature resistivity measurements indicate that, for the 500°C implantation, annealing of the set 2 sample ($\rho = 15$ μΩ cm) yields a better silicide layer than the set 1 sample ($\rho = 27$ μΩ cm). This is in agreement with the smaller strain relaxation observed for the set 2 implantations. At lower implantation temperatures, resistivity variations are too small to make any conclusions. No XTEM data for set 2 are available yet.

4. Conclusions

We have shown that for IBS of $CoSi_2$ an optimum implantation temperature interval exists, which lies well above the limit where amorphization occurs. Outside this interval, problems arise probably because the evolution of the precipitate size distribution and/or strain situation in the as-implanted state effectively reduce the necessary depth variation in precipitate stability. Ion beam current density is also a critical parameter, in the sense that it influences both the damage production rate and precipitate growth (through implantation time). A higher current density will therefore probably raise the optimum implantation temperature. Our data suggest that for a current density of 1.6 μA/cm^2, the optimum temperature interval is less than 100°C wide and centered around 350°C.

Acknowledgements

We are indebted to A.G. Mouwen and A J. Kinneging for XRD measurements and to W.J O. Teesselink for the Raman analyses. The fruitful discussions with D.J. Oostra are much appreciated.

References

[1] A E White, K T Short, R.C Dynes, J.P Garno and J M Gibson, Appl. Phys Lett 50 (1987) 95
[2] A H van Ommen, C.W T Bulle-Lieuwma, J J M Ottenheim and A M L Theunissen, J Appl Phys 67 (1990) 1767
[3] A Vantomme, M F Wu, I Dezsi, G Langouche, K Maex and J Vanhellemont, Mat Sci Eng B4 (1989) 157
[4] K Kohlhof, S. Mantl and B Stritzker, Appl Surf Sci 38 (1989) 207.
[5] A.H. van Ommen, J.J.M. Ottenheim, A M L. Theunissen and A.G. Mouwen, Appl Phys Lett 53 (1988) 669.
[6] C W T. Bulle-Lieuwma, A H van Ommen, J J.M Ottenheim, D E W Vandenhoudt and E H.A. Dekempeneer, to be published.
[7] J. Burke, in: La Cinetique des Changements de Phase dans les Metaux (Masson, Paris, 1968) p 145
[8] H. Richter, Z P. Wang and L Ley, Solid State Commun. 39 (1981) 625.

Nuclear Instruments and Methods in Physics Research B55 (1991) 773–777
North-Holland

Cobalt silicide formation caused by arsenic ion beam mixing and rapid thermal annealing

Min Ye, Edmund Burte, Pei-Hsin Tsien [1] and Heiner Ryssel
Fraunhofer-Arbeitsgruppe für Integrierte Schaltungen, Artilleriestrasse 12, D-8520 Erlangen, FRG

Ion beam mixing and rapid thermal annealing (RTA) were used to prepare low resistivity ($\approx 23\ \mu\Omega$ cm) cobalt disilicide, $CoSi_2$, layers. Through-metal As^+ ion implantation causes some mixing between Co and Si resulting in the formation of cobalt silicides. By using RTA, the silicide formation happens in the phase sequence Co_2Si, CoSi and $CoSi_2$. Samples which were only subjected to a one-step high temperature RTA process ($T \geq 900\,^\circ C$, 1 s) show significant lateral growth of cobalt silicides. By ion beam mixing of Co and Si this lateral silicide growth could be reduced efficiently. Furthermore one can get a very homogeneous $CoSi_2$ layer.

1. Introduction

Recently metal silicides have gained an increasing interest in view of their application as ohmic contact and as interconnection materials. Up to now, titanium disilicide $TiSi_2$ is the most investigated silicide because of its low resistivity and good high temperature stability [1]. As pointed out in refs. [1,2] $CoSi_2$ could be an attractive alternative to $TiSi_2$, since they have similar film resistivities and similar high-temperature stabilities ($CoSi_2$: 16–25 $\mu\Omega$ cm up to 900 °C and $TiSi_2$: 13–25 $\mu\Omega$ cm up to 1000 °C). Although cobalt consumes more silicon than titanium to achieve the same sheet resistance R_s (for instance: to achieve a 1 $\Omega/\square$ R_s value a 150 nm thick silicide film of a resistivity of 15 $\mu\Omega$ cm of $CoSi_2$ or $TiSi_2$ is required. $CoSi_2$ consumes 156 nm silicon while $TiSi_2$ only needs 140 nm silicon) $CoSi_2$ has some other advantages. Unlike titanium, cobalt does not react with SiO_2 [3], and opposite to the formation of $TiSi_2$, in which silicon is the dominant diffusing species, the formation of $CoSi_2$ is dominated by metal diffusion [4]. These properties would make it easier to avoid the bridging between source-drain and gate in MOS VLSI technology.

For use of salicide (self-aligned silicide) [5] structures, the selective formation of silicide by the solid phase reaction of thin metal films with the patterned silicon substrate or polysilicon layers must be achieved, since the patterning of silicides is very difficult [1]. The lateral growth of silicide beyond the area of the source-drain region can cause an electrical short to the gate electrode. In the present work we studied the reaction between cobalt films and Si substrates caused by rapid thermal annealing (RTA) and through-metal ion implantation as well as the lateral growth of silicide and the influence of ion beam mixing.

2. Experimental procedure

Co films were deposited onto p-type $\rho = 1$–$2.5\ \Omega$ cm (100)-Si wafers by dc magnetron sputtering. The silicon wafers were chemically cleaned and dipped in 1% HF for 2 min immediately before loading into the sputtering chamber to minimize the thickness of the native oxide. The sputtering chamber was evacuated to 2×10^{-6} Torr prior to the introduction of high purity (99.999%) argon to a pressure of 7×10^{-4} Torr. The sputtering was performed at a current of 0.9 A and a target potential of 1.5 kV, resulting in a deposition rate of approximate 3 Å/s. The thickness of the cobalt films was about 230 Å and the sheet resistance about 16 $\Omega/\square$. To study the lateral growth of cobalt silicides, square windows ($20 \times 20\ \mu m^2$) were opened in thermally grown silicon dioxide of 400 nm thickness prior to the deposition of cobalt and the silicidation process. After removing the unreacted cobalt, the wafer surfaces were studied by SEM.

To investigate the influence of the through-metal ion implantation, some samples (both Co/Si and Co/SiO_2) were As^+ implanted with an energy of 200 keV and doses of 1, 2, 5, $7 \times 10^{15}\ cm^{-2}$, and $1 \times 10^{16}\ cm^{-2}$ using an implantation current of 1 mA, resulting in a current density of 12.7 $\mu A/cm^2$. Subsequently, heat treatment was performed at temperatures between 700 and 1100 °C in flowing nitrogen atmosphere for 1 s by using an AG Associate Heatpulse 610 halogen lamp RTA system.

[1] Permanent Address: Institute of Microelectronics, Tsinghua University, Beijing 10084, People's Republic of China.

0168-583X/91/$03.50 © 1991 – Elsevier Science Publishers B.V. (North-Holland)

The metallurgical analysis was performed by Rutherford backscattering spectrometry (RBS) with a 1.5 MeV $^4He^+$ ion beam. X-ray diffraction (XRD) employing Cu K_α radiation ($\lambda = 1.5418$ Å) was used to identify the silicide phases present in the films. The behavior of silicide lateral growth and the silicide surface morphology were studied by scanning electron microscopy (SEM) The sheet resistance of $CoSi_2$ was measured by four-point probe measurements.

3. Results and discussion

The sheet resistance R_s of the annealed Co/Si samples versus the RTA temperatures is shown in fig. 1. At 700 °C, R_s decreased from 16 Ω/□, the value of the as-deposited samples, to 4 Ω/□. This is due to the formation of Co_2Si. Then R_s began to rise with increasing temperature and reached its maximum value of 80 Ω/□ at 800 °C. This maximum resistance coincided with the complete conversion of cobalt into $CoSi$, which is known to be the highest resistivity cobalt silicide [6]. At temperatures above 800 °C, R_s decreased very rapidly, indicating the transformation of CoSi into $CoSi_2$, and reached a very low value of about 3.8 Ω/□ at 900 °C. For temperatures between 900 and 1100 °C, R_s was almost constant, but showed a small decrease with increase in temperature. As no further phase transition occurred at temperatures above 900 °C, this R_s-behaviour may be due to the formation of $CoSi_2$ of better crystallinity at elevated temperatures resulting in

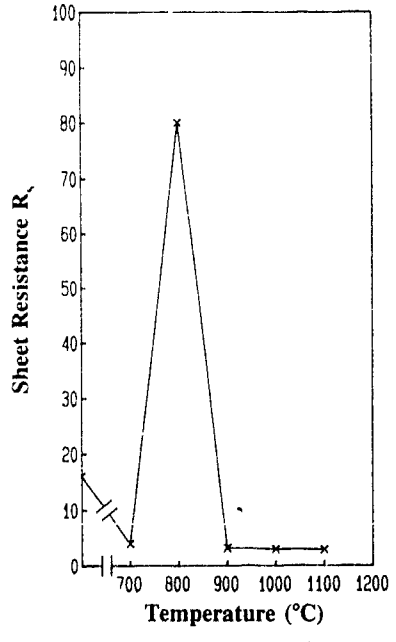

Fig 1. The sheet resistance of Co/Si samples versus the RTA temperatures

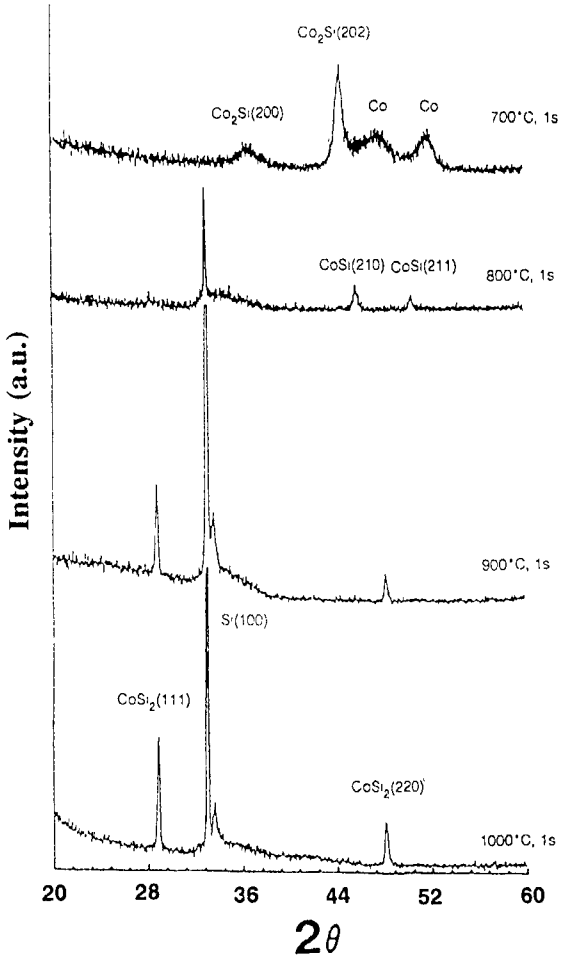

Fig 2 The X-ray diffraction spectra of annealed Co/Si samples

the observed decrease of R_s. The XRD spectra (shown in fig. 2) gave the same results: at 700 °C almost all the cobalt film reacted with the silicon substrate to form the metal-rich Co_2Si; at temperatures between 700 and 800 °C Co_2Si was transformed into CoSi by the continued reaction with Si, and at 800 °C all Co_2Si was converted into CoSi; at temperatures above 800 °C, the formation of the final phase $CoSi_2$ happened, and at 900 °C all CoSi was converted into $CoSi_2$. These results reveal that the reaction of Co and Si caused by RTA also occurs in the phase sequence of Co_2Si, CoSi and $CoSi_2$, the same as that caused by conventional furnace annealing [7].

RBS measurements were also used to investigate the reaction of Co and Si. Fig. 3 shows the RBS spectra with normal incidence of $^4He^+$ ions. At 700 °C, a slight reaction between Co and Si was observed. At 800 °C the spectra height ratio of Co and Si showed that the CoSi phase was formed. At $T \geq 900$ °C, $CoSi_2$ was the

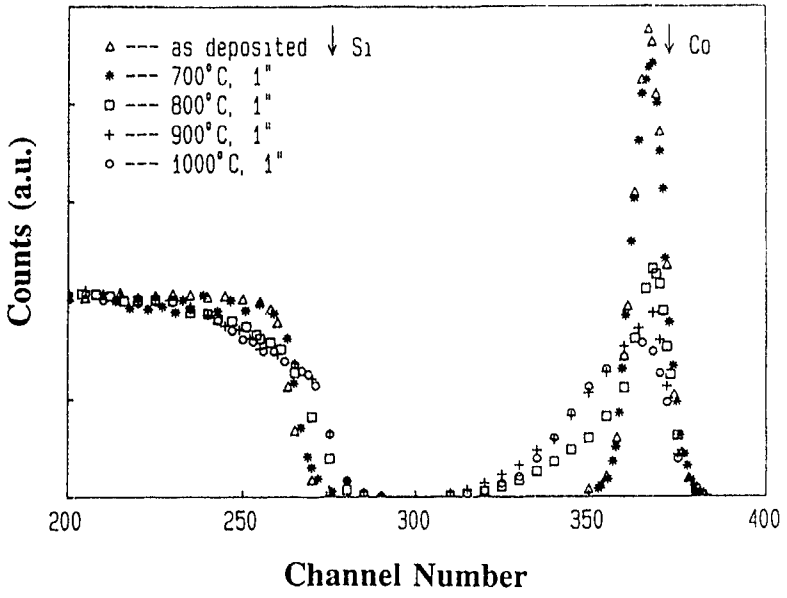

Fig 3 The RBS spectra of annealed Co/Si samples

only silicide phase, but there was no clear shoulder in the high energy edge of Si spectra, and the Co spectra also seemed to show a diffusion profile of cobalt in silicon. These findings were associated with poor depth resolution on account of the lateral inhomogeneity of the $CoSi_2$ thickness. The resistivity of $CoSi_2$ was 23.2 $\mu\Omega$ cm.

The R_s values and the XRD results of As^+ implanted samples are listed in table 1 The RBS spectra of these samples are shown in fig. 4. For the sake of clarity we omitted the spectrum corresponding to 7×10^{15} cm^{-2}. Although there are few changes in the R_s values and the normal incident RBS spectra of the samples implanted with doses of 1 and 2×10^{15} cm^{-2} with respect to those of the as-deposited samples, XRD spectra show that some silicide phases are already present in the as-implanted films. In the samples implanted with doses of 5, 7×10^{15} cm^{-2} and 1×10^{16} cm^{-2}, the R_s values are about 3 $\Omega/\square$, equal to those of $CoSi_2$ formed by RTA. The RBS spectra corresponding to

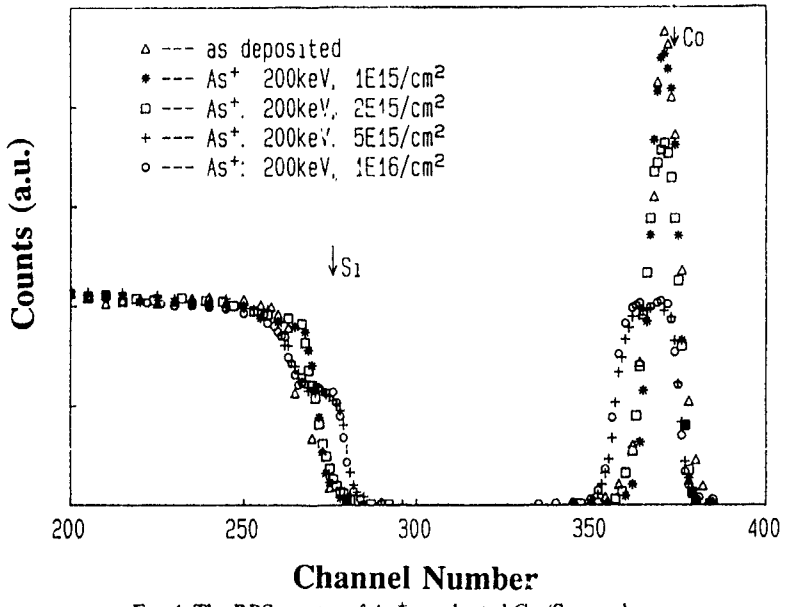

Fig. 4. The RBS spectra of As^+ implanted Co/Si samples

Table 1
The sheet resistance values and the XRD results of As^+ implanted samples (E = 200 keV)

Dose [10^{15} cm^{-2}]	1	2	5	10
R_s [Ω/□]	14	17	3.6	2.8
Phase (XRD)	Co, Co_2Si	Co_2Si, CoSi, $CoSi_2$	$CoSi_2$	$CoSi_2$

these samples show a distinct shoulder, the signal height illustrates that the atom ratio of Co to Si is 1 : 2 in the films. The XRD peaks show clearly that $CoSi_2$ has already been formed. This phenomenon may be due to the thermal effects during ion beam mixing, as the implantation current was rather high [8].

The main motivation for using $CoSi_2$ as a substitute for $TiSi_2$ in VLSI circuits is that it is easier to avoid the lateral growth of silicides with cobalt than with titanium,

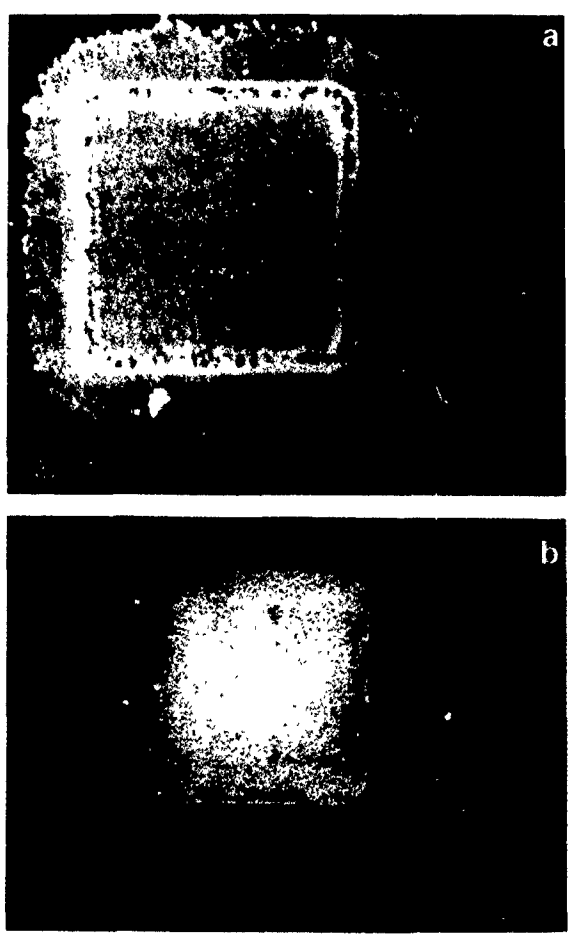

Fig. 5. SEM figures of Co silicide selective formation (RTA: 900 °C, 1 s): (a) without As^+ implantation and (b) with As^+ implantation.

since $CoSi_2$ is formed by metal atom diffusion [5,9]. Our experiments reveal that the one-step high temperature RTA ($T \geq 900$ °C, 1 s) can cause significant lateral growth of silicides in the samples without As^+ implantation before the annealing. Fig. 5a clearly demonstrates the overgrowth of cobalt silicides beyond the edges of the patterned SiO_2. This phenomenon was observed in the formation of $CoSi_2$ by conventional furnace annealing [10]. There is, however, little lateral growth of silicides in the samples which were As^+ implanted after the deposition of cobalt (fig. 5b). This lateral growth of cobalt silicide originates from the fact that $CoSi_2$ is formed via the formation of CoSi, in which the silicon atom is the dominant diffusion species [11]. By As^+ implantation, the cobalt film is mixed with the silicon substrate and a presilicidation probably occurs prior to the thermal treatment of the samples. One may speculate that by this As^+ implantation some cobalt silicide phases, most probably Co_2Si, are produced, which are transformed into $CoSi_2$ by the following RTA step. In this process the dominant diffusion species is cobalt Therefore, the through-metal As^+ implantation can prevent the lateral growth of $CoSi_2$. Furthermore, ion beam mixing results in a smoother surface of $CoSi_2$ (see fig. 5) and a more homogeneous $CoSi_2$ layer (see fig. 4). This may be due to a very high number of nucleation centers generated by implantation of As^+ ions resulting in smaller $CoSi_2$ grains formed during the RTA step.

4. Conclusion

Our experiments reveal that cobalt silicides can be formed by rapid thermal annealing (RTA) in the phase sequence of Co_2Si, CoSi and $CoSi_2$, the same as in the case of conventional furnace annealing. One-step high temperature RTA without ion beam mixing results in significant lateral growth of cobalt silicide beyond the edge of the SiO_2 windows. The through-metal arsenic implantation causes the mixing of Co with Si and forms some silicides. This implantation can effectively prevent the lateral growth of silicides and results in a very smooth silicide surface and a homogeneous $CoSi_2$ thickness.

Acknowledgements

Pei-Hsin Tsien wishes to thank the Deutsche Akademische Austauschdienst (DAAD) for financial support during his stay in the Federal Republic of Germany. The assistance of Silvia Fuchs, Rudolf Berger, Rainer Schork and Erich Pauer in sample preparation is gratefully acknowledged. The authors are greateful to Jing-Ping Zhang and Peter Hemment for performing

the RBS measurements, to Hui-Wang Lin for the XRD analysis and to Li Gong for helpful discussions.

References

[1] S.P Murarka, Silicides for VLSI Application (Academic Press, New York, 1983).
[2] S.P Murarka, in: Semiconductor Silicon 1986, Electrochem. Soc. Softbound Proc. Ser. (Penrington, NJ, 1986) p. 297.
[3] R Pretorius, J.M. Harris and M.-A Nicolet, Solid State Electron. 21 (1978) 667
[4] C -D Lien, M. Bartur and M.-A Nicolet, Mater. Res. Soc Symp. Proc. 25 (1984) 51.
[5] Y Murao, S. Mihara, M. Kikuchi, R Sase and T. Furuhashi, IEEE IEDM Techn. Dig 83 (1983) 518
[6] C -D. Lien, M. Finetti M.-A. Nicolet and S S. Lau, J Electron. Mater. 13 (1984) 95
[7] S.S. Lau, J.W. Mayer and K.N. Tu, J. Appl. Phys 49 (1978) 4005.
[8] H Ryssel and I. Ruge, Ion Implantation (Wiley, 1986) p 114.
[9] F.M. d'Heurle and C.S. Petersson, Thin Solid Films 128 (1985) 283.
[10] S.P Murarka, J. Vac. Sci. Technol. 17 (1980) 775.
[11] G.J. van Gurp, W.F. van der Weg and D Sigurd, J. Appl Phys. 49 (1978) 4011

Nuclear Instruments and Methods in Physics Research B55 (1991) 778–781
North-Holland

The application of a 600 keV heavy ion implanter

Jiang Xinyuan, Zhao Qihua [1], Guan Anmin, Shao Tianhao and Lin Chenglu
Shanghai Institute of Metallurgy, Academia Sinica, 865 Chang Ning Road, Shanghai 200050, People's Republic of China

The application of a 600 keV heavy ion implanter is described. High energy B^+ and high energy doubly charged P^{2+} were implanted in silicon for p- and n-wells isolation in CMOS ICs. 600 keV Ar^+ was implanted in silicon to form a damage layer, the perfect layer near the surface of the Si-wafer was made by defect gettering. Si^+, Mg^+ and O^+ were implanted in GaAs, and the uniformity of the threshold voltage (V_{th}) of GaAs MESFETs buried with Mg or O layers was improved. High activation efficiencies of Mg^+ and Si^+ implanted GaAs after RTA were obtained by using a specially designed graphite heater, and the activation efficiencies were 100% and 92%, respectively. The isolation of GaAs and InGaAsP/InP and other compound semiconductors, the characteristics of $LiNbO_3$ and other insulators after high energy ion implantation and molecular ion implantation have also been investigated using this implanter.

1. Introduction

Ion implantation technology has been developed since 1952. At first Bell Laboratory used H^+ implantation to form p- n junctions and fabricate solar batteries. At first, application of ion implantation in silicon devices was by low energy implantation ($\leqslant 10$ keV). With the development of ion implantation technology, high energy ion implantation and applications in other materials became more and more attractive. The new implantation technologies stimulated applications in SOI structures, Si, GaAs and other compound semiconductor devices, materials and insulator materials.

A 600 keV heavy ion implanter (pre-accelerating and post-analyzing implanter) has been built at the Shanghai Institute of Metallurgy, Academia Sinica [1]. The implanter has the following characteristics: energy above 600 keV and stable (long-time drift less than 1×10^{-4}), mass range of 1–210 and mass resolving power over 210, beam stability better than 100 μA $\pm$ 2.5% per hour. This ion implanter has been put into use in ion implantation applications.

The applications of ion implantation using the 600 keV heavy ion implanter are now in silicon materials and devices, GaAs and other compound semiconductor materials and devices, and $LiNbO_3$ optical wave-guides, and other insulator materials.

[1] Present address: Institute of Information Display and Transducer, Shanghai Jiao Tong University, Shanghai 200030, People's Republic of China.

2. Applications

2.1. Application in silicon materials and devices

High energy doubly charged phosphorus (P^{2+}) was implanted in a $\langle 100 \rangle$ p-type silicon wafer to form an isolation well in CMOS technology [2]. This technique results in a significant reduction of thermal treatment time for n- and p-wells. Also, the better control over the well dopant profiles in implantation can be used to decrease latch-up susceptibility, while simultaneously increasing packing density. However, accompanying the production of P^{2+} during the discharge of red phosphorus in the ion source, P_2^+ is also produced. P_2^+ could turn into P^+ and P with half energy each in the silicon. Contamination is introduced, which results in another peak in the carrier concentration profile of the annealed samples. The contamination of low energy P^+ ions has been effectively avoided by using PF_3 gas as discharge material in the ion source. As shown in fig. 1, where the low peak refers to the implanted P^+ of 300 keV (the half energy of the P_2^+ ion) and the P^{2+} energy is 1.2 MeV. The samples were annealed both by RTA (1200 °C, 10 s). Fig. 2 shows carrier concentration profiles of the samples (RTA, 1200 °C, 10 s) obtained by spreading resistance probe measurements. The implantation energy is from 0.8 to 1.2 MeV, at the same dose of 4×10^{13} cm^{-2}. The results of 1.0 MeV implantation meet the requirements for the retrograde well in CMOS technology: the peak concentration is 10^{18} cm^{-3} located 1.0 μm from the surface, the junction is about 1.7 μm, and the carrier concentration at the surface is less than

0168-583X/91/$03.50 © 1991 – Elsevier Science Publishers B.V. (North-Holland)

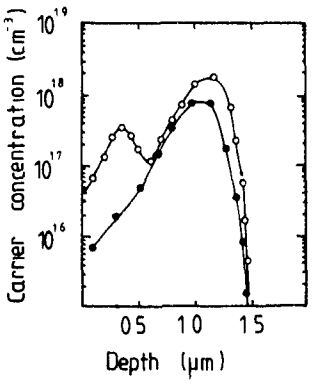

Fig 1 The carrier concentration profiles of silicon implanted with 1.2 MeV P^{2+} and annealed (RTA, 1200 °C, 10 s); (○) ion source material is red phosphorus; (●) ion source material PF_3-gas.

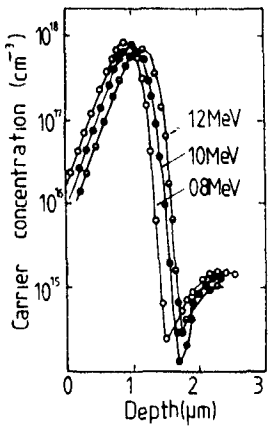

Fig 2 The carrier concentration profiles of annealed samples which are implanted with different ion energies ($P^{2+} \rightarrow P$ ⟨100⟩Si, 4×10^{13} cm^{-2}, RTA 1200 °C, 10 s)

2×10^{16} cm^{-3}. From the performances of CMOS inverter specimen, the holding current ($I_p = \infty$) and holding voltage ($V_h = \infty$) for latch-up of the CMOS specimen by P^{2+} implantation are much higher than those ($I_p = 11$ mA, $V_h = 2.9$ V) by conventional CMOS technology. Furthermore, P^-/P^+ epitaxy to form isolation wells is latch-up free.

The radiation damage introduced in the Ar^+ implanted silicon and the damage layer cannot be annealed by both RTA and FA. The high energy 600 keV Ar^+ implantation will create a buried damage layer, which could trap the defects [3]. Fig. 3 is the RBS-channelling spectrum of 600 keV Ar^+ implantation. After the high energy 600 keV Ar^+, to a dose of 4×10^{15} cm^{-2} and low energy 30 keV B^+, to a dose of 1×10^{15} cm^{-2} double implantation, and annealing at 1100 °C, 15 s, the perfect layer has been obtained by defect-gettering near the surface. Silicon photo-diode (SPD) devices can be fabricated in this layer with low leakage current.

2.2 The application in GaAs and other compound semiconductor materials and devices

Samples used in the investigation are semi-insulated (S.I.) GaAs. Si^+ and Mg^+ were implanted into GaAs and RTA was performed with improved graphite heater. After using this technique, a high activation efficiency has been obtained, the activation efficiencies of Si-implanted GaAs and Mg-implanted GaAs are 92 and 100% respectively [4]. Carrier concentration profiles of Mg-implanted GaAs wafer annealed by RTA and FA are shown in fig. 4. It can be seen that higher peak concentrations with negligible redistribution can be achieved after RTA at 1120 °C for 20 s. Also the high energy Mg^+ implantation creating a p-type buried layer

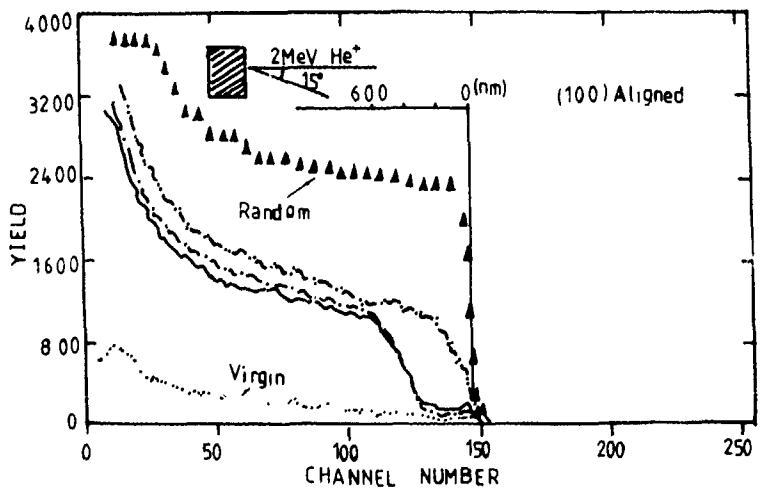

Fig 3 RBS-channelling spectrum of a 600 keV Ar^+ implanted Si-wafer. —·: Ar^+ 600 keV, 4×10^{15} cm^{-2} and B^+ 30 keV, 1×10^{15} cm^{-2} 1100 °C, 15 s; –··–: B^+ 30 keV, 1×10^{15} cm^{-2}, 1100 °C, 50 s.

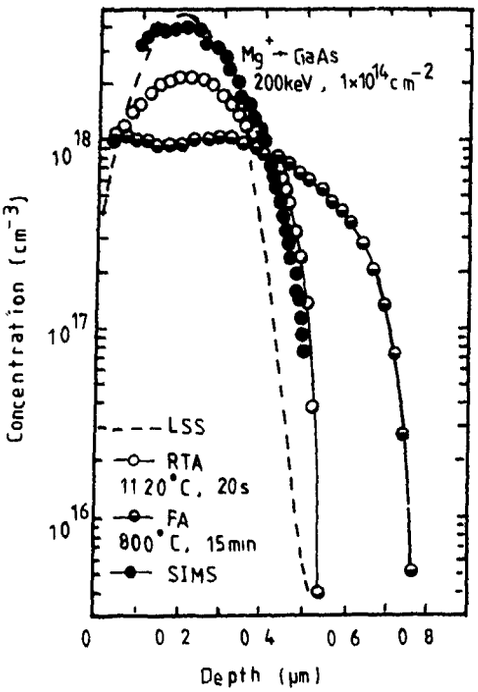

Fig. 4 The carrier concentration profiles of Mg-implanted GaAs.

and high energy O^+ implantation creating a compensation layer in S.I. GaAs have been used to improve the low concentration tails in Si-implanted GaAs [5]. Using Si^+ and Mg^+ double implantation, the carrier profiles and the p–n junction are determined as shown in fig. 5. The Si-implanted carrier concentration profile is nearly unaffected by the p-buried layer when the Mg-implanted dose is lower than 2×10^{12} cm^{-2}, but apparently this changes and the p–n junction moves towards the surface when the Mg-implanted dose is higher than 5×10^{13} cm^{-2}. The GaAs MESFETs with $L_g = 1$ μm, $L_{DS} = 4$ μm and different widths were fabricated on a Si and Mg double-implanted wafer, and the uniformity of the threshold voltage (V_{th}) of the GaAs MESFET was improved 27% compared to that of Si single-implanted GaAs MESFETs. GaAs MESFETs with a buried oxygen layer also have been fabricated and the uniformity of the threshold voltage (V_{th}) of the GaAs MESFET was improved 31% compared to that of Si single-implanted GaAs MESFETs.

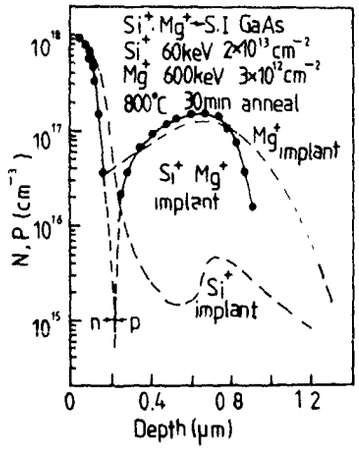

Fig. 5. Carrier concentration distribution plotted with respect to depth.

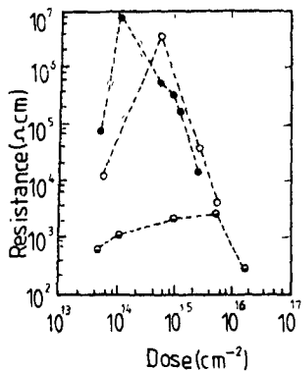

Fig. 6. Relations of resistance and implantation dose after 180 keV H^+ $In_{1-x}Ga_xAs_yP_{1-y}$/InP (●: P–InP doped Zn, 1×10^{18} cm^{-3}; ○: P–InGaAsP doped Zn, 1×10^{18} cm^{-3}; ◒: P–InGaAsP doped Zn, 1×10^{18} cm^{-3})

The production of high-resistivity regions in GaAs and other related compounds by high energy (600 keV) proton bombardment has been well investigated. The isolation depth was very deep and the isolation resistances were very high. GaAs devices were fabricated by using H^+ implantation to produce isolation and planar technology and achieved high performances of the characteristics. Fig. 6 shows the resistance after H^+ implantation into $In_{1-x}Ga_xAs_yP_{1-y}$/InP. The isolation resistances changes from 10^3 to 10^7 Ω cm to meet the needs of $In_{1-x}Ga_xAs_yP_{1-y}$/InP devices.

2.3. The application in $LiNbO_3$ and other insulator materials

$LiNbO_3$ is the optical material widely used in integrated optical circuits. The optical devices also can be made by ion implantation. We have investigated the damage distribution, the changes of chemical composition near the surface and after annealing, after H^+, N^+, Ar^+ and Xe^+ implantation in $LiNbO_3$. The experiments shows that damage distribution and nuclear energy deposition will change the refraction of the $LiNbO_3$ material and an optical wave-guide can be made because of these refraction changes. The more successful $LiNbO_3$ planar wave-guides have been fabricated by

Table 1
Parameters of $LiNbO_3$ planar waveguide after high-energy H^+ implantation

Implant energy [keV]	Implant dose [$\times 10^{16}$ cm^{-2}]	t_g (theor.) [μm]	Excited mode (TE)	βk^{-1}
180	3	0.64	TE_0	2.1892
180	5	0.64	TE_0	2.1881
500	3	2.85	TE_0	2.1881
			TE_1	2.1736
600	3	3.66	TE_0	2.1892
			TE_1	2.1703
600	3	3.66	TE_0	2.1858
650	3		TE_1	2.1725
			TE_2	2.1680

H^+ implantation [6]. The H^+ implantation in $LiNbO_3$ formed a buried radiation-damage layer because the damage by nuclear stopping is at the end of the range. The refraction will decrease because of lattice expansion by the stress in the buried layer, and a wave-guide layer is formed between the surface and the buried layer. The proton implantation will introduce light damage in the wave-guide layer because of electron stopping and there are no impurities as scattering centers in the waveguide layer. Also the damage can be annealed out by annealing at 350 °C, 30 min in an oxygen atmosphere. Table 1 shows the parameters of a $LiNbO_3$ planar wave-guide, where t_g is the thickness of the planar waveguide, TE is the excited waveguide mode, and (βk^{-1}) is the constant of wave propagation.

3. Conclusion

This paper has attempted to review recent work in ion implantation by using a 600 keV heavy ion implanter. The research has been performed for silicon, GaAs and other compound semiconductors, $LiNbO_3$ and other insulator materials. The research will be developed to meet the necessity for Si and GaAs integrated circuits, optical wave-guides and devices and other new materials and new device fabrication.

References

[1] Jiang Xinyuan, Lu Shi Wan and Shi Zhi Zu, Nucl. Instr. and Meth. B21 (1987) 310
[2] Guan Anmin, Geng Haiyang, Yu Bo, Cheng Jinyi, Lin Chenglu and Zhang Ming, Proc Shanghai Workshop on Ion Implantation, Hangzhou, China, 1988, P. 164
[3] J.C Zhou, X.Y Jiang and J L Zhu, ibid, p. 63
[4] Wei Dong Fan, Xin Yuan Jiang, Guan Qun Xia and Wei Yuan Wang, Inst. Phys Conf Ser. (1987) 277
[5] Ou Haijiang, Wang Weiyuan, Zhao Qihua and Jiang Xinyuan, Chin J Semicond. 10 (1989) 309
[6] Shao Tianhao, Proc 7th Int. Conf. on Ion Beam Modification of Materials, Knoxville, TN, 1990, Nucl. Instr. and Meth B, to be published

Nuclear Instruments and Methods in Physics Research B55 (1991) 782–784
North-Holland

Preparation of W–Th films by ion beam sputtering

M. Griepentrog, R.-A. Noack, M. Rosengarten and W. Schneider
Department of Physics, Humboldt University, Berlin 1040, Germany

In the present work ion beam sputtering of polycrystalline W/Th targets with a well-defined Th content by 12 keV Xe^+ ions was used for the preparation of W–Th films in order to produce a new material for cathodes in light-emitting devices. The films, deposited on silicon and Al_2O_3, were investigated by secondary ion mass spectrometry (SIMS), electron probe micro-analysis (EPMA), and Auger electron spectroscopy (AES). The films are close-packed and have the density of tungsten bulk material. It was established that the thorium distribution in the films is homogeneous. The thorium is always activated. The W/Th ratio is proportional to the thorium content in the target. Because of the poor vacuum conditions during the deposition (10^{-4} Pa) oxygen and carbon were found in the films. The films are mostly amorphous and seem to be a new exciting cathode material with interesting properties.

1. Introduction

The life-time of cathodes in light-emitting devices is in general limited by the erosion rate of the material used. At present powder-metallurgically made polycrystalline tungsten is often used for the production of cathodes because of the interesting thermal and electrical properties of tungsten. To obtain lower erosion rates and better emission characteristics the tungsten matrix is doped by an activator, i.e. a material with a low work-function (e.g. thorium oxide or barium oxide) [1]. Investigations of thoriated tungsten cathodes [2] show that the thorium oxide forms irregularly distributed particles with a diameter of a few micrometers. Size, concentration, and distribution of the activator particles determine the ignition, emission, and erosion behaviour of the cathodes.

The intention of the present paper is to show that W–Th films produced by ion beam sputter deposition (IBSD) are an interesting material for improving cathode performance. IBSD is a well established deposition technique [3,4]. In IBSD a collimated beam of energetic noble gas ions strikes a target. The sputtered particles impinge on a nearby substrate and form a thin film there. According to the energy distribution of the sputtered particles in IBSD the energy of the particles impinging on the substrate is much higher than in conventional evaporation processes. The sputtered particles leave the target with a near-cosine distribution. The energy and angular distribution of the sputtered particles depend on the energy, mass, and angle of incidence of the sputtering ions, and on the mass, chemical bonding states, and crystalline structure of the target [5]. There are different interactions between the impinging particles, the substrate surface, and the growing film [6,7]. Using highly energetic particles for film formation even at low temperatures films with good adhesion, high density, and low contamination can be prepared [8,9]. The sputtering of a target by energetic ion bombardment often results in the reflection of a significant fraction of incident ions as energetic neutrals into the growing film. These energetic neutrals also influence the growing film [10]. There are some additional advantages of IBSD in comparison with other sputtering techniques, for example, lower background pressure, independent control of the ion energy and ion current density, no interaction between substrate and plasma, and better control of the process.

2. Experimental

In this work ion beam sputtering by 12 keV Xe^+ ions was used. The beam was 8 mm in diameter. The current density of the ion beam was 1 mA/cm^2. The normal of the target was oriented at 45° with respect to the primary ion beam. Substrates for deposition were mounted on a sample holder placed 25 mm from the target. The deposition chamber was pumped by an ion getter pump. The pressure within the vacuum chamber was 1×10^{-4} Pa and 5×10^{-4} Pa during ion source operation.

W–Th films with thicknesses from 50 to 250 nm were deposited on crystalline silicon and on polycrystalline Al_2O_3 substrates. The surface of the silicon substrates was polished. The surface of the Al_2O_3 substrates showed a high roughness. Polycrystalline tungsten with different contents of thorium oxide (1.8 to 10 mass%) was used as target material. Various methods for surface analysis have been used for investigating

0168-583X/91/$03.50 © 1991 – Elsevier Science Publishers B.V. (North-Holland)

formation processes and properties of W–Th films by determining composition, structure and chemical bonding states. The techniques mostly used are electron probe microanalysis (EPMA), secondary ion mass spectrometry (SIMS), and Auger electron spectroscopy (AES). These techniques have both special features and disadvantages in investigations of thin films.

3. Results and discussion

As shown by studies of scanning electron microscopy the W–Th films on Al_2O_3 and Si are continuous. The films on the Al_2O_3 substrate have the same roughness as the substrate. A direct determination of the film thickness is thus not possible. The films deposited on Si are characterized by a smooth surface and a high adhesion to the substrate surface.

The thickness of films was determined by a surface profiling device due to masking a fixed area of the substrate surface during deposition. A symmetric distribution of film thickness with a gradient of 10%/cm was found. The maximum of the distribution is located opposite the centre of the area sputtered by the Xe^+ ion beam. The average film growth rate is 1.2 nm/min for W–Th films where the film is thickest.

The films show good electrical conductivity. The specific resistance determined from four-point probe measurements is two orders of magnitude higher than that of metallic tungsten (5.5 μΩ cm)

Because the application of EPMA, SIMS, and AES for the characterization of thin films on rough Al_2O_3 substrates is complicated and not always possible. Results are limited, in some cases, to films on Si substrates.

The SIMS depth profiling for W and Th allows an assessment of the homogeneity of the films. The depth profiles exhibit an increase in secondary ion signals at the surface and at the interface between film and substrate. Constant signals of secondary ions of the bulk species indicate the homogeneous nature of the film.

Investigations by SIMS, AES, and measurements with an electron probe microanalyzer showed that there are no additional impurities in the layers with the exception of carbon (< 10 at.%) and oxygen (< 3 at.%). Measurements by X-ray photoelectron spectroscopy (XPS) carried out for some samples indicate the existence of thorium oxide, various tungsten oxides and tungsten carbides in the tungsten film.

The thorium oxide will work as the activator. It is possible to obtain information concerning the lateral homogeneity of the distribution of activators by X-ray microanalysis [2]. These investigations show that the thorium oxide is distributed totally homogeneously through the films. Precipitates are not traceable (fig. 1).

The concentration of activators in the films can be determined by means of X-ray microanalysis [11]. The concentration of Th in a W–Th film produced by IBSD of a polycrystalline tungsten target with 5% thorium oxide (mass%) was determined to be (4 ± 1)% Th. In general, the concentration of activator in the films is proportional to the content of the activator in the target material. Measurements of the cathodoluminescence signal (CL) show an almost homogeneous distribution.

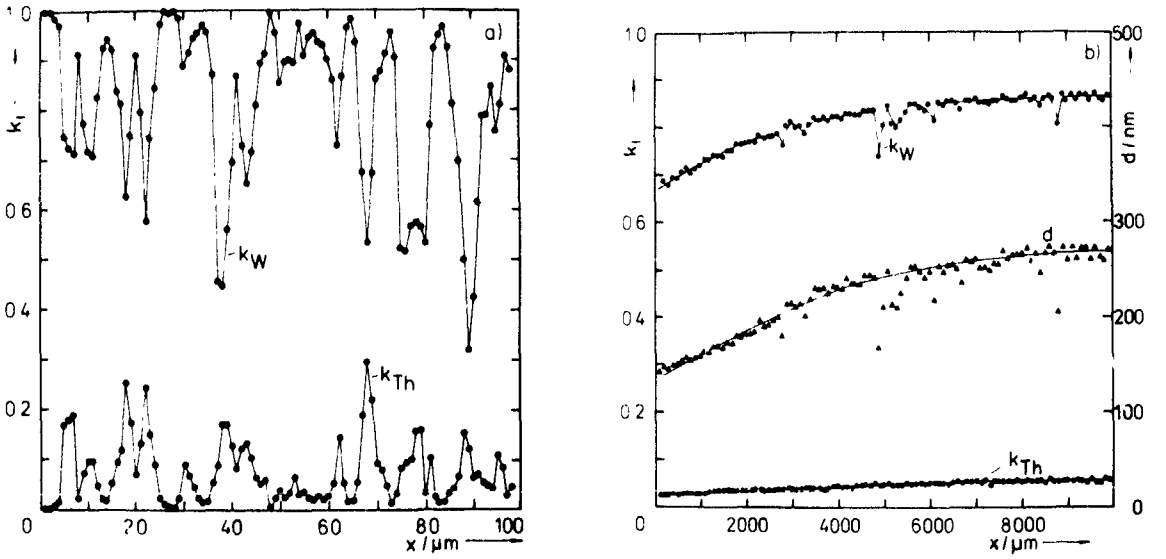

Fig 1. X-ray microanalysis of the W and Th distribution in the films (k-values for the $W_{M\alpha}$ and the $Th_{L\alpha}$ line, $E = 25$ keV) along the surface (a) of a WTh target (distance between the measuring points 1 nm), and (b) of a W–Th film on Si (target WTh 50) and the resulting distribution of the thickness d (distance between the measuring points 100 μm).

This indicates that the activators in the films are crystalline without needing to heat to high temperatures [2]. If the thickness of the film is known, the density of the deposited film can be determined using the AES concentration data. The density of the deposited films of about 16 g/cm^3 is near to the density of bulk tungsten (19.3 g/cm^3).

4. Conclusions

The ion beam sputter deposition has proven to be a useful technique for producing a new material for cathodes with exciting properties. However, compared to other deposition techniques, several problems remain to be solved, such as low deposition rates and the problem of contamination.

References

[1] V.M. Amosow, B.A. Karelin and V.V. Kubyskin, Material for Cathodes on the Basis of High Melting Metals (Metalurgija, Moscow, 1976) in Russian

[2] H. Düsterhöft, W. Schneider and V. Steinbrück, Exp. Tech. Phys. 25 (1981) 447.

[3] P. Mazzoldi and G.W. Arnold (eds.), Ion beam modification of insulators, in: Beam Modification of Materials, vol. 2 (Elsevier, New York, 1987).

[4] T. Itoh (ed.), Ion beam assisted film growth, in: Beam Modification of Materials, vol. 3 (Elsevier, New York, 1989).

[5] R Behrisch (ed.), Sputtering by Ion Bombardment – Physics and Application, (Springer, Berlin 1981).

[6] T. Tagaki, Proc. Int. Ion Engineering Congress – ISIAT '83, Kyoto, 1983, ed. T. Tagaki (Institute of Electrical Engineerings of Japan, Tokyo, 1983) p 785.

[7] T Tagaki, J Vac. Sci Technol. A2 (1984) 382.

[8] J M.E. Harper, Solid State Technol. 30 (1987) 129.

[9] J.E. Greene, Solid State Technol 30 (1987) 115

[10] E. Kay, F Parmigiani and W Parrish, J. Vac Sci Technol. A5 (1987) 44

[11] W Weisweiler and J Eck, Beitr Elektronmikr. Direktabb Oberfl. 18 (1985) 1.

Nuclear Instruments and Methods in Physics Research B55 (1991) 785–788
North-Holland

X-ray diffraction studies of radiation damage in gallium arsenide

W.H. van Berlo and T. Pihl
Swedish Institute of Microelectronics, Box 1084, S-164 21 Kista, Sweden

X-ray diffraction was used to study the damage caused by ion implantations in gallium arsenide The dependence of damage induced strain (DIS) on various implantation parameters was investigated It was found that the amount of DIS increases with ion mass, dose and dose rate, while it decreases with substrate temperature The thickness of the damaged layer was found to depend approximately linearly on implantation energy Results obtained from these studies were used to interpret the annealing behaviour of n-type impurities (sulphur and selenium) in GaAs. After implantation these elements showed upon annealing an activation energy which decreased with increasing implantation temperature. As the annealing may be considered to consist of regrowth of the damaged layer and activation of the impurities, the activation energies obtained from annealing experiments should reflect these two processes This means that the activation energies found may vary for different experimental conditions. This should be generally valid for compound semiconductors

1. Introduction

Ion implantation in compound semiconductors has been studied extensively in the past. Annealing behaviour and activation mechanisms for various elements in these materials have been investigated, but with not always consistent results [1–3]. Because of this, implantation technology seems to become something of an art; the implantations needed to obtain certain material properties often cannot be predicted, but have to be determined by trial and error, plus a great deal of experience. Part of the confusion seems to be due to a lack of knowledge of the influence various implantation parameters have on the resulting material properties. While a great deal of information has been obtained for silicon over the years, and therefore much is known about its behaviour and properties after implantation, this seems not to be the case for compound semiconductors like GaAs and InP. Just because these materials are compounds with a very narrow stoichiometric solubility range, and their electrical properties strongly depend on stoichiometric composition, their behaviour after implantation is much more delicate and complex than that of silicon. Especially the number of possible defects after implantation is, because of their structure, much larger than for silicon, and this number is greatly affected by the way the implantation parameters are chosen. It will be clear that in order to understand the behaviour of these compounds, information is needed about the influence various implantation parameters have on the defects generated during implantation.

There are various techniques for studying defects in semiconductor crystals. For low defect concentrations techniques like deep level transient spectroscopy (DLTS) or photo-luminescence (PL) may be used, while for nearly or completely amorphous layers Rutherford back scattering (RBS) is mainly used, often combined with channeling of the ion beam. There are also studies where ellipsometry has been used for measuring the thickness of damaged layers [4]. Recently X-ray diffraction (XRD) was used by Speriosu to study the strain induced by implantation damage in semiconductor material [5–7].

The advantage of using XRD is that it is sensitive to low defect concentrations while also high concentrations can be measured (up to the threshold of amorphization). Furthermore, it does not require any sample preparation. The main disadvantage of this technique lies in the fact that it is not a direct one. Defect concentrations can not be obtained directly from measurements. Rather the diffractograms (rocking curves) have to be simulated by computer until a fit is obtained between them and the measurements. The technique being quite sensitive also means, unfortunately, that simulation may become rather time consuming. Nevertheless, it seems a good alternative to be used besides other techniques.

We present here a study of the influence of various implantation parameters on the strain that is induced by the created damage, and the implications these have on the annealing behaviour of n-type impurities in GaAs.

2. Experimental

Undoped LEC-grown GaAs substrates were cut into approximately 2 cm^2 pieces and then implanted, in a

0168-583X/91/$03.50 © 1991 – Elsevier Science Publishers B V. (North-Holland)

nonchanneling direction, with noble gas ions (helium, neon, argon or krypton). For most implantations the energy was chosen proportional to the ion mass; typically 7–9 keV/amu. For energies below 300 keV singly charged ions were used, but for higher energies doubly charged ions had to be used. The implantation temperature was either room temperature or higher (100 °C to 600 °C). Doses were chosen in the range 1×10^{12} to 3×10^{15} cm^{-2}, depending on the ion. The dose rate was chosen such that substrate heating was avoided.

Immediately after implantation the amount of strain in the crystal was measured using a Philips five-crystal diffractometer [8]. The rocking curve around the ⟨004⟩ Bragg reflection was used to determine the amount of strain.

For some of the implantations the strain profile was obtained by simulating the rocking curves using Bede Scientific Instruments dynamical simulation program (RADS), which solves the Takagi–Taupin equations [9,10]. Strain profiles were compared to recoil and deposited energy profiles obtained from Monte Carlo calculations (TRIM-89) [11] for the case of an argon implant in an unheated substrate.

In order to study the annealing behaviour of n-type impurities in GaAs, 2×10^{14} cm^{-2} sulphur or selenium ions were implanted in undoped substrates at room temperature or at 400 °C. Sulphur was implanted at an energy of 140 keV and selenium at 300 keV. The samples where annealed in a Heatpulse RTP furnace for 5 s in an H_2/Ar ambient, using a silicon wafer as cap. Hall measurements was used to obtain the activated fraction of dopant atoms.

3. Results and discussion

A typical diffractogram, in this case of a 1×10^{13} cm^{-2} argon implantation at 300 keV into a substrate at room temperature, is shown in fig. 1, together with a simulated diffractogram. The signal of the implanted layer lying on the low angle side of the substrate peak indicates an expansion of the lattice after implantation. The amount of strain is determined from the position of the largest peak relative to the substrate peak, using the equation

$$\frac{\delta a}{a} = \frac{-\delta\theta}{\tan\theta_B}, \qquad (1)$$

where $\delta\theta$ is the angle between the substrate peak and the peak of the strained layer, and θ_B is the Bragg angle (33° for the GaAs ⟨004⟩ reflection). For the case shown in fig. 1, an angle of 300 arc sec between the substrate peak and the peak of the strained layer gives a strain corresponding to a 0.22% lattice mismatch. The thickness of the strained layer may be determined from

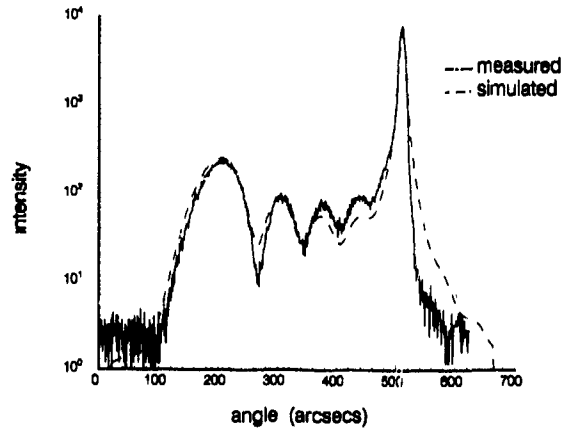

Fig. 1. Measured (———) and simulated (— — —) rocking curve for argon implantation at 300 keV and room temperature

the interference fringes (Pendellösung) between the substrate and strained layer peak, using the equation

$$t = \frac{\lambda \sin(2\theta_B - \theta)}{\delta\theta \sin 2\theta_B}, \qquad (2)$$

where λ is the wavelength (1.54 Å for Cu$K_{\alpha 1}$), θ the angle at which the period is measured and $\delta\theta$ the fringe period. The simulated strain profile is shown in fig. 2, together with the profile of recoils and argon ions, as determined by Monte Carlo calculation. We found that the strain profile follows the recoil profile closer than the deposited energy profile from the same Monte Carlo calculations, in disagreement with other work [5].

Fig. 3 shows the strain versus dose for different ion species, implanted at room temperature. As also reported by other workers [6], the strain increases with increasing dose up to a certain saturation level. Increasing the dose above this level does not appreciably alter

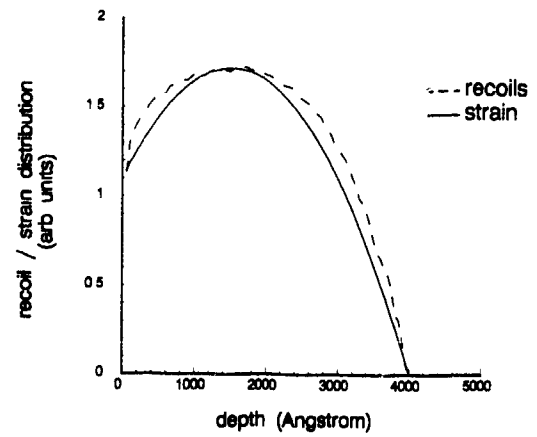

Fig. 2. Strain (———) and recoil (— — —) profile for argon implantation at 300 keV and room temperature.

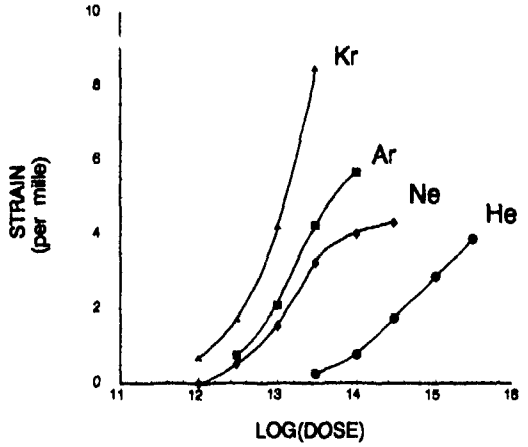

Fig. 3 Strain versus ion dose (cm^{-2}) for He (●), Ne (◆), Ar (■) and Kr (▲) implanted at room temperature. Dose is shown in log units.

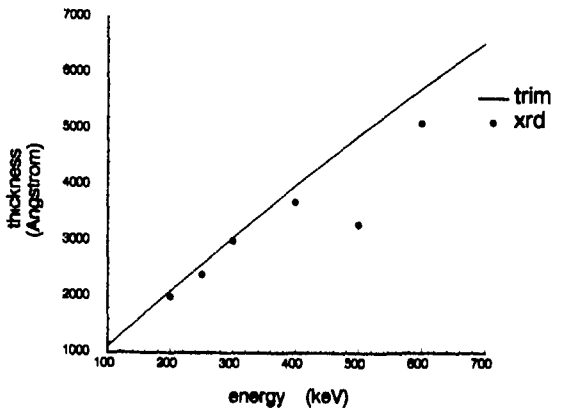

Fig. 5. Thickness versus implantation energy for an argon implant at room temperature, fluence $1 \times 10^{13}\,cm^{-2}$.

the strain, but affects the reflecting power of the strained layer. We suggest that this is either due to plastic deformation or partial amorphization of the implanted material. Also shown in the figure is the dependence of the strain on ion species. The amount of strain increases with ion mass, as would be expected.

Increasing the substrate temperature during implantation has a pronounced effect on the strain, as shown in fig. 4. The strain decreases when the temperature is increased, even for temperatures below 100 °C. For sufficiently high temperatures the strain vanishes almost completely, even for the heaviest ions. This would indicate that the radiation damage may be reduced considerably by increasing the substrate temperature during implantation. As it is generally more difficult to anneal substrates implanted with heavy ions, and the activated fraction of heavy dopant atoms after annealing tends to be much lower than that of light atoms, much may be gained by implanting heavy atoms at elevated temperatures, as will be shown later on.

The thickness of the strained layer increases almost linearly with ion energy, as shown in fig. 5. The values were obtained from the diffractograms by means of eq. (2), for an implantation of $1 \times 10^{13}\,cm^{-2}$ argon ions at room temperature. Also shown in this figure, as reference, is the projected range plus standard deviation according to TRIM calculations. The amount of strain, not shown here, was found to be independent of energy.

The amount of strain does, however, depend on dose rate, as is shown in fig. 6. For an argon implant at 300 keV and room temperature, the strain first increases gradually with increasing dose rate, until a threshold rate is reached, after which the amount of strain increases dramatically. The decrease in strain for the

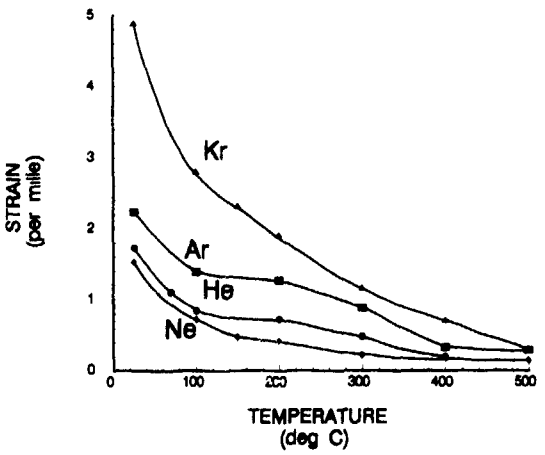

Fig 4. Strain versus temperature for He (●), Ne (◆), Ar (■) and Kr (▲), fluence $1 \times 10^{13}\,cm^{-2}$, except for He ($3 \times 10^{14}\,cm^{-2}$).

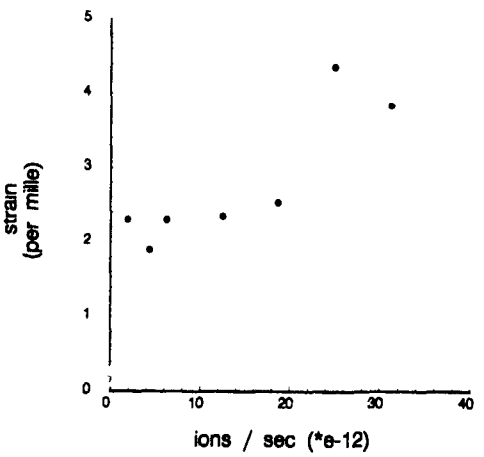

Fig 6 Strain versus ion current for $1 \times 10^{13}\,cm^{-2}$ argon implant at 300 keV and room temperature.

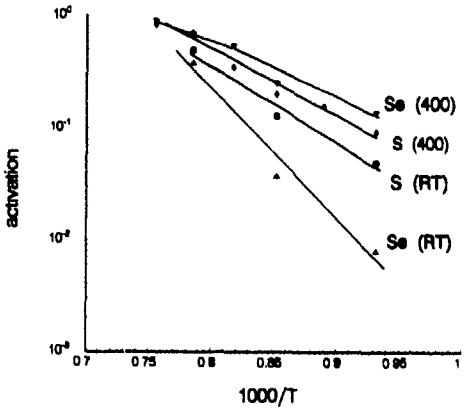

Fig. 7. Active fraction for sulphur and selenium implanted 2×10^{14} cm^{-2} in GaAs at room temperature or 400°C and annealed for 5 s.

highest dose rate measured, as shown in fig. 6, may be due to substrate heating.

In order to see more clearly what these studies imply for the effect of implantation parameters on the annealing behaviour of dopant atoms, we implanted sulphur and selenium in GaAs substrates, both at room temperature and at 400°C. The activation after a 5 s heat treatment is shown in fig. 7. Implanted at room temperature, the two dopant species show a different annealing behaviour, characterized by a different activation energy. Implanted at high temperature, this difference disappears completely. As the figure also shows, the effect of increased implantation temperature is much stronger for heavy ions, consistent with the results shown in fig. 4.

4. Conclusions

X-ray diffraction was used for studying radiation damage in compound semiconductors. It was found that various implantation parameters have a pronounced effect on the amount of strain in the material after implantation. This is reflected in the annealing behaviour of n-type impurites. It also means that care must be taken when trying to model the activation mechanism of dopants in compound semiconductors, such as gallium arsenide.

References

[1] N. Morris and B.J. Sealy, Inst. Phys. Conf. Ser. 91 (1988) 145
[2] N.J. Barrett, J.D. Grange, B.J. Sealy and K.G. Stephens, J. Appl. Phys. 57 (1985) 5470.
[3] K.D. Cummings, S.J Pearton and G.P Vella-Coliero, J. Appl. Phys. 60 (1986) 163.
[4] T Motooka and K. Watanabe, J Appl. Phys 51 (1980) 4125.
[5] B.E. MacNeal and V S. Speriosu, J. Appl Phys 52 (1981) 3935
[6] V S Speriosu, B M. Paine, M-A. Nicolet and H.L. Glass, Appl. Phys Lett. 40 (1982) 604
[7] M. Nemiroff and V S. Speriosu, J Appl. Phys. 58 (1985) 3735.
[8] W.J. Bartels, Philips Tech. Rev. 41 (1983/84) 183
[9] S. Takagi, J. Phys Soc. Jpn 26 (1969) 1239
[10] D. Taupin, Bull. Soc Fr. Mineral. Cristallogr 87 (1964) 469.
[11] J.F. Ziegler, J P Biersack and U Littmark, The Stopping and Range of Ions in Solids (Pergamon, 1985)

Nuclear Instruments and Methods in Physics Research B55 (1991) 789–793
North-Holland

Defect production in ion implanted GaAs, GaP and InP

E. Wendler, W. Wesch and G. Götz

Friedrich-Schiller-Universitat Jena, Institut für Festkörperphysik, Max-Wien-Platz 1, Jena, O-6900, Germany

The defect production in InP, GaP and GaAs after room temperature and 80 K implantation is investigated by means of Rutherford backscattering (RBS) and optical absorption spectroscopy The influence of defect transformation and annealing processes during the implantation is much more essential in GaAs than in the other two $A_{III}B_V$ compounds. In the phosphides the primarily produced defect clusters seem to be almost stable, and the crystalline-to-amorphous transition proceeds via an accumulation process In GaAs first of all point defects and point defect complexes are produced, amorphous regions being generated by a collapse-like process.

1. Introduction

In $A_{III}B_V$ semiconductors the influence of the implantation parameters on the defect structure resulting after ion implantation are much more pronounced than in the elementary semiconductor Si. In GaAs, a remarkable decrease of the resulting defect concentration for implantation temperatures near room temperature as compared to low temperature implantation occurs. In several $A_{III}B_V$ compounds defect annealing after warming up of low temperature implants to room temperature is observed (see, e.g., refs. [1–4]). Furthermore, the current density influences the defect concentration produced [5–7].

Most of the investigations concerning defect production in $A_{III}B_V$ semiconductors were performed at room temperature,and the problem of low temperature implantation is discussed only in a few papers Furthermore, a direct comparison of defect generation in different $A_{III}B_V$ compounds implanted at identical conditions is lacking. Preliminary investigations of the defect production in various compounds indicate remarkable differences pointing at different defect creation mechanisms occurring in these materials [8]. To give a contribution to the understanding of these processes, in this paper results of a comparative study of the defect production in InP, GaP and GaAs at room temperature and at 80 K are presented.

2. Experimental

Single crystals of ⟨100⟩ n-doped GaAs, GaP and InP were implanted with 200 keV Ar^+ ions at implantation temperatures of $T_I = 80$ and 300 K. The different materials were implanted together under identical conditions.

The implanted samples were analyzed by means of Rutherford backscattering spectrometry in combination with the channeling technique (RBS) using 1.4 MeV He^+ ions and a backscattering angle of $\theta = 170°$. From the energy spectra of the backscattered He^+ ions the relative defect concentration N'/N_0 (N_0: atomic density) was calculated in the framework of the two-beam approximation introduced by Bøgh (see, e.g., [9]) as a function of the depth z. The integral concentration of defects N_d contributing to the direct backscattering of the He^+ ions was obtained by integrating $N'(z)/N_0$ over the damaged depth region.

Additionally, the optical transmission of the implanted samples was measured in the frequency range below the fundamental absorption edge ($0.5 \leq \hbar\omega \leq 1.3$ eV in the case of GaAs and InP; $1.4 \leq \hbar\omega \leq 2.2$ eV in the case of GaP). The absorption exponent Kd (K: absorption coefficient and d: thickness of the implanted layer) was calculated on the basis of a two-layer approximation [10], taking into account a refractive index change in the implanted layer between $\Delta n/n_c \approx 1\%$ for weakly damaged layers and $\Delta n/n_c \approx 10\%$ in the case of amorphized material [11,12].

For several GaAs samples the optical absorption measurements were combined with successive chemical etching of the implanted layer to determine the depth distribution of the absorption coefficient [13].

In order to compare the results for the various semiconductors the depth profile of the total vacancy concentration $N_{vac}(z)$ was calculated using the TRIM 87 Monte Carlo code [14]. By normalizing the vacancy concentration N_{vac}, which is connected with the energy deposited in nuclear processes, to the atomic density N_0 one has a useful quantity to compare the defect production in the various $A_{III}B_V$ compounds.

0168-583X/91/$03 50 © 1991 – Elsevier Science Publishers B V (North-Holland)

3. Results and discussion

In fig. 1 the depth distributions of the relative defect concentration N'/N_0 are depicted for implantation at $T_I = 80$ K in InP (fig. 1a), GaP (fig. 1b) and GaAs (fig. 1c). Comparing these profiles with the profiles of the total vacancy concentration calculated by TRIM, a good accordance is to be seen concerning the shape and the depth position of the profiles for all compound materials investigated. Therefore, it can be concluded that primary defect production as well as secondary processes, which occur during implantation and during warming up of the samples to room temperature, can be related to the energy density deposited in nuclear processes.

In the case of InP (see fig. 1a) the concentration of defects increases nearly linearly with the total concentration of vacancies produced. Such a behaviour points at amorphization via heterogeneous defect nucleation [15]. Processes of defect transformation and annealing do not seem to be essential, at least the influence of them does not depend on the vacancy concentration primarily produced during the implantation

Comparing with the results obtained with InP the situation is changed for GaAs and GaP. No linear relation occurs between N'/N_0 and N_{vac}. From figs. 1b and c it can be seen that the concentration of defects per number of vacancies primarily produced increases with increasing ion dose.

The total vacancy concentration necessary for amorphization at $T_I = 80$ K is 5.7×10^{21} cm^{-3} for InP, 5.2×10^{21} cm^{-3} for GaP and 13×10^{21} cm^{-3} for GaAs (see fig. 1), which corresponds to 15%, 11% and 29% of the atomic density of the respective material. The value for GaAs is significantly higher than that for the two phosphides. Taking further into account the nonlinear relation between N'/N_0 and N_{vac} as mentioned above, it can be concluded that in GaAs defect transformation and annealing during the implantation are of greatest importance.

The results obtained for GaP indicate that the defect clusters primarily produced are almost stable, at least at high ion doses and therefore, the relative vacancy concentration necessary for amorphization is lower than for GaAs but comparable to the value estimated for InP.

Fig. 2 shows the dose dependence of the integral defect concentration N_d and of the absorption exponent Kd (at a frequency near the band edge: $\hbar\omega = 1.3$ eV for GaAs, $\hbar\omega = 2.1$ eV for GaP and $\hbar\omega = 1.24$ eV for InP) normalized to their maximum values N_d^{max} and $(Kd)_{max}$, respectively, for $T_I = 80$ K and $T_I = 300$ K. It should be mentioned that N_d is mainly sensitive to heavily damaged and amorphous regions whereas Kd is caused simultaneously by point defects and by amorphous regions. Therefore, the comparison of N_d/N_d^{max} and

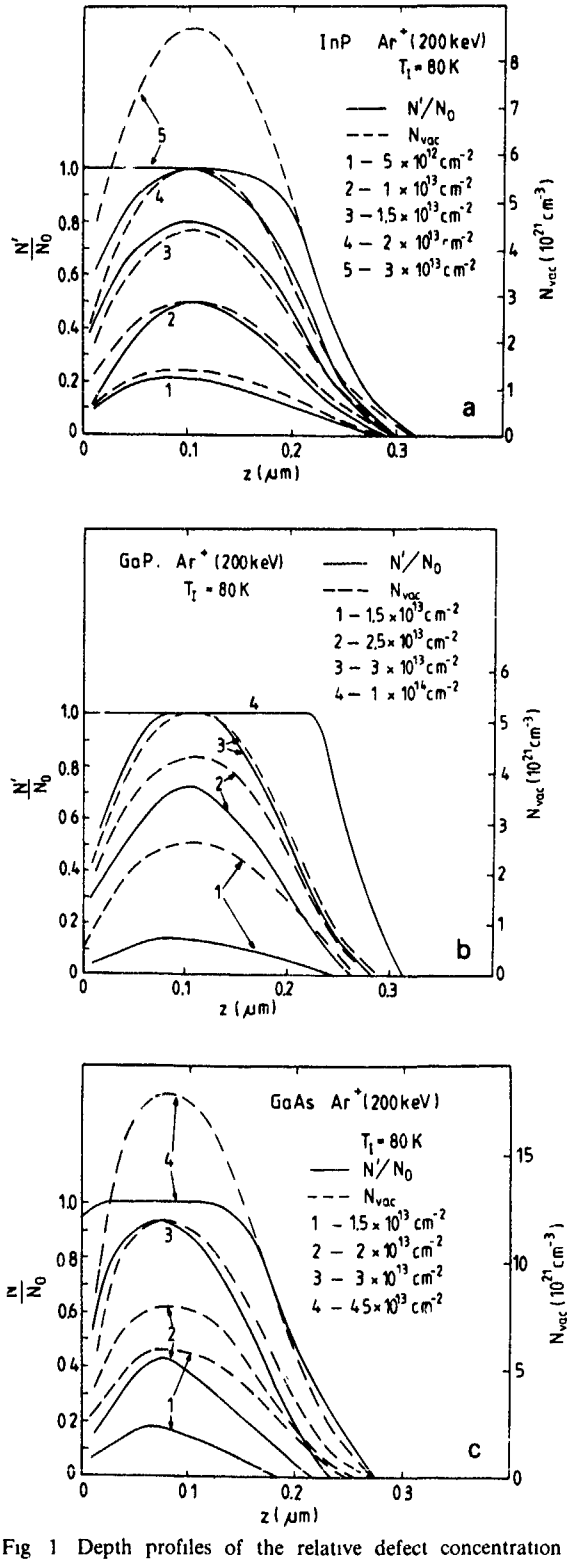

Fig 1 Depth profiles of the relative defect concentration N/N_0 and of the total vacancy concentration N_{vac} calculated by TRIM 87 for 200 keV Ar^+ implantation in (a) InP, (b) GaP and (c) GaAs at $T_I = 80$ K.

$Kd/(Kd)_{max}$ yields information about the kind of defects existing in the implanted layers.

In the case of Ar^+ implantation in InP at both temperatures N_d/N_d^{max} and $Kd/(Kd)_{max}$ are in good accordance with each other in a wide dose range (lower part of fig. 2). Only for small fluences ($N_I \leq 1 \times 10^{13}$ cm^{-2}) $Kd/(Kd)_{max}$ exceeds N_d/N_d^{max}. As mentioned above this should be a consequence of the existence of point defects and point defect complexes.

That means in InP for ion fluences $N_I \geq 1 \times 10^{13}$ cm^{-2} almost only heavily damaged clusters occur. The influence of the implantation temperature is weak; for room temperature implantation the damage production is only shifted to higher ion fluences by a factor of about 1.4. These results confirm the already drawn assumption of heterogeneous defect nucleation in InP in connection with a weak influence of defect annealing during the implantation.

In Ar^+ implanted GaP the differences between N_d/N_d^{max} and $Kd/(Kd)_{max}$ as well as between the results obtained for $T_I = 80$ K and $T_I = 300$ K are more pronounced than in InP (cf. middle and lower part of fig. 2). For $T_I = 300$ K, N_d/N_d^{max} is shifted to higher ion fluences, and the slope of the curve is smaller than for $T_I = 80$ K. The more significant dose shift observed for $T_I = 300$ K in GaP compared to InP indicates a higher influence of defect transformation and annealing on the damage production in GaP than in InP. This assumption is confirmed by the fact that for room temperature implantation in GaP point defects are more essential than in InP, which can be deduced from the considerably higher values of $Kd/(Kd)_{max}$ for GaP.

In the upper part of fig. 2 N_d/N_d^{max} and $Kd/(Kd)_{max}$ are illustrated for implantation in GaAs per-

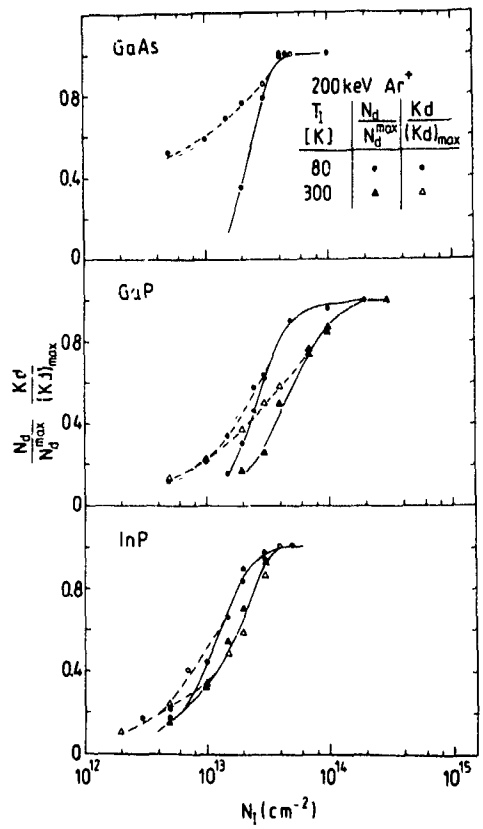

Fig. 2 Normalized integral defect concentration N_d/N_d^{max} and normalized absorption exponent $Kd/(Kd)_{max}$ ($\hbar\omega = 1.24$ eV for InP, $\hbar\omega = 2.1$ eV for GaP and $\hbar\omega = 1.3$ eV for GaAs) versus the ion fluence N_I for 200 keV Ar^+ implantation in InP, GaP and GaAs at $T_I = 80$ K and in InP and GaP at $T_I = 300$ K

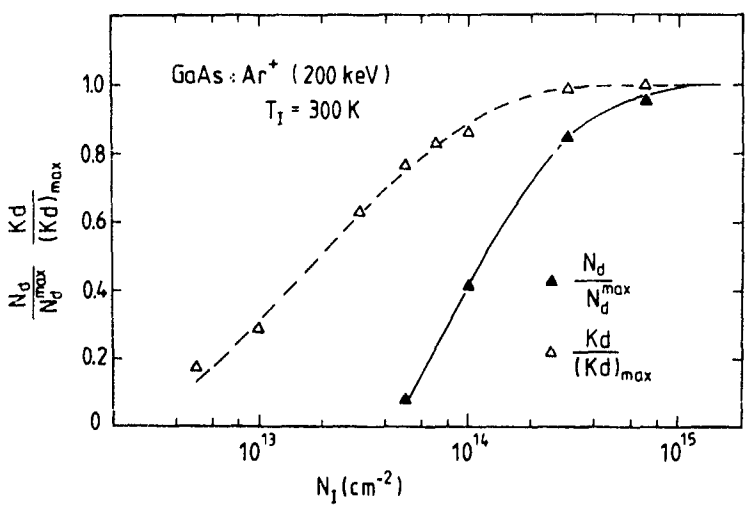

Fig. 3. Normalized integral defect concentration N_d/N_d^{max} and normalized absorption exponent $Kd/(Kd)_{max}$ ($\hbar\omega = 1.3$ eV) versus the ion fluence N_I for 200 keV Ar^+ implantation in GaAs at $T_I = 300$ K

formed at $T_I = 80$ K. Comparing these curves with the corresponding curves for GaP and InP it is obvious that in GaAs the strongest increase of N_d occurs with increasing ion fluence and the highest difference in the shape of N_d/N_d^{max} and $Kd/(Kd)_{max}$ is observed there. Within the overlap damage model of amorphization [16] the sharp increase of N_d with the ion fluence indicates a high number of overlaps to be necessary for the amorphization of GaAs. Further, considering the high concentration of point defects for ion fluences $N_I \leq 1.5 \times 10^{13}$ cm^{-2}, these results give a hint of collapse-like processes of amorphization in GaAs during Ar^+ implantation at $T_I = 80$ K. This also correlates with the nonlinear increase of the defect concentration N'/N_0 (see fig. 1c) as a function of the total vacancy concentration produced during the implantation.

The results for room temperature implantation in GaAs are shown in fig. 3. This implantation was performed at another implanter and therefore, the experimental data are not included in fig. 2. Nevertheless, the most pronounced difference between N_d/N_d^{max} and $Kd/(Kd)_{max}$ for Ar^+ implantation in GaAs at $T_I = 300$ K is clearly illustrated. Heavily damaged regions occur only for fluences $N_I \geq 4 \times 10^{13}$ cm^{-2}, whereas the absorption exponent reaches already about 70% of its maximum value at this ion fluence. This high amount of absorption is caused by point defects as it was determined by the analysis of the spectral dependence of $Kd(\hbar\omega)$ [8]. To investigate the origin of these point defects depth-dependent absorption measurements were performed on GaAs samples implanted with $N_I = 1 \times 10^{13}$ cm^{-2} and $N_I = 3 \times 10^{13}$ cm^{-2} at $T_I = 300$ K. The resulting profiles of the absorption coefficient K are given in fig. 4. A good correspondence with the vacancy concentration N_{vac}, i.e., to the energy density deposited in nuclear processes (dashed lines in fig. 4) is observed. Furthermore, it can be seen that the effectiveness of the creation of point defects decreases with increasing N_{vac}: an absorption coefficient in the maximum of the profile of 1.9×10^4 cm^{-1} is related to a vacancy concentration of $N_{vac} = 4 \times 10^{21}$ cm^{-3} at $N_I = 1 \times 10^{13}$ cm^{-2}, whereas at $N_I = 3 \times 10^{13}$ cm^{-2} a value of $K = 3.1 \times 10^4$ cm^{-1} corresponds to $N_{vac} = 12 \times 10^{21}$ cm^{-3}. This effect reflects the saturation behaviour of point defect production in ion implanted GaAs [11]. Further, point defects are mobile to some extent and diffuse deeper into the crystal than it would be expected from the profile $N_{vac}(z)$. This effect intensifies with increasing ion fluence (cf. the profiles of K for $N_I = 1 \times 10^{13}$ cm^{-2} and $N_I = 3 \times 10^{13}$ cm^{-2} in fig. 4, see ref. [13]).

These results show that in GaAs at both temperatures for low ion fluences the energy deposition in nuclear processes results in the production of point defects and point defect complexes. For implantation at $T_I = 80$ K amorphization seems to be achieved in the form of collapse-like processes. For $T_I = 300$ K,

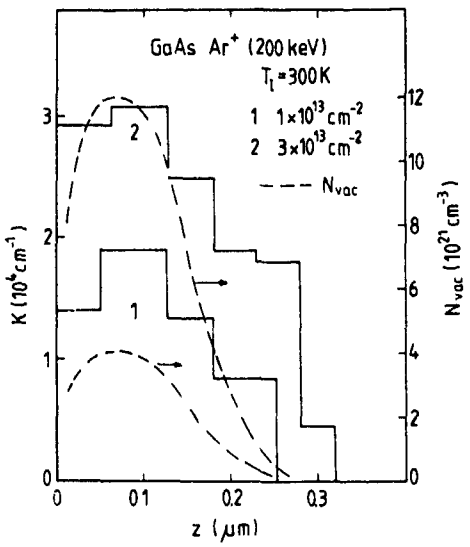

Fig 4 Depth profiles of the absorption coefficient K ($\hbar\omega = 1.3$ eV) and of the total vacancy concentration N_{vac} calculated by TRIM 87 for 200 keV Ar^+ implantation in GaAs at $T_I = 300$ K with ion fluences $N_I = 1 \times 10^{13}$ cm^{-2} and 3×10^{13} cm^{-2}

N_d/N_d^{max} increases, but not so strongly as for $T_I = 80$ K, indicating that heavy clusters created are able to dissociate, possibly due to the high mobility of point defects during implantation at room temperature.

4. Summary

The results of RBS and optical absorption measurements of identically implanted InP, GaP and GaAs samples show that the three materials behave differently with respect to defect creation.

In GaAs the influence of defect transformation and annealing processes during the implantation is much more essential than in the two phosphides investigated. As a consequence of these processes a high concentration of point defects and point defect complexes occurs before amorphous clusters are produced, thus pointing at amorphization via collapse-like processes, especially for $T_I = 80$ K.

On the contrary, in InP defect transformation and annealing during the implantation seem not to be essential and the defect clusters primarily produced are almost stable at both temperatures investigated. These results indicate a crystalline-to-amorphous transition via an accumulation process (heterogeneous defect nucleation).

In the case of GaP the difference between defect production at $T_I = 80$ K and $T_I = 300$ K is more pronounced than in InP. During room temperature implantation defect transformation and annealing are of importance, possibly resulting in a reduction of the size of

the clusters primarily produced, and amorphization seems to be achieved by accumulation of the remaining defect clusters. For $T_1 = 80$ K the increase of the integral defect concentration as a function of the ion fluence is stronger than it would be expected for heterogeneous defect nucleation. A possible explanation of this behaviour may be given by a model proposed by Carter and Webb [17]. In this paper amorphization was assumed to occur by the accumulation of heavily damaged clusters primarily produced, *and* by the overlap of weakly damaged regions existing in the outer part of the damaged regions.

Up to now, no conclusive explanation can be given concerning the substantial differences in the defect production during implantation into arsenides on the one hand, and into phosphides on the other hand [8]. Similar results were found by investigating defects in flash-evaporated amorphous III–V compounds [18,19]. In these papers the different results obtained for InP and GaP on the one hand and for GaAs on the other hand were related to the different binding properties of P and As atoms. It seems to be possible that this is also the reason responsible for the differences observed in the case of ion implantation induced defects

References

[1] J S Williams and M W Austin, Nucl Instr and Meth 168 (1980) 307

[2] N A Ahmed, G Carter, C E Christodoulides, M.J Nobes and A Titov, Nucl Instr and Meth 168 (1980) 283

[3] M.G. Grimaldi, B.M. Paine, M A. Nicolet and D.K. Sadana, J. Appl. Phys. 52 (1981) 4038

[4] N.P Tognetti, G. Carter, D V. Stevanovich and D.A Thompson, Radiat. Eff 66 (1982) 15

[5] J.E. Westmoreland, O.J. Marsh and R.G Hunsperger, Radiat. Eff 5 (1970) 245.

[6] S T. Johnson, J.S. Williams, R.G. Elliman, A P Pogany, E. Nygren and G.L. Olsen, Mater Res Soc Proc. 82 (1987) 127.

[7] E. Wendler, W Wesch and G Götz, Nucl Instr. and Meth. B52 (1990) 57.

[8] W Wesch, E Wendler, G. Götz and N P Kekelidse, J. Appl. Phys. 65 (1989) 519

[9] G. Götz and K. Gärtner (eds.), High Energy Ion Beam Analysis of Solids (Akademieverlag, Berlin, 1988).

[10] K. Hehl and W Wesch, Phys Status Solidi A51 (1980) 181

[11] E. Wendler, W Wesch and G Götz, Phys Status Solidi A93 (1986) 207

[12] W Wesch, E Wendler and G Gotz, Nucl Instr and Meth. B22 (198-) 532.

[13] E Wilk, W Wesch and K. Hehl, Phys Status Solidi A76 (1983) K197

[14] J P Biersack and L G Haggmark, Nucl Instr and Meth 174 (1980) 257.

[15] L T Chadderton, Radiat Eff 8 (1981) 77

[16] J F Gibbons, Proc IEEE 60 (1972) 1062

[17] G Carter and R Webb, Radiat Eff 43 (1979) 19

[18] M-L Theye and A Gheorghiu, Solar Energy Mater 8 (1982) 331

[19] A Gheoghiu, M Ouchene, T Rappeneau and M-L Theye, J Non-Cryst Solids 59 & 60 (1983) 621

Nuclear Instruments and Methods in Physics Research B55 (1991) 794–797
North-Holland

Characterization of Si-implanted gallium antimonide

Y.K. Su [a], K.J. Gan [a], F.S. Juang [a] and J.S. Hwang [b]

[a] *Department of Electrical Engineering and* [b] *Department of Physics, National Cheng Kung University, Tainan, Taiwan*

Ion implantation is of technological importance in the preparation of doped semiconductors. Raman spectroscopy is a very sensitive and nondestructive tool useful for obtaining information about the state of a material and to distinguish the original crystalline structure and the damaged lattice. In this paper, the variations of the Raman spectra for Si-implanted (100)GaSb with various doses and energies were investigated. In order to heal the damage layer, conventional furnace annealing (FA) as well as rapid thermal annealing (RTA) were used. From these spectra we found that the quality of the recovered layer will be improved with higher annealing temperatures and longer annealing times. Also, rapid thermal annealing showed better results in comparison with conventional furnace annealing. The best recovery of the damage layer for Si-implanted (1×10^{15} cm^{-2}, 150 keV) GaSb was at 600°C for 30 s by rapid thermal annealing.

1. Introduction

In recent years, ion implantation technology has become very important in the preparation of doped semiconductors. It has numerous advantages over diffusion, the most important of these being reproducibility, good dopant profile control, uniformity and the high speed of the doping process. During ion implantation, the lattice damage produced by the energetic ions must be removed by a subsequent annealing process to achieve electrical activation of the dopants.

Raman spectroscopy is probably the most useful method available to study lattice vibrations and their interactions with other excitations [1]. Many experiments have shown the characterization of ion-implanted III–V semiconductors based on Raman spectra [2,3]. The Raman spectra measurements were made at room temperature in a quasi-backscattering geometry with the 5145 Å line of an Ar^+ laser. The penetration depth of the light is about 1000 Å, which is approximately the same as the density distribution of the implanted ions. Therefore, Raman scattering is a convenient tool to evaluate the structural properties after ion implantation.

GaSb is a zincblende-type semiconductor which at the $q=0$ (center of the first Brillouin zone) optical phonon mode splits into longitudinal (LO) and transverse (TO) modes [4]. In this paper, we report a series of Raman spectra from GaSb samples which have been implanted with Si ions. We will consider the broadening of Raman spectra with increasing dose and energy, and investigate the change of Raman intensity from subsequent annealing-induced "healing" of the damage layer by conventional furnace annealing (FA) and rapid thermal annealing (RTA).

2. Experimental

The materials studied were undoped (100)GaSb unimplanted and implanted with Si at a dose of 1×10^{13} to 1×10^{15} cm^{-2} at room temperature with the ion beam at 7° off the normal, and energy ranging from 70 keV to 150 keV.

For the annealing studied, some of the Si-implanted samples (1×10^{15} cm^{-2}, 150 keV) were annealed at 500°C from 20 min to 40 min with flowing nitrogen and no encapsulate in a conventional furnace, while the other samples were annealed in an RTA furnace with the surface protected by the proximity method [5] at temperatures of 400°C, 500°C and 600°C, respectively.

The Raman scattering experiments were performed in backscattering geometry from the (100) surface of the samples using an Ar^+ ion laser. For III–V compound semiconductors having the zincblende crystal structure, in scattering by the (111) orientation both TO and LO modes are allowed in the Raman spectra, while in scattering by the (100) orientation only the LO mode is permitted and the TO mode is forbidden by the selection rules [6].

The laser output power was fixed at 200 mW so as to avoid excess heating of the samples and was focused

0168-583X/91/$03.50 © 1991 - Elsevier Science Publishers B.V. (North-Holland)

onto the samples using a cylindrical lens. The scattered light was analyzed using a standard double-grating spectrometer in photo-counting mode, with a spectral resolution of about 2 cm^{-1}.

3. Results and discussion

Fig. 1 displays the Raman spectrum of the unimplanted GaSb wafer. In our experiments, we found a strong peak at 226 cm^{-1} and a weak peak at 220 cm^{-1} which belong to the LO and TO mode, respectively. As we have mentioned above, only the LO mode is allowed for (100)-oriented material and the TO mode is forbidden. However, a small peak due to the TO mode is also observed. This is probably a result of slight substrate misorientation or imperfection, but it may be also due to a small experimental deviation from backscattering However, this phenomenon is also observed for other semiconductors in the (100) orientation [7,8].

Fig 2 shows the Raman spectra results of GaSb for 125 keV Si implantation with a dose ranging from 1×10^{13} to 1×10^{15} cm^{-2}. As we know, when the implanted dose increases the local damaged regions begin to overlap and result in the formation of a highly damaged region From the spectra, we find that the intensity of the LO modes approaches zero with increasing implantation dose The TO modes broaden with increasing dose

In fig. 3 we display a series of Raman spectra of GaSb implanted with Si (1×10^{15} cm^{-2}) for energies of 70, 100, 125 and 150 keV, respectively. From these spectra, we also observed that the TO and LO modes broaden and the intensity decreases gradually with increasing energy Therefore, there are two reasons for the broadening and weakening of the TO and LO lines. Firstly, the symmetry of the unimplanted samples will be destroyed by point defects and dislocations after implantation. Secondly, it may be due to inhomogeneity of the strain [6].

From these results, we can conclude that point defects and dislocations increase with increasing dose and energy. An amorphous layer [9] will occur when the dose is increased to 1×10^{15} cm^{-2} or the energy is over 150 keV. If amorphous layers are formed, both the TO

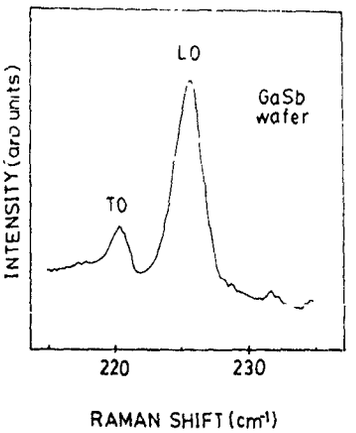

Fig. 1. Raman spectra of an unimplanted GaSb wafer

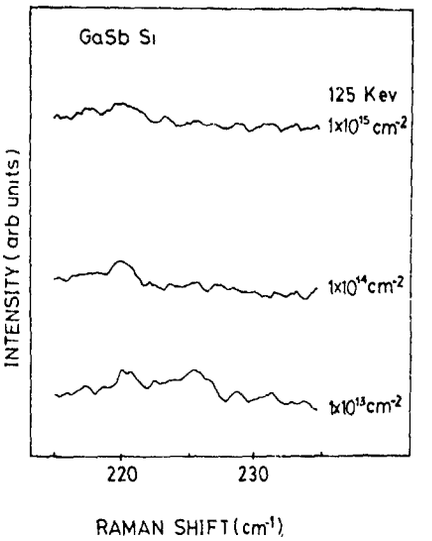

Fig 2. Raman spectra of Si-implanted GaSb as a function of dose

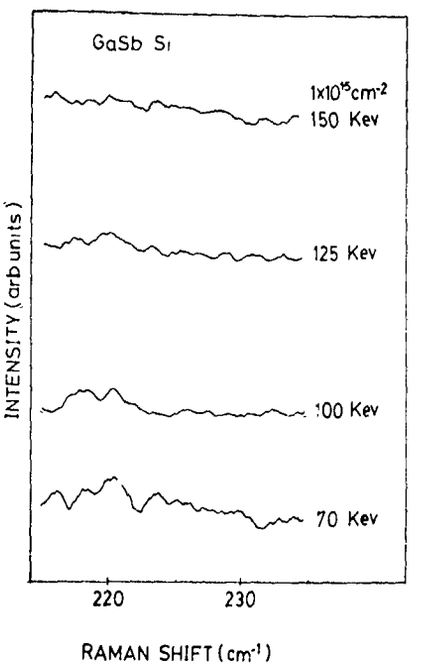

Fig 3. Raman spectra of Si-implanted GaSb as a function of energy.

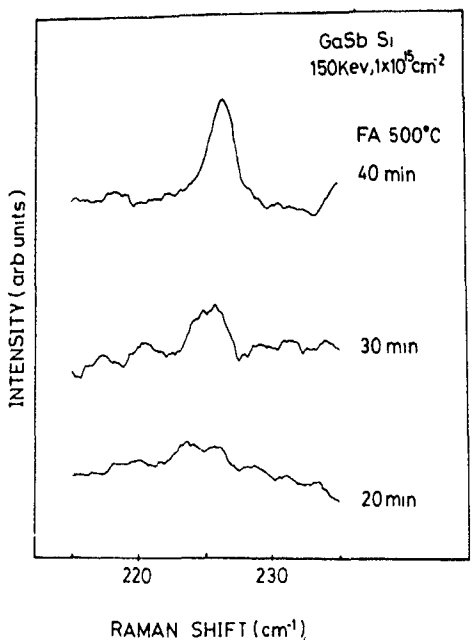

Fig 4 Series of Raman spectra for furnace annealing at 500 °C for different times

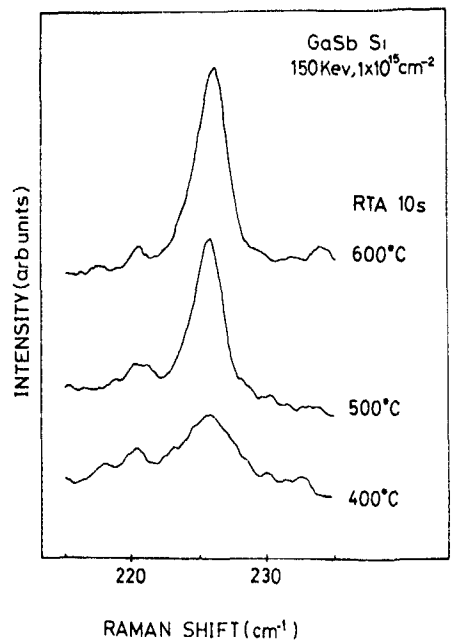

Fig 6 Series of Raman spectra for rapid thermal annealing at different temperature for 10 s

and LO modes will be decreased in intensity, asymmetrically broadened, and may be shifted in frequency.

The Raman spectra depend on the annealing time for temperatures of 500 °C and 600 °C, as shown in fig. 4 and fig. 5, when the dose is 1×10^{15} cm^{-2} at 150 keV. These annealing processes are carried out by conventional furnace annealing (FA). We can observe that the intensity of the LO phonon increases with the annealing time from 20 min to 40 min. However, it seems that the intensity of the LO mode is not strong enough in comparison with that of the unimplanted wafer.

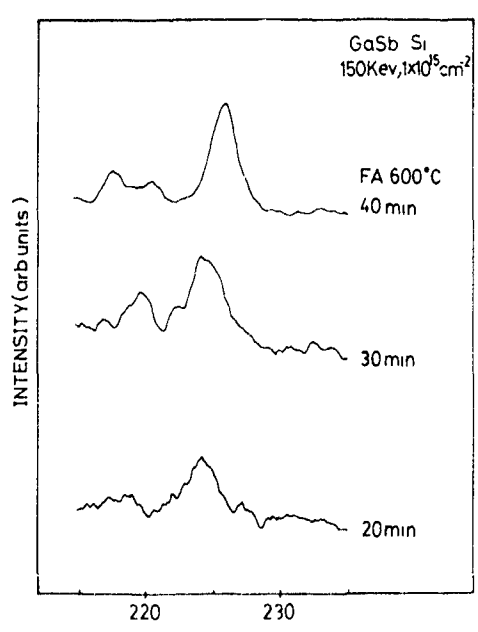

Fig 5. Series of Raman spectra for furnace annealing at 600 °C for different times.

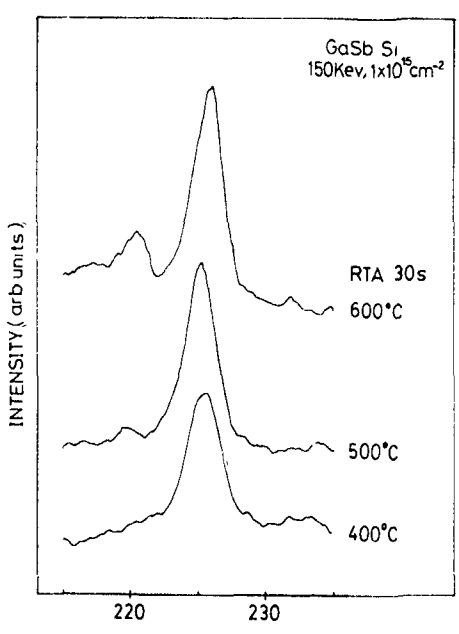

Fig. 7 Series of Raman spectra for rapid thermal annealing at different temperature for 30 s.

Figs. 6 and 7 show the Raman spectra of GaSb implanted with Si ions under the same implantation conditions as in fig. 4, and followed by rapid thermal annealing (RTA) at temperatures of 400 °C, 500 °C and 600 °C for 10 s and 30 s, respectively. Upon rapid thermal annealing, we observed that the intensity of the LO modes are increased with increasing annealing temperature and/or annealing time. The spectra are better than those that were obtained by furnace annealing. Therefore, the rapid thermal annealing process could recover the highly damaged layer and improve the crystalline quality more effectively. From fig. 7, we observe that a better recovery of the damage layer after Si implantation (1×10^{15} cm^{-2}, 150 keV) is obtained by rapid thermal annealing at 600 °C for 30 s.

4. Conclusion

We have investigated the Raman spectra of (100)GaSb bombarded by Si ions with different doses and energies, which was followed by recovering the amorphous samples with conventional furnace annealing or rapid thermal annealing technology. These phenomena showed that the Raman scattering measurements are a convenient and sensitive tool to probe the damage situation after ion implantation and the annealing process. We have shown that the scattering phonon modes are broadened and weakened with increasing dose and energy. This indicates the existence of a highly disordered or amorphous regime in these samples.

The damage layer must be healed after ion implantation by annealing. Here, we used a furnace annealing process as well as rapid thermal annealing, and found the intensities of the Raman spectra increased gradually with higher annealing temperature and longer annealing time. A better recovery of the damage layer was obtained by rapid thermal annealing at a temperature of 600 °C for 30 s, when comparing the scattering phonon intensities with those of the unimplanted wafer.

Acknowledgements

The authors would like to thank Mr. Y.C Chou for his assistance with ion implantation during this experiment. This project was supported by the National Science Council under contract NSC79-0417-E006-04.

References

[1] V.J. Zemski, E.L. Ivshenko, D.N. Mirlin and J J Reshina, Solid State Commun. 16 (1975) 221.
[2] P.S. Peercy, Appl. Phys. Lett. 18 (1971) 574.
[3] A.H. Kachare, J.M. Cherlow, T T. Yang, W.G. Spitzer and F.K. Euler, J. Appl. Phys. 47 (1976) 161.
[4] F.H. Pollak, reprinted from Test and Measurement World (May 1985)
[5] K.D Cummings, S J Pearton and G.P Vella-Coleiro, J Appl. Phys. 60 (1986) 163.
[6] C.S. Rama Rao, S. Sundaram, R.L. Schmidt and J. Comas, J. Appl. Phys. 54 (1983) 1808
[7] K.K. Tiong, P.M. Amirtharaj, F.H Pollak and D E Aspnes, Appl Phys. Lett. 44 (1984) 122
[8] M. Holtz, R. Zallen and R.A Sodler, J Appl. Phys 59 (1986) 1946.
[9] T Nakamura and T Katoda, J Appl Phys 53 (1982) 5870

Nuclear Instruments and Methods in Physics Research B55 (1991) 798–801
North-Holland

Rapid thermal annealing of Mg^+ and P^+ dually implanted InP

Honglie Shen, Genqing Yang, Zuyao Zhou and Shichang Zou

Ion Beam Laboratory, Shanghai Institute of Metallurgy, Academia Sinica, Shanghai 200050, People's Republic of China

125 keV Mg^+ ions and 160 keV P^+ ions were implanted at RT, 100 °C and 200 °C with doses ranging from 1×10^{14} to 1×10^{15} cm^{-2} to study the effect of the dual implantations on the electrical properties of Fe doped InP. The samples were characterized by electrochemical $C-V$ measurement and RBS-channelling techniques. It has been found that $Mg^+ + P^+$ dual implantations into InP can result in an enhanced activation of implanted dopants. The highest peak hole concentration and dopant activation obtained in this work were 1.1×10^{19} cm^{-3} and 68% in the case of $Mg^+ + P^+$ dual implantations at a dose of 1×10^{15} cm^{-2} while that for Mg^+ single implantation at the same dose were 5.4×10^{18} cm^{-3} and 40%. A thin n-type layer was found in the carrier concentration profile of Mg^+ singly implanted samples whereas there was not such a layer in that of $Mg^+ + P^+$ dually implanted ones. RBS spectra showed that the implantation at 100 °C leads to damage similar to that in the sample implanted at 200 °C. A deep penetration of Mg into InP during annealing, which is supposed to be related to the (Mg,Fe) complex, can be suppressed to some extent by P^+ co-implantation

1. Introduction

InP is a promising material for use in optoelectronic and microwave devices. When doping in selected areas is necessary in the fabrication of such devices, ion implantation is the most commonly used technique. Generally speaking, it is easier to obtain highly doped n-type layers than p-type layers in InP by ion implantation [1–3], which is contrary to results obtained in work on GaAs [4–6]. For p-type doping in InP, Be^+ implant is commonly used. Wang [7] has reported that Be in-diffusion can be eliminated through rapid thermal annealing (RTA) of a P^+/Be^+ co-implantation, but the highest peak hole concentration reported in his paper was 2×10^{18} cm^{-3}. Zn^+ and Cd^+ are also p-type species for InP, but from the point of view of atomic mass, Mg is more appropriate for implantation than Zr or Cd. The lower mass of Mg should result in less damage and afford greater variation in the location of projected range than with heavier ions. From the Phillips values for covalent tetrahedral radii and electronegativity [8], Mg should be a better substitutional impurity for In than Be. An InP pn-junction waveguide made by Mg^+ implantation has been reported [9].

As for GaAs, Choudhury [10] showed an improved activation of Mg^+ and As^+ dual implants by capless rapid thermal annealing. For high dose Mg^+ implant (1×10^{15} cm^{-2}, 100 keV), the activation increased from 18% for Mg^+ single implant to 61% for $Mg^+ + As^+$ dual implants. In this paper, we report the electrical properties of Mg^+ and P^+ dually implanted into InP. It is found that the peak hole concentration and activation in Mg^+ implanted InP can be much enhanced by $Mg^+ + P^+$ dual implantations. Also the n-type buried layer which appeared in Mg^+ singly implanted samples can be eliminated by P^+ co-implantation. RBS-channelling measurements showed that the implantation at 100 °C leads to less damage than for room temperature implant.

2. Experimental

All implantations were performed into semi-insulating ⟨100⟩ oriented Fe doped InP wafers cut from crystals grown by the Czochralski method with liquid encapsulation. The wafers were degreased using organic solvents and etched by a solution of $H_2O_2:H_2O:H_3PO_4 = 9:1:1$ to remove surface damage caused by polishing. Mg^+ ions were implanted at 125 keV with doses ranging from 1×10^{14} to 1×10^{15} cm^{-2} at room temperature (RT). The co-implant wafer was preimplanted with phosphorus at 200 °C with an energy of 160 keV at the same dose of magnesium The purpose of an implantation at elevated temperature is to reduce the lattice damage introduced by a heavier ion, i.e., phosphorus. For some samples, Mg^+ and P^+ were implanted at 200 or 100 °C, respectively. The energy of 160 keV was chosen for the distribution of implanted P atoms to overlap that of Mg atoms. This is according to the results for Mg^+ and As^+ dual implants into GaAs [10] and for Si^+ and P^+ dual implants into InP [11]. The samples were tilted by 7° from the ⟨100⟩ axis during implantation to avoid possible channelling. After implantation, Si_3N_4 film of about 100 nm in thickness was deposited on all wafers by plasma enhanced chemical

0168-583X/91/$03.50 © 1991 – Elsevier Science Publishers B.V. (North-Holland)

vapour deposition (PECVD). RTA was performed in a KST-2 tungsten halogen lamp heating system in flowing N_2 at temperatures ranging from 800 to 900 °C with samples face down on a silicon wafer. The annealing time was from 5 to 15 s. The annealing temperature and time profile were monitored by a thermocouple cemented onto the Si wafer. The annealing cycle could be chosen using the computer-controlled system. The electrical properties of the implanted layer were characterized by electrochemical C–V measurements. The damage and its annealing were evaluated using the RBS-channelling technique with a 2 MeV He^+ probe beam.

3. Results and discussion

Fig. 1 shows the carrier concentration profiles in Mg^+ singly implanted samples. After annealing at 825 °C for 5 s, a buried n-type layer appeared in the sample implanted with a dose of 1×10^{15} cm^{-2} Mg^+ at RT. Reducing the Mg^+ dose to 5×10^{14} cm^{-2} and annealing at the same condition, we found that the buried n-type layer became narrower. For still lower dose implant (1×10^{14} cm^{-2}), the buried n-type layer disappeared but the activation was only 8%. These results are similar to the behaviour occurring in 1 MeV Mg^+ implantation into InP [12], where a resistive layer broadened with increasing implantation dose. For $Mg^+ + P^+$ dually implanted samples, there was no n-type layers existing after annealing at 825 °C for 5 s (fig. 2). In the sample implanted with doses of 1×10^{15} cm^{-2}, the peak hole concentration was 5.5×10^{18} cm^{-3}. The

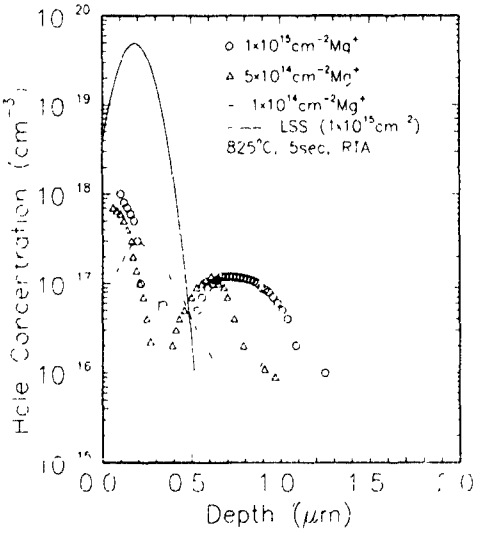

Fig. 1. Hole concentration depth profiles in samples implanted with 125 keV Mg^+ (RT) at the indicated doses and annealed at 825 °C for 5 s.

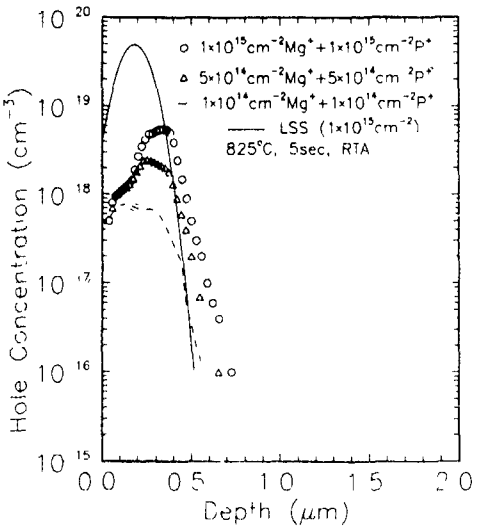

Fig. 2 Hole concentration depth profiles in samples implanted with 125 keV Mg^+ (RT) and 160 keV P^+ (200 °C) at the indicated doses and annealed at 825 °C for 5 s.

low hole concentration at the region near the surface in samples implanted with doses of 1×10^{15} or 5×10^{14} cm^{-2} may be due to either the residual disordered layer, remaining in the high dose implanted samples after annealing, providing donors to compensate the holes [13], or large out-diffusion of implanted Mg during annealing in the case of high Mg concentration [14]. For the sample implanted with doses of 1×10^{14} cm^{-2}, the activation was 24%, which is much larger than that of Mg^+ implanted alone. From fig. 2, on the other hand, one can also find that the in-diffusion of Mg in dually implanted samples is less than that in singly implanted ones. From the results discussed above, the buried n-type seems related to the radiation damage. Therefore the high dose implanted samples were annealed at higher temperature for a longer time. The result of 1×10^{15} cm^{-2} Mg^+ implanted samples after annealing at 875 °C for 15 s is shown in fig. 3. It indicates that there is no longer a buried n-type layer in the singly implanted sample. The activation and peak hole concentration in Mg^+ singly implanted sample are 40% and 5.4×10^{18} cm^{-3}, respectively, while, in the $Mg^+ + P^+$ dually implanted sample, the values are 68% and 1.1×10^{19} cm^{-3}. To the best of our knowledge, such a high hole concentration in InP by ion implantation has never been reported. This can be attributed to the fact that more Mg atoms have been forced to occupy the In sublattice sites owing to the decrease in the concentration ratio of P and In vacancies ($[V_P]/[V_{In}]$) resulting from the P^+ co-implant. It is also worth noticing that, when annealing at high temperatures for a long time, the Mg in-diffuses considerably. The peak hole concentration reaches about 700 nm in

depth. Another feature in fig. 3 is that there are deep hole distribution tails at about $10^{17}\,cm^{-3}$ in both Mg^+ singly, and $Mg^+ + P^+$ dually implanted samples.

To reduce radiation damage, implantations of Mg^+ at elevated temperature were also investigated. We found that, after annealing at 825 °C for 5 s the hole concentration distribution near the peak position is quite flat for a sample implanted with $1 \times 10^{15}\,cm^{-2}$ Mg^+ at 200 °C, which suggests that both out-diffusion and in-diffusion of Mg have taken place. There is also a deep hole distribution tail about $10^{17}\,cm^{-3}$ in the distribution. For an implantation dose of $5 \times 10^{14}\,cm^{-2}$, the hole concentration in the sample implanted at 100 °C is much higher than that in the sample implanted at 200 °C. The former is even as high as that for implantation with $1 \times 10^{15}\,cm^{-2}$ Mg^+ at 200 °C, only without the tail. These results indicate that hot implantation can also avoid the formation of an n-type layer. But higher temperature implantation will result in an apparent redistribution of dopant and lower activation though the reason for the latter needs to be studied further. The RBS-channelling spectra for samples implanted with $1 \times 10^{15}\,cm^{-2}$ Mg^+ at RT, 100 and 200 °C are shown in fig. 4. Though an amorphous layer was formed in RT implanted samples, the radiation damage in the samples implanted at elevated temperature (even at 100 °C) was quite small.

Increasing the annealing temperature and time produced a deeply penetrating profile in samples implanted at 100 °C. For samples implanted with doses of $5 \times 10^{14}\,cm^{-2}$ Mg^+ at 100 °C and annealed at 875 °C for 10 s, the activation for Mg^+ single implant was 55% and that for $Mg^+ + P^+$ dual implants was 67%. Mg penetrated

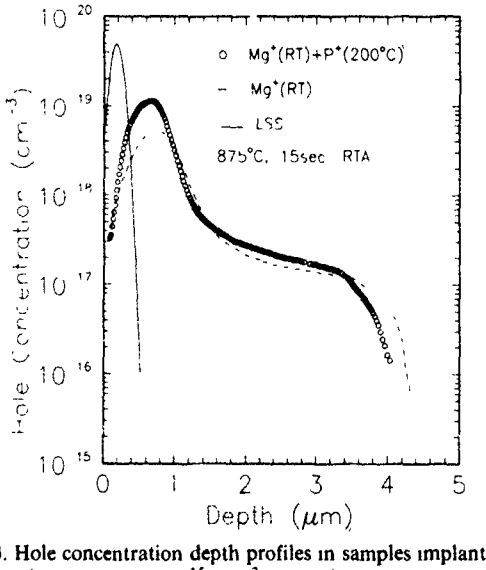

Fig. 3. Hole concentration depth profiles in samples implanted with Mg^+ (125 keV, $1 \times 10^{15}\,cm^{-2}$) and P^+ (160 keV, $1 \times 10^{15}\,cm^{-2}$) and annealed at 875 °C for 15 s.

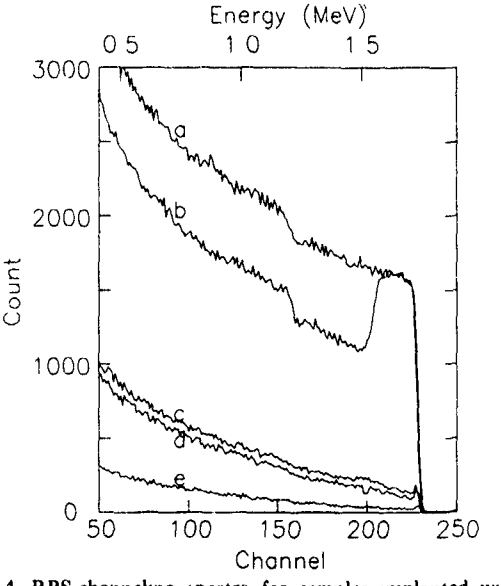

Fig. 4. RBS-channeling spectra for samples implanted with Mg^+ (125 keV, $1 \times 10^{15}\,cm^{-2}$) at indicated target temperatures (a) Random, (b) RT; (c) 100 °C, (d) 200 °C; (e) virgin.

into the InP substrate as deep as 2 μm but a P^+ co-implant can reduce the tail to some extent. These results showed that a high annealing temperature is one of the causes for the deep in-diffusion of the Mg. Moreover, in a sample annealed in a furnace (750 °C, 10 min), the hole tail, at $1 \times 10^{17}\,cm^{-3}$, was found to be deeper than 3.5 μm, so that a long annealing time is another cause for the deep in-diffusion. The fast diffusion of Mg in InP was reported by Koing et al. [15] and a diffusion coefficient of $1 \times 10^{-10}\,cm^2/s$ was calculated. Surprisingly, the value of the hole distribution tails is the same as the one in our experiment, i.e., about $1 \times 10^{17}\,cm^{-3}$. In Mg-doped InP grown by MOCVD [16], Mg penetrated into Fe doped InP substrates with a concentration level of $10^{17}\,cm^{-3}$ resulting in the same level of hole concentration, while in S doped InP substrates, there was no such Mg distribution. The similarity mentioned above suggests that the mechanism is the same for Mg diffusion in both types of substrates. Considering the Fe doping level of the substrates in the range of 5×10^{16}–$1 \times 10^{17}\,cm^{-3}$ (data provided by the manufacturer), we can deduce that there is an association of the diffusing Mg with the Fe species, with the formation of immobile (Fe,Mg) pairs or complexes.

4. Conclusions

After RTA, an extremely high hole concentration of $1.1 \times 10^{19}\,cm^{-3}$ in InP has been obtained by $Mg^+ + P^+$ dual implantations. A buried n-type layer in Mg^+ singly implanted InP was observed and could be eliminated by

the P^+ co-implant. The deep diffusion of Mg into InP, which increases with increasing dose, implantation temperature, annealing temperature, and time, was explained to be related to the Fe impurities in the substrate. The radiation damage for implantation at 100 °C proved to be very small by RBS-channelling measurements.

Acknowledgement

The authors thank Yonggang Zhang for the measurement of the electrochemical $C-V$.

References

[1] J.P. Donnelly and C.E Hurwitz, Appl. Phys. Lett. 31 (1977) 418.
[2] C W Farley and B G Streetman, J Electrochem. Soc. 134 (1987) 498.
[3] M V. Rao, M P. Keating and P E Thompson, J. Electron Mater. 17 (1988) 315
[4] J.M. Woodcock, Appl. Phys. Lett. 28 (1976) 226.
[5] S. Gill and B.J. Sealy, J. Electrochem Soc. 133 (1986) 2590
[6] C.W. Farley, T.S. Kim and B.G. Streetman, J Electron. Mater 16 (1987) 79.
[7] K.W. Wang, Appl Phys. Lett. 51 (1987) 2127
[8] J D. Oberstar, B.G. Street, J.E. Baker and P. Williams, J Electrochem Soc 129 (1982) 1320.
[9] K. Ogawa, S. Uekusa, Y. Sugiyama and M. Tacano, J Appl. Phys. 25 (1986) 1902.
[10] A.N.M.M. Choudhury and C.A Armiento, Appl Phys. Lett. 50 (1987) 448.
[11] Shen Honglie, Yang Genqing, Zhou Zuyao and Zou Shichang, Semicond. Sci. Technol. 4 (1989) 951.
[12] D.E. Davies, J. Cryst. Growth 54 (1981) 150
[13] T Inada, S Taka and Y Yamamoto, J. Appl. Phys 52 (1981) 6623.
[14] W.H. van Berlo and G. Landgren, J Appl Phys 66 (1989) 3117.
[15] U. Koing, J. Hilgarth, H.H. Tiemann, J Electronic Mater. 14 (1985) 311
[16] C. Blaauw, R A Bruce, C J. Miner, A.J Howand, B Emmerstorfer and A.J. Springthorpe, J. Electron Mater. 18 (1989) 567

Nuclear Instruments and Methods in Physics Research B55 (1991) 802–810
North-Holland

Section VII. Future trends and applications

The technology of finely focused ion beams *

L.R. Harriott
AT&T Bell Laboratories, Murray Hill, NJ 07974, USA

Focused ion beam machine technology is generally divided into two distinct categories according to the intended applications These are: (1) low-energy (10–30 keV) heavy-ion beam (usually Ga) systems used in sputtering and ion-induced material deposition and (2) high-energy (50–200 keV) systems with generally more complex ion optics for implantation and lithography applications State-of-the-art focused ion beam systems are capable of minimum beam diameters (FWHM) on the order of 500 Å with a chromatic aberration-limited current density of about 1 A/cm^2. While continuing progress in ion optics and the computer automation of both these types of focused ion beam systems has enabled them to emerge from the laboratory and into limited production uses, some new approaches are also on the horizon. These new approaches include the use of achromatic quadrupole lenses to improve the maximum achievable beam current density perhaps by a factor of 10, and the use of immersion lenses for producing finely focused beams at very low (100 eV or less) energy to minimize substrate damage during processing. This paper will review some of the recent developments in focused ion beam machine technology in the context of existing and emerging processing techniques

1. Introduction

Finely focused ion beam (FIB) systems and their applications have been reviewed previously [1–5] and it is not the intention of this paper to provide a comprehensive review of the subject. The purpose of this paper is to give a brief introduction followed by a snapshot review of some recent focused-ion-beam applications and then discuss ongoing developments in FIB machine technology driven by current and future needs.

Current focused ion beam technology is based on the development of liquid-metal ion sources (LMIS). LMISs offer high brightness and small virtual source size, making them suitable for probe-forming systems. The limiting factor in the performance of finely focused ion beam systems is generally chromatic aberration due to the moderate energy spread (10–40 eV) inherent in LMIS. The performance of a probe-forming optical system is most generally characterized by the current density in the focused spot. In practical applications the processing throughput is a direct function of the total ion current on the target. Since the beam size is usually dictated by the application requirements, the current density achievable offers a good measure of the overall performance of the ion optical column.

For typical electrostatic ion focusing lenses chromatic aberration is dominant and is the limiting factor in the performance of ion microbeam systems [1]. The current density (J) in the focused spot is given by

$$J = \frac{\mathrm{d}I/\mathrm{d}\Omega (E/\Delta E)^2}{C^2}, \qquad (1)$$

where $\mathrm{d}I/\mathrm{d}\Omega$ is the angular current density of the ion source, C is the chromatic aberration of the lens, ΔE is the energy spread of the ions, and E the beam energy Note that the current density is independent of the lens acceptance angle. In other words, it is constant for a given focusing system and does not depend on the focal spot size. The focal spot size increases with the solid angle of acceptance of the lens in just such a way as to keep the current density in the spot the same. As can be seen from the above equation, the current density increases with increasing beam energy This improvement is limited, however, by the maximum voltage of the particular lens. As the maximum lens voltage is increased by using larger gaps, the quantity (E/C) tends to remain constant due to increases in C [1]. Furthermore, increasing the source emission current also increases the energy spread These factors combine to limit the maximum current densities in practical LMIS round-lens focusing systems to about 1 A/cm^2. Beam spot sizes in state-of-the-art ion-focusing columns are in the range of 50–200 nm with the smaller spot sizes being obtained at the price of reduced beam current Current densities of 1 A/cm^2 or higher are usually achieved at beam energies of 20 keV or higher

Applications for finely focused beams cover a wide range of processing techniques in industry and research These applications generally exploit one or more of three basic aspects of the ion–solid interactions. The desired effect of the ion beam may be produced by: (1) pseudoelastic collisions between the energetic ions and target atoms where momentum transfer results in displacements (damage) and sputtering, (2) inelastic scattering of the ions with electrons in the solid producing excitations which may cause chemical changes such

* Invited paper

0168-583X/91/$03.50 © 1991 – Elsevier Science Publishers B.V. (North-Holland)

as in polymer resist exposure, or (3) the presence of the ion in the solid after it has come to rest such as in semiconductor doping The design of ion focusing columns and choice of LMIS species is usually dictated by the application. The two major classes of FIB systems are the low-energy (10–50 keV) type with heavy-ion species (usually Ga) where momentum transfer and sputtering are important, and the higher-energy (50–200 keV) type where electronic excitation and doping are the desired effects.

Fig. 1a shows an example of a simple focusing system used mainly for applications employing sputtering such as mask repair [1,6], circuit restructuring [7–9] and micromachining [10]. Ions from the LMIS are extracted at an energy of 3–6 keV and pass through a beam-limiting aperture to a three-element asymmetric electrostatic lens designed for low chromatic aberration [11]. The ion column also employs an electrostatic beam deflector. A system of this type operates at 20–50 keV with 100–200 nm spot size and a beam current of 100–300 pA. The beam can be scanned over fields of up to 1 mm usually with computer control for imaging with secondary electrons (or ions) and patterned exposures. The doses required for sputtering applications are quite high, 10^{17}–10^{18} cm^{-2} limiting practical applications to those where the area to be exposed to the ion beam is small, such as defect repair of lithographic masks.

Fig 1b illustrates the other major type of ion-focusing column. It is designed to operate with an alloy LMIS so that may ion species can be produced in the beam Ions from the source are focused to a crossover at an intermediate aperture Crossed electric and magnetic (EXB) fields act as a velocity filter, effectively separating the ion species by mass. The EXB filter is adjusted to allow only the desired ion species to pass through the intermediate aperture and the rest of the ion column The objective lens then focuses the mass-selected beam onto the target.

This type of mass-separating column is usually designed to run at energies from 50 to 200 keV [13,14]. These systems are used for maskless implantation [15] and lithography producing minimum feature sizes of 100 nm [16,17]. Again, there is a trade-off between beam diameter and current with the minimum practical spot size of such a system at about 50 nm. Eutectic alloy sources such as AuSi or AuSiBe are commonly used in such systems. The AuSiBe LMIS can provide beams of both n- and p-type dopants for III–V semiconductors.

2. Recent developments

As mentioned in the previous section, there are several applications of finely focused ion beams which have been proven to be valuable over the last several years For production related to integrated circuits, defect repair of photomasks is well established. More recently the idea of using a focused ion beam to aid in the process of diagnosing failures and testing of fully processed wafers has gained in popularity. The ion beam is used for minor circuit editing by either cutting metal lines by sputtering or depositing conductive lines by ion induced metal deposition In the research laboratory, focused ion beams have proven useful for fine-line resist lithography. In addition, the flexibility of scanning beam implantation doping where parameters such

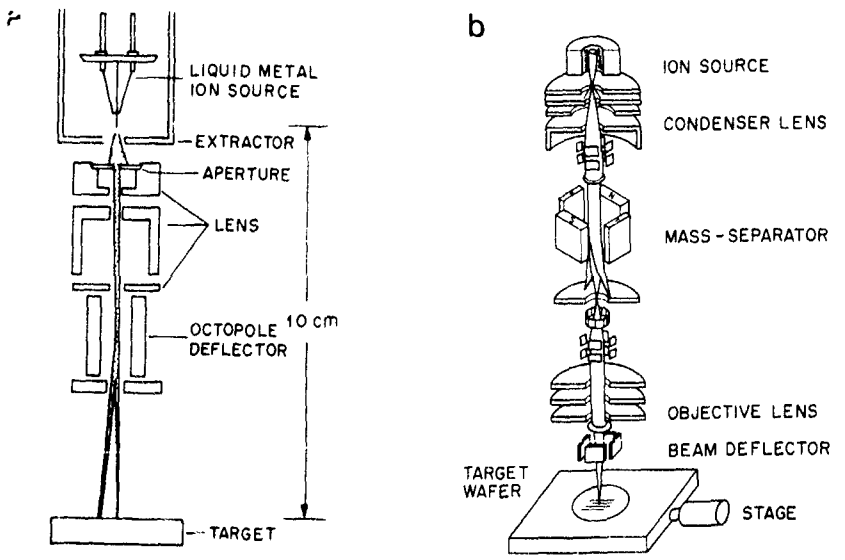

Fig 1 (a) A single-lens column for a focused-ion-beam system including a liquid-metal ion source, lens, beam and deflector (after ref. [1]) (b) A two-lens focusing column including an EXB mass filter for use with alloy LMIS (after ref. [12])

as species, energy and dose can be varied across a single wafer or even a single device can be very useful in prototyping new device structures. In this section, several relatively new applications of finely focused ion beams are discussed with the thought that some of them will become established as being important in the future.

2.1. Integrated-circuit microsectioning and inspection

Micromachining of integrated circuits for the purpose of in-process inspection with a focused ion beam is a very straightforward process [1,20,21]. The ion beam is scanned over a fairly large (compared to the FIB diameter) area repeatedly to mill a crater several μm deep and 10–50 μm on a side. The crater is positioned so that a sidewall cuts through the area of interest in the circuit. After the milling process the sidewall is imaged by tilting the sample to obtain a cross section of the device. During the sputtering process, some of the material removed from the bottom of the crater is redeposited on the sidewalls, possibly obscuring the sectioned device. This problem is usually solved by milling in two steps. First the large crater is milled to its final depth, resulting in sidewalls contaminated by redeposition Next a "fine cut" is made only along the sidewall of interest to expose a clean surface for later imaging. The extent of the redeposition is further reduced by increasing the number of scans used to deliver the ion dose [10] for both the initial large feature and the final "fine cut".

Fig. 2 shows an example of FIB microsectioning of an integrated circuit. This approach to sectioning has many advantages over the conventional method of cleaving and polishing preparation for electron-microscope imaging:

(1) despite times of several minutes to produce a suitable crater, it is still much faster than cleaving and polishing;
(2) since the edges of the crater can be located precisely (usually within 0.1 μm), the section can be placed where they are needed and actual working devices can be inspected without the need of including special "test transistors" on the wafer;
(3) since it is not necessary to cleave the wafer, this method is destructive only to the device sectioned, leaving the remainder of the wafer intact; this is particularly important where production involves a large number of chip designs but a small number of wafers of each

Fig. 2 Cross section of an aluminum conductor covered with SiO_2 and silicon nitride from an integrated circuit The section was prepared by focused ion beam micromachining (M J Vasile, AT&T Bell Laboratories, unpublished)

2.2 X-ray mask defect repair

As the minimum lateral dimensions of integrated-circuit features continue to decrease toward 0.5 μm and below, X-ray lithography may become a dominant manufacturing tool [22]. The most likely form of X-ray lithography is proximity printing of small fields using a membrane-type mask in a step-and-repeat fashion across the wafer. A typical mask structure is a thin membrane (boron nitride, silicon carbide or silicon) of low-atomic-number material supporting a thick (0 3–1 0 μm) patterned X-ray absorber layer of high-atomic-number material (gold or tungsten). Because the mask may contain only a few chips (perhaps as few as one), economics demands that the masks contain zero defects

Focused ion beam repair of X-ray mask defects is in two forms [23,24]: milling to remove excess material or ion-induced metal deposition [25] to fill in missing features. This may seem to be a straightforward extension of the methods used in focused-ion-beam photomask repair [6], but there are several difficult problems presented by X-ray masks. Some of these problems include:

(1) ion channeling in the polycrystalline Au absorber obscures the ion imaging used to precisely locate the defect prior to repair;

(2) channeling also results in spatially nonuniform sputtering during defect repair;
(3) the small lateral dimensions (down to 0.1 μm) require a much smaller ion beam diameter (25–50 nm) than that (250 nm) typically used in photomask repair;
(4) the high aspect ratio of the mask features (as much as 10:1) can be difficult to reproduce in repaired features due to redeposition during milling and in general during ion-induced deposition.

The problems of redeposition of material during ion milling can be mostly overcome by choice of the scanning strategy [10,24–26]. Multiple raster scans used in milling are somewhat effective but more elaborate strategies may be needed for some cases in X-ray masks. An example of such a strategy is to mill the center portion of the defect first, leaving a "wall" around its perimeter to stop material from being deposited on nearby features, and then, in a second milling step, remove the wall. Another approach is to allow material to be redeposited on the surrounding features and then remove it as necessary after the defect has been repaired.

The problem of filling in high-aspect-ratio features to repair "clear" defects by FIB-induced metal deposition is a more difficult task. For FIB-induced deposition, a precursor gas is introduced to the FIB vacuum chamber through a small-diameter (~ 100–200 μm) tube or gas jet. The end of the gas jet is positioned just above the target (50–100 μm) at the place where the ion beam strikes. This arrangement allows equivalent pressures of the precursor gas to be in the range of hundreds of mTorr while the ion gun remains at high vacuum. For X-ray mask repair metal–organic precursors such as dimethylgold hexafluoro acetylacetonate (DMG(hfac)) are used. The adsorbed layer of the precursor is decomposed by the action of the ion beam to produce a deposit. At the same time, however, the ion beam sputters the adlayer and previously deposited material. Careful control of the kinetics of this process is necessary to ensure that net deposition of material occurs rather than net material removal [29]. The most critical parameter is the beam scanning strategy. Again, the feature is exposed in multiple scans of the beam. To ensure net deposition, the dwell time of the beam at each point in the feature during each pass of the beam is kept short (0.1–1 μs) so that only enough dose to decompose the surface adlayer (one monolayer at best) is delivered. Time is allowed between each pixel exposure (1–10 ms) to replenish the precursor adlayer coverage. The optimum conditions are determined by the gas pressure, beam current density and sticking coefficient of the precursor.

Deposition yields as high as 100 deposited atoms per incident ion have been reported [23,29]. High yield is important for several reasons: (1) the time required to produce an adequate deposit is reduced, (2) the amount of redeposited material on surrounding features is reduced (there is always sputtering occurring during deposition) and (3) if the balance between sputtering and deposition is shifted heavily in favor of deposition, then the $1/\cos\theta$ angular dependence of the deposition yield can result in very-high-aspect-ratio features. Fig. 3 shows an example (taken from ref. [23]) of Au features deposited with very high aspect ratio under high yield (75–100 atoms deposited per incident ion) conditions.

2.3. Damage patterning

In the previous examples, ion sputtering was used as the patterning mechanism. At much lower doses and perhaps higher energies, crystal damage can be readily produced with a finely focused ion beam. The damage caused by the ion beam can be used for patterning by creating defects which modify or destroy the conductivity of a previously doped semiconductor layer. With the small diameter of available FIB systems, this method has been applied recently to the fabrication of quantum-effect structures. An example of a simple method for producing a one-dimensional conductor is shown in fig. 4 [36]. In this case, a conductive current bar is first created with ion implantation and annealing. Nonconducting regions are then created by a second implant using FIB where the damage is not annealed out. The conducting channel between the damaged areas is further narrowed by the depletion region and can be made as small as 20 nm despite the fact that a 100 nm beam was used by adjusting the distance between the implanted regions and the dose. A variation of this damage patterning method has been used recently to fabricate an in-plane-gated quantum wire transistor [31].

Compositional disordering of multi-quantum well (MQW) structures is a related technique of interest in the fabrication of quantum-effect structures and devices [32]. When the multilayer GaAs/AlGaAs structures are implanted with high-energy Ga ions (100 keV), the defects produced cause enhanced interdiffusion of the Al and Ga within the implanted area at moderate doses [33] of 10^{13}–10^{15} ions/cm^2. After annealing, the implanted regions are structureless, leaving intact the unimplanted MQW structures. The ultimate limitations on the spatial resolution of this technique are from ion scattering and diffusion. There is some evidence that channeling effects significantly reduce the lateral broadening of the implanted regions with depth predicted by simulations of ion implants into amorphous material [34]. MQW structures with lateral dimensions of about 100 nm have been produced so far and were probably limited by the ion beam diameter. It is expected that 50 nm features could be made with this technique.

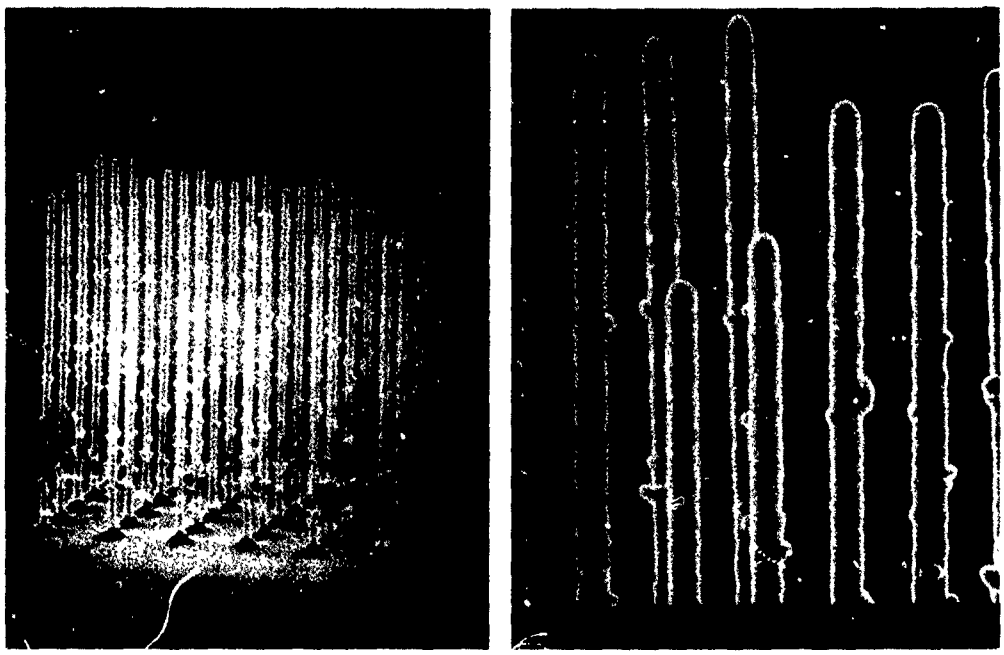

Fig 3 Gold microstructures deposited by a 100 keV Ga ion beam The beam diameter was approximately 100 nm The structures are about 150–200 nm in diameter and 10 μm tall (after ref [23])

2 4. Patterning of high-T_c superconductor thin films

Conventional lithographic patterning of these materials tends to have detrimental effects on the superconducting properties of the films such as superconducting transition temperature (T_c) and critical current density (J_c). Mostly, the films are effected at the edges of features so that when small features (less than 5–10 μm) are fabricated, the patterned material is no longer a good superconductor. Focused ion beams have been used for micron- and submicron-sized patterning of high-T_c superconductor thin films in two major ways [35] which are discussed below

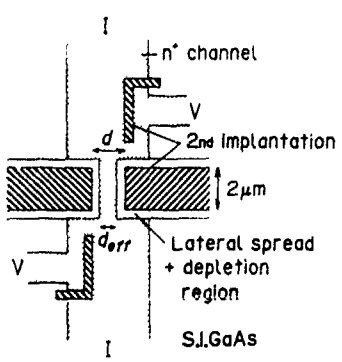

Fig 4. Implanted quantum wire structure A narrow conducting channel is formed between the high-resistivity implanted areas (2nd implantation) The damage from the second implantation has not been annealed out (after ref. [30])

Focused-ion-beam micromachining has been used to pattern features down to sizes less than 0.5 μm without degradation in T_c or J_c [36]. In this case, fine patterns are formed by sputtering away superconductor material leaving behind the desired pattern The resolution limit for forming narrow lines was related to the diameter of the FIB used (200 nm). Since material is removed on either side of the line with a large (5×10^{17}) ion dose, the roughly Gaussian beam profiles will produce a significant (10% of the milling dose) ion exposure at the center of the line when the width of the line is on the order of the beam diameter or slightly more. The general observation was that feature sizes down to about 1.5 times the beam diameter can be produced without significant degradation of the superconducting properties of the remaining material. Although FIB micromachining has proven to be a valuable method for making micron and submicron experimental device and test structures [37], the major limitation is the time required to produce the patterns. For a typical 2000 Å thick YBaCuO film patterned with a 200 nm Ga focused ion beam at 1 A/cm^2 (160 pA on the target), the milling dose is $(5–6) \times 10^{17}$ cm^{-2}, requiring $10^7–10^8$ s/cm^2 processing times. Patterning by ion beam damage offers a speed improvement of 1000 or more at similar spatial resolution [38].

It has been demonstrated that transition-temperature and critical-current properties of high-T_c superconductors can be modified in a controlled way by broad-area bombardment with high-energy (MeV) heavy ions such

as Ne, As and O [39,40]. The transition temperature and critical current can be adjusted downwards with increasing ion dose usually in the 10^{13} to 10^{14} range. These high-energy ions generally penetrate through the film and are stopped in the substrate. Their effect on the superconducting properties of the thin films is primarily through lattice damage from the nuclear stopping process. At ion doses of about 10^{14} cm^{-2}, the implanted material is no longer a superconductor at any temperature and shows increasing electrical resistance with decreasing temperature (semiconductor-like behavior).

Maskless implantation of thin film superconductors with high-energy light ions from a focused ion beam system [14] such as 300 keV Si^{2+} can produce a similar effect to the MeV broad-beam implants [35,38] (see fig. 5). In this case the superconductor pattern is formed by implanting regions at doses of 10^{14} cm^{-2} or higher, leaving unimplanted areas as superconducting regions. The spatial resolution of this technique is probably limited by the large-angle scattering of the incoming light ions by the heavier elements in the superconducting film such as Ba. Linewidths of 0.5 μm have been demonstrated using a 300 keV Si^{2+} beam (nominally 100 nm diameter) on 2000 Å thick films of YBaCuO (1–2–3) [38]. It is possible that finer patterns could be made using heavier ions and/or thinner films.

2.5 All-vacuum processing

Three-dimensional nanostructure fabrication for optoelectronic and quantum-effect devices can benefit from the greatly improved surface and interface layer quality and low contamination offered by all-vacuum processing [41–43]. Ultrathin epitaxial layers can be grown with excellent uniformity with techniques such as molecular beam epitaxy (MBE) to produce planar structures. Devices using these structures are usually made by subtractive patterning after crystal growth. This processing however renders the surface of the structures damaged and contaminated, unsuitable for epitaxial overgrowth. As the feature sizes are decreased, the condition of the surface has a large effect on the electrical and optical properties of the devices. Overgrowth on the patterned substrate is often desirable for surface passivation. However, once the surface has been exposed to contaminants from the atmosphere, resist used in patterning, or etchants, the quality of overgrowth is poor.

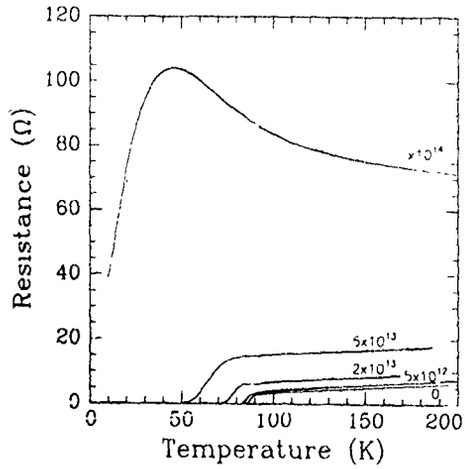

Fig. 5. Resistance vs temperature for a thin film (2000 Å) of YBaCuO (1–2–3) superconductor implanted with various doses of 300 keV Si^{2+} (after ref. [38]).

Focused ion beams offer a number of possible patterning techniques useful in device fabrication which are compatible with the ultrahigh-vacuum (UHV) and surface-contamination requirements of MBE crystal growth.

One of the first ideas for combining focused-ion-beam patterning with MBE crystal growth was for maskless implantation [44,45]. The system consists of a 10 keV focused-ion-beam implanter line the one in fig. 1b and an MBE growth chamber connected by an UHV sample transfer tube. The EXB equipped focusing column and a AuSiBe LMIS allows both n- and p-type of patterned doping under computer control. The purpose of this system is to produce GaAs-based optoelectronic integrated circuits (OEIC) by implanting both electrical (FET) and optical (laser) structures in multiple epitaxial layers with atomically abrupt interfaces.

Vacuum compatible lithographic patterning is also required for in-situ processing which includes overgrowth on patterned substrates. One approach to this is chemically enhanced sputter etching [46]. A gas inlet tube similar to that used in FIB-induced deposition is used to introduce an etchant gas such as Cl_2 into the chamber in the vicinity where the ion beam strikes the target. Enhanced material removal rates are observed particularly at elevated substrate temperatures. The enhancement may be as much as 100 times over the removal rate for physical sputtering alone. However, this technique still requires large ion doses to create micron-sized features such as laser facets (10^{16} cm^{-2} or more), making large-area patterning impractical. In addition, since energetic heavy ions are typically used (e.g., 20 keV Ga), the bottom surfaces of the etched features have considerable crystal damage [47], leaving them unsuitable for epitaxial overgrowth.

A two-step process for vacuum compatible lithography has also been described using a 20 keV Ga focused ion beam and Cl_2 etching [48,49]. In this method, a thin (20–40 Å) oxide layer is grown on the surface of the III–V crystal (InP in this case). The FIB defines the pattern on the substrate by sputtering and/or modifying the oxide layer locally. When the sample is then placed in a Cl_2 etching chamber, the exposed substrate

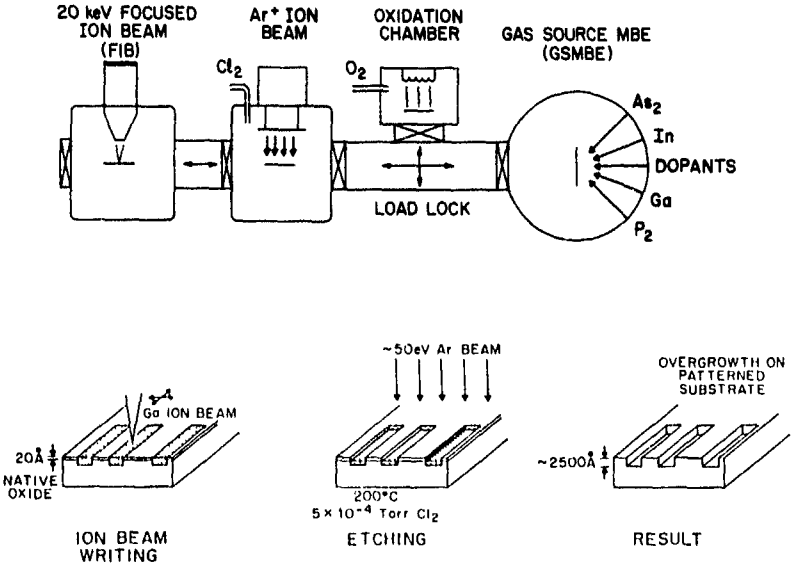

Fig. 6 Apparatus for vacuum lithography and in-situ processing The four main elements are: molecular beam epitaxy (MBE) crystal growth, oxidation, FIB patterning and dry etching (after ref. [49])

(the areas which have been exposed to the FIB) are etched while the oxide-covered areas are not etched. After the pattern is transferred to the substrate by the etching (40 Å of oxide is sufficient to etch features up to 3 μm deep), the oxide is thermally desorbed in the MBE growth chamber as first step in the growth procedure. The system used for this method is shown in fig. 6 schematically. This method has been used to pattern and overgrow features in InP/InGaAs heterostructures with dimensions as small as 200 nm, limited by the ion beam diameter. The features show excellent morphology and luminescence properties indicating the quality of the interface between the patterned substrate and overgrown layers [50].

3. New developments in focused ion beam systems

The most obvious improvement to make to a serial writing instrument such as a focused ion beam system is to increase the current density. If the total beam current can be increased without a penalty in spot size, the processing throughput is improved, always an important consideration in serial processing. If the beam diameter can be decreased without having to sacrifice total beam current, higher-resolution patterning is possible. Ideally both a smaller spot and higher current are advantageous. This problem can be approached from at least three directions for chromatically limited optics:

(1) an improved source can be developed with inherently low energy spread;
(2) the chromatic aberration of the focusing lenses can be reduced or eliminated;
(3) existing or conventional optics designs can be operated in a more optimum way.

Examples of these ideas are presented in the following section.

The analysis of ion optical systems using LMIS usually assumes that the final beam-current distribution will be Gaussian and can be described by only a full-width-at-half-maximum (FWHM) usually used as the beam diameter. In addition, it is usually assumed that the effects of finite virtual source size, chromatic aberration, and spherical aberration are statistically independent and the net effect calculated by a root-mean-square (RMS) method. It is clear that both of these assumptions are not valid and are in effect only approximations. A more careful treatment of the beam profile and how it is affected by lens aberrations [51,52] can lead to both improved optics designs and more optimal use of current designs. In one example [53], the system magnification was reduced by reducing the distance from the second lens (in a two-lens column) to the sample [53]. In this configuration beam diameters (FWHM) as small as 15 nm were obtained and 20 nm wide lines were written in PMMA resist. In addition to reducing the FWHM of the beam profile the shape of the profile was also improved. That is, the deviation of the profile from a Gaussian was improved, resulting in much lower current at large distances from the peak of the beam current (beam tails).

One approach to improving the current density in chromatically limited FIB systems is to reduce the chromatic aberration of the lenses. A combined electrostatic and magnetic quadrupole lens can be operated such that the chromatic aberration is exactly zero [54,55]. A

single quadrupole lens will focus in one plane and defocus in the perpendicular plane. Therefore, to make a round image of a point source such as a LMIS, a multiplet system is required. A doublet lens results in unequal magnifications in the two planes but a triplet configuration can be operated with equal magnifications to produce a round beam spot. The idea of an achromatic quadrupole triplet focusing system has been recently applied to LMIS [56,57]. This approach offers perhaps an order of magnitude increase in current density compared to electrostatic round lenses at the cost of increased complexity. The current density is then limited by parasitic aberrations (mechanical tolerances, power stability) and third-order aperture aberrations (roughly analogous to spherical aberration in round lenses) This performance is available at much lower energies that typical electrostatic systems (since the focal properties are independent of energy to first order) which may offer some advantages as well.

Gas field ionization sources (GFIS) offer the potential of higher current density in the focused spot due to a lower energy spread (~ 1 eV) than that for a LMIS [58–62] GFIS are derived from the field ion microscope. Like a field ion microscope a GFIS operates by biasing a cryogenically cooled sharpened metal tip in a gas atmosphere. When a high positive potential is applied to the tip, the electric field concentration in its vicinity causes electrons to tunnel into the tip from the surrounding gas molecules, resulting in ions being accelerated away from the tip. These tips are very sharp with emission sites sometimes consisting of only a few atoms. Unlike the field ion microscope, the GFIS is optimized for high-current emission from a single site rather than low-current imaging of crystal planes on the tip. The technical difficulties of operating a high-voltage, low-temperature source with adequate gas supply, low residual gas pressure and an atomically sharp tip have limited its practical application to date. The potential improvement in current density of as much as a factor of 100 over LMIS-based systems is, however, a strong driving force for further work.

A practical system would probably use He ions at 100 keV for polymer resist exposure lithography. Such a system would offer advantages over electron beam exposure. One would expect reduced lateral- and backscattering which can limit resolution and the greater per-particle sensitivity of resists to ions over electrons to improve throughput

In addition to improvements in beam current density, a reduction in the defects and damage caused during chemically assisted processes such as etching and deposition is important. Low-energy focused ion beam systems address this problem [63,64,65]. These focusing systems operate by first forming a probe in the usual 10–70 keV energy range and decelerating the beam just before it strikes the target to minimize beam broadening by chromatic aberration. The decelerating is accomplished by biasing the substrate with a positive potential with respect to one or more lens apertures above the target. By careful design of the deceleration lens, a 300 nm diameter beam with 10 pA at 1 keV has been demonstrated [65]. In this case, the beam was decelerated from 30 keV. It is expected that improved designs for the decelerating lenses will result in improved performance. In order for such a system to significantly reduce the number of defects created in FIB processing, energies of less than 100 eV are required and it is not clear whether this type of an approach can produce submicron beam diameters at these energies.

4. Summary

The emerging focused ion beam applications described in the previous sections rely on the current state of the art of commercially available systems. These machines can be quite sophisticated and highly automated with computer controls. A photomask repair system has a large amount of control software to allow consistent location and repair of defects down to the resolution limits of the ion beam The systems built for maskless implantation and lithography have "front-end" hardware and software for processing chip design data and directing the beam writing in very much the same way as an electron beam lithography system does. As the technology matures, and the useful applications become more well defined, the major system improvements will probably be in the controls and software. Fortunately, this technology is relatively young and there are still a number of interesting improvements in the ion beam part of the systems which are still needed.

Acknowledgements

I would like to thank W. Thompson, H. Sawaragi and R Aihara of JEOL, B Ward and D. Stewart of Micrion Corp., A. Wagner and P. Blauner of IBM, and M.J Vasile of AT&T Bell Laboratories for their help in assembling the material for this paper I also acknowledge many helpful discussions with Y.L. Wang of AT&T Bell Laboratories

References

[1] A. Wagner, Nucl Instr and Meth 218 (1983) 355.
[2] W.L Brown, Microelectron Eng 9 (1989) 269
[3] J. Melngailis, J. Vac. Sci. Technol. B5 (1987) 469.
[4] L.R Harriott, Appl. Surf. Sci. 36 (1989) 432
[5] L.R Harriott, in: VLSI Electronics. Microstructure Science, vol 21 (Academic Press, New York, 1989) p 157

[6] A Wagner and J.P Levin, Nucl. Instr. and Meth. B37/38 (1989) 224.
[7] L.R Harriott, A. Wagner and F Fritz, J Vac. Sci. Technol B4 (1986) 181
[8] J. Melngailis, C R Musil, E.H. Stevens, M Utlaut, E.M. Kellogg, R.T Post, M.W Geis and R W. Mountain, J Vac Sci Technol B4 (1986) 176
[9] D.C Shaver and B W. Ward, J. Vac Sci Technol. B4 (1986) 185.
[10] L.R. Harriott, R.E. Scotti, K.D. Cummings and A.F. Ambrose, J. Vac. Sci. Technol. B5 (1987) 207.
[11] J Orloff and L.W Swanson, J. Appl. Phys. (1979) 2494
[12] E Miyauchi, H. Arimoto, H Hashimoto, T. Furuya and T Utsumi, Jpn. J Appl. Phys. 22 (1983) L287
[13] R Aihara, H. Sawaragi, B. Thompson and M H. Shearer, Nucl Instr and Meth B37/38 (1989) 212.
[14] N W Parker, W P Robinson and J.M Snyder, Proc. SPIE 632 (1986) 76
[15] W M Clark and M W Utlaut, J. Vac Sci. Technol B6 (1988) 1014
[16] T Kato, A Yasuoka and K Fujikawa, Nucl Instr. and Meth B37/38 (1989) 218
[17] S Matsui, Y Kojima and Y. Ochiai, Appl Phys Lett 53 (1988) 868
[18] D K. Stewart, L A Stern and J C Morgan, Proc SPIE 1089 (1989) 18
[19] J.R.A Cleaver, E C G Kirk, R J Young and H. Ahmed, J. Vac Sci Technol B6 (1988) 1026
[20] P Sudraud and G Ben Assayag, J Vac Sci Technol B6 (1988) 234
[21] B W Ward, Micron Corp., private communication
[22] J Warlaumount, J. Vac Sci. Technol B7 (1989) 1634.
[23] A. Wagner, J.P. Levin, J L. Mauer, P.G Blauner, S J Kirch and P Longo, J Vac Sci Technol (1990) to be published
[24] K P. Muller, Jpn. J Appl Phys 28 (1989) 2348
[25] K Gamo and S Namba, Proc Mater Res Soc 131 (1988) 531
[26] H. Betz, A Heuberger, N.P Economou and D C. Shaver, Proc SPIE 632 (1986) 67.
[27] L R Harriott and M J. Vasile, J Vac Sci Technol B6 (1988) 1035
[28] G M Shedd, H Lezec, A D Dubner and J. Melnagilis, Appl Phys Lett 49 (1986) 1584
[29] J P Levin, P G Blauner and A Wagner, Proc SPIE 1263 (1990).
[30] T Hiramoto, K Hirakawa and T Ikoma, J Va. Sci. Technol. B6 (1988) 1014
[31] A D. Wiek and K Ploog, Appl. Phys Lett 56 (1990) 928.
[32] Y Hirayama, Y Suzuki and H Okamoto, Surf Sci 174 (1986) 98.
[33] F Laruelle, P. Hu, R. Simes, R Kubena, W. Robinson, J Merz and P M Petroff, J Vac Sci Technol B7 (1989) 2034
[34] F. Laruelle, A. Bagchi, M. Tsuchiya, J. Merz and P M Petroff, Appl Phys Lett. 56 (1990) 1561.
[35] S. Matsui, Y. Ochiai, Y. Kojima, H. Tsuge, N. Takado, K Asakawa, H. Matsutera, J. Fujita, T. Yoshitake and Y. Kubo, J Vac. Sci. Technol. B6 (1988) 900
[36] L.R. Harriott, P.A Polakos and C.E. Rice, Appl Phys. Lett. 55 (1989) 495.
[37] P L. Gammel, P.A. Polakos, C.E Rice, L R Harriott and D.J. Bishop, Phys Rev. B41 (1990) 2593.
[38] L.R. Harriott, P.A. Polakos, C E. Rice, P L. Gammel, W.P Robinson and C. Hiner, Proc. SPIE 1263 (1990) 53
[39] A E White, K.T. Short, A F.J. Levi, M Anzlowar, K W Baldwin, P.A. Polakos, T A Fulton and L.N Dunkleberger, Appl Phys Lett. 53 (1988) 200.
[40] G.J Clark, A.D. Marwick, R.H Koch and R.B Laibowicz, Appl Phys. Lett 51 (1987) 139.
[41] I. Hayashi, in Emerging Technologies for In-Situ Processing, eds D Ehrlich and V.T Nguyen (Nijhoff, Dordrecht, 1988) p 13
[42] H Ahmed, Microelectron. Eng. 9 (1989) 313
[43] L R. Harriott, Proc. SPIE 1284 (1990) 132
[44] E. Miyauchi and H. Hashimoto, Nucl. Instr and Meth B7/8 (1985) 851
[45] E. Miyauchi, H. Arimoto, Y. Bamba, A Tahamori and H. Hashimoto, Nucl. Instr. and Meth. B6 (1985) 183
[46] N. Takado, K Asakawa, T Yuasa, S Sugata, E. Miyauchi, H Hashimoto and M Ishii, Appl Phys Lett. 50 (1987) 1891.
[47] M Taneya, Y Sugimoto and K. Akita, Jpn. J Appl Phys 66 (1989) 1375
[48] H Temkin, L.R. Harriott, R.A Hamm, J Weiner and M.B. Panish, Appl Phys. Lett 54 (1989) 54
[49] L.R Harriott, H Temkin, Y L Wang, R A Hamm and J.S Weiner, J Vac Sci Technol. (1990) to be published.
[50] J.S Weiner, Y L. Wang, H. Temkin, L R Harriott, R A Hamm and M B Panish, J Vac Sci. Technol (1990) to be published.
[51] Z Shao and Y L Wang, J Vac Sci Technol B8 (1990) 95
[52] Z Shao and Y.L Wang, Advances in Electronics and Electron Physics, ed. P W. Hawkes (Academic Press, New York, 1990)
[53] R.L. Kubena, F P Stratton, J W Ward, G M. Atkinson and R.J Joyce, J Vac Sci Technol. B7 (1989) 1798
[54] V.M Kelman and S Yavor, Sov Phys Tech Phys 6 (1962) 1052.
[55] F W Martin and R Goloskie, Appl. Phys Lett. 40 (1982) 191
[56] L R Harriott, W L Brown and D.L. Barr, J. Vac Sci. Technol A8 (1990) 3279
[57] L R. Harriott, W L Brown and D L Barr, J Vac Sci. Technol. B (1990) to be published
[58] J Orloff and L W Swanson, J Vac. Sci. Technol 12 (1975) 1209
[59] P R Schwoebel and G R Hanson, J Vac Sci Technol B3 (1985) 214.
[60] M Konishi, M Takizawa and T Tsumori, J Vac. Sci Technol. B6 (1988) 498
[61] K Horiuchi, T Itakura and H Ishikawa, J Vac Sci Technol. B6 (1988) 937
[62] K Bohringer, K. Jousten and S Kalbitzer, Nucl Instr. and Meth B30 (1988) 289.
[63] D.H. Narum and R.F W. Pease, J. Vac Sci. Technol B6 (1988) 966.
[64] R Aihara, H. Kasahara, H. Sawaragi, M H. Shearer and W.B Thompson, J Vac Sci Technol. B7 (1989) 79.
[65] H. Sawaragi, R. Mimura, H. Kasahara, R. Aihara, W.B Thompson and M H. Shearer, J Vac Sci Technol (1990) to be published.

Nuclear Instruments and Methods in Physics Research B55 (1991) 811–820
North-Holland

Plasma immersion ion implantation for ULSI processing *

Nathan W. Cheung

Department of Electrical Engineering and Computer Sciences, University of California, Berkeley, CA 94720, USA

With a high ion-density plasma produced by electron cyclotron resonance (ECR) sources, the space charge region between the plasma and a negatively biased target can sustain a potential difference up to 50 kV, with an implantation flux as high as $10^{16}/cm^2$ s. Other unique features of this plasma immersion ion implantation (PIII) technique include, no ion mass selection, no beam transport optics, and the ion energy and angular distributions controlled by the plasma gas pressure and the applied bias waveforms. By adding a sputtering electrode into the plasma which is powered by a separate voltage supply (i.e., a triode configuration) the implantation chamber can also be converted into an ion-assisted physical vapor deposition system. In this review paper, we outline the physical mechanisms and operation modes of PIII and discuss applications of PIII's unique features for ultra-large-scale integrated circuit fabrication. Recent successes of using PIII for conformal doping of nonplanar device structures, sub-100-nm p^+/n junction formation, backside damage impurities gettering, and selective electroless plating of metal interconnects are presented.

1. Introduction

Recent advancement in ultra-large-scale integrated circuits (ULSI) concerns the fabrication of more than 10^7 device elements per circuit. This high packing density of devices needs reduced doping geometry for both the lateral and vertical dimensions. For example, quarter-micron complementary MOS (CMOS) circuits will require source/drain junction depths below 100 nm for proper scaling. For p^+/n junction formation where boron implantation is used, preamorphization of the crystalline Si is preferred together with large doses of boron to minimize the source/drain resistance. It is interesting to point out that the final junction depth of these ultra-shallow junctions depends more on the post-annealing thermal cycle rather than the as-implanted depth profile. Other high-dose implantation applications such as doping of poly-Si or silicides share similar requirements - dose control is more important than details of the implanted profile. These new processing developments may open up new opportunities for ion beam technologies with non-monoenergetic ion energies.

To increase the signal-to-noise margin of the circuits, usage of the vertical sidewalls becomes more popular for active transistor channels and trench capacitors. The doping of these nonplanar surfaces poses new challenges for conventional ion implantation which is basically a line-of-sight doping process. Another technology bottleneck for ULSI is the fabrication of multilevel metallization. Due to lithography depth of focus limitations and step coverage problems with thin film deposition, planarized surface topography management adds new complexity to the processing sequence. Bilayer or trilayer metals are also used to improve interface adhesion, interfacial diffusion barriers, and electromigration resistance. Although ion beam technology is still not commonly utilized in these thin-film processing steps by the semiconductor industry because of the high doses needed (10^{17}–10^{18} cm^{-2}), ion-assisted deposition techniques can offer simpler process designs if the throughput of implanters can be improved.

Conrad et al. [1] and Tendys et al. [2] have recently demonstrated a new ion implantation technique, the *plasma immersion ion implantation* (PIII) technique. Using a high ion density plasma produced by Penning discharge and by applying negative voltage pulses up to 100 kV to the substrate, they successfully applied this technique to improve the wear and corrosion resistance of metals. The principle of PIII is illustrated in the schematic shown in fig. 1. With a high ion density (10^{10}–10^{11} cm^{-3}) plasma produced by efficient ionization sources, the ion-matrix sheath between the plasma boundary and a negatively biased substrate can sustain a potential difference of many kilovolts. The positive ions inside the ion sheath will accelerate towards the substrate by the negatively biased substrate. Depending on the ion–neutral scattering mean free path, the ions will implant the substrate with energy and angular distributions determined by the plasma gas pressure, bias voltage, the ion charge state, and substrate surface contours. In its simplest configuration, PIII does not provide ion mass selection or beam transport optics. However, the PIII implant dose-rate can be very high ($\sim 10^{16}$ cm^{-2} s^{-1}) and large implant workpieces can

* Invited paper

0168-583X/91/$03.50 © 1991 - Elsevier Science Publishers B.V. (North-Holland)

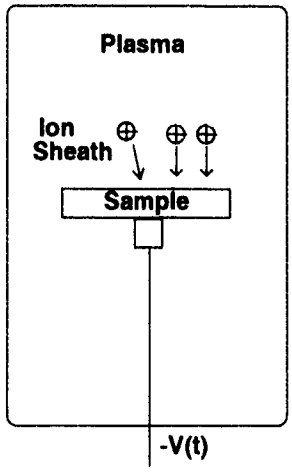

Fig 1 Schematic showing the principles of plasma immersion ion implantation

easily be accommodated inside the plasma without any need for beam raster

2. PIII mechanisms

Fig 2 shows the time development of the ion-matrix sheath during PIII. With an abrupt negative bias applied to the substrate, electrons near the substrate surface are repelled in the time scale of the inverse electron plasma frequency ω_e^{-1} (10^{-9} s), leaving behind a uniform density ion sheath The negatively biased substrate will accelerate the ions within a time scale of the inverse of the ion plasma frequency ω_i^{-1} (10^{-6} s) This ion movement will lower the ion density and the sheath–plasma boundary will expand to sustain the applied potential drop, exposing more ions to be extracted

An analytical model of PIII for collisionless ion flow has been developed by Lieberman [3] The collisionless assumption will be valid for PIII conditions where the gas pressure is low In the case where the applied bias has a duration much longer than ω_i^{-1}, a steady-state Child–Langmuir sheath will develop with the ion current density j limited by the space-charge [4]:

$$j = \frac{4}{9}\epsilon_0 \frac{2q^{1/2}}{M} \frac{V_0^{3/2}}{s_\infty^2}, \qquad (1)$$

where ϵ_0 is the free-space permittivity, q the ion charge, M the ion mass, V_0 the applied bias, and s_∞ the steady state sheath thickness. With a plasma density of n_0 and electron temperature of T_e, it can be shown that j is equal to en_0u_B where the ion Bohm velocity u_B is equal to $(qT_e/M)^{1/2}$ [3]. The time t_s required to establish the steady-state condition is $\sim(\sqrt{2}/9)\omega_i^{-1}(2V_0/T_e)^{3/4}$.

For pulse durations on the order of $3\omega_i^{-1}$, the time dependence of current density is given by,

$$J = \frac{\sinh T}{\cosh^2 T} + \frac{2}{9}\frac{1 + T\sinh T - \cosh T}{\cosh^2 T}, \qquad (2)$$

with the normalized current density $J = j/(2n_0u_0)$, the normalized time $T = \omega_i t$. The characteristic ion velocity for bias V_0 is equal to $(2qV_0/M)^{1/2}$ This analytical solution is valid for those ions in the initial sheath matrix before expansion.

For ions originally located outside the sheath at time = 0, their contribution to current density is given by:

$$J = \frac{1}{\frac{2}{9}\left(x_0^2/s_0^2\right) + 3}, \qquad (3)$$

where s_0 is the initial sheath thickness and x_0 is the expanding sheath boundary thickness.

Results from the Lieberman model (dashed lines) are plotted in fig. 3 together with those from numerical solutions of the plasma equations [5] It is interesting to note that most of the implant current comes from original sheath and the current density peaks at around ω_i^{-1}. Lieberman's model also predicts the energy distri-

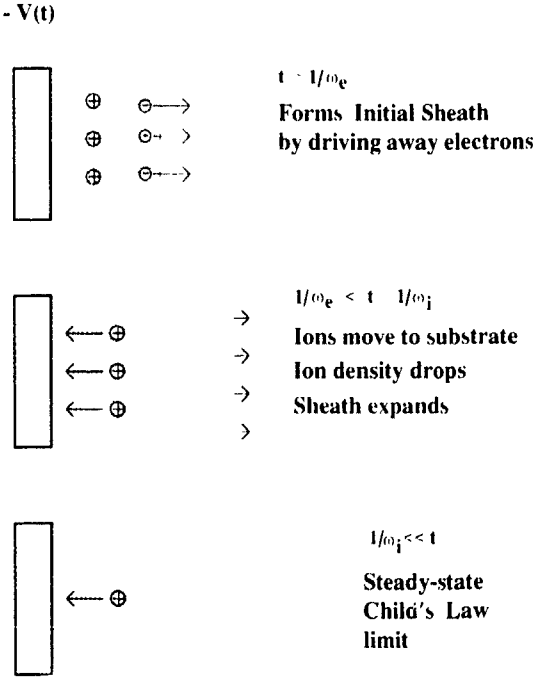

Fig 2 Schematic showing the time development of the ion-matrix sheath when a negative step pulse is applied to the substrate at time = 0. (i) Initial sheath formation within nanoseconds (ii) Sheath expansion within microseconds (iii) Steady-state Child–Langmuir sheath after long duration

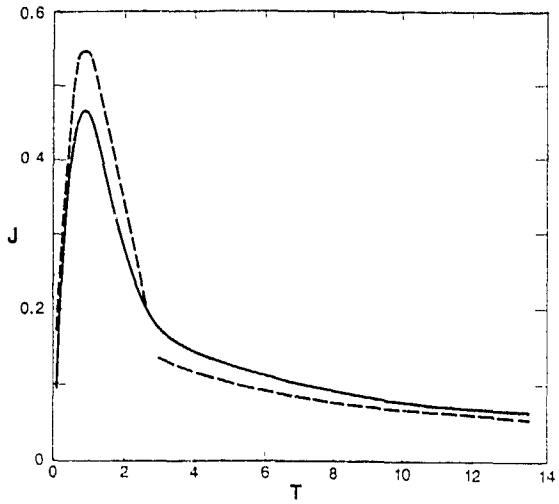

Fig 3 Plot of normalized current density J versus normalized time T The dashed lines show the analytical solution from the Lieberman model [3], the solid line shows the numerical solution of the plasma equations by Conrad [5]. The asymptotic J value for large T indicates the Child's law limit

bution dN/dE of the implantation is proportional to $(V_0 - E)^{3.5}$ for a collisionless sheath This functional form can be used to produce a convoluted implantation profile if desired.

For higher gas pressures, collisional effects within the ion sheath will affect the energy and angular distributions Simulation programs based on Monte Carlo techniques have been developed for PIII modeling [6,7]. Results from the simulations show that ion–neutral scattering is important for pressures in the mTorr range.

3. PIII configurations and operation modes

Figs. 4a and b illustrate the two PIII system configurations compatible with ULSI processing requirements. To avoid hot filament contamination, an ECR source operating at 2.45 GHz will provide the high ion density ($\sim 10^{10}$–10^{11} cm^{-3}) to supply the high implantation current. The substrate is biased from a time-varying or dc negative voltage to accelerate the ions towards the substrate surface. These two operation modes are called pulsed PIII and dc-PIII respectively

With the diode configuration, gaseous sources such as Ar, N_2, BF_3, B_2H_6 can be used to provide the ionization medium. The diode configuration is most convenient for doping applications such as shallow junction formation and conformal doping of nonplanar device structures because many dopant gaseous sources are available When metal-containing gas are used (e.g. WF_6), the diode configuration can operate as an ion-assisted chemical vapor deposition system (IACVD)

By adding another negatively biased target controlled by a separate power supply to form a triode configuration, the target atoms will be sputtered by the carrier gas plasma ions. Part of the emitted target atoms will be ionized in the ECR plasma and eventually be implanted into the substrate. In fig. 5, we show the differential optical emission spectrum from a Pd sputtering target with Ar as the ECR plasma gas The differential spectrum was obtained by subtracting the emission spectrum of an Ar plasma operating under identical ECR conditions but with the Pd target removed. Prominent emission lines of Pd^+ can be detected together with the emission lines of neutral Pd This optical emission technique can provide valuable

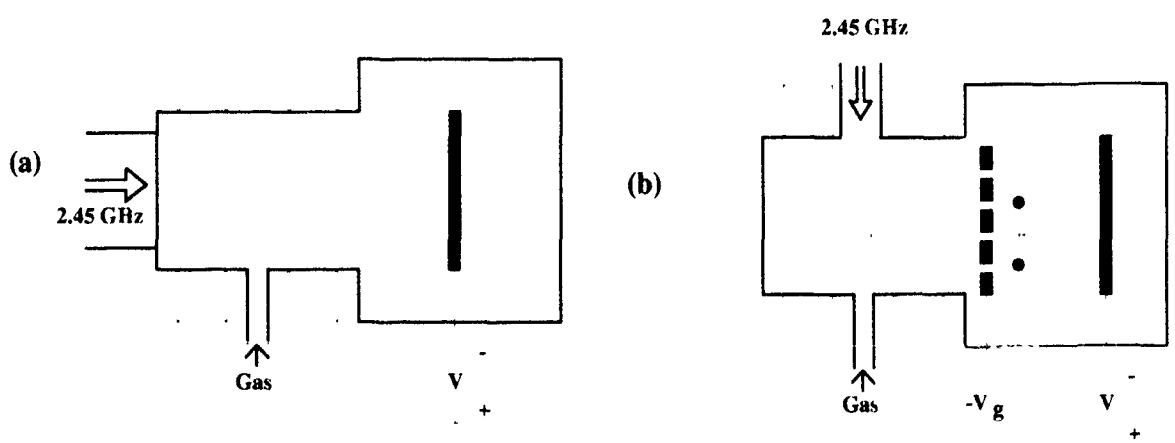

Fig 4 PIII with ECR to generate the plasma (a) The diode configuration uses ionized gas for the implant species (b) The triode configuration uses ionized sputtered atoms of solid source for the implant species

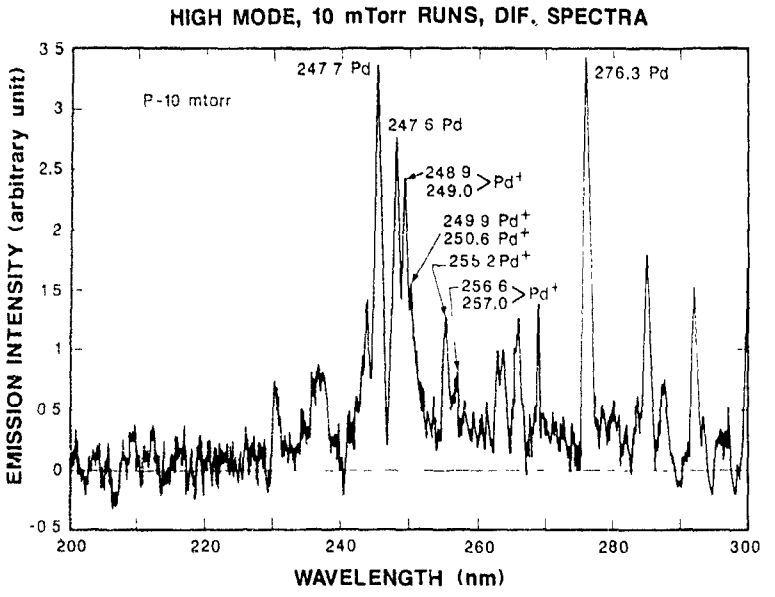

Fig. 5. Differential optical emission spectrum of a triode PIII configuration with Pd sputtered off from a biased target in an Ar plasma.

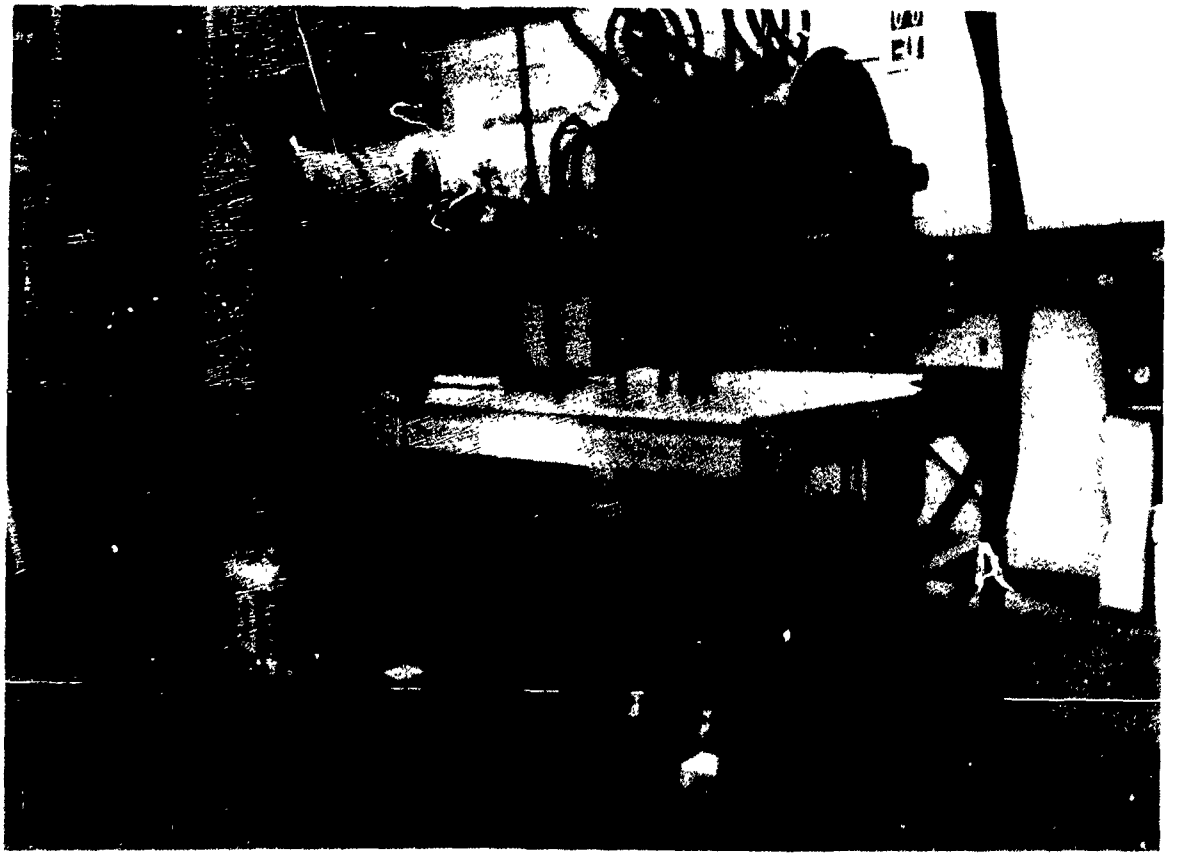

Fig. 6. Photograph of the UCB engineering PIII reactor.

information on the ionization efficiency of sputtered atoms for various PIII conditions.

This ion-assisted physical vapor deposition (IAPVD) is very attractive for processing multilevel metallization in ULSI. Example applications for ULSI processing are seeding implantation for selective deposition of interconnects and ion beam mixing of interfaces. Compound thin-film deposition formed by reactive sputtering is also possible if the ECR plasma gas has the chemical constituents of the desired compound.

The pulsed PIII mode is necessary if dielectric coatings are present on the substrate surface. Otherwise, the dielectric surface will acquire a potential close to zero at steady-state, with all the applied potential drop across the dielectric layer. The tradeoff with pulse mode operation is a smaller time-average dose rate unless the voltage supply can maintain high duty factors for the bias pulses. For conductive substrates, the dc-PIII mode is advantageous for high throughput applications because the implantation current is no longer restricted by the duty factor and repetition rate of the pulse power supply.

Performance of a prototype PIII reactor has been reported by Qian et al. [8]. Shown in fig. 6 is the photograph of an engineering PIII reactor recently constructed in the Plasma Assisted Materials Processing Laboratory of the University of California at Berkeley. The reactor is designed to study PIII issues such as implant uniformity over large areas, processing development, and reactor materials compatibility with IC process requirements. The system is powered by a commercial, well-regulated 1500 W ASTEX ECR 2.45 GHz microwave source. The power is coupled into the 6-inch diameter source chamber using a TE_{10} rectangular to TM_{01} circular mode converter which eliminates azimuthal plasma non-uniformities and provides increased radial uniformity over conventional coupling schemes. The plasma expands into an 18-inch diameter, 30-inch long process chamber where the implantation takes place. The vacuum system consists of a 1000 ℓ/s turbomolecular pump for corrosive gas handling backed by a mechanical pump. Both the source and process chambers are aluminum for materials compatibility with the usual IC processes. The 12-inch diameter wafer holder can be cryogenically cooled to control the temperature during implantation and has been designed to accommodate wafers up to 10 inches in diameter. Initial testing of the reactor indicates an ion density of 10^{10} to 10^{11} cm^{-3} at the wafer holder with a microwave power from 500 to 1000 W.

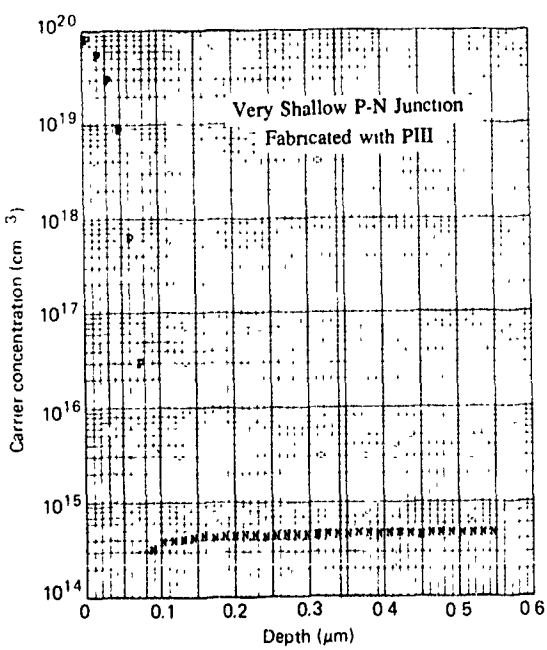

Fig. 7 SRP profile of 80 nm p^+/n junction formed by PIII. The preamorphization was performed in a SiF_4 plasma (4 kV, 25 mC, dc) followed by BF_3 plasma (2 kV, 10 mC, dc) for doping. RTA: 1060 °C, 1 s. Sheet resistance, 447 Ω.

4. Applications for ULSI processing

4.1 Sub-100-nm junction formation

Because of PIII's high current and low energy capabilities, it is well suited for ultra-shallow junction formation. Qian et al. [9] have reported results of sub-100-nm p^+/n junction formation in Si. They have tried both (i) direct PIII from BF_3 plasma, and (ii) SiF_4 PIII for preamorphization followed by BF_3 PIII. Secondary ion mass spectrometry (SIMS) profiling shows the PIII profiles peaks at the surface, follow by a rapid decrease of the implant concentration. This decaying profile is characteristic of the energy distribution of PIII. Rapid thermal annealing was used for the post-implantation step to minimize the diffusion thermal budget. For the direct PIII samples, the dopant activation behavior is very similar to conventional implantation of BF_2^+. Without preamorphization, rapid initial diffusion of the boron was observed for the first few seconds of the diffusion cycle, giving a junction depth in excess of 100 nm [10].

To circumvent the rapid boron diffusion process, the Si substrate was preamorphized with SiF_4 PIII prior to the boron implantation. In fig. 7, we show the spreading resistance profiling (SRP) results of samples annealed at 1060 °C for 1 s. An extremely low junction depth of 80 nm was obtained with a sheet resistance of 447 Ω/□.

4.2 Conformal doping of non-planar Si structures

The high packing density of devices in ULSI is made possible by making use of vertical sidewalls for active

Fig. 8 SEM micrograph of an Si trench after BF_3 PIII and junction staining The junctions were formed by annealing at 1000 °C for 30 s The implant area is about 50 cm^2

transistor channels and charge storage elements such as trench capacitors. Conventional implantation techniques have focused on multi-step implants with collimated beam at controlled beam incidence angles [11] Using an ECR source and RF substrate bias, Mizuno et al. have shown excellent trench doping uniform for trenches with 0.5 μm openings [12].

Taking advantage of the beam divergence angle of PIII, Qian et al have demonstrated conformation doping of high aspect-ratio Si trenches with BF_3 doping [13]. In this experiment, Si trenches about 1 μm wide and 5 μm deep were etched into n-type Si wafers by reactive ion etching. A blanket PIII of BF_3 plasma was performed with a bias voltage of −10 kV at a gas pressure of 5 mTorr After annealing at 1000 °C for 30 s in nitrogen, the wafers were cleaved and stained in a 30 $(HNO_3)\cdot 1$ (HF) solution to delineate the p^+/n junction. Shown in fig. 8 is a scanning electron microscopy (SEM) micrograph of the stained Si trenches The uniform formation of p^+-layers with a junction depth of 300 nm along the trench sidewall was observed. Since the junction depths on the planar regions and the sidewall are identical, this clearly demonstrates the applicability of PIII for the conformal doping process.

Three mechanisms have been proposed to explain the conformal doping of vertical structures by PIII: (i) specular reflection of impinging ions by internal sidewalls, (ii) angular divergence of the incident ion flux due to ion–neutral scattering, and (iii) electrostatic defocusing of ion beams due to protruded surface structures. Further work is needed to clarify the contributions of the proposed mechanisms.

4.3 Seeding for planarized selective metal deposition

To minimize *RC* time delays in ULSI circuits, multilevel interconnects are a necessity. The fine features of

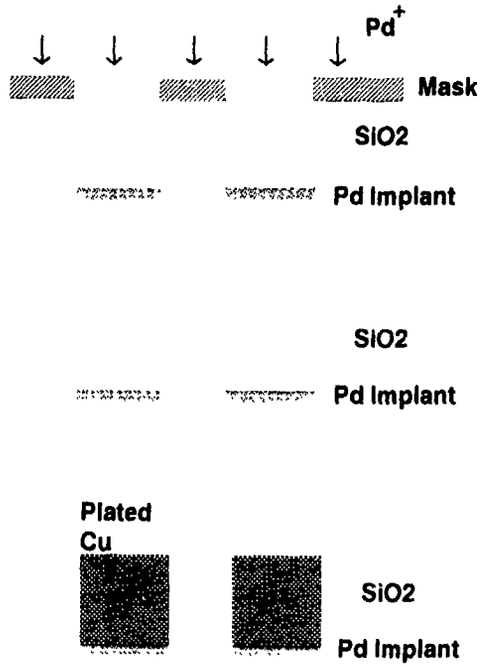

Fig 9. Process flow for selective plating of copper interconnects in SiO_2 trenches with Pd PIII seeding

the interconnects and the small metal-to-metal pitch also requires planarized dielectric isolation and vertical filling of contact vias. Recently, selective deposited tungsten and electroless plated copper have been investigated extensively for this purpose. Seeding by Si or W implantation for selective tungsten deposition was first demonstrated by Thomas et al. [14,15]. Both conventional implantation and MEVVA implantation have been used in these investigations [16].

Since copper has a very low electrical resistivity (2 μΩ-cm) and exhibits good electromigration properties, it

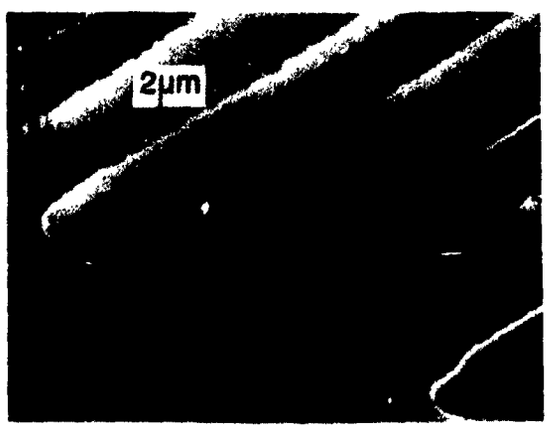

Fig. 10. SEM micrograph showing plated Cu interconnects in SiO_2 trenches. The interconnect linewidth is 3 μm.

is an ideal conductor for IC interconnects. Unfortunately, reactive ion etching of copper has not been successful so far due to the lack of suitable volatile copper etching by-products. Using PIII, Qian et al. have recently reported selective electroless plating of copper interconnects with Pd seeding [17]. With conventional copper electroless plating, a Ti layer is first deposited on the SiO_2 substrate. The Ti surface is then activated by a Pd exchange process with a PdCl solution, followed by the plating process which uses a mixture of $CuSO_4$ and KCN solution [18]. Since both the activation and plating steps depend critically on the seeding surface chemistry, the process window is extremely narrow, giving irreproducible deposition from run to run. Hence, the direct implantation of Pd by PIII greatly simplifies the plating process by eliminating the Pd activation solution for seeding copper plating.

For Pd PIII, a triode configuration is used with Ar gas to excite the plasma source. A Pd sputtering target is immersed in the plasma and has an independently controlled negative bias to regulate the sputtering rate. The sputtered neutral Pd will form a continuous flux for deposition while the Ar^+ and Pd^+ will assist the penetration of deposited Pd into the substrate via the ion beam mixing and direct implantation mechanisms. Rutherford backscattering spectroscopy (RBS) analyses show that the threshold Pd dose required to seed Cu plating is about 4×10^{14} cm^{-2} and Pd penetration below the SiO_2 surface is about 10 nm when a substrate bias of -6 kV was used. For pure Ar PIII, no Cu plating can be detected on the SiO_2. This result indicates the seeding process is controlled by the Pd enriched surface and is not related to implantation damage.

Using masking to define the SiO_2 trenches as well as an implantation mask, Pd PIII was then used to seed the bottom of the trenches. After mask removal, electroless copper will only be selectively deposited inside the trenches but not on the masked area. The process flow is shown in fig. 9. Fig. 10 shows the SEM micrograph of the plated Cu lines inside the SiO_2 trenches.

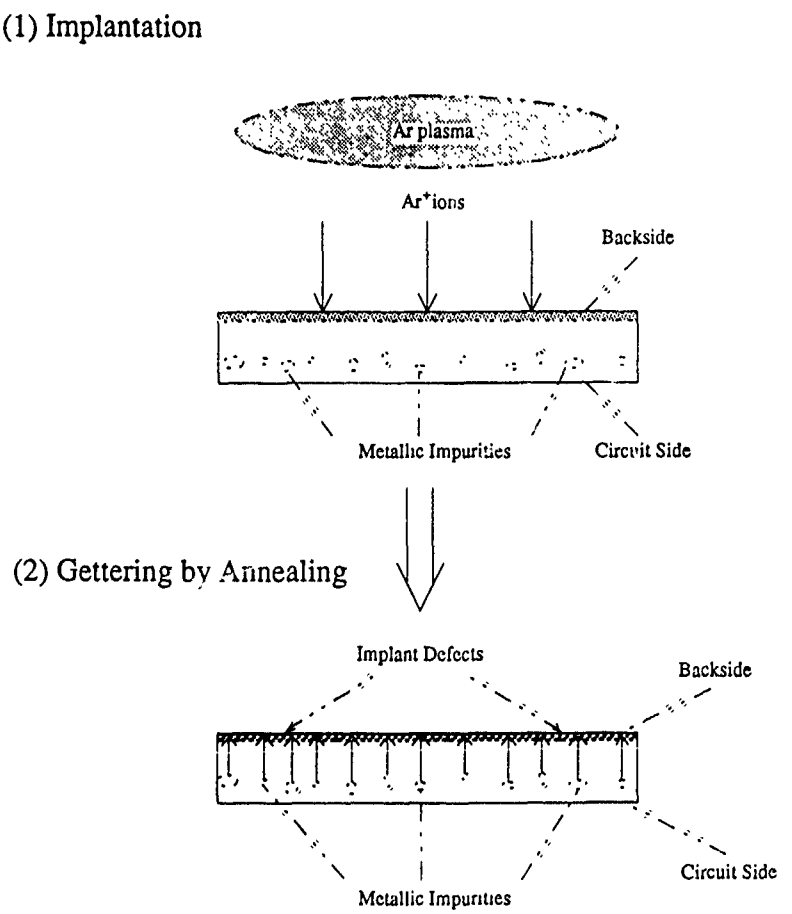

Fig. 11. Process flow showing backside damage impurity gettering using PIII.

4.4 Impurity gettering with implant damage

It is well-known that damage created by ion implantation of noble gas at the backside of Si wafers can form gettering centers for metallic impurities [19]. However, this backside gettering technique is not cost-effective using conventional implanters because of the high dose needed. Since the implant damage profile is not important and the dose uniformity requirement across the whole wafer is not stringent, PIII is well-suited for this application with its extremely high implantation dose-rate.

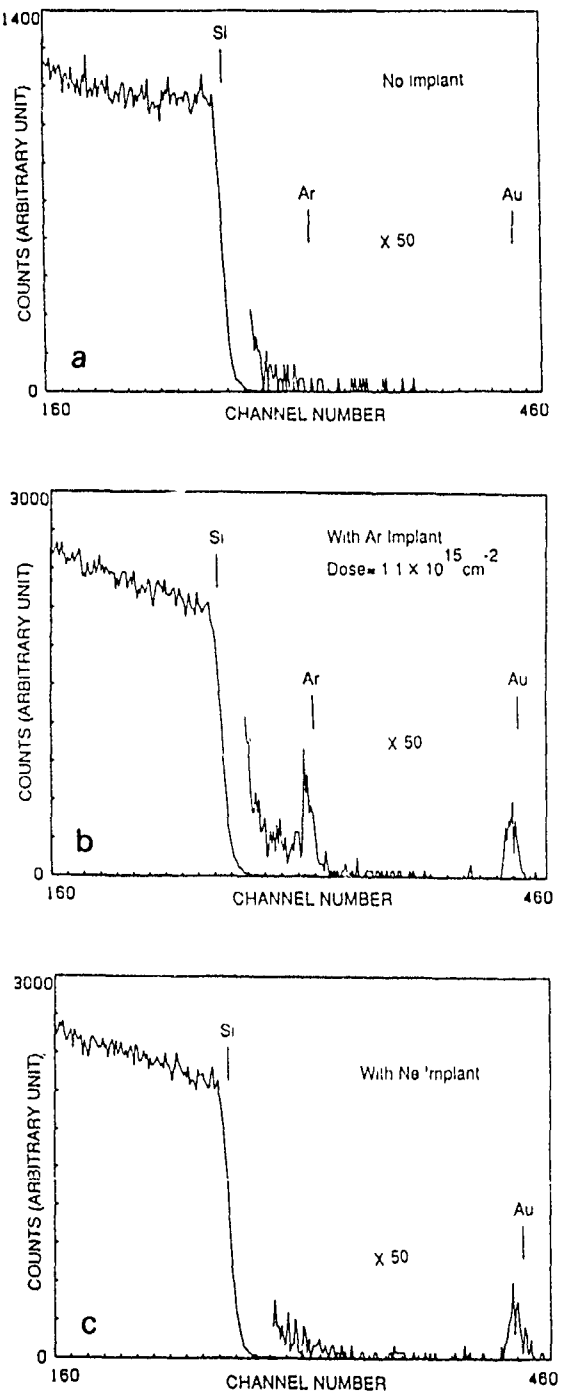

Fig. 12. RBS spectra of Au-doped Si wafers. (a) Without implant. (b) With Ar implant at a dose of 1.1×10^{15} cm^{-2} and peak voltage of -38 kV. The amount of gettered Au was 4.4×10^{13} cm^{-2}. The surface peak positions of Ar and Au are marked in the figure. The portion of the spectra containing Ar and Au peaks was magnified 50 times. (c) With Ne implant. The bias pulse peak voltage was -38 kV. The amount of gettered Au was 4.5×10^{13} cm^{-2}. The Au surface peak position is marked in the figure. The portion of the spectrum containing the Au peak was magnified 50 times. The wafers were annealed at 1000 °C for 1 h.

Wong et al. [20] and Qian et al. [21] have recently demonstrated the effectiveness of using PIII to getter Au, Ni and Cu in silicon wafers. The process sequence of PIII backside gettering is illustrated in fig. 11. In their experiments, p-type CZ silicon wafers with (100) orientation and resistivity of 15 Ω cm were used. After metal marker diffusion, the surface of the wafers were subjected to ion implantation with Ar or Ne PIII at a negative dc or pulsed voltage of 20–40 kV. During operation, the gas pressure was about 10^{-3} Torr, and the microwave power was 700 W. The gettering thermal annealing was performed at 1000 °C for 1 h in a N_2 ambient.

Two RBS spectra of Au doped wafers with and without the Ar implantation are shown in figs. 12a and b. The gettering effect of Au at the silicon surface due to PIII is evident. The gettered Au areal density is about 4.4×10^{13} cm^{-2} for an Ar implant dose of 1.1×10^{15} cm^{-2} after annealing. Fig. 12c shows the Ne implant gettering effect. The implanted Ne atoms cannot be measured by RBS due to their light mass. The implanted dose is comparable to the Ar dose in fig. 12b based on wafer charge integration measurements. An areal density of 4.5×10^{13} cm^{-2} of Au was detected in the surface of Ne implanted wafer. PIII of Ar into Si also shows more efficient gettering of Ni and Cu, an effect probably due to the larger diffusivities of these metals in silicon.

5. Wafer charging considerations

For MOS devices used in ULSI circuits, thin gate oxides on the order of 5 to 10 nm will be used. For self-aligned source/drain implants, of great concern is whether the gate will accumulate enough charge during

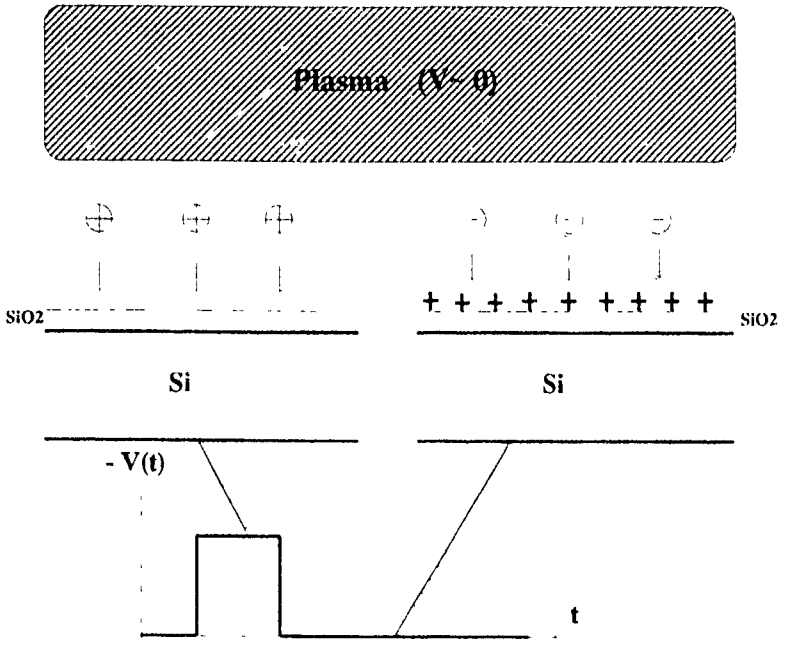

Fig 13 Schematic showing the wafer charging sequence with PIII operating in the pulse mode. Electrons will be attracted towards the substrate by positive surface charge during off-cycle of pulse

implantation causing oxide breakdown. Similar wafer charging problem have also been reported for poly-Si doping implants. With conventional heavy current implanters, electron flood guns are often employed to neutralize the accumulated positive ion charge with various degree of success.

It is important to point out that the PIII process has a built-in mechanism to neutralize surface positive charge accumulation. Fig. 13 shows a simplified wafer charging sequence of a SiO_2 on Si structure during PIII. As discussed previously in the PIII operation mode section, pulsed mode is required for substrates with insulating surface coatings. At the onset of the negative pulse, the surface potential of SiO_2 will be equal to $-V(t)$ since the voltage across the oxide capacitor cannot be changed instantaneously. This negative surface potential will induce the ion implantation, creating a positive surface charge and attracting the plasma electrons for neutralization during the off cycle of the pulse. If we define Q_{max} to be the maximum positive surface charge per unit area acquired for each PIII pulse which will create oxide breakdown, Q_{max} is the equal to.

$$Q_{max} = E_{breakdown}(SiO_2) \times \epsilon_{ox}, \quad (4)$$

where $E_{breakdown}(SiO_2)$ and ϵ_{ox} are the breakdown field and dielectric constant of SiO_2 respectively. Using a conservative breakdown field of 5 MV/cm, Q_{max} is on the order of 1×10^{13} q/cm^2-pulse. This worst-case consideration strongly suggests that for MOS PIII applications, it is preferable to use short duty-factor and high frequency pulses.

To investigate the wafer charging problem and to study PIII oxide damage effects, aluminum $C-V$ dots with diameters from 100–1000 μm were deposited on SiO_2/n-Si substrates. The gate oxide thickness was 20 nm. These test wafers were subjected to blanket PIII with conditions similar to those of shallow p^+/n junction formation using SiF_4 preamorphization and BF_3 doping. Oxide breakdown testing was then carried out without post-implant annealing. The breakdown field is the same (8 MV/cm) for samples without implantation and with PIII dose of 10^{16} cm^{-3}. $C-V$ tests of the MOS capacitors also show no threshold shift due to the high dose PIII.

6. Conclusions

The motivation for developing the PIII technology is primarily driven by recent processing and manufacturing requirements for ULSI device structures. From the machine design point of view, the simplicity of PIII reactors makes it an ideal candidate for cluster-tool development. The impurity contamination issue will need reactor design improvement but the technical difficulties are similar to those of reactive ion etching and plasma enhanced chemical vapor deposition. Uniformity requirements on the order of 1% across 8-inch Si wafers is difficult to attain with present ECR sources

but distributed ECR sources, magnetic plasma confinement, and substrate holder design are potential candidates for better uniformity [24].

Recent processing research shows very favorable results to use PIII for conformal doping, preamorphization, high dose doping, selective plating of metal interconnects, and damage induced impurity gettering. Although the dose-rate capability of PIII is extremely high, wafer heating will be the limiting factor for throughput considerations in ULSI processing. PIII is also unlikely to replace conventional implanters for applications such as threshold voltage tailoring or bipolar base doping, where energy and beam purity are of utmost concern. However, for applications where the implant depth profile is noncritical such as source/drain formation, poly-silicide doping, trench capacitor doping, and multilevel metallization, PIII does offer many unique features for fabricating new device structures.

References

[1] J.R. Conrad, J.L. Radtke, R A. Dodd, F.J. Worzala and N C. Tran, J Appl. Phys. 62 (1987) 4591

[2] J Tendys, I J Donnelly, M J. Kenny and J T.A Pollock, Appl Phys Lett 53 (1988) 2143.

[3] M A Lieberman, J Appl Phys 66 (1989) 2926.

[4] C D Child, Phys Rev 32 (1911) 492

[5] J R Conrad, J Appl Phys 62 (1987) 777

[6] M.V Alves, V Vahedi and C K Birdsall, Bull. Am Phys Soc 34 (1989) 2028

[7] C K Birdsall and A B Langdon, Plasma Physics via Computer Simulation (McGraw-Hill, New York, 1985)

[8] X.Y. Qian, H. Wong, D Carl, N W Cheung, M.A Lieberman, I G. Brown a M I Current, these Proceedings (8th Int Conf on Ion Implantation Technology, Guildford, UK, 1990) Nucl. Instr and Meth B55 (1991) 884.

[9] X.Y. Qian, N.W. Cheung, M.A Lieberman and M I Current, ibid., p. 821

[10] A E Michel, W. Rausch, P.A Ronsheim and R.H. Kastl, Appl Phys Lett. 50 (1987) 416.

[11] I. Kaim, Solid State Technol 33 (1990) 103

[12] B. Mizuno, I Nakayama, N Aoi, M Kubota, and T Komeda, Appl. Phys. Lett. 53 (1988) 2059

[13] X.Y. Qian, N.W Cheung, M A Lieberman and M I. Current, these Proceedings (8th Int. Conf on Ion Implantation Technology, Guildford, UK, 1990) Nucl. Instr and Meth B55 (1991) 898.

[14] D.C Thomas and S.S Wong, IEDM 86 (1986)

[15] D.C. Thomas, N.W Cheung, I G. Brown and S S. Wong, in. Tungsten and other Advanced Metals for VLSI/ULSI Applications V, eds. S S Wong and S Furukawa (Mat. Res Soc., Pittsburgh, 1990) p 233

[16] I Brown and J Washburn, Nucl Instr and Meth B21 (1987) 201.

[17] X.Y Qian, M H. Kiang, D Carl, N.W Cheung, M A Lieberman, I.G Brown, K M Yu and M I Current, these Proceedings (8th Int Conf on Ion Implantation Technology, Guildford, UK, 1990) Nucl Instr and Meth. B55 (1991) 888

[18] C H. Ting, M Paunovic, P.L Pai and G Chiu, J Electrochem. Soc 136 (1989) 462.

[19] T E Seidel, in· Material Issues in Silicon Integrated Circuit Processing, eds M Wittmer, J Stimmell and M Strathman (Mat. Res. Soc Pittsburgh, 1986) p 3

[20] H. Wong, X Y. Qian, D. Carl, N.W Cheung, M.A. Lieberman, I.G Brown and K.M Yu, Mater Res Soc. Symp Proc. 147 (1989) 91.

[21] X.Y Qian, H Wong, D Carl, N W Cheung, M A Lieberman, I.G Brown and K M Yu, Proc ECS Symp on Ion Implantation for Elemental and Compound Semiconductors, vol. 90-13 (1990) p. 268

Nuclear Instruments and Methods in Physics Research B55 (1991) 821–825
North-Holland

Sub-100 nm p +/n junction formation using plasma immersion ion implantation

X.Y. Qian, N.W. Cheung and M.A. Lieberman

Plasma Assisted Materials Processing Laboratory, Department of Electrical Engineering and Computer Sciences, University of California, Berkeley, CA 94720, USA

M.I. Current

Applied Materials, Inc., Implant Division· MS0907, 3050 Bowers Avenue, Santa Clara, CA 95054, USA

P.K. Chu

Charles Evans and Associates, 301 Chesapeake Drive, Redwood City, CA 94063, USA

W.L. Harrington, C.W. Magee and E.M. Botnick

Evans East, Inc., The Office Center, 666 Plainsboro Road, Suite 1236, Plainsboro, NJ 08536, USA

Using plasma immersion ion implantation (PIII), sub-100 nm p+/n junctions were fabricated with SiF_4 preamorphization followed by BF_3 doping. With this technique, the dose rate can be as high as $10^{16}/cm^2$ per second. The silicon wafer was immersed in SiF_4 or BF_3 plasma and biased with a negative voltage. The positively charged ions were accelerated by the electric field in the plasma sheath and implanted into the wafer. The junction depth can be controlled by varying the negative voltage applied to the wafer holder and thermal annealing conditions.

1. Introduction

Extremely shallow (less than 100 nm) p+/n junction formation is a key issue in the development of submicron CMOS technology. With conventional ion implanters, molecular ion BF_2^+ has been used as the implant species to lower the boron effective kinetic energy [1]. In order to reduce the channeling effect and to activate dopants without excessive diffusion, an implantation step to preamorphize the silicon substrate prior to BF_2^+ implantation is also required [2]. Since relatively large doses are needed for both preamorphization and doping, the overall implantation process can be time consuming.

A large dose rate ion implantation technique, plasma immersion ion implantation (PIII), has been used to implant nitrogen and other ion species into the surface of machine parts to improve wear or corrosion resistance [3–4]. Recently, a prototype plasma PIII apparatus dedicated to integrated circuit processing has been developed, and was successfully applied to implant noble gas ions into Si for metallic impurity gettering [5,6]. In this paper, we show that PIII can be used for sub-100 nm p+/n junction fabrication. Both SiF_4 preamorphization and BF_3 doping were carried out in sequential steps by switching the plasma gases.

2. Experiment

Shown in fig. 1 is a schematic of the p+/n junction fabrication process using the PIII technique. The silicon wafer was immersed in a SiF_4 plasma for preamorphization, then in a BF_3 plasma for doping. The wafer was biased with a dc or pulsed negative voltage. A plasma sheath around the wafer was generated by the applied

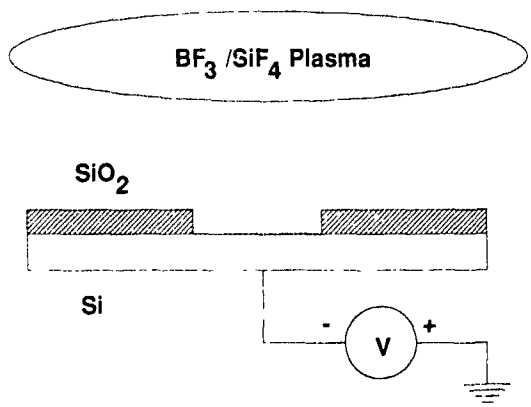

Fig. 1. Schematic of p+/n junction fabrication process using plasma immersion ion implantation.

0168-583X/91/$03.50 © 1991 – Elsevier Science Publishers B.V. (North-Holland)

negative potential. The positively charged ions were accelerated by electric field in the sheath and implanted into the wafer. The plasma was excited in an electron cyclotron resonance (ECR) discharge chamber with an 800 W, 2.45 GHz microwave power supply. The charge flow per pulse, including ions and secondary electrons, was measured with a current transformer (Rogowski loop) connected to an integrator. The total dose was later calibrated against the number of pulses When a dc bias is used, the dose was monitored with a current meter serially connected in the circuit. For this shallow p+/n junction study, we have investigated both dc and pulsed bias methods To avoid wafer heating and to obtain better dose control, a lower microwave power of 100 W was used. A detailed description of the PIII apparatus has been presented elsewhere [7]

After the PIII doping process, the Si wafer was rapid thermal annealed (RTA) to activate the boron dopant. RTA was performed in a N_2 ambient at a flow rate of 3 SCCM to prevent sample surface oxidation Sheet resistance was then measured with a four point probe, and the carrier profiles were measured using the spreading resistance (SPR) technique Secondary ion mass spectroscopy (SIMS) was used to analyze the implant depth profiles before and after annealing

3. Results and discussion

Experimental results of sheet resistance and junction depth dependence on dosage and bias potential are presented in figs 2, 3 and 4 P-type CZ wafers with resistivity of 10–50 Ω cm were used The BF_3 gas pressure was set at 1 mTorr A dc voltage from −500 V to −20 kV was applied as the wafer bias. After PIII, all samples were annealed for 20 s at various temperatures.

Fig 2 shows the sheet resistance dependence on PIII dose as charge per unit wafer area. The wafer bias was set at −5 kV for this group of samples As shown in fig 2, the sheet resistance decreases monotonically with the dose As the dose was raised from 0.05 mC/cm^2 to 0.5 mC/cm^2, the sheet resistance dropped from 1050 Ω/□ to 100 Ω/□ However, the curve flattened out as the dose exceeded 4 mC/cm^2. The minimum sheet resistance obtained was 50 Ω/□ with −5 kV bias and RTA at 1060°C for 20 s From SIMS and SPR profile studies, it was found that the boron atomic concentration near the silicon surface of the samples was well above the activation limit of 2×10^{20} cm^{-2} at 1060°C [8]. Lower sheet resistance was achieved by annealing these samples at higher temperature or for a longer time, because a larger fraction of boron atoms was driven-in to a concentration below the activation limit. With our experimental PIII system, the standard deviation of sheet resistance across a 2 in. wafer was about 40% when a pulsed bias was used. In dc mode, the uniformity is poorer, especially when the bias voltage is high A much better uniformity is expected with the recently constructed 10 in. reactor in UC Berkeley

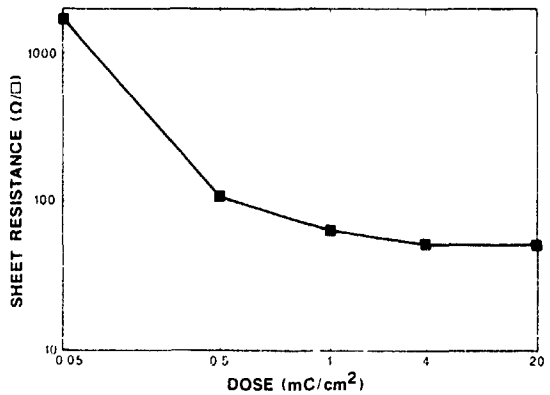

Fig 2. The sheet resistance dependence on BF_3 PIII dose The wafer bias was −5 kV and RTA was performed at 1060°C for 20 s for this group of samples. The minimum sheet resistance obtained was 50 Ω/□ under this condition

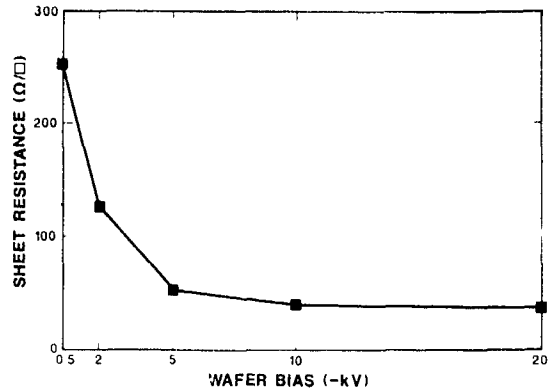

Fig 3 The sheet resistance dependence on wafer bias voltage Samples were implanted with BF_3 PIII at a dose of 4 mC/cm^2 and annealed at 1060°C for 20 s A dc bias from −500 V to −20 kV was applied during implantation

Sheet resistance dependence on wafer bias is shown in fig 3 At a dose of 4 mC/cm^2, sheet resistance dropped from 250 Ω/□ to 50 Ω/□ as the negative bias increased from 500 V to 5 kV. Using SIMS analysis, it was found that a large portion of boron atoms was localized near the surface region with a concentration above the activation limit for the −500 V and −2 kV samples, so that higher sheet resistances were observed in these samples. However, in higher biased samples, dopants were more evenly distributed due to the deeper penetration of the more energetic ions, which led to a higher percentage of activated boron. Further raising of the voltage did not affect the resistance much for this particular dose condition because a full activation was nearly reached

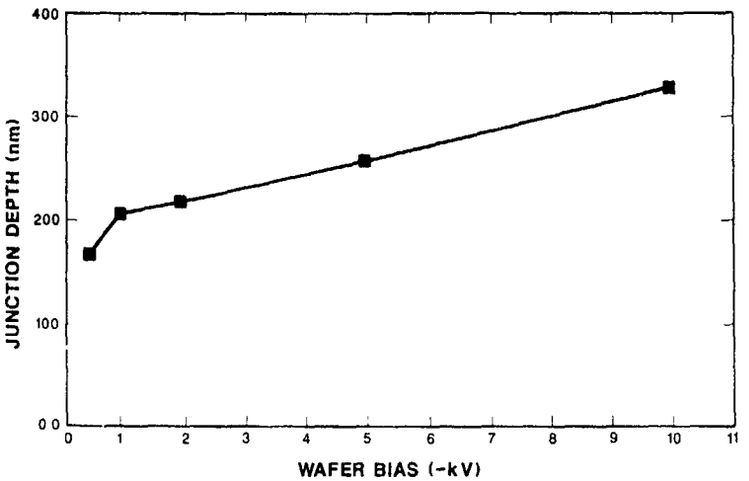

Fig. 4 The electrical junction depth dependence on wafer bias Samples were implanted with bias from −500 V to −10 kV at a fixed dosage of 4 mC/cm^2 and annealed at 1060°C for 20 s

Shown in fig 4 is the effect of bias voltage on electrical junction depth, as defined by a junction carrier concentration of 10^{15}/cm^3. As expected, the higher bias potential increased the implantation ion energy, which in turn resulted in a deeper junction However, the junction depth in all samples annealed at 1060°C

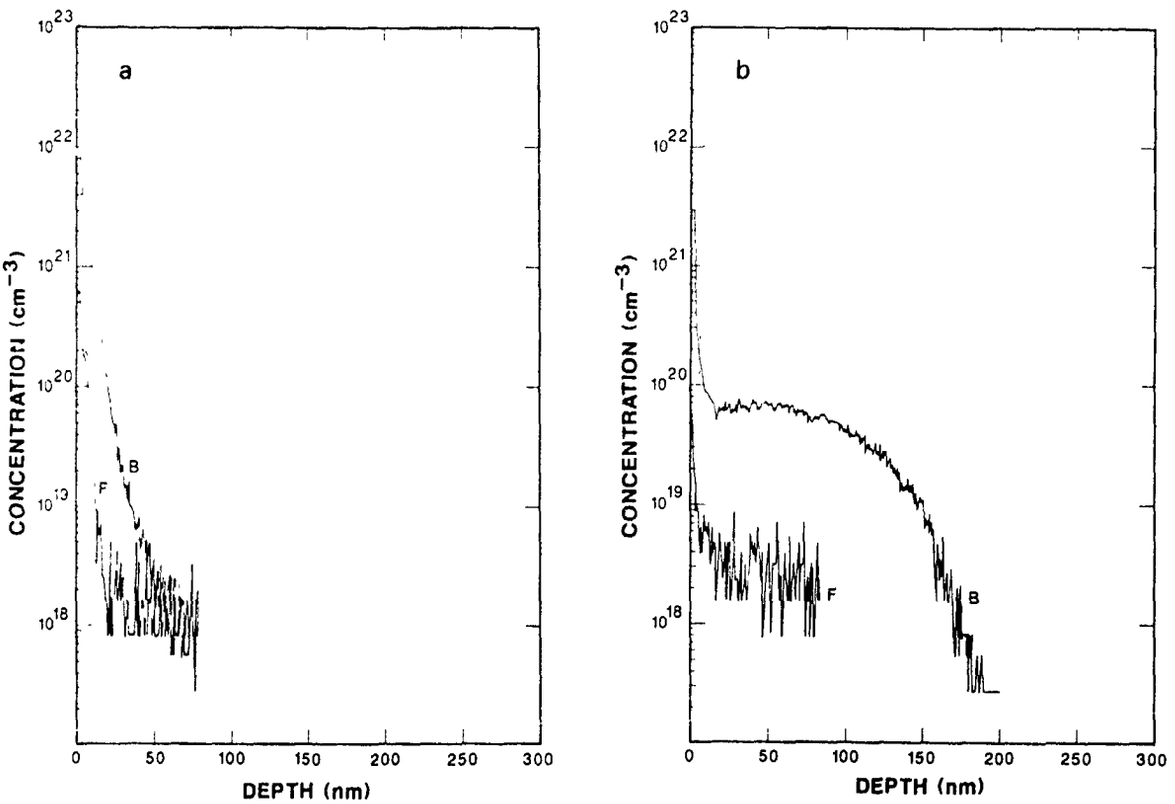

Fig 5 SIMS profiles of BF_3 plasma immersion ion implanted Si wafers before (a) and after (b) thermal annealing. The "B" and "F" in the figures represent boron and fluorine concentrations, respectively The doping was carried out at a −2 kV dc bias with a gas pressure of 3 mTorr. The implantation dose was 4 mC/cm^2 The sample in (b) was annealed at 1060°C for 20 s

for 20 s was much deeper than the prediction of LSS theory [9]. Moreover, extrapolation of x_j to zero bias voltage gives a value of 140 nm. The apparently high x_j with a low-energy implantation suggests that sub-100 nm p + /n junction formation in crystalline Si substrate with the above annealing condition is not feasible, even when the applied bias voltage is reduced to zero.

A pair of SIMS profiles from a sample before and after annealing are presented in figs. 5a and 5b. BF_3 PIII doping was performed at 3 mTorr gas pressure with a dc bias of -2 kV. The dose was 4 mC/cm^2. As shown in fig. 5a, the boron profile peak was very close to the wafer surface. The boron concentration decreased by three orders of magnitude to 1.5×10^{19}/cm^3 at a depth of 30 nm below the surface. However, this boron concentration was located at 130 nm after a thermal annealing at 1060°C for 20 s as shown in fig. 5b. This rapid diffusion of shallow implanted boron during annealing is in agreement with observations in conventional implantation experiments [10,11]. Apparently, a shorter RTA cycle or lower annealing temperature is required for sub-100 nm p + /n junction fabrication.

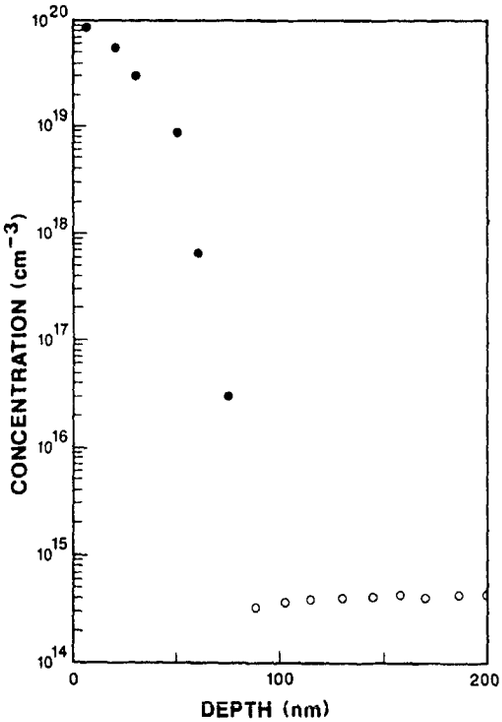

Fig. 6. The SPR profile of sub-100 nm p+/n junctions fabricated with PIII. The preamorphization was performed in SiF_4 plasma at -4 kV dc bias with a dose of 3×10^{15}/cm^2. The doping implantation was then performed in BF_3 plasma at -2 kV dc bias with a dose of 1.2×10^{15}/cm^2. The post-implantation annealing was performed at 1060°C for 1 s.

An interesting observation to be noted from the SIMS measurements was the fluorine depth distribution of the as-implanted samples. Due to a moderate electron temperature of 4–8 eV in ECR plasmas, most ions generated are presumably in the form of one-fluorine-stripped, singly charged BF_2^+. However, the total amount of fluorine measured in fig. 5a was much less than the boron dose. The existence of a small concentration of double-fluorine-stripped ions and fluorine outdiffusion during PIII may be responsible. As shown in fig. 5b, most fluorine outdiffused after RTA at 1060°C for 20 s.

To check the effect of ion channeling during the PIII process, we have compared the SIMS profiles of BF_3 PIII into crystalline and amorphous CVD silicon samples. A steeper decay of the SIMS profile tail for the amorphous sample indicates that a preamorphization step will help to reduce the junction depth.

To demonstrate the feasibility of fabricating sub-100 nm p + /n junctions, we have used SiF_4 PIII preamorphization followed by BF_3 PIII doping. To show the real p + /n junction, n-type CZ wafers with resistivity of 8–12 Ω cm were used in this experiment. DC wafer bias was applied for both implantation steps. The preamorphization was performed in SiF_4 plasma with a -4 kV dc wafer bias at the gas pressure of 3 mTorr. A preamorphization dose of 3×10^{15}/cm^2 was obtained in about 10 s. The doping implantation was then performed in BF_3 plasma at a bias of -2 kV to a dose of 1.2×10^{15}/cm^2. The post-implantation annealing was performed at 1060°C for 1 s. As shown in the SPR profile of fig. 6, the observed peak carrier concentration is 1×10^{20} cm^{-3}. The electrical junction depth is only 80 nm and the sheet resistance is 447 Ω/□.

4. Conclusion

Sub-100 nm p +/n junctions were fabricated with PIII. Using PIII, the dose rate can be much larger than with conventional ion implanters. The sheet resistance and junction depth can be regulated with implantation dosage, wafer bias and RTA conditions. For extremely shallow p +/n junction formation, sample preamorphization, moderate boron dose and short-cycle RTA are required. With SiF_4 PIII preamorphization followed by a -2 kV BF_3 PIII at a dose of 1.2×10^{15}/cm^2 and RTA at 1060°C for 1 s, 80 nm p + /n junctions were successfully obtained.

Acknowledgement

This work was supported by Applied Materials, Inc. and a grant from the California State MICRO program.

References

[1] S.N Hong, G A. Ruggles, J.J Paulos, J J Wortman and M.C. Ozturk, Appl Phys Lett 53 (1988) 1741

[2] C M Lin, A J Steck and T.P. Chow, Appl Phys. Lett 54 (1989) 1790

[3] J R. Conrad, J.L. Radtke, R A Dodd, F J Worzala and N.C Tran, J. Appl Phys 62 (1987) 4591

[4] J. Tendys, I.J. Donnelly, M.J. Kenny and J T.A. Pollock, Appl Phys. Lett 53 (1988) 2143.

[5] H Wong, X Y Qian, D Carl, N W Cheung, M.A Lieberman, I G Brown and K.M Yu, MRS Symp Proc 147 (1989) 91

[6] X Y Qian, H Wong, D Carl, N W Cheung, M A Lieberman, I G Brown and K M Yu, Proc. Symp on Ion Implantation and Dielectrics for Elemental and Compound Semiconductors, vol. 90-13 (Electrochemical Soc., 1990) p. 268

[7] X.Y. Qian, D Carl, J. Benasso, N W Cheung, M A. Lieberman, I G. Brown, J E. Galvin, R A. MacGill and M.I. Current, these Proceedings (8th Int Conf. on Ion Implantation Technology, Guildford, UK, 1990) Nucl. Instr. and Meth B55 (1990) 884

[8] H Ryssel, K Muller, K. Haberger, R Henkelmann and F Jahael, Appl. Phys. 22 (1980) 3

[9] J Lindhard, M. Scharff and H Schiott, K. Dan Vidensk Selsk. Mat.-Fys Medd. 33 (no 14) (1963) 1

[10] T.E Seidel, D J Lischner, C S Pai, R V Knoell, D.M Maher and D C Jacobson, Nucl. Instr and Meth B7/8 (1985) 251

[11] R.T. Hodgson, V R Deline, S. Mader and J.C Gelpey, Appl. Phys Lett 44 (1984) 589.

Nuclear Instruments and Methods in Physics Research B55 (1991) 826-830
North-Holland

SIMOX-material quality in a semi-industrial production

J.M. Lamure, J. Margail, B. Biasse, J.F. Michaud, A. Soubie, C. Pudda, F. Gusella and C. Jaussaud

Laboratoire d'Electronique, de Technologie et d'Instrumentation, Commissariat à l'Energie Atomique, Centre d'Etudes Nucleaires de Grenoble, 85X, 38041 Grenoble Cedex, France

Based on the results of five years of research on the SIMOX process, a complete facility for production of SIMOX wafers on a semi-industrial basis has been set up at LETI. This facility which is located in a class-100 clean room comprises an EATON NV 200 implanter, a high-temperature annealing furnace and nondestructive characterization tools. As-implanted wafers are characterized from the point of view of particles, implanted oxygen dose and dose homogeneity. After annealing, the silicon overlayer thickness and homogeneity are measured. Destructive characterization tools such as nuclear reaction analysis (NRA) for absolute oxygen-dose monitoring and secondary-ion mass spectrometry (SIMS) for metallic-impurity controls are also used. HEM and XTEM are used to monitor the dislocation density and the Si/SiO_2 interface quality. The SIMOX wafers have typically a 200 nm thick silicon layer on top of a 380 nm thick buried oxide and a dislocation density smaller than 5×10^5 cm^{-2}. This facility is also used for research on SIMOX material with a view to producing very thin (< 100 nm) silicon overlayers that will be required for the future CMOS/SOI circuit generations.

1. Introduction

LETI has been involved in producing silicon-on-insulator wafers formed by oxygen ion implantation (SIMOX) since 1984. Oxygen implantation was first performed on a conventional machine (1 mA current) equipped with a modified target chamber [1] that allowed wafer temperature control up to 700°C before and during the implantation. In 1985, high-temperature annealing was introduced [2], and a furnace specially designed for annealing up to 1350°C became available at LETI in 1986. Based on the results obtained on devices, the decision to set up a facility for SIMOX production was made in 1986. This facility has been operational since mid-1989. Before this date, most circuits processed in our laboratory used IBIS implanted wafers, annealed at LETI.

2. SIMOX wafer fabrication

The facility includes all the equipment for implantation, annealing and nondestructive characterizations. The process flow of wafer fabrication is the following.

2.1 Oxygen implantations

Oxygen implantations are done on an Eaton NV 200 implanter [3] equipped with an electron cyclotron resonance source. The beam is stationary, but a small dither is used to improve the homogeneity. The beam current on the wafers is 40 mA, and the implantations are performed into bare wafers.

2.2 Post-implantation control

Both destructive and nondestructive tests are done after implantation.

Nondestructive tests. Particles are counted on every wafer and the implanted dose is measured by infrared (IR) spectroscopy in one wafer, at 17 points. The wafers are observed at grazing incidence for detection of large defects such as scratches, and under an optical microscope for observation of small defects.

Destructive tests on one wafer in one batch out of five. Since IR is not an absolute measurement, the dose is controlled by nuclear reaction analysis [4], metallic contamination (Fe, Cr, Cu) is controlled by secondary-ion mass spectroscopy (SIMS) and the material quality is assessed by transmission electron microscopy (TEM) observation.

2.3 Annealing

High-temperature annealing is performed under a 600 nm thick SiO_2 cap at 1320°C in an argon atmosphere with a small percentage of oxygen. The furnace uses a SiC tube, and 100 wafers can be annealed per run. The maximum wafer size that can be annealed is 150 mm.

After cap-etching, the silicon thickness is measured by reflectivity, with a home-made program, at 17 points

0168-583X/91/$03.50 © 1991 – Elsevier Science Publishers B.V. (North-Holland)

on one wafer in each batch. The thickness is then adjusted to the required value by sacrificial oxidation.

Before delivery, the silicon thickness is controlled by reflectivity: measurements are performed at 1 point on each wafer, and at 17 points on one wafer The wafers are observed under an optical microscope and one wafer is taken for destructive control by SIMS, TEM and cross-sectional TEM (XTEM). Since two wafers are kept for destructive control, the delivered batches contain 23 wafers.

3. Production

3.1 Standard production

2500 wafers, which corresponds to 75% of the wafers produced, are standard, stabilized products. This production started in April 89, and has rapidly improved, compared to the specifications given by the implanter manufacturer (in particular dose homogeneity and particle levels) The more serious problem that stopped the machine for a long period was related to the target-chamber rotation system. An unusual number of particles were added during the implant, and it was found that the origin of this problem was a leak at the seal between the rotating shaft and the target chamber. The characteristics of the standard production that we can guarantee on 100 mm, ⟨100⟩ wafers, for a 190 keV implant energy into bare silicon are the following:

- dose, 1.8×10^{18} O^+/cm^2, ±2% on each wafer, ±3% batch to batch;
- temperature, 600 °C,
- SiO_2 thickness 380 nm;
- final silicon thickness: average value 200 ± 6 nm; ±8 nm uniformity on each wafer;
- total particle count: < 5 particles/cm^2 (for particles larger than 0.5 μm, measured before annealing).

Typical values for the dose and thickness across a wafer are shown in fig. 1. For the other parameters, we do not give the specifications, but typical values are the following:

- metallic contamination: smaller than the SIMS threshold;
- dislocation density: $< 5 \times 10^5$ cm^{-2};
- stacking faults: $< 10^4$ cm^{-2}.

Complementary tests are carried out on unimplanted substrates that went through all the other processing steps. These tests are particle count at every step and $C(V)$ characterization after high-temperature annealing

3.2 Nonstandard production

This facility is also used for research on the implantation, annealing, and thinning processes The research directions that are presently under way are the following.

(1) *Multistep implantations*: Implantation in two or three steps with annealing between the implants [5] has been performed to improve the material quality. We first observed that a two-step process on our research implanter was successful to obtain SIMOX structures with very low dislocation densities, and very few silicon islands at the lower Si/SiO_2 interface [6]. The same experiment carried out on an NV 200 implanter showed that silicon islands are still present in the buried SiO_2 after two-step implants, and three-step implants are

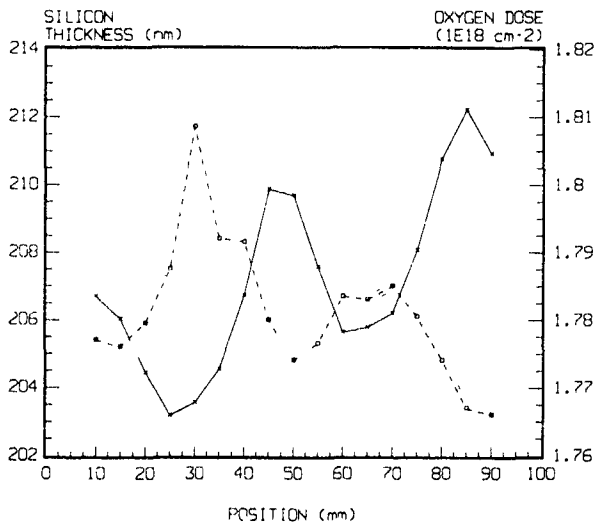

Fig. 1 Oxygen implantation dose (×) and silicon thickness (□) across a 100 mm wafer These measurements are taken along a diameter parallel to the larger beam dimension, which corresponds to the larger nonhomogeneities.

necessary to get the same result as on the research machine.

(2) *Implantation at lower energies*: the NV200 is designed to operate at 200 keV, and since the homogeneity relies on the energy distribution in the beam, any change in the implantation conditions (current or acceleration energy) requires a delicate optimization of the machine parameters. But the trend towards thinner silicon overlayers leads us to decrease the implantation energy, and the implantation can now be performed at 160 keV, leading after annealing to a silicon thickness of 150 nm These implantation conditions correspond to different values of beam current densities and temperature, which may have an impact on the material quality. Investigation of the quality of this material is presently under way

4. Characterization

The necessity of delivering batches with more and more exacting specifications has led us to increase the number of characterization steps, with emphasis on nondestructive tools. Most of these tools required an adaptation to the particular SIMOX structure

4 1 Particles

The counting of particles on wafers is based on the measurement of light diffused by the particles. This diffused light has two components. light scattered in the backward direction and light scattered in the forward direction and reflected at the silicon surface The latter is much stronger than the former, and for highly reflective substrates, the intensity received by the detector is roughly proportional to the substrate reflectivity. Unannealed substrates have very smooth Si/SiO_2 interfaces, and the total reflectivity is close to that of bulk silicon On the other hand, annealed substrates have very sharp Si/SiO_2 interfaces, and their reflectivity varies strongly, which leads to very large errors in the particle count. Calibrations done on unannealed SIMOX substrates with 0.36 μm latex spheres are very close to those on bulk silicon, whereas they are very different on annealed substrates. So, at the present time, we can count particles on unannealed wafers only. The measurements use a laser beam at 633 nm, a wavelength which is not strongly absorbed by silicon The use of a shorter wavelength strongly absorbed in the 200 nm thick silicon layer would eliminate the interferences with light reflected at the buried Si/SiO_2 interfaces but might be more sensitive to surface roughness. Systems working at a wavelength of 500 nm should soon be available on the market

4 2 Dose

Nondestructive dose control is performed by infrared (IR) spectroscopy The position and the shape of the SiO_2 absorption band around 1060 cm^{-1} depend on the nature of the Si–O bond and changing the implantation conditions such as temperature and energy will change the absorption for a given implanted dose. Fig. 2 shows an example of a calibration curve for a standard 190 keV implantation. The calibration points at 160 keV are outside the calibration curve and the IR measurement therefore has to be calibrated against an ab-

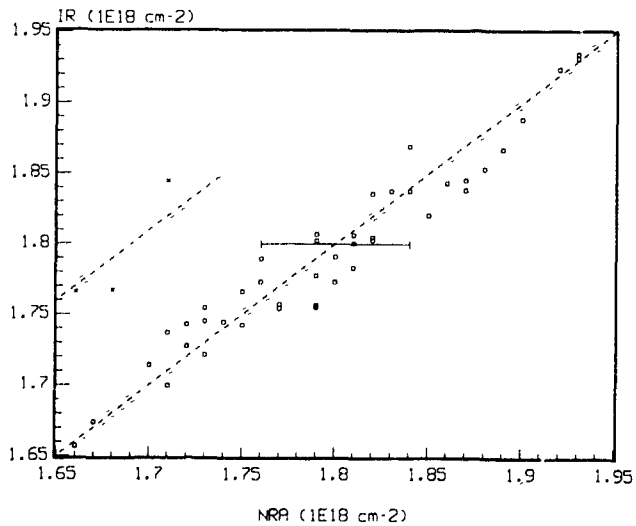

Fig 2. Infrared versus nuclear-reaction analysis calibration curves (×: 160 keV, □: 190 keV) The horizontal bar corresponds to the nuclear-reaction measurement error

solute measurement technique such as nuclear reaction analysis

4.3 Thickness

Reflectivity in the visible range is a convenient way to measure the silicon film thickness. Nevertheless, due to interferences with the light reflected at the lower SiO_2/Si interface, automatic measurements are difficult for thicknesses below 100 nm. This technique does not readily give the SiO_2 thickness, which at the moment is only estimated from the dose measurement. Fig. 1 gives the thickness and dose values obtained on a typical wafer

Spectroscopic ellipsometry offers an alternative to reflectivity Besides the Si thickness, it can give the SiO_2 thickness, and information about the structure of the layers (presence of a polycrystalline layer, buried silicon islands in the SiO_2 layer, etc.). Recent developments such as the use of diode arrays have reduced the acquisition time from 20 min to a few seconds. Nevertheless, the interpretation of the spectrum still has to be improved to allow a rapid and automatic access to the information that this technique can provide. Spatial resolution limits its use to substrate characterization, while the availability of very small spots allows the use of reflectivity for silicon thickness control during circuit processing

5. Characterizations to be developed

There are two important fields in which the lack of characterization tools is particularly obvious: metallic contamination and crystalline quality evaluation

5.1 Metallic contamination

Secondary-ion (or neutral) mass spectroscopy is the only method that gives information on the nature of the contaminant, its concentration and depth profile. But besides being destructive, the residual levels are too high (between 10^{15} and 10^{17} cm^{-3}, depending on the ion) and not very reproducible. Methods based on lifetime measurement are being developed, but they can only measure the bulk lifetime, and the correlation with the SIMOX material quality is not straightforward. Total X-ray fluorescence analysis is a potentially interesting method (it has very high sensitivities: in the 10^{9}–10^{12} cm^{-2} range), but the analysis is limited to a surface layer of a few nanometers thickness. An estimation of its applicability to SIMOX contamination control is under way

5.2 Dislocations

The crystalline quality of SIMOX has improved from 10^{9}–10^{10} dislocations/cm^2 for the first SIMOX structures [7] to 10^{3}–10^{4} cm^{-2} for the best published results [8]. TEM can be used to measure defect densities larger than 10^{5} cm^{-2}. Better sensitivities can be obtained at the expense of a very long observation time. For example, 16 h of observation were necessary to confirm that the dislocation density was less than 10^{4} cm^{-2} on a sample implanted in three steps. Several methods such as chemical or electrochemical etching and X-ray topography [9] have been tried to measure dislocation densities less than 10^{5} cm^{-2}.

Chemical etching based on the differential etching rates between perfect silicon and localized regions of higher chemical potential (dislocations, precipitates, etc.) has been currently used to reveal crystallographic defects on bulk silicon. But the standard etchants used on bulk silicon are difficult to use on SIMOX silicon overlayers (usually less than 250 nm thick) because of the small differential etching rate between perfect silicon and defect regions. The results published on very low dislocation densities observed by pitch counting after chemical etching on multistep implants [9,10,11] were obtained on thick silicon overlayers obtained by epitaxy.

Recently, the method has been improved using electrochemical etching to improve the differential etching rate between perfect and defective crystals [12]. This technique appears to be powerful, but etch pits are correlated to both dislocations and metallic impurities [13]. So more work on the correlation between etch pit densities and known dislocation densities or metallic impurity concentrations is required to assess this technique.

However, the real need is in nondestructive characterization methods Such methods have been proposed to evaluate the dislocation density from as-implanted samples: Raman line shifts have been shown to correlate with the dislocation density observed after annealing [14,15], but too few studies of this method have been made to assess it for dislocation density measurements in SIMOX structures. Other methods such as thermal waves, spectroscopic ellipsometry and X-ray topography have been suggested, but no evidence has been given that a clear correlation exists between the observed signals and the dislocation density.

6. Material-quality impact on devices

6.1. Silicon thickness influence on threshold voltage

Fig. 3 shows the influence of silicon overlayer thickness on the threshold voltage, V_t, of NMOS transistors.

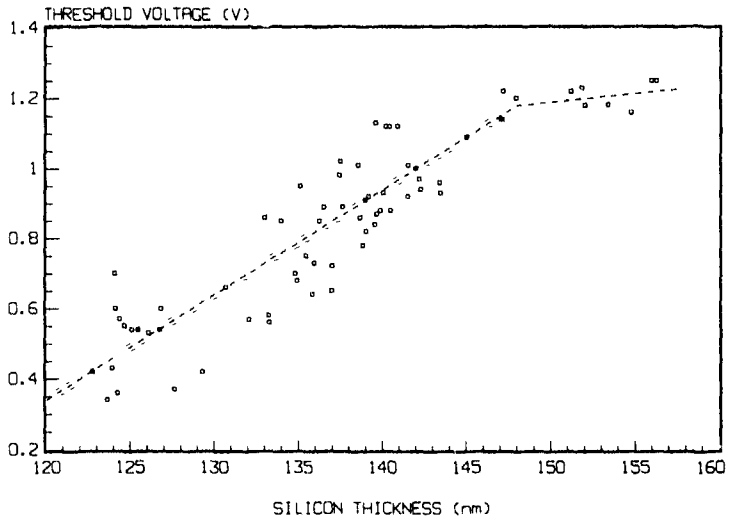

Fig. 3 Threshold voltage variations of NMOS transistors as a function of silicon film thickness

For silicon thicknesses less than 150 nm, there is a strong variation of V_t with silicon thickness (30 mV/nm). These V_t-variations are due to a rapid variation with the silicon thickness of the boron percentage implanted in the buried SiO_2, which leads to variations of the boron concentrations under the gate. To avoid this, for the process parameters that we use, the silicon thickness must be larger than 150 nm.

6.2 *Yield*

Medium-complexity circuits (16K SRAMs having more than 100000 transistors) are processed at LETI. The yields are usually around 60%, which is quite similar to what we obtain on bulk silicon, and yields of 90% have been obtained. This shows that for medium-complexity circuits, parameters such as dislocation and particle densities, though much more important than on bulk silicon, have no significant influence on yield.

7. Conclusion

A complete SIMOX wafer fabrication line is now operational at LETI. Particular emphasis has been put on wafer quality control which uses both nondestructive optical techniques and heavy destructive methods such as TEM and SIMS. Yields of up to 90% have been obtained on 16K SRAM (100000 transistors) and no difference between yields on SIMOX and bulk silicon has been observed, indicating that very-high-quality SIMOX material can now be produced. The more and more exacting requirements of process engineers on SIMOX wafer specifications will require more on-line nondestructive characterization tools. Some such as spectroscopic ellipsometry are already under development but some others are still lacking, in particular for metallic-contamination monitoring.

References

[1] M. Bruel, J. Margail, J. Steomenos, P. Martin and C. Jaussaud, Vacuum 35(12) (1985) 589.
[2] J. Stoemenos, C. Jaussaud, M. Bruel and J. Margail, J. Cryst. Growth 73 (1985) 546.
[3] J.P. Ruffel, D.H. Douglas-Hamilton, R.E. Kaim and K. Izumi, Nucl. Instr. and Meth. B21 (1987) 229.
[4] M. Dubus, J. Margail and P. Martin, Nucl. Instr. and Meth. B15 (1986) 559.
[5] J. Margail and J. Stoemenos, patent no. 2616590 (1987).
[6] J. Margail, J. Stoemenos, C. Jaussaud and M. Bruel, Appl. Phys. Lett. 54 (1989) 526.
[7] P.L.F. Hemment, E. Maydell-Ondrusz and K.G. Stephens, Vacuum 34 (1) (1984) 203.
[8] D. Hill, P. Fraundorf and G. Fraundorf, Appl. Phys. Lett. 63 (1988) 4933.
[9] B.L. Jiang, F. Shimura and C.A. Rozgonyi, Appl. Phys. Lett. 56 (1990) 352.
[10] C.A. Rozgonyi, Z.J. Radzimski, T. Higuchi, B.L. Jiang, D.M. Lee, T. Zhou, D. Schmidt and J. Blake, Electrochem. Soc. Meeting, Abstract No. 229 (1989).
[11] T.F. Cheek, Jr. and D. Chen, Mater. Res. Soc. Symp. Proc. 107 (1988) 53.
[12] M.J. Kelly, T.R. Guilinger, J.W. Medernach, S.S. Tsao, H.D.T. Jones and J.O. Stevenson, Electrochem. Soc. Meeting, Abstract No. 298 (1990).
[13] T.R. Guilinger, M.J. Kelly, J.W. Medernach, S.S. Tsao, J.O. Stevenson and H.D.T. Jones, Electrochem. Soc. Meeting, Abstract No. 239 (1990).
[14] A.H. Van Ommen, Mater. Res. Soc. Symp. Proc. 107 (1987) 43.
[15] L. Jastrebski, J.T. McGinn and P. Zanzucchi, J. Electrochem. Soc. 124 (1990) 306.

Nuclear Instruments and Methods in Physics Research B55 (1991) 831–835
North-Holland

Annealing behaviour of BF_2^+ implanted (001) and (111)Si inside miniature size oxide openings

C.W. Nieh [1] and L.J. Chen

Department of Materials Science and Engineering, National Tsing Hua University, Hsinchu, Taiwan

Both planview and cross-sectional transmission electron microscopy have been applied to study the annealing behaviour of (001) and (111)Si inside miniature size oxide openings implanted with 110 keV BF_2^+ to a dose of 2×10^{15} cm^{-2}. In (001) samples, dislocations were observed to form at the intersections of the lateral and vertical regrowth fronts. The type and density of residual defects were found to be largely independent of the size of the oxide opening. The effects of lateral growth in (111) samples were found to be much more pronounced than those for (001) samples. The presence of the lateral interface drastically altered the distribution of residual d ts. The effects of lateral growth on the distribution of residual defects were found to be more prominent with decreasing size of the oxide opening.

1. Introduction

Ion implantation has become a standard processing step in fabricating shallow junctions in very large scale integrated circuits (1). Previous studies of the post-implantation annealed silicon were almost exclusively conducted on laterally unconfined films. In practical applications, the ion implanted silicon is often laterally confined. Because the implanted area is finite in extent, the recovery process ceases to be planar. A precise knowledge of the spatial distributions of dopants and damage in annealed samples is important for the fabrication of small-dimension devices. An experimental study of the effects of lateral confinements is more demanding than the investigation of extended layers, because a good depth perception as well as a good lateral resolution is now required. Progress in understanding reactions in laterally confined implanted layers has been correspondingly slow. The information obtained from Rutherford backscattering spectrometry, transient reflectivity and conductance measurements are the average properties of a relatively large area ($\sim$ mm^2) [2]. Therefore, the annealing behaviour of amorphous silicon in a small region formed by ion implantation through miniature size oxide opening can only be obtained by using transmission electron microscopy (TEM).

A localized amorphous region inside a miniature size oxide opening is bounded by vertical and lateral amorphous/crystalline (a/c) interfaces. Stress is induced by the volume expansion of the amorphous phase as well as by the dopant size effect. The annealing behaviour of B^+ and As^+ implanted silicon in laterally confined regions have been reported recently [3–5]. In this paper, we report the results of a TEM investigation of the annealing behaviour of samples implanted with 110 keV BF_2^+ to a dose of 2×10^{15} cm^{-2}. We note that BF_2^+ implantation has been commonly utilized to form p^+/n shallow junctions in microelectronics devices. The residual defects in annealed (001) and (111)Si samples without confinement were well characterized by TEM [6,7].

2. Experimental procedures

Single-crystal, 3–5 Ω cm, phosphorus-doped (001) or (111) oriented silicon wafers with 0.6–10 μm wide oxide openings were implanted with 110 keV BF_2^+ to a dose of 2×10^{15} cm^{-2} at room temperature. The patterned wafers were supplied by the Xerox Palo Alto Research Center. The beam current density was maintained to be less than 1.4×10^{12} cm^{-2} s^{-1} to alleviate the beam heating effect. The wafers were oriented 7° off the incident beam direction to minimize the channeling effect. Almost all samples were annealed isothermally in flowing dry nitrogen in a diffusion furnace at temperatures ranging from 600 to 1100°C. The annealing time was 0.5 h unless otherwise specified. The high purity nitrogen gas was first passed through a titanium getter tube, maintained at 800°C, to reduce the O_2 content.

Cross-sectional TEM (XTEM) samples were prepared following the procedures outlined by Marcus and Sheng [8]. Planview samples were also examined whenever it was deemed helpful in gaining information on residual defects. Detailed procedures for polishing of planview specimens were reported previously [9]. A JEOL-200CX scanning transmission electron micro-

[1] Present address: Hughes Research Laboratory, Malibu, CA, USA.

0168-583X/91/$03.50 © 1991 – Elsevier Science Publishers B.V. (North-Holland)

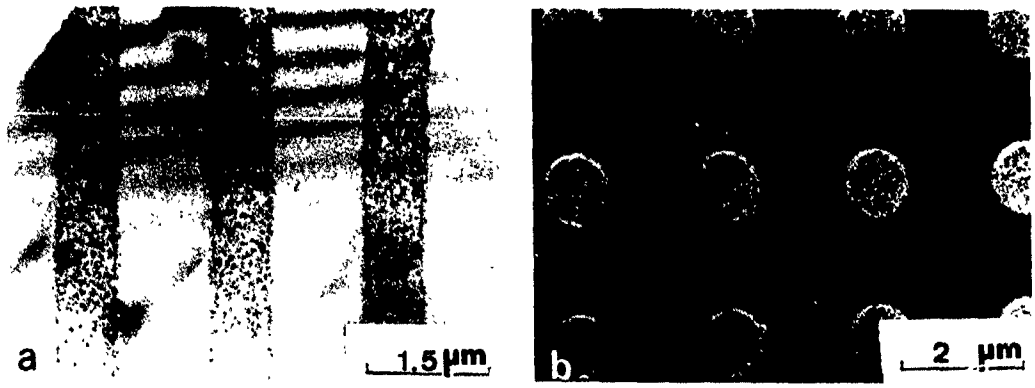

Fig 1 Planview micrographs, (001)Si, 800 °C: (a) bright field, 0.6 μm linear and (b) weak beam dark field (WBDF), 1 μm circular regions

scope operating at 200 keV was used for the TEM examinations. The defect distribution has been investigated by both cross-sectional and planview microscopy. The weak beam dark field technique was used to reveal the true shape of the defects [10]. The detection limit in terms of adequate contrast for the small loops is about 3 nm.

3. Results and discussion

The thickness of the SiO_2 layer was about 500 nm which is expected to be effective in shielding the underlying silicon from ion bombardment. Amorphization of the surface layer to a depth of 140 nm was observed No difference in the solid phase epitaxial growth (SPEG) rate was found among samples with oxide openings of different sizes. The stress level apparently was not high enough to cause detectable change in the a/c regrowth rate

3.1 (001) samples

After annealing at 600°C for 30 min, SPE regrowth was completed. A 50 nm thick band with a high density of point defect clusters was observed beneath the original a/c interface. In the 600–800°C annealed samples, both equiaxial and irregular dislocation loops were found to be distributed near the original lateral and vertical a/c interfaces In addition, dislocations were observed near the original lateral a/c interface Their Burgers vectors were determined as $\frac{1}{2}\langle 110\rangle$. Examples are shown in fig. 1. It is thought that the dislocations were formed at the intersections of the vertical and lateral a/c regrowth front owing to a slight misorientation between the two regrowth fronts. With the exception of the linear defects near the original lateral a/c

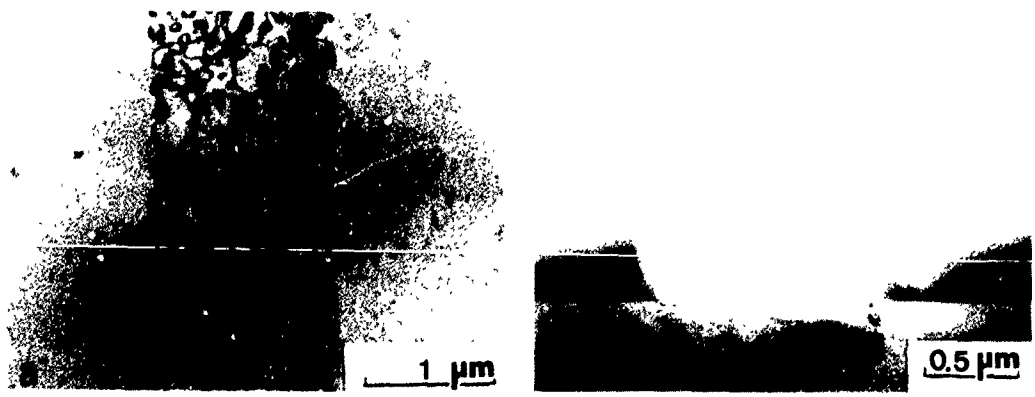

Fig 2. (001)Si, 900 °C, bright field: (a) planview micrograph, 1.4 μm and (b) cross-sectional micrograph, 1 μm linear regions

interface, the regrowth regions are essentially defect free. After 900°C annealing, equiaxial and intersecting dislocation lines were annealed out. Irregular dislocation loops were found to be confined to the implanted regions Examples are shown in fig. 2.

In 1000–1100°C annealed samples, the density of irregular dislocations was significantly reduced Dislocations were observed to be confined within the implanted region Most of the dislocations were located at a depth corresponding to the original a/c interface Similar to those found in broad area samples, fluorine bubbles were formed in bands, about 30 nm in thickness, centered at depths corresponding to the R_p and original a/c interface

The annealing behaviour of the end-of-range defects were similar to those in broad area samples The type and density of the residual defects were found to be largely independent of the size of the oxide opening. The main differences in the distribution of residual defects between broad-area and laterally confined samples are the conspicuous additional band of dislocation loops at the original lateral interface and the intersecting dislocations in the latter case.

3.2 (111) samples

Complete amorphization to a depth of 140 nm was found A band with a high density of defect clusters was observed near the lateral and vertical a/c interfaces An example is shown in fig 3

In samples annealed at 600–900°C, a high density of defect clusters was observed near the lateral and vertical a/c interfaces Lateral growth along the [110] direction was revealed by the presence of a 200 nm wide defect-free region The SPEG behavior along the [111] direction was similar to that of extended area samples A layer free from any defects was formed for the initial 15 nm growth A high density of twins was found for the subsequent regrowth The presence of both primary and

Fig 3 Cross-sectional micrograph: (111)Si, bright field, as implanted

secondary twins was revealed by the analysis of diffraction patterns. Examples are shown in figs. 4 and 5.

In 1000–1100°C annealed samples, no irregular dislocation loops were observed. Twins were formed in the regions regrown on (111)Si. Fluorine bubbles were observed A 200 nm wide band with a low density of bubbles was observed near the original lateral a/c interface Examples are shown in fig 6

The effects of lateral growth in (111) samples were found to be much more pronounced than those for (001) samples. The volume fraction of laterally regrown regions was much higher than that for (001) samples inside oxide openings of the same size As the size of the implanted region decreased, the lateral regrowth became the dominant growth process. The defect distribution clearly reflects the influence of the regrowth direction Twins were observed only in the region regrown on (111)Si. The widths of the lateral regrowth regions were about 200 nm along the $\langle 01\bar{1} \rangle$ directions independent of the annealing temperature and the size of the oxide opening.

For extended area samples, the volume fractions of bubbles were higher than those in (001) samples In (111) samples, a high density of twins was present, whereas it was absent in (001) samples Twin boundaries may act as the nucleation sites for bubbles and facilitate the growth of bubbles The regions near the lateral original a/c interface with a low density of bubbles

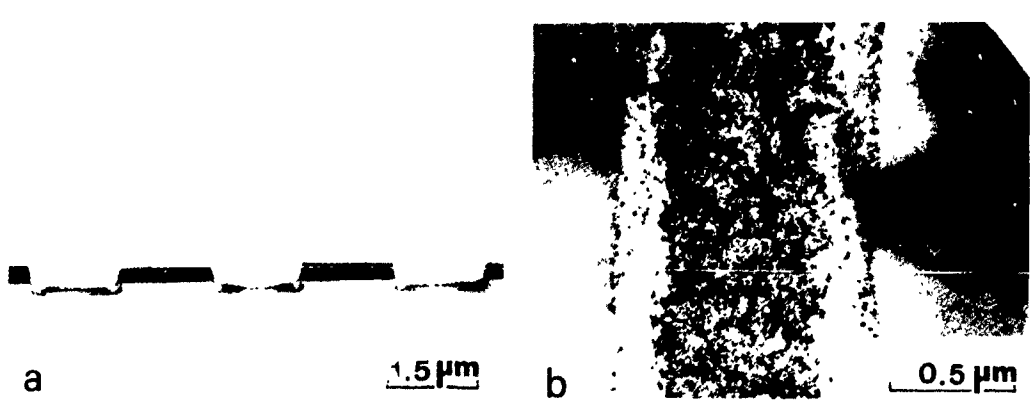

Fig 4 (111)Si, bright field, 700°C (a) cross-sectional and (b) planview micrographs, 1 μm linear regions

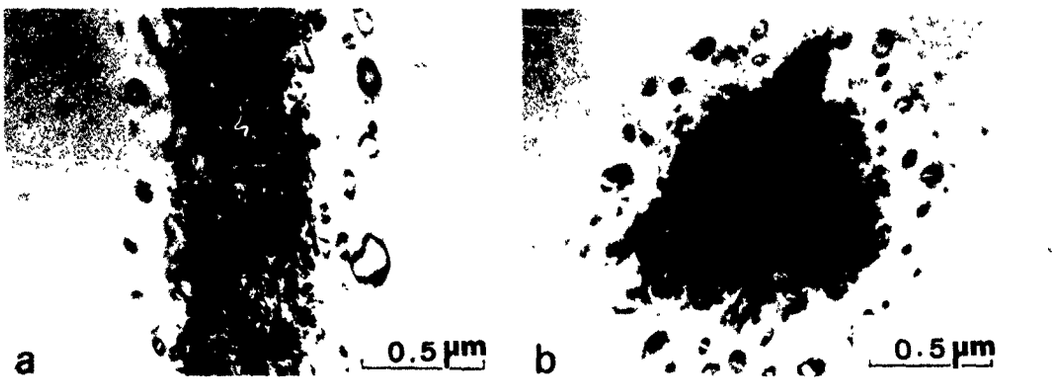

Fig 5 Planview micrograph, (111)Si, bright field, 900 °C: (a) 1 μm linear and (b) 1 2 μm circular regions.

coincides with the lateral regrowth region which is free from twins The results provide strong evidence for the significant influence of twins on the formation of bubbles

4. Summary and conclusions

Both planview and cross-sectional TEM have been applied to study the annealing behaviour of (001) and (111)Si inside miniature size oxide openings implanted with 110 keV BF_2^+ to a dose of 2×10^{15} cm^{-2} The effects of the substrate orientation, annealing temperature, size and shape of the oxide opening on the formation of residual defects have been investigated

In (001) samples, dislocations were observed to form at the intersections of the lateral and vertical regrowth fronts The annealing behaviour of the end-of-range defects were similar to those in broad area samples The type and density of residual defects were found to be largely independent of the size of the oxide opening.

The effect of lateral growth in (111) samples was found to be much more pronounced than that for (001) samples. Twins were observed only in the region regrown on (111)Si The widths of the lateral regrowth regions were about 200 nm along the $\langle 01\bar{1} \rangle$ directions independent of the annealing temperature and the size of the oxide opening. The region near the lateral original a/c interface with a low density of bubbles coincides with the lateral regrowth region which is free from twins The results provide strong evidence for the significant influence of twins on the formation of bubbles The presence of the lateral interface drastically altered the distribution of residual defects The effects of lateral growth on the distribution of residual defects were found to be more prominent with decreasing size of the oxide opening

Acknowledgement

The research was supported by the Republic of China National Science Council

Fig. 6 Cross-sectional micrograph, (111)Si, bright field (a) 1000 °C, 1 μm and (b) 1100 °C, 0 8 μm linear regions

References

[1] J M Poate and J S Williams, in Ion Implantation and Beam Processing, eds. J.S Williams and J M Poate (Academic Press, Sydney, 1984) p. 13

[2] G L. Olson and J.A Roth, Mater. Sci. Rep 3 (1988) 1

[3] A.C Ajmera and G A Rozgonyi, Appl Phys Lett. 49 (1986) 1269.

[4] M Tamura, M Horiuchi and Y Kawamoto, Nucl Instr and Meth. B37/38 (1989) 329

[5] M Horiuchi, M. Tamura and S. Aoki, Nucl Instr and Meth B37/38 (1989) 285

[6] C W Nieh and L J Chen, J. Appl Phys 60 (1986) 3546

[7] C W Nieh and L.J Chen, J Appl Phys 62 (1987) 4421

[8] R.B. Marcus and T T. Sheng, Transmission Electron Microscope of Silicon VLSI Circuits and Structures (Wiley, New York, 1983)

[9] I W Wu and L J Chen, J Appl Phys 58 (1985) 3032

[10] G Thomas and M J Goringe, Transmission Electron Microscopy in Materials (Wiley, New York, 1979)

Nuclear Instruments and Methods in Physics Research B55 (1991) 836–841
North-Holland

Dose dependence of crystallinity and resistivity in ion beam synthesised $CoSi_2$ layers

R.S. Spraggs [a], K.J. Reeson [a], R.M. Gwilliam [a], B.J. Sealy [a], A. De Veirman [b 1] and J. van Landuyt [b]

[a] *Department of Electronic and Electrical Engineering, University of Surrey, Guildford, Surrey GU2 5XH, England*
[b] *University of Antwerp (RUCA), Groenenborgerlaan 171, B-2020 Antwerpen, Belgium*

Epitaxial $CoSi_2$ layers have been fabricated in silicon by implanting 200 keV cobalt ions to doses of 2×10^{17}–7×10^{17} Co^+ cm^{-2}. For the lower doses (2×10^{17} and 3×10^{17} Co^+ cm^{-2}) the synthesised layers, after implantation, are silicon-rich and consist of A- and B-type $CoSi_2$ precipitates interwoven by silicon. For the medium doses (4×10^{17} and 5×10^{17} Co^+ cm^{-2}) an epitaxial aligned layer of $CoSi_2$ is formed after implantation, with any excess cobalt being incorporated in small CoSi inclusions at the peak of the distribution. For the highest doses (6×10^{17}–7×10^{17} Co^+ cm^{-2}) preferential sputtering of the silicon at the surface of the synthesised layer means that this region is cobalt-rich and grains of CoSi form above the epitaxial $CoSi_2$ layer.

As the dose is increased up to 5×10^{17} Co^+ cm^{-2}, the crystallinity of the layer improves, after which it deteriorates again as the thickness of the layer of CoSi grains increases. The degradation in crystallinity is accompanied by a rise in resistivity and this can be correlated to the value of x in $CoSi_x$. When $x \neq 2$ then the resistivity of the layer increases and there is a corresponding deterioration in crystal quality. After annealing the resistivity of the $CoSi_2$ layer decreases and the crystallinity improves as the ratio of Co:Si approaches that in the stoichiometric compound ($CoSi_2$).

1. Introduction

The fabrication of high quality $CoSi_2$ layers using ion beam synthesis (IBS) has been successfully performed by a number of groups [1–16] and is rapidly becoming an area of significant interest in microelectronics research. This is mainly due to the fact that very high quality, single crystal silicide layers can now be produced using IBS. IBS $CoSi_2$ layers have several other advantages over layers fabricated by other techniques, for example, the only reports of successful epitaxial $CoSi_2$ growth on device-compatible (100) silicon, are those using IBS. IBS layers also display some of the lowest resistivities reported for $CoSi_2$.

Potential microelectronic applications of IBS $CoSi_2$ include its use in low resistance interconnects and contacts and fast bipolar devices [17–18]. The low resistivity and close lattice match of $CoSi_2$ to silicon (mismatch = 1.22%) and its compatibility with silicon processing technology makes it particularly attractive for these purposes. However, before successful devices can be fabricated it is important to understand how the physical properties and dimensions of the IBS $CoSi_2$ layers are affected by the implantation parameters, both before and after annealing. In this paper we undertake a detailed examination of how the microstructural and electrical properties of IBS $CoSi_2$ layers depend upon the implanted dose and the annealing conditions.

2. Experimental

Cobalt ions with an energy of 200 keV were implanted into 3 in. device-quality n-type (100) silicon (resistivity of 17–23 Ω cm). During implantation, the ion beam was used to heat the wafer so that the substrate temperature rose to approximately 350 °C, and to minimise conductive heat losses during implantation, the wafer was mounted on silicon tips. The implanted doses ranged between 2×10^{17} and 7×10^{17} Co^+ cm^{-2}. Following implantation, the implanted region was cleaved into a number of smaller specimens which were then annealed at either 600 °C for one hour or 600 °C for one hour and 1000 °C for 30 min, in a conventional furnace with a flowing nitrogen ambient.

Rutherford backscattering (RBS) with 1.5 MeV He^+ ions was used to analyse the cobalt depth distribution and to calculate the cobalt:silicon ratio within the implanted region. Ion channelling allowed the crystalline quality of the structure to be assessed and also enabled the degree of coherency between the synthesised $CoSi_2$ layer and the silicon overlayer and substrate to be established. To determine the resistivity of the synthesised layer, sheet resistance measurements were made using a four-point probe.

[1] Now at Philips Research Laboratories, 5600 JA Eindhoven, The Netherlands.

0168-583X/91/$03.50 © 1991 – Elsevier Science Publishers B.V. (North-Holland)

3. Results and discussion

3.1 As-implanted

Fig. 1a shows the random and channelled RBS spectra for a sample implanted with a dose of 2×10^{17} Co^+ cm^{-2}, prior to annealing. The spectra in fig. 1a can be divided into four main regions, labelled (I), (II), (III) and (IV). In the random spectrum, region (I) corresponds to the depth distribution of the implanted cobalt atoms, which in this case resembles a Gaussian, with the peak of the implant lying ~ 1200 Å beneath the silicon surface. In order to quantify the degree of crystallinity within the silicide layer, we use the term χ_{ave}. This is defined as the ratio of the channelled to random yields in region (I) (channels 300–380). The presence of the implanted cobalt atoms is also manifested by a dip in the silicon yield, region (III) (channels 232–258), which corresponds to a reduced concentration of silicon atoms within the synthesised layer. The position of this dip in fig. 1a indicates that the synthesised layer is buried beneath a thin silicon overlayer (region (II)). The value of x in $CoSi_x$ calculated for fig. 1a, is 3.63, which indicates that either a noncontinuous layer has been formed, or that the silicide layer is silicon-rich. Previous studies [4,7–11,15] have shown that the former is in fact the case, with the synthesised "layer" consisting of a mixture of A-(aligned with the matrix) and B-(rotated 180° in a {111} plane with respect to the silicon matrix) type precipitates interwoven by single crystal silicon. This type of noncontinuous structure makes channelling difficult and hence leads to a high value for χ_{ave} (86%).

From the channelled spectrum in fig. 1a, it can be seen that at the back interface of the synthesised layer (region (IV)) the dechannelled yield rises. This appears in all of the spectra in figs. 1a–d and can be attributed to the presence of defects, created by the condensation of silicon self-interstitials, which lie along silicon ⟨311⟩ lattice planes [4,7–11,15].

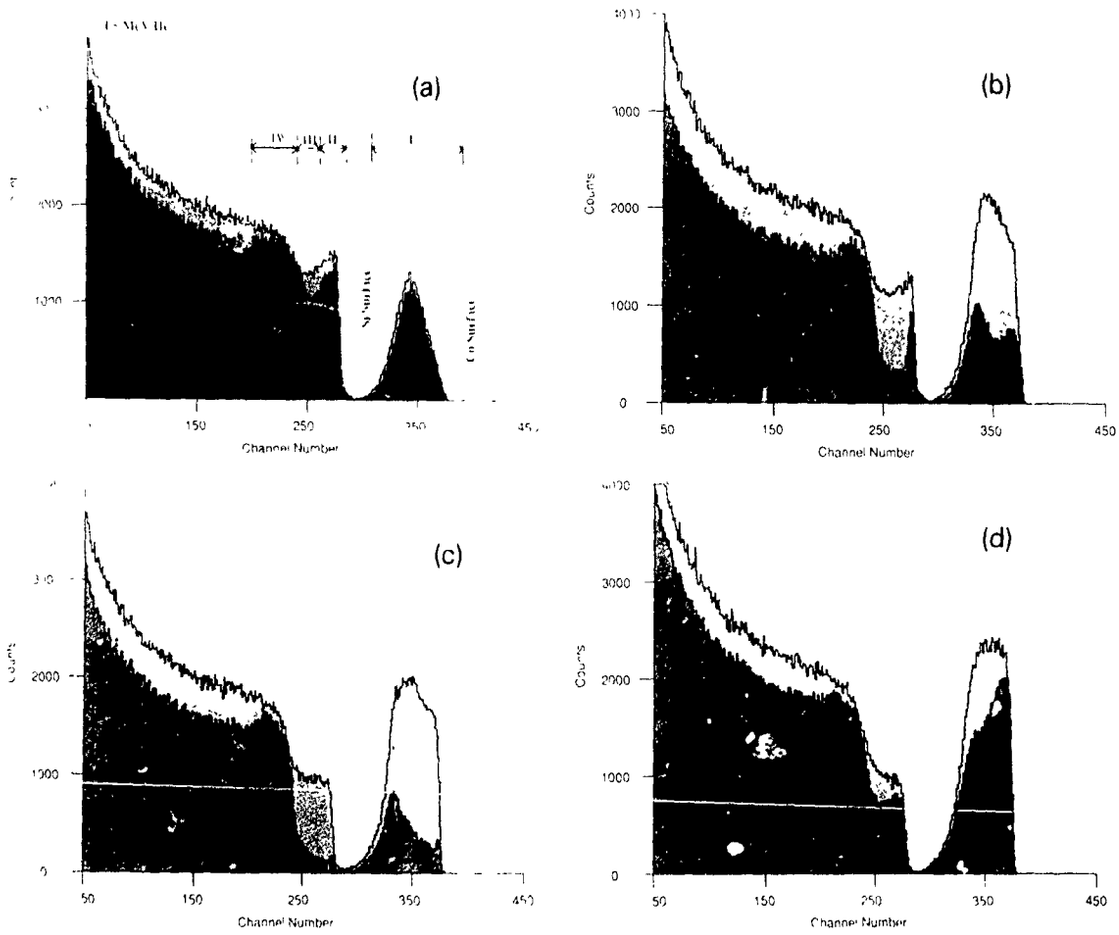

Fig. 1. Random (light shading) and channelled (dark shading) RBS spectra for specimens implanted with doses of (a) 2×10^{17} Co cm^{-2}, (b) 4×10^{17} Co^+ cm^{-2}, (c) 5×10^{17} Co cm^{-2} and (d) 6×10^{17} Co^+ cm^{-2}, after implantation.

Figs 1b–d, respectively, show the random and channelled RBS spectra for specimens implanted with cobalt doses of 4×10^{17} Co^+ cm^{-2}, 5×10^{17} Co^+ cm^{-2} and 6×10^{17} Co^+ cm^{-2}, prior to annealing. For the samples implanted with doses of 4×10^{17} Co^+ cm^{-2} and 5×10^{17} cm^{-2}, a continuous epitaxial layer is formed during implantation, in which the value of x, in $CoSi_x$, is close to 2. For the dose of 5×10^{17} Co^+ cm^{-2}, the $CoSi_2$ layer extends right up to the silicon surface (i.e. region (II) is no longer present) and there is a slight excess of cobalt at the peak of the distribution, which is probably in the form of small CoSi inclusions [8,11,12,15]. It is also apparent, from the channelled spectra in figs 1b and 1c, that once the disilicide layer becomes continuous it exhibits a lower dechannelled yield than the specimen in fig. 1a, implanted with a lower dose.

Fig 2 shows how χ_{ave} varies with dose, from which it can be seen that as the dose is increased from 2×10^{17} to 5×10^{17} Co^+ cm^{-2} there is an improvement in the

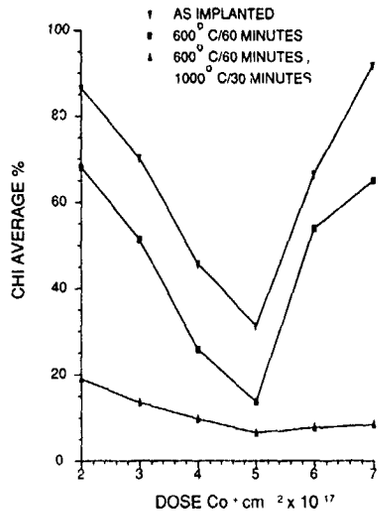

Fig 2 Variation in χ_{ave} with dose, after implantation and annealing at 600 °C (1 h) and 600 °C (1 h) + 1000 °C (30 min)

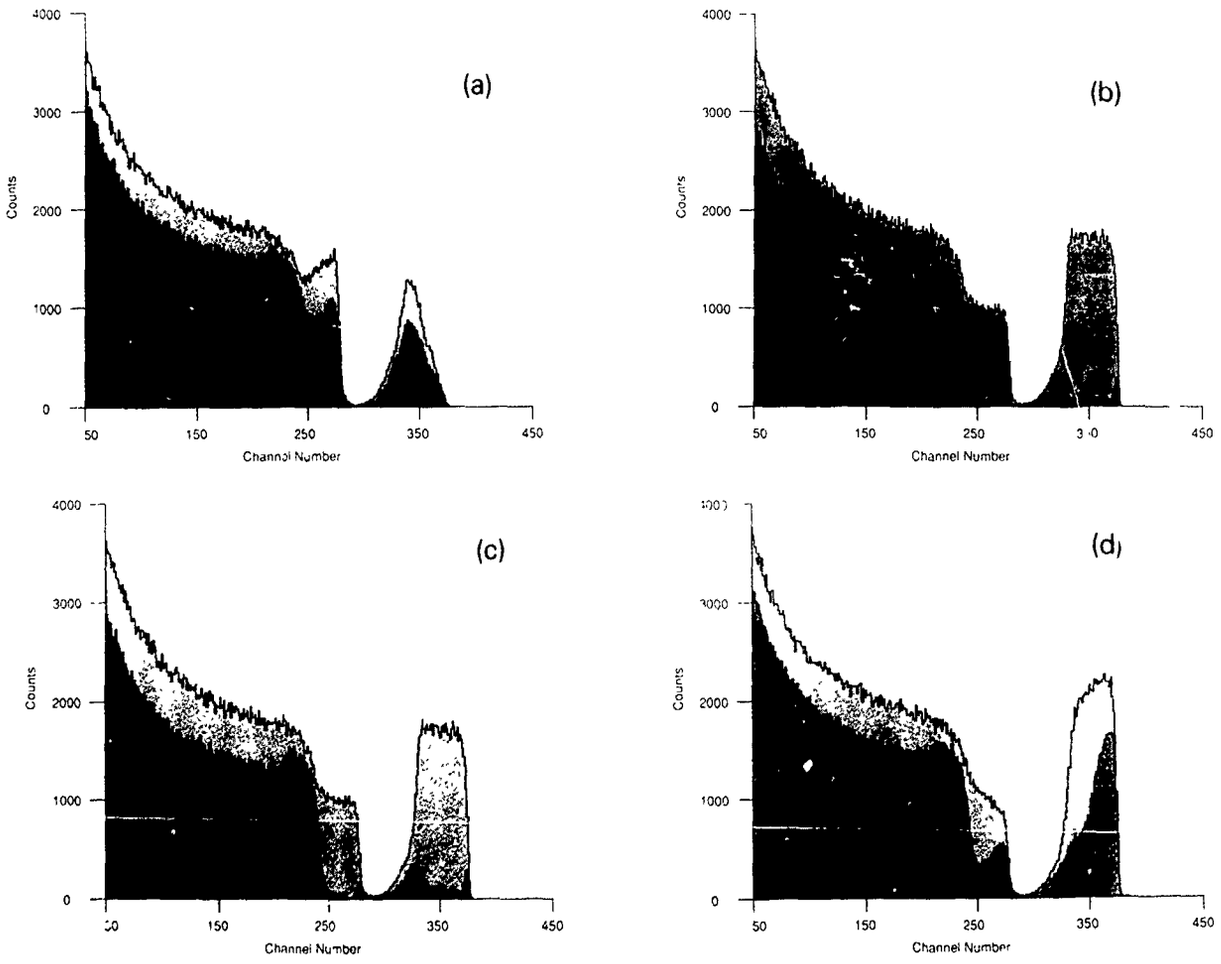

Fig 3 Random (light shading) and channelled (dark shading) RBS spectra for specimens implanted with doses of (a) 2×10^{17} Co^+ cm^{-2}, (b) 4×10^{17} Co^+ cm^{-2}, (c) 5×10^{17} Co^+ cm^{-2} and (d) 6×10^{17} Co^+ cm^{-2}, after annealing at 600 °C for 1 h.

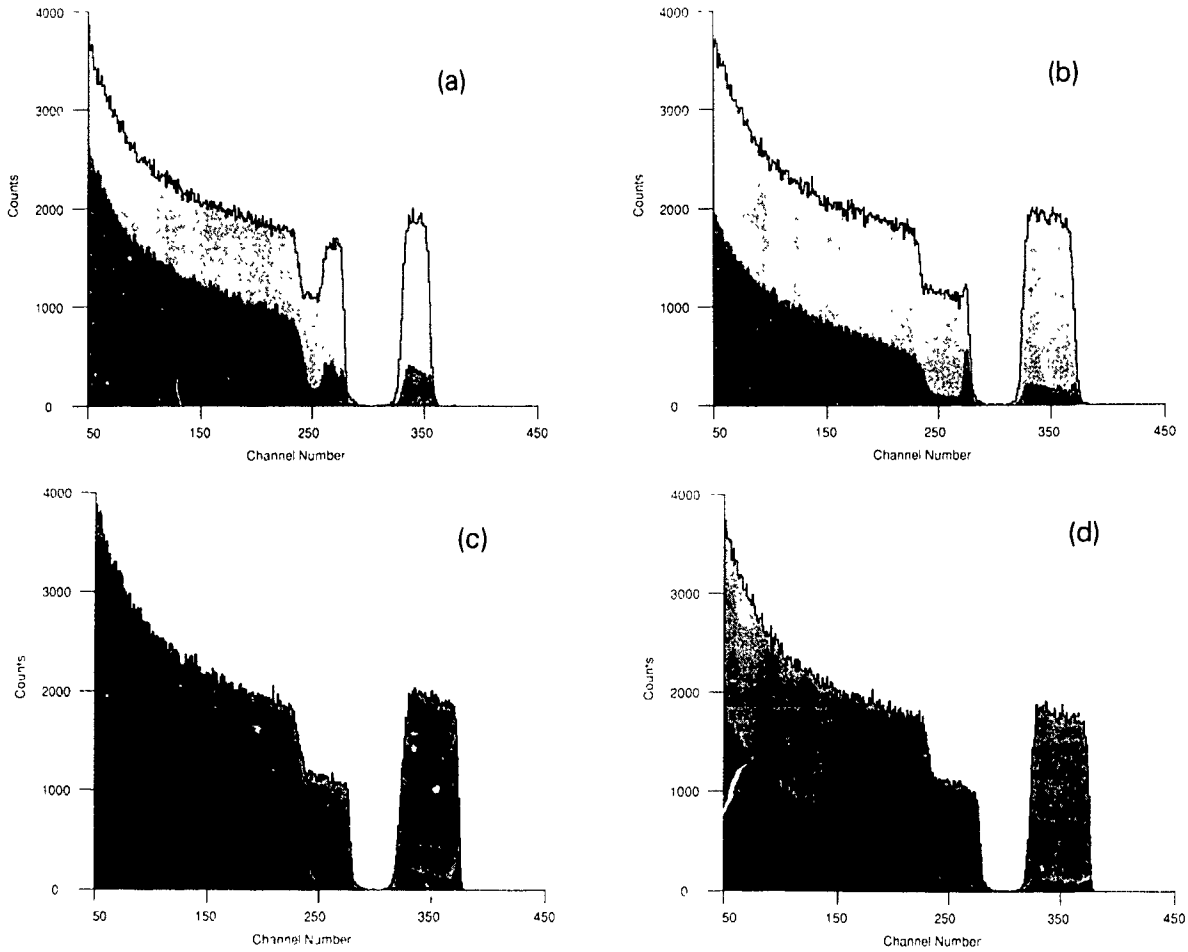

Fig 4 Random (light shading) and channelled (dark shading) RBS spectra for specimens implanted with doses of (a) 2×10^{17} Co^+ cm^{-2}, (b) 4×10^{17} Co^+ cm^{-2}, (c) 5×10^{17} Co^+ cm^{-2} and (d) 6×10^{17} Co^+ cm^{-2}, after annealing at 600 °C (1 h) and 1000 °C (30 min)

crystalline quality of the synthesised layer and a corresponding drop in χ_{ave}. Above 5×10^{17} Co^+ cm^{-2}, any further increase in dose results in an increase in χ_{ave}. The reason for this increase can be found by examining the channelled spectrum in fig 1d (for a dose of 6×10^{17} Co^+ cm^{-2}) which shows that the dechannelled yield near the surface is high. This is because silicon is preferentially sputtered from the surface of the synthesised layer by the impinging ion beam, which means that the resulting layer is cobalt-rich. XTEM analysis of this "cobalt-rich layer" shows that it consists of CoSi grains which overlie a layer of epitaxial $CoSi_2$ [19].

3.2 *Annealed 600 °C 60 min*

Fig. 3 shows the random and channelled RBS spectra for the same specimens described above, but after annealing at 600 °C for one hour. For the lowest dose specimen (2×10^{17} Co^+ cm^{-2}) the value of χ_{ave} has decreased to 68% and fig. 3a (random spectrum) shows that the cobalt in the tails of the distribution has begun to redistribute towards the peak. This effect is even more pronounced for a dose of 3×10^{17} Co^+ cm^{-2} (not shown) where a continuous layer of stoichiometric $CoSi_2$ is formed at the peak of the distribution. This redistribution against the concentration gradient probably occurs in an analogous manner to that described by Jaussaud et al. [20] for high dose oxygen implantation.

For the samples implanted with 4×10^{17} Co^+ cm^{-2} and 5×10^{17} Co^+ cm^{-2} (figs 3b and 3c, respectively) the cobalt distribution have become more rectangular in profile and the values of χ_{ave} in fig. 2 have decreased with respect to their "as-implanted" values. This occurs by the gettering action of the synthesised layer and the

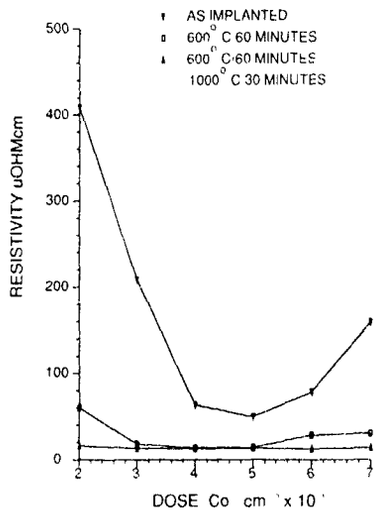

Fig 5 Variation in resistivity with dose, after implantation and annealing at 600 °C (1 h) and 600 °C (1 h) + 1000 °C (30 min)

redistribution of any "excess" cobalt released by the dissolution of the CoSi inclusions For the highest doses, the 600 °C one hour anneal creates a marked improvement in the value of χ_{ave} (fig 2) because the CoSi grains near the surface start to undergo a phase transformation to $CoSi_2$ at this temperature (fig. 3d)

3.3 Annealed 600 °C 60 min, 1000 °C 60 min

For all doses, annealing at 1000 °C has a major effect on the cobalt distribution. Figs 4a–d indicate that in all cases these distributions are now essentially rectangular in profile. A temperature of 1000 °C, therefore, appears to be sufficient to anneal out most of the damage in the tail of the implant profile and to allow the cobalt to redistribute to give a stoichiometric $CoSi_2$ layer XTEM studies [7,8,11,12,15] have shown that after annealing at 1000 °C for 30 min, the $CoSi_2$ precipitates in the tails of the distribution have completely dissolved and, for the higher doses, the phase transformation from CoSi to $CoSi_2$ is complete

3.4 Resistivity

Fig. 5 shows a plot of the variation in resistivity with dose for the "as-implanted" and annealed specimens. A comparison of figs 2 and 5 indicates that the resistivity varies in a similar way to χ_{ave} For the lower doses (2×10^{17} and 3×10^{17} Co^+ cm^{-2}), after implantation, the discontinuous nature of the synthesised layer contributes to the relatively high resistivity Once the $CoSi_2$ layer becomes continuous and Co : Si ~ 1 · 2, i.e. for doses of 4×10^{17} and 5×10^{17} Co^+ cm^{-2}, the resistivity drops. For the higher dose specimens (6×10^{17} and 7×10^{17} Co^+ cm^{-2}) the layer of CoSi grains near the surface causes the resistivity to rise again.

Annealing produces a dramatic decrease in resistivity, especially for the low (2×10^{17} and 3×10^{17} Co^+ cm^{-2}) and high (6×10^{17} and 7×10^{17} Co^+ cm^{-2}) dose specimens. The reasons for this improvement are similar to those described previously for χ_{ave} and it is worth noting that the lowest values of resistivity (13.7 ± 0.5 Ω cm) and χ_{ave} are obtained when Co : Si = 1 : 2.

4. Conclusions

It has been shown that after implantation the resistivity and crystallinity of layers synthesised by high dose cobalt implantation are very dependent on the implanted dose and the cobalt to silicon ratio within the layer. For doses of 4×10^{17} and 5×10^{17} Co^+ cm^{-2}, a continuous epitaxial layer of aligned $CoSi_2$ is formed after implantation, with any excess cobalt being accommodated in CoSi inclusions at the peak of the distribution For lower (2×10^{17} and 3×10^{17} Co^+ cm^{-2}) and higher (6×10^{17} and 7×10^{17} Co^+ cm^{-2}) doses the resulting layers are silicon-rich and cobalt-rich, respectively These layers display higher χ_{ave} values and have correspondingly higher resistivity values After annealing at 600 °C for 1 h, stoichiometric $CoSi_2$ layers result for layers fabricated with doses of 3×10^{17}, 4×10^{17} and 5×10^{17} Co^+ cm^{-2}, whilst after annealing at 600 °C (1 h) and 1000 °C (30 min) stoichiometric layers of $CoSi_2$ are found for all doses In addition to this, for each layer, the crystallinity improves (i.e. χ_{ave} improves) and the resistivity decreases as the value of x in $CoSi_x$ approaches 2 This shows that even though the "as-implanted" specimens display marked differences in resistivity, crystallinity and stoichiometry, after annealing at 600 °C (1 h) and 1000 °C (30 min), the structural and electrical properties of the layers are very similar, with only a slight memory effect being apparent.

References

[1] A E. White, K.T Short, R C Dynes, J P Garno and J M Gibson, Appl Phys Lett 50 (1987) 95
[2] J C Barbour, S Picraux and B L Doyle, Mater. Res Soc Proc 107 (1988) 269
[3] D K Brice and J C Barbour, Nucl Instr and Meth B36 (1989) 431
[4] C W T Bulle-Lieuwma, A F. de Jong, A H van Ommen, J F van der Veen and J Vrijmoeth, Appl Phys Lett 55 (1989) 648
[5] K Kohlhof, S Mantl, B Stritzker and W Jager, Nucl Instr and Meth B39 (1989) B39.
[6] K Kohlhof, S. Mantl, B Stritzker and W Jager, Appl Surf. Sci 38 (1989) 207.

[7] K J Reeson, A De Veirman, R M Gwilliam, C Jeynes, B J Sealy and J van Landuyt, Inst. Phys. Conf Ser 100 (1989) 627
[8] K J Reeson, A De Veirman, R.M Gwilliam, C Jeynes, B J Sealy and J van Landuyt, Mater Res Soc Proc 147 (1989) 217
[9] A H van Ommen, J J.M Ottenheim, A.M L Theunissen and A G Mouwen, Appl Phys. Lett 53 (1988) 669
[10] B.J. Sealy, B L Tan, R M Gwilliam, K J Reeson and C Jeynes, Electron Lett 25 (189) 1532
[11] K G. Stephens, K J. Reeson, R M. Gwilliam, B.J. Sealy and P L.F Hemment, Nucl Instr and Meth B50 (1990) 368
[12] A De Veirman, J van Landuyt, K J Reeson, R M Gwilliam, C Jeynes and B.J Sealy, accepted for publication in J Appl Phys
[13] C W T Bulle-Lieuwma, A H van Ommen and L J van Ijzendoorn, Appl Phys Lett. 54 (1989) 244.
[14] A E. White, K T Short, R C Dynes, J M Gibson and R Hull, Mater Res Soc Proc 107 (1988) 3
[15] A De Veirman, Ph.D Thesis, RUCA, University of Antwerp (1990)
[16] A.H van Ommen, C W.T. Bulle-Lieuwma, J J.M Ottenheim and A.M L Theunissen, J Appl Phys. 67 (1990) 1767.
[17] A F J. Levi, R T Tung, J L Batstone and M Anzlowar, Mater. Res Soc Proc 107 (1988) 259
[18] P Hunt, personal communication
[19] A De Veirman, unpublished results.
[20] C Jaussaud, J Margail, J Stoemenos and M Bruel, Mater Res. Soc Proc 107 (1988) 17

Nuclear Instruments and Methods in Physics Research B55 (1991) 842–846
North-Holland

Contouring of SIMOX profiles by oxygen ion energy change *

A. Wittkower, M. Guerra, B. Cordts, R. Dolan and P. Sandow
Ibis Technology Corporation, 32A Cherry Hill Drive, Danvers, MA 01923, USA

The objective of this work was to determine if, by changing the ion energy during the implant, depth distribution profiles could be contoured to produce improved SIMOX material In the SIMOX process, oxygen ions are implanted into bare silicon or into silicon through a silicon dioxide capping layer During the course of the implant, the incoming fast ions sputter silicon atoms from the surface Through this mechanism, by the end of the implant, the apparent depth of penetration with respect to the original surface will have increased. However, a competing action is at work oxygen ions retained by the formation of the buried oxide layer will cause swelling. Detailed calculations have been performed, which show that the sputtering effect is approximately compensated by the swelling. Experimentally, by increasing the oxygen beam energy during the implant, improved SIMOX material was formed without the silicon islands normally observed

1. Introduction

In the SIMOX process, oxygen ions are implanted into bare silicon or into silicon through a SiO_2 capping layer In the first approximation, these ions come to rest below the surface at an average range R_p in a quasi-Gaussian distribution with range straggling (standard deviation) ΔR_p As an example for O^+ ions in Si at 150 keV, $R_p \approx 3220$ Å and $\Delta R_p \approx 909$ Å (see fig. 1).

During the implantation, the incoming fast ions sputter silicon atoms from the surface This is always the case in implantation, but since SIMOX requires doses 100 times greater than for doping applications, the sputtering effect is now significant, typically 1500 Å of material is removed in a SIMOX implant Although the range defined by R_p has not, of course, changed (unless other effects are at work) at the end of the implant, the implant depth with respect to the original surface has increased by 1500 Å. This effect would also cause a broadening in the effective range straggle. Visualization of the problem is somewhat simplified by the fact that the range of oxygen into either Si or SiO_2 is similar, implying that the shape of the instantaneous as-implanted oxygen profile is not appreciably skewed by the change in target composition. Presumably then, by reducing the beam energy as the implant progresses, one can superimpose the peaks of the distributions, thereby narrowing the final distribution. This would improve the quality of the SIMOX material, since:

(i) the total applied dose necessary to form a continuous buried layer can be expected to be reduced; thus there will be fewer faults in the surface silicon layer,
(ii) the implant time will be reduced,
(iii) defects at both Si/SiO_2 interfaces may be reduced since the incoming oxygen ion profile is more precisely located and the distribution tails are less diffuse.

An increase in the effective range is indeed the case for implantation of ion species which diffuse out of the material (e.g. H^+ or Ar^+) But with O implantation, the incoming ions are retained through the reaction.

$$Si + 2O = SiO_2,$$

and the formation of this buried oxide layer causes swelling. Thus, there are competing actions. If the swell-

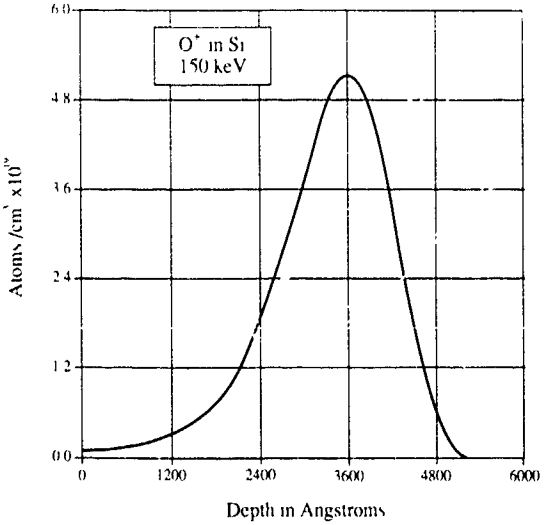

Fig 1 A typical dose versus depth implantation profile.

* Work performed under an SBIR contract issued by the Defense Nuclear Agency, Dr Lewis Cohn, Technical Monitor

0168-583X/91/$03 50 © 1991 – Elsevier Science Publishers B V (North-Holland)

ing is less than the sputtering, the energy reduction scheme described above should operate; but if the swelling is greater than the sputtering, an increase in implant energy during the implant would improve the profile overlap.

2. Sputtering rates

There are not many sources of data for sputtering coefficients of the oxygen/silicon system in the 150--200 keV range. A few values have been published by authors specifically interested in SIMOX, and one general review paper has been produced. To some degree these data are inconsistent, sometimes grossly so.

The available data are summarized in fig. 2 for oxygen bombarding both silicon and silicon dioxide. The curve of Matsunami et al. [1] is calculated from theory with specific material properties and data taken at lower energies taken into account. This is the data used in the Profile Code calculation of this work. Additional experimental sputtering data have been obtained by Hemment et al. [2] and Bussmann [3].

The two earlier measurements of oxygen into silicon sputtering by Hayashi et al. [4] and Maydell-Ondrusz and Wilson [5] appear to be rather far from the Matsunami predictions. The Maydell-Ondrusz paper describes an indirect measurement technique which examines the change in step height between an implanted zone and a neighboring unimplanted region. This method, as pointed out by the authors, is sensitive to assumptions about the material swelling taking place during implantation, and this makes it difficult to interpret the data.

The two data points for oxygen implantation into SiO_2 are based on more reliable techniques. Since the SiO_2 layer will not change thickness during implantation, a simple step height or optical measurement is sufficient for good accuracy. Both the results of Douglas-Hamilton et al. [6] and Bunker [unpublished] are based on tabulating the total dose seen to just remove the SiO_2 capping layer during actual SIMOX implantations.

3. Swelling

An indication of the amount of swelling can be extracted from handbook data of the relative density of Si and SiO_2. The data suggests that 1000 Å of Si will swell to 2170 Å of SiO_2 during the SIMOX process, using a dose of 1×10^{18} oxygen ions.

The code was used to estimate the balance between sputtering and swelling by calculating, at different energies, the minimum dose needed to reach stoichiometry. When a series of energies were entered which caused the profiles to overlap best, the total dose to stoichiometry was less than the total dose needed for poorly overlapping profiles. The effect could most easily be checked by using only two energies: a fixed dose of $0.8 \times 10^{18}/cm^2$ at 200 keV was entered, and the code used to calculate the extra dose which was needed to reach stoichiometry at the second energy. In this way, it

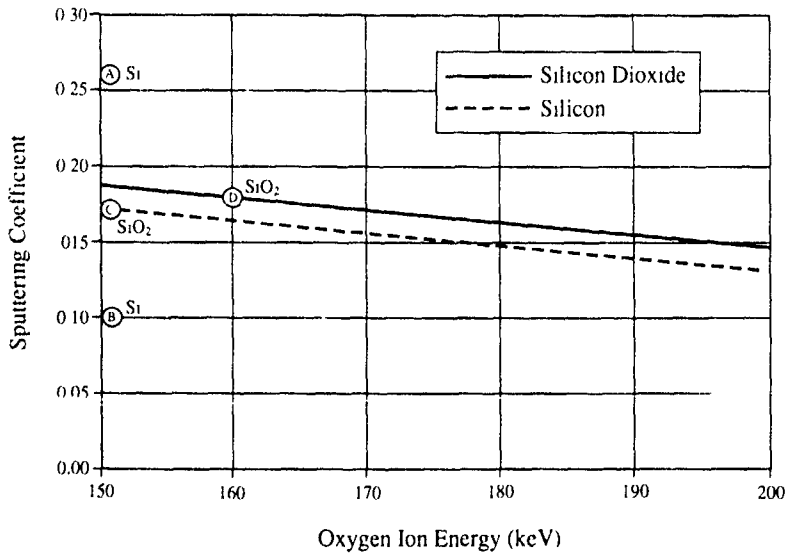

Fig 2 Sputtering of O^+ on Si and SiO_2 The continuous curves are theoretical [1] The experimental data points are, for O^+ on Si, from (A) ref [2], (B) ref. [3], and for O^+ on SiO_2, from (C) ref [4], (D) Bunker [unpublished]

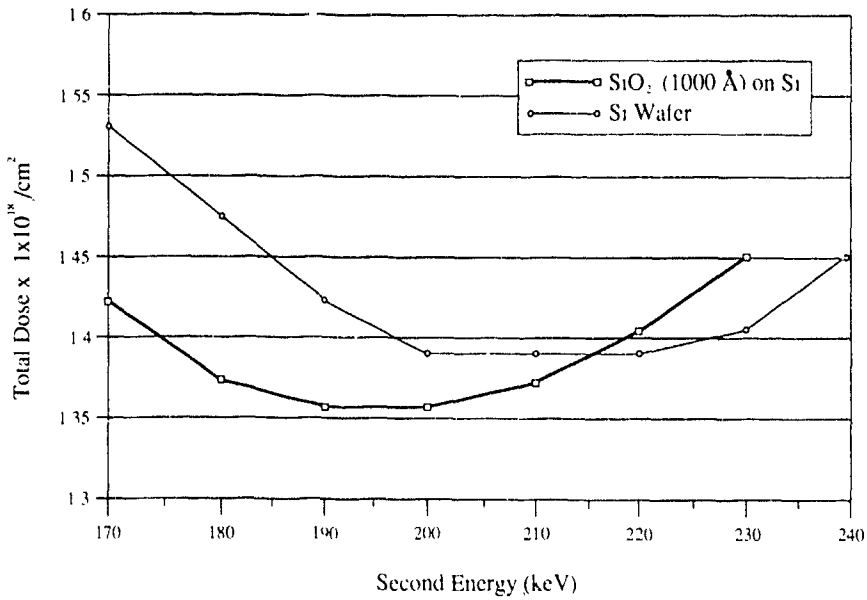

Fig 3 The total calculated dose required to reach stoichiometry using two beam energies The first implant was always $0\,8\times10^{18}$/cm^2 at 200 keV

was possible to determine whether a higher energy (excess swelling) or a lower energy (excess sputtering) was more appropriate

Fig. 3 shows the results for both capped and uncapped wafers It can be seen from the vertical scale that the effect of changing energy is not very sensitive.

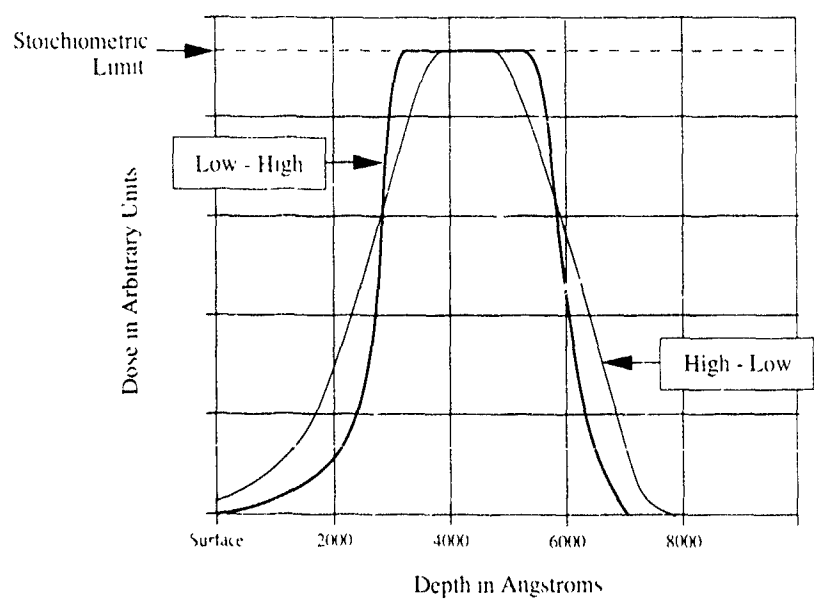

Fig 4 Calculated composite dose versus depth profiles for two cases. 150 keV to 200 keV in ten steps (low-high), and 200 keV to 150 keV in ten steps (high–low)

Fig 5 TEM photomicrograph of SIMOX, total dose $1.8 \times 10^{18}/cm^2$ using five stepwise increases in energy from 150 keV to 200 keV (low–high), annealed at 1325 °C for 6 h.

amounting at best to only a few percent over a wide range of computer calculations. For uncapped wafers, it is slightly better to increase the energy, whereas for capped wafers, a decrease in energy is preferred.

For a pure silicon target, the swelling is slightly larger than the sputtering, but for a capped wafer, it is slightly smaller. This is a strong indication that adjustment of energy will have little effect.

Fig. 6 TEM photomicrograph of SIMOX, dose $1.8 \times 10^{18}/cm^2$, energy 200 keV, annealed at 1325 °C for 6 h

4. Simulation profiles of high to low and low to high energy

Even with the minimal impact on dose reduction predicted by these simulations, it was decided that further simulations and actual experiment, over the energy range of 150 to 200 keV, might prove interesting and potentially have an impact on buried oxide quality. The ten-energy simulation plot in fig. 4 shows the composite profile for the case of high energy first, followed by a decrease in energy from 200 to 150 keV (high–low).

Fig. 4 also shows the equivalent composite profile for the low energy first followed by an increase in energy from 150 to 200 keV (low–high). A significant difference is observed in these two composite plots in that the low–high is much sharper and more "box-like" with less broadening than the high–low case. It can be seen that more oxygen atoms pile up at the back interface where oxygen depletion is likely to occur during annealing.

5. Experimental results

Wafers were implanted to a dose of 1.8×10^{18} with five stepwise increases in energy from 150 to 200 keV during the implant (low–high). The wafers were then annealed at 1325°C for 6 h and TEM photomicrographs made for the resultant material (fig. 5). These TEMs suggest that a buried oxide of better quality was formed than at a single fixed energy (fig. 6) where silicon islands can be seen clearly near the lower surface of the buried oxide. It is believed that the simulation data (low–high) of fig 4 may help to explain these data. The greater concentration of oxygen that results deep within the silicon helps to restore the oxygen that depletes toward the surface during annealing, hence allowing a more continuous stoichiometric film to be formed. This is confirmed by the experimental results obtained in fig. 5.

6. Conclusions

An increase in energy during oxygen implantation may provide an improved technique for producing SIMOX layers in silicon. Simulation results confirm actual TEM findings that buried oxides of improved quality are obtained.

Acknowledgement

The profile code calculations were performed by Dr S. Bunker of Implant Sciences Corp. The authors thank him for his contribution to this work.

References

[1] I. Matsunami, At. Data Nucl. Data Tables 31 (1984) 1.
[2] P.L.F. Hemment, K.J. Reeson, A.K. Robinson, J.A. Kilner, R.J. Chater, C.D. Marsh, K.N. Christensen and J.R. Davis, Nucl. Instr. and Meth. B37/38 (1989) 766.
[3] U. Bussmann, Proc. 4th Int. Symp. on Silicon-on-Insulator Technology and Devices, Electrochem. Soc. 90-6 (1990) 85.
[4] T. Hayashi, H. Okamoto and Y. Homma, Defects and Radiation Effects in Semiconductors 1980, Inst. Phys. Conf. Ser. 59 (1981) 533.
[5] E.A. Maydell-Ondrusz and I.H. Wilson, Thin Solid Films 114 (1984) 357.
[6] D.H. Douglas-Hamilton, R.P. Dolan and H.E. Friedman, Nucl. Instr. and Meth. B21 (1987) 158.

Nuclear Instruments and Methods in Physics Research B55 (1991) 847–851
North-Holland

SIMOX wafers with low dislocation density produced by a 100-mA-class high-current oxygen implanter

S. Nakashima and K. Izumi

NTT LSI Laboratories, 3-1, Morinosato Wakamiya, Atsugi 243-01, Japan

The dislocation density and the structure of SIMOX wafers formed under different implantation conditions have been investigated using Secco etching and cross-sectional transmission electron microscopy (XTEM). The relationship between the breakdown voltage of the buried oxide layer and the oxygen dose has also been studied. The dislocation density decreases as the dose decreases and the wafer temperature, during implantation, increases. The SIMOX wafer implanted at 180 keV with a low dose of 0.4×10^{18} cm^{-2} at 550 °C and subsequently annealed at temperatures higher than 1300 °C has an extremely low dislocation density on the order of 10^2 cm^{-2}. The buried oxide layer of this SIMOX wafer has a breakdown voltage of 40 V.

1. Introduction

Ever since the development of the 100-mA-class high-current oxygen implanter, NV-200 [1], SIMOX technology [2] has been actively studied at many research institutes [3–5]. SIMOX has come to be regarded as one of the most promising SOI technologies for future VLSIs and ULSIs as well as for the fabrication of radiation-hardened devices.

In this technology a great number of oxygen ions penetrate the superficial silicon layer, which is used as the active layer of a semicondutor device. The crystallinity, or more precisely, the dislocation density of the superficial silicon layer strongly depends on the implantation conditions such as the dose, the wafer temperature during implantation, and so on. A SIMOX wafer generally has a dislocation density of $10^8 - 10^9$ cm^{-2} [6]. By using a multiple implantation and annealing technique, the dislocation density can be reduced to 10^4–10^5 cm^{-2} [7]. This technique is, however, troublesome and far from practical. In addition, a number of dust particles generated by the processes in the technique results in contamination of the SIMOX wafers. Therefore, it is important to develop a practical way of reducing the dislocation density, which affects the long-term reliability of LSIs.

One optimized method of producing SIMOX wafers with an extremely low dislocation density and with an abrupt interface between the superficial silicon layer and the buried oxide layer is proposed in this study.

2. Experiment

Oxygen-ion implantation was performed using a NV-200 [1]. Oxygen ions ($^{16}O^+$) were implanted into 100 mm (100) silicon wafers at an acceleration energy of 180 keV with doses from 0.1–2.4×10^{18} cm^{-2}. The wafer temperature during oxygen implantation was controlled at between 400 and 720 °C. The fundamental technique applied to measure the wafer temperature during implantation has been described elsewhere [8].

The implanted wafers were annealed at 1150 °C for 2 h in an N_2 ambient and at either 1300 °C or 1350 °C for 4 h in an Ar–O_2 gas mixture. 500 nm thick epitaxial silicon layers were grown on some of the annealed wafers for Secco etching, which was employed to estimate the dislocation density in the superficial silicon layers. Etch pits produced by Secco etching, which were directly related to the dislocations, were observed using a microscope and by scanning electron microscopy (SEM). The structure of the SIMOX wafers was analyzed by XTEM. The breakdown voltage of the buried oxide layers was also measured to estimate the electrical characteristics of the layers.

3. Results

3.1. Oxygen dose effect

Fig. 1 shows XTEM photomicrographs of as-implanted and annealed wafers implanted with different oxygen doses. The wafer temperature was kept at 550 °C during implantation. High-temperature annealing was performed at 1350 °C for 4 h in an Ar–O_2 gas mixture. For the as-implanted wafers a buried oxide layer begins to form with a dose of 1.3×10^{18} cm^{-2}. The high-temperature anneal changes the oxygen distribution of the as-implanted wafers. Redistribution can be clearly observed in the relatively low dose region of 0.2–1.3×10^{18} cm^{-2}, by comparing photomicrographs of both the

0168-583X/91/$03.50 © 1991 – Elsevier Science Publishers B V (North-Holland)

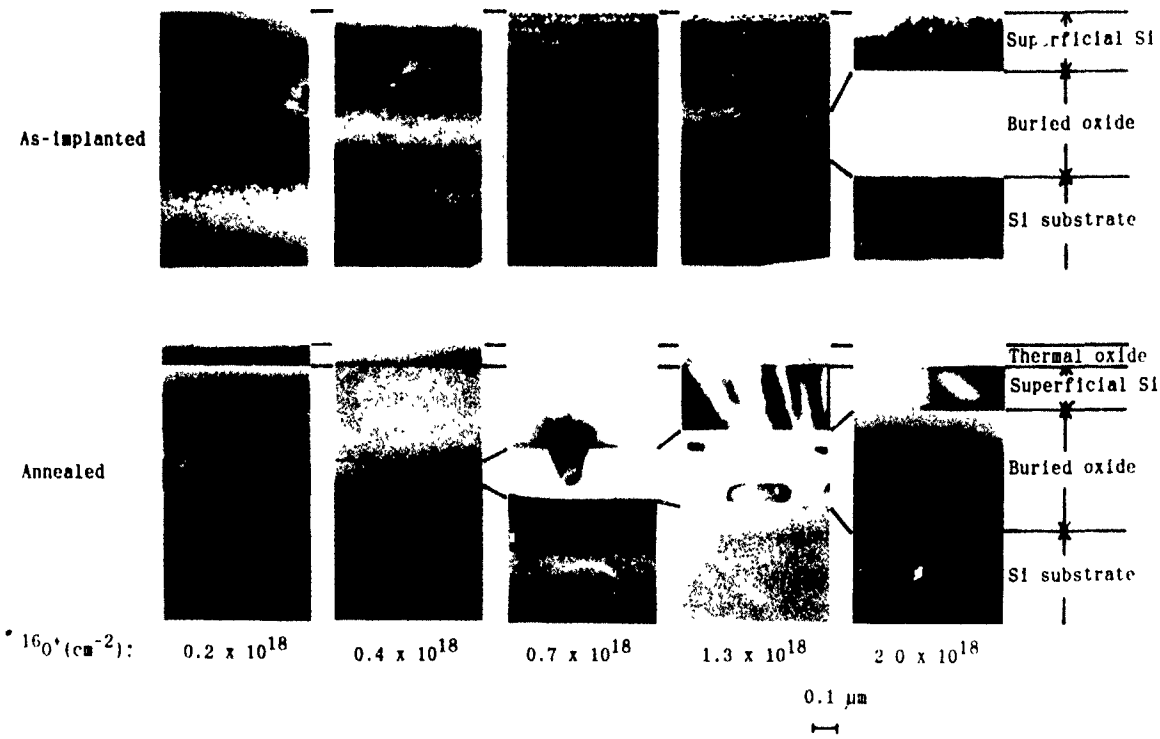

Fig 1 XTEM photomicrographs of as-implanted and annealed wafers implanted with different oxygen doses at an acceleration energy of 180 keV at 550 °C Post-implantation annealing was performed at 1350 °C for 4 h in an $Ar-O_2$ mixture

as-implanted and the annealed wafers Even after high-temperature annealing, no continuous buried oxide layer is formed in the wafer implanted with a dose of 0.2×10^{18} cm^{-2}, though hexagonal oxide precipitates are observed A uniform continuous buried oxide layer of approximately 80 nm is formed with a dose of 0.4×10^{18} cm^{-2}. In the case of a dose of 0.7×10^{18} cm^{-2}, the front interface between the superficial silicon layer and the buried oxide layer is uneven and silicon precipitates are observed within the buried oxide layer The front interface is even, for a dose of 1.3×10^{18} cm^{-2}, although silicon precipitates remain in the buried oxide layer. As the dose increases, the number of silicon precipitates is reduced. Almost all the precipitates disappear with a dose of 2.0×10^{18} cm^{-2}. In this case, a threading dislocation is found in the superficial silicon

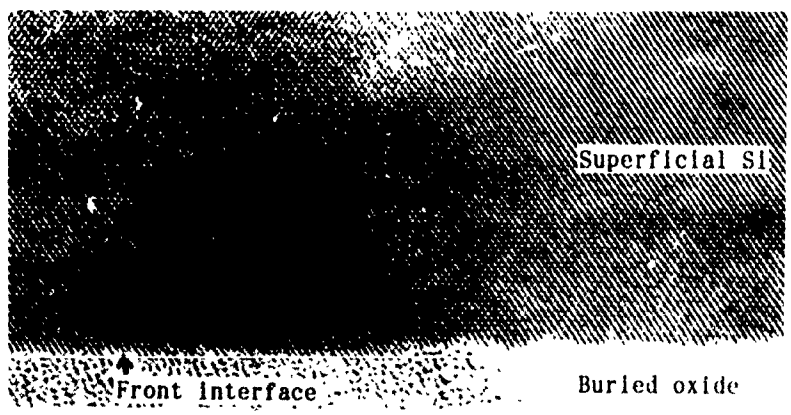

Fig 2 High resolution XTEM photomicrograph of a SIMOX wafer implanted at 180 keV with a dose of 0.4×10^{18} cm^{-2} at 550 °C The anneal was performed under the same conditions as described in the caption of fig. 1.

layer. All the defects observed in the annealed wafers were dislocations. Similar cross-sectional structures were obtained for wafers annealed at 1300 °C.

Fig. 2 shows a high resolution XTEM photomicrograph of an annealed wafer implanted with a dose of 0.4×10^{18} cm^{-2}. The high-temperature anneal was performed at 1350 °C for 4 h in an Ar–O_2 gas mixture. The front interface is abrupt with an undulation of less than 3 lattices.

The relationship between the dislocation density and the oxygen dose is exhibited in fig. 3. Oxygen ions were implanted at 550 °C. Subsequent annealing was performed at 1150 °C for 2 h in an N_2 ambient or at 1300 °C for 4 h in an Ar–O_2 gas mixture. The dislocation density is approximately 10^9 cm^{-2} with a dose of 2.0×10^{18} cm^{-2}, which is standard, at both anneal temperatures. As the dose decreases, the density drastically decreases. For the wafers annealed at 1300 °C, the dislocation density falls to a value on the order of 10^2 cm^{-2} for doses lower than 1.2×10^{18} cm^{-2}. For the wafers annealed at 1150 °C, however, such a drastic decrease in dislocation density is not observed in this dose range. This result suggests that the redistribution of the implanted oxygen atoms during the high-temperature anneal should play an important role in reducing the dislocation density.

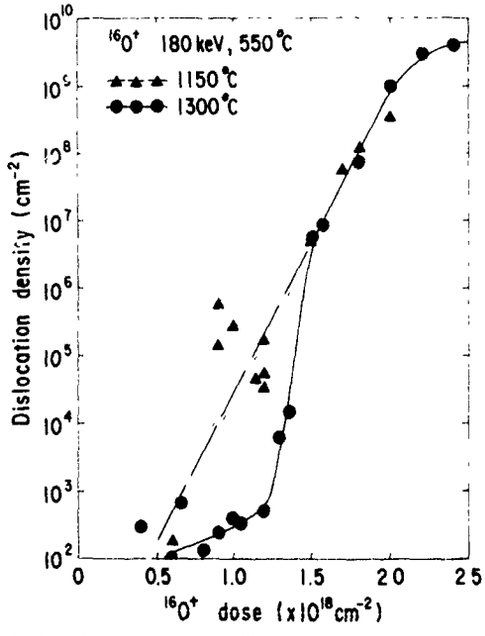

Fig. 3. Relationship between the dislocation density of the superficial Si layer and the oxygen dose. Oxygen ions were implanted at 180 keV and 550 °C. SIMOX wafers were annealed at 1300 °C for 4 h in an Ar–O_2 mixture or at 1150 °C for 2 h in an N_2 ambient.

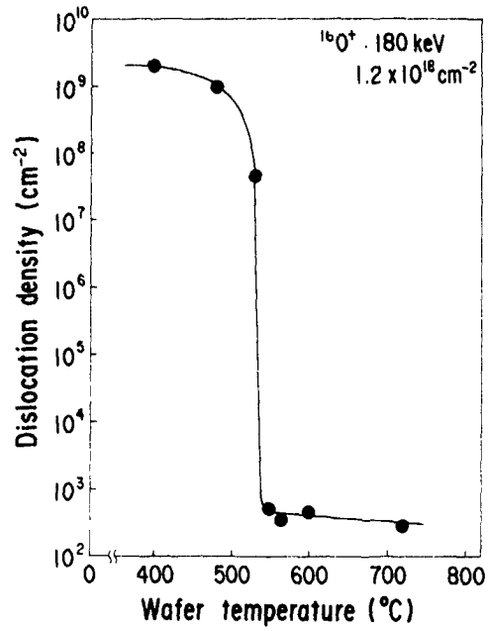

Fig. 4. Relationship between the dislocation density and the wafer temperature during oxygen implantation. Oxygen ions were implanted at 180 keV with a dose of 1.2×10^{18} cm^{-2}. SIMOX wafers were annealed at 1300 °C for 4 h in an Ar–O_2 mixture.

3.2 *Effects of wafer temperature*

Fig. 4 shows the relationship between the dislocation density and the wafer temperature during oxygen implantation. The dose was fixed at 1.2×10^{18} cm^{-2}. Post-implant annealing was performed at 1300 °C for 4 h in an Ar–O_2 gas mixture. The dislocation density shows strong dependence on the wafer temperature. For the wafers implanted at wafer temperatures lower than 500 °C, the dislocation density is approximately 10^9 cm^{-2}. The density is drastically reduced to an order of 10^2 cm^{-2} at wafer temperatures higher than 550 °C. The dislocation density dependence on wafer temperature was observed only in a region of doses lower than 1.5×10^{18} cm^{-2}. In the case of a high dose, such as 2.0×10^{18} cm^{-2}, the dislocation density remains on the order of 10^9 cm^{-2}, independent of the wafer temperature.

Fig. 5 shows XTEM photomicrographs of as-implanted wafers prepared at three different temperatures with a dose of 1.2×10^{18} cm^{-2}. For the wafers implanted at 400 and 480 °C, a number of defects and stress contrast related to the defects are observed in the superficial silicon layer. At 550 °C, numerous cavities are formed in the superficial silicon layer and no stress contrast associated with defects is found in the vicinity of the cavities. These cavities exist in all wafers implanted at temperatures higher than 550 °C [9]. It is

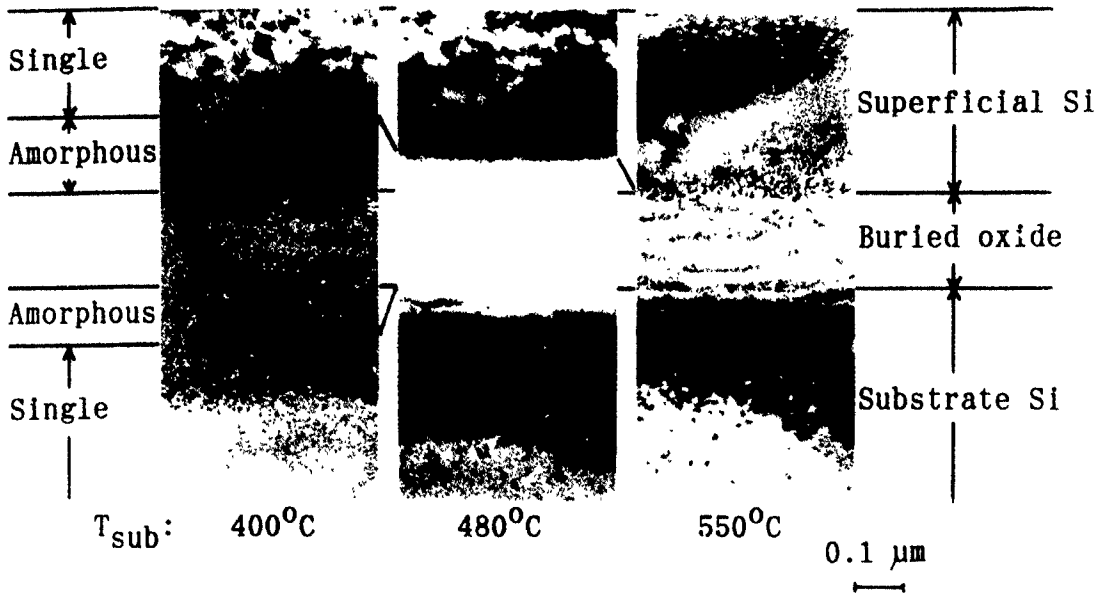

Fig 5 XTEM photomicrographs of as-implanted wafers prepared with a dose of 1.2×10^{18} O^+ cm^{-2} at 180 keV The wafer temperature was kept at 400, 480 and 550 °C, respectively

considered that the generation of cavities should relax the stress induced by high-dose oxygen implantation. This results in the drastic reduction in the dislocation density

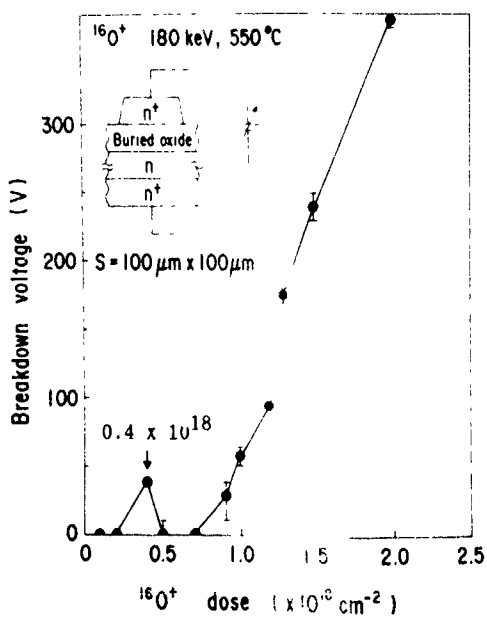

Fig. 6. Relationship between the breakdown voltage of the buried oxide layer and the oxygen dose Oxygen ions were implanted at 180 keV and 550 °C Implanted wafers were annealed at 1350 °C for 4 h in an $Ar-O_2$ mixture.

3.3 Breakdown voltage of buried oxide layers

The relationship between the breakdown voltage of the buried oxide layer and the oxygen dose is shown in fig 6. Implantation and subsequent annealing were performed under the same conditions as described in the caption of fig. 1 The area of the buried oxide for each device is 100 μm × 100 μm. For wafers implanted with doses lower than 0.2×10^{18} cm^{-2}, the breakdown voltage is 0 V because no buried oxide layer is formed, as shown in fig. 1. In case of a dose of 0.4×10^{18} cm^{-2}, the buried oxide layer has a breakdown voltage of approximately 40 V This breakdown voltage is sufficiently high for usual LSI applications. This dose is one-fifth the standard dose. Accordingly, the oxygen-implantation time can be shortened to one-fifth of what is usually used. In other words, this result is practically equivalent to implantation by an ion-beam current five times higher than that of NV-200, i.e., 500 mA.

The breakdown voltage is again 0 V in spite of the higher dose range from $0.5–0.7\times10^{18}$ cm^{-2}. In this range, the front interface is uneven and the buried oxide layer has a lot of silicon precipitates, as described previously. These reduce the effective thickness of the oxide layer, which causes a leakage current to flow through the layer. With doses ranging from $0.9–2.0\times10^{18}$ cm^{-2}, the effective buried oxide layer is thick enough and the breakdown voltage increases as the dose increases.

4. Summary

The relationships between the oxygen implantation conditions and the structure of SIMOX wafers in addition to the dislocation density in the superficial silicon layer have been clarified A SIMOX wafer implanted with a dose of 0.4×10^{18} O^+ cm^{-2}, which is one-fifth the standard dose, has an extremely low dislocation density on the order of 10^2 cm^{-2}. In this case, the breakdown voltage of the buried oxide layer is approximately 40 V, which is sufficiently high for usual LSI applications. This has enabled a five-fold increase in the throughput of SIMOX-wafer production.

The authors would like to thank T. Sakai for his guidance and encouragement.

References

[1] J.P Ruffell, D H. Douglas-Hamilton, R.E Kaim and K. Izumi, Nucl Instr and Meth B21 (1987) 229

[2] K. Izumi, M. Doken and H Ariyoshi, Electron Lett 14 (1978) 593

[3] P.S. Fecher, G Gardner, J. Yue, S T Liu and B Cordts, Proc IEEE SOS/SOI Techn Conf. (1989) 70.

[4] T.W Houston, H. Lu, P Mei, G W Blake, L.R Hite, R Sundaresan, W.E. Bailey, J Liu, A Peterson and G Pollack, Proc IEEE SOS/SOI Techn. Conf (1989) 137.

[5] J Belz, G. Burbach, H Vogt and J Pieczynski, Proc. 4th Int Symp. SOI Techn and Devices 90-6 (1990) 518

[6] G K Celler, P.L F Hemment, K.W. West and J M. Gibson, Appl. Phys. Lett. 48 (1986) 532.

[7] F. Namavar, E. Cortesi and P Sioshani, Proc IEEE SOS/SOI Techn. Workshop (1988) p. 19

[8] S. Nakashima, S Kanamori and K. Izumi, Electron Lett 21 (1989) 1229

[9] S. Nakashima and K Izumi, J Mater Res. 5 (1990) 1918

Nuclear Instruments and Methods in Physics Research B55 (1991) 852–855
North-Holland

Energy and dose dependence of silicon top layer and buried oxide layer thicknesses in SIMOX substrates

U. Bussmann, A.K. Robinson and P.L.F. Hemment

Department of Electronic and Electrical Engineering, University of Surrey, Guildford GU2 5XH, UK

The formation of SIMOX (separation by implanted oxygen) substrates involves the implantation of very high doses of oxygen into silicon. A model has been developed to predict the evolution of the oxygen depth profile taking into account sputtering, swelling and oxygen redistribution during implantation as well as chemical segregation during high temperature annealing. The resulting computer code IRIS (implantation of reactive ions into silicon) enables a fast calculation of oxygen profiles to be made. The simulation results discussed in this paper cover the energy range 50–300 keV and doses of up to 2.5×10^{18} O^+ cm^{-2}.

1. Introduction

During the past decade SIMOX (separation by implanted oxygen) [1] has emerged as one of the most promising SOI (silicon-on-insulator) technologies [2]. The implantation of high doses of oxygen is followed by high temperature annealing leading to the formation of a buried insulating layer beneath a silicon top layer. These layer thicknesses can be varied by adjusting the implantation energy and dose, thus making SIMOX a technology of great versatility. A predictive model which enables a calculation of the final oxygen distribution is desirable. However, standard tables and computer codes, which deliver satisfactory profiles for low doses, are not applicable as sputtering, swelling and diffusion during implantation as well as chemical segregation during annealing all lead to oxygen redistribution.

Different approaches to develop dedicated models for this special ion–target combination are reported in the literature. Hayashi et al. [3] found simple formulas to reproduce measured layer thicknesses. Maydell-Ondrusz et al. [4] calculated as-implanted profiles in a stepwise procedure by taking into account the changes of the target composition after successive implantations of small incremental doses. Jager et al. [5] solved the partial differential equations describing the mass transport during the implantation. As a common disadvantage, these models include fitting parameters and, therefore, they cannot be applied in the absence of experimental data.

Recently, the computer model IRIS (implantation of reactive ions into silicon) [6] has been developed, which enables a fast calculation of oxygen distributions after implantation. During high temperature annealing the implanted oxygen segregates to form a buried oxide layer. Assuming total thermal segregation the thicknesses of the silicon top layer and buried oxide can be calculated [7]. In this paper the evolution of the oxygen profiles and resulting layer thicknesses is investigated as a function of implantation energy (50–300 keV) and dose (up to 2.5×10^{18} O^+ cm^{-2}).

2. IRIS

In the programme IRIS, the target is divided into 100 channels, each representing a particular depth interval of the original silicon wafer. A stepwise procedure is applied to simulate the evolution of the implantation profile. After each deposition of a small incremental dose (typically 1/1000 of the total dose) into the appropriate channels, the composition and width of each channel is recalculated taking into account all the major high dose effects. The justification for the assumptions made in the design of this model have been extensively discussed elsewhere [6,7] and therefore only a brief summary will be given here.

Incremental dose profile: The implantation profiles, which are generated by the Monte Carlo simulation programme TRIM [8,9], are the most reliable theoretical low dose profiles known so far. Advantage is taken of the high similarity of the profiles of O in Si and O in SiO_2 (fig. 1). Throughout the simulation procedure the incremental dose profile is always represented by that of O in Si.

Swelling: The internal oxidation of the silicon leads to volume expansion. The resulting swelling is assumed to be linear with the local oxygen concentration. In order

0168-583X/91/$03.50 © 1991 – Elsevier Science Publishers B.V. (North-Holland)

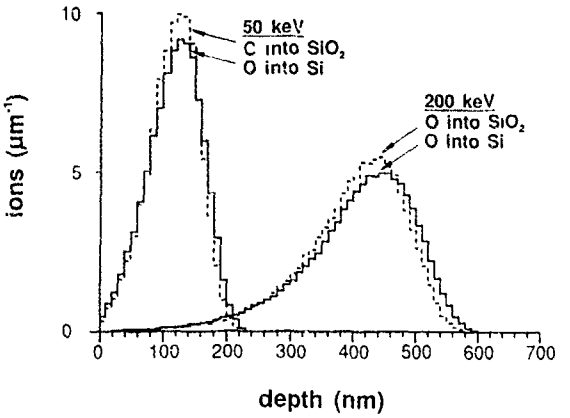

Fig 1. TRIM [10] profiles of O in Si and O in SiO_2 (target density = 2.33 g cm^{-3})

to calculate its absolute value a SiO_2 density of 2.33 g cm^{-3} is used.

Sputtering: The energy-dependent sputter yields used in the present calculations (e.g. 0.32 atoms/ion at 50 keV and 0.13 atoms/ion at 300 keV) were generated by the programme TRIM89 [11]. It has been shown, that for an implantation energy of 200 keV the theoretical yield matches the experimental result for silicon. Care has to be taken if an oxide surface layer exists. In this case a much higher sputter yield can lead to a different buried layer formation mechanism [6,12].

Diffusion: Diffusion is neglected in substoichiometric regions. However, if oxygen is deposited into an already existing stoichiometric oxide, the excess oxygen is immediately redistributed to the profile flanks and the profile becomes flat topped. For the presented calculations it is assumed that this oxygen is bound at the upper interface, which thereby moves towards the surface.

Thermal segregation: High temperature annealing (> 1300°C) leads to complete segregation of the implanted oxygen towards the buried oxide layer [13]. The simulated implantation profile is transformed into a rectangular profile. When, for doses above the critical dose, which is necessary to reach stoichiometry at the profile maximum, the as-implanted oxygen distribution already includes a stoichiometric layer, the oxygen from each profile flank is redistributed to the nearest interface. The stoichiometric layer grows towards the surface and towards the bulk silicon until all the implanted oxygen has been incorporated. For implantation doses less than the critical dose, it is assumed that the formation of the stoichiometric layer starts at the profile maximum. However, if the implantation dose is too low lateral as well as vertical segregation is taking place during annealing leading to a non-continuous oxide. For example, it has been shown that for an implantation energy of 200 keV the buried oxide layer is interrupted for doses $\leq 0.5 \times 10^{18}$ O^+ cm^{-2}) [14]. In such a case the simulation programme is not applicable.

3. Results and discussion

For an implantation energy of 200 keV the evolution of the oxygen implantation profile with increasing dose is shown in fig. 2. Swelling dominates over sputtering, shifting target material downwards relative to the current surface. While the incremental dose profile (peak position at 440 nm) is not allowed to change, the maximum of the implantation profile slowly moves to greater depths. This movement leads to an increase of the critical dose for stoichiometry at the profile maximum to 1.35×10^{18} O^+ cm^{-2} (0.95×10^{18} O^+ cm^{-2} if swelling and sputtering are ignored). Above this critical dose a buried oxide layer is formed. The upward movement of the upper interface (the upper boundary of the stoichiometric layer) is mainly due to the redistribution of excess oxygen deposited inside the SiO_2 layer. This redistribution also transforms the gradient of the implantation profile into a step. On the other side of the stoichiometric layer the lower interface is slowly moving downwards due to the effect of swelling minus sputtering. Eventually the lower flank moves out of the range of the implanted oxygen ions and its shape stays constant.

Fig. 3 summarizes the results of many calculations performed for an implantation energy of 200 keV. The peak position of the as-implanted profile is shown for subcritical doses and interface positions are shown for higher doses. The final interface positions, as reached after thermal segregation, are compared to experimental data points taken from the literature (annealing temper-

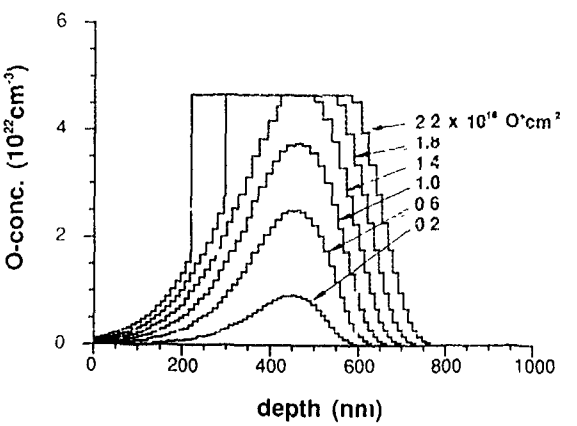

Fig. 2 IRIS results for 200 keV O into Si

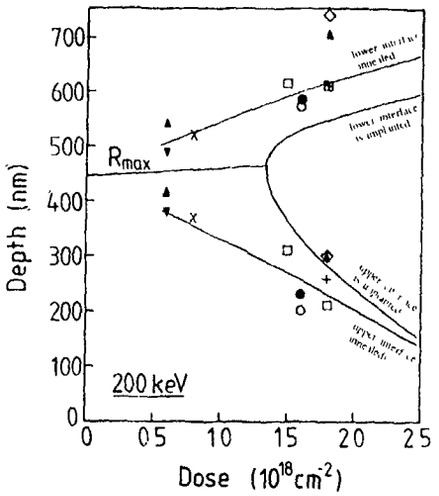

Fig. 3 Calculated depths [7] of the maximum O-concentration (R_{max}) and interface positions for 200 keV O into Si. The symbols represent experimental data points for annealing temperatures ≥ 300°C, taken from XTEM micrographs and SIMS measurements as found in the literature (see ref. [7] for details).

ature ≥ 1300°C, see ref. [7] for details). Each of the later curves consists of two approximately linear parts. The slight change in the slopes reflects the onset of the redistribution of excess oxygen inside the SiO_2 layer during the implantation process itself. This redistribution also leads to the consumption of an increasing part of the substoichiometric SiO_x layer above the buried SiO_2 layer during the implantation leaving less oxygen in the top layer to be redistributed during the annealing

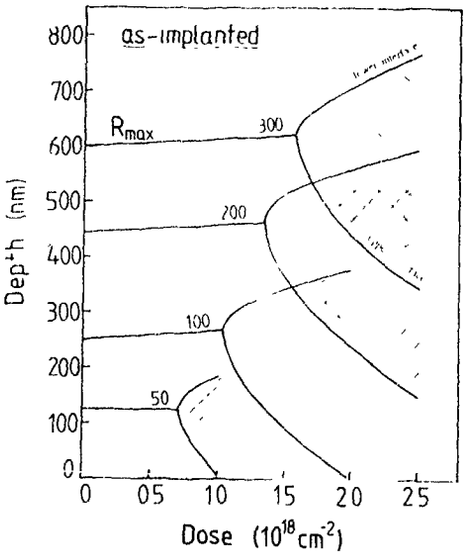

Fig 4. As-implanted (IRIS results): Depth of the maximum O-concentration and interface positions for different energies in keV.

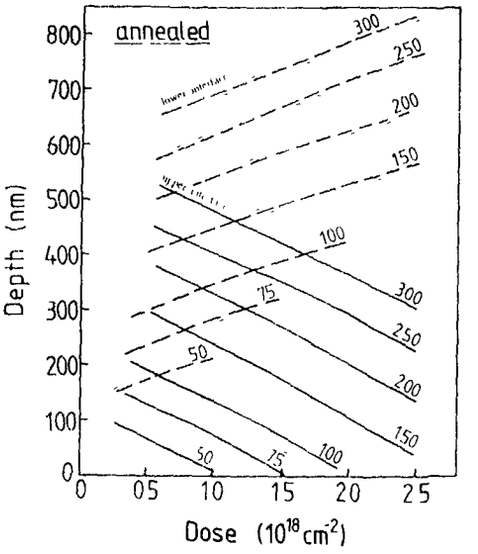

Fig 5 Annealed (IRIS results): Interface positions for different energies in keV

Therefore, the gap between the curves representing the as-implanted and the annealed state is closing. Taking into account the scatter in the experimental data, there is good agreement between the simulation and experiment.

Simulations have been performed for the energy range 50–300 keV. Fig. 4 shows the results for the as-implanted state All curves follow a trend similar to the discussed 200 keV case. With increasing implantation energy the critical dose increases due to the larger straggle in the incremental dose distribution.

Fig. 5 shows the interface positions after high temperature annealing. The thickness of the silicon overlayer shows a strong dependence on both the implantation energy and the dose. In contrast, the buried oxide thickness depends on the implantation dose only. This is due to the fact, that after annealing all the implanted oxygen is found within the buried stoichiometric layer. Only a small proportion of oxygen is lost during the implantation due to the oxygen atoms which are deposited close to the surface and subsequently removed by surface erosion.

4. Summary

A predictive model of the evolution of high dose oxygen implantation profiles in silicon has to take into account swelling, sputtering and diffusion (rapid redistribution of excess oxygen in SiO_2 to the profile flanks leading to flat topped profiles). The new computer code IRIS enables this evolution to be simulated and the layer thicknesses of the silicon top layer and the buried

oxide layer, as found after high temperature annealing, to be calculated. It has been shown that for an implantation energy of 200 keV, the model reproduces the experimental results. Predictions have been made for the energy range 50–300 keV.

Acknowledgements

This work was funded by the US Air Force Office of Scientific Research (grant AFO-88-0356), and received support from the UK Science and Engineering Research Council.

References

[1] K. Izumi, M. Doken and H. Ariyoshi, Electron. Lett. 14 (1978) 593
[2] A.H. van Ommen, Nucl. Instr. and Meth. B39 (1989) 194
[3] T. Hayashi, H. Okamoto and Y. Homma, Proc. Conf. on Defects and Radiation Effects in Semiconductors 1980, Inst. Phys. Conf. Ser. 59 (1981) 533
[4] E.A. Maydell-Ondrusz and I.H. Wilson, Thin Solid Films 114 (1984) 357
[5] H.U. Jäger, J.A. Kilner, R.J. Chater, P.L.F. Hemment, R.F. Peart and K.J. Reeson, Thin Solid Films 161 (1988) 333
[6] U. Bussmann and P.L.F. Hemment, Nucl. Instr. and Meth. B47 (1990) 22.
[7] U. Bussmann and P.L.F. Hemment, Appl. Phys. Lett. 57 (1990) 1200
[8] J.P. Biersack and L.G. Haggmark, Nucl. Instr. and Meth. 174 (1980) 257
[9] J.F. Ziegler, J.P. Biersack and U. Littmark, in: The Stopping and Ranges of Ions in Solids, vol. 1, ed. J.F. Ziegler (Pergamon, New York, 1985).
[10] The version used in this calculation is based on the original TRIM [8], but using the universal nuclear interaction potential and the ZBL electronic stopping power of ref. [9]. The cutoff energy was set to 25 eV.
[11] J.F. Ziegler, J.P. Biersack and G. Cuomo, TRIM89
[12] P.L.F. Hemment, K.J. Reeson, A.K. Robinson, J.A. Kilner, R.J. Chater, C.D. Marsh, K.N. Christensen and J.R. Davies, Nucl. Instr. and Meth. B37/38 (1989) 766.
[13] C. Jaussaud, J. Margail, J. Stoemenos and M. Bruel, Mater. Res. Soc. Symp. Proc. 100 (1988) 17
[14] C.D. Marsh, J.L. Hutchison, G.R. Booker, K.J. Reeson, P.L.F. Hemment and G.K. Celler, Inst. Phys. Congr. Ser. 87 (1987) 409

Nuclear Instruments and Methods in Physics Research B55 (1991) 856–859
North-Holland

Oxygen implantation through patterned masks: a method for forming insulated silicon device islands while maintaining a planar wafer surface

U. Bussmann, P.L.F. Hemment, A.K. Robinson and V.V. Starkov [1]

Department of Electronic and Electrical Engineering, University of Surrey, Guildford GU2 5XH, UK

SIMOX (separation by implanted oxygen) is a recognized technology to produce silicon on insulator substrates Laterally isolated device islands are formed by subsequent mesa etching or selective local oxidation of the silicon top layer. Alternatively, isolation can be achieved by using patterned masking layers in the implantation process, leading to continuous but nonplanar buried oxide layers In order to ease device fabrication, it is desirable to achieve a planar wafer surface. Special test structures have been implanted with 200 keV oxygen to doses up to 2.4×10^{18} O^+ cm^{-2}. The formation of TDI (total dielectric isolation) structures has been analyzed by Talystep and cross-sectional TEM The successful formation of isolated islands in combination with a planar surface is demonstrated for an oxygen implantation through an oxide mask formed in a LOCOS process.

1. Introduction

Devices in dielectrically isolated islands have many advantages compared to those in bulk silicon, including higher switching speeds and improved radiation tolerance A recognized technique to produce silicon on insulator substrates is SIMOX (separation by implanted oxygen) (review in ref. [1]) The implantation of a high dose of oxygen ions (typically 1.8×10^{18} O^+ cm^{-2} at an implantation energy of 200 keV and temperature of 500 °C) is followed by a high temperature annealing stage (typically $\geq$ 1300 °C), where the implanted oxygen segregates towards a buried layer. Thereby, a buried insulator is formed, which vertically isolated the crystalline silicon top layer against the substrate (fig. 1a). Subsequent trench isolation by plasma etching (fig 1b) or selective oxidation of the silicon overlayer (fig. 1c) are conventional techniques to form laterally isolated silicon device islands

TDI (Total Dielectric Isolation) has been introduced as a variation of SIMOX technology [2–4], where both vertical and lateral isolation is achieved in a single implantation stage. This approach uses patterned masking layers (fig. 1d). In the window region (i.e. in the unmasked area) the substrate structure corresponds to that of the standard SIMOX substrate. However, in the mask region the oxygen ions lose part of their energy while penetrating the mask and therefore the buried oxide layer is formed closer to the original wafer surface. A nonplanar but continuous buried oxide layer can be formed [3]. Processing parameters, which determine the final structure, include mask material, mask thickness and the edge topography in the transition region (TR) between mask and window

For further device processing, it is desirable to maintain a planar wafer surface. This cannot be achieved

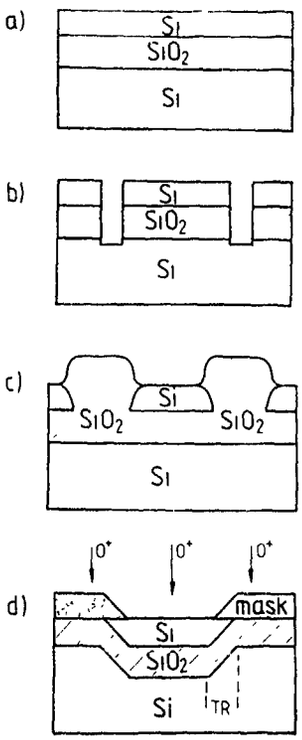

Fig 1 Schematic showing (a) SIMOX structure, (b) trench isolation, (c) LOCOS isolation and (d) TDI structure.

[1] On leave from Institute of Problems of Microelectronics Technology and Superpure Materials, Academy of Science, 142432 Chernogolovka, Moscow District, USSR.

0168-583X/91/$03 50 © 1991 – Elsevier Science Publishers B.V. (North-Holland)

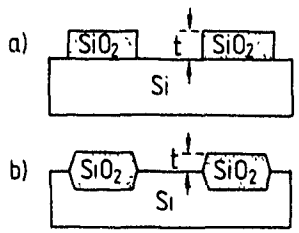

Fig 2. Schematic of prepared masks: (a) patterned thermal oxide and (b) LOCOS oxide.

with conventional methods for lateral isolation (trench etching or LOCOS). In this paper we exploit the different sputter rates for oxygen into silicon and oxygen into SiO_2 to planarize the surface during the formation of the TDI structure.

2. Experiment

Periodic test structures with SiO_2 masks of varying thickness were prepared on 3 in. device grade (100) silicon wafers The patterns were formed by etching windows into a thermally grown oxide or by local oxidation (LOCOS) of the silicon wafer (fig. 2). Molecular oxygen ions were implanted with an energy of 200 keV/atom in the dose range $0.4\text{–}2.4 \times 10^{18}$ O^+ cm^{-2}. The implantation temperature was held at 500 °C by beam heating. Some samples were capped with a 500 nm thermal oxide cap and subsequently annealed at 1300 °C for 5 h or at 1350 °C for 4 h.

The formation of the TDI structure has been studied by Talystep measurements of the step height and cross-sectional TEM investigations of the microstructure of the transition between the mask and window regions.

3. Results and discussion

In SIMOX samples the movement of the free surface is determined by the amount of swelling (i.e. the volume expansion due to the internal oxidation of the silicon) and surface erosion. The step height between the mask and window regions is given by the resulting relative movements in both regions. The sputter yield is approximately 0.15 atoms/ion for silicon and 1.1 atoms/ion for SiO_2 [4], corresponding to erosion rates of 30 and 165 nm per 1×10^{18} O^+ cm^{-2}, respectively. Assuming, that the target density stays constant during oxidation, a layer of silicon will increase its thickness by a factor of 2.15 upon oxidation. The resulting upwards movements of the surface with respect to the bulk silicon is 123 nm per 1×10^{18} O^+ cm^{-2} implanted oxygen.

Periodic thermal oxide masks of various thicknesses, t, (470, 800 and 1820 nm) were implanted with different doses of 200 keV oxygen ions (projected range 410 nm, range straggling 90 nm [5]). The resulting step height between the silicon surface and the remaining oxide was measured by Talystep. Their dependence upon the implantation dose is shown in fig. 3, curves a, b and c. For the thick masks of 1820 (curve a) and 800 nm (curve b), the gradient of the curves is found to be 230 nm per 1×10^{18} O^+ cm^{-1}. If no swelling occurs beneath the oxide mask, a value of 258 nm per 1×10^{18} O^+ cm^{-2} would be expected. Thus we conclude that approximately 90% of the implanted oxygen, which is at first deposited into the thick masking layer, is subsequently lost through the wafer surface.

For an initial mask thickness of 470 nm (fig. 3, curve c), most of the implanted oxygen ions are deposited close to the interface between masking oxide and silicon wafer. In this case most of the implanted ions oxidize the silicon, leading to substantial swelling beneath the mask. Therefore, the resulting step height is determined by the difference in the surface erosion rates. This is reflected by the gradient of the corresponding step height curve being 110 nm per 1×10^{18} O^+ cm^{-2} (135 nm per 1×10^{18} O^+ cm^{-2} expected with identical swelling in both regions).

In order to planarize the surface (i.e. to reduce the step height to zero) a smaller initial step is required. On the other hand the oxide thickness, t, (see the schematic in fig. 2) cannot simply be decreased, because this would leave an unwanted silicon overlayer below the masking material. Masks formed by a LOCOS oxidation process offer the alternative. In this case only about 55% of the total oxide thickness is located above the original wafer surface. Thus a small initial step height, t, can be combined with an adequately thick oxide layer. The step height decrease with increasing dose, as measured for a LOCOS mask of $t = 380$ nm initial step

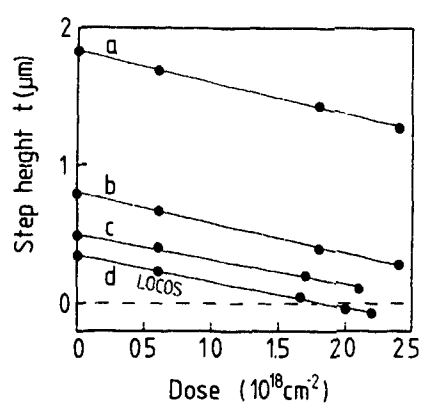

Fig 3. Dose dependence of residual step height as measured by Talystep for (a)–(c) patterned thermal oxide masks of different thicknesses and (d) a LOCOS oxide mask.

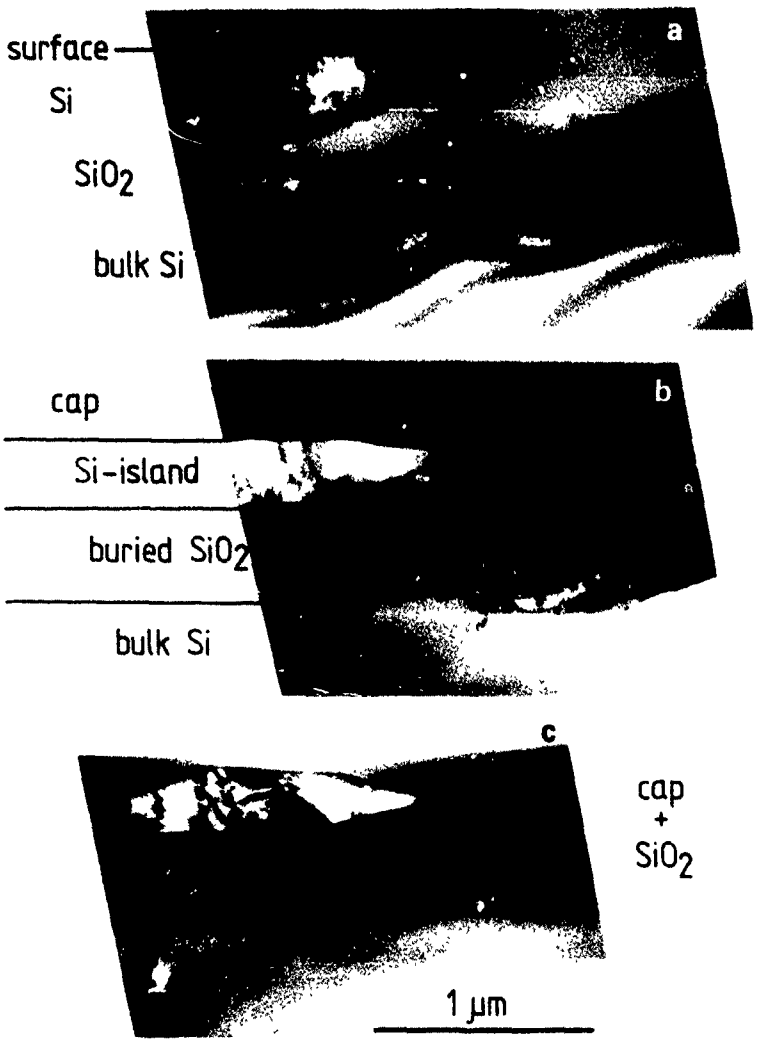

Fig. 4 XTEM micrographs (a) after implantation of 1.8×10^{18} O^+ cm^{-2}, (b) after annealing at 1300 °C and (c) after annealing at 1350 °C.

height, is shown in fig 3, curve d. Planarization is achieved for a dose of about 1.8×10^{18} O^+ cm^{-2}, for higher doses the step is reversed.

In the transition region (marked "TR" in fig. 1d) between mask and window, the structure of the implanted wafer is laterally nonhomogeneous. During high temperature annealing, lateral as well as vertical segregation will play an important role in this region. Therefore, the buried oxide formation mechanism will be different from that in planar SIMOX substrates.

The segregation of the implanted oxygen during high temperature annealing has been studied by cross-sectional transmission electron microscopy. Fig. 4 shows the microstructure of the transition region after the implantation of 1.8×10^{18} O^+ cm^{-2} into a wafer with a LOCOS oxide mask of 500 nm total thickness (the wafer is already covered by a deposited oxide, which is required as a protective cap during the subsequent high temperature annealing process). A highly defective but single crystalline silicon island is formed. Silicon inclusions are found within the buried oxide. The agglomeration of such inclusions near the edge of the masked region extends upwards chain-like to the tip of the silicon island. After annealing at 1300 °C (fig. 4b) the window region consists of a 400 nm thick buried oxide beneath a 300 nm silicon overlayer with threading dislocations as in conventional SIMOX samples. The silicon included in the oxide is now found in discrete precipitates. After the 1350 °C anneal (fig. 4c) most of these precipitates have dissolved and the interfaces between

silicon and oxide have sharpened further. Some crystalline silicon inclusions remain close to the interface between the buried oxide and the substrate, similar to those in conventional SIMOX substrates. A few inclusions are also found near the tip of the silicon island, which remains as a single crystal, but the precipitates forming the chain-like structure have disappeared.

4. Conclusions

(i) Oxygen implantation through patterned masking layers has been successfully applied to form dielectrically isolated silicon device islands.
(ii) Using a LOCOS mask in the implantation process, a planar wafer surface can be maintained.
(iii) For a high quality synthesized nonplanar oxide without detrimental silicon inclusions at the mask edge annealing temperatures above 1300 °C are required.
(iv) The best TDI microstructure observed so far has been achieved by implanting 1.8×10^{18} O^+ cm^{-2} through a LOCOS oxide mask (500 nm total thickness) with subsequent annealing at 1350 °C.

Acknowledgements

The authors gratefully acknowledge the assistance of F. Manning (preparation of test structures) and the staff of the D.R. Chick Laboratory (oxygen implantation). The work of one of the authors (U.B.) is supported in part by the Air Force Office of Scientific Research (grant AFO-88-0356)

References

[1] A.H. van Ommen, Nucl. Instr. and Meth B39 (1989) 194.
[2] J.R. Davis, A K. Robinson, K.J Reeson and P L F Hemment, Appl Phys. Lett 51 (1987) 1419
[3] P.L F. Hemment, A K Robinson, K.J Reeson, J.R Davis, J.A Kilner, R J Chater and J Stoemenos, Mater. Res Soc Symp Proc. 107 (1988) 87
[4] P.L.F Hemment, K J Reeson, A K. Robinson, J.A Kilner, R.J Chater, C.D. Marsh, K N Christensen and J R Davis, Nucl Instr and Meth B37/38 (1989) 766.
[5] J F Ziegler, J P Biersack and G Cuomo, TRIM89

Nuclear Instruments and Methods in Physics Research B55 (1991) 860–865
North-Holland

Nitrogen implantation for local oxidation (NILO) of silicon

P. Molle, C. Jaussaud and M. Bruel

Laboratoire d'Électronique, de Technologie et d'Instrumentation, Commissariat à l'Energie Atomique, Centre d'Etude Nucleaire de Grenoble, 85X, 38041 Grenoble cedex, France

Complete physical and electrical characterisation of nitrogen implantation for local oxidation (NILO) of silicon technology is detailed. Nitrogen implantation is performed at 20 keV through 25 nm of thermal oxide with doses within the range of 5×10^{16}–1.5×10^{17} cm^{-2}. Physical characterisation of the sealed nitride films is performed using secondary ion mass spectroscopy, transmission electron microscopy, nuclear reaction analysis and X-ray photoelectron spectroscopy. Nitrogen implantation in silicon can provide sealed nitride films of thicknesses around 20–25 nm, capable of masking a 550 nm field oxidation. Physical characterisation shows that implanted nitride films are composed of elemental Si–Si$_4$ bonds, silicon oxynitride and diffused oxygen. The nitrogen concentration in such films is lower than that of a stoichiometric nitride. "Bird's beak" lengths as short as 0.08 μm can be obtained. For a 950°C field oxide temperature, dislocations are observed at the edge of the nitride mask. At a higher temperature (1050°C) no dislocations are observed; on the other hand, stacking faults with a density of 0.05 faults per μm of mask length are observed at the edge of the nitride mask. Because of the presence of the stacking faults, high leakage currents are measured on n$^+$p diodes.

1. Introduction

Local oxidation of silicon (LOCOS) [1] is the dominant isolation technology for large-scale integrated circuits. This technology uses a deposited film of silicon nitride on a thin layer of buffer oxide as an oxidation mask. But this kind of selective oxidation is limited, in submicronic circuits, by lateral diffusion of oxidising species under the nitride mask. This transition region from thin oxide to thick oxide, commonly known as the "bird's beak", is enhanced by the presence of the buffer oxide. A solution consists in forming a silicon nitride in intimate contact with the silicon substrate. Because of the absence of any buffer oxide, this technique, called SILO (sealed interface local oxidation), can provide "bird's beak" lengths close to zero. Different methods have been explored to form films of silicon nitride directly sealed to the silicon surface and able to mask field oxidation. Among them we can find low-pressure chemical vapor deposition (LPCVD) [2], plasma-enhanced thermal nitridation [3] and nitrogen implantation in silicon [4–7].

We propose to study the nitrogen implantation for local oxidation (NILO) process in which N_2^+ implantation is performed at high dose (in the range of 10^{17} cm^{-2}) and low energy (in the range of 20 keV) which leads to direct nitridation of silicon. Oxidation masking properties of such layers have already been explored [7]. Nitrogen profiles, chemical composition and behaviour under oxidation are studied by complete physical characterisation. Nitride films are then patterned in order to perform selective oxidation; "bird's beak" lengths and oxidation-induced defects are investigated for different process parameters (nitrogen implantation dose and oxidation temperature). The NILO process has been implemented in a MOS technology. Electrical results are then discussed.

2. Experimental procedure

The substrates used for the experiments are ⟨100⟩ p-type wafers. The main processing steps required to obtain the NILO structure are shown in fig. 1. Wafers are oxidised in dry oxygen to grow an initial oxide of 25 nm. Molecular nitrogen ions are then implanted, at an energy of 20 keV, with doses between 5×10^{16} and 1.5×10^{17} cm^{-2} in order to form a thin film of sealed nitride. Nitrogen implantations are performed on high-current (Vecco VHC 120) or medium-current (Varian DF4) implanters. After annealing for 30 min at 950°C in N_2, wafers are patterned to define active areas. Initial oxide and implanted nitride are dry etched in a $CHF_3/C_2F_6/Ar$ mixture. Oxygen plasma, followed by diluted HF cleaning is then performed in order to eliminate carbonate or fluorate compounds, due to the dry etch, at the silicon surface. A 550 nm field oxide is obtained by steam oxidation at 950 or 1050°C. Initial oxide and implanted nitride are removed with the same process as before field oxidation. A 45 nm sacrificial oxide precedes the gate oxide growth. A classical NMOS process is then performed.

0168-583X/91/$03.50 © 1991 – Elsevier Science Publishers B.V. (North-Holland)

3. Physical characterisation

3.1. Implant parameters

3.1.1. Secondary ion mass spectroscopy (SIMS)

The SIMS profiles are shown in fig. 2. Nitrogen implantation is performed at 3 doses: 5×10^{16}, 10^{17} and 1.2×10^{17} cm^{-2}. All the samples are annealed for 30 min at 950 °C. We can observe that, except for the increase of the maximum nitrogen concentration with dose, the nitrogen profiles are similar. They are all composed of 3 characteristic regions: region 1, in the oxide film, where the nitrogen concentration strongly increases with depth, region 2, where the nitrogen concentration is a maximum and slightly decreases as a function of depth, and region 3, when the nitrogen concentration rapidly decreases as a function of depth. The region 2 width does not significantly increase when the implant dose is increased whereas the maximum

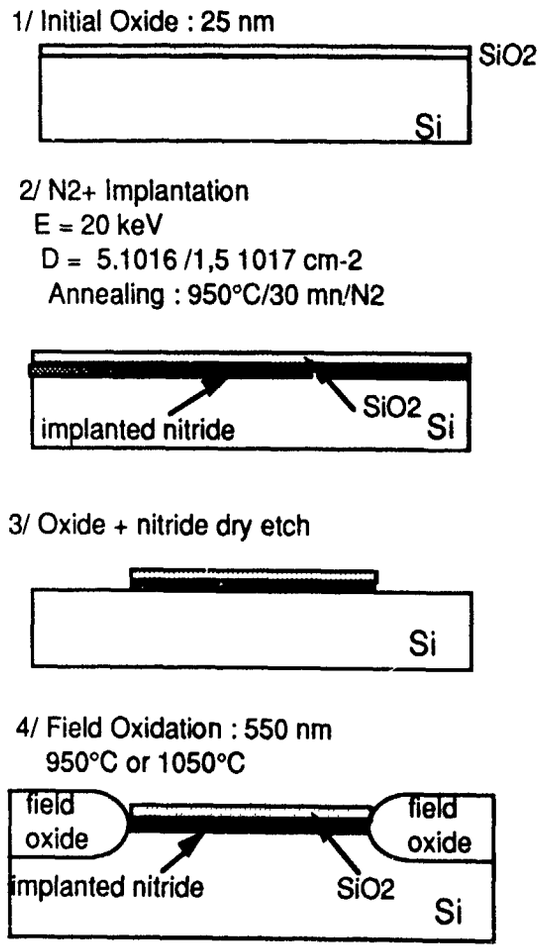

Fig. 1. NILO isolation processing sequence. Processing is performed at 20 keV through 25 nm SiO_2. $D = 5 \times 10^{16}$, 10^{17} and 1.2×10^{17} cm^{-2}.

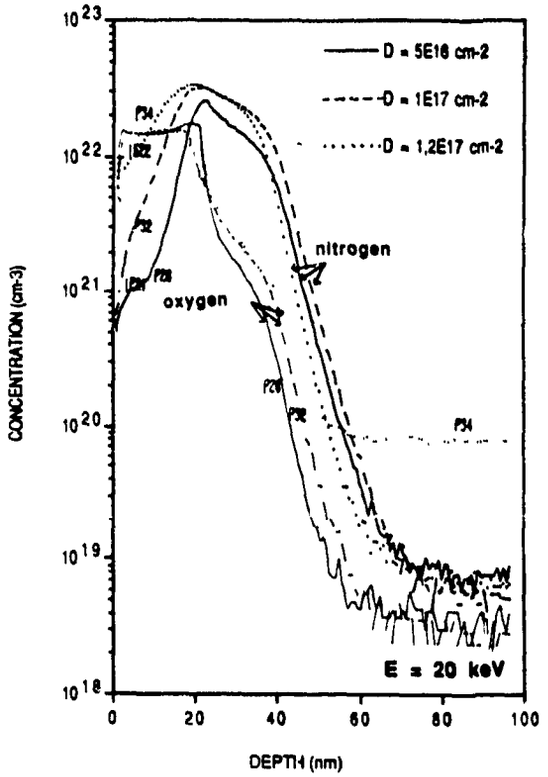

Fig. 2 SIMS profiles N_2^+ implantation is performed at 20 keV through 25 nm of SiO_2 $D = 5 \times 10^{16}$, 10^{17}, and 1.2×10^{17} cm^{-2}.

nitrogen concentration increases in this region with implant dose. This means that the increase of N_2^+ dose does not induce a significant increase in the implanted nitride film thickness but induces a change in the chemical composition of the film. Nevertheless nitrogen concentration never reaches the stoichiometric nitride value ($C_{N/Si_3N_4} = 6 \times 10^{22}$ cm^{-3}).

From oxygen profiles we observe a weak decrease of the initial oxide thickness: 20-nm-thick SiO_2 after 10^{17} cm^{-2} N_2^+ implantation instead of 25-nm-thick initial oxide. This decrease probably results from a sputter phenomenon due to the low-energy N_2^+ beam. Finally, we can see that the oxygen concentration is not negligible in the nitride film and slightly decreases as a function of depth. That is probably due to a recoil effect of oxygen atoms during nitrogen implantation.

3.1.2. Transmission electron microscopy (TEM)

TEM cross sections of 20 keV N_2^+ implantation are shown in fig. 3. Both samples, 5×10^{16} and 10^{17} cm^{-2}, exhibit two dielectric films The thickness of the top one decreases while that of the bottom one increases and the total thickness remains constant when the dose is increased. According to the SIMS profiles the top-

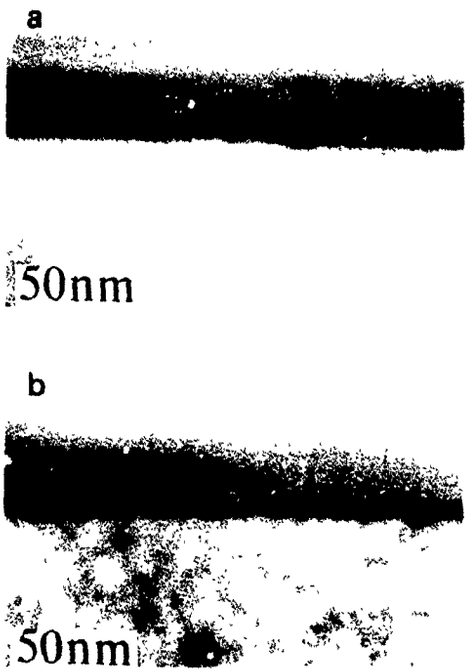

Fig 3 TEM cross sections N_2^+ implantation is performed at 20 keV through 25 nm SiO_2. (a) $D = 5 \times 10^{15}$ and (b) 10^{17} cm^{-2}

film/bottom-film interface corresponds to a limit of the nitrogen concentration in the initial oxide film, an important increase of the nitrogen concentration in the oxide being observed between 5×10^{16} and 10^{17} cm^{-2} on SIMS profiles. On the other hand, both nitrogen profiles in silicon are very similar which explains the same total thicknesses obtained for both nitrogen implantation doses.

3.1.3 Nuclear reaction analysis (NRA)

NRA has been performed after 30 min annealing in N_2 at 950 °C and removal (in diluted HF) of the initial oxide. The nitrogen dose as measured by NRA is shown in fig. 4 as a function of implant dose. The points follow a straight line with a 0.7 slope. This means that 30% of the implanted dose is eliminated after oxide removal. The weak percentage of nitrogen in the oxide film is due to nitrogen diffusion during annealing. SIMS profiles have shown that nitrogen concentration in the nitride film increases with the increase of the implant dose. From NRA dose measurements and TEM thickness measurements we can evaluate the mean nitrogen concentration value in the nitride film. If we consider an average consumption of 3 and 5 nm during a 20 keV N_2^+ implantation of respectively 5×10^{16} and 10^{17} cm^{-2}, the oxide thicknesses are then respectively 22 and 20 nm. TEM micrographs show a total thickness (nitride + oxide) of 43 nm. The nitride thicknesses are then 21 nm for a 5×10^{16} cm^{-2} implant dose and 23 nm for a 10^{17} cm^{-2} implant dose. From NRA measurements we obtain an average nitrogen concentration in the film: $C_N = 1.6 \times 10^{22}$ cm^{-3} for $D = 5 \times 10^{16}$ cm^{-2} and $C_N = 3.2 \times 10^{22}$ cm^{-3} for $D = 10^{17}$ cm^{-2}. These values are in good agreement with those obtained by SIMS and are below those of a stoichiometric nitride.

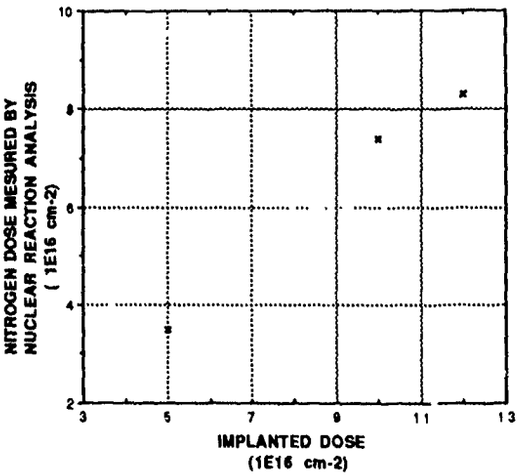

Fig. 4. Nitrogen dose measured by nuclear reaction analysis as a function of implanted dose.

3.1.4. X-ray photoelectron spectroscopy (XPS)

N_2^+ ion implantation through 25 nm SiO_2 has been performed at doses of 10^{17} and 1.5×10^{17} cm^{-2}. Both wafers have been annealed for 30 min under N_2 at 950 °C. XPS analyses are performed after removal of the initial oxide. The Si(2p) photoelectron line of a 10^{17} cm^{-2} implanted wafer is shown in fig. 5. We can observe that the Si(2p) line exhibits two components, Si1 and Si2. A complete study of depth profiling and

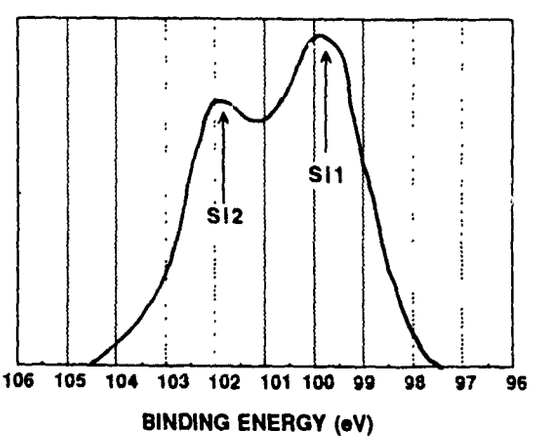

Fig. 5. XPS analysis: Si(2p) line, $D = 10^{17}$ cm^{-2}.

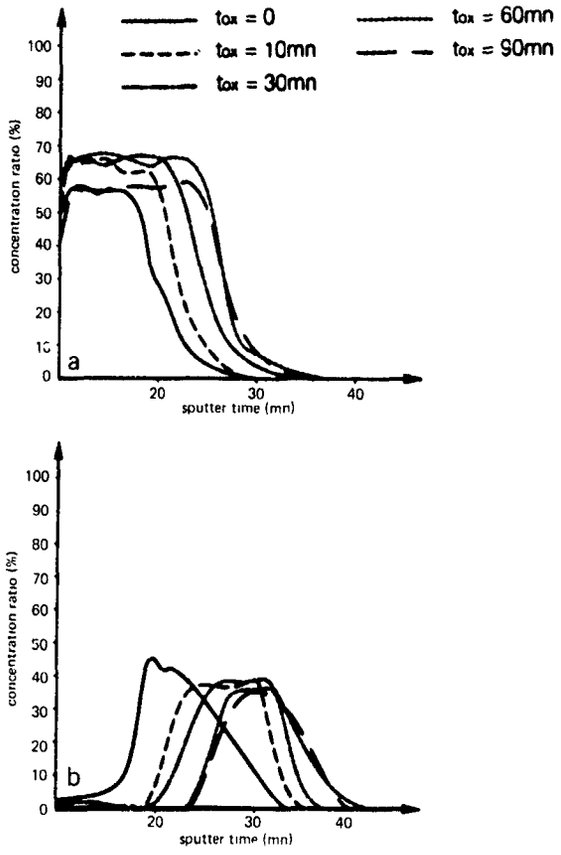

Fig 6 Auger profiles· oxygen (a) and nitrogen (b) concentrations for different oxidation times (t_{ox} = 0, 10, 30, 60 and 90 mn) Field oxide temperature = 1050 °C.

chemical composition of these wafers has already been published [8]. This paper points out the complex structure of these implanted nitride films: they are composed of elemental Si–Si_4 (Si1 component), silicon oxynitride (Si2 component) and diffused oxygen mixture. Oxygen, presumably due to recoil implantation, is always present in the nitride layer in an exponentially decreasing amount The respective concentrations of both silicon components are nearly constant in the film.

3.2 *Behaviour under oxidation*

Oxidation resistance of implanted nitride films has already been studied as a function of implant parameters (dose and energy) [7]. It has been established that a dose of 5×10^{16} cm^{-2} implanted at 20 keV through 25 nm of SiO_2 is sufficie nt to mask a field oxidation of 3 h at 950 °C.

3.2.1. *Profiles*

Auger profiles are shown in fig. 6. The initial nitride films are obtained by 20 keV N_2^+ ion implantation into silicon through 25 nm of SiO_2 and 30 min annealing in pure N_2. They are then oxidised under steam at 1050 °C, for various times (0, 10, 30, 60 and 90 min). We can observe a decrease of the width of the nitrogen profile and an increase of the width of the oxygen profile when the oxidation time is increased. Each nitrogen profile exhibits two sharp interfaces and a constant maximum concentration around 40%. These profiles show the oxidation of the nitride film under oxidising ambient. We can note that, in spite of the complex structure (presence of Si–Si bonds) of the implanted nitride, the oxidation of the film takes place at the oxide/nitride interface and that 23 nm of the nitride are not completely consumed after 90 min of steam oxidation.

3.2.2. *Bird's beak*

Implanted wafers are then patterned. The initial oxide and the implanted nitride are etched selectively to the silicon substrate. Local oxidation is performed at

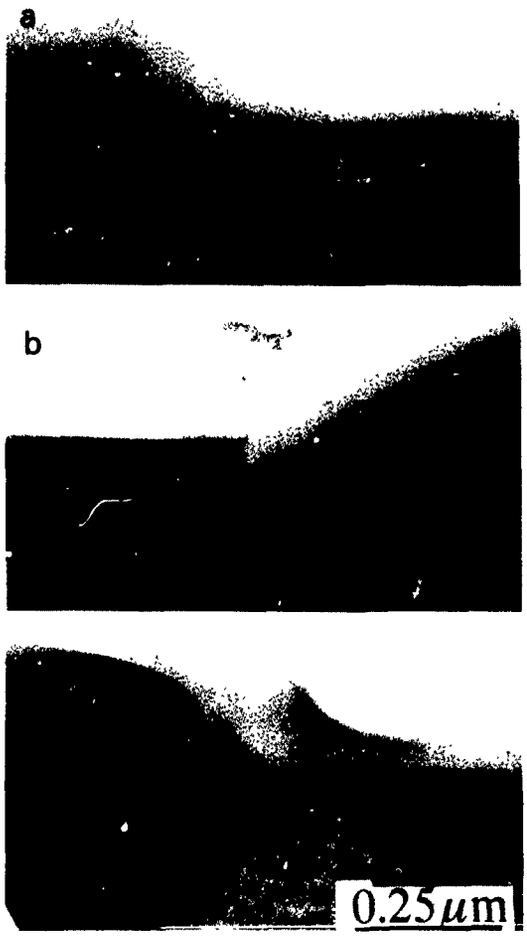

Fig. 7. NILO process. TEM cross sections. Field oxide temperature: 950 °C (a, b), 1050 °C (c) Nitrogen implantation: E = 20 keV, $D = 5 \times 10^{16}$ cm^{-2} (a), $D = 10^{17}$ cm^{-2} (b, c)

950 or 1050 °C in order to grow a 550 nm field oxide. Nitride films are obtained by implantation at 5×10^{16} or 10^{17} cm^{-2}. TEM cross-sections are shown in fig. 7. We observe first that the "bird's beak" length strongly decreases with the increase of implant dose (from 0.28 μm at 5×10^{16} cm^{-2} to 0.08 μm at 10^{17} cm^{-2}). On the other hand, the "bird's beak" length slightly increases with oxidation temperature. In the case of sealed nitride technologies such as NILO, the "bird's beak" growth is mainly governed by nitride induced stress. Oxygen diffusivity in the oxide and reaction rate are strongly affected by stress and this leads to an important decrease of lateral oxidation rate. The increase of stress with implant dose explains the decrease of the "bird's beak" with the dose. The increase of the "bird's beak" length with implant dose can be explained by the fact that, at temperatures above 960 °C, stress in SiO_2 is relaxed by viscous flow [11]. The lower stress favours lateral diffusion of oxygen species under the nitride mask and leads to a longer "bird's beak". This behaviour is different from those observed with the conventional LOCOS where the "bird's beak" length decreases with the increase of oxidation temperature. Deroux-Dauphin [9] explained that point by the great influence of the linear growth of the well-known linear-parabolic model of Deal and Grove on the "bird's beak" growth. He showed that most of the "bird's beak" grows during the linear growth. For a given oxide thickness the linear time/parabolic time ratio decreases with the increase of the oxidation temperature, which explains the decrease of the "bird's beak".

3.2.3. Oxidation-induced defects

Oxidation-induced defects are observed by optical microscopy after a SECCO etch. Wafers are implanted at a dose of 10^{17} cm^{-2} and oxidised at 950 or 1050 °C. The 950 °C oxidised wafers exhibit dislocations at the edge of the nitride mask. Their density is about 30 dislocations per μm of mask length. The dislocation generation is due to the strong nitride-induced stress during oxidation. Bogh and Gaind [12] showed that, without a buffer oxide and at a 950 °C oxidation temperature, dislocation generation cannot be avoided with nitride thicknesses above 20 nm. At a higher oxidation temperature (1050 °C) no dislocations are observed, meaning that the stress is relaxed by the viscous flow of SiO_2. On the other hand, stacking faults are observed at the edge of the nitride mask. Franz et al. [13] and Katcki et al. [14] assign the nucleation of such stacking faults to impurities, etching residues or point defects at the edge of the nitride mask. In our case we can assume that oxygen plasma plus HF cleaning is not sufficient to remove carbonate or fluorate compounds resulting from the dry etch. We can also deduce that stress and point defects due to N_2^+ implantation favour the nucleation of stacking faults.

4. Electrical results

NMOS devices have been applied on NILO-processed active areas. N_2^+ implantation is performed at 20 keV at a dose of 10^{17} cm^{-2}. A 550 nm field oxide is obtained by steam oxidation at a 1050 °C temperature.

The difference between the mask and the finished electrical width of *N* channel narrow transistors is 0.15 ± 0.02 μm, which confirms the value of 0.08 μm for the "bird's beak" measured by TEM. Junction leakages have been measured on n^+/p diodes. The perimeter and surface area of the diodes are respectively 16 cm and 40 000 μm^2. Leakage currents as high as a few mA/cm have been measured on these devices. These high leakage currents can be assigned to the presence of stacking faults at the edge of the nitride mask

Field doping conditions lead to larger than 20 V V_{Goff} values for 1.2 μm finished n-type field transistors (V_{Goff} is defined as the gate voltage for sustaining a leakage current less than 10 pA/μm of transistor width). On the other hand, low punch-through voltages are measured because of high n^+/p junction leakage.

Gate oxide breakdown is about 7 MV/cm for 90% of tested capacitances. This value is lower than that obtained with a conventional LOCOS (about 10 MW/cm).

5. Conclusion

Complete physical characterisation has been performed on nitride films obtained by low-energy (20 keV), high-dose (5×10^{16} cm^{-2}/1.5×10^{17} cm^{-2}) nitrogen implantation into silicon. From SIMS profiles, TEM micrographs, and NRA measurements we can assume that 20 keV N_2^+ implantation in silicon can provide nitride films with thicknesses around 20 to 25 nm. Nitrogen concentration of these films is lower (3.2×10^{22} cm^{-3} for a 10^{17} cm^{-2} implant dose) than the nitrogen concentration of a stoichiometric nitride ($C_{Si_3N_4} = 6 \times 10^{22}$ cm^{-3}). XPS analyses demonstrate the complex structure of formed silicon nitride films. Implanted nitride is composed of Si–Si bonds, silicon oxynitride and diffused oxygen. In spite of the presence of Si–Si bonds, 23 nm of silicon nitride (obtained by 20 keV/10^{17} cm^{-2} N_2^+ implantation through 25 nm of SiO_2) can resist steam oxidation at 1050 °C for 90 min. "Bird's beak" lengths as short as 0.08 μm can be obtained. Generation of dislocations is favoured by a 950 °C field oxide temperature. At 1050 °C no dislocations are observed but stacking faults are present at the edge of the nitride mask. The presence of these stacking faults leads to a high junction leakage.

References

[1] J.A. Appels, E. Kooi, M M. Paffen, J.J H. Schatorje and W.H.C.G. Verkuylen, Philips Res. Rep. 25 (1970) 1118.

[2] P. Deroux-Dauphin and J P. Gonchond, IEEE Trans. Electron Devices ED-32 (11) (1985).

[3] P Delpech, B Vuillermoz, M. Berenguer, A. Straboni and T Ternisien, J. Phys. (Paris) 49, C4 (1988).

[4] J.C Hui, T.Y. Chui, S.S. Wong and W G. Oldham, IEEE Trans. Electron Devices ED-329 (4) (1982)

[5] M.J Kim and M Ghezzo, J. Electrochem. Soc 131 (1984) 1935

[6] M. Ramin, H Ryssel and H. Kranz, Appl. Phys. 22 (1980) 393.

[7] P Berruyer and M. Bruel, Appl Phys. Lett 50 (1987) 89

[8] A Ermolieff, P. Molle and S Marthon, Appl Phys. Lett 56 (1990) 2672

[9] P. Deroux-Dauphin, thesis, Université de Grenoble, 1984.

[10] Deal and Grove, J. Appl Phys. 36 (12) (1965)

[11] E.P. Eernisse, Appl. Phys. Lett. 30 (1977) 290.

[12] A. Bogh and A.K. Gaind, Appl Phys. Lett 33 (1978) 895.

Nuclear Instruments and Methods in Physics Research B55 (1991) 866–869
North-Holland

Channeling contrast analysis of local damage distributions induced by maskless implantation

A. Kinomura, M. Takai, K. Hirai and S. Namba

Faculty of Engineering Science and Research Center for Extreme Materials, Osaka University, Toyonaka, Osaka 560, Japan

Channeling contrast analysis using a 400 keV helium-ion microprobe was used to locally investigate lateral damage distributions induced by maskless ion implantation. Angular spreads and incident angles of the microprobe were found to be an order of magnitude smaller than the critical angle of channeling. Channeling contrast images of a damage distribution induced by focused gallium implantation at 100 keV to a dose of 3×10^{15} Ga^+/cm^2 in silicon could be obtained with a low microprobe dose of 6×10^{14} He^+/cm^2.

1. Introduction

The focused-ion-beam (FIB) technology has realized maskless microfabrication such as lithography, doping, etching and deposition for semiconductor integrated circuits [1]. However, FIB processes induce damages localized not only in an in-depth direction but also in lateral directions, because of the nonuniform beam profiles and instability of the beam current. Therefore, it is necessary to analyze local damage distributions for the maskless processes using FIB.

Rutherford backscattering (RBS) using a microprobe has been successfully used for elemental analysis and three-dimensional local analysis [2]. The microprobe RBS with channeling also makes it possible to analyze local crystallinity [3]. Furthermore, when the microprobe is aligned to a crystalline axis of the sample, channeling contrast images to investigate lateral damage distributions can be obtained by scanning the microprobe [3,4].

However, angular spreads larger than the critical angle give rise to dechanneling, and damages induced by microprobe irradiation itself [4] change the minimum scattering yield during measurements. Therefore, angular spreads and a high dose, by focusing and scanning of the microprobe, must be taken into account for channeling measurements.

In this study, angular spreads of an incident beam were calculated to investigate the influence of dechanneling due to focusing and scanning of the beam. Channeling contrast analysis of local damage distributions, induced by a focused 100 keV gallium-ion implantation in silicon, was performed by a 400 keV helium-ion microprobe.

2. Experimental setup

A Dynamitron accelerator was used to generate 400 keV helium-ion beams for the microprobe [6]. A microbeam line for the microprobe channeling consists of object slits and a magnetic quadrupole doublet [7]. The object slits are driven by stepping motors and can be automatically positioned with a precision of 1 μm, so that an arbitrary spot size can be obtained. Demagnification factors of the quadrupole doublet are 3.5 and 13.8 for horizontal and vertical planes, respectively. The minimum spot size of the beam line was 0.9×0.7 μm^2 [7].

Samples were mounted on a holder attached to a five-axes goniometer consisting of three translational and two rotational axes. The translational and rotational resolutions were 1 μm and 0.01°, respectively. The microprobe was scanned over the sample by two pairs of electrostatic scanning plates inserted between the object slits and the quadrupole lens. A maximum scanning area was 450×450 μm^2 for 400 keV helium ions.

RBS signals were detected by a silicon solid-state detector (SSD) with an energy resolution of 15 keV. The scattering angle and the acceptance of the SSD were 130° and 28 msr, respectively. Detected RBS signals were discriminated by a single-channel analyzer (SCA). An incident angle of the microprobe was aligned to a crystalline axis by monitoring a rate meter combined to the SCA. The channeling contrast image was obtained in the same way with an RBS-mapping image [2], in which the RBS signals from the SCA were counted during the scanning of the microprobe. The microprobe dose was calculated from the integrated beam current and spot size measured by a knife-edge method [8].

0168-583X/91/$03.50 © 1991 – Elsevier Science Publishers B V. (North-Holland)

3. Results and discussion

Fig. 1 shows the trajectories of 400 keV helium ions for horizontal (x) and vertical (y) planes in the microbeam line. These trajectories were numerically calculated by a matrix method [9]. Two sets of trajectories corresponding to straight and deflected beams are indicated in fig. 1. The trajectories of the deflected beam assume a displacement of 225 μm, which corresponds to the maximum scanning area. Divergences of the beam at the object slits were measured to be 0.18 mrad (0.010°) and 0.8 mrad (0.046°) for horizontal and vertical planes, respectively. Since incident angles of ions are proportional to the demagnification factor of the quadrupole lens, the incident angle for the y-plane is larger than that of the x-plane.

The critical angle for the ⟨100⟩ axis of silicon was measured to be 1.2° by the 400 keV helium-ion beam [10]. Angular spreads of the incident beam were 0.036° and 0.063° for horizontal and vertical planes, respectively. These spreads were sufficiently smaller than the critical angle for the channeling. The deflection of 225 μm gave rise to changes in the incident angles, while the angular spreads did not change. The change in the incident angles were 0.041° and 0.096° for horizontal and vertical planes, respectively. These changes in the incident angle were an order of magnitude smaller than the critical angle. Therefore, both the angular spread and the change in the incident angle were negligible for the channeling contrast analysis.

The damage distribution induced by gallium FIB implantation at 100 keV to a dose of 3×10^{15} Ga^+/cm^2 in silicon was analyzed. Fig. 2 shows an optical micrograph of the implanted surface. The upper and lower fringes are gold electrode patterns. The gallium ions were implanted into two regions as shown in fig. 2. The upper region (1) is a rectangular pattern of 100×10 μm^2 with three overlapping line patterns with widths of 1, 2 and 5 μm. The lower region (2) consists of three rectangular patterns with widths of 5, 8 and 10 μm.

Channeling contrast analysis of the masklessly implanted silicon was performed by the 400 keV helium-ion microprobe. The energy window of the SCA was adjusted to a silicon spectrum. Fig. 3 shows the channeling contrast images of the damage patterns. The vertical scale stands for backscattering yields, where yields lower than an offset value of one count were not indicated. The analyzed area in fig. 3 corresponds to the optical micrograph in fig. 2. Fig. 3b is the four times magnified image of the upper implanted region (1). The microprobe was aligned to the crystalline axis by a focused beam with a spot size of about 10 μm. The spot size of the microprobe during measurements was 3×3 μm^2 with a beam current of 30 pA. Data acquisition time

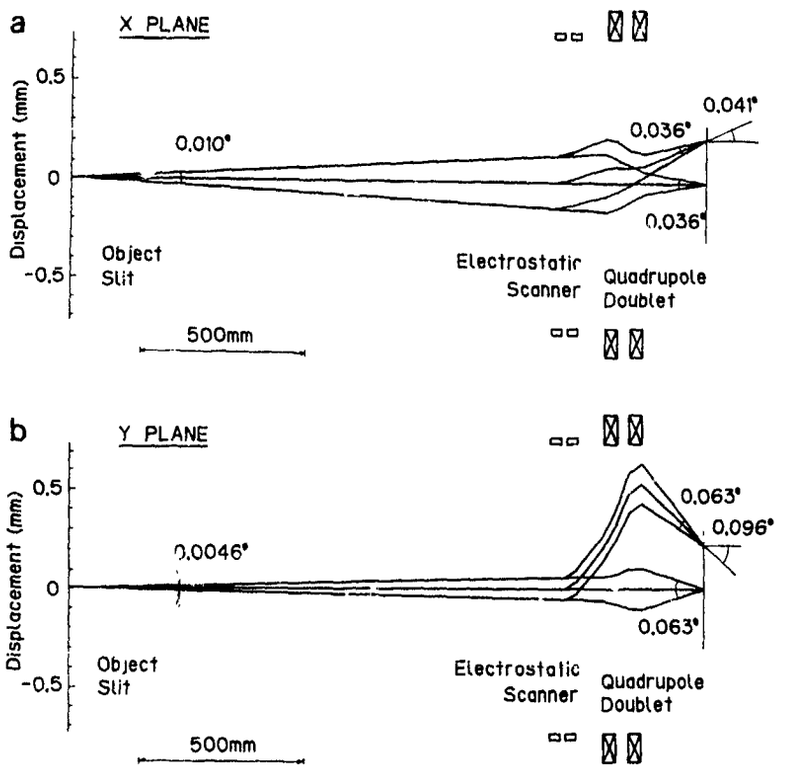

Fig. 1. Ion trajectories for straight and deflected beams in a microbeam line; (a) horizontal (x) plane; (b) vertical (y) plane

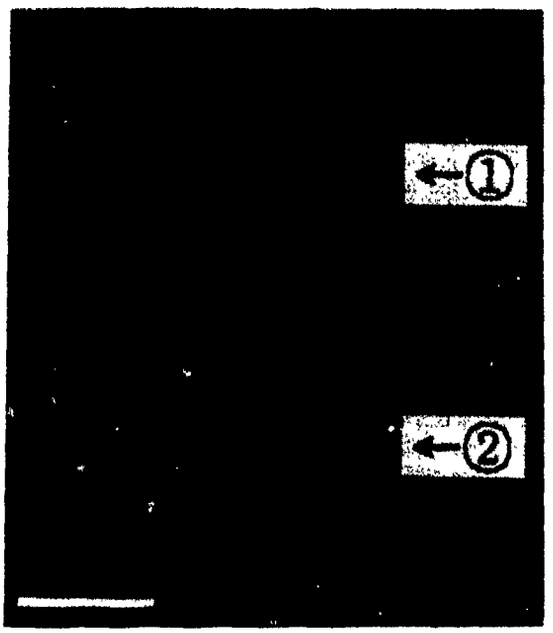

Fig. 2. Optical micrograph of masklessly gallium-implanted silicon. The gallium ions were implanted in two regions (1 and 2). The upper and lower fringes are gold electrode patterns.

was 7 min. Higher backscattering yields due to the dechanneling by the gold electrodes were observed at the upper and lower fringes in fig. 3a. This is not due to the change in crystallinity. Yields in a crystalline region (i.e., not implanted region) were uniformly low. In spite of the large scanning area of $450 \times 450\ \mu m^2$, changes in the incident angle of the microprobe to the crystalline axis were sufficiently low and no dechanneling occurred even at the edges of the scanning area. The increase in minimum scattering yields of the implanted region was also detected in fig. 3b. The precise shape of the implanted patterns could not be resolved because of low backscattering yields in this case.

Although microprobe irradiation degrades crystallinity of a sample, drastic increase in the minimum scattering yield of an aligned RBS spectrum was not observed by a microprobe irradiation of less than 5×10^{17} He^+/cm^2 in our previous study [10]. Since the microprobe dose of 6×10^{14} He^+/cm^2 for fig. 3b was three orders of magnitude lower than the critical dose (5×10^{17} He^+/cm^2), a change in minimum scattering yield during measurements was not observed. Therefore, the microprobe dose can be further increased to obtain higher yield and suppress statistical errors. However, clear image of the damage distribution, indicating positions and shapes, could be obtained by a low microprobe dose (6×10^{14} He^+/cm^2) and a short data-acquisition time (7 min).

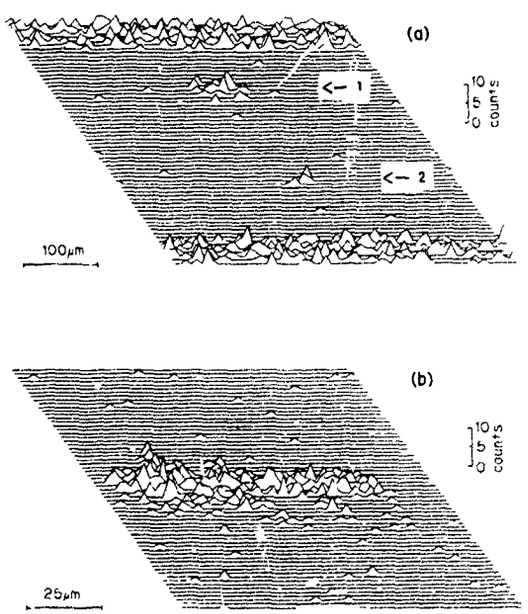

Fig. 3. Channeling contrast images of masklessly gallium-implanted silicon. The scanning area of (a) corresponds to the optical micrograph in fig. 2; (b) is an enlarged image of the upper implanted region (1).

4. Conclusion

Channeling contrast analysis using a 400 keV helium-ion microprobe was performed to investigate locally induced damages by maskless ion implantation. Angular spreads and change in incident angles during the channeling contrast analysis were, at most, 0.096°, which was sufficiently smaller than the critical angle of 1.2° for 400 keV helium to the silicon ⟨100⟩ axis. Local damage distributions induced by 100 keV focused gallium-ion implantation to a dose of 3×10^{15} Ga^+/cm^2 in silicon could be detected by the channeling contrast analysis with a low microprobe dose of 6×10^{14} He^+/cm^2.

Acknowledgements

The authors are indebted to K. Kawasaki for his assistance to a stable operation of the Disktron accelerator. We wish to thank K. Gamo and T. Kakuta for useful discussions and preparation of the gallium-implanted sample.

References

[1] T. Shiokawa, P.H. Kim, K. Toyoda, S. Namba, K. Gamo, R. Aihara and N. Anazawa, Jpn. J. Appl. Phys. 24 (1985) L566.

[2] A. Kinomura, M. Takai, K Inoue, K. Matsunaga, M. Izumi, T. Matsuo, K. Gamo, S. Namba and M. Satou, Nucl. Instr. and Meth. B33 (1988) 862.
[3] J.C. McCallum, C D. McKenzie, M.A. Lucas, K.G. Rossiter, K.T. Short and J.S. Williams, Appl. Phys. Lett. 42 (1983) 827
[4] J.A. Cookson, Nucl. Instr. and Meth. B30 (1988) 324.
[5] J.S. Williams, J.C. McCallum and R.A. Brown, Nucl. Instr and Meth. B30 (1988) 480.
[6] Y. Agawa, T. Uchiyama, A. Hoshino, H. Tsuboi, R. Fukui, K. Takagi, H Yamakawa, T. Matsuo, M. Takai and S Namba, Nucl. Instr. and Meth. B45 (1990) 540.
[7] M Takai, T. Matsuo, A Kinomura, S. Namba, K. Inoue, K. Ishibashi and Y. Kawata, Nucl Instr. and Meth. B45 (1990) 553.
[8] A. Kinomura, M. Takai and S. Namba, Jpn. J. Appl. Phys. 28 (1989) L1644.
[9] G.W. Grime and F Watt, Beam Optics of Quadrupole Probe Forming Systems (Adam Hilger, Bristol, 1984).
[10] K. Inoue, M. Takai, K. Ishibashi, Y. Kawata, N. Suzuki and S. Namba, Proc. Mat Res. Soc Symp 157 (1990) 329.

Nuclear Instruments and Methods in Physics Research B55 (1991) 870–872
North-Holland

Effect of deposition temperature of arsenic implanted poly-Si-on-insulator on grain size and residual stress

M. Takai, K. Kato [1] and S. Namba

Faculty of Engineering Science and Research Center for Extreme Materials, Osaka University, Toyonaka, Osaka 560, Japan

U. Pfannenmüller and H. Ryssel

Lehrstuhl für Elektronische Bauelemente, Universität Erlangen-Nürnberg, Fraunhofer AIS, Artilleriestrasse 12, D8520 Erlangen, FRG

Poly-Si layers were deposited on thermal oxides of Si at various temperatures from 560 to 700 °C. Arsenic was implanted at 100 keV to a dose of 1×10^{16} cm^{-2} in poly-Si layers, followed by annealing at 1000 °C. The grain size was found to range from 10 to 220 nm for deposition temperatures from 620 to 700 °C Implantation, followed by annealing, resulted in grain sizes of 200–250 nm independent of deposition temperature. An optimum deposition temperature range for poly-Si layers was found by Raman measurement to be 660–680 °C, in which arsenic-implanted layers have residual tensile stresses of 0.75–3.0 kbar after annealing at 1000 °C for 20 min.

1. Introduction

Poly-silicon-on insulator (poly-SOI) structures have recently attracted great attention because of their potential for application in thin-film transistors (TFTs) such as switching devices for flat-panel displays or driving circuits for image sensors. Improvement in device performance of poly-Si TFTs is possible by optimizing TFT structures [1], or by increasing grain size and reducing defects in poly-Si layers. Aspects of crystallinity, i.e., grain boundary defects and grain sizes of poly-Si layers, depending on deposition and annealing temperature, affect device performance such as switching speeds.

Arsenic (As) implantation, followed by annealing, is one of the possible doping processes for TFT in poly-Si layers with SOI structures, where precise controls of impurity profiles, i.e., junction depth, are necessary. Diffusion of implanted As in poly-Si layers also depended on the grain size [2–5].

In this study, the deposition temperature dependence of the grain size, crystallinity and residual stress in poly-Si layers before and after As implantation has been investigated by transmission electron microscopy (TEM) and Raman-scattering spectroscopy.

2. Experimental procedures

Boron-doped poly-Si layers with a thickness of 500–800 nm were deposited by a low-pressure CVD method on a 100 nm thick oxide of (100) Si wafers. The pressure during deposition was 0.25 Torr, while the deposition temperature was varied between 560 °C and 700 °C. The deposition rate ranged from 2.5 to 9.0 nm/min, depending on the deposition temperature. In poly-Si layers 100 keV As ions were implanted to a dose of 1×10^{16}/cm^{-2}. Conventional furnace-annealing in a flowing nitrogen atmosphere was performed for 20 min at 1000 °C.

Transmission electron microscopy (TEM) was used to measure the grain sizes of poly-Si layers before and after implantation followed by annealing. The grain size was determined at near-surface regions of the samples.

Raman scattering spectroscopy was used before and after implantation followed by annealing, to measure residual stress and crystallinity, i.e., grain boundary defects in poly-Si layers [4,5]. The relative peak position can be determined with an accuracy of about 0.1 cm^{-1}. A 488 nm line of an Ar laser with a penetration depth of about 500 nm was used to excite the sample, in which Raman signals come from only poly-Si layers. The experimental arrangement was described in detail elsewhere [6].

3. Results and discussion

Table 1 compares the grain sizes of deposited poly-Si layers on insulators for various deposition temperatures from 560 to 700 °C before and after implantation, obtained from cross-sectional TEM observation. At 560 °C the cross-sectional TEM photograph showed no con-

[1] On leave from Glory Ltd., Himeji, Hyogo 670, Japan.

0168-583X/91/$03.50 © 1991 – Elsevier Science Publishers B.V. (North-Holland)

Table 1
A comparison of grain sizes for poly-Si layers deposited at 560, 620, 660 and 700 °C before and after implantation and annealing

Deposition temperature [°C]	Grain size [nm]	
	As-deposited	Implanted [a]
560	amorphous	200
620	10	250
660	200	– [b]
700	220	– [b]

[a] Samples were annealed at 1000 °C for 20 min
[b] Not measured.

trast, indicating that the deposited Si layer was amorphous. An average grain size of 10 nm was observed for Si layers deposited at 620 °C. Further increase in the deposition temperature to 660–700 °C resulted in grain sizes of 200–220 nm. These results indicate that the deposition temperature must be held above 620 °C to obtain poly-Si layers on insulators.

As ion implantation in deposited Si-layers gave rise to a dark contrast in cross-sectional TEM images with a thickness of 150 nm, corresponding to the amorphous layer induced by implanted As in Si [5]. Annealing at 1000 °C for 20 min after As implantation showed the contrast to change in the cross-sectional TEM images, indicating grain sizes of 200–250 nm even for Si-layers deposited at 560–620 °C. These results indicate that As implantation followed by annealing causes grain enlargement.

In order to clarify the influence of deposition temperature on the crystallinity after the implantation and annealing processes, Raman-scattering measurements have been performed, since TEM methods require tedious and time-consuming sample preparation.

Fig. 1 shows the comparison of the Raman spectra for Si layers deposited at 560, 640 and 680 °C, respectively. A spectrum for bulk crystalline Si is also shown for comparison. The Raman spectrum for crystalline Si has a peak at about 520 cm^{-1} with a half-width (FWHM) of 4.0 cm^{-1}, while the peak for a Si-layer deposited at 560 °C is not observed. This result is in good agreement with that of grain size measurement by TEM, in which the deposited layer did not show any contrast, indicating that the deposited layer is amorphous. A Raman peak with a half-width of 7.2 cm^{-1} appears for the Si-layer deposited at 640 °C. The broadening of the half-width is due to the grains in poly-Si layers. The peak intensity increases by about three times for the Raman signal from poly-Si layers deposited at 680 °C and the half-width is 6.8 cm^{-1},

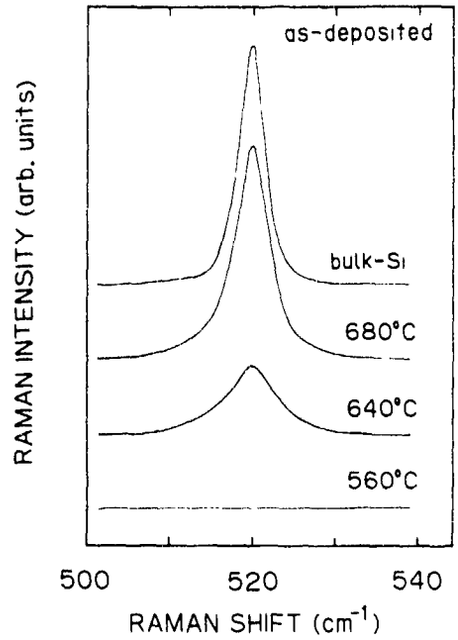

Fig. 1. Raman scattering spectra for single-crystalline bulk Si and poly-Si layers deposited at 560, 640 and 680 °C.

This indicates that the grain size becomes larger by elevating the deposition temperature from 560 °C to 680 °C.

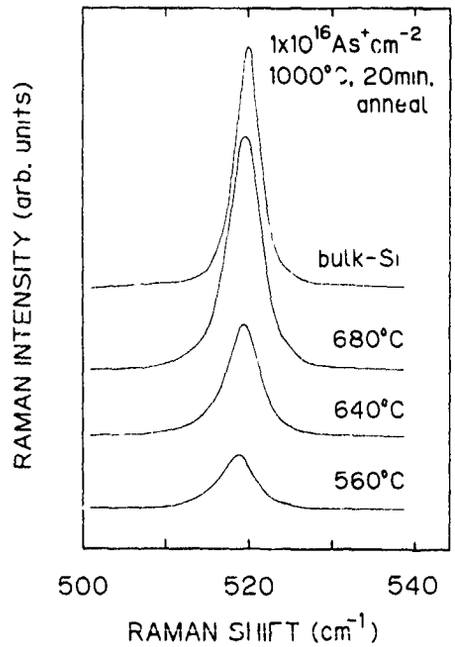

Fig. 2. Raman scattering spectra for poly-Si layers deposited at 560, 640 and 680 °C and implanted with As^+ ions to a dose of $1 \times 10^{16}/cm^{-2}$ after annealing at 1000 °C for 20 min. A Raman spectrum for bulk Si is also shown.

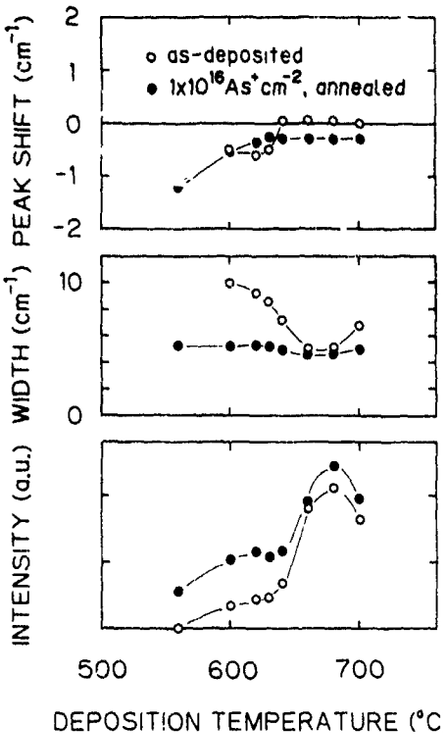

Fig. 3. Raman peak intensity, half-width and shift as a function of deposition temperature for poly-Si before and after As^+ implantation. Implanted poly-Si samples were annealed at 1000 °C for 20 min

Fig. 2 shows the comparison of the Raman spectra for poly-Si layers deposited at 560, 640 and 680 °C and implanted with As ions to a dose of $1 \times 10^{16}/cm^{-2}$ after annealing at 1000 °C for 20 min. A Raman peak with a half-width of 5.3 cm^{-1} is observed for poly-Si layers deposited at 560 °C and implanted with As ions after annealing at 1000 °C for 20 min. This is in good agreement with TEM observation, in which implantation and annealing resulted in a grain size of 200 nm for Si-layers deposited at 560 °C. The increase in deposition temperature to 640–680 °C enhanced the peak intensity of Raman signals by 2–4 times. These results suggest that higher deposition temperatures are superior in obtaining better crystallinity even after implantation and annealing.

Fig. 3 shows Raman peak intensity, half-width, and shift as a function of deposition temperature for poly-Si layers before and after As implantation followed by annealing at 1000 °C for 20 min. The Raman peak intensity, indicating crystallinity, gradually increases with the increase in deposition temperature of poly-Si layers from 600 °C and shows a maximum at 680 °C for both as-deposited and implanted layers. At 700 °C the peak intensity decreases. The halfwidth for as-deposited layers changes with deposition temperature, while that for layers implanted with As ions after annealing shows a constant value of about 5.0 cm^{-1}. The peak shift ranges from 1.2 to 0.3 cm^{-1}. Such peak shifts are induced by different mechanisms: for as-deposited layers at 560–640 °C the grain size is less than 10 nm, which induces the relaxation of the phonon wave vector, giving rise to the shift in peak wave number [7], while the implanted layers after annealing have grain sizes greater than 200 nm, so that the shift is due to the stress in the layer [6–8]. The peak shift of 0.3 to 1.2 cm^{-1} to lower wave numbers for implanted layers after annealing corresponds to tensile stresses of 0.75 to 3.0 kbar [8]. The optimum deposition temperature of poly-Si layers is, thus, 660–680 °C.

4. Conclusions

Poly-Si layers were deposited on thermal oxides of Si at various temperatures from 560 to 700 °C. Arsenic was implanted at 100 keV to a dose of 1×10^{16} cm^{-2}. Grain size, crystallinity, and residual stress in poly-Si layers were investigated before and after implantation followed by annealing, by transmission electron microscopy and Raman scattering spectroscopy.

Grain size was found to range from 10 to 220 nm for deposition temperatures from 620 to 700 °C. Implantation, followed by annealing at 1000 °C for 20 min, resulted in grain sizes of 200–250 nm, independent of deposition temperature. An optimum deposition-temperature range for poly-Si layers was found by Raman measurement to be 660–680 °C, in which arsenic-implanted layers have tensile stresses of 0.75–3.0 kbar after annealing.

References

[1] T. Noguchi, H. Hayashi and T. Ohshima, in: Polysilicon Films and Interfaces, eds. C.Y. Wong, C.V. Thompson and K.N. Tu (Materials Research Society, Pittsburgh, 1988) p. 293.

[2] B. Swaminathan, K.C. Saraswat, R.W. Dutton and T.I Kamins, Appl. Phys. Lett. 40 (1982) 795.

[3] M. Takai, M. Izumi, K. Matsunaga, K. Gamo, S. Namba, T. Minamisono, M. Miyauchi and T. Hirao, Nucl Instr. and Meth. B19/20 (1987) 603.

[4] M. Takai, M. Izumi, T. Yamamoto, A. Kinomura, K. Gamo, T. Minamisono and S. Namba, in: Polysilicon Films and Interfaces, eds. C.Y. Wong, C.V. Thompson and K.N. Tu (Materials Research Society, Pittsburgh, 1988) p. 341.

[5] M. Takai, M. Izumi, T. Yamamoto, S. Namba and T. Minamisono, Nucl. Instr. and Meth. B39 (1989) 352

[6] M. Takai, T. Tanigawa, M. Miyauchi, S. Nakashima, K. Gamo and S. Namba, Jpn. J. Appl. Phys. 23 (1984) L365.

[7] H. Richter, Z P. Wang and L. Ley, Solid State Commun. 39 (1981) 625.

[8] T. Englert, G. Abstreiter and J. Pontcharra, Solid-State Electron. 23 (1980) 31.

Nuclear Instruments and Methods in Physics Research B55 (1991) 873–875
North-Holland

Epitaxial growth of carbon-doped p-type GaAs films by ionized cluster beam

Gikan H. Takaoka [a], Yasuhiko Haga [b], Hiroshi Tsuji [b] and Junzo Ishikawa [b]

[a] *Ion Beam Engineering Experimental Laboratory, Kyoto University, Sakyo, Kyoto 606, Japan*
[b] *Department of Electronics, Kyoto University, Sakyo, Kyoto 606, Japan*

Carbon-doped GaAs films with p-type conduction on GaAs(100) substrates were grown by the ICB technique. The carrier concentration of the films was in the range of 10^{18} to 10^{20} cm^{-3}, and the Hall mobility increased from 50 to 100 $cm^2/(Vs)$ with decreasing carrier concentration. In Rutherford backscattering spectroscopy (RBS) analysis, highly carbon-doped films had a low value of χ_{min}, i.e. 4.5%, which was almost the same as that of the GaAs substrate. It was also found that these films had a high activation ratio of carbon as an acceptor.

1. Introduction

Epitaxial growth of p-type GaAs films with a high carrier concentration has been of interest in electronic devices such as the hetero bipolar transistor (HBT), negative electron affinity (NEA) devices, etc. [1,2]. Fabrication of these devices requires high quality GaAs films with a flat surface and a high carrier concentration. In order to obtain p-type GaAs films by conventional methods, impurities such as Be, Zn and Mg have been used as a dopant [3,4]. These materials have a high diffusion coefficient resulting in the segregation, and highly doped GaAs films showed a rough surface. On the other hand, carbon is an effective dopant [5] because of a low diffusion coefficient and a high activation ratio. Methane (CH_4) gas can be dissociated by ionization process to produce radical species such as CH, CH_2 and CH_3, and the radical species can be used to provide carbon as an acceptor in the GaAs films.

The ionized cluster beam (ICB) technique [6] is an ion-assisted technique for film formation by using low-energy ion beams. It has several advantages in film formation, one of which is the capability of controlling the film properties by adjusting the acceleration voltage and the electron current for ionization. Therefore, ionization and acceleration for Ga and As clusters in the CH_4 gas atmosphere are effective to obtain the p-type GaAs films with a high carrier concentration. In this paper, we investigate the crystalline state and the electrical properties of the carbon-doped GaAs films prepared by the ICB technique.

2. Deposition conditions

High-purity gallium (7N-Ga) and arsenic (6N-As) were used as source materials. The carbon crucibles for Ga and As were heated up to 1250 and 360 °C, respectively. Ga and As clusters, which are expected to be formed by an adiabatic expansion from the individual crucibles [7] and consist of 100–1000 atoms loosely coupled together [8,9], were ionized and accelerated together with high-purity methane (3N-CH_4) gas. The ionization ratio of clusters could be changed to several tens percent by increasing the electron current for ionization [10]. The CH_4 gas was introduced into the ionization region of As clusters through the leak valve. Carbon could be doped effectively in the film as an acceptor, because the ionized and radical species of CH, CH_2 and CH_3 produced by the electron current for the ionization of As clusters could be used for the enhancement of chemical bonding between gallium and carbon atoms. The electron current (I_e) for ionization and the acceleration voltage (V_a) were adjusted at $I_e = 0$–700 mA and $V_a = 0$–1 kV, respectively. The substrate was Cr-doped semi-insulating GaAs(100). The GaAs substrate was cleaned by standard organic solvents, etched by the H_2SO_4–H_2O_2–H_2O solution, and rinsed in deionized water. It was prebaked while being exposed to the As cluster beam, which was effective in removing the oxygen contaminant from the substrate. The substrate temperature (T_s) during the growth was adjusted in the range of $T_s = 470$–700 °C. The growth rate was about 25 nm/min, and the film thickness was about 1

0168-583X/91/$03.50 © 1991 – Elsevier Science Publishers B.V. (North-Holland)

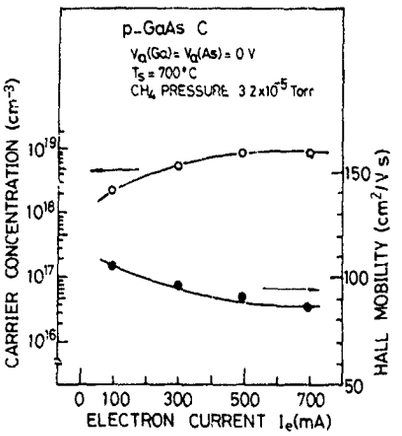

Fig. 1. Dependence of the carrier concentration and Hall mobility as a function of the electron current for ionization.

μm. The background pressure in the chamber evacuated by the cryopump was 4×10^{-7} Torr

3. Results and discussion

Doping effects of CH_4 gas into GaAs films prepared at different deposition conditions were investigated. Fig. 1 shows the dependence of the Hall mobility and the carrier concentration on the electron current for ionization. By increasing the electron current for ionization, the carrier concentration was increased and the Hall mobility was decreased. This is due to the enhancement of the chemical reaction between CH_4 gas and gallium atoms by ionization which resulted in the effective doping of carbon as an acceptor. In the case of the films prepared by using neutral Ga and As clusters in the CH_4 gas atmosphere, the films showed high resistivity,

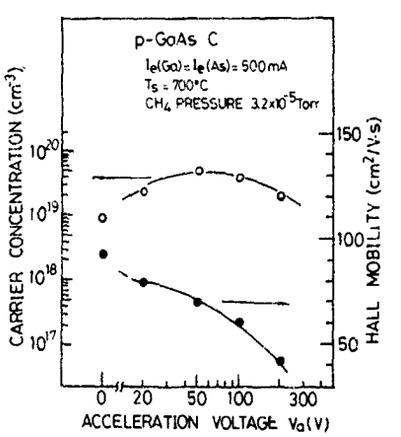

Fig. 2 Dependence of the carrier concentration and Hall mobility as a function of the acceleration voltage for ionized cluster beams.

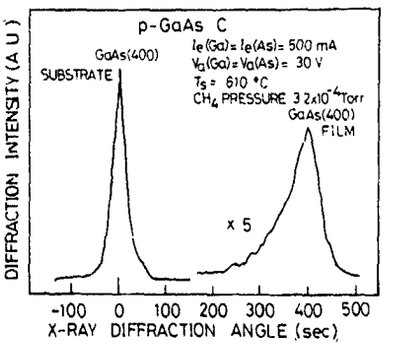

Fig. 3. X-ray rocking curves at the (400) plane of GaAs substrate and p-GaAs:C film

and it was difficult to measure the Hall mobility and the carrier concentration.

The CH_4 gas could be dissociated by ionization, and ionized and radical species such as CH, CH_2 and CH_3 were produced. From the point of the repulsion force for lone pairs and bonding pairs of electrons, the electron of the radical is considered to be localized near the carbon atom [11]. This effect induces the displacement of the electric charge of carbon atom in parallel to the direction of the dangling bond. Therefore, carbon atoms can form the bond with gallium rather than with arsenic [11] because the electronegativity of carbon is larger than that of arsenic. In addition, the ionization of anion material in the compound material can enhance the chemical reaction with the cation material. Thus, carbon can attract more electrons from gallium because the ionic state of carbon has more net charge [12]. Therefore, ionization of the CH_4 gas is effective for doping of carbon as an acceptor.

The Hall mobility and the carrier concentration of the films could be controlled by adjusting the acceleration voltage as well as the electron current for ionization. This is a preferred characteristic for the carbon-doped GaAs films prepared by ICB in comparison with

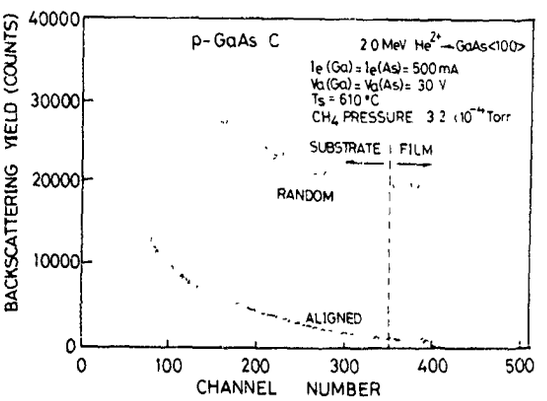

Fig. 4 RBS spectra of p-GaAs:C film.

the films by MBE and other techniques. As shown in fig. 2, the carrier concentration has a maximum at $V_a = 50$ V, and the Hall mobility decreases with the increase of acceleration voltage. At higher acceleration voltages, the excess kinetic energy of atomic and molecular gas ions included in the beam may produce defects in the films, decreasing the Hall mobility.

With respect to the substrate temperature dependence, the carrier concentration was almost constant in the range of 470 to 700 °C, which was about 10^{19} cm^{-3}. On the other hand, the Hall mobility increased with the increase of substrate temperature. The films grown at higher substrate temperatures showed an improvement of the crystallinity.

The increase of CH_4 gas pressure can increase the carrier concentration. In the condition of $I_e = 500$ mA, $V_a = 30$ V, $T_s = 610$ °C and a CH_4 gas pressure of 3.2×10^{-4} Torr, films with a carrier concentration of 1.6×10^{20} cm^{-3} and a Hall mobility of 51 cm^2/(V s) could be obtained. In addition, the relationship between the Hall mobility and the carrier concentration was investigated for the films prepared at different growth conditions. Hall mobility at higher carrier concentrations than 10^{18} cm^{-3} had a good agreement with the empirical curve, which was obtained from the good-quality GaAs films prepared by several other methods [3–5,13]. This suggests that the CH_4 gas could be heavily doped as an acceptor and a good-quality GaAs film could be formed.

We evaluated the activation ratio of carbon as an acceptor in the GaAs films by measuring the double crystal X-ray rocking curve [14]. Fig. 3 shows the X-ray rocking curve at the (400) plane for the films grown at $I_e = 500$ mA, $V_a = 30$ V, $T_s = 610$ °C and a CH_4 gas pressure of 3.2×10^{-4} Torr. In comparison with the GaAs substrate, a large shift of the peak position in the X-ray rocking curve is observed. From the peak shift, the activation ratio of carbon as an acceptor could be expected to be high by applying Begard's rule [14].

In order to investigate the crystallinity of the carbon-doped GaAs films, the Rutherford backscattering spectroscopy (RBS) analysis was made. Fig. 4 shows RBS spectra of the GaAs film having a carrier concentration of 1.6×10^{20} cm^{-3}. In the figure, the dashed line corresponds to the interface between the film and the substrate. As shown in the figure, there is no step in the spectra near the interface. Furthermore, the surface peak, that is χ_{min}, is found to be 4.5%, which was almost the same as that of the GaAs substrate used. This indicates the good quality of GaAs films prepared even with a very high carrier concentration.

4. Conclusions

Carbon-doped GaAs films with p-type conduction have been grown on GaAs(100) substrates by the ICB technique. The films had a high carrier concentration and a flat surface. The carrier concentration of the films was in the range of 10^{18} to 10^{20} cm^{-3}, and the Hall mobility increased from 50 to 100 cm^2/(V s) with the decrease of carrier concentration. In the RBS analysis, the highly carbon-doped GaAs films had a low value of χ_{min}, i.e. 4.5%, which was almost the same as that of the GaAs substrate used. It was also found that these films showed a large shift of peak position in the X-ray rocking curve in comparison with the GaAs substrate, indicating a high activation ratio of carbon as an acceptor. In addition, characteristics of the films were improved by the ICB method, and the kinetic energy and the ionic charge of cluster ions were effective to obtain the high-quality carbon-doped GaAs films.

Acknowledgment

The authors are grateful to the research group at the Nuclear Engineering laboratory on the Uji campus of Kyoto University for RBS measurements

References

[1] J J Scheer and J van Laar, Solid State Commun. 3 (1965) 189.
[2] T.Z Zuiphen, IEEE Trans Electron Devices ED-36 (1989) 2715
[3] K. Proog, A Fischer and H. Kunzel, J Electrochem. Soc. 128 (1981) 400.
[4] J L Lievin and F Alexander, Electron Lett 21 (1985) 413.
[5] K Saito, E. Tokumitsu, T. Akatsuka, M Miyauchi, T. Yamada, M. Konagai and K Takahashi, J Appl Phys 64 (1988) 3975
[6] T Takagi, Ionized-Cluster Beam Deposition and Epitaxy (Noyes Publ, Park Ridge, 1988)
[7] I. Yamada, H Usui and T. Takagi, J. Phys Chem 91 (1987) 2463
[8] M. Sosnowski, S. Krommenhoek, J. Sheen and R.H Cornely, J. Vac. Sci. Technol. A8 (1990) 1458.
[9] K. Kim, K.C. Hsieh, M.J Fornek, L.C. Yang and C.H Wu, Proc. Spec. Seminar on ISIAT'90, Tokyo (Ion Engineering Soc. of Japan, 1990) p. 71
[10] T. Takagi, I. Yamada and A Sasaki, Inst Phys. Conf. Ser 38 (1978) 229.
[11] G C Pimentel and R.D Spratley, Chemical Bonding – Clarified Through Quantum Mechanics (Holden-Day, 1969) chap. 6.
[12] J C Phillips Bonds and Bands in Semiconductors, (Academic Press, New York and London, 1973) chap 2.
[13] M Ilegems, J. Appl. Phys. 48 (1977) 1278.
[14] K. Saito, E. Tokumitsu, T. Akatsuka, M. Miyauchi, T. Yamada, M Konagai and K Takahashi, Inst. Phys. Conf. Ser. 96 (1989) 69

Nuclear Instruments and Methods in Physics Research B55 (1991) 876–879
North-Holland

Preparation of atomically flat gold films by ionized cluster beam

I. Yamada [a], G.H. Takaoka [a], H. Usui [a], F. Satoh [a], Y. Itoh [a], K. Yamashita [b], S. Kitamoto [c], Y. Namba [d], Y. Hashimoto [c], Y. Maeyama [e] and K. Machida [e]

[a] *Ion Beam Engineering Experimental Laboratory, Kyoto University, Sakyo, Kyoto 606, Japan*
[b] *Institute of Space and Astronautical Science, Sagamihara, Kanagawa 229, Japan*
[c] *Department of Physics, Osaka University, Toyonaka, Osaka 560, Japan*
[d] *Department of Mechanical Engineering, Chubu University, Kasugai, Aichi 487, Japan*
[e] *Manufacturing Development Laboratory, Mitsubishi Electric Corp., Amagasaki, Hyogo 661, Japan*

We have prepared atomically flat Au films by using an ionized cluster beam. The films were deposited on polyimide and SiO_2 at room temperature in an ultrahigh vacuum of 4×10^{-9} Torr using different electron currents for ionization and different acceleration voltages. Using scanning tunneling microscopy (STM) and scanning electron microscopy (SEM), the film surface was found to be improved with increasing acceleration voltage. The root-mean-square roughness measured was 0.25 nm for the films deposited on SiO_2 at $I_e = 100$ mA and $V_a = 3$ kV. The films showed high reflectivity for X-rays at a wavelength of 0.834 nm.

1. Introduction

The formation of an atomically flat surface has become important in optical devices such as X-ray telescopes, synchrotron radiation sources, LSI devices, etc. [1]. For example, X-ray reflectivity from a mirror surface is strongly related to the surface and interface characteristics of the films as well as the film quality. The control of these characteristics has attracted much interest because of the application to optical mirrors operating over a wide range of wavelengths and this has stimulated the development of film preparation techniques.

The ionized cluster beam (ICB) technique is an ion-assisted technique for film formation by using low energy ion beams [2–4]. The basic mechanism of cluster formation is described elsewhere [5]. The ionization ratio of clusters can be changed to several tens of percents by adjusting the electron current for ionization [6]. The cluster size and density distribution are not exactly clear, but the ICB technique has the advantage of providing low-temperature growth with the aid of the kinetic energy and ionic charge of the cluster ions. Another advantage is the capability of controlling the surface and interface characteristics of the films, as well as the film properties. In this paper we describe the preparation of Au films on SiO_2 and polyimide by the ICB technique, and the surface and interface characteristics of these films.

2. Experimental

Gold (Au) films were prepared in an ultrahigh vacuum (UHV) system consisting of three chambers; a growth chamber, an analysis chamber and an exchange chamber. The growth chamber, which was evacuated by an ion pump, was equipped with an ICB source. The analysis chamber was also evacuated by an ion pump, and it has an X-ray photoemission spectroscopy (XPS) instrument.

High purity (99.99%) Au was charged in a carbon crucible, which was heated to 1750–1800 °C by electron bombardment. The Au beam ejected from a 2 mm nozzle of the crucible was ionized and accelerated to the substrate. The electron current (I_e) for ionization was kept at 100 mA. The acceleration voltage (V_a) was varied from 0 to 5 kV. The deposition rate was kept at 3 nm/min by adjusting the crucible temperature. The substrates used were thermally grown SiO_2 and polyimide, and the substrate temperature (T_s) during deposition was room temperature. Acetone and trichloroethylene were used to clean the SiO_2 substrate whilst the polyimide substrate was cleaned using methyl alcohol. The vacuum pressure during deposition was 4×10^{-9} Torr.

3. Results and discussion

3.1. Au on polyimide

X-ray photoemission spectroscopy (XPS) analysis was made to investigate the initial state of deposition of Au films on the polyimide substrate. Fig. 1 shows the dependence of C_{1s} signal intensity on the coverage of the Au films. C_{1s} is the XPS signal from the 1s orbital of carbon atoms, which are constituent atoms of the polyimide substrate. In comparison with the case of

0168-583X/91/$03.50 © 1991 – Elsevier Science Publishers B.V. (North-Holland)

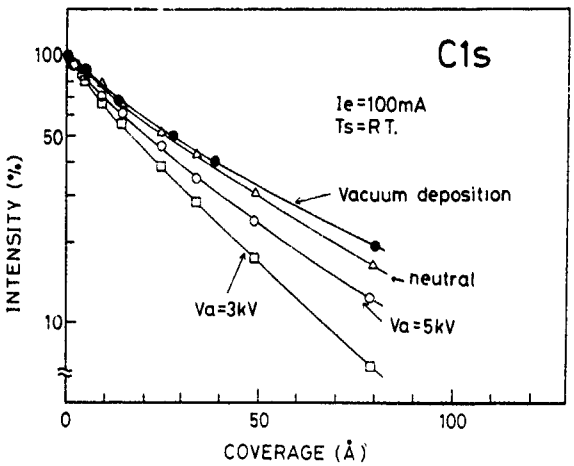

Fig. 1 Dependence of the C_{1s} intensity on the coverage of the Au films prepared on polyimide substrate using different deposition conditions.

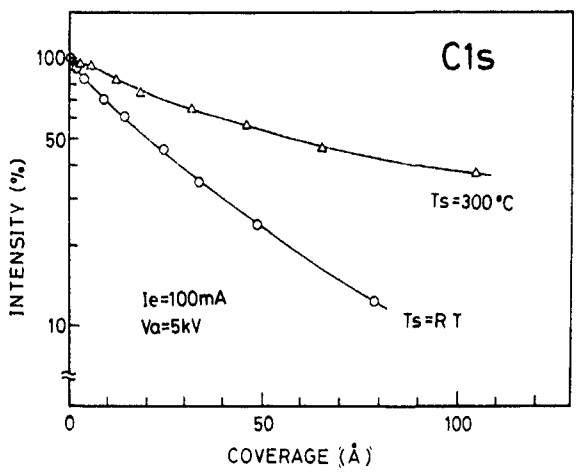

Fig. 2 Dependence of C_{1s} intensity on the coverage of the Au films prepared on polyimide substrate at T_s = RT and T_s = 300 °C.

vacuum deposition [7], the film prepared at I_e = 100 mA and V_a = 3 kV by ICB shows much decrease in the C_{1s} intensity with the increase of coverage. In ICB deposition, both the migration effect and the nucleation density increase with increasing acceleration voltage. This indicates the approach of two-dimensional growth for the films, resulting in the effective formation of a smooth surface. For the case of V_a = 5 kV, however, the C_{1s} intensity decreases gradually. This is considered to be due to the increase of the surface roughness by the excess kinetic energy of incident beams.

Fig. 2 shows the dependence of the C_{1s} signal intensity on the coverage of the Au films prepared at T_s = RT and T_s = 300 °C. In comparison with the case of T_s = RT, the C_{1s} intensity for T_s = 300 °C decreases gradually with the increase in coverage. The polyimide surface becomes soft at T_s = 300 °C, and the migration effect of the Au clusters decreases compared to that of the flat surface at T_s = RT. Therefore, the Au film deposited at higher substrate temperature approaches that for three-dimensional growth. As a result, the C_{1s} signal from the polyimide substrate was still observed even when the coverage of the Au film was larger than 10 nm.

In order to investigate the surface state of the Au films prepared at different substrate temperatures, scanning electron microscopy (SEM) analysis was used. Fig. 3 shows the SEM images of the Au films prepared at (a) T_s = RT and (b) T_s = 300 °C. The electron current (I_e) for ionization and the acceleration voltage (V_a) were I_e = 100 mA and V_a = 5 kV, respectively. The film thickness was 10 nm for both films. As shown in the figure, the film at T_s = RT is continuous and it has a flat surface. On the other hand, the film at T_s = 300 °C has many island-like grains. This is due to the increase of condensation and coalescence of Au adatoms at T_s = 300 °C.

3.2 Au on SiO_2

Au films deposited on SiO_2 were investigated by scanning tunneling microscopy (STM) and transmission

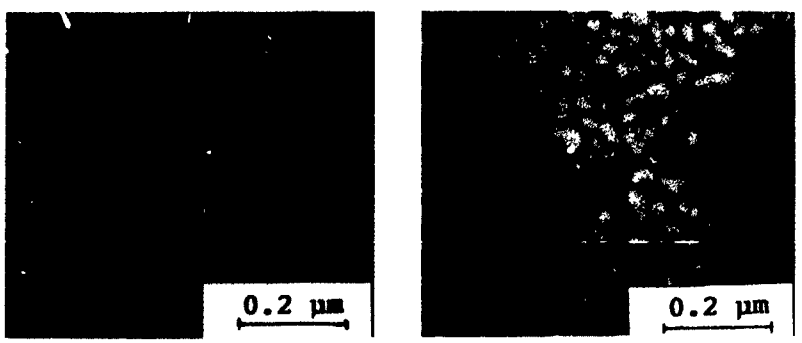

Fig. 3. SEM images of the Au films prepared on polyimide substrate at (a) T_s = RT and (b) T_s = 300 °C

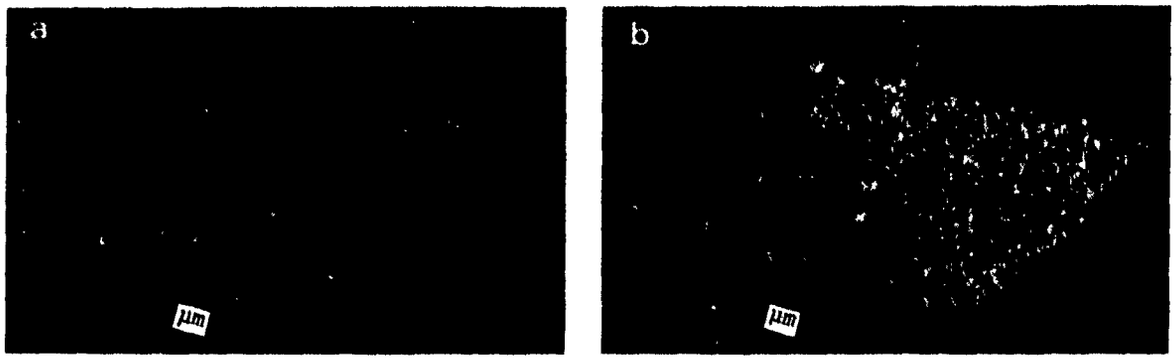

Fig. 4. STM images of the Au films prepared on SiO_2 substrate at (a) $V_a = 3$ kV and (b) $V_a = 5$ kV.

electron microscopy (TEM). Fig. 4 shows the STM images for the films prepared at (a) $V_a = 3$ kV and (b) $V_a = 5$ kV. In the case of $V_a = 3$ kV, the film is found to have an atomically flat surface. On the other hand, the surface roughness of the film prepared at $V_a = 5$ kV increases. The root-mean-square roughness calculated by using the X-ray reflectivities, which were measured at different incident angles, was 0.25 nm at $V_a = 3$ kV. The surface roughness of the substrate was 0.3 nm. The increase of the surface roughness occurs because of the excess kinetic energy of incident beams on the substrate surface

Fig. 5 shows the TEM images for Au films prepared by (a) ICB and (b) vacuum deposition. The film prepared by ICB has grains larger than those obtained by vacuum deposition. In the case of ICB deposition, the grain size and the packing density of the films increased with increasing acceleration voltage.

Fig. 6 shows the X-ray reflectivity for the Au films deposited at an acceleration voltage of 3 kV. The film thickness was 23 nm. The X-ray used was Al Kα at a wavelength of 0.834 nm. The film shows a reflectivity of 95% at an incident angle of 0.75°. This is 10% larger than the calculated value using Fresnel's equation, which assumed that the surface roughness is zero [8]. It should be noted that the X-ray reflectivity decreases rapidly at an incident angle less than 0.5°, because the spot size of the X-ray on the reflecting surface becomes larger than the area of the film, i.e., 4×4 cm^2.

4. Conclusions

We prepared atomically flat Au films which had high reflectivity for X-rays by using the ionized cluster beam (ICB). The films were deposited on polyimide and on SiO_2. For the main study the substrate was kept at room temperature, and the vacuum was 4×10^{-9} Torr. The root-mean-square roughness was 0.25 nm for the films deposited on SiO_2 at $I_c = 100$ mA and $V_a = 3$ kV The films showed a high reflectivity for X-rays (Al Kα) at a wavelength of 0.834 nm. The reflectivity was 95% at

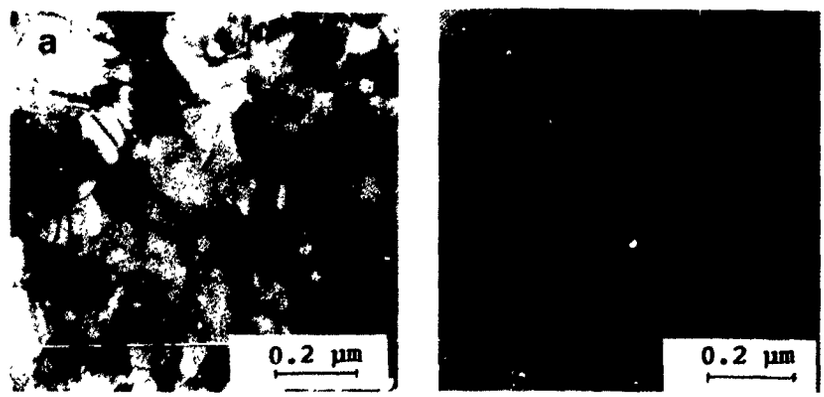

Fig. 5. TEM images of the Au films prepared on SiO_2 substrate (a) at $I_c = 100$ mA and $V_a = 3$ kV by ICB and (b) by vacuum deposition.

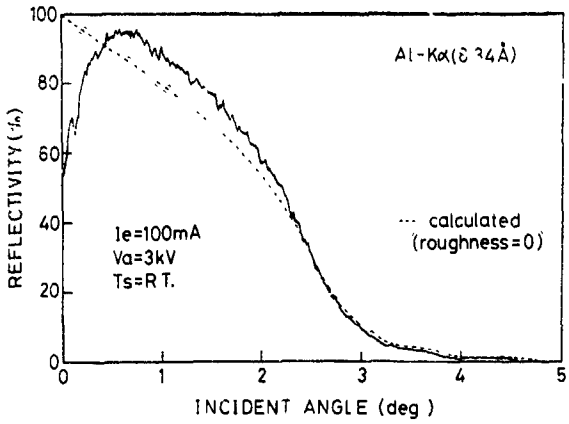

Fig 6 X-ray reflectivity for the Au film prepared on an SiO_2 substrate at $I_e = 100$ mA and $V_a = 3$ kV

an incident angle of 0.75°. This was 10% larger than the calculated value by using Fresnel's equation, which assumed that the surface roughness is zero.

Acknowledgement

This work was supported in part by the Grant-in-Aid for Scientific Research on Priority Areas, "X-ray Imaging Optics", Contract Number 01651006 from the Japanese Ministry of Education, Science and Culture, Japan.

References

[1] D.H Bilderback, SPIE 315 (1981) 90.
[2] I. Yamada, Mater. Res. Soc. Symp. Proc. 128 (1989) 113.
[3] I. Yamada, Nucl. Instr and Meth. B37/38 (1989) 770
[4] T Takagi, Ionized-Cluster Beam Deposition and Epitaxy (Noyes, New Jersey, 1988).
[5] I. Yamada, H Usui and T Takagi, J Phys Chem 91 (1987) 2463.
[6] T. Takagi, I. Yamada and A. Sasaki, Inst Phys. Conf Ser. 38 (1978) 229.
[7] H.M. Mayer III, S G Anderson, L J Atanasoska and J H Weaver, J Vac Sci. Technol A6 (1988) 30
[8] L.G. Darratt, Phys. Rev 95 (1954) 359.

Nuclear Instruments and Methods in Physics Research B55 (1991) 880–883
North-Holland

A system for complex processing of semiconductor structures in vacuum

E.B. Yankelevich and V.S. Budishevsky
Institute of Semiconductor Devices, Tomsk, G34042, USSR

A description of the installation is presented, which allows complex, piece by piece double-sided treatment of ~76 mm ⌀ semiconductor structures to be performed in a single vacuum cycle, including the surface cleaning, multilayer metallizing and rapid isothermal electron-beam heating. The installation has been successfully used to form ohmic and barrier contacts for discrete devices and integral schemes on GaAs, in making Ge on GaAs structures, as well as for rapid electron-beam thermal annealing of ion-doped Si and GaAs layers on ~100 mm ⌀ plates

1. Introduction

In recent years there has been a tendency away from equipment used for batch processing of semiconductor structures when producing microelectronic devices, to the use of equipment designed for step by step processing. Special attention is now paid to the use of equipment capable of performing as many technological operation as possible in a single vacuum cycle [1]

One of the process stages in the construction of discrete semiconductor devices (e.g. radiating diodes) is the formation of ohmic junctions including semiconductor substrate cleaning, double-sided contact metallizing of the substrate and intermelting. This work describes an installation constructed on the basis of standard spraying equipment. The installation makes it possible to realize the above-mentioned process in a single vacuum cycle and, moreover, to produce Ge on GaAs heterostructures and anneal ion-implanted Si and GaAs layers.

2. Technical description

A schematic representation of the modernized installation is shown in fig. 1. A pumping system used in the installation allows an ultimate vacuum in the operating volume of $(4–6) \times 10^{-5}$ Pa to be obtained.

Preparatory surface cleaning of the semiconductor substrate, prior to the metallizing process, is performed either in a glow discharge plasma, or by electron-beam heating. It is experimentally established that combining these methods of substrate surface cleaning results in better electrophysical parameters of the contacts formed.

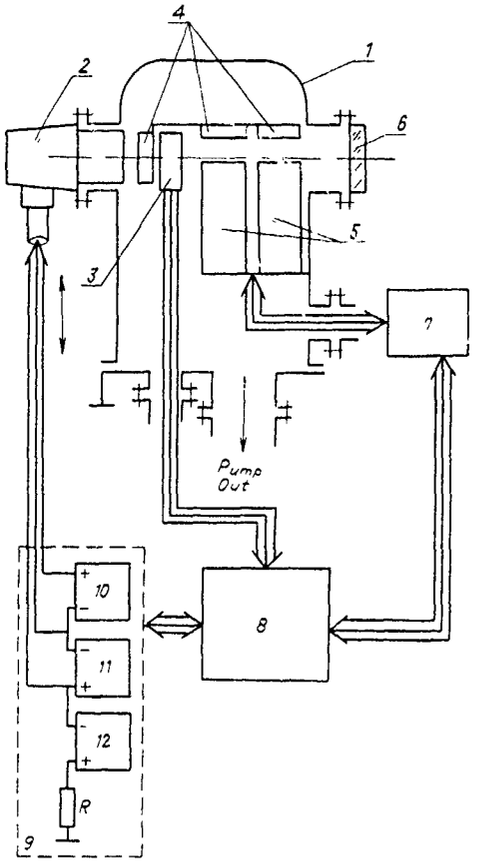

Fig. 1. (1) metal hood, (2) electron-beam heater, (3) primary element, (4) displacement device with semiconductor plate holders, (5) blocks of thermal evaporators and magnetron spraying, (6) observation window, (7) feed sources for spraying system, (8) controlling computing system, (9) block of feed sources for electron-beam heater, (10,11) sources to form a plasma emission surface, (12) accelerating voltage source.

0168-583X/91/$03 50 © 1991 – Elsevier Science Publishers B.V. (North-Holland)

To increase the technological potential, a small-size magnetron spraying unit was additionally introduced into the installation, including four thermal evaporators. The construction of the magnetron unit, the operating principle of which is described in ref. [2], as well as its electric supply system make it possible to carry out both successive and joint sputtering of the three different materials. A controlling computing system realized the control and monitoring of semiconductor substrate metallization.

For thermal treatment of semiconductor structures, a heater based on a plasma electron emitter is used [3], which forms a wide-aperture quasi-continuous beam having the following parameters: electron energy 1–10 keV; power density 0.1–40 W/cm^2; density distribution nonuniformity over the beam cross section ±5%; beam diameter 100 mm; and beam current pulse duration 0.5–100 s.

The advantage of plasma emitters over other kinds of emitters is explained by their high emission efficiency and reliability, long operation capability, nonsensitivity to gas-release from substrates treated and pressure surges in the installation operation volume. In the electron-beam heater a large-area plasma emitting surface is created in a special hollow electrode due to charged particles being injected into it through a small hole from a discharge cell, where a reflective discharge plasma with cold electrodes is generated [4]. This principle of plasma emitter construction allows a large cross section electron beam to be obtained with power density sufficient for a thermal treatment and a uniformity within operating pressure range of 10^{-2}–1 Pa.

The heater is supplied from three sources, situated in the common unit (labelled 9 in fig. 1). Two identical sources (10, 11) are used to form a large-area plasma emission surface and provide at the output a voltage up to 1 kV at a nominal current of ~1 A. The third high-voltage source (12) is connected to a special hollow heater electrode by its negative pole, while its positive pole is grounded. It allows the electron energy to be regulated smoothly from 1 to 10 keV and provides a nominal current up to 0.4 A. The heater control is performed both in "manual" and automatic regimes. In the "manual" regime at the specified electron beam parameters, the heater control is performed by setting the running time. In the automatic regime, heater control is provided by the controlling computing system (8) due to a signal from the combined primary element 3 (fig. 1). The primary element allows measurement of the beam current density and uniformity over the cross section, as well as the semiconductor plate temperature during fast isothermal heating. The primary element consists of a multiaperture collimator with a unit of Faraday cylinders and a photodiode. The Faraday cylinders are situated in such a way that they allow the current density distribution to be controlled over the beam cross section in two mutually perpendicular planes. Photodiode signals, which are proportional to the temperature of the irradiated semiconductor plate [5] provide the electron heater control in the automatic regime.

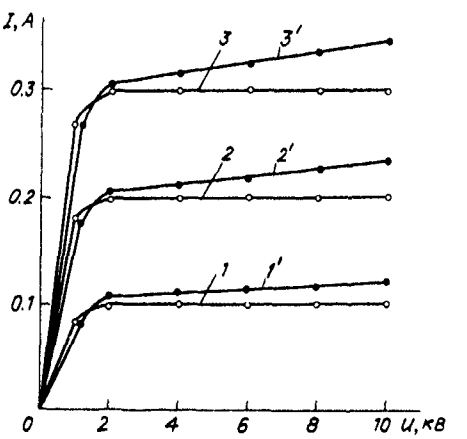

Fig. 2. Voltage–current characteristic of a plasma electron-beam source. Discharge current: (1, 1′) 0.4 A; (2, 2′) 0.5 A; (3, 3′) 0.7 A. (1, 2, 3) Beam current stabilization included; (1′, 2′, 3′) beam current stabilization excluded.

The voltage–current characteristic of the heater (fig. 2) shows an insufficient beam current I dependence on the accelerating voltage U, when $U > 2$ kV, but by introducing current stabilization one can practically eliminate this dependence. The efficiency of the electron-beam heater constructed using such a scheme achieves 80–90%. This is practically provided by using diaphragms of different diameters, confining the plasma emitting surface area. The diaphragms introduced do not reduce the current density distribution over the beam cross section. In all cases the nonuniformity of the current density distribution does not exceed ±5% (fig. 3). The diameter of the diaphragm used is defined by the diameter of the semiconductor structures treated.

The electron-beam heater makes it possible to finely change the electron beam power density, thus corresponding to requirements of a fast isothermal annealing of large-diameter semiconductor structures.

A holder is used for fixing semiconductor plates, which is constructed to allow double-sided treatment of the substrates. Two pairs of thin strings of a refractory metal are the fixing elements of the holder. This provides minimal shadowing of the plate operating field, as well as minimal influence of the supports on the temperature distribution over the plate. A 100 mm ∅ semiconductor plate treated is introduced into the holder, squeezed by strings just at the edges, and is fixed rigidly by regulated stretching of the strings.

The movement of holders from one treatment position to another is performed using a special device. It

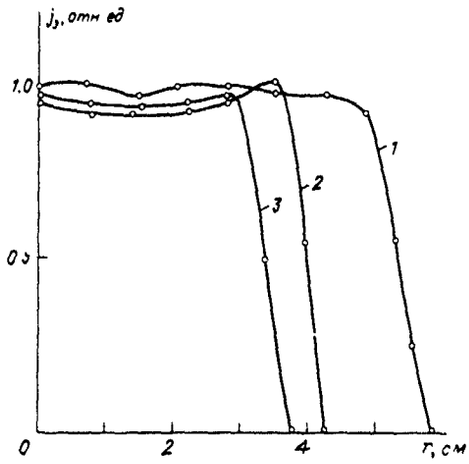

Fig. 3. Current density distribution along the beam section 50 mm from the emission electrode. Diaphragm hole diameter: (1) 85 mm; (2) 65 mm; (3) 45 mm.

allows the plates to be moved in the horizontal plane and to rotate by 180° (fig. 4). It consists of a support (2) in the form of a star with six rays, and a guide (4). Plate holders H1–H6 are attached to the support using a bracket (3) and special axles. The bracket (3) is connected with the holder by means of an axle screw,

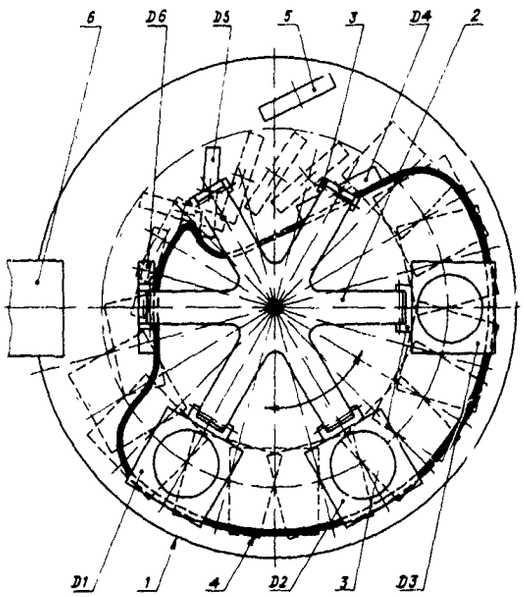

Fig. 4. Schematic diagram of the device for semiconductor plate displacement and their treatment positions (plan view). (1) Vacuum chamber frame, (2) support, (3) bracket with axle, (4) guide, (5) anode assembly of the ion-cleaning block, (6) electron-beam heater; (H1–H6) semiconductor substrate holders, (7) the appearance of guide 4 on the side of the electron-beam heater.

making it possible for the holder to have an additional degree of freedom. The guide (4), which specifies a definite orientation for each holder with respect to the units of treatment positions, is situated in parallel under the holder (2). In fig. 4 the holders H1–H3 are in a horizontal position above the metal-spraying units. The holders H1 and H2 are situated above the thermal evaporation units, each having two evaporators, and the holder H3 is situated above the magnetron spraying unit. The holders H4–H6 are in a vertical position, e.g. in the plane, which is perpendicular to the support plane (2). This position of the holders H4–H6 is determined by the form of the guide (4) at a given section of the support movement. The ion cleaning unit (5) is situated opposite the holder and is parallel to it. The holder H5 is in such a position that due to the form of the guide (4) in the given sector of the support anti-clockwise movement (between H4 and H6), there occurs a 180° holder turn with respect to its longitudinal axis. Preheating of substrates and their rapid isothermal heating using the electron beam from the heater (6) occurs when the holder is in the position H6. Due to the form of the guide in the sector between H6 and H1 and the holder hinge attachment to the support (2), the holders exchange their vertical position for a horizontal one, with respect to the support when it moves anti-clockwise, while in the sector between H3 and H4 the holder changes its horizontal position for a vertical one. Therefore, with the support rotating, the holders with the substrates fixed in them move from one treatment position to another, thus providing a double-sided multioperational step by step treatment of the substrates in a single vacuum cycle.

3. Installation use

The possibilities of the designed installation are well illustrated by the process of ohmic junction formation at both sides of a GaAs semiconductor structure when making radiating diodes. After a chemical treatment ~100 μm thick GaAs structures were fixed in the holders and placed into the vacuum chamber of the installation. Them the following operations were performed in a single vacuum cycle:

(a) structure planar side cleaning by the electron beam;
(b) layer by layer spraying of the clean structure surface with AuGe–Ta–Au contact metal system;
(c) turning the components over and performing the above-mentioned operations on the opposite side;
(d) thermal treatment using a second electron beam from the substrate side.

Ohmic junctions created in such a way have a low contact resistance ($R_c < 10^{-6}$ Ω cm^2) and high thermal stability.

The installation has been successfully used for the electron-beam annealing of ion-implanted GaAs [6] and Si [7] layers, as well as for investigations on Ge on GaAs structure formation.

4. Conclusions

(1) The installation constructed makes it possible to perform complex technological operations in a single vacuum cycle, thus providing engineers developing microelectronic devices with new possibilities.

(2) An electron-beam heater with a plasma emitter forming a large cross sectional beam, is essentially more simple than a heater with a scanning electron beam from the constructional and operational viewpoints.

Acknowledgements

The authors are sincerely grateful to Dr. D.I. Proskurovsky for his valuable suggestions, and thank S.I. Beljuk, V.Ya. Martens and Yu.V. Pomitkin for their help in creating the installation.

References

[1] U. Iversen, Electronics 62 (1989) 3.
[2] K. Char, A.D. Kent, A. Kapitulnik, M.R. Beasley and T H Geballe, Appl. Phys. Lett. 51 (1987) 1370.
[3] Yu.E. Kreindel, V.Ya. Martens and V.Ya. S'edin, Prib. Tekh. Eksp. 4 (1982) 178.
[4] S.P. Bugaev, Yu.E. Kreindel and P.M. Schanin, in: Electron Beams with Large Cross sections (Energoatomizdat, Moscow, 1984) p. 112.
[5] R.A. McMagon, D.G. Hasko and X. Ahmed, Pribory dlya Nauchnykh Issledovanii [Apparatus for scientific investigations] 6 (1985) 136.
[6] D. Panknin, N.I. Lebedeva and D.I. Proskurivsky, Abstracts Symp. on Microelectronics, Minsk, USSR, 1988, p. 42.
[7] V.S. Budishevsky, R. Grötchel, V.A. Kagadey, N.I. Lebedeva, D.I. Proskurovsky and E.B. Yankelevich, Phys Res. 8 (1988) 262

Nuclear Instruments and Methods in Physics Research B55 (1991) 884–887
North-Holland

A plasma immersion ion implantation reactor for ULSI fabrication

X.Y. Qian, D. Carl, J. Benasso, N.W. Cheung and M.A. Lieberman

Plasma Assisted Materials Processing Laboratory, Department of Electrical Engineering and Computer Sciences, University of California, Berkeley, CA 94720, USA

I.G. Brown, J.E. Galvin and R.A. MacGill

Lawrence Berkeley Laboratory, University of California, Berkeley, CA 94720, USA

M.I. Current

Applied Materials Inc., Implant Division, MS0907, 3050 Bowers Avenue, Santa Clara, CA 95054, USA

A plasma immersion ion implanation (PIII) reactor compatible with integrated-circuit fabrication has been developed Using this system, metallic impurity gettering with a noble gas plasma, sub-100-nm p+/n junction formation with SiF_4 plasma for preamorphization and BF_3 plasma for doping, trench conformal p+ doping, and Pd ion seeding implantation for selective Cu electroless plating were successfully carried out. The PIII system consists of an electron cyclotron resonance plasma source, a processing chamber with wafer bias supply, a sputtering target with bias supply, gas handling and plasma diagnostic tools. The apparatus is described in this paper. Plasma characterization and reactor performance are also presented.

1. Introduction

Plasma immersion ion implantation (PIII) has been used to implant nitrogen and metallic impurities into the surfaces of machine parts to improve corrosion and wear resistance [1,2]. PIII possesses several desirable characteristics such as large dose rate (up to tens of mA/cm^2), large implant area and a wide range of implanation energy (eV to 100 keV). PIII is also capable of implantating targets with irregular shapes, and allows for rapid changing or combination of various ion species and adjustment of beam angular distribution by varying the gas pressure. These properties make PIII very attractive for fabricating ultralarge-scale integration (ULSI) device structures.

A prototype PIII reactor dedicated to integrated-circuit processing has been developed at the University of California. This system has successfully demonstrated metallic impurity gettering with noble gas implantation [3,4], sub-100-nm p+/n junction formation with SiF_4 plasma for preamorphization and BF_3 plasma for p+ doping [5], trench conformal doping with BF_3 plasma [6], and seeding layer implantation using Pd ions sputtered from a solid target for selective Cu electroless plating [7]

2. Reactor description and ion density measurements

Fig. 1 shows a schematic of the prototype PIII reactor. The system consists of five subsystems: (1) a 2.45 GHz microwave power supply with power adjustable from 0 to 800 W and a matching network, (2) an electron cyclotron resonance (ECR) plasma source, (3) a processing chamber with wafer holder and bias supply, (4) gas handling units and (5) plasma diagnostic tools. Both the ECR chamber and the processing chamber were fabricated with aluminum. The inner diameter of ECR chamber was 7.6 cm. To compensate for plasma heating, the source chamber was constructed with a cooling water jacket. Microwave from the power supply was transmitted via WR284 rectangular waveguide into the ECR chamber through a quartz window. The reactor was pumped to a base pressure of 10^{-7} Torr before the working gas was introduced. The gas pressure in the ECR chamber could be controlled in the 0.1–10 mTorr range with a pressure controller. An ECR zone was generated at the center of the source chamber by an applied magnetic field of 875 G with a mirror field configuration. The plasma density was adjusted by varying the microwave power. The processing chamber could accommodate three different wafer holders designed for 2 and 4 in. wafers and irregular slices. The wafer holders were made of Al blocks for heat absorption; no special wafer cooling was used. The wafer holder could be biased with a negative pulsed high voltage (pulsed mode) or a negative dc voltage (dc mode), as discussed later.

Langmuir-probe measurements using Laframboise's analysis [8] were carried out to evaluate the ion density in the reactor. It was found that the ion density was a

0168-583X/91/$03.50 © 1991 – Elsevier Science Publishers B.V (North-Holland)

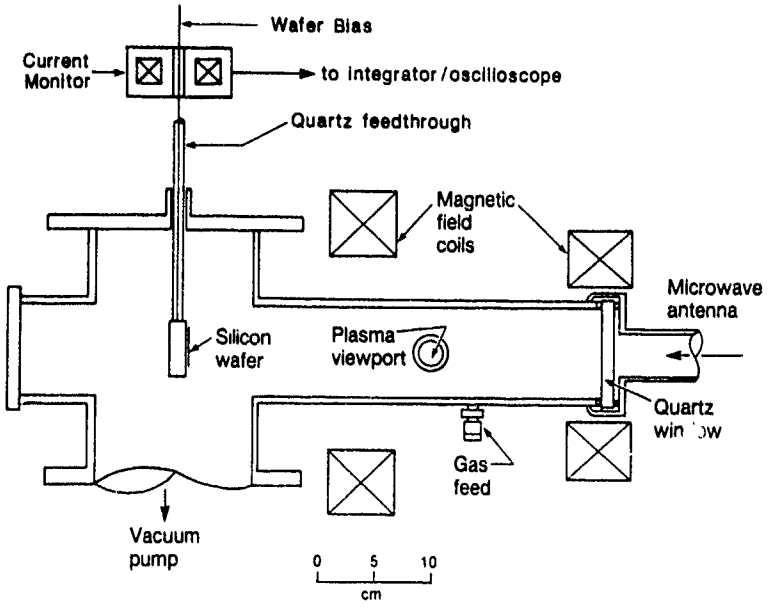

Fig. 1. Schematic of plasma immersion ion implantation apparatus.

sensitive function of microwave power, magnetic field strength, gas pressure and species, probing position and microwave tuning condition. For a full-power Ar plasma, a density of $10^{12}/cm^3$ in the ECR chamber near the resonance zone and $10^{11}/cm^3$ at the centerline of the processing chamber near the wafer can be achieved. Fig 2a shows the ion density dependence near the wafer versus forward microwave power for a BF_3 plasma. The magnetic coil current was set at 125 A, and the Langmuir probe was 3.2 cm from the center line at the plane where the wafer sits during normal implantation. The measured ion density increased linearly with microwave power, and no saturation was observed. This behavior has been observed in other similar systems with different gases [9,10]. Fig. 2b shows the ion density dependence versus BF_3 pressure for a forward microwave power of 490 W. The measurements were taken at the same position as for fig. 2a. The ion density increased rapidly with pressure from 0.1 to 1 mTorr. However, beyond a critical pressure around 1 mTorr, the ion density dropped as the pressure increased, most probably due to ambipolar ion diffusion (to the chamber wall) at high pressures.

3. System performance

3.1. Pulsed mode

A negative high-voltage pulser using an *LC* pulse line and a high-voltage step-up pulse transformer was connected to the wafer holder to supply the bias voltage for implantation.The pulse width was approximately 1 μs, and the pulse repetition frequency was adjustable up to 1 kHz. Shown in fig. 3a is a schematic of the monitoring circuit. The applied voltage was measured with an oscilloscope through a 1000 : 1 high-voltage probe. The charge flow per pulse, including ions and secondary electrons, was measured with an integrator connected to a 1 A-to-1 V current transformer (Rogowski loop). Since the input voltage to the integrator, V_I, was much larger than its output voltage V_Q, the charge flow Q per pulse through the wafer holder was equal to RCV_Q or $2.2 \times 10^{-4} V_Q$. Thus the dose rate per pulse [C/cm^2] was $2.75 \times 10^{13} V_Q$ [V] for a 50 cm^2 wafer-holder surface area. The total dose was later calibrated against the number of pulses. Shown in fig. 3b are typical voltage pulse and implantation charge pulse measured with this circuit for a BF_3 plasma powered at 250 W. The measured total charge per pulse was 1.8 μC, or a dose rate per pulse of $2.34 \times 10^{11}/cm^2$ with a -6.4 kV wafer bias.

Fig. 4a shows the dose-rate dependence on the forward microwave power with various applied biases for a BF_3 plasma. The pressure was set at 1 mTorr and the magnetic coil current was 125 A. The abrupt change in dose rate between 200 and 300 W was due to a plasma mode switch. Very similar results were obtained for an Ar plasma, as shown in fig. 4b.

3.2. DC mode

As an alternative means of wafer biasing, a dc negative voltage can be directly applied to the wafer holder

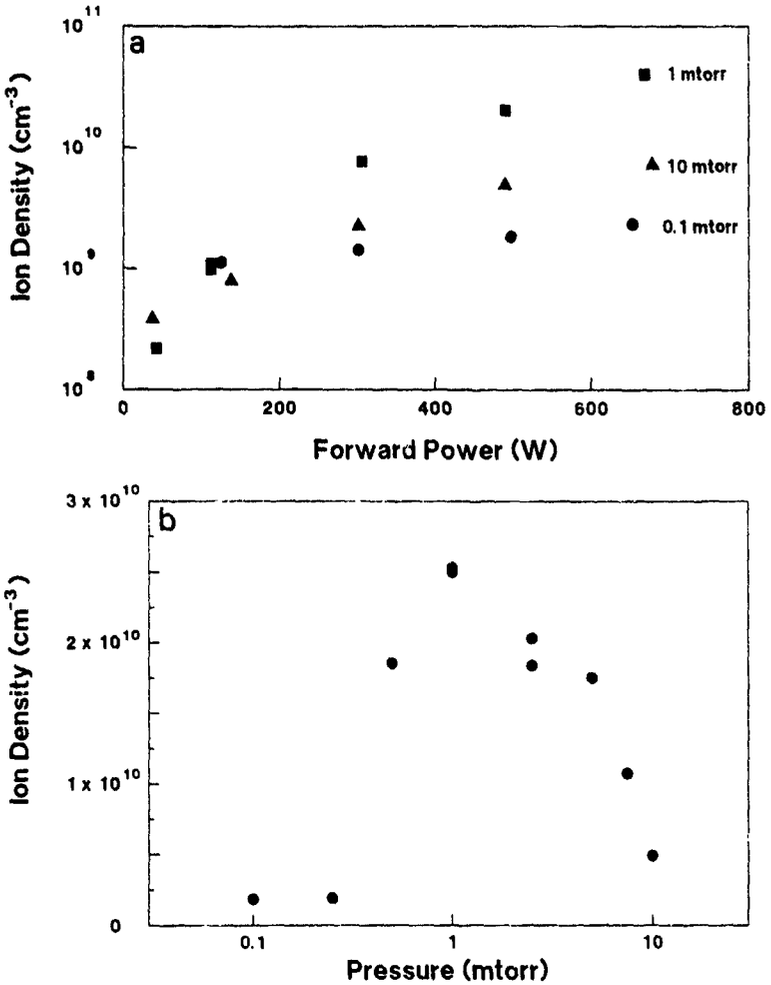

Fig. 2 (a) Ion density dependence on forward microwave power for $p = 0.1$, 1 and 10 mTorr BF_3 ECR plasma. (b) Ion density dependence on BF_3 pressure with 490 W forward microwave power. In both cases, the magnetic coil current was 125 A. The Langmuir probe was 3.2 cm from the center line at the plane where the wafer sits during normal implanation. BF_2^+ ions were assumed for the ion density calculation

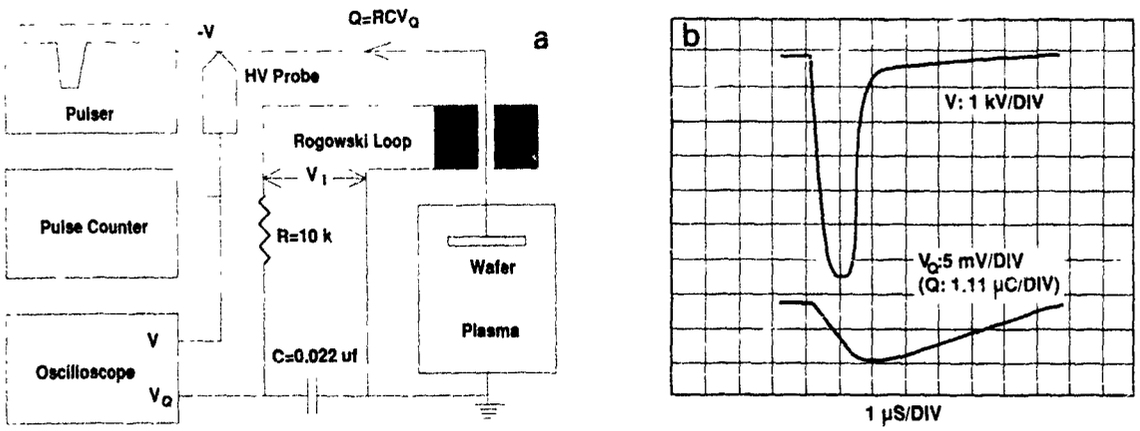

Fig. 3. (a) Monitoring circuit of the pulsed mode The applied voltage was measured with an oscilloscope through a 1000:1 high-voltage probe. The charge flow per pulse was measured with an integrator connected to a 1 A-to-1 V Rogowski loop. (b) A typical voltage pulse and implantation charge pulse measured with the circuit shown in (a).

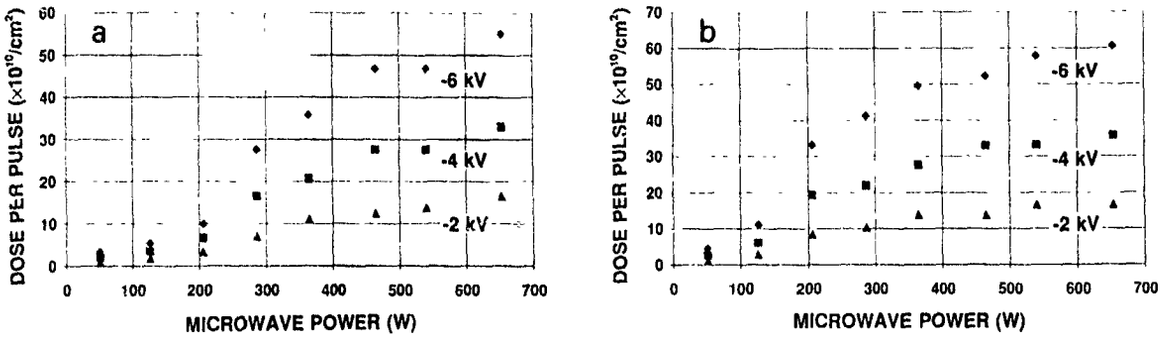

Fig. 4 Dose-rate dependence on forward microwave power with wafer biases at −2, −4 and −6 kV for a BF_3 plasma (a) and an Ar plasma (b) The pressure was set at 1 mTorr and the magnetic coil current at 125 A

as shown in the inset of fig. 5 The bias voltage was measured with a digital voltmeter through a 1000 : 1 high-voltage probe. The dose rate was monitored by a microammeter serially connected in the circuit. In this configuration, an extremely high dose rate can be achieved For example, the current density was 6.1 mA/cm^2 for a −2 kV bias at a microwave power of 650 W, corresponding to a dose rate of 3.8×10^{16} cm^{-2} s^{-1}. This high-dose-rate capability is very attractive for some applications in ULSI processing such as backside impurity gettering. When precise dose control is needed or wafer heating has to be minimized, a lower dose rate can be used by reducing the microwave power.

4. Conclusions

A plasma immersion ion implanation (PIII) reactor suitable for integrated-circuit fabrication has been developed. The ion density can reach 10^{12} cm^{-3} in the ECR chamber and 10^{11} cm^{-3} in the processing chamber. The dose rate can be varied up to 5×10^{11} cm^{-2} per pulse for a −6 kV bias or as high as 3.8×10^{16} cm^{-2}s^{-1} for a −2 kV dc bias. The bias potential can be adjusted from zero to −70 kV.

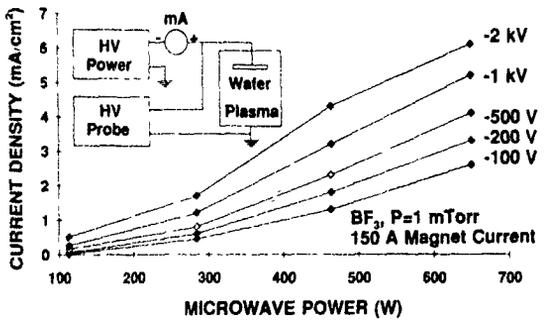

Fig. 5. Implantation current-density dependence on forward microwave power with BF_3 plasma in dc mode The bias voltage was measured with a digital voltmeter through a 1000 1 high-voltage probe. The dose rate was monitored by a microampere meter serially connected in the circuit as shown in the inset

Acknowledgements

This work was supported by Applied Materials, Inc. and a grant from the California State MICRO program

References

[1] J R. Conrad, J.L Radtke, R A Dodd, F J Worzala and N C. Tran, J Appl Phys 62 (1987) 4591
[2] J Tendys, I J Donnelly, M.J. Kenny and J T.A. Pollock, Appl Phys Lett 53 (1988) 2143
[3] H Wong, X.Y. Qian, D. Carl, N W Cheung, M A Lieberman, I.G Brown and K M Yu, Mater Res. Soc Proc. 147 (1989) 91
[4] X Y Qian, H. Wong, D Carl, N W. Cheung, M A Lieberman, I G Brown and K M. Yu, Proc Symp. on Ion Implantation and Dielectrics for Elemental and Compound Semiconductors, vol 90-13 (Electrochem Soc., 1990) p. 268.
[5] X Y Qian, N W Cheung, M A. Lieberman, M.I Current, P.K. Chu, W.L Harrington, C.W. Magee and E.M Botnick, these Proceedings (8th Int. Conf. on Ion Implantation Tecl.nology, Guildford, UK, 1990) Nucl. Instr and Meth. B55 (1991) 821.
[6] X.Y. Qian, N W. Cheung, M A. Lieberman, R Brennen, M I Current and N Jha, ibid , p 898.
[7] X.Y. Qian, M.H. Kiang, J Huang, D Carl, N W Cheung, M.A. Lieberman, I.G. Brown, K M Yu and M I Current, ibid., p. 888.
[8] J G Laframboise, Inst for Aero Stud , Univ of Toronto, Rep. no 100 (1966)
[9] J. Forster and W. Holber, J Vac Sci Technol A7 (1989) 899
[10] D.A. Carl, D.W. Hess and M.A Lieberman, J. Vac. Sci. Technol. A8 (1990) 2924

Nuclear Instruments and Methods in Physics Research B55 (1991) 888–892
North-Holland

Plasma immersion Pd ion implantation seeding pattern formation for selective electroless Cu plating

X.Y. Qian, M.H. Kiang, J. Huang, D. Carl, N.W. Cheung and M.A. Lieberman

Plasma Assisted Materials Processing Laboratory, Department of Electrical Engineering and Computer Sciences, University of California, Berkeley, CA 94720, USA

I.G. Brown and K.M. Yu

Lawrence Berkeley Laboratory, University of California, Berkeley, CA 94720, USA

M.I. Current

Applied Materials, Inc., Implant Division. MS0907, 3050 Bowers Avenue, Santa Clara, CA 95054, USA

Selective plating of Cu for interconnects was carried out using plasma immersion Pd ion implantation and Cu electroless plating. Pd ions were sputtered from a negatively biased target and ionized in an Ar electron cyclotron resonance (ECR) plasma. The Pd ions were implanted into the SiO_2 substrates biased with negative high pulsed voltages. In our studies, we found the required Pd seeding dose for Cu plating was on the order of $5\times10^{14}/cm^2$. With a direct Pd implantation, an intermediate activation step using a $PdCl_2$ solution was eliminated.

1. Introduction

Because of its low electrical resistivity and good electromigration property, copper has been proposed as the interconnect material of choice for submicron IC metallization [1]. However, reactive ion etching of copper is difficult because the etching products are usually non-volatile. This constraint led to some recent investi-

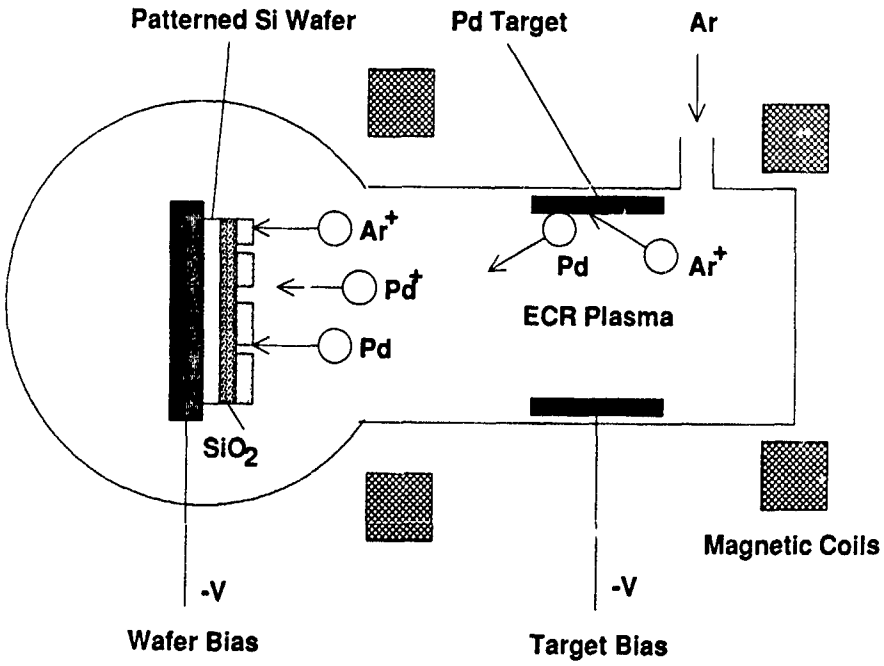

Fig. 1. Schematic of plasma immersion Pd ion implanter for selective Cu plating seeding layer formation.

0168-583X/91/$03.50 © 1991 – Elsevier Science Publishers B.V (North-Holland)

gations of selective copper deposition by chemical vapor deposition [2] or electroless plating [1]. To initiate the nucleation process for electroless plating, catalyst atoms are required as the seeds on the SiO_2 substrate to be plated. The plasma immersion ion implantation (PIII) technique is well suited for this purpose [3–5]. With PIII, seed metallic materials can be supplied directly from a sputtering target and implanted into the substrate. The implantation dose rate of PIII can be much higher than with a conventional implanter. In addition, by choosing the proper substrate bias voltage, the peak concentration of implanted ions can be on the surface so that no intermediate etching steps are needed to expose the profile peak for Cu plating. The gradual transition from a Pd-rich surface to a pure SiO_2 substrate is also expected to improve the adhesion of the plated Cu film. In this paper, we report the feasibility of using PIII to form seeding patterns for selective electro-

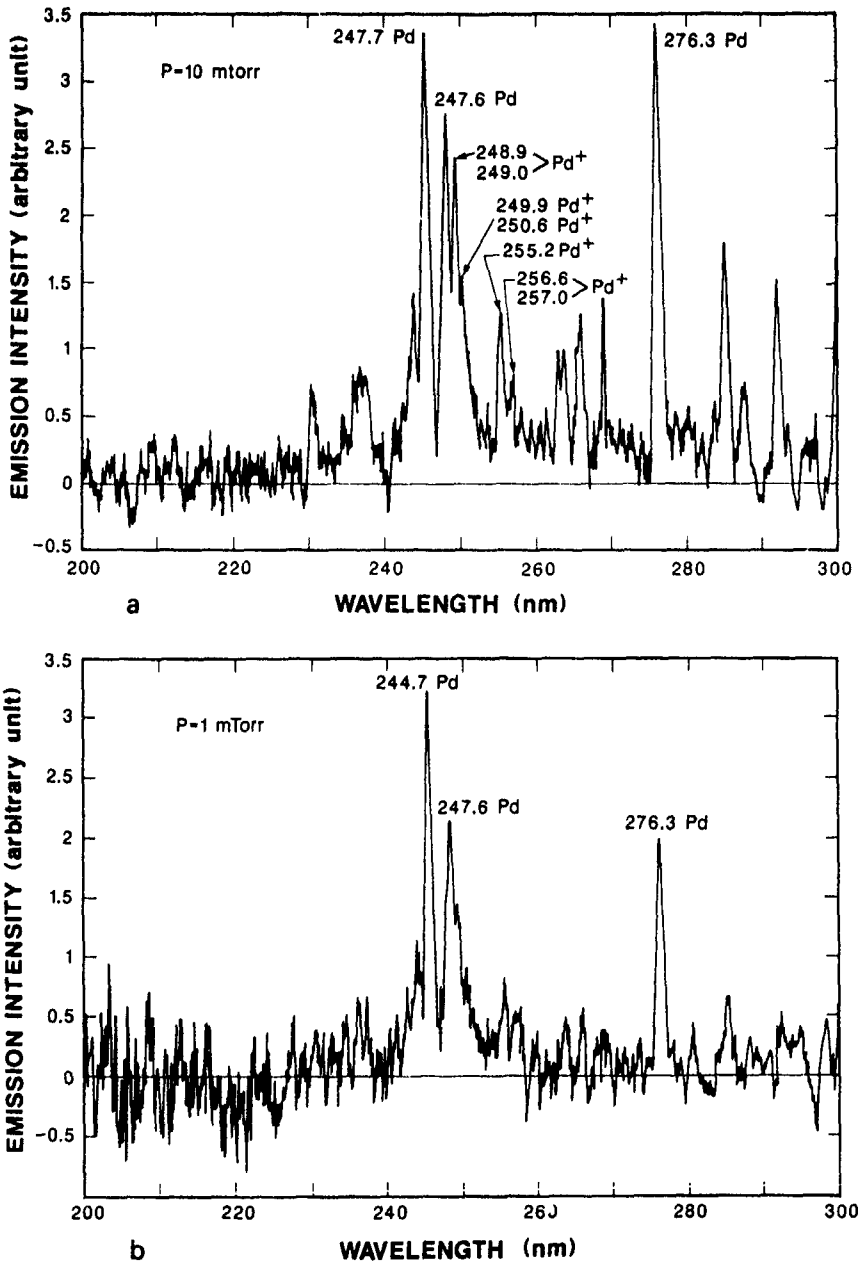

Fig 2 Differential optical emission spectra from plasma immersion Pd ion implanter with Ar pressures at 10 mTorr (a) and 1 mTorr (b) The emission from Ar has been subtracted Strong emission peaks from excited Pd neutral atoms and Pd^+ are marked.

less Cu plating on SiO_2, and show that direct Cu plating is feasible without an intermediate $PdCl_2$ solution activation process.

2. Experiments

A schematic of the plasma immersion Pd ion implanter developed at the University of California, Berkeley, is shown in fig. 1. A Pd target was introduced into an electron cyclotron resonance (ECR) Ar plasma. The plasma was generated with 700 W microwave power at 2.45 GHz. The magnetic field needed for the electron cyclotron resonance was supplied by two coils surrounding the ECR chamber. The Ar gas pressure was regulated with a pressure controller in the 1–10 mTorr range. A dc negative bias from 50 to 400 V was applied to the Pd sputtering target; sputtered Pd atoms were ionized in the Ar plasma. An optical emission spectrometer was used to monitor photoemission from neutral and ionized species. A pulsed negative bias of several kV was applied to a Si wafer in the downstream plasma to facilitate the implantation process.

Blanket and patterned SiO_2 substrates were used for this Pd PIII implantation study. The SiO_2 substrate film

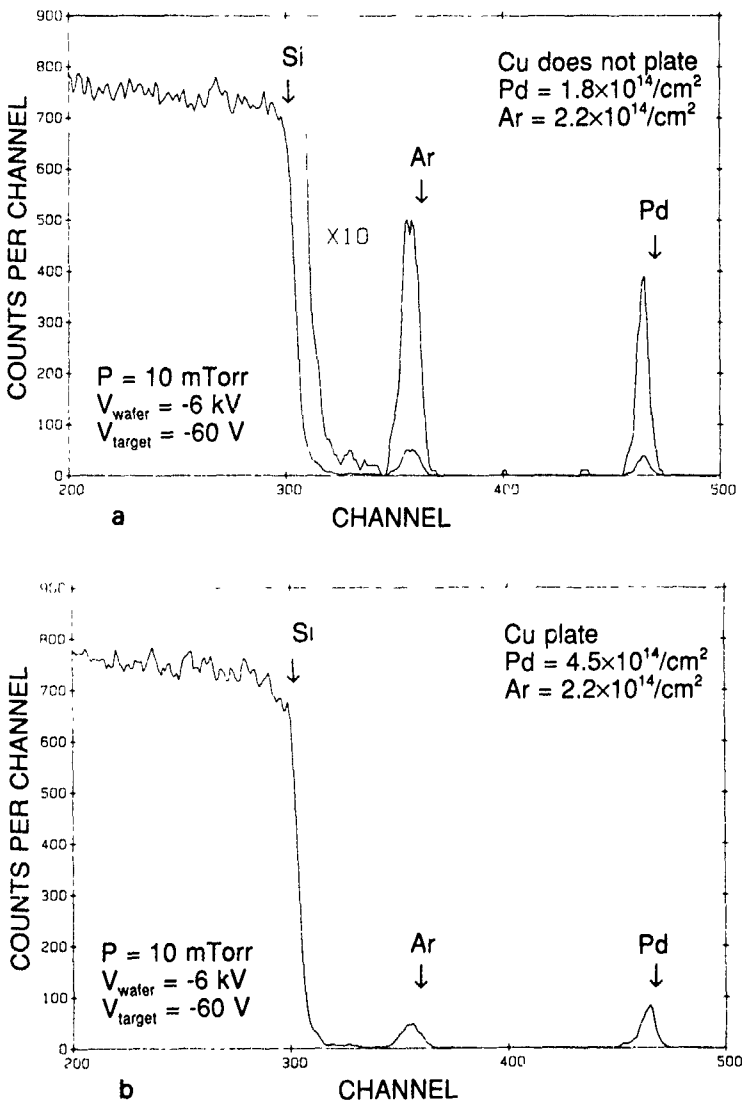

Fig. 3 RBS spectra of two samples implanted with Pd and Ar using PIII Both samples were implanted in a 10 mTorr Ar plasma. The Pd target bias was −60 V dc The wafer was biased with 1 μs pulses at 1 kHz The pulse peak was at −6 kV RBS spectra were taken with a 2 MeV He beam at a normal incident angle to the wafer surface No plating of Cu was observed in 30 min for the samples with a Pd dose of $1.8\times10^{14}/cm^2$ (a) The sample with a Pd dose of $4.5\times10^{14}/cm^2$ rapidly seeded Cu (b)

was formed on Si wafers with wet oxidation at 1000 °C for 2 hours. Rutherford backscattering spectroscopy (RBS) was used to analyze implanted Pd and Ar profiles. The electroless Cu plating was performed in a mixture of $CuSO_4$ and KCN solution [6]. In the case of patterned SiO_2 substrates, a photoresist stripping step was added before Cu plating.

3. Results and discussion

Optical emission spectroscopy was carried out with Ar plasma at various pressures and target biases. Shown in fig. 2 is a pair of differential spectra where the emission from Ar has been subtracted. Emission lines at wavelengths of 244.7, 247.6 and 276.3 nm from excited Pd neutral atoms are prominent. The intensities from these peaks are similar for Ar pressures of 1 and 10 mTorr. However, emission lines from Pd ions at 248.9 and 249.0 nm, 249.9 and 250.6 nm, and 255.2 nm for the case of Ar pressure of 10 mTorr in fig. 2a are more pronounced than at 1 mTorr as shown in fig. 2b. This increase of Pd ionization with higher gas pressure is in agreement with the ion density measurements where a higher plasma density has been found in a 10 mTorr Ar plasma [7].

Blanket Si wafers with 1 μm SiO_2 were used for the initial PIII and plating condition studies. Shown in figs. 3a and 3b are RBS spectra of two samples implanted with Pd and Ar using PIII. Both samples were implanted in a 10 mTorr Ar plasma at 700 W. The Pd target was connected to a dc power supply at −60 V; 500 mA target current was measured. The wafer was biased to a −6 kV peak potential at 1 kHz with a high voltage pulser. The pulse width was 1 μs. It was found that for such a low energy, both Ar and Pd were implanted in the SiO_2 surface. The electroless Cu plating was performed at 72 °C with a pH value of the plating solution equal to 13. No plating of Cu was observed with more than 30 minutes of plating time for the samples with a Pd dose of $1.8 \times 10^{14}/cm^2$ as measured by RBS. However, the sample with a slightly higher Pd dose of $4.5 \times 10^{14}/cm^2$ rapidly seeded Cu. Fig. 4 shows that a threshold Pd dose at $(3–4) \times 10^{14}/cm^2$ is required for Cu plating to occur. The plated Cu films are continuous with mirror finishes

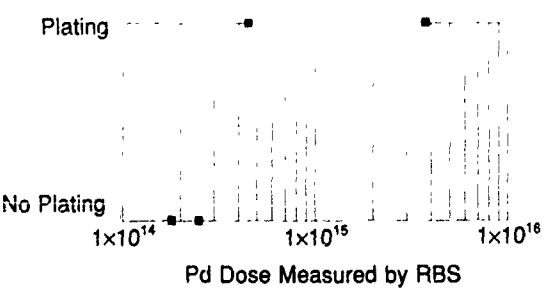

Fig. 4. Threshold Pd dose for electroless Cu plating

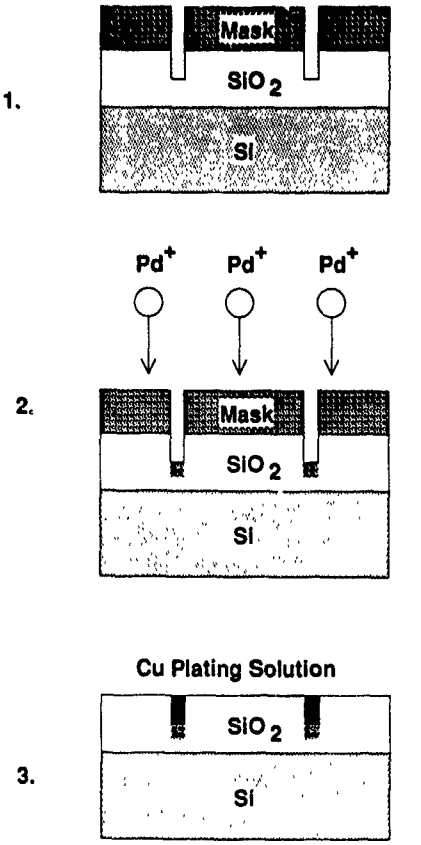

Fig 5 Process sequence of selective Cu plating: (1) Wet oxidation followed by photoresist patterning and reactive ion etching; (2) Pd ion implantation and photoresist removal; (3) electroless Cu plating

For multilevel interconnection technology, maintaining a planar interconnect structure will improve lithography definition and metal step-coverage The process flow of planarized Cu interconnect based on electroless plating is shown in fig. 5. Si wafers with 1 μm thermal SiO_2 were patterned with photoresist. Then, 4500 Å deep trenches on the SiO_2 layer were formed with dry etching. Pd ion implantation was carried out in the PIII reactor with the patterned photoresist as implantation mask. After the mask was stripped, Cu electroless plating was performed. Fig. 6a shows an optical micrograph of the Cu film grown in the Pd implanted trenches. The Cu plated lines shown were 2 μm wide

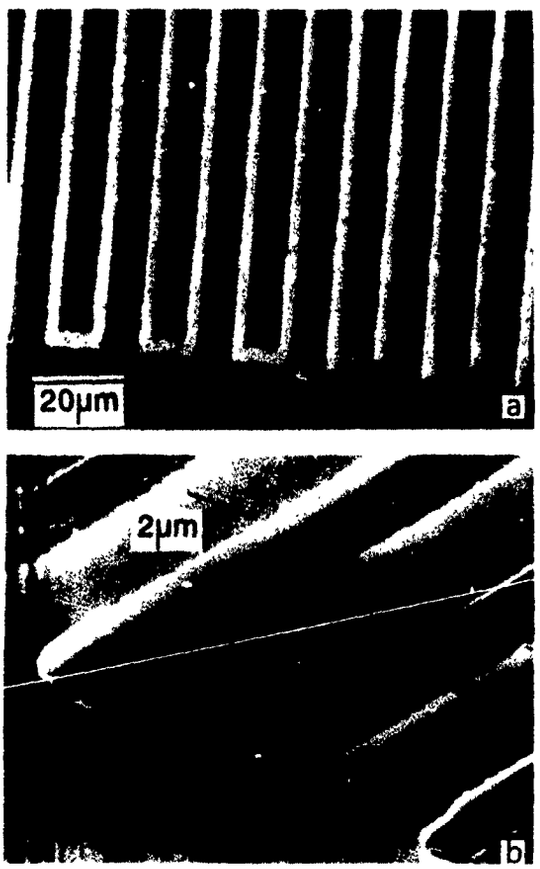

Fig 6. Optical (a) and scanning electron microscopy (b) pictures of Cu plated trenches

and no Cu plating was found on the SiO_2 surface. In fig 6b, the scanning electron microscopy micrograph shows that the plated Cu was about 2000 Å thick.

4. Conclusion

We have demonstrated the selective plating of Cu interconnects using Pd PIII for the seeding process The required Pd PIII dose is on the order of $(3-4) \times 10^{14}/cm^2$. With direct Pd implantation, an intermediate activation step using a $PdCl_2$ solution is not necessary. Other implanted species such as Pt, Au and Cu are also expected to work with this selective plating process.

Acknowledgement

This work was supported by Applied Materials, Inc and a grant from the California State MICRO program.

References

[1] P L. Pai and C.H Ting, IEEE Electron Device Lett. 10 (1989) 423
[2] A. Awaya and Y. Arita, Proc VLSI Symp., Kyoto, Japan, 1989, p. 103
[3] J.R Conrad, J.L. Radtke, R.A Dodd, F.J Worzala and N.C Tran, J Appl Phys. 62 (1987) 4591
[4] J Tendys, I J Donnelly, M J Kenny and J T A. Pollock, Appl Phys. Lett 53 (1988) 2143
[5] X.Y Qian, D Carl, J. Benasso, N.W Cheung, M.A Lieberman, I.G Brown, J E. Galvin, R A MacGill and M I. Current, these Proceedings (8th Int Conf on Ion Implantation Technology, Guildford, UK, 1990) Nucl Instr and Meth B55 (1991) 884
[6] X Y. Qian, M.H. Kiang, N W Cheung, M.A Lieberman, I G Brown, X. Godechot and K.M Yu, ibid , p 893
[7] D Carl, private communication.

Nuclear Instruments and Methods in Physics Research B55 (1991) 893–897
North-Holland

Metal vapor vacuum arc ion implantation for seeding of electroless Cu plating

X.Y. Qian, M.H. Kiang and N.W. Cheung

Plasma Assisted Materials Processing Laboratory, Department of Electrical Engineering and Computer Sciences, University of California, Berkeley, CA 94720, USA

I.G. Brown, X. Godechot [1], J.E. Galvin, R.A. MacGill and K.M. Yu

Lawrence Berkeley Laboratory, University of California, Berkeley, CA 94720, USA

A metal vapor vacuum arc (MEVVA) ion source has been used to implant Pd into SiO_2 substrates. The ion implanted area formed a seeding layer on which a Cu film was successfully plated through an electroless plating process. It was found that the required Pd dose for Cu plating to occur is on the order of 3×10^{15} cm^{-2} when the implantation was performed with a 20 kV extraction voltage. Taking advantage of the large pulsed ion current capability (up to 1 A) of the MEVVA ion source, the needed Pd dose for seeding was achieved in minutes. With direct Pd implantation, an intermediate activation step using $PdCl_2$ solution can be eliminated. The Cu plating rate was not a sensitive function of temperature and no incubation period was found in our experiments.

1. Introduction

Simulation studies [1] on the circuit performance have shown that the delay time contributed by interconnection gradually takes over as the dominant factor when the device dimensions go down to the deep-submicron regime. The low electrical resistivity and expected high resistance to electron and stress migration have made copper a promising candidate for future interconnection material for its superiority over aluminum in operating speed and reliability. Therefore, copper has been investigated as a potential interconnect material for some time. Recently, the processing difficulty in patterning copper has been solved by employing the selective electroless plating technique [1]. Deposited and implanted Si, W and Ti have been used to initiate the copper nucleation process.

A high current metal ion implantation facility using a metal vapor vacuum arc (MEVVA) ion source [2–8] has been developed at Lawrence Berkeley Laboratory. With this apparatus, the relatively high Pd dose needed for the seeding process of electroless Cu plating can be achieved in minutes. Moreover, instead of depositing a seeding layer on the substrate, the "buried" seeds might even help the adhesion of the plated Cu film. In this report, we have demonstrated that MEVVA can be applied to form Pd seeding patterns for selective electroless Cu plating on SiO_2 substrates, and that direct Cu plating is feasible without a $PdCl_2$ activation step.

2. Experiments

The MEVVA ion source is operated in a pulsed mode, with pulse width 0.25 ms and repetition rate up to 100 pps. The beam current can be as high as several amperes at peak and around 10 mA on a time average. Implantation was done in a broad-beam mode using the MEVVA ion source version V without magnetic charge-to-mass analysis of beam components, and the ion trajectories were line-of-sight from ion source to target.

In fig. 1 a schematic of the MEVVA ion implanter is shown. The vacuum pressure during implantation was typically in the low-to-mid 10^{-6} Torr range. The target to be implanted was introduced into the vessel through an air lock, and was mounted on a water-cooled holder. A magnetically suppressed Faraday cup can be inserted into the beam immediately in front of the target; the beam current can thus be adjusted prior to implantation and the number of beam pulses needed to accumulate the required dose can be calculated.

The ion beam charge state distribution was measured using a time-of-flight diagnostic technique [9]. The detector measured the electrical current in the different charge/mass (Q/A) states and provided a good mea-

[1] On leave to Lawrence Berkeley Laboratory from SODERN; present address: SODERN, 1 Ave. Descartes, 94451 Limeil-Brevannes, France. Supported by a grant from the French Ministère des Affaires Etrangères, Bourse Lavoisier, and a grant from SODERN.

0168-583X/91/$03.50 © 1991 – Elsevier Science Publishers B.V. (North-Holland)

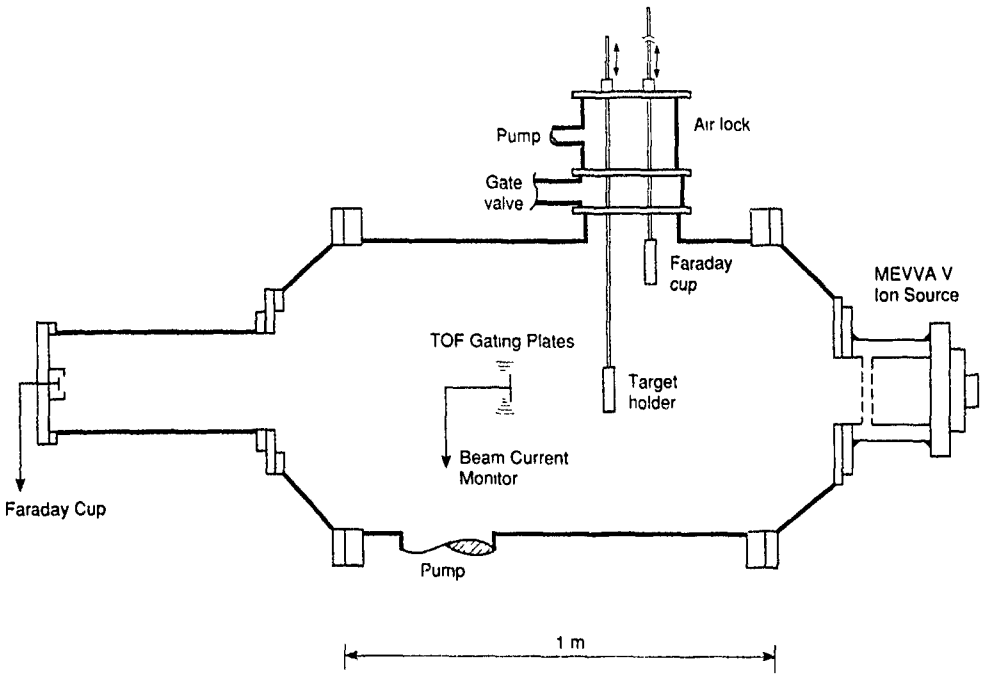

Fig 1 Schematic of the MEVVA ion implanter

surement of the ion composition of the extracted ion beam. An oscillogram of the time-of-flight charge state spectrum for a Pd ion beam is shown in fig. 2. The fractions of 23, 67, 9 and 1% of Pd ions in the beam were in 1+, 2+, 3+ and 4+ charge states, and hence, with implantation energies of 20, 40, 60 and 80 keV, respectively.

The implanted Pd profile was analyzed with Rutherford backscattering spectroscopy (RBS). Since the implantation was performed at a relatively low energy, the

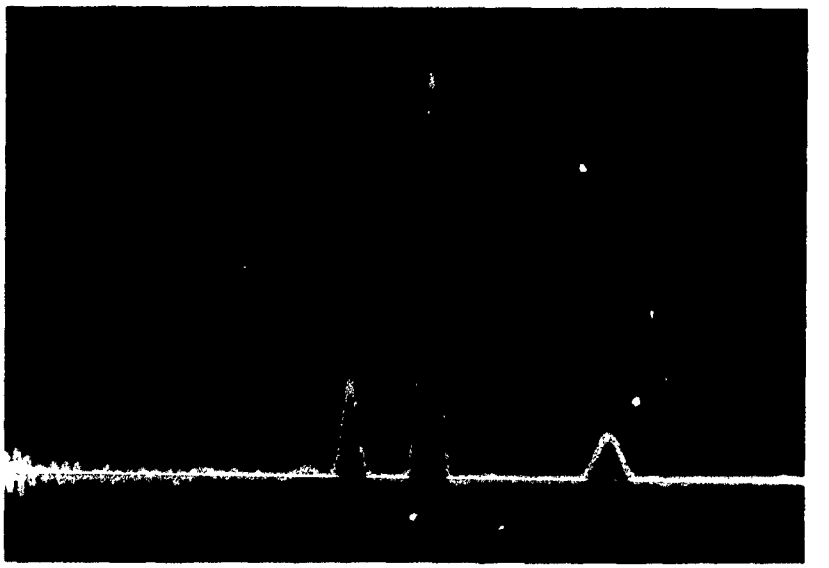

Fig. 2. Charge state distribution for Pd ion beam. The peaks correspond to $Q=1+$, 2+ (maximum), 3+ and 4+, right to left. The signal is the electrical current collected by a Faraday cup.

Pd profile was shallow. For a 20 kV extraction voltage, the profile peak was only 26 nm below the SiO_2 surface with a relatively high surface Pd concentration. Therefore, the electroless Cu plating was then carried out directly, without a stripping process to expose the Pd peak concentration. The electroless Cu plating bath composition is as follows:

$CuSO_4 \cdot 5H_2O$	7.5 g/l,
NaOH	23 g/l,
CH_2O (37%)	10 ml/l,
EDTA	25 g/l,
KCN(1 g NaOH, then 1 g KCN to 1 l water)	10 ml,
Gafac (3%)	75 ml/l.

The pH value of the plating solution was 13. With formaldehyde as the reducing agent, the overall electroless plating process on the palladium surface can be resolved into two electrochemical half reactions [10]:

$$HCHO + 3OH^- \rightarrow HCOO^- + 2H_2O + 2e^-,$$

$$Cu^{2+} + 2e^- \rightarrow Cu.$$

By directly using Pd as the seeding for electroless plating, we eliminated the need for $PdCl_2$ treatment conventionally employed to activate the substrate before plating. This not only simplifies the electroless plating to a one-step process, but it also eliminates the possibility of undesirable metal deposition on nonselected area in the substrate.

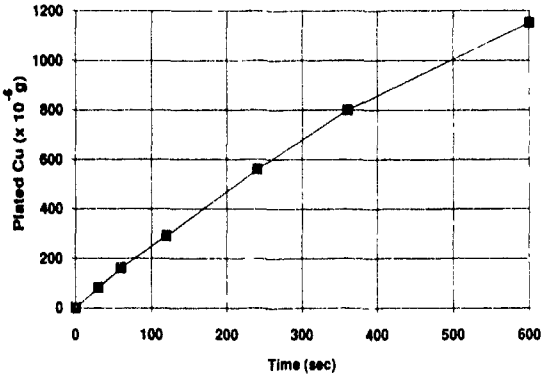

Fig. 4 Cu deposition rate versus time. Pure Pd foils with 5 cm^2 surface area were used. The "plated Cu" means the total amount of Cu deposited on the whole Pd foil in the indicated time period. The plating bath was kept at 60 °C.

3. Results and discussion

It has been reported that the rate constant of the oxidation reaction is an exponential function of temperature [11]. To study the sensitivity of Cu deposition rate on temperature variation, we have conducted a series of electroless plating experiments at various temperatures. Pure Pd foils with 5 cm^2 surface area were plated in the

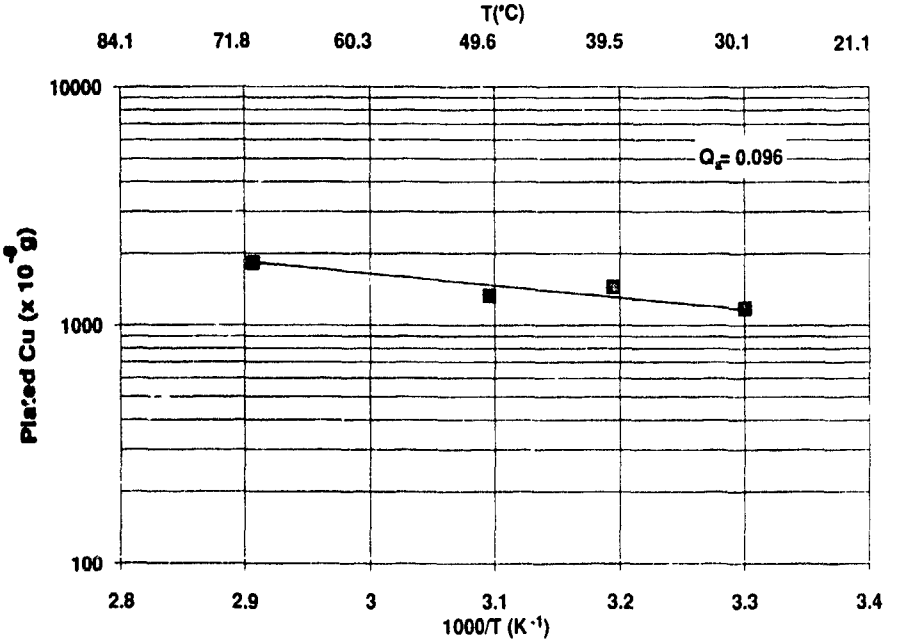

Fig. 3. Cu deposition rate versus temperature. Pure Pd foils with 5 cm^2 surface area were used. The "plated Cu" means the total amount of Cu deposited on the whole Pd foil in 100 s. The calculated activation energy Q_a was 0.096 eV.

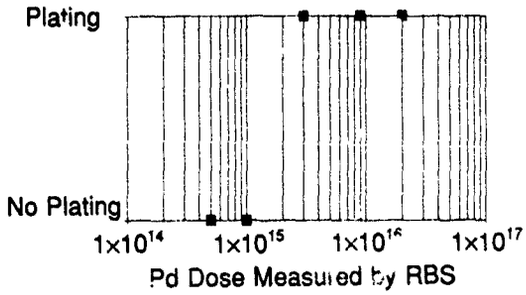

Fig. 5. Cu-plating behavior on Pd dose. Pd was implanted into SiO_2 substrate with the MEVVA implanter at a 20 kV beam extraction voltage. The threshold Pd dosage is on the order of 3×10^{15} cm^{-2}

bath at temperatures ranging 30 to 70 °C for 100 s. The weights of the Pd samples were measured before and after plating. The difference represented the amount of plated copper. The results are given in fig. 3. On the semilog plot, a roughly linear dependence is observed. However, the activation energy Q_a was calculated to be 0.096 eV, a rather small value to have a significant effect on the plating rate. At 60 °C, the amount of plated Cu was approximately 1600 μg in 100 s. This corresponds to a solid Cu deposition rate of 3.6 nm/s. Fig. 4 shows the deposition rate dependence versus plating time on pure Pd foils. The plating bath was kept at 60 °C. As shown in the figure, copper grew almost linearly with time, and no significant incubation period was observed.

Blanket Si wafer with 1 μm thermal oxide was used for the initial seeding test. Pd was implanted into SiO_2 substrates at various doses from 5×10^{14} to 2×10^{16} cm^{-2} with the MEVVA implanter using a 20 kV beam extraction voltage. As shown in fig. 5, a threshold Pd dosage on the order of 3×10^{15} cm^{-2} was required for Cu plating to occur.

For multilevel interconnection technology, maintaining a planar structure would facilitate the metallization by eliminating processing steps such as planarization. Therefore, selective Cu plating on trenches with Pd implanted seeds was tested. The experimental procedure is shown in fig. 6. A SiO_2 substrate film was formed on Si wafer with wet oxidation at 1000 °C for 2 h. Photoresist was used as mask. Then, 0.45 μm deep trenches on

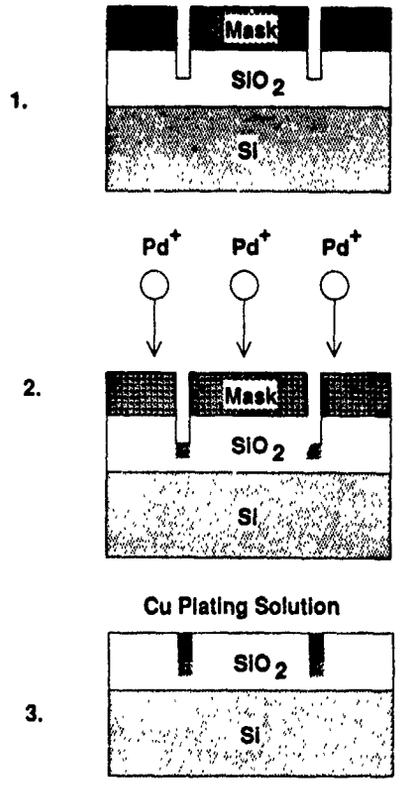

Fig. 6 The process flow of selective electroless copper plating: (1) wet oxidation followed by photoresist pattern and reactive ion etching; (2) Pd ion implantation and photoresist removal; (3) electroless Cu plating.

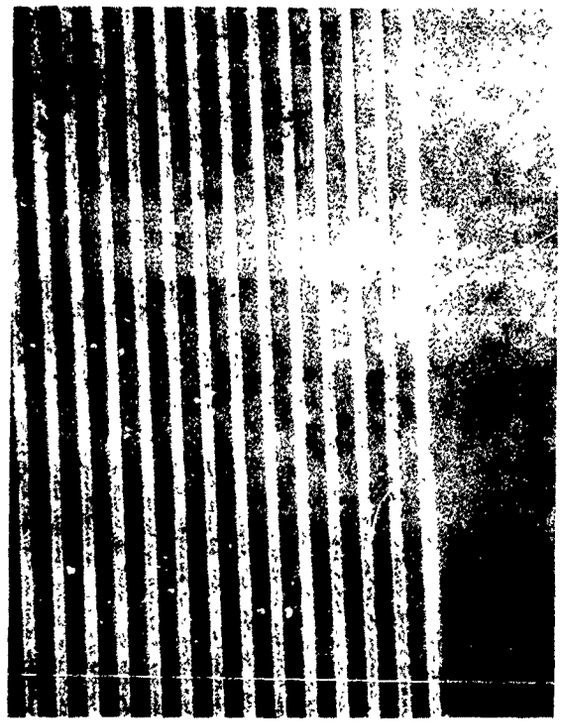

Fig. 7. Optical picture of selective electroless Cu plated on Pd-implanted trenches. The Cu-plated lines seen in the picture are 2 μm wide.

SiO_2 film were fabricated with dry etching. Pd ion implantation was carried out at 20 kV. After photoresist stripping by acetone, Cu electroless plating was performed. Fig. 7 shows a picture of Cu film grown in Pd-implanted trenches. The Cu plated lines shown are 2 μm wide.

4. Conclusion

We have demonstrated that selective Cu plating on SiO_2 substrate can be achieved with implanted Pd seeding using a high current MEVVA ion source. At 20 kV extraction voltage, the threshold Pd dose required for Cu plating is about 3×10^{15} cm^{-2}. With direct Pd implantation, an intermediate activation step using $PdCl_2$ solution can be eliminated. The Cu plating rate was not a sensitive function of temperature and no incubation period was found in our process.

References

[1] P.L. Pai and C.H. Ting, IEEE Electron Device Lett. 10 (1989) 423

[2] I.G. Brown (ed.), in: The Physics and Technology of Ion Sources (Wiley, New York, 1989) p. 331.

[3] I.G. Brown, J.E. Galvin and R.A. MacGill, Appl. Phys. Lett. 47 (1985) 358.

[4] I.G. Brown, J.E. Galvin, B.F. Gavin and R.A. MacGill, Rev. Sci. Instr. 57 (1986) 1069.

[5] R.A. MacGill, I.G. Brown and J.E. Galvin, Rev. Sci. Instr. 61 (1990) 580.

[6] I.G. Brown, J.E. Galvin, R.A. MacGill and F.J. Paoloni, Rev. Sci. Instr. 61 (1990) 577.

[7] I.G. Brown, J.E. Galvin, R.A. MacGill and R.T. Wright, Appl. Phys. Lett. 49 (1986) 1091.

[8] I.G. Brown, M.R. Dickinson, J.E. Galvin, X. Godechot and R.A. MacGill, these Proceedings (8th Int. Conf. on Ion Implantation Technology, Guildford, UK, 1990) Nucl. Instr. and Meth. B55 (1991) 506.

[9] I.G. Brown, J.E. Galvin, R.A. MacGill and R.T. Wright, Rev. Sci. Instr. 58 (1987) 1589.

[10] J.E.A.M. van den Meerakker and J.W.G. de Bakker, J. Appl. Electrochem. 20 (1990) 85.

[11] S. Glasstone, An Introduction to Electrochemistry (Van Nostrand, New York, 1960) p. 466.

Nuclear Instruments and Methods in Physics Research B55 (1991) 898–901
North-Holland

Conformal implantation for trench doping with plasma immersion ion implantation

X.Y. Qian, N.W. Cheung and M.A. Lieberman

Plasma Assisted Materials Processing Laboratory, Department of Electrical Engineering and Computer Sciences, University of California, Berkeley, CA 94720, USA

R. Brennan

Solecon Laboratory, Inc., 2241 Paragon Drive, San Jose, CA 95131, USA

M.I. Current and N. Jha

Applied Materials, Inc., 3050 Bowers Avenue, Santa Clara, CA 95054, USA

Taking advantage of the moderate beam divergence angle of plasma immersion ion implantation (PIII), we demonstrated conformal doping of boron in high aspect ratio Si trenches. A uniformly doped p^+ layer all around the side walls and bottom of trenches with an aspect ratio of 6:1 was observed with scanning electron microscopy (SEM) after junction staining. To test the limit of this conformal doping technique, an extremely high aspect ratio macroscopic trench model (0.5 mm wide and 12.5 mm deep) made with Si wafer slices was implanted using similar PIII conditions. After rapid thermal annealing, sheet resistance along trench top and sidewalls was evaluated with the four-point probe method. The average sheet resistance of trench sidewalls was about twice of that of the trench top. The deviation of the sidewall sheet resistance was ±60% with respect to the mean value.

1. Introduction

Doping of trench capacitors by ion implantation has focused on the use of multi-step implants at controlled beam incidence angles [1–4]. This approach has led to development of a number of implanter designs for control of implantation angle and changes in wafer orientation [5]. With conventional ion implantation techniques, using a collimated ion beam at energies of 50 to 150 keV, effects of ion reflection, sputtering and damage compound the stringent alignment requirements imposed by the high aspect ratio geometries of trench capacitors [4,5].

This work describes a fundamentally different approach to trench doping using a directly extracted beam from a plasma, referred to as plasma immersion ion implantation (PIII), to achieve conformal doping profiles throughout the trench sidewall surface area [6]. The use of PIII has been demonstrated for metallurgical surfaces and semiconductor processing [7–10]. Since the PIII beam is believed to have an angular divergence of at least several degrees with operation in the mTorr pressure range, it will have an advantage over conven-

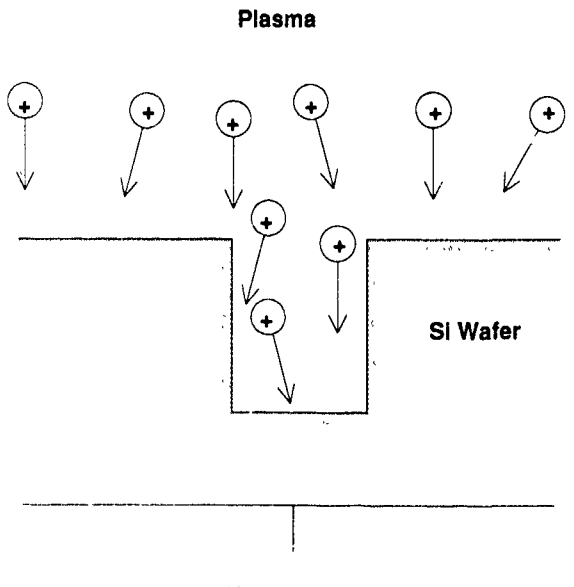

Fig. 1. Schematic showing trench conformal doping with plasma immersion ion implantation.

0168-583X/91/$03.50 © 1991 – Elsevier Science Publishers B.V. (North-Holland)

tional implantation with collimated beams. Fig. 1 shows the schematic of the trench doping technique using the beam divergence characteristics of PIII. The trench samples were immersed in a BF_3 plasma, with a negative high voltage applied to the substrate. Ions in the plasma sheath were accelerated by the negative potential and implanted into the wafer. Since the gas pressure was maintained in the mTorr range, the accelerated ions presumably have a mean free path of several cm due to the charge transfer and elastic scattering. Therefore, a certain angular distribution of bombarding ions is expected. The full width at half maximum of this angular distribution was found to be about 3° at a gas pressure of 1 mTorr with −500 V bias according to computer simulation results from a Monte Carlo simulator PDP1 developed at UC Berkeley [11].

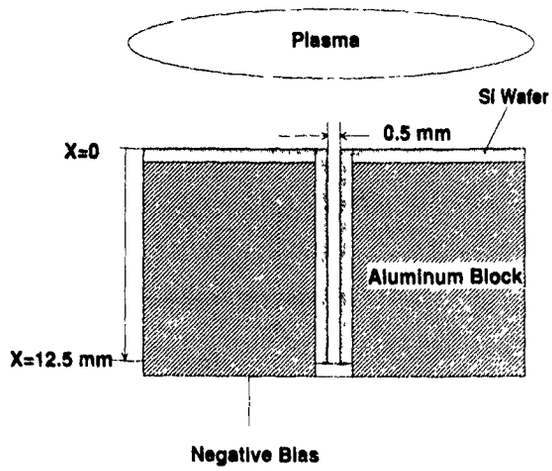

Fig. 3. Sample geometry to simulate the trench on a macroscopic scale.

2. Experiment and results

The prototype PIII reactor used in this study consists of: (1) an 800 W, 2.45 GHz microwave power supply, (2) an electron cyclotron resonance (ECR) source, (3) a processing chamber with wafer holder and bias supply, and (4) gas handling and diagnostic tools. The reactor was pumped to a base pressure at 10^{-7} Torr before BF_3 was introduced into the chamber. The gas pressure was controlled in the mTorr range. An ECR zone was generated at the center of the source chamber by an applied magnetic field of 875 G. The plasma density was adjusted by varying the microwave power input to the ECR chamber. A negative dc or pulsed high voltage was connected to the wafer holder to supply the bias voltage for implantation. In pulsed mode, the charge flow per pulse was measured with an integrator connected to a current transformer (Rogowski loop). The total dose was later calibrated against the number of pulses. When a dc bias is used, the dose rate was monitored by a current meter serially connected in the circuit. To avoid wafer heating and to obtain better dose control, a lower microwave power of 100–200 W with a current density of 0.5–1 mA/cm^2 was used for the dc mode. The detailed description of PIII apparatus has been presented elsewhere [12].

Fig. 2. Cross section SEM picture of Si trench doped in BF_3 plasma using PIII. The pressure was maintained at 5 mTorr and the wafer bias was −10 kV during PIII. The wafer accumulated charge was 4 mC/cm^2.

N-type Si wafers were etched with reactive ion etching to form 1 μm wide and 5–6 μm deep trenches. After boron implantation in the PIII reactor, rapid thermal annealing (RTA) in an N_2 ambient at 1060 °C for 30 s was used to activate the dopant. The annealed sample was carefully cleaved to expose the trench cross sections. A Si etchant of 30 (HNO_3) : 1 (HF) solution was then used to stain the p^+/n junction. The boron dopant uniformity and p^+/n junction depth along the trench after staining were examined with a scanning electron microscope (SEM). Fig. 2 is a SEM picture showing the cross section of the doped trench. This sample was biased with a −10 kV dc voltage during PIII. The BF_3 gas pressure was kept at 5 mTorr. The accumulated areal charge of the implantation current was 4 mC/cm^2. As seen from the SEM pictures, the trench top, sidewalls and bottom were uniformly doped. The thickness of the doped layer is about 2500–3000 Å. Uniformly doped layers were observed in samples implanted with −4 kV and −2 kV dc bias or −3.6 kV pulsed bias. There was not much difference in doped layer thickness as observed with SEM within this bias range. However, the doped layer thickness increased to 4500 Å for a sample with ten times the dose. This is probably due to the fact that the implantation profiles in all cases were very shallow, the dopant distribution was dominantly controlled by a driven-in mechanism during RTA, which is concentration dependent. This transient rapid diffu-

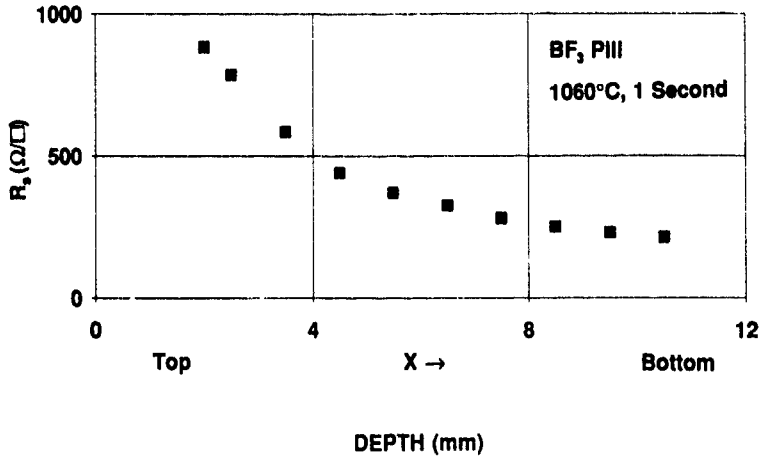

Fig 4 Sheet resistance of the doped layer along a sidewall of the macroscopic model trench.

sion of shallow boron dopant has been reported by Qian et al. [13].

3. Macroscopic trench simulation

We have also investigated the limit of PIII conformal doping with extremely high aspect ratio. Since it is difficult to determine the dopant profile or carrier concentration on a 1 μm wide, 6 μm deep trench sidewall, a macroscopic trench of aspect ratio 25 : 1, made with Si slices, was used for the study. Shown in fig. 3 is the illustration of the macroscopic trench. N-type CZ wafers with resistivity of 10 Ω-cm were used to form the trench. The width and depth of the trench were 0.5 and 12.5 mm respectively. BF_3 PIII was carried out with the same bias as for the microscopic trench sample shown in fig. 2. After RTA at 1060 °C for 1 s, sheet resistance along trench top and sidewalls were evaluated with the four-point probe method. The sheet resistance of the doped layer on the trench top was 225 Ω/□, while the average value on the sidewall was 436 Ω/□. The variation of sheet resistance along trench sidewall is shown in fig. 4. The area near the trench bottom was doped heavier than the area near the trench top. This could be understood as a result of ion multi-reflection from trench sidewalls and bottom. It is well known that when an incident ion collides with a surface at a glancing angle, the reflection probability is high. A large portion of the ion beam hitting the sidewall was presumably reflected, leaving the top part of the sidewall lightly doped. The large dose on the lower sidewall can be attributed to reflected ions from the trench bottom as well as from the top part of the sidewalls

With our experimental PIII systems, the standard deviation of sheet resistance across a two inch wafer was about 40% with a pulsed bias. The uniformity was poorer in the dc mode, especially when the bias voltage was high. A much better uniformity is expected with the recently constructed ten inch reactor in UC Berkeley.

4. Conclusions

We have demonstrated conformal doping of boron in high aspect ratio Si trenches using PIII. A uniformly doped p^+ layer all around the sidewalls and bottom of trenches of aspect ratio 6 : 1 was observed with scanning electron microscopy after junction staining. To test the limit of PIII for conformal doping, the macroscopic trench results showed that the average sheet resistance of trench sidewalls was about twice of that of the trench top and the deviation of the sheet resistance of sidewall was ±60% with an aspect ratio of 25 : 1.

Acknowledgements

This work was supported by Applied Materials, Inc. and a grant from the California State MICRO program.

References

[1] R. Kakoschke, H. Binder, S. Rohl, K. Masseli, I.W. Rangelow, S. Saler and R. Kassing, Nucl. Instr. and Meth. B21 (1987) 142.

[2] G. Fuse, H. Ummoto, S. Okanaka, M. Wakabayashi, M. Fukumoto and T. Ohzone, J. Electrochem. Soc. 133 (1986) 996

[3] G. Fuse, K. Tateiwa, S. Odanaka, T. Yamada, I. Nakao, H. Shimoda, O. Shippou, M. Fuumoto, J Yasui, Y. Naito and T. Ohzone, in: 19th Conf. on Solid State Devices and Materials, Tokyo, 1987, p. 11

[4] G Fuse, H. Ogawa, K Tamura, Y. Naito and H. Iwasaki, Appl. Phys Lett 54 (1989) 1534.
[5] R E. Kaim, Solid State Technol 33 (1990) 103.
[6] M.A. Lieberman, J Appl Phys. 66 (1989) 2926.
[7] J.R Conrad, J L. Radtke, R A. Dodd, F J Worzala and N C Tran, J Appl. Phys 62 (1987) 4591.
[8] B Mizuno, I Nakayama, N Aoi, M Kubota and T Komeda, Appl Phys Lett. 53 (1988) 2059
[9] H Wong, X.Y Qian, D Carl, N.W Cheung, M A. Lieberman, I G Brown and K M. Yu, MRS Proc 147 (1989) 91.
[10] X Y Qian, H Wong, D. Carl, N.W Cheung, M.A. Lieberman, I G Brown and K.M Yu, Proc. Symp. on Ion Implantation and Dielectrics for Elemental and Compound Semiconductors, vol 90-13 (Electrochemical Soc., 1990) p. 268.
[11] V. Vahedi, M.A. Lieberman, M A. Alves, J.P. Verboncoeur and C.K. Birdsall, A Collisional Model for Plasma Immersion Ion Implantation, 1990 IEEE Int. Conf. on Plasma Science (Oakland, CA, 1990) p. 185.
[12] X Y Qian, D Carl, J Benasso, N.W Cheung, M A. Lieberman, I G. Brown, J.E. Galvin, R A. MacGill and M.I. Current, these Proceedings (8th Int Conf on Ion Implantation Technology, Guildford, UK, 1990) Nucl Instr and Meth. B55 (1991) 884.
[13] X Y Qian, N.W. Cheung, M.A. Lieberman, M I. Current, P K. Chu, W L Harrington, C.W. Magee and E.M Botnick, ibid , p 821

Nuclear Instruments and Methods in Physics Research B55 (1991) 902–904
North-Holland

Ion projection lithography process on dry resist

A.I. Kholopkin, M.N. Lyakhov, D.A. Pankratenko and V.V. Simonov
Scientific and Industrial Amalgamation "Vacuummashpribor", Nagorny Proezd 7, Moscow 113105, USSR

A.F. Vyatkin
Institute of Microelectronics Technology and High Purity Materials, USSR Academy of Sciences, Chernogolovka 142432, Moscow District, USSR

The ion projection lithography processes have been studied on octasilsesquioxanes-based dry resists. The investigations were carried out on an experimental ion projection lithography system in the gallium ion dose range of 10^{12}–10^{14} ions/cm^2. Resist thickness was varied from 0.01 to 0.3 μm. It is shown that the lithography process offers prospects for further developments for VLSI technology.

1. Introduction

Ion beam lithography (IBL) offers new prospects for submicron device fabrication [1]. It has been developed in three forms: focused (FIBL) [2], masked (MIBL) [3], and ion projection lithography (IPL) [4]. FIBL has a very low throughput capability and can be used for mask repairing and special device fabrication. MIBL and IPL have relatively high throughput capabilities and can be used for VLSI circuit manufacturing. Further progress in VLSI microfabrication technology can be achieved by the application of the IPL process on dry resists. This process can be realized fully automatically and could lead to cost-effective VLSI production. The logical extension of IPL is ion projection implantography (IPI), which is a process of local ion implantation in the IC construction materials to form areas with desirable geometrical sizes and physical and chemical properties. However, IPI can only find applications in the resistless technology of VLSI manufacturing once a number of fundamental and technical problems have been solved.

This paper describes the results of investigations of the MIBL process on dry negative resists.

2. Exposure apparatus

Exposure was carried out with an ion beam condenser lens system which was part of an IPI machine. The ion beam condenser system consists of a liquid metal ion source, an ion optical system for forming a parallel homogeneous ion beam, and an arrangement for precise conjunction of silicon stencil mask and resist coated wafer. It has the following specifications: ion species Ga^+, Al^+, P^+, B^+; ion energy 5–20 keV; ion current 0.1–50 μA; ion beam divergence less than 10^{-4}; image field diameter 60 mm; dose non-uniformity less than 3.0%; distance between mask and wafer 5–1000 μm.

For preparing silicon stencil masks a special technology based on electron beam lithography methods, ion implantation, dry selective etching, and vacuum metallization was used. The stencil masks had the following characteristics: thickness 0.5–4.5 μm; field size 45 × 45 mm^2; vertical absorber wall profiles; size of elements (openings) up to 0.5 μm; mismatching of different masks less than 0.3 μm; ion resistance up to 10^{19} ions/cm^2.

3. Two-level resist system for MIBL

To perform the MIBL process on dry resist it is desirable to use a two-level resist system. The first layer is a thick organic resist which flattens out surface features. It is a radiation insensitive layer. The second layer is a uniform thin radiation sensitive dry resist. The pattern is transferred to this top resist which can be developed normally. A final reactive ion etching in O_2 etches the thick nonuniform organic resist layer under the mask of the dry resist. This dry etching procedure is highly anisotropic so the original pattern is transferred linearly through the thick resist.

The first layer of polystyrene was deposited on a silicon wafer by plasma enhanced polymerization of styrene from He and CCl_4 gas mixture under 0.5 Torr

0168-583X/91/$03.50 © 1991 – Elsevier Science Publishers B.V. (North-Holland)

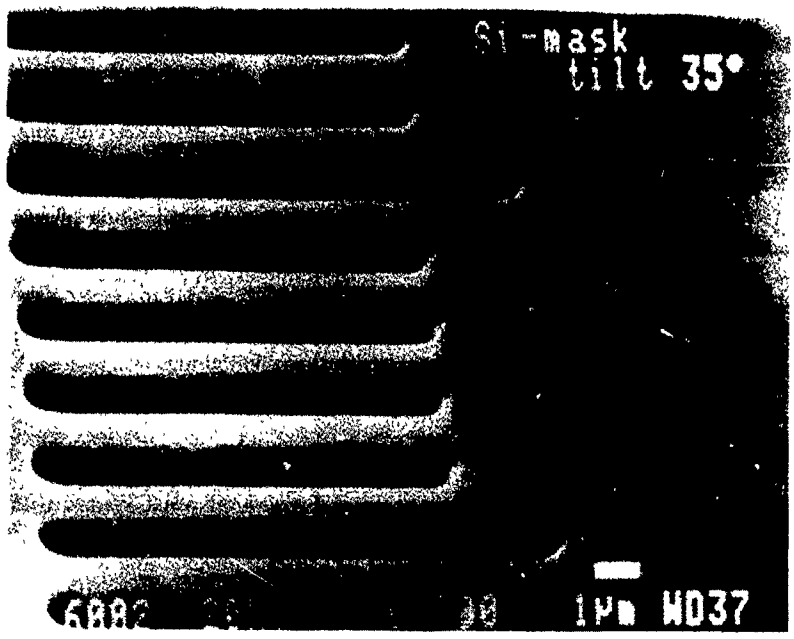

Fig 1. SEM photograph of a silicon stencil mask with 1 0 μm openings.

and 100 W rf power conditions Reactive ion etching was carried out in O_2 gas under 2×10^{-2} Torr and 500 W rf power conditions.

The dry negative resist, which belongs to the class of octasilsesquioxanes, was deposited in a specially designed module by vacuum thermal evaporation at 150 °C The module of dry resist deposition had the following characteristics: resist thickness 0.01–0.6 μm, thickness nonuniformity 5%, wafer diameter up to 100 mm, particle contamination in the range of 0.05–0.3 parti-

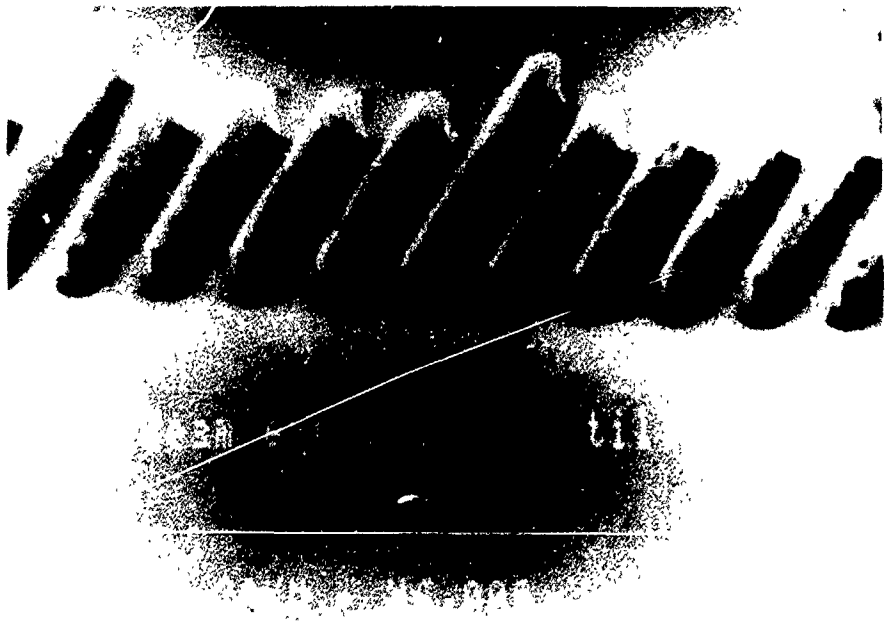

Fig 2 SEM photograph of $1\,0 \times 10\ \mu m^2$ patterns formed in a 1 0 μm thickness two-level resist system

cles/cm^2 with diameter more than 0.3 μm. Development of the dry resist was carried out in a specially designed module by heating the exposed wafers in vacuum at 107°C. All process modules could be integrated in one line of dry electron or ion lithography with a vacuum wafer transport system.

4. Experimental results

In the experiments with dry resists, the dry resist thickness was varied from 0.01 to 0.3 μm. In the experiments with a two-level resist system, the thickness of the bottom layer was varied in the 0.3–3.0 μm range, and the thickness of the upper dry resist layer was about 50 nm. The dry resist was exposed to about 20 keV accelerated gallium ions at 3.5–10.0 μA current and in the 10^{12}–2×10^{14} ions/cm^2 dose range. Exposure was carried out through a silicon stencil mask with a test pattern in the form of rectangular 1.0×10.0 μm^2 holes with a 2.0 μm period over the 40×40 mm^2 work field (fig. 1).

The first experiments have shown that the thickness of the exposed and polymerized dry resist layer did not exceed 50 nm. During the development of thick dry resist (more than 100 nm) the polymerized patterns became separated from the silicon wafer. This is the main reason why two-level resist systems were used in the further experiments. Fig 2 shows a scanning electron microscope observation of 1.0 μm width lines and spaces fabricated in a 1.0 μm thick two-level resist system. The measured dry resist sensitivity is about 8×10^{12} ions/cm^2. In the 8×10^{12}–4×10^{13} ions/cm^2 dose range, the two-level resist patterns repeat patterns on the silicon stencil mask completely. With increase in dose from 4×10^{13} ions/cm^2 to 2×10^{14} ions/cm^2, the pattern dimensions increase by about 0.1 μm. In comparison with electron projection lithography, MIBL does not require the application of any additional treatment after dry resist development because of the absence of scattering electrons. The two-level resist system ensures the manufacture of thick polystyrene patterns up to 3.0 μm thickness under a dry resist mask with a thickness of about 30–50 nm.

5. Conclusions

A two-level resist system with 50 nm thick upper layer of dry negative resist, which belongs to the class of octasilsesquioxanes, and a lower 0.3–3.0 μm thick polystyrene layer can be used in fully dry MIBL and IPL processes for manufacturing submicron VLSI devices

References

[1] W.L. Brown, T., Venkatesan and A Vagner, Nucl Instr and Meth. 191 (1981) 157
[2] H Kuwano, J Appl Phys 55 (1984) 1149.
[3] J.L Bartlet, Solid State Technol. (May 1986) 215
[4] G Stengl, H Loschner, W. Maurer and P Wolf, J Vac Sci. Technol B4 (1986) 194.

Author Index

Abril, I., see Jimenez-Rodriguez, J.J 681
Adibi, B., see Leung, S. 35
Adibi, B., see Wauk, M.T. 413
Adibi, B , see Crook, J.P 593
Agawa, Y., M. Takai, S. Namba, T. Uchiyama, R. Fukui and H. Yamakawa, A 500 keV ion accelerator with two types of ion source 502
Aitken, D , The phased linear scanner 517
Alderman, J., see Reeson, K.J. 718
Alves, E , M.F Da Silva, J.C. Soares, A.A. Melo, J May, V. Hašlar, P Seidl, U Feuser and R. Vianden, Expitaxial regrowth and lattice location of indium implanted in arsenic-preamorphized silicon 580
Amemiya, K., K. Tokiguchi, Y. Hakamata and N. Sakudo, Ion beam injection system for a variable energy RFQ accelerator 339
Angel, G., N. Meyyappan, F. Sinclair and W. Tu, Charging measurement and control in high-current implanters 211
Angel, G , see Nasser-Ghodsi, M 398
Anjum, M , G S Sandhu, S Cherekdjian and W Weisenberger, Thermal wave characterization of silicon implanted with MeV phosphorus ions 266
Armour, D.G., see Gordon, J.S. 314
Armour, D G., see Bousetta, A. 565
Asari, M , see Hirakimoto, A. 493

Bachmann, T , see Wesch, W 625
Badenes, G , see Bausells, J. 666
Baisse, B , see Lamure, J M. 826
Balek, D , see McIntyre, E 473
Bartoš, M , see Hazdra, P. 637
Bartsch, H., see Skorupa, W. 224
Battaglia, A , F Priolo, C. Spinella and E Rimini, Evolution of low-fluence heavy-ion damage in Si under high energy ion irradiation 611
Bausells, J , see Montserrat, J 261
Bausells, J., G Badenes and E. Lora-Tamayo, Calculation of channeling effects in ion implantation 666
Baxter, G , see Kenny, M.J. 522
Belgorokhov, A.I , A.B Danilin, Yu.N Erokhin, A.A. Kalinin, V N Mordkovich, V.V. Saraikin and I.I Khodos, The peculiarities of the new phase formation by O^+ ion implantation into silicon under thermo-ionization excitation 750
Benasso, J., see Qian, X.Y 884
Bergholz, W., see Kolbesen, B.O. 124
Bernhardt, D , see Nasser-Ghodsi, M. 398
Black, T., see Lundquist, P 243
Boisseau, P , see McIntyre, E. 473
Bond, P , D. Duckworth, R.G Elliman, R Henshaw, S.T Johnson, M.C Ridgway, R P. Thornton, J.S Williams, P. Byers and D J. Chivers, A versatile WIBS 200 kV ion implanter for materials modification . 511
Booker, G.R., see Robinson, A K. 555
Booker, G.R., see Reeson, K.J. 718
Borwn, I.G., see Qian, X.Y. 893
Botnick, E.M., see Qian, X.Y 821
Bousetta, A., see Gordon, J.S 314
Bousetta, A., J.A Van den Berg, R. Valizadeh, D G Armour and P.C. Zalm, Ultra low energy (100–200 eV) boron implantation into crystalline and silicon-preamorphized silicon 565
Bowe, T., see Nasser-Ghodsi, M. 398
Brennan, R , see Qian, X.Y. 898
Brown, D.A , P. Sferlazzo and J.F O'Hanlon, Possible mechanisms for particle transport in ion implanters . . 348

Brown, I.G., M.R. Dickinson, J.E. Galvin, X. Godechot and R A MacGill, A broad-beam, high-current metal-ion implantation facility 506
Brown, I.G., see Qian, X.Y. 884
Brown, I.G., see Qian, X.Y. 888
Bruel, M., see Molle, P. 860
Budishevsky, V.S., see Yankelevich, E.B 880
Bulle-Lieuwma, C W.T., see Dekempeneer, E H A. 769
Buravlyov, A.V., A.F. Vyatkin, V.K. Egorov, V.V. Kireiko and A P. Zuev, Some properties of amorphous silicon produced by helium ion implantation 642
Burte, E., see Ye, M. 773
Bussmann, U., see Robinson, A.K. 555
Bussmann, U., see Zhang, J.P. 691
Bussmann, U., see Castle, J.E. 697
Bussmann, U., see Hatzopoulos, N. 734
Bussmann, U , A K. Robinson and P.L.F. Hemment, Energy and dose dependence of silicon top layer and buried oxide layer thickness in SIMOX substrates 852
Bussmann, U., P.L.F. Hemment, A.K. Robinson and V V. Starkov, Oxygen implantation through patterned masks· a method for forming insulated silicon device islands while maintaining a planar wafer surface . . 856
Byers, P., see Bond, P. 511

Capizzi, S., see Rainieri, V. 661
Carl, D., see Qian, X Y 884
Carl, D., see Qian, X Y 888
Carnera, A , see La Ferla, A. 561
Carnera, A., see Rainieri, V 661
Castle, J.E., see Zhang, J P 691
Castle, J.E , H.D. Liu, J.F. Watts, J.P. Zhang, P L.F Hemment, U Bussmann, A K Robinson, S.M Newstead, A R Powell, T E. Whall and E.H C Parker, An investigation of $Si_{0.5}Ge_{0.5}$ alloy oxidation by high dose oxygen implantation 697
Cerva, H , see Küsters, K H. 9
Cerva, H , see Kolbesen, B O 124
Chang, H -C. and W -S Chen, Effects of P^+-implanted poly-Si electrodes on the gate dielectric characteristics of thin oxides 216
Chao, W Y., see Chu, C.H 193
Chater, R.J., J A Kilner, K J. Reeson, A K Robinson and P L F Hemment, High-dose oxygen implantation into silica 686
Chater, R J., see Reeson, K J. 718
Chen, L.J , see Chu, C.H 193
Chen, L.J., see Hsu, S N 620
Chen, L.J., see Hsu, C T 758
Chen, L.J., see Nieh, C W. 831
Chen, W -S , see Chang, H.-C 216
Cherekdjian, S and W. Weisenberger, Energetic neutral contamination in modern high-current implanters . 30
Cherekdjian, S., see Lukaszek, W. 143
Cherekdjian, S. and W Weisenberger, Daily 2×10^{12} monitoring of an ion implanter 178
Cherekdjian, S., see Anjum, M. 266
Cheung, N W., Plasma immersion ion implantation for ULSI processing (*Invited paper*) 811
Cheung, N W., see Qian, X Y. 821
Cheung, N W., see Qian, X Y 884
Cheung, N W., see Qian, X Y 888
Cheung, N W., see Qian, X.Y 893
Cheung, N W., see Qian, X Y 898
Chivers, D.J., see Bond, P 511
Chotokudani, M , see Kawai, T. 4
Christensen, K., see Reeson, K J. 718
Chu, C H , E.L Tsai, W.Y. Chao and L.J Chen, Annealing behaviors of residual defects in high-dose BF_2^+-implanted (001)Si under different implantation conditions 193
Chu, P.K., see Qian, X.Y. 821
Ciavola, G., see La Ferla, A. 561
Claverie, A., see Marou, F. 655
Cleff, B., see Gottdang, A. 310

Clissold, R.A., see Kenny, M.J. 522
Coffa, S., see Poate, J.M. 533
Cole, P.D , G.M. Crean, J. Lorenz and L. Dupas, Comparison of models for the calculation of ion implantation moments of implanted boron, phosphorus and arsenic dopants in thin film silicides 763
Cordts, B., see Wittkower, A 842
Cornet, A., see Pérez, A. 714
Crean, G.M., see Cole, P.D 763
Criddle, A.J., see Reeson, K.J. 718
Crook, J P., M.I. Current, B. Adibi, S. Leung and L.A. Larson, Custom profiles by automated multi-step implantation 593
Cubina, A. and M. Frost, Effects of molybdenum contamination resulting from BF_2 implantation 160
Cummings, J J. and D.T. Enloe, A RGA study of the cross-contamination of dopant species and low level impurities and the use of the RGA as a process monitor in a Varian 180XP 55
Current, M., see Wauk, M.T 413
Current, M I., T. Guitner, N. Ohno, K. Hurley, W.A Keenan, W Johnson, R J. Hillard and C. Jeynes, Monitoring the micro-uniformity performance of a spinning disk implanter 173
Current, M I., see Crook, J.P. 593
Current, M.I., see Qian, X.Y 821
Current, M.I., see Qian, X Y. 884
Current, M I , see Qian, X.Y 888
Current, M.I., see Qian, X Y 898
Custer, J.S , see Poate, J M. 533

Da Silva, M F , see Alves, E 580
Damilin, A B , see Belgorokhov, A I. 750
Dart, A., see McIntyre, E 473
Davies, J A., see Williams, J.S. 602
De Veirman, A , see Spraggs, R.S 836
Dekempeneer, E H A., J.J.M. Ottenheim, D E.W Vandenhoudt, C.W T Bulle-Lieuwma and E G.C Lathouwers, Ion beam synthesis of cobalt silicide. effect of implantation temperature 769
Denholm, A S , see McIntyre, E 473
Diamond, M , see Tami, T 408
Dickinson, M R , see Brown, I G. 506
Dixit, K., see Nasser-Ghodsi, M. 398
Doherty, B., see Tami, T 408
Dolan, R , see Wittkower, A 842
Donovan, E , see Poate, J.M 533
Downey, D F. and R.B Liebert, Control of BF_2 dissociation in high-current ion implantation 49
Downey, D.F , see Liebert, R B. 71
Downey, D.F., see Satoh, S 77
Duckworth, D., see Bond, P 511
Dupas, L , see Cole, P.D 763
Dvurechenskii, A V , see Karanovich, A A 630
Dykstra, J P , A M Ray and R B. Simonton, A versatile ion implanter for planar and 3D device construction . 478
Dykstra, J.P., see Ray, A.M 488

Eddy, R., see Yarling, C 104
Eddy, R J , see Taylor, M.C. 20
Egorov, V.K., see Buravlyov, A.V. 642
Eich, K., see Gottdang, A. 310
Elliman, R G , see Bond, P 511
Elliman, R G., see Thornton, R P. 598
Elliman, R.G , see Williams, J.S 602
Enloe, D T., see Cummings, J.J 55
Erokhin, Yu.N , see Belgorokhov, A.I 750
Evans, E , see Liebert, R.B. 71

Fairbairn, K.P , see Jaffe, P.R. 448
Farley, M., see Nasser-Ghodsi, M. 398
Felch, S.B , see Satoh, S. 77
Felch, S B., S. Mehta, S Kikuchi and S Kitahara, Device charge-to-breakdown studies on a high-current implanter 82

Felch, S.B., see Nee, R. ... 137
Ferla, G., see La Ferla, A. ... 561
Ferla, G., see Rainieri, V. ... 661
Feuser, U., see Alves, E. ... 580
Fiegl, B., see Kolbesen, B.O. ... 124
Fishkin, B., see Leung, S. ... 35
Foley, M., see Nasser-Ghodsi, M. ... 398
Foley, M., see Nasser-Ghodsi, M. ... 469
Freeman, J.H., Ion beams in retrospect (*Special invited talk*) ... ix
Fried, M., T. Lohner, E. Jároli, C. Hajdu and J. Gyulai, Nondestructive determination of damage depth profiles in ion-implanted semiconductors by multiple-angle-of-incidence single-wavelength ellipsometry ... 257
Frost, M., see Cubina, A. ... 160
Fujishita, N., K. Noguchi, S. Sasaki and H. Yamamoto, A high-resolution beam profile measuring system for high-current ion implanters ... 90
Fujita, J., see Sasao, M ... 318
Fujita, J., see Maeno, S. ... 359
Fujiwara, S., see Tanjyo, M. ... 86
Fukao, K., see Ishiwara, H. ... 585
Fukui, R., see Agawa, Y. ... 502
Furuta, H., see Yokota, K. ... 633

Galvagno, G., see Rainieri, V. ... 661
Galvin, J.E., see Brown, I.G. ... 506
Galvin, J.E., see Qian, X.Y. ... 884
Galvin, J.E., see Qian, X.Y. ... 893
Gan, K.J., see Su, Y.K. ... 794
Gasparotto, A., see La Ferla, A. ... 561
Gelsdorf, F., see Kolbesen, B.O. ... 124
Ghibaudo, G., see Said, J. ... 576
Giles, A.D. and A. van de Steege, Ion implantation challenges in the drive towards 65 Mb and 256 Mb memory cell type devices (*Invited paper*) ... 379
Glavish, H., see McIntyre, E. ... 473
Godechot, X., see Brown, I.G. ... 506
Godechot, X., see Qian, X.Y. ... 893
Gorbatov, Yu.B., A.F. Vyatkin and V.I. Zinenko, A low-energy fast-atom beam source ... 328
Gordon, J.S., A. Bousetta, J.A. van den Berg, D.G. Armour, R. Kubiak and E.H.C. Parker, A silicon MBE-compatible low-energy ion implanter ... 314
Gordon, K.C., see Leung, K.N. ... 94
Gotoh, Y., see Ishikawa, J. ... 343
Gottjang, A., K. Eich, A. Hassenbürger, W.H. Schulze, B. Cleff, D.J.W. Mous, R. Koudijs, G.F.A. van de Walle and J. Politiek, A dual source low-energy ion implantation system for use in silicon molecular beam epitaxy ... 310
Götz, G., see Wesch, W. ... 625
Götz, G., see Wendler, E. ... 789
Grant, J., see Nasser-Ghodsi, M. ... 398
Gras-Marti, A., see Jimenez-Rodriguez, J.J. ... 681
Griepentrog, M., R.-A. Noack, M. Rosengarten and W. Schneider, Preparation of W–Th films by ion beam sputtering ... 782
Grötzschel, R., V.A. Kagadey, N.I. Lebedeva and D.I. Proskurovsky, Sublimation and diffusion of arsenic implanted into silicon at rapid electron beam annealing ... 573
Guan Anmin, see Jiang Xinyuan ... 778
Guerra, M., see Wittkower, A. ... 842
Guitner, T., see Current, M.I. ... 173
Gusella, F., see Lamure, J.M. ... 826
Gwilliam, R., see Hašlar, V. ... 569
Gwilliam, R.M., see Spraggs, R.S. ... 836
Gyulai, J., see Fried, M. ... 257

Haga, Y., see Takaoka, G.H. ... 873
Hagemann, F., see Wesch, W. ... 625
Hagiwara, H., see Hara, T. ... 250
Hahn, S.K., see Hara, T. ... 250

Hajdu, C., see Fried, M. . . . 257
Hakamata, Y., see Amemiya, K. . . . 339
Hara, T., H. Hagiwara, R. Ichikawa, W.L. Smith, C. Welles, S.K. Hahn and L. Larson, Monitoring of dose in low dose ion implantation . . . 250
Harrington, W.L., see Qian, X.Y. . . . 821
Harriott, L.R., The technology of finely focused ion beams (*Invited paper*) . . . 802
Harris, M., Advances in the Extrion 1000 and XP Series high-current ion implantation systems . . . 428
Hashimoto, S., see Shibuya, T. . . . 305
Hashimoto, S., see Shibuya, T. . . . 364
Hashimoto, Y., see Yamada, I. . . . 876
Hašlar, V., P. Seidl, P. Hazdra, R. Gwilliam and B. Sealy, Shallow junction formation by dual Ge/B, Sn/B and Pb/B implants . . . 569
Hašlar, V., see Alves, E. . . . 580
Hašlar, V., see Hazdra, P. . . . 637
Hassenbürger, A., see Gottdang, A. . . . 310
Hatzopoulos, N., U. Bussmann, A.K. Robinson and P L F. Hemment, Buried insulator formation by nitrogen implantation at elevated temperatures . . . 734
Hayden, C., see McIntyre, E. . . . 473
Hazdra, P., see Hašlar, V. . . . 569
Hazdra, P., V. Hašlar and M. Bartoš, The influence of implantation temperature and subsequent annealing on residual implantation defects in silicon . . . 637
Heft, A., see Wesch, W. . . . 625
Heinonen, A., see Mehta, S. . . . 457
Hemment, P.L.F., see Robinson, A K . . . 555
Hemment, P.L.F., see Chater, R.J. . . . 686
Hemment, P.L.F., see Zhang, J P. . . . 691
Hemment, P.L.F., see Castle, J.E. . . . 697
Hemment, P.L.F., see Starkov, V V. . . . 701
Hemment, P L F., see Lu Diantong . . . 705
Hemment, P.L F., see Pérez, A . . . 714
Hemment, P.L.F., see Yu, Y. . . . 730
Hemment, P.L.F., see Hatzopoulos, N. . . . 734
Hemment, P.L.F., see Zheng Lirong . . . 754
Hemment, P.L.F., see Bussmann, U . . . 852
Hemment, P.L.F., see Bussmann, U. . . . 856
Henshaw, R., see Bond, P. . . . 511
Hill, C. and P. Hunt, Ion implantation in bipolar technology (*Invited paper*) . . . 1
Hillard, R.J., see Current, M.I. . . . 173
Hirai, K., see Kinomura, A. . . . 866
Hirakimoto, A., H. Nakanishi and M. Asari, The MeV ion implantation system "RFQ-1000" and its applications . . . 493
Hiramatsu, T., see Kawai, T . . . 443
Hodul, D., see Keenan, W.A . . . 269
Holden, S., see Nasser-Ghodsi, M . . . 398
Holden, S., see Nasser-Ghodsi, M . . . 469
Holmes, A.J.T. and G. Proudfoot, Negative-ion sources for ion implantation . . . 323
Homewood, K.P., see Pérez, A. . . . 714
Horvath, J and S. Moffatt, Maximization of DRAM yield by control of surface charge and particle addition during high dose implantation . . . 154
Howard, K., Implant uniformity evaluation using a Varian/Extrion scan compensator module on an electrostatic scanning ion implanter . . . 202
Hsu, C.T., C.J. Ma and L.J. Chen, Radiation damage in As^+ implanted $TiSi_2$ films . . . 758
Hsu, S.N. and L.J. Chen, Annealing behavior of dislocation loops near the projected ion range in high-dose As^+- and P^+-implanted (001) Si . . . 620
Huang, J., see Qian, X.Y. . . . 888
Hucknall, D.J. and M. Kuhn, Vacuum system design for ion implanters . . . 439
Hunt, P., see Hill, C. . . . 1
Hurley, K., see Current, M.I. . . . 173
Hurley, K., see Taylor, M. . . . 725
Hwang, J.S., see Su, Y.K. . . . 794

Ichikawa, R., see Hara, T. 250
Inami, H., Y. Inouchi, H Tanaka, T Yamashita, K. Matsunaga and K. Matsuda, Development of a high current and high energy metal ion beam system 370
Inouchi, Y., see Inami, H. 370
Ishihara, S., see Yokota, K. 633
Ishii, S., Improvement of an ECR multicharged ion source 296
Ishikawa, J., H. Tsuji and Y. Gotoh, Milliampere metal ion beam formation using multipoint emission by an impregnated-electrode-type liquid-metal ion source 343
Ishikawa, J., see Takaoka, G.H. 873
Ishiwara, H. and K. Fukao, Effect of SiN_x coating in lateral solid phase epitaxy of implanted amorphous Si films 585
Isobe, M., see Nagai, N. 393
Ito, H. and N R White, Computer modelling for ion-beam system design 527
Itoh, Y., see Yamada, I. 876
Izumi, K., see Nakashima, S. 847

Jackson, D., see Lundquist, P. 243
Jacobson, D.C., see Poate, J M. 533
Jaffe, P.R. and K.P Fairbairn, System and process enhancements of the Applied Materials Precision Implant 9200 448
Janssen, K T F, see Schreutelkamp, R.J 615
Jároli, E, see Fried, M. 257
Jaussaud, C., see Lamure, J.M. 826
Jaussaud, C, see Molle, P. 860
Jeynes, C., see Current, M.I. 173
Jha, N., see Qian, X. 898
Jiang Xinyuan, see Znao Qihua 374
Jiang Xinyuan, Zhao Qihua, Guan Anmin, Shao Tianhao and Lin Chenglu, The application of a 600 keV heavy ion implanter 778
Jimenez, J., see Pérez, A 714
Jimenez-Rodriguez, J.J., I. Abril, J.A Peinador and A Gras-Marti, Transport-theoretical studies of static and dyanmic recoil mixing 681
Jin Yuqing, see Li Jinghua 746
Johnson, S.T., see Bond, P 511
Johnson, W., see Current, M I 173
Johnson, W.H., W.A. Keenan and T. Wetteroth, Gauge-capability study of ion-implant monitors . 148
Johnson, W.H, see Keenan, W A. 166
Johnson, W.H., see Keenan, W.A 230
Johnson, W.H., see Keenan, W A. 269
Johnson, W H, see Larson, L.A 275
Johnston, S.T., see Williams, J.S. 602
Juang, F.S., see Su, Y.K. 794

Kachurin, G A., see Karanovich, A A 630
Kagadey, V A, see Grötzschel, R. 573
Kaim, R.E., see Van der Meulen, P.F.H M 45
Kaim, R.E. and P.F H.M van der Meulen, The EXTRION 220 parallel scan magnet 453
Kaim, R.E., see Schreutelkamp, R J. 615
Kalinin, A.A, see Belgorokhov, A I. 750
Kamenitsa, D.E., see Simonton, R.B. 39
Kamenitsa, D E., see Simonton, R B. 188
Kaminski, L., see McIntyre, E 473
Karanovich, A A., A.V. Dvurechenskii, I.E. Tyschenko and G.A Kachurin, Centers of spin-dependent recombination in structures formed by N^+ ion implantation into Si 630
Kase, M., M. Kimura, Y. Kikuchi, H Mori and T. Ogawa, BF_2^+ implantation in predamaged Si with Ge^+ or Si^+ at doses lower than amorphization 550
Kato, K, M. Takai, S. Namba, R. Schork and H. Ryssel, Raman measurement of local SOI structure by SIMOX 710
Kato, K., see Takai, M. 870
Kawai, T., see Nagai, N. 393
Kawai, T., M. Chotokudani, M. Naito, T. Hiramatsu, M. Sasaki, T. Sunouchi, Y. Nishigami, T. Matsumoto, M. Nakaya and M. Nakazawa, The Nissin PR-80A high current ion implantation system 443

Kawakami, H., see Nagai, N. 393
Keenan, W.A., see Johnson, W.H 148
Keenan, W.A., W.H. Johnson, L. Mantalas, L. Nguyen and L.A. Larson, A micro-uniformity test structure . . 166
Keenan, W.A., see Current, M.I. 173
Keenan, W.A., W.H. Johnson and C B. Yarling, Comparison of modern uniformity-mapping techniques 230
Keenan, W A., see Yarling, C.B. 235
Keenan, W A., W.H. Johnson, D. Hodul and D. Mordo, RTP temperature uniformity mapping 269
Keenan, W.A , see Larson, L.A. 275
Kenny, M.J., L.S Wielunski, M.D. Scott, R.A. Clissold, D Stevenson and G. Baxter, A universal sample manipulator with 50 kV negative bias 522
Khodos, I.I., see Belgorokhov, A.I. 750
Kholopkin, A.I., see Vyatkin, A.F. 386
Kholopkin, A.I., M N. Lyakhov, D.A. Pankratenko, V.V. Simonov and A F Vyatkin , Ion projection lithography process on dry resist 902
Kiang, M.H., see Qian, X.Y. 888
Kiang, M.H., see Qian, X.Y. 893
Kibi, Y , see Nagai, N. 393
Kikuchi, S., see Felch, S.B 82
Kikuchi, S , see Nee, R. 137
Kikuchi, Y., see Kase, M. 550
Kilner, J.A , see Robinson, A.K. 555
Kilner, J.A., see Chater, R.J. 686
Kilner, J.A., see Reeson, K.J. 718
Kimura, I , see Yokota, K 633
Kimura, M., see Kase, M. 550
Kinney, P , see Leung, S. 35
Kinomura, A , M Takai, K. Hirai and S. Namba, Channeling contrast analysis of local damage distributions induced by maskless implantation 866
Kireiko, V.V , see Buravlyov, A V 642
Kitahara, S., see Felch, S B. 82
Kitamoto, S., see Yamada, I. 876
Klein, K.M., see Simonton, R.B 39
Kögler, R., see Skorupa, W 224
Koike, H , see Sakudo, N 300
Kolbesen, B.O , W. Bergholz, H Cerva, B Fiegl, F Gelsdorf and G Zoth, Process-induced defects in VLSI (*Invited paper*) 124
Koudijs, R , see Gottdang, A. 310
Kröner, F , Knock-on of contaminants causing instabilities of transistor characteristics 198
Kubiak, R , see Gordon, J S. 314
Kuhn, M , see Hucknall, D.J 439
Kunkel, W B., see Leung, K.N 94
Küsters, K H , H.M. Mühlhoff and H Cerva, Application of ion implantation in submicron CMOS processes (*Invited paper*) 9
Kwok, C B , see Mathur, M S 671

La Ferla, A , E Rimini, A. Carnera, A. Gasparotto, G. Ciavola and G. Ferla, Measurements and applications of high energy boron implants in silicon 561
La Ferla, A , see Raineri, V. 661
Lamure, J.M., J. Margail, B Baisse, J F Michaud, A. Soubie, C. Pudda, F. Gusella and C Jaussaud, SIMOX-material quality in a semi-industrial production 826
Larson, L., see Hara, T. 250
Larson, L.A., M. Sakshaug and W. Weiner, The use of tertiarybutylarsine (TBA) and tertiarybutylphosphine (TBP) as liquid reagents for ion implantation 109
Larson, L.A., A survey of implant particulate process control and yield effects (*Invited paper*) 132
Larson, L.A , see Keenan, W.A. 166
Larson, L.A., see Yarling, C.B. 235
Larson, L A., W.A. Keenan and W.H. Johnson, Ion implant standard 275
Larson, L.A., see Crook, J P. 593
Lathouwers, E.G.C., see Dekempeneer, E.H.A. 769
Lebedeva, N.I., see Grötzschel, R 573
Lee, K., see Taylor, M. 725

LeMere, M., see Taylor, M. . . . 725
Leung, K.N., K.C. Gordon, W.B. Kunkel, C.M. McKenna, S.R. Walther and M.D. Williams, An electron-beam charge neutralization system for ion implanters . . . 94
Leung, S., B. Adibi, S. Moffat, B. Fishkin and P. Kinney, Real time, in situ particle monitoring of the Applied Materials PI9200 ion implanter . . . 35
Leung, S., see Crook, J.P. . . . 593
Li Jinghua, see Lin Chenglu . . . 742
Li Jinghua, Lin Chenglu, Lin Zhixing, Jin Yuqing and Zou Shichang, The effects of epitaxy and oxidation on the properties of SIMNI and SIMOX materials . . . 746
Li Xiaoqin, Lin Chenglu, Yang Genqin, Zhou Zuyao and Zhou Shichang, Near-surface damage created in silicon by BF_2^+ implantation . . . 589
Li, Y., see Robinson, A.K. . . . 555
Li, Y.H., see Thornton, R.P. . . . 598
Libby, B., see McIntyre, E. . . . 473
Lieberman, M.A., see Qian, X.Y. . . . 821
Lieberman, M.A., see Qian, X.Y. . . . 884
Lieberman, M.A., see Qian, X.Y. . . . 888
Lieberman, M.A., see Qian, X.Y. . . . 898
Liebert, R.B., see Downey, D.F . . . 49
Liebert, R.B., S. Satoh, B.O. Pedersen, D.F. Downey, T. Sakase and E. Evans, Control of metal contamination in the Varian Extrion 1000 ion implantation system . . . 71
Liebert, R.B., see Satoh, S. . . . 77
Lin, C., see Yu, Y. . . . 730
Lin, C., see Zhang, S. . . . 738
Lin Chenglu, see Zhao Qihua . . . 374
Lin Chenglu, see Li Xiaoqin . . . 589
Lin Chenglu, Li Jinghua, Zhang Shunkai, Yu Yuehui and Zou Shichang, SOI structure formed by 95 keV N_2^+ and N^+ implantation and epitaxial growth . . . 742
Lin Chenglu, see Li Jinghua . . . 746
Lin Chenglu, see Jiang Xinyuan . . . 778
Lin Zhixing, see Li Jinghua . . . 746
Lindsey, D., see Lukaszek, W. . . . 143
Liu, H.D., see Zhang, J.P. . . . 691
Liu, H.D., see Castle, J.E. . . . 697
Liu, X., see Yu, Y. . . . 730
Lohner, T., see Fried, M. . . . 257
Lora-Tamayo, E., see Montserrat, J. . . . 261
Lora-Tamayo, E., see Bausells, J. . . . 666
Lorenz, J., see Cole, P.D. . . . 763
Lu Diantong, Zheng Lirong, Wang Zhonglie and P.L.F. Hemment, The IR properties in SOI wafers formed by oxygen implantation into silicon . . . 705
Lu Diantong, see Zheng Lirong . . . 754
Lukaszek, W., R.K. Nahar, A. McCarthy, W. Weisenberger, S. Cherekdjian and D. Lindsey, Charging studies with "CHARM" . . . 143
Lundquist, P., S. Mehta, T. Black and D. Jackson, Techniques for dose matching between ion implanters . . . 243
Lyakhov, M.N., see Kholopkin, A.I. . . . 902

Ma, C.J., see Hsu, C.T. . . . 758
Ma, M., J.E. Mynard, B.J. Sealy and K.G. Stephens, A cold-hollow-cathode lateral-extraction Penning ion source . . . 335
MacGill, R.A., see Brown, I.G. . . . 506
MacGill, R.A., see Qian, X.Y. . . . 884
MacGill, R.A., see Qian, X.Y. . . . 893
Machida, K., see Yamada, I. . . . 876
Mack, M.E., see Renau, A. . . . 61
Mack, M.E., see O'Connor, J.P. . . . 207
Mack, M.E., see Tokoro, N. . . . 434
Maeno, S., M. Tanjyo, K. Tanaka and J. Fujita, Development of a four-electrode extraction system for a large area ion source with a wide range of operational conditions . . . 359
Maes, H.E., see Vanhellemont, J. . . . 183
Maeyama, Y., see Yamada, I. . . . 876

Magee, C.W., see Qian, X.Y. ... 821
Mantalas, L., see Keenan, W.A. ... 166
Margail, J., see Lamure, J.M. ... 826
Marou, F., A. Claverie, Ph. Salles and A. Martinez, The enhanced diffusion of boron in silicon after high-dose implantation and during rapid thermal annealing ... 655
Marsh, C.D., see Robinson, A.K. ... 555
Martinez, A., see Marou, F. ... 655
Mathur, M.S., J.S.C. McKee and C.B. Kwok, Molecular complexes on implanted surfaces: unenhanced surface Raman study ... 671
Matsuda, K., see Inami, H. ... 370
Matsumoto, T., see Kawai, T. ... 443
Matsunaga, K., see Inami, H. ... 370
May, J., see Alves, E. ... 580
McCarron, D., see Nasser-Ghodsi, M ... 469
McCarthy, A., see Lukaszek, W ... 143
McIntyre, E., D. Balek, P. Boisseau, A Dart, A.S. Denholm, H. Glavish, C. Hayden, L. Kaminski, B. Libby, N. Meyyappan, J. O'Brien, F. Sinclair and K. Whaley , Initial performance results from the NV1002 high energy ion implanter ... 473
McKee, J.S.C., see Mathur, M S. ... 671
McKenna, C.M., see Leung, K.N. ... 94
McKenna, C.M., see Mehta, S. ... 457
McOmber, J.I. and R.S. Nair, Development of a process to achieve residue-free photoresist removal after high-dose ion implantation ... 281
Mehta, S., see Taylor, M.C. ... 20
Mehta, S., see Van der Meulen, P.F H.M. ... 45
Mehta, S , see Felch, S.B. ... 82
Mehta, S., see Nee, R. ... 137
Mehta, S., see Lundquist, P. ... 243
Mehta, S., R F Outcault, C M. McKenna and A. Heinonen, Improved wafer charge neutralization system in Varian high current implanters ... 457
Melo, A.A., see Alves, E ... 580
Meyyappan, N., see Angel, G. ... 211
Meyyappan, N., see McIntyre, E. ... 473
Michaud, J.F , see Lamure, J.M. ... 826
Mihara, Y , K Niikura, O. Tsukakoshi and Y Sakurada, Parallel beam ion implanter· IPX-7000 ... 417
Milgate, R. and J Pollock, Particle contamination control in the EXTRION 220 ... 66
Moffatt, S., see Leung, S ... 35
Moffatt, S., see Horvath, J. ... 154
Mohadjeri, B , see Svensson, B G. ... 650
Molle, P., C. Jaussaud and M. Bruel, Nitrogen implantation for local oxidation (NILO) of silicon ... 860
Montserrat, J , J. Bausells and E. Lora-Tamayo, Limitations of the spreading resistance technique for ion implant profile measurements ... 261
Mooney, S., see Nasser-Ghodsi, M. ... 469
Morante, J.R., see Pérez, A. ... 714
Mordkovich, V.N., see Belgorokhov, A.I. ... 750
Mordo, D., see Keenan, W A. ... 269
Mori, H., see Kase, M. ... 550
Mous, D.J W., see Gottdang, A. ... 310
Mühlhoff, H.M., see Küsters, K.H. ... 9
Mynard, J.E , see Ma, M. ... 335

Nagai, N., Implant dose uniformity simulation program ... 253
Nagai, N , T Kawai, M Nogami, T Shin'yama, T. Yuasa, Y. Kibi, H. Kawakami, K. Nishikawa and M. Isobe, The Nissin NH-20SP medium-current ion implanter ... 393
Nahar, R.K., see Lukaszek, W. ... 143
Nair, R.S., see McOmber, J.I. ... 281
Naito, M., see Tanjyo, M. ... 86
Naito, M., see Kawai, T. ... 443
Nakanishi, H., see Hirakimoto, A. ... 493
Nakashima, S and K. Izumi, SIMOX wafers with low dislocation density produced by a 100 mA-class high-current oxygen implanter ... 847

Nakaya, M., see Kawai, T. 443
Nakazawa, M., see Kawai, T. 443
Namba, S , see Agawa, Y. 502
Namba, S., see Kato, K. 710
Namba, S., see Kinomura, A. 866
Namba, S., see Takai, M. 870
Namba, Y., see Yamada, I. 876
Nasser-Ghodsi, M., M. Farley, J. Grant, D. Bernhardt, M. Foley, S. Holden, T Bowe, C. Singer, K. Dixit and G. Angel, A high-current ion implanter system 398
Nasser-Ghodsi, M., D. McCarron, M. Foley, S. Holden, D. Veinbachs, S Mooney and S. Ward, Particulate performance for robotics-based wafer handing ion implant system 469
Natsuaki, N., see Yajima, Y. 607
Nee, R., S. Mehta, S.B. Felch and S. Kikuchi, Wafer charging study on a Varian 160 XP ion implanter with charge-sensitive devices 137
Newstead, S.M., see Zhang, J.P. 691
Newstead, S.M., see Castle, J.E. 697
Nguyen, L., see Keenan, W A. 166
Nieh, C.W. and L.J. Chen, Annealing behaviour of BF_2^+ implanted (001) and (111)Si inside miniature size oxide openings 831
Niikura, K., see Mihara, Y. 417
Nishigami, Y., see Kawai, T. 443
Nishikawa, K., see Nagai, N. 393
Nishimatsu, S., see Yajima, Y. 607
Noack, R.-A., see Griepentrog, M. 782
Nogami, M., see Nagai, N. 393
Noguchi, K., see Fujishita, N. 90

O'Brien, J , see McIntyre, E. 473
O'Brien, T., see Taylor, M 725
O'Connor, J.P , see Renau, A 61
O'Connor, J P , M.E. Mack, A. Renau and N Tokoro, The use of negative ions to enhance beam currents at low energies in an MeV ion implanter 207
O'Connor, J.P., see Tokoro, N 434
Ogata, S., see Tsukakoshi, O. 355
Ogawa, T., see Kase, M 550
O'Hanlon, J F , see Brown, D A. 348
Ohno, N., see Current, M.I 173
Olson, G L., see Poate, J.M 533
Opsal, J , see Taylor, M. 725
Ottenheim, J.J.M , see Dekempeneer, E.H A 769
Otto, G , see Posselt, M 220
Outcault, R.F , see Mehta, S 457
Outcault, R F , see Walther, S R. 465

Palmer, G R., see Williams, J.S 602
Pankratenko, D.A., see Kholopkin, A.I. 902
Park, C , see Simonton, R.B 39
Parker, E.H.C , see Gordon, J.S. 314
Parker, E H C., see Zhang, J P 691
Parker, E.H.C., see Castle, J E. 697
Pearson, P , see Reeson, K.J. 718
Pedersen, B O , see Liebert, R.B 71
Pedersen, B.O., see Satoh, S. 77
Peinador, J.A., see Jiménez-Rodriguez, J J. 681
Pérez, A., J. Portillo, A. Cornet, J. Jimenez, J.R. Morante, P.L.F. Hemment and K.P. Homewood, Raman scattering and photoluminescence analysis of SOI/SIMOX structures obtained by sequential implantation and annealing correlated with cross sectional TEM 714
Pfannenmüller, U., see Takai, M. 870
Pihl, T., see Van Berlo, W.H. 785
Pippins, M.W., A system and performance overview of the EXTRION 220 medium-current ion implanter . . . 423

Poate, J.M , S Coffa, D.C Jacobson, A. Polman, J.A. Roth, G.L. Olson, S. Roorda, W. Sinke, J.S Custer, M.O Thompson, F. Spaepen and E Donovan, Amorphous Si – the role of MeV implantation in elucidating defect and thermodynamic properties (*Invited paper*) 533
Politiek J., see Gottdang, A. . . . 310
Pollock, J., see Milgate, R. . . . 66
Polman, A., see Poate, J.M. . . . 533
Portillo, J., see Pérez, A. . . . 714
Posselt, M., E. Sobeslavsky and G. Otto, Investigation of backscattering and re-implantation during ion implantation into deep trenches . . . 220
Posselt, M , A new method to calculate range and damage distributions by direct numerical solution of Boltzmann transport equations . . . 676
Powell, A.R., see Zhang, J.P. . . . 691
Powell, A R., see Castle, J.E. . . . 697
Priolo, F , see Battaglia, A. . . . 611
Ploskurovky, D.I., see Grötzschel, R. . . . 573
Proudfoot, G., see Holmes, A J.T . . . 323
Pudda, C , see Lamure, J.M. . . . 826

Qian, X Y , N.W Cheung, M.A. Lieberman, M.I. Current, P.K Chu, W L Harrington, C W Magee and E.M. Botnick, Sub-100 nm p + /n junction formation using plasma immersion ion implantation . . . 821
Qian, X.Y , D Carl, J. Benasso, N W. Cheung, M.A. Lieberman, I G. Brown, J E. Galvin, R A. MacGill and M.I. Current, A plasma immersion ion implantation reactor for ULSI fabrication . . . 884
Qian, X.Y., M.H. Kiang, J. Huang, D. Carl, N.W. Cheung, M.A. Lieberman, I.G Brown, K M Yu and M.I. Current, Plasma immersion Pd ion implantation seeding pattern formation for selective electroless Cu plating . . . 888
Qian, X.Y , M.H. Kiang, N.W. Cheung, I.G Borwn, X. Godechot, J.E. Galvin, R.A. MacGill and K.M. Yu, Metal vapor vacuum arc ion implantation for seeding of electroless Cu plating . . . 893
Qian, X.Y , N.W Cheung, M.A Lieberman, R. Brennan, M.I. Current and N Jha, Conformal implantation for trench doping with plasma immersion ion implantation . . . 898

Raineri, V , see Schreutelkamp, R J. . . . 615
Rainieri, V., G Galvagno, E. Rimini, A La Ferla, S. Capizzi, A. Carnera and G Ferla, Channeling implants of boron in silicon . . . 661
Ray, A M , see Simonton, R.B. . . . 39
Ray, A.M , see Simonton, R B. . . . 188
Ray, A.M , see Dykstra, J.P . . . 478
Ray, A.M. and J.P. Dykstra, Beam incidence variations in spinning disk ion implanters . . . 488
Reeson, K J., see Robinson, A K. . . . 555
Reeson, K J., see Chater, R.J. . . . 686
Reeson, K J., A.J. Criddle, P. Pearson, R J. Chater, K Christensen, J. Alderman, G R Booker and J.A. Kilner, Microscope-spectrophotometric analysis to determine the origins of the colour variations on SIMOX wafers 718
Reeson, K J., see Spraggs, R.S. . . . 836
Renau, A , M.E. Mack, J.P. O'Connor and N. Tokoro, An analysis of vacuum effects on ion implanter performance . . . 61
Renau, A , see O'Connor, J.P . . . 207
Renau, A., see Tokoro, N. . . . 434
Ridgway, M.C., see Bond, P. . . . 511
Ridgway, M.C., see Williams, J S. . . . 602
Rimini, E., see La Ferla, A . . . 561
Rimini, E , see Battaglia, A . . . 611
Rimini, E , see Rainieri, V. . . . 661
Robinson, A K., C D. Marsh, U Bussmann, J.A. Kilner, Y. Li, I. Vanhellemont. K.J. Reeson, P.L.F Hemment and G R Booker, Formation of thin silicon films using low energy oxygen ion implantation . . . 555
Robinson, A.K., see Chater, R.J . . . 686
Robinson, A.K., see Zhang, J P. . . . 691
Robinson, A.K., see Castle, J.E. . . . 697
Robinson, A.K., see Hatzopoulos, N . . . 734
Robinson, A.K , see Bussmann, U. . . . 852
Robinson, A.K , see Bussmann, U. . . . 856
Roorda, S., see Poate, J.M. . . . 533
Rosengarten, M., see Griepentrog, M. . . . 782

Roth, J.A., see Poate, J.M. 533
Roussel, Ph., see Vanhellemont, J. 183
Ryssel, H., see Kato, K. 710
Ryssel, H., see Ye, M 773
Ryssel, H., see Takai, M. 870

Said, J , G. Ghibaudo, I. Stoemenos and P. Zaumseil, Thermal-annealing effects on the structural and electrical properties of heavy-ion-implanted silicon layers 576
Sakamoto, H., see Tanjyo, M. 86
Sakase, T., see Liebert, R.B. 71
Sakase, T , see Satoh, S. 77
Sakshaug, M , see Larson, L.A 109
Sakudo, N , H. Koike, T. Seki and K. Tokiguchi, An increased implant current by combining a long-slit microwave ion source with a converging lens 300
Sakudo, N., see Amemiya, K. 339
Sakurada, Y., see Mihara, Y. 417
Salles, Ph , see Marou, F. 655
Sandhu, G.S., see Anjum, M 266
Sandow, P., see Wittkower, A 842
Saraikin, V.V , see Belgorokhov, A.I. 750
Saris, F.W., see Schreutelkamp, R.J. 615
Sasaki, M., see Kawai, T 443
Sasaki, N , see Tsukakoshi, O. 355
Sasaki, S , see Fujishita, N. 90
Sasao, M., H. Yamaoka, M. Wada and J Fujita, Direct extraction of a Na^- beam from a sodium plasma . . . 318
Satoh, F., see Yamada, I. 876
Satoh, S , see Liebert, R.B. 71
Satoh, S., B.O. Pedersen, D.F. Downey, T. Sakase, R.B. Liebert and S.B Felch, Control of wafer charging on the Varian EXTRION 1000 ion implanter 77
Schmalz, K., see Skorupa, W 224
Schneider, W , see Griepentrog, M 782
Schork, R., see Kato, K. 710
Schreutelkamp, R.J , V. Raineri, F.W Saris, R.E Kaim, J.F. Westendorp, P F H.M. van der Meulen and K T F. Janssen , Channeling implantation of B and P in silicon 615
Schulte, W H., see Gottdang, A. 310
Scott, M.D., see Kenny, M J 522
Sealy, B., see Hašlar, V 569
Sealy, B.J , see Ma, M 335
Sealy, B J., see Tang , S 647
Sealy, B.J., see Spraggs, R S 836
Seidel, T.E., Implantation in the 1990s (*Invited paper*) 17
Seidl, P., see Hašlar, V 569
Seidl, P., see Alves, E. 580
Seki, T , see Sakudo, N 300
Sferlazzo, P., see Brown, D.A 348
Shao Tianhao, see Jiang Xinyuan 778
Shen, H , G. Yang, Z. Zhou and S Zou, Rapid thermal annealing of Mg^+ and P^+ implanted InP 798
Shibuya, T., S Hashimoto, E. Yabe and K. Takayama, Plasma cathode oxygen ion source 305
Shibuya, T., S Hashimoto, E. Yabe and K Takayama, Production of oxygen plasmas using radio-frequency magnetron-discharge 364
Shimizu, S., see Tsukakoshi, O. 355
Shin'yama, T , see Nagai, N. 393
Simonov, V V., see Vyatkin, A.F. 386
Simonov, V.V , see Kholopkin, A.I. 902
Simonton, R.B., D.E. Kamenitsa, A M. Ray, C. Park, K M Klein and A.F Tasch, Channeling control for large tilt angle implantation in Si ⟨100⟩ 39
Simonton. R.B., D.E Kamenitsa and A.M. Ray, Process control issues for ion implantation using large tilt angles 188
Simonton, R.B., see Dykstra, J.P. 478
Sinclair, F , Gate oxides in high curent implanters: how do they survive? (*Invited paper*) 115
Sinclair, F., see Angel, G. 211

Sinclair, F., see McIntyre, E. 473
Sinclair, F., Simulation of the geometrical characteristics of a mechanically scanned high current implanter . . 482
Singer, C., see Nasser-Ghodsi, M. 398
Sinke, W., see Poate, J.M. 533
Skorupa, W., R. Kögler, K. Schmalz and H. Bartsch, Proximity gettering by MeV-implantation of carbon: microstructure and carrier lifetime measurements 224
Smith, W.L., see Hara, T. 250
Soares, J.C., see Alves, E. 580
Sobeslavsky, E., see Posselt, M. 220
Soubie, A., see Lamure, J.M. 826
Spaepen, F., see Poate, J.M 533
Spinella, C., see Battaglia, A. 611
Splinter, P., see Tami, T. 408
Spraggs, R.S., K.J. Reeson, R.M. Gwilliam, B.J. Sealy, A De Veirman and J van Landuyt , Dose dependence of crystallinity and resistivity in ion beam sythesised $CoSi_2$ layers 836
Starkov, V V., P L.F. Hemment and A.F Vyatkin, Amorphisation and solid phase epitaxial regrowth of the silicon overlayer in SIMOX structures 701
Starkov, V V., see Bussmann, U. 856
Stephens, K G., see Ma, M 335
Stevenson, D., see Kenny, M.J 522
Stoemenos, I., see Said, J. 576
Strain, J., see Wauk, M.T. 413
Strain, J.A., Y Tanaka, N.R. White and R J Woodward, New approaches to charging control 97
Su, Y.K , K J. Gan, F S Juang and J.S Hwang, Characterization of Si-implanted gallium antimonide . . . 794
Sunouchi, T , see Kawai, T 443
Svensson, B G and B. Mohadjeri, Isotope effects for ion-implantation profiles in silicon . . . 650

Taguchi, H., see Tonegawa, A 331
Takai, M , see Agawa, Y 502
Takai, M , see Kato, K 710
Takai, M , see Kinomura, A. 866
Takai, M , K. Kato, S Namba, U. Pfannenmüller and H Ryssel, Effect of deposition temperature of arsenic implanted poly-Si-on-insulator on grain size and residual stress 870
Takaoka, G H , Y. Haga, H Tsuji and J Ishikawa, Epitaxial growth of carbon-doped p-type GaAs films by ionized cluster beam 873
Takaoka, G H , see Yamada, I 876
Takayama, K., see Shibuya, T 305
Takayama, K , see Tonegawa, A. 331
Takayama, K , see Shibuya, T 364
Tami, T , M. Diamond, B Doherty and P Splinter, Mechanically scanned ion implanters with two-axis disk tilt capability 408
Tanaka, H , see Inami, H 370
Tanaka, K., see Maeno, S 359
Tanaka, Y., see Strain, J A. 97
Tang, Y S. and B J Sealy, Electrical activation process of erbium implanted in silicon and SIMOX . 647
Tanguy, P., see Zhao Qihua 374
Tanjyo, M , S. Fujiwara, H. Sakamoto and M Naito, Control of ion beam density and profile for high current ion implantation systems 86
Tanjyo, M., see Maeno, S. 359
Tasch, A.F., see Simonton, R B 39
Taylor, M K. Hurley, K Lee, M LeMere, J Opsal and T O'Brien, Thermal-wave measurements of high-dose ion implantation 725
Taylor, M.C , S Mehta and R.J Eddy, A detailed study of elemental contamination in a Varian 180XP high-current implanter 20
Thompson, M O , see Poate, J.M. 533
Thornton, R.P., see Bond, P 511
Thornton, R.P., Y H. Li, R.G. Elliman and J.S Williams, The annealing behaviour of ion-implanted Si studied using time-resolved reflectivity 598
Tokiguchi, K., see Sakudo, N 300
Tokiguchi, K., see Amemiya, K 339
Tokoro, N , see Renau, A 61

Tokoro, N., see O'Connor, J.P. 207
Tokoro, N., J.P. O'Connor, A. Renau and M.E. Mack, The beam performance of the Genus G-1500 ion implanter 434
Tonegawa, A., H. Taguchi and K. Takayama , Double hollow cathode ion source for metal ion-beam production 331
Tsai, E.L., see Chu, C H. 193
Tsien, P-H., see Ye, M. 773
Tsuji, H., see Ishikawa, J. 343
Tsuji, H., see Takaoka, G.H. 873
Tsukakoshi, O , S. Shimizu, S. Ogata, N Sasaki and H. Yamakawa, A high-current low-energy multi-ion beam deposition system 355
Tsukakoshi, O , see Mihara, Y. 417
Tu, W., see Angel, G. 211
Turner, J., see Yarling, C 104
Tyschenko, I E., see Karanovich, A.A 630

Uchiyama, T., see Agawa, Y 502
Usui, H., see Yamada, I. 876

Valizadeh, R., see Bousetta, A. 565
Van Berlo, W.H and T Pihl, X-ray diffraction studies of radiation damage in gallium arsenide . . . 785
Van de Steege, A , see Giles, A.D. 379
Van de Walle, G.F.A , see Gottdang, A 310
Van den Berg, J.A., see Gordon, J S. 314
Van den Berg, J A., see Bousetta, A. 565
Van der Meulen, P.F H M., S Mehta and R E. Kaim, Energy contamination of P^{2+} ion beams on the Varian, EXTRION 220 medium current implanter 45
Van der Meulen, P F H.M , see Kaim, R E 453
Van der Meulen, P F H M., see Schreutelkamp, R J 615
Van der Steege, A N., see Van Herk, J 25
Van Herk, J , A N n der Steege, M L.C. van Meyl and P C. Zalm, Energy contamination in ion implantation 25
Van Landuyt, J , see Spraggs, R.S 836
Van Meyl, M L C , see Van Herk, J. 25
Vandenhoudt, D.E.W., see Dekempeneer, E.H A. 769
Vanhellemont, J , Ph. Roussel and H.E Maes, Spectroscopic ellipsometry for depth profiling of ion implanted materials 183
Vanhellemont, J., see Robinson, A.K. 555
Veinbachs, D , see Nasser-Ghodsi, M. 469
Vianden, R , see Alves, E 580
Vyatkin, A F , see Gorbatov, Yu B. 328
Vyatkin, A F., V V Simonov and A I Kholopkin, Development of ion implantation equipment in the USSR (*Invited paper*) 386
Vyatkin, A.F., see Buravlyov, A V. 642
Vyatkin, A.F., see Starkov, V.V. 701
Vyatkin, A.F., see Kholopkin, A.I. 902

Wada, M., see Sasao, M. 318
Walther, S R., see Leung, K.N 94
Walther, S R and R F. Outcault, Operating procedure for improving ion source lifetime for the 80-180XP ion implanter 465
Wang Zhonglie, see Lu Diantong 705
Wang Zhonglie, see Zheng Lirong 754
Ward, S., see Nasser-Ghodsi, M 469
Watts, J F , see Zhang, J P 691
Watts, J F., see Castle, J E. 697
Wauk, M T , N. White, B. Adibi, M. Current and J Strain, Charge neutralisation in the PI9000 series implanters 413
Weiner, W., see Larson, L.A 109
Weisenberger, W., see Cherekdjian, S. 30
Weisenberger, W , see Lukaszek, W 143
Weisenberger, W., see Cherekdjian, S. 178

Weisenberger, W., see Anjum, M. ... 266
Welles, C., see Hara, T ... 250
Wendler, E., W. Wesch and G. Götz, Defect production in ion implanted GaAs, GaP and InP ... 789
Wesch, W., T. Bachmann, G. Götz, F. Hagemann and A. Heft, Activation of shallow implants in Si by pulse laser irradiation ... 625
Wesch, W., see Wendler, E. ... 789
Westendorp, J.F., see Schreutelkamp, R.J ... 615
Wetteroth, T., see Johnson, W.H. ... 148
Whaley, K., see McIntyre, E. ... 473
Whall, T E., see Zhang, J.P. ... 691
Whall, T.E., see Castle, J.E ... 697
White, N., see Wauk, M.T. ... 413
White, N.R., see Strain, J A. ... 97
White, N.R., Ion beam systen design for ULSI device requirements (*Invited paper*) ... 287
White, N.R., see Ito, H ... 527
Wielunski, L.S., see Kenny, M.J. ... 522
Williams, J S., see Bond, P. ... 511
Williams, J S, see Thornton, R.P. ... 598
Williams, J S, M.C Ridgway, R.G Elliman, J A. Davies, S T Johnston and G.R Palmer, MeV ion-beam annealing of semiconductor structures ... 602
Williams, M.D., see Leung, K N ... 94
Wittkower, A, M. Guerra, B. Cordts, R Dolan and P Sandow, Contouring of SIMOX profiles by oxygen ion energy change ... 842
Woodward, R.J., see Strain, J.A. ... 97

Yabe, E, see Shibuya, T ... 305
Yabe, E, see Shibuya, T ... 364
Yajima, Y, N Natsuaki, K Yokogawa and S Nishimatsu, Distribution of paramagnetic defects formed in silicon by MeV ion implantations ... 607
Yamada, I, Recent progress in depositing epitaxial metal films by an ionized cluster beam (*Invited paper*) ... 544
Yamada, I., G H Takaoka, H Usui, F Satoh, Y Itoh, K Yamashita, S Kitamoto, Y Namba, Y Hashimoto, Y Maeyama and K Machida, Preparation of atomically flat gold films by ionized cluster beam ... 876
Yamakawa, H., see Tsukakoshi, O ... 355
Yamakawa, H., see Agawa, Y ... 502
Yamamoto, H., see Fujishita, N ... 90
Yamaoka, H., see Sasao, M. ... 318
Yamashita, K, see Yamada, I. ... 876
Yamashita, T., see Inami, H. ... 370
Yang, G, see Shen, H ... 798
Yang Genqin, see Li Xiaoqin ... 589
Yankelevich, E B. and V S Budishevsky, A system for complex processing of semiconductor structures in vacuum ... 880
Yarling, C, R Eddy and J Turner, Implantation-equipment data management for cost reduction, equipment optimization and process enhancement ... 104
Yarling, C B., see Keenan, W A ... 230
Yarling, C B, W A Keenan and L A Larson, The history of uniformity mapping in ion implantation ... 235
Ye, M., E. Burte, P-H Tsien and H Ryssel, Cobalt silicide formation caused by arsenic ion beam mixing and rapid thermal annealing ... 773
Yokogawa, K, see Yajima, Y. ... 607
Yokota, K, H Furuta, S. Ishihara and I Kimura, Anomalous redistributions of As and Sb atoms in As-implanted Sb-doped and Sb-implanted As-doped Si during annealing ... 633
Yu, K M., see Qian, X Y ... 888
Yu, K M, see Qian, X.Y. ... 893
Yu, Y., C. Lin, X. Liu, S. Zou and P L F Hemment, Optical characteristics of multi-layer structures formed by ion beam synthesis and their computer simulation ... 730
Yu Yuehui, see Lin Chenglu ... 742
Yuasa, T., see Nagai, N. ... 393

Zalm, P.C., see Van Herk, J ... 25
Zalm, P C, see Bousetta, A ... 565
Zaumeil, P, see Said, J. ... 576

Zhang Bei, see Zheng Lirong 754
Zhang, J.P., P.L.F. Hemment, U. Bussmann, A.K. Robinson, J.E. Castle, H.D Liu, J.F. Watts, S.M. Newstead, A.R. Powell, T.E. Whall and E.H.C. Parker, The study of $Si_{0.5}Ge_{0.5}$ alloy implanted by high dose oxygen . 691
Zhang, J.P., see Castle, J.E. 697
Zhang, S., C. Lin, Z. Zhou and S. Zou, Studies on $Si^+ + B^+$ dual implantations into the top silicon layer of SIMNI material 738
Zhang Shunkai, see Lin Chenglu 742
Zhao Qihua, Jiang Xinyuan, Lin Chenglu and P Tanguy, Beam optics research for a 600 keV heavy ion implanter 374
Zhao Qihua, see Jiang Xinyuan 778
Zheng Lirong, see Lu Diantong 705
Zheng Lirong, Lu Diantong, Wang Zhonglie, Zhang Bei and P.L.F. Hemment, SOI structures produced by oxygen ion implantation and their annealing behaviour 754
Zhou Shichang, see Li Xiaoqin 589
Zhou, Z., see Zhang, S. 738
Zhou, Z., see Shen, H. 798
Zhou Zuyao, see Li Xiaoqin 589
Zinenko, V.I., see Gorbatov, Yu.B. 328
Zoth, G., see Kolbesen, B.O. 124
Zou, S., see Yu, Y. 730
Zou, S., see Zhang, S. 738
Zou, S., see Shen, H. 798
Zou Shichang, see Lin Chenglu 742
Zou Shichang, see Li Jinghua 746
Zuev, A.P., see Buravlyov, A.V. 642